Encyclopedia of Nanoscience and Nanotechnology

Volume 2 Number 1 2004

Cluster-Assembled Nanostructured Carbon

P. Milani, A. Podestà, E. Barborini

Università degli Studi di Milano, Milan, Italy

CONTENTS

1. INTRODUCTION

Since the discovery of fullerenes and carbon nanotubes and the recent progress in the synthesis of diamond-like nanostructures, carbon has occupied a strategic position in materials science and technology as one of the most versatile and far-reaching materials [1–3]. An arsenal of advanced growth methods now has the potential to provide a large variety of novel carbon materials with tailored properties and functions. In particular, the recent development of cluster assembling techniques has greatly contributed to the notion and practice of nanostructured materials [4]. Nanostructured carbon, in particular, offers a growing number of applications, which apparently depend on its nanoscale constitution. In order to establish a link between nanostructure and materials performances, characterization and manipulation techniques have to be developed and fully mastered on the nanometric scale. In particular, the structural and functional properties of carbon critically depend on the ratio between the numbers of sp (carbyne-like), sp^2 (graphite-like), and sp^3 (diamond-like) bonds. The control of such a ratio, which has become possible through the most recent growth techniques such as, for example, the one based on supersonic cluster beam assembling [4–6], enables one to synthesize a variety of carbon thin films of great interest in tribology (self-lubrication, wear-resistant, superhard coatings), electronics (field emission for flat-panel displays), or electrochemistry (molecular sieves, ionic and molecular insertion for various applications, including supercapacitors) [5].

Carbon particles and soot attracted the attention of the scientific community well before the discovery of fullerenes [7]. The synthesis and characterization of soot are of particular relevance in many fields of pure and applied science such as astrophysics, electrochemistry, and catalysis [5, 7]. Hundreds of different carbon soots generated by arc discharge, pyrolisis, or sooting flames have been studied since the 1960s [7]. The unifying point of all of the different approaches is the nanoscale structure of these materials, where one hopes to recognize universal building blocks and to determine assembling strategies for the production of materials with tailored properties. The structural and functional properties of carbon thin films assembled atom by atom and, in particular, the sp^2/sp^3 ratio, are largely determined by the kinetic energy of the particles impinging on the substrate during the film growth [3]. The use of clusters instead of atoms, as building blocks, can open new possibilities for the synthesis of materials where the structural and functional properties are also determined by the hierarchical organization of units with dimensions ranging from the nanoscopic to the mesoscopic scale [4, 5].

Experimental and theoretical investigations have shown that small carbon clusters (roughly below 40 atoms) have chain or ring structures, whereas larger clusters have the tendency to form three-dimensional cage-like structures characterized by sp^2 coordination [8–17]. The low-energy deposition of different carbon clusters preserving the original structure thus would be a very powerful technique for the creation of materials with controlled hybridization, and hence controlled physicochemical properties [4]. For example, films grown using a cluster mass distribution depleted by the large fullerene-like clusters are expected to have a very disordered compact structure; on the other hand, films grown with a cluster distribution rich in the large fullerene-like component should be characterized by a disorder graphitic structure with a large porosity [18, 19].

2. GAS-PHASE SYNTHESIS OF CARBON CLUSTERS

The deposition process of nanostructured carbon films starting from clusters produced in the gas phase can be divided into the following steps:

1. cluster formation
2. cluster extraction
3. cluster selection
4. cluster deposition.

Gas-phase synthesis of clusters is a very efficient method based on the growth of particles from a monomeric vapor [4, 20, 21]. Typically, a Knudsen cell for the production of atomic beams of thermally vaporizable substances can be used for the generation of cluster beams. However, the presence of clusters in a standard effusive beam as produced by a thermal evaporation source is residual, and therefore a gas-aggregation process should be activated by nonequilibrium cooling [20]. This consists of mixing in a condensation cell the atomic vapor with a cold buffer gas (usually a noble gas). The clusters are then extracted by letting the mixture expand through a nozzle. The geometry and dimensions of the source influence the residence time of the clusters before expansion, and hence the cluster-size distribution [4].

Generally speaking, the requisites that one should look at for assembling nanoparticles are the control of mass distribution, structure, and chemical reactivity. Moreover, one should be able to control the degree of coalescence of the clusters during the formation of the nanostructured materials [4].

The production of clusters of refractory materials like carbon requires an efficient vaporization method, such as laser ablation, arc discharge, sputtering, and so on [4, 22, 23]. These methods must be coupled with an efficient cluster extraction, which can be obtained by a gas stream.

Cluster mass selection is also very important in order to obtain films and materials with tailored properties. This can be achieved by varying the particle condensation conditions prior to extraction; however, only a coarse control of mass distribution is possible with this method [4, 20]. Clusters can also be selected, once extracted from the source, by mechanical or electromagnetic filtering methods [20, 21]. These have the disadvantage of considerably lowering the cluster flux, and thus being impractical for many applications where mass production is required.

2.1. Sputtering and Laser Ablation

The production of carbon-based systems having a structure at the nanoscale due to the incorporation of clusters can be obtained using arc-discharge methods [22, 24]. Carbon films with inclusions of fullerene-like structures and nanotube fragments have been produced with a filtered cathodic arc apparatus, where the arc occurs in a localized high-pressure (10 torr) region. Due to the presence of the inert gas, condensation takes place, and a beam of monomer ions and clusters is formed and deposited. The incorporation of three-dimensional networks, consisting of buckled planes with fullerene-like features, induces the formation of films with very high values of hardness and elasticity [5, 22, 24].

Figure 1 shows a schematic representation of the experimental configuration of the so-called anodic jet carbon arc (AJCA) deposition technique used to deposit nanocomposite carbon films. Nitrogen is injected into the chamber, and is directed toward the arcing region through an orifice at the side of a specially machined hollow anode. During the discharge, the ionization of nitrogen takes place [5, 22, 24]. The working pressure in the chamber is kept below 10^{-3} mbar. The electric arc is driven by an ac voltage of 22–24 V, with the arc current typically between 70 and 100 A. The use of an ac voltage is not very common, and effectively results in each electrode oscillating between being an anode and a cathode [5].

The production of cluster-assembled carbon foams has been reported by using high-repetition-rate laser ablation in inert gas atmosphere [25, 26]. A silicon substrate placed at a distance of 17 cm was used to collect the particles ablated from a graphite target [27]. This form of cluster-assembled carbon is characterized by a coexistence of sp^2 and sp^3 bonds and a very low density similar to that of carbon aerogels [28].

Pulsed laser deposition with an excimer laser (KrF) has also been used to produce a form of nanoporous carbon films. By varying the pressure in the deposition chamber, control of density and porosity has been demonstrated [29].

The above-mentioned approaches do not have control of cluster mass distribution produced during the ablation process or of the kinetic energies of the nanoparticles.

2.2. Supersonic Cluster Beams

Supersonic cluster beam deposition (SCBD) allows a reasonably precise control of cluster mass distribution and kinetic energy, with the possibility of obtaining very large deposition rates [4, 24]. The availability of intense and stable cluster sources makes cluster beam deposition a viable technique for the synthesis of cluster-assembled carbon films [30, 31].

A supersonic beam is schematically described as a gas stream expanding very rapidly from a high-pressure region
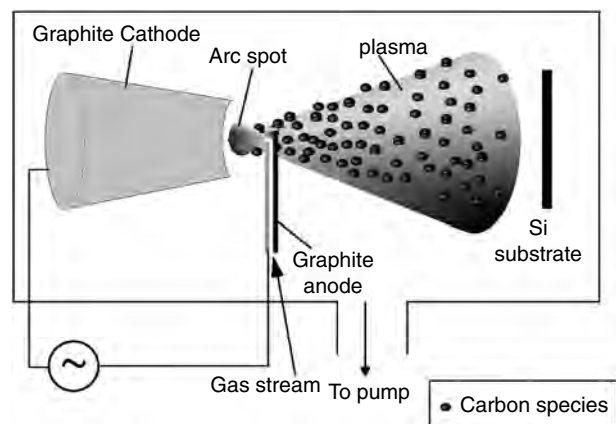

Figure 1. Schematic representation of the experimental configuration of the so-called anodic jet carbon arc (AJCA) deposition technique. Reprinted with permission from [5], G. A. J. Amaratunga et al., in "Nanostructured Carbon for Advanced Applications." Kluwer, Dordrecht, 2001. © 2001, Kluwer Academic.

(source), through a nozzle, to a low-pressure region [32]. The characteristics of the beam are mainly determined by the size and shape of the nozzle and by the pressure difference between the two regions. Compared to effusive beams used in molecular beam epitaxy, supersonic beams provide higher intensity and directionality, allowing the deposition of films with very high growth rates [32].

When a heavy species is diluted in a lighter one (as in the case of clusters diluted in He or another inert gas) and the mixture is expanded, there is formation of a seeded supersonic beam. Seeded supersonic beams are extensively used to cool and to accelerate heavy species such as clusters, and they are particularly attractive for cluster beam deposition [4, 33, 34].

A supersonic expansion can be obtained by imposing a pressure ratio less than $P_b/P_0 = 0.478$ across a convergent nozzle driving an isentropic flow expansion, where P_0 and P_b are the stagnation and the background pressures, respectively. The expansion through a convergent nozzle will always take place in a subsonic regime regardless of the amount of the applied pressure ratio. Outside the converging nozzle, depending on the pressure ratio, the flow will supersonically expand to pressures even much lower than the background. A normal shock, known as the Mach disk, matches the pressure inside the jet to the background, and closes an area called the zone of silence. The location of the Mach disk has been empirically determined as being only a function of the pressure ratio, and independent of the fluid nature and nozzle geometry [32].

In general, an isentropic supersonic jet led by a shock-free converging–diverging nozzle is advantageous compared to a nonisentropic underexpanded jet obtained by a convergent nozzle. However, depending on the Reynolds number, a converging–diverging nozzle requires a slow increase in cross-sectional area to avoid boundary layer separation and backflow, which enlarges the nozzle length to inconvenient dimensions. Furthermore, the conical converging part (either in converging–diverging or pure converging nozzles) usually produces some focal points after which particles may diverge [35, 36]. The location of these focal points depends greatly on the particle size and initial position prior to the nozzle.

The sudden free expansion of the flow produces a high outward radial velocity at the beginning of the free jet close to the nozzle outlet. This radial velocity (drag) greatly varies with the radial position, both in the jet and at the nozzle outlet. It is weak at the centerline, and very strong close to the nozzle wall at the outlet. Hence, in contrast to the particles located in the central regions, those far from the axis are exposed to a strong radial drag. Consequently, the trajectories of particles concentrated on the centerline can remain approximately unchanged, while particles far from the axis may strongly diverge in the free expansion. It also should be noted that the response of the particles to these radial drags is a function of the particle size. The above-mentioned radial drag can effectively separate the particles of different sizes, especially if they are not concentrated on the centerline [37]. Small particles can follow the expanding carrier gas, while large particles persist in their original trajectories.

If the particles can be concentrated on the nozzle centerline, only the Brownian diffusion (and lift-force effects

in case of nonspherical particles [38, 39] can perturb/spread the configuration obtained by aerodynamic focusing. Focusing the clusters on the beam center will directly improve the beam intensity, while also having an influence on the other characteristics of the supersonic part of the expansion [40].

Figure 2 shows the principle of operation of the typical apparatus used for a cluster beam, and based on a supersonic cluster source. It consists of three differentially evacuated chambers, and it can operate in the high- and ultrahigh-vacuum regimes. The first chamber hosts the cluster source; the supersonic cluster beam enters the second chamber through an electroformed skimmer. The second chamber can be equipped with a sample holder, which can intersect the beam, a quartz microbalance for beam intensity monitoring; it can also host a beam chopper or a fast ionization gauge for time-of-flight measurements of the velocity distribution of particles in the beam [32]. The third chamber usually hosts a linear time-of-flight mass spectrometer (TOF/MS), which is placed collinearly or orthogonally to the beam axis [4].

3. CARBON CLUSTER BEAM SOURCES

3.1. Laser Vaporization Cluster Source

Carbon clusters can be condensed from species obtained by laser ablation of a solid target [9]. A laser vaporization cluster source (LVCS) was originally developed for the production of clusters in molecular beams by Smalley [41–43]. Since this pioneering work, laser vaporization has become one of the most common techniques for generating cluster beams of refractory materials [4].

The design and realization of LVCS are very simple (Fig. 3), especially if compared to classical hot oven sources. LVCSs are conceptually similar to the chambers used for laser ablation for thin-film deposition [44]; the only relevant difference is that the plasma plume expands in a buffer gas. In an LVCS, the light of a high-intensity pulsed laser is focused onto a target rod, and a small amount of material is vaporized into a flow of an inert carrier gas. The inert gas quenches the plasma, and cluster condensation is promoted. The mixture is then expanded in vacuum, and forms a supersonic beam. LVCSs are operated in a pulsed regime; hence, pulsed valves are used for delivering the carrier gas. This allows the use of a relatively economical apparatus with moderate pumping speed.
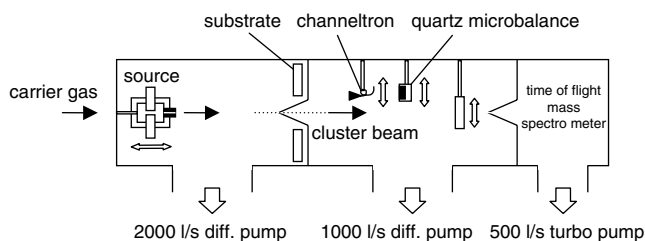

Figure 2. Schematic representation of the supersonic beam apparatus for the deposition of cluster beams. Reprinted with permission from [5], P. Milani et al., in "Nanostructured Carbon for Advanced Applications." Kluwer, Dordrecht, 2001. © 2001, Kluwer Academic.
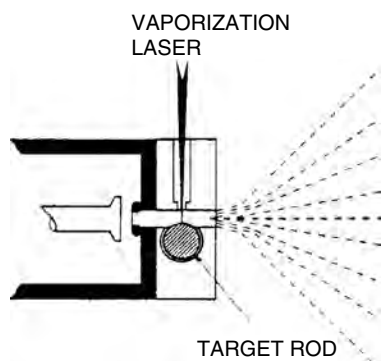
Figure 3. Schematic representation of the laser vaporization cluster source (LVCS). Reprinted with permission from [45], P. Milani and W. A. de Heer, *Rev. Sci. Instrum.* 61, 1835 (1990). © 1990, American Institute of Physics.

Several factors affect the LVCS performance in terms of intensity, stability, and the cluster mass range attainable: quantity of ablated material, plasma–buffer gas interaction, plasma–source wall interaction, and cluster residence time prior to expansion [45].

The characteristics of the cluster population are controlled by the local gas pressure during plasma production, and by the residence time of the particles in the source body. The plasma–gas interaction affects not only the final cluster distribution, but also the subsequent expansion and beam formation.

Increasing the pressure during the ablation results in a shift of the cluster distribution toward larger masses. Laser pulse characteristics influence the quantity and the state of the matter removed from the target. Pellarin et al. showed that the use of a Ti:sapphire laser (790 nm, 30 ns pulse width) can produce very intense cluster beams over a wider mass range [46]. Although the microscopic mechanisms underlying this improvement have not been characterized in detail, the longer pulse duration should be responsible for a more efficient material removal from the target [44].

Smalley and Kroto and co-workers used a disk LVCS for producing carbon clusters and C_{60} [47]. A modified version of this source, with a computer-controlled disk motion and a fast pulsed valve, has been coupled with a Fourier transform ion cyclotron resonance apparatus to characterize large carbon clusters in the beam [10].

Cluster-assembled carbon films have been produced using clusters generated by an LVCS by the group of Melinon [48].

3.2. Pulsed Microplasma Cluster Source

The pulsed microplasma cluster source (PMCS) is based on a microplasma ablation. By confining a plasma in a well-defined region of the target, it is possible to achieve material vaporization with high efficiency. Source geometry and dimensions can be optimized to produce intense and stable cluster beams, while using a relatively low carrier–gas load [30].

Due to its extremely high intensity and stability, the PMCS is a unique tool for the synthesis of nanostructured carbon-based materials, providing long-time stability and high deposition rates [30].

The PMCS is schematically shown in Figure 4. It consists of a ceramic cubic body in which a few cubic centimeters cylindrical cavity is drilled. A channel of 6 mm diameter is drilled perpendicular to the axis of the cavity, and hosts two rods (electrodes) of the material to be vaporized, facing each other and separated by a small gap. A solenoid pulsed valve injects helium at the pressure of several tens of bars through a ceramic nozzle on the back of the cavity. The gap between the electrodes is off axis, in such a way that the gas flushes on the cathode surface. A removable nozzle with a cylindrical shape closes the front of the source.

The principle of operation of the cluster source is the following: the valve delivers an intense He pulse with an opening time of a few hundreds of microseconds, thus forming a small high-gas density region at the cathode surface. After that, a very intense discharge (hundreds of amperes) lasting for few tens of microseconds is fired between the electrodes by applying a voltage ranging from 500 up to 1500 V. Ionized helium sputters a small area of cathode surface at the point where the He flux impinges on the electrode. The mixture of helium-vaporized atoms quenches, and cluster nucleation takes place. The clusters are then carried out through the nozzle by supersonic expansion [30].

Due to the source internal cavity configuration, the ablation process can be localized on a small region of the target, and hence it is very efficient. As in laser vaporization sources [45], the cathode is continuously rotated by means of an external motor in order to allow constant ablation conditions for all pulses and a homogeneous consumption of the rod.

Deposition rates, up to 65 μm/h over an area of 1 cm^2, can be obtained substituting the simple cylindrical nozzle with a more complex one, called a focuser [49]. Exploiting inertial aerodynamic effects [40, 49], the focuser reduces the angular semiaperture of the beam from ~12 to less than 1°, concentrating the cluster on the center of the beam.

Using the typical mass distributions of a PMCS, it is possible to grow films with a density ranging from 0.9 up to 1.4 g/cm^3, depending on the precursor clusters. BET analysis shows a surface specific area of roughly 750 m^2/g [50–52].

Time-of-flight mass spectrometry performed on carbon cluster beams shows that the length of a single pulse is about 10 ms, and the beam intensity decreases exponentially, resembling the gas pressure fall in the source. The velocity
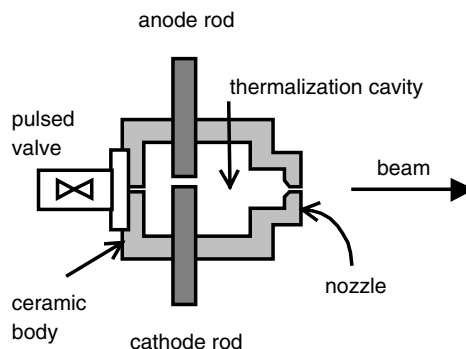

Figure 4. Expanded view of the PMCS. Reprinted with permission from [56], E. Barborini et al., *Chem. Phys. Lett.* 300, 633 (1999). © 1999, Elsevier.

of the carrier gas is about 2000 m/s in the head of the pulse, and slows down to 1000 m/s in the tail. A velocity slip of the clusters with respect to the carrier gas is present, but becomes of some relevance only for the last clusters exiting from the nozzle. The kinetic energy of the clusters is lower than 0.4 eV/atom [53].

The intensity and mass distribution of carbon clusters in the beam can be controlled and optimized by a precise synchronization between gas injection and discharge firing. Cluster intensity is also strongly dependent on the quantity of ablated material, which increases as function of the discharge voltage.

Cluster mass distribution is lognormal, as usually observed in gas-phase-grown particles [21]. For typical operation parameters, it is peaked around 550 atoms/cluster, with a mean size of 850 atoms/cluster, as shown in Figure 5. The mass distribution moves toward larger masses as the residence time increases; for this reason, the population found in the front of the pulse differs from the one in the tail. Figure 5 is representative of the average spectrum obtained by integrating over the whole cluster pulse.

Depending on the application, the PMCS can operate under different conditions. An ultrahigh-vacuum (UHV) PMCS has been developed in order to allow *in-situ* characterization of cluster-assembled carbon [54].

4. CONTROL OF FILM NANOSTRUCTURE BY CLUSTER SELECTION

The assembling of carbon cluster beams has been investigated both experimentally and theoretically in view of the creation of a new class of solids based on nanoscopic structures (chains, fullerene-like units, etc.), otherwise difficult to produce by assembling the film atom by atom [6, 18, 31, 55, 56]. This could be achieved by control of the cluster size distribution prior to deposition. Novel structural and functional properties could be displayed by solids, retaining some of the cluster characteristics [6, 18].

The growth of carbon films via low-energy cluster deposition can be viewed as a random stacking of particles as for ballistic deposition [53, 57]. The resulting material is characterized by a low density compared to that of films assembled atom by atom, and it shows different degrees of order, depending on the scale of observation [25, 26, 31].

The morphology of cluster-assembled carbon films shows different degrees of order and structures, depending on the scale of observation. The characteristic length scales are determined by cluster dimensions and by their fate after deposition: cluster beams are characterized by the presence of a finite mass distribution and by the presence of different isomers with different stabilities and reactivities. Once on the substrate, stable clusters can survive almost intact, while reactive isomers can coalesce to form a more disordered phase.

Classical molecular dynamics simulations tailored for SCBD experiments have been used to characterize and predict the growth of carbon thin films assembled by SCBD [18]. The simulations show that, depending on the cluster mass distribution, films with fullerene structures embedded in an amorphous matrix characterized by threefold coordination and hexagonal bond rings are obtained with large clusters (Fig. 6). Smaller and more fragile clusters such as linear chains produce disordered structures characterized by nonhexagonal rings with twofold coordinated atoms. Structural and elastic properties are in good agreement with the experiments. The large porosity allows the accommodation of mechanical stresses, thus permitting the growth of films with very large thicknesses (>10 μm) [29, 53].

Molecular dynamics simulations have also been performed to describe the deposition of small fullerene-like carbon clusters. C_{28} [19] and C_{20} [58] have been used as elemental building blocks. The growth of hydrocarbon thin films has also been simulated, starting from the deposition of small clusters at various kinetic energies [59].
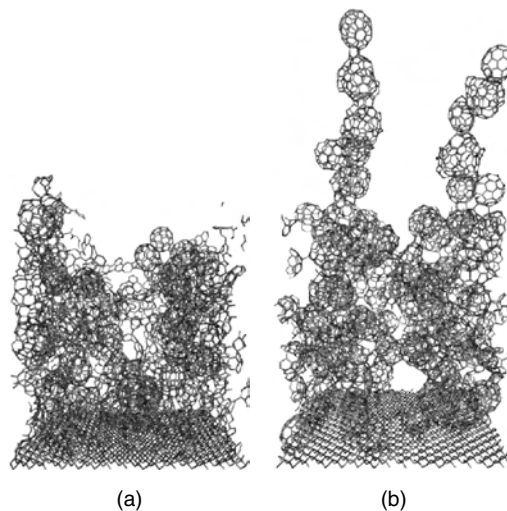
Figure 6. Atomic structure of amorphous film obtained by deposition of beams with bimodal cluster mass distribution in the range 1–23 atoms/cluster and 46–120 atoms/cluster with relative weight 5:1 [sample (a)] and 1:10 [sample (b)], respectively. Reprinted with permission from [18], D. Donadio et al., *Phys. Rev. Lett.* 83, 776 (1999). © 1999, American Physical Society.
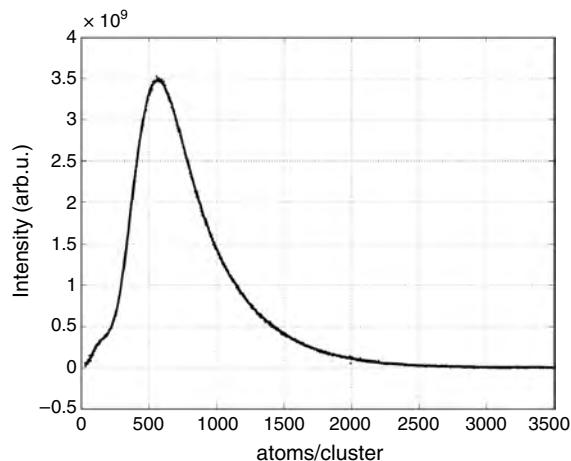

Figure 5. Typical mass spectrum for a supersonic beam of carbon cluster produced by a PMCS. Mass distribution is peaked at about 550 carbon atoms/cluster, with a mean size of 850 atoms/cluster.

5. STRUCTURAL AND FUNCTIONAL CHARACTERIZATION

5.1. Raman Scattering

An enormous number of papers have been devoted to the Raman characterization of different forms of disordered and nanocrystalline carbon, and many reviews can be found on this subject [60–63]. Raman scattering is perhaps the most popular method for the routine characterization of carbon-based materials [64, 65]. From Raman spectra, it is, in principle, possible to detect the coexistence of different carbon allotropic forms, the degree of order of different structures, the nature of the local bonding, and to follow the structural evolution as a function of the physicochemical treatments of the samples. The popularity of Raman scattering for the study of carbon, however, does not correspond to well-established models for the interpretation of all of the features observed in carbon-based materials: up to now, especially for disordered carbonaceous materials, no satisfactory theory of the Raman effect has been provided [60].

Raman scattering is very sensitive to structural changes that modify the translational symmetry of the perfect crystal. Different carbonaceous materials, characterized by the degree of disorder, ranging from the atomic scale, typical of noncrystalline systems, to nano- and microcrystalline assemblies, should display different Raman spectra.

The coexistence of the contributions coming from localization effects and structural disorder renders it very difficult to extract, from Raman spectra of disordered carbon, information on the structure and dimensions of domains. In particular, the sp^2/sp^3 ratio in amorphous and diamond-like carbon cannot be derived solely from Raman spectra analysis [60].

Raman scattering can be easily interpreted in terms of crystallites dimensions when G and D bands are well separated and distinct. These bands have relatively narrow bandwidths, whereas "nonorganized" or disordered carbon contributes to their broadening. In the case of large broadening and merging of the G and D bands, the extraction of structural information is very difficult, and interpretation of the Raman spectra must be performed very carefully to disentangle the different contributions to the line shapes. Several factors, such as crystallite dimensions and size distribution, bond angle disorder, and stress, affect the Raman line shape with a weight, which is predictable with difficulty [65].

In amorphous carbon, the G and D bands broaden and coalesce; the Raman spectra can be interpreted as being originated by an amorphous carbon matrix of threefold and fourfold coordinated carbon atoms in which a small region of hexagonal rings is embedded [65]. Different synthetic methods can change the sp^2/sp^3 ratio [63]; however, Raman spectra only exhibit small changes, confirming that they are mainly sensitive to the sp^2 content.

The Raman characterization of cluster-assembled materials must address the problem of cluster coalescence and their organization in structures spanning length scales from the nanometer up to the micrometer. The different structures in which the precursor clusters are organized need

experimental probes sensitive to the different length scales typical of intracluster and intercluster interactions. For carbon-based materials, Raman spectroscopy can be used for the characterization on a nanometer scale [66].

Melinon and co-workers [33, 48] characterized the structural and mechanical properties of cluster-assembled carbon films obtained with an LVCS at different operating conditions, which should correspond to different cluster mass distributions. The observation of mass spectra peaked at C_{20}, C_{60}, and C_{900} has been interpreted as an indication of different size distributions; however, a systematic characterization of the cluster beams has not been made by taking into account the residence time of the clusters in the source.

Low-density films (1 g/cm^3), characterized by a granular structure on a scale of several tens of nanometers, show Raman spectra evolving from a graphitic character when large clusters (C_{900}) are used to an amorphous character as the cluster size distribution is reduced to a few tens of atoms per cluster [48].

Melinon and co-workers assumed, from Raman spectra taken with excitation at 532 nm, that films formed with small clusters have an sp^3 character due to the formation of a diamond-like phase by the assembling of cage-like C_{20} clusters. Unfortunately, the available experimental evidence does not support this hypothesis. Despite the uncertainty on the final film structures, these studies showed the existence of a "memory effect" that is the dependence of the final structure of the film on the mass distribution of the precursor clusters [48].

Raman characterization has been performed on nanostructured carbon films deposited with clusters of several hundreds atoms at low kinetic energy by a PMCS [31, 55, 56, 66]. The original graphitic structure of the clusters was essentially conserved after the landing on the surface, producing a porous graphite-like film.

Micro-Raman spectroscopy indicates that the films are formed at a submicrometric scale by two coexisting phases, one amorphous and the other one more graphitic. Figure 7 shows a typical micro-Raman spectrum of a cluster-assembled film. The spectrum can be described as a superposition of contributions coming from amorphous carbon (B) and disordered graphite (C). These two phases are uniformly distributed, and coexist over the whole sample.

The more ordered phase probably originates from the aggregation of large graphitic clusters prior to deposition. Macro-Raman spectra of macroscopic portions of the films show an increase of the graphitic character when the cluster growth conditions favor the formation of large particles. In these films, the graphitic microregions are more abundant.

By changing the PMCS operation parameters, different structures have been grown (Fig. 8). The two main Raman features at about 1550 and 1350 cm^{-1} can be, respectively, identified as the G-band peak of crystalline graphite and the D-band peak due to crystal disorder. It is evident that source parameters (in this case, the amount of He filling PMCS, increasing from A to C) change cluster size distribution and determine different film structures. Spectrum A is typical of amorphous sp^2 carbon, having a broad G structure shifted at 1540 cm^{-1} (G peak of crystalline graphite appears at 1581 cm^{-1}) and just a shoulder as a D structure. Spectrum C shows a well-defined D peak, and a narrow G peak
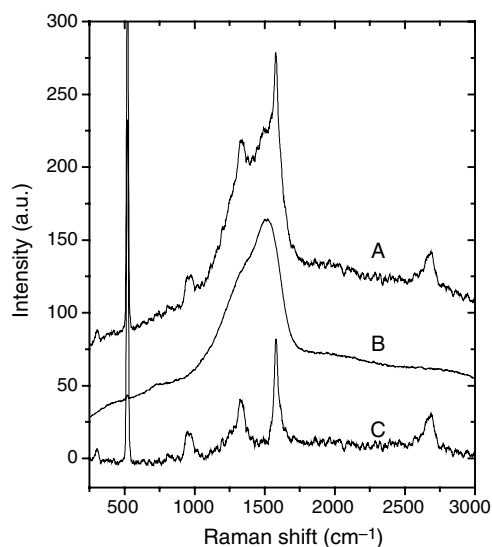
Figure 7. (A) Micro-Raman spectra of *ns*–C film. This is a superposition of a spectrum typical of amorphous carbon (B), and one typical of polycrystalline graphite (C) with defined *D* and *G* bands. Spectrum (C) was obtained by subtracting (B) from (A). Reprinted with permission from [103], C. Ducati et al., *J. Appl. Phys.* 92, 5482 (2002). © 2002, American Institute of Physics.

centered at 1581 cm^{-1}. This is consistent with a disordered graphitic structure. Different film structures are related to different relative abundances of small (few atoms) clusters and larger fullerene-like clusters.

Keeping constant the thermodynamic conditions in the cluster source, it has been demonstrated that a selection of clusters can be made in the beam by using aerodynamical gas effects [56]. It is possible to separate light clusters from the heavy ones by forcing gas flux lines to make sudden
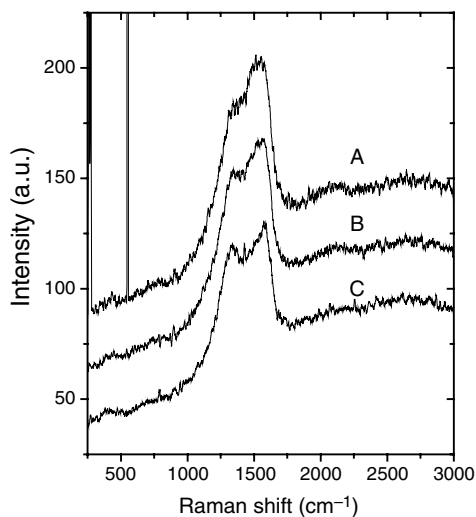
Figure 8. Micro-Raman spectra of *ns*–C films showing the influence of the PMCS helium pressure during cluster formation. The He pressure increases from (A) to (C) from 8 to 16 torr, and this parameter controls the number of large graphitic nanoparticles present in the beam. Reprinted with permission from [103], C. Ducati et al., *J. Appl. Phys.* 92, 5482 (2002). © 2002, American Institute of Physics.

turns. The light particles will be able to follow the flux line trajectories, whereas the large ones will maintain their original trajectories. By varying the background pressure in the source chamber, a shock wave can be produced in front of the skimmer, causing mass separation effects and changing the final characteristics of the beam (Fig. 9). In particular, due to their different inertia, light species follow diverging streamlines after the shock front, while heavy species are not diverted and can follow straight trajectories through the skimmer. Due to this effect, large clusters are concentrated in the central portion of the beam, whereas the lighter ones are at the periphery. By placing substrates in different portions of the beam, films from different precursor clusters can be grown [56].

Figure 10 reports Raman spectra of films deposited with different portions of the beam. The top spectrum is taken on a region rich with small clusters deposited with the periphery of the beam. The shape and the shift of the peak (*G* band) are typical of amorphous *sp*^{2} carbon. The *D* peak is present as a broad shoulder on the left of the *G* band. Going from the top to the bottom spectrum in Figure 10, one can follow the evolution from an amorphous toward a disordered graphitic structure by shifting the mass distribution from small to large clusters (from the periphery to the center of the beam). This evolution is confirmed by hardening of the *G* peak, the appearance of a well-defined *D* band, and by the narrowing of the two lines. All of these parameters are in agreement with a graphitization of the sample [60].

Cluster separation can also be obtained by using an appropriate nozzle configuration (focusing nozzle) [49]. Films grown using a cluster mass distribution depleted by the large fullerene-like clusters are expected to show a very disordered structure; on the other hand, films grown with a cluster distribution rich in the fullerene-like component should be characterized by a disordered graphitic structure.

Raman spectra show that films deposited with large clusters are characterized by the presence of a high number of distorted *sp*^{2} bonds, whereas when depositing small clusters (few tens of atoms), *sp*^{3} and *sp* coordination is present. These results are in qualitative agreement with XPS measurements [67], although photoemission spectroscopy is
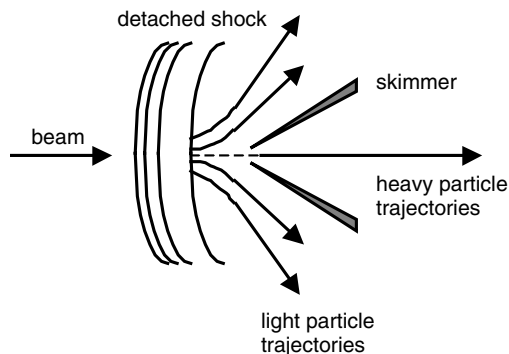
Figure 9. Varying the background pressure in the source chamber, a shock wave can be produced in front of the skimmer, causing mass separation effects and changing the final characteristics of the beam. Reprinted with permission from [56], E. Barborini et al., *Chem. Phys. Lett.* 300, 633 (1999). © 1999, Elsevier.
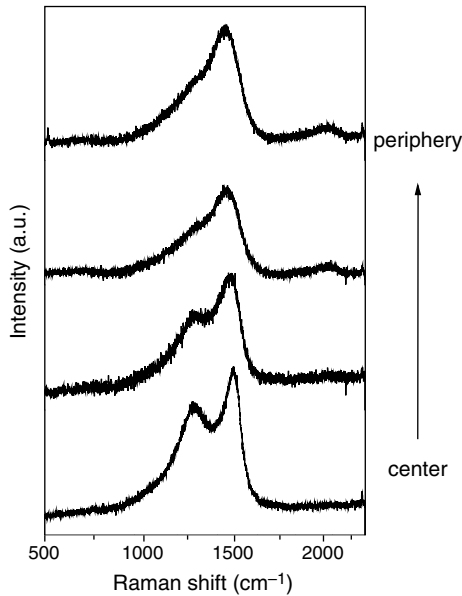
Figure 10. First-order Raman spectra of films deposited with different cluster mass distributions in the beam. Selection is obtained by using different regions of the beam. In the center, there is a concentration of large clusters, whereas small clusters are at the periphery. Going from the bottom (internal part of the beam, i.e., large clusters) to the top spectrum (external part of the beam, i.e., small clusters), one can see the evolution from a disordered graphitic structure to an amorphous one. Reprinted with permission from [56], E. Barborini et al., *Chem. Phys. Lett.* 300, 633 (1999). © 1999, Elsevier.

sensitive to a scale smaller than that of Raman. For large clusters, optical spectra confirm the disordered sp^2 structure, and show the presence of a gap of 0.6 eV [55].

5.2. Brillouin Scattering

Although Raman spectroscopy is a powerful tool for studying the structure of carbon-based materials, the information is restricted to the scale of a few nanometers. The experimental characterization and theoretical modeling of cluster-assembled granular materials must address the problem of cluster coalescence and their organization in structures spanning length scales from the nanometer up to the micrometer. The different structures in which the precursor clusters are organized needs experimental probes sensitive to the different length scales typical of intracluster and intercluster interactions. In order to study the organization of clusters on a scale of hundreds of nanometers, which is the typical scale of thermally excited long-wavelength acoustic phonons, Brillouin light scattering can be used [52]. Films of graphite [68], polycrystalline diamond [69], diamond-like a–C:H [70], fullerite [71], and phototransformed C_{60} [72] have also been studied by Brillouin scattering. From Brillouin spectra, the elastic properties of the material can also be extracted with a higher accuracy compared to nanoindentation measurements, which require a complex analysis and a careful interpretation.

Bulk and surface Brillouin scattering signals have been obtained from cluster-assembled carbon films characterized by a complex structure from the atomic to the hundreds of

nanometers level, showing that this technique also can be used for nanostructured materials with irregular surfaces. The bulk and shear modulus of the material have been determined, giving information on the acoustic properties on a mesoscopic scale. This allows us to infer the nature of the bonding between the carbon aggregates.

Cluster-assembled films are characterized by a mesostructure with low density and high porosity, originated by the coalescence of the primeval clusters. Films produced with large clusters show a surface roughness higher than films produced with small clusters, with comparable thickness. Moreover, roughness evolves more rapidly with respect to thickness in films produced with large clusters. Films produced with small clusters show a more close-packed structure, as revealed by AFM measurements [73].

Thick films (thickness >0.5 μm) and thin films (thickness <0.3 μm) have been studied [51, 52]. In thick films, only damped bulk acoustic phonons have been observed, giving rise to coherent Brillouin scattering of laser light [74]. This indicates that thick films can be modeled as a continuum with translational invariance and effective elastic constants, although structural disorder at smaller scales scatters the phonons significantly. The presence of a rather strong central peak in the spectra has been tentatively ascribed to nonpropagating (overdamped) or to confined vibrational excitations within the films, probably coupled to the confined modes by a relaxation mechanism. In thin films, surface Brillouin spectra have been observed [51, 52].

For films thicker than 1 μm, no surface peaks related to the propagation of surface acoustic phonons could be observed (only a weak longitudinal bulk peak was detectable); in the latter, surface acoustic phonons (Rayleigh wave, RW) together with a longitudinal bulk phonon peak (LB) and a longitudinal resonance peak (LR), were observed. This is the evidence that, at the typical scale of the Brillouin probe (about 200 nm), the film structure changes dramatically as a function of the cluster size distribution: in large clusters, film structural disorder acts as a damping factor for the phonon propagation so that the film cannot be considered as an elastic continuum with well-defined elastic constants. On the other hand, in small-cluster films, the surface is well described by an elastic continuum model, and the elastic constants can be evaluated by direct analysis of the Brillouin spectra.

Other physical properties can be investigated by the analysis of the Brillouin spectra of thick films deposited with small clusters. The presence of both the longitudinal bulk wave and the surface resonance reveals a nonnegligible elastooptic effect. This occurrence permits us to estimate the real part of the refractive index at 514.5 nm ($n = 1.45$ in agreement with ellissometry measurements). A rough evaluation of the elastooptic constants and the imaginary part of the refractive index can be obtained with the calculation of the Brillouin scattering cross section.

5.3. X-Ray Diffraction

The density of films deposited by SCBD has been measured for focused and nonfocused film by means of X-ray reflectivity, showing a low density value (probably due to the high fraction of voids). No interference fringes have been

detected, due to the high surface roughness. The refractive index for X-rays in solids is smaller than unity, and total external reflection occurs at low angles of incidence [75]. From the critical angle, the density of the material can be obtained. If a thick layer is deposited on a substrate, and its density is lower than the density of the substrate (as in the case of cluster-assembled carbon on silicon), X-rays start to penetrate when the incidence angle θ_i becomes greater than the film critical angle (and the reflected intensity sharply falls due to absorption in the film), but they undergo total external reflection at the film–substrate interface. When the incidence angle θ_i becomes greater than the substrate critical angle, they penetrate into the substrate, and a second intensity fall is seen in the reflectivity curve at the substrate critical angle. From the first critical angle, the density of the film can be obtained [76]. The density in the case of films grown by large clusters has a value of 0.8–1.0 g/cm^3, while in the case of films grown using small clusters, the more compact nature of the films is confirmed by the higher density value of $\rho = 1.25 \pm 0.05$ g/cm^3.

5.4. Scanning Electron Microscopy

It is well known that the morphology of thin films shows, regardless of the material, universal characteristics [77]. These ubiquitous features, consisting of arrays of columnar and conical structures, are correlated with low adatom mobility. Since deposition is usually performed on substrates kept at temperatures considerably lower than the melting point of the deposited material, a regime where the impinging particles have a low mobility is common. The general occurrence of morphological similarities, not only between different materials, but also on different length scales, as the growth takes place, suggests that a nonspecific mechanism is responsible for the observed morphologies, and that the formation, growth, and dynamics of film surfaces can be described in terms of scaling relations and universality classes [57]. Different growth mechanisms have been proposed, such as random and ballistic deposition, the critical ingredient for all of the models being surface diffusion.

Cluster beam deposition allows one to investigate how the precursor particle dimensions affect thin-film morphologies and, more generally, whether there is any influence of the particle dimensions on the scaling parameters. Nanostructured carbon film growth mechanisms with cluster beam deposition have been studied experimentally for the very initial stages at submonolayer coverages [33, 78]. The evolution of film structure and film surface roughness is of particular interest for thick films since these parameters evolve with thickness in a way that is not yet clear. In Figure 11, the surface and a section of cluster-assembled carbon films are shown. In Figure 11(a), the surface of a thin film (roughness of approximately 1 μm) is fairly flat at this scale of magnification, whereas, at the same scale, a film 15 mm thick shows a disordered and highly corrugated structure [Fig. 11(b)]. The roughness evolution, characterized by scanning electron microscopy (SEM) and atomic force microscopy (AFM), indicates that the surface may be self-affine. The film section reported in Figure 11(c) shows conical and nodular features typical of a low-mobility deposition regime [57]. Cones and
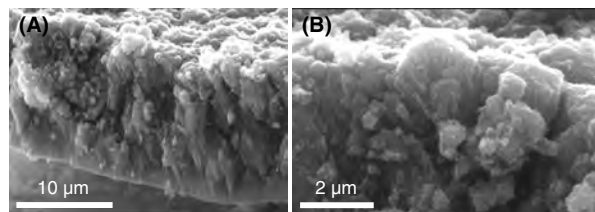
Figure 11. SEM micrographs of a section of *ns*–carbon film. In (A), conical and nodular defects are visible. The magnification of a region near the film surface is also shown in (B), where the dendritic structure of a protruding nodular defect is apparent. Reprinted with permission from [5], P. Milani et al., in "Nanostructured Carbon for Advanced Applications." Kluwer, Dordrecht, 2001. © 2001, Kluwer Academic.

spherical nodules develop as the film grows. At higher magnification, the cones are composed of dendritic structures. As in the case of atom-assembled films [77, 79], the large number of these defects seems to indicate that the mobility of clusters is very low. The formation of nodular defects is also related to the presence of substrate imperfections or minute distortions in the growth pattern of atom-assembled films. In the case of cluster assembling, one should remember that, due to finite cluster mass distribution, relatively large clusters are somehow "diluted" among small particles. Large clusters can act as seeds for the formation of nodular defects, which evolve like isolated structures protruding from the average thin-film surface. Depending on the initial density of defects, there is a critical film thickness where the nodular structures start to merge. These defects have a profound influence on the evolution of the surface morphology [31, 53].

5.5. Transmission Electron Microscopy

Figure 12 shows a low magnification TEM image of a film deposited using the AJCA technique [5, 24, 80]. The electron beam has been strongly underfocused in order to obtain stronger contrast. Under such conditions, the diffracting species appear darker than the background. Two kinds of diffracting features can be seen in this image. The two very
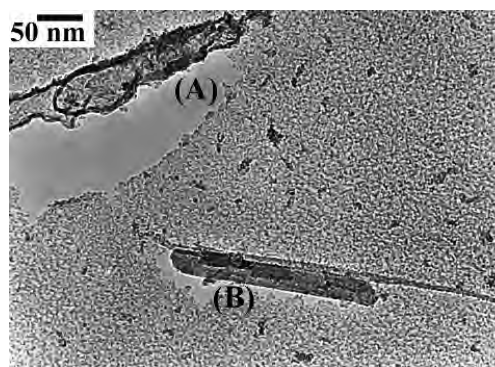
Figure 12. Low magnification TEM image of a film deposited using the AJCA technique with an N$_2$ jet creating a pressure of 0.8×10^{-3} mbar. Reprinted with permission from [5], G. A. J. Amaratunga et al., in "Nanostructured Carbon for Advanced Applications." Kluwer, Dordrecht, 2001. © 2001, Kluwer Academic.

large diffracting areas (labeled *A* and *B*) are micron-scale macroparticles containing long graphitic layers reminiscent of turbostratic carbon. Secondly, there are numerous small diffracting areas dispersed almost uniformly throughout the film, their size varying between 10 and ~20 nm. Observation at higher magnification under phase contrast imaging conditions (such as in Fig. 13) revealed that most of the latter areas are agglomerates of fullerene-like nanoparticles. Sets of concentric graphene sheets with an interlayer spacing of 3.4 Å are clearly seen in Figure 13. The pattern formed resembles closely packed multiwalled carbon nanotubes imaged along their axes (i.e., aligned along the direction of film growth). Alternatively, the particles seen in Figure 12 could also be more spherical bucky "onion"-type entities. Some of them are distorted with several graphene planes buckling away (at least in projection) toward other nanoparticles. It is proposed that the observed nanoparticle agglomerates are included in the condensing flux [24], rather than formed on the film.

When the same film was examined after it had been etched for 10 min, the surface density of large macroparticles such as *A* and *B* shown in Figure 12 decreased dramatically, and pinholes became apparent in the film surface. Figure 14 shows a plan-view HREM image from an area thinned by the chemical etching. In the majority of cases, we could image fullerene-like fringe structures in the vicinity of the pinhole. The removal of the large graphitic particles suggests that they were not strongly bonded to the film, but simply lying on the film surface. Also, the preferential thinning of some areas, and particularly the existence of nanoparticles at the edge of the pinholes, suggests that the amorphous material surrounding the embedded nanoparticles was preferentially removed by chemical etching.

Figure 12 shows that the featureless matrix takes up most of the film volume. In the interest of electron transport, it is important to examine the microstructure and carbon bonding in it. Figure 15 shows an HREM image of a thin part of the matrix. Figure 15(a) is the image taken directly from the film, while image (b) has resulted from (a) after image processing to remove any contributions to the image from scattered electrons. Although the matrix looks featureless in low magnification, the HREM images of Figure 15 reveal
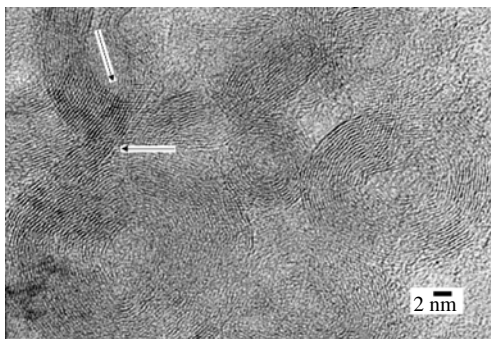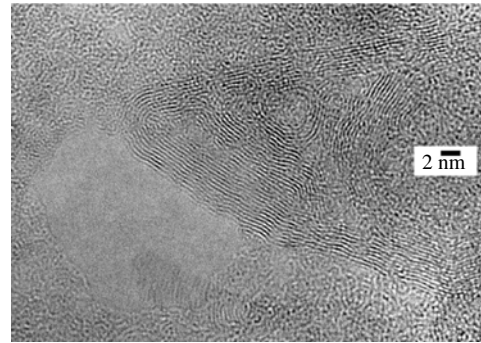

Figure 14. Plan-view HREM image showing a characteristic pinhole in the film surface observed after 10 minutes of chemical etching. Graphene sheets can be clearly seen on one side of the hole. Reprinted with permission from [5], G. A. J. Amaratunga et al., in "Nanostructured Carbon for Advanced Applications." Kluwer, Dordrecht, 2001. © 2001, Kluwer Academic.

that the film matrix consists of a mixture of amorphous carbon nitride and features that look similar to fullerene fragments. Since the arcing conditions are shown to definitely result in the formation of cage-like carbon nanoparticles, it can be suggested that these fragments are the seeds needed for nanoparticles to start forming in a carbon arc in the presence of a high gas pressure.

TEM analysis of carbon foam produced by pulsed laser deposition revealed that the foam has a fractal-like structure consisting of particles with average dimaters of 6 nm randomly interconnected into a web-like foam [25, 26].

TEM analysis of naostructured films produced by SCBD has shown that films grown without any selection of the cluster mass distribution contain ordered structures of various sizes, such as nanotubes and onions, embedded into an amorphous matrix, as shown in Figure 16(a). The amorphous matrix in which the nanoparticles are embedded is formed by the coalescence of highly metastable small clusters present with different isomers in the beam [18]. The structure of *ns–C* films obtained with the filtering nozzle does not show the presence of ordered particles, and it is characterized by an amorphous structure where only a few ordered graphene layers are distinguishable [Fig. 16(b)].

A transmission electron microscope analysis of the cluster-assembled films shows that, at this scale, the morphology is reminiscent of the precursor clusters. TEM

Figure 13. HREM image of a typical cluster of nanoparticles in a film deposited using AJCA. High magnification and phase contrast imaging conditions revealed that most of these agglomerates are made of fullerene-like nanoparticles. Reprinted with permission from [5], G. A. J. Amaratunga et al., in "Nanostructured Carbon for Advanced Applications." Kluwer, Dordrecht, 2001. © 2001, Kluwer Academic.

Figure 15. HREM image of a thin part of the matrix. (a) is the image taken directly from the film, while (b) is a part of image (a) after image processing in order to remove any contributions to the image from scattered electrons. Reprinted with permission from [5], G. A. J. Amaratunga et al., in "Nanostructured Carbon for Advanced Applications." Kluwer, Dordrecht, 2001. © 2001, Kluwer Academic.

Figure 18. (A) Grain size distributions of films deposited with large (white bars) and small (black bars) clusters. (B) Relative weight of roughness (RWR) for films deposited with different cluster mass distributions with different thicknesses. Open circles: small clusters; black squares: large clusters.
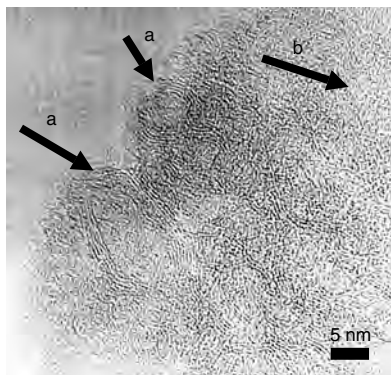
Figure 16. TEM micrograph showing the structure at the nanoscale of an *ns*–carbon film. Onions (a), closed graphitic particles, and graphene sheets are dispersed among a less structured amorphous-like material (b).

micrographs show the presence of an amorphous matrix with small closed shell particles and bundles of graphene sheets [Fig. 16(a)]. The presence of larger onion-like and tubular particles has also been observed.

5.6. Atomic Force Microscopy

Roughness, scale invariance, and spatial correlation of the film surface depend on the cluster precursor size and film thickness. Surface roughness, defined as the standard deviation of surface height (the width of the surfaces), is a function of the growth process. The evolution of the roughness during deposition and the extension of spatial correlation on the surface plane are peculiar to a growth mechanism, and largely independent of the specific physical system [57]. This makes the roughness a useful parameter to describe film morphology, and to obtain a deeper understanding of the aggregation mechanisms of clusters leading to the film formation.

Figure 17 shows typical surface morphologies of cluster-assembled carbon films measured by the atomic force microscope. The observed grains are larger than single clusters in the beam, and they result from an aggregation mechanism. The grain size depends on the precursor size: typical dimensions are shown in Figure 18(A), where the whole size distribution for films grown by small and large clusters is reported. The difference in grain size distribution suggests
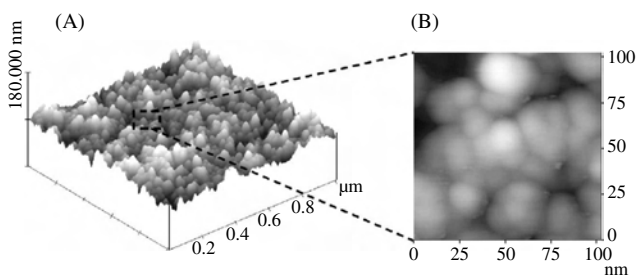
Figure 17. Tapping mode AFM topographies at different magnifications of a cluster-assembled carbon film. Typical granular morphology characterized by grain diameter of 10–20 nm can be observed. (A) Scan size 1000 nm × 1000 nm. (B) Scan size 100 nm × 100 nm.
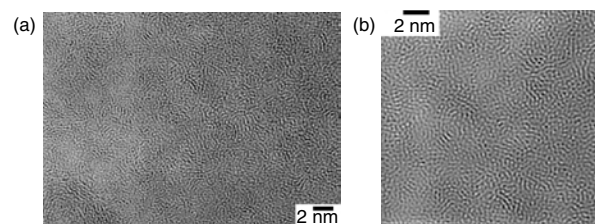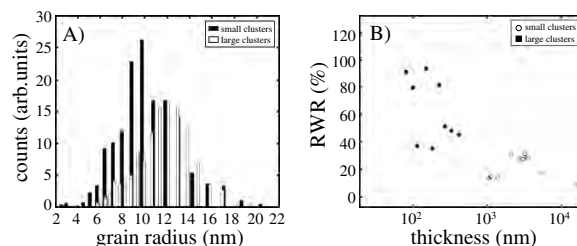
that large precursors aggregate in larger basic units. The grain size distribution seems to be independent of film thickness for a given cluster mass distribution. This fact further corroborates the assumption that grains are the basic units of nanostructured carbon film morphology in the dimension range observed by AFM.

On a micrometric scale, the morphology at a given thickness is the result of the coalescence of the primeval grains into larger units. This observation directly suggests the existence of a statistically scale-invariant morphology repeating itself across a limited number of decades. The scaling range depends on the deposition duration, and hence on the film thickness.

The cluster size strongly affects the velocity of film roughening. This can be seen in Figure 18(B), where the relative weight of roughness (RWR), defined as the ratio of twice the roughness on the film thickness, for films assembled with small and large clusters of different thicknesses, is shown. Extrapolating the two sets of data in the range 100–1000 nm, it can be noticed that the RWR of films grown with large clusters is systematically larger over the whole range of thickness. Films grown with large clusters are generally rougher than films grown with small clusters with the same thickness.

Among a rather smooth distribution of grain dimensions, AFM pictures show the presence of larger isolated features randomly distributed over the film surface. These random nodular defects are protruding from the film surface, in analogy to what is observed for atom-assembled films; their density increases with film thickness until they start to coalesce. The film thickness where coalescence takes place depends on the precursor size. The density of these nodules appears to be higher in the films grown from large clusters.

The presence of nodular defects plays an important role in the development of a rough scale-invariant morphology, where the larger units can no longer be distinguished as isolated. This happens over typical critical thicknesses around 200 and 2000 nm for samples assembled by small and large clusters, respectively. Figure 19 qualitatively shows the roughening process leading to scale-invariant morphology. This process is qualitatively similar for films grown with clusters of different sizes. Small grains and nodular defects coexist at low coverage (Fig. 19, left). At high coverage (Fig. 19, right), a cauliflower-like scale-invariant morphology develops. The tuning of the precursor mass distribution
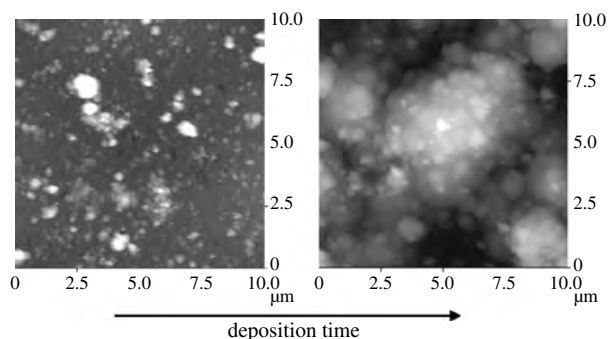
Figure 19. Tapping mode AFM pictures showing the roughening process during the growth of nanostructured carbon. A fine raster of grains and isolated nodular defects coexist at low coverage (left), while a cauliflower-like scale-invariant surface develops at high coverage (right). The behavior is similar for films grown with clusters of different sizes, although the thicknesses at which roughening occurs are different.

allows controlling the relative weight of roughness in the film, together with the film granularity [73].

In a simple picture of growth, basic morphological units (the grains) aggregate in larger and larger superunits, leading to a scale-invariant morphology. Such a morphology is self-affine, rather than self-similar because of its anisotropy due to the existence of a preferred direction, the direction of growth [57]. Scale invariance extends up to three decades in our thick films. Typical correlation lengths for films assembled by small clusters range from 50 nm to 4 μm. The lowest value refers to film where the density of nodular defects is low and their coalescence has not taken place. Apart from isolated nodules, large structures are not present, and consequently, the correlation length closely reflects the size of the basic morphological units. As long as the morphology develops and larger and larger features appear, the correlation length increases. A similar behavior is seen for films assembled by large clusters, and it is observed at considerably lower thickness.

5.7. Scanning Tunnel Microscopy

The first stages of growth of films assembled by carbon cluster deposition have been investigated by scanning tunnel microscopy (STM) in ultrahigh-vacuum conditions ($P < 8 \times 10^{-10}$ torr) [78]. Carbon clusters have been deposited at room temperature on a stepped Ag (110) surface in a regime of submonolayer coverage to study the consequent formation of islands. Figure 20 shows an STM image of carbon particles on the terraces of the silver substrate. A preferential location of the islands at the step edges is found. From this observation and from the analysis of the size distribution of the islands, it has been concluded that the clusters can diffuse on the metallic surface. A simulation of the cluster aggregation mechanism highlights that a mere two-dimensional case is incompatible with the experimental data [78]. We observe a correlation between the averaged apparent height of the islands and the corresponding mean diameter well matched with a preferential three-dimensional growth of the islands together with a small contribution of the two-dimensional aggregation mechanism.
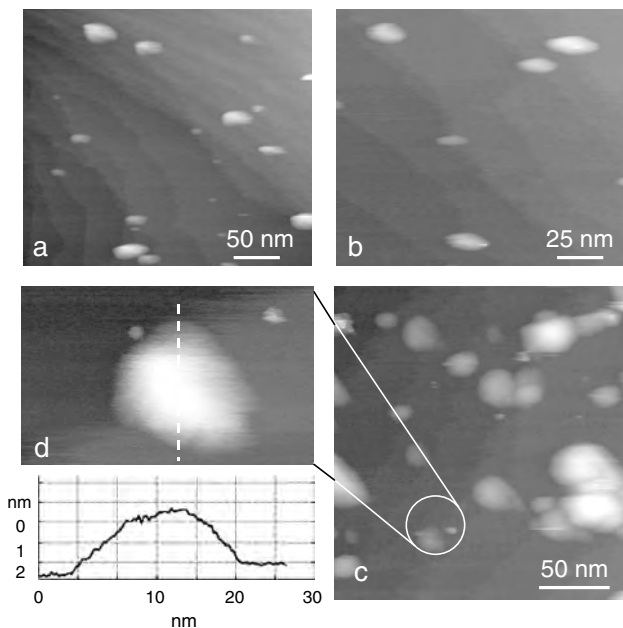
Figure 20. STM images of cluster aggregates on stepped Ag(1 1 0) surface ($T_{dep} = 300$ K, $t_{dep} = 20$ s) for several scanning area: (a) 300×300 nm^2, (b) 150×150 nm^2, (c) 210×210 nm^2, and (d) 50×50 nm^2. The last one is the acquired image corresponding to the zone surrounded by a circle in (c). The graph represents the profile corresponding to the dashed line. Reprinted with permission from [78], F. Siviero et al., *Surf. Sci.* 513, 381 (2002). © 2002, Elsevier Science.

A transition from two different growth modes occurs, and the final appearance of the film can be strongly affected by the first stages of growth. As reported in Section 5.6, AFM analysis of nanostructured films (from about 100 nm up to a few microns) shows that their morphology evolves toward a self-affine structure with increasing surface roughness. This suggests the possibility of changing the growth dynamics of a thick film acting on the parameters that determine the first stages of nanostructured carbon growth.

5.8. Electronic Spectroscopy

X-ray photoemission spectroscopy (XPS) and electron-energy-loss spectroscopy (EELS) can provide information on how the nanostructure influences the electronic properties of cluster-assembled carbon [67].

The XPS valence-band (VB) spectra of polycrystalline diamond, of the HOPG sample, and of the nanostructured sample are shown in Figure 21. Despite the structural inhomogeneities of the film, no significant changes have been observed in the VB spectra for materials deposited with small or large clusters. In Figure 21, each spectrum shows a broad and intense peak (1) at about 20 eV, a second peak (2) between 10 and 15 eV, and a third not well-defined shoulder (3) between 10 eV and the top of the valence band. The first peak is ascribed to structures of primarily C 2s character, the second peak has a mixed sp origin, while the structure (3) can be related to 2p_σ and 2p_π orbitals [81]. The NS sample spectrum also shows a structure at 26 eV, which is assigned to O 2s due to contamination. On the other hand,
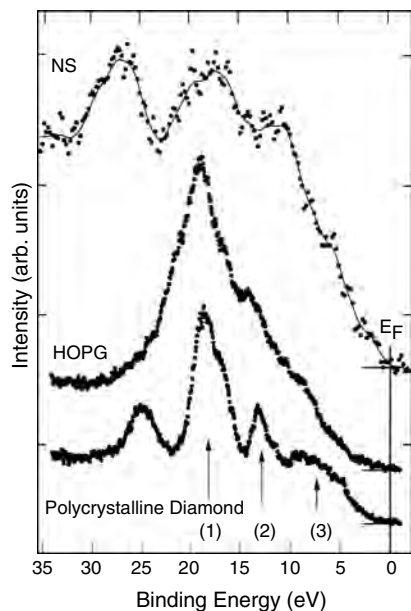
Figure 21. Valence band XPS spectra of HOPG, polycrystalline diamond, and the nanostructured carbon sample. The solid line is obtained after smoothing, and it is shown as an eye guide. Reprinted with permission from [67], E. Riedo et al., *Solid State Commun.* 116, 287 (2000). © 2000, Elsevier Science.

the O $2p$ structure is significantly attenuated with respect to the O $2s$ feature due to its smaller cross section [82].

Electron-energy-loss spectra of nanostructured films produced with large and small clusters and a HOPG sample are shown in Figure 22 after subtracting the contributions from double scattering and the background. It is worth
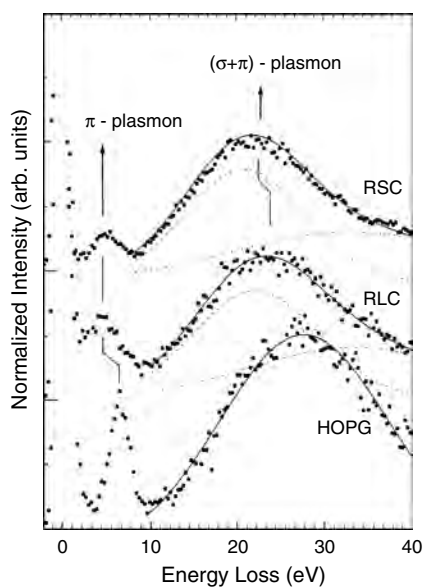
Figure 22. Electron-energy-loss spectra of nanostructured films produced with large and small clusters and an HOPG sample. RLC: rich in large clusters region; RSC: rich in small clusters region. The $\sigma + \pi$ peak is resolved into Gaussian components. Reprinted with permission from [67], E. Riedo et al., *Solid State Commun.* 116, 287 (2000). © 2000, Elsevier Science.

observing that, differently from the XPS analysis and similarly to Raman characterization, EELS reveals some important differences between small clusters and large clusters. The spectrum of HOPG shows loss features at 6.6 and 27.6 eV, representing the collective excitations of two groups of valence electrons present in the sp^2 bonded system. The former is a π plasmon due to the π electrons alone, and the latter is the plasmon due to all of the valence electrons [83]. The loss spectra of the RLC and RSC regions display two loss features attributed to the π and $\sigma + \pi$ plasmons. The $\sigma + \pi$ plasmon appears at 23.4 and 21.7 eV for the RLC and RSC regions, respectively. This is, in both cases, at a reduced energy as compared to HOPG. This can be due to the lower atomic density of cluster-assembled carbon with respect to graphite.

These data indicate that XPS is not sensitive to different structures originating from different cluster precursors at variance with Raman and EELS, which show spectral signatures of the predominant precursor clusters. In cluster-assembled systems, a mixture of various chemical environments local to the carbon site is always present. The density of states, as probed by XPS, is thus expected to average over a variety of spectral contributions representative of these carbon site inhomogeneities. Even though different weights of these specific components are expected to vary depending on the precursor mass distribution, it is likely that the overall DOS is not significantly affected. In contrast, EELS is much more specific in its spectral response since it sees primarily how many "delocalized electrons" are present in different systems with respect to the valence-band electron bound into more localized configurations, as might be the case for fivefold or sevenfold rings.

In-situ electron spectroscopy investigation of carbon clusters produced via SCBD and deposited on Ag(100) and Si(100)–(2 × 1) surfaces has been reported [84]. This avoids oxygen or moisture contaminations. Already at very low coverages, the cluster-assembled material shows an electronic structure dominated by features typical of amorphous sp^2 carbon. No significant changes of the electronic structure have been observed up to the formation of a thick film. The resulting nanostructured carbon is characterized by a semimetallic behavior. Postdeposition thermal annealing of nanostructured carbon deposited on Si(100)–(2 × 1) brings about the formation of an SiC film (Fig. 23). The conversion to SiC initiates at temperatures lower than usually seen when the precursors are fullerene molecules.

The coordination of carbon atoms in a nanostructured film can be obtained by near-edge X-ray absorption fine structure spectroscopy (NEXAFS). X-ray absorption at the carbon K edge depends principally on the atomic number Z, and consequently, the cross section is independent of the carbon atom coordination. The $1s \rightarrow \pi^*$ and $1s \rightarrow \sigma^*$ resonances in sp^2 carbon and $1s \rightarrow \sigma^*$ resonance in sp^3 carbon present a distinguishable difference in energy, and a simple identification of each contribution can be made. Thus, a quantitative determination of the amount of sp^2 can be performed [66].

The NEXAFS C K-edge spectra of as-deposited nanostructured (SCBD) and amorphous (a–C) films are shown in Figure 24. For comparison, the spectra of graphite and diamond are also reported.
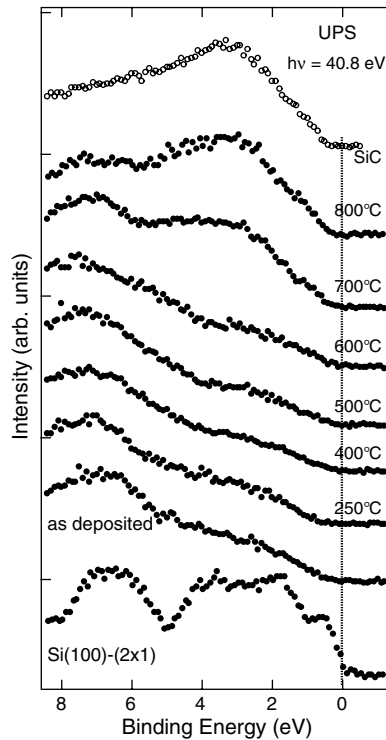
Figure 23. UPS spectra of a thin film (≈ 1 nm) deposited on Si(100)–(2×1) at different annealing steps. The typical features of an SiC layer appear above 700 °C. An SiC spectrum obtained with a different technique is also shown for comparison. Reprinted with permission from [84], E. Magnano et al., *Phys. Rev. B* (in press). © American Physical Society.

Figure 24. NEXAFS C *K*-edge spectra of as-deposited nanostructured and amorphous carbon films. The samples of the two pairs [S#3(CBD)–S#4(CBD) and S#1(*a*–C)–S#2(*a*–C)] differs with respect to the growth conditions (see text). The anodic deposit grown in the cluster source is indicated as "Anode." It has been used as a 100% sp^2 reference sample for the evaluation of the sp^2 content of the carbon films. For comparison, the spectra of graphite and diamond powder are also shown. Reprinted with permission from [66], C. Lenardi et al., *J. Appl. Phys.* 85, 7159 (1999). © 1999, American Institute of Physics.

The shape of the graphite spectrum is similar to that of graphite spectra reported in the literature [85]. The diamond spectrum shows the characteristic feature at 302.7 eV related to the second absolute gap [86]. Nevertheless, the sharp core exciton peak [87] at about 0.2 eV below the onset of $1s \rightarrow \sigma^*$ transitions (~ 288.5 eV) cannot be resolved. In Figure 24, the spectra of *a*–C and SCBD samples show a preedge resonance at about 285.3 eV due to transitions from the C $1s$ level to unoccupied π^* states of sp^2 (C=C) sites, with eventually, also, the contribution of sp (C≡C) sites if present. This peak is also present in the diamond spectrum, and originates from a graphitic phase contained in the material already detected by X-ray diffraction measurements. Another relevant peak arises at 288.8 eV, more evident in the amorphous carbon films and reduced after etching in the SCBD samples. The as-deposited SCBD samples also show a prominent resonance at 286.8 eV partially reduced after etching and implantation. The amorphous nature of the films induces a spread of the σ^* resonances, and no recognizable structures can be identified. Thus, the broad band between 290 and 310 eV is the result of overlapping C $1s \rightarrow \sigma^*$ transitions at sp, sp^2, and sp^3 sites.

The position of the peaks in the preedge region can be determined by means of the second-order derivative of the spectrum, as described in [86]. Four principal minima appear, and the corresponding energies can be used as the initial inputs of the peak positions in the fit procedure. The preedge resonances can be fitted with symmetrical Gaussian

curves. The width of these peaks is dominated by the disordered nature of the deposit. The edge jump at the ionization potential is represented by an erf function multiplied by an exponential decay. Since various shifts of the C $1s$ due to different chemical states are present, the use of only one step edge could be regarded as too rough an approximation. For this reason, it may be useful to consider the step width as a free parameter in the fit in order to include many different ionization potentials within a single broad step. For the best fit, a step width of about 0.9 eV is obtained. The σ^* resonance region has been fitted with two Gaussian curves having an exponential tail at higher energies, and dropping down in a similar fashion to the step function at the absorption edge. The first peak (at 285.3 eV) is due to π^* antibonding orbitals principally originating from C=C bonds. The amount of this bond type can be partially overestimated in the case of CBD films since, in these layers, a certain proportion of C≡C bonds seems to be present (usually disregarded in amorphous films), and may therefore contribute to the area of $1s \rightarrow \pi^*$ resonance of the C=C bond. The averaged full width at half maximum (FWHM) of the peak at 285.3 eV for the as-deposited *a*–C films is 1.9 eV, and for the as-deposited CBD films is 1.7 eV. After the *N* implantation and/or sputtering, the value is 1.9 eV. For the graphite, the FWHM is evaluated to be 1.1 eV, and for the anode, 1.3 eV. The width of the $1s \rightarrow \pi^*$ resonance of the C=C bond is

thus considered as an index of disorder on a local scale. This effect is correlated with the presence of different distorted sp^2 sites and defects. Furthermore, the peak position lies at lower energy (a shift of 0.4 eV) with respect to the graphite and the anode for both types of prepared samples. From NEXAFS peak analysis, an sp^2 of 63% can be evaluated.

6. PROPERTIES AND APPLICATIONS

6.1. Electrical Transport

Conductivity in disordered carbon materials has been ascribed to the segregation of sp^2 phases with conjugation of π bonds that in a mixed sp^2/sp^3 system can cause the appearance of complex transport phenomena [61, 88]. Carbon materials with resistivities rather uniformly distributed in the whole range from graphite to diamond have been observed [89]. The development of an industrially scalable carbon film deposition technique providing a continuous tuning of the conductivity, over even a part of this range, would be a valuable tool for the production of electronic devices. The study of electrical conduction in nanostructured carbon-based materials is thus of great interest, both for developing new applications and for fundamental studies.

The electrical conductivity of cluster-assembled films is quite sensitive to the properties of the deposited clusters: the resistivity may change by up to three orders of magnitude by changing the cluster dimensions, and even more by introducing metallic impurities in the beam [90]. This feature suggests the possibility of producing materials with tailored electrical properties.

Moreover, due to the high porosity, the conductivity of ns–C films is strongly sensitive to the gaseous environment: this property should make this nanostructured material suitable for the production of gas sensors.

The I–V characteristic of nanostructured carbon films deposited by SCBD indicates a strict ohmic behavior all over the measured electric field range. Conductivity values ranging from 7×10^{-6} to 4×10^{-4} $(\Omega \cdot m)^{-1}$ have been measured in-$situ$. Different behaviors have been observed, depending on the substrate roughness and precursor clusters used for deposition. In particular, films grown with small clusters exhibit a lower conductivity. Exposure to air causes a decrease of the conductivity whose evolution has been followed up to six months after deposition. The difference between films assembled with large and small clusters significantly reduces after air exposure. Current–temperature characteristics measured in-$situ$ at various temperatures indicate a thermally activated conductivity with energy of 0.3 eV. The different conductivity regimes and their dependence on film thickness suggest that this cluster-assembled material has transport properties significantly different from atom-assembled thin films [91, 92].

The electrical conduction properties of ns–C films have been studied under different thermal and environmental conditions, showing a clear ohmic behavior when I–V characteristics were recorded at any experimental condition. The conductivity appears to be influenced by the gaseous environment, and in particular, it is strongly reduced after the first exposure of the sample to ambient air. This evidences that electrical characterization on porous carbon systems should be carried out under accurately controlled environments. Furthermore, very slow kinetics of adsorption–desorption processes have been observed, sometimes on the scale of several days.

6.2. Field Emission

Electron field emission (FE) of carbon-based materials has been widely investigated in view of the production of stable and inexpensive cold flat cathodes [93]. Interesting emission properties in terms of low turn-on fields and high emission currents are typical of various systems such as a–C:H, a–C:N, and diamond-like films [94–96]. However, these materials show severe limitations in terms of site emission density.

FE properties are determined by the coexistence of sp^2 and sp^3 bonding to form "chemical inhomogeneities" [97] and, more generally, by the presence of a structure at the nanoscale. Systems based on carbon nanotubes, nanocrystalline diamonds, and carbon clusters have been proposed as a promising alternative to more conventional materials in terms of extraction fields, current densities, and site emission densities [98–101].

The presence of sp^2 clusters and their organization play a very important role in determining the FE performances; it is then important to control the size, structure, density, and mutual interaction of these clusters in order to understand the basic mechanisms underlying the observed phenomena, and to produce materials with tailored properties [102].

Figure 25 shows representative current density J versus electric field E curves obtained during field-emission measurements. The sample was first measured as grown, and was remeasured after chemical etching in an HF:NH$_4$F solution for 10 min. By defining the threshold field Eth as that required to get a field emission current density of 10^{-9} A/cm^2, Eth was 3.8 V/μm for the as-grown film, decreasing to 2.6 V/μm after chemical etching.

Carbon thin films were deposited using a modified carbon arc method, where a jet of nitrogen gas was used to create a high-pressure region in the vicinity of the electric
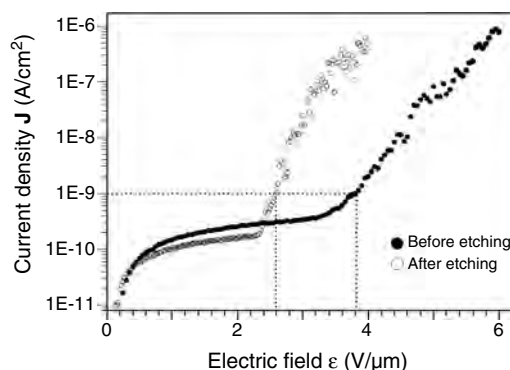
Figure 25. Current density (J) versus applied electric field (E) for the AJCA material before and after etching. In this case, the material has been deposited at room temperature, using an arc current of 140 A with a nitrogen jet creating a background pressure of 1×10^{-3} mbar. Reprinted with permission from [5], G. A. J. Amaratunga et al., in "Nanostructured Carbon for Advanced Applications." Kluwer, Dordrecht, 2001. © 2001, Kluwer Academic.

arc. HREM analysis demonstrated that the material includes clusters of fullerene-like nanoparticles. Field-emission measurements revealed that the resultant material has a relatively low threshold field and a high field-emission current. Correlating the HREM and field-emission results suggests that the good field-emission properties are related to the protrusion of clusters of nanoparticles, which are topographically and electronically suitable to cause a concentration of the external electric field over their tips. This is further supported by the fact that the field-emission characteristics of the nanocomposite films examined were broadly similar to those achieved with nanotube suspension films. Chemical etching of the material deposited by the AJCA method resulted in a further improvement of the field-emission characteristics. It is proposed that the removal of the amorphous material from the vicinity of the carbon nanoparticles during chemical etching results in an increase in the number of emission sites that are close to the dielectric matrix–vacuum interface, while the change of the dielectric medium around the tips of the nanoparticles that are exposed to vacuum leads to an increase of the local value of the electric field applied over the exposed tip. This consequently leads to easier emission of electrons from the protruding nanoparticles [5].

The field-emission properties of cluster-assembled carbon films deposited by SCBD have been investigated [101, 103]. A typical example of the emission stages for a cluster-assembled film is shown in Figure 26. Initially, the current is constant, or weakly increasing with the applied field. Above a certain value of the field, about 15 V/μm in this case, an irreversible process occurs, and the dependence becomes stronger, leading to a large hysteresis between the upward and downward voltage ramps. The next cycles follow the new track with little hysteresis, and give stable emission characteristics. This process is often called conditioning [104]. In the cycles after conditioning, the emitted current increases exponentially up to 10^{-6} A, and then saturates to about $5 \cdot 10^{-4}$ A. High-resolution SEM confirmed that no morphological damage, that is, crater formation, on the nano- and mesoscale occurred upon conditioning.

The cluster-assembled films show an emission behavior, characterized by an initial turn-on field above 10 V/μm,
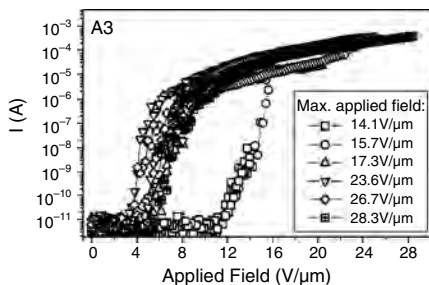
Figure 26. *I–F* characteristics of a cluster-assembled carbon film. The relevant steps of the conditioning process are shown (the cycles are named after the max voltage applied during the ramp). The turn-on field is 12.5 V/mm in the first cycles, and decreases to 4 V/mm after high field conditioning. Reprinted with permission from [103], C. Ducati et al., *J. Appl. Phys.* 92, 5482 (2002). © 2002, American Institute of Physics.

decreasing to 2–5 V/μm at the end of the conditioning process. The average threshold field, that is, the field that corresponds to an emission current density J of 1 μA/cm^2, ranges between 9.4 and 16 V/μm for the samples deposited at room temperature, and between 6 and 10 V/μm for the samples heated during the deposition. For the latter case, threshold fields as low as 4 V/μm were measured at the end of the conditioning process. The emission site density (ESD) measured in a parallel-plate configuration is on the order 10^2 cm^{-2} after a long conditioning process.

Films deposited with small clusters (that means with no large graphitic particles) showed a poor emission performance: a high turn-on and threshold field, a low saturation current (one–two orders of magnitude lower) and an ESD of 1 cm^{-2}. Since the filtering nozzle eliminates the high-mass component from the cluster beam, it leads to a low number of graphitic inclusions in the film, and hence to a more resistive, amorphous material that is hard to condition.

A strong correlation exists between substrate heating and the effectiveness of the conditioning process, leading to a larger variation of the field-emission parameters for the samples annealed during or after deposition. A similar trend was observed for the ESD: thicker samples heated during deposition showed a larger increase in the number of emitting spots. Upon annealing, unsaturated or defective metastable clusters undergo bonding rearrangements and aggregation. This could cause the clusters to sinter together and to eliminate defects (dangling bonds, nonsix-member rings), decreasing their series resistance. The higher connectivity of the heated samples seems to make their conditioning process softer and more effective, with the final turn-on field shifting to 2 V/μm (compared to 5 V/μm of the unheated samples).

An interpretation of the results might follow the model proposed by Ilie et al. [102] for sp^2 bonded clusters in an amorphous matrix. Cluster-assembled films can be modeled as a nanostructured matrix containing graphitic nanoparticles in analogy with the systems described by Alexandrou et al. [24]. The density, size, and spatial distribution of these particles affect the field-emission properties. Tubes, onions, and, in general, large graphitic clusters can be linked together to form an sp^2 correlated conductive channel perpendicular to the surface plane. The field lines focus onto the gap states of the sp^2 channel, creating a negative space charge in the film. The large local field lowers the surface barrier, giving rise to preferential emission from the channel tip.

Heating during deposition seems to favor intercluster linking and rearrangement of metastable species toward more ordered conductive structures. This sintering increases the size of the emission channels, either in length or in gap state density, relative to those of the unheated samples. The difference between the two growth conditions is evident at the first stages of emission, where the field enhancement for the heated samples is nearly twice as large as for the unheated ones (i.e., double channel "length" for the same film thickness). In the intermediate regime, the applied field might induce an extension in the sp^2 channels in the unheated samples to a size comparable to that of the heated ones, so that they exhibit the same field enhancement. The final stage of the measurement not only opens new emission

channels, but also completely develops the sp^2 channels of the heated samples, whereas the unheated ones do not show any further development either in the slope/channel length or in the intercept/emission area. The material deposited with the filtering nozzle, lacking ordered sp^2-bonded regions on the mesoscopic scale, proved to be highly resistive and unsuitable for field-emission applications [103].

6.3. Mechanical and Tribological Properties

The hardness of carbon films containing fullerene and onion-like nanoparticles has been measured by nanoindentation using a 5 nN load. The elastic recovery was obtained by load-displacement curves [22]. The hardness and elasticity values were found to be 42 ± 4 Gpa and 60%, respectively, while the same parameters for conventional carbon films obtained by arc deposition were found to be 27 ± 3 Gpa and 40%. This suggests that the incorporation of fullerenes and nanotubes in the amorphous matrix improves the mechanical properties of the system.

From Brillouin scattering data, the mesoscopic elastic properties of SCBD carbon films have been obtained [51, 52]. The shear modulus and the bulk modulus turned out to be, respectively, $\mu = 4.0$ GPa and $B = 3.67$ GPa, corresponding to a very low Poisson's ratio ν. The numerical value of μ is in the range of the C_{44} elastic constant of hexagonal crystalline graphite, and equals the value of its shear modulus along the c axis, as reported in [105–107]. This last result can be compared with Raman measurements discussed above, which point out the mainly sp^2 carbon bonding present in the disordered granular structure of the films on a nanometer scale. Yet the cluster-assembled carbon is not elastically identical to nanocrystalline graphite: in fact, the values of B (and, consequently, of the Poisson's ratio) are significantly different [106, 107].

Elastic properties of films grown with small clusters can be evaluated from the propagation velocities of the observed modes in the thick film spectrum. Knowing the longitudinal velocity v_L and using $v_L = \sqrt{C_{11}/\rho}$ (with the previously discussed density value $\rho = 1.25 \pm 0.05$ g/cm^3), we found 5.4 ± 0.4 GPa for the C_{11} elastic constant. The value 2.5 ± 0.2 GPa for the shear modulus $\mu = C_{44}$ was determined using the relation $v_T = \sqrt{C_{44}/\rho}$. Since for a semi-infinite medium the transverse bulk wave velocity v_T depends only on v_L and on the Rayleigh wave velocity v_R, we found v_T solving numerically the corresponding equation. Knowing C_{11} and C_{44} allows completely characterizing the elastic properties of an isotropic material and other elastic constants such as the bulk modulus B, Poisson ratio ν, and Young modulus E. We found $E = 5.3$ GPa, $B = 2.1$ GPa, and $\nu = 0.07$. The comparison with diamond elastic constants $E = 1141$ GPa, $B = 442$ GPa, and $\nu = 0.07$ indicates a very soft and highly deformable material [76].

Cluster-assembled carbon films have also shown the capability of accommodating mechanical stresses. This provides the opportunity to grow films with a thickness of several microns without delamination [18, 29, 53].

The understanding and control of friction, adhesion, lubrication, and wear in nanostructured systems are essential requisites to validate the use of nanomaterials for highly demanding structural applications [107, 108]. The rapidly growing number of applications based on micro-electromechanical systems (MEMS) and the new perspectives opened by the production of nanoelectromechanical systems (NEMS) make necessary the development of an entirely novel class of protective and lubricant coatings with improved mechanical properties at the nanoscale [109]. Diamond and the various types of amorphous carbon show interesting tribological properties such as high elastic moduli, good lubrication properties, low stiction surfaces, and so on [110]. These properties are controlled by a combination of physicochemical properties of the surfaces such as sp^2/sp^3 ratio, surface roughness and porosity, and by the presence of contaminant layers [111]. Because of the peculiar control of these parameters, which is allowed by the SCBD technique, the tribological properties of SCBD nanostructured carbon are worth being investigated.

Friction force microscopy [112, 113] is the state-of-the-art technique for the quantitative characterization of important friction parameters, such as the friction coefficient, and other tribological parameters, such as adhesion and wear at the submicrometer scale. At these scales, moreover, the mechanical behavior is influenced by several parameters that must be taken into account in order to extract quantitative and reproducible results. Among them, the morphological parameters, such as roughness, granularity, and power spectrum of the surface, play an important role [114–116]. Because of its ability to simultaneously acquire topographic and friction maps, AFM turns out to be a privileged candidate to perform quantitative nano- and microtribological characterization of materials having a corrugated surface. The case of nanostructured materials is somehow peculiar since the typical size of the AFM probe is close to or even comparable to cluster size. In this case, peculiar tip–sample interactions and topographic effects should be expected. Eventually, it must be considered that the sub-micron tribological properties measured with an FFM–AFM apparatus are not directly comparable to the macroscopic ones. However, a study at the submicron scale may help identify the effects of physicochemical and environmental parameters on the tribological performances at larger scales.

The tribological properties of nanostructured carbon films grown by SCBD have been characterized [117]. Films grown with large and small clusters in dry and humid nitrogen environments have been investigated. It has been found that the friction behavior of nanostructured carbon at the nanoscale is well described by a modified Amonton's law (linear dependence on *total* load plus offset), typical of a multi-asperity friction regime, demonstrating that a nanometer-sized contact such as the one realized in FFM experiments does not necessarily lead to a single-asperity friction regime. The value of the friction coefficient measured in FFM experiments was about 0.081–0.086 ± 0.01. Friction coefficients measured on carbon-based materials span from 0.009 (for HOPG in air) to 1 for DLC in UHV [118]. Molecular dynamics simulations of FFM experiments on the same samples (simulated themselves with MD [18]) support this interpretation, and show a qualitative agreement with the experiments. Simulations show a linear trend of the friction versus load curve with a finite offset, different from zero in the limit of the experimental error. The quantitative discrepancy between theoretical and experimental results is not

surprising, and it can be attributed to the parameterization of the interaction potentials and in the choice of using carbon tips in the simulations of the FFM experiments.

As confirmed also by MD simulations, in the limit of the experimental error, the nanostructure of the films seems to have very weak or no influence on the friction coefficient. In analogy to the macroscale, one could expect that films grown with large clusters, and hence containing a larger number of well-organized graphitic regions, should show a lower friction coefficient [118]. This is not observed. The friction coefficient is also found to be independent of relative humidity. Null or weak dependence of friction coefficient and adhesion on the relative humidity was reported in literature for carbon-based materials [119–121]. One possible explanation for the behavior of our films in a dry environment is the hydrophilic nature of cluster-assembled carbon [122]. The low density and large porosity of these systems in conjunction with a nonnegligible wettability may favor the formation of a water layer lasting even in dry nitrogen, with the formation of a water meniscus between the tip and the surface.

Buzio and co-workers also reported on the friction characterization on cluster-assembled carbon films produced by SCBD [123, 124]. A nonlinear dependence of friction on load, well fitted by the Hertzian-plus-offset model, using a silicon tip with a radius of 30 nm and a scan length of 50 nm, has been found. On the other hand, a linear dependence of friction on load is found by scanning on an area of 1 μm square, with a friction coefficient of about 0.13–0.20. The nonlinear dependence has been attributed to a possible passivation of the sample surface, and to the presence of a water layer, which would induce a transition from a multiasperity to a single-asperity contact (i.e., from a linear to a power-law dependence), as explained in the framework of the composite-tip model [125]. For a larger scan length and relatively larger scan velocity, the tip–sample interface is broken and reformed rapidly, and the smoothing action of water and impurities is less effective. This hypothesis is confirmed by the results of Podestà et al. [117], apart from differences observed in the numerical values of the friction coefficients.

Summarizing, FFM experiments on nanostructured carbon films grown by SCBD show that a modified Amonton's law, typical of a multiasperity contact, can describe the friction behavior at the submicron scale. The presence of water and the high reactivity of sp^2–sp^3 material play an important role in determining a multiasperity-like contact also at these very small scales. Molecular dynamics simulations support this interpretation, and show a qualitative agreement with the experiments. On smaller scales, the passivation of the surface by contaminants and water can lead to a single-asperity friction regime. The friction regime was thus found to depend on the length scale considered. This suggests that the tribological behavior of a nanostructured solid is "scale sensitive," and one should always consider the scale factor before making a comparison or extrapolations. Although numerical comparison with other carbon-based systems must be considered with high caution, cluster-assembled carbon shows a low friction coefficient, even in a dry environment.

6.4. Gas Storage

The nanostructured carbon films under investigation exhibit a specific surface area of 665.3 m^2/g, and a mesoporous structure with the pore size distribution showing a maximum at 34 Å.

NEXAFS measurements indicate the presence of chemisorbed hydrogen. With this technique, we cannot assess if the chemisorption is induced by the photon beam, which is able to disrupt (with unknown efficiency) physisorbed water or hydrogen molecules, or is a process taking place during exposures. However, the mechanism of hydrogen chemisorption can be favored by the high number of defects contained in our carbon films. They cause electronic localization which can induce a sacrificial donor effect for the photosplitting of water or a hydrogen molecule. Moreover, at present, information on the sorption kinetics is still missing. The exposure parameters (pressure less than 1 bar, 30 min, room temperature) could not be suitable for a relevant adsorption of hydrogen from the nanostructured carbon. In any case, the capacity of these films to adsorb hydrogen and releasing it, under moderate heating treatment, in a reversible way is evident. On the other hand, TPD analysis completes the picture, showing the population of physisorption sites. The hydrogen content of the sample exposed to H$_2$, as estimated from NEXAFS spectra, was about 0.5 wt%, in good agreement with the values for not alkali-doped carbon nanotubes and graphite reported in [126]. Nevertheless, the large area under the C–H* peak in the as-deposited sample indicates that nanostructured carbon could have a bigger adsorbing capacity with respect to the evaluated one. In spite of the limits in data interpretation addressed above, the obtained results on the absorption of hydrogen in nanostructured carbon material are encouraging with regard to the possible use of this material in hydrogen storage devices. Further investigations are planned for a deeper understanding of the sorption mechanism, and for an accurate evaluation of the hydrogen uptake capacity.

The hydrogen uptake by carbon-based materials has aroused large interest in the scientific community [127, 128]. Very high adsorption of molecular hydrogen in carbon nanotubes [129–131] and in alkali-doped nanotubes [132] was reported. Similarly, pure graphite nanofibers (GNF) [133, 134] seem to show a very high H$_2$ adsorption capacity [128]. Theoretical work [135–137] was also stimulated by experimental results since the mechanism of adsorption of such a high quantity of hydrogen is not completely explained.

The porous structure of nanostructured carbon makes this material a good candidate for the storage of gases such as hydrogen. The porosity of the films and their absorptive capacity were investigated by a gas adsorption–desorption technique (BET) model. Particular attention was paid to establishing if the process is reversible. The hydrogen adsorption was observed by temperature-programmed desorption (TPD) and a near-edge X-ray absorption fine structure (NEXAFS) [50]. Since the hydrogen absorption seems smaller in films deposited with large clusters, and a high deposition rate is a fundamental requirement for competitive applications, the investigations on hydrogen uptake capacity involved the films assembled with small-sized carbon clusters.

The adsorption of H_2 has been probed by means of TPD analysis. The specific surface area has been determined by BET characterization. The obtained value for the specific surface area was 665.3 m^2/g. The pore size distribution showed a maximum for pores having a diameter of 34 Å.

TPD analysis for a blank sample and an H-exposed sample shows a correlation between the increment of the TPD signal and the increase of the line for the sample exposed to hydrogen (Fig. 27). In addition, no correspondent increments were observed for other monitored lines, principally related to water, molecular oxygen, and a few hydrocarbon fragments. The TPD peak at approximately 230 °C represents a population of physisorbed H_2 sites. This peak was very small in the first cycle due to the sorption of water and hydrocarbon radicals during air exposure after the deposition. The heating up to 700 °C allowed the release of sites suitable for physisorption. The exponential behavior starting at approximately 500 °C is related to the desorption of chemisorbed hydrogen. This branch is present in both samples, and its intensity decreases from cycle to cycle. This can be due to the presence of hydrogen-containing contaminants which are strongly reduced by iterating the TPD processes. The mass of each sample was very low, and no reliable quantification of the desorbed hydrogen can be made with the experimental apparatus used.

A series of X-ray absorption measurements was performed in order to verify the capacity of nanostructured carbon deposits in absorbing and releasing hydrogen in a reversible way, and the possible structural changes induced by the thermal treatments. In the carbon K-edge NEXAFS spectra, it was followed by the evolution of the C–H peak 288.5 eV of a film grown with the focalizer for different sample treatments (see Fig. 28). The $1s \rightarrow \sigma^*_{C-H}$ resonance indicates the presence of C–H carbon hydrogen bonds. Dissociation of hydrogen-containing physisorbed species, in particular water and H_2, can be induced by X-ray beam photons or by catalytic properties of the deposits themselves. Thus, with these measurements, it is not possible to discriminate the cause of the hydrogen sorption; nevertheless, the response of the nanostructured carbon to hydrogen exposure can be reliably analyzed, as will be described in the following.
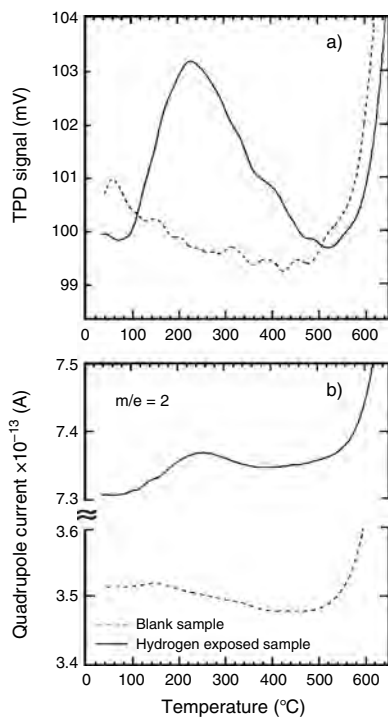
In Figure 28, the NEXAFS spectra are presented in the order with which they were acquired from bottom to top, together with two reference samples: natural diamond, and highly oriented pyrolitic graphite (HOPG). The sample was subjected to a first degassing (500 °C, 20 min). Subsequently, the sample was exposed first to air, and then to air with high relative humidity. Afterwards, the sample was again degassed under the same conditions, and finally exposed, inside a prechamber, to hydrogen maintained at a pressure of 800 mbar for 30 min at room temperature. The trend of the C–H peak is evident: after the first annealing, the resonance is strongly reduced, and only partially restored after air exposure; the second air exposure does not lead to an increase of the peak, indicating a sort of saturation of the sorption sites; the second degassing again reduces the peak, whereas the hydrogen exposure partially restores it. Moreover, there was no evidence of relevant modifications of the film structure, even if the heating yields to an increment of

Figure 27. Second cycle of temperature-programmed desorption (TPD). (a) Thermal conductivity detector (TCD) signal. (b) Quadrupole current–temperature dependence of the $m/e = 2$ line. Solid line: sample exposed to hydrogen; dashed line: blank sample. Reprinted with permission from [50], C. Lenardi et al., *Diamond Rel. Mater.* 10, 1195 (2001). © 2001, Elsevier.

Figure 28. Carbon K-edge NEXAFS spectra of a carbon film subjected to a series of treatments: degassing, air exposure, and hydrogen exposure. The measured reference spectra of HOPG and natural diamond are also shown. Reprinted with permission from [50], C. Lenardi et al., *Diamond Rel. Mater.* 10, 1195 (2001). © 2001, Elsevier.

sp^2 sites, as can be argued from the small increase of the C–C resonance at 285.3 eV. In order to point out the C–H contribution of the sample after the different treatments, a subtraction between the spectra has been made.

After calculations on NEXAFS measurements, the presence of chemisorbed hydrogen in nanostructured carbon films is clearly evident. With NEXAFS, it is not possible to assess if the chemisorption is induced by the photon beam, which is able to disrupt with unknown efficiency physisorbed water or hydrogen molecules, or is a process taking place during exposures. However, the mechanism of hydrogen chemisorption can be favored by the high number of defects contained in our carbon films. They cause electronic localization, which can induce a sacrificial donor effect for the photosplitting of water or hydrogen molecule.

The exposure parameters (pressure less than 1 bar, 30 min, room temperature) could not be suitable for a relevant adsorption of hydrogen from the nanostructured carbon. In any case, it is evident that the capacity of these films is able to adsorb hydrogen and then release it, under moderate heating treatments and in a reversible way. The hydrogen content of the sample exposed to H_2, as estimated from NEXAFS spectra, was approximately 0.5 wt%, in good agreement with the values for not alkali-doped carbon nanotubes and graphite reported in [132].

6.5. Electrochemical Properties (Supercapacitors)

Electrical energy can be stored in faradaic (redox) batteries and in electrostatic capacitors. Batteries are characterized by high-energy density, that can rise up to 150 W·h/kg, but poor power density, that with difficulty reaches 100 W/kg. The batteries suffer from several weaknesses that cause a rapid decrease of their performances. The origin may be the fast charging and discharging or the cold environmental temperature. Moreover, they also have a limited lifetime, and require expensive maintenance. Conversely, due to the completely different physical principle on which electrical energy storage is based, a capacitor has lower energy density but higher power density. Power density depends on the velocity characterizing the energy transfer: capacitors are much faster than batteries in delivering or accumulating their energy. Therefore, while slow storage processes may be performed with batteries, the fast ones have to be realized with capacitors. Examples of technological applications that could benefit from the employing of capacitors as fast energy storage devices are the following.

- Engine starter: Today, the energy required to crank a small or a big engine is stored in batteries, either Pb or Ni–Cd. Because of their high internal resistance, which limits the initial peak current, they have to be oversized. Fast discharges and the cold environmental temperature could heavily affect battery properties.
- Hybrid vehicle: The mean power of a small car is about 30 kW, and its peak power should be about 60 kW. Capacitors may supply the power to the electrical vehicle required to meet the city road traffic conditions, where power is suddenly requested or could be taken from braking.

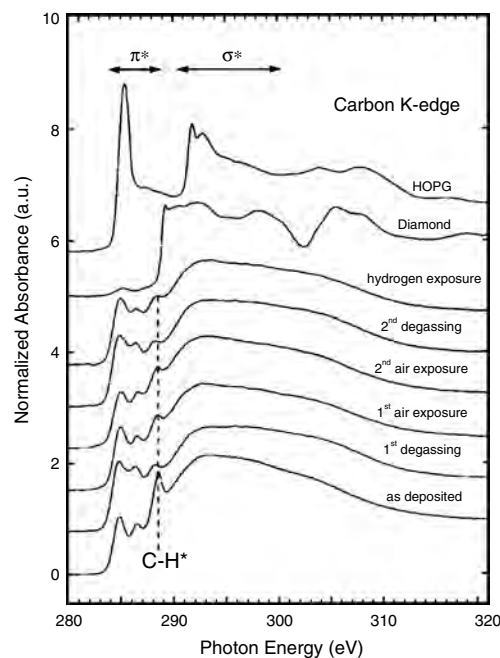- UPS: The uninterruptible power supplies may have some economical interests by using capacitors, thanks to the suppression of an inverter and the suppression of the maintenance. The energy supply during a limited time, at a voltage much higher than that of batteries, is easy to perform with capacitors. The limit of actual capacitor technology lies in the fact that the capacitance values obtained in real devices is too low for most of the practical requirements. In fact, the energy in a capacitor, being proportional to the capacitance, the achievable energy density values are problematically small.

Besides different types of capacitor technology, the electrochemical double-layer capacitor (EDLC), also designed as a supercapacitor or supercaps, shows the highest energy density. The performances of this device could fill the gap between the batteries and the classical capacitors: it shows the properties of a capacitor, but has the technology design of a battery. Supercaps are attractive for their high energy and power densities, and their long cycle life (>100,000). In addition to the high specific power, the energy storage in supercapacitors is simpler and more reversible than in conventional batteries [138].

Supercapacitors are formed by two polarizable electrodes: a separator and an electrolyte. The electrical field is stored at the interfaces between the electrolyte and the electrodes. The layer of the charges in the electrode and the layer of solvated ions of opposite sign constitute the so-called "double layer." The dielectric medium is the high-permittivity electrolyte. The electrode surface is extremely huge, and the distance between the opposite charges is in the nanometer scale due to the double layer. The double-layer phenomenon at the boundary between an ionic liquid and a solid was been discovered in 1879 by Helmholtz, and studied by several authors [139]. A theoretical treatment can be easily found in electrochemistry textbooks, for example, [140, 141].

At the surface of a metal in an electrolyte, the following exchange reaction occurs, depending on the energies of the different species in the electrode and in the electrolyte:

$$Me^{z+} + Ze^- \leftrightarrow Me$$
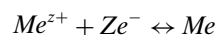
Here, Me^{z+} is the solvated metal ion (Z indicates the valence), Ze^- are the exchanged electrons, and Me is the solid metal constituting the electrode. The positive or negative charges in the electrode are compensated by a layer of cations or anions adsorbed at the surface of the electrode (the double layer). If a potential is applied, the charge of the double layer can be changed, that is, increased or decreased, or even the sign of the charge may change. If the electrode is immersed in an inert electrolyte, no reaction can occur upon a potential change; only the double layer is charged. There is no charge transfer between the electrode and an electrolyte as long as the potential is smaller than the dissociation potential of the electrolyte.

As reported in Figure 29, the double-layer thickness is defined as half the diameter ($a/2$) of the adsorbed solvated ions. This simple model of the Helmholtz double layer is called a rigid double layer [142], and corresponds to a two-plate capacitor where the plates are at a distance of $a/2$.
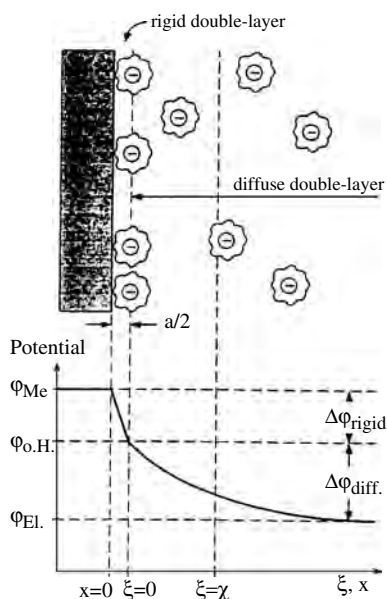
Figure 29. Helmholtz double layer in the approximation of rigid layer. Correspondingly, the electric potential is reported as a function of the distance from the electrode surface: ϕ_{Me} is the electrode potential, ϕ_{oH} is the potential at the outer Helmholtz layer, and ϕ_{El} is the potential of the electrolyte. Reprinted with permission from [142], O. Stern, *Z. Electrokem.* 30, 508 (1924). © 1924,

The potential decreases linearly with distance to the electrolyte potential within the adsorbate rigid layer (also called the Stern layer). Due to thermal diffusion, the potential decreases exponentially outside the outer Helmholtz surface ($\xi = 0$). At $\xi = \chi$, the potential is decreased to $1/e$ of the total potential ($\Delta\phi = \Delta\phi_{rigid} + \Delta\phi_{diff}$). The value of χ is approximately 10 nm, and decreases with increasing ionic concentration of the electrolyte. For an electrolyte concentration greater than 0.1 mol/l, χ decreases to the outer Helmholtz surface (0.1 nm). Therefore, the Helmholtz double layer is a capacitor in which the charges of different sign are separated by just a few nanometers: this allows EDLC to have a high capacity.

The working voltage of an ECDL capacitor is determined by the decomposition voltage of the electrolyte. For a single cell and an organic electrolyte, it is approximately 2.5 V_{DC}. In addition, the operating voltage depends mainly on the environmental temperature, the current intensity, and the required lifetime. The capacitance of an ECDL capacitor can be very large, for example, several thousands of farads, thanks to the very small distance which separates the opposite charges at the interfaces between the electrolyte and the electrodes, and thanks to the very huge surface of the electrodes. These capacitances are several orders of magnitude greater than that of conventional capacitors.

The goal of ECDL capacitor research is to reach the highest energy and power densities to get the smallest component volume and weight for a given application. These goals have been fixed by the U.S. Department of Energy (DOE) to 15 W·h/kg for the energy density and 2000 W/kg for the power density. To meet these values, it is necessary to increase the capacitance density, to reduce the series resistance (see below), and to increase the cell operating voltage. The efforts are concentrated on the study of the electrode surface, the electrode accessibility, and the electrolyte decomposition voltage.

Nanostructured materials based on the assembly of carbon nanotubes are attracting increasing interest in view of energy storage applications [143]. Several requirements still remain to be fulfilled before the development of a nanotube-based technology, in particular, the production and manipulation of macroscopic quantities of nanotubes with controlled structure and dimensions. In this sense, if compared with other applications, electrochemical ones are less demanding since a controlled nanostructure is required without internal atomic perfection. The use of nanotube mats and, in general, of nanostructured carbon materials thus offers great potential for electrochemistry and, in particular, for the production of porous electrodes for supercapacitors.

Since the capacitance is proportional to the surface area, electrochemical inert materials with the highest specific surface area are utilized for supercap electrodes in order to form a double layer with a maximum number of electrolyte ions [144]. Therefore, carbonaceous materials in their various forms have been studied as electrodes for the construction of rechargeable ECDL capacitor energy storage devices. Activated carbon composites and fibers [145] with surface areas up to 2000 m^2/g (measured by gas absorption), as well as carbon aerogels [138] with surface areas up to 850 m^2/g have been investigated. Unfortunately, a significant part of the surface area resides in nanopores (sizes below 2 nm) which are not accessible to the electrolyte ions. The surface area that remains electrochemically accessible (mesopores, macropores) reveals capacitance values well below the estimated values. Therefore, the pore size distribution, together with the surface area, are important for the determination of the double-layer capacitance.

Niu et al. [143] realized supercap electrodes with free-standing mats of catalytically grown nanotubes. The nanotube electrodes (diameter of 0.5 in) have shown a surface area of 430 m^2/g, and a measured specific capacitance up to 113 F/g with an aqueous electrolyte, resulting in a power density above 8 kW/kg. Although very promising, the use of nanotubes in practical devices is limited by the complex production/purification method, the small area of the free-standing nanotube films, and the adhesion of nanotube mats to large surfaces which have to be wound into a capacitor.

The morphological features of nanostructured carbon films match the requirements on supercap electrodes. The hierarchical organization of clusters in grain structures covering a wide range of length scales (from nanoscopic up to mesoscopic) accounts for high porosity and low density, and particularly fulfills the demand for a high specific surface. As other forms of carbon, this material appears to be inert with respect to the electrochemical processes involved in a supercap. Difficulties could arise from the high resistivity of cluster-assembled nanostructured carbon film [146], which limits the power density.

With respect to nanotube-based technology, requiring a complex sequence of steps to obtain the electrodes from the as-grown material, supersonic cluster beam deposition appears to be a simpler and versatile technique. Moreover, the presence in the beam of clusters of different masses

could allow the selection of precursors, thus modifying the properties of the deposited electrode. Granularity and conductivity should be the main properties to be controlled.

A single ECDL cell device was fabricated with two nanostructured carbon electrodes with a thickness $d = 0.8$ μm and a surface of 6 cm $\times$ 6.6 cm (for each electrode) deposited on an aluminum substrate (30 μm thick) serving as a collector. The two carbon electrodes were separated by a 36 μm thick polymer separator as a membrane. The cell is impregnated using a quartenary ammonium salt soluted in propylene carbonate (PC) as an organic electrolyte. Impregnation was performed under controlled conditions (argon inert atmosphere) in a glove box. The carbon-coated electrodes and the separator were stacked between two 3 mm thick aluminum plates. Finally, the stack was pressed together for better contact, and was sealed. A dc voltage is used to charge the supercapacitor to its nominal voltage $V_0 = 2.7$ V. The capacitance C and the equivalent series resistance ESR are determined by measuring the voltage over the contacts of the ECDL cell during discharge over an external circuit resistance R_e of 100 Ω. A schematic view of the cell and the setup for the C and the ESR measurement methodology is shown in Figure 30.

The equivalent circuit of an ECDL capacitor consists of a capacitance C, a parallel resistance Rp responsible for the self-discharge, an inductivity L, and the equivalent series resistance ESR representing the internal resistance of the capacitor. The series resistance keeps the current low, and therefore limits the power of the component and is responsible for the electric losses. The key factors determining the high energy and power density are the capacity (maximum C is required) and the series resistance (minimal ESR is required), respectively. The time constants of the charging and discharging circuits are equal to $(R_e + \text{ESR}) \times C$, while the time constant of the self-discharge is equal to $R_p \times C$. In order to minimize the self-discharge, R_p should be as large as possible.

The electrolyte itself strongly influences the capacity as well as the series resistance of the ECDL capacitor. Tanahashi et al. [145] did a comparison between aqueous and organic electrolytes, showing on one side that organic electrolytes can operate at higher voltages (up to 3 V compared to 1.2 V for aqueous electrolyte), desirable for high energy and power densities. On the other side, the aqueous electrolyte reveals a higher capacity and an ESR lower by a factor of 10. The lower ESR of the aqueous electrolyte, desirable for high-power densities, is due to the higher conductance of the ions, resulting in a voltage drop by a factor

of 10 lower than for organic electrolytes at the beginning of the capacitor discharge.

During tests, the nanostructured carbon ECDL prototype was discharged over an external circuit resistance R_e. The voltage drop ΔU at the beginning of the discharge of the capacitor allows us to determine ESR, while C is determined on the basis of ESR after 20 and 30 s of discharge. The capacity C and the equivalent series resistance ESR were determined with the following equations:

$$C = \frac{-t}{(\text{ESR} + R_e) \cdot \ln\left((\text{ESR} + R_e) \cdot \frac{U_t}{U_{1,\,t=0} \cdot R_e}\right)}$$

$$\text{ESR} = \frac{\Delta U}{i_{t=0}} = \Delta U \cdot \frac{R_e}{U_{1,\,t=0} - \Delta U}$$

where t is the time, and U_t is the voltage at time t.

For the single-cell device, the best results are ESR $= 1.13 \pm 0.09$ Ω and $C = 0.099 \pm 0.004$ F; per surface unit: ESR $= 45.7$ Ω/cm^2 and $C = 0.003$ F/cm^2. Based on these values and with a density of 1 g/cm^3, the specific capacity of one electrode is $c = 2C/d = 75$ F/g. The maximal energy density is given by $P = U_{\max}^2/(4 \times \text{ESR})$, and with its nominal voltage $V_0 = 2.7$ V, it results in 76 W·h/kg. The maximal power density is 506 kW/kg [147]. These results demonstrate that cluster-assembled carbon films are very attractive for supercapacitor realization. The optimization of parameters such as electrolyte accessibility, film conductivity, and interface resistance is currently underway. The scale up of the cluster deposition parameters to match industrial requirements will also be explored.

6.6. Nano- and Microfabrication with Carbon Cluster Beams

The fabrication of functional devices based on nanostructured materials requires the ability to assemble nanoparticles in micrometer and submicrometer patterns with high precision and compatibility with planar technology [148]. Physical and chemical deposition techniques are used for the patterning of semiconductor, metallic, and polymeric films and the production of dot arrays. These techniques require putting resists or stamps in contact with a substrate that undergoes different pre- or postdeposition etching or thermal treatments [149–151].

The effect of etching or thermal treatments on cluster-assembled materials has not been investigated systematically; however, several problems due to the "granularity" of nanostructured materials can be expected.

For nanostructured films, a noncontact patterning has been demonstrated based on the principle of depositing particle beams on a substrate through a stencil mask [152]. Due to the use of supersonic cluster beams, this process has a high lateral resolution, large area deposition, high deposition rate, and low temperature processing [153].

SCBD can be used for the fabrication of patterns of micrometer-size cluster-assembled objects. By exploiting the high intensity and collimation typical of supersonic expansions, it is possible to create structures with a high aspect ratio and controlled shape, arranged in ordered arrays on any kind of substrate at room temperature.
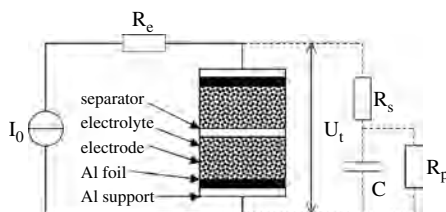

Figure 30. Schematic view of an ECDL cell and the setup for the capacity C and the equivalent series resistance ESR measurement methodology.
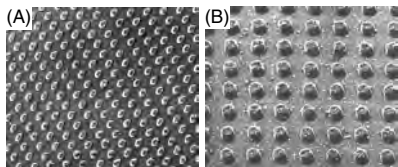
Figure 31. (A) SEM images of *ns*–carbon pillars deposited on a polymeric substrate. A standard metallic TEM grid with round holes of 20 μm diameter is used as a mask. The mask–substrate distance is about 0.3 mm. (B) The same sample is tilted to show the 3-D nature of the deposit.

Figure 31 shows SEM images of a pattern of nanostructured carbon pillars obtained by deposition of carbon clusters. The pattern has been obtained by using a round hole grid. Atomic force microscope analysis reveals granularity at a nanometer scale based on the assembling of grains with a mean diameter of 20 nm. Dots with complex geometries and a high aspect ratio, as well as self-standing microstructures can be obtained with this technique.

Key issues for micropatterning applications of SCBD are process speed, resolution, surface finish, and substrate compatibility [152]. Supersonic cluster beam sources are characterized by high directionality and high intensity. These properties have been used for the thin-film metallization of flat and microstructured surfaces [152]. SCBD allows the creation of micrometer-size objects having a structure on the nanoscale. The stencil mask is not in contact with the substrate; patterns on different substrates such as silicon, aluminum, copper, stainless steel, and polyethylene can be deposited at room temperature.

Lateral resolution depends not only on the sharpness of the mask edges, but also on the beam collimation. Supersonic expansions have a higher collimation compared to effusive beams [49]; however, clusters in supersonic beams can still have a nonnegligible thermal divergence and a broad mass distribution [49]. With a standard supersonic beam, a step produced with a straight edge mask is very noisy, and not well defined [49]. In order to increase the step sharpness, one should increase the degree of supersonicity of the beam, but this will require a huge pumping system [4, 49]. The use of a focusing nozzle can circumvent this problem by concentrating the clusters on the center beam, keeping intact the other expansion parameters. A step with a width of 450 nm using a mask placed at 0.33 mm from the substrate has been reported.

7. APPLICATIONS OF CLUSTER-ASSEMBLED CARBON

Nanostructured carbon-based materials and, in particular, those assembled from nanotubes, are attracting an increasing interest in view of a wide variety of applications ranging from micromechanics to electronics and energy storage [154]. The use of cluster-assembled carbon films can be an interesting alternative for applications in the above-mentioned fields.

Nanostructured carbon films are good field emitters, showing reasonably high current densities and stability [101, 103]. The use of supersonic beams allows deposition at very high rates over sizable areas at room temperature. This is a considerable advantage since it allows us to overcome limitations for the thermal sensitivity of many substrates. Compared to other emissive carbon films, cluster-assembled carbon films can be deposited, for example, onto glass substrates. In contrast, nanotubes can so far be formed only under high-temperature conditions [155].

Pulsed-laser-induced electron emission has also been observed from *ns*–carbon films. These properties may be of interest for the construction of photoemitting cathodes with applications for accelerator injectors [156].

Due to its high porosity and highly accessible surface area, *ns*–carbon is a good candidate for the production of supercapacitors [147]. Films with a density of 1 g/cm^3 have shown, in a dc regime, a specific capacitance per electrode of 75 F/g and energy and power densities of 76 W/kg and 506 kW/kg, respectively [147]. *ns*–carbon films, once deposited, do not require further chemical purification or thermal annealing. The use of cluster beams allows the deposition of films on thin foil films compatible with the actual manufacturing processes for supercapacitors [157].

Cluster-assembled carbon grown by pulsed laser deposition has been used for the production of preconcentrators for gas trace analysis by gas chromatography microsensors [29].

GLOSSARY

Cluster Aggregate of atoms, whose number of constituents can vary from a few units to many thousands.

Nanostructured materials Materials whose building blocks, instead of single atoms, are nanometer-sized units (i.e. clusters).

(Supersonic) molecular beam A stream of molecules or atoms, possessing high directionality, propagating in a vacuum environment. In the case of supersonic beams, mean velocity is larger than the local velocity of sound.

Supersonic cluster beam deposition (SCBD) Technique for the deposition of films exploiting a supersonic beam of clusters. The film is grown in high or ultra-high vacuum, intercepting the cluster beam with a suitable substrate.

REFERENCES

1. A. M. Rao and M. S. Dresselhaus in "Nanostructured Carbon for Advanced Applications" (G. Benedek, P. Milani, and V. G. Ralchenko, Eds.), NATO Science Series, Vol. 24. Kluwer, Dordrecht, 2001.

2. H. S. Nalwa, Ed., "Handbook of Nanostructured Materials and Nanotechnology." Academic Press, San Diego, 2000.

3. R. E. Clausing, L. L. Norton, J. C. Angus, and P. Koidl, Eds., "Diamond and Diamond-like Films and Coatings," NATO ASI Series B: Physics 266. Plenum, New York, 1991.

4. P. Milani and S. Iannotta, "Cluster Beam Synthesis of Nanostructured Materials." Springer, Berlin, 1999.

5. G. Benedek, P. Milani, and V. G. Ralchenko, Eds., "Nanostructured Carbon for Advanced Applications," NATO Science Series, Vol. 24. Kluwer, Dordrecht, 2001.

6. L. Ravagnan, F. Siviero, C. Lenardi, P. Piseri, E. Barborini, P. Milani, C. Casari, A. Li Bassi, and C. E. Bottani, *Phys. Rev. Lett.* 89, 28 (2002).

7. J. B. Donnet, R. C. Bansal, M. J. Wang, Eds., "Carbon Black." Marcel Dekker, New York, 1993.

8. E. A. Rohlfing, D. M. Cox, and A. Kaldor, *J. Chem. Phys.* 81, 3322 (1984).

9. R. F. Curl and R. E. Smalley, *Science* 242, 1017 (1988).

10. S. Maruyama, R. L. Anderson, and R. E. Smalley, *Rev. Sci. Instrum.* 61, 3686 (1990).

11. E. A. Rohlfing, *J. Chem. Phys.* 89, 6103 (1988); *J. Chem. Phys.* 93, 7851 (1990).

12. W. R. Creasy and J. T. Brenna, *J. Chem. Phys.* 92, 2269 (1990).

13. G. von Helden, M. T. Hsu, P. R. Kemper, and M. T. Bowers, *J. Chem. Phys.* 95, 3835 (1991).

14. G. von Helden, P. R. Kemper, N. G. Gotts, and M. T. Bowers, *Science* 259, 1300 (1993).

15. J. M. Hunter, J. L. Fye, and M. F. Jarrold, *J. Chem. Phys.* 99, 1785 (1993).

16. J. M. Hunter, J. L. Fye, and M. F. Jarrold, *Science* 260, 784 (1993).

17. J. M. Hunter, J. L. Fye, E. J. Roskamp, and M. F. Jarrold, *J. Phys. Chem.* 98, 1810 (1994).

18. D. Donadio, L. Colombo, P. Milani, and G. Benedek, *Phys. Rev. Lett.* 83, 776 (1999).

19. A. Canning, G. Galli, and J. Kim, *Phys. Rev. Lett.* 78, 4442 (1997).

20. H. Haberland, Ed., "Clusters of Atoms and Molecules." Springer, Berlin, 1994.

21. J. M. Bonard and A. Chatelain, Eds., "Small Particles and Inorganic Clusters." Springer, Berlin, 1999.

22. G. A. J. Amaratunga, M. Chowalla, and C. J. Kiely, I. Alexandrou, R. Aharonov, and R. M. Devenish, *Nature* 383, 321 (1996).

23. T. Hihara and K. Sumiyama, *J. Vac. Sci. Technol. B* 17, 1923 (1999).

24. I. Alexandrou, H. J. Scheibe, C. J. Kiely, A. J. Papworth, G. A. J. Amaratunga, and B. Schultrich, *Phys. Rev. B* 60, 10903 (1999).

25. A. V. Rode, S. T. Hyde, E. G. Gamaly, R. G. Elliman, D. R. McKenzie, and S. Bulcock, *Appl. Phys. A* 69, S755 (1999).

26. A. V. Rode, E. G. Gamaly, and B. Luther-Davies, *Appl. Phys. A* 70, 135 (2000).

27. A. V. Rode, B. Luther-Davies, and E. G. Gamaly, *J. Appl. Phys.* 85, 4222 (1999).

28. G. A. M. Reynolds, Z. H. Wang, M. S. Dresselhaus, A. W. P. Fung, and R. W. Pekala, *Phys. Rev. B* 49, 15027 (1994).

29. M. P. Siegal, D. L. Overmeyer, R. J. Kottenstette, D. R. Tallant, and W. G. Yelton, *Appl. Phys. Lett.* 80, 3940 (2002).

30. E. Barborini, P. Piseri, and P. Milani, *J. Phys. D: Appl. Phys.* 52, L105 (1999).

31. P. Milani, P. Piseri, E. Barborini, A. Podestà, and C. Lenardi, *J. Vac. Sci. Technol. A* 19, 2025 (2001).

32. G. Scoles, Ed., "Atomic and Molecular Beam Methods." Oxford University Press, Oxford, 1988.

33. A. Perez, P. Melinon, V. Dupuis, P. Jensen, B. Prevel, J. Tuaillon, L. Bardotti, C. Martet, M. Treilleux, M. Broyer, M. Pellarin, J. L. Vaille, B. Palpant, and J. Lerme, *J. Phys. D: Appl. Phys.* 30, 709 (1997).

34. F. Huisken, B. Kohn, and V. Paillard, *Appl. Phys. Lett.* 74, 3776 (1999).

35. J. Fernandez de la Mora and P. Riesco-Chueca, *J. Fluid. Mech.* 195, 1 (1988).

36. J. Fernandez de la Mora, N. Rao, and P. H. McMurry, *J. Aerosol Sci.* 21, 889 (1990).

37. V. H. Reis and J. B. Fenn, *J. Chem. Phys.* 39, 3240 (1963).

38. P. Liu, P. J. Ziemann, D. B. Kittelson, and P. H. McMurry, *Aerosol Sci. Technol.* 22, 293 (1995).

39. P. Liu, P. J. Ziemann, D. B. Kittelson, and P. H. McMurry, *Aerosol Sci. Technol.* 22, 314 (1995).

40. H. Vahedi Tafreshi, P. Piseri, S. Vinati, E. Barborini, G. Benedek, and P. Milani, *Aerosol Sci. Technol.* 36, 593 (2002).

41. T. G. Dietz, M. A. Duncan D. E. Powers, and R. E. Smalley, *J. Chem. Phys.* 74, 6511 (1981).

42. R. E. Smalley, *Laser Chem.* 2, 167 (1983).

43. R. E. Smalley, *Acc. Chem. Res.* 25, 98 (1992).

44. J. C. Miller, Ed., "Laser Ablation." Springer, Berlin, 1994.

45. P. Milani and W. A. de Heer, *Rev. Sci. Instrum.* 61, 1835 (1990).

46. M. Pellarin, E. Cottancin, J. Lermé, J. L. Vialle, J. P. Wolf, M. Broyer, V. Paillard, V. Dupuis, A. Perez, J. P. Perez, J. Tuaillon, and P. Melinon, *Chem. Phys. Lett.* 224, 338 (1994).

47. H. V. Kroto, J. R. Heath, S. C. O'Brien, R. F. Curl, and R. E. Smalley, *Nature* 318, 162 (1985).

48. V. Paillard, P. Melinon, V. Dupuis, J. P. Perez, A. Perez, and B. Champagnon, *Phys. Rev. Lett.* 71, 4170 (1993).

49. P. Piseri, A. Podestà, E. Barborini, and P. Milani, *Rev, Sci. Instrum.* 72, 2261 (2001).

50. C. Lenardi, E. Barborini, V. Briois, L. Lucarelli, P. Piseri, and P. Milani, *Diamond Rel. Mater.* 10, 1195 (2001).

51. C. E. Bottani, A. C. Ferrari, A. Li Bassi, P. Milani, and P. Piseri, *Europhys. Lett.* 42, 431 (1998).

52. C. S. Casari, A. Li Bassi, C. E. Bottani, E. Barborini, P. Piseri, A. Podestà, and P. Milani, *Phys. Rev. B* 64, 085417/1 (2001).

53. P. Milani, E. Barborini, P. Piseri, C. E. Bottani, A. Ferrari, and A. Li Bassi, *Eur. Phys. J.* D9, 63 (1999).

54. E. Barborini, F. Siviero, S. Vinati, C. Lenardi, P. Piseri, and P. Milani, *Rev. Sci. Instrum.* 73, 2060 (2002).

55. P. Milani, M. Ferretti, P. Piseri, C. E. Bottani, A. Ferrari, A. Li Bassi, G. Guizzetti, and M. Patrini, *J. Appl. Phys.* 82, 5793 (1997).

56. E. Barborini, P. Piseri, A. Li Bassi, A. Ferrari, C. E. Bottani, and P. Milani, *Chem. Phys. Lett.* 300, 633 (1999).

57. A. L. Barabasi and H. E. Stanley, "Fractal Concepts in Surface Growth." Cambridge University Press, Cambridge, 1995.

58. A. J. Du et al., *Phys. Rev. B* 66, 035405 (2002).

59. T. A. Plaisted, B. Ni, J. D. Zahrt, and S. B. Sinnott, *Thin Solid Films* 381, 73 (2001).

60. J. Robertson, *Prog. Solid State Chem.* 21, 199 (1991).

61. J. Robertson, *Semicond. Sci. Technol.* 18, S12 (2003).

62. M. W. Geis and M. A. Tamor, "Diamond and Diamondlike Carbon," Encyclopedia of Applied Physics, Vol. 5, VCH Publishers, Weinheim, 1993.

63. D. R. McKenzie, *Rep. Prog. Phys.* 59, 1611 (1996).

64. M. A. Tamor and W. C. Vassel, *J. Appl. Phys.* 76, 3823 (1994).

65. A. C. Ferrari and J. Robertson, *Phys. Rev. B* 61, 14095 (2000).

66. C. Lenardi, P. Piseri, V. Briois, A. Li Bassi, C. E. Bottani, and P. Milani, *J. Appl. Phys.* 85, 7159 (1999).

67. E. Riedo, E. Magnano, S. Rubini, M. Sancrotti, E. Barborini, P. Piseri, and P. Milani, *Solid State Commun.* 116, 287 (2000).

68. M. Grimsditch, *J. Phys. C* 1, L143 (1983).

69. X. Jiang, *Phys. Rev. B* 43, 2372 (1990).

70. X. Jiang, J. W. Zou, K. Reichelt, and P. Gruenberg, *J. Appl. Phys.* 66, 4729 (1989).

71. D. Fioretto, G. Carlotti, G. Socino, S. Modesti, C. Cepek, L. Giovannini, O. Donzelli, and F. Nizzoli, *Phys. Rev. B* 52, R8707 (1995).

72. M. Manfredini, C. E. Bottani, and P. Milani, *Chem. Phys. Lett.* 226, 600 (1994).

73. P. Milani, A. Podestà, P. Piseri, E. Barborini, C. Lenardi, and C. Castelnovo, *Diamond Rel. Mater.* 10, 240 (2001).

74. A. Pinczuk and E. Burstein, in "Light Scattering in Solids" (M. Cardona, Ed.), Topics in Applied Physics. Springer, Berlin, 1975.

75. B. Lengeler, in "X Ray Absorption and Reflection in the Hard X-Ray Range" (M. Campagna and K. Rosei, Eds.). North-Holland, Amsterdam, 1990.

76. C. Casari, A. Li Bassi, C. E. Bottani, E. Barborini, A. Podestà, and P. Piseri, *Diamond Rel. Mater.* 12, 856 (2003).

77. D. A. Glocker and S. I. Shah, Eds., "Handbook of Thin Film Process Technology." IoP, Bristol, 1995.

78. F. Siviero, E. Barborini, C. Boragno, R. Buzio, E. Gnecco, C. Lenardi, P. Piseri, S. Vinati, U. Valbusa, and P. Milani, *Surf. Sci.* 513, 381 (2002).

79. K. H. Guenther, *Appl. Opt.* 23, 3806 (1984).

80. M. Chowalla, R. A. Aharonov, C. J. Kiely, I. Alexandrou, and G. A. J. Amaratunga, *Phil. Mag. Lett.* 75, 329 (1997).

81. J. Schäfer, J. Ristein, R. Graupner, L. Ley, U. Stephan, Th. Frauenheim, V. S. Veerasamy, G. A. J. Amaratunga, M. Weiler, and H. Ehrhardt, *Phys. Rev. B* 53, 7762 (1996).

82. J. J. Yeh and I. Lindau, *Atomic Data Nucl. Tables* 32, 1 (1985).

83. P. Kovarik, E. B. D. Bourdon, and R. H. Prince, *Phys. Rev. B* 48, 12123 (1993).

84. E. Magnano, C. Cepek, M. Sancrotti, F. Siviero, S. Vinati, C. Lenardi, P. Piseri, E. Barborini, and P. Milani, *Phys. Rev. B* 67, 125414 (2003).

85. P. E. Batson, *Phys. Rev. B* 48, 2608 (1993).

86. M. Jaouen, G. Tourillon, J. Delafond, N. Junqua, and G. Hug, *Diamond Rel. Mater.* 4, 200 (1995).

87. J. F. Morar, F. J. Himpsel, G. Hollinger, G. Hughes, and J. L. Jordan, *Phys. Rev. Lett.* 54, 1960 (1985).

88. J. Robertson, *Philos. Mag. Lett.* 57, 143 (1988).

89. V. Paillard, M. Meaudre, P. Melinon, V. Dupuis, J. P. Perez, S. Vignoli, A. Perez, and R. Meaudre, *J. Non-Cryst. Solids* 191, 174 (1995).

90. M. Bruzzi, P. Piseri, S. Miglio, G. Bongiorno, E. Barborini, C. Ducati, J. Robertson, and P. Milani, *Euro. Phys. J. B*, in press.

91. N. F. Mott and E. A. Davis, "Electronic processes in noncrystalline materials", Oxford University Press, Oxford, 1979.

92. K. Shimakawa and K. Miyake *Phys. Rev. B* 39, 7578 (1989).

93. J. Robertson, J. P. Sullivan, O. Zhou, T. B. Allen, and B. F. Coll, "Amorphous and Nanostructured Carbon." *MRS Symp. Proc.*, Vol. 593, 2000.

94. G. A. J. Amaratunga and S. R. P. Silva, *J. Non-Cryst. Solids* 198, 611 (1996).

95. B. S. Satyanarayana, A. Hart, W. I. Milne, and J. Robertson, *Appl. Phys. Lett.* 71, 1430 (1997).

96. O Groening, O. M. Kuettel, P. Groening, and L. Schlapbach, *Appl. Phys. Lett.* 71, 2253 (1997).

97. J. Robertson, *J. Vac. Sci. Technol. B* 17, 695 (1999).

98. W. A. deHeer, A. Chatelain, and D. Ugarte, *Science* 270, 1179 (1995).

99. O. Gröning, O. M. Küttel, Ch. Emmenegger, P. Gröning, and L. Schlapbach, and *J. Vac. Sci. Technol. B* 18, 665 (2000).

100. W. Zhu, G. P. Kochanski, and S. Jin, *Science* 282, 1471 (1998).

101. A. C. Ferrari, B. S. Satyanarayana, J. Robertson, W. I. Milne, E. Barborini, P. Piseri, and P. Milani, *Europhys. Lett.* 46, 245 (1999).

102. A. Ilie, A. C. Ferrari, T. Yagi, S. E. Rodil, J. Robertson, E. Barborini, and P. Milani, *J. Appl. Phys.* 90, 2024 (2001).

103. C. Ducati, E. Barborini, P. Piseri, P. Milani, and J. Robertson, *J. Appl. Phys.* 92, 5482 (2002).

104. T. W. Mercer, N. J. DiNardo, J. B. Rothman, M. P. Siegal, T. A. Friedman, and L. J. Martinez-Miranda, *Appl. Phys. Lett.* 72, 2244 (1998).

105. O. L. Blakslee, D. G. Proctor, E. J. Seldin, G. B. Spence, and T. Weng, *J. Appl. Phys.* 41, 3373 (1970).

106. E. J. Seldin and C. W. Nezbeda, *J. Appl. Phys.* 41, 3389 (1970).

107. B. Bhushan, "Handbook of Micro and Nano Tribology." Chemical Rubber, Boca Raton, FL, 1995.

108. R. Carpick and M. Salmeron, *Chem. Rev.* 97, 1163 (1997).

109. MEMS Issue, *Mater. Res. Soc. Bull.* 26 (2001), pp. 282–337.

110. J. Sullivan, T. Friedmann, and K. Hjort, *Mater. Res. Soc. Bull.* 26, 309 (2001).

111. S. Sundararajan and B. Bhushan, *Wear* 225/229, 678 (1999).

112. B. Bhushan, *Trans. ASME, J. Tribol.* 116, 378 (1994).

113. G. Dedkov, *Phys. Stat. Sol. (a)* 179, 3 (2000).

114. S. Sundararajan and B. Bhushan, *J. Appl. Phys.* 88, 4825 (2000).

115. V. Koinkar and B. Bhushan, *J. Appl. Phys.* 81, 2472 (1997).

116. A. Podestà, G. Fantoni, and P. Milani, Quantitative nanofriction characterization of corrugated surfaces by atomic force microscopy (unpublished).

117. A. Podestà, G. Fantoni, P. Milani, M. Ragazzi, D. Donadio, and L. Colombo, *J. Nanosci. Nanotechnol.* 2, (2002).

118. A. Grill, *Surf. Coat. Technol.* 94/95, 507 (1997).

119. M. Binggeli and C. Mate, *Appl. Phys. Lett.* 65, 415 (1994).

120. V. Koinkar and B. Bhushan, *J. Vac. Sci. Technol. A* 14, 2378 (1996).

121. B. Bhushan and C. Dandavate, *J. Appl. Phys.* 87, 1201 (2000).

122. L. Ostrovskaya, A. Podestà, P. Milani, and V. Ralchenko, *Europhys. Lett.* 63, 401 (2003).

123. E. Gnecco, R. Buzio, C. Boragno, and U. Valbusa, *Acta Phys. Slovaca* 50, 423 (2000).

124. R. Buzio, E. Gnecco, C. Boragno, and U. Valbusa, *Carbon* 40, 883 (2002).

125. C. Putman and M. Igarashi, *Appl. Phys. Lett.* 66 (1995).

126. L. Schlapbach and A. Zuettel, *Nature* 414, 353 (2001).

127. S. Hynek, W. Fuller, and J. Bentley, *Int. J. Hydrogen Energy* 22, 601 (1997).

128. M. S. Dresselhaus, K. A. Williams, and P. C. Eklund, *MRS Bull.* 45 (1999).

129. A. C. Dillon, K. M. Jones, T. A. Bekkedahl, C. H. Kiang, D. S. Bethune, and M. J. Heben, *Nature* 386, 377 (1997).

130. C. Liu, Y. Y. Fan, M. Liu, H. T. Cong, H. M. Cheng, and M. S. Dresselhaus, *Science* 286, 1127 (1999).

131. Y. Ye, C. C. Ahn, C. Witham, B. Fultz, J. Liu, A. G. Rinzler, D. Colbert, K. A. Smith, and R. E. Smalley, *Appl. Phys. Lett.* 74, 2307 (1999).

132. P. Chen, X. Wu, J. Lin, and K. L. Tan, *Science* 285, 91 (1999).

133. A. Chambers, C. Park, R. T. K. Baker, and N. M. Rodriguez, *J. Phys. Chem. B* 102, 4253 (1998).

134. C. Park, P. E. A. A. Chambers, C. D. Tan, R. Hidalgo, and N. M. Rodriguez, *J. Phys. Chem. B* 103, 10572 (1999).

135. F. Darkrim and D. Levesque, *J. Chem. Phys.* 109, 4981 (1998).

136. Q. Wang and J. K. Johnson, *J. Chem. Phys.* 110, 577 (1999).

137. S. M. Lee, K. S. Park, Y. C. Choi, Y. S. Park, J. M. Bok, D. J. Bae, K. S. Nahm, Y. G. Choi, S. C. Yu, N. Kim, T. Frauenheim, and Y. H. Lee, *Synth. Met.* 113, 209 (2000).

138. S. T. Mayer, R. W. Pekala, and J. L. Kaschmitter, *J. Electrochem. Soc.* 140, 446 (1993).

139. A. F. Burke, "1st International Seminar on Double Layer Capacitor and Similar Energy Storage Devices," Florida Educational Seminars, Boca Raton, FL, 1991.

140. A. W. Adamson, "Physical Chemistry of Surfaces." Wiley, New York, 1976.

141. S. R. Morrison, "The Chemical Physics of Surfaces." Plenum, New York, 1990.

142. O. Stern, *Z. Electrokem.* 30, 508 (1924).

143. C. Niu, E. K. Sichel, R. Hoch, and H. Tennent, *Appl. Phys. Lett.* 70, 1480 (1997).

144. A. Kornyshev, W. Schmickler, and M. Vorotyntsev, *Phys. Rev. B* 25, 5244 (1982).

145. I. Tanahashi, A. Yoshida, and A. Nishino, *J. Electrochem. Soc.* 137, 3052 (1990).

146. M. Bruzzi, P. Piseri, E. Barborini, G. Benedek, and P. Milani, *Diamond Rel. Mater.* 10, 989 (2001).

147. L. Diederich, E. Barborini, P. Piseri, A. Podestà, P. Milani, A. Schneuwly, and R. Gallay, *Appl. Phys. Lett.* 75, 2662 (1999).

148. Y. Mihara, in "Frontiers of Nano-Optoelectronic Systems," (L. Pavesi and E. Buzaneva Eds.). NATO ASI, Kluwer, Dordrecht, 275, 2000.

149. S. M. Rossnagel, D. Mikalsen, H. Kinoshita, and J. J. Cuomo, *J. Vac. Sci. Technol.* A9 261 (1991).

150. Y. Xia and G. M. Whitesides, *Angew. Chem., Int. Ed.* 37, 550 (1998).

151. D. C. Liu and C. P. Lee, *Appl. Phys. Lett.* 63, 3503 (1993).

152. P. Gatz and O. F. Hagena, *Appl. Surf. Sci.* 91, 169 (1995).

153. E. Barborini, P. Piseri, A. Podestà, and P. Milani, *Appl. Phys. Lett.* 77, 1059 (2000).

154. A. A. Zakhidov, R. H. Baughman, Z. Iqbal, C. Cui, I. Khayrullin, S. O. Dantas, J. Marti, and V. G. Ralchenko, *Science* 282, 897 (1998).

155. E. Franckowiac, S. Gautier, H. Gaucher, S. Bonnamy, and F. Beguin, *Carbon* 37, 61 (1999).

156. I. Boscolo, P. Milani, M. Parisotto, G. Benedek, and F. Tazzioli, *J. Appl. Phys.* 87, 4005 (2000).

157. B. E. Conway, "Electrochemical Supercapacitors: Scientific Fundamentals and Technological Applications." Kluwer, New York, 1999.

Colloidal Gold

Victor H. Perez-Luna, Kadir Aslan, Pravin Betala

Illinois Institute of Technology, Chicago, Illinois, USA

CONTENTS

1. INTRODUCTION

There is currently enormous interest in the field of nanoscale science and engineering because of (i) the novel properties of matter found at the intermediate scale between molecules and bulk materials and (ii) phenomena that occur only at the nanoscale regime. Over the last decade the number of publications in the field of nanoparticle synthesis has increased enormously. Gold nanoparticles in particular are receiving renewed interest because of novel applications being developed with this material. One of the reasons for this renewed interest is the attractive combination of its optical properties, which depend on the electronic properties rather than molecular structure, and the facile functionalization of this material with a variety of molecules. Despite being known and used for centuries, the use of this material is currently exhibiting a boom, particularly in the field of materials science.

1.1. History

Accounts on the use of colloidal gold can be found throughout history. The oldest object containing gold nanoparticles is frequently cited as being the Lycurgus Chalice from fifth century Rome [1, 2]. However, accounts of colloidal gold preparations may extend further back in time. Colloidal gold is found in treatments in the alternative medicine Ayurveda

(the traditional medical system of India), which has its written origins in the Vedas, the sacred texts of India. The Vedas are believed to be the oldest writings in the world. More recent accounts of colloidal gold are its uses in alchemia by Paracelsus around 1600 [3], incorporation of gold into molten silica to create "ruby glass" [attributed to Johann Kunckel (1638–1703)] [4, 5], and the experiments by Michael Faraday that led him to attribute the color of ruby glass and his aqueous solutions of gold (colloidal gold) to finely divided gold particles [6, 7].

In addition to the early experiments by Faraday, colloidal gold was considered a useful research tool for particle science in the early 19th century. This led to important advances in the development of novel synthetic methods for colloidal gold [8]. However, its main applications were still relegated to the production of dyes for glass and fabrics. The development of a reproducible method through the sodium citrate reduction method to produce colloidal gold with controlled and reproducible properties [9] eventually made possible its application to the fields of particle science and cell biology [10–14]. Until recently, the wide use of colloidal gold for labeling studies in cell biology was one of the more important applications of this material with a good number of textbooks devoted to the subject [10–14]. However, during the last few years there has been a resurgence of interest in colloidal gold because of the potential of this material for a variety of applications related to nanoscale science and engineering. The scope of this chapter will concentrate on these latest developments, particularly in their relationship to nanoscale science and engineering.

1.2. Properties

Due to its large free electron density, colloidal gold has been used extensively in applications involving electron microscopy. As it turns out, the free electrons of metallic nanoparticles also impart them with unique optical properties, which can be explained in terms of classical free-electron theory and simple electrostatic models of electrostatic polarizability [7, 14]. It was Michael Faraday who first explained the characteristic colors of colloidal dispersions of gold and ruby glass. Although his theoretical framework was mostly qualitative, it formed the foundations for

more elaborate theories on the colors of metallic colloidal dispersions.

The optical properties of metallic nanoparticles with radius, R, much smaller than the wavelength, λ, of light ($2R/\lambda \ll 1$) can be estimated by assuming that the size dependent interaction of the particles with light is static (a direct result of $2R/\lambda \ll 1$) while the dielectric properties of the free electrons in metallic nanoparticles are considered dynamic. Under these assumptions, the theory predicting the optical properties of metallic clusters is represented by the sets of equations known as the Maxwell-Garnett formula [14–18].

The polarizability α of a small spherical particle in a static electric field is

$$\alpha = 4\pi\varepsilon_0\varepsilon_m R^3 \frac{\varepsilon - \varepsilon_m}{\varepsilon + 2\varepsilon_m} \qquad (1)$$

with ε_0 being the dielectric constant of vacuum, ε_m the dielectric constant of the media the nanoparticles are embedded into, and ε the dielectric constant of the particle (assumed equal to that of the bulk metal). For metals, the dielectric constant is a complex number related to the index of refraction n and absorption coefficient k as

$$\varepsilon = \varepsilon_1(\omega) + i\varepsilon_2(\omega) = (n + ik)^2 \qquad (2)$$

and the magnitude of ε_1 and ε_2 are strong functions of the frequency of the applied electric field (wavelength of the incident light).

A direct result of Eqs. (1) and (2) is that the polarizability of a metallic nanoparticle will be maximum when the term $\varepsilon + 2\varepsilon_m$ is minimum, that is, when $(\varepsilon_1 + 2\varepsilon_m)^2 + \varepsilon_2^2 =$ minimum. During a typical ultraviolet-visible measurement the extinction coefficient γ is related to k as $\gamma = 4\pi k/\lambda$. The overall absorption was obtained first by Mie [19] by integrating over a medium filled with nanoparticles according to

$$k = 9/2\varepsilon_m^{3/2}(N4/3\pi R^3)\frac{\varepsilon_2}{(\varepsilon_1 + 2\varepsilon_m)^2 + \varepsilon_2^2} \qquad (3)$$

where N is the number density of the nanoparticles. The term in parentheses represents the filling factor $f = (N4/3\pi R^3)$.

For dilute dispersions, Eq. (3) describes the absorption of noninteracting particles. However, when the filling factor is large, each particle will be subjected to an average polarization field due to surrounding particles. Under these conditions, it is helpful to calculate an effective dielectric constant

$$\varepsilon_{\text{eff}} = \varepsilon_m \frac{1 + 2N\alpha/(3\varepsilon_0\varepsilon_m)}{1 - N\alpha/(3\varepsilon_0\varepsilon_m)} = \varepsilon_m \frac{1 + 2f\Lambda}{1 - f\Lambda} \qquad \text{with}$$

$$\Lambda = \frac{\varepsilon - \varepsilon_m}{\varepsilon + 2\varepsilon_m} = \frac{\alpha}{3\varepsilon_0\varepsilon_m V} \qquad (4)$$

Equation (4) is known as the Maxwell–Garnett formula. A direct consequence of the static approximation is that the effective optical properties are independent of particle size. The imaginary part of the refractive index is

$$k = \sqrt{0.5\left(-\varepsilon_{\text{eff},1} + \sqrt{\varepsilon_{\text{eff},1}^2 + \varepsilon_{\text{eff},2}^2}\right)} \qquad (5)$$

In order to calculate an extinction coefficient it is necessary to first obtain an estimate of the dielectric constants. For metals, the dielectric constants can be approximated by the Drude model [20]. According to this model the real and imaginary parts of the dielectric constant are given by

$$\varepsilon_1 = 1 - \frac{\omega_p^2}{\omega} \qquad \text{and} \qquad \varepsilon_2 = 1 - \frac{\omega_p^2}{\omega^3}\omega_d \qquad (6)$$

where $\omega_p = \sqrt{ne^2/\varepsilon_0 m_e}$ is the bulk plasma frequency, n is the concentration of free electrons in the metal, and m and e are the effective mass and charge of the electron respectively. The term $\omega_d = v_F/l$ represents the relaxation or damping frequency with v_F being the velocity of the electrons at the Fermi level and l the electron mean free path [14–17, 20, 21]. The Drude model allows an estimation of the dielectric constants. In addition, tabulated values of experimentally determined dielectric constants for bulk metals can be found in the literature [22]. Figure 1 shows the simulated extinction coefficient of 10 nm gold nanoparticles embedded in media with different dielectric constants. Tabulated experimental values of the dielectric constants of gold were used to simulate the spectra [22]. This figure shows the sensitivity of the absorbance of the nanoparticles to the dielectric medium surrounding them. Two features that emerge from this figure are a slight redshift in the surface plasmon resonance (SPR) peak position and an increased intensity of the SPR absorption band. Thus, changing the dielectric constant of the media surrounding the nanoparticles results in changes on their optical absorption spectra. Interactions of other materials with the nanoparticles' surfaces can induce similar changes.

The optical properties of gold nanoparticles are also susceptible to the degree of interaction (aggregation) among the particles. For a particle pair with a small enough center-to-center separation, D, the oscillations of the surface plasmons differ significantly from those of isolated particles. In aggregated pairs, two excitation modes can exist, parallel or perpendicular relative to the axis pair. Longitudinal in-phase oscillations differ significantly from transversal oscillations with the former being significantly different from noninteracting particles while the latter is only slightly redshifted. When interacting nanoparticle pairs are exposed to
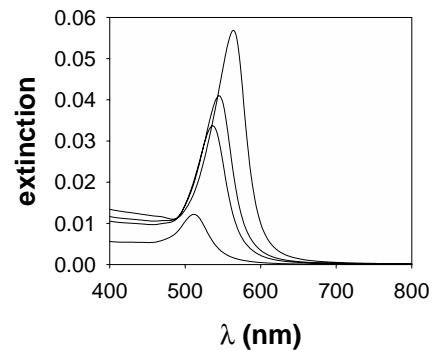

Figure 1. Simulated optical absorption spectra for 10 nm gold particles embedded in media with $\varepsilon_m = 1.0, 1.77, 2.0,$ and 2.5.

an applied electrical field E, the resulting dipole moments, μ_{1j} and μ_{2j}, of the two spheres are given by

$$\mu_{1j} = \alpha_1 E^* + \frac{\alpha_1 \mu_{2j} j}{4\pi\varepsilon_0\varepsilon_m D^3} \qquad \text{and}$$

$$\mu_{2j} = \alpha_2 E^* + \frac{\alpha_2 \mu_{1j} j}{4\pi\varepsilon_0\varepsilon_m D^3} \qquad (7)$$

with $j = 1$ representing the transversal mode and $j = 2$ the longitudinal mode of oscillation. If the angle between the electric field vector and the longitudinal axis of the particle pair is θ, then $E^* = E\cos\theta$ for the longitudinal mode and $E^* = E\sin\theta$ for the transversal mode. The pair polarizability for the longitudinal and transversal modes can be calculated with these equations.

For nanoparticle pairs in a two-dimensional (2D) plane, the average polarizability $\Lambda_{\text{pair, 2D}}$ is obtained when integrating over all possible orientations of the longitudinal and transversal modes, giving

$$\Lambda_{\text{pair, 2D}} = \frac{\eta}{2}((1 - 2\eta(R/D)^3)^{-1} + (1 + \eta(R/D)^3)^{-1}) \quad (8)$$

where $\eta = (\varepsilon - \varepsilon_m)(\varepsilon + 2\varepsilon_m)$. With the average polarizability $\Lambda_{\text{pair, 2D}}$, an effective dielectric constant and the absorption can be calculated with Eqs. (4) and (5), respectively. Figure 2 shows the simulated absorption spectra of 10 nm gold nanoparticles embedded in dielectric medium with $\varepsilon_m = 2.5$ at various separation distances between the nanoparticles. When the particles are separated by a large distance they behave as independent particles and the simulated spectrum is similar to that obtained from Eq. (3). However, when the separation becomes comparable to the radius of the particle, longitudinal and transversal resonance peaks can coexist. The longitudinal mode is significantly redshifted while the transversal mode is only slightly redshifted from that of noninteracting particles. Furthermore, the magnitude and shift of the longitudinal mode become significant when the separation distance is smaller than the diameter of the particles and this effect becomes stronger as the separation distance of the particles becomes smaller. The previous approximation is valid for 2D particle-pair aggregates. For many particle aggregates, more complex calculations are
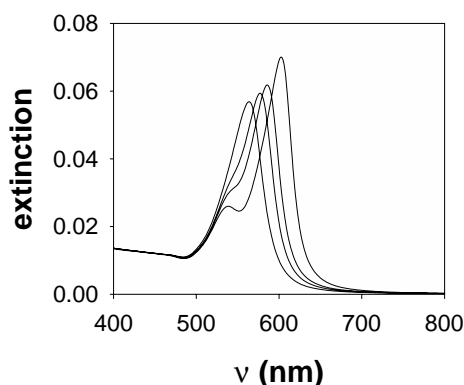
Figure 2. Simulated optical absorption spectra of 10 nm gold nanoparticles at varying separation distances between the particles with $R/D = 0.0001, 0.444, 2.5,$ and 2.0.

necessary [23, 24]. In this case, additional resonances appear at lower frequencies (longer wavelengths) that are even more separated than those calculated for 2D particle pairs. In fact, their optical absorption spectra can show broad bands that extend into the near infrared region depending on the size of the aggregates and the number of particles in the aggregate [17, 18, 23–25].

Because particle size, degree of aggregation, and the dielectric constant of the media determine its optical properties, applications of colloidal gold exploiting the strong dependence of optical properties with aggregation and surrounding dielectric media have been implemented through proper surface modification of the nanoparticles or by embedding them in different dielectric media. The following sections summarize preparation methods, surface modification, characterization, and modern applications. Traditional applications (e.g., immunostaining) are only briefly discussed since there is already a wide body of literature on these applications and the techniques are well established [10–14].

2. PREPARATION METHODS

2.1. Gold Nanoparticle/Colloidal Gold Synthesis

Metallic nanoparticles can be synthesized by a variety of methods such as chemical [10, 12–14, 17], sonolytic [26], radiolytic [27–30], and photolytic reactions [31–37]. However, the reduction of metal salts by added reducing agents is the oldest established procedure for the preparation of aqueous suspensions of nanoparticles. A wide range of reducing agents have been used in gold nanoparticle synthesis; the most frequently used ones include sodium citrate [38, 39], sodium borohydride [10, 12–14, 40], tannic acid [10, 12–14], white phosphorus [6, 10, 41] hydrazine [42–44], hydrogen [45, 46], carbon monoxide [47], hydroxylamine [48–50], and mild agents like ascorbic acid [51, 52]. Reducing solvents such as alcohols [53–55], formamide [56], and ethers [54, 57] can also be used in the synthesis of metallic nanoparticles.

In 1951, Turkevich et al. [58]. established the first reliable procedure for the preparation of gold sols with well-controlled size distributions. Such a method is based on reduction of chloroauric acid by trisodium citrate and has become a standard for histological staining applications.

Other approaches to the synthesis of colloidal gold nanoparticles have been used. Among those is a two-phase system, first introduced by Faraday [6], who reduced aqueous gold salt with phosphorus vapor in carbon disulfide. Later, a combination of the two-phase approach with the more recent techniques of ion extraction and formation of self-assembled monolayers (SAMs) of alkanethiols on gold led to a one-step method for the synthesis of derivatized gold nanoparticles by Brust et al. [59, 60]. The technique consists of simultaneous reduction of gold salts and SAM formation. The redox reactions can be carried out by an appropriate choice of reducing and phase-transfer reagents in the two phases. In the original procedure, an aqueous solution of chloroaurate is mixed with a solution of the phase-transfer reagent tetraoctyl ammonium bromide in

toluene and the mixture is vigorously stirred until all tetra-chloroaurate was transferred to the organic layer. The alka-nethiol is then added to the organic phase followed by the reducing agent. This procedure led to the formation of sta-ble gold nanoparticles protected by a self-assembled mono-layer that imparted the nanoparticles different properties depending on the functional group at the surface. These lat-ter systems are also commonly referred to as monolayer pro-tected clusters, which have the characteristic that they can be treated as unique chemical entities because they can be manipulated with a variety of physicochemical procedures while maintaining their identity (*vide infra*) [59–61].

2.2. Polymers in the Synthesis of Gold Nanoparticles

The preparation of nanocomposites with an inorganic core such as metal nanoparticles and a protective organic shell of small molar mass compounds or polymers is a route to obtain materials suitable for hierarchical self-organization into nanoassemblies. Incorporation of nanoparticles into polymer matrices is particularly advantageous for materials engineering and the study of nanoparticle–matrix interac-tions. The adsorption of polymers onto a wide variety of nanoparticles is of broad industrial relevance in such areas as pharmaceuticals, photography, paints and coatings, foods, wastewater treatment, rubbers, and composite materials and is ubiquitous in natural aqueous environments as well as in many biological organisms. Recently, nanocomposites of π-conjugated polymers and inorganic particles have received much attention [62–68], due to the interesting high electrical conductivity [69] and redox properties [70] of π-conjugated polymers and their extensive applications ranging from bat-teries to light-emitting devices [71]. The adsorption or graft-ing of environmentally responsive "smart" polymers onto surfaces holds potential applications in controlled modula-tion of interfacial properties, as demonstrated in thermally switchable cell culture of anchorage-dependent mammalian cells [72, 73] and to control bacteria fouling [74]. Consid-ering the wide range of applications, the combination of polymers with nanoparticles has driven lot of interest in its research.

Overall there have been two different approaches to achieve nanoparticle–polymer composites. The first tech-nique consists of the *in-situ* preparation of the nanoparticles in the matrix. This is effected either by the reduction of metal salts dissolved in the polymer matrix [75–77] or by the evaporation of metals on the heated polymer surface [78]. A second technique involves polymerizing the matrix around the nanoparticles [79].

Lennox et al. [80]. proposed a desirable approach that involved blending premade nanoparticles into a presynthe-sized polymer matrix. Coating gold nanoparticles first with a polymer ligand chemically similar to the polymer matrix made mixing of the gold nanoparticles with the polymeric matrix thermodynamically more favorable and thus more compatible as compared to coatings with polymer ligands that were chemically different from the matrix [81]. The sur-faces of gold nanoparticles were decorated with covalently bound thiol-capped polystyrene macromolecules (PS–SH) and these were dispersed in a PS matrix. Because of its

high glass-transition temperature, PS allows for the for-mation of robust films at room temperature. The PS–SH macromolecules were synthesized by anionic polymeriza-tion and the polystyrene anion was titrated with one unit of propylene sulfide to generate the thiol end group [82]. The PS–Au nanoparticles were prepared following modi-fied Ulman reaction conditions [83], using lithium triethyl-borohydride as a reducing agent. Incorporation into the PS matrix was effected by dissolving both PS–Au and PS matrix in a small amount of chloroform. The PS–Au nanoparticles were found to be evenly dispersed. This method provided for the full synthetic control over both the nanoparticles and the matrix.

Novel π-conjugated polymer-protected metal (Pd, Au, Pt) nanoparticles have been prepared via reduction of the metal ions by a π-conjugated poly(dithiafulvene) (PDF) having strong electron-donating properties. For the synthesis of gold nanoparticles, the PDF is dissolved into a dimethyl sulfoxide solution of $HAuCl_4$ and the reaction mixture is stirred for 24 hours at room temperature. The reaction mixture changes gradually from yellow to purple, indicat-ing nanoparticle formation. It has been proposed that elec-tron transfer from the π-conjugated PDF to the Au ions results in the formation of Au nanoparticles embedded in the polymeric matrix. The oxidized π-conjugated polymer might possess a delocalized positive charge and provide both steric and electrostatic stabilization, protecting the Au in stable colloidal form [84]. Nanoparticles encapsulated in π-conjugated polymers show interesting characteristics, particularly in dielectric properties, energy storage, catalytic activity, and magnetic susceptibility [85].

Hybrid polymeric systems with metal nanoparticles located inside specific areas of the material have been developed by Svergun et al. [86]. In this approach, a self-assembled multilayered polymer, poly(octadecylsiloxane), provided a nanostructured matrix for the incorporation of gold and platinum compounds and for metal nanoparticle formation. The size distributions of the nanoparticles and the changes in the internal structure of the matrix as a result of nanoparticle formation for different reducing agents and reaction media were studied.

In addition to the examples mentioned, a variety of other polymers used for the preparation and study of polymer–gold nanocomposites can be found in the literature [87–91]. Further uses of polymers also involve surface modification of nanoparticles as described in Section 3.5.

2.3. Laser Ablation

In recent years, gold nanoparticles with diameters less than 10 nm have attracted much attention because of their size dependent physical and chemical properties: a gold nanoparticle in the size range of less than 5 nm in diame-ter shows a dramatic decrease of the melting point [92, 93], exhibits intense photoluminescence [94], and catalyzes CO oxidation even at low temperatures (200 K) when used with TiO_2 [95, 96]. Traditionally, chemical reduction of gold salt into gold nanoparticles in reverse micelles has been one of the most successful methods to obtain gold nanoparti-cles with diameters less than 10 nm in solution [97]. In this method, the size of the nanoparticles depends on that of the

reversed micelles, so that nanoparticles with a desired size can be obtained by introducing a proper amount of water inside the reverse micelles through adjustment of the molar ratio of water to nonpolar solvent.

Alternatives to chemical synthesis for the preparation of gold nanoparticles with diameters less than 10 nm have been developed that involve laser ablation of a gold plate in solution [98]. These methods are currently under investigation by several research groups [99–102]. In this method, a gold metal plate, which is placed at the bottom of a glass vessel filled with an aqueous solution of a surfactant (e.g., sodium dodecyl sulfate or SDS), is irradiated with a Nd:YAG pulsed laser (1064 nm) and gold nanoparticles are formed [101].

Formation of gold nanoparticles occurs by a SDS concentration dependent mechanism [103]. After laser ablation, a dense cloud of gold atoms is built over the laser spot of the metal plate and the atoms aggregate as fast as they are supplied. This continues until the atoms in close vicinity are depleted almost completely. As a result an embryonic particle is formed in a region void of atoms. However, the supply of atoms outside the region by diffusion causes the particle to grow slowly even after rapid growth ceases. The surfactant (SDS) plays an important role determining the stability and size of the nanoparticles, because the termination of the particle growth is controlled by the diffusion and attachment rates of SDS on the nanoparticle. Gold nanoparticles end up coated with a double layer of SDS, such that in the first layer the SDS molecules orient with the hydrophilic $-SO_4^-$ end toward the nanoparticle and the hydrophobic $-C_{12}H_{25}$ end outward while in the second layer they orient in the opposite direction. The fact that the nanoparticles end up coated with a double layer of SDS ensures the stability of gold nanoparticles in solution.

Gold nanoparticles produced upon laser irradiation (1064 nm) to the gold plate have typical size distributions of 1–15 nm with average diameters less than 10 nm. However, when the nanoparticles form, it is very difficult to change their size, and the aggregation of the ablated atoms can hardly be controlled. In order to address this problem, further size reduction of the gold nanoparticles can be induced by laser irradiation (532 nm) in the vicinity of the wavelength of SPR excitation of the gold nanoparticles (520 nm) [98, 104, 105]. Gold nanoparticles in solution do not absorb photons at 1064 nm, but they absorb photons at 532 nm and fragment into smaller particles. Dissociation of the gold nanoparticles by absorption of 532 nm photons can be achieved by first preparing nanoparticles by laser ablation of the metal at 1064 nm followed by irradiation with a 532 nm laser. The mechanism of laser-induced size reduction along with experimental evidence of the hypothesis was proposed by Takami et al. [106]. In this scheme, when the laser (532 nm) irradiates the gold nanoparticles, the plasmons in the gold nanoparticles absorb photons and the electrons are excited. The temperature of the nanoparticles rises above the melting point such that they melt and become liquid. Further size reduction takes place due to vaporization of the gold nanoparticles when the temperature rises to the boiling point such that atoms and/or small particles are ejected via vaporization. The amount of ejected atoms depends on the absorbed laser energy. The maximum diameter is determined by the equilibrium between the ejected atoms and the deposition of ejected atoms back onto the nanoparticle surface. Because the ejected atoms are very unstable in aqueous solution, they tend to agglomerate and/or deposit on the gold nanoparticles remaining in the solution.

Laser-induced size reduction of gold nanoparticles that are produced by laser ablation of gold plates is a promising new technique for the preparation of size-selected nanoparticles with diameters less than 10 nm in solution. This technique is very simple, is versatile compared to other preparation techniques, and can be applied to other metals.

2.4. Ultrasonic Irradiation

In the preceding sections, stabilizers were used to control the particle nucleation and growth processes along with parameters such as the initial concentration of the reactants. Although there is an enormous amount of research being conducted with nanoparticles prepared by these methods, there are only few reports elucidating the relationship between the rates of reduction of metal ions and the size of the formed gold nanoparticles due to experimental difficulties in solution systems. Some of the difficulties include (a) the precise determination of the rate of reduction of metal ions because the reaction is often too fast to track the course of the reduction experimentally, and (b) the quantitative analysis for the concentration of unreduced metal ions that are still present in the reaction medium.

In recent years the formation of gold nanoparticles in an ultrasound field has been studied as an alternative to other methods [98, 107–109]. Caruso et al. [98]. summarizes the description of the ultrasonic irradiation phenomenon and the details of this method can be found in the references therein. The mechanisms of formation of gold nanoparticles have also been proposed before. [106, 107] In short, ultrasonic irradiation causes pyrolysis of water and other organic compounds present in an aqueous solution resulting in formation of free radicals at extremely high temperatures and pressures. These radicals reduce the gold (III) ions into gold (II), gold (I), and finally gold (0). The reduction of gold (III) with sonochemically formed radical species can be followed by a colorimetric method using NaBr. The rate of gold (III) reduction and the size of the gold nanoparticles can be controlled by the ultrasound irradiation conditions such as temperature, intensity of the ultrasound, and positioning of the reactor. However, this method yields polydisperse gold nanoparticles, which is an important problem for some applications where monodisperse solutions of gold nanoparticles are required.

2.5. Anisometric Gold Nanoparticles

The preparation and characterization of nanostructured materials has grown constantly because of their distinctive properties and potential use in technological applications. Since the electronic, magnetic, catalytic, and optical properties of metallic nanoparticles depend mainly on their size and shape (or morphology), shape control is one of the alternative tools to adjust these properties for various applications.

Nonspherical gold nanoparticles in the shapes of plate-like triangles [58, 110, 111], rods [112, 113], oblate or pancakelike [114–117], prolate or needlelike [114–117], hexagonal [110], ellipsoidal, quasi-ellipsoidal [110], and noncentrosymmetric [118] have been prepared and studied by a number of groups around the world. Some of the techniques that have been exploited to prepare shape controlled gold nanoparticles include the template synthesis method [115–117, 119–125], ultraviolet (UV) irradiation photoreduction [110], electrochemical synthesis [126], poly(tetrafluoroethylene) (PTFE) friction transfer approach [127], and grazing incidence vacuum deposition [128, 129].

In the template method, different materials are used as templates for the synthesis of anisometric gold nanoparticles. Schönenberger et al. [130]. reported the synthesis of Au nanowires using polycarbonate track-etched membranes as templates. Martin and co-workers [114–117, 119–122, 125] have explored the properties of gold nanowires prepared by electrochemically depositing Au within the pores of alumina membranes. Noncentrosymmetric gold nanoparticle structures with diameters of 26–28 nm were prepared in porous anodic aluminum films via a modified template synthesis procedure [118]. Figure 3 shows the schematic preparation of nanoparticles in an alumina template. The electrochemical preparation of nanoporous alumina films utilized a two-electrode temperature-controlled anodization cell with lead foil serving as the cathode and the polished aluminum plate as the anode. With constant stirring of the cell, anodic aluminum oxide film was grown to produce pores with 32 nm diameter and film thickness of 40–60 μm. Separation of the alumina film was achieved using a voltage reduction procedure, which created small branched pores in the barrier layer of oxide film. After rinsing and drying, the barrier side of the film was sputtered with silver and gold was potentiostatically
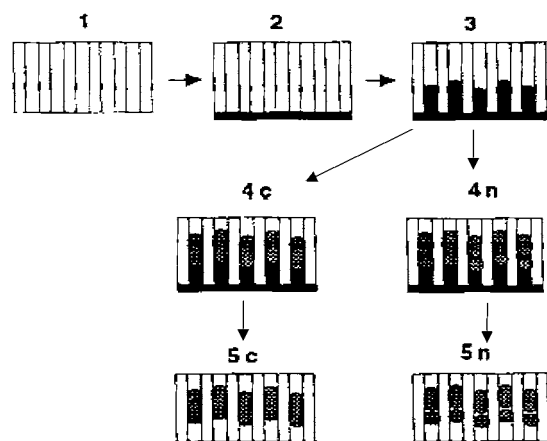
Figure 3. Schematic of nanoparticle synthesis: (1) porous anodic alumina film after detachment from Al substrate; (2) one face of alumina film coated with silver using plasma deposition; (3) electrodeposit silver foundation into pores; (4c) electrodeposit gold onto silver foundation to form centrosymmetric gold particles; (4n) electrodeposit layers of gold, silver, and then a second gold layer to form noncentrosymmetric gold particles; (5c and 5n) immerse film in nitric acid to remove silver foundation and silver spacing segments. Reprinted with permission from [118], M. L Sandrock et al., *J. Phys. Chem. B.* 103, 2668 (1999). © 1999, American Chemical Society.

deposited on a silver foundation to produce centrosymmetric and noncentrosymmetric gold nanoparticles [118].

Esumi et al. [112]. used hexadecyltrimethylammonium chloride (HTAC) (25–30 wt%) as a template for an ultraviolet irradiation technique to synthesize colloidal Au particles with morphologies ranging from spherical to needle shapes. For a 25% (w/w) HTAC concentration, spherical particles were obtained for $HAuCl_4$ concentration below 1 mM and rodlike gold particles at concentrations 5 mM and above. It was discussed that when an aqueous solution of $HAuCl_4$ is added to an aqueous solution of a cationic surfactant, $AuCl_4^-$ forms a 1:1 complex with the cationic surfactant, resulting in a precipitate. With a further increase of the surfactant concentration, the precipitate is redispersed and the solution becomes clear. This situation is understood by the view that $AuCl_4^-$ binds preferentially to the surface of rodlike micelles because of the hydrophilic property of $AuCl_4^-$ and the neutralization of micellar charge. It seems likely that binding of $AuCl_4^-$ to the surface of rodlike micelles reduced by UV irradiation results in formation of rodlike gold particles.

In the procedure developed by Chen et al. [110], an aqueous solution of $HAuCl_4$ is mixed with polyvinyl alcohol (PVA), which is used as capping material and irradiated for 48 h, resulting in platelike triangular Au nanoparticles, which developed into hexagonal shapes of about 25 nm with increased $HAuCl_4$ concentration. Also the increase in the duration of irradiation resulted in the formation of more regular platelet triangular shapes. It was reasoned that there was enough time for the reduction of $HAuCl_4$ into elemental Au, which aggregated and grew into more regular triangular shapes. But further study revealed that the crystal morphology of Au nanoparticles was predominantly hexagonal rather than triangular. The variation in Au morphology might be the result of excess gold in the solution, which facilitates the formation of hexagonal Au nanoparticles. The concentration of the capping material played an important role in the formation and morphology of Au nanoparticles. The polymer capping materials acted as molecularly dissolved surface modifiers and steric stabilizers, which influenced the crystallization of the growing Au nucleus site in a specific manner. For PVA concentrations smaller than 1.0 wt%, spherical particles were obtained and a further increase in PVA concentration was found to favor the formation of polyhedral-shaped Au nanoparticles. When polyethylene glycol was used in place of PVA as the capping material, Au nanoparticles with quasi-ellipsoidal morphology were obtained.

Gold nanorods with different aspect ratios have also been prepared with the aid of shape-inducing micelles using an electrochemical oxidation/reduction method [126]. Appropriate surfactants were employed as both the supporting electrolyte and the stabilizer for the resulting Au nanoparticles. In this approach, a gold metal plate is used as an anode and a platinum plate is used as a cathode. Both plates are immersed in an electrolytic solution consisting of a cationic surfactant (e.g., hexadecylmethylammonium bromide) and a rod-inducing cosurfactant (e.g., tetraoctylammonium bromide/tetradecylammonium bromide). A controlled-current electrolysis is carried out under constant ultrasonication and controlled temperature, resulting in the formation of cylindrical nanoparticles with a typical transverse diameter of 10 nm. The ratio of the two surfactants controls the length of

the gold nanorods formed. Hence the surrounding medium, often referred to as capping material, is of great importance as it prevents aggregation and provides the formation of the desired nanorods [113]. It has been observed, in general, that the particle size and shape are influenced by the concentrations of the capping "micellar" materials. Gold nanorods with very large aspect ratios (up to 18) have been prepared following a seed-mediated growth procedure [131, 132].

Wittman and Smith developed the friction-transfer method [133], wherein a block of PTFE is translated across the surface of a glass slide. As a result the glass surface is coated with highly oriented chains of PTFE, which can in turn orient a wide variety of substances from small molecules to polymers [133, 134] and liquid crystals [135]. Alkanethiol coated gold nanoparticles in organic solvents were introduced onto the polymer substrate and subsequently rubbed and flame treated, resulting in strong linear dichroism in the visible spectrum. The gold structures appeared as chains of spherical and rodlike particles with definite gross alignment. The elongated structures appear to be the result of heat-induced particle agglomeration [127].

Ravaine et al. [136]. demonstrated that gold nanoparticles could be formed upon UV irradiation of Langmuir–Blodgett (LB) films of positively charged amphiphiles deposited from an aqueous $HAuCl_4$ subphase. Different LB templates led to different types of Au particles. Single crystals, irregularly shaped crystals, or multiply twinned particles of different size are formed depending on the nature of the amphiphile used to prepare the LB matrix [137, 138]. Most of the particles prepared by this method are platelike particles with sizes ranging from 20 to 800 nm.

2.5.1. Optical Properties of Anisometric Gold Nanoparticles

In addition to the interest in controlling the shape of gold nanoparticles, the optical properties of these particles have attracted many researchers since the early 20th century. The optical properties of spherical gold nanoparticles were briefly discussed in Section 1.2 in terms of the surface plasmon resonance absorption peak. The surface plasmon depends on the size of the nanoparticles and many attempts have been made to experimentally correlate the absorption maximum and plasmon bandwidth to the actual size. Several factors, such as nonhomogeneous size distribution and surrounding media, complicate a strict correlation between the theory and experimental results.

The optical properties of anisometric gold particles are also of interest because, in addition to size, the absorption spectra are also strongly dependent on the shape of the nanoparticle. In the case of gold nanorods, the optical absorption spectra become split into two SPR modes: a longitudinal mode along the long axis of the rod and a transverse mode perpendicular to the first mode. The magnitude of these modes is also sensitive to the orientational order of the gold rods. With incident light polarized parallel to the main axis of the particles that are fully aligned, the spectrum displays only the longitudinal resonance. In the case of perpendicular polarization of the incident light, the spectrum displays only transverse resonance [113]. The first theoretical calculations were made by Gans [139], who extended

Mie's theory [19] to prolate and oblate spheroidal particles averaged over all orientations. The Gans theory predicts that the longitudinal resonance shifts to longer wavelengths with increasing aspect ratio (length to diameter ratio), whereas the transverse resonance shifts only slightly to shorter wavelengths [139]. Experimental evidence supporting this theory was obtained by Skillman et al. [140]. who studied the optical properties of silver ellipsoids embedded in gelatin. They found a shift in the longitudinal resonance at longer wavelengths with increasing aspect ratios of the particles.

Figure 4 shows a transmission electron microscopy (TEM) picture of gold nanorods synthesized by electrochemical reduction of $AuCl_4H$ in a micellar solution [113, 141, 142]. The same figure shows the UV-visible (UV-vis) absorption spectrum of this system. The presence of transverse and longitudinal SP modes is evident and points out to the special optical properties of these nanoparticles.

In summary, spherical gold nanoparticles differ from gold nanorods not only in shape but also in terms of the optical properties. Spherical gold nanoparticles display only one size dependent absorption maximum, whereas gold rods have two maximums depending on the aspect ratio with the longitudinal mode being more intense and shifted to longer wavelengths.

2.6. Nanoshells

Nanoshells are nanoparticles normally composed of a dielectric core (usually silica) coated by a thin metallic film, from which the term nanoshell is derived. Synthesis of these particles usually involves formation of dielectric cores (silica nanoparticles) followed by further attachment of very small colloidal gold particles on their surface that will act as nucleation sites for further reduction of gold chloride so that the dielectric nanoparticles become covered by a continuous metallic film. These colloidal systems have similar optical properties to colloidal gold in the sense that they also exhibit SPR absorption. The optical properties of these materials strongly depend on the size of the dielectric core, the thickness of the metallic thin film, and the surrounding media [143–159]. In contrast to colloidal gold, however, where the SPR peak is weakly dependent on particle size, nanoshells allow tuning the SPR peak across the visible and infrared
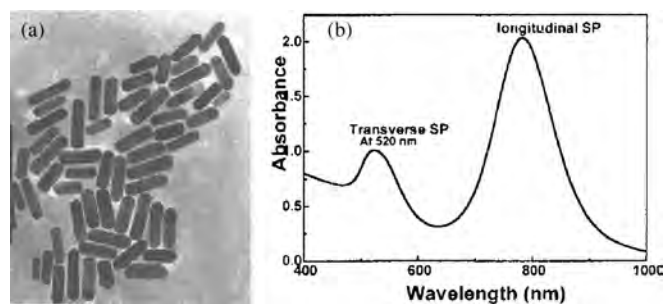

Figure 4. Right: Experimental UV-vis absorption spectrum of a gold nanorod sample is referred to as the transverse plasmon resonance, while the one centered at 740 nm is called the longitudinal plasmon absorption. Left: TEM image of the same solution. Reprinted with permission from [142], M. A. El-Sayed, *Acc. Chem. Res.* 34, 257 (2001). © 2001. American Chemical Society.

region over a wavelength range of hundreds of nanometers [143, 144, 147, 148, 151, 152, 156]. Thus, while nanoshells have similar properties to colloidal gold, they also allow flexibility in "tuning" their optical properties. Because of this, nanoshells have been investigated as platforms for surface enhanced raman spectroscopy [146], to decrease the rate of photo oxidation of semiconducting polymers [150], and in controlled drug delivery applications [149, 153]. In the latter, the nanoshells can be conjugated to a thermoresponsive polymer carrying a drug. Since tissue can transmit light in the near infrared region with little attenuation, transmitting infrared light to the site where release of the bioactive substance is desired can induce drug release from the thermoresponsive hydrogel [149].

In addition to the tunable optical properties of gold nanoshells composed of a dielectric core, gold nanoshells consisting of a metallic core have also been recently reported [159]. Gold nanoshells with a silver core show larger sensitivity to changes in the properties of the surrounding medium, which makes them attractive materials for biosensing applications. Additionally, these silver/gold core/shell particles also have the advantage of being tunable in their optical properties, in very much the same way as those formed with a dielectric core. Since the outer shell consists of gold, they can also be functionalized in a way similar to conventional colloidal gold [159].

2.7. Other Methods

Apart from the chemical and physical synthesis methods, biological production of gold nanoparticles using microorganisms has also been studied by several research groups utilizing the ability of these living organisms to convert Au^{3+} ions into gold nanoparticles. Beveridge and co-workers [160–163] have shown that gold nanoparticles readily precipitate in bacterial cells when the cells are incubated with Au^{3+} ions. Mukherjee et al. [164]. demonstrated that the exposure of fungus, *Verticillium sp*. (AAT-TS-4), to aqueous $AuCl_4^-$ ions resulted in the reduction of the metal ions and formation of gold nanoparticles (diameter of 20 nm). Although the exact mechanism is not known it is speculated that the gold nanoparticles are formed on both the surface and within the fungal cells (on the cytoplasmic membrane) by means of reductases. According to this speculation, the first step involves the trapping of the $AuCl_4^-$ on the surface of the fungal cells. Then, the gold ions are reduced by enzymes within the cell leading to the aggregation of metal atoms and the formation of gold nanoparticles. TEM images of the cells show the presence of gold nanoparticles on the cytoplasmic membrane, which indicates that some of the metal ions/gold nanoparticles diffuse across the cell wall and are localized on the cytoplasmic membrane. It is possible that the enzymes present on the cytoplasmic membrane also participate in the reduction of gold ions.

Following this report the same group [165] demonstrated the extracellular formation of gold nanoparticles using another fungus, *Fusarium oxysporum*. In this case, the formation of gold nanoparticles is believed to be due to reductases released by the fungus into the solution, which causes the reduction of gold ions in the solution. Although these results are promising, more research has to be done in order

to understand the mechanisms of the formation of gold nanoparticles.

Braun et al. [166] have also demonstrated that gold nanoclusters can be formed on specific surface sites of protein molecules in analogy to thin film formation of noble metals on inorganic substrates. In the early stages of thin film growth during vacuum deposition, metals first form nanometer size clusters or islands on the substrate if the condensing atoms are more strongly bound to each other than to the substrate (Volmer–Weber mode) [167]. These adsorbed metal atoms are mobile on the surface until they encounter other mobile atoms and come across special sites that have high adsorption and diffusion energies compared to the neighboring places where they are "trapped" and form clusters or islands. Nucleation theories and experimental evidence demonstrate that these clusters are formed in linear arrays (or so-called "decoration lines"), which are caused by steps on the substrate surface as well as the deviation from the perfect crystal surface leading to preferred nucleation of metal clusters on predetermined sites. These principles are also valid for metal condensation on protein molecules and their crystals. During vacuum condensation of gold on frozen enzyme complexes of lumazine synthase (from *B. subtilis*), proteasome (from *T. acidophilum*), and GTP cyclohydrolase (from *E. Coli*), nanoclusters are formed at specific surface sites (decoration). It was found that, under the experimental conditions outlined by Braun et al. [164], gold decorates the surface areas consisting of polar but uncharged residues. The quality of the decoration pattern can be influenced by the temperature of the substrate as well as by attaching dominant trapping sites onto the surface via chemisorption of small molecules or ions such as a polytungstate complex. The decoration sites on the enzyme complexes can be viewed by electron microscopy and their atomic surface structures can be determined with X-ray crystallography. These results opened ways to analyze the binding mechanism of nanoclusters to small specific sites on the surface of hydrated bio-macromolecules by physical–chemical methods. Although very little is known about the nature of the special sites on protein surfaces and why they enhance or impede cluster formation, understanding the binding mechanism may lead to decoration techniques with much fewer background clusters. This would improve the analysis of single molecules with regard to their symmetries and their orientation in the adsorbed state and in precrystalline assemblies as well as facilitate the detection of point defects in crystals caused by misorientation or by impurities.

3. SURFACE MODIFICATION AND FUNCTIONALIZATION OF GOLD NANOPARTICLES

In order to fully take advantage of the unique properties of gold nanoparticles, it is necessary to impart them with different surface functionalities. This allows the nanoparticles to be readily dispersed in nonpolar media and make them more compatible with a matrix during the formation of nanocomposites, or it can provide the nanoparticles with the specific molecular recognition capabilities of biomolecules.

A variety of methods for surface modification exist that can be implemented with nanoparticles.

Maintaining the stability of the nanoparticles upon surface modification is important. However, gold nanoparticles often tend to aggregate upon surface modification, especially when the surface functionalization proceeds with elimination of the negative charges on colloidal gold that normally keeps these particles from aggregating in aqueous solutions. Such is the case with the formation of self-assembled monolayers of alkanethiolates on colloidal gold [168, 169]. Chemical modification of gold surfaces can be performed by using alkanethiols, polymers, dendrimers, and other molecules as stabilizers. This can be achieved either by surface modification of already available colloidal gold or by the synthesis of colloidal gold with an organic monolayer in a one-step procedure. The following section gives a brief description of surface modification techniques for colloidal gold.

3.1. Monolayer Protected Clusters

Chemisorption of alkane thiols offers a facile route for creating well-defined surface chemistries on gold substrates. This area of research has been extensively explored during the last two decades [170–177]. Surface modification of colloidal gold using alkane thiols would appear to be a logical choice to modify the surface chemistry of these nanoparticles. However, chemisorption of alkane thiols eliminates the charges on colloidal gold that impart these particles with their stability in aqueous environments, leading to destabilization and hence irreversible flocculation [168, 169].

It is possible to synthesize stable thiol-functionalized gold nanoparticles in a one-step procedure. Common synthetic procedures to achieve this goal are most commonly based on modifications to the synthetic procedure originally reported by Brust et al. (described briefly in Section 2) [59, 60]. This method results in nanoparticles protected by an organic monolayer, which are commonly referred to as monolayer-protected clusters (MPCs). The alkanethiolate molecules protecting the gold nanoparticles have the potential to develop novel technological applications such as chemical sensing, catalysis, colorimetric assays for DNA detection, biosensors, etc [61, 178]. Understanding the properties of the alkanethiolate ligands may expand the range of applications of these nanoparticles. A wide variety of thiol molecules such as straight-chain alkanethiols [179, 180], glutathione [181], tiopronin [182], thiolated poly(ethylene glycol) [183], p-mercaptophenol [184], aromatic alkane thiol [185], phenyl alkanethiols [186], and γ-mercaptopropyl)-trimethoxysilane [187] have been used to prepare MPCs.

Several research groups have undertaken extensive efforts toward the synthesis and characterization of MPCs. Notable among these are the papers of Murray et al. who followed the first reports of Brust et al. [59, 60]. to develop elaborate characterizations of the gold clusters stabilized by monolayers of alkane thiols and a route to mixed monolayers of alkane thiols and ω-alkane thiols ligands on these nanometer-sized clusters [188]. The monolayers on these nanoparticles confer these systems with new surface properties and with extraordinary stability. In fact, they can be isolated and manipulated with a variety of chemical and physical procedures to the extent that they can be dried

and resuspended in solution again without compromising the stability of MPCs. Subsequent reports by this group have shown that a variety on alkanethiol chain lengths (C_3–C_{24}) [179, 180], ω-functionalized alkane thiols [189], and dialkyl disulfides [190] can be employed in the same protocol. Several groups in the world are now actively involved in the study and synthesis of these nanoparticles [40, 61, 191–197].

3.2. Place-Exchange Reaction

Although the synthesis of a number of alkanethiolate functionalized MPCs is reported in detail in the literature, more diverse surface properties can be achieved by altering the surface with different chemical groups. One method to accomplish further functionalization of MPCs is the place-exchange reaction, which has been used to obtain a wider variety of MPCs by various research groups [61, 188, 198–203]. Noteworthy are the efforts during the last decade of Murray et al. to produce MPCs with a variety of ligands by the place-exchange reaction [198, 199, 202]. In this method, the alkanethiolates of MPCs are displaced by chemisorption of other alkanethiols during incubation in a concentrated solution of alkanethiols. Two routes can be applied toward producing poly-hetero-ω-functionalized clusters: (a) *simultaneous*, exchange of a mixture of thiols onto an MPC and (b) *stepwise*, progressive exchange of different thiols, isolating and characterizing the cluster product after each step. During a typical place-exchange reaction, MPCs with alkanethiolate monolayers (RS) are functionalized with $R'S$ groups according to

$$x(R'SH) + (RS)_m MPC \rightarrow x(RSH) + (R'S)_x(RS)_{m-x} MPC$$
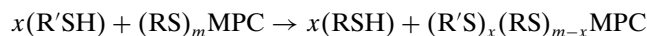
where x and m are the numbers of new and original ligands [188], respectively.

The rate and equilibrium stoichiometry, x, of this reaction, are controlled by factors such as the mole ratio of R′SH to RS, their relative steric bulk, and R versus R′ chain lengths [199]. The stepwise place-exchange reaction additionally reveals the extent to which an exchange reaction can displace ω—functionalized versus nonfunctionalized alkanethiolate ligands from a cluster. An important observation is that ligands with longer chains tend to displace those with short linker chains, but the displacement of ligands with long linker chains by those with short linker chains is less likely to occur. Also, short chain length, bulky, ω-functionalized alkanethiolates are the least thermodynamically stable ligands, consistent with the fact that they have a varying density of chain packing around the gold core [199].

Detailed studies of the dynamics and the mechanism revealed that the place-exchange reaction (a) has a 1:1 stoichiometry, (ii) is an associative reaction, (iii) yields the displaced ligand in solution as a thiol, and (iv) does not involve disulfides or oxidized sulfur species [198]. The time-dependent rate of place exchange has been interpreted as reflecting a hierarchy of different core surface binding sites with associated susceptibility (vertexes, edges, terraces) to place exchange [193, 198, 199]. These observations are similar to the displacement of alkanethiols on self-assembled monolayers on flat substrates [204].

3.3. Chemisorption of Alkanethiols

As mentioned, surface modification of gold nanoparticles by chemisorption of alkane thiols is a logical choice for surface functionalization of gold nanoparticles provided that the proper steps to avoid irreversible aggregation are taken. The interaction of alkanethiols with the gold nanoparticle surface causes the thiol molecules self-assemble in a well ordered, densely packed manner on the nanoparticle surface (similar to SAMs on flat substrates). Common precursors of these SAMs are aliphatic thiols with the structure of $HS–(CH_2)_nR$, where the functional group, R, stands for a variety of functionalities [172–181]. In principle, these groups can allow for further functionalization of the gold nanoparticles with ligands, proteins, and other biomolecules.

Direct chemisorption of alkanethiols on already synthesized colloidal gold produces functionalized nanoparticles similar to MPCs. However, there are some disadvantages associated with this method. Under some conditions (pH, ionic strength, alkane thiol chain length, and alkane thiol functionality) and during their functionalization, the nanoparticles can undergo irreversible aggregation or flocculation [172, 173]. This limits the use of this method for surface modification purposes. Although used to some extent by several research groups [25, 205–207], the conditions under which this method is employed usually require dilute solutions and the modified particles lack stability over long periods of time or under extreme conditions of pH, ionic strength, and temperature.

Our group has recently proposed a method that greatly facilitates the formation of SAMs of alkanethiols on colloidal gold [208]. The approach to obtain stable alkanethiol modified gold nanoparticles using this method consists of performing the chemisorption of carboxyl terminated alkane thiols in the presence of a nonionic surfactant [polyoxyethylene (20) sorbitan monolaurate (Tween 20)]. This method was developed from the observation that the physisorption of Tween 20 prior to chemisorption of alkanethiols provides a protective, stabilizing layer around the nanoparticles preventing them from aggregation by means of steric hindrance caused by the oligo(ethylene glycol) moieties on this surfactant molecule. Since the physisorption of Tween 20 on the gold nanoparticles is weak compared to the chemisorption alkane thiols, the weakly adsorbed surfactant can be displaced by alkanethiols chemisorbing onto the gold surface. The alkane thiol modified gold nanoparticles obtained by this method have remarkable stability in the sense that they can be frozen or dried and resuspended with mild sonication without suffering irreversible aggregation. Further derivatization of these particles with other molecules is possible and it is accomplished easily without formation of particle aggregates.

Often, surface functionalization with alkanethiols is only an intermediate step toward further functionalization of nanoparticles. This is the case for the place exchange reaction and further derivatization of chemically reactive groups. [182, 198–203] Another strategy involves a noncovalent coupling of ligands by means of hydrophobic interactions that consists on the formation of interdigitated bilayers [209–212]. The latter appears to be versatile enough for derivatization with a variety of compounds and the modified surfaces are remarkably stable in aqueous environments which makes this method attractive for biological applications.

3.4. Proteins and Antibodies (Immunogold)

Identification and localization of components of biological systems (e.g., visualization of proteins within a cell) using gold nanoparticles attached to an antibody that binds specifically to a protein is a commonly used method in electron microscopy studies of cells. The combination of the reliable immunological methods for producing good quality monoclonal and polyclonal antibodies and the techniques for complexing proteins onto gold nanoparticles to form immunological probes allows the investigation of a vast range of antigens in cells and tissues.

These gold conjugates can be used in a wide range of applications. The major reason for their use in electron microscopy studies is the high electron density of the gold nanoparticles coupled with the ease with which different particle sizes can be used for examination at different magnifications. Also the strong emission of secondary electrons and backscattered electrons from gold nanoparticles make the gold probes ideal for study of surface antigens and macromolecules with scanning electron microscopy (SEM) [213]. Immunogold probes give the highest possible spatial resolution to obtain structural information at the macromolecular level. Also nanogold is known to produce a more punctuate labeling pattern than eosin photo-oxidation and thus has advantages in electron microscopic quantitation and resolution of binding sites. Immunogold gives more intense stains compared to other stains and this permits much higher dilutions of primary antibody and gold conjugate, resulting in lower background.

Colloidal gold labeling techniques were first introduced by Faulk and Taylor when they absorbed antisalmonella rabbit gamma globulins to gold particles for one-step identification and localization of salmonella antigens [214]. Indirect labeling techniques with gold probes were subsequently introduced by Romano et al. who also reported gold labeling with protein A for detection of primary immunoglobulins [215]. The application to thin sections for electron microscopy was described in detail by Roth et al. and since then colloidal gold has been used in TEM for ultrastructural studies of cellular antigens [216]. Electron imaging of gold particles has also been combined with X-ray emission using an energy dispersive analyzer in SEM for immunolabeling studies [217]. To date, the method of application of gold probes to the tissues has been well documented [218]. Gold probes in sizes ranging from 1 to 40 nm have been in use for electron microscopy. But the possibility of ambiguity between small gold particles and tissue structures indicates that larger particle sizes are preferred and are best visualized by backscattered electron imaging. While all sizes of gold probes may be used to label tissue proteins, the sizes most commonly employed for SEM studies are 20–30 nm.

Gold nanoparticles may be conjugated to primary antibodies for one-step identification of antigens (e.g., with anti Human IgG) but are more usually employed as secondary antibody/protein labels. Also multiple labeling of different

cellular proteins on the same structures using different sizes of gold probes or gold probes in conjunction with other labels has become a popular method [219, 220].

On cells of eukaryotic origin, which have a net negative surface charge from anionic plasma membrane components, the membrane charge distribution is thought to be important in the movement of various soluble macromolecules across cell walls. Various methods have been employed to analyze the spatial distribution of anionic sites in tissues and to study the role played by surface charges in intracellular and intercellular dynamics. Cationic colloidal gold is one of the most used probes for this study [221–224].

Cationic gold results from the conjugation of colloidal gold particles with poly-L-lysine, which exhibits a strong positive charge at physiological pH [223]. A one-step incubation with these conjugates reveals subcellular sites bearing a net negative charge and such gold probes may be used at physiological pH and ionic strength. Cationic gold can also be tested for use in paraffin and resin embedded sections.

Gold cluster complexes offer several advantages over conventional colloidal gold for labeling. A number of different reactive groups may be incorporated during synthesis and used for covalent, site-specific attachment to biomolecules. An example of this nanogold cluster is a gold core of 1.4 nm in diameter, stabilized by tris(aryl)phosphine ligands. This is a neutral molecule, stable over a wide range of pH and ionic concentrations. It has been used to label IgG molecules, Fab' fragments, streptavidin, and other proteins, as well as smaller molecules such as peptides [225], oligonucleotides [226], and lipids [227], which cannot be directly labeled with colloidal gold.

3.5. Dendrimers and Polymers

Dendrimers and polymers can also be used to functionalize gold nanoparticles. Section 2.2 provided a description on the use of polymers for the preparation of colloidal gold. From that, it is obvious that gold nanoparticles can also be functionalized with polymers and examples of this abound in the literature. Citrate-capped gold nanoparticles have been efficiently grafted with nonionic hydrophilic polymers bearing hydroxyl groups, using disulfide anchors by the "grafting-to" strategy (in which a covalently attached polymer monolayer is formed by simple contact of the metal surface with dilute solutions of polymers) enabling their use in biological applications [228]. The resulting monolayers can be derivatized for specific recognition of analytes using unsymmetrical bifunctional linker groups or directly when the polymer bears activated sites. Two monomers used in this approach are N-[tris(hydroxymethyl)methyl]acrylamide (NTHMMAAM) and N-(isopropyl)acrylamide (NIPAAM). Derivatization of the gold surface by the disulfide bearing polymers (NTHMMAAM or NIPAAM) improved the stability of nanoparticles toward aggregation. They remained water-soluble during all the synthesis steps and could also be lyophilized and redispersed in water, indicating the complete protection of gold colloids by the polymer monolayer. Additionally, gold nanoparticles coated with the thermoresponsive polymer poly(NIPAAM) underwent conformational collapse with increased temperature, resulting

in controlled and reversible thermally induced aggregation [228].

End functionalized 3D SAMs on gold nanoparticles have been used to initiate a living cationic ring-opening polymerization reaction directly on gold nanoparticle surfaces, by the "grafting-from" technique (in which a reactive group is created on the surface that is able to initiate the polymerization, and the propagating polymer chain is growing *from* the surface) [229, 230]. Using appropriate initiators and 2-oxazoline monomers (2-phenyl-2-oxazoline/2-ethyl-2-oxazoline), ring-opening polymerization can proceed in a living manner in a "one-pot multistage" reaction, creating complex core–shell morphologies of amphiphilic nanocomposites [231]. This combination of a grafting–from reaction resulting in polymer "brush-type" shells of linear macromolecules and the introduction of a terminal mesogen by means of a termination reaction can result in stable, amphiphilic, core–shell materials with a well defined hydrophilic/lipophilic balance. Based on the synthetic concept developed for preparing dense polymer brushes on planar gold substrates [232, 233], the exposure of 11-hydroxyundecane-1-thiol (HUT)-functionalized gold nanoparticles to a trifluoromethanesulfonic anhydride vapor/nitrogen stream results in the conversion of the HUT hydroxyl groups to triflate functional groups. Addition of dry chloroform and the freshly distilled monomer (2-ethyl-2-oxazoline or 2-phenyl-2-oxazoline) at 0 °C under vigorous stirring followed by subsequent heating in an oil bath allows for polymerization to take place on the surface of the nanoparticles. The polymerization can be terminated by addition of N, N-di-n-octadecylamine (for 2-ethyl-2-oxazoline) solution in dry chloroform or piperidine [for poly(2-ethyl-2-oxazoline)] at 0 °C. The surface-bound triflate SAM is a highly efficient initiator for the cationic ring-opening polymerization of oxazolines and the triflate gegenion ensures a strictly ionic mechanism of the propagation reaction, ensuring a living and stoichiometric polymerization [232, 233].

A similar procedure for the preparation of terminally functionalized poly (N-propionylethylenimine) (PPEI) by cationic living ring-opening polymerization of 2-ethyl-2-oxazoline in a one-pot multistep reaction, by the so called "grafting-onto" approach (which involves the chemisorption of macromolecules), involves a direct combination of the fast initiation technique and a selective quantitative termination reaction [234]. The chain ends of the linear hydrophilic polymers can be further functionalized with different lipophilic moieties (methyl-, n-hexadecyl- (C_{16}), and 1,2-O-dioctadecyl-sn-glyceryl- [(C_{18})$_{2-}$]) and a monofunctional silane-coupling group. By varying the length of the double functionalized hydrophilic PPEI chain ($n = 10$, 20), surface active amphiphilic lipopolymers of controlled hydrophilic–lipophilic balance for surface functionalization can be obtained in high overall yields [234].

The fabrication of surfaces with controlled modulation of interfacial properties (e.g., wettability) involving the adsorption or grafting of "smart" (environmentally responsive) polymers onto surfaces has also been implemented on metallic nanoparticles. Chilkoti et al. [235]. used the change in optical properties of colloidal gold upon aggregation to develop an experimentally convenient colorimetric method

to study the interfacial phase transition of an elastinlike polypeptide (ELP). This thermally responsive, genetically encoded biopolymer was covalently attached to mercaptoundecanoic acid functionalized gold nanoparticles. Raising the solution temperature from 10 to 40 °C thermally triggered the hydrophilic-to-hydrophobic phase transition of the adsorbed ELP resulting in formation of large aggregates due to interparticle hydrophobic interactions, causing a color change from red to violet. Below the phase transition temperature, the Au–ELP colloids in suspension have an average interparticle distance several times greater than the colloid radius and hence appear red. Upon raising the temperature of an Au–ELP suspension, the adsorbed ELP undergoes an intramolecular hydrophilic to hydrophobic transition and the interparticle distance of the colloids in the aggregated state approaches the colloidal radius, which results in a redshift in the absorbance spectrum (*vide supra*, Section 1.2), and the suspension consequently appears violet. Cooling the suspension back to 10 °C causes the ELP to transition back to the hydrophilic state, which dissociates the colloidal aggregates and returns the absorbance maximum to 535 nm. Figure 5 shows the schematic of the reversible aggregation of ELP-functionalized gold nanoparticles [235].

In addition to linear polymers, hyperbranched molecules called dendrimers can also be used to functionalize gold nanoparticles. Dendrimers are attracting increasing attention because of their unique structures and properties [236–243]. These aesthetically appealing synthetic macromolecules are monodispersed and hyperbranched polymers constructed from AB_n monomers (AB is a monomer, n usually 2 or 3) rather than the standard AB monomers, which produce linear polymers. Their synthesis in an iterative fashion leads to a nonlinear, stepwise synthetic growth wherein the number of monomer units incorporated in each successive iteration roughly doubles (AB_2) or triples (AB_3) that in the previous cycle. Thus each repetition cycle leads to the addition of one more layer of branches—called a *generation*—to the dendrimer framework. The generation

number of the dendrimer is equal to the number of repetition cycles performed and may be easily determined by counting the number of branch points as one proceeds from the core to the periphery [236–243].

Dendrimer stabilized nanocomposite materials have unique potential for applications such as catalysis which require stable colloidal particles having surfaces that are not completely passivated by a stabilizing adsorbate. Because of the low mass density within the dendrimer interior, such monolayers are highly permeable to small molecules [244]. Thus, dendrimers can serve the dual purpose of acting as a "nanofilter" that passes small and specifically charged species, prevents other molecules from interacting with the colloid, and can function as a stabilizer.

Dendrimers are also recognized as monodispersed nanoreactors, possessing architectures that allow the preorganization of metal ions within their interiors [245]. Several noble metal nanoparticles have been prepared in the presence of dendrimers, in which the size of the nanoparticle can be controlled by the size of the dendrimers [246–250].

Two molecules of this type that are frequently used are polyamidoamine (PAMAM) dendrimers and polypropylene imine dendrimers. Au colloids in the 2–3 nm size regime have been prepared by one-phase *in-situ* reduction of an aqueous solution of $HAuCl_4$ in the presence of either second- or fourth-generation (G2 or G4, respectively) PAMAM dendrimers using $NaBH_4$ as the reducing agent. The dendrimers encapsulated the colloids, imparting stability to the aqueous colloidal solutions. The driving force for the interaction of the colloids with the dendrimers was an association of Au with the primary amine terminal groups (and perhaps the interior secondary and tertiary amines) of the dendrimer. The dendrimer generation used in such syntheses controlled the size of the resultant colloids: lower generation dendrimers gave rise to larger, less monodisperse and more aggregated colloids than those prepared using higher generation dendrimers, for a constant ratio of primary amine groups to $AuCl4^-$. Also the stability of nanoparticles decreased sharply when either the solvent or the excess free dendrimer was removed from the solution [247, 251].

Sugar-persubstituted PAMAM dendrimers (sugar balls) were synthesized by Aoi et al. [252]. Since sugar balls have highly ordered structure with arranged saccharides on the peripheries of the dendrimers and terminal hydroxyl residues that can operate as reductants, sugar balls were used to act as protective agents for gold nanoparticles, against flocculation. When Au^{3+} ions are reduced with the hydroxyl groups of the sugar balls, the hydroxyl groups are oxidized to carbonyl groups. Thus it is found that sugar balls can act as protective agents as well as reductants for the preparation of gold nanoparticles [253].

Fourth-generation PAMAM dendrimers [254] having terminal groups partially or fully functionalized with thiol groups have also been explored for the functionalization and synthesis of gold nanoparticle [255]. Diluted solutions of thiolated dendrimers and tetrachloroauric acid can be mixed and reduced with $NaBH_4$ to produce stable dendrimer functionalized gold nanoparticles. The enhanced stability with thiolated dendrimers compared to amine-stabilized materials is due to the low concentration of dendrimer required to prepare the nanocrystals.

Figure 5. Reversible aggregation of gold nanoparticles caused by the environmentally triggered phase transition of adsorbed ELP: (A) Au–ELP in the hydrophilic phase with spectra typical of isolated gold colloid and (B) aggregates which exhibit a redshift in their absorbance spectra compared to that of individual colloid in (A). Reprinted with permission from [235], N. Nath et al., *J. Am. Chem. Soc.* 123, 8197 (2001). © 2001. American Chemical Society.

3.6. Sol–Gels

As explained in the previous sections, surface modification of gold nanoparticles imparts these systems with a variety of functionalities that makes them useful on a wide variety of applications. Surface modification can be achieved as a series of sequential steps starting with the synthesis of the particles or in a one-step procedure. For most applications the ligands are selected such that they are used both as stabilizing agents and as functional surface groups for the immobilization of other molecules onto the nanoparticle surface. With the availability of a variety of ligands, the choice of ligands is almost entirely dependent on the application in which the gold nanoparticle will be used. Most of the time, alkane thiols, polyelectrolytes, and dendrimers are used for the purpose of both surface modification and stabilization of gold nanoparticles. Often, the ligands employed may affect the electronic (optical, chemical) properties of the nanoparticles, for example, adsorption of a nucleophilic molecule on gold nanoparticles results in a redshift in surface plasmon resonance and an increase in absorbance at higher wavelengths [22, 99].

Alternative methods of preparing surface modified gold nanoparticles have been explored such as functionalization with silica by sol–gel processing. Silica has recently been utilized for the stabilization of metallic nanoparticles [256–261]. Sol–gel processing is a powerful technique that offers unique opportunities for the synthesis of optical materials in the form of thin films, fibers, and fine powders [262]. Several general approaches have been reported for the functionalization of gold nanoparticles with silica by sol–gel processing. Martino et al. used sol–gel processing in reverse micelle solutions and sequential reduction of gold salt for the creation of gold–silicate nanodispersions [263]. However, the presence of gel precursors destabilizes the inverse micelles resulting in larger nanoparticles and wider particle size distributions. Liz-Marzan et al. synthesized silica coated gold nanoparticles in a two-step process, where gold nanoparticles are first reduced by citrate and the nanoparticles are coated with silica using a silane coupling agent [256].

During the synthesis of silica coated gold nanoparticles a monolayer of a silane coupling agent [e.g., (3-aminopropyl) trimethoxysilane or *N*-(3-trimethoxysilyl) propyl ethylenediamine] is allowed to adsorb onto gold nanoparticles where the strong affinity of gold for amine groups is exploited [187, 256, 261]. In a second step, active silica (sodium silicate) is added to the dispersion promoting the formation of a thin, dense, and relatively homogeneous silica layer around the nanoparticles using the silanol groups as anchor points. At this stage, the nanoparticles can be transferred into ethanol and the silica layer thickness can be increased in a controlled way. With this method, the morphology and the concentration of gold nanoparticles over a wide range can be controlled without sacrificing the stability, and the optical properties of the gold nanoparticles agree extremely well with the predictions of Mie theory [256]. Thus, the preparation and surface modification of gold nanoparticles via sol–gel processing is another alternative to the well-established gold–alkane thiol method. Moreover, similar procedures can be used for other nanoparticles such as platinum, silver, and palladium and semiconductor particles.

4. CHARACTERIZATION

A variety of techniques are used to characterize gold nanoparticles. In general a combination of techniques is needed in order to characterize these systems because no single analytical technique can provide complete information on nanoparticles.

One of the most commonly used techniques in the study of colloidal gold is UV-vis spectroscopy. The absorption maximum, which is due to excitation of surface plasmons on the metallic nanoparticles, is observed around 520 nm for spherical gold nanoparticles. The position of this peak is only weakly dependent on the size of the gold nanoparticles [22]. However, changes in the dielectric medium around the particles can have a significant effect on the position of the SPR peak, shifting to longer wavelengths with increased values of the dielectric constant of the medium. Additionally, the SPR position also depends on the shape of the particles and their proximity to each other [17, 18, 22–25, 139]. When the separation distance between metallic nanoparticles is smaller than their radius additional resonances occur at longer wavelengths. Thus, if the individual particles approach each other to within less than one particle diameter the absorption spectra broadens and shifts to longer wavelengths. These changes in the absorption spectrum are routinely used to determine the presence of interparticle interactions such as aggregation and have also been exploited for DNA detection.

Optical absorption spectroscopy can give semiquantitative information on colloidal gold aggregation. However, the state of aggregation and the size distribution of the nanoparticles can be more accurately assessed with TEM. TEM is a very effective (and commonly used) technique for the characterization metallic nanoparticles due to their high density of free electrons. TEM gives immediate visualization of the gold nanoparticles by capturing the contrast created when a high-energy electron beam is passed through them. As electrons hit the nanoparticles on the sample grid, some of them will be scattered while the remainder are focused onto a photographic film to form an image. Unfocussed electrons are blocked out by the objective aperture resulting in an enhancement of the image contrast. The resolution limits of modern TEM are sufficient enough to image gold nanoparticles in the 1–10 nm size range. Although atomic resolution and lattice imaging are required for detailed structural analysis, a particle size distribution can be obtained at moderately low resolution for gold nanoparticles with mean diameter less than 10 nm [264–268].

Since modern applications of colloidal gold have exploited the capability to functionalize their surfaces with a variety of ligands the composition of the nanoparticles also needs to be characterized. It may be necessary to find the oxidation state of gold or the entire composition of the monolayer. X-ray photoelectron spectroscopy (XPS) is a surface sensitive technique that can provide this information [269]. Additionally, XPS can help determine the presence of contaminants remaining from the preparation procedures for gold nanoparticles (e.g., adsorption of unreduced gold cations and their corresponding anions during gold salt reduction). XPS can also be used to determine the composition of these species with high accuracy [268, 270].

Nuclear magnetic resonance (NMR) can also be used for the characterization of gold nanoparticles. This technique is based on the difference between the resonant frequency of a metal and a diamagnetic compound such as a complex or ionic solid. This difference (NMR shift or the Knight shift) is a consequence of the interaction of a metal nucleus with the conduction electrons and is measured as a fraction of the applied field. The NMR shift for [197] Au is +1.4%. This means that in a field in which a standard such as $[PtI_6]^2$ resonates at 100 MHz, the ^{197}Au resonance for metallic gold is shifted by 1.4 MHz. The measurement of the NMR shift of gold in small particulate form provides crucial information on the size at which gold nanoparticles begin to develop metallic properties, which is an important topic in nanotechnology. Moreover, NMR spectroscopy is particularly informative about the structure and chemical composition of MPCs and alkane thiol modified gold nanoparticles [180, 182, 183, 186, 271, 272]. For monolayer characterization ^{1}H and ^{13}C NMR resonances are usually measured, since mostly hydrogen and carbon are present in the monolayers adsorbed on the gold clusters/nanoparticles. In this case, strong NMR shifts are observed due to the interaction of the adsorbate nuclei with the conduction electron density of the gold surface.

Fourier transform infrared spectroscopy (FTIR) can also be used to elucidate the surface chemistry of molecules adsorbed on gold nanoparticles [272–274]. Information on the order–disorder (*gauche* defects) of the chains of the molecules or the defects near gold nanoparticle surface is obtained by measuring the vibrational energy levels of each bond (C–H, C–C, C–N) in the infrared region of the spectrum. These energy modes are characteristic to each bond and shifts in the vibration modes provide the necessary information on the structure and content of the molecules adsorbed on gold nanoparticles.

Fourier transform infrared spectroscopy can provide valuable information on the conformation and order of alkyl chains on monolayers, particularly through analysis of the (CH_2) bands. However, symmetrical bonds such as C–C appear as very weak bands or may not be detectable at all by FTIR. Thus, FTIR normally does not produce this information [275]. Symmetrical bonds, however, are readily detected using Raman spectroscopy. Thus, this technique can provide complementary information on the C–C backbones of monolayers. Other bands present in alkanethiol SAMs such as C–S and S–H bands can be analyzed easily by Raman spectroscopy, thus providing structural and chemical insight into the interaction between the alkanethiolates and the metal substrate [128, 246, 275–277]. For example, the S–H bond of alkanethiols is cleaved upon chemisorption to gold [275]. Thus, the relative intensity of the (S–H) band of free thiol and gold thiolates samples can indicate the progression of alkanethiol chemisorption. The (C–S) band in the Raman spectrum also indicates the chemisorption process and the resultant structure of the alkyl chains near the surface of gold [275, 278]. Thus, FTIR and Raman spectroscopy provide complementary information on the vibration modes in the chemisorbed monolayers on metallic nanoparticles. In this context, it is a fortunate fact that metallic nanoparticles further enhance the Raman signals [128, 146].

5. APPLICATIONS

Although colloidal gold has been used for hundreds of years, the number of applications has been limited until recently. For centuries, its main applications were as a stain for glass and fabrics and to a minor extent as a purported therapeutic agent. However, there is currently a boom on its applications, particularly within the realm of nanoscale science and engineering. In the following, a number of newer applications developed within the last decade are described. It is likely that newer applications will be developed because of the large interest in nanotechnology.

5.1. Colorimetric Assays

One of the most remarkable applications of gold nanoparticles reported in recent years is the colorimetric detection of oligonucleotides based on the optical properties of the gold nanoparticles [206, 279]. This simple and highly selective detection method has many advantages over other sequence-specific DNA detection methods currently applied in the diagnosis of pathogenic and genetic diseases. Most of the current systems make use of the hybridization of an immobilized target oligo- or polynucleotide probes labeled with radioactive ^{32}P or ^{35}S reporter groups [280–283]. Although this technique offers high sensitivity, the use of radioactive labels creates certain problems such as the disposal of the probes, the requirement of specially trained personnel, and the short shelf life. In other techniques, the radioactive labels are replaced with nonradioactive labels such as organic dyes, and the hybridization of target DNA molecules is detected by fluorescence or luminescence spectroscopy with high sensitivity [280–283]. However, the labels and the monitoring equipment are relatively expensive increasing the cost of the method.

The detection of oligonucleotides using gold nanoparticles has many desirable features such as rapid detection, a colorimetric response, and little or no required instrumentation [206, 284]. This approach involves two gold nanoparticle probes with covalently bound oligonucleotides that are complementary to a target of interest. When exposed to target strands, these nanoparticle probes are cross-linked through DNA hybridization and form networks of aggregates composed of thousands of nanoparticles. The aggregation process is accompanied by red-to-blue color change of the solution, which occurs due to changes in the SPR frequency of the gold nanoparticles. The detection mechanism is based upon the fact that when the interparticle distance between the nanoparticles is greater than the average nanoparticle diameter, the color of the aggregated appears red, but as the interparticle distance decreases the color shifts to blue providing a means of detection. Also, the melting characteristics of these networks (they have sharp melting transitions) allow one to differentiate a perfectly complementary target strand from a strand with a single base mismatch. Moreover, the color changes associated with hybridization are significantly enhanced and easily visualized even with the naked eye if the hybridized sample is processed on a solid support [284]. This method provides a simple, fast, qualitative response for the detection of mismatches in the DNA sequence [206, 284–286].

With this approach, quantitative responses can be obtained using larger gold nanoparticles [285] and incorporating silver nanoparticles into the system that allows the responses to be obtained by an inexpensive flatbed scanner [286, 287]. Since the molar extinction coefficient of 50 nm gold nanoparticles is 10^{11} M^{-1} cm^{-1} (10^8 M^{-1} cm^{-1} in case of 13 nm nanoparticles), the use of larger gold nanoparticles provides higher sensitivity assays and allows quantitative colorimetric detection. It was shown that increasing the nanoparticle size resulted in significant improvement in the extinction dampening of the surface plasmon band (indicative of oligonucleotide hybridization-induced nanoparticle aggregation) as evidenced via melting analyses. A detection range of 50 pM to 5 nM was obtained [286]. Another way to increase the sensitivity of detection and quantify the hybridization process is by incorporation of silver (Ag) to gold (Au) nanoparticles in a so-called "core–shell" scheme. In this method, silver ions are reduced to silver metal on gold nanoparticles creating core–shell Au/Ag nanoparticles that can be easily modified alkylthiol-oligonucleotides. The molar extinction coefficient of the core–shell nanoparticles is very similar to that for the silver nanoparticles alone and is larger than that for gold nanoparticles of the same size. These oligonucleotide-modified core–shell nanoparticles show similar but enhanced changes in the optical spectrum and has similar melting properties as oligonucleotide-modified gold nanoparticles when they are aggregated due to hybridization. This process increases the scanned intensity by a factor as large as 10^5 and target oligonucleotides concentrations as low as 50 fM can be measured [287].

The strong dependence of the SPR absorption band on the degree of aggregation of gold nanoparticles has also been exploited to detect heavy metals. Various metal ions like zinc, manganese, nickel, lead, cadmium, and mercury may be present in water at parts per million concentrations or higher. Some of these are toxic metal ions that pose significant public health hazards when present in drinking water. For absolute identification and total concentration assessment, ion-coupled-plasma spectroscopy is commonly used as a characterization method. However, more efficient detection can be implemented using colloidal gold.

In gold nanoparticles covered with capping agents like mercaptocarboxylic acid, the surface carboxyl groups can enable chelation of metal ions [288–290]. The principle of metal-cation based aggregation has been used by Murray and co-workers to initialize the formation of metal films and solution-phase aggregates [291, 292] similar to the aggregation of DNA-functionalized metal nanoparticles that has been used for the sequence-specific detection of the oligonucleotides [206, 279].

A colorimetric technique, particularly appropriate for otherwise largely spectroscopically silent species like trace mercury, cadmium, and lead has been demonstrated using the principle of change in color from red to blue due to the ion-chelation based aggregation of functionalized gold nanoparticles. The aggregation process produces a shift in plasmon band energy and a substantial increase in long wavelength Rayleigh scattering, which has been employed for visual detection of these ions. In this method functionalized gold nanoparticles are aggregated in solution in the presence of divalent metal ions by an ion-templated chelation process.

This caused a measurable change in the absorption spectrum of the particles. The aggregation also enhanced the hyper-Rayleigh scattering (HRS) response from the nanoparticles solutions, providing an inherently more sensitive method of detection. The increase in the HRS intensity appeared to be due to both symmetry lowering and an increase in the effective size of the chromophoric entity responsible for plasmon-enhanced HRS [293].

One of the challenges in devising colorimetric methods for the identification of these ions has been the identification of appropriately strongly binding leuco dyes capable of yielding sufficiently intensely absorbing metal/dye complexes. Thus appropriately functionalized gold nanoparticles could be used as exceptionally high extinction dyes for colorimetric sensing of heavy metal ions [293].

Rao et al. [294] investigated the effect of concentration of metal ions on the interaction of nanoparticles and chelation of ions. Figure 6 shows the ion-chelation mechanism binding two nanoparticles. Gold nanoparticles capped with α-lipoic acid were interacted with various metal ions like Cu, Fe, Ni, Mn, Cd, Zn, and Pb. It was found that in the dilute metal-ion concentration regime the metal ions bound to the carboxyl functional group of the α-lipoic acid and thereby caused observed dampening of the plasmon band. The chelation/aggregation process was reversible via addition of a strong metal ion chelator such as EDTA. The intermediate metal-ion concentration regime was characterized by the aggregation and irreversible chelation accompanied by an increase flocculation. Further increase in concentration resulted in precipitation.

Another study by Szulczewski et al. [295] on the adsorption of Hg atoms on the gold and silver nanoparticles revealed the influence of particle size on the properties of the nanoparticles. The adsorption of Hg on nanoparticles resulted in a blueshift of the surface plasmon mode, the shift being more pronounced for the smaller particles than the larger particles for the same Hg shell thickness. More research in this field is to be done in terms of improving the modest colorimetric detection limits, enhancing the chemical selectivity and sensitivity, and study of properties in the presence of metal ions.

5.2. Fluorescence Assays

Besides their unique optical properties, metallic nanoparticles metals can also exert an important influence in the fluorescence emission characteristics of fluorophores positioned in their vicinity. Two different phenomena can be observed depending on the separation distance between the surface of gold nanoparticles and the fluorophores. In general, when the separation distance is smaller than 5 nm,
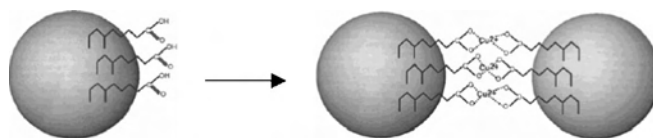

Figure 6. Ion–chelation binding of two nanoparticles. Reprinted with permission from [294], S. Berchmans et al., *J. Phys. Chem. B* 106, 4647 (2002). © 2002, American Chemical Society.

strong quenching of the emission of fluorescence and dramatic reduction in the lifetimes of the excited states of fluorophores is observed [296–299]. On the other hand, when the separation distance is between 10 and 20 nm, enhanced emission of fluorescence is observed due to local concentration of the incident excitation field by the gold nanoparticles [299–303]. Although these phenomena are well known, to date, only a very limited number of applications involving nanoparticles are reported in the literature for the detection of molecules [303, 304].

In 2002, Maxwell et al. [303] reported the use of gold nanoparticles in the detection of DNA sequences and single-base mutations based on the quenching of fluorescence emission of fluorophores that are attached to the oligonucleotides. The gold nanoparticles were 2.5 nm in diameter and functioned as a "nanoscaffold" for the attachment of fluorophore-labeled oligonucleotides and as a quencher (or energy acceptor). The fluorophore-labeled oligonucleotides assembled into a constrained archlike conformation on the gold nanoparticle surface such that the thiol group and the fluorophore adsorb on the same nanoparticle. In this state, the fluorescence emission of the fluorophore is quenched by the gold nanoparticle. Upon binding of the target DNA, the constrained conformation opens, and the fluorophores separate from the surface because of the structural rigidity of the hybridized DNA, leading to an increased emission of fluorescence. Desorption of the fluorophore from the gold surface was attributed to the fact that the hybridization energy of the DNA ($\Delta H = 80$–100 kcal/mol) is considerably larger than that of adsorption energies of organic dyes on gold ($\Delta H = 8$–16 kcal/mol) [305]. Since the separation distance between the fluorophore and the gold nanoparticle in the open state is about 10 nm, nonradiative energy transfer from the excited fluorophores to gold nanoparticles was considerably decreased upon hybridization because when the nanoparticles are small (2–3 nm), nonradiative energy transfer occurs within 1–2 nm from the gold nanoparticle surface, thus resulting in a dramatic increase of fluorescence upon hybridization [306, 307].

Our group has researched how to use gold nanoparticles as platforms for displaying ligands in fluorescence-based assays that exploit the quenching phenomena exerted by gold nanoparticles on fluorophores. For this, alkanethiol functionalized gold nanoparticles are used in this detection scheme because the thickness of the SAMs is in the order of 1–3 nm [174–177], which positions the fluorophores in a region from the gold surface where the fluorescence emission is more sensitive to changes in the separation distance [296–299]. Proof on concept demonstration of this biosensing system is shown in Figure 7. The specific interaction of biotinylated gold nanoparticles with fluorophore-labeled antibiotin caused a decrease in the fluorescence emission intensity. Upon addition of soluble D-biotin, competitive dissociation of bound antibiotin caused a recovery in the fluorescence emission intensity. When the binding sites of antibiotin were saturated with D-biotin prior to the interaction with biotinylated gold nanoparticles, there was no change in the fluorescence emission, which further shows the specific nature of the interactions taking place between the biotinylated gold nanoparticles and the labeled antibody.
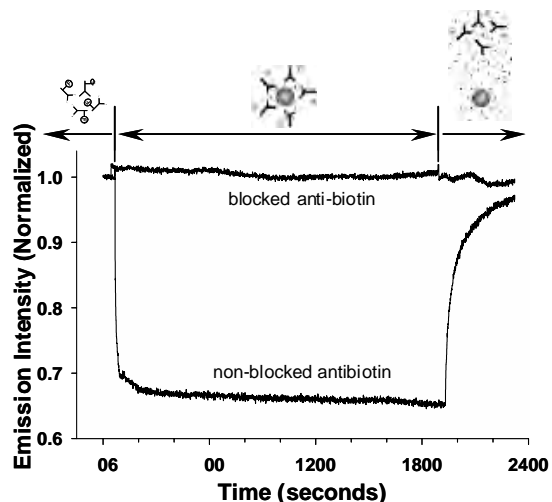
Figure 7. Binding and dissociation of fluorescently labeled antibiotin to biotinylated gold nanoparticles.

The biosensing scheme described could be easily generalized to other ligand–protein pairs where specific molecular interactions at the surface of the gold nanoparticles cause the separation of fluorophore labeled biomolecules from the gold nanoparticle.

5.3. Monolayers

In addition to their use in surface-enhanced Raman scattering gold nanoparticles can have uses in electro-optics and molecular electronics in the form of thin films. These applications require the assembly of the nanoparticles on solid surfaces in the form of desired one-, two-, and three-dimensional structures. Some of the strategies for the formation of gold nanoparticle thin films on solid surfaces take advantage of the ionic nature of gold [308] as well as its affinity toward thiol or amine molecules, while in some applications polymers such as poly(allylaminehydrochloride), poly(sodium 4-styrene sulfonate), and poly(ethylene imine) are used [309].

Natan and his research group exploited one of the earliest approaches to assemble gold nanoparticles onto chemically functionalized substrates [264–266, 308, 310]. In this approach, organosilanes with different functional groups are used as the linker between the glass substrates and the gold nanoparticles. Gold nanoparticles are strongly bound to the surface through covalent bonds to pendant functional groups such as CN, NH_2, or SH. The general assembly protocol is carried out completely in solution: clean glass substrates are immersed in methanolic solutions (or in toluene) of organosilanes, rinsed, and subsequently immersed in aqueous gold nanoparticle solutions. Two-dimensional arrays spontaneously form on the organosilane surface. The resulting substrates can be characterized by UV-vis spectroscopy, TEM or atomic force microscopy, and SERS. The flexibility and control that this method provides are noteworthy, such that by manipulating the particle size, particle–silane interactions and the physical and chemical properties of the substrate the nanoscale architecture can be controlled. This solution-based assembly protocol makes the substrate

fabrication routine and it also allows one to fabricate substrates with any shape or size. Therefore, gold nanoparticles monolayers can be prepared on glass/quartz slides and TEM grids. The same strategy has also been used by other groups [311–313].

Another approach to making thin films of gold nanoparticles on solid substrates is by functionalization of both substrate and the nanoparticles and chemically coupling them via functional groups [273]. Gold nanoparticles can be functionalized with a ligation partner such as ketone and then chemoselectively immobilizing them onto planar gold substrates presenting SAMs of aminooxy groups. Ketone and aminooxy groups react selectively to form a chemically stable oxime, and they are unreactive toward thiol that is essential for the preparation of gold nanoparticles as well as the monolayer film. The resulting films of ketone-functionalized gold nanoparticles are fairly stable and can be characterized with ellipsometry, grazing-angle infrared spectroscopy, and electrochemistry. Since this technique requires mutually exclusive reactivity of pairs of functional groups, even among a number of potentially reactive functional groups, only the two chemoselective ligation partners will react with each other. Because the reaction can tolerate the presence of a diverse functionality so that protecting-group manipulations are unnecessary, it has been also used to conjugate peptides and proteins onto surfaces [314].

Metal nanoparticle loading on surfaces can be increased by the use of additional linker molecules to bind more nanoparticles to the surface [265, 292, 315] by the modification of the surface by preadsorption of polyelectrolytes (layer-by-layer adsorption) [316, 317] or by repeated washing and reexposure of the substrates to nanoparticles solutions [318, 319]. In the layer-by-layer adsorption method, functionalized molecular linkers are first immobilized onto a substrate followed by dipping into a solution of unmodified gold nanoparticles to immobilize a layer of nanoparticles on the linker layer. The resulting nanoparticle layer is then immersed again into the solution of linkers for further immobilization. Repeating sequentially the adsorption processes results in a multilayer film. While this method is attractive for producing well-defined multilayers, corruption of the films may occur via the repetitive immersion and rinsing process and the issue of how this method can be applied to thin film fabrication on any desired substrates is yet to be addressed. In order to overcome this problem, Leibowitz et al. [313]. suggested an alternative and simpler pathway for the production of thin films on substrates of any type. The procedure involved a one-step, exchange–cross-linking–precipitation route, where ligands (that is, alkanethiols) on gold nanoparticles were place-exchanged with α, ω-functionalized dithiols, which in turn caused crosslinking and precipitation of gold nanoparticles on the surface of the substrates. This route may be written as

$$(Au)_n - SR + HSR'SH \rightarrow SR'S - (Au)_n \cdots$$
$$\rightarrow -[SR'S - (Au)_n]_m - precipitation$$
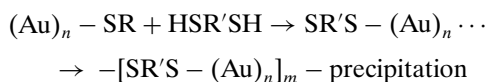
in which (HSR'SH) is the dithiol and (SR) is the alkane thiol. The structural and electronic properties of the thin films produced by this method were found to be comparable with thin films derived from a stepwise layer-by-layer

method. Moreover, since one can produce thin films in a single step using this method, it offers a much simpler route for preparing nanoparticle thin films on almost any substrate.

5.4. Biosensors

Current research in biosensor technology is leaning toward the use of gold nanoparticles as an important component of biosensing platforms due their unique optical and electronic properties. Recently, Jia et al. [320]. constructed a horseradish peroxidase (HRP) biosensor using sol–gel processing and gold nanoparticles in a three-dimensional network. In this study, gold nanoparticles were chemisorbed onto thiol groups on the sol–gel network, and HRP was adsorbed onto the surface of gold nanoparticles. Here, gold nanoparticles acted as tiny conduction centers that facilitated the transfer of electrons (produced in the enzymatic reaction where hydrogen peroxide was oxidized) to the electrode surface. Since gold nanoparticles were assembled into a multilayer, the enzyme loading on the biosensor was increased resulting in better signals. Also, both gold nanoparticles and sol–gel had little effect on enzyme activity, imparting the biosensor with high sensitivity and good stability.

In 1996, Chen et al. [321] reported that the addition of gold nanoparticles with sizes ranging from 10 to 30 nm to a glucose biosensor resulted in the enhancement of glucose oxidase (GOD) activity. They found that 10 nm gold nanoparticles caused more increase in the GOD activity than 30 nm gold nanoparticles. In their following report, they used even smaller gold nanoparticles (less than 10 nm) to investigate further enhancement in the enzymatic activity. The enhanced activity of GOD was attributed to the quantum size effect, which is related to electron transfer between the nanoparticles and protein molecules, which could elucidate the enhancement of enzyme activity. According to this concept, the surface of metallic clusters is always electron deficient, and the redox potential of nanoparticles is closely related to particle size and is relatively high. When the atoms contained in a particle decrease as the particle size decreases, the redox potential of the nanoparticle increases causing stronger affinity to electrons. Although the enhancement effect of gold nanoparticles on enzyme activity is observed qualitatively and further investigation is necessary, it was an important step for the development of better glucose biosensors.

Based on the observations made on the glucose sensor in which gold nanoparticles enhanced the enzymatic activity, it was considered that gold nanoparticles could also be useful for DNA sensors [322–328] considering that gold nanoparticles allow immobilization of biomolecules and could be assembled on gold substrates. The quartz crystal microbalance (QCM) is widely used for DNA sensing and allows real-time measurement of DNA binding and hybridization at the nanogram level. Its potential for DNA hybridization detection has been demonstrated recently. The detection limit of this device could be improved by using DNA-functionalized gold nanoparticles in a probe/target/probe-nanoparticle sandwich fashion where the amount of DNA hybridized is increased significantly by introducing DNA-functionalized gold nanoparticles on the QCM surface. This

method causes an amplified frequency shift and substantially extends the sensitivity limits of the QCM detection system. Liu et al. [327] studied the effect of the size of gold nanoparticles on the detection sensitivity enhancement of a QCM system, and they found that the amount of mass change on the QCM sensor increased as the gold nanoparticle size increased until 40 nm and decreased thereafter.

Signal enhancement using gold nanoparticles is not just limited to QCM; Lyon et al. [329] utilized gold nanoparticles in the signal enhancement of SPR immunosensing. When gold nanoparticles are incorporated into the SPR biosensing surface such that surface immobilized antibody interacts with antigen–gold nanoparticle conjugate, an increased SPR sensitivity to protein–protein interactions was observed. Picomolar (pM) detection of human IgG has been realized using gold nanoparticle enhancement, with theoretical detection limits for this technique being much lower [328].

6. CONCLUSIONS

The rapid growth in the number of applications that colloidal gold has found during the last decade has expanded to new levels. It is likely that this material will be considered more than a simple stain for glass, a marker for TEM studies in molecular biology, or a good model system for colloidal science. Novel applications will be found in the field of nanotechnology and particularly in combination with biological molecules. Ordered assemblies and arrays of these particles may provide materials with novel properties. Supramolecular crystals have been explored and may find novel applications. More importantly, novel technologies will emerge that use this material and exploit its unique optical and electronic properties. One of the fields that will likely encounter fast growth in the near future is the implementation of metallic nanoparticles in fluorescence detection schemes. Nanoparticle alloys of gold and other noble metals such as silver will allow further flexibility in fine-tuning the optical and electronic properties of this material. Additionally, the optical properties of anisotropic nanoparticles could be implemented to great advantage in surface enhancement of fluorescent emission and Raman scattering. For example, nanorods of this material would concentrate the electric field at the end of the nanorod and this could be exploited to greatly increase the natural fluorescence of biological molecules such as DNA. It is likely that electronic properties such as coupling of SPR modes could be directed at the nanoscale level using assemblies of nanorods for spatially directed transduction of electronic and/or optical excitations. The boom in the number of applications of this material is only likely to continue expanding into more sophisticated applications during the coming years.

GLOSSARY

Anisometric gold nanoparticles   Nonspherical gold nanoparticles.

Deoxyribonucleic acid (DNA)   A macromolecule consisting of one or two strands of linked deoxyribonucleotides.

DNA hybridization   Formation of the double helical structure of DNA by pairing of two complementary single strands of DNA.

Fluorescence   The emission of light by a substance after absorbing energy from light of usually shorter wavelength. When an incident light source excites the electrons of a substance these will jump to higher excited levels. When they return to the ground level then energy is released as photons.

Fluorescence resonance energy transfer (FRET)   The radiationless transfer of excitation energy from a donor to an acceptor. When this transfer occurs the emission of fluorescence by the donor is decreased. The acceptor may or may not be fluorescent. If the acceptor is fluorescent, emission will occur from the acceptor instead of the donor. FRET is a distance-dependent interaction that occurs over distances of 1–10 nm.

Monolayer protected clusters (MPCs)   Metallic clusters covered by an organic monolayer that prevents their irreversible aggregation. These nanoparticles are most commonly formed by reduction of a noble metal salt in the presence of a surface-active substance that forms a monolayer on the surface of the growing clusters, thus limiting their further growth and stabilizing them against aggregation.

Nanoshells   Metallic nanoparticles consisting of a metallic shell surrounding a dielectric core. Recently nanoshells have also been prepared that consist of a metallic core surrounded by a metallic shell consisting of a different metal.

Self-assembled monolayers   Molecular assemblies that are formed spontaneously by immersion of a substrate in to a solution of active surfactant in a solvent.

Surface enhanced emission of fluorescence   The increased emission of fluorescence resulting when fluorophores interact with the enhanced electromagnetic field around metallic nanoparticles.

Surface enhanced Raman spectroscopy (SERS)   The dramatic increase in the intensity of an otherwise weak Raman signal produced by rough metallic surfaces. This increase can be as high as 10^4–10^6 or even 10^8–10^{14} for some systems. The main contribution to this enhancement is due to the concentration of the electromagnetic field in the vicinity of rough metallic surfaces.

Surface plasmons   The free electrons on the surface of a metal that behave like a quasi-free electron gas. They represent the quanta of the oscillations of surface charges and can behave like real surface waves. They can be excited by the electric field of electromagnetic radiation.

Surface plasmon resonance (SPR)   The condition at which the frequency of the incident electromagnetic radiation couples with that of the oscillating electrons on the surface of a metal.

REFERENCES

1. L. Lee, G. Seddon, and F. Stephens, "Stained Glass." Crown, New York, 1976.
2. G. Savage, "Glass and Glassware." Octopus Books, London, 1975.
3. H. B. Wesier, "Inorganic Colloidal Chemistry," Vol. 1. Wiley, New York, 1933.
4. F. Mehlman, "Phaidon Guide to Glass." Prentice Hall, Englewood Cliffs, NJ, 1983.
5. N. H. Moore, "Old Glass." Tudor, New York, 1935.
6. M. Faraday, *Philos. Trans. Roy. Soc. London* 147, 145 (1857).
7. L. P. Williams, Ed., "The Selected Correspondence of Michael Faraday," Vol. 2. Cambridge Univ. Press, London, 1971.
8. W. Ostwald, "Practical Colloid Chemistry," 4th ed. Dutton, New York, 1924.
9. G. Frens, *Nature* (*London*) 241, 20 (1973).
10. M. A. Hayat, Ed., "Colloidal Gold: Principles, Methods, and Applications," Vols. 1, 2, and 3. Academic Press, San Diego, 1989.
11. L. C. Javois, Ed., "Immunocytochemical Methods and Protocols." Humana Press, Clifton, NJ, 1999.
12. J. E. Beesley, "Colloidal Gold: New Perspective for Cytochemical Marking." Oxford Univ. Press, Oxford, UK, 1999.
13. M. Bendayan, "Colloidal Gold Post-Embedding Immunocytochemistry," Vol. 29. Wiley, Stuttgart, 1995.
14. C. A. Foss and D. L. Feldheim, "Metal Nanoparticles: Synthesis, Characterization, and Applications." Dekker, New York, 2001.
15. J. Schmitt, P. M. Mächtle, D. Eck, H. Möwald, and C. A. Helm, *Langmuir* 15, 3256 (1999).
16. D. Eck and C. A. Helm, *Langmuir* 17, 957 (2001).
17. U. Kreibig and M. Vollmer, "Optical Properties of Metal Clusters." Springer-Verlag, Berlin, 1995.
18. C. F. Bohren and D. R. Huffman, "Absorption and Scattering of Light by Small Particles." Wiley, New York, 1983.
19. G. Mie, *Ann. Phys.* 25, 307 (1908).
20. C. Kittel, "Introduction to Solid State Physics," 2nd ed. Wiley, New York, 1956.
21. P. Mulvaney, *Langmuir* 12, 788 (1996).
22. "Handbook of Chemistry and Physics." CRC Press, Cleveland, 1986.
23. M. Quinten and U. Kreibig, *Surface Sci.* 172, 557 (1986).
24. J. Wiesner and A. Wokaun, *Chem. Phys. Lett.* 157, 569 (1989).
25. J. J. Storhoff, A. A. Lazarides, R. C. Mucic, C. A. Mirkin, R. L. Letsinger, and G. C. Schatz, *J. Am. Chem. Soc.* 122, 4640 (2000).
26. K. S. Suslick, *Science* 247, 1439 (1990).
27. A. Henglein, *Langmuir* 15, 6738 (1999).
28. A. Henglein and D. Meisel, *Langmuir* 14, 7392 (1998).
29. J. Belloni, M. Mostafavi, H. Remita, J. L. Marignier, and M. O. Delcourt, *New J. Chem.* 22, 1239 (1998).
30. M. Treguer, C. de Cointet, H. Remita, J. Khatouri, M. Mostafavi, J. Amblard, J. Belloni, R. de Keyzer, and J. Belloni, *J. Phys. Chem. B* 102, 4310 (1998).
31. A. Henglein and R. J. Tausch-Treml, *J. Colloid Interface Sci.* 80, 84 (1981).
32. J. L. Marignier, J. Beloni, M. O. Delcourt, and J. P. Chevalier, *Nature* 317, 344 (1985).
33. Y. Yonezawa, T. Sato, M. Ohno, and H. J. Hada, *Chem. Soc., Faraday Trans.* 83, 1559 (1987).
34. K. Torigoe and K. Esumi, *Langmiur* 8, 59 (1992).
35. T. Sato, S. Kuroda, A. Takami, Y. Yonazawa, and H. Hada, *Appl. Organomet. Chem.* 5, 261 (1991).
36. K. Kurihara, J. Kizling, P. Stenius, and J. J. Fendler, *J. Am. Chem. Soc.* 105, 2574 (1983).
37. A. Henglein, *Chem. Mater.* 10, 444 (1998).
38. S. L. Cumberland and G. F. Strouse, *Langmuir* 18, 269 (2002).
39. J. W. Slot and H. J. Geuze, *Europ. J. Cell Biol.* 38, 87 (1985).
40. S. Chen and K. Kimura, *Langmuir* 15, 1075 (1999).
41. G. T. Hermanson, "Bioconjugate Techniques." Academic Press, San Diego, 1996.
42. J.-A. He, R. Valluzzi, K. Yang, T. Dolukhanyan, C. Sung, J. Kumar, S. K. Tripathy, L. Samuelson, L. Balogh, and D. A. Tomalia, *Chem. Mater.* 11, 3268 (1999).
43. H. Ishizuka, T. Tano, K. Torigoe, K. Esumi, and K. Meguro, *Colloids Surf.* 63, 337 (1992).
44. K. Esumi, N. Sato, K. Torigoe, and K. Meguro, *J. Colloid Interface Sci.* 149, 295 (1992).
45. A. Henglein, *J. Phys. Chem. B* 104, 2201 (2000).
46. A. Henglein, *J. Phys. Chem. B* 104, 6683 (2000).
47. D. J. Elliot, D. N. Furlong, F. Grieser, P. Mulvaney, and M. Giersig, *Coll. Surf. A* 130, 141 (1997).
48. K. R. Brown, D. G. Walter, and M. J. Natan, *Chem. Mater.* 12, 306 (2000).
49. D. G. Duff, A. Baiker, and P. P. Edwards, *Langmuir* 9, 2310 (1993).
50. K. R. Brown, L. A. Lyon, A. P. Fox, B. D. Reiss, and M. J. Natan, *Chem. Mater.* 12, 314 (2000).
51. E. C. Stathis and A. Fabrikanos, *Chem. Ind.* 47, 860 (1958).
52. V. Privman, D. V. Goia, J. Park, and E. Matijevic, *J. Coll. Int. Sci.* 213, 36 (1999).
53. H. Hirai, Y. Nakao, and N. Toshima, *J. Macromol. Sci.-Chem. A* 12 1117 (1978).
54. H. Hirai, *J. Macromol. Sci.-Chem. A* 13, 633 (1979).
55. H. Hirai, Y. Nakao, and N. Toshima, *J. Macromol. Sci.-Chem. A* 13, 727 (1979).
56. M. Y. Han, C. H. Quek, W. Huang, C. H. Chew, and L. M. Gan, *Chem. Mater.* 11, 1144 (1999).
57. L. Longenberger and G. Mills, *J. Phys. Chem.* 99, 475 (1995).
58. J. Turkevich, P. C. Stevenson, and J. Hillier, *Discuss. Faraday Soc.* 11, 55 (1951).
59. M. Brust, M. Walker, D. Bethell, D. J. Schiffrin, and R. Whyman, *J. Chem. Soc. Chem. Commun.* 801 (1994).
60. M. Brust, J. Fink, D. Bethell, D. J. Schiffrin, and C. Kiely, *J. Chem. Soc. Chem. Commun.* 1655 (1995).
61. A. C. Templeton, W. P. Wuelfing, and R. W. Murray, *Acc. Chem. Res.* 33, 27 (2000).
62. N. C. Greenham, X. G. Peng, and A. P. Alivisatos, *Phys. Rev. B* 54, 17628 (1996).
63. V. L. Colvin, M. C. Schlamp, and A. P. Alivisatos, *Nature* 370, 354 (1994).
64. T. Cassagneau, T. E. Mallouk, and J. H. Fendler, *J. Am. Chem. Soc.* 120, 7848 (1998).
65. M. Gao, B. Richer, and S. Kirstein, *Adv. Mater.* 9, 802 (1997).
66. M. Gao, B. Richer, S. Kirstein, and H. Möhwald, *J. Phys. Chem. B* 102, 4096 (1998).
67. H. Mattoussi, L. H. Radzilowski, B. O. Dabbousi, E. L. Thomas, M. G. Bawendi, and M. F. Rubner, *J. Appl. Phys.* 83, 7965 (1998).
68. R. Gangopadhyay and A. De, *Chem. Mater.* 12, 608 (2000).
69. R. Singh, R. P. Tandon, and S. Chandra, *J. Appl. Phys.* 70, 243 (1991).
70. Y. P. Ting, K. G. Neoh, E. T. Kang, and K. L. Tan, *J. Chem. Technol. Biotechnol.* 59, 31 (1994).
71. E. K. Miller, C. J. Brabee, H. Neugebauer, A. J. Heeger, and N. S. Sariciftci, *Chem. Phys. Lett.* 335, 23 (2001).
72. A. Kushida, M. Yamato, C. Konno, A. Kikuchi, Y. Sakurai, and T. Okano, *J. Biomed. Mater. Res.* 51, 216 (2000).
73. K. Uchida, O. H. Kwon, E. Ito, T. Aoyagi, A. Kikuchi, M. Yamato, and T. Okano, *Macromol. Rapid Comm.* 21, 169 (2000).
74. L. K. Ista, V. H. Perez-Luna, and G. P. Lopez, *Appl. Environ. Microbiol.* 65, 1603 (1999).
75. A. B. R. Mayer, *Mater. Sci. Eng. C* 6, 155 (1998).
76. S. T. Selvan, J. P. Spatz, H.-A. Klok, and M. Moller, *Adv. Mater.* 10, 132 (1998).
77. J. J. Watkins and T. J. McCarthy, *Chem. Mater.* 7, 1991 (1995).
78. K. Sayo, S. Deki, and S. Hayashi, *Eur. Phys. J. D* 9, 429 (1999).
79. J. Lee, V. C. Sundar, J. R. Heine, M. G. Bawendi, and K. F. Jensen, *Adv. Mater.* 12, 1102 (2000).

80. M. K. Corbierre, N. S. Cameron, M. Sutton, S. G. J. Mochrie, L. B. Lurio, A. Ruhm, and R. B. Lennox, *J. Am. Chem. Soc.* 123 10411 (2001).
81. J. M. G. Cowie, "Polymers: Chemistry and Physics of Modern Materials 2." Blackie, New York, 1991.
82. J. M. Stouffer and T. J. McCarthy, *Macromolecules* 21, 1204 (1988).
83. N. C. Greenham, X. G. Peng, and A. P. Alivisatos, *Phys. Rev. B.* 54, 17628 (1996).
84. Y. Zhou, H. Itoh, T. Uemura, K. Naka, and Y. Chujo, *Langmuir* 18, 277 (2002).
85. R. Gangopadhyay and A. De, *Chem. Mater.* 12, 608 (2000).
86. D. I. Svergun, M. B. Kozin, P. V. Konarev, E. V. Shtykova, V. V. Volkov, D. M. Chernyshov, P. M. Valetsky, and L. M. Bronstein, *Chem. Mater.* 12, 3552 (2000).
87. A. B. Lowe, B. S. Sumerlin, M. S. Donovan, and C. L. McCormick, *J. Am. Chem. Soc.* 124, 11562 (2002).
88. B. S. Sumerlin, M. S. Donovan, Y. Mitsukami, A. B. Lowe, and C. L. McCormick, *Macromolecules* 34, 6561 (2001).
89. Y. Mitsukami, M. S. Donovan, A. B. Lowe, and C. L. McCormick, *Macromolecules* 34, 2248 (2001).
90. M. S. Donovan, A. B. Lowe, B. S. Sumerlin, and C. L. McCormick, *Macromolecules* 35, 4123 (2002).
91. M. S. Donovan, T. Sanford, A. B. Lowe, Y. Mitsukami, B. S. Sumerlin, and C. L. McCormick, *Macromolecules* 35, 4570 (2002).
92. M. Tagaki, *J. Phys. Soc. Jpn.* 9, 359 (1954).
93. D. A. Buffat and J. P. Bonel, *Phys. Rev. A* 13, 2289 (1976).
94. J. P. Wilcoxon, J. E. Martin, F. Parsapour, B. Wiedenman, and D. F. Kelley, *J. Chem. Phys.* 108, 9137 (1998).
95. M. Haruta, S. Tsubota, T. Kobayashi, H. Kayegama, M. J. Genet, and B. Delmon, *J. Catal.* 144, 175 (1993).
96. H. Sakurat and M. Haruta, *Appl. Catal. A: General* 127, 93 (1995).
97. C. Petit, P. Lixon, and M. P. Pileni, *J. Phys. Chem.* 97, 12974 (1993).
98. R. A. Caruso, M. Ashokkumar, and F. Grieser, *Langmuir* 18, 7831 (2002).
99. A. Henglein, *J. Phys. Chem.* 97, 5457 (1993).
100. F. Mafune, J.-Y. Kohno, Y. Takeda, and T. Kondow, *J. Phys. Chem. B* 105, 9050 (2001).
101. F. Mafune, J.-Y. Kohno, Y. Takeda, and T. Kondow, *J. Phys. Chem. B* 106, 8555 (2002).
102. H. Kurita, A. Takami, and S. Koda, *Appl. Phys. Lett.* 72, 789 (1998).
103. F. Mafune, J.-Y. Kohno, Y. Takeda, T. Kondow, and H. Sawabe, *J. Phys. Chem. B* 105, 5114 (2001).
104. H. Eckstein and U. Kreibig, *Z. Phys. D* 26, 239 (1993).
105. Y. Takeuchi, T. Ida, and K. Kimura, *J. Phys. Chem. B* 101, 1322 (1997).
106. A. Takami, H. Kurita, and S. Koda, *J. Phys. Chem. B* 103, 1226 (1999).
107. K. Okitsu, A. Yue, S. Tanabe, H. Matsumoto, and Y. Yobiko, *Langmuir* 17, 7717 (2001).
108. W. Chen, W. Cai, L. Zhang, G. Wang, and L. Zhang, *J. Coll. Int. Sci.* 238, 291 (2001).
109. Y. Nagata, Y. Mizukoshi, and K. Okitsu, *Radiation Res.* 146, 333 (1996).
110. Y. Zhou, C. Y. Wang, Y. R. Zhu, and Z. Y. Chen, *Chem. Mater.* 11, 2310 (1999).
111. W. O. Milligan and R. H. Morriss, *J. Am. Chem. Soc.* 86, 3461 (1964).
112. K. Esumi, K. Matsuhisa, and K. Torigoe, *Langmuir* 11, 3285 (1995).
113. S. Link, M. B. Mohamed, and M. A. El-Sayed, *J. Phys. Chem. B* 103, 3073 (1999).
114. C. A. Foss, G. L. Hornyak, J. A. Stockert, and C. R. Martin, *J. Phys. Chem.* 96, 7497 (1992).
115. C. A. Foss Jr., G. L. Hornyak, J. A. Stockert, and C. R. Martin, *J. Phys. Chem. B* 98, 2963 (1994).
116. G. L. Hornyak, C. J. Patrissi, and C. R. Martin, *J. Phys. Chem. B* 101, 1548 (1997).
117. G. L. Hornyak and C. R. Martin, *Thin Solid Films* 303, 84 (1997).
118. M. L. Sandrock, C. D. Pibel, F. M. Geiger, and C. A. Foss Jr., *J. Phys. Chem. B* 103, 2668 (1999).
119. C. R. Martin, *Science* 266, 1961 (1994).
120. G. L. Hornyak, C. J. Patrissi, and C. R. Martin, *J. Phys. Chem. B* 101, 1548 (1997).
121. J. C. Hulteen, C. J. Patrissi, D. L. Miner, E. R. Crosthwait, E. B. Oberhauser, and C. R. Martin, *J. Phys. Chem. B* 101, 7727 (1997).
122. C. A. Foss, G. L. Hornyak, M. J. Tierney, and C. R. Martin, *J. Phys. Chem.* 96, 9001 (1992).
123. C. K. Preston and M. Moskovits, *J. Phys. Chem.* 92, 2957 (1988).
124. C. K. Preston and M. Moskovits, *J. Phys. Chem.* 97, 8405 (1993).
125. M. J. Tierney and C. R. Martin, *J. Phys. Chem.* 93, 2878 (1989).
126. Y.-Y. Yu, S.-S. Chang, C.-L Lee, and C. R. C. Wang, *J. Phys. Chem. B* 101, 6661 (1997).
127. A. H. Lu, G. H. Lu, A. M. Kessinger, and C. A. Foss Jr., *J. Phys. Chem. B* 101, 9139 (1997).
128. P. F. Liao, R. K. Chang, and T. E. Furtak, "Surface Enhanced Raman Scattering." Plenum Press, New York, 1982.
129. M. C. Buncick, R. J. Warmack, and T. C. Ferrell, *J. Opt. Soc. Am. B* 4, 927 (1988).
130. C. Schönenberger, B. M. I. Van der Zande, L. G. J. Fokkink, M. Henny, C. Schmid, M. Krüger, A. Bachtold, R. Huber, H. Birk, and U. Staufer, *J. Phys. Chem. B* 101, 5497 (1997).
131. N. R. Jana, L. Gearheart, and C. J. Murphy, *J. Phys. Chem. B* 105, 4065 (2001).
132. N. R. Jana, L. Gearheart, S. O. Obare, and C. J. Murphy, *Langmuir* 18, 922 (2002).
133. J. C. Wittman and P. Smith, *Nature* 352, 414 (1991).
134. R. E. Gill, G. Hadziioannou, P. Lang, F. Garnier, and J. C. Wittman, *Adv. Mater.* 9, 331 (1997).
135. P. Hubert, H. Dreyfus, D. Guillon, and Y. Galerne, *J. Phys. II* 5, 1371 (1995).
136. S. Ravaine, G. E. Fanucci, C. T. Seip, J. H. Adair, and D. R. Talham, *Langmuir* 14, 708 (1998).
137. L. D. Marks and D. J. Smith, *J. Crystal Growth* 54, 425 (1981).
138. D. J. Smith and L. D. Marks, *J. Crystal Growth* 54, 433 (1981).
139. R. Gans, *Ann. Phys.* 47, 270 (1915).
140. D. C. Skillman and C. R. Berry, *J. Chem. Phys.* 48, 3297 (1968).
141. M. B. Mohamed, Z. L. Wang, and M. A. El-Sayed, *J. Phys. Chem. A* 103, 10255 (1999).
142. M. A. El-Sayed, *Acc. Chem. Res.* 34, 257 (2001).
143. R. D. Averitt, D. Sarkar, and N. Halas, *J. Phys. Rev. Lett.* 78, 4217 (1997).
144. S. J. Oldenburg, R. D. Averitt, S. L. Westcott, and N. J. Halas, *J. Chem. Phys. Lett.* 288, 243 (1998).
145. R. D. Averitt, S.L. Westcott, and N. J. Halas, *J. Phys. Rev. B* 58, 10203 (1998).
146. S. J. Oldenburg, S. L. Westcott, R. D. Averitt, and N. Halas, *J. Chem. Phys.* 111, 4729 (1999).
147. R. D. Averitt, S. L. Westcott, and N. J. Halas, *J. Opt. Soc. Am. B* 16, 1824 (1999).
148. S. J. Oldenburg, J. B. Jackson, S. L. Westcott, and N. J. Halas, *Appl. Phys. Lett.* 75, 2897 (1999).
149. S. R. Sershen, S. L. Westcott, N. J. Halas, and J. L. West, *J. Biomed. Mater. Res.* 51, 293 (2000).
150. G. D. Hale, J. B. Jackson, O. E. Shmakova, T. R. Lee, and N. J. Halas, *Appl. Phys. Lett.* 78, 1502 (2001).
151. J. B. Jackson and N. J. Halas, *J. Phys. Chem. B* 105, 2743 (2001).
152. D. D. Smith, L.A. Snow, L. Sibille, and E. Ignont, *J. Non-Cryst. Solids* 285, 256 (2001).
153. V. C. Coffey, *Laser Focus World* 37, 46 (2001).
154. J. J. Diao and G. D. Chen, *J. Phys. D* 34, L79, (2001).
155. M. C. Netti, S. Coyle, J. J. Baumberg, M. A. Ghanem, P. R. Birkin, P. N. Bartlett, and D. M. Whittaker, *Adv. Mater.* 13, 1368 (2001).
156. S. Lal, S. L. Westcott, R. N. Taylor, J. B. Jackson, P. Nordlander, and N. J. Halas, *J. Phys. Chem. B* 106, 5609 (2002).

157. T. Pham, J. B. Jackson, N. J. Halas, and T. R. Lee, *Langmuir* 18, 4915 (2002).

158. E. Prodan, A. Lee, and P. Nordlander, *Chem. Phys. Lett.* 360, 325 (2002).

159. Y. G. Sun and Y. N. Xia, *Anal. Chem.* 74, 5297 (2002).

160. T. J. Beveridge and R. G. E. Murray, *J. Bacteriol.* 141, 876, (1980).

161. T. J. Beveridge and R. J. Doyle, "Metal Ions and Bacteria." Wiley, New York, 1989.

162. G. Southam and T. J. Beveridge, *Geochim. Cosmochim. Acta* 60, 4369 (1996).

163. D. Fortin and T. J. Beveridge in "Biomineralization; From Biology to Biotechnology and Medical Applications" (E. Baeuerlein, Ed.), p. 7. Wiley–VCH, Weinheim, 2000.

164. P. Mukherjee, A. Ahmad, D. Mandal, S. Senapati, S. R. Sainkar, M. I. Khan, R. Ramani, R. Parischa, P. V. Ajayakumar, M. Alam, M. Sastry, and R. Kumar, *Angew. Chem. Int. Ed.* 40, 3585 (2001).

165. P. Mukherjee, S. Senapati, D. Mandal. A. Ahmad, M. I. Khan, R. Kumar, and M. Sastry, *Chem. Biochem.* 5, 461 (2002).

166. N. Braun, W. Meining, U. Hars, M. Fischer, R. Ladenstein, R. Huber, A. Bacher, S. Weinkauf, and L. Bachmann, *J. Mol. Biol.* 321, 341 (2002).

167. Z. Zhang and M. G. Lagally, *Science* 76, 377 (1997).

168. C. S. Weisbecker, M. V. Merritt, and G. M. Whitesides, *Langmuir* 12, 3763 (1996).

169. K. S. Mayya, V. Patil, and M. Sastry, *Langmuir* 13, 3944 (1997).

170. J. E. Houston and H. I. Kim, *Acc. Chem. Res.* 35, 547 (2002).

171. N. K. Chaki and K. Vijayamohanan, *Biosens. Bioelectr.* 17, 1 (2002).

172. C. M. Knobler and D. K. Schwartz, *Curr. Opinion. Coll. Interf. Sci.* 4, 46 (1999).

173. M. J. Hostetler and R. W. Murray, *Curr. Opinion. Coll. Interf. Sci.* 2, 42 (1997).

174. A. R. Bishop and R. G. Nuzzo, *Curr. Opinion. Coll. Interf. Sci.* 1, 127 (1996).

175. A. Ulman, *Chem. Rev.* 96, 1533 (1996).

176. M. Mrksich and G. M. Whitesides, *Ann. Rev. Biophys. Biomol. Struct.* 25, 55 (1996).

177. A. Ulman, "An Introduction to Ultrathin Organic Films: From Langmuir–Blodgett to Self Assembly." Academic Press, Boston, 1991.

178. S. J. Green, J. J. Stokes, M. J. Hostetler, J. Pietron, and R. W. Murray, *J. Phys. Chem. B* 101, 2663 (1997).

179. M. J. Hostetler, J. E. Wingate, C.-J. Zhong, J. E. Harris, R. W. Vachet, M. R. Clark, J. D. Londono, S. J. Green, J. J. Stokes, G. D. Wignall, G. L. Glish, M. D. Porter, N. D. Evans, and R. W. Murray, *Langmuir* 14, 17 (1998).

180. R. H. Terrill, T. A. Postlethwaite, C. Chen, C. Poon, A. Terzis, A. Chen, J. E. Hutchison, M. R. Clark, G. W., J. D. Londono, D. Superfine, M. Falvo, C. S. Johnson, E. T. Samulski, and R .W. Murray, *J. Am. Chem. Soc.* 117, 12537 (1995).

181. T. G. Schaaff, G. Knight, M. N. Shafigullin, R. F. Borkman, and R. L. Whetten, *J. Phys. Chem. B* 102, 10643 (1998).

182. A. C. Templeton, S. Chen, S. M. Gross, and R. W. Murray, *Langmuir* 15, 66 (1999).

183. W. P. Wuelfing, S. M. Gross, D. T. Miles, and R. W. Murray, *J. Am. Chem. Soc.* 120, 12696 (1998).

184. M. Brust, J. Fink, D. Bethell, D. J. Schiffrin, and C. Kiely, *J. Chem. Soc., Chem. Commun.* 1655 (1995).

185. S. R. Johnson, S. D. Evans, S. W. Mahon, and A. Ulman, *Langmuir* 13, 51 (1997).

186. S. Chen and R. W. Murray, *Langmuir* 15, 682 (1999).

187. P. A. Buining, B. M. Humbel, A. P. Philipse, and A. J. Verkleij, *Langmuir* 13, 3921 (1997).

188. M. J. Hostetler, S. J. Green, J. J. Stokes, and R. W. Murray, *J. Am. Chem. Soc.* 118, 4212 (1996).

189. S. R. Johnson, S. D. Evans, and R. Brydson, *Langmuir* 14, 6639 (1998).

190. L. A. Porter, Jr., D. Ji, S. L. Westcott, M. Graupe, R. S. Czernuszewicz, N. J. Halas, and T. R. Lee, *Langmuir* 14, 7378 (1998).

191. Y. S. Shon, C. Mazzitelli, and R. W. Murray, *Langmuir* 17, 7735 (2001).

192. D. E. Cliffel, F. P. Zamborini, S. M. Gross, and R. W. Murray, *Langmuir* 16, 9699 (2000).

193. A. Aguila and R. W. Murray, *Langmuir* 16, 5949 (2000).

194. A. C. Templeton, S. Chen, S. M. Gross, and R. W. Murray, *J. Phys. Chem. B* 104, 564 (2000).

195. N. Kometani, M. Tsubonishi, T. Fujita, K. Asami, and Y. Yonezawa, *Langmuir* 17, 578 (2001).

196. C. Yee, M. Scotti, A. Ulman, H. White, M. Rafailovich, and J. Sokolov, *Langmuir* 15, 4314 (1999).

197. H. Imahori, M. Arimura, T. Hanada, Y. Nishimura, I. Yamazaki, Y. Sakata, and S. Fukuzumi, *J. Am. Chem. Soc.* 123, 335 (2001).

198. M. J. Hostetler, A. C. Templeton, and R. W. Murray, *Langmuir* 15, 3782 (1999).

199. R. S. Ingram, M. J. Hostetler, and R. W. Murray, *J. Am. Chem. Soc.* 119, 9175 (1997).

200. M. G. Warner, S. M. Reed, and J. E. Hutchison, *Chem. Mater.* 12, 3316 (2000).

201. P. Ionita, A. Caragheorgheopol, B. C. Gilbert, and V. Chechik, *J. Am. Chem. Soc.* 124, 9048 (2002).

202. S. J. Green, J. J. Pietron, J. J. Stokes, M. J. Hostetler, H. Vu, W. P. Wuelfing, and R. W. Murray, *Langmuir* 144, 5612 (1998).

203. M. S. Fleming and D. R. Walt, *Langmuir* 17, 4836 (2001).

204. J. B. Schlenoff, M. Li, and H. Ly, *J. Am. Chem. Soc.* 117, 12528 (1995).

205. M. Sastry, N. Lala, V. Patil, S. P. Chavan, and A. G. Chittiboyina, *Langmuir* 14, 4138 (1998).

206. J. J. Storhoff, R. Elghanian, R. C. Mucic, C. A. Mirkin, and R. L. Letsinger, *J. Am. Chem. Soc.* 120, 1959 (1998).

207. S. Connolly, S. Cobbe, and D. Fitzmaurice, *J. Phys. Chem. B* 105, 2222 (2001).

208. K. Aslan and V. H. Pérez-Luna, *Langmuir* 18, 6059 (2002).

209. N. Lala, A. G. Chittiboyina, and S. P. Chavan, *Coll. Surf. A* 205, 15 (2002).

210. M. Sastry, K. S. Mayya, and V. Patil, *Langmuir* 14, 5921 (1998).

211. V. Patil and M. Sastry, *Langmuir* 14, 2707 (1998).

212. V. Patil, K. S. Mayya, S. D. Pradhan, and M. Sastry, *J. Am. Chem. Soc.* 119, 9281 (1997).

213. E. De Harven, R. Leung, and H. Christensen, *J. Cell Biol.* 99, 53 (1984).

214. W. Faulk and G. Taylor, *Immunochemistry* 8, 1081 (1979).

215. E. Romano, C. Stolinsky, and N. Hugh-Jones, *Immunochemistry* 11, 521 (1974).

216. J. Roth, M. Bendayan, and L Orci, *J. Histochem. Cytochem.* 28, 55 (1980).

217. S. Eskelinen and R. Peura, *Scan. Electr. Microsc.* 2, 1765 (1988).

218. R. M. Albrecht and G. M. Hodges, Eds., "Biotechnology and Bioapplications of Colloidal Gold." Scanning Microscopy International, IL, 1988.

219. M. M. Kay, in "Principles and Techniques of Scanning Electron Microscopy" (M. A. Hayat, Ed.), Vol. 6, p. 338. Van Nostrand Reinhold, New York, 1978.

220. R. S. Molday and P. Maher, *J. Histochem.* 12, 273 (1980).

221. E. Skutelsky and J. Roth, *J. Histochem. Cytochem.* 34, 693 (1986).

222. A. W. Vorbrodt, *J. Histochem. Cytochem.* 35, 1261 (1987).

223. N. Thurauf, R. Dermietzel, and P. Kalweit, *J. Ultrastruct Res.* 84, 103 (1983).

224. J. Beesley, "Royal Microscopical Society Handbook," Vol. 17. Oxford Univ. Press, London, 1989.

225. T. Wenzel and W. Baumeister, *Nat. Struct. Biol.* 2, 199 (1995).

226. A. P. Alivisatos, K. P. Johnson, X. Peng, T. E. Wilson, C. J. Loweth, M. P. Bruchez Jr., and P. G. Schultz, *Nature* 382, 609 (1996).

227. J. F. Hainfield, in "Proc. 54th Ann. Mtg., Micr. Soc. Amer." (G. W. Bailey, J. M. Corbett, R. V. W. Dimlich, J. R. Michael, N. J. Zaluzec, Eds.), p. 898. San Francisco Press, San Francisco, 1996.

228. C. Mangeney, F. Ferrage, I. Aujard, V. Marchi-Artzner, L. Jullien, O. Ouari, E. D. Rekai, A. Laschewsky, I. Vikholm, and J. W. Sadowski, *J. Am. Chem. Soc.* 124, 5811 (2002).

229. A. Laschewsky, O. Quari, C. Mangeney, and L. Jullien, *Macromol. Symp.* 164, 323 (2001).

230. R. Jordan, A. Ulman, J. F. Kang, M. H. Rafailovich, and J. Sokolov, *J. Am. Chem. Soc.* 121, 1016 (1999).

231. R. Jordan, N. West, A. Ulman, Y.-M. Chou, and O. Nuyken, *Macromolecules* 34, 1606 (2001).

232. R. Jordan and A. Ulman, *J. Am. Chem. Soc.* 120, 243 (1998).

233. R. Jordan, A. Ulman, J. F. Kang, M. Rafailovich, and J. Sokolov, *J. Am. Chem. Soc.* 121, 1016 (1999).

234. R. Jordan, K. Martin, H. J. Rader, and K. K. Unger, *Macromolecules* 34, 8858 (2001).

235. N. Nath and A. Chilkoti, *J. Am. Chem. Soc.* 123, 8197 (2001).

236. D. A. Tomalia, *Angew. Chem. Int. Ed. Engl.* 29, 138 (1990).

237. F. Zeng and S. C. Zimmerman, *Chem. Rev.* 97, 1681 (1997).

238. D. A. Tomalia, A. M. Naylor, and W. A. Goddard, *Angew. Chem.* 102, 119 (1990).

239. D. A. Tomalia and H. D. Durst, *Top. Curr. Chem.* 165, 193 (1993).

240. G. R. Newkome, C. N. Moorefield, and F. Vögtle, "Dendritic Macromolecules: Concepts, Syntheses, Perspectives." VCH, Weinheim, 1996.

241. J. M. J. Fréchet, *Science* 263, 1710 (1994).

242. B. I. Voit, *Acta Polym.* 46, 87 (1995).

243. N. Ardoin and D. Astruc, *Bull. Soc. Chim. Fr.* 132, 875 (1995).

244. M. Zhao, H. Tokuhisa, and R. M. Crooks, *Angew. Chem. Int. Ed. Engl.* 36, 2596 (1997).

245. M. F. Ottaviani, F. Montalti, N. J. Turro, and D. A. Tomalia, *J. Phys. Chem. B* 101, 158 (1997).

246. K. Esumi, A. Suzuki, N. Aihara, K. Usui, and K. Torigoe, *Langmuir* 14, 3157 (1998).

247. M. E. Garcia, L. A. Baker, and R. M. Crooks, *Anal. Chem.* 71, 256 (1999).

248. L. Balogh, R. Valluzzi, K. S. Laverdure, S. P. Gido, G. L. Hagnauer, and D. A Tomalia, *J. Nanopart. Res.* 1, 353 (1999).

249. K. Esumi, A. Suzuki, A. Yamahira, and K. Torigoe, *Langmuir* 16, 2604 (2000).

250. F. Grohn, B. J. Bauer, Y. A. Akpalu, C. L. Jackson, and E. J. Amis, *Macromolecules* 13, 6042 (2000).

251. J.-A. He, R. Valluzzi, K. Yang, T. Dolukhanyan, C. Sung, J. Kumar, S. K. Tripathy, L. Samuelson, L. Balogh, and D. A. Tomalia, *Chem. Mater.* 11, 3268 (1999).

252. K. Aoi, K. Itoh, and M. Okada, *Macromolecules* 28, 5391 (1995).

253. K. Esumi, T. Hosoya, A. Suzuki, and K. Torigoe, *Langmuir* 16, 2978 (2000).

254. A. Manna, T. Imae, K. Aoi, M Okada, and T. Yogo, *Chem. Mater.* 13, 1674 (2001).

255. V. Chechik and R. M. Crooks, *Langmuir* 15, 6364 (1999).

256. L. M. Liz-Marzan, M. Giersig, and P. Mulvaney, *Langmuir* 12, 4329 (1996).

257. S. T. Selvan, T. Hayakawa, M. Nogami, Y. Kobayashi, L. M. Liz-Marzan, Y. Hamanaka, and A. Nakamura, *J. Phys. Chem. B*, 106, 10157 (2002).

258. F. Garcia-Santamaria, V. Salgueirino-Maceira, C. Lopez, and L. M. Liz-Marzan, *Langmuir* 18, 4519 (2002).

259. Y. Kobayashi, M. A. Correa-Duarte, and L. M. Liz-Marzan, *Langmuir* 17, 6375 (2001).

260. S. Bharathi and O. Lev, *Chem. Comm.* 23, 2303 (1997).

261. S. Bharathi, N. Fishelson, and O. Lev, *Langmuir* 15, 1929 (1999).

262. C. J. Brinker and G. W. Scherer, "Sol–Gel Science." Academic Press, New York, 1990.

263. A. Martino, S. A. Yamanaka, J. S. Kowala, and D. L. Loy, *Chem. Mater.* 9, 423 (1997).

264. K. C. Grabar, R. G. Freeman, M. B. Hommer, and M. J. Natan, *Anal. Chem.* 67, 735 (1995).

265. K. C. Grabar, P. C. Smith, M. D. Musick, J. A. Davis, D. G. Walter, M. A. Jackson, A. P. Guthrie, and M. J. Natan, *J. Am. Chem. Soc.* 118, 1148 (1996).

266. K. C. Grabar, K. J. Allison, B. E. Baker, R. M. Bright, K. R. Brown, R. G. Freeman, A. P. Fox, C. D. Keating, M. D. Musick, and M. J. Natan, *Langmuir* 12, 2353 (1996).

267. P. Mukherjee, A. Ahmad, D. Mandal, S. Senapati, S. R. Sainkar, M. I. Khan, R. Ramani, R. Parischa, P. V. Ajayakumar, M. Alam, M. Sastry, and R. Kumar, *Angew. Chem. Int. Ed.* 40, 3585 (2001).

268. D. V. Leff, L. Brandt, and J. R. Heath, *Langmuir* 12, 4723 (1996).

269. B. D. Ratner and D. G. Castner, Electron spectroscopy for chemical analysis, in "Surface Analysis–Techniques and Applications" (J. C. Vickerman, Ed.), pp. 43–98. Wiley, Chichester, UK, 1997.

270. J. A. Harnisch, A. D. Pris, and M. D. Porter, *J. Am. Chem. Soc.* 123, 5829 (2001).

271. O. Kohlmann, W. E. Steinmetz, X-A, Mao, W. P. Wuelfing, A .C. Templeton, R. W. Murray, and C. S. Johnson, *J. Phys. Chem. B* 105, 8801 (2001).

272. M. J. Hostetler, J. J. Stokes, and R. W. Murray, *Langmuir* 12, 3604 (1996).

273. E. W. L. Chan and L. Yu, *Langmuir* 18, 311 (2002).

274. F. X. Zhang, W. Zheng, M. M. Maye, Y. Lou, L. Han, and C.-J. Zhong, *Langmuir* 16, 9639 (2000).

275. M. A. Bryant and J. E. Pemberton, *J. Am. Chem. Soc.* 113, 8284 (1991).

276. P. C. Lee and D. Meisel, *J. Phys. Chem.* 86, 3391 (1982).

277. H. Xu, C.-H. Tseng, T. J. Vickers, C. K. Mann, and J. B. Schlenoff, *Surf. Sci.* 311, L707 (1994).

278. C. J. Sandroff, S. Garoff, and K. P. Leung, *Chem. Phys. Lett.* 96, 547 (1983).

279. C. A. Mirkin, R. L. Letsinger, R. C. Mucic, and J. J. Storhoff, *Nature* 382, 607 (1996).

280. L. J. Kricka, "Nonisotopic DNA Probe Techniques." Academic Press, San Diego, 1992.

281. B. D. Hames and S. J. Higgins, "Gene Probes 1." IRL Press, New York, 1995.

282. J. Wang, E. Palecek, P. E. Nielsen, G. Rivas, X. Cai, H. Shiraishi, N. Dontha, D. Luo, and P. A. M Farias, *J. Am. Chem. Soc.* 118, 7667 (1996).

283. S. Tyagi and F. R Kramer, *Nat. Biotechnol.* 14, 303 (1996).

284. R. Elghanian, J. J. Storhoff, R. C. Mucic, R. L. Letsinger, and C. A. Mirkin, *Science* 277, 1078 (1997).

285. R. A. Reynolds, III, C. A. Mirkin, and R. L. Letsinger, *J. Am. Chem. Soc.* 122, 3795 (2000).

286. T. A. Taton, G. Lu, and C. A. Mirkin, *J. Am. Chem. Soc.* 123, 5164 (2001).

287. Y. Cao, R. Jin, and C. A. Mirkin, *J. Am. Chem. Soc.* 123, 7961 (2001).

288. H. Schmitt, A. Badia, L. Dickson, L. Reven, and R. B. Lennox, *Adv. Mater.* 10, 475 (1998).

289. C. Templeton, F. P. Zamborini, W. P. Wuelfing, and R. W. Murray, *Langmuir* 16, 6682 (2000).

290. J. Simard, C. Briggs, A. K. Boal, and V. M. Rotello, *Chem. Commun.* 1943 (2000).

291. F. P. Zamborini, J. F. Hicks, and R. W. Murray, *J. Am. Chem. Soc.* 122, 4514 (2000).

292. W. P. Wuelfing, F. P. Zamborini, A. C. Templeton, X. Wen, H. Yoon, and R. W. Murray, *Chem. Mater.* 13, 87 (2001).

293. Y. Kim, R. C. Johnson, and J. T. Hupp, *Nano Lett.* 1, 165 (2001).

294. S. Berchmans, P. J. Thomas, and C. N. R. Rao, *J. Phys. Chem. B* 106, 4647 (2002).

295. T. Morris, H. Copeland, E. McLinden, S. Wilson, and G. Szulczewski, *Langmuir* 18, 7261 (2002).

296. P. Avouris and B. N. J. Persson, *J. Phys. Chem.* 88, 837 (1984).

297. B. N. J. Persson and S. Anderson, *Phys. Rev. B* 29, 4382 (1984).
298. G. Cnossen, K. E. Drabe, and D. A. Wiersma, *J. Chem. Phys.* 98, 5276 (1993).
299. J. R. Lakowicz, *Anal. Biochem.* 298, 1 (2001).
300. K. Sokolov, G. Chumanov, and T. M. Cotton, *Anal. Chem.* 70, 3898 (1998).
301. T. Liebermann and W. Knoll, *Colloids Surf. A* 171, 115 (2000).
302. I. Gryczynski, J. Malicka, Y. Shen, Z. Gryczynski, and J. R. Lakowicz, *J. Phys. Chem. B* 106, 2191 (2002).
303. D. J. Maxwell, J. R. Taylor, and S. Nie, *J. Am. Chem. Soc.* 124, 9606 (2002).
304. G. Wang, J. Zhang, and R. W. Murray, *Anal. Chem.* 74, 4320 (2002).
305. P. Hindebrandt and M. Stockburger, *J. Phys. Chem.* 88, 5935 (1984).
306. A. C. Pineda and D. Ronis, *J. Chem. Phys.* 83, 5330 (1985).
307. I. Pockrand, A. Brillante, and D. Mobius, *Chem. Phys. Lett.* 69, 499 (1980).
308. R. G. Freeman, K. C. Grabar, K. J. Allison, R. M. Bright, J. A. Davis, A. P. Guthrie, M. B. Hommer, M. A. Jackson, P. C. Smith, D. G. Walter, and M. J. Natan, *Science* 267, 1629 (1995).
309. M. D. Musick, D. J. Pena, S. L. Botsko, T. M. McEvoy, J. N. Richardson, and M. J. Natan, *Langmuir* 15, 844 (1999).
310. K. C. Grabar, K. R. Brown, C. D. Keating, S. J. S., S.-L. Tang, and M. J. Natan, *Anal Chem.* 69, 471 (1997).
311. N. Nath and A. Chilkoti, *Anal. Chem.* 74, 504 (2002).
312. H. X. He, H. Zhang, Q. G. Li, T. Zhu, S. F. Y. Li, and Z. F. Liu, *Langmuir* 16, 3846 (2000).
313. F. L. Leibowitz, W. Zheng, M. M. Maye, and C.-J. Zhong, *Anal. Chem.* 71, 5076 (1999).
314. L. Scheibler, P. Dumy, M. Boncheva, K. Leufgen, H. J. Mathieu, M. Mutter, and H. Vogel, *Angew. Chem.* 38, 696 (1999).
315. M. D. Musick, C. D. Keating, L. A. Lyon, S. L. Botsko, D. J. Pena, W. D. Holliway, T. M. McEvoy, J. N. Richardson, and M. J. Natan, *Chem. Mater* 12, 2869 (2000).
316. J. F. Hicks, Y. Seok-Shon, and R. W. Murray, *Langmuir* 18, 2288 (2002).
317. J. Schmitt, G. Decher, W. J. Dressick, S. L. Brandow, R. E. Geer, S. Shashidhar, and J. M. Calvert, *Adv. Mater.* 9, 61 (1997).
318. S. Pathak, M. T. Greci, R. C. Kwong, K. Mercado, G. K. S. Prakash, G. A. Olah, and M. E. Thompson, *Chem. Mater.* 12, 1985 (2000).
319. M. Brust, D. Bethell, C. J. Kiely, and D. J. Schiffrin, *Langmuir*, 14, 5425 (1998).
320. J. Jia, B. Wang, A. Wu, G. Cheng, Z. Li, and S. Dong, *Anal. Chem.* 74, 2217 (2002).
321. Z. J. Chen, X. M. Ou, F. Q. Tang, L. Jiang, *Colloids and Surfaces B* 7, 173 (1996).
322. L. Lin, H. Zhao, J. Li, J. Tang, M. Duan, and L. Jiang, *Biochem. Biophys. Res. Comm.* 274, 817 (2000).
323. F. Patolsky, K. T. Ranjit, A. Lichtenstein, and I. Willner, *Chem. Comm.* 12, 1025 (2000).
324. I. Willner, F. Patolsky, Y. Weizmann, and B. Willner, *Talanta* 56, 847 (2002).
325. X. C. Zhou, S. J. O'Shea, and S. F. Y. Li, *Chem. Comm.* 11, 953 (2000).
326. T. Liu, J. Tang, and L. Jiang, *Biochem. Biophys. Res. Comm.* 295, 14 (2002).
327. T. Liu, J. Tang, H. Zhao, Y. Deng, and L. Jiang, *Langmuir* 18, 5624 (2002).
328. H.-Y. Gu, A.-M. Yu, S.-S. Yuan, and H.-Y. Chen, *Anal. Lett.* 35, 647 (2002).
329. L. A. Lyon, M. D. Musick, and M. J. Natan, *Anal. Chem.* 70, 51774 (1998).

Computational Atomic Nanodesign

Michael Rieth, Wolfram Schommers

Forschungszentrum Karlsruhe, Karlsruhe, Germany

CONTENTS

1. INTRODUCTION

Only a few years ago technology had mainly to do with macroscopic systems and aggregates with micrometer-scale properties. The situation changed fundamentally with the rise of nanotechnology; this technology will have an essential influence on the development of new devices in all or almost all fields of technology, medicine, biology etc., and these developments will influence our future life considerably.

It is well known that nanosystems can have properties which are distinctly different from those of macroscopic systems: properties which are well defined and clearly fixed in the bulk are very often no longer typical features in nanophysics and nanotechnology. If the particle number is decreased so that the size of the system is in the nanometer region, new effects emerge which have no counterpart in other fields of physics, chemistry, and technology.

Let us give an example. The melting temperature of a macroscopic system is usually well defined, and the system is thermally stable up to the melting point. Of course there can be phase transitions but the various phases define stable configurations. In contrast to macroscopic systems, the melting temperature of a nanosystem in general depends on the particle number and is also a function of the outer shape of the system. Moreover, the melting temperature of certain nanosystems is not defined and not clearly fixed, which can be explained by the faster occurrence of sublimation compared to the melting process.

This is a completely new situation, in particular in connection with materials research. Clearly, the construction of nanomachines and other aggregates is based on components whose material properties have an essential influence on the function on such systems. Therefore, the definition and classification of material properties at the nanolevel is a particular challenge and is just at the beginning. Within such a program not only do further sophisticated experiments have to be prepared, but also specific methods for the theoretical treatment of such systems have to be selected and refined carefully.

Nanotechnology will also lead to drastic new insights in connection with biological systems, not only by the manipulation of the features of existing biological structures, but also with respect to questions as "What is a biological system?" or, quite generally "What is life?" It is usually assumed that biological features are strongly correlated with systems of sufficiently large complexity, in particular, in connection with complex molecules. But do we really need complex systems and complex organic molecules, respectively, for all phenomena which arise in connection with biological (living) systems? Obviously this must not be the case [1], a sufficiently small system consisting of an inorganic monatomic material (aluminum) shows surprisingly new effects in analogy to those which are typical for biological systems. How far has such an Al system to be reduced in order to show such features? In the micrometer realm the system behaves completely nonbiologically. However, if the size is of the order of a few nanometers, such new effects emerge.

What is the adequate theoretical treatment of such and similar nanoeffects? How relevant in this context are the usual methods of solid state physics, which have been successfully applied to the bulk state? In order to be able to answer these questions more specifically, let us mention the following often observed characteristics of nanosystems.

The properties of nanosystems vary strongly with temperature—much more than in the bulk of the crystal. This fact can lead to the effect that certain nanosystems (e.g., nanomachines) work properly only within a relatively

small temperature window, since components (or even the whole nanosystem) lose their stability outside this temperature window.

The reason for this temperature sensitivity is obvious and is explained by the following fact [2]. As the surface atoms are, in general, less bonded than bulk particles we expect that the structure and dynamics are more sensitive to variations in temperature. This is for example, the case for the mean-square displacements at the surface and also for anharmonic effects, leading to the effect of premelting; that is, the crystal is molten in the surface region already below the melting temperature. Since the relative number of surface atoms increases with decreasing size of the system, these effects are large in the case of nanosystems and, as we have already remarked, the melting temperature T_{mn} of the whole nanosystem is in general far below the melting temperature T_m of the bulk. Furthermore, below T_{mn} various specific structure transformations [3] can take place in connection with systems of nanometer size. All these effects can influence the function of nanosystems and have to be considered carefully.

Also this behavior of nanosystems makes clear that the basic principles of solid state physics can hardly be extended to the realm of systems with nanometer size. For example, the concept of phonons cannot be extended to nanosystems and we have to use other methods for the determination of the particle dynamics in such systems. Only a few concepts, which work well in the description of bulk states, can be used for the characterization of nanosystems. In conclusion, the typical features of the solid in the bulk (periodic structure, harmonic behavior) can be no basis for the theoretical description of nanosystems, and the system under investigation has to be analyzed carefully with respect to the theoretical treatment.

However, the principles of modern surface physics are often useful within the analysis of nanometer-scale properties. The reason is obvious: In the case of nanosystems a great fraction of atoms belong to the surface region of the system and determine essentially their behavior, and such nanosurface effects can be much larger than those of semi-infinite surface systems. For example, in the case of sufficiently small nanoclusters no particle of the system can be considered as a bulk particle since the distances of all the particles to the surface are smaller then the cutoff radius for the interaction.

In this chapter we introduce methods which are adequate for the theoretical treatment of nanosystems. These methods have been discussed critically and, in some cases, proposals are made to improve them under consideration of recent research results. The material is not only an introduction to the state of the art for researchers and professors, but is also benefits advanced students.

In this work we had to restrict ourselves to the study of the structure and dynamics of the atoms which form nanosystems (machines, aggregates, clusters etc.); we do not deal with nanostructured materials or with electronic properties of nanosystems (quantum dots, quantum computers, etc.). Clearly, the structure and dynamics of atoms are determined by the electrons, but only in connection with the interaction

between the particles, and these interactions are of fundamental importance for the understanding of the structural and dynamical behavior of nanosystems.

In the study given here we will concentrate on the *molecular dynamics* method, since this method is the most powerful tool in the theoretical treatment of nanosystems; within this method the structure and dynamics of the particles can be investigated as a function of temperature. This is important since the nanometer-scale properties are in general very sensitive to small variations in temperature, as we have already outlined above. The molecular dynamics method is described in detail, and also models and methods for the description of interaction potentials which are needed in connection with molecular dynamics calculations.

We also discuss the Monte Carlo method. While this tool is restricted to the study of structural properties, it has, on the other hand, the advantage that it can be used to treat quantum systems.

We start our considerations with the quantum-theoretical treatment of nanosystems, that is, with the methods of quantum chemistry. Here the discussion concentrates on the Hartree–Fock method and the density-functional formalism. However, we have restricted ourselves to a few brief statements. The reason is the following: until now, these methods only allowed the determination of *zero-temperature* properties, and as we have already discussed, temperature effects are of considerable importance in connection with nanosystems. In particular, the nanoproperties are in general very sensitive to small variations in temperature and, therefore, it should hardly be possible to conclude from *zero-temperature* data (Hartree–Fock method, density-functional formalism) to *non-zero-temperature* properties.

2. QUANTUM-THEORETICAL TREATMENT OF NANOSYSTEMS

2.1. Approximations

For sufficiently small systems, that is, systems with a particle number not larger than a few hundred, the methods of theoretical quantum chemistry are useful. The main disadvantage of these approaches is that they are only applicable for systems at zero temperature, and this is a far-reaching restriction in connection with nanosystems, since temperature effects play a central role here, at least for metallic nanosystems. Furthermore, quantum chemistry is not able to say something about the dynamics of the atoms as, for example, the phonons.

The central problem of quantum chemistry is to find an approximation for the electronic Schrödinger equation. The nuclei are fixed at first; only the electrons are treated quantum mechanically (Born–Oppenheimer approximation). In a further step the displacements of the nuclei can be easily treated.

The direct solution of the electronic Schrödinger equation

$$\widehat{H}\Psi = E\Psi \tag{1}$$

is not possible, either in an analytical way nor within the frame of numerical methods. The approximate solution of

(1) can only be achieved on the basis of relatively drastic simplifications for the wave function Ψ. The loss of precision is only then acceptable when a certain inaccuracy is compensated by another; only in this way can we obtain useable results for the structure and the binding energies of the system under investigation [4].

2.1.1. Hartree–Fock Approximation

For systems with more than 300 electrons only the most simple ansatz for the wave function Ψ is applicable, and this is expressed by the Hartree–Fock approximation [5] which has the following form:

$$\Psi_{HF} = [\varphi_1(\mathbf{r}_1), \ldots, \varphi_n(\mathbf{r}_n)] \tag{2}$$

where n is the number of electrons. Each electron is modeled by a wave function $\varphi_i(\mathbf{r}_i)$ and includes a spin function. The brackets $[\cdots]$ in (2) denote antisymmetrization and consider the Pauli principle. The optimization of the wave functions $\varphi_i(\mathbf{r}_i)$, which is necessary because ansatz (2) is very simple, leads within the frame of the variational procedure to the Hartree–Fock equations

$$\widehat{F}\varphi_i = \varepsilon_i\varphi_i \tag{3}$$

In other words, the three-dimensional Hatree–Fock Eq. (3) replaces the $3n$-dimensional Schrödinger equation (1), and this is a drastic simplification. However, the Fock operator depends on the wave functions $\varphi_i(\mathbf{r}_i)$ which one actually wants to know and, therefore, for the solution of (3) an iteration procedure is needed.

Despite the enormous simplifications the Hartree–Fock equations are only applicable to simple cases, for example, atoms or small molecules. Therefore, it is necessary to approximate the wave functions $\varphi_i(\mathbf{r}_i)$ by a superposition of basis functions $b_\nu(\mathbf{r})$:

$$\varphi_i(\mathbf{r}) = \sum_\nu B_{\nu i}b_\nu(\mathbf{r}) \tag{4}$$

This approach is called linear combination of atomic orbitals (LCAO) since for the functions $b_\nu(\mathbf{r})$ atomic orbitals have been used in the early stage. Presently almost exclusively "contracted Gauss-type orbitals" (CGTOs) are used,

$$b_\nu = \left\{\sum_\gamma d_\gamma \exp(-\eta_\gamma r^2)\right\} x^k y^l z^m \tag{5}$$

which are centered at the nuclei of the system. By the use of these basis functions the Hartree–Fock method becomes an efficient procedure [4]. More details and specific techniques, respectively, are given in the solid state literature, in particular in [5].

2.1.2. Density-Functional Formalism

The theoretical foundations of this method have been developed by Hohenberg and Kohn in 1964 [6]. Within the conventional treatment of the n-electron system the external potential $v_{ex}(\mathbf{r})$, produced by the charge of the nuclei, determines uniquely—together with the n electrons—the Hamiltonian of the system and, therefore, the properties of the ground state, at least in principle. In the work by Hohenberg and Kohn it is outlined that in the case of a nondegenerated ground state instead of n and $v_{ex}(\mathbf{r})$ also the one-particle density $n(\mathbf{r})$ can be used for the unique characterization of the many-electron system.

The external potential $v_{ex}(\mathbf{r})$ of the n-electron system is uniquely determined by the one-electron density $n(\mathbf{r})$. Also the energy E_0 of the ground state is a unique functional of this density $n(\mathbf{r})$:

$$E_0 = E_0[n(\mathbf{r})] \tag{6}$$

Since the one-particle density $n(\mathbf{r})$ determines the number of electrons (with the normalization condition $n = \int n(\mathbf{r})d\mathbf{r}$), it contains the information about the wave function of the ground state. Here, the external field $v_{ex}(\mathbf{r})$ is not restricted to Coulomb potentials; $v_{ex}(\mathbf{r})$ has merely to be local and, therefore, it can also be applied to external electrical fields. Further, a variational principle exists for the one-particle density $n(\mathbf{r})$: The functional of the total energy $E[n(\mathbf{r})]$ becomes stationary if $n(\mathbf{r})$ is given by the density of the ground state. Let us consider the electron density $n'(\mathbf{r})$ with $n'(\mathbf{r}) \geq 0$ and $n = \int n'(\mathbf{r})d\mathbf{r}$. Then, the energy $E[n'(\mathbf{r})]$ is always larger than the exact energy of the ground state E_0: $E[n'(\mathbf{r})] \geq E_0$, and we have $E[n'(\mathbf{r})] = E_0$ in the case of the exact ground state density $n(r) = n'(r)$. If $E[n(\mathbf{r})]$ can be differentiated, the Euler–Lagrange equation

$$\frac{\delta E[n(\mathbf{r})]}{\delta n(\mathbf{r})} = \mu \tag{7}$$

can be deduced if the particle number n remains constant; μ is the chemical potential.

Although the details of the density-functional formalism are not given here, it should be mentioned that Kohn and Sham proposed a method for the treatment of the kinetic energy [7]: In the treatment of the many-particle problem the kinetic energy is not easy to determine since this energy part is large in comparison to the entire energy and, therefore, the kinetic energy has to be calculated very precisely. Kohn and Sham proposed a method for that which is presently the basis for most numerical calculations in connection with the density-functional formalism.

2.1.3. Discussion

The Hartree–Fock method begins conceptionally with the description of individual electrons interacting with the nuclei and all the other electrons of the system. In contrast to this picture within the density-functional formalism the total energy of the whole electron system is considered. There are three terms: the kinetic energy, the Coulomb energy due to the electrostatic interactions among all the charged particles, and the so-called exchange-correlation energy for which the actual expressions are unknown. Within the LDA

the exchange-correlation energy is taken from the many-electron interactions in an electron system of constant density, which are known, or more specifically: Within the LDA it is assumed that the exchange-correlation energy of an inhomogeneous system is given in an infinitesimal volume $d\mathbf{r}$ by that of a homogeneous system. The LDA turned out to be convenient in connection with numerical calculations and is surprisingly accurate. The LDA is exact for an ideal metal where the electron density is a constant and, therefore, this approximation is less precise for systems with a varying electron density. Within the density-functional formalism instead of the electron density we have the one-electron densities, which are expressed by one-electron wave functions which are similar to those used within the Hartree–Fock approximation, that is, the wave functions $\varphi_i(\mathbf{r}_i)$ (Section 2.1.1).

It is not clear *a priori* which of the two approaches, the Hartree–Fock method or the local density-functional formalism, gives a better description. For the applicability of both methods the effective interaction range of the electrons is of importance. The Hartree–Fock method works better if the interaction range is of the order of several interatomic distances. This is because the molecular orbitals, which are used in Hartree–Fock based methods for the description of correlation effects, are quite large (they are extended over several interatomic distances). On the other hand, if the range of many-body effects is short, that is, smaller than interatomic distances, then the local density-functional formalism should be applied; in such cases a description with mathematical objects like molecular orbitals is extremely slowly converging.

For large molecules there is a further method which has been applied successfully [4]. This approach extends the Hartree–Fock method and is known as the MP2 approach (MP2: Möller–Plesset, second order perturbation theory). This MP2 approach can only be applied if already a good Hartree–Fock result for the system under investigation could be obtained. On the basis of this Hartree–Fock result an improved description is possible if the approximations typical for the Hartree–Fock approach are corrected by means of perturbation theory (MP2). It turned out that results based on MP2 calculations are more accurate than those obtained by the density-functional formalism [4].

2.1.4. Applications

Hartree–Fock Method A lot of interesting applications exist in connection with the Hartree–Fock method. Here we would like to list some selected works that are typical for various topics in connection with this method.

Specific Nanosystems Articles include: theoretical study of the catalytic properties of Pt/Fe nanoclusters [8], ion channeling on nanofilms [9], structure and thermodynamics of carbon and carbon/silicon precursors to nanostructures [10], size-dependent oxidation of hydrogenated silicon clusters [11], tomonaga–luttinger parameters for quantum wires [12], interactions in chaotic nanoparticles [13], Hartree–Fock dynamics in highly excited quantum dots [14], and Coulomb interactions in carbon nanotubes [15]. Further information is given in [16–40].

Surface Investigations Articles include: Hartree–Fock studies of surface properties of $BaTiO_3$ [41], effect of basis set superposition error on the water-dimer surface [42], *ab initio* Hartree–Fock study on surface desorption process in tritium release [43], *ab initio* Hartree–Fock study of Bronsted acidity at the surface of oxides [44], and structure and bonding of bulk and surface theta-alumina from periodic Hartree–Fock calculations [45]. More information concerning surface investigations is given in [46–54].

Molecules Articles include: a comparison of finite difference and finite basis set Hartree–Fock calculations for the N_2 molecule [55], exact solution of the Hartree–Fock equation for the H_2 molecule in the linear-combination-of-atomic-orbitals approximation [56], from the nonplanarity of the amino group to the structural nonrigidity of the molecule [57], and coupled Hartree–Fock calculations of origin-independent magnetic properties of benzene molecule [58]. Further information is given in [59–67].

Metals Articles include: metal dissolution in aqueos electrolyte: semi-empirical Hartree–Fock and *ab initio* molecular dynamics calculations [68], density-functional computations of transition metal NMR chemical shifts: dramatic effects of Hartree–Fock exchange [69], electronic structure and orbital ordering in perovskite-type $3d$ transition metal oxides studied by Hartree–Fock band structure calculations [70], Hartree–Fock ground state of the composite fermion metal [71], and localized-orbital Hartree–Fock description of alkali-metal clusters [72]. More information about metals is given in [73–84].

Biological Systems Articles include: *ab initio* quantum mechanical study of hydrogen-bonded complexes of biological interest [85], combining implicit solvation models with hybrid quantum mechanical/molecular mechanical methods: a critical test with glycine [86], and an efficient coupled Hartree–Fock computational scheme for parity-violating energy differences in enantiomeric molecules [87]. Further information about biological systems is given in [88–95].

Islands Articles include: shape and stability of heteroepitaxial metallic islands: effects of the electronic configuration [96], spin depolarization in quantum dots [97], and magnetic-field dependence of the level spacing of a small electron droplet [98]. More information is given in [99–103].

Specific Application (Hartree–Fock)

Ab Initio Models for ZnS Clusters The Hartree–Fock molecular orbital method has been applied in the study of ZnS clusters [104–106]. The electronic structure of ZnS is localized; this can be shown, for example, by the density matrix approximation. The influence of vacancies and cluster edges on the charge distribution have distinct damping effects on it. The influence of the ZnS vacancy on the electronic structure of the $6 \times 6^*2$ cluster is shown in Figure 1, where the cluster is labeled according to the rings and layers [104–106]. According to Figure 1 the changes are local and there is a distinct damping near the vacant site on both the sulfur and the more metallic Zn ending surfaces.
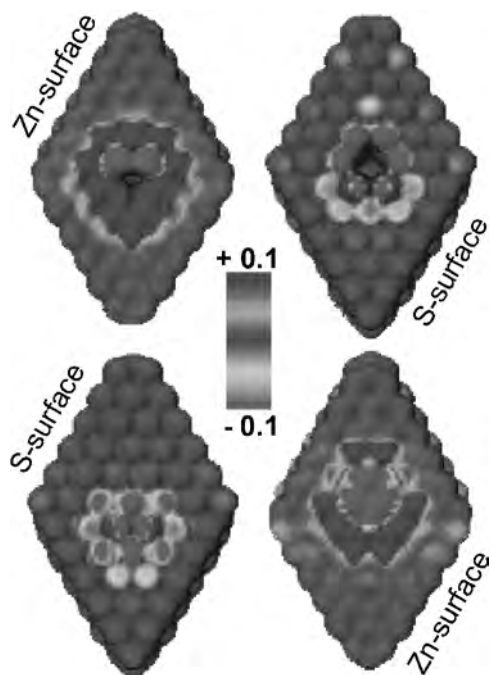
Figure 1. Charge density isosurface of the $6 \times 6^{*}2$ cluster, where the ZnS monomer is removed from the middle of the zinc (left) and sulfur (right) surfaces. The isosurface is colored according to the density difference between the clean and the defect clusters. Courtesy of J. Muilu, Biomedicum, Helsinki.

Density-Functional Formalism Also, many interesting studies in connection with the density-functional formalism have been published. We have selected some of them which we think are important. The density-functional formalism has been applied to the following problems.

Nanostructures Articles include: organic and inorganic nanostructures: an atomistic point of view [107], *ab initio* study of quantum confined unpassivated ultrathin Si films [108], surface effective-medium approach to the magnetic properties of 3d adatoms on metals [109], towards controlled production of specific carbon nanostructures—A theoretical study on structural transformations of graphitic and diamond particles [110], and semiclassical density functional theory: Strutinsky energy corrections in quantum dots [111]. More information about this topic is given in [112–123].

Nanoparticles, Nanoclusters, and Clusters, Including Cluster Methods Articles include: theoretical study of the catalytic activity of bimetallic RhCu surfaces and nanoparticles towards H_2 dissociation [124], adhesion of nanoparticles to vesicles: a Brownian dynamics simulation [125], influence of quantum confinement on the electronic and magnetic properties of (Ga,Mn)As diluted magnetic semiconductors [126], first mixed valence cerium-organic trinuclear cluster as a possible molecular switch: synthesis structure and density functional calculations [127], Structures of small gold clusters cations: Ion mobility measurements versus density functional calculations [128], a theoretical study of Si_4H_2 cluster with *ab initio* and density functional theory methods [129], new insights into the structure of supported bimetallic nanocluster catalysts prepared from carbonylated precursors: a

combined density functional theory and EXAFS study [130], and Structures and spectra of gold nanoclusters and quantum dot molecules [131]. Further information is given in [132–181].

Molecules Articles include: infrared spectra and density functional calculations of the $SiCO_4$ molecule in solid argon [182], a density functional model for tuning the charge transfer between a transition metal electrode and a chemisorbed molecule via electrode potential [183], a density functional study of possible intermediates of the reaction of dioxygen molecule with non-heme iron complexes [184], and van der Waals interaction of the hydrogen molecule: an exact implicit energy density functional [185]. More information about molecules is given in [186–197].

Biological Systems Articles include: density functional theory-based molecular dynamics of biological systems [198], a self-consistent charge density functional based tight binding scheme for large biomolecules [199], density functional theory and biomolecules: a study of glycine, alanine, and their oligopeptides [200], compared performances of the molecular orbital and density functional theories for fragments of biomolecules [201], DFT calculations on the energy thresholds of DNA damages under irradiation conditions [202], and electronic structure of wet DNA [203]. Further information about biological systems can be found in [204–229].

Droplets and Islands Articles include: heterogeneous nucleation on mesoscopic wettable particles: a hybrid density functional theory [230], electronic properties of model quantum-dot structures in zero and finite magnetic fields [231], structure and stability of superfluid He_4 systems with cylindrical symmetry [232], effect of oxide vacancies on metal island nucleation [233], arsenic flux dependence of island nucleation on InAs(001) [234], and first-principles studies of kinetics in epitaxial growth of III–V semiconductors [235]. Further information is given in [236–253].

Metals Articles include: investigation of the metal binding site in methionine aminopeptidase by density functional theory [254], generalized spin orbital density functional study of multicenter metal systems [255], density functional theory study on the geometric, electronic and vibrational structures of alkali metal porphyrin complexes [256], and infrared spectra and density functional theory calculations of group 4 transition metal sulfides [257]. More information about metals is given in [258–270].

Nanotubes Articles include: first principles calculations for electronic band structure of single-walled nanotube under uniaxial strain [271], theoretical study of structure-dependent Coulomb blockade in carbon nanotubes [272], theoretical tools for transport in molecular nanostructures [273], electronic structures of capped carbon nanotubes under electric fields [274], and Fullerene based devices for molecular electronics [275]. More information concerning nanotubes is given in [276–290].

Nanowires Articles include: Fe nanowires on vicinal Cu surfaces: *Ab initio* study [291], Pentagonal nanowires: A first principles study of the atomic and electronic structure [292], Simulation of quantum transport in nanoscale systems: Application to atomic gold and silver wires [293], Quantum transport through one-dimensional aluminum wires [294]. Further information about wires and nanowires, respectively, is given in [295–304].

Specific Application (Density-Functional Theory)

1. Electronic conductance through monatomic Na wires coupled to electrodes has been studied using the LDA and the Friedel sum rule. Conductance (G) is found to exhibit even–odd behavior. When the number L of atoms in wires is odd, G has the quantized value of

$$G_0 = \frac{e^2}{\hbar \pi}$$

which is stable with respect to variations of the wire geometry. On the other hand, G is smaller than G_0 for even L and is dependent on the wire geometry in this case. This behavior results from the charge neutrality and resonant character due to the sharp tip structure of the electrodes and may appear in other monovalent atomic wire such as gold. More details concerning this study are given in [305, 306] and in Figure 2.

2. On the basis of density-functional calculations of model systems for the active site, Rod et al. have suggested a mechanism for the ammonia synthesis catalyzed by the enzyme nitrogenase [307, 308] (see also Fig. 3). The mechanism can explain many experimental observations including the obligatory H_2 release. The authors have also suggested a mechanism behind the observed CO frequency shift upon CO adsorption on the FeMo co-factor [308]. In [309] the enzyme catalyzed reaction with the reaction catalyzed by a Ru surface is compared and it is explained why the two reactions need different conditions (low temperature and pressure as opposed to high pressure
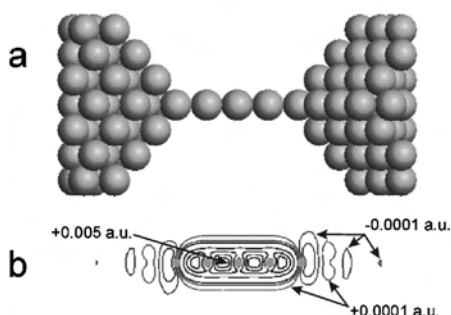

Figure 3. Left panel: The MoFe protein, component of the enzyme nitrogenase, which catalyzes the ammonia synthesis from atmospheric nitrogen. The active sites, where the synthesis is going on, are depicted by atom specific coloring, while the remaining atoms are colored green. Atoms have been removed from the structure in order to make the active sites visible. Right panel: The FeMo cofactor $MoFe_7S_9$ (homocitrate) is the active site, where N_2 bins and react with protons and electrons. Courtesy of T. H. Rod, The Scripps Research Institute, Department of Molecular Biology, La Jolla.

and temperature). On the basis of that, the authors give suggestions to how the ammonia synthesis can be (electro)catalyzed at low temperature and pressure on a surface; they also discuss the properties that such a surface should have. Reference [310] is basically a summary of the above plus work by Per Siegbahn, but with emphasis on what we can learn from the cross interaction between surface science and biological science.

The methods, which the authors have applied, are pretty much standard surface science density-functional theory methods, namely density functional calculations using a plane wave basis with cutoff energy of 25 Rydberg. They have used Vanderbilt ultrasoft pseudopotentials [311] and soft pseudopotentials [312] (for sulfur) to describe the core part of the atoms. The generalized gradient approximation in the form of Perdew–Wang [313] and revised Perdew–Burke–Enzerhoff [314] has been used to describe the exchange-correlation term. The FeMo co-factor is antiferromagnetic, so spin dependent exchange-correlation functionals have been used.

Remarks Concerning Metallic Systems

The quantum theoretical treatment of metal systems, for example, clusters, is a particular challenge. The reason is that the electronic structure of such systems is rather complex which is directly connected with the features of metals. Metal clusters obviously cannot be treated within the Hartree–Fock method [4]; accurate calculations are only available for very small clusters (up to Al_6). However, the density-functional formalism works well and reliable for larger clusters (for example, Al_{146}). More details are given in [315].

Figure 2. (a) The atomic structure for a $L = 5$ Na wire connected to electrodes with the inversion symmetry. (b) Contour plot of the difference of the total charge densities between the systems with and without the $L = 5$ wire (marked by green dots); black contours for 0.001 to 0.005 a.u. with the increment of 0.001 a.u., whereas blue and red ones for −0.0003 to 0.0003 a.u. with the increment of 0.0002 a.u. Courtesy of Heung-Sun Sim, School of Physics, Korea Institute for Advanced Study, Seoul.
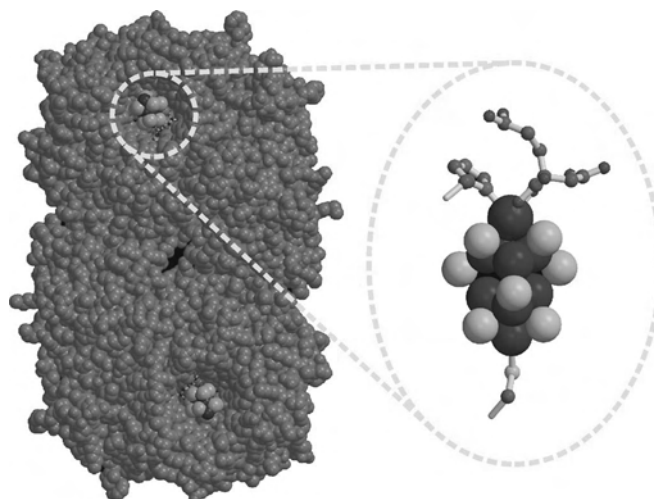
2.1.5. Density-Functional Formalism at Nonzero Temperature

The Hartree–Fock method and the density-functional formalism are only able to describe systems at zero temperature. However, the structure and also the dynamics of metallic nanosystems (for example, Al clusters) are sensitive to small variations in temperature: Relatively small changes in temperature can lead to drastic effects in connection with the atomic structure and dynamics, and the properties at zero temperature can become meaningless. Therefore, the following question arises: Can the methods of theoretical quantum chemistry be extended to nonzero temperatures? In principle, this is possible within the framework of density-functional formalism. Since this point is important for future developments, let us discuss the situation in somewhat more detail, in particular, with respect to the changes in the formalism when we go from zero to nonzero temperatures.

Within the density-functional formalism the density $n(\mathbf{r})$ is of relevance and its determination is in any case a quantum mechanical problem for all temperatures. Let us consider a system of N electrons of mass m and charge $-e$ which are distributed around positive charges of magnitude $Z_1 e, Z_2 e, \ldots$ at positions $R_1, R_2, \ldots$. The Hamiltonian $\widehat{H}$ is given in the second-quantized representation by

$$\widehat{H} = \widehat{T} + \widehat{U} + \widehat{W} \tag{8}$$

where

$$\widehat{T} = \frac{\hbar^2}{2m} \int \nabla \psi^+(\mathbf{r}) \nabla \psi(\mathbf{r}) \, d\mathbf{r} \tag{9}$$

is the kinetic energy operator. $\psi(\mathbf{r})$ and $\psi^+(\mathbf{r})$ are annihilation and creation operators. The operator $\widehat{U}$ describes the mutual repulsion, both among the electrons and the ions:

$$\widehat{U} = \frac{1}{2} \iint d\mathbf{r} \, d\mathbf{r}' \frac{e^2}{|\mathbf{r} - \mathbf{r}'|} \psi^+(\mathbf{r}) \psi^+(\mathbf{r}') \psi(\mathbf{r}') \psi(\mathbf{r})$$
$$+ \frac{1}{2} \sum_{\substack{i,j \\ i \neq j}} \frac{Z_i Z_j e^2}{|\mathbf{R}_i - \mathbf{R}_j|} \tag{10}$$

$\widehat{W}$ in (8) is given by

$$\widehat{W} = \int dr \, v(\mathbf{r}) \psi^+(\mathbf{r}) \psi(\mathbf{r}) \tag{11}$$

where $v(\mathbf{r})$ is an external potential arising from the nuclei. The electron density $n(\mathbf{r})$ is given in the ground state $|\phi\rangle$ by the expectation value

$$n(\mathbf{r}) = \langle \phi | \psi^+(\mathbf{r}) \psi(\mathbf{r}) | \phi \rangle \tag{12}$$

For *zero temperatures* Kohn and co-workers [6, 7] showed that for a nondegenerate $|\phi\rangle$, $v(\mathbf{r})$ is (to within a constant) a unique functional of $n(\mathbf{r})$ and the correct $n(\mathbf{r})$ minimizes the ground state energy

$$E_0 = \langle \phi | \widehat{H} | \phi \rangle \tag{13}$$

which is a unique functional of $n(\mathbf{r})$:

$$E_0 = E_0[n(\mathbf{r})] \tag{14}$$

With (12) we have

$$E_0[n(\mathbf{r})] = \int v(\mathbf{r}) n(\mathbf{r}) \, dr + F[n(\mathbf{r})] \tag{15}$$

where

$$F[n(\mathbf{r})] = \langle \phi | \widehat{T} + \widehat{U} | \phi \rangle \tag{16}$$

Equation (15) defines a variational principle for the ground state energy of an electron gas in an external potential $v(\mathbf{r})$, in which $n(\mathbf{r})$ is the variable function. However, from this density-functional formalism we can only extract *zero-temperature properties* for an electron gas, which fundamentally determines the system properties; all calculations reported in literature have been done on the basis of this zero-temperature approach.

It is, however, possible to extend this formalism to nonzero temperatures, and this has been done by Mermin [316]. In the case of nonzero temperatures the equilibrium electron density in a grand canonical ensemble is given by

$$n(\mathbf{r}) = \text{Tr}\{\rho_0 \psi^+(\mathbf{r}) \psi(\mathbf{r})\} \tag{17}$$

where ρ_0 is the grand canonical density matrix

$$\rho_0 = \frac{\exp\left[-\frac{\widehat{H} - \mu \widehat{N}}{k_B T}\right]}{\text{Tr}\left\{\exp\left[-\frac{\widehat{H} - \mu \widehat{N}}{k_B T}\right]\right\}} \tag{18}$$

μ is the chemical potential, and $\widehat{N}$ is the particle number operator. Mermin showed [316] that in a grand canonical ensemble for a given temperature T, chemical potential μ, and external potential $v(\mathbf{r})$ the quantity

$$\Omega[n(\mathbf{r})] = \int d\mathbf{r} \, v(\mathbf{r}) n(\mathbf{r}) + G[n(\mathbf{r})] - \mu \int d\mathbf{r} \, n(\mathbf{r}) \tag{19}$$

with

$$G[n(r)] = \text{Tr}\{\rho_0 (T + U + k_B T \ln \rho_0)\} \tag{20}$$

is equal to the grand potential

$$\Omega = k_B T \ln \text{Tr}\left\{\exp\left(-\frac{\widehat{H} - \mu \widehat{N}}{k_B T}\right)\right\} \tag{21}$$

when $n(\mathbf{r})$, expressed by (17), is the correct equilibrium density. In particular, Merwin showed that the correct density minimizes (19) over all density functions that can be associated with an external potential $v(\mathbf{r})$.

Since the properties of systems with surface (for example nanosystems) are very sensitive to variations in temperature, zero-temperature approaches, such as the Kohn–Hohenberg–Sham formalism, are not appropriate for the treatment of such systems (in particular metallic nanosystems). It is, in our opinion, in many cases an insufficient approximation to use zero-temperature methods for

the determination of the electronic properties, which determine chiefly the entire properties of the system. Such an analysis is only correct for zero temperatures but has often been used for the determination of the structure and dynamics for nonzero temperatures, in particular in connection with molecular dynamics calculations (see Sections 5.3.4 and 5.3.5, embedded-atom method and quantum molecular dynamics introduced by Car and Parrinello). Such calculations can be misleading since nonzero temperature data are coupled with zero-temperature properties. Therefore, instead of the Kohn–Hohenberg–Sham approach Mermin's formalism, briefly discussed above, should be used in such calculations. But to the authors knowledge there exists no analysis on the basis on Mermin's non-zero-temperature formalism.

3. BASIC PROPERTIES AT THE NANOLEVEL

Specific material properties of nanosystems can be essentially different from the corresponding properties of macroscopic systems (the solid in the bulk). This has been demonstrate in [317] in connection with the thermal stability and the melting temperature of specific nanostructures.

An essential reason for this tendency is the fact that a great fraction of the particles (atoms, molecules) of such small systems belong to the surface region and the surface particles are less bonded than the particles in the bulk, leading to relatively strong anharmonicities even at low temperatures, that is, far below the melting temperature. Even the melting process takes place far below the bulk melting temperature or is simply not defined as has been demonstrated in connection with the nanosystem discussed in [317]. The thermal behavior of such systems is a complex function of the particle number and the outer shape of the systems. This must have consequences for the theoretical description of the material properties for systems of nanometer size. Let us discuss this point in more detail.

3.1. Relevance of the Theoretical Bulk Methods for the Description of Nanosystems

In modern materials research, solid-state physics becomes more and more relevant, in particular, the microscopic structure and dynamics. For sufficiently large systems, the *standard model* of solid-state physics is in most cases adequate for the description of material properties. The standard model of solid-state physics is based on the *ordered structure* and on the assumption that the vibrational amplitudes of the atoms are sufficiently small, so that it can work within the *harmonic approximation*. In other words, the dynamics is expressed by phonons. For example, the specific heat at constant volume is expressed in terms of phonons by the expression [318, 319]

$$c_V = k_B \sum_{p,q} \frac{\alpha^2 \exp(\alpha^2)}{(\exp(\alpha) - 1)^2} \qquad (22)$$

with

$$\alpha = \frac{\hbar \omega_p(\mathbf{q})}{k_B T} \qquad (23)$$

where $\omega_p(\mathbf{q})$ are the phonon frequencies, $\mathbf{q}$ is the wave vector, and p labels the phonon branches.

Electronic properties are of course also essential. For example, for the understanding of superconductivity, the electron–phonon interaction is important.

In conclusion, within conventional materials research, the basis for the microscopic description of the material properties is the ordered structure and the harmonic approximation; the properties of a solid are given in terms of phonons $\omega_p(\mathbf{q})$, where the phonon frequencies $\omega_p(\mathbf{q})$ are dependent on the crystal structure and the electronic properties.

That is the situation in connection with macroscopic systems. But this can no longer be the basis for the description of the properties of nanosystems.

As was outlined in [317], nanosystems do not behave in such a simple way: They are in most cases disordered and the dynamics cannot be approximated by phonons because the harmonic approximation is not applicable. Therefore, at the nanolevel materials research gets a new dimension. Even the melting temperature is no longer a fixed material property, as is demonstrated in connection with the nanostructure discussed in [320].

Nanosystems are already disordered at relatively low temperatures and the harmonic approximation breaks down completely; that is, even at relatively low temperatures, phonons are no longer definable. In such cases the anharmonicities cannot be considered as small perturbations to the harmonic case.

In other words, the standard model of solid-state physics breaks down at the nanolevel in many cases, and we have to introduce other methods and quantities for the description of material properties. This is the case for any anharmonic and disordered system (for example, liquids in the bulk) and, for simplicity, we want to explain the principal points by means of a bulk liquid.

In the case of liquids, usual crystallography and phonons are not relevant but the structure must be described by statistical mechanics, that is, in terms of correlation functions, for example, the pair correlation function $g(r)$, which can be measured; r is the relative distance between the atoms and molecules, respectively. In the case of metals, the interaction is given by the pair potential $v(r)$, where r is again the relative distance between two particles.

In conclusion, instead of the phonons $\omega_p(\mathbf{q})$, correlation functions like $g(r)$ and the interaction potential $v(r)$ become the relevant quantities:

$$\omega_p(\mathbf{q}) \rightarrow g(r), v(r)$$

For example, the isothermal compressibility χ_T is defined by the expression [320]

$$\frac{1}{\chi_T} = -\frac{1}{V} \left(\frac{\partial p}{\partial V} \right)_T \qquad (24)$$

and we need an expression for the pressure p (V is the volume); that is, we need the "equation of state," which can be formulated in terms of $g(r)$ and $v(r)$ as follows:

$$p = \rho k_B T - \frac{\rho^2}{6} \int r \frac{\partial v(r)}{\partial r} g(r) \, d\mathbf{r} \qquad (25)$$

If we apply Eq. (25) to Eq. (24), the isothermal compressibility χ_T can be expressed in terms of $g(r)$ and $v(r)$:

$$g(r), v(r) \rightarrow \chi_T$$

In the case of nanosystems, the anharmonicities are very strong and the thermal expansion becomes a relevant quantity. Moreover, a great fraction of the atoms belong to the surface region and it turns out that the thermal expansion at the surface is distinctly larger than in the bulk. Therefore, the theoretical picture must be able to describe the thermal expansion.

The thermal expansion coefficient α_p can be expressed by the isothermal compressibility χ_T and the thermal pressure coefficient γ_V:

$$\alpha_p = \chi_T \gamma_V \qquad (26)$$

In order to get the thermal expansion coefficient α_p, we have to calculate both the quantities χ_T and γ_V. We already did that for χ_T, and for the description of

$$\gamma_V = \left(\frac{\partial p}{\partial T} \right)_V \qquad (27)$$

we need again the pressure p, that is, the equation of state, which is given for the bulk by Eq. (25).

In other words, the thermal expansion coefficient α_p can also be expressed in terms of $g(r)$ and $v(r)$,

$$g(r), v(r) \rightarrow \alpha_p$$

and this is the case for all material properties (in some cases, higher order correlation functions are needed).

It should be mentioned that the thermal expansion is zero for the harmonic case; that is, within the phonon picture the thermal expansion cannot be described.

In conclusion, in the case of disordered systems with strong anharmonicities (e.g., liquids in the bulk and nanosystems), phonons are not suitable for the adequate description of such systems but must be expressed in terms of $g(r)$ and $v(r)$.

In the case of nanosystems, a great fraction of particles belong to surface regions, and the quantities of $g(r)$ and $v(r)$ are not simply dependent on the relative distance r of the particles but are also dependent on the distance of the particles from the surface. Because there is in general more than one surface in the vicinity of a particle the situation can be very complex.

Even for systems with only one surface—for example, a semi-infinite liquid—the situation is already rather complex. In this case, the surface (defining the x, y plane) separates the liquid from the vapor phase, and the density ρ varies with respect to the coordinate z (the coordinate perpendicular to the surface), so that we have $\rho = \rho(z)$.

In the liquid–vapor transition zone, the pressure p cannot be described by Eq. (25); that is, p is no longer a constant and independent of the coordinates but becomes an anisotropic quantity [321]: At any point z in the transition zone, we have a normal pressure component p_1 and a tangential component p_2. While p_1 and p_2 are different from each other in the liquid–vapor transition zone both quantities are of course identical in the isotropic bulk phases. With $\mathbf{r}_{12} = (x_{12}, y_{12}, z_{12})$, the statistical mechanical expressions for p_1 and p_2 take the form [321, 322]

$$p_1 = \rho(z)k_B T - \frac{1}{2} \int \rho(z)^2 \rho^{(2)}(\mathbf{r}, z) \nabla v(r) \frac{z_{12}^2}{r} \, d\mathbf{r} \quad (28)$$

$$p_2 = \rho(z)k_B T - \frac{1}{2} \int \rho(z)^2 \rho^{(2)}(\mathbf{r}, z) \nabla v(r) \frac{x_{12}^2}{r} \, d\mathbf{r} \quad (29)$$

where we assumed for simplicity that the pair potential at the surface is the same as in the bulk. In Eqs. (28) and (29) the distribution function $\rho^{(2)}(\mathbf{r}, z)$ is used instead of the correlation function $g(\mathbf{r}, z)$.

The pressure components p_1 and p_2 can be used for the determination of the surface tension γ which is expressed by

$$\gamma = \gamma(T) = \int_{-\infty}^{\infty} [p_1 - p_2(z)] \, dz \qquad (30)$$

With Eqs. (28) and (29), the statistical mechanical expression for the surface tension is expressed by

$$\gamma(T) = \frac{1}{2} \int_{-\infty}^{\infty} \rho^{(2)}(\mathbf{r}, z) \nabla v(r) \frac{x_{12}^2 - z_{12}^2}{r} \, d\mathbf{r} \, dz \qquad (31)$$

As outlined in [321], the surface tension and its temperature dependence are of particular interest in the description of thermodynamic properties.

In the case of nanosystems, the situation concerning the statistical mechanical description is more complex than for semi-infinite systems. This is because various surfaces, which are most often close together, have to be considered. Therefore, the statistical mechanical expressions [in analogy to Eqs. (28), (29) and (31)] will hardly be relevant in connection with theoretical investigations. A certain potential for applications should be given in the case of disordered nanofilms that are positioned on surfaces.

The more direct way is to perform *molecular dynamics* calculations (details of this computational method are given in the next section). In such calculations the interaction potential, in particular the pair potential $v(r)$, is of fundamental relevance and, therefore, in Section 5 we will give a brief overview of this topic.

3.2. Wear at the Nanolevel

Within the frame of Hamiltonian systems, such as molecular dynamics systems, *friction* in the macroscopic sense is not defined. At the microscopic, molecular dynamics level, the forces are formulated as quantities which are dependent on the structural configuration (particle positions) but not on the particle velocities. Therefore, a force which is proportional to the velocity cannot be introduced at the microscopic level and, therefore, a friction constant in the macroscopic sense is not definable at the microscopic

level of modern materials research. In the case of non-Hamiltonian systems friction can be studied by nonequilibrium molecular dynamics; this topic is briefly discussed in Section 4.2.4.

At the nanolevel, wear is described by specific complex processes. Let us discuss this point by means of an example: Figure 4 shows a molecular dynamics model for a wheel which is pressed on a surface. The wheel rotates with 10^{12} revolutions in a second. The wheel has a temperature of 300 K and it has a diameter of approximately 10 nm. If the wheel is pressed on a surface, wear effects emerge and, according to the magnitude of the force vertically applied, the wheel can even be destroyed, as can be observed in Figure 4.

In summary, friction (wear) at the microscopic level is a complex process and cannot be characterized by only one constant as is the case of macroscopic friction. In our example (Fig. 4), wear is dependent on the specific structure of the surface and also on the shape of the wheel.

3.3. Conclusions

Theoretical materials research at the nanolevel not only needs solid-state physics but due to the strong anharmonicities and the strongly disturbed structure of many nanosystems (even far below the melting temperature of the corresponding bulk state) the basics of statistical mechanics and the theory of liquids are very often more appropriate as the basis for the theoretical description of such systems. In such cases the standard model of solid-state physics [ordered structure and harmonic approximation, here summarized by the symbol $\omega_p(\mathbf{q})$] is not suitable, and we come to the description in terms of correlation functions and interaction potentials that we have briefly characterized by $g(r)$ and $v(r)$. Within this statistical mechanical description time correlations are of course included, for example, the velocity autocorrelation function whose Fourier transform has to be considered as the generalized phonon density of states.
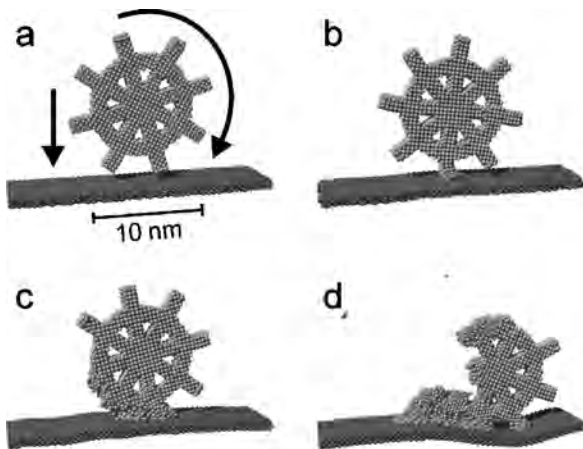

Figure 4. A molecular dynamics model for a wheel consisting of aluminum atoms; it rotates with 10^{12} rev/s and its diameter is approximately 10 nm. The molecular dynamics method is discussed in more detail in Section 4.

However, due to the strong anharmonicities, the dynamics of such systems is characterized by a broad range of different dynamical states including small local vibrations and complex diffusion processes. This situation indicates that the development of a suitable *standard model* for the theoretical description of nanosystems will hardly be possible; even in the case of liquids in the bulk a standard model could not be found up to now.

Therefore, the most important tool for the investigation of nanosystems is the molecular dynamics method since anharmonicities are treated within this method without approximation, and this is important because the typical anharmonicities in connection with nanosystems cannot be considered as small perturbations to the harmonic approximation. No other microscopic method in condensed matter physics allows one to treat anharmonicities without approximation; this is only possible in connection with phenomenological models. Thus, the molecular dynamics methods should be considered as the *standard method* for the theoretical description of nanosystems. On the basis of these considerations we come to the following rough classification scheme:

$$
\begin{array}{c}
\omega_p(\mathbf{q}) \\
\text{(standard model for the solid)} \\
\downarrow \\
g(r),\, v(r) \\
\text{(statistical mechanics)} \\
\downarrow \\
\text{molecular dynamics} \\
\text{(standard method for nanosystems)}
\end{array}
\tag{32}
$$

In other words, with decreasing particle number disorder effects and anharmonicities increase and this has an influence on the theoretical treatment. In Section 4.2.3 more details concerning the molecular dynamics method will be given.

4. MODELING OF NANOSYSTEMS

4.1. The Hamiltonian

4.1.1. General Formulation

The quantum mechanical modeling of a system with N particles of masses m leads to the Hamiltonian

$$
\widehat{H} = \sum_{i=1}^{N}\left(-\frac{\hbar^2}{2m_i}\nabla_i^2 + V_i(\mathbf{r}_i)\right) + \sum_{\substack{i,\,k=1 \\ i\neq k}}^{N} V_{ik}(\mathbf{r}_i,\mathbf{r}_k)
\tag{33}
$$

Here $V_i(\mathbf{r}_i)$ is an externally applied potential in which the ith particle is located, where $\mathbf{r}_i = (x_i, y_i, z_i)$ is the position of the ith particle; $V_{ik}(\mathbf{r}_i,\mathbf{r}_k)$ denotes the interaction potential between the two particles i and k. To analyze or to describe the characteristics of the system one has to solve the according many-particle Schrödinger equation

$$
\widehat{H}\psi = E\psi
\tag{34}
$$

where E is the total energy of the N-particle system. The wave function ψ depends on the $3N$ coordinates (configuration space) of all particles:

$$\psi = \psi(x_1, y_1, z_1, \ldots, x_N, y_N, z_N) \qquad (35)$$

If we consider nanosystems, most often external potentials are not present and the particles involved are atoms which in turn have to be divided into nuclei and electrons. In this case the interaction potential in Eq. (33) is given by the Coulomb potential

$$V_{ik}(\mathbf{r}_i, \mathbf{r}_k) = \frac{Z_i Z_k e^2}{|\mathbf{r}_i - \mathbf{r}_k|} \qquad (36)$$

where Z is the according particle charge number including the sign of the charge.

With a closer look at this many-particle problem it becomes clear that an exact quantum mechanical solution can probably never be achieved. Here is an example: A relatively small nanocluster of only 100 argon atoms consists of 100 nuclei and 1800 electrons, which is a total of 1900 particles. In this case the configuration space consists of 5700 dimensions. The key point with numerical solutions of the Schrödinger equation is the spatial integration. With the assumption that a division of each dimension into 100 steps is sufficient for an accurate calculation we would have to compute the summation of 10^{11400} volume elements. Needless to say, this is not possible without further, most intensive simplifications and approximations.

4.1.2. Approximations

The treatment of many-particle systems in condensed matter physics is usually based on the fact that core electrons do not influence the properties of such many-particle systems and, therefore, the system can be divided into ions and valence electrons. A further approximation is to treat the ions and electrons separately (Born–Oppenheimer approximation) which leads to two Schrödinger equations—one for the electrons, where the ion positions appear as parameters only, and another for the nuclei, where the electron energy E_{el} acts as an effective potential—so that the Hamiltonian for the ions takes the form

$$\widehat{H} = \sum_{i=1}^{N_I} \left(-\frac{\hbar^2}{2m_i} \nabla_i^2 + V_i(\mathbf{r}_i) \right) + V(\mathbf{r}_1, \ldots, \mathbf{r}_{N_I}) \qquad (37)$$

with

$$V(\mathbf{r}_1, \ldots, \mathbf{r}_{N_I}) = V_I(\mathbf{r}_1, \ldots, \mathbf{r}_{N_I}) + E_{\text{el}}(\mathbf{r}_1, \ldots, \mathbf{r}_{N_I}) \qquad (38)$$

where N_I is the number of ions. Equation (38) means that the dynamics of the ions take place within an effective potential V which is formed by the potential energy of the direct ion–ion interaction V_I and the entire electronic energy E_{el}, where E_{el} depends on the coordinates of the ions and therefore plays the role of an indirect ion–ion interaction. But it must be emphasized that an unique splitting into ions and valence electrons is not always possible.

Under the assumption that the change of the electronic arrangement (core electrons) around each ion or atom is sufficiently small the potential energy V may be expanded:

$$V(\mathbf{r}_1, \ldots, \mathbf{r}_{N_I}) = \frac{1}{2} \sum_{\substack{i,j=1 \\ i \neq j}}^{N_I} v_{ij} + \frac{1}{6} \sum_{\substack{i,j,k=1 \\ i \neq j \neq k}}^{N_I} v_{ijk} + \cdots \qquad (39)$$

Here the terms on the right of Eq. (39) represent pair, triplet, and many-body contributions of the ionic or atomic interactions and $\mathbf{r}_1, \ldots, \mathbf{r}_N$ are the positions of the N ions or atoms.

If the polarization of the core electrons is negligibly small, then—compared with the pair terms—the triplet and higher terms diminish rapidly in significance. Then the obvious final step of approximation is to neglect them entirely. This is called the pair potential approximation,

$$V(\mathbf{r}_1, \ldots, \mathbf{r}_{N_I}) = \frac{1}{2} \sum_{\substack{i,j=1 \\ i \neq j}}^{N_I} v_{ij} = \frac{1}{2} \sum_{\substack{i,j=1 \\ i \neq j}}^{N_I} v(|\mathbf{r}_i - \mathbf{r}_j|) \qquad (40)$$

with $|\mathbf{r}_i - \mathbf{r}_j| = r_{ij}$.

Referring to our example with the 100 argon atoms, with Eq. (40) the problem has been reduced to a 9900-fold sum of values from one pair potential function v with only one dimension, which is the distance of two particles. This simplification expands the calculability of the many-particle problem with today's computer power up to millions of particles—at least under certain conditions. On the other hand, such a far-reaching, if not to say brute simplification, has a strong influence on the applicability as can be easily imagined [323].

In almost all cases the ions or atoms behave classically and, furthermore, only the pair interaction is effective. Then, instead of the Hamiltonian (39) we get the classical Hamilton function in the pair potential approximation. For monatomic systems it reads

$$H = \sum_{i=1}^{N_I} \frac{p_i^2}{2m} + \frac{1}{2} \sum_{\substack{i,j=1 \\ i \neq j}}^{N_I} v(r_{ij}) \qquad (41)$$

If three or higher body forces are effective, instead of the pair potential approximation for the potential energy the expansion (39) has to be used. Pair potentials and many-body forces will be discussed in more detail below.

4.2. Description of Nanosystems

4.2.1. Simple Models

How can we determine the properties of a many-particle system on the basis of a given Hamiltonian? In the conventional treatment of this problem we need simple models. Quite generally, simple models can be obtained by controlled approximation from the general cases (37) and (41). In connection with many-particle systems the general mathematical formulation of the problem is in most cases so complex that simplifying models have to be chosen but often cannot be obtained by controlled simplifying steps from the

general cases (37) and (41), respectively. It is therefore a rule to introduce simple models just for convenience.

The "simple model" of solid state physics is the crystalline solid in the harmonic approximation (Section 3.1). On the basis of this model one is able to determine successfully the properties of a lot of materials. However, there are also a lot of cases where this simple model is not applicable, even when it is extended by specific assumptions. For example, the silver subsystem of the solid electrolyte α-AgI is highly disordered and shows strongly anharmonic behavior [324–326]; a simple model for α-AgI and similar materials is not available. Also in the case of liquids and gases "simple models" have not been found. Even in the case of gases with low densities we cannot simply restrict ourselves to the first terms in the virial expansion in the calculation of the pressure. This is because the expansion obviously converges slowly and, therefore, even in the case of low density one has to consider more than the first two terms [327]. The virial coefficients can be expressed in terms of the pair potential $v(r)$ [see Eq. (40)], but the expressions are getting complicated for the higher order virial coefficients and in practical calculations only the first terms are accessible. The virial expansion would define a "simple model" if for a broad class of gases a restriction on the first two terms would be realistic.

In summary, only for a specific class of many-particle systems could a "simple model" be found: It is the crystalline solid in the harmonic approximation, but in most cases anharmonicities cannot be considered as small perturbations to the harmonic approximation (see also the discussion in Section 3.1). This is also the case for typical nanosystems since a great fraction of atoms are more or less close to the surface region of the system, and surface particles behave strongly anharmonically. In small nanosystems (for example, clusters with a few hundred of atoms) even the innermost particles cannot be treated as bulk particles since the cutoff radius for the interaction potential is larger than the distance to the surface. The atoms at surfaces are less bonded than in the bulk and, therefore, the mean-square amplitudes of the atoms are significantly larger than at the surface leading to relatively strong anharmonicities. This phenomenon can be observed even at low temperatures—low in comparison to the melting temperature of the bulk system.

4.2.2. Dynamical-Matrix Solutions

Surfaces not only give rise to *quantitative* effects but can also be the source for new qualitative phenomena. For example, the phonons, which describe the dynamics of the system, are expressed by the dynamical-matrix solutions, and these solutions are obviously not complete for systems with surfaces.

In order to show that in more detail let us consider a monatomic crystal with a free surface and let M be the mass of the atoms of the crystal. In this semi-infinite system there is only a two-dimensional invariance of the force constants which implies that the normal-mode solutions of the equation of motion

$$\ddot{u}_\alpha(\mathbf{l}) = -\sum_{l',\beta} \frac{1}{M} \Phi_{\alpha\beta}(\mathbf{l},\mathbf{l}')u_\beta(\mathbf{l}') \qquad \alpha,\beta = x,y,z \qquad (42)$$

is a superposition of two-dimensional Bloch functions

$$u_\alpha(l_{12},m) = \sum_{n_1,n_2,j} u_{\alpha,j}(m,\mathbf{q})\exp\{i[\mathbf{q}\cdot\mathbf{r}_0^{l_{12}} - \omega_j(\mathbf{q})t]\} \qquad (43)$$

where $\mathbf{l} = (l_1,l_2,m)$. Here u_α is the displacement from the equilibrium positions in the α-direction, $l_{12} = (l_1,l_2)$ specifies the points in the layers parallel to the surface, and m labels the planes of the crystal which are parallel to the surface starting with $m = 1$ for the outermost layer. The frequencies $\omega_j(\mathbf{q})$ are given by the solutions of the dynamical matrix, where j is the branch index. Further, n_1, n_2, denotes summation over the wave vectors $\mathbf{q} = (n_1,n_2)$; the allowed values of n_1 and n_2 are determined by the periodic boundary conditions: $n_i = 0,\pm1,\ldots,\pm N_i/2$, $(i = 1,2)$ where N_1 is the particle number in the x-direction and N_2 in the y-direction of layer m.

Now we consider the center-of mass velocity of layer m, and we want to distinguish between the bulk and surface contributions. Summation of $u_{\alpha=z}(l_{12},m)$ over all the particles in layer m and the use of well-known identities yields

$$\varepsilon_z(m) = \sum_{l_{12}} \dot{u}_z(l_{12},m) = \varepsilon_{b,z}(m) + \varepsilon_{s,z}(m) \qquad (44)$$

where

$$\varepsilon_{a,z}(m) = -i\sum_{n_1,n_2,k} \omega_k(\mathbf{q})u_{z,k}(m,\mathbf{q})\exp\{-i\omega_k(\mathbf{q})t\}$$
$$\times N_1 N_2 \delta_{n_1,0}\delta_{n_2,0} \qquad a = b,s \qquad (45)$$

which leads to

$$\varepsilon_{a,z}(m) = -i\sum_k \omega_k(0)u_{z,k}(m,0)\exp\{-i\omega_k(0)t\}$$
$$a = b,s \qquad (46)$$

$\varepsilon_{b,z}(m)$ and $\varepsilon_{s,z}(m)$ are the contributions of the bulk modes b and the surface modes s to the center-of-mass motion. $\varepsilon_{b,z}(m)$ is by definition not localized at the surface and, therefore, it is independent of m. From Eq. (46) follows that only those surface modes contribute to $\varepsilon_{s,z}(m)$ for which $\omega \neq 0$ in the limit of $\mathbf{q} \to 0$; that is, only optical surface modes contribute to $\varepsilon_{s,z}(m)$ (the acoustic surface phonons only give rise to a uniform translational motion at $\mathbf{q} \to 0$).

From the analysis of the motion of the atoms relative to each other follows that the excitation described by the amplitude $A_\varepsilon(m)$ of $\varepsilon_{s,z}(m)$ cannot be an optical surface mode. Moreover, it has been discussed in literature (see, for example, [328]) that in the long-wave limit monatomic systems with only one particle in the three-dimensional unit cell admit only acoustic surface waves which do not contribute to $\varepsilon_{s,z}(m)$. In other words, the dynamical-matrix solutions would lead to

$$\varepsilon_{s,z}(m) = 0 \qquad (47)$$

and the center-of-mass motion is entirely given by $\varepsilon_{b,z}(m)$ and must be independent of m. However, molecular dynamics calculations (see Section 4.2.3) show that the amplitude $A_\varepsilon(m)$ of the center-of-mass motion is strongly dependent on m [323]. In particular, it is shown in [323] that this

excitation is localized at the surface: Its amplitude $A_\varepsilon(m)$ decreases with increasing m, and its penetration depth into the crystal is only a few interatomic distances. All this is in contrast to Eq. (47). In other words, the center-of-mass motion at the surface, described by $\varepsilon_{s,z}(m)$, cannot be described by the dynamical-matrix solutions, and it is shown in [323] that this effect is large; the dynamical-matrix solutions are obviously not complete for systems with surfaces, and in connection with *nanosystems* a relatively great fraction of atoms belong to surface regions.

4.2.3. Molecular Dynamics

The relatively strong anharmonicities in nanosystems are not negligible even at low temperatures. Furthermore, we have discussed in the last section in connection with the center-of-mass motion that surfaces can be the source for new qualitative phenomena. Since the dynamical-matrix solutions are obviously not complete the following questions arise: How can the dynamics of nanosystems be described? What method or basic model is adequate? Since only for the ideal solid does such a basic model exist [other simplifying principles at the microscopic level could not be found for many-particle systems (Section 4.2.1)], we have to describe such systems on the basis of the most general formulation. In the case of classical systems this can be done on the basis of Eq. (41) if the pair potential approximation can be applied and if many-body interactions can be neglected [Eq. (39)]. Such a general description can be achieved within the framework of *molecular dynamics calculations* which have to be performed for the characterization of nanosystems. We already came in Section 3.1 to this conclusion [scheme (32)]. In the following we would like to give more details concerning the molecular dynamics method.

Basic Information Only on the basis of the general formulation the relatively strong anharmonicities can be treated without approximation. In other words, the general description of the properties of classical many-particle systems (for example, nanosystems) can be done by means of molecular dynamics calculations without the use of "simple models" (Section 4.2.1) or other simplifying assumptions (Fig. 5). As already mentioned several times, such "simple models" and simplifying assumptions, respectively, are not known at the microscopic level and can only be introduced in a phenomenological or empirical way.

Within the framework of molecular dynamics Hamilton's equations

$$\dot{p}_{x_i} = -\frac{dH}{dx_1}, \ \ldots, \ \dot{p}_{z_N} = -\frac{dH}{dz_N}$$
$$\dot{x}_1 = \frac{dH}{dp_{x_i}}, \ \ldots, \ \dot{z}_N = \frac{dH}{dp_{z_{Ni}}} \tag{48}$$

are solved by iteration with the help of a high speed computer, and we obtain the following information for the
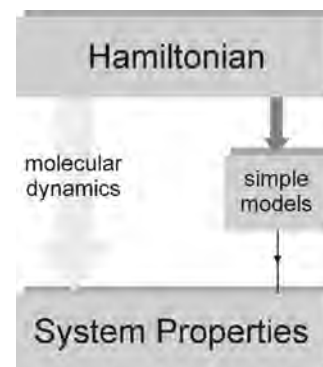

Figure 5. If a "simple model" is available, the properties of many-particle systems—including those of nanometer size—can be determined on the basis of such a model; in most cases additional assumptions are necessary. The advantage of molecular dynamics is that the description can be done without simple models and other additional assumptions. This is important since in most cases such systems are so complex that simplifying models have often been chosen for convenience and could not always be obtained by controlled simplifying steps from the general case (41). For nanosystems a simple model could not be found up to now. Therefore, the molecular dynamics methods is of particular importance in the nanometer-scale realm.

$N = N_I$ atoms:

$$q(t_1), p(t_1)$$
$$q(t_2), p(t_2)$$
$$\vdots$$
$$q(t_i), p(t_i) \tag{49}$$
$$\vdots$$

where

$$q(t_i) = (x_1, y_1, z_1, \ldots, x_N, y_N, z_N)$$
$$p(t_i) = (p_{x_1}, p_{y_1}, p_{z_1}, \ldots, p_{x_N}, p_{y_N}, p_{z_N}) \tag{50}$$

In other words, as solutions of the classical equations of motion we obtain the coordinates and momenta for all particles of the system as a function of time t. The time step in the iteration process is $\Delta t = t_{i+1} - t_i$. With k iteration steps the information about the system consisting of N particles is given in the time interval $\tau = k \cdot \Delta t$. Equation (49) contains the total information of the many-particle system. On the basis of this information the properties of the system, in particular experimental data, can be determined—at least in principle. In the following we will give some remarks about the determination of typical functions on the basis of information (49).

Correlation Functions In the analysis of many-particle systems correlation functions

$$\langle a(t')b(t'') \rangle \tag{51}$$

of two quantities $a(t')$ and $b(t'')$ are of particular interest, where

$$a(t') = a(q(t'), p(t'))$$
$$b(t'') = b(q(t''), p(t'')) \tag{52}$$

The angular brackets $\langle \cdots \rangle$ in (51) denote a thermodynamic average, which will be discussed in connection with molecular dynamics calculations in the next section. The time evolution of the system is given in statistical mechanics by the operator $\widehat{S}(t)$:

$$a(q(t'), p(t')) = \widehat{S}(t' - t'')a(q(t''), p(t'')) \quad (53)$$

where $\widehat{S}(t)$ can be written in terms of the Liouville operator $\widehat{L}$,

$$\widehat{S}(t) = \exp(i\widehat{L}t) \quad (54)$$

with

$$\widehat{L} = i\sum_{i=1}^{3N}\left[\frac{\partial H}{\partial q_i}\frac{\partial}{\partial p_i} - \frac{\partial H}{\partial p_i}\frac{\partial}{\partial q_i}\right] \quad (55)$$

where q_i and p_i denote all the $3N$ coordinates and momenta, respectively.

In general it is difficult to determine the time evolution of many-particle systems on the basis of Eq. (54). However, on the basis of the molecular dynamics information (49) it is straightforward to determine correlation functions of type (51).

In connection with time correlation functions of type (51) it is important to mention that they are not dependent on the time origin; that is, in Eq. (51) $t'' - t'$ are relevant but not t' and t'':

$$\langle a(t')b(t'')\rangle = \langle a(0)b(t'' - t')\rangle \quad (56)$$

Let us briefly discuss an example: With $a(0) = \mathbf{v}(0)$ and $b(t) = \mathbf{v}(t)$ we get the velocity autocorrelation function

$$\phi(t) = \langle \mathbf{v}(0) \cdot \mathbf{v}(t)\rangle \quad (57)$$

where $\mathbf{v}(t)$ is the velocity at time t for one atom of the ensemble. With $\phi(t) = \phi(-t)$ the Fourier transform of $\phi(t)$ is given by

$$f(\omega) = \frac{2}{\langle \mathbf{v}(0)^2\rangle \pi}\int_0^\infty \phi(t)\cos \omega t \, dt \quad (58)$$

where $f(\omega)$ is normalized to unity:

$$\int_0^\infty f(\omega)d\omega = 1 \quad (59)$$

In the case of the harmonic solid $f(\omega)$ is just the frequency spectrum of the normal modes, that is, the phonons. The frequency spectrum $f(\omega)$ defined by (57) is quite general and is applicable to systems with strong anharmonicities like nanosystems. $f(\omega)$ describes the complete dynamics of many-particle systems; that is, all kinds of excitation are included—even diffusion processes. The diffusion constant is directly expressed by $f(\omega)$ [329]:

$$D = \frac{\pi}{2}\frac{k_B T}{m}f(\omega = 0) \quad (60)$$

In particular, using $f(\omega)$ in the description of the dynamics no problems appear in connection with systems with surfaces where the dynamical matrix solutions are obviously not complete as we have demonstrated in Section 4.2.2.

How can we calculate the velocity autocorrelation function $\phi(t)$ and other properties from the basic molecular dynamics information (49)? In order to answer this question we have to outline how thermodynamic averages $\langle \cdots \rangle$ can be treated within the framework of molecular dynamics, which we have introduced in the context with Eq. (51). In the next section we will give some principal remarks.

Average Values Imagine a space of $6N$ dimensions whose points are determined by $3N$ coordinates $q(t_i) = (x_1, y_1, z_1, \ldots, x_N, y_N, z_N)$ and $3N$ momenta $p(t_i) = (p_{x_1}, p_{y_1}, p_{z_1}, \ldots, p_{x_N}, p_{y_N}, p_{z_N})$. This space is the so-called phase space where each point at time t corresponds to a mechanical state of the system. The evolution with time of the system is completely determined by Hamilton's equations (40) and is represented by a trajectory in phase space. The trajectory passes through the element $dq\,dp$ at point (q,p) of the phase space and it can pass it several times. This process defines a "cloud" of phase points indicating how often the elements of the phase space have passed through by the trajectory. In other words, instead of the trajectory we have now a "cloud" of phase points. The "cloud" is a great number of systems of the same nature, but differing in the configurations and momenta which they have at a given instant.

In summary, instead of considering a single dynamic system we consider a collection of systems, all corresponding to the same Hamilton function. This collection of systems is the so-called statistical ensemble (see also, for example, [330–337]). The introduction of the statistical ensemble is very useful in regard to the relationship between dynamics and thermodynamics.

The statistical ensemble can be described by a density function

$$\rho(q_1, \ldots, q_{3N}, p_1, \ldots, p_{3N}) \quad (61)$$

in phase space. The number of points in the statistical ensemble is arbitrary and, therefore, $\rho(q, p)$ has to be normalized:

$$\int \rho(q, p, t)\,dq\,dp = 1 \quad (62)$$

The quantity

$$\rho(q, p, t)\,dq\,dp \quad (63)$$

can be considered as the probability of finding at time t a system of the ensemble in the element $dq\,dp$ at the point (q,p) of the phase space. The introduction of the density (61) is meaningful only if the density takes an asymptotic value for long times t:

$$\lim_{t\to\infty}\rho(q, p, t) = \rho(q.p) \quad (64)$$

where $\rho(q, p)$ is the density function of the statistical ensemble. When the trajectory $q(t), p(t)$ is able to produce, over

a long period of time, the function $\rho(q, p)$ (ergodic hypothesis) then we have equivalence between the time average and the average over the statistical ensemble of a function $f(q(t), p(t))$:

$$\langle f \rangle = \frac{\int f(q, p)\rho(q, p)\, dq\, dp}{\int \rho(q, p)\, dq\, dp} \tag{65}$$

$$\langle f \rangle = \lim_{t \to \infty} \frac{1}{\tau} \int_0^x f(t)\, dt \tag{66}$$

Different expressions exist for the density function $\rho(q, p)$. These expressions depend on the thermodynamic environment: (1) *microcanonical ensemble* (an isolated system, N, V, and E are given, where E is the energy and V the volume); (2) *canonical ensemble* (a closed isothermal system, N, V, and T are given, where T is the temperature); (3) *grand canonical ensemble* (V, T, and μ given, where μ is the chemical potential). In molecular dynamics calculations in most cases N, V, and E are given and, therefore, such models represent microcanonical ensembles.

In connection with nanosystems the following discussion is relevant: Within the thermodynamic limit

$$\begin{aligned} N &\to \infty \\ V &\to \infty \\ \frac{N}{V} &= \text{const} \end{aligned} \tag{67}$$

the microcanonical, the canonical, and the grand canonical ensemble are equivalent; that is, within the thermodynamic limit we obtain in all three cases the same value for the statistical average of $\langle f \rangle$ of $f(q, p)$. This is not fulfilled in the case of nanosystems since the properties of nanosystems are in general dependent on the particle number N.

For nanosystems two points are important:

(1) What can we say about the dependence of the particle number N?
(2) What does a long period of time [$\tau \to \infty$ in Eq. (66)] mean?

Discussion Concerning Point (1)   The properties of nanosystems are in general dependent on the particle number. This is the reason we investigate nanosystems. In order to study this point in more detail one has to study the statistical average $\langle g \rangle$ of a suitable quantity $g(q, p)$ as a function of N and if there is

$$\langle g \rangle_{N'} = \langle g \rangle_{N''} = \langle g \rangle_{N'''} \tag{68}$$

with

$$N' < N'' < N''' \tag{69}$$

we may consider the system under investigation for $N \geq N'$ no longer as a nanosystem. On the other hand, if N' is the critical particle number we may consider the system for $N < N'$ as a nanosystem.

Discussion Concerning Point (2)   With Eq. (64) and using the well-known expression for the velocity distribution

$$\rho(q, p) = \rho(v) = 4\pi \left(\frac{m}{2\pi k_B T} \right)^{3/2} v^2 \exp\left(-\frac{mv^2}{2k_B T} \right) \tag{70}$$

we obtain for the mean-square velocity

$$\begin{aligned} \langle v^2 \rangle &= 4\pi \left(\frac{m}{2\pi k_B T} \right)^{3/2} \int_0^\infty v^4 \exp\left(-\frac{mv^2}{2k_B T} \right) dv \\ &= 3\frac{k_B T}{m} \end{aligned} \tag{71}$$

On the other hand let us consider a single particle of the N-particle system and let $v_i(t)$ be the velocity of the ith particle at time t where the index i has been chosen arbitrarily. If we define a function $v^2(\tau)$ by

$$v_i^2(\tau) = \int_0^\tau v_i^2(t)\, dt \tag{72}$$

we expect [according to (65) and (66)] that

$$\lim_{\tau \to \infty} v_i^2(\tau) = \langle v^2 \rangle \tag{73}$$

That is, there is equivalence between the average over the time and the average over the statistical ensemble [Eq. (71)]. In other words, we expect that after a sufficiently large time τ the velocity $v_i(t)$ of a single atom of the N-particle system, which can be arbitrarily chosen, has passed through all the states given by Maxwell's distribution (70).

In connection with molecular dynamics calculation the following question is of particular interest: How large is the time τ in order to fulfill (73) in a good approximation? Specific calculations showed that τ is relatively small; to fulfill Eq. (73) one needs not more than 10^3 iteration steps (i.e., τ is of the order of 10^{-11} s if the time step is 10^{-14} s).

Clearly, within molecular dynamics calculations averages will not be calculated on the basis of a statistical ensemble (65) or with Eq. (66). The calculated information expressed by (49) already represents the data in thermal equilibrium. Therefore, it is straightforward to determine averages on the basis of (49). For the mean-square velocity [see Eq. (71)] the molecular dynamical average is

$$\langle v^2 \rangle = \frac{1}{N_\theta} \frac{1}{N} \sum_{j=1}^{N_\theta} \sum_{i=i}^{N} v_i^2(\theta_j) \tag{74}$$

The average is formed over all N particles and various times θ_j.

Time Evolution of Molecular Dynamics Systems   From the solutions of Hamilton's equations (48) we obtain the coordinates and momenta (velocities) of all N particles as a function of time [see Eq. (49)]; this is the total *microscopical* information of the system under investigation. However, the solutions of Hamilton's equations require *initial values* for the coordinates and the velocities of the N particles.

In the case of gases and liquids the initial values for the coordinates can be distributed randomly with the appropriate density. In connection with crystals (with and without surfaces, and nanosystems) the particles will be situated

within the array so that the perfect lattice structure appropriate to the system under investigation is generated.

Without external forces acting on the system, the *directions* of the initial values for the velocities should be distributed randomly so that the momentum of the whole system is approximately zero at the initial time t_0, and it must remain zero for all times t (conservation of momentum).

In thermal equilibrium the *magnitudes* of the particle velocities are distributed according to Maxwell's distribution. However, it is more convenient to choose for all particles the same magnitude of the velocities, and this means that the system is initially not in thermal equilibrium. With the help of the function

$$\alpha(t) = \frac{\frac{1}{N} \sum_{i=1}^{N} \left[\mathbf{v}_i(t)^2 \right]^2}{\left[\frac{1}{N} \sum_{i=1}^{N} \mathbf{v}_i(t)^2 \right]^2} \tag{75}$$

where $\mathbf{v}_i(t)$, $i = 1, \ldots, N$, are the velocities obtained from the molecular dynamics calculations, we can study at which point in time Maxwell's distribution (70) is reached. In the case of (71) the function $\alpha(t)$ in (75) takes the value of

$$\alpha(t) = \frac{5}{3} \tag{76}$$

for all times t. However, if all particles have the same initial magnitude of the velocities we get for $\alpha(t)$ at time t_0

$$\alpha(t) = 1 \tag{77}$$

It can be demonstrated by realistic molecular dynamics calculations that thermal equilibrium ($\alpha(t) = 5/3$) is reached after a few hundred time steps if we start from $\alpha(t_0) = 1$. Due to the finite number of particles $\alpha(t)$ fluctuates around its equilibrium value of 5/3 (see also Fig. 6); these fluctuations are getting small with increasing particle number N and are physically realistic. Clearly, in the case of macroscopic systems ($N \to \infty$) the fluctuations are zero.
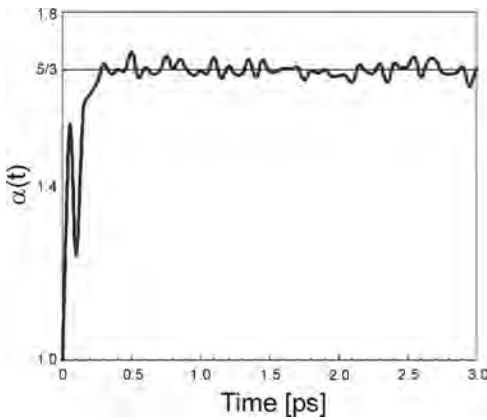

Figure 6. Schematic representation of $\alpha(t)$. The system is initially ($t_0 = 0$) not in thermal equilibrium ($\alpha \neq 5/3$). After a few hundred molecular dynamics time steps thermal equilibrium (Maxwell's distribution) is reached. Due to the finite number of particles the system fluctuates around 5/3.

The *temperature* of molecular dynamics systems is dependent on time t and is defined by the relation

$$\frac{1}{2} m \overline{\mathbf{v}(t)^2} = \frac{3}{2} k_B T(t) \tag{78}$$

With

$$\overline{\mathbf{v}(t)^2} = \frac{1}{N} \sum_{i=1}^{N} \mathbf{v}_i(t)^2 \tag{79}$$

we get for the temperature as a function of time

$$T(t) = \frac{m}{3 N k_B} \sum_{i=1}^{N} \mathbf{v}_i(t)^2 \tag{80}$$

As in the case of $\alpha(t)$ also the temperature $T(t)$ fluctuates in finite systems around the mean temperature (see Fig. 7):

$$T = \lim_{\theta \to \infty} \frac{1}{\theta - \theta_1} \int_{\theta_1}^{\theta} T(t) \, dt \tag{81}$$

θ_1 is the time where the system has reached equilibrium, and θ is the time of investigation (i.e., for which Hamilton's equations have been solved after equilibrium is reached).

As in the case of $\alpha(t)$, the temperature fluctuations (see Fig. 7) are physically real. From these fluctuations we can extract the specific heat at constant volume (per particle)

$$c_V = \frac{1}{N} \left(\frac{\partial E}{\partial T} \right)_V \tag{82}$$

It is straightforward to show that in the case of a microcanonical ensemble the specific heat is expressed by [338, 339]

$$c_V = \frac{3}{2} \left[1 - \frac{3N}{2\overline{T^2}} (\overline{T^2} - \overline{T}^2) \right]^{-1} \tag{83}$$

where $\overline{T}$ and $\overline{T^2}$ are obtained by averaging over a sufficiently large time interval. For example, $\overline{T^2}$ is given by

$$\overline{T^2} = \lim_{\theta \to \infty} \frac{1}{\theta - \theta_1} \int_{\theta_1}^{\theta} T(t)^2 \, dt \tag{84}$$
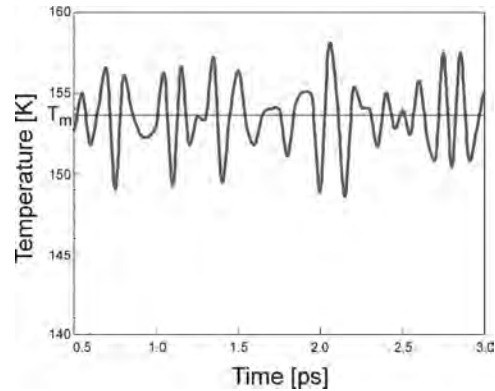

Figure 7. The temperature as a function of time (schematic representation). T is the mean temperature; θ_1 is the time where the system has reached equilibrium. Due to the finite number of particle the temperature fluctuates around its mean value T.

In other words, the temperature fluctuations are a direct measure of the specific heat, indicating that these fluctuations are not an artificial element of the method.

4.2.4. Nonequilibrium Molecular Dynamics

A few remarks should be given in connection with nonequilibrium molecular dynamics which has been developed in addition to equilibrium molecular dynamics (Section 4.2.3) and which has been known since the early 1970s [340–342]. This method was introduced in order to compute efficiently transport coefficients. To establish the nonequilibrium situation of interest, an external force is applied to the system. Then the response of the system to these forces is determined from the simulation. This method has been used for the calculation of diffusion coefficients, the shear and bulk viscosity, and thermal conductivity [343]. Further basic literature concerning nonequilibrium molecular dynamics is given by [344–349]. Recent interesting results can also be found in [350–355].

Non-Hamiltonian systems can be studied by means of nonequilibrium molecular dynamics [356], for example, dissipative systems, that is, systems which involve friction in one of its various forms. In such cases, particle trajectories are calculated from the equations of motion which are, however, not consistent with any Hamilton function.

5. INTERACTION POTENTIALS

Clearly, in order to be able to perform molecular dynamics calculations not only are the initial values for the coordinates and momenta (velocities) for all the N particles of the system needed as input (Section 4.2.3), but in particular the interaction potential between the particles, which reflects the specific characteristics of the system under investigation.

For a reliable description of material properties precise knowledge of the interaction potential is required. We will outline below that surface properties in general, as well as in connection with nanosystems, are particularly sensitive to potential variations. Both the repulsive and the attractive parts of the potential have to be determined carefully. However, the determination of accurate pair potentials for systems of interest (e.g., metals and materials with covalent bonding) is rather difficult even for the bulk, and the nanoproblem, where a great fraction of atoms belong to the surface region, is much harder because of the change in electronic states and other relevant properties near the surfaces of the nanosystem.

In this section we would like to discuss methods which—from the authors point of view—are relevant for the determination of interaction potentials. In literature a lot of theoretical studies can be found—in particular, in connection with molecular dynamics calculations—in which the potentials are used in a rather uncritical way: The potentials have not been tested carefully, in some cases even not at all. Serious research in nanoscience requires just the opposite: Since the properties of nanosystems are particularly sensitive to potential variations, the potentials have to be determined thoroughly for such systems.

5.1. Types of Interactions in Condensed Matter Physics

Basically, in condensed matter physics we have to distinguish between four binding types (see, for example, [357]): (1) *ionic interactions* (4–14 eV), (2) *metallic bonds* (0.7–6 eV), (3) *van der Waals interactions* (0.02–0.3 eV), and (4) *covalent bonds* (1–10 eV), where the numbers denote the typical binding energies. Also the *hydrogen bridge bond* (0.1–0.5 eV) is a characteristic binding type but will not be discussed in the following.

5.1.1. Ionic Binding

The ionic interaction is characterized by different atoms (for example, Na and Cl) which have exchanged electrons, so that the many-particle systems consist of positive and negative charged ions. The interaction law as a function of distance r between the ions is simply described by Coulomb's law if the distances are larger than $r_+ + r_-$, where r_+ and r_- are the radii of the positively and negatively charged particles. For distances $r < r_+ + r_-$ the interaction is repulsive due to the overlap of the electron cores.

5.1.2. Metallic Binding

In the case of certain atoms (for example, Al) the electrons of the outer shell are only weakly bonded. If a many-particle system is formed with such atoms the weakly bonded electrons leave the according atoms and move through the whole system. These are the conduction electrons. In other words, in metals we have the following situation: There are positively charged ions which move through the sea of conduction electrons. In metals the ion–ion interaction is not simply given by the Coulomb potential since the ions are screened by the conduction electrons and that makes its determination complicated. Such a modeling of the ion–ion potential can be performed, for example, within the frame of pseudopotential theory; in Section 5.3.1 we give some details concerning this method.

5.1.3. Van der Waals Interaction

The motion of the electrons around the atomic nucleus means that there is a certain probability that the atoms have at instant t an electrical dipole moment which, however, becomes zero when it is averaged over the time. In a many-particle system these momentary dipole moments interact with each other leading to an attractive potential between the atoms of the system. Typical van der Waals systems are noble gases. Clearly, repulsive core effects have to be considered also in the description of the interaction potential at small distances.

5.1.4. Covalent Bonds

In the case of covalent binding the interaction between particles is given by the fact that part of their electrons belong to several particles at the same instant. The probability of finding an electron, which is responsible for binding, is relatively large in the environment between the particles leading to the interaction between them. In most cases this process is based on the formation of spin saturated electron

pairs, where each atom contributes an electron so that the electron shells take a noble gas configuration. Examples for substances with covalent bonds are carbon, amorphous semi-conductors, hydrogen molecules, etc.

Remarks Concerning Phenomenological Potentials
In connection with realistic calculations phenomenological potential functions are used very often, which are most often not strictly constructed with respect to the basic inter-action types discussed above. As a typical example for a phenomenological potential let us briefly discuss the poten-tial of Morse [358] which has been extensively used in the study of lattice dynamics [359], the defect structure in metals [360–368], the inert gases in metals [369, 370], the equa-tion of state [371, 372], elastic properties of metals [373], the interaction between gas atoms and crystal surfaces [374], and in studies of other specific problems [375–381].

In order to calculate the energy levels for diatomic molecules, Morse required some conditions for the inter-atomic potential of the atoms of the molecule [323] which describes the spectroscopy of the molecules. Morse chose the potential function

$$v(r) = \alpha_0 \exp[-2\alpha(r - r_0)] - 2\alpha_0 \exp[-\alpha(r - r_0)] \quad (85)$$

where r_0 is the intermolecular separation. The solution of the radial part of Schrödinger's equation using this potential yielded the correct energy level representation.

In conclusion, the Morse potential has not been con-structed on the basic interaction types discussed above but is based on the spectroscopy of molecules. Nevertheless, the potential has been used extensively in the study of various many-particle properties, but there is no physical justifica-tion for that.

There are many other phenomenological approaches for the interaction (for example, the Buckingham potential [382–385]), but we do not want to discuss these functions here because in most cases there is no or almost no physi-cal background for their introduction; these potentials have often been chosen for purely pragmatic reasons and, there-fore, they have to be considered only as fitting functions.

Since there is a strong potential sensitivity in connection with the properties of systems with surfaces (for example, nanosystems), we have to construct the potentials very care-fully. In the next sections we would like to discuss some relevant theoretical methods for the construction of model potentials.

5.2. Sensitivity of System Properties against Potential Variations

Before we discuss specific model potentials let us first give some remarks about the sensitivity of the system properties on the interaction between the particles which form the sys-tem. It turned out that the properties of many-particle sys-tems are very sensitive to small variations in the interaction potentials. Therefore, in the description of system properties on the basis of the particle interaction the potentials have to be modeled very carefully. What does "sensitive to small variations in the interaction potentials" mean?

Let us demonstrate that by means of krypton [386]. In connection with nanosystems surface properties are of par-ticular interest and, therefore, let us study the sensitivity of surface properties on the potential function.

As is well known, krypton is a noble gas, and in con-trast to metals, the potential functions of noble gas systems (solid, liquids, nanosystems, etc.) do not depend on density and temperature, respectively, and they are the same at the surface as in the bulk of the crystal. At free metal surfaces the local background may be changed from its average bulk value and produces concomitant changes in the potential functions. Such difficulties do not arise at noble gas surfaces and, therefore, in the study of the potential sensitivity we want to restrict our study to noble gas (krypton) surfaces.

For krypton a reliable potential, the so-called Barker potential, is available [387]; its form is rather complex and will not be outlined here. The Barker potential is more real-istic than the famous Lennard-Jones potential

$$v(r) = 4\varepsilon\left[\left(\frac{\sigma}{r}\right)^{12} - \left(\frac{\sigma}{r}\right)^{6}\right] \quad (86)$$

because it undoubtedly correlates accurately a much wider range of experimental data. Although the shapes of the Lennard-Jones potential and the Barker potential are sim-ilar (see Fig. 8) the results for the relaxation are *qualita-tively different* from each other: The Barker potential leads to a *contraction* and, on the other hand, the Lennard-Jones potential leads to an *expansion*, as has been demonstrated by molecular dynamics calculations for the Kr (111) sur-face and 539 atoms [388]. The contraction is confirmed by low energy electron diffraction (LEED) data [388]. Figure 9 shows that the molecular dynamics model calculations agree well with the experimental data. The interlayer spacing $d_\perp$ at the surface is always smaller than the corresponding value for the bulk within the temperature range studied. As already mentioned above, the lattice contraction result-ing from the model and the experiments is in contradiction to the results of model calculations with the Lennard-Jones potential (leading to an expansion), indicating that investigations—for example, in connection with dynamical
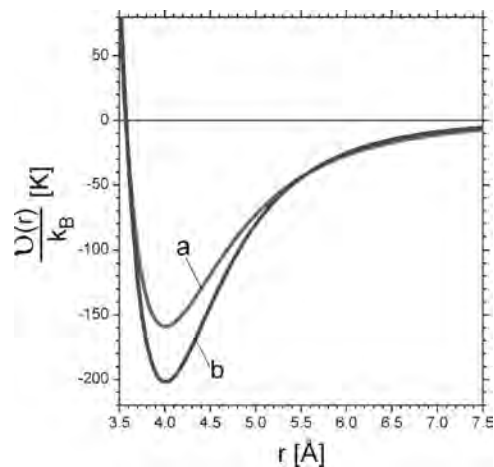

Figure 8. Pair potentials for krypton: (a) Barker potential, (b) Lennard-Jones potential.
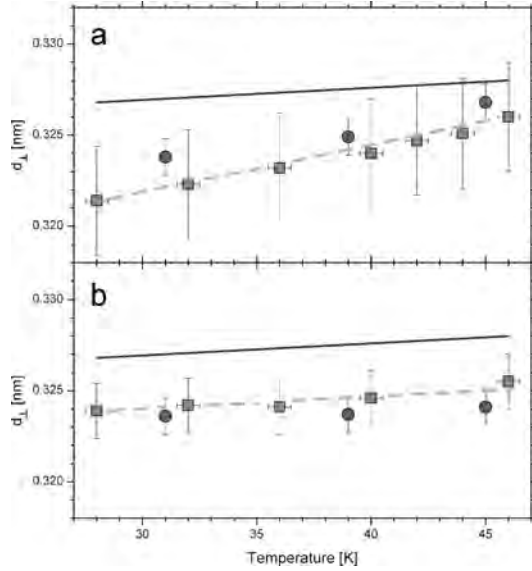
Figure 9. Temperature dependence of the interlayer spacing $d_\perp$ measured by LEED experiments ($\Diamond$) for electron energies $E = 53$ eV (a) and $E = 125$ eV (b) together with the results obtained by molecular dynamics calculations ( ) [in (a) for the outermost interlaying spacing and in (b) averaged for the outermost two layer spacings]. The solid lines show the interlayer spacings for the bulk as determined by X-ray experiments. The error bars in the experimental data are mainly due to the error for the effective inner potential. The error bars with respect to the molecular dynamics results are due to the statistical fluctuations.

processes in nanosystems—on the basis of the Lennard-Jones potential can be seriously in error.

It should be emphasized here that the Lennard-Jones potential is the most used interaction function in literature, and sometimes it is even used for the description of metals [389], but there is no physical basis for that since the interaction type (van der Waals forces) described by the Lennard-Jones potential has nothing to do with the interaction type dominant in metals.

In conclusion, the properties of many-particle systems (in particular those with surfaces like nanosystems) are obviously very sensitive to small variations in the interaction between the particles. We have shown that the relatively small quantitative differences between the Lennard-Jones potential and the Barker potential (Fig. 8) give rise not only to quantitative effects but also to qualitative differences. This example shows that one has to be very careful in the selection of interatomic potentials, especially when modeling nanosystems, since a great fraction of particles belong to the surface region.

With respect to the interaction problem we have still to mention that the Lennard-Jones potential as well as the Barker potential are descriptions within the pair potential approximation (Section 4.1.2). However, in principle many-body forces [three-body interactions etc.; see Eq. (39)] might also play a role. What can we say about the influence of three-body interactions?

The calculations in connection with Figure 9 have been done for the noble gas krypton which is a typical van der Waals system. For such systems a three-body potential exists

(Axilrod–Teller potential [390])

$$v_3(i, j, k) = \nu \frac{1 + 3\cos\theta_1 \cos\theta_2 \cos\theta_3}{r_{ij}^3 r_{il}^3 r_{jl}^3} \tag{87}$$

where ν is a constant; r_{ij}, r_{il}, r_{jl} and θ_1, θ_2, θ_3 are the sides and angles of the triangle formed by the particles i, j and l. $v_3(i, j, l)$ can be repulsive and attractive, which depends on the shape of the triangle formed by the three atoms i, j, and l. Are those Axilrod–Teller interactions relevant in connection with the results given in Figure 9?

We cannot exclude that the three-body potential (87) together with the Lennard-Jones potential may lead to good results for the relaxation at the surface. However, it is shown in [391] that the influence of $v_3(i, j, l)$ on structural data is relatively small and, therefore, we cannot expect that the Lennard-Jones potential together with $v_3(i, j, l)$ gives good results for the relaxation and other quantities of relevance.

On the other hand, the Barker potential is expressed by a lot of parameters, and these parameters were fitted by a lot of experimental data; this fact can be expressed formally by

$$v = v(r, a, b, \dots) \tag{88}$$

where a, b, etc. are the fit parameters. In other words, such kinds of potentials should not be considered as pure pair potentials in the sense of Eq. (39) in Section 4.1.2 but rather play the role of effective interaction potentials $v(r, a, b, \dots) = v_{\text{eff}}(r, a, b, \dots)$ which in particular consider approximately many-body forces. Therefore, we may express Eq. (39) in Section 4.1.2 by

$$V(\mathbf{r}_1, \dots, \mathbf{r}_N) = \frac{1}{2} \sum_{\substack{i, j \\ i \neq j}}^{N} v_{ij} + \frac{1}{6} \sum_{\substack{i, j, k \\ i \neq j \neq k}}^{N} v_{ijk} + \cdots$$

$$\cong \frac{1}{2} \sum_{\substack{i, j \\ i \neq j}}^{N} v_{\text{eff}}(r_{ij}, a, b, \dots) \tag{89}$$

That is, the effective potential simulates approximately many-body forces. This is due to the fact that the potential parameters a, b, etc. are fitted to experimental data which may be more or less sensitive to many-body forces.

5.3. On the Determination of Pair Potentials in Metals

5.3.1. Remarks Concerning Pseudopotential Theory

As outlined in Section 5.1 metals consist of ions of positive charge and electrons. In the case of the ionic interaction the potential between the particles is simple and is given by the Coulomb potential. In metals the situation is more complicated since the ions are surrounded of conduction electrons. The ions are screened by the electrons; in particular, there are quantum-mechanical correlation and exchange effects among the electrons. All these facts have to be considered in the construction of ion–ion potentials $v(r)$ in metals, where r is the distance between the two ions of the system. Within the framework of pseudopotential theory

(see, for example, [392]) all these effects (screening, correlation, and exchange effects) can be adequately considered.

The pseudopotential method is often used for the determination of the interaction between the ions in metals. Within the frame of this theory the problem can be treated on various levels, and a lot of pseudopotential models exist in literature. Let us briefly discuss here a typical example for a monatomic system. This example shows how all the previously mentioned effects (screening, correlation, and exchange effects) can be treated mathematically and how they are interrelated.

As already outlined, the metal system has to be considered as a conglomerate of ions which are embedded in an uniform compensating background of negative charge (conduction electrons). Within the framework of pseudopotential theory the ion–ion potential $v(r)$ can be divided into two parts [392, 393],

$$v(r) = v_d(r) + v_{ind}(r) \tag{90}$$

where $v_d(r)$ is the so-called direct interaction between the ions, and $v_{ind}(r)$ is the ion–electron–ion interaction, which has the meaning of an indirect interaction. In most cases $v_d(r)$ is approximated by the Coulomb potential

$$v_d(r) = \frac{Z^{*2}e^2}{r} \tag{91}$$

of the point charges Z^*e [392]. The deviations of the effective valency Z^* from the valency Z are in most cases less than 10% [393]. The difference Z^*–Z can be thought of as resulting from the orthogonalization of plane waves to the core states which gives an extra charge on the ion.

The local approximation of the indirect ion–ion interaction $v_{ind}(r)$ [see Eq. (90)] can be expressed by [392]

$$v_{ind}(r) = \frac{\Omega_0}{\pi^2} \int_0^\infty F(q) \frac{\sin qr}{qr} q^2 \, dq \tag{92}$$

Following Sham [394] and Heine and Abarenkov [395] for the function $F(q)$ the following ansatz can be chosen:

$$F(q) = -\frac{\Omega_0 q^2}{8\pi e^2} |\langle k+q|k\rangle|^2 \frac{\varepsilon(q)-1}{\varepsilon(q)[1-C(q)]} \tag{93}$$

with

$$\varepsilon(q) = 1 + [1-C(q)] \frac{me^2}{2\pi k_F \hbar^2 x^2} \left(1 - \frac{1-x^2}{2x} \ln\left|\frac{1+x}{1-x}\right|\right) \tag{94}$$

and

$$C(q) = \frac{q^2}{2[q^2 + k_F^2 + k_s^2]} \tag{95}$$

where Ω_0 is the specific volume, k_F is the Fermi wave number vector, $x = q/2k_F$, $k_s = 2k_F/\pi a_0$, and a_0 is the Bohr radius.

The matrix element $\langle k+q|w_0|k\rangle$ is the unscreened pseudopotential form factor, which is independent of k in the local approximation. With $C(q)$ exchange and correlation effects among the electrons are taken into account approximately in the dielectric function $\varepsilon(q)$. If $C(q)$ is taken equal

to zero in Eq. (94), $\varepsilon(q)$ is equal to the static Hartree dielectric function. It should be mentioned that there exist various models for the dielectric function $\varepsilon(q)$ in literature [392], and the form of $\varepsilon(q)$ essentially depends on the material under investigation.

The Fourier transform $w_0(R)$ of the matrix element $\langle k+q|w_0|k\rangle$ can be considered as the unscreened potential $v_0(R)$ between the ion and the conduction electron at distance R. $v_0(R)$ must be corrected by an orthogonalization potential $v_{orth}(R)$ in the core region due to the orthogonalization of the plane waves to the core states [392],

$$w_0(R) = v_0(R) + v_{orth}(R) \tag{96}$$

where $w_0(R)$ is related to $\langle k+q|w_0|k\rangle$ by

$$\langle k+q|w_0|k\rangle = \frac{4\pi}{\Omega_0} \int_0^\infty w_0(R) \frac{\sin qR}{qR} R^2 \, dR \tag{97}$$

$v_0(R)$ in Eq. (96) is expressed by the Coulomb interaction between the conduction electron and the excessive point charge Ze of the ion:

$$v_0(R) = -\frac{Ze^2}{R} \tag{98}$$

The function $v_{orth}(R)$ in Eq. (96) has to be modeled. For example, within the often used Ashcroft model [396] we have

$$v_{orth}(R) = \frac{Ze^2}{R} [1 - \theta(R - r_c)] \tag{99}$$

with

$$\theta(R - r_c) \begin{cases} = 0 & R \leq r_c \\ = 1 & R > r_c \end{cases} \tag{100}$$

where r_c is the core radius. Within the Ashcroft model the Coulomb potential is canceled within the core region.

A typical feature of the ion–ion potential $v(r)$ in metals is that, due to the conduction electrons, the long-range part oscillates. This is schematically shown in Figure 10 in comparison to a Lennard-Jones-type potential which
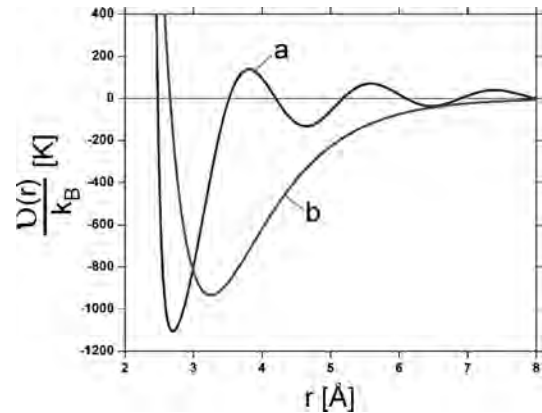

Figure 10. The schematic representation of different potential types: (a) the ion–ion interaction $v(r)$ for a metal; (b) the typical atom–atom potential in a noble gas.

describes noble gases, that is, systems without conduction electrons.

Equations (90)–(100) represent the basic model, but it turned out [397] that there can obviously be additional effects which are due to the cores of the ions. These are van der Waals-type interactions. Without going into detail the analysis of this problem [397] leads to additional inter-action terms with respect to the direct interaction $v_d(r)$ between the ions [see Eq. (91)] and the unscreened inter-action $v_0(R)$ between the conduction electron and the ion [see Eq. (96)],

$$v_d(r) = \frac{Z^{*2}e^2}{r} - \frac{\alpha_1}{r^6} - \frac{\alpha_2}{r^4} \tag{101}$$

$$v_0(R) = -\frac{Ze^2}{R} - \frac{\alpha}{R^4} \tag{102}$$

where the r^{-6} term in (101) represents a dipole–dipole inter-action, and the r^{-4} and R^{-4} terms in (101) and (102) reflect monopole–dipole potentials. The constants α, α_1, and α_2 can be estimated quantum mechanically [397].

Pseudopotentials have often been applied to various prob-lems. Some typical articles are: Avoided crossings in the interaction of a Xe Rydberg atom with a metal surface [398], The theoretical spin-orbit structure of the RbCs molecule [399], *ab initio* study of the adsorption of In on the Si(001)-(2 × 2) surface [400], *ab initio* study of iron and Cr/Fe001 [401], and Dilute Bose gas in a quasi-two-dimensional trap [402]. Further information is given in [403–415].

5.3.2. Model-Independent Potentials

The interaction models which are based on pseudopotential theory work well in many cases [392, 397], provided the var-ious terms, which compose the model, have been carefully prepared. Nevertheless, such models are complicated and contain a lot of assumptions and simplifications which are often based on more or less uncontrolled calculation steps. Therefore, it would be desirable to find methods which allow one to determine *model-independent* interaction potentials. Such a way is still less developed but should attract more attention in the future since the properties of systems are in general very sensitive to small variations in the interac-tion potential (Section 5.2); this is in particular the case in connection with nanosystems where a great fraction of the particles belong to the surface of the system. However, model-independent potentials can already be determined for liquids. The according method could in principle also be applied to nanofilms. Because of its principal meaning let us briefly discuss this method.

The method [416] is based on experimental data for the liquid structure and allows one to determine the interaction without the use of any parameter in a self-consistent way. Since the method is model-independent, it is applicable for all interaction types. The liquid structure is characterized by the pair correlation function $g(r)$, which can be deter-mined experimentally. $g(r)$ is an essential quantity because important thermodynamic functions (pressure, energy, etc.) are only dependent on $g(r)$—provided we can work within the pair potential approximation.

Let us start from the expansion for $g(r)$ in powers of the particle number density n (see, for example, [417, 418]),

$$g(r) = \exp\left[-\frac{v(r)}{k_B T}\right]\gamma(r) \tag{103}$$

with

$$\gamma(r) = 1 + na(r) + n^2 b(r) + \cdots \tag{104}$$

where k_B is Boltzman's constant and T is the absolute tem-perature of the system. The coefficients of each power of n are cluster integrals (more details concerning Eq. (104) are given in [417]). The detailed form of $v(r)$ will only have a small influence on $\gamma(r)$ because $\gamma(r)$ plays the role of an integral quantity in the determination of $\gamma(r)$. This means that different pair potentials can lead to the same function $\gamma(r)$—at least in principle. In other words, if we know a potential $v_1(r) \neq v(r)$ which satisfies the condition

$$\gamma_1(r) \cong \gamma(r) \tag{105}$$

we can calculate the unknown pair potential $v(r)$ by

$$v(r) \cong v_1(r) - k_B T \ln\left[\frac{g(r)}{g_1(r)}\right] \tag{106}$$

where

$$g_1(r) = \exp\left[-\frac{v_1(r)}{k_B T}\right]\gamma_1(r) \tag{107}$$

and $g(r)$ in (106) is the experimentally determined $g(r)$. Since Eq. (107) is in general an expansion with slow conver-gence, $g_1(r)$ should be calculated from the known potential $v_1(r)$ by molecular dynamics and not by (107) on the basis of (104). It is difficult to fulfill Eq. (105) in the first step and, therefore, instead of (106) we get the following itera-tion scheme:

$$\begin{aligned}
v_2(r) &= v_1(r) - k_B T \ln\left[\frac{g(r)}{g_1(r)}\right] \\
v_3(r) &= v_2(r) - k_B T \ln\left[\frac{g(r)}{g_2(r)}\right] \\
&\quad\vdots \\
v_i(r) &= v_{i-1}(r) - k_B T \ln\left[\frac{g(r)}{g_{i-1}(r)}\right] \\
v_i(r) &= v_{i-1}(r) \\
&= v(r)
\end{aligned} \tag{108}$$

with

$$g_{i-1}(r) = g(r) \tag{109}$$

The unknown pair correlation functions $g_k(r)$, $k = 1, \ldots, i - 1$, can be calculated using $v_k(r)$, $k = 1, \ldots, i - 1$, by molecular dynamics. After the $(i - 1)$th iteration the molecular dynamical calculated pair correlation function $g_{i-1}(r)$ agrees with the experimental $g(r)$ [Eq. (109)] within the limit of accuracy dictated by the molecular dynamics calculation.

For the applicability of the self-consistent method con-vergence of the scheme (108) is necessary. This depends on

the potential $v_1(r)$ which we have to know in the first iteration step. In all calculations (see, for example, [416]) the approximation for low densities [$\gamma(r) = 1$, Eq. (103)]

$$v_1(r) = -k_B T \ln g(r) \tag{110}$$

worked well, where $g(r)$ is again the experimental pair correlation function.

The pair potential $v(r)$ is sensitive to small variations in $g(r)$ which means that $g(r)$ has to be measured very accurately. This has been done for liquid gallium [419]. In [416] the self-consistent method has been applied to liquid gallium; the details are discussed there.

The self-consistent method could also be applied to nanosystems. For example, it should be possible to determine the pair potential for the particles of nanostructures on surfaces. On the other hand, other model-independent methods should be developed which correlate the potential with suitable measurable quantities, that is, methods which are not based on the experimentally determined pair correlation function $g(r)$ but on other relevant experimental input data leading to new schemes.

5.3.3. Microscopic Considerations

The pseudopotential theory as discussed in Section 5.3.1 leads to more or less phenomenological potentials with parameters which can be fitted to experimental data, in particular to data for systems with surfaces, for example, nanosystems. However, the surface properties can be considered from the beginning if we work more microscopically within the framework of first principles calculations. Let us briefly discuss this point.

The electron density in metals must drop from a characteristic interior average value within the system to zero outside the surface. The ion–ion potential in metals is dependent on the electron density, and the charge redistribution at the surface has the effect that the potential at the surface is different from that in the bulk of metals. How can we determine the pair potential at metal surfaces, that is, in connection with nanosystems? Let us give an example.

For sufficiently low temperatures the pair interactions outside and inside the metal surface have been calculated microscopically in [420] on the basis of the static electronic response function. The basic points of the approach are the following: An ensemble of ions with the positions $\mathbf{R}_i$, $i = 1, \ldots, N$, are surrounded by a neutralizing electron charge of density $n(\mathbf{r})$. An infinitesimal displacement of ion k with the position $\mathbf{R}_k$ introduces a perturbating potential $\delta V_k(\mathbf{r} - \mathbf{R}_k)$ and an energy change which is given by

$$\Delta E = -\frac{1}{2} \sum_{\mathbf{R}_i, \mathbf{R}_j} \int d\mathbf{r} \int d\mathbf{r}' \, \delta V_i(\mathbf{r} - \mathbf{R}_i)$$
$$\times \chi(\mathbf{r}, \mathbf{r}') \, \delta V_j(\mathbf{r} - \mathbf{R}_j) \tag{111}$$

where $\chi(\mathbf{r}, \mathbf{r}')$ is the static electronic response function appropriate to the electronic density $n(\mathbf{r})$. $n(\mathbf{r})$ can be determined by the density functional formalism (see also Sections 2.1.2 and 2.1.5). How is the function $\chi(\mathbf{r}, \mathbf{r}')$ correlated to the quantities defined by the density functional theory? As we have already outlined in Section 2.1.5, within

this approach instead of the complicated wave function $\psi(\mathbf{r}_1, \ldots, \mathbf{r}_N)$ for the N-particles the electron density

$$n(\mathbf{r}) = \frac{\int d\mathbf{r}_1 \cdots d\mathbf{r}_N \sum_{i=1}^{N} \delta(\mathbf{r} - \mathbf{r}_i) \psi^*(\mathbf{r}_1, \ldots, \mathbf{r}_N) \psi(\mathbf{r}_1, \ldots, \mathbf{r}_N)}{\psi^*(\mathbf{r}_1, \ldots, \mathbf{r}_N) \psi(\mathbf{r}_1, \ldots, \mathbf{r}_N)} \tag{112}$$

is introduced as a variable. According to Kohn, Hohenberg, and Sham [6, 7] $n(\mathbf{r})$ is given in the ground state by

$$n(\mathbf{r}) = \sum_{i=1}^{N} \phi_i^*(\mathbf{r}) \phi_i(\mathbf{r}) \tag{113}$$

with

$$\int n(\mathbf{r}) \, d\mathbf{r} = N \tag{114}$$

The wave functions $\phi_i(\mathbf{r})$ satisfy

$$\left\{ -\frac{\hbar^2}{2m} \nabla^2 + V_{\text{eff}}(\mathbf{r}) \right\} \phi_i(\mathbf{r}) = \varepsilon_i \phi_i(\mathbf{r}) \tag{115}$$

where

$$V_{\text{eff}}(\mathbf{r}) = V(\mathbf{r}) + V_H(n(\mathbf{r})) + V_{\text{xc}}(n(\mathbf{r})) \tag{116}$$

with $V(\mathbf{r})$ being an arbitrary external potential. $V_H(n(\mathbf{r}))$ and $V_{\text{xc}}(n(\mathbf{r}))$ are the usual Hartree and exchange-correlation potentials which are functionals of $n(\mathbf{r})$.

The static susceptibility $\chi(\mathbf{r}, \mathbf{r}')$ in (111) is a ground state response and, therefore, it is a functional of $n(\mathbf{r})$ and can be described by $\phi_i(\mathbf{r})$. On the basis of (111) the ion–ion interaction outside and inside a metal jellium surface has been calculated [420].

In order to check the reliability of such potentials it would be most helpful to use them in molecular dynamics calculations for the description of nanosystems and compare the results carefully with experimental data. In this way, valuable insight into the validity of such potentials can be achieved. Another approach, extensively used in connection with molecular dynamics, is given by the so-called embedded-atom method; in the next section we discuss the basic principles of this method.

5.3.4. Embedded-Atom Method

An alternative to the pair potential description has been proposed by Daw and Baskes [421, 422]; as in Section 5.3.3 also within this approach density-functional ideas are used. This approach, the so-called embedded-atom method, has also been used in connection with molecular dynamics for the description of various complex physical situations. First we give a brief description of the method and after that we quote some applications.

The basic idea behind the embedded-atom method is the following (see, for example, [423]): The density-functional formalism allows one to formulate the total electronic energy for an arbitrary arrangement of nuclei as a unique functional of the total electron density. The method starts with the approximation that the total electron density in a metal can be expressed by the linear superposition of contributions from the individual atoms. Then, the electron density around each atom can be described as a sum of the

density contributed by all the surrounding atoms plus the electronic density of the atom in question. The first contribution is assumed to be a slowly varying function of position. If the problem is simplified by the assumption that this background electron density is a constant, the energy of the atom in question is given by the energy associated with the electron density of the atom plus the constant background density. On the basis of this ideas the total energy of a system with N atoms is given by

$$E_{\text{tot}} = \sum_{i=1}^{N} \left[F_i(\bar{\rho}_i) + \frac{1}{2} \sum_{\substack{j=1 \\ j \neq i}}^{N} u(r_{ij}) \right] \tag{117}$$

where $F_i(\bar{\rho}_i)$ is the energy required to embed atom i into the background electron density $\bar{\rho}_i$ at side i, and $u(r_{ij})$ is the core–core pair interaction potential between atom i and j separated by the distance r_{ij}.

As already remarked, the host electron density $\bar{\rho}_i$ is approximated by a linear superposition of the spherically averaged electron densities of the n_i atoms neighboring atom i,

$$\bar{\rho}_i = \sum_{\substack{j=1 \\ j \neq i}}^{N} \rho(r_{ij}) \tag{118}$$

where $\rho(r_{ij})$ is the electron density of atom j at a distance r_{ij} from the nucleus of atom i. If the atomic density $\rho(r)$ and the pair interaction $u(r)$ are both known, the embedding energy F can be uniquely defined by matching a certain equation for the cohesive energy of the metal as a function of the lattice constant. This can be used to fit $F(\bar{\rho})$ to experimental results.

The embedded-atom method has been applied with success to several problems: for face-centered cubic (fcc) metals and their alloys [423], phonon spectra in metals [424], and the structure of liquid metals [425]. It has also successfully been used for the determination of surface energies and geometries including reconstruction phenomena [426]. Other relevant topics have been studied on the basis of the embedded-atom method. In this connection let us quote the following selected studies: Numerical evaluation of the exact phase diagram of an empirical Hamiltonian: embedded-atom model for the Au–Ni system [427], Development of modified embedded-atom potentials for the Cu–Ag system [428], Atomistic process on hydrogen embrittlement of a single crystal of nickel by the embedded-atom method [429], Kinetic pathways from embedded-atom-method potentials: Influence of the activation barriers [430], and Structural and thermodynamic properties of liquid transition metals with different embedded-atom method models [431]. More information concerning the embedded-atom method is given in [432–444] and in Section 6.1.

5.3.5. Quantum Molecular Dynamics

An interesting procedure has been developed by Car and Parrinello (see [445] and, for example, [446–448]) which directly combines quantum theory with classical mechanics: The equations of the density-functional formalism [6, 7] are solved simultaneously to the classical equations of motion, so that a time-consuming iterative self-consistent procedure is not needed. This method, designated as quantum molecular dynamics, is equivalent to the self-consistent solution of the equations of the density-functional theory.

Within quantum molecular dynamics the classical Lagrange equations of the atomic positions R_j and velocities $\dot{R}_j$ are extended by a fictitious dynamics of the Kohn–Sham wave functions ϕ_i [6, 7] and their time derivations $\dot{\phi}_i$:

$$L = \sum_i \mu \int d\mathbf{r} |\dot{\phi}_i(\mathbf{r})|^2 + \frac{1}{2} \sum_j m_j \dot{R}_j^2 - E[\{\phi(\mathbf{r})\}, \{\mathbf{R}_i\}]$$
$$+ \sum_{i,j} \Lambda_{ij} \left\{ \int d\mathbf{r} \, \phi_i^*(\mathbf{r}) \phi_i(\mathbf{r}) - \delta_{ij} \right\} \tag{119}$$

The first two terms describe the kinetic energy of the nuclei and that of the orbital motion with the fictitious mass μ. The third term contains the functional of the energy as an element of the density functional formalism. The fourth term of Eq. (119) guarantees orthonormality of the wave functions, where the quantities Λ_{ij} are the Lagrange multipliers. Using this Lagrange equation we obtain the equation of motion for the nuclei

$$m_j \ddot{\mathbf{R}}_j = -\frac{\partial E}{\partial \mathbf{R}_j} \tag{120}$$

as well as the "equation of motion" for the electronic system:

$$\mu \ddot{\phi}_i(\mathbf{r}, t) = -\frac{\partial E}{\partial \phi_i(\mathbf{r}, t)} + \sum_j \Lambda_{ij} \phi_j(\mathbf{r}, t) \tag{121}$$

Equation (121) enables one to determine the wave functions $\phi_i(\mathbf{r}, t)$ as a function of time with a simultaneous motion of the atoms. It must be emphasized that this equation describes the fictitious dynamics of the electronic system and does not reflect the motion of the electrons in the field of the nuclei.

The essential difference between quantum molecular dynamics and classical molecular dynamics is that within the classical approach the forces are calculated by more or less empirically determined potentials (see Sections 5.3.1 and 5.3.2), whereas in the quantum case the forces are directly calculated from the quantum-mechanically determined potential ($E[\mathbf{R}_1, \mathbf{R}_2, \dots]$) of the system. More details concerning the principles of quantum molecular dynamics are given, for example, in [447, 448].

For a system of about 100 atoms such calculations (accurately performed) are about 1000 times slower than force field calculations and the time scale is reduced considerably. Therefore, the Car–Parrinello method in general is reduced to the picosecond time range.

Selected Studies Articles include: Wannier function analysis for understanding disordered structures generated using Car–Parrinello molecular dynamics [449], Hybrid Car–Parrinello/molecular dynamics modelling of transition metal complexes: Structure, dynamics and reactivity [450], Car–Parrinello molecular dynamics simulation of liquid water [451], A Hamiltonian electrostatic coupling scheme for hybrid Car–Parrinello molecular dynamics simulations [452], and Nonadiabatic Car–Parrinello molecular dynamics [453]. More details are given in [454–467] and in Section 6.1.

Final Remarks Molecular dynamics is in any case a *non-zero-temperature* method. On the other hand, within quantum molecular dynamics the density-functional formalism is used which is a *zero-temperature* approach and, therefore, in the case of quantum molecular dynamics non-zero-temperature data are coupled to the zero-temperature properties of the electronic part of the system. Since systems with surfaces (for example nanosystems) are in general very sensitive to small variations in temperature (in particular in connection with metals) such a treatment can lead to misleading and less relevant results, respectively, because non-zero-temperature data are mixed with zero-temperature properties. Therefore, instead of the density-functional formalism given within the Kohn–Hohenberg–Sham approach (Section 2.1.2) Mermin's formalism, briefly discussed in Section 2.1.5, should be used within quantum molecular dynamics calculations. To the authors' knowledge no calculations are reported yet on the basis on Mermin's non-zero-temperature formalism.

5.4. Covalent Binding

Many-body potentials have to be used mainly for the description of interactions within covalent bonded systems and materials, respectively, and for phenomena at higher energy levels. In metals many-body forces are less relevant because the interactions due to the conduction electrons (Section 5.3.1) are dominant.

Allinger developed widely used models (MM2, MM3) for a broad range of organic structures [468–471] which are based on the separation of the total interactions between the particles, that are significant for a bond, into a sum of single potentials with respect to *bond stretching*, *bond angle bending*, and *bond torsion*. Within the MM2 model nonbonded interactions are described by the well-known Buckingham (exp-6) potential (Section 5.1).

For the development of the interaction of such bond models a lot of *a priori* knowledge is necessary to classify all the different bond types and to treat the special cases. The MM2 and MM3 models are established to characterize within *molecular mechanics* the minimum energy configuration of structures, their stiffness, bearing properties, and the like [471], and they have become standards in literature.

The term "molecular mechanics" means the following: "Many of the properties of molecular systems are determined by the molecular potential energy function. Molecular mechanics models approximate this function as a sum of 2-atom, 3-atom, and 4-atom terms, each determined by the geometries and bonds of the component atoms. The 2-atom and 3-atom terms describing bonded interactions roughly correspond to linear springs" [471]. Molecular mechanics studies are given, for example, in [471].

Because of the basic meaning of *bond stretching*, *bond angle bending*, and *bond torsion* let us briefly discuss often used models for these interaction types [471]:

Bonds tend toward an equilibrium length r_0 and, therefore, they resist stretching and compression. Bond stretching is treated with cubic pair potentials; that is, within the MM2

model anharmonicities are taken into account. The potential energy of *bond stretching* is given by the expression

$$v_s = \frac{1}{2}k_s(r - r_0)^2\{1 - k_{cubic}(r - r_0)\} \qquad (122)$$

where r is the actual bond length, k_s is the stretching stiffness, and k_{cubic} is the parameter for describing anharmonicities.

Bond angle bending is modeled in the form of sextic three-body potentials (MM2 model) depending on the angle between two bonds to a shared atom. The potential energy v_θ for this model is given by

$$v_\theta = \frac{1}{2}k_\theta(\theta - \theta_0)^2\{1 + k_{sextic}(\theta - \theta_0)^4\} \qquad (123)$$

where θ_0 is the equilibrium bond angle, θ is actual bond angle, k_θ is the angular spring constant, and k_{sextic} is the sextic bending constant.

Bond torsion follows an expression depending on the torsion angle between two bonds within the same plane and a third one, thus acting as four-body potential; this potential describes the variation in energy associated with rotation about a bond and is expressed by

$$v_\omega = \frac{1}{2}\{V_1(1 + \cos\omega) + V_2(1 - \cos 2\omega)$$
$$+ V_3(1 + \cos 3\omega)\} \qquad (124)$$

Parameters for all the models described by (122), (123), and (124) are quoted for some common bond types in [471].

5.4.1. Models for Many-Body Potentials

Due to their complexity and difficult derivation there are basically just a few three-body potentials available which are well suited for molecular dynamics calculations and Monte Carlo studies. A comparative study and discussion of some of these empirical potentials, which have been applied mainly to carbon and silicon and other semiconductor materials, is given in [472] and the references therein.

The potentials discussed here are those of Pearson, Takai, Halicioglu, and Tiller (PTHT) [473], Stillinger and Weber (SW) [474], Biswas and Hamann (BH) [475], Tersoff (T2 and T3) [476, 477], and Dodson (DOD) [478]. These potentials constitute a good representative sample among the existing potentials (Brenner's potential will be discussed seperately); they differ in their degree of physical level, mathematical form, and range of interaction. In [472] the potentials have been tested with respect to clusters (for example, Si_2–Si_6), bulk states, and surface properties. Similarities and differences between these potentials are discussed by a systematic comparison, although a theoretical justification for the potential functions can hardly be given. They have to be considered more or less as fitting functions, since they have mostly been chosen for purely pragmatic reasons.

The potentials given by PTHT, BH, and SW can be classified as cluster potentials, the others as cluster functionals. The SW, DOD, T2, and T3 models only consider first-nearest neighbors (by the bond bending term second-neighbor interactions are implicitly considered). Interactions up to the third and seventh shell, respectively, are included in the potentials of BH and PTHT.

Cluster Potentials The cluster potentials describe bonding by means of classical two- and three-body interactions. The potential energy V can be written as

$$V = \frac{1}{2} \sum_{i,j}{}' V_2(r_{ij}) + \sum_{i,j,k}{}' V_3(r_{ij}, r_{ik}, r_{jk}) \qquad (125)$$

where all summations are distinct which is indicated by the primes. In connection with the PTHT model the potential $V_3(i, j, k)$ is symmetric with respect to an interchange of i, j, k and we have to use $i < j < k$ in the triple sum. The BH and SW models are only symmetric in j and k and the condition $j < k$ has to be used. The two-body potential is generally given by

$$V_2(r) = f_c(r)[A_1\phi_1(r) - A_2\phi_2(r)] \qquad (126)$$

where f_c is a cutoff function and ϕ_s, $s = 1, 2$, decays monotonically with r. The forms of the three-body interactions differ from each other and will be given for each potential discussed next.

The PTHT Potential Within this model the functions which define V_2 and V_3 are given by

$$f_c(r) \begin{cases} = 1 & \text{if } r < R_c \\ = 0 & \text{otherwise} \end{cases}$$

$$\phi_s(r) = r^{-\lambda_s}, \qquad s = 1, 2$$

$$V_3(r_{ij}, r_{ik}, r_{jk}) = Z\psi(r_{ij})\psi(r_{ik})\psi(r_{jk})g(\theta_i, \theta_j, \theta_k) \qquad (127)$$

$$\psi(r) = \frac{f_c(r)}{r^3}$$

$$g(\theta_i, \theta_j, \theta_k) = 1 + 3\cos\theta_i \cos\theta_j \cos\theta_k$$

where R_c is the cutoff radius and θ_1, θ_2, and θ_3 are the angles of the triangle formed by the particles i, j, and k. Within the PTHT model the two-body interaction V_2 is the Lennard-Jones potential (Section 5.2) since the exponents of $\phi_s(r)$ were chosen to be $\lambda_1 = 12$ and $\lambda_2 = 6$. V_3 is the Axilrod–Teller potential (Section 5.2).

The use of these potentials for the description of V_2 and V_3 is more than doubtful since both potentials are appropriate for noble gases but not to describe bonding in covalent system; there is simply no physical justification for that. Thus, these potentials must be viewed as fitting functions.

The PTHT model has been extensively used in the description of various materials, with and without surfaces, and it has been extended to binary and ternary systems (e.g., GaAs); more details are given in [472].

The BH Potential Within this model for the radial functions $\phi_s(r)$ Gaussians have been used, and for the cutoff function f_c a Fermi-like expression; the three-body potential function is separable. In particular, we have

$$f_c(r) \begin{cases} = \left[1 + \exp\left\{\frac{r - \sigma}{\mu}\right\}\right]^{-1} & \text{if } r \le R_c \\ = 0 & \text{otherwise} \end{cases}$$

$$\phi_s(r) = \exp(-\lambda_s r^2) \qquad s = 1, 2$$

$$V_3(r_{ij}, r_{ik}, \theta_i) = \sum_{s=1}^{2} Z_s\psi_s(r_{ij})\psi_s(r_{ik})g_s(\theta_i) \qquad (128)$$

$$\psi_s(r) = \exp(-\alpha_s r^2)f_c(r)$$

$$g_s(\theta_i) = [\cos\theta_i - \cos\phi_0]^{s+1}$$

The BH model has been used for the study of bulk and surface effects, for example, in connection with microclusters and bulk point defects [475]. More details are given in [472], in particular with respect to the determination of the parameters.

The SW Potential The radial function $\phi_s(r)$ is identical with that of the PTHT potential. The other expressions are given by

$$f_c(r) \begin{cases} = \exp\left[\frac{\mu}{r - R_c}\right] & \text{if } r \le R_c \\ = 0 & \text{otherwise} \end{cases}$$

$$V_3(r_{ij}, r_{ik}, r_{jk}) = Z\psi(r_{ij})\psi(r_{ik})g(\theta_i) \qquad (129)$$

$$\psi(r) = [f_c(r)]^{\alpha}$$

$$g(\theta_i) = (\cos\theta_i - \cos\theta_0)^2$$

f_c not only acts as a cutoff function but also defines the attractive branch of V_2 (since $\lambda_2 = 0$) and the radial components of V_3 and, therefore, the model is very sensitive to small variations in R_c.

The SW potential is mostly used in the description of systems with covalent bonds, for example, in connection with clusters, lattice dynamics, bulk point defects, etc. The potential has been applied to Si, Ge, sulfur, and fluorine and to the Si–F system [472].

Cluster Functionals Of particular interest are the cluster functionals of Tersoff type, where the bonding is described by means of pairwise interactions, but many-body interactions are effectively included with respect to the attractive term of the pair interaction which is dependent on the local environment. The potential energy takes the form

$$V = \frac{1}{2} \sum_{i,j}{}' f_c(r_{ij})\{A_1\phi_1(r_{ij}) - A_2\phi_2(r_{ij})p(\xi_{ij})\} \qquad (130)$$

where ξ_{ij} is the effective coordination number and determines p which is a measure of the bond order, where we have to consider that p has in general the property

$$p(\xi_{ij}) \ne p(\xi_{ji})$$

ξ_{ij} is given by

$$\xi_{ij} = \sum_{k \ne i,j} V_3(r_{ij}, r_{ik}, \theta_i) \qquad (131)$$

with

$$V_3(r_{ij}, r_{ik}\theta_i) = \psi(r_{ij}, r_{ik})g(\theta_i) \qquad (132)$$

Rewriting (130) the two-body energy term can be extracted and we get

$$V = \frac{1}{2}\sum_{i,j}{}' V_2(r_{ij}) + \frac{1}{2}\sum_{i,j}{}' A_2\phi_2(r_{ij})f_c(r_{ij})$$
$$\times \{1 - p(\xi_{ij})\} \qquad (133)$$

It can be shown by simple manipulations that the second term of (133) effectively includes many-body effects [472].

The DOD Potential Dodson chose the following form for the model functions:

$$f_c(r)\begin{cases} = \frac{1}{2}\left[1 - \cos\left(\frac{\pi(r - R_c)}{\mu}\right)\right] \\ \qquad \text{if}\quad R_c - \mu < r < R_c \\ = 1 \qquad \text{if}\quad r \le R_c - \mu \\ = 0 \qquad \text{otherwise} \end{cases}$$

$$\phi_s(r) = \exp(-\lambda_s r) \qquad s = 1, 2$$
$$p(\xi_{ij}) = \exp(-\xi_{ij}^n) \qquad (134)$$
$$\psi(r_{ij} r_{ik}) = \left[\frac{\phi_2(r_{ik})f_c(r_{ik})}{\phi_2(r_{ij})f_c(r_{ij})}\right]^\alpha$$
$$g(\theta_i) = \frac{\beta}{\eta + \exp(-\delta \cos\theta_i)}$$

This potential has been used for studying surface reconstructions and low-energy beam deposition of Si. It should be mentioned that the DOD potential is similar to the first Tersoff potential [479].

The Tersoff Potential (T_2 and T_3) Here two different parametrizations are used for the same potential, leading to the T_2 and T_3 potentials. The expressions for f_c and ϕ_s are identical with those used within the DOD potential. The other functions have been chosen as follows:

$$p(\xi_{ij}) = (1 + \xi_{ij}^n)^{-1/2n}$$
$$\psi(r_{ij}, r_{ik}) = f_c(r_{ik})\exp(\alpha^3(r_{ij} - r_{ik})^3) \qquad (135)$$
$$g(\theta_i) = \beta + \frac{\eta^2}{\delta^2} - \frac{\eta^2}{\delta^2 + (\cos\theta_i - \cos\theta_0)^2}$$

The potential parameters for Si were fitted to the cohesive energy, lattice parameter, and bulk modulus of the diamond structure, and the cohesive energy of bulk polytypes of silicon [480, 481]. In connection with the T_3 model an additional constraint was used in order to fit the three elastic constants.

The T_2 and T_3 potentials have been used to study lattice dynamics, microclusters, bulk point defects, the liquid and amorphous states, surface reconstructions, etc. More details are given in [472].

It should be emphasized that the Tersoff formalism is obviously similar to the embedded-atom method (Section 5.3.4) since by a proper choice of functional forms and model parameters the two expressions for the potential energy can be made identical [482].

Other Potentials Further expressions for the potential form exist in the case of covalent binding, but here we only want to quote the empirical potential by Brenner [483] which has often been used in the description of numerous processes including the nanometer-scale indentation of diamond surfaces, the deformation of carbon nanotubes, the formation of fullerenes from graphitic ribbons, etc. [484]. The Brenner potential (the so-called hydrocarbon potential) can be formulated as follows [483]: The binding energy for the potential is formulated as a sum over bonds as

$$E_b = \sum_i \sum_{j>i}[V_R(r_{ij}) - \overline{B}_{ij}V_A(r_{ij})] \qquad (136)$$

where the repulsive pair term is given by

$$V_R(r_{ij}) = f_{ij}(r_{ij})D_{ij}^{(e)}/(S_{ij} - 1)e^{-\sqrt{2S_{ij}}\beta_{ij}(r - R_{ij}^{(e)})} \qquad (137)$$

and the attractive pair term has the form

$$V_A(r_{ij}) = f_{ij}(r_{ij})D_{ij}^{(e)}S_{ij}/(S_{ij} - 1)e^{-\sqrt{2S_{ij}}\beta_{ij}(r - R_{ij}^{(e)})} \qquad (138)$$

The function $f_{ij}(r)$ restricts the pair potential to nearest neighbors and is given by

$$f_{ij}(r)\begin{cases} = 1 \qquad r < R_{ij}^{(1)} \\ = \frac{1}{2}\left[1 + \cos\left\{\frac{\pi(r - R_{ij}^{(1)})}{(R_{ij}^{(2)} - R_{ij}^{(1)})}\right\}\right] \\ \qquad R_{ij}^{(1)} < r < R_{ij}^{(2)} \\ = 0 \qquad r > R_{ij}^{(2)} \end{cases} \qquad (139)$$

We do not want to discuss the details of this potential and refer to [483], but the following should mentioned: If $S_{ij} = 2$, then the pair terms have the form of the usual Morse potential (Section 5.1) and, furthermore, the equilibrium distance $R_{ij}^{(e)}$, the well depth $D_{ij}^{(e)}$, and the parameter β_{ij} are equal to the parameters for the usual Morse potential (independent of the value of S_{ij}). Critical remarks concerning the Morse potential are given in Section 5.1.

Applications The potentials introduced above are important for the description of covalent systems, in particular, in connection with carbon and silicon systems, respectively. Let us quote here some selected studies which are based on the often used potentials by Stillinger and Weber, Tersoff, and Brenner.

Stillinger–Weber Potential Articles include: Nearest neighbor considerations in Stillinger–Weber type potentials for diamond [485], Development of an improved Stillinger–Weber potential for tetrahedral carbon using *ab initio* (Hartree–Fock and MP2) methods [486], Computed energetics for etching of the Si(100) surface by F and Cl atoms [487], Boson peak in amorphous silicon [488], and Strain profiles in pyramidal quantum dots by means of atomistic simulation [489]. Further information is given in [490–499].

Tersoff Potential Articles include Modeling chemical and topological disorder in irradiation-amorphized silicon carbide [500], Atomic diffusion at solid/liquid interface of silicon: Transition layer and defect formation [501], Predictive study of thermodynamic properties of GeC [502], Orientation dependence in C_{60} surface-impact collisions [503], Parameter optimization of Tersoff interatomic potentials using genetic algorithm [504], etc. [505–522].

Brenner Potential Articles include: Monte Carlo simulations of carbon-based structures on an extended Brenner potential [523], Numerical study of shapes of fullerenes with symmetrically arranged defects [524], Energy window effect in chemisorption of C_{36} on diamond (001)-(2 × 1) surface [525], Reconstruction of diamond (100) and (111) surfaces: Accuracy of the Brenner potential [526], Phonon spectra in model carbon nanotubes [527], and Interaction among C_{28} clusters and diamond (002) surfaces [528]. More information is given in [529–541].

6. MOLECULAR DYNAMICS

In this section we give an overview about recent results in the field of molecular dynamics. Clearly, not all studies could be considered but we selected interesting investigations which, on the other hand, also reflect a broad variety of applications in connection with nanometer-scale molecular dynamics. First a brief overview about various topics is given. Then some specific molecular dynamics models will be discussed which is followed by a more detailed study of metallic nanosystems.

6.1. Design at the Nanolevel

6.1.1. Recent Developments

Selected studies about the following topics are compiled: nanomachines, metallic nanosystems, biological systems, nanostructures and nanostructured materials, nanoclusters and nanoparticles, nanotubes and fullerenes, nanowires, and silicon and carbon.

Nanomachines Articles include: Molecular mechanics and molecular dynamics analysis of Drexler–Merkle gears and neon pump [542], Docking envelopes for the assembly of molecular bearings [543], dynamics of He/C_{60} flow inside carbon nanotubes [544], On the importance of quantum mechanics for nanotechnology [545], dynamics and fluid flow inside carbon nanotubes [546], Dynamics of a laser-driven molecular motor [547], and The dynamics of molecular bearings [548].

Metallic Nanosystems Articles include: Simulation of chemical mechanical planarization of copper with molecular dynamics [549], Atomistic simulations of solid-state materials based on crystal-chemical potential concepts: Applications for compounds, metals, alloys, and chemical reactions [550], Metallic nanoislands: Preferential nucleation, intermixing and electronic states [551], Large-scale molecular dynamics study of the nucleation process of martensite in Fe–Ni alloys [552], Molecular dynamics simulation of the grain-growth in nano-grained metallic polycrystals [553], and Melting and freezing of gold nanoclusters [554]. Further studies can be found in [555–594].

Biological Systems Articles include: Completion and refinement of 3-D homology models with restricted molecular dynamics [595], Simulation of biological ionic channels by technology computer-aided design [596], Interfacing molecular dynamics with continuum dynamics in computer simulation: Towards an application to biological membranes [597], Structural properties of a highly polyunsaturated lipid bilayer from molecular dynamics simulations [598], Comparison of aqueous molecular dynamics with NMR relaxation and residual dipolar couplings favors internal motion in a mannose oligosaccharide [599], Molecular dynamics simulation of thymine glycol-lesioned DNA reveals specific hydration at the lesion [600], A molecular dynamics study based post facto free energy analysis of the binding of bovine angiogenin with UMP and CMP ligands [601], and Molecular dynamics of DNA quadruplex molecules containing inosine, 6-thioguanine and 6-thiopurine [602]. More information about molecular dynamics in connection with biological systems is given in [603–637].

Nanostructures and Nanostructured Materials Articles include: Molecular dynamics in nanostructured polyimide–silica hybrid materials and their thermal stability [638], Computer simulation of displacement cascades in nanocrystalline Ni [639], Mechanical properties of nanostructured materials [640], Sintering, structure, and mechanical properties of nanophase SiC: A molecular dynamics and neutron scattering study [641], Multiresolution algorithms for massively parallel molecular dynamics simulations of nanostructured materials [642], Computer modeling the deposition of nanoscale thin films [643], and Molecular dynamics simulation of lattice distortion region produced by rounded grain boundary in nanocrystalline materials [644]. Further information about this topic is given in [645–689].

Nanoclusters, Nanoparticles Articles include: Charge dependence of temperature-driven phase transitions of molecular nanoclusters: Molecular dynamics simulation [690], Theoretical study of the atomic structure of Pd nanoclusters deposited on a MgO(100) surface [691], Melting of bimetallic Cu–Ni nanoclusters [692], Structure and properties of silica nanoclusters at high temperatures [693], Platinum nanoclusters on graphite substrates: A molecular dynamics study [694], and Study of self-limiting oxidation of silicon nanoclusters by atomic simulations [695]. More information about molecular dynamics in connection with nanoclusters and nanoparticles is given in [696–731].

Nanotubes and Fullerenes Articles include: Computational studies of gas–carbon nanotube collision dynamics [732], Binding energies and electronic structures of adsorbed titanium chains on carbon nanotubes [733], Microscopic mechanisms for the catalyst assisted growth of single-wall nanotubes [734], Nanotube and nanohorn nucleation from graphitic patches: Tight binding molecular dynamics simulations [735], Carbon nanotubes as masks against ion irradiation: An insight from atomistic simulations [736], Molecular dynamics and quantum mechanics investigation on mechanic-electric behaviors of nanotubes [737], Molecular dynamics study of the fragmentation of silicon-doped fullerenes [738], Fullerene cluster between graphite walls— Computer simulation [739], and Se atom incorporation in

fullerenes by using nuclear recoil and *ab initio* molecular dynamics simulation [740]. Further information is given in [741–821].

Nanowires Articles include: Thermal properties of ultra-thin copper nanobridges [822], Atomic-scale simulations of copper polyhydral nanorods [823], Size effect on the thermal conductivity of nanowires [824], Structural transformations, amorphization, and fracture in nanowires: A multimillion-atom molecular dynamics study [825], and Large deformation and amorphization of Ni nanowires under uniaxial strain: A molecular dynamics study [826]. More information about molecular dynamics in connection with nanowires is given in [827–842].

Silicon and Carbon Articles include: Structural transition in nanosized silicon clusters [843], Molecular dynamics studies of plastic deformation during silicon nanoindentation [844], Computational nanotechnology with carbon nanotubes and fullerenes [845], Neck formation processes of nanocrystalline silicon carbide: A tight-binding molecular dynamics study [846], Amorphization and anisotropic fracture dynamics during nanoindentation of silicon nitride: A multimillion atom molecular dynamics study [847], Non-equilibrium molecular dynamics simulation study of the behavior of hydrocarbon-isomers in silicalite [848], Pressure-controlled tight-binding molecular dynamics simulation of nanoscale nanotubes [849], and Effect of chirality on the stability of carbon nanotubes: Molecular dynamics simulations [850]. Further information is given in [851–921].

6.1.2. Specific Molecular Dynamics Investigations on Nanosystems

Nanogears Concerning nanogears interesting models have been studied by Globus and co-workers from the NASA Advanced Supercomputing Division (see, for example, [922]). A typical example is given in Figure 11: The operation of these nanogears was simulated using molecular dynamics calculation and Brenner's hydrocarbon force field (Section 5.4.1). The study showed that if one gear is turned by an external force, the second gear will turn as well. Furthermore, if the gears are driven too fast (input rate >0.4
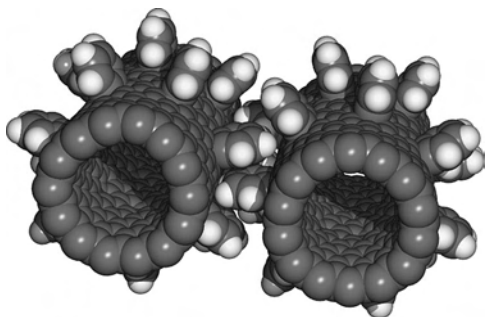

Figure 11. On the basis of fullerene nanotechnology it is possible to construct nanomachines, for example, nanogears. A typical gear configuration, designed by A. Globus (NASA Advanced Super-computing Division), is shown in the figure (see, for example, also [822]). The operation of these nanogears was simulated using molecular dynamics calculation on the basis of Brenner's hydrocarbon force field (Section 5.4.1). Courtesy of NASA.

rotations per picosecond), then slippage occurs but bonds do not break and normal operation will resume when the rotation rate slows.

Bending of Nanotubes The bending of a (8,8) nanotube has been simulated in [923]. The study was performed on the basis of molecular dynamics calculations. For the interatomic interaction Brenner's potential has been used (Section 5.4.1). The results are shown in Figure 12. The 21 nm long tube contained 2688 atoms. In the simulation a portion of 3.6 Å was fixed from both ends of the tube. One of the ends was forced to move on a half-circular path at a constant rate. The radius of the circular path was a half of the tube length. The total bending time was 250,000 fs during which the simulation temperature was kept at 300 K.

Atomistic Simulations of Plastic Deformations in Glassy Amorphous Polymers [924] as the demand for polymers with superior properties increases, an understanding of the fundamental connections between the mechanical behavior and underlying chemical structure becomes imperative. In this work, the thermo-mechanical behavior and the molecular-level origins of elastic and plastic deformation in an amorphous glassy polymer were studies using molecular dynamics simulations (Fig. 13a). A velocity Verlet integration scheme with a Berendsen barostat and a Nose–Hoover thermostat were used to study a system of united atom polyethylene. These simulations provide detailed atomic information that has been used to verify experimental results. Stress-induced mobility has been directly observed within these simulations (Fig. 13b), corroborating similar observations in nuclear magnetic resonance experiments of Loo et al. [925]. Dihedral angle transition rates are observed to increase during active deformation and drop off again when deformation ceases. These simulations also show that there is no correlation between local volume and dihedral angle transitions in this system.

Models of the Dodecamer DNA Double Stranded Segment Molecular dynamics simulations were performed on models of the dodecamer DNA double stranded segment [d(CGCGAATTCGOG)], in which each of the adenine residues, individually or jointly, was replaced by the water-mimicking analog 2′-deoxy-7-(hydroxymethyl)-deazaadenosine (hmdA). The simulations, when compared to the dodecamer itself, show that incorporation of the analog affects neither the overall DNA structure nor its
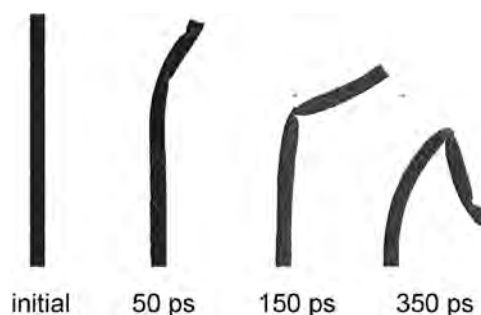

initial   50 ps   150 ps   350 ps

Figure 12. Bending of a (8,8) nanotube by molecular dynamics. reprinted with permission from [923] M. Huhtala et al., *Comp. Phys. Comm.* 147, 91 (2002). © 2002, Elsevier Science.
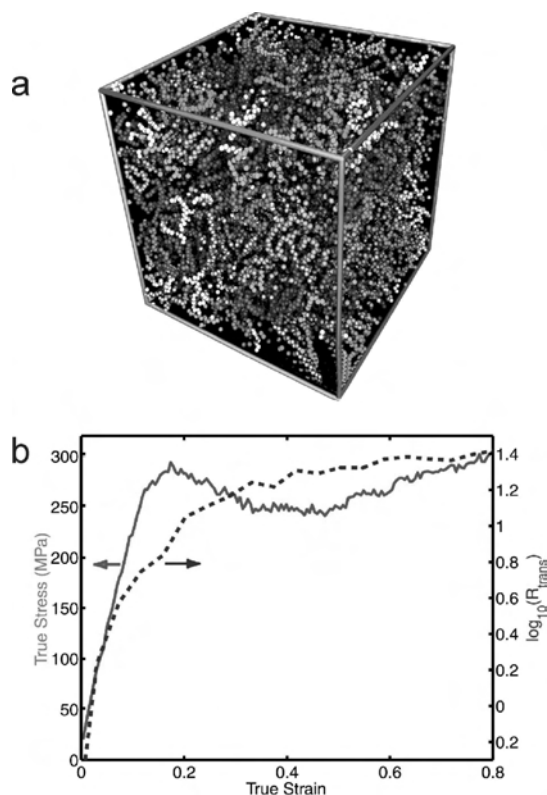
Figure 13. (a) Snapshot of a simulation cell containing a united atom representation of 160 polyethylene chains each with 250 beads. (b) Compressive true stress (red line) and the logarithm of transition rate per bond per nanoseconds, R_{trans} (blue line), versus true strain for a system deformed at a constant true strain rate of 5×10^{10} per second along the x-axis at 200 K while the lateral faces were held at atmospheric pressure. Courtesy of F. M. Capaldi, M. C. Boyce, G. C. Rutledge, Massachusetts Institute of Technology (MIT), Department of Chemical Engineering, Cambridge, MA.

hydrogen-bonding and stacking interactions when a single individual base is replaced by the analog. Furthermore, the water molecules near the basis in the single-substituted oligonucleotides are similarly unaffected (Fig. 14). Double substitution lead to differences in all the aforementioned parameters with respect to the reference sequence [926].

Visualization of the Pathway of Diffusants in Amorphous Polymers   The diffusion in nanoconfined polymers has been studied by Boshoff and co-workers [527] in order to study the effects of polymer structure and dynamics on the molecular mechanism of diffusion (see also Fig. 15).

6.2. Metallic Nanosystems

As we have outlined, the interaction potentials for nanosystems have to be constructed carefully since surface properties are in general very sensitive to small variations in the potential shape, and in the case of nanosystems a great fraction of atoms belongs to the surface region of the system. This effect is particularly significant in the case of metals.

The determination of pair potentials for metals can be done, for example, by means of pseudopotential theory that
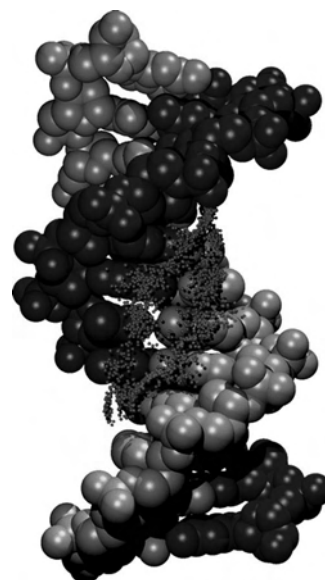

Figure 14. Molecular dynamics simulations were performed on models of the dodecamer DNA double-stranded segment, in which each of the adenine residues, individually or jointly, was replaced by the water-mimicking analog 2′-deoxy-7-(hydroxymethyl)-deazaadenosine (hmdA). Water molecules within hydrogen bonding distance (proton–acceptor distances < 2.5 Å and angle donor–proton acceptor > 120 to the acceptor/donor groups of the GAATIC bases) were selected and are shown superimposed (for a better understanding the oxygen atoms of the water molecules are shown as vdW spheres with a reduced radius). The DNA atoms are vdW representation. The analog bases are shown in gray. More details are given in the text. This image was made by the Theoretical Biophysics group at the Beckman Institute, Courtesy of University of Illinois at Urbana–Champaign.

we have discussed in Section 5.3.1. In this section we would like to study molecular dynamics results for Al (as a typical example for a metal system); the specific behavior of *clusters* will be discussed, but also some remarks in connection with
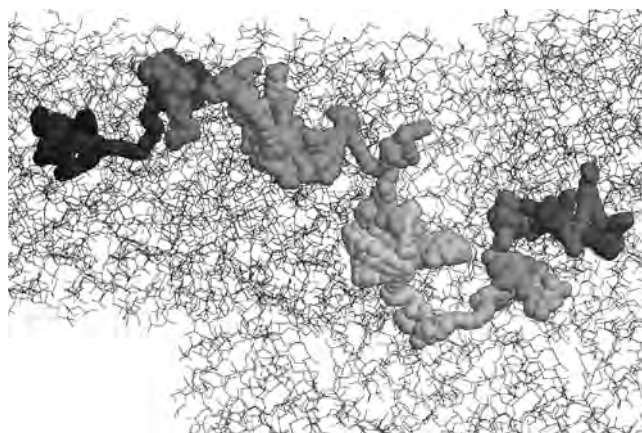
Figure 15. A diffusion pathway of a tracer He atom in a glassy, amorphous polypropylene model. Each colored sphere represents a snapshot of the He atom's position along a 150 ps trajectory (starting at blue and ending at red), as calculated by molecular dynamics at 233 K. Snapshot are spaced 0.1 ps apart. The polymer is represented by carbon–carbon bond for clarity. Courtesy of J. Boshoff, Chemical Engineering, University of Delaware.

nanoengineering will be given. The potential for Al used in this study has been determined in accordance with the principles outline in Section 5.3.1.

6.2.1. Interaction Potential for Al

In the case of noble gases (for example, krypton [928]) the temperature dependence of system properties can be treated in a good approximation on the basis of temperature-independent pair potentials. That is in general not possible in the case of metals. Why?

As we have already outlined in Section 5.3.1, a metal consists of ions and conduction electrons. The interactions between the ions are strongly influenced by the *screening* of the conduction electrons, and the screening is sensitive to the density of the conduction electrons, which is, on the other hand, temperature dependent. Therefore, we may conclude that the pair potential in metals is in general dependent on temperature. This property is reflected in the dielectric function $\varepsilon(q)$, which in turn is important for the determination of the pair potential within the framework of pseudopotential theory.

How large are such temperature effects for Al? In a first attempt [929] a pseudopotential was used, developed by Dagens et al. [930]. This potential is a nonlocal pseudopotential; the screening is described by the Geldart–Taylor dielectric function. However, this potential was not sufficient to describe certain properties at the surface. Therefore, another model has been chosen for the pseudopotential which is obviously more realistic [931]. Concerning this model, the essential point is the consideration of interactions of *van der Waals type* in the determination of the direct ion–ion potential as well as in the ion–electron part of the interaction. (Numerical calculations for liquid rubidium near the melting point showed that van der Waals-type interactions are distinctly reflected in the metal potential [932].)

The pair potential for Al based on this kind of potential is shown in [933] for two temperatures (300 and 1000 K; the melting temperature is 933 K). The free parameters were fitted with the help of crystal and liquid data for various temperatures and, therefore, the temperature-dependent Al potential describes a wide range of experimental bulk and surface properties:

(1) The crystal is stable up to the melting point. The phonon density of states at $T = 300$ K is described well. (2) The structure and dynamics of the liquid state are also described adequately by the potential: The structure factor (Fourier transform of the pair correlation function) of the liquid state agrees well with experimental data, and the correct value of the diffusion constant is obtained. (3) The melting temperature (933 K) of Al is reproduced by the potential. (4) We found for the outermost layer an inward relaxation, which is confirmed by experiments [934]. (5) The mean-square displacements at the surface agree well with LEED data [934]. (6) The molecular dynamics results indicate that there are relatively strong anharmonic effects already at low temperatures; this is confirmed by experiments [934], too. (7) The onset of premelting ($T > 650$ K) resulting from the molecular dynamics calculations agrees excellently with the experimental observations.

6.2.2. Metastable Cluster-States

Molecular dynamics calculations have been performed for cubic nanoclusters with (001) surfaces consisting of $N = 500$ atoms [935]. For this system the classical Hamilton equations were solved by iteration. The time step in the calculation was 10^{-15} s. The number of time steps was 4000 (4 ps). The initial values for the positions were chosen to be the bulk structure. In the case of Al and $N = 500$ particles, the box size of the clusters is approximately 20 Å. The cutoff radius for the interaction potential was chosen as the sixth nearest neighbor distance.

The initial velocities have been set according to a temperature of 50 K followed by an equilibration phase of 2000 time steps (2 ps). In the following $t = 0$ refers to the end of the equilibration phase (i.e., the time at which the system has reached thermal equilibrium). The initial directions of the velocities were distributed randomly, so that the velocity averaged over all particles was zero and remained zero for all time steps.

The amplitudes of the velocities determine the temperature T of the system [Eq. (80), Section 4.2.3] and also the α-function [Eq. (75), Section 4.2.3] which can be used for the study of the thermodynamic state. As already outlined in Section 4.2.3, due to the finite number of particles T and α fluctuate around mean values.

Figure 16 shows the temperature T and the α-function as a function of time t. As can be seen, there are three different phases: (1) In the interval $0 \leq t \leq 1$ ps the cluster remains in thermal equilibrium (α fluctuates around 5/3) at a mean temperature of 50 K (with the usual, stable fluctuations). (2) Within the interval $1 \leq t \leq 2$ ps a transition takes place without any external influence, and within this time interval the temperature rises up to 160 K. (3) Finally, for $t > 2$ ps
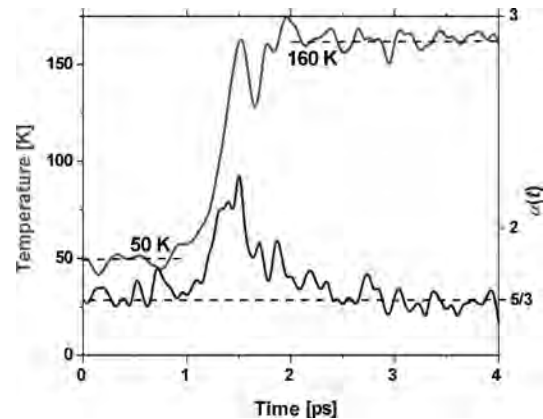
Figure 16. Temporal development of the temperature and the α-function for a cubic Al_{500} cluster with (001) surfaces. Initially, the cluster remains in thermal equilibrium at about 50 K for 1 ps ($\alpha = 5/3$ indicates thermal equilibrium, Section 4.2.3). Then, during a transition phase the cluster temperature increases to 160 K. During the transition phase of 1 ps the cluster leaves equilibrium. After this process, the mean temperature remains at 160 K for all times and the system also remains in thermal equilibrium. It should be emphasized that the whole process takes place without external influence; that is, there is no outer effect causing the transition.

the cluster temperature remains at 160 K and in thermal equilibrium (α fluctuates around 5/3).

How can we interpret this transition? What is the driving force behind this phenomenon and, furthermore, under what conditions does it occur?

The cluster is obviously in a metastable state within the first phase (50 K), and in the third phase (160 K) it is in a stable state. Further, due to the energy conservation of the system the potential energy of the cluster in the stable state has to be smaller compared to that in the metastable state. Therefore, the structure of the metastable state should be different from that of the stable state, since the potential energy depends on the relative distances of the atoms. Let us first study the structure and after that the Dynamics of the cluster in the metastable state as well as in the stable state.

Structure The structure of the different cluster states has been studied by means of the structure factor (see, for example, [393])

$$S(q) = \frac{1}{N} \sum_{i,\,j=1}^{N} \langle \exp[i\mathbf{q}(\mathbf{r}_i - \mathbf{r}_j] \rangle \qquad (140)$$

where $\langle \cdots \rangle$ denotes again statistical averaging, $\mathbf{q}$ is the wave vector, and $\mathbf{r}_i$ is the position vector of the ith particle. By averaging of $\mathbf{q}$ over all directions, $S(\mathbf{q})$ only depends on the magnitude of $\mathbf{q}$: $S(q)$ with $q = |\mathbf{q}|$.

Figure 17 shows the results of $S(q)$ for the metastable and the stable state together with the results for the bulk state (500 particles with periodic boundary conditions). As can be seen, the typical double peak of fcc-structured materials at about 2.7 and 3.1 Å^{-1} appears also for the other states (indicated in Fig. 17 by gray bars). However, the metastable cluster state additionally exhibits a well pronounced peak at 3.4 Å^{-1} which is missing in the stable state as well as in the bulk (indicated by the yellow bar). This peak can be interpreted as a superstructure that has been formed within the metastable cluster due to a periodical particle shift.

Dynamics The cluster dynamics has been studied by means of the generalized phonon density of states $f(\omega)$, and this quantity can be calculated from the velocity autocorrelation function $\phi(t)$ by means of a Fourier transform (Section 4.2.3). As already outlined in Section 4.2.3, the Fourier transform of $\phi(t)$ yields a frequency spectrum which is, in the case of the *harmonic* solid, the frequency spectrum of the normal modes. Thus, for an *anharmonic* system, for example, clusters, we can define a generalized phonon density of states $f(\omega)$ by means of the Fourier transform of $\phi(t)$.

$\phi(t)$ has been calculated by molecular dynamics, and its Fourier transform is shown in Figure 18. In Figure 18 the generalized phonon density of states is given as a function of ν with $\omega = 2\pi\nu$. For the metastable state $f(\nu)$ at 50 K is quite different from that of the stable state at 160 K. In particular, the pronounced peak at 2 THz (metastable state) does not appear in the frequency spectrum of the stable state (and also not in the bulk). Thus, we may conclude that the appearance of the superstructure in the metastable state (Fig. 17) is accompanied with the appearance of the low frequency mode at 2 THz. This mode is completely missing
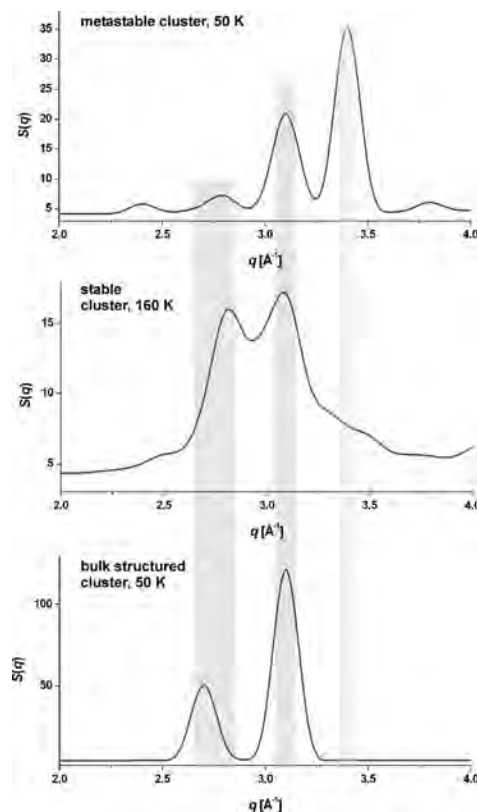
Figure 17. Structure factor $S(q)$ of a cubic Al$_{500}$ cluster with (001) surfaces which is in the metastable and stable state, compared with $S(q)$ for the bulk (also here 500 particles have been used but with periodic boundary conditions). The light blue bars indicate peaks which are common for all phases; they are typical for Al. The yellow bar emphasizes the well pronounced peak at 3.4 Å^{-1} that appears only in the metastable phase and could be a hint for a superstructure.

Figure 18. Generalized phonon density of states $f(\nu)$ of a cubic Al$_{500}$ cluster in the metastable and stable state. The well pronounced peak at 2 THz in the frequency spectrum of the metastable state is recognizable to some extent only in the stable state. This peak results from surface oscillations at the metastable cluster.

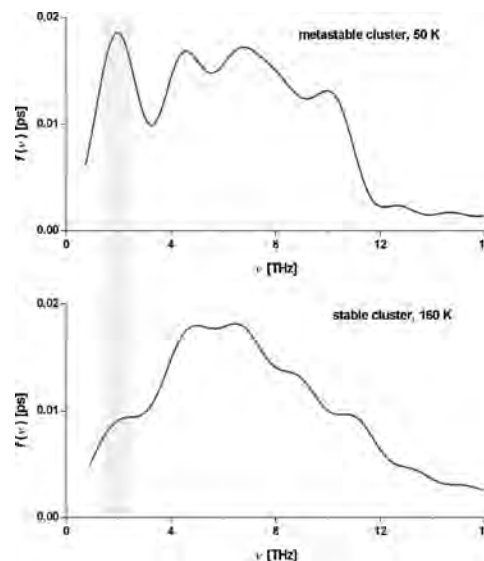in the spectrum of the solid in the bulk as well as in the liquid bulk state. The low frequency mode is probably the cause for the transition from the metastable to the stable cluster state. Let us briefly discuss this.

The outer dimensions of the metastable cluster are smaller compared to the initial bulk-structured cluster. Therefore, during the equilibration phase the whole cluster passes through a "shrinking process," and due to the repulsion, this shrinking process should be followed by a "recoiling effect"; that is, there is an oscillation reflected in a temporal change of shrinking and recoiling leading to a "breathing" of the whole cluster.

In connection with Figure 16 we discussed that the potential energy V_{ms} of the metastable state must be larger than the potential energy V_s of the stable state. Since the transition takes place after a certain time and not at once, we can conclude that there is a certain potential barrier ΔV_{ms} which the cluster has to overcome. The "breathing" of the cluster can lead to the effect that the system has, at a certain time, the potential energy $V \geq V_{ms} + \Delta V_{ms}$, and then the transition from the metastable to the stable state can take place; it is only a question of time until a fitting configuration has established by chance which yields a potential energy high enough ($V \geq V_{ms} + \Delta V_{ms}$) to overcome the potential-energy barrier.

Analogies to Atomic Excitations There is a certain analogy between metastable states of clusters and of atoms in an excited electron state: (1) The potential energy in the excited (metastable) state is larger than in the ground (stable) state. (2) The systems (atoms, clusters) leave their excited (metastable) state without external influence after a certain time interval: the atoms by emiting photons, the clusters by increasing their temperature (see also Fig. 16).

The atoms are in an excited state for 10^{-8} s while the clusters are in a metastable state for approximately 10^{-12} s. The time interval of 10^{-12} s is much smaller than 10^{-8} s (excitation time of atoms). Nevertheless, the lifetime of 10^{-12} s of the metastable state is relatively large; it is distinctly larger than the time interval (0.4×10^{-12} s) that a sound wave needs for the propagation across the nanosystem. The lifetime of such metastable states is a function of the particle number and is also a function of the outer shape of the nanosystem [3].

6.2.3. Bifurcation Phenomena

In connection with metastable states of clusters the following effect is of particular interest: When a cluster transforms from the metastable to the stable state, there are several possibilities for that. In other words, the local minimum in the potential energy of the metastable state is surrounded by numerous deeper minima which correspond to numerous stable states. Which of these stable states the cluster will finally take cannot be predicted in principle. Due to the unavoidable fluctuations in the potential energy of such nanosystems it is completely a matter of chance (Section 6.2.2).

In other words, in connection with cluster state transitions there is a *bifurcation* in the sense of chaos theory (Fig. 19): At the bifurcation point nature plays dice to decide on which
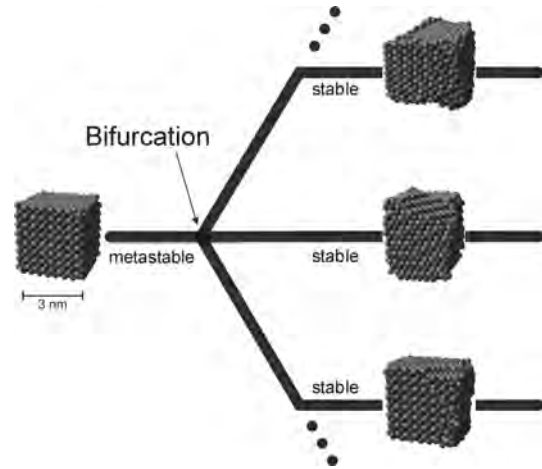

Figure 19. Illustration of the bifurcation phenomenon: In principle it cannot be predicted in what stable state the metastable systems transits. At the bifurcation point nature plays dice in order to decide on which of the various branches the cluster will finally rest.

of the various branches (stable states) the cluster will finally rest.

Stable cluster configurations may differ in both the inner structure as well as the outer shape. In general, the inner structures show multicrystalline compositions (i.e., there are grain boundaries, dislocations, and other lattice defects). The outer shapes of the clusters strongly depend on the arrangement of these lattice defects.

This is an interesting phenomenon and there is no counterpart in micro- and macrotechnique. In macrotechnique, a system (for example, a machine) will always be destroyed after a certain time, if the mechanic does not keep the machine in good condition; this degradation of the system is due to its interaction with the systems surrounding. There are no other transitions in micro- and macrotechnique. As we have seen, the situation is different in connection with nanosystems: The transition at the bifurcation point is constructive; the system will not simply be destroyed but there emerge new forms, namely one of the possible stable states (see Fig. 19).

As said, in micro- and macrotechnique we do not observe such phenomena, and this is because there are no such metastable states. If there were, nevertheless, metastable states also established in the macroscopic realm, in principle a screwdriver could transform spontaneously into a hammer or a nippers; Nature plays dice; a screwdriver becomes either a hammer or a nippers, and such transitions would take place without any external influence. We know that such phenomena are not possible in micro- and macrotechniques but should be real phenomena in nanotechnology, in particular, within the frame of materials research at the nanolevel.

The bifurcation phenomenon is the behavior of single clusters. This specific behavior comes into play by the mutual influence of temperature and the interaction between the particles forming the cluster. There is a certain kind of independent creativity which does not come from outside; that is, it is not forced by the observer or by other factors of the

environment but is an inherent characteristic of the system itself. Such behavior is also known in connection with biological systems, which are, however, much more complex compared to the Al clusters studied here. Since this specific behavior (creativity) is essentially influenced by the temperature and the interaction potential between the particles, nanosystems at zero temperature have to be considered as "dead" systems without any creativity.

6.2.4. Final Remarks

Although the Al clusters represent *inorganic* systems there are certain analogies to biological systems:

(1) A nanosystem can be creative; that is, it can meet individual decisions which cannot be influenced from outside; the bifurcation phenomena (Fig. 18) can be interpreted in this way.
(2) A nanosystem is able to transform spontaneously; it can transform from a metastable state to a stable state without external influence. Spontaneous transformations are also typical phenomena within biology, in particular in connection with embryology.
(3) New forms, new shapes, which were not existent before, emerge without external influence. Also within biology (e.g., in embryology) new forms appear, which were not existent before.
(4) The shapes of such nanosystems transform to more complex forms. This behavior too is typical for biological systems and is a feature of biological evolution. The nanosystems transform, for example, from a cube to a cuboid, and a cuboid is more complex than a cube because one needs more description elements to characterize it.

6.3. Nanoengineering

6.3.1. Nanomodels

So far the general procedures and different elements for designing molecular dynamics models have been discussed. As long as there are just single and simple shaped objects of interest, like cubical nanoclusters, the setup of an appropriate molecular dynamics model is relatively easy. Since the initial positions are given by the perfect lattice structure such objects can be built by using any programming language to implement the according algorithms. Depending on the variety of materials, characterized by the lattice constant and structure (fcc, body-centered cubic, hexagonal, etc.), and depending on the possible orientations [(001), (011), (111), and so on] the software development is more or less extensive. For the generation of (semi-infinite) surface models the additional application of periodic boundary conditions (within two dimensions) is necessary.

But obviously such simple objects are only of minor interest within the field of nanoengineering, where either structures with complex shapes or interactions (cluster–cluster or surface–cluster) under various conditions play an important role. Especially for studies of nanomachines (but for others too) the molecular dynamics (MD) models have to contain moving parts in addition to objects of miscellaneous materials, and therefore, the software should be able to combine single structures, each with different initial values.

Quite clearly, the development of a computer program that can generate MD models for all the above-mentioned topics is rather extensive. While the setup of simple structures (cuboids, spheres, surfaces) and the setup of the initial values according to rotational or transitional movements and for the construction (positioning, centering, adjusting) of individual objects may be fixed by usual programming, the nanodesigning part of complex shapes has been accomplished by a common commercial software.

The idea arose from the fact that for metallic nanostructures—unlike covalent bonded materials—there are basically no restrictions concerning their initial shapes (i.e., in this case a molecular dynamics model can be built first by defining the outer shape and then by filling it up with atoms according to the crystal lattice). Since the design of three-dimensional shapes is a very common topic within mechanical engineering—the so-called computer aided design (CAD)—one can use a suitable CAD software with a programming interface to perform such a task.

Here the choice fell on the commercial software package Genius Desktop® (in combination with Mechanical Desktop®) that includes a LISP derivative as programmable interface. At first, two additional system functions have been developed, one to compute the outer limits of a three-dimensional CAD object, the other to determine whether a given spatial point lays within a selected object or not. Then, with the help of these functions the implementation of various filling, scaling, and storage algorithms for different lattice structures has been performed.

But in contrast to common mechanical engineering the nanodesign does not end here. The nanomodel with its initial atomic perfect lattice positions corresponds to a temperature of 0 K. So the next step is to accelerate the atoms until an equilibrium is reached according to a prescribed specific model temperature. Such an equilibration is performed during a sufficient number of MD calculation steps by rescaling the particle velocities:

$$\mathbf{v}_i(t) \leftarrow \sqrt{\frac{T_d}{T}}\mathbf{v}_i(t) \qquad i = 1, \ldots, N \qquad (141)$$

where T_d is the desired model temperature, and T and $\mathbf{v}_i$ are the current temperature value and velocity vectors. During such an isothermal equilibration phase, the rescaling needs to be applied after about each tenth time step only.

The rescaling of velocities is not only useful for the equilibration of nanomodels but can be applied during molecular dynamics calculations too, where varying T_d with time leads to artificial tempering or cooling processes.

6.3.2. Differences Between Nanoengineering and Common Mechanical Engineering

Most often the initial molecular dynamics model, according to the perfect lattice structure, is not a stable configuration. Figure 20 illustrates the typical design steps in the case of metallic nanostructures. First, a CAD model is established which defines the rough layout, known from common mechanical engineering. Then the molecular dynamics model is created by filling the CAD design with single atoms.
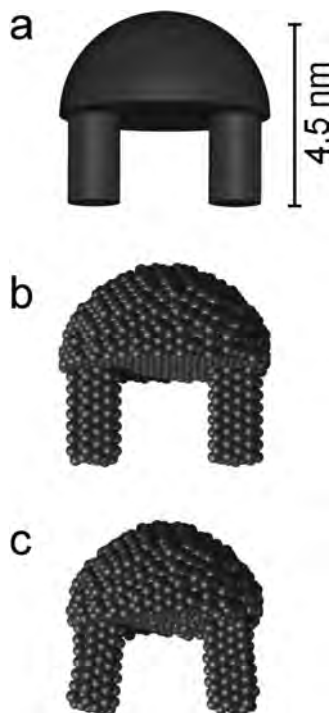
Figure 20. The three steps of nanodesign: First, a CAD model has to be established. Then, the molecular dynamics model is created by filling the CAD object with 1958 aluminum atoms. Finally, temperature is applied on the model during an equilibrium phase (in this case 300 K).

Finally, the realistic nanostructure results from the equilibration process which applies a prescribed temperature to the molecular dynamics model.

As can be seen quite clearly, the final shape differs significantly from the CAD model. How can this be explained?

The atomic positions of the molecular dynamics model are set according to the perfect lattice structure. While such a structure is a stable configuration in macroscopic realms this is no longer valid for nanometer-sized objects. Therefore, the atoms of the molecular dynamics model rearrange their positions during the equilibration phase until a stable configuration is reached. Most often this leads to quite different results compared to the initial design.

In conclusion, one has to recognize that, in comparison to common mechanical engineering nanodesign strongly depends on the outer shape of the considered structure.

Another difference is significant too: While in mechanical engineering sharp edges or plane surfaces or any shape and also continuous calibrations are common, nanodesign is limited to certain positions of single atoms (i.e., the shape of structures is restricted to certain measures dependent on the material). This becomes obvious, if one thinks about such trivial mechanical parts like fittings and bearings.

And in addition, the initial shape of a nanomodel which may have more or less pronounced edges can change considerably during the equilibration phase (as well as later on during the molecular dynamics calculation) and, therefore, the layout of the model would have to be redesigned. That is, building nanomodels or performing nanoengineering is an iterative process of nanodesign, molecular dynamics

calculation, and redesign, and there is almost nothing in common with common mechanical engineering.

6.3.3. Nanomachines

The synthesis of real nanomachines has not yet been performed, but it is a most interesting topic to perform molecular dynamics studies and, therefore, to determine how and under what conditions nanomachines could be working—regardless of the question of how to assemble them in reality.

An example of such a study is illustrated in Figure 21. This is a model of a simple nanoturbine that consists of a paddle wheel with an axle and two bearings resting on a substrate. The propulsion of the turbine could be established by a particle or laser beam.

When comparing Figure 21a with Figure 21b the differences between common mechanical engineering and nanodesign again become obvious. While mechanical engineering
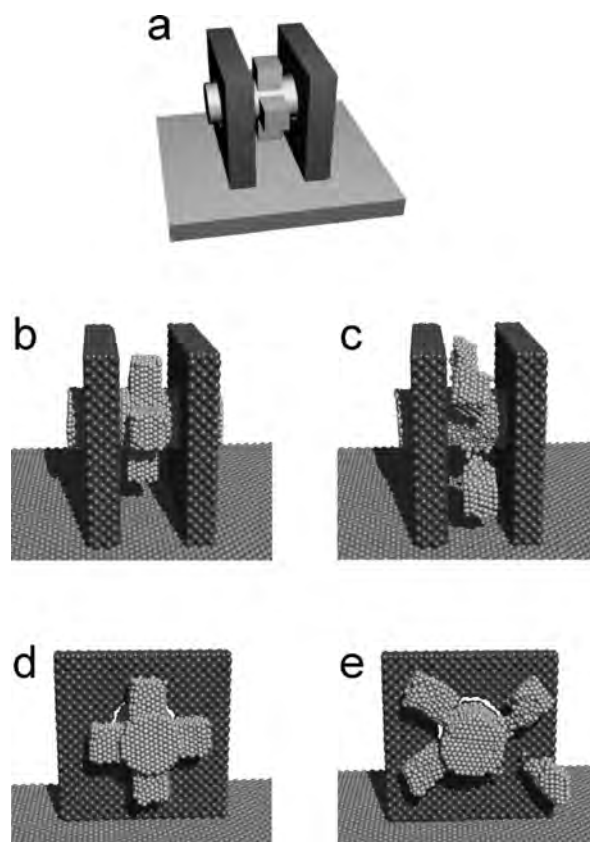
Figure 21. Nanoengineering of a simple turbine. The turbine consists of a paddle wheel with an axle and two bearings. (a) Mechanical engineering model build with common CAD software. (b) Perspective view and cross-section of the MD model [the corresponding side view is shown in (c)]. The paddle wheel rotates with 5×10^{10} revolutions per second. (d) The paddle wheel ruptures, if the number of revolutions is increased to 10^{11} per second model [the side view of (d) is shown in (e)]. The bearings (blue) consist of 4592 silicon atoms, each with ideal shaped surfaces. Due to the strong covalent bonds of silicon the bearings have been treated as rigid objects within the MD calculations. The axle with the attached paddle wheel (yellow) has been assembled with 5226 aluminium atoms and the substrate (green) consists of krypton.

usually works with sharp edges and smooth surfaces, nano-design is restricted to the use of single atoms which leads to the typical grainy appearance of nanostructures. Moreover, tolerances may be kept very small with mechanical engineering, but nanodesign allows measures only in certain steps where the steps depend on the according material. Therefore, the fit of axle and bearing is rather loose as can be seen in the cross-sections of Figure 21. However, the MD studies have shown that such nanoturbines could be working stable for revolutions of up to about 5×10^{10} per second.

7. MONTE CARLO METHOD

In contrast to molecular dynamics calculations, where we have completely deterministic algebraic equations, the Monte Carlo method is a numerical approach in which specific stochastic elements are used. The Monte Carlo method was introduced by Metropolis et al. [936] in 1953. The method and results have been extensively reviewed in the literature (see, for example, [937]). Since we have concentrated in this chapter mainly on molecular dynamics, we only want to discuss here some basic characteristics.

Whereas the molecular dynamics method enables the investigation of *static* and *dynamic* properties, the Monte Carlo method only deals with *static* properties; these are configurational averages and thermodynamics quantities. The results produced by the two methods should be in agreement to order N^{-1} and, therefore, one can expect agreement of the two methods within statistical error. It should be emphasized that the Monte Carlo method may be easily extended to quantum mechanical systems.

The widespread applications of the Monte Carlo method made it to an important tool in science and technology. In connection with condensed matter physics typical applications are (see, for example, [937]): fluids and plasmas, thermal properties and scattering functions for solids, liquids, and dense gases; properties of metallic alloys (in particularly in connection with short- and long-range-order properties); relaxation phenomena and diffusion processes; kinetics of crystal growth; phase transitions; magnetic properties of surfaces; kinetics of adsorption on surfaces; structural and thermal properties of glasses and amorphous magnets and of other disordered systems; ground state properties of certain quantum systems; etc.

The Monte Carlo method has been used in a diverse number of ways. For example, in connection with molecular calculations five types have often been used: classical Monte Carlo, quantum Monte Carlo, path-integral quantum Monte Carlo, volumetric Monte Carlo, and simulation Monte Carlo. But there are still many variations of these five types in literature. Here we only want to give the main principles of the classical Monte Carlo method and those of the quantum Monte Carlo method.

7.1. Classical Many-Particle Problems

The Monte Carlo method enables the determination of *configurational averages*. Let us consider a quantity α which depends on the configuration $\Gamma = \Gamma(\mathbf{r}_1, \ldots, \mathbf{r}_N)$ of the N particles of the system: $\alpha = \alpha(\Gamma)$. The configurational average of α is given in a canonical ensemble by

$$\langle \alpha \rangle = \int d\Gamma\, \rho(\Gamma) \alpha(\Gamma) \tag{142}$$

where

$$\rho(\Gamma) = \frac{\exp\left\{-\frac{V(\Gamma)}{k_B T}\right\}}{\int d\Gamma\, \exp\left\{-\frac{V(\Gamma)}{k_B T}\right\}} \tag{143}$$

The Monte Carlo method enables the determination of integrals of type (142). Below we discuss the main points of this procedure.

Let us split the configurational space into k cells with sufficiently small elements $\Delta\Gamma$, and let Γ_m, $m = 1, \ldots, k$, be the corresponding configurational states. Then, the average (142) may be approximated by

$$\langle \alpha \rangle_{\text{MC}} = \frac{\sum_{m=1}^{k} \alpha(\Gamma_m) \exp\left\{-\frac{V(\Gamma_m)}{k_B T}\right\}}{\sum_{m=1}^{k} \exp\left\{-\frac{V(\Gamma_m)}{k_B T}\right\}} \tag{144}$$

We can estimate (144) by selecting at random a certain number $L\ (<k)$ of configurational states, average α over these configurations, and weigh each configuration with the appropriate Boltzman factor [938]:

$$\langle \alpha \rangle = \frac{\sum_{m=1}^{L} \alpha(\Gamma_m) \exp\left\{-\frac{V(\Gamma_m)}{k_B T}\right\}}{\sum_{m=1}^{L} \exp\left\{-\frac{V(\Gamma_m)}{k_B T}\right\}} \tag{145}$$

However, this method is only practicable if the occupation probabilities do not differ very much from each other, and this is not fulfilled in the case of

$$\frac{\exp\left\{-\frac{V(\Gamma_m)}{k_B T}\right\}}{\sum_{m=1}^{L} \exp\left\{-\frac{V(\Gamma_m)}{k_B T}\right\}} \tag{146}$$

Thus, this method is not practicable because in the case of (146) the number of configurations required for reasonable averaging would be enormous.

In the Monte Carlo approach, however, configurations are selected with a frequency proportional to (146), and one has to average over the selected configurations with equal weight and, instead of (145), we get

$$\langle \alpha \rangle_{\text{MC}} = \frac{1}{L} \sum_{m=1}^{L} \alpha(\Gamma_m) \tag{147}$$

In the Monte Carlo approach ensemble averages are estimated by taking a random walk in configuration space. A Markov chain is produced in which the individual Markov states are points in the usual configuration space of statistical mechanics. Without going in detail, the steps in a Monte Carlo calculation for a system consisting of N atoms at temperature T are the following:

(1) The initial position vectors of the N are given:

$$\mathbf{r}_1^a, \ldots, \mathbf{r}_N^a$$

(2) The potential energy

$$V^a = \frac{1}{2} \sum_{\substack{i,\,j=1 \\ i \neq j}}^{N} \upsilon\big(|\mathbf{r}_i^a - \mathbf{r}_j^a|\big) \qquad (148)$$

and the Boltzmann factor

$$b^a = \exp\left\{-\frac{V^a}{k_B T}\right\} \qquad (149)$$

are calculated on the basis of the initial coordinates.

(3) A particle (say 1) of the system is selected, either serially or at random, and random atomic displacements $\Delta x_1, \Delta y_1, \Delta z_1$ are selected, each uniformly distributed over the interval $(-\Delta/2, \Delta/2)$.

(4) On the basis of the new configuration the potential energy V^n is given by

$$V^n = V^a - \sum_{j=2}^{N} \big[\upsilon_{1j}^a - \upsilon_{1j}^n\big] \qquad (150)$$

and for the Boltzmann factor we have

$$b^n = \exp\left\{-\frac{V^n}{k_B T}\right\} \qquad (151)$$

(5) If

$$\Delta V = V^n - V^a \qquad (152)$$

is negative, the new configuration is accepted and the old configuration is replaced by the new one. It is evidently more probable than the former one.

(6) If ΔV is positive the move is accepted only with the probability

$$\exp\left\{-\frac{\Delta V(\Gamma)}{k_B T}\right\} \qquad (153)$$

The computer selects a uniformly distributed random number h from the interval $(0,1)$ and compares it to (153). If the exponential expression is greater, the new configuration and the new potential energy become the current properties of the system. Otherwise the old configuration is counted again.

In a sufficiently long chain produced by these rules, configurations Γ appear with a probability of

$$\exp\left\{-\frac{V(\Gamma)}{k_B T}\right\} \qquad (154)$$

as is required in a canonical ensemble.

7.1.1. Applications

Articles include: Decay of pyramidal nano-island formed on Si(100) studied by kinetic Monte Carlo simulation [939], Particle size distribution of nanospheres by Monte Carlo fitting of small angle X-ray scattering curves [940], The structure of frozen phases in slit nanopores: A grand canonical Monte Carlo study [941], Simulation of nanocolloid chemical potentials in a hard-sphere polymer solution: Expanded ensemble Monte Carlo [942], Study of molecular shape and non-ideality effects on mixture adsorption isotherms of small molecules in carbon nanotubes: A grand canonical Monte Carlo simulation study [943], and Nanodroplets on a solid plane: Wetting and spreading in a Monte Carlo simulation [944]. Further information can be found in [945–997]. An interesting Monte Carlo study is given in [998, 999]. It is a simulation of long, thin molecules in a periodic box. The system shows two phases: a nematic liquid crystal and an isotropic liquid (see also Fig. 22).

7.2. Quantum Many-Particle Problems

The expectation value of an operator is given by

$$\overline{F} = \frac{\int d\mathbf{r}_1 \cdots d\mathbf{r}_N \, \psi_T^*(\mathbf{r}_1, \ldots, \mathbf{r}_N) \widehat{F} \psi_T(\mathbf{r}_1, \ldots, \mathbf{r}_N)}{\int d\mathbf{r}_1 \cdots d\mathbf{r}_N |\psi_T(\mathbf{r}_1, \ldots, \mathbf{r}_N)|^2} \qquad (155)$$

where $\mathbf{r}_1, \ldots, \mathbf{r}_N$ are again the N position vectors of the N particles, and $\psi_T(\mathbf{r}_1, \ldots, \mathbf{r}_N)$ is a trial wave function which can be determined by means of the variational principle. The variational method enables the computation of the ground-state properties of many-particle systems. The variational energy is given by

$$E_T = \frac{\int d\Gamma \, \psi_T^*(\Gamma) \widehat{H} \psi_T(\Gamma)}{\int d\Gamma |\psi_T(\Gamma)|^2} \qquad (156)$$

Figure 22. The image shows a snapshot from a Monte Carlo simulation of long, thin molecules in an elongated periodic box. The molecules are color-coded by orientation. The system shows two phases at equilibrium: a nematic liquid crystal (in the center) and an isotropic liquid (on either side) separated by planar interfaces. These simulations allowed the first determination of the surface tension of the equilibrium nematic–isotropic interface and confirmed that the molecules in the nematic phase are preferentially aligned in the plane of the surface. Subsequent simulations, using the molecular dynamics method, investigated capillary-wave fluctuations of this interface as a function of cross-sectional area.

where $\widehat{H}$ is the Hamiltonian. E_T will be the minimum when $\psi_T(\Gamma)$ is the ground-state solution of Schrödinger's equation. $\psi_T(\Gamma)$ must be either symmetric or antisymmetric with respect to the coordinates depending on the statistics. The parameters of $\psi_T(\Gamma)$ are optimized so that the energy E_T is minimized.

The problem is to construct realistic trial wave functions $\psi_T(\Gamma)$ [1000]. For a Bose system at zero temperature Bijl [1001] proposed the form

$$\psi_T(\Gamma) = \prod_{i<j=1}^{N} f(r_{ij})$$
$$= \exp\left[-\frac{1}{2}\sum_{i<j=1}^{N} u(r_{ij})\right] \qquad r_{ij} = |\mathbf{r}_i - \mathbf{r}_j| \quad (157)$$

That is, the trial function $\psi_T(\Gamma)$ was chosen to be a product of pair functions, where $u(r)$ is an unknown function. Equation (157) has been generalized to Fermi systems [1002–1004],

$$\psi_T(\Gamma) = D(\Gamma)\exp\left[-\frac{1}{2}\sum_{i<j=1}^{N} u(r_{ij})\right] \qquad (158)$$

where $D(\Gamma)$ is the ideal Fermi gas wave function. Another form for the trial wave function is given by [937]

$$\psi_T(\Gamma) = \exp\left[-\frac{1}{2}\sum_{i<j=1}^{N} u(r_{ij})\right]$$
$$\times \sum_p (\pm 1)^p \phi(\mathbf{r}_i - \mathbf{s}_{p_i})\eta_{\sigma_i \sigma_{p_i}} \qquad (159)$$

η is a spinor, p is a permutation of the pairing of particles to lattice sites $\mathbf{s}$, $\phi(\mathbf{r})$ is a single-particle orbital about a lattice site, and the $\pm$ sign is for Bose or Fermi statistics.

The integrals required to evaluate expectation values [Eq. (155)] can be carried out by the Monte Carlo method (see, for example, [937]). The Monte Carlo simulation of quantum many-particle systems is very similar to that of classical systems (Section 7.1). For quantum systems an algorithm is needed for the production of configurations with the probability proportional to the square of the trial wave function $\psi_T(\Gamma)$. The probability distribution

$$\frac{\psi_T^*(\Gamma)\psi_T(\Gamma)}{\int d\Gamma \, |\psi_T(\Gamma)|^2} \qquad (160)$$

for quantum systems is completely equivalent to the probability for classical systems which is given for the canonical ensemble by (143).

7.2.1. Applications

Articles include: Quantum Monte Carlo methods [1005], A quantum Monte Carlo study of the Josephson effect in a quantum dot [1006], Benchmark quantum Monte Carlo calculations [1007], The behavior of correlation functions in trans-polyacetylen: Quantum Monte Carlo study [1008], and Various spin-polarization states beyond the maximum-density droplet: A quantum Monte Carlo study [1009]. More

information can be found in [1010–1028]. An interesting study, also in connection with density functional theory (Section 2.1.2), is given in [1029] for carbon clusters.

Carbon clusters are very difficult to model accurately due to the wide range of geometries and because there are single, double, and triple bonds. In [1029] the energetics of various clusters have been studied as, for example, C_{24} clusters. This study has been done on the basis of highly accurate diffusion quantum Monte Carlo calculations. To search for structural isomers it is proposed in [1029] to use a hierarchy of methods of increasing accuracy. The first step is to apply empirical methods based on bond counting and geometrical considerations. The second step is to refine the selection by quantum mechanics calculations using, for example, density-functional formalism. The final energetic ordering of different isomers can be obtained on the basis of highly accurate calculations; for this purpose in [1029] the diffusion quantum Monte Carlo method has been used. The results in connection with C_{24} are shown in Figure 23. There are five isomers: ring, sheet, bowl, O_h cage, and D_6 fullerene. Figure 23 shows that the results obtained from the density-functional methods scatter considerably about the curve resulting from the diffusion Monte Carlo method. It is stated in [1029] that an accurate treatment of electron correlations is critical for accurate results.
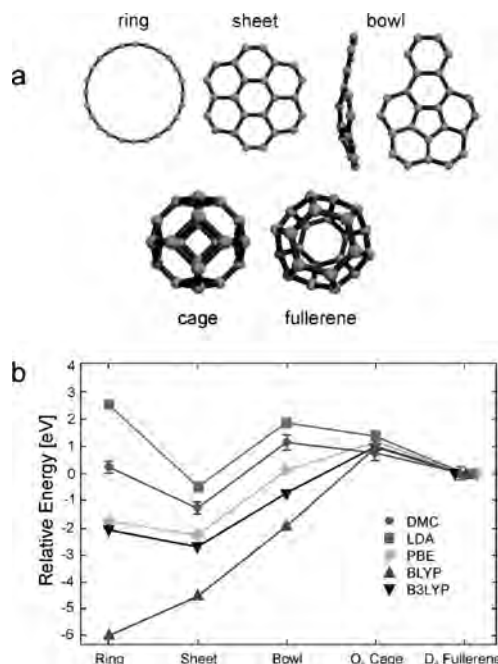

Figure 23. (a) C_{24} isomers: ring, sheet, bowl, O_h cage, D_6 fullerene. (b) The energies and structures of the C_{24} isomers given relative to the D_6 fullerene. It can be seen that the results obtained from the density functional methods (LDA, PBE, BLYP, B3LYP) scatter considerably about the curve resulting from the diffusion quantum Monte Carlo method (DMC). (LDA: local density approximation; PBE: Perdew, Burke, Enzerhof generalized gradient approximation for the exchange-correlation energy within the density functional formalism; BLYP: generalized gradient approximation density functional; B3LYP: hybrid density functional). Courtesy of R. J. Needs, Theory of Condensed Matter Group, Cavendish Laboratory, University of Cambridge.

8. SUMMARY

Nanosystems behave in general very differently from macroscopic systems: Properties which are well defined and clearly fixed in the bulk are often no longer typical features in nanophysics and nanotechnology. New effects emerge which have no counterpart in other fields of physics, chemistry, and technology. For example, the melting temperature of a macroscopic system is usually well defined, and the system is thermally stable up to the melting point. In contrast to that, the melting temperature of a nanosystem is in general dependent on the particle number and can also be a function of the outer shape of the system. Moreover, the melting temperature of certain nanosystems is not defined and not clearly fixed, respectively. And there are other surprising effects in the nanometer-size realm, for example, bifurcation phenomena: Nanosystems (e.g., nanoclusters) can transform *spontaneously* from a metastable to a stable state, and the transformed state may differ from the metastable state in both the inner *atomic* structure as well as the outer shape. When such a nanosystem transforms from the metastable to the stable state there are several possibilities for that. Which of these stable states the system will finally take is completely a matter of chance (Section 6.2.2). This is an interesting phenomenon and has no counterpart in micro- and macrotechnique, but there is rather a certain vicinity to biological systems (Section 6.2.4).

This is a completely new situation, and the new nanophysical effects reflect a huge potential for technological applications. This process is just at the beginning but presupposes, on the other hand, a good theoretical understanding of the systems under investigation. Therefore, in nanophysics and nanotechnology not only do sophisticated experiments and methods have to be established, but also specific methods for the theoretical treatment of such systems have to be selected and refined.

What is the adequate theoretical treatment of typical atomic nanoeffects? How relevant in this context are the usual methods of solid state physics, which have been successfully applied to the bulk state? We discussed this question and came to the result that the standard model of solid-state physics (ordered structure, harmonic behavior) can be no basis for the treatment of nanosystems, which is due to the strong anharmonicities even at relatively low temperatures. These anharmonicities cannot be considered as small perturbation to the harmonic approximation and are caused by the atoms at the surface which are less bonded than in the bulk. Therefore, the mean-square amplitudes of the atoms at the surface are significantly larger than in the bulk leading to relatively strong anharmonicities. This phenomenon can be observed even at low temperatures. This behavior is also typical for nanosystems since a great fraction of atoms are more or less close to the surface region of the system. In small nanosystems (for example, clusters with a few hundred of atoms) even the innermost particles cannot be treated as bulk particles since the cutoff radius for the interaction potential is larger than its distance to the surface.

This phenomenon leads to complex situations, much more than in the case of macroscopic systems. For example, a typical feature of nanosystems is that their properties vary strongly with temperature which are moreover a sensitive function of particle number. For the theoretical treatment of such phenomena methods are needed which in general cannot be based on the standard model of solid-state physics (ordered structure, harmonic behavior).

In Section 3.1 we argued that for the theoretical treatment of nanosystems we have to recourse to the most general method in order to be able to analyze the diversity of structural and dynamical atomic effects which are typical for such systems. Therefore, the most important tool for the investigation of nanosystems is the molecular dynamics method. No other microscopic method in condensed matter physics allows one to treat anharmonicities without approximation. Thus, the molecular dynamics method should be considered as the *standard method* for the theoretical description of nanosystems. Not only can anharmonicities be treated without approximation within this method but also the temperature effects and their dependence on the particle number.

We started our considerations with the quantum-theoretical treatment of nanosystems, that is, with the methods of quantum chemistry. Here the discussion concentrated on the Hartree–Fock method and the density-functional formalism, and we restricted ourselves to a few brief statements. The reason is the following: Up to now, these methods only allow the determination of *zero-temperature* properties. However, as we have stated above, temperature effects are of considerable importance in connection with nanosystems. In particular, nanoproperties are in general very sensitive to small variations in temperature and, therefore, it should hardly be possible to conclude from *zero-temperature* data (Hartree–Fock method, density-functional formalism, etc.) to *non-zero-temperature* properties. It would be most fruitful to consider in future investigations also the non-zero-temperature density-functional formalism by Mermin. Also the embedded-atom method (Section 5.3.4) and quantum molecular dynamics introduced by Car and Parrinello (Section 5.3.5) can lead to misleading results since here too non-zero-temperature data are coupled with zero-temperature properties.

On the other hand, in order to be able to perform a molecular dynamics calculation the interaction potential between the particles is needed as input. For a reliable description of the properties of nanosystems the precise knowledge of the interaction potential is required. We showed in Section 5.2 that surface properties are in general sensitive to small potential variations—more than in the bulk of the crystal. Both the repulsive and the attractive part of the potential have to be determined carefully. However, the determination of accurate pair potentials for systems of interest (e.g., metals and materials with covalent bonding) is rather difficult even for the bulk, and the nanoproblem, where a great fraction of atoms belong to the surface region, is much harder because of the change in electronic states and other relevant properties near the surfaces of the nanosystem.

A lot of realistic molecular dynamics calculations have been performed for various systems, but the physical basis for the used interaction potentials is often not recognizable and serves merely as fitting functions which is unsatisfactory. Furthermore, often the potentials have not been tested carefully, in some cases even not at all. Serious research in

nanoscience requires just the opposite: Since the properties of nanosystems are particularly sensitive to potential variations, the potentials have to be determined as carefully as possible for such systems.

There exist many phenomenological approaches for the interaction, but we did not discuss these functions in detail because in most cases there is no or almost no physical background for their introduction—these potentials have often been chosen for purely pragmatic reasons. For example, the Morse potential has not been constructed on the basic interaction types (ionic interaction, van der Waals forces, metallic interaction, covalent binding) discussed in Section 5 but it is based on the spectroscopy of molecules. Nevertheless, the potential has been used extensively in the study of various many-particle properties, and there is obviously no physical justification for that.

The potential functions should be constructed on the basis of the physical features of the system under investigation. These potential functions will in most cases be dependent on certain model parameters which have to be fitted accurately. This has been done, for example, for Al by means of the pseudopotential method (Section 6.2), and the parameters were fitted by a wide range of experimental data.

In conclusion, for a realistic atomic description of nanosystems there is no alternative to the molecular dynamics method. However, the situation in connection with interaction potentials has to be improved. For the design of nanosystems and also in connection with nanoengineering reliable potential functions with an adequate physical background are needed, and they should not merely be used as fitting functions.

GLOSSARY

Correlation energy The modification of the Coulomb energy of a system that results from the tendency of electrons to stay apart from each other.

Coulomb blockade Current respectively tunneling suppression at low bias, caused by charging effects.

Deoxyribonucleic acid (DNA) A macromolecule consisting of one or two strands of linked deoxyribonucleotides.

Electronic band structure A quantum-theoretical approach of the dynamics of the electrons in solids that predicts certain restricted ranges (bands) for the electronic energies.

Electron X-ray absorption fine structure (EXAFS) A variation of the X-ray absorption of a material as a function of energy. The energies are just above those required for photons to bring core electrons into the continuum. The method is based on the interference between the outgoing photoelectrons waves and electron waves backscattered from atoms adjacent to the adsorbing atoms.

Exchange effects Effects which are due to an exchange of space and/or spin coordinates of the particles involved, for example, electrons.

Fullerene A form of carbon consisting of an empty cage of atoms. Fullerene derivatives can be created by adding endo- or exohedral substituents. This opens the possibility of obtaining a wide range of building blocks for developing new materials with unique properties.

Harmonic approximation The dynamics of a many-particle system can be formulated within the harmonic approximation if the displacements x of the atomic structure from its equilibrium geometry can be described with linear restoring forces $F(Fx)$. In this case the potential energy is proportional to x^2.

Law energy electron diffraction (LEED) An experimental scattering technique for the study of the atomic surface structure by electrons of uniform energy within a range of 5–500 eV.

Nanotube A one-dimensional fullerene (a convex cage of atoms with only hexagonal and/or pentagonal faces) with a cylindrical shape. Depending on the direction that the tubes appear to have been rolled (quantified by the "chiral vector"), they are known to act as conductors or semiconductors. Nanotubes are proving to be useful as molecular components for nanotechnology.

NMR The effect is due to a large number of nuclei in a static magnetic field which absorb energy from a radiofrequency field at certain characteristic frequencies.

Pair correlation function The pair correlation function $g(r)$ is the probability of finding an atom (or molecule) at r if there is another atom at the origin. $g(r)$ is normalized to unity at large r.

Screening The reduction of the electric field about a charge (for example, an ion of a metal) by the space charges of the surrounding electrons (e.g., conduction electrons).

Statistical ensemble A collection of systems of atoms (or molecules) which are used for the description of an individual system. Time averages for the individual system can be expressed by averaging over the systems of the collection (ensemble) at a fixed time.

Virial coefficients For a given temperature T, the virial coefficients are defined as constants in the expansion of P/RT in powers of the particle number density, where P is the pressure and R is the gas constant.

REFERENCES

1. M. Rieth and W. Schommers, in "What is Life?" (H.-P. Dürr, F.-A. Popp, and W. Schommers, Eds.). World Scientific, Singapore, 2002.
2. W. Schommers and P. von Blanckenhagen (Eds.), "Structure and Dynamics of Surfaces." Springer-Verlag, Berlin, 1986 (part I), 1987 (part II).
3. M. Rieth, "Nano-Engineering in Science and Technology." World Scientific, Singapore, 2002.
4. R. Ahlrichs, "Nachrichten 2-3." Forschungszentrum Karlsruhe, Karlsruhe, 1999.
5. N. Szabo and S. Ostlund, "Modern Quantum Chemistry: Introduction to Advanced Electronic Structure Theory." Macmillan, New York, 1982.
6. P. Hohenberg and W. Kohn, *Phys. Rev. B* 136, 864 (1964).
7. W. Kohn and L. J. Sham, *Phys. Rev. A* 140, 1133 (1965).
8. A. Fortunelli and A. M. Velasco, *J. Mol. Struct.* 586, 17 (2002).
9. L. J. M. Selen, L. J. van IJzendoorn, P. J. M. Smulders, and M. J. A. de Voigt, *Nucl. Instrum. Methods B* 190, 570 (2002).
10. V. A. Glezakou, J. A. Boatz, and M. S. Gordon, *J. Am. Chem. Soc.* 124, 6144 (2002).
11. R. Q. Zhang, W. C. Lu, and S. T. Lee, *Appl. Phys. Lett.* 80, 4223 (2002).

12. W. Hausler, L. Kecke, and A. H. MacDonald, *Phys. Rev. B* 65, 085104 (2002).

13. D. Ullmo and H. U. Baranger, *Phys. Rev. B* 64, 245324 (2001).

14. A. Puente, L. Serra, and V. Gudmundsson, *Phys. Rev. B* 64, 235324 (2001).

15. M. P. L. Sancho, M. C. Munoz, and L. Chico, *Phys. Rev. B* 63, 165419 (2001).

16. R. Vivas-Reyes, F. De Proft, P. Geerlings, M. Biesemans, R. Willem, F. Ribot, and C. Sanchez, *New J. Chem.* 26, 1108 (2002).

17. M. Alfredsson, K. Hermansson, and R. Dovesi, *PCCP* 4, 4204 (2002).

18. V. F. Elesin, *J. Exp. Theor. Phys.* 95, 114 (2002).

19. E. Trabert, *Phys. Scr. T* 100, 88 (2002).

20. J. S. Loring and W. H. Casey, *J. Colloid Interface Sci.* 251, 1 (2002).

21. L. Colletti, F. Pederiva, E. Lipparini, and C. J. Umrigar, *Eur. Phys. J. B* 27, 385 (2002).

22. A. C. de Dios and A. E. Abraham, *J. Mol. Struct.* 602, 209 (2002).

23. W. J. Liang, M. Bockrath, and H. Park, *Phys. Rev. Lett.* 88, 126801 (2002).

24. A. Abdurahman, A. Shukla, and M. Dolg, *Phys. Rev. B* 65, 115106 (2002).

25. O. Ivanciuc, L. Bytautas, and D. J. Klein, *J. Chem. Phys.* 116, 4735 (2002).

26. N. R. Brinkmann, H. F. Schaefer, C. T. Sanderson, and C. Kutal, *J. Phys. Chem. A* 106, 847 (2002).

27. H. H. Kwong, Y. P. Feng, and T. B. Boo, *Comput. Phys. Commun.* 142, 290 (2001).

28. Y. L. Li, C. W. Lee, D. Q. Wang, K. H. Leung, and D. L. Phillips, *Chem. Phys. Lett.* 350, 78 (2001).

29. C. Trindle, D. Shillady, J. Craig, and S. Rutan, *J. Cluster Sci.* 12, 473 (2001).

30. E. Prodan and P. Nordlander, *Chem. Phys. Lett.* 349, 153 (2001).

31. R. Tamura, *Phys. Rev. B* 64, 201404 (2001).

32. S. Bednarek, B. Szafran, and J. Adamowski, *Phys. Rev. B* 64, 195303 (2001).

33. T. Kar, J. Pattanayak, and S. Scheiner, *J. Phys. Chem. A* 105, 10397 (2001).

34. A. Peeters, C. Van Alsenoy, N. H. March, D. J. Klein, and V. E. Van Doren, *J. Phys. Chem. B* 105, 10546 (2001).

35. W. Z. Liang, S. Yokojima, M. F. Ng, G. H. Chen, and G. Z. He, *J. Am. Chem. Soc.* 123, 9830 (2001).

36. K. Kral, Z. Khas, and C. Y. Lin, *Phys. Status Solidi B* 224, 453 (2001).

37. C. Steinebach, C. Schuller, E. Ulrichs, C. Heyn, and D. Heitmann, *Phys. Status Solidi B* 224, 97 (2001).

38. I. Grigorenko and M. E. Garcia, *Physica A* 291, 439 (2001).

39. D. L. Strout, *J. Phys. Chem. A* 105, 261 (2001).

40. A. K. Rajagopal and M. Mochena, *Phys. Rev. B* 62, 15461 (2000).

41. L. Fu, E. Yaschenko, L. Resca, and R. Resta, *Phys. Rev. B* 60, 2697 (1999).

42. S. Simon, M. Duran, and J. J. Dannenberg, *J. Phys. Chem. A* 103, 1640 (1999).

43. M. Taniguchi and S. Tanaka, *J. Nucl. Mater.* 263, 531 (1998).

44. P. Nortier, A. P. Borosy, and M. Allavena, *J. Phys. Chem. B* 101, 1347 (1997).

45. A. P. Borosy, B. Silvi, M. Allavena, and P. Nortier, *J. Phys. Chem.* 98, 13189 (1994).

46. M. P. Lara-Castells and J. L. Krause, *J. Chem. Phys.* 115, 4798 (2001).

47. W. C. Mackrodt and C. Noguera, *Surf. Sci.* 457, L386 (2000).

48. N. H. March, D. J. Klein, A. K. Ray, and X. Wu, *Int. J. Quantum Chem.* 75, 829 (1999).

49. J. F. Sanz and C. M. Zicovich-Wilson, *Chem. Phys. Lett.* 303, 111 (1999).

50. A. Markovits and C. Minot, *J. Mol. Catal. A* 119, 185 (1997).

51. M. Taniguchi and S. Tanaka, *Fusion Technol.* 30, 874 (1996).

52. M. J. T. Jordan and M. A. Collins, *J. Chem. Phys.* 104, 4600 (1996).

53. F. Frechard and P. Sautet, *Surf. Sci.* 336, 149 (1995).

54. G. I. Csonka and L. Sztraka, *Chem. Phys. Lett.* 233, 611 (1995).

55. J. Kobus, H. M. Quiney, and S. Wilson, *J. Phys. B* 34, 2045 (2001).

56. A. V. Mitin, *Phys. Rev. A* 62, 010501 (2000).

57. D. M. Hovorun, L. Gorb, and J. Leszczynski, *Int. J. Quantum Chem.* 75, 245 (1999).

58. J. Kobus, D. Moncrieff, and S. Wilson, *Mol. Phys.* 92, 1015 (1997).

59. P. Lazzeretti, M. Malagoli, and R. Zanasi, *J. Chem. Phys.* 102, 9619 (1995).

60. B. Hernandez, R. Navarro, A. Hernanz, and G. Vergoten, *Biopolymers* 67, 440 (2002).

61. H. Takashima, K. Kitamura, K. Tanabe, and U. Nagashima, *J. Comput. Chem.* 20, 443 (1999).

62. D. T. Nguyen, A. C. Scheiner, J. W. Andzelm, S. Sirois, D. R. Salahub, and A. T. Hagler, *J. Comput. Chem.* 18, 1609 (1997).

63. D. Moncrieff and S. Wilson, *J. Phys. B* 29, 6009 (1996).

64. R. Rencsok, K. A. Jackson, T. A. Kaplan, J. F. Harrison, and M. R. Pederson, *Chem. Phys. Lett.* 262, 207 (1996).

65. C. Gatti, B. Silvi, and F. Colonna, *Chem. Phys. Lett.* 247, 135 (1995).

66. D. Moncrieff and S. Wilson, *J. Phys. B* 28, 4007 (1995).

67. B. Champagne, V. Deguelle, and J. M. Andre, *Theochem. J. Mol. Struct.* 332, 93 (1995).

68. R. I. Eglitis, S. V. Izvekov, and M. R. Philpott, *Comp. Mater. Sci.* 17, 275 (2000).

69. M. Buhl, *Chem. Phys. Lett.* 267, 251 (1997).

70. T. Mizokawa and A. Fujimori, *Phys. Rev. B* 54, 5368 (1996).

71. P. Sitko and L. Jacak, *Mod. Phys. Lett. B* 9, 889 (1995).

72. O. Sugino and H. Kamimura, *Z. Phys. D* 19, 67 (1991).

73. M. Kurokawa and T. Mizokawa, *Phys. Rev. B* 66, 024434 (2002).

74. A. Lyalin, A. Solov'yov, and W. Greiner, *Phys. Rev. A* 65, 043202 (2002).

75. A. Lyalin, A. Solov'yov, W. Greiner, and S. Semenov, *Phys. Rev. A* 65, 023201 (2002).

76. C. Degli Esposti-Boschi and L. Ferrari, *Philos. Mag. B* 80, 1693 (2000).

77. T. Mizokawa and A. Fujimori, *Phys. Rev. B* 53, R4201 (1996).

78. M. C. Holthausen, M. Mohr, and W. Koch, *Chem. Phys. Lett.* 240, 245 (1995).

79. M. C. Holthausen, C. Heinemann, H. H. Cornehl, W. Koch, and H. Schwarz, *J. Chem. Phys.* 102, 4931 (1995).

80. B. N. Plakhutin and A. B. Trofimov, *J. Struct. Chem.* 33, 786 (1992).

81. M. Bermejo, J. M. Recio, M. Florez, V. Luana, and L. Pueyo, *J. Solid State Chem.* 102, 226 (1993).

82. M. Casarin, E. Ciliberto, S. Dibella, A. Gulino, I. Fragala, and T. J. Marks, *Inorg. Chem.* 31, 2835 (1992).

83. O. Sugino and H. Kamimura, *Phys. Rev. Lett.* 65, 2696 (1990).

84. M. B. Lepetit, J. P. Malrieu, and F. Spiegelmann, *Phys. Rev. B* 41, 8093 (1990).

85. N. Huang and A. D. MacKerell, *J. Phys. Chem. A* 106, 7820 (2002).

86. Q. Cui, *J. Chem. Phys.* 117, 4720 (2002).

87. M. Gnani, P. Lazzeretti, A. Ligabue, U. Pincelli, and A. Soncini, *Comput. Phys. Commun.* 144, 130 (2002).

88. F. Bernardi, A. Bottoni, and M. Garavelli, *Quant. Struct. Act. Relat.* 21, 128 (2002).

89. D. M. Gasparro, D. R. P. Almeida, S. M. Dobo, L. L. Torday, A. Varro, and J. G. Papp, *J. Mol. Struct.* 585, 167 (2002).

90. S. L. S. Stipp, *Mol. Simulat.* 28, 497 (2002).

91. B. M. Cabrera-Vivas, J. C. Ramirez, L. M. R. Martinez-Aguilera, and C. Kubfi-Garfias, *J. Mol. Struct.* 584, 5 (2002).

92. N. Ferre, X. Assfeld, and J. L. Rivail, *J. Comput. Chem.* 23, 610 (2002).

93. P. Chaudhuri and S. Canuto, *J. Mol. Struct.* 577, 267 (2002).

94. G. Fischer and T. Wydrzynski, *J. Phys. Chem. B* 105, 12894 (2001).

95. T. Kameda, M. Kobayashi, J. M. Yao, and T. Asakura, *Polymer* 43, 1447 (2002).

96. A. M. Mazzone and G. Mattei, *Appl. Surf. Sci.* 188, 140 (2002).

97. A. S. Sachrajda, C. Gould, P. Hawrylak, Y. Feng, P. Zawadzki, and Z. Wasilewski, *Braz. J. Phys.* 29, 639 (1999).

98. O. Klein, D. GoldhaberGordon, C. D. Chamon, and M. A. Kastner, *Phys. Rev. B* 53, R4221 (1996).

99. R. F. Aroca, R. E. Clavijo, M. D. Halls, and H. B. Schlegel, *J. Phys. Chem. A* 104, 9500 (2000).

100. G. S. Jeon, S. Wu, M. Y. Choi, and H. W. Lee, *Phys. Rev. B* 59, 2841 (1999).

101. C. Gould, P. Hawrylak, A. S. Sachrajda, Y. Feng, and Z. Wasilewski, *Physica B* 258, 141 (1998).

102. R. Jaeger and G. J. Vancso, *Macromol. Theory Simul.* 5, 673 (1996).

103. R. Nada, A. C. Hess, and C. Pisani, *Surf. Sci.* 336, 353 (1995).

104. J. Muilu and T. A. Pakkanen, *Phys. Rev. B* 49, 11185 (1994).

105. J. Muilu and T. A. Pakkanen, *Appl. Surf. Sci.* 75, 75 (1994).

106. J. Muilu and T. A. Pakkanen, *Surf. Sci.* 364, 439 (1996).

107. A. Di Carlo, *Phys. Status Solidi B* 232, 5 (2002).

108. M. I. Trioni, Q. Sun, G. P. Brivio, Z. X. Yang, and R. Q. Wu, *Phys. Rev. B* 65, 104408 (2002).

109. B. K. Agrawal and S. Agrawal, *Appl. Phys. Lett.* 79, 4366 (2001).

110. H. Hermann, F. Fugaciu, and G. Seifert, *Appl. Phys. Lett.* 79, 63 (2001).

111. D. Ullmo, T. Nagano, S. Tomsovic, and H. U. Baranger, *Phys. Rev. B* 63, 125339 (2001).

112. J. J. Zhao, B. C. Liu, H. J. Zhai, R. F. Zhou, G. Q. Ni, and Z. Z. Xu, *Solid State Commun.* 122, 543 (2002).

113. A. Di Carlo, *Physica B* 314, 211 (2002).

114. G. Seifert, T. Kohler, Z. Hajnal, and T. Frauenheim, *Solid State Commun.* 119, 653 (2001).

115. V. Bellini, N. Papanikolaou, R. Zeller, and P. H. Dederichs, *Phys. Rev. B* 64, 094403 (2001).

116. M. Weissmann, A. M. Llois, and M. Kiwi, *J. Magn. Magn. Mater.* 234, 19 (2001).

117. A. Zoroddu, F. Bernardini, P. Ruggerone, and V. Fiorentini, *Phys. Rev. B* 64, 045208 (2001).

118. G. Seifert, T. Frauenheim, T. Kohler, and H. M. Urbassek, *Phys. Status Solidi B* 225, 393 (2001).

119. G. Materzanini, P. Saalfrank, and P. J. D. Lindan, *Phys. Rev. B* 63, 235405 (2001).

120. R. J. Gottschall, *Mater. Trans.* 42, 548 (2001).

121. G. Seifert, T. Kohler, H. M. Urbassek, E. Hernandez, and T. Frauenheim, *Phys. Rev. B* 63, 193409 (2001).

122. K. Suenaga, E. Sandre, C. Colliex, C. J. Pickard, H. Kataura, and S. Iijima, *Phys. Rev. B* 63, 165408 (2001).

123. J. M. Soler, I. L. Garzon, and J. D. Joannopoulos, *Solid State Commun.* 117, 621 (2001).

124. S. Gonzalez, C. Sousa, M. Fernandez-Garcia, V. Bertin, and F. Illas, *J. Phys. Chem. B* 106, 7839 (2002).

125. H. Noguchi and M. Takasu, *Biophys. J.* 83, 299 (2002).

126. S. Sapra, D. D. Sarma, S. Sanvito, and N. A. Hill, *Nano Lett.* 2, 605 (2002).

127. Y. K. Gun'ko, S. D. Elliott, P. B. Hitchcock, and M. F. Lappert, *J. Chem. Soc. Dalton Trans.* 1852 (2002).

128. S. Gilb, P. Weis, F. Furche, R. Ahlrichs, and M. M. Kappes, *J. Chem. Phys.* 116, 4094 (2002).

129. W. N. Wang, H. R. Tang, K. N. Fan, and S. Iwata, *J. Chem. Phys.* 114, 1278 (2001).

130. S. T. Bromley, G. Sankar, C. R. A. Catlow, T. Maschmeyer, B. F. G. Johnson, and J. M. Thomas, *Chem. Phys. Lett.* 340, 524 (2001).

131. R. N. Barnett, C. L. Cleveland, H. Hakkinen, W. D. Luedtke, C. Yannouleas, and U. Landman, *Eur. Phys. J. D* 9, 95 (1999).

132. J. E. Monat, J. H. Rodriguez, and J. K. McCusker, *J. Phys. Chem. A* 106, 7399 (2002).

133. H. Tada, F. Suzuki, S. Ito, T. Kawahara, T. Akita, K. Tanaka, and H. Kobayashi, *Chem. Phys. Chem.* 3, 617 (2002).

134. Y. D. Glinka, A. S. Zyubin, A. M. Mebel, S. H. Lin, L. P. Hwang, and Y. T. Chen, *Chem. Phys. Lett.* 358, 180 (2002).

135. J. A. Larsson, M. Nolan, and J. C. Greer, *J. Phys. Chem. B* 106, 5931 (2002).

136. G. Belomoin, E. Rogozhina, J. Therrien, P. V. Braun, L. Abuhassan, M. H. Nayfeh, L. Wagner, and L. Mitas, *Phys. Rev. B* 65, 193406 (2002).

137. V. K. Dobruskin, *Langmuir* 18, 4356 (2002).

138. M. J. Yacaman, J. A. Ascencio, S. Tehuacanero, and M. Marin, *Top. Catal.* 18, 167 (2002).

139. T. V. Albu, A. B. Anderson, and J. C. Angus, *J. Electrochem. Soc.* 149, E143 (2002).

140. H. Schweiger, P. Raybaud, G. Kresse, and H. Toulhoat, *J. Catal.* 207, 76 (2002).

141. K. Michaelian, M. R. Beltran, and I. L. Garzon, *Phys. Rev. B* 65, 041403 (2002).

142. R. B. Thompson, V. V. Ginzburg, M. W. Matsen, and A. C. Balazs, *Macromolecules* 35, 1060 (2002).

143. A. S. Zyubin, Y. D. Glinka, A. M. Mebel, S. H. Lin, L. P. Hwang, and Y. T. Chen, *J. Chem. Phys.* 116, 281 (2002).

144. T. Jacob, S. Fritzsche, W. D. Sepp, B. Fricke, and J. Anton, *Phys. Lett. A* 300, 71 (2002).

145. P. Weis, T. Bierweiler, S. Gilb, and M. M. Kappes, *Chem. Phys. Lett.* 355, 355 (2002).

146. Y. Ferro, F. Marinelli, and A. Allouche, *J. Chem. Phys.* 116, 8124 (2002).

147. L. Pejov, *Int. J. Quantum Chem.* 86, 356 (2002).

148. J. Campbell, H. P. A. Mercier, H. Franke, D. P. Santry, D. A. Dixon, and G. J. Schrobilgen, *Inorg. Chem.* 41, 86 (2002).

149. A. Valcarcel, J. M. Ricart, A. Clotet, A. Markovits, C. Minot, and F. Illas, *J. Chem. Phys.* 116, 1165 (2002).

150. D. Geschke, T. Bastug, T. Jacob, S. Fritzsche, W. D. Sepp, B. Fricke, S. Varga, and J. Anton, *Phys. Rev. B* 64, 235411 (2001).

151. V. A. Nasluzov, V. V. Rivanenkov, A. B. Gordienko, K. M. Neyman, U. Birkenheuer, and N. Rosch, *J. Chem. Phys.* 115, 8157 (2001).

152. A. Haras, M. Witko, D. R. Salahub, K. Hermann, and R. Tokarz, *Surf. Sci.* 491, 77 (2001).

153. J. Moc and J. Panek, *Chem. Phys. Lett.* 345, 497 (2001).

154. H. Isobe, T. Soda, Y. Kitagawa, Y. Takano, T. Kawakami, Y. Yoshioka, and K. Yamaguchi, *Int. J. Quantum Chem.* 85, 34 (2001).

155. R. Tokarz-Sobieraj, K. Hermann, M. Witko, A. Blume, G. Mestl, and R. Schlogl, *Surf. Sci.* 489, 107 (2001).

156. T. Jacob, D. Geschke, S. Fritzsche, W. D. Sepp, B. Fricke, J. Anton, and S. Varga, *Surf. Sci.* 486, 194 (2001).

157. S. Kruger, S. Vent, F. Nortemann, M. Staufer, and N. Rosch, *J. Chem. Phys.* 115, 2082 (2001).

158. X. Y. Wu and A. K. Ray, *Physica B* 301, 359 (2001).

159. S. H. Cai, K. M. Neyman, H. Knozinger, and N. Rosch, *Surf. Sci.* 479, 169 (2001).

160. A. Ghosh, T. Vangberg, E. Gonzalez, and P. Taylor, *J. Porphyrins Phthalocyanines* 5, 345 (2001).

161. X. Y. Wu and A. K. Ray, *Physica B* 293, 362 (2001).

162. D. Begue and C. Pouchan, *J. Comput. Chem.* 22, 230 (2001).

163. J. L. Wang, G. H. Wang, and J. J. Zhao, *Phys. Rev. B* 66, 035418 (2002).

164. C. Majumder, T. M. Briere, H. Mizuseki, and Y. Kawazoe, *J. Chem. Phys.* 117, 2819 (2002).

165. N. A. Lambropoulos, J. R. Reimers, and N. S. Hush, *J. Chem. Phys.* 116, 10277 (2002).

166. A. Puzder, A. J. Williamson, J. C. Grossman, and G. Galli, *Phys. Rev. Lett.* 88, 097401 (2002).

167. S. Y. Park, J. D'Arcy-Gall, D. Gall, Y. W. Kim, P. Desjardins, and J. E. Greene, *J. Appl. Phys.* 91, 3644 (2002).

168. J. D'Arcy-Gall, D. Gall, I. Petrov, P. Desjardins, and J. E. Greene, *J. Appl. Phys.* 90, 3910 (2001).

169. A. Aguado, L. M. Molina, J. M. Loez, and J. A. Alonso, *Eur. Phys. J. D* 15, 221 (2001).

170. M. van Schilfgaarde and O. N. Mryasov, *Phys. Rev. B* 63, 233205 (2001).

171. I. Vasiliev, S. Ogut, and J. R. Chelikowsky, *Phys. Rev. Lett.* 86, 1813 (2001).

172. J. M. Soler, I. L. Garzon, and J. D. Joannopoulos, *Solid State Commun.* 117, 621 (2001).

173. E. Canadell, P. Ordejon, E. Artacho, D. Sanchez-Portal, A. Garcia, and J. M. Soler, *J. Mater. Chem.* 11, 1 (2001).

174. R. Rousseau and D. Marx, *Chem.-Eur. J.* 6, 2982 (2000).

175. P. J. Dyson, J. E. McGrady, M. Reinhold, B. F. G. Johnson, J. S. McIndoe, and P. R. R. Langridge-Smith, *J. Cluster Sci.* 11, 391 (2000).

176. J. M. Soler, M. R. Beltran, K. Michaelian, I. L. Garzon, P. Ordejon, D. Sanchez-Portal, and E. Artacho, *Phys. Rev. B* 61, 5771 (2000).

177. J. R. Sabin, S. B. Trickey, S. P. Apell, and J. Oddershede, *Int. J. Quantum Chem.* 77, 358 (2000).

178. J. Vega, K. Michaelian, I. L. Garzon, M. R. Beltran, and L. Hernandez, *J. Mol. Struct. Theochem.* 493, 275 (1999).

179. M. Seth, P. M. Margl, and T. Ziegler, *Macromolecules* 35, 7815 (2002).

180. N. Lopez and J. K. Norskov, *J. Am. Chem. Soc.* 124, 11262 (2002).

181. S. Park, S. A. Wasileski, and M. J. Weaver, *Electrochim. Acta* 47, 3611 (2002).

182. J. Dong, L. Miao, and M. F. Zhou, *Chem. Phys. Lett.* 355, 31 (2002).

183. X. Crispin, V. M. Geskin, C. Bureau, R. Lazzaroni, W. Schmickler, and J. L. Bredas, *J. Chem. Phys.* 115, 10493 (2001).

184. M. Torrent, K. Mogi, H. Basch, D. G. Musaev, and K. Morokuma, *J. Phys. Chem. B* 105, 8616 (2001).

185. T. C. Choy, *Phys. Rev. A* 62, 012506 (2000).

186. Z. Y. Zhou, Y. H. Qu, A. P. Fu, B. N. Du, F. X. He, and H. W. Gao, *Int. J. Quantum Chem.* 89, 550 (2002).

187. N. Jorge, E. A. Castro, L. F. R. Caffferata, and M. E. G. Vara, *B. Pol. Acad. Sci.-Chem.* 49, 255 (2001).

188. D. C. Ghosh, J. Jana, and S. Bhattacharyya, *Int. J. Quantum Chem.* 87, 111 (2002).

189. Y. Okamoto, *J. Phys. Chem. B* 106, 570 (2002).

190. F. J. Owens, *J. Mol. Struct. Theochem.* 546, 261 (2001).

191. M. Torrent, D. G. Musaev, K. Morokuma, and H. Basch, *J. Phys. Chem. B* 105, 4453 (2001).

192. A. Karpfen, *J. Phys. Chem. A* 105, 2064 (2001).

193. G. N. Vayssilov, A. Hu, U. Birkenheuer, and N. Rosch, *J. Mol. Catal. A* 162, 135 (2000).

194. R. Colle and A. Curioni, *J. Phys. Chem. A* 104, 8546 (2000).

195. J. Kortus, M. R. Pederson, and S. L. Richardson, *Chem. Phys. Lett.* 322, 224 (2000).

196. S. Zelek, J. Wasilewski, and J. Heldt, *Comput. Chem.* 24, 263 (2000).

197. M. R. Pederson and N. Laouini, *J. Cluster Sci.* 10, 557 (1999).

198. P. Carloni, *Quant. Struct. Act. Relat.* 21, 166 (2002).

199. M. Elstner, T. Frauenheim, E. Kaxiras, G. Seifert, and S. Suhai, *Phys. Status Solidi B* 217, 357 (2000).

200. R. Kaschner and D. Hohl, *J. Phys. Chem. A* 102, 5111 (1998).

201. G. Berthier, B. Cadioli, E. Gallinella, A. Aamouche, and M. Ghomi, *Theochem. J. Mol. Struct.* 390, 11 (1997).

202. M. W. Zhao, Y. Y. Xia, Y. C. Ma, M. J. Ying, X. D. Liu, and L. M. Mei, *Phys. Lett. A* 300, 421 (2002).

203. F. L. Gervasio, P. Carloni, and M. Parrinello, *Phys. Rev. Lett.* 89, 108102 (2002).

204. Z. W. Qu, H. Zhu, X. D. Zhang, X. C. Ai, J. P. Zhang, X. K. Zhang, and Q. Y. Zhang, *Chem. Phys. Lett.* 360, 283 (2002).

205. X. L. Yin, L. Calderin, M. J. Stott, and M. Sayer, *Biomaterials* 23, 4155 (2002).

206. R. K. Szilagyi, D. G. Musaev, and K. Morokuma, *Inorg. Chem.* 40, 766 (2001).

207. L. Alexandrova, O. G. D'yachenko, G. M. Kazankov, V. A. Polyakov, P. V. Samuleev, E. Sansores, and A. D. Ryabov, *J. Am. Chem. Soc.* 122, 5189 (2000).

208. T. Frauenheim, G. Seifert, M. Elstner, Z. Hajnal, G. Jungnickel, D. Porezag, S. Suhai, and R. Scholz, *Phys. Status Solidi B* 217, 41 (2000).

209. J. A. Cogordan, M. Mayoral, E. Angeles, R. A. Toscano, and R. Martinez, *Int. J. Quantum Chem.* 71, 415 (1999).

210. R. Stranger, J. E. McGrady, and T. Lovell, *Inorg. Chem.* 37, 6795 (1998).

211. S. Ono, K. Okazaki, M. Sakurai, and Y. Inoue, *J. Phys. Chem. A* 101, 3769 (1997).

212. N. M. Maurits and J. G. E. M. Fraaije, *Z. Angew. Math. Mech.* 76, 475 (1996).

213. J. H. Wu and C. A. Reynolds, *Anti-Cancer Drug Des.* 11, 415 (1996).

214. T. Simonson and N. Calimet, *Proteins* 49, 37 (2002).

215. N. Lehnert, F. Neese, R. Y. N. Ho, L. Que, and E. I. Solomon, *J. Am. Chem. Soc.* 124, 10810 (2002).

216. M. R. Fuchs, E. Schleicher, A. Schnegg, C. W. M. Kay, J. T. Torring, R. Bittl, A. Bacher, G. Richter, K. Mobius, and S. Weber, *J. Phys. Chem. B* 106, 8885 (2002).

217. Y. H. Jang, W. A. Goddard, K. T. Noyes, L. C. Sowers, S. Hwang, and D. S. Chung, *Chem. Res. Toxicol.* 15, 1023 (2002).

218. F. Bernardi, A. Bottoni, M. De Vivo, M. Garavelli, G. Keseru, and G. Naray-Szabo, *Chem. Phys. Lett.* 362, 1 (2002).

219. M. Mertig, L. C. Ciacchi, R. Seidel, W. Pompe, and A. De Vita, *Nano Lett.* 2, 841 (2002).

220. N. A. Richardson, S. S. Wesolowski, and H. F. Schaefer, *J. Am. Chem. Soc.* 124, 10163 (2002).

221. G. B. Jones, J. M. Wright, G. Hynd, J. K. Wyatt, P. M. Warner, R. S. Huber, A. W. Li, M. W. Kilgore, R. P. Sticca, and R. S. Pollenz, *J. Org. Chem.* 67, 5727 (2002).

222. S. Martins and J. F. Stilck, *Physica A* 311, 23 (2002).

223. P. Damle, A. W. Ghosh, and S. Datta, *Chem. Phys.* 281, 171 (2002).

224. M. E. Costas and R. Acevedo-Chavez, *J. Mol. Struct. Theochem.* 587, 129 (2002).

225. S. X. Tian and K. Z. Xu, *Int. J. Quantum Chem.* 89, 106 (2002).

226. M. Plazanet, N. Fukushima, and M. R. Johnson, *Chem. Phys.* 280, 53 (2002).

227. C. F. Guerra and F. M. Bickelhaupt, *Angew. Chem. Int. Ed.* 41, 2092 (2002).

228. Z. E. R. Newby, E. Y. Lau, and T. C. Bruice, *Proc. Natl. Acad. Sci. USA* 99, 7922 (2002).

229. C. B. Martin, M. L. Tsao, C. M. Hadad, and M. S. Platz, *J. Am. Chem. Soc.* 124, 7226 (2002).

230. T. V. Bykov and X. C. Zeng, *J. Chem. Phys.* 117, 1851 (2002).

231. H. Saarikoski, E. Rasanen, S. Siljamaki, A. Harju, I. J. Puska, and R. M. Nieminen, *Eur. Phys. J. B* 26, 241 (2002).

232. L. Szybisz and S. M. Gatica, *Phys. Rev. B* 64, 224523 (2001).

233. A. Bogicevic and D. R. Jennison, *Surf. Sci.* 515, L481 (2002).

234. F. Grosse, W. Barvosa-Carter, J. Zinck, M. Wheeler, and M. F. Gyure, *Phys. Rev. Lett.* 89, 116102 (2002).

235. P. Kratzer, E. Penev, and M. Scheffler, *Appl. Phys. A* 75, 79 (2002).

236. M. Schmidt and C. von Ferber, *Phys. Rev. E* 64, 051115 (2001).

237. H. Morita, T. Kawakatsu, and M. Doi, *Macromolecules* 34, 8777 (2001).

238. R. K. Murarka and B. Bagchi, *J. Chem. Phys.* 115, 5513 (2001).

239. B. Partoens and F. M. Peeters, *Physica B* 298, 282 (2001).

240. M. Pi, A. Emperador, M. Barranco, and F. Garcias, *Phys. Rev. B* 63, 115316 (2001).

241. V. V. Pogosov, A. Kiejna, and D. P. Kotlyarov, *Physica A* 293, 59 (2001).

242. M. Borg, A. Mikkelsen, M. Birgersson, M. Smedh, E. Lundgren, D. L. Adams, C. O. Almbladh, and J. N. Andersen, *Surf. Sci.* 515, 267 (2002).

243. K. A. Fichthorn, M. L. Merrick, and M. Scheffler, *Appl. Phys. A* 75, 17 (2002).

244. P. Kratzer and M. Scheffler, *Phys. Rev. Lett.* 88, 036102 (2002).

245. B. Giese and D. McNaughton, *J. Phys. Chem. B* 106, 101 (2002).

246. P. J. Feibelman and T. Michely, *Surf. Sci.* 492, L723 (2001).

247. P. Varga, E. Lundgren, J. Redinger, and M. Schmid, *Phys. Status Solidi A* 187, 97 (2001).

248. P. O. Nilsson, S. Mankefors, J. Guo, J. Nordgren, D. Debowska-Nilsson, W. X. Ni, and G. V. Hansson, *Phys. Rev. B* 64, 115306 (2001).

249. E. Penev, P. Kratzer, and M. Scheffler, *Phys. Rev. B* 64, 085401 (2001).

250. M. Kiguchi, K. Saiki, T. Sasaki, Y. Iwasawa, and A. Koma, *Phys. Rev. B* 63, 205418 (2001).

251. B. O. Skadtchenko and R. Aroca, *Spectrochim. Acta A* 57, 1009 (2001).

252. S. M. Lee, Y. H. Lee, and N. G. Kim, *Surf. Sci.* 470, 89 (2000).

253. A. Michaelides and P. Hu, *J. Chem. Phys.* 114, 513 (2001).

254. A. T. Jorgensen, P. O. Norrby, and T. Liljefors, *J. Comput. Aided Mol. Des.* 16, 167 (2002).

255. S. Yamanaka, R. Takeda, and K. Yamaguchi, *Mol. Cryst. Liq. Cryst.* 379, 537 (2002).

256. D. M. Chen, X. Liu, T. J. He, and F. C. Liu, *Chem. Phys. Lett.* 361, 106 (2002).

257. B. Y. Liang and L. Andrews, *J. Phys. Chem. A* 106, 6295 (2002).

258. C. W. Bauschlicher and G. L. Gutsev, *Theor. Chem. Acc.* 108, 27 (2002).

259. B. Y. Liang and L. Andrews, *J. Phys. Chem. A* 106, 6945 (2002).

260. Y. Ishikawa, M. S. Liao, and C. R. Cabrera, *Surf. Sci.* 513, 98 (2002).

261. F. Nunzi, A. Sgamellotti, and N. Re, *Organometallics* 21, 2219 (2002).

262. S. Virko, T. Petrenko, A. Yaremko, R. Wysokinski, and D. Michalska, *J. Mol. Struct. Theochem.* 582, 137 (2002).

263. Y. Li, J. E. McGrady, and T. Baer, *J. Am. Chem. Soc.* 124, 4487 (2002).

264. T. B. Freedman, X. L. Cao, D. A. Young, and L. A. Nafie, *J. Phys. Chem. A* 106, 3560 (2002).

265. B. Y. Liang and L. Andrews, *J. Phys. Chem. A* 106, 3738 (2002).

266. A. Vierheilig, D. Moigno, W. Kiefer, and A. Materny, *J. Mol. Spectrosc.* 211, 58 (2002).

267. B. Kiran and M. T. Nguyen, *J. Organomet. Chem.* 643, 265 (2002).

268. L. Andrews and X. F. Wang, *J. Phys. Chem. A* 106, 1196 (2002).

269. L. Pejov, *Int. J. Quantum Chem.* 86, 356 (2002).

270. H. Harris, K. Fisher, and I. Dance, *Inorg. Chem.* 40, 6972 (2001).

271. T. Ito, K. Nishidate, M. Baba, and M. Hasegawa, *Surf. Sci.* 514, 222 (2002).

272. Y. Q. Feng, R. Q. Zhang, K. S. Chan, H. F. Cheung, and S. T. Lee, *Phys. Rev. B* 66, 045404 (2002).

273. A. Di Carlo, M. Gheorghe, P. Lugli, M. Sternberg, G. Seifert, and T. Frauenheim, *Physica B* 314, 86 (2002).

274. C. Kim, B. Kim, S. M. Lee, C. Jo, and Y. H. Lee, *Phys. Rev. B* 65, 165418 (2002).

275. G. Cuniberti, R. Gutierrez, G. Fagas, F. Grossmann, K. Richter, and R. Schmidt, *Physica E* 12, 749 (2002).

276. A. Ricca and J. A. Drocco, *Chem. Phys. Lett.* 362, 217 (2002).

277. C. Carraro, *Phys. Rev. Lett.* 89, 115702 (2002).

278. C. Kim, Y. S. Choi, S. M. Lee, J. T. Park, B. Kim, and Y. H. Lee, *J. Am. Chem. Soc.* 124, 9906 (2002).

279. R. Car, *Quant. Struct.-Act. Relat.* 21, 97 (2002).

280. A. G. Marinopoulos, L. Reining, V. Olevano, A. Rubio, T. Pichler, X. Liu, M. Knupfer, and J. Fink, *Phys. Rev. Lett.* 89, 076402 (2002).

281. M. Di Ventra, N. D. Lang, and S. T. Pantelides, *Chem. Phys.* 281, 189 (2002).

282. J. S. Arellano, L. M. Molina, A. Rubio, M. J. Lopez, and J. A. Alonso, *J. Chem. Phys.* 117, 2281 (2002).

283. T. Heine and F. Zerbetto, *Chem. Phys. Lett.* 358, 359 (2002).

284. K. Murata, M. Yudasaka, S. Iijima, M. El Merraoui, and K. Kaneko, *J. Appl. Phys.* 91, 10227 (2002).

285. O. Dubay, G. Kresse, and H. Kuzmany, *Phys. Rev. Lett.* 88, 235506 (2002).

286. H. Richter and J. B. Howard, *PCCP* 4, 2038 (2002).

287. T. Hayashi, M. Terrones, C. Scheu, Y. A. Kim, M. Ruhle, T. Nakajima, and M. Endo, *Nano Lett.* 2, 491 (2002).

288. M. Brandbyge, J. L. Mozos, P. Ordejon, J. Taylor, and K. Stokbro, *Phys. Rev. B* 65, 165401 (2002).

289. T. Miyake and S. Saito, *Phys. Rev. B* 65, 165419 (2002).

290. S. Reich, C. Thomsen, and P. Ordejon, *Phys. Rev. B* 65, 153407 (2002).

291. D. Spisak and J. Hafner, *Phys. Rev. B* 65, 235405 (2002).

292. P. Sen, O. Gulseren, T. Yildirim, I. P. Batra, and S. Ciraci, *Phys. Rev. B* 65, 235433 (2002).

293. J. L. Mozos, P. Ordejon, M. Brandbyge, J. Taylor, and K. Stokbro, *Nanotechnology* 13, 346 (2002).

294. I. P. Batra, P. Sen, and S. Ciraci, *J. Vac. Sci. Technol. B* 20, 812 (2002).

295. H. Nakanishi, H. Kasai, T. Kishi, F. Komori, and A. Okiji, *Surf. Sci.* 514, 161 (2002).

296. A. Ayuela, H. Raebiger, M. J. Puska, and R. M. Nieminen, *Phys. Rev. B* 66, 035417 (2002).

297. S. K. Nielsen, M. Brandbyge, K. Hansen, K. Stokbro, J. M. van Ruitenbeek, and F. Besenbacher, *Phys. Rev. Lett.* 89, 066804 (2002).

298. J. Y. Song and M. Choi, *Phys. Rev. B* 65, 241302 (2002).

299. R. H. Miwa, T. M. Schmidt, and G. P. Srivastava, *Surf. Sci.* 507, 368 (2002).

300. J. K. Kang and C. B. Musgrave, *J. Chem. Phys.* 116, 9907 (2002).

301. C. A. Stafford, *Phys. Status Solidi B* 230, 481 (2002).

302. S. B. Legoas, D. S. Galvao, V. Rodrigues, and D. Ugarte, *Phys. Rev. Lett.* 88, 076105 (2002).

303. S. R. Bahn and K. W. Jacobsen, *Phys. Rev. Lett.* 87, 266101 (2001).

304. S. Tsukamoto, Y. Fujimoto, T. Ono, K. Inagaki, H. Goto, and K. Hirose, *Mater. Trans.* 42, 2253 (2001).

305. H.-S. Sim, H. W. Lee, and K. J. Chang, *Phys. Rev. Lett.* 87, 096803 (2001).

306. H.-S. Sim, H. W. Lee, and K. J. Chang, *Physica E* 14, 347 (2002).

307. T. H. Rod, B. Hammer, and J. K. Nørskov, *Phys. Rev. Lett.* 82, 4054 (1999).

308. T. H. Rod and J. K. Nørskov, *J. Am. Chem. Soc.* 122, 12751 (2000).

309. T. H. Rod, A. Logadottir, and J. K. Nørskov, *J. Chem. Phys.* 112 (2000).

310. T. H. Rod and J. K. Nørskov, *Surf. Sci.* 500, 678 (2002).

311. D. Vanderbilt, *Phys. Rev. B* 41, 7892 (1990).

312. N. Troullier and J. L. Martins, *Phys. Rev. B* 43, 1993 (1991).

313. J. P. Perdew et al., *Phys. Rev. B* 46, 6671 (1992).

314. B. Hammer, L. B. Hansen, and J. K. Nørskov, *Phys. Rev. B* 59, 7413 (1999).

315. R. Ahlrichs and D. Elliott, *Phys. Chem. Chem. Phys.* 1, 13 (1999).

316. N. D. Mermin, *Phys. Rev. A* 137, 1441 (1965).

317. M. Rieth, W. Schommers, S. Baskoutas, C. Politis, and A. Jannussis, *Chinese Phys.* 10, 137 (2001).

318. R. E. Allen and F. W. de Wette, *J. Chem. Phys.* 51, 4820 (1969).

319. A. A. Maradudin, E. W. Montroll, G. H. Weiss, and I. P. Ipatova, "Theory of Lattice Dynamics in the Harmonic Approximation," Solid State Physics (Suppl. 3). Academic Press, New York, 1967.

320. N. H. March, in "Theory of Condensed Matter." International Atomic Agency, Vienna, 1968.

321. W. Schommers, in "Structure and Dynamics of Surfaces II" (W. Schommers and P. von Blanckenhagen, Eds.). Springer-Verlag, Berlin, 1987.

322. C. A. Croxton, "Statistical Mechanics of the Liquid Surface." Wiley, Chichester, 1980.

323. M. Torrens, "Interatomic Potentials." Academic Press, New York, 1972.

324. W. Schommers, *Phys. Rev. Lett.* 38, 1536 (1977).

325. W. Schommers, *Phys. Rev. B* 21, 847 (1980).

326. W. Schommers, *Phys. Rev. B* 22, 1058 (1980).

327. W. Schommers, *Phys. Rev. A* 22, 2855 (1980).

328. R. E. Allen, G. P. Alldredge, and F. W. de Wette, *Phys. Rev. B* 4, 1648 (1971).

329. W. Schommers, *Solid State Commun.* 16, 4 (1975).

330. O. Krisement, "Vorlesungen über Statistische Mechanik und Thermodynamik." Münster Univ. Press, Münster, 1966.

331. L. D. Landau and E. M. Lifshitz, "Statistical Physics." Pergamon, London, 1963.

332. I. Prigogine, "From Being to Becoming." Freeman, San Francisco, 1979.

333. A. Münster, "Statistical Thermodynamics 1." Springer, Berlin, 1969.

334. A. Münster, "Statistical Thermodynamics 2." Springer, Berlin, 1974.

335. T. L. Hill, "An Introduction to Statistical Thermodynamics." Addison–Weesley, Reading, MA, 1960.

336. K. Huang, "Statistische Mechanik," Bd. 1-3. Bibliographisches Institut, Mannheim, 1964.

337. R. Becker, "Theorie der Wärme." Springer, Berlin, 1985.

338. J. L. Lebowitz and J. K. Percus, *Phys. Rev.* 153, 250 (1965).

339. J. R. D. Copley and S. W. Lovesey, *Rep. Progr. Phys.* 38, 461 (1975).

340. A. W. Lees and S. F. Edwards, *J. Phys. C* 5, 1921 (1972).

341. E. M. Gosling and I. R. McDonald, *Mol. Phys.* 26, 1475 (1973).

342. W. T. Ashurst and W. G. Hoover, *Phys. Rev. Lett.* 31, 206 (1973).

343. W. G. Hoover, *Annu. Rev. Phys. Chem.* 34, 103 (1983).

344. W. G. Hoover, "Molecular Dynamics, Lecture Notes in Physics 258." Springer-Verlag, Berlin, 1986.

345. W. G. Hoover, "Computational Statistical Mechanics." Elsevier, Amsterdam, 1991.

346. D. J. Evans and G. Morriss, "Statistical Mechanics of Nonequilibrium Liquids." Academic Press, New York, 1990.

347. R. M. Hockney and J. W. Eastwood, "Computer Simulation Using Particles." McGraw–Hill, New York, 1981.

348. G. Coccotti and W. G. Hoover (Eds.), "Molecular-Dynamics Simulations of Statistical-Mechanical Systems." North-Holland, Amsterdam, 1986.

349. M. P. Allen and G. J. Tildesley, "Computer Simulation of Liquids." Clarendon, Oxford, 1987.

350. M. Mareschal, S. McNamara, J.-B. Maillet, and R. Soto, *Am. Inst. Phys. Conf. Proc.* 574, 155 (2001).

351. S. Butler and P. Harrowell, *Nature* 415, 1008 (2002).

352. J. D. Kress, S. R. Bickham, L. A. Collins, B. L. Holian, and S. Goedecker, *Am. Inst. Phys. Conf. Proc.* 505, 381 (2000).

353. E. Molinari and M. Tomellini, *Chem. Phys.* 277, 373 (2002).

354. Yu. K. Tovbin, R. Ya. Tugazakov, and V. N. Komarov, *Colloids Surfaces A* 206, 377 (2002).

355. M. Ernst, in "Dynamics: Models and Kinetic Methods for Non-equilibrium Many Body Systems" NATO Science Series E: Applied Sciences Vol. 371 (J. Karkheck, Ed.), p. 361. Kluwer Academic, Dordrecht, 2000.

356. J. M. Haile, "Molecular Dynamics Simulation." Wiley, New York, 1997.

357. E. Lüscher, in "Die feste Materie." Umschau Verlag, Frankfurt am Main, 1973.

358. P. M. Morse, *Phys. Rev.* 34, 57 (1929).

359. K. Mohammed, M. M. Shukla, F. Milstein, and J. L. Merz, *Phys. Rev. B* 29, 3117 (1984).

360. M. Eichler and M. Peyzl, *Phys. Status Solidi* 35, 333 (1969).

361. H. D. Diener, R. Heinrich, and W. Schellenberger, *Phys. Status Solidi B* 44, 403 (1971).

362. V. Vitzk, C. R. Perrin, and D. K. Bown, *Philos. Mag.* 21, 1049 (1970).

363. C. Gehlen, A. R. Rosenfeld, and G. T. Hahn, *J. Appl. Phys.* 39, 5346 (1968).

364. R. Chang, *Philos. Mag.* 16, 1021 (1967).

365. R. M. J. Cotterill and M. Doyama, *Phys. Rev.* 145, 465 (1966).

366. M. Doyama and R. M. J. Cotterill, *Phys. Rev. A* 137, 994 (1965).

367. R. A. Johnson, *Phys. Rev. A* 134, 1329 (1964).

368. L. A. Gififalco and V. G. Weizer, *J. Phys. Chem. Solids* 12, 260 (1960).

369. W. D. Wilson and C. L. Bisson, *Phys. Rev. B* 3, 2979 (1971).

370. A. Anderman and W. G. Gehman, *Phys. Status Solidi* 30, 283 (1968).

371. R. Furth, *Proc. Roy. Soc. London* 183, 87 (1944).

372. L. A. Gififalco and V. G. Weizer, *Phys. Rev.* 114, 687 (1959).

373. R. G. Lincoln, K. M. Koliwad, and P. B. Ghate, *Phys. Rev.* 157, 463 (1967).

374. F. O. Goodman, *Phys. Rev.* 164, 1113 (1967).

375. M. Moody, J. R. Ray, and A. Rahman, *Phys. Rev. B* 35, 557 (1987).

376. A. Strachan, T. Cagin, and W. A. Goddard, *Phys. Rev. B* 60, 15084 (1999).

377. S. Azizian and F. Gobal, *React. Kinet. Catal. L* 76, 43 (2002).

378. C. L. Kao, J. F. Weaver, and R. J. Madix, *Surf. Sci.* 505, 115 (2002).

379. T. H. Fang, C. I. Wenig, and J. G. Chang, *Surf. Sci.* 501, 138 (2002).

380. C. L. Kao, A. Carlson, and R. J. Madix, *Surf. Sci.* 497, 356 (2002).

381. A. Vijay and H. Metiu, *J. Chem. Phys.* 116, 60 (2002).

382. R. A. Buckingham, *Proc. Roy. Soc. London Ser. A* 168, 264 (1938).

383. R. A. Buckingham, *J. Plan. Space Sci.* 3, 205 (1961).

384. U. Burkert and N. L. Allinger, "Molecular Mechanics," ACS Monograph 177. Am. Chem. Soc., Washington, DC, 1982.

385. J. O. Hirschfelder, C. F. Curtis, and R. B. Bird, "Molecular Theory of Gases and Liquids." Wiley, New York, 1954.

386. W. Schommers, *Int. J. Modern Phys. B* 8, 3411 (1994).

387. J. A. Barker, R. O. Watts, J. K. Lee, T. P. Schafer, and Y. T. Lee, *J. Chem. Phys.* 61, 3081 (1974).

388. U. Romahn, H. Göbel, W. Schommers, and P. von Blanckenhagen, *Mod. Phys. Lett. B* 5, 1873 (1991).

389. D. Wolf, J. Wang, S. R. Phillpot, and H. Gleiter, *Phys. Rev. Lett.* 74, 4686 (1995).

390. B. M. Axilrod and E. Teller, *J. Chem. Phys.* 11, 229 (1943).

391. W. Schommers, *Phys. Rev.* 22, 2855 (1980).

392. W. Harrison, "Pseudopotentials in the Theory of Metals." Benjamin, New York, 1966.

393. P. A. Egelstaff, "An Introduction to the Liquid State." Academic Press, New York, 1970.

394. L.-J. Sham, *Proc. Roy. Soc. London Ser. A* 33, 283 (1965).

395. V. Heine and I. Abarenkov, *Philos. Mag.* 9, 451 (1965).

396. N. W. Ashcroft, *J. Phys. C* 1, 232 (1965).

397. W. Schommers, *Z. Phys. B* 24, 171 (1976).

398. C. Oubre, P. Nordlander, and F. B. Dunning, *J. Phys. Chem. B* 106, 8338 (2002).

399. H. Fahs, A. R. Allouche, M. Korek, and M. Aubert-Frecon, *J. Phys. B* 35, 1501 (2002).

400. Z. S. Yuan, L. F. Zhu, X. Tong, W. B. Li, X. J. Liu, and K. Z. Xu, *J. Mol. Struct. Theochem.* 589, 229 (2002).

401. G. Csanyi and T. A. Arias, *Chem. Phys. Lett.* 360, 552 (2002).

402. K. Kassali and N. Bouarissa, *Mater. Chem. Phys.* 76, 255 (2002).

403. Y. Ciftci, M. Cakmak, G. P. Srivastava, and K. Colakoglu, *Surf. Sci.* 507, 23 (2002).
404. J. Gonzalez, E. Calderon, C. Power, F. Capet, A. Munoz, O. F. Sankey, and M. Fuentes-Cabrera, *High Pressure Res.* 22, 361 (2002).
405. H. Takeda, N. Mori, and C. Hamaguchi, *Physica B* 314, 377 (2002).
406. H. C. Herper, E. Hoffmann, and P. Entel, *Phase Transit.* 75, 185 (2002).
407. A. A. Mamun and P. K. Shukla, *Phys. Scr. T* 98, 107 (2002).
408. B. P. van Zyl, R. K. Bhaduri, and J. Sigetich, *J. Phys. B* 35, 1251 (2002).
409. L. Banci, I. Bertini, G. Cavallaro, and C. Luchinat, *J. Biol. Inorg. Chem.* 7, 416 (2002).
410. C. M. Fang, H. T. Hintzen, and G. de With, *J. Alloys Compd.* 336, 1 (2002).
411. U. P. Wad, A. V. Limaye, and S. B. Ogale, *Solid State Commun.* 121, 505 (2002).
412. L. Serra, P. G. Reinhard, and E. Suraud, *Eur. Phys. J. D* 18, 327 (2002).
413. M. Hjiaj, G. de Saxce, and Z. Mroz, *Eur. J. Mech. A* 21, 49 (2002).
414. J. F. McKenzie, *Phys. Plasmas* 9, 800 (2002).
415. M. Merawa and M. Rerat, *Eur. Phys. J. D* 17, 329 (2001).
416. W. Schommers, *Phys. Rev. A* 28, 3599 (1983).
417. S. A. Rice and P. Gray, "The Statistical Mechnics of Simple Liquids." Wiley, New York, 1965.
418. A. Münster, "Statistical Thermodynamics," Vols. 1 and 2. Springer, Berlin, 1969, 1974.
419. A. H. Narten, *J. Chem. Phys.* 56, 1185 (1972).
420. M. Rasolt and F. Perrot, *Phys. Rev. B* 28, 6749 (1983).
421. M. S. Daw and M. I. Baskes, *Phys. Rev. Lett.* 50, 1285 (1983).
422. M. S. Daw and M. I. Baskes, *Phys. Rev.* 29, 6443 (1984).
423. S. M. Foiles, M. I. Baskes, and M. S. Daw, *Phys. Rev.* 33, 7983 (1986).
424. M. S. Daw and R. L. Hatcher, *Solid State Commun.* 56, 697 (1985).
425. S. M. Foiles, *Phys. Rev. B* 32, 3409 (1985).
426. M. S. Daw, *Surf. Sci. Lett.* 166, L161 (1986).
427. E. O. Arregui, M. Caro, and A. Caro, *Phys. Rev. B* 66, 054201 (2002).
428. H. Feraoun, H. Aourag, T. Grosdidier, D. Klein, and C. Coddet, *Superlattices Microstruct.* 30, 261 (2001).
429. X. J. Xu, M. Wen, Z. Hu, S. Fukuyama, and K. Yokogawa, *Comp. Mater. Sci.* 23, 131 (2002).
430. Y. Le Bouar and F. Soisson, *Phys. Rev. B* 65, 094103 (2002).
431. J. Z. Wang, M. Chen, and Z. Y. Guo, *Chinese Phys. Lett.* 19, 324 (2002).
432. Y. Mishin, M. J. Mehl, and D. A. Papaconstantopoulos, *Phys. Rev. B* 65, 224114 (2002).
433. M. Karabacak, S. Ozcelik, and Z. B. Guvenc, *Surf. Sci.* 507, 636 (2002).
434. F. Fang, M. Q. Zeng, X. Z. Che, and M. Zhu, *J. Alloys Compd.* 340, 252 (2002).
435. B. J. Thijsse, *Phys. Rev. B* 65, 195207 (2002).
436. G. M. Gusinskii and A. V. Matyukov, *Tech. Phys.* 47, 578 (2002).
437. H. R. Cong, X. F. Bian, J. X. Zhang, and H. Li, *Mater. Sci. Eng. A* 326, 343 (2002).
438. K. Mae, T. Nobata, H. Ishida, S. Motoyama, and Y. Hiwatari, *Modell. Simul. Mater. Sci. Eng.* 10, 205 (2002).
439. W. Y. Hu, H. D. Xu, X. L. Shu, X. J. Yuan, and B. W. Zhang, *Int. J. Mater. Prod. Tec.* 107 (2001).
440. T. Wang, F. X. Zhou, and Y. W. Liu, *Chinese Phys.* 11, 139 (2002).
441. E. Lundgren, G. Leonardelli, M. Schmid, and P. Varga, *Surf. Sci.* 498, 257 (2002).
442. J. Zhuang, T. Kojima, W. H. Zhang, L. Liu, L. Zhao, and Y. F. Li, *Phys. Rev. B* 65, 045411 (2002).
443. M. F. Horstemeyer, M. I. Baskes, and S. J. Plimpton, *Theor. Appl. Fract. Mec.* 37, 49 (2001).
444. X. J. Xu, M. Wen, S. Fukuyama, and K. Yokogawa, *Mater. Trans.* 42, 2283 (2001).
445. R. Car and M. Parrinello, *Phys. Rev. Lett.* 55, 2471 (1985).
446. G. Seifert, in "Physik der Nanostrukturen." Schriften des Forschungszentrums Jülich, Jülich, 1998.
447. R. Car and M. Parrinello, in "Simple Molecular Systems at Very High Density," NATO Advanced Study Institute Ser. 455. Plenum Press, New York, 1988.
448. G. Pastore, E. Smargiassi, and F. Buda, *Phys. Rev. A* 44, 6336 (1991).
449. S. H. N. Lim, D. G. McCullooch, A. R. Merchant, N. A. Marks, M. M. M. Bilek, and D. R. McKenzie, *Mol. Simulat.* 28, 971 (2002).
450. L. Guidoni, P. Maurer, S. Piana, and U. Rothlisberger, *Quant. Struct. Act. Relat.* 21, 119 (2002).
451. M. Boero, M. Parrinello, K. Terakura, and H. Weiss, *Mol. Phys.* 100, 2935 (2002).
452. S. Izvekov and G. A. Voth, *J. Chem. Phys.* 116, 10372 (2002).
453. A. Laio, J. VandeVondele, and U. Rothlisberger, *J. Chem. Phys.* 116, 6941 (2002).
454. N. L. Doltsinis and D. Marx, *Phys. Rev. Lett.* 88, 166402 (2002).
455. B. Ensing, F. Buda, P. E. Blochl, and E. J. Baerends, *PCCP* 4, 3619 (2002).
456. M. Pagliai, S. Raugei, G. Cardini, and V. Schettino, *J. Chem. Phys.* 117, 2199 (2002).
457. M. C. Colombo, L. Guidoni, A. Laio, A. Magistrato, P. Maurer, S. Piana, U. Rohrig, K. Spiegel, M. Sulpizi, J. VandeVondele, M. Zumstein, and U. Rothlisberger, *Chimia* 56, 13 (2002).
458. T. Oda, *J. Phys. Soc. Jpn.* 71, 519 (2002).
459. T. K. Woo, P. Margl, P. E. Blochl, and T. Ziegler, *J. Phys. Chem. A* 106, 1173 (2002).
460. W. Langel, *Surf. Sci.* 496, 141 (2002).
461. P. Tangney and S. Scandolo, *J. Chem. Phys.* 116, 14 (2002).
462. M. Pagliai, S. Raugei, G. Cardini, and V. Schettino, *PCCP* 3, 4870 (2001).
463. Y. A. Mantz, F. M. Geiger, L. T. Molina, M. J. Molina, and B. L. Trout, *Chem. Phys. Lett.* 348, 285 (2001).
464. D. Frigyes, F. Alber, S. Pongor, and P. Carloni, *J. Mol. Struct. Theochem.* 574, 39 (2001).
465. H. Weiss, M. Boero, and M. Parrinello, *Macromol. Symp.* 173, 137 (2001).
466. M. Boero, K. Terakura, T. Ikeshoji, C. C. Liew, and M. Parrinello, *Progr. Theor. Phys. Supp.* 259 (2000).
467. U. Rothlisberger, P. Carloni, K. Doclo, and M. Parrinello, *J. Biol. Inorg. Chem.* 5, 236 (2000).
468. N. L. Allinger, *J. Am. Chem. Soc.* 99, 8127 (1977).
469. N. L. Allinger, *J. Am. Chem. Soc.* 99, 8127 (1989).
470. N. L. Allinger, Y. H. Yuh, and J. Lii, *J. Am. Chem. Soc.* 111, 8551 (1989).
471. K. Eric Drexler, "Nanosystems, Molecular Machinery, Manufacturing, and Computation." Wiley, New York, 1992.
472. H. Balamane, T. Halicioglu, and W. A. Tiller, *Phys. Rev. B* 46, 2250 (1992).
473. E. M. Pearson, T. Takai, T. Halicioglu, and W. A. Tiller, *Cryst. Growth* 70, 33 (1984).
474. F. H. Stillinger and T. A. Weber, *Phys. Rev. B* 31, 5262 (1985).
475. R. Biswas and D. R. Hamann, *Phys. Rev. B* 36, 6434 (1987).
476. J. Tersoff, *Phys. Rev. B* 37, 6991 (1988).
477. J. Tersoff, *Phys. Rev. B* 38, 9902 (1988).
478. B. W. Dodson, *Phys. Rev. B* 35, 2795 (1987).
479. J. Tersoff, *Phys. Rev. Lett.* 56, 632 (1986).
480. J. Tersoff, *Phys. Rev. B* 61, 2879 (1988).
481. J. Tersoff, *Phys. Rev. B* 64, 1757 (1988).
482. D. W. Brenner, *Phys. Rev. Lett.* 63, 1022 (1989).
483. D. W. Brenner, *Phys. Rev. B* 42, 9458 (1990).

484. A. Garg and S. B. Simon, *Phys. Rev. B* 60, 13786 (1999).
485. A. S. Barnard, S. P. Russo, and G. I. Leach, *Mol. Simulat.* 28, 761 (2002).
486. A. S. Barnard and S. P. Russo, *Mol. Phys.* 100, 1517 (2002).
487. S. P. Walch, *Surf. Sci.* 496, 271 (2002).
488. F. Finkemeier and W. von Niessen, *Phys. Rev. B* 63, 235204 (2001).
489. Y. Kikuchi, H. Sugii, and K. Shintani, *J. Appl. Phys.* 89, 1191 (2001).
490. S. Kret, J. Chen, P. Ruterana, and G. Nouet, "Microscopy of Semiconducting Materials," IOP, London, 2001, p. 319.
491. S. Kret, P. Dluzewski, G. Maciejewski, V. Potin, J. Chen, P. Ruterana, and G. Nouet, *Diamond Relat. Mater.* 11, 910 (2002).
492. L. Colombo and F. Cleri, *Key Eng. Mat.* 5, 307 (2002).
493. V. M. Glazov and L. M. Pavlova, *Scand. J. Metall.* 31, 52 (2002).
494. M. H. Liang, X. Xie, and S. Li, *Int. J. Mod. Phys. B* 16, 227 (2002).
495. J. L. Feldman, C. S. Hellberg, G. Viliani, W. Garber, and F. M. Tangerman, *Philos. Mag. B* 82, 133 (2002).
496. J. Chen, G. Nouet, and P. Ruterana, *Phys. Status Solidi B* 228, 411 (2001).
497. R. L. C. Vink, G. T. Barkema, W. F. van der Weg, and N. Mousseau, *J. Non-Cryst. Solids* 282, 248 (2001).
498. S. Costantini, P. Alippi, L. Colombo, and F. Cleri, *Phys. Rev. B* 63, 045302 (2001).
499. Y. L. Song, R. Malek, and N. Mousseau, *Phys. Rev. B* 62, 15680 (2000).
500. X. L. Yuan and L. W. Hobbs, *Nucl. Instrum. Methods B* 191, 74 (2002).
501. T. Motooka, K. Nishihira, R. Oshima, H. Nishizawa, and F. Hori, *Phys. Rev. B* 65, 081304 (2002).
502. W. Sekkal and A. Zaoui, *New J. Phys.* 4, 9 (2002).
503. Q. H. Tang, K. Runge, H. P. Cheng, and F. E. Harris, *J. Phys. Chem. A* 106, 893 (2002).
504. Y. Saito, N. Sasaki, H. Moriya, A. Kagatsume, and S. Noro, *JSME Int. J. A* 44, 207 (2001).
505. F. Gao and W. J. Weber, *Phys. Rev. B* 66, 024106 (2002).
506. F. El Mellouhi, W. Sekkal, and A. Zaoui, *Physica A* 311, 130 (2002).
507. W. Yu, X. Y. Teng, X. W. Li, and G. S. Fu, *Chinese Phys. Lett.* 19, 492 (2002).
508. M. A. Migliorato, A. G. Cullis, M. Fearn, and J. H. Jefferson, *Phys. Rev. B* 65, 115316 (2002).
509. L. Malerba and J. M. Perlado, *Phys. Rev. B* 65, 045202 (2002).
510. S. Munetoh, K. Moriguchi, A. Shintani, K. Nishihara, and T. Motooka, *Phys. Rev. B* 64, 193314 (2001).
511. R. Devanathan, W. J. Weber, and F. Gao, *J. Appl. Phys.* 90, 2303 (2001).
512. C. Koitzsch, D. Conrad, K. Scheerschmidt, F. Scharmann, P. Maslarski, and J. Pezoldt, *Appl. Surf. Sci.* 179, 49 (2001).
513. M. Posselt, V. Belko, and E. Chagarov, *Nucl. Instrum. Methods B* 180, 17 (2001).
514. F. Gao, W. J. Weber, and R. Devanathan, *Nucl. Instrum. Methods B* 180, 176 (2001).
515. F. Gao, E. J. Bylaska, W. J. Weber, and L. R. Corrales, *Nucl. Instrum. Methods B* 180, 286 (2001).
516. M. Koster and H. M. Urbassek, *Phys. Rev. B* 63, 224111 (2001).
517. S. Munetoh, K. Moriguchi, K. Kamei, A. Shintani, and T. Motooka, *Phys. Rev. Lett.* 86, 4879 (2001).
518. M. Mazzarolo, L. Colombo, G. Lulli, and E. Albertazzi, *Phys. Rev. B* 63, 195207 (2001).
519. J. Cai and J. S. Wang, *Phys. Status Solidi B* 223, 773 (2001).
520. F. Gao and W. J. Weber, *Phys. Rev. B* 63, 054101 (2001).
521. L. Malerba, J. M. Perlado, A. Sanchez-Rubio, I. Pastor, L. Colombo, and T. D. de la Rubia, *J. Nucl. Mater.* 283, 794 (2000).
522. S. Ueda, T. Ohsaka, and S. Kuwajima, *J. Nucl. Mater.* 283, 1100 (2000).
523. J. H. Los and A. Fasolino, *Comput. Phys. Commun.* 147, 178 (2002).
524. A. Perez-Garrido, *J. Phys.* 14, 5077 (2002).
525. A. J. Du, Z. Y. Pan, Y. K. Ho, Y. X. Wang, and Y. Xu, *Nucl. Instrum. Methods B* 180, 153 (2001).
526. A. V. Petukhov and A. Fasolino, *Phys. Status Solidi A* 181, 109 (2000).
527. V. P. Sokhan, D. Nicholson, and N. Quirke, *J. Chem. Phys.* 113, 2007 (2000).
528. W. J. Zhu, Z. Y. Pan, and Y. K. Ho, *Surf. Coat. Tech.* 128, 170 (2000).
529. A. Delcorte, B. Arezki, P. Bertrand, and B. J. Garrison, *Nucl. Instrum. Methods B* 193, 768 (2002).
530. N. Winograd, *Izv. Akad. Nauk Fiz.* 66, 462 (2002).
531. A. Perez-Garrido, J. D. Catala, and F. Alhama, *Phys. Solid State* 44, 598 (2002).
532. N. A. Marks, N. C. Cooper, D. R. McKenzie, D. G. McCulloch, P. Bath, and S. P. Russo, *Phys. Rev. B* 65, 075411 (2002).
533. N. Winograd and B. J. Garrison, *Int. J. Mass Spectrom.* 212, 467 (2001).
534. A. J. Du, Z. Y. Pan, Y. K. Ho, Z. Huang, Z. X. Zhang, and Y. X. Wang, *Chem. Phys. Lett.* 344, 270 (2001).
535. I. Laszlo and A. Rassat, *Int. J. Quantum Chem.* 84, 136 (2001).
536. W. J. Zhu, Z. Y. Pan, Y. K. Ho, and Y. X. Wang, *J. Appl. Phys.* 88, 6836 (2000).
537. S. R. Schofield, M. W. Radny, and P. V. Smith, *Phys. Rev. B* 62, 10199 (2000).
538. J. Tanaka, C. F. Abrams, and D. B. Graves, *J. Vac. Sci. Technol. A* 18, 938 (2000).
539. A. V. Petukhov, D. Passerone, F. Ercolessi, E. Tosatti, and A. Fasolino, *Phys. Rev. B* 61, 10590 (2000).
540. J. Z. Que, M. W. Radny, P. V. Smith, and A. J. Dyson, *Surf. Sci.* 444, 123 (2000).
541. J. Z. Que, M. W. Radny, and P. V. Smith, *Surf. Sci.* 444, 140 (2000).
542. T. Cagin, A. Jaramillo-Botero, G. Gao, and W. A. Goddard, *Nanotechnology* 9, 143 (1998).
543. R. E. Tuzun, K. Sohlberg, D. W. Noid, and B. G. Sumpter, *Nanotechnology* 9, 37 (1998).
544. R. E. Tuzun, D. W. Noid, B. G. Sumpter, and R. C. Merkle, *Nanotechnology* 8, 112 (1997).
545. D. W. Noid, R. E. Tuzun, and B. G. Sumpter, *Nanotechnology* 8, 119 (1997).
546. R. E. Tuzun, D. W. Noid, B. G. Sumpter, and R. C. Merkle, *Nanotechnology* 7, 241 (1996).
547. R. E. Tuzun, D. W. Noid, and B. G. Sumpter, *Nanotechnology* 6, 52 (1995).
548. R. E. Tuzun, D. W. Noid, and B. G. Sumpter, *Nanotechnology* 6, 64 (1995).
549. Y. Ye, R. Biswas, A. Bastawros, and A. Chandra, *Appl. Phys. Lett.* 81, 1875 (2002).
550. B. Eck, Y. Kurtulus, W. Offermans, and R. Dronskowski, *J. Alloys Compd.* 338, 142 (2002).
551. A. L. V. de Parga, J. M. Gallego, J. J. de Miguel, and R. Miranda, *J. Phys.* 14, 4187 (2002).
552. K. Kadau, P. Entel, T. C. Germann, P. S. Lomdahl, and B. L. Holian, *J. Phys. IV* 11, 17 (2001).
553. H. Ogawa and F. Wakai, *Mater. Trans.* 42, 2266 (2001).
554. Y. G. Chushak and L. S. Bartell, *J. Phys. Chem. B* 105, 11605 (2001).
555. L. J. Yang, W. A. Beard, S. H. Wilson, B. Roux, S. Broyde, and T. Schlick, *J. Mol. Biol.* 321, 459 (2002).
556. A. Strachan, T. Cagin, and W. A. Goddard, *J. Comput. Aided Mater. Des.* 8, 151 (2002).
557. B. D. Wirth, V. V. Bulatov, and T. D. de la Rubia, *J. Eng. Mater. T ASME* 124, 329 (2002).
558. A. Pundt, M. Dornheim, M. Guerdane, H. Teichler, H. Ehrenberg, M. T. Reetz, and N. M. Jisrawi, *Eur. Phys. J. D* 19, 333 (2002).

559. R. Rinaldi, E. Branca, R. Cingolani, R. Di Felice, A. Calzolari, E. Molinari, S. Masiero, G. Spada, G. Gottarelli, and A. Garbesi, *Mol. Electron. II* 960, 184 (2002).

560. R. Komanduri, L. M. Raff, and A. Chandrasekaran, *Philos. Mag. Lett.* 82, 247 (2002).

561. S. E. Donnelly, R. C. Birtcher, C. W. Allen, I. Morrison, K. Furuya, M. H. Song, K. Mitsuishi, and U. Dahmen, *Science* 296, 507 (2002).

562. A. Casnati, F. Sansone, J. F. Dozol, H. Rouquette, F. Arnaud-Neu, D. Byrne, S. Fuangswasdi, M. J. Schwing-Weill, and R. Ungaro, *J. Inclusion Phenom.* 41, 193 (2001).

563. H. Wang, Y. Z. Hu, K. Zou, and Y. S. Leng, *Sci. China Ser. A* 44, 1049 (2001).

564. M. Baaden, R. Schurhammer, and G. Wipff, *J. Phys. Chem. B* 106, 434 (2002).

565. X. J. Xu, M. Wen, S. Fukuyama, and K. Yokogawa, *Mater. Trans.* 42, 2283 (2001).

566. Y. Ashkenazy, R. S. Averback, and K. Albe, *Phys. Rev. B* 64, 205409 (2001).

567. M. F. Horstemeyer, M. I. Baskes, and S. J. Plimpton, *Acta Mater.* 49, 4363 (2001).

568. A. N. Andriotis, M. Menon, D. Srivastava, and G. Froudakis, *Phys. Rev. B* 64, 193401 (2001).

569. Z. H. Yao, C. C. Zhu, M. Cheng, and J. H. Liu, *Comp. Mater. Sci.* 22, 180 (2001).

570. P. M. Derlet, R. Meyer, L. J. Lewis, U. Stuhr, and H. Van Swygenhoven, *Phys. Rev. Lett.* 87, 205501 (2001).

571. D. C. Sorescu, K. D. Jordan, and P. Avouris, *J. Phys. Chem. B* 105, 11227 (2001).

572. P. Vashishta, M. Bachlechner, A. Nakano, T. J. Campbell, R. K. Kalia, S. Kodiyalam, S. Ogata, F. Shimojo, and P. Walsh, *Appl. Surf. Sci.* 182, 258 (2001).

573. X. W. Zhou, H. N. G. Wadley, R. A. Johnson, D. J. Larson, N. Tabat, A. Cerezo, A. K. Petford-Long, G. D. W. Smith, P. H. Clifton, R. L. Martens, and T. F. Kelly, *Acta Mater.* 49, 4005 (2001).

574. J. Cai and J. S. Wang, *Surf. Rev. Lett.* 8, 581 (2001).

575. K. Yashiro and Y. Tomita, *J. Phys. IV* 11, 3 (2001).

576. D. R. Jennison, O. Dulub, W. Hebenstreit, and U. Diebold, *Surf. Sci.* 492, L677 (2001).

577. J. A. Zimmerman, C. L. Kelchner, P. A. Klein, J. C. Hamilton, and S. M. Foiles, *Phys. Rev. Lett.* 87, 165507 (2001).

578. B. Reincke, C. Perez, P. Pristovsek, C. Lucke, C. Ludwig, F. Lohr, V. V. Rogov, B. Ludwig, and H. Ruterjans, *Biochemistry* 40, 12312 (2001).

579. M. Jaouen, J. Pacaud, and C. Jaouen, *Phys. Rev. B* 64, 144106 (2001).

580. J. H. He and E. Ma, *Phys. Rev. B* 64, 144206 (2001).

581. J. Cai and J. S. Wang, *Phys. Rev. B* 64, 113313 (2001).

582. X. W. Zhou and H. N. G. Wadley, *J. Appl. Phys.* 90, 3359 (2001).

583. F. Baletto and R. Ferrando, *Surf. Sci.* 490, 361 (2001).

584. R. Komanduri, N. Chandrasekaran, and L. M. Raff, *Int. J. Mech. Sci.* 43, 2237 (2001).

585. J. A. Ascencio, M. Perez-Alvarez, S. Tehuacanero, and M. Jose-Yacaman, *Appl. Phys. A* 73, 295 (2001).

586. Y. Shimizu, K. S. Ikeda, and S. Sawada, *Phys. Rev. B* 64, 075412 (2001).

587. C. G. Zimmermann, K. Nordlund, M. Yeadon, J. M. Gibson, R. S. Averback, U. Herr, and K. Samwer, *Phys. Rev. B* 64, 085419 (2001).

588. J. L. Yang, H. J. Liu, and C. T. Chan, *Phys. Rev. B* 64, 085420 (2001).

589. H. Rafii-Tabar and K. Ghafoori-Tabrizi, *Progr. Surf. Sci.* 67, 217 (2001).

590. A. N. Andriotis and M. Menon, *J. Chem. Phys.* 115, 2737 (2001).

591. M. B. Mohamed, T. S. Ahmadi, S. Link, M. Braun, and M. A. El Sayed, *Chem. Phys. Lett.* 343, 55 (2001).

592. J. B. Adams, L. G. Hector, D. J. Siegel, H. L. Yu, and J. Zhong, *Surf. Interface Anal.* 31, 619 (2001).

593. L. C. Ciacchi, W. Pompe, and A. De Vita, *J. Am. Chem. Soc.* 123, 7371 (2001).

594. G. Rubio-Bollinger, S. R. Bahn, N. Agrait, K. W. Jacobsen, and S. Vieira, *Phys. Rev. Lett.* 87, 026101 (2001).

595. J. A. Flohil, G. Vriend, and H. J. C. Berendsen, *Proteins* 48, 593 (2002).

596. K. Hess, U. Ravaioli, M. Gupta, N. Aluru, T. Van Der Straaten, and R. S. Eisenberg, *VLSI Design* 13, 179 (2001).

597. G. S. D. Ayton, S. Bardenhagen, P. McMurtry, D. Sulsky, and G. A. Voth, *IBM J. Res. Dev.* 45, 417 (2001).

598. L. Saiz and M. L. Klein, *Biophys. J.* 81, 204 (2001).

599. A. Almond, J. Bunkenborg, T. Franch, C. H. Gotfredsen, and J. O. Duus, *J. Am. Chem. Soc.* 123, 4792 (2001).

600. M. Pinak, *J. Comput. Chem.* 22, 1723 (2001).

601. M. S. Madhusudhan, S. Vishveshwara, A. Das, P. Kalra, and B. Jayaram, *Indian J. Biochem. Biol.* 38, 27 (2001).

602. R. Stefl, N. Spackova, I. Berger, J. Koca, and J. Sponer, *Biophys. J.* 80, 455 (2001).

603. M. Kuttel, J. W. Brady, and K. J. Naidoo, *J. Comput. Chem.* 23, 1236 (2002).

604. D. Mazumder, K. Kahn, and T. C. Bruice, *J. Am. Chem. Soc.* 124, 8825 (2002).

605. D. Gersappe, *Phys. Rev. Lett.* 89, 058301 (2002).

606. B. de Foresta, L. Tortech, M. Vincent, and J. Gallay, *Eur. Biophys. J. Biophys.* 31, 185 (2002).

607. J. G. Renisio, J. Perez, M. Czisch, M. Guenneugues, O. Bornet, L. Frenken, C. Cambillau, and H. Darbon, *Proteins* 47, 546 (2002).

608. B. J. Premraj, S. Raja, and N. Yathindra, *Biophys. Chem.* 95, 253 (2002).

609. E. Marco, R. Garcia-Nieto, J. Mendieta, I. Manzanares, C. Cuevas, and F. Gago, *J. Med. Chem.* 45, 871 (2002).

610. A. Kumar, S. Shankar, and V. Kothekar, *J. Biomol. Struct. Dyn.* 19, 449 (2001).

611. O. Beckstein, P. C. Biggin, and M. S. P. Sansom, *J. Phys. Chem. B* 105, 12902 (2001).

612. J. C. Pizarro, B. Vulliez-le Normand, M. M. Riottot, A. Budkowska, and G. A. Bentley, *FEBS Lett.* 509, 463 (2001).

613. C. T. Choma, D. P. Tieleman, D. Cregut, L. Serrano, and H. J. C. Berendsen, *J. Mol. Graph. Model.* 20, 219 (2001).

614. B. Li, D. O. V. Alonso, B. J. Bennion, and V. Daggett, *J. Am. Chem. Soc.* 123, 11991 (2001).

615. F. J. Barrantes, *Curr. Sci. India* 81, 983 (2001).

616. I. P. Sugar, E. Michanova-Alexova, and P. L. G. Chong, *Biophys. J.* 81, 2425 (2001).

617. K. Ishikawa, T. Nakamura, and Y. Koga, *J. Mass Spectrom.* 36, 937 (2001).

618. M. Rieth, W. Schommers, S. Baskoutas, and C. Politis, *Chinese Phys.* 10, S132 (2001).

619. R. A. Bryce, I. H. Hillier, and J. H. Naismith, *Biophys. J.* 81, 1373 (2001).

620. S. Chowdhury and M. Bansal, *J. Phys. Chem. B* 105, 7572 (2001).

621. A. Mai, G. Sbardella, M. Artico, R. Ragno, S. Massa, E. Novellino, G. Greco, A. Lavecchia, C. Musiu, M. La Colla, C. Murgioni, P. La Colla, and R. Loddo, *J. Med. Chem.* 44, 2544 (2001).

622. F. Massi and J. E. Straub, *Biophys. J.* 81, 697 (2001).

623. F. Rodriguez-Barrios, C. Perez, E. Lobaton, S. Velazquez, C. Chamorro, A. San Felix, M. J. Perez-Perez, M. J. Camarasa, H. Pelemans, J. Balzarini, and F. Gago, *J. Med. Chem.* 44, 1853 (2001).

624. T. M. Raschke, J. Tsai, and M. Levitt, *Proc. Natl. Acad. Sci. USA* 98, 5965 (2001).

625. M. T. Hyvonen, K. Oorni, P. T. Kovanen, and M. Ala-Korpela, *Biophys. J.* 80, 565 (2001).

626. M. V. Berjanskii, M. I. Riley, and S. R. Van Doren, *J. Mol. Biol.* 321, 503 (2002).

627. J. X. Duan and L. Nilsson, *Eur. Biophys. J. Biophys.* 31, 306 (2002).

628. H. Ishida, *J. Biomol. Struct. Dyn.* 19, 839 (2002).

629. M. Paulino, P. Esperon, M. Vega, C. Scazzocchio, and O. Tapia, *J. Mol. Struct. Theochem.* 580, 225 (2002).

630. S. Schumm, M. Prevost, D. Garcia-Fresnadillo, O. Lentzen, C. Moucheron, and A. Kirsch-De Mesmaeker, *J. Phys. Chem. B* 106, 2763 (2002).

631. P. Kalra, T. V. Redd, and B. Jayaram, *J. Med. Chem.* 44, 4325 (2001).

632. A. N. Kapanidis, Y. W. Ebright, R. D. Ludescher, S. Chan, and R. H. Ebright, *J. Mol. Biol.* 312, 453 (2001).

633. M. Katahira, Y. Miyanoiri, Y. Enokizono, G. Matsuda, T. Nagata, F. Ishikawa, and S. Uesugi, *J. Mol. Biol.* 311, 973 (2001).

634. S. Chowdhury and M. Bansal, *J. Biomol. Struct. Dyn.* 18, 647 (2001).

635. N. Spackova, I. Berger, and J. Sponer, *J. Am. Chem. Soc.* 123, 3295 (2001).

636. A. K. Mazur, *J. Comput. Chem.* 22, 457 (2001).

637. K. Drukker, G. S. Wu, and G. C. Schatz, *J. Chem. Phys.* 114, 579 (2001).

638. V. A. Bershtein, L. M. Egorova, P. N. Yakushev, P. Pissis, P. Sysel, and L. Brozova, *J. Polym. Sci. Pol. Phys.* 40, 1056 (2002).

639. M. Samaras, P. M. Derlet, H. Van Swygenhoven, and M. Victoria, *Phys. Rev. Lett.* 88, 125505 (2002).

640. K. A. Padmanabhan, *Mat. Sci. Eng. A* 304, 200 (2001).

641. A. Chatterjee, R. K. Kalia, A. Nakano, A. Omeltchenko, K. Tsuruta, P. Vashishta, C. K. Loong, M. Winterer, and S. Klein, *Appl. Phys. Lett.* 77, 1132 (2000).

642. R. K. Kalia, T. J. Campbell, A. Chatterjee, A. Nakano, P. Vashishta, and S. Ogata, *Comput. Phys. Commun.* 128, 245 (2000).

643. C. M. Gilmore and J. A. Sprague, *Nanostruct. Mater.* 9, 643 (1997).

644. X. W. Wang, J. Y. Wang, and D. X. Li, *J. Mater. Sci. Technol.* 18, 254 (2002).

645. A. J. Du, Z. Y. Pan, Y. K. Ho, Z. Huang, and Z. X. Zhang, *Phys. Rev. B* 66, 035405 (2002).

646. U. Stuhr, W. Wagner, J. Kohlbrecher, and H. Van Swygenhoven, *Acta Phys. Pol. A* 102, 109 (2002).

647. L. Zoppi, L. Colombo, and D. Donadio, *Eur. Phys. J. B* 27, 335 (2002).

648. B. Lehner, M. Hohage, and P. Zeppenfeld, *Phys. Rev. B* 65, 165407 (2002).

649. D. V. Shtansky, K. Kaneko, Y. Ikuhara, and E. A. Levashov, *Surf. Coat. Tech.* 148, 206 (2001).

650. I. Cendoya, D. Lopez, A. Alegria, and C. Mijangos, *J. Polym. Sci. Pol. Phys.* 39, 1968 (2001).

651. D. Srivastava, M. Menon, and K. Cho, *Phys. Rev. B* 63, 195413 (2001).

652. M. Bogana, D. Donadio, G. Benedek, and L. Colombo, *Europhys. Lett.* 54, 72 (2001).

653. J. G. Wan, M. Han, J. F. Zhou, and G. H. Wang, *Phys. Lett. A* 280, 357 (2001).

654. H. E. Schaefer, K. Reimann, W. Straub, F. Phillipp, H. Tanimoto, U. Brossmann, and R. Wurschum, *Mater. Sci. Eng. A* 286, 24 (2000).

655. Q. Hou, M. Hou, L. Bardotti, B. Prevel, P. Melinon, and A. Perez, *Phys. Rev. B* 62, 2825 (2000).

656. L. Bardotti, B. Prevel, P. Melinon, A. Perez, Q. Hou, and M. Hou, *Phys. Rev. B* 62, 2835 (2000).

657. J. Mijovic, M. Z. Shen, J. W. Sy, and I. Mondragon, *Macromolecules* 33, 5235 (2000).

658. P. Vashishta, M. E. Bachlechner, T. Campbell, R. K. Kalia, H. Kikuchi, S. Kodiyalam, A. Nakano, S. Ogata, F. Shimojo, and P. Walsh, *Progr. Theor. Phys. Supp.* 175 (2000).

659. S. Ogata, H. Iyetomi, K. Tsuruta, F. Shimojo, R. K. Kalia, A. Nakano, and P. Vashishta, *J. Appl. Phys.* 86, 3036 (1999).

660. C. K. Loong, *J. Phys. Chem. Solids* 60, 1397 (1999).

661. D. Donadio, L. Colombo, P. Milani, and G. Benedek, *Phys. Rev. Lett.* 83, 776 (1999).

662. A. Nakano, M. E. Bachlechner, T. J. Campbell, R. K. Kalla, A. Omeltchenko, K. Tsuruta, P. Vashishta, S. Ogata, I. Ebbsjo, and A. Madhukar, *IEEE Comput. Sci. Eng.* 5, 68 (1998).

663. P. Melinon, P. Keghelian, B. Prevel, A. Perez, G. Guiraud, J. LeBrusq, J. Lerme, M. Pellarin, and M. Broyer, *J. Chem. Phys.* 107, 10278 (1997).

664. J. K. Kruger, R. Jimenez, K. P. Bohn, and C. Fischer, *Phys. Rev. B* 56, 8683 (1997).

665. A. Perez, P. Melinon, V. Dupuis, P. Jensen, B. Prevel, J. Tuaillon, L. Bardotti, C. Martet, M. Treilleux, M. Broyer, M. Pellarin, J. L. Vaille, B. Palpant, and J. Lerme, *J. Phys. D* 30, 709 (1997).

666. R. E. Tuzun, D. W. Noid, and B. G. Sumpter, *Trend Polym. Sci.* 4, 223 (1996).

667. K. Fujita, A. Inoue, T. Zhang, and N. Nishiyama, *Mater. Trans.* 43, 1957 (2002).

668. D. Farkas, H. Van Swygenhoven, and P. M. Derlet, *Phys. Rev. B* 66, 060101 (2002).

669. K. Kadau, P. Entel, and P. S. Lomdahl, *Comput. Phys. Commun.* 147, 126 (2002).

670. W. Stier and O. V. Prezhdo, *J. Phys. Chem. B* 106, 8047 (2002).

671. H. Van Swygenhoven, P. M. Derlet, and A. Hasnaoui, *Phys. Rev. B* 66, 024101 (2002).

672. V. Ranjan, M. Kapoor, and V. A. Singh, *J. Phys.* 14, 6647 (2002).

673. P. Keblinski, *Acta Phys. Pol. A* 102, 123 (2002).

674. L. G. Wang, S. J. Pennycook, and S. T. Pantelides, *Phys. Rev. Lett.* 89, 075506 (2002).

675. T. Fujita, Z. Horita, and T. G. Langdon, *Philos. Mag. A* 82, 2249 (2002).

676. M. C. Beard, G. M. Turner, and C. A. Schmuttenmaer, *J. Phys. Chem. B* 106, 7146 (2002).

677. Y. W. Liu, R. Zhou, and S. Q. Lu, *Int. J. Nonlinear Sci. Numer. Simul.* 3, 531 (2002).

678. C. Powell, N. Fenwick, F. Bresme, and N. Quirke, *Colloid. Surface A* 206, 241 (2002).

679. S. Sriraman, S. Agarwal, E. S. Aydil, and D. Maroudas, *Nature* 418, 62 (2002).

680. J. Schiotz, T. Leffers, and B. N. Singh, *Radiat. Eff. Defects Solids* 157, 193 (2002).

681. R. Meyer, S. Prakash, and P. Entel, *Phase Transit.* 75, 51 (2002).

682. A. J. Haslam, D. Moldovan, S. R. Phillpot, D. Wolf, and H. Gleiter, *Comp. Mater. Sci.* 23, 15 (2002).

683. P. Zapol, M. Sternberg, L. A. Curtiss, T. Frauenheim, and D. M. Gruen, *Phys. Rev. B* 65, 045403 (2002).

684. A. K. Mukherjee, *Mater. Sci. Eng. A* 322, 1 (2002).

685. V. Yamakov, D. Wolf, S. R. Phillpot, and H. Gleiter, *Acta Mater.* 50, 61 (2002).

686. A. J. Haslam, S. R. Phillpot, H. Wolf, D. Moldovan, and H. Gleiter, *Mater. Sci. Eng. A* 318, 293 (2001).

687. K. Tsuruta, H. Totsuji, and C. Totsuji, *Mater. Trans.* 42, 2261 (2001).

688. H. Van Swygenhoven and P. A. Derlet, *Phys. Rev. B* 64, 224105 (2001).

689. P. M. Derlet and H. Van Swygenhoven, *Philos. Mag. A* 82, 1 (2002).

690. S. Pisov and A. Proykova, *Comput. Phys. Commun.* 147, 238 (2002).

691. W. Vervisch, C. Mottet, and J. Goniakowski, *Phys. Rev. B* 65, 245411 (2002).

692. S. P. Huang and P. B. Balbuena, *J. Phys. Chem. B* 106, 7225 (2002).

693. I. V. Schweigert, K. E. J. Lehtinen, M. J. Carrier, and M. R. Zachariah, *Phys. Rev. B* 65, 235410 (2002).

694. S. P. Huang and P. B. Balbuena, *Mol. Phys.* 100, 2165 (2002).

695. J. Dalla Torre, J. L. Bocquet, Y. Limoge, J. P. Crocombette, E. Adam, G. Martin, T. Baron, P. Rivallin, and P. Mur, *J. Appl. Phys.* 92, 1084 (2002).

696. T. X. Li, S. M. Lee, S. J. Han, and G. H. Wang, *Phys. Lett. A* 300, 86 (2002).

697. C. Roland, V. Meunier, B. Larade, and H. Guo, *Phys. Rev. B* 66, 035332 (2002).

698. T. Koike, S. Watanabe, M. Hoshino, T. Suda, S. Ohnuki, H. Takahashi, and N. Q. Lam, *Mater. Trans.* 43, 1716 (2002).

699. U. Tartaglino, E. Tosatti, D. Passerone, and F. Ercolessi, *Phys. Rev. B* 65, 241406 (2002).

700. J. A. Ascencio, M. Mendoza, T. Santamaria, M. Perez, I. Nava, C. Gutierrez-Wing, and M. Jose-Yacaman, *J. Cluster Sci.* 13, 189 (2002).

701. F. Baletto, C. Mottet, and R. Ferrando, *Chem. Phys. Lett.* 354, 82 (2002).

702. F. Baletto, J. P. K. Doye, and R. Ferrando, *Phys. Rev. Lett.* 88, 075503 (2002).

703. F. Baletto, R. Ferrando, A. Fortunelli, F. Montalenti, and C. Mottet, *J. Chem. Phys.* 116, 3856 (2002).

704. A. Tamashiro, J. Rodriguez, and D. Laria, *J. Phys. Chem. A* 106, 215 (2002).

705. M. G. Del Popolo, E. P. M. Leiva, and W. Schmickler, *Angew. Chem. Int. Ed.* 40, 4674 (2001).

706. J. H. Werth, S. M. Dammer, Z. Farkas, H. Hinrichsen, and D. E. Wolf, *Comput. Phys. Commun.* 147, 259 (2002).

707. V. V. Prokhorov, *Phys. Low-Dim. Struct.* 5–6, 209 (2002).

708. M. Mertig, L. C. Ciacchi, R. Seidel, W. Pompe, and A. De Vita, *Nano Lett.* 2, 841 (2002).

709. J. H. Shim, B. J. Lee, and Y. W. Cho, *Surf. Sci.* 512, 262 (2002).

710. D. C. Sayle, J. A. Doig, S. A. Maicaneanu, and G. W. Watson, *Phys. Rev. B* 65, 245414 (2002).

711. E. Rabani and S. A. Egorov, *J. Phys. Chem. B* 106, 6771 (2002).

712. H. Noguchi and M. Takasu, *Biophys. J.* 83, 299 (2002).

713. N. Nishiguchi, *Physica B* 316, 441 (2002).

714. M. Schmidt and H. Haberland, *Comptes Rendus Phys.* 3, 327 (2002).

715. C. A. Bearchell and D. M. Heyes, *Mol. Simulat.* 28, 517 (2002).

716. K. Kadau and P. Entel, *Phase Transit.* 75, 59 (2002).

717. F. W. Starr, T. B. Schroder, and S. C. Glotzer, *Macromolecules* 35, 4481 (2002).

718. M. B. Knickelbein, *J. Chem. Phys.* 116, 9703 (2002).

719. H. Shinto, D. Iwahara, M. Miyahara, and K. Higashitani, *Langmuir* 18, 4171 (2002).

720. J. P. Devlin, N. Uras, J. Sadlej, and V. Buch, *Nature* 417, 269 (2002).

721. H. Kasemagi, M. Klintenberg, A. Aabloo, and J. O. Thomas, *Solid State Ionics* 147, 367 (2002).

722. D. C. Sayle and G. W. Watson, *J. Phys. Chem. B* 106, 3916 (2002).

723. H. Schweiger, P. Raybaud, G. Kresse, and H. Toulhoat, *J. Catal.* 207, 76 (2002).

724. B. C. Hathorn, B. G. Sumpter, M. D. Barnes, and D. W. Noid, *Polymer* 43, 3115 (2002).

725. R. Guirado-Lopez, F. Aguilera-Granja, and J. M. Montejano-Carrizales, *Phys. Rev. B* 65, 045420 (2002).

726. B. C. Hathorn, B. G. Sumpter, D. W. Noid, and M. D. Barnes, *Macromolecules* 35, 1102 (2002).

727. M. A. Osman, M. Ernst, B. H. Meier, and U. W. Suter, *J. Phys. Chem. B* 106, 653 (2002).

728. K. E. J. Lehtinen and M. R. Zachariah, *J. Aerosol Sci.* 33, 357 (2002).

729. S. J. Zhao, S. Q. Wang, D. Y. Cheng, and H. Q. Ye, *J. Phys. Chem. B* 105, 12857 (2001).

730. H. H. Kwong, Y. P. Feng, and T. B. Boo, *Comput. Phys. Commun.* 142, 290 (2001).

731. P. Keblinski, S. R. Phillpot, S. U. S. Choi, and J. A. Eastman, *Int. J. Heat Mass Transfer* 45, 855 (2002).

732. K. Bolton and A. Rosen, *PCCP* 4, 4481 (2002).

733. C. K. Yang, J. J. Zhao, and J. P. Lu, *Phys. Rev. B* 66, 041403 (2002).

734. J. Gavillet, A. Loiseau, F. Ducastelle, S. Thair, P. Bernier, O. Stephan, J. Thibault, and J. C. Charlier, *Carbon* 40, 1649 (2002).

735. T. Kawai, Y. Miyamoto, O. Sugino, and Y. Koga, *Phys. Rev. B* 66, 033404 (2002).

736. A. V. Krasheninnikov, K. Nordlund, and J. Keinonen, *Appl. Phys. Lett.* 81, 1101 (2002).

737. W. L. Guo, Y. F. Guo, and L. F. Wang, *Int. J. Nonlinear Sci. Numer. Simul.* 3, 469 (2002).

738. C. C. Fu, J. Fava, R. Weht, and M. Weissmann, *Phys. Rev. B* 66, 045405 (2002).

739. M. Skrzypek and Z. Gburski, *Europhys. Lett.* 59, 305 (2002).

740. T. Ohtsuki, K. Ohno, K. Shiga, Y. Kawazoe, and H. Yuki, *Phys. Rev. B* 65, 073402 (2002).

741. J. L. Wang, X. S. Chen, G. H. Wang, B. L. Wang, W. Lu, and J. J. Zhao, *Phys. Rev. B* 66, 085408 (2002).

742. T. Ito, K. Nishidate, M. Baba, and M. Hasegawa, *Surf. Sci.* 514, 222 (2002).

743. M. Huhtala, A. Kuronen, and K. Kaski, *Comput. Phys. Commun.* 147, 91 (2002).

744. T. Kawai, Y. Miyamoto, O. Sugino, and Y. Koga, *Phys. Rev. Lett.* 89, 085901 (2002).

745. R. Car, *Quant. Struct.-Act. Relat.* 21, 97 (2002).

746. S. Y. Bhide and S. Yashonath, *J. Phys. Chem. A* 106, 7130 (2002).

747. M. Terrones, F. Banhart, N. Grobert, J. C. Charlier, H. Terrones, and P. M. Ajayan, *Phys. Rev. Lett.* 89, 075505 (2002).

748. M. C. Gordillo and J. Marti, *J. Chem. Phys.* 117, 3425 (2002).

749. T. Y. Astakhova, G. A. Vinogradov, O. D. Gurin, and M. Menon, *Russ. Chem. Bull.* 51, 764 (2002).

750. A. Berezhkovskii and G. Hummer, *Phys. Rev. Lett.* 89, 064503 (2002).

751. L. Chernozatonskii, E. Richter, and M. Menon, *Phys. Rev. B* 65, 241404 (2002).

752. E. Salonen, A. V. Krasheninnikov, and K. Nordlund, *Nucl. Instrum. Methods B* 193, 603 (2002).

753. A. N. Andriotis, M. Menon, and D. Srivastava, *J. Chem. Phys.* 117, 2836 (2002).

754. M. J. O'Connell, S. M. Bachilo, C. B. Huffman, V. C. Moore, M. S. Strano, E. H. Haroz, K. L. Rialon, P. J. Boul, W. H. Noon, C. Kittrell, J. P. Ma, R. H. Hauge, R. B. Weisman, and R. E. Smalley, *Science* 297, 593 (2002).

755. L. D. Gelb, *Mol. Phys.* 100, 2049 (2002).

756. M. Huhtala, A. Kuronen, and K. Kaski, *Comput. Phys. Commun.* 146, 30 (2002).

757. R. Che, L. M. Peng, S. Zhang, S. Wang, and J. Luo, *Chem. Phys. Lett.* 358, 103 (2002).

758. T. Halicioglu and R. L. Jaffe, *Nano Lett.* 2, 573 (2002).

759. C. Y. Wei, D. Srivastava, and K. J. Cho, *Nano Lett.* 2, 647 (2002).

760. I. Narita and T. Oku, *Diamond Relat. Mater.* 11, 945 (2002).

761. L. G. Zhou and S. Q. Shi, *Comp. Mater. Sci.* 23, 166 (2002).

762. Y. C. Ma, Y. Y. Xia, M. W. Zhao, and M. J. Ying, *Chem. Phys. Lett.* 357, 97 (2002).

763. S. V. Rotkin and Y. Gogotsi, *Mater. Res. Innovations* 5, 191 (2002).

764. T. Duren, F. J. Keil, and N. A. Seaton, *Chem. Eng. Sci.* 57, 1343 (2002).

765. W. H. Noon, Y. F. Kong, and J. P. Ma, *Proc. Natl. Acad. Sci. USA* 99, 6466 (2002).

766. B. Ni, S. B. Sinnott, P. T. Mikulski, and J. A. Harrison, *Phys. Rev. Lett.* 88, 205505 (2002).

767. C. E. Capener and M. S. P. Sansom, *J. Phys. Chem. B* 106, 4543 (2002).

768. D. J. Mann and M. D. Halls, *J. Chem. Phys.* 116, 9014 (2002).

769. S. Erkoc and O. B. Malcioglu, *Int. J. Mod. Phys. C* 13, 367 (2002).

770. F. Z. Cui, Z. J. Chen, J. Ma, G. R. Xia, and Y. Zhai, *Phys. Lett. A* 295, 55 (2002).

771. A. N. Andriotis, M. Menon, D. Srivastava, and L. Chernozatonskii, *Phys. Rev. B* 65, 165416 (2002).

772. A. V. Krasheninnikov, K. Nordlund, and J. Keinonen, *Phys. Rev. B* 65, 165423 (2002).

773. C. Y. Wei, D. Srivastava, and K. Cho, *CMES-Comp. Model. Eng.* 3, 255 (2002).

774. W. H. Noon, K. D. Ausman, R. E. Smalley, and J. P. Ma, *Chem. Phys. Lett.* 355, 445 (2002).

775. Y. F. Zhao, B. I. Yakobson, and R. E. Smalley, *Phys. Rev. Lett.* 88, 185501 (2002).

776. S. Berber, Y. K. Kwon, and D. Tomanek, *Phys. Rev. Lett.* 88, 185502 (2002).

777. Y. Y. Xia, M. W. Zhao, Y. C. Ma, M. J. Ying, X. D. Liu, P. J. Liu, and L. M. Mei, *Phys. Rev. B* 65, 155415 (2002).

778. Y. C. Ma, Y. Y. Xia, M. W. Zhao, and M. J. Ying, *Phys. Rev. B* 65, 155430 (2002).

779. B. X. Li, P. L. Cao, R. Q. Zhang, and S. T. Lee, *Phys. Rev. B* 65, 125305 (2002).

780. P. K. Schelling, S. R. Phillpot, and P. Keblinski, *Phys. Rev. B* 65, 144306 (2002).

781. M. Menon, A. N. Andriotis, and G. Froudakis, *Nano Lett.* 2, 301 (2002).

782. C. Gu, G. H. Gao, Y. X. Yu, and T. Nitta, *Fluid Phase Equilib.* 194, 297 (2002).

783. J. Marti and M. C. Gordillo, *Chem. Phys. Lett.* 354, 227 (2002).

784. M. Terrones, P. M. Ajayan, F. Banhart, X. Blase, D. L. Carroll, J. C. Charlier, R. Czerw, B. Foley, N. Grobert, R. Kamalakaran, P. Kohler-Redlich, M. Ruhle, T. Seeger, and H. Terrones, *Appl. Phys. A* 74, 355 (2002).

785. D. Asthagiri and D. Bashford, *Biophys. J.* 82, 1176 (2002).

786. T. Werder, J. H. Walther, R. L. Jaffe, T. Halicioglu, F. Noca, and P. Koumoutsakos, *Nano Lett.* 1, 697 (2001).

787. N. H. Green, S. Allen, M. C. Davies, C. J. Roberts, S. J. B. Tendler, and P. M. Williams, *TRAC-Trend. Anal. Chem.* 21, 64 (2002).

788. H. F. Bettinger, T. Dumitrica, G. E. Scuseria, and B. I. Yakobson, *Phys. Rev. B* 65, 041406 (2002).

789. M. Wilson, *J. Chem. Phys.* 116, 3027 (2002).

790. M. K. Kostov, H. Cheng, R. M. Herman, M. W. Cole, and J. C. Lewis, *J. Chem. Phys.* 116, 1720 (2002).

791. S. Y. Bhide and S. Yashonath, *J. Chem. Phys.* 116, 2175 (2002).

792. B. Ni, R. Andrews, D. Jacques, D. Qian, M. B. J. Wijesundara, Y. S. Choi, L. Hanley, and S. B. Sinnott, *J. Phys. Chem. B* 105, 12719 (2001).

793. G. E. Froudakis, A. N. Andriotis, and M. Menon, *Chem. Phys. Lett.* 350, 393 (2001).

794. J. Gavillet, A. Loiseau, C. Journet, F. Willaime, F. Ducastelle, and J. C. Charlier, *Phys. Rev. Lett.* 87, 275504 (2001).

795. L. A. Chernozatonskii, M. Menon, T. Y. Astakhova, and G. A. Vinogradov, *JETP Lett.* 74, 467 (2001).

796. T. Oku, M. Kuno, H. Kitahara, and I. Narita, *Int. J. Inorg. Mater.* 3, 597 (2001).

797. A. Dawid and Z. Gburski, *J. Mol. Struct.* 614, 183 (2002).

798. M. Gu, T. B. Tang, and D. Feng, *Phys. Rev. B* 66, 073404 (2002).

799. E. Nardi, Z. Zinamon, T. A. Tombrello, and N. M. Tanushev, *Phys. Rev. A* 66, 013201 (2002).

800. R. Astala, M. Kaukonen, R. M. Nieminen, G. Jungnickel, and T. Frauenheim, *Phys. Rev. B* 65, 245423 (2002).

801. Y. Murata, M. Ito, and K. Komatsu, *J. Mater. Chem.* 12, 2009 (2002).

802. D. I. Schuster, P. D. Jarowski, A. N. Kirschner, and S. R. Wilson, *J. Mater. Chem.* 12, 2041 (2002).

803. G. Y. Sun and M. Kertesz, *J. Phys. Chem. A* 106, 6381 (2002).

804. E. E. B. Campbell, A. V. Glotov, A. Lassesson, and R. D. Levine, *Comptes Rendus Phys.* 3, 341 (2002).

805. Y. Takahashi, T. Hattori, H. Kashiwagi, T. Hata, N. Hayashizaki, I. Sugai, and K. Noda, *Nucl. Instrum. Methods B* 188, 278 (2002).

806. W. Eberhardt, *Surf. Sci.* 500, 242 (2002).

807. S. Tomita, P. Hvelplund, S. B. Nielsen, and T. Muramoto, *Phys. Rev. A* 65, 043201 (2002).

808. R. M. Nieminen, *J. Phys.* 14, 2859 (2002).

809. S. Erkoc, *Nano Lett.* 2, 215 (2002).

810. D. Costa, C. Caccamo, and M. C. Abramo, *J. Phys.* 14, 2181 (2002).

811. G. A. Domrachev, Y. A. Shevelev, V. K. Cherkasov, E. G. Domracheva, and G. V. Markin, *Phys. Solid State* 44, 518 (2002).

812. V. A. Davydov, L. S. Kashevarova, A. V. Rakhmanina, V. M. Senyavin, N. N. Oleinikov, and V. N. Agafonov, *Phys. Solid State* 44, 557 (2002).

813. S. Palucha, K. Kaczor, and Z. Gburski, *J. Phys.* 14, 1223 (2002).

814. V. Schettino, M. Pagliai, and G. Cardini, *J. Phys. Chem. A* 106, 1815 (2002).

815. M. Mattesini and S. F. Matar, *Phys. Rev. B* 65, 075110 (2002).

816. P. Espeau, M. Barrio, D. O. Lopez, J. L. Tamarit, R. Ceolin, H. Allouchi, V. Agafonov, F. Masin, and H. Szwarc, *Chem. Mater.* 14, 321 (2002).

817. S. Erkoc and L. Turker, *Int. J. Mod. Phys. C* 12, 1391 (2001).

818. Y. E. Lozovik and A. M. Popov, *Phys. Solid State* 44, 186 (2002).

819. B. X. Li and P. L. Cao, *J. Phys.* 13, 10865 (2001).

820. B. Song and P. L. Cao, *Phys. Lett. A* 291, 343 (2001).

821. K. Shiga, K. Ohno, T. Ohtsuki, and Y. Kawazoe, *Mater. Trans.* 42, 2189 (2001).

822. J. W. Kang and H. J. Hwang, *Nanotechnology* 13, 503 (2002).

823. J. W. Kang and H. J. Hwang, *Nanotechnology* 13, 524 (2002).

824. X. Lu, W. Z. Shen, and J. H. Chu, *J. Appl. Phys.* 91, 1542 (2002).

825. P. Walsh, W. Li, R. K. Kalia, A. Nakano, P. Vashishta, and S. Saini, *Appl. Phys. Lett.* 78, 3328 (2001).

826. P. S. Branicio and J. P. Rino, *Phys. Rev. B* 62, 16950 (2000).

827. Y. Qi, Y. T. Cheng, T. Cagin, and W. A. Goddard, *Phys. Rev. B* 66, 085420 (2002).

828. J. W. Kang and H. J. Hwang, *Mol. Simulat.* 28, 1021 (2002).

829. W. W. Kim, J. W. Kang, T. W. Kim, H. J. Hwang, and G. Y. Lee, *J. Korean Phys. Soc.* 40, 889 (2002).

830. J. W. Kang and H. J. Hwang, *J. Korean Phys. Soc.* 40, 946 (2002).

831. X. Lu and J. H. Chu, *Eur. Phys. J. B* 26, 375 (2002).

832. J. W. Kang and H. J. Hwang, *J. Phys.* 14, 2629 (2002).

833. A. Hasmy and E. Medina, *Phys. Rev. Lett.* 88, 096103 (2002).

834. H. J. Hwang and J. W. Kang, *J. Korean Phys. Soc.* 40, 283 (2002).

835. S. R. Bahn and K. W. Jacobsen, *Phys. Rev. Lett.* 87, 266101 (2001).

836. E. Z. da Silva, A. J. R. da Silva, and A. Fazzio, *Phys. Rev. Lett.* 87, 256102 (2001).

837. S. Tsukamoto, T. Ono, Y. Fujimoto, K. Inagaki, H. Goto, and K. Hirose, *Mater. Trans.* 42, 2257 (2001).

838. G. Rubio-Bollinger, S. R. Bahn, N. Agrait, K. W. Jacobsen, and S. Vieira, *Phys. Rev. Lett.* 87, 026101 (2001).

839. M. Diaz, J. L. Costa-Kramer, P. A. Serena, E. Medina, and A. Hasmy, *Nanotechnology* 12, 118 (2001).

840. A. Hasmy, E. Medina, and P. A. Serena, *Phys. Rev. Lett.* 86, 5574 (2001).

841. B. L. Wang, S. Y. Yin, G. H. Wang, A. Buldum, and J. J. Zhao, *Phys. Rev. Lett.* 86, 2046 (2001).

842. E. Canadell, P. Ordejon, E. Artacho, D. Sanchez-Portal, A. Garcia, and J. M. Soler, *J. Mater. Chem.* 11, 1 (2001).

843. D. K. Yu, R. Q. Zhang, and S. T. Lee, *Phys. Rev. B* 65, 245417 (2002).

844. A. Gannepalli and S. K. Mallapragada, *Nanotechnology* 12, 250 (2001).

845. D. Srivastava, M. Menon, and K. Cho, *Comput. Sci. Eng.* 3, 42 (2001).

846. K. Tsuruta, H. Totsuji, and C. Totsuji, *Philos. Mag. Lett.* 81, 357 (2001).

847. P. Walsh, R. K. Kalia, A. Nakano, P. Vashishta, and S. Saini, *Appl. Phys. Lett.* 77, 4332 (2000).

848. S. Furukawa, C. McCabe, T. Nitta, and P. T. Cummings, *Fluid Phase Equilib.* 194, 309 (2002).

849. T. Ito, K. Nishidate, M. Baba, and M. Hasegawa, *J. Phys. Soc. Jpn.* 70, 2593 (2001).

850. S. Erkoc and O. B. Malcioglu, *Int. J. Mod. Phys. C* 12, 865 (2001).

851. F. Liu, M. H. Huang, P. P. Rugheimer, D. E. Savage, and M. G. Lagally, *Phys. Rev. Lett.* 89, 136101 (2002).

852. A. M. Lomonosov and P. Hess, *Phys. Rev. Lett.* 89, 095501 (2002).

853. S. M. Nakhmanson and N. Mousseau, *J. Phys.* 14, 6627 (2002).

854. L. Z. Zhang and S. Y. Jiang, *J. Chem. Phys.* 117, 1804 (2002).

855. E. R. Fuoco and L. Hanley, *J. Appl. Phys.* 92, 37 (2002).

856. Y. J. Lee and R. M. Nieminen, *Defect. Diffus. Forum* 194-1, 261 (2001).

857. P. Raiteri, F. Valentinotti, and L. Miglio, *Appl. Surf. Sci.* 188, 4 (2002).

858. U. Kaiser, J. Biskupek, D. A. Muller, K. Gartner, and C. Schubert, *Cryst. Res. Technol.* 37, 391 (2002).

859. G. S. Painter, P. F. Becher, H. J. Kleebe, and G. Pezzotti, *Phys. Rev. B* 65, 064113 (2002).

860. R. Komanduri, N. Chandrasekaran, and L. M. Raff, *Philos. Mag. B* 81, 1989 (2001).

861. A. M. Mazzone, *Int. J. Mod. Phys. C* 12, 1139 (2001).

862. G. S. Smith, E. B. Tadmor, N. Bernstein, and E. Kaxiras, *Acta Mater.* 49, 4089 (2001).

863. L. Liu, C. S. Jayanthi, and S. Y. Wu, *J. Appl. Phys.* 90, 4143 (2001).

864. L. Z. Zhang, K. Wesley, and S. Y. Jiang, *Langmuir* 17, 6275 (2001).

865. E. Lidorikis, M. E. Bachlechner, R. K. Kalia, A. Nakano, P. Vashishta, and G. Z. Voyiadjis, *Phys. Rev. Lett.* 87, 086104 (2001).

866. C. R. S. da Silva and A. Fazzio, *Phys. Rev. B* 64, 075301 (2001).

867. J. P. Crocombette and D. Ghaleb, *J. Nucl. Mater.* 295, 167 (2001).

868. K. E. J. Lehtinen and M. R. Zachariah, *Phys. Rev. B* 63, 205402 (2001).

869. X. T. Su, R. K. Kalia, A. Nakano, P. Vashishta, and A. Madhukar, *Appl. Phys. Lett.* 78, 3717 (2001).

870. A. R. Burns, R. W. Carpick, D. Y. Sasaki, J. A. Shelnutt, and R. Haddad, *Tribol. Lett.* 10, 89 (2001).

871. A. J. Perry, S. J. Bull, A. Dommann, M. Michler, B. P. Wood, D. Rafaja, and J. N. Matossian, *Surf. Coat. Tech.* 140, 99 (2001).

872. W. C. D. Cheong, L. C. Zhang, and H. Tanaka, *Key Eng. Mater.* 196, 31 (2001).

873. J. Jurga, M. Nowicki, K. Bula, B. Susla, and S. S. Rejeibi, *Mol. Cryst. Liq. Cryst.* 354, 631 (2000).

874. M. C. Troparevsky and J. R. Chelikowsky, *J. Chem. Phys.* 114, 943 (2001).

875. G. Milano, G. Guerra, and F. Muller-Plathe, *Chem. Mater.* 14, 2977 (2002).

876. C. Mathioudakis, P. C. Kelires, Y. Panagiotatos, P. Patsalas, C. Charitidis, and S. Logothetidis, *Phys. Rev. B* 65, 205203 (2002).

877. C. D. Bruce, M. L. Berkowitz, L. Perera, and M. D. E. Forbes, *J. Phys. Chem. B* 106, 3788 (2002).

878. F. Claeyssens, M. N. R. Ashfold, E. Sofoulakis, C. G. Ristoscu, D. Anglos, and C. Fotakis, *J. Appl. Phys.* 91, 6162 (2002).

879. J. Hilding, E. A. Grulke, S. B. Sinnott, D. L. Qian, R. Andrews, and M. Jagtoyen, *Langmuir* 17, 7540 (2001).

880. S. Grigoras, A. A. Gusev, S. Santos, and U. W. Suter, *Polymer* 43, 489 (2002).

881. D. Qian, W. K. Liu, and R. S. Ruoff, *J. Phys. Chem. B* 105, 10753 (2001).

882. Z. G. Lu and C. L. Luo, *Phys. Lett. A* 289, 121 (2001).

883. G. Hummer, J. C. Rasaiah, and J. P. Noworyta, *Nature* 414, 188 (2001).

884. K. Masuda-Jindo, M. Menon, and V. Van Hung, *J. Phys. IV* 11, 11 (2001).

885. Y. G. Seo, G. H. Kum, and N. A. Seaton, *J. Membrane Sci.* 195, 65 (2002).

886. J. H. Walther, R. Jaffe, T. Halicioglu, and P. Koumoutsakos, *J. Phys. Chem. B* 105, 9980 (2001).

887. G. Arya, H. C. Chang, and E. J. Maginn, *J. Chem. Phys.* 115, 8112 (2001).

888. Y. C. Ma, Y. U. Xia, M. W. Zhao, M. J. Ying, X. D. Liu, and P. J. Liu, *J. Chem. Phys.* 115, 8152 (2001).

889. Y. C. Ma, Y. Y. Xia, M. W. Zhao, M. Ying, X. D. Liu, and P. J. Liu, *Phys. Lett. A* 288, 207 (2001).

890. J. D'Arcy-Gall, D. Gall, I. Petrov, P. Desjardins, and J. E. Greene, *J. Appl. Phys.* 90, 3910 (2001).

891. J. A. Soderhall and A. Laaksonen, *J. Phys. Chem. B* 105, 9308 (2001).

892. S. Bogusz, R. M. Venable, and R. W. Pastor, *J. Phys. Chem. B* 105, 8312 (2001).

893. S. Erkoc and D. C. Vural, *Int. J. Mod. Phys. C* 12, 685 (2001).

894. J. Marti and M. C. Gordillo, *Phys. Rev. E* 64, 021504 (2001).

895. V. P. Sokhan, D. Nicholson, and N. Quirke, *J. Chem. Phys.* 115, 3878 (2001).

896. A. N. Andriotis, M. Menon, D. Srivastava, and L. Chernozatonskii, *Phys. Rev. Lett.* 87, 066802 (2001).

897. M. B. Sweatman and N. Quirke, *Langmuir* 17, 5011 (2001).

898. B. Ni and S. B. Sinnott, *Surf. Sci.* 487, 87 (2001).

899. Z. G. Mao and S. B. Sinnott, *J. Phys. Chem. B* 105, 6916 (2001).

900. A. Maiti, *Phys. Status Solidi B* 226, 87 (2001).

901. C. Kubel and D. C. Martin, *Philos. Mag. A* 81, 1651 (2001).

902. D. Christopher, R. Smith, and A. Richter, *Nucl. Instrum. Methods B* 180, 117 (2001).

903. A. N. Andriotis, M. Menon, D. Srivastava, and L. Chernozatonskii, *Appl. Phys. Lett.* 79, 266 (2001).

904. A. V. Krasheninnikov, K. Nordlund, M. Sirvio, E. Salonen, and J. Keinonen, *Phys. Rev. B* 63, 245405 (2001).

905. M. C. Gordillo and J. Marti, *Chem. Phys. Lett.* 341, 250 (2001).

906. J. Marti and M. C. Gordillo, *J. Chem. Phys.* 114, 10486 (2001).

907. D. L. Hu, B. C. Pan, and J. M. Li, *Chinese Phys. Lett.* 18, 653 (2001).

908. Y. Kawazoe, K. Ohno, K. Esfarjani, Y. Maruyama, K. Shiga, and A. Farajian, *J. Mol. Graph. Model.* 19, 270 (2001).

909. J. Marti and M. C. Gordillo, *Phys. Rev. B* 63, 165430 (2001).

910. M. A. Osman and D. Srivastava, *Nanotechnology* 12, 21 (2001).

911. M. G. Martin, A. P. Thompson, and T. M. Nenoff, *J. Chem. Phys.* 114, 7174 (2001).

912. L. F. Xu, T. T. Tsotsis, and M. Sahimi, *J. Chem. Phys.* 114, 7196 (2001).

913. M. J. Lopez, A. Rubio, J. A. Alonso, L. C. Qin, and S. Iijima, *Phys. Rev. Lett.* 86, 3056 (2001).

914. Y. C. Ma, Y. Y. Xia, M. W. Zhao, R. J. Wang, and L. M. Mei, *Phys. Rev. B* 63, 115422 (2001).

915. M. Y. Li, E. J. Knystautas, and M. Krishnadev, *Surf. Coat. Tech.* 138, 220 (2001).

916. M. W. Zhao, Y. Y. Xia, Y. C. Ma, S. Y. Li, R. J. Wang, H. D. Zhang, and L. M. Mei, *Chinese Phys. Lett.* 18, 82 (2001).

917. S. J. V. Frankland and D. W. Brenner, *Chem. Phys. Lett.* 334, 18 (2001).

918. T. Kawai, Y. Miyamoto, O. Sugino, and Y. Koga, *Phys. Rev. B* 62, R16349 (2000).

919. S. Erkoc, *Int. J. Mod. Phys. C* 11, 1247 (2000).

920. L. Sun and R. M. Crooks, *J. Am. Chem. Soc.* 122, 12340 (2000).

921. S. Y. Bhide and S. Yashonath, *J. Phys. Chem. B* 104, 11977 (2000).

922. J. Han, A. Globus, R. Jaffe, G. Deardorff, *Nanotechnology* 8, 95 (1997).

923. M. Huhtala, A. Kuronen, and K. Kaski, *Comp. Phys. Comm.* 147, 91 (2002).

924. F. M. Capaldi, M. C. Boyce, and G. C. Rutledge, *Phys. Rev. Lett.* 89, 175505 (2002), F. M. Capaldi, Master's Thesis, Massachusetts Institute of Technology, 2001.

925. L. S. Loo, R. C. Cohen, and K. K. Gleason, *Science* 288, 116 (2000).

926. D. Kosztin, R. Gumport, and K. Schulten, *Nucleic Acids Res.* 27, 3550 (1999).

927. J. H. D. Boshoff, R. F. Lobo, and N. J. Wagner, *Macromolecules* 34 (2001).

928. W. Schommers, *Appl. Phys. A* 68, 187 (1999).

929. P. von Blanckenhagen, W. Schommers, and V. Voegele, *J. Vac. Sci. Technol. A* 5, 649 (1987).

930. L. Dagens, M. Rasolt, and R. Taylor, *Phys. Rev. B* 11, 134 (1975).

931. W. Schommers, C. Mayer, H. Gšbel, P. von Blanckenhagen, *J. Vac. Sci. Technol. A* 13, 1413 (1995).

932. W. Schommers, *Z. Phys. B* 24, 171 (1976).

933. W. Schommers, *Nanostruct. Mater.* 9, 693 (1997).

934. H. Göbel and P. von Blanckenhagen, *Phys. Rev. B* 47, 2378 (1993).

935. W. Schommers and M. Rieth, *J. Vac. Sci. Technol. B* 15, 1610 (1997).

936. N. Metropolis, A. W. Rosenbluth, M. N. Rosenbluth, A. H. Teller, and E. Teller, *J. Chem. Phys.* 21, 1067 (1953).

937. K. Binder (Ed.), 'Monte Carlo Methods in Statistical Physics." Springer-Verlag, Berlin, 1979.

938. F. Vasely, "Computerexperimente an Flüssigkeitsmodellen." Physik Verlag, Weinheim, 1978.

939. T. Kawamura, S. Toyoshima, and A. Ichimiya, *Surf. Sci.* 514, 60 (2002).

940. S. Martelli and P. E. Di Nunzio, *Part. Part. Syst. Char.* 19, 247 (2002).

941. K. G. Ayappa and C. Ghatak, *J. Chem. Phys.* 117, 5373 (2002).

942. M. K. Tej and J. C. Meredith, *J. Chem. Phys.* 117, 5443 (2002).

943. A. Heyden, T. Duren, and F. J. Keil, *Chem. Eng. Sci.* 57, 2439 (2002).

944. A. Milchev, A. Milchev, and K. Binder, *Comput. Phys. Commun.* 146, 38 (2002).

945. J. D. Romero and L. F. Fonseca, *Intergr. Ferroelectr.* 42, 385 (2002).

946. Y. Wang, T. P. Pearl, S. B. Darling, J. L. Gimmell, and S. J. Sibener, *J. Appl. Phys.* 91, 10081 (2002).

947. S. V. Divinski, F. Hisker, Y. S. Kang, J. S. Lee, and C. Herzig, *Z. Metallkd.* 93, 256 (2002).

948. O. Crisan, Y. Labaye, L. Berger, J. M. D. Coey, and J. M. Greneche, *J. Appl. Phys.* 91, 8727 (2002).

949. R. Komanduri, L. M. Raff, and A. Chandrasekaran, *Philos. Mag. Lett.* 82, 247 (2002).

950. H. Shinto, K. Uranishi, M. Miyahara, and K. Higashitani, *J. Chem. Phys.* 116, 9500 (2002).

951. H. K. Lee, T. C. Shulthess, D. P. Landau, G. Brown, J. P. Pierce, Z. Gai, G. Farnam, and J. Shen, *J. Appl. Phys.* 91, 6926 (2002).

952. J. H. Shim, B. J. Lee, J. P. Ahn, Y. W. Cho, and J. K. Park, *J. Mater. Res.* 17, 925 (2002).

953. C. J. Jameson, *J. Chem. Phys.* 116, 8912 (2002).

954. S. Tanimori and S. Shimamura, *J. Phys. Soc. Jpn.* 71, 797 (2002).

955. I. Brovchenko and A. Geiger, *J. Mol. Liq.* 96-7, 195 (2002).

956. F. Porcheron, M. Schoen, and A. H. Fuchs, *J. Chem. Phys.* 116, 5816 (2002).

957. O. Crisan, Y. Labaye, L. Berger, and J. M. Greneche, *Phys. Status Solidi A* 189, 845 (2002).

958. J. Boronat, M. C. Gordillo, and J. Casulleras, *J. Low Temp. Phys.* 126, 199 (2002).

959. T. Suzuki and S. Oishi, *Synth. Met.* 125, 265 (2001).

960. S. R. Challa, D. S. Sholl, and J. K. Johnson, *J. Chem. Phys.* 116, 814 (2002).

961. Y. G. Seo, G. H. Kum, and N. A. Seaton, *J. Membrane Sci.* 195, 65 (2002).

962. A. Vishnyakov and A. V. Neimark, *J. Phys. Chem. B* 105, 7009 (2001).

963. V. Vao-soongnern, R. Ozisik, and W. L. Mattice, *Macromol. Theory Simul.* 10, 553 (2001).

964. O. Iglesias and A. Labarta, *Phys. Rev. B* 63, 184416 (2001).

965. P. A. Serena and J. L. Costa-Kramer, *Rev. Mex. Fis.* 47, 72 (2001).

966. H. Tsuchiya and U. Ravaioli, *J. Appl. Phys.* 89, 4023 (2001).

967. D. S. Mainardi and P. B. Balbuena, *Langmuir* 17, 2047 (2001).

968. M. Vacatello, *Macromolecules* 34, 1946 (2001).

969. D. Hinzke and U. Nowak, *J. Magn. Magn. Mater.* 221, 365 (2000).

970. H. Kanda, M. Miyahara, and K. Higashitani, *Langmuir* 16, 8529 (2000).

971. L. E. Ocola, W. Y. Li, R. J. Kasica, M. I. Blakey, P. A. Orphanos, W. K. Waskiewicz, A. E. Novembre, and M. Sato, *Microelectron. Eng.* 53, 433 (2000).

972. M. Chen, C. Yang, and Z. Y. Guo, *Chinese Phys. Lett.* 17, 313 (2000).

973. K. A. Williams and P. C. Eklund, *Chem. Phys. Lett.* 320, 352 (2000).

974. M. Miyahara, T. Yoshioka, J. Nakamura, and M. Okazaki, *J. Chem. Eng. Jpn.* 33, 103 (2000).

975. S. Tanimori, K. Ishida, O. Sueoka, and S. Shimamura, *J. Phys. Soc. Jpn.* 68, 3556 (1999).

976. A. M. D. Assa'D, M. M. El Gomati, and J. Dell, *Ultramicroscopy* 79, 141 (1999).

977. T. Suzuki, T. Iiyama, K. E. Gubbins, and K. Kaneko, *Langmuir* 15, 5870 (1999).

978. F. Porcheron, B. Rousseau, A. H. Fuchs, and M. Schoen, *PCCP* 1, 4083 (1999).

979. H. Persson, P. Thormahlen, V. P. Zhdanov, and B. Kasemo, *J. Vac. Sci. Technol. A* 17, 1721 (1999).

980. P. E. Di Nunzio and S. Martelli, *J. Appl. Crystallogr.* 32, 546 (1999).

981. F. Lelarge, G. Biasiol, A. Rudra, A. Condo, and E. Kapon, *Microelectron. J.* 30, 461 (1999).

982. P. Thormahlen, H. Persson, V. P. Zhdanov, and B. Kasemo, *Abstr. Pap. Am. Chem. S* 217, 058-COLL (1999).

983. M. Strobel, K. H. Heinig, and W. Moller, *Nucl. Instrum. Methods B* 148, 104 (1999).

984. C. Tojo, M. C. Blanco, and M. A. Lopez-Quintela, *Langmuir* 14, 6835 (1998).

985. C. F. Mellot, A. K. Cheetham, S. Harms, S. Savitz, R. J. Gorte, and A. L. Myers, *Langmuir* 14, 6728 (1998).

986. A. Drefahl, O. Seidel, and H. J. Mogel, *Thin Solid Films* 329, 850 (1998).

987. Y. Z. Shao, C. H. Shek, and J. K. L. Lai, *Phys. Status Solidi B* 209, R1 (1998).

988. F. Darkrim and D. Levesque, *J. Chem. Phys.* 109, 4981 (1998).

989. I. A. Khan and K. G. Ayappa, *J. Chem. Phys.* 109, 4576 (1998).

990. J. L. Rousset, A. J. Renouprez, and A. M. Cadrot, *Phys. Rev. B* 58, 2150 (1998).

991. V. M. Samsonov, S. D. Murav'ev, and P. G. Khalatur, *Colloid J.* 60, 367 (1998).

992. V. P. Zhdanov and B. Kasemo, *Surf. Sci.* 405, 27 (1998).

993. K. G. Ayappa, *Chem. Phys. Lett.* 282, 59 (1998).

994. C. L. Liu, G. R. Odette, B. D. Wirth, and G. E. Lucas, *Mater. Sci. Eng. A* 238, 202 (1997).

995. C. Tojo, M. C. Blanco, and M. A. LopezQuintela, *Langmuir* 13, 4527 (1997).

996. T. Tadaki, T. Kinoshita, Y. Nakata, T. Ohkubo, and Y. Hirotsu, *Z. Phys. D* 40, 493 (1997).

997. H. Li, F. Czerwinski, and J. A. Szpunar, *Nanostruct. Mater.* 9, 673 (1997).

998. A. J. McDonald, M. P. Allen, and F. Schmid, *Phys. Rev. E* 63, 010701(R) (2001).

999. N. Akino, F. Schmid, and M. P. Allen, *Phys. Rev. E* 63, 041706 (2001).

1000. D. M. Ceperley and M. H. Calos, in "Monte Carlo Methods in Statistical Physics" (K. Binder, Ed.). Springer-Verlag, Berlin, 1979.

1001. A. Bijl, *Physica* 7, 869 (1940).

1002. R. B. Dingle, *Philos. Mag.* 40, 573 (1949).

1003. R. Jastrow, *Phys. Rev.* 98, 1479 (1955).

1004. N. F. Mott, *Philos. Mag.* 40, 61 (1949).

1005. N. Kawashima, *Progr. Theor. Phys. Supp.* 138 (2002).

1006. K. Kusakabe and Y. Tanaka, *J. Phys. Chem. Solids* 63, 1511 (2002).

1007. J. C. Grossman, *J. Chem. Phys.* 117, 1434 (2002).

1008. S. Goumri-Said, H. Aourag, L. Salomon, and J. P. Dufour, *Solid State Sci.* 4, 757 (2002).

1009. S. Siljamaki, A. Harju, R. M. Nieminen, V. A. Sverdlov, and P. Hyvonen, *Phys. Rev. B* 65, 121306 (2002).

1010. J. E. Hirsch, *Phys. Rev. B* 65, 214510 (2002).

1011. L. M. Almeida, J. P. Perdew, and C. Fiolhais, *Phys. Rev. B* 66, 075115 (2002).

1012. M. Mella, M. Casalegno, and G. Morosi, *J. Chem. Phys.* 117, 1450 (2002).

1013. D. Bressanini, G. Morosi, L. Bertini, and M. Mella, *Few-Body Syst.* 31, 199 (2002).

1014. L. Shifren and D. K. Ferry, *Physica B* 314, 72 (2002).

1015. J. Riera, *Physica B* 312, 569 (2002).

1016. A. J. F. de Souza and M. L. Lyra, *Phys. Rev. B* 65, 100405 (2002).

1017. F. Schautz and H. J. Flad, *J. Chem. Phys.* 116, 7389 (2002).

1018. H. X. Huang and Z. H. Zhao, *Chinese Chem. Lett.* 13, 55 (2002).

1019. M. Neumann and M. Zoppi, *Phys. Rev. E* 65, 031203 (2002).

1020. F. Alet and E. S. Sorensen, *Phys. Rev. B* 65, 092408 (2002).

1021. F. F. Assaad, *Phys. Rev. B* 65, 115104 (2002).

1022. D. Bressanini, G. Morosi, and M. Mella, *J. Chem. Phys.* 116, 5345 (2002).

1023. A. Harju, S. Siljamaki, and R. M. Nieminen, *Phys. Rev. B* 65, 075309 (2002).

1024. J. Boronat, M. C. Gordillo, and J. Casulleras, *J. Low Temp. Phys.* 126, 199 (2002).

1025. T. Tsuchiya, *Int. J. Mod. Phys. B* 15, 3985 (2001).

1026. M. Mella, S. Chiesa, and G. Morosi, *J. Chem. Phys.* 116, 2852 (2002).

1027. W. K. Leung, R. J. Needs, G. Rajagopal, S. Itoh, and S. Ihara, *VLSI Design* 13, 229 (2001).

1028. W. M. C. Foulkes, L. Mitas, and R. J. Needs, *Rev. Mod. Phys.* 73, 33 (2001).

1029. P. R. C. Kent, M. D. Towler, and R. J. Needs, *Phys. Rev. B* 62, 15394 (2000).

Conducting Polymer Nanostructures

Rupali Gangopadhyay

Hokkaido University, Sapporo, Japan

CONTENTS

1. INTRODUCTION

With the advancement of science and technology the world around us is shrinking and the importance of nanostructures is increasing. Attaining the nanoscale control over the spatial arrangement of the building blocks of materials has become an important objective of material scientists, because organization of materials on nanoscale very often leads to materials with physical properties distinctly different from the bulk counterpart. A new branch of science has been established for studying the preparation, properties, and application of such smaller objects of different size, shape, and origin. In view of this recently emerging field of nanoscience and nanotechnology, a nanomaterial is defined as one consisting of a substance or structure, at least one of the dimensions of which is less than 100 nm (0.1 μm). It has been repeatedly established that materials with such reduced dimension are especially important for showing fascinating electronic, optical, and magnetic properties. Science and technology of such micro- and nano-sized materials and objects are studied under different titles *viz.* micro- and nano-electronics, microelectromechanical systems (MEMS), micromolding in capillaries (MIMIC), etc. [1–4]. In parallel with the progress of nanotechnology, importance of multifunctional and lightweight materials, suitable for fabrication of smaller devices, is also increasing. Inherently conducting polymers (ICP) top the list of the smart and intelligent materials that can be successfully utilized for fabrication of different optical devices (LED and ECD), rectifying diodes, transistors, photovoltaic cells, rechargeable batteries, sensors for chemical and biochemical species, and so on [5–12]. However, some inherent difficulties in the nature of conducting polymers, such as their insolubility and infusibility, brittleness, poor mechanical property, etc. have primarily obstructed their successful and widespread application. For the same reason, to get conducting polymer-based nanomaterials in hand was not as easy as other polymers, at least up to the first 15 years after their discovery. These polymers are synthesized only in macroscopic precipitate form or in brittle and intractable film form, both which are highly disordered; but fabrication of nanodevices, particularly those relevant to micro- and/or nanoelectronics, demand some ultimate control over the synthesis leading to the defect-free and highly ordered form of the polymer. At the same time, the method of obtaining such defect-free materials with reduced dimension should be highly reproducible and controllable so that the synthesized materials are always identical. Therefore, the origin of synthesis of conducting polymer-based nanomaterials lies in the desire of attaining the nanoscale control over the structure and property of these polymers and to combine them with established nanotechnological systems. On the other hand, this attempt is also in pace with the attempt to overcome the intractability of the same.

Over the last 15 years, there have been a series of attempts to overcome the intractability of conducting polymers and to bring them in solution and/or in melt. Some of these attempts have directly launched some ICP-based nanomaterials. Depending upon the approach of synthesis, shape, size, and properties of the nanomaterials are varied. However, almost all possible forms of nanostructures *viz.* nanoparticle, nanotubule, nanofiber, nanowire, nanolayer (sometimes monolayer also), and patterned structures have thus far been prepared from ICPs. These materials were widely characterized from different aspects and were sometimes subjected to very interesting and sophisticated

applications. Principles and objectives of different techniques followed, for the development of such nanomaterials are the subject of discussion in this article. Structures of the synthesized materials, some of their fundamental properties, and interesting applications, as well as application potential have also been mentioned in this context. Investigations regarding synthesis, characterizations, and suitable applications of such materials encompass the field of chemistry, materials science, solid state physics, and even biological sciences. The subject is highly interdisciplinary and has rarely been reviewed thus far with such large purview. In the present context, versatility of this subject has been presented with careful selection and compilation of works.

2. OVERVIEW

Before entering a detailed discussion of the different techniques followed for obtaining ICP nanomaterials, the subject of discussion should be outlined so that it can be followed systematically. The quest for obtaining conducting polymers in microscopic/nanoscopic form has primarily given birth to the core-shell type nanoparticles with different size and morphology. Depending upon the synthesis techniques and other conditions, the ICP component could form either the core or the shell of the system. However, in such works, the prime achivement was prevention of the macroscopic precipitation of the ICP, thereby overcoming its lack of processability to some extent; the nanoparticles were mainly stabilized by the support polymers and were not separate entities. Different processable polymers like poly(vinyl alcohol) (PVA), polystyrene (PS), some surfactants, etc. were used as the stabilizers in these works. Later on, the synthesis of ICP nanoparticles have encountered multidirectional advancement and true nanoparticles—hollow or filled up, have been synthesized with different physical properties and applications. A broad spectrum of inorganic nanoparticles with versatile properties (colloidal stability, catalytic activity, magnetic susceptibility, etc.) were used for supported growth of the conducting polymers and also to combine their inherent properties. This section has been reviewed earlier in detail [13–15].

Channeled growth of conducting polymers within different inorganic/organic templates has given rise to ICP-based hybrid materials of some different types. Polymers could be grown chemically/electrochemically within three-dimensional templates like zeolite, porous glass, polymeric membrane, etc. in the form of nanotubules or nanowires. After removal of the host, the polymeric nanomaterials are set free in solution. If the host is a two-dimensional (layered) one like FeOCl, V_2O_5, etc., the polymer is in the form of a single chain or monolayer. Regardless, the template essentially introduces some control over the growth of the conducting polymer and brings it to nanoscopic form. All these inorganic-organic hybrid materials (nanoparticles and nanostructured materials) are collectively designated as "nanocomposites" which constitute a branch in advanced materials science. Various aspects of this particular class of ICP nanomaterials have also been peer-reviewed many times by different groups [16–20]. Formation of the three most widely investigated nanocomposites has been schematically shown in Figure 1.
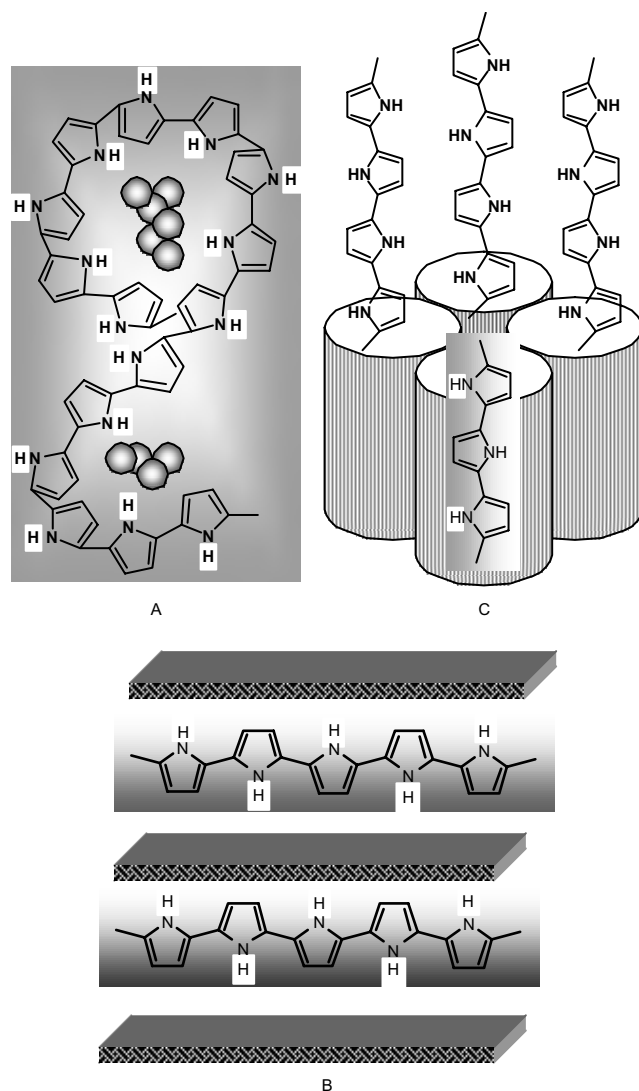
Figure 1. Schematic presentation of formation of three major categories of nanocomposites: A. Nanoparticles incorporated; B. 2-D (layered) template guided; C. 3-D template guided.

Template-guided methods are replaced later by more advanced template-free techniques of synthesis and materials with more advanced properties were obtained. Thin film and monolayer is another form of assemblence of conducting polymers in nanolevel; this has also been performed by both template-guided and template-free methods. Moscovite mica, some chemically designed surfaces, etc. have been used for templated monolayer growth. On the other hand, Langmuir–Boldgett (LB) technique is applied for template-free growth of monolayers. Fundamental electrical properties of such nanomaterials are different from their bulk counterparts to different extents which have been revealed by critical analyses. Nanomaterials of this type are a very recent addition to the list of advanced materials. At the same time, some very especial applications of such nanomaterials in electrically driven nanodevices like junctions, actuators, circuitry, etc. have been designed. An outline of the different materials synthesized and methodology followed has been presented in Table 1. However, these smaller objects are

Table 1. Conducting polymer nanostructures at a glance.
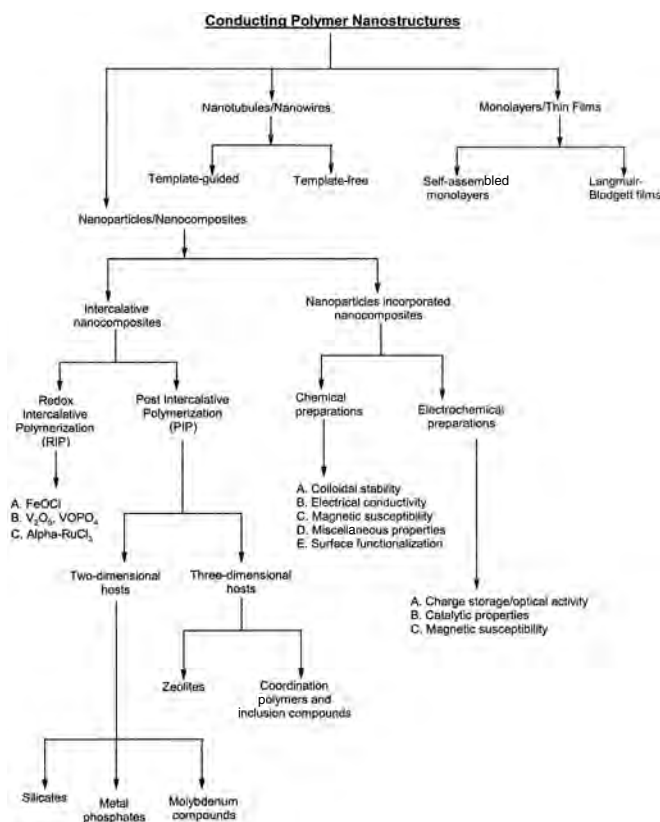
recent developments and have not been presented collectively thus far. In this article, these materials and devices are also introduced. It should be mentioned that this article is not solely decided to "nanoscale" materials only and addresses both micro- and nano-dimensional materials and devices under the title of "Nanostructures" because both are smaller materials and it is meaningless to draw a clear line of demarcation between them.

3. NANOPARTICLES

3.1. Colloidal Dispersions Guided by Steric Stabilization

The general feature, as well as the obvious problem with conducting polymers, is that during their chemical polymerization, they are precipitated out from the medium as intractable solid and cannot be turned to usable forms like films and coating. After discovery of these polymers and their promising properties and application potential, there has been a continuous effort to keep them in solution by controlling their particle size and morphology. The principles followed in this direction were steric stabilization or colloid formation. The former technique generally provides a bi-component or a tricomponent system, while the latter route may produce a bi-component and/or a tri-component system, depending upon the nature of components.

The most elementary approach is the bi-component steric stabilization which is nothing but to polymerize aniline

or pyrrole in presence of the solution (generally aqueous) of a suitable polymer so that the macroscopic precipitation of the former is prevented by the latter. This stream of investigation was started in the early 1980s and is still active. During these years, a number of low Tg polymers were utilized in this respect and colloidal dispersion having different extent of stability and versatile properties were introduced. Depending upon the nature of the reacting polymers, reaction conditions like temperature, solvent morphology, and size of the conducting polymer, etc. were varied. As revealed from the transmission electron microscopy (TEM) images, the conducting polymer was present in nanoparticle form and its dimension was within 300 nm. Water soluble polymers *viz.* methylcellulose (MC) [21], PVA [22], poly(ethylene oxide) (PEO) [23], poly(vinyl acetate) (PVAc) [24], poly(vinyl pyrrolidone) (PVP) [25], etc. were utilized elaborately and adsorption of these polymers onto the surface of the growing, conducting polymer particles was the key to their stabilizing property. This way, the conducting polymer nuclei were prevented from further aggregation, thereby giving rise to core-shell morphology where conducting polymer resides within the core.

The earliest report in this particular field of work was published in 1986; in this work MC (Mol. Wt. 95,000) was used as the steric stabilizer to the growing PPy particles in aqueous medium using $FeCl_3$ as the oxidant [21]. From scanning electron microscopy (SEM) images, globular PPy particles with $\sim$100–200 nm diameter were detected and maximum conductivity $\sim$0.2 S/cm was obtained. This work was followed by a series of works published by Vincent and Armes et al. [22–27], who could stabilize both PAn and PPy more efficiently using PVA, PVP, PEO, and some other polymers and copolymers. General synthesis technique was to add the monomer solution dropwise into the mixture of oxidizing agent and stabilizer under stirring. In few works the oxidant solution was added dropwise to the mixture of monomer and stabilizer. Depending upon the stabilizer, solvent, and other conditions (like the order of addition of reactants), size and morphology of PAn and PPy particles were varied. For example, using PVA as a stabilizer, spherical PPy particles of the size range 50–250 nm were obtained [22], while for PEO, the particle size changed to 390–490 nm [23]. Using $K_2S_2O_8$ as the oxidant much smaller particles $\sim$30 nm were detected. On the other hand, using polymer of 2- and 4-(vinyl pyridine-co-p-amino styrene) (VPAS) sterically stabilized PPy and PAn particles having rice grain shape and $\sim$120 nm length were obtained [24–26]. Electrical conductivity of these composites were nearby to each other; PPy-PVA : 1.5 S/cm, PPy-PEO : 1-2 S/cm, PPy-MC : 0.2 S/cm, PAn-VPAS : 0.5 S/cm. In a later publication [27], Aldissi and Armes have shown the effect of different stabilizers on the particle size of PPy; in this work PEO, PVA (two different molecular weight), PVP, P2VP-BM (butyl methacrylate), and P4VP-BM were used under similar reaction conditions. Spherical particles appeared in each case and it was observed that PVA resulted in smallest particles. Particle diameter varied from $\sim$60 nm to $\sim$350 nm and particles with larger diameter resulted in lower conductivity.

Since then, this field of investigation has been widely and elaborately cultivated and has produced a number of

fruitful results. PAn is the most exclusively studied polymer in this respect, and lot of composites with good processability and high electrical conductivity were obtained [28–31]. Vincent and Waterson and Stejskal et al. have published a series of works on synthesis and characterization of PAn nanoparticles under different chemical environment [32, 33]. Banerjee and Mandal [34] have introduced a novel method of obtaining PAn nanoparticles using ultrasonication, and subsequently used the nanoparticles to give rise to composites with extremely low percolation threshold. However, in all such works, although conducting polymer is present in nanoparticle form, it has no separate identity as nanoparticle. Its macroscopic form in combination with the support polymer is only considered and it is only studied as composites.

Recently, there have been a few publications reporting stabilization of PAn nanoparticles in the micelle of SDS and dodecylbenzene sulphonic acid (DBSA) [35, 36]. In such cases, aniline is polymerized in the presence of SDS or DBSA so that growing PAn chains are surrounded by the micelles and are prevented from macroscopic precipitation. Very recently, Ghosh et al. [37] have also published a novel technique for obtaining PAn nanoparticles in DMSO medium, which formed a stable solution without any stabilizer. These works are somewhat different from the core-shell type solutions.

There is a second stream of synthesis of core-shell type materials in which a conducting polymer component serves the outer layer or "shell." In other words, these works are analogous to coating some polymeric or inorganic nanoparticles with conducting polymers. As the polymeric latex particles are concerned (as the core materials), the objective of the work is to synthesize stable dispersion of conducting polymers with good film forming property and high electrical conductivity. The first report of this series of work was published by Yassar et al. [38] who could obtain aqueous dispersion of –COOH or –SO$_3$H functionalized polystyrene latex particles coated with PPy; this dispersion could be film-casted and maximum conductivity 0.25 S/cm was obtained. Similarly, styrene-butadiene rubber (SBR) with a small amount of methacrylic acid formed the latex pyrrole; aniline and methyl thiophene (MT) were polymerized on the latex particles using FeCl$_3$, CuSO$_4$, etc. different catalysts [39]. Conductivity of PPy and PAn containing blends were of the order of 10^{-1} S/cm, while PMT containing composites showed 10^{-4} S/cm. However, these two reports were not supported by successive investigators at least in the point of stability of dispersion.

Later on, the research group of Lascelles and Armes have carried out a widespread investigation on this stream of work aiming at successful synthesis of a stable core-shell type of composites having the shell of conducting polymers. In contrast to the earlier reports, they have started with sterically stabilized latexes *viz.* polystyrene (PS) stabilized by PVP or PEG [40, 41]. A simple chemical polymerization technique was followed in each case, and three important conducting polymers—PAn, PPy, and poly(3,4 ethylene dioxy thiophene, (PEDOT))—were utilized. Respective monomers were added to the PS dispersion having micron- and submicron-sized PS particles followed by the addition of oxidant solution. The reaction was carried

out for 24 h, and in each case a parallel reaction scheme was also followed in which the oxidant was taken in PS latex and monomer was added from the outside. The composites were obtained as a stable dispersion in which conducting polymer-coated PS latex particles more or less preserve the colloidal stability. In contrast, chlorinated copolymer latex (Haloflex EP 252) without any steric stabilizer resulted in macroscopic precipitation [42]. A detailed study on the synthesis-structure-property relationship has been carried out by this research group using different dimensions of PS latex, different experimental conditions, etc. and all these materials were studied from different aspects to build up a thorough understanding on this subject. The most interesting part of the work was the verification of core-shell morphology from SEM. Initially, the composite particles appeared in globular shape but after prolonged immersion in THF, the PS core was dissolved and "broken egg shell" like morphology of the composites was identified from the SEM image (Fig. 2). This confirms the real core-shell configuration of the composite particles where PS forms the core. All these composites were found to be highly conducting and classical percolation
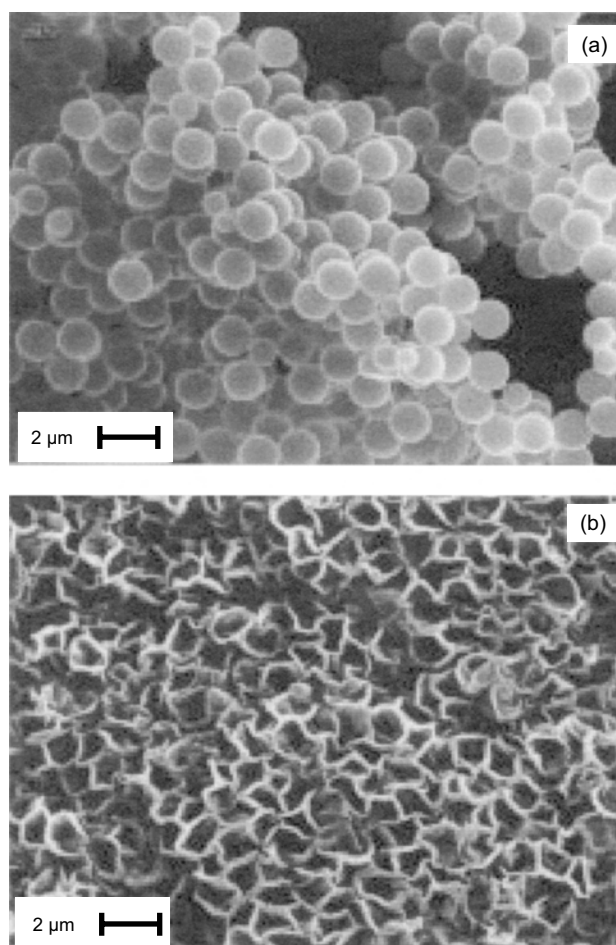

Figure 2. SEM images of (a) PPy-coated PS latex, and (b) resulting PPy residues after extraction of the inner PS (core) particles by THF; a "broken egg-shell" morphology, a clear evidence of "core-shell" type orientation. Reproduced with permission from [41], S. F. Lascelles et al., *J. Mater. Chem.* 7, 1349 (1997). © 1997, RSC.

behavior was obtained in each case. The order of lowering in conductivity, as well as rising in percolation concentration, was as follows:

$$PPy\text{-}PS > PAn\text{-}PS > PEDOT\text{-}PS$$

There are a few other works in this direction that concern the coating of 60–100 μm polyurethane (PU) latex, stabilized by PEO and hydroxyethyl cellulose, with PPy; this presents a system with good film-forming capability and solid-state conductivity of 10^{-5} to 10 S/cm. In a recent work, stabilization of uniform, micron-sized PAn particles in a multicomponent system was reported, one of the components being porous PS particles. Colloidal stability at a higher PAn loading is an important achievement of this system although the other characterizations are forthcoming.

3.2. Combination with Inorganic Particles

The idea of synthesizing conducting polymer-based, core-shell type materials in which the polymer serves the shell has been most widely implemented on nanocomposites in which inorganic nanoparticles or nanoclusters (*viz.* metals, metallic oxides, sulphides, etc.) serve the core. These nanocomposites can be considered elegant hybrid materials, which play a bridging role between the world of conducting polymers with that of the inorganic nanoparticles, and which can successfully combine the physical properties of both. The work in this direction was started with the aim of combining the colloidal stability of a few inorganic colloids with optical and electrical properties of conducting polymers; later on, other characteristic properties like catalytic activity, magnetic susceptibility, etc. were also considered important for combination. Different inorganic particles used for the formation of nanocomposites, their dimensions, and important physical properties are tabulated in Table 2.

It was mentioned earlier that the insoluble and infusible nature of conducting polymers have kept them away from combining with foreign materials in a simple blending technique; *in-situ* polymerization was a more convenient way of combination. The same route was followed and is still being followed by the scientists as an efficient way of incorporating inorganic nanoparticles into conducting a polymer matrix. The pioneering work in this direction was reported by Armes et al. who were able to encapsulate silica particles of different dimension into the core of PPy and PAn [43]. Spherical silica particles of three different sizes—1 μm [43], ~38 nm [44], and 20 nm [45]—and "stringy" (elongated 40–300 nm long, 5–20 nm in diameter) silica particles [46] were utilized for this purpose. The general synthesis technique was to add the oxidant (or monomer) solution into the colloid containing the monomer (or oxidant) on stirring, and almost in all experiments the resulting composite was synthesized in the form of a stable colloid. The principle of synthesis in each case was to polymerize respective monomers (aniline or pyrrole) in the presence of the pre-formed inorganic colloid using some appropriate oxidant, generally ammonium peroxodisulphate (APS) (HCl) for aniline and FeCl$_3$ for pyrrole. Controlled polymerization of the monomer, preferably on the surface of the colloidal particles rather than in bulk, using low concentration of both

the monomer and the oxidant, was the key to the formation of a colloidal nanocomposite. Interestingly, a critical silica concentration was required for the formation of the nanocomposite colloid which was 2.0–2.3% (w/v) for larger silica (~38 nm) and ~1.0% for smaller (20 nm) silica particles. Composite particles were 1.5–3.0 μm in diameter and a maximum ~21% polymer loading was primarily obtained (with 38 nm silica). Gill et al. [45] were the first to reveal a unique "raspberry" morphology of the composites by high resolution TEM images that appeared reproducibly in other publications of the same group. This image apparently reveals that silica particles are connected or rather "glued" by the conducting polymer chain and such orientation accounts for the high silica loading in these materials (Fig. 3). Even on changing the morphology of silica colloid from spherical to elongated (stringy) silica the "raspberry"-like orientation of colloid has not changed much (Fig. 4). Later on, there was a thorough investigation [47–50] about the different reaction parameters like nature of oxidant, concentration of reactants, etc. and a colloid with 20 nm silica (1%) was used as an almost standard condition for succeeding works. Depending upon other conditions, polymer loading in these composites could be varied from ~37% to ~70%. Electrical conductivity of most of these samples fall within a broad range from 10^{-5}–1.0 S/cm and a maximum value 4.0 S/cm was obtained for the nanocomposites prepared with 20 nm silica and FeCl$_3$ oxidant in the presence of p-toluene sulphonate (PTS).

Later on, this field of investigation was extended to a series of other colloids, namely, SnO$_2$, TiO$_2$, Sb$_2$O$_3$, ZrO$_2$, and Y$_2$O$_3$, with the appearance of raspberry morphology in each case. But a nanocomposite in stable colloid form could be prepared only with two dispersants—SiO$_2$ and SnO$_2$—the reason of which was not very obvious [51, 52]. Extensive studies on different aspects of different pure colloids, as well as their respective nanocomposite colloids using inverse gas chromatography (XPS) and electrokinetic measurements, have revealed some unique surface features of SiO$_2$ and SnO$_2$ that can only account for the prolonged stability of the respective nanocomposites against precipitation. Brunauer–Emmet–Teller (BET) surface area measurements [53] have shown that a larger surface area of the supporting colloid is a necessary, but not sufficient condition, for the formation of colloidal nanocomposite. However, both these colloids possess significant porosity, as revealed from inverse gas chromatographic data [54] for which their specific surface area is always larger than expected. X-ray photoelectron spectroscopy (XPS) measurements and electrokinetic measurements have revealed that in both these nanocomposites, the Si/N or Sn/N ratio on the surface was found to be higher than that in bulk, which signifies that the surface of these composites is silica (or SnO$_2$)-rich rather than polymer-rich [55, 56]. Therefore, particles of the composites can be considered as associated particles of SiO$_2$ or SnO$_2$ connected by polymer chains, in which the surface feature of inorganic support materials is retained. The effect of other synthesis parameters like temperature, reagent concentration, nature of oxidant, effect of stirring, etc. were also studied in the succeeding articles and only the stirring was found to have any effect on particle size, polymer content, and conductivity of the composites [57]. A larger surface area

Table 2. An overview of the composition and properties of the nanoparticles incorporated nanocomposites.

Polymer used	Inorganic nanoparticles	Physical appearance	Significant characteristics/applications
PPy and PAn	SiO_2 (1 μm, 35 nm, and 20 nm), Stringy SiO_2 (40–300 nm long)	Stable colloid, can be spin-coated	Raspberry morphology (in TEM) showing inorganic particle-rich surface and monolayer of polymer
PPy and PAn	CeO_2 (0.52 μm), CuO (1.6 nm), α-Fe_2O_3 (spherical, polyhedral, and spindle-shaped), NiO (3.8 μm), SiO_2 (0.46 μm)	Stable colloid with core-shell type orientation	Oxidizing property of the core materials was exploited; no polymerization initiator was required. Nanocomposite with extremely low dc conductivity was obtained.
PPy and PAn	Colloidal gold (7–9 nm and 25 nm), silicon-titanium zeolite (TS-1,~100 nm) and $BaSO_4$ (20 nm)	Stable colloid or emulsion having core-shell morphology	Nanocomposite supported in membrane or in microemulsion. Variable thickness of the polymer coating; for 25 nm gold core, 10 nm thick shell was obtained.
PPy and PPV	ZrO_2 (20–30 nm), α-Fe_2O_3 (25–50 nm), SiO_2 (nm), n-TiO_2 (~10 nm), Al_2O_3 (35–50 nm), MgO (2–4 nm), carbon black	Macroscopic precipitation or colloid with limited stability	Improved thermal stability and dc electrical conductivity. Novel transport properties and applications
PPy and PAn	SiO_2 (20 nm)	Stable colloid with functional groups	Surface functionalized with –NH_2or–COOH group, important for immunodiagnostic assay
PPy and PAOABSA	MS (5–30 nm), Fe_xO_y (14 nm), Fe_2O_3 (15–50 nm), γ-Fe_2O_3(~85 nm)	Nanocomposite colloid or film (electro-chemical)	Nanocomposite powder or film, both having significant magnetic susceptibility.
PPy and PAn	Barium titanate (1 μm), Fe_2O_3 (4 nm, 40 nm), β-MnO_2, TiO_2, $LiMnO_2$, $LiMn_2O_4$, V_2O_5, WO_3, PMo_{12}, Ta_2O_5, prussian blue	Powdered solid (chemical) and/or film on electrode	Solids having appreciable electrical conductivity, improved charge storage, dielectric and optical properties; materials suitable for cathode and ECD.
PPy, PAn, and PEDOT	SiO_2 (20 nm), Pt (~4 nm), Pd, Cu, Pd, and a few other metals and bimetallic couples	Nanocomposite colloid/film	Nanocomposites with catalytically important metals; important for heterogeneous catalysis

of nanocomposites has offered them better performance as bio-adsorbent as compared to pure PPy. In one of the publications of these series [58], PPy and PPy-SnO_2 nanocomposites were both allowed to adsorb a model protein human serum albumin (HSA), and the spectrophotometric method has proven that colloidal nanocomposite possesses better adsorptive capacity compared to PPy itself.

When one group of scientists exploited the unique colloidal stability of a few nanoparticles toward synthesis of colloidal nanocomposite, the other group utilized the oxidative nature of some other particles for a similar purpose. In a series of publications, Matijevic et al. [59–61] have reported the formation of a colloidal nanocomposite by *in-situ* oxidative polymerization of pyrrole and aniline, where

Figure 3. TEM image of dried, diluted PPy-silica nanocomposite colloid using spherical silica particle (20 nm): typical "raspberry" morphology. Reproduced with permission from [48], S. Maeda and S. P. Armes, *J. Coll. Interface Sci.* 159, 257 (1993), © 1993, Elsevier Science.
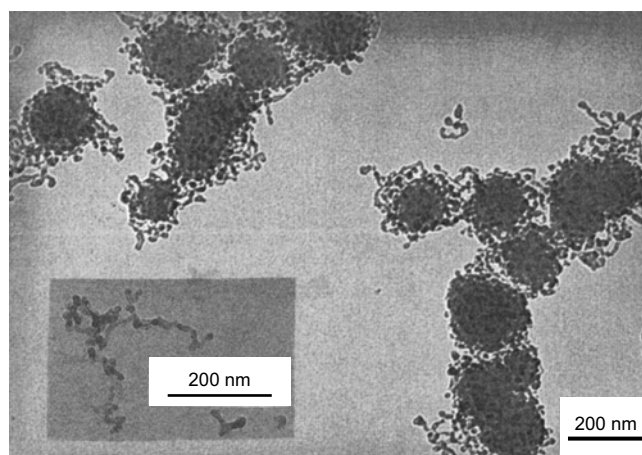
Figure 4. TEM image of dried and diluted PPy-silica nanocomposite colloid using "stringy" silica Colloid; pure stringy silica colloid in inset. Reproduced with permission from [46], R. Flitton et al. *J. Coll. Interface Sci.* 173, 135 (1995). © 1995, Elsevier Science.

nanoparticles of CeO_2, α-Fe_2O_3, CuO, NiO, and hematite-coated silica served the core materials as well as the oxidant. Aqueous suspensions of the inorganic particles containing pyrrole were heated up to $\sim$100 °C in a closed vessel to initiate polymerization leading to black colloidal suspension. Nanoparticles having no oxidative site (*e.g.*, SiO_2) cannot form such a colloidal composite, which indicates that the active participation of the oxidative centers of the inorganic colloid is the key to the formation of the colloid in these works. However, harshness of reaction condition is responsible for the extremely poor conductivity of these solids. CuO was also used to form colloid with PAn in insulating leucoemeraldine form. For experiments performed in air, aerial oxygen promotes polymerization of pyrrole to some extent even with silica particles with no catalytic property.

Works so far discussed present the "first generation nanocomposites" as the prime objective of synthesis of which was to encapsulate the inorganic particle and keep the composite in stable colloid form. Later on, diversity was brought to different aspects of the work; the synthesis technique as well as the objective of the work was varied. The synthesis technique was modified with the aim of enhancing microstrucrural homogeneity in composites. Emulsion polymerization and different types of template-guided polymerization replaced the simple reaction techniques. For example, *in-situ* formation and encapsulation of $BaSO_4$ nanoparticles within PAn shell and simultaneous stabilization of the whole in an oligo-ethylene oxide-based microemulsion was reported by Gan et al. [62]. Similarly, the *in-situ* formation of gold nanoparticles and their simultaneous stabilization within the core of a diblock copolymer was also reported by Selvan et al. [63, 64]. In contrast to two component composites in earlier publications, these systems present three component composites/nanocomposites in stable solution form.

Template-guided synthesis provides some control over the growth of the conducting polymer chain; two types of substrates were used as templates *viz.* inorganic nanoparticles embedded in polymeric/organic membranes and a self-assembled array of some modified inorganic hosts. In the former example, gold nanoparticles are arranged within the pores of an Al_2O_3 membrane and pyrrole is polymerized within the latter using the vapor phase polymerization technique [65]. The gold particles are acting as the nucleation center for polymerization and after slow removal of the membrane, the PPy-Au particles are set free in the solution. Further extending the work to filtration of KCN or $K_3[Fe(CN)_6]$ solution through the PPy-Au assembly, Au particles are removed and hollow capsules of PPy are obtained [66, 67]. The arrangement of Au nanoparticles coated with PPy and the hollow PPy capsule after removal of the Au core has been nicely shown in a TEM picture (Fig. 5). A conventional technique for synthesis can also be applied by adding oxidant solution into suspension of gold-containing pyrrole, but in that case some stabilizer (*e.g.*, PVP) should be added from outside. The PPy capsules obtained this way have potential application in entrapment of small and reactive molecules without hampering reactivity. The second example of a template utilizes self-assembly of pyrrole on some inorganic substrates like Al_2O_3 or synthetic zeolite,
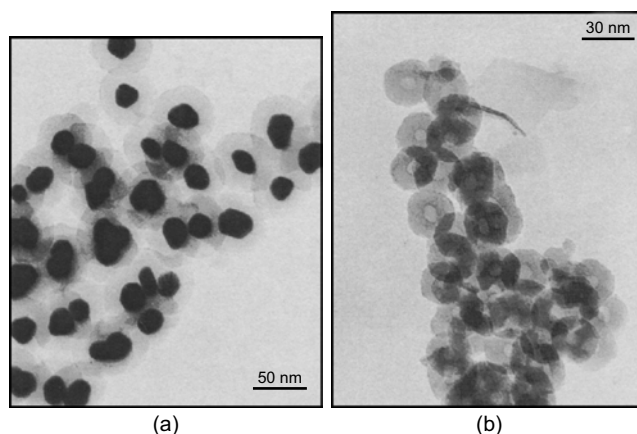
Figure 5. TEM images of PPy-Au nanocomposite using Au particle of 30 nm diameter: (a) PPy-coated Au, (b) after removal of Au core by complexation. Reproduced with permission from [66], S. M. Marinakos et al. *Adv. Mater.* 11, 34 (1999). © 1999, Wiley-VCH.

desirably modified by some surface-active agents *viz.* hexanoic acid (HA) or cetyl pyridinium chloride (CPC) [68, 69]. These reagents themselves can form a self-assembled monolayer on the inorganic host by a semi-chemisorption mechanism; pyrrole molecules, on the other hand, have some affinity towards HA and CPC by which they can also form a monolayer (or a thin layer) on the modified substrate. With the addition of APS or $FeCl_3$, pyrrole is polymerized and the nanocomposite is grown. High electrical conductivity (of the order of 10^{-1} S/cm) indicates that PPy is present in highly ordered form. The synthesis of an optically active nanocomposite of PAn-silica was reported by a single publication following an electrochemical synthesis technique. The electropolymerization of aniline in the presence of colloidal silica (20 nm) and optically active camphor sulphonic acid in a flow through-electrochemical cell resulted in a desired nanocomposite in stable colloidal form with a characteristic "raspberry" morphology (TEM) and a core-shell type orientation [70].

The objective of synthesis of conducting polymer-based nanocomposites has been shifted to versatile directions other than simply obtaining the polymer in a stable colloid or in ordered structures. Colloids were designed having a wide range of characteristic physical and chemical properties, and the resulting nanocomposites could combine the desirable properties of the components in a single material. An apparently surprising result was obtained from the combination of ZrO_2 [71] and Fe_2O_3 [72] with PPy; these colloidal nanoparticles could enhance the electrical conductivity of PPy to an appreciable extent. The reason behind such an anomalous result was an improvement of compactness of the polymer after nanocomposite formation, the effect of which was reflected in improved thermal and environmental stability also. Nanodimensional TiO_2 [73, 74] was sometimes combined with PAn-DBSA (solution) to reduce the size of composite particles to as low as 35 nm; this combination, however, failed to improve the solid-state properties of the polymer. Very recently, Xia and Wang have published a novel approach

towards synthesis of spherical PAn-TiO$_2$ core shell type nanocomposites, using nanocrystalline TiO$_2$ having a diameter $\sim$27 nm [75]. Polymerization of aniline was performed chemically using APS (HCl) in the presence of TiO$_2$ particles and a surfactant solution. Ultrasonic irradiation was maintained during the polymerization and the nanocomposite was obtained as a dark green dispersion of particles with a dimension up to 200 nm. Electrical conductivity of the nanocomposite with 21.6% TiO$_2$ was 0.72, larger than that prepared without ultrasound assistance.

Carbon black (CB) is a very important material considering its filler properties to plastics and rubber. This material has been used as core of conducting nanocomposites in a series of works published by Wampler et al. [76, 77], using simple solution polymerization of pyrrole in the presence of CB. At a low concentration, CB hampers conductivity of PPy but after a critical CB loading, conductivity rises and saturation at $\sim$60% loading is observed. Deposition of PPy and PAn on other allotropes of carbon $viz.$ graphite and carbon nanotube (CNT) has also been reported in a number of publications [78–82].

Magnetic susceptibility of the well-known magnetic materials $viz.$ γ-Fe$_2$O$_3$, Fe$_3$O$_4$, etc. has been nicely combined with important physical properties of conducting polymers in a significant number of articles. Butterworth et al. [83, 84] have designed a novel technique by which silica-coated magnetite particles (prepared as described elsewhere [85]) were combined with PPy to give rise to magnetic nanocomposites. These ultrafine particles are expected to combine unique dispersing ability of silica with magnetic susceptibility of magnetite and the composite showed superparamagnetic behavior with an appreciable magnetic susceptibility of 6.5 emu/g. Higher silica loading enhanced the colloidal stability, although the conductivity and magnetic property were sincerely hampered. Superparamagnetic γ-Fe$_2$O$_3$ particles (9 nm) were included in a PPy-based composite by copolymerizing pyrrole and pyrrole-N-propylsulphonate with FeCl$_3$, and subsequently treating the materials by NH$_4$OH at 70 °C [86]. Incorporation of nanocrystalline Fe$_x$O$_y$ (14 nm) into a PAn matrix could be performed by mixing an aqueous solution of FeSO$_4$ with a NMP solution of PAn (EB) under N$_2$ atmosphere [87–89]. However, magnetic susceptibility of these materials could be observed only in high pH ($>$7) condition because of the appearance of Fe$_3$O$_4$ in such conditions. In a very recent publication, the in-$situ$ formation of a ferric oxide embedded nanocomposite of PPy was described following the sol–gel technique. Fe(NO$_3$)$_2$, 9H$_2$O was used as the precursor of ferric oxide, which (in 2-hydroxy ethanol medium) is converted to α- and γ-Fe$_2$O$_3$ (or Fe$_3$O$_4$) with simultaneous polymerization of pyrrole [90]. The resulting black powder shows electrical conductivity and magnetic property and both are enhanced on annealing to 250 °C and then diminishing. On changing the medium to 2-methoxy ethanol, a similar result is obtained although the conductivity and magnetic susceptibility is found to increase up to $\sim$350 °C.

A sophisticated method of obtaining superparamagnetic nanocomposite film with appreciable electrical conductivity was designed by Tang et al. [91]. γ-Fe$_2$O$_3$ particles (10 nm) were coated with anionic surfactant prior to mixing with solutions of PAn containing different anions ($e.g.$, DBSA, CSA, etc.) in different solvents. Highly conducting films (maximum conductivity 237 S/cm) with very high magnetic susceptibility (maximum saturation magnetization 40 emu/g) were thereby obtained. Another novel method of synthesis of magnetically susceptible nanocomposites was reported by Bidan et al. [92, 93] using electropolymerization principle. In this work, γ-Fe$_2$O$_3$ was surrounded by some anionic complexing agents so that core-shell type macro-anions are prepared with γ-Fe$_2$O$_3$ in core. As pyrrole is subjected to electropolymerization, in the presence of the dispersion of such macro-anions stabilized by some surfactant, the nanocomposite having good magnetic property is grown in-$situ$. An overall evaluation of the efforts of producing conducting polymer composites and nanocomposites has been done by Kryszewski and Jeszka in a contemporary review [94].

The quest for obtaining conducting composites with unique redox properties like conducting polymers and significant charge-discharge properties have led scientists to combine cathode-active materials like LiMn$_2$O$_4$, V$_2$O$_5$, etc. with PPy and PAn. Both chemical and electrochemical polymerization technique was followed and spectrums of different inorganic materials were combined in this respect. For combination with PPy, pyrrole was polymerized in the presence of V$_2$O$_5$, LiMn$_2$O$_4$, and β-MnO$_2$, etc., utilizing the oxidative power of the inorganic materials while PAn-NMP was solution blended with inorganic components. Interestingly, in such nanocomposites conducting polymers and the inorganic materials are participating as active components having complementary redox properties [95–102].

Catalytically important nanoparticles could be combined with conducting polymers to give rise to nanocomposites having catalytic activity. Pt [103] and PtO$_2$ [104, 105] are the two most important materials in this respect, and they were combined with PPy and PEDOT by the chemical polymerization technique. Later on, Au and Pd nanoparticles were also included into the PPy and PAn bed, sometimes using a solution-blending technique and sometimes by simultaneous oxidation-reduction reactions. Sometimes, even the PPy-SiO$_2$ nanocomposite (rather than only PPy or PAn) were also used to entrap Pd or Au nanoparticles with retention of catalytic activity and the nanocomposites having a larger surface area were found to be better adsorbents for catalytic particles. The electrochemical incorporation of other metallic and bimetallic elements in the ICP films and their subsequent application in chemical sensing ($e.g.$, glucose) and gas sensing, etc. are described in a few publications [106–111].

It was already mentioned that the surface of the first generation SiO$_2$-based nanocomposites containing PPy and PAn (introduced mainly by Armes et al.) was silica-rich rather than polymer-rich. These composites were considered as agglomerates of silica particles bound or a "glued" by polymer chains. Later on, there have been numerous efforts to synthesize nanocomposites with a PPy rich surface. In a very recent publication, large glass beads (diameter $\sim$550 μm) were coated with PPy by a chemically polymerizing pyrrole on the surface of beads treated with FeCl$_3$ [112]. The treatment was repeated to thicken the PPy coating, and coating thickness was found to increase from

6.2 μm to 20.2 μm after coating the beads twice. The surface is obviously PPy-rich, and thereby positively charged and capable of the removal of Humic acid from water. Chriswanto et al. [113, 114] and Perruchot et al. [115–117] have attempted to modify the composite surface by using porous silica particles but ended up with a silica-rich surface. The latter group has tried to functionalize silica particles with –COOH and –NH_2 groups so that adhesion of PPy to silica increased, and thereby a nanocomposite with PPy-rich surface is obtained. Different methodologies to introduce functionalized silica particles are grouped in Figure 6. Aminopropyl triethoxy silane (ATS) is a specific reagent for introducing –NH_2 groups to silica; silica particles were treated with ATS prior to deposition of PPy on them, which ultimately led to a PPy-rich surface of nanocomposites. PPy loading and electrical conductivity of the composite were found to be increased with ATS loading, and in the future the technique could be applied to form PPy coating (20–50 nm thick) on E-glass fibers as well [118, 119]. Functionalization of nanocomposite particles themselves with –NH_2 or –COOH groups (rather than only the core) could be performed with the objective of improving their performance in immunodiagnostic assay. Aminopropyl triethoxy silane was again used for this purpose, and stirring the preformed nanocomposites with an aqueous solution of ATS could add a –NH_2 functional group to them [120, 121]. In a modified technique, Goller et al. have described –NH_2 functionalization of PPy-SiO_2 nanocomposites through copolymerization of pyrrole and 1-(3-aminopropyl pyrrole) in the presence of silica; the amination was established from varying evidence [122]. On the other hand, in order to add a –COOH functional group to the composites, the reaction had to be started from copolymerization of pyrrole with 1-(2-carboxyethyl)-pyrrole or pyrrole-3-acetic acid, in the presence of ultrafine silica sol as described by Maeda et al. [124], the 3-substituted derivative presented better stability and other properties as compared to the other one [123–125]. The –COOH functionalized colloid proved itself to be an excellent candidate for immunodiagnostic
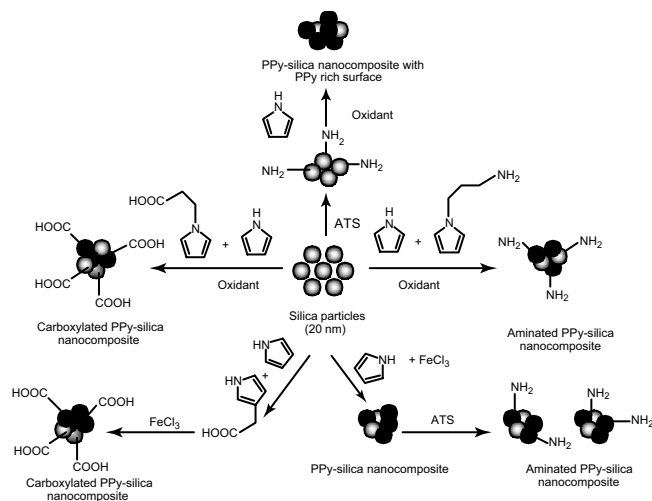
assays [126]. Amino-functionalized nanocomposites are also expected to show better performance in immobilization of biomolecules like hormones, antigens, antibodies, DNA, etc. [127].

4. NANOTUBULES AND NANOWIRES

Over the last one and a half decades, the world of conducting polymers has been enriched with a number of nanostructured objects in different forms like nanotubules, nanowires, nanorods, etc. The prime objective of synthesis in most of the cases, however, was to achieve the perfect control over the growth of polymers, which ultimately helps to reveal the unexplored fundamental properties of them. Inorganic and polymeric substrates having nanodimensional pores, channels, and gaps were used as a support for this purpose and conducting polymers were led to grow chemically or electrochemically within them. These ICP-loaded substrates are examples of a different kind of nanocomposite, in which the nanodimensional conducting polymer is the guest. After removal of the supporting matrix by selective dissolution, the nanomaterials are set free and can be collected in solid state and/or subjected to different studies. Depending upon the nature of the support and some other factors, these materials can be classified into two major classes *viz*. intercalative polymerization and template-guided polymerization.

There are two major differences between the intercalative nanocomposites, which depend on whether the supporting substrate itself is oxidative or not. In the former category, there are only a few layered materials possessing substantial oxidative property that is utilized for oxidative polymerization of the monomer within the substrate. The majority of the hosts are devoid of oxidative property and require oxidant (for the polymerization) to be applied from outside after incorporation of the monomer into the host. In each case, the reaction gives rise to solids with nanodimensional-conducting polymers confined in the host materials. The synthesis techniques are obviously named as redox intercalative polymerization (RIP) and post-intercalative polymerization (PIP), respectively. Template-guided polymerization should be discussed under a separate title because the related works very often present simultaneous polymerization and incorporation as will be clarified later. This classification, however, is not very applicable and very often, overlaps are observed.

4.1. Template-Guided Synthesis

Considering the simplicity of the system and the interesting properties of the resulting materials, the discussion should be started with template-guided polymerization. The underlying principle of this branch of synthesis is to allow chemical/electrochemical growth of conducting polymers within some chemically inert microporous/nanoporous membrane matrices. In most of the works, after the reaction is over the polymer-membrane hybrid is subjected to selective dissolution of the membrane (using appropriate solvent) in order to set the nanodimensional polymers free. Different synthesis techniques followed for template-guided polymerization

Figure 6. Schematic presentation of different routes of surface functionalization of PPy-silica nanocomposites by amino and carboxyl groups.

and properties of the polymeric nanomaterials have been presented collectively in Table 3. This stream of investigation was started in 1986 when Penner and Martin were able to polymerize pyrrole electrochemically within the pores of a polycarbonate (nucleopore) membrane having a thickness of 1 μm [128, 129]. This technique obviously controls the macroscopic growth of the polymer and leads the polymer to adopt fibrillar or microporous morphology. After dissolution of the matrix in chloroform, the fibrils or tubules are set free and could be separated. The availability of the support membranes in different pore sizes ranging 100 Å– 12 μM results in a variety of the dimension of the nanomaterials; at the same time, uniformity of the pore diameter leads to a uniform dimension of the conducting polymers synthesized under each confinement. The chemical polymerization technique has also been applied for the synthesis of these membrane-based polymeric nanomaterials; in that system, the membrane is placed as a separator of two compartments containing aqueous solutions of monomer and the oxidant. The solutions diffuse towards each other through the pores and react to form the polymer within. These techniques were applied for growth of a variety of conducting polymers, namely, PA [130], PPy [131, 132], PAn [133], and P3MT [134]. Tubular growth of PPy and N-methyl-PPy within a porous membrane under chemical and electrochemical synthesis conditions has been revealed by the respective SEM images (Fig. 7). In each case, however, nucleation of
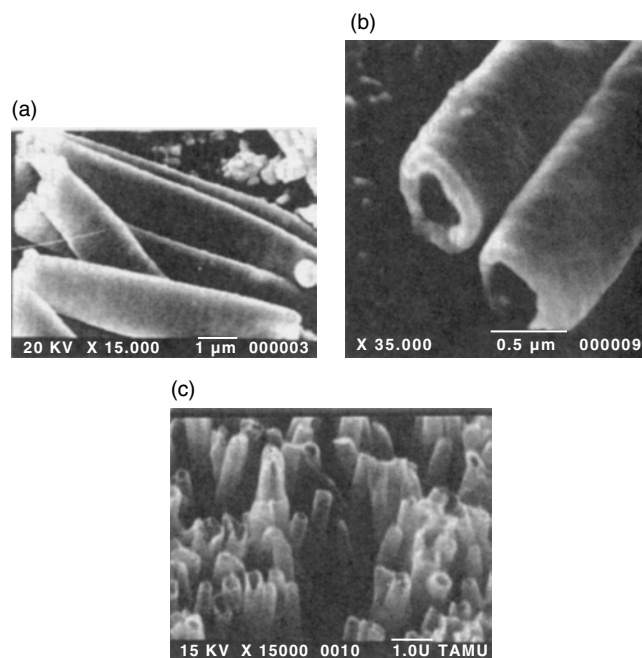
Figure 7. SEM images of chemically synthesized PPy nanotubules (a & b) and electrochemically synthesized poly (n-methyl pyrrole) microtubules (c). Reproduced with permission from [132], C. R. Martin et al., *J. Am. Chem. Soc.* 112, 8976 (1990). © 1990, American Chemical Society.

Table 3. Synthesis techniques and important properties of template synthesized conducting polymer nanocomposites.

Polymer used	Template/host	Synthesis technique	Nature of isolated polymer	Important properties/applications
PPy, PTh, and PAn	Porous membranes: nucleopore, milipore, Gore-Tex, polycarbonate, Al$_2$O$_3$, stainless steel mesh	Both chemical and electrochemical polymerization	Nanotubules with diameter of the membrane pores, variable thickness, and very high conductivity (up to 3000 S/cm)	1. High conductivity of composites (up to 50 S/cm) 2. Excellent nanotubules with uniform size and thickness 3. Promising for application in biosensor
PAn	Al$_2$O$_3$	Two-step synthesis; Chemical polymerization followed by electro-deposition	PAn nanotubules loaded with Fe or Co nanowires	1. Polymer envelope protects the metallic core from environmental effects 2. Highly promising vertical recording materials
PPy	Porous PMMA membrane	Chemical polymerization	Interconnecting tubules	1. PPy-PMMA IPN-like structure 2. High conductivity (0.05–19.86 S/cm)
PPy, PAn, and PTh	Polystyrene colloid film	Electro-polymerization	Macroporous solid film	1. Conductivity similar to bulk polymer 2. Easy mass transport and rapid switching
PPy and PAn	Porous Vycor glass	Chemical polymerization	Uniform rod-like tubules	No macroscopic conductivity (10^{-7}S/cm) indicating no polymer on surface
PAn	SiO$_2$ network from TEOS	Electro-polymerization	Tubules (not isolated)	Electrochemically identical to bulk polymer
PA, PTh, PPy, and PAn	Zeolites (Z-Y, MOR, MCM, ZSM-5, etc).	Mainly chemical polymerization, little electropolymerization	Tubules and wires	Isolated polymers are chemically identical to bulk polymers but shorter in chain length and poorer in conductivity

polymerization starts at the wall of the pores and therefore hollow polymeric tubules are formed at each end. Controlling the duration of polymerization, the length as well as the thickness of the tubules can be controlled. For poly(3-methyl thiophene) (P3MT), prolonged polymerization resulted in the growth of polymer tubules out of the membrane in spiral form; for PPy, on increasing the duration of polymerization, the thickness of the tubule is increased, ultimately resulting in a closed polymeric wire, while for PAn only the tubules are obtained which does not close. Nanotubules of PPy can form stable colloidal dispersion if the dissolution of the substrate can be done in the presence of any stabilizer/surfactant; such a report is also available using dimethyl sulphosuccinate (DMSS) as dispersant [135].

Confined growth of polymers under such template-guided polymerization results in highly ordered/oriented form—the same as is revealed from their high solid-state electrical conductivity. Despite their large insulating fraction, the composites show conductivity as high as 50 S/cm and the isolated tubules show exceptionally high value as 3000 S/cm. The value is higher for tubules with a narrower dimension, all of which can be attributed to enhancement in ordering of the tubules [136–138]. Martin et al. have suggested that the nanotubules consist of a highly ordered, thin outer layer surrounding a disordered inner part or core. The outer layer or skin is highly conductive while the core is less conductive. Therefore, in the narrow tubules (diameter ∼50 nm), the highly conductive fraction is larger resulting in its high conductivity. The effect of different experimental parameters on the nature and morphology of the polymeric nanotubules were also studied and reported by another group; interestingly, they have even measured the elastic modulus of the nanotubules [139–141]. The mechanism of electrical transport in these materials was also studied and will be discussed in proper context.

Template-guided synthesis of a conducting polymer turned to a new direction with novel application potential recently when a two-step synthesis technique was designed for a three-component hybrid material [142–144]. This can be considered as an extension of the earlier methods followed by Martin et al. and others. Conducting polymer PAn, PPy, etc. are synthesized within microporous Al_2O_3 membrane using a chemical polymerization route similar to earlier ones. The array of conducting polymeric tubules in an Al_2O_3 matrix is subjected to electrodeposition of different metals *viz.* Fe, Co, Ni, etc. covering one side by silver and using the Al_2O_3-ICP array as the working electrode. As a result, the metallic nanowires are grown within the polymeric nanotubules confined in the inorganic membrane. After dissolution of the outer membrane, metallic nanowires encapsulated in a polymeric envelope are obtained; these materials are expected to bring revolution to vertical recording materials.

The templates discussed so far present systems with uniform cylindrical pores, which ultimately produce conducting polymers with fibriller morphology. Variation in the structure of the template, on the other hand, can obviously bring some change in the ultimate morphology of the nanomaterial. There are reports of producing templates with interconnected pores so that ultimately the interconnected, polymeric nanotubules are obtained. Such template

membranes made of PMMA and Vycor glass were reported from two different research groups. In the PMMA, two porogens—NaCl and PEG—were incorporated as foreign materials following solution bending technique; after leaching out the porogens in proper solvent, the required porous membrane with open pore structure [145] is obtained. Porous Vycor glass (PVG) is obtained by acid leaching of a phase-separated borosilicate glass; the soluble borate phase is dissolved in acid, leaving an open porous structure with narrow pore size distribution (∼80 Å) and made up of almost pure silica. Mainly, chemical polymerization of aniline and pyrrole were done within such open porous membranes, which in the former case produced composites with conductivity as high as 19.86 S/cm [146, 147]. For PVG, the redox polymerization (initiated by pre-exchanged Cu^{2+}) takes place mainly within the pores leaving the PVG surface highly resistive (10^{-7} S/cm). These interconnecting polymers were not isolated, however, from the matrix which seems to be difficult also, owing to the complexity of the system.

It is here relevant to mention the work that produced a conducting polymer in macroporous form. Polystyrene latex having PS spheres with a diameter 0.5 μm and 0.75 μm was used to coat the working electrode of a cell prior to electropolymerization of aniline, pyrrole, and bithiophene. Polymers grow on the electrode leaving the PS spheres free, and completion of polymerization followed by dissolution of the PS matrix leaves the polymer in macroporous form with large voids. Conductivity of the macroporous polymer is similar to the bulk one, although the high surface area provides them improved mass transport ability and rapid switching. Another very relevant work was published recently which describes the fabrication of "PAn inverse opals" via templating colloidal PS assemblies [148]. Wet colloidal sediment of PS spheres (which spontaneously self-organize into different crystal structures, *e.g.*, cubic, FCC, BCC, etc.) with a diameter of 640 nm was used as the host template, the interstices of which were used as the submicrometer-sized reactor array. Aniline hydrochloride and $K_2S_2O_8$ solutions were subsequently infiltrated through the PS array at a constant speed to initiate the oxidation polymerization of aniline within the voids. Afterwards, the host was dissolved in THF in order to get the self-supported, specially designed 3D network of PAn specifically termed as "inverse opals." This synthesis is a truly chemical technique and a successful step towards formation of photonic bandgap (PBG) crystals. Very recently, the same group has reported electrochemical synthesis of inverse opals from PPy or PTh [149]. The principle of synthesis is very similar to the chemical technique, only the polymerization of pyrrole or thiophene within PS assembly was performed electrochemically. Electro-entrapment of PAn in sol–gel derived porous silica films (prepared from tetraethyl ortho-silicate +1,1,3,3, tetramethyl-1,3, diethoxy-disiloxane + methanol + HCl) was recently reported [150].

4.2. Intercalative Polymerization

It was mentioned earlier that a second stream of template-guided polymerization consists of intercalative polymerization that describes the confined growth of conducting polymers (chemical/electrochemical) within the layers/networks of naturally occurring 2-D or 3-D inorganic

materials. Depending upon the chemical nature of the host (oxidative or neutral), such polymerization can be grouped as RIP and PIP. Different inorganic hosts used for intercalative polymerization and the few important observations on this system have been tabulated in Table 4. Redox intercalative polymerization of aniline and pyrrole has been performed with only a few layered hosts having substantial oxidizing power *viz.* FeOCl, V_2O_5, and α-RuCl$_3$. As mentioned earlier, the system is based on chemical polymerization by exploiting oxidative properties of the host matrix. The stream of investigation was started around 1987 when Kanatzidis et al. were able to guide RIP of pyrrole within the van Der Walls gaps of FeOCl layers [151]. FeOCl is a layered solid having an interlayer gap of 7.98 Å, and upon intercalating variety of chemical species, namely, amines, erathiafulvalene, pyridine, etc., the interlayer distance is found to be increased [152]. This particular research group was able to intercalate each of PPy, PAn, and PTh in FeOCl with the simultaneous reduction of a fraction of Fe (III) as evidenced by the Maussbauer spectroscopy, and in each case the interlayer spacing was also increased to different extents as an evidence of intercalation. The synthesis technique is as simple as stirring the respective monomers (Py, An, Th) with FeOCl crystals, although

the other conditions like reaction temperature, solvent, duration of reaction, etc. are varied for different monomers. For example, stirring FeOCl with neat pyrrole at 60 °C leads to the formation of $(PPy)_{0.34}$FeOCl [151–153] while synthesis of $(PAn)_{0.20}$FeOCl needs stirring with 10% aniline (in acetonitrile) in the air for 1 week [154, 155]. Intercalation of polythiophene could be done in a similar way by stirring 2–2′ bithiophene with FeOCl in acetonitrile [152, 153]. In each case, the interlayer distance of FeOCl increased by 6.54 Å (PAn), 5.23 Å (PPy), and 5.33 Å (PTh), respectively. The crystal structure of FeOCl and the possible arrangement of PAn chains within this host has been shown in Figure 8 (I & II). Intercalation of polyfuran in FeOCl was done by stirring 2,2′,5′,2″ tetrafuran with FeOCl at 100 °C in methanol, and in this instance, the interlayer distance is increased by 7.7 Å. The order of electrical conductivity of these materials follows:

$$PFu_{0.67-0.75}FeOCl < PAn_{0.20}FeOCl < PPy_{0.34}FeOCl < PTh_{0.27}FeOCl$$

$$0.001 \text{ S/cm} \qquad 0.007 \text{ S/cm} \qquad 0.15 \text{ S/cm} \qquad 5.0 \text{ S/cm}$$

In each of these works the polymers synthesized under the confinement could be separated by dissolution of the host

Table 4. Composition and important properties of a few intercalative nanocomposites involving laminar hosts.

Inorganic host	Polymer used	$\Delta d^{\#}$ (°A)	Conductivity (S/cm)	Important information/remarks
FeOCl (RIP)	PPy	5.23	0.150	1. Monolayer intercalation with monomer units oriented perpendicular to crystal plane
	PAn	6.54	0.007	
	PTh	5.33	5.000	2. Profound effect of aerial oxygen, appearance of α- and β-phases
	PFu	7.70	10^{-4}–10^{-3}	
	PNMP*	5.84		
V_2O_5 (RIP)	PAn	5.1	10^{-4}–10	1. Formation of polymer monolayer
	PTh	5.95	0.1	2. Influence of aerial oxygen detected
V_2O_5 Dried gel (RIP)	PAPSA	Not clearly mentioned	10^{-4}–10^{-3}	Both water soluble and insoluble parts of composites are available with good film-forming character
VOPO$_4$ (RIP)	PAn	4.9	Not	Aniline intercalates and polymerizes while Pyrrole does not.
	PPy	2.1	mentioned	
	P3MP*	8.7		Pyrrole derivatives intercalate.
	P 3, 4, DMP*	9.7		
α-RuCl$_3$ (RIP)	PAn	6.2	2.0	1. Effect of aerial oxygen was observed.
	PPy	6.0	—	2. PPy is formed in highly defective form.
MMT (PIP)	PAn	5.3	5×10^{-2} (Cu^{2+}) 10^{-6}–10^{-3} (APS)	1. Fixing An$^+$ followed by exposure to APS or fixing Cu^{2+} followed by exposure to An$^+$.
	PPY	4.5–5.0	2×10^{-5} (Cu^{2+}) 1.2×10^{-2} (I$_2$)	2. I$_2$ encourages surface polymerization to some extent.
Porous silicon (PIP)	PAn		20–30Ω (resistance)	Electroentrapment of PAn within host layers Lowering of resistance by $\sim$20–25 times
α-ZrP (PIP)	PAn	7.6, 13.6	10^{-4}–10^{-3}	Monolayer and bi-layer formation is possible.
MoS$_2$	PPy	4.5	$\sim10^{-1}$	Monolayer formation occurring, polymer chains are not perpendicular.
	PAn	4.2		
MoO$_3$	PAn	6.8	5×10^{-3}–3×10^{-3}	1. Monolayer formation with retention of high crystallinity of host.
	PPV	5.6	0.5	2. Formation of H$^+$-doped PPV (conducting).

*PNMP: poly(N-methyl pyrrole); P3MP: poly(3-methyl pyrrole); P 3, 4 DMP: poly(3,4 dimethyl pyrrole).
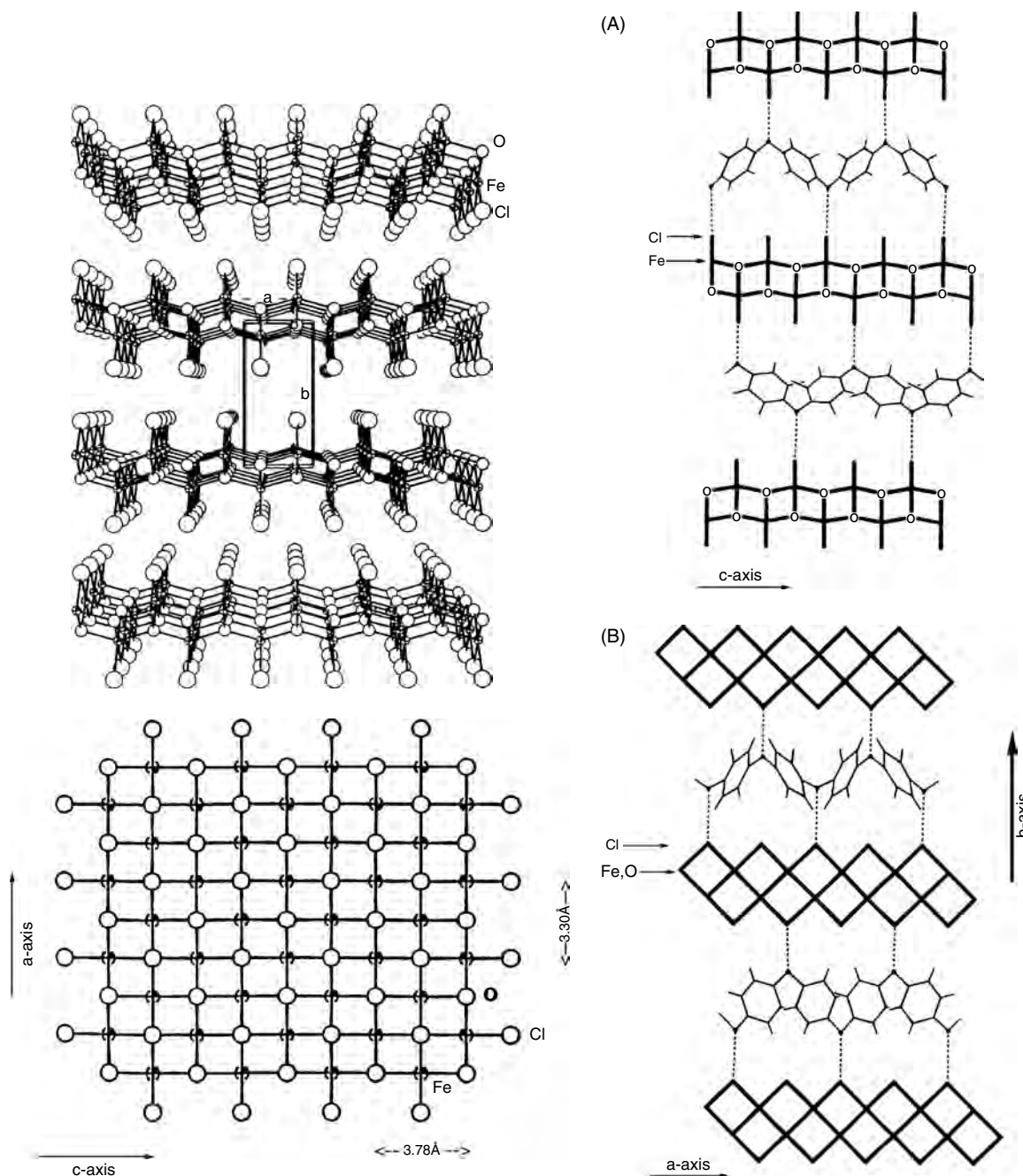$^{\#}\Delta$d: increase in d-spacing.

Figure 8. (I) Crystal structure of FeOCl. Top: view perpendicular to the b-axis (large open circles represent chlorine, small open circles represent oxygen, and crossed circles represent iron). Bottom: view down the b-axis. (II) Proposed arrangement of PAn chains in the galleries of FeOCl viewed from two different directions. Reproduced with permission from [155], C. G. Wu et al., *J. Am. Chem. Soc.* 117, 9229 (1995). © 1995, American Chemical Society.

and were found to be chemically identical to that of the bulk polymers [156] synthesized conventionally.

V_2O_5, nH_2O xerogels present a group of layered materials that have been extensively used for the synthesis of hybrid materials by intercalation of PAn, PPy, and PTh. The investigation was started in 1989 when the interaction of aniline with water-swollen V_2O_5, nH_2O films changed color from dark red to bluish black indicating intercalation of PAn by oxidative polymerization of aniline [157]. Subsequent characterizations have proved that the conductive form of PAn

was generated with simultaneous reduction of the host frame but without disrupting the structural features of the latter. This work opened the way to a series of works highlighting the mechanism of polymerization, orientation of the polymer chains, and the effect of different external parameters like aerial oxygen, etc. In almost all these nanocomposites (including the FeOCl systems), the aniline and pyrrole units of polymer chains are oriented perpendicular to the layer. In the V_2O_5 system, an interlayer expansion of 5.14 Å was observed and a pronounced effect of aerial oxygen was also

found [158, 159]. The intercalation of PTh within V_2O_5 layers was possible on refluxing solution of thiophene (in acetonitrile) with the host for 24 h; in this case, interlayer expansion of 5.95 Å was observed. $PTh-V_2O_5$ composites are highly conducting (0.1 S/cm), while that of $PAn-V_2O_5$ composites vary over a wide range (10^{-4}–1 S/cm) [160].

$VOPO_4$, $2H_2O$ presents another system having substantial oxidizing power and intercalating capability. This layered system has been used up in the formation of intercalative nanocomposites in combination with PAn and PPy [161, 162]. For PAn, it requires stirring with neat aniline for 1–5 days in the dark at a temperature range over 1–35 °C; aniline is intercalated and subsequently polymerized to anilinium cation (An^+) with the simultaneous reduction of V(V) to V(IV). On exposure of this An^+-loaded $VOPO_4$ to oxidizing agents like $CuCl_2$, aniline polymerizes and the ultimate nanocomposite is formed. Instead of aniline, if ethanolic solution of An^+ is taken initially, then intercalation and subsequent polymerization of aniline takes place with simultaneous reduction of V(V) and the formation of the nanocomposite. Interlayer distance increases by 4.9 Å on the intercalation of PAn which also indicates monolayer formation. Pyrrole itself, under the similar conditions, gives polymerization only on the surfaces of the host while 3-methyl and 3,4-dimethyl derivatives of pyrrole give an intercalative nanocomposite formation with an interlayer expansion of 8.7 Å and 9.7 Å, respectively [163–165].

α-$RuCl_3$ offers another layered system having interesting catalytic, photochemical, and magnetic properties. This system was capable of undergoing RIP of aniline and forming $PAn/RuCl_3$ nanocomposite on stirring α-$RuCl_3$-aniline mixture in acetonitrile for 1 week in open air [166]. For PPy intercalation, to an aqueous suspension of pyrrole and Li_xRuCl_3, $FeCl_3$ solution is added dropwise to complete polymerization. Conductivity of PAn-α-$RuCl_3$ is 2.0 S/cm, while PPy formed under this condition is highly defective and almost insulating [167].

From the discussion on nanocomposite formation by the RIP method, it is obvious that the host material should possess sufficient redox activity to initiate the oxidative polymerization of the conducting polymer. Therefore, structured hosts not having oxidative property are incapable of taking part in nanocomposite formation in this technique. However, a large variety of such hosts including the oxides, silicates, phosphates, dichalcogenides, etc. has been utilized for nanocomposite formation by using suitable oxidants (for polymerization). This technique suggests intercalation of the monomer within interlayer spaces of the host by adsorption or ion exchange, etc. followed by exposure of the entire thing to oxidants: The total scheme is properly termed as PIP.

The inorganic host materials used for confinement of conducting polymers following the PIP method can be divided into two groups depending on whether it is two dimensional (2-D) or three dimensional (3-D). Two-dimensional hosts encompass a large variety of materials viz. the natural and synthetic silicates, phosphates, oxides, sulphides, etc. while 3-D hosts are mainly different zeolites and only a few coordination polymers and inclusion compounds. Among the layered silicates, the most extensively used are montmorillonite (MMT) and hectorite. All these clays contain a large number of hydrated cations in their interlayer space which are exchangeable with metal ion or organic cations, which is the key to the intercalation as well as polymerization of aniline, pyrrole, etc. This series of work was started with inclusion of PPy within MMT exchanged with Cu^{2+}. This report was published in the Ph.D. thesis of Van de Poel in 1975 when conducting polymers themselves were yet to be discovered properly [168]. This work was followed by a similar work describing the synthesis of $PAn-MMT-Cu^{2+}$ from aqueous aniline solution [169]. Polymerization of aniline or pyrrole in these materials is achieved at the cost of reduction of exchanged Cu^{2+} ions. Later on, there were numerous works regarding the synthesis and characterization of PAn or PPy intercalated, MMT-based nanocomposites [170–174]. The general synthesis technique of these materials can be described by a two-step process; at first, MMT containing metal ions like Na^+, Cs^+, etc. (having no oxidizing power) is exchanged with monomer cations in order to fix them onto the host, followed by their exposure to oxidants like APS or $FeCl_3$. Interlayer expansion of 5.3 Å for PAn-MMT and 4.5–5.0 Å for PPy-MMT were observed. As the conducting polymer fraction is mainly in the interlayer places, macroscopic conductivity of some of these composites is as low as 10^{-6} S/cm. All these composites are highly anisotropic in nature and maximum anisotropy as high as 10^5 was observed. The polymer confined in MMT layers is analytically identical to the bulk polymer, although few properties like molecular weight, dc conductivity, etc. are strongly dependent on different experimental parameters.

Montmorillonite is a layered silicate having very high swelling ability suitable for intercalation of polymers with bulky dopants. This capability has been utilized in intercalation of PAn having dopants like DBSA, camphor sulphonic acid (CSA), etc. following solution/emulsion polymerization of aniline in the presence of MMT [175–178]. On the other hand, some preformed colloids of PPy and PTh could also be intercalated into MMT simply by mixing the preformed latexes with the clay [179–185]. In a few experiments, electropolymerization of aniline has been followed for the synthesis of nanocomposite based on MMT or PS layers [186]. All these materials were explored from different aspects and important physical properties were observed.

Phosphates of different transition metals viz. Zr, Ti, Sn, U, etc. offer a large variety of layered materials which were extensively used for intercalative polymerization. Techniques of polymerization can be broadly classified into two main categories: either the monomer cation is fixed onto the host by cation exchange followed by exposure to oxidants or an oxidative cation (e.g., Fe^{3+}) is fixed by cation exchange followed by exposure to the monomer. α- and γ-zirconium phosphates (ZrP) [187, 188] and some of their organo derivatives (ZPS) [189] present layered systems with exchangeable hydrogen, which are first exchanged with NaOH or NaCl to form Na-derivatives of ZrP. The latter can then be exchanged with aniline to fix the same in ZrP. Then the aniline-loaded ZrP is exposed to APS or $FeCl_3$ in order to polymerize aniline within the matrix. It is interesting to note that aniline forms mono- and bi-layers in α-ZrP and after intercalation of the aniline interlayer, spacing increased by 6 Å. After dissolution of the host in HF, the PAn separated is similar to emeraldine salt and emeraldine base, respectively, within layers of ZrP(H) and

ZrP(Na) and electrical conductivity around 10^{-1} S/cm. The composites prepared with ZrP(H) are moderately conductive (10^{-4}–10^{-3} S/cm), but those with ZrP(Na) have poorer conductivity. Nanocomposites with ZPS (S indicates –SO$_3$H group) possess higher conductivity (0.1–4.2 S/cm) because of more efficient protonation with acidic H$^+$.

Tin (IV) phosphonates (SnP-C) also offer a layered host system with exchangeable acidic protons and have therefore been used for intercalation of aniline [190–192]. However, with this host, the fixation of Fe^{3+} prior to exposure to aniline was extensively followed and nanocomposites with poor conductivity (10^{-9} S/cm) were obtained, which indicates that PAn was formed only in the interlayer spaces. When α-tin bis (hydrogen phosphate monohydrate), Sn(HPO$_4$)$_2$, H$_2$O (α-SnP) is used as the host ($d = 7.89$ Å), the synthesis technique does not work well with prefixation of Fe^{3+} and fixation of aniline followed by exposure to APS+HCl gives a better result. α-SnP was also used to form a nanocomposite with PPy when it was exposed to pyrrole after being exchanged with Cu^{2+}. Electrical conductivity of these composites were not reported, although they were proven to have less branching/crosslinking as revealed by cyclic voltammetry (CV). In a parallel synthesis route, some layered hosts *viz.* α-Zr (HOPO$_3$)$_2$, α-Ti (HOPO$_3$)$_2$, H$_2$O and HUPO$_2$PO$_4$, 4H$_2$O (HUP) [193, 194] were combined with aniline using the help of aerial oxidation. The hosts were shaken with aniline and left in the air for the polymer to form. Composites formed in such a way are poorly conducting because of complete intercalation of polyaniline and the range of conductivity is within 10^{-5}–10^{-1} S/cm.

Molybdenum-based, layered compounds *viz.* MoS$_2$ and MoO$_3$ have been extensively used for intercalation of conducting polymers like PPy, PAn, and PPV. The interesting thing about MoS$_2$ was that it was earlier used for intercalation of only the highly reducing alkali metals and not the organic molecules. But it could be successfully used to intercalate PAn (from NMP solution) and PPy (by sequencial addition of pyrrole and FeCl$_3$ to the aqueous dispersion of MoS$_2$) to form single-phase hybrid materials [195, 196]. For PAn intercalation, an interlayer expansion of 4.2 Å is observed, while the same is 4.5 Å for PPy incorporation. Both these values are in pace with the dimension of the monolayer of PAn and PPy. Both these materials are highly conducting, the absolute value going to $\sim10^{-1}$ S/cm. The FTIR spectrum of the PPy-MoS$_2$ system shows a blue shift of ~10 cm^{-1}, which indicates that the molecular weight of PPy grown under such restricted conditions is lower than the bulk polymer.

MoO$_3$ presents a highly crystalline system having the potential application as an electrode in high-energy, density rechargeable Li batteries. This property has been successfully combined with electrical conductivity of PAn and PPV giving rise to a series of hybrid materials. The synthesis technique is the most conventional one as described earlier. MoO$_3$ solid was shaken with aniline and the An-MoO$_3$ was subsequently exposed to APS or FeCl$_3$ solution so that the aniline polymerizes and the dark green solid is formed [197, 198]. After dissolution of the host framework (in NaOH), the molecular weight of the PAn was found to be lower than the bulk. Conductivity of this system could be measured from polycrystalline thin films rather than pressed

pellets; the range of conductivity was found to be 10^{-4} to 10^{-3} S/cm. Formation of a PAn-MoO$_3$ nanocomposite and the arrangement of PAn chains within the MoO$_3$ layers is shown in Figure 9 (I & II). The interlayer expansion in PAn-MoO$_3$ is 6.8 Å, which is in agreement with the orientation of PAn rings perpendicular to MoO$_3$ layers. However, the PAn chains are lying parallel to each other in the troughs or valleys of the oxide sheets so that the incorporation of PAn does not hamper the crystallinity of MoO$_3$.

PPV is a highly conducting polymer that does not undergo oxidative polymerization. This polymer has been intercalated in MoO$_3$ framework using indirect technique, incorporation of the precursor poly (p-xylene-α-dimethyl sulphonium chloride), followed by the elimination of HCl and S(CH$_3$)$_2$ by heating. An interlayer expansion of 5.6 Å was observed and the sample shows a unique high conductivity ~0.5 S/cm,
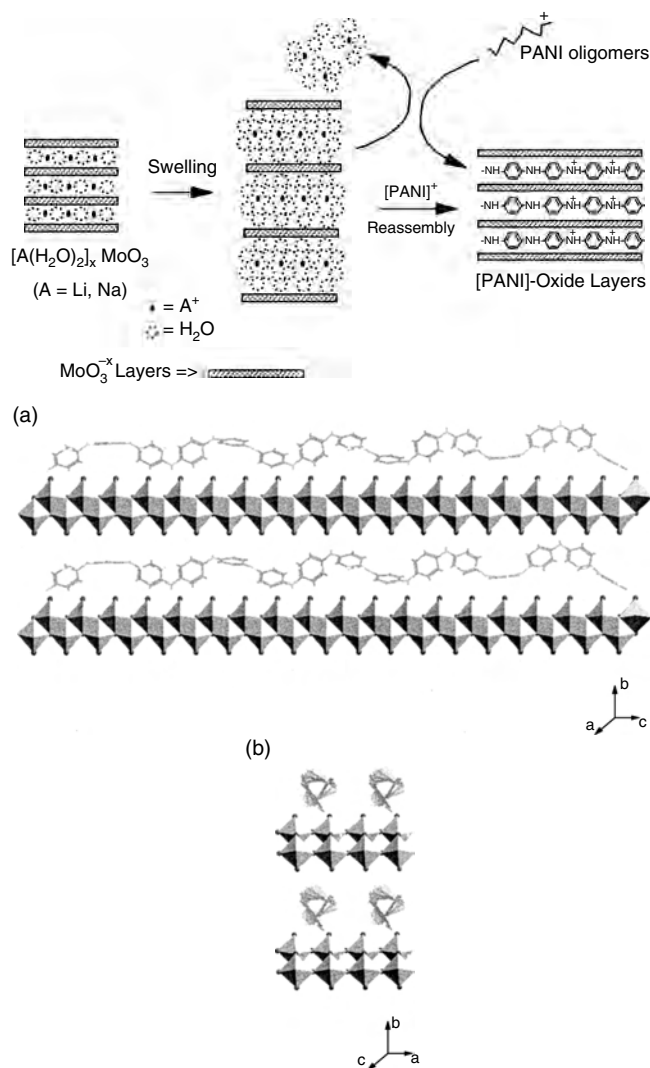

Figure 9. (I) Schematic diagram of the synthesis of (PAn)$_{0.24}$MoO$_3$: swelling and reassembly of MoO$_3$ layers. (II) Possible ordering of PAn chains in every other "trough" of MoO$_3$ lattice: (a) view along [100], and (b) view along [001]. Reproduced with permission from [198], T. A. Kerr, H. Wu, and L. F. Nazar, *Chem. Mater.* 8, 2005 (1996). © 1996, American Chemical Society.

which indicates that PPV is present in a highly doped form [199, 200].

All these examples discussed thus far relate to the confinement of conducting polymers within layered solids. But the synthesis of nanotubules or nanowires is most likely to take place within cylindrical or tubular pores which is available in some naturally occurring 3-D systems like zeolites. Zeolites are crystalline, aluminosilicate lattices formed from adjoining SiO_4 and AlO_4 tetrahedral building units which have given rise to open pores, voids, and channels in their structure. The pores and channels may have different shape and orientation and their size can vary from a few angstroms to ~20 Å. Versatile structural features are shown by the zeolites and depending upon their structure and chemical composition, physical properties are also varied [201, 202]. Zeolites are the only 3-D framework that have been extensively used as templates for growing conducting polymers, especially polyacetylene (PA) in nanoscopic form. The beginning of this stream of investigation dates back to 1978 when one research group reported the formation of PA within the channels of zeolite-X (Z-X) and studied the influence of exchangeable cations on the system [203]. Later on, different research groups have reported intercalation of PA in different zeolites *viz.* Y-, L-, A-, Ω-, ZSM-5, SAPO-5, Mordenite (M), etc.

The protonated form of ZSM-5, that is, H-ZSM-5 is a highly acidic zeolite capable of initiating cationic polymerization of acetylene. However, acetylene, being a gaseous one, the monomer loading in the host should be done at a high temperature (298 K to 550 K) under high pressure (10 torr to 1000 torr) [204]. Polyacetylene fills up the pores of zeolite and a color change from white or light gray to black or dark gray is observed. Methyl acetylene (MA) can be similarly polymerized within H-ZSM-5 and both the PA- and PMA-rich zeolite can show reversible change of color with exposure to NH_3. A comparative study on polymerization and spectroscopic properties of PA and its derivatives (methyl and ethyl) in H-ZSM-5 has been published by a contemporary research group [205]. Z-Y exchanged with Co and Ni has also been used for intercalative polymerization of acetylene [206].

This very attractive field of research has been very regularly cultivated by Bein and Enzel [207]. Over a period of few years, they have attempted polymerization of pyrrole, aniline, thiophene, and a few other monomers within different zeolite structures, producing a series of hybrid materials with versatile importance. The general technique followed for confining conducting polymers within zeolite spaces is a two-step one. At first, Na ions of the zeolite are exchanged with an oxidizing cation, for example, Cu^{2+}, Fe^{3+}, etc. followed by subsequent drying and exposure of the zeolite to monomer vapor or solution. Polymerization proceeds spontaneously and the nanocomposite is formed *in-situ*. Z-Y, Z-A, and M were the most widely used matrices for this purpose. Na^+ of these hosts are first exchanged with Cu^{2+} (from a $Cu(NO_3)_2$ solution) and subsequently equilibrated with pyrrole vapor (1 torr) for 1 h at 295 K and placed in a vacuum for 1 h. The yellowish or greenish color of zeolites gradually changes to different shades of green and black with the progress of polymerization. The Fe (III) form of zeolites could be used similarly but the monomer is to be

fed from solution instead of vapor. The polymer essentially forms in interstitial spaces rather than on the surfaces. That is why electrical conductivity values of these samples are as low as almost 10^{-9} S/cm, although the PPy isolated from these composites have conductivity around 10^{-4} S/cm. For the same reason, Z-A having a pore diameter less than a PPy chain cannot host the PPy. Isolated PPy is structurally similar to the bulk polymer, only the molecular weight is substantially lower which accounts for its poor conductivity. Later on, H-Fe-FAU was also used for PPy intercalation following an almost identical technique. L-Z is another form of zeolite that possesses parallel channels leading to one-dimensional growth of PPy [208–212]. Pd and SnO_2 were deposited randomly within the channels of the zeolite, which in the following step acted as an initiator for pyrrole polymerization [213]. Polymerization of thiophene and furfural could be done following similar techniques and almost similar results were obtained [210–211, 214–215]. The bulk conductivity of PTh-Z composite was too low to be reported, but the isolated PTh has shown a conductivity value of 0.01 S/cm. The effect of chain length played an important role in this respect also, and PTh confined in Pentasil-Z was found to vary from two to nine molecular units [215]. On the other hand, the pore size of Z-A was too low to allow PTh formation to take place inside.

Intercalation of PAn within zeolite is a bit different from that of PPy and PTh, because of the necessity of the presence of acidic medium during polymerization. However, it was possible to intercalate PAn in Z-Y, MOR, MCM-4, Halloysite, and a few other zeolites [216–220]. The synthesis technique is very similar to the PIP in nonoxidizing hosts; aniline or anilinium cation is adsorbed into the host followed by exposure to APS. The acid form of zeolite (Na^+ exchanged with H^+), however, is essential for the initiation of polymerization of aniline, and the acidic protons of zeolite can provide sufficient acidity for the formation of a green colored-emeraldine salt form of PAn. Other aspects of the synthesis of PAn-Z nanocomposite are similar to those of PPy-Z or PTh-Z; different properties of the isolated polymer are identical to bulk PAn although the chain length is much shorter. Bulk conductivity of the composite is as low as 10^{-8} S/cm and volume conductivity of the isolated PAn is as high as 10^{-2} S/cm, which indicates the formation of a polymer in interstitial spaces rather than on a surface. Interestingly, the chain length of PAn in Z-Y (six units) is shorter than that formed in interstitial spaces of MMT (15 units), which can be considered as limitation imposed by a 3-D network. In MCM-41 PAn chains with, several hundred units of length were obtained and around 20 PAn wires were found to exist together within a single pore [218].

There is a single report on electrochemical polymerization of aniline within Z-Y. This approach, is different from general electrochemical intercalation of PAn in a nonoxidizing host as described earlier. Here, the zeolite moiety is used as the solvent of the monomer rather than the host. Na-form of Z-Y was exchanged with aniline hydrochloride for 12 h to immobilize the aniline on the zeolite bed followed by filtration and washing. The working electrode (Pt) of the conventional electrochemical cell was then coated with aniline-loaded Z-Y from suspension in

THF using polystyrene as a binder [219]. Electropolymerization under a potentiodynamic condition was carried out in a 0.1 M HCl medium leading to an ordered growth of PAn within zeolite. Therefore, the monomer here is present only within the zeolite host, which is the novelty of the system. However, the amount of polymer synthesized under such conditions is too small to carry out further characterizations. In a recent report, intercalative polymerization of aniline in a Cu^{2+} exchanged natural zeolite named Halloysite has been published [220]. This host possesses a spiral cross-section and relatively thin walls, which did not affect the intercalation and polymerization, and a high resistance of composite again reveals complete intercalation of PAn.

Therefore, confinement of conducting polymers within different oxidizing/nonoxidizing 2-D and 3-D hosts has given birth to a variety of hybrid nanocomposites from which the polymer can be separated in nanostructured form. The stream of investigation is still alive and versatile modifications are in progress. It has already been mentioned that the quest for getting conducting polymers in nanostructured form has primarily led the scientists towards the nanostructured hybrid materials or nanocomposites. However, after the dissolution of the template, the chance of undesired aggregation remains, which very often disturbs the important characterizations of the nanodimensional polymer. Keeping this point in view, the nature of the template has gradually changed during this time and, recently, some molecular templates have become very popular providing very accurate nanoscale control over the conducting polymer. β-cyclodextrin (CD), having a basket-like structure, has been selected as a molecular template for both chemical and electrochemical growth of PAn and PPy nanowires [221, 222]. The template molecule provides some cavities for the pseudo, one-dimensional growth of the polymer ~10 nm in diameter and a few μm long. Electrical conductivity of the polymer is enhanced compared to the bulk polymer.

4.3. Template-Free Synthesis

Very recently, techniques for template-free synthesis of conducting polymers has also been published which describes direct-and single-step synthesis of ICP nanotubules, nanowires, etc. The stream was almost pioneered by Langer and Czajkowski, who have electrochemically synthesized PAn micro-and nano-rods following a novel technique [223, 224]. A movable Ir or Pt needle with a tip less than 10^{-2} mm was used as the working electrode in their work. After commencement of the polymerization, the electrode is slowly moved out of the reaction area so that the PAn is deposited on the PAn electrode only and the PAn microrod grows. Electrochemical synthesis of a single nanofibrillar and giant microfibrillar form of PAn, doped by fullerene derivatives, have been reported by Langer et al., which is one of the pioneering works in this direction [225, 226]. By suitable modification of the synthesis technique, a compact 3-D nano-network array could also be prepared. Later on, chemical synthesis of PAn nanotubules has been described by Dai et al. [227] and Wan et al. [228–230] who have used both fullerene derivatives and naphthalene sulphonic acid (NSA) derivatives for chemical synthesis of

PAn micro- and nanotubules (Fig. 10). The most conventional oxidizing agent, APS, was used for polymerizing aniline in these works. PPy microtubules were also prepared by the polymerization of pyrrole in the presence of β-NSA using APS as an oxidizing agent; controlling the concentration of NSA, the morphology of PPy could be altered from particles to fibers and tubules. Therefore, selection of a particular concentration of NSA was the key to synthesize PPy nanostructures in the present template-free method. Electrochemical synthesis of PPy microtubules (0.8–2.0 μm diameter and 15–30 μM length) could also be performed in the presence of β-NSA; electrical conductivity of chemically and electrochemically prepared microtubules are comparable (1–10 S/cm). Electrochemical deposition of PAn as concentric nanowire within multiwalled carbon nanotube (MWCNT) has been reported by Hassanien et al. [231]. However, the simplest self-formation of PPy microtubules has been published recently; electrochemical polymerization of pyrrole in the presence of Na-p-toluene sulphonate
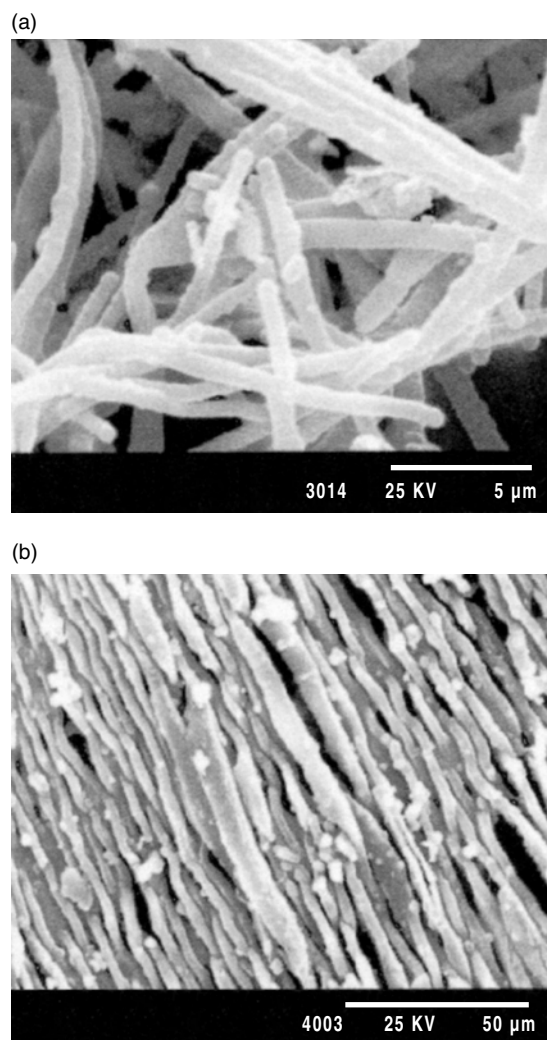
(a)

(b)

Figure 10. Growth of PPy-β-NSA nanotubules on noncorrosive steel electrode, (a) nonpolished electrode, and (b) polished electrode. Reproduced with permission from [229], Y. Yang and M. Wan, *J. Mater. Chem.* 11, 2022 (2001). © 2001, RCS.

(NaPTS) resulted in the formation of hollow tubules of PPy a few mm in length and several hundred μm in diameter [232]. These tubules are grown on the surface of simultaneously grown PPy film and are strong enough to tolerate free movement along Pt wire. These tubules are highly conducting (498 S/cm) and conductivity is extremely anisotropic (conductivity ratio 10^3 and 10^5 along two different planes). There is another report that describes spontaneous formation of tubular nanostructures of PAn through self-assembly in the presence of azobenzenesulphonic acid (ABSA) [233]. Therefore, synthesis of conducting polymer nanomaterials is easier and cheaper after the advent of template-free techniques; these technique are expected to bring revolution to the world of ICP nanomaterials.

5. MONOLAYERS AND THIN FILMS

Remembering the level of intractability of conducting polymers, it need not explain that it is highly difficult to obtain such polymers in thin film or monolayer form. However, considering the importance of highly organized and specifically arranged forms of conducting polymers in molecule-based electronic devices, there have been continuous efforts toward obtaining thin films of conducting polymers. Special interest was gathered on PAn owing to its low cost, easy preparation, environmental stability, and electronic properties. PTh has also been appreciably studied, while PPy is the least explored one in this respect. Two techniques are mainly applied here, one of which is the self-assembly and another is the Langmuir–Blodgett (LB) technique.

5.1. Langmuir–Blodgett Technique

Langmuir–Blodgett (LB) technique is a highly established technique for preparation of ultra-thin organic films as it offers unique control over the thickness and molecular orientation of the films. Fabrication of thin films following LB technique requires a very particular instrumental set-up and at the same time the polymer should have good solubility and amphiphilic nature. The principle is to dissolve the material of interest in a suitable solvent and to spread the solution onto the water surface as a monolayer [234, 235]. Owing to the lack of processability and amphiphilicity of conducting polymers, preparation of LB films from ICP has become highly restricted. Over the last few years, however, there were some successful molecular engineering approaches for obtaining the same. Such techniques include derivatization of the polymer with long alkyl chains, doping with an amphiphilic dopant, and co-LB deposition along with typical film forming materials [236–240]. This technique for thin film deposition has almost exclusively utilized PAn, while PTh was also used in a few examples but PPy is not used till now. In most of the works on LB film of PAn, the polymer is initially synthesized in a conventional technique, dedoped, and solvated in NMP [241] or NMP-CHCl$_3$ mixture [242, 243] (following its limited solubility in these solvents), the solution is then used for film formation following the established techniques. Few surface active amphiphilic molecules like stearic acid [237], cadmium stearate, cadmium arachidate, etc. [238, 240] were used as codeposition materials expected to improve the structural order of the polymeric film. In other streams of

work, PAn is derivatized with acid like camphor sulphonic acid (CSA), dodecylbenzene sulhonic acid (DBSA), toluene sulphonic acid (TSA), etc. [244] in order to improve the solubility of PAn in organic solvents like CHCl$_3$, and to use the solution for fabrication of LB film. For PTh, the work is easier because 3-alkyl detivatives of PTh have good solubility in CHCl$_3$ and some other organic solvents. Therefore the formation of PTh monolayers from CHCl$_3$ solutions by LB technique, sometimes using surface active agents like cadmium stearate, etc., is available in the literature [245–247]. All these monolayers were characterized from their structural and electrochemical aspects and their material properties were revealed. Spontaneous folding of an especially designed PTh monolayer to the corresponding nanowire was also reported in an excellent publication [248].

5.2. Self-Assembly Technique

The second method exploits the self-assembled monolayers (SAMs) of a support material as a template for the patterned growth of ICP thin films. This technique, in principle, is nothing but selective deposition of conducting polymers on some especially modified surfaces. For example, in related work, a glass surface was modified with patterned SAM of octadecyltrichlorosilane (OTS) following sophisticated techniques [249]. Afterwards, the surface was immersed in a solution of FeCl$_3$, followed by the addition of pyrrole, and PPy film grows on the modified surface with good adhesive property. For aniline, the addition of reactants was in reversed order—aniline followed by APS— although the result was the same. In another work published from the same group, PAn-NMP solution has been used for the formation of a patterned surface of PAn using a polymeric template [250]. The procedure is shown in Figure 11. In a related work, the glass surface was modified with a sulphonate group so that anilinium ions are selectively deposited on the surface followed by exposure to APS and the formation of a monolayer of polyaniline [251]. There is a single publication describing an sophisticated method for formation of PAn monolayers on the lattice-matched surface of Moscovite Mica, one special type of a phyllosilicate host matrix, having good lattice matching with the growth of PAn [252]. Although the synthesis technique is as simple as *in-situ* polymerization of aniline in the presence of a freshly cleaved mica sample, it provides the complete alignment of PAn chains relative to each other and also to the substrate. This work is similar to the intercalative polymerization of PAn within different oxidative/nonoxidative layered hosts discussed earlier; however, the complete alignment of PAn chains have given the work a new dimension. Overall, the synthesis of conducting a polymer-based monolayer or thin film is still confined in a few techniques and there is ample scope of exploring the stream of work in depth.

6. CONDUCTION MECHANISM IN INHERENTLY CONDUCTING POLYMER (ICP) NANOMATERIALS

From the foregoing discussions about conducting polymer-based nanomaterials of versatile origin, it is now established that the conducting polymers present in the hybrid
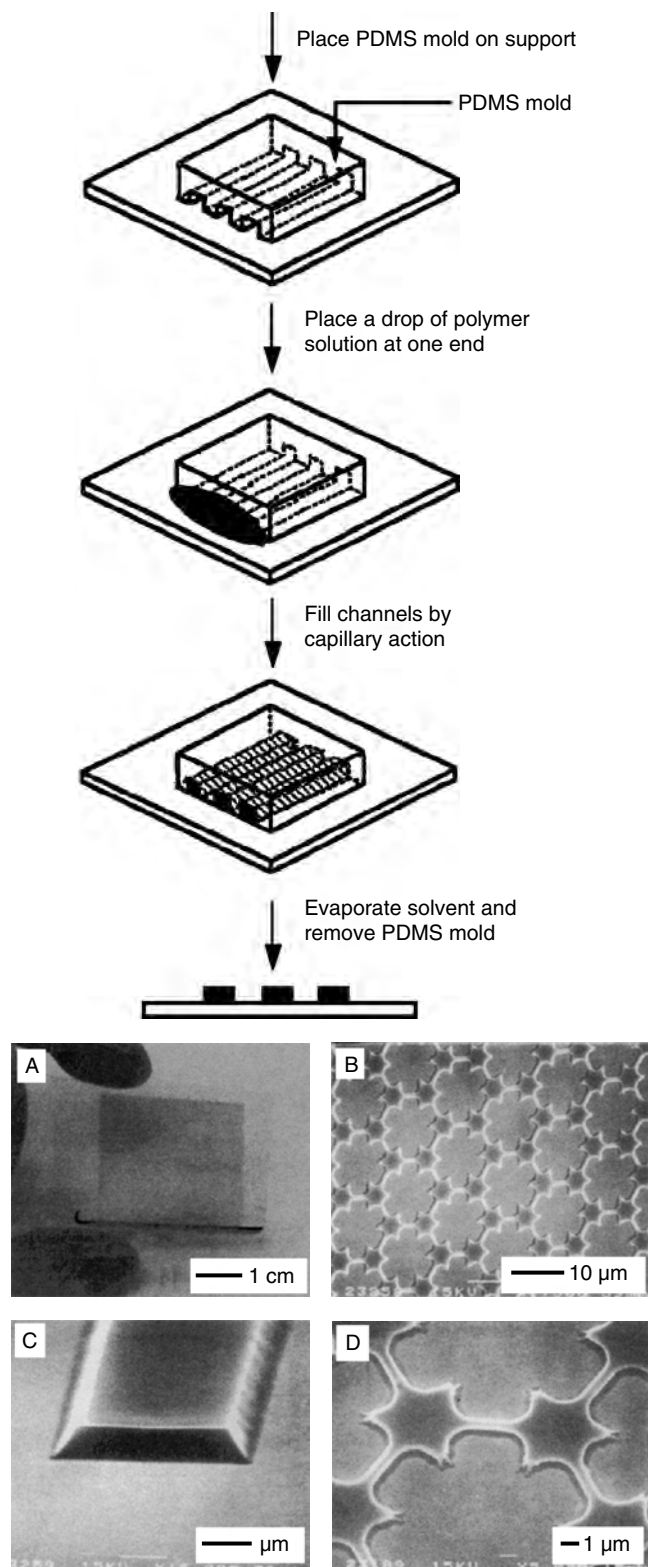
Figure 11. (I) Schematic diagram for the formation of patterned microstructures of PAn (EB) by MIMIC (II) A. Photograph of parallel lines of PAn-ES formed on polyester film using MIMIC, B, C, D. SEM images of PAn-ES structures formed on Si-SiO$_2$ using MIMIC. Reproduced with permission from [250], W. S. Beh et al., *Adv. Mater.* 11, 1038 (1999). © 1999, Wiley-VCH.

nanocomposites or the polymers synthesized under a template-guided, synthesis technique possess some structural and physical differences from their bulk counterpart. These polymers, however, are analytically identical to the latter. Whether the confined growth has some effect on the electrical conduction mechanism of the nanodimensional polymers is a subject of very elaborate study. Thus for, this field has been cultivated only to a limited extent, results of which will be presented here briefly. For the sake of convenience of discussion of this part, ICP nanomaterials are grouped into two categories: the template-guided, nanodimensional polymers, separated from the template (nanotubules, nanowires, etc.) and the template-polymer assembly as a whole (ICP-inorganic nanoparticles, ICP-layered solids, etc.).

Before entering into categorized discussions it should be mentioned that the important model commonly applied for 1-D, 2-D, and 3-D conduction in solids is the Mott's variable range hopping (MVRH) theory [253]. According to this model temperature (T), dependence of electronic conductivity (σ) of a system is given by

$$\sigma = K_0 T^{-1/2} \exp[-(T_0/T)^{1/n}]$$

where K_0 and T_0 are constants and $n = 4, 3$, and 2 for 3-D, 2-D, and 1-D conduction, respectively. According to this theory, resistance (R) of a conducting polymer-based material can be analyzed from the plot of ln ($RT^{-1/2}$) vs $T^{-1/n}$. The value of "n" can be obtained from the fitting of the plot which indicates the dimensionality of the conduction. The Mott temperature parameter T_0 is directly proportional to the density of states at Fermi level and is inversely proportional to the localization length.

Carrying out the temperature-dependent conductivity measurements and analyzing the results with appropriate fitting with the MVRH model, it was found that for PPy and PAn tubules with a 400 nm diameter, 3-D electronic conduction is taking place (considering $T^{-1/4}$ dependence) [254]. Also for the bulk polymers synthesized under conventional chemical synthesis, the same conduction mechanism is prevailing. However, for the tubules with a 50 nm diameter, the conduction is predominantly 2-D because of the $T^{-1/3}$ dependence of the model equation [255]. Similar dimesnsionality of conduction was observed for the amorphous semiconductors also. For the semiconductors, the authors have suggested that when the film thickness becomes larger relative to the hopping distance, 3-D conduction takes place while film thickness being relatively smaller than the hopping distance, the conduction is constrained to two dimensions. An analogous argument is applied for the nanostructures. It can be recalled that nanotubules consist of a highly ordered, thinner outer layer (~5 nm) surrounding a relatively disordered core. For smaller diameter tubules, owing to the lager proportion of the ordered material, conduction is constrained to the layer and 2-D conduction is occurring; conversely, for larger diameter tubules, the conduction in a disordered phase predominates and the 3-D conduction takes place.

Intercalative nanocomposites in which PAn and PPy are confined within different 2-D and 3-D hosts like FeOCl, V$_2$O$_5$, MoO$_3$, etc. were widely investigated, with respect to their electrical transport properties using variable temperature electrical conductivity and thermoelectric power (TEP)

as probes. It can be recalled that these nanocomposites are two types: one containing FeOCl, V_2O_5, and α-RuCl$_3$ hosts that are synthesized by the RIP method and others that are synthesized by the PIP method using nonoxidizing hosts like MoO_3, MoS_2, ZrP, zeolites, etc. Normally, the electrical conductivity of the hybrid materials is poor and very often are completely insulating ($>10^{-7}$ S/cm) which can account for the lack of interpolymer contact in the composite or complete encapsulation of the polymer within the layers of the host. On the other hand, conductivity of the polymers extracted from the composite is generally lower than those synthesized by conventional technique; a smaller chain length of the polymers synthesized under confinement is the reason for that. All these hybrid materials are highly anisotropic which confirms their specific orientation. Conductivity measurements were done on PPy-FeOCl (which itself has relatively high conductivity, 10^{-1} S/cm) [151], α- and β- PAn-FeOCl (10^{-2}–10^{-3} S/cm), and PTh-FeOCl, all of which have shown thermally activated-type conductivity suggesting the materials to be semiconductors [151, 153–156]. However, all these materials possess grain boundary and, therefore, TEP is a more reliable probe to decide the nature of conduction. PPy-FeOCl and PTh-FeOCl along with bulk PPy and PAn (ES) show p-type metallic conduction. For PPy-FeOCl, the TEP is positive at 260 °C and falls steadily at lower temperatures and ultimately becomes negative below 340 K, indicating valence band to conduction-band carrier excitation within FeOCl framework becoming increasingly important. But TEP measurement on an α-(I) form of PAn-FeOCl both in single crystal and pressed pellet form shows p-type semiconducting nature with TEP ~ 7 μV/K at room temperature, increasing steadily with lowering temperatures reaching a value 100 μV/K at 140 K [153–155]. Therefore, in α-(I) PAn-FeOCl, the reduced FeOCl framework, rather than the PAn component, dominates the charge transport properties of the system. Short-chain PAn molecules in the interlayer space give rise to too many carrier-hopping barriers and lead the charge transport possibly through the FeOCl layers which accounts for this result. Thermoelectric power of β-PAn-FeOCl is dramatically changed and a change in the conduction mechanism from p-type to n-type is observed which is similar to bulk PAn. Therefore, the β-phase is considered a mixture of PAn and β-FeCOOH which is mainly owing to the higher chain length of PAn in β-phase.

Temperature-dependent (5–300 K) conductivity measurement on polyaniline-V_2O_5, H_2O suggests thermally activated behavior. A representative curve showing the variation of electrical conductivity (four probe) as a function of temperature is shown in Figure 12. Thermoelectric power data at the same temperature range is small and negative (~ -30 μV/K), which approaches 0 with an increasing temperature indicating (Fig. 13) the presence of a metallic density of states similar to PAn itself. PAn-V_2O_5 hybrid material is a combined system with two low-dimensional electrical conductors presenting two types of carriers—the small polarons (V^{4+}) and the large polarons (on PAn backbone). Films of PAn-V_2O_5 possess 100–1000 times higher conductivity than the pressed pellets [157–159]. On temperature-dependent conductivity measurement all samples show semiconducting nature and thermally activated
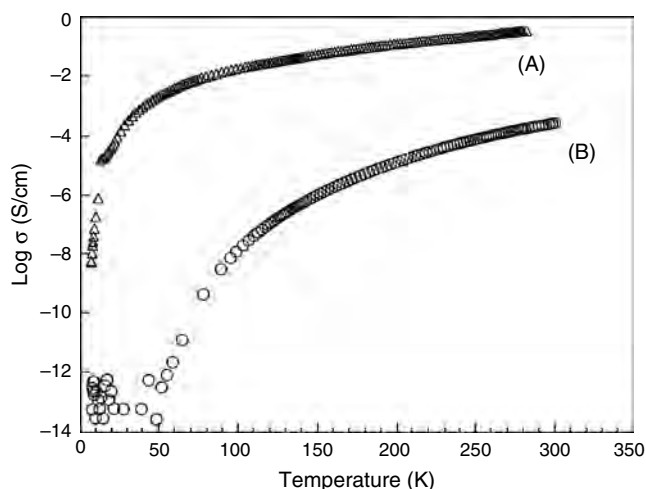
Figure 12. Four probe variable temperature electrical conductivity data of (A) (PAn)$_{0.48}$V$_2$O$_5$, nH$_2$O (film), and (B) (PAn)$_{0.48}$V$_2$O$_5$, nH$_2$O (pressed pellet) [n varies from 0.5 to 1.3]. Reproduced with permission from [159], C. G. Wu et al., *Chem. Mater.* 8, 1992 (1996). © 1996, American Chemical Society.

property. Thermoelectric power, is large and negative and very weak temperature dependence is shown. The freshly prepared samples reveal n-type semiconducting property similar to the reduced xerogel itself and a relatively weaker effect of PAn is observed which is strongly dependent on the extent of protonation, molecular weight, and the aging of polymer.

Composites of α-RuCl$_3$ with both PPy and PAn are highly conductive (23 S/cm and 1 S/cm, respectively) as compared to the host (α-RuCl$_3$ = 5×10^{-4} and its Li salt is 0.3 S/cm) [166, 167]. Therefore, electrical transport in these composites takes place through the ICP component, although some contribution from the [RuCl$_3$]$^{x-}$ may also occur. Variable temperature-conductivity measurements have shown a thermally activated-type transition, normal for the materials with
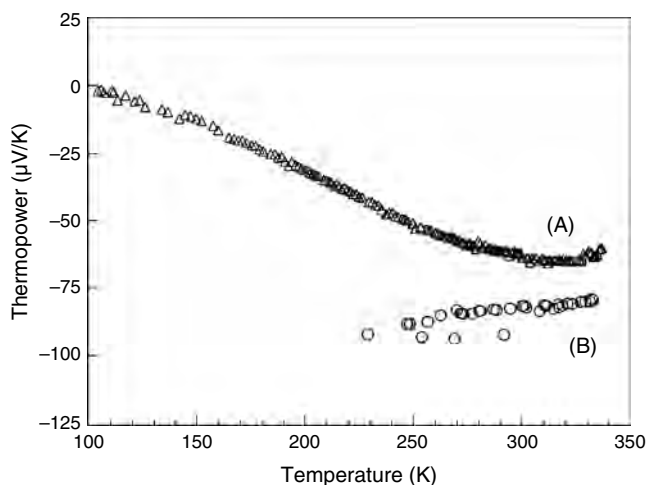

Figure 13. Variable temperature TEP data of (A) (PAn)$_{0.44}$V$_2$O$_5$, 1.3H$_2$O (film), and (B) (PAn)$_{0.44}$V$_2$O$_5$, 0.33 H$_2$O (pressed pellet). Reproduced with permission from [159], C. G. Wu et al., *Chem. Mater.* 8, 1992 (1996). © 1996, American Chemical Society.

a grain boundary. The activation energy is 0.3 eV and 0.35 eV for PAn and PPy samples. At a higher temperature (>100 K), the log (σ) versus $1/T$ curves fit to a straight line indicating the evidence of thermal activation, while at lower temperatures the deviation from a straight line indicated a more complicated transport process. Thermoelectric power is positive and increases steadily at a higher temperature indicating a metal-like transition in these materials; however, overall p-type behavior is observed, which is consistent with the behavior of the components. Thermally activated transport is commonly observed for Mo-compounds (MoS_2 and MoO_3) also containing nanocomposites. For MoS_2-PPy and MoS_2-PAn [195, 196], very similar behavior—p-type metallic nature—although the relatively large value of Seebeck coefficient (S) suggests a deviation from ideal metallic behavior. For MoO_3-based composites containing PAn and PPV [197–200], the activated transition is observed with activation energy 0.2 eV. There are a few other relevant studies on some other nanocomposites; however, considering the poor room temperature conductivity of the materials the lower temperature measurements do not seem to be convincing.

The mechanism of electrical transport has rarely been studied in nanoparticle-incorporated nanocomposites. Earlier on, there were a few reports on PPy-carbon black composites, which showed a deviation from existing models like MVRH or thermal fluctuation-induced tunneling of carriers (TFTC) [76, 77]. In another work, Gangopadhyay et al. [256] have studied variable temperature ac and dc conductivity and TEP measurements on PPy-Fe_2O_3 nanocomposites. Results have shown that dc conductivity fits the MVRH model satisfactorily, while ac conductivity TEP data shows complex behavior. At a lower temperature ($\leq$225 K), TEP varied linearly showing metal-like behavior while it deviates from linearity at a higher temperature. The results suggested that a single model is quite inadequate for explaining the overall behavior of the system; a heterogeneous model with a highly conducting island, connected by poorly conducting barriers, was suggested.

7. NANODEVICES

It has now been well established that conducting polymers, owing to their considerable technological potential, have occupied a very important position in the arena of materials science. Versatile applications of these polymers encompass electronics, sensors, actuators, optical bioanalytical devices, displays, etc. On the other hand, miniaturization of the optical, mechanical, and electronic devices has fueled the present revolution in information and biotechnology. This is because such microstructured devices are suitable for application in areas where an extremely small quantity is handled, and especially where many small simultaneous experiments are required. Therefore, it is very obvious that nanomaterials obtained from conducting polymers will possess rather enhanced application potential as compared to the bulk counterpart. As described earlier, these nanomaterials are synthesized in two general synthesis techniques—template-guided synthesis and self-assembly. Template-guided synthesis is easier although the self-assembly technique is more favored because it is free from the inconvenience of removing the template. Numerous applications of such

nanomaterials are possible, few examples of which will be discussed here. It should be mentioned here that very often nanodevices based on conducting polymers do not utilize the nanostructured forms of polymers described so far; rather the chemical/electrochemical deposit of the polymer, sometimes patterned suitably, are used as the active part of the devices. Few of these devices will also be mentioned here.

It has already been discussed that nanomaterials, obtained from conducting polymers, are generally of three types: nanoparticles, nanotubules/nanowires, and nanolayers. Immediately after the synthesis of the nanotubules, they were subjected to an excellent application as a bioanalytical device. The PPy nanotubules (within the membrane) were loaded with an enzyme (GOD) by simple immersion and one side of the membrane was coated by silver. This assembly was subjected to the successful measurement of glucose in the concentration range 1–25 mmol dm^{-3} [257]. In a modified version of this work, Parthasarathy and Martin have synthesized capped PPy nanotubules and have performed different bioanalyses after loading the nanotubules with enzymes like glucose oxidase, catalase, subtilisin, trypsin, and alcohol dehydrogenase by vacuum filtration [258]. This assembly works almost as an enzymatic bioreactor in both aqueous and nonaqueous medium as described by Figure 14. In a relatively recent publication, Sukeerthi and Contractor have demonstrated [259] the fabrication of biosensor arrays based on PAn microtubules grown within a microporous polycarbonate membrane. In this single device, three different enzymes were immobilized
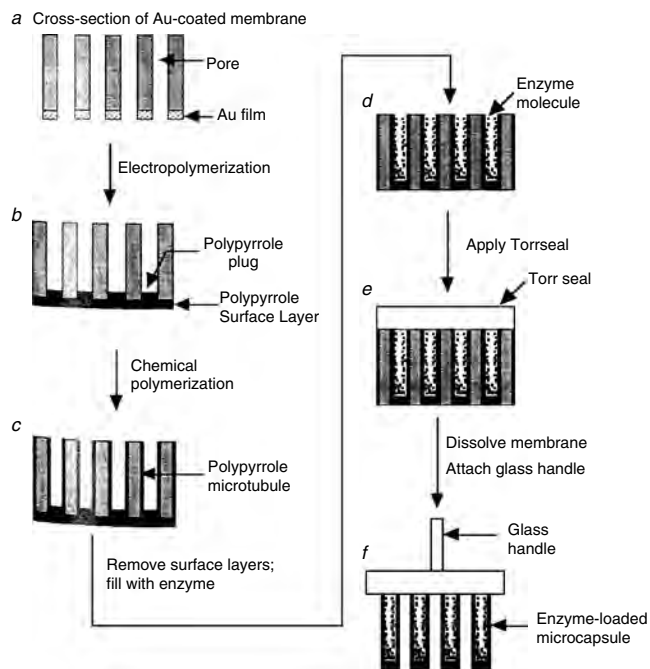

Figure 14. Schematic diagram of methods used for synthesis and enzyme loading of microcapsule arrays: (a) Au-coated template membrane, (b) electropolymerization of pyrrole, (c) immersion into Fe^{3+} and pyrrole solution for formation of PPy tubules, (d) enzyme loading, (e) epoxy capping, and (f) dissolution of the template. Reproduced with permission from [258], R. V. Parthasarathy and C. R. Martin, *Nature* 369, 298 (1994). © 1994, Macmillan Magazines Ltd.

so that in a single measurement, the array can recognize glucose, urea, and triglyceride from a mixture. In a different approach, a thin PAn film, electrochemically deposited on a nanometer-sized carbon fiber electrode, has been designed to form an ultra-micro pH sensor [260]. In another report, PPy containing hydrogel microelectrodes were proved to be interesting materials for neural communications [261].

There are different useful methods for the fabrication of conducting polymer junctions or nanoscale fibers/devices suitable for application in nanoelectronics, namely, electrospinning (electrostatic fabrication), etc. [262]. On the other hand, line-patterning is a method suitable for fabricating patterns from conducting polymers. The particular conducting polymers may either be electrodeposited or solution-casted on the specific regions. A very intelligent nonphotolithographic technique for the formation of patterned microstructures from conducting polymers (PAn) on a Si/SiO$_2$ wafer has been described by Beh et al. [263] and Krawice et al. [264]. The width of the smallest structure of PAn fabricated using this procedure was ∼350 nm. The schematic presentation of such a patterning technique and the different patterns fabricated are already shown in Figure 11. All these fibers, lines, patterns, etc. can play excellent electrodes for high quality optical displays and transistors. Earlier, Granstrom et al. have demonstrated the formation of micrometer- (10 μm) and nanometer-sized (100 μm) structures from a polythiophene derivative and their function as LED [265]. In a recent work, a movable electrochromic "pixel" was constructed from a microfabricated PPy deposited on an Au electrode. Depending upon the applied potential and thickness, the color of the PPy layer was changed from red to yellow. This particular device can have potential application in studying living cells or a single-cell organism [266]. Therefore, it is obvious that both electrical conductivity and potential, dependent light-emitting and color change properties of conducting polymers are exploited in the fabrication of such nanodevices. In a separate publication, Zhang et al. have reported the fabrication of nanowires and nanodots from PEDOT-PSS on a glass plate or silicon wafer. The fabrication was done by a soft lithographic method (MIMIC) and the nanowires (833 nm or 278 nm in width) are important for using in optoelectronic devices, where light propagation and electronic paths are defined by patterning [267].

Redox activity of conducting polymers and the relevant volume change has been successfully explored in the fabrication of miniaturized actuator devices from conducting polymers. Smela et al. have reported a series of works on the construction of microrobotic arms and microactuators for uplifting, gripping, and positioning of micrometer-sized objects. The conducting polymer (PPy-DBS$^-$) nanolayer (but not the monolayer) deposited on gold is the active material in such works. Through the series, the polymer is deposited and patterned following a standard micromachining technique. The PPy-Au bilayer actuator has a dimension of 30 μm to 100 μm, and it can execute very sharp but controlled folding of microsized plates by redox-induced, reversible oxidation and bending. This system is an excellent manipulation of a folding arm suitable for working with micrometer-sized objects [268]. Later on, this work was further modified and a complete arm including functions of
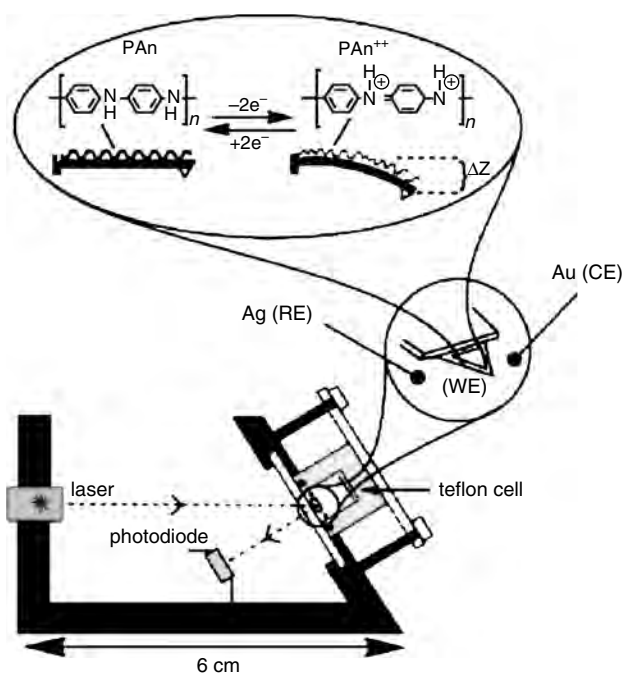
Figure 15. The system used for *in-situ* electrochemically induced stress measurements on the cantilever. Reversible electrochemical redox reaction of PAn and resulting lever deflection is shown in inset. Reproduced with permission from [272], M. Lahav et al., *Angew. Chem. Int. Ed.* 40, 4095 (2001). © 2001, Wiley-VCH.

elbow, wrist, and hand with fingers was constructed by a suitable modification of the earlier system [269–271]. This system works in micrometer dimension and can move with micrometer-sized objects within an area of about 250 μm × 100 μm, making the microrobot an excellent tool for single cell manipulation. The handling, transport, separation, and detection of cells and biomolecules, which should be essentially done in a very small volume of liquids, should be easier by these actuators. These microactuators, also termed as micromuscles, could be further modified so that they can be used to move plate, open and close boxes, and close microvials under complete control.

Very recently, the designing of an electrodriven cantilever has been reported [272] by the electrochemical deposition of PAn on one side as shown in Figure 15. On oxidation of the polymer, the micromachine is subjected to a stress generated by the electrostatic repulsion and the corresponding swelling of the polymer layer. As a result, the cantilever undergoes deflection and on reduction of the polymer the stress is released and the cantilever is retracted to the original position. This way, the micrometer-sized cantilever (length 160 μm, thickness 0.6 μm) can generate a stress of ∼2–∼4 Nm^{-1}. These examples can establish that conducting polymers in their nanoscopic forms are extremely intelligent candidates for versatile applications.

8. CONCLUSIONS

Keeping pace with the ongoing trend of miniaturization, a group of conducting polymer-based nanomaterials has also been launched—synthesis, characteristics, and a few

applications of which are described in this article. However, parallel with their application potential, ICP-based nanomaterials have raised excellent scientific interest favoring the true understanding of fundamental properties of themselves. At the same time, synthesis of these nanomaterials and successful designing of the nanodevices indicate the successful steps toward overcoming intractability of conducting polymers.

It is interesting to note that the attempt to obtain conducting polymers in different nanodimensional forms (nanoparticles, nanotubules, nanolayers) was started more or less at the same period by different research groups. Attempts to synthesize each of these materials were commenced with the template-guided polymerization route, which at a later stage, was replaced by more efficient, template-free routes. However, the template-free methods very often give rise to materials poorer in quality. Considering the scientific and technological aspects, the versatility of synthesis techniques and application aspects, the present status of research and development on these different branch nanomaterials is almost at the same stage. The conduction mechanism in these hybrid materials and/or nanostructured materials has not been properly explored until now.

The interesting point to observe is that the research on conducting polymer nanostructures was primarily centered on optimization of the synthesis techniques; the application aspect of the synthesized materials was explored later on. Therefore, the application potential of a large fraction of the earlier work on nanocomposites and nanotubules, etc. was not properly explored. But the recent trend in this respect is to synthesize the nanomaterial according to its specific use. This difference in the trend of work is very obvious from the present discussion on the ICP nanodevices. Recently, there has been wealth of research and development on the synthesis and application of such nanomaterials, and new polymers with novel application potential are also being introduced day by day [273, 274]. Nanostructures formed from inherently conducting polymers have recently been reviewed by Wallace and Innis [275]. It seems that conducting polymer nanomaterials are no longer difficult to get in hand: proper utilization of them should bring revolution to the world of lightweight, miniaturized devices.

GLOSSARY

Actuator   A device that performs through conversion of electrical energy into mechanical energy.

Ammonium peroxodisulphate (APS) $(NH_4)_2S_2O_8$, efficient oxidant for aniline polymerization.

Biosensor   An analytical device that detects biomolecules in the system or biologically produced signals.

Brunauer–Emmet–Teller (BET)   equation meant for multilayer adsorption of gases on solid surface. Total surface area of a granular solid can be derived from this equation.

Colloid   A stable dispersion of nanodimensional particles in a solvent. The dispersion can pass through ordinary filter paper.

Inherently conducting polymers (ICP)   Polymers with conjugated double-bonded backbone that can show significant electronic conductivity after doping with suitable dopants. ICPs are generally semiconductors (p-type) having versatile novel properties and important applications.

Microelectronics   Branch of electronics that deals with electronic junctions and devices smaller than 50 μm.

Nanocomposite   A composite that combines at least one nanodimensional component with a polymer or other material.

Nanoparticle   A particle with diameter $\leq$100 nm.

Nanotube/nanowire/nanorod   A tube/wire/rod having diameter $\leq$100 nm.

Percolation threshold   In an insulator-conductor, bi-component system, a critical fraction of conducting component is reached above which macroscopic conductivity of the system shows an inflexion. This particular limit is termed as percolation threshold.

Scanning electron microscopy (SEM)   that reveals the surface morphology of a solid by analyzing the electron beam reflected from the surface.

Steric stabilization   Prevention of macroscopic percipitation of a growing polymeric solid by using a soluble polymeric support. The precipitated polymer is supposed to be covered by the shell of the soluble polymer.

ACKNOWLEDGMENTS

REFERENCES

1. G. M. Chow and K. Gonslaves, "Nanotechnology: Molecularly Designed Materials." American Chemical Society, Washington, DC, 1996.
2. Nanostructured Materials, Special Issue of *Chem. Mater.* 8 (1996).
3. G. Timp, "Nanotechnology." Springer, New York, 1999.
4. M. Gross, "Travels to the Nanoworld: Miniature Machinary in Nature and Technology." Plenum, New York, 1999.
5. T. A. Skotheim, R. L. Elesenbaumer, and J. R. Reynolds (Eds.), "Handbook of Conducting Polymers" (2nd Ed.) Section V. Marcel Dekker, New York, 1998.
6. A. Dodadabalapour, L. Torsi, and H. E. Katz, *Science* 268, 270 (1995).
7. Y. Yang and A. J. Heeger, *Nature* 372, 344 (1994).
8. M. Barggren. O. Inganas, G. Gustafsson, J. Rasmusson, M. R. Andersson, T. Hjertberg, and O. Wennerstrom, *Nature* 372, 444 (1994).
9. G. Horowitz, *Adv. Mater.* 10, 365 (1998).
10. M. J. Sailor, F. L. Klavetter, R. H. Gubbs, and N. S. Lewis, *Nature* 346, 155 (1990).
11. F. Garnier, R. Hajlaoui, A. Yassar, and F. Srivastava, *Science* 265, 1684 (1994).
12. M. C. Lonergan, E. J. Severin, B. J. Doleman, S. A. Beaber, R. H. Grubbs, and N. S. Lewis, *Chem. Mater.* 8, 2298 (1996).
13. S. P. Armes, in "Handbook of Conducting Polymers" (2nd ed.), (T. A. Skotheim, R. L. Elesenbaumer, and J. R. Reynolds, Eds.), Chapter 17. Marcel Dekker, New York, 1998.
14. M. A. Khan and S. P. Armes, *Adv. Mater.* 12, 671 (2000).
15. R. Gangopadhyay and A. De, *Chem. Mater.* 12, 608 (2000).
16. E. R. Hitzky and P. Aranda, *Anales de Quim. Int. Ed.* 93, 117 (1997).

17. P. G. Romero, *Adv. Mater.* 13, 163 (2001).
18. C. R. Martin, *Acc. Chem. Res.* 28, 61 (1995).
19. C. R. Martin, *Chem. Mater.* 8, 1739 (1996).
20. R. Gangopadhyay and A. De, Handbook of Organic-Inorganic Hybrid Materials and Nanocomposites (H. S. Nalwa Ed.). American Scientific Publishers. Los Angeles (2003), Vol. 2, pp. 217–263.
21. R. B. Bjorklund and B. Liedberg, *J. Chem. Soc., Chem. Commun.* 1293 (1986).
22. S. P. Armes and B. Vincent, *J. Chem. Soc., Chem. Commun.* 288 (1987).
23. N. Cawdery, T. M. Obey, and B. Vincent, *J. Chem. Soc., Chem. Commun.* 1189 (1988).
24. M. Aldissi and S. P. Armes, U.S. Patent Number U.S. 5021193 (1991).
25. M. Aldissi and S. P. Armes, U.S. Patent Number U.S. 305816 (1990).
26. S. P. Armes and M. Aldissi, *J. Chem. Soc., Chem. Commun.* 88 (1989).
27. M. Aldissi and S. P. Armes, U.S. Patent Number U.S. 305817 (1990).
28. S. P. Armes, M. Aldissi, G. C. Idzorek, P. W. Keaton, L. J. Rowton, G. L. Stradling, M. T. Collopy, and D. B. Mccoll, *J. Coll. Interface. Sci.* 141, 119 (1991).
29. R. Gangopadhyay and A. De, *Synth. Met.* 123, 21 (2001).
30. P. Ghosh, A. Chakrabarti, and S. K. Siddhanta, *Eur. Polym. J.* 35, 803 (1999).
31. J.-B. Jun, J.-W. Kim, J.-W. Lee, and K.-D. Suh, *Macromol. Rapid. Commun.* 22, 937 (2001).
32. B. Vincent and J. Waterson, *J. Chem. Soc., Chem. Commun.* 683 (1990).
33. J. Stejskal, P. Kratochvil, and M. Helmstedt, *Langmuir* 12, 3389 (1996).
34. P. Banerjee and B. M. Mandal, *Macromolecules* 28, 3940 (1995).
35. B. J. Kim, S.-G. Oh, M.-G. Han, and S.-S. Im, *Synth. Met.* 122, 297 (2001).
36. M.-G. Han, S. K. Cho, S.-G. Oh, and S.-S. Im, *Synth. Met.* 126, 53 (2002).
37. P. Ghosh, S. K. Siddhanta, S. R. Haque, and A. Chakrabarti, *Synth. Met.* 123, 83 (2001).
38. A. Yassar, J. Roncali, and F. Garnier, *Polym. Commun.* 28, 103 (1987).
39. C.-F. Liu, T. Maruyama, and T. Yamamoto, *Polym. J.* 25, 363 (1993).
40. S. F. Lascelles and S. P. Armes, *J. Mater. Chem.* 7, 1339 (1997).
41. S. F. Lascelles, S. P. Armes, P. A. Zhdan, S. J. Greaves, A. M. Brown, J. F. Watts, S. R. Leadley, and S. Y. Luk, *J. Mater. Chem.* 7, 1349 (1997).
42. P. Beadle, S. P. Armes, S. Gottesfeld, C. Mombourquete, R. Houlton, W. D. Andrews, and S. F. Agnew, *Macromolecules* 25, 2526 (1992).
43. S. P. Armes, S. Gottesfeld, J. G. Beery, F. Garzon, and S. F. Agnew, *Polymer* 32, 2325 (1991).
44. M. Gill, J. Mykytiuk, S. P. Armes, J. L. Edwards, T. Yeats, P. Moreland, and C. Mollett, *J. Chem. Soc., Chem. Commun.* 108 (1992).
45. M. Gill, S. P. Armes, D. Fairhurst, S. N. Emmett, G. Idzork, and T. Pigott, *Langmuir* 8, 2178 (1992).
46. R. Flitton, J. Johal, S. Maeda, and S. P. Armes, *J. Coll. Interface Sci.* 173, 135 (1995).
47. N. J. Terrill, T. Crowley, M. Gill, and S. P. Armes, *Langmuir* 9, 2093 (1993).
48. S. Maeda and S. P. Armes, *J. Coll. Interface Sci.* 159, 257 (1993).
49. S. Maeda and S. P. Armes, *J. Mater. Chem.* 4, 935 (1994).
50. J. Stejskal, Kratochvil, S. P. Armes, S. F. Lascelles, A. Riede, M. Helmstedt, J. Prokes, and I. Krivka, *Macromolecules* 29, 6814 (1996).
51. S. Maeda and S. P. Armes, *Synth. Met.* 69, 499 (1995).
52. S. Maeda and S. P. Armes, *Chem. Mater.* 7, 171 (1995).
53. S. Maeda and S. P. Armes, *Synth. Met.* 73, 151 (1995).
54. C. Perruchot, M. M. Chehimi, M. Delamar, S. F. Lascelles, and S. P. Armes, *J. Coll. Interface Sci.* 193, 190 (1997).
55. S. Maeda, M. Gill, S. P. Armes, and I. W. Fletcher, *Langmuir* 11, 1899 (1995).
56. M. D. Butterworth, R. Corradi, J. Johal, S. F. Lascelles, S. Maeda, and S. P. Armes, *J. Coll. Interface Sci.* 174, 510 (1995).
57. S. F. Lascelles, G. P. McCarthy, M. D. Butterworth, and S. P. Armes, *Coll. Polym. Sci.* 276, 893 (1998).
58. A. Azioune, K. Pech, B. Soudi, M. M. Chehimi, G. P. McCarthy, and S. P. Armes, *Synth. Met.* 102, 1419 (1999).
59. R. Partch, S. G. Gangolli, E. Matijevic, W. Cai, and S. Arajs, *J. Coll. Interface Sci.* 144, 27 (1991).
60. C. L. Huang, R. E. Partch, and E. Matijevic, *J. Coll. Interface Sci.* 170, 275 (1995).
61. C. L. Huang and E. Matijevic, *J. Mater. Res.* 10, 1327 (1995).
62. L. M. Gan, L. H. Zhang, H. S. O. Chan, and C. H. Chew, *Mater. Chem. Phys.* 40, 94 (1995).
63. S. T. Selvan, *Chem. Commun.* 351 (1998).
64. S. T. Selvan, J. P. Spatz, H. A. Klok, and M. Moller, *Adv. Mater.* 10, 132 (1998).
65. S. M. Marinakos, L. C. Brousseau, A. Jones, and D. A. Feldheim, *Chem. Mater.* 10, 1214 (1998).
66. S. M. Marinakos, D. A. Schultz, and D. L. Feldheim, *Adv. Mater.* 11, 34 (1999).
67. S. M. Marinakos, J. P. Novak, L. C. Brousseau III, A. B. House, E. M. Edeki, J. C. Feldhans, and D. L. Feldheim, *J. Am. Chem. Soc.* 121, 8518 (1999).
68. G. Cho, D. T. Glatzhofer, B. M. Fung, W. L. Yuan, and E. A. O'Rear, *Langmuir* 16, 4424 (2000).
69. G. Cho, B. M. Fung, D. T. Glatzhofer, J. S. Lee, and Y. G. Shul, *Langmuir* 17, 456 (2001).
70. V. Aboutaneos, J. N. Barisci, L. A. P. Kane-Maguir, and G. G. Wallace, *Synth. Met.* 106, 89 (1999).
71. A. Bhattacharya, K. M. Ganguly, A. De, and S. Sarkar, *Mater. Res. Bull.* 31, 527 (1996).
72. R. Gangopadhyay and A. De, *Eur. Polym. J.* 35, 1985 (1999).
73. M. I. Baraton, L. Merhari, J. Wang, and K. E. Gonslaves, *Nanotechnology* 9, 356 (1998).
74. W. Fang, E. Sun, A. Fuji, H. Wu, K. Niihara, and K. Yoshino, *Bull. Chem. Soc. Jpn.* 73, 2627 (2000).
75. H. Xia and Q. Wang, *Chem. Mater.* 14, 2158 (2002).
76. W. A. Wampler, K. Rajeshwar, R. G. Pethe, R. C. Hyer, and S. C. Sharma, *J. Mater. Res.* 10, 1811 (1995).
77. W. A. Wampler, S. Basak, and K. Rajeshwar, *Carbon* 34, 747 (1996).
78. S. Higashika, K. Kimura, Y. Matsuo, and Y. Sujie, *Carbon* 37, 351 (1999).
79. J. K. Avlyanov, *Synth. Met.* 102, 1272 (1999).
80. J. Fan, M. D. Wan, D. Zhu, B. Chang, Z. Pan, and S. Xu, *Synth. Met.* 102, 1266 (1999).
81. I. Musa, Baxendale, G. A. J. Amaratuga, and W. Eccleston, *Synth. Met.* 102, 1250 (1999).
82. M. Hughes, G. Z. Chen, M. S. P. Shaffer, D. J. Fray, and A. H. Windle, *Chem. Mater.* 14, 1610 (2002).
83. M. D. Butterworth, S. P. Armes, and A. W. Simpson, *J. Chem. Soc., Chem. Commun.* 2129 (1994).
84. M. D. Butterworth, S. A. Bell, S. P. Armes, and A. W. Simpson, *J. Coll. Interface Sci.* 183, 91 (1998).
85. A. P. Philipse, M. P. B. van Bruggen, and C. Pathmamonoharan, *Langmuir* 10, 92 (1994).
86. M. T. Nguyen and A. Diaz, *Adv. Mater.* 6, 858 (1994).
87. M. Wan, W. Zhou, and J. Li, *Synth. Met.* 78, 27 (1996).
88. M. Wan and J. Li, *J. Polym. Sci., Part A: Polym. Chem.* 36, 2799 (1998).

89. M. Wan and J. Fan, *J. Polym. Sci., Part A: Polym. Chem.* 36, 2749 (1998).
90. K. Suri, S. Annapoorni, R. P. Tandon, and N. C. Mehra, *Synth. Met.* 126, 137 (2002).
91. B. Z. Tang, Y. Geng, J. W. Y. Lam, B. Li, X. Jing, X. Wang, F. Wang, A. B. Pakhomov, and X. X. Zhang, *Chem. Mater.* 11, 1581 (1999).
92. G. Bidan, O. Jarjayes, J. M. Fruchart, and E. Hannecart, *Adv. Mater.* 6, 152 (1994).
93. O. Jarjayes, P. H. Fries, and G. Bidan, *Synth. Met.* 69, 343 (1995).
94. M. Kryszewski and J. K. Jeszka, *Synth. Met.* 94, 99 (1998).
95. V. D. Pokhodenko, V. A. Krylov, Y. I. Kurys, and O. Y. Posudievsky, *Phys. Chem. Chem. Phys.* 1, 905 (1999).
96. S. Kuwabata, A. Kishimoto, T. Tanaka, and H. Yoneyama, *J. Electrochem. Soc.* 141, 10 (1994).
97. S. Kuwabata, A. Kishimoto, T. Tanaka, and H. Yoneyama, *J. Electrochem. Soc.* 141, 4190 (1994).
98. A. H. Gemeay, H. Nishiyama, S. Kuwabata, and H. Yoneyama, *J. Electrochem. Soc.* 142, 4190 (1994).
99. M. Nishiwaza, K. Mukai, S. Kuwabata, C. R. Martin, and H. Yoneyama, *J. Electrochem. Soc.* 144, 1923 (1997).
100. S. Kuwabata, T. Idzu, C. R. Martin, and H. Yoneyama, *J. Electrochem. Soc.* 145, 2707 (1998).
101. S. Kuwabata, S. Masui, and H. Yoneyama, *Electrochim. Acta* 44, 4593 (1999).
102. S. Kuwabata, S. Masui, H. Tomiyori, and H. Yoneyama, *Electrochim. Acta* 46, 91 (2000).
103. Z. Qi and P. G. Pickup, *J. Chem. Soc., Chem. Commun.* 15 (1998).
104. Z. Qi and P. G. Pickup, *J. Chem. Soc. Chem. Commun.* 2299 (1998).
105. Z. Qi, M. C. Lefebvre, and P. G. Pickup, *J. Electroanal. Chem.* 459, 9 (1998).
106. K. G. Neoh, T. T. Young, N. T. Looi, E. T. Kang, and K. L. Tan, *Chem. Mater.* 9, 2906 (1997).
107. S. W. Huang, K. G. Neoh, E. T. Kang, H. S. Han, and K. L. Tan, *J. Mater. Chem.* 8, 1743 (1998).
108. S. W. Huang, K. G. Neoh, C. W. Shih, D. S. Lim, E. T. Kang, H. S. Han, and K. L. Tan, *Synth. Met.* 96, 117 (1998).
109. K. G. Neoh, K. K. Tan, P. L. Goh, S. W. Huang, E. T. Kang, and K. L. Tan, *Polymer* 40, 887 (1999).
110. J. G. Wang, K. G. Neoh, and E. T. Kang, *J. Coll. Interface Sci.* 239, 78 (2001).
111. A. Drelinkiewicz, M. Hasik, and M. Choczynski, *Mater. Res. Bull.* 33, 739 (1998).
112. R. Bai and X. Zhang, *J. Coll. Interface Sci.* 241, 52 (2001).
113. H. Chriswanto, H. Ge, and G. G. Wallace, *Chromatographia* 37, 423 (1993).
114. H. Chriswanto and G. G. Wallace, *Chromatographia* 42, 191 (1996).
115. C. Perruchot, M. M. Chehimi, M. Delamar, and F. Fievet, *Surf. Interface Anal.* 26, 689 (1998).
116. C. Perruchot, M. M. Chehimi, D. Mordenti, M. Briand, and M. Delamar, *Surf. Interface Anal.* 8, 2185 (1998).
117. C. Perruchot, M. M. Chehimi, M. Delamar, P. C. Lacaze, A. J. Eccles, T. A. Steale, and C. D. Mair, *Synth. Met.* 102, 1194 (1999).
118. F. Faverolle, O. Le Bars, A. J. Attias, and B. Bloch, *J. Chim. Phys.* 92, 943 (1995).
119. F. Faverolle, O. Le Bars, A. J. Attias, and B. Bloch, "Organic Coatings" (P. C. Lacaze, Ed.), p. 267. Woodbury, NY, 1996.
120. J. W. Goodwin, R. S. Habron, and P. A. Reynolds, *Coll. Polym. Sci.* 268, 766 (1990).
121. A. P. Philipse and A. Vrig, *Coll. Interface Sci.* 165, 519 (1994).
122. M. I. Goller, C. Barthet, G. P. McCarthy, R. Corradi, B. P. Newby, S. A. Wilson, S. P. Armes, and S. Y. Luk, *Coll. Polym. Sci.* 276, 1010 (1998).
123. P. J. Tarcha, D. Misun, D. Finley, M. Wong, and J. J. Donovan, "Polymer Latexes, Preparation, Characterization and Applications" (E. S. Danniels, E. D. Sudol, and M. S. El-Assar, Eds.), ACS Symposium Series, 492, p. 347. American Chemical Society, Washington, DC, 1992.
124. S. Maeda, R. Corradi, and S. P. Armes, *Macromolecules* 28, 2905 (1995).
125. B. Soudi, N. Jammul, M. M. Chehimi, G. P. McCarthy, and S. P. Armes, *J. Coll. Interface Sci.* 192, 269 (1997).
126. G. P. McCarthy, S. P. Armes, S. J. Greaves, and J. F. Watts, *Langmuir* 13, 3686 (1997).
127. M. R. Pope, S. P. Armes, and P. J. Tarcha, *Bioconjugate Chemistry* 7, 436 (1996).
128. R. M. Penner and C. R. Martin, *J. Electrochem. Soc.* 133, 2206 (1986).
129. R. M. Penner and C. R. Martin, *J. Electroechem. Soc.* 133, 310 (1986).
130. Z. Cai and C. R. Martin, *J. Am. Chem. Soc.* 111, 4138 (1989).
131. W. Liang and C. R Martin, *J. Am. Chem. Soc.* 112, 9666 (1990).
132. C. R. Martin, L. S. van Dyke, Z. Cai, and W. Liang, *J. Am. Chem. Soc.* 112, 8976 (1990).
133. C. R. Martin, R. Parthasarathy, and V. Menon, *Synth. Met.* 55–57, 1165 (1993).
134. W. Cahalane and M. M. Labes, *Chem. Mater.* 1, 519 (1989).
135. S. De Vito and C. R. Martin, *Chem. Mater.* 10, 1738 (1998).
136. Z. Cai, J. Lei, W. Liang, V. Menon, and C. R. Martin, *Chem. Mater* 3, 960 (1991).
137. R. V. Parthasarathy and C. R. Martin, *Chem. Mater.* 6, 1627 (1994).
138. V. P. menon, J. Lei, and C. R. Martin, *Chem. Mater.* 8, 2382 (1996).
139. S. Demoustier-Champagne, E. Ferain, C. Jerome, R. Jerome, and R. Legras, *Eur. Polym. J.* 34, 1767 (1998).
140. S. Demoustier-Champagne and P. Y. Stavaux, *Chem. Mater.* 11, 829 (1999).
141. S. Cuenot, S. Demoustier-Chempagne, and B. Nysten, *Phys. Rev. Lett.* 85, 1690 (2000).
142. H. Q. Cao, Z. Xu, D. Sheng, J. Hong, H. Sang, and Y. Du, *J. Mater. Chem.* 11, 958 (2001).
143. H. Q. Cao, Z. Xu, H. Sang, D. Sheng, and C. Tie, *Adv. Mater.* 13, 121 (2001).
144. H. Q. Cao, C. Y. Tie, Z. Xu, J. M. Hong, and H. Sang, *Appl. Phys. Lett.* 78, 1592 (2001).
145. M. Nikpour, H. Chaouk, A. Mau, D. J. Chung, and G. Wallace, *Synth. Met.* 99, 121 (1999).
146. A. J. Gorgatti Zarbin, M. A. de Paoli, and O. L. Alves, *Synth. Met.* 84, 107 (1997).
147. A. J. Gorgatti Zarbin, M. A. de Paoli, and O. L. Alves, *Synth. Met.* 99, 227 (1999).
148. P. N. Bartlet, P. R. Birkin, M. A. Ghanem, and C. S. Toh, *J. Mater. Chem.* 849 (2001).
149. S. das Neves and M. A. de Paoli, *Synth. Met.* 96, 49 (1998).
150. S. das Neves, S. I. Cordoba de Torresi, and R. A. Zoppi, *Synth. Met.* 101, 754 (1999).
151. M. G. Kanatzidis, L. M. Tonge, T. J. Marks, H. O. Marcy, and C. R. Kanneworf, *J. Am. Chem. Soc.* 109, 3797 (1987).
152. M. G. Kanatzidis, H. O. Marcy, W. J. McCarthy, C. R. Kanneworf, and T. J. Marks, *Solid State Ionics* 32/33, 594 (1989).
153. R. H. Herber, *Acc. Chem. Res.* 15, 216 (1982) and references therein.
154. M. G. Kanatzidis, C. G. Wu, H. O. Marcy, D. C. DeGroot, C. R. Kanneworf, A. Kostikas, and V. Papaefthymiou, *Adv. Mater.* 2, 364 (1990).
155. C. G. Wu, D. C. DeGroot, H. O. Marcy, J. L. Schindler, C. R. Kannewurf, T. Bakas, V. Papaefthymiou, W. Hirpo, J. P. Yesinowski, Y. J. Liu, and M. G. Kanatzidis, *J. Am. Chem. Soc.* 117, 9229 (1995).
156. C. G. Wu, H. O. Marcy, D. C. DeGroot, J. L. Schindler, C. R. Kannewurf, W. Y. Leung, M. Benz, E. LeGoff, and M. G. Kanatzidis, *Synth. Met.* 41–43, 797 (1991).

157. M. G. Kanatzidis, C. G. Wu, H. O. Marcy, and C. R. Kannewurf, *J. Am. Chem. Soc.* 111, 4139 (1989).

158. Y. J. Liu, D. C. DeGroot, J. L. Schindler, C. R. Kannewurf, and M. G. Kanatzidis, *J. Chem. Soc., Chem. Commun.* 593 (1993).

159. C. G. Wu, D. C. DeGroot, H. O. Marcy, J. L. Schindler, C. R. Kannewurf, Y. J. Liu, W. Hirpo, and M. G. Kanatzidis, *Chem. Mater.* 8, 1992 (1996).

160. M. G. Kanatzidis, C. G. Wu, H. O. Marcy, D. C. DeGroot, and C. R. Kannewurf, *Chem. Mater.* 2, 222 (1990).

161. S. A. Chen and G. W. Hwang, *J. Am. Chem. Soc.* 117, 10056 (1995).

162. H. Nakajima and G. Matsubayashi, *Chem. Let.* 423 (1993).

163. G. Matsubayashi and H. Nakajima, *Chem. Let.* 31 (1993).

164. H. Nakajima and G. Matsubayashi, *J. Mater. Chem.* 4, 1325 (1994).

165. H. Nakajima and G. Matsubayashi, *J. Mater. Chem.* 5, 105 (1995).

166. L. Wang, P. Brazis, M. Rocci, C. R. Kannewurf, and M. G. Kanatzidis, *Chem. Mater.* 10, 3298 (1998).

167. L. Wang, M. Rocci, P. Brazis, C. R. Kannewurf, Y. Kim, W. Lee, J. H. Choy, and M. G. Kanatzidis, *J. Am. Chem. Soc.* 122, 6629 (2000).

168. D. van de Poel, Ph.D. thesis, Catholic University of Louvain, Louvain, Belgium, 1975.

169. P. Cloos, A. Moreale, and C. Badot, *Clay Min.* 14, 307 (1979).

170. A. Moreale, P. Cloos, and C. Badot, *Clay Min.* 20, 29 (1985).

171. Y. Soma and M. Soma, *Clay Min.* 23, 1 (1988).

172. V. Merhotra and E. P. Giannelis, *Solid State Commun.* 77, 155 (1991).

173. V. Merhotra and E. P. Giannelis, *Solid State Ionics* 51, 115 (1992).

174. T. C. Chang, S. Y. Ho, and K. J. Chao, *J. Chinese Chem. Soc.* 39, 209 (1992).

175. B. H. Kim, J. H. Jung, J. W. Kim, H. J. Choi, and J. Joo, *Synth. Met.* 117, 115 (2001).

176. B. H. Kim, J. H. Jung, J. W. Kim, H. J. Choi, and J. Joo, *Synth. Met.* 121, 1311 (2001).

177. H. J. Choi, J. W. Kim, J. Joo, and B. H. Kim, *Synth. Met.* 121, 1325 (2001).

178. Q. Wu, Z. Xue, Z. Qi, and F. Wang, *Polymer* 41, 2029 (2000).

179. J. M. Yeh, S. J. Liou, C. Y. Lai, and P. C. Wu, *Chem. Mater.* 13, 1131 (2001).

180. D. K. Lee, S. H. Lee, K. Char, and J. Kim, *Macromol. Rapid Commun.* 21, 1136 (2000).

181. J. H. Park, Y. T. Lin, and O. O. Park, *Macromol. Rapid Commun.* 22, 606 (2001).

182. H. Inoue and H. Yoneyama, *J. Electroanal. Chem.* 38, 815 (1987).

183. C. de Armitt and S. P. Armes, *Langmuir* 9, 652 (1993).

184. C. O. Oriakhi and M. M. Lerner, *Mater. Res. Bull.* 30, 723 (1995).

185. K. Ramachandran and M. M. Lerner, *J. Electrochem. Soc.* 144, 3739 (1997).

186. V. P. Parkhutik, J. M. Martinez-Duart, R. D. Calleja, and E. M. Marveeva, *J. Electrochem. Soc.* 140, L 94 (1993).

187. K. J. Chao, T. C. Chang, and S. Y. Ho, *J. Mater. Chem.* 3, 427 (1993).

188. T. C. Chang, S. Y. Ho, and K. J. Chao, *J. Phys. Org. Chem.* 7, 371 (1994).

189. T. C. Chang, W. Y. Shen, and S. Y. Ho, *Microporous Mater.* 4, 335 (1995).

190. D. J. Maia, O. L. Alves, and M. A. de Paoli, *Synth. Met.* 90, 37 (1997).

191. A. J. Gorgatti Zarbin, D. J. Maia, M. A. de Paoli, and O. L. Alves, *Synth. Met.* 102, 1277 (1999).

192. A. B. Gonclaves, A. S. Mangrich, and A. J. Gorgatti Zarbin, *Synth. Met.* 114, 119 (2000).

193. Y. J. Liu and M. G. Kanatzidis, *Inorg. Chem.* 32, 2989 (1993).

194. Y. J. Liu and M. G. Kanatzidis, *Chem. Mater.* 7, 1525 (1995).

195. M. G. Kanatzidis, R. Bissessur, D. C. Degroot, J. L. Schindler, and C. R. Kannewurf, *Chem. Mater.* 5, 595 (1993).

196. L. Wang, J. Schindler, C. R. Kannewurf, and M. G. Kanatzidis, *Chem. Mater.* 7, 1753 (1995).

197. R. Bissessur, D. C. Degroot, J. L. Schindler, C. R. Kannewurf, and M. G. Kanatzidis, *J. Chem. Soc., Chem. Commun.* 687 (1993).

198. T. A. Kerr, H. Wu, and L. F. Nazar, *Chem. Mater.* 8, 2005 (1996).

199. L. F. Nazar, Z. Zhang, and D. Zinkweg, *J. Am. Chem. Soc.* 114, 6239 (1992).

200. T. A. Kerr, F. Leroux, and L. F. Nazar, *Chem. Mater.* 10, 2588 (1998).

201. G. A. Ozin, A. Kuperman, and A. Stein, *Angew. Chem. Int. Ed. Engl.* 28, 359 (1989).

202. G. A. Ozin, *Adv. Mater.* 5, 334 (1993).

203. J. Heaviside, P. J. Hendra, P. Tsai, and R. P. Cooney, *J. Chem. Soc. Farad. Trans* (*I*) 74, 2542 (1978).

204. C. Pereira, G. T. Kokotailo, and R. J. Gorte, *J. Phys. Chem.* 95, 705 (1991).

205. S. D. Cox and G. D. Stuky, *J. Phys. Chem.* 95, 710 (1991).

206. S. Bordiga, G. Ricchiardi, G. Spoto, D. Scaravo, L. Carnelli, A. Zecchina, and C. Otero, *J. Chem. Soc., Farad. Trans.* 89, 1843 (1993).

207. T. Bein and P. Enzel, *Angew. Chem. Int. Ed. Engl.* 28, 1692 (1989).

208. R. Roque, J. Onate, E. Requera, and E. Navarro, *J. Mater. Sci.* 28, 2321 (1993).

209. R. Roque, J. Onate, and E. Navarro, *J. Mater. Sci. Lett.* 12, 1037 (1993).

210. G. J. Millar, G. F. McCann, C. M. Hobbis, G. A. Bowmaker, and R. P. Coonne, *J. Chem. Soc. Farad. Trans.* 90, 2579 (1994).

211. G. F. McCann, G. J. Millar, G. A. Bowmaker, and R. P. Coonne, *J. Chem. Soc. Farad. Trans.* 91, 4321 (1995).

212. H. Uehara, M. Miyake, M. Matsuda, and M. Sato, *J. Mater. Chem.* 8, 2133 (1998).

213. G. Larsen, G. L. Haller, and M. Marquez, *J. Phys. Chem.* 96, 4145 (1992).

214. P. Enzel and T. Bein, *J. Chem. Soc. Chem. Commun.* 1326 (1989).

215. J. V. Casper, V. Ramamurthy, and D. R. Corbin, *J. Am. Chem. Soc.* 113, 600 (1991).

216. T. Bein and P. Enzel, *Synth. Met.* 29, 163 (1989).

217. P. Enzel and T. Bein, *J. Phys. Chem.* 93, 6270 (1989).

218. C. G. Wu and T. Bein, *Science* 264, 1757 (1994).

219. K. L. N. Phani, S. Pitchumani, and S. Ravichandran, *Langmuir* 9, 2455 (1993).

220. V. Luca and S. Thomson, *J. Mater. Chem.* 10, 2121 (2000).

221. M. Ma and D. Li, *Chem. Mater.* 11, 872 (1999).

222. S.-J. Choi and S. M. Park, *Adv. Mater.* 12, 1547 (2000).

223. J. J. Langer and I. Czajkowski, *Adv. Mater. Opts. Electronics* 7, 149 (1997).

224. J. J. Langer, *Adv. Mater. Opts. Electronics* 9, 1 (1999).

225. J. J. Langer, G. Framski, and R. Joachimiak, *Synth. Met.* 121, 1281 (2001).

226. J. J. Langer, G. Framski, and S. Golczak, *Synth. Met.* 121, 1319 (2001).

227. L. Dai, J. Lu, B. Matthews, and A. W. H. Mau, *J. Phys. Chem. B* 102, 4049 (1998).

228. H. Qiu and M. Wan, *Macromolecules* 34, 675 (2001).

229. Y. Yang and M. Wan, *J. Mater. Chem.* 11, 2022 (2001).

230. J. Liu and M. Wan, *J. Mater. Chem.* 11, 404 (2001).

231. A. Hassanien, M. Gao, M. Tokumoto, and L. Dai, *Chem. Phys. Lett.* 342, 479 (2001).

232. H. Yan, T. Ishida, and N. Toshima, *Chem. Lett.* 816 (2001).

233. K. Huang and M. Wan, *Chem. Mater.* 14, 3486 (2002).

234. A. Ulman, "An Introduction to Ultrathin Organic Films—from Langmuir–Blodgett to Self Assembly (Part 2)." Academic Press, New York, 1991.

235. J. H. Cheung, E. Punkka, M. Rikukawa, R. B. Rosner, A. T. Royappa, and M. F. Rubner, *Polymer. Mater. Sci., Eng.* 64, 263 (1991).

236. T. L. Porter, D. Thompson, and M. Bradley, *Thin Solid Films* 288, 268 (1996).

237. J. H. Cheung and M. F. Rubner, *Thin Solid Films* 244, 990 (1994).
238. T. Suwa, M. Kakimoto, Y. Imai, I. Araki, and K. Yriyama, *Mol. Cryst. Liq. Cryst.* 255, 45 (1994).
239. N. E. Agbor, M. C. Petty, A. P. Monkmann, and M. Harris, *Synth. Met.* 55–57, 3879 (1993).
240. A. Dhanabalan, R. B. Dabke, S. N. Datta, N. Prasanta Kumar, S. S. Major, S. S. Talwar, and A. Q. Contractor, *Thin Solid Films* 295, 255 (1997).
241. A. Dhanabalan, R. B. Dabke, S. S. Major, R. Lal, S. S. Talwar, and A. Q. Contractor, *Langmuir* 13, 4395 (1997).
242. M. K. Ram, N. S. Sundaresan, and B. D. Malhotra, *J. Phys. Chem.* 97, 11580 (1993).
243. R. B. Dabke, A. Dhanabalan, S. Major, S. S. Talwar, R. Lal, and A. Q. Contractor, *Thin Solid Films* 335, 203 (1998).
244. A. Riul, Jr., L. H. C. Mattoso, S. V. Mello, G. D. Telles, and O. N. Oliviera, Jr., *Synth. Met.* 71, 2067 (1995).
245. I. Watanabe, K. Hong, and M. F. Rubner, *Langmuir* 6, 1164 (1990).
246. M. Rikukawa, M. Nakagawa, H. Abe, K. Ishida, K. Sanui, and N. Ogata, *Thin Solid Films* 273, 240 (1996).
247. T. Bjornholm, D. R. Greve, N. Reitzel, T. Hassenkam, K. Kjaer, P. B. Howes, N. B. Larsen, J. Bogelund, M. Jayraman, P. C. Ewbank, and R. D. McCullough, *J. Am. Chem. Soc.* 120, 7643 (1998).
248. T. Bjornholm, T. Hassenkam, D. R. Greve, R. D. McCullough, M. Jayraman, S. M. Savoy, C. E. Jones, and J. T. McDevitt, *Adv. Mater.* 11, 1218 (1999).
249. Z. Huang, P-C. Wang, A. G. MacDiarmid, Y. Xia, and G. Whitesides, *Langmuir* 13, 6480 (1997).
250. W. S. Beh, I. T. Kim, D. Qin, Y. Xia, and G. M. Whitesides, *Adv. Mater.* 11, 1038 (1999).
251. R. Sfez, L. De-Zhong, I. Turyan, D. Mandler, and S. Yitzchaik, *Langmuir* 17, 2556 (2001).
252. J. Y. Josefowicz, J. K. Avlyanov, and A. G. Macdiarmid, *Thin Solid Films* 393, 186 (2001).
253. N. F. Mott and E. A. Davis, "Electronic Processes in Noncrystalline Solids, 2nd Ed.," p. 32. Clarendon Press, Oxford, 1979.
254. J. P. Spatz, B. Lorenz, K. Weishaupt, H. D. Hochheimer, V. P. Menon, R. V. Parthasarathy, C. R. Martin, J. Bechtold, and P. H. Hor, *Phys. Rev. Lett.* 50, 14,888 (1994).
255. M. L. Knotek, M. Pollak, T. M. Donovan, and H. Kurtzman, *Phys. Rev. Lett.* 30, 853 (1973).
256. R. Gangopadhyay, A. De, and S. N. Das, *J. Paal. Phys.* 87, 2363 (2000).
257. C. G. J. Koopal, B. de Ruiter, and R. J. M. Nolte, *J. Chem. Soc., Chem. Commun.* 1691 (1991).
258. R. V. Parthasarathy and C. R. Martin, *Nature* 369, 298 (1994).
259. S. Sukeerthi and A. Q. Contractor, *Anal. Chem.* 71, 2231 (1999).
260. X. Zhang, B. Ogorevc, and J. Wang, *Anal. Chim. Acta* 452, 1 (2002).
261. T. Nyberg, O. Inganas, and H. Jerregard, *Biomed. Microdevices* 4, 43 (2002).
262. D. H. Reneker, A. L. Yarin, H. Fong, and S. Koombhongse, *J. Appl. Phys.* 87, 4531 (2000).
263. W. S. Beh, I. T. Kim, D. Qin, Y. Xia, and G. M. Whitesides, *Adv. Mater.* 11, 1038 (1999).
264. B. S-Krawice, T. Cassagneau, and J. H. Fendler, *Adv. Mater.* 11, 659 (1999).
265. M. Granstrom, M. Berggren, and O. Inganas, *Science* 267, 1479 (1995).
266. E. Smela, *Adv. Mater.* 11, 1343 (1999).
267. F. L. Zhang, T. Nyberg, and O. Inganas, *Nano Lett.* 2, 1373 (2002).
268. E. Smela, O. Inganas, and I. Lundstrom, *Science* 268, 1735 (1995).
269. E. W. H. Jager, E. Smela, and O. Inganas, *Science* 290, 1540 (2000).
270. E. W. H. Jager, O. Inganas, and I. Lundstrom, *Science* 288, 2335 (2000).
271. E. W. H. Jager, O. Inganas, and I. Lundstrom, *Adv. Mater.* 13, 76 (2001).
272. M. Lahav, C. Durkan, R. Gabai, E. Katz, I. Willner, and M. E. Welland, *Angew. Chem. Int. Ed.* 40, 4095 (2001).
273. L. Liang, J. Liu, C. F. Windisch, G. J. Exarhos, and Y. H. Lin, *Angew. Chem. Int. Ed.* 41, 3665 (2002).
274. T. Nyberg, F. Zhang, and O. Inganas, *Curr. Appl. Phys.* 2, 27 (2002).
275. G. G. Wallace and P. C. Innis, *J. Nanosci. Nanotech.* 2, 441 (2002).

Conducting Polymeric Nanomaterials

Silmara Neves

Universidade São Francisco, Itatiba, SP, Brazil

Wilson A. Gazotti

Universidade Estadual do Norte Fluminense,
Campos dos Goytacazes, RJ, Brazil

Marco-A. De Paoli

Universidade Estadual de Campinas, Campinas, SP, Brazil

CONTENTS

1. INTRODUCTION

Because new structures and properties are obtained when dimensions are reduced to nanometric sizes, considerable effort is being devoted to produce nanomaterials and to exploit their special properties. Materials with nanoscopic dimensions not only have potential technological applications in various areas but also are of fundamental interest in that the properties of a material can change in this transition from bulk to molecular scale.

Polymeric systems are a field of increasing scientific and technical interest, offering the opportunity to obtain a broad variety of promising new materials, with a wide range of properties and potential applications. The properties of these polymers are strongly dependent on their microstructure and morphology, which are mainly determined by their synthesis conditions [1–23]. The most important consideration from a chemical viewpoint is that tailored properties are obtained when polymers are prepared with enhanced molecular and supermolecular order and, consequently, contain fewer conjugation-interrupting defects, such as sp^3-hybrid carbons or twists and kinks in the polymer chain [4–56].

Among the different strategies to synthesize ordered materials reported in the literature, template synthesis is a very promising and powerful tool [7]. This technique consists of including inorganic or organic constituents (guests) inside the void spaces of host materials. These void spaces act as a template, determining the shape, size, and in many cases the orientation of the compound produced. A composite is obtained when the host matrix maintains its integrity. Details and the most recent advances of this technology applied to obtain conducting polymers on the nanoscale are described in this chapter.

2. CONDUCTING POLYMERS

2.1. History and Applications

Since the first studies on the chemistry and production of synthetic polymers were related to saturated macromolecules, which are excellent electrical insulators, the technological applications of these materials with respect to their electrical properties are often directed to exploit their capacity as insulators. However, electronically conducting polymers possess different properties related to their redox behavior. In these materials, unsaturated chemical bonds contain unpaired electrons, which can be delocalized along the polymer chain. This characteristic provides interesting electronic properties, which can be exploited in several applications. In 2000 the world scientific community recognized the importance and the potential applications of

this class of materials when Shirakawa, Heeger, and Mac-Diarmid (prominent scientists in conducting polymer studies) were awarded the Nobel Prize in Chemistry for their research in this field [8].

Although conducting polymers are considered to be new materials within the most recent generation of polymeric materials [9], the first work describing the synthesis of what is now recognized as a conducting polymer was published in 1862 [10]. "Aniline black" was prepared from the anodic oxidation of aniline and, although its electronic properties were not established, a color change observed upon switching potential (later defined as electrochromism) was also reported [11]. Despite these initial works, the discovery of conducting polymers as materials which present reasonable electrical conductivity is attributed to Shirakawa et al. [12], who exposed freestanding films of polyacetylene to vapors of chlorine, bromine, iodine, arsenic pentafluoride, or sodium, obtaining an increase of 12 orders of magnitude in the electrical conductivity at room temperature. This amazing discovery was based on several studies initiated by Natta et al. [13] and Hatano et al. [14]. Natta's group described the synthesis of polyacetylene (PA) and Hatano et al. obtained the first results on the electrical conductivity of PA. Nowadays, the field of conducting polymerns is well established, and researchers are striving to arrive at materials with optimized properties so that all possible commercial applications can be fully exploited.

Conducting polymers are interesting materials because they present the electrical, electronic, magnetic, and optical properties inherent to metals or semiconductors, while retaining mechanical properties close to those observed for conventional polymers. These properties open new possibilities for technological applications. For example, the color change induced by the electrochemical doping–undoping enables the use of these materials in the manufacture of multichromic displays or electrochromic windows [15]. Taking the hole-injecting properties of these polymers under an applied potential or current, flexible light emitting diodes (LED) [16, 17] and light emitting photoelectrochemical cells have been developed [18, 19]. The photovoltaic effect observed in a conducting polymer|electrolyte interface, by irradiating it with energy higher than the polymer bandgap, has been a focus of attention due to the possibility of producing photoelectrochemical cells [20–23]. Other properties also suggest the use of conducting polymers as active components in batteries and capacitors [24–26], biosensors [27, 28], drug-releasing agents [29], gas separation membranes [30], electromagnetic radiation shielding [31], and conductive textiles [32].

Such unique properties are different from those that originate from a physical mixture of insulating polymers with conducting fillers. In intrinsic conducting polymers, the conductivity is related to the delocalization of π-bonded electrons over the polymeric backbone, coexisting with unusual electronic properties, such as low energy optical transitions, low ionization potentials, and high electron affinities [33]. This phenomenon is a consequence of the presence of the conjugated C=C double bonds in the polymer backbone,

as seen in the molecular structures of the repeating units of some conducting polymers (Fig. 1) [34].

2.2. Electrical Conductivity: Electron Delocalization, Oxidation, and Doping Processes

After the Nobel laureates' pioneering work on highly conductive polyacetylene [12], much effort has been devoted toward finding a satisfactory explanation for this phenomenon. Electronic conduction in conjugated C=C double bonds is achieved with electron delocalization, which only occurs if charge carriers have the mobility to carry the charge throughout the chains. Shirakawa et al. [12] showed that the electronic conductivity of polyacetylene changes dramatically when cations or anions are incorporated into the polymer. In analogy to inorganic semiconductors, where an external agent is also incorporated into the matrix to promote conductivity, the species that increased the electronic conductivity of conducting polymers were designated "dopants." Thus, by "doping" a semiconductor organic polymer, the conductivity changes from 10^{-15}–10^{-10} S cm^{-1} to values arriving at 10^4 S cm^{-1}. The doping process distinguishes conducting polymers from all other kinds of polymers. The controlled addition of known, small ($<10\%$) nonstoichiometric amounts of chemical species results in dramatic changes in the electronic, electrical, magnetic, optical, and structural properties of the polymer. The initial studies involving doping are now defined as chemical doping
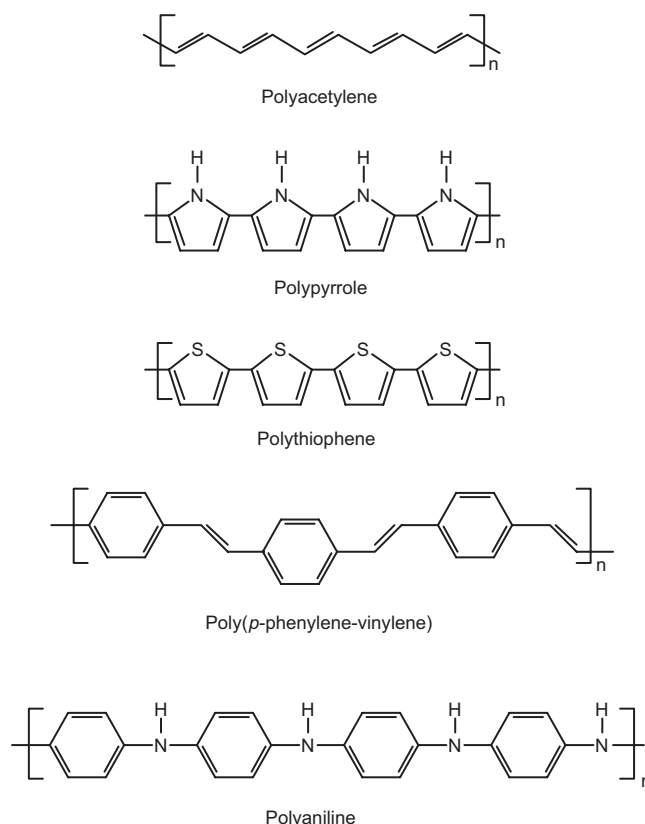
Figure 1. Structure of the π-conjugated conducting polymers.

by charge transfer [9], and an example is the treatment of *trans*-polyacetylene with an oxidizing agent to produce the *p*-doped parent polymer [35].

The phenomenon of electronic conduction in polymers was based on early theories on the same phenomenon seen in studies of inorganic semiconductors, the band model. Basically, the electrical properties were related to the width of the energy gap (E_g) between the valence band and the conduction band. Based on these concepts, Su et al. [36] proposed a unidimensional model based on the existence of structural defects in the polymer backbone originating during polymerization, with the formation of radicals in the undoped state. This delocalized defect can move as a solitary wave in *trans*-polyacetylene and is called a neutral "soliton" in field theory and, by oxidation or reduction, it is possible to remove or add electrons, giving rise to positively or negatively charged solitons (Fig. 2). These species can move along the PA backbone carrying charge but no spin (spinless). If an electron is added to the cation or taken away from the anion, a neutral radical soliton is again established.

In a mechanism involving solitons, electron conduction involves only fully occupied bands in the ground state and leads to the formation of a half-occupied electronic level (one electron) within the gap. This model was initially challenged [37] as it did not explain the fact that the conductivity of PA, poly(*p*-phenylene), poly(*p*-phenylene vinylene), poly(*p*-phenylene sulfide), and polypyrrol (PPy) could be associated with charge carriers having zero spin (spinless) and not to unpaired electrons [38]. Furthermore, polyheterocyclic conducting polymers do not possess degenerate ground states, making conduction by solitons improbable in these materials.

The initial species formed by ionizing polyheterocycles is a radical ion that has both spin and charge, called a "polaron" [39–42]. A polaron is a positively charged hole site (radical cation) or a negatively charged electron site (radical anion), plus a lattice relaxation (distortion) around the charge producing electronic levels within the gap. Theoretical models demonstrate that two radical ions (polarons) react exothermically to produce a dication or a dianion (bipolaron). The former is thermodynamically more stable than two polarons, due to electronic repulsion exhibited by two charges confined in the same site, and causes strong lattice distortions.

Briefly, there are two models concerning the conductivity of conducting polymers. The first has a degenerate ground state and solitons as the most important phenomenon. The second model, used for polyheterocyles, has polarons and bipolarons as the charge carriers and the dominant charge-storage configurations.
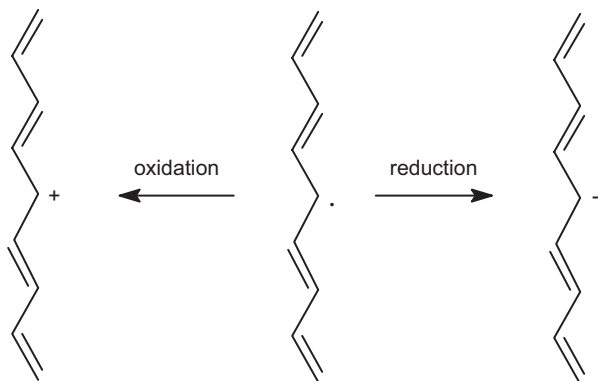
Solitons and polarons–bipolarons explain the electronic motion along the same segments of a polymer chain, but Mateeva [43] proposed that charge transport also occurs by interchain hopping of charges, as seen in Figure 3. In this model, three elements contribute to the overall conducitvity: (A) single chain or intramolecular transport, (B) interchain transport, and (C) interparticle contact. These elements comprise a complicated resistive network, which determines the effective mobility of the carriers.

Thus, the mobility and the conductivity are determined on both microscopic (intra- and interchain) and macroscopic (interparticle) levels [44]. Experimental determinations of mobility of the charge carriers in PA films confirmed that interchain and interparticle transports are the limiting factors for conduction [45]. It can be seen that, although a particular molecular structure theory might predict a lower conductivity based on single-chain conjugation, the conductivity observed could occur due to morphologically controlled interparticle effects. Briefly, interchain interactions are the most important fact that contributes to the occurrence of charge transport in polymer films [46, 47].

As stated before, electron delocalization along the polymer chain requires the partial oxidation or reduction of the chain by introducing an external agent called a dopant. In the first work concerning electronic conductivity in polyacetylene, the polymer was submitted to oxidizing and reducing agents, as shown in the scheme

$$(\mathrm{CH})_n + ny\mathrm{X} \longrightarrow [(\mathrm{CH})^{+y}\mathrm{X}_{y-}]_n$$
$$(\mathrm{CH})_n + ny\mathrm{M} \longrightarrow [(\mathrm{CH})^{-y}\mathrm{M}_{y+}]_n$$
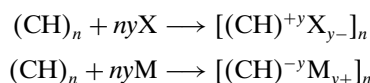
This process was called "chemical doping." Although this method produces highly conductive materials, one of the most interesting properties of conducting polymers is the possibility of modulating the electrical (and other) properties
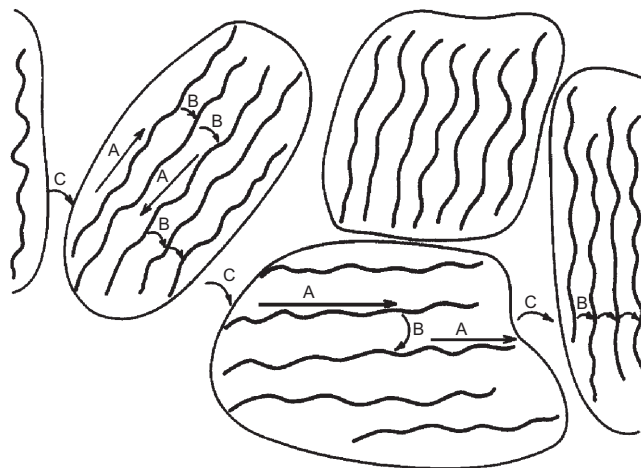
Figure 3. Several mechanisms of charge transport in a conducting polymer: (A) single chain or intramolecular transport, (B) interchain transport, and (C) interparticle contact.

Figure 2. Schematic representation of solitons in *trans*-polyacetylene.

by controlling the doping process and the concentration of the dopant. Unfortunately, chemical doping generally leads to completely doped polymers.

To solve this problem, "electrochemical doping" is an alternative to be considered. In this method, the doping level is precisely controlled by an external potential applied though an electrode. It supplies the charge necessary to oxidize or reduce the polymer film conveniently deposited on a conductive substrate [9]. The first work concerning this concept was published by the same group who introduced the chemical doping as a way to achieve high conductivity in polymers [48]. In electrochemical doping processes, the charge generated in the polymer chain is compensated by ionic diffusion from the electrolyte to the polymer film and these ions play the role of dopants. Figure 4 shows both p- and n-electrochemical doping processes in a poly(3-methylthiophene) film.

In certain cases (e.g., in polyanilines), the doping processes can take place with no redox reactions. The degree of oxidation of polyaniline (PAni) and its derivatives can range from a fully reduced form to a completely oxidized one [49]. Figure 5 shows the oxidation degree of the polyanilines: leucoemeraldine (fully reduced), emeraldine (partially oxidized), and pernigraline (fully oxidized). In this case, all oxidation states are in the so-called "base form" and, although the oxidation degree was altered, the electronic conduction does not reach reasonable values.

The emeraldine base form reacts with dilute acids (e.g., HCl) to give rise to the corresponding salts, with protonation occurring mainly at the imine nitrogen atoms. This reaction is accompanied by an increase of approximately 9–10 orders of magnitude in conductivity of the polymer, reaching 5 S cm^{-1}. Thus, instead of redox reactions, electronic conductivity in polyanilines occurs only for the emeraldine form and is dependent on the protonation degree. This is interpreted on the basis of a p-type doping process and, in contrast to other polymers, does not induce changes in the number of electrons associated with the polymer chain. According to MacDiarmid and Espstein [49], the high conductivity of PAni emeraldine salt is mainly related to a highly symmetrical π-delocalized structure.

"Photodoping" in conducting polymers is achieved when the material is exposed to radiation with energy greater than its bandgap. This kind of doping does not involves dopant insertion into the backbone and the doped material quickly returns to the parent-undoped polymer if the incident radiation is discontinued [35]. The polymer chain is simultaneously oxidized and reduced, producing free electrons and holes. Recombination of the charge carriers can occur as
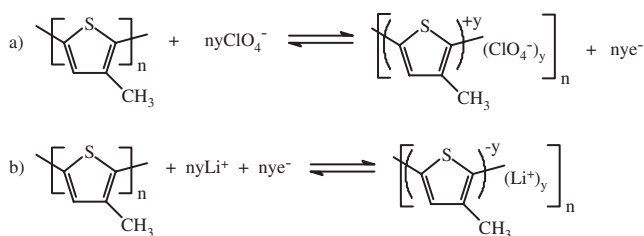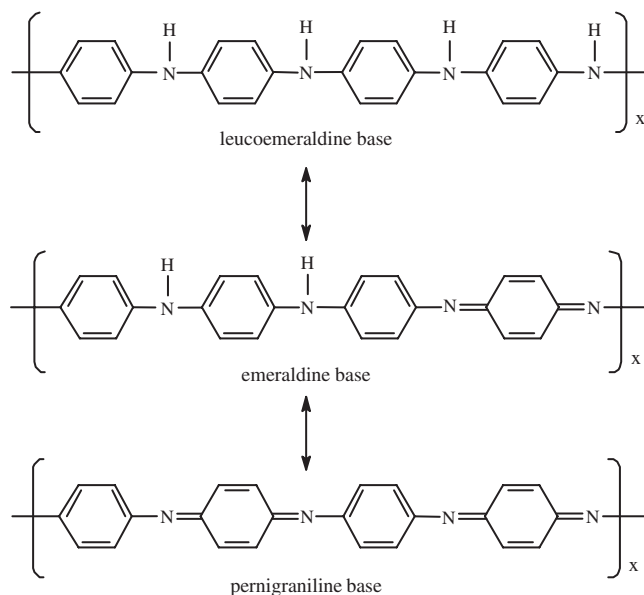
Figure 5. Polyaniline in different states of oxidation, ranging from leucoemeraldine to pernigraniline.

either radiative or nonradiative decay. When one of the photogenerated charge carriers (electron or hole) is collected by other species, the photodoping method finds application in several devices to convert light into electricity, such as photovoltaic devices and photoelectrochemical cells.

The basic processes to achieve efficient solar energy conversion in photoelectrochemical cells are well understood [50] and charge carriers generated in the photodoping processes can be conveniently converted into electricity if the electrolyte contains redox species to collect and transport the charge. The photodoping phenomenon in conducting polymers and the energy position of the bands govern the nature of the redox species to be used. Solution species are reduced at the surface of an irradiated p-doped polymer, while oxidation occurs at an irradiated n-doped polymer [51, 52]. Redox species are not incorporated into the polymer because the photodoping phenomenon is not accompanied by dopant insertion. Figure 6 shows an example of the charge generated (and collected by the external circuit) by photodoping of poly(4,4′-dipentoxy-2,2′-bithiophene) [53]. In this experiment, oxygen dissolved in the electrolytic medium plays the role of the redox species. Furthermore, if a potential is applied during irradiation, electrons and holes separate and photoconductivity is observed [35].

The doping process can occur by charge injection at the metal–semiconductor interface. In the case of the photodoping method, electron–hole pairs exist only while light is shining on the polymer. For charge injection at a metal|semiconductor interface, electron–hole pairs are separated while a bias voltage is applied across the heterojunction. By this method, the conducting polymer can be used as active material in field effect transistors and LEDs.

Doping processes in conducting polymers lead to a new material, with little or no degradation of the polymer chain, and reversibility of this phenomenon is one of the most important features of these materials. This ability to be cycled between charged and neutral states forms

Figure 4. Electrochemical (a) p- and (b) n-doping processes observed for poly(3-methylthiophene) in an electrolyte containing LiClO$_4$.
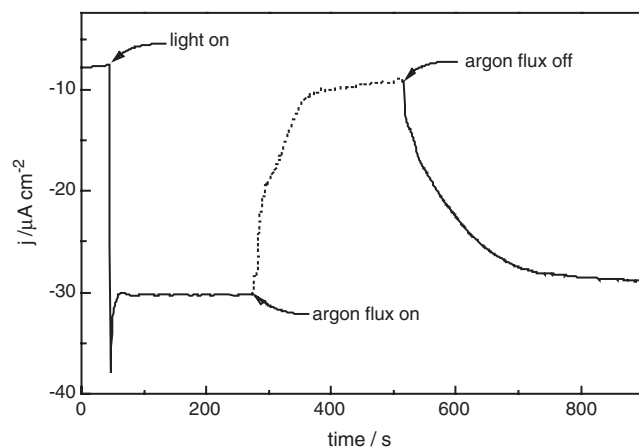
Figure 6. Photoresponse of a poly(4,4′-dipentoxy-2,2′-bithiophene) film submitted to −0.3 V (vs. Ag\AgCl) and polychromatic irradiation of 100 mW cm^{-2} using a 0.1 mol L^{-1} (C$_4$H$_9$)$_4$NClO$_4$ solution in CH$_3$CN as electrolyte.

the basis of the applications of conducting polymers in secondary (rechargeable) batteries and electrochromic displays. Indeed, the large spectrum of applications of conductive polymers using the variation of their properties upon "doping" has attracted the attention of many researchers. Recently, Heeger [9] associated the method used to dope conducting polymers with possible technological applications for these materials, as can be seen in Table 1.

2.3. Synthesis

Since the first reports on the conductivity in polymers, many alternatives have been proposed to produce these materials. Although polyacetylene was the first conducting polymer to be studied in detail, other polymers also have been extensively investigated because of the low environmental stability of polyacetylene. Thus, polyheterocycle polymers, such as polypyrrole, polyaniline, polythiophene, and their substituted derivatives, are nowadays materials in the spotlight. Indeed, much of the work relating the encapsulation of conducting polymers in hosts (which is the scope of this chapter) is devoted to composites based on these three families of polymers. Thus, we have limited this discussion only to the most used methods to prepare these conducting polymers.

Table 1. Doping mechanisms in conducting polymers and the related applications [9].

Doping mechanism	Applications
Chemical doping	transparent electrodes, antistatics
	EMI shielding
Photodoping	photoinduced electron transfer
	photovoltaic devices
	tunable NLO properties
Electrochemical doping	electrochemical batteries and capacitors
	electrochromic devices
	light-emitting electrochemical cells
Interfacial doping	FET
	tunneling injection in LED

There are two ways to synthesize conducting polymers: the "classical chemical synthesis" and the "electrochemical method." The polymerization process occurs by oxidation of the monomer and, for the chemical methods, an oxidizing agent is used. In electrochemical synthesis, an external potential or current is used to oxidize the monomer. When choosing one methodology instead of the other, one must take into account the final properties of the resulting products as well as the applications where the material will be used. For example, *in-situ* electrochemical polymerization is usually preferred in technological applications where a modified electrode is required. Otherwise, chemical synthesis of conducting polymers usually leads to larger quantities of material. As will be seen, a new approach to chemical synthesis also enables the preparation of regioregular polymers. Chemical synthesis of soluble polymers also permits the deposition of films by spin-coating, spraying, or casting.

Chemical methods consist of the direct oxidation of the monomer with an appropriate chemical oxidant. Anilines and pyrroles require a lower potential to be oxidized when compared to thiophenes. Pyrrole is one of the most easily oxidized monomers and there is a great variety of oxidizing agents that can be used in the polymer synthesis, such as the salts of Fe(III) and Cu(II). Polypyrrole powder with a conductivity of 200 S cm^{-1} has been prepared by oxidizing the monomer with FeCl$_3$ [54].

Polythiophenes can also be obtained by direct oxidation of the monomer by an oxidizing agent, such as Fe(III) or other transition metals. However, it is difficult to control the final properties of the first in direct oxidation of thiophenes, and other reactants have been explored for use in the preparation of polythiophenes by chemical polymerization. Organometallic coupling reactions have been used with success to produce polythiophenes, based on Ni or Pd catalyzed reactions. For example, in Ni-catalyzed reactions, dibromothiophenes react with Mg to produce the corresponding Grignard reagent, and the polymerization occurs by polycondensation catalyzed by Ni(bipyridine)$_2^{2+}$ [55]. For polythiophenes, regioregular structures have been obtained by chemical methods. Hoffmann et al. [56] synthesized a series of poly(3,3′-dialkyl-2,2′-bithiophenes) by chemical oxidation of regioregular alkylated thiophenes and verified that the length of the alkyl chain could be related to the solubility and the electrical conductivity of the product.

Chemical methods are also largely used to produce polyanilines by oxidizing the monomer with a great variety of agents, such as ammonium persulfate, manganese oxide, chromium oxide, and hydrogen peroxide. Unlike pyrroles and thiophenes, the oxidation of anilines is usually done in aqueous acid media [57]. The acid medium is necessary because, as mentioned, polyanilines are doped by nonredox processes and electrical conductivity only occurs if the polymer is protonated. The monomer/oxidant ratio has a strong influence on the electrical conductivity of the former and on the polymerization yield [58]. According to Geniès et al. [59], polymer degradation takes place if a high concentration of oxidant is used. The emeraldine salt obtained by chemical synthesis of polyaniline in a HCl medium presents electrical conductivity of 5 S cm^{-1} and treatment with a weak base, typically NH$_4$OH, leads to the emeraldine base with a conductivity of ca. 10^{-9} S cm^{-1}.

Electrochemical synthesis is convenient to produce polymer films deposited on electrodes. The electrochemical synthesis of a given conducting polymer can be achieved by galvanostatic or potentiostatic methods in three-electrode/one-compartment electrochemical cells. The synthesis solution, generally nonaqueous, contains the monomer and a supporting electrolyte. The latter provides the conductive medium and the dopant anions. An important feature of the oxidative electropolymerization reaction is that it proceeds with electrochemical stoichiometry, with values generally in the range of 2.1–2.6 F mol^{-1}, depending on the type of polymer and the electrosynthesis conditions. Polymer formation requires two electrons per monomer and the excess charge corresponds to p-doping of the polymer. By controlling the charge in the cell it is possible to monitor the thickness of the polymer film. Moreover, by changing the nature of the dopant ion (electrolyte salt) or the value of the electrodeposition current density or voltage the physicochemical properties and the morphology of the final polymer can also be controlled [60]. Electropolymerization is the preferential method for preparing conducting polymers because the resulting products are "clean" and generally do not require extraction from the initial monomer/oxidant/solvent mixtures. Besides, electrochemical synthesis offers the additional advantage of homogeneous incorporation of the dopant counterions into the polymer films.

PPy can be obtained by electrochemical synthesis on Pt substrates, producing a strongly adherent, durable film with good electronic and conductivity properties [61]. PAni can be easily prepared by electrodeposition of the film from highly acidic (e.g., H_2SO_4 or $HClO_4$) aqueous solutions, since its electroactivity is promoted by protons [62]. Depending on different solvent/acid media the films of PAni display significant variations in structure and properties [59]. Thiophene, benzene, phenol, and other aromatic hydrocarbons have also been electrochemically polymerized [63]. The use of functionalized acids as dopants in PAni and its derivatives has contributed to increase solubility, promoting a better compatibility between polymer and solvent [58].

Although chemical and electrochemical syntheses require different conditions for the production of high quality polymers, the mechanism accepted for polymerization is basically the same for both methods. Figure 7 shows a typical mechanism for the polymerization of pyrroles and thiophenes. The initial step in the process is monomer oxidation to form a radical cation. For polypyrroles and polythiophenes, ideal chain growth is obtained by 2,5-coupling of the pyrrolic or thiophenic rings (Fig. 7). In this case, the linear product has the highest conjugation in the chain and all properties are optimized. Although the 2,5-coupling is preferential, it is also possible that the reactions proceed at positions 3 and 4 of the rings. This alternative path can lead to branched polymers with undesirable properties. Basically, attaching substituent groups to the 3- and/or 4-positions minimizes the occurrence of α,β coupling during the polymer synthesis, resulting in more regular structures with enhanced properties [64]. Fewer α,β linkage defects in the final structures lead to more effective conjugation, which is an essential feature for more conductive final products. Furthermore, other effects derived specifically from the
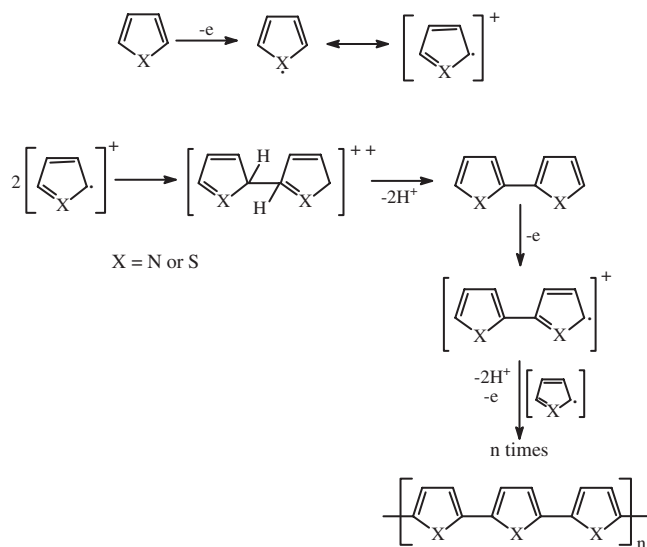
Figure 7. Mechanism for the formation of polypyrroles and polythiophenes.

substituent group also contribute to increase the electrical conductivity.

A similar mechanism was proposed by Geniès et al. [65] for the polymerization of aniline. 1,4-Couplings are needed to produce linear polymers with this monomer. Figure 8 presents this mechanism, supposing that only 1,4-couplings occur in the polymerization. As mentioned, branched polymers are not desirable because electron delocalization is precluded in nonlinear chains.

The next section discusses the effect of the structure on the properties of the polymers.
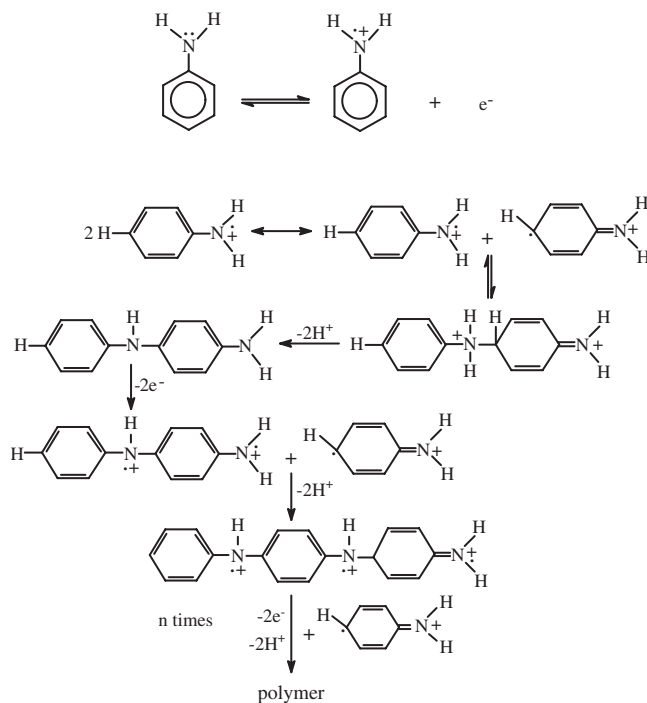
Figure 8. Polymerization mechanism accepted for the synthesis of polyaniline.

2.4. Structure–Property Relationship

The close relationship between polymer properties and their structures is the most interesting characteristic of such materials because few variations in the polymer chains, such as the inclusion of pendant groups or the modification of the molar mass, lead to the preparation of materials with different characteristics. Among the several characteristics that make conducting polymers unique materials, electrical conductivity was the first property studied. This property is basically related to the presence of conjugated double bonds along the polymer backbone, as can be seen in Figure 1. These bonds can be aliphatic (as in PA) or aromatic (in PAni) and allow π-electron delocalization along the polymer structure. Electrical conductivity is strongly dependent on the doping agent and can be changed by several orders of magnitude as the dopant nature or concentration is altered [66].

The nature of the doping agent also affects the mechanical properties of conducting polymers. Self-standing films of polypyrrole are obtained using surfactant salts as doping agents [67]. Polyaniline is a nonmelting and nonprocessable material when doped with HCl; however, it shows elastomeric behavior when doped with sulfonic acids [68, 69] or phosphoric acid esthers [70, 71]. Changes in the mechanical behavior are associated with plastification effects induced by amphifilic dopants. Microcrystalline domains obtained by casting polyaniline solutions induce pseudo-cross-linking that permits the formation of flexible films [72].

The strongly conjugated π-electron system present in conducting polymers makes most of these materials insoluble in ordinary organic solvents. Changing their structures by introducing pendant groups is an alternative to make them more soluble. Qiao et al. [73] studied the influence of different alkyl substituents on the properties of polythiophenes and concluded that alkyl chain lengths up to about 10–12 carbons induce the formation of layered structures in the parent polythiophene. Alkyl side chains of appropriate length also contribute to making the polymer more soluble, in organic solvents, which broadens the possibility of using it in technological applications [73, 74].

As increases in the length of the polymer chain intensify electron delocalization, it could be supposed that the electrical conductivity is proportional to the chain length. However, Gruber and Utley [75] prepared several oligomers of p-phenylene-vinylene and showed that the electrical conductivity remains unchanged independent of the number of monomeric units. These results indicate that Matteva's proposition [43], about the conductivity occurring by intermolecular carrier mobility, is probably correct for this polymer. On the other hand, another article reported that increasing the molar mass of polyaniline from 15,000 to 174,000 g mol^{-1} changed the conductivity from 1.2 to 17 S cm^{-1}. However, there is no consensus on whether the enhanced conductivity is a function of the increased molar mass or is due to the crystallinity degree [76].

As stated, electrical conductivity is also proportional to the crystallinity degree because closer intermolecular distances occurring in the crystalline phase make it easier for the carriers to hop among the chains [76]. Thus, branched chains produced by α,β coupling during polymer synthesis induce lower conductivity values, because branched macromolecules are less crystalline. Besides, the presence of branching also generates traps that hamper the charge carrier mobility along the polymer backbone. Basically, attaching substituent groups to the 3- and/or 4-positions minimizes the occurrence of α,β coupling during polymer synthesis, producing more regular structures [64]. Fewer α,β linkage defects in the final structures lead to a more effective conjugation, which is an essential feature to arrive at more conductive final products. Furthermore, other effects derived specifically from the substituent group also contribute to increasing the electrical conductivity. Moreover, those functionalized polymers with longer alkyl chains have been used to produce more regioregular structures. Roncali et al. [77] verified that no irregular head-to-head or tail-to-tail couplings are observed in the product obtained from the electrochemical polymerization of 3-(3,6-dioxaheptyl)thiophene.

As discussed, the complex morphology of conducting polymers plays a crucial role in their physical properties. In general, conjugation length, interchain interactions, and the extent of disorder are significant parameters that govern the final characteristics of the resulting polymer [78].

Figures 7 and 8 show the mechanisms for the ideal growth of conducting polymer chains to obtain linear backbones. However, other kinds of coupling can occur during the polymerization. Although preferential couplings during polymerization of pyrroles and thiophenes occur in positions 2 and 5, secondary reactions are possible in positions 3 and/or 4, leading to branched products. Figure 9 shows possible structural defects that can occur in a polypyrrole chain [79]. A similar phenomenon is observed in polyaniline synthesis, where polymerization in position 2 leads to pendant groups that affect electron delocalization.

Electrical conductivity in solid-state systems is dependent on the number of charge carriers and on the mobility of these carriers. Inorganic semiconductors possess few charge carriers, but these carriers have high mobility, due to the high crystallinity degree and purity presented by these materials. Otherwise, conducting polymers have a high number of charge carriers with low mobility. The low mobility of
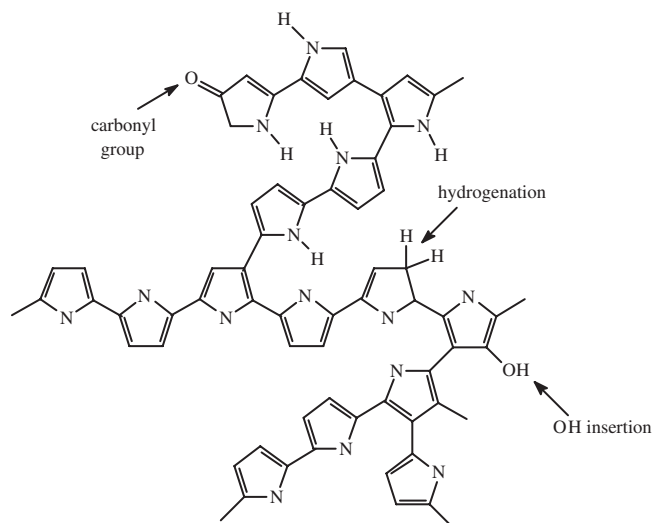
Figure 9. Scheme of structural defects presented by polypyrrole.

charge carriers is attributed to structural defects, as shown in Figure 9. For this reason, the production of polymers with optimized values of electrical conductivity is directly related to the increase of the mobility of the carriers. Indeed, the possibility of controlling the electronic and optical properties of a conducting polymer by tailoring the organic molecular structure (precluding structural defects) will open new possibilities of using these materials in technological applications.

One of the most promising alternatives to produce conducting polymers with fewer structural defects is the encapsulation of the polymer chains in the internal cavities of host structures. Among the possibilities of achieving encapsulated polymers, the "template synthesis" of the conducting polymers in cavities, pores, and lamellae has been explored to produce highly ordered polymer chains with optimized characteristics.

3. CONDUCTING POLYMERIC NANOMATERIALS

3.1. Preparing Conducting Polymers by Template Synthesis

Conjugated polymers have many potential applications, most of which are related to their conductivity. In these materials, the chemical bonding leads to one unpaired electron per carbon atom. Moreover, π-bonding, in which the carbon orbitals are in the $sp^2 p_z$ configuration and in which the orbitals of successive carbon atoms along the backbone overlap, leads to electron delocalization along the backbone of the polymer. This electronic delocalization provides the "highway" for charge mobility along the backbone of the polymer chain. Consequently, doped conjugated polymers are good conductors for two reasons [9]:

i. Doping introduces carriers into the electronic structure. Since every repeating unit is a potential redox site, conjugated polymers can be n-type (reduced) or p-type (oxidized) doped to a relatively high density of charge carriers [80].
ii. The attraction of an electron in one repeating unit to the nuclei in the neighboring unit leads to carrier delocalization along the polymer chain and to charge carrier mobility, which is extended into three dimensions through interchain electron transfer.

Disorder, however, limits carrier mobility and, in the metallic state, limits the electrical conductivity. In most of the cases, this disorder consists of the presence of conjugation-interrupting defects, such as sp^3-hybridized carbons or twists and kinks in the polymer chain [38, 81]. Ioffe and Regel [82] argued that, as the extent of disorder increased in a metallic system, there was a limit to metallic behavior; when the mean free path becomes equal to the interatomic spacing, coherent metallic transport would not be possible. Thus, the Ioffe–Regel criterion is defined in Eq. (1), where k_F is the Fermi wave number and l is the mean free path:

$$k_F \cdot l \approx 1 \qquad (1)$$

In Eq. (1), the metallic regime corresponds to $k_F \cdot l \gg 1$; however, this truly metallic regime has not yet been achieved with conducting polymers. Based on the Ioffe–Regel criterion, Mott and Davis [83] proposed that a metal–insulator transition must occur when the disorder is sufficiently large that $k_F \cdot l < 1$. In the limit, where $k_F \cdot l \ll 1$ (i.e., where the strengh of the random disorder potential is large compared to the bandwidth), all states become localized and the system is called a "Fermi glass." Fermi glass is an insulator with a continuous density of localized states occupied according to Fermi statistics. Although there is no energy gap, the behavior is that of an insulator because the states of the Fermi energy are spatially localized.

Generally, conjugation-interrupting defects are introduced during the synthesis that, as previously mentioned, involves in the first step the formation of cation radicals. The further fate of this highly reactive species depends on the experimental conditions. In favorable cases the next step is a dimerization reaction and stepwise chain growth proceeds via association of radical ions (RR route) or of a cation radical with a neutral monomer (RS route) [84, 85]. Even in these cases, parallel dimerization reactions might occur, leading to different products or to a polymer with a disordered structure. If the synthesis conditions are not carefully optimized, a mixed material is obtained, containing electrochemically active and conducting as well as inactive and insulating portions [86]. It has been demonstrated that, in the synthesis of polypyrrole, the current density is a crucial parameter. At low current densities its structure is dominated by one-dimensional chains, while at high current densities two-dimensional microscopic structures of the polymer are formed. The structure substantially affects the conductivity of the polymer phase. The conductivity of the two-dimensional (2D) form is higher and its temperature dependence is lower, which is of importance when this polymer is used for practical purposes. Detailed studies have shown that short 1D chain segments acting as tunneling barriers interconnect the higher conductive 2D islands [87, 88].

In the case of polyaniline, assuming that polymerization does occur via a radical intermediate, coupling is possible at all three positions on the ring (albeit with differing probabilities) and a number of alternative products to the emeraldine-based structure can be envisaged, including both head-to-head and head-to-tail coupling of the monomer units. The conductivity can be varied over 15 orders of magnitude under appropriate synthesis conditions, up to a maximum of 10^2 S cm^{-1}, typical values being 10^{-3}–10^{-2} S cm^{-1} when oxidized and 10^{-2}–10^{-1} when reduced, although material with predominantly meta-coupling has a very low conductivity (10^{-15}–10^{-14} S cm^{-1}) [84].

Indeed, research directed toward conjugated polymers with improved structural order and hence higher mobility is a focus of current activity in the field. In principle, disorder can be controlled. Experimental studies have established that, for conducting polymers, the electrical properties improve as the degree of chain extension and chain alignment are improved. In polymers with enhanced supermolecular order, the polymer chains are ordered via stretching and/or crystallization of the polymer. Using these approaches, conductivity values in excess of 100,000 S cm^{-1} have been achieved for highly ordered polyacetylene [89],

which is near that of copper. Unfortunately, the doped forms of polyacetylene are so reactive that it appears unlikely that this material will be useful for any of the proposed applications of conductive polymers [90, 91]. Conductivity values for more chemically stable materials (heterocyclic conjugated polymers) are many orders of magnitude lower. Hence, developing strategies for improving the conductivity of these polymers is an important research objective. In this context template synthesis appears to be an "elegant approach" for controlling the extent of molecular and supermolecular order in electronically conductive polymers.

The underlying principle of the template synthesis technique is akin to that of producing components through the use of replication (e.g., die-casting or mold casting, like making ice candies out of molds) [92]. The term "replica" polymerization was first used by Szwarc in 1954 [93]; this term was then displaced by "matrix" or "template" polymerization. In this technique, materials can be deposited within the void spaces of the host materials. These void spaces act as a template that determines the shape, size, and, in many cases, the orientation of the produced particle. Thus, by carrying out the synthesis of conducting polymers in a confined medium, the polymer chains are forced to align within the environment of the host matrix and an enhancement of the conductivity can be expected.

The strategy in using template synthesis involves the judicious selection of the host material and suitable precursors to the desired guest(s). There now exists a huge range of choice of hosts. They can be inorganic, organic, or organometallic compositional types, with 1D tunnels, 2D layers, or 3D framework structures [7, 94]. Hosts may be of insulating, semiconducting, metallic, or superconducting types or may attain these properties following inclusion of the chosen guest. On surveying known host structures, one finds that channel, interlamellar, and cavity dimensions vary widely in size, separation, and perfection, spanning the size range from barely being able to accommodate the smallest ionic or molecular guest all the way to having channel dimensions of about 5–10,000 Å, interlamellar spaces of 3–50 Å, and cavity diameters of 6–10,000 Å.

The template method has a number of interesting and useful features [95]. First, it is very general and can be used to prepare tubules and fibrils composed of electronically conductive polymers [96–104], metals [105–109], semiconductors [110, 111], carbons [112], and other materials. Furthermore, nanostructures with extraordinarily small diameters can be prepared. In addition, when membranes with monodisperse diameter pores are used as templates, monodisperse nanostructures are obtained. Finally, the tubules or fibrils synthesized within the pores can be freed from the template membrane and collected. Alternatively, an ensemble of micro- or nanostructures that protrude from a surface like the bristles of a brush can be obtained. When the host matrix is not dissolved, a nanocomposite is produced.

Nanocomposites can be defined as a combination of two or more phases containing different compositions or structures, where a least one of the phases is in the nanoscale regime [7, 113, 114]. Size effects in nanostructured materials are of great importance from both fundamental considerations and modern practice. It seems of interest to consider

the upper and lower limits of the nanosizes [115, 116]. By nanomaterials, materials are commonly meant to have the size of the grains or phases (D) composing their structure not exceeding 100 nm, in at least one direction. This upper limit is very arbitrary and its value is dictated by convenience considerations rather than by physical ones. However, simple estimations show that, starting from this size, the fraction of disordered interface regions becomes increasingly noticeable (this fraction is about $3s/D$, where s is the width of the grain-boundary region and D is the characteristic size); at reasonable values of $s \approx 0.5$–1 nm, this fraction reaches several percent. On the other hand, the upper limit of D should correspond to the size that is a characteristic length of a physical phenomenon (e.g., the free path of carriers for transport properties, the domain features for magnetic characteristics, etc.). It is clear that the limiting D values would differ for different physical–chemical properties and different materials.

The field of polymer nanocomposites has attracted considerable attention due to the small size of the structural unit and the high surface-to-volume ratio can result in properties not found in bulk materials [117–119]. In this way, new materials with new properties can be obtained and have wide ranging implications for a variety of areas, including chemistry, physics, electronics, optics, materials science, and biomedical science.

The research in polymer-intercalated composites is not exclusively directed toward obtaining high-conductivity materials. Other important properties could also be interesting for a variety of applications. All of these aspects will be discussed in the next sections.

3.2. Development of the Technique

There are several examples in the literature of depositing materials within the pores of microporous membranes. Bean [120] first demonstrated the art of filling the pores of a membrane with silver, followed by Possin [121], who used an electrodeposition technique in the fabrication of thin wires as small as 400 Å, using mica with etched pores as templates for the growth of elements of the microstructures. Williams and Giordano [122] claimed to have reduced the size to 80 Å after some refinements to this technique. Penner and Martin began their template-synthesis work in 1985 by electrochemically synthesizing the electronically conductive polymer polypyrrole within the pores of a nanoporous polycarbonate filtration membrane [96]. Martin et al. coined the term "template synthesis " to describe the process whereby electronically conductive polymers (or other material) are synthesized within the pores of microporous support membrane [98, 123–127]. Most of the initial work entailed the use of two types of membranes: "track-etch" polymeric membranes and porous aluminas.

Nowadays a wide variety of nanoporous solids have been used as template materials. Tonucci et al. [128] have described a nanochannel array glass with pore diameters as small as 33 nm and pore densities as high as 3×10^{10} pores per square centimeter. Douglas et al. [129] have shown that the nanoscopic pores in a protein derived from a bacterium can be used to transfer an image of these pores to an underlying substrate.

Recently, several papers have reported the use of the uniform and straight channels of anodic aluminum oxide (AAO) films as a template [130–133]. Conducting polymers and the copolymer nanofibrils obtained have uniform and well-aligned arrays and their diameters and lengths can be controlled by changing the aspect ratios of the AAO membrane.

3.3. Hosts

"[T]he possibility of assembling a conducting polymer chain within a non-polarizable porous channel is a fascinating one, not only because it would yield a true molecular nanowire, but also it would allow us to study selectively the charge transport mechanisms operating along the polymer chains. . . " [134].

When contemplating how to make template synthesis or "well-defined" host–guest inclusions systems, it is pivotal to really appreciate the effects of the topology and reactivity of the internal surface of the host on the occluded guest [7]. These factors will control, for instance, details of the chemistry between the host and the guest inside the host lattice. Representative examples of the hosts that have been used in template synthesis of conducting polymers are shown in Figure 10.

3.3.1. One-Dimensional Tunnel Hosts

The synthesis of nanoscale organic polymer fibers, cylinders, and wires has created a tremendous amount of excitement in several segments of the scientific community [95, 135, 136].

a)

1-D tunnel hosts:
– Graphite tubes
– Nuclepore membranes
– Inorganic tunnels
– Zeolites, molecular sieves
– Soft chemistry
– Aligned polymer channels

2-D layered hosts:
– Graphite
– Oxide, halide and halcogenide layers
– Organic, inorganic LB films
– Self-assembled mono- and multilayers
– Miscellaneous inorganic layers

b)

3-D framework hosts:
– Carbon sieves
– Porous glasses
– Polymer cavities
– Block-copolymer nanodomains
– Zeolites, molecular sieves
– Protein cages
– Inorganic insertion materials
– Buckyball endohedral complexes and
– insertion compounds

c)

Figure 10. Representative examples of (a) one-dimensional tunnel hosts, (b) two-dimensional layered hosts, and (c) three-dimensional framework hosts.

Such nanoscale sculptures are intrinsically interesting systems with a myriad of potential applications.

A variety of materials that contain one-dimensional pores are known (Fig. 10a) but most of the initial work in this area has entailed the use of two types of membranes: "track-etch" polymeric membranes and porous aluminas (Fig. 11).

Track-Etch Membranes A number of companies, such as Nuclepore and Poretics, sell microporous and nanoporous polymeric filtration membranes that have been prepared by the track-etch method [135, 137]. This method entails bombarding a nonporous sheet of the desired material with nuclear fission fragments, to create damage tracks in the material, and then chemically etching these tracks into pores. These membranes contain randomly distributed cylindrical pores of uniform diameter. Membranes with pore diameters as small as 10 nm are available commercially; pore densities approach 10^9 pores per square centimeter (Fig. 11a and b). The commercially available membranes are prepared from polycarbonate or polyester; however, a number of other materials are amenable to the track-etch process.

Porous Alumina Membranes of this type are prepared electrochemically from Al metal [138]. Pore densities as high as 10^{11} pores per square centimeter can be achieved [139]. Nanomaterials produced by the template method, membranes with high pore density, allow a greater number of nanostructures to be produced per unit area of template membrane (Fig. 11c and d). While such membranes are sold commercially, only a limited number of pore diameters are available. Foss et al. [106, 140] have, however, prepared membranes of this type with a broad range of pore diameters. Membranes with pores as small as 5 nm were made and smaller pores can be prepared.

Most of the work of Martin et al. has focused on polypyrrole, poly(3-methylthiophene), and polyaniline. These polymers can be synthesized by oxidative polymerization of the corresponding monomer. This may be accomplished either electrochemically or with a chemical oxidizing agent. Both of these methods can be used to do template synthesis of conductive polymers. The easiest way to do electrochemical templating is to coat one surface of the templating membrane with a metal film and then use this metal film as anode to electrochemically synthesize the polymer within the pores of the membrane [107, 141, 142]. Chemical template synthesis can be accomplished by simply immersing the membrane in a solution of the desired monomer and its oxidizing agent. This fabrication procedure is shown schematically in Figure 12. Other groups have since used such methods [109, 133].

In developing these template-synthetic methods, an interesting discovery was made. When these polymers are synthesized (either chemically or electrochemically) within the pores of the track-etched polycarbonate membranes, the polymer preferentially nucleates and grows on the pore walls [98–100, 123, 143]. As a result, polymeric tubules are obtained. By controlling the polymerization time, tubules with thin walls (short polymerization times) or thick walls (long polymerization times) can be produced. For polypyrrole, the tubules ultimately "close up" to form solid fibrils. In contrast, polyaniline tubules will not close up, even after long polymerization times [143].
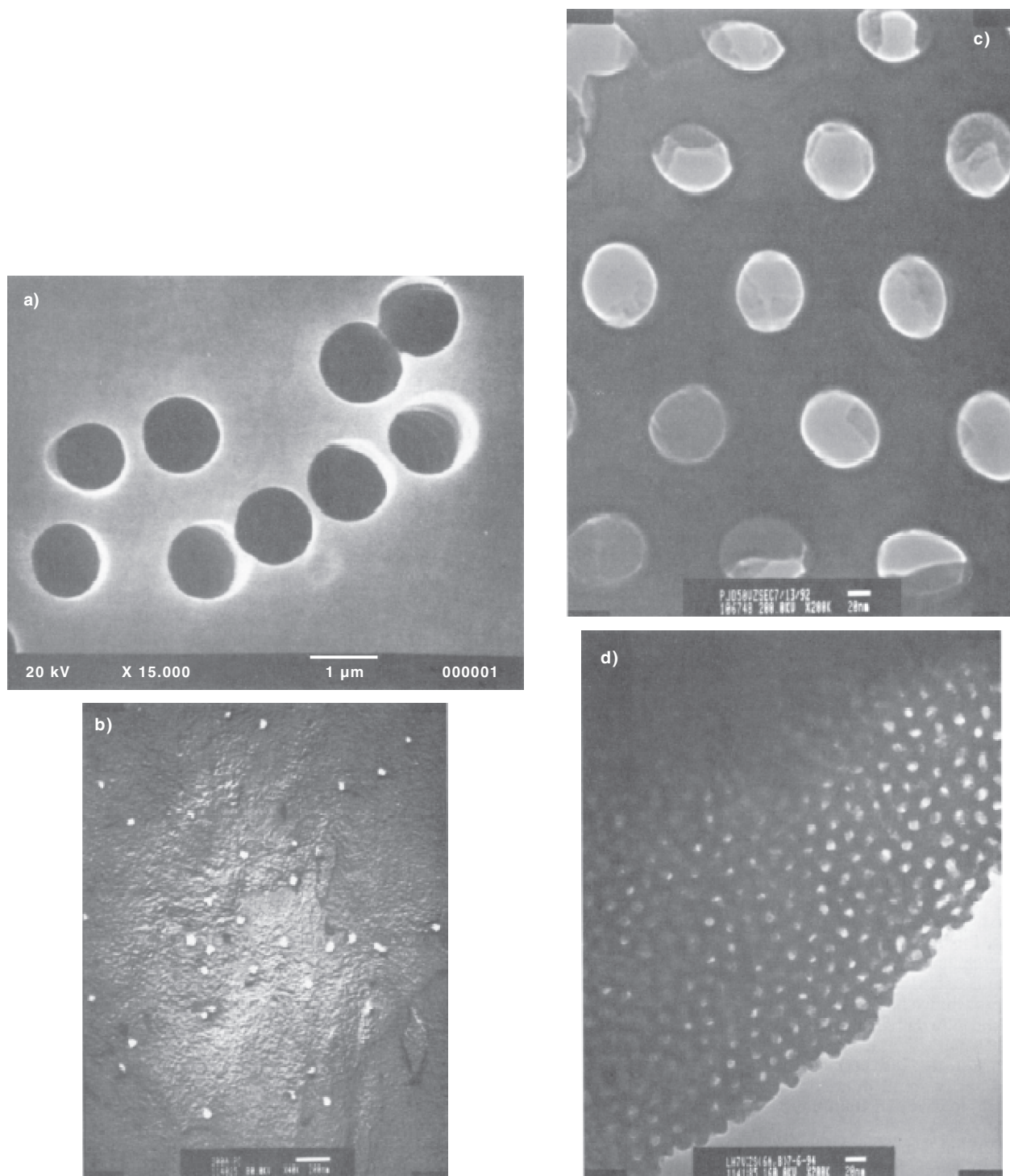
Figure 11. Electron micrographies of polycarbonate (a and b) and alumina (c and d) template membranes. For each type of membrane, an image of a larger pore membrane is presented (a and c) so that the characteristics of the pores can be clearly seen. An image of a membrane with extremely small pores is also presented (b and d). (a) Scanning electron micrograph of the surface of a polycarbonate membrane with 1 μm diameter pores. (b) Transmission electron micrography (TEM) of a graphite replica of the surface of a polycarbonate membrane with 30 nm diameter pores. The pores appear "raged." This is an artifact of the graphite replica. (c and d) TEMs of microtomed section of alumina membranes with (c) 70 and (d) 10 nm diameter pores. Reprinted with permission from [136], C. R. Martin, *Chem. Mater.* 8, 1739 (1996). © 1996 American Chemical Society.

The reason that the polymer preferentially nucleates and grows on the pore walls is straightforward [99]. Although the monomers are soluble, the polycationic forms of these polymers are completely insoluble. Hence, there is a solvo-phobic component to the interaction between the polymer and the pore wall. There is also an electrostatic component because the polymers are cationic and there are anionic sites on the pore walls [99]. This illustrates an important
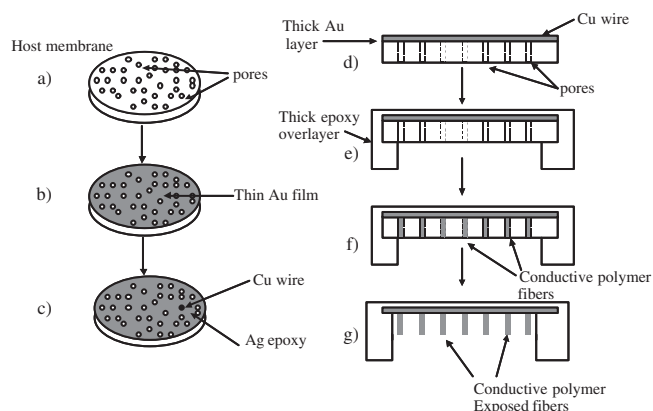
Figure 12. Schematic of the procedure for preparing fibers from anopore alumina membranes.

point: If a "molecular anchor" that interacts with the material being deposited is present on the pore wall, a hollow tubule (as opposed to a solid fibril) will be obtained. This concept of a molecular anchor provides a general route for template synthesis of tubular micro- and nanostructures [125]. A plot of conductivity versus diameter for template-synthesized polypyrrole fibrils is shown in Figure 13.

Whereas fibrils with large diameters have conductivities comparable to those of bulk samples of polypyrrole, the conductivities of the nanofibrils, which have the smallest diameters, are more than an order of magnitude greater. The template-synthesized materials have higher conductivities because the polymer chains on the outer surfaces of the tubules or fibrils are aligned. This can be proven with a technique called polarized infrared absorption spectroscopy (PIRAS) [98, 126, 144].

The PIRAS method entails measurement of the absorption by a polymeric sample of two orthogonally polarized beams of infrared radiation. One beam is polarized perpendicular to the axes of the fibrils, and the other has a
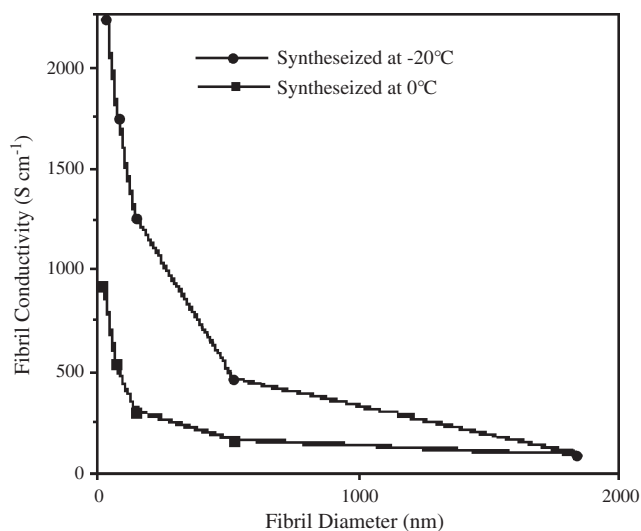
component that is parallel to the fibril axes. In general, if the integrated absorption intensities of the perpendicular and parallel polarizations are the same, the polymer chains show no preferred orientation. In contrast, if equal absorption is not observed, the polymer chains show some degree of alignment. The extent of this alignment can be assessed by calculating a parameter called the dichroic ratio, which is the ratio of the integrated absorption intensities of the parallel and perpendicular polarizations [126, 144]. In this case, the smaller the dichroic ratio, the greater the extent of polymer chain alignment.

By controlling the polymerization time it is possible to prepare tubules with very thin or very thick walls [145]. The PIRAS data were obtained as a function of polymerization time and the extent of polymer chain alignment in the layer of conductive polymer that was deposited directly onto the polycarbonate (short polymerization times) or on subsequently deposited layers (long polymerization times). Figure 14 shows the results of experiment. Parthasarathy and Martin found that the layer of polypyrrole that is deposited directly on the pore wall is ordered (low dichroic ratio) but that the extent of order decreases in subsequently deposited layers (dichroic ratio approaches unity). Analogous results were obtained with polyaniline tubules [143].

These data show that template-synthesized conductive polymer fibrils or tubules have a layer of ordered polymer chains at their outer surface and that the extent of this chain order decreases toward the center of the nanostructure. The chains on the outer surface of the conductive polymer tubules and fibrils are ordered because the polycarbonate chains that make up the pore walls in the template membranes are likewise ordered. Hence, the first layer of conductive polymer chains deposits in accordance with the

Figure 13. Conductivity versus diameter for polypyrrole fibrils. Data for two different synthesis temperatures are shown: lower curve, 0 °C; upper curve, −20 °C. Reprinted with permission from [135], C. R. Martin, *Science* 266, 1961 (1994). © 1994, American Chemical Society.
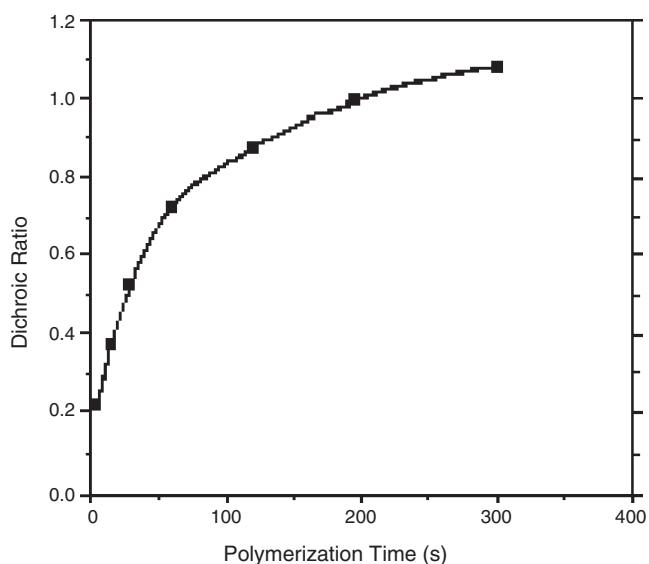
Figure 14. Dichroic ratio for polypyrrole tubules synthesized in a polycarbonate membrane with 400 nm diameter pores, as a function of polymerization time. Since polymerization time controls tubule wall thickness, the *x*-axis is also a wall thickness axis. The band at 1560 cm^{-1} was used to obtain the data. Reprinted with permission from [145], C. R. Martin, *Acc. Chem. Res.* 28, 61 (1995). © 1995, American Chemical Society.

polycarbonate chains on the pore wall. The central core of a fibril is disordered because the order-inducing influence of the pore wall is lost in subsequently deposited layers. The thinnest template-synthesized fibrils have the highest conductivity (Fig. 13) because they contain a relatively higher proportion of ordered material (and a smaller amount of disordered material) than the larger diameter fibrils.

Although particle track-etched membranes are commercially available, the technology has recently been improved in some laboratories [109, 146], in order to produce reliable and reproducible nanoporous particle track-etched membranes (nano-PTM). These lab-scale samples exhibit controlled properties: mean pore size in the range of 15–1000 nm, low pore size distribution, perfectly cylindrical pores with smooth walls, and a parallel arrangement across the membrane. With such optimized properties, nano-PTMs are considered excellent templates for the preparation of controlled nanoscale materials.

Scanning electron micrographs of the "as-prepared" polypyrrole nanostructures after dissolution of the PC membrane clearly show that nanotubules are obtained (Fig. 15) [147]. The nascent polymer is preferentially deposited as thin layers on the pore walls and thus produces hollow polymer tubules that run through the entire thickness of the membrane. It must be noted that the tubules form a continuum with the outer polypyrrole films (i.e., surface layers) and so are strongly fixed.

As shown in Figure 16, two kinds of morphology are observed in terms of the Ppy nanotubule outside diameter. For diameters higher than 100 nm, the tubules are rigid and form a brush supported by the surface layers. At the other extreme, for diameters below 100 nm, the polymer tubules become very flexible and are lying on the surface when the PC membrane is dissolved [147].

The marked difference in morphology between the alumina membrane-templated nanostructures and polycarbonate membrane-templated nanocylinders observed by Mativetsky and Datars [133] reflects a difference in the surface chemistry taking place at the pore walls. A scanning

Figure 16. Scanning electron micrographies of polypyrrole tubules in terms of the pore diameter: (a) for a 40 nm diameter; (b) for a 1000 nm diameter. Reprinted with permission from [147], J. Duchet et al., *Synth. Met.* 98, 113 (1998). © 1998, Elsevier Science.

electron micrograph providing an edge-on view of a filled alumina membrane is shown in Figure 17.

The basic shape of the nanostructures is that of a linear aggregate of irregular blobs. The blobs measured 290 ± 50 nm across, had an elongated shape, and were packed closely together. Few of the nanostructures extended from end-to-end of the template membrane. As no molecular anchor sites are present on the alumina pore walls, there is no preferential growth along the pore walls; instead, the nucleation appears to be at random positions within the pores. The polypyrrole subsequently grows radially outward from the nucleation site, until a pore wall or another polypyrrole mass is contacted. Once in close proximity, the blobs can grow together [133].

The Mott characteristic temperature T_0 was the same as that for similar diameter polycarbonate membrane-templated nanocylinders. This suggests that the two types of samples have similar charge carrier localization lengths, similar densities of states at the Fermi level, and similar conductivities. This supports the argument that there

Figure 15. Scanning electron micrography of typical polypyrrole tubules. Reprinted with permission from [147], J. Duchet et al., *Synth. Met.* 98, 113 (1998). © 1998, Elsevier Science.
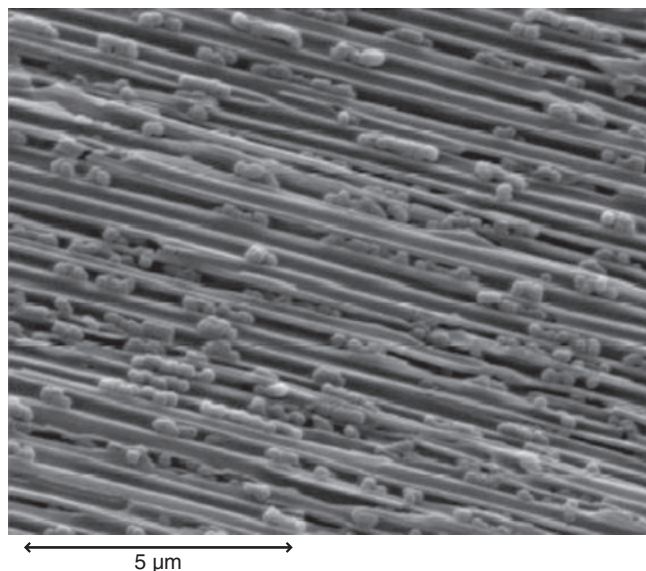
Figure 17. Scanning electron micrography providing a cross-sectional view of a polypyrrole-filled alumina membrane. Reprinted with permission from [133], J. M. Mativetsky and W. R. Datars, *Solid State Commun.* 122, 151 (2002). © 2002, Elsevier Science.

is no conductivity-enhancing order in the polycarbonate membrane-templated nanocylinders [133].

Micro- and nanotubules of conducting polymers have been reported by several groups [130, 132, 148, 149]; however, few large-area, high-quality bilayer films have been reported in detail. In this sense, Fu et al. [150] used templates of microporous alumina membranes having a thickness of 60 μm and pore diameters of 20 and 200 nm. Flexible polythiophene micro- and nanotubules, and aligned tubule/gold bilayer films with an area of 1.8 cm^2, were obtained by direct oxidation of thiophene in freshly distilled boron trifluoride diethyl etherate solutions. Raman spectroscopic studies give evidence for polymer chain orientation in the skin of the nanotubules (20 nm). The micro- or nanotubule/gold bilayer film shows broad and strong redox responses and its charge/discharge capacity is about 30 times that of the usual polythiophene film. These results imply that such films are advanced materials for fabricating capacitors with high energy density.

Li et al. [131, 151] have recently used a template to prepare pyrrole/aniline and pyrrole/3-methylthiophene copolymer nanofibrils by the chemical copolymerization technique and have investigated the structure and morphology of the copolymer fibrils. The copolymerization has a high potential for modifying the physical properties because it provides materials with intermediate properties between two or more monomers. Copolymer nanofibrils were successfully synthesized in the pores of micropores of an AAO template by the chemical copolymerization technique [32]. Electron scanning microscopy results showed that the template technique could control the length, diameter, and thickness of copolymer nanofibrils, which had uniform and well-aligned arrays. A thermogravimetric study demonstrated that the copolymer was thermally stable, as compared to the homopolymers and mixtures. In addition, the conductivity of the copolymers is higher than that observed for homopolymers.

Among the huge range of hosts, many studies were performed using carbon nanotubes [104, 152, 153]. The formation of nanotube/polymer composites is considered a promising approach to an effective incorporation of carbon nanotubes into devices with possible synergetic effects.

Organic LEDs with lower current densities and better thermal stabilities than the corresponding pure polymer devices [154], and photovoltaic cells of a reasonably high quantum efficiency (1.8% at 2.9–3.2 eV) [155], have recently been fabricated. Chen et al. [104] obtained polypyrrole-coated carbon nanotube electrodes that showed significantly improved electrochemical redox performance. Specifically, when the formation charge is around 680 mC cm^{-2}, the redox charge improves 2.5 to 23 times, compared to the flat Ti and Pt substrates. In all these cases the coaxial nanowire structure and the ease with which several conducting polymers can be deposited onto the aligned carbon nanotubes suggest a wide range of potential applications for the conducting polymer–carbon nanotube nanowires, especially in optoelectronic devices and high-performance, lightweight rechargeable batteries.

There has been considerable technological interest in conducting polymers with tubular or fibrillar nanostructures. Areas of application that can be foreseen to benefit from the small size and organization of conducting polymers include electrochemistry, optoelectronics, microelectronics, sensors [156], and bioencapsulation (drug delivery systems involving microencapsulation) [135, 157].

3.3.2. Two-Dimensional Layered Hosts

The ability of nitrogenated bases to penetrate into the interlayer space of different layered solids is the basis for the so-called "intercalatation polymerization" of molecules like aniline and pyrrole [158]. It is a promising strategy to study the confinement of polymer chains in nanometer size inorganic galleries. As conjugated polymers have many potential applications, their insertion in the layered (two-dimensional) inorganic hosts has received extensive attention over the past few years and many conjugated polymer/inorganic host hybrid composites have been synthesized and studied. In intercalation polymerization the inorganic host serves as template within which a guest molecule of nanometer dimensions is assembled. Host lattices such as FeOCl [159], uranyl phosphates [160], transition-metal oxides [161–163], and aluminosilicates [164], with lamellar structures, have been successfully used. The constrained environment is expected to lead to a high degree of polymer ordering and to useful properties [165].

The protons of the carboxylic groups present in the interlayer space of tin (IV)-2-carboxyethylphosphonate (SnP-C) can be ionically exchanged by transition metals (e.g., Fe^{3+}) that act as oxidizing agents for the polymerization of aniline. This process made possible the synthesis of polyaniline in the interlayer spaces producing the composite Pani/SnP-C, which showed electroactive properties characteristic of polyaniline, although the amount of polymer does not exceed 4.0 wt%. The formation of the polymer in the interlayer space of the host material was confirmed by Fourier transform infrared and X-ray diffraction [166]. The photoelectrochemical behavior of the composite was investigated as a function of applied potential, polyaniline

concentration, and the direction of polychromatic radiation [167]. As shown in Figure 18, the photoelectrochemical response was observed as an anodic or cathodic photocurrent, depending on the applied potential [168].

The variation in the sign of the photocurrent with the potential indicates that not only does the bandgap energy change with the potential, but also there is a change of the position of the band edge in relation to the standard potential of the redox pair present in the solution. The photoelectrochemical response showed good stability to prolonged irradiation times and is comparable to the values reported in the literature for other materials, although only 4 wt% of active material was present in the composite.

An alternative route for preparation of PAni-phosphate intercalation materials was reported by Zarbin et al. [169], which consists of submitting the host to a saturated aniline atmosphere. Subsequently the sample was immersed into an oxidant solution and a dark green solid was isolated. The characterization results demonstrated strong evidence for the formation of nanocomposites, indicating that the polymeric chain had high linearity and negligible cross-linking or branching.

The polymerization of aniline in the interlayer space of hosts has also been induced electrochemically [170]. In this way, aniline-intercalated montmorillonite/Pt systems were used as electrodes for aniline anodic oxidation operating in an acid medium. Redox peaks observed in the cyclic voltammograms of the resulting intercalated PAni are associated with polymer protonation/deprotonation processes. This technique can also give information about the oxidation mechanisms occurring either in the interlayer region or on the external surface of the host. Furthermore, it is very important to extend the use of these electrochemical polymerization procedures to other systems, although the required acidic medium could be a limitation with regard to the structural stability of host lattices [158].

The unusual combination of polypyrrole, vanadium oxides, and bentonites has never been reported before the work of Fontes et al. [171]. This promising new ternary composite, formed by the redox/intercalative reaction of polypyrrol with the lamellar bentonite/V_2O_5 [172, 173],
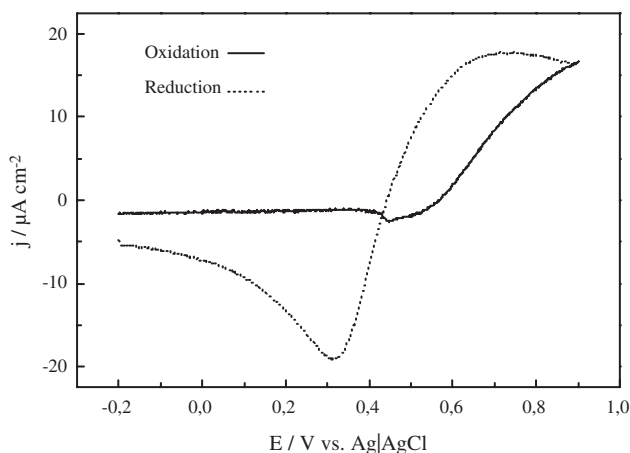
Figure 18. Photoelectrochemical response of the PAni/SnP-C/Fe composite in 0.1 mol L^{-1} $HClO_4$/0.1 mol L^{-1} $LiClO_4$ electrolyte and 0.2 mmol L^{-1} KI/KI 0.02 I_2 mmol L^{-1} redox pair, at 5 mV s^{-1}.

exhibits a characteristic green color and keeps the lamellar structure and electrochemical/electronic properties of the starting materials. The main advantage is its good stability and conductivity as well as its poor solubility in water, in addition to its good adherence to most electrode surfaces. All of these properties ensure potential applications as electrode modifiers, for analytical and sensor purposes.

The research in polymer-intercalated nanocomposites is not exclusively directed toward obtaining stable, electroactive, and highly conductive materials. Intercalation polymerization is also a promising strategy to study the chain structure of conducting polymers and their polymerization mechanisms. According to Wu et al. [174], when polyaniline is inserted into inorganic galleries the strong intermolecular interaction of the polymer chains is eliminated by the host barriers and a polyaniline single chain can be obtained. This is nearly impossible in the classical chemical polymerization of aniline. In addition, the polymerization rate is much slower in the confined environment. Aniline polymerization is a somewhat complicated process; it is a typical precipitation polymerization with a high reaction rate. These features make it difficult to identify and characterize the reaction intermediates and monitor the reaction rate. Thus, in intercalation polymerization the slow kinetic diffusion retards the reaction rate and possibly allows a novel method to study the mechanism during the polymerization induction period, the formation of dimers, and the propagation of polymer chains.

3.3.3. Three-Dimensional Framework Hosts

The design and understanding of well-defined conducting structures of nanometer dimensions and developments along this line could ultimately reduce the size of electronic circuits to molecular dimensions. In this way, conducting polymers have been synthesized within several kinds of hosts.

A material that can be used as a three-dimensional host matrix to obtain conducting polymer nanocomposites is porous vycor glass (PVG—Corning 7930). PVG is a highly transparent porous glass obtained by acid leaching of phase-separated alkaline borosilicate glass [175]. The soluble borate phase is dissolved leaving an open porous structure of essentially pure silica. It has interconnecting pores with a narrow pore size distribution (approximately 80 Å), and a pore of nearly 26%. Si—O—H groups, with acid hydrogens that permit an ion-exchange reaction with Cu^{+2}, form the internal surface of the pores. When pyrrole is added to PVG/Cu^{+2}, the monomer diffuses through the pores, starting oxidative polymerization. Polymer formation is shown by the color change from light blue to black, after 30 min of immersion of PVG/Cu^{+2} in pyrrole solutions.

A PVG/polyaniline nanocomposite was obtained in an inverse way; the monomer was first introduced inside the PVG pores and, after that, the PVG containing the monomer was immersed in an acid oxidizing solution, to promote polymerization. The green color observed in the final product is evidence for polyaniline formation in its conducting state, the emeraldine salt.

In both cases, the polymers are obtained with linear chains, with a very low incidence of structural defects and cross-linking. The very narrow pore size distribution in the glass prevents the occurrence of intermolecular interactions, structural defects, and cross-linking, providing the formation

of molecularly isolated polymer chains. Therefore, these nanocomposites could be produced with high reproducibility, without modifying the chemical properties of polypyrrole or polyaniline. The reversible color change of PAni/PVG composite from dark green (emeraldine salt) to dark blue (emeraldine base) when the glass is immersed in an acid solution or a basic solution, respectively, indicates the usefulness of this material as a sensing phase for an optical pH sensor [176].

Sotomayor et al. [177] describe the use of PAni/PVG nanocomposite as a sensing phase in an optical fiber pH sensor. The optical sensor was constructed by fixing a PVG slide onto the distal end of bifurcated optical fiber bundle, with a cyanoacrylic resin. The sensor response was found to be reversible in the pH range from 5 to 12 and linear from 7.4 to 9.5. Response times of 4, 8, and 16 min were obtained for slide thicknesses of 0.5, 4, and 1.5 mm, respectively. Changes of temperature, ranging from 20 to 40 °C, showed only minor effects on the dynamic range. Similarly, the ionic strength and the nature of the ions showed only small effects on the sensor response. Leaching of PAni was not observed and the sensor lifetime was ca. 5 months. These results indicated that the PAni–PVG nanocomposite is really suitable for the construction of optical pH sensors, with good analytical performance, since the glass slides can be prepared with good reproducibility and durability.

Due to structural complementarity, zeolites have also been recognized to be suitable host compounds to stabilize conducting polymers on the nanoscale. They are a class of crystalline aluminosilicates based on rigid anionic frameworks with well-defined channels and cavities. These cavities contain exchangeable metal cations and can also hold removable and replaceable guest molecules [178]. The primary building units of zeolites are $[SiO_4]^{4-}$ and $[AlO_4]^{5-}$ tetrahedra linked together by corner-sharing, forming bent oxygen bridges. It is possible for the tetrahedra to link by sharing two, three, or all four corners, thus forming a variety of different structures. The important structural feature of zeolites, which can be exploited for template matrices, is the network of linked cavities or pores forming a system of channels throughout the structure. These cavities are of molecular dimensions (approximately 300 to 1200 pm) and a controlling factor in whether molecules can be adsorbed in the cavities is the size of the window or pore opening into the channel.

Early reports on the encapsulation of conjugated polymers in zeolites relate to polypyrrole [179], polythiophenes [180], and polyaniline [181]. Polyacetylene is an interesting case, not only because the bulk polymer is particularly sensitive to atmospheric attack, but also because the doped material can have both the highest conductivity for an organic polymer, and the lowest weight per conducting chain. Bein [182] showed that polyacetylene could be obtained in a variety of microporous hosts, under a variety of conditions, and using different forms of zeolite, including protonated, alkali metal, and transition metal exchanged forms. Recently, Cardin et al. [183] have shown that, in zeolites exchanged with Ni^{2+} or Co^{2+}, ethyne polymerizes rapidly at low temperatures to give complete filling of the voids. The materials were characterized by several techniques (Raman, thermogravimetry and electronic spectra,

infrared and X-ray photoelectron spectroscopy) and shown to form polyacetylene that fully fills the voids of the host, so that the composites are stable to air indefinitely, presumably because oxygen cannot gain access to the polyene chain.

Heterogeneous materials, which have a wide range of void space sizes, can also be used as hosts in template synthesis. Neves et al. [184, 185] have explored the idea of using the heterogeneous porosity of inorganic (sol–gel silica) and organic [poly(vinylidine fluoride)] films as templates for preparation of polyaniline (nano)composites. The large size pore distribution (∼2.5–800 nm) in both template matrices results in a fraction of polyaniline growing more ordered than in films synthesized without spatial restriction. Small-angle X-ray scattering and scanning electron microscopy experiments were done to determine the pore diameters. Cyclic voltammetry experiments confirmed the electroactivity of the composites. In Figure 19 the voltammetric peaks correspond to the changes in the oxidation state of the polyaniline that can be related to the ratio between amine and imine content in the film. There are two characteristic redox couples: at the cathodic extreme the conversion leucoemeraldine to the emeraldine salt and at the anodic extreme from the emeraldine to the pernigraniline form. From analysis of the voltammograms it could be also observed that the redox charge is more intense in the order PAni < PAni/silica < PAni/PVDF. The film porosity increases in the same order, indicating that the swelling of composite bulk by the electrolyte solution should also be considered. The higher bulk interaction of the film with the electrolyte solution results in redox process intensification.

Diffuse reflectance spectra of PAni and the respective composites films (Fig. 20) show two distinct bands, one centered at ∼380 nm and other at ∼800 nm. According to Xia et al. [186] these bands can be ascribed to the π^*-polaron and π-polaron transitions. Note that the more significant differences between the spectra are an increasing absorption tail extending toward the near infrared region, observed only in the composites. This extended "free carrier tail" corresponds to a decrease in the bandgap, which is a direct consequence of an increase in the conjugation length [187]. Since no near-infrared (NIR) absorption tail is observed for
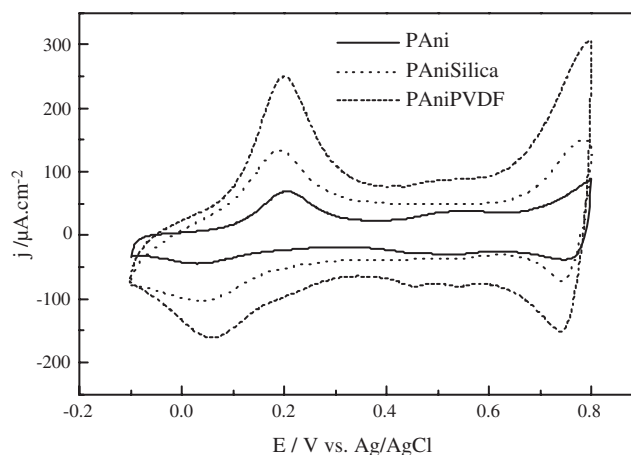
Figure 19. Steady-state cyclic voltammograms of polyaniline film and (nano)composites films in 1.0 mol L^{-1} HCl/1.0 mol L^{-1} NaCl electrolyte, at 5 mV s^{-1}.
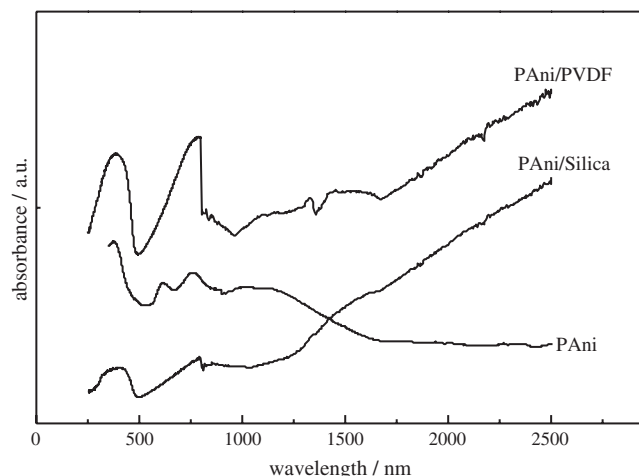
Figure 20. Ultraviolet-visible NIR spectra for polyaniline film and (nano)composite films.

PAni films, the authors [185] concluded that polarons (dominant charge carriers in polyaniline) are more localized in the composite films.

The same authors [188] also investigated the charge/discharge performance of a lithium battery using PAni or PAni/silica as the cathode. For the PAni/silica film, the discharge in the first cycle was 352 mA h g^{-1} and reached a stable value of 223 mA h g^{-1} after the 25th cycle, when the Coulombic efficiency was 95%. In contrast, the initial discharge capacity for the PAni film was 94 mA h g^{-1} and then stabilized at 52 mA h g^{-1}, with the same Coulombic efficiency as the composite. The values are in good agreement with those reported by Venancio et al. [189] for electrochemical thin films with a discharge capacity of 107 mA h g^{-1} and a Coulombic efficiency of 97.5%.

Due to a larger pore size distribution in both template matrices, the polymer formed a continuous conducting network within the composite films but porous morphologies were still observed. The formation of a continuous conducting network within the porous silica matrix increases the electroactive surface area exposed to the electrolyte, thereby providing parallel ionic and electronic conduction pathways which improve the process of charge transfer and mass transport. The balance between these processes is responsible for the good performance of the composite as an electrochemical device.

4. CONCLUSIONS

The goal of this chapter was to present template synthesis as an elegant approach to obtain conducting polymers on the nanoscale. A wide variety of polymers and hosts can be combined to produce materials with the desired properties. This method provides a route for controlling the extent of molecular and supermolecular order in electronically conductive polymers. This allows predictable control not only of the magnitude of the conductivity but also of the conduction mechanism within the material. Hence, these template-synthesized nanostructures are proving to be useful materials for exploring the fundamentals of the conduction

processes in conductive polymers. On the other hand, this method also provides protection from atmospheric attacks to sensitive polymers.

Future research could focus on the preparation of new nanomaterials involving novel kinds of hosts as well as alternative polymeric guest species. Nevertheless, much work should also be devoted to optimizing the preparation by controlling the steps and parameters during template synthesis; increasing understanding of the intercalation mechanisms of monomers, the polymerization driving force, and the nature of host–guest interactions; providing a more profound characterization of the systems; and developing new applications for template-synthesized nanomaterials.

This promising technology could show practical utility early in this century, provided the huge challenge of rapidly and reproducibly moving matter at the atomic level can be surmounted. This interdisciplinary field of research needs creative imagination and should receive increasing attention in the exciting nanoscale world of the future.

This field is now growing rapidly and in just one chapter it is not possible to be entirely comprehensive. Thus, we apologize to those authors whose contributions have not been included.

GLOSSARY

Nanocomposite A combination of two or more phases containing different compositions or structures, where a least one of the phases is on the nanometer scale.

One-dimensional tunnel hosts Host materials that contain one-dimensional channels or pores with internal diameter on the nanometer scale.

Template synthesis Inclusion of inorganic or organic constituents (guests) inside the void spaces of a host material. These void spaces act as a template, determining the shape, size, and in many cases the orientation of the compound produced.

Three-dimensional framework hosts Crystalline or amorphous host materials with channels and/or cavities extending to the three dimensions. The internal diameter of the channels or cavities is on the nanometer scale.

Two-dimensional layered hosts Host materials with a bidimensional structure and an interlayer space on the nanometer scale.

ACKNOWLEDGMENTS

REFERENCES

1. K. Koziel and M. Lapkowski, *Synth. Met.* 55–57, 1011 (1993).
2. G. T. Andrade, M. J. Aguirre, and S. R. Biaggio, *Electrochim. Acta* 44, 633 (1998).
3. G. Inzelt and G. Horanyi, *J. Electrochem. Soc.* 136, 1747 (1989).

4. W. Fosong, T. Jinsong, W. Lixiang, Z. Hongfang, and M. Zhishen, *Mol. Cryst. Liq. Cryst.* 160, 175 (1988).

5. J. Lei, Z. Cai, and C. R. Martin, *Synth. Met.* 46, 53 (1992).

6. A. G. MacDiarmid, in "Conjugated Polymers and Related Materials" (W. R. Salaneck, I. Lundstrom, and B. Ranby, Eds.), Oxford Univ. Press, Oxford, 1993.

7. G. A. Ozin, *Adv. Mater.* 4, 612 (1992).

8. www.nobel.se/chemistry/laureates/2000/index.html.

9. A. J. Heeger, *Synth. Met.* 125, 23 (2002).

10. H. Letheby, *J. Chem. Soc.* 224, 161 (1862).

11. M. F. Goppelsröder, *Compt. Rend.* 82, 331 (1876).

12. H. Shirakawa, E. J. Louis, A. G. MacDiarmid, C. K. Chiag, and A. J. Heeger, *J. Chem. Soc. Chem. Commun.* 578 (1977).

13. G. Natta, G. Mazzanti, and P. Corradini, *Atti. Accad. Nazl. Lincei. Rend. Classe Sci. Fis. Mat Nat.* 25, 3 (1958); *Chem Abstr.* 53, 13985 (1959).

14. M. Hatano, S. Kambara, and S. Okamoto, *J. Polym. Sci.* 51, S26 (1961).

15. W. A. Gazotti, G. Casalbore-Miceli, A. Geri, and M.-A. De Paoli, *Adv. Mater.* 10, 60 (1998).

16. G. Yu and A. J. Heeger, *Synth. Met.* 85, 1183 (1997).

17. J. H. Burroughes, D. D. C. Bradley, A. R. Brown, R. N. Marks, K. Mackay, R. H. Friend, P. L. Burns, and A. B. Holmes, *Nature* 347, 539 (1990).

18. Q. Pei, G. Yu, C. Zhang, Y. Yang, and A. J. Heeger, *Science* 269, 1086 (1995).

19. Q. Pei, Y. Yang, G. Yu, C. Zhang, and A. J. Heeger, *J. Am. Chem. Soc.* 118, 3922 (1996).

20. L. Micaroni and M.-A. De Paoli, *Sol. Energy Mater. Sol. Cells* 43, 79 (1996).

21. M.-A. De Paoli, L. Micaroni, M. Martini, F. L. C. Miquelino, A. M. Rocco, W. A. Gazotti, R. C. D. Peres, and E. A. R. Duek, in "Current Trends in Polymer Photochemistry" (N. S. Allen, M. Edge, I. R. Bellobono, and E. Selli, Eds.), p. 328. Ellis Horwood, London, 1995.

22. T. Yohannes, T. Solomon, and O. Inganäs, *Synth. Met.* 82, 215 (1996).

23. T. Yohannes and O. Inganäs, *Sol. Energy Mater. Sol. Cells* 51, 193 (1998).

24. T. Matsunaga, H. Daifuku, T. Nakajima, and T. Kavagoi, *Polym. Adv. Techn.* 1, 33 (1990).

25. B. Scrosati, *Polym. Int.* 47, 50 (1998).

26. P. Kathirgamanathan and S. Ravichandran, *Synth. Met.* 74, 165 (1995).

27. C. G. J. Koopal, B. de Ruiter, and R. J. M. Nolte, *J. Chem. Soc. Chem. Commun.* 1691 (1991).

28. J. N. Barisci, C. Conn, and G. G. Wallace, *Trend Polym. Sci.* 4, 307 (1996).

29. Y. Li and S. Dong, *J. Chem. Soc. Chem. Commun.* 827 (1992).

30. N. Langsam and L. M. Robeson, *Polym. Eng. Sci.* 29, 44 (1989).

31. R. Racicot, R. Brown, and S. C. Yang, *Synth. Met.* 85, 1263 (1997).

32. R. V. Gregory, W. C. Kimbrell, and H. H. Kuhn, *Synth. Met.* 28, C823 (1989).

33. J. D. Stenger-Smith, *Progr. Polym. Sci.* 23, 57 (1998).

34. W. A. Gazotti, A. F. Nogueira, E. M. Girotto, L. Micaroni, M. Martini, S. Neves, and M.-A. De Paoli, in "Handbook of Advanced Electronic and Photonic Materials and Devices" (H. S. Nalwa, Ed.), Vol. 10, p. 54. Academic Press, San Diego, 2001.

35. A. G. MacDiarmid, *Synth. Met.* 125, 11 (2002).

36. W. P. Su, J. R. Schirieffer, and A. J. Heeger, *Phys. Rev. Lett.* 42, 1698 (1979).

37. Y. Tomkiewicz, T. D. Schultz, H. B. Broom, T. C. Clarke, and G. B. Street, *Phys. Rev. Lett.* 43, 1532 (1979).

38. J. L. Brédas and G. B. Street, *Acc. Chem. Res.* 18, 309 (1985).

39. J. L. Brédas, R. R. Chance, and R. Silbey, *Phys. Rev. B* 26, 58431 (1982).

40. J. L. Brédas, J. C. Scott, K. Yakushi, and G. B. Street, *Phys. Rev. B* 30, 1023 (1984).

41. H. Kaufman, N. Colaneri, J. C. Scott, and G. B. Street, *Phys. Rev. Lett.* 53, 1005 (1984).

42. S. Stafstrom, J. L. Brédas, A. J. Epstein, H. S. Woo, D. B. Tanner, W. S. Huang, and A. G. MacDiarmid, *Phys. Rev. Lett.* 59, 1464 (1987).

43. E. S. Matveeva, *Synth. Met.* 79, 127 (1996).

44. J. I. Kroschwitz, "Encyclopedia of Polymers: Science and Engineering," Vol. 5, p. 462. Wiley, New York, 1986.

45. C. R. Fincher, M. Ozaki, M. Tanaka, D. Peebles, L. Lauchlan, A. J. Heeger, and A. G. MacDiarmid, *Phys. Rev. B* 20, 1589 (1979).

46. S. Kivelson, *Phys. Rev. Lett.* 46, 1344 (1981).

47. R. R. Chance, J. L. Brédas, and R. Silbey, *Phys. Rev. B* 29, 4991 (1984).

48. P. J. Nigrey, A. G. MacDiarmid, and A. J. Heeger, *J. Chem. Soc. Chem. Commun.* 96, 594 (1979).

49. A. G. MacDiarmid and A. J. Epstein, *Faraday Discuss. Chem. Soc.* 88, 317 (1989).

50. H. Gerischer, in "Solar Energy Conversion. Solid-State Physics Aspects" (B. O. Seraphin, Ed.), Vol. 31. Springer-Verlag, Berlin, 1979.

51. H. O. Finklea, *J. Chem. Educ.* 60, 325 (1983).

52. D. Vanmaekelbergh, *Electrochim. Acta* 42, 1121 (1997).

53. W. A. Gazotti, E. M. Girotto, A. F. Nogueira, and M.-A. De Paoli, *Sol. Energy Mater. Sol. Cells* 69, 315 (2001).

54. V. Bocchi and G. P. Gardini, *J. Chem. Soc. Chem. Commun.* 148 (1996).

55. J. W. P. Lin and L. P. Dudek, *J. Polym. Sci. Polym. Chem. Ed.* 18, 2869 (1980).

56. K. J. Hoffmann, E. Bakken, E. J. Samuelsen, and P. H. J. Carlsen, *Synth. Met.* 113, 39 (2001).

57. L. H. C. Mattoso, *Quím. Nova* 19, 388 (1996).

58. W. A. Gazotti and M.-A. De Paoli, *Synth. Met.* 80, 263 (1996).

59. E. M. Geniès, A. A. Syed, and C. Tsintavis, *Mol. Cryst. Liq. Cryst.* 121, 181 (1985).

60. C. Arbizzani, M. Mastragostino, and B. Scrosati, in "Handbook of Organic Conductive Molecules and Polymers" (H. S. Nalwa, Ed.), Vol. 4, pp. 595–619. Wiley, New York, 1997.

61. A. F. Diaz, K. K. Kanazawa, and G. P. Giardini, *J. Chem. Soc. Chem. Commun.* 635 (1979).

62. A. Watanabe, K. Mori, Y. Iwasak, and Y. Nakamura, *J. Chem. Soc. Chem. Commun.* 3 (1987).

63. N. Oyama, T. Ohsaka, T. Hirokawa, and T. Suzuki, *J. Chem. Soc. Chem. Commun.* 1133 (1987).

64. M. Dietrich, J. Heinze, G. Heywang, and F. Jonas, *J. Electroanal. Chem.* 369, 87 (1994).

65. E. M. Geniès, A. Boyle, M. Lapkowski, and T. Tsintavis, *Synth. Met.* 36, 139 (1990).

66. O. Ikkala, J. Ruokolainen, R. Makinen, M. Torkkeli, R. Serimaa, T. Makela, and G. ten Brinke, *Synth. Met.* 102, 1498 (1999).

67. M.-A. De Paoli, S. Panero, S. Paserini, and B. Scrosati, *Adv. Mater.* 2, 480 (1990).

68. T. Vikki and O. T. Ikkala, *Synth. Met.* 69, 235 (1995).

69. O. T. Ikkala, T. M. Lindholm, H. Ruohonen, M. Selantau, and K. Väkiparta, *Synth. Met.* 69, 135 (1995).

70. J. Laska, A. Pron, M. Zagórska, M. Lapkowski, and S. Lefrant, *Synth. Met.* 69, 113 (1995).

71. A. Pron, J. Laska, J.-E. Österholm, and P. Smith, *Polymer* 34, 4235 (1995).

72. M. Angelopoulos, G. E. Asturias, S. P. Ermer, A. Ray, E. M. Scherr, A. G. MacDiarmid, M. Akhtar, Z. Kiss, and A. J. Epstein, *Mol. Cryst. Liq. Cryst.* 160, 151 (1988).

73. X. Qiao, X. Wang, and Z. Mo, *Synth. Met.* 118, 89 (2001).

74. X. Hu and L. Xu, *Polymer* 41, 9147 (2000).

75. J. Gruber and J. H. P. Utley, in "Proceedings of the 17th Meeting of the Brazilian Chemical Society," Caxambu, 1994, p. QO-106.

76. A. G. MacDiarmid and A. J. Epstein, in "Proceedings of the 2nd Brazilian Polymer Congress," São Paulo, 1993, p. 544.
77. J. Roncali, R. Garreau, D. Delabouglise, F. Garnier, and M. Lemaire, *J. Chem. Soc. Chem. Commun.* 679 (1989).
78. R. Kiebooms, R. Menon, and K. Lee, in "Handbook of Advanced Electronic and Photonic Materials and Devices" (H. S. Nalwa, Ed.), Vol. 8, p. 1. Academic Press, San Diego, 2001.
79. D. J. Maia, M.-A. De Paoli, O. L. Alves, A. J. G. Zarbin, and S. Neves, *Quím. Nova* 23, 204 (2000).
80. C. K. Chiang, S. C. Gau, C. R. Fincher, Jr., Y. W. Park, and A. G. MacDiarmid, *Appl. Phys. Lett.* 33, 18 (1978).
81. S. Kivelson and A. J. Heeger, *Synth. Met.* 22, 371 (1988).
82. A. F. Ioffe and A. R. Regel, *Progr. Semicond.* 4, 237 (1960).
83. N. F. Mott and E. A. Davis, in "Electronic Processes in Non-crystalline Materials." Oxford Univ. Press, Oxford, 1979.
84. G. P. Evans, "Electrochemical Science Engineering" (H. Gerischer and C. W. Tobias, Eds.), Vol. 1, p. 1. VCH, Weinheim, 1990.
85. R. J. Forster and J. G. Vos, in "Comprehensive Analytical Chemistry," Vol. 27. Elsevier, Amsterdam, 1992.
86. T. F. Otero and J. Rodriguez, *Electrochim. Acta* 39, 245 (1994).
87. K. West, T. Jacobsen, B. Zachau Christiansen, M. A. Careem, and S. Skaarup, *Synth. Met.* 55/57, 1412 (1993).
88. G. Paasch, D. Smeisser, A. Bartl, H. Naarman, L. Dunsch, and W. Göpel, *Synth. Met.* 66, 135 (1994).
89. H. Naarmann and N. Theophilou, *Synth. Met.* 22, 1 (1987).
90. J. S. Miller, *Adv. Mater.* 5, 587 (1993).
91. A. Pron and P. Rannou, *Progr. Polym. Sci.* 27, 135 (2002).
92. A. B. Frazier and M. G. Allen, *J. Microelectromech. Syst.* 2, 87 (1993).
93. M. Szwarc, *J. Polym. Sci.* 13, 317 (1954).
94. G. Farrington and D. F. Shriver, *Chem. Eng. News* 63, 42 (1985).
95. S. K. Chakarvati and J. Vetter, *Rad. Measurem.* 29, 149 (1998).
96. R. M. Penner and C. R. Martin, *J. Electrochem. Soc.* 133, 2206 (1986).
97. L. S. Van Dyke and C. R. Martin, *Langmuir* 6, 1123 (1990).
98. W. Liang and C. R. Martin, *J. Am. Chem. Soc.* 112, 9666 (1990).
99. C. R. Martin, *Adv. Mater.* 3, 457 (1991).
100. R. V. Parthasarathy and C. R. Martin, *Nature* 369, 298 (1994).
101. V. P. Menon, J. Lei, and C. R. Martin, *Chem. Mater.* 8, 2382 (1996).
102. A. J. G. Zarbin, M.-A. De Paoli, and O. L. Alves, *Synth. Met.* 99, 227 (1999).
103. M. Delvaux, J. Duchet, P.-Y. Stavaux, R. Legras, and S. Demoustier-Champagne, *Synth. Met.* 113, 275 (2000).
104. J. H. Chen, Z. P. Huang, D. Z. Wang, S. X. Yang, W. Z. Li, J. G. Wen, and Z. F. Ren, *Synth. Met.* 125, 289 (2002).
105. R. M. Penner and C. R. Martin, *Anal. Chem.* 59, 2625 (1987).
106. C. A. J. Foss, G. L. Hornyak, J. A. Stockert, and C. R. Martin, *Adv. Mater.* 5, 135 (1993).
107. C. J. Brumlik, V. P. Menon, and C. R. Martin, *J. Mater. Res.* 9, 1174 (1994).
108. U. Simon and M. E. Franke, *Micropor. Mesopor. Mater.* 41, 1 (2000).
109. S. Demoustier-Champagne, *Mater. Sci. Eng. C* 15, 269 (2001).
110. J. D. Klein, R. D. I. Herrick, D. Palmer, M. J. Sailor, C. J. Brumlik, and C. R. Martin, *Chem. Mater.* 5, 902 (1993).
111. B. B. Lakshmi, P. K. Dorhout, and C. R. Martin, *Chem. Mater.* 9, 857 (1997).
112. R. V. Parthasarathy and C. R. Martin, *Adv. Mater.* 7, 896 (1995).
113. J. W. Schultze and A. Bressel, *Electrochim. Acta* 47, 3 (2001).
114. H. Iahida, S. Campbell, and J. Blackwell, *Chem. Mater.* 12, 1260 (2000).
115. R. A. Andrievski and A. M. Glezer, *Scripta Mater.* 44, 1621 (2001).
116. D. Chakravorty, S. Banerjee, and T. K. Kundu, *Appl. Surf. Sci.* 182, 251 (2001).
117. A. S. Edelstein, J. S. Murday, and B. B. Rath, *Progr. Mater. Sci.* 42, 5 (1997).
118. H. Gleiter, *Acta Mater.* 48, 1 (2000).
119. M. Kryszewski, *Synth. Met.* 109, 47 (2000).
120. C. P. Bean, U.S. Patent 3, 483, 095, 1969.
121. G. E. Possin, *Rev. Sci. Instrum.* 41, 772 (1970).
122. W. D. Williams and N. Giordano, *Rev. Sci. Instrum.* 53, 410 (1984).
123. Z. Cai and C. R. Martin, *J. Am. Chem. Soc.* 111, 4138 (1989).
124. C. R. Martin, L. S. Van Dyke, Z. Cai, and W. Liang, *J. Am. Chem. Soc.* 112, 8976 (1990).
125. C. J. Brumlik and C. R. Martin, *J. Am. Chem. Soc.* 113, 3174 (1991).
126. Z. Cai, J. T. Lei, V. Menon, and C. R. Martin, *Chem. Mater.* 3, 457 (1991).
127. C. R. Martin, L. S. Van Dyke, and Z. Cai, *Electrochim. Acta* 37, 1611 (1992).
128. R. J. Tonucci, B. L. Justus, A. J. Campilo, and C. E. Ford, *Science* 258, 783 (1992).
129. K. Douglas, G. Devaud, and N. A. Clark, *Science* 257, 642 (1992).
130. C. Wang, Z. Wang, M. Li, and H. Li, *Chem. Phys. Lett.* 341, 431 (2001).
131. M. Lu, X.-H. Li, and H.-L. Li, *Mater. Sci. Eng. A* 334, 291 (2002).
132. Z. Wang, M. Chen, and H.-L. Li, *Mater. Sci. Eng. A* 328, 33 (2002).
133. J. M. Mativetsky and W. R. Datars, *Solid State Commun.* 122, 151 (2002).
134. P. J. Langley and J. Hulliger, *Chem. Soc. Rev.* 28, 289 (1999).
135. C. R. Martin, *Science* 266, 1961 (1994).
136. C. R. Martin, *Chem. Mater.* 8, 1739 (1996).
137. R. L. Fleischer, P. B. Price, and R. M. Walker, "Nuclear Tracks in Solids." Univ. of California Press, Berkeley, CA, 1975.
138. A. Despic and V. P. Parkhutik, in "Modern Aspects of Electrochemistry" (J. O. Bockris, R. E. White, and B. E. Conway, Eds.), Vol. 20. Plenum, New York, 1989.
139. D. AlMawiawi, N. Coombs, and M. Moskovits, *J. Appl. Phys.* 70, 4421 (1991).
140. C. A. Foss, Jr., G. L. Hornyak, J. A. Stockert, and C. R. Martin, *J. Phys. Chem.* 96, 7497 (1992).
141. L. S. Van Dyke and C. R. Martin, *Synth. Met.* 36, 275 (1990).
142. V. P. Menon and C. R. Martin, *Anal. Chem.* 67, 1920 (1995).
143. R. V. Parthasarathy and C. R. Martin, *Chem. Mater.* 6, 1627 (1994).
144. J. Lei, V. P. Menon, and C. R. Martin, *Polym. Adv. Technol.* 4, 124 (1992).
145. C. R. Martin, *Acc. Chem. Res.* 28, 61 (1995).
146. E. Ferain and R. Legras, *Nucl. Instrum. Methods B* 131, 97 (1997).
147. J. Duchet, R. Legras, and S. Demoustier-Champagne, *Synth. Met.* 98, 113 (1998).
148. J. W. Schultze, T. Morgenstern, D. Schattka, and S. Winkels, *Electrochim. Acta* 44, 1847 (1999).
149. M. Xan, J. Huang, and Y. Shen, *Synth. Met.* 101, 708 (1999).
150. M. Fu, Y. Zhu, R. Tan, and G. Shi, *Adv. Mater.* 13, 1874 (2001).
151. X. H. Li, X. G. Zhang, and H.-L. Li, *J. Appl. Polym. Sci.* 81, 3002 (2001).
152. J. Sandler, M. S. P. Shaffer, T. Prasse, W. Bauhofer, K. Schulte, and A. H. Windle, *Polymer* 40, 5967 (1999).
153. D. B. Romero, M. Carrard, W. A. de Heer, and L. Zuppiroli, *Adv. Mater.* 8, 899 (1996).
154. S. A. Curran, P. M. Ajayan, W. J. Blau, D. L. Carroll, J. N. Coleman, A. B. Dalton, A. P. Davey, A. Drury, B. McCarthy, S. Maier, and A. Strevens, *Adv. Mater.* 10, 1091 (1998).
155. H. Ago, K. Petritsch, M. S. P. Shaffer, A. H. Windle, and R. H. Friend, *Adv. Mater.* 11, 1281 (1999).
156. R. V. Parthasarathy, V. P. Menon, and C. R. Martin, *Chem. Mater.* 9, 560 (1997).
157. R. Pool, *Science* 247, 1410 (1990).
158. E. Ruiz-Hitzky, *Adv. Mater.* 5, 334 (1993).
159. M. G. Kanatzidis, C. G. Wu, H. O. Marcy, D. C. DeGroot, and C. R. Kannewurf, *Adv. Mater.* 2, 364 (1990).
160. Y. J. Liu and M. G. Kanatzidis, *Inorg. Chem.* 7, 1525 (1993).
161. Y. J. Liu, D. C. DeGroot, J. L. Schindler, C. R. Kannewurf, and M. G. Kanatzidis, *J. Chem. Soc. Chem. Commun.* 593 (1993).

162. M. G. Kanatzidis, C. Wu, H. O. Marcy, and C. R. Kannewurf, *J. Am. Chem. Soc.* 111, 4139 (1989).

163. T. A. Kerr, H. Wu, and L. F. Nazar, *Chem. Mater.* 8, 2005 (1996).

164. V. Mehrotra and E. P. Giannelis, *Solid State Commun.* 51, 115 (1992).

165. V. Mehrotra and E. P. Giannelis, *Solid State Commun.* 7, 155 (1991).

166. D. J. Maia, O. L. Alves, and M.-A. De Paoli, *Synth. Met.* 90, 37 (1997).

167. D. J. Maia, S. Neves, O. L. Alves, and M.-A. De Paoli, *Synth. Met.* 102, 1153 (1999).

168. D. J. Maia, S. Neves, O. L. Alves, and M.-A. De Paoli, *Electrochim. Acta* 44, 1945 (1999).

169. A. J. G. Zarbin, D. J. Maia, M.-A. De Paoli, and O. L. Alves, *Synth. Met.* 102, 1277 (1999).

170. H. Inoue and H. Yoneyama, *J. Electroanal. Chem.* 233, 291 (1987).

171. G. J.-F. Demets, F. J. Anaissi, H. E. Toma, and M. B. A. Fontes, *Mater. Res. Bull.* 37, 683 (2002).

172. F. J. Anaissi, G. J.-F. Demets, H. E. Toma, and A. C. V. Coelho, *J. Electroanal. Chem.* 464, 48 (1999).

173. F. J. Anaissi, G. J.-F. Demets, S. Dovidauskas, A. C. Vieira, and H. E. Toma, *Mater. Res. Bull.* 36, 289 (2001).

174. Q. Wu, Z. Xue, Z. Qi, and F. Wang, *Polymer* 41, 2029 (2000).

175. Corning Glass Works, *Mater. Eng.* 90, 92 (1979).

176. K G. Neoh and E. T. Kang, *Polymer* 34, 1630 (1993).

177. P. T. Sotomayor, I. M. Raimundo, Jr., A. J. G. Zarbin, J. J. R. Rohwedder, G. Oliveira Neto, and O. L. Alves, *Sens. Actuators B* 74, 157 (2001).

178. L. Smart and E. Moore, "Solid State Chemistry: An Introduction," Ch. 7. Chapman & Hall, London, 1995.

179. T. Bein and P. Enzel, *Angew. Chem. Int. Ed. Engl.* 28, 1692 (1989).

180. P. Enzel and T. Bein, *J. Chem. Soc. Chem. Commun.* 18, 1326 (1989).

181. P. Enzel and T. Bein, *J. Phys. Chem.* 93, 6270 (1989).

182. T. Bein, *Stud. Surf. Sci. Catal.* 102, 295 (1996).

183. D. J. Cardin, S. P. Constantine, A. Gilbert, A. K. Lay, M. Alvaro, M. S. Galletero, H. Garcia, and F. Marquez, *J. Am. Chem. Soc.* 123, 3141 (2001).

184. S. Neves, S. I. Córdoba de Torresi, and R. A. Zoppi, *Synth. Met.* 101, 754 (1999).

185. S. Neves, C. Polo Fonseca, R. A. Zoppi, and S. I. Córdoba de Torresi, *J. Solid State Electrochem.* 5, 412 (2001).

186. Y. Xia, J. M. Wiesinger, A. G. MacDiarmid, and A. J. Epstein, *Chem. Mater.* 7, 443 (1995).

187. M. Zagorska, A. Prón, and S. Lefrant, in "Handbook of Organic Conductive Molecules and Polymers" (H. S. Nalwa, Ed.), Vol. 3, pp. 183–218. Wiley, Chichester, UK, 1997.

188. S. Neves and C. Polo Fonseca, *J. Power Sources* 107, 13 (2002).

189. E. C. Venancio, A. J. Motheo, F. A. Amaral, and N. Bocchi, *J. Power Sources* 94, 36 (2001).

Conducting Polymer Nanotubes

Meixiang Wan

Chinese Academy of Sciences, Beijing, China

CONTENTS

1. INTRODUCTION

Since the discovery of carbon nanotubes (CNTs) by Iijima in 1991 [1], nanotubes, nanofibers, and even molecular wires have received great attention because of their unique properties. First, the properties of the nanotubes differ from the analogous properties of their bulk materials due to size, surface, and quantum effects. Second, a nanotube is an excellent template or "nanoreactor" to prepare molecule wires or molecule rings, which are fundamental units of molecule devices. Third, coated or filled nanotubes with electrical, optical, and magnetic materials can be as multifunctionalized nanomaterials. As a result, tubular nanomaterials including carbon nanotubes have promising potential applications in electronic, optical, and mechanical devices [2–6], drug delivery [7], and bioencapsulation [8].

Meanwhile, since the invention of conducting polyacetylene (PA) doped with iodine by Shirakawa et al. [9] in 1977, which was awarded the Nobel in chemistry in 2000, conducting polymer as a new field has been established and developed. Compared with other materials, some advantages of conducting polymers are shown as follows [10]: (1) Their conductivity at room temperature can be changed from the insulating through the semiconducting to the metallic range (10^{-9}–10^5 S/cm) by a doping process resulting in covering the whole range from the insulator to metal range. (2) The metallic state can also be brought back to its insulating state

by a dedoping process, and the doping/dedoping process is reversible. (3) Changing the doping degree can control the structure and physical properties. (4) Besides these, conducting polymers remain lightweight and the processability of conventional polymers [10]. These unique properties result in extensive investigations for commercial applications in energy storage devices, electrochemical/chemical sensors, and electrochromic devices [10–12]. Nowadays conducting polymers are the forth generation of polymers.

Currently, conducting polymer nanotubes or nanowires as moleculer wires have attracted attention because of their highly conjugated length and metal-like conductivity (10^0–10^5 S/cm) [10]. However, some fundamental issues on conducting polymer nanotubes or nanowires, such as synthesis, characterization, and property of the nanotubes, need to be understood. So far, many research works dealing with these issues have been reported in the literature; especially their potential application in nanodevices has been developed.

In this chapter, the synthetic method, spectroscopic characterization, and physical properties of the conducting polymer nanotubes including nanofibers, multifunctionalized nanotubes, as well as nanotube dendrites are overviewed in detail. The formation mechanism of self-assembled nanotubes and their multifunctionalized nanotubes, especially nanotube dendrites, is discussed briefly.

2. CONDUCTING POLYMER NANOTUBES

2.1. Synthetic Methods

In principle, utilization of application of conducting polymer nanotubes in nanodevices is limited by development of the synthetic method for conducting polymer nanotubes. As a result, a template-synthesis method [13], an electrospinning method [14], a template-free method [15], and electrochemical polymerization with a scanning microelectrodes [16] have been used to synthesize or prepare conducting polymer nanotubes or nanofibers. In particular, a new approach to synthesize the nanostructures by using organized assemblies or self-assemblies of supramolecular system as nanoreactors or templates has been developed rapidly and demonstrated to be full of promise for preparing the nanostructures of materials [16, 17]. In this section, synthetic methods dealing

with the template-synthesis method and self-assembly process, characterization, and physical properties of the conducting polymer nanotubes are discussed.

2.1.1. Template-Synthesis Method

Among those synthetic methods described, the template-synthesis method is one effective and common route to synthesize or prepare conducting polymer nanotubes or nanowires. Martin and his co-workers have successfully obtained PA, polythiophene (PTH), polypyrrole (PPy), and polyaniline (PANI) nanotubes or nanofibers by using this method [13, 18–24]. Moreover, other papers dealing with template-synthesized conducting polymer nanotubes have also been reported in the literature [25–39]. The moleculer structure of some typical conducting polymer nanotubes obtained is shown in Figure 1.

In general, template-synthesized conducting polymer nanotubes can be prepared either electrochemically [55–58] or by using a chemical oxidizing agent [59–61]. The easiest way to do electrochemical template synthesis is to coat a metal film onto one surface of the membrane and then use this thin film to electrochemically synthesize the desired polymer within the membrane [59]. Chemical template synthesis can be accomplished by simply immersing the membrane into solution of the desired monomer and its oxidizing agent [44, 45]. This method has advantage of controlling diameter and length by porous diameter and thickness of the membranes respectively. Moreover, changing the polymerization time can control the wall thickness of the nanotubes. Especially, it is a powerful method to prepare oriented arrays of the conducting polymer nanotubes, which are fundamental conditions to fabricate nanodevices. On the other hand, a membrane as a template is required in this method. Sometime post-treatment for removal of the template is required after polymerization, resulting in disorder or destruction of the nanotubes.

In general, a porous membrane for the template-synthesis method is required as a template, which allows monomer polymerization inside the pore individually. A typical schematic of the template-synthesis method is shown in Figure 2. Usually, porous alumna prepared electrochemically from aluminum metal is used as the common template [47]. The pore in these membranes is arranged in a regular hexagonal lattice. Pore densities as high as 10^{11} pores/cm^2 can be achieved [48]. Although such membranes are sold commercially, only a limited number of pore diameters are available. Foss et al. [49–51] have made membranes with pores as small as 5 nm.
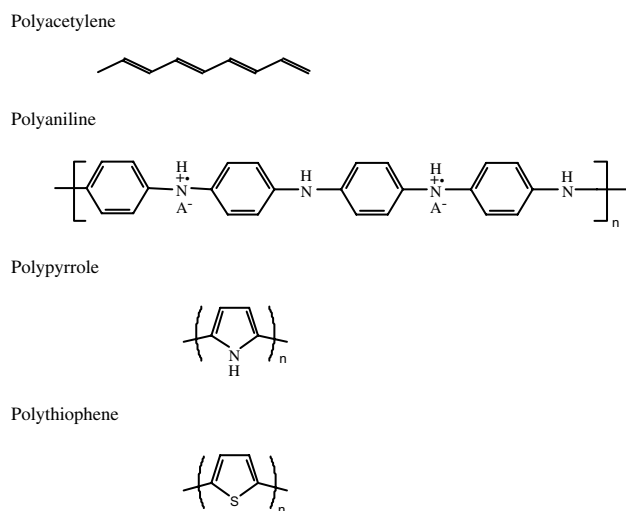
Track-etched membranes, such as polycarbonate (PC) [52], are also used as common templates to synthesize nanotubes or nanofibers of conducting polymers. Track-etched membranes present a significant advantage because they lead to the production of different kinds of nanotubes or nanowires with monodisperse diameter and length. Those track-etched membranes with a wide range of pore diameters (0.03 to 12 μm) and pore densities (10^5–10^9 pore/cm^2) can be achieved. Except for the previously described membranes, glass membranes have been reported. Tonic et al. [53], for instance, described a nanochannel array glass membrane which contains pores with diameters as small as 33 nm and densities as high as 3×10^{10} pore/cm^2. Beck et al. [54] prepared a new large pore diameter zeolite; Wu and Bein [55, 56] have used zeolite as a membrane to synthesize polyaniline and graphitic nanofibers. In addition, Ozin [57] discussed a wide variety of other nonporous solids that could be used as template materials.

Furthermore, synthesis or preparation of oriented nanotube arrays of conducting polymers is also one of the aspects in the field of conducting polymer nanotubes because it is a fundamental condition for fabricating nanodevices. The template-synthesis method is a powerful route to prepare nanotube arrays. Marinakos et al. [58] described two methods for assembling one-dimensional (1D) arrays of Au nanoparticles. Both methods involve aligning nanoparticles in the pores of Al$_2$O$_3$ or PC filtration membranes. The first strategy is to entrap and align particles in the pores by vacuum

Figure 1. Molecule structure of some typical conducting polymer nanotubes.
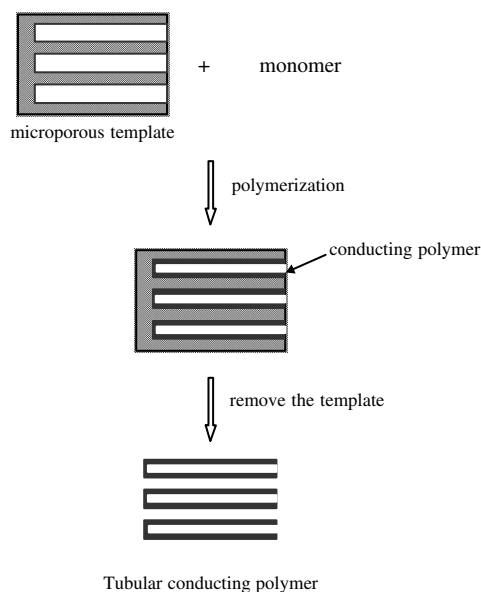
Figure 2. Schematic of template-synthesized conducting polymer nanotubes.

filtration. Hornyak and co-workers [59] have also reported a similar method.

2.1.2. Self-Assembly Process

Recent advances in the control via self-assembly of synthetic molecules has generated numerous molecular architectures by applying principles such as hydrogen bonding, hydrophobic interaction, molecular recognition, and solvent–molecule interaction [73]. Research on self-assembled nanotubes or nanowires through hydrogen bonding, amphiliphilic block copolymer, and supermacromolecules as templates is discussed. The formation mechanism of the self-assembled nanotubes is also discussed briefly.

Hydrogen Bonding   As one knows, calyx[4]hydroquinone (CHQ) is a reducing form of calyx[4]quinine [31], which has four hydroquinone moieties with eight –OH groups. Four inner –OH groups form a circular proton-tunneling resonance of H-bond stabilized "cone" structures. The four free –OH groups can lead to self-assembled structures with intermolecular H-bonds. Hong et al. [62] investigated the assembling phenomena of CHQ with density functional calculations of various possible combinations of assembled structures derived from previously reported calixarene based dimers, trimers, tertramers, hexarence, and polymers by using the computer-aided molecular design approach based on intermolecular interaction forces. Their results suggest that in the presence of water molecules, a linear tubular polymeric structure be highly stabilized by the formation of H-binged bridges between repeating tubular actamer units. In particular, nanotubes arrays composed of electrochemically/photochemically active CHQ can be synthesized through a hydrogen bonding reaction. They also found that addition of water molecules into CHQ in acetone resulted in stable self-assembling thin needlelike nanotubes whose size depends on the evaporation rate and temperature.

Nanoscale conducting cylinders of polyaniline doped with camphoresulfonic acid (CSA), where 4-hexylresorcianol (Heres) (PANI $(CSA)_{0.5}(Heres)_y$, reported by Kosonen et al. [63]) is another typical sample of self-organization of the hydrogen-bonding reaction because Heres is hydrogen bonded to form supramolecules, which further undergo self-organization. Highly ordered hexagonal cylindrical structures were observed with a distance between the cylinders of 35 Å. This method would allow an easy preparation of nanoscale organic conducting wires, just by mixing the components together.

Amphiphilic Block Copolymer   Up to now, various morphologies including spheres, cylinders, vesicles, and layers that can be formed through self-assembly of amphiphilic block copolymers in block-selective solutions have been reported in the literature [64–69]. The reported results indicate that the self-assembly of block copolymers is clearly a potentially powerful route for the generation of nanostructured materials. However, virtually all the studies have focused on organic block polymers. Since the discovery of the living anionic-opening polymerization of strained silicon-bridged ferrocenophanes, it has become possible to access polyferrocene block copolymers, which combine organometallic segments with inorganic or organic co-blocks

[70, 71]. The incorporation of the polyferrocene block offers the opportunity to access self-assembled materials with redox-active, semiconducting, or preceramic nanodomains, or large periodic variation in the refractive index suitable for optical and phonic applications [72–74]. Manners [75], for example, has reported the self-assembly of poly-(ferrocenyldimethelsilane-*b*-dimethylsiloxane) cylinders. In particular, the first organometallic nanotubes using a different block ratio was reported by Raez et al. [76].

Supermacromolecules as Templates   In fact, surfactant [77–87], block copolymers [64–68], and colloidal particles [88, 89] have been successfully used as templates to obtain self-assembling nanostructural materials under adequate conditions. Langer et al. [90] reported that micro- and nano-fibril structures were obtained in PANI copolymers doped with fullerene derivatives prepared by electro-oxidative polymerization. The fibrils of 10 to 100 nm thickness are usually as long as 30,000 nm. Fibrils of PANI–C_{60} derivatives can also be obtained at the surface of the PANI nanolayer under controlled charge polymerization conditions, which can reach lengths from 1000 to 3000 to 15,000 nm and thickness of about 1000 nm. These complex structures support a fractal growth model and a modified diffusion-limited aggregation growth mechanism.

Wan and co-workers found that PANI and PPy micro/nanotubes could be synthesized electrochemically and chemically by *in-situ* doping polymerization in the presence of β-naphthalene sulfuric acid (β-NSA) as a dopant [91]. This method was called a template-free method because it did not use an external membrane as template. In fact, the essence of this method is a self-assembly process because of the dopant acting as a dopant and template function at the same time. Therefore, it is simple and cheap compared with the template–synthesis method. The schematic of the chemical and electrochemical self-assembly process to synthesize conducting polymer nanotubes or nanowires is shown in Figure 3. In a typical chemical self-assembly process, for example, aniline or pyrrole monomer was mixed in aqueous solution with ultrasonic stirring at room temperature. Then oxidant [e.g., $(NH_4)_2S_2O_8$ or $FeCl_3$] was added to this mixture by stirring at 0–5 °C for about 8–10 hours. Finally, the resulting precipitate was filtered and washed with deionized water, methanol, and ethyl ether several times, then dried in a dynamic vacuum at room temperature for 24 hours. Moreover, the reliability and practicality of this
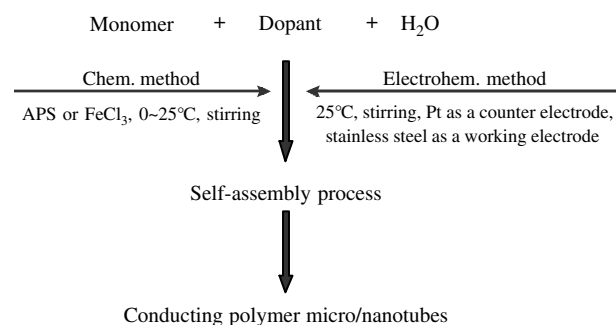
Figure 3. Schematic of chemical and electrochemical self-assembly process to synthesize conducting polymer nanotubes.

method for synthesizing conducting polymer nanotubes by changing the polymer chain and dopant structure as well as the polymerization method have been demonstrated [92–111]. In their studies, PANI and PPy as well as their derivatives were used as the conducting polymers because of their high conductivity, stability in air, and easy preparation. Two kinds of dopant were used: one was inorganic acid, including HCl, H_2SO_4, H_3PO_4, and HBF_4 [108] without surfactant function; another was organic functionalized acid with surfactant function (e.g., $–SO_3H$ group). Naphthalene sulfuric acid and its derivatives [93–100, 105–107, 109, 111], hydrogen sulfated–fullerene [$C_{60}(OSO_3H)_6$] [102], 6-disulfo-nanpthyl-thiorea (PMMA4) [102], 4-{n-[4-(4-nitrophenylazo)phenyloxy]alkyl} aminobenzene sulfonic acid (represented by Cn–ABSA and n = 2, 3, 4, 6, 8, and 10) [103, 104], and p-toluenesulfonate acid (PTSA) [101] were used as organic functionalized acids. Chemical and electrochemical polymerization were used as polymerization methods because both methods are common and useful routes to synthesize conducting polymers. Scanning electron microscopy (SEM) images of some typical self-assembled nanotubes obtained by the author are shown in Figure 4. As one can see the resulting PANI and PPy are fibers and their average diameters are in the range of 50–1000 nm, depending on the polymer chain, dopant, polymerization method, and synthesis conditions [92–111]. Transmission electron microscopy (TEM) measurements showed that most of those nanofibers are hollow. For a given polymer chain and dopant, however, sometimes those fibers are solid depending on the synthesis conditions [92–111]. In addition, the formation yield, morphologies, and size strongly depend on the polymer chain, dopant structure, and synthesis conditions. In particular, the molar ratio of monomer to dopant and the concentration of dopant significantly affect the morphology and size of the resulting nanostructures [92–111].

Although without using external membrane as template, controlling the size of the self-assembled nanotubes is possible. In case of PANI–$C_{60}(OSO_3H)_6$ nanotubes, for example, changing the addition of water in the reaction system can control the diameter, and length of the nanotubes decreases with increasing the addition of water during the polymerization [102] as shown in Figure 5. Moreover, the diameter of PANI–H_3PO_4 nanotubes decreases with increase of the molar ratio of aniline to H_3PO_4 [108] as shown in Figure 6, which is a typical sample to show that the diameter of the self-assembled nanotubes is affected by the molar ratio of monomer to dopant. Of course, one can change the dopant structure and dopant concentration at the same time to control the size of the nanotubes. For instance the diameter of PANI nanotubes doped with different naphthalene sulfonic acids (e.g., α-NSA, β-NSA, and 1,5-DNSA, whose which position and number of $–SO_3H$ groups attached to the naphthalene ring are different) increases with increase of the concentration of dopant [109]. For a given concentration of dopant, however, the diameter of the nanotubes depends on the dopant structure, showing order PANI-(α-NSA) > PANI-(β-NSA) > PANI-(1,5-DNSA) [109] due to their different solubilities in aqueous solution [112]. Especially, PANI–Cn-(ABSA) reported by Qiu and Wan [103] provided another good example that the diameter of the
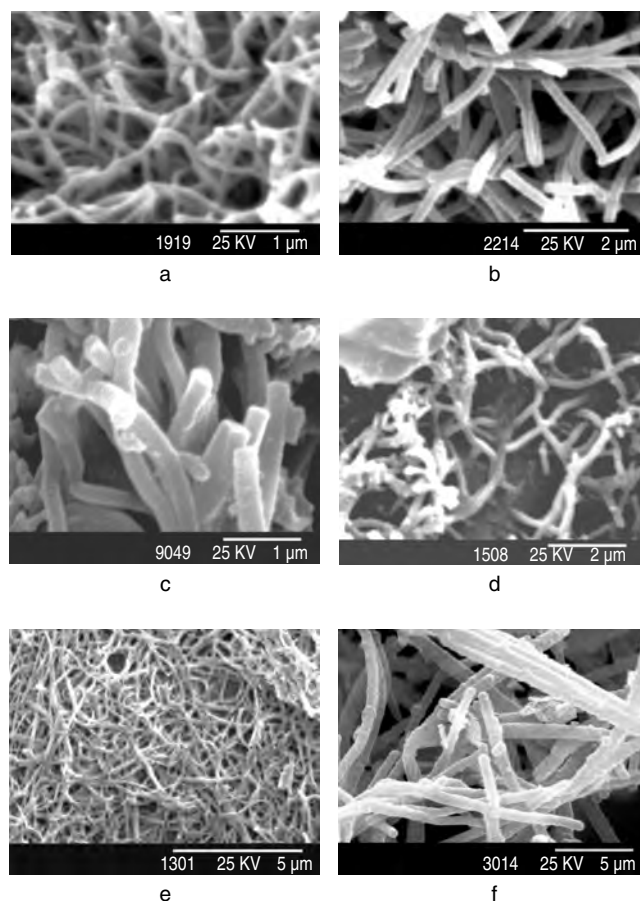
Figure 4. Typical SEM images of conducting polymer nanotubes synthesized by a self-assembly process: (a) PANI–NSA. Reprinted with permission from [106], Z. X. Wei and M. X. Wan, *Langmuir* 18, 917 (2002). © 2002, American Chemical Society. (b) PANI–H_3SO_4. Reprinted with permission from [108], Z. M. Zhang et al., *Macromolecules* 35, 5937 (2002). © 2002, American Chemical Society. (c) PANI–$C_{60}(OSO_3H)_6$. Reprinted with permission from [102], H. J. Qiu et al., *Macromolecules* 34, 675 (2001). © 2001, American Chemical Society. (d) PANI–C_8-ABSA. Reprinted with permission from [103], H. J. Qiu and M. X. Wan, *J. Polym. Sci. Part A: Polym. Chem.* 39, 3485 (2001). © 2001, Wiley. (e) PPy–NSA synthesized by chemical method. Reprinted with permission from [97], J. Liu and M. X. Wan, *J. Mater. Chem.* 11, 404 (2001). © 2001, Royal Society of Chemistry. (f) PPy–NSA synthesized by electrochemical method. Reprinted with permission from [100], Y. S. Yang and M. S. Wan, *J. Mater. Chem.* 11, 2022 (2001). © 2001, Royal Society of Chemistry.

nanotubes is affected by the dopant structure, showing the diameter decreased from 275 to 200 nm when the n value of Cn–ABSA dopant changed from 2 to 10.

C_{60} or Carbon Nanotube Derivatives as Dopants In principle, C_{60} or CNT derivatives with $–OSO_3H$ groups can be used as the dopant for conducting polymers, especially PANI because of its proton-doping characteristic [112–123]. Obviously, self-assembly of conducting polymer nanotubes doped with C_{60} or CNT derivative as a dopant is a challenge in the field of nanomaterials. Up to now, only a few papers dealing with these issues have been reported in the literature [102, 114]. Qiu et al. [102], for example, reported that PANI
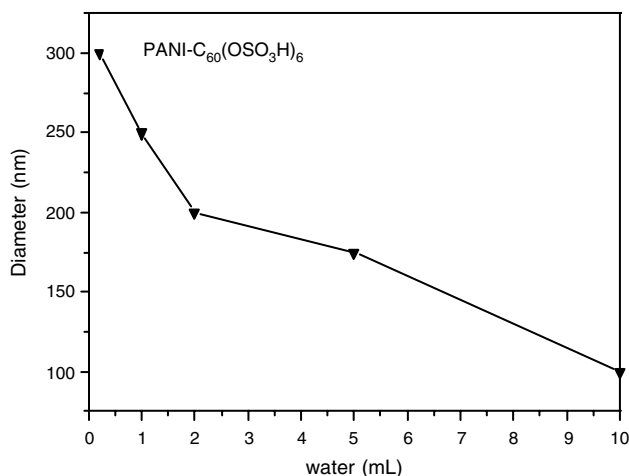
Figure 5. Effect of addition water on the diameter of self-assembled PANI–$C_{60}(OSO_3H)_6$ nanotubes. Reprinted with permission from [102], H. J. Qiu et al., *Macromolecules* 34, 675 (2001). © 2001, American Chemical Society.

nanotubes can be synthesized by *in-situ* doping polymerization in the presence of sulfated C_{60} [$C_{60}(OSO_3H)_6$] as a dopant. It was reported that the PANI–$C_{60}(OSO_3H)_6$ nanotubes are formed through a self-assembly process because of $C_{60}(OSO_3H)_6$ acting as template in the formation of PANI–$C_{60}(OSO_3H)_6$ nanotubes and as a dopant at the same time due to the hydrophilicity of $C_{60}(OSO_3H)_6$. When water is absent in the reaction system, however, only grains are obtained, indicating addition of water during polymerization is a necessary condition for self-assembly of PANI–$C_{60}(OSO_3)H_6$ nanotubes. Moreover, changing the addition of water during polymerization can control the size of the resulting PANI–$C_{60}(OSO_3H)_6$ nanotubes (see Fig. 5). Meanwhile, the flexibility of the nanotubes is enhanced slightly by increasing the addition of water during polymerization. The effect of water during the polymerization on the formation,
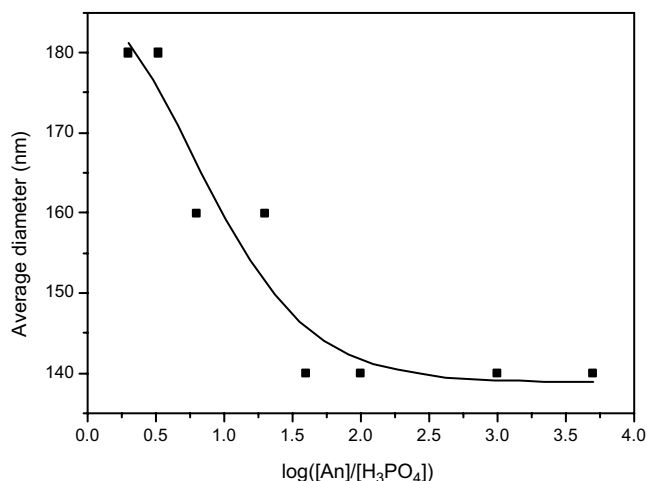
size, and flexibility of the nanotubes might be due to hydrogen bonding of water and polymer chains of PANI.

In particular, Wei and Wan [114] synthesized the PANI nanotubes doped with sulfated multiwall carbon nanotubes [MWNT–$(OSO_3H)_n$] as the dopant by *in-situ* doping polymerization without using any external template. It was noted that by changing only the molar ratio of aniline to MWNT–$(OSO_3H)_n$ one could obtain two kinds of PANI nanotubes. One is PANI coated MWNT–$(OSO_3H)_n$ [represented by PANI–*c*-MWNT–$(OSO_3H)_n$]; another is MWNT–$(OSO_3H)_n$ doped PANI nanotubes [represented by PANI–*d*-MWNT–$(OSO_3H)_n$]. When the molar ratio of aniline to MWCNT–$(OSO_3H)_n$ is less than or equal to 1 (e.g., 1/2 or 1/1), for instance, the polymerization of aniline occurs dominantly on the surface of MWNT–$(OSO_3H)_n$, resulting in formation of PANI coated MWNT–$(OSO_3H)_n$ [i.e., PANI–*c*-MWNT–$(OSO_3H)_n$]. The coaxial structures of the resulting PANI–*c*-MWNT–$(OSO_3H)_n$ nanotubes are conformed by TEM images and electronic diffraction. Moreover, TEM images clearly show a thin layer of PANI is coated on the surface of MWNT–$(OSO_3H)_n$ nanotubes, indicating MWNT–$(OSO_3H)_n$ nanotubes only act as templates for PANI polymerization to form PANI–*c*-MWNT–$(OSO_3H)_n$ nanotubes due to hydrophilicity of aniline. When the aniline/MWNT–$(OSO_3H)_n$ ratio became high (e.g., 2/1, 4/1, and 8/1), on the other hand, MWNT–$(OSO_3H)_n$ doped PANI nanotubes [i.e., PANI–*d*-MWCNT–$(OSO_3H)_n$] formed via a self-assembly process, which was proved by SEM and TEM measurements. Their outer diameter is 100–150 nm and inner diameter is several nanometers down to even zero, depending on the polymerization conditions. Compared with PANI–*c*-MWNT–$(OSO_3H)_n$, however, the surface of the PANI–*d*-MWNT–$(OSO_3H)_n$ nanotubes is very rough. Electronic diffraction revealed that either PANI–*c*-MWNT–$(OSO_3H)_n$ or PANI–*d*-MWNT–$(OSO_3H)_n$ nanotubes are amorphous, which differs from crystal MWNT–$(OSO_3H)_n$ nanotubes.

Formation Mechanism of Self-Assembled Nanostructures Wan et al. proposed a template-like model to interpret the formation of the self-assembled conducting polymer nanotubes without using external porous membranes as templates [102]. The schematic of the formation mechanism of self-assembled nanotubes or nanofibers is given in Figure 7a. The template-like model means that the micelles formed by dopant and/or monomer/dopant salt or supermolecules act as templates in the formation of the nanotubes. Based on this model, it is easy to understand that the essence of the method proposed by the author is a typical self-assembly process because of dopant providing counterions for doping and acting as a template in the formation of nanotubes at the same time. Now let us discuss the formation mechanism of the self-assembled nanotubes when dopant is with and without surfactant function in detail.

Dopant with surfactant function, such as NSA, $C_{60}(OSO_3H)_6$, PMMA4, PTSA, and Cn–ABSA, is easy to form micelles in an aqueous solution due to its hydrophilicity of –SO_3H group of the dopants. The micelles are expected to form spherical micelles through micellerization due to lower surface energies. Moreover, aniline monomer reacts with dopant to form an aniline/dopant salt through

Figure 6. Inference of [An]/[H_3PO_4] on the average diameter of self-assembled PANI–H_3PO_4 nanotubes. [SDBS] = 2.4×10^{-3} M, at 0–4 °C. Reprinted with permission from [167], Z. M. Zhang and M. X. Wan, *Synth. Met.* 175, 135 (2003). © 2003, Elsevier.

acid/base reaction at the same time. As a result, the anilinium cations coexist in the reaction solution. Those anilinium cations can diffuse into the surface of the spherical micelles by electrostatic interaction. Moreover, these spherical micelles are further aggregated to form cylindrical micelles through a self-assembly process. It is reasonable to believe that the self-assembled cylindrical micelles might act as templates in the formation of nanotubes. After adding oxidant [e.g., $(NH_4)_2S_2O_8$], the polymerization only takes place at the micelle/water interface due to the hydrophilicity of oxidant [115]. The growth of the nanotubes is accessed [116] or enlongated [117] by polymerization and aggregation. When the molar ratio of aniline to dopant is high, however, free aniline can diffuse into the micelles to form aniline filled micelles. Those aniline filled micelles might act as templates in forming nanofibers. That is why both nanotubes and nanofibers can be observed in the experiment, and their yield depends upon the synthesis conditions, especially the molar ratio of aniline to dopant. See Figure 7.

In the aniline/MWNT–$(OSO_3H)_n$ system, however, the H_2O-dispersed MWNT–$(OSO_3H)_n$ might play two roles. One

acts as the supramolecular template with anilinium cations [108] in the formation of the nanotubes. Another acts as a dopant, which in turn is generated by H^+ transfer form the –SO_3H groups to enhance the electrical conductivity of PANI. In fact, the doped PANI or its oligomer is a kind of cationic polyelectrolyte with a very rigid backbone structure, which has the tendency to form self-assembled cylindrical micelles induced by the anionic-type MWNT–$(OSO_3H)_n$ in the process of polymerization, leading to the formation of PANI–d-MWCNT–$(OSO_3H)_n$ nanotubes [118, 119].

2.2. Spectroscope Characterization

Scanning electron microscopy (SEM) and transmission electron microscopy (TEM) are used to measure the morphology of the resulting materials. In particular, TEM is a powerful route to prove if the resulting nanofibers are hollow. Moreover, elemental analysis, the ultraviolet-visible (UV-vis) absorption spectrum, X-ray photoelectron spectroscopy (XPS), and Fourier transform infrared (FTIR) spectra as well as X-ray diffraction are used to characterize the molecular structure of the resulting nanotubes. It was found that the main chain of the nanotubes is identical to that of conventional conducting polymers (i.e., granular conducting polymers). However, it is expected that the polymer chain of nanotubes synthesized by the template method should be reined due to template pores. How can we prove it? Usually X-ray diffraction, Raman spectra, and polarized infrared absorption spectroscopy (PIRAS) are used to prove that the template-synthesized nanotubes show supermolecular order [120]. PIRAS entails measuring the absorbance by the sample of two orthogonal polarizations of IR radiation [121]. In PIRAS measurements, one polarization is perpendicular to the axes of the nanotubes ($I_\perp$) and the other has a component that is parallel to the nanotube axes ($I_\parallel$). In general, if $I_\perp$ and $I_\parallel$ are absorbed to the same extent, the polymer chain shows no preferred orientation. Unequal absorbance indicates that the polymer chains are preferentially aligned. PIRAS data can be quantified by calculating a parameter called the dichroic ratio (R). If the R value is equal to 1, meaning no preferential chain alignment, while an R value less than 1 means some degree of alignment, the lower the R, the greater the extent of alignment. Martin et al. [125] reported that the R value of PPy nanotubes reduced with decreasing temperature, indicating the alignment degree of polymer chain at lower temperature is higher than that at high temperature. Moreover, the Raman spectrum is also a powerful tool to prove the orientation of polymer chains. Fu et al. [123] proved that the polymer chain in the skin of polythiophene nanotubes (20–200 nm in diameter), which were synthesized electrochemically by a template-synthesis method (microporous alumna membranes as templates) in the presence of boron trifluoride dietetheate as a dopant, is oriented [123]. Wei and Wan [105] reported that the electronic structure of PANI–$C_{60}(OSO_3H)_6$ nanotubes is identical to that of either doped or dedoped PANI, depending on the solvent used. But influence of morphology on the electronic structure of PANI–$C_{60}(OSO_3H)_6$ nanotubes can be legible. In general, the crystallinity of the nanotubes depends on the polymer chain, dopant and polymerization method [92–111].

a. In case of dopant with or without surfactant function

Anilinium cations: ——⊕ Dopant anion: ∿∿Ⓘ Free aniline: ——

a. Spherical micelles are formed through aggregation process due to surface energy

b. Free aniline can be diffused into the micelles to form aniline filled micelles

b. In case of composite nanotubes containing inorganic nanoparticles

NSA as shell and tail

∿∿◉ ← Fe_3O_4 and TiO_2 as core

Figure 7. Schematic of the formation mechanism of self-assembled nanostructures. (a) Dopant with or without surfactant function; (b) composite nanostructures containing inorganic nanoparticles.

In most case, the nanotube is partially crystalline due to special tubular morphology. In particular, it was found that the crystallinity of the nanotubes is affected by the self-assembled micelles, which act as templates in the formation of the nanotubes. Yang and Wan [101] reported that PPy–PTSA nanotubes are partially crystalline and all sharp peaks observed in the PPy–PTSA nanotubes are in excellent agreement with that of pyrrole/PTSA supermacromolecular clusters, which act as templates in the formation of PPy–PTSA nanotubes. On the other hand, their grains are amorphous [101]. In addition, Wei and Wan [114] found that the Raman spectra of PANI–d-MWNT–$(OSO_3H)_n$ nanotubes differs from that of PANI–c-MWNT–$(OSO_3H)_n$ nanotubes, which might result from the different conformation of PANI in both of the nanotubes [124]. This is further confirmed by UV-vis spectra, showing more extended conformation of the PANI chain in the PANI–d-MWNT–$(OSO_3H)_n$ nanotubes due to its nanotubular structure [114].

2.3. Properties

2.3.1. Electrical Properties

Conductivity of conducting polymer nanotubes at room temperature is one of the important parameters to be understood. The four-probe method on pallet or freestanding film is usually used to measure the conductivity of the conducting polymers. However, the conductivity of nanotubes synthesized inside the pores is obtained by measuring bulk resistance across the filled membrane by the two-probe method. The surface layer of conducting polymers on the membrane can contribute to the resistance measurement but cannot be completely removed because it ensures contact between the tubes and the electrical wires [126] when the thickness of this surface layer is thin (∼100 nm) because such a thin layer did not contribute to the membrane resistance [13]. By measuring the bulk resistance across the filled membrane using the two-probe method, one can calculate the conductivity of a single nanofiber or nanotube when the diameter (d) and length (L) of the pores are known. Usually, one side of the membrane is held on a copper electrode, and two copper wires contact the other side of the membrane. Silver paste ensures a good contact and allows a well-defined cross section for calculating the conductivity. Therefore, the conductivity along a single fiber or tube can be calculated from the resistance measurement (R), which can be written as

$$1/R = 1/R_f + 1/R_m \qquad (1)$$

where R_f is the parallel sum of the resistance of the conductive polymer fibers or tubes, and R_m is the resistance of the membrane. In most cases, R_m can be neglected because $R_m \gg R_f$. As a result, Eq. (1) can be simplified into

$$1/R = 1/R_f = n/R_I \qquad (2)$$

where n is the number of nanotubes or nanofibers in the measurement area, and R_i is the resistance of an individual fiber or tube. Knowing the diameter (R) and length (L) of the pores, the conductivity (σ) of a single fiber or tube can be calculated according to the following equation:

$$\sigma = L/(R_i \pi d^2/4) \qquad (3)$$

Martin [13] reported that conductivity of PANI nanotubes measured by this method was enhanced by one or two orders of magnitude when the diameter decreased, showing a size effect on the electrical properties of the nanotubes or nanowires. Similar phenomena have also been observed from PPy nanotubes [125–127]. In principle, the electrical properties of conducting polymers are determined by their electronic structure. The charge transport occurs via mobility of charge carriers (polaron and bipolaron) along segments of the conjugated polymer chains and by hopping of these charges from chain to chain. The carrier mobility is the limiting parameter of the electrical conductivity and depends mainly on two factors: the interchain distance and the frequency of interchain hopping. The frequency of interchain hopping can be reduced either by increasing the conjugation length or by orienting the polymer chain. Thus, the polymer chains of the nanotubes synthesized inside of pores are forced to align within the environment of the host matrix and an enhancement of the conductivity can be expected. The enhancement of conductivity is attributed to the presence of a large ratio of polymer chain within narrow conducting polymer tubes.

Except for size effects on the conductivity of the nanotubes, the conductivity is also dependent upon the synthesis conditions, especially the molar ratio of monomer to dopant. Qui et al. [102] reported that changing the addition of water during polymerization can control the size of the resulting PANI–$C_{60}(OSO_3H)_6$ nanotubes (i.e., the diameter decreases with increase of the addition of water during polymerization). Moreover, it was found that room-temperature conductivity of self-assembled conducting polymer nanotubes depends on not only the doping degree but also the dopants used. For instance, the conductivity of PANI nanotubes (150–340 nm in diameter) doped with HCl, H_2SO_4, HBF_4, and H_3PO_4 is in the range of 0.49–6.38 S/cm, and an order of PANI–HCl > PANI–H_2SO_4 ≈ PANI–HBF_4 > PANI–H_3PO_4 is observed [108]. Moreover, the conductivity of PANI–H_3PO_4 nanotubes deceases with increase of the molar ratio of aniline to H_3PO_4 due to deceasing doping degree measured by XPS as shown in Figure 8. Obviously, the polymer also affects the conductivity of the nanotubes. Qiu [103] reported that the conductivity of PANI–Cn–ABSA ($n = 2, 4, 6, 8$, and 10) depends on the number of alkyl groups on the ABSA dopant, showing a maximum conductivity at $n = 6$. Moreover, Kosonen et al. [63] observed that the electrical conductivity of $(PANI–CSA)_{0.5}(Heres)_y$ increases two orders of magnitude upon formation of cylindrical structures potentially due to conformation of PANI chains within the cylinders. This is a good example of the effect of tubular morphology on the conductivity of conducting polymers.

Temperature dependence of conductivity measured by the four-probe method is an important route to understanding the conducting mechanism of conducting polymer nanotubes. It exhibits a metallic behavior if the conductivity increases with decrease of temperature ($\partial\sigma/\partial T < 0$), but it is semiconducting when conductivity increases with increase of temperature ($\partial\sigma/\partial T > 0$). Temperature dependence of conductivity for the self-assembled conducting polymer nanotubes always exhibits semiconducting behavior and obeys a
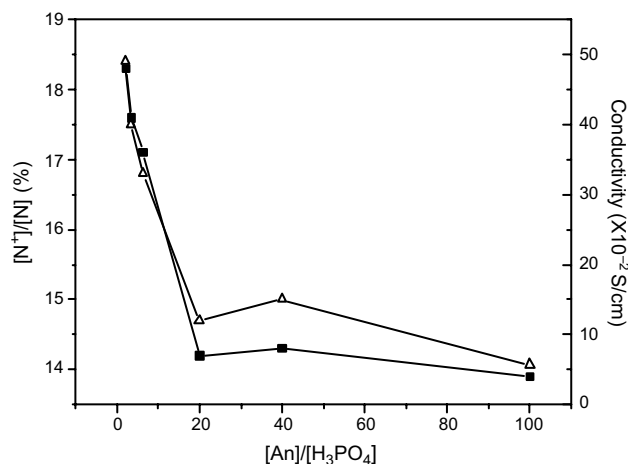
Figure 8. Effect of [An]/[H$_3$PO$_4$] on room temperature conductivity and doping degree of PANI–H$_3$PO$_4$ nanotubes, x room temperature, O doping degree. [An]/[H$_3$PO$_4$] = 2, [SDBS] = 2.4 × 10^{-3} M, at 0–4 °C. Reprinted with permission from [108], Z. M. Zhang et al., *Macromolecules* 35, 5937 (2002). © 2002, American Chemical Society.

variable range hopping (VRH) model proposed by Mott and Davis [128], which is expressed as

$$\sigma(T) = \sigma_0 \exp[(-T_0/T)^{1/n+1}] \qquad n = 1, \ 2, \ \text{and} \ 3 \quad (4)$$

where $T_0 = 8\alpha/ZN(E_F)K_B$, α^{-1} is the localization length, $N(E_F)$ is the density of state at the Fermi level, K_B is the Boltzmann constant, and Z is the number of nearest neighbor chains. The T_0 value corresponds to the hopping energy barriers of charge carriers, which can be obtained from the slope of the straight line of Log σ vs $T^{1/n+1}$. The T_0 value and n number (corresponding to 1D, 2D, and 3D at $n = 1, 2$, and 3 respectively) are affected by the polymer chain, dopant, and polymerization [93–97, 99–101, 108, 111]. It noted that PPy nanotubes obey the 3D-VRH model [99–101], while PANI nanotubes always show a 1D-VRH model [93, 108, 109]. The temperature dependence of conductivity of PANI self-assembled nanotubes doped with different inorganic acids is shown in Figure 9. As one can see, the data are best fit to the relationship of ln σ plotted vs $T^{-1/2}$, showing a 1D-VRH model [128]. The T_0 values follow the order PANI–H$_3$PO$_4$ > PANI–HBF$_4$ > PANI–H$_2$SO$_4$ > PANI–HCl. This is consistent with a trend of their room-temperature conductivity [108].

However, the room-temperature conductivity data, especially its temperature dependence, obtained based on this described method is not intrinsic due to large contact resistance between nanotubes. Therefore, direct measurement of single nanotube conductivity is necessary in order to obtain intrinsic conductivity of the nanotubes and its temperature dependence is required. Park [129] Recently reported that the conductivity of a single nanotube or nanowire can be measured by scanning tunneling microscopy technology, showing the conductivity of the single nanotube or nanowire is one or two orders of magnitude larger than that of bulk materials. However, modification of this method or development of new methods is required.
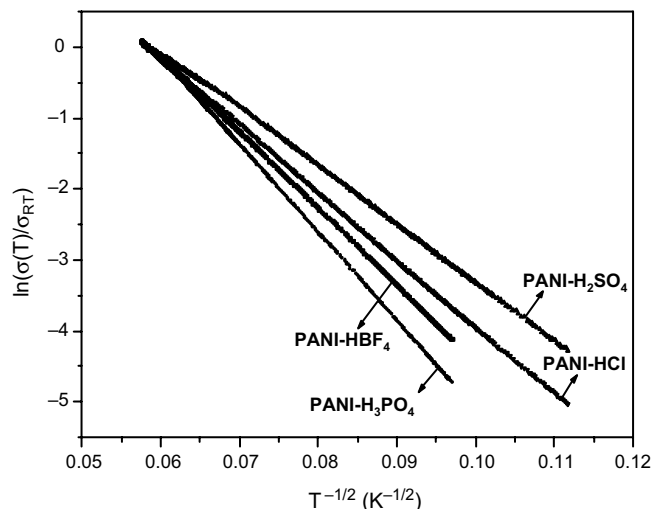
Figure 9. Temperature dependence of conductivity for PANI self-assembled nanotubes doped with different inorganic acids. [An]/[acid] = 1.0.5, [SDBS] = 2.4 × 10^{-3} M, at 0–4 °C. Reprinted with permission from [108], Z. M. Zhang et al., *Macromolecules* 35, 5937 (2002). © 2002, American Chemical Society.

2.3.2. Other Properties

Fu et al. [123] reported that the aligned polythiophene nanotube/gold layered film shows broad and strong redox response and its charge/discharge capacity is about 30 times that of the usual polythiophene. These results present new opportunities for studying the electronic and optical properties of well-organized nanoparticle superstructures. Wan et al. found that PANI self-assembled micro/nanotubes exhibit an unusual magnetic loss at microwave frequency ($f = 1$–18 GHz) [92]. This is quite different from conventional conducting polymers that only have electrical loss without any magnetic loss at the same frequency. The unusual electromagnetic loss at the microwave frequency observed from nanotubes may be related to a special tubular morphology, arising from ordering caused by charge carrying polarons [92]. This result indicates that conducting polymer micro/nanotubes can be used as new stealth materials with advantages being lightweight with wide frequency band and high absorption, which are important in stealth technology. In addition, Zhang et al. [108] observed that PANI–H$_3$PO$_4$ nanotube films deposited on the glass substrate exhibited hydrophilic behavior, which was conformed by measuring contact angle with water ($O = 32°$), especially the hydrophilicity of PANI nanotubes is affected by the dopant used. For example, PANI–HCl, PANI–H$_2$SO$_4$, and PANI–HBF$_4$ films all are hydrophilic, and their contact angles with water are 40°, 38°, and 27°, respectively.

Hong et al., utilizing the redox reaction of CHQ nanotubes with novel metal ions, have made silver nanowires arrays which would be useful for molecular electronic devices [62]. Moreover, they have also reported that the organic nanotubes could also be used as a model for selective water/ion channels in biological systems and a nanohost to include size–specific guest molecules. Lui [70] and Ni et al. [71] reported that the incorporation of the polyferrocene block offers the opportunity to access self-assembled materials with redox-active, semiconducting, or preceramic

nanodomains, or large periodic variation in the refractive index suitable for optical and phonic applications [72–74].

3. CONDUCTING POLYMER NANOFIBERS

3.1. Synthetic Methods

In principle, the template-synthesis method can be used to prepare conducting polymer nanofibers. However, the length of the resulting nanofibers is limited by the thickness of the porous membrane as templates. As a result, it is difficult to prepare long conducting polymer nanofibers by using the template-synthesis method. On the other hand, the electrospinning method invented in the 1930s [130] is a route to prepare ultrafine fibers of conventional polymers. This technique has been recently rediscovered for applications such as high performance filters [131, 132] and for scaffolds in tissue engineering [133] that utilized the unique characteristic of the high surface area (10^3 m^2/g) provided by the fibers.

In the electrospinning method to prepare fibers, in general, a high electrical field is generated between a polymer fluid contained in a glass syringe with a capillary tip and a metallic collection screen. When the voltage reaches a critical value, the charge overcomes the surface tension of the deformed drop of the suspended polymer solution from on the tip of the syringe, and a jet is produced. The electrically charged jet resulting in the hyperstretching of the jet undergoes a series of electrically induced bending instabilities during its passage to the collection screen that results in the hyperstretching of the jet. These stretching processes accompanied by the rapid evaporation of the solvent molecules reduce the diameter of the jet. The dry fibers are accumulated on the surface of the collection screen, resulting in a nonwoven mesh of nano- to microdiameter fibers. The length of the nanofibers by the electro-spinning method is larger than that of the template-synthesis method.

It has been demonstrated that the fiber shape can be influenced by many parameters, such as the polymer, solvent, surface tension, solution viscosity, and solution conductivity. Changing the charge density and polymer solution concentration can control the fiber diameter [133]. For example, Norris et al. [134] reported the influence of solution viscosity on the formation of PANI–CSA fibers by the electrospinning method. They found that without the addition of PEO to PANI/CSA dissolved in chloroform no fiber formation occurred, as the viscosity and surface tension of the solution were not high enough to maintain a stable drop at the end of the capillary tip. Adding more doped PANI also could not increase the viscosity of the polymer solution, as the capillary tip had a very low solubility in chloroform. A stable drop at the end of the capillary tip was achieved once 2 wt% PEO was added to the solution.

Based on the electrospinning concept, Bognitzki et al. [135] have developed a straightforward and highly versatile template method for the production of polymer, metal, and hybrid nano- and mesotubes. The general concept is to take such extremely thin degradable template polymer fibers, which are prepared by the electrospinning method, and coat them with the desired wall materials using various types of deposition techniques. MacDiarmid et al. [136] have

recently reported polycrylonitrile and polyrene fiber can be easily and informally coated from aqueous solution with conducting polypyrrole or with Au by electrolyse deposition. In particular, polycrylonitrile fibers can be thermally converted to conducting carbon nanofibers, which may be a new route to prepare carbon nanofibers.

3.2. Characterization and Properties

Since only a few studies are on conducting polymer fibers prepared by an electrospinning method, structural characterization and physical properties of electrospun conducting polymer fibers have seldom been reported in the literature. However, MacDiarmid et al. [136] investigated the molecular structure and electrical properties of electrospun PANI/PEO blend ultrafine fibers. They reported that absorption spectra of PANI/PEO fibers were consistent with those of PANI in the emeraldine salt oxidation state and no other absorption bands were observed, indicating that the high voltage used in this electrostatic process did not result in any overoxidation of the PANI chains. Moreover, dedoping of the electrospun PANI/PEO fibers could not be achieved by suspending the nonwoven mat in 0.1 M ammonium hydroxide aqueous solutions since the water dissolved the PEO and caused the fibrous network in the nonwoven mat to break apart. Instead, dedoping of the electrospun mat PANI/PEO fibers was achieved by suspending the nonwoven mat in ammonia vapor.

In addition, they observed that the conductivity of electrospun PANI/PEO fibers was lower than that for a cast film at the same concentration of PANI, which was unexpected. There may be two reasons for that: one is that measuring the conductivity of the nonwoven mat was considerably more difficult than measuring the conductivity of the cast film due to the difficulty in obtaining an accurate thickness. Another is that the nonwoven mat is highly porous and therefore the "fill factor" of PANI filberts is less than that of a cast film. However, the dependence of conductivity of PANI/PEO filberts with the weight of PANI in blend is similar to that of a PANI/PEO blend film [137].

4. MULTIFUNCTIONALIZED NANOTUBES

Multifunctionalization of conducting polymer nanotubes with electrical, optical, and magnetic properties is another aspect of nanomaterials and nanotechnology because of the unique properties and promising potential applications in nanotechnology. Recently, some PANI multifunctionalized nanotubes with electrical, optical, and magnetic properties via the self-assembly process have been reported [138, 139]. In this section, the synthesis method, characterization, and physical properties are discussed, especially the formation mechanism of the self-assembled electrical, optical, and magnetic composite nanotubes containing inorganic nanoparticles.

4.1. Synthetic Methods

Two methods can fabricate multifunctionalized conducting polymer nanotubes with electrical, optical, and magnetic properties. The first method is to co-structure multifunctionalized nanotubes by using functionalized dopant. The second

method is self-assembly of composite nanotubes of conducting polymers in the presence of optic and magnetic inorganic nanoparticles.

4.1.1. Functionalized Dopant as a Template

As described, one can prepare multifunctionalized nanotubes with electrical, optical, and magnetic properties through a self-assembly process by using functionalized dopants as templates. In this method, the dopant acts as a doping and template function at the same time. That is to say, functionalized dopants not only contribute multifunction but also act as templates in the formation of the nanotube.

As one knows, azobenzene and its derivatives are generally characterized by reversible transformations from the more state *trans* to the less state *cis* form upon irradiation with UV light [140]. Moreover, the photoinduced isomerization of azobenzene moiety is always accompanied by a structural change as reflected in the changes of dipole moment and geometry [141]. In addition, azobenzene can be selectively attached to the side chains, main chain, cross–links, or chain ends of the polymers with photochromic characteristics. The photochromic characteristic may provide light control the chemical characteristic by an "on–off" light switch. Thus, it is expected that azobenzene derivatives with $-OSO_3H$ groups can be used to dope PANI, resulting in electro-optical PANI. Huang et al. [138] recently reported that conductive PANI nanotubes 110–130 nm in diameter can be synthesized via a self-assembly process in the presence of azobenzene sulfonic acid as a dopant for the fist time. They found that the formation probability and size of PANI–ABSA nanotubes depend on the molar ratio of aniline to ABSA and the concentration of ABSA.

Furthermore, chiral conducting polymers are of considerable interest because of their potential applications. Electrodes for electrochemical asymmetric synthesis [142, 143], modified electrodes capable of performing stereoselective analysis [143, 144], novel chiral stationary phases for chromatographic separation of enantiomers [145–147], microwave absorbents [148, 149], and electroactive chiral membranes for selective transport enantiomer chemicals [150] have been reported. Optically active conducting polymers, such as PPy [151], polythiophene [152], and polyaniline [153], have been reported in the literature. However, nanotubes of these chiral conducting polymers have seldom been investigated. Yang et al. [139] recently reported chiral nanotubes of PANI doped with (S)-$(-)$-2-pyrrolidone-5-carboxylic acid [(S)-PCA] or (R)-$(+)$-2-pyrrolidone-5-carboxylic acid (R)-PCA as a dopant via a self-assembly process for the first time. SEM and TEM images proved that most of the nanotubes with 80–220 nm outer diameter and 50–130 nm inner diameter are hollow along the whole length, and the aspect ratio of these nanotubes varies from 6 to 12. Those chiral nanotubes are independent upon the configuration of PCA dopant. However, morphology, size, and yield of PANI–(S)-PCA and PANI–(R)-PCA nanotubes are affected by the synthesis conditions, especially the aniline concentration and the molar ratio of aniline to PCA. When the concentration of aniline monomer was about 0.04 mol L^{-1}, for instance, the resulting PANI–(S)-PCA was

tubes, but as the concentration of aniline was higher (e.g., 0.1 or 0.35 mol L^{-1}), only granular PANI–(S)-PCA was obtained. Moreover, when the molar ratio of aniline to PCA was 2, the percentage of the nanotubes in both cases was decreased. If the molar ratio of aniline to PCA was higher or lower than 2, on the other hand, almost no tubes were observed.

4.1.2. Dopant Containing Inorganic Nanoparticles as a Template

Another easy way to costructure multifunctionalized conducting polymer nanotubes synthesis through a self-assembly process in the presence of optic and magnetic inorganic nanoparticles. Zhang and Wan [154] recently reported that PANI–NSA/TiO_2 nanotubes with average diameters of 90–130 nm were synthesized through the self-assembly process in the presence of β-NSA as the dopant. The morphologies and formation yield of the composite nanotubes were affected by the content of TiO_2 in the composites. In particular, the diameter of the composite nanotubes decreases with increasing the content of TiO_2 nanoparticles in the composites.

Obviously, preparation of conducting polymers containing magnetic nanoparticles has also attracted attention because of their unique electrical, optical, and magnetic properties, which result in many potential applications in electromagnetic interference shielding [155], electrochromic devices [157], and optical systems [158]. A lot of papers dealing with electromagnetic composites of conducting polymers have been reported [159–166]. Yaneyama et al. [159] and Partch et al. [160], for instance, reported an incorporation of metal oxide particles into PPy during electrochemical polymerization. In particular, Tang et al. [161] have developed a versatile process employing anionic surfactants to prepare processable freestanding films of PANI containing nanomagnets of γ-Fe_2O_3 as high as 50%. Moreover, Wan et al. [162–166] also reported a series of PANI and its derivative or PPy composites containing nanomagnetic particles (Fe_3O_4) prepared by a chemical method, showing high saturated magnetization ($Ms = 10$–40 emu/g) with a superparamagnetic behavior (i.e., $Mr = 0$ and $Hc = 0$), and high conductivity (10^{-1}–10^1 S/cm). However, nanotube or nanowire composites of conducting polymers containing magnetic nanoparticles have seldom been reported. Zhang and Wan [167] recently reported that composite nanowires of PANI–NSA containing Fe_3O_4 nanoparticles ($\sim$10 nm in diameter) with an average diameter of 80–100 nm were prepared by a self-assembly process in the presence of β-NSA as a dopant. However, TEM shows most of them are solid, but a small quantity is hollow. Here, it should be noted that the self-assembled composite nanotubes containing inorganic nanoparticles (e.g., PANI–NSA/TiO_2 or PANI–NSA/Fe_3O_4) described previously are quite different from the coated carbon nanotubes with other materials. In case of coated or filled carbon nanotube composites, carbon nanotubes only act as templates. In case of self-assembled composite nanotubes (e.g., PANI–NSA/TiO_2 or PANI–NSA/Fe_3O_4), however, conducting polymers and inorganic nanoparticles costructure to form composite nanotubes through a self-assembly process. There is evidence to

prove it. One is that some black dots ~10 nm in diameter embedded in the nanofibers or in the skin of PANI–NSA/Fe_3O_4 nanotubes are observed by means of TEM measurements [163]. Moreover, electronic diffraction patterns further proved that those black dots are Fe_3O_4 because those dots are not present in PANI–NSA nanotubes [163]. Further evidence is that the Ti element is only observed on the skin of PANI–NSA/TiO_2 composite nanotubes by an energy distribution spectrum [154].

4.1.3. Formation Mechanism

In Section 1, author proposed a template-like model to interpret the formation of the self-assembled conducting polymer nanostructures including nanotubes and nanowires without using external membranes as templates [102]. The template-like model means that the micelles formed by dopant and/or monomer/dopant salt or supermolecules act as templates in the formation of the nanostructures. Now it is easy to understand the formation mechanism of the self-assembled composite nanotubes or nanofibers containing inorganic nanoparticles. However, the substance of the templates in the composite nanotubes is quite different from that of the self-assembled nanotubes without inorganic nanoparticles.

In case of PANI–NSA/Fe_3O_4 [109] or PANI–NSA/TiO_2 nanostructures [154], Fe_3O_4 or TiO_2 nanoparticles are dispersed in NSA solution before polymerization. As a result, it is possible to form a "core–shell" structural mixture in which Fe_3O_4 or TiO_2 nanoparticles act as "core" and NSA dopant act as "shell." So aniline/NSA micelles containing Fe_3O_4 or TiO_2 nanoparticles might form due to the hydrophobility of aniline and hydrophilicity of –SO_3H group of NSA. If NSA is assigned as a "tail" and aniline containing Fe_3O_4 or TiO_2 nanoparticles as a "head," the micelles with "head–tail" structure can be formed. Therefore it is reasonable to believe that the resulting "head–tail" micelles might act as templates in forming composite nanostructures containing inorganic nanoparticles. The formation process of the composite nanotubes is as same as that of self-assembled nanostructures in the absence of inorganic nanoparticles, and a possible formation schematic of PANI–NSA/Fe_3O_4 or PANI–NSA/TiO_2 nanostructures is shown in Figure 7b.

4.2. Characterization

Elemental analysis, FTIR, UV-vis absorption, XPS, and X-ray diffraction are also used to characterize the molecular structure of multifunctionalized nanotubes of conducting polymers. The molecular structure of the multifunctionalized nanotubes of conducting polymer is identical to that of conventional conducting polymers. For instance, FTIR measurements indicated that the main chain of chiral PANI–(s)-PCA or PAN–(D)-PCA nanotubes [139] is similar to that of conventional doped PANI [112]. However, some differences in the FTIR spectrum between chiral and conventional PANI were observed [139]. Meanwhile, the electronic structure of chiral PANI nanotubes measured by UV-vis absorption spectra is identical to that of conventional PANI [112]. However, inference of the configuration of the chiral dopant (PCA) on its electronic structure is not observed. X-ray scattering patterns of the chiral nanotubes observed

a very sharp peak at $2\theta = 6.43$ ($d = 13.73$ Å), which is assigned to the periodicity distance between the dopant and N atom on the adjacent main chain of PANI. This results from tubular morphology because it is absent from its grains [139].

Similarly, the molecular structure of composite nanotubes containing inorganic nanoparticles is also identical to that doped conducting polymers. However, X-ray scattering peaks of those inorganic nanoparticles can always be observed from that of composite nanotubes. For instance, both characteristic peaks of PANI–NSA nanotubes and Fe_3SO_4 nanoparticles can be observed from that of PANI–NSA/Fe_3O_4 nanotubes [109]. This indicates that there is no chemical interaction between Fe_3O_4 and PANI–NSA in the composites. In addition, a sharp peak at $2\theta = 8.8$ assigned to the scattering along the orientation parallel to the PANI chain [168] can be observed in the composite nanotubes. Interestingly, it is absent from doped PANI by a common method [112], indicating the polymer chain in the nanotubes is partially oriented along the polymer chain due to tubular morphology.

4.3. Properties

In general, the room-temperature conductivity of multi-functionalized nanotubes depends on the polymer chain, dopant, synthesis method, and conditions, which are similar to those in the nanotubes described in Sections 1 and 2. In most cases, the conductivity of functionalized nanotubes containing inorganic nanoparticles is lower than that without inorganic nanoparticles due to the electrical insulating behavior of those inorganic nanoparticles. For example, the conductivity of PANI–NSA/Fe_3O_4 nanotubes decreases with increasing content of Fe_3O_4 in the composites [109]. In some cases, however, adding nanoparticles in the composites can enhance the conductivity of composite nanotubes containing inorganic nanoparticles. A typical sample is that the conductivity of PANI–NSA–TiO_2 nanotubes increases with increase of the content of TiO_2 nanoparticles in the composites [154], which is consistent with results reported by Su and Kurumoto [169]. The temperature dependence of the conductivity for those multifunctionalized nanotubes shows semiconducting behavior and obeys the VRH model [128], which is similar to that of nanotubes described in Sections 1 and 2.

It is expected that the multifunctionalized nanotubes exhibit some new interesting properties except for electrical properties. The resulting multifunctionalized nanotubes, such as chiral PANI–PCA [139], PANI–ABSA [138], PANI–NSA/Fe_3O_4 [167], and PANI–NSA/TiO_2 nanotubes [154], show very interesting optic and magnetic properties. For electro-optic nanotubes, for example, PANI–ABSA [138] nanotubes exhibited *trans–cis* photoisomerization, which is similar to that of azobenzene moiety, upon irradiation with UV light ($\lambda = 365$ nm). However, the rate of photoisomerization of PANI–ABSA is reduced in comparison to that of ABSA by measuring the kinetics of photoisomerization, indicating the doped *trans*-azobenzene moieties along the PANI backbone, probably owing to steric hindrance, are more resistant to the photoisomerization process in comparison with small molecular ABSA [138]. In addition, Yang

and Wan [139] recently reported chiral nanotubes of PANI–(S)-PCA and PANI–(D)-PCA nanotubes showing a positive and negative Cotton effect measured by circular diachroism, indicating helical screw of the polymer chain is observed in the chiral nanotubes. Moreover, Zhang and Wan [154] reported that the PANI–NSA/TiO_2 composite nanotubes are hydrophobic, proved by measuring water contact angle, but the PANI–NSA nanotubes are hydrophilic. Especially, the hydrophobility of the composite nanotubes increases with increase of the content of TiO_2 nanoparticles in the composites. This result suggests that adding TiO_2 nanoparticles can change the hydrophilicity of PANI. Moreover, Zhang and Wan [167] recently reported that PANI–NSA/Fe_3O_4 composite nanofibers exhibited a superparamagnetic behavior (i.e., no hysteretic loop), and their electrical and magnetic properties can be adjusted by changing the content of Fe_3O_4 in the composites.

5. CONDUCTING POLYMER COATED CARBON NANOTUBES

Coating or filling of nanotubes with other materials is a simple and effective method to prepare electrical, optical, and magnetic composite nanotubes. In most cases, carbon nanotubes have been used to impart electrical properties to insulating materials (e.g. polymers) for electronic applications [170, 171]. On the other hand, conducting polymer coated CNTs have recently received great attention because of their unique electrical, optic, and magnetic properties and potential applications in a wide range of devices, including nanoelectronic and biomedical devices [172, 173]. Due to the mass production of CNTs [174] and soluble derivatives [175] of the carbon nanotubes, composite CNTs containing other materials have been developed rapidly. Especially, conducting polymer coated CNTs are expected to be new way to prepare new types of nanotubes. In fact, a combination of CNTs with conducting polymers has been demonstrated to lead to composite materials processing of properties of each constituent component with a significant effect [175–178]. As a result, highly efficient photovoltaic cells [179, 180], light emitting diodes with low current density and good thermal stability [181], and aligned coaxial nanowires with high surface and interface [182] based on composites of CNTs with conducting polymers have been reported.

In this section, synthesis method, characterization, and properties of conducting polymer coated CNTs are introduced.

5.1. Synthesis

In principle, conducting polymer coated CNTs can be fabricated chemically or electrochemically by *in-situ* doping polymerization in the presence of CNTs. For example, Fan et al. [183] synthesized PPy coated carbon nanotubes using *in-situ* polymerization of pyrrole on carbon nanotubes in 0.1 M HCl solution containing $(NH4)_2S_2O_8$ as oxidant at 0–5 °C. A typical synthesis process was described as follows: 0.1 M HCl solution (150 ml) containing CNTs was ultrasonically stirred at room temperature for about 0.5 h to disperse CNTs. Pyrrole monomer (0.67 g) in 100 ml HCl (0.1 M)

solution was added to the CNT suspension system with ultrasonic stirring. Then 50 ml HCl (0.1 M) solution containing $(NH_4)_2S_2O_8$ was slowly added drop by drop into the suspension system with a constant sonication. The reaction mixture was sonicated for an additional 4 h at 0–5 °C, after which the CNT/PPy powder formed was filtered and rinsed with distilled water and methanol until the filtrate was colorless. The obtained black CNT/PPy powder was dried under vacuum for 24 h. In order to prepare uniform PPy coated CNTs, the following conditions are required: (1) The reaction solution should be dilute so that CNTs can be dispersed very well. (2) The oxidant (e.g., ammonium persulfate) must be dropped very slowly so that the polymerization of pyrrole on the surface of CNTs is not too rapid. (3) Supersonic stirring is easy to disperse CNTs in the reaction, which is much better than magnetic stirring due to its insoluble in any solvent. The diameter of PPy/CNT nanotubes is about 80–100 nm, and a uniform layer of PPy on the surface of CNTs was proved by TEM measurements, indicating CNTs only act as templates for polymerization of pyrrole monomer. Especially, Pamamurthy et al. [184] recently fabricated PANI/CNT composites for Schottky electronic device application. They described the preparation of Schottky diodes in detail as follows: the mixture of the emeraldine base form of PANI with different weights present of CNTs was procured onto ITO coated glass slides. Then the slides were placed in an oven under a vacuum of 20 mm Hg at 50 °C to remove the solvent. Vapor doping of the dried films was achieved by placing the films in a closed chamber with 1 M HCl solution for 48 hr. Aluminum was then evaporated onto the front side of the samples to form Schottky contacts. Moreover, Chen et al. [185] reported thin and very uniform PPy films are successfully coated on the surface of each carbon nanotube by electrochemical polymerization. They also synthesized uniformly PPy films coated over each carbon nanotube of the well–aligned carbon nanotubes arrays by electrochemical polymerization in the aligned arrays.

5.2. Characterization

SEM, TEM, elemental analysis, FTIR, and X-ray are used to characterize the molecular structure of the resulting conducting polymer coated CNTs. Especially the Raman spectrum is a powerful tool to characterize CNTs. Fan et al. [183] used FTIR and Raman spectra to characterize the structure of PPy–CNTs. They reported that the characteristic peaks of PPy could be observed in the CNT/PPy samples, which are similar to those of PPy using a chemical and electrochemical polymerization method. The Raman spectrum of CNTs has two significant peaks at 1348 and 1578 cm^{-1}, indicating the used CNTs are multiwall carbon nanotubes because 1601 cm^{-1}, corresponding to single wall carbon nanotubes, is absent. The Raman spectrum of PPy–CNT nanotubes is similar to that of CNTs, but the intensity of those peaks in PPy–CNT nanotubes is decreased. On the other hand, the Raman spectrum of PPy shows a broad band at 1300–1600 cm^{-1} in the C=C stretching vibration range. Moreover, X-ray scattering patterns of PPy–CNT nanotubes not only have characteristic peaks of CNTs (3.42, 2.13, 1.70 A), but also show PPy amorphous characteristics (broad peak). There is no

new peak in X-ray scattering patterns of PPy–CNT nanotubes, indicating no interactions between PPy and CNTs took place.

5.3. Properties

Pamamurthy et al. [184] also reported that the electrical characteristics of PANI/CNT Schottky diodes are nearly an order of magnitude higher than those of PANI devices. Chen et al. [185] reported that the growth current of PPy on the well-aligned carbon nanotubes is much larger than that on the flat Ti/Pt substrate. Moreover, PPy-coated carbon nanotube electrodes show significantly improved electrochemical redox performance, showing that the redox charge of PPy films is enhanced significantly by carbon nanotubes. These results may lead to the possibility of using the hybrid material in high-performance, lightweight, rechargeable batteries. This is very promising that the electrode developed in this study could be used as high performance electrode in rechargeable batteries [186]. Huges et al. [187] also reported that arrays of aligned MWNTs coated with conducting polymer composites (e.g., PPy) are not only well suited for energy applications such as super capacitors and secondary batteries but also for use in devices such as sensors that would benefit from this desirable combination of properties. Fan et al. [183] measured the electrical, magnetic, and thermal properties of PPy–CNT nanotubes, but no new physical properties were observed, indicating CNTs only act as templates for pyrrole polymerization. However, they found that homogeneous solution of CNTs dispersed in PPy dissolved in m-cresol with ethanol could be formed. Based on this result, Liu et al. [188] measured third-order optical nonlinearity ($\chi^{(3)}$) of CNTs by degenerate four-wave mixing for the first time. They reported that $\chi^{(3)}$ of CNTs is about 6.460×10^{-14} esu at 1064 nm, and considering the local field correction, the contribution of one carbon atom to third-order nonlinearity is about 5.921×10^{-36} esu, which is larger than that of C_{60} (5.000×10^{-36} esu).

6. SELF-ASSEMBLED NANOTUBE DENDRITES OF CONDUCTING POLYMERS

Dendrite tubes, such as the vessels in the bodies of animals and plants, are a very popular structure in the nature [189]. Although many metal, metal oxide, and polymer dendrites have been produced by fractal growth [190–192], they are all composed of solid particles, not tubes. Recently, dendrites of carbon nanotubes have been reported [193], in which a carbon nanotube grows up from the outer walls of another one, but it is not a popular phenomenon and cannot form complete dendrites with many branches. However, Wei and Wan [194] have recently found that nanotube dendrites of PANI doped with chiral D-camphor-10-sulfonate acid (D-CSA), α-NSA, β-NSA, 1,5-DNSA, and H_3PO_4 as the dopant can be synthesized in stationary state through a self-assembly process. Typical SEM and TEM images of PANI–CSA nanotube dendrites synthesized through a self-assembly process are shown in Figure 10. In the meantime, PPy nanotube dendrites doped with PTSA were also obtained by the same
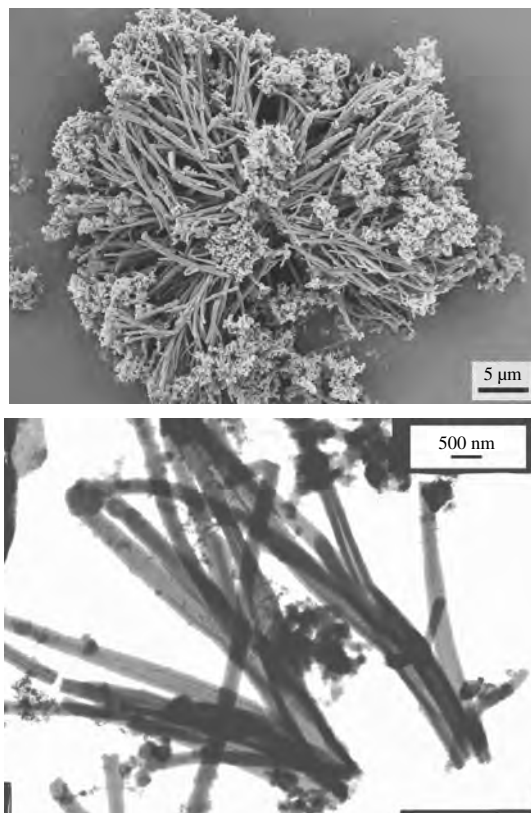
Figure 10. Typical SEM and TEM images of PANI–(D)-CSA nanotube dendrites synthesized through a self-assembly process.

method. SEM images confirmed that all resulting PANI and PPy are of fibrous morphology, but these fibers are aggregated to form dendrite morphology. Those branches spread out from the boot and each big branch has thinner branches. The diameters of the branches are in the range of 230 to 540 nm, but they become thinner and thinner along the direction from the boot to the top. Interestingly, the TEM images revealed that these branches are hollow; especially their inner diameters decreased from the boot to the top and become zero at the end. Moreover, it was found that the diameter of the branches and the aggregated morphology of the nanotube dendrites are affected by the synthesis conditions, including dopant structure, the concentration of dopant and monomer, as well as their molar ratio. The diameter of PANI–D-CSA nanotubes decreases with increase of mole ratio of aniline to D-CSA, for instance, while the branch number increases with increase of the interaction along the polymer chain. They proposed that the nanotubes are derived from an *in-situ* polymerization on a micelle template consisting of dopant and/or dopant/monomer salt through a self-assembly process [127]. Dendrite morphologies are induced by the interactions among conducting polymer chains, including interaction of hydrogen bond and ionic bond through aggregation. This method shows a possibility to prepare nanotube dendrites of conducting polymers through a self-assembly process for the first time.

7. SUMMARY

In summary, the nanomaterials, especially nanostructures (e.g., nanotubes and nanofibers, even molecule wires), of conducting polymers have attracted attention due to their unique properties and promising potential applications in nanodevices especially molecule devices. However, this field is only at the beginning because many fundamental issues need to be studied in detail. First, synthesis or preparation of new materials with unique properties, including electrical, optic, and magnetic functions, thermal and air stability, as well as process ability, is required. Second, modification of old methods and development of new methods to synthesize or fabricate nanostructures are needed. Especially, controlling morphology and size of nanotubes or nanowires through the self-assembly process is a key issue. Meanwhile, development of methods for oriented arrays of nanotubes or nanowires is a key technology to fabricate nanodevices. Furthermore, searching for new characterization routes to measure molecular structure and physical properties of nanotubes or nanowires is also a fundamental scientific issue. In particular, measurements of physical properties of single nanotubes or nanowires are required in order to understand size, surface, and quantum effects on the physical properties of single nanotubes or nanowires. Utilization of nanodevices and molecule devices strongly depends on the development of these scientific issues.

GLOSSARY

Carbon nanotubes (CNTs) Essentially tiny strips of graphite sheet rolled into tubes and capped with half a fullerene at the each end. Their diameter is just a few billionths of a meter.

Conducting polymer Fourth generation of polymer that has semiconducting and metallic properties and retains polymer's lightweight and processability. In principle, the π-conjugated polymers can be converted to the semiconducting and even metallic state by using a chemical or electrochemical doping method. The characteristic of the molecule structure consists of π-conjugated polymer chains and counterions, depending on doping type (p- or n-type).

Doping In the conducting polymers this is an important route to convert the electrical insulating state to the conducting state of the conducting polymers. On the other hand, the doping concept in conducting polymers differs from that of inorganic semiconductors. For instance, the intrinsic conducting polymer doping is a chemical or electrochemical redox reaction, while it is atom replacement in inorganic semiconductors. Moreover, dedoping can be performed in the conducting polymers, and the doping/dedoping process for conducting polymers is reversible. Thus, the conducting polymers are called intrinsic conductive polymers, which quietly differ from the conducting plastic polymers containing inorganic conducting particles (Ag and Cu nanoparticles as well carbon powders) as conducting fillers.

External template Made of porous micromembrane, which allows monomer polymerization inside the pore individually. Porous alumna prepared electrochemically from aluminum metal or track-etched polycarbonate is widely applied as an external template to synthesize nanostructures by using the template-synthesis method.

Fullerene C_{60} is a pure carbon molecule composed of at least 60 atoms of carbon and contains only hexagonal and pentagonal faces. The name is a homage to R. Buckminster Fuller for his writing on geodesic domes. Also they are referred to as Buckyballs. Fullerenes are seen as promising components of future microelectromechanical systems and in nanotechnology. Current work on fullerenes is largely theoretical and experimental.

Hydrophilic/hydrophobic Describes a contact behavior of materials with water or oil, which can be determined by water or oil contact angle, depending on the surface energies and the surface roughness of the materials.

Nanostructures Material size is in the range of 1–100 nm, and the micromorphology is complex including tubes, fibers, hollow spheres, and even nanotube junctions.

Organic light-emitting diodes (OLEDs) One of the electronic devices which can electroluminesce from conjugated polymer or organic molecule layers sandwiched between metallic electrodes. Operation of a LED is achieved when the diode is biased sufficiently to achieve injection of positive and negative charge carriers from opposite electrodes. Capture of oppositely charged carriers within the region of the polymer layer can then result in the formation of the singlet excitation, which is generated by photoexcitation across the π–π^* gap, and this can then decay radioactively to produce the same emission spectrum as that produced by photoexcitation. Charge carrier injection, transportation, and recompilation are important processes in LEDs. Especially equilibrium injection of positive (hole) and negative (electron) charge is a key to enhance the electroluminescence efficacy and brightness.

Polyaniline PANI is an unusual member of π-conjugated conducting polymer in which nitrogen atoms are incorporated between phenyl (C_6H_4) rings. It consists of three different types, depending on the oxidation state (represented as y, and $0 < y < 1$), for instance, reduced lecucoemeradine base for $y = 1$, partially oxidized emeraldine base form for $y = 0.5$, and fully oxidized pernigraniline for $y = 0$, respectively. Moreover, the electrical properties of PANI are controlled by both oxidation and protonation states, which is different from many other conducting polymers (e.g., polyacetylene) whose electrical properties are well understood by simply considering the properties of conjugated backbones.

Self-assembly Molecules can self-construct nanostructures through intermolecular weak interaction, such as van der Waals force, hydrogen bond, hydrophilic/hydrophobic interface. Recently, the self-assembly process has been widely used to synthesize or prepare nanostructures including nanotubes, nanofibers, hollow spheres, and even nanotube junctions.

Superparamagnet A type of magnetic material in which both remnant magnetization (Mr) and coercive force (Hc) are very low, even equated to zero. Sometimes they are called soft magnets.

Template-synthesis method A common and effective route for synthesizing nanostructural materials. A porous membrane as a template is required, which allows nanostructural

materials to be synthesized inside porous micromembranes, resulting in controllable size of the nanostructural materials. Especially, it is a powerful route to prepare aligned nano-structural arrays, which are fundamental units for preparing nanodevices. However, post-treatment for removing template is required, which results in disorder or destruction of the resulting nanostructures.

Van der Waals force A weak intermolecular attractive force which cannot result from ionic charges.

REFERENCES

1. S. Iijima, *Science* 354, 56 (1991).
2. G. A. Ozin, *Adv. Mater.* 4, 612 (1992).
3. G. A. Ozin, *Science* 29, 29 (1991).
4. M. H. Devorel, J. P. Harbison, and A. Scherer, *Sci. Am.* 265, 86 (1991).
5. M. H. Devorer, D. Esteve, and C. Uribina, *Nature* 360, 547 (1992).
6. M. Delvaux, J. Duchet, P. Y. Stavaux, R. Legras, and S. D. Champagne, *Synth. Met.* 113, 275 (2000).
7. R. Gref, Y. Trubetskoy, V. Torchilin, and R. Langer, *Science* 263, 1600 (1994).
8. R. Parhasarathy and C. R. Martin, *Nature* 369, 298 (1994).
9. H. Shirakawa, E. J. Louis, A. G. MacDiarmid, C. K. Chiang, and and A. J. Heeger, *J. Chem. Soc. Chem. Commun.* 578 (1977).
10. "Handbook of Organic Conductive Molecules and Polymers" (H. S. Nalwa, Ed.), Vols. 1–4, Wiley & Sons, Ltd., Chichester, 1997.
11. "Handbook of Conducting Polymers" (T. A. Skotheim, R. L. Elsenbaumer, and J. R. Reynolds, Eds.), Vols. 1 and 2. Dekker, New York, 1998.
12. S. M. Park, "Handbook of Organic Conductive Molecules and Polymers" (H. S. Nalwa, Ed.), Vol. 3, pp. 429–469, Wiley, Chichester, 1997.
13. C. R. Martin, *Science* 266, 1961 (1994).
14. S. Shirators, S. Moriand, and K. Ikeyaki, *Sens. Actuators B* 49, 30 (1998).
15. M. X. Wan, Y. Q. Shen, and J. Huang, Chinese Patent 98109916.5, 1998.
16. A. J. Horsewill, N. H. Jones, and R. Caciuffo, *Science* 291, 100 (2000).
17. E. R. Zubarev, M. U. Pralle, E. D. Sone, and S. I. Stupp, *J. Am. Chem. Soc.* 123, 4105 (2001).
18. Z. Cai, J. Lei, W. Liang, V. Menon, and C. R. Martin, *Chem. Mater.* 3, 860 (1991).
19. C. Zeoliters, W. Wu, and T. Bein, *Science* 264, 1757 (1994).
20. C. R. Martin, *Chem. Mater.* 8, 1739 (1996).
21. J. C. Hulteen and C. R. Martin, *J. Mater. Chem.* 7, 1075 (1997).
22. V. M. Cepak and C. R. Martin, *J. Mater. Sci.* 87, 23J (1994).
23. C. R. Martin, *Acc. Chem. Res.* 28, 61 (1995).
24. V. P. Menon, J. Lei, and C. R. Martin, *Chem. Mater.* 8, 2382 (1996).
25. J. Manford and R. P. Baurford, *J. Mater. Sci.* 87, 23 (1994); J. Manford and R. P. Baurford, *J. Mater. Sci.* 29, 2500 (1994).
26. M. Granstrom and O. Inganas, *Polymer* 36, 2867 (1995).
27. M. Granstrom, J. C. Carlberg, and O. Inganas, *Polymer* 36, 3191 (1995).
28. E. Ferain and R. Legras, *Nucl. Instrum. Methods B* 131, 97 (1997).
29. J. Duchet, R. Legras, and S. Demoustier-Champagne, *Synth. Met.* 98, 113 (1998).
30. S. Demoustier-Champagne, E. Ferain, R. Legras, C. Jrme, and R. Jrme, *Eur. Polym. J.* 34, 1767 (1998).
31. S. Demoustier-Champagne and P. Y. Stavaux, *Chem. Mater.* 11, 829 (1999).
32. T. Bien and P. Enzed, *Angew. Chem. Int. Edit.* 28, 1692 (1989).
33. G. A. Ozin, *Adv. Mater.* 4, 61 (1992).
34. M. Delvaux, J. Duchet, P. Y. Stavaux, R. Legras, and S. Demoustier-Champagne, *Synth. Met.* 113, 275 (2000).
35. M. Granstrom and O. Inganas, *Polymer* 36, 2867 (1995).
36. M. Granstrom, J. C. Carlberg, and O. Inganans, *Polymer* 36, 3191 (1995).
37. E. Ferain and R. Legras, *Nucl. Instrum. Methods B* 131, 97 (1997).
38. J. Duchet, R. Legras, and S. Demoustier-Champagne, *Synth. Met.* 98, 113 (1998).
39. J. Joo, K. T. Park, B. H. Kim, M. S. Kim, S. Y. Lee, C. K. Jeong, J. K. Lee, D. H. Park, W. K. Yi, S. H. Lee, and K. S. Ryu, in "International Conference of Synthetic Metals (ICSM'2002)," June 30–July 5, 2002, Shanghai, China.
40. R. M. Penner and C. R. Martin, *J. Electrochem. Sci.* 133, 2206 (1986).
41. L. S. Van Dyke and C. R. Martin, *Langmuir* 6, 1123 (1990).
42. R. M. Pernner, L. S. Van Dyke, and C. R. Martin, *J. Phys. Chem.* 92, 5274 (1988).
43. J. Lei, Z. Cai, and C. R. Martin, *Synth. Met.* 46, 53 (1992).
44. R. V. Parthasarathy and C. R. Martin, *Chem. Mater.* 6, 1627 (1994).
45. J. Lei, V. P. Menon, and C. R. Martin, *Phys. Adv. Tech.* 4, 124 (1992).
46. P. Parthasarathy and C. R. Martin, *Nature* 369, 298 (1994).
47. A. Despic and V. P. Parkhutik, in "Modern Aspects of Electrochemistry" (J. O. Bockris, R. E. White, and B. E. Conway, Eds.), Vol. 20, Ch. 6. Plenum, New York, 1989.
48. D. Almawiawi, N. Coornbs, and M. Moshovits, *J. Appl. Phys.* 70, 4421 (1991).
49. C. A. J. Foss, G. L. Hornyak, A. Stockert, and C. R. Martin, *J. Phys. Chem.* 1992, 7497 (1992).
50. C. A. J. Foss, G. L. Hornyak, J. A. Strockert, and C. R. Martin, *Adv. Mater.* 5 135 (1993).
51. C. R. Foss, G. L. Hornyak, J. A. Stackert, and C. R. Martin, *J. Phys. Chem.* 8, 2963 (1994).
52. R. L. Fleischer, P. B. Price, R. M. Wallker, "Nuclear Tracks in Solids: Principles and Applications." Univ. of California Press, Berkeley, 1975.
53. R. J. Tonic, B. L. Justus, A. J. Campillo, and C. E. Ford, *Science* 258, 783 (1992).
54. J. S. Beck, J. C. Vartul, W. J. Roth, M. E. Leonowicz, C. T. Kresge, K. D. Schmitt, C. T. W. Chu, D. H. Olson, E. W. Scheppard, S. B. McCullen, J. B. Hisgins, and J. L. Schlenker, *J. Am. Chem. Soc.* 114, 10834 (1992).
55. C. G. Wu and T. Bein, *Science* 264, 1757 (1994).
56. C. G. Wu and T. Bein, *Science* 266, 1013 (1994).
57. G. A. Ozin, *Adv. Mater.* 4, 612 (1992).
58. S. M. Marinakos, L. C. Brousseau III, A. Jones, and D. L. Feldheim, *Chem. Mater.* 10, 1214 (1998).
59. G. L. Hornyak, M. Kroll, R. Pugin, T. Sawitowski, G. Schmid, J. O. Bovin, G. Karsson, H. Hofmeister, and S. Hopfe, *Chem. Eur. J.* 3, 19 (1997).
60. G. Omerz-Kaifer, P. A. Reddy, C. D. Gutsche, and L. Echegoyen, *J. Am. Chem. Soc.* 120, 2486 (1998).
61. B. H. Hong, J. T. Lee, C. W. Lee, J. C. Kim, S. C. Bae, and K. S. Kim, *J. Am. Chem. Soc.* 123, 10748 (2001).
62. B. H. Hong, S. C. Bae, T. S. Lee, and K. S. Kim, *Science* 194, 348 (2001).
63. H. Kosonen, J. Ruokolainen, M. Knaapila, M. Torkkeli, K. Jokela, R. Serimaa, G. T. Brinke, W. Bras, A. P. Monkman, and O. Ikkala, *Macromolecules* 33, 8671 (2000).
64. C. Price, *Pure Appl. Chem.* 55, 1563 (1983).
65. F. S. Bates, *Science* 251, 898 (1991).
66. M. Templin, A. Franck, A. D. chesene, A. Leist, A. Zhang, R. Vlrich, V. Schadler, and U. Winsner, *Science* 278, 1795 (1997).
67. S. A. Jenekhe, J. Feng, Q. Huo, N. Melosh, G. H. Fredrickson, B. F. Chemelka, and G. O. Stucky, *Science* 279, 548 (1998).

68. P. Leclere, A. Calderone, D. Marsitzky, V. Francke, Y. Geerts, K. Mullen, J. L. Bredas, and R. Lazaronic, *Adv. Mater.* 12, 1042 (2000).
69. J. Dig and G. Liu, *Chem. Mater.* 10, 537 (1998).
70. G. Liu, *Adv. Mater.* 9, 437 (1997).
71. Y. Ni, R. Rulkens, and I. Manners, *J. Am. Chem. Soc.* 118, 4102 (1996).
72. R. Rulkens, Y. Ni, and I. Manners, *J. Am. Chem. Soc.* 116, 1212 (1994).
73. J. A. Massey, K. N. Power, M. Winnik, and I. Manners, *Adv. Mater.* 10, 1559 (1998).
74. I. Mannes, *Chem. Commun.* 857 (1999).
75. I. Manners, *Pure Appl. Chem.* 71, 1471 (1999).
76. J. Raez, R. Barjovanu, J. A. Massey, M. A. Winnik, and I. Manners, *Angew. Chem. Int. Ed.* 39, 3862 (2000).
77. T. M. Yao, N. E. Kim, Y. Xia, G. M. Whitesides, and I. A. Aksay, *Nature* 390, 674 (1997).
78. P. Yager and P. E. Schoen, *Mol. Cryst. Liq. Cryst.* 106, 381 (1984).
79. T. Yanagisawa, T. Shimizu, K. Kuroda, and C. Kato, *Bull. Chem. Soc. Jpn.* 63, 988 (1990).
80. C. T. Kresge, M. E. Leonowicz, W. J. Roth, J. C. Vartuli, and J. S. Beck, *Nature* 359, 710 (1992).
81. J. S. Beck, J. C. Vartuli, W. J. Roth, M. E. Leonowicz, C. T. Kresge, K. D. Schmitt, C. T.-W. Chu, D. H. Olson, E. W. Sheppard, S. B. McCullen, J. B. Higgins, and J. L. Schlenker, *J. Am. Chem. Soc.* 114, 10834 (1992).
82. J. M. Schnur, *Science* 262, 1669 (1993).
83. M. Ghadiri, J. R. Granja, and L. Buehler, *Nature* 369, 301 (1994).
84. H. P. Lin and C-Y. Mou, *Science* 273, 765 (1996).
85. M. S. Spector, R. R. Price, and J. M. Schnur, *Adv. Mater.* 11, 337 (1999).
86. D. M. Antonelli, *Adv. Mater.* 11, 487 (1999).
87. M. Harada and M. Adachi, *Adv. Mater.* 12, 839 (2000).
88. A. Imhor and D. J. Pine, *Nature* 389, 948 (1997).
89. J. E. G. J. Wijnhoven and W. L. Vos, *Science* 281, 802 (1998).
90. J. J. Langer, G. Framski, and S. Golczak, *Synth. Met.* 121, 1319 (2001).
91. M. X. Wan, Y. C. Shen, and J. Huang, Chinese Patent 98109916.5, 1989.
92. M. X. Wan, J. C. Li, and S. Z. Li, *Polym. Adv. Tech.* 12, 561 (2001).
93. J. Huang and M. X. Wan, *J. Polym. Sci. Part A: Polym. Chem.* 37, 151 (1999).
94. J. Huang and M. X. Wan, *J. Polym. Sci. Part A: Polym. Chem.* 37, 165 (1999).
95. Y. Q. Shen and M. X. Wan, *J. Polym. Sci. Part A: Polym. Chem.* 37, 1443 (1999).
96. Y. Q. Shen and M. X. Wan, *Synth. Met.* 96, 127 (1998).
97. J. Liu and M. X. Wan, *J. Mater. Chem.* 11, 404 (2001).
98. J. Liu and M. X. Wan, *J. Polym. Chem. Sci. Part A: Polym. Chem.* 39, 997 (2001).
99. J. Liu and M. X. Wan, *Synth. Met.* 124, 317 (2001).
100. Y. S. Yang and M. X. Wan, *J. Mater. Chem.* 11, 2022 (2001).
101. Y. S. Yang and M. X. Wan, unpublished.
102. H. J. Qiu, M. X. Wan, B. Matthews, and L. Dai, *Macromolecules* 34, 675 (2001).
103. H. J. Qiu and M. X. Wan, *J. Polym. Sci. Part A: Polym. Chem.* 39, 3485 (2001).
104. J. Qiu and M. X. Wan, *Chinese J. Polym. Sci.* 19, 65 (2001).
105. Z. X. Wei and M. X. Wan, *J. Appl. Polym. Sci.*, in press.
106. Z. X. Wei and M. X. Wan, *Langmuir* 18, 917 (2002).
107. Z. X. Wei and M. X. Wan, *Adv. Mater.* 14, 1314 (2002).
108. Z. M. Zhang, Z. X. Wei, and M. X. Wan, *Macromolecules* 35, 5937 (2002).
109. Z. M. Zhang and M. X. Wan, *Synth. Met.*, unpublished.
110. Y. S. Yang and M. X. Wan, *J. Chem. Mater.* 12, 897 (2002).
111. M. X. Wan et al., *Synth. Met.*, 175, 135 (2003).

112. A. G. MacDiarmid, M. Halpern, and W. S. Huang, *Mol. Cryst. Liq. Cryst.* 121, 173 (1985).
113. M. X. Wan, *J. Polym. Sci. Part A: Polym. Chem.* 30, 543 (1992).
114. Z. X. Wei and M. X. Wan, *Adv. Mater.* January, 15 (2003).
115. B. J. Kim, Q. S. Han, M. G. Han, and S. S. Im, *Synth. Met.* 122, 297 (2001).
116. B. J. Kim, S. G. Oh, M. G. Han, and S. S. Im, *Langmuir* 1, 5841 (2000).
117. M. Harada and M. Adachi, *Adv. Mater.* 12, 839 (2000).
118. M. Bockstaller, W. Kohler, G. Wegner, D. Vassopoulos, and G. Fytas, *Macromolecules* 33, 3951 (2000).
119. O. Krathaus, N. Maruyama, X. Cieren, M. Shimomura, H. Hasegawa, and T. Hasshimoto, *Langmuir* 16, 6071 (2000).
120. C. F. Liu, D.-K. Moon, T. Maruyama, and T. Yamamoto, *Polym. J.* 25, 775 (1993).
121. N. Gospodinova, L. Terlemezyan, P. Mokreva, J. Stejskal, and P. Kratochvil, *Eur. Polym. J.* 29, 1305 (1993).
122. "Handbook of Conducting Polymers" (T. A. Skotheim, R. L. Elsenbaumer, and J. R. Reynolds, Eds.), 2nd ed., p. 415. Dekker, New York/Basel/Hong Kong, 1998.
123. M. X. Fu, Y. F. Zhu, B. Q. Tan, and G. Q. Shi, *Adv. Mater.* 13, 651 (2001).
124. Yucca, Posit, and A. J. Heeger, *Synth. Met.* 32, 263 (1989).
125. C. R. Martin, R. Parthasarathy, and V. Menon, *Synth. Met.* 55–57, 1165 (1993).
126. V. M. Cepak and C. R. Martin, *J. Mater. Sci.* 87, 23 (1994).
127. Z. Cai, J. Lei, W. Liang, V. Menon, and C. R. Martin, *Chem. Mater.* 3, 960 (1991).
128. N. F. Mott and E. A. Davis, "Electronic Processes in Non-crystalline Materials," 2nd ed., p. 34. Clarendon, Oxford, 1979.
129. Y. W. Park, in "The International Conference of Synthetic Metals" (ICSM'2002), June 30–July 5, 2002, Shanghai, China.
130. A. Formhals, U.S. Patent 1975.504, 1934.
131. J. Doshi and D. H. Rencker, *J. Electrost.* 35, 151 (1995).
132. P. W. Gibson, H. L. Schreuder-Gibson, and D. Riven, *AICHE J.* 45, 190 (1999).
133. E. K. Ko, C. T. Laurencin, M. D. Borden, and D. H. Renecker, The dynamic of cell-fiber architecture interaction, in "Proceedings, Annual Meeting, Biomaterials Research Society," San Diego, April, 1998.
134. I. D. Norris, M. M. Shaker, F. K. Ko, and A. J. MacDiarmid, *Synth. Met.* 114, 109 (2000).
135. M. Bognitzki, H. Hou, M. Ishaque, T. Frese, M. Hellwing, C. Sechwarte, A. Schaper, J. H. Wendroff, and A. Greiner, *Adv. Mater.* 12, 637 (2000).
136. A. G. MacDiarmid, W. E. Jone, I. D. Norris, J. Gao, A. T. Johnson, N. J. Pinto, J. Hone, B. Han, F. K. Ko, Okuzaki, and M. Llauno, *Synth. Met.* 119, 27 (2001).
137. B. Sixou, J. P. Travers, C. Barthet, and M. Gugliemi, *Phys. Rev. B* 56, 4604 (1997).
138. K. Huang and M. X. Wan, *Chem. Mater.* 14, 3486 (2002).
139. Y. S. Yang and M. X. Wan, *J. Mater. Chem.* 12, 897 (2002).
140. G. Hunner and D. C. Neckers, *Chem. Rev.* 89, 1915 (1989).
141. G. Zimmerman, L. Chow, and U. Paik, *J. Am. Chem. Soc.* 80, 3528 (1985).
142. M. Schwientek, S. Plens, and C. H. Hamann, *J. Electroanal. Chem.* 461, 94 (1999).
143. S. Pleus and M. Schwientek, *Synth. Met.* 95, 233 (1998).
144. Z. D. Chen, Y. Takei, B. A. Deo Ye, and T. Nagaoka, *Analyst* 125, 2249 (2000).
145. Y. X. Zhou, B. Yu, and G. Y. Zhu, *Polymer* 38, 5493 (1997).
146. H. S. Lee and J. Hong, *J. Chromatogr. A* 868, 189 (2000).
147. Z. D. Chen, A. Okimoto, T. Kiyonaga, and T. Nagaoka, *Anal. Chem.* 71, 1834 (1999).
148. H. L. Guo, C. M. Nobler, and R. B. Kaner, *Synth. Met.* 101, 44 (1999).

149. G. C. Sun, K. L. Yao, H. X. Liao, Z. C. Hiu, and Z. L. Liu, *Int. J. Electron.* 87, 735 (2000).
150. L. A. P. Kane-Maguire, I. D. Norris, and G. G. Wallance, *Synth. Met.* 101, 817 (1999).
151. F. Chen, P. Akhta, L. A. P. Kane-Maguire, and G. G. Wallance, *Aust. J. Chem.* 50, 939 (1997).
152. D. Kotkar, V. Joshi, and P. K. Ghosh, *J. Chem. Soc. Chem. Commun.* 917 (1988).
153. I. D. Norris, L. A. P. Kane-Maguire, G. G. Wallence, and L. H. C. Mattaso, *Aust. J. Chem.* 153, 89 (2000).
154. L. J. Zhang and M. X. Wan, *J. Polym. Sci. Part A: Polym. Chem.*, in press.
155. S. Su and N. K. Kuramoto, *Synth. Met.* 114, 147 (2000).
156. S. Miyauchi, H. Aiko, Y. Sorimashi, and I. Tsubuta, *J. Appl. Polym. Sci.* 37, 289 (1989).
157. P. K. Shen, H. T. Huang, and A. C. C. Tseung, *J. Electrochem. Soc.* 139, 1840 (1992).
158. X. Peng, Y. Zhang, B. Zou, L. Xiao, T. Li, and J. Yang, *J. Phys. Chem.* 96, 3412 (1992).
159. H. Yaneyama, Y. Shoji, and K. Kawai, *Chem. Lett.* 1069 (1997).
160. R. S. G. Partch, E. Ganglli, and W. Matijevic, *J. Coll. Int. Sci.* 144, 27 (1991).
161. B. Z. Tang, Y. H. Geng, Q. H. Sun, X. X. Zhang et al., *Pure Appl. Chem.* 72, 157 (2000).
162. M. X. Wan and W. G. Li, *J. Polym. Sci. Part. A: Polym. Chem.* 35, 2129 (1997).
163. M. X. Wan, W. Zhou, and J. C. Li, *Synth. Met.* 78, 27 (1996).
164. M. X. Wan and J. H. Fan, *J. Polym. Sci. Part A: Polym. Chem.* 36, 2749 (1998).
165. M. X. Wan and J. C. Li, *Synth. Met.* 101, 844 (1999).
166. J. Liu and M. X. Wan, *J. Polym. Sci. Part A: Polym. Chem.* 38, 2724 (2000).
167. Z. M. Zhang and M. X. Wan, *Synth. Met.*, 205, 132 (2003).
168. Y. B. Moon, Y. Cao, P. Smith, and A. Heeger, *Polym. Commun.* 30, 196 (1989).
169. S. Su and N. K. Kuramoto, *Synth. Met.* 114, 147 (2000).
170. J. Sandler, M. Shaffer, T. Prasse, W. Bauhofer, K. Schulte, and A. H. Windle, *Polymer* 40, 5967 (1999).
171. A. Hachtold, P. Hadeky, T. Nakanish, and C. Dekker, *Science* 294, 1317 (2001).
172. S. Fan, M. G. Chapline, N. R. Frankline, T. W. Tomber, A. M. Cassell, and H. Dai, *Science* 283, 512 (1999).
173. S. Frank, P. Poncharal, Z. L. Wang, and W. A. Heer, *Science* 280, 1744 (1998).
174. C. Juornet and P. Bernier, *Appl. Phys. A* 67, 1160 (1998).
175. J. L. Barth, E. T. Mickelsom, M. J. Bronikowaki, R. E. Smally, and J. M. Tour, *Chem. Commun.* 93, 2001.
176. J. Fan, M. X. Wan, D. B. Zhu, Z. Pan, and S. Xie, *Synth. Met.* 102, 1266 (1999).
177. M. S. P. Shatter, D. Coleby, G. Dixon, W. Zhou, D. J. Fray, and A. H. Windel, *Adv. Mater.* 12, 522 (2000).
178. C. Douns, J. Nugnet, P. M. Ajayan, D. J. Duguette, and K. S. V. Santhanam, *Adv. Mater.* 11, 1028 (1999).
179. H. Ago, K. Pertrisch, S. P. Shaffer, A. H. Windle, and R. H. Friend, *Adv. Mater.* 11, 1281 (1999).
180. E. Kymakis and G. A. Amaratunga, *J. Appl. Phys.* 80, 112 (2002).
181. S. Curran, P. M. Ajayan, W. J. Blau, D. L. Carroll, J. N. Coleman, A. B. Dalton, A. P. Davey, A. Drury, B. McCarthy, S. Maier, and A. Strevens, *Adv. Mater.* 10, 1091 (1998).
182. M. Gao, S. Huang, L. Dai, G. Wallace, R. Gao, and Z. Wang, *Angew. Chem. Int. Ed.* 39, 3664 (2000).
183. J. H. Fan, M. X. Wan, D. B. Zhu, B. H. Chang, Z. W. Pan, and S. S. Xie, *Synth. Met.* 102, 1266 (1999).
184. P. C. Pamamurthy, W. R. Harrall, R. V. Gregory, B. Sadanadan, and A. M. Rao, in "ICSM'2002," June 30–July 5, 2002, Shanghai, China.
185. J. H. Chen, Z. P. Huang, D. Z. Wang, S. X. Yang, W. Z. Li, J. G. Wen, and Z. F. Ren, *Synth. Met.* 125, 294 (2002).
186. J. H. Chen, Z. P. Huang, D. Z. Wang, S. X. Yang, W. Z. Li, J. G. Wen, and Z. F. Ren, *Synth. Met.* 125, 294 (2002).
187. M. Huges, M. S. P. Shaffer, A. C. Renouf, C. Singh, G. Z. Chen, D. J. Fray, and A. H. Windle, *Adv. Mater.* 14, 382 (2002).
188. X. C. Liu, J. H. Si, B. H. Chang, G. Xu, Q. Yang, Z. W. Pan, P. X. Ye, and S. S. Xie, *Appl. Phys. Lett.* 74, 164 (1999).
189. B. B. Mandelborot, "The Fractal Geometry of Nature." Freeman, San Francisco, 1982.
190. A. Harrison, "Fractals in Chemistry." Oxford Univ. Press, Oxford, 1995.
191. J. J. Langer and I. Cazikowski, *Adv. Mater. Opt. Electron.* 7, 149 (1997).
192. I. Mogi and M. kamiko, *Bull. Chem. Jpn.* 69, 1889 (1996).
193. A. Cao, X. Zhang, C. Wu, J. Liang, D. Wu, and B. Wei, *Mater. Res. Bull.* 36, 2519 (2001).
194. Z. X. Wei and M. X. Wan, *Adv. Mater.* 15, 15 (2003).

Confined Molecules in Nanopores

H. Tanaka, M. El-Merraoui, H. Kanoh, K. Kaneko

Chiba University, Chiba, Japan

CONTENTS

1. PRINCIPLE OF DYNAMICS OF CONDENSED MOLECULES

The band shape analysis of vibrational spectra provides useful information about the dynamics of a molecule in liquids and solutions. Since the original works of Gordon [1] and Shimizu [2], in which vibrational line profiles of dense gases, liquids, and solutions are represented by Fourier transformation of a time correlation function, many studies on molecular motion in the condensed phase have been reported [3–14]. A molecule in a condensed phase changes its temporal equilibrium orientation and vibrational phase of transition moment, owing to frequent collisions with its surroundings. In this section, such a fluctuating rotational-vibrational transition moment is considered. Here, a relevant transition moment operator $\mu(t)$ can be developed into a series in terms of the atomic displacement coordinate Q (normal coordinate) of vibrational mode ν

$$\mu(t) = \mu_0(t) + \left[\frac{\partial \mu(t)}{\partial Q(t)}\right]_{Q=0} Q(t) + \cdots \quad (1)$$

For a rotational-vibrational transition, the relevant term is

$$\left[\frac{\partial \mu(t)}{\partial Q(t)}\right]_{Q=0} Q(t) \equiv \mathbf{m}(t) \quad (2)$$

The vector $\mathbf{m}(t)$ can be written as a product of its unit vector $\hat{\mathbf{m}}$ and its modulus m

$$\mathbf{m}(t) = \hat{\mathbf{m}}(t)m(t)$$
$$m(t) = |\mathbf{m}(t)| \quad (3)$$
$$\hat{\mathbf{m}}(t) = \mathbf{m}(t)/m(t)$$

Clearly $\hat{\mathbf{m}}$ and m denote, respectively, the angle-dependent and amplitude-dependent factors of the transition moment vector. Therefore, $\hat{\mathbf{m}}(t)$ can be assigned to the purely orientational coordinate and $m(t)$ to the purely vibrational coordinate of the fluctuating rotational-vibrational transition moment. When the reorientational (rotational) relaxation and the vibrational relaxation of the transition moment are independent of each other, the infrared absorption spectral intensity $I(\omega)$ can be written as [1–3]

$$I(\omega) = \int_{-\infty}^{\infty} dt \, \exp\{-i(\omega - \omega_0)t\}$$
$$\times \langle \hat{\mathbf{m}}(0)\hat{\mathbf{m}}(t)\rangle \langle m(0)m(t)\rangle \quad (4)$$

where ω is the angular frequency and ω_0 is the band center. The function $\langle \hat{\mathbf{m}}(0)\hat{\mathbf{m}}(t)\rangle$ corresponds to the reorientational correlation function, and $\langle m(0)m(t)\rangle$ to the vibrational correlation function. Here the reorientational and vibrational relaxation times, τ_r and τ_v, are defined as

$$\tau_r = \int_0^{\infty} dt \langle \hat{\mathbf{m}}(0)\hat{\mathbf{m}}(t)\rangle \qquad \text{and}$$
$$\tau_v = \int_0^{\infty} dt \langle m(0)m(t)\rangle \quad (5)$$

If we assume that the reorientational and vibrational relaxation do not depend on each other and the reorientational and vibrational correlation functions have an exponential form, $I(\omega)$ has a Lorentzian shape, and thus the measured half-band width $\Delta\nu_{1/2}$ (cm^{-1}) of $I(\omega)$ is expressed as a sum

$$\Delta\nu_{1/2} = \Delta\nu_r + \Delta\nu_v \quad (6)$$

where

$$\Delta\nu_r = (2\pi c\tau_r)^{-1} \qquad \text{and} \qquad \Delta\nu_v = (2\pi c\tau_v)^{-1} \qquad (7)$$

Then the half-band width of the infrared band for a single vibrational transition has information about the reorientational and vibrational relaxation of a condensed molecule. Although the infrared measurement cannot divide spectroscopically the reorientational and vibrational relaxation processes, the vibrational relaxation time obtained from the isotropic part of Raman scattering can be diverted to evaluate the reorientational relaxation time [3]. These principles should also be applied to study the dynamics of molecules confined in nanoscale pores.

2. THEORETICAL DESCRIPTION OF CONFINED MOLECULES

Confined fluids in nanopores have received considerable attention in recent decades. The molecule-nanopore interaction should induce interesting phenomena, such as micropore filing and capillary condensation. Modern methods, such as grand canonical Monte Carlo (GCMC) simulation [15–17], molecular dynamics (MD) [18], and density functional theory (DFT) [19, 20], have led to substantial progress in understanding adsorption phenomena. In particular, the DFT method is quite effective for the study of adsorption in nanopores. In this section, we introduce DFT and discuss the capillary condensation of fluids in mesopores.

2.1. Density Functional Theory

DFT is a useful tool for the description of inhomogeneous classical fluids. Such systems are characterized by spatial variation of the average single particle density $\rho(\mathbf{r})$. DFT methods are based on the idea that the free energy of an inhomogeneous fluid can be reproduced by a functional of the local density $\rho(\mathbf{r})$. The basic formulations of DFT can be found in [21], and [22] provides the review. The simplest version of DFT using the local density approximation (LDA), which does not take into account short-range correlations in the repulsive part of the free energy functional, has been used successively in the study of wetting phenomena [23], liquid-gas interfaces [24], and capillary condensation [25–27]. However, it has been recognized that LDA fails to predict the strong oscillations that are present in the density profile of a fluid in contact with a solid substrate [28]. These oscillations are a reflection of short-range correlations in a fluid. Tarazona and co-workers [29, 30] developed a nonlocal version of DFT, which is based on the weighted-density approximation (WDA) including such correlations. The basis of WDA is that hard-sphere Helmholtz free energy can be expressed as a function of a smoothed density $\rho_s(\mathbf{r})$, which is a nonlocal functional of the true density profile $\rho(\mathbf{r})$. WDA yields realistic oscillatory density profiles, which reflect packing constraints on the arrangements of particles in the case of a fluid in simple confining geometries. Moreover, it was shown that WDA generally yields results comparable to those obtained by GCMC simulations [28], which are regarded as reference computer experiments. Tarazona's version of DFT has recently been

employed for theoretical predictions of adsorption isotherms in porous materials and phase transitions, such as micropore filling, capillary condensation in pores, layering, and wetting transitions on solid substrates [20, 31–39]. The nonlocal density functional theory has also been used to study the high-pressure adsorption of supercritical gases [40–42] and to calculate the pore size distribution (PSD) of porous materials, such as activated carbons, mesoporous silica, and pillared interlayered clays [19, 43–47]. In particular, DFT-based methods for the pore size characterization of activated carbons from nitrogen adsorption isotherms have become a standard characterization method in recent years.

Different versions of WDA have been introduced by several authors (e.g., Rosenfeld [48], Denton and Ashcroft [49], and Kierlik and Rosinberg [50]). The WDA method of Rosenfeld-Kierlik-Rosinberg has been employed for the theoretical study of adsorption, mainly for the adsorption of mixtures [51–58]. The WDA method of Tarazona has also been applied for the adsorption of mixtures [59–61], although it should require more computation time than that for Rosenfeld-Kierlik-Rosinberg.

In this section, the nonlocal DFT based on WDA, which was developed by Tarazona, is treated. In the conventional DFT approach, it is assumed that the pore has a fixed geometry and is open and in contact with bulk fluid. For this system, a grand canonical ensemble provides an appropriate description of the thermodynamics. In this ensemble, system volume V, temperature T, and chemical potential μ are specified. For a fluid in the presence of a spatially varying external potential $V_{ext}(\mathbf{r})$, the grand potential functional Ω can be expressed as

$$\Omega[\rho(\mathbf{r})] = F[\rho(\mathbf{r})] + \int d\mathbf{r}\, \rho(\mathbf{r})[V_{ext}(\mathbf{r}) - \mu] \qquad (8)$$

where $F[\rho(\mathbf{r})]$ is the intrinsic Helmholtz free energy functional. At thermodynamic equilibrium, $\Omega[\rho(\mathbf{r})]$ is a global minimum with respect to variations in $\rho(\mathbf{r})$. The minimum value is equal to the thermodynamic grand potential of the system. It is customary to divide $F[\rho(\mathbf{r})]$ into two parts, which are due to repulsive and attractive interactions. The repulsive interaction is modeled by a hard sphere of diameter d, and the attractive interaction is treated in a mean-field fashion

$$F[\rho(\mathbf{r})] = F_{hs}[\rho(\mathbf{r}); d]$$
$$+ \tfrac{1}{2} \iint d\mathbf{r}\, d\mathbf{r}'\, \rho(\mathbf{r})\rho(\mathbf{r}')\Phi_{att}(|\mathbf{r} - \mathbf{r}'|) \qquad (9)$$

Here $\Phi_{att}(|\mathbf{r}|)$ is the attractive part of the pairwise potential between two fluid molecules. The attractive part of the fluid-fluid potential is represented by the WCA form of the Lennard-Jones (LJ) potential [62]

$$\Phi_{att}(r) = \begin{cases} -\varepsilon, & r < r_m \\ \Phi_{LJ}(r), & r_m < r < r_c \\ 0, & r_c < r \end{cases} \qquad (10)$$

$$\Phi_{LJ}(r) = 4\varepsilon\left[\left(\frac{\sigma}{r}\right)^{12} - \left(\frac{\sigma}{r}\right)^{6}\right] \qquad (11)$$

where $r_{\mathrm{m}} = 2^{1/6}\sigma$ is the location of the minimum of the LJ potential and r_{c} is the cutoff distance. The hard-sphere free energy functional $F_{\mathrm{hs}}[\rho(\mathbf{r})]$ is not known exactly for the three-dimensional fluid. Therefore, further approximations must be made with respect to the free energy functional. The hard-sphere term is often divided into an ideal gas component and an excess (configurational) component

$$F_{\mathrm{hs}}[\rho(\mathbf{r}); d] = F_{\mathrm{id}}[\rho(\mathbf{r})] + F_{\mathrm{ex}}[\rho(\mathbf{r}); d] \qquad (12)$$

The ideal contribution $F_{\mathrm{id}}[\rho(\mathbf{r})]$ is given exactly by the local density expression

$$F_{\mathrm{id}}[\rho(\mathbf{r})] = kT \int d\mathbf{r}\, \rho(\mathbf{r})[\ln(\Lambda^3 \rho(\mathbf{r})) - 1] \qquad (13)$$

where $\Lambda = h/(2\pi m kT)^{1/2}$ is the thermal de Broglie wavelength of a molecule of mass m, h is the Planck constant, and k is the Boltzmann constant. The excess component is expressed as

$$F_{\mathrm{ex}}[\rho(\mathbf{r}); d] = \int d\mathbf{r}\, \rho(\mathbf{r}) f_{\mathrm{ex}}[\rho_{\mathrm{s}}(\mathbf{r}); d] \qquad (14)$$

where $f_{\mathrm{ex}}[\rho_{\mathrm{s}}(\mathbf{r}); d]$ is the excess free energy per molecule in the hard-sphere fluid, which is calculated from the Carnahan-Starling equation of state [63]

$$f_{\mathrm{ex}}[\rho_{\mathrm{s}}(\mathbf{r}); d] = kT \frac{\eta(4 - 3\eta)}{(1 - \eta)^2} \qquad (15)$$

with $\eta = \pi \rho_{\mathrm{s}} d/6$. The smoothed density $\rho_{\mathrm{s}}(\mathbf{r})$ is given by an average of $\rho(\mathbf{r})$ weighted by a suitable function w, which is allowed to depend on $\rho_{\mathrm{s}}(\mathbf{r})$ [29]

$$\rho_{\mathrm{s}}(\mathbf{r}) = \int d\mathbf{r}'\, \rho(\mathbf{r}') w[|\mathbf{r} - \mathbf{r}'|; \rho_{\mathrm{s}}(\mathbf{r})] \qquad (16)$$

The weight function w is specified by requiring the direct correlation function of a uniform hard-sphere fluid (which is calculated from functional differentiation of Eq. (12) with Eq. (16)) to be close to the corresponding Percus-Yevick result. The Tarazona prescription for the weight function uses a (truncated) power series expansion in the smoothed density

$$w[|\mathbf{r} - \mathbf{r}'|; \rho_{\mathrm{s}}(\mathbf{r})] = w_0(|\mathbf{r} - \mathbf{r}'|) + w_1(|\mathbf{r} - \mathbf{r}'|)\rho_{\mathrm{s}}(\mathbf{r})$$
$$+ w_2(|\mathbf{r} - \mathbf{r}'|)[\rho_{\mathrm{s}}(\mathbf{r})]^2 \qquad (17)$$

The expansion coefficients w_i ($i = 0, 1, 2$) are given in [29, 30]. Then Eq. (16) reduces to a quadratic equation for $\rho_{\mathrm{s}}(\mathbf{r})$

$$\rho_{\mathrm{s}}(\mathbf{r}) = \rho_{\mathrm{s}0}(\mathbf{r}) + \rho_{\mathrm{s}1}(\mathbf{r})\rho_{\mathrm{s}}(\mathbf{r}) + \rho_{\mathrm{s}2}(\mathbf{r})[\rho_{\mathrm{s}}(\mathbf{r})]^2 \qquad (18)$$

with coefficients

$$\rho_{\mathrm{s}i}(\mathbf{r}) = \int d\mathbf{r}'\, \rho(\mathbf{r}') w_i(|\mathbf{r} - \mathbf{r}'|) \qquad (19)$$

for $i = 0, 1, 2$. The physical root of Eq. (18) is

$$\rho_{\mathrm{s}}(\mathbf{r}) = \frac{1 - \rho_{\mathrm{s}1}(\mathbf{r}) - \left[(1 - \rho_{\mathrm{s}1}(\mathbf{r}))^2 - 4\rho_{\mathrm{s}0}(\mathbf{r})\rho_{\mathrm{s}2}(\mathbf{r})\right]^{1/2}}{2\rho_{\mathrm{s}2}(\mathbf{r})}$$

$$= \frac{2\rho_{\mathrm{s}2}(\mathbf{r})}{1 - \rho_{\mathrm{s}1}(\mathbf{r}) - \left[(1 - \rho_{\mathrm{s}1}(\mathbf{r}))^2 - 4\rho_{\mathrm{s}0}(\mathbf{r})\rho_{\mathrm{s}2}(\mathbf{r})\right]^{1/2}}$$
$$(20)$$

where the second form is more convenient for calculations when $\rho_{\mathrm{s}1}(\mathbf{r})$ and $\rho_{\mathrm{s}2}(\mathbf{r})$ approach zero. Here the normalization condition for Eq. (17)

$$\int d\mathbf{r}\, w[|\mathbf{r} - \mathbf{r}'|; \rho_{\mathrm{s}}(\mathbf{r})] = 1 \qquad (21)$$

implies that

$$\int d\mathbf{r}\, w_i(|\mathbf{r} - \mathbf{r}'|) = \begin{cases} 1, & i = 0 \\ 0, & i = 1, 2 \end{cases} \qquad (22)$$

Therefore, in the limit of a uniform fluid, $\rho_{\mathrm{s}i}(\mathbf{r})$ becomes $\rho_{\mathrm{s}0}(\mathbf{r}) = \rho$ (bulk fluid density) and $\rho_{\mathrm{s}1}(\mathbf{r}) = \rho_{\mathrm{s}1}(\mathbf{r}) = 0$.

The problem of finding an equilibrium density distribution $\rho(\mathbf{r})$ can be solved by minimizing the grand potential functional (Eq. (8)) with respect to $\rho(\mathbf{r})$. The standard method employed first by Tarazona [29] is based on the Euler–Lagrange equation; the minimization requirement is satisfied by differentiating the grand potential functional with respect to density and equating to zero. The resulting Euler–Lagrange equation is

$$\mu = V_{\mathrm{ext}}(\mathbf{r}) + kT \ln(\Lambda^3 \rho(\mathbf{r})) + f_{\mathrm{ex}}(\rho_{\mathrm{s}}(\mathbf{r}))$$
$$+ \int d\mathbf{r}'\, \rho(\mathbf{r}') f_{\mathrm{ex}}'(\rho_{\mathrm{s}}(\mathbf{r}')) \frac{\delta \rho_{\mathrm{s}}(\mathbf{r}')}{\delta \rho(\mathbf{r})}$$
$$+ \int d\mathbf{r}'\, \rho(\mathbf{r}') \Phi_{\mathrm{att}}(|\mathbf{r} - \mathbf{r}'|) \qquad (23)$$

where the functional derivative of $\rho_{\mathrm{s}}(\mathbf{r})$ with regard to $\rho(\mathbf{r})$ can be represented as

$$\frac{\delta \rho_{\mathrm{s}}(\mathbf{r}')}{\delta \rho(\mathbf{r})} = \frac{w[|\mathbf{r} - \mathbf{r}'|; \rho_{\mathrm{s}}(\mathbf{r}')]}{1 - \rho_{\mathrm{s}1}(\mathbf{r}') - 2\rho_{\mathrm{s}2}(\mathbf{r}')\rho_{\mathrm{s}}(\mathbf{r}')} \qquad (24)$$

The terms on the right-hand side of Eq. (23) must be imposed to the chemical potential of the bulk fluid at all points in the system. For the homogeneous system, the chemical potential of the bulk fluid of a uniform density ρ_{b} is

$$\mu = \mu_{\mathrm{hs}}(\rho_{\mathrm{b}}) + \rho_{\mathrm{b}} \int d\mathbf{r}\, \Phi_{\mathrm{att}}(|\mathbf{r}|) \qquad (25)$$

Here, $\mu_{\mathrm{hs}}(\rho_{\mathrm{b}})$ is the chemical potential of the hard-sphere fluid calculated from the Carnahan-Starling equation of state

$$\mu_{\mathrm{hs}}(\rho_{\mathrm{b}}) = kT \ln\left(\Lambda^3 \rho_{\mathrm{b}}\right) + f_{\mathrm{ex}}(\rho_{\mathrm{b}}, d) + \rho_{\mathrm{b}} f_{\mathrm{ex}}'(\rho_{\mathrm{b}}, d)$$

$$= kT \left[\ln\left(\Lambda^3 \rho_{\mathrm{b}}\right) + \frac{8\eta - 9\eta^2 + 3\eta^3}{(1 - \eta)^3}\right] \qquad (26)$$

with $\eta = \pi \rho_{\rm b} d / 6$. The integral over r of attractive interactions (which is the second term on the right-hand side of Eq. (25)) can be performed analytically as follows

$$\int_{|\mathbf{r}| < r_{\rm c}} d\mathbf{r}\, \Phi_{\rm att}(|\mathbf{r}|)$$

$$= -\frac{32}{9}\pi\varepsilon(r_{\rm m})^3 + \frac{16}{9}\pi\varepsilon\sigma^3 \left[3\left(\frac{\sigma}{r_{\rm c}}\right)^3 - \left(\frac{\sigma}{r_{\rm c}}\right)^9 \right]$$

$$= -\alpha \qquad (27)$$

For numerical calculations, Eq. (23) with Eq. (25) can be rearranged as

$$kT \ln\left(\frac{\rho(\mathbf{r})}{\rho_{\rm b}}\right)$$

$$= f_{\rm ex}(\rho_{\rm b}) + \rho_{\rm b} f'_{\rm ex}(\rho_{\rm b}) - \rho_{\rm b}\alpha - V_{\rm ext}(\mathbf{r}) - f_{\rm ex}(\rho_{\rm s}(\mathbf{r}))$$

$$- \int d\mathbf{r}'\, \rho(\mathbf{r}') f'_{\rm ex}(\rho_{\rm s}(\mathbf{r}')) \frac{\delta\rho_{\rm s}(\mathbf{r}')}{\delta\rho(\mathbf{r})}$$

$$- \int d\mathbf{r}'\, \rho(\mathbf{r}') \Phi_{\rm att}(|\mathbf{r} - \mathbf{r}'|) \qquad (28)$$

or, denoting the right-hand side of Eq. (28) as Ψ

$$\rho(\mathbf{r}) = \rho_{\rm b} \exp(\Psi/kT) \qquad (29)$$

This equation can be solved by iterations of substituting the initial or current density in the right-hand side and getting a better estimate on the left-hand side. This calculation is repeated until the required accuracy is attained. However, this iteration process is not efficient, because it usually diverges in a few steps if the full new density obtained from Eq. (29) is used for the next step. To avoid this, the weighted iteration method can be employed for a better convergence as follows [29]

$$\rho_{(i)} = \omega \rho_{(i)}^{\rm out} + (1 - \omega)\rho_{(i-1)} \qquad (30)$$

where $\rho_{(i)}^{\rm out}$ is the quantity calculated by substituting the initial guess $\rho_{(i-1)}$ into Eq. (29) without employing weights ω. The density $\rho_{(i)}$ is used for the next step iteration. The weight ω can be optimized to reduce the time of computations. Then, for the successive iterations, it may be better to change the value of ω depending on the changing rate: $|\rho_{(i)}^{\rm out}(\mathbf{r}) - \rho_{(i-1)}(\mathbf{r})|/\rho_{(i-1)}(\mathbf{r})$. Another method for minimizing the grand potential functional in the nonlocal DFT has recently been developed by Neimark [64]. The method is based on the implementation of indeterminate Lagrange multipliers (ILMs). The ILM method gives a substantial advantage when the functional derivative $\delta\rho_{\rm s}(\mathbf{r}')/\delta\rho(\mathbf{r})$ cannot be expressed explicitly.

The pressure of a bulk fluid is described by the following equation of state

$$P = P_{\rm hs}(\rho_{\rm b}) + \tfrac{1}{2}\rho_{\rm b}^2 \int d\mathbf{r}\, \Phi_{\rm att}(|\mathbf{r}|)$$

$$= P_{\rm hs}(\rho_{\rm b}) - \tfrac{1}{2}\rho_{\rm b}^2 \alpha \qquad (31)$$

with

$$P_{\rm hs}(\rho_{\rm b}) = \rho_{\rm b} kT \frac{1 + \eta + \eta^2 - \eta^3}{(1 - \eta)^3} \qquad (32)$$

Here $P_{\rm hs}(\rho_{\rm b})$ is the pressure of the hard-sphere fluid, which is calculated from the Carnahan-Starling equation of state, and $\eta = \pi \rho_{\rm b} d / 6$. The chemical potential of the bulk fluid is represented by Eq. (26). The equation of state given by Eqs. (26) and (31) is essentially a two-parameter equation that depends on the hard-sphere diameter d and the product $\varepsilon\sigma^3$ (see Eq. (27)). In this mean-field approximation, the hard-sphere fluid serves as the reference system. That is, the fluid-fluid potential is split at the minimum $r_{\rm m} = 2^{1/6}\sigma$ in the WCA fashion, and the repulsive part of the potential is modeled by an equivalent hard-sphere potential with an appropriate hard-sphere diameter. Then the equivalent hard-sphere diameter should be temperature and density dependent according to WCA. Three prescriptions for the choice of the hard-sphere diameter are usually considered. The first choice is made such that d equals σ. The first choice of the hard-sphere diameter (d_1) has been used in nonlocal DFT by several authors [28, 31]. The second one is given by the well-known Barker-Henderson (BH) [65] expression

$$d_2 = \int_0^{r_m} dr\, \{1 - \exp[-\Phi_{\rm rep}(r)/kT]\} \qquad (33)$$

where $\Phi_{\rm rep}(r)$ is the repulsive part of the LJ potential

$$\Phi_{\rm rep}(r) = \Phi_{\rm LJ}(r) - \Phi_{\rm att}(r) \qquad (34)$$

The second choice (d_2) is only temperature dependent. However, the hard-sphere diameter d_2 from the BH expression may be overestimated when one deals with the nonuniform situations, that is, fluid in confining geometries, which shows high-density oscillation in contact with a solid substrate. The third one (d_3) originates from the works of Lu et al. [24] and Verlet and Weis [66]. The form of d_3 approximates the BH diameter

$$\frac{d_3}{\sigma} = \frac{\xi_1 kT/\varepsilon + \xi_2}{\xi_3 kT/\varepsilon + \xi_4} \qquad (35)$$

where the coefficients ξ_i ($i = 1$–4) are parameters chosen such that the theory yields a good fit for the liquid density along the coexistence curve. The coefficients $\xi_1 = 0.3837$, $\xi_2 = 1.035$, $\xi_3 = 0.4249$, and $\xi_4 = 1$, which fit the liquid branch simulated by use of the LJ fluid, are reported in [19].

The liquid-vapor equilibrium conditions are determined from the equality of pressures and chemical potentials in the two phases. Simultaneous solution of Eqs. (25) and (31) gives the equilibrium gas and liquid densities, chemical potential, and saturated vapor pressure. Thus, the chemical potential of Eq. (25) must adequately describe the behavior of the bulk fluid at different temperatures and satisfy the Maxwell relation. Ravikovitch et al. have determined the fluid-fluid interaction parameters of the LJ potential ($\sigma_{\rm ff}$ and $\varepsilon_{\rm ff}$) and the hard-sphere diameter d suitable for nitrogen fluid [20]. First, they determined the parameters so that the theory could reproduce the experimental liquid-gas coexisting densities, saturation pressure, and surface tension of the free liquid-gas interface at the normal boiling point of 77.347 K. The fitted parameters $\sigma_{\rm ff}$, $\varepsilon_{\rm ff}$, and hard-sphere diameter d are listed in Table 1. Then parameters of the LJ potential were fixed and a subsequent optimization was

Table 1. Parameters of the fluid-fluid interaction potentials.

Fluid	$\varepsilon_{\mathrm{ff}}/k_B$ (K)	σ_{ff} (nm)	d (nm)	Ref.
N_2	94.45	0.3575	0.3575	[20, 42]
Ar	118.05	0.305	0.338	[42]

Note: The cutoff distance for the fluid-fluid interaction is $5\sigma_{\mathrm{ff}}$. d is the equivalent hard-sphere diameter.

Table 2. Parameters of the solid-fluid interaction potentials.

Solid-fluid	$\rho_v \varepsilon_{\mathrm{ff}}/k_B$ (K/nm^2)	σ_{sf} (nm)	Ref.
O-N$_2$	0.2253	0.317	[20, 42]
O-Ar	0.262	0.30	[42]

Note: The effective diameter of oxygen atoms in the wall is $\sigma_{\mathrm{ss}} = 0.276$ nm.

made only with respect to the hard-sphere diameter d as a function of temperature. The thermal dependence of the equivalent hard-sphere diameter was calculated with the use of Eq. (35) with the coefficients $\xi_1 = 0.3837$, $\xi_3 = 0.4249$, and $\xi_4 = 1$. The fitted parameter ξ_2 has been found to be 1.034. Ravikovitch et al. have reported that the theory describes the liquid-vapor densities and saturation pressure of nitrogen within 5% accuracy in the temperature range 63–90 K [44].

2.2. Adsorption on Cylindrical Mesopores

Recently, new families of mesoporous materials have been synthesized. Mesoporous molecular sieves, known as M41S, exhibit uniform pore structures and can be synthesized to consist of a regular array of hexagonal and unidimentional mesopores (MCM-41) [67, 68] or cubic structures (MCM-48) [69]. The mesopores of MCM-41 materials can be systematically varied in size from around 2 nm to 10 nm [68]. The siliceous mesoporous material SBA-15 also possesses a regular two-dimensional array of cylindrical channels [70, 71]. SBA-15 can have larger pores (up to 30 nm), which are larger than those of MCM-41 materials.

Recently Neimark et al. have studied capillary condensation in mesopores of MCM-41 and calculated pore size distributions, using nonlocal DFT [20, 36, 43, 44]. They approximated the mesopore of MCM-41 with a cylindrical pore composed of oxygen [20, 44], although its pores actually have a hexagonal cross section [67, 68].

The adsorbent-adsorbate interactions, V_{ext}, for the cylindrical pore geometry can be modeled with the use of the LJ potential integrated over an infinitely long cylinder [72, 73]

$$V_{\mathrm{ext}}(r, R) = \pi^2 \rho_s \varepsilon_{\mathrm{sf}} \sigma_{\mathrm{sf}}^2$$

$$\times \left[\frac{63}{32} \frac{F(-4.5, -4.5, 1.0; \beta^2)}{[R^*(1-\beta^2)]^{10}} - 3 \frac{F(-1.5, -1.5, 1.0; \beta^2)}{[R^*(1-\beta^2)]^4} \right] \quad (36)$$

where $\beta = r/R$ and $R^* = R/\sigma_{\mathrm{sf}}$, and then r, R, and $F(\alpha, \beta, \gamma; \chi)$ are the distance from the center, radius of the cylinder, and a hypergeometric function, respectively. Here the excess adsorption per unit pore volume is calculated as

$$\Gamma_v = \frac{2}{(R - \sigma_{\mathrm{ss}}/2)^2} \int_0^{R-\sigma_{\mathrm{ss}}/2} r \, dr [\rho(r) - \rho_b] \quad (37)$$

where $\sigma_{\mathrm{ss}} = 0.276$ nm is the effective diameter of oxygen atoms in the pore wall.

Ravikovitch et al. have determined the solid-fluid interaction parameters so that the theory could provide the best fit to nitrogen and argon standard isotherms on nonporous siliceous materials [20, 44] (see Table 2). They also

calculated fluid-fluid interaction parameters for nitrogen and argon such that the theory fit the experimental liquid-gas coexistence densities, saturation pressure, and surface tension of the free liquid-gas interface (see Table 1). Figure 1 shows the nitrogen adsorption isotherm in the cylindrical pore (diameter: $D^* = D/\sigma_{\mathrm{ff}} = 16.8$) at 77 K, calculated by the nonlocal DFT, using the interaction parameters reported in [20] (see Tables 1 and 2). In Figure 1, the grand potential changes along the adsorption and desorption are also shown. According to Neimark et al. [36], the DFT isotherm in a mesopore allows one to determine three characteristic points on adsorption-desorption isotherms: the pressure (P_{eq}) of the equilibrium capillary condensation transition; the starting point (P_{sc}) of spontaneous capillary condensation (vapor-like spinodal); and the starting point (P_{sd}) of spontaneous desorption (liquid-like spinodal) (see Fig. 1). For MCM-41 materials with pores wider than $\sim$5 nm, it has been reported that the experimental adsorption-desorption hysteresis loop is in agreement with the branches at P_{sc} and P_{eq} from the theoretical prediction [36].

3. ROTATIONAL AND VIBRATIONAL RELAXATION OF CONFINED MOLECULES

Although a capillary condensation theory has been devoted to the determination of pore size distribution of mesopores, adsorption studies of regular mesoporous silica such as MCM-41 or FSM [74, 75] demonstrated that classical capillary condensation theory could not explain the dependence of adsorption hysteresis on the pore width [76]. It has also been assumed that condensates in mesopores have the same
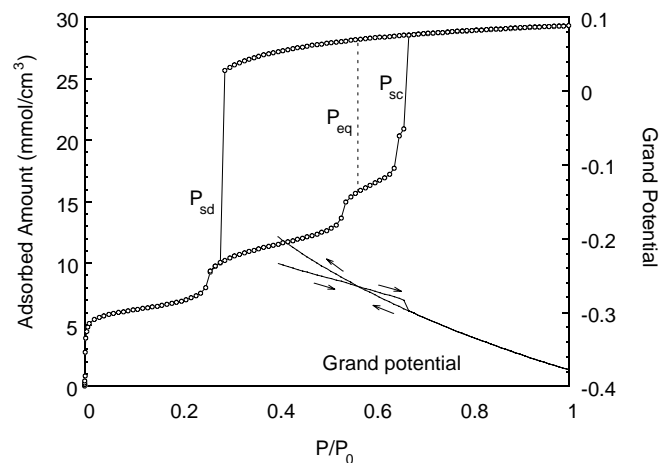
Figure 1. DFT isotherm for nitrogen in a cylindrical pore of diameter $D^* = 16.8$ (6.01 nm) at 77 K.

structure and density as bulk liquid. In the case of molecules adsorbed in micropores it was found that they formed a molecular assembly whose structure is different from that of liquid [77–79]. Hence, there is a possibility that molecular states of molecules adsorbed even in small mesopores are different from those of bulk liquid. Therefore, we should get microscopic information on adsorbed molecules in mesopores with the use of spectroscopic methods. In this section, nitrogen adsorption and argon adsorption on MCM-41 at 77 K are treated by means of DFT to gain an understanding the capillary condensation of fluids in small mesopores, and then the motional state of acetonitrile (CH_3CN) in mesopores of MCM-41 at 303 K is assessed by infrared band shape analysis. Acetonitrile is a symmetrical top molecule and has a very large dipole moment (3.92 D), which plays a key role in the reorientational relaxation [11].

3.1. Nitrogen and Argon Adsorption

The MCM-41 sample was prepared by Johannes Gutenberg University. The detailed preparation procedure of MCM-41 has been given elsewhere [80]. Nitrogen and argon adsorption isotherms at 77 K were measured with a conventional volumetric apparatus, manufactured by Quantachrome Corp. (Autosorb-1). Figure 2 displays the nitrogen adsorption isotherm on MCM-41 at 77 K. A distinct step in the isotherm occurs at a relative pressure of about 0.3 with no adsorption hysteresis. The slight inclination of the condensation step is due to a narrow pore size distribution. The total surface area S_t, external surface area S_{ex}, and primary mesopore volume V_p of MCM-41 were calculated with the α_s-plot method [81]. The α_s-plot method is based on a comparison of the adsorption isotherm for a given porous material with adsorption data for a reference nonporous solid. In the α_s-plot calculation, the nitrogen adsorption isotherm on macroporous silica gel LiChrospher Si-1000 (BET surface area: $S_{BET} = 26$ m^2/g) at 77 K was used as a standard isotherm [82]. The primary mesopore volume V_p and external surface area S_{ex} were calculated from the slope of a linear portion of the α_s-plot above the pressure of nitrogen condensation (α_s above 1.2) in primary mesopores (Fig. 3).
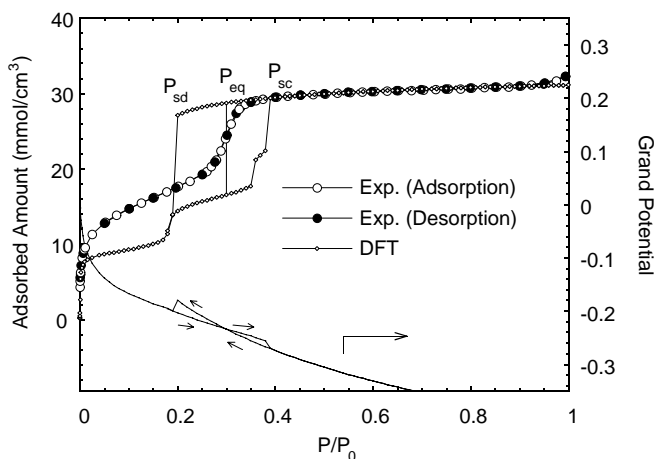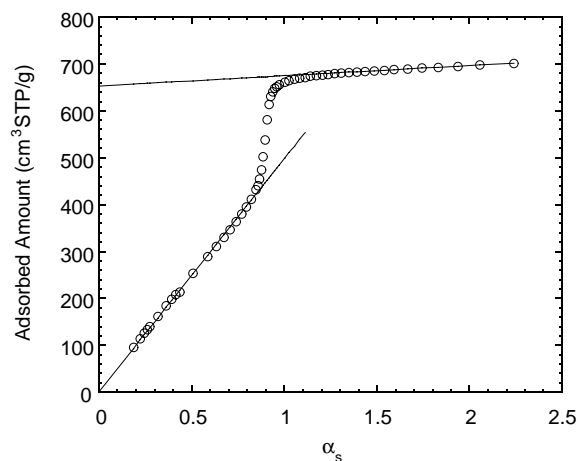
Figure 3. α_s plot for nitrogen adsorption on MCM-41.

The total surface area S_t was calculated from the slope of the initial part of the α_s-plot, that is, for α_s below 0.8. The mean pore diameter d_p was evaluated from the relations between the surface area, pore diameter, and pore volume for circular pores ($d_p = 4V_p/(S_t - S_{ex})$). The calculated total surface area S_t, external surface area S_{ex}, mesopore volume V_p, and mean pore diameter d_p are listed in Table 3.

In Figure 2, we also present the DFT isotherm of nitrogen at 77 K in the cylindrical pore of 3.92 nm (internal diameter: $d = 2R - \sigma_{ss}$) in comparison with the experimental isotherm on MCM-41. The theoretical isotherm exhibits metastable adsorption (P_{sc}) and desorption (P_{sd}) branches of the hysteresis loop and equilibrium transition (P_{eq}). Comparison with the experimental isotherm shows that the inflection point of the reversible experimental condensation branch does not coincide with the theoretical vapor-like spinodal line, but agrees satisfactorily with the equilibrium transition. Thus, this suggests that the capillary condensation and evaporation of nitrogen in the MCM-41 mesopore occur in a thermodynamic equilibrium state. However, the diameter of the model cylindrical pore used in the DFT calculation ($d = 3.92$ nm) is a little larger than that experimentally determined from the α_s-plot method ($d = 3.2$ nm, see Table 3). This may be attributed to an overestimation of the internal surface area ($S_t - S_{ex}$) obtained from the α_s-plot method. The correlation between theoretical and experimental isotherms of argon on the same MCM-41 sample at 77 K is shown in Figure 4. The theoretical isotherm was calculated from the same DFT model with a pore diameter of 3.92 nm, using the interaction parameters listed in Tables 1 and 2. The experimental adsorption branch is placed within the loop formed by the theoretical equilibrium transition and vapor-like spinodal, and then the

Figure 2. Adsorption isotherms of nitrogen on MCM-41 at 77 K: experimental data and DFT calculation for a cylindrical pore of internal diameter $d = 3.92$ nm.

Table 3. Structural parameters of MCM-41.

S_t (m^2/g)	S_{ex} (m^2/g)	V_p (cm^3/g)	d_p [α_s] (nm)	d [DFT] (nm)
1427	62	1.0	3.2	3.9

Note: S_t, total surface area; S_{ex}, external surface area; V_p, primary mesopore volume; d_p, mean pore diameter; d_p, $4V_p/(S_t - S_{ex})$. d is the pore diameter determined by fitting the DFT isotherm to the experimental one.
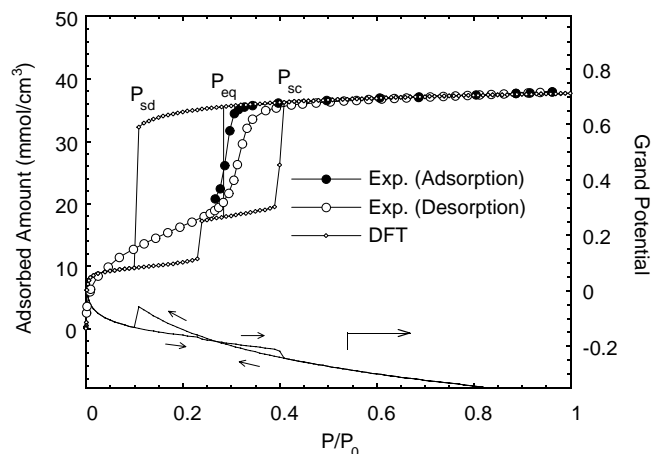
Figure 4. Adsorption isotherms of argon on MCM-41 at 77 K: experimental data and DFT calculation for a cylindrical pore of internal diameter $d = 3.92$ nm.

Figure 6. Local density profiles for argon adsorbed in a cylindrical pore of diameter $d = 3.92$ nm at 77 K. Dashed line: $P/P_0 = 0.2$; solid line: $P/P_0 = 0.6$.

experimental desorption branch is close to the theoretical equilibrium capillary condensation. This suggests that the metastable state on adsorption cannot be easily achieved for small mesopores, and the deviations between theoretical and experimental isotherms for the small mesopores are likely caused by neglect of the intrinsic energetic and geometrical heterogeneities of the pore walls in the theory. Local density profiles for nitrogen and argon adsorption in the cylindrical pore are shown in Figures 5 and 6. At $P/P_0 = 0.2$, nitrogen and argon molecules form a two-layer structure on the pore wall. Then, at $P/P_0 = 0.6$, the two fluids condense in the pore and the density profiles have six highly pronounced layers. The oscillations suggest that the condensates are more structured in the pore compared with bulk fluids. On the other hand, the structureless feature of the condensed phase can be seen for the case of the capillary condensation of a fluid in a fairly large mesopore. In Figure 7 we present the density profile of condensed nitrogen in a slit pore (internal width = 6.81 nm or $\sim 19\sigma_{\text{ff}}$) composed of two graphitic substrates at 77 K. The density profile has a weaker fluid

structure in the center of the slit pore, and the local density is consistent with the average density of bulk liquid nitrogen. This indicates that the structure of the condensed phase in the pore center is similar to that of the bulk liquid. However, it is possible that the molecular motion of the condensed molecules in the mesopore (smaller than $\sim 10\sigma_{\text{ff}}$ in diameter) is more restricted or hindered than that of liquid molecules because of the highly ordered structure as mentioned before.

3.2. Acetonitrile Adsorption

The adsorption isotherm of acetonitrile on MCM-41 (Fig. 8) was measured at 303 K with a computer-aided volumetric apparatus. The adsorption isotherm had a sharp jump at $P/P_0 = 0.3$ without adsorption hysteresis, indicating capillary condensation in regular mesopores. Moreover, the adsorption isotherm had a well-defined plateau, which provides clear evidence for the upper limit of capillary condensation. The value of the BET monolayer capacity, n_{m},

Figure 5. Local density profiles for nitrogen adsorbed in a cylindrical pore of diameter $d = 3.92$ nm at 77 K. Dashed line: $P/P_0 = 0.2$; solid line: $P/P_0 = 0.6$.
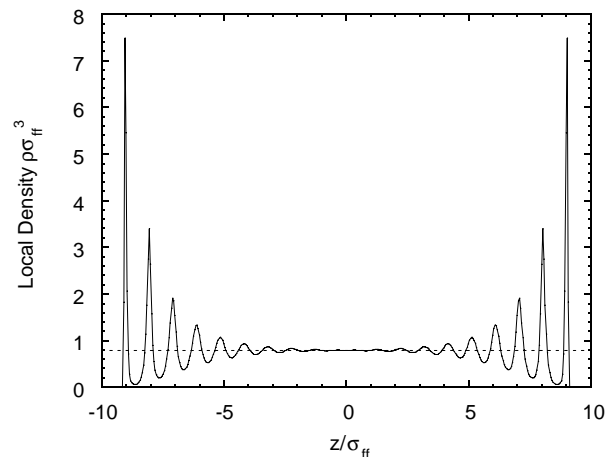
Figure 7. Local density profiles for nitrogen adsorbed in a slit pore composed of graphite substrates of inner width $w = 6.81$ nm at 77 K and $P/P_0 = 1$. The dashed line denotes the density of bulk liquid nitrogen.
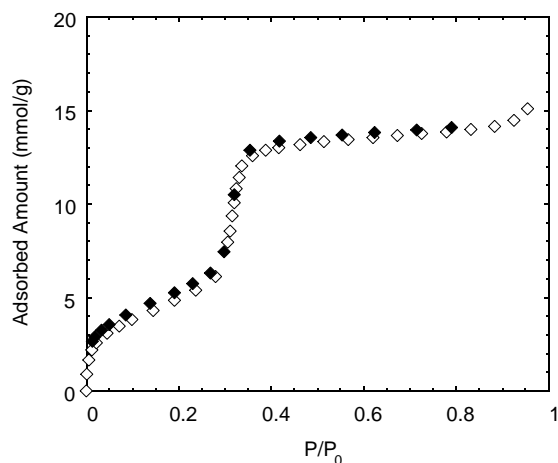
Figure 8. Acetonitrile adsorption isotherm on MCM-41 at 303 K. Open and closed symbols denote adsorption and desorption, respectively.

Figure 9. Changes in infrared adsorption of acetonitrile adsorbed on mesopores of MCM-41 as a function of P/P_0 at 303 K (C≡N stretching ν_2 region).

for acetonitrile was 4.5 mmol g^{-1}. By assuming the surface area ($S_t - S_{ex}$; see Section 3.1) determined from the nitrogen adsorption isotherm to be available for the adsorption of acetonitrile, the apparent molecular area, a_m, of adsorbed acetonitrile can be calculated from the value of n_m. The value of a_m for adsorbed acetonitrile (0.37 nm^2) was quite different from the value 0.22 nm^2, which was calculated from the liquid density by assuming close packing as in a bulk liquid. This result indicates that the BET monolayer cannot be regarded as a perfect close-packed monolayer, and a specific adsorption of acetonitrile takes place. The later infrared (IR) data will show that acetonitrile molecules are adsorbed on the surface hydroxyls in the monolayer adsorption stage.

3.3. Infrared Spectra of Confined Acetonitrile

The infrared spectra of acetonitrile adsorbed on MCM-41 were measured at 303 K with an *in-situ* IR cell with KRS-5 windows, with the aid of an Fourier transform IR spectrometer (Jasco FT/IR-550). The IR spectra were measured with the summation of 256 consecutive scans and a resolution of 1 cm^{-1}. The MCM-41 powder was uniformly coated on the KBr disk under a pressure of 5 MPa for the IR measurement, which does not induce the destruction of the pore structure of MCM-41 [83]. Acetonitrile of spectroscopic grade reagent from Wako Pure Chemicals was used. Figure 9 shows the IR spectra of adsorbed acetonitrile in the C≡N stretching ν_2 region over the range of $P/P_0 = 0.05–0.33$. The adsorbed amounts at $P/P_0 = 0.05$ and 0.15 are 70% and 98% of the monolayer capacity. Hence the absorption bands at $P/P_0 = 0.05$ and 0.15 are assigned to acetonitrile molecules in the monolayer. The band at 2265 cm^{-1} can be associated with the C≡N stretching ν_2 band of acetonitrile molecules interacting with surface hydroxyls of MCM-41, because the growth of the 2265 cm^{-1} band coincides with the disappearance of the absorption band of free surface hydroxyls at 3744 cm^{-1}. According to Purcell and Drago [84], the C≡N frequency increases when acetonitrile forms a coordination complex with an electron acceptor molecule,
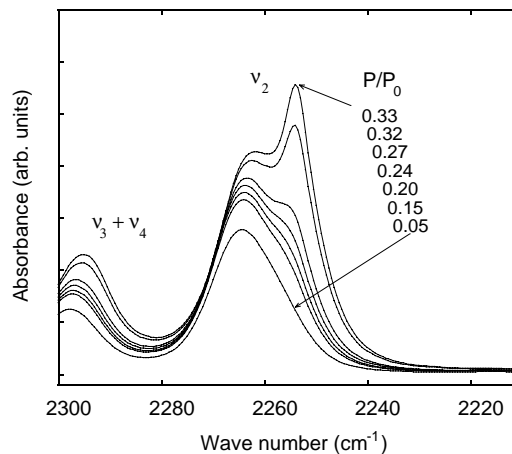
that is, overlapping of the N_{2S} orbital with the C_{2s} and $C_{2p\sigma}$ orbitals is responsible for the observed strengthening of the C≡N bond upon coordination of an acetonitrile molecule to Lewis acids. The C≡N stretching ν_2 band (2265 cm^{-1}) of acetonitrile adsorbed on MCM-41 shifts upward by 11 cm^{-1} from the bulk liquid phase value (see Fig. 9). Therefore, the upward shift should be due to the increase in the C≡N force constant of the acetonitrile molecule hydrogen-bonded to surface hydroxyls. In the case of a decationized zeolite sample with OH groups, similar spectral features were reported [85]. Above $P/P_0 = 0.3$, a new band is explicitly observed at a low-frequency side of the 2265 cm^{-1} band. This band becomes predominant above the adsorption jump (after capillary condensation). Furthermore, the band position of the lower frequency band agrees with that of the bulk liquid acetonitrile (2254 cm^{-1}). This suggests that the band at 2254 cm^{-1} can be assigned to the vibrational transition of the physisorbed molecule with nonspecific interactions.

The observed spectra in the C≡N stretching ν_2 region were carefully analyzed to assign the absorption bands of adsorbed acetonitrile exactly. As a first step of the analysis of the ν_2 band, the second-derivative curves were calculated from the observed spectra in the 2320–2220 cm^{-1} range (Fig. 10). At $P/P_0 = 0.05$, the second-derivative curve has minima at 2298 and 2265 cm^{-1} that correspond to the band positions. The curve around 2298 cm^{-1}, which originates from the band of the combination $\nu_3 + \nu_4$ transition, is very symmetrical, whereas the curve around 2265 cm^{-1} (ν_2 transition of the hydrogen-bonded acetonitrile) is slightly asymmetrical, owing to another component of the low-frequency side. At $P/P_0 = 0.15$, the minimum at 2254 cm^{-1} becomes quite apparent, indicating the presence of physisorbed acetonitrile (Fig. 10b). Nevertheless the 2254 cm^{-1} band is smeared out in the case of the infrared spectrum at $P/P_0 = 0.15$ (see Fig. 9); it is clear that there are at least two kinds of molecular states of hydrogen-bonded and physisorbed acetonitrile above $P/P_0 = 0.15$. In this section the ν_2 band of hydrogen-bonded acetonitrile is designated as the $\nu_2\alpha$ band, and that of physisorbed acetonitrile as the $\nu_2\beta$ band. Although the low-frequency component of
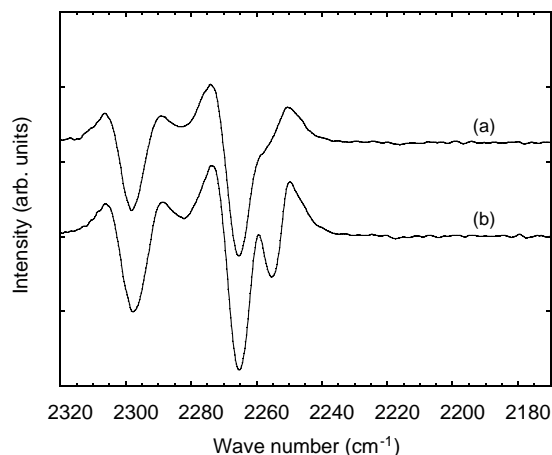
Figure 10. Second-derivative curves from the observed spectra of adsorbed acetonitrile in the 2220–2320 cm^{-1} range at (a) $P/P_0 = 0.05$, (b) 0.15.

the 2265 cm^{-1} band at $P/P_0 = 0.05$ cannot be attributed to physisorbed molecules, there is another possibility, to be described later.

3.4. Band Shape of the ν_2 Band of Liquid Acetonitrile

It is well known that the ν_2 band of liquid acetonitrile is significantly asymmetrical because of overlap of hot band transitions on the low-frequency side (Fig. 11). From a study of the gas phase rotation-vibration spectrum [86], the hot band transition from the first excited state of the degenerate C—C≡N bending ν_8 mode, $\nu_2^{h1} = \nu_2 + \nu_8 - \nu_8$, has its center 4.944 cm^{-1} lower than that of the fundamental transition, ν_2^f. Also the existence of a $\nu_2^{h2} = \nu_2 + 2\nu_8 - 2\nu_8$ transition is expected. Hashimoto et al. studied the ν_2 band of liquid acetonitrile [11] to determine the reorientational and vibrational relaxation times of liquid acetonitrile. They showed
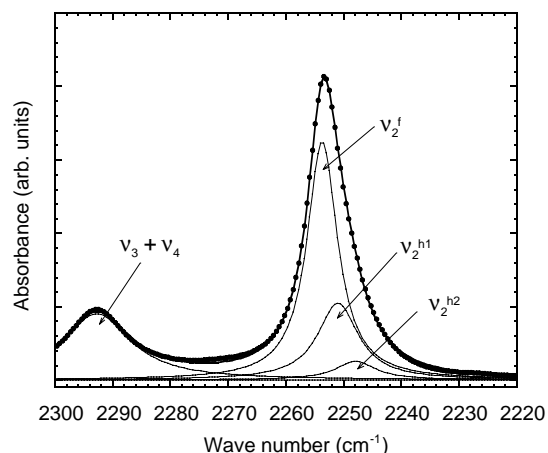
Figure 11. Infrared spectra of liquid acetonitrile in the C≡N stretching ν_2 region at 298 K, and the deconvolution using four Lorentzian curves. ∘, Observed intensity; —, calculated total intensity; —, calculated component intensity.

that the peak position and bandwidth of the hot band transitions were not the same as those of the fundamental transition, but those contributions to the fundamental transition could be corrected by using the Boltzmann distribution; they succeeded in separating the component bands. In this section, their method was applied to analyze the ν_2 band of adsorbed acetonitrile in the MCM-41 mesopores.

3.5. Band Shape Analysis of the ν_2 Band of Confined Acetonitrile

As the hot band transitions should exist in both of the ν_2 bands of hydrogen-bonded and physisorbed acetonitrile, it is actually required to separate the fundamental ν_2 bands from the hot band transitions. Therefore, the analytical functions for fundamental transitions of $\nu_2^f \alpha$ and $\nu_2^f \beta$ and for hot band transitions should be determined upon the least-squares procedure. Here, it is assumed that the reorientational-vibrational relaxation processes of physisorbed acetonitrile can be described as a diffusion process similar to that of the bulk liquid molecule, whose spectral density has a Lorentzian form. Accordingly it is supposed that the $\nu_2 \beta$ band can be reproduced as a sum of three Lorentzian curves of the $\nu_2^f \beta$, $\nu_2^{h1} \beta$, and $\nu_2^{h2} \beta$ bands. Then, it is also assumed that the $\nu_2 \alpha$ band shapes over the range of $P/P_0 = 0.15$–0.37 are represented by the band profile measured at $P/P_0 = 0.05$. The band at $P/P_0 = 0.05$ should include both $\nu_2^{h1} \alpha$ and $\nu_2^{h2} \alpha$ bands, and the bands that come from a few kinds of α-species because of the surface heterogeneity. Then, the observed spectra in the 2320–2220 cm^{-1} range were deconvoluted with the use of the observed band profile at $P/P_0 = 0.05$ for the $\nu_2 \alpha$ band; three Lorentzian curves for $\nu_2^f \beta$, $\nu_2^{h1} \beta$, and $\nu_2^{h2} \beta$ bands; one Lorentzian curve for the $\nu_3 + \nu_4$ band of physisorbed acetonitrile, and a horizontal base line. The least-squares fitting was carried out under the following assumptions to reduce adjustable parameters: only the intensity and peak frequency of the $\nu_2 \alpha$ band, which are measured at $P/P_0 = 0.05$, are variable; the intensity ratios of the $\nu_2^f \beta$, $\nu_2^{h1} \beta$, and $\nu_2^{h2} \beta$ bands are 1:0.332:0.083 (the calculation of the relative intensities will be described in detail in Section 4); and the bandwidth of $\nu_2^{h1} \beta$ is equal to that of $\nu_2^{h2} \beta$. Examples of the resolved spectra are shown in Figure 12. The calculated composite curves shown by a bold solid line reproduce well the observed spectra. The band shape of the ν_2 band at $P/P_0 = 0.15$ is nearly similar to that at $P/P_0 = 0.05$ (Fig. 12a), as expected. However, we should regard with caution the change in the $\nu_2 \beta$ band in the low P/P_0 region, because the $\nu_2 \beta$ band below $P/P_0 = 0.24$ may have inevitable uncertainties.

The absorbance of the $\nu_2^f \beta$ and $\nu_2 \alpha$ bands obtained by the least-squares fitting was plotted against P/P_0 in Figure 13. The relation between the absorbance of the $\nu_2^f \beta$ band and P/P_0 undergoes a steep upward jump at $P/P_0 = 0.3$. This steep jump stems from the capillary condensation, whereas other gradual increases in the absorbance below $P/P_0 = 0.3$ correspond qualitatively to the multilayer adsorption. On the other hand, the absorbance curve of the $\nu_2 \alpha$ band gradually increases above $P/P_0 = 0.15$, suggesting that the effect of adsorbate-adsorbate interaction increases the dipole moment of the C≡N bond of the molecule concerned.
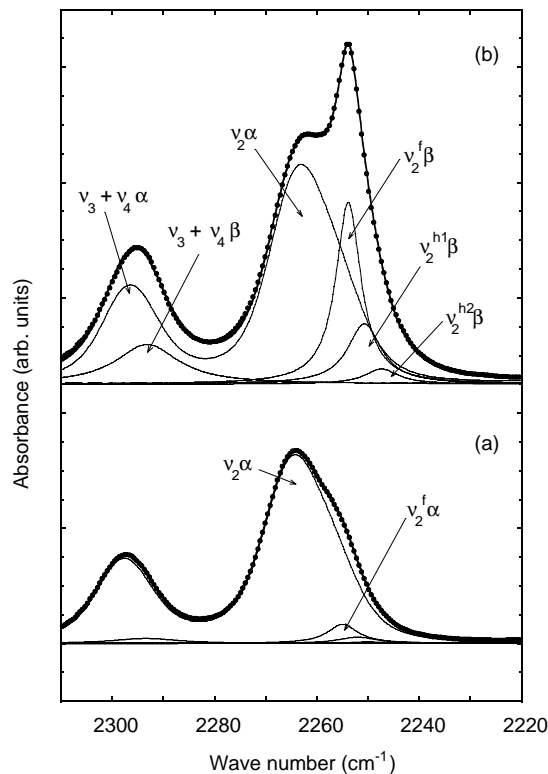
Figure 12. Resolved infrared absorption spectra of adsorbed acetonitrile on MCM-41 in the C≡N stretching ν_2 region at (a) $P/P_0 = 0.15$ and (b) 0.37 (after capillary condensation). ○, Observed intensity; —, calculated total intensity; —, calculated component intensity.

3.6. Motional States of Confined Acetonitrile

The relationship between the half-band width (half width at half-maximum heights) of the $\nu_2^f\beta$ band and P/P_0 is plotted in Figure 14. The half-band width of the $\nu_2^f\beta$ band drops steeply at $P/P_0 = 0.3$. This sudden decrease is in beautiful agreement with the adsorption isotherm. Hence, the change
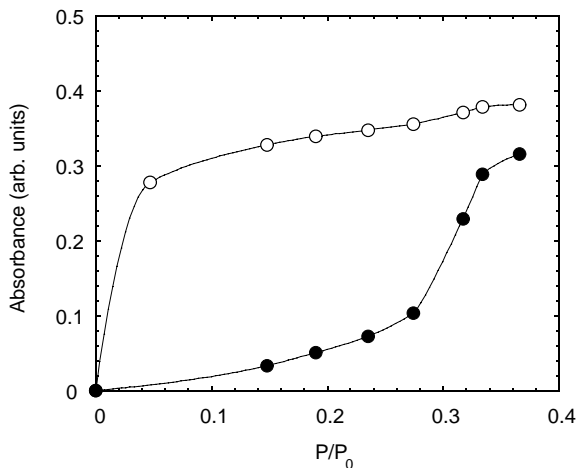
Figure 13. Changes in absorbance of the $\nu_2^f\beta$ band with adsorption. Open and solid symbols denote the $\nu_2\alpha$ and $\nu_2^f\beta$ bands, respectively.
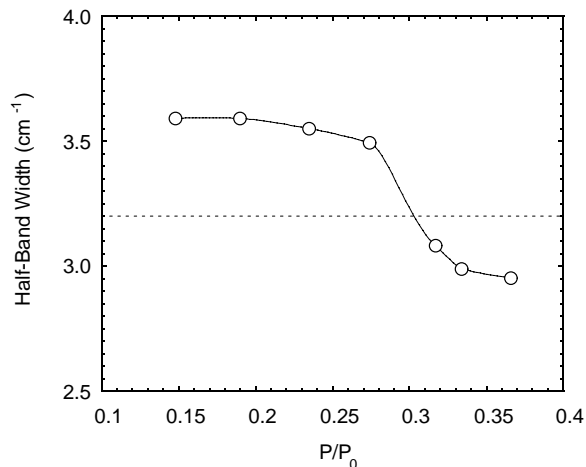
Figure 14. Changes in half-band width of the $\nu_2^f\beta$ band with adsorption. A dashed horizontal line denotes the half-band width of the ν_2 band of liquid acetonitrile at 298 K.

in half-band width of the $\nu_2^f\beta$ band suggests that the relaxation process of an acetonitrile molecule transforms with capillary condensation. If the reorientational and vibrational time correlation functions of the single vibrational transition have an exponential form and thus the infrared band profile is given by a Lorentzian, the relaxation time is expressed by

$$\tau = (2\pi c\Delta\nu_{1/2})^{-1} \qquad (38)$$

$$\tau^{-1} = \tau_r^{-1} + \tau_v^{-1} \qquad (39)$$

where $\Delta\nu_{1/2}$ is the half-band width (cm^{-1}), and τ_r and τ_v are the reorientational relaxation and vibrational relaxation times, respectively. The measured half-band width is represented as a sum: $\Delta\nu_r + \Delta\nu_v$ (see Eqs. (6) and (7)). Therefore, the half-band width of the $\nu_2^f\beta$ band has information about the reorientational-vibrational relaxation of the physisorbed acetonitrile. The τ values for the $\nu_2^f\beta$ bands calculated by Eq. (38) are summarized in Table 4. It is expected that the physisorbed acetonitrile just below the steep rising of the adsorption isotherm prior to the capillary condensation undergoes fewer collisions with its surroundings than in the liquid state. However, the τ values of the physisorbed acetonitrile in the range of $P/P_0 = 0.15$–0.27 are smaller than that of the bulk liquid. In this relative pressure range, it is unlikely that the vibrational relaxation of the physisorbed acetonitrile is faster than that of the liquid acetonitrile, because the vibrational phase should be retained because

Table 4. Relaxation time of acetonitrile molecule adsorbed on mesopores of MCM-41.

State	Temp. (K)	τ (ps)
Adsorbed state over the range $P/P_0 = 0.15$–0.27	303	1.5
Adsorbed state over the range $P/P_0 = 0.32$–0.37	303	1.7–1.8
Liquid	298	1.7

there are fewer collisions between adsorbates. Therefore, the $\Delta\nu_v$ value of the physisorbed acetonitrile in the relative pressure range should be smaller than that of the liquid acetonitrile. Hence, this result suggests that the reorientational motion of acetonitrile molecules in this state is comparatively fast (larger $\Delta\nu_r$) because of the small intermolecular torque. Above $P/P_0 = 0.3$, the half-band widths of the $\nu_2^f\beta$ band tend to be narrower than that of the bulk liquid (Fig. 14). That is, the τ values are slightly longer than that of the bulk liquid at the same temperature. In this condensed state, it is supposed that intermolecular collisions of adsorbates in small mesopores cannot be more frequent than that of liquid molecules. If only collisions between acetonitrile molecules confined in small mesopores are restricted, the vibrational phase relaxation may be slow (smaller $\Delta\nu_v$), and the reorientational relaxation should be fast (larger $\Delta\nu_r$), owing to the free rotation of adsorbates. That is, the orientation of adsorbed acetonitrile should be retained more than that of liquid molecules in terms of the longer reorientational-vibrational relaxation time. Therefore, it is concluded that the reorientational motion of acetonitrile molecules condensed in mesopores is prevented more than that of the bulk liquid because of the large intermolecular torque, which comes from the confinement in small mesopores.

4. VIBRATIONAL DEPHASING OF CONFINED FLUIDS

Vibrational phase relaxations in condensed phases have received considerable attention in recent decades, because they are recognized as a powerful probe of intermolecular interaction dynamics [2, 87]. In Kubo-Rothschild theory a given stochastic process is defined by the rms magnitude of the Bohr frequency modulation Δ and its correlation time τ_c. The accurate determination of these Kubo parameters yields interesting information on molecular dynamics. Vibrational dephasing is especially suited to describing the dynamics of a hydrogen bonding. In the H-bonded systems, such as O—H$\cdots$Y and C≡N$\cdots$Y in solution, the modulation of the O—H and C≡N frequency (vibrational dephasing) occurs though the coupling to hydrogen bridge stretching ν_σ (H$\cdots$Y and N$\cdots$Y) modes, which undergoes energy exchange with the bath. In these cases, the τ_c-value reflects the lifetime of the hydrogen bond [2]. The simple dephasing model of Kubo-Rothschild theory can also be extended to describe an adsorbed molecule, which interacts with the solid surface [2]. The vibrational dephasing of translationally immobilized adsorbates can be simple, because there is no influence of the fluctuating bath. Therefore, pure vibrational dephasing should be observed in such a system. On the other hand, the concentration, reactivity, and accessibility of internal surface hydroxyl groups (SiOH) of MCM-41 or FSM-16 [88] are responsible for ion exchange and post-modification, such as silylation and chemical deposition. It is consequently indispensable to elucidate the molecule–SiOH group interactions at the molecular level.

It is well known that acetonitrile forms a coordination complex with an electron acceptor molecule [84], such as Brønsted sites and surface hydroxyls in zeolites [85, 89].

The C≡N group can also form a hydrogen bond of the ≡N$\cdots$HO type with SiOH groups of MCM-41, as discussed in Section 3. Hydrogen bonding affects the C≡N stretching mode significantly. The infrared band width of the C≡N stretching ν_2 mode of hydrogen-bonded acetonitrile is larger than that of unassociated acetonitrile by a factor of about 2. This indicates that the vibrational dephasing rate of the ν_2 mode is strongly influenced by hydrogen-bond formation.

In this section, the infrared adsorption bands of the ν_2 mode of hydrogen-bonded acetonitrile on SiOH groups of MCM-41 are treated.

4.1. Theoretical Methodology

The normalized spectral function of an infrared absorption band $\widehat{I}(\nu)$ is a Fourier transform of a dipole correlation function [2]

$$\widehat{I}(\nu) = c \int_{-\infty}^{\infty} \exp(-i2\pi c\nu t)\Phi(t)\,dt \qquad (40)$$

where c is light velocity and ν is the wave number. The following product is assumed as for $\Phi(t)$

$$\Phi(t) = \Phi_r(t) \cdot \Phi_{res}(t) \cdot \Phi_{ph}(t) \qquad (41)$$

where $\Phi_r(t)$, $\Phi_{res}(t)$, and $\Phi_{ph}(t)$ are the reorientational, resonance energy transfer, and vibrational dephasing correlation functions, respectively. It seems that it is difficult for the hydrogen-bonded acetonitrile on the SiOH group of MCM-41 to undergo a free reorientational motion around the main C_{3V} symmetry axis because of the hydrogen bonding. The resonant vibrational energy transfer process can also be negligible because the hydrogen-bonded acetonitrile may be isolated. Therefore, it is expected that the vibrational relaxation process of the hydrogen-bonded acetonitrile mainly shows aspects of pure vibrational dephasing. Hence, relaxation processes other than vibrational phase relaxation can be neglected. Therefore, the correlation function is rewritten as

$$\Phi(t) = \Phi_{ph}(t) \qquad (42)$$

Vibrational dephasing is expressed by the following Kubo relaxation function [2]

$$\Phi_{ph}(t) = \exp\{-\Delta^2[\tau_c^2(\exp(t/\tau_c) - 1) + \tau_c t]\} \qquad (43)$$

Here Δ and τ_c are the Kubo parameters. The correlation time τ_c determines the average time between perturbative events (such as "collisions" and "librations"). Here, the factor $\Delta h/2\pi$ can be looked upon as a root mean square intermolecular energy, reflecting the static distribution of the interaction. Then the spectral function $I(\nu)$ is

$$I(\nu) = \Gamma \int_0^{\infty} \cos 2\pi c t(\nu - \nu_0)\Phi_{ph}(t)\,dt \qquad (44)$$

where ν_0 is the band center and Γ is associated with the absolute intensity of the band. The observed spectral function is given by the convolution integrals of Eq. (44) as follows

$$I(\nu')_{obs} = \int_{-\infty}^{\infty} I(\nu)\text{ILS}(\nu' - \nu)\,d\nu \qquad (45)$$

Here $ILS(\nu)$ is the instrumental line shape function, which is the Fourier transform of the apodization function used. In this study, the Hamming function $[f(x) = a + b\cos(\pi x/L),$ where $a = 0.54$, $b = 0.46$, and L is the maximum retardation] was adopted for the apodization function. The ILS function is represented by

$$ILS(\nu) = 2L\frac{\sin(2\pi\nu L)}{(2\pi\nu L)}\left[a - \frac{b(2\pi\nu L)^2}{\{(2\pi\nu L)^2 - \pi^2\}}\right] \quad (46)$$

On the other hand, the observed spectral function of an infrared absorption band $I(\nu)_{\text{obs}}$ is measured by

$$I(\nu)_{\text{obs}} = \sigma(\nu)/\nu[1 - \exp(-hc\nu/kT)] \quad (47)$$

where $\sigma(\nu)$ is the absorption coefficient and $I(\nu)$ is called the "spectral density." Therefore, the Kubo parameters in Eq. (43) can be determined by curve fitting of Eq. (45) to the measured band profile represented by Eq. (47).

4.2. Band Shape Analysis

The observed spectra in the 2230–2305 cm^{-1} ranges were resolved into fundamental (ν_2^{f}), hot band ($\nu_2^{\text{h1}} = \nu_2 + \nu_8 - \nu_8$, $\nu_2^{\text{h2}} = \nu_2 + 2\nu_8 - 2\nu_8$), and combination band ($\nu_3 + \nu_4$) transitions (see Section 3 and [11]) of the form of Eq. (45). The least-squares fitting (DLS method) was carried out under restrictions from the following assumptions:

(1) The relative intensities I_{f}, I_{h1}, and I_{h2} of the ν_2^{f}, ν_2^{h1}, and ν_2^{h2} transitions are represented by

$$
\begin{aligned}
I_{\text{f}} &= 1 \\
I_{\text{h1}} &= 2\exp[-(\nu_8 \times 1.9865)/kT] \quad (48) \\
I_{\text{h2}} &= 3\exp[-(2\nu_8 \times 1.9865)/kT]
\end{aligned}
$$

The fundamental frequency of the ν_8 mode is estimated as

$$\nu_8 + x_{28} = (\nu_2 + \nu_8) + \nu_2 \quad (49)$$

where x_{28} is a constant that is associated with the nonharmonic term. In the case of bulk liquid ($\nu_8 = 378$ cm^{-1}, $\nu_2 + \nu_8 = 2628$ cm^{-1}, and $\nu_2 = 2254$ cm^{-1}), the constant x_{28} is -4 cm^{-1}. Then the fundamental frequency of the ν_8 mode of hydrogen-bonded acetonitrile can be calculated as

$$
\begin{aligned}
\nu_8 &= (\nu_2 + \nu_8) + \nu_2 - x_{28} \\
&= 2640 - 2263 - x_{28} \quad (50) \\
&\approx 381 \text{ cm}^{-1}
\end{aligned}
$$

(2) The peak frequency of ν_2^{h2} is given by $\nu_2^{\text{h2}} = 2\nu_2^{\text{h1}} - \nu_2^{\text{f}}$.
(3) The correlation time τ_{c} and Bohr frequency modulation Δ of ν_2^{h2} are equal to that of ν_2^{h1}. The example of the resolved spectra of hydrogen-bonded acetonitrile is shown in Figure 15. The calculated composite curve shown by a bold solid line reproduces well the observed spectra.
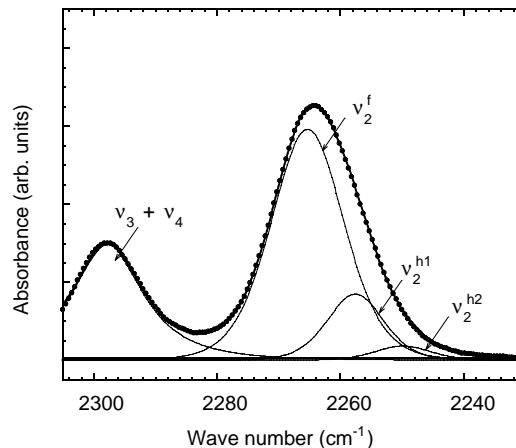
Figure 15. Resolved infrared absorption spectra of hydrogen-bonded acetonitrile on MCM-41 in the C≡N stretching ν_2 region at $P/P_0 = 0.001$ and $T = 283$ K. ∘, Observed intensity; —, calculated total intensity; —, calculated component intensity.

4.3. Vibrational Dephasing of Confined Acetonitrile

Figure 16 shows difference spectra for MCM-41 between the acetonitrile-adsorbed and adsorption-free samples in the O—H stretching (ν_{OH}) region at 303 K, as a function of relative pressure. The ν_{OH} bands of the free SiOH (3738 cm^{-1}) and terminal SiOH (3715 cm^{-1}) groups of MCM-41 were shifted downward by about 300 cm^{-1}, when they formed hydrogen bonds with acetonitrile molecules. Then the difference spectra between the acetonitrile-adsorbed sample and the outgassed one (background spectra) gave negative bands at 3738 cm^{-1} and 3715 cm^{-1}. Figure 17 shows infrared spectra of hydrogen-bonded acetonitrile in the C≡N stretching ν_2 region at 303 K as a function of relative pressure. As the negative ν_{OH} bands grow, the ν_2 band of the hydrogen-bonded acetonitrile (2264 cm^{-1}) increases. The integrated absorbance of the negative ν_{OH} bands has a linear correlation with that of the ν_2 band in the range of $P/P_0 = 0.001$–0.004 (surface coverage $\theta = 0.15$–0.32). This indicates that
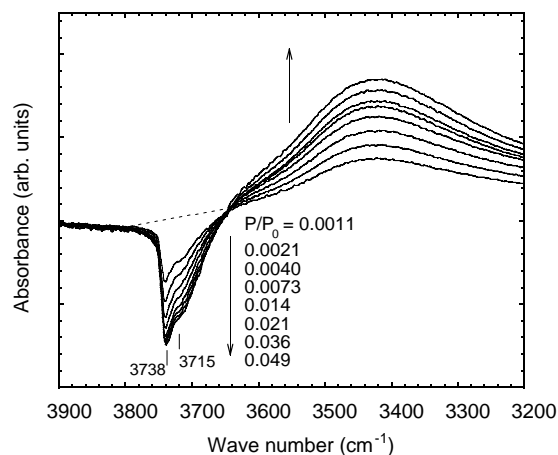
Figure 16. Difference spectra of MCM-41 between acetonitrile adsorbed and adsorption free samples at 303 K (ν_{OH} region).
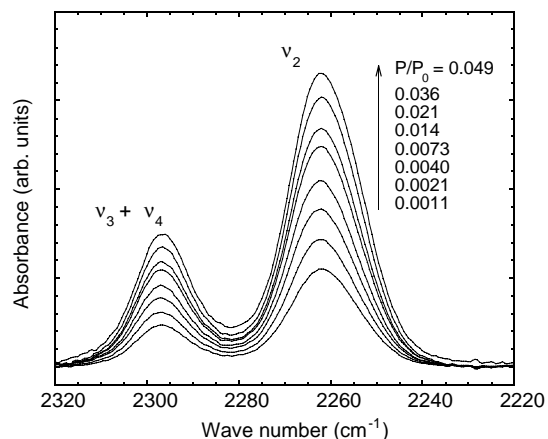
Figure 17. Infrared spectra of hydrogen-bonded acetonitrile on surface hydroxyls of MCM-41 in the C≡N stretching ν_2 region at 303 K.

Figure 19. Temperature effect on frequency shift of the ν_2 band of hydrogen-bonded acetonitrile.

a 1:1 hydrogen-bonded complex is formed in this pressure range. The correlation between the integrated absorbance of the ν_2 and negative ν_{OH} bands in the temperature range between 283 K and 333 K is shown in Figure 18. When the temperature was lowered (from 333 K to 283 K), a linear correlation was observed, although the surface coverage should be increased. Therefore, this indicates the formation of a 1:1 hydrogen-bonded complex in these temperature and pressure ranges.

The $\tau_c \Delta$ value, which is the product of τ_c and Δ, denotes the modulation regime of the system. If $\tau_c \Delta \ll 1$, the system is in a fast modulation limit; the perturbation of a vibrating molecule over a very short time does not intensively vary the phase, so its phase is retained for a long time. In this case $I(\nu)$ (Eq. (44)) is a Lorentzian curve. If $\tau_c \Delta \gg 1$, it is in a slow modulation limit; the phase is rapidly lost and $I(\nu)$ is a Gaussian form [2, 87]. As calculated $\tau_c \Delta$ values at 303 K are approximately 1.0, the system is in an intermediate modulation regime. The correlation time τ_c for the ν_2 band of hydrogen-bonded acetonitrile at 303 K is about 0.6 ps and is

independent of the surface coverage. The independence of τ_c of the surface coverage suggests that adsorbed molecules are highly isolated and the correlation time, τ_c, should be associated with the interaction with the SiOH group. The observed τ_c agrees with typical lifetimes of hydrogen bonds in liquid systems including solvent water [90]. Furthermore, in the case of a pyridine (C$_5$H$_5$N)—water system [91], the 988 cm^{-1} band of C$_6$H$_5$N is sensitive to hydrogen bonding of the N···HO type, the τ_c value of the mode is about 1.2 ps, and $\tau_c \Delta$ is approximately 0.8 over the whole concentration range. Accordingly, the observed vibrational dephasing must be ascribed to hydrogen bonding with the surface SiOH group. The ν_0 value decreases linearly with increasing temperature, as shown in Figure 19. When acetonitrile forms a coordination complex with an electron acceptor molecule, the C≡N bond force constant of acetonitrile is strengthened and the stretching frequency always increases, according to Purcell and Drago [84]. Therefore, in the case of hydrogen-bonded acetonitrile on the surface hydroxyl of MCM-41, the upward shift of the C≡N stretching frequency depends

Figure 18. Correlation between the integrated absorbance of the ν_2 and negative ν_{OH} band.
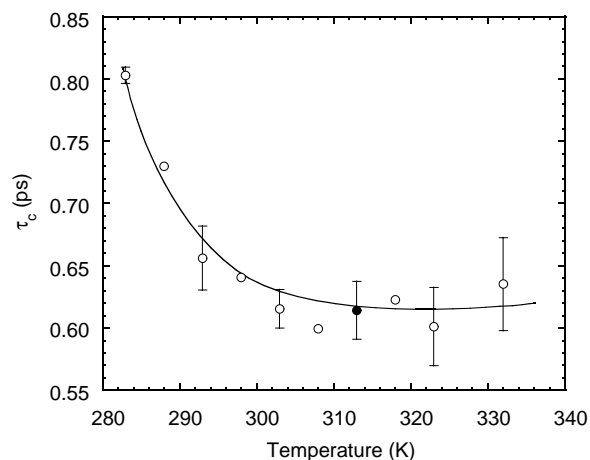
Figure 20. Temperature dependence of the modulation time τ_c.
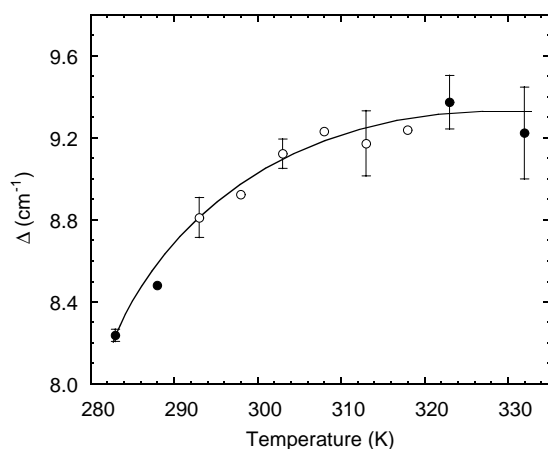
Figure 21. Temperature dependence of average magnitude of the frequency modulation Δ.

on the electron transfer interaction of the nitrogen atom of the acetonitrile with the surface hydroxyl due to hydrogen bonding. The ν_2 band of hydrogen-bonded acetonitrile shifts upward by 12 cm^{-1} at 283 K and 10 cm^{-1} at 332 K from the bulk liquid phase value. Therefore, the downward frequency shift shows that the hydrogen bond becomes weaker with increasing temperature.

Figures 20 and 21 show the temperature dependence of τ_c and the Δ value, respectively. The τ_c value decreases with increasing temperature, while the Δ value increases. τ_c is the modulation time, which is related to the time scale of the molecular fluctuations (in this system, it should be the lifetime of the hydrogen bond), and the Δ is the average magnitude of the frequency modulation, that is, the frequency distribution of the CN stretching mode due to the coupling to the hydrogen bridge stretching ν_σ mode. Therefore, these results suggest that the lifetime of the hydrogen bond becomes shorter with increasing temperature. This is clearly consistent with the fact that the hydrogen bond becomes weaker with increasing temperature (see Fig. 19).

5. CONCLUSIONS

We found, through DFT, that condensates were highly structured in small cylindrical mesopores (diameter: $d = 3.9$ nm) compared with bulk fluids. This suggests that the molecular motion of the condensed molecules in such a small mesopore is more restricted or hindered than that of the bulk liquid because of the tightly ordered structure formation induced by the strong solid-fluid interaction. Then we explored the dynamics of adsorbed acetonitrile in the small mesopore of MCM-41 ($d = 3.9$ nm) by use of IR spectroscopy.

The IR spectra of adsorbed acetonitrile on MCM-41 were measured at 303 K. In the CN stretching ν_2 region, two bands were observed at 2265 cm^{-1} and 2254 cm^{-1}, assigned to hydrogen-bonded molecules on surface hydroxyls of MCM-41 and physisorbed molecules in mesopores, respectively. In this study, the 2265 cm^{-1} band was denoted as the $\nu_2\alpha$ band and the 2254 cm^{-1} band as the $\nu_2\beta$ band. The band width of the fundamental transition $\nu_2^f\beta$ was

obtained by removing the overlap with hot band transitions of the same mode, $\nu_2\alpha$ band, and other modes by least-squares fitting. Before the capillary condensation, the relaxation time τ obtained from the band width of the $\nu_2^f\beta$ band was smaller than that of the bulk liquid, indicating the presence of weakly hindered rotation. After the capillary condensation, the τ value was slightly longer than that of the bulk liquid, suggesting that the motion of acetonitrile molecules condensed in mesopores is prohibited in comparison with that of liquid acetonitrile at the same temperature.

The IR-band shapes of the ν_2 mode of the hydrogen-bonded acetonitrile on the surface hydroxyls (SiOH) of MCM-41 were analyzed with the Kubo-Rothschild theory to understand the vibrational dephasing dynamics. The rms magnitude of the Bohr frequency modulation Δ and its correlation time τ_c were determined for the vibrational dephasing of the ν_2 mode. The correlation time τ_c for the ν_2 band of hydrogen-bonded acetonitrile at 303 K was about 0.8 ps, which was independent of the surface coverage. The independence of τ_c of the surface coverage suggests that adsorbed molecules are highly isolated and the correlation time, τ_c, should be associated with the interaction with the SiOH group. The observed τ_c agrees with typical lifetimes of hydrogen bonds in liquid systems including solvent water. The τ_c value decreases with increasing temperature, whereas the Δ value increases. The τ_c is the modulation time, related to the time scale of the molecular fluctuations, and it should be the lifetime of the hydrogen bond in this system; the Δ is the average magnitude of the frequency modulation, that is, the frequency distribution of the CN stretching due to the coupling to the hydrogen-bond stretching mode. Therefore, these results suggest that the τ_c values obtained by this analysis reflect the pure vibrational dephasing of the CN stretching mode induced by the coupling to the stretching mode of the hydrogen bond with no influence of a fluctuating bath, and then the lifetime of the hydrogen bond becomes shorter with increasing temperature.

Although there are active studies on adsorption in nanopore systems such as MCM-41, one still cannot understand the molecular states of molecules adsorbed in mesopores. This article shows one aspect of molecular motional states of molecules adsorbed in mesopores. This type of research should be planned in the future.

GLOSSARY

Capillary condensation A phenomenon that liquid-like dense sate is formed in a pore (the pore size is larger than 2 nm) when a porous solid is exposed to a vapor. This occurs at a gas pressure smaller than the saturated vapor pressure at the given temperature.

MCM-41 One of the molecular sieves that have been discovered by Mobil scientists. It is composed of amorphous silica walls and possesses an array of uniform channels arranged in a two-dimensional hexagonal lattice. The diameter of the channel can be controlled in the range of 2–10 nm.

Mesopore A pore that has the size in the range of 2–50 nm by IUPAC classification.

Reorientational relaxation A diffusion of the direction of rotational-vibrational transition moment of adense molecule that is caused by intermolecular collisional steps.

Rotational-vibrational transition A change in rotational energy of a polyatomic molecule accompanying a vibrational transition ($v = 0$ to $v = 1$) induced by infrared irradiation.

Vibrational dephasing One of the different vibrational relaxation processes. A phase loss of the initial coherence of the autocorrelation of the vibrational amplitude.

Vibrational relaxation A coherence decay of fluctuations of a rotational-vibrational transition moment of a molecule in a dense phase.

REFERENCES

1. R. G. Gordon, *J. Chem. Phys.* 43, 1307 (1965).
2. H. Shimizu, *J. Chem. Phys.* 43, 2453 (1965).
3. W. G. Rothschild, "Dynamics of Molecular Liquids." Wiley, New York, 1984.
4. A. I. Burshtein and S. I. Temkin, "Spectroscopy of Molecular Rotation in Gases and Liquids." Cambridge University Press, Cambridge, UK, 1994.
5. M. Kakimoto and T. Fujiyama, *Bull. Chem. Soc. Jpn.* 45, 3021 (1972).
6. W. G. Rothschild, *J. Chem. Phys.* 57, 991 (1972).
7. J. E. Griffiths, *J. Chem. Phys.* 59, 751 (1973).
8. A. M. Amorim Da Costa, M. A. Norman, and J. H. R. Clarke, *Mol. Phys.* 29, 191 (1975).
9. T. Bien, M. Possiel, G. Döge, J. Yarwood, and K. E. Arnold, *Chem. Phys.* 56, 203 (1981).
10. H. J. Böhm, R. M. Lynden-bell, P. A. Madden, and I. R. Mcdonald, *Mol. Phys.* 51, 761 (1984).
11. S. Hashimoto, T. Ohba, and S. Ikawa, *Chem. Phys.* 138, 63 (1989).
12. A. A. Stolov, A. I. Morozov, and A. B. Remizov, *Spectrochim. Acta.* 54A, 589 (1998).
13. E. Marri, A. Morresi, G. Paliani, R. S. Cataliotti, and M. G. Giorgini, *Chem. Phys.* 243, 323 (1999).
14. A. Morresi, P. Sassi, M. Paolamtoni, S. Santini, and R. S. Cataliotti, *Chem. Phys.* 254, 337 (2000).
15. R. F. Cracknell and K. E. Gubbins, *Langmuir* 9, 824 (1993).
16. R. F. Cracknell, K. E. Gubbins, M. Maddox, and D. Nicholson, *Acc. Chem. Res.* 28, 281 (1995).
17. W. A. Steele and M. J. Bojan, *Adv. Colloid Interface Sci.* 76–77, 153 (1998).
18. M. W. Maddox and K. E. Gubbins, *J. Chem. Phys.* 107, 9659 (1997).
19. C. Lastoskie, K. E. Gubbins, and N. Quirke, *J. Phys. Chem.* 97, 4786 (1993).
20. P. I. Ravikovitch, S. C. Ó Domhnaill, A. V. Neimark, F. Schüth, and K. K. Unger, *Langmuir* 11, 4765 (1995).
21. J. P. Hansen and I. R. McDonald, "Theory of Simple Liquids." Academic Press, London, 1990.
22. R. Evans, in "Fundamentals of Inhomogeneous Fluids" (D. Henderson, Ed.). Dekker, New York, 1992.
23. D. E. Sullivan, *J. Chem. Phys.* 74, 260 (1981).
24. B. Q. Lu, R. Evans, and M. M. Telo da Gama, *Mol. Phys.* 55, 1319 (1985).
25. R. Evans, U. Marini Bettolo Marconi, and P. Tarazona, *J. Chem. Soc., Faraday Trans. 2* 82, 1763 (1986).
26. B. K. Peterson, J. P. R. B. Walton, and K. E. Gubbins, *J. Chem. Soc., Faraday Trans. 2* 82, 1789 (1986).
27. R. Evans and U. Marini Bettolo Marconi, *J. Chem. Phys.* 86, 7138 (1987).
28. B. K. Peterson, K. E. Gubbins, G. S. Heffelfinger, Marini Bettolo Marconi, and F. van Swol, *J. Chem. Phys.* 88, 6487 (1988).
29. P. Tarazona, *Phys. Rev. A* 31, 2672 (1985); 32, 3148 (1985).
30. P. Tarazona, U. Marini Bettolo Marconi, and R. Evans, *Mol. Phys.* 60, 573 (1987).
31. P. C. Ball and R. Evans, *J. Chem. Phys.* 89, 4412 (1988).
32. P. B. Balbuena and K. E. Gubbins, *Langmuir* 9, 1801 (1993).
33. C. Lastoskie and K. E. Gubbins, *Langumiur* 9, 2693 (1993).
34. J. P. Olivier, *J. Porous Mater.* 2, 9 (1995).
35. A. Vishnyakov, P. I. Ravikovitch, and A. V. Neimark, *Langmuir* 15, 8736 (1999).
36. A. V. Neimark, P. I. Ravikovitch, and A. Vishnyakov, *Phys. Rev. E* 62, 1493 (2000).
37. P. I. Ravikovitch and A. V. Neimark, *J. Phys. Chem.* 105, 6817 (2001).
38. P. I. Ravikovitch, A. Vishnyakov, and A. V. Neimark, *Phys. Rev. E* 64, 011602 (2001).
39. H. Tanaka, M. El-Merraoui, T. Kodaira, and K. Kaneko, *Chem. Phys. Lett.* 351, 417 (2002).
40. Z. Tan and K. E. Gubbins, *J. Phys. Chem.* 94, 6061 (1990).
41. A. V. Neimark and P. I. Ravikovitch, *Langmuir* 13, 5148 (1997).
42. H. Tanaka, M. El-Merraoui, W. A. Steele, and K. Kaneko, *Chem. Phys. Lett.* 352, 334 (2002).
43. P. I. Ravikovitch, D. Wei, W. T. Chueh, G. L. Haller, and A. V. Neimark, *J. Phys. Chem.* 101, 3671 (1997).
44. P. I. Ravikovitch, G. L. Haller, and A. V. Neimark, *Adv. Colloid Interface Sci.* 76–77, 203 (1988).
45. M. El-Merraoui, M. Aoshima, and K. Kaneko, *Langmuir* 16, 4300 (2000).
46. P. I. Ravikovitch, A. Vishnyakov, R. Russo, and A. V. Neimark, *Langmuir* 16, 2311 (2000).
47. J. P. Olivier and M. L. Occelli, *J. Phys. Chem.* 105, 623 (2001).
48. Y. Rosenfeld, *Phys. Rev. Lett.* 63, 980 (1989).
49. A. R. Denton and N. W. Ashcroft, *Phys. Rev. A* 44, 8242 (1991).
50. E. Kierlik and M. L. Rosinberg, *Phys. Rev. A* 44, 5025 (1991).
51. S. Jiang, K. E. Gubbins, and P. B. Balbuena, *J. Phys. Chem.* 98, 2403 (1994).
52. S. Jiang, J. A. Zollweg, and K. E. Gubbins, *J. Phys. Chem.* 98, 5709 (1994).
53. E. Kierlik, Y. Fan, P. A. Monson, and M. L. Rosinberg, 102, 3712 (1995).
54. S. L. Sowers and K. E. Gubbins, *Langmuir* 11, 4758 (1995).
55. M. W. Maddox, S. L. Sowers, and K. E. Gubbins, *Adsorption* 2, 23 (1996).
56. M. Sliwinska-Bartkowiak, R. Sikorskie, S. L. Sowers, L. D. Gelb, and K. E. Gubbins, *Fluid Phase Equilib.* 136, 93 (1997).
57. H. Pan, J. A. Ritter, and P. B. Balbuena, *Langmuir* 15, 4570 (1999).
58. P. Bryk, A. Patrykiejew, J. Reszko-Zygmunt, and S. Sokolowski, *Mol. Phys.* 96, 1509 (1999).
59. Z. Tan, F. van Swol, and K. E. Gubbins, *Mol. Phys.* 62, 1213 (1987).
60. U. Marini Bettolo Marconi and F. van Swol, *Mol. Phys.* 72, 1081 (1991).
61. E. Kierlik, M. Rosimberg, J. E. Finn, and P. A. Monsoon, *Mol. Phys.* 75, 1435 (1992).
62. J. D. Weeks, D. Chandler, and H. C. Andersen, *J. Chem. Phys.* 54, 5237 (1971).
63. N. F. Carnahan and K. E. Starling, *J. Chem. Phys.* 51, 635 (1969).
64. A. V. Neimark, *Langmuir* 11, 4183 (1995).
65. J. A. Barker and D. Henderson, 47, 4714 (1967).
66. L. Verlet and J. J. Weis, *Phys. Rev. A* 5, 939 (1972).
67. C. T. Kresge, M. E. Leonowicz, W. J. Roth, J. C. Vartuli, and J. S. Beck, *Nature* 359, 710 (1992).
68. J. S. Beck, J. C. Vartuli, W. J. Roth, M. E. Leonowicz, C. T. Kresge, K. D. Schmitt, C. T.-W. Chue, D. H. Olson. E. W. Sheppard, S. B. MacCullen, J. B. Higgins, and J. L. Schelender, *J. Am. Chem. Soc.* 14, 10824 (1992).
69. Q. Huo, D. I. Margolese, U. Ciesla, D. G. Demuth, P. Feng, T. E. Gier, P. Sieger, A. Firouzi, B. F. Chmelka, F. Schüth, and G. D. Stucky, *Chem. Mater.* 6, 1176 (1994).
70. D. Y. Zhao, J. L. Feng, Q. S. Huo, N. Melosh, G. H. Fredrickson, B. F. Chmelka, and G. D. Stucky, *Science* 279, 548 (1998).

71. D. Y. Zhao, Q. S. Huo, J. L. Feng, B. F. Chmelka, and G. D. Stucky, *J. Am. Chem. Soc.* 120, 6024 (1998).
72. G. J. Tjatjouls, D. L. Feke, and J. A. Mann, Jr., *J. Phys. Chem.* 92, 4006 (1988).
73. W. A. Steele and M. J. Bojan, *Adv. Colloid Interface Sci.* 76–77, 153 (1998).
74. T. Yanagisawa, T. Shimizu, K. Kuroda, and C. Kato, *Bull. Chem. Soc. Jpn.* 63, 1535 (1990).
75. S. Inagaki, Y. Fukushima, and K. Kuroda, *J. Chem. Soc., Chem. Commun.* 681 (1993).
76. P. L. Llewellyn, Y. Grillet, F. Schüthe, H. Reichert, and K. K. Unger, *Microporous Mater.* 3, 345 (1994).
77. T. Iiyama, K. Nishikawa, T. Otowa, T. Suzuki, and K. Kaneko, *J. Phys. Chem.* 99, 10075 (1995).
78. T. Iiyama, K. Nishikawa, T. Suzuki, and K. Kaneko, *Chem. Phys. Lett.* 274, 152 (1997).
79. T. Ohkubo, T. Iiyama, K. Nishikawa, T. Suzuki, and K. Kaneko, *J. Phys. Chem.* 103, 1859 (1999).
80. M. Grün, K. K. Unger, A. Matsumoto, and K. Tsutsumi, *Microporous Mesoporous Mater.* 27, 207 (1999).
81. K. Kaneko, C. Ishii, M. Ruike, and H. Kuwabara, *Carbon* 30, 1075 (1992).
82. M. Jaroniec, M. Kruk, and J. P. Olivier, *Langmuir* 15, 5413 (1999).
83. Y. G. Vladimir, F. Xiaobing, B. Zimei, L. H. Gary, and A. O. James, *J. Phys. Chem.* 100, 1985 (1996).
84. K. F. Purcell and R. S. Drago, *J. Am. Chem. Soc.* 88, 919 (1965).
85. C. L. Angell and M. V. Howell, *J. Phys. Chem.* 73, 2551 (1969).
86. I. Suzuki, J. Nakagawa, and T. Fuzikawa, *Spectrochim. Acta* 33A, 689 (1977).
87. A. Morresi, L. Mariani, M. R. Distefano, and M. G. Giorgini, *J. Raman Spectrosc.* 26, 179 (1995).
88. S. Inagaki, Y. Fukushima, and K. Kuroda, *J. Chem. Soc., Chem. Commun.* 680 (1993).
89. Jelena Šepa, R. J. Gorte, B. H. Suits, and David White, *Chem. Phys. Lett.* 289, 281 (1998).
90. J. Lascombe and M. Perrot, *Faraday Discuss. Chem. Soc.* 66, 216 (1978).
91. W. Shindler and H. A. Posch, *Chem. Phys.* 43, 9 (1979).

Copper Chloride Quantum Dots

Keiichi Edamatsu, Tadashi Itoh

Osaka University, Osaka, Japan

CONTENTS

1. INTRODUCTION

Copper chloride (CuCl) crystal is one of the best-investigated materials from the early days of the optical study of semiconductors, because of its rich optical properties produced by excitons and exciton complexes such as biexcitons [1]. The exciton spectrum of CuCl and its assignment to the electronic band structure was first reported by Cardona [2]. He assigned the lowest exciton absorption band appearing at $\sim$3.20 eV ($T = 4$ K) to the singlet (Z_3) exciton band split by the spin–orbit coupling from the doublet band (Z_{12}) at $\sim$3.27 eV. Thus, unlike other semiconductor materials in which the doublet excitons are the lowest, the singlet lowest exciton in CuCl has the simplest configuration. Also, since the binding energy of the exciton ($\sim$200 meV) [3] in CuCl is one of the largest in semiconductor materials, the exciton is very stable even at room temperature. The stability as well as the simplicity of the lowest exciton state in CuCl makes the material very unique and important in the study of excitons and exciton complexes. These interesting features of CuCl also invited us to investigate the properties of excitons confined in nanometer-sized crystals, that is, quantum dots (QDs) of this material. In QDs, since the exciton wavefunction is confined three-dimensionally, distinct quantum confinement effects are expected. Again, due

to the small excitonic Bohr radius in CuCl, the confinement of excitons in CuCl QDs is much different from that in other semiconductor materials [4, 5]. Thus, it is worthwhile to explore the optical properties of CuCl QDs not only for a deep understanding of this characteristic material, but also from the general point of view of the study of semiconductor QDs.

In this chapter, we review a number of important works on the optical study of CuCl quantum dots and see how this material provides unique and important information in the study of semiconductor quantum dots. In Section 2, we introduce and discuss the quantum confinement effects on the lowest exciton states and its radiative decay process. In Section 3, we review the experimental and theoretical studies on the higher excited states of the confined exciton. In Section 4, we consider the enhancement of the optical nonlinearity and its mechanisms including its size dependence. In Section 5, we see the confinement of lattice vibrations (phonons) in the QDs and discuss their influence on the confined exciton states (exciton–phonon coupling). In relation to the exciton–phonon coupling, in Section 6, we discuss the phase relaxation or decoherence mechanisms of the confined exciton states. In Section 7, we see some extraordinary effects caused by the interfaces between the QDs and matrices. Finally, in Section 8, we summarize the current status of the study on CuCl QDs and give some perspectives.

2. EXCITON CONFINEMENT IN COPPER CHLORIDE (CuCl) QUANTUM DOTS

CuCl-like exciton spectra appearing in NaCl heavily doped with Cu^+ ions were first reported by Gross and Kaplyanski [6] in 1957, followed by Ueta et al. [7] and Kishishita [8]. The spectra were explained by the formation of CuCl microcrystals in NaCl matrix by the coagulation of Cu^+ ions. However, no clear explanation was given for high-energy shift of the spectra compared to the bulk one. The first experimental manifestation of the quantum size effect on the confined excitons in CuCl nanocrystals, or QDs, was performed by Ekimov et al. in glass matrix [9–12] in the 1980s and later on by Itoh et al. in NaCl matrix [13–15]. The effect was theoretically explained by Efros and Efros [16] in 1982. Exciton confinement of II–VI semiconductor colloidal nanocrystals was also reported by Brus [17] in 1984. Quantum confinement for the lowest 1S exciton state in a CuCl QDs affects

essentially the exciton translational motion with less influence on the internal motion because of the very small exciton Bohr radius $a_B^* = 0.7$ nm [9, 13]. This situation is called the "weak confinement" regime and quite different from the "strong confinement" regime applicable to II–VI or III–V nanocrystals where the exciton radius easily exceeds the particle size and the exciton internal motion is much modified by the confinement [16].

In the weak confinement regime, the energy of the lowest exciton, $E(a)$, is approximately given by

$$E(a) = E_g - Ry^* + \frac{\hbar^2}{2M}\left(\frac{\pi}{a}\right)^2 \tag{1}$$

where E_g is the bandgap energy, Ry^* is the effective Rydberg energy of the exciton, M is the translational mass of the exciton, and a is the radius of the QD [16]. Ekimov et al. [9, 11, 12] experimentally studied the absorption and luminescence spectra of CuCl QDs embedded in silicate glass matrices and discussed for the first time the exciton confinement of this material. Later, Itoh et al. [13–15] studied the optical spectra of CuCl QDs embedded in NaCl matrices. As shown in Figure 1, they measured the blueshifts of the Z_3 exciton luminescence and compared them with the mean radii of the QDs, which are estimated by means of the small-angle X-ray scattering method. Although they found that the QDs become somewhat oblate for larger sizes, they estimated the mean radii assuming that the QDs have spherical shapes. The observed blueshift $\Delta E = E(a) - E(\infty)$ of the confined exciton was well reproduced by Eq. (1), if the QD's radius a is replaced by an "effective radius" [14]

$$a^* = a - \eta a_{\mathrm{ex}} \tag{2}$$

where a_{ex} is the Bohr radius of the exciton, and η is a constant of order of unity. The qualitative explanation of the effective radius is that the exciton cannot reach the surface because of the finite size (i.e., internal motion of the exciton). This "dead layer" effect was explained theoretically by Kayanuma [18, 19] in a more quantitative way. This finding indicates that even in the weak confinement regime such as realized in CuCl QDs, the internal motion of the exciton must be taken into account. Kayanuma and Momiji extended their variational calculation to the cases of incomplete potential barriers [20], cylindrical shaped QDs [21], and quantum microsphere shells [22].

The three-dimensional confinement of the exciton wavefunction causes not only the blueshift of the exciton energy, but also the drastic modification of the radiative decay of the exciton. In bulk CuCl crystal, it is well known that the exciton strongly couples with radiation fields, thus forming exciton polaritons [1]. The oscillator strength of the exciton was distributed over the polariton states, and the radiative decay of the exciton must be treated in a framework of the polariton picture. In the QD, however, the polariton effect is not important because the size of the QD is much smaller than the wavelength of light. Consequently, the QD acts as a mesoscopic atom, in which the exciton exists as a coherent superposition of the electronic excitation over the QD's volume. In this situation, the oscillator strength of the exciton should be proportional to the QD's volume [23, 24]. Hanamura [24] showed that the radiative lifetime τ_r for the spherical QD is expressed by

$$\tau_r = \frac{3}{64\pi\varepsilon}\left(\frac{\lambda}{a}\right)^3 \frac{\hbar}{\Delta E_{\mathrm{LT}}} \tag{3}$$

where ΔE_{LT} is the longitudinal-transverse splitting of the exciton, ε is the background dielectric constant, and λ is the luminescent wavelength. This size-dependent radiative lifetime, which is sometimes referred to as "exciton superradiance" in QDs, has been confirmed by experiments [25–27]. Itoh et al. [26, 27] measured the radiative lifetimes of the confined excitons for various sizes between $a^* = 1.6$ and 15 nm, by means of selective excitation using a picosecond pulsed laser. They found that the observed radiative lifetime was in good agreement with Eq. (3), for smaller ($a^* \leq 4$ nm) QDs. For larger QDs, however, the observed radiative lifetime deviated from the theoretical value, approaching the constant value around $\tau_r \sim 50$ (130) ps at 10 (77) K. Although the reason for the deviation from the theoretical value was not fully understood, it was suggested that the deviation is attributable to the decoherence of the lowest exciton state originating from the admixture of the higher confinement states via thermal excitation and/or exciton–phonon scattering, which is expected to be more frequent for larger sizes because the splitting between the confined sublevels becomes smaller [24, 26, 27]. However, it is also worth considering that, in the range of the QD sizes concerned, the excitonic polarization is strongly coupled with electromagnetic fields. The exciton-field coupling in spherical QDs was theoretically examined by Ekimov et al. [28], and later on by Ajiki et al. [29, 30]. They pointed out that the oscillator strength, which is concentrated at the lowest confined exciton state for smaller ($a^* \leq 5$ nm) QDs, is transferred to higher confined states that become energetically resonant with a "surface mode" with the increase of QD size. From this point of view, it is natural that the radiative lifetime of the lowest confined exciton deviates from the simple theory, Eq. (3), in which the strong exciton-field coupling is not taken into account. It is suggestive that the size at which the observed lifetime started to deviate from the theory corresponds to the expected size at which the oscillator strength
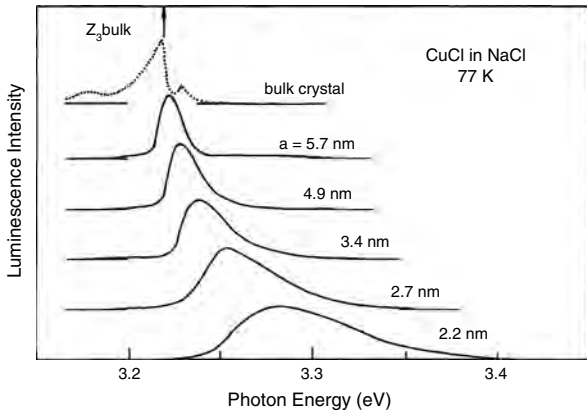
Figure 1. Luminescence spectra of CuCl quantum dots (a) mean dot radius, embedded in NaCl matrices measured at 77 K. Dotted curve is the luminescence spectrum of bulk CuCl crystal.

begins to transfer from the lowest exciton state to other states. Recently, Cho and Ajiki [31, 32] have shown an unified picture in which the coupled modes between the exciton polarization and the radiation field are smoothly connected to those in microsphere cavities for larger sizes, and also to the exciton polariton picture in bulk crystal. In connection to the "exciton superradiance" or "giant oscillator strength" of the confined exciton, it is very interesting that the giant oscillator strength was recently predicted [33] and observed [34–36] in larger QDs based on III–V materials.

3. HIGHER EXCITED STATES OF THE CONFINED EXCITON

In the recent decade a lot of works on CuCl QDs mainly concentrated on the investigation of the optical properties of the lowest $1S$ exciton state as a typical example of the weak confinement. As far as the weak confinement regime in spherical QDs is concerned, the notation of the quantum number such as "$1S$" has two different meanings. One is for the Rydberg states of the internal motion of the exciton, and the other is for the confinement states of the translational motion of the exciton. Hereafter, we denote the former as small capital letters N, L as $1S$, $2S$, $2P$, $\ldots$, and the latter as lowercase letters n, l as $1s$, $1p$, $1d$, $2s$, $\ldots$, where N and n are the main quantum number, and L and l denote the angular momentum. In the limit of the weak confinement of spherical QDs with infinite potential barrier, the exciton energy ΔE_{NLnl} of the confined state ($NLnl$) is given as an extension of Eq. (1) by [16]

$$\Delta E_{(NLnl)} = E_g - \frac{Ry^*}{N^2} + \frac{\hbar^2}{2M}\left(\frac{\phi_{nl}}{a}\right)^2 \qquad (4)$$

where ϕ_{nl} gives the nth zero of the spherical Bessel function $j_l(x)$, satisfying

$$j_l(\phi_{nl}) = 0 \qquad (5)$$

From Eq. (4), one can see that the exciton internal motion (second term) is independent of its translational motion (third term), as in the bulk crystal. This approximation works well, as long as the exciton Bohr radius is much smaller than that of the dot size, or, in other words, the absolute value of the second term of Eq. (4) is much larger than the third term. This condition is fulfilled for the lowest $1S$ exciton in the QD with the size of a few nm. However, if the dot size is sufficiently small, or if the exciton is in the higher Rydberg state, the condition would not be satisfied. In these cases, the internal motion and the translational motion of the confined exciton are not separable, and thus the total angular momentum $J = L + l$ will be a good quantum number. Kayanuma [19] performed the variational calculation that includes both internal and translational motion of the excitons in spherical QDs and showed for the first time how the well-separated quantum states of Rydberg and confinement states in the weak confinement regime mix with each other when the dot size decreases toward the strong confinement regime. More recently, Uozumi et al. [37, 38] calculated the ground and excited states of the confined excitons with a much larger set of basis functions and examined their optical properties.

From the experimental side to observe the higher excited states of the confined exciton, since measurements of standard optical absorption and luminescence excitation spectra are strongly influenced by the inhomogeneous broadening of the exciton bands due to the wide size distribution [13], one must achieve more sophisticated experiments to reveal the optical responses originating from higher excited states. Itoh et al. [14, 15] performed the size-selective excitation of CuCl QDs using monochromated ultraviolet (UV) light. They observed several peaks in the excitation spectra depending on the detection photon energy of the inhomogeneously broadened photoluminescence. By selecting the detection photon energy, one can select the size of QDs for the detection, as expressed by Eq. (1). From the relationship between the energy position of the peaks in the excitation spectra and the detection energy of the photoluminescence, they found that these peaks originate from the confined states of the Z_{12} excitons, which split into three (including two heavy-hole and one light-hole) components. Also, they found the components that converge to the higher energy position for larger sizes. As described later, from comparison with other experimental results, they were attributed to the confined states of the Coulombic $2S$ states of the Z_3 and Z_{12} excitons. Later on, by means of the size-selective luminescence spectra, Itoh et al. [39] revealed the luminescence structure that is attributed to the excitons that are initially excited to the $1p$ confinement states. As described in Section 5, it is interesting that this confinement state strongly couples with the optical phonons in the QD.

Another useful technique to investigate higher excited states of the confined exciton is the two-photon excitation technique. Generally, the two-photon excitation has a different selection rule from that of one-photon excitation. For instance, exciton states with S type symmetry are optically allowed under one-photon excitation, whereas those with P type symmetry are allowed under two-photon excitation. Thus, individual structures associated with the exciton excited states are expected to be more distinctly observed without the disturbance from the contribution of the lowest strong exciton states with S type symmetry. Also, with two-photon excitation, one can spectrally eliminate the strong scattering of the excitation light, which sometimes causes difficulties in resolving the small signal close to the excitation photon energy. Fröhlich et al. [40] measured the two-photon excitation spectra of the confined exciton luminescence and found that the $1S$ exciton states are weakly two-photon active for the linear polarized light parallel to [110] axes but forbidden for [100] axes of the NaCl matrix. Considering that the $1S$ exciton of the bulk CuCl crystal is weakly two-photon active for the polarized light parallel to [110] but not to the [100], this finding indicates that the crystalline axes [100] of the CuCl QDs are parallel to that of the NaCl host crystal. Edamatsu et al. [41] observed the two-photon excitation spectra for CuCl QDs with different mean radii and found a steep increase of the two-photon excitation efficiency at a few hundreds mV higher than the lowest $1S$ exciton energy. Furthermore, the energy positions of the steep rise depended on the mean dot size of the samples. From the energy separation between the steep rise and the lowest $1S$ exciton, and from the comparison with the results of excited-state absorption described later, they

concluded that this steep rise of two-photon excitation originates from the nP Rydberg-like states of the confined exciton. This attribution was also in good agreement with the theory [19, 38, 42]. The confinement effect on the higher Rydberg-like states will be discussed later in this section. Edamatsu et al. [43] also studied the luminescence spectra of CuCl QDs in NaCl matrices under size-selective one- and two-photon excitation. As in the excitation spectra reported by Itoh et al. [14, 15], several structures, the positions of which were dependent on the excitation photon energies, were observed in the luminescence spectra. These structures were likely to originate from the confined exciton that was initially excited to higher confinement states. However, the energy positions of the observed structures did not follow the theoretical ones that assumed the spherical shape of the QDs. Instead, the experimental result might indicate that the shape of CuCl QDs in NaCl matrices would be more oblate, as previously suggested by Itoh et al. [13–15]. On the contrary, the luminescence structure that is attributable to the excitons that are initially excited to the $1p$ confinement states of the spherical QD in glass matrices was observed in size-selective one-photon [39] and two-photon [44] excitation. From these results, it is likely that CuCl QDs embedded in glass matrices have mostly spherical shapes. It is also noteworthy that, in the two-photon excitation, the size-selective luminescence spectra of the QDs in both NaCl and glass matrices exhibited an unknown structure, whose Stokes shift is nearly half that originates from the $1p$ confinement state [41, 44]. Baranov et al. [44] attributed the structure to the confined longitudinal excitons in the QDs. However, this attribution is inconsistent with the recent theory [29, 30] that dealt with the coupling between the polarization of confined exciton states and electromagnetic fields, as described in Section 2. Thus, the origin of this unidentified luminescence structure appearing in two-photon excitation is still a open question to be clarified in the future.

As well as the two-photon excitation, transient two-step excitation is a powerful method to investigate the higher excited states of the confined exciton. In this method, a strong UV pump pulse excites the confined excitons at their lowest states, and a succeeding weak pulse probes the transient absorption arising from the transition from the lowest to higher states of the confined excitons. Mimura et al. [45] found the infrared transient absorption attributable to the transition from Rydberg $1S$ to $2P$ states of the confined excitons in CuCl QDs embedded in NaCl matrices. The absorption spectra depended on the mean size of the QDs: the peak position of the absorption for QDs with mean radius $a^* = 3.5$ nm was located at 0.28 eV, while that for $a^* = 1.3$ nm QDs was at 0.39 eV. Yamanaka et al. [46, 47] studied the size dependence of the transient absorption by means of size-selective excitation, and the result was compared with the theory [37, 38]. In general, the agreement between the experiment and theory is very good: the observed blueshift of the transient absorption with the decrease of dot size is reproduced by the theory. The change of the Rydberg $1S$–$2P$ absorption with the dot size indicates that the effective Rydberg energy of the confined exciton depends on the dot size. In other words, the $2P$ state of the confined exciton in CuCl QDs in the size region under study (a few nm) is no more classified into the ideal weak confinement regime,

in which the internal motion of the exciton is assumed not to be affected by the confinement. Instead, since the effective exciton radius of the $2P$ exciton state is much larger than that of the $1S$ state, the confinement effect on the $2P$ state deviates from the weak confinement toward the strong confinement regime. The theoretical calculation [37, 38] presented the optical properties including two-photon and transient absorption spectra and predicted the drastic change of the optical spectra between the two extreme regimes. In addition to the transient absorption of the confined excitons in the QDs, transient absorption originating from the confined biexcitons in CuCl QDs was recently observed [48]. The excited state of the biexciton is not stable in bulk crystal because the excess energy of the excited states (a few hundred meV) is larger than the binding energy of the biexciton (32 meV). However, in the QDs, the excited biexciton can exist because the two excitons in one QD are never dissociated from each other. Since the observed transient absorption spectra of the confined biexcitons was very similar to those of the confined excitons, it was suggested that the excited states of the confined biexciton is approximately composed of one excited and one lowest excitons [48].

4. NONLINEAR OPTICAL RESPONSE AND CONFINED BIEXCITON

Control of nonlinear optical response is one of the most important aspects of semiconductor QDs for the application to optically functional devices. It is expected that multiply created excitons in a QD strongly interact with each other, because the two excitons are confined in a tiny space. The spatial closeness and strong interaction between the two excitons breaks the bosonic nature of the confined excitons, thus generating large optical nonlinearity even in the "weak confinement" regime [49–55].

Experimentally, the nonlinear optical response of CuCl QDs was first reported by Gilliot et al. [56, 57], and soon followed by other groups [58–64]. In these early experiments, strong nanosecond lasers were used as pump sources to examine the nonlinear response. The main features of these experiments are bleaching and blueshift of the exciton absorption bands. Since the exciton binding energy in CuCl is very large, these nonlinear effects were believed to be caused by many-body effects (i.e., creation of two or more excitons in a QD), rather than the formation of electron–hole plasma. In fact, the saturation intensity, from which the saturation of the exciton absorption takes place, was almost inversely proportional to $(a^*)^3$ [58, 62], indicating that the number of excitons per QD is an essential parameter to govern the optical nonlinearity of the QD. Edamatsu et al. [64] investigated the temporal evolution of the nonlinear optical response by means of subpicosecond pump-probe spectroscopy. They revealed that the nonlinear optical response was composed of saturation, blueshift, and broadening of the exciton absorption band. The saturation and broadening components almost disappeared within several picoseconds after the pump pulse, indicating that these components arise from hot carriers, or higher excited states of the exciton, which are initially generated in the QD by the pump that had considerably higher photon energy than the lowest Z_3 exciton energy. In contrast, the time evolution of blueshift had

longer decay times (60 and 380 ps), which are identical to the lifetimes of a biexciton (excitonic molecule) and an exciton, respectively. This finding is the first clear evidence that the blueshift component of the optical nonlinearity is mainly caused by the existence of a biexciton and an exciton in the QD. Furthermore, they observed that the exciton luminescence grows with a rise time that is consistent with the decay time of the biexciton, indicating a cascade radiative decay process of the biexciton via the exciton. In bulk CuCl crystal, the luminescence decay time of the biexciton was usually measured to be about half that of the excitons, reflecting the population equilibrium between the excitons and biexcitons brought by frequent exciton–exciton collisions [65]. In QDs, however, such collisions never occur between excitons isolated in different QDs, and thus the observed decay time represents the real lifetime of the excitonic molecule confined in a QD, which is of the same order as those in bulk crystal [66, 67]. Thus, the cascade radiative decay of the biexciton via the exciton is characteristic of the confined exciton and biexciton system in the QD. Similar results on the temporal evolution of the blueshift and the cascade decay of the biexciton were also obtained by Ikezawa and Masumoto [68]. By these experiments, it was clarified that the main origin of the optical nonlinearity of CuCl QDs is the blueshift of the exciton energy caused by the presence of another exciton in the same QD. However, the agreement of the observed amount of blueshift with existing theories had not been satisfactory [64] until Nair and Takagahara [54, 55] proposed the concept of "weakly correlated exciton pair states" in the QD, as will be discussed.

It is expected that the two excitons created in a QD interact with each other and form exciton pair states that are somewhat different from the ideal uncorrelated two exciton state. Especially, the existence of a biexciton (or excitonic molecule: a bound state of the two excitons) in a QD and the size dependence of the biexciton binding energy have been intensively discussed in several theoretical works [50, 69–75]. Since it is well known that the biexciton is very stable in bulk CuCl crystal, one can also expect the existence of biexcitons in CuCl QDs. In fact, the luminescence originating from the radiative decay from the biexciton to the exciton was observed in CuCl QDs under strong excitation using a pulsed laser [27, 76, 77]. Provided that the weak confinement regime is also applicable to the biexciton, one would expect that the blueshift of the biexciton energy is almost half that of the exciton, because the translational mass of the biexciton is approximately twice the exciton mass [see Eq. (1)]. As a result, the luminescence photon energy would decrease with the increase of dot size, because the luminescence is caused by the radiative decay from the biexciton to the exciton states [75]. Itoh [27] measured the peak position of the biexciton luminescence as a function of the dot size and found that the biexciton luminescence exhibits the redshift from the bulk value with the decrease of the dot size in the range $a \geq 3$ nm, whereas it shows blueshift for smaller sizes. The redshift for larger sizes is consistent with the consideration described previously. However, this size-dependent redshift was not clearly observed in other reports [76, 77]. Interestingly, the energy position of the biexciton luminescence for larger sizes did not converge to that of the

biexciton luminescence in the bulk crystal leaving a transverse exciton, but even closer to that leaving a longitudinal exciton [27, 77]. This phenomenon is likely to be explained by the previously mentioned consideration that the oscillator strength of larger QDs concentrates at the surface mode, which is located between the transverse and longitudinal excitons in the bulk crystal [28–30]. As a result, the biexciton luminescence of the QDs with larger sizes ($a \geq 10$ nm) is energetically closer to that of the bulk crystal leaving a longitudinal exciton. The blueshift for smaller sizes is attributable to the deviation from the weak confinement regime of the biexciton for the QDs of such small sizes. This consideration is consistent with the fact that the size at which the redshift turns to blueshift almost coincides with the Bohr radius of the biexciton (3.5 nm [78]). The binding energy of the biexciton is defined by

$$\Delta E_{BX} = 2E_X - E_{BX} = E_X - (E_{BX} - E_X)$$
$$= E_X - h\nu_{BX} \qquad (6)$$

where E_X, E_{BX}, and $h\nu_{BX}$ are the energies of exciton, biexciton, and biexciton luminescence, respectively. Even though the biexciton luminescence exhibits the blueshift, larger blueshift of exciton energy results in the increase of the binding energy with the decrease of dot size, as predicted by the theoretical calculations [69–75]. Concerning the biexciton state in CuCl QDs, it is also noteworthy that the optical gain and lasing associated with the transitions from the biexciton to the exciton states were observed [63, 64].

In addition to the lowest bound state of the biexciton, since the two excitons in a QD cannot separate entirely from each other, one may consider the excited states of the biexciton. These excited states correspond to a kind of antibonding state and thus are not stable in the bulk crystal. Nair and Takagahara [54, 55] pointed out that this "weakly correlated exciton pair state" plays an crucial role in the optical nonlinearity of the QDs. Ikezawa et al. [79, 80] observed the excited-state absorption from the exciton state to these excited biexciton states by means of a size-selective pump-probe technique. They found the absorption signals to the excited biexciton states ($J = 2$), as well as to the bound biexciton ($J = 0$). The blueshift of the excited biexciton was approximately twice as large as that of the exciton, indicating that each exciton constituting the excited biexciton effectively occupies half the volume of the QD [80]. Furthermore, they observed the absorption from the biexciton state to a triexciton states consisting of three excitons in a QD. In relation to the excited states of the biexcitons, it is also interesting that another kind of excited state of the biexciton composed of one Rydberg excited and one lowest exciton was observed in the infrared transient absorption, as described in Section 3.

To consider the size dependence of the optical nonlinearity, one must take account of two contradictory effects. One is the anharmonicity or nonbosonic nature of the exciton states, and the other is the superradiant oscillator strength of the confined exciton that is discussed in Section 2. The former decreases with the increase of dot size because the correlation between the two excitons in a QD decreases [54, 55]. On the other hand, the latter increases with increasing dot size because the oscillator strength of the confined exciton

increases with the dot size. Kataoka et al. [60] measured the third order optical susceptibility $\chi^{(3)}$ of CuCl QDs and its size dependence by means of the degenerate four-wave mixing method. The observed values of $\chi^{(3)}/\alpha$, where α is the linear absorption coefficient, increased with the increase of dot size until $\chi^{(3)}/\alpha = 3.4 \times 10^{-9}$ esu cm at $a \sim 5$ nm and decreased for larger sizes. They also discussed the size dependence of the oscillator strength of the confined exciton, which is derived from the observed $\chi^{(3)}$, and showed that the size dependence of $\chi^{(3)}$ mainly depends on that of the oscillator strength. The size (4–5 nm) at which the obtained values of $\chi^{(3)}/\alpha$ and oscillator strength exhibited the maximum value was in good agreement with the size where the luminescence lifetime started to deviate from the theoretical value [26, 27], as discussed in Section 2. Also, Yano et al. studied the size dependence of the absorption saturation and obtained a similar size dependence [61]. Thus, the saturation of the oscillator strength is likely to be one reason for the suppression of the optical nonlinearity in larger dots. For the other reason, Nair and Takagahara [54, 55] pointed out that when the energy difference $E_{XX} - 2E_X$ (where E_X and E_{XX} are the energies of confined exciton and correlated exciton pair state, respectively) is comparable or smaller than the homogeneous width of the states concerned, strong cancellation of the two terms (via the ground state and via the exciton pair state) on $\chi^{(3)}$ takes place and causes the suppression of the optical nonlinearity.

5. PHONON CONFINEMENT AND EXCITON–PHONON COUPLING

In addition to the exciton confinement, it has also been reported that lattice vibrations, of both acoustic [81–83] and optical [39, 43, 84–87] phonons, are confined and quantized in the CuCl quantum dots. Masumoto et al. [81, 82] investigated the confined acoustic phonons by means of the persistent spectral hole-burning spectroscopy. They found that the energy separation of the phonon sidebands from the zero-phonon bands to be inversely proportional to the radius of the quantum dots that were excited resonantly by a narrow-line laser. Similar results were also obtained by resonant luminescence spectroscopy, in which it was confirmed that the phonon sidebands originate from the confined acoustic phonons by means of the temperature dependence of the Stokes and anti-Stokes sideband intensities [83]. The inverse proportion of the confined phonon energy to the dot size is explained by the theoretical works on the confinement of acoustic phonons in isolated elastic spheres [88–92]. For the simplest case, the vibrational frequencies $\omega_{n,l}^S$ and $\omega_{n,l}^T$ of an elastic sphere in a free boundary condition are given by

$$\omega_{n,l}^S = \frac{\eta_{n,l}^S}{a} v_t \tag{7}$$

$$\omega_{n,l}^T = \frac{\eta_{n,l}^T}{a} v_t \tag{8}$$

where the superscripts S and T indicate the spheroidal and torsional modes, respectively, l is the angular momentum index, n is the branch number, a is the sphere radius, v_t

is the transverse sound velocity of the elastic medium, and $\eta_{n,l}^S$ and $\eta_{n,l}^T$ are the eigenvalues satisfying appropriate equations [88–92]. These lowest frequency modes with $n = 0$ are called surface modes, since these modes have a large amplitude at the surface. The amount of the observed Stokes shift for the QDs in glass matrices was in good agreement with the calculated value of $\hbar\omega_{0,0}^S$, or even with $\hbar\omega_{0,2}^T$ or $\hbar\omega_{0,2}^S$. Since only the spheroidal modes with $l = 0$ contribute to the resonant Raman scattering via the Z_3 exciton state [93], the observed phonon sideband was assigned as the lowest spheroidal mode $\omega_{0,0}^S$ [83]. For the QDs embedded in NaCl matrices, however, the observed energy shift is not explained by vibrational modes assuming simple boundary conditions [81–83]. Given that the sound velocities of the NaCl and CuCl are similar, the vibrational mode of the CuCl QD in the NaCl matrix might be extended further into the matrix, which would explain why the energy estimation is more complicated than that in glass matrix. Such matrix effects that might cause the disappearance of the lowest surface modes ($n = 0$) and the softening of the torsional modes were discussed by Tamura et al. [90].

In the case of the confinement of optical phonons, the situation is somewhat different. Since the optical phonon frequency depends less on its wave number, its dependence on dot size is also quite small. Ekimov obtained slight but positive dot-size dependence of the longitudinal optical (LO) phonon frequency in Raman spectra and interpret it as quantization along the dispersion curves of the LO phonon [86, 87]. As described later in this section, the confined LO phonon and the exciton strongly interact with each other, forming exciton–phonon complexes [39, 43, 84]. The strong exciton–phonon interaction also results in the renormalization of the LO phonon energy associated with the exciton [84, 85].

It is valuable to discuss the exciton–phonon coupling in the QD. For several QD materials, there are a number of works on the enhancement of exciton–acoustic–phonon coupling [92–96] and exciton–optical–phonon coupling [97–103]. Because of the different origins of the coupling— deformation potential for exciton–acoustic–phonon coupling and Fröhlich interaction for exciton–optical–phonon coupling—the mechanisms of the enhancement are also different. Since the confined excitonic state in CuCl QDs is much different from those in other materials, it is very interesting to examine the exciton–phonon coupling in CuCl QDs. In bulk CuCl crystal, the coupling between phonons and excitons is relatively week so that the exciton absorption and emission spectra are mainly composed of the zero-phonon line of the free exciton. The value of the exciton–acoustic–phonon coupling constant g defined by Toyozawa [104] for bulk CuCl was estimated to be the order of 0.001 [105]. Itoh and Furumiya [105] evaluated the exciton–phonon coupling constant for CuCl QDs (effective radius $a^* = 1.5$ nm) in NaCl matrix to be $g = 0.35$ from linear temperature dependence of homogeneous broadening of the resonant exciton luminescence. Kuroda et al. [106] obtained the approximately doubled value of g for CuCl QDs ($a^* = 2.3$ nm) in glass matrix by two-photon excitation. Edamatsu et al. [83] evaluated the Huang–Rhys parameter S [107] of the phonon sidebands originating from the confined acoustic phonons in resonant luminescence spectra.

The estimated values of S at $T = 0$ K are 0.24 and 0.30 for glass ($a^* = 2.4$ nm) and NaCl ($a^* = 3.2$ nm) matrices, respectively. In the case of deformation potential coupling, the Huang–Rhys parameter is related to the exciton–lattice coupling constant g [104]. The resulting values were $g = 0.07$ and 0.08 for the QDs in glass and NaCl matrices, respectively. Although these obtained values of g are slightly different from each other, they are all much larger than that estimated for the bulk CuCl crystal. This result indicates the strong enhancement of the coupling between the confined excitons and acoustic phonons in the QD. Although such enhancement of the exciton–acoustic–phonon coupling is intensively discussed for various QDs [92–96], it seems that there are not consentaneous conclusions at present. Further theoretical and experimental investigations will be necessary to clarify the mechanism of the enhancement of exciton–acoustic–phonon coupling in semiconductor QDs.

In the case of exciton–optical–phonon coupling, drastic effects have been observed in CuCl QDs as noted above previously. Itoh et al. [39] found that the confined excitons and LO phonons form exciton–phonon complexes; they observed in resonant luminescence spectra the anticrossing between the LO phonon sideband and the sideband arising from the excitation to higher confined states of the exciton. This anticrossing was also observed in two-photon excitation [43] and persistent hole-burning [84] spectra. The strong exciton–optical–phonon interaction in the QD also results in the renormalization of the LO phonon energy [84, 85], which means that the confined LO phonon associated with an exciton suffers considerable ($\sim$10%) [84] softening. In fact, the LO phonon sidebands observed in persistent hole burning [84], resonant luminescence [43, 84], and the beat frequency in four-wave mixing experiment [85] exhibited reduced LO phonon energies from that observed in off-resonant Raman spectra [87]. This is one of the unique phenomena originating from the strong exciton–optical–phonon interaction in CuCl QDs.

6. PHASE RELAXATION OF THE CONFINED EXCITON

The excitonic states confined in semiconductor QDs are sometimes referred to as artificial atoms or mesoscopic atoms, since they have discrete energy spectra and their wavefunctions are coherent superposition of the electronic excitation over the QD's volume. It is also expected that those states are more or less isolated from environment because of the three-dimensional confinement. If the excitonic states are well isolated form environment, it is expected that the phase relaxation, or decoherence, of the confined excitonic states will be very slow compared with that in bulk crystals. In fact, there are a number of experimental works reporting very long phase relaxation time in CuCl and other QDs [108–111]. The amount of phase relaxation time is crucial for the application of confined excitonic states to quantum information processing, because the phase relaxation essentially destroys quantum information held in excitonic wavefunctions. Thus, it is very important to study the phase relaxation mechanisms of the confined excitons.

To measure the phase relaxation time of the confined exciton, there two methods: frequency-domain and time-domain measurements. The former includes resonant luminescence and persistent hole-burning spectroscopy, and the latter does four-wave mixing and photon echo spectroscopy. Masumoto et al. [112] reported for the first time the homogeneous width of the Z_3 exciton in CuCl QDs embedded in NaCl crystal. They measured the homogeneous width by means of laser saturation spectroscopy of the exciton absorption and reported that the homogeneous width of the QD (mean dot radius = 6.1 nm) was 0.18 meV at 77 K. Itoh and Furumiya [105] measured the homogeneous width and its temperature and size dependence of the resonant luminescence of CuCl QDs in NaCl crystal. The homogeneous width Γ_0 extrapolated to 0 K was 0.32 meV for the QD (effective dot radius $a^* = 4.0$ nm), and Γ_0 increased with the decrease of dot size. Wamura et al. [113] measured the homogeneous width of CuCl QDs in NaCl crystal by means of persistent hole-burning spectroscopy. The obtained Γ_0 for the QD with $a^* = 4.1$ nm was 0.30 meV and increased with decreasing dot size, in accordance with that obtained from the resonant luminescence spectra described previously. Later on, Masumoto et al. [114] reexamined the persistent hole-burning experiment with high spectral resolution and obtained $\Gamma_0 = 0.07$ meV for the QDs ($a^* = 3.5$ nm) in NaCl. In addition, Kuroda et al. [106] measured the homogeneous width of CuCl QDs in a glass matrix by means of two-photon-excited resonant luminescence. The obtained Γ_0 was 2.1 meV for $a^* = 2.3$ nm. Since the homogeneous widths obtained from these frequency-domain experiments do not show good consistency, the corresponding phase relaxation time (T_2) ranges from subpicoseconds to over 10 picoseconds. This discrepancy is probably caused by the difference in experimental conditions, most probably in excitation intensity, which might affect the homogeneous width. In fact, Edamatsu et al. [83] recently reported that the homogeneous widths of the resonant luminescence of CuCl QDs in both glass and NaCl matrices were less than 30 μeV, which is limited by the experimental spectral resolution, at sufficiently weak excitation power. Meanwhile, the phase relaxation time of CuCl QD was measured by time-domain experiments: four-wave mixing or accumulated photon echo (see Section 7). Kuribayashi et al. [108] measured the phase relaxation time of a CuCl QD (mean dot radius = 5.4 nm) in a glass matrix and obtained $T_2 = 130$ ps at 2 K. Ikezawa and Masumoto [109] measured the phase relaxation time of CuCl QDs in NaCl and glass matrices. The obtained T_2 was very long: T_2 reached 1.3 and 2.6 ns at low temperature below 1 K (i.e., $\Gamma_0 = 1$ and 2 μeV) for the QDs in NaCl and glass matrices, respectively. Following to the finding of the very long T_2 in CuCl QDs, it has recently been reported that QDs of III–V materials also exhibit very long phase relaxation times of several hundred picoseconds [110, 111].

It is an very interesting subject to observe the mechanism of the very long phase relaxation of the confined excitons in relation to the exciton–phonon interaction. In a low excitation regime, where at most one exciton is to be created in a QD, it is expected that the phase relaxation mainly originates from interaction with phonons. At low temperature,

the main origin of the phase relaxation would be exciton–acoustic–phonon coupling while the coupling with optical phonons may be important at high temperature. In bulk semiconductors, the contribution of the acoustic phonon on the temperature dependence of the homogeneous width $\Gamma(t)$ is often expressed by

$$\Gamma(T) = \Gamma_0 + AT \qquad (9)$$

where A is a constant, and Γ_0 is the temperature-independent width that remains even at $T = 0$ K. The temperature-linear term originates from the contribution of the acoustic phonons that have continuous density of states from zero energy. On the contrary, the phase relaxation in CuCl QD is characteristic because, as described in Section 5, not only the excitonic states but the acoustic phonons are also quantized so as to have discrete energy spectra. Once both are quantized, the usual phase-relaxation mechanism via one-phonon emission or absorption can occur only when the energy separation between the lowest and higher excitonic states happens to coincide with one of the discrete phonon energies. As a result, the two-phonon process which involves almost simultaneous emission and absorption of the confined acoustic phonons becomes dominant in the phase-relaxation mechanism in this system. In a temperature region where the two-phonon process is a dominant mechanism, the homogeneous width of the zero-phonon line of the confined exciton is expressed by

$$\Gamma(T) = \Gamma_0 + A\sinh^{-2}\left(\frac{\hbar\omega}{2kT}\right) \qquad (10)$$

where $\hbar\omega$ is the energy of the confined acoustic phonon concerned, A is a constant, and Γ_0 is the temperature-independent width. The contribution of the two-phonon process on the homogeneous width in the CuCl QD system has been reported by recent photon echo [109] and resonant luminescence [83] studies. This contribution is characteristic of the QD system in which the electronic system is confined and the vibrational energies are actually quantized. The nature of the phase-relaxation process of CuCl quantum dots is much different from that of III–V compounds, in which the dot size is so large that the true zero-phonon line is not resolvable from the sidebands of the confined acoustic phonons.

In a higher temperature region, the zero-phonon band merges with the confined-acoustic-phonon sidebands, and the total homogeneous width is governed by the contribution of the phonon sidebands and is thus expressed by the one-phonon process of the acoustic phonons. When the spectral resolution is not good enough, this one-phonon contribution would be the dominant part of the homogeneous width measured in earlier experiments. In a lower temperature region, another mechanism of the phase relaxation with lower energy excitation might take place. Ikezawa and Masumoto [109] suggested the phase relaxation due to the coupling to a two-level system (TLS), which had been often used to explain the anomalous temperature dependences of the homogeneous widths of impurity atoms or molecules in glassy or polymer matrices [115]. With the contributions from the TLS and two-phonon process (10) taken together,

the low-temperature homogeneous width of the exciton confined in the CuCl QD system is expressed by [109]

$$\Gamma(T) = \Gamma_0 + A\sinh^{-2}\left(\frac{\hbar\omega}{2kT}\right) + B\cosh^{-2}\left(\frac{\hbar\omega'}{2kT}\right) \qquad (11)$$

where $\hbar\omega'$ is the excitation energy of the TLS, and B is a constant. The contribution of the TLS indicates that the interaction between the excited electron/hole and the surrounding matrices plays an important role in phase relaxation in the low-temperature region, as described in the next section.

7. INTERACTION WITH MATRICES

In the previous section, we described that the electronic states in semiconductor QDs are more or less isolated from environment and thus the phase relaxation time of the electronic excitation becomes very long. However, in general, real semiconductor QDs are not fully isolated from environment. In many cases, the QDs are suspended in surrounding matrix substances. As a result, the electronic excitation of the QDs sometimes interacts with matrices. For instance, it is known that colloidal QDs of II–VI materials exhibit intermittent ("random telegraph") photoluminescence [116] or spectral diffusion [117]. These phenomena are caused by Auger ionization of the QDs and succeeding carrier trapping in the matrix site near the QD [118]. In CuCl QDs, such phenomena as photofatigue [119] and persistent hole burning [120] also suggest the efficient ionization and trapping of the carriers in the matrices. Also, Kuroda et al. [121] found that CuBr QDs in glass matrices exhibit an extraordinary strong photon echo signal that originates from the accumulation effect due to the presence of long-lived excited states. The accumulated photon echo was also observed for CuCl QDs [108, 109], as stated in the previous section. Another strong indication of the interaction with the matrices is the contribution of the TLS on the low-temperature phase relaxation of the confined exciton described in the previous section.

Recent progress of the microspectroscopy technique has enabled us to observe and analyze photoluminescence signals from a single QD. The single QD spectroscopy has allowed the opportunity to study the electronic states of individual QDs interacting with the matrices and environment. Thus far, photoluminescence signals from single QDs of various kinds of materials were widely studied. Generally speaking, the stability of the photoluminescence signal from single QDs depends on many factors, such as material, environment, interface, temperature, excitation power, and so on. For instance, as described, colloidal QDs of II–VI materials exhibit intermittent photoluminescence [116] or spectral diffusion [117], depending strongly on the excitation power and on the surface treatment of the QDs. Adequately passivated colloidal QDs have very high quantum yields and low intermittent frequencies. It is worth studying such optical properties of single QDs for further understanding of the role of interaction with matrices. However, unfortunately, stable photoluminescence from single CuCl QDs has not been reported so far. In this context, Edamatsu et al. [122] observed frequently intermittent photoluminescence from a single QD, or a small number of QDs, of CuCl embedded

in NaCl crystal. The frequent intermittency suggested that the excited electrons or holes of this material easily escape from the QD and then are captured by some traps in the matrix, even at low temperature.

More important progress in the recent study of CuCl QDs is the sample preparation and characterization methods. The traditional methods to grow the CuCl QDs are thermal treatments of the supersaturated solid solution of CuCl in silicate glass [9, 10] or NaCl [13, 14] matrices. Haselhoff et al. [123, 124] studied the growth condition and size distribution of CuCl QDs in NaCl crystals. It is also noteworthy that the topographical investigations of CuCl clusters at the surface of NaCl crystal were made by near-field optical microscopy and atomic force microscopy observations [125]. However, the sizes of the observed clusters were rather large compared to the typical size of the QDs, and there are no optical or topographical observations of the individual QDs that have sufficiently small sizes. The serious disadvantage of the traditional growth methods is their poor controllability in size and concentration of the QDs. For instance, so as to observe single QD luminescence, we need sufficiently low concentration of the QDs. However, the concentration of the CuCl QDs thermally grown in glass or NaCl matrices is usually too high. As described, Edamatsu et al. [122] prepared CuCl QDs contained in thin films of NaCl crystals grown between two silica plates. However, the result indicated that we need QDs that have lower concentrations and are stable against autoionization of the photoinduced carriers to prevent the frequent luminescence intermittency. Up to now, there are a limited number of trials that intend to obtain well-characterized samples of the CuCl QD. Kurisu et al. [126] reported the growth of CuCl QDs embedded in SiO_2 film by means of a sputtering method. Kawamori et al. [127] reported the formation of CuCl island structures on CaF_2 substrates by means of molecular beam epitaxy. We hope that these efforts will succeed in growing well-characterized and well-controlled samples of CuCl QDs in the future.

8. CONCLUSION

In this chapter we have reviewed the optical properties of CuCl quantum dots associated with quantum confinement effects and related phenomena. Due to the confinement of exciton translational motion which is peculiar to this material, many kinds of intrinsic natures of coherent excitons, such as blueshift and splitting of exciton states, rapid radiative decay of exciton, size-dependent optical nonlinearity, etc., only appear in the quantum dots because of their small sizes similar to or smaller than the exciton coherence length. The exciton coherence is pronounced not only because of very small size and small number of impurities or crystal imperfections but also the dramatic decrease of exciton–phonon interaction. Those are the main reasons coherent control of confined excitons becomes practical [128]. The quantum control of photons in quantum dots will also be practical due to long coherence time of excitons. The aforementioned quantum size effects are all caused by the wave natures of confined excitons inside the quantum dots. The quantum dots are essentially typical open systems which

are easily affected by the physical properties of the surroundings, such as matrices. The shape of the quantum dot itself depends critically on the matrices: cubic in crystalline matrix and/or spherical in amorphouses. The confined excitons can interact with outer optical phonons by the Frölich interaction. The exciton energy and/or photogenerated carriers can be transferred through the interface between the quantum dots and their surroundings that cause the ionization of quantum dots, blinking, and the photofatigue effect on exciton luminescence. The charge transfer through the interface is nothing but the function of photocatalysis, and the energy transfer is similar to that on a reaction center.

In the near future, one can surely expect that the research fields of the quantum dots will be further expanded into many kinds of new fields not only in physics but also towards chemistry, biology, and information technology.

GLOSSARY

Biexciton A quasiparticle consisting of two excitons, or two electrons and two holes, combined together. It is also called an "excitonic molecule".

Exciton An elementary excitation (quasiparticle) of electronic states in semiconductors. An exciton consists of an electron and a hole combined by Coulomb interaction. As in the general treatment of two-particle systems, the exciton wave function can be separated into two parts: the internal (relative) motion of the electron and hole, and the translational motion as a combined particle. In most semiconductors, the internal motion of an exciton causes a series of discrete absorption bands similar to that of a hydrogen atom. This type of exciton is called Wannier exciton, and the series of absorption bands is called Wannier (or Rydberg) series of the exciton.

Quantum dot A nanometer-sized particle of semiconductor material in which the quantum nature of electronic behavior becomes dominant. In a quantum dot, the electronic wave function is confined in all dimensions. As a result, electronic and optical properties of quantum dots deviate from those of bulk crystal as a function of dot size. "Nanocrystal" is a synonym of "quantum dot".

Weak confinement The quantum confinement effect of the Wannier exciton in a quantum dot is characterized by the relationship between the exciton Bohr radius and the dot size. When the dot size is sufficiently larger than the exciton Bohr radius, it is a good approximation to treat the exciton as a particle whose translational motion is confined in the dot, with much less influence on its internal motion. This situation is called the "weak confinement" regime.

REFERENCES

1. "Excitonic Processes in Solids" (M. Ueta, H. Kanzaki, K. Kobayashi, Y. Toyozawa, and E. Hanamura, Eds.), Ch. 3. Springer-Verlag, Berlin, 1986.
2. M. Cardona, *Phys. Rev.* 129, 69 (1963).
3. J. Ringeissen and S. Nikitine, *J. Phys.* 28, C3-48 (1967).
4. A. D. Yoffe, *Adv. Phys.* 42, 173 (1993).
5. L. E. Brus, Al. L. Efros, and T. Itoh, *J. Lumin.* 70 (1996).
6. E. Gross and A. A. Kaplyanskii, *Soviet Phys.—Opt. Spectrosc.* 2, 204 (1957).

7. M. Ueta, M. Ikezawa, and S. Nagasaka, *J. Phys. Soc. Jpn.* 20, 1724 (1965).

8. H. Kishishita, *Phys. Status Solidi B* 55, 399 (1973).

9. A. I. Ekimov, A. A. Onushchenko, and V. A. Tzehomskii, *Soviet Phys.—Chem. Glass* (*Fiz. Khim. Stekla*) 6, 511 (1980).

10. V. V. Golubkov, A. I. Ekimov, A. A. Onushchenko, and V. A. Tzehomskii, *Soviet Phys.—Chem. Glass* (*Fiz. Khim. Stekla*) 7, 265 (1981).

11. A. I. Ekimov and A. A. Onushchenko, *Soviet Phys.—Semicond.* 16, 775 (1982).

12. A. I. Ekimov, Al. L. Efros, and A. A. Onushchenko, *Solid State Commun.* 56, 921 (1985).

13. T. Itoh and T. Kirihara, *J. Lumin.* 31 & 32, 120 (1984).

14. T. Itoh, Y. Iwabuchi, and M. Kataoka, *Phys. Status Solidi B* 145, 567 (1988).

15. T. Itoh, Y. Iwabuchi, and T. Kirihara, *Phys. Status Solidi B* 146, 531 (1988).

16. Al. L. Efros and A. L. Efros, *Soviet Phys.—Semicond.* 16, 772 (1982).

17. L. E. Brus, *J. Chem. Phys.* 79, 5566 (1983); *ibid.* 80, 4403 (1984); *ibid*. 90, 2555 (1986).

18. Y. Kayanuma, *Solid State Commun.* 59, 405 (1986).

19. Y. Kayanuma, *Phys. Rev. B* 38, 9797 (1988).

20. Y. Kayanuma and H. Momiji, *Phys. Rev. B* 41, 10261 (1990).

21. Y. Kayanuma, *Phys. Rev. B* 44, 13085 (1991).

22. Y. Kayanuma, *Solid State Commun.* 84, 771 (1992).

23. T. Takagahara, *Phys. Rev. B* 36, 9293 (1987).

24. E. Hanamura, *Phys. Rev. B* 37, 1273 (1988); *Phys. Rev. B* 38, 1228 (1988).

25. A. Nakamura, H. Yamada, and T. Tokizaki, *Phys. Rev. B* 40, 8585 (1989).

26. T. Itoh, M. Furumiya, T. Ikehara, and C. Gourdon, *Solid State Commun.* 73, 271 (1990).

27. T. Itoh, *Nonlinear Opt.* 1, 61 (1991).

28. A. I. Ekimov, A. A. Onushchenko, M. É. Raĭkh, and Al. L. Efros, *Zh. Eksp. Teor. Fiz.* 90, 1795 (1986); *Sov. Phys. JETP* 63, 1054 (1986).

29. H. Ajiki and K. Cho, *Phys. Rev. B* 62, 7402 (2000).

30. K. Cho, H. Ajiki, and T. Tsuji, *Phys. Status Solidi B* 224, 735 (2001).

31. K. Cho, *J. Phys. Soc. Jpn.* 68, 683 (1999).

32. H. Ajiki and K. Cho, unpublished.

33. L. C. Andreani, G. Panzarini, and J. M. Gérard, *Phys. Rev. B* 60, 13276 (1999).

34. T. H. Stievater, X. Li, D. G. Steel, D. Gammon, D. S. Katzer, D. Park, C. Piermarocchi, and L. J. Sham, *Phys. Rev. Lett.* 87, 133603 (2001).

35. H. Kamada, H. Gotoh, J. Temmyo, T. Takagahara, and H. Ando, *Phys. Rev. Lett.* 87, 246401 (2001).

36. H. Htoon, T. Takagahara, D. Kulik, O. Baklenov, A. L. Holmes Jr., and C. K. Shih, *Phys. Rev. Lett.* 88, 087401 (2002).

37. T. Uozumi, Y. Kayanuma, K. Yamanaka, K. Edamatsu, and T. Itoh, *Phys. Rev. B* 59, 9826 (1999).

38. T. Uozumi and K. Kayanuma, *Phys. Rev. B* 65, 165318 (2002).

39. T. Itoh, M. Nishijima, A. I. Ekimov, C. Gourdon, Al. L. Efros, and M. Rosen, *Phys. Rev. Lett.* 74, 1645 (1995).

40. D. Fröhlich, M. Haselhoff, K. Reimann, and T. Itoh, *Solid State Commun.* 94, 189 (1995).

41. K. Edamatsu, K. Hisakawa, and T. Itoh, *Phys. Rev. B* 59, 15868 (1999).

42. T. Itoh, K. Yamanaka, K. Edamatsu, T. Uozumi, and Y. Kayanuma, *Int. J. Mod. Phys. B* 15, 3569 (2001).

43. K. Edamatsu, M. Tsukii, K. Hayashibe, M. Nishijima, T. Itoh, B. P. Zhang, Y. Segawa, and A. I. Ekimov, *Nonlinear Opt.* 18, 295 (1997).

44. A. V. Baranov, Y. Masumoto, K. Ioue, A. V. Fedorov, and A. A. Onushchenko, *Phys. Rev. B* 55, 15675 (1997).

45. Y. Mimura, K. Edamatsu, and T. Itoh, *J. Lumin.* 66 & 67, 401 (1996).

46. K. Yamanaka, K. Edamatsu, and T. Itoh, *J. Lumin.* 76 & 77, 256 (1998).

47. K. Yamanaka, K. Edamatsu, and T. Itoh, *Int. J. Mod. Phys. B* 15, 4005 (2001).

48. K. Miyajima, K. Edamatsu, and T. Itoh, *Phys. Status Solidi C*, 1275 (2003).

49. L. Banyai and S. W. Koch, *Phys. Rev. Lett.* 57, 2722 (1986).

50. L. Banyai, Y. Z. Hu, M. Lindberg, and S. W. Koch, *Phys. Rev. B* 38, 8142 (1988).

51. E. Hanamura, *Phys. Rev. B* 37, 1273 (1987).

52. L. Belleguie and L. Banyai, *Phys. Rev. B* 44, 8785 (1991).

53. L. Belleguie and L. Banyai, *Phys. Rev. B* 47, 4498 (1993).

54. S. V. Nair and T. Takagahara, *Phys. Rev. B* 53, R10516 (1996).

55. S. V. Nair and T. Takagahara, *Phys. Rev. B* 55, 5153 (1997).

56. P. Gilliot, J. C. Merle, R. Levy, M. Robino, and B. Hönerlage, *Phys. Status Solidi B* 153, 403 (1989).

57. P. Gilliot, B. Hönerlage, R. Levy, and J. B. Grun, *Phys. Status Solidi B* 159, 259 (1990).

58. Y. Masumoto, S. Ideshita, and T. Wamura, *Phys. Status Solidi B* 159, 133 (1990).

59. L. G. Zimin, S. B. Gaponenko, V. Yu. Lebed', I. E. Malinovskii, and I. N. Germanenko, *J. Lumin.* 46, 101 (1990).

60. T. Kataoka, T. Tokizaki, and A. Nakamura, *Phys. Rev. B* 48, 2815 (1993).

61. S. Yano, T. Goto, and T. Itoh, *J. Appl. Phys.* 79, 8216 (1996).

62. T. Itoh, S. Iwai, K. Edamatsu, S. Yano, and T. Goto, *Jpn. J. Appl. Phys.* 34, 1 (1995).

63. Y. Masumoto, T. Kawamura, and K. Era, *Appl. Phys. Lett.* 62, 225 (1993).

64. K. Edamatsu, S. Iwai, T. Itoh, S. Yano, and T. Goto, *Phys. Rev. B* 51, 11205 (1995).

65. E. Ostertag and J. B. Grun, *Phys. Status Solidi B* 82, 335 (1977).

66. H. Akiyama, T. Kuga, M. Matsuoka, and M. Kuwata-Gonokami, *Phys. Rev. B* 42, 5621 (1990).

67. T. Ikehara and T. Itoh, *Solid State Commun.* 79, 755 (1991).

68. M. Ikezawa and Y. Masumoto, *Phys. Rev. B* 53, 13694 (1996).

69. L. Banyai, *Phys. Rev. B* 39, 8022 (1989).

70. Al. L. Efros and A. V. Rodina, *Solid State Commun.* 72, 645 (1989).

71. T. Takagahara, *Phys. Rev. B* 39, 10206 (1989).

72. Y. Z. Hu, S. W. Koch, M. Lindberg, N. Peyghambarian, E. L. Pollock, and F. F. Abraham, *Phys. Rev. Lett.* 64, 1805 (1990).

73. Y. Z. Hu, M. Lindberg, and S. W. Koch, *Phys. Rev. B* 42, 1713 (1990).

74. E. L. Pollock and S. W. Koch, *J. Chem. Phys.* 94, 6776 (1991).

75. Y. Kayanuma and K. Kuroda, *Appl. Phys. A* 53, 475 (1991).

76. R. Levy, L. Mager, P. Gilliot, and B. Hönerlage, *Phys. Rev. B* 44, 11286 (1991).

77. Y. Masumoto, S. Okamoto, and S. Katayanagi, *Phys. Rev. B* 50, 18658 (1994).

78. B. Hönerlage, R. Levy, J. B. Grun, C. Klingshrm, and K. Bohnert, *Phys. Rep.* 124, 161 (1985).

79. M. Ikezawa and Y. Masumoto, *Jpn. J. Appl. Phys.* 36, 4191 (1997).

80. M. Ikezawa, Y. Masumoto, T. Takagahara, and S. V. Nair, *Phys. Rev. Lett.* 79, 3522 (1997).

81. S. Okamoto and Y. Masumoto, *J. Lumin.* 64, 253 (1995).

82. J. Zhao and Y. Masumoto, *Phys. Rev. B* 60, 4481 (1999).

83. K. Edamatsu, T. Itoh, K. Matsuda, and S. Saikan, *Phys. Rev. B* 64, 195317 (2001).

84. L. Zimin, S. V. Nair, and Y. Masumoto, *Phys. Rev. Lett.* 80, 3105 (1998).

85. H. Ohmura and A. Nakamura, *Phys. Rev. B* 59, 12216 (1999).

86. A. I. Ekimov, *J. Lumin.* 70, 1 (1996).

87. A. I. Ekimov, private communication.

88. H. Lamb, *Proc. London Math. Soc.* 13, 187 (1882).

89. N. Nishiguchi and T. Sakuma, *Solid State Commun.* 38, 1073 (1981).

90. A. Tamura, K. Higeta, and T. Ichinokawa, *J. Phys. C* 15, 4975 (1982).

91. A. Tanaka, S. Onari, and T. Arai, *Phys. Rev. B* 47, 1237 (1993).

92. T. Takagahara, *J. Lumin.* 70, 129 (1996).

93. S. V. Goupalov and I. A. Merkulov, *Fiz. Tverd. Tela* 41, 1473 [*Phys. Solid State* 41, 1349] (1999); *Phys. Status Solidi B* 224, 649 (2001).

94. T. Takagahara, *Phys. Rev. Lett.* 71, 3577 (1993).

95. A. P. Alivisatos, A. L. Harris, N. J. Levinos, M. L. Steigerwald, and L. E. Brus, *J. Chem. Phys.* 89, 4001 (1988).

96. X.-Q. Li and Y. Arakawa, *Phys. Rev. B* 60, 1915 (1999).

97. M. C. Klein, F. Hache, D. Ricard, and C. Flytzanis, *Phys. Rev. B* 42, 11123 (1990).

98. S. Nomura and T. Kobayashi, *Phys. Rev. B* 45, 1305 (1992).

99. V. M. Fomin, V. N. Gladilin, J. T. Devreese, E. P. Pokatilov, S. N. Balaban, and S. N. Klimin, *Phys. Rev. B* 57, 2415 (1998).

100. R. Heitz, I. Mukhametzhanov, O. Stier, A. Madhukar, and D. Bimberg, *Phys. Rev. Lett.* 83, 4654 (1999).

101. M. A. Odnoblyudov, I. N. Yassievich, and K. A. Chao, *Phys. Rev. Lett.* 83, 4884 (1999).

102. U. Woggon, F. Gindele, W. Langbein, and J. M. Hvam, *Phys. Rev. B* 61, 1935 (2000).

103. A. Lemaître, A. D. Ashmore, J. J. Finley, D. J. Mowbray, M. S. Scolnick, M. Hopkinson, and T. F. Krauss, *Phys. Rev. B* 63, 161309-1 (2001).

104. Y. Toyozawa, *Progr. Theor. Phys.* 27, 89 (1962).

105. T. Itoh and M. Furumiya, *J. Lumin.* 48 & 49, 704 (1991).

106. T. Kuroda, S. Matsushita, F. Minami, K. Inoue, and A. V. Baranov, *Phys. Rev. B* 55, R16041 (1997).

107. For example, B. Henderson and G. F. Imbusch, "Optical Spectroscopy of Inorganic Solids," Clarendon, Ch. 5. Oxford, 1989.

108. R. Kuribayashi, K. Inoue, K. Sakoda, V. A. Tsekhomskii, and A. V. Baranov, *Phys. Rev. B* 57, R15084 (1998).

109. M. Ikezawa and Y. Masumoto, *Phys. Rev. B* 61, 12662 (2000).

110. P. Borri, W. Langbein, S. Schneider, and U. Woggon, *Phys. Rev. Lett.* 87, 157401 (2001).

111. D. Birkedal, K. Leosson, and J. M. Hvam, *Phys. Rev. Lett.* 87, 227401 (2001).

112. Y. Masumoto, T. Wamura, and A. Iwaki, *Appl. Phys. Lett.* 55, 2535 (1989).

113. T. Wamura, Y. Mausmoto, and T. Kawamura, *Appl. Phys. Lett.* 59, 1758 (1991).

114. Y. Masumoto, T. Kawazoe, and N. Matsuura, *J. Lumin.* 76 & 77, 189 (1998).

115. R. M. MacFarlane and R. M. Shelby, *J. Lumin.* 36, 179 (1987).

116. M. Nirmal, B. O. Dabbouski, M. G. Bawendi, J. J. Macklin, J. K. Trautmann, T. D. Harris, and L. E. Brus, *Nature* 383 (1996) 802;

117. S. A. Empedocles, D. J. Norris, and M. G. Bawendi, *Phys. Rev. Lett.* 77 (1996) 3873.

118. Al. L. Efros and M. Rosen, *Phys. Rev. Lett.* 78 (1997) 1110.

119. T. Itoh, S. Yano, N. Katagiri, Y. Iwabuchi, C. Gourdon, and A. I. Ekimov, *J. Lumin.* 60 & 61, 396 (1994).

120. M. Masumoto, *J. Lumin.* 70, 386 (1996).

121. T. Kuroda, F. Minami, K. Inoue, and A. V. Baranov, *Phys. Rev. B* 57, R2077 (1998).

122. K. Edamatsu, T. Itoh, S. Hashimoto, B. P. Zhang, and Y. Segawa, *J. Lumin.* 87–89, 387 (2000).

123. M. Haselhoff and H.-J. Weber, *Mater. Res. Bull.* 30, 607 (1995).

124. M. Haselhoff, K. Reimann, and H.-J. Weber, *J. Crystal Growth* 196, 135 (1999).

125. A. Diegeler, M. Haselhoff, W. Rammensee, and H.-J. Weber, *Solid State Commun.* 105, 269 (1997).

126. H. Kurisu, K. Nagoya, N. Nakayama, S. Yamamoto, and M. Matsuura, *J. Lumin.* 87–89, 390 (2000).

127. A. Kawamori, K. Edamatsu, and T. Itoh, *J. Crystal Growth* 237–239, 1615 (2002).

128. N. H. Bonadeo, J. Erland, D. Gammon, D. Park, D. S. Katzer, and D. G. Steel, *Science* 282, 1473 (1998).

Core-Shell Nanoparticles

Guido Kickelbick

Technische Universität Wien, Vienna, Austria

Luis M. Liz-Marzán

Universidade de Vigo, Vigo, Spain

CONTENTS

1. INTRODUCTION

Core-shell nanoparticles have recently been the focus of a lot of scientific efforts because of the combination of different properties in one particle based on different compositions of the core and the shell. Furthermore, many interesting technological applications can be foreseen for this kind of material, in addition to others in analytical chemistry (chromatography), separation technology (ion exchange), catalysis, biochemistry and medicine, etc. [1, 2]. These types of particles can be defined by their different core and shell compositions. The core often (though not always, as will be discussed below) shows the relevant property (e.g. semiconductors, metals, magnetic oxides, encapsulated molecules), while the shell can stabilize the core; create compatibility between the core and the environment; or can change the charge, functionality, or reactivity of the surface. This is especially important if the shell is a polymer and the final core-shell particle can be homogeneously dispersed in a polymer on the nanoscale [3]. In recent years, especially for medical purposes, the shell has become more and more important (e.g., for drug delivery applications).

Core-shell nanoparticles are classified within this chapter according to their chemical composition, as follows:

- *Inorganic–Inorganic Nanoparticles*: This category mainly comprises metallic, magnetic, or semiconductor core particles surrounded by a semiconductor, insulating, or metal shell.
- *Inorganic–Organic Nanoparticles*: Hybrid systems that contain an inorganic core such as a metal or a metal oxide and an organic shell of a polymer or layers of molecules on the surface of the core.
- *Organic–Organic Nanoparticles*: Most of these systems contain cross-linked polymers as the core and a different polymer or functional molecule as the shell.
- *Organic–Inorganic Nanoparticles*: Entities with an organic cross-linked polymeric core surrounded by an inorganic shell.
- *Inorganic–Biomolecule:* The inorganic core is covered by biorelated molecules such as DNA sequences.

Core-shell architectures are the result of either a two-step approach, consisting of preparation of nanoparticles and then modification of their surface, or an *in-situ* approach during particle formation. The shell can be formed by surface chemical reactions, by simple adsorption of molecules or small nanoparticles or the whole core-shell nanoparticle can be formed by subsequent self-assembly and crosslinking of macro molecules.

This chapter provides an overview of the synthetic procedures and some selected properties that make core-shell nanoparticles a very interesting class of nanomaterials. Because of the many different possible ways to prepare such particles, we shall limit the description to the most common synthetic techniques, which in most cases will make use of solution chemistry.

For simplicity, in some occasions we shall make use of the terminology core@shell to represent the composition of the composite particles.

2. INORGANIC–INORGANIC CORE-SHELL NANOPARTICLES

2.1. Core-Shell Semiconductor Quantum Dots

One very important class within these all-inorganic nanoparticles is constituted by core-shell quantum dots. Quantum dots are semiconductor particles in which quantum size effects can be observed [4]. Such quantum size effects arise from the size-dependent separation between the valence and conduction bands characteristic of the semiconductor, which gives rise to very interesting optical properties, especially with respect to luminescence at well-defined and narrow spectral ranges, which depend on particle size. Although the luminescent properties are characteristic of neat quantum dots, it has been observed that the formation of core-shell structures leads to an enhancement of the luminescent properties of the core [5–9]. Coating of II–VI nanoparticles with a different semiconducting material has a profound impact on the photophysics of the nanocrystalline cores [4, 10–17]. A broad range of intensities and spectral emission characteristics can be obtained by varying the thickness and the bandgap of the overlayer. Deposition of a semiconductor with a larger bandgap than that of the core typically results in luminescence enhancement due to the suppression of radiationless recombination mediated by surface states [4, 10–18], while the degree of charge carrier confinement does not change. The absorption bands redshift only slightly, even for quite thick layers of ZnS on CdSe [10], ZnSe on CdSe [11], and CdS on CdSe [12], as expected for a minimum variation of the confinement. Conversely, a layer of a small bandgap semiconductor provides an additional area of delocalization for both the electron and the hole [14–20]. The relaxation of the confinement regime results in a red-shift of spectral features. These studies have been carried out with PbS and HgS layers deposited on CdS and CdSe nanoparticles. Recently, CdS nanoparticles with a monomolecular coating of MoS_4 have been investigated, which demonstrated both enhancement of the excitonic emission and a noticeable red-shift of absorption features [21].

Several methods have been developed for the synthesis of core-shell II–VI nanoparticles. Successive reactions within microemulsions were used by Hoener et al. [22] to prepare ZnSe-coated CdSe nanoparticles. The microemulsion method was used again by Han et al. [19] for the coating of CdS with Ag_2S, and by Tian et al. [20] for the synthesis of CdS@CdSe and CdSe@CdS. More recently, Hao et al. [23] also used microemulsions to prepare CdSe and CdSe@CdS nanoparticles, attaining a notable enhancement of the excitonic luminescence upon coating.

The most popular method for synthesis and coating of quantum dots was initially developed by Murray et al. [24]. This procedure also makes use of surfactants (trioctylphosphine (-TOP-) and trioctylphosphine oxide (-TOPO)), which act as solvents during the nanoparticle formation, making it possible to use high temperatures (on the order of 300 °C), which are necessary to yield highly crystalline materials, but also bind to the nanoparticle surface, limiting its growth [24]. Variations of this technology were subsequently devised to prepare core-shell nanoclusters [10–12].

One example would be the addition of preformed CdS particles in pyridine to a dispersion of CdSe in TOP/TOPO at 100 °C, which leads to a core-shell CdSe@CdS structure accompanied by a large increase in the photoluminescence quantum yield (see Fig. 1). A similar procedure was used for the synthesis of CdSe@ZnS with a very high luminescence quantum yield [10].

The group of O'Brien [25] simplified the quantum dot synthesis with the use of single-molecule precursors for each semiconductor material, and they prepared, for instance, highly monodispersed CdSe@CdS through the successive thermolysis of $[Cd\{Se_2CNMe(Hex)\}_2]$ and $[Cd\{S_2CNMe-(Hex)\}_2]$ in TOPO. Other core-shell combinations followed, such as CdSe@ZnS, CdSe@ZnSe, through the use of the corresponding single-molecule compounds [26].

Apart from the II–VI semiconductors, core-shell quantum dots were also made with InAs cores, with bandgaps tunable in the near-IR, which can be useful as IR biological luminescent markers. Cao and Banin [27, 28] explored the coating of these quantum dots with InP and CdSe, using pyridine or benzylamine as solvents at a high temperature. A drop in luminescence quantum yield was found after coating with InP, but an enhancement was found with CdSe, which was reasoned to be due to the quality of the outer surface.
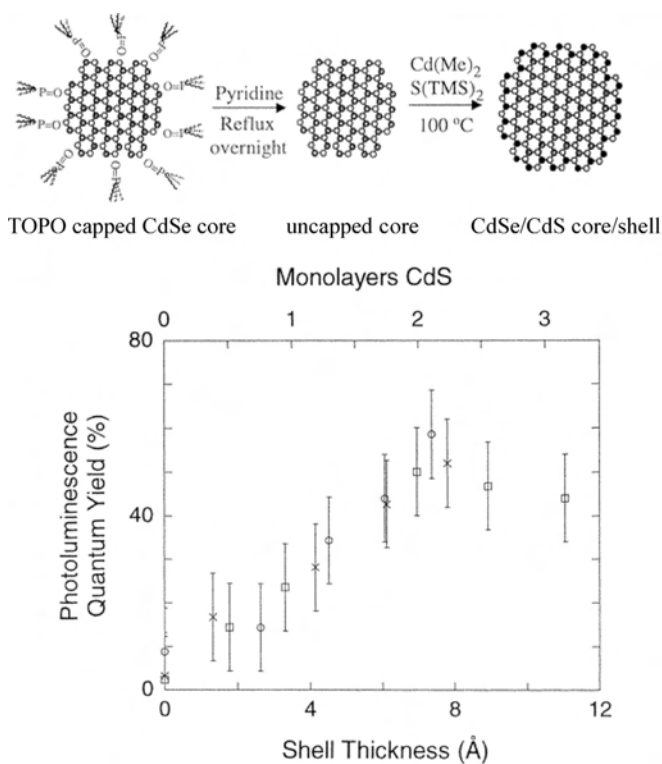
Figure 1. Top: Schematic synthesis of CdSe@CdS core-shell nanocrystals. Bottom: Photoluminescence quantum yield variation with shell thickness for three different core-shell systems, starting with core diameters of 23 Å (circles), 34 Å (X's), and 39 Å (squares). Reprinted with permission from [12], X. Peng et al., *J. Am. Chem. Soc.* 119, 7019 (1997). © 1997, American Chemical Society.

2.2. Bimetallic Nanoparticles

The main properties of metal nanoparticles reside in their optical and catalytic properties. Therefore, within this section we separate the discussion of bimetallic core-shell nanoparticles according to the type of properties that have been investigated during their study.

2.2.1. Optical Properties

Metal nanoparticles display very interesting optical and electronic properties, which are mainly due to the collective oscillation of conduction electrons, when interacting with an electromagnetic radiation of certain frequency [29]. Since this is mainly a surface phenomenon, it is affected by the medium surrounding the nanoparticles, which can be a solvent, a solid matrix, or adsorbed molecules/coating shells [30]. Each metal is characterized by a particular, wavelength-dependent, dielectric function, which determines the frequency at which the plasmon resonance takes place. The whole optical picture is altered when one metal is deposited on the surface of nanoparticles made of a different metal, and plenty of deposition methods and optical studies can be found in the literature.

Morriss and Collins [31] pioneered this field with the synthesis of Au@Ag nanospheres of constant gold core diameter and epitaxially grown silver shells with varying thickness. The initial plasmon absorption band (pure gold, 518 nm) progressively blue-shifted and broadened until a single broad peak around 400 nm was observed for sufficiently thick silver shells. These experimental results were in reasonable agreement with the theory, with some discrepancy, which was likely due to simplifications in the theory. Kreibig and co-workers carried out more refined calculations on the Au-Ag system [32], which yielded a much closer agreement with the experimentally measured spectra.

Synthesis of Au@Ag and Ag@Au was also carried out recently by various chemical methods in solution, such as that of Rivas et al. [33], who achieved both structures by citrate reduction. Silver shells were also deposited on citrate-stabilized 12-nm gold nanoparticles in aqueous solution, with ascorbic acid as a reductant and cetyltrimethylammonium chloride as an additional stabilizer during the growth [34], which yielded quite monodisperse core-shell particles with controlled shell thickness.

The opposite structure (Ag@Au) is harder to achieve, since Au^{3+} ions can completely oxidize 10-nm colloidal silver, forming colloidal gold [35]. To avoid this problem, Cao et al. [36] have shown that by simple reduction of gold salts by sodium borohydride, in the presence of preformed silver nanoparticles passivated with bis(p-sulfonatophenyl) phenylphosphine, Ag@Au nanoparticles were formed. Such core-shell particles proved useful for DNA diagnosis. An interesting recent report on the Au/Ag system was made by Xia et al. [37], who observed that the addition of Au^{3+} ions to colloid dispersions of larger Ag nanoparticles leads to oxidation of the silver cores and reduction of gold on the surface, so that hollow gold particles are obtained that retain the shape of the original silver cores. Another interesting design for the synthesis of Au/Ag colloids was realized by Schierhorn and Liz-Marzán [38], who deposited an insulating silica shell on uniform gold cores and then applied an electroless plating procedure [39] to deposit silver on the outer silica surface, so that the spectral features of both metals can be preserved if the silica interlayer is thick enough, as shown in Figure 2.

Very extensive work on noble metal and core-shell bimetallic nanoparticles was carried out by Henglein and co-workers, who used γ-radiolysis to generate free radicals in aqueous solution, leading to a very well-controlled reduction of metal salts, normally in the presence of a suitable stabilizer. Examples of bimetallic coated particles include Au@Cd [40], Au@Pb [40, 41], Au@Sn [42], Au@Tl [40], Ag@Pb [43, 44], Ag@Cd [45], and Ag@In [43]. They observed a variety of optical and chemical properties of the particles in dilute aqueous solutions. As each of the less noble metals (Cd, Pb, Sn, Tl, and In) was deposited as shells on either of the noble core particles (Au and Ag), the absorption band of the core particles blue-shifted toward that of a pure colloid of the shell material because of the donation of electron density from atoms to the core metal particle [43, 45].

In a later study, Henglein et al. [46] used silver particles as a template to deposit mercury by γ-radiolysis. However, only a couple of layers of mercury can be deposited on the silver particles before mercury precipitates. A similar experiment was later performed in the presence of gold nanoparticles [47], with a limited penetration of mercury and again formation of a thin mercury layer on the surface. Henglein has also demonstrated the generation of Au@Pt and Pt@Au nanoparticles [48]. Although a gold layer on platinum clusters could be deposited radiolitically, the deposition of platinum on gold had to be performed by hydrogen reduction of aged $PtCl_4^-$, and the resulting core-shell structures seem to be formed by Pt islands that join together if a sufficient amount of the metal is deposited. Successive
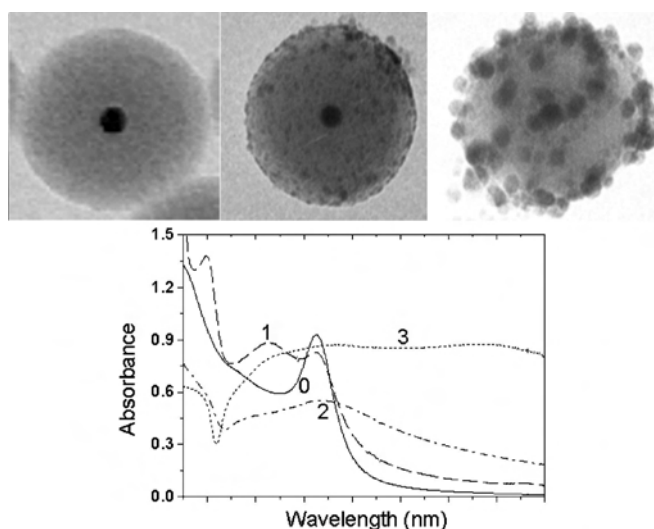
Figure 2. Top: Representative transmission electron micrographs of silica-coated gold nanoparticles (core diameter 15 nm), before and after one and two electroless plating experiments. Bottom: Spectral evolution during the deposition of silver on silica-coated gold spheres by electroless plating. The labels indicate the number of deposition cycles. Adapted with permission from M. Schierhorn and L. M. Liz-Marzán, *NanoLetters* 2, 13 (2002). © 2002, American Chemical Society.

radiolytic reduction has also led to trimetallic Pd@Au@Ag nanoparticles with interesting optical features [49].

2.2.2. Catalytic Properties

Toshima and co-workers have been very active in this field [50]. Apart from intensive research on the catalytic activity of several metal nanoparticles, they also studied the influence of various bimetallic geometries on catalytic activity [51]. For the synthesis of metal nanoparticles, they developed a reduction method based on the use of an alcohol as a solvent and reducing agent (at reflux) and a polymer (typically polyvinylpyrrolidone, PVP) as a ligand. In the case of bimetallic structures, they typically worked through simultaneous reduction of the two metals. The mechanism for the formation of core-shell structures by simultaneous reaction was proposed [52], based on two principal factors: redox potential (the metal more easily reduced would form the core), and a coordination ability of the ligand polymer upon the metal (the metal more strongly coordinated by the ligand polymer would form the shell). Pd-Pt bimetallic nanoparticles with various Pd/Pt ratios were produced in the presence of PVP [53, 54], resulting in similar sizes, but with quite different catalytic activities for selective partial hydrogenation of 1,3-cyclooctadiene to cyclooctene. The highest catalytic activity was achieved by the bimetallic nanoparticles with Pd/Pt = 4/1. This is the nanoparticle with the perfect core-shell structure. The catalytic activity decreases with decreasing Pd/Pt ratio, in other words, with decreasing number of Pd atoms. If the total catalytic activity is divided by the number of Pd atoms in a bimetallic nanoparticle, the catalytic activities of the Pd atoms are nearly equal to each other. This means that all Pd atoms are located in the surface layer of the Pd-Pt bimetallic nanoparticles. In addition, the Pd atom in the bimetallic nanoparticles has a much higher catalytic activity than the surface Pd atom in Pd monometallic nanoparticles. This fact demonstrates that the Pt atom, located in the core of bimetallic nanoparticles and adjacent to the surface Pd atom, affects the catalytic activity of the surface Pd atoms. This cannot be an ensemble effect but should be a ligand effect. The inner Pt atom should change the electronic density and/or structure of the surface Pd atoms, resulting in the higher catalytic activity of Pd-Pt bimetallic nanoparticles than Pd monometallic ones.

Studies have also been performed by Lee et al. [55], who deposited a very thin palladium shell on 5-nm gold colloids, to prepare bimetallic particles which should be more effective catalysts. The palladium shell was structurally different from its bulk counterpart, because of the electronic perturbation of the shell by the gold core, leading to a very large increase in the catalytic performance for the cyclization of acetylene to form various isomers of butane, *n*-hexane, and benzene, at room temperature.

2.3. Metallic Shells

We describe in this section the synthesis and some properties of encapsulated colloids composed of dielectric cores and metal shells. The interest in such particles is basically due to their optical properties, which differ from those of standard nanoparticles. Early work by Barnickel and co-workers [56] showed that particles made of silver layers on polystyrene

(PS) and polymethacrylate (PMA) displayed strongly red-shifted and broader absorption bands than those of standard 10-nm colloidal silver in solution. However, the coating was not homogeneous enough to provide a good model system for testing optical theories.

A much more consistent study was performed by Oldenburg et al. [57, 58], who managed to coat SiO_2 particles of various diameters with continuous gold shells. They found that the plasmon bands depend on the core-to-shell thickness ratio as well as on absolute core size. Their observation was reported to agree quantitatively with Mie theory [59]; for the calculation of this it was necessary to take into account the quadrupolar components, because of the large sizes. Later studies by the same group showed that the plasmon resonances in the shells can be tuned across the IR region, up to 2.2 μm [60], which was useful for demonstrating surface-enhanced Raman scattering (SERS) with these systems [61]. An example of the spectacular plasmon band shifts that can be obtained by varying the core-to-shell ratio is shown in Figure 3. Later studies on the formation of Au shells on silica were performed by Graf and van Blaaderen, who reported a higher colloid stability, which allowed their use for the assembly as colloid crystals [62].

The Halas group also reported the deposition of silver shells on silica spheres, with optical behavior in agreement with Mie theory [63]. Another method that has recently been designed [39] for the deposition of metal nanoparticles on silica spheres is electroless plating [64]. This method comprises as a first step the adsorption of a sensitizer (Sn^{2+} ions) on the silica surface, followed by the addition of Ag^+. Oxidation of Sn(II) to Sn(IV) takes place at the surface, while Ag^+ is reduced to Ag^0 in the form of small nanoparticles that remain attached to the surface. No full contact between adjacent metallic particles has been observed in this case, and therefore no spectacular optical shift was produced.

2.4. Coated Magnetic Nanoparticles

Magnetic nanoparticles are interesting for a number of different applications, both in the form of ferrofluids (new refrigerators that employ the magneto caloric effect [65], new inks for inkjet printers [66], novel spin valves [67], or for new cancer therapies, such as hyperthermia [68]
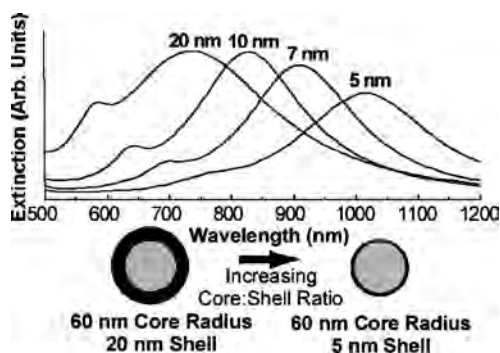
Figure 3. Example of the red shift in the plasmon resonance of Au nanoshells with increasing core-to-shell ratio. Reprinted with permission from [58], S. J. Oldenburg et al., *Chem. Phys. Lett.* 288, 243 (1998). © 1998, Elsevier.

and apheresis [69]) or in thin films [70–73], basically for magnetic storage. Most of these possible applications of ferrofluids require high remanent magnetization and high anisotropy at room temperature. High remanent magnetization is a characteristic feature of soft ferromagnetic materials with diameters above a critical minimum dependent on the material (>10 nm for Co). On the other hand, hard ferromagnetic materials, which often exist as alloys, exhibit high anisotropies. Soft ferromagnetic materials embedded in a noble metallic matrix show a technologically important effect called giant magnetoresistance (GMR). The ability to prepare air-stable ferromagnetic/noble metal bimetallic particles is therefore a challenge. Well-known ferromagnetic alloys consist of ferromagnetic 3d and noble metal elements of the platinum group. They are known to have large magnetic moments and large magnetic anisotropies [74]. Accordingly, the synthesis of monodisperse ferromagnetic/noble metal bimetallic particle alloys (especially Fe/Pt) or core-shell particles and their assembly into ordered arrays have been investigated intensely in recent years.

Rivas et al. [75] reported the synthesis of cobalt nanoparticles coated with silver, based on the successive reduction of Fe^{2+} or Co^{2+} and Ag^+ within the aqueous microdroplets of inverse microemulsions. A similar approach was later used by Seip and O'Connor [76, 77] for the synthesis of Fe@Au using cationic surfactants, with magnetic measurements showing superparamagnetic behavior.

Klabunde and co-workers [78] reported the formation of core-shell structures upon heat treatment of metastable alloy nanoparticles of immiscible metals prepared through the so-called solvated metal-atom dispersion (SMAD) method. For the case of Fe-In and Fe-Nd, but with Fe-Au, Fe-Bi, Fe-Ca, Co-Mg, and Ni-Mg, either stable alloys or segregated particles were formed. Magnetic studies of the Fe@In and Fe@Nd samples showed low coercivities and Fe crystallite size-dependent saturation magnetization, though apparently there was always an increase in stability against core oxidation.

More recently, the synthesis of well-defined, core-shell Co-Pt nanoparticles was reported by Park and Cheon [79]. The formation of these alloys is driven by redox transmetalation reactions between the reagents without the need for any additional reductants. While the reaction between $Co_2(CO)_8$ and Pt hexafluoroacetylacetonate results in the formation of alloy nanoparticles such as $CoPt_3$, the reaction of Co nanoparticles with Pt hexafluoroacetylacetonate in solution results in Co@Pt morphologies, which is schematically shown in Figure 4.

Core-shell nanoparticles with an *inverted* morphology were prepared by Sobal et al. [80], with Ag cores coated with uniform Co shells. These authors report an unexpected stabilization of the Co shell against oxidation, which can be due to electron transfer from the core. In this case, the higher electron density of the core allows a sufficient contrast in TEM to distinguish the core-shell morphology (Fig. 5).

2.5. Silica-Coated Nanoparticles

We have decided to discuss silica-coated nanoparticles separately because of their special interest, which is also the reason for the extensive work that has been performed on
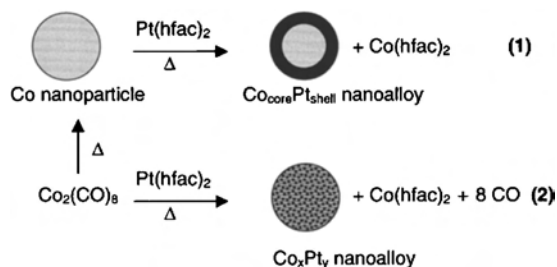
Figure 4. Synthetic routes of core-shell and alloy nanoparticle formation via transmetallation reactions. Reprinted with permission from [79], J.-I. Park and J. Cheon, *J. Am. Chem. Soc.* 123, 5743 (2001). © 2001, American Chemical Society.

these systems. One of the major reasons for silica coating is the anomalously high stability of silica colloids, especially in aqueous media, but other reasons are the easy control on the deposition process (and therefore on the shell thickness) and its processibility, chemical inertness, controllable porosity, and optical transparency. All of these properties make silica an ideal and costless material for tailoring surface properties, while maintaining the physical properties of the underlying cores.

This technique was pioneered in the late 1950s by Iler [81], who described a method for coating with silica "particles with at least one dimension which is less than about 5 microns," and the nature of which is typically metal oxides and silicates. Silicate solutions with suitable concentration, pH, and temperature were termed *active silica*, which easily sticks to the surface of oxide colloids in suspension. The slow reaction ensured deposition of thin silica shells, thus retaining the surface shape of the core particles. An alternative to Iler's silica coating procedure was developed by Ohmori and Matijevic [82], following the already classical Stöber method [83] (base catalyzed hydrolysis and condensation of tetraethoxysilane (TES)) to coat hematite (Fe_2O_3) spindles in ethanol. This procedure was later modified by Thies-Weesie [84]. Later work by Philipse et al. used a combination
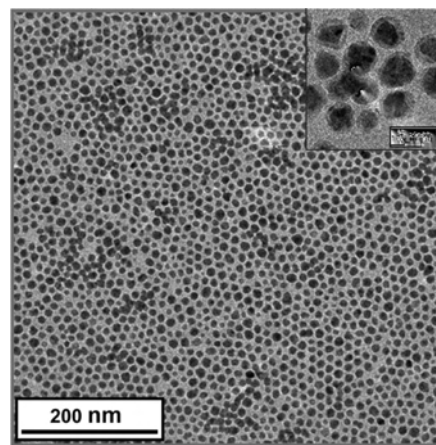
Figure 5. TEM image at low magnification of a monolayer of Ag@Co nanoparticles deposited on a carbon-coated copper grid by drying of a drop of solution. The core-shell structure is visible at higher magnification (see inset). Reprinted with permission from [80], N. S. Sobal et al., *NanoLetters* 2, 621 (2002). © 2002, American Chemical Society.

of the previously described procedures for coating magnetite (Fe_3O_4) superparamagnetic nanoparticles [85] and boehmite (AlOOH) rods [86]. Following Philipse's work, the silica coating of magnetite was later modified independently by Liu et al. [87] and by Correa-Duarte et al. [88], both achieving more homogeneous and well-defined shells. The control of magnetic interactions is an important consequence of the coating of magnetic particles, which was demonstrated by Donselaar et al. for particles in solution [89] and by Aliev et al. in close-packed thin films [72].

A different approach was followed by Schmidt and co-workers, who used various organosilanes as building blocks and spacers to introduce functionalities within the nanoparticle structure, which can be subsequently employed for preparing more complex materials [90, 91].

Silica coating of metal colloids was also studied in detail, specially during the last decade. This type of core-shell particle presents as an additional difficulty the chemical mismatch between the core and the shell materials. Thus, a procedure must be devised to link the core and shell materials with each other. Several routes have been followed with better or worse results. Ohmori and Matijevic [92] prepared $Fe@SiO_2$ particles by an indirect path comprising the initial coating of hematite spindles [82], followed by reduction of the core within a furnace in the presence of hydrogen. The high temperature promoted sealing of the pores of the silica shell, thus avoiding further oxidation of the metallic core. Liz-Marzán and Philipse [93] first approached the synthesis of $Au@SiO_2$ particles through the formation of nanosized gold particles on the surface of small silica spheres, followed by extensive growth in ethanol, so that Au was embedded as a core. However, a large proportion of pure silica spheres was also produced, which were difficult to separate.

A method that has provided substantially better results was later designed by Liz-Marzán et al. [94, 95], with the use of bifunctional molecules to anchor silanol groups on the nanoparticle surface, followed by a slow deposition of a thin silica layer in water, and subsequent growth in ethanol, resulting in monodisperse colloids with one Au core at their center and an outer silica shell of controlled thickness. An example of the concentric geometry achieved is shown in Figure 6. This system proved ideal for a systematic study of optical properties [95, 96]. The same method was later extended to $Ag@SiO_2$ by Ung et al. [35], though dissolution of the Ag cores was observed when concentrated ammonia was added to increase the thickness of the silica shell. The same team [35, 97–98] demonstrated that dissolution by ammonia is due to the possibility of chemical reactions taking place on the cores because of the porosity of the shells.
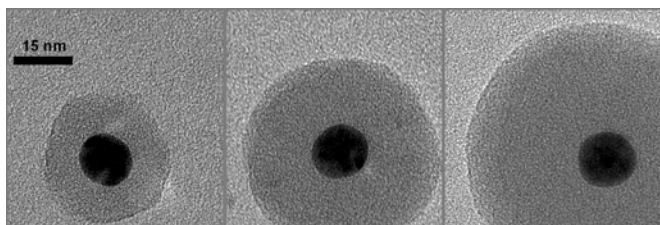
Figure 6. TEM micrographs of $Au@SiO_2$ nanoparticles with constant core size and increasing shell thickness, grown by TES hydrolysis.

Another advantage of this method is that the first deposition in water is so slow that the shape of the original core is preserved in the initial stages, which was shown first by Chang et al. [99] and then by Obare et al. [100] by coating gold nanorods with the same procedure. The method was also modified by Hall et al. [101], who used silane coupling agents during the growth of the shell to obtain particles with amino groups on the outer surface. Hardikar and Matijevic [102] demonstrated that for larger silver particles (60 ± 5 nm) stabilized with a complicated compound (Daxad 19), no coupling agent is necessary for silica coating through TES hydrolysis in 2-propanol, and this was also recently shown by Xia and co-workers for PVP-stabilized Ag nanorods [103]. Mine et al. have also recently found [104] that standard, citrate-stabilized Au nanoparticles can be homogeneously coated with relatively thick shells without the use of a silane coupling agent, through careful tailoring of the concentrations of ammonia and TES, as well as choosing the proper addition sequence. This leads to a cleaner system (no chemical alteration of the metal surface), but almost invariably implies the formation of some core-free silica particles in addition, which is undesirable for some applications. Ostafin and co-workers have recently devised a procedure to create mesoporous silica shells on Au nanoparticles coated with a thin silica layer by using surfactants during shell formation [105].

The same method was also applied [106] to coat CdS nanoparticles, observing that the silica shell not only enhanced the colloidal stability of the quantum dots, but also the photostability, so that no photodegradation took place, even under light and in the presence of oxygen. A similar procedure was used by the Alivisatos group [107, 108] with the aim of using highly luminescent quantum dots coated with silica for biological labeling. A new variation of the same method was used by Rogach et al. [109] for the coating of CdTe and $CdSe@CdS$ nanocrystals, which resulted in the inclusion of multiple cores within every silica sphere, as well as a dramatic drop in luminescence intensity upon coating.

Other methods were later designed for the preparation of $Ag@SiO_2$. The group of Adair [110] reported the coating through consecutive reactions within microemulsion droplets. The problem with this technique is that removal of surfactants is expensive, tedious, and time consuming. Pastoriza-Santos and Liz-Marzán prepared $Ag@SiO_2$ particles through reduction of Ag^+ by N,N-dimethylformamide (DMF) [111] in the presence of an amino-silane. High temperatures were needed to achieve fast reduction of the silver salt, prior to condensation of the organo-silica shell, but rather monodisperse silver cores were obtained, and the particles could be extracted into water or ethanol.

2.6. Semiconductor Shells on Metal Cores

Research has also been carried out to deposit other oxide shells on nanoparticles, particularly on metal nanoparticles. In this way, it is intended to make use of semiconducting properties of some oxides, such as TiO_2 or SnO_2, in combination with the conducting properties of the core. This can be exploited for biological and electronic applications, as detailed below.

One example is the synthesis of Ag@TiO$_2$ by Pastoriza-Santos et al. [112] through the reduction of AgNO$_3$ in DMF/ethanol mixtures, in the presence of titanium tetrabutoxide, which condensed on the surface of the silver cores. Layer-by-layer assembly of the resulting core-shell nanoparticles, followed by dissolution of the silver cores with ammonia, subsequently led to the development of ion-selective and biocompatible titania nanoshell films [113], which were found to be useful for monitoring the diffusion of dopamine, an important compound for neurochemical processes.

Coating of gold nanoparticles with titania was also achieved by Mayya et al. [114], who used a different TiO$_2$ precursor (titanium(IV) bis(ammonium lactato) dihydroxide), which is negatively charged and readily complexes with a positively charged polyelectrolyte, poly(dimethyldiallyl ammonium chloride), previously assembled on the nanoparticle surface, and can then be hydrolyzed, providing a good control on the morphology of the shell. The same authors applied this procedure to coat Ni nanorods with titania [115], and upon dissolution of the Ni cores they were able to obtain uniform TiO$_2$ nanotubes. Typical electron micrographs of the core-shell nanorods and titania nanotubes are shown in Figure 7.

Another interesting application of metal nanoparticles surrounded by semiconductor shells is the fabrication of composite nanoparticles with a large electronic capacitance. The idea is that there is a large difference between the Fermi level of the core and the conduction band energy of the shell, so that electrons diffusing through the shell can be trapped in the core for a long time. Mulvaney et al. [116] explored this possibility with Au nanoparticles encapsulated in a polycrystalline SnO$_2$ shell. These authors demonstrated that charge can be injected by cathodic polarization through γ-radiolysis, which resulted in a blue-shift of the plasmon band (as predicted by theory), which remained blue-shifted in the absence of oxygen, but red-shifted back when open to air because of oxygen reduction by the electrons stored in the core.
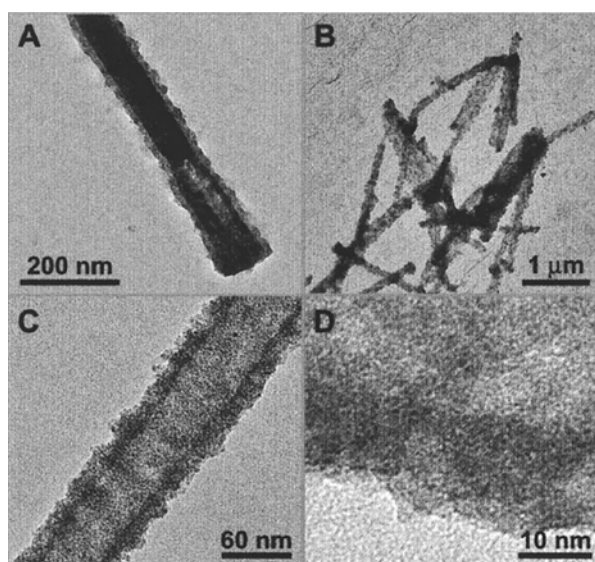
We finally include in this subsection metals surrounded by semiconductor shells which are not composed of oxides, but rather of chalcogenides. Kamat and Shanghavi [117] prepared Au@CdS nanoparticles by surface modification of Au colloids with mercaptonicotinic acid followed by the addition of Cd^{2+} and exposure to H$_2$S. The result was the formation of very small CdS particles attached to the surface of the Au cores, but also free in solution. To prepare particles with novel optical properties due to both local field effects of the metal and further enhancing nonlinear optics of quantum dots, Nayak et al. [118] generated Au@CdSe particles in TOP/TOPO organic solvents, though a large proportion of particles were a mixture of individual Au and CdSe particles, as detected by TEM. Hirano et al. [119] encapsulated nanosized gold with boron nitride at extremely high temperatures and proposed that these particles would have potential applications for single-electron transistors.

3. INORGANIC–ORGANIC CORE-SHELL NANOPARTICLES

Principally inorganic-organic nanoparticles can be divided into systems with an organic core and an inorganic shell or vice versa. Although this differentiation seems to be necessary for the specific properties of the prepared materials, similar methodologies are often used for their synthesis. A prominent technique for the preparation of such cores is the use of microemulsions [2, 120]. In this approach, in which the dispersed stabilized phase can be considered as a nanoreactor, the size, shape, and curvature of the surfactant-stabilized phase determine the shape of the nano-objects obtained. With this technique the core and the shell are formed with the use of the same microemulsion by simply subsequently building up the two moieties in the micelles. In a different approach the core is formed first, isolated, and modified with the shell in a separate step by covalent anchoring or adsorption of organic groups on the surface. For the synthesis of defined core-shell systems it is crucial to obtain in a first step well-defined cores. Water-in-oil microemulsions, sometimes also called reversed micelles, are probably the most widely investigated emulsion systems for the preparation of spherical inorganic nanoparticles. The metal precursor is usually dissolved inside the water droplets and reacts in this confined arrangement to the final particle. Two different methods were used for the formation of the nanoparticles: either all chemicals for the nanoparticle formation are already included in the water phase and the metal precursor is added, or two water-in-oil microemulsions, both containing precursors for the nanoparticle formation, are mixed. In the latter case, the exchange of substances occurs in the united microemulsion by diffusion and droplet collision. With the microemulsion method a variety of nanoparticles were synthesized, such as SiO$_2$ [121–124], TiO$_2$ [125–128], ZrO$_2$ [129], CdS [130], magnetite [131], or mixed metal oxide systems [132].

Surfactants are crucial for the stabilization of the microemulsions; they produce compatibility between the two

Figure 7. TEM images of (A) a nickel nanorod coated with titania, (B) titania-based nanotubes obtained by dissolution of coated nickel nanorods, (C) a higher magnification image of a nanotube. (D) A high-resolution image showing the presence of titania nanoparticles. Reprinted with permission from [115], K. S. Mayya et al., *Chem. Mater.* 13, 3833 (2001). © 2000, American Chemical Society.

phases and act as barriers against the agglomeration of the final particles. These molecules cover the surface of the particles formed and often interact with it, which can directly affect the local structure of the surface [133]. If the particles have diameters in the lower nanometer range, this interaction can result in a significant change of the particle properties. The capping of the surface with the surfactant is frequently used for the stabilization of the particles formed. With this methodology, for example, surface-capped Pd [134], Fe_2O_3 [135, 136], and CeO [137] particles were formed.

Emulsion polymerization has the potential to produce a stable and compact polymer layer, completely enclosing the particle and improving its chemical resistance. This is particularly important for pure metal particles that have a tendency to undergo oxidation reactions. Changing the concentration of monomers can readily control the thickness of the layer, which usually protects the core very efficiently. With this method, for example, Ag nanoparticles were encapsulated in styrene and copolymers of styrene and methacrylate. Encapsulated particles retain their optical properties and display a remarkable chemical stability [138].

Dense silica nanoparticles can be prepared by the Stöber process, as already mentioned [83]. The size of the nanoparticles formed can be controlled over a wide range with a narrow size distribution. Therefore, this method is often the source for dense silica nanoparticles, which can be subsequently surface modified after isolation. Additionally, the formed alcosol can also be used as a reaction medium for the direct surface modification of the particles, for example, with trialkoxy-substituted silane coupling agents (Fig. 8) [139]. Depending on the coupling agent, a change of the particles' properties, such as their solubility, coagulation behavior, or their reactivity, can be observed. Furthermore, the use of organically modified trialkoxysilanes in the synthesis of the silica core provides a method for decreasing the cross-linking density and/or to incorporating additional functionalities, such as dyes, into the core [90, 140]. For example, the use of $MeSi(OR)_3$ and $Me_2Si(OR)_2$ instead of $Si(OR)_4$ can subsequently decrease the cross-linking density of the particle core; therefore these particles can mimic a behavior, for example, with respect to solvent uptake that is between those of pure silica and cross-linked polymers [90]. Polymer chains were grafted to organosilicon nanoparticles that carried a Si-H surface modification [141]. PS with a terminal unsaturated bond was reacted with these particles by the application of a hydrosilation reaction. With this method particles with a radius of 10 nm were reacted with PS chains with gram molecular weights up to 20,000 g/mol. The resulting core-shell particles reveal a high compatibility with linear PS polymers if the molecular weight of the free polymer is equal to or smaller than that of the grafted polymers. In these cases, an optical transparent film
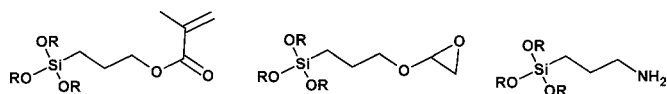
is obtained, while the pure organosilicon particles are totally incompatible.

3.1. Metal Nanoparticles with Capping Ligands

Probably the oldest nanoparticle system known is that of gold colloids, which were already used hundreds of years ago for the coloring of window glass. Because of their relatively simple preparation and exceptional stability, gold nanoparticles have also become an important research issue in the present time. In addition, gold nanoparticles are particularly easy to modify because they are often stabilized with weakly binding layers of charged ligands (e.g., citrate) that can be replaced with molecules with chemical functionalities that bind more strongly (e.g., thiols, amines, and disulfides) to their surfaces than these ligands. A two-phase synthesis approach results in monodisperse, stable, and soluble gold nanoparticles with a core size of a few nanometers [142]. The synthesis is based on the transfer of $AuCl_4^-$ from an aqueous phase into an organic phase under phase transfer conditions followed by reduction in the presence of thiols. This methodology produces thiol-capped gold nanoparticles. If the thiol employed has additional reactive functionalities attached, the surface-modified nanoparticles can undergo chemical reactions [142]. Another advantage of thiol-capped gold nanoparticles is that the ligands can undergo ligand-exchange reactions with other thiols [143]. The thiol-stabilized Au nanoparticles showed spontaneous self-assembly phenomena depending on the surface modification [144]. Mixtures of different thiol-capped metal cores (i.e., Ag and Au) were used for the formation of ordered two-dimensional arrays, so-called nanoalloys [145]. More information on aspects of the self-assembly of nanoparticles can be found in some recent reviews [146, 147].

Similar to the gold nanoparticles, other metals and semiconductors can serve as cores and bind organic molecules with anchor groups, allowing a strong interaction with the metal surface. Among others, platinum nanoparticles were prepared with the use of alkyl isocyanides as capping ligands, or the self-assembly of films of CdS nanoparticles was enhanced by dithiol ligands [148, 149].

A very interesting property of thiol-encapsulated gold nanoparticles is their activity in catalytic reactions [150]. From a chemical point of view, the attached thiol molecules should passivate the active gold surface. However, the thiolate encapsulation did not block the catalytic sites in a significant way, as proved by electrooxidation experiments. An explanation for this unusual behavior is the encapsulation of gold oxides formed in the organic layer. The uptake of oxygen and the subsequent expansion of the microstructure of the gold oxides led to an increase in particle size and the formation of nanoporosity in the shell.

3.2. Surface Modification of Metal Oxide Nanoparticles with Monomolecular Layers

Often the surface atoms of metal oxide nanoparticles carry terminal or bridging O^- or OH groups, less often Cl, OR, or carboxylate and other complexing groups. These surface

Figure 8. Silane coupling agents often used in the surface modification of silica particles.

groups are typical reactive sites for the attachment of suitable organic groups. Coordinative bonds are less favorable because the interactions are too weak and because the metal atoms at the surface usually have no pronounced Lewis-acidic properties, that is, no empty coordination sites.

Many metal oxide nanoparticles contain chemical reactive hydroxy groups on their surface. These can easily react with organically substituted silane molecules of the principal formula R_nSiX_{4-n}, where X is a hydrolyzable group, such as a halogen, alkoxy, or amine group. The rest R is connected by a hydrolytically stable bond, for example, a Si—C bond. The OH groups on the surface of the nanoparticles react via hydrolysis and condensation reactions with these so-called silane coupling agents. A plethora of functional groups can be deposited on the particle surface with this approach, and it is beyond the scope of this chapter to mention all possible combinations. Depending on the functional group, specific surface properties can be introduced which are often important for further modifications, for example, to enhance the interfacial interaction between the inorganic particle and a polymer shell. Most of the work done with these compounds was on the modification of silica systems; however, in principal reactions with other nanoparticles that contain hydroxy groups on their surface can also be imagined, such as alumina [151].

The work on organic surface modification of metal oxide nanoparticles by approaches other than those previously mentioned is limited. However, the chemical and structural principles behind the various surface modification methods can be discussed for clusters in which the overall geometry and surface structure are well defined. Because most of the modification methods of clusters can also be transferred to particles, and, based on the fact that there is a fluent transition between clusters and nanoparticles, a clear distinction between these two systems cannot be made. Therefore, we will also present here possibilities of surface modification of clusters with organic molecules to form core-shell-type architectures.

In the postsynthesis modification approach, the functionalized cluster or particle is formed in two steps that are distinctly separate from each other: the cluster/particle core is formed first, and the functional organic groups are introduced later in a different reaction. The alternative method is synthesis of the oxo clusters or particles in the presence of functional organic molecules (i.e., the functionalization of the clusters/particles occurs *in-situ*). The assembly of the cluster occurs in such a way that the organic groups are exclusively bonded to the surface atoms. The advantage of this method is that the process is based on a self-limiting organization of the inorganic and organic building blocks as the formation of the cluster core and the capping of the cluster surface by the organic groups mutually influence each other. The growth of the core is controlled and limited by the organic groups, and, vice versa, the incorporation of the organic groups on the cluster surface is controlled by the chemical reactions by which the cluster is formed. This technique is especially valuable for transition metal oxo systems formed in sol–gel reactions. For example, the surface-modified clusters $Zr_6(OH)_4O_4(OMc)_{12}$ (OMc = methacrylate) are formed when $Zr(O^nPr)_4$ is reacted with

4 molar equivalents of methacrylic acid. The molecular structure reveals the existence of chelating and bridging methacrylate ligands which cover the cluster surface [152]. Clusters of different sizes and shapes and a different degree of substitution by organic ligands can be obtained by modifying the reaction conditions. The main parameters appear to be the nature of the metal alkoxide, the metal alkoxide/carboxylic acid ratio, and the type of carboxylate groups [153–161]. The results obtained for isolated and structurally characterized metal oxide clusters are models for the chemistry leading to the functionalization of larger metal oxide particles. An example of the use of bidendate ligands in the synthesis of surface-modified nanoparticles is the hydrolysis of different metal alkoxides in the presence of acetylacetone and a noncomplexing organic acid, which, after aging, led to nanoparticles with tunable sizes in the range of 2 to 4 nm [162–164].

3.3. Polymer Shells
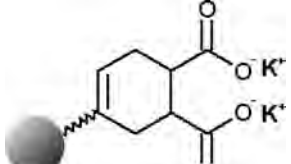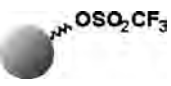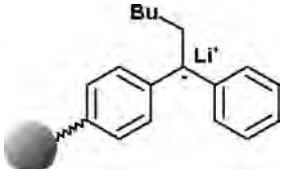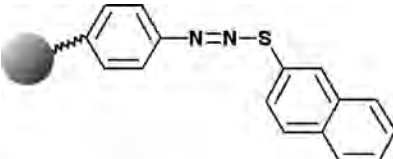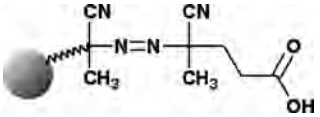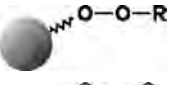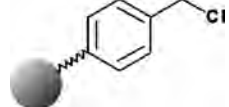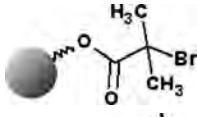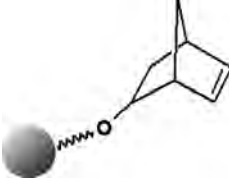
The attachment of polymers to the surface of nanoparticles is obtained by the initiation of the polymerization via a surface-immobilized initiator "grafting-from" approach, by the attachment of the polymer via active sites to the particle surface "grafting-to" approach, or by encapsulation techniques in dispersions. The "grafting-from" method has advantages over the "grafting to" method particularly because the latter has limits in the surface coverage due to diffusion restrictions caused by already immobilized macromolecules. Ionic and radical polymerizations were performed from the surfaces of nanoparticles. In general, these polymerization techniques can be divided into controlled and free radical polymerizations. The controlled polymerizations have the advantage that they possess the possibility to grow polymer shells with the desired thickness and composition. In contrast, free radical polymerizations usually show a very fast kinetics with many termination reactions occurring that do not allow a distinct control over the shell morphology.

3.3.1. Grafting-From Approach

Several polymerization techniques were used for the grafting-from approach (Table 1). Generally this method allows the highest density of polymer chains on the surface of a particle. For this technique the initiator molecules are usually attached to the particle surface in a first step, and afterward the polymerization is promoted.

Ionic Polymerizations Polyesters were grafted from various ultrafine inorganic particles such as silica, titania, and ferrite by anionic ring-opening copolymerization of epoxides and cyclic acid anhydrides [165]. The silica, titania, and ferrite particles had sizes of 16, 120, and 15 nm, respectively, and surface hydroxy group concentrations of 1.37, 0.77, and 0.55 mmol/g. The initiating group was a potassium carboxylate, which was attached to the surface by a series of modifications. The amount of initiating groups on the surface of the silica, titanium oxide, and ferrite particles was 1.92, 0.94, and 0.62 mmol/g, respectively. The organic monomers used were styrene oxide, chloromethyloxirane, gylcidyl methacrylate, gylcidyl phenyl ether, phthalic anhydride, succinic anhydride, and maleic anhydride.

Table 1. Examples of polymerization reaction initiated from inorganic particles.

Initiator	Inorganic particle	Polymerization method	Monomer	Ref.
	SiO$_2$, TiO$_2$, Ferrite	Anionic Ring Opening	Styrene oxide, chloromethyloxirane, gylcidyl methacrylate, gylcidyl phenyl ether, phthalic anhydride, succinic anhydride, maleic anhydride	[166]
	Au	Living cationic	2-Ethyl-2-oxazoline, 2-Phenyl-2-oxazoline	[167]
	SiO$_2$	Living anionic	Styrene	[168]
	SiO$_2$	Free radical	Styrene	[169]
	SiO$_2$	Free radical	MMA	[170]
	SiO$_2$	Free radical	MMA	[173]
	SiO$_2$	Controlled radical	Styrene	[174]
	SiO$_2$, Au	Controlled radical	N-Butyl acrylate	[176, 178]
	Au	Ring-opening metathesis polymerization	Different norbornenyl-containing monomers	[181]

Surface-modified gold nanoparticles were used to initiate the living cationic ring-opening polymerization of 2-ethyl-2-oxazoline and 2-phenyl-2-oxazoline [166]. The grafting-from polymerization was initiated by 11-hydroxyundecane-1-thiol attached to the surface, which was activated by triflate. In this manner, dense polymer brushes were prepared in a so-called one-pot multistep reaction. *Ex situ* kinetic studies of the polymerization of 2-phenyl-2-oxazoline using Fourier transform infrared spectroscopy and matrix-assisted laser desorption ionization time-of-flight mass spectrometry resulted in a linear relation between the reaction time and degree of polymerization of the grafted polymer. The

polymers were successfully end-functionalized by termination with secondary amines.

Living anionic polymerization was initiated from 12–20-nm 1,1-diphenylethylene (DPE) surface-modified silica nanoparticles [167]. *N*-BuLi was used to activate the DPE, which allowed the anionic polymerization of styrene in benzene. A high-vacuum reactor was used to allow polymerization from the surface of silica particles under anhydrous solution conditions.

Free Radical Polymerizations Diazo groups capable of initiating free radical polymerization were attached to the surface of pyrogenic amorphous silica (Aerosil) by a

multistep synthesis [168]. PS was grafted from the thus modified surface. It should be noted that in free radical polymerizations with the described macroinitiators, polymerization also occurs in the solution because the surface-attached initiator decomposes into two radicals from which one initiates polymerization in solution. Therefore, with this technique a purification step is necessary to separate the core-shell systems from the homopolymer. A linear dependence between the monomer and initiator concentration and the polymer coverage was observed.

In several studies, silane coupling agents such as alkoxysilanes [169] or chlorosilanes [170] have been used to modify the surface of silica particles. For example, 4,4'-azobis(4-cyanopentanoic acid) was immobilized on the surface of pyrogenic silica via amide bonds through attached aminophenyltrimethoxysilane. The concentration of diazo groups at the surface reached 0.2 mmol/g. DSC measurements proved that the stability of the initiator decreased upon immobilization. Poly(methyl methacrylate) (PMMA) with a molecular weight of up to 8.7×10^5 was grafted from the particle surface. The polymerization was highly affected by the Trommsdorff effect [171], which was also thought to be responsible for the higher molecular weights of the grafted polymer compared with the homopolymer formed in solution.

Surface-anchored peroxide initiators were used for the grafting of MMA [172]. This type of initiator was attached to the surface by treatment of silica particles with thionyl chloride to obtain surface Si-Cl groups, which were then reacted with tert-butylhydroperoxide or diisopropylbenzene hydroperoxide to form the initiating groups. Depending on the type of peroxide, the concentration of initiators on the surface was 0.08 mmol/g for tert-butylperoxide and 0.29 mmol/g for diisopropylbenzene peroxide. Both peroxide groups were able to initiate the polymerization and led to the grafting of PMMA.

The study of the kinetics and mechanism of an azo-initiated free radical styrene polymerization from modified silica particles was part of more detailed studies for the grafting of polymers from surfaces [170]. In these studies initiators with a cleavable ester group were attached to the surface.

Atom Transfer Radical Polymerizations In contrast to free radical polymerizations, in which, polymerization also occurs in the solution, this is not the case for controlled radical polymerization, such as transition metal-mediated atom transfer radical polymerization (ATRP). Dense silica spheres with a diameter of 70 nm were produced with the Stöber process and modified by reaction with the silane coupling agent [2-(4-chloromethylphenyl)ethyl]dimethylethoxysilane [173]. A surface concentration of the initiator of 0.14 mmol/g was thus achieved. The particles obtained were used as macroinitiators for ATRP of styrene. In a similar approach (11'-chlorodimethylsilylundecyl)-2-chloro-2-phenylacetate was covalently attached to the surface of commercially available silica particles, and ATRP grafting of styrene from the surface was achieved. The grafted polymers were detached from the solid particles for analysis. After polymerization of a first generation of grafts

and work-up of the hybrid particles, the chain ends of the grafts were still active in initiating a second monomer feed [174]. A soft polymer shell around 12-nm silica particles was formed with the use of a chlorodimethylsilyl-functionalized 2-bromo-2-methylpropionate derivative and n-butylacrylate as the monomer [175]. Hyperbranched polymer-silica hybrid nanoparticles were synthesized by surface-initiated self-condensing ATRP of an acrylic AB* inimer from 16-nm silica nanoparticles [176]. About 0.13 mmol initiator/g of silica particles and 0.4 initiator molecules/nm^2 were immobilized on the silica particles, corresponding to about 320 initiator molecules per silica particle. 2-(2-Bromopropionyloxy)ethylacrylate and tert-butylacrylate were used as monomers. Gold nanoparticles were modified with thiole-functionalized initiators for ATRP, and n-butylacrylate was polymerized from the surface [177]. Furthermore, CdS/SiO$_2$ core-shell nanoparticles were prepared and modified with an ATRP initiator, followed by the polymerization of MMA [178]. These hybrid inorganic polymer nanoparticles could be cast into films that retained the photoluminescence of the precursor CdS particles and showed an even distribution of the CdS/SiO$_2$ cores throughout the PMMA matrix. An alternative controlled/"living" radical polymerization technique that was used in the grafting of polymers from silica surfaces is the alkoxyamine-based method that also allowed the controlled synthesis of polymer brushes with variable sizes on the surface of the inorganic core [179].

Ring-Opening Metathesis Polymerizations Transition-metal-catalyzed ring-opening metathesis polymerization (ROMP) was used to graft different norbornenyl-containing monomers from the surface of colloidal gold particles [180]. The two-step preparation of metathesis-ready gold nanoparticles includes the preparation of 1-mercapto-10-(exo-5-norbornen-2-oxy)decane and its immobilization on the metal particles. Metathesis of the norbornene rings on the particles with catalyst Cl$_2$Ru(PCy$_3$)$_2$CHPh was achieved in less than 10 min in CDCl$_3$; subsequent addition of a redox-active ferrocenyl norbornene complex led to copolymerization. ROMP was also carried out from the surface of cadmium selenide nanoparticles stabilized by functional phosphine oxides [181]. These phosphine oxides bear a vinyl group that allows a carbene exchange with the metathesis catalyst and the subsequent polymerization of a variety of cyclic olefins.

3.3.2. Grafting-to Approach

The grafting-to approach is based on the reaction of preformed functional polymers containing reactive groups with the surface of inorganic particles. This includes the reaction with the bare surface, for example, in the case of silica with silanol groups at the surface, or the reaction of chemically modified surfaces that have already been treated with silane coupling agents. Either weak (hydrogen bonds, van der Waals) or strong (covalent, coordinative) chemical interactions are feasible.

The reaction of colloidal silica of 10-, 45-, and 120-nm diameter with trimethoxysilyl-terminated poly(maleic anhydride-co-styrene) and poly(maleic anhydride-co-MMA) in THF resulted in surface modification. The maximum

graft densities of 5 and 3.5 chains/nm^2 were obtained in the reaction of the silica colloids of 10- and 45-nm diameter [182].

Citrate-capped gold nanoparticles can be efficiently grafted with a covalently attached polymer monolayer a few nanometers thick, by simple contact of the metal surface with diluted aqueous solutions of hydrophilic polymers that are end-capped with disulfide moieties [183]. The end-functionalized polymers were synthesized with the use of disulfide-functionalized diazo initiators and *N*-[tris-(hydroxymethyl)methyl]acrylamide as well as *N*-(isopropryl)acrylamide as monomers. The hydrophilic polymer-coated gold colloids can be freeze-dried and stored as powders that can be subsequently dissolved to yield stable aqueous dispersions, even at very large concentration.

Another interesting approach to polymer-capped nanoparticles is the use of end-functionalized polymers, which can interact with the metal species as so-called macroligands, control the final particle size, and stabilize the particles in solution. Nanoscopic CdS entities were produced with this approach, with a thiol-modified poly(caprolactone) as the macroligand [184]. The clusters were grown through the reaction of thiourea with cadmium acetate, and the macroligands were in competition with this reaction by the surface stabilization of the formed particles.

There are a variety of other methods that allow the grafting of polymers to particle surfaces; the interested reader is referred to reviews on this topic [185–188].

3.3.3. Polymer Encapsulation

One of the major problems in the formation of polymer shells on the surfaces of inorganic particles is the chemical incompatibility of the surface and the monomers (Fig. 9). To overcome this difficulty, coupling agents with functional groups, as specified previously, are allowed to react with the surface functional groups. These groups either participate in the polymerization process or simply change the hydrophobicity of the surface. Another possibility for enhancing the polymerization on the particle surface in a heterophase polymerization is the growth of the macromolecules on the surface by the adsorption of required components, namely, surfactants, monomers, or initiator molecules. Interactions that typically take place with the compounds are charge-charge attractions, hydrogen bonding, or hydrophobic interactions.

Polymerization occurs primarily at the surface of unmodified particles because of the adsorption of the monomer on the surface, followed by polymerization in the adsorbed layer [189–191]. The formation of an initial hydrophobic layer on the surface of the particles seems to be crucial for the formation of the polymer shell. Methods for the introduction of such a layer include the use of nonionic surfactants, amphiphilic block copolymers, etc. Furthermore, these surface-active molecules fulfill another task: they avoid agglomeration of the particles. The concentration of such compatibilizing molecules in solution must be carefully tuned because a latex formation in free micelles in the emulsion can be observed at higher concentrations. Moreover, these molecules are usually only weakly bonded to the surface and can therefore desorb easily. Hence, the covalent attachment of organic groups, which
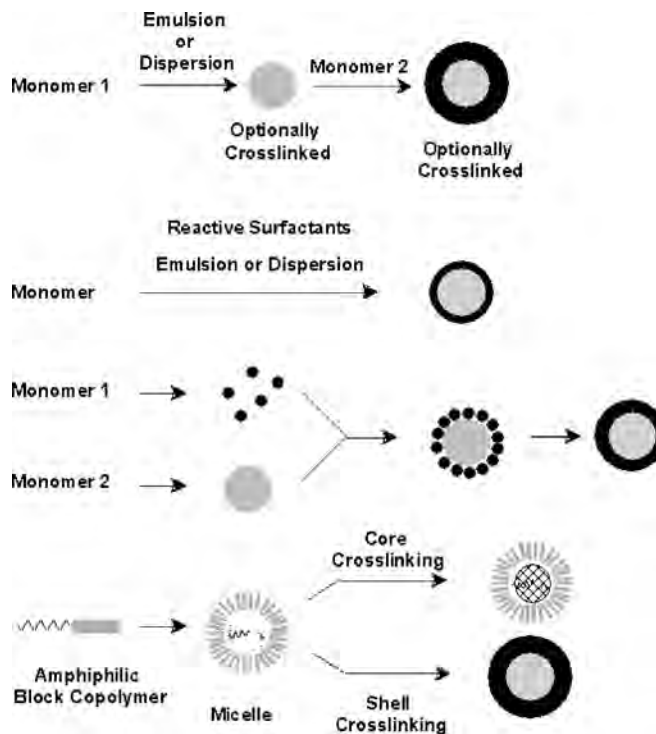
Figure 9. Common approaches to core-shell particles. Adapted with permission from [216], J.-E. Jönsson et al., *Macromolecules* 27, 1932 (1994). © 1994, American Chemical Society.

potentially can interact in the polymerization reaction, is used for surface modification. Silane coupling agents are ideal for this purpose, especially in the case of oxidic inorganic particles containing reactive groups on their surface [192–199]. With a one-pot process Nanosized surface-modified silica particles encapsulated with a polymeric layer have been formed (Fig. 10). Depending on the reaction conditions like stabilizer concentration, different products were obtained, for example, those in which a few particles were encapsulated in a polymer shell and those where only single-shell particles were formed. Additionally, pure polymer latex particles can also be formed in an emulsion. Spherical CaCO$_3$-PS composite nanoparticles were obtained by pretreating CaCO$_3$ particles with stearic acid or γ-methacryloxypropyltrimethoxysilane to make them more hydrophobic and using these precursors in different emulsion polymerizations [200, 201].

Polymerization in microemulsions is probably the most promising versatile technique for the synthesis of a wide variety of nanoparticles with polymeric shells because this
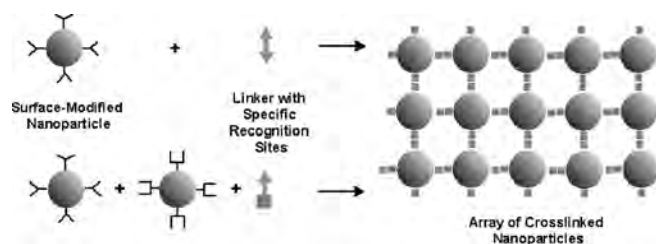
Figure 10. Principle of the formation of 3D networks by site-specific interactions in the shell of nanoparticles.

technique offers the possibility of controlling precisely both the size of the core and that of the polymeric shell formed. This is especially important if the properties of the core-shell particles are dependent on both parameters. One example is magnetite particles, which are employed in biology and medicine for the magnetic separation of biochemical products and cells as well as the magnetic guidance of particle systems for site-specific drug delivery. Because the size, charge, and surface chemistry of magnetic particles could strongly influence their biodistribution, it is important to have good control over all of these parameters. In a recent study it was proved that magnetite nanoparticles with a core radius as small as 15 nm and a PMA-poly(hydroxyethyl methacrylate) random copolymer shell size between 80 and 320 nm can be synthesized in a single microemulsion [202].

An interesting unconventional technique used for the formation of organic shells is sonochemistry [203, 204]. This method was used for the quantitative coating of γ-Fe_2O_3 nanoparticles with octadecyltrihydrosilane and the formation of titania nanoparticles with a polyaniline shell. The advantage of this approach is that the aggregation of nanoparticles can be broken down under ultrasonic irradiation, and through the formation of a shell a new aggregation is avoided.

Armes et al. reported the synthesis of colloidal silica-conducting polymer core-shell nanocomposites by the oxidative polymerization of either aniline or pyrrole via dispersion polymerization in aqueous media on spherical or "stringy" silica nanoparticles [205–210]. The authors found that both the particle size and the chemical composition depend markedly on the type of chemical oxidant selected for the *in-situ* polymerization of the monomers. In addition, other functional cores were also used for the surface pyrrole polymerization, such as silica-coated magnetite particles [211] or tin oxide particles [212]. The resulting colloidal poly(pyrrole)-silica-magnetite nanocomposites have a conducting polymer content of 75 mass% and exhibit superparamagnetism. Furthermore, it was shown that a strong acid-base interaction between vinyl monomers such as 2-vinylpyridine, 4-vinylpyridine, and 2-(diethylamino)ethyl methacrylate and the silica surface promotes the formation of nanocomposites in the aqueous media [213]. In addition to studies on silica cores trapped in conducting polymers, other inorganic cores were also used. For example, $HAuCl_4$ was used as an oxidizing agent for the polymerization of pyrrole and the simultaneous formation of Au nanoparticles within the core [214].

4. ORGANIC–ORGANIC CORE-SHELL NANOPARTICLES

4.1. Polymer–Polymer Core-Shell Systems

In recent years spherical polymer cross-linked particles (microgels) have attracted attention in the production of micro- and nanostructured materials. In addition to their specific properties, such as the swelling behavior in certain solvents, a variety of functionalizations can be attached to the surface of these particles for further modifications. The major advantage of the microgel systems compared with other colloids is their stabilization by the solution. If the

appropriate solvent is used the particles are filled and surrounded by the solvent and therefore are practically dissolved within the molecular medium on a nanoscopic scale. The cross-link density can easily control the volume swelling behavior.

One of the most commonly used polymer cores consists of cross-linked PS, but other monomers for latex particles are also in use, which are typically formed by applying free radical emulsion polymerization in combination with selected quantities of cross-linking agents. An overview of different routes towards core-shell polymer nanoparticles is given in Figure 9. The methodologies used are (i) two-stage seeded emulsion polymerization; (ii) emulsion polymerization using reactive surfactants; (iv) stepwise heterocoagulation of smaller particles onto larger ones, followed by heat treatment at a temperature above the T_g of the shells; and (v) the use of reactive block copolymers that allow polymerization [215]. These routes are generally employed for micrometer-sized particles but can also be employed for nanoparticles. Because of the plethora of different systems already investigated, we will limit the description here to some principal modifications of the latex particles.

Some recent examples of different core-shell nanoparticles that were prepared by various types of emulsion polymerizations are PMMA-PS [216], polypyrrole-PS [217], PS-poly(*p*-vinylphenol) [218], poly(dimethylsiloxane)-poly(butadiene) [219], and cross-linked PS-poly-(*tert*-butyl acrylate) [220].

Some of these polymer–polymer core-shell architectures have potential applications for biomaterials. For example, PS-poly(glycidyl methacrylate) core-shell nanoparticles with mean diameters of about 85 nm were modified with a number of different ligands, including diamines of increasing chain length, amino acids and corresponding amines, and higher molecular weight ligands like polymyxin B [221]. The modified particles were tested for their endotoxin (ET) binding capacity in water and physiological sodium chloride solution with the *Limulus amebocyte lysate* assay. It was found that the ET binding properties of the different surface modifications depend on the ability of the ligand to form Coulomb and van der Waals interactions with the ET molecule influenced by the nature of the suspension medium. Therefore, the choice of ligands for particle modification has to consider minutely the conditions under which ET has to be removed, for example, removal from pure water, dialysis fluids, plasma, or blood.

PS latexes were functionalized with halogen-containing groups at their surface capable for initiating ATRP and applied as macroinitiators in this polymerization technique. With this method hydrophobic core-hydrophilic shell nanoparticles were prepared with the use of hydroxyethyl acrylate, 2-(methacryloxy)ethyl trimethylammonium chloride, or methacrylic acid as monomers [222, 223].

A technologically important issue for the application of conducting polymers is to increase their processibility by attaching them to latex particles. Because many of the conducting polymers are water-soluble the surface of the microgel needs at least to be partially polar. To reach this property latex particles were, for example, synthesized from carboxylic or sulfonic derivatized PS. These particles (120 nm)

are soluble in aqueous solutions and were used as a seed in a second stage for the synthesis of the core-shell particles. Polypyrrole, for example, can be polymerized around the core in an oxidative chemical *in-situ* polymerization [224]. In a similar approach styrene-butadiene-methacrylate latex (200 nm) was covered with polyaniline, polypyrrole, and poly(3-methoxythiophene) [225]. Polypyrrole was deposited from aqueous media on a poly(ethylene oxide)-stabilized PS latex with a mean diameter of 129 nm. The polypyrrole loading was varied systematically. The resulting polypyrrole-PS composites did not possess the expected "core-shell" morphology previously observed for other polypyrrole-coated PS particles. Instead, TEM studies indicated that the conducting polymer component was present as discrete 20–30-nm nanoparticles, which were adsorbed to the PS latex [217].

An example of core-crosslinked micelles is the use of amphiphilic poly(ethylene glycol)-*b*-polylactide (PEG/PLA) copolymers with an aldehyde group at one chain end and a methacryloyl group at the other terminal end. The methacryloyl groups located in the core of the micelle were polymerized to form core-shell-type nanoparticles with diameters between 20 and 30 nm and reactive aldehyde groups on the surface [226].

Microgels composed of environmentally responsive polymers continue to attract attention because of their potential applications in numerous fields, including drug delivery, chemical separations, catalysis, and sensors. Perhaps the most studied class of responsive polymers is thermoresponsive poly(alkylacrylamides). Hence, these polymers were also used in the synthesis of stimuli-responsive core-shell latexes [227]. Many of the synthesized systems contain a responsive and a nonresponsive component. Furthermore, multiresponsive systems were also investigated that are composed of two or more environmentally sensitive polymers [228]. For example, core particles composed of cross-linked poly(*N*-isopropylacrylamide) or mixtures of the latter with acrylic acid were synthesized via precipitation polymerization and then used as nuclei for subsequent polymerization for the formation of a shell. These hydrogel particles display both a strong temperature and pH dependence on swelling. Through a change of the composition of the core and the shell, for example, by copolymerizing other monomers, the response of these hydrogels is made tunable [229].

As already mentioned, the sol–gel process is a versatile tool if an oxidic shell should be formed around a particle. The advantage of this process is its applicability for a lot of different metals (e.g., Si, Ti, Zr, Sn, etc.) and the mild reaction conditions that allow the incorporation of organic groups into the networks formed. An interesting aspect of these coated polymer particles is the removal of their core by calcination and the production of hollow spheres.

4.2. Cross-Linked Micelles

Amphiphilic block copolymers can aggregate in solutions into spherical micelles depending on the solvents and concentrations between solvent and block copolymers. If the copolymers contain functional groups that are able to undergo cross-linking reactions, stable spherical core-shell nanostructures can be formed with either a cross-linked core

or shell and with differing physical and chemical properties of the core and the shell that can be tailored over a wide range.

Wooley et al. prepared several examples of so-called shell cross-linked knedel-like (SCK) polymer assemblies with diameters between 5 and 100 nm [230]. Based on the cross-linked shell, these nanostructures have a robust character and surface stability under changing environmental conditions. In addition, the shell serves as a membrane that has a permeability that can be tailored to control the transport of guests to and from the core. Furthermore, the lack of cross-links in the core region maintains chain mobility and access to the core volume. Hence these systems are nanoscale scaffolds that can mimic several biological systems. One important parameter that influences the properties of these systems is the composition and structure of the amphiphilic block copolymer. Another parameter is the composition and cross-link density of the shell that determines the extent of swelling, controls the interactions with the environment, and influences the shell's permeability. The core provides a unique nanoenvironment for guests that are able to pass the shell barrier. Typical examples of such systems comprise assemblies of PS-poly(4-vinylpyridine) block copolymers in which the shell was cross-linked by applying quaternization reactions of the pyridine segments [231] or PS-poly(acrylic acid) cross-linked via amidation reactions in the shell [232]. Other reports used micelles of PS-poly(2-cinnamoylethyl methacrylate) or polyisoprene-poly(2-cinnamoylethyl methacrylate) diblock copolymers with photo-cross-linked shells [233], poly(solketal methacrylate)-block-poly(2-(dimethylamino)ethyl methacrylate) with 1, 2-bis(2-iodoethoxy)ethane cross-linked shells [234], 1, 2-bis(2-iodoethoxy)ethane cross-linked partially quaternized 2-(dimethylamino)ethyl methacrylate-*N*-(morpholino)ethyl methacrylate diblock copolymer micelles [235], or zwitterionic diblock copolymers [236].

5. POLYMER–INORGANIC CORE-SHELL NANOPARTICLES

Because of the simple availability of polymer latexes in combination with a wide range of sizes and functionalities, they are ideal building blocks for complex functional materials. For the deposition of precursors for inorganic shells the latex particles often require a charge. This charge can be introduced by applying ionic initiators in the free radical polymerizations. With this technique stable colloidal core-shell particles consisting of a PS core and a titania coating were prepared in one step by the hydrolysis of a titanium alkoxide in the presence of a cationic PS latex. The coatings obtained were very smooth and uniform and varied in thickness from just a few nanometers up to 50 nm [237].

The surface modification with magnetic compounds attracted much interest because of their possible applications for therapeutic or analytical purposes. In the first case, magnetic particle carriers permit either the guiding and release of a drug in a specific site of the body or the extraction of tumor cells from the organism and their curing *in vitro* [238, 239]. For this purpose different latex particles were covered with magnetic substances. For example, PS-poly(*N*-isopropylacrylamide) core-shell nanoparticles were

prepared, and iron oxide was adsorbed on the outer shell via electrostatic interactions [240].

Gold shells on PS latex were prepared by adsorbing polyethyleneimine polyelectrolyte to the polymer core via electrostatic and hydrogen-bonding attraction, followed by the adsorption of negatively charged Au particles with sizes of 3 nm or 15 nm [241]. The coverage of gold was increased by a seeding procedure, resulting in a Au shell thickness of 10 ± 5 nm.

The coating of anionic or cationic latexes with metals or metal salts is a general approach to core-shell nanoparticles. Examples of such systems are PS latexes with shells of Y basic carbonate [242], Zr compounds [243], TiO_2 [244], iron compounds [245], or copper and copper compounds [246]. These particles were synthesized via absorption and reaction of metal salts on the surface of the latexes. In several cases these particles were calcined and hollow spheres were obtained.

A different method for producing multilayer particles, for example, of a latex core with a corona of inorganic nanoparticles capping its surface, is the layer-by-layer method. Magnetite, titanium dioxide, silica, and laponite nanoparticles were used as the inorganic building blocks for multilayer formation on PS sphere templates [247, 248]. Composite organic–inorganic particles were formed by the controlled assembly of the preformed nanoparticles in alternation with oppositely charged polyelectrolytes onto PS microspheres. Inorganic nanoparticles with different diameters were shown to work effectively in this coating process. In addition, hollow capsules can be obtained from the precursor polymer–inorganic core-shell particles by direct removal of the core material by chemical or physical methods.

6. INORGANIC BIOMOLECULE CORE-SHELL SYSTEMS

In recent years nature motivated intense efforts to develop assembly methods that mimic or exploit the recognition capabilities and interactions found in biological systems. Many studies concentrated on fundamental principles by applying surface-modified nanoparticles with complementary receptor-substrate sites on their surface for the detection of biological molecules and/or for the recognition-driven self-assembly of ordered aggregates. The basic idea for the latter approach was transferred from biological systems in which organic molecules show a remarkable level of control over the nucleation and mineral phase of inorganic materials such as calcium carbonate and silica, and over the assembly of crystallites and other nanoscale building blocks into complex structures required for biological functions. Of particular value are methods that could be applied to materials with interesting electronic or optical properties. Similar to the interactions in enzymes, organic ligands can interact with the surface of metal or semiconductor nanoparticles. With this approach peptides with limited selectivity for binding to metal and semiconductor surfaces can, for example, be used for the particle modification [249].

A general approach is to prepare nanoparticles by wet chemistry in the presence of stabilizing agents that coordinate to the surface, such as citrates, phosphines, or thiols, of the resulting nanoparticles. These molecules prevent an uncontrolled growth and aggregation and are substituted in a further step with ligands that have a stronger interaction with the metal atoms at the surface. For example, gold nanoparticles were reacted with thiol-modified DNA sequences that allow recognition by specific particles of each other through the hydrogen bonds typical for these biomolecules. This technique in particular was used as a method for assembling colloidal nanoparticles rationally and reversibly into macroscopic aggregates [250, 251]. The method involves attachment of two batches of non-complementary DNA oligonucleotides capped with thiol groups as linkers to the surface of nanometer gold particles. When oligonucleotide duplexes with complementary ends are added to the two grafted sequences, the nanoparticles self-assemble into aggregates (Fig. 10). The assembly process can be reversed by thermal denaturation. This material synthesis approach has been extended to a wide range of biomolecules, including peptides and proteins [252–254], and a collection of nanoparticles, including gold and semiconductor quantum dots [255, 256]. However, gold proved to be ideal for this kind of materials since, for example, it was more difficult to modify CdSe and CdS quantum dots because of a surfactant layer that is very strongly bound to their surfaces and, consequently, difficult to displace [257]. Hence, if nanoparticle compositions different from Au were required, a typical route is to cover their surface with a gold layer and immobilize the oligonucleotides on this layer afterward [258]. Another possibility for activating the surface of quantum dots for the coupling of biomolecules is their coverage with silane coupling agents, which was used in the capping of core(CdSe)-shell(CdS) nanoparticles [107]. Other biorelated interaction techniques, for example, antibody-antigen recognition, were also applied for the directed self-assembly of Au and Ag nanoparticles [259]. The absorption of the biomolecules in these cases was carried out at a pH above the isoelectric point of the stabilizing citrate groups. The proteins then show a strong interaction with colloids by the positively charged amino acid side chains.

In addition to the possibility of enhancing the self-assembly of larger arrays, the use of recognition chemistry has found wide application in the development of highly sensitive and selective diagnostic methods [107, 260–264].

Major problems in the synthesis of biomolecule-capped nanoparticles are the avoidance of harsh reaction conditions, which often lead to the inactivation of the biofunctionalization and the strong fixation of the molecules to the surface of the particles.

Only a few examples from the field of nanoparticle-biomolecule interactions were given in this chapter. The interested reader is referred to a comprehensive review that shows the possibilities of combining inorganic materials with biomolecules [265].

As a summary of the different materials described within this chapter, we have collected in Table 2 most of the combinations, as well as their properties of interest and corresponding references.

Table 2. Summary of material combinations and properties.

Core	Shell	Synthesis method	Relevant property	Ref.
CdSe	ZnS	Microemulsions	Luminescence	[10]
CdSe	ZnS	TOPO	Luminescence	[10]
CdSe	ZnSe	Single-molecule precursors	Luminescence	[26]
CdSe	ZnSe	TOPO	Luminescence	[11, 22, 26]
CdSe	CdS	TOPO	Luminescence	[12, 25]
CdSe	CdS	Single-molecule precursors	Luminescence	[25]
CdSe	CdS	Microemulsions	Luminescence	[20, 23]
CdS	Ag_2S	Microemulsions	Luminescence	[19]
CdS	CdSe	Microemulsions	Luminescence	[20]
InAs	InP	TOPO	IR luminescence	[27]
InAs	CdSe	TOPO	IR luminescence	[27]
Au	Ag	Chemical reduction	Optical absorption	[31, 33, 34, 38]
Ag	Au	Chemical reduction	Optical absorption	[33, 36]
Au	Cd	γ-Radiolysis	Optical absorption	[40]
Au	Pb	γ-Radiolysis	Optical absorption	[40, 41]
Au	Sn	γ-Radiolysis	Optical absorption	[42]
Ag	Pb	γ-Radiolysis	Optical absorption	[43, 44]
Ag	Cd	γ-Radiolysis	Optical absorption	[45]
Ag	In	γ-Radiolysis	Optical absorption	[43]
Ag	Hg	γ-Radiolysis	Optical absorption	[46]
Au	Pt	Chemical reduction	Optical absorption	[48]
Pt	Au	γ-Radiolysis	Optical absorption	[48]
Pd	Pt	Ethanol reduction	Catalysis	[53, 54]
Au	Pd		Catalysis	[55]
PS	Ag	Chemical reduction	Optical absorption	[56]
SiO_2	Au	Chemical reduction	Optical absorption	[57–62]
SiO_2	Ag	Chemical reduction	Optical absorption	[63]
SiO_2	Ag	Electroless plating	Optical absorption	[39]
Fe	Ag	Microemulsions	Magnetic	[75]
Co	Ag	Microemulsions	Magnetic	[75]
Fe	Au	Microemulsions	Magnetic	[76, 77]
Fe	In	Solvated metal-atom dispersion	Magnetic	[78]
Fe	Nd	Solvated metal-atom dispersion	Magnetic	[78]
Co	Pt	Redox transmetalation	Magnetic	[79]
Ag	Co	Thermal decomposition + transmetalation	Magnetic	[80]
Fe_2O_3	SiO_2	Sol–gel	Magnetic	[82, 84]
Fe_3O_4	SiO_2	Sol–gel	Magnetic	[72, 85, 87–89]
Fe	SiO_2	Sol–gel	Magnetic	[92]
Au	SiO_2	Sol–gel	Optical absorption	[93–96, 99–101, 104, 105]
Ag	SiO_2	Sol–gel	Optical absorption	[35, 97, 98, 102, 103]
Ag	SiO_2	Microemulsions	Optical absorption	[110]
Ag	SiO_2	DMF reduction	Optical absorption	[111]
CdS	SiO_2	Sol–gel	Luminescence	[106, 109]
CdSe	SiO_2	Sol–gel	Luminescence	[107, 108]
Ag	TiO_2	DMF reduction	Optical absorption	[112]
	TiO_2	DMF reduction	Biocompatible membranes	[113]
Au	TiO_2	Layer-by-layer	Optical absorption	[114]
Au	SnO_2	Sol–gel	Capacitance	[116]
Au	CdS	Chemical precipitation	Optical absorption	[117]
Fe_2O_3	Surfactant	Microemulsion	Nonlinear optical response	[133, 135, 136]
Pd	Surfactant	Microemulsion		[134]
CeO_2	Surfactant	Microemulsion		[137]
Ag	PS, PMMA	Emulsion	Functionalization with bio-molecules	[138]
SiO_2	3-Aminopropyltriethoxysilane	Stöber process		[139]
$SiO_{2-n}R_n$	PS	Dispersion/hydrosilation		[141]
Au	p-Mercaptophenol	*In-situ* reduction		[142]
Au	ω-Substituted alkanethiolates	*In-situ* reduction/ligand exchange		[143]
Pt	Alkyl isocyanides	Coordination		[148]
CdS	Hexanedithiol	Coordination	Film formation	[149]

Table 2. Continued

Core	Shell	Synthesis method	Relevant property	Ref.
Al_2O_3	PS, polyacrylamide	Dispersion		[151]
Zr, Ti, Nb Metal oxo clusters	Carboxylic acids	Coordination		[152–161]
ZrO_2	Acetylacetone	Coordination		[162]
TiO_2	Acetylacetone	Coordination		[163, 164]
SiO_2, TiO_2, Ni-Zn ferrite	Polyesters	Grafting from polymerization		[165]
Au	Polyoxazoline	Grafting from polymerization		[166]
SiO_2	PS	Grafting from polymerization		[167, 168, 170, 173, 174, 179]
SiO_2	PMMA	Grafting from polymerization		[169, 172, 179]
SiO_2	Poly(n-butyl acrylate)	Grafting from polymerization		[175]
SiO_2	PAA, poly(t-butyl acrylate)	Grafting from polymerization		[176]
Au	Poly(n-butyl acrylate)	Grafting from polymerization		[177]
CdS/SiO_2	PMMA	Grafting from polymerization		[178]
Au	Polynorbornene	Grafting from polymerization		[180]
CdSe	Polycyclooctene	Grafting from polymerization		[181]
SiO_2	Poly(maleic anhydride-co-styrene), Poly(MA-co-Me methacrylate)	Grafting to		[182]
Au	Poly(N-[tris-(hydroxymethyl) methyl]-acrylamide), poly(N-(isopropryl)-acrylamide)	Grafting to		[183]
CdS	Poly(caprolactone)	Grafting to		[184]
SiO_2	Poly(ethyl acrylate)	Encapsulation		[192–195]
SiO_2	PS	Encapsulation		[196–198]
SiO_2	Poly(t-butyl acrylate)	Dispersion		[199]
$CaCO_3$	PS	Emulsion		[200, 201]
Fe_3O_4	Cross-linked copolymer of methacrylic acid and hydroxyethyl methacrylate	Microemulsion	Magnetic	[202]
Fe_2O_3	Octadecyltrihydrosilane	Sonochemistry	Magnetic	[203]
TiO_2	Polyaniline	Sonochemistry	Conductivity	[204]
SiO_2	Polyaniline	Surface polymerization	Conductivity	[205, 206, 210]
SiO_2	Polypyrrole	Surface polymerization	Conductivity	[207–209]
SiO_2/magnetite	Polypyrrole	Surface polymerization	Superparamagnetism	[211]
SnO_2	Polypyrrole	Surface polymerization	Conductivity	[212]
SiO_2	Poly(vinylpyridine) and copolymers with styrene and MMA, poly(2-(diethylamino)ethyl methacrylate)	Surface polymerization		[213]
Au	Polypyrrole	Polymerization in diblock copolymer micelles		[214]
PMMA	PS	Emulsion		[216]
PS	Polypyrrole	Emulsion		[217, 224]
PS	Poly(p-vinylphenol)	Emulsion		[218]
Poly (dimethyl-siloxane)	Poly(butadiene)	Emulsion		[219]
PS Poly (t-butyl acrylate)	Poly(t-butyl acrylate) PS	Emulsion		[220]
PS	Poly(glycidyl methacrylate)	Emulsion	Endotoxin binding	[221]
PS	Poly(2-hydroxyethyl acrylate) poly(2-(methacryloyloxy)ethyl trimethylammonium chloride)	Emulsion		[222]
PS	PMA, PMMA	Grafting from		[223]
Thermoplastic rubber latexes	Polyaniline polypyrrole poly(3-methoxythiophene)	Emulsion		[225]
Poly (ethylene glycol)	Polylactide	Cross-linked micelle		[226]

Table 2. Continued

Core	Shell	Synthesis method	Relevant property	Ref.
PS	Poly(*N*-isopropylacrylamide)	Emulsion	Stimuli responsive	[227]
Poly (*N*-isopropylacrylamide) poly (NIPAm-*co*-acrylic acid)	Poly (*N*-isopropulacrylamide) poly(NIPAm-*co*-acrylic acid)	Precipitation polymerization	Stimuli responsive	[228]
Poly (*N*-isopropylacrylamide)	Poly(*N*-isopropylacrylamide) copolymerized with butyl methacrylate	Precipitation polymerization	Thermoresponsive	[229]
PS	Poly(4-vinylpyridine)	Shell-cross-linked micelle		[231]
PS	Poly(acrylic acid)	Shell-cross-linked micelle		[232]
Polyisoprene	Poly(2-cinnamoyethyl methacrylate)	Shell-cross-linked micelle		[233]
Poly (solketal methacrylate)	Poly(2-(dimethylamino)ethyl methacrylate)	Shell-cross-linked micelle		[234]
Poly (2-dimethylamino) ethyl methacrylate	Poly(*N*-(morpholino)ethyl) methacrylate	Shell-cross-linked micelle		[235]
Poly (2-dimethylamino) ethyl methacrylate	Poly(2-tetrahydropyranyl methacrylate)	Shell-cross-linked micelle		[236]
PS	TiO_2	Sol–gel		[237]
PS-poly(N-isopropylacrylamide)	Iron oxide	Surface deposition	Magnetic	[240]
PS	Au	Surface deposition		[241]
PS	Yttrium basic carbonate	Surface deposition		[242]
PS	Zirconium compounds	Surface deposition		[243]
PS	TiO_2	Surface deposition		[244]
PS	Iron compounds	Surface deposition		[245]
PS	Copper and copper compounds	Surface deposition		[246]
PS	Fe_3O_4	Layer-by-layer deposition	Magnetic	[247]
PS	TiO_2, SiO_2, laponite	Layer-by-layer deposition		[248]
Au	DNA oligonucleotides	Coordination		[250, 251, 254]
ZnS@CdSe	Proteins and other biomolecules	Electrostatic binding	Ultrasensitive biological detection	[253, 256]
Au@Ag	Oligonucleotides	Electrostatic binding		[258]

7. CONCLUSIONS

In this chapter we have reviewed the synthesis and properties of core-shell nanoparticles of various composition. A classification based on the nature of the core and the shell lead us to distinguish mainly between organic and inorganic materials, but also to find clear subdivisions taking into account the metallic, semiconductor, or dielectric nature of the inorganic materials, or the relative configuration of organic and inorganic material within the composite particles. We have shown that there is a plethora of possible combinations leading to nanomaterials with various functionalities, which has a great potential for applications in technology and life sciences.

GLOSSARY

Colloid A substance consisting of very tiny particles that are usually between 1 nm and 1000 nm in diameter and that are suspended in a continuous medium, such as a liquid, a solid, or a gaseous substance.

Core-shell nanoparticles Particles with size below 1 μm, composed of an inner, typically spherical core homogeneously surrounded by a shell of a different material.

Emulsion Drop-shaped distribution of one liquid in another while both of them are not miscible.

Latex A homogeneous colloidal dispersion of polymeric particles in water.

Nanoshells Spherical colloid particles with a hollow interior, usually filled with solvent.

Plasmon resonance Collective oscillation of conduction electrons in metal nanoparticles, induced by an electromagnetic wave.

Quantum dot Particle of matter so small that quantum size effects can be observed.

Silica coating Deposition of an amorphous silicon dioxide shell on a preformed colloid particle.

Surfactant Abbreviation for surface-active agent; soluble compound that reduces the surface tension of liquids, or reduces interfacial tension between two liquids or a liquid and a solid.

REFERENCES

1. C.-J. Zhong and M. M. Maye, *Adv. Mater.* 13, 1507 (2001).
2. E. Bourgeat-Lami, *J. Nanosci. Nanotechnol.* 2, 1 (2002).
3. G. Kickelbick, *Prog. Polym. Sci.*, 28, 83 (2003).
4. A. P. Alivisatos, *J. Phys. Chem.* 100, 13226 (1996).
5. A. P. Alivisatos, *Science* 271, 933 (1996).
6. L. L. Beecroft and C. K. Ober, *Chem. Mater.* 9, 1302 (1997).
7. N. Herron and D. L. Thorn, *Adv. Mater.* 10, 1173 (1998).

8. U. Woggon, "Optical Properties of Semiconductor Quantum Dots." Springer-Verlag, Berlin, 1997.

9. T. Vossmeyer, S. Jia, E. Delonno, M. R. Diehl, X. Peng, A. P. Alivisatos, and J. R. Heath, *J. Appl. Phys.* 84, 3664 (1998).

10. B. O. Dabbousi, J. Rodriguez-Viejo, F. V. Mikulec, J. R. Heine, H. Mattoussi, R. Ober, K. F. Jensen, and M. G. Bawendi, *J. Phys. Chem. B* 101, 9463 (1997).

11. M. Danek, K. F. Jensen, C. B. Murray, and M. G. Bawendi, *Chem. Mater.* 8, 173 (1996).

12. X. Peng, M. C. Schlamp, A. V. Kadavanich, and A. P. Alivisatos, *J. Am. Chem. Soc.* 119, 7019 (1997).

13. M. A. Hines and P. Guyot-Sionnest, *J. Phys. Chem.* 100, 468 (1996).

14. A. Eychmüller, A. Hasselbarth, and H. Weller, *J. Lumin.* 53, 113 (1992).

15. A. Hasselbarth, A. Eychmüller, M. Eichberger, M. Giersig, A. Mews, and H. Weller, *J. Phys. Chem.* 97, 5333 (1993).

16. V. F. Kamalov, R. Little, S. L. Logunov, and M. A. El-Sayed, *J. Phys. Chem.* 100, 6381 (1996).

17. H. S. Zhou, H. Sasahara, I. Homma, H. Komiyama, and J. Haus, *Chem. Mater.* 6, 1534 (1994).

18. G. Counio, S. Esnouf, T. Gacoin, and J. P. Boilot, *J. Phys. Chem.* 100, 20021 (1996).

19. M. Y. Han, W. Huang, C. H. Chew, L. M. Gan, X. J. Zhang, and W. Ji, *J. Phys. Chem. B* 102, 1884 (1998).

20. Y. Tian, T. Newton, N. A. Kotov, D. M. Guldi, and J. H. Fendler, *J. Phys. Chem.* 100, 8927 (1996).

21. D. Diaz, J. Robles, T. Ni, S.-E. Castillo-Blum, D. Nagesha, O.-J. A. Fregoso, and N. A. Kotov, *J. Phys. Chem. B* 103, 9854 (1999).

22. C. F. Hoener, K. A. Allan, A. J. Bard, A. Campion, A. M. Fox, T. E. Mallouk, S. E. Webber, and J. M. White, *J. Phys. Chem.* 96, 3812 (1992).

23. E. Hao, H. Sun, Z. Zhou, J. Liu, B. Yang, and J. Shen, *Chem. Mater.* 11, 3096 (1999).

24. C. B. Murray, D. J. Norris, and M. G. Bawendi, *J. Am. Chem. Soc.* 115, 8706 (1993).

25. N. Revaprasadu, M. A. Malik, P. O'Brien, and G. Wakefield, *Chem. Commun.* 1573 (1999).

26. M. A. Malik, P. O'Brien, and N. Revaprasadu, *Chem. Mater.* 14, 2004 (2002).

27. Y.-W. Cao and U. Banin, *Angew. Chem., Int. Ed.* 38, 3692 (1999).

28. Y.-W. Cao and U. Banin, *J. Am. Chem. Soc.* 122, 9692 (2000).

29. A. Henglein, *J. Phys. Chem.* 97, 54 (1993).

30. P. Mulvaney, *Langmuir* 12, 788 (1996).

31. R. H. Morriss and L. F. Collins, *J. Chem. Phys.* 41, 3357 (1964).

32. J. Sinzig, U. Radtke, M. Quinten, and U. Kreibig, *Z. Phys. D* 26, 242 (1993).

33. L. Rivas, S. Sánchez-Cortes, J. V. García-Ramos, and G. Morcillo, *Langmuir* 16, 9722 (2000).

34. L. Lu, H. Wang, Y. Zhou, S. Xi, H. Zhang, J. Hu, and B. Zhao, *Chem. Commun.* 144 (2002).

35. T. Ung, L. M. Liz-Marzán, and P. Mulvaney, *Langmuir* 14, 3740 (1998).

36. Y. W. Cao, R. Jin, and C. A. Mirkin, *J. Am. Chem. Soc.* 123, 7961 (2001).

37. Y. Sun, B. T. Mayers, and Y. Xia, *NanoLetters* 2, 481 (2002).

38. M. Schierhorn and L. M. Liz-Marzán, *NanoLetters* 2, 13 (2002).

39. Y. Kobayashi, V. Salgueiriño-Maceira, and L. M. Liz-Marzán, *Chem. Mater.* 13, 1630 (2001).

40. F. Henglein, A. Henglein, and P. Mulvaney, *Ber. Bunsenges. Phys. Chem.* 98, 180 (1994).

41. P. Mulvaney, M. Giersig, and A. Henglein, *J. Phys. Chem.* 97, 7061 (1993).

42. A. Henglein and M. Giersig, *J. Phys. Chem.* 98, 6931 (1994).

43. A. Henglein, P. Mulvaney, A. Holzwarth, T. E. Sosebee, and A. Fojtik, *Ber. Bunsenges. Phys. Chem.* 96, 754 (1992).

44. A. Henglein, A. Holzwarth, and P. Mulvaney, *J. Phys. Chem.* 96, 8700 (1992).

45. A. Henglein, P. Mulvaney, and A. Holzwarth, *J. Phys. Chem.* 96, 2411 (1992).

46. L. Katsikas, M. Gutiérrez, and A. Henglein, *J. Phys. Chem.* 100, 11203 (1996).

47. A. Henglein and M. Giersig, *J. Phys. Chem. B* 104, 5056 (2000).

48. A. Henglein, *J. Phys. Chem. B* 104, 2201 (2000).

49. A. Henglein, *J. Phys. Chem. B* 104, 6683 (2000).

50. N. Toshima, in "Fine Particle. Synthesis, Characterization, and Mechanism of Growth" (T. Sugimoto, Ed.), pp. 430–459. Dekker, New York, 2000.

51. N. Toshima and T. Yonezawa, *New J. Chem.* 22, 1179 (1998).

52. T. Yonezawa and N. Toshima, *J. Chem. Soc., Faraday Trans.* 91, 4111 (1995).

53. N. Toshima, K. Kushihashi, T. Yonezawa, and H. Hirai, *Chem. Lett.* 1769 (1989).

54. N. Toshima, Y. Shiraishi, A. Shiotsuki, D. Ikenaga, and Y. Wang, *Eur. Phys. J. D* 16, 209 (2001).

55. A. F. Lee, C. J. Baddeley, C. Hardacre, R. M. Ormerod, R. M. Lambert, G. Schmid, and H. West, *J. Phys. Chem.* 99, 6096 (1995).

56. P. Barnickel and A. Wokaun, *Mol. Phys.* 67, 1355 (1989).

57. S. L. Westcott, S. J. Oldenburg, L. Randall, and N. J. Halas, *Langmuir* 14, 5396 (1998).

58. S. J. Oldenburg, R. D. Averitt, S. L. Westcott, and N. J. Halas, *Chem. Phys. Lett.* 288, 243 (1998).

59. G. Mie, *Ann. Phys.* 25, 337 (1908).

60. S. J. Oldenburg, J. B. Jackson, S. L. Westcott, and N. J. Halas, *Appl. Phys. Lett.* 75, 2897 (1999).

61. S. J. Oldenburg, S. L. Westcott, R. D. Averitt, and N. J. Halas, *J. Chem. Phys.* 111, 4729 (1999).

62. C. Graf and A. van Blaaderen, *Langmuir* 18, 524 (2002).

63. J. B. Jackson and N. J. Halas, *J. Phys. Chem. B* 105, 2743 (2001).

64. G. O. Mallory and J. B. Hajdu, Eds., "Electroless Plating: Fundamentals and Applications." American Electroplaters and Surface Finishers Society, Orlando, FL, 1990.

65. V. K. Pecharsky and K. A. Gschneidner, Jr., *J. Magn. Magn. Mater.* 200, 44 (1999).

66. C. Kormann, E. Schwab, F.-W. Raulfs, and K. H. Beck, U.S. Patent 5,500,141, 1996.

67. J. C. Lodder, D. J. Monsma, R. Vlutters, and T. Shimatsu, *J. Magn. Magn. Mater.* 198–199, 119 (1999).

68. A. Jordan, R. Scholz, P. Wust, H. Schirra, T. Schiestel, H. Schmidt, and R. Felix, *J. Magn. Magn. Mater.* 194, 185 (1999).

69. M. Y. Mapra, I. J. Körner, M. Hildebrandt, R. Bargou, D. Krahl, P. Reichardt, and B. Dörken, *Blood* 89, 337 (1997).

70. S. A. Iakovenko, A. S. Trifonov, M. Giersig, A. Mamedov, D. K. Nagesha, V. V. Hanin, E. C. Soldatov, and N. A. Kotov, *Adv. Mater.* 11, 388 (1999).

71. T. Fried, G. Shemer, and G. Markovich, *Adv. Mater.* 13, 1158 (2001).

72. F. G. Aliev, M. A. Correa-Duarte, A. Mamedov, J. W. Ostrander, M. Giersig, L. M. Liz-Marzán, and N. A. Kotov, *Adv. Mater.* 11, 1006 (1999).

73. M. Giersig and M. Hilgendorff, *J. Phys. D: Appl. Phys.* 32, L111 (1999).

74. R. D. Shull and L. H. Bennet, *Nanostruct. Mater.* 1, 83 (1992).

75. J. Rivas, R. D. Sánchez, A. Fondado, C. Izco, A. J. García-Bastida, J. García-Otero, J. Mira, D. Baldomir, A. González, I. Lado, M. A. López-Quintela, and S. B. Oseroff, *J. Appl. Phys.* 76, 6564 (1994).

76. C. T. Seip and C. J. O'Connor, *Nanostruct. Mater.* 12, 183 (1999).

77. E. E. Carpenter, C. Sangregorio, and C. J. O'Connor, *IEEE Trans. Magn.* 35, 3496 (1999).

78. D. Zhang, G. Glavee, K. J. Klabunde, G. C. Hadjipanayis, and C. M. Sorensen, *High Temp. Mater. Sci.* 36, 93 (1997).

79. J.-I. Park and J. Cheon, *J. Am. Chem. Soc.* 123, 5743 (2001).

80. N. S. Sobal, M. Hilgendorff, H. Moehwald, M. Giersig, M. Spasova, T. Radetic, and M. Farle, *NanoLetters* 2, 621 (2002).
81. R. K. Iler, Patent 2,885,366, 1959.
82. M. Ohmori and E. Matijevic, *J. Colloid Interface Sci.* 150, 594 (1992).
83. W. Stöber, A. Fink, and E. Bohn, *J. Colloid Interface Sci.* 26, 62 (1968).
84. D. M. Thies-Weesie and A. P. Philipse, *Langmuir* 11, 4180 (1995).
85. A. P. Philipse, M. P. van Bruggen, and C. Pathmamanoharan, *Langmuir* 10, 92 (1994).
86. A. P. Philipse, A. M. Nechifor, and C. Pathmamanoharan, *Langmuir* 10, 4451 (1994).
87. Q. Liu, Z. Xu, J. A. Finch, and R. Egerton, *Chem. Mater.* 10, 3938 (1998).
88. M. A. Correa-Duarte, M. Giersig, N. A. Kotov, and L. M. Liz-Marzán, *Langmuir* 14, 6430 (1998).
89. L. N. Donselaar and A. P. Philipse, *J. Colloid Interface Sci.* 212, 14 (1999).
90. C. Graf, W. Schärtl, K. Fischer, N. Hugenberg, and M. Schmidt, *Langmuir* 15, 6170 (1999).
91. C. Roos, M. Schmidt, J. Ebenhoch, F. Baumann, B. Deubzer, and J. Weis, *Adv. Mater.* 11, 761 (1999).
92. M. Ohmori and E. Matijevic, *J. Colloid Interface Sci.* 160, 288 (1993).
93. L. M. Liz-Marzán and A. P. Philipse, *J. Colloid Interface Sci.* 176, 459 (1995).
94. L. M. Liz-Marzán, M. Giersig, and P. Mulvaney, *J. Chem. Soc., Chem. Commun.* 731 (1996).
95. L. M. Liz-Marzán, M. Giersig, and P. Mulvaney, *Langmuir* 12, 4329 (1996).
96. L. M. Liz-Marzán and P. Mulvaney, *New J. Chem.* 1285 (1998).
97. M. Giersig, L. M. Liz-Marzán, T. Ung, D. Su, and P. Mulvaney, *Ber. Bunsenges. Phys. Chem.* 101, 1617 (1997).
98. M. Giersig, T. Ung, L. M. Liz-Marzán, and P. Mulvaney, *Adv. Mater.* 9, 570 (1997).
99. S. S. Chang, C. W. Shih, C. D. Chen, W. C. Lai, and C. R. Wang, *Langmuir* 15, 701 (1999).
100. S. O. Obare, N. R. Jana, and C. J. Murphy, *NanoLetters* 1, 601 (2001).
101. S. R. Hall, S. A. Davis, and S. Mann, *Langmuir* 16, 1454 (2000).
102. V. V. Hardikar and E. Matijevic, *J. Colloid Interface Sci.* 221, 133 (2000).
103. Y. Yin, Y. Lu, Y. Sun, and Y. Xia, *NanoLetters* 2, 427 (2002).
104. E. Mine, A. Yamada, Y. Kobayashi, M. Konno, and L. M. Liz-Marzán, manuscript submitted for publication.
105. R. I. Nooney, T. Dhanasekaran, Y. Chen, R. Josephs, and A. E. Ostafin, *Adv. Mater.* 14, 529 (2002).
106. M. A. Correa-Duarte, M. Giersig, and L. M. Liz-Marzán, *Chem. Phys. Lett.* 286, 497 (1998).
107. M. Bruchez, Jr., M. Moronne, P. Gin, S. Weiss, and A. P. Alivisatos, *Science* 281, 2013 (1998).
108. D. Gerion, F. Pinaud, S. C. Williams, W. J. Parak, D. Zanchet, S. Weiss, and A. P. Alivisatos, *J. Phys. Chem. B* 105, 8861 (2001).
109. A. L. Rogach, D. K. Nagesha, J. W. Ostrander, M. Giersig, and N. A. Kotov, *Chem. Mater.* 12, 2676 (2000).
110. T. Li, J. Moon, A. A. Morrone, J. J. Mecholsky, D. R. Talhman, and J. H. Adair, *Langmuir* 15, 4328 (1999).
111. I. Pastoriza-Santos and L. M. Liz-Marzán, *Langmuir* 15, 948 (1999).
112. I. Pastoriza-Santos, D. Koktysch, A. Mamedov, N. A. Kotov, and L. M. Liz-Marzán, *Langmuir* 16, 2731 (2000).
113. D. S. Koktysh, X. Liang, B.-G. Yun, I. Pastoriza-Santos, R. L. Matts, M. Giersig, C. Serra-Rodríguez, L. M. Liz-Marzán, and N. A. Kotov, *Adv. Funct. Mater.* 12, 255 (2002).
114. K. S. Mayya, D. I. Gittins, and F. Caruso, *Chem. Mater.* 13, 3833 (2001).

115. K. S. Mayya, D. I. Gittins, A. M. Dibaj, and F. Caruso, *NanoLetters* 1, 727 (2001).
116. G. Oldfield, T. Ung, and P. Mulvaney, *Adv. Mater.* 12, 1519 (2000).
117. P. V. Kamat and B. Shanghavi, *J. Phys. Chem. B* 101, 7675 (1997).
118. R. Nayak, J. Galsworthy, P. Dobson, and J. Hutchinson, *J. Mater. Res.* 13, 905 (1998).
119. T. Hirano, T. Oku, and K. Suganuma, *J. Mater. Chem.* 9, 855 (1999).
120. V. Pillai and D. O. Shah, *Surfactant Sci. Ser.* (*Ind. App. Microemulsions*), 66, 227 (1997).
121. F. J. Arriagada and K. Osseo-Asare, *Colloids Surf.* 69, 105 (1992).
122. F. J. Arriagada and K. Osseo-Assare, *J. Colloid Interface Sci.* 170, 8 (1995).
123. J. Esquena, T. F. Tadros, K. Kostarelos, and C. Solans, *Langmuir* 13, 6400 (1997).
124. F. J. Arriagada and K. Osseo-Asare, *J. Colloid Interface Sci.* 211, 210 (1999).
125. P. D. Moran, J. R. Bartlett, J. L. Woolfrey, G. A. Bowmaker, and R. P. Cooney, *Ceram. Trans.* (*Ceram. Processing Sci. Technol.*) 51, 27 (1995).
126. V. Chhabra, V. Pillai, B. K. Mishra, A. Morrone, and D. O. Shah, *Langmuir* 11, 3307 (1995).
127. G. L. Li and G. H. Wang, *Nanostruct. Mater.* 11, 663 (1999).
128. M. Wu, J. Long, A. Huang, Y. Luo, S. Feng, and R. Xu, *Langmuir* 15, 8822 (1999).
129. H. Schmidt, C. Kropf, T. Schiestel, H. Schirra, S. Sepeur, and C. Lesniak, *Ceram. Trans.* 95, 49 (1998).
130. M. L. Curri, G. Palazzo, G. Colafemmina, M. Della Monica, and A. Ceglie, *Prog. Colloid Polym. Sci.* (*Trends Colloid Interface Sci. XII*) 110, 188 (1998).
131. P. A. Dresco, V. S. Zaitsev, R. J. Gambino, and B. Chu, *Langmuir* 15, 1945 (1999); L. Liz, M. A. López-Quintela, J. Rivas, and J. Mira, *J. Mater. Sci.* 29, 3797 (1994).
132. H. Herrig and R. Hempelmann, *Mater. Lett.* 27, 287 (1996).
133. L. Guo, Z. Wu, T. Liu, and S. Yang, *Physica E* 8, 199 (2000).
134. V. Arcoleo, M. Goffredi, A. Longo, and V. Turco Liveri, *Mater. Sci. Eng., C* 6, 7 (1998).
135. T. Liu, L. Guo, Y. Tao, Y. B. Wang, and W. D. Wang, *Nanostruct. Mater.* 11, 487 (1999).
136. T. Liu, L. Guo, Y. Tao, T. D. Hu, Y. N. Xie, and J. Zhang, *Nanostruct. Mater.* 11, 1329 (2000).
137. Z. Wu, R. E. Benfield, L. Guo, H. Li, Q. Yang, D. Grandjean, Q. Li, and H. Zhu, *J. Phys.: Condens. Matter* 13, 5269 (2001).
138. L. Quaroni and G. Chumanov, *J. Am. Chem. Soc.* 121, 10642 (1999).
139. A. Van Blaaderen and A. Vrij, *J. Colloid Interface Sci.* 156, 1 (1993).
140. W. Schärtl, *Adv. Mater.* 12, 1899 (2000).
141. W. Schärtl, G. Lindenblatt, A. Strack, P. Dziezok, and M. Schmidt, *Prog. Colloid Polym. Sci.* 110, 285 (1998).
142. M. Brust, J. Fink, D. Bethell, D. J. Schiffrin, and C. Kiely, *J. Chem. Soc., Chem. Commun.* 1655 (1995).
143. M. J. Hostetler, S. J. Green, J. J. Stockes, and R. W. Murray, *J. Am. Chem. Soc.* 118, 4212 (1996).
144. C. J. Kiely, J. Fink, M. Brust, D. Bethell, and D. J. Schiffrin, *Nature* 396, 444 (1998).
145. C. J. Kiely, J. Fink, J. G. Zheng, M. Brust, D. Bethell, and D. J. Schiffrin, *Adv. Mater.* 12, 640 (2000).
146. M. Sastry, in "Handbook of Surfaces and Interfaces of Materials" (H. S. Nalwa, Ed.), Vol. 3, p. 87. Academic Press, San Diego, 2001.
147. M. Brust and C. J. Kiely, *Colloids Surf., A* 202, 175 (2002).
148. S. L. Horswell, C. J. Kiely, I. A. O'Neil, and D. J. Schiffrin, *J. Am. Chem. Soc.* 121, 5573 (1999).
149. K. Hu Kai, M. Brust, and A. J. Bard, *Chem. Mater.* 10, 1160 (1998).
150. C.-J. Zhong and M. M. Maye, *Adv. Mater.* 13, 1507 (2001).
151. M. Z. Rong, L. Q. Ji, M. Q. Zhang, and K. Friedrich, *Eur. Polym. J.* 38, 1573 (2002).
152. G. Kickelbick and U. Schubert, *Chem. Ber.* 130, 473 (1997).

153. G. Kickelbick and U. Schubert, *Eur. J. Inorg. Chem.* 159 (1998).

154. G. Kickelbick, P. Wiede, and U. Schubert, *Inorg. Chim. Acta* 284, 1 (1999).

155. G. Kickelbick and U. Schubert, *J. Chem. Soc., Dalton Trans.* 1301 (1999).

156. B. Moraru, S. Gross, G. Kickelbick, G. Trimmel, and U. Schubert, *Monatsh. Chem.* 132, 993 (2001).

157. U. Schubert, E. Arpac, W. Glaubitt, A. Helmerich, and C. Chau, *Chem. Mater.* 4, 291 (1992).

158. B. Moraru, N. Hüsing, G. Kickelbick, U. Schubert, P. Fratzl, and H. Peterlik, *Chem. Mater.* 14, 2732 (2002).

159. G. Kickelbick and U. Schubert, *Eur. J. Inorg. Chem.* 159 (1998).

160. B. Moraru, G. Kickelbick, and U. Schubert, *Eur. J. Inorg. Chem.* 1295 (2001).

161. L. G. Hubert-Pfalzgraf, V. Abada, S. Halut, and J. Roziere, *Polyhedron* 16, 581 (1997).

162. M. Chatry, M. In, M. Henry, C. Sanchez, and J. Livage, *J. Sol-Gel Sci. Technol.* 2, 233 (1994).

163. E. Scolan and C. Sanchez, *Chem. Mater.* 10, 3217 (1998).

164. E. Scolan, C. Magenent, D. Massiot, and C. Sanchez, *J. Mater. Chem.* 9, 2467 (1999).

165. N. Tsubokawa, A. Kogure, and Y. Sone, *J. Polym. Sci.: Part A: Polym. Chem.* 28, 1923 (1990).

166. R. Jordan, N. West, A. Ulman, Y.-M. Chou, and O. Nuyken, *Macromolecules* 34, 1606 (2001).

167. Q. Zhou, S. Wang, X. Fan, R. Advincula, and J. Mays, *Langmuir* 18, 3324 (2002).

168. R. Laible and K. Hamann, *Angew. Makromol. Chem.* 48, 97 (1975).

169. G. Boven, M. L. C. M. Oosterling, G. Chella, and A. J. Schouten, *Polymer* 31, 2377 (1990).

170. O. Prucker and J. Rühe, *Macromolecules* 31, 602 (1998).

171. G. V. Schulz and G. Harborth, *Makromol. Chem.* 1, 106 (1948).

172. N. Tsubokawa and H. Ishida, *J. Polym. Sci.: Part A: Polym. Chem.* 30, 2241 (1992).

173. T. von Werne and T. E. Patten, *J. Am. Chem. Soc.* 121, 7409 (1999).

174. H. Böttcher, M. L. Hallensleben, S. Nuß, and H. Wurm, *Polym. Bull.* 44, 223 (2000).

175. G. Carrot, S. Diamanti, M. Manuszak, B. Charleux, and J.-P. Vairon, *J. Polym. Sci., Part A: Polym. Chem.* 39, 4294 (2001).

176. H. Mori, D. C. Seng, M. Zhang, and A. H. E. Müller, *Langmuir* 18, 3682 (2002).

177. S. Nuß, H. Bottcher, H. Wurm, and M. L. Hallensleben, *Angew. Chem., Int. Ed.* 40, 4016 (2001).

178. S. C. Farmer and T. E. Patten, *Chem. Mater.* 13, 3920 (2001).

179. M. Husseman, E. E. Malmström, M. McNamara, M. Mate, D. Mecerreyes, D. G. Benoit, J. L. Hedrick, P. Mansky, E. Huang, T. P. Russell, and C. J. Hawker, *Macromolecules* 32, 1424 (1999).

180. K. J. Watson, J. Zhu, S. T. Nguyen, and C. A. Mirkin, *J. Am. Chem. Soc.* 121, 462 (1999).

181. H. Skaff, M. F. Ilker, E. B. Coughlin, and T. Emrick, *J. Am. Chem. Soc.* 124, 5729 (2002).

182. K. Yoshinaga, Y. Tani, and Y. Tanaka, *Colloid Polym. Sci.* 280, 85 (2002).

183. C. Mangeney, F. Ferrage, I. Aujard, V. Marchi-Artzner, L. Jullien, O. Ouari, E. D. Rekaie, A. Laschewsky, I. Vikholm, and J. W. Sadowski, *J. Am. Chem. Soc.* 124, 5811 (2002).

184. G. Carrot, S. M. Scholz, C. J. G. Plummer, and J. G. Hilborn, *Chem. Mater.* 11, 3571 (1999).

185. R. Laible and K. Hamann, *Adv. Colloid Interface Sci.* 13, 65 (1980).

186. K. Ryan, *Chem. Ind.* 359 (1988).

187. B. Vincent, *Chem. Eng. Sci.* 48, 429 (1993).

188. K. Yoshinaga, *Surf. Sci. Ser.* (*Fine Particles*) 92, 626 (2000).

189. W. D. Hergeth, M. Peller, and P. Hauptmann, *Acta Polym.* 37, 468 (1986).

190. W. D. Hergeth, P. Starre, and K. Schmutzler, *Polymer* 29, 1323 (1988).

191. W. D. Hergeth, U. J. Steinau, H. J. Bittrich, G. Simon, and K. Schmutzler, *Polymer* 30, 254 (1989).

192. E. Bourgeat-Lami, P. Espiard, A. Guyot, S. Briat, C. Gauthier, G. Vigier, and J. Perez, *ACS Symp. Ser.* (*Hybrid Organic–Inorganic Composites*) 585, 112 (1995).

193. E. Bourgeat-Lami, P. Espiard, and A. Guyot, *Polymer* 36, 4385 (1995).

194. P. Espiard and A. Guyot, *Polymer* 36, 4391 (1995).

195. E. Bourgeat-Lami, P. Espiard, A. Guyot, C. Gauthier, L. David, and G. Vigier, *Angew. Makromol. Chem.* 242, 105 (1996).

196. E. Bourgeat-Lami and J. Lang, *J. Colloid Interface Sci.* 197, 293 (1998).

197. E. Bourgeat-Lami and J. Lang, *J. Colloid Interface Sci.* 210, 281 (1999).

198. E. Bourgeat-Lami and J. Lang, *Macromol. Symp.* 151, 377 (2000).

199. I. Sondi, T. H. Fedynyshyn, R. Sinta, and E. Matijevi, *Langmuir* 16, 9031 (2000).

200. N. Bechthold, F. Tiarks, M. Willert, K. Landfester, and M. Antonietti, *Macromol. Symp.* 151, 549 (2000).

201. J. Yu, J. Yu, Z.-X. Guo, and Y.-F. Gao, *Macromol. Rapid Commun.* 22, 1261 (2001).

202. P. A. Dresco, V. S. Zaitsev, R. J. Gambino, and B. Chu, *Langmuir* 15, 1945 (1999).

203. K. V. P. M. Shafi, A. Ulman, A. Dyal, X. Yan, N.-L. Yang, C. Estournes, L. Fournes, A. Wattiaux, H. White, and M. Rafailovich, *Chem. Mater.* 14, 1778 (2002).

204. H. Xia and Q. Wang, *Chem. Mater.* 14, 2158 (2002).

205. M. Gill, Michael, J. Mykytiuk, S. P. Armes, J. L. Edwards, T. Yeates, P. J. Moreland, and C. Mollett, *J. Chem. Soc., Chem. Commun.* 108 (1992).

206. M. Gill, F. L. Baines, and S. P. Armes, *Synth. Met.* 55, 1029 (1993).

207. S. Maeda and S. P. Armes, *J. Colloid Interface Sci.* 159, 257 (1993).

208. S. Maeda and S. P. Armes, *J. Mater. Chem.* 4, 935 (1994).

209. R. Flitton, J. Johal, S. Maeda, and S. P. Armes, *J. Colloid Interface Sci.* 173, (1995).

210. J. Stejskal, P. Kratochvil, S. P. Armes, S. F. Lascelles, A. Riede, M. Helmstedt, J. Prokes, and I. Krivka, *Macromolecules* 29, 6814 (1996).

211. M. D. Butterworth, S. P. Armes, and A. W. Simpson, *J. Chem. Soc., Chem. Commun.* 2129 (1994).

212. S. Maeda and S. P. Armes, *Synth. Met.* 69, 499 (1995).

213. C. Barthet, A. J. Hickey, D. B. Cairns, and S. P. Armes, *Adv. Mater.* 11, 408 (1999).

214. S. T. Selvan, J. P. Spatz, H.-A. Klok, and M. Möller, *Adv. Mater.* 10, 132 (1998).

215. W.-H. Li and H. D. H. Stöver, *Macromolecules* 33, 4354 (2000).

216. J.-E. Jönsson, H. Hassander, and B. Törnell, *Macromolecules* 27, 1932 (1994).

217. D. B. Cairns, S. P. Armes, and L. G. B. Bremer, *Langmuir* 15, 8052 (1999).

218. C. Lu and R. Pelton, *Colloids Surf., A* 201, 161 (2002).

219. M. Okaniwa, *Polymer* 41, 453 (1999).

220. S. Kirsch, A. Doerk, E. Bartsch, H. Sillescu, K. Landfester, H. W. Spiess, and W. Maechtle, *Macromolecules* 32, 4508 (1999).

221. R. Darkow, T. Groth, W. Albrecht, K. Lützow, and D. Paul, *Biomaterials* 20, 1277 (1999).

222. M. M. Guerrini, B. Charleux, and J.-P. Vairon, *Macromol. Rapid Commun.* 21, 669 (2000).

223. K. Min, J. Hu, C. Wang, and A. Elaissari, *J. Polym. Sci.: Part A: Polym. Chem.* 40, 892 (2002).

224. A. Yassar, J. Roncali, and F. Garnier, *Polym. Commun.* 28, 103 (1987).

225. C. F. Liu, T. Maruyama, and T. Yamamoto, *Polym. J.* 25, 363 (1993).
226. M. Iijima, Y. Nagasaki, T. Okada, M. Kato, and K. Kataoka, *Macromolecules* 32, 1140 (1999).
227. C. Pichot, A. Elaissari, D. Duracher, F. Meinier, and F. Sauzedde, *Macromol. Symp.* 175, 285 (2001).
228. C. D. Jones and L. A. Lyon, *Macromolecules* 33, 8301 (2000) and references therein.
229. D. Gan and L. A. Lyon, *J. Am. Chem. Soc.* 123, 7511 (2001).
230. K. L. Wooley, *J. Polym. Sci.: Part A: Polym. Chem.* 38, 1397 (2000).
231. K. B. Thurmond II, T. Kowalewski, and K. L. Wooley, *J. Am. Chem. Soc.* 118, 7239 (1996).
232. H. Huang, T. Kowalewski, E. E. Remsen, R. Gertzmann, and K. L. Wooley, *J. Am. Chem. Soc.* 119, 11653 (1997).
233. J. Tao, G. Liu, J. Ding, and M. Yang, *Macromolecules* 30, 4084 (1997).
234. Z. Zhang, G. Liu, and S. Bell, *Macromolecules* 33, 7877 (2000).
235. V. Buetuen, N. C. Billingham, and S. P. Armes, *J. Am. Chem. Soc.* 120, 12135 (1998).
236. V. Buetuen, A. B. Lowe, N. C. Billingham, and S. P. Armes, *J. Am. Chem. Soc.* 121, 4288 (1999).
237. A. Imhof, *Langmuir* 17, 3579 (2001).
238. R. Langer, *Science* 249, 1527 (1990).
239. T. Lea, F. Vartdal, K. Nustad, S. Funderud, A. Berge, T. Ellingsen, R. Schmid, P. Stenstad, and J. Ugelstad, *J. Mol. Recognit.* 1, 9 (1988).
240. F. Sauzedde, A. Elaissari, and C. Pichot, *Colloid Polym. Sci.* 277, 846 (1999).
241. T. Ji, V. G. Lirtsman, Y. Avny, and D. Davidov, *Adv. Mater.* 13, 1253 (2001).
242. N. Kawahashi and E. Matijevic, *J. Colloid Interface Sci.* 138, 534 (1990).
243. N. Kawahashi, C. Persson, and E. Matijevic, *J. Mater. Chem.* 1, 577 (1991).
244. H. Shiho and N. Kawahashi, *Colloid Polym. Sci.* 278, 270 (2000).
245. H. Shiho and N. Kawahashi, *J. Colloid Interface Sci.* 226, 91 (2000).
246. N. Kawahashi and H. Shiho, *J. Mater. Chem.* 10, 2294 (2000).
247. F. Caruso, M. Spasova, A. Susha, M. Giersig, and R. A. Caruso, *Chem. Mater.* 13, 109 (2001).
248. R. A. Caruso, A. Susha, and F. Caruso, *Chem. Mater.* 13, 400 (2001).
249. S. R. Whaley, D. S. English, E. L. Hu, P. F. Barbara, and A. M. Belcher, *Nature* 405, 665 (2000).
250. C. A. Mirkin, R. L. Letsinger, R. C. Mucic, and J. J. Storhoff, *Nature* 382, 607 (1996).
251. S.-J. Park, A. A. Lazarides, C. A. Mirkin, and R. L. Letsinger, *Angew. Chem., Int. Ed.* 40, 2909 (2001).
252. S. Mann, W. Shenton, M. Li, S. Connolly, and D. Fitzmaurice, *Adv. Mater.* 12, 147 (2000).
253. H. Mattoussi, J. M. Mauro, E. R. Goldman, G. P. Anderson, V. C. Sundar, F. V. Mikulec, and M. G. Bawendi, *J. Am. Chem. Soc.* 122, 12142 (2000).
254. A. P. Alivisatos, K. P. Johnsson, X. Peng, T. E. Wilson, C. J. Loweth, M. P. Bruchez, Jr., and P. G. Schultz, *Nature* 382, 609 (1996).
255. D. Gerion, W. J. Parak, S. C. Williams, D. Zanchet, C. M. Micheel, and A. P. Alivisatos, *J. Am. Chem. Soc.* 124, 7070 (2002).
256. W. C. W. Chan and S. Nie, *Science* 281, 2016 (1998).
257. G. P. Mitchell, C. A. Mirkin, and R. L. Letsinger, *J. Am. Chem. Soc.* 121, 8122 (1999).
258. Y. Cao, R. Jin, and C. A. Mirkin, *J. Am. Chem. Soc.* 123, 7961 (2001).
259. W. Shenton, S. A. Davis, and S. Mann, *Adv. Mater.* 11, 449 (1999).
260. T. A. Taton, R. L. Letsinger, and R. C. Mirkin, *Science* 289, 1757 (2000).
261. T. A. Taton, G. Lu, and C. A. Mirkin, *J. Am. Chem. Soc.* 123, 5164 (2001).
262. J. J. Storhoff, R. Elghanian, R. C. Mucic, C. A. Mirkin, and R. L. Letsinger, *J. Am. Chem. Soc.* 120, 1959 (1998).
263. Y. C. Cao, R. Jin, and C. A. Mirkin, *Science* 297, 1536 (2002).
264. J.-M. Nam, S.-J. Park, and C. A. Mirkin, *J. Am. Chem. Soc.* 124, 3820 (2002).
265. C. M. Niemeyer, *Angew. Chem., Int. Ed.* 40, 4128 (2001).

Crystal Engineering of Metallic Nanoparticles

A. Hernández Creus, Y. Gimeno

Universidad de La Laguna, La Laguna, Spain

R. C. Salvarezza, A. J. Arvia

Universidad Nacional de La Plata—CONICET, La Plata, Argentina

CONTENTS

1. INTRODUCTION

Metallic nano/mesoparticles supported on conducting substrates such as carbons are of interest due to their unique physical chemistry properties, making them of importance in different fields of applied science [1–10] and for the eventual development of new techniques. The technology used to produce preformed mass selected atomic clusters on carbons involves nanometer-sized systems in which, as a result of the reduced average atomic coordination, the quantum size effect, and the modified screening response, clusters display novel electronic and magnetic properties [11–12]. The physicochemical properties of nano/mesoparticles depend strongly on the perturbations that arise from the large area/volume atom ratio in relation to bulk metals. Therefore, the manageability of pattern morphology of nano/mesoislands is of importance in dealing with catalysts, electrocatalysis, and nano/microfabrication and in developing materials with interesting properties such as giant magneto resistances, high saturation-moments, and high anisotropic binary clusters. A great research effort has been made to develop a predictive understanding of the relationship between particle size and structure, and physicochemical properties such as electronic and magnetic properties.

The understanding of the reactivity of supported nanometer-sized particles in heterogeneous catalysis can be approached by either a molecular standpoint in which small soft-landed metal clusters of 5–50 atoms are considered, or by taking into account the reactivity of extended single-crystal surfaces. Both approaches have advantages and limitations, particularly to explain the behavior of supported clusters a few nm in diameter, due to their intrinsic heterogeneities [11–12]. Significant progress in this direction has been made in the understanding of size-dependent catalytic behavior, showing that the high activity requires the minimum size compatible with metallic properties. In contrast, the fabrication of the nano/mesoparticles remains at present a rather empirical task due to the fact that the physical processes that determine shape and size at the nanometer scale are not systematically identified.

Metal nano/mesoparticles can be prepared by different techniques, such as vapor deposition, ultrahigh vapor deposition, chemical vapor deposition, chemical impregnation, homogeneous reactions in solution, electroless deposition, and electrodeposition. The success in obtaining particles with defined physicochemical properties relies on the possibility of obtaining a narrow particle size distribution. Precisely, major efforts in nano/microparticle preparation by electrochemical methods have focused on improving particle size distribution. At present, very homogeneous size particles can be prepared by nucleation and growth from solution [1–10], although this goal is still a pending issue for obtaining metallic particles supported on solid substrates [13–14]. For the latter, most of the present methods result in the formation of particles with a broad particle size distribution function, the broadening being dependent on growth conditions.

In principle, metal electrodeposition appears as an excellent route for nano/mesoparticle preparation on conducting substrates due to the easy control of the experimental variables [13–18]. In this method the reaction rate can be easily adjusted either for a surface reaction or for a reaction under a mass-transport kinetic regime. Therefore, metal electrodeposition can be taken as a model system to investigate possible relationships between particle size and shape, and growth kinetics. Recently, the preparation of narrowly dispersed particles with average diameter at the nano/micro scale and relative standard deviation RSD $\leq$ 30% by electrodeposition has been accomplished [13–14]. In this case, mesoparticles have been modeled as simple hemispherical objects produced either by using double pulse electrodeposition to nucleate first a large number of particles that later are allowed to grow slowly on the substrate, or metal and hydrogen codeposition under forced convection due to bubbles at the microscale [13–14].

For further advances in the above mentioned matters, one should understand the entire kinetics and mechanisms of the process at different length and time scales. This fundamental knowledge would provide a rational approach to prepare mesoparticles with different structures and shapes, to discover how physical and chemical processes determine particle structure and shape, and to determine the dependence of the physicochemical properties of mesoparticles on their structure and shape. Manipulation of mesoparticles is a "nanostructuring" problem, deserving theoretical and experimental consideration. Therefore, a combination of theoretical models that have been developed to understand the relationship between growth kinetics, shape, and structure based on both Euclidean and fractal concepts, and powerful experimental techniques able to image these objects at the nanometer scale, such as scanning tunneling microscopy (STM) and atomic force microscopy (AFM), is required.

In this contribution, the state-of-the-art concerning our ability to handle physical variables of remarkable influence in determining the structure/shape of metal nano/mesoparticles produced by electrodeposition on highly oriented pyrolytic graphite (HOPG), that is, the basal plane of graphite (C(0001)), and to evaluate their catalytic activity for some test reactions is reviewed. Among the different carbon substrates HOPG exhibits unique properties for studies at the nanometer level by scanning probe microscopies (STM and AFM) because it is atomically smooth and chemically inert. Metal electrodeposition on HOPG was taken as a model system to disperse metallic particles, because it is a smooth substrate in which no metal underpotential deposition takes place, as in no complete metallic adlayer is produced [19]. In fact, due to the large difference between the metal and the carbon surface tension, metal particle deposition on HOPG follows the Volmer–Weber mechanism [20] rather than the Stranski–Krastanov [21] and the van der Merwe mechanisms [22] (Fig. 1). Furthermore, metallic particles dispersed on carbon are important in dealing with a number of electrocatalytic and heterogeneous catalytic systems [23]. Metal electrodeposition on HOPG has also been taken as a model system for the development of a new technology for nanostructure fabrication1 at wafer scale [24] and for the preparation of
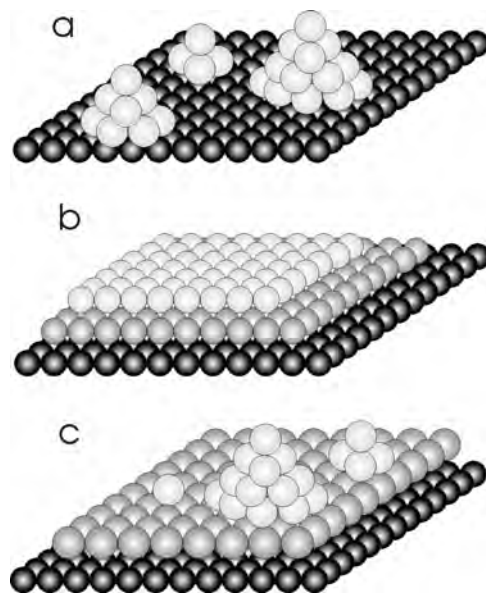
Figure 1. Different growth modes of metal deposition on foreign substrate. (a) Volmer–Weber mechanism, 3-D metallic islands. (b) Frank–van der Merwe mechanism, layer by layer growth. (c) Stranski–Krastanov mechanism, 3-D islands on top of 2-D layer.

metallic wires [25, 26] as promising interconnectors in future nanoscale electronics. Metal-patterned HOPG has also been considered for directly embossing different polymeric materials [27].

The presentation of the material is organized as follows. First, some fundamental aspects of electrochemistry related to metal electrodeposition are described. Then, the preparation methods of metal nano/mesoparticles are considered. Special attention to the electrodeposition of crystals of platinum, palladium, and gold on HOPG is paid. These are typical examples of metal electrodeposition from which kinetic conclusions applicable to the growth of other metallic phases can be drawn. The correlation between kinetics and particle structure from the early stages of growth onward is described. Later, the electrodeposition parameters and the size and shape of HOPG-supported crystals are related to the physicochemical processes that determine the shape and structure at different temporal and length scales. In the third section, we compare nanoparticle growth by electrochemical techniques with vapor deposition methods. The influence of the applied electric potential on crystal shape is discussed. Finally, typical applications of metallic deposits supported on HOPG in nanowires, embossing, and electrocatalysis are given.

2. BASIC ELECTROCHEMICAL ASPECTS

2.1. Substrate Characterization

HOPG is commonly used in STM and AFM studies [28] because it exhibits micrometer-sized atomically smooth terraces separated by steps 0.35 nm in height (Fig. 2a) that
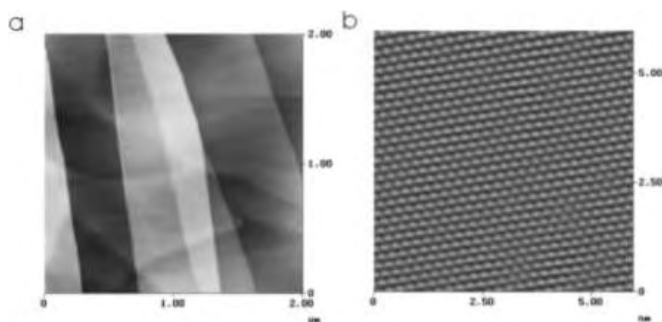
Figure 2. STM images of freshly exfoliated HOPG surface. (a) $2 \times 2 \ \mu m^2$, large and smooth terraces separated by steps are clearly seen. (b) Atomic resolution, $6 \times 6 \ nm^2$. Bright spots correspond to carbon atoms.

correspond to the interlayer spacing. Also, HOPG is chemically inert and can be handled in the atmosphere with negligible contamination. It is used for (x, y) piezoelectric calibration at the atomic level in STM. The STM imaging of a HOPG surface originates reproducible atomically resolved hexagonal lattices with $d = 0.246$ nm, where three of the six carbon atoms of the honeycomb structure of graphite are imaged (Fig. 2b). The smoothness of the HOPG surface in relation to other carbon substrates such as mechanically polished vitrous carbon, fractured vitrous carbon, and amorphous carbon turns it into the best substrate to study the morphology of nano/mesometallic particles.

2.2. Electrochemical Deposition of Metals

Metal particles dispersed on a HOPG surface can most frequently be obtained by electrodeposition from aqueous electrolyte solutions containing a relatively small concentration of depositing ions as either cations or anions. The electrochemical cell (Fig. 3) usually consists of a working cathode, such as a freshly exfoliated HOPG surface, a large area noble metal counter electrode, and a reference electrode.
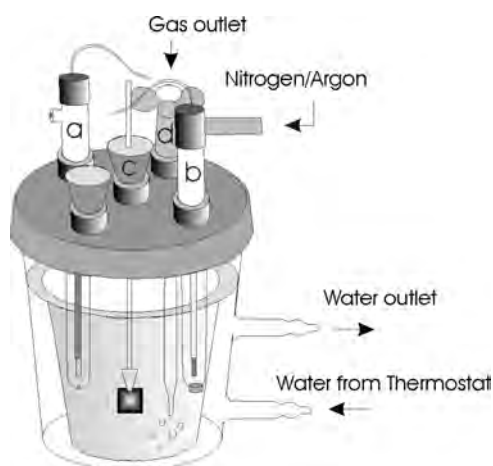
Figure 3. Conventional three-electrode water-jacket electrochemical cell. (a) Reference electrode. (b) Counter electrode. (c) Working electrode. (d) Inert gas bubbler.

In general, the plating solution is deareated and kept under an inert atmosphere (argon or nitrogen) to suppress any interference of the oxygen electroreduction reaction at the cathode. The electrochemical cell is operated by a potentiostat that permits one to select either a constant potential or a constant current regime under nonstationary conditions when the electrolysis time (t_d) is properly adjusted to avoid both the coalescence of growing particles and the formation of a continuous metal layer.

Electrodeposition under potential control can be made by applying either a constant potential (E_d) or a linear potential sweep ($E_d = E_o - vt_d$, where E_o is the starting potential and v is the potential sweep rate). In the former case, the current transient (I_c versus t_d, where I_c is the electrodeposition current) is recorded. The integration of this transient yielding the electrodeposition charge (Q_c) passes between $t = 0$ and $t = t_d$. For the latter, the electrodeposition voltammogram is obtained, that is, the E versus I_c plot at the rate v, and the value of Q_c can also be determined from the voltammogram.

For electrodeposition under a constant current (galvanostatic), the potential transient (E_c versus t_d) is recorded. This procedure is interesting for electrodeposition under a constant flow of discharging ions on the cathode. The values of I_c and Q_c are usually referred to as the unit surface area (A) of the substrate as current density (j_c) and charge density (q_c) because a reliable definition of A for dispersed particles on a solid surface is not always feasible. Further details on electrochemical deposition techniques are given in reference [29].

3. ELECTROCHEMICAL PREPARATION

3.1. Previous Work

Metal particles of silver, gold, palladium, molybdenum, copper, and platinum can be easily electrodeposited on HOPG [13–18, 25, 26, 30–33]. Platinum mesoparticles (ca. 0.1 μm in diameter) on glassy carbon have been electrodeposited from H_2PtCl_6 in the potential of the first electroreduction wave (0.2 to 0.5 V versus SCE). At loading levels 10–20 μg cm^{-2}, these electrodes exhibit high particle stability and an exchange current density value for hydrogen evolution comparable to that for bulk platinum [34, 35]. Platinum particles of 2–2.5 nm diameter can also be formed by spontaneous reduction of H_2PtCl_6 at the plane edges and basal plane of HOPG caused by the incompletely oxidized surface functional carbon group [36]. Potentiostatic deposition on pyrolytic graphite of roughly circular platinum particles 0.3–1 μm in diameter, spatially distributed in a random fashion, has also been reported [37].

The electrodeposition of platinum on HOPG has been followed by AFM tapping mode. In the absence of a supporting electrolyte, two-dimensional (2-D) nanoparticles aggregate after reaching a critical mobile particle size. Subsequent growth is dominated by surface diffusion of mobile platinum particles. In aqueous perchloric acid, three-dimensional (3-D) growth is the dominant mechanism competing with 2-D/3-D growth. This leads to various morphologies. The process is also influenced by the presence of specifically adsorbed anions [38].

Platinum nanoparticles have been electrocrystallized on HOPG by a first reactant electrostatic adsorption, followed by electrochemical reduction on a 4-aminophenyl monolayer-grafted carbon substrate. The STM imaging shows a good size monodispersivity and particles well separated from one another [39].

Metal nano- and microparticles of silver, gold, platinum, molybdenum, and nickel narrowly dispersed by electrodeposition on HOPG have been formed by a two-step method—a 5 msec potential step to nucleate particles at an overvoltage $\eta_c = -0.5$ V, and a growth pulse set in the range $-0.02 \leq \eta_c \leq 0.250$ V to reach the desired particle diameter. The slow growth process leads to a particle dispersion ranging from 50 nm to 2 μm in diameter with a RSD as low 7% [13–14].

Carbon electrodes with an effective fiber radius of 1 nm can be prepared by different procedures: electrochemical etching of a carbon fiber, deposition of electrophoretic paint, and an inverted deposition technique for insulating the tip. Thus, the complete insulation of the whole body of the carbon fiber, except tip pinhole formation, is avoided [40].

3.2. Potentiodynamic Electrodeposition

A typical potentiodynamic polarization curve (j_c versus E_d) for metal electrodeposition on HOPG is shown in Figure 4 [41]. The values of E_d are referred to the standard calomel electrode scale. This example corresponds to palladium electrodeposition at $v = 5 \times 10^{-3}$ V/s from a palladium chloride-containing aqueous solution at 298 K [41]. The electrochemical deposition of a metal (Me) can be produced either from the discharge metal of ions (Me^{z+}) of charge z,

$$\text{Me}^{z+}(\text{aq}) + z\text{e}^- = \text{Me}(0) \qquad (1a)$$

or from the discharge of a metal-containing complex anion (MeX$_n^{z-}$) containing n ligands and charge z,

$$\text{MeX}_n^{z-}(\text{aq}) + z'\text{e}^- = \text{Me}(0) + n\text{X}^{(z+z')-} \qquad (1b)$$
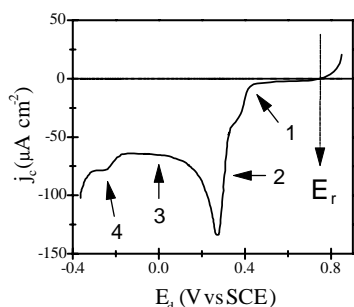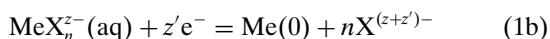
Figure 4. Potentiodynamic polarization curve of HOPG in aqueous 7.5×10^{-4} M palladium chloride $+ 5 \times 10^{-2}$ M sodium perchlorate $+ 5 \times 10^{-3}$ M perchloric acid run from 0.85 V to -0.35 V at $v = 5 \times 10^{-3}$ V/s; 298 K. The cathodic current density (j_c) is referred to the working electrode geometric area. (1) Beginning of metal electrodeposition. (2) Main cathodic current peak. (3) Cathodic limiting current. (4) Hydrogen evolution reaction. The reversible potential (E_r) for Pd electrodeposition is indicated.

The reversible potential E_r of Equations (1a) and (1b) are given by the following Nernst equations, respectively,

$$E_r(1a) = E^o(1a) + (\mathbf{R}T/z\mathbf{F})\ln a[\text{Me}^{z+}]/a[\text{Me}(0)] \qquad (2a)$$

and

$$E_r(1b) = E^o(1b) + (\mathbf{R}T/z'\mathbf{F})\ln a[\text{MeX}_n^{z-}]$$
$$/a[\text{Me}(0)]a[\text{X}^{(z+z')-}]^n \qquad (2b)$$

$E^o[N]$, $N = $ (1a), (1b), and $a[i]$ being the standard potential and the activity of species i, and z, $\mathbf{F}$ and T the number of electrons per reacting species involved in the reaction, the Faraday constant (96,500 C/equivalent) and the absolute temperature, respectively. The activity of the metal is taken as 1. For values of E_d more negative than E_r, the cathodic potentiodynamic polarization curve first exhibits a low current portion (Fig. 4, region 1) extending from E_r to a value of E_d where a rapid increase in j_c leading to a current maximum (Fig. 4, region 2) is observed. As E_d is further increased negatively, the cathodic current density attains a limiting value j_L (Fig. 4, region 3) that extends to the potential range where the hydrogen electrode reactions on electrodeposited palladium commence (Fig. 4, region 4). Often, the first low current region approaches a E_d versus $\ln j_c$ linear relation indicating that the kinetics of metal electrodeposition is under charge-transfer control. However, as E_d is shifted more negatively, the kinetics of the electrodeposition reaction turns into a mass transport regime from the solution side to the cathode surface.

3.3. Potentiostatic Electrodeposition

Detailed information of the nucleation and growth of metallic particles on foreign substrates can be obtained from potentiostatic current transients. In this case, for diluted solutions, these transients exhibit a rapid increase in current that is frequently observed for the nucleation and growth of metal particles under mass transport control. Thus, following the potential step at E_d, the diffusion zones built up around growing nuclei begin to overlap, and after a time (t_M) the growth kinetics become a linear diffusion-controlled process. Finally, for a t_c that depends on E_d, the contribution of free convection increases, and j_c approaches the j_L value (Fig. 4, region 3).

Potentiostatic current transients run at different E_d can be analyzed with growth models that are applicable to the electrochemical formation of a new solid phase on a conducting substrate. Further details related to this subject are extensively described in the literature (see, e.g., [19]).

Current transients for palladium electrodeposition on HOPG were obtained by stepping the potential from $E \geq E_r$ to values of E_d lying within the different potential windows of the palladium electrodeposition regions (Fig. 4) [41]. For the potential regions 2–4 (Fig. 4), the current transients (Fig. 5a) exhibit an initial fast current decay due to the contribution of the double-layer charging that is significant for $t_d < 1$ sec. Subsequently, a fast increase in current up to a maximum value j_M at time t_M is observed. Subsequently, a slow decay characterized by a j_c versus $t_d^{-1/2}$ dependence is observed (Fig. 5b), as expected for a diffusion kinetic regime
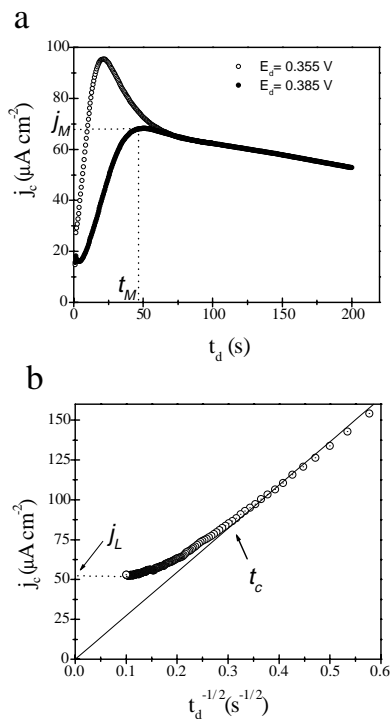
Figure 5. Potentiostatic current transients (j_c versus t_d) for palladium electrodeposition on HOPG using the same solution as in Figure 4. (a) $E_d = 0.355$ V (o), $E_d = 0.385$ V (•). The current maximum j_M at t_M is indicated. (b) j_c versus $t_d^{-1/2}$ plot from current transient run at $E_d = -0.100$ V. The straight line corresponds to Cottrell–Sand equation for linear diffusion. The arrows indicate the j_L and t_c values. Reprinted with permission from [41], Y. Gimeno et al., *J. Phys. Chem. B* 106, 4232 (2002). © 2002, American Chemical Society.

from the solution. As E_d is negatively increased j_M increases and t_M decreases. In all cases, after an E_d-dependent time t_c that is usually less than 30 sec, free convection sets in and all transients tend to approach the quasisteady convective-diffusion regime (Figs. 4 and 5b). Therefore, depending on t_d, the kinetics of palladium electrodeposition changes from a linear diffusion to convective diffusion control.

4. CRYSTAL GROWTH KINETICS

4.1. Initial Stages of Growth

Current transients similar to those described above for palladium electrodeposition have also been obtained for the electrodeposition of silver, palladium, gold, platinum, cadmium, and copper on HOPG from diluted aqueous solutions for $t_d \ll t_c$ [13, 33, 41]. These transients often fit equations predicted by either instantaneous or progressive nucleation and 3-D growth models under diffusion control [42–45]. The j_c versus t_d relationship can be expressed by the equations proposed by Scharifker and Hills [44], either for instantaneous nucleation,

$$j_c = (z\mathbf{F}c_i D_i^{1/2}/\pi^{1/2}t_d^{1/2})[1 - \exp(-\pi K_e D_i N_o t_d)] \quad (3a)$$

or for progressive nucleation,

$$j_c = (z\mathbf{F}c_i D_i^{1/2}/\pi^{1/2}t_c^{1/2})$$
$$\times [1 - \exp(-\pi K_e' D_i N_o A_c t_d^2/2)] \quad (3b)$$

In Equations (3a) and (3b), D_i, and c_i are the diffusion coefficient and the concentration of the electroactive species (i) in the bulk of the solution, respectively; N_o is the number of sites available for nucleation on the HOPG substrate; $K_e = (8\pi c_i M/\rho)^{1/2}$ and $K_e' = 4/3(8\pi c_i M/\rho)^{1/2}$; M and ρ are the molar mass and the density of the deposited metal, respectively; and A_c is the site-to-nucleous conversion frequency. Equations (3a) and (3b) reproduce the current transients for different metal electrodepositions. Figure 6 shows current transients for gold electrodeposition on HOPG and the comparison of these data to predictions from the models. More refined models including "clear field" effects around growing nuclei have been proposed [46, 47].

The nucleation rate ($A_c N_o$) for progressive nucleation can be determined from the current density transient maxima resulting from relatively low cathodic overvoltages, $\eta_c = E_d - E_r$. However, as very often current density maxima at high values of η_c are not observable at the time scale of conventional transient measurements, values of $A_c N_o$ can be estimated from the N_c versus t_d plots derived from STM and AFM imaging, and SEM micrograph data, using equation [44, 45, 48]

$$N_c = N_o[1 - \exp(-A_c t_d)] \quad (4)$$

N_c being the number of nuclei at t_d. Data from palladium electrodeposition were plotted according to Equation (4) (Fig. 7). In this case, for -0.10 V $< E_d < 0.365$ V, values of $A_c N_o$ fulfill equation [19, 47] (Fig. 8)

$$A_c N_o = K_1 \exp(-K_2/\eta_c^2) \quad (5)$$

In Equation (5), K_1 depends on both the nucleous dimension (2-D, 3-D) and nucleation mechanism, as in, whether the metal lattice grows under diffusion or charge transfer
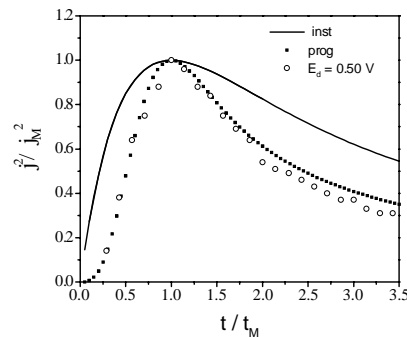
Figure 6. Comparison of normalized current transient data (j_c/j_M versus t_d/t_M) for gold electrodeposition on HOPG at $E_d = 0.500$ V from aqueous 5×10^{-4} M gold chloride + 0.5 M sodium perchlorate + 1×10^{-2} M perchloric acid. Predictions from equations [3a and 3b] for the instantaneous (—) and progressive (...) nucleation and growth model under diffusion control are indicated.
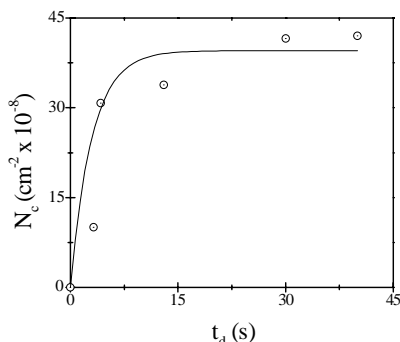
Figure 7. N_c versus t_d plot for palladium electrodeposition on HOPG from the same solution as in Figure 4 and $E_d = -0.100$ V. The solid line corresponds to Eq. (4). Reprinted with permission from [41], Y. Gimeno et al., *J. Phys. Chem. B* 106, 4232 (2002). © 2002, American Chemical Society.

control. The constant K_2 is related to A_c by the following relationship [48]

$$K_2/\eta_c^2 = A_c/\mathbf{k}T \qquad (6)$$

$\mathbf{k}$ being Boltzmann constant. Equation (6) implies a linear $A_c N_o$ versus η_c^{-2} relationship (Fig. 8), and the value of K_2 can be determined from the slope of this linear plot. Likewise, the number of atoms (n^*) involved in the formation of the critical nucleus can be calculated from the expression

$$n^* = 2A_c/z\mathbf{e}_o(E_d - E_r) \qquad (7)$$

with $\mathbf{e}_o = 1.60 \times 10^{-19}$ Coulomb. Then, by combining Equations (6) and (7), it is possible to estimate values of n^* at different E_d. For palladium electrodeposition it results in $n^* = 2$ for $E_d = 0.38$ V, and $n^* = 0$ for $E_d = -0.1$ V. Comparable values of n^* have been reported for the electrocrystallization of several metals on foreign substrates [19]. In all these cases, the decrease in n^* with E_d has been related to a decrease in the activation energy for nucleation with η_c. Thus, combined electrochemical and microscopy data can be used to obtain reliable information about the very early stages of growth of metal nucleus on HOPG.
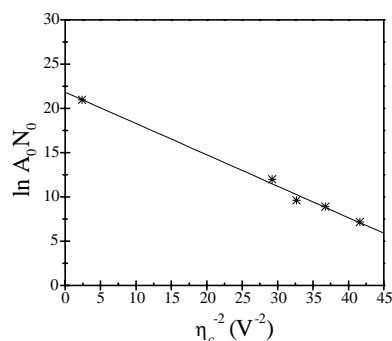
Figure 8. $\mathrm{Ln}(A_c N_0)$ versus $1/\eta_c^2$ plot to estimate the number of atoms at the critical nucleus (n^*). Data obtained from the same solution as in Figure 4. Reprinted with permission from [41], Y. Gimeno et al., *J. Phys. Chem. B* 106, 4232 (2002). © 2002, American Chemical Society.

The preceding analysis points out that model predictions exclusively derived from electrochemical data should be checked against direct data from either STM or AFM imaging or SEM micrographs. In fact, for a number of metal electrodeposits, large discrepancies between values of N_o from imaging data and the number density of nuclei resulting from electrochemical data have been observed [32]. Likewise, for a particular system, the value of N_o depends on the carbon substrate. For silver electrodeposition on HOPG, the value of N_o increases from 5.7×10^6 to 3×10^7 cm^{-2} as E_d is shifted negatively, whereas values of N_o one order of magnitude smaller have been determined on mechanically polished vitrous carbon.

For an isolated nucleus, Equations (3a) and (3b) imply a radial growth equation of the form $\langle r \rangle \approx t_d^{1/2}$, where $\langle r \rangle$ is the average radius of the growing nucleous. This equation is obeyed by data from the initial stages of platinum electrodeposition on HOPG [38]. Furthermore, for $t_d > t_M$ the current decay obeys a $j_c \approx t_d^{-1/2}$ relationship (Fig. 6) as expected for pure diffusion. This behavior for j_c, which is observed in the range $t_M \leq t_d \leq t_c$, has also been found for the electrodeposition of different metals from diluted solutions [32, 33, 41, 42]. Deviations from the $j_c \approx t_d^{1/2}$ behavior are observed for $t_d \geq t_c$, as in when j_c tends asymptotically to j_L.

4.2. Electrodeposition Parameters: Shape and Size of Metal Crystals

The initial stages of metal electrodeposition on HOPG have been extensively studied by *in-situ* and *ex situ* STM and AFM combined with electrochemical techniques [19, 30, 31]. When electrodeposition proceeds close to equilibrium conditions, such as when E_d is slightly more negative than E_r, and a small charge density is involved, in the initial stages already metallic agglomerates (clusters) 1–2 nm in average diameter preferentially nucleated at step edges are produced. Under these conditions, there is agreement that the electrodeposition process takes place by the Volmer–Weber [20] growth mechanism (Fig. 1). For silver electrodeposition from acid plating solutions, the appearance of small ordered metallic domains has also been observed near step edges, probably acting as precursors to clustering [30]. For copper electrodeposition on HOPG, the formation of periodic arrays of clusters 2 nm in diameter following step edges has been observed [24]. Similar results have been obtained for platinum electrodeposition from acid plating baths on the same substrate [31], yielding clusters of average diameter $\langle d \rangle$ that roughly increases with t_d as $\langle d \rangle \approx t_d^{1/2}$ [49]. The aspect ratio (f) defined as the average height-to-average radius ratio is always small, $f = \langle h \rangle / \langle r \rangle \approx 0.1$.

The increase in either t_d or q_d as E_d is made slightly more negative than E_r, as in still maintaining a slow growth rate, results in the development of larger crystals that tend to develop regular patterns. Thus, at this stage, silver electrodeposition on HOPG yields triangular islands with closely packed (111) faces [31], whereas palladium electrodeposition on the same substrate produces quasi-hexagonal crystals [41]. Under comparably applied potential conditions [50], tetragonal tin crystals on both vitreous carbon and on

HOPG were grown from aqueous tin sulphate-sulphuric acid solution.

The increase in metal electrodeposition rate dramatically affects the shape and density of growing crystals. As a typical example, let us consider palladium electrodeposits on HOPG obtained for $q_d = 5$ mC/cm^2 as the electrodeposition rate is increased by shifting E_d negatively (Fig. 9). Thus, for $E_d = 0.380$ V ($E_d < E_r$), faceted hexagonal crystals with $\langle r \rangle = 200$–500 nm are grown (Fig. 9a) [41]. The corresponding crystal density evaluated from SEM micrographs is $N_c = 0.4 \times 10^8$ cm^{-2}. For $E_d = 0.125$ V, N_c increases to 3.6×10^8 cm^{-2} and $\langle r \rangle$ decreases markedly (Fig. 9b). The size distribution of these crystals is rather homogeneous with $\langle r \rangle \cong 80$ nm. The average height of these crystals measured from STM images is $\langle h \rangle = 35$ nm. Accordingly, the value f is still low enough to describe crystals as compact rounded disks rather than hemispherical crystals. On the other hand, for $E_d = -0.1$ V ($E_d \ll E_r$), such as when E_d is set in the potential range just preceding the hydrogen evolution reaction threshold potential, a large number, $N_c = 4 \times 10^9$ cm^{-2}, of small branched palladium crystals with $\langle r \rangle = 70$ nm is formed (Fig. 9c). The detailed structure of these small islands can only be resolved by STM imaging (Fig. 9d). A similar dependence of the crystal shape and size on E_d has also been observed for gold electrodeposits on HOPG [33].

The growth of the branched gold and palladium crystals for $E_d = -0.1$ V and different values of q_d was followed by sequential STM imaging. It should be noted that $q_d \propto t_d$. Thus, for $q_d = 1$ mC/cm^2 (Fig. 10a), irregular crystals with protrusions either randomly distributed over HOPG terraces or aligned and coming into contact with neighboring crystals, decorating HOPG steps are observed. The palladium crystals grown along step edges form metallic mesowires that have been recently used as hydrogen sensors [25]. Higher
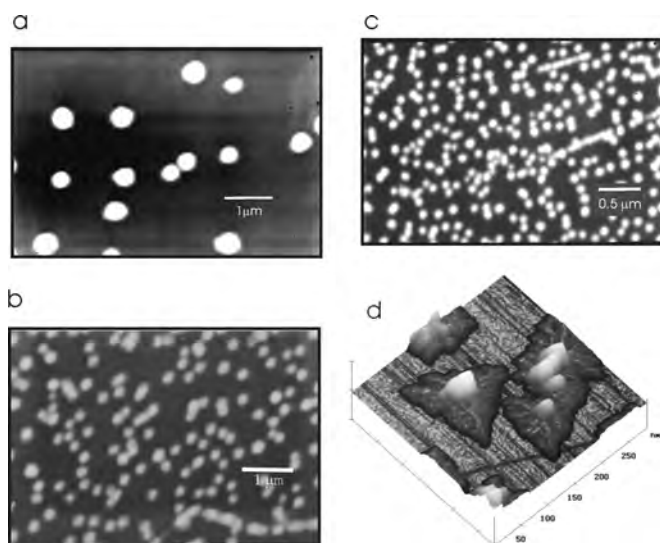
Figure 9. SEM micrographs of palladium electrodeposits on HOPG obtained from the same solution as in Figure 4; $q_d = 5$ mC/cm^2. (a) $E_d = 0.380$ V. (b) $E_d = 0.125$ V. (c) $E_d = -0.100$ V. (d) STM image (280 × 280 nm^2) of palladium branched islands ($E_d = -0.100$ V) $q_d = 3$ mC/cm^2. The bar corresponds to $z = 40$ nm. Reprinted with permission from [41], Y. Gimeno et al., *J. Phys. Chem. B* 106, 4232 (2002). © 2002, American Chemical Society.
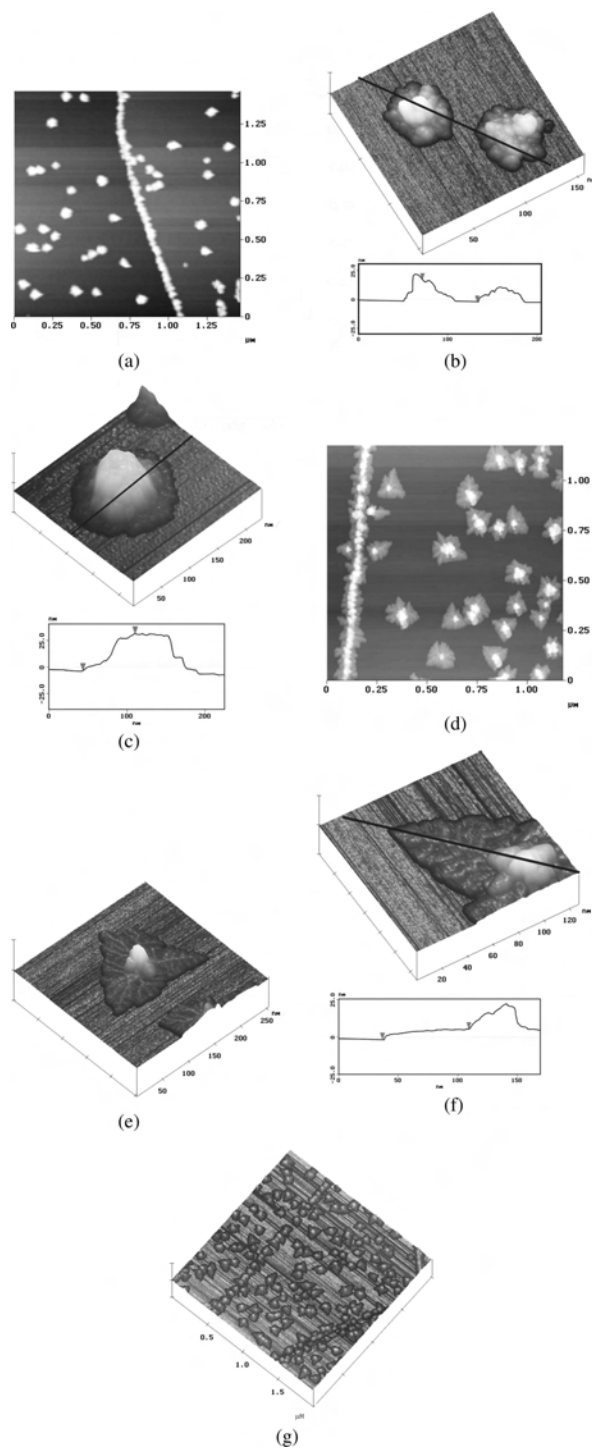
Figure 10. STM images of palladium islands on HOPG electrodeposited at $E_d = -0.100$ V from the same solution as in Figure 4. (a) 1.5×1.5 μm^2; $q_d = 1$ mC/cm^2. (b) Higher resolution 3-D STM image (156×156 nm^2), $q_d = 1$ mC/cm^2, $z = 40$ nm, and cross section. (c) 0.23×0.23 nm^2 STM image, $q_d = 1.5$ mC/cm^2, $z = 40$ nm, and cross section. (d) STM image of branched islands (1.25×1.25 μm^2), $q_d = 3$ mC/cm^2, $z = 40$ nm. (e) 3-D STM image of a triangular island (0.25×0.25 μm^2), $q_d = 3$ mC/cm^2, $z = 40$ nm. (f) 3-D detail and cross section of a palladium main branch, $q_d = 3$ mC/cm^2, $z = 40$ nm. (g) Branched islands (2×2 μm^2), $q_d = 4$ mC/cm^2, $z = 200$ nm. Reprinted with permission from [41], Y. Gimeno et al., *J. Phys. Chem. B* 106, 4232 (2002). © 2002, American Chemical Society.

resolution STM images (Fig. 10b) show that each metallic island consists of an agglomeration of small quasispherical particles with $5 \leq \langle d \rangle \leq 15$ nm forming a 3-D core. For $q_d = 1.5$ mC/cm^2 instabilities at crystal edges can be seen (Fig. 10c), and for $q_d = 3$ mC/cm^2, a net distinction between the central 3-D core and the 2-D branched pattern originated by instabilities around the core is observed (Fig. 10d). The quasi-2-D branched pattern is revealed by the fact that the maximum height of crystals remains almost the same as that of the 3-D core initially formed. Consistent with a (111) metallic lattice, the 2-D pattern around the core shows a net tendency to develop triangular crystals with most of the 2-D branches merging at 120° (Fig. 10e). Similar gold and palladium islands with preferential orientation (111) were grown on HOPG by vapor phase deposition at room temperature [51].

As recently reported [52, 53], STM images of palladium triangular crystals on HOPG produced from the vapor phase deposition demonstrate that for every stage before and after heating, irrespective of the degree of surface coverage, the deposit grows epitaxially in the fcc(111) direction. For palladium, secondary branches are separated by thin "fjords" 10 nm in width emerging from each main branch that have a tendency to produce a dense growth pattern. These patterns closely resemble those dense radial morphologies that have been observed for several metallic electrodeposits with a non-fractal mass and a self-affine fractal perimeter [54, 55]. Considering the crystal as a 2-D object, the fractal dimension (D_F) of branched crystal edge is $D_F = 1.3$. On the other hand, gold crystals tend to produce dendritic patterns with $D_F = 1.76$ [55]. Procedures for calculation of the fractal dimension of metallic crystals are given in [54–58].

For both gold and palladium electrodeposits, the cross section of crystals taken from the core border down to the tip of a main branch (Fig. 10f) approaches a 2-D profile with terraces almost atomically smooth (Fig. 10f, cross section). The height of each main branch decreases only about 5 nm in going from the core border to the branch tip with an average slope close to 3–4°. These tapering effects of the main branches mostly involve steps one atom high. Typical branch tip radii are close to 10 nm, whereas the tip height fluctuates between 2 and 4 nm. Finally, for $q_d = 4$ mC/cm^2 (Fig. 10g), the increase in both N_c and $\langle r \rangle$ leads to the partial overlap of neighbor branch centers.

The full width at one-half maximum height value (FWHM) from the crystal size distribution function of these palladium crystals increases with q_d (Fig. 11a–c) [13–14]. Thus, the relative standard deviation (RSD) in crystal diameter increases from 8.7% to 15.4% as $\langle d \rangle$ increases from 70 nm ($q_d = 1$ mC/cm^2) to 140 nm ($q_d = 3$ mC/cm^2).

4.3. Quantitative Kinetic Data from Different Stages of Growth

Quantitative kinetic data for the different stages of metal crystal growth can be obtained from the time dependence $\langle r \rangle$ and $\langle h \rangle$ derived by sequential STM and AFM images, as well as SEM micrographs. For the latter, in the case of 2-D-type deposits, only values of $\langle r \rangle$ can be derived. In general, both $\langle r \rangle$ and $\langle h \rangle$ fulfill power law dependences with
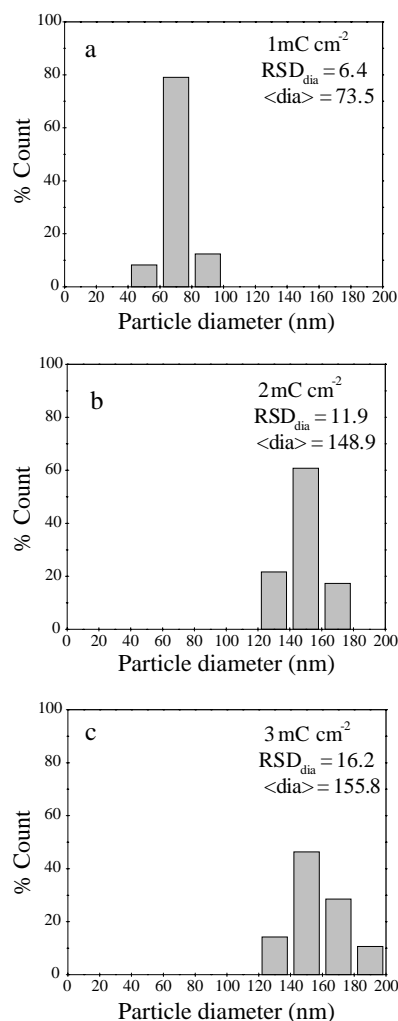
Figure 11. Particle size histograms for palladium electrodeposits. Data taken from Figure 10. (a) $q_d = 1$ mC/cm^2. (b) $q_d = 2$ mC/cm^2. (c) $q_d = 3$ mC/cm^2.

time, namely, $\langle r \rangle \propto t_d^n$ and $\langle h \rangle \propto t_d^m$, respectively. The values of the coarsening exponent, n and m, depend on E_d and q_d as the relative contribution of different rate processes to crystal growth changes with E_d and t_d. Correspondingly, for m $\neq$ n the value of f turns into a function of t_d, that is, $f(t_d) = \langle h \rangle(t_d)/\langle r \rangle(t_d)$. Values of n and m for gold and palladium are assembled in Table 1.

Table 1. Values of m, n, and f resulting from the electrochemical growth of palladium, gold, silver and platinum particles on HOPG at 298 K.

	Palladium	Gold	Platinum	Silver
m	$E_d < E_{pzc}$: 0.15	$E_d > E_{pzc}$: 0.40 $E_d < E_{pzc}$: 0.25	–	–
n	$E_d < E_{pzc}$: 0.40 $E_d > E_{pzc}$: 0.40	$E_d > E_{pzc}$: 0.40 $E_d < E_{pzc}$: 0.25	1/2	1/3
f	$f(t)$	0.3	0.1	–
Reference	[41]	[33]	[49]	[13–14]

For the early stages of a hemispherical or spherical cluster grown under diffusion from the solution side and $t_d \leq t_c$, a $\langle r \rangle \propto t^n$, dependence on n = 1/2 should be expected [44]. In this case $f = 1$, irrespective of t_d. On the other hand, for a 2-D-shaped cluster the same radial growth kinetic equation is obeyed, although in this case $f(t_d)$ approaches zero as t_d increases.

At later stages, for $t_d \geq t_c$, as in when crystal growth is under a convective-diffusion regime, growth models predict a $\langle r \rangle \propto t^n$ relationship with n = 1/3 [2]. Conversely, when particle growth proceeds under surface reaction kinetics, a $\langle r \rangle \propto t$ relationship is fulfilled [56–58].

Values of n for electrodeposition of various metals have been reported (Table 1). These figures for $E_d \approx E_r$ are consistent with diffusion and convective-diffusion regimes [13, 14, 49], whereas for $E_d < E_r$ values of n and m ranging from 1/4 to 2/5 are found [33, 41]. Otherwise, for gold crystal growth $f \approx 0.3$, a figure that is independent of t_d as n = m. The reverse situation occurs for the growth of palladium crystals as n > m, and f decreases rapidly with t_d. Values of f smaller than 1 indicate that a relatively fast surface metal atom relaxation takes place during crystal growth. It is well established that metal atom relaxation becomes a significant kinetic contribution for $T \ll 0.5T_m$, T_m being the melting temperature of bulk metal. Therefore, it is reasonable to consider that under this situation surface diffusion of metal adatoms contributes to crystal growth [59]. This conclusion is supported by the value n = 2/5 [60, 61] that was determined for disk-shaped gold and palladium crystals grown at E_d more positive than E_{pzc}, the potential of zero charge of the electrodepositing metal. For the growth of branched gold crystals at $E_d < E_{pzc}$, the value n = 1/4 [62] also sustains a surface diffusion contribution to the process, although in this case there is a significant influence of activation energy barriers for surface diffusion via step edges on the global process [63], as discussed later.

4.4. Models for Crystal Growth

In principle, as a first approach it seems reasonable to analyze the physical processes that determine the structure, shape, and size of crystals within the framework of the surface diffusion, deposition and aggregation (DDA) model [56–58]. This model is widely used for interpreting cluster growth data resulting from vapor phase deposition (Fig. 12a) [11, 64]. According to the DDA model, metal atoms impinging on the solid substrate diffuse as adatoms toward growing crystals to be captured at edges. Otherwise, adatoms impinging at the top of crystals diffuse downward to be captured at crystal edges. These processes occur without restrictions, as no activation energy barriers for adatom surface diffusion at step edges exist [63]. When a bump at a crystal edge is formed, it has a greater chance of capturing arriving atoms from the substrate rather than a reentrant, thus favoring tip growth and crystal branching (Fig. 12b) [56]. In the DDA model, tip splitting rather than tip stabilization becomes dominant, although tip stabilization resulting in dendritic patterns could also be produced by including the noise reduction technique in the model [65].

In principle, the DDA model could describe the growth of metal crystals on HOPG. For $E_d \rightarrow E_r$, the low flux of arriving particles implies a small nucleation rate (Equation (6))
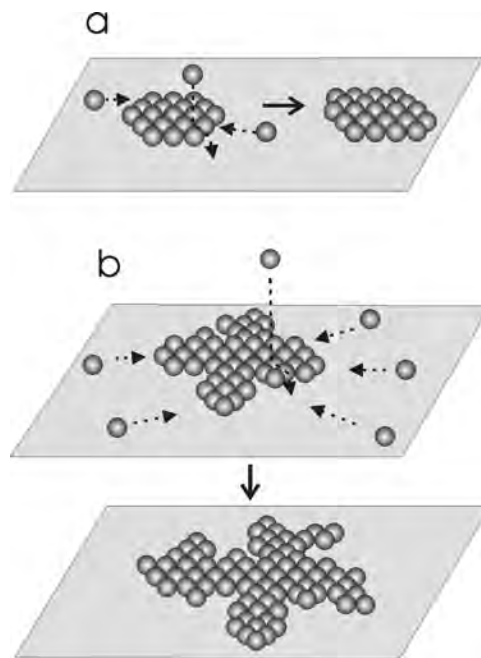
Figure 12. Scheme of particle displacement in the DDA growth model. (a) Initial stages. (b) Advanced stages showing branching development.

and internuclei distances relatively large, so that the direct discharge of reactants on the susbtrate becomes possible. However, experimental compact disk-shaped island patterns with unstable edges that are formed for $E_d \rightarrow E_r$ do not evolve according to the predictions of a DDA-like model including dendrite formation. On the other hand, when the surface diffusion of adatoms at crystal edges is enhanced by increasing the substrate temperature, it results in a transition from DDA-like to rounded compact, kinked islands [56–58]. These results, therefore, support the idea that for $E_d \rightarrow E_r$, metal adatom surface diffusion at crystal edges plays a key role in eliminating either the DDA or dendrite-like structure.

Another drawback in describing experimental results in terms of the DDA model lies in the fact that it predicts perfect 2-D patterns, as there is no restriction for moving adatoms on growing crystals to reach crystal edges. For gold electrodeposition, the value $f = 0.3$, irrespective of E_r, indicates that gold adatoms produced by discharging $AuCl_4^-$ ions on crystal tops must surmount an activation energy barrier at gold crystal steps [63]. A scheme showing the location and the relative magnitude of activation energy barriers for intra- and interterrace diffusion at metal surfaces is shown in Figure 13. The activation energy barrier at step edges is due to the decrease in the coordination number of adatoms along their interterrace trajectories across step edges. For barrierless surface diffusion, the development of a completely flat interface similar to that predicted by the Edwards–Wilkinson model [66] should be expected (n = 1/2). For gold adatom interterrace diffusion, the corresponding energy barrier is larger than that for intraterrace diffusion [67, 68]. Therefore, in this case, interterrace adatom diffusion becomes rate determining. Accordingly, a clear deviation in the crystal shape from a perfect 2-D pattern should be expected. It should be noted that for isotropic
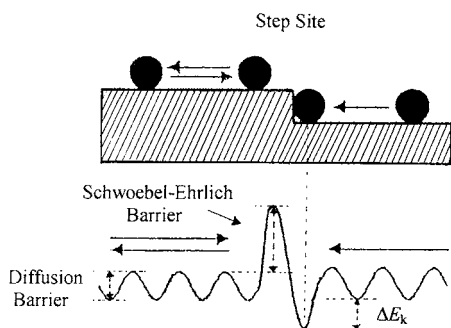
Figure 13. Qualitative scheme of Schwoebel–Erlich barrier for interterrace and intraterrace adatom surface diffusion. ΔE_k corresponds to the energy contribution to kink formation.

Figure 14. (a) Scheme of isotropic growth model. (b) Ball scheme of adatom surface diffusion across steps A and B on a (111) substrate. (c) Ball scheme of adatom surface diffusion at corner (1) and edges (2).

surface diffusion that implies the existence of a single activation energy barrier, the crystal evolves maintaining its original rounded or hexagonal shape.

The height of the activation energy barrier at step edges is closely related to the value of n. Values n ≈ 2/5 have been related to low activation energy barriers at step edges [60, 61]. The influence of the latter in determining the departure of the crystal shape from a perfect 2-D pattern can also be derived from the analysis of $f(t)$ values. Thus, as $f(t)$ decreases with t_d, crystals tend to approach 2-D patterns as in the case of palladium (111) (Table 1). In this case, mean-field calculations have shown that the height of step-edge activation energy barriers is considerably lower than that for gold (111), so that for palladium (111) intraterrace diffusion becomes rate controlling [68].

From the above discussion, for $E_d \rightarrow E_r$, it can be concluded that any DDA-like model applicable to the growth of metal electrodeposits on HOPG should include the presence of activation energy barriers at step edges to account for shape evolution. Therefore, to explain the nearly compact disks found in this potential region, either enhanced edge surface diffusion and/or an isotropic activation energy barrier at steps should be included. A scheme of this type of crystal growth under isotropic adatom surface diffusion is depicted in Figure 14a.

For E_d, which is more positive than the potential of zero charge of the depositing metal (E_{pzc}), the role played by metal adatom surface diffusion is sustained by the fact that the presence of a small amount of additive such as citric acid ($c = 0.1$ mM) in the plating solution eliminates branching and promotes the formation of rounded 3-D islands. As seen by *in-situ* STM imaging [69], this effect is caused by the adsorption of additive molecules at step edges, which hinders surface diffusion of gold atoms.

On the other hand, for fcc(111) surfaces, two different step edges, A- and B-type, should be distinguished [70]. The height of the activation energy barrier for interterrace adatom surface diffusion across A-type step edges is greater than across B-type step edges. This anisotropy in interterrace adatom surface diffusion results in the growth of triangular crystals. A scheme for anisotropic surface diffusion is shown in Figure 14b. Experimental data from gold and palladium electrodeposition show that anisotropic surface diffusion is approached for $E_d < E_{pzc}$. In this case, for $E_d \ll$
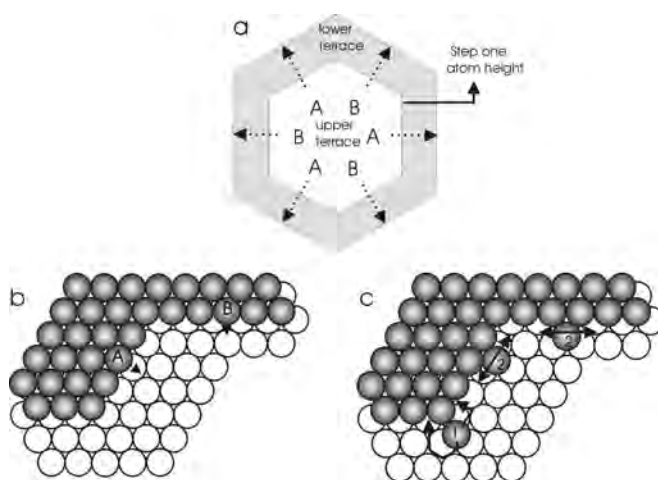
E_r, as a large number of nuclei is initially formed (Equations (4)–(6)), most of the ions coming from the solution are discharged on crystal tops, and the descending flux of adatoms across B-type steps is favored. Therefore, triangular crystals are by far preferentially formed. Hence, the existence of activation energy barriers of different height at A- and B-step edges leading to anisotropic surface diffusion of metal adatoms can explain the island shape obtained for $E_d < E_{pzc}$.

For $E_d \ll E_r$, dendritic patterns that are observed for both palladium and gold crystals also indicate the presence of anisotropic activation energy barriers at step edges [70]. From an atomistic standpoint, it is possible to distinguish two surface diffusion processes at island edges, depending on whether an adatom starts from a site that is laterally twofold (edge diffusion) (Fig. 14c) or onefold coordinated to the crystal edge (corner diffusion) [70]. Hexagonal lattice dendritic patterns with trigonal symmetry have been generated introducing anisotropic corner surface diffusion, whereas edge surface diffusion leads mainly to a thickening of island branching. For these surface diffusion processes, the symmetry of the substrate also plays a key role in the development of dendritic patterns [70]. This fact can explain, for instance, why under comparable experimental conditions, no dendritic crystals for gold electrodeposition onto amorphous carbon can be observed [71].

The preceding analysis provides a reasonable explanation to results obtained for $E_d < E_{pzc}$, but the question of why anisotropic surface diffusion is no longer observed for $E_d > E_{pzc}$ still remains open. In this case, an answer can be given after paying attention to the influence of the applied electric potential on surface diffusion processes.

4.5. The Electric Potential Influence

For metal electrodeposition processes, the height of activation energy barriers for adatom surface diffusion across step edges depends on the applied electric potential. Accordingly, it is possible to control the nanostructure and shape of metal

islands by properly adjusting the electrodeposition conditions, particularly the applied electric potential in potentiostatic experiments. For a potential-dependent metal island shape on HOPG, the adsorption of anions plays an important role. It is well known that anions in solution interact with the metal surface either electrostatically or specifically adsorbed. Both interactions depend on the electric potential applied to the electrochemical interface [72]. In principle, for $E_d < E_{pzc}$, the degree of metal surface coverage by adsorbed anions is negligible, as in this case the metal surface is negatively charged with respect to the solution. The reverse situation occurs for $E_d > E_{pzc}$. Then, as E_d is shifted positively, the electron density at the metal surface decreases and the degree of surface coverage by anions increases, eventually leading to the formation of a well-defined ordered anion adlattice [73]. For example, for either chloride or metal-chloride complex-containing plating solution, at $E_d > E_{pzc}$, anions accumulate at the metal/solution interface in the course of metal electrodeposition, and either chloride or metal-chloride complex ions become specifically adsorbed at growing metal islands. The global metal electrodeposition reaction from chloride containing metal anions is represented by Equation (1b) for Me = palladium, X = chlorine, and $1 \leq x \leq 6$.

When $E_d < E_{pzc}$, as the metal surface is negatively charged with respect to the solution, chloride ions produced by Equation (1b), as well as anions in general, diffuse outward from the metal/solution interface, and therefore, the influence of anion adsorption on metal electrodeposition becomes negligible. Then, the metal deposit approaches a dendritic growth pattern, as expected when an anisotropic corner diffusion regime operates. It is interesting to note that the same growth pattern has been observed for vapor phase deposition of silver islands on platinum (111) [70]. Conversely, at $E_d > E_{pzc}$, the metal being positively charged, chloride anions produced by Equation (1b) become specifically adsorbed on the growing crystal surface. Under these particular conditions, it is well-established that specific adsorption phenomena are enhanced at step edges. The increase in chloride ion adsorption with E_d correlates with an increase in the surface diffusion coefficient of metal adatoms, leading to an enhancement of both adatom surface mobility [72] and step displacement [73]. In fact, when E_d is increased from 0.30 V ($E_{pzc} \approx 0.25$ V versus SCE) to 0.80 V, the surface diffusion coefficient of gold adatoms on gold immersed in acid solution increases from $D_s = 1 \times 10^{-12}$ cm^2/s to $D_s = 8 \times 10^{-12}$ cm^2/s [74]. Hence, the specific adsorption of anions at step edges produces a decrease in the height of energy barriers for adatom surface diffusion, that is, isotropic surface diffusion conditions are then approached that favor the growth of kinked rounded crystals. For gold island electrodeposition, this explanation is consistent with the change of n from 1/4 to 2/5 [75]. On the other hand, values of D_s for palladium adatom surface diffusion on palladium, either in the presence or in the absence of chloride ions are not available yet, but they can be estimated from the Gjostein–Rhead equation [76–78]

$$D_s = 749 \times 10^{-4} \exp(-30 T_m / \mathbf{R} T)$$
$$+ 0.014 \times 10^{-4} \exp(-13 T_m / \mathbf{R} T) \qquad (8)$$

In Equation (8), T_m is the melting point of the surface species, and $\mathbf{R} = 1.987$ cal/mol K.

Let us consider Equation (8) to determine whether the most likely surface-diffusing species is closely related to palladium adatoms or to palladium-chloride-complex adsorbates. Based on electrochemical kinetic data [41], let us assume that for $E_d > E_{pzc}$, a PdCl$_2$ adsorbate on palladium is formed [77, 78]. Then, from the application of Equation (8) for palladium ($T_m = 1827$ K) and PdCl$_2$ ($T_m \approx 773$ K), it results in $D_s = 1.3 \times 10^{-14}$ cm^2/s for PdCl$_2$, and $D_s = 5.7 \times 10^{-24}$ cm^2/s for palladium at 298 K. Therefore, we can conclude that a palladium-chloride complex species [79] is responsible for the surface relaxation process occurring during the palladium crystal electrochemical growth. The increase in the value of D_s for palladium-chloride-complex-ion-containing solution follows the same tendency that has already been reported for the surface mobility of gold adatoms on gold under comparable conditions [74]. For such a high value of D_s, the average traveling rate of [PdCl$_2$] species on the palladium surface is about 1 nm/s. This figure is consistent with the surface relaxation rate that contributes to the formation of rounded islands for $E_d > E_{pzc}$. It should be noted that the high value of D_s referred to above is of the same order of magnitude as that of D_s that has recently been found for the surface diffusion of disk-shaped aggregates of cadmium sulfide nanocrystals on HOPG at 50–100 °C [80].

The role of chloride ions in the surface diffusion rate was confirmed by increasing their concentration in the plating solution. In fact, the addition of chloride salt promotes 2-D growth, that is, it decreases the value of f, and tends to hinder dendritic growth [69] as found from AFM imaging for the growth of flat cobalt crystals on HOPG by electrodeposition from chloride-containing solutions [50].

5. APPLICATIONS

5.1. Nanowires

Among the different methods for fabricating long metallic nano- and mesowires, the most successful ones are template synthesis [81–83] and step-edge decoration [84–87].

The electrochemical method for preparation of metallic meso- and nanowires is based on the selective electrodepositon of the metal directly at step edges utilizing HOPG substrate. This step-edge decoration method has been proposed by Liu et al. [13], Penner [14], Penner et al. [25], and Zach et al. [26] from either metal or metal oxide electrodeposition on HOPG.

For the preparation of palladium meso- and nanowires, the solid solution interface is perturbed by a routine consisting of three successive potential steps. The first step is adjusted to oxidize step edges on HOPG just prior to deposition; the second step, which involves a large cathodic overvoltage for metal deposition of about 0.3 V for 5–10 ms, favors metal nucleation; the third step involves a low cathodic overvoltage for metal growth of less than 0.1 V. The radius of the nanowires is controlled by the electrodeposition time [88, 89].

Metallic palladium meso- and nanowires can also be produced by a two-stage electrochemical process involving first the potentiostatic electrodeposition of palladium followed

by a controlled anodic stripping stage. A typical palladium nano/mesowire array prepared by this method is shown in Figure 15.

The preparation of metallic nanowires also proceeds via the electrodeposition of a metal oxide. This is the case of the electrodeposition of molybdenum dioxide on HOPG from dilute molybdate solution at pH 6.5. This process is followed by hydrogen reduction at 500 °C yielding HOPG-supported metallic molybdenum meso- and nanowires [88, 89].

Nanoparticles and nanowires are potentially very efficient chemical sensors. The chemical sensing mechanism is envisioned as the adsorption and eventually diffusion of the analyte species at the surface inducing there a change in a measurable property. An example of a chemical sensor operating on the above principle, which has been described recently [88, 89], is that of gold nanowires showing changes in the electrical conductivity upon exposure to thiols of amines.

Arrays of mesoscopic palladium wires have been applied as hydrogen sensors and hydrogen-actuated switches [25]. These devices have been constructed by transferring the palladium nanowire arrays from HOPG onto a cyanoacrylate or polyurethane film. In contrast to hydrogen sensors based on macroscopic palladium resistors, which become more resistive in the presence of hydrogen, the resistance of the palladium mesowire array decreases under hydrogen. From AFM and SEM observations, the likely mechanism that has been proposed for the operation of the palladium mesowire array to account for its response as a hydrogen-actuated switch involves the closing of nanoscopic break junctions along the step edges caused by the dilation of wire grains undergoing the reversible conversion of palladium to palladium hydride. Accordingly, in the absence of hydrogen, each break junction reverts to open circuit [25].

5.2. Pattern Transfer to Polymeric Materials

HOPG patterned with electrodeposited nanometer-sized metallic crystals has been used as a template to fabricate nanocavities on polymeric materials [27]. The procedure for
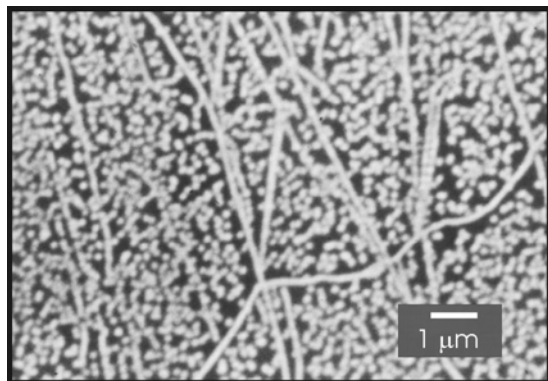
Figure 15. SEM micrograph of palladium islands on HOPG electrodeposited at $E_d = -0.100$ V, from the solution indicated in Figure 4, for $q_d = 5$ mC/cm^2, after anodic stripping in 0.1 M aqueous perchloric acid to reach $q_d = 1.3$ mC/cm^2.

pattern transfer is simple. It consists of pouring a prepolymer solution onto the patterned HOPG surface. After evaporation, a polymer film that can be easily released from the HOPG surface is formed. The inner face of the polymer film, which has been in contact with the HOPG surface, exhibits nanocavities—the pattern transfer from the HOPG surface to the polymeric material takes place. It should be noted that this simple method to produce nanocavities onto polymeric surfaces has also been performed using either patterned silicon or patterned metallic substrates. However, in these cases, the template surface has to be modified by a self-assembled monolayer of alkanethiols (metals) or silanes (silicon) in order to release the polymer film from the template without damage. The advantage of using patterned HOPG arises from the fact that, due to its extremely low chemical reactivity, no surface chemistry modification is needed to avoid damage. Note that depending on the metal-polymer interactions, the electrodeposited metal particles can either be transferred to the polymeric film (as described in Section 5.1) or remain on the HOPG surface forming cavities on the polymer (nanocavity fabrication).

5.3. Heterogeneous Catalysis

The reactivity of the nanometer-sized compact disks and branched palladium particles for hydrogen atom electroadsorption/electrodesorption reactions in aqueous 0.1 M perchloric acid was investigated by cyclic voltammetry at $v = 0.1$ V/s [90]. For the sake of comparison, blanks were run that utilized massive either palladium or platinum electrodes. For massive palladium, the voltammogram recorded from 0 V to -0.3 V (Fig. 16a) shows a cathodic current, essentially related to hydrogen absorption by palladium, and to some extent the initial formation of molecular hydrogen at higher cathodic overvoltage [91]. The reverse potential scan shows the electro-oxidation of absorbed hydrogen as the main anodic process with a broad anodic current peak at -0.075 V. This voltammogram shows no trace of adsorbed hydrogen as might be expected at -0.30 V and -0.15 V (Fig. 16a, inset). Therefore, in contrast to the voltammogram of polycrystalline platinum that exhibits conjugated pairs of current peaks related to weakly and strongly bound hydrogen adatoms at approximately -0.05 V and -0.20 V, respectively, no hydrogen atom electroadsorption/electrodesorption can be concluded from the voltammogram of smooth massive palladium.

Comparable voltammograms were recorded for nanometer-sized palladium crystals of different morphologies on HOPG, namely, compact disk-shaped crystals prepared at $E_d = 0.125$ V ($q_d = 5$ mC/cm^2) (Fig. 16b), and branched particles produced at $E_d = -0.100$ V ($q_d = 5$ mC/cm^2) (Fig. 16c). In contrast to massive palladium, both types of palladium islands exhibit voltammetric features resembling those for hydrogen atom electroadsorption/electrodesorption on platinum [92]. For palladium crystals supported on HOPG electrodes, these processes are characterized by peaks I and II at approximately -0.25 V and -0.15 V, respectively (Fig. 16c), and the anodic-to-cathodic voltammetric charge ratio approaches 1 as expected for relatively fast surface electrochemical processes [93, 94]. It can also be observed that for branched palladium islands
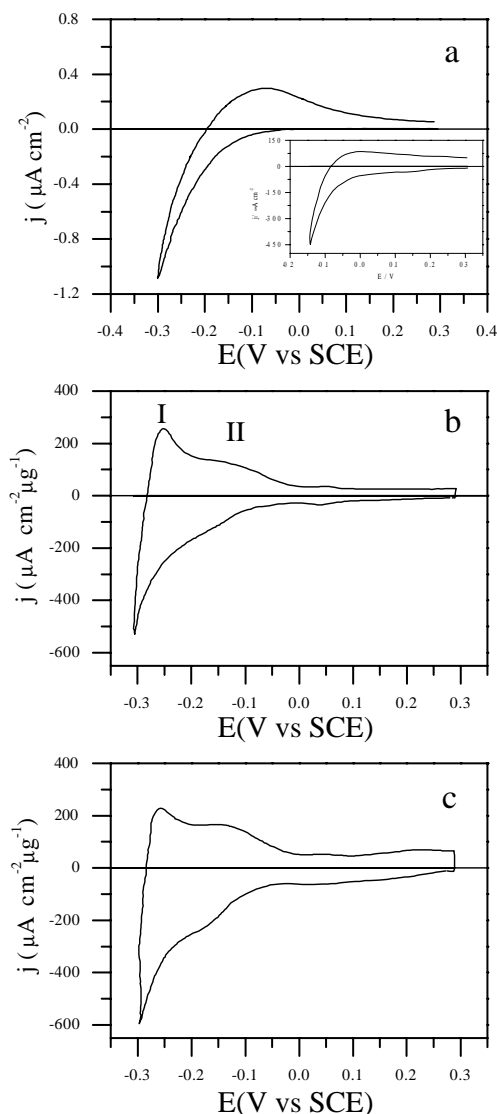
Figure 16. Current density versus potential curves recorded at 0.1 V/s from 0.30 to −0.30 V to reach the region where hydrogen atom electrosorption/electrodesorption reactions are observed. Aqueous 0.1 M perchloric acid. (a) Polycrystalline palladium electrode (0.125 cm² geometric area). The voltammogram (inset) corresponds to the cathodic potential limit −0.15 V. (b) Quasi-hemispherical palladium islands on HOPG, $E_d = 0.125$ V, $q_d = 5$ mC/cm². (c) The continuous trace corresponds to branched palladium islands on HOPG, $E_d = -0.10$ V, $q_d = 5$ mC/cm². 298 K. Electrodeposits have been obtained as indicated in Figure 9. Reprinted with permission from [90], Y. Gimeno et al., *Chem. Mater.* 13, 1857 (2001). © 2001, American Chemical Society.

supported on HOPG, the peak I/peak II charge ratio is increased, as compared to that resulting from compact disk-shaped crystals. Therefore, the contribution of the hydrogen adatom electrodeposition reaction

$$\mathrm{Pd(H)_{ad} = Pd + H^+ + e^-} \qquad (9)$$
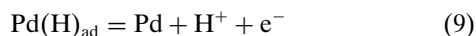
as compared to hydrogen absorption is considerably enhanced on nanometer-sized palladium crystals supported on

HOPG, particularly on branched crystals. It should be noted that the voltammogram resulting from a palladium-plated HOPG electrode at $E_d = -0.100$ V ($q_d = 20$ mC/cm²) shows a contribution of hydrogen electroadsorption/electrodesorption much smaller than that observed for branched palladium crystals [95].

To confirm the high electrochemical reactivity of nanometer-sized branched palladium crystals, the electrochemical oxidation of hydrazine on massive palladium, nanometer-sized compact disk-shaped particles and nanometer-sized branched palladium crystals ($q_d = 5$ mC/cm²) supported on HOPG were also investigated [90]. For this purpose, aqueous 6×10^{-3} M hydrazine + 0.1 M potassium sulphate at 298 K was employed. For massive palladium (Fig. 17a), the voltammogram shows a broad anodic current peak at 0.31 ± 0.01 V related to the electro-oxidation of hydrazinium ions [90]. This peak is followed by another broad peak at approximately 0.6 V, which corresponds to the formation of the oxygen-containing layer on palladium [96, 97]. The latter is electroreduced as the potential scan is reversed, as seen by the broad current peak at approximately 0.5 V. For nanometer-sized compact disk crystals produced at $E_d = 0.125$ V (Fig. 17b), the anodic current peak potential related to hydrazinium ion electro-oxidation is 0.33 ± 0.01 V, whereas for branched palladium crystals (Fig. 17b) it is 0.26 ± 0.01 V. In this case, the conjugated cathodic reaction can also be observed at the same potential during the reverse potential scan. Furthermore, the initial portion of the voltammogram fits a linear E_d versus $\ln j_c$
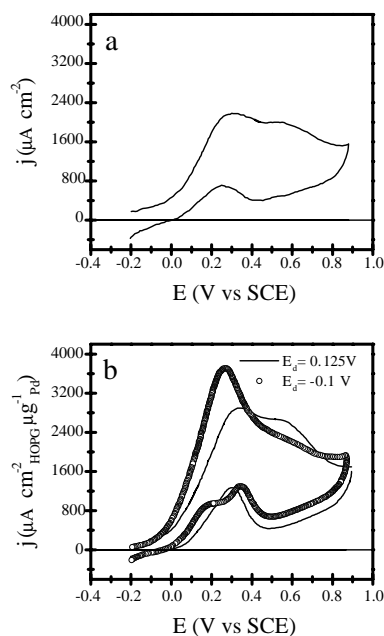
Figure 17. Current density versus potential curves for hydrazine electro-oxidation recorded at 0.2 V/s. Aqueous 6×10^{-3} M hydrazinium sulphate + 0.1 M potassium sulphate. (a) Polycrystalline palladium electrode. (b) Quasi-hemispherical, $E_d = 0.125$ V (full trace), and branched, $E_d = -0.10$ V (open circles) palladium islands on HOPG ($q_d = 5$ mC/cm²). 298 K. The current density in (b) is also referred to the weight of electrodeposited palladium calculated from q_d. Reprinted with permission from [90], Y. Gimeno et al., *Chem. Mater.* 13, 1857 (2001). © 2001, American Chemical Society.

plot, with the slope $\Delta E_d/\Delta \ln j_c$ decreasing from 0.15 ± 0.01 to 0.09 ± 0.01 V/ln unit in going from smooth to branched crystals. These results are consistent with electrochemical kinetics under intermediate control [98].

Under the above-mentioned conditions, the voltammetric electrochemical oxidation of hydrazine is a 4-electron reaction

$$N_2H_5^+ = N_2 + 5H^+ + 4e^- \tag{10}$$
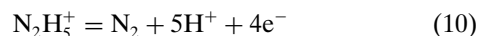
with a pair of conjugated peaks at the range 0.26–0.33 V. This complex electrochemical reaction depends on the crystallography, state, and history of the electrode surface, as has been concluded for platinum electrodes in the same solution [99]. The decrease in the value of the slope $\Delta E_d/\Delta \ln j_c$, the increase in height of conjugated peaks, and the displacement of their peak potentials by 0.07 V negatively indicate an increased catalytic effect of nanometer-sized branched-palladium crystals on HOPG-supported electrodes. Therefore, electrodes behave as the electrochemically most active material for both test reactions.

6. CONCLUSIONS

The electrodeposition of metallic crystals on carbon HOPG has been reviewed, in particular, in relation to crystal structure and shape. At the mesoscale, narrow particle size distributions of metal crystals can be obtained by conventional potentiostatic electrodeposition of metal ions from aqueous solutions. The shape and structure of mesocrystals depend on the applied electric potential. Over a wide potential range, the aspect ratio of crystals differs considerably from that of hemispherical particles. This departure can be explained by growth models, including surface adatom diffusion and step-dependent activation energy barriers at step edges. Anions adsorption from the solution plays a key role in determining the height of activation energy barriers for surface diffusion. The electrocatalytic activity of branched mesocrystals for different processes is considerably greater than that of compact disk-shaped mesocrystals of comparable size. Metallic electrodeposition on carbons can also be used for nano/mesowire fabrication with potential applications as chemical sensors, and promising interconnectors for nanoelectronic devices and polymer embossing. The discussion of these issues is important for facing problems related to the crystal engineering of metalic nanoparticles.

GLOSSARY

Exchange current density Value of the current density at the equilibrium potential of the electrochemical interface.

Mesoparticles Particles with size comprised between 100 to 1000 nm.

Nanoparticles Particles with size up to 100 nm.

Overvoltage The potential difference between the applied electric potential and the reversible potential of the electrochemical interface.

Potentiodynamic polarization curve A current versus potential record obtained under a single linear potential scan.

Voltammogram Current versus potential record obtained under a triangular potential scan between an upper and a lower switching potential.

REFERENCES

1. G. Frens, *Nature* 20, 241 (1973).
2. A. Henglein, *Chem. Rev.* 89, 1861 (1989).
3. M. T. Reetz and W. J. Helbing, *J. Am. Chem. Soc.* 116, 7401 (1994).
4. T. S. Ahmadi, Z. L. Wang, T. C. Green, A. Henglein, and M. A. El Sayed, *Science* 272, 1924 (1996).
5. T. S. Ahmadi, Z. L. Wang, A. Henglein, and M. A. El-Sayed, *Chem. Mater* 8, 1161 (1996).
6. A. Henglein and M. Giersig, *J. Phys. Chem. B* 103, 9533 (1999).
7. M. B. Mohamed, Z. L. Wang, and M. A. El-Sayed, *J. Phys. Chem. A* 103, 10255 (1999).
8. G.-Q. Lu and A. Wieckowski, *Colloid and Interface Science* 5, 95 (2000).
9. V. F. Puntes, K. M. Krishnan, and A. P. Alivisatos, *Science* 291, 2115 (2001).
10. A. Henglein, *J. Phys. Chem. B* 104, 1206 (2000).
11. C. Binns, *Surf. Sci. Rep.* 44, 1 (2001), and references therein.
12. C. R. Henry, *Appl. Surf. Sci.* 164, 252 (2000).
13. H. Liu, F. Favier, K. Ng, M. P. Zach, and R. M. Penner, *Electrochim. Acta* 47, 671 (2001).
14. R. M. Penner, *J. Phys. Chem. B* 106, 3339 (2002).
15. K. Itaya, S. Sugawasa, and K. Higaki, *J. Phys. Chem.* 92, 6714 (1988).
16. M. Aindow and J. P. G. Farr, *Trans. Inst. Mater. Finish.* 70, 171 (1992).
17. A. R. Layson and M. R. Columbia, *Microchem. J.* 56, 103 (1997).
18. P. Garrido, E. Gomez, and E. Valles, *J. Electroanal. Chem.* 441, 147 (1998).
19. E. Budevski, G. Staikov, and W. J. Lorenz, "Electrochemical Phase Formation and Growth." VCH, Weinheim, Germany, 1996.
20. M. Volmer and A. Z. Weber, *Phys. Chem.* 119, 277 (1926).
21. J. N. Stranski and L. Krastanov, *Ber. Akad. Wiss. Wien* 146, 797 (1938).
22. F. C. Frank and J. H. van der Merwe, *Proc. R. Soc. London A* 198, 205 (1949).
23. G. A. Somorjai, "Introduction to Surface Chemistry and Catalysis." John Wiley & Sons, New York, 1994; N. Memmel, *Surf. Sci. Rep.* 32, 91 (1998).
24. T. Tanii, K. Ishibashi, K. Ohta, and I. Ohdomari, *Appl. Surf. Sci.* 162–163, 662 (2000).
25. R. M. Penner, F. Favier, E. C. Walter, and M. P. Zach, *Science* 293, 2227 (2001).
26. M. P. Zach, K. H. Ng, and R. M. Penner, *Science* 290, 2120 (2000).
27. P. L. Schilardi, O. Azzaroni, and R. C. Salvarezza, *Nano-tech.* submitted.
28. "Scanning Tunneling Microscopy I," edited by H.-J. Guntherodt and R. Wiesendanger, Springer-Verlag, Berlin, 1992.
29. M. Paunovic and M. Schlesinger, in "Fundamentals of Electrochemical Deposition." Wiley, New York, 1998.

30. L. Vázquez, A. Hernández-Creus, P. Carro, P. Ocón, P. Herrasti, C. Palacio, J. M. Vara, R. C. Salvarezza, and A. J. Arvia, *J. Phys. Chem.* 96, 10454 (1992).
31. J. L. Zubimendi, L. Vázquez, P. Ocon, J. M. Vara, W. E. Triaca, R. C. Salvarezza, and A. J. Arvia, *J. Phys. Chem.* 97, 5095 (1993).
32. M. Miranda-Hernández, I. González, and N. Batina, *J. Phys. Chem.* 105, 4212 (2001).
33. H. Martin, P. Carro, A. Hernández Creus, S. González, R. C. Salvarezza, and A. J. Arvia, *Langmuir* 13, 100 (1997).
34. K. Shimazu, D. Weisshaar, and T. Kuwana, *J. Electroanal. Chem.* 223, 223 (1987).
35. K. Shimazu, K. Uosaki, H. Kita, and Y. Nodasaka, *J. Electroanal. Chem.* 256, 481 (1988).
36. J. V. Zoval, *J. Phys. Chem. B* 102, 1166 (1998).
37. A. C. Hill, R. E. Patterson, J. P. Sefton, and M. R. Columbia, *Langmuir* 15, 4005 (1999).
38. I. Lee, K.-Y. Chan, and D. L. Phillips, *Appl. Surf. Sci.* 136, 321 (1998).
39. S. Liu, Z. Tang, E. Wang, and S. Dong, *Electrochem. Commun.* 2, 800 (2000).
40. S. Chen and A. Kucernak, *Electrochem. Commun.* 4, 80 (2002).
41. Y. Gimeno, A. Hernández Creus, P. Carro, S. González, R. C. Salvarezza, and A. J. Arvia, *J. Phys. Chem. B* 106, 4232 (2002).
42. A. Hernández-Creus, A. E. Bolzán, P. Carro, S. González, R. C. Salvarezza, and A. J. Arvia, *Electrochim. Acta* 38, 1545 (1993).
43. A. Hernández-Creus, P. Carro, S. González, R. C. Salvarezza, and A. J. Arvia, *Electrochim. Acta* 37, 2215 (1992).
44. B. Scharifker and G. Hills, *Electrochim. Acta* 28, 879 (1983).
45. B. Scharifker and J. Mostany, *J. Electroanal. Chem.* 177, 13 (1984).
46. L. Heerman and A. Tarallo, *J. Electroanal. Chem.* 470, 70 (1999).
47. L. Heerman and A. Tarallo, *Electrochem. Commun.* 2, 85 (2000).
48. E. B. Budevski, in "Comprehensive Treatise of Electrochemistry" edited by B. E. Conway, J. O'M. Bockris, E. Yeager, S. U. M. Khan, and R. M. White, Vol. 7, Plenum Press, New York 1983, p. 399.
49. I. Lee, K.-Y. Chan, and D. L. Phillips, *Ultramicroscopy* 75, 69 (1998).
50. E. Gómez, E. Guaus, F. Sanz, and E. Vallés, *J. Electroanal. Chem.* 465, 63 (1999).
51. R. Q. Hwang, J. Schroder, G. Gunther, and R. J. Behm, *Phys. Rev. Lett.* 67, 3279 (1991).
52. I. Kojima, A. K. Srivastava, and M. J. Kurahashi, *J. Appl. Phys.* 30, 1852 (1991).
53. M. Bonet, E. Boschung, J. Hayoz, T. Pillo, G. Dieter, and P. Aebi, *Surf. Sci.* 473, 17 (2001).
54. "The Fractal Approach to Heterogeneous Chemistry," edited by D. Avnir, John Wiley & Sons, New York, 1989.
55. J. M. Gómez-Rodríguez, A. M. Baró, L. Vázquez, R. C. Salvarezza, J. M. Vara, and A. J. Arvia, *J. Phys. Chem.* 96, 347 (1992).
56. A. L. Barabasi and H. E. Stanley, in "Fractal Concepts in Surface Growth." Cambridge University Press, Cambridge, 1995, and references therein.
57. "Dynamics of Fractal Surfaces," edited by F. Family and T. Vicsek, World Scientific, Singapore, 1991.
58. F. Family, *Physica A* 168, 561 (1990), and references therein.
59. H. P. Bonzel, in "Surface Chemistry of Materials," edited by J. M. Blakeley, Academic Press, New York, 1975, p. 280.
60. P. Smilauer and D. D. Vvedenski, *Phys. Rev. B* 52, 14263 (1995).
61. S. Majaniemi, T. Ala-Nissila, and J. Krug, *Phys. Rev. B* 53, 8071 (1996).
62. M. Siegert and M. Plischke, *Phys. Rev. Lett.* 73, 1517 (1994).
63. R. Schwoebel, *J. Appl. Phys.* 40, 614 (1969).
64. J. Jacobsen, K. W. Jacobsen, S. Stoltze, and J. K. Norskov, *Phys. Rev. Lett.* 74, 2295 (1995).
65. P. Meakin, in "The Fractal Approach to Heterogeneous Chemistry," edited by D. Avnir, John Wiley & Sons, New York, 1990, p. 131.
66. S. F. Edwards and D. R. Wilkinson, *Proc. R. Soc. London A* 381, 17 (1982).
67. G. Erlich, *Surf. Sci.* 299/300, 628 (1994), and references therein.
68. Y. Li and E. DePristo, *Surf. Sci.* 351, 189 (1996).
69. H. Martín, P. Carro, A. Hernández Creus, S. Gonzalez, G. Andreasen, R. C. Salvarezza, and A. J. Arvia, *Langmuir* 16, 2915 (2000).
70. H. Brune, H. Roder, K. Bromann, K. Kern, J. Jacobsen, P. Stoltze, K. Jacobsen, and J. Norskov, *Surf. Sci.* 349, L115 (1996), and references therein.
71. D.-I. Lu, Y. Okawa, M. Ichihara, A. Aramata, and K.-I. Tanaka, *J. Electroanal. Chem.* 406, 101 (1996).
72. D. J. Trevor, C. E. D. Chidsey, and D. N. Loiacono, *Phys. Rev. Lett.* 62, 929 (1989).
73. X. Gao, G. J. Edens, and M. J. Weaver, *J. Electroanal. Chem.* 376, 21 (1994), and references therein.
74. M. P. García, M. M. Gómez, R. C. Salvarezza, and A. J. Arvia, *J. Electroanal. Chem.* 347, 237 (1993).
75. H. Martin, P. Carro, A. Hernández Creus, S. González, R. C. Salvarezza, and A. J. Arvia, *J. Phys. Chem. B* 103, 3900 (1999).
76. N. A. Gjostein, in "Surfaces and Interfaces," edited by J. J. Burke, N. L. Reed, and V. Weiss, Syracuse University Press, Syracuse, New York, 1967, p. 271.
77. G. E. Rhead, *Surf. Sci.* 15, 353 (1969).
78. G. E. Rhead, *Surf. Sci.* 22, 223 (1970).
79. L. G. Sillén, in "Stability Constant of Metal-Ion Complexes, Section 1: Inorganic Ligands," The Chemical Society, Burlington House, London, 1964, p. 288.
80. G. Ge and L. E. Brus, *Nano Lett.* 1, 219 (2001).
81. C. A. Foss, M. J. Tierney, and C. R. Martin, *J. Phys. Chem.* 96, 9001 (1992).
82. C. K. Preston and M. Moskovits, *J. Phys. Chem. B* 97, 8495 (1993).
83. L. Sun, P. C. Searson, and C. L. Chien, *Phys. Rev. B* 61, R6463 (2000).
84. T. Jung, R. Schlittler, J. K. Gimzewski, and F. J. Himpsel, *Appl. Phys. A* 61, 467 (1995).
85. M. Blanc, K. Kuhnke, V. Marsico, and K. Kern, *Surf. Sci.* 414, L964 (1998).
86. R. J. Nichols, D. M. Kolb, and R. J. Behm, *J. Electroanal. Chem.* 313, 109 (1991).
87. S. Morin, A. Lachenwitzer, O. M. Magnussen, and R. J. Behm, *Phys. Rev. Lett.* 83, 5066 (1999).
88. F. Favier, E. C. Walter, M. P. Zach, T. Benter, and R. M. Penner, *Science* 293, 2227 (2001).
89. E. C. Walter, F. Favier, and R. M. Penner, *Anal. Chem.* 74, 1546 (2002).
90. Y. Gimeno, A. Hernández Creus, S. González, R. C. Salvarezza, and A. J. Arvia, *Chem. Mater.* 13, 1857 (2001).
91. R. C. Salvarezza, C. Montemayor, E. Fatas, and A. J. Arvia, *J. Electroanal. Chem.* 313, 291 (1991).
92. N. Hoshi, M. Kuroda, and Y. Hori, *J. Electroanal. Chem.* 521, 155 (2002).
93. S. Srinivasan and E. Giliadi, *Electrochim. Acta* 11, 321 (1966).
94. N. Baldauf and D. M. Kolb, *Electrochim. Acta* 38, 2145 (1993).
95. Y. Gimeno, A. Hernandez Creus, R. C. Salvarezza, A. J. Arvia, to be submitted.
96. A. Bolzan, M. E. Martins, and A. J. Arvia, *J. Electroanal. Chem.* 172, 221 (1984).
97. A. Bolzan, A. C. Chialvo, and A. J. Arvia, *J. Electroanal. Chem.* 179, 71 (1984).
98. A. J. Bard and L. Faukner, "Electrochemical Methods." John Wiley & Sons, New York, 1960.
99. R. Gómez, J. M. Orts, A. Rodes, J. M. Feliú, and A. J. Aldaz, *J. Electroanal. Chem.* 358, 287 (1993).

Crystallography and Shape of Nanoparticles and Clusters

J. M. Montejano-Carrizales

Universidad Autónoma de San Luis Potosí, México

J. L. Rodríguez-López

Instituto Potosino de Investigación Científica y Tecnológica, San Luis Potosí, México

C. Gutierrez-Wing

*Instituto Nacional de Investigaciones Nucleares, Mexico,
and University of Texas at Austin, Austin, Texas, USA*

M. Miki-Yoshida

*University of Texas at Austin, Austin, Texas, USA,
and Centro de Investigación en Materiales Avanzados, Chichuahua, México*

M. José-Yacaman

*University of Texas at Austin, Austin, Texas, USA,
and Instituto de Física, UNAM, México*

CONTENTS

1. INTRODUCTION

Nanotechnology is a leading interdisciplinary science that is emerging as a distinctive field of research. Its advances and applications will result in technical capabilities that will allow the development of novel nanomaterials with applications that will revolutionize the industry in many areas [1, 2]. It is now well established that dimensionality plays a critical role in determining the properties of materials and its study has produced important results in chemistry and physics [3].

Nanoparticles are one of the cornerstones of nanotechnology. Indeed, even though the research in this field has been underway for a long time, many present and future applications are based on nanoparticles. For instance, the electron tunneling through quantum dots has led to the possibility of fabricating single-electron transistors [4–9]. One concept particularly appealing is a new three-dimensional periodic table based on the possibility of generating artificial atoms from clusters of all of the elements [10]. This idea is based on the fact that several properties of nanoparticles show large fluctuations, which can be interpreted as electronic or shell-closing properties with the appearance of magic numbers. Therefore, it is conceivable to tailor artificial superatoms with given properties by controlling the number of shells on a nanoparticle.

The development of nanotechnology can be approached from several directions; mesoscopic physics, microelectronics, materials nanotechnology, and cluster science. The different fields are now coming together, and a completely new area is emerging [11, 12]. Figure 1 illustrates how the different approaches are converging; it exhibits the domains of clusters and nanoparticles with different structures that result from an increase in the number of atoms. The different possible structures include nanorods, nanoparticles, fullerenes, nanotubes, and layered materials.

One of the most remarkable advances in this field has been the synthesis of ligand-capped metallic clusters. In a seminal contribution, Brust et al. [13] used the classical two-phase Faraday colloid separation combined with contemporary phase-transfer chemistry to produce small gold nanoclusters coated with alkanethiolate monolayers. Several groups have pursued this technique [14–21], and have introduced improvements and modifications to the original technique. Whetten and his group [15, 16] made important contributions to this technique.

A significant property of ligand-capped clusters is that they can be repeatedly isolated from and redissolved in common organic solvents without irreversible aggregation or decomposition. The properties of the monolayer-protected nanoparticles (MPNs and MPANs) allow handling in ways that are familiar to the molecular chemist since they are stable in air conditions. The MPNs of some metals such as Pt [22], Ag [23], Rh, and Pd [24] have been synthesized.

2. GEOMETRIC CONSIDERATIONS

2.1. Clusters and Nanoparticles

Since the pioneering work of Ino and Ogawa [25, 26], it was clear that, in most cases, the structure of nanoparticles cannot be described by the bulk crystallography of the used material. The concept of multiple twins was used to explain many of the structures, Such as the icosahedron and the decahedron. This concept was directly imported from the macroscopic metallurgical studies, and was certainly very useful for a first understanding of the structure of nanoparticles. Another related research field was the study of clusters formed by few atoms. From that field, we learned that structures are formed by shells, and the concept of a magic number was introduced [27]. Nanoparticles referred
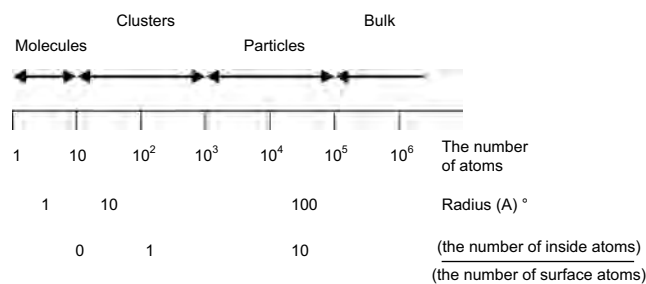
to sizes of ∼5–10 nm, and clusters referred to sizes of ∼1 nm. In recent times, the computational tools for study clusters allow the analysis of a large number of atoms, and the methods to study nanoparticles allow interrogating smaller nanoparticles. The two fields are merging into one. In this chapter we will use the term particle and cluster indistinctly.

2.2. Clusters with Cubic Symmetry

When considering atom clusters of nanometric dimensions, it can be supposed that they correspond to some symmetry group. In previous works, small clusters (up to tents of atoms) of diverse forms (tetrahedron, hexahedron, octahedron, decahedron, dodecaheltahedron, trigonal, trigonal prism, and hexagonal antiprism, with and without a central site) have already been studied [28]. Partially and totally capped clusters were also considered (clusters to which a site has been added to each face of the polyhedron, equidistant to every site of the face), in order to vary the number of sites for all of the polyhedrons, and thus allowing the comparison as a function of the number of sites.

Geometric characteristics of the clusters formed by concentric layers can be considered, as formed by equivalent sites: sites located at the same distance from the origin, which occupy the same geometric place and have the same environment, that is, the same number and type of neighbors. These layers can be arranged in such a way that they group in shells forming clusters of different sizes, retaining the original geometric structure. The number of shells in the cluster is called the order of the cluster, and is represented by letter ν. The studied structures were: the icosahedron, the face-centered cubic structure fcc (the cubooctahedron), the body-centered cubic bcc, and the simple cubic sc [29].

In order to determine the stability of the structures from an energetic point of view, a study of the cubo-octahedral and icosahedral structure was performed using the embedded atom method (EAM) for the transition metals Cu, Pd, Ag, and Ni [30]. It was determined that for sizes smaller than 2000 atoms, the icosahedron is the most stable structure, and for larger sizes, the cubooctahedron. For this study, the advantage of having equivalent sites in the clusters was used to reduce computation time. In a latter study, based upon the same metals, small clusters of less than 100 atoms with regular polyhedron geometries were used, and to change the cluster size, partially and totally capped clusters were considered. Tetrahedral clusters showed the highest stability for sizes of less than 18 atoms, and icosahedra for larger sizes [31].

In this work, the structural stability competition among different regular structures of the concentric shell type is searched. Here, the studied geometries are reproduced, considering some other arrays of the layers in shells, which give rise to other geometries. The fcc structure considers many structures, which are divided into two groups: (1) with a central site, and (2) without a central site. Among the centered ones, the cubooctahedron, octahedron, and truncated octahedron are considered. For the ones not centered, the

Figure 1. Domains of nanoparticles and clusters with different structures.

octahedron and the truncated octahedron are considered. The bcc structure has the dodecahedron. The sc structure does not allow a study like the one presented here because, when a truncation is tried, second neighbor distances are obtained. Once the geometric properties of the structures are determined, the EAM is applied to them, and their stability is discussed.

2.3. Geometric Characterization

The following procedure was used to determine the geometric characteristics of the structures: (1) First, identify the structures, that is, their geometric shape; (2) the nature of the site coordinates which conform the structures; and (3) their neighbors with surrounding layers, in order to identify the equivalent sites and generate the concentric shell-type structures. Once this previous stage is completed, the geometric properties to be determined are defined, the structures are presented, and the geometric properties of each structure are numbered. Afterwards, based on the geometric characteristics of each structure, the analytic expressions are deduced as a function only of the cluster order for the defined properties.

An example of the concentric shell-type structures is shown in Figure 2, which presents the cubooctahedron in three different sizes. In this figure, a central site surrounded by 12 sites forming a cubooctahedron with one first shell can be seen; Figure 2(a). Then it is covered with another shell of sites distributed in three layers of equivalent sites, as will be seen later, but retaining the original geometric shape; Figure 2(b). And finally, Figure 2(c) presents a three-shell cubooctahedron.

The structures considered are the face-centered cubic fcc, [Fig. 3(a)], and the body-centered cubic bcc [Figs. 3(d) and (e)]. Although both are cubic, in Figure 3(a) the fcc does not seem to be cubic, but the face-centered cubic structure with a central site fccc [Fig. 3(b)], and the face-centered cubic structure without a central site fccs [Fig. 3(c)], show that they do have a cubic shape: 8 vertexes, 6 square faces, and 12 edges. The bcc structure has a central site, while the fcc structure can be considered with and without a central site. Truncating each one of them in a certain direction, noncubic structures are obtained, they have, besides vertexes (V), edges (E), and square faces (S), faces of different shapes: a triangular face (T), a hexagonal face (H), and a rombohedral face (R). The resulting structures are: the

Figure 3. Structures (a) face-centered cubic fcc, (b) face-centered cubic with central site fccc, (c) face-centered cubic without central site fccs, and (d), (e) body-centered cubic bcc.

cubooctahedron [Fig. 4(a)], the octahedron [Fig. 4(b)], the truncated octahedron [Fig. 4(c)], and the dodecahedron [Fig. 4(d)]. For the fccc, the obtained structures are the cubooctahedron CO, the octahedron OCTAC, and the truncated octahedron OCTTC; for the fccs, the structures obtained are the octahedron OCTAS, and the truncated octahedron OCTTS; and for the bcc, only the decahedron is obtained, DODE.

Table 1 presents the number of characteristic sites of each structure, in such a way that each structure is read as: the structure is formed by V vertexes attached by E edges forming X faces of different types, where $X = S$, T, H, R, as it corresponds. The icosahedron is included [Fig. 4(e)], because it can be obtained by an adequate distortion of the CO, and it is useful as a reference for a comparison of results. ICO, the fccc and its derivates, as well as the bcc and the DODE, present a central site. The OCTTC is centered over an octahedron with a central site of 19 sites, and the OCTTS over a regular octahedron of 6 sites.

2.3.1. Standard Coordinates

Each of the structures studied here, except the ICO, corresponds to a well-defined crystalline structure, fcc or bcc, so that the coordinates of the geometric sites which compose them are characteristic of each one of them. In each structure, the standard coordinates are described by triads (a, b, c), a, b and c are integers, where the total number of sites is obtained by doing permutations and commutations

Figure 2. Cubooctahedrons formed by a central site and (a) one layer, (b) two layers, and (c) three layers.
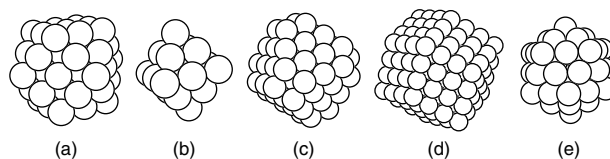
Figure 4. Polyhedrons resulting from truncation of fcc and bcc structures. (a) cubooctahedron, (b) octahedron, (c) truncated octahedron, and (d) dodecahedron. (e) as a result of an adequate distortion of the cubooctahedron, the icosahedron is obtained.

Table 1. Number of geometric sites corresponding to the structures of the first column. Last column presents the number of central sites of the structure.

	V	E	S	T	H	R	Central site
ICO	12	30	—	20	—	—	1
fccc	8	12	6	—	—	—	1
CO	12	24	6	8	—	—	1
OCTAC	6	12	—	8	—	—	1
OCTTC	24	36	6	—	8	—	19
fccs	8	12	6	—	—	—	—
OCTAS	6	12	—	8	—	—	—
OCTTS	24	36	6	—	8	—	6
bcc	8	12	6	—	—	—	1
DODE	14	24	—	—	—	12	1

of the positive and negative values of a, b and c. Table 2 presents the characteristics of standard coordinates for each structure as a function of the cluster order ν. Sites ES [EH] in OCTTC are the sites on edges between hexagonal and squared [hexagonal] faces.

2.3.2. First Neighbors

There will be different types of equivalent sites, depending on the geometric structure, and each type will occupy a geometric position which will be of type vertex (V), edge (E), square face (S), triangular face (T), hexagonal face (H), and rombohedral faces (R), and it will have a total number of neighbors, coordination z, which will correspond to the structure, but the number of neighbors with layers of its same shell, with interior and exterior shells, will be characteristic of each site. Table 3 presents the different types of sites in the studied structures, as well as the number of first neighbors with layers of interior shells ($\downarrow$), in the same shell ($\leftrightarrow$), and with exterior shells ($\uparrow$). Also, total coordination z

Table 2. Standard coordinates characteristics for each of the structures.

	Site	a	b	c	$b + c$	$a + b + c$
fccc	S	$[2\nu - 1, 2\nu]$		$[0, 2\nu - 1]$		even $[2\nu, 6\nu - 2]$
	E		$[2\nu - 1, 2]$	$[0, 2\nu - 2]$ (even)		$[2\nu, 6\nu - 2]$
	V		2ν			6ν
CO	S	ν		$[0, \nu - 2]$	$[\nu - 2]$	even $[\nu, 2\nu - 2]$
	T		$[1, \nu)$			2ν
	E	ν		$[1, \nu]$	ν	2ν
	V		ν	0		2ν
OCTAC	T		$[1, 2\nu - 2]$			2ν
	E		$[1, 2\nu - 1)$	0		2ν
	V	2ν	0	0		2ν
OCTTC	S	$\nu + 2$	$[0, \nu - 2]$	$[0, (\nu - 2)/2], \nu$ even $[0, (\nu - 3)/2], \nu$ odd		$[\nu + 2, 2\nu]$
	H	$[\nu - 2, \nu + 1]$	$[(\nu/2) + 1, \nu], \nu$ even $[(\nu + 1)/2, \nu], \nu$ odd	$[1, (\nu/2) + 2], \nu$ even $[1, (\nu + 3)/2], \nu$ odd		$2\nu + 2$
	ES	$\nu + 2$		$[1, \nu]$	ν	$2\nu + 2$
	EH		$\nu + 1$	0		$2\nu + 2$
	V	$\nu + 2$	ν	0		$2\nu + 2$
fccs	S	$[2\nu - 2, 2\nu - 1]$		$[0, 2\nu - 2]$		odd $[2\nu - 1, 6\nu - 5]$
	E		$[2\nu - 2, 2\nu - 1]$	$[1, 2\nu - 1]$ (odd)		$[4\nu - 3, 6\nu - 3]$
	V		$2\nu - 1$			$6\nu - 3$
OCTAS	T		$[1, \nu - 1]$			$2\nu - 1$
	E		$[1, 2\nu - 1]$	0		$2\nu - 1$
	V	$2\nu - 1$	0	0		$2\nu - 1$
OCTTS	S	$\nu + 1$	$[0, \nu - 2]$	$[0, \nu/2], \nu$ even $[0, (\nu - 1)/2], \nu$ odd	$[\nu - 4, \nu - 2]$	
	H		$[1, \nu]$			$2\nu + 1$
	E	$\nu + 1$	$[\nu/2, \nu)$ $[(\nu - 1)/2, \nu)$	$[1, \nu/2]$ $[1, (\nu - 1)/2]$		$2\nu + 1$
	V	$\nu + 1$	ν	0		$2\nu + 1$
bcc	S	ν		$[0, \nu - 2]$		even, ν even odd, ν odd $[\nu, 3\nu - 4]$
	E		ν	$[0, \nu - 2]$ (even) $[1, \nu - 2]$ (odd)		$[2\nu, 3\nu - 2]$ $[2\nu + 1, 3\nu - 2]$
	V		ν			3ν
DODE	R		$[1, \nu - 1]$			$2\nu - 1$
	E		$[0, 2\nu/ - 2]$	0		$2\nu - 1$
	V	$2\nu - 1$	0	0		$2\nu - 1$

Table 3. Number of first neighbors with shell on external layers ↑ (internal ↓) and with layers in the same shell ↔ for the different types of sites of the structures fcc, icosahedral, and bcc. The total coordination z is given by $(\uparrow) + (\downarrow) + (\leftrightarrow)$.

		dir	S	T	H	R	A		V		z
		↑	↑	↑	↑	↑	↑		↑		
		↔	□	△	H	◇	\		•		
		↓	↓	↓	↓	↓	↓		↓		
			4	4	4	—	—	—	7	9	
			4	5	6	—	—	—	4	3	12
			4	3	2		—	—	1	0	
fcc	CO		4	3	—	—	5		7		
			4	6	—	—	5		4		12
			4	3	—	—	2		1		
	OCTAC		—	3	—	—	5		8		
			—	6	—	—	6		4		12
			—	3	—	—	1		0		
	OCTTC		4	—	3	—	5	5	6		
			4	—	6	—	5	6	5		12
			4	—	3	—	2	1	1		
			4	4	4	—	—	—	7	9	
			4	5	6	—	—	—	4	3	12
			4	3	2		—	—	1	0	
fccs	OCTAS		—	3	—	—	5		8		
			—	6	—	—	6		4		12
			—	3	—	—	1		0		
	OCTTS		4	—	3	—	5		6		
			4	—	6	—	5		5		12
			4	—	3	—	2		1		
	ICO		—	3	—	—	4		6		
			—	6	—	—	6		5		12
			—	3	—	—	2		1		
bcc			4	—	—	—	6		7		
			0	—	—	—	0		0		8
			4	—	—	—	2		1		
	DODE		—	—	—	2	3	4	4		
			—	—	—	4	4	4	3		8
			—	—	—	2	1	0	1		

Figure 5. fcc polyhedrons of (a) 13 sites (central site plus a sublayer of 12 sites), (b) 63 sites (a complete layer of 62 sites), (c) 171 sites (a sublayer of 108 sites over the order 1 fccc), and (d) 365 sites (two complete layers).

1×12 E sites, 5×6 S and 8 V, but looking carefully it will be noticed that the S sites are not equivalent because the one in the center of the squared face has a coordination of 4 with the surface sites, while the other has a coordination of 6, but both have a coordination of 4 toward external layers. It is also observed that in Figure 5(c) the four sites of type S at the center of the face have a coordination of 4 with the surface sites, and the other eight sites of type S have a coordination of 5 with surface layers, but all of them have 4 toward external layers, while in Figure 5(d) it is observed that the S sites near the vertexes have a coordination of 6 with sites over the same surface shell, and the ones close to sites E have a coordination of 5, this is why in Table 3 the coordination for S sites can be of three types, but all of them with a coordination of 4 toward external layers. That is why in fccc and fccs there are shells composed of two subshells, one that will contain the surface sites, and the other that will remain internal. Surface sites will interact with the internal sites, and these internal ones with those of the cluster and the surface ones.

From Fig. 4d it is worth noticed that the vertex sites for the dodecahedron are of two types: one on which four edges converge and another on which three edges converge. This is why in Table 3 the coordination for the V sites for the DODE structure are of two types.

2.3.3. Definition of Geometric Properties

Table 4 presents definitions and their mathematical expressions for the general geometric characteristics, which can be expressed analytically as a function of only the order of the cluster ν, for each structure or geometric array. The upper section of Table 4 refers to the geometric characteristics of the cluster, the middle section to the bonds, and it relates Table 3, and the superior part of Table 4, and the lower section of Table 4 to the average coordination based on the rest of Table 4.

The cluster can be defined as a nucleus and a surface over the nucleus. The number of I sites, the number of types of I sites and what refers to dispersions is over the surface, and the average number of bonds and coordination is over the involved sites of the cluster. In the expressions for $\mathcal{N}_{CC}$ and $\mathcal{N}_{SS}$, $(\uparrow)_I$ means the number of I site bonds in the internal layer (the nucleus surface) with sites in the external layer (the cluster surface), $(\downarrow)_I$ means the number of I-site bonds in the external layer (the cluster surface) with sites in the internal layer (the nucleus surface), and $(\leftrightarrow)_I$ means the number of I-site bonds in the surface of the cluster with

in the structure is presented. The truncated octahedron with a central site presents two types of edges, the edges between squared and hexagonal faces, ES, with coordination $(2, 5, 5)$, and the edges between hexagonal faces, EH, with coordination $(1, 6, 5)$, while all of the other structures have only one. It should be noticed that, in order to obtain structures of the concentric shell type in the fccc and fccs structures, two shells will be needed, as shown on Figure 5 for fccc (similarly for fccs); Figure 5(a) presents the fccc "cube" of 13 sites; Figure 5(b) shows the fccc of 63 sites, which will be a complete shell of 62 sites $(12 + 50)$ over the central site; Figures 5(c) and (d) present the fccc of 171 sites and the fccc of 365 sites, the latter is the one with two shells, one with 108 sites and the other with 194 sites. The surface sites in the fccc of 13 sites become internal when adding 50 to complete the fccc of 63 sites, the same happens for that one of the 171 sites when covering it to complete the one with 365. From Figure 5(b), it is observed that there will exist

Table 4. General definitions of geometric parameters for different structures.

Symbol	Definition	Mathematical expression
N	Total number of atoms in a cluster of order ν	
N_σ	Number of atoms in a crust or on the surface	
$\mathscr{D}$	Dispersion;	N_σ/N
N_I	Number of surface atoms on site I, $I = S, T, H, R, E, V$	
R_I^a	Number of shells in which are contained the I-sites (a = even, odd)	
N_{shell}^ν	Number of shells at the surface	
N_{shell}^T	Total number of shells in the cluster	
$\mathscr{D}_I$	Dispersion due to surface I sites;	N_I/N_σ
$\mathscr{N}_{CO}$	Number of internal bonds in a cluster of order ν;	$\frac{1}{2} \times z \times N(\nu - 1)$
$\mathscr{N}_{CC}$	Number of bonds between two adjacent crusts ($\nu - 1$) and ν;	$\sum_I (\uparrow)_I \times N_I(\nu - 1) = \sum_I (\downarrow)_I \times N_I(\nu)$
$\mathscr{N}_{SS}$	Number of bonds on the surface of a cluster of order ν;	$\frac{1}{2} \sum_I (\leftrightarrow)_I \times N_I(\nu)$
$\mathscr{N}_C$	Number of bonds in a cluster of order ν;	$\mathscr{N}_{CO} + \mathscr{N}_{CS} + \mathscr{N}_{SS}$
$\overline{Z}$	cluster average coordination;	$2\mathscr{N}_C(\nu)/N(\nu)$
$\overline{Z}_{CO}$	Core average coordination;	$2\mathscr{N}_{CO}(\nu)/N(\nu - 1)$
$\overline{Z}_{CS}$	Core–surface average coordination;	$\mathscr{N}_{CC}(\nu)/N_\sigma(\nu - 1)$
$\overline{Z}_{SC}$	Surface–core average coordination;	$\mathscr{N}_{CC}(\nu)/N_\sigma(\nu)$
$\overline{Z}_{SS}$	Surface average coordination;	$2\mathscr{N}_{SS}(\nu)/N_\sigma(\nu)$

sites in the same surface. It must be clear that, due to the fact that there are many ways to coordinate S sites in the surface for fccc and fccs structures, the formula for $\mathscr{N}_{CC}$ must only be used as $\sum_I (\uparrow)_I \times N_I(\nu - 1)$, and only for these two structures, the proposed equity does not apply.

2.4. fcc Structure

An fcc structure is that in which the unit cell is a cube with sites in the vertexes and in the center of squared faces, this means that there are 14 sites on a cube, 8 vertexes, and 6 squared faces [Fig. 3(a)], also, it can be seen as a completely capped octahedron. When attaching many of these arrays with common or shared sites in faces and vertexes, clusters are obtained with sites in vertexes, edges, and squared faces. The origin of coordinates can be chosen to be at the center of the cube or on a vertex, obtaining structures with and without a central site, respectively.

2.4.1. fcc Structure with a Central Site

In the fcc structure with a central site, the cubic cluster of order 1 is a cube with 63 sites, distributed in 5 layers around a central site [Fig. 5(b)]; it can be seen that it is an array of 6 unit cells with common sites. The order 2 cluster is obtained when covering the one of order 1 with 302 sites distributed in 13 layers to obtain a total of 365 sites [Fig. 5(d)], and so on. Layers of equivalent sites can be identified (Table 1): squared face (S), edges (E) and vertexes (V). Table 2 presents the standard coordinates and its characteristics, it can be seen that the sum of the standard coordinates a, b and c is an even number, and in Table 3 the coordination of each site. From Figures 5(a)–(d) it can be seen that a shell is composed of two subshells. Table 5 lists the geometric characteristics of the fccc structure, separating each shell into subshells to allow the calculus of surface dispersions and the number of bonds as defined in Table 4, and for each shell. General expressions for the geometric characteristics of Table 4 are presented in Table 6. These are shown when they are being considered as shells or subshells,

in both columns corresponding to subshells, the first one is for the internal, and the second one is for the external or surface. N_σ represents the number of sites added to the cluster of order $\nu - 1$, N_{sup} is the number of sites forming the surface, and it is the same for either of the considered cases because the internal shell does not form part of the surface. Besides this, the distinction is made among the different types of sites S forming the surface, N_S^j, where j is the coordination of the S sites with sites in the same layer, $j = 4, 5, 6$. In the calculus of the number of bonds between the two sublayers, the coordination from inside to outside was considered, because all of the types of S sites have a coordination of 4 with the exterior shell.

When grouping the layers of equivalent sites in shells in a different manner than the one given in fccc, geometries that present, besides squared faces, triangular and hexagonal faces will rise. Here, the cubooctahedron, octahedron, and truncated octahedron are considered.

2.4.2. Cubo-octahedra

The cubo-octahedron can be obtained by truncating an fcc structure in direction (111), this is shown in Figure 6(b), where a cubo-octahedron of 55 sites is presented, and is the result of removing the 8 corners of a cube of 63 sites. It is

Table 5. Geometrical characteristics for the face-centered cubic and with central site structure, fccc.

ν	N_S	N_E	N_V	R_S	R_E	R_V	N_{shell}^σ	N_{shell}^T	N_σ	N
1	0	12	0	0	1	0	1	2	12	13
	30	12	8	2	1	1	4	6	50	63
	30	24	8	2	2	1	5	6	62	63
2	72	36	0	2	2	0	4	10	108	171
	150	36	8	6	2	1	9	19	194	365
	222	72	8	8	4	1	13	19	302	365
3	240	60	0	6	3	0	9	28	300	665
	366	60	8	12	3	1	16	44	434	1099
	606	120	8	18	6	1	25	44	734	1099

Table 6. Particular expressions of the geometric characteristics for the face-centered cubic with a central site structure, fccc.

	Layer	Sublayers	
N		$32\nu^3 + 24\nu^2 + 6\nu + 1$	
N_σ	$96\nu^2 - 48\nu + 14$	$48\nu^2 - 48\nu + 12$	$48\nu^2 + 2$
N_{sup}	$48\nu^2 + 2$	$48\nu^2 - 48\nu + 12$	$48\nu^2 + 2$
$\mathscr{D}$	$\dfrac{48\nu^2 + 2}{32\nu^3 + 24\nu^2 + 6\nu + 1}$	$\dfrac{48\nu^2 - 48\nu + 12}{32\nu^3 + 24\nu^2 + 6\nu + 1}$	$\dfrac{48\nu^2 + 2}{32\nu^3 + 24\nu^2 + 6\nu + 1}$
N_S^6	24	—	24
R_S^6	1	—	1
N_S^5	$48(\nu - 1)$	—	$48(\nu - 1)$
R_S^5	$\nu - 1$	—	$\nu - 1$
N_S^4	$24[(2\nu 1)^2 + (2\nu - 2)^2]$	—	$24[(2\nu - 1)^2 + (2\nu - 2)^2]$
R_S^4	ν^2	—	ν^2
N_E	$24(2\nu - 1)$	$12(2\nu - 1)$	
R_E^p	2ν	ν	
N_V	8	0	8
R_V	1	0	1
$\mathscr{N}_{CO}$		$6(32\nu^3 - 24\nu^2 + 6\nu - 13)$	
$\mathscr{N}_{CC}$		$12(16\nu^2 - 10\nu + 1)$	
$\mathscr{N}_{SS}$		$48\nu(4\nu + 48)$	
$\mathscr{N}_C$		$4(48\nu^3 + 60\nu^2 - 9\nu - 14)$	

formed by 8 triangular faces and 6 squared ones, attached by 24 edges and 12 vertexes; see Table 1. Consequently, the surface sites are localized in squared faces (S), triangular faces (T), edges (E), and vertexes). The CO of order 1 has a central site and a first shell with one single layer of 12 vertexes, Figure 6(a). The CO of order 2 is formed by adding one shell formed by 42 sites in order to complete 55 [Fig. 6(b)], distributed in three layers: one layer of 6 S sites, another of 24 E sites and a third one of 12 V sites. When adding a third shell of 92 sites, the third order CO of 147 sites is completed [Fig. 6(c)], sites are distributed in four layers: one of 24 S sites, another of 8 T sites, one more of 48 E sites, and a fourth one of 12 V sites. Successively, complete shells are added this way, forming clusters of order ν.

The standard coordinates for the cubo-octahedron are listed in Table 2, the number of neighbors for each site can be found in Table 3, and the geometric characteristics of the CO are listed in Table 7; from this table, it is possible to obtain the general expressions for the geometric characteristics of the cubooctahedron defined in Table 4. These expressions are presented in Table 11, for the cubo-octahedron and all the other fccc structures to be studied.

Figure 6(e) presents an icosahedron of 923 sites of order 6. When comparing with the CO, which has the same number of sites, from Figure 6(d), the distortion made to obtain the ICO can be observed. Table 3 shows the number of neighbors for each site, and Table 8 reproduces the geometric characteristics corresponding to the icosahedron, which have been reported previously [29]. A great similarity can be noticed between Tables 7 and 8, in the columns referring to the types of sites or layers by shell (columns for T, E, V), and in the sites at the surface, in the total (the two last columns of tables N_σ and N), and in the expressions for both in Table 11. Based on these latter, it is possible to obtain the dispersions due to the surface sites of both structures obtaining the graphic in Figure 7. Surface and vertex dispersion is exactly the same for both structures, they start close to 1 and in 1, respectively, and then they decrease. Dispersion in triangular faces, for both structures, shows a very similar behavior, they start in the same value, and increase with the size of the cluster, but D_T in the ICO increases

Figure 6. Cubo-octahedron of (a) order 1 of 13 sites, (b) order 2 of 55 sites, (c) order 3 of 147 sites, and (d) order 6 of 923 sites. Observe the distortion of CO (d) to obtain (e) an icosahedron of order 6 of 923 sites.

Table 7. Geometrical characteristics for the cubo-octahedra.

ν	N_S	N_T	N_E	N_V	R_S	R_T	R_E	R_V	N_{shell}^σ	N_{shell}^T	N_σ	N
1	0	0	0	12	0	0	0	1	1	1	12	13
2	6	0	24	12	1	0	1	1	3	4	42	55
3	24	8	48	12	1	1	1	1	4	8	92	147
4	54	24	72	12	3	1	2	1	7	15	162	309
5	96	48	96	12	3	2	2	1	8	23	252	561
6	150	80	120	12	6	3	3	1	13	36	362	923
7	216	120	144	12	6	4	3	1	14	50	492	1415
8	294	168	168	12	10	5	4	1	20	70	642	2057
9	384	224	192	12	10	7	4	1	22	92	812	2869
10	486	288	216	12	15	8	5	1	29	121	1002	3871

Table 8. Geometrical characteristics for the icosahedra.

ν	N_T	N_E	N_V	R_T	R_E	R_V	$N_{\text{shell}}^{\sigma}$	N_{shell}^{T}	N_{σ}	N
1	0	0	12	0	0	1	1	1	12	13
2	0	30	12	0	1	1	2	3	42	55
3	20	60	12	1	1	1	3	6	92	147
4	60	90	12	1	2	1	4	10	162	309
5	120	120	12	2	2	1	5	15	252	561
6	200	150	12	3	3	1	7	22	362	923
7	300	180	12	4	3	1	8	30	492	1415
8	420	210	12	5	4	1	10	40	642	2057
9	560	240	12	7	4	1	12	52	812	2869
10	720	270	12	8	5	1	14	66	1002	3871

faster. Similarly for the edges, they increase rapidly from zero to a maximum value, and decrease slowly almost parallel. The predominance of D_T and D_C for large sizes has to be noticed for ICO and CO, respectively.

2.4.3. Octahedron with a Central Site

The octahedron with a central site has 6 vertexes (V), 12 edges (E), and 8 triangular faces (T), Figure 8. In this figure, the sides of the triangular faces have a length of $2\nu d_{NN}$, an even number times the distance to first neighbors; this means that the triangular faces do not present a central site, and the number of sites for each edge is odd. The number of neighbors for each site with sites in other layers can be found in Table 3, the standard coordinates in Table 2, and the geometric characteristics for the octahedron with a central site are listed in Table 9. From this latter, the general expressions of the geometric characteristics for the octahedron with a central site (OCTAC) can be deduced and are presented in Table 11. Figure 8(c) shows an octahedron of 891 sites with a central site.

With the same method applied for the CO and the ICO, the dispersions due to surface sites can be calculated from Table 5, and the results are presented in the graphic of Figure 9. It can be observed that the surface dispersion
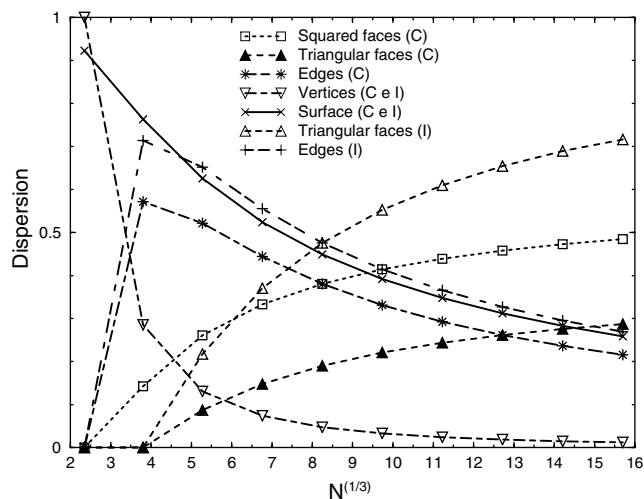
Figure 8. Octahedron of 19 atoms with central site. Smaller atoms are presented in (a) to allow observation of first neighbor bonds and central site in (b). (c) Octahedron of 891 atoms, order 5, and with a central site.

and dispersions due to edges and vertexes decrease, while the one due to the triangular faces starts from zero and increases rapidly, being predominant for larger sizes.

2.4.4. Truncated Octahedron with a Central Site

A truncated octahedron is a structure centered over an octahedron of 18 sites (2 layers) with a central site (layer 0), and has 24 vertexes (V) 36 edges (E), 6 squared faces (S), and 8 hexagonal faces (H); Figure 10. Edges are of two types: 24 between squared and hexagonal faces (ES), and 12 between hexagonal faces (EH); the number of EH sites N_{EH} is always equal to 12, one site in each edge (EH), while the one in ES sites N_{ES} depends on the order of the cluster, this means that the length of the edges ES is variable, and the one of EH edges is $2d_{NN}$. And so, the hexagonal faces are irregular, except when the number of ES sites is 24 and the number of EH sites is 12, which occurs in the cluster of order 2. The number of first neighbors for each site can be found in Table 3, standard coordinates are in Table 2, and Table 10 presents the geometric characteristics of each structure. Figure 10(c) shows the truncated octahedron of 711 sites with a central site.

From Table 10 it can be observed that the number of EH sites is 12 and of V sites is 24 for all ν, besides this, it is possible to obtain the general expressions of the geometric characteristics for the truncated octahedron with a central site, as presented in Table 11.

Figure 7. Dispersions due to surface sites of the cubooctahedron (C) and icosahedron (I) as a function of the cubic root of the number of sites.

Table 9. Geometrical characteristics for the octahedra with a central site.

ν	N_T	N_E	N_V	R_T	R_E	R_V	$N_{\text{shell}}^{\sigma}$	N_{shell}^{T}	N_{σ}	N
1	0	12	6	0	1	1	2	2	18	19
2	24	36	6	1	2	1	4	6	66	85
3	80	60	6	3	3	1	7	13	146	231
4	168	84	6	5	4	1	10	23	258	489
5	288	108	6	8	5	1	14	37	402	891
6	440	132	6	12	6	1	19	56	578	1469
7	624	156	6	16	7	1	24	80	786	2255
8	840	180	6	21	8	1	30	110	1026	3281
9	1088	204	6	27	9	1	37	147	1298	4579
10	1368	228	6	33	10	1	44	191	1602	6181
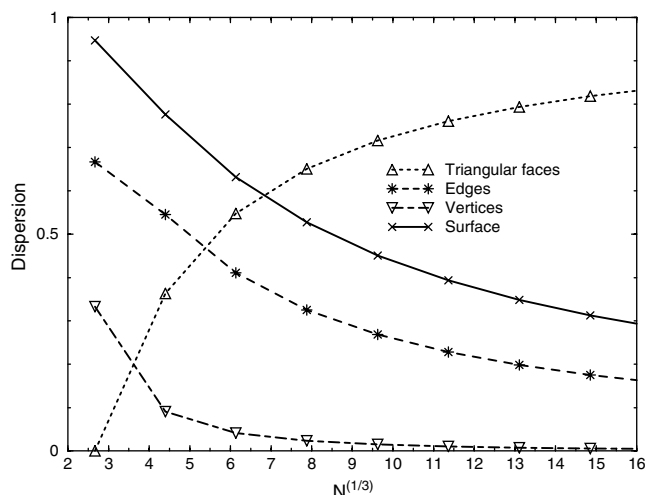
Figure 9. Dispersions due to surface sites of the octahedron with a central site.

Figure 11 presents the dispersions for the truncated octahedron and with a central site, derived from the data of Table 10. The predominance of the dispersion due to the sites in hexagonal and squared faces for large sizes can be observed. Dispersions due to other sites and the surface one decrease with the size of the cluster.

With support from Tables 4 and 6–10, it is possible to obtain the characteristics defined in the middle and lower parts of Table 4 for each and every studied structure. Characteristics in the middle part of Table 4 are presented in Table 11, and Figures 12–15 present the obtained graphics of the dependence of the number of bonds at the surface $\mathcal{N}_{SS}$, the number of bonds between the surface and the internal cluster $\mathcal{N}_{SC}$, the number of bonds in the internal cluster $\mathcal{N}_{CO}$, and of the total number of bonds in the cluster $\mathcal{N}_C$, respectively, for all of the structures studied here, the curves for the ICO and CO practically coincide, so that just the curve of CO will be presented, except for $\mathcal{N}_{CO}$. It is observed that for the structures with a central site, and taking as reference the CO and the ICO, the OCTAC has a larger number of surface bonds and the OCTTC has fewer. But for $\mathcal{N}_{SC}$, the CO and ICO surpass the OCTAC and the OCTTC. For $\mathcal{N}_{CO}$, the OCTAC and the OCTTC surpass the CO. For $\mathcal{N}_C$, there are some crossings for smaller sizes, while for larger sizes the OCTAC and OCTTC surpass the CO.
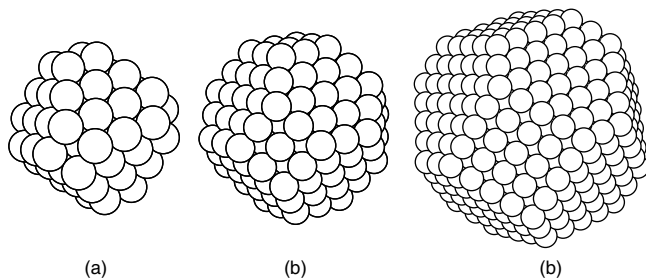
Figure 10. Truncated octahedron with central site of (a) order 1 and 79 atoms, (b) order 2 and 201 atoms, and (c) order 4 and 711 atoms.

2.4.5. EAM Applied to fcc Structures

The embedded atom method is applied, in the Foiles version [32] and with the parameters of copper, to clusters with central site fcc structures in order to calculate the cohesion energy per atom, determining in this way the stability of the clusters. The results are compared with the ones from the icosahedra and cubooctahedra previously reported [30]. Figure 16 presents the cohesive energy graphic as a function of $N^{1/3}$ for the octahedron and truncated octahedron clusters of fcc with central site type, for sizes from 300 to 3400 atoms. From Figure 16 it can be seen that the truncated octahedra ($\triangle$) have a higher stability than the icosahedra ($\bullet$) and cubooctahedra ($\blacksquare$), while the octahedra ($\diamond$) have it until sizes larger than 900 atoms.

In a previous work, it was found that the CO presented a higher stability than the ICO for larger sizes; when analyzing the number of bonds in the clusters, it is found that this condition is present when the number of bonds of CO surpasses the ICO ones. The competition among fcc structures with a central site and the icosahedron observed in the graphic of Figure 16 must have the same origin.

2.5. fcc Structure without a Central Site

In the fcc structure without a central site, the cubic cluster of order 1 has the same unit cell as the fcc structure of Figure 5(a), a cube with 14 sites, 8 in vertexes and 6 in the center of the squared faces. The second order cluster has 172 sites [Fig. 3(c)], which results from covering the first-order cluster with one shell of 158 sites, distributed in 8 layers; the second-order cluster is an array of 9 cubes attached by faces and common sites. The next cubic cluster is formed by the second-order one and a shell of 494 sites in 18 layers covering it, and so on. Equivalent sites layers can be identified: Table 1: squared face (S), edges (E) and vertexes (V). As in the fccc structure, each shell is composed of two subshells. Table 12 lists the geometric characteristics of the fccs structures, and the separation of subshells for each shell is done in order to allow the calculus of the number of bonds as defined in Table 2, and for each shell also. General expressions for the geometric characteristics of Table 12 are presented in Table 13. Table 2 presents the standard coordinates and their characteristics, it can be seen that the sum of the standard coordinates a, b and c is an odd number, and in Table 3 the coordination of each site is presented.

When grouping the layers of equivalent sites in shells, in a different way than given for fccs, the geometries presented are given: besides the squared faces, triangular and hexagonal faces are included. Here, the cubooctahedron, octahedron, and truncated octahedron will be considered.

2.5.1. Octahedron without a Central Site

The octahedron is formed by 6 vertexes, 12 edges, and 8 triangular faces. Figure 17 shows the octahedrons of 44 and 146 sites, without a central site. In these figures, it can be seen that there are sites in vertexes (V), edges (E), and in triangular faces (T). In this structure, the sides of the triangular faces have a length of $(2\nu - 1)d_{NN}$, an odd number times the distance to first neighbors d_{NN}, this means that the triangular faces can present a central site, and the number

Table 10. Geometric characteristics for the truncated octahedra with a central site.

ν	N_S	N_H	N_{ES}	N_{EH}	N_V	R_S	R_H	R_{ES}	R_{EH}	R_V	$N_{\text{shell}}^{\sigma}$	N_{shell}^{T}	N_{σ}	N
1	0	24	0	12	24	0	1	0	1	1	3	5	60	79
2	6	56	24	12	24	1	3	1	1	1	6	11	122	201
3	24	96	48	12	24	1	3	1	1	1	7	18	204	405
4	54	144	72	12	24	3	4	2	1	1	11	30	306	711
5	96	200	96	12	24	3	6	2	1	1	13	43	428	1139
6	150	264	120	12	24	6	7	3	1	1	18	61	570	1709
7	216	336	144	12	24	6	9	3	1	1	20	81	732	2441
8	294	416	168	12	24	10	11	4	1	1	27	108	914	3355
9	384	504	192	12	24	10	13	4	1	1	29	137	1116	4471
10	486	600	216	12	24	15	15	5	1	1	37	174	1338	5809

of sites in each edge is even. The number of first neighbors is presented in Table 3, the standard coordinates in Table 2 and the geometric characteristics for the octahedron without a central site are listed in Table 14. Figure 17(c) shows the octahedron of 1156 sites without a central site.

The number of V sites N_V is equal to 6 for all ν, and they are of just one type. From Table 14, it is possible to determine, for the octahedron without a central site, the dependence of the geometric characteristics on the order of the cluster ν, and it is reported in Table 14. This same

Table 11. Particular expressions of the geometric characteristics for the icosahedra and fcc with central site structures.

	CO	ICO	OCTAC	OCTTC
N	$\dfrac{10}{3}\nu^3 + 5\nu^2 + \dfrac{11}{3}\nu + 1$		$\dfrac{16}{3}\nu^3 + 8\nu^2 + \dfrac{14}{3}\nu + 1$	$\dfrac{10}{3}\nu^3 + 21\nu^2 + \dfrac{107}{3}\nu + 19$
N_{σ}	$10\nu^2 + 2$		$16\nu^2 - 48\nu + 2$	$10\nu^2 + 32\nu + 18$
$\mathscr{D}$	$\dfrac{30\nu^2 + 6}{10\nu^3 + 15\nu^2 + 11\nu + 3}$		$\dfrac{3(\nu^2 - 48\nu + 2)}{16\nu^3 + 24\nu^2 + 14\nu + 3}$	$\dfrac{3(10\nu^2 + 32\nu + 18)}{10\nu^3 + 63\nu^2 + 107\nu + 57}$
N_S	$6(\nu - 1)^2$	—	—	$6(\nu - 1)^2$
R_S^{even}	$\dfrac{\nu(\nu + 2)}{8}$	—	—	$\dfrac{\nu(\nu + 2)}{8}$
R_S^{odd}	$\dfrac{\nu^2 - 1}{8}$	—	—	$\dfrac{\nu^2 - 1}{8}$
N_T	$4(\nu - 1)(\nu - 2)$	$10(\nu - 1)(\nu - 2)$	$8(\nu - 1)(2\nu - 1)$	$4\nu^2 + 20\nu$
R_T^m	A	B	—	
N_H	—	—	—	$4\nu^2 + 20\nu$
R_H^m	—	—	—	C
N_E	$24(\nu - 1)$	$30(\nu - 1)$	$12(2\nu - 1)$	$24(\nu - 1)$
R_E^{even}	$\dfrac{\nu}{2}$		$\nu - 1$	$\dfrac{\nu}{2}$
R_E^{odd}	$\dfrac{\nu - 1}{2}$		$\nu - 1$	$\dfrac{\nu - 1}{2}$
$\mathscr{N}_{CO}$	$4\nu(5\nu^2 + 3\nu + 1)$	$20\nu^3 + 15\nu^2 + 7\nu$	$32\nu^3 - 48\nu^2 + 28\nu11$	$20\nu^3 + 66\nu^2 + 22\nu + 6$
$\mathscr{N}_{CC}$	$12(3\nu^2 - 3/nu + 1)$	$6(5\nu^2 - 5/nu + 2)$	$12(4\nu^2 - 4\nu + 1)$	$12(3\nu^2 + 5\nu + 1)$
$\mathscr{N}_{SS}$	$24\nu^2$	$30\nu^2$	$48\nu^2$	$24(\nu^2 + 4\nu + 2)$
$\mathscr{N}_C$	$4(5\nu^3 - 12\nu^2 + 10\nu - 3)$	$20\nu^3 - 45\nu^2 + 37\nu - 12$	$2(16\nu^3 + 24\nu^2 - 10\nu + 3)$	$2(10\nu^3 + 63\nu^2 + 89\nu + 33)$

$$A = \begin{cases} \displaystyle\sum_{\alpha=1}^{m/2}(3\alpha + a) + \sum_{\alpha=1}^{(m/2)-1} 3\alpha; & m \text{ even} \\ & \begin{cases} \nu = 3m + a; \\ a = -1, 0, 1; \end{cases} \\ \dfrac{1+a}{1+|a|} + \displaystyle\sum_{\alpha=1}^{(m-1)/2}(6\alpha + a); & m \text{ odd} \end{cases}$$

$$B = \begin{cases} \displaystyle\sum_{\alpha=1}^{m/2}(3\alpha + a) + \sum_{\alpha=1}^{(m/2)-1} 3\alpha; & m \text{ even} \\ & \begin{cases} 2\nu = 3m + a; \\ a = -1, 0, 1; \end{cases} \\ \dfrac{1+a}{1+|a|} + \displaystyle\sum_{\alpha=1}^{(m-1)/2}(6\alpha + a); & m \text{ odd} \end{cases}$$

$$C = \begin{cases} \displaystyle\sum_{\alpha=1}^{m/2}(3\alpha + a) + \sum_{\alpha=1}^{(m/2)-1} 3\alpha + \sum_1^b 1; & m \text{ even} \\ & \begin{cases} \nu = 3m + a; \\ a = -1, 0, 1; \end{cases} \\ \dfrac{1+a}{1+|a|} + \displaystyle\sum_{\alpha=1}^{(m-1)/2}(6\alpha + a) + \sum_1^b 1; & m \text{ odd} \end{cases}$$

where b is the integer of $(\nu + m + |a| + 1)/2$
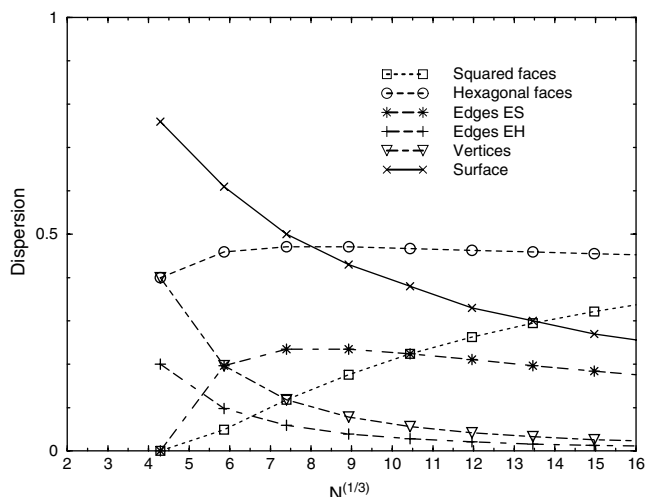
Figure 11. Dispersions due to surface sites of truncated octahedron with central site.

Figure 13. Number of bonds between the surface and the internal cluster as a function of the number of sites.

procedure is applied for the truncated octahedron, and without a central site and with the ones from the dodecahedron, which will be studied afterwards. The surface dispersion and the one due to each surface site also can be obtained from Table 14, and are presented in the graphic of Figure 18. The strong predominance of the sites of triangular faces and the fast decrease of the dispersions due to the vertexes and edges can be observed.

2.5.2. Truncated Octahedron without a Central Site

The truncated octahedron without a central site, Figure 19, is formed by a central octahedron surrounded by 6 squared faces and 8 irregular hexagonal faces (3 sides of length 1 and 3 of length equal to the order of the cluster ν, in units of d_{NN}, alternated) attached by 24 vertexes and 36 edges, so the edges are of two types: 24 between squared and hexagonal faces and 12 between hexagonal faces; the first ones are

Figure 14. Number of internal bonds as a function of the number of sites.

Figure 12. Number of surface bonds as a function of the number of sites.
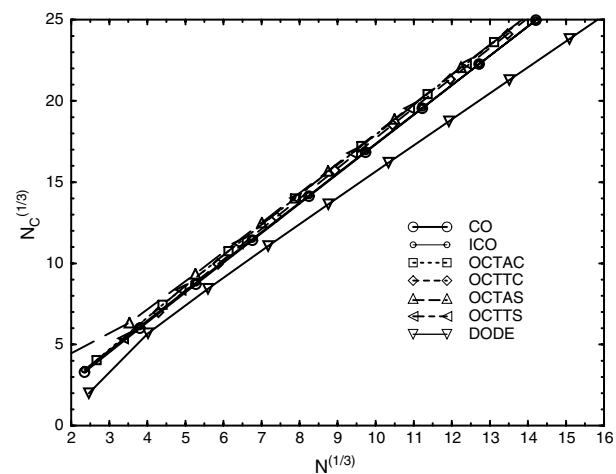
Figure 15. Total numbers of bonds as a function of the number of sites.
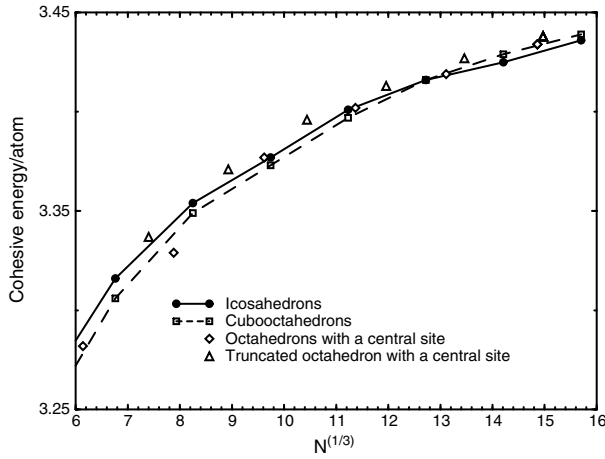
Figure 16. Cohesive energy per atom as a function of the cubic root of the number of atoms in the cluster for the octahedrons and truncated octahedrons type fcc with a central site.

length dependent on the cluster order, and the second ones on length $1d_{NN}$, this means that there is not a single site in them, so the first 24 are simply called E. The number of first neighbors of each site is presented in Table 3, the standard coordinates in Table 2, and the geometric characteristics for the truncated octahedron without a central site are listed in Table 15. Figure 19(b) shows the truncated octahedron of 1288 without a central site.

The number of V sites N_V is equal to 24 for all ν, and they are of just one type. From Table 15 the expressions for the geometric characteristics for the truncated octahedron without a central site can be determined, and are presented in Table 16. Also, the surface dispersions can be determined, and are presented in the graphic of Figure 20. A not so strong predominance of the sites in squared and hexagonal faces can be observed, while the other dispersions decrease as the cluster size increases.

With support from Tables 4 and 15 it is possible to obtain expressions for the number of bonds for the different types of bonds in the truncated octahedron without a central site, which are presented in Table 16 and whose graphics are shown in Figures 12–15.

Table 12. Geometric characteristics for the face-centered cubic without a central site structure, fccs.

ν	N_S	N_E	N_V	R_S	R_E	R_V	$N_{\text{shell}}^{\sigma}$	N_{shell}^{T}	N_{σ}	N
1	0	0	0	0	0	0	0	0	0	0
	6	0	8	1	0	1	2	2	14	14
	6	0	8	1	0	1	2	2	14	14
2	24	24	0	1	1	0	2	4	48	62
	78	24	8	4	1	1	6	10	110	172
	102	48	8	5	2	1	8	10	158	172
3	144	48	0	4	2	0	6	16	192	364
	246	48	8	9	2	1	12	28	302	666
	390	96	8	13	4	1	18	28	494	666

2.5.3. EAM Applied to fcc Structures without a Central Site

The embedded atom method is applied, in the Foiles version [32] and with the parameters of copper, to clusters with fcc structures without a central site to calculate the cohesion energy per atom, determining in this way the stability of the clusters. The results are compared with the ones from the icosahedra and cubooctahedra previously reported [30]. Figure 21 presents the cohesive energy graphic as a function of $N^{1/3}$ for the octahedron and truncated octahedron clusters of fcc without central site type, for sizes from 300 to 3400 atoms. From Figure 21, it can be seen that the truncated octahedra ($\triangle$) as well as the octahedra ($\diamond$) compete in stability with the icosahedra ($\bullet$) and cubooctahedra ($\square$). And most of all, the truncated octahedra show a higher stability than the octahedra.

2.6. bcc Structure

The body-centered cubic structure is a cube with sites in the vertexes and in the center of the cube, that is, there are 9 sites over a cube, 8 in vertexes, and 1 in the center of it; this is a cluster of order 1 with cubic arrays [Fig. 22(a)]. When attaching many of these arrays, clusters with sites in vertexes, edges, and squared faces are obtained. The cubic cluster of second order consists of an array of 8 cubes, which results from covering the first cube with a shell of sites distributed in three layers: 6 in squared face (S), 12 in edge (E), and 8 in vertexes (V) [Fig. 22(b)]. The next cluster has 56 sites distributed in 3 layers, and so on. From here, it is deduced that it is possible to identify layers of equivalent sites; these layers can be grouped into shells yielding noncubic geometries which present sites in vertexes, edges, and in rombohedral faces, such as in the dodecahedron.

2.6.1. Dodecahedra

The dodecahedron is formed by a central site, 14 vertexes of two types ($V1$ and $V2$), 24 edges (E) and 12 rombohedral faces (R), Figure 23. The two types of vertexes are: (1) 6 vertexes (V_1) of coordination 4 with sites of their own shell and of4 with sites of exterior shells; an (2) 8 vertexes (V_2) of coordination 1 towards sites of interior shells, 3 with sites of its own shell, and 4 with sites of exterior shells.

The number of first neighbors is found in Table 3, standard coordinates in Table 2, and the geometric characteristics of the decahedron are listed in Table 17, from which the dependence of geometric characteristics for the decahedron can be determined and are presented in Table 16. Surface dispersions originating from the different types of sites in the surface of the decahedron can also be shown graphically; Figure 24.

Based on Tables 3 and 17, it is possible to construct the expressions for the number of bonds for the different types of bonds in the dodecahedron, and are presented in Table 16 and their graphics in Figures 12–15.

2.6.2. EAM Applied to bcc Structures

The embedded atom method is applied, in the Foiles version [32] and with the parameters of copper, to clusters with bcc structures to calculate the cohesion energy per atom,

Table 13. Particular expressions of the geometric characteristics for the face-centered cubic without a central site structure, fccs.

	Layer	Sublayers	
N		$32\nu^3 - 24\nu^2 + 6\nu$	
N_σ	$96\nu^2 - 144\nu + 62$	$48(\nu - 1)^2$	$48\nu^2 - 48\nu + 14$
N_{sup}	$48\nu^2 - 48\nu + 14$	$48(\nu - 1)^2$	$48\nu^2 - 48\nu + 14$
$\mathscr{D}$	$\dfrac{48\nu^2 - 48\nu + 14}{32\nu^3 + 24\nu^2 + 6\nu + 1}$	$\dfrac{48(\nu - 1)^2}{32\nu^3 + 24\nu^2 + 6\nu + 1}$	$\dfrac{48\nu^2 - 48\nu + 14}{32\nu^3 + 24\nu^2 + 6\nu + 1}$
N_S^6	24	—	24
R_S^6	1	—	1
N_S^5	$24(2\nu - 3)$	—	$24(2\nu - 3$
R_S^5	$\nu - 1$	—	$\nu - 1$
N_S^4	$6[(2\nu - 2)^2 + (2\nu - 3)^2]$	—	$6[(2\nu - 2)^2 + (2\nu - 3)^2]$
R_S^4	$\nu(\nu - 1)$	—	$\nu(\nu - 1)$
N_E	$48(\nu - 1)$	$24(\nu - 1)$	
R_E^p	$2(\nu - 1)$	$\nu - 1$	
N_V	8	0	8
R_V	1	0	1
$\mathscr{N}_{CO}$		$12(16\nu^3 - 36\nu^2 + 27\nu - 7)$	
$\mathscr{N}_{CC}$		$24(8\nu^2 - 13\nu + 5)$	
$\mathscr{N}_{SS}$		$24(8\nu^2 - 6\nu + 1)$	
$\mathscr{N}_C$		$12(16\nu^3 - 4\nu^2 - 11\nu + 5)$	

determining in this way the stability of the clusters. The results are compared with the ones from the icosahedra and cubooctahedra previously reported [30]. Figure 25 presents the cohesion energy graphic as a function of $N^{1/3}$ for dodecahedral clusters, for sizes from 300 to 3400 atoms. From Figure 25 it can be seen that the dodecahedra ($\diamond$) compete in stability with the icosahedra ($\bullet$) and cubooctahedra ($\square$).

3. CLUSTERS AND NANOPARTICLES WITH PENTAGONAL SYMMETRY

3.1. Introduction

A cluster is defined as an aggregate of atoms; this can lead to clusters from two atoms (diatomic molecules), a lineal array of atoms, bidimensional, or three-dimensional arrays. This work presents the study of clusters with pentagonal symmetry, with sizes up to thousands of atoms in arrays of spherical or concentric layer types.

Arrays of linked atoms forming three-dimensional clusters are considered here as sites in geometric positions attached by the edges in such a way that faces of diverse forms are generated (triangular, squared, rombohedral, etc.). The distance between the sites is considered as the distance to first neighbors d_{NN}, which is normalized to one. There could be sites in the vertexes, edges, and faces, either in the surface or internals; also, there could be different types of sites, depending on their position and the number and type of neighbors in the geometric array. There also could be equivalent sites, which present the same geometric characteristics: to the same distance from the center of the geometric array, in the same type of site and with the same number and type of neighbors.

From the bicaped hexahedron or decahedron, Figure 26(a), pentagonal symmetry structures can be obtained. Among the clusters with structures of pentagonal symmetry, the following structures are considered: decahedra with and without a central site, icosahedra, pentadecahedra,

Figure 17. Octahedron without central site of (a) order 2 with 44 sites, (b) order 3 with 146 sites, and (c) order 6 with 1156 atoms.

Table 14. Geometric characteristics for the octahedra without a central site.

ν	N_T	N_E	N_V	R_T	R_E	R_V	N_{shell}^σ	N_{shell}^T	N_σ	N
1	0	0	6	0	0	1	1	1	6	6
2	8	24	6	1	1	1	3	4	38	44
3	48	48	6	2	2	1	5	9	102	146
4	120	72	6	4	3	1	8	17	198	344
5	224	96	6	7	4	1	12	29	326	670
6	360	120	6	10	5	1	16	45	486	1156
7	528	144	6	14	6	1	21	66	678	1834
8	728	168	6	19	7	1	27	93	902	2736
9	960	192	6	24	8	1	33	126	1158	3894
10	1224	216	6	30	9	1	40	166	1446	5340
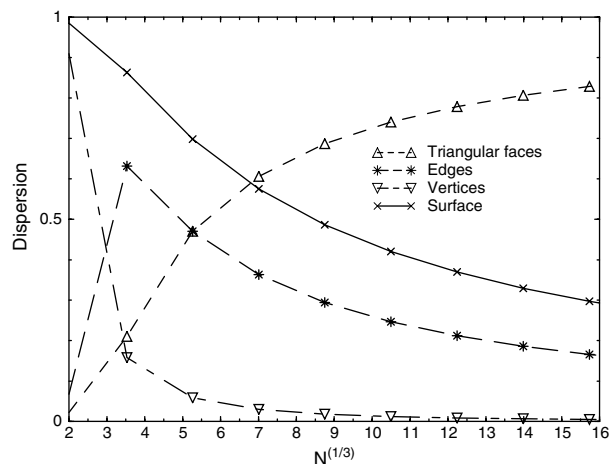
Figure 18. Dispersions caused by surface sites of octahedron without a central site as a function of the cluster size.

truncated decahedra (Marks decahedra), star-type decahedra, modified and developed decahedra, truncated icosahedra, and the *decmon*.

3.2. Decahedra

Decahedra are obtained from the bicapped hexahedra, and also from attaching two pentagonal-based pyramids from their bases and sharing their sites (which form the equator of the cluster), yielding geometrical bodies of 7 vertexes (2 at poles and 5 at equator), 15 edges (all from the same length, 5 at the equator), and 10 triangular equilateral faces: 5 of them converge on each pole, and by pairs, they form the edges of the equator. Decahedra can be without a central site, Figures 26(a) and (c), and with a central site, Figure 26(b), without losing the decahedral form. So, decahedra have the vertexes at the poles *VP*, vertexes at the equator *VE*, at the edges over the equator *EE*, edges at poles *EP*, and in triangular faces *T*. It has to be noticed that coordination, that is, distribution to first neighbors (NN), is what makes the difference in each type of sites, although the total coordination is the same for all of the sites of the corresponding cluster. Table 18 presents the coordination of each site, for example, the poles (*VP*) have 4 first neighbors (NN)
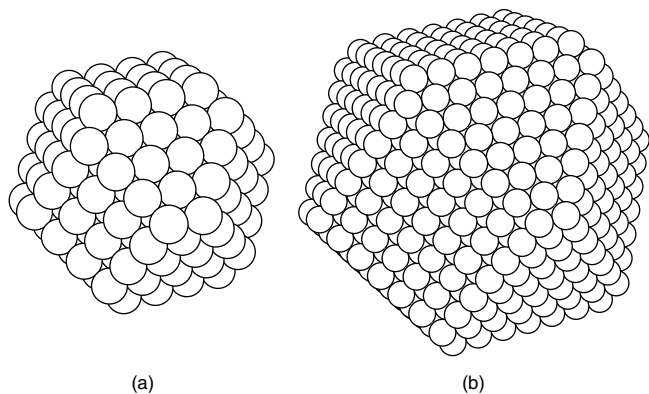
Figure 19. Truncated octahedron without a central site of (a) order 3 with 260 sites and (b) order 6 with 1288 sites.

Table 15. Geometric characteristics for the truncated octahedra without a central site.

ν	N_S	N_H	N_E	N_V	R_S	R_H	R_E	R_V	N_{shell}^σ	N_{shell}^T	N_σ	N
1	0	8	0	24	0	1	0	1	2	3	32	38
2	6	24	24	24	1	1	1	1	4	7	78	116
3	24	48	48	24	1	2	1	1	5	12	144	260
4	54	80	72	24	3	3	2	1	9	21	230	490
5	96	120	96	24	3	4	2	1	10	31	336	826
6	150	168	120	24	6	5	3	1	15	46	462	1288
7	216	224	144	24	6	7	3	1	17	63	608	1896
8	294	288	168	24	10	8	4	1	23	86	774	2670
9	384	360	192	24	10	10	4	1	25	111	960	3630
10	486	440	216	24	15	12	5	1	33	144	1166	4796

with sites at their same shell, 1 NN toward the inner shell, and 4 toward the exterior shell. The decahedron of order 1, without a central site, Figure 26(a), has only 7 vertexes in two layers; the one from order 2, Figure 26(c), is obtained from covering the one of order 1 with a shell of 47 sites distributed as follows: 7 *V* sites of two types, 30 *E* sites in three layers (10 sites of one type ant the equator), and 10 at triangular faces (sites *T*, one for each triangular face) in one single layer, for a total of 54 sites in the cluster. Decahedra of superior order are formed by coverage of this cluster of order 2 with successive shells of many layers in each one.

The decahedron with central site of order 1, Figure 26(b), has 15 sites *E*, one per edge, of two types, 5 sites of one type at the equator, and 7 sites *V*, a total of 22 sites and the central one in five layers. The second-order cluster results from the order 1 cluster covered by a shell of 82 sites distributed in 8 layers: 45 *E* sites in 5 layers, 30 *T* sites in one single layer, and 7 *V* sites in two layers, for a total of 105 sites in the cluster, and so on for cluster of superior order.

Table 19 presents the geometric characteristics of decahedra with and without a central site. The first column, common for all decahedra, lists the cluster order ν. This is followed by two groups of 9 columns each, which correspond to the decahedron with and without central site. The first three columns of each group list the number of sites on each type of site in the cluster: triangular face (*T*) N_T, edge (*E*) N_E, and vertex (*V*) N_V. The two following columns show the number of sites per shell N_{SE}, and the total of sites in the plane just above the equator N_{tSE}, (the *SE* sites). The following two columns list the number of sites at the equator (sites *EC*) per shell N_{EC}, and in the whole cluster, N_{tEC}; the joint between *SE* and *EC* sites form the *SEC* layer, which will be needed afterwards, and they both form a pentagonal flat layer. Finally, the two last columns of each group, the number of sites in the shell N_σ, and the total of sites in the cluster *N*. Decahedra with (without) a central site have an odd (even) number of sites per edge, which is important for the star and truncated-type decahedra, detailed later.

From Table 19 it is observed that, for both decahedron types, the number of vertexes per shell is 7, 2 type *VP* and 5 type *VE*; We can also obtain, for each type of decahedra, the dependence with the cluster order of the number of *T* sites, *E* sites, the number of sites in the layer at the equator, as well as the total sites in the shell (or of the surface), and from the total of sites over the equator, at the equator and in the decahedron. Such dependency is expressed in the

Table 16. Particular expressions of the geometric characteristics for the fcc without a central site and dodecahedral structures.

	OCTAS	OCTTS	DODE
N	$\frac{16}{3}\nu^3 + \frac{2}{3}\nu$	$\frac{10}{3}\nu^3 + 13\nu^2 + \frac{47}{3}\nu + 6$	$4\nu^3 + 6\nu^2 + 4\nu + 1$
N_σ	$16\nu^2 - 16\nu + 6$	$10\nu^2 + 16\nu + 6$	$12\nu^2 + 2$
$\mathscr{D}$	$\dfrac{3(16\nu^2 - 16\nu + 6)}{16\nu^3 + 2\nu}$	$\dfrac{3(10\nu^2 + 16\nu + 6)}{10\nu^3 + 39\nu^2 + 47\nu + 18}$	$\dfrac{12\nu^2 + 2}{4\nu^3 + 6\nu^2 + 4\nu + 1}$
N_S	—	$6(\nu - 1)^2$	—
R_S^p	—	$\dfrac{\nu(\nu + 2)}{8}$	—
R_S^i	—	$\dfrac{\nu^2 - 1}{8}$	—
N_T	$8(2\nu - 3)(\nu - 1)$	—	—
R_T^m	A	—	—
N_H	—	$4\nu(\nu + 1)$	—
R_H^m	—	C	—
N_R	—	—	$12(\nu - 1)^2$
R_R^p	—	—	$\dfrac{\nu^2}{4}$
R_R^i	—	—	$\dfrac{\nu^2 - 1}{4}$
N_E	$24(\nu - 1)$	$24(\nu - 1)$	$24(\nu - 1)$
R_E^p	$\nu - 1$	$\dfrac{\nu}{2}$	$\nu - 1$
R_E^i	$\nu - 1$	$\dfrac{\nu - 1}{2}$	$\nu - 1$
$\mathscr{N}_{CO}$	$4(8\nu^3 - 24\nu^2 + 25\nu + 7)$	$2\nu(10\nu^2 + 9\nu - 1)$	$4(4\nu^3 - 6\nu^2 + 4\nu - 7)$
$\mathscr{N}_{CC}$	$48(\nu - 1)^2$	$6(5\nu^2 - 5\nu + 2)$	$24\nu(\nu - 1)$
$\mathscr{N}_{SS}$	$12(4\nu^2 - 4\nu + 1)$	$24\nu(\nu + 2)$	$4(6\nu^2 + 1)$
$\mathscr{N}_C$	$4(8\nu^3 - 11\nu + 40)$	$2\nu(10\nu^2 + 39\nu + 29)$	$8(2\nu^3 + 3\nu^2 - \nu - 3)$

following relations for the decahedra with a central site; it is to be noticed that, for $\nu = 1$, there are 11 sites at the equator because the central site is included:

$$N_E(\nu) = 15(2\nu - 1) \begin{cases} N_{EP}(\nu) = 10(2\nu - 1) \\ N_{EE}(\nu) = 5(2\nu - 1) \end{cases}$$

$$N_T(\nu) = 10(2\nu^2 - 1)(\nu - 1)$$

Figure 20. Dispersions due to surface sites of the truncated octahedron without a central site as a function of the cubic root of the cluster size.

$$N_{SE}(\nu) = 10(\nu - 1) + 5$$

$$N_{t_{SE}}(\nu) = 5\nu^2$$

$$N_{EC}(\nu) = 10\nu$$

$$N_{t_{EC}}(\nu) = 5\nu(\nu + 1) + 1$$

$$N_\sigma(\nu) = 20\nu^2 + 2$$

$$N(\nu) = \frac{20}{3}\nu^3 + 10\nu^2 + \frac{16}{3}\nu + 1$$

and for decahedra without a central site,

$$N_E(\nu) = 30(\nu - 1) \begin{cases} N_{EP}(\nu) = 20(\nu - 1) \\ N_{EE}(\nu) = 10(\nu - 1) \end{cases}$$

$$N_T(\nu) = 20\nu^2 - 50\nu + 30$$

$$N_{SE}(\nu) = 10(\nu - 1)$$

$$N_{t_{SE}}(\nu) = 5\nu(\nu - 1) + 1$$

$$N_{EC}(\nu) = 5(2\nu - 1)$$

$$N_{t_{EC}}(\nu) = 5\nu^2$$

$$N_\sigma(\nu) = 20\nu^2 - 20\nu + 7$$

$$N(\nu) = \frac{20}{3}\nu^3 + \frac{\nu}{3}.$$
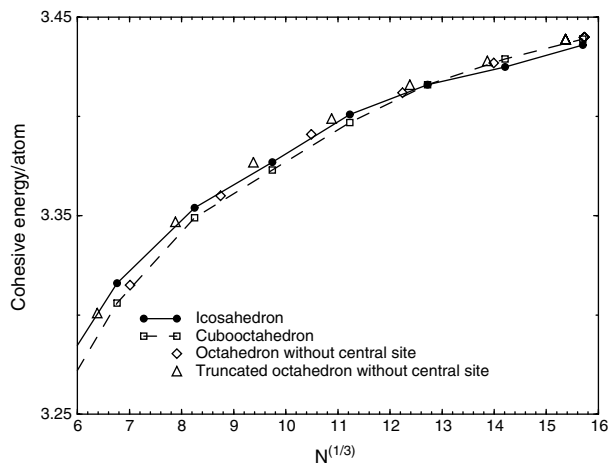
Figure 21. Cohesion energy per atom as a function of the square root of the number of atoms in the cluster, for the octahedron and truncated octahedron with central site, type fcc.

Note that from the expression for N_A, and from Figures 26(c) and (d), the number of EP and EE per edge is $2\nu - 1$ $[2\nu - 2]$ for decahedra with [without] a central site.

If, instead of attaching the base of the two pentagonal base pyramids to form the decahedron, they are separated, two types of geometrical figures can be obtained, depending on the way the sites of the bases are connected: the pentadecahedron and the icosahedron.

3.3. Pentadecahedra

If the pentagonal pyramids which generate the decahedron when they are joined, are separated, they are in a position in which the vertexes of the base of both can be attached by 5 edges (EC) perpendicular to the base, yielding 5 rectangular faces, which form the pentadecahedra, Figure 27, that is, a decahedron with a wide waist or a developed decahedron. Separation can be done by adding intermediate layers of type SEC (formed by a layer of sites SE and another of sites EC as mentioned previously). The number of SEC intermediate layers, and the length of the edges perpendicular to the bases, depend on the desired separation. For example, the pentadecahedron from Figure 27 has 5 layers in the waist; to obtain it, 4 layers of type SEC are added to the order 6 decahedron of 1442 sites without a central site, which results
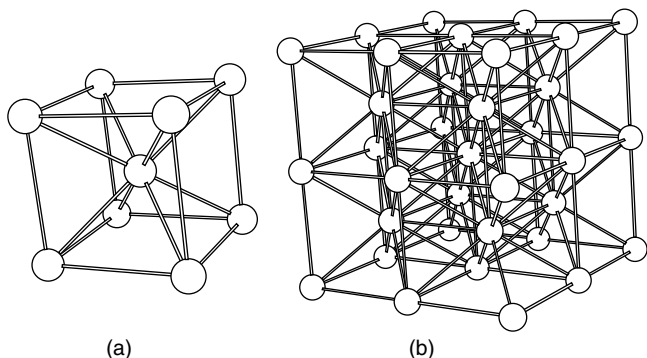
Figure 22. bcc structure of (a) 9 sites, and (b) 35 sites.
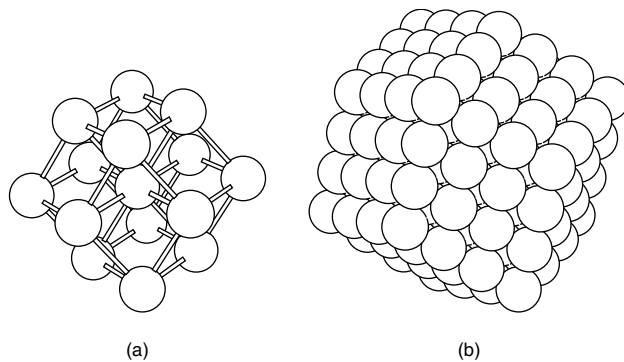
Figure 23. bcc dodecahedron of (a) order 1 with 15 sites, and (b) order 2 with 175 sites.

in edges $4d_{NN}$ long. It has to be noticed that, upon widening of the waist of a decahedron, from one equatorial layer to two equatorial layers, an SEC-type layer is added, when widening three equatorial layers, two SEC-type layers are added, that is, for each equatorial layer wanted to widen the decahedra waist, one type of SEC layer is added.

The pentadecahedra are polyhedra of 12 vertexes (2 poles and 10 in vertexes at the waist), 25 edges (20 of one type and 5 of the other, which join the vertexes of the two pyramids, and whose length depends on the number of intermediate layers added), 10 equilateral triangular faces and, 5 rectangular lateral faces (or squared, depending on the number of intermediate layers added) (Fig. 27). The number of sites in these pentadecahedra depends on the size of the original decahedron and how many intermediate layers are added; also, whether they are with and without a central site is considered, depending on the original decahedron from which they were generated. So, at the surface of the pentadecahedra, there are the same type and number of sites as in the decahedra, plus the N_{EC} sites added (because the N_{SE} are not at the surface), which are divided in sites type VE, sites EE, sites at vertical edges at the width of the waist EV and in rectangular faces RF. Table 20 presents the coordination of each type of site in the pentadecahedron. Notice that, upon comparison of Table 18, as expected, only the sites corresponding to the pentadecahedron are added, and those of the decahedron are not. Sites N_{SE} added, originally 5 EP sites, and the rest T sites (except for the pentadecahedron of order 11, without a central site) are converted in internal sites of coordination 12.

Table 17. Geometric characteristics for the dodecahedra.

ν	N_R	N_E	N_V	R_R	R_E	R_V	$N_{\text{shell}}^{\sigma}$	N_{shell}^{T}	N_{σ}	N
1	0	0	14	0	0	2	2	2	14	15
2	12	24	14	1	1	2	4	6	50	65
3	48	48	14	2	2	2	6	12	110	175
4	108	72	14	4	3	2	9	21	194	369
5	192	96	14	6	4	2	12	33	302	671
6	300	120	14	9	5	2	16	49	434	1105
7	432	144	14	12	6	2	20	69	590	1695
8	588	168	14	16	7	2	25	94	770	2465
9	768	192	14	20	8	2	30	124	974	3439
10	972	216	14	25	9	2	36	160	1202	4641
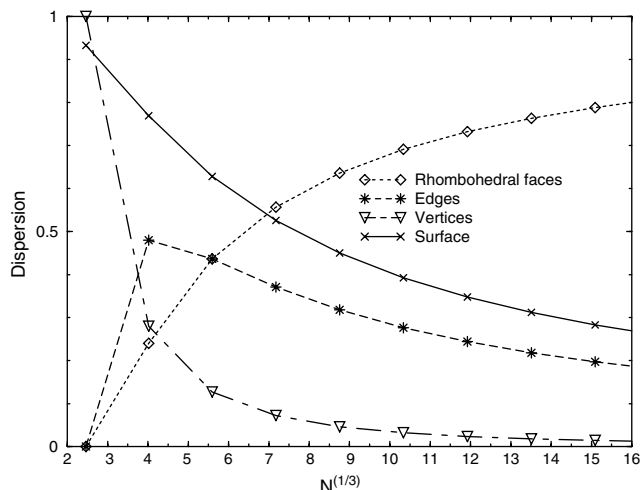
Figure 24. Dispersion due to surface sites of the dodecahedron as a function of the cubic root of the cluster size.

For pentadecahedron order, we can use $\nu\mu$, ν for the decahedron order from which comes and μ for the number of layers at the waist, so regular decahedra would be pentadecahedra with $\mu = 1$. The number of layers of type *SEC* which are added to the decahedron referred to generate the pentadecahedron is $\mu - 1$, so that the number of sites added is equal to the sum of the total of sites *SE* and the total of *EC* sites of the corresponding decahedron, columns 6 and 8, and 15 and 17 of Table 19. So, in order to have a pentadecahedron of order 55 with a central site, one has to start with a decahedron of order 5, 111 sites, and an aditional 4 layers of type *SEC* of $125 + 151 = 276$ sites each, for a total of 1104 added sites and 2215 sites in the cluster.

The number of sites *T*, *EP*, and *VP* is the same as in the decahedron which originated from the pentadecahedron. The number of sites *EE* and *VE* is duplicated with respect to the original decahedron. The number of *EV* and *RF* sites
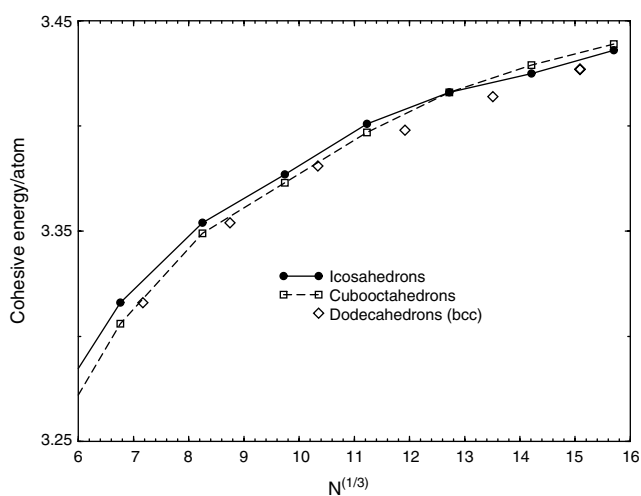
Figure 25. Cohesive energy per atom as a function of the cubic root of the number of atoms in the cluster for decahedron bcc type.
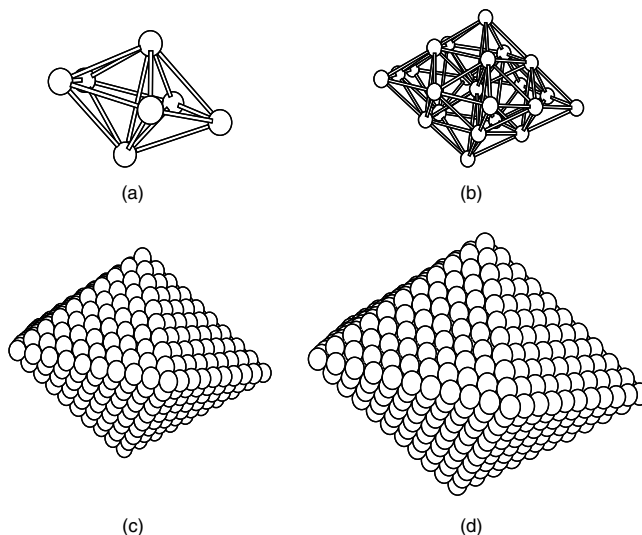
Figure 26. Decahedral polyhedrons. (a) bilayered hexahedron or decahedron of 7 atoms of order 1, without central site. (b) Decahedron of 23 atoms of order 1 with central site. (c) Decahedron of 835 sites of order 5, without central site. (d) Decahedron of 1111 atoms of order 5 with central site.

for the pentadecahedra with and without a central site is the same, and is presented in Table 21, which shows the geometric characteristics of the pentadecahedra with and without a central site respectively; only some of μ values are presented. There are three groups of three, four, and five columns, respectively. In the columns of the first group are listed the quantities common to the two types of pentadecahedra: cluster order ν and μ, and the number of sites *EV*, N_{EV}; for both polyhedra, in each following group, the geometric characteristics for each polyhedron are presented, those of the pentadecahedron both with and without a central site. A list of the number of *RF* sites N_{RF}, the number of sites added N_{ag}, of sites at the surface $N\sigma$, and the total of sites N in the cluster of order $\nu\mu$ is given. Note that, for $\mu = 1$, the values from Table 19 are obtained.

From Table 21, the analytic expressions for the number of sites *EV* can be obtained as a function of ν and v:

$$N_{EV}(\mu) = 5(\mu - 2)$$

as well as the number of *RF* sites, sites which are added, sites in the surface, and the total of sites for pentadecahedra

Table 18. Coordination or number of first neighbors (NN) of the different types of sites in the decahedron with sites in external, the same, and internal shell.

Shell	T	EE	EP	VE	VP
External	3	6	4	8	6
Same	6	6	6	4	5
Internal	3	0	2	0	1

Table 19. Geometric characteristics for the decahedra with and without a central site. ν is the order of the cluster, N_I with $I = T$, E and V, is the number of sites I. The number of sites SE and EC in each layer, the number of sites in each layer, the total number of SE and EC sites and the total number of sites in the cluster are also listed.

ν	With a central site									Without a central site								
	N_T	N_A	N_V	N_{SE}	N_{tSE}	N_{EC}	N_{tEC}	N_σ	N	N_T	N_A	N_V	N_{SE}	N_{tSE}	N_{EC}	N_{tEC}	N_σ	N
1	0	15	7	5	5	10	11	22	23	0	0	7	1	1	5	5	7	7
2	30	45	7	15	20	20	31	82	105	10	30	7	10	11	15	20	47	54
3	100	75	7	25	45	30	61	182	287	60	60	7	20	31	25	45	127	181
4	210	105	7	35	80	40	101	322	609	150	90	7	30	61	35	80	247	428
5	360	135	7	45	125	50	151	502	1111	280	120	7	40	101	45	125	407	835
6	550	165	7	55	180	60	211	722	1833	450	150	7	50	151	55	180	607	1442
7	780	195	7	65	245	70	281	982	2815	660	180	7	60	211	65	245	847	2289
8	1050	225	7	75	320	80	361	1282	4097	910	210	7	70	281	75	320	1127	3416
9	1360	255	7	85	405	90	451	1622	5719	1200	240	7	80	361	85	405	1447	4863
10	1710	285	7	95	500	100	551	2002	7721	1530	270	7	90	451	95	500	1807	6670

with a central site

$$N_{RF}(\nu, \mu) = 5(2\nu - 1)(\mu - 2)$$

$$N_{\text{ag}}(\nu, \mu) = (\mu - 1)(10\nu^2 + 5\nu + 1)$$

$$N_\sigma(\nu, \mu) = 20\nu^2 + 2 + 10\nu(\mu - 1)$$

$$N(\nu, \mu) = \frac{20}{3}\nu^3 + 10\nu^2 + \frac{16}{3}\nu + 1 + N_{\text{ag}}(\nu, \mu)$$

and for pentadecahedra without a central site

$$N_{RF}(\nu, \mu) = 10(\nu - 1)(\mu - 2)$$

$$N_{\text{ag}}(\nu, \mu) = (\mu - 1)(10\nu^2 - 5\nu + 1)$$

$$N_\sigma(\nu, \mu) = 20\nu^2 - 20\nu + 7 + 5(2\nu - 1)(\mu - 1)$$

$$N(\nu, \mu) = \frac{20}{3}\nu^3 + \frac{\nu}{3} + N_{\text{ag}}(\nu, \mu).$$

3.4. Modified Decahedra

In a certain decahedron, with or without a central site, the number of sites per edge increases in 2 sites per shell increased. For example, in the decahedron of 287 sites of order 3 with a central site, Figure 28(a), in the surface shell there are 5 sites in each edge, and in the one of order 4, there are 609 sites, Figure 28(b), there are 7 sites per edge. The decahedron modification can be done in two ways: (1) as channels at the surface, and (2) as surface reconstruction. Besides, modified and developed decahedra can be obtained, adding SEC-type layers in order to widen the waist of the modified decahedra.
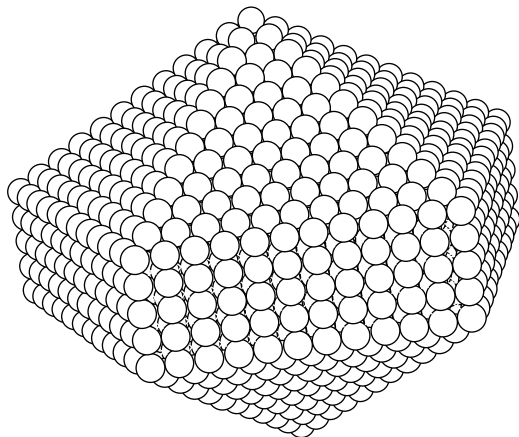
3.4.1. Decahedra with Additional Faceting (*Channels at Twin Boundaries*)

When suppressing surface sites from the edges converging in the poles (*EP* sites) and from all of the vertexes in a decahedron, a one-channel decahedron is obtained, for example, from the decahedron of 609 sites of order 4 with a central site [Fig. 28(b)], a decahedron of 532 sites is obtained with one channel convergent to the pole, Figure 29(a), eliminating 77 sites. These result in a polyhedron formed by a decahedron of order 3 with triangular faces covered with sites corresponding to the decahedron of order 4, in a way that some surface sites that were T type are now type E. If, now, the following edges (which were type T sites) are eliminated from the surface, a triple-channel decahedron of 412 sites is obtained, 120 sites were eliminated [Fig. 29(b)]. It can be continued in this way until the desired number of channels is reached. The construction of the first channel, eliminating vertexes and *EP* edges from the surface, in other words, remains with a coordination lower than 12, which implies that there are free bonds. Type *VP* sites from the internal decahedron have two free bonds, sites *VE* have three and sites *EP* have four. So, surface sites are not only the difference between surface sites and the ones that

Figure 27. Pentadecahedron of 2766 atoms of order 65, obtained from a decahedron without a central site of order 6 with 5 layers in the waist, which means adding 4 *SEC*-type layers to the original decahedron.

Table 20. Coordination or number of first neighbors (NN), of the different types of sites in the pentadecahedra with sites in shells in external, the same and internal layers.

Crust	T	EE	EP	EV	RF	VE	VP
externa	3	6	4	6	4	8	6
la misma	6	6	6	4	4	4	5
interna	3	0	2	2	4	0	1

Table 21. Geometric characteristics for pentadecahedra with and without a central site, obtained from the corresponding decahedron of order ν.

				With a central site			Without a central site			
ν	μ	N_{AV}	N_{RF}	N_{ag}	N_σ	N	N_{RF}	N_{ag}	N_σ	N
1	1	0	0	0	22	23	0	0	7	7
	2	0	0	16	32	39	0	6	12	13
2	1	0	0	0	82	105	0	0	47	54
	2	0	0	51	102	156	0	31	62	85
	3	5	15	102	122	207	10	62	77	116
3	1	0	0	0	182	287	0	0	127	181
	2	0	0	106	212	393	0	76	152	257
	3	5	25	212	242	499	20	142	177	333
4	1	0	0	0	322	609	0	0	247	428
	2	0	0	181	362	790	0	141	282	569
	4	10	70	543	442	1152	60	423	352	851
5	1	0	0	0	502	1111	0	0	407	835
	2	0	0	276	552	1387	0	226	452	1061
	3	5	45	552	602	1663	40	452	497	1287
	5	15	135	1104	702	2215	120	904	587	1739

Note: μ is the number of equatorial layers in the cluster. Number of sites AV, N_{AV}, R sites N_R, of sites added N_{ag}, surface site N_σ, and of total sites N in the cluster of order $\nu\mu$. Notice that, for $\mu = 1$, values of Table 1 are obtained. Even when μ can have any value higher than zero, here only some values are presented.

were eliminated, but the interior decahedron sites are added which have a coordination lower than 12.

Table 22, lists the geometric characteristics for the decahedra, with and without a central site, modified with surface channels. ν is the original cluster order. The only characteristics presented are for an $n = 1$, a single channel and 2, a triple channel. Eliminating the sites for the channel in the decahedron affects the number of sites *SE* and *EC* of the original decahedron. Table 22 lists the number of sites that are eliminated N_{el}, the number of sites *SE* and *EC*, per shell and in total, and the number of sites at the surface and in total in the final cluster. The number of sites *SE* and *EC* is needed in order to generate the decahedra with channels and developed, as was done for the pentadecahedron.

From Table 22 are deduced the analytic expressions for the number of sites eliminated in a decahedron in order to obtain the decahedron with channels, the number of *SE* and *EC* sites, and the number of sites in the surface and the number of total sites in the cluster, which are presented next

(a)   (b)
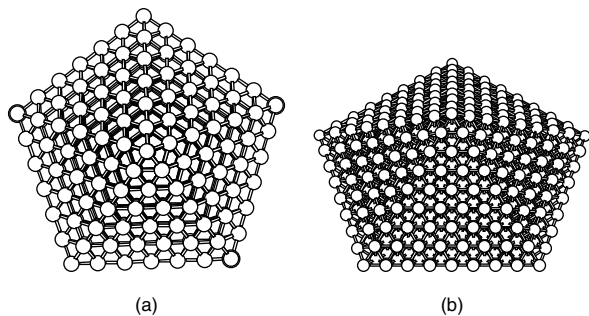
Figure 28. (a) Decahedron of 287 sites, of order 3, with a central site,(b) Decahedron of 609 sites, of order 4, with a central site.

(a)   (b)
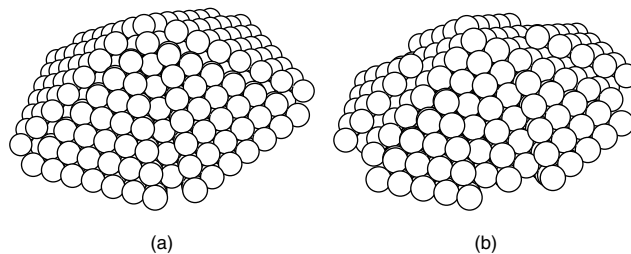
Figure 29. Decahedron of 609 sites of order 4 and (a) a single channel, and (b) a triple channel per edge converging to the pole, of 532 sites and 412 sites, respectively.

for the decahedron with a central site and a simple channel:

$$N_{el}(\nu) = 20\nu - 3, \qquad N_{SE}(\nu) = 10(\nu - 1)$$
$$N_{t_{SE}}(\nu) = 5\nu^2 - 5, \qquad N_{EC}(\nu) = 10\nu - 5$$
$$N_{t_{EC}}(\nu) = 5\nu(\nu + 1) - 4, \qquad N_\sigma(\nu) = 20\nu^2 - 18$$
$$N(\nu) = \frac{20}{3}\nu^3 + 10\nu^2 - \frac{44}{3}\nu + 4$$

for the decahedron with a central site and a triple channel:

$$N_{el}(\nu) = 60\nu - 43, \qquad N_{SE}(\nu) = 10\nu - 20$$
$$N_{t_{SE}}(\nu) = 5\nu^2 - 15, \qquad N_{EC}(\nu) = 10\nu - 15$$
$$N_{t_{EC}}(\nu) = 5\nu(\nu + 1) - 14, \qquad N_\sigma(\nu) = 20\nu^2 - 58$$
$$N(\nu) = \frac{20}{3}\nu^3 + 10\nu^2 - \frac{164}{3}\nu + 44$$

and for the decahedron without a central site and a simple channel:

$$N_{el}(\nu) = 20\nu - 13, \qquad N_{SE}(\nu) = 10\nu - 15$$
$$N_{t_{SE}}(\nu) = 5\nu(\nu - 1) - 4, \qquad N_{EC}(\nu) = 10(\nu - 1)$$
$$Nt_{EC}(\nu) = 5\nu^2 - 5, \qquad N_\sigma(\nu) = 20\nu^2 - 20\nu - 13$$
$$N(\nu) = \frac{20}{3}\nu^3 - \frac{59}{3}\nu + 13$$

for the decahedron without a central site and a triple channel,

$$N_{el}(\nu) = 60\nu - 73, \qquad N_{SE}(\nu) = 10\nu - 25$$
$$N_{t_{SE}}(\nu) = 5\nu(\nu - 1) - 14, \qquad N_{EC}(\nu) = 10\nu - 20$$
$$N_{t_{EC}}(\nu) = 5\nu^2 - 15, \qquad N_\sigma(\nu) = 20\nu^2 - 20\nu - 53$$
$$N(\nu) = \frac{20}{3}\nu^3 - \frac{179}{3}\nu + 73.$$

In the same way used to generate the pentadecahedra, by modifying the decahedra, the new type of decahedra can be obtained, (Fig. 30). In order to do this, a layer of type *SEC* is added for each layer desired to increase the waist of the decahedron with channels. Table 22 lists the number of sites *SE* and *EC*, which are used to construct Table 23 for the decahedra with channels and developed.

Table 22. Geometric characteristics of decahedra with and without a central site, modified with surface channels.

		With a central site							Without a central site						
ν	n	N_{el}	N_{SE}	$N_{t_{SE}}$	N_{EC}	$N_{t_{EC}}$	N_σ	N	N_{el}	N_{SE}	$N_{t_{SE}}$	N_{EC}	$N_{t_{EC}}$	N_σ	N
2	1	37	10	15	15	26	62	68	27	5	6	10	15	27	27
3	1	57	20	40	25	56	162	230	47	15	26	20	40	107	134
	2	137	10	30	15	46	122	150	107	5	16	10	30	67	74
4	1	77	30	75	35	96	302	532	67	25	56	30	75	227	361
	2	197	20	65	25	86	262	412	167	15	46	20	65	187	261
5	1	97	40	120	45	146	482	1014	87	35	96	40	120	387	748
	2	257	30	110	35	136	442	854	227	25	86	30	110	347	608

Note: ν is the cluster order. Here are presented only the characteristics for a single channel, $n = 1$, and a triple channel, $n = 2$. The number of eliminated sites N_{el}, the number of sites *SE* and *EC* per shell, and the number of sites in the surface and in total in the final cluster are listed.

When adding layers to widen the waist, the number of sites *EE* and *VE* is duplicated with respect to the original polyhedron, and different type *EV* and *RF* sites are generated, as happened with pentadecahedra, and the number of sites is given by

$$N_{EV}(\nu, \mu) = 10(\mu - 2)$$

while the number of sites *RF*, the number of sites added N_{ag}, of which $N_{\sigma_{\text{ag}}}$ are added to the surface for μ equatorial layers for the polyhedron with central site and a single channel is:

$$N_{RF}(\nu, \mu) = 5(2\nu - 3)(\mu - 2)$$
$$N_{\text{ag}}(\nu, \mu) = (\mu - 1)(10\nu^2 + 5\nu - 9)$$
$$N_{\sigma_{\text{ag}}}(\nu, \mu) = (\mu - 1)(10\nu - 5)$$

with a central site and a triple channel

$$N_{RF}(\nu, \mu) = 5(2\nu - 5)(\mu - 2)$$
$$N_{\text{ag}}(\nu, \mu) = (\mu - 1)(10\nu^2 + 5\nu - 39)$$
$$N_{\sigma_{\text{ag}}}(\nu, \mu) = (\mu - 1)(10\nu - 15)$$

without central site and a single channel

$$N_{RF}(\nu, \mu) = 10(\nu - 2)(\mu - 2)$$

(a)   (b)
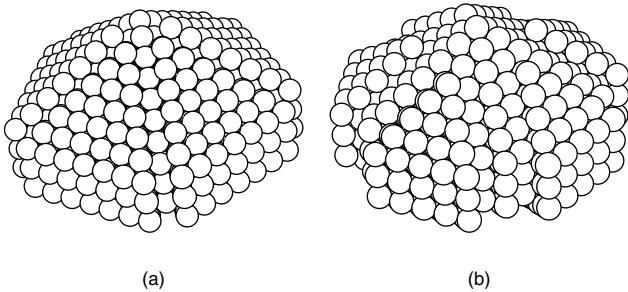
Figure 30. Decahedron of order 4 of 609 sites with a central site, with (a) one single channel, and (b) with a triple channel per edge converging to the pole, with three layers in the waist, of 874 sites and 714 sites, respectively.

$$N_{\text{ag}}(\nu, \mu) = (\mu - 1)(10\nu^2 - 5\nu - 9)$$
$$N_{\sigma_{\text{ag}}}(\nu, \mu) = (\mu - 1)[10(\nu - 1)]$$

with central site and a triple channel

$$N_{RF}(\nu, \mu) = 5(2\nu - 3)(\mu - 2)$$
$$N_{\text{ag}}(\nu, \mu) = (\mu - 1)(10\nu^2 - 5\nu - 39)$$
$$N_{\sigma_{\text{ag}}}(\nu, \mu) = (\mu - 1)(10\nu - 20).$$

3.4.2. Modified Decahedra with Surface Reconstruction

Surface reconstruction of a decahedron is obtained if each triangular face of the decahedron proceeds as follows: a triangular face is obtained exactly as the one from the original decahedron; it is transported outwards to the same distance as the one between parallel triangular faces, $0.7953d_{NN}$, which is the height of a tetrahedron with a base of $1.05d_{NN}$ from one side and the other sides of $1.0d_{NN}$, then in a parallel way is shifted to the waist to a distance of $0.606d_{NN}$, which is 2/3 of the height of the equilateral triangle of $1.05d_{NN}$ from one side, until the generated sites coincide with the triangle centers of the original triangular face, and finally, the complete edge of the waist is eliminated. Hereafter these polyhedra are called *mrdec* (Montejano's reconstructed decahedron) [33]. Figure 31 shows an example of a decahedron of 287 sites of order 3, to which 21 sites are added per face, this is 210 sites in total, for a *mrdec* of 497 sites. It should be noted that it seems that a decahedron with a surface channel is obtained, although the sites which seem to form the channel are at a distance of $1.13d_{NN}$, while in a decahedron with a simple channel they are at $1.63d_{NN}$. This is why, in this modification, a long bond is considered, and the *EP* sites of the interior decahedron do not form part of the surface. In fact, the surface of the resulting polyhedron is formed by the added sites and the sites *VE*, *VP*, and *EE* of the internal decahedron, which are those which also can be considered as surface because they remain with free bonds.

It should be noted that the planes above the equator and the sites in the plane of the equator of the original decahedron are not modified. The characteristics of these polyhedra are presented in Table 24. ν is the original cluster order,

Table 23. Geometric characteristics for the decahedra with and without a central site, modified with surface channels and with added layers in the waist.

| | | | With a central site | | | | | | | | | Without a central site | | | | | | | |
| | | | A single channel | | | | A triple channel | | | | A single channel | | | | A triple channel | | | |
ν	μ	N_{EV}	N_{RF}	N_{ag}	N_σ	N	N_{RF}	N_{ag}	N_σ	N	N_{RF}	N_{ag}	N_σ	N	N_{RF}	N_{ag}	N_σ	N
2	1	0	0	0	62	68	—	—	—	—	0	0	27	27	—	—	—	—
	2	0	0	41	77	109	—	—	—	—	0	21	37	48	—	—	—	—
	3	10	5	82	92	150	—	—	—	—	10	42	47	69	—	—	—	—
3	1	0	0	0	162	230	0	0	122	150	0	0	107	134	0	0	67	74
	2	0	0	96	187	326	0	66	137	216	0	66	127	200	0	36	77	110
	3	10	15	192	212	422	5	132	152	282	20	132	147	266	15	72	87	146
4	1	0	0	0	302	532	0	0	262	412	0	0	227	361	0	0	187	261
	2	0	0	171	337	703	0	141	287	553	0	131	257	492	0	101	207	362
	4	20	50	513	407	1045	30	423	337	835	60	393	317	754	50	303	247	564
5	1	0	0	0	482	1014	0	0	442	854	0	0	387	748	0	0	347	608
	2	0	0	266	527	1280	0	236	477	1090	0	216	427	964	0	186	377	794
	3	10	35	532	572	1546	25	472	512	1326	40	432	467	1180	35	372	407	980
	5	30	105	1064	662	2078	75	944	582	1798	120	864	547	1612	105	744	467	1352

Note: ν is the cluster order, μ is the number of equatorial layers added. Only the characteristics for a single channel, $n = 1$, and a triple channel, $n = 2$ are presented. Notice that for $\mu = 1$ Table 22 values are obtained. Although μ can take any value higher than zero, here are only presented some values.

N_{ag} is the number of sites added, N_σ is the number of sites in the surface, and N is the total number of sites in the cluster.

From Table 24, it is possible to obtain the analytic expressions as a function of the order of the original cluster for the different characteristics listed here, and they are presented next for the polyhedron with a central site:

$$N_{\text{ag}}(\nu) = 20\nu^2 + 10\nu$$

$$N_\sigma(\nu) = 20\nu^2 + 20\nu + 2$$

$$N(\nu) = \frac{20}{3}\nu^3 + 30\nu^2 + \frac{46}{3}\nu + 1,$$

and without a central site

$$N_{\text{ag}}(\nu) = 20\nu^2 - 10\nu$$

$$N_\sigma(\nu) = 20\nu^2 - 3$$

$$N(\nu) = \frac{20}{3}\nu^3 + 20\nu^2 - \frac{29}{3}\nu.$$
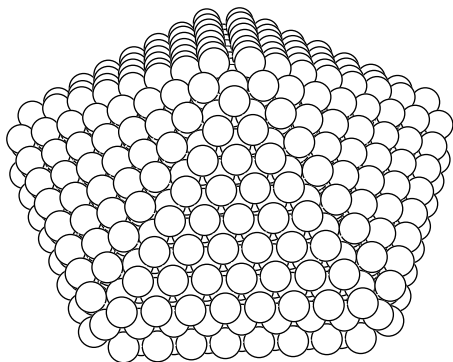
Figure 31. Decahedron of order 4 with 609 sites and with a central site, with 360 sites aggregated for a *mrdec* of 969 sites.

Alternatively, it is possible to generate the decahedra with surface reconstruction and developed. For this, simply add one *SEC*-type layer for each layer wanted to increase the waist of the decahedron with surface reconstruction, Figure 32. Table 19 presents the sites of type *SE* and *EC* of the original decahedron, used to construct Table 25 for the decahedra with surface reconstruction and developed.

When adding the layers to widen the waist of the sites *EE* and *VE* of the original decahedron, they duplicate and generate the sites of type *EV* and *RF*, as occurred with the pentadecahedra, and the number of sites is the same. The number of added sites N_{ag} from which $N_{\sigma_{\text{ag}}}$ are added to the surface for μ equatorial layers for the polyhedron with a central site is

$$N_{\text{ag}}(\nu, \mu) = (\mu - 1)[10\nu^2 + 5\nu + 1]$$

$$N_{\sigma_{\text{ag}}}(\nu, \mu) = (\mu - 1)(10\nu),$$

and without central site

$$N_{\text{ag}}(\nu, \mu) = (\mu - 1)[10\nu^2 - 5\nu + 1],$$

$$N_{\sigma_{\text{ag}}}(\nu, \mu) = (\mu - 1)[5(2\nu - 1)].$$

Table 24. Geometric characteristics for the *mrdec*, decahedra with and without a central site, modified with surface reconstruction.

| | With a central site | | | Without a central site | | |
ν	N_{ag}	N_σ	N	N_{ag}	N_σ	N
2	100	122	205	60	77	114
3	210	242	497	150	177	331
4	360	402	969	280	317	708
5	550	602	1661	450	497	1285

Note: ν is the cluster order. The number of added sites N_{ag}, of surface sites N_σ, and the total number of sites N in the cluster are listed.
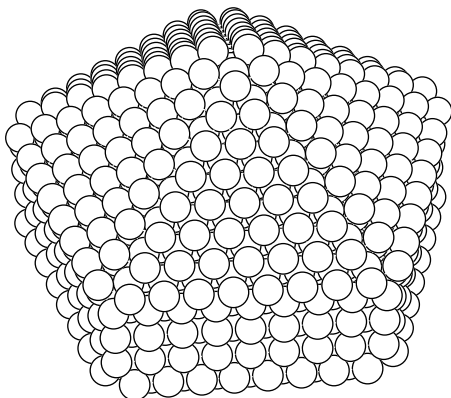
Figure 32. *mrdec* decahedron with a central site of order 4 (609 sites), with surface reconstruction (969 sites) and three equatorial layers (two layers *SEC* of 181 sites each one) for a total of 1331 sites in the polyhedron.
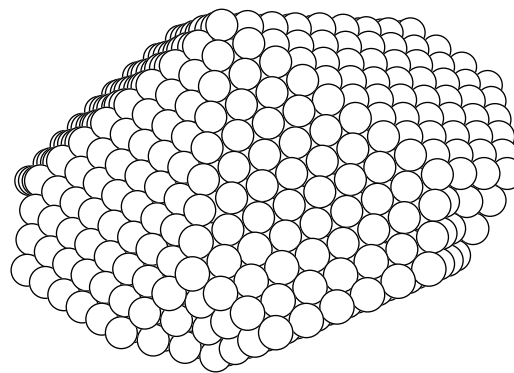
3.5. Truncated Decahedra (Marks Decahedra)

These result from the adequate elimination of some sites of a certain decahedron. The resulting geometry is a figure of 22 vertexes (of three types), 40 edges (of 4 types, 15 from the original decahedron, but shorter, and 25 which are generated by elimination of the adequate sites), 10 pentagonal faces (triangular faces from the original decahedron are converted to irregular pentagons), and 10 equilateral triangular faces (at the equator and joint by pairs) (Fig. 33).

The adequate elimination of sites is equivalent to eliminating the end sites of the edges which converge in the vertexes of the equator of the corresponding decahedron. Notice that in, each elimination, the equatorial edges lose two sites, while the edges which converge also toward the poles only lose one; this causes edges converging to the poles to be larger than the equatorial ones, but shorter then the ones from the original decahedron.

Table 25. Geometric characteristics for the *mrdec*, decahedra with and without a central site, modified with surface reconstruction and added layers in the waist.

ν	μ	N_{EV}	N_{RF}	N_{ag}	N_{σ}	N	N_{RF}	N_{ag}	N_{σ}	N
			With a central site				Without a central site			
2	1	0	0	0	122	205	0	0	77	114
	2	0	0	51	142	256	0	31	92	145
	3	5	15	102	162	307	10	62	107	176
3	1	0	0	0	242	497	0	0	177	331
	2	0	0	106	272	603	0	76	202	407
	3	5	25	212	302	709	20	152	227	483
4	1	0	0	0	402	969	0	0	317	708
	2	0	0	181	442	1150	0	141	352	849
	4	10	70	543	522	1512	60	423	422	1131
5	1	0	0	0	602	1661	0	0	497	1285
	2	0	0	276	652	1937	0	226	542	1511
	3	5	45	552	702	2213	40	452	587	1737
	5	15	135	1104	802	2765	120	904	677	2189

Note: ν is the cluster order, μ is the number of equatorial layers in the polyhedron. Notice that, for $\mu = 1$, Table 24 values are obtained. Although μ can take any value higher than zero, here are presented only some values.

Figure 33. Truncated decahedron of 1372 sites of order 63, without a central site.

In the first step, $n = 1$, the equator vertexes from the equator of the exterior shell are eliminated, the last shell, 5 sites. In the second step, $n = 2$, two sites per equatorial edge are eliminated, and one of the rest of the edges, 20 sites of the previous stage are converted into 25. In the third step, $n = 3$, the step of the edges of the last shell is repeated, 20 sites, plus two sites of each triangular face, 20 sites, besides, in one shell before the last, the interior decahedron, the equator vertexes are eliminated, 5 more sites are needed in order to obtain 40 sites to be eliminated in this step, and there is a complete total of 70 eliminated sites in three steps. And so on, for $n < \nu$ because $N_{EE} = 5(2\nu - 1)[= 5(2\nu - 2)]$ for decahedra with [without] a central site, for $\nu = n - 1$, there are only 3 [2] sites *EE*, see Table 26.

Table 26 lists the truncated decahedra, resulting from decahedra with and without a central site, respectively. The order of the truncated decahedron consists of two numbers corresponding to the first and second columns of Table 26, the first column is the order of the decahedron generated ν, and the second column is the number of steps n needed to eliminate the adequate sites, or is half of the sites eliminated from each edge at the equator: $n = 1$ means that only the vertexes at the equator are eliminated, the first step in the elimination process. The third column lists the total number of sites eliminated from the original decahedron to obtain the truncated decahedron of order νn, $N_{(-)}$, in the fourth [eighth], the number of sites per equatorial site *EE* remaining in the originals are presented (taking into account that in these sites are included the two new vertexes *VE*) per edge, for the polyhedron with a central site [without a central site] (for $n = 1$ is the number of sites in edges in the original decahedron); finally, the fifth, sixth, and seventh columns [ninth, tenth, and eleventh] present the number of sites *SE* and *EC* and the total in the resulting truncated decahedron with a central site [without a central site]. For example, the truncated decahedron without a central site of order 63, Figure 33, is generated from the decahedron with a central site of order 6 (1442 sites, 10 sites per edge, 151 sites *SE* and 180 sites *EC*), and eliminating the 5 sites *VE*, 4 sites *EE* of each one of the equatorial edges of the surface, 2 sites *EP* from each edge toward the poles and the 5 *VE* sites from the immediate interior shell, so the truncated decahedron of order 63 has 6 sites per equatorial edge, 70

Table 26. Geometric characteristics for the truncated decahedra, constructed from a certain decahedra of order ν, with and without a central site.

Order			With a central site				Without a central site			
ν	n	$N_{(-)}$	N_{EE}	$N_{t_{SE}}$	$N_{t_{EC}}$	N	N_{EE}	$N_{t_{SE}}$	$N_{t_{EC}}$	N
1	1	5	1	5	6	18	—	—	—	—
2	1	5	3	20	26	100	2	11	15	49
3	1	5	5	45	56	282	4	31	40	176
	2	25	3	40	46	262	2	26	30	156
4	1	5	7	80	96	604	6	61	75	423
	2	25	5	75	86	584	4	56	65	403
	3	70	3	65	71	539	2	46	50	358
5	1	5	9	125	146	1106	8	101	120	830
	2	25	7	120	136	1086	6	96	110	810
	3	70	5	110	121	1041	4	86	95	765
	4	150	3	95	101	961	2	71	75	685
6	1	5	11	180	206	1828	10	151	175	1437
	2	25	9	175	196	1808	8	146	165	1417
	3	70	7	165	181	1763	6	136	150	1372
	4	150	5	150	161	1683	4	121	130	1292
	5	275	3	130	136	1558	2	101	105	1167

Note: n is the half of sites eliminated from each equator edge.

sites are eliminated, and it has a total of 136 sites SE, 150 sites EC and, 1372 in total.

The number of eliminated sites, the third column of Table 26, is the same for the two polyhedra, with and without a central site, and depends only on the number of steps n given and is obtained by

$$N_{(-)}(n) = \frac{5}{6}n(n+1)(2n+1).$$

Expressions for the number of sites SE, sites EC, and in total for the truncated decahedra with a central site

$$N_{t_{SE}}(\nu, n) = 5\nu^2 - \frac{5}{2}n(n-1)$$

$$N_{t_{EC}}(\nu, n) = 5\nu(\nu+1) + 1 - \frac{5}{2}n(n+1)$$

$$N(\nu, n) = \frac{20}{3}\nu^3 + 10\nu^2 + \frac{16}{3}\nu + 1 - N_{(-)}(n)$$

and for the truncated decahedra without a central site

$$N_{t_{SE}}(\nu, n) = 5\nu(\nu-1) + 1 - \frac{5}{2}n(n-1)$$

$$N_{t_{EC}}(\nu, n) = 5\nu^2 - \frac{5}{2}n(n+1)$$

$$N(\nu, n) = \frac{20}{3}\nu^3 + \frac{\nu}{3} - N_{(-)}(n).$$

The truncated decahedron is a polyhedron formed by 22 vertexes, joined by 22 vertexes, attached by 40 edges, forming 10 pentagonal faces and 10 triangular. Vertexes are of three types: VP, VE, and V'; VP (2 vertexes), and are the same as in the original decahedron, VE and V' (10 vertexes each) result by pairs from elimination of the original VE and from elimination of sites from EE and EP; sites V' are

found to be the end of the edges that converge toward the poles, that is, the edges EP join sites VP and V'. Edges are of 4 types: the original EP edges (10 edges) and EE (5 edges), but the shorter ET (20 edges) and EV' (5 edges) which make up the triangular faces TF (10 faces) formed upon elimination of the equatorial sites, the edges EV' join the vertexes V' by pairs, and the edges ET join sites VE and V'. So, any truncated decahedron will have vertex sites of type VP, VE, V', edges type EP, EE, ET, EV', and faces type TF and pentagonal face PF. The number of VP sites is 2, of V' is 10, and of VE is also 10. The number of remaining sites is variable, and is listed in Table 27 for the truncated decahedra with and without a central site. The number of surface sites is also listed as well as the total sites of the polyhedron. Columns 1 and 2 correspond to the order of the cluster ν and n respectively. Columns 3–8 [11–16] correspond to sites EP, N_{EP}, EE, N_{EE}, ET, N_{ET}, EV', $N_{EV'}$, PF, N_{PF}, and TF, N_{TF}, respectively, and the two last columns to the surface sites N_σ and the total of sites N for truncated decahedra with [without] a central site.

From Table 27 it is possible to deduct the analytic expressions for the number of sites of the different types of sites as a function of the order of the truncated decahedron, the resulting expressions, common for the polyhedra with and without a central site, but depending on the number of steps made for the elimination of the sites, are N_{ET}, $N_{EV'}$, and N_{TF}

$$N_{ET}(n) = 20(n-1)$$

$$N_{EV'}(n) = 5(n-1)$$

$$N_{TF}(n) = 5(n-2)(n-1).$$

The expressions for the other types of sites are as follows for the one with a central site:

$$N_{EP}(\nu, n) = 10(2\nu - 1) - 10n$$

$$N_{EE}(\nu, n) = 5(2\nu - 1) - 10n$$

$$N_{PF}(\nu, n) = 10(2\nu - 1)(\nu - 1) - 10n(n-1)$$

$$N_\sigma(\nu, n) = 20\nu^2 - 5n^2 + 2$$

and without a central site:

$$N_{EP} = 20(\nu - 1) - 10n$$

$$N_{EE} = 10(\nu - 1) - 10n$$

$$N_{PF} = 10(2\nu - 3)(\nu - 1) - 10n(n-1)$$

$$N_\sigma = 20\nu^2 - 20\nu - 5n^2 + 7.$$

3.5.1. Developed Truncated Decahedra

The same method used to generate pentadecahedra is used here. Intermediate layers can be added to the truncated decahedra in order to obtain polyhedra with 15 lateral faces, 5 rectangular, and 10 trapezoidal (before triangular) (Fig. 34). This means that a layer of SEC type is added per each layer wanted to widen the polyhedron, so the polyhedron of Figure 34 has 4 equatorial layers; this means that 3 SEC

Table 27. Geometric characteristics for the truncated decahedra with and without a central site. The number of surface sites for each type of site, the number of total surface sites, and in the polyhedron are listed.

ν	n	N_{ET}	$N_{EV'}$	N_{TF}	With a central site					Without a central site				
					N_{EP}	N_{EE}	N_{PF}	$N\sigma$	N	N_{EP}	N_{EE}	N_{PF}	N_{σ}	N
2	1	0	0	0	20	5	30	77	100	10	0	10	42	49
3	1	0	0	0	40	15	100	177	282	30	10	60	122	176
	2	20	5	0	30	5	80	162	262	20	0	40	107	156
4	1	0	0	0	60	25	210	317	604	50	20	150	242	423
	2	20	5	0	50	15	190	302	584	40	10	130	227	403
	3	40	10	10	40	5	150	277	539	30	0	90	202	358
5	1	0	0	0	80	35	360	497	1106	70	30	280	402	830
	2	20	5	0	70	25	340	482	1086	60	20	260	387	810
	3	40	10	10	60	15	300	457	1041	50	10	220	362	765
	4	60	15	30	50	5	240	422	961	40	0	160	327	685

layers were added. So, in a developed truncated decahedron, there will be the same sites as in one without development, except for the *TF* sites, triangular face, which convert into sites *TR* trapezoidal face, and the sites generated when adding the *SEC* layers, sites in the rectangular faces *RF* and in the vertical edges *EV*, joining the *VE* sites which are duplicated. The number of sites that will be added depends on the number of equatorial layers that the polyhedron will have, $N_{t_{SE}} + N_{t_{EC}}$ sites from the original truncated decahedron are added per each layer to widen them. It is to be noticed that, in this case, the *SE* sites corresponding to *EV'* and *ET* sites will be added to the surface also, that is, they will not remain internal, along with the *EC* sites. Table 28 lists the number of sites of the different types of sites in the truncated decahedron with and without a central site and developed.

When adding *SEC* layers to grow the truncated decahedron, the number of sites *VP*, *EP*, *ET*, *V'*, and *PF* are not modified, while the number of sites *VE*, and *EE* are duplicated, sites *EV'* increase and sites *TF* are converted to *TR* and they increase with respect to the original truncated decahedron. Sites *RF* and *EV* appear. From Table 28 it is possible to obtain the analytic expressions for the different number of sites in the developed truncated decahedron. The number of sites *EV'*, *EV*, and *TR* is common for the two

polyhedra with and without a central site, that is, they only depend on n and μ, and their analytic expression is the following:

$$N_{EV'}(\mu, n) = 5(n + \mu - 2)$$
$$N_{EV}(\mu) = 10(\mu - 2)$$
$$N_{TR}(\mu, n) = 5(n-1)(n + 2\mu - 4),$$

and the expressions for the other types of sites, for the one with a central site,

$$N_{RF}(\nu, \mu, n) = 5(2\nu - 2n - 1)(\mu - 2)$$
$$N_{ag}(\nu, \mu, n) = (\mu - 1)[5\nu(2\nu + 1) + 1 - 5n^2]$$
$$N_{\sigma}(\nu, \mu, n) = 10\nu(2\nu + \mu - 1) - 5n^2 + 2$$

and without a central site

$$N_{RF}(\nu, \mu, n) = 10(\nu - n - 1)(\mu - 2)$$
$$N_{ag}(\nu, \mu, n) = (\mu - 1)[5\nu(2\nu - 1) + 1 - 5n^2]$$
$$N_{\sigma}(\nu, \mu, n) = 10\nu(2\nu + \mu - 3) - 5n^2 - 5\mu + 12.$$

the total number of sites is equal to the total number of sites in the original decahedron plus the N_{ag} sites.

3.6. Star-Type Decahedra

If the method to obtain a truncated decahedron is applied to a decahedron without a central site, which has an odd number of edges, it could be possible to eliminate all of the sites from the equatorial edges, except one, obtaining the star-type decahedron, named after the shape it represents (Fig. 35). For this decahedron, the equator edges from the original decahedron are practically eliminated, with one site remaining which converts to a vertex. The edges toward the poles are reduced to a half. The resulting figure has 17 vertexes, 30 edges, 10 rhombohedral-shaped faces, and 10 lateral triangular faces (over the equator and joint in pairs). The types of sites present are the same as in the truncated decahedron, although the *PF* sites, pentagonal faces, change to *R* sites, rhombohedral faces. The number of *VP* sites is 2, of *V'* is 10, and of *VE* is 5; the number of sites *EP*, *ET*,

Figure 34. Truncated decahedron without a central site of order 63 with four equatorial layers, for a total of 2230 sites.

Table 28. Geometric characteristics for the truncated decahedra with and without a central site and developed.

ν	n	μ	$N_{EV'}$	N_{EV}	N_{TR}	With a central site				Without a central site			
						N_{RF}	N_{ag}	N_σ	N	N_{RF}	N_{ag}	N_σ	N
2	1	1	0	0	0	0	0	77	100	0	0	42	49
	1	2	5	0	0	0	46	97	146	0	26	57	65
3	1	1	0	0	0	0	0	177	282	0	0	122	176
	1	2	5	0	0	0	101	207	383	0	71	147	247
	1	3	10	10	0	15	202	237	484	10	142	172	318
	2	1	5	0	0	0	0	162	162	0	0	107	156
	2	2	10	0	10	0	86	192	248	0	56	132	212
	2	3	15	10	20	5	172	222	334	0	112	157	268
4	1	1	0	0	0	0	0	317	604	0	0	242	423
	1	2	5	0	0	0	176	357	780	0	136	277	559
	1	3	10	10	0	25	352	397	956	20	272	312	695
	1	4	15	20	0	50	528	437	1132	40	408	347	831
	2	1	5	0	0	0	0	302	584	0	0	227	403
	2	2	10	0	10	0	161	342	745	0	121	262	524
	2	3	15	10	20	15	322	382	906	10	242	297	645
	2	4	20	20	30	30	483	422	1067	20	363	332	766
	3	1	10	0	10	0	0	277	539	0	0	202	358
	3	2	15	0	30	0	136	317	675	0	96	237	454
	3	3	20	10	50	5	272	357	811	0	192	272	550
	3	4	25	20	70	10	408	397	947	0	288	307	646

Note: νn is the cluster order, μ is the number of equatorial layers in the polyhedra. Notice that, for $\mu = 1$, Table 27 values are obtained. Although μ can take any value higher than zero, here are only presented some values.

and EV' per edge is the same, not the number of edges of each type.

Table 29 describes the geometric characteristics of the star-type decahedra, notice that they correspond to the truncated decahedron with a central site with $\mu = \nu$ (only one site remanins in the equatorial edges).

From Table 29 it is possible to obtain the analytic expressions for the star-type decahedra, and they are presented next:

$$N_{EP}(\nu) = 10(\nu - 1), \qquad N_R(\nu) = 10(\nu - 1)^2$$

$$N_{ET}(\nu) = 20(\nu - 1), \qquad N_{TF}(\nu) = 5(\nu - 2)(\nu - 1),$$

$$N_{EV'}(\nu) = 5(\nu - 1), \qquad N_{(-)}(\nu) = \frac{5}{6}\nu(\nu + 1)(2\nu + 1)$$

$$N_{t_{SE}}(\nu) = \frac{5}{2}\nu(\nu + 1), \qquad N_{t_{EC}}(\nu) = \frac{5}{2}\nu(\nu + 1) + 1$$

$$N_\sigma(\nu) = 15\nu^2 + 2, \qquad N(\nu) = 5\nu^3 + \frac{15}{2}\nu^2 + \frac{9}{2}\nu + 1.$$

To these decahedra, it is possible to add intermediate layers. The resulting figure has 10 trapezoidal lateral faces (which were triangular), and besides the 10 rhombohedral, 5 edges more, (Fig. 36). When adding layers of type *SEC*, the number of sites *VP*, *EP*, *ET*, *V'*, and *RF*, are not modified, while the number of sites *EE* and *VE* are duplicated; the number of sites EV' increases and the *TF* sites, triangular face, change to *TR*, trapezoidal face. Besides, sites *EV* appear. Table 30 lists the geometric characteristics of these polyhedra. Analytical expressions for the number of sites for the modified sites are presented next:

$$N_{EV'}(\nu, \mu) = 5(\nu + \mu - 2)$$

$$N_{TR}(\nu, \mu) = 5(\nu - 1)(\nu + 2\mu - 4)$$

$$N_{EV}(\mu) = 5(\mu - 2)$$

$$N_{ag}(\nu, \mu) = (\mu - 1)[5\nu(\nu + 1) + 1]$$

Figure 35. Star-type decahedron of order 4.

Table 29. Geometric characteristics for the star-type decahedra.

ν	N_{EP}	N_R	N_{ET}	N_{TF}	$N_{EV'}$	$N_{(-)}$	$N_{t_{SE}}$	$N_{t_{EC}}$	N_σ	N
1	0	0	0	0	0	5	5	6	17	18
2	10	10	20	0	5	25	15	16	62	80
3	20	40	40	10	10	70	30	31	137	217
4	30	90	60	30	15	150	50	51	242	459
5	40	160	80	60	20	275	75	76	377	836
6	50	250	100	100	25	455	105	106	542	1378
7	60	360	120	150	30	700	140	141	737	2115
8	70	490	140	210	35	1020	180	181	962	3077
9	80	640	160	280	40	1425	225	226	1217	4294
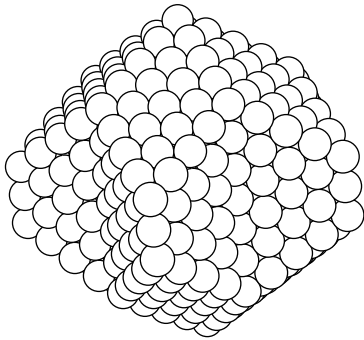
Figure 36. Star-type decahedron of order 4 and three equatorial layers added, with 661 sites.

$$N_{t_{SE}}(\nu) = \begin{cases} \dfrac{5}{2}\nu(\nu+1) & \nu \text{ impar} \\ \dfrac{5}{2}\nu(\nu+1)+1 & \nu \text{ par} \end{cases}$$

$$N_{t_{EC}}(\nu) = \begin{cases} \dfrac{5}{2}\nu(\nu+1)+1 & \nu \text{ impar} \\ \dfrac{5}{2}\nu(\nu+1) & \nu \text{ par} \end{cases}$$

$$N_{\sigma}(\nu, \mu) = 5(\nu-1)(3\nu+2\mu+1) + 10\mu + 7$$

$$N(\nu, \mu) = 5\nu^3 + \frac{15}{2}\nu^2 + 1 + \frac{9}{2}\nu + 1 + N_{\text{ag}}(\nu, \mu)$$

the total number of sites is equal to the total number of sites in the original star-type decahedron plus the N_{ag} sites.

Table 30. Geometric characteristics for the star-type decahedra.

ν	μ	$N_{EV'}$	N_{TR}	N_{EV}	N_{ag}	$N_{t_{SE}}$	$N_{t_{EC}}$	N_{σ}	N
1	1	0	0	0	0	5	6	17	18
2	1	5	0	0	0	15	16	62	80
2	2	10	10	0	31	16	15	82	111
3	1	10	10	0	0	30	31	137	217
3	2	15	30	0	61	31	30	167	278
3	3	20	50	5	122	30	31	197	339
4	1	15	30	0	0	50	51	242	459
4	2	20	60	0	101	51	50	282	560
4	3	25	90	5	202	50	51	322	661
4	4	30	120	10	303	51	50	362	762
5	1	20	60	0	0	75	76	377	836
5	2	25	100	0	151	76	75	427	987
5	3	30	140	5	302	75	76	477	1138
5	4	35	180	10	453	76	75	527	1289
5	5	40	220	15	604	75	76	577	1440
6	1	25	100	0	0	105	106	542	1378
6	2	30	150	0	211	106	105	602	1589
6	3	35	200	5	422	105	106	662	1800
6	4	40	250	10	633	106	105	722	2011
6	5	45	300	15	844	105	106	782	2222
6	6	50	350	20	1055	106	105	842	2433

3.7. Additional Truncations in Decahedra

Just as in the decahedra, it is possible to add or eliminate sites to obtain modified structures of all of the types of decahedra previously described to obtain new structures. This is achieved by eliminating the sites on the edges which converge to a pole in a truncated decahedron, for example, the one of order 74 without a central site with 2139 sites, a truncated decahedron with one channel per edge converging to a pole is obtained, Figure 37(a), of 2032 sites, having an elimination of 107 sites, sites EP, VP, EV, and V'. If only the sites EP, VP, and V' are eliminated, Figure 38(a), a polyhedron of 2047 sites is obtained. If, now, the following edges are eliminated, the result is a truncated decahedron with a triple channel of 1822 sites, 210 sites were eliminated [Fig. 37(b)], and also, it is possible to eliminate only the sites at edges without eliminating the EV sites [Fig. 38(b)]. This process can continue until obtaining the desired number of channels.

Elimination of only the EP, VP, and V' sites does not affect the number of SE and EC sites from the original polyhedron, listed in Table 26, while upon elimination of the sites EV they do modify. Table 31 lists the geometric characteristics of some truncated decahedra with and without a central site and the resulting ones with single and triple channels when sites EP, VP, EV, and V' are eliminated. For the case when sites EP, VP, and V' are eliminated the geometric characteristics are listed in Table 32.
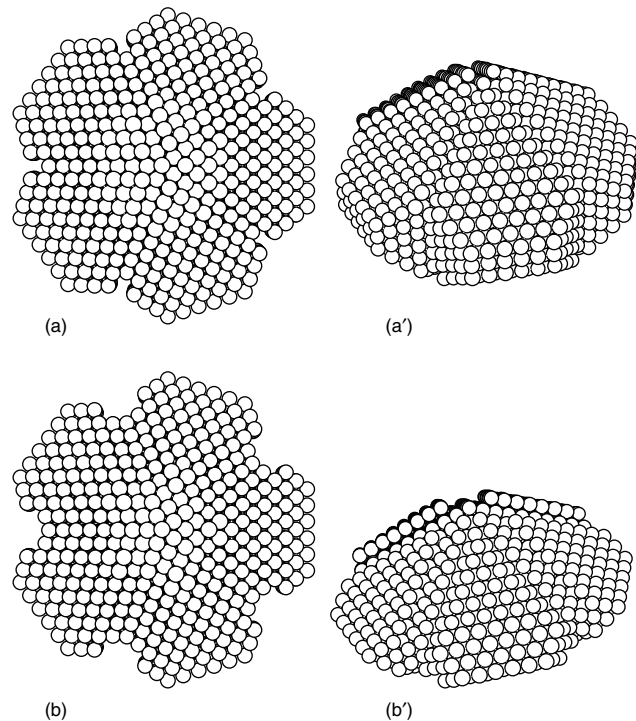
Figure 37. Truncated decahedron without a central site of order 74 with (a) one single channel and 2032 sites, and (b) a triple channel and 1822 sites, eliminating AP, VP, AV, and V' sites. [(a') and (b') are lateral views of superior (a) and (b) views, respectively].
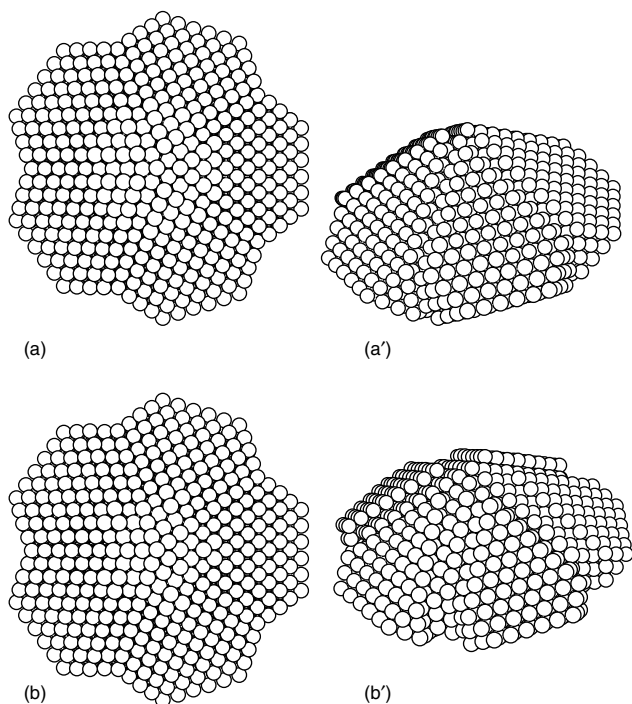
Figure 38. Truncated decahedron without central site of order 74 with (a) one single channel and 2047 sites, and (b) a triple channel and 1857 sites, eliminating *AP*, *VP*, and *V'* sites. [(a') and (b') are lateral views of superior (a) and (b) views, respectively).

In both Tables the number of eliminated sites and the total number of sites in the cluster are enumerated. Besides that in Table 31 the total number of sites *SE* and *EC* are also enumerated.

From Tables 31 and 32, in both cases it is possible to obtain the analytical expressions for the total number of sites eliminated from these clusters. When sites *EP*, VP, EV and V' are eliminated from a truncated decahedron with a central site and a simple channel

$$N_{\rm el}(\nu, n) = 20\nu - 5n - 3,$$

for a triple channel,

$$N_{\rm el}(\nu) = 10(4\nu - 5),$$

for a truncated decahedron without a central site and a simple channel,

$$N_{\rm el}(\nu, n) = 20\nu - 5n - 13,$$

and for a triple channel,

$$N_{\rm el}(\nu) = 10(4\nu - 7).$$

And when only sites *EP*, *VP*, and *V'* are eliminated from a truncated decahedron with a central site and a simple channel,

$$N_{\rm el}(\nu, n) = 20\nu - 10n + 2,$$

for a triple channel,

$$N_{\rm el}(\nu, n) = 10(4\nu - n - 3),$$

for a truncated decahedron without a central site and a simple channel,

$$N_{\rm el}(\nu, n) = 20\nu - 10n - 8,$$

and for a triple channel,

$$N_{\rm el}(\nu, n) = 10(4\nu - n - 5),$$

Also from Table 31 it is possible to obtain the analytical expressions for the total number of *EC* and *SE* sites when sites *EP*, *VP*, *EV*, and *V'* are eliminated from a truncated decahedron. It can be notice that the behavior of these quantities do not depend if the polyhedron has or not a central site. For the case of a simple channel,

$$(N_{t_{SE}})_{\rm sc} = (N_{t_{SE}})_{\rm Marks} - \begin{cases} 5, & n \text{ odd} \\ 0, & n \text{ even} \end{cases}$$

$$(N_{t_{EC}})_{\rm sc} = (N_{t_{EC}})_{\rm Marks} - \begin{cases} 0, & n \text{ odd} \\ 5, & n \text{ even} \end{cases}$$

Table 31. Geometric characteristics for the truncated decahedra with and without a central site modified with a single and a triple channel, eliminating *EP*, *VP*, *EV*, and *V'* sites.

| | | With a central site | | | | | | | | Without a central site | | | | | | | |
| | | A single channel | | | | A triple channel | | | | A single channel | | | | A triple channel | | | |
ν	n	$N_{\rm el}$	$N_{t_{SE}}$	$N_{t_{EC}}$	N	$N_{\rm el}$	$N_{t_{SE}}$	$N_{t_{EC}}$	N	$N_{\rm el}$	$N_{t_{SE}}$	$N_{t_{EC}}$	N	$N_{\rm el}$	$N_{t_{SE}}$	$N_{t_{EC}}$	N
2	1	32	15	26	68	30	15	16	38	22	6	15	27	10	6	5	17
3	1	52	40	56	230	70	40	46	160	42	26	40	134	50	26	30	84
	2	47	40	41	215	70	30	41	145	37	26	25	119	50	16	25	69
4	1	72	75	96	532	110	75	86	422	62	56	75	361	90	56	65	271
	2	67	75	81	517	110	65	81	407	57	56	60	346	90	46	60	256
	3	62	60	71	477	110	60	61	367	52	41	50	306	90	41	40	216
5	1	92	120	146	1014	150	120	136	864	82	96	120	748	130	96	110	618
	2	87	120	131	999	150	110	131	849	77	96	105	733	130	86	105	603
	3	82	105	121	959	150	105	111	809	72	81	95	693	130	81	85	563
	4	77	95	96	884	150	85	96	734	67	71	70	618	130	61	70	488

Table 32. Geometric characteristics for the truncated decahedra with and without a central site modified with a single and a triple channel, eliminating *EP*, *VP*, and *V′* sites.

		With a central site				Without a central site			
				Channel					
Order		Single		Triple		Single		Triple	
ν	n	N_{el}	N	N_{el}	N	N_{el}	N	N_{el}	N
2	1	32	68	40	28	22	27	20	7
3	1	52	230	80	150	42	134	60	74
	2	42	220	70	150	32	124	50	74
4	1	72	532	120	412	62	361	100	261
	2	62	522	110	412	52	351	90	261
	3	52	487	100	387	42	316	80	236
5	1	92	1014	160	854	82	748	140	608
	2	82	1004	150	854	72	738	130	708
	3	72	969	140	829	62	703	120	583
	4	62	899	130	769	52	633	110	523

and for a triple channel,

$$(N_{t_{SE}})_{tc} = (N_{t_{SE}})_{cs} - \begin{cases} 0, & n \text{ odd} \\ 10, & n \text{ even} \end{cases}$$

$$(N_{t_{EC}})_{tc} = (N_{t_{EC}})_{cs} - \begin{cases} 10, & n \text{ odd} \\ 0, & n \text{ even} \end{cases}$$

The total number of sites in the cluster is the total number of sites in the truncated decahedron minus the eliminated sites.

With this, it is possible to add the layers type *SEC* to obtain truncated decahedra with channels and developed [Figs. 39(a) and (b)].

Another modification of a truncated decahedron with surface reconstruction, as explained for the decahedron, can be achieved by shifting the pentagonal face outwards and to the waist, eliminating then the sites *EE*, *VE*, *ET*, and *V′*, which reflects in adding N_{ag} sites (Fig. 40). Table 33 lists the geometric characteristics of the truncated decahedra modified by surface reconstruction. From this Table can be deduced that for the truncated decahedron with a central site the number of sites added, the number of surface sites and the total number of sites in the cluster are

$$N_{ag}(\nu, n) = 10[2\nu^2 + \nu - 2 - (n-1)(n+2)]$$
$$N_{\sigma}(\nu, n) = 20\nu(\nu+1) - 5n(n+2) + 2$$
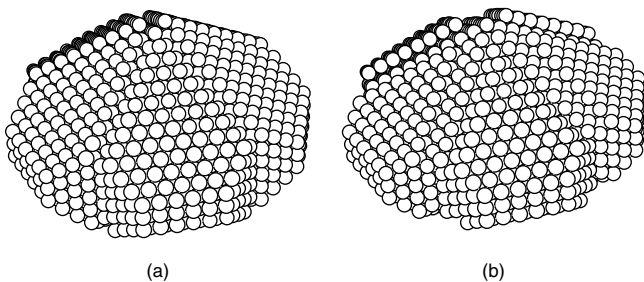
Figure 39. Truncated decahedron without a central site of order 74 with (a) one single channel, and (b) a triple channel and three layers in the waist.
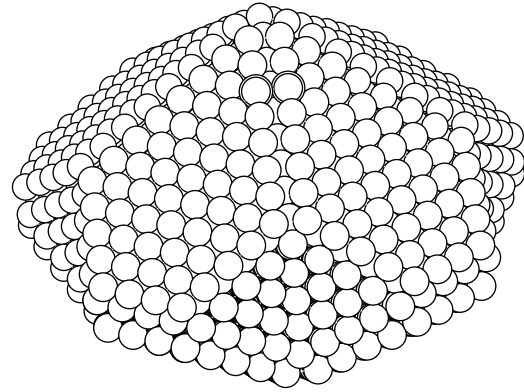
Figure 40. Truncated decahedron with surface reconstruction.

$$N(\nu, n) = \frac{20}{3}\nu^3 + 30\nu^2 + \frac{46}{3}\nu - \frac{5}{3}n^3 - \frac{25}{2}n^2 - \frac{65}{6}n + 1,$$

and for the truncated decahedron without a central site

$$N_{ag}(\nu, n) = 10[(2\nu - 3)(\nu + 1) - (\mu - 1)(\mu + 2) + 1]$$
$$N_{\sigma}(\nu, n) = 20\nu^2 - 5n^2 - 10n - 3$$
$$N(\nu, n) = \frac{20}{3}\nu^3 + 20\nu^2 - \frac{29}{3}\nu - \frac{5}{3}n^3 - \frac{25}{2}n^2 - \frac{65}{6}n.$$

When adding the sites for the surface reconstruction, the number of sites *SE* and *EC* is not affected. So, layers of type *SEC* can be added to obtain truncated decahedra with surface reconstruction and developed (Fig. 41). Table 34 lists the geometric characteristics for the truncated decahedron with and without a central site modified with surface reconstruction and with *SEC* layers added. From this table it is

Table 33. Geometric characteristics for the truncated decahedra with and without a central site modified with surface reconstruction.

| | | With a central site | | | Without a central site | | |
ν	n	N_{ag}	N_{σ}	N	N_{ag}	N_{σ}	N
3	2	150	202	412	90	137	246
4	2	300	362	884	220	277	623
	3	240	327	779	160	242	518
5	2	490	562	1576	390	457	1200
	3	430	527	1471	330	422	1095
	4	350	482	1311	250	377	935
6	2	720	802	2528	600	677	2017
	3	660	767	2423	540	642	1912
	4	580	722	2263	460	597	1752
	5	480	667	2038	360	542	1527
7	2	990	1082	3780	850	937	3114
	3	930	1047	3675	790	902	3009
	4	850	1002	3515	710	857	2849
	5	750	947	3290	610	802	2624
	6	630	882	2990	490	737	2324

Note: νn is the cluster order. Number of agregated sites, N_{ag}, of surface sites, N_{σ}, and of the total of sites, N, in the polyhedron are listed.
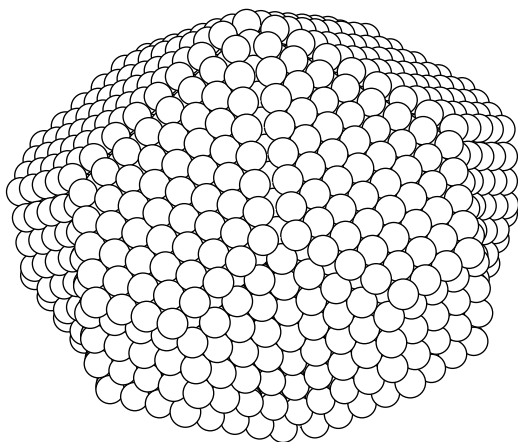
Figure 41. Truncated decahedron with surface reconstruction and with three *SEC* layers.

possible obtain expressions for the number of sites aggregated, the number of surface sites and the total number of sites in the cluster, for polyhedra with a central site they are

$$N_{ag}(\nu,\mu,n) = (10\nu^2 + 5\nu - 10n + 6)(\mu - 1)$$

$$N_\sigma(\nu,\mu,n) = 20\nu^2 + 5n^2 - 10\mu^2 + 10\nu - 20\mu + 10\nu\mu + 2$$

Table 34. Geometric characteristics for the truncated decahedra with and without a central site modified with surface reconstruction and developed.

ν	n	μ	With a central site			Without a central site		
			N_{ag}	N_σ	N	N_{ag}	N_σ	N
3	2	1	0	233	262	0	177	156
3	2	2	91	234	353	60	142	216
3	2	3	182	235	444	120	87	276
4	2	1	0	393	584	0	317	403
4	2	2	166	404	750	125	292	528
4	2	3	332	415	916	250	247	653
4	2	4	498	426	1082	375	182	778
4	3	1	0	418	539	0	342	358
4	3	2	156	429	695	115	317	473
4	3	3	312	440	851	230	272	588
4	3	4	468	451	1007	345	207	703
5	2	1	0	593	1086	0	497	810
5	2	2	261	614	1347	210	482	1020
5	2	3	522	635	1608	420	447	1230
5	2	4	783	656	1869	630	392	1440
5	2	5	1044	677	2130	840	317	1650
5	3	1	0	618	1041	0	522	765
5	3	2	251	639	1292	200	507	965
5	3	3	502	660	1543	400	472	1165
5	3	4	753	681	1794	600	417	1365
5	3	5	1004	702	2045	800	342	1565
5	4	1	0	653	961	0	557	685
5	4	2	241	674	1202	190	542	875
5	4	3	482	695	1443	380	507	1065
5	4	4	723	716	1684	570	452	1255
5	4	5	964	737	1925	760	377	1445

Note: ν is the cluster order. Number of agreggated sites, N_{ag}, of surface sites, N_σ, and of the toal of sites, N, in the polyhedron are listed.

$$N(\nu,\mu,n) = \frac{20}{3}\nu^3 + 10\nu^2 + \frac{16}{3}\nu + 1 - \frac{5}{6}n(n+1)(2n+1) + N_{ag},$$

and for polyhedra without a central site

$$N_{ag}(\nu,\mu,n) = (10\nu^2 - 5\nu - 10n + 5)(\mu - 1)$$

$$N_\sigma(\nu,\mu,n) = 20\nu^2 + 5n^2 - 10\mu^2 - 10\nu - 35\mu + 10\nu\mu + 22$$

$$N(\nu,\mu,n) = \frac{20}{3}\nu^3 + + \frac{1}{3}\nu - \frac{5}{6}n(n+1)(2n+1) + N_{ag}(\nu,\mu,n).$$

3.8. Icosahedra

The icosahedron (ICO) is a geometric figure with a central site, 12 vertexes, connected with 30 edges, and formed by 20 triangular faces; Figure 42 shows a 561 icosahedron. From this figure, it can be seen that the icosahedron can also be considered as two pentagonal pyramids with a rotation of 36° of one with respect to the other, and with intermediate layers, to adequately join the vertexes of both pyramids. Each icosahedral cluster presents a certain number of sites, but distributed in different layers, which are formed by equivalent sites: sites at the same distance from the origin, which have the same environment, and the same type of neighbors. Sites in the ICO are localized in triangular faces (*T*), edges (*E*), and vertexes (*V*). The order-1 ICO is formed by one central site and one first shell with only one layer of 12 vertexes. The second-order ICO is formed by the addition of one shell formed by 42 sites, to complete 55 sites, distributed in two layers: one layer of 30 sites *E* and a second layer of 12 sites *V*. When adding a third shell of 92 sites, the ICO of third order of 147 sites is completed, the added sites are distributed in three layers: one of 20 sites *T*, one more of 60 sites *E* and the third of 12 sites *V*. And successively, complete shells are added, forming clusters of order ν.

The geometric characteristics of the ICO are listed in Table 35, to clusters of order 10. The first column lists the order of the cluster ν. The following columns list the number of sites in each type of sites in the cluster. Next, is the number of sites of each site or the layers of each type of site. Finally, the number of sites in the shell and in the total
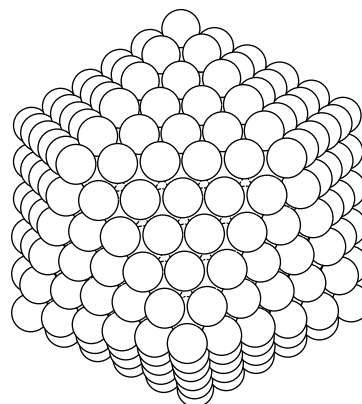
Figure 42. Icosahedron of order 5 with 561 atoms.

Table 35. Geometric characteristics for icosahedra.

ν	N_T	N_E	N_V	R_T	R_E	R_V	N_{shell}^{ν}	N_{shell}^{T}	N_{σ}	N
1	0	0	12	0	0	1	1	1	12	13
2	0	30	12	0	1	1	2	3	42	55
3	20	60	12	1	1	1	3	6	92	147
4	60	90	12	1	2	1	4	10	162	309
5	120	120	12	2	2	1	5	15	252	561
6	200	150	12	3	3	1	7	22	362	923
7	300	180	12	4	3	1	8	30	492	1415
8	420	210	12	5	4	1	10	40	642	2057
9	560	240	12	7	4	1	12	52	812	2869
10	720	270	12	8	5	1	14	66	1002	3871

of sites in the cluster is given. From this table, it is possible to obtain the dependence on the cluster order ν from the total number of sites N, on the number of surface sites N_{σ}, the number of sites T N_T and of sites E N_E, as well as the number of layers of sites T R_T, and sites E R_E, which are expressed as

$$N(\nu) = \frac{10}{3}\nu^3 + 5\nu^2 + \frac{11}{3}\nu + 1, \qquad N_{\sigma}(\nu) = 10\nu^2 + 2$$

$$N_T(\nu) = 10(\nu - 1)(\nu - 2), \qquad N_E(\nu) = 30(\nu - 1)$$

$$R_T^m(\nu) = \begin{cases} \displaystyle\sum_{\alpha=1}^{m/2}(3\alpha + a) + \sum_{\alpha=1}^{(m/2)-1} 3\alpha; & m \text{ even} \\[6pt] & \begin{cases} \nu = 3m + a; \\ a = -1, 0, 1; \end{cases} \\[6pt] \displaystyle\frac{1+a}{1+|a|} + \sum_{\alpha=1}^{(m-1)/2}(6\alpha + a); & m \text{ odd,} \end{cases}$$

$$R_E(\nu) = \begin{cases} \nu/2; & \nu \text{ even,} \\ \nu - 1/2; & \nu \text{ odd.} \end{cases}$$

3.9. Decmon-Type Polyhedra

In contrast with previous polyhedra, decmon polyhedra are based on a decmon-type pyramid, which is constituted by 16 vertexes joined by 30 edges which form 15 faces: 5 rectangular type (100) and 10 triangular of type (111), 5 of which are equilateral and 5 isosceles; Figure 43. The 5 equilateral triangular faces (*TE*) have m edge sites per side, and each
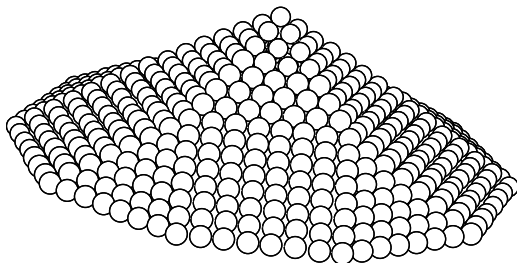
Figure 43. Decmon type pyramid.

side of length $1.05(m+1)d_{NN}$, where d_{NN} is the distance to the first neighbors; the 10 isosceles triangle faces (*TI*) have n edge sites per side, two sides of length $(n+1)d_{NN}$ and one of length $1.05(n+1)d_{NN}$; the 10 rectangular faces (*RF*), with $m \times n$ sites, have sides $1.0(n+1)d_{NN}$ and $1.05(m+1)d_{NN}$. Equal sides of faces *TI* coincide with the sides of faces *RF*, and the different side forms part of the equator along with one of the sides of *RF* faces. Faces *TE* coincide with the pole, and have a common side; also, each face has a common face with one *RF* face. The angle between the planes of *RF* and *TE* faces is 190.66°, and between *RF* and *TI* faces is 161.94°. The 16 vertexes (*V*) are of three types: 1 pole, where the 5 TE faces converge, 5 where the three types of faces (*V*3) converge, and 10 at the equator, and where an *R* and a *TI* face converge (*V*4). These vertexes are joined by 30 edges (*E*) of 5 types: 5 of length $1.05(m-1)$, between *TE* faces and which converge at the poles and join the *VP* and *V*3 vertexes (*EE*); 5 of length $1.05(m-1)$, between *TE* and *RF* faces and join vertexes *V*3 (*E*3); 10 of length $1.0(n-1)$ between *TI* and *RF* faces and join vertexes *V*3 and *V*4 (*E*34); and 10 at the equator, 5 of them of length $1.05(m-1)$ of one *RF* (*ER*) face and 5 of length $1.05(n-1)$ of one *TI* (*EI*) face, which joins *V*4 vertexes.

Based on the decmon pyramid, many polyhedra can be obtained: the truncated icosahedron, the decmon, and the decmon with intermediate aggregated layers.

3.9.1. Decmon Icosahedra

The truncated icosahedron or icosahedron of decmon type is a polyhedron obtained upon adequate truncation and in a symmetric way of an icosahedron (however, they can be truncated asymmetrically also). An asymmetric truncation of an icosahedron is done in the following manner: surface sites forming a cover with a pentagonal pyramid shape over a vertex, yielding a decmon-type pyramid, with rectangular faces and a side with a length of d_{NN}. In order to perform a symmetrical truncation, first a cover like that previously presented has to be eliminated, but from the vertex diagonally opposite. The following truncations have to be done by elimination of sites which form a pyramid-shaped cover of decmon type. Figure 44 shows two icosahedra with their corresponding truncations. Figure 44(a) [Fig. 44(d)] shows a 561 (309) site icosahedron that, upon truncation, yields the 409 (207) sites TI_h (observe in this one the decmon-type pyramid); Figure 44b [Fig. 44(e)], which, when truncated, again yields the 257 (105) sites TI_h, Figure 44(c) [Fig. 44(f)]. From this figure, it can be observed that it is possible to obtain the TI_h of two different kinds: (1) the TI_{ha} [Fig. 44(f) and (b)], and (2) the TI_{hb} [Figs. 44(b), (c), and (e)].

3.9.2. Truncated Icosahedra TI_{ha}

As shown in Figure 44(f), it is formed by 22 vertexes, joined by 50 edges, forming faces of three types: rectangular, *RF* type (110), and two triangular of type (111), one equilateral (*TE*) and the other isosceles (*TI*). Also, from this figure it can be noticed that the TI_{ha} can be formed by attaching two decmon-type pyramids, with *TI* faces coinciding with *TI* faces at the equator or waist.
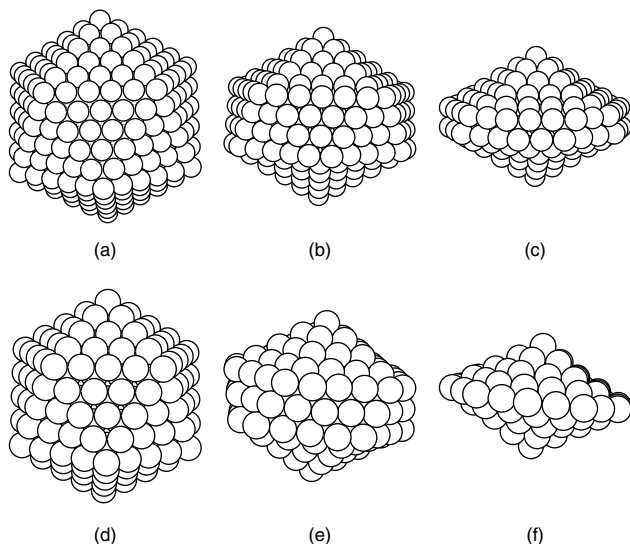
Figure 44. (a) Icosahedron I_h of 561 atoms. (b) Truncated icosahedron, TI_h of 409 atoms. (c) TI_h of 257 atoms. (d) I_h of 309 atoms. (e) TI_h of 207 atoms. (f) TI_h of 105 atoms.

3.9.3. Truncated Icosahedra TI_{hb}

As shown in Figures 44(b), (c), and (e), it is formed by 32 vertexes, joinrd by 80 edges of I order to form 50 faces. 10 vertexes, 30 edges, and 20 faces more than TI_{ha}. The 10 vertexes form one plane, and are of equator type from TI_{ha} and the 20 edges connect the vertexes from the two planes forming the 20 extra faces of trapezoidal type TR, now having the waist of the TI_{hb}.

TI_h are characterized by three numbers (m, n, r) where m (n) $[r]$ is the number of sites in one edge between faces TE, $(RF$ and $TI)$ $[TR]$, including vertexes, for example, in Figure 44(f), there is TI_{ha} $(3, 3, 1)$, and in Figures 44(b), (e), and (f), there are the TI_{hb} $(5, 2, 4)$, $(4, 3, 2)$, and $(4, 2, 3)$. It is clear that, based on this notation, to the icosahedron corresponds an $m = r$ and an $n = 1$, for example, $(6, 1, 6)$ and $(5, 1, 5)$ from Figures 44(a) and (d), respectively. From Figure 44, it can be seen also that TI_{ha} results from complete truncation (when there is only one or two edge sites from the original icosahedron) of an icosahedron with an odd number of sites in the edges.

By truncation of an icosahedron, only some TI_h are obtained, and upon truncation of another icosahedron, others are obtained; in each truncation, a certain number of sites are eliminated, but the same number in each truncation. Table 36 presents some of the geometric characteristics of TI_h. The first column shows the order of the icosahedron from where the ν comes, the second column shows the number of truncations done n_t, the third column shows the three characteristic numbers, in the fourth column is the number of sites eliminated from the original icosahedron n_-, in the fifth column the number of sites remaining in the surface N_σ is shown, and in the sixth column, the total number of sites in TI_h, N is shown. So, for example, the TI_h $(5, 3, 3)$, comes from the icosahedron of order 6, to which 424 sites were eliminated in two truncations, yielding a TI_h of 499 sites, of which 242 are at the surface.

Table 36. Geometric characteristics for truncated icosahedra TI_h.

ν	n_t	mnr	n_-	N_σ	N
1	0	2,1,2	0	12	13
2	0	3,1,3	0	42	55
	1	2,2,1	32	22	23
3	0	4,1,4	0	92	147
	1	3,2,2	62	62	85
4	0	5,1,5	0	162	309
	1	4,2,3	102	122	207
	2	3,3,1	204	82	105
5	0	6,1,6	0	252	561
	1	5,2,4	152	202	409
	2	4,3,2	304	152	257
6	0	7,1,7	0	362	923
	1	6,2,5	212	302	711
	2	5,3,3	424	242	499
	3	4,4,1	636	182	287

Note: n_t is the number of truncations made.

From Table 36 it can be seen that the maximum number of truncations is $\nu/2$ $[(\nu - 1)/2]$, for ν even [odd]; besides the values for m, n, r, and $m + n + r$ show the next characteristics

$$\left.\begin{array}{l}(\nu + 2)/2, \ \nu \ \text{even} \\ (\nu + 3)/2, \ \nu \ \text{odd}\end{array}\right\} \leq m \leq \nu + 1$$

$$1 \leq n \leq \begin{cases}(\nu + 2)/2, \ \nu \ \text{even} \\ (\nu + 1)/2, \ \nu \ \text{odd}\end{cases}$$

$$\left.\begin{array}{l}1, \ \nu \ \text{even} \\ 2, \ \nu \ \text{odd}\end{array}\right\} \leq r \leq \nu$$

$$\left.\begin{array}{l}\nu + 3, \ \nu \ \text{even} \\ \nu + 4, \ \nu \ \text{odd}\end{array}\right\} \leq m + n + r \leq 2(\nu + 1) + 1.$$

It is worth also notice that the parity of r is equal to the one for ν, and the maximum values of m and r coincide with the minimum value of n; m and n take values of one to one, while r takes values of 2 to 2. The analytical expressions for n_-, N_σ and N are

$$n_-(\nu) = 2n_t\left[1 + \frac{5\nu(\nu + 1)}{2}\right]$$

$$N_\sigma(\nu) = (N_\sigma)_{\text{ico}} - 10\nu n_t = 10\nu^2 - 10\nu n_t + 2$$

$$N(\nu) = (N)_{\text{ico}} - n_-$$

$$= \frac{10}{3}\nu^3 + 5\nu^2 + \frac{11}{3}\nu + 1 - 2n_t\left[1 + \frac{5\nu(\nu + 1)}{2}\right].$$

For the truncated icosahedra TI_{ha}, $r = 1$ and $m = n = (\nu + 2)/2$, ν even, based in the structure itself there are sites on vertexes VP, $V3$, and $V4$, on edges EE, $E3$, $E34$, ER, and EI, on triangular faces TE and TI, and on squared faces RF. The number of sites on vertexes are 2, 10 and 10, respectively. The number of sites for the other type of sites,

which is given in function of m, and the number of surface atoms can be obtained from the following expressions

$$N_{EE} = N_{E3} = 10(m-2), \quad N_{ER} = N_{EI} = 5(m-2)$$

$$N_{E34} = 20(m-2), \quad\quad N_{TE} = N_{TI} = 5(m-2)(m-3)$$

$$N_R = 10(m-2)^2, \quad\quad N_\sigma = 20(m-1)^2 + 2.$$

For the truncated icosahedra TI_{hb}, the number of sites $V4$, ER, and EI are duplicated with respect to the original polihedron, the number of surface sites is modified and the sites EL and TR, sites on lateral edges and on trapezoidal faces, are aggregated, and they are given by

$$N_{EL} = 10(r-2)$$

$$N_{TR} = \begin{cases} 0 & r = 2 \\ 10[n(r-1) - n - 1], & r \geq 3, \end{cases}$$

$$N_\sigma = \begin{cases} 5(m+n-2)(m+n-1) + 2, & r = 2 \\ 5(m+n-2)(m+n-1) \\ \quad + 10(r+nr-2n) - 28, & r \geq 3. \end{cases}$$

3.9.4. Decmon Polyhedra

A decmon polyhedra, Figure 45, is very similar to TI_{ha}, it has the same number of vertexes, edges, and faces, and the same type of sites. Also, it can be constructed by two decmon-type pyramids. The difference is that, at the equator or at the waist, faces TI have TI faces, and RF have RF faces.

The lengths of decmon edges, even when they are of three sizes, are related to the values m and n of the decmon pyramid, characterizing each particular decmon. mn can be considered as the order of the decmon (decmon mn), and the values taken by m and n are not limited. m and n are the (number-1) of edge sites EE and $E34$, respectively. Indeed, every decmon is formed by centered shells in one decmon of an order in which: (1) $m = 1$ and $n = 1$, (2) $m > 1$ and $n = 1$, or (3) $m = 1$ and $n > 1$, which are the smallest. For example, decmon of Figure 45 is of order 78, decm78, which in turn is a decm67 + one shell, decm67 is a decm56 + one shell, decm56 is a decm45 + one shell, decm45 is a decm34 + one shell, and decm34 is decm23 + one shell, decm23 is a decm12 + one shell, decm12 being the smallest of this family.

Decmon of order 11 (decm11) is the smallest of all decmons, and the edges at the equator are all the same;

Figure 46. Decmon-type decahedron of order 11. In (b) the sizes of the atoms of (a) were reduced to more clearly observe the squared and triangular faces by bondings to first neighbors, and to show that this is a polyhedron with a central site. (c) Decmon-type decahedron of order 44, decm44, of 609 sites.

Figure 46. It only has sites in vertexes, and is centered in one site, having a cluster of 23 sites. There is a decmon family mm, based on decm11, and the possible decmons to be created are decm22, decm33, decm44, decm55, and so on.

The geometric characteristics of a decahedra-type decmon of order mm are listed in Table 37. The first column lists the m value, the four following columns list the number of sites in each type of sites, rectangular face sites RF, in triangular faces T, in edges E, and in vertexes V. It should be clear that T sites include TE and TI sites, which in number are equal. Besides, the 5 types of edges are included in E, corresponding $1/5$ to each one of EE and $E3$, $1/10$ to ER, and another to EI and $2/5$ to $E34$. Vertexes are always 22, and from the three kinds already mentioned, 2 poles, 10 $V3$, and 10 $V4$. The following three groups of two columns list the number of sites in the plane above the equator, at the equator, and for the number of sites in clusters, for each shell and in total. Figure 46(c) shows the decmon for $m = 4$ and of 609 atoms.

From Table 37, it can be seen that, for a decmon of order m, the dependency with m values of the number of sites in a rectangular face N_{RF}, triangular face N_T, edges N_E, surface N_σ, and total N is given by the following expressions:

$$N_{RF} = 10(m-1)^2, \quad\quad N_T = 10(m-1)(m-2)$$

$$N_E = 50(m-1), \quad\quad N_\sigma = 20m^2 + 2$$

$$N = \frac{20}{3}m^3 + 10m^2 + \frac{16}{3}m + 1$$

Figure 45. Decmon-type polyhedron.

Table 37. Geometric characteristics for decmons of family of order mm based on decmons of order 11, decm11.

m	N_{RF}	N_T	N_E	N_V	N_{SE}	$N_{t_{SE}}$	N_{EC}	$N_{t_{EC}}$	N_σ	N
1	0	0	0	22	5	5	10	11	22	23
2	10	0	50	22	10	15	20	31	82	105
3	40	20	100	22	20	35	30	61	182	287
4	90	60	150	22	30	65	40	101	322	609
5	160	120	200	22	40	105	50	151	502	1111
6	250	200	250	22	50	155	60	211	722	1833
7	360	300	300	22	60	215	70	281	982	2815
8	490	420	350	22	70	285	80	361	1282	4097
9	640	560	400	22	80	365	90	451	1622	5719
10	810	720	450	22	90	455	100	551	2002	7721

also, expressions for the number of sites *SE* and *EC* can be calculated for each m, N_{SE}, N_{EC}, and total $N_{t_{SE}}$ and $N_{t_{EC}}$:

$$N_{SE} = 10(m-1), \qquad N_{t_{SE}} = 5(m^2 - m + 1)$$

$$N_{EC} = 10m, \qquad N_{t_{EC}} = 5m(m+1) + 1.$$

The next family decmon size, following the decmon family *mm*, is the decmon family *mn*, with $n = m - 1$ or $n = m + 1$, and based on the decm12 and decm21, respectively. Decm12 and decm21 have the same number of sites, a total of 54, although decm21 is more elongated toward the poles; Figure 47. Decm12 has 20 sites in edges *E34* and 5 in *EI*, while decm21 has 10 sites in edges *EE*, 10 in *E3*, and 5 in *ER*, and both are centered in a decahedron of 7 sites, regular for decm12 and more elongated toward the poles for decm21. From decm12, other decm can be generated: decm23, decm34, decm45, decm56, and so on. From decm21, the decm generated are decm32, decm43 decm54, decm65, and so on.

The geometric characteristics of decmon-type decahedra, of order *mn*, with $m = n - 1$ and $m = n + 1$, are listed in Table 38. The first two columns list the *m* and *n* values, and in the following 10 columns, the number of sites of each type of site, which considers only the sites in rectangular faces *RF*, equilateral triangular faces *TE*, isosceles triangular faces *TI*, of two types of edges: short edges *Em*, and large edges *En*, and in vertex *V*. It should be clear that sites in *Em* [*En*] include sites *EE*, *ER*, and *E3* [*EI* and *E34*], corresponding (2/5) to *EE*, (2/5) to *E3*, and (1/5) to *ER* [(4/5) to *EI* and (1/5) to *E34*]. The vertexes are always 22, and come from the three types already mentioned. The number of sites *RF* and *V* is common for the two decmon *mn* families, with $m = n - 1$ and $m = n + 1$, while the number of sites *TE* and *TI*, *Em*, and *En* are interchanged. Columns 8–11 correspond to the interchange of values of *m* and *n*; this is what happens with decmon families of order *mn* with $m = n + 1$. The following three groups of two columns list the number of sites in the plane above the equator (SE sites), at the equator (EC sites), and the numbers of sites in the cluster, per shell and in total, these values are common to the *m* and *n* values and are interchanged. Figures 47(c) and (d) show decmons of order 45 and 54, of 835 atoms.

After the *mn* decmon families, with $m = n - 1$ and $m = n + 1$, follow in size the ones of decmon of order *mn*, with $m = n - 2$ and $m = n + 2$, and are based on decm13 and decm31, respectively. The decm13 and decm31 decmon have the same number of sites, 105 in total, although decm31 is more elongated toward the poles, Figure 48. Decm13 has 40 sites in edges *E34*, 10 in *EI*, and 10 in faces *TI*, while decm31 presents 20 sites in edges *EE*, 20 in *E3*, 10 in *ER*,

and 10 in faces *TE*, and both are centered at a decahedron of 23 sites with central site, regular for the decm13 and more elongated toward the poles for the decm31. From the decm13, it is possible to generate the decm24, decm35, decm46, decm57, and so on. From decm 31, it is possible to obtain the decm42, decm53, decm64, decm75, and so on. The geometric characteristics of the decahedra type decmon of order *mn*, with $m = n - 2$ and $m = n + 2$, are listed in Table 39, with the same indications for the columns as in Table 38. Figures 48(c) and (d) show the 1111 atoms decmon of order 46 and 64.

From Tables 37–39, it is deduced that, for a decmon order *mn*, the dependency on the *m* and *n* values of the number of sites in rectangular face N_{RF}, sites in the equilateral triangular face N_{TE}, of sites in an isosceles triangular face N_{TI}, of sites in the edge type *Em* (*EE*, *E3*, and *ER*), N_{Em}, of sites in the edge type *En* (*EI* and *E34*) N_{En}, and of sites in the surface N_σ is given by the following expressions:

$$N_{RF} = 10(m-1)(n-1), \qquad N_{TE} = 5(m-1)(m-2)$$

$$N_{TI} = 5(n-1)(n-2), \qquad N_{Em} = 25(m-1)$$

$$N_{En} = 25(n-1), \qquad N_\sigma = 5(m+n)^2 + 2.$$

Also, it is possible to obtain the number of sites in the immediate superior plane over the equator for each *m* and *n*, N_{SE} and in total $N_{t_{SE}}$, and in the equator N_{EC} and $N_{t_{EC}}$ for the number of sites in the surface and the number of sites for each *m* and *n* and in total for the decmon for each combination of *m* and *n* used here. For $m = n \pm 1$

$$N_{SE} = 10m, \qquad N_{t_{SE}} = 5m(m+1) + 1$$

$$N_{EC} = 10m + 5, \qquad N_{t_{EC}} = 5(m+1)^2$$

$$N_\sigma = 20m^2 \pm 20m + 7, \qquad N = \begin{cases} \dfrac{20}{3}m^3 + 20m^2 + \dfrac{61}{3}m + 7; \\ \qquad\qquad\qquad \text{for } (+) \\ \dfrac{20}{3}m^3 + \dfrac{1}{3}m; \quad \text{for } (-) \end{cases}$$

and for $m = n \pm 2$

$$N_{SE} = 10m + 5, \qquad N_{t_{SE}} = 5m(m+2) + 5$$

$$N_{EC} = 10(m+1), \qquad N_{t_{EC}} = 5m^2 + 15m + 11$$

$$N_\sigma = 20m^2 \pm 40m + 22, \qquad N = \begin{cases} \dfrac{20}{3}m^3 + 30m^2 + \dfrac{136}{3}m + 23; \\ \qquad\qquad\qquad \text{for } (+) \\ \dfrac{20}{3}m^3 - 10m^2 + \dfrac{16}{3}m - 24; \\ \qquad\qquad\qquad \text{for } (-) \end{cases}$$

3.9.5. Modified Decmon

To obtain decmon type decahedra, widened with extra layers, the same procedure is followed as with the decahedra, separating the decmon as two pyramids with parallel bases, making the vertexes coincide, and adding layers of type *SEC*, Figure 49. The obtained figure has 10 regular lateral faces besides the ones previously mentioned, and 10 more edges.

Figure 47. Decmon-type decahedrons of (a) order 12, and (b) order 21 with 54 sites. Decmon-type decahedron of 835 sites of (c) order 45, decm45, and (d) order 54, decm54.

Table 38. Geometric characteristics for decmons of family of order mn with $m = n - 1$ and $m = n + 1$ based on decmons of order 12, decm12, and of order 21, decm21.

			mn				nm										
m	n	N_{RF}	N_{TE}	N_{TI}	N_{Em}	N_{En}	N_{TE}	N_{TI}	N_{Em}	N_{En}	N_V	N_{SE}	$N_{t_{SE}}$	N_{EC}	$N_{t_{EC}}$	N_σ	N
1	2	0	0	0	0	25	0	0	25	0	22	10	11	15	20	47	54
2	3	20	0	10	25	50	10	0	50	25	22	20	31	25	45	127	181
3	4	60	10	30	50	75	30	10	75	50	22	30	61	35	80	247	428
4	5	120	30	60	75	100	60	30	100	75	22	40	101	45	125	407	835
5	6	200	60	100	100	125	100	60	125	100	22	50	151	55	180	607	1442
6	7	300	100	150	125	150	150	100	150	125	22	60	211	65	245	847	2289
7	8	420	150	210	150	175	210	150	175	150	22	70	281	75	320	1127	3416
8	9	560	210	280	175	200	280	210	200	175	22	80	361	85	405	1447	4863
9	10	720	280	360	200	225	360	280	225	200	22	90	451	95	500	1807	6670
10	11	900	360	450	225	250	450	360	250	225	22	100	551	105	605	2207	8877

Besides to the type of sites for decmon-type polyhedra, the modified decmon presents the lateral and vertical edges sites EV, sites on rectangular faces that join triangular faces RI, and sites on rectangular faces that join rectangular faces RR. The number of sites $V4$, ER, and EI are duplicated with respect to the original polyhedron, and the number of surface sites is modified. The analytical expressions for them are the following

$$N_{V4} = 20, \qquad N_{Em} = 30(m-1)$$
$$N_{En} = 30(n-1), \qquad N_{EV} = 10(\mu - 2)$$
$$N_{RI} = 5(n-1)(\mu-2), \qquad N_{RR} = 5(m-1)(\mu-2)$$
$$N_\sigma = 5(m+n)(m+n+1) + 2 + 5(\mu-2)(m+n).$$

The number of sites that are aggregated to the surface and to the total number of sites in the cluster for $n = m \pm 1$ are given for

$$N_{ag} = (10m^2 + 15m + 6)(\mu - 1)$$
$$N_{\sigma_{ag}} = (10m + 5)(\mu - 2)$$

and for $n = m \pm 2$

$$N_{ag} = (10m^2 + 25m + 16)(\mu - 1)$$
$$N_{\sigma_{ag}} = 10(m + 1).$$

4. SYNTHESIS OF NANOPARTICLES

Metal clusters have been formed in a supersonic beam, this method to prepare colloidal metals in nonaqueous media was first reported by the group of Andres at Purdue
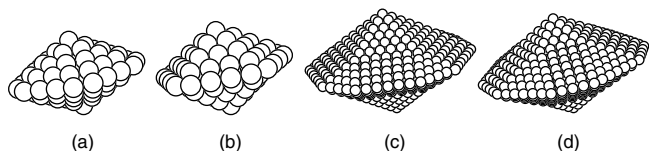
Figure 48. Decmon-type decahedra of (a) order 13 and (b) order 31. Decmon-type decahedron of 1111 sites of (c) order 46, decm46, and (d) order 64, decm64.

University [34–36]. A supersonic beam source was used; this instrument produces metal clusters with a controlled mean diameter in the range of 1–20 nm in size. Once the clusters have nucleated, the cluster aerosol is directed through a spray chamber to be placed in contact with a fine spray of organic solvent and surfactant.

However, conceptually, the simplest method of preparing colloidal metals is the condensation of atomic metal vapor into a dispersing medium [37]. Given the high oxidation potential of most atomic metals (for example, the oxidation potential for atomic gold is −1.5 V), the use of water as the diluent's phase can be ruled out, so exclusively inert organic liquids are going to be used in this procedure. Since the activation energy for the agglomeration of metal atoms is very low, the possibility for competing molecular complex formation processes which have higher activation energies can be mitigated by operating at low temperatures.

The use of metal vapors cocondensed with organic vapors to prepare colloidal metals in nonaqueous media was first reported by Roginski and Schalnikoff in 1927 [38], some 50 years before the recent wave of activity in metal vapor chemistry. The organosols were prepared at reduced pressure by the evaporation of relatively volatile metals such as cadmium, lead, and thallium, and a subsequent cocondensation of these with the vapors of organic diluents such as benzene and toluene on a liquid air cooled cold finger. After cocondensation was complete, a colloidal suspension of the metal was obtained by warming up the frozen matrix and collecting the liquid (Fig. 50).

A new metal vapor synthesis system for the preparative scale cocondensation of metal vapors with aerosols of organic liquids was recently achieved by Bradley's group [39]. The use of aerosol overcomes one limitation of the other methods, in which the organic diluent must be either volatile or has a liquid range which extends to a temperature low enough to reduce its vapor pressure to a useful value. The aerosol droplets, *ca.* 1μm in diameter, are generated by feeding the organic liquid (neat liquid, polymer solutions, solutions of nonvolatile ligands) into an ultrasonic atomizing nozzle from which they fall onto a rotating plate cooled to 77 K in a vacuum chamber, as shown in Figure 50. Vapors of one or more metals, obtained by simultaneous sputtering from metal or alloy targets, are then cocondensed with the aerosol. This results in the formation of a frozen organometallic matrix, which is then warmed up to allow the

Table 39. Geometric characteristics for decmons of family of order mn with $m = n - 2$ and $m = n + 2$ based on decmons of order 13, decm13, and of order 31, decm31.

		mn					nm											
m	n	N_{RF}	N_{TE}	N_{TI}	N_{Em}	N_{En}	N_{TE}	N_{TI}	N_{Em}	N_{En}	N_V	N_{SE}	$N_{t_{SE}}$	N_{EC}	$N_{t_{EC}}$	N_σ	N
1	3	0	0	10	0	50	10	0	50	0	22	15	20	20	31	82	105
2	4	30	0	30	25	75	30	0	75	25	22	25	45	30	61	182	287
3	5	80	10	60	50	100	60	10	100	50	22	35	80	40	101	322	609
4	6	150	30	100	75	125	100	30	125	75	22	45	125	50	151	502	1111
5	7	240	60	150	100	150	150	60	150	100	22	55	180	60	211	722	1833
6	8	350	100	210	125	175	210	100	175	125	22	65	245	70	281	982	2815
7	9	480	150	280	150	200	280	150	200	150	22	75	320	80	361	1282	4097
8	10	630	210	360	175	225	360	210	225	175	22	85	405	90	451	1622	5719
9	11	800	280	450	200	250	450	280	250	200	22	95	500	100	551	2002	7721
10	12	990	360	550	225	275	550	360	275	225	22	105	605	110	661	2422	10143

aggregation of the metal atoms. The resulting colloid solution is removed from the reactor under helium atmosphere for characterization and further studies.

In the 1980's, several research groups in Japan prepared metal particles of Al, Mg, Mn, Be, Te, Fe, Pb, Co, Ni, Cd, Ag, In, Pd, and Au by this method [40–49]. The work most recently performed was by Uyeda in 1991 [50]. This study demonstrated the feasibility of producing films of almost any metal or semiconductor by metal vapor deposition in a noble gas high-pressure atmosphere.

Another method to produce nanoparticles is the bioreduction method. Several researchers established that live and nonlive biologic systems such as algae have the ability to absorb metal ions from solutions through their cell walls and various cellular constituents [51, 52]. Studies have shown that algae are able to bind gold ions from aqueous solutions and form colloidal particles on their surfaces, yet the mechanisms have not been fully understood [53–57]. Several plants have been studied for their unique biochemical ability to accumulate metal compounds over extended periods. In fact, plant species such as *Douglas-fir* and *rye grass* are utilized as biological indicators of geologic gold deposits [58, 59]. Some other plants such as Indian mustard have been utilized for phytomining; the accumulation of valuable metals comes from low concentrations in soils by plants [60, 61]. Furthermore, Lujan and co-woekers reported that a purple color, similar to "Purple of Cassius", resulted when aqueous

Au(III) was reacted with the biomaterials in their study, indicating the formation of gold colloids [62–64]. Plants may possess a unique natural chemical stabilization mechanism that allows the formation of nanoparticles. In addition, the plant biomaterials may be isolated for a more thorough study of the colloidal information mechanisms. Therefore, by taking advantage of the naturally occurring compounds found within the plant systems, a novel method may be found to generate similarly sized stable metal colloids. While consistency in nanoparticle size and shape is important to many materials, differences in nanoparticle synthesis may also lead to changes in particle conformation and spatial arrangement, which may provide better nanoscopic building blocks to form new raw materials with distinctly different properties than their macroscaled counterparts.

Recently, it was shown that live plants can uptake metal solutions and produce nanoparticles [65]. This approach is very promising for further developments in nanotechnology.

All of the particles reposited in the present work were produced by the methods described above.

A third way to prepare metal nanoparticles is the colloidal methods discussed in the introduction. In the original Brust reaction [13], the addition of dodecanethiol to the organic-phase $AuCl_4^-$ (1:1 molecule), followed by reduction
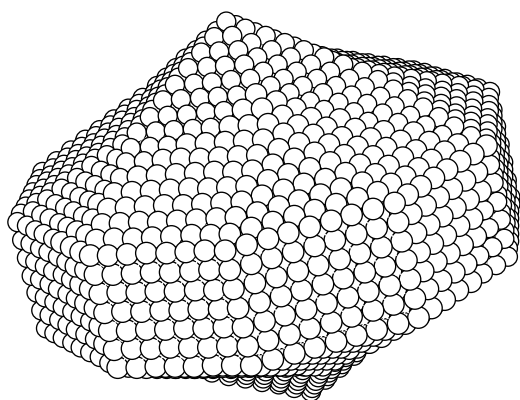
Figure 49. Decmon-type decahedron of order 78 with 6 intermediate layers added.
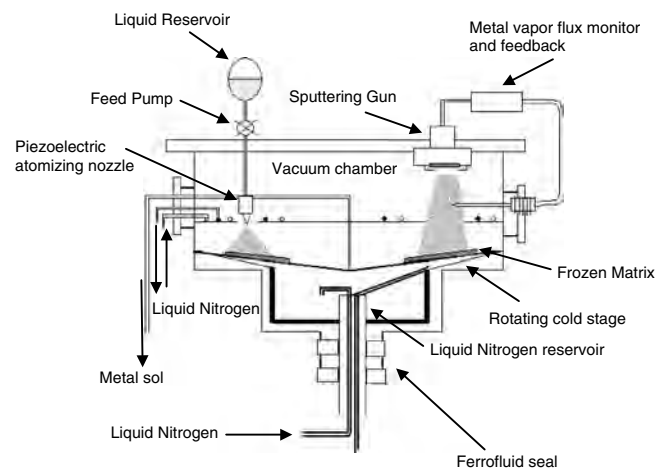
Figure 50. Schematic of sputtering source metal vapor/aerosol for metal colloid preparation with permission from [39], J. S. Bradley, 1994. © 1994, VCH, Weinheim.

with BH_4^-, led to dodecanethiolate protected Au clusters having a 1–3 nm range of core diameters

$$AuCl_4^- (\text{toluene}) + RSH \rightarrow (-AuSR^-)_n (\text{polymer})$$

$$(-AuSR^-)_4 + BH_4 \rightarrow Au_x(SR)y$$
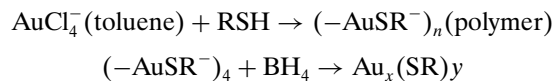
Subsequent reports have shown that a wide range of alkanethiolate chain lengths ($C3$–$C24$) [66], ω-functionalized alkanethiolates, and dialkyl disulfides [67] can be employed in this same protocol. An example of a passivated nanoparticles formula is $Au_{145}(S(CH_2)_5CH_3)_{50}$.

Pt, Rh and Pd salts can be used following the same method. One of the possible reactions is

$$AuCl_4^- (\text{toluene}) + PtCl^- + R - SH$$

$$\rightarrow (-Au_xPt_ySR^-)_n (\text{polymer})$$

$$(Au_xPt_ySR^-)_4 + BH_4 \rightarrow Au_xPt_y(SR)_z$$
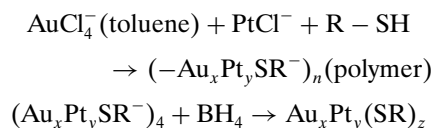
The details of these reactions have not been completely understood; however, the behavior of the reaction is consistent with a nucleation-growth-passivation process: (1) larger thiol: gold mole ratios give smaller average nanoparticle metal core sizes [68, 69], and (2) fast reductant addition and cooled solutions produce smaller, more monodisperse nanoparticles [70, 71], and (3) quenching the reaction immediately following reduction produces higher abundances of very small core sizes (≤ 2 nm).

The Schiffrin reaction tolerates considerable modification with regard to the protecting ligand structures. While alkanethiolate passivated nanoparticles (a) are nonpolar, highly polar ligands (b–d) can yield water-soluble passivated nanoparticles in modified synthesis. Nanoparticles passivated with arenethiolate [72–75] (e–g) and (γ–mercaptopropyl) trimethyloxysilane ligands (h) have also been prepared. Sterically bulky ligands tend to produce smaller Au core sizes (relative to alkanethiolate-passivated nanoparticles prepared using equal thiol/$AuCl_4^-$ ratios), suggesting a steric connection (as yet unproven) with the dynamics of core passivation [76].

The core metal of passivated nanoparticles can also be modified. Alloy nanoparticles with Au/Ag, Au/Cu, Au/Ag/Cu, Au/Pt, Au/Pd, and Au/Ag/Cu/Pd cores [77] have been reported.

It is well known for the case of bare particles that noncrystallographic structures are formed in many cases, these being predominantly icosahedral and decahedral. In other cases fcc, bcc, or single twinned particles are also produced. Extensive literature is found on shape observations and the kinetic growth conditions in which the different types of particles are produced [78–90].

5. TRANSMISSION ELECTRON MICROSCOPY (TEM) AND SIMULATIONS OF IMAGES OF NANOPARTICLES

5.1. Introduction

Since its inception in the 20th century, electron microscopy has developed into a powerful tool for scientific research. Indeed, the use of electron microscopy has facilitated many

fundamental discoveries. This technique has itself been subject to constant evolution thanks to unceasing design efforts in the scientific and manufacturing transmission electron microscopy (TEM) community. The advances in this field have been characterized by a series of quantum leaps in technology. For instance, the double condenser lens and tilting stages revolutionized the study of defects in metals in the late 1950s and early 1960s. The high lattice resolution achieved in the 1970s, along with improvements in vacuum methods and lens control, produced a less complicated instrument capable of achieving rapid results with minimal training. Consequently, the TEM (Transmission Electron Microscopy) gained enormous popularity in the materials community. In the second half of the 1980s, a new quantum leap was realized by the achievement of atomic resolution on a routine basis. Microscopes with a point resolution of 0.17 nm coupled with spectacular advances in diffraction theory led to many fine examples of materials characterization. In the 1990s another quantum leap occurred with the introduction of highly coherent field emission electron sources and electron loss analyzers. Combined with X-ray analysis, this established the TEM as a powerful analytical machine. For the first time, images, diffraction, and spectroscopy could be obtained from a single instrument. The TEM has become a standard instrument for many scientific fields. During the second half of the 1990s, the substantial increase in the number of papers published in *Physical Review Letters* containing electron microscopy studies attests to this fact. Other important developments include the introduction of electron holography and dark field images produced using incoherently scattered electrons (*Z*Contrast).

The next quantum leap in electron microscopy will be produced by the introduction of aberration correctors for the objective lens and STEM lens-forming system, and by the development of monochromators for the incident beam. These techniques will undoubtedly usher in a new era for TEM. Improved point resolution of 0.007 nm, an increased information limit, enhanced energy resolution, and improved stages using MEMS technology will allow 3D reconstruction of amorphous materials such as glasses. Refined X-ray techniques will facilitate chemical analysis essentially at the single atom level. Still more exciting, $\mathscr{C}_s$-corrected microscopes will allow more space in the objective lens gap, thus making it possible to construct stages for the *in-situ* examination of materials at atomic resolution and analysis with atomic accuracy [91]. The most recent developments in TEM coincide with the emergence of nanotechnology [92], and because the TEM probe size is ideal for nanoscale studies, it is clear that advanced TEM will be a major instrument in subsequent nanotechnological developments. The TEM will also be fundamental in areas of rapid development such as advanced materials research, biotechnology, and microelectronics. The automation of modern TEM has led to applications in semiconductor fabrication processes, and energy filtering will permit the study of polymers and biological materials with unprecedented accuracy.

Transmission electron microscopy is one of the most important techniques to study nanoparticles. The resolution of the TEM is well below the size of most of the

particles and in the order of magnitude of the metal–metal bonds. There are several papers which have explained in a very detailed way the electron microscopy methods to study nanoparticles. We will not discuss in this chapter dynamical diffraction methods, but we rather refer the reader to those publications [93–96].

Images were obtained using a JEOL 2010-FEG microscope, with a resolution of 0.19 nm and a tilting possibility of ±30°, and a JEOL 4000EX with a resolution of 0.17 nm. HREM (High Resolution electron microscopy) images of nanoparticles were obtained at the first optimum defocus (Scherzer focus) or at the second optimum defocus condition, resulting in images of atomic columns as black (first maximum) or white (second maximum) dots. Molecular Dynamics software was used to build theoretical models of the particles. Simulated images were obtained using the Simula TEM software of the Institute of Physics at UNAM, which is especially adequate for studying nanoparticles with noncrystallographic symmetries. A comparison of experimental and simulated data will allow us to interpret the experimental images.

In general, in order to recognize a nanoparticle in a nonambiguous fashion, it is necessary to obtain a tilting sequence of HREM. Figure 51 illustrates the changes in contrast when the orientation of the particle is changed with respect to the electron beam. This case corresponds to a cubooctahedral particle. This image illustrates a remarkable difference between nanoparticles and large crystals. In the latter case, the image will be very sensitive to tilting, and will disappear with small tilts. The nanoparticle, on the other hand, always shows images despite the large angle of tilting. In many cases, the images correspond to pseudolattice images. Considerable caution should be taken when analyzing fringe images of nanoparticles. The images out of a low-index direction do not necessarily reflect a structural feature. In diffraction terms, the finite size of the nanoparticles in real space results in real rods in reciprocal space. The Ewald sphere will always cut the reciprocal space points despite the angle.
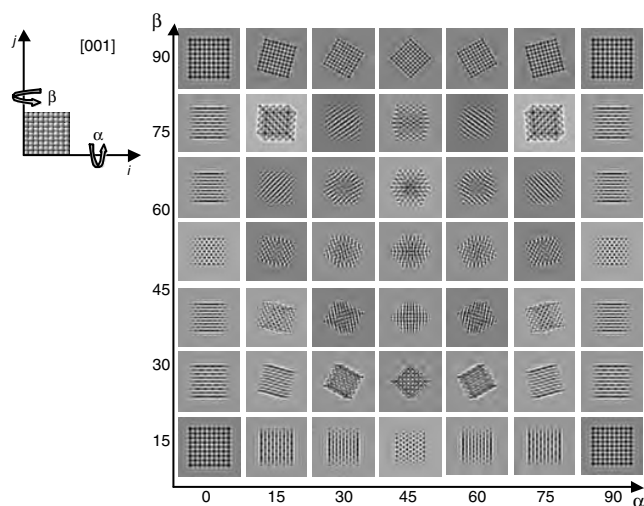
5.2. fcc Particles

The fcc particles are straightforward to identify. Figure 52 illustrates the contrast produced by an fcc by a pyramid formed by two tetrahedrons and their diffraction pattern (which in most instances is identical to the FFT, Fast Fourier Transform, of the image). Experimental examples of a pyramidal and of a tetrahedral particle are shown in Figure 53.

5.3. Decahedral Particles

Very important cases to consider are the images produced by pentagonal particles such as the one shown in Figure 54.

Typical TEM images of pentagonal particles are shown in Figure 55. The fivefold symmetry of the FFT can be observed. However, these patterns are a combination of the diffraction patterns of different portions of the particle, as shown in Figure 56. This indicates that the overall structure of the particle has a fivefold symmetry but this is not the result of fivefold symmetry in each portion of the particle. Because of that, it is more correct to consider that the particle has a pseudofivefold symmetry. This is in sharp contrast with the case of quasicrystals [97].

It should be remembered that another important effect in the images observed in a TEM is due to the defocus condition which can change the image significantly. Figure 57 illustrates this effect for the case of a regular decahedron. In this case the calculations were made for a JEOL 4000 microscope. As is known from image theories [98], there are two defocus conditions in which the image represents the true atomic columns which correspond on the figure to −40.5 nm (black atoms) and −70.2 nm (white atoms). If another defocus is used, the image does not necessarily reflect the atomic positions, but useful information still can be obtained. For instance, a defocus of −35.5 increases the grain boundary contrast, and the nature of the interfaces can be examined. At an even lower defocus of −20.5 nm, the pentagonal particle structure is reflected on the image.

An experimental example of a pentagonal particle showing well-defined atomic resolution is shown in Figure 58. In this case, some of the twin boundaries are incoherent. An example of the structure formed at a defocus condition below the optimum value is shown in Figure 59.

Figure 51. Simulation of HREM images of a cubooctahedral particle in different orientations with respect to the electron beam.
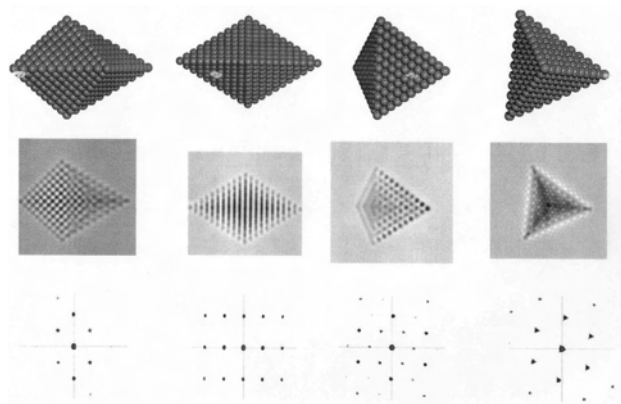
Figure 52. Models of a fcc pyramid formed by two tetrahedra. Observe their contrast in the second row and their diffraction pattern in the third row.
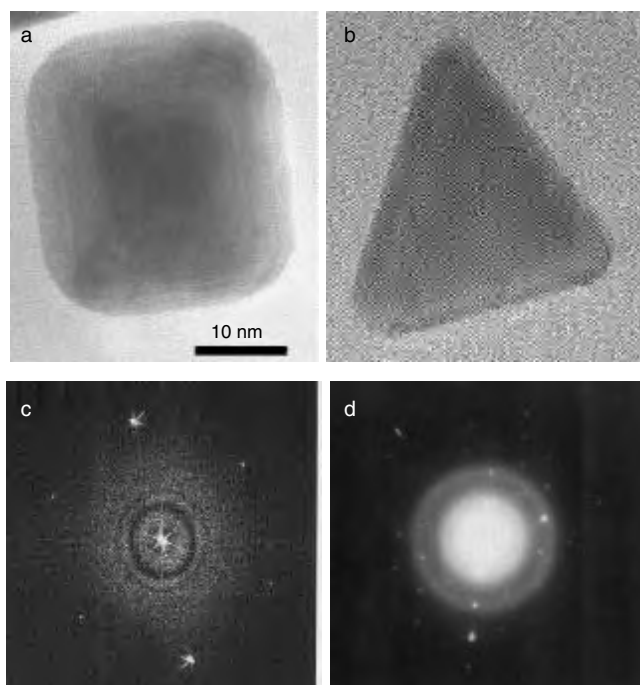
Figure 53. Bright field images of: (a) pyramidal particle, (b) Tetragonal particle, (c) FFT of (b), (d) diffraction pattern of (b).

A commonly observed type of pentagonal particle corresponding to a rounded shape and the respective model of the particle are shown in Figures 60(a) and (b), respectively. A complete set of images at different tilting angles is shown in Figure 61. Obtaining different images at different tilting angles and referring to this sequence should be enough data to fully identify the structure of that particle.

In the previous sections, we described a new type of pentagonal structure that was described originally by Montejano [99] and was termed a decmon type of particle. This type of structure belongs to a more general family of decahedral nanoparticles, which includes the truncated decahedron
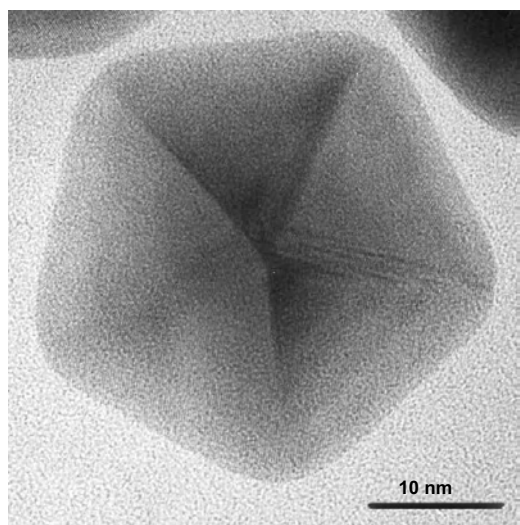
Figure 54. Bright field image of a pentagonal gold particle.
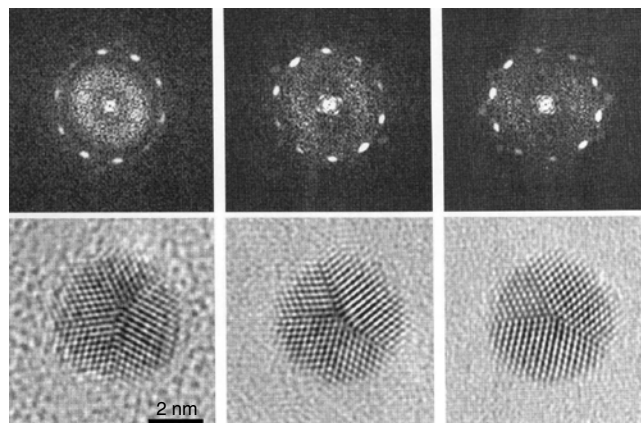
Figure 55. High-resolution images showing atomic contrast of ∼2 nm pentagonal gold nanoparticles and their corresponding FFT showing the fivefold symmetry.
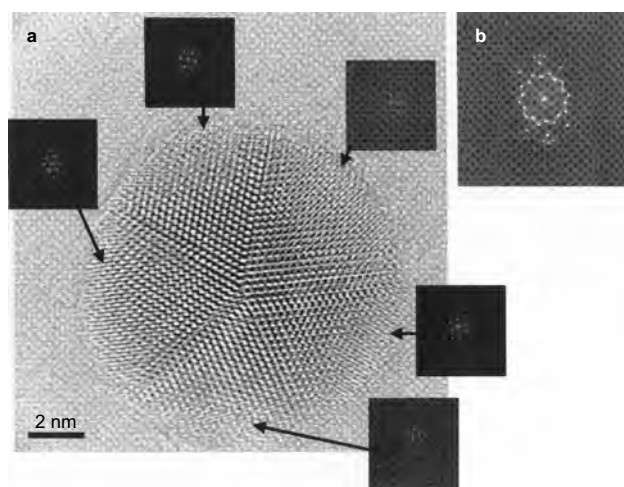
Figure 56. (a) Pentagonal particle showing the FFT of different sections. (b) Overall FFT.
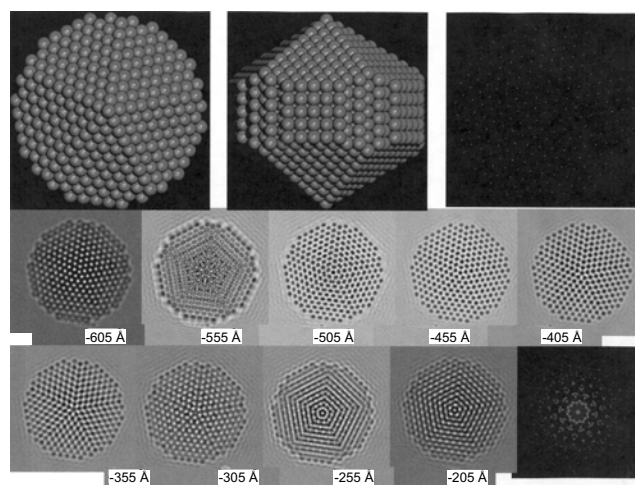
Figure 57. Effect of defocus on TEM images. Calculations made for a truncated decahedron and for a JEOL 4000 microscope.
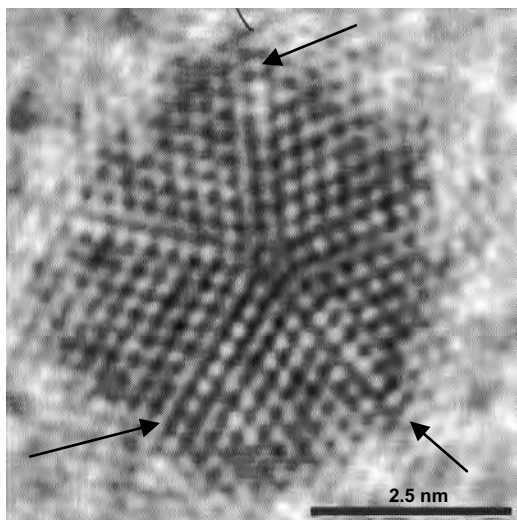
Figure 58. HREM image of a pentagonal particle, showing incoherent twin boundaries indicated by arrows.

(Marks) [100], the pancake structure of Koga and Sugarawa [101], and the truncated icosahedron of Ascencio et al. [102].

A tilting sequence for three different decmon structures is shown in Figures 62–64. We also include the calculation a 64-order pentadecahedron in Figure 65. An experimental example of this type of particle is shown in Figure 66. This image corresponds to a dark field taken in a weak beam condition. In this case, a continuous set of thickness fringes is expected. However, because of the decmon shape, a pentagonal profile is formed at the center of the particle.

Another experimental example is shown in Figure 67(a). The particle marked by an arrow can be identified using a model with surface reconstruction, as shown in Figure 67(b). We have found that surface reconstruction particles are formed very frequently when the sample approaches the equilibrium condition. For instance, the particle in Figure 67(a) was obtained after heating the sample with an electron beam and allowing recrystallization. In this process, the total surface energy of the nanoparticle will tend to be a minimum. There are several ways to achieve this surface energy minimization. Marks described truncations on the decahedron structure [100] that result in a more stable structure.
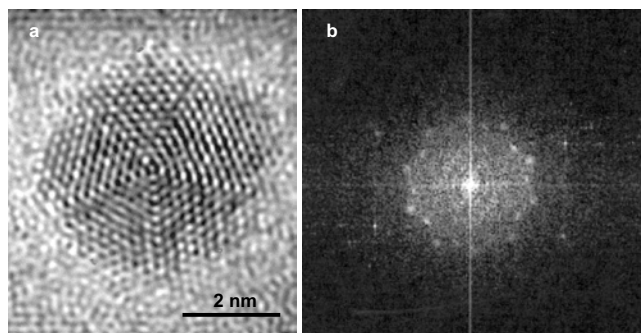
Figure 59. (a) High-resolution image of a pentagonal particle with a defocus below the optimal value. (b) Corresponding FFT indicating the fivefold symmetry.
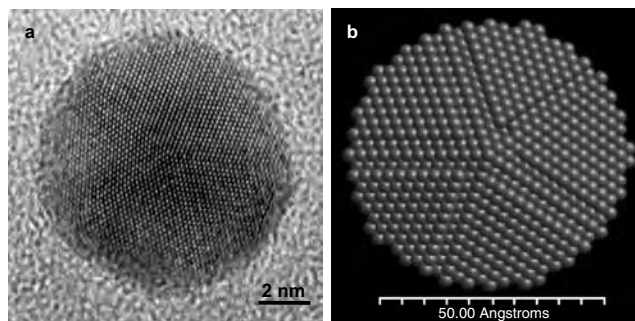
Figure 60. Pentagonal particle with rounded shape. (a) HREM image, (b) model of particle.
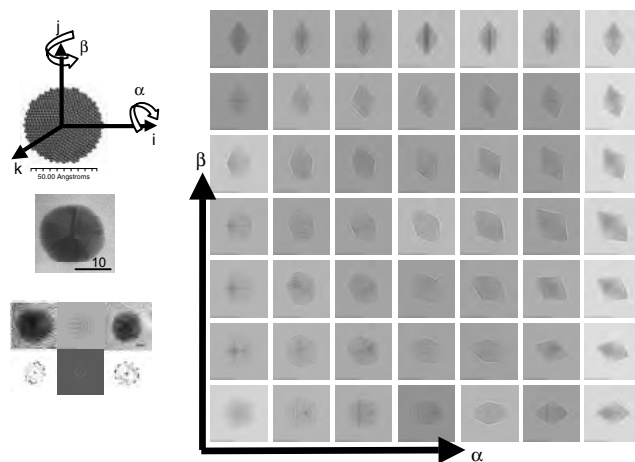
Figure 61. Images of a pentagonal particle obtained as a function of the tilting angles α and β. The origin of the coordinate system indicates a 0, 0 position, and the range of the angles is 90°. The model and typical bright field and HREM image (including FFT) are shown in the left portion of the figure.
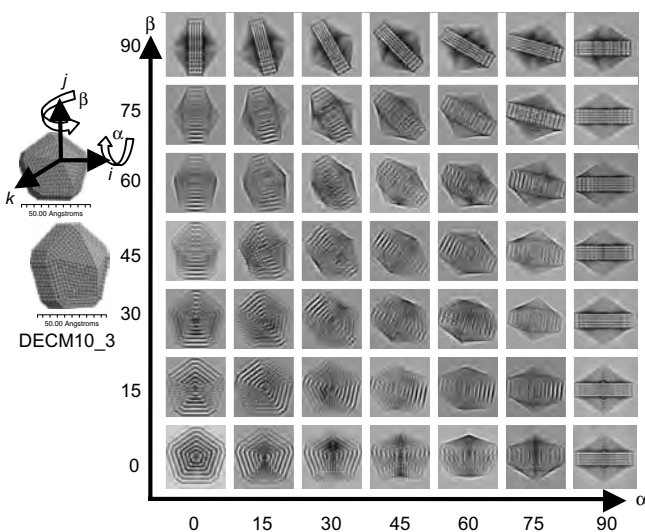
Figure 62. HREM images calculated for a decmon 10 structure shown in the left portion of the figure. The rotation angles α and β go from 0 to 90°.
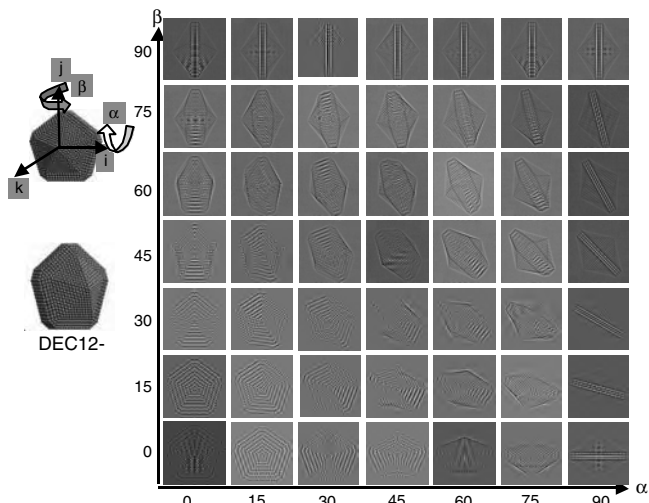
Figure 63. HREM images calculated for a decmon 12 structure shown in the left portion of the figure. The rotation angles α and β go from 0 to 90°.

However, the energy landscape has many structures with similar energy. Another possibility is to introduce faceting along the twin boundaries of the decahedra, resulting in the structure shown in Figure 68(a). If images are formed at the Scherzer condition, the channels can be visualized [Fig. 68(b)], in contrast to the case of the regular decahedron. We have described these particles previously in this chapter.

A full map of images for these channeled structures as a function of the tilting angle for the optimum defocus is shown in Figures 69(a) and (b). This type of decahedron is often observed in larger particles, as shown in Figure 70.

Another very interesting possibility has been suggested by molecular dynamic simulations of Chushak and Bartell [103] and other group [104]. This work indicates that, in the twin boundaries, a stacking fault is formed. In other words, the
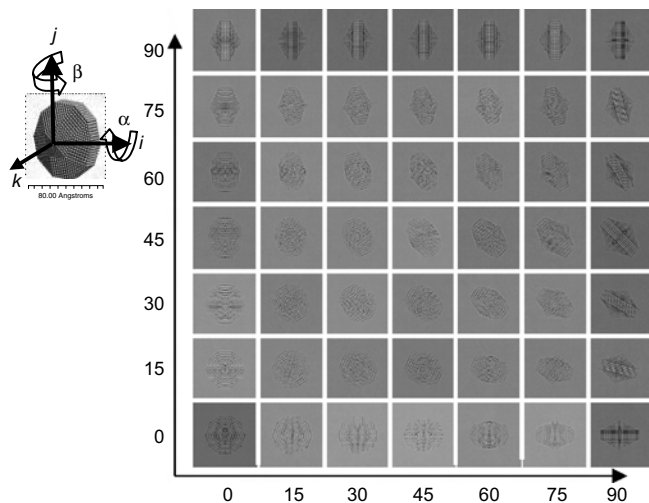
Figure 64. HREM images calculated for a decmon structure with less degree of truncation, as the model shown in the left portion of the figure. The rotation angles α and β go from 0 to 90°.
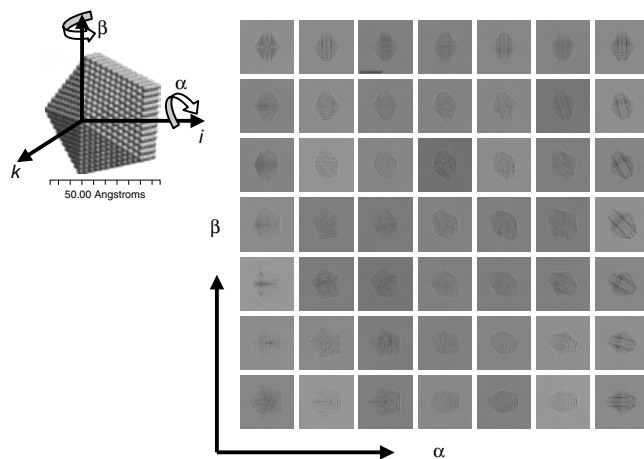
Figure 65. HREM images calculated for a pentadecahedral structure as the model shown in the left portion of the figure. The rotation angles α and β go from 0 to 90°.
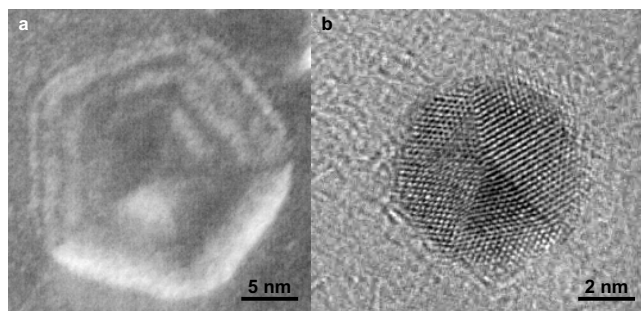
Figure 66. (a) A weak multibeam dark field image of a decmon type of decahedron obtained in a gold particle synthesized by bioreduction. (b) An HREM image of a decmon-type particle.
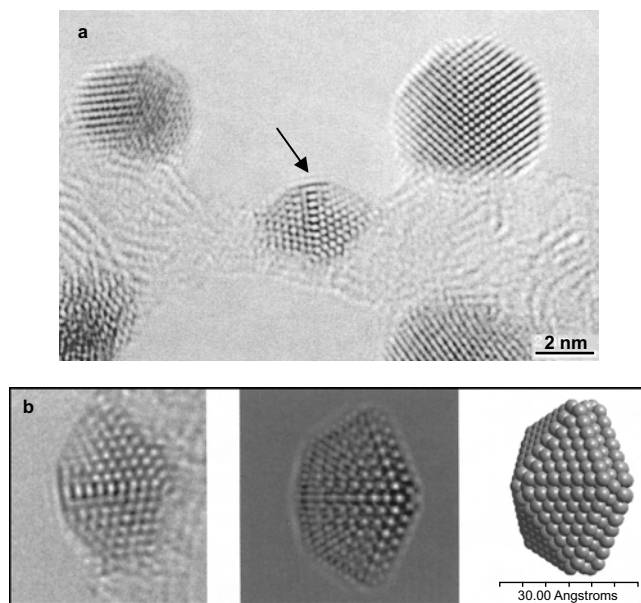
Figure 67. Analysis of a decmon type particle supported on a thin portion of a carbon film (indicated by an arrow). (a) TEM Image, (b) Identification of particle using a model with surface reconstruction.
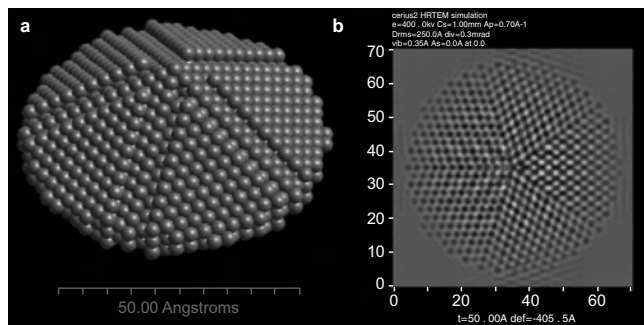
Figure 68. (a) Model of decahedron showing faceting along the twin boundaries. (b) Simulated TEM image of a decahedron in Scherzer condition, where the channels can be observed.

ABC stacking will be converted to *ABAB* stacking in the boundary region.

A different situation corresponds to the structure reported in Figure 68. In this case, the stacking is altered only in the last layer of the packing. This is illustrated in
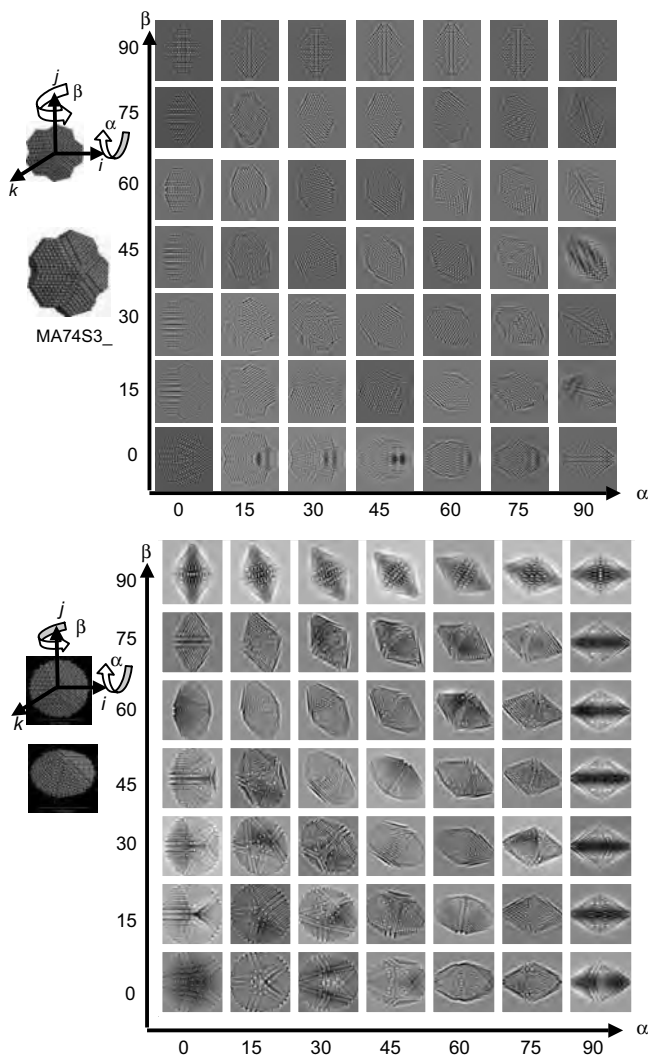
Figure 69. (a) Map of images for the truncated decahedron as function of the tilting angle for the optimum defocus.
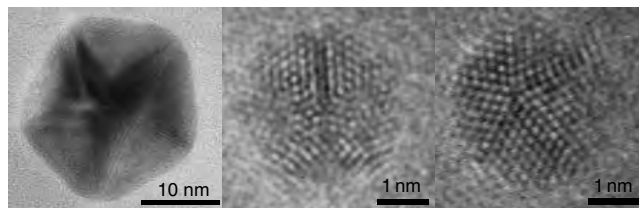
Figure 70. (a) Bright field image of a large particle produced by biore-duction showing a typical contrast of channels in the twin boundaries in the interface. (b) and (c) show the high-resolution image of deca-hedral shape in which the contrast at the boundaries does not change with defocus and can be explained by the model of interface channels discussed in the theoretical section.

Figure 71 in which a regular stacking in a unit of the dec-ahedra is altered in the surface. In other words, the *ABCA* sequence becomes *ABCB*. In Figure 71, each layer is illus-trated in a different color. The yellow atoms correspond to the surface sites. We have found experimentally that this type of decahedron is very stable, especially at small sizes.

The contrast of this particle is very peculiar, and is shown in Figure 72 for a different defocus. In this case, the bound-aries show a very strong contrast at all defocus conditions. This provides a practical way to distinguish this particle from other types of decahedra which, under some focus condi-tions, can produce boundary contrast, as shown before. The contrast of the boundaries will be very strong, as shown in Figure 72. This type of particle is often observed experi-mentally in nanoparticles with sizes ~1.5 nm, as shown in Figure 73(a), or when two metals are present. Figures 73(b)
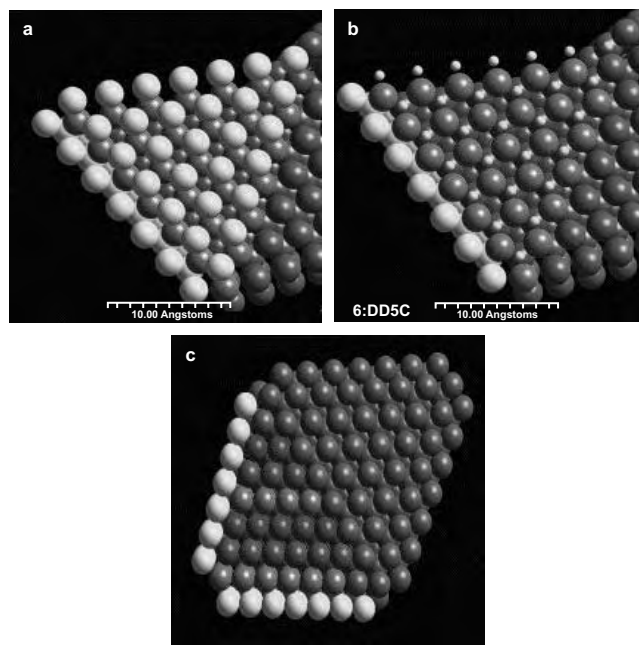
Figure 71. (a) Packing of atoms in a decahedron showing a stacking fault in the last atomic layer. Different colors correspond to differ-ent layers of the packing sequence, and the *ABCA* sequence becomes *ABCB*. (b) Another view of the same packing, in which the surface atoms are drawn in a smaller size. (c) Side view of the resulting stricture in which a missing atom in the center can be observed.
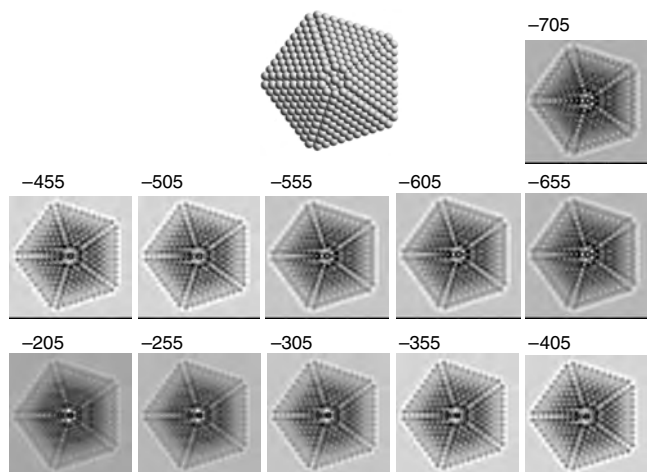
Figure 72. Sequence of simulated images of a decahedron particle with a missing atom in the center (fivefold site) as the result of surface recontruction. The image is calculated at a different defocus.

and (c) show the HREM image of a particle of Au-Pd at 50%–50% in which, in many places, it is possible to observe the surface atom vacancy. In general, it can be said that the central atom vacancy is a unique feature of this type of particle.

Finally in some cases irregular or asymmetric decahedral shape is produced. This was described by Uppenbrink and Wales [105] and most likely is the result of the kinetics of growth; a typical example is shown in Figure 74. When the particles grow larger some special shapes are seen as indicated in Figure 75.

5.4. Icosahedral Particles

One of the most frequently observed particles at small sizes corresponds to the icosahedral structure. A typical TEM image of these particles is shown in Figure 76. The profile is typically hexagonal in the threefold orientation.

The most common images are in the two- and three-fold orientation. The calculations of these images are shown in Figure 77 and are consistent with previous calculations [106]. Experimental images of a gold icosahedral particle in a threefold orientation and a twofold orientation are presented in Figures 78(a), (b) and (c), (d) including the FFT, which indicates the symmetry. A less commonly observed orientation is the fivefold. This is probably due to the fact
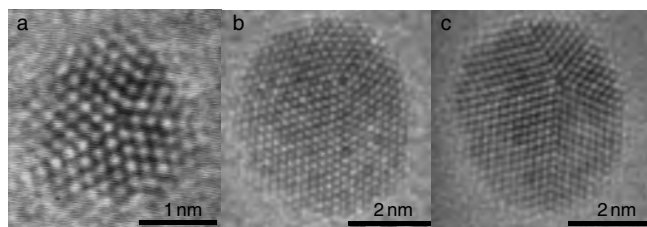
Figure 73. Decahedral particles, in which a defect was formed in the last layer of atoms. Notice that the particle in (a) does not have a central atom in the fivefold site. The particles in (b) and (c) correspond to an Au-Pd system, and atom vacancies in several sites are observed.
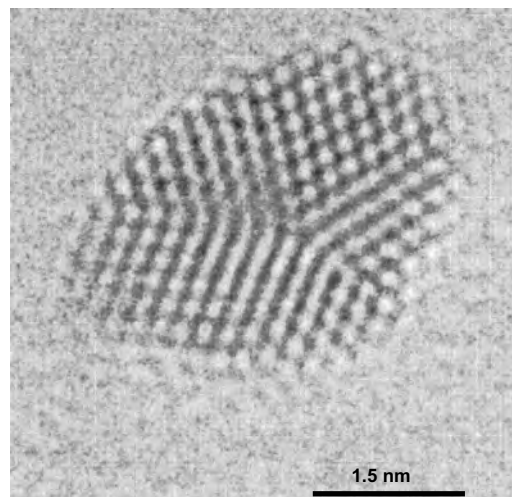
Figure 74. Distorted decahedral particle.

that, under flat surfaces, particles will be tilted until one triangular face (111) becomes in contact with the substrate. This results in most cases in a twofold orientation.

However when the particles are around 1–2 nm, it is possible to observe the fivefold orientation more frequently. This is probably due to truncations on the surface in contact with the substrate. An example of this contrast and an experimental example are shown in Figure 79.

When a bimetallic particle is synthesized, the frequency of the icosahedral particle increases, particularly at the smallest sizes [107].

5.5. Single Twinned and Complex Particles

Twinning is a very general phenomenon which might happen in the very early stages of growth and does not necessarily result in a decahedral or icosahedral particle. In many cases,
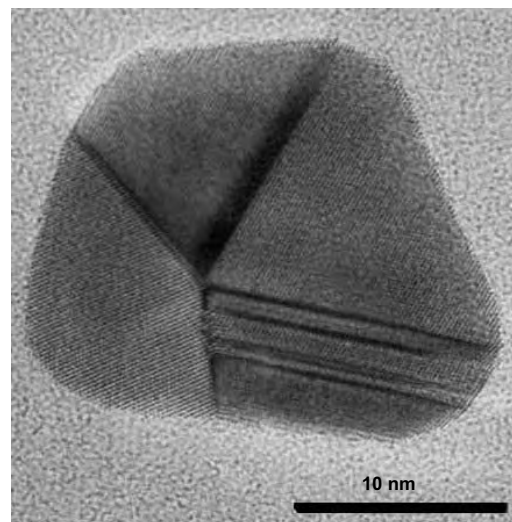
Figure 75. Large irregular decahedral particle grown from a distorted decahedral particle.
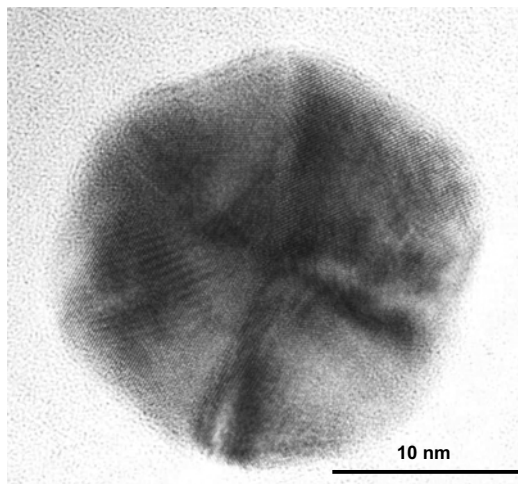
Figure 76. Bright field of an icosahedral gold particle showing a typical hexagonal profile.

we can observe a pyramidal particle with a single twin. This particle is shown in Figure 80.

We have observed particles down to 1.5 nm in size which present single twins. Therefore, it is safe to assume that, in some cases, twinning proceeds in the very early stages of growth. However, when the particles grow to larger sizes, coalescence can occur, leading to a more complex type of particles. We have found by molecular dynamics that a double icosahedral structure can be produced very often. In this structure, we have two interpenetrating icosahedra to form a double icosahedron, as shown in Figure 81. This structure
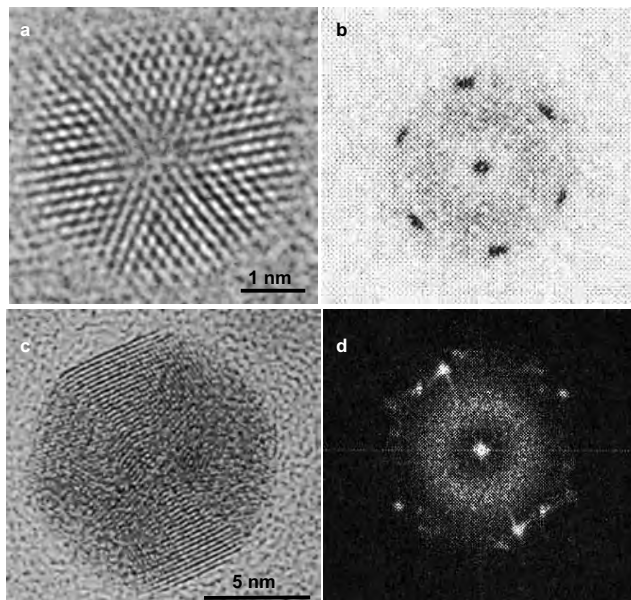
Figure 78. Experimental images of icosahedral particles and their corresponding FFT. (a), (b) threefold orientation. (c), (d) twofold orientation.
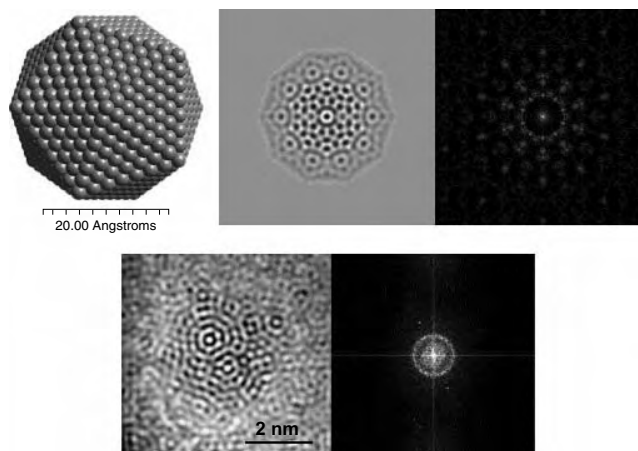
Figure 79. Model and image simulations of an icosahedral particle in fivefold symmetry (upper portion) and experimental images for a gold particle in the lower part. In both cases, we include the FFT.
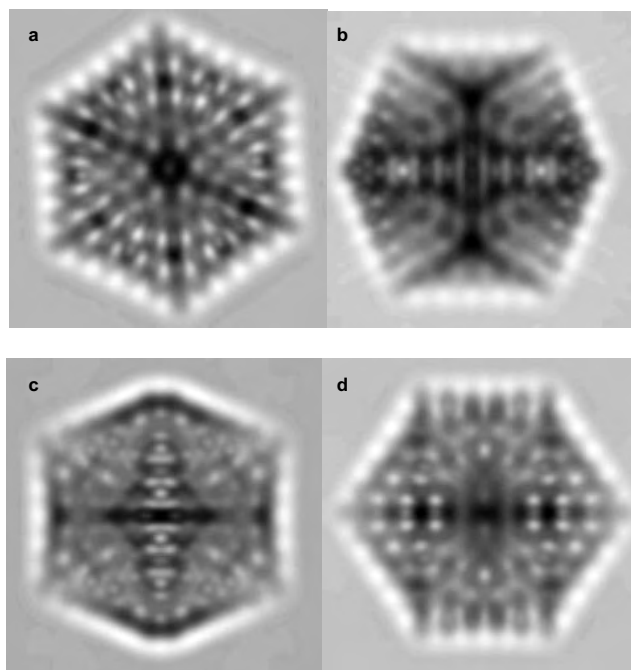
Figure 77. Calculated images of HREM icosahedral particles at (a) threefold orientation, and (b)–(d) different twofold orientations.
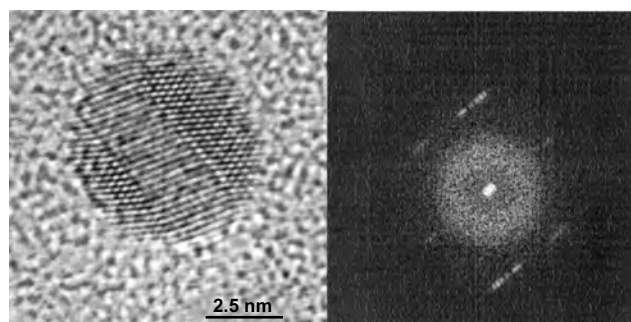
Figure 80. HREM image of a single twin particle and its corresponding FFT.
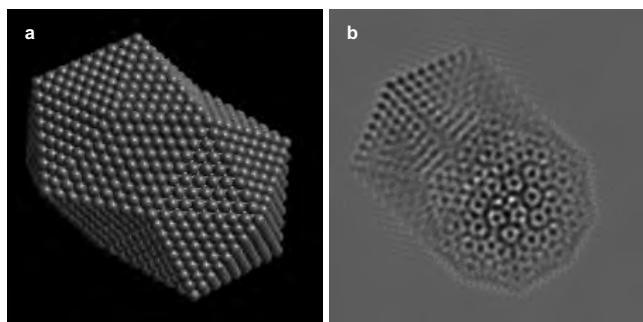
Figure 81. (a) Model for a double icosahedron obtained by molecular dynamics. (b) simulated image. As can be seen, one part of the structure is a fivefold orientation and the other one is at fivefold orientation.
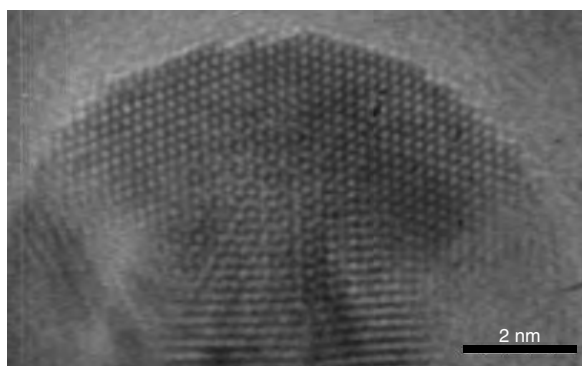
Figure 82. HREM image of a gold particle showing surface faceting.

corresponds to a minimum in the total energy, and has been observed experimentally by Hofmeister's group [108].

5.6. Surface Faceting in Nanoparticles

In many cases, the particles can present a surface faceting, especially when they are annealed or heated *in-situ*. This faceting is relevant since it can be related to the catalytic activity of the particles; an example is shown in Figure 82. The presence of steps will increase the particle curvature, yielding an almost spherical particle. We have observed that faceting results in (110) and (112) faces.

6. CONCLUSIONS

We have made a systematic description of the most significant geometries which are formed in nanoparticles. We have calculated the number of different atomic sites and growth characteristics of the nanoparticles. It has been shown that the models correspond closely with the experimental HREM and diffraction data. New types of particles have been described in this work, which correspond to a new family of decahedral structures. We expect that, as the field advances and new synthesis routes for particles ~1 nm are developed, all the if predicted clusters will be observed. This work also illustrates the richness of the crystallography of nanoparticles and clusters. Unlike the bulk materials, fivefold symmetry in nanoparticles produces a very rich landscape of structures.

LIST OF SYMBOLS

ν	Order of the cluster of Number of crusts in the cluster
z	Total coordination
N_σ	Number of surface sites
N	Total number of sites in the cluster
N_{shell}^ν	Number of layers in the shell ν
N_{shell}^T	Total number of shells in the cluster of order ν
S	Squared face
T	Triangular face
H	Hexagonal face
RF	Rectangular face
R	Rhombohedral face
TR	Trapezoidal face
PF	Pentagonal face
TF	Equatorial triangular face
TI	Isosceles triangular face
TE	Equilateral triangular face
E	Edge
EE	Edge on the equator
EV	Vertical edges on the equator
ET	Edges between PF and TF
EI	Edge between TI faces
ER	Edge between R faces
EP	Edge toward pole sites
ES	Edges between square and hexagonal faces in truncated octahedrons
EH	Edges between hexagonal faces in truncated octahedrons
EV'	Edges joining V'
$E34$	Edges joining V3 and V4
V	Vertex
V'	Vertex at the end of truncated *EP*
VE	Vertex on the equator
VP	Vertex on pole sites
$V3$	Vertex where converge TI, TE and RF
$V4$	Vertex where converge TI and RF
SE	Sites in a plane just over the equator
EC	Sites on the equator
SEC	Layer of the total of SE sites plus the total of EC sites
N_I	Number of I sites, I= S, T, H, R, RH,
$N_{t_{SE}}$	Total number of SE sites in the cluster
$N_{t_{EC}}$	Total number of EC sites in the cluster
fcc	Face-centered cubic
fccc	Face-centered cubic with a central site
OCTAC	Octahedron with a central site type fccs
OCTTC	Truncated octahedron with a central site type fccs
fccs	Face-centered cubic without a central site
OCTAS	Octahedron without a central site type fccs
OCTTS	Truncated octahedron without a central site type fccs
bcc	Face-centered cubic
DODE	Dodecahedron
CO	cubooctahedron
ICO	Icosahedron
TI_h	Truncated icosahedron
decmon	Decahedron of Montejano, described originally by J. M. Montejano-Carrizales

mrdec Montejano's reconstructed decahedron, described originally by J. M. Montejano-Carrizales and J. L. Rodríguez-López

TEM Transmission electron microscope/microscopy

STEM Scanning transmission electron microscope/microscopy

HREM High resolution electron microscope/microscopy

MEMS Micro-electro-mechanical system

FFT Fast Fourier transform

GLOSSARY

Equivalent sites Sites located at the same distance from the origin, which occupy the same geometric place and have the same environment, that is, the same number and type of neighbors.

EC layer The layer formed by the total of sites in the plane of the equator of decahedral structures.

Geometric characteristics The set of the number of the different type of sites, the number of sites for each type of site, the number of sites by shell, of surface sites and the total of sites for each structure.

SE layer The layer formed by the total of sites in the plane just above the equator of decahedral structures.

SEC layer The layer formed by the joint between the SE layer and the EC layer.

Site coordination The number of first nearest neighbors of the site with layers of its same shell, with interior and exterior shells, and it will be characteristic of each site.

Standard coordinates Site coordinates described by triads (a, b, c), a, b and c are integers, where the total number of sites is obtained by doing permutations and commutations of the positive and negative values of a, b and c.

ACKNOWLEDGMENTS

REFERENCES

1. M. Gross, "The Nanoworld, Miniature Machinery in Nature and Technology," p. 254. Plenum Trade, New York, 1999.
2. H. S. Nalwa, "Handbook of Nanostructured Materials and Nanotechnology," Vol. 1–4, Academic, San Diego, 2000.
3. S. Sugano and H. Koizumi, "Microcluster Physics," Springer-Verlag, Berlin, 1998.
4. S. a. P. Das-Sarma, "Perspectives in Quantum Hall Effects," p. 430. Wiley, New York, 1997.
5. H. L. Stormer, *Solid State Comun.* 107, 617 (1998).
6. H. Grabert, "Single Charge Tunneling," Plenum, New York, 1992, p. 335.
7. M. H. Dvoret, D. Esteve, and C. Urbina, *Nature* 547 (1992).
8. R. C. Ashoori, *Nature* 413 (1996).
9. A. P. Alivisatos, *Science* 933 (1996).
10. A. Rosen, Nanostructured Materials Made from Self-Assembled Particles, Chalmers University of Sweeden, 2000.
11. H. Haberland, "Clusters of Atoms and Molecules I and II: Solvation and Chemistry of Free Clusters, Embeded, Supported and Compressed Cluster," Springer-Verlag, Berlin, New York, 1994, p. 412.
12. W. A. de Heer, *Rev. Mod. Phys.* 65, 611 (1993).
13. M. Brust, M. Walker, D. Bethel, D. Schiffrin, and R. Whyman, *J. Chem. Soc.* 801 (1994).
14. A. C. Templeton, M. J. Hostetler, E. K. Warmoth, S. Chen, C. M. Hartshorn, V. M. Krishnamurty, M. D. E. Forbes, and R. W. Murray, *J. Am. Chem. Soc.* 120, 4845 (1998).
15. R. Whetten, T. Khoury, M. Alvarez, S. Murthy, I. Vezmar, Z. L. Wang, P. W. Stephens, C. L. Cleveland, W. D. Luedtke, and U. Landman, *Adv. Mater.* 8, 428 (1996).
16. T. G. Schaaff, M. N. Shafigullin, J. T. Khoury, I. Vezmar, R. L. Whetten, W. Cullen, P. N. First, C. Gutierrez-Wing, J. Ascencio, and M. José-Yacamán, *J. Phys. Chem. B* 101, 7885 (1997).
17. D. V. Leff, L. Brandt, and J. Heat, *Langmuir* 12, 4723 (1996).
18. S. L. Logunov, T. S. Ahmadi, M. A. El-Sayed, J. T. Khoury, and R. L. Whetten, *J. Phys. Chem.* 101, 3713 (1997).
19. C. J. Kiely, J. Fink, M. Brust, D. Bethell, and D. J. Schiffrin, *Nature* 396, 444 (1998).
20. A. Mews, A. V. Kadavanich, U. Banin, and A. P. Alivisatos, *Phys. Rev. B* 53, 13242 (1996).
21. H. Bonnemann, W. Brijoux, R. Brinkmann, R. Fretzen, T. Joussen, R. Koppler, B. Korall, P. Neiteler, and J. Richter, *J. Molec. Catal.* 86, 129 (1994).
22. Z. L. Wang, *Adv. Mater.* 10, 13 (1998).
23. B. Korgel and D. Fitzmaurice, *Phys. Rev. B* 59, 14191 (1999).
24. H. Bonnemann and R. M. Richards, *Eur. J. Inorg. Chem.* 2455 (2001).
25. S. Ino and S. Ogawa, *J. Phys. Soc. Jpn.* 22, 1365 (1967).
26. S. Ogawa, S. Ino, T. Katar, and H. Ota, *J. Phys. Soc. Jpn.* 21, 1963 (1966).
27. T. P. Martin, *Phys. Rep.* 273, 199 (1996).
28. J. M. Montejano-Carrizales and F. Aguilera-Granja, *Rev. Mex. Fís.* 44 S3, 59 (1998).
29. J. M. Montejano-Carrizales, F. Aguilera-Granja, and J. L. Morán-López, *Nanostructured Materials* 8, 269 (1997).
30. J. M. Montejano-Carrizales, M. P. Iñiguez, and J. A. Alonso, *J. Cluster Sci.* 5, 287 (1994).
31. L. García González and J. M. Montejano-Carrizales, *Phys. Stat. Sol. (A)* 230, 357 (2000).
32. M. Foiles, M. I. Baskes, and M. S. Daw, *Phys. Rev. B* 33, 1285 (1983).
33. J. M. Montejano-Carrizales and J. L. Rodríguez-López, Institute of Physics University of San Luis Potosi, Internal report (2002) and personal communication. Surface reconstruction and decahedral structure of bimetallic nanoparticles, S. L. Rodríguez-López, J. M. Montejano-Carrizales, U. Pal, J. F. Sánchez-Ramírez, D. García, M. Miki-Yoshida, and M. José-Yacamán, to be published.
34. R. Andres, J. Bielefeld, J. Henderson, D. Janes, V. Kolagunta, C. Kubiak, W. Mahoney, and R. Osifchin, *Science* 273, 1690 (1996).
35. D. Janes, V. Kolagunta, R. Osifchin, J. Bielefeld, R. Andres, J. Henderson, and C. Kubiak, *Superlatt. Microstruct.* 18, 275 (1995).
36. R. Osifichin, W. Mahoney, R. Andres, J. Henderson, C. Kubiak, and R. Dominey, *Superlatt. Microstruct.* 18, 283 (1995).
37. J. R. Blackborow and D. Young, "Metal Vapor Synthesis," Springer-Verlag, New York, 1979.
38. S. Roginsky, A. Schalnikoff, *Kolloid Z.* 43, 67 (1927).

39. J. S. Bradley in "Clusters and Colloids: From Theory to Applications." (G. Schmid , Ed.). VCH, Weinheim, 1994.
40. K. Kimoto, *J. Phys. Soc. Jpn.* 9, 762 (1953).
41. H. Morimoto, *J. Phys. Soc. Jpn.* 13, 1015 (1958).
42. K. Mihama and Y. Yasuda, *J. Phys. Soc. Jpn.* 21, 1166 (1966).
43. T. Hayashi, T. Ohno, S. Yatsuya, and R. Uyeda, *Japanese J. App. Phys.* 16, 705 (1977).
44. K. Kimoto and I. Nishida, *Japanese J. App. Phys.* 6, 1047 (1967).
45. K. Kimoto and I. Nishida, *J. Phys. Soc. Jpn.* 22, 940 (1967).
46. T. Okazaki, *Japanese J. App. Phys.* 27, 2037 (1988).
47. N. Wada, *Japanese J. App. Phys.* 8, 551 (1969).
48. R. Uyeda, in "Phys.-Math Society," Japan, 1942.
49. A. Tasaki, S. Tomiyama, S. Iida, and R. Uyeda, *Japanese J. App. Phys.* 4, 707 (1965).
50. R. Uyeda, *Progr. Mater. Sci.* 35, 1 (1991).
51. J. Chang and J. Huang, *Biotech. Prog.* 14, 735 (1998).
52. D. W. Darnall, B. Greene, M. T. Henzl, M. J. Hosea, R. A. McPherson, and J. Sneddon, *Environ. Sci. Technol.* 20, 206 (1986).
53. D. W. Darnall, B. Greene, and J. L. Gardea-Torresdey, *BioHydroMetall.* 487 (1988).
54. A. V. Pethkar and K. M. Paknikar, *J. Biotech.* 63, 121 (1998).
55. N. Kuyucak and B. Volesky, *Biorecovery* 1, 189 (1989).
56. N. Kuyucak and B. Volesky, *Precious Metals* 211 (1986).
57. M. J. Hosea, B. Greene, R. A. McPherson, M. T. Henzl, M. D. Alexander, and D. W. Darnall, *Inorgan. Chem. Acta* 161 (1986).
58. J. A. Erdman, B. F. Leonard and D. M. Mckown, A case for Plants in Exploration: Gold in Douglas-fir at the Red Mountain Stockwell, U.S. Department of the Interior Geological Survey, Yellow Pine Distric, ID, 1985, p. 85.
59. K. C. Jones and P. J. Peterson, *Biogeochem.* 7, 3 (1989).
60. C. W. Anderson, R. R. Brooks, A. Ciarucci, C. J. LaCoste, M. Leblanc, B. H. Brobinson, R. Simcock, and R. B. Stewart, *J. Geochem. Explor.* 67, 407 (1999).
61. A. L. Kovalebskii and O. M. Kovalevskaya, *Appl. Geochem.* 4, 369 (1989).
62. J. R. Lujan, D. W. Darnall, P. C. Stark, G. D. Rayson, and J. L. Gardea-Torresdey, *Solvent Extract. Ion Exchange* 12, 803 (1994).
63. J. L. Gardea-Torresdey, K. J. Tiemann, J. G. Parsons, G. Gamez, and M. Yacamán, *Adv. Environmental Res.* 00, 1 (2001).
64. J. R. Peralta, J. L. Gardea-Torresdeay, K. J. Tiemann, E. Gómez, S. Arteaga, E. Rascón, and J. G. Parsons, *Bull. Environ. Contam. Toxicol.* 66, 727 (2001).
65. J. L. Gardea-Torresdey, J. G. Parsons, E. Gómez, J. Peralta-Videa, H. Troiani, P. Santiago, and M. J. Yacamán, *Nano Lett.* 2, 397 (2002).
66. M. J. Hostetler, J. E. Wingate, C. J. Zhong, J. E. Harris, R. W. Vachet, R. M. Clark, J. D. Londono, S. J. Green, J. J. Stokes, G. D. Wignall, G. L. Glish, M. D. Porter, N. D. Evans, and R. W. Murray, *Langmuir* 14, 17 (1998).
67. L. A. Porter, Jr. D. Ji, S. Westcott, M. Graupe, R. Czernuszewicz, N. Halas, and T. Lee, *Langmuir* 14, 7378 (1998).
68. D. V. Leff, P. C. Ohara, J. R. Heat, and W. M. Gelbart, *J. Phys. Chem.* 99, 7036 (1995).
69. M. Hostetler, S. Green, J. Stokes, and R. Murray, *J. Am. Chem. Soc.* 118, 4212 (1996).
70. M. Alvarez, J. Khoury, T. Schaaff, M. Shafigullin, I. Vezmar, R. L. Whetten, *Chem. Phys. Lett.* 266, 91 (1997).
71. R. S. Ingram, M. Hostetler, and R. Murray, *J. Am. Chem. Soc.* 119, 9175 (1997).
72. P. Buning, B. Humbel, A. Philipse, and A. Verklej, *Langmuir* 18, 3921 (1997).
73. S. Chen and K. Kimura, *Langmuir* 15, 686 (1999).
74. S. R. Johnson, S. D. Evans, S. Mahon, and A. Ulman, *Langmuir* 13, 51 (1997).
75. M. Brust, D. Bethell, D. Schiffrin, C. Kiely, and L. Novel, *Adv. Mater.* 7, 795 (1995).
76. A. Templeton, M. Hostetler, C. Craft, and R. Murray, *J. Am. Chem. Soc.* 120, 1906 (1998).
77. I. Srnová-loufová, F. Lednick, A. Gemperle, and J. Gemperlová, *Langmuir* 16, 9928 (2000).
78. M. J. Yacamán, K, Heinemann, and H. Popa, *Crit. Rev. Sol. Stat. Mater.* 10, 243. (1983).
79. K. Yagi, "High resolution Electron Microscopy and Associated Techniques," Oxford, 1988, p. 568.
80. K. Yagi, K. Takanayagi, K. Kobayashi, and G. Honjo, *J. Cryst. Growth* 28, 117 (1975).
81. M. José-Yacamán, J. A. Ascencio, H. B. Liu, and J. L. Gardea-Torresdey, *J. Vac. Sci. Technol. B* 19, 1091 (2001).
82. Z. L. Wang, "Characterization of Nanophase Materials." Wiley-VCH, Weinheim, 2000.
83. S. A. Harfenist, Z. L. Wang, R. L. Whetten, I. Vezmar, and M. Alvarez, *Adv Mater.* 9, 817 (1997).
84. J. Spiller Metois and J. A. Venables, *Philos. Mag.* 46, 1015 (1982).
85. M. Gillet, *Surf. Sci.* 67, 139 (1977).
86. L. D. Marks, "The structure of small silver particles." Cambridge University Press, Oxford, 1980.
87. M. J. Yacamán and J. M. Domínguez, *J. Catal.* 213 (1980).
88. Z. L. Wang, T. S. Ahmad, and M. A. El-Sayed, *Surf. Sci.* 380, 302 (1996).
89. M. José-Yacamán, J. A. Ascencio, H. B. Liu and J. Gardea-Torresday, *J. Vac. Sci. Technol. B* 19, 1091 (2001).
90. S. Giorgio and J. Urban, *Appl. Phys. Lett.* 52, 1467 (1988).
91. See "Nanoscale Characterization of Materials," *MRS Bulletin* 22, 8 (1997).
92. "Handbook of Nanostructured Materials and Nanotechnology." (H. S. Nalwa, Ed.). Vols. 1–5, Academic Press, London, 1999.
93. J. A. Ascencio, C. Gutierrez-Wing, M. E. Espinosa, M. Marín, S. Tehuacanero, C. Zorrilla, and M. José-Yacamán, *Surf. Sci.* 396, 349 (1998).
94. E. J. Kirkland, "Advanced Computing in Electron Microscopy." Plenum, New York, 1998.
95. Z. L. Wang, "Elastic and Inelastic Scattering in Electron Diffraction and Imaging." Plenum, New York, 1995.
96. L. D. Marks, *Rep. Prog. Phys.* 57, 603 (1994).
97. "Extended Icosahedral Structures." (M. V. Jaric and D. Gratias, Eds.). Academic, 1987.
98. O. Krivanek, in "High Resolution Electron Microscopy." (P. Busec, J. Cowley, and L. Eyring, Eds.). Oxford University Press, 1988.
99. J. M. Montejano-Carrizales, Institute of Physics University of San Luis Potosí, Internal report and personal communication, 2000.
100. L. D. Marks, *J. Cryst. Growth* 61, 556 (1984).
101. K. Koga and K. Sagawara, *Surf. Sci.* 529, 23 (2003).
102. J. Ascencio, M. Perez, and M. José-Yacamán, *Surf. Sci.* 447, 73 (2000).
103. Y. Chushak and L. S. Bartell, *Eur. Phys. J. D* 16, 43 (2001).
104. K. Manninen and M. Manninen, *Eur. Phys. J. D* 20, 243 (2002).
105. J. Uppenbrik and D. J. Wales, *J. Chem. Phys.* 96, 8520 (1992).
106. J. Urban, H. Sack-Kongehl, and K. Weiss, *Z. Phys. D* 28, 247 (1993).
107. D. Lu and K. Tanaka, *Surf. Sci.* 409, 283 (1998).
108. S. A. Nepijko, H. Hofmeister, H. Sack-Kongehl, and R. Schlogl, *J. Cryst. Growth* 312, 129 (2000).

Cyclodextrins and Molecular Encapsulation

J. Szejtli

Cyclolab Ltd., Budapest, Hungary

CONTENTS

1. INTRODUCTION

The interaction of two or more molecules which results in significant changes in their properties without establishing covalent chemical bond(s) between them is the subject of the supramolecular chemistry. Because one molecule is the possible smallest unit of any compound, the smallest nanostructure is a few nanometer sized molecular structure. A larger cylinder-shaped molecule, which is able to include another smaller molecule (of adequate size and polarity) into its axial cavity itself is a capsule of molecular size.

The temporary or static inclusion of other molecules into the cavity of a so-called "host" molecule without establishing covalent bond results in broadly and practically very well utilizable effects, which belong to the ultimate limits of the nanotechnology.

The cyclodextrins are toroidal (conical cylinder) shaped hollow molecular structures; their outer diameter is 13.7 to 16.9 nanometers, height uniformly 7.8 nanometers, and their axial cavity about 0.57 to 0.95 nanometers wide. They are produced by a relatively simple enzymic conversion technology from starch.

A cyclodextrin (CD) molecule is the possible smallest (nano)capsule: in most cases another, smaller molecule can be inserted into its axial cavity. This "molecular encapsulation" results in smaller or larger changes in the physical and chemical properties of the encapsulated molecules.

While in the 1970s this possibility was not more than a scientific curiosity, by the beginning of the 21st century it became a widely used industrial technology; cyclodextrins are produced and utilized in thousand ton amounts. The number of cyclodextrin containing products and cyclodextrin utilizing technologies increases steadily—the cyclodextrin market increases yearly by about 15 to 20%.

By end the of 2002, the number of CD-related publications is more than 26.000, representing more than 170,000 printed pages [1–26].

While 30 years ago about four to five CD papers were published monthly, in 2002 that many are published daily.

About 16% of all CD-relevant publications are dedicated to the fundamentals of cyclodextrin chemistry and technology (i.e., the physical and chemical properties of cyclodextrins, their enzymology, toxicology, production, and derivatives). This section also includes the numerous review articles on CDs.

Nearly 22% of the publications are dedicated to studies of the CD-inclusion phenomena. These works are generally not directly practice-oriented, dealing with energetics and kinetics of inclusion, X-ray, Fourier transform infrared, liquid and solid phase nuclear magnetic resonance (NMR), electron paramagnetic resonance, circular dichroism, Raman spectroscopy, enhancement of luminescence and phosphorescence, thermal analysis, interaction of CDS with specific guest types, enzyme modelling with CDs and CD derivatives, preparation, analysis of cyclodextrin complexes, etc. These methods, as well as the correlation between the complexation and various structural and external parameters, form the basis for all practical applications of CDs.

The largest group of CD papers, nearly 25%, is dedicated to the pharmaceutical application of CDs. The large number (nearly 5000) of drug/CD related papers and patents is a little misleading, because many authors publish the same result in different journals under different titles, but with virtually identical content. Rediscoveries are published frequently, simply because the authors did not read the earlier literature; in essence they have discovered something that was published earlier. Because of the many repetitions, and the

nonfeasible ideas, only about 30% of the published papers disclose really new and significant results.

Actually only 7% of the CD-related papers are dedicated directly to the food, cosmetic, and toiletry applications of CDs, but at the same time about 70% of all cyclodextrins produced are used in this field. The approval process for CD-containing products in this field is much simpler and faster than in the case of the drug/CD formulations. The amount of CD used in a single cosmetic or toiletry product might be larger, by orders of magnitude, than the total amount used in drugs.

Presently, about 11% of the CD literature is dedicated to the application of CDs in the chemical and biotechnological industries.

About 25% of the CD literature involves the application of cyclodextrins in analytical chemistry and diagnostic preparations. The analytical applications of CDs refer mainly to the application of cyclodextrins in gas chromatography, in high performance liquid chromatography, and in capillary zone electrophoresis, but some dozen papers are dedicated to thin-layer chromatography, to enhancement of ultraviolet-visible (UV-VIS) absorption, luminescence/phosphorescence by CDs, and to increasing the sensitivity of the related analytical methods. Apparently, it is difficult to find a separation problem on an analytical scale which could not be solved by using the appropriate CD.

2. CYCLODEXTRINS

2.1. Chemistry

Cyclodextrins comprise a family of three well known industrially produced major and several rare, minor cyclic oligosaccharides [1, 4, 9, 19]. The three major cyclodextrins are crystalline, homogeneous, nonhygroscopic substances, which are toruslike macrorings built up from glucopyranose units (Fig. 1). The α-cyclodextrin (Schardinger's α-dextrin, cyclomaltohexaose, cyclohexaglucan, cyclohexaamylose, αCD, ACD, C6A) comprises six glucopyranose units, βCD (Schardinger's β-dextrin, cyclomaltoheptaose, cycloheptaglucan, cycloheptaamylose, βCD, BCD, C7A) comprises seven such units, and γCD (Schardinger's γ-dextrin, cyclomaltooctaose, cyclooctaglucan, cyclooctaamylose, γCD, GCD, C8A) comprises eight such units (Fig. 1). The most important characteristics of the CDs are summarized in Table 1.

As a consequence of the $^4C_1$ conformation of the glucopyranose units, all secondary hydroxyl groups are situated on one of the two edges of the ring, whereas all the primary ones are placed on the other edge. The ring, in reality, is a cylinder or, better said, a conical cylinder, which is frequently characterized as a doughnut or wreath-shaped truncated cone. The cavity is lined by the hydrogen atoms and the glycosidic oxygen bridges, respectively. The nonbonding electron pairs of the glycosidic oxygen bridges are directed toward the inside of the cavity producing a high electron density there and lending to it some Lewis-base characteristics.

The C-2-OH group of one glucopyranoside unit can form a hydrogen bond with the C-3-OH group of the adjacent
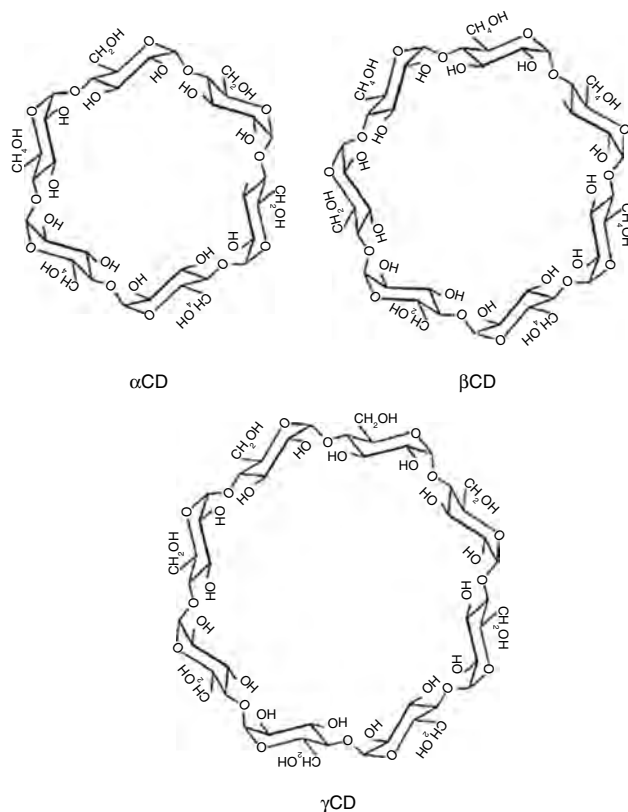
Figure 1. Chemical structure of α-, β-, and γCDs.

glucopyranose unit. In the βCD molecule, a complete secondary belt is formed by these H-bonds; therefore the βCD is a rather rigid structure. This intramolecular hydrogen bond formation is probably the explanation for the observation that βCD has the lowest water solubility of all CDs.

The hydrogen-bond belt is incomplete in the αCD molecule, because one glucopyranose unit is in a distorted position. Consequently, instead of the six possible H-bonds, only four can be established simultaneously. The γCD is a noncoplanar, more flexible structure; therefore it is the more soluble of the three CDs.

Figure 2 shows a sketch of the characteristic structural features of CDs. On the side where the secondary hydroxyl groups are situated, the cavity is wider than on the other side where free rotation of the primary hydroxyls reduces the effective diameter of the cavity.

The cyclodextrins are produced from starch by enzymic conversion [9, 17].

The starch might be of any origin: maize, potato, tapioca, etc. All starch consists of two essential components: the amylose (2 to 70%), which is a linear glucose polymer (several hundreds or thousands of D-glucopyranose units are linked by α-1,4 glucosidic linkages), and the amylopectin, which is a ramified structure. The main linkage type between the D-glucopyranoside units is also of α-1-4 type, but every 20th to 30th glucose is connected to another polyglucan chain by an α-1,6-glucosidic linkage.

Splitting the glucosidic linkage (catalyzed by acid, or enzyme) the formed free carbenium cation will react immediately with another hydroxyl-containing molecular entity. If

Table 1. Characteristics of α-, β-, and γCD.

Parameter	α	β	γ
No. of glucose	6	7	8
Mol. wt.	972	1135	1297
Solubility in water (g/100 ml^{-1}) at room temp.	14.5	1.85	23.2
$[\alpha]_D$ 25°	150 ± 0.5	162.5 ± 0.5	177.4 ± 0.5
Cavity diameter (Å)	4.7–5.3	6.0–6.5	7.5–8.3
Height of torus (Å)	7.9 ± 0.1	7.9 ± 0.1	7.9 ± 0.1
Diameter of outer periphery (Å)	14.6 ± 0.4	15.4 ± 0.4	17.5 ± 0.4
Approx. volume of cavity (Å)^3	174	262	427
Approx. cavity volume in 1 mol CD (ml)	104	157	256
In 1 g CD (ml)	0.10	0.14	0.20
Crystal forms (from water)	hexagonal plates	monoclinic parallelograms	quadratic prisms
Crystal water wt%	10.2	13.2–14.5	8.13–17.7
Diffusion constants at 40 °C	3.443	3.224	3.000
Hydrolysis by A. oryzae α-amylase	negligible	slow	rapid
pK (by potentiometry) at 25 °C	12.332	12.202	12.081
Partial molar volumes in solution (ml mol^{-1})	611.4	703.8	801.2
Adiabatic compressibility in aqueous solutions (ml mol^{-1} bar^{-1} 10^4)	7.2	0.4	−5.0

the reaction partner is water, the reaction is called hydrolysis; the final product is glucose. If the reaction partner is, for example, methanol, the reaction product is methyl-glucopyranoside. If the reaction partner is the sixth, seventh, or eighth glucopyranose unit of the same amylose

Figure 2. Dimensions and hydrophilic/hydrophobic regions of the CD molecules.

molecule or amylopectin molecule side chain, the product is a cyclodextrin. Because the minimum energy conformation for both the amylose as well as the segments of the amylopectin molecule is the helical (wormlike) structure, one turn is composed of six, seven, or eight glucose units. Consequently the sixth, seventh, or eighth glucopyranose unit will be in the immediate vicinity of the newly formed carbenium cation. This "splitting and the ring closing" process is catalyzed by the so called cyclodextrin-glucosyl-transferase enzyme.

2.2. Production

The cyclodextrin glucosyl transferase enzyme (CGT-ase) is produced by a large number of microorganisms, like Bacillus macerans, Klebsiella oxytoca, Bacillus circulans, Alkalophylic bacillus No. 38-2, etc. Genetic engineering has provided more active enzymes, and probably, in the future, mostly these enzymes will be used for industrial CD production [17].

The first step in CD production is the liquefaction of the starch at elevated temperature. To reduce the viscosity of the rather concentrated (around 30% dry weight) starch solution, it has to be hydrolyzed to an optimum degree. The prehydrolyzed starch must not contain glucose or low molecular oligosaccharides, because they strongly reduce the yield of the formed CDs. After cooling to the optimum temperature, CGT-ase enzyme is added to the starch solution. In the so-called nonsolvent technology, the formed α-, β-, and γCDs have to be separated from the complicated partially hydrolyzed mixture. In the case of the solvent technology, an appropriate complex-forming agent is added to the conversion mixture. If toluene is added to this system, the formed toluene/βCD complex is separated immediately, and the conversion is shifted toward the formation of βCD (Fig. 3). If n-decanol is added to the conversion mixture, mainly αCD will be produced, while in case of cyclohexadecenol the main product is γCD. Various other complex-forming agents can be used. The selection depends on price,
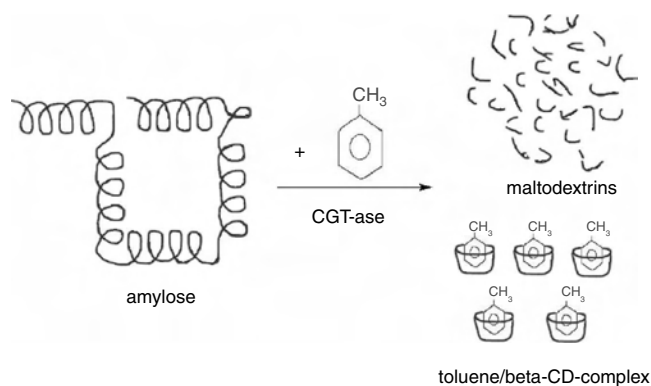
Figure 3. Production of βCD: in the presence of toluene the formed βCD is converted immediately to a water-insoluble toluene/βCD complex. Therefore the main product will be βCD. In the presence of decanol αCD, hexadecenol γCD is the isolated final product.

toxicity, and explosivity, but mainly on the efficiency of the removal of the solvents from the crystalline end-product. The insoluble complexes are separated from the conversion mixture by filtration. The removal of the solvents from the filtered and washed complex is generally made after suspending it in water by distillation or extraction. The aqueous solution obtained after removal of the complexing solvent is treated with activated carbon and filtered. The cyclodextrins are then separated from this solution by crystallization and filtration. The homegeneity of the industrially produced cyclodextrins is generally better than 99%.

2.3. Biological Effects

2.3.1. Absorption and Metabolism

For application of cyclodextrins in the pharmaceutical and food industry, the fate of cyclodextrins in the mammal organisms is a crucial question. Cyclodextrins are consumed by humans or animals (as orally administered pharmaceuticals, or as food additives) either as free cyclodextrins or their inclusion complexes, containing some drug, flavor, or other guest substance. The inclusion complexes undergo very rapid dissociation under physiological conditions in the gastrointestinal tract; therefore only the absorption of the free cyclodextrin deserves attention [8, 16, 17].

Summarizing the available data and experimental observations the following conclusions can be drawn. The CD molecule is a relatively large molecule. Its outer surface is strongly hydrophilic. It is a true carrier. It brings the hydrophobic guests into solution, keeps them in dissolved state, and transports them to the lipophilic cell membrane, but after delivering the guest to the cell (because it has higher affinity to the guest than the cyclodextrin), the cyclodextrin remains in the aqueous phase.

Only an insignificant amount of orally administered CD is absorbed from the intestinal tract in intact form. The source of eventual CD-elicited toxic phenomena might be that CDs can solubilize and facilitate the otherwise insoluble, nonabsorbable toxic compounds, like polyaromatic hydrocarbons, pesticides, etc. The preponderant part of orally administered cyclodextrin is metabolized in the colon, by

the colon microflora. The primary metabolites (acyclic maltodextrins, maltose, and glucose) are then further metabolized, absorbed like the starch, and finally excreted as CO_2 and H_2O.

While the metabolism of starch takes place in the small intestines, the cyclodextrin is metabolized in the colon. Correspondingly the maximum intensities of metabolism are observed for starch around 1 to 2 hours and for CDs 6 to 8 hours after consumption, respectively.

The metabolism of αCD is slower and that of γCD is much faster than that of βCD. The chemically modified CDs are, however, very resistant to enzymic degradation. Methylated and hydroxypropylated CDs (and probably all other more or less substituted CD derivatives) can be absorbed from the intestinal tract to a quite considerable extent and can get into the circulation.

2.3.2. Toxicology

Upon parenteral administration all CDs can interact with the components of cell membranes, but the extent of this interaction is very different. This cell-damaging effect can be characterized by CD concentration, which results in an 50% haemolysis of the erythrocytes or which reduces to 50% the luminescence of an Escherichia coli suspension. In these experiments, the more hydrophobic (but very well soluble) derivatives like dimethyl βCD showed the largest effects. Because the cell-damaging effect is a consequence of CD complexation of cell-wall components like cholesterol and phospholipids, βCD and particularly its more hydrophobic derivatives, like the dimethyl βCD, show the strongest cell-membrane damaging effect among all CDs. The γCD and its derivatives are less toxic, because their affinity (through the wider CD cavity) to cholesterol and phospholipids is lower. Administering the CDs at a rate that their actual concentration does not reach the haemolytic threshold concentration (slow infusion, or absorption from the intestinal tract, or through the skin), this immediate toxic consequence can be avoided, but not the kidney-toxic effect. Parenteral administration of βCD is not possible, because it forms the most stable cholesterol/CD complex, which will be accumulated in the kidneys, destroying cells. Apparently γCD is free from this noxious property: it is well soluble and does not form stable, easily crystallizable complexes with any vital component of the circulation. The cavity of γCD is too large and that of the αCD is too small for cholesterol.

HPβCD (hydroxypropyl βCD) does not form insoluble kidney-damaging cholesterol complex crystals; therefore it can be injected even in rather large doses without any irreversible consequences, but chronic treatment again showed unwanted side-effects: it forms soluble cholesterol/HPβCD complex in the circulation. In the kidneys this less stable complex dissociates. The HPβCD will be excreted, but the cholesterol remains in the kidneys. Long-term parenteral administration of HPβCD will heavily load the kidneys with cholesterol—not considering other toxic effects of HPβCD.

Parenterally only such CDs can be administered that have a low affinity to cholesterol. The best CD would be the one that is stable in aqueous solution, has a high drug solubilizing and stabilizing capacity, but after injecting into the circulation rapidly decomposes. Regrettably we have not yet such a derivative.

3. CYCLODEXTRIN DERIVATIVES

3.1. Aim of Derivatization

For a series of reasons (price, availability, approval status, cavity dimensions, etc.) the βCD is the most widely used and represents at least 95% of all presently produced and consumed CDs. It is used for many purposes; however, its anomalous low aqueous solubility (and the low solubility of most of its complexes) is a serious barrier in its wider utilization. Fortunately by chemical or enzymatic modifications the solubility of all CDs can be strongly improved, and instead of the 18 g/L aqueous βCD solutions 500 g (or more)/L aqueous βCD derivative solutions can easily be prepared.

In the cyclodextrins every glucopyranose unit has 3 free hydroxyl groups which differ in both their functions and reactivity. The relative reactivities of C(2) and C(3) secondary and C(6) primary hydroxyls depend on the reaction conditions (pH, temperature, reagents). In βCD 21 hydroxyl groups can be modified substituting the hydrogen atom or the hydroxyl group with a large variety of substituting groups like alkyl-, hydroxyalkyl-, carboxyalkyl-, amino-, thio-, tosyl-, glucosyl-, maltosyl-, etc. groups, thousands of ethers, esters, anhydro-deoxy-, acidic, basic, etc. derivatives can be prepared by chemical or enzymatic reactions. The aim of such derivatizations may be:

- to improve the solubility of the CD derivative (and its complexes)
- to improve the fitting and/or the association between the CD and its guest, with concomitant stabilization of the guest, reducing its reactivity and mobility
- to attach specific (catalytic) groups to the binding site (e.g., in enzyme modeling),
- to form insoluble, immobilized CD-containing structures, polymers, (e.g. for chromatographic purposes).

3.2. Derivate Types

From the thousands of CD derivatives described in hundreds of scientific papers and patents only a few can be taken into consideration for industrial scale synthesis and utilization. Complicated multistep reactions, using expensive, toxic, environment-polluting reagents and requiring purification of the products by chromatography, are feasible to prepare derivatives only on laboratory scale. To produce tons at an acceptable price only about a dozen of the known CD derivatives can be taken into consideration.

Among industrially produced, standardized, and available (even in ton amounts) βCD derivatives the most important ones are the heterogeneous, amorphous, highly water soluble methylated βCD and 2-hydroxypropylated βCDs (Fig. 4). Due to its heterogeneity the HPβCD cannot be crystallized, which is an important advantage (e.g., at producing liquid drug formulations).

The first hydroxypropyl-βCD and hydroxypropyl-γCD containing drug formulations are already approved and marketed in several countries.

A methylated βCD is more hydrophobic than the βCD itself; therefore it forms a more stable (but soluble) complex with cholesterol. Its affinity to cholesterol is so strong that it extracts cholesterol from the blood cell membranes, resulting in hemolysis already at around 1 mg/mL concentration.
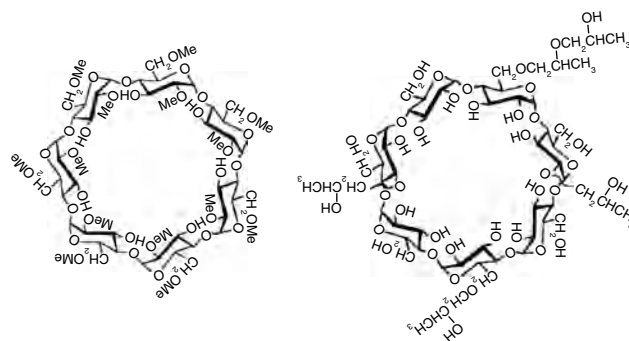
Figure 4. Structure of the heptakis (2,6-O-dimethyl)-βCD and of a hydroxypropyl βCD of DS∼4.

A particular methylated βCD, the heptakis (2,6-di-O-methyl-βCD) is a crystalline product (Fig. 4). It is extremely soluble in cold water but insoluble in hot water. Therefore, its purification, and also the isolation, of its complexes is technically very simple. Up to now no better solubilizer has been found among the CDs. It is available in better than 95% isomeric purity for injectable drug formulation (for example radio-pharmaceuticals) but for widespread industrial application the cheaper noncrystalizable randomly methylated βCD (called RAMEB) is produced and marketed.

Enzymatically modified CDs are produced, for example, by reacting βCD with starch in the presence of pullulanase enzyme. One or two maltosyl or glucosyl groups will be attached to the primary side of the CD ring with α-1,6 glycosidic linkage. The product is the so-called "branched" CD (mono- or dimaltosyl or mono- or diglucosyl CD) which is very well soluble in water, being a heterogeneous, noncrystallizable substance. It is produced and used in the food industry, mainly in Japan, for example, for production of stable flavor powders.

There has been increasing interest toward the per-acyl-CDs. All acetylated CDs from per-acetyl to per-octanoyl esters have been studied partly as retarding drug carriers and partly as bioadhesive, film-forming substances to be used in transdermal drug delivery systems. The heptakis-(sulfobutyl)-βCD is very well soluble in water, is noncrystallizable, and even at extreme high doses seems to be free from any toxic side-effects. It can be used as a chiral separating agent in capillary zone electrophoresis, but the aim of the intensive research is to use it as a parenteral drug carrier, for preparation of aqueous injectable solutions of poorly soluble drugs. A few such drug complexes are already approved and marketed.

The CD sulfates possess many similar properties as the heparin without its anticoagulating effect. Apparently they can reduce the blood supply of tumor tissues through inhibiting the formation of new arteries (=antiangiogenesis).

The monochloro-triazinyl βCD is produced on industrial scale from CDs and cyanuric chloride. It is reactive with cellulose fibers in alkaline medium (see at the application of CDs in textiles).

To elongate the actual CD cavity substituents are attached to the primary or secondary side. This elongation may be hydrophylic in which case hydroxyalkyl groups are attached

to the ring, or it might be hydrophobic. For example substituting the primary hydroxyl groups with long fatty-acid chains, "medusa"-like molecules can be prepared. These molecules behave as detergents while retaining their complex forming ability. The coming years will decide how utilizable these derivatives are.

The chair conformation of the CD ring can be modified by inverting the position of some hydroxyl groups. For example eliminating the tosyl group in alkaline medium from a CD-tosyl derivative, 2,3-anhydro derivatives can be prepared. Opening the anhydro ring one hydroxyl group will take up an inverted position, and this way cycloaltrins are formed. Eliminating an appropriate leaving group from the primary side, 3,6-anhydro-CDs are formed. Because of the twisted conformation of the anhydro glucopyranose unit the properties of CDs—for example, their solubility—are strongly increased.

It is possible to close one side of the CD cavity, for example, by overbridging the primary or secondary side with an appropriate bifunctional substituent. It is expected that these overbridged CDs will form more stable complexes with certain guests.

A dozen various CD derivatives are used in gas chromatography, liquid chromatography, and capillary zone electrophoresis.

For other industrial purposes where toxicological demands do not play a decisive role, epichlorohydrin cross-linked, hydroxyethylated, or sometimes (apparently rather fancy, but by its use justified) mixed ethers–esters, like heptakis (2,6-di-O-methyl)-3-O-trifluoroacetyl-βCD and similar derivatives, are produced and utilized.

It seems to be very probable that for drug carrier purposes four or five different CD derivatives will be developed and produced in the future, because no one of them is able to fulfill alone all the very strict requirements, which are usual in the case of a parenteral drug carrier.

For other industrial purposes the production of hundreds of tons of alkylated, hydroxyalkylated, and acylated CDs is prognosticated by end of first decade of the 21st century.

4. INCLUSION COMPLEXES

4.1. Mechanism and Equilibria

In an aqueous solution, the slightly apolar cyclodextrin cavity is occupied by water molecules which are energetically unfavored (polar–apolar interaction) and therefore can be readily substituted by appropriate "guest molecules" which are less polar than water (Fig. 5). The dissolved cyclodextrin is the "host" molecule, and the "driving force" of the complex formation is the substitution of the high-enthalpy water molecules by an appropriate "guest" molecule. One, two, or three cyclodextrin molecules contain one or more entrapped "guest" molecules. Most frequently the host:guest ratio is 1:1. This is the essence of "molecular encapsulation" [17].

This is the simplest and most frequent case. However, 2:1, 1:2, 2:2, or even more complicated associations and higher order equilibria exist, almost always simultaneously.
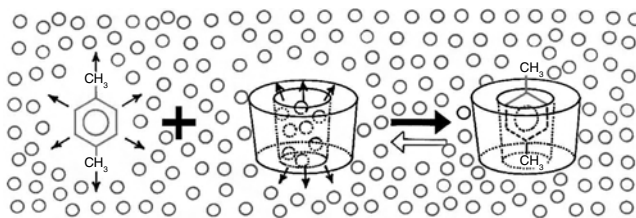
Figure 5. Schematic representation of the association–dissociation of the host (CD) and guest (p-xylene). The formed guest/host inclusion complex can be isolated as a microcrystalline powder.

The formed inclusion complexes can be isolated as stable crystalline substances. Upon dissolving these complexes, an equilibrium is established between dissociated and associated species, and this is expressed by the complex stability constant K_a. The association of the CD and guest (D) molecules, and the dissociation of the formed CD/guest complex is governed by a thermodynamic equilibrium:
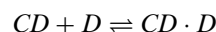
$$CD + D \rightleftharpoons CD \cdot D$$

$$K_{1:1} = \frac{[CD \cdot D]}{[CD][D]}$$

Generally, the study of the interaction between a CD and a potential guest begins with registration of the solubility isotherm (phase solubility diagram, Fig. 6). Adding the potential "guest" to an aqueous solution and agitating (stirring, shaking) until the equilibrium is attained
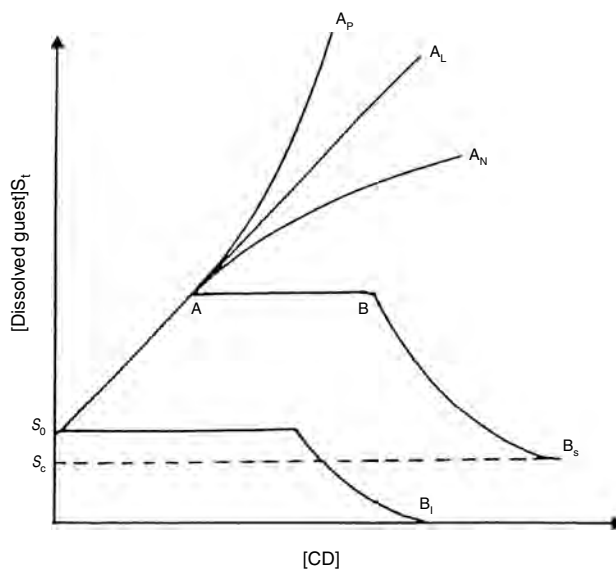
Figure 6. Registering the solubility of a poorly water soluble guest as a function of the CD concentration in aqueous solution, different solubility isotherms can be obtained, depending on the type of CD and properties of the guest. Solubility isotherm types: S_o = solubility of guest in the absence of CD; S_t = concentration of dissolved guest (free + complexed); and S_c = solubility limit of the poorly soluble complex. Isotherm types A_p, A_L, and A_N = very soluble complexes formed (solubility limit determined by solubility of the CD). Isotherm B_S = complex of limited solubility is formed. Isotherm B_I = insoluble complex is formed.

(from 3 h to 1), the following visual observations may be expected:

If the guest is *well soluble* in water then

- No visual change, but a shift in the UV spectrum, a change in the NMR chemical shift values, enhanced fluorescence, or induced circular dichroism, etc. may recorded.
- Precipitate is formed already at low concentrations of the guest which allows one to conclude to the complex formation. (The majority of water miscible solvents at high concentration precipitate the CDs, but it does not necessarily mean complex formation.)
- Solubility of the CD increases significantly (e.g., solubility of βCD increases from 18 to over 100 mg/ml) which points to a strong interaction with the CD, but not necessarily inclusion.

If the guest is *poorly soluble* in water, and it is able to form complex with the CD, then its solubility as a function of the CD concentration in most cases will change. This change may be an increase, either monotonously or only to a certain limit, or it may even decrease. The correlation between guest solubility and CD concentration is illustrated by Figure 6.

If only dissolved complex is formed the phase-solubility isotherm is of "A" type, whereas if the solubility of the formed complex is limited, then the isotherm is of the "B" type. In cases where the formed complex is insoluble (type B_I, Fig. 6) the solubility of the guest remains unaltered until all guest molecules are converted into insoluble complexes. Thereafter the concentration of dissolved guest begins to decrease.

When the complex is more soluble than the free guest, but its solubility limit can be reached within the studied CD concentration range, the (S_t) first increases from the aqueous solubility of the guest (S_O) until point "A," where the solubility limit of the complex is reached.

Any further increase in the CD concentration results in no further increase in solubility, but in precipitation of the microcrystalline complex (B_S-type isotherm). Reaching point "B" means that all solid guest has been converted to a less soluble inclusion complex, therefore adding even more CD to the system. The association–dissociation equilibrium will be shifted to association, and the solubility asymptotically approximates to the inherent solubility limit of the complex (S_c).

Theoretically the concentration increase from S_o to A should be identical with the one from zero to S_c (i.e., at point "A" the solution is just saturated for both the guest and its complex). This is, however, only a theoretical case, because in many instances the stoichiometry of a formed complex depends on the concentration ratios. While at the beginning only a 1:1 complex is formed, at higher CD concentration the stoichiometry is more complicated (1:2, 2:3, etc.).

The prevailing complex structure and stoichiometry are not necessarily identical in solution and in the solid state.

If within the studied CD-concentration range the solubility limit of the complex is not reached, the isotherm is of type "A," and "A_L" means a linear increase with unchanged stoichiometry. The "A_P"-type isotherm shows a positive deviation from linearity and this indicates a continuous increase in the stoichiometry of the complex, (i.e., the original 1:1 complex tends to associate with further guests, forming 2:3, etc. compositions). If the isotherm is of "A_N" type, the system is even more complicated because it can point either to an increase of the host ratio within the complex (1:1 to 2:1) or a change in the solute-solvent interaction (hydration, ionization of the guest) or both.

The determination of the complex stability constants and the problems associated with their interpretation are treated in Section 6. The theoretically incorrect, but for practical purposes utilizable, apparent complex stability constant K_C (association constant) for a 1:1 complex can be calculated from the slope and intercept of the initial straight line portion of the diagram as follows:

$$K_c \frac{(S_t - S_o)}{S_o\{[CD]_t - (S_t - S_o)\}} = \frac{\tan \alpha}{S_o(1 - \tan \alpha)}$$

The stoichiometry of the inclusion compound can be deduced by analyzing the length of the plateau region, AB, according to the following equation:

$$\frac{[\text{guest}]}{[\text{CD}]} = \frac{(\text{total guest added to system}) - (\text{guest in solution at point A})}{[\text{CD}]_t \text{ corresponding to plateau region}}$$

This equation means that the concentration of CD, corresponding to the plateau, is equal to that of the host which is consumed for the conversion to the solid inclusion compound, with no free solid guest remaining at point A. The stoichiometry thus estimated by this method should be confirmed by isolation and chemical analysis of the solid inclusion compound. In the case of the B_1-type diagram, the initial rise is not detectable because the inclusion compound is practically insoluble. In the same way, the K_c value is calculated from the A_L-type diagram according to the first equation. From the A_p-type diagram K_c is calculated by iteration. The value of K_c cannot be calculated from an A_N-type diagram.

4.2. Stoichiometry and Crystal Structure

Geometrical rather than chemical factors are decisive in determining the kind of guest molecules which can penetrate into the CD cavity [9, 17]. The α-, β-, and γCDs, with different internal diameters, are able to accommodate molecules of different size. Naphthalene is too bulky for αCD, and anthracene fits only into γCD. Propionic acid is compatible with αCD, but it has no satisfactory fitting in the large cavities. (Fig. 7). The included molecules are normally oriented in the host in such a position as to achieve the maximum contact between the hydrophobic part of the guest and the CD cavity. The hydrophilic part of the guest molecule remains, as far as possible, at the outer face of the complex. This ensures maximum contact with both the solvent and the hydroxyl groups of the host.

Complex formation with molecules significantly larger than the cavity may also be possible. This is done in such a way that only certain groups or side chains penetrate into
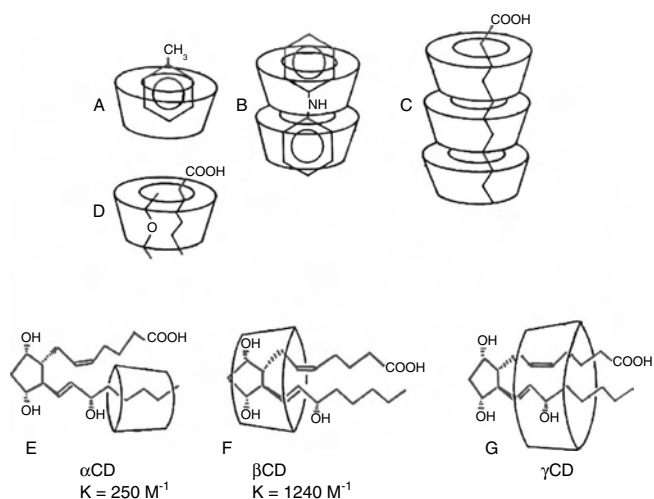
Figure 7. Examples of CD complexes: the same CD with different guests, and the same guest with different CDs. Toluene/βCD (A), diphenylamine/βCD (B), long-chain fatty acid/CD (C), short chain fatty acid + diethyl ether ternary βCD complex (D), prostaglandin E2/αCD (E), prostaglandin E2/βCD complex (F), prostaglandin E2/γCD (G) [9].

the carbohydrate cavity (e.g., aromatic amino acid moieties of a polypeptide or protein).

The fitting between host and guest can be visualized by computer graphics. Computer programs are available which, using crystallographically determined bond length and bond angle values and appropriate interaction energy functions, can rapidly ascertain the most probable conformations of a complex. However, if an inclusion can be established on the screen of a computer monitor, it does not necessarily mean that the complex can really be prepared, because the crystallographic data cannot take into account those factors that exist only in aqueous solutions: hydration, ionization, and concomitant torsion of the conformation.

A 2:1 complex of CD and a guest molecule may be formed when the guest is too large (long) to find complete accommodation in one cavity, and its other end is also amenable to complex formation. Such complexes are formed in the case of the vitamin D_3/βCD complex and the much "slimmer" aliphatic chains of n-alkanes and αCD.

In solution both the α- and βCD are highly associated with benzoic acid, but only the βCD complex can be readily crystallized. A crystalline 2:1 complex with αCD and benzoic acid will give a low yield. βCD will perfectly include a benzoic acid molecule; the carboxyl group forms a hydrogen bond with one secondary CD hydroxyl.

The role of substituents in complex formation is demonstrated by the methylnitrophenols. Relative to 4-nitrophenol, methyl groups in positions 2 and 6 have no significant influence on the stability of the αCD complex, but one methyl group in the 3-position will lower the stability of the complex by about two orders of magnitude. 3,5-Dimethyl-4-nitrophenol fails to give a complex at all.

Strongly hydrophilic molecules (very soluble in water) and strongly hydrated and ionized groups are not or are only very weakly complexable. Only molecules which are less polar than water can be complexed by CDs.

Excessively strong cohesive forces between the molecules of the guest impede their separation, which is a precondition for the inclusion. A measure of the cohesion between the molecules of a crystalline substance is the melting point. When the melting point is higher than 250 °C a stable CD complex cannot generally be prepared.

The structure of crystalline CD complexes is not necessarily identical to that of the complexes in solution. In the dissolved state the guest molecule or its corresponding group is located within the cavity of the CD and the whole complex is surrounded by a multilayer hydrate shell. In the crystalline state, however, guest molecules and also some CD molecules include only water molecules; consequently they are incorporated into the crystal lattice as water complexes. Therefore, the isolated amorphous or crystalline complexes are practically never of strictly stoichiometric composition; however, they are stable even if the ring cavities are only partially saturated by apolar guest molecules.

In solution the association–dissociation equilibrium determines the uncomplexed/complexed ratio for the guest and the host. However, depending on properties such as size and shape of the guest, not only 1:1, but also 1:2, 2:1, or 2:2 host:guest complexes may coexist in solution. This will also depend on the CD and/or guest concentration. Even two identical or different guest molecules may be included in one host (ternary complex). For example sodium 1-pyrenesulphonate with βCD forms a 1:1 low stability ($k = 1$ M^{-1}) complex, but with γCD a very stable ($k = 10^6$ M^{-1}) 2:1 complex is formed. At higher γCD concentrations, however, one further γCD will react, resulting in a 2:2 complex. Similarly, γCD forms a 1:1 complex with methyl orange in dilute solution; depending on the concentration 1:2 and 2:2 complexes can also occur. Generally, in aqueous solution with no extreme concentrations, the 1:1 complex is predominant.

CD inclusion complexes always contain water as crystal hydrate. For example, the p-iodoaniline/αCD complex contains four and the krypton and the methanol/αCD complexes contain five molcules of water of crystallization.

In crystalline αCD inclusion complexes, the packing depends largely on the type of guest molecule. The cage-type structure (see Fig. 8) is characteristic for small guests, which fit completely into the cavity. The channel type is observed when the guest is so large that it protrudes on both sides of the cavity.

The structure of the complex changes from the cage to channel type in the homologous series of carboxylic acids. Acetic, propionic, and butyric acids form cage-type structures, but valeric acid is too long to be accommodated in the cage, and from valeric acid onward, only channel-type structures are formed. The ionization of a small guest also results in the conversions of the cage to channel structure. Thus, acetic acid forms a cage-type structure, whereas the ionic potassium acetate prefers a channel-type arrangement.

The brickwork-type cage structure is characteristic of small, neutral, but not fully incorporated guests, which only weakly protrude on one side of the cavity (e.g., monocyclic aromatic compounds). This kind of brick-type cage arrangement has so far only been observed with α- and not with β- and γCD.
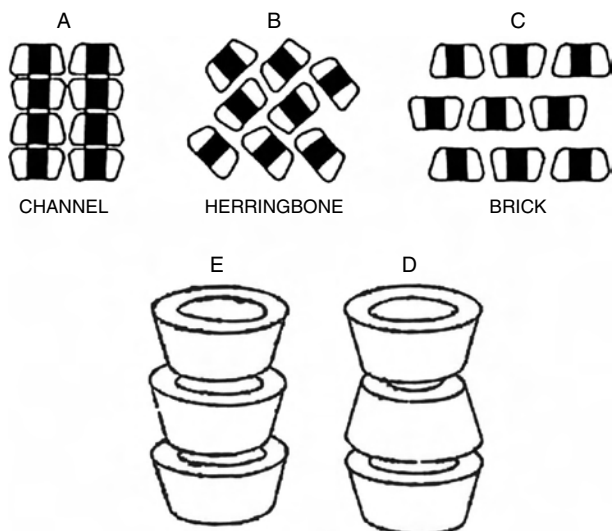
Figure 8. Channel (A), herringbone (B), brick-wall (C), head-to-tail (D), and head-to-head (E) alignment of CD rings in their complex crystal structures.

The βCD complexes crystallize with a fishbone, dimeric cage or channel structure.

The typical fishbone structure has been observed only with a few small guests: water, methanol, and ethanol. Larger guests, such as n-propanol, are accommodated in cavities which are formed by two βCD molecules arranged in a head-to-head fashion, although n-propanol is small enough to be enclosed in a monomeric cavity. It appears that the head-to-head dimer formation is favored by βCD.

These "double volume cages" (i.e. head-to-head arranged dimers or even tetramers) are arranged side-by-side in layers. Such adjacent layers are displaced so that the cavities of the dimers or tetramers are closed at both ends, or they are stacked on top of each other. This leads to cage-type structure formation, although the βCD molecules are arranged in a channel-type form. In fact, all the channels formed by βCD are more or less irregular because this molecule has seven glucose units in one ring.

If γCD is crystallized as an "empty" molecule from water, it arranges in a fishbone-type cage structure similar to that observed for α- and βCDs. If, however, a small guest, such as n-propanol, is added, a channel-type structure is formed in which the γCD molecules, with an eightfold symmetry, are stacked along a fourfold symmetry axis, and exactly linear channels are produced.

4.3. Effects of Inclusion

The most important primary consequences of the interaction between a poorly soluble guest and a CD in aqueous solution are as follows:

(a) The concentration of the guest in the dissolved phase increases significantly, while the concentration of the dissolved CD decreases. This latter point is not always true, however, because ionized guests, or hydrogen-bond establishing (e.g., phenolic) compounds may enhance the solubility of the CD.

(b) The spectral properties of the guest are modified. For example, the chemical shifts of the anisotropically shielded atoms are modified in the NMR spectra. Also, when achiral guests are inserted into the chiral CD cavity, they become optically active and show strong induced Cotton effects on the circular dichroism spectra. Sometimes the maximum of the UV spectra are shifted by several nm and fluorescence is very strongly improved, because the fluorescing molecule is transferred from the aqueous milieu into an apolar surrounding.

(c) The reactivity of the included molecule is modified. In most cases the reactivity decreases (i.e., the guest is stabilized), but in many cases the CD behaves as an artificial enzyme, accelerating various reactions and modifying the reaction pathway.

(d) The diffusion and volatility (in case of volatile substances) of the included guest decreases strongly.

(e) The formerly hydrophobic guest, upon complexation, becomes hydrophilic; therefore its chromatographic mobility is also modified.

And in the solid state:

(f) The complexed substance is molecularly dispersed in a carbohydrate matrix forming a microcrystalline or amorphous powder, even with gaseous guest molecules.

(g) The complexed substance is effectively protected against any type of reaction, except that with the CD hydroxyls, or reactions catalyzed by them.

(h) Sublimation and volatility are reduced to a very low level.

(i) The complex is hydrophilic, easily wettable, and rapidly soluble.

When, in an aqueous system, the formation of the CD-inclusion complex can be detected (e.g., by NMR or circular dichroism, or through a catalytic effect), this does not mean necessarily that a well-defined crystalline inclusion complex can be isolated. The two main components of the driving force of the inclusion process are the repulsive forces between the included water molecules and the apolar CD cavity, on the one hand, and between the bulk water and the apolar guest, on the other hand. This second factor does not exist in the crystalline (dry) state. Therefore it is not uncommon that the complex formation is convincingly proven in solution, but the isolated product is nothing other than a very fine dispersion of the CD and the guest.

The absolute majority of all practical applications of CDs are based on their inclusion complex forming capacity.

4.4. Preparation of CD Complexes

The preparation of cyclodextrin inclusion complexes is simple; however, the conditions have to be "tailor made" for any guest substances [2, 4, 17]. The complexation may be performed in homogeneous solution, or in a suspension, under pressure, or by simple mixing of the components, by melting together the potential guest with the CD. The principle is illustrated in Figure 9.

When preparing a CD complex in solution the presence of water is absolutely necessary. Either pure water or some
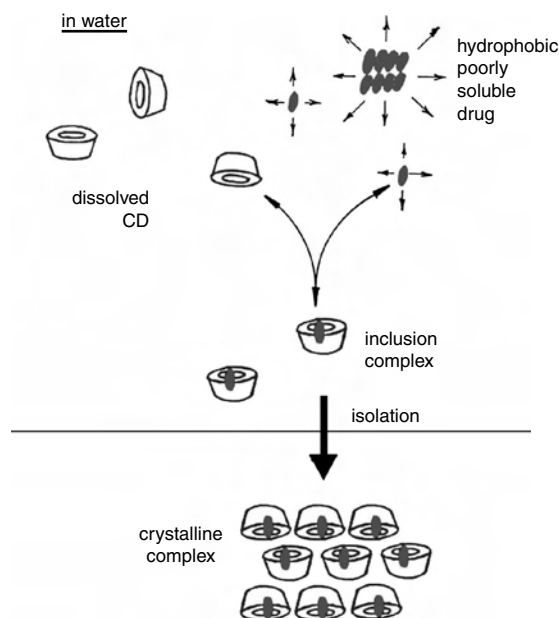
Figure 9. Schematic representation of the production of a CD complex.

aqueous system containing an organic solvent can be used. The use of organic solvent is necessary when the guest molecule is hydrophobic, or its melting point is over 100 °C. Therefore it cannot be dispersed finely in an aqueous CD solution. In such a case, organic solvents have to be used for solubilization of the guest.

Only a very limited number of organic solvents can be used, because the majority of them are excellent complex-forming partners. Using ethanol, at least a small amount of it will be retained very firmly in the formed complex (seldom more than 1–2% by weight of the product). Other solvents, like diethyl ether, do not form a stable complex with βCD; however, together with, for example, prostaglandin-$F_{2\alpha}$, a small amount of a ternary complex is formed, and then the diethyl ether cannot be removed, even at 105 °C in *vacuo*.

Complex for gases (xenon, chlorine, ethylene, krypton, carbon, dioxide, etc.) can be prepared by exposing a saturated αCD solution to the gas at 7–120 atm for 5–8 days at 20 °C.

In the so-called "slurry" method the CD and the guest are not dissolved but only finely suspended in water at ambient temperature with vigorous stirring. (The use of ultrasonification may even improve the procedure by accelerating the dispersion of solid phase.)

The reaction mixture is stirred intensively for 4–8 h (generally in the case of light oils, e.g., essential oils, terpenoids), or even for several days (24–72 h) in the case of heavy oils (e.g., natural waxes, higher terpenoids, balms) or when the guest substance is solid and no solvent is used. This method is the most feasible for industrial purposes.

A variation of this method uses even less water.

In the so-called "kneading" method the cyclodextrin is intensively kneaded with a small amount of water to which the calculated amount of the guest component is added directly without using any solvent. Because the initial cyclodextrin–water complex is energetically less favored than the CD–guest complex, the cavity water molecules will

be substituted by the guests. Besides this, the crystal lattice of the complex is also different from that of the water–CD complex. Therefore the reaction runs toward inclusion. Owing to their different crystal structure, the molecular layers of the inclusion complex formed on the surface of the parent cyclodextrin will dissociate from the crystal. Thus the entire cyclodextrin crystal quickly becomes disorganized and transformed into the guest–CD complex.

Industrially the solution or slurry is freeze-dried in the case of expensive and very sensitive guests, like prostaglandins, vaccines, and taxanes, or spray-died like omeprazole, or simply kneaded and dried in air or *in vacuo* like nitroglycerin, essential oils, etc.

5. INDUSTRIAL APPLICATIONS

5.1. Pharmaceutical Industry

The complexation of a drug molecule with a CD should be taken into consideration when the bioavailability and/or the chemical stability of the drug is not satisfactory, or the usual formulation methods do not result in an acceptable product. Indications for CD complexation include:

- The bioavailability of the drug (upon oral, dermal, pulmonar, mucosal, etc. application) is incomplete or irregular, because the drug is poorly soluble.
- The rate of dissolution is low; even in case of a complete absorption, the time to reach the effective blood level of the orally administered drug is too long.
- The drug is chemically unstable (on account of its autodecomposition, polymerization, or degradation by atmospheric oxygen, absorbed humidity, light, etc.). No marketable formulation with satisfactory shelf-life can be produced.
- The drug is physically unstable. Volatilization or sublimation result in losses. By migration the originally homogeneous product becomes heterogeneous. On account of its hygroscopicity it liquifies by atmospheric humidity.
- Because of the low solubility no aqueous eye-drop or injectable solution (or other liquid formulation) can be prepared.
- The drug is a liquid, but its preferred pharmaceutical form would be a stable tablet, powder, aqueous spray, etc.
- The drug is incompatible with other components of the formulation.
- The dose of the lipid(like) hardly homogenizable drug is extremely low. Therefore content uniformity of the product is problematic.
- The acceptability of the drug is bad, because of bad smell, bitter, astringent, or irritating taste.
- Relief of serious side-effects (throat, eye, skin, or stomach irritation) is required.
- Because of the extreme high biological activity (in case of drugs of extremely low doses) working with such powder is rather dangerous.

The advantageous results of CD complexation of (CD-complexable) drugs are as follows:

- improved bioavailability from solid or semisolid formulations (Fig. 10),
- enhanced stability, elongated shelf-life,
- reduced side-effects,
- uniform, easy to handle powders, even from liquids, and
- aqueous, injectable solution from poorly soluble drugs.

Speaking only of the numerous advantages of drug/CD complexation can be bitterly misleading, because there are just as many limiting factors which restrict the applicability of CDs to certain types of drugs, because not all drugs are suitable for CD complexation. Many compounds cannot be complexed, or complexation results in no essential advantages. Inorganic compounds generally are not suitable for CD complexation. Exceptions are nondissociated acids (HCl, HI, H_3PO_4, etc.) halogens, and gases (CO_2, C_2H_4, Kr, Xe, etc.). Inorganic salts as KCl, Fe salts, etc. can not be complexed.

General preconditions (not without exceptions!) to form a medicinally useful CD complex of a drug molecule are the following:

- More than five atoms (C, P, S, N) form the skeleton of the drug molecule.
- Its solubility in water is less than 10 mg/ml.
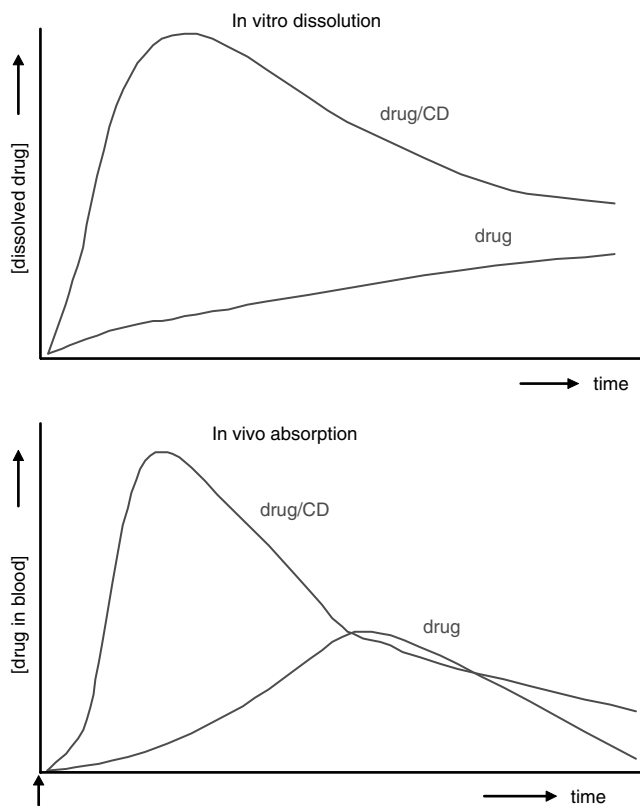
Figure 10. The bioavailability of a poorly soluble drug will be improved by CD complexation, because it will be dissolved faster, will attain a higher solubility, will be absorbed faster [the time between administration and onset of biological effect (e.g., pain reduction) will be shorter], and will result in a more complete absorption.

- Its melting point temperature is below 250 °C (otherwise the cohesive forces between the molecules are too strong).
- The molecule consists of less than five condensed rings.
- Its molecular weight should be between 100 and 400 (with smaller molecules the drug content of the complex is too low; large molecules do not fit the CD cavity).

Strongly hydrophilic, too small or too large molecules (e.g., peptides, proteins, enzymes, sugars, polysaccharides, etc.) generally cannot be complexed. Nevertheless, when large water soluble molecules contain appropriate complex forming side-chains (e.g., an aromatic aminoacid in a polypeptide) it will react with CDs in aqueous solutions, resulting in modified solubility and stability (e.g., the stability of an aqueous solution of insulin or many other peptides, proteins, hormones, and enzymes is significantly improved in presence of an appropriate CD).

An unavoidable limiting factor in selecting the drug for complexation is the dose of the complex that has to be administered. A fundamental requirement is that the mass of a tablet should not exceed 500 mg. Since the drugs to be complexed have molecular weights between 100 and 400, and the CDs have rather large molecular weights (972, 1132, and 1297 for α-, β-, and γCDs) a 100 mg complex contains only about 5–25 mg of active ingredient. If the single dose of a drug is not more than 25 mg then even a complex of 5% active substance content can carry the necessary dose in a single tablet of 500 mg weight. Otherwise the possibility of a powder sachet or sparkling-tablet formulation has to be taken into consideration. Thus, in the case of complex forming drugs, the relationship of the required dose and the molecular weight determines the feasibility of oral administration in CD complexed form.

Similarly, the volume of an injection should be less than 5 ml, or even better not more than 2–3 ml (i.e., to dissolve the necessary amount of the drug in 2–3 ml of 40% HPBCD solution 800–1200 mg HPBCD can be used). In liquid formulations the use of CD derivatives in large excess is possible. For example, in the case of prostavasin injection the molar ratio of prostaglandin E_1 to αCD is 1:11 (20 μg PGE_1 + 646 μg αCD/dose). In slow infusion the parenteral administration of several grams of a noncrystallisable CD derivative is possible. For example, in a liquid itraconazole formulation the weight ratio of the drug to hydroxypropyl βCD is 1:40! One single intravenous infusion dose of the commercial product Sporanox® contains 250 mg itraconazole and 10,000 mg HPβCD.

A 3000 I.U. D_3-vitamin tablet contains only 0.075 mg cholecalciferol. A prostarmon-E tablet contains only 0.5 mg PGE_2. The active ingredient content of a nitroglycerin tablet is 0.5–4 mg. These and similar drugs are ideal for CD complexation, but even the 20 mg piroxicam containing Brexin® tablet is a widely marketed, successful product.

If the K_a stability constant of a complex is low (less than 10^2 mol^{-1}) the existence of the complex can be evidenced in solution, but removing the water the obtained product is not seldom only a mixture (e.g., a coprecipitate) which contains the host and guest in an intimately fine dispersion. Removing the water is also an important component, as the driving force for complexation is

eliminated: the repulsive forces between water and the hydrophobic drug. Upon contacting with water the complex formation is an instantaneous process (i.e., in solution the guest is really included in the CD cavity, and the dissociation–association equilibrium is reached within seconds). In such cases the guest is not protected against external destructing factors, like oxygen or humidity, but if the guest is stable enough, only its low solubility means problems. Such intimate mixtures can be utilized for preparation (e.g., solid formulations of improved bioavailability). If, however, the guest is instable then only a full, also in anhydrous state prevailing complexation can help.

In the case of extremely high complex stability constants (over about 10^4 M^{-1}) the bioavailability can even be reduced. The complex is practically not absorbed, only the released, molecularly dispersed (=dissolved) drug molecules. In such cases the co-administration of an even better complex forming competitor molecule (e.g., phenylalanine) can help.

Hundreds of published examples illustrate the stabilizing, solubility, and bioavailability enhancing, side-effect reducing, and advantageous technological effects of CD complexation of the instable, poorly soluble, locally irritating drugs. Table 2 illustrates a selection of CD containing drugs, approved and marketed in various countries.

5.2. Food Industry

Flavor substances are generally volatile, easily deteriorating substances. Most of them (e.g., terpenoids, phenylpropan derivatives) form stable complexes with CDs and in dry complexed form remain stable for long time, without any further protection, at room temperature. Such powder flavors are approved, produced, and used in several countries like France, Japan, and Hungary. For example lemon-peel oil/βCD complex mixed with powdered sugar is used in pastries or spice-flavor mixtures complexed with CDs in preparation of canned meat and sausages. Peppermint oil/βCD complex is used in chewing gum, etc. In Germany garlic oil/βCD complex is marketed as odorless dragées (to substitute garlic and a number of various unstable garlic preparations, consumed to reduce blood cholesterol level).

βCD cannot be considered tasteless. Its taste threshold value is lower than that of sucrose (detection: 0.039% cf. 0.27%; recognition: 0.11% cf. 0.52%). An aqueous solution of a 0.5% βCD was as sweet as sucrose, and a 2.5% solution was as sweet as a 1.71% sucrose solution. When βCD is used in food processing, its sweetness cannot be ignored. Sucrose sweetness and βCD sweetness are additives.

Emulsion stability, water retention, and storability can be improved in many cases by addition of cyclodextrins to the food component or food. A solid composition containing sugars and amino acids for food or pharmaceutical purposes is known to undergo browning and caking. This can be prevented by incorporating in such a composition at least 40% of an oligo- or polysaccharide, such as dextrin, starch, or CD, with a water content of not more than 3%. For example the addition of 20% βCD to a powdered juice consisting of anhydrous glucose, sodium L-aspartate, DL-alanine, citric acid, and inorganic salts resulted in a product of excellent stability. After 30 days at 40 °C there was no apparent discoloration or caking. The control, without βCD, began to cake on the second day and to turn brown on the fourth.

CD can be utilized for the preparation of stable water-in-oil emulsions, such as mayonnaise and salad dressing. Natural food coloring components in tomato ketchup can be stabilized by adding 0.2% β-CD. The ketchup thus prepared

Table 2. Some approved and marketed CD-containing pharmaceutical products.

Drug	Trade name	Formulation	Indication	Company/country
PGE$_1$-αCD 20 μg/amp.	Prostavasin	intraaterial	chronic arterial occlusive disease, etc.	Ono, J. Schwarz, D.
PGE$_1$-αCD 500 μg/amp.	Prostadin 500	infusion	controlled hypotension during surgery	Ono, J.
PGE$_1$-βCD	Prostarmon E	sublingual tablet	induction of labor	Ono, J.
OP-1206-γCD	Opalmon	tablet	Buerger's disease	Ono, J.
Piroxicam-βCD	Brexin, Cicladol	tablet, sachet, and suppository	Analgesic, antiinflammatory	Chiesi, I, Masterpharma, I.D., B., NL., etc.
Garlic oil-βCD	Xund, Tegra, Allidex, Garlessence	dragées	antiatherosclerotic	Bipharm, Hermes, D., Pharmafontana, H., D., USA
Benexate-βCD	Ulgut, Lonmiel	capsules	anti-ulcerant	Teikoku, J., Shionogi, J.
Iodine-βCD	Mena-Gargle	garling	throat disinfectant	Kyushin, J.
Dexamethanose, Glyteer-βCD	Glymesason	ointment	analgesic, antiinfammatory	Fujinaga, J.
Niroglycerin-βCD	Nitropen	sublingual tablet	coronary dilator	Nippon Kayaku, J.
Cefotiam-hexatil-αCD	Pansporin T	tablet	antibiotic	Takeda, J.
New oral cephalosporin (ME 107)-βCD	Meiact	tablet	antibiotic	Meiji Seika, J.
Thiaprofenic acid-βCD	Surgamyl	tablet	analgesic	Roussel-Maestrelli, I.
Chlordiazepoxide-βCD	Transillium	tablet	tranquilizer	Gabor Ar.
Hydrocortisone-HPβCD	Dexacort	liquid	mouthwash against ahpta, gingivitis, etc.	Icelandic Pharm., Isl.
Itraconazol-HPβCD	Sporanox	liquid	AIDS, oesophagal candidiosis	Janssen, B
Diclofenac-Na	Voltaren Ophtha	eyedrop	anti-inflammatory	Novartis CH,D,F, etc.

did not discolor on heating at 100 °C for 2 hours, whereas the control did. Addition of CDs to emulsified foods or cheese can increase water retention and shelf life. In processed meat products CD improves water retention and texture.

The addition of 0.005 to 1% βCD to canned citrus products prevents precipitate formation, which is mainly due to the poorly soluble, bitter tasting hesperidin and naringin. When the concentration of these substances is too high in grapefruit juice resulting in a bitter taste, they can be selectively removed by passing the fruit juice through a cyclodextrin polymer filled chromatographic column.

In Belgium low-cholesterol butter is produced. The molten butter is mixed with βCD which does not react with triglicerides but forms complexes with cholesterol, and the βCD complex is easily removable from the butter. More than 90% of the cholesterol can be removed in one step. The butter does not retain any CD. Other low-cholesterol milk products, like cheese, cream, or even low-cholesterol eggs, are produced by this technology.

CDs, incorporated into food packaging plastic films very effectively, reduce the loss of aroma substances. Incorporating fungicide CD complexes into films—for example, packaging of hard cheeses—significantly elongates the shelf life of the product by inhibiting the rapid development of mold colonies on the surface of the packaged cheese.

5.3. Cosmetics and Toiletry Industry

Many active principles of interest in cosmetics have been complexed with cyclodextrins achieving very positive, interesting results. For instance, the inclusion of retinol in hydroxypropyl-β-cyclodextrin leads to a water-soluble product, sufficiently stable, of higher bioavailability and lower toxicity compared to free retinol. Similarly to retinol, it is possible to include in cyclodextrins almost all (fat-soluble) vitamins, with unquestionable advantages as concerns their stability and bioavailability. The main advantages of using CD complexes in functional dermocosmetics are similar to those in the pharmaceutical formulations:

- increase of the bioavailability of incorporated active components (vitamins, hormones, glycolic acid, depigmenting agents, etc.)
- protection from oxidation (vitamin A, retinol, hydroquinone, arbutin, DHA, etc.)
- reduction of toxicity and aggressivity (glycolic acid, hydroquinone, essential oils, fragrances, etc.)
- formation of hydrosoluble complexes even if the incorporated molecule is liposoluble
- increased stability of emulsion and gel products
- easy formulation (the complex is added to the final formulation, dispersing it in the aqueous phase at 35–40 °C)
- no added preservatives

Some special advantages were observed for the sunscreen agent/CD complexes:

- increased stability (photostability) of cream formulations
- decreased cytotoxicity

- increased/improved functional activity
- reduced smell
- reduced fabric staining

Thus the markedly increased photostability is associated with decreased phototoxicity and/or photosensitization risk coming from the production of free radicals primed by the sun photochemical attack on the filter molecule itself.

Cyclodextrins are suitable not only for real skin treatment products, but also for the formulation of make-up cosmetics which are to stay on the face and skin for a number of hours (about one whole day).

CD complexation can be used to stabilize emulsion, color, and perfume or aroma. For instance, most perfume concentrates, such as rose oil, citral, and citronellal, can form complexes and can be used in any solid preparation, such as powdered detergents. The collateral irritant effect caused by a scent in a shampoo can be reduced through the use of CD complexes. A solution of iodine-βCD can be used as a deodorant for the body, for baths, or as a refresher for the oral cavity. CD complexes with detergent molecules can act as antifoam agents, etc.

5.4. Textile Industry

The first cellulose-CD copolymer was described in 1980. Alkali-swollen cellulose fibers were reacted with CD and epichlorohydrin. The chemically bound CD retained its complex forming ability and could be "loaded" with biologically active guests, like drugs (to prepare medical bandages), insect repellents, antimicrobial agents, etc. The drug is adsorbed partly to cellulose and partly complexed with CD. Upon contact with skin the fabrics made from such fibers ensure immediate drug release from cellulose and a sustained drug release from CD.

α-, β-, and γCD has been grafted onto a nonwoven polypropylene support. The fabric was first activated by electron beam irradiation, followed by the graft polymerization of glycidyl methacrylate, a polymerizable monomer carrying epoxide groups. CDs were then fixed onto the fibers by reaction with the epoxide groups. The final CD content after this second step of the reaction increased to 150 mmol per gram of support (20% in weight). 2-Naphtol and p-nitrophenol were sorbed in batch and dynamic filtration systems by the CD grafted supports.

Polycarboxylic acids such as citric acid, 1,2,3,4-butanetetracaboxylic acid, or polyacrylic acid have been used as cross-linking agents of cyclodextrins depending on the reaction conditions, and according to the adapted experimental process, polyesters of CDs or textiles carrying CDs could be obtained. Permanent fixation of CDs onto textiles occurred either through reaction of the functional groups of the fibers (covalent bonding), or through the formation of a cross-linked polymer that is tangled up in the fibers (noncovalent bonding) (Fig. 11).

Presently the use of monochlorotriazinyl-βCD seems to be the most promising approach. βCD was condensed with cyanuric chloride in an aqueous medium at 0–5 °C in the presence of NaOH to give a 4-chloro-6-hydroxy-triazin-2-yl-βCD Na salt with degree of substitution of active Cl 0.4. This product is a reactive CD derivative that can be
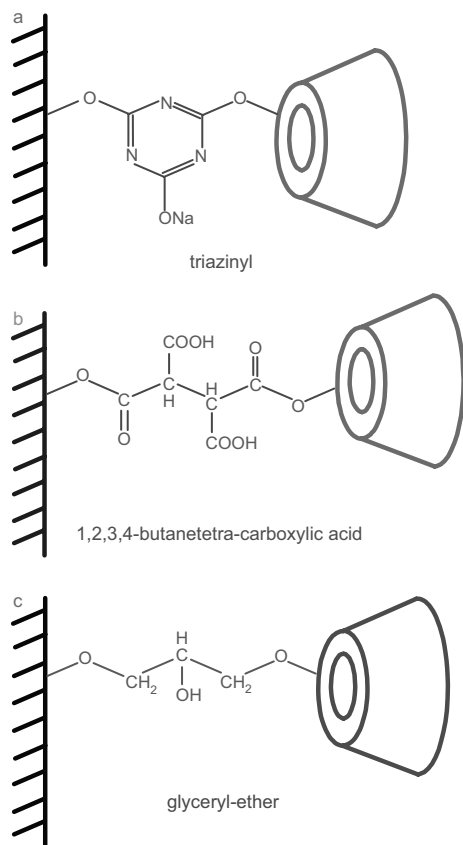
Figure 11. Fiber-cyclodextrin binding types: (a) triazinyl chloride reacted with cyclodextrin and the product reacted with the fiber; (b) polycarboxylic acid reacted with the fiber, the formed ester converted to cyclic anhydride, and then it reacted with cyclodextrin; and (c) the cyclodextrin and epichlorohydrine reacted with strong alkaly treated cellulose.

covalently fixed to nucleophilic substrates by a condensation reaction carried out by the usual finishing procedure. This new type of surface modification means a permanent transfer of CD properties to the treated materials. The finish is applied by standard methods—analogous to those of reactive dyeing—on conventional equipment. The dissolved monochlorotriazinyl-βCD (MCT-βCD) is drawn up from a dipping bath, the textile is squeezed, and the CD is fixed on the fiber at elevated temperature. Unattached CD is simply removed by washing. Both alkaline and acidic methods for MCT-βCD finishes have been developed. While fixing temperatures and times are the main parameters for the fixing reaction, other variables such as dampness of the fabric and the MCT-βCD concentration are also important. An MCT-βCD finish is wash resistant. Cotton for T-shirts, sports socks, and so forth is particularly amenable to CD modification. However, the latest studies also reveal that very good fixing results may be obtained with blended fabrics, such as cotton/polyurethane and cotton/polyurethane/polyamide. This is especially important for top-of-the range lingerie. Given suitably adapted processes, moreover, wool can also be finished with MCT-βCD. Encapsulation of sweat or cigarette smoke greatly reduces the intensity of odors on articles of clothing or furniture textiles. In the washing machine, the encapsulated substances are washed out, and

the CD is free again to trap odors. CD textiles can be recharged selectively with the most diverse guest substances by dipping or spraying. Particularly interesting is the treatment with fragrances and antimicrobial or pharmaceutical preparations which can be released continuously over a long period on exposure to moisture. The higher the level of moisture, the more guest substance is liberated. CD-modified fabrics, therefore, "respond" to varied ambient conditions (Fig. 12).

In Germany 5 million people suffer from neurodermitis, 2 million from psoriasis, and a further 3 million from dermal diseases of occupational origin (like hairdressers' allergic reactions on the hands, athlete's foot, etc.). The corresponding article of clothing (underwear, gloves, socks) can be loaded with the necessary antifungal, antihistaminic, anti-inflammatory, etc. agents.

A further application is towels, which start smelling after drying one's hands. Also bed linen may release a pleasant odor after going to bed. Curtains with cyclodextrins
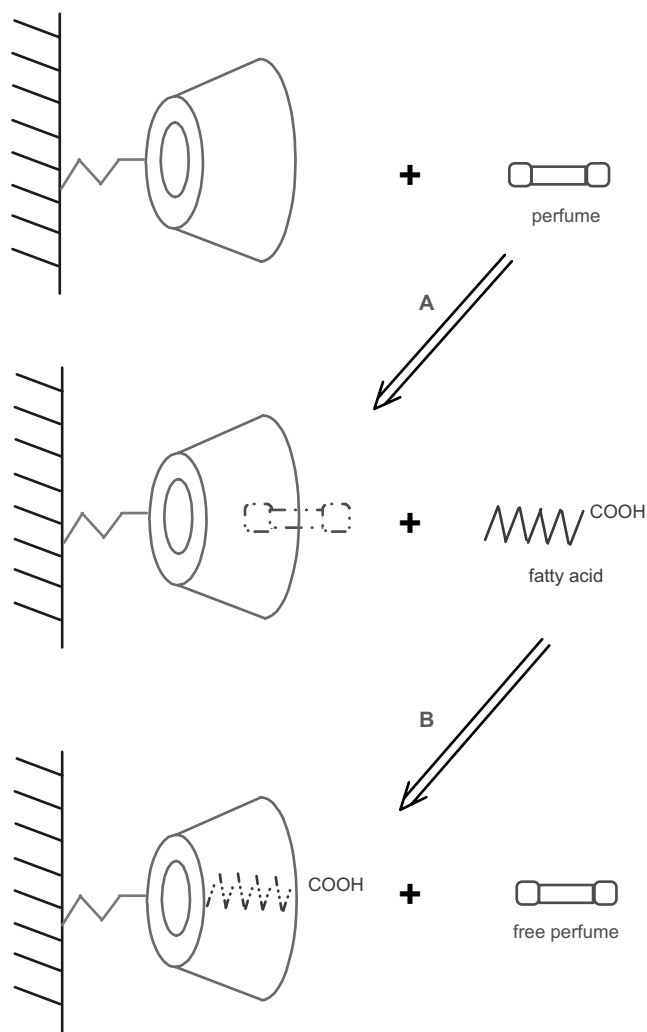
Figure 12. Guest exchange, for example, perfume release and sweat component entrapment. (A) Loading the fixed cyclodextrin with perfume. (B) During wearing, upon the effect of sweat, humidity, and excreted short chain fatty acids, the guest will be exchanged, the perfume gets released, and the fatty acids are entrapped.

can be used to improve the air in rooms or offices with smokers.

The identification of the organic compounds excreted from patients through their skin enables new methods in medical diagnostics. Up to now blood or urine tests have normally been used due to the problems of taking a sweat probe from a patient. This becomes easy by wearing for 24 hours a T-shirt which contains chemically bound βCD. After extraction of the T-shirt, the substances—characteristic, for example, of metabolic disorders—excreted through the skin are detectable by gas chromatography. The complexation of organic substances from sweat results in a preconcentration and their identification becomes easier.

Mixing CD or CD–polymer fragrance complexes to the melt mixtures of synthetic fiber polymers (e.g., polyester) and weaving the fabric from such fibers, washfast fragrant fabrics can be produced.

5.5. Biotechnology

The majority of biotechnology processes mean an enzyme-catalyzed transformation of a substrate in aqueous medium. The main difficulties which used to arise were the following:

- The substrate is hydrophobic, sparingly (or hardly) soluble in water.
- The enzyme or the enzyme-producing microbial cells are sensitive to the toxic effects of the substrate or to inhibitors which can even be the product of the transformation.
- The substrate or the product is unstable under the conditions of the enzymatic transformation.
- Isolation of the product from the very heterogeneous system is difficult.

Cyclodextrins and their derivatives enhance the solubility of complexed substrates in aqueous media and reduce their toxicity, but they do not damage the microbial cells or the enzymes. As a result, the enzymatic conversion of lipophilic substrates can be intensified (accelerated, or performed at higher substrate concentrations), both in industrial processes and in diagnostic reagents, the yield of product-inhibited fermentation can be improved, organic toxic compounds are tolerated and metabolized by microbial cells at higher concentrations, and compounds in small amounts can be isolated simply and economically from complicated mixtures.

Examples illustrate the rapidly growing and promising uses of cyclodextrins in various operations: the intensification of the conversion of hydrocortisone to prednisolone, the improvement in the yield of fermentation of lankacidine and podophyllotoxin, the stereoselective reduction of benzaldehyde to L-phenylacetyl carbinol, and the reduction in toxicity of vanillin to yeast, or organic toxic substances to detoxificating microorganisms. In the presence of an appropriate cyclodextrin derivative (e.g., 2,6-dimethyl-β-cyclodextrin), lipidlike inhibitor substances are complexed. The propagation of *Bordatella pertussis* and the production of pertussis toxin therefore increases up to a hundredfold. Cyclodextrin and their fatty acid complexes can substitute mammalian serum in tissue cultures.

In recent years Leprae bacillus (Mycobacterium leprae) was considered to be not cultivable under *in vitro* conditions. The most important energy source for bacillus is palmitic (or stearic) acid which, however, cannot penetrate through the thick strongly hydrophilic shell of the Mycobacterium. Solubilizing, however, the fatty acids (or fatty alcohols) with dimethyl-β-cyclodextrin, the Mycobacterium can be cultivated *in vitro*, on synthetic medium. This discovery will facilitate the screening of drugs against similar difficultly cultivable microorganisms.

The biological remediation of carcinogenic polyaromatic hydrocarbon polluted soils is a very slow process, because the dangerous polluting hydrocarbons are adhered very strongly to the soil particles. They are not available for the soil micro-organisms. Adding CDs (for example, the randomly methylated βCD) to such soils, the CD mobilizes the hydrocarbons and makes them available for the micro-organisms, resulting in an accelerated remediation of the soil.

5.6. Chemical Industry

Fragrant paper or paper containing protective substances can be prepared using CD complexes of perfumes, insecticides, rust inhibitors, mold- and mildew-proofing agents, fungicides, and bactericides. For example, fenitrothion βCD complex sprayed on a wet paper web, passed between drying rollers heated to 100 °C, resulting in an insecticide containing paper, was shown to be effective for more than 6 months.

Conservation of wood-made products which are prone to attack of micro-organisms, like frames of windows, doors, and buildings constructed from wood, usually has been made by impregnating the wood with fungicides, which are generally water insoluble. Therefore they had to be dissolved in organic solvents. After impregnation the solvents escaped into the atmosphere. A new process dissolves the fungicides in aqueous CD solutions; the impregnation and conservation of the woods can be made without using organic solvents.

Emulsion-type coatings (paints) contain emulsion polymer binders, to give—after drying—a resistant, continuous protecting film on the coated surface. To ensure the formation of a good film, the applied layer has to contain various compatible components, like solvent, pigment, thickener, and binder. The rheological properties of the paint are determined by the thickener, which is usually a hydrophobically modified polymer, like polyurethane, polyacrylamides, cellulose ethers, etc. To avoid a concomitant too high viscosity (which makes difficult the formation of a uniform coating of the surface to be covered) viscosity suppressors has to be added to the emulsion. Adding organic solvent to such emulsions, the viscosity can be reduced, but use of organic solvents has to be avoided because of safety, health-damaging, environmental polluting effects. Also surfactants can strongly reduce the viscosity of such emulsions, but their use results in the formation of a less resistant coating.

The viscosity enhancing effect of hydrophobically modified macromolecules in aqueous emulsions is based on the hydrophobic–hydrophobic interactions between these molecules. Adding CDs to this emulsion the CD molecules

will associate with the hydrophobic sites and, being strongly hydrated, inhibit the association of the macromolecules, resulting in a strong reduction of the viscosity. The RAMEB was shown to be the most effective viscosity suppressor.

The CD complexes are compatible with thermoplastic resins. Mixing a dry pulverized CD complex of a perfume, for example, a geraniol αCD complex, with a thermoplastic resin (polyethylene), and molding it yielded plastic products with a long lasting (at least 6 months) fragrance. Rapid loss of the perfume by volatility and thermal decomposition can be avoided in this way.

Mixing CD complexes of thymol, eugeneol, isobutylquinoline, etc., to molten PVC (=polyvinylchloride) a natural leather odor emitting (leatherlike) material was prepared (e.g., for automobile door internal coverings).

The epoxyresin adhesives are produced and stored as separated components mixed just before utilization. Complexing the curing agent (polymerization catalyst) with βCD a one-package composition can be prepared. Upon layering such a composition between metal plates and heating to 130 °C for 5 min, binding will take place.

Properties of cyanacrylate adhesives can be improved significantly by heptakis(2,6-di-O-butyl-3-O-acetyl)-βCD. The ethyl-2-cyanacrylate monomer is stabilized with 20 ppm phosphoric acid, 20 ppm SO_2, and 100 ppm hydrochinon. Various amounts of the dibutyl-acetyl-βCD were added to this mixture, and using an adhesive, for example, to bind hard cartoon papers by quick heating to 200 °C, the polymerization (binding) of cyanacrylate has been accelerated, and the tear-strength of the binding increased significantly.

Explosive substances, like nitroglycerin or isosorbidedinitrate, when complexed can be handled without any danger. The pernitro-γCD complex of the extremely explosive nitramine can be used as a controlled missile propellant.

Important properties such as relative sensitivity and the fog of silver halide containing photographic materials can be improved by adding CDs to the light sensitive photographic gelatin layers.

Additives, dyes, stabilizers, and fog inhibitors used in the photographic industry should be fixed to a certain layer of the film or photopaper. This can be achieved by using derivatives with "heavy" side chains. It seems to be more convenient to prepare the water soluble polymer complexes of these substances. In complexed form their mobility is markedly reduced, and they become fixed to the required layer. A diminished diffusion can be observed either on preparing, processing, or storing the film. Another advantage of the soluble polymer complex is that poorly soluble or even water insoluble stabilizers can be applied to the film in aqueous solutions. A CD-gelatin composition as photographic layer shows a lower water absorption and accelerated diffusion of the developing agents.

Silane resins are made using a 1,5-cyclooctadieneplatinum catalyst. Once the catalyst is added, the reaction proceeds. Complexing the catalyst with βCD, it became possible to produce a single component heat-curable silicone with a shelf life exceeding 7 months since complexation prevented immediate catalysis and reaction. No gelation occurred at ambient temperature, only when the mixture was heated up to 150 °C.

Active ingredients of pesticides (insecticides, fungicides, herbicides, etc.) can be complexed with the same technologies and same consequences as drug molecules.

The selectivity of an insecticide can be improved. For example, complexing an insecticide, which kills herbivorous insects, will not be toxic for the honey-bee. Stability against sunlight accelerated decomposition of pyrethroids can be improved ensuring a longer lasting insecticidal effect. Wettability or solubility of poorly soluble benzimidazole type antifungicides can be improved, allowing the reduction of the dose and the pollution of the environment. The possibilities of utilization of CDs in pesticide formulations have already been elucidated in numerous scientific papers. However, until recent years the price of βCD did not allow its utilization for such purposes because the pesticide industry is very cost sensitive. By the end of the 20th century the price of βCD dropped to such a low level that the price will no longer be a restricting factor in its utilization for pesticide formulations.

The preparative- and technical-scale chiral resolution of enantiomers is one of the biggest challenges in industrial utilization of CDs. The utilization of CDs in this area is still in its infancy but some results are encouraging. For example, a continuous method for separation of dichlorophenyldichloronapthalenone enantiomers has been published using different γCD derivatives in a multiple solvent extraction technology. A continuous, easy to scale up preparative chiral separation device, a slowly moving "chiral" belt coated with 3,5-dimethyl-phenyl-carbamoyl-βCD, enters into and passes through different solutions in separate troughs. The solutions contain different solvents: trough 1 contains the racemic analyte (R,S-oxprenolol), troughs 2 and 3 are filled with a hexane:i-propanol mixture for enantioselective desorption of analyte, while only hexane is in trough 4 for rinsing/regenerating the belt. The continuous process results in 2 hours in the enrichment of R-oxprenolol isomer in trough 1, while trough 3 becomes rich in the S-isomer (about 68%). Despite the encouraging results in the preparative scale resolution a reliable and economic technology for the routine enantiomer separations in 1 or 10 g pure enantiomer per batch still remains a challenging task of the future.

5.7. Analytical Chemistry

5.7.1. Chromatographic Separations

CDs and mainly specific derivatives are widely used in chromatographic separations. In 1990–2000 about 25 papers were published monthly on successful application of CD in gas or liquid chromatography. In gas chromatography the CDs are used only in the stationary phase, while in high pressure liquid chromatography (HPLC) the CD is used either as dissolved in the mobile phase or bound to the surface of the stationary phase. In capillary zone electrophoresis the most used chiral selectors are the CDs and their anionic, cationic, or alkylated derivatives.

5.7.2. Diagnostics

The actually used and marketed chiral separation products include HPLC, gas chromatographic columns, and capillary electrophoresis buffer additives.

In medicinal diagnostic kits frequent problems are the limited, uncertain solubility of some essential component, the stability, and the storability of the kit. Complexing with CDs as the typical components, such problems can be eliminated. Frequently intensity of color reactions or of fluorescence can be significantly enhanced by the presence of CDs, resulting in a higher sensitivity of the method.

In the following a few examples illustrate the application of CDs in clinical sample preparation, in enhancement of sensitivity of analytical methods, CDs used for solubilization and/or stabilization of reagents, and CD based sensors and indicators.

In clinical chemistry:

- βCD is used for the selective and highly effective extraction of serum Digoxine in one single run enabling the convenient determination of the drug in biological samples by the RIA method.
- βCD is also used for the determination of steroid hormones in human serum traditional solvent extraction of serum samples, followed by a re-extraction of the steroids into an aqueous cyclodextrin solution.
- A pre-column containing immobilized βCD-sulfate was successfully applied for the on-line enrichment and separation of heparin binding proteins.
- The treatment of lipemic serum with aqueous solutions of CDs will produce an immediate and quantitative precipitation of the lipoproteins. αCD was found to precipitate chylomicrons, very low, low, and high density lipoproteins.
- CDs can selectively remove disturbing components from complex biological samples. The presence of fatty acids in blood samples disturbs colorimetric analysis and causes an underestimation of the actual Ca^{2+} level. αCD was found to eliminate this interference, completely.
- An automated LDL-cholesterol assay has been recently marketed that employs αCD together with Mg ions to effectively mask interfering lipoproteins present in clinical samples.

Through complexation of analyte and/or the color-forming reagent by CDs in the spectrophotometric determination of a wide variety of compounds, the sensitivily of the method is significantly improved. For example:

- The spectrophotometric determination of copper in leaves and in human hair was improved by CDs, as the sensitivity of the color reaction of Cu(II) and mesotetrakis-(4-methoxy-3-sulfophenyl) porphyrin was enhanced by 50% in the presence of αCD.
- In the determination of microamounts of Zn based on the Zn-dithizone color reaction sensitized with βCD, the apparent molar absorptivity at 538 nm is 8.37 times larger than that in the absence of βCD.
- CDs often can result in significant enhancement of the fluorescence or phosphorescence of the complexed analyte. A substantial enhancement of the fluorescence emission of aflatoxins in the presence of aqueous solutions of α- and β-di-O-methyl-βCD and hydroxypropyl-βCD was observed, which enabled the determination of minute amounts of these toxins in food samples.

- Determination of selenium in biological matrices was improved using βCD by which the relative fluorescence of the reagent 4,5-benzopiaselenol is about 150-fold higher than that without CD.
- The application of βCD in beryllium analysis allowed the determination of 10–40 ng/mL beryllium, compared to 60–500 ng/mL in the absence of the CD.
- CD-assisted spectrofluorimetric assay enabled the detection of mescaline in the 0.8–1.4 ppm range.
- The application of CD enabled a limit of detection of 0.07 μg/ml zirconium.
- βCD stabilizes dichlorofluorescein against autoxidation and enhances its fluorescence, a dual benefit that can be used to improve the determination of serum uric acid and glucose.
- Improved sensitivity was reported on trace cadmium determination from hair, nails, water, etc., which was based on the enhancement of the chromogenic reaction due to βCD complexation. This method enabled the determination of about 0.4 ng/ml cadmium.

The solubilizing effect of cyclodextrin complexation for lipophilic reagents or analytes provides the possibility to replace organic solvents and detergents with aqueous CD solutions. For example:

- Complexation of the unstable, insoluble substrate L-γ-glutamyl-4-nitroanilide with CDs eliminated the errors occurring in the determination of γ-glutamyl-transferase activity caused by its poor solubility.
- Poorly soluble antigens can be solubilized by βCD in immunoassay used for determination of progesterone in human serum by the solid phase EIA (enzyme immunoassay) method.
- Fluorescent labeling of proteins done with dansyl-chloride organic water-soluble complex with βCD enables the labeling of proteins in aqueous solutions.
- SIN-1A/γCD complex is a stable analytical standard suitable for reliable determination of NO and calibration of NO detectors.
- By complexing highly unstable ortho-phenylene-diamine, an immunodiagnostic reagent with βCD, and simply tabletting the solid complex, a stable reagent with extended shelf life was prepared.

5.7.3. Sensors

CD-based supramolecular assemblies or covalent new chemical entities have been developed as selective sensors, detectors, and indicators. For example:

- A benzene-vapor detecting piezoelectric quartz crystal was constructed by coating the surface with 2,6-O-$tert$-butyl-dimethyl-silyl-αCD. This detector is highly selective for benzene even in large excess of methane, propane, butane, pentane, ammonia, nitrobenzene, and toluene.
- βCD fixed on a quartz oscillator surface was shown a very sensitive sensor for cholesterol suitable for determination of blood cholesterol level.
- Various compounds including steroids, bile acids, terpenes, etc. have been selectively detected with a specifically designed cromphore bearing CD derivatives.

- Voltammetric responsive sensors based on organized self-assembled βCD derivatives in monolayers on gold electrodes were studied for analysis of electroinactive organic analytes.
- A fiber-optic CD-based sensor was developed using laser excitation and fluorescence detection, with βCD as the reagent phase immobilized at the tip of an optical fiber. The sensitivity of the fiber-optic CD-based sensor was found to be 14 times greater than that of a bare optical fiber.
- Lipophilic cyclodextrins were used for construction of guanidinium ions and choline, acetylcholine selective sensors.

5.7.4. Standards

CD complexation offers the possibility for preparation of flavor standards.

There are cases when human taste and smell sensors cannot be substituted even by the most sophisticated analytical instruments. In organoleptic evaluation, comparison of identical food products of different origin—for example, beers—the dosing of extremely small but exactly known amounts of flavor components (for example ppm amounts of mercaptanes, butyric acid, hydrogen sulphide, etc.) is necessary. To store and dose these volatile, unstable substances becomes very simple when they are complexed with CDs, diluted with inert excipient to the appropriate grade, and filled in known amounts into hard gelatine capsules. Adding the content of one or more capsules of different flavors to the sample at sensoric "titration," the differences between the products can be expressed unambiguously and numerically.

6. CYCLODEXTRIN BASED NANOSTRUCTURES

Cyclodextrins belong to the most appropriate rotaxane forming molecules. A long slim guest molecule can be threaded through the CD cavity. Then both ends can be terminated by bulky groups or the terminal group can be ionized and therefore the threaded molecule cannot slip out of the cavity (Fig. 13). Upon various environmental effects (pH, irradiation, electric field, etc.) this threaded molecule may rotate
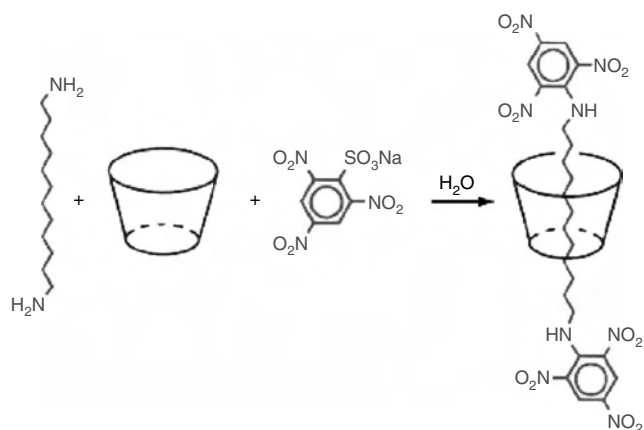
Figure 13. Principle of the CD-rotaxane formation.
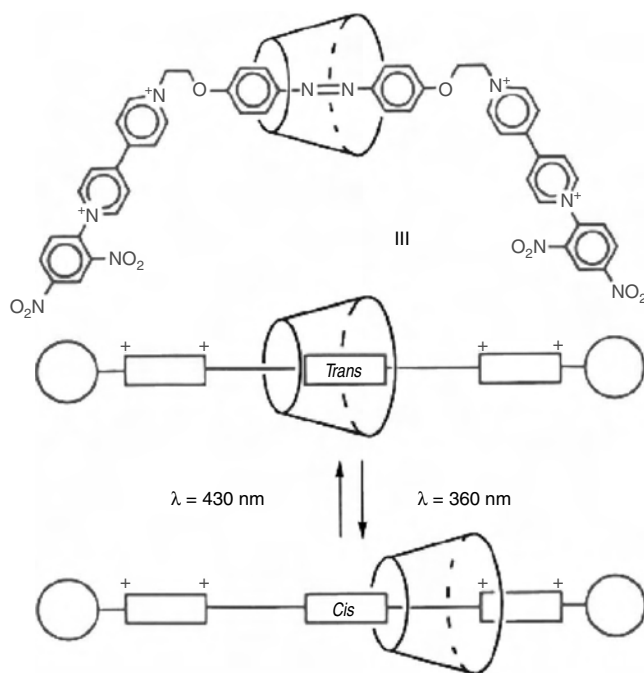
Figure 14. A light driven shuttle.

around its axis; otherwise its mobility is restricted. Similarly the CD-ring mobility is also restricted; it can move only along the axis.

This way a molecular "shuttle" or "switch" can be constructed. Threading an azobenzene derivate through an αCD ring, the azo-bridge will be allocated in the CD cavity. Attaching 2,4-dinitrophenyl-bipyridinium "stoppers" to both ends of the threaded axis molecule, a shuttle rotaxane is formed. Irradiation of its aqueous solution with UV light (360 nm) causes isomerization of the azobenzene moiety from a *trans* to *cis* configuration: the isomerization can be reversed when the solution is irradiated with visible light (430 nm). This configuration change is reflected in a dramatic alteration of the geometry (Fig. 14). The αCD ring resides around the azo-bridge; when the azobenzene unit adopts the *trans* configuration the αCD ring migrates toward one of the bis-(methylene) spacers. The photoswitching process is reversible, and this is an excellent example of a light driven molecular shuttle.

Threading a long slim guest through a number of CD rings, a "molecular necklace" can be prepared (Fig. 15). Recently the nylon/CD complex, by reacting the βCD complex of hexamethylene diamine with CD-complexed diacylchloride, has been published. This way new materials with quite interesting properties can be produced.

"Molecular tubes" can be prepared for example by complexing polyethylene glycol-bis-amin with αCD; then the formed polyrotaxane is reacted with 2,4-dinitrofluoro benzene. This way both ends of the long chain guest are terminated by bulky groups. Reacting this polyrotaxane with epichlorohydrine the vicinal CD rings will be interconnected through glyceryl bridges between the primary and secondary sides of the CDs. Finally, upon the effect of strong alkali, the dinitrofluorobenzene groups will split off and the long polymer chain will slip out from the polymeric tube (Fig. 15).
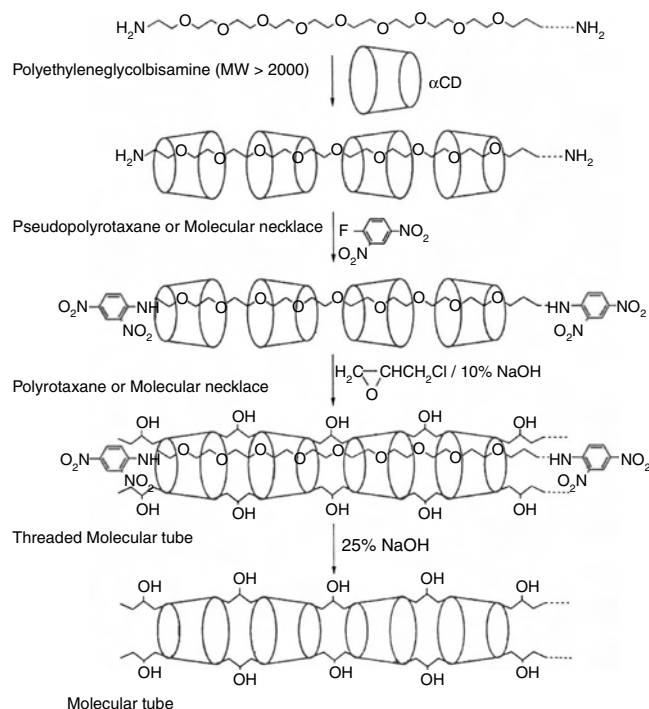
Figure 15. Scheme for the sequential formation of αCD pseudopolyrotaxane, polyrotaxane (molecular necklace), and molecular tube.

If the threaded molecule itself is closed to form a closed ring, then the formed structure is called catenane or, if it includes more than one CD ring, polycatenane (Fig. 16).

Metal ions can be complexed with CDs in different ways:

- The metal ion reacts with the hydroxyl groups of the CD molecule.
- The metal ion forms a coordination complex with the usual organic ligands and this coordination complex will be included in the CD cavity.
- The metal atom is bound covalently in a metallorganic compound which will form a regular inclusion complex with a CD molecule.
- The metal ion is bound by an anhydro-CD.

In the first case, a hydroxo complex is not an inclusion complex; more likely it is an outer sphere complex (e.g., Cu^{2+} or Mn^{2+} ions in alkaline solutions form such CD-hydroxo-metal complexes).

The second case means the formation of ternary complexes: CD + organic ligand + metal ion. This is a real second sphere coordination metal complex. For example, a ferrocene is a coordination complex which consists of an iron ion, sandwiched between two cyclopentadiene molecules, forming a stable iron-coordination complex. This coordination complex can form a true inclusion complex with CDs and this inclusion strongly modifies the physical and chemical properties of the included coordination complex. The technecium-99 ethylcysteinate dimer for brain imaging or the technecium-99 nitrido-dithiocarbamate for myocardial scintigraphy can be used only after solubilizing them with an appropriate CD.
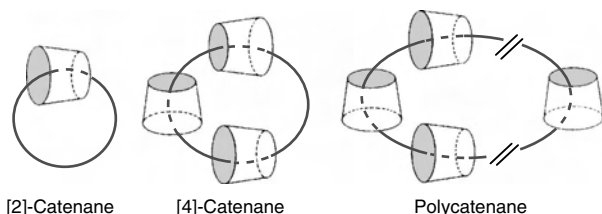
In the third case, the complexation of organometallic compounds—this is a binary complex—also results in the modification of important properties of the included compound (e.g. in pharmaceutical preparations).

The ferrocene complexes can be prepared easily, in crystalline form, with good yield. The excess of sublimable ferrocene can easily be removed by vacuum sublimation, while the CD-bound ferrocene is stable up to the temperature of the caramelization of CDs.

The orientation of an ionizable ferrocene within the CD cavity depends on the pH of the solution (Fig. 17). On the basis of circular-dichroism spectra the ferrocene carboxylic acid was assumed to orient itself inside the CD cavity parallel to its axis, while the ionized carboxylate ion was perpendicular to it (at pH 9 in water).

In aqueous solution the antitumor carboplatin forms an 1:1 complex only with αCD, but not with β- or γCD (Fig. 18). The cyclobutane ring penetrates the CD cavity, with additional stability arising from hydrogen bonds between the ammine ligands and hydroxyls. Also dimethyl-αCD forms a similar complex with carboplatin. In contrast, the platinum phosphine complex trans-Pt(PMe$_3$) Cl$_2$(NH$_3$) forms an 1:1 complex with βCD but not with αCD, and the hydrophobic trimethylphosphine ligand resides in the CD cavity.

The 3,6-peranhydro-2-O-methyl-αCD showed a surprisingly high affinity for lead (1.2×10^7 M^{-1}) and for strontium (1.8×10^4 M^{-1}). Eventually this and similar CD derivatives will be utilizable for decontamination or detoxication by sequestering selectively certain metal ions from the contaminated environment, or even from intoxicated organisms.

The essence of the photodynamic tumor therapy is that such compounds have to be delivered to the tumor tissues, which upon strong light irradiation become toxic through isomerization, splitting, etc. In this case upon strong light irradiation the photosensitive molecules will become toxic just for the tumor cells. For such targeting of the drug very stable (10^5–10^7 M^{-1}) complexes are needed. The duplex or triplex homo- or heterodimers of CDs (constructed only from one or two different CDs) form complexes which are

Figure 16. Various catenanes.
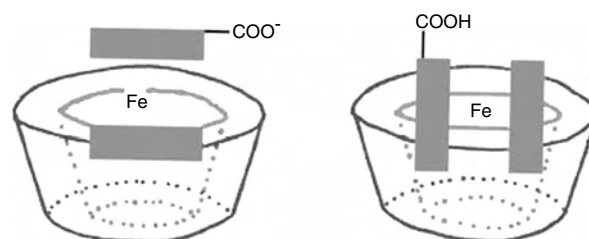
Figure 17. Orientation of an included ionizable ferrocene depends on the pH of the solution.
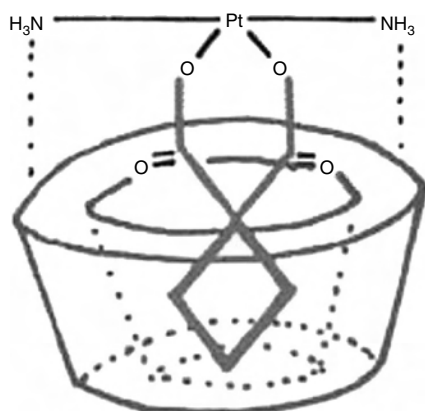
Figure 18. Structure of carboplatin.

more stable by orders of magnitude than the singular CDs (Fig. 19). Interconnecting two CDs with appropriate bridges such duplex CD derivatives have been prepared which can form stable complexes with photosensitive porfirinoid structures and to transport them to the target organs.

In "antennae" bearing CDs receptor specific oligosaccharide units are attached to the CDs, which will be bonded in the living organism only to certain specific receptors. The aim of this effort is to synthetize a receptor-targeting carrier; that is, the drug complexed with an antenna bearing duplex CD would transport the specific drug just to the target organ.

CDs are considered to be not very selective receptors for a very large number and variety of relatively small (CD-cavity compatible) molecules. A promising new challenge is the synthesis of such artificial receptors, which will show selectivity for nanometer scale large molecules. One promising approach is molecular imprinting. Polymerizing (with appropriate cross-linking agents) the cholesterol/βCD complex and then removing the guest (e.g., by excessive organic solvent extraction) the obtained "empty" polymer will show an interesting specific affinity for cholesterol. No other potential guest will fit so correctly into the cavity of the ordered assembly than cholesterol. A nonimprinted βCD polymer hardly bounds any cholesterol.

The assembly of CDs is ordered by the template (=guest) molecule, which facilitates the fixing of the position and orientation of the CD units by cross-linking just in the most advantageous position for maximum cooperation in
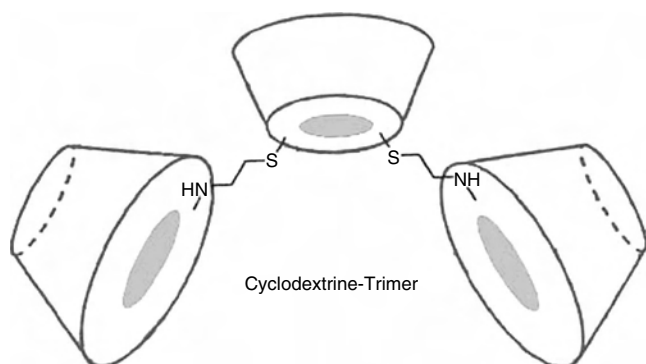
binding the guest. Using this principle a large variety of single molecule specific "accommodations" can be memorized by such ordered and fixed assemblies (Fig. 20).

The most complicated CD derivatives are synthetized for enzyme-modeling experiments. For all enzymes it is characteristic that they have a substrate binding site and an active, catalytic group. The CDs are similar; the axial cavity is the binding site, and the hydroxyl group can attack, for example, an ester linkage of an included ester-type guest. This enzymelike activity is, however, weak and restricted to only a few well studied examples. Very active and specific artificial enzymes can be constructed by using the CD molecule as a scaffold. The axial cavity can be elongated (e.g., by alkaline substitution on the primary face) and one or more CD hydroxyls can be substituted by active, prosthetic groups. This way artificial hydrolase, isomerase, lyase, transferase, oxydoreductase, etc. enzyme models have been synthesized. In some cases their activity approaches well the activity of natural enzymes. Combining the molecular imprinting technique with enzyme modeling, very probably artificial enzymes of high activity and specificity will be produced, both for industrial applications and for *in vivo* (e.g., detoxicating) purposes.

A βCD dimer (Fig. 21) with a linker containing a bipyridil group can form a coordination complex with metal ions. These are very effective at hydrolyzing ester substrates which have two hydrophobic arms that can be fixed by the CD cavities of the catalyst.
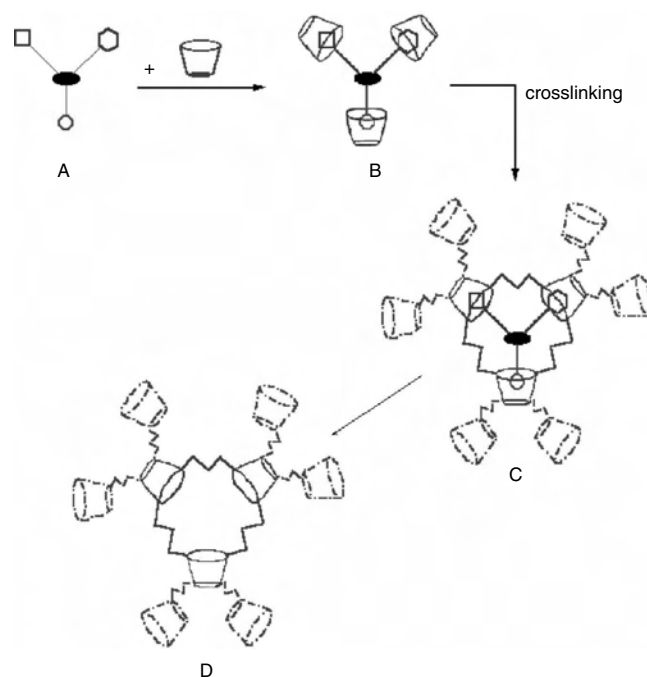
Figure 20. Principle of molecular imprinting: a guest (A) is complexed with a CD in solution (B). Then the CDs will be cross-linked with an appropriate agent (C) forming either a water-soluble oligomer ($M_w < \sim 10,000$) or a water-insoluble polymer ($M_w > \sim 10,000$). Finally the guest is removed (e.g., by an appropriate organic solvent) from the imprinted structure. The size, shape, and allocation of binding sites are memorized. This cavity hardly fits with other potential guests but shows high selectivity for the original "template" guest.

Figure 19. A triplex CD.
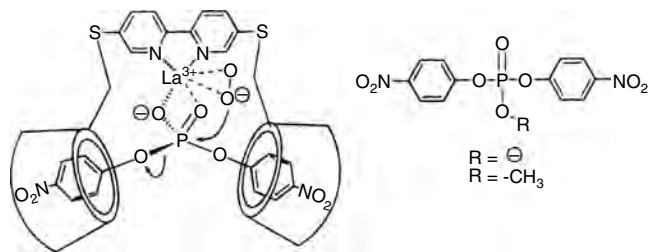
Figure 21. A cyclodextrin dimer which can bind both ends of a substrate and hold it onto a catalytic metal ion (La³⁺) is a very effective catalyst for ester hydrolysis.

Attaching four CD molecules to a porphyrin, or only 2 but in the A–C (or B–D) position, it will bind sufficiently long bifunctional "inclusion" guests (E of F) and keep them stretched with their aliphatic or olefinic section in close proximity to the center of the porphyrin structure. If the nitrogens of prophyrin are coordinated with an Mn(III) atom, then the aliphatic segment of the guest will be hydroxylated or the olefinic segment will be epoxidated (Fig. 22). When the two CDs are linked at the vicinal (A–B, B–C, C–D) positions no guest binding takes place.
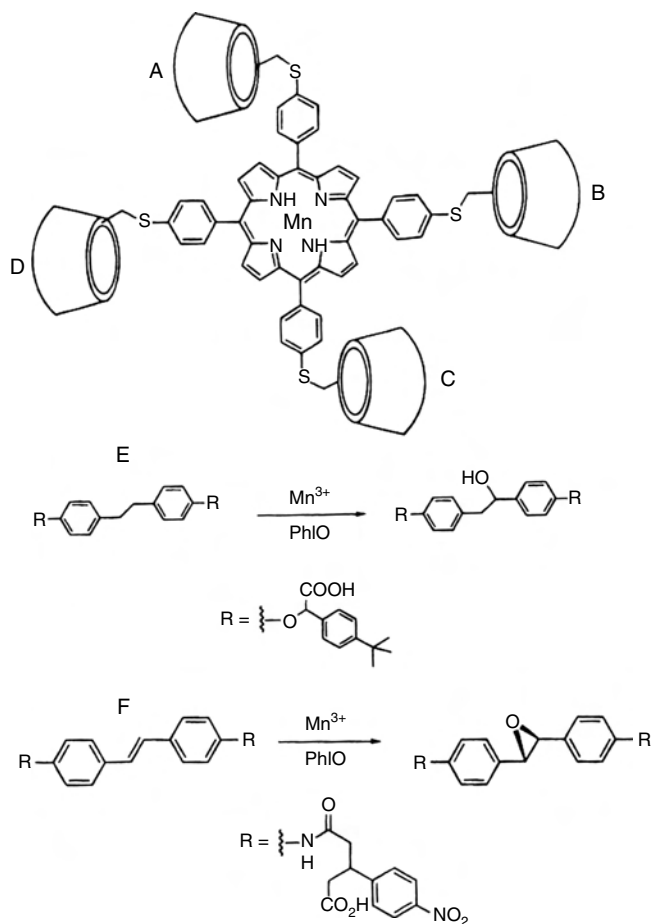
Figure 22. Porphyrin carrying four attached CD rings binds strongly to an appropriate two-armed guest and, forcing its oxidizable center near to the Mn³⁺ ion atom, results in hydroxylation of a –CH₂– unit or epoxidation of an olefinic bond.

GLOSSARY

Administration routes Mode of incorporation of a drug into the organism: i.v. = intravenous, p.o. = per oral, i.m. = intramuscular, s.c. = subcutaneous, i.p. = intraperitoneal, etc.

AUC value (area under curve) The integrated area under the curve blood level versus time (counted from time of administration till end of the observation, e.g. 24 h).

Bioavailability The absorption (penetration) of drugs through the absorption sites (gastrointestinal system, skin, lung, mucous membranes, etc.) is frequently far from being complete, and biological utilizability (bioavailability) depends on numerous factors, but the prevailing one is the solubility, and dissolution rate of the administered drug.

CTG ase (cyclodextrin trans glucosylase enzyme) This enzyme splits the glucosidic linkages between the sixth, seventh, eight (etc.) glucopyranose units in the amylose or amylopectin molecules (components of starch of any origin) then establishes new glucosidic linkages between both ends of the formed break-down products resulting in formation of cyclic dextrins = cyclodextrins.

Cyclodextrin 6,7,8 (or more) glycopyranose units are bound through α-1,4-glycosidic linkages. The outer surface of these conical torus-shaped (doughnut shaped) molecules is hydrophilic, in aqueous solution strongly hydrated but the internal cavity of well defined diameter and length is apolar, ready to incorporate appropriate apolar guest molecules.

Cyclodextrin catalysis Cyclodextrins similarly to all enzymes have a substrate binding site (the CD cavity) and active catalytic moieties, the secondary and/or primary hydroxyl groups. Substituting one or more CD hydroxyls with appropriate substituents aritificial enzyme models can be synthetized.

Cyclodextrin derivatives The hydrogen from one or more hydroxyl group or the complete hydroxyl group are replaced by substituent(s), resulting in ester, ether, deoxy-, amino-, carboxy-, halogen-, etc. derivatives of CDs.

Degree of substitution Number of substituents, attached to the CD ring.

Guest molecule A molecule, which at least one part of it can penetrate into the CD-cavity, to form an "inclusion" complex.

Host molecule A molecule, which has an open cavity of appropriate size and polarity for incorporation of an appropriate "guest" molecule.

Inclusion complex A guest molecule (or a part of appropriate size and polarity of it) is included, and bound by non-covalent forces in the cavity of a host molecule.

Molecular necklace Rotaxane, which consists of long slim axis guest molecule and several CD-hosts around it.

Molecular encapsulation Inclusion complexation.

Molecular switch (or shuttle) In a rotaxane the host CD changes its position along the axis guest molecule, upon external effects (light, pH) or the orientation of the (partly) included guest is modified relative to the CD-cavity.

Outer-sphere complex The host (cyclodextrin) is linked through a non-covalent bond to a non-incorporated guest (e.g., by hydrogen bond, through the CD-hydroxyls).

Rotaxane   A long slim guest molecule threaded through one or more CD cavity, then both ends are terminated by "stopper" moieties, which cannot penetrate through the CD-cavity, impeding the "slip out" of the axis guest molecule.

REFERENCES

1. D. French, *Adv. Carbohydrate Chem.* 12, 189 (1957).

2. M. L Bender and M. Komiyama, "Cyclodextrin Chemistry." Springer-Verlag, Berlin, 1978.

3. "Proc. First Int. Symp. on Cyclodextrins," Budapest, 1981 (J. Szejtli, Ed.), Reidel, Dordrecht, 1982, p. 544.

4. J. Szejtli, "Cyclodextrins and Their Inclusion Complexes," p. 296. Akadémiai Kiadó, Budapest, 1982.

5. "Inclusion Compounds" (J. L. Atwood, J. E. D. Davies, and D. D. MacNicol, Eds.), Vols. 1–3, Academic Press, London, 1984.

6. J. L. Atwood, J. E. D. Davies, and T. Osa, Clathrate compounds, molecular inclusion phenomena and cyclodextrins, in "Proc. of Third Int. Symp. on Clathrate Compounds and Molecular Inclusion and the Second Int. Symp. on Cyclodextrins," Tokyo, 1984, Reidel, Dordrecht, 1985, p. 426.

7. Inclusion phenomena in inorganic, organic and organometallic hosts, in "Proc. Fourth Int. Symp. on Inclusion Phenomena and the Third Int. Sympt. on Cyclodextrins," Lancaster, 1986 (J. L. Atwood and E. D. Davies, Eds.), p. 455. Reidel, Dordrecht, 1987.

8. "Cyclodextrins and Their Industrial Uses" (D. Duchene, Ed.), Editions de Santé, Paris, 1987, p. 448.

9. J. Szejtli, "Cyclodextrin Technology," Kluwer Academic, Dordrecht, 1988, p. 450.

10. "Proc. Fourth Int. Symp. on Cyclodextrins," Munich, 1988, (O. Huber and J. Szejtli, Eds.), p. 576. Kluwer Academic, Dordrecht, 1988.

11. "Minutes of the Fifth Int. Symp. on Cyclodextrins," Paris, 1990 (D. Duchene, Ed.), Editions de Santé, Paris, 1990. p. 722.

12. "New Trends in Cyclodextrins and Derivatives" (D. Duchene, Ed.), Editions de Santé, Paris, 1991, p. 635.

13. "Minutes of the Sixth Int. Symp. on Cyclodextrins," Chicago, 1992 (A. R. Hedges, Ed.), Editions de Santé, Paris, 1992, p. 693.

14. K. H. Frömming and J. Szejtli, "Cyclodextrins in Pharmacy." Kluwer Academic, Dordrecht, 1993.

15. "Proc. of the Seventh International Cyclodextrin Symposium," Tokyo, 1994 (T. Osa, Ed.), p. 554. Publ. Office of Business Center for Academic Societies, Tokyo, Japan.

16. J. Szejtli, *Med. Res. Rev.* 14, 353 (1994).

17. "Comprehensive Supramolecular Chemistry" (J. Szejtli and T. Osa, Eds.), Vol. 3, p. 693. Pergamon, Oxford, 1996.

18. "Proc. of the Eighth International Cyclodextrin Symposium," Budapest, 1996 (J. Szejtli and L. Szente, Eds.), p. 685. Kluwer Academic, Dordrecht, 1996.

19. J. Szejtli, *Chem. Rev.* 5 1743 (1998).

20. S. A. Nepogodiev and J. F. Stoddart, *Chem. Rev.* 5, 1959 (1998).

21. R. Breslow and S. D. Dong, *Chem. Rev.* 5, 1997 (1998).

22. K. Uekama, F. Hirayama, and T. Irie, *Chem. Rev.* 5, 2045 (1998).

23. "Proc. Ninth Int. Symp. on Cyclodextrins," Santiago de Compostella (J. J. Torres-Labandeira and J. L. Vila-Jato, Eds.), p. 707. Kluwer Academic, Dordrecht, 1999.

24. N. J. Easton and S. F. Lincoln, "Modified Cyclodextrins, Scaffolds and Templates for Supramolecular Chemistry," p. 293. Imperial College Press/World Scientific, London/Singapore, 1999.

25. T. Loftsson, in "Proc. Eleventh Int. Symp. on Cyclodextrins," Reykjavik, 2002.

26. *Cyclodextrin News* (a monthly abstracting newsletter since 1986, dedicated exclusively to cyclodextrin literature, production, marketing, related conferences, etc.), edited and published by Cyclolab Ltd., Budapest.

Deformation Behavior of Nanocrystalline Materials

Alla V. Sergueeva, Amiya K. Mukherjee

University of California, Davis, California, USA

CONTENTS

1. INTRODUCTION

1.1. Nanocrystalline Materials

Nanostructure science and technology is a broad and inter-disciplinary area of research, and development in this field has been growing very significantly worldwide in the past few years. It has the potential for revolutionizing the ways in which materials and products are created and the range and nature of functionalities that can be accessed. It is already having a significant commercial impact, which will assuredly increase in the future. Nanotechnology implies direct control of materials and devices on molecular and atomic scales, including fabrication of functional nanostructures with engineered properties, that takes advantage of physical, chemical, and biological principles that originate in the nanometer scale. New observed properties are attributed to a reduction in length scales to the point where known models for physical phenomena and interactions become larger than the actual size of the structure. New behavior at the nanoscale is not necessarily predictable from that observed at large size scales. The most important changes in behavior are caused not by the order of magnitude size reduction, but by newly observed phenomena intrinsic to or becoming predominant at the nanoscale, such as size confinement, predominance of interfacial phenomena, and quantum mechanics effects. Once it is possible to control feature size, it is also possible to enhance material properties and device functions beyond those that we currently know or even consider as feasible.

Few reviews on the basic concepts, physics, structural features, properties, and applications of nanocrystalline materials (NCM) have been written in the past few years [1–8]. Many researchers in recent years have increasingly focused on the synthesis and processing of NCM, which have a great potential for functional applications (see next Section).

Mechanical testing of NCM is characterized by features that are different from those documented for coarse-grained materials. The amount of the NCM produced by advanced processing methods is often small, and it is therefore difficult to prepare large bulk samples with nanocrystalline structures in comparison with those for conventional materials. The gauge length of testing specimens, unlike those used in testing coarse-grained materials, is usually on the order of several tens of micrometers to a few millimeters. However, due to the fact that the grain size is in scale of nanometers, it is anticipated that the experimental data obtained from these miniature specimens would still represent the bulk behavior of materials.

1.2. Severe Plastic Deformation

There are many different methods developed for the production of NCM such as mechanical alloying [9], evaporation and condensation [6], precursor decomposition [10], powder consolidation [6], electrodeposition [11, 12], sputter deposition [13, 14], thermal or plasma spraying [15], crystallization from the amorphous state [16], and severe plastic deformation [17, 18]. Reviews on some of these methods were made by Morris [8] and by Froes et al. [19]. Nevertheless, as it was determined by recent investigations [20, 21], properties in NCM are very sensitive to their initial microstructures. Two grades of a nanocrystalline material (same composition and structure) that are prepared by different procedures and that have a similar grain size may exhibit different mechanical properties. On this basis, discrepancies may exist when comparing experimental data reported by investigators who used different processing techniques in producing the same nanocrystalline material.

Moreover, it is very difficult to produce large bulk NCM that is free from porosity and other flaws and that has a wide range of grain size. Because of this difficulty, the dependence of strain rate on stress, grain size, and temperature in NCM is at present unclear and can be controversial. From the methods mentioned above, the technique of severe deformation under pressure (SePD) can produce bulk NCM free of porosity and surface flaws. This technique includes such methods as equal channel angular pressing (ECAP) [17], high pressure torsion (HPT) [17], and multiple forging (MF) [18, 22], and has been intensively applied for producing of NCM. The current analysis on superplastic behavior is made for NCM produced mostly by HPT. The basic idea of torsion straining (Fig. 1) is to apply a very large pressure (5–7 GPa) to a sample and then twist to introduce large amount of torsion strain (up to true strain of 7) into the sample. The detailed description of this method can be found in [17].

1.3. Theoretical Predictions

NCM materials contain a very large density of interfaces, causing them to differ structurally from crystals and glasses with the same chemical composition. Based on the classical scaling laws developed for conventional coarse-grained materials (grain size, $d > 10 \ \mu$m), expected behavior would include very high yield strength, σ_y, at low temperature due to constraints on dislocation motion (e.g., the Hall–Petch model predicts $\sigma_y \propto d^{-1/2}$) and low strength/high ductility at higher temperatures due to short diffusion paths (e.g., the strain rate, $\dot{\varepsilon}$, in Coble creep scales as $\dot{\varepsilon} \propto d^{-3}$). In addition, one might expect deviations from the classical scaling laws as grain size decreases. For example, when grain size becomes so very small, usual predictions based on dislocation theory may not be valid, and Hall–Petch behavior is expected to break down when the crystallite size becomes smaller than the average dislocation spacing or stable loop size. Diffusional flow might also deviate as the volume fraction of triple junctions increases.

Past, experimental studies focused on (a) whether the Hall–Petch relation, which is well-established for coarse-grained materials, is valid for grain sizes in the nanocrystalline range [23]; (b) whether grain boundary diffusion creep [24], which is expected to be dominant at moderate temperatures (0.4–$0.6T_m$), where T_m is the melting point

of the material, and low stresses, becomes significant at low temperatures (for example, room temperature); and (c) whether structural superplasticity [25], which has been observed at high temperatures ($T > 0.5T_m$) and moderate strain rates (10^{-5}–10^{-2} s^{-1}), can be observed at low temperatures and high strain rates.

There have been several reports on the variation of hardness with grain size that deviates from the normal Hall–Petch relationship [20, 21]. Attempts have been made to calculate an approximate value for the grain size at which the Hall–Petch relationship breaks down (see for example [26]). Several derivations of the Hall–Petch equation are based on the concept of dislocation pile-ups at grain boundaries. (For a review of Hall–Petch theories, see for example [27].) However, transmission electron microscopy (TEM) evidence indicates that yielding involves the emission of dislocations from grain boundaries, rather than pile-ups against them [28, 29]. As it was shown by Gryaznov and Trusov [30], parametric dependencies for the Hall–Petch relationship in NCM will be different from that for typical polycrystals, because the basic defects responsible for nanocrystal deformation are interface dislocations having Burgers vectors smaller than lattice dislocations. The large volume fraction of intercrystalline regions must strongly affect mechanical behavior. The nature of the structure of grain boundaries in NCM has been a controversial area. Early studies [31] proposed that interfaces in NCM represent a new class of solid-state structure lacking both short- and long-range orders. More recent studies [28, 32, 33] have disputed this view, and it is now concluded that the boundaries in NCM do not differ fundamentally in nature from those in coarser-grained materials. However, specific interface structures with a large amount of atomic disorder have been observed by Ranganathan et al. [33] in nanocrystalline palladium and titanium thin films.

Theoretical discussion of nanomaterial at ambient temperature usually relates to the following: Starting with the concept of intragranular dislocation plasticity, as the grain size is progressively decreased, the formation of continuum dislocation pile-ups should become more difficult, and transition to discrete pile-up behavior will occur (end of Hall–Petch correlation). At smaller values of grain size, a pile-up approaches the limit of one dislocation. Then only an Orowan bowing type of mechanism is admissible. Finally, at some critical and yet lower length scale, no dislocations can be formed. Beyond this point, these authors believe [34] along with Masumura et al. [35] that plasticity, if it still exists, has to be interface driven. All of these transitions from traditional dislocation behavior can lead to a new grain size dependence of strength and plasticity, which may cause a fundamental change in deformation behavior of NCM.

Intensive investigation of the deformation processes in NCM focuses on the main question of whether lattice dislocations exist and play the same role in nanograin interiors as with conventional coarse grains. As pointed out in the literature [36–38], the existence of dislocations in either free nanoparticles or nanograins composing a nanocrystalline aggregate is energetically unfavorable if their characteristic size, nanoparticle diameter, or grain size is lower than some critical size. And the critical size depends on such material characteristics as the shear modulus and the resistance to
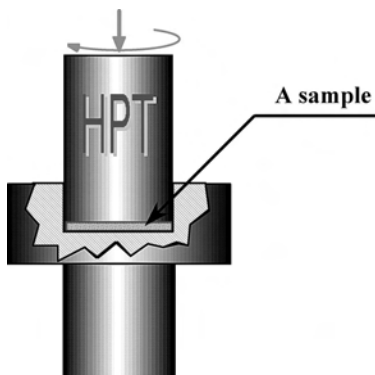
Figure 1. High pressure torsion (HPT).

dislocation motion. The dislocation instability in nano-volumes is related to the effect of the so-called image forces occurring due to the elastic interaction between dislocations and either free surface of nanoparticle or grain boundaries adjacent to a nanograin [36–38]. The lack of mobile dislocations in nanograins has been well documented in electron microscopy experiments [21, 39]. Moreover, it was suggested that mechanisms of plastic flow may be different in nanocrystals in comparison to usual polycrystals [40, 41].

However, if the available literature concerning deformation behavior of NCM at room temperature was intensively investigated, we would find that very little is known about creep behavior and the actual diffusional accommodation at elevated temperatures [41]. At very low stresses and small grain sizes, early theoretical considerations indicated that vacancies, rather than dislocations, may be responsible for the production of creep strain. Two models, Nabarro–Herring creep [42, 43] and Coble creep [24], have been formulated to account for such plastic flow. Nabarro–Herring creep [42, 43] involves the diffusion of vacancies through the grain volume; the creep rate is given by

$$\dot{\varepsilon}_{NH} = A_{NH} \frac{D_l G b}{KT} \left(\frac{b}{d} \right)^2 \frac{\sigma}{G} \qquad (1)$$

where A_{NH} is a dimensionless constant, D_l is the lattice diffusivity, G is the shear modulus, b is the Burger's vector, K is Boltzmann's constant, T is the absolute temperature, d is grain size, and σ is the applied stress. In Coble creep [24], vacancies diffuse along the grain boundaries; the creep rate is given by

$$\dot{\varepsilon}_{Co} = A_{Co} \frac{D_{gb} G b}{KT} \left(\frac{b}{d} \right)^3 \frac{\sigma}{G} \qquad (2)$$

where A_{Co} is a dimensionless constant and D_{gb} is the grain boundary diffusion coefficient.

The Nabarro–Herring and Coble processes represent two independent and parallel mechanisms, so the faster process controls the creep behavior. Coble creep should predominate over Nabarro-Herring creep when

$$\left(\frac{b}{d} \right) \frac{D_{gb}}{D_l} > \frac{A_{Co}}{A_{NH}} \qquad (3)$$

This condition prevails at low homologous temperatures and very small normalized grain sizes. On this basis, it is expected that due to the ultrafine grain size and the large fraction of intergrain areas in NCM, Coble creep (diffusional creep along grain boundaries) would become important in these materials when crept at low temperatures. Room temperature diffusional creep, however, predicted to be appreciable in nanocrystalline samples, was not confirmed in subsequent investigation [44]. At the smallest grain sizes the significant volume associated with triple points must also become important [45]. However, according to a model proposed by Suryanarayana et al. [46], when the grain size is about 30 nm, which is very close to the grain size in Ni-P and Fe-B-Si used by Wang et al. [47], Deng et al. [48], and Xiao and Kong [49], the volume fraction of triple junctions is less than 1%, while the fraction of grain boundaries is about 10% by assuming grain boundary thickness of

1 nm. Based on this information, the triple junction process is likely to be important when the grain size is less than 10 nm [45].

Another important prediction for NCMs is their high ability for superplastic deformation. The ability of some materials to exhibit extensive plastic deformation, often without the formation of a neck prior to fracture, is generally known as structural superplasticity. Superplastic behavior is indicated in tension tests by large elongations, usually greater than 200 percent and sometimes in excess of 2000 percent. The two basic requirements for the observation of structural superplasticity are (a) a temperature greater than about one-half of the melting temperature, T_m, and (b) a fine and equiaxed grain size (<10 μm) that does not undergo significant growth during high-temperature deformation. In addition to these two requirements, grain boundaries need to be mobile, high-angled, and able to resist tensile separation.

Superplasticity in microcrystalline materials is well established as a grain size dependent phenomenon that can be described by the constitutive equation for conventional superplasticity [25]

$$\dot{\varepsilon} = A \frac{DGb}{kT} \left(\frac{b}{d} \right)^p \left(\frac{\sigma}{E} \right)^2 \qquad (4)$$

where $\dot{\varepsilon}$ is the strain rate, D is the appropriate diffusivity (lattice or grain boundary), G is the shear modulus, b is the Burger's vector, K is the Boltzmann's constant, T is the test temperature, d is the grain size, p is the grain size exponent (usually 2 for lattice diffusion controlled flow and 3 for grain boundary diffusion controlled flow) and σ is the applied stress. Behavior described by this equation has been observed for metals, intermetallics, and ceramics materials. According to this relationship between grain size, superplastic strain rate, and superplastic temperature, a shifting of the optimum strain rate to higher values and/or the optimum temperatures to lower values with microstructural refinement has been predicted. Both aspects happen to have attractive technological significance and were extensively studied. For example, mechanically alloyed aluminum alloys having a typical grain size of 0.5 μm exhibit superplasticity at strain rates >1 s^{-1}, which is comparable to conventional hot forming rates. In comparison, the superplastic strain rates of a material with a typical grain size of 15 μm are 10^{-4}–10^{-3} s^{-1} [50]. The relationship between grain size and optimum strain rate of aluminum alloys is shown in Figure 2a (data taken from [50]) while Figure 2b shows the variation of superplastic temperature with grain size (data taken from [51, 52]). From these figures, it is clear that by manipulating the grain size it is possible to (a) increase the superplastic strain rate and (b) decrease the superplastic temperature.

The purpose of this chapter is to review the experimental data reported for deformation behavior of SePD processed NCM at elevated temperatures including our own results.

2. DEFORMATION BEHAVIOR

Because of specific microstructural features (very small grain sizes, high volume fraction of grain boundaries and triple points, lattice distortions, etc.), it is not surprising
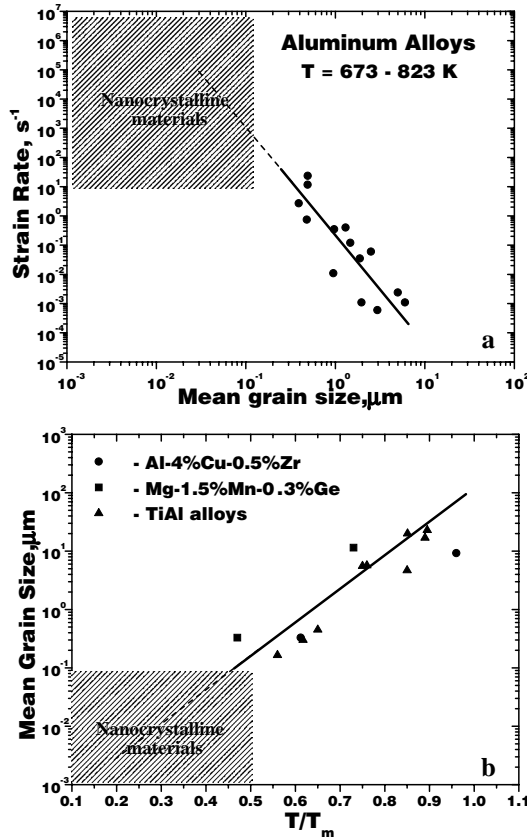
Figure 2. The relationship between grain size and (a) optimum strain rate or (b) superplastic temperature demonstrates that by reducing the grain size it is possible to increase the strain rate or decrease the superplastic temperature (data taken from [50–52]). Both effects have technological significance.

that NCMs reveal specific variations of several fundamental physical parameters as compared to their large-grained counterparts, such as Curie and Debye temperatures, elastic modulus, diffusion coefficients [53], etc. Consequently, novel

physical and mechanical properties are obtained; for example, brittle ceramics may become ductile in nanocrystalline state [54]. However, it should be noted that data on mechanical properties of nanocrystals show contradictory trends. The possible reason for this is an expected difference in structure (porosity, density gradients, contaminations, internal stresses, defects including microcracks, etc.) of samples prepared in different laboratories even for the same grain size. Often this difference in structure is due to uncertain processing history and/or lack of proper control of process variables. Thus, most of the novel properties are found to be very sensitive to the procedure for sample preparation [20, 21]. Thus, NCM produced by the powder sintering procedure did not demonstrate any superplasticity [55]. Moreover, among the NCM produced by other methods, some of them have shown the ability for superplastic flow, while others did not. The summary of our data and some additional literature data on deformation behavior of SePD NCM are given in Table 1.

On the basis of the experimental results on SePD NCM, Mishra et al. [56] proposed an "exhaustion plasticity" mechanism. It is known that severe plastic deformation introduces a large population of dislocations into the specimen. In this "exhaustion plasticity" mechanism, the flow stress at the initial stage of deformation is not high enough to nucleate new dislocations for slip accommodation because of the very small value of grain size. The applied stress moves the pre-existing dislocations, and grain boundary sliding is accommodated by the movement of these dislocations. As the easy paths of grain boundary sliding and dislocation movement get exhausted, the flow stress increases, which is indicated by a strain hardening stage observed in the superplastic deformation of the NCM. According to Mishra et al. [56], the peak flow stress can be viewed as the critical stress required to generate new dislocations during grain boundary sliding. Hence, the experimental results on commercially pure Ti and NiTi alloy have confirmed that nanostructure as well as excess of dislocations are not sufficient conditions for SePD materials to show superplasticity.

Table 1. A summary of observation of superplasticity in nanocrystalline materials.

Material and reference	Gain size[a] (nm)	Strain rate (s^{-1})	Temp. (°C)	Stress at $\varepsilon = 0.1$ (MPa)	Max. stress (MPa)	Elong. (%)	Remarks
Al-Ni-Mm[b] (Higashi et al., 1993)	70	7×10^{-1}	600	18	—	500	
Ti-6 Al-3.2 Mo (Salishchev et al., 1993)	60	5×10^{-4}	600	150	—	600	Stress at $\delta = 40\%$
Zn-Al (Mishra et al., 1997)	80	5×10^{-4}	120	18	—	230	
Ni$_3$Al alloy (Mishra et al., 1998)	50	1×10^{-3}	650	400	1530	380	Extensive strain
			725	270	790	560	hardening
Al-Mg-Li-Zr alloy (Mishra et al., 1998)	100	1×10^{-1}	250	106	154	330	Extensive strain
			300	33	146	850	hardening
Ti-6 Al-4 V (Unpublished, 1998)	70	1×10^{-3}	575	165	—	215	

[a] Denotes the starting average grain size.
[b] This alloy showed significant coarsening during heating, so the microstructure during testing was not nanocrystalline.

According to literature [57], the deformation of microcrystalline commercially pure Ti is associated with dislocation climb controlled by lattice diffusion. The stress exponent obtained by different investigators is close to 5, and activation energy is found to be 210–250 kJ/mol. This mechanism of deformation, namely five-power-law creep seems to be also operative in Ti in the nanocrystalline range at temperatures higher than $0.4T_m$ and at "conventional" strain rates ($10^{-4} \cdots 10^{-2}$ s^{-1}) [12]. Apparent activation energy for both microcrystalline and nanocrystalline states seems to be higher than that for lattice diffusion reported for commercially pure Ti (153 kJ/mol [58]). In a NiTi alloy with nanostructure obtained by the same method (HPT), the deformation mechanism seems to be related to viscous glide of dislocations with a stress exponent of 3 [12]. Such a deformation mechanism is common for ordered structures. There is a lack of data on diffusion related processes in NiTi in the literature, but an approximate estimation of activation energy for self-diffusion gives a value of 220–230 kJ/mol [12]. So, the apparent activation energy of 210 kJ/mol calculated from the experimental data is in good agreement with such estimation, assuming that the activation energy for viscous glide, which is controlled by Darken interdiffusivity, is close to volume self-diffusivity in this case. Despite the fact that the grain size of this material is on the nanometer scale, and the volume fraction of grain boundaries is therefore significant, it seems that grain boundary sliding or operation of Coble creep are suppressed in NiTi.

The results on NCM that did undergo superplastic deformation have established a number of general trends of the mechanical behavior of NCM at elevated temperatures such as excessive strain hardening during tensile tests, high flow stresses (compared to microcrystalline materials at comparable temperature and strain rate), a correlation between microstructural instability (in terms of onset of grain growth), and superplasticity, which will be discussed below.

In microcrystalline superplasticity, the stress concentration that arises at grain boundary triple points (or ledges) due to grain boundary sliding is accommodated by diffusional processes or by (dislocation) slip processes. One of the fundamental issues in nanocrystalline superplasticity is: Which of the two accommodation processes is most important? In recent years, the possibility of superplasticity in NCM has been discussed in terms of diffusional flow. However, a grain boundary sliding mechanism with diffusional accommodation will not be able to explain all of the trends described above. These trends indicate that the mechanism of superplasticity in NCM is significantly different from the well-established mechanisms in microcrystalline materials.

2.1. Significant Differences

2.1.1. Excessive Strain Hardening

Figure 3 shows flow curves of SePD 1420-Al and Ni$_3$Al alloys, commercially pure Ti, Ti-6Al-4V, and NiTi alloys. Excessive strain hardening was observed for all these materials when their grain size does not exceed 100 nm. Intensive grain growth at high temperatures (Fig. 3c and e) or low testing strain rate (Fig. 3d) leads to dramatic change in the deformation flow, and no strain hardening was observed. It is important to note that the strain hardening in the 1420-Al
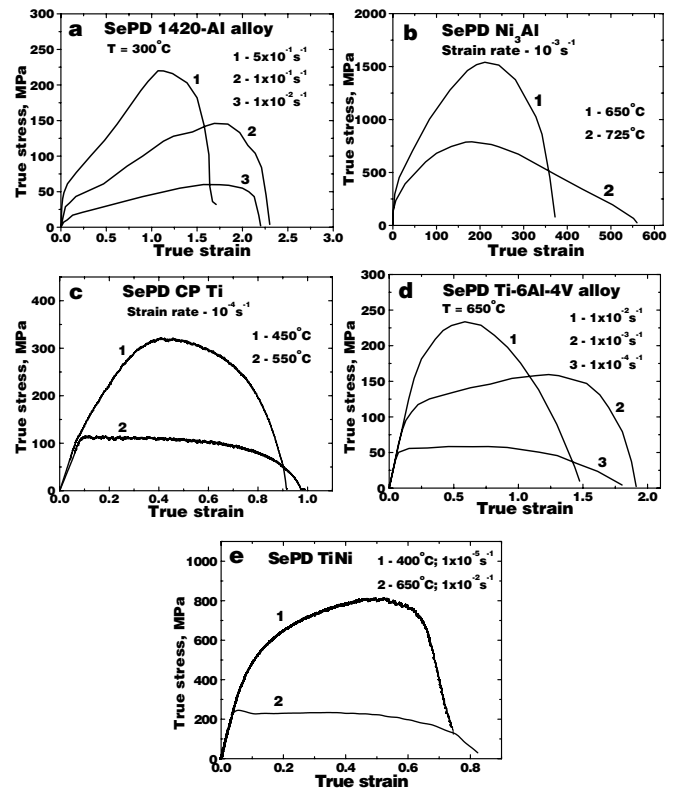
Figure 3. Flow curves for (a) 1420-Al alloy at different strain rates, (b) Ni$_3$Al alloy at different temperatures, (c) CP Ti at different temperatures, (d) Ti-6Al-4V alloy at different strain rates, and (e) NiTi intermetallic at different temperatures show excessive strain hardening. Note the increase in strain hardening with increasing strain rate in 1420-Al alloy and Ti-6Al-4V alloy.

alloy (Fig. 3a) and Ti-6Al-4V alloy (Fig. 3d) increases with increasing strain rate. We have observed a similar trend in other SePD processed materials as well, for example, Zn-Al and 2124-Al alloys [59, 60].

Similar elongations were reached in CP Ti (with initial grain size of about 120 nm) at 450 and 550 °C and at a strain rate of 1×10^{-4} s^{-1} (157% and 166% respectively, but the shape of the flow curve has changed dramatically with decrease of test temperature (Fig. 3c). The flow curve at 450 °C shows an extensive hardening period and stress dependence on strain (Fig. 3c, curve 1), whereas the curve at 550 °C, when grain size was already more than 200 nm, has a shape typical for nearly steady state flow with relatively low stress flow (Fig. 3c, curve 2).

These observations establish a trend. There is some grain growth in these NCMs during superplastic deformation. Because of the grain size dependence in the constitutive relationship for superplastic flow, strain hardening during superplasticity has been conventionally explained in terms of grain growth. However, such an explanation would not predict higher strain hardening at higher strain rate. A detailed microstructural investigation is required to explain this trend.
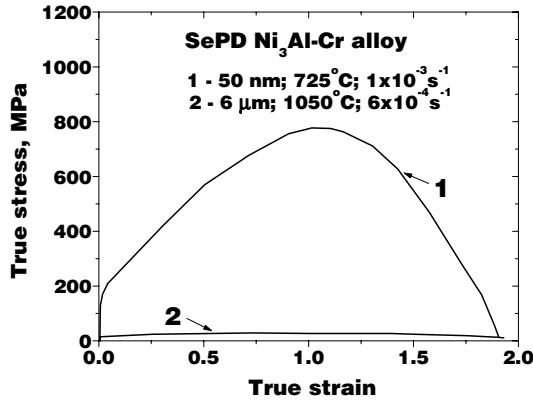
Figure 4. A comparison of flow curves for Ni_3Al alloy in microcrystalline and nanocrystalline state. Note the higher flow stress in the nanocrystalline state, although both specimens showed similar ductility.

2.1.2. High Flow Stresses

Figure 4 shows a comparison of the flow curves during superplasticity in a Ni_3Al alloy. This alloy was tested in both microcrystalline and nanocrystalline states. The high flow stresses during superplasticity of the nanocrystalline Ni_3Al alloy are apparent. Although the test temperature and grain size is different for the two microstructural conditions, the comparison is interesting because the overall ductility in both cases is similar. One of the features of conventional superplasticity in microcrystalline material is low flow stress. The observation of superplasticity with high flow stresses in NCM needs a new approach to explain the origin of such high flow stresses. First, the starting flow stress is around 170 MPa. Second, after significant strain hardening, the flow stress reaches the level of 780 MPa at 725 °C. At 650 °C, the flow stress values are even higher (Fig. 3b).

Figure 5 shows the variation of normalized stress with temperature and grain size compensated strain rate for Ti-6Al-3.2Mo alloy. The raw stress-strain rate data were taken from Salishchev et al. [18, 22]. Also, the data for a microcrystalline Ti-6Al-4V alloy [61] and the expected behavior from the grain boundary diffusion controlled mechanisms of deformation [62] are included. Titanium alloys
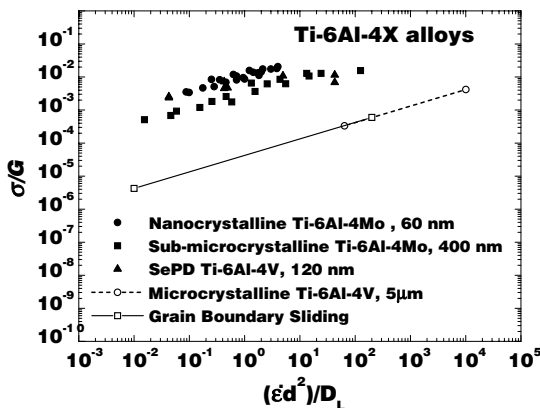
Figure 5. The variation of normalized flow stress with temperature and grain size compensated strain rate for Ti alloys (data taken from [18, 22, 61, 62]).

exhibit slip accommodated lattice-diffusion controlled grain-boundary sliding. Two things are apparent from Figure 5: (a) the data for microcrystalline alloy agree well with the expected trend for slip accommodated lattice-diffusion controlled grain-boundary sliding, and (b) the data for the submicrocrystalline alloy and nanocrystalline material show higher flow stress. Higher flow stresses have been also observed for NCM, produced by other methods [63]. This suggests a transition in micromechanisms or additional difficulty in grain boundary sliding, which is opposite to some of the earlier expectations of enhanced superplasticity in NCM.

One way to explain the origin of higher flow stresses for superplasticity in NCM is to consider the possible influence of grain size on slip accommodation during grain boundary sliding. Recently, Mishra and Mukherjee [64] have suggested that dislocation nucleation is difficult in NCM. A preliminary estimate of the stress required for nucleating such a dislocation can be obtained by using a relationship proposed by Hirth and Lothe [65] for dislocation generation by a Frank–Read source in the crystal lattice, which after simplification can be written as

$$\tau = \frac{\mu b}{4\pi L(1-\nu)}\left(\ln\frac{L}{b} - 1.67\right) \qquad (4)$$

where L is the distance between the pinning points, ν is the Poisson's ratio, and τ is the shear stress required to generate the dislocations. For superplastic deformation, the tensile stress needed to nucleate dislocation for slip accommodation can be calculated by approximating $L = d/3$, $\nu = 0.33$, and $\sigma = \sqrt{3}\,\tau$. The choice of $L = d/3$ is based on the fact that the edge of the tetrakaidecahedron grain is one-third of the distance between the faces of the grains [66]. Equation (4) does not have (a) strain rate dependence (which is an integral part of high temperature deformation), (b) temperature dependence other than the modulus, and (c) the details of dislocation generation from grain boundaries. These effects can be significant, as the flow stress at high temperatures is known to be strain rate and temperature dependent in the superplastic region.

2.1.3. Parametric Dependencies

In general, in order to understand the nature and origin of deformation mechanisms at high temperatures, information related to the dependence of strain rate on stress, temperature, and grain size is essential, and constitutive equations are very helpful in this case. For superplasticity, it is customary to evaluate the stress exponent, activation energy, and grain size exponent. Based on the values of these parametric dependencies, one can decide on the dominant micro mechanism of deformation. So far, there is very limited data on stress exponent and activation energy for superplastic flow in NCM. These data are listed in Table 2. We note that during some of the tests used to obtain the values mentioned below, significant grain growth occurred. The extent to which the results summarized below are influenced by concurrent grain growth is not clear. The stress exponent values for the alloys are close to the theoretically expected value of 2 for grain boundary sliding mechanisms. The activation energy in some cases is significantly higher than the activation energy for grain boundary diffusion. This is intriguing, because with

Table 2. Parametric dependencies for superplastic flow in nanocrystalline materials.

Material and reference	Superplastic parameters		Activation energy[a] (kJ/mol)	
	Stress exponent	Activation energy (kJ/mol)	For lattice diffusion	For grain boundary diffusion
Al-Ni-Mm alloy (Higashi et al., 1993)	~2	151	142	84
Ti-6 Al-3.2 Mo alloy (Salishchev et al., 1993)	2.3	315	150	97
Al-Mg-Li-Zr alloy (Mishra et al., 1998)	~2.5	90	142	84
CP Ti (Sergueeva et al., 2001)	5.8	270	150	97
Ti-6 Al-4V alloy (Sergueeva et al., 2001)	~2.5	ND	150	97
NiTi (Sergueeva et al., 2001)	3	210	14[b]	44.9[c]

[a] The activation energy values are for self diffusion of matrix element and these values are taken from *Deformation Mechanism Maps* by Frost and Ashby (1982).
[b] The activation energy for diffusion of Ni in Ti (taken from *Smithells Metals Reference book*, 7th ed., 1992).
[c] The activation energy for grain boundary diffusion in Ni (taken from *Smithells Metals Reference Book*, 7th ed., 1992).

the abundance of grain boundaries in NCM, an activation energy for grain boundary related deformation mechanism is expected at elevated temperatures.

2.1.4. Effect of Short Annealing

A unique experimental observation is related to the effect of a short anneal on the flow behavior. An example of this is shown in Figure 6. The annealing of SePD processed nanocrystalline Ni$_3$Al does not change the grain size significantly, but it has a dramatic effect on the flow behavior. The initial flow stress increases and the shape of the flow curve changes. The overall ductility reduces from 350% in the as received condition to ~100% after the short anneal.

It should be noted, that a strong effect of the short annealing of SePD Ti was revealed at room temperature tensile tests. Thus, short annealing of SePD Ti at 300 °C results in a 30% increase in strength combined with adequate plasticity (Fig. 7, curve 2) as compared to as-deformed state

(Fig. 7, curve 1) [67]. Annealing for a longer time even at lower temperature decreases strength (Fig. 7, curve 3). A number of tensile tests of severe plastic deformed CP Ti after annealing at different temperatures for 10 min revealed a strong dependence of strength characteristics on annealing temperature with a peak in the range of 250 °C to 300 °C. Microstructural analysis revealed a formation of specific ordered structure in grain boundary regions (Fig. 8) [68], which was not observed in as-deformed SePD Ti. In the sample, which has demonstrated the highest strength, about 80% of grain boundaries have a such special structure.

2.1.5. Correlation Between Microstructural Instability and Superplasticity

The driving force for grain growth is quite high in NCM because of the high interfacial area per unit volume. We have observed a nice correlation between the temperature for microstructural instability and onset of superplasticity in
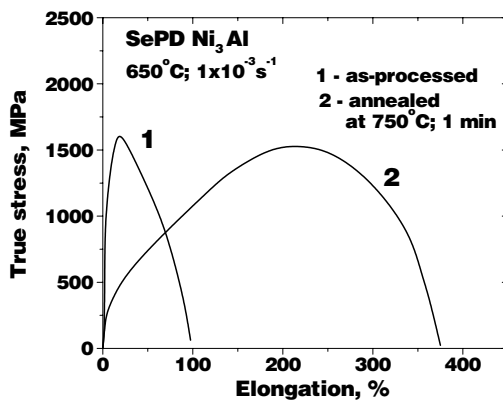
Figure 6. Effect of a short anneal on flow behavior of a nanocrystalline Ni$_3$Al alloy.
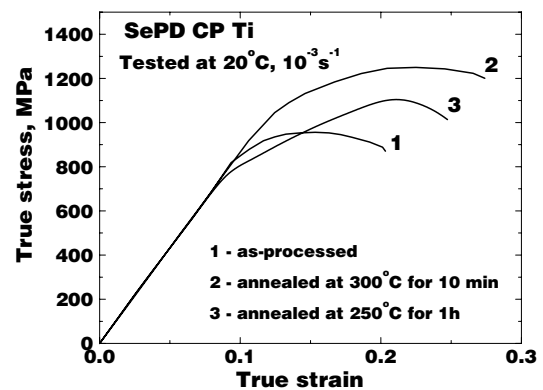
Figure 7. True stress-true strain curves of CP Ti after HPT and annealing.
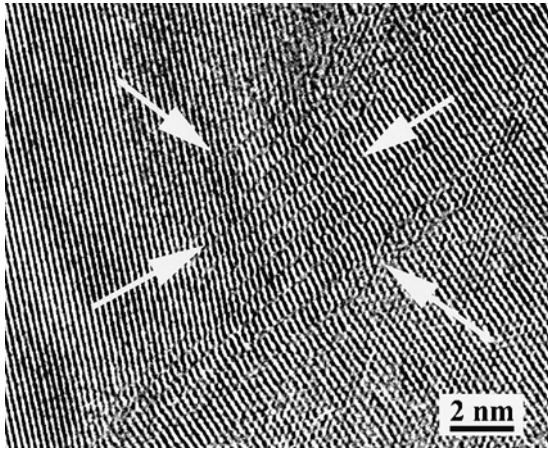
Figure 8. HREM of GB region in CP Ti after HPT and annealing at 250 °C for 10 min.

Figure 9. Combined plots showing variation of DSC signal and elongation with temperature for SePD (a) 1420-Al alloy and (b) NiTi.

NCM. In some ways this is to be expected because both grain boundary migration and grain boundary sliding involve diffusion. An important implication of this is that one needs to establish the narrow temperature range in which there is enough thermal activation for grain boundary sliding but the grain growth rate is relatively low. This is important for observing the grain boundary sliding regime without significant influence of grain growth, particularly from the viewpoint of obtaining parametric dependencies for constitutive modeling. We are investigating the microstructural instability by three different methods: differential scanning calorimetry (DSC), *in-situ* TEM heating, and TEM of heat treated specimens. The correlation between the DSC signal for thermal stability and increase in ductility is shown for SePD processed 1420-Al and NiTi alloys in Figure 9. The onset of grain growth was independently established by analyzing the video recording of *in-situ* TEM heating. The results show that the DSC can work as a very good tool to establish the optimum superplastic temperature for NCM.

2.1.6. Microstructural Observations

We have conducted two types of TEM investigations: (a) microstructural investigation of thin foils at room temperature and (b) video recording of microstructural changes during *in-situ* heating. We have established that the present results at some temperatures reflect superplasticity in the truly nanocrystalline state, as the microstructure remained nanocrystalline during the entire test. For example, Figure 10 shows the microstructure of the nanocrystalline Ni$_3$Al alloy after testing at 650 °C to 380% elongation. In general the dislocation activity appears to quite limited. A few lattice dislocations were visible, as marked in Figure 10. It is interesting to note that dislocation 2 has one end in the grain boundary. The appearance of these types of dislocations suggests the grain boundaries as sources of dislocations. This would be consistent with slip accommodation during grain boundary sliding. The 1420-Al alloy showed high strain rate superplasticity at a relatively low temperature where the nanostucture was relatively stable. It is necessary to note that in the earlier studies [69, 70]
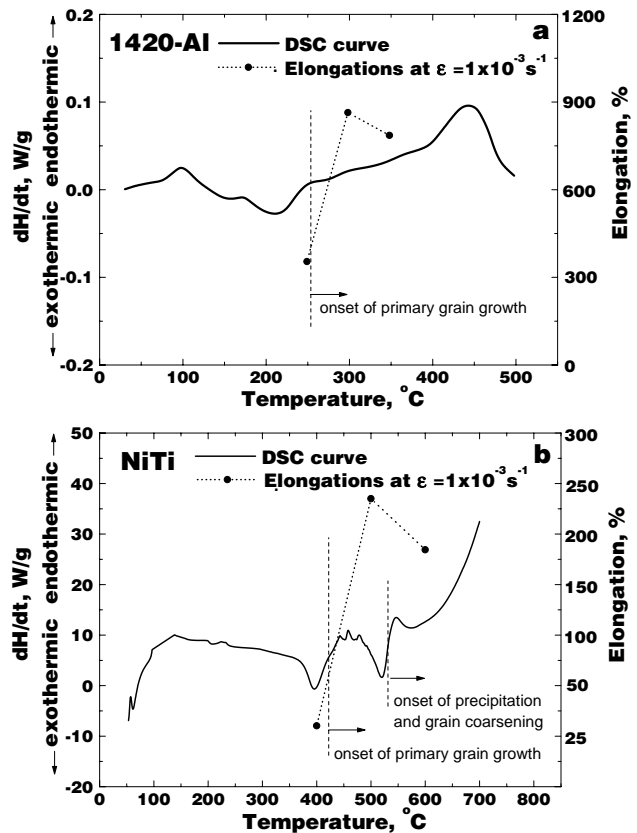
intensive grain growth prior to testing or during testing to the submicrocrystalline range was detected.

Microstructural investigation was also conducted of nanocrystalline commercially pure Ti, which showed high elongation but with parametric dependencies different from that for classical superplasticity (Table 2). This material has demonstrated a five-power-law creep that associated with dislocation climb controlled by lattice diffusion. The enhanced plasticity observed in this pure metal and TEM
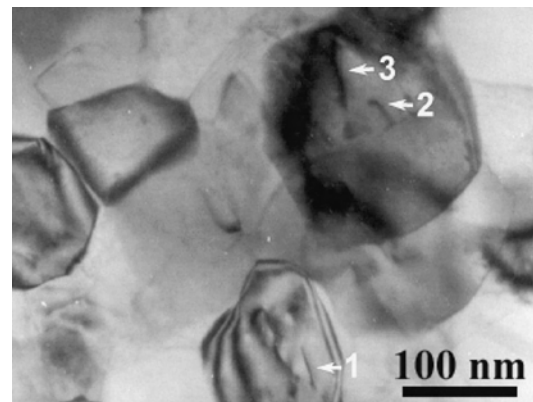
Figure 10. A bright field transmission electron micrograph of a Ni$_3$Al specimen superplastically deformed at 650 °C to an elongation of 380%. Some of the lattice dislocations are marked by arrows.

observations of the structure after deformation suggest that grain boundary sliding also took place during deformation at elevated temperatures. Figure 11 presents the microstructure of Ti produced by severe plastic deformation and deformed at 350 °C (Fig. 11a and b) and 600 °C (Fig. 11c, d, and e) to strain of 65% and 190%, respectively. It is seen that despite such high elongations the grains remain equaxied in both cases. Twinning was not observed during deformation at 350 °C (Fig. 11a and b), while at 600 °C twins were formed (Fig. 11c). Moreover, some twins emerging from grain boundaries were revealed (Fig. 11d). Such twinning can be formed as a result of grain boundary sliding in order to resolve stress concentration on grain boundary. So, during elevated temperature deformation there seems to be a competition between these two mechanisms and both of them play a role in the deformation process. As shown by analysis of stress-strain curves, the rate controlling deformation mechanism in investigated range of strain rates and temperatures is dislocation glide controlled by dislocation climb. High dislocation activity should be noted in the deformed structures (Fig. 11a and d). In the sample deformed at higher temperature, stacking faults have been also observed (Fig. 11e). Some of them look like regular extended dislocation (marked as "A"), whereas the others

have triangular shape and might be formed by dissociation of stair rod dislocations (marked as "B").

2.1.7. Absence of Cavitations

Microcrystalline superplastic materials have shown clear evidence for intergranular cavitation. This includes observation on Al-Cu-Li-Zr alloy [71] and Ni_3Al alloy [72]. However, current investigation on NCM fails to reveal any evidence of cavitation. A critical question may be: Can one maintain the stress concentration at grain boundary triple points, grain boundary ledges, or at particles on the grain boundary long enough so that cavity nucleation can take place? Or can it be that diffusional relaxation in NCM is so fast that one cannot maintain that condition? In an analysis of cavity nucleation in superplasticity [73], the authors have proposed a competition between the characteristic relaxation time for grain boundary sliding leading to the development of stress concentration at ledges. Cavities may nucleate at these sites, if the incubation period for cavity nucleation is less than the characteristic time for the relaxation of stress concentration by localized diffusion creep. The analysis yields a quantitative cavity nucleation map in terms of normalized stress versus normalized cavity height/spacing. The analysis also suggests that in such ultrafine grain materials, it is possible for cavities to nucleate under some rather limited experimental conditions.

3. MAIN ISSUES

3.1. Effect of Processing

On the basis of the experimental results on SePD NCM, Mishra et al. [56] proposed an "exhaustion plasticity" mechanism. It is known that severe plastic deformation introduces a large population of dislocations into the specimen. In this "exhaustion plasticity" mechanism, the flow stress at the initial stage of deformation is not high enough to nucleate new dislocations for slip accommodation because of the very small value of grain size. The applied stress moves the pre-existing dislocations, and grain boundary sliding is accommodated by the movement of these dislocations. As the easy paths of grain boundary sliding and dislocation movement get exhausted, the flow stress increases, which is indicated by a strain hardening stage observed in the superplastic deformation of the NCM. According to Mishra et al. [56], the peak flow stress can be viewed as the critical stress required to generate new dislocations during grain boundary sliding. Mishra et al. [56] further predicted that the NCM prepared by sintering of nanocrystalline powders would not exhibit large tensile plasticity due to the lack of the large population of pre-existing dislocations.

From the evaluation of the behavior of NCM, it is clear that a nanocrystalline grain size does not appear to be a sufficient condition for superplasticity. A number of pure metals and alloys processed by severe plastic deformation to grain sizes <100 nm did not exhibit classical superplasticity (Table 1). The effect of short annealing on deformation behavior (see above) has clearly demonstrated that microstructural features other than grain size can play a considerable role. Moreover, the ability of NCMs to deform

Figure 11. Microstructure of CP Ti produced by severe plastic deformation and deformed at 350 [(a) bright field; (b) dark field images] and at 600 °C [(c)–(e): (d) is enlarged image of the selected area on (c); (e) is enlarged image of the selected area on (d).]

by superplastic flow seems to be strongly dependent on the method of their synthesis [74].

What are the necessary conditions for obtaining superplasticity in nanocrystalline materials? The answer is not clear at present, but obviously some microstructural features other than just grain size also can be responsible for the material behavior.

3.2. Deformation Mechanisms

The specific characteristics of dependency of the hardness and yield stress on grain size in NCM are definitely caused by their structural details related to the nanoscale dimension and the extremely high volume fraction of the grain boundaries. In this context, adequate theoretical understanding of the grain size dependency of the yield stress in NCM will essentially contribute, on one hand, to the understanding of the fundamentals of structure-property relationships in nanoscale solids, and, on the other hand, will serve as a basis for development of newer technologies that exploit the outstanding mechanical properties of NCM.

Slip accommodation is an important feature in superplastic deformation of microcrystalline metallic materials. Most of the superplastic models incorporate this feature [62, 75] and transmission electron microscopy does indicate intragranular dislocation activity. However, as the grain size is decreased, slip accommodation should become more difficult. In that case, the grain size dependence of superplasticity may show a fundamental change for NCM. The most fundamental question for the accommodation for stress concentration due to grain boundary sliding is: Diffusional accommodation or Slip accommodation? In recent years the possibility of superplasticity in NCM has been discussed in terms of diffusional flow. However, a grain boundary sliding mechanism with diffusional accommodation will not be able explain all of the trends. The only way to explain strain hardening by diffusional mechanisms is grain growth. Our TEM investigation of a Ni_3Al alloy before and after deformation at 650 °C suggests that grain growth alone would not be able to explain this behavior.

One of the open questions on the micromechanism of superplasticity in NCM is the role of slip accommodation. As noted earlier, the micrograined materials do show significant intragranular dislocation activity, and these dislocation features are interpreted as evidence for slip accommodation. On the other hand deformed NCMs have shown very little dislocation activity, and theoretical calculations [36–38] appear to support this lack of dislocation activity.

3.3. Modeling

The preliminary experimental data (Table 1) indicate that the stress exponent and activation energy for superplastic flow is similar for microcrystalline and NCM, although the details are not clear at this stage. The initial results in the last two years have established a number of trends: excessive strain hardening, high flow stresses, a strong annealing effect on flow behavior, and a correlation between microstructural instability and superplasticity (Section 3). Based on the limited data, the kinetics of superplastic flow is suggested to undergo a transition at a critical grain size.

The key points that are interesting for the future theoretical studies of plastic deformation processes and associated phenomena in NCM are as follows:

- A theoretical description of the critical grain size at which the general equations for superplastic deformation will break down.
- A theoretical analysis of the specific features of plastic flow in NCM.
- A development of the generalized model that will describe the combined action of different deformation mechanisms (such as lattice dislocation motion in grain interiors, grain boundary sliding, grain rotation, and diffusion based plasticity mechanisms associated with grain boundary diffusion and triple junction diffusion) whose contribution to plastic flow in NCM is dependent on the material characteristics, grain size distribution, and conditions of loading.

One of the problems in modeling of the deformation behavior of NCMs is related to their high thermal instability and a lack of experimental data on elevated temperature properties. Another problem is the limited data on diffusion coefficients in the materials at significantly diminished length scale. Recent analysis of the existing models based on classical diffusion creep and grain boundary sliding controlled by dislocation climb from the head of a pileup [76] has shown to be ruled out as not being consistent with the experimental observations. In concept of the increasing role of grain boundaries with decreasing grain size, the model based on the grain boundary structure seems reasonable. For example, a model of secondary grain boundary dislocations [76], which is based on the basic theory of grain boundary structure, was shown to cover such processes as grain rotation and grain boundary migration. These mechanisms are predicted to play a sufficient role in deformation of materials with grains in the nanometer range.

An increasing role of grain boundaries in NCM, especially as source and sink of mobile dislocations, was also demonstrated by molecular dynamics simulation [77]. The authors observed grain boundary generation of dislocations in a 45 nm grain size high stacking fault energy metal (12% strain) at room temperature (Fig. 12). Such dislocation motion has already been captured by videocamera at room
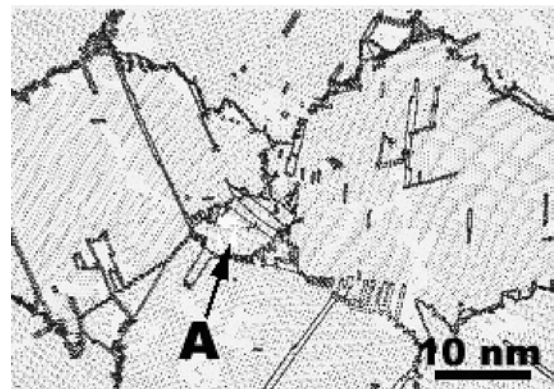
Figure 12. Dislocation nucleation at grain boundary. Molecular dynamics simulation of room temperature deformation of fcc high stacking fault energy metal. Grain size = 45 nm.
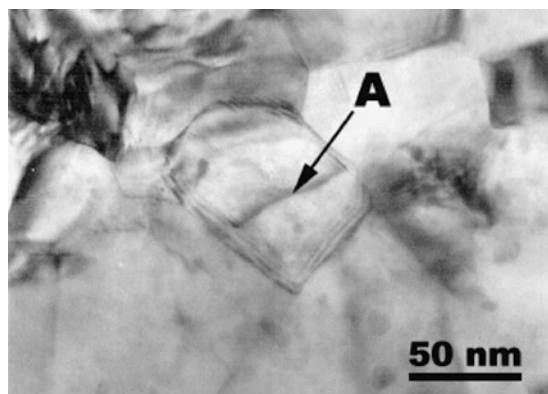
Figure 13. *In-situ* tensile testing of Ni$_3$Al at room temperature. Note dislocation A in nanosized grain. The dislocation was generated in the grain boundary, moved through the grain interior, and disappeared in the opposite grain boundary.

temperature in Ni$_3$Al ordered matrix (Fig. 13). More detailed information can be found in [78].

4. CONCLUDING REMARKS

Although NCMs are a subject of intensive investigation nowadays, there are no systematic data on their mechanical behavior and superplasticity. The size limit of nanocrystalline materials is often a matter of debate. In some publications and reviews [3], only materials with a microstructure the characteristic length scale of which is on the order of a few (typically 1–10) nanometers are determined as nanocrystalline or nanostructured materials. According to others [79] the grain size for nanocrystalline and nanostructured materials should be smaller than 500 nm. A most common definition for NCM is materials having average grain sizes below 100 nm, and this review includes mostly data on mechanical behavior of this type of materials. Nevertheless, it seems reasonable to connect this definition with characteristic features or quality changes in the material properties. The critical grain size for such changes can be slightly different for different materials but for most of them it is in the range of 20–30 nm (deviation from Hall–Petch relationship, sharp changes in magnetic properties, etc.). This seems to be the lower grain size limit for most well-known constitutive models on mechanical behavior of the materials including superplasticity. Nanomaterials seem also to have a limit in a minimum grain size, which is determined by the grain size limit of the crystalline state, and, for example, for selenium was determined to be about 4 nm [80]. It was also suggested by D. Wolf et al. [81] that below a critical grain size NCM should be unstable with respect to the amorphous phase.

Theoretical models of plastic deformation processes in NCM are mostly restricted to room temperature behavior with emphasis on Hall–Petch relationship [82]. Thus, an elevated temperature behavior of NCM is an area of high potential interest that has not been studied yet. Decreasing grain size leads to changes in deformation mechanism of the materials by eliminating some of them (a classical dislocation glide, twinning) and activation of others (grain boundary sliding, grain rotation, triple junction diffusion).

The analysis of their effect on the material properties and a development of the generalized model, which will describe the combined action of different deformation mechanisms, are the major subjects of the oncoming theoretical and experimental investigations.

GLOSSARY

Creep Time-dependent plasticity under a fixed stress at an elevated temperature.

Equal channel angular pressing (ECAP) Deformation of massive billets via pure shear that introduces an intense plastic strain into materials without changing the cross section area of billets.

High-pressure torsion (HPT) Torsion straining of the materials under high pressure.

Nanocrystalline materials (NCM) Materials with grain size in nanometer range.

Severe plastic deformation (SePD) A plastic deformation of the materials under high pressure (up to 7 GPa) to high strain (up to 7).

Superplasticity The ability of a polycrystalline material to exhibit, in a generally isotropic manner, very high tensile elongations prior to failure.

ACKNOWLEDGMENTS

REFERENCES

1. R. N. Bhargava, *J. Lumin.* 70, 85 (1996).
2. H. Gleiter, *Nanostruct. Mater.* 1, 1 (1992).
3. H. Gleiter, *Acta Materialia* 48, 1 (2000).
4. R. Schulz, *Mater. Res. Soc. Symp. Proc.* 400, 245 (1996).
5. R. W. Siegel and G. E. Fougere, in "Grain Size and Mechanical Properties-Fundamentals and Applications" (M. A. Otooni, R. W. Armstrong, N. J. Grant, and K. Ishizaki, Eds.), Materials Research Society Series, Vol. 362, p. 219 (1995).
6. C. Suruanarayana, *Int. Mater. Reviews* 40, 41 (1995).
7. N. Wang, Z. Wang, K. T. Aust, and U. Erb, *Acta Materialia* 43, 519 (1995).
8. D. G. Morris, "Mechanical Behavior of Nanostructured Materials," Vol. 2, Trans. Tech. Publ., Switzerland 1998.
9. N. Senkov, N. Srisukhumbowornchai, M. L. Ovecoglu, and F. H. Froes, *J. Mater. Res*. 13, 3339 (1998).
10. B. H. Kear and L. E. McCandlish, *Nanostruct. Mater.* 3, 19 (1993).
11. N. Wang, Z. Wang, K. T. Aust, and U. Erb, *Mater. Sci. Eng., A* 237, 150 (1997).
12. A. V. Sergueeva and A. K. Mukherjee, in "Creep Deformation: Fundamentals and Applications" (R. S. Mishra, J. C. Earthman, and S. V. Raj, Eds.), p. 137. TMS, 2002, Warrendale, PA.
13. J. B. Savader, M. R. Scanlon, R. C. Cammarata, D. T. Smith, and C. Hayzelden, *Scripta Materials* 36, 29 (1997).
14. A. Misra, H. Kung, and R. G. Hoagland, *Mat. Res. Soc. Symp. Proc.* 695, L13.9.1 (2002).
15. V. L. Tellkamp, M. L. Lau, A. Fabel, and E. J. Lavernia, *Nanostruct. Mater.* 9, 489 (1997).

16. J. C. Foley, D. R. Allen, and J. H. Perepezko, *Mater. Sci. Eng., A* 226–228, 569 (1997).

17. R. Z. Valiev, R. K. Islmgaliev, and I. V. Alexandrov, *Progress in Materials Science* 45, 103 (2000).

18. G. A. Salishchev, O. R. Valiakhmetov, V. A. Valitov, and S. K. Mukhtarov, *Mater. Sci. Forum* 170–172, 121 (1994).

19. F. H. Froes, O. N. Senkov, and E. G. Baburaj, *Mater. Sci. Eng., A* 301, 44 (2001).

20. R. W. Siegel and G. E. Fougere, in "Nanophase Materials" (G. G. Hadjipanayis and R. W. Siegel, Eds.), Kluwer, Netherlands, 1994, p. 233.

21. R. W. Siegel and G. E. Fougere, *Nanostruct. Mater.* 6, 205 (1995).

22. G. A. Salischev, R. M. Galeyev, S. P. Malisheva, and O. R. Valiakhmetov, Mater. Sci. Forum 243–245, 585 (1997).

23. E. O. Hall, *Proc. Phys. Soc. London*, B64, 747 (1951).

24. R. L. Coble, *J. Appl. Phys.* 34, 1679 (1963).

25. J. E. Bird, A. K. Mukherjee, and J. E. Dorn, in "Quantitative Relation Between Properties and Microstructure," Proceedings of an International Conference, Haifa, Israel University Press, 1969, p. 255.

26. T. G. Nieh and J. Wadsworth, *Scr. Metall. Mater.* 25, 955 (1991).

27. M. A. Meyers and K. K. Chawla, "Mechanical Metallurgy," Prentice Hall, Englewood Cliffs, NJ (1984).

28. G. J. Thomas, R. W. Siegel, and J. A. Eastman, *Scripta Metallurgica et Materialia* 24, 201 (1990).

29. M. A. Meyers and E. Ashworth, *Philos. Mag. A* 46, 737 (1982).

30. V. G. Gryazniv and L. I. Trusov, *Progress in Materials Science* 37, 289 (1993).

31. X. Zhu, R. Birringer, U. Herr, and H. Gleiter, *Phys. Rev. B* 35, 9085 (1987).

32. M. R. Fitzimmons, J. A. Eastman, M. Muller-Stach, and G. Wallner, *Phys. Rev. B* 44, 2452 (1991).

33. S. Ranganathan, R. Divakar, and V. S. Raghunathan, *Scripta Materialia* 44, 1169 (2001).

34. A. K. Mukherjee, *Mater. Sci. Eng., A* 322, 1 (2002).

35. R. A. Masumura, P. M. Hazzledine, and C. S. Pande, *Acta Materialia* 46, 4527 (1998).

36. V. G. Gryaznov, A. M. Kaprelov, and A. E. Ramanov, *Scripta Metallurgica* 23, 1443 (1989).

37. V. G. Gryaznov, I. A. Polonsky, A. E. Ramanov, and L. I. Trusov, *Phys. Rev. B* 44, 42 (1991).

38. A. E. Romanov, *Nanostruct. Mater.* 6, 125 (1995).

39. R. W. Siegel, in "Encyclopedia of Applied Physics" (G. L. Trigg, Ed.), Vol. 11, p. 1. VCH, Weinheim, 1994.

40. J. R. Weertman and P. G. Sanders, *Solid State Phenomena* 35–36, 249 (1994).

41. J. R. Weertman, *Mater. Sci. Eng., A* 166, 161 (1993).

42. F. R. N. Nabarro, "Report on a Conference on Strength on Solids," Physical Society, London (1948).

43. C. Herring, *J. Appl. Phys.* 21, 437 (1950).

44. G. W. Nieman, J. R. Weertman, and R. W. Siegel, *J. Mater. Res.* 6, 1012 (1991).

45. G. Palumbo, S. J. Thorpe, and K. T. Aust, *Scripta Metallurgica et Materialia* 24, 1347 (1990).

46. C. Suryanarayana, D. Mukhopadhyay, S. N. Patankar, and F. H. Froes, *J. Mater. Res.* 7, 2114 (1992).

47. D. L. Wang, Q. P. Kong, and J. P. Shui, *Scripta Metallurgica et Materialia* 31, 47 (1994).

48. J. Deng, D. L. Wang, Q. P. Kong, and J. P. Shui, *Scripta Metallurgica et Materialia* 32, 349 (1995).

49. M. Xiao and Q. P. Kong, *Scr. Mater.* 36, 299 (1997).

50. R. S. Mishra, T. R. Bieler, and A. K. Mukherjee, *Acta Metall. Mater.* 43, 877 (1995).

51. R. Z. Valiev, A. V. Korznikov, and R. R. Mulyukov, *Mater. Sci. Eng., A* 168, 141 (1993).

52. R. S. Mishra, W. B. Lee, A. K. Mukherjee, and Y.-W. Kim, in "International Symposia on Gamma Titanium Aluminides," (Y.-W. Kim, R. Wagner, and M. Yamaguchi, Eds.), p. 571. TMS, 1995.

53. H. Gleiter, *Progress in Materials Science* 33, 223 (1990).

54. J. Karch, R. Birringer, and H. Gleiter, *Nature* 330, 556 (1987).

55. P. G. Sanders, M. Rittner, E. Kiedaisch, J. R. Weertman, H. Kung, and Y. C. Lu, *Nanostruct. Mater.* 9, 433 (1997).

56. R. S. Mishra, R. Z. Valiev, S. X. McFadden, and A. K. Miukherjee, *Mater. Sci. Eng., A* 252, 174 (1998).

57. A. Ramesh and S. Ankem, "Advanced Materials and Processing," The Minerals, Metals and Materials Society, Hawaii, USA, PRICM 3 (1998), p. 757.

58. R. Boyer, G. Welsch, and E. W. Collings, Eds., "Materials Properties Handbook: Titanium Alloys," p. 165. ASM International Materials Park, OH, 1994.

59. R. S. Mishra, R. Z. Valiev, A. K. Miukherjee, *Nanostruct. Mater.* 9, 473 (1997).

60. A. K. Miukherjee, R. S. Mishra, T. R. Bieler, *Acta Materialia* 45, 561 (1997).

61. M. L. Meier, D. R. Lesuer, and A. K. Mukherjee, *Mater. Sci. Eng., A* 154, 165 (1992).

62. O. D. Sherby and J. Wadsworth, *Progress in Materials Science* 33, 169 (1989).

63. H. A. Calderon, V. Garibay-Febles, M. Umemoto, and M. Yamaguchi, *Mater. Sci. Eng., A* 329–331, 196 (2002).

64. R. S. Mishra and A. K. Miukherjee, "Superplasticity in nanomaterials," Minerals, Metals and Materials Society/AIME, (1998), p. 109.

65. J. P. Hirth and J. Lothe, "Theory of Dislocations," John Wiley & Sons, New York (1982), p. 752.

66. E. E. Underwood, "Metals Handbook," 9th edition, vol. 9 (1989).

67. A. V. Sergueeva, R. Z. Valiev, and A. K. Mukherjee, in "Ultrafine Grained Materials II," (Y. T. Zhu, T. G. Langdon, R. S. Mishra, S. L. Semiatin, M. J. Saran, and T. C. Lowe, Eds.), p. 515. The Minerals, Metals and Materials Society, 2002.

68. D. B. Williams, C. B. Carter, Transmission electron microscopy: a textbook for Material Science II, NY: Plenum Press, 1996, p.160.

69. K. Higashi, A. Uoya, T. Mukai, and S. Tanimura, *Mater. Sci. Eng., A* 181–A182, 1068 (1994).

70. G. A. Salishchev, R. M. Galeyev, S. P. Malisheva, and O. R. Valiakhmetov, *Mater. Sci. Forum* 243–245, 585 (1997).

71. A. H. Chokshi and A. K. Mukherjee, *Mater. Sci. Eng., A* 110, 49 (1989).

72. J. Mukhopadhyay, G. C. Kaschner, and A. K. Mukherjee, in "Superplasticity in Aerospace," (T. R. McNelley and H. C. Heikkenen Eds.), CTMS-AIME, Warrendale, PA (1990) p. 33.

73. A. H. Chokshi and A. K. Mukherjee, *Acta Materialia* 37, 3007 (1989).

74. F. A. Mohamed and Y. Li, *Mater. Sci. Eng., A* 298, 1 (2001).

75. A. K. Mukherjee, in "Plastic Deformation and Fracture of Materials," (H. Mughrabi, Ed.), vol. 6, p. 407. Materials Science and Technology. Pub, VCH, Weinheim, 1993.

76. R. I. Todd, *Mater. Sci. Technol.* 16, 1287 (2000).

77. V. Yamakov, D. Wolf, S. R. Philpot, A. K. Mukherjee, and H. Gleiter, *Nature Materials*, Vol. 1, 2002, p. 45.

78. A. K. Mukherjee, in "Creep Deformation: Fundamentals and Applications," (R. S. Mishra, Ed.), p. 3. TMS-AIME, Pittsburgh, PA, 2002.

79. Y. R. Kolobov, G. P. Grabovetskaya, K. V. Ivanov, and M. B. Ivanov, *Interface Science* 10, 31 (2002).

80. N. X. Sun and K. Lu, *Phys. Rev. B* 59, 5987 (1999).

81. D. Wolf, S. R. Phillpot, and P. Keblinski, *Mat. Res. Soc. Symp. Proc.* 400, 115 (1996).

82. M. Y. Gutkin, I. A. Ovid'ko, C. S. Pande, *Reviews on Advanced Materials Science* 2, 80 (2001).

ENN
Encyclopedia of Nanoscience and Nanotechnology
www.aspbs.com/enn

Dendrimer–Metal Nanocomposites

Kunio Esumi

Tokyo University of Science, Tokyo, Japan

CONTENTS

1. INTRODUCTION

Dendrimers are macromolecules with a regular and highly branched three-dimensional architecture. The first example of an iterative synthetic procedure toward well-defined branched structures was reported by Vögtle et al. [1], who named this procedure a "cascade synthesis." In the early 1980s, Denkewalter et al. [2] patented the synthesis of L-lysine-based dendrimers. A paper concerning dendrimers, which have received widespread attention, was presented by Tomalia et al. in the first international polymer conference at Kyoto in 1984 and was published in *Polymer Journal* in 1985 [3]. At the same time, Newkome et al. [4] reported on "arborol" for branched polymers. In 1980s, many different dendrimers were synthesized. Tomalia's poly(amidoamine) (PAMAM) dendrimers and Newkome's arborol have been obtained by the divergent method, while Fréchet et al. [5] introduced the convergent approach for precise synthesis of dendrimers. In the 1990s, for intriguing properties of dendrimers as well as their synthesis and possible applications, many types of dendrimers systems were developed [6–11].

Since dendrimers consisting of a regularly branched structure are controlled by chemical structure, molecular weight, and its distribution as well as molecular size and molecular shape, dendrimers are classified as unique macromolecules with many functional properties. In addition, it is possible to make molecular design of dendrimers from the standpoint of core, branched chain, and surface functional groups, and the pore space of dendrimers can also be utilized. Dendrimers can provide a dimensional functionality which is different from conventional linear polymers; although conventional linear polymers can be modified by grafting branched chains, dendrimers have superior properties to build up three-dimensional molecular architectures.

Through intensive research developments, dendrimers have been recognized to be important and interesting materials from the standpoint of basic and applicable new material. For example, dendrimers have many applicable potentials such as nanocapsules, gene vectors, catalysis, magnetic resonance imaging agents, electron conduction, and photon transduction. Large scale production of dendrimers can also promote dendrimers as a new generation material. Furthermore, the science of dendrimers has grown through a deep connection with disciplines that include physical and materials chemistry, biotechnology, and applied physics. At the present, poly(amidoamine) dendrimers and poly(propyleneimine) dendrimers are available commercially which are made by the divergent method.

Since dendrimers can interact with many chemicals which can be applied to many fields, synthesis and characterization of dendrimer–metal nanocomposites are discussed in this chapter.

2. SYNTHESIS AND CHARACTERIZATION

Before discussing synthesis of dendrimer–metal nanocomposites it is better to show some information about the evolution of the size and shape of dendrimers. Figure 1 shows transmission electron microscope (TEM) images of PAMAM dendrimers stained positively for G10 to G5, respectively [12]. The dendrimer molecules appear as dark objects on a light background of the amorphous carbon substrate and they are spherical to a first approximation for G10 to G7, with some molecules showing "edges" or slightly polyhedral shapes. For G6 and G5, the shapes become more indistinct because the substrate is closer in size to the molecule and the edges become more difficult to delineate. The mean and median diameters of each generation are listed in Table 1, along with the standard deviation of the measurement. In general, the agreement between the mean and median diameters is good, indicating that the distribution is approximately Gaussian in shape. The mean diameters range from 14.7 nm for G10 to 4.3 nm for G5. The
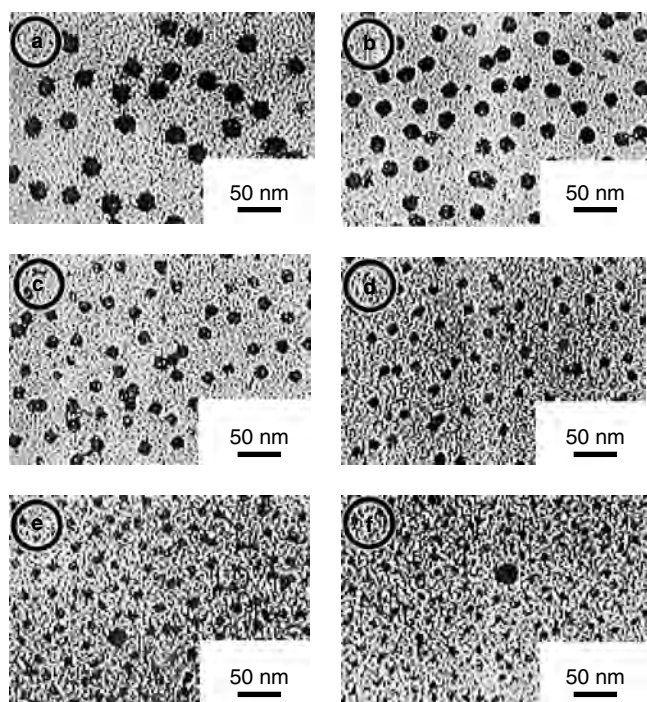
Figure 1. PAMAM dendrimers positively stained with 2% aqueous sodium phosphotungstate imaged by conventional TEM: (a) G10, (b) G9, (c) G8, (d) G7, (e) G6, (f) G5. The scale bars indicate 50 nm. For G6 and G5, a small amount of G10 has been added as a focusing aid. Reprinted with permission from [12], C. J. Jackson et al., *Macromolecules* 31, 6259 (1998). © 1998, American Chemical Society.

diameters of PAMAM determined by size-exclusion chromatography are much smaller than those by TEM. Further, the diameters of PAMAM dendrimers are larger than the equivalent poly(propyleneimine) dendrimers [13].

Preparation of metal particles has been intensively investigated because metal nanoparticles have been applied in electrooptical devices, electronic devices, imaging materials, catalysis, and so on [14–20]. Fabrication of nanoparticles becomes one of the important topics in nanotechnology. For that purpose, it is required that reliable nanoscale devices control particle size, shape, and size distribution of metal nanoparticles.

Since dendrimers contain a large number of regularly spaced internal and external functional groups, it is expected that they operate as templates to grow inorganic crystal in

Table 1. Size measurements on PAMAM dendrimers from computer analysis of TEM images.

Generation	Mean diameter (nm)	Median diameter (nm)	No. of dendrimers	Standard deviation
10	14.7	14.8	413	1.1
9	12.4	12.5	1331	0.8
8	10.2	10.3	459	0.8
7	8.0	8.0	576	0.7
6	6.9	6.9	239	0.5
5	4.3	4.3	285	0.7

Source: Reprinted with permission from [12], C. J. Jackson et al., *Macromolecules* 31, 6259 (1998). © 1998, American Chemical Society.

the internal or external region of the dendrimer which provides organic–inorganic hybrid nanostructures [21–44].

When metal ions are mixed with PAMAM dendrimers in solutions complex formation by ligand–metal ion interaction, acid–base interaction, and other interactions might occur at the surface or inside of the dendrimers. After the reduction the location of metal particles in nanocomposites strongly depends on the place of the complex formation. Accordingly dendrimer–metal nanocomposite structures are schematically illustrated in Figure 2. In Figure 2a, metal ions interact with surface functional groups of the dendrimers and the resulting nanoparticles are present on the surface of the dendrimers. Also, for lower generation dendrimers whose diameters are smaller than those of metal particles a nanocomposite structure as in Figure 2a might be suggested. On the other hand, when metal ions are diffused into the dendrimers complexed with the binding sites, metal particles after the reduction are encapsulated into the dendrimers as shown in Figure 2b. Such encapsulation might occur in higher generation dendrimers. In addition, there is
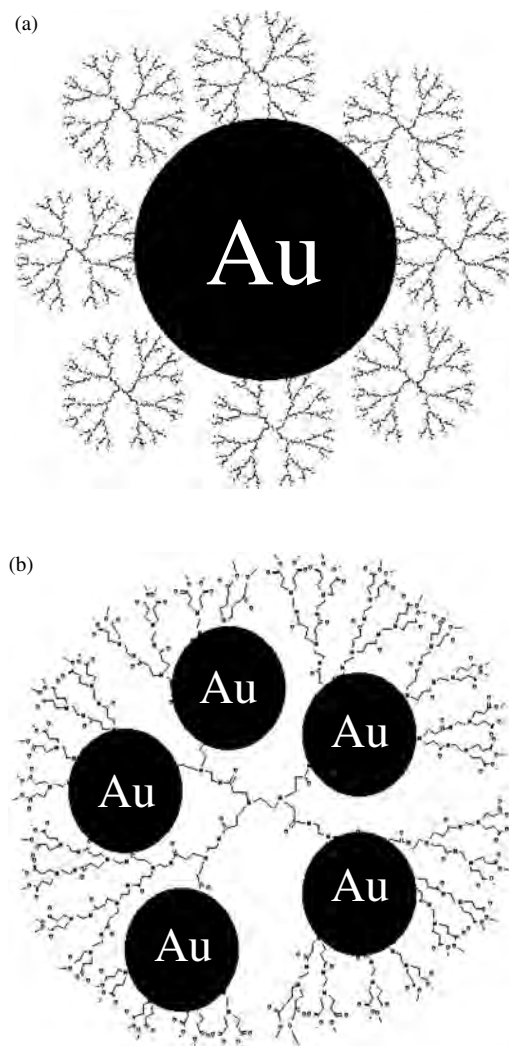
Figure 2. Schematic illustration of dendrimer–metal nanocomposite structures: (a) gold nanoparticle surrounded by dendrimers; (b) dendrimer-encapsulated gold nanoparticles.

a possibility of a mixed structures of Figure 2a and b. The results of dendrimer–metal nanocomposites synthesized so far are discussed below.

The dendrimer–copper nanocomposites were first synthesized using PAMAM dendrimers with various surface functional groups in aqueous solution [22, 23]. In the case of copper sulfate and dendrimer with surface hydroxyl group, chemical reduction of Cu^{2+}-loaded G4 dendrimer (G4-OH) with a fivefold molar excess of sodium borohydride results in intradendrimer Cu clusters. The solution color immediately changes from blue to golden brown: the absorbance bands originally present at 605 and 300 nm disappear and are replaced with a monotonically increasing spectrum of nearly exponential slope toward shorter wavelengths. This behavior results from the appearance of a new interband transition arising from the formation of intradendrimer Cu clusters. TEM results indicate the presence of intradendrimer Cu clusters after reduction. Micrographs of Cu clusters within G4-OH reveal particles having a diameter less than 1.8 nm, much smaller than the 4.5 nm diameter of G4-OH. Clusters formed in the presence of G4-OH are stable for at least 1 week in an oxygen-free solution. However, in air-saturated solutions the clusters revert to intradendrimer Cu^{2+} ions overnight. When G4 dendrimers with surface amino group are used as templates, they adsorb Cu^{2+} ions which bind primarily to the surface amino groups. Reduction of a solution shows a formation of Cu clusters having diameters more than 5 nm. This large size is a consequence of agglomeration of Cu particles adsorbed to the unprotected dendrimer exterior. Another study for the synthesis of dendrimer–copper nanocomposites using copper acetate and hydrazine as a reductant agent suggests that copper particles are present at both the interior and exterior of the dendrimer with surface amino groups. Dendrimer–copper nanocomposites are also synthesized using amine-terminated poly(propyleneimine) dendrimer with a diaminobutane core. The size of copper clusters decreases with increasing dendrimer generation. In the case of fourth generation of dendrimer it is possible to have some degree of encapsulation of the copper clusters. Thus, depending on the polarity of the dendrimer surface substitutes, the metallic particles may be directed near the dendrimer surface or deeper into the interior.

The dendrimer–gold nanocomposites have been synthesized by reduction of $AuCl_4^-$ with ultraviolet (UV) irradiation in aqueous solution [21]. The absorption band of colloidal gold appears at around 520 nm, and its intensity increases with an increase of the irradiation time. In the case of the low generation PAMAM dendrimers the plasmon band is shifted to longer wavelength with increasing UV irradiation time due to coagulation of gold particles. Typical TEM images of gold colloids obtained in the presence of G5 dendrimer with surface amino group (G5-NH2) and their particle size distributions are shown in Figure 3. At the ratio of [surface amino]/[HAuCl₄] = 1 : 1, the particle size of gold colloids is in the 2–18 nm range, having a broad size distribution. When the ratio is increased to 4 : 1, monodispersed gold particles with a diameter less than 1 nm are obtained. The average particle sizes of gold colloids obtained in the presence of G(0-5)-NH2 are shown in Figure 4. The average
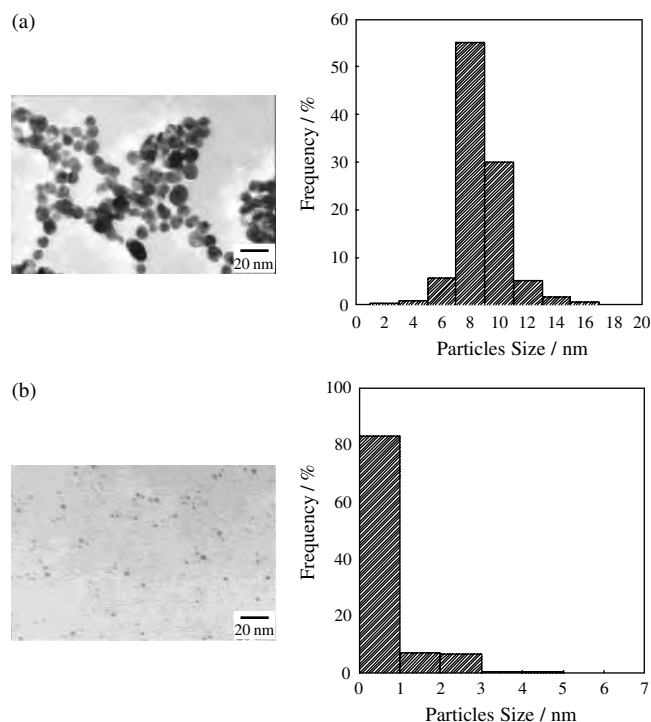
Figure 3. TEM images and particle size distribution of gold nanoparticles, molar ratio of surface amino group of PAMAM G5 and HAuCl₄: (a) 1 : 1; (b) 4 : 1. Reprinted with permission from [21], K. Esumi et al., *Langmuir* 14, 3157 (1998). © 1998, American Chemical Society.

particle size decreases with increasing concentration of surface amino group for each dendrimer. In particular, it is interesting to note that ultrafine gold colloids with a diameter less than 1 nm are obtained in the presence of a higher
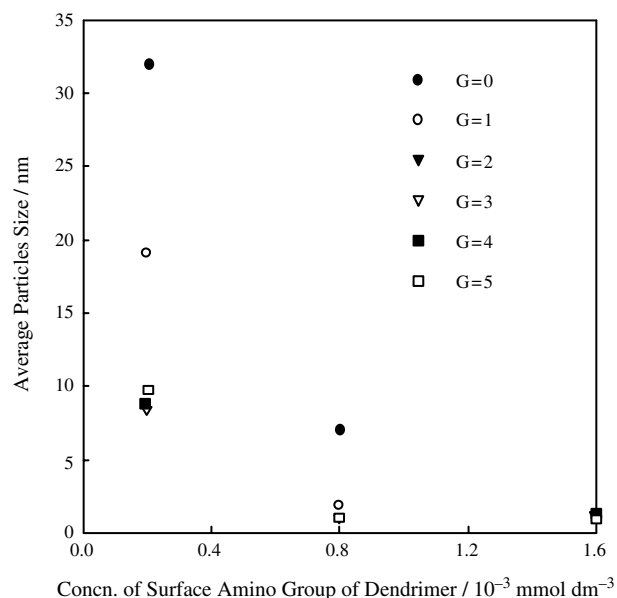
Figure 4. Variation of average particle size of gold nanoparticles with concentration of surface amino group of PAMAM dendrimers G(0-5). Reprinted with permission from [21], K. Esumi et al., *Langmuir* 14, 3157 (1998). © 1998, American Chemical Society.

concentration surface amino group of higher generation dendrimers. These results suggest that the dendrimers of lower generation G0 do not operate as effective protective colloids, but dendrimers of higher generations provide sites for complex formation with $AuCl_4^-$ as well as an effective protective action. Dendrimer–silver nanocomposites are also synthesized in the presence of amino- (G4) or carboxylate-terminated (G3.5) PAMAM dendrimers by UV irradiation [38]. The silver nanoparticles with average size of about 7 nm diameter are obtained using amino-terminated dendrimers, while a larger size (about 31 nm) is observed in the case of carboxylate-terminated dendrimer.

By addition of reductants such as sodium borohydride into noble metal ion–dendrimer aqueous solutions, dendrimer–noble metal particles nanocomposites (gold, silver, platinum, palladium) have also been synthesized [24–27, 30, 32, 37, 40–42, 44]. The average sizes of gold decrease with an increase of the concentration of surface amino groups for G(3–5) dendrimers, while the average sizes of platinum particles are independent of the generation of the dendrimers above a certain ratio of [amino group]/[Pt^{4+}] [30]. It should be mentioned that a much higher concentration of the dendrimers is required to stabilize platinum colloids compared to that for gold colloids. Since it is expected that Ag$^+$ ions strongly adsorb on the dendrimers having surface carboxyl groups through electrostatic attractive forces, the reduction of AgNO$_3$ by addition of sodium borohydride in the presence of G(3.5–5.5) dendrimers has been carried out. Figure 5 shows the change in optical spectra of silver colloids obtained in the presence of G5.5 dendrimer with various concentrations. Although a typical plasmon band of silver colloids is observed at 380 nm at the ratio of
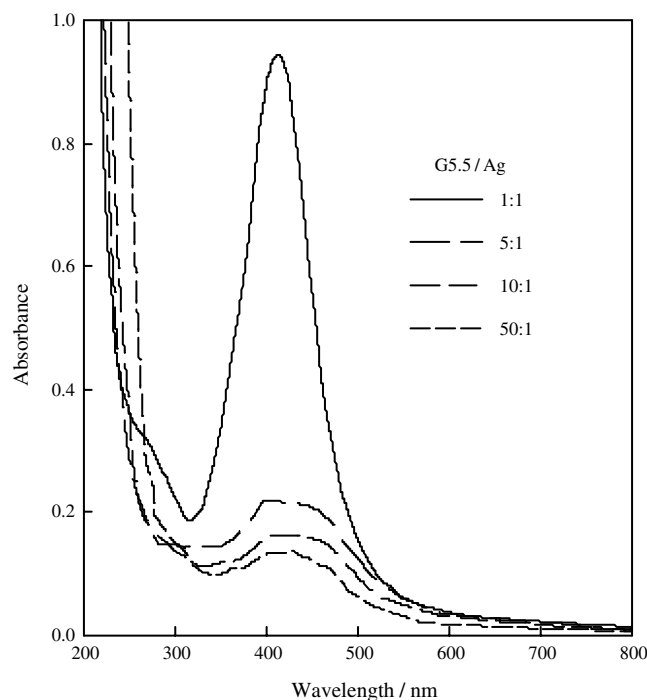
[G5.5]/[Ag$^+$] = 1 : 1, another band at around 450 nm appears. Further, the absorbance at both bands considerably decreases. The color of silver colloids also changes with increasing concentration of G5.5 dendrimer; yellow at the ratio of [G5.5]/[Ag$^+$] = 1 : 1 turns to orange at the higher ratios. In the case of G3.5 and G4.5 dendrimers, a result similar to that of G5.5 dendrimer is observed. At above the ratio of [G5.5]/[Ag$^+$] = 5/1 we cannot observe any silver particles by TEM because the particle size is too small to detect in the condition used. From Fourier transform infrared (FTIR) spectra it may be suggested that metal colloids adsorb on the exterior of the dendrimers. On the other hand, by using fourth-generation PAMAM with surface hydroxyl group, it has been reported [24] that platinum or palladium nanoparticles can be encapsulated inside the dendrimer. This is probably due to different interactions of metal nanoparticles with various functional groups of dendrimers. In addition, it has also been suggested [33] that the structure of dendrimer–gold or –silver nanocomposites is a function of the dendrimer structure and surface functional groups as well as the formation mechanism and the chemistry involved.

To verify the structure of dendrimer–gold nanocomposites gold nanoparticles synthesized by reduction of HAuCl$_4$ with sodium borohydride in the presence of PAMAM with surface amino groups (G2–G10) have been characterized by TEM, SANS, and SAXS [32]. Figure 6 shows a TEM image of gold particles containing G9 PAMAM dendrimer. The image indicates that gold colloids are formed inside the dendrimer. Under slow reaction conditions, one gold particle per dendrimer is predominantly formed. The sizes estimated

Figure 5. Absorption spectra of AgNO$_3$ in the presence of PAMAM dendrimer, G5.5, after reduction with NaBH$_4$. Reprinted with permission from [30], K. Esumi et al., *Langmuir* 16, 2604 (2000). © 2000, American Chemical Society.
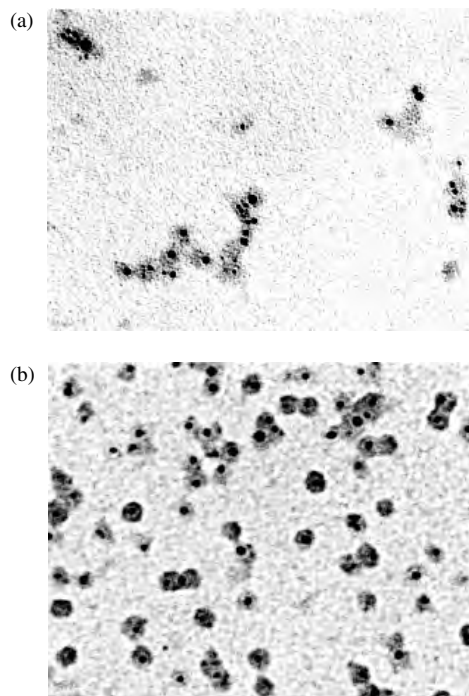
Figure 6. TEM images of gold containing G9 PAMAM dendrimer obtained for 1:1 loading. The dendrimers have been stained with phosphotungstic acid and appear gray; the gold colloids appear black. (a) Fast reduction (NaBH$_4$ in 0.1 M NaOH); (b) slow reduction (NaBH$_4$ in 0.3 M NaOH). Reprinted with permission from [32], F. Grohn et al., *Macromolecules* 33, 6042 (2000). © 2000, American Chemical Society.

for the dendrimer and gold are 13 and 4 nm, respectively. SANS measurements have been performed on solutions of dendrimer–gold hybrid particles in deuterium oxide. The radius of gyration obtained from Guinier extrapolation is 5.1 ± 0.1 nm. This is within the same experimental error as the unmodified dendrimer, indicating that the hybrid particles also do not form larger aggregates in solution. Furthermore, the higher order sphere form factor features, which are pronounced in the case of the unmodified dendrimer, nearly completely disappear for the hybrid samples. SAXS provides more detailed information about the colloid structures; an estimate of the dimensions of the inner-sphere and outer-sphere diameter by SAXS confirms the diameters of the gold (4 nm) and the dendrimer (13 nm) estimated by TEM. More importantly, this result proves that the gold is formed inside the dendrimer. Further, it has been suggested for the dendrimers with various generations that several dendrimers surround the surface of gold particle formed for G2–G4 dendrimers, while gold particles are completely formed inside individual dendrimers for G6–G10 dendrimers. For G10, multiple gold particles within one dendrimer molecule are formed due to the more crowded volume inside the dendrimer. Thus, such a transition has been shown from colloid stabilization by low molecular mass molecules to polymer nanotemplating with an increase of molecular mass but unchanged chemistry of the stabilizing species.

For metal ions that do not form either covalent bonds or strong complexes with the interior amine groups of PAMAM dendrimers a method for preparing dendrimer-encapsulated metal nanoparticles has been reported [26]. For example, when G6 dendrimer (with surface hydroxyl group)-encapsulated copper is exposed to a solution containing ions more noble than copper, the copper is displaced and the more noble ions are reduced. By using this method, silver, gold, palladium, and platinum dendrimer-encapsulated metal particles have been obtained.

Gold and silver nanoparticles can also be synthesized in the presence of sugar-persubstituted PAMAM dendrimers (sugar ball) without reductants [34]. Actually, the hydroxyl groups of glucose residue of sugar balls can operate as reductants. In the case of silver nanoparticles, the addition of NaOH is required to reduce Ag$^+$ ions. It is suggested that gold or silver nanoparticles having diameters between 2 and 6 nm are present on the surface of sugar balls. In addition, the kinetics of the formation of gold and silver nanoparticles is affected by the generation of sugar balls as well as the concentration of sugar balls. The observed rate constants increase with the concentration of sugar balls, where the rate constants for low-generation sugar balls are greater than those for higher generation. Such noble metal–sugar nanocomposites are of considerable interest in biochemical and medical applications.

Dendrimer–gold and –platinum nanocomposites have been synthesized [31, 36] in ethyl acetate by reduction of respective metal salts with dimethylamineborane, where PAMAM dendrimers with surface methyl ester groups have been used. When ethyl acetate solution of HAuCl$_4$ is added to dendrimers in ethyl acetate, the formation of dendrimer–Au^{3+}complex is observed. HAuCl$_4$ shows an intense absorption at 324 nm which can be assigned to the LMCT band of

AuCl$_4^-$. On the other hand, G5.5 dendrimer shows a small absorption maximum at 278 nm. On mixing Au^{3+} with the dendrimer, a new band develops at 280 nm at the expense of the 324 nm band and the latter completely disappears in 15 minutes of stirring. In addition, an isobestic point is found at 304 nm, indicating that a ligand substitution from AuCl$_4^-$ to another Au^{3+} complex occurs through a participation of the dendrimer. It is also found from FTIR measurements that the bands for surface methyl ester groups at 1044, 1200, 1438, and 1736 cm^{-1} do scarcely change by introducing Au^{3+}, while the amide I band at 1647 cm^{-1} for interior amide groups undergoes a high-frequency shift to 1649 cm^{-1} and a single peak for the amide II band splits into two peaks by addition of Au^{3+}. A similar result for the formation of complex of dendrimer–Au^{3+} is obtained for G3.5 dendrimer. Au^{3+} ions in the presence of the dendrimers in ethyl acetate are readily reduced by adding an excess amount of dimethylamineborane. Interestingly, it is found that at above the ratio of [G]/[Au^{3+}] $\geq$ 10 the maximum particle size of gold is less than the hydrodynamic diameter of the dendrimer (G3.5 and G5.5), while in the case of G1.5 dendrimer the maximum size of gold is larger than the hydrodynamic diameter of G1.5. These results may suggest that the encapsulation of gold nanoparticles by G3.5 or G5.5 dendrimer occurs, while gold nanoparticles are stabilized by adsorbing G1.5 dendrimers. These suggestions are supported by the results of interactions between Au^{3+} and several model compounds such as acrylamide, N-methylpropionamide, trimethylamine, and N,N-dimethylglycine methyl ester.

Gold nanoparticles have also been obtained by addition of sodium borohydride into formamide solution of HAuCl$_4$ in the presence of PAMAM dendrimer with surface methyl ester group [39]. The particle size decreases with an increase of the dendrimer concentration as well as the generation. Further, the particle size of gold is affected by the elapsed time for the solution before reduction because HAuCl$_4$ in formamide is reduced to some extent without reductant. In N,N-dimethylformamide in the presence of the dendrimers relatively monodispersed gold nanoparticles are obtained. It may be suggested that stable gold nanoparticles are prepared by adsorbing a low dendrimer on the nanoparticles, while dendrimer-encapsulated gold nanoparticles are obtained in the case of a higher generation dendrimer.

Platinum nanopaticles have also been synthesized in ethyl acetate in the presence of PAMAM dendrimers with surface methyl ester group [31]. The elapsed time after mixing of H$_2$PtCl$_6$ and PAMAM dendrimers in ethyl acetate is very important to control the particle size, which is different from the preparation of gold nanoparticles. Figure 7 shows TEM images of platinum nanoparticles obtained in the presence of PAMAM 5.5 at 5 min of elapsed time after mixing. One can see that even at different concentrations of dimethylamineborane large (about 18 nm in diameter) and small (about 3 nm in diameter) platinum particles are formed. In particular, when the concentration of dimethylamineborane is 90 times that of H$_2$PtCl$_6$, it is visualized that the large particles are coated by PAMAM G5.5, where the thickness of coating is about 4–5 nm and is smaller than the hydrodynamic diameter (7.6 nm) of PAMAM G5.5 determined by dynamic light scattering measurements in ethyl acetate. It is suggested that PAMAM G5.5 dendrimers
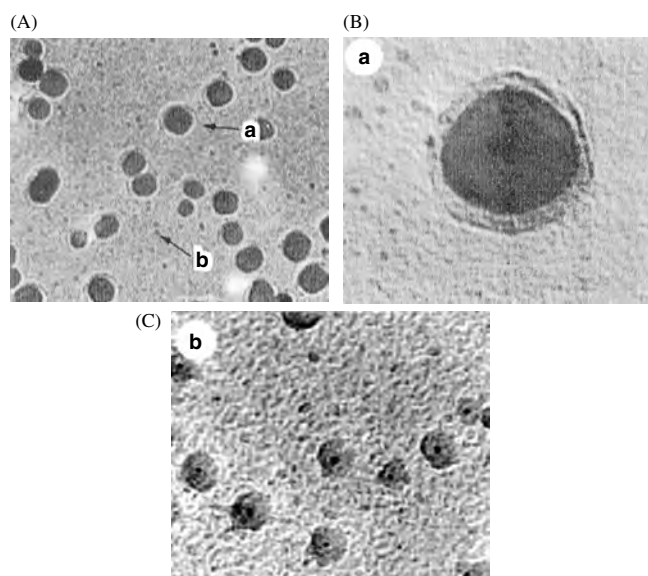
Figure 7. TEM images of (A) platinum nanoparticles obtained in the presence of PAMAM G5.5 after 5 min elapsed time. (B) Enlargement of the particle in (A). (C) Enlargement of the particle in (B). Reprinted with permission from [31], K. Esumi et al., *Langmuir* 16, 7842 (2000). © 2000, American Chemical Society.

are flattened on the surface of the platinum particle. Actually, the structural distortion of the dendrimers on gold surfaces has been reported [45]: the height of PAMAM G8 on a naked gold surface ranges from 3.5 to 4.0 nm, which is less than the ideal-sphere diameter of 9.7 nm. On the other hand, it is seen that the small platinum particles are encapsulated by PAMAM G5.5 in which the diameter of a PAMAM G5.5-encapsulated platinum particle is about 10 nm. It seems that the PAMAM G5.5-encapsulated platinum particle is flattened on the grid surface [46]. When the concentration of dimethylamineborane is reduced to 10 times that of H_2PtCl_6, the image of visualized dendrimers is not observed, although similar large and small platinum particles are obtained. It is speculated that the visualization of PAMAM G5.5 dendrimer by TEM is caused by the interaction between dimethylamineborane and PAMAM G5.5 dendrimer. It should be mentioned that the visualization of PAMAM G5.5 dendrimer from mixtures of dimethylamineborane and PAMAM G5.5 dendrimer is not observed, suggesting that platinum particles play an important role for the visualization of PAMAM G5.5 dendrimer to some extent. Such a formation of large and small platinum particles at short elapsed time may occur due to nonuniform distribution of Pt^{4+} ions in the solution and in the PAMAM G5.5 dendrimer. When the elapsed time after mixing is increased, the average particle diameter decreases: the average diameters are about 1.7 nm (standard deviation 0.3 nm) at 1 day of elapsed time and 0.8 nm (standard deviation 0.1 nm) at 3 days of elapsed time. Since the particle size is considerably smaller than the diameter of PAMAM G5.5 dendrimer, it is conceivable that many clusters of platinum are entrapped in the interior of the PAMAM G5.5 dendrimer. When the ratio of [G5.5]/[H_2PtCl_6] is varied from 150/1 to 50/1, the average diameter of platinum is not appreciably changed.

Also, from the results of the reduction of $PtCl_6^-$ in the presence of PAMAM G3.5 or PAMAM G1.5 dendrimer in ethyl acetate it is suggested that PAMAM G3.5-encapsulated platinum particles are formed, while PAMAM G1.5 dendrimers adsorb on the surface of platinum particles because the particle size of platinum obtained is larger than the diameter of PAMAM G1.5 dendrimer.

In toluene, which is a less polar organic solvent than ethyl acetate, dendrimer–gold nanocomposites have been synthesized in which a hydrophobically modified PAMAM dendrimer has been used [35]. The hydrophobically modified PAMAM is synthesized by reaction of PAMAM with surface amino group with 1,2-epoxydodecane [47, 48]. Solution of the hydrophobically modified PAMAM dendrimer in toluene is carefully layered on top of $HAuCl_4$ aqueous solution. After the solution stood for several hours at room temperature, a bright yellow color emerges in toluene. The extraction experiment is continued for 1 day. Since $HAuCl_4$ is not soluble in toluene solution, it is reasonable to consider that $AuCl_4^-$ ions should be incorporated in the interior of the hydrophobically modified PAMAM in toluene. Then, by addition of dimethylamineborane–toluene solution, $AuCl_4^-$ ions are reduced. The average diameters of gold nanoparticles obtained range between 2.5 and 3.4 nm which is smaller than the diameter (4.5 nm) of PAMAM G4. This suggests that gold nanoparticles are encapsulated in the hydrophobic PAMAM dendrimer. A similar result has also been obtained using chloroform as an organic solvent.

Another approach for the preparation of dendrimer–metal nanocomposites in toluene is a process driven by acid–base chemistry and ion pairing [28]. At first, palladium nanoparticles are synthesized by reducing aqueous K_2PdCl_4 with sodium borohydride in the presence of PAMAM G4 dendrimer where the pH of dendrimer solution is adjusted to about 2. The low pH protonates the exterior amines to a greater extent than the less basic interior tertiary amines. Accordingly, Pd^{2+} binds preferentially to the interior tertiary amines and upon reduction palladium particles form within the dendrimer interior. After complete reduction, the pH of solutions is adjusted back to about 8.5. Then, these nanocomposites can be quantitatively transported from the aqueous phase into toluene containing 10–20% of dodecanoic acid. The transition is visualized by the color change: the brown aqueous solution of PAMAM dendrimer–palladium nanocomposites becomes clear after addition of the acid, while the toluene layer turns brown.

In addition, dendron-stabilized gold nanoparticles have been synthesized using Fréchet-type dendrons possessing a single thiol group at the focal point, and their diameters are 2.4–3.1 nm [49].

3. PROPERTIES

Since dendrimers act as template and stabilizer for synthesizing metal nanoparticles, we can control particle size and particle stability. In addition, for dendrimer–metal nanocomposites metal nanoparticles are present in the interior or exterior of the dendrimer. These two different structures allow different interactions with substrates. Accordingly, dendrimer–metal nanocomposites would exhibit an unique property in the field of catalysis.

Dendrimer-encapsulated metal nanoparticles such as platinum and palladium have been examined as catalysts for hydrogenation and Heck reactions [40, 50–54]. The catalytic hydrogenation of allylic alcohol to 1-propanol has been carried out by dendrimer-encapsulated palladium nanoparticles in water. The turnover frequency calculated from the rate of hydrogen uptake is 218 mol of H_2(mol of Pd)$^{-1}$ h^{-1} at 20 °C [55]. Similar data have been obtained for dendrimer-encapsulated platinum nanoparticles. In addition, the turnover frequency for the allyic alcohol reduction using toluene solutions of dendrimer-encapsulated palladium nanoparticles is 760 mol H_2 at 20 °C [28], which compares favorably with the value in water.

Dendrimer-encapsulated palladium nanoparticles has been applied to fluorous biphasic catalysis [56–58] in order to facilitate recovery and recycling of soluble catalysts. These catalysts are active in fluorous biphasic systems for the hydrogenation of alkenes and for the isomerization of terminal alkenes and are also recycled 12 times without appreciable loss of catalytic activity [28].

Perfluorinated catalysts also allow the use of supercritical CO_2 in which they are soluble. Using perfluorinated dendrimer-encapsulated palladium nanoparticles, Heck coupling between aryl halides and n-butylacrylate has been carried out and it is 100% selective for the production of n-butyl-$trans$-formylcinnamate with unoptimized isolated yields up to 70% [59].

The effect of dendrimer generation on the catalytic activity using dendrimer–platinum nanocomposites has been reported [60]. The time course of hydrogenation of cyclohexene using PAMAM–dendrimer–platinum nanocomposites synthesized in ethanol is shown in Figure 8. It is clearly demonstrated that PAMAM G1.5–platinum nanocomposites
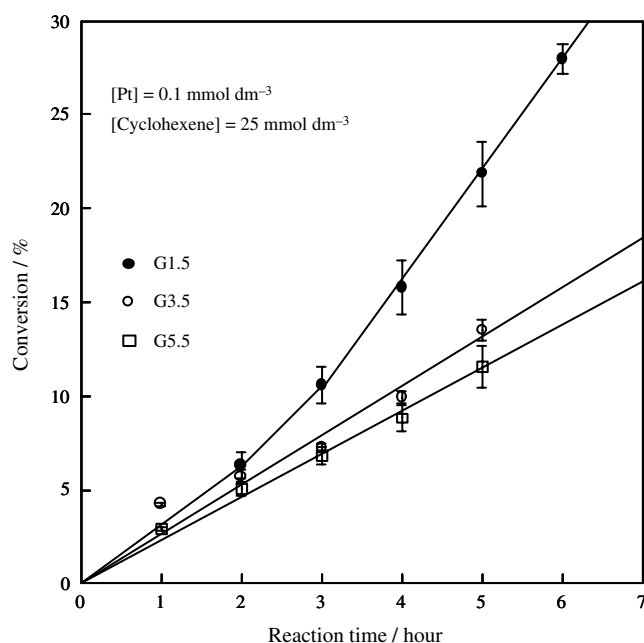
Figure 8. Hydrogenation of cyclohexene by platinum nanoparticles prepared in the presence of PAMAM dendrimers in ethanol. Reprinted with permission from [60], K. Esumi et al., *J. Jpn. Soc. Colour Mater* 73, 434 (2000). © 2000, Japan Society of Colour Material.

have much higher catalytic activity than those of PAMAM G3.5 or G5.5–platinum nanocomposites. At a reaction time of 24 h, the conversion to cyclcohexane is about 86% for PAMAM G1.5 dendrimer and 48% for PAMAM G3.5 and G5.5, respectively. Thus, the catalytic reaction can be controlled using dendriemers of various generations. Such characteristics may be derived from a unique structure of dendrimer so that cyclohexene molecules are less able to penetrate into the interior platinum nanoparticles of dendrimers when the generation of dendrimer increases.

Optical properties of nanoscale metal domains in dendrimer–metal nanocomposites are interesting and strongly influenced by the surface plasmon resonance of metal nanoparticles [61, 62]. In particular, gold, silver, and copper nanoparticles exhibit characteristic plasmon bands. This is relevant for the case of optical limiting where the material's absorption is dependent upon the intensity of the input beam. It is demonstrated [63] that PAMAM dendrimer–silver nanocomposites can exhibit large optical limiting at 532 nm by factors up to 115. The mechanism governing the optical limiting observed is nonlinear scattering, most probably due to bubble formation at the small laser spot. This important finding indicates the feasibility of using novel dendrimer–metal nanocomposites for application in optical limiting devices and medicine. Further, time-resolved fluorescence from dendrimer–gold or –silver nanocomposites has been measured [64]. The dendrimer architecture allows for strongly enhanced measurable fluorescence intensity from the metal nanoclusters. It is suggested by fluorescence anisotropy measurements that the metal emission shows a relatively polarized character while the dendrimer host shows a relatively polarized emission. The proposed mechanism of the emission decay is due to electron–electron and electron–surface scattering processes, and there may also be a contribution from the interaction of emission dipoles of the dendrimer host and surface plasmon of the metal.

Dendrimer–gold nanocomposites can be used to remarkably change the laser-induced optical breakdown threshold of a material, owing to a large enhancement of the local electric field [65]. The observed statistical behavior of the breakdown process is attributed to a laser-driven aggregation of individual nanocomposite particles. The breakdown threshold value of the nanocomposites has been found to be up to two orders of magnitude lower than that of pure dendrimers.

4. APPLICATIONS

Since fabrication of ordered semiconductor and metallic nanoparticles on solid substrates has recently been a topic for substantial research due to their multifunctional electronic, optical, and catalytic properties, it is important to explore a method to assemble dendrimer–metal nanocomposites to form well-defined thin films. Formation of multilayer thin film using dendrimer–metal nanocomposites has been reported [66]. The dendrimer–gold nanocomposites have been deposited as a multilayer thin film using electrostatic layer-by-layer deposition techniques. The fabrication procedure of poly(sodium 4-styrenesulfonate) (PSS)/dendrimer–gold nanocomposite multilayers is schematically presented

in Figure 9. A negatively charged solid support is primed by adsorbing a poly(dimethyldiallylammonium chloride) (PDAC) layer onto its surface. The primed substrate is then immersed in PSS solution. The modified substrate is then rinsed with water and dried using nitrogen. It is subsequently immersed in a dendrimer–gold nanocomposite solution. This process is repeated. The multilayer formation has been confirmed by using ultra violet-visible (UV-vis), TEM, and atomic force microscopy.

Also, other methods for multiplayer construction using dendrimers should be noted. The procedure involves the deposition of PAMAM dendrimer with surface amino group onto a Pt^{2+}-bearing surface, followed by reactivation with K_2PtCl_4 [67]. In a typical preparation, a silicon wafer is first silylated with (3-aminopropyl)triethoxysilane, immersed in a solution of K_2PtCl_4, and rinsed with water and methanol. Repetition of this procedure yields corresponding multilayers. The formation of multilayers of dendrimers has been confirmed by ellipsometry and X-ray photoelectron spectroscopy studies. Multilayer films of dendrimers are also fabricated by self-assembly of dendritic macromolecules of two adjacent generations using electrostatic layer-by-layer deposition [46]. PAMAM with surface amino groups for generations 4, 6, and 10 and with surface carboxyl groups for generations 3.5, 5.5, and 9.5 has been used as building units. All even generations are observed to form homogeneous, stable monolayers on a silicon surface. The thickness of a single monolayer varies with generation from 1.8 (G4) to 2.8 (G6) and 5.6 nm (G10). The average thickness of a molecular layer in multilayer films is much smaller than the diameter of ideal spherical dendritic macromolecules. The model of molecular ordering of dendrimer films assumes compressed dendritic macromolecules of oblate shape with the axial ratio in the range from 1:3 to 1:6. A tendency to higher spreading of high generation dendrimers corresponds to the surface behavior predicted by molecular dynamic simulations.

In addition, it is also important to describe preparation and characterization of dendrimer monolayers adsorbed to gold [68]. Single-component monolayers of PAMAM are prepared by exposing an Au substrate to ethanolic solutions of amine- or hydroxy-terminated PAMAM dendrimers.
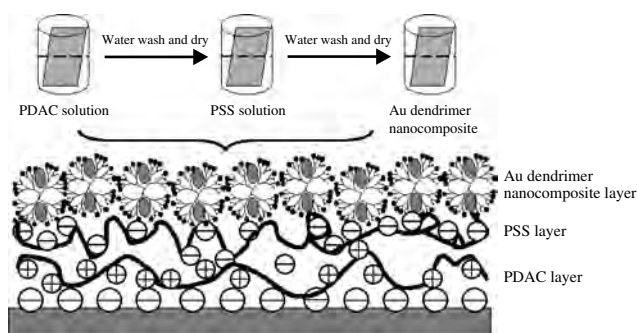
Figure 9. Schematic illustration of the procedure for fabrication of the PSS/gold–dendrimer nanocomposite film on the negatively charged substrate and the architecture of the resulting film. Reprinted with permission from [66], J.-A. He et al., *Chem. Mater.* 11, 3268 (1998). © 1999, American Chemical Society.

The resulting monolayers are highly stable and nearly close-packed for dendrimer generations ranging from G4 to G8. Electrochemical ac-impedance measurements indicate that the dendrimer surface is very porous toward the electroactive redox couple $Fe(CN)_6^{3-/4-}$. Exposure of higher generation dendrimer monolayers to ethanolic solutions of hexadecanethiol results in a dramatic compression of the dendrimers and causes them to reorient on the surface from an oblate to prolate configuration. The dendrimers originally present on the surface do not desorb as a consequence of this configurational change. It is also suggested that the structure and ion-transport function of the mixed dendrimer/alkanethiol monolayers is somewhat analogous to that of phospholipid/protein membranes. It is interesting to note for the stability of dendrimer surfaces as chemically sensitive interfaces that the response to volatile organic compounds decreases in the order acid > alcohols > hydrophobic dosants. This response order is more pronounced for the G4–G8-modified surfaces and is dictated by the PAMAM structure which possesses hydrogen-bonding exoreceptors and endoreceptors. The G4-modified surface is the most responsive material probably; although it is the smallest of the spheroidal dendrimers, its interior endoreceptors are most accessible. G0 and G2 dendrimer films are not as effective at discriminating between the three different classes of probes since these surfaces have few or no free amine terminal groups and no coherent endoreceptors ability. An atomic force microscopy investigation of PAMAM G4 and G8 dendrimers adsorbed on Au surfaces has been carried out [69]. Heights measured for isolated, adsorbed dendrimers indicate that they are substantially more oblate than expected from their spherical shapes in solution. By controlling dendrimer concentration and exposure time during adsorption, modified surfaces ranging from isolated molecules to near-monolayer coverage are obtained. Exposure of surfaces bearing adsorbed isolated dendrimers to hexadecanethiol solutions changes their conformation from oblate to prolate as more stable thiol–Au bonds replace some of the amine–Au bond. Surfaces of near-monolayer coverage gradually agglomerate, forming dendrimer "pillars" up to 30 nm high.

Vapor-sensitive thin-film resistors comprising gold nanoparticles and different types of dendrimers such as polyphenylene, poly(propyleneimine), and poly(amidoamine) have been prepared via layer-by-layer self-assembly and characterized by UV-vis spectroscopy, atomic force microscopy, and conductivity measurements [70]. Dosing the films with vapors of toluene, 1-propanol, and water significantly increases the film resistances. It is demonstrated that the chemical selectivity of this response is controlled by the solubility properties of the dendrimers.

Interactions between alkanethiols and dendrimer–gold nanocomposites in ethyl acetate have been investigated by adding alkanethiols such as 1-decanethiol and 1,10-decanedithiol into PAMAM dendrimers with surface methyl ester group–gold nanocomposites [71]. In the case of PAMAM G1.5 dendrimer–gold nanocomposites (diameter: 2.1 nm), the addition of 1-decanethiol leads to smaller gold particles, while that of 1,10-decanedithiols provides the formation of large, highly regular, spherical clusters with diameters of 40–60 nm. On the other hand, in the case

of PAMAM G5.5 dendrimer–gold nanocomposites (diameter: 2.4 nm), the addition of 1-decanethiol shows a distinct tendency into smaller and larger spheres, whereas that of 1,10-decanedithiols gives irregular spherical clusters with diameters of 30 nm. Such morphology changes by addition of alkanethiols occur due to stronger interaction between gold and alkanethiols than that between PAMAM dendrimer and gold.

Finally, bioapplications of dendrimer–metal nanocomposites are briefly described. Since PAMAM dendrimers are able to solubilize many organic materials or inorganic materials, bioactive materials may be combined in one nanoscopic delivery vehicle such as dendrimer. Studies using antibody/dendrimer conjugates *in vitro* and *in vivo* in experimental animals have demonstrated these conjugates to be nontoxic and able to target biologic agents to specific cells [72, 73]. Dendrimer–silver nanocomposites display antimicrobial activity comparable to or better than those of silver nitrate solutions [74]. Interestingly, increased antimicrobial activity is observed with dendrimer carboxylate salts. This effect may be caused by the very high local concentration of nanoscopic size silver composite particles that are accessible for microorganisms. PAMAM dendrimers have been used for imaging but only after appropriate surface modification. The potential of PAMAM–metal chelate–antibody constructs in radioimmunotherapy and imaging has been recognized [75]. Generally, fluorescent markers, such as fluorescein, or chelated metal ions, such as Gd^{3+} for magnetic resonance imaging, are used to generate a measurable signal [76, 77]. Radioactive dendrimer nanocomposites also have the potential to be delivered to the tumor.

GLOSSARY

Dendrimer Macromolecules with a regular and highly branched three-dimensional architecture.

Dendrimer–metal nanocomposite Organic–inorganic hybrid structure consisting of metal nanoparticles in the internal or external region of dendrimer.

Plasmon resonance band of gold An extinction maximum band due to the dipole resonance of small gold spheres.

Transmission electron microscopy Transmitted-light microscopy using an electron beam and magnetic lenses to produce a magnified image on a fluorescent screen.

REFERENCES

1. E. Buhleier, W. Wehner, and F. Vögtle, *Synthesis* 155 (1978).
2. R. G. Denkewalter, J. F. Kolc, and W. J. Lukasavage, U. S. Patent 4, 410, 688, 1979; 4, 289, 872, 1981; 4, 360, 646, 1982; 4, 410, 688, 1983.
3. D. A. Tomalia, H. Baker, J. Dewald, M. Hall, G. Kallos, S. Martin, J. Roeck, J. Ryder, and P. Smith, *Polym. J.* 17, 117 (1985).
4. G. R. Newkome, Z. Yao, G. R. Baker, and V. K. Guota, *J. Org. Chem.* 50, 2004 (1985).
5. C. J. Hawker and J. M. J. Fréchet, *J. Am. Chem. Soc.* 112, 7638 (1990).
6. J. M. J. Fréchet, *Science* 263, 1710 (1994).
7. G. R. Newkome, E. He, and C. N. Moorefield, *Chem. Rev.* 99, 1689 (1999).
8. "Dendrimers II: Architecture, Nanostructure and Supramolecular Chemistry" (F. Vögtle, Ed.), Topics in Current Chemistry, Vol. 210. Springer-Verlag, Berlin, 2000.
9. F. Zeng and S. C. Zimmermann, *Chem. Rev.* 97, 1681 (1997).
10. A. W. Bosman, H. M. Janssen, and E. W. Meijer, *Chem. Rev.* 99, 1665 (1999).
11. D. Astruc and F. Chardac, *Chem. Rev.* 101, 2991 (2001).
12. C. J. Jackson, H. D. Chanzy, F. P. Booy, B. J. Drake, D. A. Tomalia, B. J. Bauer, and E. J. Amis, *Macromolecules* 31, 6259 (1998).
13. R. M. Crooks, B. I. Lemon III, L. K. Yeung, and M. Zhao, in "Topics in Current Chemistry" (F. Vögtle, Ed.), pp. 81–135. Springer, Heidelberg, 2000.
14. "Clusters and Colloids" (G. Schmid, Ed.), VCH Verlag, Weinheim, 1994.
15. Y. Xia, J. A. Rogers, K. E. Paul, and G. M. Whitesides, *Chem. Rev.* 99, 1823 (1999).
16. A. P. Aliviasatos, *Science* 271, 933 (1996).
17. L. L. Beecoft and C. K. Ober, *Chem. Mater.* 9, 1302 (1997).
18. X. K. Zhao, S. Barai, R. Rolandi, and J. H. Fendler, *J. Am. Chem. Soc.* 110, 1012 (1988).
19. N. Toshima, M. Harada, T. Yonezawa, K. Kushihashi, and K. Asakura, *J. Phys. Chem.* 95, 7448 (1991).
20. K. Torigoe, Y. Nakajima, and K. Esumi, *J. Phys. Chem.* 97, 8304 (1993).
21. K. Esumi, A. Suzuki, N. Aihara, K. Usui, and K. Torigoe, *Langmuir* 14, 3157 (1998).
22. M. Zhao, L. Sun, and R. M. Crooks, *J. Am. Chem. Soc.* 120, 4877 (1998).
23. L. Bologh and D. A. Tomalia, *J. Am. Chem. Soc.* 120, 7355 (1998).
24. M. Zhao and R. M. Crooks, *Angew. Chem. Int. Ed.* 38, 364 (1999).
25. M. Zhao and R. M. Crooks, *Adv. Mater.* 11, 217 (1999).
26. M. Zhao and R. M. Crooks, *Chem. Mater.* 11, 3379 (1999).
27. M. E. Garcia, L. A. Baker, and R. M. Crooks, *Anal. Chem.* 71, 256 (1999).
28. V. Chechik, M. Zhao, and R. M. Crooks, *J. Am. Chem. Soc.* 121, 4910 (1999).
29. V. Chechik and R. M. Crooks, *J. Am. Chem. Soc.* 122, 1243 (2000).
30. K. Esumi, A. Suzuki, A. Yamahira, and K. Torigoe, *Langmuir* 16, 2604 (2000).
31. K. Esumi, R. Nakamura, A. Suzuki, and K. Torigoe, *Langmuir* 16, 7842 (2000).
32. F. Gröhn, B. J. Bauer, Y. A. Akpalu, C. L. Jackson, and E. J. Amis, *Macromolecules* 33, 6042 (2000).
33. L. Bologh, R. Valluzzi, K. S. Laverdure, S. P. Gido, G. L. Hagnauer, and D. A. Tomalia, *J. Nanoparticles Res.* 1, 353 (1999).
34. K. Esumi, T. Hosoya, A. Suzuki, and K. Torigoe, *J. Colloid Interface Sci.* 226, 346 (2000).
35. K. Esumi, T. Hosoya, A. Suzuki, and K. Torigoe, *J. Colloid Interface Sci.* 229, 303 (2000).
36. K. Torigoe, A. Suzuki, and K. Esumi, *J. Colloid Interface Sci.* 241, 346 (2001).
37. A. Manna, T. Imae, K. Aoi, M. Okada, and T. Yogo, *Chem. Mater.* 13, 1674 (2001).
38. S. Kéki, J. Török, G. Deák, L. Daróczi, and M. Zsuga, *J. Colloid Interface Sci.* 229, 550 (2000).
39. K. Esumi, A. Kameo, A. Suzuki, and K. Torigoe, *Colloids Surf. A* 189, 155 (2001).
40. R. M. Crooks, M. Zhao, L. Sun, V. Chechik, and L. K. Yeung, *Acc. Chem. Res.* 34, 181 (2001).
41. K. Esumi and K. Torigoe, *Progr. Colloid Polym. Sci.* 117, 80 (2001).
42. P. N. Floriano, C. O. Noble IV, J. M. Schoonmaker, E. D. Poliakoff, and R. L. McCarley, *J. Am. Chem. Soc.* 123, 10545 (2001).
43. F. Gröhn, G. Kim, B. J. Bauer, and E. J. Amis, *Macromolecules* 34, 2179 (2001).

44. J. Zheng, M. S. Stevenson, R. S. Hikida, and P. G. Van Patten, *J. Phys. Chem. B* 106, 1252 (2002).
45. A. Hierlemann, J. K. Campbell, L. A. Baker, R. M. Crooks, and A. J. Ricco, *J. Am. Chem. Soc.* 120, 5323 (1998).
46. V. V. Tsuruk, F. Rinderspacher, and V. N. Bliznyuk, *Langmuir* 13, 2171 (1997).
47. Y. Sayer-Sweet, D. M. Hedstrand, R. Spinder, and D. A. Tomalia, *J. Mater. Chem.* 7, 1199 (1997).
48. Y.-S. Seo, K.-S. Kim, K. Shin, H. White, M. Rafailovich, J. Sokolov, B. Lin, H. J. Kim, C. Zhang, and L. Balogh, *Langmuir* 18, 5927 (2002).
49. M.-K. Kim, Y.-M. Jeon, W. S. Jeon, H.-J. Kim, S. G. Hong, C. G. Park, and K. Kim, *Chem. Commun.* 667 (2001).
50. L. K. Yeung and R. M. Crooks, *Nano Lett.* 1, 14 (2001).
51. Y. Li and A. El-Sayed, *J. Phys. Chem. B* 105, 8938 (2001).
52. E. H. Rahim, F. S. Kamounah, J. Frederiksen, and J. B. Christensen, *Nano Lett.* 1, 449 (2001).
53. T. Mizugaki, M. Ooe, K. Ebitani, and K. Kaneda, *J. Mol. Catal. A* 145, 329 (1999).
54. M. Ooe, M. Murata, T. Mizugaki, K. Ebitani, and K. Kaneda, *Nano Lett.*, 2, 999 (2002).
55. Y. Niu, L. K. Yeung, and R. M. Crooks, *J. Am. Chem. Soc.* 123, 6840 (2001).
56. I. T. Horvath and J. Rabai, *Science* 266, 72 (1984).
57. B. Cornils, *Angew. Chem. Int. Eg. Engl.* 36, 2057 (1997).
58. D. P. Curran, *Angew. Chem. Int. Eg. Engl.* 37, 1174 (1998).
59. L. K. Yeung, C. Lee, K. P. Johnston, and R. M. Crooks, *Chem. Commun.* 2290 (2001).
60. K. Esumi, K. Satoh, A. Suzuki, and K. Torigoe, *J. Jpn. Soc. Colour Mater.* 73, 434 (2000).
61. U. Kreibig and M. Vollmer, "Optical Properties of Metal Clusters." Springer, Berlin, 1995.
62. C. F. Bohren and D. R. Huffman, "Absorption and Scattering of Light by Small Particles." Wiley-Interscience, New York, 1983.
63. R. G. Ispasoiu, L. Balogh, O. P. Varnavski, D. A. Tomalia, and T. Goodson III, *J. Am. Chem. Soc.* 122, 11005 (2000).
64. O. Varnavski, R. G. Ispasoiu, L. Balogh, D. A. Tomalia, and T. Goodson III, *J. Chem. Phys.* 114, 1962 (2001).
65. J. Y. Ye, L. Balogh, and T. B. Norris, *Appl. Phys. Lett.* 80, 1713 (2002).
66. J.-A. He, R. Valluzzi, K. Yang, T. Dolukhanyan, C. Sung, J. Kumar, S. K. Tripathy, L. Samuelson, L. Balogh, and D. A. Tomalia, *Chem. Mater.* 11, 3268 (1999).
67. S. Watanabe and S. Regen, *J. Am. Chem. Soc.* 116, 8855 (1994).
68. H. Tokuhisa, M. Zhao, L. A. Baker, Vy T. Phan, D. L. Dermody, M. E. Garcia, R. F. Peez, R. M. Crooks, and T. M. Mayer, *J. Am. Chem. Soc.* 120, 4492 (1998).
69. A. Hierlemann, J. K. Campbell, L. A. Baker, R. M. Crooks, and A. J. Ricco, *J. Am. Chem. Soc.* 120, 5323 (1998).
70. N. Krasteva, I. Besnard, B. Guse, R. E. Bauer, K. Mullen, A. Yasuda, and T. Vossmeyer, *Nano Lett.* 2, 551 (2002).
71. K. Esumi, K. Satoh, and K. Torigoe, *Langmuir* 17, 6860 (2001).
72. D. Page and R. Roy, *Bioconjugate Chem.* 8, 714 (1997).
73. A. Bielinska, J. F. Kukowska-Latallo, J. Johnson, D. A. Tomalia, and J. R. Baker, Jr., *Nucl. Acids Res.* 24, 2176 (1996).
74. L. Balogh, D. R. Swanson, D. A. Tomalia, G. L. Hagnauer, and A. T. McManus, *Nano Lett.* 1, 18 (2001).
75. C. Wu, M. W. Brechbiel, R. W. Kozak, O. A. Gansow, *Bioorganic Med. Chem. Lett.* 4, 449 (1994).
76. L. D. Margerum, B. K. Campion, M. Koo, N. Shargill, J. Lai, A. Marumoto, and P. C. Sontum, *J. Alloys Compd.* 249, 185 (1997).
77. Y. Kim and S. C. Zimmerman, *Curr. Opin. Chem. Biol.* 2, 733 (1998).

Dendritic Encapsulation

Christopher S. Cameron, Christopher B. Gorman

North Carolina State University, Raleigh, North Carolina, USA

CONTENTS

1. INTRODUCTION

The search for new materials with unusual properties is a vital area of research. Since the original reported syntheses by Newkome et al. [1] and Tomalia et al. [2], dendrimers have assumed a prominent role in this search for new materials. In the past four years, this role has grown rapidly as evidenced by the large numbers of papers appearing in literature since 1998. A cursory review of cited journals indicates the importance and level of interest in the scientific community concerning dendrimer research. The research on dendrimers is now a multidiscipline effort involving synthetic chemistry, inorganic chemistry, organometallic chemistry, analytical chemistry, and polymer science.

This level of scientific interest is driven by several properties of dendrimers. Among these are an unusual melt viscosity due to the hyperbranched structure (as described below), unusual properties when studied as thin films on surfaces, the ability to hold catalysts and influence the catalytic properties of catalysts within them, an emerging ability to foster cavities within them that can be used to bind small molecules, and the ability to mimic biomolecules and potential for drug and gene delivery. Several of these properties derive from the encapsulating abilities of dendrimers. The phenomenon of encapsulation can be observed in a multitude of different situations from atomic to macro scale. Medicines are regularly encapsulated within water-soluble capsules for delivery. Life exists because the components of cells are encapsulated by plasma membranes. Enzymes exhibit remarkable substrate binding specificity and perform remarkable organic chemistry in aqueous environments because active sites are encapsulated by the protein structure. Power cords are encapsulated by insulating material so that electric current can be channeled to power computers and lab equipment. In the broadest terms, encapsulation is the establishment of a barrier to control the access of some system to its surroundings.

Dendrimers represent a way to accomplish encapsulation on the molecular scale. Molecules with potentially useful physical and/or chemical properties can be encapsulated as the core of dendrimers. Ideally, dendritic encapsulation will result in new properties for the core molecules and ultimately new materials. This is the essence of materials research.

1.1. Synthesis of Dendrimers

Dendrimers are a class of macromolecules consisting of one or more polymeric, regularly branching arms, known as dendrons, which radiate from a central core (Fig. 1). They are synthesized in a stepwise iterative fashion which follows either divergent or convergent methodology [3]. In the divergent methodology, first used by Newkome et al. and Tomalia et al. [1, 2], the core molecule serves as a polyvalent initiation point and the dendrons are grown outward from the core in a repetitive activate/couple cycle. Each time a coupling cycle occurs, a new layer of branch points, referred to as a "generation," is added to the growing dendrimer. The divergent methodology is fast, efficient, and can yield large dendrimers. Its principal disadvantage is that the yield of complete coupling decreases as the generation and thus the number of reaction sites increases, creating some polydispersity in the molecular weight of the final product.

In the convergent methodology, first reported by Hawker and Fréchet [4], the dendrons are synthesized by starting at the tips, which will be the periphery of the dendrimer, and working backwards to a single reactive functional group. Again, each time a coupling cycle occurs, a new layer of branch points is added and the "generation" of the dendrimer increases. Once the dendrons are fully synthesized, they are linked to the core in a final activate/couple cycle. Monodisperse dendrimers can be obtained this way, but the purification after each step renders a practical limit to the size of the molecules that can be synthesized. Furthermore, steric congestion may limit the efficiency of coupling in this approach as well. The essential difference between the two methodologies is in the fashion in which the dendrimer is assembled. In the divergent methodology, as soon as the activate/couple cycle begins, an actual dendrimer is synthesized and subsequent repetitions of the activate/couple cycle

Focal linker   Branching repeat unit   Peripheral functional group
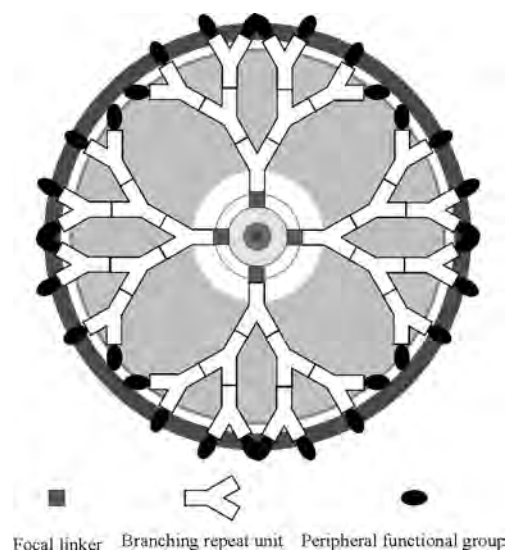
Figure 1. Conceptual Dendrimer—The relative spatial orientation of the various parts of the dendrimer are shown. The central core is attached to the dendrons, which define the nanoenvironment around the core. The peripheral functional groups define the solubility of the dendrimer and/or provide multiple reactive sites for chemistry. The dendrimer shown here has three layers of branch points in the interior and would thus be designated a third-generation dendrimer.

serve to increase the size of the dendrimer. With the convergent methodology, a dendrimer is not actually assembled until dendrons of a desired size have been synthesized and then coupled to a core. Numerous reviews and articles have thoroughly covered dendrimer synthesis and the many types of dendrimers that have been prepared using both methodologies [3, 5–12].

Dendrimers are particularly well suited for the function of encapsulation (Fig. 1). When a dendrimer becomes sufficiently large, normally measured by generation number, it adopts a globular shape. This globular shape is the natural result of an architecture in which large bulky dendrons are focally attached to a central core. DeGennes dense packing, sterics, and simple mass effect cause the dendrons to envelope the core molecule, thus leading to encapsulation. While encapsulation by dendrimers can lead to alteration of physical and chemical properties, there is some scientific and semantic difficulty in defining the critical size or generation or molecular weight required to effect this change [13]. The term "site isolation" is often used when encapsulation is determined to be complete; this term is subject to interpretation.

For dendrimers, it is possible to encapsulate many different types of core molecules in different types of "nanoenvironments" for the purpose of understanding structure–property relationships. A basic understanding of structure–property relationships is the key to the development of new materials with unusual properties and is one of the core tenets of scientific research. This ultimately is the basis for the broad-based, multidisciplinary interest in dendrimers.

1.2. Advantages of Dendrimers

As stated previously, encapsulation begins by surrounding a core molecule with a material. This effect could be achieved using conventional polymers. However, studies comparing dendrimer versus polymeric encapsulation have shown considerable differences between the two systems [14]. Structurally, dendrimers are composed of a core moiety surrounded by dendrons radiating from the core (Fig. 1). Such a structural arrangement predisposes dendrimers towards encapsulation when compared to linear polymers. There is substantial precedent for the synthesis of dendrimers as monodisperse or nearly monodisperse species. Linear polymers could be synthesized in the same, stepwise fashion, but protocols to isolate and to purify these types of molecules are less precedented. The mode of synthesis of dendrimers also facilitates the installation of different functionalities at the center and periphery. Dendrimers are modular in construction and composition, thus allowing the core, the interior dendrimer nanoenvironment, and the dendrimer peripheral functional groups to be changed independently of each other with relative ease [15]. The value of the "modular" nature of dendrimers and the potential applications for encapsulation lead to a number of possibilities for design of new functional molecules [16].

1.3. Dendrimer Cores

Dendrimer cores can be classified as "nonfunctional" or "functional." "Nonfunctional" cores are molecules that have no specifically interesting chemical or physical properties; and serve only as a polyvalent focal point of the dendrimer. Dendrimers assembled with "nonfunctional" cores either focus on materials applications other than encapsulation [17], such as supramolecular constructs [18] and self-assembly processes [19–23] or utilize the dendrimer as a polyvalent scaffold, as in DNA transfection [7, 24, 25], drug delivery [26–28], or even soluble solid-state synthesis [29]. In some of these applications, the dendrimer is used for encapsulation of small molecule guests. This type of non-covalent encapsulation is interesting and potentially useful, especially for extraction, solubility, and drug delivery. It is not, however, treated in any detail here.

A second class of encapsulating dendrimers is based on functional cores. "Functional" cores are moieties which, in addition to serving as the polyvalent focal point for the dendrimer, have some observable and potentially useful physical and/or chemical property. For dendrons containing a "functional" core, encapsulation is the predominant research focus. Observable physical/chemical properties fall into three broad categories [30]: photophysics (absorbance, luminescence, fluorescence, and phosphorescence), electrochemistry (kinetic electron transfer rate and thermodynamic redox potential) [9, 31, 32], and ligand binding (ligands, gas binding, and catalysis) [6, 8, 33, 34].

A wide variety of molecules have been employed as "functional" cores (Table 1). Most can be classified in one of four categories: porphyrins/phthalocyanines, inorganic clusters, ionic complexes/organometallics, and fluorescent dyes. Porphyrin and phthalocyanine moieties [30, 35, 36] are especially useful because they exhibit three classes

of observable properties: photophysics, electrochemistry, and ligand binding. Many dendrimers have been synthesized with porphyrin/phthalocyanine cores. Several different types of inorganic clusters have served as cores. One impetus behind the use of clusters as cores is ligand binding and when mimicking and studying enzyme active sites [37, 38]. Clusters that have been used include iron-sulfur, Fe_4S_4 [39], rhenium-selenide, Re_6Se_8 [40, 41], molybdenum-chloride, Mo_6Cl_8 [42], oxymolybdo-sulfur, $MoOS_4$ [37], and metal nanoparticles [34, 43]. Ionic complexes and organometallics [44, 45] have been popular because of the well-established synthetic conditions by which a dendrimer may be assembled around such a core. Examples of ions used to make ionic/organometallic cores complexes include ruthenium(II), osmium(II), iron(II), iridium(II), and various lanthanides. The influence of the dendrimer on the photophysical and electrochemical response of these cores has been studied. Lastly, fluorescent dyes have been employed as cores for their light emission properties. Tremendous interest in fluorescent dye core dendrimers has developed in the field of organic light-emitting diode (OLED) research.

Table 1. Classification of the functional cores used in dendrimer chemistry.

Molecule	Properties	Ref.
Porphyrins/Phthalocyanines		
Si- Phthalocyanine	U	[36]
Zn-Porphyrin	U, E, F, LB	[47, 64, 65, 74–76]
Pd-Porphyrin	P, LB	[80]
Fe-Porphyrin	U, E	[72]
Free-base Porphyrin	F	[50, 63]
Inorganic Clusters		
Mo^VOS_4	EPR, E	[37]
Fe_4S_4	E	[39, 66]
Mo_6Cl_8		[42]
Re_6Se_8	U, E	[40, 41]
Organometallic/Ionic Complexes		
$Ir(ppy)_3$	L, U	[15]
Lanthanide, (Ln^{3+})–$(RCOO^-)_3$	FT-IR, U, E	[59, 60]
Ferrocene	E	[67, 68]
Methyl Viologen	E	[69, 70]
Dyes		
4-(N-methylamino)-1-nitrobenzene	U	[46]
p-dimethoxybenzene	F	[48]
Tryptophan	F	[49]
Coumarin 343, Pentathiophene	L	[51]
Rhodamine B	F	[52]
4-(dicyanomethylene)-2-methyl-6- (4-dimethylaminostyrl)-4H-pyrane	F	[81]
3-[dimethylamino]phenoxy group	F	[57]
Coumarin 343	F	[62]
Dansyl chloride	FQ	[77]
(S)-1,1′-bi-2-naphthol	F, LB	[78]

Note: U = UV-vis absorbance, F = fluorescence, FQ = fluorescence quenching, P = phosphorescence, L = luminescence, E = electrochemistry, LB = ligand binding, EPR = electron paramagnetic resonance, FT-IR = FT-IR.

2. ENCAPSULATION

Encapsulation has been defined as altering an observable physical/chemical property of a molecule by surrounding it with material. The very simplest example of encapsulation is changing the solubility of a core molecule. Although influencing solubility can be accomplished via methods other than encapsulation, in the case of dendrimers, such control of solubility has turned out to be extremely useful, especially in OLED research. Most experiments that study the role of dendritic encapsulation focus on the influence of encapsulation on photophysical behavior, electrochemical behavior, and the kinetics and thermodynamics of ligand binding. Altering these properties is less straightforward than making something soluble and influencing them requires controlling the nanoenvironment around the core [30]. Generally, correlation of a change in one of these three properties, for any given core molecule, to an increase in the generation of a dendrimer indicates encapsulation.

2.1. Effects on Photophysical Properties

Observation of photophysical properties has been an extremely useful tool for the evaluation of dendritic encapsulation. The absorbance and/or emission of light by a core is easy to measure, is nondestructive, and is extremely sensitive to the effects of dendritic encapsulation. Fréchet and co-workers first reported dendrimer encapsulation when shifts in the UV-vis absorbance maxima were observed for a *p*-dimethylamino-nitrobenzene core aryl-ether based-dendrimer (Fig. 2) in a variety of solvents [46]. In all solvents used for UV absorbance, a noticeable increase in the absorbance maximum occurred between the third- and fourth-generation dendrimers. This increase was interpreted
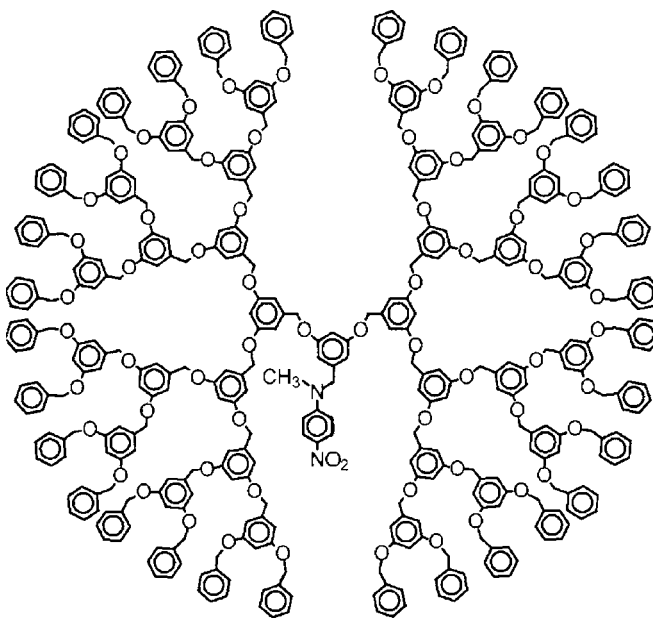
Figure 2. First Demonstration of Encapsulation—Shifts in UV absorbance maxima were observed between generation 3 and generation 4 of this molecular architecture in various solvents. Adapted with permission from [46], C. J. Hawker et al., *J. Am. Chem. Soc.* 115, 4375 (1993). © 1993, American Chemical Society.

to mean a significant change in the nanoenvironment around the core indicative of encapsulation.

Initial evidence for actual "site isolation" was reported by Aida and co-workers for aryl-ether-based dendrimers with Zn-porphyrin cores [47]. In fluorescence studies, quenching was observed between first-generation free-base dendrimers and first-generation zinc porphyrin dendrimers. No quenching was observed in the same experiments with fourth-generation zinc porphyrin dendrimers substituted. Attenuation of quenching was not universal as it was observed that quenching by vitamin K_3, a much smaller molecule, was actually enhanced as the dendrimer grew larger. Moore and co-workers reported shifts in the fluorescence maximum for phenylacetylene dendrimers with a *p*-dimethoxybenzene core [48]. Expected bathochromic shifts were observed for lower-generation dendrimers while at higher generations, abnormal shifts were observed that were very solvent dependent. From Aida and Moore's work it was clear that encapsulation was not just a general effect and could possibly be controlled.

Smith and co-workers demonstrated a level of control of encapsulation using dendrimers with tryptophan cores. The dendrons were designed to present a hydrogen bonding environment (Fig. 3) [49]. Thus, in solvents that were not hydrogen donors or acceptors, a dendritic effect was observed as a shift in the maximum emission wavelength for tryptophan. The shift was due to hydrogen bonding between the dendron and the tryptophan core. In solvents that were hydrogen
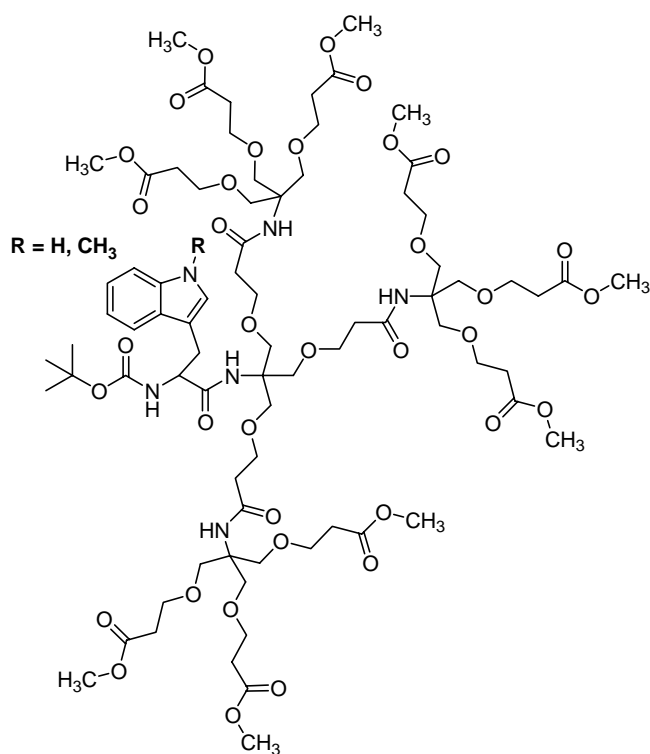
Figure 3. Controlled Encapsulation—A second-generation dendrimer for which controlled encapsulation was demonstrated. By altering the solvent from a non-hydrogen bonding to a type that was hydrogen bond donating and/or accepting, the emission spectra of the core tryptophan could be shifted [49].

bonding donors or acceptors, the dendritic effect was not observed due to competitive binding between the solvent and the dendron. Vinogradov and Wilson also demonstrated control of encapsulation through pH manipulation of a zinc porphyrin core polyglutamate dendrimer [50]. A substantial decrease in the fluorescence emission for the porphyrin core was reported as the pH of the solution was decreased. The shift in the periphery from anionic to neutral eliminated electrostatic shielding on the surface of the dendrimer and allowed the porphyrin cores to behave more like free porphyrins. Substantial amounts of self-quenching of the porphyrin cores occurred at lower pH values.

Encapsulation and site isolation by dendrimers have been used with great effect in the field of organic light-emitting diode (OLED) research. After an initial illustration by Thompson and Fréchet and co-workers [51], several groups have capitalized on the use of dendrimers to isolate chromophores and prevent exciton quenching which reduces efficiency. Otomo and co-workers synthesized Fréchet-type dendrimers with rhodamine B cores [52]. Dendrimer thin films spun onto silica, 10% by weight of dendrimer, had no loss in fluorescence emission intensity and demonstrated mirrorless laser emission. Site isolation and laser emission were also observed in a dendrimer host/guest system with reported nonlinear increases in emission in response to excitation [53]. Following several previous illustrations [54–56], Markham et al. most recently illustrated green phosphorescence in LEDs made from *fac*-tris-2phenylpyridine iridium, Ir(ppy)$_3$, core dendrimers [15]. In addition to increased luminescence efficiency due to site isolation of the core, the dendrimers altered the solubility of the Ir(ppy)$_3$ core. This allowed the Ir(ppy)$_3$ normally evaporated to form an OLED, to be spin-cast in thin layers up to 20% by weight.

Dendrimer encapsulation also can have a pronounced energy-harvesting "antenna" effect on photoactive cores. Stewart and Fox [57] and Devadoss et al. [58] first illustrated that energy could be collected from chromophores in the periphery of the dendrimer and funneled the core of the molecule. Kawa and Fréchet demonstrated that this effect correlated to increasing generation in lanthanide ion/tricarboxylate core dendrimers (Fig. 4) [59, 60]. Enhanced luminescence could be observed by (a) changing the lanthanide ion used to form the dendrimer complexes, (b) site isolation of the core by the dendrimer blocking self quenching, and (c) increasing dendrimer generation leading to enhanced energy collection and transfer to the core. Fréchet and co-workers have also used the polyvalent nature of dendrimers to enhance the generation-dependent "antenna" effect by attaching light-harvesting chromophores to the periphery of the dendrimer. Energy transfer from the periphery chromophores to the core dye was highly efficient [61, 62]. The "antenna" effect appears to be influenced greatly by dendrimer conformation. Jiang and Aida reported fully substituted dendritic porphyrins had much greater quantum yields for energy transfer than the partially substituted analogues [63]. Fluorescence emission from the series of porphyrin dendrimers was nonlinear in response to the number of dendritic substituents.
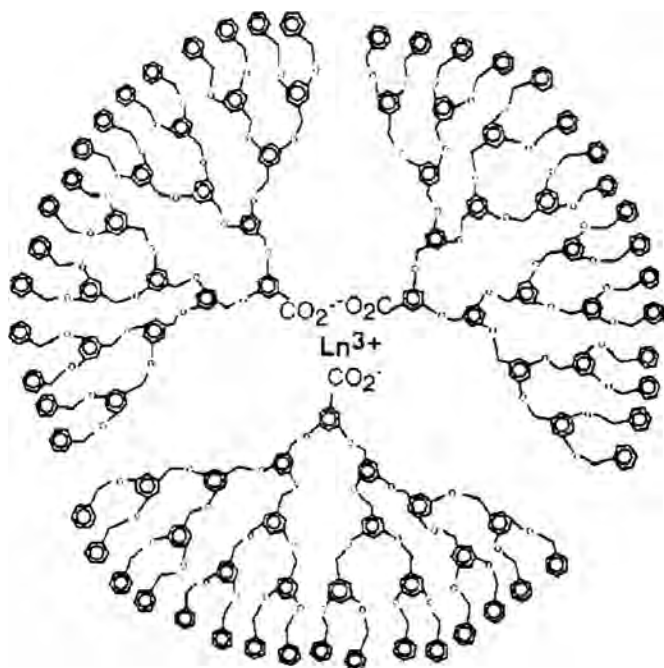
Figure 4. Dual-Purpose Encapsulation—A fourth-generation dendrimer that achieves two effects. The aromatic rings serve as light-harvesting units and funnel the energy to the lanthanide core resulting in emission. This emission was enhanced due to the steric shielding provided by the dendrimer which prevents self-quenching by the lanthanide cores. Reprinted with permission from [60], M. Kawa and J. M. J. Fréchet, *Chem. Mat.* 10, 286 (1998). © 1998, American Chemical Society.

Figure 5. Site Isolation of a Zn-Porphyrin Core—A zinc–porphyrin core was encapsulated by an aryl-ether-based dendrimer. Electrochemical characterization of the core showed a considerable attenuation of the kinetic electron transfer rate upon going from the second-generation to the third-generation dendrimer. The rate of electron transfer was attenuated past that observable by cyclic voltammetry by the fourth generation. Reprinted with permission from [65], K. W. Pollak et al., *Chem. Mat.* 10, 30 (1998). © 1998, American Chemical Society.

2.2. Effects on Electrochemical Properties

Electrochemically active cores have also been instrumental for investigating dendritic encapsulation [9, 31]. Electrochemically active cores have proven useful because two properties, the rate of electron transfer and thermodynamic redox potential, can be altered by encapsulation. Attenuation of electron transfer rates is primarily influenced by steric hindrance and is distance dependent. However, the type of units within the dendrons also has an effect. Encapsulation effects on redox potential, in contrast to electron transfer attenuation, have been less well understood, though some progress has been made [13].

Multiple dendrimer systems with different types of cores and architectures have been reported in which electron transfer rates were attenuated. Diederich and co-workers reported the first attenuation of electron transfer rates for porphyrin core dendrimers [64]. This attenuation increased as the dendrimer generation increased. Fréchet, Abruña, and co-workers demonstrated electrochemical site isolation for Zn-porphyrin dendrimers (Fig. 5) [65]. Third-generation and larger dendrimers attenuated the rate of electron transfer such that it could not be observed using cyclic voltammetry.

Gorman and co-workers elucidated structure–property relationships for electron attenuation using Fe_4S_4 cores with two different dendrimer architectures (Fig. 6) [39]. These dendrimer architectures exhibited remarkable, and seemingly contradictory, behaviors in solution and in thin films. In N,N-dimethylformamide (DMF) solution, attenuation of the heterogeneous electron transfer rates was observed from the Fe_4S_4 cores to a Pt electrode for both "flexible" and "rigid" dendrimers as generation increased (Fig. 6). The "rigid" architecture was more effective at encapsulating the core than the "flexible" architecture. Correlating this behavior with the results of computational conformational searches, it was suggested that the distance of electron transfer in the "rigid" architecture was greater than that of a "flexible" architecture for a given molecular weight as the former held the core more towards the center of the molecule than the latter. When the electron transfer rates were correlated to an approximation of the average distance of electron transfer, the "flexible" architecture attenuated the rate more than the "rigid" architecture for that given, approximate distance.

In these experiments, in solution, very little shift was observed in the thermodynamic redox potential of the Fe_4S_4 core with increasing dendrimer generation. However, when the same series of "flexible" dendrimers were spin-cast onto a platinum electrode surface, the thermodynamic redox potential shifted dramatically with increasing dendrimer generation [66]. It was proposed that, in solution, solvent could penetrate the dendrimer and define the microenvironment around the iron-sulfur cluster. In the film,
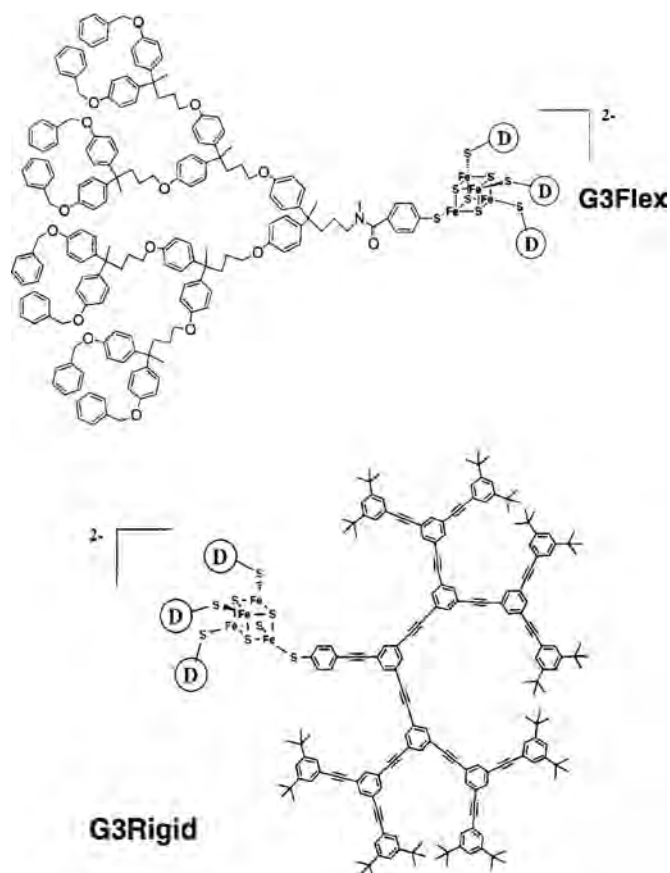
Figure 6. Effects of Repeat Unit on Encapsulation—"Flexible" and "rigid" Fe_4S_4 core dendrimers were studied to determine the effect of repeat unit on conformation and subsequent electron transfer rate attenuation. Generation 3 dendrimers are shown (where the circled-D represent arms identical to the one drawn). Analogous generation one through four dendrimers were studied. Reprinted with permission from [39], C. B. Gorman et al., *J. Am. Chem. Soc.* 121, 9958 (1999). © 1999, American Chemical Society.

however, solvent was largely excluded, and the differing size of dendrimers provided a difference in microenvironment at different generations. As the generation of the dendrimer increased, the effective microenvironment around the iron-sulfur cluster became more hydrophobic, making the cluster thermodynamically more difficult to reduce.

Kaifer and co-workers have demonstrated controlled encapsulation using ferrocene core single-arm offset dendrimers (Fig. 7) [67]. By altering the pH of the solution in which electrochemistry was performed, it was proposed that the carboxylate periphery could be made to orient towards an amine-SAM covered electrode surface, effectively stopping free rotation of the molecule. This net effect was detected as attenuation of electron transfer of the ferrocene core which had been correspondingly oriented away from the electrode surface. In further experiments with similar ferrocene core single-arm offset dendrimers, attenuation of electron transfer in both organic and aqueous solvents was demonstrated [68].

While these experiments provide a good basis to rationalize the factors for altering electron transfer via encapsulation, some recent results do not fit the simple pattern that increasing size results in increasing encapsulation. Kaifer and co-workers and Balzani and co-workers independently synthesized identical methylviologen core dendrimers up to the third generation (Fig. 8) [69, 70]. Both groups found no correlation between the electron transfer kinetics and dendrimer generation. The simplest explanation for this behavior would be that the dendrimers were not sufficiently large to encapsulate the core. However, Alvarro et al. worked with the same molecules and reported that electron transfer quenching with anthracene was inhibited by the second-generation dendrimer [71]. The interpretation of this data with regards to encapsulation remains unresolved.

The other aspect of electrochemistry influenced by encapsulation is the thermodynamic redox potential. Fréchet, Abruña, and co-workers have observed shifts in redox potential in Zn-porphyrin core dendrimers [65]. Diederich and co-workers reported solvent-dependent effects for various Fe-porphyrin dendrimers [64, 72]. Stone and co-workers reported similar effects for ferrocene core dendrimers [73]. Gorman and co-workers, however, reported no effect on the redox potential of Fe_4S_4 cores for two different dendrimer architectures in solution [39]. The same dendrimers in thin films, however, exhibited tremendous changes in redox potential [66]. A model in which the difference in charge states between the oxidized and reduced forms of a core and the relative hydrophobicity of a dendrimer has been advanced to rationalize the results [13]. However, it is unclear how generally applicable this model will be.

2.3. Effects on Ligand Binding

The effects of encapsulation on ligand binding to core molecules have been exhibited in diverse dendrimer–core systems. The principal influence is primarily steric in nature. The type of pockets that a dendrimer architecture establishes around the core is not well understood. Aida and co-workers demonstrated inhibition binding of a dendritic imidazole to a Zn-porphyrin core dendrimer [74]. Suslick and co-workers reported shape selective ligand binding in a series of Zn-porphyrin dendrimers [75, 76]. Pockets are built around the Zn-porphyrins with dendrons, limiting, but not completely eliminating access. Kaifer and co-workers also demonstrated hindrance of cyclodextrin binding for their ferrocene-core offset dendrimers [68, 77]. Pugh et al. reported the ability to discriminate chiral compounds with fluorescent dendrimers [78]. Vinogradov and co-workers showed control of O_2 binding to a Pd-porphyrin core through prudent selection of the encapsulating dendrimer [79]. In this last example, of three different water-soluble dendrimers synthesized, only the Fréchet-style aryl ether dendrimer was capable of inhibiting O_2 quenching of the porphyrin fluorescence emission (Fig. 9). The other two dendrimer architectures permitted O_2 access to the core.
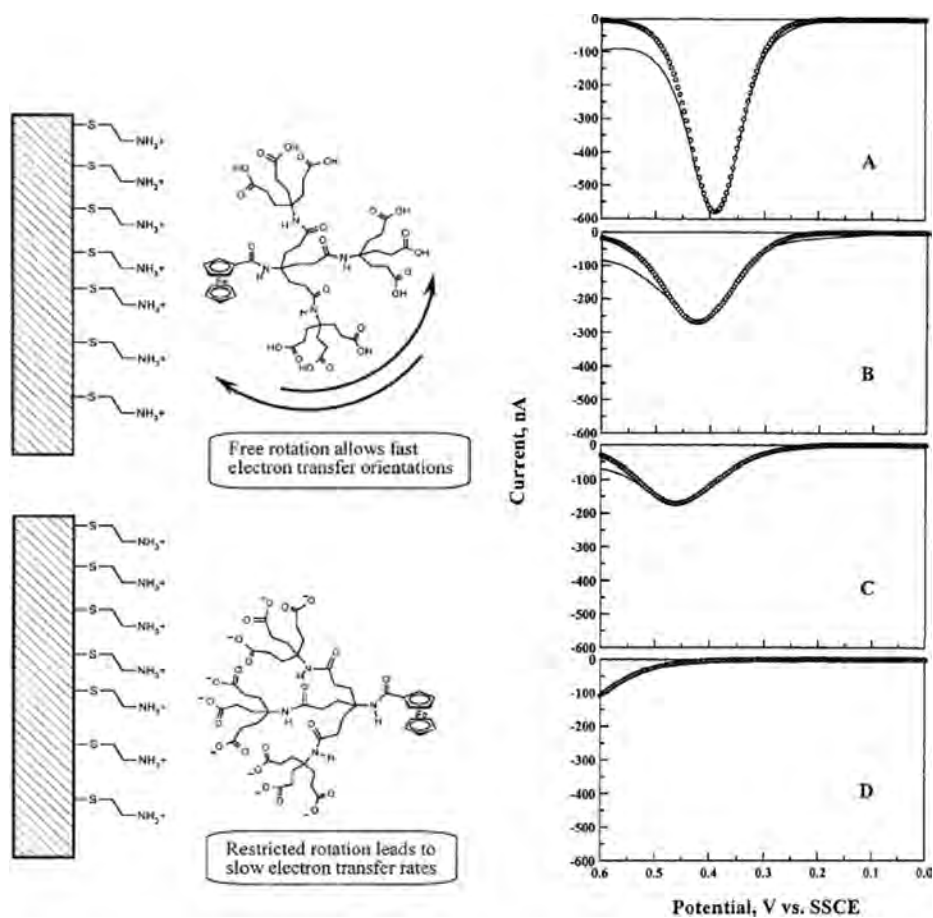
Figure 7. Controlled Encapsulation with an "On-Off" Effect—By controlling the pH of solution, electron transfer to and from the ferrocene core could be controlled. The dendrimer was proposed to control the orientation of the ferrocene with respect to the electrode. Plots A though D are Osteryoung Square Wave Voltammograms obtained at pHs 4.2, 5.3, 6.0, and 7.0, respectively. Reprinted with permission from [67], Y. Wang et al., *J. Am. Chem. Soc.* 121, 9756 (1999). © 1999, American Chemical Society.
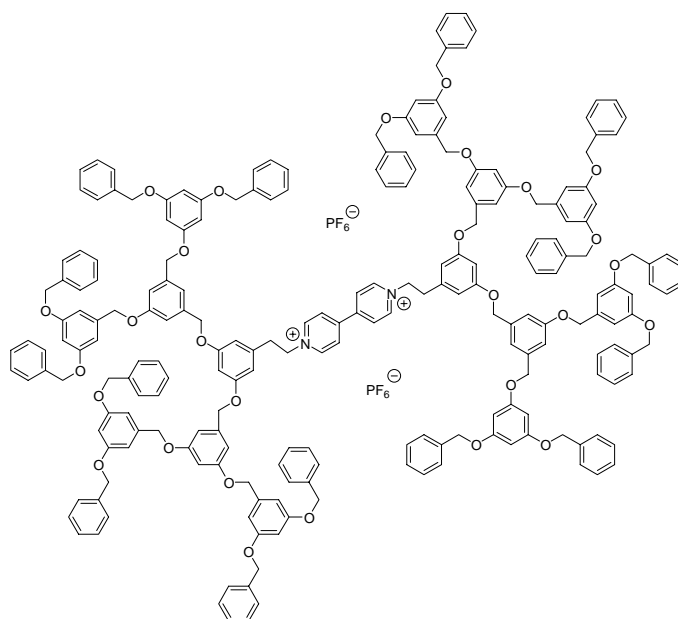
Figure 8. Unusual Methyl Viologen Core Dendrimer—A 4,4′-bipyridinium (viologen) core dendrimer which exhibited no apparent electron transfer rate attenuation in a series of molecules up to the size shown.
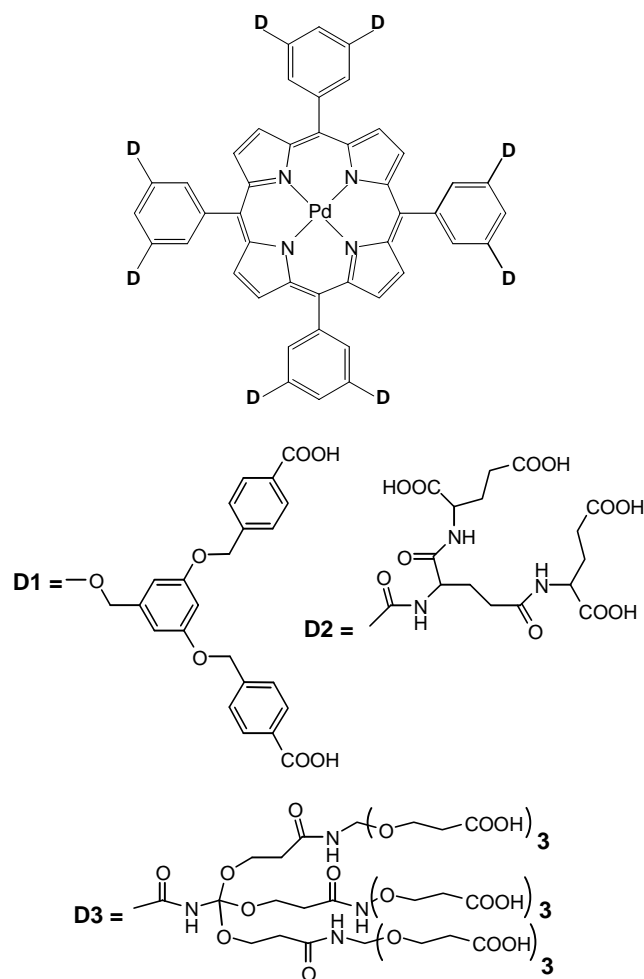
Figure 9. Differential Encapsulation—Three series of water-soluble palladium porphyrin core dendrimers with units illustrated by D1, D2, and D3, respectively. Only the aryl-ether-based dendrimers (repeat unit D1) could prevent quenching of emission from the core by O_2. Reprinted with permission from [79], V. Rozhkov et al., *Macromolecules* 35, 1991 (2002). © 2002, American Chemical Society.

3. CONCLUSIONS

Encapsulation has become a significant role that has been studied for dendrimers. A number of architectures have been explored. Several significant phenomena have been illustrated. In the most general sense, the role of the dendrimer in surrounding and encapsulating the core has been rationalized with simple models. However, in each case discussed above, there are examples that do not neatly fit a simple paradigm. Future work to enlarge the number and type of dendrimer architectures studied will facilitate extension of these models and establishment of more general paradigms for dendritic encapsulation.

GLOSSARY

Chromophore   Any chemical moiety that absorbs and/or emits light.

Convergent   A method of chemical synthesis that begins at the edge point of a molecule and builds inwards.

Dendrimer   A macromolecule consisting of a core moiety surrounded by one or more arms known as dendrons.

Dendron   A hyperbranched polymeric arms that form the bulk material of a dendrimer. They are attached to and radiate from the core moiety.

Divergent   A method of chemical synthesis that begins at the center point of a molecule and builds outwards.

Encapsulation   The process of influencing access by surrounding with a material.

Generation   A reference to the number of layers of a dendrimer. A layer is defined by the number of branch points found in the dendrons between the core and the periphery of a dendrimer. Thus, a "generation 4 dendrimer" would have dendrons with four branch points.

Monodisperse   A collection of objects that all have the same size. With regards to dendrimers, all molecules have the same molecular formula and molecular weight.

Nanoenvironment   The immediate surroundings around a moiety defined by molecular structure.

ACKNOWLEDGMENTS

REFERENCES

1. G. R. Newkome, Z. Q. Yao, G. R. Baker, and V. K. Gupta, *J. Org. Chem.* 50, 2003 (1985).
2. D. A. Tomalia, H. Baker, J. Dewald, M. Hall, G. Kallos, S. Martin, J. Roeck, J. Ryder, and P. Smith, *Polym. J.* 17, 117 (1985).
3. S. M. Grayson and J. M. J. Fréchet, *Chem. Rev.* 101, 3819 (2001).
4. C. J. Hawker and J. M. J. Fréchet, *J. Am. Chem. Soc.* 112 (21), 7638 (1990).
5. C. B. Gorman, *Adv. Mater.* 10, 295 (1998).
6. L. J. Twyman, A. S. H. King, and I. K. Martin, *Chem. Soc. Rev.* 31, 69 (2002).
7. R. Kircheis, L. Wightman, and E. Wagner, *Adv. Drug Deliv. Rev.* 53, 341 (2001).
8. D. Astruc and F. Chardac, *Chem. Rev.* 101, 2991 (2001).
9. C. M. Cardona, S. Mendoza, and A. E. Kaifer, *Chem. Soc. Rev.* 29, 37 (2000).
10. G. R. Newkome, E.-F. He, and C. N. Moorefield, *Chem. Rev.* 99, 1689 (1999).
11. A. W. Bosman, H. M. Janssen, and E. W. Meijer, *Chem. Rev.* 99, 1665 (1999).
12. M. Venturi, A. Credi, and V. Balzani, *Coord. Chem. Rev.* 186, 233 (1999).
13. C. B. Gorman and J. C. Smith, *Acc. Chem. Res.* 34, 60 (2001).
14. E. M. Harth, S. Hecht, B. Helms, E. E. Malmstrom, J. M. J. Fréchet, and C. J. Hawker, *J. Am. Chem. Soc.* 124, 3926 (2002).
15. J. P. J. Markham, S. C. Lo, S. W. Magennis, P. L. Burn, and I. D. W. Samuel, *Appl. Phys. Lett.* 80, 2645 (2002).
16. G. M. Dykes, *J. Chem. Technol. Biotechnol.* 76, 903 (2001).
17. H. Kawaguchi, *Prog. Polym. Sci.* 25, 1171 (2000).
18. S. C. Zimmerman and L. J. Lawless, *Top. Curr. Chem.* 217, 95 (2001).
19. M. Fischer and F. Vögtle, *Angew. Chem.-Int. Edit.* 38, 885 (1999).
20. T. Emrick and J. M. J. Fréchet, *Curr. Opin. Colloid Interface Sci.* 4, 15 (1999).

21. V. Percec, C. H. Ahn, G. Ungar, D. J. P. Yeardley, M. Möller, and S. S. Sheiko, *Nature* 391, 161 (1998).
22. S. D. Hudson, H. T. Jung, V. Percec, W.-D. Cho, G. Johansson, G. Ungar, and V. S. K. Balagurusamy, *Science* 278, 449 (1997).
23. V. Percec, P.-W. Chu, G. Ungar, and J.-P. Zhou, *J. Am. Chem. Soc.* 117, 11441 (1995).
24. R. Esfand and D. A. Tomalia, *Drug Discov. Today* 6, 427 (2001).
25. E. Tomlinson and A. P. Rolland, *J. Control. Release* 39, 357 (1996).
26. C. Z. Chen and S. L. Cooper, *Adv. Mater.* 12, 843 (2000).
27. M. J. Liu and J. M. J. Fréchet, *Pharm. Sci. Technol. Today* 2, 393 (1999).
28. K. Uhrich, *Trends Polym. Sci.* 5, 388 (1997).
29. R. M. Kim, M. Manna, S. M. Hutchins, P. R. Griffin, N. A. Yates, A. M. Bernick, and K. T. Chapman, *Proc. Natl. Acad. Sci. USA* 93, 10012 (1996).
30. S. Hecht and J. M. J. Fréchet, *Angew. Chem.-Int. Edit.* 40, 74 (2001).
31. C. S. Cameron and C. B. Gorman, *Adv. Funct. Mater.* 12, 17 (2002).
32. C. B. Gorman, J. C. Smith, R. Sachdeva, W. Y. Su, and H.-W. Jiang, *Macromol. Symp.* 156, 61 (2000).
33. F. Diederich and B. Felber, *Proc. Natl. Acad. Sci. USA* 99, 4778 (2002).
34. C. J. Zhong and M. M. Maye, *Adv. Mater.* 13, 1507 (2001).
35. F. Diederich, *Chimia* 55, 821 (2001).
36. N. B. McKeown, *Adv. Mater.* 11, 67 (1999).
37. S. Mondal and P. Basu, *Inorg. Chem.* 40, 192 (2001).
38. M. J. Hannon, P. C. Mayers, and P. C. Taylor, *J. Chem. Soc.-Perkin Trans.* 1, 1881 (2000).
39. C. B. Gorman, J. C. Smith, M. W. Hager, B. L. Parkhurst, H. Sierzputowska-Gracz, and C. A. Haney, *J. Am. Chem. Soc.* 121, 9958 (1999).
40. B. K. Roland, C. Carter, and Z.-P. Zheng, *J. Am. Chem. Soc.* 124, 6234 (2002).
41. R. Y. Wang and Z.-P. Zheng, *J. Am. Chem. Soc.* 121, 3549 (1999).
42. C. B. Gorman, W. Y. Su, H. W. Jiang, C. M. Watson, and P. Boyle, *Chem. Commun.* 10, 877 (1999).
43. R. M. Crooks, B. I. Lemon, L. Sun, L. K. Yeung, and M. Q. Zhao, *Top. Curr. Chem.* 212, 81 (2001).
44. V. Balzani, P. Ceroni, A. Juris, M. Venturi, S. Campagna, F. Puntoriero, and S. Serroni, *Coord. Chem. Rev.* 219, 545 (2001).
45. S. Serroni, S. Campagna, F. Puntoriero, C. Di Pietro, N. D. McClenaghan, and F. Loiseau, *Chem. Soc. Rev.* 30, 367 (2001).
46. C. J. Hawker, K. L. Wooley, and J. M. J. Fréchet, *J. Am. Chem. Soc.* 115, 4375 (1993).
47. R. H. Jin, T. Aida, and S. Inoue, *J. Chem. Soc.-Chem. Commun.* 16, 1260 (1993).
48. C. Devadoss, P. Bharathi, and J. S. Moore, *Angew. Chem.-Int. Edit. Engl.* 36, 1633 (1997).
49. S. Koenig, L. Müller, and D. K. Smith, *Chem.-Eur. J.* 7, 979 (2001).
50. S. A. Vinogradov and D. F. Wilson, *Chem.-Eur. J.* 6, 2456 (2000).
51. A. W. Freeman, S. C. Koene, P. R. L. Malenfant, M. E. Thompson, and J. M. J. Fréchet, *J. Am. Chem. Soc.* 122, 12385 (2000).
52. A. Otomo, S. Yokoyama, T. Nakahama, and S. Mashiko, *Appl. Phys. Lett.* 77, 3881 (2000).
53. S. Yokoyama, A. Otomo, and S. Mashiko, *Appl. Phys. Lett.* 80, 7 (2002).
54. M. Halim, J. N. G. Pillow, I. D. W. Samuel, and P. L. Burn, *Adv. Mater.* 11, 371 (1999).
55. J. M. Lupton, I. D. W. Samuel, M. J. Frampton, R. Beavington, and P. L. Burn, *Adv. Funct. Mater.* 11, 287 (2001).
56. J. M. Lupton, I. D. W. Samuel, P. L. Burn, and S. Mukamel, *J. Chem. Phys.* 116, 455 (2002).
57. G. M. Stewart and M. A. Fox, *J. Am. Chem. Soc.* 118, 4354 (1996).
58. C. Devadoss, P. Bharathi, and J. S. Moore, *J. Am. Chem. Soc.* 118, 9635 (1996).
59. M. Kawa and J. M. J. Fréchet, *Thin Solid Films* 331, 259 (1998).
60. M. Kawa and J. M. J. Fréchet, *Chem. Mat.* 10, 286 (1998).
61. A. Adronov and J. M. J. Fréchet, *Chem. Commun.* 18, 1701 (2000).
62. A. Adronov, S. L. Gilat, J. M. J. Fréchet, K. Ohta, F. V. R. Neuwahl, and G. R. Fleming, *J. Am. Chem. Soc.* 122, 1175 (2000).
63. D. L. Jiang and T. Aida, *J. Am. Chem. Soc.* 120, 10895 (1998).
64. P. J. Dandliker, F. Diederich, M. Gross, C. B. Knobler, A. Louati, and E. M. Sanford, *Angew. Chem.-Int. Edit. Engl.* 33, 1739 (1994).
65. K. W. Pollak, J. W. Leon, J. M. J. Fréchet, M. Maskus, and H. D. Abruña, *Chem. Mat.* 10, 30 (1998).
66. C. B. Gorman and J. C. Smith, *J. Am. Chem. Soc.* 122, 9342 (2000).
67. Y. Wang, C. M. Cardona, and A. E. Kaifer, *J. Am. Chem. Soc.* 121, 9756 (1999).
68. C. M. Cardona, T. D. McCarley, and A. E. Kaifer, *J. Org. Chem.* 65, 1857 (2000).
69. R. Toba, J. M. Quintela, C. Peinador, E. Román, and A. E. Kaifer, *Chem. Commun.* 9, 857 (2001).
70. P. Ceroni, V. Vincinelli, M. Maestri, V. Balzani, W. M. Müller, U. Müller, U. Hahn, F. Osswald, and F. Vögtle, *New. J. Chem.* 25, 989 (2001).
71. M. Alvaro, B. Ferrer, and H. Garcia, *Chem. Phys. Lett.* 351, 374 (2002).
72. P. Weyermann, F. Diederich, J. P. Gisselbrecht, C. Boudon, and M. Gross, *Helv. Chim. Acta* 85, 571 (2002).
73. D. L. Stone, D. K. Smith, and P. T. McGrail, *J. Am. Chem. Soc.* 124, 856 (2002).
74. Y. Tomoyose, D. L. Jiang, R. H. Jin, T. Aida, T. Yamashita, K. Horie, E. Yashima, and Y. Okamoto, *Macromolecules* 29, 5236 (1996).
75. P. Bhyrappa, G. Vaijayanthimala, and K. S. Suslick, *J. Am. Chem. Soc.* 121, 262 (1999).
76. J. Sen and K. S. Suslick, *J. Am. Chem. Soc.* 122, 11565 (2000).
77. C. M. Cardona, J. Alvarez, A. E. Kaifer, T. D. McCarley, S. Pandey, G. A. Baker, N. J. Bonzagni, and F. V. Bright, *J. Am. Chem. Soc.* 122, 6139 (2000).
78. V. J. Pugh, Q. S. Hu, and L. Pu, *Angew. Chem.-Int. Edit.* 39, 3638 (2000).
79. V. Rozhkov, D. Wilson, and S. Vinogradov, *Macromolecules* 35, 1991 (2002).
80. S. A. Vinogradov, L. W. Lo, and D. F. Wilson, *Chem.-Eur. J.* 5, 1338 (1999).
81. S. Yokoyama, T. Nakahama, A. Otomo, and S. Mashiko, *Colloid Surf. A—Physicochem. Eng. Asp.* 198, 433 (2002).

Diamond Nanocrystals

Tarun Sharda

Seki Technotron Corporation, Tokyo, Japan

Somnath Bhattacharyya

Indian Institute of Technology, Kanpur, India

CONTENTS

1. INTRODUCTION

"Diamond," first mined in India thousands of years ago, has been known as the "king of gemstones" by the public for its beauty for centuries. It probably will not be long until in the 21st century the same diamond with a different morphological structure will be known as the "king of materials" to engineers and scientists for its extreme properties with their unique combinations and practical use in manufacturing in the form of films and coatings [1, 2]. The extreme material properties of diamond with some potential applications from their unique combinations can be found in some review articles (for example, see K. V. Ravi in [1] and P. Chalker and S. Lande in [2]), and in addition some new areas of applications such as surface acoustic wave (SAW) devices [2, 3], and micro/nanoelectromechanical systems (MEMS and NEMS, respectively) [4–6] have started emerging. In brief, diamond is very hard and least compressible, is optically transparent from the deep ultraviolet (UV) to the far infrared, has the highest known thermal conductivity of all materials at room temperature, has low thermal expansion coefficient at room temperature (0.8×10^{-6} K) that is comparable to that of invar, exhibits low or "negative" electron affinity, and is biologically compatible and very resistant to chemical

corrosion [1, 2, 7, 8]. Diamond is much more resistant to X-rays, γ radiation, UV light, and nuclear radiation than the other semiconductors such as Si and Ge. Also, it is a very good electrical insulator (with room temperature resistivity of $\sim 10^{16}$ Ω cm). However, its resistivity can be changed over the range 10–10^6 Ω cm by doping, thus becoming a semiconductor with a wide bandgap of 5.5 eV. The great interest in diamond also comes from its applications in electronic devices as it has very high mobility (about 2000 cm^2/V s), breakdown field (10 MV/cm), and saturation velocity (about 2.5×10^7 cm/s) compared to other semiconductors [8]. At the same time, there are other diamond related carbon materials that have properties in between those of diamond and graphite. The properties of these hard carbon materials vary, depending on the concentration of sp^3-(diamond) and sp^2-(graphite) bonded carbon in the films. A classification of diamond and related materials in terms of their structure, resistivity, and energy gap is given in Table 1. The energy difference between thermodynamically stable graphite and metastable diamond is 0.9 kcal/mole. Nanodiamond is a metastable material with intermediate energy, close to *ta*-C having sp^3 bonds more than 90% [9, 10]. Before progressing further let us discuss diamond and related materials in some more detail.

1.1. Synthetic Diamond

Scarcity and cost of the natural diamond led scientists to find means of making diamond in the laboratory. Although there have been several attempts to synthesize diamond from various sources of carbon since it was discovered to be an allotrope of carbon, two main techniques were invented, both in the 1950s; high pressure and high temperature (HPHT) synthesis [1, 7] and chemical vapor deposition (CVD) synthesis [1, 2]. To date, since its discovery, most of the demands to supply diamond for industrial uses, primarily for material cutting, grinding, and polishing, are met by the HPHT technique. In this technique graphite is subjected to tens of thousands of atmosphere and heated to over 2000 K in the presence of some metal catalyst crystallizing it in diamond. However, this process is intrinsically

Table 1. Properties of diamond, graphite, and amorphous carbon.

Material	Structure	Resistivity (Ω cm)	Energy gap (eV)
Diamond	100% sp^3-C	$>10^{10}$	5.5
Nanocrystalline diamond	$>90\%$ sp^3-C	$>10^6$	2–5.5
Tetrahedral amorphous carbon	$>80\%$ sp^3-C	$\sim10^4$	~2
Amorphous carbon	~10–50% sp^3-C	$\sim10^{-1}$	a few meV
Graphite	0% sp^3-C	10^{-4}	0

limited in its ability to cover surfaces in the form of thin film coatings and to produce large sizes. These limitation are overcome by another technique (i.e., CVD synthesis of diamond) in which diamond is grown at subatmospheric pressures in the form of thin films [2]. Although the invention of this technique dates back to 1950s, its early impracticalities in terms of economical viability due to extremely low growth rate and co-deposition of graphitic phase of carbon did not allow it to develop [11]. In late 1960s to early 1980s it was discovered that presence of atomic hydrogen can preferentially etch the co-depositing graphitic phase and can improve the growth rate significantly [12, 13]. The current surge in CVD diamond research can be traced back to 1982 when the Japanese group at the National Institute for Research in Inorganic Materials (now the National Institute of Advanced Industrial Science and Technology) published details of their work clearly indicating the ways and means of generating atomic hydrogen in the growth chamber to grow good quality diamond on nondiamond substrates at significant rates (~1 μm/hr) [14]. Following this the same group came up with another technique in 1983 and this stimulated the worldwide interest in CVD diamond [15].

In general, in this technique, diamond can be nucleated on nondiamond substrates and an oriented or polycrystalline thin film can be deposited by dissociating the precursor gases at low pressures. These polycrystalline films show the same characteristics as natural and synthetic diamond and have high potential for various applications [1, 2, 8]. Generation of atomic hydrogen and the excitation of hydrocarbons can be achieved by various means and can broadly be classified as thermal CVD and plasma CVD. In thermal CVD processes, decomposition of precursor gases is accomplished by thermal activation whereas in plasmas it occurs by electron–molecule reactions. In high temperature plasma torches both mechanisms can be important. Thermal activated CVD includes hot filament and oxyacetylene torches. Plasma CVD includes low and medium pressure microwave (2.45 and 0.915 GHz) and dc plasma, dc plasma jet, low pressure radio frequency (rf) plasma, etc. [2].

1.2. Nanocrystalline Diamond

The high surface roughness of the conventionally grown polycrystalline CVD diamond films prevents their immediate use in spite of having outstanding properties with their unique combinations suitable for many applications. The high surface roughness is a major roadblock using these CVD diamond films for various applications [16, 17] such as machining and wear, optical, and thermal management

applications. For example, diamond is well suited for use as a protective optical coating but diamond films with high surface roughness cause attenuation and scattering of the transmitted signals restricting their use in optical coatings. In order to overcome the problem of surface roughness of diamond films either postpolishing is to be adopted or naturally grown smooth films are to be developed without compromising much of their hardness and other useful properties. However, postpolishing is expensive and time consuming [18–20] and it may be better to concentrate on as-grown smooth diamond films [19–51]. One way to reduce the surface roughness during growth is to control crystalline orientation with (100) facets being parallel to the film plane [52], or by reduction of the grain size (i.e., reduction of grain sizes from micrometers to nanometers) [9, 35, 37, 53].

This is the reason that in the last few years efforts in the area of diamond films grown by CVD have diverted from conventional microcrystalline diamond (MCD) films, having a grain size of a few hundred nanometers to several tens of micrometers [9, 35, 53–55], to nanocrystalline diamond (NCD) films, having a grain size from 2 nm to a few hundred nanometers [9, 19–51, 53, 56–62]. Moreover, this change of perception is a result of NCD films not only being smooth but also being more adaptive to the CVD diamond applications and having enhanced electronics and other properties. This is reflected in their cost effective and superior performances in the areas of electron field emission [63–69], optical transparency and protective coatings [21–23, 28, 38–40, 45, 51, 53, 70–72], tribology [19, 33, 34, 36, 37, 48, 73–75], SAW devices [3], and MEMS [5, 6]. Some of these properties of NCD films and a comparative study with single crystal diamond (SCD)/MCD are listed in Table 2. Moreover, as the size of the grains is changing from micrometer to nanometer, a factor of a million in volume, new properties have started emerging, exploring new areas of applications [76], for example, in X-ray optics, X-ray physics, particle physics, etc.

Some important properties of nanocrystalline diamond films are

- large surface area of diamond and high density of grain boundaries
- drastic increase in surface smoothness relative to microcrystalline diamond
- presence of more defects, however, less disorder in the interface
- better electron emission than conventional diamond films
- less highly oriented grains
- important grain boundary conduction
- enhanced optical transmission.

1.3. Diamond-like Carbon and Tetrahedral Amorphous Carbon

There is another class of hard carbon materials [1, 77, 78], essentially amorphous in nature and consisting of a mixture of sp^2 and sp^3 carbon, broadly termed "diamondlike carbon" (DLC). A significant amount of sp^3 carbon in the films gives them attractive physical and mechanical properties such as high hardness, high wear resistance, low coefficient of friction, chemical inertness, a high optical bandgap, and high

Table 2. Some properties of NCD films.

Properties	SCD/MCD[a]	NCD	Ref.[b]	Potential applications of NCD[c]
Electronic properties				
1. Bandgap (eV)	5.5	2–5.5	[30, 53, 70]	electronic devices
2. Electron affinity	negative	negative	[153]	
3. Onset of field emission (V/μm)	160	3–4	[63]	field emission display
4. Resistivity (Ω cm)	$>10^{10}$	$>10^6$	[56]	
5. Doping	p-type possible	both p- and n-type possible	[56, 162]	electrochemical electrodes
Optical properties				
1. Transmission	transparent from UV to far IR	$\sim$78–84% transmittance beyond 700 nm	[45, 53]	optical coatings
2. Refractive index (@ 633)	2.41	$\sim$2.27–2.35	[53] (@ 830 nm), [201]	IR windows
Mechanical properties				
1. Hardness (GPa)	$\sim$100	>90	[5]	
2. Young's modulus (GPa)	1054	$\sim$1000	[5, 6]	wear resistant, protective coatings
3. Wear resistance	high	high	[19, 34]	
4. Coefficient of friction	<0.1	0.1 (8000 cycles) to 0.01 (2.2×10^6 cycles)	[5]	MEMS/NEMS
Structural properties				
1. Bonding character	100% sp^3-C	$>90\%$ sp^3-C	[5]	
2. Grain size (nm)	—	2–100	this work	
3. Surface roughness (nm)	—	2–50	this work	
4. Hydrogen content (%)	—	<1	[5]	
Other properties				
1. Thermal conductivity (W/cm K)	20	12	[6]	thermal devices
2. Thermal stability (°C)	>1000	>800	[47, 170]	SAW devices
3. SAW phase velocity (km/s)	10	10	[3]	bioelectronic sensing System
4. Biological properties	biocompatible	biocompatible, highly selective, and stable	[232]	
Unique characteristics	hardness, thermal conductivity, breakdown voltage, etc. (for details see [1, 2, 7, 8])	smoothness, structural defects, high density of GB, conductivity, hardness, strong adhesion, large stress	this work, [9, 56, 76]	

[a] Data for SCD/MCD are taken mostly from [1, 2, 7, 8].
[b] References for NCD.
[c] Potential applications are a result of combinations of various properties in most of the cases.

electrical resistivity. These properties in the DLC films vary with the concentration of sp^2 and sp^3 carbon in the films. It has been shown that the properties of DLC films, such as hardness, optical transparency, etc., approach the value of diamond with high concentration of sp^3 carbon [79, 80]. The DLC films with high sp^3 concentration are termed tetrahedral carbon (ta-C) or amorphous diamond (a-D). The term DLC is mostly used to designate the hydrogenated amorphous carbon (a-C:H) whereas the term ta-C is mostly used to designate the nonhydrogenated amorphous carbon (a-C) [78]. The a-C:H films may contain 50% sp^3 carbon whereas it may be as high as 85% in ta-C films. Pulsed laser deposition [72–74, 79, 81, 82], cathodic arc deposition [80, 83], and ion deposition methods [84] have been employed to grow this new class of carbon material.

Considering the smooth surfaces having properties close to diamond, NCD and ta-C have emerged from their respective branches of CVD diamond and DLC, as described, as

the materials for intense current and future activities. As mentioned, it is not only because these films are smooth but also because they are more adaptive to the CVD diamond applications, having enhanced electronics and other properties. This makes the basis of this chapter in which some properties of NCD are discussed, emphasizing, in particular, transport and electronic properties, and are compared with the properties of ta-C. First, various deposition routes of NCD are discussed. Second, transport and electronic properties of NCD will be discussed in detail followed by a discussion on optical and mechanical properties. At the end, various other emerging aspects of NCD are also presented.

2. DEPOSITION ROUTES

A common feature of the majority of the deposition techniques of CVD diamond films is a high concentration of hydrogen gas (H_2) used as one of the constituents with some

hydrocarbon gas such as CH_4. A concentration of H_2 in excess of 99% (of the gas mixture) is required for the growth of high quality MCD films. The high concentration of H_2 results in the generation of a large flux of atomic hydrogen, which is generally believed to play a central role in the various diamond CVD processes. The growth of diamond is said to take place mostly via surface processes of addition and abstraction of radicals from the gas phase [8, 85–87]. Initially, after the nucleation of diamond, the growing diamond surface is to be protected from reconstruction into the graphitelike form. Therefore a high concentration of H is needed to satisfy the dangling bonds left unsatisfied on the growing diamond surface. Subsequently, vacancies are created by hydrogen atoms, which interact with the bonded hydrogen and remove it by converting it into H_2. Methyl radicals (CH_3), also generated by gas-phase hydrogen abstraction by H, are considered as diamond precursors are then placed on the vacancies in order to promote growth. In addition, atomic H preferentially etches the graphitic phase co-depositing with diamond. Generally, before realizing the importance of growing naturally smooth surfaces, the aim in the area of CVD diamond was to maximize the crystalline quality of CVD diamond. However, diamond grown under nonoptimum conditions, such as lower hydrogen concentration or higher carbon activity in the plasma, gives films with small grain size (e.g., several nanometers).

Also, ions are not considered to be good for diamond growth as they enhance lattice disorders and also promote graphitic content in the deposit. On the other hand, in the growth of carbon films by hyperthermal species, ions with energy in the range 40–200 eV produce a high concentration of sp^3 carbon in the films [83, 88, 89]. In this case the growth is dictated by a subplantation mechanism, which relies on the shallow subsurface implantation of the carbon ions [88]. Thus the two routes of growth of carbon films are totally different (i.e., one relies on surface and the other on subsurface processes). Moreover, the deposits are predominantly crystalline and amorphous respectively in the two processes. Interestingly, it was shown recently that both the routes can be coupled not only to generate diamond nuclei in the process called biased enhanced nucleation but can also be used to grow smooth NCD films [41, 42].

In the already existing ways to grow NCD, a number of techniques and conditions have been employed [9, 26, 27, 36, 37, 42, 44, 45, 48, 49, 57, 76]. As the need for as-grown smooth diamond films has been realized in the last few years, new routes have also emerged that mostly aim to grow smooth NCD or NCD embedded in a *ta*-C or *a*-C matrix. Based on the literature, a brief description of these new routes is as follows.

2.1. Hydrogen Deficient Gas Phase

As explained, high hydrogen concentration gives high quality MCD films and one route adopted to reduce the crystalline size to obtain NCD films is to reduce the concentration of hydrogen or increase the carbon activity in the gas phase and on the growing surfaces either by increasing the hydrocarbon constituent in the gas phase or by substituting the hydrogen with other gases, partially or completely. The resultant films vary from phase pure NCD to NCD embedded in *ta*-C or *a*-C matrix.

2.1.1. Hydrogen Deficient CH_4/Ar, C_{60}/Ar, CH_4/N_2, CH_4/He

One such process that has been studied in detail was developed at Argonne National Laboratory, USA [5, 9, 10, 19, 24, 31, 32, 35, 46, 56]. In this process, carbon dimer (C_2) is used as a reactive species in hydrogen deficient (CH_4/Ar or C_{60}/Ar) microwave plasma CVD [9]. C_2 is produced by replacing molecular hydrogen by argon and using CH_4 or C_{60} as precursor gases and also by using N_2/CH_4 as the reactant gases in a microwave plasma CVD system. The NCD films grown on seeded substrates by this technique are composed of 3–15 nm diamond crystallites with up to 1–10% sp^2 carbon residing at the boundaries [9]. Konov et al. [25] also reported growth of smooth NCD films using $CH_4/H_2/Ar$ mixtures with a methane percentage $CH_4/(CH_4 + H_2)$ varied in the range of 10 to 100% in a dc arc plasma deposition system. Their NCD films grown on Si substrates, seeded with ultrafine (5 nm) diamond particles, consisted of 30–50 nm size diamond crystallites. In the partially substituted hydrogen Nistor et al. [29] produced 1–2 μm thick NCD films from $CH_4/H_2/Ar$ mixtures by direct current plasma CVD. The Ar concentration was kept constant at 50% and methane concentration $CH_4/(CH_4 + H_2)$ was varied from 3 to 100%. Similar to Konov et al. [25] they also obtained nanodiamond films without even using hydrogen in the feed gas. Smooth NCD films with grain size of 10–50 nm were obtained on substrates seeded with 5 nm diamond powder. Although their transmission electron microscopy (TEM) studies did not reveal amorphous carbon in significant amounts, the nanocrystallites were found to be highly defective with many twins and other planar defects. The grain boundaries were presumably decorated with disordered sp^3-bonded carbon and sp^2-bonded amorphous carbon. Lin et al. [90] studied the $CH_4/H_2/Ar$ process in a hot filament CVD (HFCVD) system and proposed a compositional map demarcating regions for well-faceted diamond growth, NCD growth, and nondiamond deposition. Well-faceted MCD (2–10 μm) grow using Ar up to 90%. They report a change in microstructure from MCD to NCD, with a grain size smaller than 50 nm, at 95.5% Ar addition. Yang et al. [91] also used the $CH_4/H_2/Ar$ process to grow NCD films and observed decreasing grain size and that the surface morphology of the films changes gradually from faceted to ballastlike diamond with increasing Ar concentration. The formation of NCD was seen when more than 90% Ar was added in the $CH_4/H_2/Ar$ plasma. In another study [92] a low concentration (10–15%) of nonuniform distribution of nanodiamonds in amorphous carbon was detected at temperatures as low as 15 °C from decompositions of CH_4/Ar-rich plasmas generated at 35 kHz.

Amaratunga et al. [93, 94] reported mixed phase films containing diamond crystallites (10–200 nm) embedded in a nondiamond carbon matrix while using CH_4/He plasmas. Bi et al. [3] used Ar, H_2, and CH_4 in the ratios 100:4:1, respectively, to grow thick NCD films for a SAW device. The root mean square (rms) surface roughness in their case was 50 nm while the mean average grain size, estimated by scanning electron microscopy (SEM), was approximately 30 nm.

2.1.2. CH₄-Rich CH₄/H₂ with or without N₂ and O₂

2.1.2. CH$_4$-Rich CH$_4$/H$_2$ with or without N$_2$ and O$_2$

Yoshikawa et al. [48] prepared smooth NCD films having approximately 10 nm size grains, as observed by field emission SEM, by a microwave plasma CVD (MPCVD) system using a high methane concentration (10 vol%) in hydrogen on substrates pretreated by diamond powder of sizes 5 and 250 nm. Heiman et al. [47] used 9.91% methane in hydrogen gas mixture in a dc glow discharge. Smooth NCD films of 1 μm thickness with grain size in the range of 3–5 nm were obtained. Catledge and Vohra [36, 37] reported a new regime for synthesis of nanostructured diamond films on Ti-6Al-4V substrates. They used high pressures (125 Torr) and high methane concentration (5–15%) in balanced hydrogen and nitrogen in a MPCVD system to obtain predominantly diamond nanocrystallites of 13 nm average size, as estimated by X-ray diffraction (XRD) patterns, in a matrix of ta-C. The films are shown to be significantly smooth compared to the conventionally grown MCD films. At these processing conditions the microwave plasma is more highly activated with C$_2$ and atomic hydrogen. In another report they added varying concentrations of nitrogen in the plasma with 15% CH$_4$ and found that the grain size decreases up to the ratio of 0.1 of N$_2$/CH$_4$ before saturating at higher nitrogen concentrations. The amount of ta-C also increases in the same fashion and, as expected, the surface roughness also follows the same trend. It was suggested that the change in the film morphology is not a result of N$_2$ incorporation in the films but is a result of N$_2$ related surface processes such as microtwinning due to changes in gas-phase chemistry and surface kinetics. The same group, in their another study [95], modeled the gas-phase composition for MPCVD grown diamond with H$_2$/CH$_4$/N$_2$ mixtures using a thermodynamic equilibrium package and compared it with their experimental results by growing diamond films using the same mixture with the MPCVD system. A correlation was shown between the calculated composition of CN radical in the gas phase and the experimentally determined nanocrystallinity of the samples grown with different N$_2$ additions in the H$_2$/CH$_4$ plasma indicating the role of CN radical in the nitrogen-induced diamond nanocrystallinity in MPCVD.

Yang et al. [51] grew transparent diamond films with crystallite size below 70 nm in hydrogen and methane microwave plasma CVD on quartz substrates, ultrasonically pretreated by 0.5 μm diamond powder for 30 min. They studied surface morphology and optical and mechanical properties of the films by varying methane concentration in hydrogen plasma in the range of 1 to 4% while introducing 0.2% oxygen after the nucleation and keeping the substrate temperature 500 °C at 4 kPa pressure and 1.5 kW microwave power constant. Grain size and surface roughness were observed to decrease with methane concentration with a significant reduction in grain size occurring at 3% methane, which further reduced at 4% methane though the nanodiamond concentration in the films also goes up. The crystallite size, as estimated by TEM, near the interface was 30 nm and increases to 65 nm near the growth side. A thickness of 1–1.2 μm was obtained in 4 h growth of the films. Chen et al. [38–40, 45] used the MPCVD system to grow NCD films on quartz substrates, ultrasonically pretreated (using 4 nm diamond powder) for 8 h, using CH$_4$/H$_2$/O$_2$ plasmas in which CH$_4$ was varied between 1.5 and 42% while keeping O$_2$ constant at 0.1%. The average surface roughness of their 0.5 to 1 μm film varied between 6 and 13 nm. They showed that the surface roughness of the NCD films decreases with increasing methane concentration and has a great impact on the optical transmittance of the NCD films. Wu et al. [22] demonstrated growth of NCD (20–100 nm grain size) having a surface roughness of ∼15 nm by low pressure (5 Torr) and low microwave power (450 W). Erz et al. [23] used 10% CH$_4$ in hydrogen to grow 800 nm NCD film. Zarrabian et al. [28] used electron cyclotron resonance (ECR) plasma to grow NCD grains of size 4–30 nm embedded in DLC. Jiang et al. [59] showed that NCD can be grown with MPCVD using 5% CH$_4$ on Si ultrasonically pretreated by diamond or SiC powders. The average grain size estimated by TEM analysis revealed a NCD grain size of 30–40 nm. The substrates, mechanically abraded by Al$_2$O$_3$ grit, give NCD embedded in a-C matrix at the same conditions.

Wu et al. [66, 67] grew NCD films using N$_2$/CH$_4$/H$_2$ in a MPCVD system. In the first series the CH$_4$ was varied between 2.1 to 8.4 sccm in 150 sccm of nitrogen without any hydrogen. In the second series hydrogen was introduced and was varied in the range of 0–10 sccm while keeping the methane constant at 3.5 sccm. NCD films with grain size of 8 nm embedded in a-C matrix were obtained without any hydrogen which increases to 20 and 50 nm respectively at 5 and 10 sccm of hydrogen.

In another interesting development, composite diamond films with smooth surfaces, was achieved by alternatively depositing conventional MCD and NCD films in a HFCVD reactor [50]. The structure of the layers was such that the bottom and top layers were respectively MCD and NCD. SEM and atomic force microscopy (AFM) analyses of the films revealed 2–3 μm granules consisting of 10–100 nm diamond grains unlike the well-faceted micrometer size grains observed in conventional MCD films. The surface roughness was less than 100 nm. These films have dielectric properties similar to conventional MCD films with smooth surfaces and are considered to be promising for MEMS devices.

2.1.3. CO-Rich CO/H₂ Mixtures

2.1.3. CO-Rich CO/H$_2$ Mixtures

Lee et al. [26, 27] developed a low temperature process (350 °C < T < 500 °C) for low power but high growth rate (up to 2.5 μm/hr) NCD film by MPCVD. Instead of high methane concentration they used CO-rich CO/H$_2$ mixtures and obtained smooth NCD films consisting of 30–40 nm grain size. They observed an interesting growth trend with respect to substrate temperature while using the CO-rich CO/H$_2$ mixture. There is a narrow temperature window, different for different CO/H$_2$ ratios. The temperature at which the peak growth rate is obtained in this window decreases with increasing CO/H$_2$ ratio. For example, the peak of the growth rate is observed to occur at 500 °C at a ratio of 8 of CO/H$_2$ that decreases to 450 °C at a ratio of 18. Moreover, the growth rate also increases with increasing ratio. Although the growth of NCD was obtained at low temperatures the bulk void fraction also increased significantly compared to the films grown at higher temperatures. Recently,

growth of NCD films of size 20 nm was also reported by Teii et al. [57] at low pressure (80 mTorr) at 700 °C by inductively coupled plasma employing CO/CH$_4$/H$_2$ and O$_2$/CH$_4$/H$_2$. In this case a positive biasing of 20 V was applied to the substrate to reduce the influence of ion bombardment. The films consist of ball shape grains of size 100 nm, which are composed of 20 nm NCD grains.

2.2. Biased Enhanced Growth

As the reader may have noticed, in the growth route for NCD by hydrogen deficient plasmas, mostly the substrates were pretreated externally before deposition ultrasonically or mechanically using diamond or other abrasive powders. There is another well-established method to nucleate diamond internally in conventional growth of MCD films called biased enhanced nucleation (BEN) [96] in which the substrates are biased negatively in a relatively hydrocarbon-rich mixture of hydrocarbon–hydrogen precursor gases. This method, which results in a high density of diamond nucleation (10^{10}/cm^2 or more), is the first step followed by another step or two steps to grow heteroepitaxial diamond films. In order to achieve overgrowth of diamond on these nuclei, the BEN process is followed by conventional growth in which the bias is put off and the growth is continued with lower hydrocarbon percentage in the gas phase. It is found out that in this later stage of growth only the stable parts of the nuclei continue growing with while the remaining getting etched off in the process due to high concentration of hydrogen in the conventional step of growth [97].

To obtain an NCD film, Sharda and Soga [61] considered achieving higher densities of diamond nucleation, similar to the BEN process, followed by their continuous growth in the later stages while maintaining the high density. In order to achieve this they extended the BEN in microwave plasma CVD for the whole growth process and termed their process biased enhanced growth (BEG) in which they obtained diamond nucleation and growth on silicon substrates in a single process [41–43, 76]. They used 5% CH$_4$ in balanced H$_2$ and controlled the bias current density in a special arrangement in a MPCVD system to study the growth in a different combination of conditions (bias current density, bias voltage, and microwave power). A different regime of growth was indeed observed which resulted in NCD films having rms surface roughness of 5–30 nm composed of grains of 2–30 nm with growth rates of 0.5–2 μm/hr at 1000 W microwave power and at substrate temperatures in the range of 400–700 °C. In a similar development, Gu and Jiang [44] also used biasing to not only nucleate diamond but also to grow films. Their growth process, though, uses continuous biasing to grow NCD but in three steps unlike a single step process for both nucleation and growth by Sharda et al. [41–43, 61]. No biasing and methane were used in the first stage for 40 min at 860 °C, which was meant just to remove the oxide layer, followed first by a nucleation stage in which the substrates were biased at −120 V at 5% methane (at 840 °C, 20 mbar pressure, and 800 W microwave power) and second by the growth step in which the substrate was biased up to −140 V while decreasing the methane concentration in the range of 0.5 to 5% and changing other conditions as well. It was observed that the grain size decreases from

0.3 μm at −100 V to 40 nm at −140 V. The growth rate was 0.25 μm/hr and surface roughness, as measured by a surface profilometer, of 1 μm thick film was 5 nm at −140 V. There was a marked difference in the adhesion of the films in case of Sharda et al. [62, 76, 98] and Gu and Jiang [44]. The BEG process by Sharda et al. results in a strong adhesion that allows one to grow any thickness, irrespective of amount of the stress in the films, whereas the NCD films grown by continuous biasing by Jiang and Jia [49] cannot be grown beyond 2 μm due to relatively weak adhesion as the compressive stress in the films make them delaminate from the substrate. Groning et al. [99] grew NCD films on silicon substrates to study their field emission properties with and without biasing. In case of no biasing they used high substrate temperatures (950 and 980 °C) and high methane fraction (5%) and in the case of biasing at −250 V they used a relatively low substrate temperature (850 °C) and lower methane fraction (2%). In the latter case the surface morphology was ballastlike with large ball-like structures of 2–3 μm in diameter consisting of diamond nanocrystallites of size 10–50 nm.

In an effort by Yang et al. [100], the effect of bias in forming NCD in the MPCVD system was studied. The NCD films were grown on scratched substrates unlike the films grown on externally untreated mirrorlike substrates by Sharda et al. or Jiang et al., as described. A continuous dc negative biasing in the range of 0–250 V was applied to the substrates during deposition while using a 1% CH$_4$/H$_2$ mixture for 3 hr to study crystallinity, morphology, and growth rate of the diamond films. The substrate temperature was maintained at 900 °C while using 5.3 kPa chamber pressure and 1000 W microwave power. A change in the morphology with biasing voltage was reported from triangle-faceted grains of 1–3 μm size (up to a bias of 50 V) to square-faceted grains of 1–2 μm size (at 100 and 150 V). Smooth NCD films with grain size of 20–40 nm, as measured by TEM, were obtained at 250 V. The growth rate was reported to decrease with biasing beyond 50 V with the NCD growth rate being 0.3–0.4 μm/hr. It should be noted that the effect of biasing on the growth rate in this study is different than the effect on biasing in the BEG process reported by Sharda et al. [98]. In the later study, the layer thickness in 60 min growth increases from 1 to 2 μm with increasing biasing from 200 to 320 V. In another interesting effort by Yang et al. [101] to grow NCD films, the two main methods to grow NCD, hydrogen deficient argon plasma using methane and fullerene (Section 2.1.1) and biased enhanced growth (Section 2.2), were coupled to study their combined effect on the grain size, microstructure, and growth rate of the diamond films in the MPCVD system. The NCD films with grain size of 50–100 nm were grown using an Ar concentration of 90–99 vol% while continuously biasing the substrate at −50 V. This combination gives a growth rate of 0.7–0.8 μm/hr of NCD films in the MPCVD system, apparently larger than what the authors obtained by individual processes. However, it should again be mentioned that even the maximum growth rate (0.8 μm/hr) of NCD films, with or without Ar addition, reported by Yang et al. [100, 101] is still lower than the maximum growth rate (~1.9 μm/hr) of NCD films by the BEG process reported by Sharda et al. [98].

More studies on the growth of NCD films began appearing, with Zhou et al. [58, 102] reporting growth of nanodiamond *a*-C composite in a HFCVD system. The continuous biasing process was termed as prolong biased enhanced nucleation in which they obtained NCD (∼10 nm) embedded in *a*-C matrix at 1% CH_4 in hydrogen. They obtained 1 μm thick film in 7 h of deposition. The rms surface roughness of their films measured by AFM was ∼20 nm. Nonfaceted granular structures of size 100–200 nm are seen in SEM which consists of ∼10 nm diamond grains embedded in *a*-C matrix, as seen in low magnification TEM.

In another development, growth of smooth nanodiamond films (NCD embedded in *a*-C matrix) on different substrates was reported by Kundu et al. [30] at room temperature using dc magnetron sputtering of vitreous carbon in an argon and hydrogen (0–10%) plasma in the pressure range of 45–90 mTorr. The average grain size, as examined by TEM, was found to be ∼55 nm on quartz and ∼75 nm on Si and Mo substrates. The film surface consists mostly of sp^2-bonded carbon and was removed to see the NCD embedded in the *a*-C matrix by SEM. The sp^3/sp^2 ratio, as estimated by Fourier transform infrared (IR) increased from 4 to 16 with increasing negative bias voltage applied to the substrate.

In an interesting advancement in the synthesis of diamond films, a multilayer structure of MCD and NCD was developed using growth with and without biasing [103]. It was shown in this study that size of the diamond grains could be reduced to a few nm by applying a negative bias during the growth of an MCD film and could again be increased once the bias was put off. This way a layered structure of MCD and NCD can be grown. In this study, the grain size of the initial MCD layer, which was grown for 2 hr, had a grain size of <1 μm that reduced to about 4–5 nm in the overgrown NCD layer while using biasing. The nanometer sized diamond started appearing on the facets of MCD grains right from the growth after 5 min. Application of biasing changed the faceted surface morphology of the MCD layer to a smooth surface morphology in 30 min growth. Putting off the bias after the growth of the NCD layer can again develop a faceted MCD layer on the top of the NCD layer.

2.3. Ion Implantation

A completely different route than those described in Sections 2.1 and 2.2 was adopted by Prawer et al. [104] who showed formation of a pure NCD layer in fused quartz by means of MeV ion implantation followed by annealing at suitable conditions. Unlike the previous two routes or any other route to grow diamond, this process does not require any nucleation or any external high pressure (HPHT process) to develop diamond. In this process, 1 MeV carbon ions with a dose of 5×10^{16} C/cm^2 implanted into fused quartz followed by annealing for 1 h at 1100 °C in 4% hydrogen in argon resulted in the formation of a 60 nm thick layer consisting of 5–7 nm cubic diamond crystallites at 140 nm below the quartz surface. The size of the diamond grains can be controlled by varying the implantation dose and it increases with increasing dose (8–13 nm for 2×10^{17} C/cm^2 and 15–20 nm for 5×10^{17} C/cm^2). In another development Wang et al. [105] formed nanocrystalline diamond with sizes of ∼2–70 nm by Ar$^+$ irradiation of graphite at a fluence of 10^{22}/cm^2.

2.4. Transformation

Yet another unique concept was introduced by Hirari et al. [71] to produce nanocrystalline diamond ceramics not by sintering a raw powder but by transforming C_{60} fullerene by shock compression and rapid quenching. The transformed transparent NCD platelets consist of a few nanometer-sized diamond crystallites, which are connected directly or by a thin modified sp^3 carbon layer, as revealed by TEM and electron energy loss spectroscopy (EELS). Similarly, NCD has been formed by direct transformation of multiwalled carbon nanotubes (MWCNT) under high pressure [106]. MWCNT samples in the form of a platelike shape were subjected to a pressure of 17 GPa and were heated to 2500 K by a CO_2 laser in a diamond anvil cell. The recovered product had the same platelike shape as the starting material and consisted of nanosized octahedral crystals with size less than 50 nm, which was similar to the size of the diameter of the nanotubes. The heated part by the laser was transparent. The Raman spectra of the transparent region of the sample show a broad peak at 1322–1324 cm^{-1} indicating that the converted product is diamond which was confirmed by EELS measurements of the converted sample. No amorphous or graphitic phase could be seen in the transparent region of the converted sample. It should be noted that the unheated part of the sample did not convert to NCD and remained MWCNT. The tubular structure of the unheated part of the sample remained unchanged in spite of the fact that it was subjected to a high pressure of 17 GPa. This is because of high yield strength of the curled graphitic planes.

In another interesting development, Gogotsi et al. [107] reported in the journal *Nature* synthesis of nanocrystalline diamond-structured carbon by conversion of silicon carbide at ambient pressure. In this process silicon was extracted from silicon carbide in chlorine-containing gases at ambient pressure and temperature below 1000 °C. Average crystallite size of the diamond-structured carbon was 5 to 10 nm resulting from a stable conversion from silicon carbide in the presence of hydrogen in the gas mixture.

2.5. Dielectrophoresis/Spraying Coating

A diamond layer can be coated on substrates by dielectrophoresis or a spraying method. Zhu et al. [63] attached thin nanostructured diamond films to silicon substrates by a spraying or brushing technique using commercially available, produced by explosives, 10 to 100 nm size micropolycrystalline diamond particles with each of the particles consisting of 1 to 20 nm crystallites and associated grain boundaries in aqueous suspension. Göhl et al. [65] deposited nanodiamond powder coating by a dielectrophoresis technique. They used nanodiamond powder of 1–10 nm size produced from shock synthesis on a Si tip array, rough Si stumps, and flat standard mirror-polished Si substrates. Xu et al. [108] deposited a nanostructured diamond coating on etched silicon substrates by the dielectrophoresis method using ∼5 nm nanodiamond powder, produced by explosives, by suspending them in ethanol. Mallillard-Schaller et al. [109] deposited 4–5 nm size diamond nanoparticles on flat Si(100) substrates by electrophoresis/dielectrophoresis.

In summary, various routes have been developed or adopted to grow a variety of NCD films varying from phase-pure ultrananocrystalline diamond to nanodiamond embedded in a-C or ta-C matrix. The grain size of these nanocrystals can be controlled and can be varied by different parameters studied in these different routes of their growth. Table 3 gives the range of grain size and surface roughness of NCD films reported by various research groups by adopting different deposition routes, as described in this section. In the following section we shall now discuss in detail transport and electronic properties of this material followed by some discussion of its optical and tribological properties.

3. TRANSPORT PROPERTIES

3.1. High Electrical Conductivity from Diamond and Related Materials

There are different ways to increase conductivity of carbon related materials. One of the easiest methods is to increase the percentage of graphitelike or sp^2-bonded carbon by pyrolysis. It is also observed that application of high hydrostatic pressure can increase the conductivity by a few orders of magnitude [110]. However, controlling the enhanced conductivity by pyrolysis is a very difficult task. Beside, this process gives soft material that is rich in sp^2-bonded carbon. Doping is an elegant way to improve the conductivity of diamond and related materials without changing their structure. Several donors in mono- or di-substitutional sites like Li, F, Cl, I, Xe, S, O, P, N, NO, etc. have been analyzed with calculations. Substitutional P was found to be a better donor than N. Similarly, S and Cl are better donors than O and F, respectively [111]. Interstitial Li atoms are predicted to be shallow donors whereas substitutional Li are predicted to be as acceptors. However, electrical activation by Li-doped diamond was not so high. At the same time, oxygen forms a deep thermal donor and sulfur is a shallower donor than oxygen [111]. Over several years many researchers have been hoping that diamond or diamondlike carbon, with excellent mechanical and thermal properties, would appear as good electronic materials. However, difficulties of doping n-type impurities with low activation energy have hampered their hopes and thus actual diamond devices could not be made yet [112–114]. Due to the smaller atomic radius of carbon compared to that of Si and Ge solubility of different elements in diamond is lower [113]. Nevertheless, several researchers have attempted to incorporate different kinds of dopants, like phosphorous [115], sulfur [116], oxygen [117], etc., and very recently, some reports discussed the possibility of successful n-type doping of diamond [115–120] (see Table 4).

Despite numerous efforts demonstrating that n-type doping can produce shallow donor levels close to the conduction band (CB) of diamond, the levels and the resistivity are still too high (>300 meV and 10^3 Ω cm, respectively) for application of this material at room temperature [115–118] (see Table 4). Also, the conductivity activation energy does not seem to decrease sharply with increase of dopant concentration [116–118]. To apply n-type doped diamond to a real electronic device the resistivity and activation energy should be much smaller than those of boron-doped diamond [120, 121]. In the following we shall concentrate on nitrogen for n-type conduction in diamond.

3.2. n-Type Conduction by Nitrogen Incorporation

3.2.1. Background

Nitrogen has been thought to be an ideal n-type dopant for diamond and related materials. This is because nitrogen has five valence electrons, one more than a carbon atom. This extra electron will be shared by the sp^3- or sp^2-bonded carbon atoms forming σ or π type bonds. Though theoretically

Table 3. Surface roughness and grain size of NCD films obtained by various groups by adopting different routes.

Technique	Route	Grain size (nm)	Roughness[a] (nm)	Ref.
MPCVD	$CH_4/H_2/O_2$	<300	~10	[21]
MPCVD	$CH_4/H_2/O_2$	20–100	~15	[22]
MPCVD	C_{60}/Ar, CH_4/Ar, CH_4/N_2	2–15	20–40	[5, 9]
MPCVD	$CH_4/H_2/O_2$	4–15	~8	[45]
MPCVD	$CH_4/H_2/Ar$	10–50	~13	[29]
MPCVD	$CH_4/H_2/Ar$	5	<20	[25]
MPCVD	CH_4/H_2, $CH_4/H_2/N_2$	13	50	[36, 37]
MPCVD	biasing-CH_4/H_2	2–30	~10–30	[61]
MPCVD	biasing-CH_4/H_2	~40	~5	[44, 49]
MPCVD	CH_4/H_2	~10	8.4	[48]
dc	carbon sputtering/ H_2/Ar	~55–95	~9	[30]
HFCVD	biasing-CH_4/H_2	~6–10	20	[58]
dc-CVD	CH_4/H_2	3–5	3–13.5	[47]
MPCVD	$CH_4/H_2/O_2$	<70	~9	[51]
MPCVD	CO/H_2	~10–40		[26, 27]
MPCVD	$CH_4/N_2/H_2$	8–50		[66, 67]
HFCVD	CH_3COCH_3/H_2	10–100	<100	[50]
MPCVD	$CH_4/H_2/Ar$		50	[3]
—	conversion from SiC	5–10	—	[107]
—	irradiation	~2–70	—	[106]
—	irradiation–annealing	5–7	—	[104]
—	conversion-C_{60}	few to 5 nm	—	[71]
Hot flame	biasing-O_2-C_2H_2	~8	8–30	[34]
MPCVD	CH_4/H_2	30–40		[59]

[a] Roughness is not necessarily an rms value and is also measured by different methods (AFM, profilometer).

Table 4. Comparative study of the electrical properties of doped diamond.

Type of dopant	Conductivity S cm^{-1} (RT)	Activation energy (eV)	Carrier density (cm^3)	Mobility (cm^2/V s)	Ref.
O (n)	high	0.32	5×10^{11}	~40	[117]
S (n)	1.3×10^{-3}	0.38	1.4×10^{13}	597	[116]
P (n)	0.2×10^{-3}	0.46, 0.56, and 0.81	~10^{14}	0.5–5	[115, 118]
N (n-SCD[a])	10^{-16}	1.7	10^7	5000	[113]
N (n-MCD[b])	10^{-6}	1.6		>100	[114]
B (p)	<10	0.36–0	>10^{20}	>10^2	[120]
N (a-C:N)	10^{-2}	0.2	~10^{18}	very low	[121]

[a] SCD = single crystal diamond.
[b] MCD = microcrystalline diamond.

it looks quite simple, in practice it has been quite different because defects dominate the doping effect. Altogether an increase of conductivity can be seen in N-doped materials along with some changes in the structure of the materials.

Nitrogen is a possible donor in diamond with a lower formation energy than that of phosphorous. However, it has been understood that successful nitrogen doping of SCD is quite difficult [112–114]. Because of a high degree of localization of the N wave function, nitrogen behaves as a deep impurity center in diamond, 1.7 eV below the CB. Nitrogen in diamond prefers to form bond with three neighboring carbon atoms occupying a three-coordinated substitutional site distorted along the (111) direction and two of its electrons acting as a lone pair orbital [113]. In CVD polycrystalline diamond also doping of nitrogen has been unsuccessful due to the presence of a large defect density in this material at the surface as well as in the grain boundary that forms π–π^* states in the gap region [114]. Nitrogen creates a natural charge state and remains fourfold coordinated.

Electronic properties of NCD film with ta-C and related materials are compared in the following sections. Apart from structural disorder, the sp^3 percentage of the ta-C films is not found to be different than the sp^3 percentage of the NCD films showing very good mechanical and tribological properties. The ta-C is thought to be a better candidate than other forms of carbon for electronic applications. It is because of its bandgap of about 2 eV and a small activation energy (E_σ, about 0.2 eV) suggesting nitrogen may form a shallow donor level [83, 121]. However, the concept of doping in amorphous materials (here: ta-C) is quite different from the concept of doping in crystallographic forms (e.g., diamond) [122]. The degree of disorder is very high in ta-C which gives tailing of the band in the pseudo-gap region and thus a substitutional doping is found to be difficult [123]. It was understood that the increase of dopant concentration promoted the formation of π-bonded clusters that counteracted the doping phenomena [124]. On the other hand, NCD can be grown as a phase pure diamond where the degree of disorder can be quite low and confined only to quite thin (0.2–0.4 nm) grain boundary (GB) regions and hence the effective defect density of state in the bandgap region should be very low allowing NCD to be doped.

There are several experimental methods (e.g., photoelectron spectroscopy [125], EELS [126, 127]) available to verify doping from the shift of the Fermi level. Although in some cases the Fermi level has been observed to be shifted from the midgap region, the effect of a true substitutional doping could not be seen [121]. This means that the relative shift of the Fermi level appeared due to compensation of defects and graphitization of these materials. From the change of electrical conductivity and Hall voltage, as a function of dopant concentration as well as temperature variation, one can firmly establish doping of a given material. A successful doping increases the conductivity of the material for several orders. The temperature dependent conductivity in this case should show extended state and impurity state conduction. The carrier concentration should be very high and should increase with dopant concentration. If not interfered with by the impurity states, a heavily doped material should behave as a metal. These effects have been observed

in B-doped diamond but have yet to be seen in n-type diamond and related materials. However, B-doped diamond is not considered a good electronic material as the acceptor states lie 0.36 eV above the valence band.

For clear understanding of doping measurement, carrier concentration and mobility and also density of states are very important parameters. Hall measurements are routinely used to understand quality of doping in p-type diamond. The mechanism of current conduction or change over of different types of conduction can also be predicted from temperature dependent Hall measurements. Previously, thermoelectric power (S) was successfully used to understand the type of doping in amorphous carbon films that was found to be very low at room temperature [128]. In order to establish nitrogen doping of ta-C a combined study of low temperature conductivity and thermopower of a-CN$_x$ ($x = 15$–30 at% N) has been performed [122]. A comparative study of thermoelectric power between ta-C and NCD film should be useful to understand n-type conduction.

In this chapter N-doped NCD films will be under focus. Theoretical predictions for nitrogen doping in the NCD films will be discussed first followed by its experimental demonstration and a detailed discussion on the results in the subsequent sections. Although there is not much literature available yet on the nitrogen doping of NCD films, phase-pure NCD films prepared by a MPCVD system from a mixture of argon and methane (1%) using up to 20% nitrogen in the gas phase have been extensively studied by Bhattacharya et al. [56, 129] and provide a sufficient matter to discuss in this chapter. Electrical conductivity and Hall and thermoelectric power measurements of such films as a function of temperature have been carried out [56, 129] and will be a part of the detailed discussion.

3.2.2. Theoretical Predictions

A carbon system including diamond has the ability to change hybridization in a structurally disordered environment. Relatively small bond distortions are capable of locally inducing sp^2 type bonding. This competition between structural disordering and local hybridization change, completely absent in silicon, translate into relatively more ordered GB structures in diamond than in silicon. It has already been predicted that a diamond GB has the potential for becoming electrically conductive. The idea behind this was that the GB was made of graphitelike material with up to 80% of the atoms being three-coordinated whose electrical conductivity is very high. However, because the three-coordinated C atoms are poorly connected to each other, any type of graphitelike electrical conduction through the GBs is not likely making undoped NCD as insulator.

As a representative high energy GB, the (100) $\phi = 43.60°$ ($\Sigma 29$) twist boundary has been chosen by some theoreticians, with a planar unit cell area that is $\Sigma = 29$ times larger than that of the primitive planar unit cell of diamond (100) planes. As a representative low energy GB, the same theoreticians considered that the (111) $\phi = 42.10°$ ($\Sigma 31$) twist GB, with a planar unit cell area $\Sigma = 31$ times larger than that of perfect-crystal (111) planes [10, 130]. Both boundaries are readily generated by a twist rotation of two free (100) or (111) surfaces about the GB plane normal by the respective angle ø.

According to the model developed by Keblinski et al. [131], the degree of connectivity among the three-coordinated carbon atoms clearly showed that like in the unreconstructed free (111) surface individual three-coordinated GB atoms are totally disconnected from each other in the (111) GB because all three of their bonds involve four-coordinated atoms in the same grain. Interestingly, in spite of 80% of the GB carbon atoms being threefold coordinated, other than the sp^2-bonded atom pairs connected across the GB, these atoms are almost completely disconnected from one another. The reasons for this extremely small degree of connectivity are, again, mostly geometrical. Given that within their own (100) planes, the three-coordinated GB atoms are not bonded among themselves, typically two of the three bonds of each of these GB atoms involve four-coordinated atoms within the same grain while only one bond is capable of connecting with another three-coordinated atom, however, across the GB. However, in spite of this relatively low degree of connectivity, one could easily envision dramatic changes in the electrical behavior of diamond GBs, induced, for example, by a small amount of impurities, like nitrogen.

In doped NCD "bridging" by impurities provides the missing connections making it conducting [131]. Zapol et al. [132] reported on nitrogen substitutional impurities in NCD films. They determined the position of GB carbon atoms by energy minimization of structure, where most stable nitrogen was obtained by substituting at a threefold coordinated site (trigonal) with a nonplanar arrangement of the bonds. Nitrogen saturates the original dangling bond and forms a lone pair. This causes no breaking of bonds as opposed to the bulk. Substitution in the planar threefold coordinates results in a slightly puckered nitrogen configuration and movement of the carbon bond partner across the interface into a more pyramidal shape (see the schematic diagram of GB and nitrogen incorporation in [131, 132]). Finally carbon atoms move slightly more out of plane and the bond to the nitrogen lengthens by 10%. It seems that there is a change of bonding character from a double carbon bond to a single carbon bond. As the distortion is very localized, conduction of electrons will not be hampered in the grain boundary regions. Moreover, distribution of bonds caused by the neighboring carbon atoms related to the GB make N available in the GB.

3.2.3. Experimental Demonstration

As mentioned, although not much literature is available, Bhattacharya et al. [56] have experimentally demonstrated high conductivity in their N-doped NCD. The NCD samples were prepared from a mixture of argon (99 sccm) and methane (1 sccm) in a commercial MPCVD system with a varying flow rate of nitrogen (0 to 20 sccm). All films were deposited on n-type Si wafer as well as on fused SiO_2 substrate at 100 Torr pressure, 700 W microwave power, and 800 °C substrate temperature. The deposited films were about 0.5 μm thick. Microstructure of the films was studied by high-resolution TEM (HRTEM) and the nitrogen atomic percentage in the films was determined by secondary ionization mass spectroscopy [56, 129].

HRTEM studies of the films revealed that the films consist of phase pure diamond nanocrystals of 2–4 nm size surrounded by 3–5 Å wide grain boundaries [9, 32] (see Fig. 1a and [56]). In order to distinguish these phase-pure NCD films from other kinds of NCD films that consist of predominantly NCDs embedded in ta-C matrix the former films are termed ultra-NCD (UNCD) [5]. The same term (UNCD) will be used in the remaining part of this chapter to refer the phase-pure NCD films, as described in this section. It is also understood that the GB in the UNCD films is mostly decorated by sp^2-bonded carbon and the estimated value of sp^2-bonded carbon in the films is 5–7%. With the increase of nitrogen concentration the grain size as well as the GB width increases up to 10 times (Fig. 1a and b) [56]. However, the ratio of grain size and width of GB remains fairly constant for different nitrogen concentrations. The near edge X-ray absorption fine structure (NEXAFS) spectroscopy indicated that the sp^2-bonded carbon increases up to 15% when 20% N_2 is introduced in the plasma [133].

In another study, Xu et al. [134] reported change of the microstructure of NCD, implanted with nitrogen, by AFM and XRD. Some cubic-shaped grains that were observed on the surface in the as-deposited film (with grain size in the range 70–400 nm) disappeared with an increase in the implanted fluence, and finally the diamond grains changed into ball-shaped grains, which was caused by the sputtering effect of implanted nitrogen ions. After implantation, the film surface became smooth, owing to the sputtering effect of the nitrogen ions. After nitrogen-ion implantation, the diamond (111) XRD peak broadened and its intensity decreased with increasing fluence. Meanwhile, the value of the crystal lattice increased, but no diffraction peak for graphite was observed. These results indicate that implantation-induced irradiation damage leads to a decline in diamond crystallinity and a swelling of crystal lattice, but no graphitization caused by implantation [134].

The UNCD samples prepared in the nitrogen-free atmosphere were found to be good insulating materials (resistance more than 30 MΩ), and therefore temperature dependent conductivity measurement at low temperature was rather difficult. Upon introduction of nitrogen the conductivity increases very rapidly giving a difference of more than four orders in the samples grown with 0.5 and 20% N_2, as illustrated in Figure 2a [56]. The room temperature
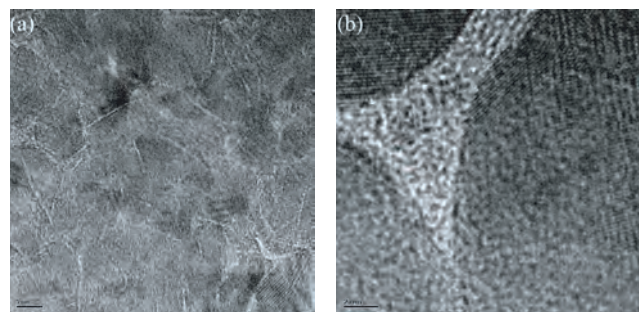
Figure 1. Plan-view HRTEM of two UNCD thin films synthesized using (a) 1% nitrogen and (b) 20% nitrogen in the plasma. The addition of nitrogen leads to an increase in both the grain size and grain-boundary width. Reprinted with permission from [56], S. Bhattacharyya et al., *Appl. Phys. Lett.* 79, 1441 (2001). © 2001, American Institute of Physics.
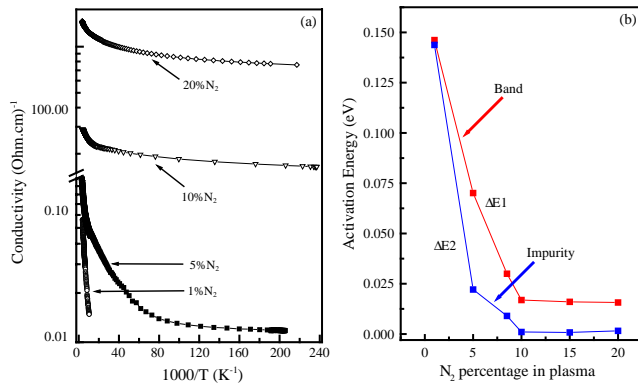
Figure 2. (a) Temperature dependent conductivity of NCD films prepared with 1, 5, 10, and 20% nitrogen. An Arrhenious plot has been attempted to fit the data. Reprinted with permission from [56], S. Bhattacharyya et al., *Appl. Phys. Lett.* 79, 1441 (2001). © 2001, American Institute of Physics. (b) Variation of activation energies E_1 and E_2 with nitrogen concentration in the plasma.

resistivity for the films grown at 20% N_2 was as low as 3.7 mΩ. This value is much lower than the lowest value reported in both *p*- and *n*-type diamond [115, 120]. With the decrease of temperature conductivity of all samples was found to decrease. But the relative change of the value of conductivity between 300 and 4.2 K was shown to decrease with increase of nitrogen concentration with the 20% N_2 sample showing the change as low as 0.66 times (Fig. 2a). Except for the 1% N_2 sample none of the curves were reported to fit in a single exponential decay or power law. The temperature dependency of the conductivity of the NCD films can be analyzed in terms of conduction of diamond grains and conduction of the grain boundary.

3.2.4. True Doping of Diamond Grains

Several researchers demonstrated the temperature dependent conductivity of MCD and SCD in different regions of conduction and a fitting of the complete conductivity versus temperature curve seems not to be possible in many cases [114, 120, 135]. At high temperatures band conduction with activation energy E_1 is dominant whereas in the intermediate region impurity conduction and in the low temperature region hopping conduction are found to be significant. Also, for B-doped diamond the low temperature conductivity was attributed to either impurity or hopping conduction [114] or to hopping conduction [135]. The conductivity as a function of inverse of temperature has been fitted in the entire range of measurements (300 to 4.2 K), in general, as a combination of three exponential decay functions expressed as $\sigma = \sigma_{ext} \exp(-E_1/kT) + \sigma_{imp} \exp(-E_2/kT) + \sigma_{hop} \exp(-E_3/kT)$ or $\sigma_1 \exp(-E_1/kT) + \sigma_2 \exp(-E_2/kT) + \sigma_3 \exp(-E_3/kT)$ using the model of nondegenarately doped semiconductor [120, 136]. The values of σ_1 and σ_2 were found to increase in a similar manner as σ with the increase of nitrogen concentration. The value of σ_1 is always higher than σ_2. The value of σ_3 is very small compared to that of other two terms and it does not change significantly with nitrogen concentration.

In the UNCD films, we find that activation energies E_1 and E_2 are almost same (~0.145 eV) for the films grown with a low amount of nitrogen (1%) in the plasma and,

as the nitrogen concentration in the films increases, E_1 decreases to 0.07 eV for 5% N_2 and thereafter it saturates at 0.016 eV for 10% and 20% N_2 [129]. A plot of variation of activation energies E_1 and E_2 as a function of nitrogen concentration is shown in Figure 2b. Activation energy E_2 decreases much faster than E_1 and ultimately tends to zero (see Fig. 2b). A similar type of variation of different activation energies (both for E_1 and E_2) with dopant concentration has been reported for B-doped diamond where diamond becomes a perfect semiconductor with almost zero activation energy at a boron concentration of more than $(2–3) \times 10^{20}/cm^3$ [135].

For N-doped diamond films the value of E_2 depends on the spacing of the donors and we observe it changing rapidly in the range between 0 and E_1 with doping level. A kink in the slope of the conductivity curve is seen (see Fig. 2a) which moves toward high temperatures with the increase of impurity level. For intermediate concentration (5% N_2), the slope of $\ln \sigma$ vs T^{-1} curve changes at about 33 K, whereas for 10% N_2 this change appears at about 50 K. It seems that for high nitrogen concentration overlapping of impurity (nitrogen) wave functions becomes appreciable and the impurity levels broaden into a band so as to make conduction within the impurity band possible. Impurity conduction at low temperature becomes dominant over the regular band conduction as all the charge carriers squeezed out of the regular band. For high carrier concentration, in 20% N_2 samples, a sharp transition in conductivity is not observed indicating the material tends to become a degenerate semiconductor, as also seen in B-doped diamond [120, 135].

From fitting of conductivity curves the values of E_3 as well as σ_3 are much lower than E_1 and σ_1 and even lower than E_2 and σ_2, suggesting that hopping conduction is negligible in the N-doped UNCD films (Fig. 2a, b). Also, for hopping conduction the value of the activation energy should rise or at least should not decrease with the increase of doping concentration. The activation energies decrease with nitrogen concentration in these samples; thus a major contribution of hopping conduction, as proposed earlier, can be ruled out [137] since hopping conduction strongly depends on the degree of compensation of carriers. As the degree of compensation (defined by $K = N_a/N_d$; N_a, N_d are acceptor and donor concentrations, respectively) is as low as 0.001, transition to hopping conduction at low temperatures may not be seen in the N-doped UNCD films. The possibility of hopping conduction will be discussed using the grain boundary model in the following.

Hall Measurements Carrier concentration and hole mobility of the oriented *p*-type diamond film as a function of temperature from 180 to 440 K have been determined by Hall effect measurements [120, 138]. The carrier concentration at room temperature was shown to be about 5.9×10^{13} cm^{-3}, and the acceptor ionization energy was calculated from the slope of the temperature dependent concentration to be ~0.346 eV. It was shown that the crystallographic morphology of the diamond films plays an important role in the electronic transport properties. The fact that the mobility is still less than that of similar B-doped films grown on single crystals suggests that the low angle grain boundaries do have deleterious effects on transport properties [138].

Hall mobility (μ) and carrier concentration (n) measurements in UNCD samples, grown with 10 and 20% N_2, at several temperatures between 400 and 5 K have been performed confirming electrons as majority carriers [129]. The results showed the highest value of carrier concentration ($\sim10^{20}$) ever found in n-type diamond or related materials indicating that nitrogen is very much soluble in these UNCD films. Therefore, formation of an impurity band at that concentration is feasible. Also noticed was a fairly high value of room temperature mobility (~10 cm^2/V s) for the sample prepared using 20% N_2. This value of room temperature mobility is obviously not comparable to that of SCD [113] because of the size difference of the crystals but is better than a-Si and much better than P-doped diamond [139]. Mobility versus carrier concentration of NCD films showed that both μ and n are increasing with nitrogen concentration. This relationship shows that N_d increases at a higher rate than N_a with nitrogen concentration. And the increase of the mobility with nitrogen concentration at room temperature suggests that μ is more affected by phonon scattering than by impurity scattering. TEM study suggested that the grain size in 20% N_2 samples is two times larger compared to that of the 10% N_2 sample (Fig. 1a and b). Therefore, the increase of mobility within the diamond grains, with the increase of nitrogen concentration, can be explained. This relatively high value of mobility is not possible from hopping conduction. Also, for a particular nitrogen concentration, n increases with temperature whereas μ decreases quite gradually with temperature (see Fig. 3). It is known that the mobility of carriers is strongly dependent on acoustic phonon scattering (at high temperature) as well as on impurity scattering (at low temperature) where the mobility varies as $T^{-3/2}$ and $T^{3/2}$, respectively [7, 140, 141]. In practice, the high temperature mobility due to lattice scattering of diamond was found to vary as $\mu(T) = \mu_0 T^{-s}$ with s varying between 1.5 and 2.8 [7, 138, 140, 141]. However, from this limited number of data points it is difficult to conclude the exact temperature dependence of μ. For the 20% N_2 sample a slight increase of μ between 400 and 50 K confirms the semimetallic nature of the sample where phonon scattering is dominant. The temperature dependence of n is similar to what is seen in boron-doped diamond [135]. The donor activation energy calculated from the carrier concentration is much smaller than that observed from any other N-doped diamond films establishing that nitrogen can create a shallow donor level in NCD.
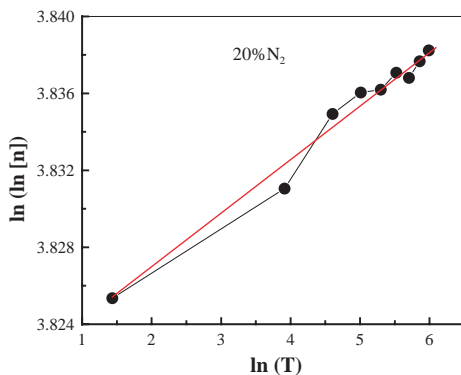
Impurity Conduction According to the complex conduction model described earlier impurity conduction refers to the direct transfer of holes between impurities without entering into the valence band. Several studies [120, 135, 142, 143] have reported impurity conduction in synthetic single-crystal diamond including very heavily B-doped MCD films. Experimentally, a transition between conduction mechanisms is indicated by a maximum in the plot of Hall coefficient (or a minimum in carrier concentration) versus inverse temperature, occurring at the same temperature as a knee in the plot of resistivity versus inverse temperature. Malta et al. [120] showed a knee in the resistivity curve and corresponding minimum in the carrier concentration. Since the mobility is not the same in different conduction regimes, mobility declined rapidly with decreasing temperature within the impurity conduction regime. It was also observed that conduction transitions always occurred at higher temperatures in the MCD films than homoepitaxial films [120]. At high temperatures, hole concentration was similar to the hole concentration in polycrystalline and homoepitaxial films [120].

Though UNCD films showed a change of slope in the temperature dependent resistivity curve of the 5% N_2 sample, no similar kind of change in Hall mobility and carrier concentration was observed. This is either due to the presence of sp^2 defect levels or no impurity conduction present in the material (unlike true doping in bulk or MCD).

Comparison with Boron-Doped Diamond B-doped type Ib synthetic diamond showed, in the range 10^{18}–10^{19} cm^{-3}, an activation energy of 185 meV between 500 and 1000 K and around 368 meV between 300 and 500 K [142]. For a doping level lower than 10^{19} cm^{-3}, the conduction process is governed by valence band conduction. For 2.5×10^{19} cm^{-3}, a new conduction process increases the conductivity at room temperature that increases strongly with the boron concentration, as seen in the MCD films with a higher doping level, and is attributed due to hopping between ionized and neutral acceptors within the impurity band. It has been suggested that hopping is of the nearest-neighbor hopping (NNH) type. For a doping level of 2.7×10^{20} cm^{-3} or higher, the conductivity decreases with temperature suggesting a metallic behavior, in accordance with the Mott transition expected around 2×10^{20} cm^{-3} [143].

Although above room temperature activated behavior has been seen for boron-doped p-type diamond, in the low temperature region conductivity is hopping type, similar to N-doped UNCD films. However, regarding Hall mobility an important difference was noticed. In P-doped SCD and MCD mobility is found to be decreasing with the increase of carrier concentration [135], whereas for N-UNCD film mobility increases with carrier concentration. Hence the doping of N-UNCD films is not exactly the same as the doping in the P-doped diamond. However, more careful work is needed in this direction.

In the case of N-doped UNCD films the change of conductivity with nitrogen concentration is different. In the low concentration regime conductivity increases with nitrogen concentration in the films. Beyond 5% N_2 in the plasma there is no increase of nitrogen concentration in the

Figure 3. Variation of carrier concentration of NCD film prepared with 20% N_2 was tried to fit with a power law of temperature.

films though conductivity and carrier concentration keep on increasing with increasing gas-phase nitrogen, as shown in Figure 4 [56].

Doping of UNCD films appears to be different from the P-doped diamond where clear distinctions between the band, hopping, and metallic conduction were observed. Therefore, the increase in conduction can be assigned to grain boundary or interface between diamond grains and the grain boundary regions. In the following section we discuss the temperature dependent conductivity by hopping conduction and percolation through the grain boundary.

Effect of Grain Boundary in n-Type Conduction Malta et al. [120] attempted to establish effect of grain boundary on the conductivity in the P-doped diamond. Due to the effect of GB scattering mobility of carriers in MCD can be significantly dropped compared to that in SCD. GBs may act as trapping centers for charge carriers leading to accumulation of charge at the interface of the crystallites thus forming a potential barrier. Traps at GBs deplete the concentration of carriers in the crystallites. Carrier trapping creates a space charge region in GB. As a result, mobility of carriers crossing the grain boundary is significantly reduced and conductivity activation energy may be reduced to a very small value.

In MCD the effective mobility of the carriers was found to change with size of grain as $1/\mu_{eff} = 1/\mu_{GB}(2W/L) + 1/\mu_{Grain}(1 - 2W/L)$, W = depletion width, L = grain size [120]. For the UNCD films both GB and grain are increasing with increase in nitrogen concentration in the plasma but μ_{Grain} is much higher than that of GB as GB is mostly made up of amorphous carbon (a mixture of sp^2- and sp^3-bonded carbon). The ratio W/L can fairly be considered as 0.1 and, therefore, the effective mobility will be dominated by μ_{Grain}. In a carefully carried out analysis by Malta et al. [120] it was observed that the carrier concentration of B-doped MCD does not change from the corresponding homoepitaxial diamond, suggesting almost no depletion of carriers. Moreover, change of mobility cannot be explained by the GB model.
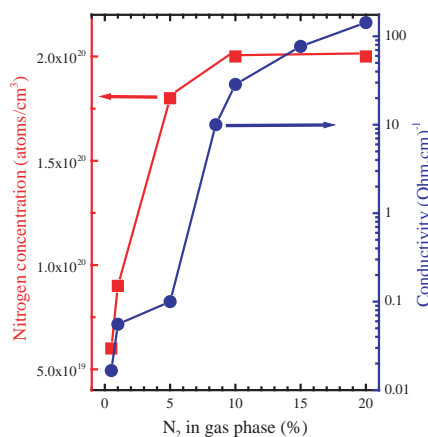
Figure 4. Total nitrogen content (left axis) and room temperature conductivity (right axis) as a function of nitrogen in the plasma. Reprinted with permission from [56], S. Bhattacharyya et al., *Appl. Phys. Lett.* **79**, 1441 (2001). © 2001, American Institute of Physics.

But GB can accommodate some impurities that can increase scattering of the carriers and reduce the mobility.

It was suggested that for heavily doped materials, as in the case of UNCD, doped with nitrogen, the depletion of carriers would be very less and hence diamond GB should have little effect on the transport properties, as also reported by Nihimura et al. [144]. However, as mentioned in the previous sections, the recent calculations, carried out by Kleblinski et al. [131] and Zapol et al. [132], showed GB playing a major role in the NCD films in current conduction. As mentioned before, nitrogen in MCD films usually forms a deep donor level with activation energy of 1.7 eV. Therefore, it is unlikely that the enhanced conductivity in UNCD is due to nitrogen doping of the grains. With the theoretical calculations indicating that nitrogen is favored by 3–5 eV for GB doping, a proposal that the nitrogen in these films is present predominantly in the GBs and not within the grains has been made [132]. In the following we review current conduction in disordered materials.

3.2.5. Transport in Disorder Material (Here Grain Boundary)

Beyond the Mobility Edge In this regime transport is governed by carriers excited beyond a mobility edge into extended state at E_c or E_v (conduction and valence band edge, respectively) giving an activation energy $E_\sigma \cong E_c - E_v$ (or $E_F - E_v$) at high temperatures. This should give an Arrhenious dependence of conductivity $\sigma = \sigma_0 \exp(-E_\sigma/kT)$. As a result, band conduction is seen at high temperatures. The second mechanism is the hopping between localized states at low temperatures.

Hopping through Localized States A number of amorphous semiconductors and amorphous carbon share temperature dependent conductivity as $\sigma = \sigma_0 \exp[-(T_0/T)^{p+1/p+4}]$ where p is a constant and depends on the distribution of states near the Fermi level as $N(E) = N_0 E^p$. For $p = 0$, 1.5, and 2 we get $\exp(-T_0/T)^{1/4}$, $\exp(-T_0/T)^{1/3}$, $\exp(T_0/T)^{1/2} \Rightarrow$ variable range hopping in three, two, and one dimension, respectively.

For the variable range in three dimensions (3D), T_0 can be expanded as $T_0 = 16\alpha^3/[k_B N(E_F)]$, where k_B corresponds to Boltzmann constant and α^{-1} is the decay length of localized states. The average hopping distance R and average energy for hopping W can be expressed as $R = 0.75[3/(2\pi\alpha N(E_F)k_B T)]^{1/4}$ and $W = 3/[4\pi R^3 N(E_F)]$.

Also, the pre-exponential factor in conductivity can be written as $\sigma_0 = e^2 N(E_F) R^2 \gamma_{ph}$ where γ_{ph} is the phonon exchange frequency [145]. From these parameters and fit of conductivity data the Bohr radius was found to be 0.3–0.8 nm at acceptor density corresponding to a resistivity of about 10^3–10^{-2} Ω cm.

Percolation Percolation or network conductivity has been used in many heterogeneous systems to explain conductivity. This type of conduction through a network of resistivity that interconnects the sites of localized states can be a substitute for conduction through a localized state as described previously. From extensive theoretical work it is understood that percolation treatment of hopping predicts behavior similar to the previous ones, like $\sigma = \sigma_0 \exp(-T_0/T)^{1/4}$ or $T^{-1/2}$ for

constant and quadratic density of states, respectively. Moreover an exponential distribution $N(E) = N(E_F) \exp(E/E_0)$ can be used to account for the downward deviation from the linear dependence of $\ln \sigma$ vs $T^{-1/4}$ [145].

In the case of UNCD films [56, 129], grown using 1% N_2, temperature dependent conductivity showed variable range hopping (VRH) in 3D (i.e., $T^{-0.25}$ law) throughout the temperature range (Fig. 5a). This can be explained by opening up some percolation path of the network or bridging by the impurity (suggested by previous models) that just crossed the percolation threshold. Typical hopping distance and density of states $N(E_F)$ for 1% N_2 sample are about 1.2 nm and 6E20 cm^{-3}, respectively. The value of the hopping distance decreases with nitrogen concentration whereas, $N(E_F)$ is found to increase. HRTEM of the sample also showed a little increase of the width of the GB in the films grown using 1% N_2 film compared to the undoped one [56, 129]. For the film grown using 5% N_2 a much wider GB has been noticed. Therefore, the percolation threshold has already been crossed. The $T^{-0.25}$ law works in the low temperature region, namely 15 to 62 K, whereas $T^{-0.5}$ law works over a wider temperature range (15 to 100 K corresponding to VRH with the presence of Coulomb gap). Conductivity of the UNCD films grown with 10 and 20% N_2 has been fitted with $\exp T^{-0.5}$. For the sample grown using 10% N_2 linearity has been found in the range between 5 and 65 K with $\exp T^{-0.5}$ fit though no such linear behavior was observed in the sample grown using 20% N_2 films. Finally, linearity has been searched for T^{β} with ln(conductivity) and it was found to be successful through the range for 10 and 20% N_2 samples with different values of β (Fig. 5b). The values of β is not close to the exponent of VRH conduction. Finally, conductivity of 10% and 20% N_2 samples throughout the temperature range has been successfully fitted as a combination of band and hopping conduction [129]. The fitted model is very much in agreement with grain boundary conduction of UNCD. More work is needed to understand the meaning of current conduction.

Recent tight-binding studies of nitrogen substitution in the GBs show that new electronic states associated with carbon π bonds and dangling bonds are introduced into the fundamental gap and that there are unoccupied states available near the Fermi level [132]. When nitrogen is introduced into the GBs, the associated carbon dangling-bond state is
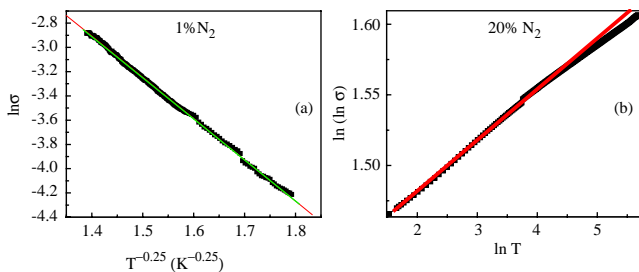
above the Fermi level and donates electron-to-carbon defect states near the Fermi level, causing it to shift upward (i.e., toward the CB). Thus, it is not unreasonable to imagine that nearest-neighbor hopping or other thermally activated conduction mechanisms could occur in the GB and result in greatly enhanced electron transport. The conduction may occur via the new carbon states in the bandgap. Therefore, a more developed theoretical model should be suggested to explain successful nitrogen doping, especially semimetallic conductivity of UNCD films at high nitrogen concentration and fairly high Hall mobility of the films [56].

Thermoelectric Power An important feature of the UNCD samples prepared with 20% N_2 in the plasma is the high thermoelectric power (S) at room temperature of about -18 μV/K. However, similar value of S with positive sign can be seen in quasi-amorphous (graphitic) carbon that was described by a model based on the series connection of regions with metallic conductivity, hopping conductivity, with variable and constant hopping length [56, 129].

For metallic conductivity, S linearly depends on temperature as $S = k_B/e\pi^2/3k_BT/\Delta(1 + p)$, where Δ is the shift of the Fermi level and p is a parameter, which depends on the predominant mechanism of carrier scattering, which in turn depends on the size of the crystallites.

Thermopower of the regions showing variable range hopping is proportional to the square root of temperature and can be expressed as $S_2 = k_B^2/2e(T_0T)^{0.5}d\ln N(E_F)/dE|_{E=EF}$. This expression does not hold good in the UNCD films reported by Bhattacharyya et al. [129].

For constant range or NNH $\sigma = \sigma_0\exp(-E/k_BT)$, thermoelectric power can be expressed as $S_3 = k_B/2e(E_c - E_F/k_BT + S_0)$ or $S = -1/|e|(E_s/T) + S_0$, where E_c is the CB mobility edge and S_0 corresponds to heat of transfer. The value of E_s is very small and close to E_σ. A shallow donor level close to CB has been suggested from these values.

In the N-doped UNCD films grown by Bhattacharyya et al. [56, 129], S showed negative sign and its temperature dependence is close to a straight line tending to zero at lower temperature [14]. For perfect fitting of the temperature dependence of S different models for metal as well as semiconductors described previously have been tried but were not successful. Finally, keeping in mind the temperature dependence of electrical conductivity, the thermoelectric power of these samples has been fitted as a combination of reciprocal temperature and temperature as follows.

$S(T) = b_1T + b_2/T$ where the first term works for metallic conductivity particularly at a high temperature regime and the second term works at a low temperature regime as observed for semiconductors with small bandgap. However, the overall trend can be attributed to metallic conduction that is more favorable for grain boundary regions. From the sign of S n-type conduction of N-doped films is confirmed. An important difference can be noticed from ta-C films where S was very small and therefore no clear temperature dependence could be observed [122].

3.2.6. Comparison with ta-C

The ta-C films were prepared, in general, by filtered cathodic arc from a graphite target with either flowing nitrogen or bombarding the growing film with nitrogen ions from

Figure 5. (a) Temperature dependent conductivity of NCD film shows variable range hopping for a low amount of nitrogen (1% N_2) in the plasma [$1/T$ is scaled to 1000/T, read abscissa as $(1000/T)^{0.25}$] and (b) temperature dependent conductivity of NCD film shows power law dependence for a high amount of nitrogen (20% N_2) in the plasma.

a Kaufman-ion source. For the discharge voltage of 50 V at the ion source, the ratio of N to C atom arrival rates (Q_r) was found to follow the relationship $Q_r = 1.7 \times j_N/j_C$, where j_N and j_C represent the current densities of nitrogen and carbon ions, respectively. The gas pressure in the chamber was maintained at about 2×10^{-2} Pa. The stoichiometry and density of all the *ta*-C films were determined by elastic recoil-detection analysis [122, 126].

It has been reported that nitrogen incorporation increases the conductivity in *ta*-C [121, 122, 146]. This could be due to either graphitization of the films or nitrogen doping. The thermoelectric power of *ta*-C is positive and acquires a low value (+0.1 mV/K, indicating that current conduction takes place via the valence band extended states), which falls to a few μV/K (a variable range type conduction) when doped by nitrogen. It seems that E_F does not move compared to CB below a doping level of about 10^{-4} where a constant density of states of the CB tail can be found [121]. In addition, it was suggested that beyond an impurity level of approximately 5%, electronic transitions take place through thermally excited electrons in the CB. The problem concerning a small amount of nitrogen incorporated into *ta*-C was investigated mostly by calculations based on schematic models [121]. It was proposed that conductivity increases by a few different routes: the first occurs by the formation of N_4^+, a nondoping configuration with a positive charged state of tetrahedrally bonded nitrogen atoms where hopping conductivity increases. Second, substitution of C in tetragonal configuration by nitrogen atoms creates N_3^0 (i.e., a nondoping and charge neutral state of trigonally bonded nitrogen atom where E_F moves with respect to the band edges, which have high density of localized states). Third, conductivity can also be enhanced by the formation of $N_{3\pi}$ and $N_{4\sigma}$ configurations which means that nitrogen in the doping configuration has three π bonds and four σ bonds, respectively, with one free electron in each case [121]. Although a quantification of doping efficiency is difficult, it is commonly believed to be very low. However, all previous ideas were developed for the low nitrogen and low concentration of sp^2-bonded carbon where the optical gap seems to remain unchanged and the nitrogen doping was suggested to be σ type [121]. It was also proposed that nitrogen doping of *ta*-C is highly compensated (i.e., connected to a large number of dangling bonds, which also need to be compensated by more nitrogen atoms bound in substitutional site) [122].

The conductivity rises by four orders of magnitude (about 4.5 S cm^{-1}) in *a*-CN15 (15% N in the film) compared to *ta*-C and fell to a local minimum in *a*-CN17 (17% N in the film). Conductivity remains almost unchanged in the range between 19% and 23% of nitrogen and increases in *a*-CN26 (26% N in the film) followed by a slight decrease in *a*-CN30 (30% N in the film). Conductivity values measured at 77 K do not change over a wide range of nitrogen concentration. The logarithmic variation of conductivity with inverse of temperature of these samples, as shown in Figure 6, in the temperature range between 80 and 300 K has been fitted with Mott's variable range hopping conduction in three dimensions. This is illustrated in Figure 7. Similar results have been obtained from the nitride carbon films prepared from magnetron sputtering [147]. Due to the high concentration of defects an Arrhenious-like plot seems to be difficult
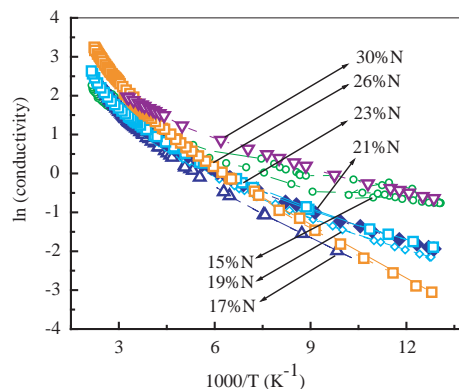
Figure 6. Temperature dependent conductivity of nitrogen doped *ta*-C films does not show Arrhenious type (activated) behavior.

in these materials. However, there are other reports [148] available where temperature dependent conductivity can be fitted as linearly dependent of inverse of temperature but only in the high temperature region. It is shown that Tauc gap first decreases sharply with nitrogen concentration followed by an increase. It seems that temperature dependent conductivity is very much dependent on the way sample is prepared (i.e., the way defects have been introduced in the materials). Chen et al. [149] also found variable range hopping type temperature dependent conductivity for nitrogen incorporated *ta*-C films where the bandgap was found to decrease from 2.5 to 1.6 eV.

One of the most important features of nitrogen (between 15 and 29%) incorporated *ta*-C is the very small value of *S* at room temperature (1–10 μV/K) for all samples and that they do not show a large change even if the temperature is lowered to 100 K. A change of *S* appears at lower temperatures, either in upward or downward direction, depending on the nitrogen concentration. At low nitrogen concentration (e.g., in *a*-CN15), *S* is negative throughout the temperature range followed by a sharp decrease below about 87 K, suggesting an *n*-type conduction as also discussed earlier. In *a*-CN17, *S* has a value very close to zero. In *a*-CN19 to *a*-CN23, *S* is positive and remains almost unchanged down to the lowest temperature of measurement suggesting a *p*-type conduction. Finally, in *a*-CN26 and *a*-CN30, *S* rises sharply below 100 K (see [122] for the temperature dependence). Only a very small variation of *S* was observed between the
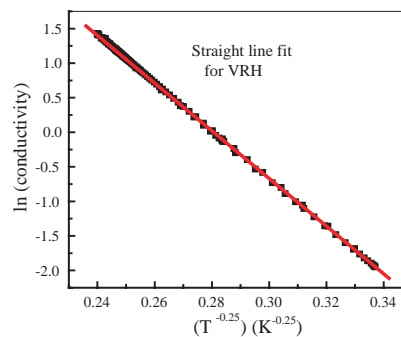
Figure 7. Temperature dependent conductivity of nitrogen doped *ta*-C films obeys variable range hopping in the low temperature regime.

nitrogen percentage of 19 and 30. Like temperature dependent conductivity thermopower, as a function of inverse of temperature, cannot be fitted as a single straight line that is normally seen in doped semiconductors. Also, S is not a linear function of temperature and does not approach to zero while lowering temperature unlike metallic samples [122]. It seems that the mechanism explaining the variation of S in the low temperature regime is quite complicated and more work is needed for a complete understanding.

At the end of this section we can accommodate discussions on the conductivity of amorphous carbon with nanodiamond inclusions where the sp^2 percentage was 60% in the undoped films. These samples are prepared at low pressure (2 mTorr) by ECR plasma from a mixture of methane, argon, and nitrogen. Nitrogen (5 at%), incorporated in the samples, increased the sp^2-bonded carbon in the films to above 80%. As a result conductivity was found to increase up to 50 times compared to the conductivity of the undoped sample. It should be noted that here the conduction takes place due to a large change of film microstructure and defects [150].

Following the approach in the previous section we look into the reasons behind the increase of conductivity in ta-C films after nitrogen incorporation. From EELS measurements, an increase of the π^* peak relative to the σ^* peak has been observed when the nitrogen percentage increases in the ta-C films. This means that graphitization took place in the films as a result of nitrogen incorporation to a large extent. From conductivity, it was shown that graphitization and defects gave rise to relatively high conductivity to doped ta-C films [151].

In summary, from the aforementioned studies we can conclude that in ta-C films conductivity arises from the sp^2-bonded carbon or from the nitrogen related (charge transfer) defects when nitrogen is introduced in the films. No truly activated conduction but only a variable range type hopping conduction can be observed. As a result, the conductivity in the films does not increase drastically with nitrogen concentration in the plasma. Hall mobility also remains very low. This is true for high nitrogen concentration in the films that form CN alloy. However, in the UNCD films the change of conductivity with nitrogen concentration is drastic in spite of the fact that the increase of percentage of sp^2-bonded carbon is very small. For the films grown with low nitrogen concentration, conductivity is explained by the percolation model and variable range hopping. In this case the nitrogen impurity in the films acts as a bridge in the grain boundary region and induces conductivity. For the films grown with higher nitrogen concentration, the grain boundary opens up and contributes to high conductivity. Both variable range hopping and activated band conduction were observed.

4. FIELD EMISSION

Field emission (FE) is considered to be one of the most interesting properties of diamond and related materials. This property can be useful for making cold cathode field emitters and other vacuum microelectronic devices. Though typical metal or semiconductor emitters posses high work functions, a negative electron affinity (NEA) of certain diamond planes allows one to emit electrons with an application of low electric field. Semiconductors and insulators can have a NEA if the minimum energy of their conduction band electrons is above the minimum energy of electrons in vacuum. At the same time, a low threshold energy can also be explained by geometric electric FE, where field can be enhanced up to 100 times. Apart from the electrons tunneling from a metal or semiconductor directly into vacuum, there are also other mechanisms proposed where electrons can tunnel from a metal to diamond surface and can be accelerated to energies sufficient to be ejected into vacuum. If a stable and reproducible emission from diamond or related materials can be obtained it would eliminate the complicated and expensive process of fabricating sharp microtips to provide geometric field enhancement.

For good FE from a diamond surface it should be conductive. Insulating undoped MCD films cannot produce sustained electron emission. MCD films with either none or with a very low percentage of sp^2-bonded carbon emit poorly with threshold emission fields typically of ~30 V/μm and having an unsatisfactory surface uniformity. There should be some conducting path for transportation of electrons. This can be achieved either by n- or p-type doping of this material [115], which could shift the Fermi level to near the CB edge, or by creation of defect states. However, p-type diamond does not emit well because the electron resides deep (>5 eV) below the Fermi level. Therefore, n-type diamond or diamond with defects, where the Fermi level is close to the CB, should be ideal for emission. Although an excellent low FE from diamond and diamondlike materials has been well known, practical application of emission is limited due to lack of reproducibility, consistency, and sustained emission for a long time. Zhu et al. [63] overcame this problem by using hydrogen plasma treated NCD and obtained electron emission of 10 mA/cm^2 at applied field of 3–5 V/μm [63]. It should be noted that the diamonds in this case are undoped and are not separated by grain boundary regions. Thus, the emission was explained to appear from inherently defective structures of nanodiamond.

Coming back to doped diamond films we find some interesting reports on their field emission character. FE of P- and B-doped diamond has been studied and it is found that doping enhances FE much more than the enhancement factor. Also, the type of doping as well as its concentration appears to be very important for the emission [152]. Okano et al. [152] reported N-doped CVD diamond (from urea) with an extremely low threshold voltage. In fact, in N-doped films the emission threshold voltage was found to be much lower than that of P- and B-doped diamond films [152]. They suggested a very low activation energy of the N-doped films. These emission characteristics are attributed mostly to the high defect density of states [63, 152–155].

Nitrogen always been found to enhance the field emission properties of nanodiamond as well [31]. In the case of UNCD, it is illustrated in a plot of variation of field emission current with electric field of UNCD films doped with 0.5 to 20% N_2 in the plasma in Figure 8. Also, in terms of film morphology and structure, NCD was found to be an excellent field emitter [32] showing the lowest onset voltage as well as the highest current density ever reported. Ultimately,
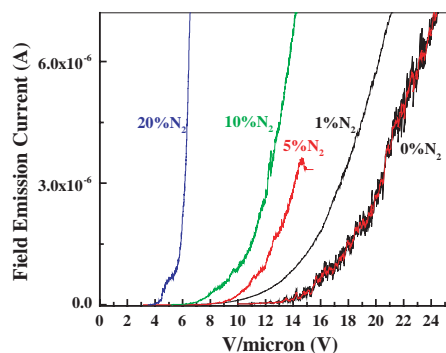
Figure 8. Variation of field emission current with electric field of NCD films doped with 0.5 to 20% N$_2$ in the plasma.

there were efforts to combine both nanostructured carbon (e.g., nanodiamond) and *n*-type conduction to observe excellent field emission in the films. We shall be discussing this effect further in this section.

As discussed, field electron-emission properties in diamond and related materials are strongly dependent on the film structure and on its composition. The emission drastically improves with better uniformity and hysteresis with an increase in *sp*^{2}-bonded carbon content in the diamond films. The best emission properties correspond to a composite structure of an MCD film, where coarse-grained diamond phase coexists with an essential amount of nanocrystalline graphite [156]. Jou et al. [157] and Zhirnov et al. [158] also observed the same phenomenon. Unfortunately, it is difficult to measure quantitative relations between the two carbon phases in the diamond films to determine a relationship between the emission threshold and an exact structure of the film. Pure nanodiamond compacts emit very poorly (thresholds were ∼200 V/μm); the optimized diamond-to-pyrocarbon relationship allows one to observe the emission at fields as low as 1 to 2 V/μm accompanied with satisfactory surface uniformity and the absence of hysteresis of *I–V* curves. From scanning tunneling microscopy it has been understood that the emission zones corresponded to the top of some grains, agglomerated from a number of smaller diamond particles and having no sharp tiplike protrusions. Moreover, the electrical resistivity on the top of the emitting grains demonstrates relatively high ("nongraphite") values, not like for an insulator (diamond), but rather typical for a semiconductor or a thin two-dimensional conducting graphitic layer. A field emission threshold as low as 3 V/μm was observed by Karabutov et al. [156] who found that emission came from the diamond/*sp*^{2}-bonded-carbon interfaces which are very conducting. It is proposed that quantum well effects at thin carbon nanolayers and insulator/graphite interfaces are responsible for the emission.

In other studies, Wang et al. [159] grew uniform NCD film, consisting of diamond grains with an average size of 10–60 nm, by the MPCVD technique using a gas mixture of nitrogen–methane–hydrogen. Field emission results showed that the threshold electric field increased, whereas the emission current density and the number of emission sites decrease with increasing mean diamond grain size. The film with a small grain size of 10 nm has a threshold electric field of 1.5 V/μm and reaches an emission current of

780 μA/cm^2 at electric field of 3.5 V/μm. The field emission characteristics of the NCD films grown on Si substrates in the MPCVD system, simply by replacing the Mo substrate holder with a graphite substrate holder using conventional diamond growth conditions [160], showed that small-grained film has low emission threshold and a high emission current. NCD field emitters were prepared using porous silicon as host matrix by Cai et al. [161]. NCD was deposited on porus Si substrates using 2% CH$_4$/H$_2$, 550 W microwave power, 30 Torr pressure, and 850 °C substrate temperature. SEM studies revealed diamond nucleation occurring at the edges of the etched pores and the nanosized grains partly embedded in the pores of the substrate. Samples with this structure showed excellent electron field emission properties. In the sample, with the smallest NCD grains, the emission current density exceeded 10 mA/cm^2 when the applied electric field was 3 V/μm.

Studies on radiation induced structural changes and electronic properties (i.e., conductivity, optoelectronic properties) of various kinds of films including amorphous carbon films have been going on for a long time. Using ion irradiation there have been efforts to increase or decrease defects in the electronic structure by changing the morphology and structure of diamond and related materials. This in turn can modify the field emission properties of the surfaces of the diamond and related films. It was shown by Jiang et al. [162] in their most recent study that heavy boron incorporation (more than 3000 ppm) using a nontoxic gaseous trimethylborane and hydrogen influences electron field emission properties and intrinsic stress of NCD films. The B-doped NCD films were continuously bombarded by H$^+$ and hydrocarbon ions. As a result of boron incorporation, the B-doped NCD films showed a lower intrinsic compressive stress. Low-field electron emission of 14 V/μm, much lower than that prepared without boron, and high emission current were also the characteristics of the B-doped NCD films consisting of nanosized diamond grains, showing a long-term stability. Gupta et al. [163] tried to improve FE properties of nanocrystalline carbon (graphite) composite by ion irradiation. They prepared MCD and nanocrystalline carbon thin films by MPCVD (a process similar to that described in Section 2) and performed gamma radiation having doses of 1, 5, and 20 Mrads in order to study the radiation-induced structural transformation and the corresponding changes in the electron field emission properties. A dramatic improvement in the emission properties was observed in MCD films only after a cumulative dose of 26 Mrad, while for nanocrystalline carbon a relatively small but systematic decrease in turn-on field was observed from 9 to 4 V/μm with increasing gamma radiation dose. The enhancement in the electron field emission properties of diamond was attributed to the structural defects with their associated electronic defect states produced by the radiation-induced microstructural transformation and *sp*^{2}-bonded carbon channels. In addition, it was observed that the nanocrystalline carbon films underwent much less significant net microstructural changes compared to MCD films upon irradiation. This was explained in terms of two known mechanisms taking place simultaneously: graphitization of diamond and conversion of graphite to diamond, both under high-energy radiation at ambient temperatures. This internal

bonding interconversion between sp^2- and sp^3-bonded carbon appears to be making their nanocrystalline carbon films relatively radiation insensitive. Based on this, the authors proposed fabricating radiation buffer materials to prevent radiations from reaching sensitive materials. Gupta et al. [164] also studied enhancement of field emission by incorporation of sulfur in MCD and nanocrystalline carbon films. The S-assisted films are shown to have lower turn-on fields and steeper rising current as compared to those grown without S addition. The lowest onset voltages achieved were 12 and 4 V/μm respectively in S-assisted MCD and nanocrystalline carbon films.

Now we come to discussion of N-doped UNCD films as described in Section 3.2.4. The highlights of these films, as also can be seen from Figures 8 and 9, are:

- Undoped UNCD films act fairly well in field emission with $V_{th} = 10$ V/μm.
- Threshold voltage of field emission decreases continuously with the increase of N_2 in plasma.
- Stable emission with V_{th} as low as 3.5 V/μm has been obtained with 20% N_2 film.
- The Fowler–Nordheim (F–N) equation, $J = 1.54 \times 10^{-6}(E^2/\phi)\exp(-6.83 \times 10^7 \phi^{3/2}/E)$, has been used to explain the emission, where $E = \beta E_0 = \beta(V/d)$, field enhancement factor $\beta = h/r$, J is current density, E is applied field, and ϕ is work function.
- The F–N equation shows multiple slopes indicating multiple conduction paths with different energy levels.
- This explains formation of more than one energy level, impurity and defect-induced levels (Fig. 9).
- Hopping conduction within the impurity band is possible. This is in agreement with nearest neighborhood hopping of electrical conduction.

There is some controversy [63, 153, 156] related to the origin of FE in diamond films; the electrons are field-emitted preferentially either from boundaries between crystal grains in diamond films or from the crystals themselves. Diamond quantum dots produced by explosive synthesis showed very

Figure 9. Schematic band diagram of conducting diamond shows enhancement of field emission.

important properties such as FE that could be used as cathodes. Combining experimental work on diamond films having nanocrystalline grain size with computations of electron properties at grain boundaries, it has been demonstrated that low threshold fields for electron emission correspond to large enhancements of the interband electronic state density [156]. The minimum threshold field (3–4 V/μm) from UNCD films is found to be the second lowest in different forms of diamond. Tight-binding electronic-structure simulations of a representative high-energy grain boundary in an NCD film show that both extended and localized electronic states are present in the energy gap region, where states are forbidden in bulk diamond [132]. The presence of these states allows significantly increased electronic transport along grain boundaries. It has been shown that hopping through localized π^*-states in sp^2-hybridized grain boundaries is a viable mechanism for transporting electrons from the interiors to the grain surface, where they can be emitted at low voltage. The demonstration of preferential electron emission from grain boundaries shows the importance of nanocrystallinity of diamond in NCD films, which has a high density and uniformity of grain boundaries. This work may have considerable technological impact on the production of materials that are capable of low voltage, uniform, high current density electron emission from large area sources for a wide range of applications, including flat panel displays, high power microwave sources, and ion thrusters for deep space missions.

For practical applications, smoothness of film surface and high mobility of carriers are considered important factors. The N-doped UNCD films prepared at Argonne National Laboratory (ANL) [31] are much more conducting and have smaller crystallites than the samples used by Zhu et al. [63] and Geis et al. [153]. The concentration of nitrogen in the UNCD film grown using 20% N_2 [129] is more than 2×10^{20}/cm³, an equivalent to 0.2% atomic concentration, which is much more than reported by Okano et al. [152, 154]. Moreover, the UNCD films grown by Bhattacharyya et al. [56] have lower surface roughness as well as reasonably good mobility suggesting that these films can offer much better applications.

Field emission of ta-C films is found to be comparable to NCD films and sometimes even better. Ta-C films prepared by filtered cathodic arc started emitting electrons by applying a bias of 250 V to the anode that was kept 60 μm away. Therefore, the threshold voltage was about 4 V/μm for undoped ta-C films. It was also found that ta-C films prepared by ECR plasma showed better field emission properties. Also nitrogen addition to the samples gave even better quality of field emission [165]. At the same time, there are other reports where nitrogen incorporated ta-C showed high threshold voltage in the range between 20 and 25 V/μm. The emitted electrons were suggested to arise from the Fermi energy where no field penetration occurred [166]. It is worth mentioning the improvement of field emission of amorphous carbon by nitrogen incorporation. Amaratunga and Silva found that the nominal onset fields for an emission current density of 10^{-3} mA cm^{-2} is 28 V/μm for 0% N, which decreases to 16 V/μm for 7% to 13 V/μm (11% N), 6 V/μm (14% N), and 4 V/μm (15% N) [167].
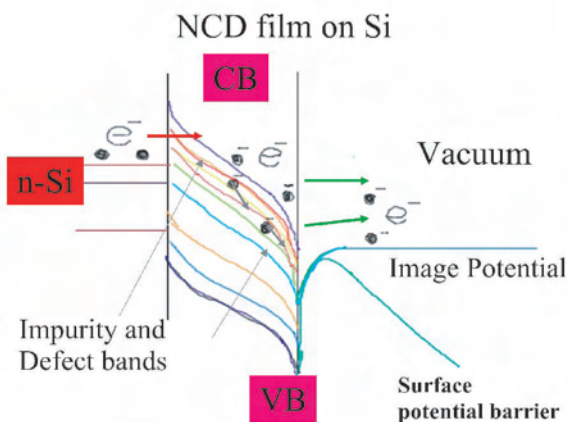
5. OPTICAL PROPERTIES

5.1. Raman Spectroscopy and Phonon Confinement

Extensive visible and UV Raman studies of NCD films find different features than bulk diamond and related films [42, 76, 168, 169]. Additional Raman features appear in NCD near 1140 and 1450–1500 cm^{-1}. The intense and sharp feature near 1332 cm^{-1} in visible Raman spectra, an unambiguous signature of cubic crystalline diamond, is found to be either completely missing or to be very weak in the NCD samples compared to single crystal or MCD films. In general, the visible Raman spectra of most of the NCD samples appear to consists of bands near 1150, 1350, 1500, and 1580 cm^{-1} [42]. Raman spectra of as-grown and annealed NCD samples grown by the BEG process (Section 2.2) [170] are shown in Figure 10. The band near 1150 cm^{-1} is mainly assigned to the presence of nanocrystalline phase of diamond [42, 76, 170–173]. It has also been observed as a weak band in the MCD films along with a sharp peak near 1332 cm^{-1} [27, 32, 36, 173]. Various groups have observed it repeatedly in the amorphous and NCD films grown by different techniques [27, 32, 36, 42, 169, 174]. For example, it has been observed in the Raman spectrum of amorphous diamond grown using low energy cluster beam deposition of carbon clusters with size distribution centered around C$_{20}$ [171] and has also been observed in the Raman spectra of NCD films grown using hydrogen deficient plasmas or by the BEG process (Fig. 10) [27, 32, 42, 170]. It was shown in the former study that the clusters keep the memory effect and, as C$_{20}$ clusters are sp^3 hybridized, the deposit turns out to be diamond in amorphous form. As described in Section 2.1.1, the latter method used a high concentration of Ar in Ar/H$_2$/CH$_4$ microwave plasmas [32], or CO/H$_2$ mixtures [27] or biasing [42] for the growth of NCD. At the same time, this Raman structure of the NCD films does not match with the Raman structure of NCD synthesized from transformation of C$_{60}$ [71] (Section 2.4) where only a cubic diamond feature was observed in the transformed
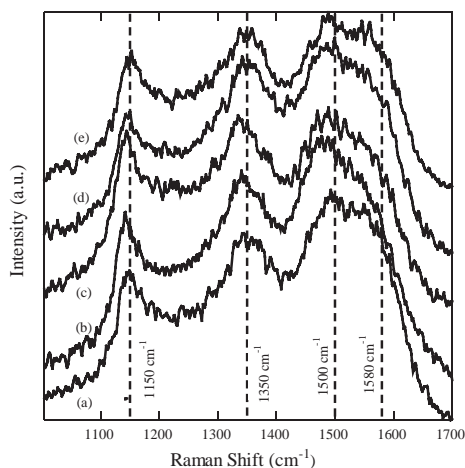
NCD platelets. The Raman intensity of the feature near 1450–1500 cm^{-1} varies proportionally with the intensity of the Raman feature near 1150 cm^{-1} as observed from most such spectra of NCD samples [29, 42, 61] and appears to be related to the disordered sp^3-bonded carbon in the films. The spectra of the samples, annealed at different temperatures, are further discussed in Section 6.

Recently the interest in the two Raman features increased when their assignment to sp^3-bonded carbon became controversial. Ferrari and Robertson argued that these two Raman features (1100–1200 and 1400–1500 cm^{-1}) cannot be related to C–C sp^3 related modes [168] and instead assigned them to *trans*-polyacetylene, or in other words, to sp^2-bonded carbon with the presence of hydrogen [168]. In another recent development, it was shown that nanophase diamond, consisting of diamond crystals of about 5 nm in diameter (Section 2.3) and largely free from aromatic sp^2-bonded carbon, displays a sharp peak near 1090 cm^{-1}, which is assigned to surface phonons of diamond [169]. It was thus concluded in the same report that a Raman feature in the range 1100–1150 cm^{-1} in NCD films, synthesized by CVD, may indicate that these films contain clusters of sp^3-bonded carbon of about 5 nm in diameter. At the same time, Sharda et al. [170] studied Raman spectra of the as-grown and annealed NCD samples (Fig. 10) grown by the BEG process (Section 2.2) and observed that the ratio of the Raman feature near 1150 cm^{-1} to the graphitic band G, which was shown in their various other studies to be related to the structural and mechanical properties of their NCD films, did not change significantly as a function of the annealing temperature. They argued, first, that if these features were related to hydrogen, their intensity should have decreased with annealing temperature, as the hydrogen should have started evolving from the samples after 200 °C [175]. Second, if these features were related to sp^2-bonded carbon, even without having any relation to hydrogen, their intensities should have increased with annealing temperature, as the concentration of sp^2-bonded carbon increases with annealing temperature [175, 176]. However, the plot of the intensity ratio of the Raman features near 1150 cm^{-1} to the graphitic G band, shown in Figure 11, did not follow the expected trends as a function of annealing temperature.

Figure 10. Raman spectra of the (a) as-grown and annealed sample at (b) 200, (c) 400, (d) 600, and (e) 800 °C. Reprinted with permission from [170], T. Sharda et al., *J. Nanosci. Nanotech.* 1, 287 (2001). © 2001, American Scientific Publishers.
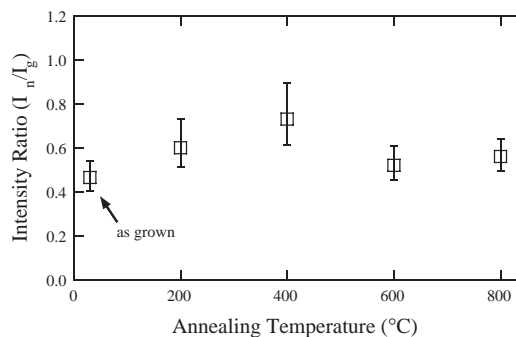
Figure 11. Plot of Raman intensity ratio of NCD (I_n) to graphitic G band (I_g) as a function of annealing temperature. The error bar is standard error in fitting the individual Raman curves. Reprinted with permission from [170], T. Sharda et al., *J. Nanosci. Nanotech.* 1, 287 (2001). © 2001, American Scientific Publishers.

Finally, cubic crystalline diamond features in the XRD patterns of their NCD films, shown in Figure 12, supported to some extent the conjecture that the Raman feature near 1150 cm^{-1} should be related to NCD. The full width at half maximum of the diamond peaks in the NCD films grown by the BEG process [41, 53] was in general observed to be high compared to the MCD films, which was well correlated with the fact that diamond nanocrystallites [32] were present in the films. No XRD peaks associated with graphite or features related to amorphous carbon were observed either in the as-grown films [41, 42, 53] or even in the annealed films in their study (Fig. 12). Therefore, they concluded that their results supported the assignment of the Raman feature near 1150 cm^{-1} to the presence of NCD (i.e., even if not originating solely from nanodiamond). Also, in the case of phase-pure UNCD films, visible Raman (514 nm excitation) shows a similar Raman structure to that described previously. Humps at about 1150 and 1450 cm^{-1} appeared for the entire sample range having different nitrogen concentration (Section 3.2). In general, Raman features in the visible range are very broad and can be analyzed only by deconvolution of the spectra. For example the peak at 1150 cm^{-1} seems to have convoluted with the 1332 cm^{-1} peak. These NCD related Raman features were much more prominent in undoped diamond.

The other bands near 1350 and 1580 cm^{-1} in the NCD samples are popularly known as graphitic D and G bands, respectively, which are related to graphitic islands. The D band appears due to the relaxation in the momentum selection rules of the Raman scattering process due to the small domain size in graphite. In fact, a similar argument is applicable to the appearance of the band near 1140 cm^{-1} due to the nanocrystallinity of diamond [173]. However, the higher or equal intensities of the graphitic bands in the NCD samples, as compared to the intensity of the band near 1140 cm^{-1}, may not represent a high amount of sp^2-bonded carbon in the NCD films. This is because the cross section
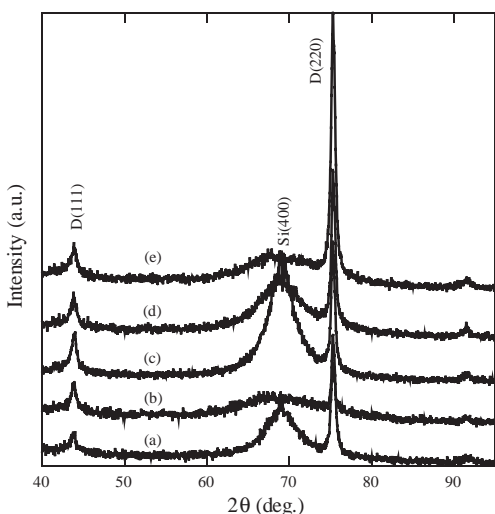
of Raman scattering is 50–60 times higher for sp^2-bonded carbon as compared to sp^3-bonded carbon, as reported by Wada and Solin [177]. In the case of the UNCD films the ratio of intensity of G to intensity of the diamond peak (near 1332 cm^{-1}) increases with addition of nitrogen [129, 178]. These results are consistent with the HRTEM picture showing an increase of grain boundary with nitrogen concentration [14, 129].

UV Raman spectroscopy has also been carried out on NCD films using 244 [129] and 257 nm lines [76]. UV-Raman spectroscopy and surface morphology of a film grown by the BEG process (Section 2.2), which shows a high intensity of the NCD related feature (1150 cm^{-1}) in the visible Raman spectroscopy (Fig. 10), are shown in Figure 13. Faceted grains of less than 30 nm in size are evident in the micrograph obtained by a high resolution SEM and the cubic crystalline feature near 1333 cm^{-1} in the UV-Raman spectroscopy is an unambiguous signature of those grains being crystalline diamond. The spectrum also shows a significant amount of the graphitic carbon in the films as evident by the G band at 1580 cm^{-1}. The additional intense feature, as observed in the visible Raman spectra (Fig. 10) of the films near 1140 and 1450–1500 cm^{-1}, was not observed, similar to what was shown by Ferrai and Robertson [168] while arguing that these features should not be assigned to any sp^3-bonded phases. In the case of undoped and doped UNCD films (Section 3.2), undoped films show a prominent diamond peak near 1330 cm^{-1}, the intensity of which is larger than the G peak [129]. The relative intensity of the G peak increases with nitrogen. In fact, the 1332 cm^{-1} peak is hardly observed in the films grown using more than 10% N$_2$. These results suggest that graphitization of the film has occurred by nitrogen incorporation.

Though the presence of the *trans*-polyacetylene at the GB of the samples cannot be verified due to the lack of extensive Raman studies, a similar sp^2 network at the GB of the sp^3-bonded carbon crystallites may be considered as the origin of the additional features observed in the visible Raman spectra of the NCD films.

Another interesting aspect of NCD films is phonon confinement in diamond nanocrystals. Researchers have

Figure 12. XRD patterns of the (a) as-grown and annealed sample at (b) 200, (c) 400, (d) 600, and (e) 800 °C. Reprinted with permission from [170], T. Sharda et al., *J. Nanosci. Nanotech.* 1, 287 (2001). © 2001, American Scientific Publishers.
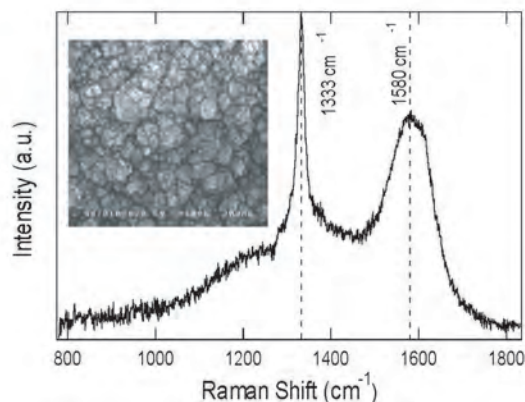
Figure 13. UV-Raman spectrum taken at 257 nm of an NCD sample. Inset is a high resolution SEM micrograph of the sample. Reprinted with permission from [76], T. Sharda et al., *Appl. Phys. Lett.* 80, 2880 (2002). © 2002, American Institute of Physics.

attempted to establish quantum confinement in nanodiamond by the upshift of the CB by the displacement of the C1s edge in the EELS spectra [179, 180]. Sun et al. [181] studied Raman spectra of diamond crystals of different sizes, calculated by a phonon confinement model originally proposed by Richter et al. [182] and extended by Campbell and Fauchet [183]. The general idea behind the downshifted and asymmetrically broadened diamond Raman line near 1332 cm^{-1} that they observed is as follows. Diamond nanocrystals should exhibit an asymmetric broadening and shift of the 1332 cm^{-1} diamond Raman peak relative to the diamond Raman peak from the bulk crystal. For an infinite crystal, only phonons near the center of the Brillouin zone ($q \sim 0$) contribute to the Raman spectrum because of momentum conservation between phonons and incident light. In a finite crystal, phonons can be confined in space by crystal boundaries or defects. This results in uncertainty in the phonon momentum, allowing phonons with $q \neq 0$ to contribute to the Raman spectrum.

The Raman line shape is calculated by superimposing Lorentzian line shapes centered at $\omega(q)$, weighted by the wavevector **q** uncertainty caused by the confinement:

$$I(\omega) \sim \int_0^1 4\pi q^2 \, dq \exp(-q^2 L^2/4)/(\omega - \omega(q))^2 + (\Gamma/2)$$

Where Γ represents the Raman line width. Here $\omega(q)$ is an approximate one-dimensional phonon dispersion curve and q can be expressed in units of $2\pi/a$. The crystallite sized L is in units of a, with $a = 3.567$ Å being the lattice constant of diamond. L was assumed to be equal to the particle size. The dispersion curve was assumed to be of the form

$$\omega(q) = A + B\cos(q\pi)$$

where $A = 1193.75$ cm^{-1} and $B = 139.25$ cm^{-1}. The Lorentzian linewidth Γ of the diamond peak was dependent on the particle size and assumed as $\Gamma = \alpha + \beta/L$ where the coefficients were calculated from the diamond peak at 1333 cm^{-1} for standard diamond particles of different sizes by UV-Raman spectroscopy. By changing particle size L, various Raman line shapes were calculated by the previous equation. Based on this, Sun et al. [181] produced, after normalizing, the calculated Raman spectra of diamond particle having sizes of 120, 45, 38, and 23 nm. The theoretical values of diamond particles in various sizes are found to be consistent with the experimental data measured by UV-Raman scattering. It is found that the asymmetric line shape, with some tailing toward low wavenumber, is well explained by the phonon confinement model. Although the scattering from defects can account for the symmetric part of the linewidth, the asymmetry part is much more than expected for a confined phonon line shape calculated according to the Gaussian confinement model for the particle sizes obtained from XRD. An alternative model for the confinement of phonons has also been discussed in the literature that involves the standing waves arising from the reflection of the phonons from the elastic–dielectric boundary [184].

Surface enhanced Raman spectroscopy (SERS) has also been employed to detect the presence of a small amount of nanodiamond in samples. Roy et al. [185] deposited MCD films by HFCVD and found broadening and shift of the 1332 cm^{-1} diamond peak in their SERS. They reported phonon confinement in their study occurring from the nanophase of diamond that was present only at the surface and was not a bulk property. Formation of nanodiamond on the surface of MCD films was confirmed by SEM measurements though the origin of the nanodiamond remained unclear.

5.2. Optical Absorption

MCD films grown by CVD methods are not used widely in the applications for optical devices and coatings because of their rough surfaces. As mentioned before, though diamond is well suited for use as protective optical coatings, diamond films with high surface roughness cause attenuation and scattering of the transmitted signals restricting their uses in optical coatings. The need for deposition of smooth surfaced as-grown CVD diamond films at low temperatures was first realized more than a decade before in 1989 by Ong and Chang [21]. They developed a low temperature process in an MPCVD system, which also resulted in a film with a grain size of less than 300 nm and surface roughness in the range of 5–20 nm (Table 3). They clearly explained in the introduction of their paper the importance of smooth surfaces of diamond films for the purpose of optical coatings with the help of theoretical formulation given by Filinski. The intensity of the transmitted beam has an exponential dependence on the scattering coefficient, which is proportional to the square of the product of rms surface roughness and refractive index. As the index of diamond is 2.4, the rms surface roughness of the films has to be extremely low to give a good intensity of the transmitted light. Ong and Chang [21] obtained over 60% optical transparency in the range 0.6–2 μm wavelength of their $\sim$0.9 μm thick diamond films grown using the different processing method developed by them. It was also shown that their films are adhered well to the quartz substrates. Another publication, realizing the importance of smooth surfaces of as-grown CVD diamond films for optical and tribological applications, appeared in 1992 when Wu et al. [22] showed synthesis of fine-grained diamond films by MPCVD having a grain size in the range of 20–100 nm and surface roughness of 15 nm (Table 3). The measured transmission in the range from 2.5 to 10 μm was found to match with the calculated transmission of $\sim$1 μm thick freestanding diamond with an index of 2.4. The 5% absorption in the films was attributed to the nondiamond carbon and hydrogen content of the film. Erz et al. [23] obtained more than 60% transmittance in their $\sim$1 μm thick NCD films with a surface roughness of 30 nm, grown by optimizing the nucleation density of diamond and methane fraction. They observed a direct correlation between the grain size used for the pretreatment of the substrate and optical transparency of the NCD films (i.e., the bigger the grain size for pretreatment, the bigger the grain size in the grown films which naturally, as explained before, results in lower transparency of the films). It was also shown in their study that the transparency of their films was not dependent on the substrate temperature below 800 °C, used in the growth of the films. Contrary to this, Chen et al. [39, 45] showed that the pretreatment, using a bigger grain size diamond powder, gives

more transparent NCD films and also that the optical transmittance at 700 nm decreases linearly in the temperature range of 600–800 °C [38]. It was shown in different papers published by the same group that the surface roughness of diamond films is the major factor that controls the optical transmittance of the films provided that the graphitic content of the films is negligible. The same group [186] showed a transmittance more than 80% beyond 700 nm in their ~1 μm thick NCD films, grown on quartz in an MPCVD system using high methane concentration (42%), with an average surface roughness of 6–7 nm grown at optimized conditions studied in their work (Table 3). In another study, Yang et al. [51] recently showed an optical transmittance of 65% in the visible light in their ~1 μm thick NCD films, grown on quartz substrate with a average surface roughness of 10 nm.

All the aforementioned studies on the optical transmittance of NCD films are grown on substrates pretreated with diamond powder. In the case of NCD films grown by the BEG process (Section 2.2), Sharda et al. [53] obtained a high transmittance of 78% in the near-IR region in their ~1 μm film, grown on mirror-polished Si substrate, at 600 °C with an rms surface roughness of ~17 nm. In the same study they also compared the optical properties of NCD and MCD films grown in the MPCVD system. Tauc's optical gap for the MCD film was shown to be ~5.5 eV. NCD grown at 700 °C had a high optical absorption coefficient in the whole spectral region and the NCD film grown at 600 °C showed, as mentioned, a high transmittance (~78 %) in the near-IR region, which is close to that of diamond. The high resolution SEM of their MCD and NCD samples showed well-shaped grains with sharp facets in the MCD film with an average grain size of about 1 μm and much smaller grains in the NCD film grown at 600 °C in the range of a few nanometers to a few tens of nanometers. The absorption spectrum of the MCD film showed a quite low absorption coefficient (10^2–10^3 cm^{-1}) in the whole spectral region demonstrating the high quality of the diamond film with the presence of a high sp^3-bonded carbon fraction and a very low sp^2-bonded carbon [53]. The optical energy gap (E_g) of indirect gap material is usually estimated from Tauc's method [187], that is, by extrapolating the linear portion of $(\alpha h\nu)^{1/2}$ vs $h\nu$ plot, where $h\nu$ is the photon energy, to $(\alpha h\nu)^{1/2} = 0$. However, $(\alpha h\nu)^{1/2}$ vs $h\nu$ plots for their NCD films did not exhibit any linear region and Tauc's method could not be applied [53]. Thus, the optical gap was defined in terms of E_{04}, the energy at which the absorption coefficient is 10^4 cm^{-1} [188]. The E_{04} energy for the NCD film grown at 600 °C was found to be around 2 eV. Interestingly, there is no indication of a sharp absorption edge in NCD films. The absorption coefficient appears to vary monotonously with the incident photon [53]. Kundu et al. [30] obtained a high bandgap (~4.2 eV) in their diamond films (predominantly NCD embedded in a-C matrix), grown at low substrate temperature (300 K) by dc magnetron sputtering of vitreous carbon. The bandgap of their films increased to 5 eV when they added 10 vol% hydrogen in the sputtering gas. The NCD ceramics fabricated from C$_{60}$ fullerene by shock compression [71] had absorbance in the wavelength range of 185 to 500 nm matched with the absorbance of natural diamond type IIa with a slightly higher absorbance in

the range of 250 to 350 nm. An abrupt increase in absorption at ~225 nm, at the absorption edge of diamond, indicated the bandgap of NCD platelets was about 5.5 eV. In the case of nitrogen-doped UNCD films (Sections 2.1.1 and 3.2.3), it was observed from the optical absorption spectroscopy that the transmission of the film decreases with nitrogen incorporation [129]. This is possible due to a decrease of the effective bandgap of the material as a result of a change of the film's microstructure. It should be noted that these optical absorption data from the nitrogen-doped UNCD films are very much consistent with the change of electrical conductivity as described in the Section 3.

NCD films were coated on both sides of a silicon wafer to increase its infrared transmission and also as a protective coating [189]. The 54% transmission in the wavenumber range from 1200 to 3600 cm^{-1} of the Si wafer increased to 66% transmission (average), especially in the range of 1500 to 2200 cm^{-1} when coated with a 0.5 μm thick NCD film at one of its surfaces. The tranmission of the one side coated Si wafer in the range of 1500 to 3000 cm^{-1} further improved to an average of 80% after applying a 0.3 μm coating at the other side of the wafer. It was also shown by a sand spraying test that the coatings are strongly adhered and that the coated wafer has better resistance to sand spraying than the Si wafer without coating.

Recently, optical properties of NCD films were obtained by demonstrating the use of a prism-coupling technique to measure the refractive index and thickness together [70]. The prism-coupling technique [190–192] is a proven technique to rapidly and accurately measure both the thickness and refractive index of dielectric and polymer films [193] and, also, has been used widely as a powerful technique to measure the optical constants of AlGaN films [194, 195] and other films [196–199]. It is understood to have unique advantages over other conventional techniques; that is, ellipsometry, spectrophotometry, etc. can be used to measure these thin film parameters as no advance knowledge of film thickness or index is required, measurements of these parameters can be done easily and rapidly (20 seconds) with extremely low standard deviation (typically 0.3% for thickness and 0.1% for index), etc. Although this technique has been used to characterize many kinds of thin films [193–199], diamond and related thin films have not been measured in detail before. The high surface roughness of the MCD films may have been a major problem in characterizing them using this technique. The NCD films grown by the BEG process (Section 2.2) were found to be absorbing for the standard operating wavelength of 633 nm and hence higher wavelengths (i.e., 830 and 1300 nm) were used to obtain sharp guided modes and refractive index and thickness of the films could be measured independently with high accuracy [70]. The index of the NCD films (2.34 at 830 nm and 2.33 at 1300 nm) was found to be homogeneous within the films with negligible changes observed at the film–substrate interface [70]. In general the index of the NCD films was a little lower compared to the index of MCD or natural diamond (2.41 at 633 nm) [200] but was in agreement of the index of fine-grained diamond films measured by the same technique [201]. The refractive index of the film grown for 60 min was also calculated by the reflectance spectrum of the same film using the basic equation for interference fringes

[202]. The index value was found out to be 2.31 ± 0.05 at 790 nm, which matches (within error of measurements) well with the value obtained by the prism-coupling method at 830 nm. Information on absorption was also obtained from the half-width of the guided modes and was correlated to the graphitic concentration in the films measured by Raman spectroscopy [70]. The thickness of the films, measured by the prism-coupling technique, was found to be in agreement with the thickness measured by cross-sectional TEM. The overall results indicated that the prism-coupling technique could be very useful for rapid, easy, and accurate measurements of refractive index and thickness of smooth diamond films [70].

By low temperature high-resolution optical spectroscopy Jelezko et al. [203] investigated individual paramagnetic defect centers in diamond nanocrystals. Optical properties of defects in, for example, diamond compared with those of atomic systems are considerably more complex. In addition to radiative decay, electron–phonon interactions and other matrix-induced relaxation processes contribute to the optical properties of electronic transitions. Previous single center spectroscopy in large diamond crystals at low temperature has revealed unexpected limitations. NCD showed a homogeneous linewidth of a single nitrogen–vacancy (N–V) center. Two sharp zero-phonon lines corresponding to fluorescence emission from single N–V centers were present in the nanocrystal. Diamond nanocrystals show an approximately four times wider spread of the spectral line positions of a single center compared to bulk diamond. The authors are hopeful that the present system may be useful for quantum information processing with individual electron spins.

6. MECHANICAL AND TRIBOLOGICAL PROPERTIES

Wear on machinery is a big problem faced by the industry, as it causes large expenses. Therefore, the wear resistant coating market is growing very fast. Already, 40% of the cutting tools in the market are coated by wear resistant coatings with the market still growing fast [204]. There is an estimated 25 billion US$ market in the United States alone for the high-performance coating industry which includes protective coatings such as thermal barriers and ultrahard or wear-resistant coatings [205]. A high-performance wear resistant coating for high speed dry machining would not only enhance the performance of the automated machines but also would save the high costs of environmentally hazardous coolants being used at present [204].

Diamond is considered to be the best candidate for wear resistant and other tribological applications because of an excellent combination of its high hardness and low friction coefficient with its high thermal conductivity. However, as mentioned in the Section 1 of this chapter, conventional CVD diamond coatings that are deposited at high temperatures have rough surfaces. The high surface roughness is a major problem using diamond films for machining and wear applications [16, 17]. Such rough films cause high friction and high wear losses on the counter surfaces. In order to overcome the problem of surface roughness of diamond films post-polishing can be adopted. The polishing of these

rough diamond surfaces can be done by various methods [16, 19, 20]. As expected, after polishing their friction coefficient becomes comparable to natural diamond [206, 207]. Another way to overcome the problem is to grow naturally smooth films without compromising their hardness and other useful properties. As the postpolishing is expensive, time consuming [18–20], and also not possible in the case of complex shapes, it might therefore be advisable to pursue the growth of naturally smooth films [19, 33, 34, 36, 37, 48, 73–75]. At the same time, a high layer adhesion to the substrate is a necessary condition to obtain a high performance of the coating in the tribological applications [208].

On the other hand, although DLC and *ta*-C films are much smoother, are equally hard as conventional diamond, and can be grown at lower temperatures [79, 209, 210], these films contain a high level of compressive stress (2–15 GPa) within the planes of the films [83, 211–216]. The stress in the films directly affects their adhesion and causes them to delaminate from the substrate [214] thus, in turn, restricting the film thickness only to a few tens of nanometers to keep the film stable on the substrate. This thickness is too low to use the films for tribological applications and also higher stress cannot be developed beyond 10–12 GPa for fundamental studies or other recently proposed related applications [76]. The high compressive stress and adhesion have been key problems, especially in their uses in tribological applications. The current research in this area in various laboratories and universities is aimed at reducing this stress and, at the same time, improving adhesion of these films to the substrate. The stresses in the DLC films are reduced by incorporating N, Si, O, or metals [78]. In *ta*-C films the stresses can be reduced by incorporation of metals [217] or boron [210], by building multilayer structure [218], or by annealing the films [209].

NCD films have superb tribological properties, meeting all the technical requirements to be an ideal wear-resistant coating material, such as smooth surfaces with their hardness being quite close to MCD or natural diamond, improved interface toughness, and material stability [5, 19, 37, 174]. Moreover, depending on the growth route the amount of stress can be controlled to grow films with low or almost no stress [5, 42]. Also, some growth routes described in Section 2 are capable of developing strong adhesion without any additional effort of engineered interfaces [62, 76]. In addition, the NCD films can be grown on a variety of substrates such as silicon, SiC, Ti-6Al-4V, Mo, W, WC, Si_3N_4, quartz, etc. [9, 30, 33, 34, 36, 38, 51, 61]. Moreover, there is a growing interest in the scientific community in the mechanical properties of the grain boundaries in nanostructured materials including NCD [131, 204, 219–222]. It is worth mentioning some interesting observations in the area of nanoscience and nanotechnology that are related to mechanical properties; highly compressed diamond grain boundaries can be harder than diamond [221], carbon nanocomposite structure films with nanometer-sized dense *a*-C regions embedded in 5–10% lower density *a*-C film shows 15% more hardness than the same higher density *a*-C film without the dense nanoregions in the film [223], and nanocrystalline TiN/SiN_x nanocomposites have been prepared with a hardness of 105 GPa [204]. We shall now look at the hardness and surface roughness of the NCD films

grown by different routes as classified in Section 2 followed by a review of their tribological properties in this section. Table 3 gives an overview of surface roughness and grain sizes of the NCD films grown by various groups.

The phase-pure UNCD, composed of randomly oriented grains of whose size distribution maximizes at 3–5 nm prepared at ANL, had a surface roughness of 20–40 nm and average hardness value of 88 GPa [5]. The NCD films prepared by Konov et al. [25] had a surface roughness of 20 nm while having a maximum hardness of 85 GPa. NCD films grown on Si by the MPCVD system using 10% methane by Yoshikawa et al. [48] showed Vickers hardness in the range of 82–99 GPa and had a rms surface roughness of 8.4 nm, as measured by AFM in a 1×1 μm^2 area. The friction coefficient of their films will be discussed while discussing tribological properties of the NCD films in the same section.

The NCD films grown by Catledge and Vohra [36] on titanium alloy (Ti-6Al-4V), a technologically important material, used in aerospace, biomedical, and chemical engineering, and on Mo substrates by MPCVD had a rms surface roughness of 50 nm, hardness of ∼90 GPa (90% that of natural diamond), and elastic modulus of 750 GPa. In another study, Catledge and Vohra [37] showed enhancement in the interface toughness with addition and increase of nitrogen in the growth process. Grogler et al. [224] showed a coating of CVD diamond using a high methane concentration of 4–10% CH_4 in balanced H_2 in the process gases in the MPCVD system exhibiting superior solid-particle erosion resistance of Ti-6Al-4V. The mass loss of Ti-6Al-4V coated with a CVD diamond layer using 6% CH_4 in balanced H_2 is shown to have decreased by a factor of 100 compared to the uncoated specimen. However, the films grown with lower and higher methane concentration showed only a modest reduction in wear. This behavior of the erosion resistance of the CVD diamond coating at different methane concentrations was explained in terms of the structural changes of the films with methane concentration as assessed by Raman spectroscopy and SEM. The high erosion resistance was explained in terms of good interconnection of diamond grains in the films grown at intermediate methane concentration. It was interpreted that at these intermediate methane concentrations twin formation is favorable which facilitates secondary nucleation resulting in good film cohesion. The coatings with a highly ordered columnar growth, at 1% methane, and the NCD coatings with a high amount of nondiamond carbon, grown at a higher methane concentrations (12% and above), showed poor erosion resistance. In another study Catledge et al. [225] showed that for a fixed flow rate of N_2, increasing the methane from 5 to 15% in hydrogen resulted in an increase in diamond crystallinity, a decrease in nondiamond carbon, and an increase in film hardness from 43 to 90 GPa. This effect of obtaining a better diamond crystallinity and higher hardness with increase in methane concentration is similar to what was reported by Sharda et al., that increasing methane in BEG growth of NCD increased NCD concentration in the films [98], and is quite a contrast to the effect of increasing methane without any nitrogen addition (i.e., in a conventional CVD diamond growth). It is quite advantageous in the case of nonconventional methods to grow NCD, as higher methane concentration not only gives higher growth rates but also results

in better adhesion of the NCD films. In the same study [225], the authors reported that at a fixed flow of methane of 88 sccm, increasing nitrogen from 0 to 26.4 sccm resulted in decreasing diamond crystallinity, increasing nondiamond carbon, and decreasing film hardness from 100 to 50 GPa. Nevertheless, a concentration of 15% CH_4 with a ratio of N_2/CH_4 of 0.10 results in a roughness of 15–30 nm, good adhesion, and a high hardness of 90 GPa. Beyond this ratio no significant changes were observed either in the diamond crystallinity or in the surface roughness of the films, which is explained in terms of saturation of concentration of CN radical beyond this ratio [95, 225]. These results of NCD coatings on metallic surfaces are quite interesting and have a great potential for use in designing articulating medical implant devices as hard and low-friction wear resistant coatings. The same group reported growth of nanostructured diamond film, as a wear resistant coating, on curved surfaces of Ti-6Al-4V alloy machined to simulate the shape of a temporomandibular joint dental implant to extend implant service lifetime [226]. It was shown that the coatings, consisting of a significant volume fraction of NCD, are hard (60 ± 5 GPa) and are uniform in composition.

The NCD films (∼1 μm thick) grown on quartz substrate by the MPCVD system for transparent protective coatings showed a Vicker's hardness of 73–93 GPa with a surface roughness of 9 nm, measured by AFM [51]. Kundu et al. [30] obtained a hardness of 50 GPa in the NCD films embedded in a-C matrix with surface roughness ∼9 nm at 300 K temperature on quartz substrate by dc magnetron sputtering of vitreous carbon.

The NCD films grown by the BEG process by Sharda et al. [42, 61, 170] had a hardness in the range of 70–90 GPa at optimized conditions with rms surface roughness, measured in an area of 5×5 μm^2 by AFM, varying in the range of 10–30 nm and a low amount of stress (<1 GPa). They were shown to have achieved a strong adhesion in their NCD films on silicon substrates that their films did not delaminate even at intentionally induced enormous amounts of in-plane stress [62, 98]. The strong adhesion may be the result of implanted carbon ions, with suitable energy, into the substrate in the initial stages of growth. Interestingly, the reduction of the grain size from micrometer to nanometer brings up unusual properties of the thin films that were never observed before. Si wafers having thicknesses in the range of 300–700 μm have been shown spherically bent up to a radius of curvature of 0.02 m by a coating of highly stressed 1–2 μm thick NCD films. The increase in the stress was correlated to the decrease in the grain size of diamond in the films [62]. The radius of curvature of the NCD/Si samples can be controlled and new applications have been proposed in the areas of X-ray physics, particle physics, etc., where bent wafers are used [76]. This subject is further discussed in Section 7.4. On the other hand, the NCD films, grown adopting the same route of biasing (Section 2.2), in multisteps, have been shown to have average surface roughness as low as 5 nm with adhesion reported to be good enough to prepare film with thickness only up to 2 μm [49]. A high amount of compressive stress and a comparatively weak thickness in the films restrict preparation of thicker films.

The nanocrystalline diamond ceramics fabricated by Hirari et al. [71] from C_{60} fullerene by shock compression have comparable hardness to type IIa diamond. It was reported that the NCD platelets were too hard to measure by the conventional micro-Vicker's method. Nanocrystalline diamond coatings by conversion of silicon carbide also show promising mechanical properties, with hardness in excess of 50 GPa and Young's moduli up to 800 GPa [107].

Thermal stability of NCD films has also been investigated by a few groups. It has been shown that the NCD films can be stable up to a temperature as high as 950 °C [47]. Heiman et al. [47] annealed their NCD samples up to a temperature of 950 °C in vacuum for 10 min and observed no change in the EELS spectrum of the film in spite of the fact that the films contained high hydrogen content. Sharda et al. [170] annealed their NCD samples up to a temperature of 800 °C in Ar ambient for one hour and, as discussed in Section 5.1, observed no or little change in the Raman spectra of their films shown in Figure 10. As shown in Figure 14, the rms surface roughness (20–25 nm) and hardness (55–75 GPa) of the NCD samples annealed at different temperatures remained fairly constant to temperatures as high as 800 °C.

Tribological properties of NCD films have also been investigated by a few research groups. Erdemir et al. [19] found out that the phase-pure NCD films, grown by MPCVD using Ar and fullerene with rms surface roughness of 20–40 nm, has tribological properties superior to the conventionally grown rough MCD films, which are even comparable to the tribological properties of the natural diamond. The sliding friction coefficients of their NCD films against Si_3N_4 balls were ~0.05 and ~0.1, respectively, in dry N_2 and air, lower by a factor of 5–10 than that of rough MCD films with rms roughness of 0.35 μm. The initial friction is always observed to be high which decreases rapidly to stabilize at lower values. In the long duration tests for 22,000 cycles of friction in dry N_2 some occasional fluctuations were observed in which the friction increases and comes back to the same value. However, such fluctuations were not observed in the tests in air. Wear rates of SiC pins and Si_3N_4 balls against the NCD films were found to be two orders of magnitude lower than the wear rates against rough MCD films. Hollman et al. [34] grew NCD films on spherical cemented carbide rock drilling

Figure 14. Plot of hardness and rms surface roughness as a function of annealing temperature. Hardness data presented in the graph are averaged from a few sets of five indents on the samples and the error bar is taken from the minimum and maximum hardness observed. Reprinted with permission from [170], T. Sharda et al., *J. Nanosci. Nanotech.* 1, 287 (2001). © 2001, American Scientific Publishers.

bits with a spherical top of 6 mm radius and tested them in dry and lubricated sliding against cemented carbide, ball-bearing steel, stainless steel (CC, BBS, and SS, respectively), titanium, and aluminum. These NCD films, grown by a hot-flame method in which the samples are negatively biased to 500 V, showed an average surface roughness of 30 nm, measured by a profilometer, and 6–10 nm, measured by AFM in an 8×8 μm^2 area. After a light polishing these NCD samples show a smoother surface with an average surface roughness in the area of 1×1 μm^2 in AFM decreased to 2.5 nm. The friction coefficient of the NCD films under dry sliding conditions was high initially, similar to what was observed by Erdemir et al. [19], and reduced after traveling a sliding distance of 5–10 m to low values (0.06–0.1) against CC, BBS, and SS. Lubrication with water and oil brought a little change in friction. There was no change in friction of CC while using oil lubrication and rather increased in the case of SS and decreased in the case of BBS. Water lubrication reduced the friction against all the materials. The friction coefficient of as-grown NCD films against Ti and Al was high (0.5–0.6) and soon resulted in seizure. The seizure occurred even with the lubrication against Ti. However, a light polishing of the NCD films gave a friction of 0.1, which further reduced to the values of 0.03–0.055 when water and oil lubrications were used. In comparison, the self-mated BBS gave a friction of 0.8, 0.4, and 0.14, respectively, in dry, water-, and oil-lubricated conditions. In the case of wear tests, the NCD films had a low wear whereas countersurfaces had almost no wear. The wear resistance of the NCD films in dry sliding against SS is shown to be 100 times higher than that of self-mated BBC with oil lubrication. This gives an idea of how excellent NCD is for wear-resistant coating. The friction coefficient of the NCD films grown at high methane concentration using the MPCVD system by Yoshikawa et al. [48] was 0.02, again after having an initial high value of approximately 0.2, similar to what was observed in the previous two cases. Hong et al. [227] studied tribological properties of their NCD film synthesized on silicon substrates using 10% CH_4/H_2 microwave plasmas. The NCD film, grown for 20 hours, consisted of 30–50 nm size diamond grain and had a surface roughness of 10 nm. The friction coefficient, measured using a SiC ball of 6.35 mm diameter with 0.5 N load, was in the range of 0.05–0.07 in dry air.

Investigations from the aforementioned studies revealed that smooth NCD films have superb tribological properties and show low friction and wear even against materials, which normally behave poorly as sliding contacts in the countersurfaces such as stainless steel, Ti, and Al. A superior performance as compared to the rough MCD films is obviously a result of the smooth surfaces of NCD films. Friction and wear can be defined, respectively, as the resistance experienced in the motion when a solid body is moving tangentially against another in contact and the damage occurring or removal of the material from one or both of the solid surfaces because of this motion. This resistance in the motion of diamond and diamondlike films has been shown to arise mainly from a combination of two main factors; physical/chemical attraction or adhesion and mechanical ploughing at the two surfaces in motion [9, 19, 34]. As mentioned, the conventionally grown MCD films have
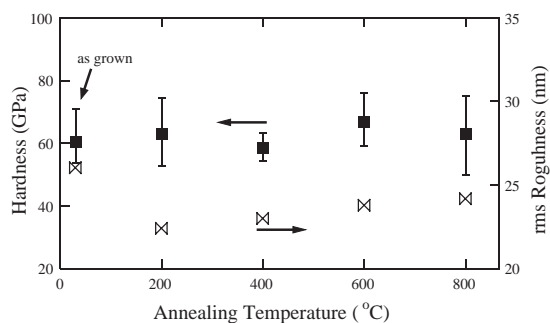
rough surfaces with sharp crystal edges. These sharp asperity tips on the rough diamond surfaces result in abrasive cutting and ploughing of the softer counterfaces giving high friction and wear from these MCD films [19]. In the case of smooth diamond surfaces the ploughing effect minimizes and thus the friction is low which is defined largely by physical/chemical interactions between the sliding surfaces or in other words by the adhesive component of the friction. There is another factor which makes NCD films superior to MCD films for tribological applications. That is its ability to become more smooth during sliding [19, 34, 48]. It can be seen while observing the initial high friction coefficient of NCD films, which rapidly decreases to stabilize at lower values [19, 34, 48]. This initial high friction comes from the as-deposited NCD surface roughness, which is still in the range of 20–40 nm. However, soon after the sliding starts these surfaces become ultrasmooth (3–6 nm [19], 0.6 nm [34]), reducing the friction coefficient, which is now purely defined by the adhesive component of the friction. The adhesive component is also minimized when the diamond surfaces are passivated. This is indeed the reason given for the low friction of smooth or cleaved diamond surfaces [228, 229]. It has been shown (Gardos in [1]) that the friction coefficient of self-mated diamond increases when adsorbed gases are desorbed. Hollman et al. [34] showed that their NCD diamond films have a higher concentration of hydrogen than the MCD films and that may have contributed to improved tribological properties. The large fluctuations of the former in the long duration sliding in dry nitrogen were attributed to the phase transformation of the moving asperity of NCD films generating micromechanical wear from the graphitic debris accumulating at the sliding interfaces. When this debris is removed by mechanical means as the sliding continues the friction again comes back to the same lower value.

In addition to modifying structural and electronic properties, as described in Section 4, ion implantation has also been employed to improve mechanical properties of NCD films. Xu et al. [230] studied the influence of nitrogen ion implantation on the friction and wear properties of NCD films. They found that the friction coefficient of their 800 nm thick NCD film on Si substrate in ambient conditions, while rubbing against a ruby ball and without any implantation, was 0.7. A wear scar of 12 mm diameter can be seen on the ruby ball in only 10 cycles of rubbing against NCD film. The friction coefficient reduces a little with sliding cycles, however, still resulting in a severe wear of the ruby ball. The NCD film broke after 250 cycles when the wear scar diameter on the ruby ball was 0.32 mm. The N ion implantation of the NCD film significantly decreased the friction coefficient and wear of the ruby ball. The friction coefficient decreased to 0.08 when the implanted fluency reached to 1×10^{17} ions/cm^2. In this case, even after 1000 cycles of rubbing against NCD films the wear scar diameter of the ruby ball was only about 0.05 mm. The adhesive component of the friction was shown to be the main reason for such a high friction between ruby ball and NCD surfaces. The N ion implantation with a typical fluency of 1×10^{17} ions/cm^2 changes the surface chemical state of NCD film thus reducing the adhesion between the two sliding surfaces resulting in improvement in the tribological properties of the NCD films. Moreover, transformation

of some part of diamond crystallites into amorphous sp^3-rich bonds and a highly disordered sp^2-rich structure, which also attributed to the decrease of the friction coefficient and wear of the ruby ball, may also contribute to decreasing the friction and wear of the ruby ball.

In summary, the NCD films have superior mechanical and tribological properties compared to the rough MCD films. The former can therefore be a superior replacement to rough MCD films in tribological applications because the as-grown smooth surfaces not only save time and cost of polishing the rough MCD surfaces but also are able to become ultrasmooth soon after the sliding starts.

7. APPLICATIONS

7.1. MEMS

MEMS is one of the most rapidly growing technologies which involves miniaturized mechanical components and devices. It has a broad range of commercial applications with a diverse collection of evolving MEMS sensors and actuators for applications in transportation, medicine, industry, and aerospace. The MEMS devices, already on the market, are sensors that trigger car airbags, nozzles for ink-jet printers, and tiny blood-pressure monitors that can be implanted in the human body.

Currently silicon is the main material used in MEMS devices because of the already available Si surface machining technology. However, because of its poor friction and wear properties it is not considered suitable for different micromachines with fast-moving parts. Thus the future MEMS applications demands a different material that possesses excellent mechanical and tribological properties and additionally that should be able to perform well in extreme environments in order to realize the range of its potential applications. Diamond with its exceptional mechanical and tribological properties in combination with high chemical inertness and high thermal conductivity has all that is needed to be an ideal tribomaterial for MEMS components, especially where significant rolling and sliding contact under harsh conditions are involved. MCD films have rough surfaces with granular morphology not suitable for MEMS applications and instead smooth NCD films will be the best suitable diamond films for MEMS applications. Krauss et al. [5] have demonstrated fabrication methods, some unique to diamond and some related to existing Si fabrication technology, to fabricate MEMS components based on their phase-pure UNCD. Butler and co-workers [6] recently demonstrated fabrication of MEMS resonators from conformal NCD coatings on Si and device processed Si wafers. They [6] reported fabrication of nanomechanical resonant structures in NCD. A different method of pretreatment was adopted in which the substrate was first exposed to the deposition conditions in the MPCVD system for 20 min followed by ultrasonic bath treatment of nanodiamond powder suspended in ethanol. Single-crystal silicon wafers were thermally oxidized to obtain a 1 μm thick silicon dioxide film before using them as substrates to grow the NCD films. The NCD films, grown at 750 °C using 3 sccm of methane and 900 sccm of hydrogen at a microwave power of 800 W, consisted of columnar grains that range in size from 5 to 15 nm

near the substrate interface to 10% of the thickness of the film at growing surface. NCD films as thin as 80 nm were obtained and by using standard lithographic and semiconductor processing techniques, NCD structures with a lateral dimensions as small as 50 nm were fabricated with the measured mechanical resonant frequencies up to 640 MHz.

7.2. SAW Devices

SAW devices that typically consist of piezoelectric substrates (quartz, lithium niobate) on which thin metal film integrated transducers are fabricated using photolithiography have key applications in microwave and rf electronics. High frequency SAW devices can be obtained with relaxed lithography criteria if diamond can be used as a substrate because of its high SAW velocity [2]. However, as-grown MCD film cannot be used because of its high surface roughness and its uses after polishing may not be considered practical since the existing SAW devices are very competitive and price sensitive [2]. Recently Bi et al. [3] showed that the NCD films could be a superior replacement to MCD films for high frequency SAW devices. NCD films have smooth surfaces that save processing time and money that are needed to polish the rough MCD films for their uses in SAW devices. In addition, interestingly, the NCD films grown in MPCVD system were shown to have superior SAW properties as well, in terms of elastic isotropy and absence of grain boundary scattering.

7.3. Electrochemical Electrodes

Diamond is an attractive material for applications in electrochemical analyses and synthesis. This attractiveness arises from its extreme electrochemical window (>3 V) and chemical inertness [231]. Some of these applications are qualitative and quantitative electrochemical analyses, water purification and disinfection, reduction of oxidants and heavy metals, synthesis of powerful oxidants like chlorine, etc. [9]. Boron-doped MCD film electrochemical electrodes exhibit superior properties in aqueous solutions compared to other material electrodes such as platinum electrodes that have a potential span of 1.5 eV. However, because of the surface morphology of the MCD films it requires a thick film of several micrometers to obtain pinhole-free films. NCD films will be advantageous to MCD films in this area mainly because doping may not be needed and also a much smaller thickness should be good enough for the corrosion protection of the underlying substrate.

7.4. DNA Modified NCD Substrates

In the most recent advancements in the area of nanocrystalline diamond, it was shown that the NCD films could be a near ideal substrate for integrating microelectronics to biological modification and sensing [232]. Two types of NCD samples, grown on silicon substrates in the MPCVD system, were investigated in this study. One of the two samples was grown using the routes described in Sections 2.1.1 and 3.2.3 with a thickness of 0.75 μm at 150 Torr using 99% Ar and 1% CH$_4$. Another NCD sample was 0.5 $\pm$ 0.2 μm thick and was grown using 900 sccm hydrogen and

1 sccm CH$_4$ at 15 Torr, also by the MPCVD system. Sequential steps taken to attach DNA to a NCD surface are illustrated in Figure 15 [232]. Initially H-terminated NCD surfaces (Fig. 15a) were chemically modified to produce a layer of amine groups using a photochemical scheme. A DNA-modified NCD surface (Fig. 15e) was produced by reacting the amine-terminated NCD surface with a heterobifunctional cross-linker sulphosuccinimidyl-4-(N-maleimidomethyl) cyclohexane-1-carboxylate (SSMCC) followed by a reaction with thiol-modified DNA (Fig. 15b–d). Hybridization studies, carried out using two different oligonucleotides attached to the surface and two fluorescently tagged complementary and noncomplementary oligonucleotides, showed no detectable nonspecific adsorption, with extremely good selectivity between matched and mismatched sequences. To demonstrate diamond's unique ability to achieve extremely high stability and sensitivity, stability studies of NCD and other commonly used surfaces for biological modification, such as gold, silicon, glass, and glassy carbon, were performed and compared. All the DNA-modified surfaces were prepared with nearly identical chemistry and were subjected to 30 successive cycles of hybridization and
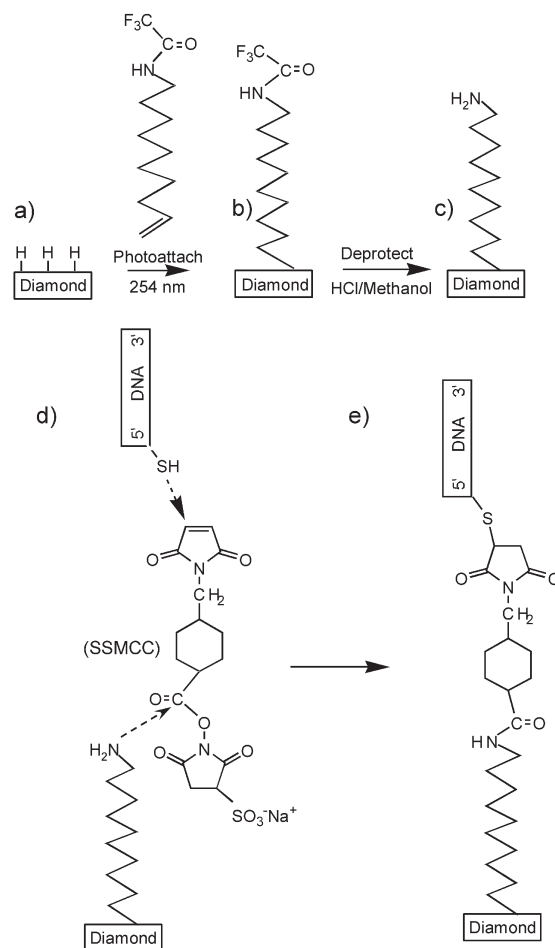
Figure 15. Sequential steps in DNA attachment to NCD surface. Reprinted with permission from [232], W. Yang et al., *Nature Mater.* 1, 253 (2002). © 2002, Macmillan Magazines Ltd.

denaturation. The fluorescence image was obtained after every cycle of hybridization and also after every cycle of denaturation. Figure 16 [232] shows no measurable decrease in the signal intensity of the UNCD sample even after 30 cycles of hybridization–denaturation, whereas there are a small but steady decrease in DNA-modified silicon surfaces and rapid degradation in DNA-modified gold and commercially available amine-terminated glass. In addition, two types of commercially available glassy carbon, prepared at 1000 and 3000 °C, respectively, showed 30% degradation and stability over 30 cycles of hybridization and denaturation. However, the latter material is not compatible with silicon microelectronics technology because of the high temperatures involved in its fabrication. This clearly demonstrated the superiority of DNA-modified NCD over others in its ability to achieve very high stability and sensitivity and, as diamond has the potential advantage of being compatible with microelectronics, the findings of this report on NCD thin film should be an important breakthrough in the development of completely integrated biological sensing systems.

Earlier in the same year, in the conference "Diamond 2002" (Granada, Spain), Takahashi [233] demonstrated in his presentation that CVD diamond is a good material to solidify and preserve DNA. A diamond chip of dimensions 3 mm × 3 mm × ∼0.3 mm was chemically modified by the amino linkage with the carboxylation. Not only was ∼4 pmole/mm^2 of oligonucleotide fixed with the amide linkage, as compared to ∼0.5 pmole/mm^2 for a silicon chip; DNA fixed on a diamond chip was also shown to be more stable than the DNA fixed on a silicon chip. Covalently bound complementary DNA libraries on diamond chips
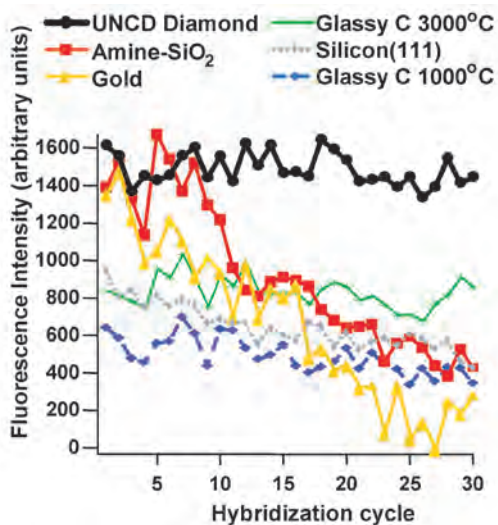
Figure 16. Stability of DNA-modified UNCD film and other materials during 30 successive cycles of hybridization and denaturation. All the DNA-modified substrates were amine-modified and then linked to thiol-terminated DNA using SSMCC as a covalent linker, as described in Section 7.4 and Figure 14. The fluorescence intensities after hybridization with perfectly matched, fluorescently labeled complements are shown. For each substrate, the fluorescence was measured after each denaturation step and was confirmed to be zero. Reprinted with permission from [232], W. Yang et al., *Nature Mater.* 1, 253 (2002). © 2002, Macmillan Magazines Ltd.

were reported to be stable for two years after solidification. DNA preservation using diamond chips was said to become the most important postgenome technology.

7.5. NCD Coated Bent Si Wafers

As mentioned in the Section 6, some interesting and unusual results were reported to emerge when NCD films were grown on Si substrates by providing controlled and continuous bias current density (BCD) in a MPCVD system [62, 98]. It was reported that NCD films grown by the BEG process can contain an enormous amount of stress when grown at high BCD. The interesting point to note was that the samples bend dramatically due to stress without delaminating. Such bending of the wafers was possible to demonstrate experimentally due to having developed strong adhesion in the films that can sustain an enormous amount of stress, which bent the whole sample. As the films show characteristics of NCD, their large grain boundary area, accommodating nondiamond carbon impurities, and the hydrogen content of the films were hypothesized to be the origin of the large stress in the films [98]. A high amount of stress in the films may cause bending of the substrates such as silicon [62]. The curved crystals find potential applications in the area of X-ray optics and particle physics [76]. A bent silicon wafer can be used in place of a magnet to deflect a beam of charged particles and ions [234–236]. In fact, this area of deflection of beams of charged particles by bent crystals has now become a mature field, both with respect to fundamental investigations as well as applications. However, to date, a heavy mechanical mechanism (crystal bender) is being used to mechanically bend the crystal to the desired radius of curvature depending upon the application [234–237]. The stress and hence the curvature of the films on silicon substrates were shown to vary by changing the BCD [61, 76]. Different growth conditions result in films with a wide range of radius of curvature (0.02 to 3.5 m). It was proposed to use these bent Si substrates in place of crystal benders, a cumbersome mechanical arrangement used for bending silicon in those areas. Data on the range of radius of curvature used in X-ray optics and particle physics were compared with the radius of curvature obtained by inducing stress in the NCD films on Si wafers. Interestingly, the radius of curvature of the NCD coated Si wafers obtained in this work falls in the range of the radius of curvature of bent crystals used in X-ray optics and particle physics experiments [76]. Therefore, these freestanding bent wafers may replace the cumbersome mechanism of crystal benders, used in the area of X-ray optics and particle physics experiments. It should be noted that this was just a proposal and can be verified only when the NCD coated bent wafers could be tested practically.

7.6. Search for Extraterrestrial Diamond

Some of the features of natural diamond are different from synthetic ones. For example, on the atomic level, natural diamonds can include paired nitrogen atoms whereas synthetic diamonds (HPHT—Section 1.1) that begin with a diamond seed have single nitrogen atoms and also metal catalysts that absorb nitrogen. These differences are the basis of the idea

of the presolar origin of natural diamond. Some researchers believe that diamond carbon came from supernovas (explosive, dying stars) that released carbon into our solar system about 5 billion years ago. From spectroscopic data on presolar diamonds and observations of dense molecular clouds, it is estimated that 10 to 20% of cosmic carbon is nanodiamond in the dense media. Meteorites transported the carbon to earth, where extreme heat and pressure transformed it into diamonds. However, neither diamonds nor fullerenes have been detected in space so far unlike in meteorites, but their presence has been predicted. Let us discuss this subject in more detail.

7.6.1. Meteoritic Diamonds

Diamond was first reported in a meteorite in 1888 from two fireballs seen to land in Siberia. The field blossomed in 1987 when John Wacker and Tang Ming, working in the laboratory of Edward Anders at the University of Chicago, discovered minuscule diamonds, only a few nanometers across, from a type of meteorite called carbonaceous chondrites.

Two types of meteorite contain diamond: stony and iron. Sometimes a large amount of diamond is collected from meteorites. The sintered, polycrystalline microdiamond from meteorites aggregates has a porous ceramic texture and ranges up to 3167 carats, which is 61 carats heavier than Cullinan, the largest single crystal diamond.

Nanodiamonds recovered from meteorites, which originate in asteroids, have been thought to be the most abundant type of presolar grain. Diamonds account for more than 99% of the identified presolar meteoritic material, with an abundance that can exceed 0.1% (1000 ppm) of the matrix, corresponding to more than 3% of the total amount of carbon in the meteorite. Presolar diamonds have been isolated from ordinary, carbonaceous, and enstatite chondrites, and the proportion of C diamond is between 3 and 4% [238]. Diamonds of meteorite and presolar origin are mostly nanocrystalline (~2 nm) but are in extraordinary high concentrations (120 to 1600 ppm) in meteorites. Such diamond is more abundant than presolar SiC (~10 ppm), graphite (~2 ppm), and other minerals. Because of the extremely fine grain sizes, analytical measurements on chondritic nanodiamond, unlike graphite and SiC, can only be obtained on aggregates and not single crystals. N concentrations in presolar diamonds range from 2000 to 12,000 ppm: an exotic source for N in presolar diamonds [238].

In addition to diamond and graphite, a-C has also been seen in meteorites. However, recent observation shows that their abundance decreases with heliocentric distance, in which large-scale transport and circulation within the early solar system is depleted [238]. Apart from presolar origin meteorite impacts on earth could have transformed carbon and graphite into diamond and lonsdaleite though there is no proof. On the other hand formation of nanodiamond in space is thought to be similar to that of passive CVD diamond and carried by meteorites to earth.

7.6.2. Presolar Diamonds

Laboratory conditions in which CVD diamonds are produced are considered to be broadly similar to stellar atmospheres in H/C and C/O ratios and temperature. If C/O > 1,

which is attained in the helium shell of massive stars, diamond is expected to condense. The CVD model is consistent with hydrogen bonding on the surfaces of presolar diamonds and with the prediction, from remote spectroscopy, that grain surfaces in C-rich circumstellar envelopes are saturated in -C–H-.

The prevailing theory for the origin of presolar diamond is that it condenses by a CVD-like process in stellar atmospheres or in atmospheric outflows from red giant stars [with solar masses (M sun) = 8 to 12] in the evolutionary sequence of becoming type II supernovae (SN). Type I SN have also been suggested as sources of diamond that involves binary stars, one of which is a dense white dwarf that gravitationally accretes material from a companion, 1 to 8 M sun C star (C/O > 2) and ultimately incinerates [238].

In the type I SN, the disruptive explosion results from the sequestering of matter from a companion star by a dense white dwarf. In a type II SN, a single star, usually a supergiant in the evolutionary sequence, undergoes a gradual and then a catastrophic collapse as core fuels in sequential layers are expended. On final implosion and rebounding, the outermost envelopes are blasted into the interstellar media. It is in these outermost expanding and cooling envelopes of type I and type II SN that nanodiamonds nucleate, perhaps a month or so after a SN event. Thermonuclear reactions in SN take place at several million Kelvin and are far in excess of temperatures of C condensation as diamond. Hence, diamond nucleation is governed by expansion and cooling of SN envelopes, which may only reach critical diamond condensation temperatures in a year or so after an SN event. C availability may also increase by ionization and dissociation of inert CO into C and O [239].

7.6.3. Experimental Evidence

Infrared stretching of an interstellar CH band (at 2880 cm^{-1}) of NGC 7538 IRS 9 indicated the presence of diamond or related material in the dense interstellar molecular cloud. The abundance of diamond in other nebula (like in the Egg nebula) and meteorites is believed that to have been produced by a shock wave of interstellar medium [240]. UV light from nearby stars suggests that diamond dust drifts in the vast spaces among stars. Diamond grains may concentrate in the cocoons of dust enshrouding young stars, because the meteorite diamonds absorb infrared light in a pattern similar to the light absorbed by grains around young stars.

8. CONCLUSIONS

This chapter reviews several aspects of nanocrystalline diamond and also presents a comparative study of related materials at relevant places. Starting from the classification of diamond and related materials, various new synthesis routes that have been developed by different groups over the last few years since realizing the importance of nanocrystalline diamond films have been described elaborately. A variety of growth from phase-pure NCD to NCD embedded in ta-C or a-C matrix is possible.

The transport property of phase-pure UNCD films is addressed in detail, as one major issues of the chapter,

with special emphasis placed on their nitrogen doping. A successful *n*-type doping, which has been quite elusive in MCD diamond, is demonstrated in nitrogen incorporated NCD films. It is shown that nitrogen is very much soluble in NCD films and that it forms a conducting percolation path through the grain boundary and a shallow donor level quite close to the CB. As a result, a very high conductivity of *n*-type diamond has been achieved. While reviewing other nitrogen-doped diamond and related materials, it was found that such an improvement in the transports properties is unique to NCD. At high doping levels this material becomes a semimetal. The low temperature dependent conductivity is explained in terms of hopping conduction and impurity conduction similar to that of boron-doped MCD diamond. Hall measurements identified electrons as majority carriers with a very high concentration as well as reasonably good mobility. With the increase of nitrogen concentration the structure of UNCD films appears to change a little making the grain boundaries wider. Theoretical prediction agrees with the results of transport properties. The nitrogen doping in the UNCD films is also shown to have enhanced their field emission properties opening up various potential applications. Optical, mechanical, and tribological properties of NCD films were reviewed. Additional features start appearing in the Raman spectroscopy of the films when the diamond grain size changes from micrometer to nanometer. The origin of these features with another interesting phenomena of phonon confinement in nanodiamond grains is discussed. Excellent optical, mechanical, and tribological properties of the NCD films with naturally grown much smoother surfaces and additional advantageous properties appear to be a superior replacement for MCD films in potential applications in areas such as optical windows, wear-resistant coatings, SAW devices, MEMS, etc. Some other aspects of NCD, such as electrochemical electrodes and DNA modified NCD substrates, are also discussed in brief. DNA-modified NCD appears to be superior to other DNA-modified materials in its ability to achieve very high stability and sensitivity and, while diamond being compatible with microelectronics, this advancement may help in the development of completely integrated biological sensing systems. Some other interesting and unique features of NCD films are also reviewed that arise when the grain size reduces to nanometers. One such feature is generation of enormous stress in a micrometer thick NCD thin film that bent Si wafers (several hundreds of micrometers thick) to a radius of curvature as low as 0.02 m. Finally, NCD in meteorites coming from deep space including a brief description of the presolar origin of nanodiamond is also reviewed.

GLOSSARY

Chemical vapor deposition (CVD)   A method to deposit thin film onto a substrate in which the deposited species are formed by chemical reactions between gaseous reactants at elevated temperature in the vicinity of the substrate.

Deoxyribonucleic acid (DNA)   A macromolecule consisting of one or two strands of linked deoxyribonucleotides.

Dielectrophoresis   It is defined as the lateral motion imparted on uncharged particles as a result of polarization induced by non-uniform electric fields.

DNA hybridization   Formation of a duplex structure by two complementary single strands of DNA.

Field emission   Emission of electron from the surface of a material by application of electric field.

Fluorescence   The emission of light by a substance immediately after the absorption of energy from light of usually shorter wavelength.

Friction and wear   Friction is the resistance to motion experienced when a solid body is moving tangentially against another in contact. Wear is the damage occurring or removal of the material from one or both the solid surfaces because of this motion (sliding, rolling or impact).

Grain boundary   Boundary between grains in polycrystalline materials.

Micro/nanoelectromechanical systems (MEMS/NEMS) The miniaturized mechanical components and devices.

Negative electron affinity   Similar to a work function, the electron affinity is defined as the energy required for an electron to escape from the conduction band edge to vacuum. The case of having vacuum level below the conduction band is termed as negative electron affinity which results in easy emission of electron from the surface of a material.

Plasma chemical vapor deposition (Plasma CVD) The chemical reactions between gaseous reactants are activated in plasma.

Surface acoustic waves (SAW)   A device in which acoustic waves propagating on the surface of a piezo-electric crystal transfer a signal between two transducers.

Thermal chemical vapor deposition (Thermal CVD)   The chemical reactions between gaseous reactants are activated using thermal energy.

ACKNOWLEDGMENTS

REFERENCES

1. K. E. Spear and J. P. Dismukes, "Synthetic Diamond: Emerging CVD Science and Technology." Wiley, Pennington, NJ, 1994.
2. B. Dischler and C. Wild, "Low-Pressure Synthetic Diamond: Manufacturing and Applications." Springer, Heidelberg, 1998.
3. B. Bi, W.-S. Huang, J. Asmussen, and B. Golding, *Diamond Relat. Mater.* 11, 677 (2002).
4. K. Holmes, J. L. Davidson, W. P. Kang, and M. Howell, p. 82; E. Kohn, M. Adamschik, P. Schmid, S. Ertl, and A. Floter, p. 90; T. Shibata, p. 98, in "Proc. of the Sixth Applied Diamond Conference/Second Frontier Carbon Technology Joint Conference," ADC/FCT, 2001.
5. A. R. Krauss, O. Auciello, D. M. Gruen, A. Jayatissa, A. Sumant, J. Tucek, D. C. Mancini, N. Moldovan, A. Erdemir, D. Ersoy, M. N. Gardos, H. G. Busmann, E. M. Meyer, and M. Q. Ding, *Diamond Relat. Mater.* 10, 1952 (2001).
6. J. E. Butler, D. S. Y. Hsu, B. H. Houston, X. Liu, J.ignola, T. Feygelson, J. Wang, and C. T.-C. Nyguen, Paper 6.2, presented at the "Eighth International Conference New Diamond Science and Technology 2002," The University of Melbourne,

Australia. The complete presentation is available online at http://www. conferences.unimelb.edu.au/icndst-8/presentations.htm; L. Sekaric, J. M. Parpia, H. G. Craighead, T. Feygelson, B. H. Houston, and J. E. Butler, *Appl. Phys. Lett.* 81, 4455 (2002).

7. J. E. Field, "Properties of Diamond." Academic Press, London, 1992.

8. L. S. Pan and D. R. Kania, "Diamond: Electronic Properties and Application." Kluwer Academic, London, 1995.

9. D. M. Gruen, *Annu. Rev. Mater. Sci.* 29, 211 (1999).

10. D. M. Gruen, P. C. Redfern, D. A. Horner, P. Zapol, and L. A. Curtiss, *J. Phys. Chem.* 103, 5459 (1999).

11. W. G. Eversole, US Patents 3, 030, 187 and 3, 030, 188, 1958.

12. J. C. Angus, H. C. Will, and W. S. Stanko, *J. Appl. Phys.* 39, 2915 (1968).

13. B. V. Deryagin, B. V. Spitsyn, L. L. Builov, A. A. Klochov, A. E. Gorodetskii, and A. V. Smolyanimov, *Dokl. Akad. Nauk. SSSR* 231, 333 (1976).

14. S. Matsumoto, Y. Sato, M. Kamo, and N. Setaka, *Jpn. J. Appl. Phys. 2* 21, 183 (1982); S. Matsumoto, Y. Sato, M. Tsutsumi, and N. Setaka, *J. Mater. Sci.* 17, 3106 (1982).

15. M. Kamo, Y. Sato, S. Matsumoto, and N. Setaka, *J. Cryst. Growth* 62, 642, 1983.

16. D. G. Bhat, D. G. Johnson, A. P. Malshe, H. Naseem, W. D. Brown, L. W. Schaper, and C.-H. Shen, *Diamond Relat. Mater* 4, 921 (1995).

17. A. K. Gangopadhyay and M. A. Tamor, *Wear* 169, 221 (1993).

18. B. Bhusan, *Diamond Relat. Mater.* 8, 1985 (1999).

19. A. Erdemir, G. R. Fenske, A. R. Krauss, D. M. Gruen, T. McCauley, and R. T. Csencsits, *Surf. Coat. Technol.* 120–121, 565 (1999).

20. S. K. Choi, D. Y. Jung, S. Y. Kweon, and S. K. Jung, *Thin Solid Films* 279, 110 (1996).

21. T. P. Ong and R. P. H. Chang, *Appl. Phys. Lett.* 55, 2063 (1989).

22. R. L. C. Wu, A. K. Rai, A. Garscadden, P. Kee, H. D. Desai, and K. Miyoshi, *J. Appl. Phys.* 72, 110 (1992).

23. R. Erz, W. Dotter, D. Jung, and H. Ehrhardt, *Diamond Relat. Mater.* 2, 449 (1993).

24. D. M. Gruen, X. Pan, A. R. Krauss, S. Liu, J. Luo, and C. M. Foster, *J. Vac. Sci. Technol. A* 12, 1491 (1994).

25. V. I. Konov, A. A. Smolin, V. G. Ralchenko, S. M. Pimenov, E. D. Obraztsova, E. N. Loubnin, S. M. Metev, and G. Sepold, *Diamond Relat. Mater.* 4, 1073 (1995).

26. J. Lee, B. Hong, R. Messier, and R. W. Collins, *Appl. Phys. Lett.* 69, 1716 (1996).

27. J. Lee, R. W. Collins, R. Messier, and Y. E. Strausser, *Appl. Phys. Lett.* 70, 1527 (1997).

28. M. Zarrabian, N. Fourches-Coulon, G. Turban, C. Marhic, and M. Lancin, *Appl. Phys. Lett.* 70, 2535 (1997).

29. L. C. Nistor, J. V. Landuyt, V. G. Ralchenko, E. D. Obraztsova, and A. A. Smolin, *Diamond Relat. Mater.* 6, 159 (1997).

30. S. N. Kundu, M. Basu, A. B. Maity, S. Chaudhuri, and A. K. Pal, *Mater. Lett.* 31, 303 (1997).

31. D. Zhou, A. R. Krauss, L. C. Qin, T. G. McCauley, D. M. Gruen, T. D. Corrigan, and R. P. H. Chang, *J. Appl. Phys.* 82, 4546 (1997).

32. D. Zhou, T. G. McCauley, L. C. Qin, A. R. Krauss, and D. M. Gruen, *J. Appl. Phys.* 83, 540 (1998).

33. S. Hogmark, O. Hollman, A. Alahelisten, and O. Hedenqvist, *Wear* 200, 225 (1996).

34. P. Hollman, O. Wanstrand, and S. Hogmark, *Diamond Relat. Mater.* 7, 1471 (1998).

35. D. Zhou, D. M. Gruen, L. C. Qin, T. G. McCauley, and A. R. Krauss, *J. Appl. Phys.* 84, 1981 (1998).

36. S. A. Catledge and Y. K. Vohra, *J. Appl. Phys.* 84, 6469 (1998).

37. S. A. Catledge and Y. K. Vohra, *J. Appl. Phys.* 86, 698 (1999).

38. D. M. Bhusari, J. R. Yang, T. Y. Wang, S. T. Lin, K. H. Chen, and L. C. Chen, *Solid State Commun.* 107, 301 (1998).

39. K. H. Chen, D. M. Bhusari, J. R. Yang, S. T. Lin, T. Y. Yang, and L. C. Chen, *Thin Solid Films* 332, 34 (1998).

40. L. C. Chen, T. Y. Wang, J. R. Yang, K. H. Chen, D. M. Bhusari, Y. K. Chang, H. H. Hsieh, and W. F. Pong, *Diamond Relat. Mater.* 9, 877 (2000).

41. T. Sharda, T. Soga, T. Jimbo, and M. Umeno, *Diamond Relat. Mater.* 9, 1331 (2000).

42. T. Sharda, M. Umeno, T. Soga, and T. Jimbo, *Appl. Phys. Lett.* 77, 4304 (2000).

43. T. Sharda, T. Soga, T. Jimbo, and M. Umeno, *Diamond Relat. Mater.* 10, 1592 (2001).

44. C. Z. Gu and X. Jiang, *J. Appl. Phys.* 88, 1788 (2000).

45. L. C. Chen, P. D. Kichambare, K. H. Chen, J.-J. Wu, J. R. Yang, and S. T. Lin, *J. Appl. Phys.* 89, 753 (2001).

46. S. Jiao, A. Sumant, M. A. Kirk, D. M. Gruen, A. R. Krauss, and O. Auciello, *J. Appl. Phys.* 90, 118 (2001).

47. A. Heiman, I. Gouzman, S. H. Christiansen, H. P. Strunk, G. Comtet, L. Hellner, G. Dujardin, R. Edrei, and A. Hoffman, *J. Appl. Phys.* 89, 2622 (2001).

48. H. Yoshikawa, C. Morel, and Y. Koga, *Diamond Relat. Mater.* 10, 1588 (2001).

49. X. Jiang and C. L. Jia, *Appl. Phys. Lett.* 80, 2269 (2002).

50. H. W. Xin, Z. M. Zhang, X. Ling, Z. L. Xi, H. S. Shen, Y. B. Dai, and Y. Z. Wan, *Diamond Relat. Mater.* 11, 228 (2002).

51. W. B. Yang, F. X. Lü, and Z. X. Cao, *J. Appl. Phys.* 91, 10068 (2002).

52. C. Wild, P. Koidl, W. Muller-Sebert, H. Walcher, R. Kohl, N. Herres, R. Locher, R. Samlemski, and R. Brenn, *Diamond Relat. Mater.* 2, 158 (1993).

53. T. Sharda, T. Soga, T. Jimbo, and M. Umeno, *Diamond Relat. Mater.* 10, 561 (2001).

54. S. Saito, N. Fujimori, O. Fukunaga, M. Kamo, K. Kobashi, and M. Yoshikawa, "Advances in New Diamond Science and Technology." MYU, Tokyo, 1994.

55. K. Hirabayashi and S. Matsumoto, *J. Appl. Phys.* 75, 1151 (1994).

56. S. Bhattacharyya, O. Auciello, J. Birrel, J. A. Carlisle, L. A. Curtiss, A. N. Goyette, D. M. Gruen, A. R. Krauss, J. Schlueter, A. Sumant, and P. Zapol, *Appl. Phys. Lett.* 79, 1441 (2001).

57. K. Teii, H. Ito, M. Hori, T. Takeo, and T. Goto, *J. Appl. Phys.* 87, 4572 (2000).

58. X. T. Zhou, Q. Li, F. Y. Meng, I. Bello, C. S. Lee, S. T. Lee, and Y. Lifshitz, *Appl. Phys. Lett.* 80, 3307 (2002).

59. N. Jiang, S. Kujime, I. Ota, T. Inaoka, Y. Shintani, H. Makita, A. Hatta, and A. Hiraki, *J. Cryst. Growth* 218, 265 (2000).

60. K. Chakrabarti, R. Chakrabarti, K. K. Chattopadhyay, S. Chaudhrui, and A. K. Pal, *Diamond Relat. Mater.* 7, 845 (1998).

61. T. Sharda and T. Soga, "Recent Developments in Applied Physics and Material Science" (S. Bhattacharyya, Ed.). Transtech, in press.

62. T. Sharda, T. Soga, T. Jimbo, and M. Umeno, *J. Appl. Phys.* 89, 4874 (2001).

63. W. Zhu, G. P. Kochanski, and S. Jin, *Science* 282, 1471 (1998).

64. J. Liu, V. V. Zhirnov, A. F. Mayers, G. J. Wojak, W. B. Choi, J. J. Hren, S. D. Wolter, M. T. McClure, B. R. Stoner, and J. T. Glass, *J. Vac. Sci. Technol. B* 13, 422 (1995).

65. A. Göhl, A. N. Alimova, T. Habermann, A. L. Mescheryakova, D. Nau, and G. Müller, *J. Vac. Sci. Technol. B* 17, 670 (1999).

66. K. Wu, E. G. Wang, J. Chen, and N. S. Xu, *J. Vac. Sci. Technol. B* 17, 1059 (1999).

67. K. Wu, E. G. Wang, Z. X. Cao, Z. L. Wang, and X. Jiang, *J. Appl. Phys.* 88, 2967 (2000).

68. C. Gu, X. Jiang, Z. Jin, and W. Wang, *J. Vac. Sci. Technol. B* 19, 962 (2001).

69. O. Gröning, L.-O. Nilsson, P. Gröning, and L. Schlapbach, *Solid State Electron.* 45, 929 (2001).

70. T. Sharda, T. Soga, and T. Jimbo, *J. Appl. Phys.* 93, 101 (2003).

71. H. Hirari, K. Kondo, N. Yoshizawa, and M. Shiraishi, *Appl. Phys. Lett.* 64, 1797 (1994); H. Hirai, K. Kondo, M. Kim, H. Koinuma, K. Kurashima, and Y. Bando, *Appl. Phys. Lett.* 71, 3016 (1997).

72. F. Davanloo, T. J. Lee, H. Park, J. H. You, and C. B. Collins, *J. Mater. Res.* 8, 3090 (1993).

73. F. Davanloo, T. J. Lee, D. R. Jander, H. Park, J. H. You, and C. B. Collins, *J. Appl. Phys.* 71, 1446 (1992).

74. F. Davanloo, C. B. Collins, and K. J. Koivusaari, *J. Mater. Res.* 14, 3474 (1999).

75. N. Toprani, S. A. Catledge, Y. K. Vohra, and R. Thompson, *J. Mater. Res.* 15, 1052 (2000).

76. T. Sharda, M. Umeno, T. Soga, and T. Jimbo, *Appl. Phys. Lett.* 80, 2880 (2002).

77. "Diamond and Diamond-Like Films and Coatings" (R. E. Clausing, L. L. Horton, J. C. Angus, and P. Koidl, Eds.). Plenum, New York, 1991.

78. A. Grill, *Diamond Relat. Mater.* 8, 428 (1999).

79. C. B. Collins, F. Davanloo, T. J. Lee, H. Park, and J. H. You, *J. Vac. Sci. Technol. B* 11, 1936 (1993).

80. R. Lossy, D. L. Pappas, R. A. Roy, J. P. Doyle, and J. Bruley, *J. Appl. Phys.* 77, 4750 (1995).

81. B. Schultrich, H. J. Scheibe, D. Drescher, and H. Ziegele, *Surf. Coat. Technol.* 98, 1097 (1998).

82. Y. K. Kong, J. J. Kim, C. Park, J. S. Kim, and J. K. Kim, *J. Vac. Sci. Technol. B* 16, 729 (1998).

83. D. R. Mckenzie, D. A. Muller, and B. A. Paithorpe, *Phys. Rev. Lett.* 67, 773 (1991).

84. Y. Lifshitz, *Diamond Relat. Mater.* 5, 388 (1996).

85. W. Banholzer, *Surf. Coat. Technol.* 53, 1 (1992).

86. T. Sharda, D. S. Misra, D. K. Avasthi, and G. K. Mehta, *Solid State Commun.* 98, 879 (1996).

87. T. Sharda, D. S. Misra, and D. K. Avasthi, *Vacuum* 47, 1269 (1996).

88. Y. Lifshitz, G. D. Lempert, and E. Grossman, *Phys. Rev. Lett.* 72, 2753 (1994).

89. P. J. Fallon, V. S. Veerasamy, C. A. Davis, J. Robertson, G. A. J. Amaratunga, W. I. Milne, and J. Koskinen, *Phys. Rev. B* 48, 4777 (1993).

90. T. Lin, Y. Yu, T. S. Wee, Z. X. Shen, and K. P. Loh, *Appl. Phys. Lett.* 77, 2692 (2000).

91. T.-S. Yang, J.-Y. Lai, C.-L. Cheng, and M.-S. Wong, *Diamond Relat. Mater.* 10, 2161 (2001).

92. J. M. Lopez, F. J. Gordillo-Vazquez, and J. M. Albella, *Appl. Surf. Sci.* 185, 321 (2002).

93. G. Amaratunga, A. Putnis, K. Clay, and W. Milne, *Appl. Phys. Lett.* 55, 634 (1989).

94. G. A. J. Amaratunga, S. R. P. Silva, and D. A. McKenzie, *J. Appl. Phys.* 70, 5374 (1991).

95. R. B. Corvin, J. G. Harrison, S. A. Catledge, and Y. K. Vohra, *Appl. Phys. Lett.* 80, 2550 (2002).

96. S. Yugo, T. Kanai, T. Kimura, and T. Muto, *Appl. Phys. Lett.* 58, 1036 (1991).

97. S. T. Lee, H. Y. Peng, X. T. Zhou, N. Wang, C. S. Lee, I. Bello, and Y. Lifshitz, *Science* 287, 104 (2000).

98. T. Sharda, T. Soga, T. Jimbo, and M. Umeno, *Diamond Relat. Mater.* 10, 352 (2001).

99. O. Groning, O. M. Kuttel, P. Groning, and L. Schlapbach, *J. Vac. Sci. Technol. B* 17, 1970 (1999).

100. T. S. Yang, J. Y. Lai, M. S. Wong, and C. L. Cheng, *J. Appl. Phys.* 92, 2133 (2002).

101. T. S. Yang, J. Y. Lai, M. S. Wong, and C. L. Cheng, *J. Appl. Phys.* 92, 4912 (2002).

102. X. T. Zhou, Q. Li, F. Y. Meng, I. Bello, C. S. Lee, S. T. Lee, and Y. Lifshitz, Paper P1.01.11, presented at the "Eighth International Conference New Diamond Science and Technology 2002," The University of Melbourne, Australia.

103. N. Jiang, K. Sugimoto, K. Nishimura, Y. Shintani, and A. Hiraki, *J. Cryst. Growth* 242, 362 (2002).

104. S. Prawer, J. L. Peng, J. O. Orwa, J. C. McCallum, D. N. Jamieson, and L. A. Bursill, *Phys. Rev. B* 62, R16360 (2000).

105. Z. Wang, G. Yu, L. Yu, F. Zhu, D. Zhu, and H. Xu, *J. Appl. Phys.* 91, 3480 (2002).

106. H. Yusa, *Diamond Relat. Mater.* 11, 87 (2002).

107. Y. Gogotsi, S. Welz, D. A. Ersoy, and M. J. McNallan, *Nature* 411, 283 (2001).

108. N. S. Xu, J. Chen, Y. T. Feng, and S. Z. Deng, *J. Vac. Sci. Technol. B* 18, 1048 (2000).

109. E. Maillard-Schaller, O. M. Kuettel, L. Diederich, L. Schlapbach, V. V. Zhirnov and P. I. Belobrov, *Diamond Relat. Mater.* 8, 805 (1999).

110. S. Bhattacharyya and S. V. Subramanyam, *Appl. Phys. Lett.* 71, 632 (1997).

111. A. B. Anderson, E. J. Grantscharova, and J. C. Angus, *Phys. Rev. B* 54, 14341 (1996).

112. Th. Frauenheim, G. Jungnickel, P. Stich, M. Kaukonen, F. Weich, J. Widnay, and D. Porezag, *Diamond Relat. Mater.* 7, 348 (1998).

113. S. A. Kajihara, A. Antonelli, J. Bernholc, and R. Car, *Phys. Rev. Lett.* 66, 2010 (1991).

114. E. Rohrer, C. F. O. Graeff, R. Janssen, C. E. Nebel, H. Guettler, and R. Zachai, *Phys. Rev. B* 54, 7874 (1996).

115. S. Koizumi, M. Kamo, Y. Sato, H. Ozaki, and T. Inuzuka, *Appl. Phys. Lett.* 71, 1065 (1999).

116. I. Sakaguchi, M. N. Gamo, Y. Kikuchi, E. Yasu, H. Haneda, T. Suzuki, and T. Ando, *Phys. Rev. B* 60, R2139 (1999).

117. J. F. Prins, *Phys. Rev. B* 61, 7191 (2000).

118. M. Nesladek, K. Meykens, K. Haenen, L. M. Stals, T. Teraji, and S. Koizumi, *Phys. Rev. B* 59, 14852 (1999).

119. T. Saito, M. Kameta, K. Kusakabe, S. Morooka, H. Maeda, Y. Hayashi, and T. Asano, *Jpn. J. Appl. Phys.* 37, L543 (1998).

120. D. M. Malta, J. A. von Windheim, H. A. Wynands, and B. A. Fox, *J. Appl. Phys.* 77, 1536 (1995).

121. J. Robertson and C. A. Davis, *Diamond Relat. Mater.* 4, 441 (1995).

122. S. Bhattacharyya, F. Richter, U. Starke, H. Griesmann, and A. Heinrich, *Appl. Phys. Lett.* 79, 4157 (2001).

123. C. Ronning, U. Griesmeier, M. Gross, H. C. Hofsäss, R. G. Downing, and G. P. Lamaze, *Diamond Relat. Mater.* 4, 666 (1995).

124. Th. Koehler, G. Jungnickel, and Th. Frauenheim, *Phys. Rev. B* 60, 10864 (1999).

125. S. Bhattacharyya, C. Vallee, C. Cardinaud, O. Chauvet, and G. Turban, *J. Appl. Phys.* 85, 2162 (1999).

126. S. Bhattacharyya, O. Madel, S. Schultze, M. Heitschold, P. Häussler, and F. Richter, *Phys. Rev. B* 61, 3927 (2000).

127. C. A. Davis, D. R. McKenzie, Y. Yin, E. Kravtchinskaia, G. A. J. Amaratunga, and V. S. Veeraswamy, *Philos. Mag. B* 69, 1133 (1994).

128. D. I. Jones and A. D. Stewart, *Philos. Mag.* 46, 423 (1982).

129. S. Bhattacharyya, unpublished data.

130. F. Cleri, P. Keblinski, L. Colombo, D. Wolf, S. R. Phillpot, *Europhys. Lett.* 46, 671 (1999).

131. P. Kleblinski, S. R. Phillpot, D. Wolf, and H. Gleiter, *Nanostruct. Mater.* 12, 339 (1999).

132. P. Zapol, M. Sternberg, L. A. Curtiss, T. Frauenheim, and D. M. Gruen, *Phys. Rev. B* 65, 045403 (2001).

133. S. Bhattacharyya, M. Lubbe, P. R. Bressler, D. R. T. Zahn, and F. Richter, *Diamond Relat. Mater.* 11, 8 (2002).

134. T. Xu, S. Yang, J. Lu, Q. Xue, J. Li, W. Guo, and Y. Sun, *Diamond Relat. Mater.* 10, 1441 (2001).

135. E. P. Visser, G. J. Bauhuis, G. Janssen, W. Vollenberg, W. J. P. van Enckevort, and L. J. Giling, *J. Phys.: Condens. Matter* 4, 7365 (1992).

136. K. J.-P. Lagrange, A. Deneuville, and E. Gheeraert, *Diamond Relat. Mater.* 7, 1390 (1998).

137. Y. F. Tsay, K. P. Ananthanarayanan, P. J. Gielisse, and S. S. Mitra, *J. Appl. Phys.* 43, 3677 (1972).

138. B. R. Stoner, C.-T. Kao, D. M. Malta, and R. C. Glass, *Appl. Phys. Lett.* 62, 2347 (1993).
139. J. O. Orwa, J. C. McCallum, S. Prawer, K. W. Nugent, and D. N. Jamieson, *Diamond Relat. Mater.* 8, 1642 (1999).
140. N. Fujimori, H. Nakahata, and T. Imai, *Jpn. J. Appl. Phys.* 29, 824 (1990).
141. A. T. Collins, *Semicond. Sci. Technol.* 4, 605 (1989).
142. K. J.-P. Lagrange, A. Deneuville, and E. Gheeraert, *Diamond Relat. Mater.* 7, 1390 (1998).
143. A. S. Williams, E. C. Lightowlers, and A. T. Collins, *J. Phys. C* 3, 1727 (1970).
144. K. Nihimura, K. Das, and J. T. Glass, *J. Appl. Phys.* 69, 3142 (1991).
145. N. F. Mott and E. A. Davis, "Electronic Processes in Non-Crystalline Solids." Clarendon Press, Oxford, 1979.
146. V. S. Veeraswamy, J. Yuan, G. A. J. Amaratunga, W. I. Milne, K. W. R. Gilkes, M. Weiler, and L. M. Brown, *Phys. Rev. B* 48, 17954 (1993).
147. M. A. Monclus, D. C. Cameron, R. Barklie, and M. Collins, *Surf. Coat. Technol.* 54, 116 (1999).
148. D. Chen, A. Weia, S. P. Wong, and S. Peng, *Diamond Relat. Mater.* 8, 1130 (1999).
149. Z. Y. Chen, Y. H. Yu, J. P. Zhao, S. Q. Yang, T. S. Shi, X. H. Liu, E. Z. Luo, J. B. Xu, and I. H. Wilson, *Thin Solid Films* 339, 74 (1999).
150. S. Bhattacharyya, C. Carinaud, and G. Turban, *J. Appl. Phys.* 83, 4491 (1998).
151. S. Bhattacharyya, M. Lubbe, and F. Richter, *J. Appl. Phys.* 88, 5043 (2000).
152. K. Okano, S. Koizumi, S. R. P. Silva, and G. A. J. Amaratunga, *Nature* 381, 140 (1996).
153. M. W. Geis, N. N. Efremow, K. E. Krohn, J. C. Twichell, T. M. Lyszczarz, R. Kalish, J. A. Greer, and M. D. Tabat, *Nature* 393, 431 (1998).
154. K. Okano, T. Yamada, H. Ishihara, S. Koizumi, and J. Itoh, *Appl. Phys. Lett.* 70, 2201 (1997).
155. A. T. Sowers, B. L. Ward, S. L. English, and R. J. Nemanich, *J. Appl. Phys.* 86, 3973 (1999).
156. A. V. Karabutov, V. D. Frolov, and V. I. Konov, *Diamond Relat. Mater.* 10, 840 (2001).
157. S. Jou, H. J. Doerr, and R. F. Bunshah, *Thin Solid Films* 280, 256 (1996).
158. V. V. Zhirnov, E. T. Givargizov, and P. S. Plekhanov, *J. Vac. Sci. Technol. B* 13, 418 (1995).
159. S. G. Wang, Q. Zhang, S. F. Yoon, J. Ahn, Q. Wang, Q. Zhou, and D. J. Yang, *J. Vac. Sci. Technol. B* 20, 1982 (2002).
160. M. Hiramatsu, C. H. Lau, A. Bennett, and J. S. Foord, *Thin Solid Films* 407, 18 (2002).
161. R. Cai, Y. Zhang, Z. Yang, D. He, and G. Chen, *Int. J. Mod. Phys. B* [*Cosmol. Nucl. Phys.*] 16, 998 (2002).
162. X. Jiang, F. C. K. Au, and S. T. Lee, *J. Appl. Phys.* 92, 2880 (2002).
163. S. Gupta, B. L. Weiss, B. R. Weiner, L. Pilione, A. Badzian, and G. Morell, *J. Appl. Phys.* 92, 3311 (2002).
164. S. Gupta, B. R. Weiner, and G. Morell, *Diamond Relat. Mater.* 11, 799 (2002).
165. U. Hoffman, A. Weber, T. Loehken, C.-P. Klages, C. Speath, and F. Richter, *Diamond Relat. Mater.* 7, 682 (1998).
166. O. Groning, O. M. Kuttel, P. Groning, and L. Schlapbach, *Appl. Phys. Lett.* 71, 2253 (1997).
167. G. A. G. Amaratunga and S. R. P. Silva, *Appl. Phys. Lett.* 68, 2529 (1996).
168. A. C. Ferrari and J. Robertson, *Phys. Rev. B* 63, 121405 (2001).
169. S. Prawer, K. W. Nugent, D. N. Jamieson, J. O. Orwa, L. A. Bursill, and J. L. Peng, *Chem. Phys. Lett.* 332, 93 (2001).
170. T. Sharda, T. Soga, T. Jimbo, and M. Umeno, *J. Nanosci. Nanotech.* 1, 287 (2001).
171. V. Paillard, P. Melinon, V. Dupuis, J. P. Perez, and A. Perez, *Phys. Rev. Lett.* 71, 4170 (1993).
172. V. Paillard, P. Melinon, V. Dupuis, A. Perez, J. P. Perez, G. Guiraud, and J. Formazero, *Phys. Rev. B* 49, 11433 (1994).
173. R. J. Nemanich, J. T. Glass, G. Lucovsky, and R. E. Shroder, *J. Vac. Sci. Technol. A* 6, 1783 (1988).
174. S. Logothetidis, *Appl. Phys. Lett.* 69, 158 (1996).
175. D. R. Tallant, J. E. Parmeter, M. P. Siegal, and R. L. Simpson, *Diamond Relat. Mater.* 4, 191 (1995).
176. T. A. Friedmann, K. F. McCarty, J. C. Barbour, M. P. Siegal, and D. C. Dibble, *Appl. Phys. Lett.* 68, 1643 (1996).
177. N. Wada and S. A. Solin, *Physica B* 105, 353 (1981).
178. J. Birrell, J. Carlisle, O. Auciello, D. M. Gruen, and J. M. Gibson, *Appl. Phys. Lett.* 81, 2235 (2002).
179. Y. K. Chang, H. H. Hsish, W. F. Pong, F. Z. Chien, P. K. Tsang, M. H. Tsai, L. C. Chen, T. Y. Wang, K. H. Chen, D. M. Bhusari, J. R. Yang, and S. T. Lin, *Phys. Rev. Lett.* 82, 5377 (1999).
180. L. Ley, J. Ristein, and R. Graupner, *Phys. Rev. Lett.* 84, 5679 (2000).
181. Z. Sun, J. R. Shi, B. K. Tay, and S. P. Lau, *Diamond Relat. Mater.* 9, 1979 (2000).
182. H. Richter, Z. P. Wang, and L. Ley, *Solid State Commun.* 39, 625 (1981).
183. I. H. Campbell and P. M. Fauchet, *Solid State Commun.* 39, 625 (1981).
184. A. K. Arora, T. R. Ravindran, G. L. N. Reddy, A. K. Sikder, and D. S. Misra, *Diamond Relat. Mater.* 10, 1477 (2001).
185. M. Roy, V. C. George, A. K. Dua, P. Raj, S. Schulze, D. A. Tenne, G. Salvan, and D. R. T. Zahn, *Diamond Relat. Mater.* 11, 1858 (2002).
186. D. M. Bhusari, J. R. Yang, T. Y. Wang, S. T. Lin, K. H. Chen, S. T. Lin, and L. C. Chen, *J. Mater. Res.* 13, 1769 (1998).
187. J. Tauc, in "Optical Properties of Solids" (F. Abeles, Ed.), Ch. 5. North-Holland, Amsterdam, 1972.
188. E. C. Freeman and W. Paul, *Phys. Rev. B* 20, 716 (1979).
189. J. Li, D. He, W. Guo, J. Zhang, Y. Sun, Q. Lei, and X. Gao, *Int. J. Mod. Phys. B* [*Cosmol. Nucl. Phys.*] 16, 1013 (2002).
190. P. K. Tien, R. Ulrich, and J. R. Martin, *Appl. Phys. Lett.* 14, 291 (1969).
191. R. Ulrich and R. Torge, *Appl. Opt.* 12, 2901 (1973).
192. X. Tang, Y. Yuan, K. Wongchotigul, and M.G. Spencer, *Appl. Phys. Lett.* 70, 3206 (1997).
193. M. Ree, C.W. Chu, and M. J. Goldberg, *J. Appl. Phys.* 75, 1410 (1994).
194. E. Dogheche, P. Ruterana, and F. Omnes, *J. Appl. Phys.* 90, 4410 (2001).
195. E. Dogheche, B. Belgacem, D. Remiens, P. Ruterana, and F. Omnes, *Appl. Phys. Lett.* 75, 3324 (1999).
196. D. C. Hall, H. Wu, L. Kou, R. J. Epstein, O. Blum, and H. Hou, *Appl. Phys. Lett.* 75, 1110 (1999).
197. K. M. Wang, B. R. Shi, N. Cue, R. F. Xiao, F. Lu, H. Hu, and Y. G. Liu, *J. Vac. Sci. Technol. A* 19, 394 (2001).
198. J. Rams, A. Tejeda, and J. M. Cabrera, *J. Appl. Phys.* 82, 994 (1997).
199. Y. Kim and A. Erbil, *Appl. Phys. Lett.* 70, 143 (1997).
200. D. F. Edwards and H. R. Philipp, in "HandBook of Optical Constants of Solid" (E. D. Palik, Ed.), p. 665. Academic, New York, 1985.
201. P. Djemia, C. Dugautier, T. Chauveau, E. Dogheche, M. I. D. Barros, and L. Vandenbulcke, *J. Appl. Phys.* 90, 3771 (2001).
202. R. Swanepoel, *J. Phys. E* 16, 1214 (1983).
203. F. Jelezko, I. Popa, A. Gruber, C. Tietz, J. Wrachtrup, A. Nizovtsev, and S. Kilin, *Appl. Phys. Lett.* 81, 2160 (2002).
204. S. Veprek, *J. Vac. Sci. Technol. A* 17, 2401 (1999).
205. J. Ouellette, *Ind. Physicist* 3, 15 (1997).
206. B. Bushan, V. V. Subramanian, A. Malshe, B. K. Gupta, and J. Ruan, *J. Appl. Phys.* 74, 41 (1993).
207. A. Erdemir, M. Halter, G. R. Fenske, A. Krauss, D. M. Gruen, S. M. Pimenov, and V. I. Konov, *Surf. Coat. Technol.* 94, 537 (1997).

208. R. K. Singh, D. R. Gilbert, J. Fitz-Geralg, S. Harkness, and D. G. Lee, *Science* 272, 396 (1996).
209. T. A. Friedmann, J. P. Sullivan, J. A. Knapp, D. R. Tallant, and D. M. Follstaedt, D. L. Medlin, and P. B. Mirkarimi, *Appl. Phys. Lett.* 71, 3820 (1997).
210. M. Chhowalla, Y. Yin, G. A. J. Amaratunga, D. R. McKenzie, and Th. Fraurnheim, *Appl. Phys. Lett.* 69, 2344 (1996).
211. P. J. Fallon, V. S. Veerasamy, and C. A. Davis, *Phys. Rev. B* 48, 4777 (1993).
212. M. Weiler, S. Sattel, and K. Jung, *Appl. Phys. Lett.* 64, 2797 (1994).
213. F. C. Marques, R. G. Lacerda, G. Y. Odo, and C. M. Lepienski, *Thin Solid Films* 332, 113 (1998).
214. R. G. Lacerda and F. C. Marques, *Appl. Phys. Lett.* 73, 617 (1998).
215. S. Sattel, J. Robertson, M. Scheib, and H. Ehrhardt, *Appl. Phys. Lett.* 69, 497 (1996).
216. S. Logothetidis, M. Gioti, P. Patsalas, and C. Charitidis, *Carbon* 37, 765 (1999).
217. O. R. Monteiro, M. P. Delplancke-Ogletree, I. G. Brown, and J. W. Ager III, *Mater. Res. Soc. Symp. Proc.* 438, 599 (1997).
218. S. Anders, D. L. Callahan, G. M. Pharr, T. Y. Tsui, and C. S. Bhatia, *Surf. Coat. Technol.* 9495, 189 (1997).
219. P. Keblinski, D. Wolf, F. Cleri, S. R. Phillpot, and H. Gleiter, *Mater. Res. Soc. Bull.* 23, 36 (1998).
220. P. Keblinski, D. Wolf, S. R. Phillpot, and H. Gleiter, *J. Mater. Res.* 13, 2077, 1998.
221. B. Palosz, S. Gierlotka, S. Stelmakh, R. Pielaszek, P. Zinn, M. Winzenick, U. Bissmayer, and H. Boysen, *J. Alloys Compounds* 286, 184 (1999).
222. V. D. Blank, S. G. Buga, N. R. Serebryanaya, G. A. Dubitsky, M. Yu. Popov, V. M. Prokohorov, N. A. Lvova, and S. N. Sulyanov, *Rev. High Pressure Sci. Tech.* 7, 972 (1998).
223. M. P. Siegal, D. R. Tallant, P. N. Provencio, D. L. Overmyer, R. L. Simpson, and L. J. Martinez-Miranda, *Appl. Phys. Lett.* 76, 3052 (2000).
224. T. Grogler, E. Zeiler, A. Franz, O. Plewa, S. M. Rosiwal, and R. F. Singer, *Surf. Coat. Technol.* 112, 129 (1999).
225. S. A. Catledge, J. Borham, Y. K. Vohra, W. R. Lacefield, and J. E. Lemons, *J. Appl. Phys.* 91, 5347 (2002).
226. M. D. Fries and Y. K. Vohra, *J. Phys. D* 35, L105 (2002).
227. S.-P. Hong, H. Yoshikawa, K. Wazumi, and Y. Koga, *Diamond Relat. Mater.* 11, 877 (2002).
228. S. V. Pepper, *J. Vac. Sci. Technol.* 20, 643 (1982).
229. S. Chandrasekar and B. Bhushan, *Wear* 153, 79 (1992).
230. T. Xu, S. Yang, M. Chen, J. Tian, Q. Xue, J. Li, and W. Guo, *J. Phys. D* 35, 788 (2002).
231. T. N. Rao and A. Fujishima, *Diamond Relat. Mater.* 9, 384 (2000).
232. W. Yang, O. Auciello, J. E. Butler, W. Cai, J. A. Carlisle, J. Gerbi, D. M. Gruen, T. Knickerbocker, T. L. Lasseter, J. N. Russel, Jr., L. M. Smith, and R. J. Hamers, *Nature Mater.* 1, 253 (2002).
233. K. Takahashi, Paper 3.1, presented at the "13th European Conference on Diamond, Diamond-Like Materials, Carbon Nanotubes, Nitrides and Silicon Carbide (Diamond 2002)," 8–13 September 2002, Granada, Spain.
234. A. A. Greeneko and N. F. Shulga, *Phys. Lett.* 454, 161 (1999).
235. N. Doble, L. Gatignon, and P. Grafstrom, *Nucl. Instrum. Methods B* 119, 181 (1996).
236. A. Baurichter, K. Kirsebom, R. Medenwaldt, S. P. Møller, T. Worm, E. Uggerhøj, U. Mikkelsen, P. Graftström, L. Gatignon, K. Elsener, N. Doble, C. Biino, A. Freund, Z. Vilakazi, M. Hage-Ali, P. Siffert, and M. Clément, *Nucl. Instrum. Methods B* 119, 172 (1996).
237. D. Pauschinger, K. Becker, and R. Ludewig, *Rev. Sci. Instrum.* 66, 2177 (1995).
238. Z. R. Dai, J. P. Bradley, D. J. Joswiak, D. E. Brownlee, H. G. M. Hill, and M. J. Genge, *Nature* 418, 157 (2002).
239. S. E. Haggerty, *Science* 285, 851 (1999).
240. L. J. Allamandola, S. A. Sandford, A. G. G. M. Tielens, and T. M. Herbst, *Science* 260, 64 (1993).

Dielectric Properties of Nanoparticles

S. Berger

Technion, Haifa, Israel

CONTENTS

1. INTRODUCTION

Dielectric properties of solids are determined by electric dipoles having a length scale of a few angstroms. A local change in microstructure or composition within this length scale affects the type and intensity of the dipole. As the particle size decreases to the nanometer scale local microstructure and composition changes relative to the bulk state are greatly increased especially at the particle surfaces and may reach 50% of the total material volume. Consequently, the dielectric properties of nanometer-sized particles are unique and different than those of bulk-sized particles. Fabrication methods of nanometer-sized particles have been developed to a mature state where high control on size and composition is achievable which enables efficient usage of their unique dielectric properties. Indeed, nanometer-sized particles are being used in various dielectric-based applications such as capacitors, electronic memories, and optical filters. In addition, intensive studies of further exploitation of their unique dielectric properties in future high-tech devices are being carried out.

In spite of the significant experimental data and knowledge gathered on dielectric properties of nanometer-sized particles the level of their understanding and modeling is far from being satisfactory. Even in simple nanostructures the theoretical models succeed in describing only qualitatively the dielectric behavior. Quantitative theoretical expressions usually depend on immeasurable parameters and fail in evaluating the experimental results. In more complicated nanostructures there is not even basic understanding of their dielectric properties due to the difficulty in identifying the different types of electric dipoles at the particle surfaces and in evaluating the contribution of each type of these dipoles to the macro dielectric properties of the materials.

This chapter makes a first attempt to review the current knowledge and understanding of dielectric properties of nanometer-sized particles. It is divided into two main sections; the first one refers to linear and the second one refers to nonlinear dielectric materials. Each section is subdivided to homogeneous and inhomogeneous systems. Each system is first defined according to microstructure and composition characteristics. The dielectric properties of each system are then summarized by presenting experimental results on the effect of decreasing the particles from bulk to nanometer size as well as changing their microstructure and composition on the dielectric permittivity, dielectric loss, and temperature-dependent dielectric response. In some cases, unique preparation methods of the particles and their technological applications are detailed. Finally, the dielectric behavior of each system is explained by presenting various theoretical models and emphasizing the limitations of each model in predicting the dielectric properties.

2. LINEAR DIELECTRICS

2.1. Homogeneous Materials

The dielectric behavior of homogeneous linear dielectric materials is changed as the particle size decreases from a typical bulk value into a nanometer scale. Experimental studies have reported that nanometer-sized particles have a higher dielectric permittivity than that of their bulk-sized particles especially at low frequencies. For example, in nanometer-sized amorphous SiO_2 particles having an average size of about 20 nm, the relative dielectric permittivity (dielectric constant $k' = \varepsilon'/\varepsilon_0$) is equal to about 13 at 1 kHz, which is higher by a factor of 3.3 than that of the bulk particles [1]. Another example shows that the dielectric constant of nanometer-sized amorphous silicon nitride particles is equal to 380 at 10 kHz, which is higher by a factor of about 48 compared to that of the micron-sized particles [2]. A similar dielectric enhancement was also reported in other materials such as Al_2O_3 [3], Si [3], and TiO_2 [4]. This dielectric enhancement is attributed to dipoles associated with the interfaces of the nanometer-sized particles. These dipoles result from different types of point defects at the particle interfaces such as dangling bonds, twisted

bonds, and bonds with adsorbed foreign polar molecules. Interface dipoles associated with dangling bonds were identified in nanometer-sized SiO_2 particles by using electron paramagnetic resonance (EPR) spectroscopy [1]. The density of these dipoles was reduced by thermal annealing, without changing the particles size, which results in a decrease of the dielectric constant [1]. A similar thermal annealing effect was observed in nanometer-sized SiC particles [5]. Interface dipoles associated with adsorbed polar molecules were identified in nanometer-sized Fe_2O_3 particles [6]. Interface dipoles have different relaxation times than those of bulk dipoles. For example, two different relaxation times that differ from each other by almost an order of magnitude were measured for two different types of interface dipoles in nanometer-sized Fe_2O_3 particles [6].

The dielectric permittivity of nanometer-sized particles can be described by the Havriliak–Negami (HN) expression [7],

$$\varepsilon^* = \varepsilon_\infty + \frac{(\varepsilon_s - \varepsilon_\infty)}{[1 + (i\omega\tau_0)^\beta]^\alpha} \qquad (1)$$

where ε_s is the static permittivity, ε_∞ is the high frequency permittivity, ω is the angular frequency, τ_0 is the mean relaxation time, and β and α are parameters that vary between 0 and 1 and describe the symmetric and asymmetric broadening of the relaxation process. The dependence of ε' and ε'' on the applied field frequency can be obtained by rearranging Eq. (1). For example, in the case of a symmetric broadening of the relaxation process ($\alpha = 1$) the dependence of ε' and ε'' on ω is as follows:

$$\varepsilon'(\omega) = \varepsilon_\infty + \frac{(\varepsilon_s - \varepsilon_\infty)(1 + (\omega\tau_0)^\beta \cos(\beta\pi/2))}{1 + 2(\omega\tau_0)^\beta \cos(\beta\pi/2) + (\omega\tau_0)^{2\beta}} \qquad (2)$$

$$\varepsilon''(\omega) = \frac{(\varepsilon_s - \varepsilon_\infty)(\omega\tau_0)^\beta \cos(\beta\pi/2)}{1 + 2(\omega\tau_0)^\beta \cos(\beta\pi/2) + (\omega\tau_0)^{2\beta}} \qquad (3)$$

The dielectric behavior of bulk-sized particles is usually characterized by a dominant polarization mechanism of bulk dipoles having a narrow distribution of relaxation times ($\beta \sim 1$). In this case, the plot of ε' vs. ω, according to Eq. (2), shows the Debye behavior characterized by a sharp decrease of ε' from ε_s to ε_∞ within a narrow range of frequencies around $\omega = \tau_0^{-1}$ (Fig. 1a). The mean dielectric loss, ε''_{mean}, is

generally composed of three contributions that depend on frequency and temperature,

$$\varepsilon''_{mean}(\omega, T) = \varepsilon''_{pol}(\omega, T) + \varepsilon''_{inter}(\omega, T) + \varepsilon''_{dc}(\omega, T) \qquad (4)$$

where $\varepsilon''_{pol}(\omega, T)$ results from dipolar reorientation, $\varepsilon''_{inter}(\omega, T)$ is associated with interface polarization, and $\varepsilon''_{dc}(\omega, T)$ results from the dc electrical conductivity. The first component of Eq. (4) is detailed by Eq. (3) for $\beta = 1$, the second component of Eq. (4) is also included in Eq. (3) for the case of $\beta < 1$, and the third component of Eq. (4) depends on the dc electrical conductivity as

$$\varepsilon''_{dc}(\omega, T) = \sigma_{dc}(T)/(\varepsilon_0\omega^{1-K}) \qquad (5)$$

where $0 \leq k \leq 1$. In the case of bulk-sized particles, the second and third components of Eq. (4) are negligible compared to the first component due to the low density of interfaces and small dc electrical conductivity ($\sigma_{dc} < 10^{-10}\ \Omega^{-1}\,m^{-1}$). In this case the plot of ε'' vs. ω according to Eq. (3) for $\beta \sim 1$ shows a peak that spans over a narrow range of frequencies and reaches its maximum value at $\omega = \tau_0^{-1}$ (Fig. 2a). At the maximum point of the peak the oscillating charges are coupled directly with the oscillating field, which results in a maximum absorption of the electrical energy. In the case of nanometer-sized particles, β is closer to zero than to one, due to a large distribution of relaxation times owing to different types of interface dipoles. The plot of ε' vs. ω for this case (Fig. 1b) shows a continuous decrease of ε' over a wide range of frequencies from few mHz up to tens of KHz as observed experimentally. In nanometer-sized particles, the contribution of $\varepsilon''_{inter}(\omega, T)$ and $\varepsilon''_{dc}(\omega, T)$ to $\varepsilon''_{meas}(\omega, T)$ is not negligible as in bulk-sized particles but rather dominant. For example [6], in nanometer-sized F_2O_3 particles, the dc electrical conductivity was found to be about $10^{-7}\ \Omega^{-1}\,m^{-1}$ which is higher by 3 orders of magnitude compared to their bulk value. The relatively high dc electrical conductivity of nanometer-sized particles is attributed to the high density of interface states. These states can contribute charge carriers due to ionization and can also function as conduction centers for the transport of charge carriers. This interface contribution to the dielectric loss is dominant at low frequencies and decreases monotonously with increasing frequency (Fig. 2b). The dielectric differences between nanometer-sized and bulk-sized particles can also be seen in the graphical presentation of ε'' vs. ε' (Cole–Cole plot). In the case of bulk-sized particles the plot of ε'' vs. ε' results in a perfect semicircle curve which indicates a single polarization mechanism of dipoles having a narrow distribution of relaxation times (Fig. 3a). However, the Cole–Cole plot for nanometer-sized particles (Fig. 3b) shows a major deviation from a perfect semicircle especially at low frequencies which indicates a large distribution of relaxation times.

2.2. Heterogeneous Materials

Heterogeneous dielectric systems consist of components having different dielectric permittivity and electrical conductivity. The presence of different types of constituents enables
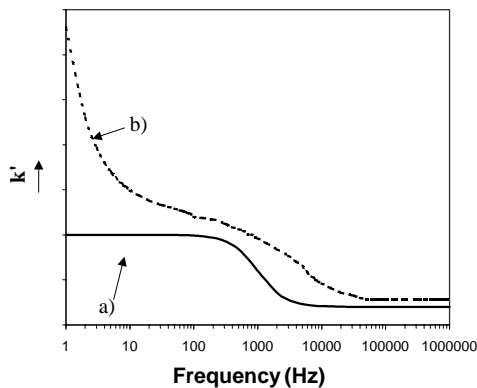
Figure 1. The dielectric constant as a function of applied field frequency for (a) bulk-sized particles and (b) nanometer-sized particles.
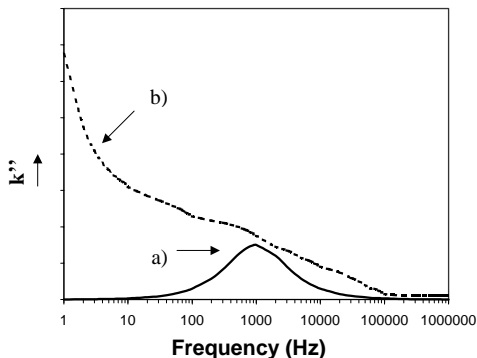
Figure 2. The dielectric loss as a function of applied field frequency for (a) bulk-sized particles and (b) nanometer-sized particles.

more degrees of freedom to change the dielectric properties and obtain unique dielectric behavior compared to homogeneous materials. At the interfaces between dissimilar particles space charges are built up and induce interfacial polarization. As the size of the particles decreases to the nanometer range and the volume fraction of the particles increases, the mechanism of interface polarization becomes more dominant in determining the dielectric behavior of the material. There is no general theoretical model that can predict the magnitude of interface polarization in heterogeneous materials due to the difficulty of defining quantitatively the particles interfaces. Current models of dielectric behavior include parameters that refer to different types of interface dipoles that can be evaluated only from experimental results. Most of the experimental studies and theoretical models of heterogeneous dielectric materials have focused on binary systems composed of metal particles embedded in an insulating matrix. These systems provide enhanced dielectric permittivity compared to the pure matrix over a wide range of metal compositions. More recently, an opposite trend has arisen, where heterogeneous systems having a dielectric permittivity lower than that of the matrix are fabricated and modeled especially for microelectronic applications. In the following section the properties of both types of heterogeneous systems are reviewed for nanometer-sized particles and compared with bulk-sized particles.
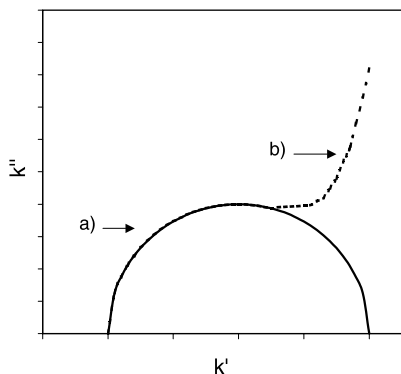
Figure 3. The Cole–Cole plot for (a) bulk-sized particles and (b) nanometer-sized particles.

2.2.1. Nanocomposites

A nanocomposite dielectric material is a heterogeneous system where at least one of the components has nanometer-sized particles. In this section the term nanocomposites will refer to a system composed of either nanometer-sized metal particles dispersed in an insulating matrix or metal particles surrounded by nanometer-sized dielectric particles. The dielectric behavior of nanocomposites can be manipulated by changing the size, shape, and composition of the particles. The effect of each of these parameters on the dielectric behavior is described in this section.

The effect of composition on the dielectric behavior of nanocomposites is characteristic of a percolation system. At the percolation threshold, there is a sharp rise of the dielectric permittivity which follows a power law dependence on the metallic phase concentration, x [8, 9],

$$\varepsilon_{\text{ef}} \propto \left| \frac{(x - x_c)}{x_c} \right|^{-q} \tag{6}$$

where q is a critical exponent and x_c is the percolation threshold. The critical exponent, q, and the percolation threshold, x_c, depend on many parameters including the particle size. Experimental studies show a large distribution of percolation threshold values for nanocomposites. For example, the percolation threshold of Au–SiO$_2$ and Ag–SiO$_2$ nanocomposites was found to be at about $x_c = 0.50$ [10, 11], which is higher than that of randomly packed bulk-sized particles [13]. On the other hand, the percolation threshold of W–SiO$_2$ nanocomposites (micron-sized W particles surrounded by nanometer-sized SiO$_2$ particles) was found to be at about $x_c = 0.2$ [12], which is lower than that of randomly packed bulk-sized particles [13]. There is no theoretical model that can predict the percolation threshold of nanocomposites, even for a relatively simple geometrical configuration of equal metal spherical particles uniformly dispersed in an insulating matrix, due to probably a strong interfacial interaction of the metal particles [10].

Below the percolation threshold, the dielectric permittivity of nanocomposites was found to be higher than that of pure bulk-sized particles of the matrix [10, 14]. For example, the dielectric constant of Au–SiO$_2$ nanocomposites was found to be higher by a factor of 10 compared to that of bulk-sized SiO$_2$ particles [15]. This finding was obtained for a composition below the percolation threshold, where the Au particles have an ellipsoidal shape, a nanometer size (80 nm length and 30 nm width), a random distribution in the SiO$_2$ matrix, and a distance of 30–200 nm between neighboring particles. ESCA measurements showed that the surfaces of the nanometer-sized Au particles are electrically charged which explains the dielectric permittivity enhancement due to an interface polarization mechanism.

Below the percolation threshold, the interface polarization contribution to the total dielectric polarization becomes more dominant as the concentration of the nanometer-sized metal particles increases which results in an increase of the dielectric permittivity [10, 14].

The dielectric loss of nanocomposites is higher than that of their bulk-sized particles. For example, in the case of Au–SiO$_2$ and Ag–SiO$_2$ nanocomposites, the dielectric loss was found to be higher by a factor of 3–7 compared to that of

their bulk-sized particles [16]. In addition, the dielectric loss increases with increasing concentration of the nanometer-sized metal particles. This result is accompanied with an increase of the ac electrical conductivity within the range of values characteristic to an insulator and not to a metal. The enhanced dielectric loss and ac electrical conductivity of nanocomposites indicate the role of the interfaces between the metal and insulator particles as charge carrier supplier and charge carrier transport medium. Another characteristic property to nanocomposites is a strong resonance in the dielectric loss, which is shifted to lower energy as the size of the particles decreases. For example, a resonance of dielectric loss was observed near 2.4 eV in Au–SiO$_2$ nanocomposites and not in their individual constituent phases [10, 17]. The resonance position was shifted to a lower energy with decreasing particle size from 6.3 to 2 nm while keeping constant their spherical shape, volume fraction, and uniform distribution in the SiO$_2$ matrix.

The effect of temperature on the dielectric behavior of nanocomposites was studied on several systems. In the case of Ag–SiO$_2$ nanocomposites [18] two different temperature dependent dielectric behaviors were observed. Below 200 K, the dielectric permittivity remains constant with decreasing temperature to 100 K. This behavior was attributed to an electronic polarization mechanism. Above 200 K, the dielectric permittivity and dielectric loss were found to increase with increasing temperature up to 300 K. A similar thermally activated behavior of the dielectric permittivity was found in W–SiO$_2$ nanocomposites at temperatures between 300 and 500 K [19]. This behavior is attributed to a thermal activation of dipoles at the interfaces of the particles. Consequently, the interface polarization, which is the dominant polarization mechanism of nanocomposites at low frequencies, increases.

The dielectric behavior of nanocomposites can be explained by theoretical models, which were originally developed for bulk-sized particles and later corrected for small-sized particles. In general, these theories consider a composite material as a medium having an effective dielectric permittivity. They present expressions for the effective dielectric permittivity as a function of dielectric permittivity, volume fraction, and shape of the particle constituents. The theoretical models refer to two cases of nanocomposites: a statistical mixture (type 1) and a matrix inclusion (type 2) systems. In the case of the type 1 system, both components are embedded in an effective medium with properties of a mixture. This system is characteristic of compacted powders, interpenetrating network structures, and heterogeneous polymer mixtures especially at high applied-field frequencies. The effective dielectric permittivity of this system can be expressed as [20]

$$\varepsilon^{1-2A} = x_1(\varepsilon_1)^{1-2L_m} + x_2(\varepsilon_2)^{1-2L_m} \qquad (7)$$

where ε_i and x_i are the permittivity and volume fraction of a component i and L_m is the depolarization factor.

In the case of the type 2 system, various models [21–26] have been presented and tested experimentally and the most widely accepted one is the Maxwell–Garnett (MG) theory [26]. The MG theory takes into account the modification of the applied electric field at any point within the medium by the dipole fields of individual polarizable entities. The theory assumes that the metal particles have spherical shape, equal size, uniform distribution in the matrix, and no interaction between them. Based on these assumptions the MG expression for the effective dielectric permittivity of the composite system is [26]

$$\varepsilon(\omega) = \varepsilon_i(\omega)\frac{(1+2xZ)}{(1-xZ)} \qquad Z = \frac{\varepsilon_m - \varepsilon_i}{\varepsilon_m + \varepsilon_i} \qquad (8)$$

where m refers to the metal and i to the insulator particles, and x is the volume fraction of the metal particles. The effect of the particle shape is taken into consideration in Eq. (9) by referring to ellipsoidal metal particles and adding a depolarization factor L_m to Eq. (8) [27]:

$$\varepsilon(\omega) = \varepsilon_i \frac{\varepsilon_i(1-x)(1-L_m) + \varepsilon_m(x+L_m(1-x))}{\varepsilon_i + L_m(1-x)(\varepsilon_m - \varepsilon_i)} \qquad (9)$$

L_m varies between 0 (perpendicular orientation) and 1 (parallel orientation) of the principal axis of the ellipsoid relative to the direction of the applied electric field. The model shows a change of dielectric permittivity for different shapes of particles. In the case of $L_m = 0$, the dielectric permittivity is equal to a weighted average of the dielectric permittivities of the components. The case of $L_m = 1$ is equivalent to an array of capacitors connected in series and the dielectric permittivity is calculated respectively. A distribution of L_m values for randomly oriented ellipsoidal particles is observed in nanocomposites by a distribution of relaxation times of the interface dipoles. The effect of particle size is hidden in Eq. (9) in the value of ε_m. A separation of the real and imaginary parts from Eq. (9) leads to the Debye-type equations with a mean relaxation time, τ_M [22]:

$$\varepsilon = \varepsilon_\infty + \frac{\varepsilon - \varepsilon_\infty}{1 + (\omega\tau_M)^2} \qquad (10)$$

$$\varepsilon'' = (\varepsilon_S - \varepsilon_\infty)\frac{\omega\tau_M}{1 + (\omega\tau_M)^2} \qquad (11)$$

τ_M, ε_S, and ε_∞ depend on volume fraction, depolarization factor, electrical conductivity, and dielectric permittivity of the metal and insulator components. This dependence leads to a decrease of ε' with increasing frequency over a wide range of frequencies due to the presence of various types of interface dipoles having different relaxation times. This behavior was observed experimentally in nanocomposites such as Au–SiO$_2$ [15] and W–SiO$_2$ [12] systems. The dielectric loss of these nanocomposites was also found to decrease with increasing frequency, and its lowest value compared to the dielectric permittivity was found at high frequencies in the range of few MHz [15].

The MG theory as expressed in Eq. (9) agrees well with the experimental results in the case of a small volume fraction ($x < 0.2$) of nanometer-sized metal particles [10, 11]. It predicts qualitatively the enhancement of the dielectric permittivity and the dielectric loss, the presence of a resonance in the dielectric loss, and the thermally activated behavior of the dielectric permittivity [26]. As the volume fraction of the nanometer-sized metal particles increases, the MG theory overestimates the dielectric permittivity and dielectric loss due to interactions between the metal particles. Other

theories [28–30], which include the interactions between the metal particles, show worse results than those obtained by the MG theory.

2.2.2. Nanoporous Materials

Nanoporous dielectric materials are heterogeneous systems composed of an insulating matrix with embedded nanometer-sized pores. The dielectric behavior of nanoporous material can be manipulated by changing the size and shape of the pores as well as by adding adsorbed polar molecules to the pore surfaces. The dielectric behavior of nanoporous materials strongly depends on the applied field frequency. At high frequencies (in the range of MHz and up) the dielectric permittivity, which is determined by bulk dipoles, decreases with increasing the concentration of pores, due to a decrease of the material density. This property is utilized in applications that require low dielectric permittivity. For example, ultra-large-scale-integration (ULSI) devices require low dielectric permittivity (low-k) materials in order to reduce the signal transition times, the power consumption, and the cross-talk. Suitable materials should have a dielectric constant of about 1.5. The pore diameter has to be about 20 nm in order to satisfy many requirements such as good mechanical and electrical strength, sufficient thermal conductivity, low adsorption of humidity, and good gap-fill capabilities [31, 32]. Nanoporous silica represents an example of a material that can be fabricated with high (50–90%) closed porosity for low dielectric constant (low-k) applications. The dielectric constant of silica can be reduced from about 4 to about 1.3 by introducing a high density of closed nanometer-sized pores and thus reducing its density from 2.2 to about 0.4 gr/cm^3 [33]. The most widely used technique to prepare nanoporous silica is the sol–gel method. This method is suitable for conventional spin-on techniques used by the microelectronic industry. Nanometer-sized pores having a narrow size distribution can be prepared by controlling the precursor chemistry, temperature, pH, reaction time, fluid, and drying conditions [34]. A different approach for the fabrication of nanopores consists of insertion of organic templates, such as surfactant arrays, emulsion droplets, or latex spheres, into various oxides during their fabrication process. In this way pores with different sizes between 5 nm and 1 μm are formed [35]. Nanoporous polyimide thin film is another example of a low-k material at high frequencies aimed for interlevel dielectrics in microelectronic packaging devices [36]. The dielectric constant of these films was found to decrease with increasing porosity from 2.9 for 0% porosity to 2.3 for 19% porosity [37].

At low frequencies, (in the range of mHz up to KHz) the dielectric permittivity of nanoporous materials, which is determined by interface dipoles, increases with increasing pore concentration, due to an increase of the pore/matrix interfaces density [38]. In this frequency range the dielectric permittivity is higher than that of the fully dense matrix. The dielectric permittivity is affected by any parameter that changes the nature of the pore/matrix interface such as temperature [37, 38].

In general, the MG theory [26] can describe the dielectric behavior of nanoporous materials as in the case of nanocomposites. However, there are discrepancies in the values of the dielectric permittivity and dielectric loss between the experimental results and the MG theory predictions, which are attributed to inaccurate approximations of the theory with regard to the effect of size and shape of pores as well as to the local electric field at the pore/matrix interfaces [25, 37].

The dielectric behavior of nanoporous materials is very sensitive to adsorbed dipolar molecules or ions on the pore/matrix interfaces [39, 40] because of the large surface-to-volume ratio, the chemical interfacial bonds, and the structural orientation of the adsorbed molecules. The adsorbed molecules can contribute to the dielectric polarization through two mechanisms: interfacial polarization and bulklike polarization [41]. The interface polarization is affected by a surface bound layer of molecules and is dominant at low frequencies. The bulklike polarization results from molecules inside a pore that are not connected directly to the pore surface. The bulklike polarization shows dielectric relaxation processes at frequencies higher than those associated with the interface polarization. An example of the effect of adsorbed molecules inside pores on the dielectric behavior can be seen in nanoporous silica. In this case, the presence of adsorbed water molecules on the surface of nanopores results in an increase of the dielectric permittivity and dielectric loss compared to those of dry pores especially at low frequencies between 100 Hz and 1 kHz [42]. Four dielectric relaxation processes associated with the adsorbed water molecules were observed at different temperatures [42]. The first relaxation process was observed at low temperatures (from −100 to +10 °C). It is characterized by a thermally activated Arrhenius behavior and a non-Debye frequency dependence. It is attributed to reorientation of adsorbed water molecules in icelike structures on the pore surfaces [39]. The second relaxation process was observed at about 60 °C. It is characterized by a non-Arrhenius behavior and is attributed to glass-forming liquids [43]. The third relaxation process was observed at low frequencies at temperatures between 20 and 80 °C. The amplitude of this process decreases with increasing frequency and the dielectric loss factor reaches a maximum value, which is independent of temperature. This relaxation process is attributed to a percolation of charge carriers within the fractal structure of connected pores [42]. The fourth relaxation process was observed at temperatures above 150 °C and is characterized by enhanced dielectric loss at low frequencies. This process is attributed to interfacial polarization due to trapping of free charge carriers at the pore/matrix interfaces causing a buildup of space charge with a relatively long relaxation time [44].

The first, second, and third relaxation processes can be fitted to a superposition of two theoretical expressions. The first one is the HN expression [Eq. (1)] [7] and the second expression is Jonscher's empirical formula [45],

$$\varepsilon(\omega) = B_1 \omega^{n-1} - i B_2 \omega^{n-1} \tag{12}$$

where B_1 and B_2 are the coefficients of asymptotic expansion, and n is the Jonscher parameter for the high frequency part of the relaxation process. The fourth relaxation process can be described by the MG theory [Eq. (9)] [26].

3. NONLINEAR DIELECTRICS

3.1. Homogeneous Materials

3.1.1. Particle Size Effect on Ferroelectric Domain Structure

A reduction of particles size into the nanometer scale changes the domain structure and consequently the dielectric behavior of ferroelectric materials. The particles size effect can be divided into three size regions [46]. The first region is characterized by multidomain crystallites having a bulk ferroelectric behavior. The second region occurs at a smaller particle size, where single-domain crystallites are present, and is characterized by a loss of spontaneous polarization, an absence of the hysteresis loop, and a nonlinear dielectric behavior. The third region is found in the smallest particles and is characterized by a disappearance of the nonlinear dielectric behavior.

The first size region, where multidomain crystallites are present, is characteristic of bulk-sized particles. In this region a decrease of the crystallites size is accompanied with a decrease of 90° domain width, as formulated in [47, 48]

$$w \propto d^m \tag{13}$$

where w is the domain width, d is the crystallite size, and m is a factor that depends on a crystallite size ($m > 1/2$ for crystallites smaller than 1 μm) [49]. Equation (13) is determined by minimizing the energies associated with the electrical and strain fields inside the domains and the domain walls [50]. In this size region the dielectric permittivity is determined by a sum of a volume contribution, $\varepsilon_{r,\mathrm{vol.}}$, which is based on the single-crystal dielectric permittivity and a domain walls contribution, $\varepsilon_{r,\mathrm{dom}}$:

$$\varepsilon_r(T) = \varepsilon_{r,\mathrm{vol.}}(T) + \varepsilon_{r,\mathrm{dom}}(T) \tag{14}$$

As the crystallite size decreases the density of 90° domain walls increases and consequently $\varepsilon_{r,\mathrm{dom}}$ increases [50]. For example [51], in BaTiO$_3$ crystallites having an average crystallite size of about 10 μm, $k_r = \varepsilon_r/\varepsilon_0 \sim 1700$ where $k_{r,\mathrm{vol.}} \sim 1000$ and $k_{r,\mathrm{dom}} \sim 700$. A decrease of the crystallite size to about 2 μm results in an increase of the dielectric constant to 2500. Based on these experimental results an expression was formulated that relates the crystallite size, d, and the contribution of the domain walls to the dielectric constant, $k_{r,\mathrm{dom}} = 2200/(d)^{0.5}$. A similar relationship was found for Pb$_{1-x}$La$_x$Zr$_{1-y}$Ti$_y$O$_3$ crystallites [52]. The number of variants determining the domain structure [53] decreases with decreasing crystallites size. At a critical size a transition from multidomain to single-domain crystallites occurs. Experimental studies show a critical size of 30 nm in PbTiO$_3$ crystallites [54] and 80 nm in BaTiO$_3$ crystallites [55]. The transition from multidomain to single-domain crystallites is accompanied by an abrupt increase of coercive field, a drop in dielectric permittivity, and a sharp decrease of domains density (Fig. 4). The increase of the coercive field is explained by a greater difficulty to form new domains in single-domain compared to multidomain crystallites by applying an external electric field [56]. This explanation is supported by an experimental observation of a smaller acti-
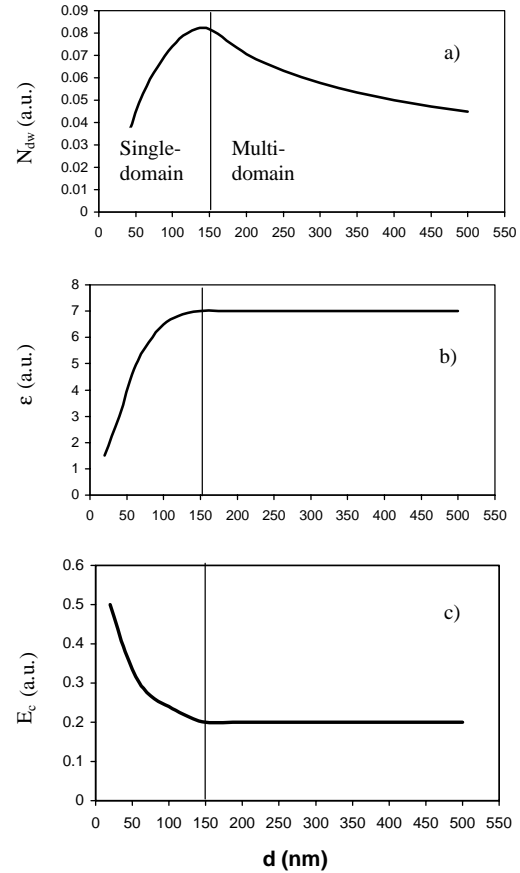
Figure 4. The effect of grain size, d, on the (a) domain wall density, N_{dw}, (b) dielectric permittivity, ε, and (c) coercive field, E_c, of a ferroelectric material.

vation energy for domain reorientation in multidomain than in single-domain PbTiO$_3$ crystallites [57]. The decrease of dielectric permittivity with decreasing crystallite size below the critical value is attributed to a lack of domain walls that can contribute to dielectric polarization via a domain wall motion mechanism. This behavior is opposite to that observed in multidomain crystallites, where the domain density increases with decreasing crystallite size according to a square-root dependence ($N_d \sim d^{-1/2}$) (Fig. 4). The transition from multidomain to single-domain crystallites can be explained by thermodynamic considerations with the aid of a schematic description (Fig. 5) [55]. The explanation starts with a reference state for the crystallites, which is a paraelectric phase. Below T_c, these crystallites transform first into single-domain crystallites. This transformation is associated with a free energy change that consists of a reduction of a volume free energy, ΔG_v, and addition of surface, ΔG_s, and strain, ΔG_ε, free energies:

$$\Delta G = -\Delta G_v + \Delta G_s + \Delta G_\varepsilon \tag{15}$$

The strain free energy in single-domain crystallites results from a volume expansion associated with a phase transformation and from clamping forces applied by the surrounding crystallites. It depends on the crystallite size and domain
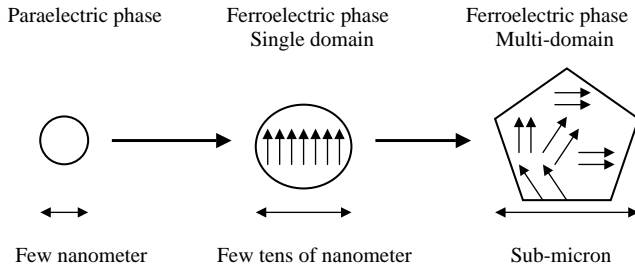
Figure 5. Schematic description of the crystallite size effect on the transition stages from a paraelectric to a multidomain ferroelectric phase.

width according to the expression [48]

$$\Delta G_\varepsilon = \frac{\sigma_{90}}{w} + \frac{2k_c \beta^2 w}{d} \qquad (16)$$

where σ_{90} is a 90° domain wall energy per unit area, k_C is a strain energy associated with the change of the crystallographic unit cell, β is the unit cell deformation ($c/a - 1$), w is the domain width, and d is the crystallite size. The dependence of the domain width on the crystallite size [Eq. (17)] is obtained by minimizing the free energy of the crystallite, ΔG:

$$w = \left(\frac{\sigma_{90} d}{2k_c \beta^2} \right)^{1/2} \qquad (17)$$

The transition from single-domain to multidomain crystallites occurs above a critical crystallite size, d_c, which is equal to the domain width at the minimum free energy state of the crystallite [Eq. (18)] (Fig. 6). This transition is accompanied with strain relaxation by a formation of twins and domain walls:

$$d_c = \frac{\sigma_{90}}{2kc\beta^2} \qquad (18)$$

Calculated values [using Eq. (18)] of the critical crystallite size were found to be in a good agreement with experimental values for $BaTiO_3$ and $PbTiO_3$ crystallites [54].

The third size region is found in the smallest crystallites and is characterized by a disappearance of the nonlinear behavior below another critical crystallite size. Various critical crystallite sizes were observed experimentally in different materials such as a 9 nm size in $PbTiO_3$ crystallites
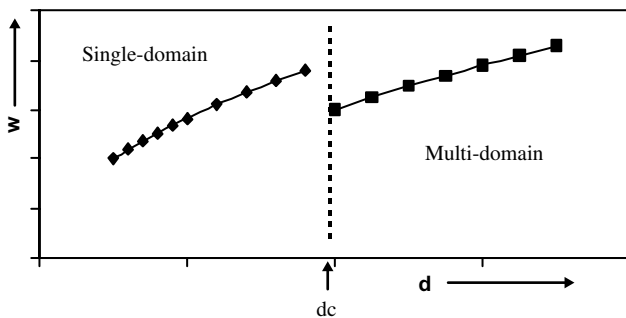
Figure 6. The effect of crystallite size, d, on domain width, w, in solid perovskites according to Eq. (17).

[58], a 150 nm size in KDP crystallites [59], and a 30 nm size in $BaTiO_3$ crystallites [55]. The transition point, which is marked by the critical size, is attributed to a surface effect, which becomes dominant as the size of the crystallites decreases into the nanometer size scale. The surface effect can be divided into two main sources: surface energy and depolarization energy. The surface energy can completely suppress the ferroelectric behavior below a critical size L_c that depends on a correlation length, ζ, and correlation factors D and α as follows [60]:

$$L_c \approx 0.85\zeta = 0.85\sqrt{\frac{D}{|\alpha|}} \qquad (19)$$

The depolarization energy can also suppress the ferroelectric behavior. It results from an accumulated charge at interfaces of neighboring crystallites and at interfaces of crystallites with external conductive electrodes. This accumulated charge partially screens the spontaneous polarization of the crystallites due to its distribution over a finite length. It becomes dominant when the polarization vector is perpendicular to the crystallite surface. In this case, L_c can be calculated as [60]

$$L_c = \frac{2\alpha C}{T_{cb} \varepsilon_0} l_s \qquad (20)$$

where α is the polarizability of the material, C is the Curie–Weiss constant, T_{cb} is the Curie temperature of the bulk ferroelectric material, ε_0 is the vacuum permittivity, and l_s is the screening length of the accumulated charge.

Calculations of L_c according to Eq. (20) result in different values than those observed experimentally. For example, L_c for $BaTiO_3$ crystallites in contact with gold electrodes [61] was calculated to be 0.53 nm, which is below the experimentally observed value (30 nm) [55]. For polyvinyliden fluoride (PVDF) copolymers, L_c was calculated to be about 0.1 nm. Crystallites with such a size cannot be fabricated and tested. The thinnest film for which full ferroelectric switching has been reported is a 0.9 nm PVDF copolymer prepared by the Langmuir–Boldgett technique [62]. The discrepancy between the calculated and experimental values of L_c in these examples indicates that the ferroelectric suppression at a critical crystallite size is not done solely by the depolarization energy but with a contribution of the surface energy.

3.1.2. Two-Dimensional Ferroelectric Behavior

Two-dimensional ferroelectric behavior means that the dielectric properties are determined by dipole interaction within a plane rather between planes in the film. It is characterized by an absence of finite size effect below a critical film thickness. Two-dimensional ferroelectric behavior was found only in ultrathin films (1–15 nm thick) of the copolymer vinyliden fluoride with trifluoroethylene, P(VDF-TrFE, 70:30) [62]. The polymer has a very high crystallinity [63, 64] due to ordered $-((CF_2\text{-}CH_2)_x\text{-}(\text{-}CF_2\text{-}CHF)_{1-x})_{n-}$ chains having a regular intrachain period of 0.26 nm controlled by C–C bonds between fluorine pairs (Fig. 7). In the ferroelectric phase, the chains are arranged in parallel rows having quasi-hexagonal close packing with an orthorhombic $mm2$
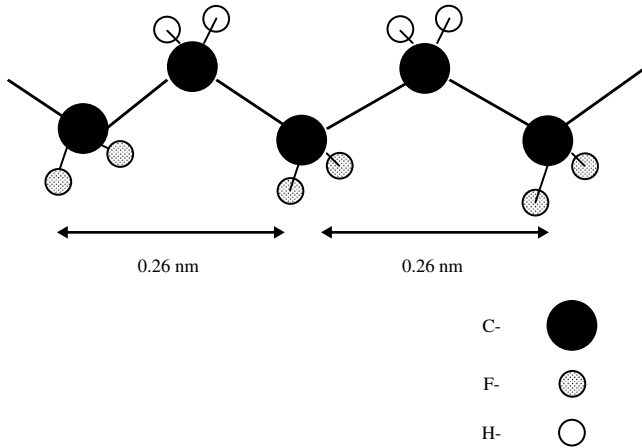
Figure 7. Schematic description of a fragment of the PVDF molecular structure having an intrachain period of 0.26 nm and dipole moments oriented from the fluorine atom side to the hydrogen atom side of the molecule chain.

structure [65]. This structure exhibits preferred polarization orientation in a direction perpendicular to the film plane. Ultrathin films of P(VDF-TrFE) were fabricated by the horizontal Schaefer variation of the Langmuir–Boldgett monolayer transfer technique, which enables precise control of the film nanostructure [66, 67]. The films show a combination of regular (bulk) and irregular ferroelectric properties. Their regular ferroelectric properties include a first-order ferroelectric–paraelectric phase transition at about 80 °C, polarization hysteresis loops with good saturation values, and complete reversible polarization switching below 80 °C [62]. The irregular properties of these films are an absence of finite size effect between 15 and 1 nm, an absence of apparent critical thickness in films as thin as 1 nm, which is much thinner than any previously reported ferroelectric film, a presence of very large coercive fields ($E_c =$ 0.6–0.9 $GV m^{-1}$) [68], and an appearance of a new phase transition at temperature of about 20 °C [62]. The absence of finite size effect and critical size in two-dimensional ferroelectric films is in contradiction to theoretical models of three-dimensional ferroelectricity. The coercive fields of two-dimensional films are much higher than in those of other ferroelectric materials; they do not depend on the film thickness and are very close to the theoretical intrinsic coercive field (~ 1 $GV m^{-1}$). This means that the switching mechanism does not depend on nucleation and growth of domains but rather on a new mechanism, which is still unknown. The new ferroelectric phase transition at 20 °C was determined as a first-order transition due to the presence of thermal polarization hysteresis loops and peaks in both dielectric constant and pyroelectric response [62]. It is attributed to a surface effect since the surface band structure is changed at about the same temperature of 20 °C [69].

Currently, there is no theoretical model that can explain the two-dimensional ferroelectric behavior of ultrathin films. It is suggested [70] to use the Ising model [71] for this purpose, since it describes restricted movement of dipoles. In the P(VDF-TrFE) case, the dipole movement is restricted to only partial rotation about the polymer chain axis due to interchain steric interactions and interchain dihedral

stiffness. The model should take into consideration the anisotropic dipole coupling within a plane in the film (strong parallel to and weak perpendicular to the plane) or the weak dipole coupling between planes in the film.

3.1.3. Effect of Crystallite Size on the Curie Temperature

The effect of crystallite size on the Curie temperature of ferroelectric materials has been investigated for a long time since 1953 [59] and the experimental results do not show a clear dependence between them. For example, one study [72] reported an increase while another study [73] reported a decrease of the Curie temperature as the crystallite size of the same material, BaTiO$_3$, decreases. However, many experimental studies reported a shift of the Curie temperature compared to its bulk value as the crystallite size decreases to the nanometer size scale [74–78]. For example, a change of a few degrees of the bulk Curie temperature was observed in the case of NaNO$_2$ nanocrystals ($d \sim$ 5–20 nm) [75] while on the other hand a change of almost 80 degrees was observed in PbTiO$_3$ nanocrystals ($d \sim$ 30 nm) [76]. An empirical expression was given in the case of PbTiO$_3$ crystallites [76] to describe the dependence between Curie temperature and crystallite size, which consists of three material-related constants, c_1, c_2, c_3:

$$T_c = c_1 - \frac{c_2}{(d - c_3)} \tag{21}$$

Equation (21) cannot describe all the observed experimental results and currently, there is no theoretical expression that can evaluate the change of T_c with crystallite size based on measurable parameters. However, there are theoretical expressions that describe this dependence on the basis of immeasurable parameters such as surface interaction strength and surface extrapolation length. These theoretical expressions, which refer to a change of order in the vicinity of the film or crystallite surface, result from two main models. The first one is known as the Ising model under a transverse field (IMTF) [78]. This model refers to a ferroelectric behavior determined by hydrogen bonds. Each bond has a double potential well for the proton. Above the Curie temperature, the protons have a random distribution between the two sides of the double potential well, while below T_c they prefer one side of it. In this way the ferroelectric phase transition becomes associated with a transition from random to ordered occupancy of the double potential wells and can be described in terms of the spin 1/2 IMTF Hamiltonian [79],

$$H = -\Omega \sum_i S_i^x - \frac{1}{2} \sum_{i,j} J_{i,j} S_i^z S_j^z \tag{22}$$

where i and j are two sites of a double potential well of the hydrogen bond, Ω is the transverse field, S_i^x and S_i^z are the x and z components of the pseudo-spin [S^z differs between occupancy of site i ($S_i^z = +\frac{1}{2}$) and site j ($S_i^z = -\frac{1}{2}$)], and J_{ij} is an effective exchange constant which represents the interaction between the ith and jth sites. The first component of Eq. (22), $\Omega \sum_i S_i^x$, corresponds to a tunneling of protons between neighboring sites

and it serves as a parameter of disorder in the material. If $\Omega \sum_i S_i^x > \frac{1}{2} \sum_{i,j} J_{i,j}$ then there is no ferroelectric phase. The second component of Eq. (22), $\frac{1}{2} \sum_{i,j} J_{i,j} S_i^z S_j^z$, is associated with the interaction between neighboring potential wells sites. Both components of Eq. (22) are affected by crystallite surfaces or interfaces, where the density and type of nearest neighbor atomic sites differ than those in the crystallite bulk regions. As the crystallite size decreases to the nanometer scale, the density of interfaces between crystallites increases, leading to a pronounced contribution of interface sites to the effective exchange constant, J_{ij} [Eq. (22)]. According to the Ising model, the relative contribution of crystallite interfaces to the overall effective exchange constant of the material, J_s/J, determines the Curie temperature.

For example [79], Eqs. (23) and (24) show the dependence of T_c on the ratio J_s/J for one and two interface layers respectively in a relatively simple case with the conditions $J_{i,j} \neq 0$ only for nearest-neighbors sites i and j, $J_{i,j} = J_s$ (if both sites are at an interface), and otherwise $J_{i,j} = J$ (nearest interactions), and the spins lie on a simple cubic lattice with the coordination axes parallel to the cube edges,

$$\text{for } n=1 \quad x=4\frac{J_s}{J} \quad \left(x=2\frac{\Omega}{J}\right)\coth\left(\frac{\Omega}{2k_B T_c}\right) \quad (23)$$

$$\text{for } n=2 \quad x=1+4\frac{J_s}{J} \quad \left(x=2\frac{\Omega}{J}\right)\coth\left(\frac{\Omega}{2k_B T_c}\right) \quad (24)$$

where n is the number of surface layers, and k_B is the Boltzman constant.

Equations (23) and (24) are compared with the bulk Curie temperature expression [Eq. (25)] obtained for a second-order phase transition, by using the Hamiltonian [Eq. (22)] under the mean-field approximation [79],

$$\tanh\left(\frac{\Omega}{2k_B T_b}\right) = 2\left(\frac{\Omega}{n_0 J}\right) \quad (25)$$

where n_0 is the coordinate number.

Curves of T_c/T_b vs. J_s/J based on Eqs. (23)–(25) show that there is a critical surface interaction strength, J_{sc}, which is higher than that of the bulk value ($J_{sc}/J = 1.25$ for a single surface layer and $J_{sc}/J = 1.08$ for two surface layers). If $J_s > J_{sc}$ then the Curie temperature increases as the size of the crystallite decreases. Otherwise, the Curie temperature decreases with decreasing the crystallite size. For a weak surface interaction, there will be no ferroelectric behavior, which was reported for nanometer-sized crystallites and ultrathin films. For a strong surface interaction, an optimum crystallite size with a maximum Curie temperature is obtained.

A second model on the effect of crystallite size on the Curie temperature of ferroelectric materials is based on the Landau–Devonshire theory [61, 80, 81]. The theory describes the free energy, F, of the bulk material as a function of polarization, P, in a formalism of a Taylor series,

$$F = \frac{1}{2}AP^2 + \frac{1}{4}BP^4 + \frac{1}{6}GP^6 \cdots \quad (26)$$

where A is a coefficient associated with a Curie temperature of a bulk material, T_b, as follows:

$$A = A_0(T - T_b) \quad (27)$$

The coefficients B and G in Eq. (26) are associated with the type of the ferroelectric phase transition. A first-order transition occurs when $B < 0$ and $G > 0$, while a second-order transition appears when $B > 0$. The effect of the particle surfaces adds more terms into Eq. (26) as detailed in

$$F = S\left\{\int d^3r\left[\frac{1}{2}AP^2 + \frac{1}{4}BP^4 + \frac{1}{6}GP^6 + \frac{1}{2}C|\nabla P|^2\right] + \frac{1}{2}C\delta^{-1}\int dS(nP)^2\right\} \quad (28)$$

where n is the number of surfaces with area S, and δ is a surface parameter. In the case of a second-order phase transition and a stationary F, Eq. (28) is changed into the following differential equation [82–84]:

$$C\frac{d^2P}{dz^2} - AP - BP^3 = 0 \quad (29)$$

The solution of Eq. (29) under the boundary condition of Eq. (30) for plane surfaces gives criteria [Eq. (31)] for the effect of the crystallite size or film thickness, d, on the Curie temperature:

$$\frac{dP}{dz} \pm \frac{1}{\delta}P = 0 \quad \text{at } z = \pm\frac{1}{2d} \quad (30)$$

$$\begin{aligned}\text{If } \delta < 0 \quad &\text{then } T_c > T_b \\ \text{If } \delta > 0 \quad &\text{then } T_c < T_b\end{aligned} \quad (31)$$

The surface parameter δ plays the same role as the normalized surface interaction strength, J_s/J, in the IMTF model. In the case of $\delta > 0$ the spontaneous polarization decreases, most pronouncedly at the crystallites surfaces, and the Curie temperature decreases with decreasing crystallite size. The opposite case occurs when $\delta < 0$, where the spontaneous polarization and Curie temperature increase with decreasing crystallite size. The dependence of T_c on the crystallite size or film thickness is usually presented by dimensionless variables of T_c/T_b vs. $1/\zeta_0$ where $\xi_0 = [CT_b/A_0]^{0.5}$ [85]. The criteria given in Eq. (31) were developed for a second-order ferroelectric phase transition. In the case of a first-order phase transition the term P^6 in Eq. (28) cannot be neglected and the model does not provide criteria for the effect of crystallite size on Curie temperature but only shows a discontinuous polarization change at the Curie temperature [85].

3.2. Heterogeneous Materials

3.2.1. Ferroelectric Relaxors

Ferroelectric relaxors (FRs) are complex oxides that belong to the family of disordered materials and most particularly to the group of mixed-cation ferroelectrics having a perovskite structure with a general chemical formula $A_{1-x} - A'_x B_{1-y} B'_y O_3$. The most intensively studied FR materials are $PbMg_{1/3}Nb_{2/3}O_3$ (PMN), $PbSc_{1/2}Ta_{1/2}O_3$, $PbSc_{1/2}Nb_{1/2}O_3$,

Pb$_2$KTa$_5$O$_{15}$ (PKT), and Pb$_{1-x}$La$_x$Zr$_{1-y}$Ti$_y$O$_3$ (PLZT). FR materials consist of nanometer-sized ferroelectric domains (10–50 nm) dispersed in a paraelectric matrix. The presence of nanometer-sized domains was verified by X-ray diffraction, neutron diffraction, and transmission electron microscopy (TEM) studies on various FR materials [86–91].

The dielectric behavior of FRs has been studied experimentally [92–94] and was found to be different than that of conventional ferroelectric materials. FRs usually exhibit high dielectric permittivity and low dielectric loss. Their dielectric permittivity has a peak-shaped dependence on temperature with a maximum value at a temperature called T_{max} (Fig. 8a) [95]. T_{max} increases with increasing applied field frequency. For example [96], in La-modified lead-based FR, an increase in frequency by one order of magnitude lead to a shift of T_{max} by about 10 °C. Below T_{max}, the dielectric permittivity shows a non-Debye dispersion over a wide range of frequencies (usually between 10 Hz and 10 MHz). The dielectric loss of FRs also has a peak-shaped dependence on temperature with a sharp rise at a temperature lower than T_{max} (Fig. 8b). The dielectric losses show frequency dependent dispersion above T_{max}, which is opposite to the direction observed for the dielectric permittivity. The dielectric loss of different frequencies merges together at low temperatures. FR materials show a diffuse phase transition from the paraelectric to the ferroelectric phase [92] and an absence of macroscopic polarization at temperatures below T_{max}. The dependence of the dielectric susceptibility, $\chi_0(T)$, on temperature in FR materials cannot be described by the known Curie–Weiss law but rather by a special quadratic law as

$$\chi_0(T) = \frac{C}{(T - T_c)^2} \tag{32}$$
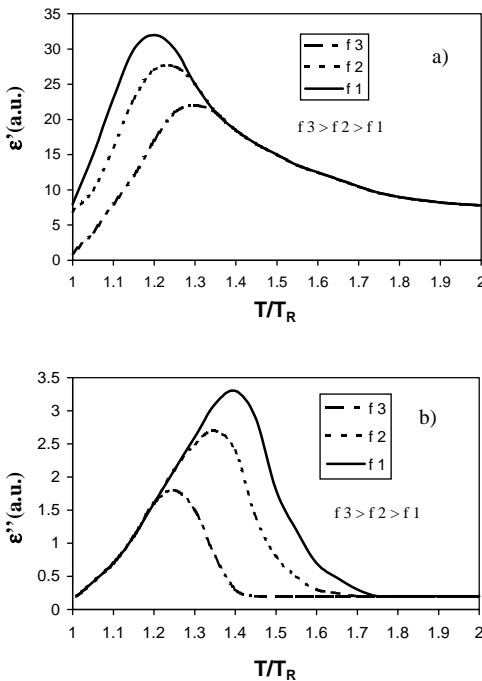
Figure 8. The effect of temperature on the dielectric permittivity [real (a) and imaginary (b) parts] of ferroelectric relaxors at different frequencies (TR is a reference temperature).

where C is the Curie constant and T_c is the Curie temperature.

The dielectric polarization of FR material was found to strongly depend on the applied field orientation relative to the crystallographic orientation. For example, an abrupt jump in polarization was found in the PMN materials by applying an electric field of about 1.7 kV/cm in the $\langle 111 \rangle$ direction. The polarization saturates at higher applied fields in this direction. Applying an electric field in the $\langle 110 \rangle$ direction resulted in a polarization jump at a higher electric filed and a lower saturation value than those observed in the $\langle 111 \rangle$ direction. Neither polarization jump nor saturation value was found when the electric field was applied in the $\langle 100 \rangle$ direction but rather a continuous increase of polarization with increasing applied field up to 6 kV/cm. Different phases have been observed in FR materials depending on the intensity and orientation of the applied field as well as on temperature. For example, in the PMN materials three different phases (paraelectric, glass, and ferroelectric) were observed when an electric field was applied in the $\langle 111 \rangle$ direction [97]. The paraelectric phase, which is controlled by a dynamic disorder, was obtained at temperatures higher than 206 K (field-free depoling temperature) under applied dc fields between 0 and 2.7 kV/cm. This phase shows a pronounced dispersive peaks of ε' and ε'' with a major maximum value at about 206 K and a minor maximum value at about 217 K in the high field regime (above 1.7 kV/cm). The amplitudes of these maxima are frequency dependent and they disappear under dc fields below 1.7 kV/cm. The glassy phase was obtained at temperatures below 206 K and under dc applied fields lower than 1.7 kV/cm. The glassy phase, which is characterized by a metastable polarization, is explained by the presence of a large distribution of dipole relaxation times. The metastable polarization increases nonlinearly with increasing applied field up to 1.7 kV/cm and can be described by the expression [97]

$$P^{ms} = \chi_0^{ms}(T)E + \frac{1}{3}\chi_2^{ms}(T)E^3 \tag{33}$$

where P^{ms} is the metastable polarization, χ is the static susceptibility, and E is the applied field. Ferroelectric phases in the PMN materials were observed at temperatures below 206 K and under dc applied fields higher than 1.7 kV/cm. The phases are classified in three groups. The first group is characterized by a ferroelectriclike behavior with a higher polarization than that of the glassy phase and it appears at lower temperatures. The second group is characterized by a field-independent value of polarization that can be reversed by an applied field. It is obtained at higher temperatures and applied fields than those of the first group. The third group shows a hysteresis loop and a usual first-order ferroelectric phase transition.

The relatively high permittivity over a wide temperature range and low sintering temperatures of FR materials make them attractive for multilayer capacitors. They are also attractive to piezoelectric applications due to their high piezoelectric coefficients [98] compared to conventional piezoelectric ceramics.

Various models have been proposed to explain the mechanism of formation and the nature of the nanometer-sized

domains that determine the unique dielectric behavior of FR materials. One model [86] suggests a unique local polarization in nanometer-sized domains without any global polarization in the crystal. The model distinguishes between short-range and long-range order effects. The short-range effect is associated with a local polar symmetry, which is correlated with local atomic shifts. The small polar regions are part of the host lattice and therefore depend on it. The structure of a polar region differs from that of the host lattice only in the atomic shifts. Thus, the crystal does not behave as a polar homogeneous structure, because the coherence length of the polar zones is spatially limited, nor does it behave as a perfectly cubic crystal because of the strong deviation from a cubic symmetry. The nanopolar regions may appear in at least two configurations. One configuration consists of islands of polar ordered nanodomains (first phase) immersed in a disordered paraelectric host lattice (second phase). Another configuration consists of an array of nanodomains (first phase) surrounded by interdomain regions (second phase). In both configurations the crystal is considered as a two phase system. The long-range effect is associated with a variation of the local polarization fields in such a way that no global polarization exists in the material. This model was tested experimentally with neutron and X-ray diffraction studies of PMN-based FR materials during cooling from 1000 to about 5 K [86, 99, 100]. The studies revealed a mean cubic structure of the matrix down to 5 K with, however, the presence of nanometer-sized rombohedral polar domains (atomic shifts along $\langle 111 \rangle$ direction of the cube, which is the rhombohedral axis). The size of the polar domains grew with increasing temperature and the correlation length was estimated to be of about 10 nm at 5 K.

Another model, called the superparaelectric model, of FR materials is based on high-resolution TEM studies that revealed nanometer-sized polar domains dispersed in a paraelectric matrix [100]. The model claims that the domains are superparaelectric regions with thermally fluctuating polarization vectors between equivalent potential wells [95]. This model was used in a phenomenological approach [101] that analyzes the behavior of FR materials throughout four stages. The first stage regards the FR as an ensemble of independent, identical, monosized superparaelectric domains. The second stage introduces a distribution of the domain size. The third stage takes into account a temperature dependence of the domain size, and the fourth stage treats the dipolar interaction of neighboring domains. This phenomenological approach was used to build a model that quantitatively describes the dielectric behavior of FR materials [102]. It is well known that the first nucleation of domains occurs hundreds of degrees above T_{max} [103]. In the case of the PMN material, it has been shown that the nucleation temperature is at about 600 K, far above $T_{max} = 265$ K [99]. At T_{max}, the size distribution of the domains is relatively narrow and the dielectric relaxation follows the Debye expressions [Eqs. (10), (11)]. Below T_{max}, the size of the domains begins to strongly increase and their size distribution is broadened upon cooling. The present model assumes homogeneous nucleation and exponential size distribution of the domains for temperatures sufficiently below T_{max}. The model also claims that the domains fluctuate under a thermal energy higher than the required polarization activa-

tion energy, E_a. E_a depends linearly on the domain volume, which means that as the domain size increases it becomes more difficult to thermally fluctuate it. The relaxation time of the domain increases exponentially with increasing E_a. The presence of a size distribution of domains below T_{max} results in a multiple relaxation times and an asymmetric dielectric response (in contrast to the Debye-type response) of FR materials. The model formulates a dependence of dielectric permittivity and dielectric loss on frequency of FR materials as

$$\varepsilon_r' \cong k_c \left[1 - \frac{n\pi}{2\sin(n\pi/2)} (\omega\tau_c)^n \right] \tag{34}$$

$$\varepsilon_r'' \cong k_c \frac{n\pi}{2\cos(n\pi/2)} (\omega\tau_c)^n \tag{35}$$

where ε_r' and ε_r'' are the real and imaginary parts of the complex dielectric permittivity, ω is the angular frequency of the applied field, k_c and τ_c are the static dielectric constant and the relaxation time of the domains, respectively, and n is a dimensionless parameter that spans between 0 and 1 and is equal to the ratio between the thermal energy and the polarization activation energy of the domains. The expression $[1 - (n\pi/2\sin(n\pi/2))(\omega\tau_c)^n]$ in Eq. (34) is known as the dispersion factor which indicates quantitatively (between 0 and 1) the degree of dielectric permittivity dispersion. The parameter n is inversely proportional to the width of the domain size distribution. Consequently, a small variation in domain size induces a dielectric dispersion over several orders of frequency magnitude. For example, a small change of the domain size from 4.5 to 5.5 nm results in a dispersion of the relaxation time over 4 orders of magnitude [104]. Equation (34) shows that the dielectric permittivity is proportional to $[1 - (\omega\tau_c)^n]$ which means that at the same temperature and domain size distribution, the dielectric permittivity increases with decreasing frequency. However, at the same frequency a decrease of temperature is associated with an increase of both n and τ_c, which results in a decrease of the dielectric permittivity. The parameter n decreases linearly from 1 to almost 0 with decreasing temperature according to Eq. (36) due to growth of domains and broadening of their size distribution,

$$n = \alpha(T - T_0) \tag{36}$$

where α and T_0 are constants. T_0 corresponds to the transition temperature from the paraelectric to the ferroelectric phase of the pure host system [105]. However, in FR materials, the nanometer-sized domains cannot grow into macrodomains without an applied electric field. Consequently, the parameter n deviates from its linear dependence on temperature below T_0, which results in a slow down of the dielectric dispersion at temperatures much lower than T_{max}. The model also claims that the dielectric permittivity peak is not associated with a true ferroelectric phase transition. The presence of the peak is explained by a growth of domains to a size where they begin to fail in following the alternating applied field. It is therefore expected that T_{max} will increase with increasing frequency. The peak of the

dielectric loss is also not associated with a true phase transition but rather corresponds to a temperature where the dielectric dispersion reaches a maximum value. This model was tested experimentally on the PMN and PKT-based FR materials and was found to be in a good agreement with the experimental results [102].

Another model of FR materials consist of random electric field [106, 107]. The dielectric behavior of ordinary ferroelectric materials can be explained by the mean-field theory, where any ion in the lattice is exposed to the same average electric field induced by the surrounding ions. However, the dielectric behavior of FR materials cannot be described by the mean field theory due to the presence of random sites and orientations of electric dipoles that result from point defects such as lattice vacancies, antisite ions, and impurities embedded in the lattice of a paraelectric phase. The dielectric behavior of FR materials is determined, according to this model, by a distribution of random electric fields where different ions are subjected to different electric fields by the surrounding ions. For example [108], La ions in a PZT lattice induce random electric fields through the formation of defects such as vacancies of Pb, Zr, and Ti, as well as dipole pairs of La^{3+}–Pb^{2+} and La^{3+}–Zr^{4+} or Ti^{4+}. The model uses three main parameters, L, nr_c^3, and temperature, to distinguish between the different phases of FR materials. L is a dimensionless order parameter that characterizes the number of coherently oriented dipoles in the material. The parameter nr_c^3 consists of the dipole concentration, n, and the host lattice correlation radius, r_c. The model shows three main phases depending on concentration of point defects and temperature. The concentration of point defects is indicated by the parameter nr_c^3. In the case of $nr_c^3 \gg 1$, there is a small concentration of defects that have a minor effect on the ferroelectric behavior of the material and therefore $T_c = T_{CMF}$ (T_c is the phase transition temperature determined by the random field theory and T_{CMF} is the phase transition temperature determined by the mean field theory). When the nr_c^3 parameter decreases to about 1, due to defects, T_c is strongly decreased relative to T_{CMF} and a mixed ferroglass phase appears. In this phase, infinite and short-range order clusters coexist and only a fraction of the dipoles are coherently oriented. Consequently, a dispersed dynamic dielectric susceptibility is obtained. On further decreasing nr_c^3, $nr_c^3 \ll 1$, the concentration of defects increases up to a critical value where the ferroelectric phase transition is completely destroyed. At this point, $T_c = 0$ and $L = 0$, the material is characterized by an absence of long-range polar clusters and a presence of a dipole glass state where only short-range clusters exist. For example, in PLZT materials this critical point was observed at a La concentration of about 6% [109, 110]. The critical concentration of defects is change with temperature. At relatively high temperatures, where $T \approx T_D$ (T_D is the transition temperature from the paraelectric to the ferroelectric phase of the pure host system), the correlation radius is large and the conditions of $nr_c^3 \gg 1$ and $L \approx 1$ are obtained. In this temperature region the material shows a ferroelectric behavior. In the intermediate temperature region, $T_c < T < T_D$, the host lattice correlation radius is small enough that the condition of $nr_c^3 \ll 1$ is obtained. In this region, short-range polar clusters appear. The size of the clusters depends on r_c and T. In this

case the interaction between dipoles can be neglected and the material consists of random sites and orientation dipoles. At high enough temperatures, the dipoles may have large reorientational velocity, which corresponds to the superparaelectric model. At low temperatures, $T < T_c$, some of the dipoles are actually frozen and cannot follow the alternating applied field. The system is confined in a certain component of phase space and its volume shrinks with decreasing the time scale of the measurement and temperature. A subphase-space of frozen dipoles is formed. Consequently, the material does not behave according to the Curie–Weiss law and shows non-Debye relaxation and non-Arrhenius temperature dependence of the dipole relaxation times [111, 112]. The fraction of frozen dipoles increases with decreasing temperature, leading to a decrease of the dielectric permittivity. A complete freezing occurs at $T \leq T_g$ (T_g is the transition temperature to the dipole glass state). This state was observed experimentally in the PMN materials [86].

The dielectric behavior of FR materials was also explained by a "breathing" boundaries model [113]. According to this model, the nanometer-sized ferroelectric regions are electrically soft and can expand or contract ("breathe"). Consequently, FR materials show a very high permittivity over a wide temperature range, large electrostrictive effects (which are believed to originate from field–activated coalescence of the polar nanoregions to macrodomains), and strong piezoelectric, pyroelectric, and electro-optic response under a bias field.

3.2.2. Core–Shell Dielectric Particles

Core–Shell (CS) dielectric particles are characterized by a special type of inhomogeneous chemical composition that spans over a limited size range [114, 115]. The core region usually consists of a pure material having a size of between few microns and tens of nanometers. The shell region usually has a smaller size, the same crystallographic structure, but a different composition than that of the core region. The composition of the shell region decreases gradually with increasing distance from the core/shell interface toward the outer surface of the shell region until it reaches a steady state value. The dielectric properties of CS particles can be varied over a wide range of values by changing the chemical composition and the size of the shell relative to the core.

Among various dielectric materials $BaTiO_3$ has gained much attention in studies of fabrication and dielectric properties of CS particles and is therefore presented here as an example of CS particles. The preparation process of $BaTiO_3$ CS particles consists of several stages including liquid phase sintering, solubility, precipitation, grain growth, and interdiffusion [115]. The first stage of preparation involves solid state mixing of $BaTiO_3$ and additives. The second stage consists of sintering the solid mixture at a temperature higher than the ternary eutectic temperature forming a liquid phase at the interfaces between the $BaTiO_3$ and additive particles. After saturation of the melt with $BaTiO_3$, a dissolution–precipitation process starts. The smaller $BaTiO_3$ particles are completely dissolved in the melt while the larger particles remain solid and grow by precipitation of a perovskite phase from the melt. The driving force for this dissolution–precipitation process is a small difference in the surface

energy between small and larger particles. The undissolved BaTiO$_3$ particles form the core regions while the precipitated perovskite phase forms the shell region, which is made of a barium titanate modified by ions occupying either the A or the B sites in the lattice [116]. It was shown experimentally [115] that the shell grows epitaxially on the BaTiO$_3$ core and the core/shell interface is enriched with additives. As the sintering time progresses the dissolution–precipitation process continues where the melt and the precipitated perovskite phases have less additives. Consequently, a diffusion of additives atoms or ions occurs from the core/shell interface inward to the core and outward to the shell due to a concentration gradient. At the diffused regions, dislocations are formed due to the volume change accompanying the formation of the solid solution. During precipitation of the perovskite phase, more and more additives pass from the melt to the solid shell. Consequently, the melting temperature of the liquid phase increases until it passes the sintering temperature and causes solidification of the remaining liquid. At this point, the formation of solid CS particles is completed. The shell phase is considered an unstable thermodynamic state due to the inhomogeneous composition distribution of additives in it. High sintering temperatures and long sintering times promote solid-state diffusion that cause homogenization of the additives and disappearance of the CS structure. The size ratio between the core and shell can be controlled through the kinetics of perovskite phase precipitation and diffusion of additives into the core and shell regions. Three types of CS structures were observed in BaTiO$_3$-based CS particles [117] that differ in microstructure of the core and in composition distribution of the shell. Type I CS particles consist of a core region that contains a high density of 90° twin domain configurations corresponding to the tetragonal ferroelectric structure of BaTiO$_3$ and a shell region that contains inhomogeneous distribution of additives. At the core/shell interface there are misfit strains that induce compressive stress on the core and affect the dielectric properties [118]. The type I structure is characteristic of particles smaller than 1 μm having a diffused ferroelectric–paraelectric phase transition. Type II CS particles have a larger shell region with a smaller distribution of additives and a higher concentration of misfit dislocations at the core/shell interface [115] than type I particles. In addition, type II particles are bigger and exhibit a less diffusive ferroelectric phase transition than type I particles. Type III CS particles do not have ferroelectric domains in the core region but only a high density of dislocations. The type III structure was found in large particles in the order of 10 μm having a relatively sharp ferroelectric phase transition. In this section only type I CS particles are considered.

The dielectric properties of type I BaTiO$_3$-based CS particles are influenced mostly by chemical inhomogeneity and internal stresses in the particles. The sources for internal stresses are mostly the lattice mismatch between the core and shell and structural changes in the shell region. Experimental studies of BaTiO$_3$-based CS particles show a weak dependence of dielectric permittivity on temperature over a wide temperature range and a diffusive phase transition around Curie temperature, which is reflected in a broad and suppressed peak of permittivity vs. temperature [114]. As the

particle size decreases below 1 μm the spontaneous polarization decreases, the Curie temperature is shifted to a lower temperature, and the permittivity peak around the Curie temperature is further broadened and suppressed due to an increase of internal stresses in the particles [119–121]. An increase of additive concentration in the shell region results in an increase of internal stresses followed by a change of dielectric properties as described above. There are systems such as the ZrO$_2$–BaTiO$_3$ CS particles [115] where the effect of additives on dielectric properties is relatively small due to limited solubility of additives in the perovskite structure. However, there are systems, such as the BaTiO$_3$–SrTiO$_3$ CS particles [122], where the dielectric properties can be varied over a wide range of values because the two perovskite oxides are completely soluble in each other. The selection of additives is done according to specific dielectric aims such as the Curie shifters, which are dopants that change the Curie temperature when entered into the BaTiO$_3$ perovskite structure [123]. The shift in Curie temperature is proportional to the concentration of the dopants. In the case of a nonuniform distribution of dopants the Curie point may span over a wide range of temperatures. However, the susceptibility-temperature dependence follows the Curie–Weiss law for all dopant concentrations, indicating the dominant role of the pure BaTiO$_3$ core on the dielectric behavior of the CS particles [124]. In this respect the dielectric behavior of CS particles differs from that of FR particles where both have different types of chemical inhomogeneity.

The dielectric behavior of BaTiO$_3$-based CS particles was explained by a model consisting of compositional inhomogeneity [124, 125]. According to the model the core is elastically clamped, which causes the phase transition to be of a second order type. The dependence of dielectric constant on temperature for the core is

$$
\begin{aligned}
K_{\text{core}}(T) &= K_{\text{av}} && \text{for } 10° \leq T \leq T_c \\
&= \frac{4\pi C}{T - T_c} && \text{for } T \geq T_c
\end{aligned}
\tag{37}
$$

where C and T_c are the Curie constant and temperature respectively. K_{core} is expected to be of the same order of magnitude of pure fine-grained BaTiO$_3$. The shell is believed to have microvolumes of various compositions and hence various ferroelectric phase transition temperatures. The shell dielectric behavior is characterized by an inhomogeneous distribution of phase transitions. The average dielectric constant of the shell is given as [126]

$$
K_{\text{shell}}(T) = \frac{\int_{-\infty}^{+\infty} K(T - T_c')f(T_c')\, dT_c'}{\int_{-\infty}^{+\infty} f(T_c')\, dT_c'}
\tag{38}
$$

where $f(T_c')$ is a general distribution function describing the spread of Curie points in the shell which is assumed to be a Gaussian distribution,

$$
f(T_c') = \exp\left\{ \frac{[-(T_c' - T_{\text{max}})^2]}{\alpha^2} \right\}
\tag{39}
$$

where α is a parameter that defines the width of the dielectric permittivity peak and T_c' is a second-order transition temperature of an individual microvolume having a constant

composition in the shell. The dielectric permittivity dependence on temperature of the shell is described as follows:

$$K_{shell}(T) = K'_{av} \qquad \text{for } T \leq T'_c$$
$$= \frac{4\pi C}{T - T'_c} \qquad \text{for } T \geq T'_c \qquad (40)$$

The dielectric permittivity of CS particles results from serial and parallel contributions of the core and shell regions that can be expressed by a semiempirical logarithmic expression:

$$\log(K) = V_{shell} \log(K_{shell}) + V_{core} \log(K_{core}) \qquad (41)$$

A good agreement was found between Eq. (41) and the experimental results of LiF–BaTiO$_3$ CS particles [124]. However, in some cases [127, 128] the calculated dielectric constant was not in good agreement with the observed values, which is attributed to a dominant effect of internal stresses on the dielectric polarization.

3.2.3. Ferroelectric Superlattices

Ferroelectric superlattices (FSs) are multilayered thin films composed of alternating epitaxial nanometer-sized layers of different ferroelectric materials. A FS can be fabricated by various techniques such as reactive evaporation [129], molecular beam epitaxy [130], pulsed laser deposition [131], metal-organic vapor deposition [132], the sol–gel method [133], and others.

Dielectric properties of FSs differ from those of their pure ferroelectric constituents and can be tailored by varying the size and periodicity of the layers. Recent experiments have shown that FSs exhibit many unusual dielectric properties such as a giant dielectric response [134] and anomalies in the domain structure and consequently in the ferroelectric–paraelectric phase transition temperature [135, 136]. A giant dielectric permittivity was reported in superlattices having alternating layers of ferroelectric and nonferroelectric epitaxial oxides [132]. This result was demonstrated on multilayer thin films composed of paraelectric Pb$_{1-x}$La$_x$TiO$_3$ (PLT) and ferroelectric PbTiO$_3$ (PT) alternating layers. Three superlattices of PT/PLT with modulation wavelengths, l, of 10, 40, and 200 nm were studied. In each superlattice, the PT and PLT layers were of equal thickness and the total film thickness was 400 nm. For the supertlattices with $l > 40$ nm the dependence of permittivity on frequency shows a Debye behavior [Eqs. (10) and (11)]. At low frequencies, a giant dielectric constant was found of about 350,000 and 420,000 for the modulation wavelengths of 200 and 40 nm respectively. However, at high frequencies the dielectric constant is equal to that of the paraelectric phase of about 750. The dielectric constant of FSs could not be calculated by assuming that the layers are serially connected capacitors [133]. This indicates that interfacial coupling should be taken into consideration in modeling the dielectric behavior of FS films. The dielectric permittivity of FS increases with increasing temperature especially at low frequencies. The dielectric loss of FSs has a peak that spans over a wide range of frequencies between 1 and 100 kHz. The peak increases in both intensity and frequency range as temperature increases. Above 75 °C the dielectric loss has no peak but rather a monotoneous increase with decreasing

frequency. A decrease of FS modulation wavelength results in an increase of dielectric permittivity and dielectric loss and a shift of the dielectric loss peak to a lower applied field frequency. However, at the modulation wavelength of 10 nm only the paraelectric phase was found in the superlattice. The paraelectric phase has a dielectric permittivity and a dielectric loss that are almost independent of frequency and are much smaller (5 orders of magnitude) than those of the ferroelectric phase at low frequencies. The effect of film thickness on the ferroelectric phase was found to be different in FSs compared to their individual ferroelectric layers [137]. For example, in the case of BaTiO$_3$/PbTiO$_3$ multilayer thin films there is no size driven ferroelectric phase transition when the interfacial coupling is strong while the pure individual layers have a critical size of about 11 and 3 nm respectively [137]. The dielectric permittivity and loss of FSs are strongly suppressed under high dc applied fields [132]. The usually measured dielectric susceptibility of FSs is the mean value of the multilayer film, which is determined by the formula

$$\frac{1}{\langle \chi \rangle} = \frac{1}{L} \int_{-d_1}^{d_2} \frac{dz}{\chi + 1} \qquad (42)$$

where $\langle \chi \rangle$ is the mean susceptibility of the film, $L = d_1 + d_2$ is the modulation wavelength, and z is the direction of applied field.

Experimental studies [138–140] show that, in ferroelectric thin films, the formation of a periodic domain pattern limits the extension of the interfacial strain field. Consequently, the total energy of the superlattice is minimized. This is in contrast to an unclamped single-crystal system, in which a single domain is the equilibrium state. The nature of the domain pattern depends very strongly on the epitaxial mismatch, the film thickness, and temperature. Experimental data for multilayers usually show that c-domains (polarization only in the c direction which is parallel to the growth direction of the layers) of one layer alternate with c-domains of the neighboring layer [136]. However, in the case of PbTiO$_3$/BaTiO$_3$ FS multilayer thin films, it was found [141] that c-domains in the BaTiO$_3$ layers alternate with a-domains (no polarization in the c direction but only in the direction perpendicular to the growth direction of the layers) in the PbTiO$_3$ layers. This domain structure, which was also found in the ferroelectric phase of the PTL/PT FS multilayer thin films [134], is responsible for their unique dielectric properties.

Currently, there are two main theoretical models that try to explain the dielectric properties of FS multilayer thin films. One model [134] consists of a rigid-body motion of domains having oscillating pinned domain walls under applied field. The dielectric behavior is analyzed by an equivalent RC electrical circuit which includes a resistor R representing the resistance for the screening current flow between the electrodes and the domain walls, a serially connected capacitor C_1 representing the polarization due to domain-wall motion, and a parallel-connected capacitor C_2 representing the polarization of the superlattice in the absence of domain walls. C_1 was determined by using an equation

of rigid-body motion for a domain-wall lattice under a sinusoidal potential [142]. The model gives expressions for the dielectric permittivity and dielectric loss of FSs as

$$
\varepsilon' =
\begin{cases}
\dfrac{\varepsilon_1 + \varepsilon_2 + \varepsilon_2 \tau^2 \omega^2}{1 + \tau^2 \omega^2} & \text{for } |V| < V_T \\[2mm]
\varepsilon_2 & \text{for } |V| > V_T
\end{cases}
\tag{43}
$$

$$
\varepsilon'' =
\begin{cases}
\dfrac{\varepsilon_1 \tau \omega}{1 + \tau^2 \omega^2} & \text{for } |V| < V_T \\[2mm]
\dfrac{\varepsilon_1}{1 + \tau \omega} & \text{for } |V| > V_T
\end{cases}
\tag{44}
$$

where ε_1 is the dielectric permittivity due to domain walls, ε_2 is the dielectric permittivity in the absence of domain walls, $|V|$ is the absolute value of the applied voltage, V_T is the threshold voltage for domain-wall motion, τ is the relaxation time, and ω is the angular frequency. Pinning occurs when the energy is lower than that needed for nucleation of new domain walls. A Gaussian distribution of V_T was assumed in order to calculate an average capacitance equal to C_1. The calculated values of dielectric permittivity and dielectric loss, according to Eqs. (43) and (44), were found to be in good agreement with experimental results obtained from the PT/PLT FS multilayer thin films at low dc bias fields [134]. However, the calculated values deviate significantly from the experimental ones at dc bias voltages higher than the threshold voltage, probably due to an inappropriate assumption of a sinusoidal pinning potential.

A second theoretical model uses interfacial coupling criteria to describe the ferroelectric behavior of FS multilayer thin films having a first-order phase transition [137]. The model is based on the thermodynamic Landau formulation for interfacial coupling combined with the transverse Ising theory. According to this model, the dielectric susceptibility of a FS can be calculated by solving numerically the two differential equations

$$
\begin{aligned}
D_1 \frac{d^2 \chi_1}{dz^2} &= \left[A_1 + 3B_1 P_1^2 + 5C_1 P_1^4 \right] \chi_1 - \frac{1}{\varepsilon_0} \\
D_2 \frac{d^2 \chi_2}{dz^2} &= \left[A_2 + 3B_2 P_2^2 + 5C_2 P_2^4 \right] \chi_2 - \frac{1}{\varepsilon_0}
\end{aligned}
\tag{45}
$$

where A, B, C, and D are thermodynamic parameters, P is the polarization, and χ is the susceptibility of layers 1 and 2 of the multilayer thin film. The model shows that when the interfacial coupling is weak there is no ferroelectric phase below a critical thickness. Above a critical thickness the film shows two different ferroelectric phase transitions corresponding to the two different layers in the multilayer film. As the interfacial coupling strength increases there will be only a single Curie temperature of the superlattice [135], which is independent of the film thickness and is characterized by a broad permittivity peak. The Curie temperature of the superlattice decreases with decreasing modulation wavelength. When the interfacial coupling is very strong, both polarization and Curie temperature increase with decreasing modulation wavelength, and the dielectric susceptibility goes down monotonically.

GLOSSARY

Core-shell dielectrics Inhomogeneous particles composed of internal (core) pure dielectric material and outer (shell) thinner cover. The shell is characterized by the same crystallographic structure but different composition than the core. The composition gradually changes from the core/shell interface towards the outer surface of the shell.

Dielectrics Materials that exhibit internal electric dipole moments under applied electric field due to a short-range movement of electric charges.

Ferroelectric relaxors Complex oxides that belong to the family of disordered materials, most particularly to the group of mixed-cation ferroelectrics having a perovskite structure with a general chemical formula $A_{1-x}A'_x B_{1-y}B'_y O_3$.

Ferroelectric superlattices Multilayered thin films composed of alternating epitaxial nanometer-sized layers of different ferroelectric materials.

Ferroelectrics Materials that exhibit spontaneous polarization and non-linear dielectric behavior.

Linear non-linear dielectrics Materials that exhibit linear/non-linear dependence of polarization on applied electric field.

Nanocomposites Heterogeneous materials composed of at least one type of nanometer-sized particles.

Nanoporous dielectrics Heterogeneous materials composed of nanometer-sized pores embedded in a dielectric matrix.

Single-domain/multi-domain structures Single ferroelectric domain/multi-ferroelectric domains in one grain.

Two dimensional ferroelectric behavior Electric dipole interactions within a plane of a thin film.

REFERENCES

1. T. Tepper and S. Berger, *Nanostruct. Mater.* 11, 1081 (1999).
2. T. Wang and L. Zhang, *Chin. Sci. Bull.* 39, 1511 (1994).
3. C. M. Mo, L. Zhang and G. Wang, *Nanostruct. Mater.* 6, 823 (1995).
4. D. Zhang, H. F. Zhang, G. Z. Wang, C. M. Mo, and Y. Zhang, *Phys. Status. Solidi A* 157, 483 (1996).
5. A. Kassiba, M. Tabellout, S. Chapentier, N. Herlin, and J. R. Emery, *Solid State Comm.* 115, 389 (2000).
6. H. Fang, B. Chen, K. Jiang, J. Sha, Z. Jiao, Q. Zhang, and L. Zhang, *Phys. Status Solidi B* 192, K11 (1995).
7. S. Havriliak and S. Negami, *J. Polym. Sci. C* 14, 99 (1966).
8. V. E. Dubrov, M. E. Levinshtein, and M. S. Shur, *Sov. Phys. JETP* 70, 2014 (1976).
9. A. L. Efrov and V. I. Shklovski, *Phys. Status Solidi B* 76, 457 (1976).
10. W. J. Kaiser, E. M. Logothetis, and L. E. Wenger, *J. Phys. C* 18, L837 (1985).
11. R. W. Cohen, G. D. Cody, M. D. Coutts, and B. Abeles, *Phys. Rev. B* 8, 3689 (1973).
12. T. Tepper and S. Berger, *Nanostruct. Mater.* 11, 895 (1999).
13. M. J. Powell, *Phys. Rev. B* 21, 3725 (1980).
14. S. Berthier and J. Lafait, *Thin Solid Films* 89, 213 (1982).
15. G. C. Vezzoli, M. F. Chen, and J. Caslavsky, *Nanostruct. Mater.* 4, 985 (1994).
16. A. Kawabata and R. Kubo, *J. Phys. Soc. Japan* 21, 1772 (1966).
17. U. J. Gibson, H. G. Craighead, and R. A. Buhrman, *Phys. Rev. B* 27, 5046 (1983).
18. B. Roy and D. Chakravorty, *J. Mater. Res.* 8, 1206 (1993).
19. T. Tepper and S. Berger, *Mater. Sci. Eng. C* 15, 195 (2001).

20. C. J. Bottcher, *Rec. Trav. Chim.* 64, 47 (1945).
21. J. C. Maxwell, "Electricity and Magnetism," Vol. 1. Clarenon, Oxford, 1892.
22. K. W. Wagner, *Arch. Electrotech.* 2, 378 (1914).
23. R. W. Sillars, *J. Inst. Electr. Eng.* 80, 378 (1937).
24. W. Lamb, D. M. Wood, and N. W. Ashcroft, *Phys. Rev. B* 21, 2248 (1980).
25. Y. Kantor and D. Bergman, *J. Phys. C* 15, 2033 (1982).
26. J. C. Maxwell-Garnett, *Philos. Trans. Roy. Soc. London Ser. A* 203, 385 (1904); 205, 237 (1906).
27. L. D. Landau and E. M. Lifshitz, "Electrodynamics of Continuous Media," pp. 20–27, 42–45. Addison–Wesley, Reading, MA, 1960.
28. W. Lamb, D. M. Wood, and N. W. Ashcroft, *Phys. Rev. B* 21, 2248 (1982).
29. J. M. Gerardy and M. Ausloos, *Phys. Rev. B* 26, 4703 (1982).
30. B. N. J. Persson and A. Liebsch, *Solid State Comm.* 44, 1637 (1982).
31. W. W. Lee and P. S. Ho, *Mater. Res. Soc. Bull.* 22, 19 (1997).
32. L. Petera, *Semicond. Inter.* 64, 11 (1998).
33. H. Fan, H. R. Bentley, K. R. Kathan, P. Clem, Y. Lu, and C. Brinker, *J. Non-Cryst. Solids* 285, 79 (2001).
34. C. Jin, J. D. Luttmer, D. M. Smith, and T. A. Ramos, *Mater. Res. Soc. Bull.* 22, 39 (1997).
35. B. T. Holland, C. F. Blanford, and A. Stein, *Science* 28, 538 (1998).
36. R. R. Tummala and E. J. Rymaszewski, "Microelectronics Packaging Handbook," Chap. 1. Van Nostrand–Reinhold, New York, 1989.
37. H. J. Cha, J. Hedrick, R. A. DiPietro, T. Blume, R. Beyers, and D. Y. Yoon, *Appl. Phys. Lett.* 68, 1930 (1996).
38. Q. Li, J. Shen, L. Chen, and B. Zhou, *IEEE Trans. Dielectr. Electr. Insul.* 5, 58 (1998).
39. P. Pissis, A. Anagnostopoulou-Konsta, l. Apekis, D. Daoukaki-Diamanti, and C. Christodoulides, *J. Non-Cryst. Solids* 131/133, 1174 (1991).
40. A. Puzenko, N. Kozlovich, A. Gutina, and Y. Feldman, *Phys. Rev. B* 60, 14348 (1999).
41. M. Arndt, R. Stannarius, W. Gorbatschow, and F. Kremer, *Phys. Rev. E* 54, 5377 (1996).
42. A. Gutina, E. Axelrod, A. Puzenko, E. R. Pasek, N. Kozlovich, and Y. Feldman, *J. Non-Cryst. Solids* 235, 302 (1998).
43. A. Schonhals and F. Kremer, *J. Non-Cryst. Solids* 172, 336 (1994).
44. S. Takashima, "Electric Properties of Biopolymers and Membranes." Hilger, Bristol, UK, 1989.
45. A. K. Jonscher, "Universal Relaxation Law." Chelsea Dielectrics Press, London, 1966.
46. R. E. Newnham and S. T. McKinstry, *Integrated Ferroelectr.* 20, 15 (1998).
47. M. Klee, U. Mackens, and A. De Veirman, *Ferroelectrics* 140, 211 (1993).
48. G. Arlt, *J. Mater. Sci.* 35, 2655 (1990).
49. W. Cao and C. A. Randall, *J. Phys. Chem. Solids* 57, 1499 (1996).
50. G. Arlt, D. Hennings, and G. de With, *J. Appl. Phys.* 58, 1619 (1985).
51. R. C. Pohanka, R. W. Rice, and B. E. Walker, Jr., *J. Amer. Ceram. Soc.* 59, 71 (1976).
52. K. Okazaki, H. Igarasi, K. Nagata, and A. Hasegawa, *Ferroelectrics* 7, 153 (1974).
53. G. Arlt, *Ferroelectrics* 104, 217 (1990).
54. W. L. Zhong, Y. X. Wang, C. L. Wang, B. Jiang, and L. A. Bursill, *Ferroelectrics* 252, 11 (2001).
55. H. i. Hsiang and F. S. Yen, *J. Amer. Ceram. Soc.* 79, 1053 (1996).
56. C. J. Lu, S. B. Ren, H. M. Shen, J. S. Liu, and Y. N. Wang, *J. Phys. Condens. Matter* 8, 8011 (1996).
57. M. H. Lee, A. Halliyal, and R. E. Newnham, *Ferroelectrics* 87, 71 (1988).
58. P. Zhang, B. Jiang, W. Zhong, J. Ma, H. Cheng, Z. Yang, and L. Li, *Guisuanyan Xuebao* 22, 141 (1994).

59. A. Jaccard, W. Kanzig, and M. Peter, *Helv. Phys. Acta* 26, 521 (1953).
60. W. Y. Shih, W.-H. Shih, and I. A. Aksay, *Phys. Rev. B* 50, 15575 (1994).
61. M. E. Lines and A. M. Glass, "Principles and Applications of Ferroelectrics and Related Materials." Clarendon, Oxford, 1977.
62. A. V. Bune, V. M. Fridkin, S. Ducharme, L. M. Blinov, S. P. Palto, A. V. Sorokin, S. G. Yudin, and A. Zlatkin, *Nature* 391, 874 (1998).
63. J. Choi, P. A. Dowben, S. Pebley, A. V. Bune. S. Ducharme, V. M. Fridkin, S. P. Palto, and N. Petukova, *Phys. Rev. Lett.* 80, 1328 (1998).
64. T. Furukawa, *Phase Transit.* 18, 143 (1989).
65. J. F. Legrand, *Ferroelectrics* 91, 303 (1989).
66. S. P. Palto, L. Blinov, A. V. Bune, E. Dubovik, V. M. Fridkin, N. Petukova, K. Verkovskaya, and S. G. Yudin, *Ferroelectr. Lett.* 19, 65 (1995).
67. S. Ducharme, *Ferroelectrics* 202, 29 (1997).
68. S. Duchrame, V. M. Fridkin, A. V. Bune, S. P. Palto, L. M. Blinov, N. Petukova, and S. G. Yudin, *Phys. Rev. Lett.* 84, 175 (2000).
69. A. V. Bune, S. Ducharme, V. Fridkin, L. Blinov, S. Palto, N. Petukhova, and S. G. Yudin, *Appl. Phys. Lett.* 67, 3975 (1995).
70. L. M. Blinov, V. M. Fridkin, S. P. Palto, A. V. Bune, P. A. Dowben, and S. Ducharme, *Phys. Usp.* 43, 243 (2000).
71. L. C. Wang, W. L. Zhong, and P. L. Zhang, *J. Phys. Condens. Matter* 3, 4743 (1992).
72. M. Anliker, H. R. Brugger, and W. Kanzig, *Helv. Phys. Acta* 27, 99 (1954).
73. T. Kanata, K. Yoshikawa, and K. Kubota, *Solid State Comm.* 62, 765 (1987).
74. K. Ishikawa, K. Yoshikawa, and N. Okada, *Phys. Rev. B* 37, 5852 (1988).
75. P. Marquardt and H. Gleiter, *Phys. Rev. Lett.* 48, 1423 (1982).
76. K. Ishikawa, K. Yoshikawa, and N. Okada, *Phys. Rev. B* 37, 5852 (1988).
77. J. F. Scott, M. S. Zheng, R. B. Godfrey, C. Araujo, and L. McMillan, *Phys. Rev. B* 35, 4044 (1987).
78. P. G. De Gennes, *Solid State Comm.* 1, 132 (1963).
79. R. Blinc and B. Zeks, "Soft Modes in Ferroelectrics and Antiferroelectrics." North-Holland, Amsterdam, 1974.
80. M. I. Kaganov and A. N. Omelyanchuk, *Sov. Phys. JETP* 34, 895 (1972).
81. C. Toledano and P. Toledano, "Landau Theory of Phase Transitions." World Scientific, Singapore, 1987.
82. C. Lubensky and M. H. Rubin, *Phys. Rev. B* 12, 3885 (1975).
83. R. Kretschmer and K. Binder, *Phys. Rev. B* 20, 1065 (1979).
84. D. R. Tilley and B. Zeks, *Solid State Comm.* 49, 823 (1984).
85. D. R. Tilley, in "Ferroelectric Thin Films: Synthesis and Basic Properties" (C. Paz de Araujo, J. F. Scott, and G. F. Taylor, Eds.). Gordin and Breach, Amsterdam, 1996.
86. N. de Mathan, E. Hussonne, C. Calvarin, J. Gavarri, A. Hewat, and A. J. Morell, *J. Phys. Condens. Matter* 3, 8159 (1991).
87. S. Vakhrushev, A. A. Naberezhov, N. M. Ouneva, and B. P. Toperverg, *Ferroelectrics* 90, 173 (1989).
88. E. Husson, L. Abello, and A. Morel, *Mater. Res. Bull.* 25, 539 (1990).
89. T. R. Shrout and J. P. Dougherty, "Dielectric Ceramics: Composition, Processing and Properties, Ceramic Transactions 8," pp. 3–19. Am. Ceram. Soc., Westerville, OH, 1990.
90. E. Husson, M. Chubb, and A. Morell, *Mater. Res. Bull.* 24, 201 (1989).
91. J. Chen, H. M. Can, and M. P. Harmer, *J. Amer. Ceram. Soc.* 72, 593 (1989).
92. Z. G. Lu, J. P. Bonnet, J. Ravez, J. M. Reau, and P. Hagenmuller, *J. Phys. Chem. Solids* 53, 1 (1992).
93. A. D. Hilton, C. A. Randall, D. J. Barber, and T. R. Shrout, *Ferroelectrics* 93, 379 (1989).
94. Y. Xi, C. Zhili, and L. Cross, *Ferroelectrics* 54, 163 (1983).

95. L. E. Cross, *Ferroelectrics* 76, 241 (1987).
96. T. Takenaka, T. Kanegae, and H. Takagi, in "Dielectric Ceramics: Processing, Properties, and Applications," Ceramic Transactions 32 (K. M. Nair, J. P. Guha, and A. Okamoto, Eds.), pp. 221–230. Am. Ceram. Soc., Westerville, OH, 1993.
97. R. Sommer, N. K. Yushin, and J. Van der Klink, *Phys. Rev. B* 48, 1323 (1993).
98. S. E. Park, T. Shrout, and S. Shrout, *IEEE. Trans. UFFC* 44, 1140 (1997).
99. P. Bonneau, P. Garnier, G. Calvrin, E. Husson, J. R. Gavarri, A. W. Hewat, and A. Morell, *J. Solid State Chem.* 91, 350 (1991).
100. N. de Mathan, E. Husson, G. Calvarin, and A. Morell, *Mater. Res. Bull.* 26, 1167 (1991).
101. A. J. Bell, *J. Phys. Condens. Matter* 5, 8773 (1993).
102. Z. G. Lu and G. Calvarin, *Phys. Rev. B* 51, 2694 (1995).
103. F. Wickenhofer, W. Kleemann, and D. Rytz, *Ferroelectrics* 124, 237 (1991).
104. D. Viehland, S. J. Jang, and L. E. Cross, *J. Appl. Phys.* 68, 2916 (1990).
105. V. A. Isupov, *Ferroelectrics* 90, 113 (1989).
106. M. D. Glinchu and R. Farhi, *J. Phys. Condens. Matter* 8, 6985 (1996).
107. V. Westphal, W. Kleemann, and M. D. Glinchuk, *Phys. Rev. Lett.* 68, 847 (1992).
108. J. M. Haun, E. Furman, J. S. Jany, and L. E. Cross, *Ferroelectrics* 99, 13 (1989).
109. G. A. Rosetti, T. Nishimura, and L. E. Cross, *J. Appl. Phys.* 69, 6595 (1991).
110. X. Dai, Z. Xu, J. F. Li, and D. Viehland, *J. Appl. Phys.* 77, 3254 (1995).
111. D. Viehland, S. J. Jang, and L. E. Cross, *J. Appl. Phys.* 68, 2916 (1990).
112. X. Duan, W. Luo, W. Wu, and J. S. Yuan, *Solid State Comm.* 114, 597 (2000).
113. N. Setter and R. Waser, *Acta Mater.* 48, 151 (2000).
114. B. S. Rawal, M. Kahn, and W. R. Buessem, in "Advanced Ceramics," (L. M. Levinson, Ed.), Vol. 1. Am. Ceram. Soc., Westerville, OH, 1981.
115. D. Hennings and G. Rosenstein, *J. Amer. Ceram. Soc.* 68, 249 (1985).
116. W. Heywang, *Ferroelectrics* 49, 3 (1983).
117. H.-Y. Lu, J.-S. Bow, and W.-H. Deng, *J. Amer. Ceram. Soc.* 73, 3562 (1990).
118. T. R. Armstrong and R. C. Buchanan, *J. Amer. Ceram. Soc.* 73, 1268 (1990).
119. R. C. Buchanan, R. D. Roseman, and T. R. Armstrong, in "Ceramic Transactions Dielectric Ceramics: Processing, Properties, and Applications" (K. M. Nair, J. P. Guha, and A. Okamoto, Eds.), Vol. 32, pp. 167–176. Am. Ceram. Soc., Westerville, OH, 1993.
120. Y. Pak, Y. Kim, and H. G. Kim, *J. Phys. D* 29, 2483 (1996).
121. K. Kinoshinta and A. Yamaji, *J. Appl. Phys.* 47, 371 (1976).
122. T. R. Armstrong, L. E. Morgens, A. K. Maurice, and R. C. Buchanan, *J. Amer. Ceram. Soc.* 72, 605 (1989).
123. B. Jaffe, W. R. Cook, and H. Jaffe, "Piezoelectric Ceramic." Academic Press, New York, 1971.
124. C. A. Randall, S. F. Wang, D. Laubscher, J. P. Dougherty, and W. Huebner, *J. Mater. Res.* 8, 871 (1993).
125. G. A. Smolenskii, *J. Phys. Soc. Japan Suppl.* 28, 26 (1970).
126. H. Diamond, *J. Appl. Phys.* 32, 909 (1961).
127. S. B. Rawal, M. Kahn, and W. R. Buessem, "Grain Boundary Phenomena in Electronic Ceramics." Am. Ceram. Soc., Columbus, OH, 1981.
128. Y. Park, Y. I. Song, and S. K. Ahn, Korean Patent 90-13543, 1990.
129. K. Iijima, T. Terashima, Y. Bando, K. Kamigaki, and H. Terauchi, *J. Appl. Phys.* 72, 2840 (1992).
130. T. Tsurumi, T. Suzuki, M. Yamane, and M. Daimon, *Japan. J. Appl. Phys.* 33, 5192 (1994).
131. H. Tabata, H. Tanaka, and T. Kawai, *Appl. Phys. Lett.* 65, 1970 (1994).
132. A. Erbil, Y. Kim, and R. A. Gerhardt, *Phys. Rev. Lett.* 77, 1628 (1996).
133. Y. Ohya, T. Ito, and Y. Takahashi, *Japan. J. Appl. Phys.* 33, 5272 (1994).
134. Y. Kim, R. A. Gerardt, and A. Erbil, *Phys. Rev. B* 55, 8766 (1997).
135. E. D. Specht, H.-M. Christen, D. P. Norton, and L. A. Boatner, *Phys. Rev. Lett.* 80, 4317 (1998).
136. J. C. Jiang, X. Q. Pan, W. Tian, C. D. Theis, and D. Schlom, *Appl. Phys. Lett.* 74, 2851 (1999).
137. B. D. Qu, W. L. Zhong, and R. H. Prince, *Phys. Rev. B* 55, 11218 (1997).
138. B. S. Kwak, A. Erbil, B. J. Wilkens, J. D. Budai, M. F. Chisholm, and L. A. Boatner, *Phys. Rev. Lett.* 68, 3733 (1992).
139. B. S. Kwak, A. Erbil, J. D. Budai, M. F. Chisholm, L. A. Boatner, and B. J. Wilkens, *Phys. Rev. B* 49, 14865 (1994).
140. J. S. Speck, A. Seifert, W. Pompe, and R. Ramesh, *J. Appl. Phys.* 76, 477 (1994).
141. M. D. Glinchuck, E. A. Eliseev, V. A. Tephanovich, M. G. Karkut, and R. Farhi, *Condens. Matter* 1, (2000).
142. G. Gruner, *Rev. Mod. Phys.* 60, 1129 (1988).

Diffusion and Thermal Vacancy Formation in Nanocrystalline Materials

U. Brossmann, R. Würschum

Technische Universität Graz, Graz, Austria

H.-E. Schaefer

Universität Stuttgart, Stuttgart, Germany

CONTENTS

1. INTRODUCTION

Since the pioneering work on nanocrystalline (n-) materials nearly twenty years ago [1], diffusion in these novel types of materials attracted permanent interest. This interest arises from the fact that material transport belongs to those physical properties of nanocrystalline materials that differ most from those of their coarse-grained or single-crystalline counterparts. In nanocrystalline materials, efficient mass transport may occur because the number density of crystallite interfaces in these materials is high, and diffusion along interfaces is usually much faster than in crystals [2].

With respect to nanotechnology, diffusion represents a key issue for a number of application-oriented properties of nanocrystalline materials, such as enhanced ductility, diffusion-induced magnetic anisotropy, enhanced ionic mass transport, or improved catalytic activity [3, 4]. On the other hand, diffusion is also relevant with respect to the basic physics of nanophase materials since diffusion represents a highly structure-sensitive atomistic process. In particular, atomic-scale free volumes in interfaces and thermal vacancies at high temperatures play crucial roles in diffusion processes. Therefore, most detailed insight into the diffusion

characteristics of nanocrystalline materials is gained from a combined study of diffusion and free volumes.

This chapter is an up-to-date review of diffusion and thermal vacancy formation in nanocrystalline metals and alloys. Focus will be on self-diffusion or diffusion of substitutional atoms and the variation of the diffusion characteristics with the routes applied for materials synthesis. The few diffusion studies on nanocrystalline oxide materials will be briefly summarized.

2. MODELING

In both nanocrystalline and coarse-grained materials, diffusion coefficients are usually deduced from the penetration profile of tracer atoms from the surface, which for example are measured by means of the radiotracer technique [see Section 3]. In general, the diffusion in polycrystalline materials involves two simultaneous diffusion processes progressing at different rates: i) rapid diffusion in the crystallite interfaces characterized by the grain boundary (GB) diffusion coefficient D_B, and ii) the usually much slower volume diffusion from the interfaces and the specimen surface into the crystallites characterized by the volume diffusion coefficient D_V. According to the classification scheme introduced by Harrison, three regimes of grain boundary diffusion denoted A, B, and C can be found in polycrystalline materials for which the evaluation of the penetration profiles is relatively simple [5, 6]. The validity of these diffusion regimes is defined by appropriate ratios of the diffusion length $L_V \propto \sqrt{D_V t}$ (t: diffusion time) in the crystallites and the crystallite size d or the interface thickness δ [6].

In the type C regime, prevalent at the low temperatures where many diffusion experiments on nanocrystalline pure metals such as n-Fe and n-Pd are performed, the diffusion is confined to the interfaces ($L_V < \delta$). Assuming an initial thin

layer of tracer atoms at the surface, the interface diffusion coefficient D_B can be directly determined from Gaussian shaped concentration profiles

$$C \propto \frac{1}{\sqrt{D_B t}} \exp\left(-\frac{z^2}{4 D_B t}\right) \qquad (1)$$

with z and t denoting the depth and time of diffusion. The same simple profile shape prevails in the type A regime where the diffusion length in the crystallites exceeds the crystallite diameter, or, $L_V > d$. In this regime, which may occur at high temperatures or at long times of diffusion annealing, the diffusion is characterized by an effective diffusion coefficient $D_{eff} = (1 - f)D_V + f D_B$ where f denotes the volume fraction of interfaces. In the type B regime $(\delta < L_V < d)$, which occurs in an intermediate temperature regime, the diffusion profiles are composed of a Gaussian part for small penetration depths, which characterizes the volume diffusion from the surface, and a deeper penetration part from which the product $s\delta D_B D_V^{-0.5}$ can be determined (s: segregation factor). Diffusion conditions falling in between these regimes can be treated numerically. Moreover, an immobilization of diffusing atoms from fast interfacial diffusion paths in the crystallites due to grain growth and GB migration can be quantitatively be taken into account, leading to an apparent diffusivity smaller than the actual value of D_B [6]. An extension of the aforementioned scheme for fine grained metals, distinguishing different interface geometries and the ratio between the diffusion length in the interfaces and the crystallite size, has been proposed by Mishin and Herzig [7].

Important aspects with respect to diffusion characteristics in nanocrystalline materials pertain to residual porosity and crystallite agglomeration, which has to be taken into account in particular for nanocrystalline materials prepared by powder routes. Residual porosity and loosely packed interfaces between larger agglomerates of nanocrystallites may provide fast diffusion paths from which diffusion into the crystallite interfaces of the nanocrystalline agglomerates occurs, as schematically shown in Figure 1. This type of diffusion characteristic can be dealt with within the framework of a cluster model, as first proposed by Bokstein et al. for studies on n-Ni [8] (see Section 4.1.1). This model takes into account two types of interfaces with fast and slow diffusivity, for which relationships analogous to GB diffusion kinetic of type B are valid [8, 9].

In view of the close correlation between atomic-scale open volumes and atomic diffusion, positron annihilation has proven to be a powerful supplementary tool for gaining additional insight into the complex material transport characteristics of nanocrystalline materials. By means of positron annihilation, open volumes on an atomic scale can be specifically detected with high sensitivity, owing to the characteristic change of the positron-electron annihilation parameters that occurs upon positron trapping at free volumes. In nanocrystalline materials with positrons being predominantly trapped and annihilated in the interfaces between the nanocrystallites, the defect-specific positron lifetime components yield unique information on the size of interfacial structural free volumes [10]. At high temperatures, the formation of thermal vacancies also can be
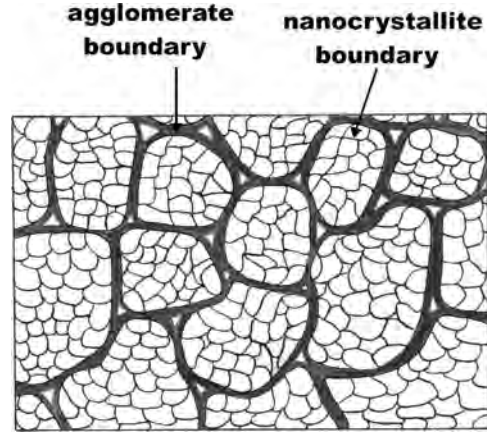
Figure 1. Agglomerate model of diffusion in nanocrystalline materials synthesized via powder routes [8]. Due to crystallite agglomeration and residual porosity, these materials show two types of interfaces with fast and slow diffusion, which can be modeled in analogy to type B kinetics of interface diffusion. The loosely packed boundaries between the densely packed agglomerates provide fast paths of diffusion, whereas the diffusion in the interfaces between the nanocrystals is similar to conventional grain boundaries.

detected. A pattern of the positron annihilation sites in nanocrystalline metals is shown in Figure 2. As outlined elsewhere [11, 12], in most high-temperature studies of nanocrystalline metals and alloys, the mean positron lifetime can

$$\bar{\tau} = \frac{\tau_V \sigma_V C_V + \tau_1 \sigma_1 C_1 + \tau_{\text{void}} \sigma_{\text{void}} C_{\text{void}}}{\sigma_V C_V + \sigma_1 C_1 + \sigma_{\text{void}} C_{\text{void}}} \qquad (2)$$
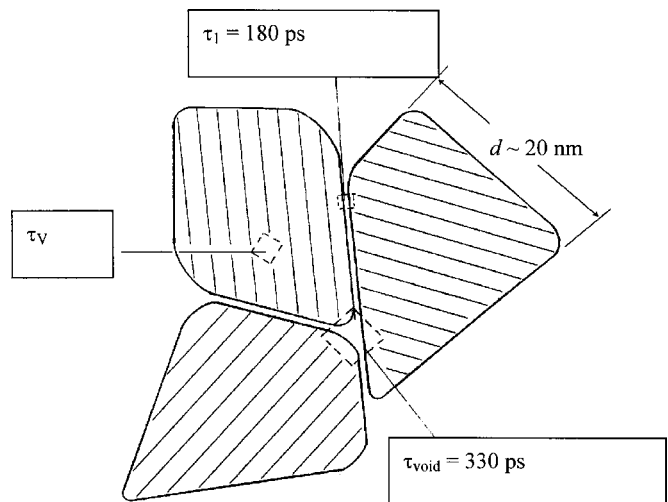
Figure 2. Positron annihilation sites in nanocrystalline metals. In nanocrystalline metals, the positrons are quantitatively trapped and annihilated at vacancy-sized defects in the interfaces or nanovoids with a size of about 5–15 missing atoms yielding the characteristic positron lifetime components τ_1 and τ_{void}. A lifetime component τ_V characterizing thermal lattice vacancies is found in thermally stable nanomaterials at higher temperatures. Reprinted with permission from [12], R. Würschum, *Mater. Sci. Forum* 363–365, 35 (2001). © 2001, Trans Tech Publications, Inc.

be described by the weighted average of the characteristic positron lifetimes in vacancy-type free volumes at interfaces (τ_1), nanovoids (τ_{void}), and thermal vacancies (τ_V). The weighting factors $\sigma_i C_i$ are given by the product of the specific positron trapping rate σ_i and the concentration C_i of the respective type i of positron trap. In order to avoid structural changes during the measuring runs, high-temperature measurements of the positron lifetime are performed after preannealing at or above the maximum measuring temperature.

3. EXPERIMENTAL TECHNIQUES

Diffusion measurements on nanocrystalline materials are carried out using a wide spectrum of well-established experimental techniques. These include the radiotracer method with sputter sectioning or mechanical sectioning, mainly used for metallic diffusors as ^{59}Fe; secondary ion mass spectroscopy (SIMS) with depth profiling for nonradioactive tracers as ^{18}O; Rutherford backscattering (RBS); or nuclear magnetic resonance (NMR) for studies on an atomic scale. Details of these experimental techniques are described in textbooks on diffusion (see, e.g., [5]) and the references quoted for the respective materials (see Table 1 and [13–30]).

Table 1. Overview of diffusion studies published on nanocrystalline metals and alloys.

Metals	Synthesis route	Ref.
Pd (Fe)	CC	[13]
Pd (Fe)	SPD	[14]
Fe (Fe)	CC	[15]
Fe (Fe)	SPD	[15]
Cu (Cu)	CC	[16]
Cu (Ag)	MS	[17]
Cu	CC	[18]
Cu (Ag)	CC	[19]
Cu (Au)	CC	[20]
Cu (Bi)	CC	[20]
Cu (Sb)	CC	[21]
Ni (Ni)	CC	[8]
Ni (Cu)	SPD	[22]
Ni (Cu)	ED	[22]
Fe (B)	CC	[23]
Alloys		
$Fe_{73.5}Si_{13.5}B_9/Nb_3Cu_1$ (Fe)	MS/CRY	[24]
$Fe_{73.5}Si_{13.5}B_9/Nb_3Cu_1$ (Ge)	MS/CRY	[25]
$Fe_{90}Zr_{10}$ (Fe)	MS/CRY	[26]
$Fe_{90}Zr_7B_3$ (Fe)	MS/CRY	[25]
$Nd_{14.2}Fe_{80.8}B_5$ (Fe)	MS/HC	[25, 27]
γ-$Fe_{61.2}Ni_{38.8}$ (Fe)	MA/HC	[9]
$Al_{91.9}Ti_{7.8}Fe_{0.3}$ (Cu)	MA/HC	[28]
$Al_{96.8}Mg_3Sc_{0.2}/Al_{99.8}Sc_{0.2}$	SPD	[29]
Ni-Cu (Interdiffusion)	PVD/ML	[30]

Note: Synthesis routes: crystallite condensation and compaction (CC), severe plastic deformation (SPD), magnetron sputtering of films (MS), electro-deposition (ED), melt-spinning and crystallization (MS/CRY), melt-spinning and hot compaction (MS/HC), mechanical alloying and hot compaction (MA/HC), or deposition of thin multi-layers in high vacuum (PVD/ML). The diffusing element is given in brackets.

For the high-temperature positron annihilation studies, a radioactive source, such as ^{58}Co, is deposited on and subsequently diffused into the consolidated specimen material. Positron lifetime spectra containing about 10^6 to 10^7 counts are recorded by means of the $\gamma\gamma$-coincidence technique using two fast scintillation detectors. A description of the positron annihilation technique and its application to nanomaterials has been given earlier [10, 12, 31, 32].

4. RESULTS ON DIFFUSION AND THERMAL VACANCY FORMATION

The structure of nanocrystalline materials in general depends greatly on the synthesis route. Therefore, the following presentation of the results on diffusion and positron annihilation in nanocrystalline metals and alloys (Section 4.1) is subdivided into the various synthesis routes, such as cluster-synthesis and compaction (Section 4.1.1), melt-spinning (Section 4.1.2) and mechanical routes (Section 4.1.3). The diffusion in nanocrystalline ceramics is addressed in Section 4.2. A compilation of diffusion and positron lifetime measurements in nanocrystalline metals, alloys, and ceramics is given in Tables 1–3.

4.1. Nanocrystalline Metals and Alloys

4.1.1. Cluster-Condensation and Compaction

A common route for the preparation of nanocrystalline metals and alloys is cluster synthesis and compaction (cf. CC in Table 1). Summarizing briefly, pure metals or alloys are vaporized in a thermal evaporation or sputtering source in a low-pressure inert gas atmosphere (mostly He or Ar). Nanocrystallites, formed by condensation in the gas atmosphere, are collected on a cold surface and subsequently consolidated *in-situ* into disk-shaped samples by uniaxial pressing. In the case of n-Pd [13] and n-Fe [15], mass densities near the theoretical value were obtained by applying a pressure of 3–4 GPa at slightly elevated temperatures in the range of 400 K under ultra-high vacuum conditions.

Due to the synthesis conditions far from thermodynamic equilibrium, structural relaxation occurs in cluster-assembled nanocrystalline metals at slightly elevated temperatures, as evidenced by a variety of structure-sensitive measuring techniques (see [4, 33]). Regarding diffusion characteristics, an influence of structural relaxation is concluded from recent studies of self-diffusion in nanocrystalline Fe prepared by cluster condensation and compaction (see Fig. 3), where a decrease of self-diffusivity with increasing time of diffusion annealing could be detected [15]. Similar observations were made for nanostructured Fe [15] or Ni [22] prepared by severe plastic deformation (see Section 4.1.3).

In the relaxed state of cluster-assembled nanocrystalline Fe, interface diffusivities are found that are quite similar to values extrapolated from high-temperature data of GB self-diffusion in coarse-grained Fe (Fig. 4). Similar conclusions were drawn from earlier diffusion studies on virtually pore-free, cluster-assembled nanocrystalline Pd [13]. The fast diffusion of ^{59}Fe in n-Fe and n-Pd is regarded as evidence that
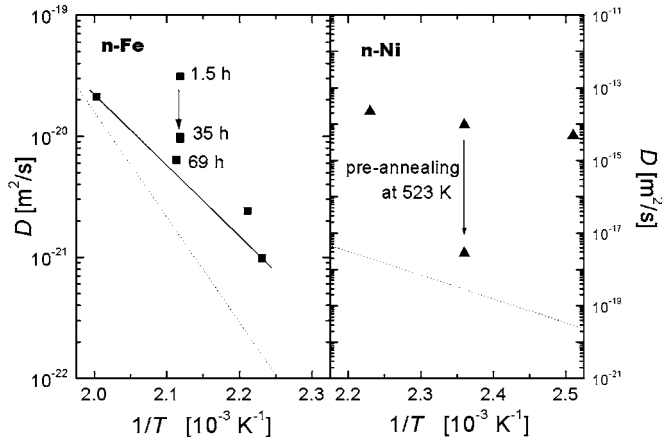
Figure 3. Correlation between structural relaxation and grain boundary diffusivities in nanocrystalline metals. Structural relaxation induced by preannealing at a temperature of 523 K leads to a significant reduction of the Cu diffusivity in nanocrystalline Ni prepared by severe plastic deformation [22]. A similar decrease of ^{59}Fe self diffusivity is noted in cluster-assembled Fe during extended diffusion annealing [15]. Dashed lines denote extrapolated values of GB diffusion in coarse-grained metals.

atomic transport occurs in the crystallite interfaces since the bulk diffusion in crystalline Pd or Fe is negligibly small at these temperatures (see Fig. 4). Moreover, the diffusion in these cluster-compacted nanocrystalline metals is probably not affected by porosity, as indicated by the high relative mass density and the observation that the data obtained in
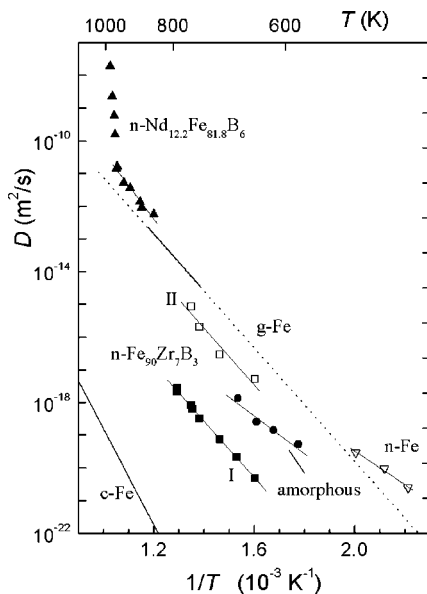
Figure 4. Overview of ^{59}Fe tracer diffusion in nanocrystalline Fe and Fe-rich alloys: n-Fe prepared by cluster and compaction [15], n-Fe$_{90}$-Zr$_7$B$_3$ [25] and n-Fe$_{73.5}$Si$_{13.5}$B$_9$Nb$_3$Cu$_1$ [24] prepared by melt-spinning and crystallization, and n-Nd$_{12.2}$Fe$_{81.8}$B$_6$ prepared by melt-spinning and hot-compaction [27]. For Fe$_{90}$Zr$_7$B$_3$ the diffusivities in two types of interfaces (I,II) are shown. Literature data of Fe diffusion in the ferromagnetic phase of crystalline α-Fe (c-Fe, [39]) and in grain boundaries of Fe (GB-Fe, [40]) are shown for comparison (extrapolations are dotted).

pore-free nanostructured metals prepared by severe plastic deformation (see Section 4.1.3) are very similar.

The major result that the diffusion characteristics are similar in relaxed interfaces of nanocrystalline metals and in conventional GBs indicates that the interfaces in nanocrystalline metals attain an equilibrium-like structure upon structural relaxation at slightly elevated temperature. The enhanced diffusivity prior to relaxation has to be ascribed to a nonequilibrium structure of the interfaces. In cold-worked bulk metals, nonequilibrium GBs have been found to exhibit a gradual relaxation or metastable characteristics [34]. In this case, the enhanced diffusivities are ascribed to the absorption of lattice dislocations at the grain boundaries [34, 35]. In nanocrystalline metals, where the dislocation activity is suppressed at small crystallite sizes [36], the enhanced diffusivity may arise from local excess free volume which, for example, is left after initial high-pressure crystallite compaction. This view is supported by positron annihilation studies providing evidence of vacancy-type interfacial free volumes and their variations upon annealing at slightly elevated temperatures [10, 31]. A similar decrease of the diffusivity upon annealing is well known in the case of amorphous alloys, where excess free volumes anneal out during structural relaxation (see [37]). The relaxed state of amorphous alloys remains stable over a relatively wide temperature range below the onset of crystallization. In nanocrystalline metals, however, the relaxed interfacial structure is prone to interface migration and grain growth [13]. This is particularly true in the case of porosity-free nanocrystalline metals of high purity where no pinning centers for interfaces are available [38].

A substantial influence of porosity on diffusion behavior in cluster-assembled nanocrystalline metals has to be taken into consideration in the case of incomplete crystallite compaction. This appears to apply particularly to the first diffusion studies in this field where extraordinarily high diffusivities were found (see [2] for discussion). More recently, residual porosity in the wake of agglomerate formation during cluster synthesis and compaction has been quantitatively considered by Bokstein et al. [8] for the analysis of Ni self-diffusion studies on cluster-assembled n-Ni with a relative density of 92–93%. Applying the cluster model described in Section 2 and schematically shown in Figure 1, a high diffusivity comparable to surface diffusion was found for the loosely packed interfaces between the agglomerates, whereas the diffusion in the nanocrystallite boundaries within the agglomerates was found to be characteristic of GB diffusion [8]. Similar conclusions were drawn most recently from a more detailed diffusion study on 98% dense γ-Fe$_{61.2}$Ni$_{38.8}$ prepared by mechanical alloying and hot compaction [9] (see Section 4.1.3 and Fig. 6).

4.1.2. Melt-Spinning

Nanocrystalline alloys can be obtained from appropriate amorphous materials by means of crystallization (cf. MS/CRY in Table 1). The amorphous alloys are prepared by rapid cooling making use of, for example, the melt-spinning technique. Upon annealing, the initially amorphous alloys transform into a nanocrystalline structure with a residual

amorphous intergranular phase. In this class of nano-materials, the attention focuses on Fe-based magnetic materials such as the soft magnetic alloys $Fe_{73.5}Si_{13.5}B_9Nb_3Cu_1$ and $Fe_{90}Zr_7B_3$ (NANOPERM^{TM}), which are already in commercial application [41, 42]. In these nanocomposites prepared by crystallization of amorphous alloys, the residual intergranular amorphous phase plays a key role in determining the diffusion and positron annihilation behavior. In the case of the permanent magnetic alloy $Fe_2Nd_{14}B$, the nanocrystalline structure can be directly obtained upon melt-spinning [43]. Fine-tuning of the magnetic properties by nanostructuring and high thermal stability make these aforementioned nanocrystalline materials both attractive choices for technical applications and important targets of scientific investigation.

The soft-magnetic alloy $Fe_{73.5}Si_{13.5}B_9Nb_3Cu_1$ shows a two-component nanocomposite structure of DO_3-type ordered Fe_3Si nanocrystallites (crystallite size $d \sim 12$ nm) embedded in an Nb and B enriched amorphous matrix. This structure is maintained until well above the annealing temperature ($T_a = 810$ K) applied for crystallization of the initially amorphous alloy [24].

Diffusion studies conducted on nanocrystalline and amorphous $Fe_{73.5}Si_{13.5}B_9Nb_3Cu_1$ under identical conditions ($T_d = 693$ K) show that the ^{59}Fe tracer diffusion in the nanocrystalline state is markedly higher than in the initially amorphous state [24]. This rather unusual behavior can be attributed to the formation of thermal vacancies in the DO_3-$Fe_{80}Si_{20}$-nanocrystallites leading to a higher diffusivity of Fe in the volume of the Fe_3Si crystallites than in the surrounding amorphous matrix. This is concluded from the observation of a reversible increase of the positron lifetime in $Fe_{73.5}Si_{13.5}B_9Nb_3Cu_1$ at temperatures above 700 K (see Fig. 5), indicating thermal vacancy formation in the DO_3-Fe_3Si nanocrystallites. The enthalpy of vacancy formation $H_V^F = 1.1$ eV determined from the high-temperature increase of the mean positron lifetime $\bar{\tau}$ is almost identical to the value in DO_3-$Fe_{79}Si_{21}$ single crystals [24]. In further analogy to single-crystalline DO_3-$Fe_{79}Si_{21}$ [44], the diffusion on the Fe sublattice of the nanocrystallites is found to be much faster than on the Si sublattice. This is deduced from a recent extension of the studies on the diffusion of Ge, which is considered to resemble the self-diffusion of Si in nanocrystalline $Fe_{73.5}Si_{13.5}B_9Nb_3Cu_1$ [25].

Regarding the interface diffusion in $Fe_{73.5}Si_{13.5}B_9Nb_3Cu_1$, a closer inspection shows the interface diffusivity of Fe in the nanocrystalline state to be similar as in the amorphous state prior to crystallization. This important observation of a slow interface diffusion, strongly reduced in comparison to that in grain boundaries of metals (Fig. 4), represents a characteristic feature of alloys that are prepared by crystallization of melt-spun amorphous ribbons. This slow diffusivity, which occurs in other crystallized alloys ($Fe_{90}Zr_{10}$, $Fe_{90}Zr_7B_3$) as well (see later), has to be attributed to residual intergranular amorphous phases [24, 26].

This view is supported by positron lifetime studies on nanocrystalline $Fe_{73.5}Si_{13.5}B_9Nb_3Cu_1$, where prior to the onset of thermal vacancy formation in the nanocrystallites, a positron lifetime $\bar{\tau}$ similar to that in the amorphous state is observed [24]. This shows that positrons are trapped in the residual intergranular amorphous phase between the
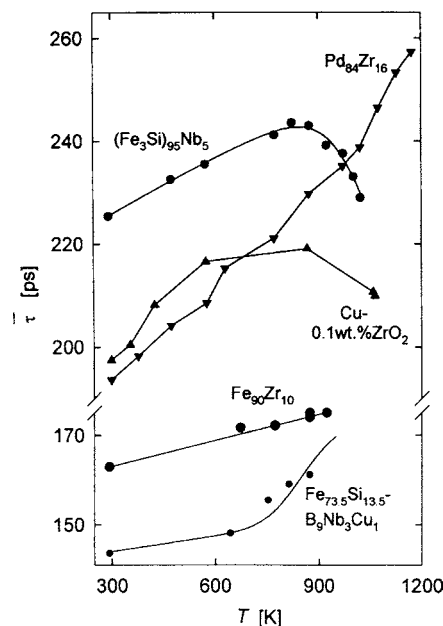
Figure 5. Overview of high temperature positron measurements (mean positron lifetime $\bar{\tau}$) in the structurally stable nanocrystalline alloys $(Fe_3Si)_{95}Nb_5$ [32], ZrO_2-doped Cu [45], $Pd_{84}Zr_{16}$ [45], $Fe_{73.5}Si_{13.5}B_9Nb_3Cu_1$ [24], and $Fe_{90}Zr_{10}$ [45]. Thermal formation of vacancies is indicated by the reversible increase $(Fe_{73.5}Si_{13.5}B_9Nb_3Cu_1)$ or decrease $((Fe_3Si)_{95}Nb_5, ZrO_2$-doped Cu) of $\bar{\tau}$ at high temperatures. Reprinted with permission from [12], R. Würschum, *Mater. Sci. Forum* 363–365, 35 (2001). © 2001, Trans Tech Publications, Inc.

nanocrystallites and annihilated at free volumes of similar size as in the amorphous alloys. The same conclusion is drawn from positron lifetime studies on n-$Fe_{90}Zr_{10}$ [45].

The Fe and Ge diffusion data on nanocrystalline $Fe_{73.5}Si_{13.5}B_9Nb_3Cu_1$ allow important conclusions on the application-relevant issue of magnetic anisotropy, which can be induced in this alloy upon annealing under mechanical stress or in an external magnetic field [46, 47]. A more detailed consideration indicates that the generation of a magnetic anisotropy is controlled by the slow diffusion of Si within the nanocrystallites [25].

Although there are common features of $Fe_{73.5}Si_{13.5}B_9Nb_3Cu_1$ and the other crystallized alloys $Fe_{90}Zr_{10}$ and $Fe_{90}Zr_7B_3$, as stated above, there are also remarkable differences which are addressed in the following. Nanocrystalline $Fe_{90}Zr_{10}$ is prepared by crystallizing melt-spun amorphous ribbons at 873 K for 48 h under high vacuum conditions. The resulting two-phase microstructure is composed of α-Fe and Fe_2Zr nanocrystallites with a mean grain size in the order of $d \sim 30$ nm [26, 48]. A more refined nanostructure of α-Fe grains with a size of $d \sim 10$–15 nm is obtained in $Fe_{90}Zr_7B_3$ [25].

In contrast to the Fe_3Si-based alloy $Fe_{73.5}Si_{13.5}B_9Nb_3Cu_1$ (as previously shown), the α-Fe based alloys $Fe_{90}Zr_7B_3$ and $Fe_{90}Zr_{10}$ show no increase of the ^{59}Fe tracer diffusivity upon crystallization (Fig. 4). This behavior reflects the much slower volume diffusion of Fe in the α-Fe nanocrystallites compared to that in Fe_3Si, as the temperature range studied is below the onset of thermal vacancy formation in α-Fe. This interpretation is supported by high-temperature

positron lifetime studies of n-Fe$_{90}$Zr$_{10}$, where no indication of thermal vacancy formation is found [45] (Fig. 5).

In addition to the slow interface diffusivity, indication for a second fast diffusion process is deduced from the tails of the diffusion profiles measured on nanocrystalline Fe$_{90}$Zr$_7$B$_3$ and Fe$_{90}$Zr$_{10}$. Assuming two types of interfaces with either high or low interface diffusivity and diffusion kinetics analogous to a type B process, similar as applied to cluster-compacted n-metals (see Section 3), the fast process is found to resemble the diffusion in conventional grain boundaries in α-Fe (see Fig. 3 and [24, 26, 49]). No fast interfacial paths are found in nanocrystalline Fe$_{73.5}$Si$_{13.5}$B$_9$Nb$_3$Cu$_1$ [24], presumably due to the higher volume fraction of the intergranular amorphous phase compared to Fe-Zr alloys.

Finally, the results on the nanocrystalline permanent magnet Nd$_2$Fe$_{14}$B will be presented. A novel type of diffusion behavior has been found in Nd$_2$Fe$_{14}$B-based alloys that shows an intergranular melting transition of Nd-enriched GBs [43]. In the technology of these hard magnetic materials, the intergranular melting transition is used in powder-metallurgical processing and to induce a crystallographic and thus magnetic texture in Nd$_2$Fe$_{14}$B [43].

Radiotracer measurements making use of the isotope ^{59}Fe show a substantial increase of the product δD_{GB} of the interfacial thickness and the interface diffusion coefficient above the intergranular melting transition [27] (Fig. 4). The increase of δD_{GB} toward the diffusivity in bulk melts occurs over an extended temperature range rather than abruptly. Such a gradual change could either be due to confinement or due to melting initially restricted locally. Both effects give rise to reduced long-range diffusivities compared to bulk melts, as long as the dimensions of the molten region are small or interconnected liquid regions have not yet formed in the initial stage of melting. Below the intergranular melting transition, GB diffusivities in n-Nd$_2$Fe$_{14}$B similar to those in α-Fe are found in the framework of GB diffusion kinetics of type B when a volume self-diffusivity of α-Fe is assumed (Fig. 4).

4.1.3. Mechanical Routes

Mechanical processing, as severe plastic deformation or mechanical attrition, represents a further important route for obtaining a wide range of nanomaterials. Fully dense, massive samples can be transformed to a nanocrystalline structure by extensive torsional deformation under high pressure or equiaxial channel pressing [50] (cf. SPD in Table 1). Powders of agglomerated nanocrystals with a wide range of alloy compositions are prepared by high-energy ball milling starting from elemental metal powders or alloy powders [51].

Diffusion experiments on porosity free, nanostructured Pd prepared by severe plastic deformation show a similar ^{59}Fe tracer diffusion behavior as found in highly dense n-Pd specimens prepared by cluster condensation and compaction (see [14] and Section 4.1.1). In the case of fully dense, nanostructured Fe prepared by severe plastic deformation—similar as in n-Fe specimens prepared by cluster condensation and compaction (see [15] and Section 4.1.1)—evidence for a reduction of the ^{59}Fe tracer diffusivity by up to one order of magnitude due to structural relaxation

was found (see Fig. 3). Similar observations were recently reported by Kolobov et al. [22] on nanostructured Ni prepared by severe plastic deformation. In that case, the diffusivity of Cu at 423 K was found to decrease by more than three orders of magnitude upon preannealing at 523 K prior to the onset of grain growth (see Fig. 3 and [22]). Both in n-Fe [15] and n-Ni [22], the interfacial diffusion coefficients in the relaxed state appear to be similar to or only slightly higher than values that are expected for conventional GBs in coarse-grained materials from an extrapolation of high-temperature data to lower temperatures.

The most detailed diffusion studies on mechanically prepared nanocrystalline alloys were recently reported by Divinski et al. [9]. In 98% dense γ-Fe$_{61.2}$Ni$_{38.8}$, prepared by mechanical alloying and hot compaction, the Fe diffusion was studied in a wide temperature range covering the GB diffusion regimes of type A, B, and C (see Fig. 6). Measurements at low diffusion temperatures indicate two different types of interfaces in this hot-compacted material. In analogy to the cluster model of Bokstein et al. [8] (see Sections 2, 4.1.1), the diffusion profiles obtained at low temperatures were analyzed by employing relationships in analogy to those of type-B kinetics of GB diffusion and taking into consideration diffusion fluxes from the inter-agglomerate to the intra-agglomerate boundaries. The diffusion coefficients of the intra-agglomerate boundaries were found to be characteristic of conventional GBs, whereas diffusivities several orders of magnitude higher were deduced for the inter-agglomerate boundaries. Diffusion coefficients
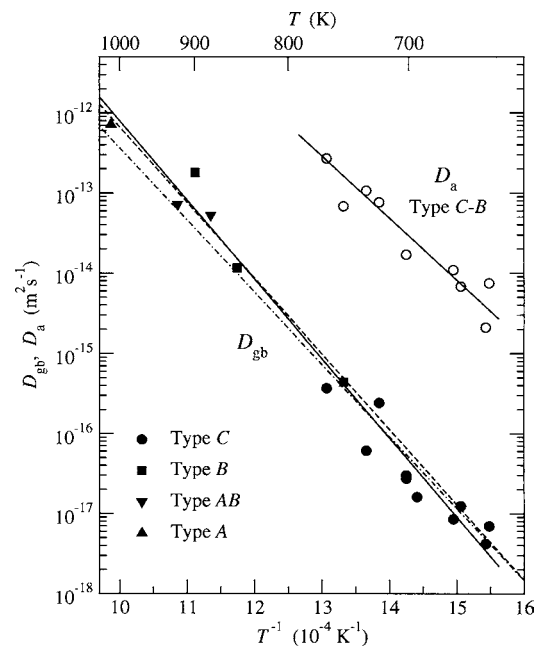
Figure 6. Arrhenius plot of the Fe GB diffusion in nanocrystalline γ-Fe-40 wt.% Ni. The results of the ^{59}Fe tracer diffusion studies show fast diffusion in inter-agglomerate boundaries (open symbols) and significantly slower diffusion in intra-agglomerate grain boundaries (filled symbols) similar as in GBs of coarse-grained γ-Fe (cf. Fig. 1 and Sect. 2 for diffusion model). Reprinted with permission from [9], S. V. Divinski et al., *Z. Metallkd.* 93, 265 (2002). © 2002, Institut für Metallkunde der Universität Stuttgart.

of the intra-agglomerate boundaries very similar to GBs in coarse-grained α-Fe were also deduced from the high-temperature diffusion measurements on γ-Fe$_{61.2}$Ni$_{38.8}$ in the type B and A regimes, where volume diffusion from the intra-agglomerate boundaries into the crystallites becomes increasingly dominant [9]. These results demonstrate the significant influence of residual porosity and agglomerate formation on the diffusion characteristics of powder-synthesized nanomaterials.

The remainder of this chapter will deal with high-temperature positron annihilation studies on structural free volumes and thermal vacancy formation in nanocrystalline alloys prepared by mechanical routes. Three different alloys—Pd$_{84}$Zr$_{16}$ [45], (Fe$_3$Si)$_{95}$Nb$_5$ [32], and ZrO$_2$-doped Cu [45]—represent model systems, due to their high structural stability allowing positron lifetime measurements up to high temperatures (Fig. 5, Table 2).

In ball-milled n-Pd$_{84}$Zr$_{16}$, the structural stability arises from Zr segregation at the grain boundaries. Positron lifetime studies on powder-compacted n-Pd$_{84}$Zr$_{16}$ samples show a substantial and fully reversible increase of the positron lifetime by more than 60 ps between ambient temperature and the maximum temperature of 1173 K (see Fig. 5 and [12, 45]). A numerical analysis of the positron lifetime spectra shows two lifetime components of $\tau_1 = 175$ ps and $\tau_2 = 360$ ps, which are ascribed to interfacial free volumes slightly smaller than a lattice vacancy and nanovoids of about 10 missing atoms, respectively. A detailed analysis shows that the high-temperature increase of the positron lifetime is primarily due to an increase of the specific trapping rate at nanovoids [45]. In particular, no indication of thermal vacancy formation is found.

In sub-microcrystalline Cu-0.1 wt.% ZrO$_2$ prepared by equichannel angular pressing, an initial increase of the mean positron lifetime $\bar{\tau}$ due to the increase of the positron trapping rate in nanovoids similar as in n-Pd$_{84}$Zr$_{16}$ is found (Fig. 5, [45]). More remarkably, the thermal formation of lattice vacancies can be deduced from the reversible decrease of $\bar{\tau}$ at high temperatures above 900 K [45].

Most detailed results on the thermal vacancy formation are available for ball-milled Nb-doped Fe$_3$Si. These studies were motivated by the observation of thermal vacancies in the crystallized soft-magnetic Fe$_3$Si based alloy

Fe$_{73.5}$Si$_{13.5}$B$_9$Nb$_3$Cu$_1$ (see Section 4.1.2). In consolidated specimens of ball-milled (Fe$_3$Si)$_{95}$Nb$_5$, the positron annihilation behavior is determined by competitive trapping and annihilation of positrons in vacancy-sized interfacial free volumes, nanovoids, and thermal vacancies as described by Eq. (2) [32]. From the reversible decrease of the positron lifetime $\bar{\tau}$ at high temperatures, a vacancy formation enthalpy of $H_V^F = 1.1$ eV as in crystalline Fe$_3$Si is deduced. This indicates identical thermal vacancy characteristics in the nanocrystallites and the coarse-grained state.

The vacancy formation and diffusion data in Fe$_3$Si allow an assessment of the DO$_3$ ordering processes that occur in this intermetallic alloy upon heat treatment after ball-milling [32]. X-ray diffraction studies show that nanocrystalline (Fe$_3$Si)$_{95}$Nb$_5$ is initially disordered after ball-milling. Long range ordering (DO$_3$ superstructure) was found to emerge at about $T_a = 623$ K and to be almost complete after annealing at $T_a = 713$ K, far below the onset of massive crystallite growth above 800 K [32]. A comparison with diffusion data measured in ordered DO$_3$-Fe$_{76}$Si$_{24}$ and in disordered A2-Fe$_{76}$Si$_{24}$ [44] shows that the ordering process in nanocrystalline (Fe$_3$Si)$_{95}$Nb$_5$ is controlled by slow Si diffusion similar to that discussed for the formation of magnetic anisotropy in n-Fe$_{73.5}$Si$_{13.5}$B$_9$Nb$_3$Cu$_1$ (Section 4.1.2). This correlation of the ordering with the Si diffusion is further supported by Mössbauer studies performed on the same (Fe$_3$Si)$_{95}$Nb$_5$ material [52].

4.2. Nanocrystalline Ceramics

Compared to nanocrystalline metals and alloys, as presented in the previous section, few diffusion data are available for nanocrystalline oxide materials (Table 3). In nanostructured ceramics, the interface diffusion is of particular importance with respect to enhanced sintering rates and improved plasticity. The electric charge of the diffusing ions and the requirement to maintain overall electric neutrality leads to a diffusion behavior substantially different from metals. Both anions and cations diffuse separately on their respective sublattices and may show significantly different diffusivities and activation enthalpies. In addition, deviations from stoichiometry or doping with aliovalent cations exert a strong influence, in particular on the diffusion of oxygen.

The diffusion of oxygen in nanostructured ZrO$_2$ and TiO$_2$ was studied using ^{18}O as a tracer and depth profiling by means of secondary ion mass spectroscopy (SIMS) [53, 54]. Samples of undoped, monoclinic ZrO$_2$ with a mass density of 97%–99% and average crystallite sizes d of 80 or

Table 2. Characteristics of nanocrystalline alloys studied by positron annihilation at high temperatures.

Alloy	Synthesis	T_{max} [K]	d [mm]	Stabilizing factor	Ref.
Fe$_{73.5}$Si$_{13.5}$B$_9$Nb$_3$Cu$_1$	CRY	880	15	amorphous phase	[24]
Fe$_{91}$Zr$_9$	CRY	970	30	two-phase structure	[45]
Pd$_{84}$Zr$_{16}$	BM	1170	120	GB segregation	[45]
(Fe$_3$Si)$_{95}$Nb$_5$	BM	1020	110	GB segregation	[32]
Cu-0.1 wt.% ZrO$_2$	ECP	1060	250	precipitates	[45]

Note: T_{max}: maximum temperature of measurement and/or pre-annealing, d: crystallite size during high temperature measuring run (see Fig. 4). Synthesis routes: crystallization (CRY), ball milling (BM), and equichannel angular pressing (ECP).

Source: Reprinted with permission from [12], R. Würschum, *Mater. Sci. Forum* 363–365, 35 (2001). © 2001, Trans Tech Publications, Inc.

Table 3. Overview of diffusion studies on nanostructured ceramics (diffusing element quoted in parentheses).

Ceramic (diffusor)	Synthesis route	Ref.
ZrO$_2$ (^{18}O)	CC	[53]
TiO$_2$ (^{18}O)	CC	[54]
TiO$_2$ (Hf)	CC	[54]
CaF$_2$ (^{19}F)	CC	[56]
LiNbO$_3$ (^{7}Li)	BM	[57]
Li$_x$TiS$_2$ (^{7}Li)	BM	[58]

Note: Synthesis routes: cluster condensation, oxidation, and consolidation (CC); high energy ball milling (BM).

300 nm were prepared from Zr metal by cluster synthesis and oxidation of Zr nanocrystallites with *in-situ* compaction and subsequent pressure-less sintering of n-ZrO$_2$ at 950 °C or 1050 °C [54]. The volume and interface diffusivities in the type B and A diffusion regime were directly determined from the ^{18}O diffusion profiles. In undoped n-ZrO$_2$, the diffusion of ^{18}O in the interfaces is 10^3 to 10^4 times faster than in the volume of the crystallites in the temperature range of 450 °C to 950 °C. No dependence on the crystallite size was found. The activation enthalpies $Q_V = 2.29$ eV and $Q_B = 1.95$ eV of the volume or interface diffusion, respectively, are considerably higher than observed in Ca- or Y-doped ZrO$_2$ where structural oxygen vacancies contribute to fast ionic conduction.

In nanocrystalline TiO$_2$, the oxygen diffusivity was found to be similar as observed in n-ZrO$_2$, whereas the oxygen diffusion in bulk rutile is considerably slower, especially if the lower melting temperature of TiO$_2$ is taken into account [53, 54]. Unlike the oxygen diffusion behavior, studies on the cation diffusion in n-TiO$_2$ using Hf as tracer show no significant enhancement of Hf diffusion in n-TiO$_2$ in comparison to extrapolated values of Ti self-diffusion in bulk TiO$_2$ [54].

In cluster-synthesized CaF$_2$ and in ball-milled LiNbO$_3$, the diffusion of the F$^-$ anions and Li$^+$ cations was studied on an atomic scale in nuclear magnetic resonance (NMR) experiments [55–57]. In both materials, nanocrystalline samples show an onset of diffusion-induced spin-lattice relaxation at substantially lower temperatures than in the corresponding bulk materials. The NMR data indicate fast interfacial diffusion with activation energies much lower than in the bulk, such as for example 0.4 eV vs. 1.6 eV for F$^-$ in CaF and 0.27 eV vs. 0.75 eV for Li$^+$ in LiNbO$_3$ [55–57]. These findings support the two-phase model for nanocrystalline materials consisting of nanometer-sized single crystals separated by a large volume fraction of grain boundaries and interfaces. In a similar fashion, NMR studies on the Li diffusion in ball-milled nanocrystalline Li$_x$TiS$_2$ indicate that the grain surfaces provide fast diffusion paths [58].

5. CONCLUSIONS

As outlined in this chapter, diffusion processes constitute a central issue in determining both the properties and future applications as well as the processing routes of nanocrystalline materials. A comparison of the diffusion data with the results of positron annihilation studies strongly contributes to a better understanding of the diffusion process and the role of structural defects and relaxation. Based on the studies of nanostructured metals, alloys, and ceramics reviewed here, the diffusion related properties of nanomaterials can be summarized as follows:

- The synthesis route and the resulting microstructure play a key role in determining the diffusion behavior and related properties of these materials.
- Structural relaxation, which, especially in the case of pure nanocrystalline metals, is accompanied by grain growth, leads to a significant reduction of the diffusivity.
- In general, the diffusivities in relaxed interfaces in nanomaterials are close to those found for grain boundaries in conventional polycrystals.

- Diffusion studies on nanomaterials prepared via powder routes may exhibit different types of interfaces, such as inter-agglomerate boundaries of high diffusivity and intra-agglomerate boundaries with a diffusivity characteristic of conventional grain boundaries.
- Intergranular amorphous phases, which occur in structurally stable nanostructured alloys prepared by melt-spinning, show a much lower diffusivity than found in grain boundaries.

GLOSSARY

Agglomerate Ensemble of densely packed crystallites formed, e.g., during ball milling.

Grain boundary An interface involving the misorientation between the adjoining crystallites.

Interface diffusion Atomic diffusion in interfaces, usually enhanced compared to lattice diffusion.

Nanocomposite Nanostructured material consisting of different nanoscale phases.

Positron annihilation Nuclear measuring technique for studying atomic free volumes and electronic properties of condensed matter by means of the characteristics of positron-electron annihilation.

Tracer diffusion Highly sensitive experimental technique for the determination of diffusion coefficients by measuring the penetration of radioactive tracer atoms in solids.

REFERENCES

1. R. Birringer, H. Gleiter, H.-P. Klein, and P. Marquardt, *Phys. Lett. A* 102, 365 (1984).
2. R. Würschum, U. Brossmann, and H.-E. Schaefer, in "Nanostructured Materials: Processing, Properties, and Applications" (C. C. Koch, Ed.), p. 267. Noyes Publications, Norwich, New York, 2002.
3. "Nanomaterials: Synthesis, Properties, and Applications" (A. S. Edelstein and R. C. Cammarata, Eds.). Institute of Physics, Bristol, 1996.
4. "Nanostructured Materials: Processing, Properties, and Applications" (C. C. Koch, Ed.). Noyes Publications, Norwich, New York, 2002.
5. "Diffusion in Condensed Matter" (J. Kärger, P. Heitjans, and R. Haberlandt, Eds.). Vieweg, Braunschweig, 1998.
6. L. Kaur, Y. Mishin, and W. Gust, "Fundamentals of Grain and Interphase Boundary Diffusion." John Wiley, Chichester, UK, 1995.
7. Y. Mishin and C. Herzig, *Nanostruct. Mater.* 6, 859 (1995).
8. B. S. Bokstein, H. D. Bröse, L. I. Trusov, and T. P. Khvostantseva, *Nanostruct. Mater.* 6, 873 (1995).
9. S. V. Divinski, F. Hisker, Y.-S. Kang, J.-S. Lee, and C. Herzig, *Z. Metallkd.* 93, 256; *Z. Metallkd.* 93, 265 (2002).
10. R. Würschum and H.-E. Schaefer, in [2], p. 277.
11. R. Würschum and A. Seeger, *Philos. Mag. A* 73, 1489 (1996).
12. R. Würschum, *Mater. Sci. Forum* 363–365, 35 (2001).
13. R. Würschum, K. Reimann, S. Gruß, A. Kübler, P. Scharwaechter, W. Frank, O. Kruse, H. D. Carstanjen, and H.-E. Schaefer, *Philos. Mag. B* 76, 401 (1997).
14. R. Würschum, A. Kübler, S. Gruß, P. Scharwaechter, W. Frank, R. Z. Valiev, R. R. Mulyukov, and H.-E Schaefer, *Ann. Chim.* 21, 471 (1996).
15. H. Tanimoto, P. Farber, R. Würschum, R. Z. Valiev, and H.-E. Schaefer, *Nanostruct. Mater.* 12, 681 (1999).

16. J. Horváth, R. Birringer, and H. Gleiter, *Solid State Commun.* 62, 319 (1987).
17. Z. Erdélyi, Ch. Girardeaux, G. A. Langer, D. L. Beke, A. Rolland, and J. Bernardini, *J. Appl. Phys.* 89, 3971 (2001).
18. W. Dickenscheid, R. Birringer, H. Gleiter, O. Kanert, B. Michel, and B. Günther, *Solid State Commun*. 79, 683 (1991).
19. S. Schumacher, R. Birringer, R. Strauß, and H. Gleiter, *Acta Metall. Mater.* 37, 2485 (1989).
20. H. J. Höfler, R. S. Averback, H. Hahn, and H. Gleiter, *J. Appl. Phys.* 74, 3832 (1993).
21. I. L. Balandin, B. S. Bokstein, V. K. Egorov, and P. V. Kurkin, *Defects Diffusion Forum* 143–147, 1475 (1997).
22. Y. R. Kolobov, G. P. Grabovetskaya, M. B. Ivanov, A. P. Zhilyaev, and R. Z. Valiev, *Scripta Mater.* 44, 873 (2001).
23. H. J. Höfler, R. S. Averback, and H. Gleiter, *Philos. Mag. Lett.* 68, 99 (1993).
24. R. Würschum, P. Farber, R. Dittmar, P. Scharwaechter, W. Frank, and H.-E. Schaefer, *Phys. Rev. Lett.* 79, 4918 (1997).
25. S. Herth and R. Würschum, to be published.
26. R. Würschum, T. Michel, P. Scharwaechter, W. Frank, and H.-E. Schaefer, *Nanostruct. Mater.* 12, 555 (1999).
27. M. Eggersmann, F. Ye, S. Herth, O. Gutfleisch, and R. Würschum, *Interface Sci.* 9, 337 (2001).
28. Y. Minamino, S. Saji, K. Hirao, K. Ogawa, H. Araki, Y. Miyamoto, and T. Yamane, *Mater. Trans., JIM* 37, 130 (1996).
29. T. Fujita, H. Hasegawa, Z. Horita, and T. G. Langdon, *Defects Diffusion Forum* 194–199, 1205 (2001).
30. R. Venos, W. Palmer, and H. Hoffmann, *Thin Solid Films* 162, 155 (1988).
31. H.-E. Schaefer, W. Eckert, O. Stritzke, R. Würschum, and W. Templ, in "Positron Annihilation" (L. Dorikens-Vanpraet, M. Dorikens, and D. Segers, Eds.), p. 79. World Scientific Publ., Singapore, 1989.
32. L. Pasquini, A. A. Rempel, R. Würschum, K. Reimann, M. A. Müller, B. Fultz, and H.-E. Schaefer, *Phys. Rev. B* 63, 134114/1–7 (2001).
33. R. Würschum, Habilitation Thesis, University of Stuttgart, Stuttgart, Germany, 1997.
34. L. G. Kornelyuk, A. Yu Lozovoi, and I. M. Razumovskii, *Defects Diffusion Forum* 143–147, 1481 (1997).
35. R. Z. Valiev, I. M. Razumovskii, and V. I. Sergeev, *Phys. Status Solidi A* 139, 321 (1993).
36. V. Yamakov, D. Wolf, S. R. Phillpot, and H. Gleiter, *Acta Mater.* 50, 61 (2002).
37. W. Frank, *Defects Diffusion Forum* 143–147, 695 (1997).
38. R. Würschum, K. Reimann, and P. Farber, *Defects Diffusion Forum* 143–147, 1463 (1997).
39. M. Lübbehusen and H. Mehrer, *Acta Metall. Mater.* 38, 283 (1990).
40. J. Bernardini, P. Gas, E. D. Hondros, and M. P. Seah, *Proc. R. Soc. Lond. A* 379, 159 (1982).
41. G. Herzer, *Scripta Metall. Mater.* 33, 1741 (1995).
42. A. Makino, A. Inoue, and T. Masumoto, *Mater. Trans., JIM* 36, 924 (1995).
43. W. Grünberger, D. Hinz, A. Kirchner, K.-H. Müller, and L. Schultz, *J. Alloys Compd.* 257, 293 (1997).
44. A. Gude and H. Mehrer, *Philos. Mag. A* 76, 1 (1997).
45. R. Würschum, E. Shapiro, R. Dittmar, and H.-E. Schaefer, *Phys. Rev. B* 62, 12021 (2000).
46. M. Emura, A. M. Severino, A. D. Santos, and F. P. Missell, *IEEE Trans. Magn.* 30, 4785 (1994).
47. B. Hofmann and H. Kronmüller, *J. Magn. Magn. Mater.* 152, 91 (1996).
48. R. Würschum, W. Greiner, R. Z. Valiev, M. Rapp, W. Sigle, O. Schneeweiss, and H.-E. Schaefer, *Scripta Metall. Mater.* 25, 2451 (1991).
49. S. Herth, T. Michel, H. Tanimoto, M. Eggersmann, R. Dittmar, H.-E. Schaefer, W. Frank, and R. Würschum, *Defects Diffusion Forum* 194–199, 1199 (2001).
50. R. Z. Valiev, R. K. Islamgaliev, and I. V. Alexandrov, *Progress in Materials Science* 45, 130 (2000).
51. J. Eckert in [4], p. 423.
52. Z. Gao and B. Fultz, *Nanostruct. Mater.* 4, 939 (1994).
53. U. Brossmann, R. Würschum, U. Södervall, and H.-E. Schaefer, *J. Appl. Phys.* 85, 7646 (1999).
54. H. J. Höfler, H. Hahn, and R. S. Averback, *Defects Diffusion Forum* 75, 195 (1991).
55. P. Heitjans and A. Schirmer, in [5], p. 130.
56. W. Puin, P. Heitjans, W. Dickenscheid, and H. Gleiter, in "Defects in Insulating Materials" (O. Kanert and J. M. Spaeth, Eds.), p. 137. World Scientific, Singapore, 1993.
57. D. Bork and P. Heitjans, *J. Phys. Chem. B* 102, 7303 (1998).
58. R. Winter and P. Heitjans, *Nanostruct. Mater.* 12, 833 (1999).

Diffusion in Nanomaterials

Yu. Kaganovskii

Bar-Ilan University, Ramat-Gan, Israel

L. N. Paritskaya

Karazin National University, Kharkov, Ukraine

CONTENTS

1. INTRODUCTION

Nanomaterials (nanocrystalline or nanostructured materials (NMs)) are solids that have a microstructure with a characteristic length-scale on the order of 1–20 nanometers [1]. Interest in this class of materials stems from their unique structure, which exhibits many desirable properties important both for the development of fundamental physical concepts and numerous technical applications.

Among the great variety of NMs [2], only two categories were extensively studied with regard to diffusion. The first one includes bulk nanostructural solids and thin polycrystalline solid films, consisting of nanometer-sized crystallites. The bulk microstructure of such NMs is similar to that of two-phase materials, where one of the phases consists of grain interiors, the other—of grain boundaries (GBs), and both have comparable volume fractures. Diffusion in NMs of this category occurs mainly along GBs and interfaces. Coherent or incoherent interfaces are formed between adjacent assembled crystallites depending on their atomic structure, crystallographic orientation, and chemical composition [3]. Such a heterogeneous microstructure, composed of nanocrystallites and interfaces between them, is crucial for many important properties and processes in NMs. Diffusion is one such process, which demonstrates the unusual behavior of NMs compared to regular polycrystals.

The other category of NMs, in which diffusion was extensively studied, includes single crystals whose surface regions structured laterally on a nanometer scale by "writing" a nanometer-sized structural pattern on the free surface or precise deposition of another material. One example of such a pattern is an array of nanometer-sized islands (e.g., quantum dots) connected by thin (nanometer scale) wires [3]. Diffusion evolution of such materials occurs mainly due to surface diffusion (SD).

Interest in diffusion in both types of NMs is stimulated by the fact that atomic motion plays an important role in the structural stability and physical properties of NMs. Grain boundary diffusion governs the kinetics of mass-transfer processes, such as sintering, phase transformation, creep, electromigration, superplastic deformation, as well as the synthesis and processing of new NMs. Surface diffusion, which happens very rapidly at high temperatures, is the main mechanism for the production of nanoscale surface structures, as well as the evolution of their surface morphology, which results in a loss of required physical properties, such as the narrow size distribution or self-assembly.

The principal difficulty in studying the kinetic properties of NMs is caused by the fact that their atomic structure (in particular, the structure of GBs and free surfaces) is far from an equilibrium state and significantly depends on the method of fabrication. Nanostructured materials created by different methods can exhibit entirely different properties, even if they are the same size as the structural element. Numerous examples of interrelations between the interfacial microstructure and the kinetic properties of NMs can be found in the literature [4–13].

High densities of incoherent interfaces and other lattice defects, such as dislocations, vacancies, enhanced free volumes at the interfaces, and surface steps produce excess free energy, which yields the driving force for the two relaxation

processes: modification of the atomic structure (in order to make it closer to the perfect crystal) and growth of the structural element [1, 2]. Relaxation processes are thermally activated, so NMs may be stable at low temperatures but become unstable at elevated temperatures. This situation has important consequences for both GB and surface diffusion measurements, which are accompanied by structural relaxation, depending on the time and temperature.

According to the results of a calorimetric analysis [1], GB relaxation processes were detected at $T \approx 0.2T_m$ (where T_m is the NMs melting temperature). This means that the GB diffusion characteristics measured at temperatures below $0.2T_m$ are related to nonequilibrium GBs, and they are very sensitive to the mode of NM preparation. At temperatures around $0.2T_m$, the diffusion coefficients should change with time due to the evolution of the GB structure. At higher temperatures ($T \geq 0.25T_m$), the structural relaxation may be attributed to grain growth. At these temperatures, the two main stages of GB diffusion can be distinguished under isothermal conditions.

The duration of the first stage is defined by the inequality $t \leq a^2/D$ (where a is the lattice parameter, D is the bulk diffusion coefficient). At this stage, GB-diffusion is still accompanied by relaxation processes and occurs along nonequilibrium GBs without the participation of bulk diffusion. Diffusion characteristics, determined at this stage, are usually highly sensitive to the preparation mode of NMs. At later stages (when $t > a^2/D$), the relaxation is practically complete and GB diffusion occurs mainly along stationary GBs and other interfaces and is accompanied by leakage into the grain bulk. A correct description of diffusion penetration at this stage demands the accounting for the small size of the structural element. The diffusion characteristics obtained at this stage may be close to those measured for conventional GBs in coarse-grained polycrystals. The difference between GB diffusion coefficients in NMs and other polycrystalline objects may indicate the "special" properties of GBs, such as specific GB structures, enhanced energies, solubilities, heats of segregation, the presence of metastable, and amorphous phases at GBs.

A SD-mediated relaxation of surface nanoscale features in the continuum approximation was derived by Herring [14] and further developed by Mullins [15]. The theory can be readily applied to amorphous materials and to single-crystal surfaces above their roughening transition [16–18] temperature T_R, where the surface is atomically rough. However, fabrication of nanoscale structures on single-crystalline substrates and diffusion evolution of these structures, as a rule, occur at temperatures below T_R, where the surfaces become atomically flat. It means that a direct application of the theory to nanoscale structures is prevented below T_R, where the surfaces consist of atomically flat terraces separated by steps, and new models involving rate equations for individual steps are necessary [19, 20].

This article is organized in the following way. Sections 2–4 describe GB diffusion in "bulk" NMs consisting of nanometer-sized crystallites. Section 2 describes the relaxation processes in GBs and grain growth, which are crucial for accurate diffusion measurements as well as for the diffusion behavior of nano-objects. Tracer diffusion along GBs

in NMs is considered in Section 3, with a theoretical analysis of size-dependent diffusion penetrability and the results of experimental measurements of diffusion characteristics. We present the diffusion data for NMs that exists in the literature and compare them with the diffusion characteristics obtained for coarse-grained polycrystals. The kinetics and mechanisms of interdiffusion and the accompanying mass transfer effects, such as the Kirkendall and Frenkel GB effects, low-temperature homogenization, and diffusion-induced processes resulting in nonstability of binary NMs, are considered in Section 4. Sections 5 and 6 analyze surface diffusion mass transfer. The important mass transfer processes, such as surface flattening, decay of rods and needles, and decomposition of thin continuous films into beaded films, are described in Section 5 in continuum approximation. In addition, specific features of surface diffusion mass transfer on atomically flat surfaces (vicinal and singular) are considered in terms of motion of elementary steps. Mass transfer in island films and reactive surface diffusion are analyzed in Section 6.

2. RELAXATION PROCESSES IN GRAIN BOUNDARIES (GBs) AND GRAIN GROWTH

Relaxation of nonequilibrium GB structures and grain growth in NMs are the most important processes, crucial for many properties of nano-objects as well as diffusion kinetics. To provide stationary conditions for diffusion study, while preserving the unique properties of NMs, it is necessary to prevent grain growth and preserve nanometer-sized morphology. There are two main tasks related to the relaxation of NMs: (1) to specify driving forces and predict the kinetics of grain growth, and (2) to prevent grain growth and stabilize the nanometer-sized structure.

The excess free energy of NMs provides the driving force for grain growth—the process that was widely studied in different nano-objects through the use of different techniques [21–29]. It is well known that boundaries in polycrystals move towards their centers of curvature and the kinetics of the resulting grain growth obeys the parabolic law:

$$l^2(t) = l_0^2 + Kt \tag{1}$$

where l and l_0 are the grain sizes at the time t and at the beginning of annealing, respectively; K is the rate constant that depends on the temperature as described by the following Arrhenius-type equation:

$$K = K_0 \exp(-Q_r/k_B T) \tag{2}$$

Here Q_r is the activation enthalpy for isothermal grain growth, k_B is the Boltzmann constant, and K_0 is a constant independent of the temperature. The normal grain growth described by (1) is a rare phenomenon, which is observed exceptionally in high pure metals at high homologous temperatures. For a description of isothermal grain growth, the empiric kinetic laws with an exponent power of $\sigma \geq 2$ are used [3] in the form:

$$l^\sigma = l_0^\sigma + K_1' t \tag{3}$$

The deviation of the exponent σ from the ideal value of 2 is attributed mainly to pore and impurity effects on grain growth. The atomic mechanism of grain growth can be identified from the value of activation enthalpy Q_r (2), which determines the temperature dependence of the rate constants K and K_1 from Eqs. (1) and (3). Experiments confirmed that the activation enthalpy of grain growth correlates well with the enthalpy for GB diffusion, which means that grain growth involves the transport of atoms not only across GB but also along the boundary.

The peculiarities of grain growth in NMs, as compared to coarse-grained polycrystals, are caused by their nanometer grain sizes (leading to a high driving force) and nonequilibrium structures of GBs (leading to an increased GB mobility). These two factors were defined and studied quantitatively by calorimetric measurements of thermal relaxation in nanocrystalline objects [1]. The isothermal heat release was recorded by the method of differential scanning calorimetry [1] for nanocrystalline platinum, compacted from inert gas condensation particles, under conditions of stepwise temperature increase from 400 to 550 K with the step of 50 K. Two large, heat-release peaks were found in this temperature range: at 400 K (of about 1.1 kJ/mol) and 500 K (1.3 kJ/mol), whereas at 450 and 550 K the exothermal reactions yielded only 0.27 and 0.24 kJ/mol, respectively. These data were compared with temperature dependence of grain growth and it was shown that at 400 and 450 K, the grain size stayed practically constant at 8–9 nm, whereas at 500 K the intensive grain growth (up to $\geq$40 nm) was observed. At 550 K, grain size got to $\geq$50 nm. From the comparison of above data on heat release and the grain growth, it was suggested that two large enthalpy releases at 400 and 500 K correspond to two different kinds of structural changes—with and without grain growth, and that there are two different relaxation processes. Nanostructured materials compacted from nano-particles, produced by inert gas condensation, contain nonequilibrium GB structures, and the spectrum of internal stresses was observed by high-resolution electron microscopy [30]. The enthalpy stored in the nonequilibrium GB structures and the internal stresses is released at 400 K. The relaxation at 500 K is associated with grain growth. If the enthalpy release of 1.3 kJ/mol at this stage is caused by the difference in the grain boundary area before and after relaxation, the specific GB enthalpy can be estimated as 1.0 J/m². This value is in good agreement with the GB tension for conventional GBs (0.94 J/m²) in coarse-grained Pt polycrystals [31]. From here, it can be concluded that the relaxed GBs in NMs are thermodynamically similar to the conventional large angular GBs. The large enthalpy stored in NMs due to the nonequilibrium GB structure and internal strain leads to grain growth at lower temperatures, especially in the beginning of the recrystallization process. The smaller are the grain sizes, the lower is the temperature of grain growth [32] and the more probable are the abnormal growth rate conditions.

Abnormal grain growth in NMs was observed at room temperature and slightly above room temperatures in nanostructured Cu, Ag, Pd [26, 32]. Anomalously fast grain growth was observed [28, 29] during the sintering of compacted Cu and Ni nanopowders (with the porosity of

about 40%) at temperatures $T \approx (0.3–0.5)T_m$. Simultaneously with the growth of the average grain size, separate single-crystalline inclusions appeared with sizes of up to 10 μm. The rate of their growth was $V \approx 10^{-8}$–10^{-7} m/s at 300 °C in n-Cu, whereas the average grain size rate was 10^{-11}–10^{-10} m/s. Single crystalline inclusions had spherical or faceted shapes, with a porous zone around them. They had appeared at early stages of active sintering, and after a few minutes of annealing, stopped growing once they had become separated from the nanosized medium by the built-up porous layer. The nuclei of single crystals appeared in the densest regions of nano-compacts [28].

There are two principal reasons for inhomogeneous grain growth [28, 32]: (a) nonuniformity of initial grain size distribution, where the larger grains act as nuclei, and (b) nonuniformity of impurity distribution, so that enhanced grain growth may occur in regions with the lowest impurity content. Abnormal grain growth only occurs at early stages of annealing (when both reasons are most effective) and becomes negligible at longer annealing times.

An important problem of grain growth in NMs is the effect of impurities and pores on the growth kinetics. It is well known that soluble impurities, insoluble inclusions, and pores restrain grain growth due to their interaction with migrating boundaries. The interaction of inclusions and pores with GB is based on the concept that the total free energy of GB segment with the inclusion (or pore) is reduced by a value on the order of $\alpha_{\iota\kappa}S$ (S is the inclusion cross section and $\alpha_{\iota\kappa}$ is the specific GB free energy). This means that if a GB tears away from the inclusion, the local "GB-inclusion" free energy of the system increases. In other words, there is a binding force that attracts the inclusion to the GB. The insoluble inclusions and pores at GBs act as stoppers and restrain boundary movement by the pinning mechanism [33, 34]. The considerable effect of pinning by pores [21, 33] was clearly observed in nanostructured TiO_2 powder compacts [35, 36]. With the initial grain size of 14 nm and the porosity of about 25%, the average grain size after annealing (for 20 h at 700 °C) became 30 nm. When the porosity was reduced to about 10% under the same conditions, the grain size increased to 500 nm.

The pinning effect by precipitates of the second phase was demonstrated in nanocrystalline Ni with Ni_3P precipitates [24] and Y-Fe alloys with YFe_2 precipitates [37] that suppressed grain growth.

Another mechanism of grain growth prevention is related to soluble impurities and results from the solute drag-effect [34, 38, 39]. In many solids, solute atoms segregate at the boundaries, reducing their energy and forming solute clouds in the vicinity of GBs. If a boundary with a cloud migrates, the following three types of motion may be in effect depending on the relative rates of GB and solute-cloud mobility: (1) if the boundary migrates slowly, it drags the solute cloud with it, reducing GB mobility and therefore grain growth; (2) if the boundary migrates very fast it breaks away from the solute atoms and moves freely; (3) at intermediate migration rates, the boundary loses its cloud and the segments free from impurity bulge ahead. The resulting increase of GB curvature reduces the segment motion rate and a continuous impurity cloud is formed again.

Some specific influence of soluble impurities on grain growth in nano-structures in comparison with coarse-grained polycrystals is attributed to the nonequilibrium configuration and the energetic state of interfaces in NMs. In general, GBs in NMs are characterized by an enhanced solubility in the core of GBs [37]. This can bring about two effects facilitating the stability of microstructure. The first one is the solute drag effect described above. The second effect is the reduction of the driving force for grain growth. The GB free energy becomes lower due to the segregation and may be even reduced to zero [40–42]. As a consequence of the solute enrichment at grain boundaries and the vanishing GB free energy, a meta-stable nanocrystalline state is distinguished when the grain growth is suppressed. It was shown that in Y-Fe alloys, the grains grew at low Fe molar fraction whereas at higher Fe concentrations the grain growth was suppressed [37].

Thus, the stability of nano-structures against grain growth can be ensured by two factors: reduction in the driving force of grain growth (by reducing GB free energy) and reduction of GB mobility (by introducing stoppers for GB migration).

3. TRACER DIFFUSION

The tracer method is based on measurements of tracer concentration-depth profiles $C(x, t)$ after diffusion annealing over time t. The diffusing matter (diffusant) is placed on a clean sample surface by vacuum evaporation or chemical deposition. The diffusion profiles are preferably measured by the methods of Rutherford back-scattering spectroscopy (RBS), Auger electron spectroscopy (AES) combined with sputter erosion, or by microsectioning (ion-beam sputtering), and analyzing the activity of radiotracers. Experimental profiles are compared with the theoretical concentration distributions calculated under certain assumptions, taking into account the small sizes of structural elements.

3.1. Diffusion Penetrability of Nanostructures

3.1.1. Analysis for Massive Nanostructured Materials

According to Harrison [43], three diffusion regimes—A, B, and C—are defined in polycrystalline objects, in dependence on the relationship between the diffusion characteristics of GBs, grain interiors, and the structural element size.

Three principal parameters govern the diffusion regime [44]:

$$\Lambda = l/(Dt)^{1/2} \qquad (4)$$

$$\alpha = s\delta/2(Dt)^{1/2} \qquad (5)$$

$$\beta = P/2D^{3/2}t^{1/2} \qquad (6)$$

where l is the size of structure element; $s = C_b/C_0$ is the segregation factor (C_b and C_0 are the respective concentrations of diffusing species inside GB and adjacent grain volume under local dynamic equilibrium conditions between them); δ is the width of GB; $P = sD_b\delta$ is the triple product; and D_b is the GB diffusion coefficient.

The diffusion of A-type refers to the case when the leakage zones of tracer atoms from GBs overlap inside the grain interior, that is, $\Lambda \ll 1$ and each tracer atom during its random walk uses a large number of grains and GBs. For instantaneous diffusion source, the concentration profile of tracer is

$$C(x, t) = \frac{M}{\sqrt{\pi D_{eff} t}} \exp\left(-\frac{x^2}{4D_{eff} t}\right) \qquad (7)$$

where M is the number of tracer atoms per unit area; D_{eff} is effective diffusion coefficient; and x is the depth coordinate in the diffusion direction. According to Hart [45],

$$D_{eff} = fD_b + (1 - f)D \qquad (8)$$

where f is the volume fraction of GBs in the sample. In recent estimates [46], the condition for A-type diffusion was defined as $\Lambda \leq 0.4$.

The B-regime refers to diffusion along GBs with limited leakage into the grain interior ($\Lambda \geq 1$). As a necessary condition for the B-regime, the parameters α and β were determined [44] as $\alpha < 0.1$ and $\beta > 10$.

For GB diffusion of B-type the concentration distribution calculated using the Fisher [47] model is [48]:

$$\overline{C}(x, t) = \overline{C}_0 \exp(-\alpha x) \qquad (9)$$

According to eq. 9, $\log \overline{C}$ is a linear function of the penetration depth x, and the slope α of the straight line is defined by [48]

$$\alpha^2 = \left(\frac{D}{\pi t}\right)^{1/2} \frac{2S}{L} \frac{1}{sD_b\delta} \qquad (10)$$

where S and L are the surface of GBs per unit volume and the length of GBs per unit area on the crosssection perpendicular to the diffusion direction. Thus, the triple product $P = s\delta D_b$ can be determined as

$$sD_b\delta = (2S/L)(D/\pi t)^{1/2}(-\partial \ln \overline{C}/\partial x)^{-2} \qquad (11)$$

A more precise analysis of the GB concentration profiles [49], made on the basis of an exact analytical solution [50], has shown that a straight line should be observed in the coordinates of $\log \overline{C} - x^{6/5}$, and the value P can be determined from the slope with a higher accuracy using the formula

$$sD_b\delta = r(D/t)^{1/2}(-\partial \ln \overline{C}/\partial x^{6/5})^{-5/3} \qquad (12)$$

where r is a numerical factor depending on the surface conditions. Although the power 6/5 has no physical meaning, accurately measured experimental profiles normally do follow the 6/5-rule over a wide concentration range [51]. The "6/5-method" is widely used for GB diffusion measurements along separate GBs.

Due to small size of structure element l in NMs, the diffusion zone $(Dt)^{1/2}$ of leakage becomes comparable with l even at relatively low temperatures, and GB-diffusion deviates from the pure B-regime. It was shown [48] that for

$1 \leq \Lambda \leq 2$, the solution (9) is still valid, with the slope α_1, defined by the formula

$$\alpha_1^2 = \frac{4DS}{Ll\,sD_b\delta} \exp\left(-\frac{\pi^2 Dt}{l^2}\right) \qquad (13)$$

Equation 13 shows that by analyzing the variation of α_1 with time, one has the ability to determine the size of the structural element l from diffusion measurements. This size was qualified as the "diffusion grain size," which is the characteristic distance between fast diffusion circuits. It usually differs from the real size determined by direct electron microscopic methods due to the strong dependence of GB diffusion penetration on the structure of GBs.

The C-regime is defined as GB diffusion not accompanied by a leakage from GBs into the grain interior. The leakage may be neglected [44] with $\alpha > 10$.

Due to the nonequilibrium state of NMs, low-temperature diffusion measurements are preferable to avoid fast relaxation processes and provide convenient conditions for the determination of GB diffusion characteristics. At low temperatures, the C-diffusion type is available with the solutions for concentration distributions in the form [44]

$$\overline{C}(x, t) = \frac{M\lambda\delta}{(\pi Dt)^{1/2}} \exp\left(-\frac{x^2}{4D_b t}\right) \qquad (14)$$

for diffusion from an instantaneous source and

$$\overline{C}(x, t) = \lambda\delta\overline{C}_0\, erfc\left(\frac{x}{2\sqrt{D_b t}}\right) \qquad (15)$$

for diffusion from a constant source. Here, $\overline{C}(x, t)$ is the average concentration; $\lambda = \pi/2l$ is the geometrical factor for a polycrystalline material with randomly oriented grains.

To extract D_b from the triple product, it is necessary to know the segregation factor s and the GB width δ. The segregation factor s can be determined by combining GB diffusion measurements in the B and C regimes. At low enough temperatures, the lattice diffusion, is negligible, so all atoms diffusing along a GB stay in the GB and the GB diffusion profile depends on D_b only (see (14) and (15). Thus, carrying out measurements under regimes B and C (by variation time of diffusion at the same temperature), one can extract the product $s\delta = (s\delta D_b)_{\text{B-reg}}/(D_b)_{\text{C-reg}}$ and determine the s (assuming $\delta \approx 0.5$ nm). Such diffusion measurements were carried out for different impurities [52, 53] in Cu and segregation factors were determined over a wide range (from 1 up to 10^5) [51]. It was shown that strong GB segregation tends to impede GB diffusion—the more so the stronger it is [52].

3.1.2. Chemical GB Diffusion

The tracer diffusion coefficient suggests a very small concentration of diffusing atoms, when interaction between them is negligible. It is always valid for selfdiffusion; in case of heterodiffusion with high segregation factors, the GB concentration of foreign atoms can be large enough and interaction between them can change the diffusion barriers. The diffusion coefficients of interacting atoms are called the intrinsic

coefficients (D_i). They differ from the tracer coefficients D^* as follows [54–56]

$$D_i = D_i^*(1 + \partial \log \gamma_\iota / \partial \log C_i) \qquad (16)$$

where γ_ι is the activity coefficient [57].

The diffusion process, in which the intrinsic coefficients are measured, is called chemical diffusion. Chemical diffusion employs diffusion sources of high capacity in the form of thick layers, in contrast to the instantaneous sources which are used for tracer diffusion. For the determination of GB diffusion parameters in chemical diffusion experiments with NMs, the same expressions (9 and 15) can be used for concentration profiles at appropriate diffusion regimes and determination of the intrinsic GB diffusion coefficients D_{bi}. As the thermodynamic data on γ for GBs are restricted even for simple binary systems, a direct comparison of the diffusion coefficients D_{bi} and D_b^* is rather difficult to achieve.

3.1.3. Thin Films

It is known that GB diffusion is the dominant transport mechanism in the majority of thin films. Unfortunately, the measurements of GB diffusion in thin films by depth-profiling methods have often been of a semi-quantitative nature since in many cases the diffusion analysis is inadequate.

Hwang and Balluffi have proposed a method of surface accumulation [58] for diffusion measurement in polycrystalline thin films, in which atoms diffused from a source (substrate) along GBs to a free surface of the film, where they tend to spread out and accumulate. The average concentration on the accumulation surface is then measured as a function of time. Grain boundary diffusion coefficients are determined from the kinetics of accumulation of diffusing species on the surface. The accumulation rate depends on two main parameters:

$$H = \frac{s_b\delta_b h}{2s_s\delta_s l}$$

and

$$G = H\frac{\tau_b}{\tau_s}$$

where h is the film thickness, l is the lateral grain size, s_b, s_s and δ_b, δ_s are the GB and the surface segregation factors and the GB width and the thickness of the surface diffusion layer, respectively, $\tau_s = D_s t/l^2$ and $\tau_b = D_b t/h^2$. The time dependence of the accumulation-surface concentration for a constant source and for $H \ll 1$ and $G \ll 1$ is

$$C_s(t) = 1 - \exp(-pt) \qquad (17)$$

where $p = H\tau_b/t = s_b D_b\delta_b/2s_s\delta_s hl$. The effective thickness of the accumulation surface, $s_s\delta_s$, can be experimentally determined by AES methods [59]. Consequently, the triple product $s_b D_b\delta_b$ can be determined by measuring the time dependence of the accumulation-surface concentration during diffusion. This method was repeatedly applied to diffusion studies in thin nanocrystalline films [60].

3.2. Experimental Data

The unusual diffusion properties of NMs can be seen in Table 1, where GB diffusion coefficients measured in different NMs are compared with those obtained in massive polycrystals with the so-called conventional GBs. The GB diffusion coefficients in NMs are 2–4 orders of magnitude larger in comparison with conventional GBs in coarse-grained polycrystals.

The data on diffusion activation energies and pre-exponent factors are presented in Table 2 and compared with the same for polycrystals and single crystals.

For self-diffusion and substitutive impurity diffusion, the activation energies in NMs are about one-half of the GB activation energy in polycrystals and about one-third of the bulk diffusion activation energy. These results can be understood in terms of enhanced free volumes in the core of the GBs in NMs [61, 62]. According to positron annihilation measurements [63], the free volumes on the order of 1–10 atomic volumes have been detected in NMs. It means that diffusion along GBs may include, as a consistent part, the diffusion along free surface of microvoids. Indeed, the self-diffusion activation energy in nanoCu is close to the activation energy for surface diffusion (see Table 2).

There is no simple correlation between hetero-diffusivity and the atomic size of the diffusing species. For instance, the relative difference in the atomic radii for diffusion into n-Cu, $(r_x - r_{Cu})/r_{Cu}$, equals ~0.13 for Ag and Au and ~0.32

for Bi (r_x is the atomic radius of a diffusing species). As one can see from Table 1, the simple correlation between diffusivity and the atomic radius exists for Bi and Ag: the larger the relative atomic radius, the smaller the diffusivity of this species. The remarkable example of a breakdown of this regularity is Au-diffusivity, which is much smaller than one of Ag with the same value of the relative radius. This deviation is explained [62, 64] by the negative heat of mixing of Au in Cu (-42 kJ/mol) in comparison with the positive values for Ag in Cu ($+10$ kJ/mol) and Bi in Cu ($+35$ kJ/mol) [84]. With a negative mixing heat, the energy barrier required for an Au-atom to jump into a site surrounded by Cu-atoms can be higher than for Bi and Ag atoms.

The difference between GB diffusivities in NMs and coarse-grained polycrystals is reduced when the temperature is increased. This can be attributed to the relaxation of GB structure, which according to positron lifetime measurements [85] consists in diminution of free volumes in the core of GBs. In addition to GB relaxation, grain growth may also influence the results of diffusion measurements at higher temperatures. Due to GB migration, the values of the diffusion coefficients calculated under the terms of the C-regime, could be reduced because moving GBs may "lose" a number of diffusing atoms, which stayed inserted into the grain bulk behind the GBs. This process impedes the diffusion penetration along GBs under the C-regime, which results in lower

Table 1. Comparison of GB diffusion coefficients in NMs and coarse-grained polycrystals.

Diffusant	Host	Temp. K	D_b, m²/s in NMs	Remarks	D_b, m²/s in polycryst.	Method	Refs.
^{67}Cu	Cu	393	$1.7 \cdot 10^{-17}$		$2.2 \cdot 10^{-19}$	Tracer	[61, 62]
		353	$2.0 \cdot 10^{-18}$		$6.2 \cdot 10^{-21}$		
		293	$2.6 \cdot 10^{-20}$		$4.8 \cdot 10^{-24}$		
Bi	Cu	393	$2.3 \cdot 10^{-19}$	Tracer	$1.2 \cdot 10^{-21}$	Tracer	[64]
		393	$1.1 \cdot 10^{-20}$	Intrinsic			[64]
Au		393	$4.8 \cdot 10^{-22}$	Tracer	$2.6 \cdot 10^{-26}$		[64–66]
Ag		393	$4.8 \cdot 10^{-17}$	Tracer	$8.1 \cdot 10^{-20}$		[67, 68]
Sb		373	$5.2 \cdot 10^{-20}$	Tracer			[69]
Sb		353	$3.3 \cdot 10^{-20}$	Tracer			[69]
Sb		323	$7.6 \cdot 10^{-21}$	Tracer			[69]
Ag	Pd	393	$3.5 \cdot 10^{-17}$	Tracer	$1.3 \cdot 10^{-21}$	SIMS	[70]
Au		393	$8.1 \cdot 10^{-19}$	Tracer	$1.5 \cdot 10^{20}$		[70]
Cu		393	$1.1 \cdot 10^{-18}$	Tracer			[70]
B		393	$3.10 \cdot 10^{-24}$	Tracer	$3.7 \cdot 10^{-22}$		[70]
O		393	$8.5 \cdot 10^{-18}$	Tracer			[70]
H		293	$5.1 \cdot 10^{-12}$	Tracer	2.10^{-10}	EMF	[71]
^{59}Fe	Fe	499	$2.9 \cdot 10^{-20}$	Tracer			[72]
^{59}Fe		472	$9.4 \cdot 10^{-21}$	Tracer			[72]
^{59}Fe		452	$2.4 \cdot 10^{-21}$	Tracer			[72]
B		298	$3.4 \cdot 10^{-21}$	Tracer	$2.5 \cdot 10^{-20}$	SIMS	[73]
^{63}Ni	Ni	293	$1.14 \cdot 10^{-20}$	Tracer	$1.4 \cdot 10^{-26}$	Tracer	[74]
^{63}Ni		373	$1.05 \cdot 10^{-18}$	Tracer	$3.3 \cdot 10^{-22}$	Tracer	[74]
^{63}Ni		423	$4.0 \cdot 10^{-18}$	Tracer	$2.7 \cdot 10^{-20}$	Tracer	[74]
^{63}Ni		473	$2.0 \cdot 10^{-17}$	Tracer	$8.4 \cdot 10^{-19}$	Tracer	[74]
Au		448	$3.3 \cdot 10^{-20}$	Tracer	$5.6 \cdot 10^{-21}$	RBS	[74]
Cu		423	$3.8 \cdot 10^{-17}$	Tracer	$4.3 \cdot 10^{-19}$	SIMS	[74]

SIMS = secondary ion mass spectrometry
RBS = Rutherford back scattering
EMF = electro-moving force measurements

Table 2. Diffusion parameters in NMs in comparison with coarse-grained polycrystals and single crystals.

Diffusant	Host	Temp. Range, K	D_0, m^2/s	Q, eV	Method	Ref.
Cu	n-Cu	293–393	$3 \cdot 10^{-9}$	0.64		[61, 62]
	pc-Cu		$9.7 \cdot 10^{-6}$	1.06		[65]
	sc-Cu		$4.4 \cdot 10^{-6}$	1.98		[75]
	Cu-SD		—	0.69		[76]
Bi	n-Cu	293–393	$1.8 \cdot 10^{-5}$	1.0	Tracer	[64]
	pc-Cu		$2.4 \cdot 10^{-8}$	0.99	Tracer	[64]
	sc-Cu		$7.7 \cdot 10^{-5}$	1.84	Tracer	[77]
Ag	n-Cu	303–343	$1.0 \cdot 10^{-12}$	0.39	Intrinsic	[67]
		353-373	$3.0 \cdot 10^{-8}$	0.63	Intrinsic	[67]
	pc-Cu		$3 \cdot 10^{-9}$	0.64		[78]
	sc-Cu		$6 \cdot 10^{-5}$	2.01		[79]
	Cu-SD		10^{-9}	0.3		[80]
Sb	n-Cu	323–383	$1.0 \cdot 10^{-17}$	0.33	Intrinsic	[69]
	pc-Cu			0.87		[65]
	sc-Cu			1.82		[81]
^{59}Fe	n-Fe	452–499	$6.0 \cdot 10^{-10}$	1.03		[72]
	n-Fe$_{90}$Zr$_{10}$		$4.3 \cdot 10^{-9}$	1.25		[82]
B	n-Fe	298–383	$1.7 \cdot 10^{-11}$	0.59		[72]
	sc-Fe		$2.3 \cdot 10^{-7}$	0.82		[83]
H	n-Pd	293–393	$2.5 \cdot 10^{-7}$	0.25		[71]
	pc-Pd		$2.9 \cdot 10^{-7}$	0.23		[71]
	sc-Pd		$2.9 \cdot 10^{-7}$	0.23		[71]

n = nano
pc = polycrystal
sc = single crystal
SD = surface diffusion

diffusion coefficients. In a relaxed state, the GB-diffusivities in nano-objects are similar to those extrapolated from high temperatures for conventional GBs in coarse-grained polycrystals. Such results were obtained for high-density n-Fe and n-Pd (0.91–0.96 of bulk density) [82, 86].

Grain boundary-diffusivity in NMs changes not only at different temperature intervals but also at constant temperatures over different annealing periods. In the course of annealing, GB-diffusivity sometimes becomes comparably low with GB-diffusion coefficients of conventional GBs in coarse-grained polycrystals [82, 86]. An increase in the annealing temperature and time causes the development of relaxation processes and the GB structure becomes closer to that in conventional GBs.

The heterodiffusion coefficients depend on the segregation factor of the diffusing impurity in GBs. There is an evident correlation between GB-diffusivity and GB-solubility of a diffusing species: the larger its solubility, the smaller the diffusivity. For instance, the Bi-diffusivity in n-Cu is two orders of magnitude smaller than self- and Ag-diffusivities [62, 64, 67] (see Tables 1 and 2). High Bi-solubility in GBs of n-Cu reduces GB energy and thus lowers the diffusion coefficient [64]. From measurements of concentration depth profiles during Bi-diffusion in n-Cu, the Bi-solubility in GBs was calculated for grain sizes of ∼10 nm as ∼32 at.%. In comparison, the Bi-solubility in Cu-lattice extrapolated to 100 °C is 10^{-6} at.% [87]. In other words, the Bi-solubility in GBs of n-Cu is seven orders of magnitude higher than its solubility in single crystalline Cu. It is known that Bi-solubility in GBs of massive Cu-polycrystals is of 5–10 at.% [31]. This

fact correlates with higher GB-energies in NMs caused by the extra free volumes in the core of GBs (compared to conventional GBs) [3]. Such a type of structure provides a high GB solubility of Bi in nano-objects. The proposed concept of correlation between GB-solubility and GB-structure was confirmed [64] by a preannealed experiment (at 100 °C for 24 h) to achieve GB relaxation. It was observed that this procedure reduced GB Bi-solubility by ∼40 at.% and the diffusion coefficient by ∼50% due to relaxation of GB structure. This also confirms the conclusion [52] that GB segregation tends to retard GB diffusion.

The important factor, which influences GB diffusivity, is intergranular phase formation due to chemical interaction of the diffusing species with the matrix substance. As a rule, the intergranular amorphous phases reduce GB diffusivity. In Table 2, the comparable data on ^{59}Fe diffusion in n-Fe and n-alloy Fe$_{90}$Zr$_{10}$ are presented to demonstrate the different diffusion characteristics obtained for these two objects [72, 82]. The ^{59}Fe-tracer diffusivity in these alloys is one-two orders of magnitude lower than in pure n-Fe, depending on the content of intergranular amorphous phases [82]. Intergranular amorphous phases reduce GB-diffusion due to their high packing density. The other reason for Fe-diffusivity reduction is the chemical interaction of Fe-tracer atoms with the alloy constituent Zr and the subsequent formation of new phase layers in the core of interfaces.

Recently, there was another important contribution to the study of high diffusivity of NMs: the discovery of the fact that high density of triple junctions may significantly change

some properties of nano-crystalline materials, and specifically, their diffusion behavior [88–90]. A triple junction is a line defect at the junction of three or more grains. Triple junctions are characterized by a line tension approximately two orders of magnitude higher than the line energy associated with lattice dislocation [88]. Triple junction lines have a positive free energy uncompensated by the joining interfaces and one can expect that they have high diffusivities, up to three orders of magnitude higher compared to GB diffusivities [89, 90]. Therefore, triple junctions in nano-objects can significantly contribute to diffusion penetration.

Interstitial impurities, such as hydrogen, boron, oxygen, which diffuse in the lattice by the interstitial mechanism, demonstrate many different diffusion regularities compared to the substitutive diffusing species described above. The principal difference is that diffusivities B, H, and O in different NMs are either comparable to or even less than B-and lattice diffusivities (Table 1). The activation energy of boron diffusion in n-Fe is about 0.2 eV lower than that for lattice diffusion (Table 2) but the pre-exponential factor is very small in comparison with the D_0 for lattice diffusion. This is typical for GB impurity diffusion with low lattice solubility and high enough GB-solubility. Low values of GB-diffusivity by interstitial mechanism are explained by interaction of diffusing atoms with GB traps as well as with one another.

The tracer and intrinsic diffusion coefficients may differ from one another (see Bi diffusion into n-Cu in Table 2). As it was noted earlier they differ by the thermodynamic factor (16), which is not available in many cases, and an exact comparison of these coefficients for some systems is difficult to achieve. For Bi-diffusion, these coefficients differ by almost one order of magnitude.

4. INTERDIFFUSION

4.1. General Remarks

Interdiffusion in binary diffusion couple A–B consists of two diffusion fluxes A and B directed towards one another and supported by concentration gradients of both components. In contrast to tracer diffusion (when concentration of diffusion species is too small whereby the diffusion zone is considered as a practically ideal solution of A in B) and chemical diffusion (when A-atoms form a nonideal solution in the B matrix, whereas the diffusion of B atoms is "frozen" or not taken into account), the interdiffusion is a process of simultaneous diffusion of both components. As a rule, it occurs in large concentration gradients (in soluble systems the concentration varies from 1 to 0) and is accompanied by macroscopic mass transfer effects [79, 91–93]. Interdiffusion employs a diffusion couple with two thick (semi-infinite) layers of components A and B or, in other words, constant (infinite) diffusion sources. The diffusion fluxes A and B, are called partial diffusion fluxes and characterized as a rule, by the unequal partial diffusion coefficients, D_A and D_B.

In the diffusion zone with large concentration gradients of both components, the partial diffusion coefficients D_A and D_B depend on the concentration, so they vary with coordinates inside the diffusion zone. The reason for this is the nonideality of solutions inside the diffusion zone, as well as

a different character of correlations for atomic jumps during interdiffusion (as opposed to tracer diffusion [79]).

With the vacancy diffusion mechanism, inequality of the coefficients D_A and D_B (and, therefore, the partial diffusion fluxes A and B), initiates a vacancy flux directed towards the component with a higher diffusivity (e.g., if $D_A > D_B$, the flux is directed towards the component A). The interaction of extra vacancies with the two different types of the sinks (dislocations and microcavities) in the crystal lattice leads to two fundamental accompanying phenomena: the flow of material in the diffusion zone (the Kirkendall effect [93]) and formation of "diffusion porosity" (the Frenkel effect [91, 94]). These two phenomena are in competition with each other. The extra vacancies captured by dislocation induce dislocation climb [91], leading to the dismantlement of lattice planes and to the Kirkendall shift of the marks in the diffusion zone. If extra vacancies are captured by pores that grow in the diffusion zone, no Kirkendall shift is observed.

The important consequence of these phenomena is the generation of stresses, which change both the structure of the diffusion zone and the values of the diffusion fluxes. By changing the conditions for generation and relaxation of stresses, one can reduce and even suppress interdiffusion [91]. The effect of stresses is immediately apparent in the systems, in which interdiffusion is accompanied by formation of intermetallic phases with large volume dilatation and, as a result, a high level of generated stresses. The accompanying phenomena caused by interdiffusion with unequal partial diffusion coefficients can significantly affect the kinetics of interdiffusion.

Using the concentration profile measured in the diffusion zone between two contacted semi-infinite layers A and B, one can obtain the so-called interdiffusion coefficient, $\widetilde{D}(C)$, which determines the diffusion flux (accounting the Kirkendall shift of the lattice):

$$J_A = -\widetilde{D}(C)\frac{\partial C_A}{\partial x} \tag{18}$$

The concentration dependence of $\widetilde{D}(C)$ is calculated by the Matano–Boltzmann method [79, 91].

The analysis of interdiffusion proposed by Darken [55] yields the following relations between the different diffusion coefficients:

$$\widetilde{D} = D_A C_B + D_B C_A \tag{19}$$

Here C_A and C_B are the dimensionless concentrations of A and B atoms, and each of the partial diffusion coefficients relates to the tracer ones according to (16).

The partial diffusion coefficients D_A and D_B can be determined from the rate of Kirkendall shift, V_K, of a marked plane in the diffusion zone using the measured interdiffusion coefficient, $\widetilde{D}(C)$, and (19):

$$V_K = (D_A - D_B)\frac{\partial C_A}{\partial x} \tag{20}$$

(here $\partial C_A/\partial x$ is the concentration gradient at the marked plane). The partial diffusion coefficients D_A and D_B can be calculated for any given concentration where the marked plane is located. The interdiffusion coefficient $\widetilde{D}(C)$ and the partial diffusion coefficients D_A and D_B determine the diffusion fluxes in all diffusion mass transfer processes

in binary and multi-component systems. These coefficients alone control the kinetics of phase transformation, sintering of powder mixtures, creep, and other types of deformation in alloys, decay of supersaturated solutions, and coalescence of precipitates [33, 79, 91].

Similarly to tracer diffusion, interdiffusion in NMs at relatively low temperatures occurs mainly inside the wide network of GBs, which are simultaneously short-circuit diffusion paths and sources and sinks of vacancies. This peculiarity provides yet another condition for the manifestation of the Kirkendall and Frenkel effects that accompany interdiffusion, as well as for generation and relaxation stresses.

The inequality of the GB partial diffusion coefficients initiates the phenomenon of diffusion-induced grain boundary migration (DIGM) [95–98], which is one of the most effective mechanisms for the formation of solid solutions and other new phases at low temperatures when bulk diffusion is practically frozen. It means that new phases in the bulk of material are formed and grow without participation of bulk diffusion. The DIGM phenomenon consists in the motion of GB, induced by unequal, opposite directed, partial diffusion fluxes of A and B atoms along GB. A GB migrating in the matrix B leaves the diffusing impurity atoms (A) in the bulk of B material behind of the GB.

The motion of GBs in the grain growth (recrystallization) process also plays a crucial role in the kinetics of interdiffusion and the formation of solid solutions at low temperatures. Due to the small size of the structural element, the grain growth4 is especially rapid at the early stages of diffusion (see Section 2). Interdiffusion along GBs, which are moving due to recrystallization, is also accompanied by low-temperature phase formation behind the migrating GBs [29, 97, 99]. However, the driving forces and the kinetics of GB motion and phase formation are different in these two cases, establishing different GB velocities and therefore, different rates of diffusion homogenization.

In this section, GB interdiffusion and the accompanying GB Kirkendall and Frenkel effects in NMs have been considered in comparison to bulk interdiffusion. The phenomenon of low-temperature homogenization (LTH) in NMs is described and the model of LTH by interdiffusion along migrating GBs is presented. The phenomenon of diffusion-induced decay of multilayered nanostructures initiated by GB migration during LTH and the ways to prevent these processes and conserve stable nanostructures are discussed.

4.2. GB Kirkendall Effect

The GB Kirkendall effect is a result of interdiffusion of A and B atoms along GBs with unequal GB partial diffusion coefficients. It consists of a change of distance between markers in the diffusion zone due to insertion or elimination of atomic planes inside GBs. Contrary to the bulk Kirkendall effect, in this process each GB is simultaneously a diffusion short-circuit path and a source or sink of vacancies. On the supposition that $D_{bA} > D_{bB}$ the flux of A-atoms coming into each GB is larger than the flux of B-atoms leaving GB. As a result, one component (B) of the diffusion couple swells, while the other one- (A) shrinks, changing distance between the marks.

Excess atoms, which appear at the B-side of the couple due to the difference of GB partial fluxes, attach to the GB walls forming extra planes. In this process, GB walls act as a vacancy source generating vacancies necessary to insert excess atoms. As a result, the B-side of diffusion zone "swells." The converse process occurs at the A-side of the diffusion couple: the flux of the A-atoms leaving the GB is larger than incoming flux of the B-atoms. Grain boundaries are the sources of atoms (i.e., the sinks of vacancies), making the distance between some marks smaller due to the shrinkage of the A-side.

An analysis of the GB Kirkendall effect similar to that for bulk interdiffusion [55] (see (20)) yields the following equation for the GB Kirkendall velocity of the contact plane [29]:

$$V_{bK} = \frac{d\Delta x_{bK}}{dt} = \frac{\delta}{l}(D_{bA} - D_{bB})\frac{\partial C_b}{\partial x}\bigg|_{x=0} \tag{21}$$

where Δx_{bK} is the Kirkendall shift of the contact plane ($x = 0$) between the nanodispersed layers A and B of the diffusion couple, δ is the GB width, and l is the grain size. Due to the random distribution of GBs in nanodispersed A and B layers, interdiffusion along GBs occurs in all directions that could provide practically equal Kirkendall shift. In massive diffusion couples, however, due to the stresses appearing near the diffusion contact and in the diffusion zone, Kirkendall effect can be realized without introduced stresses and measured only in the direction perpendicular to the contact plane.

According to (21) the GB Kirkendall shift depends on the type of the diffusion regime, which determines the value of the concentration gradient $\partial C_b/\partial x$. For the diffusion regime of type B, which at relatively low temperatures $T = (0.3–0.4)T_m$ is realistic for long diffusion times, one can obtain the kinetic law for GB Kirkendall shift in the form [29]:

$$\Delta x_{bK} = \frac{4}{3}\frac{\delta}{l}C_0(D_{bA} - D_{bB})\left(\frac{2S/L}{s\widetilde{D}_b\delta}\right)^{1/2}\left(\frac{\widetilde{D}}{\pi}\right)^{1/4}t^{3/4} \tag{22}$$

where

$$\widetilde{D}_b = D_{bA}C_{bB} + D_{bB}C_{bA} \tag{23}$$

is the GB interdiffusion coefficient. The kinetic law $\Delta x_{bK} \sim t^{3/4}$ differs from the known parabolic law for the bulk Kirkendall effect [55] and similar to the subsurface Kirkendall effect [100, 101], caused by the interdiffusion along a free surface in B-regime.

The GB Kirkendall effect was observed experimentally [29] in diffusion couples composed from n-dispersed ∼1–2 mm thick Cu and Ni layers compacted from nanopowders of 8–12 nm sizes. Small pits (3 μm in diameter) produced by a diamond indenter and located on the sample surface perpendicular to the Cu-Ni interface were used as inert marks. The increase of the distances between the pits was detected at the Ni-side near the Cu-Ni interface, whereas the distances between the pits stayed constant far from the contact interface, outside of the diffusion zone. The shift of the Cu-Ni interface was measured relatively to immobile pits at the Ni-side outside of the diffusion zone. The kinetic law $\Delta x_{bK} \sim t^{3/4}$ was obtained [29] at the temperature 500 °C for

$t = 5 \times 10^3$ s. With $D \approx 8 \cdot 10^{-23}$ m²/s [102] the bulk leakage zone, $(Dt)^{1/2} \leq 0.6$ nm, satisfied the B-type diffusion regime. The measured values of Kirkendall shifts were on the order of 1.5–2.5 μm. By substituting $\delta/l \approx 5 \times 10^{-2}$; $S/L \approx 3/2$ (for spherical powders); $s\widetilde{D}_b\delta \approx 1.4 \cdot 10^{-23}$ m³/s [65] in Eq. 22, the ratio $(D_{bA} - D_{bB})/\widetilde{D}_b$ was estimated as 0.45. Observation of the GB Kirkendall effect is evidence of the inequality of GB partial diffusion coefficients, as well as presenting a simple way for quantitative measurements of this inequality. It is important to note that NMs are unique objects for measurements of the GB Kirkendall shifts. Indeed, due to the factor δ/l in Eq. (22) this effect in coarse-grained polycrystals becomes negligible.

At the Cu-side of the diffusion zone, the distance between the pits decreased, although the Kirkendall velocity of the marks was about two times smaller than at the Ni-side. With that, microscopic porosity was detected at GBs (the GB Frenkel effect) which, being in competition with the Kirkendall effect, retarded the Kirkendall velocity at the Cu-side [91, 103].

The insertion or elimination of atomic planes inside interfaces in GB Kirkendall effect, that is, the increase or decrease of the number of atomic sites inside GBs leads to stress generation inside grain interiors. The stresses were visualized in experiments on lateral interdiffusion in nanostructured thin films. The thin film couples Au-Pd, Au-Ag, and Cu-Ni of 50–100 nm thickness were evaporated [104–106] onto a quartz substrate from two sources separated from one another by a screen perpendicular to the substrate. By variation of the distance between the screen and the substrate, one could control the width of the overlap between two thin films (varying in the range 5–20 μm). Interdiffusion occurred in both directions parallel to the free surface through the network of GBs. Unlike the usual sandwich-type thin film couples, in which interdiffusion between two films occurs perpendicular to the free surface and the width of the diffusion zone is restricted by the film thickness, in lateral interdiffusion experiments the films provide unlimited diffusion zones. In this process, inner GBs and the outer free surface serve as sinks or sources of vacancies generated by interdiffusion. The Kirkendall shift was measured as a change of distances between the pits produced by a diamond indenter and located on the film surface along the line parallel to the diffusion direction at both sides of the contact. During interdiffusion, compressive stresses developed in film B (with lower diffusivity) where the number of atomic sites inside GBs increased, whereas in film A (with faster diffusivity) the number sites decreased and tensile stresses appeared. Relaxation of these stresses is realized by different mechanisms: relaxation of compressive stresses (at the B-side of the diffusion couple) occurs through formation of surface hillocks and/or appearance of periodically located pleats near the overlap. Having the same origin, these two forms of stress relaxation are competitive. Under different conditions, different mechanisms of stress relaxation were realized: the hillocks were formed by diffusion transfer of material from adjacent regions, so that each hillock was surrounded by a concave zone [107], whereas the pleats were formed by a nondiffusion mechanism (due to tearing off of the film from the substrate). The hillock formation was the preferred relaxation way at higher temperatures, whereas the pleats were formed preferably at lower temperatures. A comparative analysis of the kinetics of hillock and pleat formation compared to the kinetics of GB Kirkendall effect was carried out. It was shown that the stresses originate from the GB Kirkendall effect and can be estimated both from the distance between pleats and from the marker shifts.

The tensile stresses in the A-film (with higher diffusivity) relaxed mainly by pore formation along GBs, that is, due to the GB Frenkel effect [105, 106]. The pores form a chain at the distance l_p from the contact, parallel to the overlap line. This effect was observed on Au-Ag thin films [106] even at room temperature. The spreading kinetics of the porous zone obeys the law $l_p \sim t^{1/4}$, that is, pore formation is controlled by GB interdiffusion. Extra vacancies produced by interdiffusion along GBs coagulate in micropores, decorating the GBs. This process is stimulated by tensile stresses, which tend to relax by pore formation.

4.3. Low Temperature Homogenization

The phenomenon of LTH in polycrystalline materials consists of the formation of solid solutions in the bulk of grains during interdiffusion of soluble A and B components at comparably low temperatures, when bulk interdiffusion is practically "frozen" $((\widetilde{D}t)^{1/2} \leq a)$. This means that solutions in the bulk are formed without participation of bulk diffusion. The LTH was detected during interdiffusion in different NMs, such as thin films [108, 109], compacts of binary nano-powder mixtures [99], diffusion couples composed from contacting layers A and B compacted from nano-powders [29, 97, 99], and multilayered objects with alternating layers A and B [110].

4.3.1. Mechanisms, Driving Forces, and Favorable Conditions

The mechanism, which explains how a solid solution is formed in the grain interior, consists of impurity diffusion along a moving boundary, which leaves the impurity atoms in the bulk of the grain behind the moving GB (Fig. 1).

Two different driving forces comparable by magnitudes may initiate GB migration. The first of them is the "chemical" driving force (which is responsible for DIGM), caused by reduction of free energy due to formation of the solution. The specific chemical energy ΔG_{ch} calculated per unit volume is [95, 98]:

$$\Delta G_{ch} \approx \frac{k_B T(C_0 - C_s)^2}{\omega C_0^2} \qquad (24)$$

where ω is the atomic volume; C_0 is the initial diffusant concentration in diffusion source, and C_s is the final concentrations of the diffusant in the forming solution. The chemical driving force is independent of the grain size. With $C_0 \approx 1$, $C_s \approx 0.2$ (Fig. 2a), $\omega \approx 1.3 \cdot 10^{-29}$ m³, and $T \approx 600$ K it is about $\Delta G_{ch} \approx 3 \cdot 10^8$ J/m³.

Another driving force of capillary origin, which is responsible for grain growth during recrystallization, is inversely proportional to the grain size l

$$\Delta G_r \approx 2\alpha_{ik}/l \qquad (25)$$
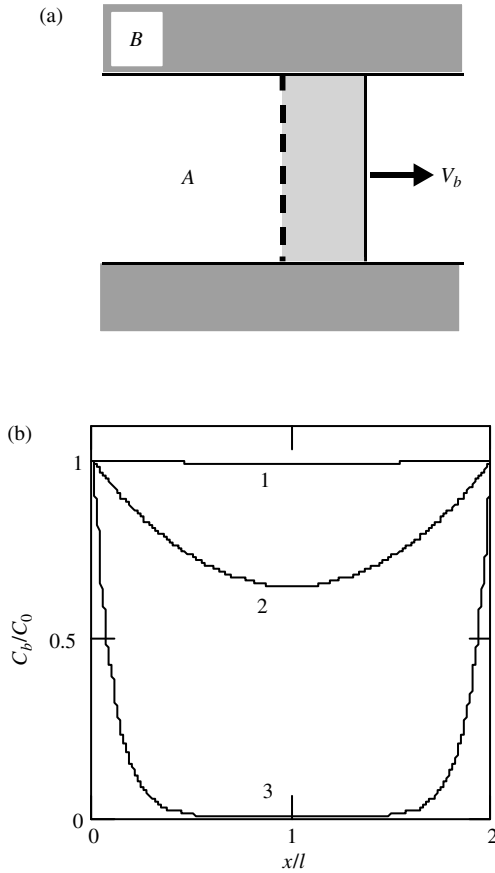
Figure 1. (a) Scheme of the plate A with the GB moving with the velocity V_b. Atoms B diffusing into moving GB stay in the grain interior behind the GB. (b) Steady state concentration distribution of atoms B in the moving GB calculated for various l/λ: 1 – $l/\lambda = 0.1$; 2–1; 3–10.

Figure 2. The time dependencies of average solution concentration (a) and the volume fraction of the solution (b) for nano-powder mixture Cu-Ni. $T = 300°$ C. Two branches are clearly seen in the plots corresponding to two stages of LTH.

where α_{ik} is the GB tension. For NMs with $l \approx 5$ nm and $\alpha_{ik} \approx 1.5$ J/m^2 (taking into account the nonequilibrium state of GBs in NMs just after preparation) the driving force is $\Delta G_r \approx 6 \cdot 10^8$ J/m^3.

Thus, at early stages of annealing the capillary force stimulating grain growth can exceed the chemical force and then interdiffusion occurs along GBs migrating due to grain growth. High GB migration rates at early stages of annealing and abnormal grain growth in NMs [29] were discussed in Section 2. This process sharply slows down in the course of annealing time both due to grain growth (l grows) and the modification of GB structure [112–115] (α_{ik} decreases in Eq. 25). As a result, at later stages of diffusion, GB migration is governed by the chemical driving force, which provides the slower DIGM mechanism.

To estimate the kinetics of LTH at early stages, an analysis of the concentration distribution during interdiffusion along moving GBs in NMs has been performed [97]. In Figure 1 the element of nanostructure is presented in the form of an A-plate of width $2l$, with the boundary moving with the recrystallization rate V_b. The diffusion sources of B-atoms are located at both surfaces of the A-plate. The B-atoms diffusing along GB are captured by the grain bulk after shift of GB for distance δ. The diffusion equation describing this process is written in the form

$$\delta \frac{\partial C_{bB}}{\partial t} = \delta D_{bB} \frac{\partial^2 C_{bB}}{\partial x^2} - C_B V_b \qquad (26)$$

Here C_{bB} and C_B are the concentrations of B-atoms in the GB and in the grain interior near the GB, respectively, $C_{bB} = sC_B$, s is the segregation factor. The second term on the right-hand side of (26) accounts for the "leakage" flux of B-atoms from the moving GB into the grain bulk. At stationary conditions, when $\frac{\partial C_{bB}}{\partial t} = 0$, the solution of (26) with the boundary conditions $C_{bB}(0) = C_{bB}(2l) = C_0$ is [97]:

$$C_{bB}(x) = C_0 \left(ch\frac{x}{\lambda} - th\frac{l}{\lambda} sh\frac{x}{\lambda} \right); \quad \lambda = \left(\frac{sD_b\delta}{V_b} \right)^{1/2} \qquad (27)$$

The parameter λ has the meaning of the characteristic diffusion length. The distribution of the diffusing B-atoms inside GB depends on the ratio l/λ. As it was shown [97], with $l/\lambda \leq 0.1$ the concentration C_{bB} slightly varies along the GB length (Fig. 1) and the solid solution with an almost constant concentration (about C_0/s) is formed behind the migrating GB.

The following conditions are necessary for the most complete LTH [99]:

$$(D_b t)^{1/2} \gg l; \quad V_b t \geq l; \quad l \ll \left(\frac{sD_b\delta}{V_b} \right)^{1/2} \qquad (28)$$

The smaller the structural element in NMs, the smaller might be the GB diffusion coefficients and the GB migration rates to provide LTH. According to the proposed scheme, formation of solid solutions occurs by "spots," in the local volumes of the sample where GBs move with favorable conditions. This means that the volume fraction of solutions cannot reach 1 by this mechanism.

The formulated conditions for LTH are valid for different NMs, such as compacts produced from disordered A and B nanopowder mixtures, binary A-B thin films, nanofibers, or alternating A and B nanolayers. They afford the possibility to predict the minimum temperature of LTH depending on the GB diffusivity, GB migration rate, and the size of the structural element.

4.3.2. LTH in Binary Powder Mixtures

In agreement with the theoretical predictions mentioned above, two stages of LTH were detected in experiments with binary (50:50) nanopowder Cu-Ni mixtures [29, 99]. The kinetics was studied at 300 °C by the method of X-ray phase analysis. The grain sizes both Cu and Ni varied in the range 8–15 nm. Two branches were clearly seen in the time dependencies of average solution concentration $C(t)$ and the volume fraction of the solution $\chi(t)$ (Fig. 2). The first rapid stage was reasonably described in the terms of interdiffusion along GBs moving due to recrystallization, whereas the slower second stage—by DIGM.

It was observed [99] that in Cu-Ni n-powder mixture with identical sizes of Cu and Ni powders the solutions were formed on the Cu base. The solutions on the Cu base is characterized by higher GB diffusivity compared to the solutions on the Ni base, and the GB velocity in Cu is higher than in Ni. By size variation of the Cu and Ni powders, it was possible to "reverse" the process of solution formation [116]. When the Ni particle size became one order of magnitude smaller than the Cu grains, the solution was formed on the Ni base, in spite of lower GB diffusivity of the Ni-atoms.

A comprehensive model of LTH in A-B n-powder mixture, available for semi-quantitative kinetic estimations, has been proposed [99]. It is based on the concept that disordered A-B powder mixtures can be considered as being composed from the A and B broken lines (chains) consisting of grains of the same kind and surrounded by grains of another kind. Each GB in the chain can move with the probability 0.5 in one of the two possible directions. Then, using the scheme of homogenization described by Eq. (27) the volume fraction of the solution was calculated as a function of time. The calculations made under the assumption that two adjacent GBs in a chain move in the opposite directions were found to be in good agreement with the experiments.

4.3.3. LTH in Multilayered Systems

In binary multilayered systems with alternating A and B layers, the wide network of the short circuit diffusion paths is composed both of GBs inside each layer and interfaces between the A and B layers. Participation of interfaces in the LTH process is turned out to be crucial for stability of the layered structure. The kinetics of LTH in multilayered systems is similar to that described for powder mixtures [110, 111].

The LTH, however, is accompanied by the decay of the layered structure and its transformation into a globular structure [110, 111]. The explanation of this phenomenon and the model of the decay initiated by LTH process has been proposed with reference to experimental results obtained for Ni-Cr multilayered systems. Due to interdiffusion of Cr and Ni along two adjacent GBs inside the Ni-layer (see scheme in Fig. 3), they move towards one another and leave behind the solution between two Ni grains. Further growth of the grain of the solution possible due to interdiffusion along the "solution-Cr-layer" and "solution-Ni-grain" interfaces. According to the scheme (Fig. 3b), the interdiffusion of Cr and Ni in opposite directions along the interfaces results in an increase of the solution grain and its separation from the layer, that is, in decay of the layered structure and its subsequent transformation into isomeric globular structure. This process is similar to well-known decay of thin rods or films under capillary force [117]. In contrast to that, the decay of the layered structure during LTH is caused by the chemical driving force ΔG_{ch}, which initiates the solution formation, so this effect may be qualified as chemically induced decay.

As the degradation of layered structures essentially lowers their functional characteristics, stability of multilayered materials at elevated temperatures becomes an extremely important problem. One of the effective ways of stabilization is doping by nanocrystalline insoluble inclusions embedded between the layers. Nanoinclusions act as stoppers
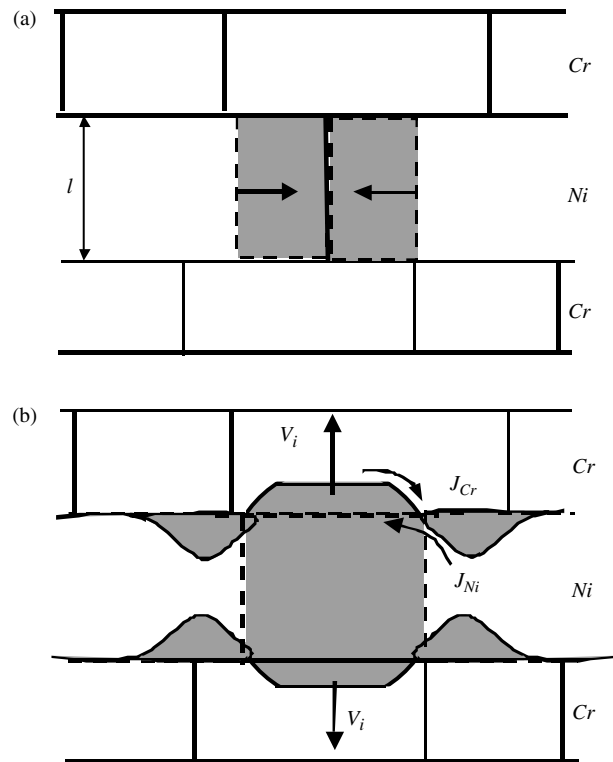
Figure 3. Scheme of decay of a layered structure Ni-Cr during LTH. (a) as a result of motion of two adjacent GBs one to another, the solid solution is formed in the hatched region; (b) the interdiffusion fluxes J_{Ni} and J_{Cr} along the interfaces "solution-Cr" and "solution-Ni" lead to the decay of the layers.

for moving interfaces, hindering decay of the layers. For example, the Y_2O_3 particles hindered decay of multilayered Cr-Ni system [118], as well as the kinetics of LTH. The physical ground of the hindering was partly discussed in Section 2. Interaction of inclusions with migrating boundaries is determined by relation between the binding force F_b, which attracts impurity to the boundary, and external driving force F_{ex}, which initiates the boundary migration. The external forces are determined by (24) or (25) depending on the size of the structural element. The condition $F_b > F_{ex}$ is favorable to the stability of the layered structures because the inclusions stay at the boundary and hinder its migration. If the boundary migrates under F_{ex}, it should drag the inclusions with it. In this case, the rate of boundary migration is limited by the Brownian mobility of inclusion as a whole [118].

5. SURFACE DIFFUSION AND MASS TRANSFER IN NANOSTRUCTURED MATERIALS

The following two sections are devoted to diffusion processes in NMs produced in the form of nanometer-sized corrugations on a single-crystalline surface of a given orientation or nanometer-sized particles (2D or 3D) located on a substrate of the same or different material. The particles (corrugations) can be produced by chemical vacuum deposition (CVD), physical vacuum deposition (PVD), inert gas condensation, various aerosol techniques, synthesized by lithography, or by the means of local probes, such as scanning tunneling microscope (STM) or atomic force microscope (AFM). The particles are produced to form an array of nanometer-sized islands on a free surface. The physical properties of such NMs are functions of the particle size, therefore understanding the diffusion processes that take place both during fabrication and exploitation is of great importance.

The kinetics of these processes is determined mainly by SD over the substrate and particle surfaces. Due to the small lateral distances between the structural elements in NMs and the small particle sizes, SD can rapidly change the particle morphology.

In Section 5, an analysis of the smoothing and coarsening of nanoscale corrugations will be given for nanoscale objects with different surface structures. The following three types of crystal surfaces are usually considered in the polar diagram of surface tension γ [14, 119]: singular, vicinal, and nonsingular surfaces. Singular surfaces are densely packed (low Muller index surfaces) and characterized by sharp minima (cusps) in the γ-diagram [14, 119, 120] (the singularity is expressed by the discontinuity of the angular derivative of γ); they are completely flat on the atomic scale. Vicinal surfaces slightly deviate from the singular ones and consist of close-packed terraces separated by elementary steps [119–122], whose linear density ρ is proportional to the angle of deviation, θ, so that $\rho(\theta) = \sin\theta/a$ (a is the height of the steps). Surface tension of vicinal surfaces grows with ρ as

$$\gamma(\theta) = \gamma_0 + \alpha\rho + f_i\rho^3 \qquad (29)$$

where α is the linear tension of an isolated step and the last term represents the interaction free energy between the steps. The cubic dependence on ρ of the interaction free energy term follows from the quadratic dependence on ρ of the interaction free energy per step for the entropic repulsion [123], elastic interaction and electric dipole interaction between the steps [124]. When the interaction free energy per step is multiplied by the step density ρ, the result is a ρ^3 term for the interaction free energy per unit area.

At low temperatures, the steps on vicinal surfaces are straight; while at higher temperatures some waviness appears due to the formation of kinks, redistribution of atoms adsorbed at steps, and the attachment-detachment of adatoms. Thermal fluctuations grow with temperature and at some temperature, T_R, the vicinal surface can undergo a roughening transition; above T_R the surface becomes atomically rough [121, 122], or non-singular.

The kinetics of flattening of corrugated nonsingular surfaces in continuum approximation was examined by Mullins [125, 126] about 40 years ago. There is an extensive body of literature devoted to the continuum description and analysis of the evolution of surface shapes driven by the reduction of surface free energy mediated by SD [15, 117, 127–133]. It was shown that the measurements of capillary-induced mass transfer could be used to extract SD coefficients.

Strictly speaking, the continuum Mullins theory is valid for relatively high temperatures, above T_R, where the surface structure and SD coefficients are independent of the crystallographic orientation. Below T_R, the mass transfer occurs mainly on atomically flat terraces separated by elementary steps. Both driving forces and the kinetics of SD mass transfer on atomically flat surfaces differ from those on nonsingular surfaces. In particular, the kinetics of surface evolution depends in this case on the mobility of steps, which can be determined either from the surface mobility of atoms or the kinetics of their attachment to the steps (or detachment from them).

5.1. Surface Diffusion Mass Transfer on Atomically Rough Surfaces

5.1.1. Flattening of a Corrugated Surface

An arbitrarily shaped crystal surrounded by a saturated vapor tends to transform its shape to that whose surface free energy, γ, is minimal for the given volume. Each macroscopically small surface region would transform its shape following the same thermodynamic tendency. Fluxes between the adjacent areas of a crystal under isothermal conditions are determined by the distribution of the chemical potential of atoms, $\mu(x, y)$, along the surface. Neglecting the anisotropy of surface energy (for atomically rough surfaces), one can write [14]

$$\mu(x, y) = \mu_0 + \gamma\Omega K(x, y) \qquad (30)$$

where $K(x, y)$ is the surface curvature, Ω is the atomic volume, and μ_0 is the chemical potential of atoms in a large equilibrium crystal, where the capillary effects are negligible. A heterogeneous distribution of μ with a given surface profile $z(x, y)$ causes atomic fluxes along the SD, in the bulk of the crystal (volume diffusion), and through the vapor phase

(evaporation-condensation or diffusion in a gas phase). The last two mechanisms are important only at high temperatures ($T > 0.7 \cdot T_m$, where T_m is the melting temperature), whereas SD is active enough at $T \geq 0.2 \cdot T_m$.

The surface flux of atoms is given as

$$J_s = -\frac{D_s n_0}{k_B T} \nabla \mu \tag{31}$$

where D_s is the surface diffusion coefficient, n_0 is the surface density of the diffusing atoms. If mass transport occurs only by SD, the time variation surface profile $z(x, y, t)$ satisfies the continuity equation

$$\frac{\partial z}{\partial t} = -\Omega \cdot div J_s \tag{32}$$

where n_0 is the surface density of the diffusing atoms. Equations (31) and (32) are written in a small-slope approximation since the spatial derivatives in these formulas should in fact be taken with respect to the surface $z(x, y, t)$. Combining (30–32), one can obtain the kinetic equation of the form [125]

$$\frac{\partial z}{\partial t} \approx -B\left(\frac{\partial^4 z}{\partial x^4} + \frac{\partial^4 z}{\partial y^4}\right) \tag{33}$$

where

$$B = D_s \gamma \Omega^2 n_0 / k_B T \tag{34}$$

Considering as an example, the flattening of a 2D periodic surface with a sinusoidal profile in two directions

$$z(x, y, 0) = z_0 \sin q_x x \cdot \sin q_y y \tag{35}$$

one can obtain a solution in the form

$$z(x, y, t) = z(x, y, 0) \cdot \exp\left[-B\left(q_x^4 + q_y^4\right)t\right] \tag{36}$$

As it is seen, the profile remains a sinusoid with an amplitude that decays exponentially with time. The flattening is extremely sensitive to the periodicity of the profile: the smaller the periods in both directions ($\lambda_x = 2\pi/q_x$; $\lambda_y = 2\pi/q_y$), the faster is the flattening kinetics ($\sim\lambda^{-4}$). Additionally, the measurements of the flattening rate could be used for extracting the SD coefficient D_s, which determines the kinetics of mass transfer on atomically rough surfaces.

Since any surface profile could be represented as a set of Fourier harmonics of the wave vectors $\boldsymbol{q}(q_x, q_y)$ and amplitudes, and because (33) is linear, solution (36) describes both flattening (and coarsening) of an arbitrary rough surface $z(x, y)$ as a simultaneous and independent smoothing of each of the Fourier expansion harmonics [125]. It is clear from this expression that high harmonics of a general profile decay rapidly, leaving the slower decaying ones fundamental.

5.1.2. Diffusion Evolution of Needles and Rods

Needles and rods are the regular components of surface nanostructures, and the kinetics of the diffusional evolution of their tips is of interest for the estimates of their structural stability.

It is known that in an isotropic approximation, needles and rods are not thermodynamically stable shapes, because the decay of rods or needles for spheres leads to a decrease of their surface free energy [134]. As it has been observed in experiments [135], the decay begins from the top of the rod due to a difference in the chemical potentials of atoms at the top ($\mu = \mu_0 + 2\gamma\Omega/R$) and at the side surface ($\mu = \mu_0 + \gamma\Omega/R$). This leads to the appearance of a current of atoms from the top to the side surface, which results in an increase of the top radius R and a shift of the top along the rod axis z (Fig. 4). In this process, a sphere on the top can separate from the rod if the principal radii of curvature, R_1 and R_2, in the neck area satisfy the inequality $R_1^{-1} - R_2^{-1} > R^{-1}$. The difference in the decay kinetics of a cylindrical rod and a conical needle is caused by the difference in the neck geometry. The growth kinetics of the top radius and the shift of the top position in the z direction are described by the following formulas [132]

$$R^4 = R_0^4 + m_1 Bt; \qquad z^4 = z_0^4 + m_2 Bt \tag{37}$$

where m_1 and m_2 are numerical coefficients that depend on the cone angle, and B is defined by (34).

5.1.3. Diffusion Decay of Continuous Thin Films

Stability of thin films is becoming increasingly important for numerous technical applications, especially in the electronics industry and catalysis, which require large surface areas of precious metals. The thin films used in such applications have a very high surface-to-volume ratio, which produces a
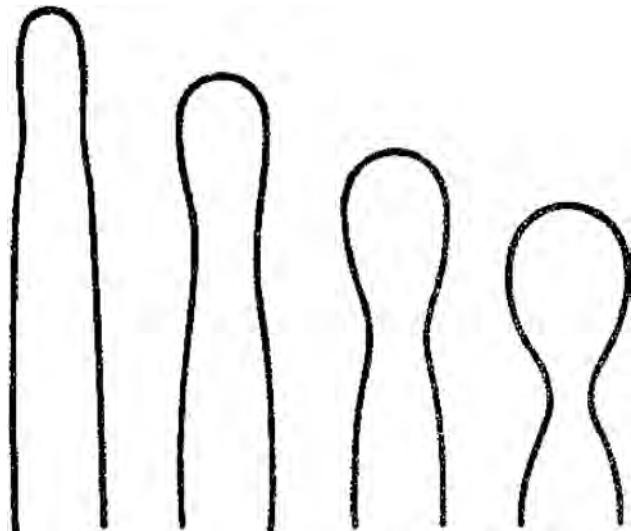
Figure 4. Scheme of blunting of a needle edge: the top radius grows and, simultaneously, the top of the needle moves down.

large driving force reducing the surface area. Due to diffusion mass transfer, the thin film changes shape and becomes discontinuous. The decomposition of a thin continuous film into a collection of beads occurs in two steps: the fluctuation of the film thickness with the formation of voids and the void growth.

There are several mechanisms responsible for the thickness fluctuation in polycrystalline thin films [117]. The main mechanisms are hillock growth [136] and the formation of grooves at GBs, which intersect the surface of the film [137].

Hillock Growth Due to the difference $\Delta\alpha_T$ in the thermal expansion coefficients between the film and the substrate (as a rule, $\Delta\alpha_T > 0$ because the thermal expansion coefficient of the film exceeds that of the substrate), compressive stresses on the order of

$$\Delta\sigma_T \approx \Delta\alpha_T E \cdot \Delta T \tag{38}$$

appear in the film during the heating of the sample over ΔT (E is Young's modulus). As the relaxation of stresses in different grains occurs differently, the stresses in the film become inhomogeneous, inducing atomic currents directed to the grains with lower stress values, both through GBs (primary recrystallization) and over the surface. The hillocks grow at the surface of grains that have become larger than the critical size

$$R^* \approx 2\gamma_f/\Delta\sigma_T \tag{39}$$

(here γ_f is the surface tension of the film material). The surface diffusion current is defined by (31) and depends on the difference between the chemical potentials of atoms in the hillock (which is assumed to be free of stresses) and the adjacent stressed grains

$$\Delta\mu \approx \Omega \cdot \Delta\sigma_T \left(1 - \frac{R^*}{R}\right) \tag{40}$$

where R is the radius or the hillock. With $R \gg R^*$ the hillock radius grows with time [107] as

$$R^2 = R_0^2 + \frac{2D_s \cdot \Delta\sigma_T \Omega^2 N_0}{k_B T \lambda} t \tag{41}$$

Here R_0 is the initial radius of the hillock and λ is a characteristic distance (on the order of the average distance between the hillocks), which determines the gradient μ in (31) ($\nabla\mu \approx \Delta\mu/\lambda$). Growth of a hillock due to mass transfer towards it leads to the thinning of the film around it, nucleation of voids, and decay of the film. Experimental studies [107] have confirmed the kinetic law [41]. It was shown that the surface diffusion coefficients and activation energies, obtained on hillock growth, were in good agreement with other experimental data [117].

Development of GB Grooves occurs because the equilibrium at the intersection of the GB with the surface is reached when the tangent angle β is defined by the obvious formula

$$\sin\beta = \gamma_b/2\gamma_s \tag{42}$$

A curvature formed near the intersection induces a surface current from the GB top to the free surface, and the depth of GB groove d grows with time, so that [126]

$$d = 0.973 \, m(Bt)^{1/4} \tag{43}$$

where $m = \tan\beta$ and B is defined by (34). As it follows from eq. (43), the top of GB groove reaches the substrate (Fig. 5) during the time

$$\tau = h^4/0.896 \, m^4 B \tag{44}$$

where h is the film thickness. For metal films at high temperatures ($T \approx 500$ K), with $D_s \approx 10^{-11}$ m^2/s [117], $\gamma \approx 1.5$ J/m^2, $\Omega \approx 10^{-29}$ m^3, $n_0 \approx 10^{19}$ m^{-2}, $B \approx 2.2 \cdot 10^{-29}$ m^4/s (as it follows from (34), and setting into (44) $m \approx 10^{-1}$ and $h = 10$ nm one can obtain $\tau = 5$ s, whereas with $h = 100$ nm $\tau = 5 \cdot 10^4$ s. It is worth noting that the groove's tip can reach the substrate only if the grain radius R exceeds the value of $3h \sin^3 \beta/(2 - 3\cos\beta + \cos^3 \beta)$ [138]. In the opposite case, when the width of GB groove becomes close to $2R$, an equilibrium configuration in the shape of spherical caps on the surface of each grain will be formed, preventing the subsequent development of GB grooves.

Void Growth. Voids that are formed in the film due to its thinning around hillocks or developing of GB grooves will grow if their radius r exceeds the film thickness h. The kinetics of growth was calculated both analytically [137, 139] and numerically for various wetting angles of the film on a substrate [140–142]. The kinetic law of the void radius growth was obtained analytically [139]

$$r \approx 1.81 \frac{(Bt)^{2/5}}{h^{3/5}} \tag{45}$$
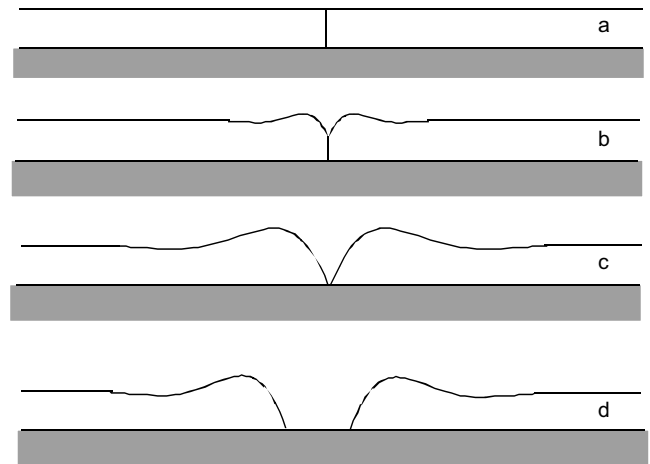
Figure 5. Scheme of development of GB grooves in thin film: (a) GB without a groove in the film surface; (b, c) successive stages of groove development; (c) the GB reaches the substrate; (d) subsequent growth of the hole.

and also confirmed by numerical calculations [142]. As seen from eq. 45, the measurements of the void growth during the decay of a thin continuous film also allow for the extraction of the SD coefficient D_s.

It follows from the above that the kinetics of SD mass transfer on nonsingular surfaces of NMs can be easily estimated and predicted if the SD coefficients D_s are known from independent measurements. One of the independent methods could be the method of "tracer" diffusion. It is worth noting, however, that the tracer method is very sensitive to the atomic structure of surfaces, even if they are nonsingular. The diffusion concentration distribution of tracer atoms depends strongly on imperfections in the periodic energetic relief, which can be considered as surface traps, that is, local sinks for the spreading atoms. The sinks should be taken into account for accurate calculations of D_s [117].

5.2. Diffusion Mass Transfer on Atomically Flat Surfaces

In contrast with atomically rough surfaces (where each point on the surface could be displaced along its normal due to mass divergence, leaving the surface structure homogeneous), the shape evolution of vicinal surfaces occurs due to lateral motion of atomic steps driven by gradients of the chemical potential along the surface. The gradients are determined both by the shape of the surface profile and the pressure of the vapor phase surrounding the crystal. Motion of steps, therefore, plays a key role in the mass transport on vicinal surfaces.

5.2.1. Dynamics of Steps

The lowest energy configuration of a step is usually straight, along a close-packed surface direction. At high temperatures, the steps deviate from the straight configuration due to the formation of kinks. At lower temperatures, the atoms adsorbed at steps have not enough thermal energy to detach from the steps and a fluctuation of the step positions occurs due to the random motion of kinks along the steps. These fluctuations have been studied experimentally, using STM, on vicinal surfaces Cu (001) [143] and (1 1 19) [144], Pb (111) [145], Pt (111) [146], and Ag (115) [147]. A tunneling tip repeatedly scanned the same line oriented perpendicularly to the step and the step position x was displayed as a function of time. A step correlation function

$$F(t) = \langle [x(t) - x(t_0)]^2 \rangle \tag{46}$$

was calculated from these data. It was shown that the experimental dependence $F(t)$ could satisfy the power law

$$F(t) = c_1(T) \, t^{1/4} \tag{47}$$

which was theoretically obtained [148] under the assumption that mass transport occurs only alongside the step. The temperature dependent factor $c_1(T)$ was determined for various temperatures and plotted in an Arrhenius graph. The activation energies for the emission of an adatom from a kink (onto the step edge) were estimated from these experiments.

Higher temperatures allow exchanges between the atoms adsorbed on the surface (adatoms) and the steps. In this case, the step correlation function calculated from the experimental measurements of step fluctuations on Au (110) [145, 149], made with a high-speed STM satisfied another power law

$$F(t) = c_2(T) n_k^{-1} \, t^{1/2} \tag{48}$$

Here $c_2(T)$ is a temperature-dependent constant, and n_k is the average number of lattice sites between the kinks on the step.

Surface diffusion of different adsorbing species can now be directly observed and studied on atomically flat surfaces with atomic resolution microscopy, such as STM and field ion microscopy (FIM). These experiments have determined the "tracer" diffusion coefficients D_a. In recent years, self-diffusion and hetero-diffusion have both been studied on various crystal surfaces and several surface diffusion mechanisms have been identified. In most cases, SD occurs due to adatom hops in directions determined by the crystal lattice. It was detected, however, that the diffusion process may sometimes involve an adatom-substrate exchange mechanism [150, 151] and atom tunneling [152, 153] when the mass of diffusing atoms is small and their interaction with the substrate is weak.

The adatom diffusion coefficient is defined as

$$D_a = \frac{1}{2d} \frac{\langle r^2 \rangle}{t} \tag{49}$$

where $\langle r^2 \rangle$ is the mean-square adatom displacement during time t, and d is the dimensional factor: $d = 1$ for linear (1D) diffusion and $d = 2$ for two-dimensional (2D) diffusion.

From the temperature dependence of D_a

$$D_a = D_{a0} \exp(-Q_m/k_B T) \tag{50}$$

one can determine the activation barrier (adatom migration energy) Q_m and the pre-exponent factor

$$D_{a0} \approx \frac{\nu_0 l^2}{2d} \tag{51}$$

Here ν_0 is the adatom oscillation frequency, l^2 is the mean square of the jump length. It is worth noting that at high temperatures, the dissipation of the extra thermal energy of the diffusing atoms may not be quick enough, which can cause adatoms to move beyond the nearest neighbor site, that is, l can exceed the interatomic space. In this case some deviation from the linear Arrhenius behavior is expected [154].

During surface self-diffusion, adatoms can attach to atomic steps, and atoms adsorbed at steps can leave them, passing to the adsorbed state on the surface. When the crystal is in a thermodynamic equilibrium with the surrounding vapor phase, this results in equilibrium fluctuations of step positions, that is, the step coordinate x becomes a function of time t. If the crystal is brought out of equilibrium, the fluctuating step moves with the drift velocity proportional to the difference $\Delta\mu$ in the chemical potentials of the crystal and the vapor.

A theoretical analysis of the step dynamics during crystal growth from the vapor phase [117, 121, 122] shows that the

velocity of a straight solitary step in the general case can be written in the form

$$v_0 = \frac{2D_s\beta_s}{2D_s + \beta_s\lambda_s}\frac{\Delta\mu}{k_BT} \qquad (52)$$

that is, v_0 is a function of the three main parameters $D_s = D_a\xi_0$, $\beta_s = \beta_a\xi_0$, $\lambda_s = (D_a\tau)^{1/2}$ and the supersaturation in the vapor phase $\sigma = \Delta\mu/k_BT$. Here, ξ_0 is the adatom equilibrium concentration on the surface, β_a is the kinetic coefficient of steps, and τ is the average adatom lifetime on the surface. The coefficient D_s has the physical meaning of a surface diffusion coefficient, which determines the kinetics of mass transfer. The factor of two in (52) appeared due to the appearance of adatoms both from the lower and upper terraces.

There are two main regimes of step motion: the diffusion regime (when the step velocity is determined by the adatom diffusion towards the step) and the kinetic regime (when the velocity is limited by the attachment-detachment kinetics). If $D_s \ll \beta_s\lambda_s$, the step follows the diffusion regime, as (52) implies,

$$v_0 = 2\frac{D_s}{k_BT}\frac{\Delta\mu}{\lambda_s} \qquad (53)$$

The ratio $\Delta\mu/\lambda_s$ determines the gradient of the adatom chemical potential in the growth process and can be considered to be the thermodynamic driving force of step motion. The diffusion mobility of steps

$$\Gamma = 2D_s/k_BT \qquad (54)$$

is determined by the SD coefficient D_s (in contrast to the adatom diffusion coefficient D_a). With $D_s \gg \beta_s\lambda_s$, the step motion is limited by the kinetics of adatom attachment-detachment (the kinetic regime) and

$$v_0 = \frac{\beta_s}{k_BT}\Delta\mu \qquad (55)$$

On a macroscopically plane vicinal surface steps are located at some distance l from one another forming a step train. If $l < \lambda_s$, the step velocity in the train under some supersaturation $\Delta\mu/k_BT$ becomes smaller compared to a solitary step because the number of adatoms absorbed by the step is limited by the distance l, whereas for the solitary step this distance is λ_s both for the upper and lower terraces. In the mixed diffusional-kinetic regime the step velocity in the step train was calculated as [117, 155]

$$v = \frac{2D_s\beta_s\tanh\frac{l}{2\lambda_s}}{2D_s\tanh\frac{l}{2\lambda_s} + \beta_s\lambda_s}\frac{\Delta\mu}{k_BT} \qquad (56)$$

As it follows from (56), if $2D_s\tanh(l/2\lambda_s) \ll \beta_s\lambda_s$, the steps in the step train move following the diffusion regime and their velocity is

$$v = \frac{2D_s}{\lambda_s}\frac{\Delta\mu}{k_BT}\tanh\frac{l}{2\lambda_s} = v_0\tanh\frac{l}{2\lambda_s} \qquad (57)$$

With the opposite sign of the inequality, steps move following the kinetic regime and their velocity is determined by (55).

The first experimental studies of elementary step motion were made on a surface of alkali halide crystals, using the method of vacuum decoration [156], which allowed the detection of monatomic steps and observation of crystal growth and evaporation on an atomic scale [157, 158]. The velocity of elementary steps was measured by studying the development of spirals of growth or evaporation around screw dislocations. Analyzing the distances between the coils in the spiral, one could determine λ_s and using the values v measured under given supersaturation $\Delta\mu/k_BT$, calculate coefficients D_s from (57) [159].

Recent experiments on step dynamics were performed with nanoscale using STM [160–163] and FIM [164–166], which allowed observation of step motion in real time. The experiments were carried out at relatively low temperatures where it was possible to neglect evaporation, so that the variation of adatom chemical potential $\Delta\mu$ and the corresponding surface fluxes were determined from the local step geometry.

In the experiments on step dynamics on the Si(111) surface, the decomposition rates of isolated silicon hillocks and the fill-up rates of craters (height or depth $a = 3.14$ Å) were measured [167] at various temperatures. It was shown that the number of atoms constituting 2D hillocks decreased linearly with time; the same kinetic law was observed for the filling-up of 2D craters. This result directly follows from (55), which describes the attachment-detachment kinetic regime. Indeed, substituting into (55) $\Delta\mu = \alpha\Omega/aR$, $v = dR/dt$, and $N = \pi aR^2/\Omega$, one can obtain after integration

$$N(t) = N_0 - \frac{2\pi\beta_s\alpha}{k_BT}t \qquad (58)$$

in agreement with experimental observations. The same kinetic law is expected for the filling rate of 2D craters. However, it was observed [167] that the filling rate of craters (vacancy islands) was smaller than the decay rate of hillocks (adatom islands) of the same size. The filling of vacancy islands occurs due to the diffusion current directed from the plane surface towards the crater restricted by a descending step. To attach the step, the adatom should first overcome the Ehrlich–Schwoebel barrier [168–171], that is, the energy barrier near the edge of the descending step, which is higher than the barrier for adatom migration on the terrace. This barrier hinders adatom jumps from the upper terrace to the lower one. In contrast, the decay of 2D hillocks occurs due to an adatom diffusion current directed towards the plane surface from the island restricted by a descending circular step. Since in this process, adatoms do not overcome the Ehrlich–Schwoebel barrier, the activation energy is smaller than in the previous case. The difference in the activation energies allowed the measuring of the Ehrlich–Schwoebel barrier.

Similar experiments were performed with two concentric monoatomic circular steps, prepared on the Ag (111) surface [163], so that the external step was formed by a vacancy island, whereas the internal one—by either an adatom or a vacancy island. By observation of dissolution of internal adatom islands or filling of the internal vacancy island (which was formed under the attachment-detachment kinetic regime), it was possible to determine the activation energy for atom detachment, the line tension of steps α, and the Ehrlich–Schwoebel barrier.

5.2.2. Flattening of Corrugated Vicinal Surfaces

A connection can be made between the macro description of surface evolution and an atomistic description by considering steps on a vicinal surface where the steps (of one sign) alternate with terraces corresponding to a neighboring facet orientation [172, 173]. In the unperturbed surface, the steps are, on the average, uniformly spaced and straight. The corrugations are assumed to be a sinusoid of sufficiently small amplitude so that all steps remain of one sign. The relaxation of the surface may then be described in terms of the reconfiguration of steps to become (on the average) straight and uniformly spaced. Neglecting atom exchange between the surface and surrounding vapor phase, SD is driven by the energetics of step configurations and takes place by the exchange of material along and between steps. This provides an atomic-scale interpretation of the dependence of the chemical potential on surface curvature and of the surface diffusion transport that results.

As it has been shown [173–176], the driving forces and the kinetics of flattening are completely different for surfaces corrugated parallel and perpendicular to the steps. When the surface is corrugated parallel to the step direction (the wave vector of the sinusoidal perturbation is normal to the steps), they remain straight on the average but vary in their spacing. The flattening of the surface profile, as seen from the geometrical scheme (Fig. 6a), occurs by the evolution of the variable step density $\rho(x, t)$ to the constant value ρ_0.

It may be shown [172, 173] that in this case the interaction free energy between steps, f_i (see (29)), corresponding to a mutual repulsion between steps, provides the driving force for step motion. The smoothing of sinusoidal profile

$$z(x, 0) = z_0 \sin q_x x$$

is given by

$$z(x, t) = z(x, 0) \cdot \exp(-B_n q_x^4 t) \qquad (59)$$

(a)

(b)
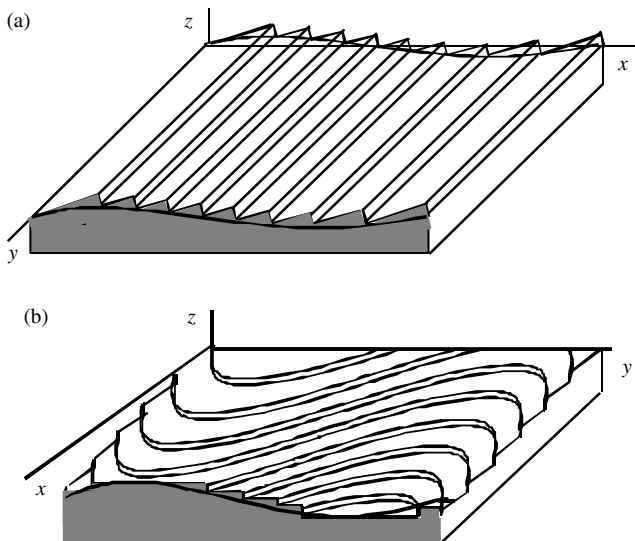
Figure 6. Surface profiles on a vicinal surface. (a) The surface is modulated normal to the steps: the step density varies; (b) modulation is parallel to the unperturbed step direction: the step profile varies.

with

$$B_n = \frac{6 D_n \Omega^2 \varepsilon \cdot n_0 \sin \theta}{k_B T \cos^4 \theta} \qquad (60)$$

where $\varepsilon = f_i / a^3$ is the free energy of step interaction per unit surface, D_n is the SD coefficient normal to the steps; of the processes discussed, only diffusion across the terraces can enter into D_n. Note that the step free energy α does not enter into B_n, since the steps do not change their average length as the perturbation decays.

If the surface corrugations are perpendicular to the step direction, that is, the wave vector of the sinusoidal perturbation is parallel to the (unperturbed) steps, they each acquire a sinusoidal shape (Fig. 6b). The relaxation of the surface is now achieved by the steps becoming both straight and uniformly spaced. Hence, the decaying sinusoidal profile is described by (59) with q_x replaced by q_y and B_n replaced by [173, 176]

$$B_p = \frac{D_p \cdot (\alpha/a + 3\varepsilon \tan^2 \theta) \cdot \Omega^2 n_0}{\sin \theta \cdot k_B T} \qquad (61)$$

in which both α and ε appear; D_p is the diffusion coefficient parallel to the unperturbed steps, and hence comprises both diffusion along the terraces and along the step edges. The factor $\sin \theta$ in the denominator of (61) reflects the increasing amplitude and curvature of the steps for the given amplitude of the surface sinusoid as the step spacing $l = a/\tan \theta$ increases. Note, however, that the condition $q_y a/\tan \theta \ll 1$ must continue to hold for the continuum treatment to be valid.

If the modulation wave vector makes an angle φ with the step direction, the decay constant B of profile smoothing can be written as [173]

$$B(\varphi) = \frac{D_s(\varphi) \cdot E(\varphi) \Omega^2 n_0}{k_B T} \qquad (62)$$

where $D_s(\varphi)$ and $E(\varphi)$ are φ-dependent SD coefficient and energy factor, respectively. They are given by

$$D_s(\varphi) = D_p \cos^2 \varphi + D_n \sin^2 \varphi \qquad (63)$$

$$E(\varphi) \approx \frac{\alpha}{a \sin \theta} \cos^2 \varphi + \frac{6\varepsilon \sin \theta}{\cos^4 \theta} \sin^2 \varphi \qquad (64)$$

Since the step interaction energy ε is smaller than the step energy α [177] and the diffusion parallel to steps is faster than normal to steps [164, 178, 179], the decay rate of such profiles is expected to be much faster when the modulation is parallel to the steps. As seen from the ratio (see (60) and (61))

$$\frac{B_p}{B_n} \approx \frac{D_p \alpha}{D_n a \varepsilon} \frac{1}{6 \tan^2 \theta} \qquad (65)$$

smaller miscuts lead to much greater anisotropy of the smoothing rates.

Experimental studies of smoothing rate anisotropy were carried out with vicinal Au surfaces, which were patterned with periodic line gratings parallel and perpendicular to steps [180, 181]. The ratio $B_p/B_n = 25$, which was found

by measuring the decay rates for two perpendicular gratings, was almost equal to the factor $1/\tan^2\theta$, in qualitative agreement with (65) and the old results [182] obtained by smoothing of scratches prepared at various angles φ with the step direction.

The analysis presented for diffusion-controlled flattening of corrugated vicinal surface may be extended [173] to include attachment-detachment kinetics, and evaporation-condensation as the transport mechanism [183, 184].

The kinetics of smoothing differs from the preceding one when average orientation of a bidirectionally modulated surface (checkerboard of hills and valleys) is equal to that of a close packed facet. In this case, development requires the facets to move in a normal direction. In the assumption of an SD mechanism of mass transfer and small slopes it was shown [185] that the height (depth) of the hills (valleys) is a linear function of time

$$z(t) \approx z_0 - \frac{D_s \alpha \Omega}{k_B T \lambda^3} t \qquad (66)$$

with a lifetime proportional to λ^3, where z_0 is the initial amplitude of the profile, and λ is the wavelength. This contrasts with the exponential decay and a lifetime proportional to λ^4 predicted by the continuum theory above T_R (see (36)). Decay of bidirectional sinusoidal profiles mediated by SD was also calculated for various λ using a Monte Carlo simulation on the base of a solid-on-solid model with the square lattice [186]. It was shown that for long wavelengths ($\lambda/z_0 > 15$), the decay can be described approximately by eq. 61; however, for shorter wavelengths ($\lambda/z_0 < 5$) the wavelength scaling exponent $n \approx 5$ gives a better fit than $n = 3$.

Similar models predicted exponential time dependence $R \propto t^\sigma$ of the radius R of the top layer of a hillock, with $\sigma = 1/4$ for a conical hillock shape both for the diffusion and kinetic regimes [187, 188], and for a parabolic hillock shape $\sigma = 1/5$ or $1/6$ for the diffusion and kinetic regimes, respectively [189, 190].

Experimental work in this direction to date has treated structures with just a small number of layers [163, 191]. For example, thermal relaxation of biperiodic μm-scale surface modulations on Si(100) and related their decay process were studied [192] using low energy electron microscopy (LEEM) [193]. The surface consisted of a biperiodic array of hills and valleys, each consisting of concentric arrays of islands and holes. The surface relaxed towards its equilibrium flat, step-free state by the islands on top of the hills shrinking and disappearing, and by the holes of the valleys filling in. It was found that the adatom attachment-detachment rate limited the kinetics of step motion.

Decay of island mounds consisting of a stack of a dozen such layers was studied on the reconstructed Si(111) surface [194]. The exponent associated with the (3D) decay of the mound height was found to be 1/4, in agreement with the predicted value for a conical hillock shape. The activation energy of the decay rate was indicated as the energy of step motion in the attachment-detachment kinetic regime.

In the case of a dimensionally modulated surface of period λ with facets at the tops and bottoms and unstable neighboring orientations, each side wall is comprised of a bundle of steps that meet the top and bottom facets at a finite angle. Alternate walls are composed of steps of opposite sign. A fluctuation is required to separate a loop of the outer steps from the bundle; the loops may then cross the facet and annihilate. The rate of decay of the modulation decreases exponentially [195] with λ, since the loop formation resembles nucleation kinetics. Again, this contrasts with the λ^4 dependence of the lifetime by surface diffusion above T_R.

If a surface is modulated randomly (statistically homogeneous surface), a coarsening of the surface structure can occur, that is, an increase in the separation of the characteristic surface features of the structure. It occurs both during growth or erosion and during volume-preserving relaxation of macroscopic surface roughness.

The coarsening of surface structures on atomically rough (nonsingular) surfaces is a trivial consequence of capillary flattening [125], which occurs mainly by the surface diffusion mechanism. A more complicated consideration is necessary to explain the coarsening on atomically flat surfaces, which contain mounds and pits consisting of concentric round or faceted steps [196]. Such surface morphology is observed on initially smooth surfaces, which became rough during homoepitaxial growth or ion erosion. In this case, the phenomenological theory [197–199] also assumes the coarsening to rely on a surface diffusion current driven by curvature-dependent differences of the surface chemical potential; however, the diffusion current may be limited by detachment of atoms from steps, their migration over terraces, and subsequent reattachment [200, 201]. At low enough temperatures, the motion of atoms along step edges without the need to lose contact with the step may also be important [202–204].

6. DIFFUSION PROCESSES IN ISLAND FILMS

An island film (IF) is a specific nanoscale object representing a system of islands of one substance located on the surface of another. Island Films attract the interest and attention of many research groups because the knowledge of their properties is needed for the understanding of the physics of formation of continuous films from the vapor phase, when an IF is just a stage in reaching the final goal. Experiments on IFs are also a source of important and sometimes unique information on the physics of surface phenomena, particularly on the SD coefficients and on the nature of the interaction between atoms migrating on crystal surfaces and elements of the real crystal structure, such as steps, kinks, and charged point defects. Moreover, IFs often provide convenient and easily visualized models of processes occurring in heterogeneous bulk NMs.

From the thermodynamic point-of-view, an IF is a system that is far from equilibrium in respect to many parameters at the same time. One of the principal signs of the lack of equilibrium in IFs is the presence of very highly developed free and interphase surfaces, with which an excess energy is associated. At elevated temperatures, when the necessary diffusion mechanisms are active, certain mass diffusive transfer processes occur in IFs, which tend to release the excess energy.

There are several ways of diffusion evolution of an IF: diffusive atomic transfer of matter from one island to another (Ostwald ripening [205]), diffusion motion of islands on the substrate accompanied by their collision and merging, ordering and disordering of islands in ensembles, and transformation of the shape of the islands. All these processes occur under real conditions and will be discussed later.

6.1. Diffusion Coalescence of Islands

Diffusion coalescence in an ensemble of dispersed particles, or Ostwald ripening is a process of diffusion redistribution of atoms between the particles, in which the particles, whose radius R is smaller than the average radius $\overline{R}$, in the ensemble are dissolved, whereas the particles with $R > \overline{R}$ grow larger. As a result, the average particle radius in the ensemble grows with time. The kinetics of this process can be calculated using the basic idea that the radius of a given island changes with time as a result of its diffusive interaction not with its nearest neighbors but with a generalized diffusion field [206–208]. In the case of IF, this means the generalized field of adatoms [209, 210].

The generalized diffusion field can be described by the adatom concentration $\bar{\xi}$, which depends on the island size distribution function $f(R, t)$ and which is in equilibrium with the islands of a critical size R^*. As it was shown, the critical radius R^* almost coincides with the average radius $\overline{R}$, so that the islands of radii $R < R^*$ dissolve in the diffusion field because the equilibrium concentration near them is $\xi_R > \bar{\xi}$, whereas the islands with $R > R^*$ grow because they are characterized by $\xi_R < \bar{\xi}$.

The problem of the kinetics of diffusive coalescence of a system of islands can be reduced to the solution of the equation of continuity in the space of island sizes for the function $f(R, t)$:

$$\frac{\partial f(R, t)}{\partial t} + \frac{\partial}{\partial R}\left[f(R, t)\frac{dR}{dt} \right] = 0 \qquad (67)$$

with the condition of mass conservation in the ensemble of islands:

$$Q = \kappa \int_0^\infty f(R, T)R^3\, dR + Q_0 \qquad (68)$$

for 3D islands and

$$Q = \pi a \int_0^\infty f(R, T)R^2\, dR + Q_0 \qquad (69)$$

for 2D islands. Here, κ is a dimensionless factor, which represents the island geometry, Q_0 is the total amount of island material present as two-dimensional gas of adatoms and in the vapor phase in contact with the IF (on the assumption that the system is closed).

Various mechanisms of 2D diffusive coalescence have been considered [211]; the main one for nanoscale objects is the mechanism of adatom SD. The same three parameters, λ_s, D_s, and β_s determine the kinetic laws of coalescence. The kinetic coefficient β_s describes the rate of adatom attachment (detachment) to the island perimeter both for 2D and 3D islands.

For nanoscale objects ($\overline{R} \ll \lambda_s$), it appears worthwhile to consider the kinetic laws for the following cases.

1. $D_s \ll \beta_s\overline{R}$ (diffusion-controlled regime). The average radius of 3D islands grows in this case as

$$\overline{R}^4 = \overline{R}_0^4 + \frac{\psi(\vartheta)}{\ln(\lambda_s/\overline{R}_1)}\frac{D_s\gamma\Omega^2 n_0}{k_B T}t \qquad (70)$$

where $\psi(\vartheta) = 2/(2 - 3\cos\vartheta + \cos^3\vartheta)$; ϑ is the contact angle of wetting, R_1 is the radius of island at its base, γ and Ω are the surface tension and the atomic volume of island material, respectively. For 2D islands, the formula is

$$\overline{R}^3 = \overline{R}_0^3 + \frac{D_s\alpha\Omega^2 n_0}{a^2 k_B T}t \qquad (71)$$

where a is the height of 2D island and α is the linear tension of the island perimeter.

If $D_s \gg \beta_s\overline{R}$ (attachment-detachment controlled regime), the average radius of 3D islands grows as

$$\overline{R}^3 = \overline{R}_0^3 + \frac{\psi_1(\vartheta)\beta_s\gamma\Omega^2 n_0}{k_B T}t \qquad (72)$$

and for 2D islands

$$\overline{R}^2 = \overline{R}_0^2 + \frac{\beta_s\alpha\Omega}{a k_B T}t \qquad (73)$$

The expressions (70)–(73) describing the dependence $\overline{R}(t)$ can be used to find the time dependencies of the two-dimensional density of islands $N_s(t)$ for each of the above cases. Since the amount of matter contained in the islands is much greater than that presented on the surface in the form of isolated adatoms, one can simplify (68) and (69) by dropping Q_0 and rewriting Q for 3D islands as $Q \approx \kappa N_s(0)\overline{R}_0^3 \approx \kappa N_s(t)\overline{R}^3(t)$, which gives

$$N_s(t) = N_s(0)\frac{\overline{R}_0^3}{\overline{R}^3(t)} \qquad (74)$$

or, for 2D islands,

$$N_s(t) = N_s(0)\frac{\overline{R}_0^2}{\overline{R}^2(t)} \qquad (75)$$

It follows from the calculations that the asymptotic island-size distribution functions are in each case independent of the initial distribution and have the form

$$f_n(R, t) = \frac{N_s(t)}{\overline{R}(t)}P_n(u),\ u = \frac{R}{\overline{R}} \qquad (76)$$

The functions $P_n(u)$ are found to be the same for a given power exponent $n(n = 2, 3,\ \text{or}\ 4)$ governing the law $\overline{R}(t)$, and they depend only on the dimensionless ratio $u = R/\overline{R}$.

Equations (70–75) can be used for determination of the kinetic coefficients controlling the coalescence process, from the known law $\overline{R}(t)$ and the shape of the asymptotic function representing the size distribution of islands.

Coalescence in metal IFs with an effective thickness between 0.1 and 100 nm has been observed experimentally on various substrates [212–217]. Typical microphotographs showing successive stages of coalescence are shown in Figure 7.

The main difficulties in the interpretation of the experimental results arise in the determination of the mechanism and rate-limiting stage of the process. They can vary with temperature, island size, and shape. For nano-islands, different rate-limiting regimes give different laws $\overline{R}(t)$ (compare (70) and (72) or (71) and (73)) and different island-size distributions, so one can determine the rate-limiting stage and the appropriate kinetic coefficients [218].

In recent years, evolution of 2D IFs was intensively studied on the atomic level using STM [219–226], which allows direct determination of the mechanism of coarsening after successive stages of film deposition. With the agent of STM studies of epitaxial growth, it has become clear that mass transport in IFs also occurs by the movement of whole islands even when the sizes become very large. While
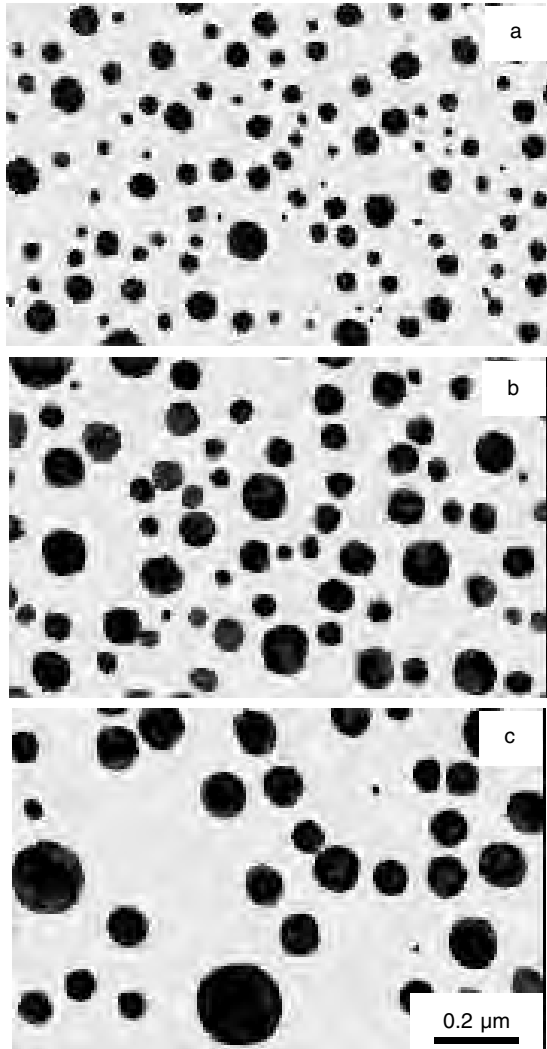
Ostwald ripening may occur when islands are far apart, the dominant mechanism for coarsening, at least at low temperatures, can be diffusion of whole islands with random collisions and merging [224, 225].

6.2. Diffusion Motion of Nanoclusters

6.2.1. Brownian Cluster Mobility

By analogy with random motion of solitary adatoms, nanoclusters and even large islands (containing 10^2–10^3 atoms) may migrate as a whole on the surface of a crystal exhibiting Brownian motion [219–223]. The Brownian diffusion coefficient of the cluster, D_B, depends on the cluster geometry (2D or 3D cluster), the number of atoms in the cluster, lattice mismatch to the substrate, and the main diffusion mechanism resulting in the motion. The cluster mobility $b = D_B/k_BT$ determines the cluster velocity v under the action of force F applied to the cluster:

$$v = \frac{D_B}{k_B T} F \qquad (77)$$

The main mechanisms for epitaxially oriented clusters are periphery diffusion (*i.e.*, linear diffusion along the cluster perimeter), diffusion over the cluster surface (or terrace in the case of 2D clusters), and SD on the substrate (due to 2D evaporation and condensation). Heteroepitaxial islands, which are not commensurate with the substrate or have misfit dislocations at the cluster-substrate interface, can also glide over the surface, limiting cluster mobility due to friction at the interface limits [227–229].

For the diffusion mechanisms of motion, the Brownian diffusion coefficient of 2D clusters can be presented in the form [230]

$$D_B = D_{B0} R^{-\alpha} \qquad (78)$$

so that for periphery diffusion (PD)

$$D_{B0}^{PD} = D_{st} N_{st} s^2 / \pi; \ \alpha = 3 \qquad (79)$$

for terrace diffusion (TD)

$$D_{B0}^{TD} = 2D_s s / \pi; \ \alpha = 2 \qquad (80)$$

and for 2D evaporation-condensation (EC)

$$D_{B0}^{EC} = \Gamma / \pi; \ \alpha = 1 \qquad (81)$$

Here D_{st} is the (tracer) diffusion coefficient of single atom diffusing along the step edge, N_{st} is the number of atoms per unit length along the step edge, s is the area of the surface unit cell, $D_s = D_a \xi_a$, ξ_a is the adatom concentration on the surface of the island, Γ is the step mobility proportional to the rate of random attachments (detachments) of adatoms at the edge of the cluster boundary [231, 232]. It is important to note that (79–81) predicting the integer exponents were obtained under highly simplified assumptions and are therefore only valid for some limited cases. In fact, noninteger behavior of the size-dependent scaling exponent α have been observed in several Monte Carlo simulations [233–235] and detailed theoretical treatments [236, 237].

Figure 7. Successive stages of the diffusion coalescence in Au IF on NaCl (100). $T = 410$ °C; (a)-$t = 0$, (b)-20 min, 3-60 min.

0.2 μm

The dependence of diffusivity upon cluster size has been extensively studied [219, 221, 223, 38] in attempts to explore the atomic mechanisms by which large 2D clusters move over surfaces. Scanning tunneling microscopy studies of vacancy island diffusion on Ag (111) have shown $\alpha \approx 2$ corresponding to the TD mechanism [223]. For adatom islands on Ag (111), a very weak dependence ($\alpha \approx 1$) was found, and the EC mechanism was suggested to be dominant [219]. A combined study of island diffusion, island coalescence, and island decay was carried out for Ag on Ag (100) and Cu on Cu (100) [221] in the submonolayer coverage regime. The rather small island decay rate was detected showing that neither the TD nor EC mechanisms could be responsible for the observed island diffusion coefficient D_B. On the other hand, within the PD diffusion, the value of D_B yielded a peripheral (along the step) mass diffusion coefficient D_{st}, which for Cu was comparable to the value obtained from independent comprehensive step fluctuation measurements [144, 239]. Experimental evidence of nonintegral values of the scaling exponent was also found: $\alpha \approx 2.28$ for Ag and $\alpha \approx 2.49$ for Cu. These results indicate that the usual assumption of a structureless island periphery, which yields $\alpha = 3$, is inadequate. The diffusion coefficient of atoms moving along the periphery depends on the detailed structure of the island edges, giving rise to a range of α values. It is worth noting that direct observations of single clusters in the field ion microscope [240] have established that mobility and even the mechanism of motion of compact clusters consisting of 7 or 19 atoms essentially differs from that for noncompact clusters (consisting, e.g., of 18 atoms). The noncompact clusters, whose peripheral step contains kinks, can move by the PD mechanism which is forbidden for compact clusters in some temperature range.

Diffusion of large 3D clusters on a foreign substrate has been also observed experimentally [213, 214, 241–247], sometimes with unexpectedly high diffusion coefficients. The unusually high diffusivity [247] was explained by weak bonds between the cluster and the substrate and smoothing of potential barriers for cluster motion due to a big difference in atomic spacing for cluster (Sb) and substrate (carbon). Indeed, the results of a molecular dynamics simulation of 3D cluster diffusion motion made for nonepitaxial cluster-substrate configurations have shown [229] that large clusters can diffuse rapidly, as experimentally observed.

It can also happen that "random" migration of islands is not associated with thermal fluctuations but occurs under the action of a randomly varying (in magnitude and direction) external force resulting from electrostatic or elastic interaction between the islands [218]. Active interaction of islands with one another via elastic stress fields was demonstrated [248–250] by measuring the radial distribution function of the islands after annealing compared to that just after film deposition. Islands migrated under the influence of elastic forces and became distributed on the surface in a somewhat ordered manner, so that the characteristic maxima appeared in the radial distribution function.

Elastic interaction between the clusters is of importance for their self-organization in periodic arrays during thin film growth. Advanced crystal growth techniques, notably molecular beam epitaxy (MBE) and metal-organic vapor phase epitaxy (MOVPE), make it possible to fabricate new types of surface structures, with lateral dimensions of order of de Broglie wavelength of electrons (50 nm for GaAs). These structures, consisting of small semiconductor clusters (quantum dots) with specific energy dependence of the density of states, manifest unique electronic and optical properties. Millions of the quantum structures, density packed and uniform on the atomic scale, are needed to achieve the appropriate active volume for practical applications [251]. One method for making quantum dots is heteroepitaxial growth of lattice-mismatched systems, such as InGaAs on GaAs [252, 253], $Si_{1-x}Ge_x$ on Si [254–257], or PbSe on PbTe [258, 259]. Growth occurs in the Stranski–Krastanow mode [260], in which after the formation of a wetting layer, growth of 3D crystallites is thermodynamically required. The islands have a well-defined pyramidal shape with (105) facets for $Si_{1-x}Ge_x$ on Si (100) and (100) facets for PbSe on PbTe (111).

Surprisingly, narrow size dispersions of PbSe islands on PbTe were obtained under certain conditions of growth. One of the proposed mechanisms explaining this result is kinetic self-limitation of island growth caused by stress concentration at the island edges, which results in kinetic barriers for adatom attachment [261, 262]. This mechanism is confirmed by investigations of Ostwald ripening of self-assembled PbSe quantum dots during annealing [263]. With increased anneal duration, the dot density was found to decrease rapidly with a simultaneous increase of the average dot size. The kinetics of ripening was limited by interface reaction, that is, the limiting process was the kinetic barrier for adatom attachment to the islands and detachment from the island edges.

6.2.2. Surface Tension Driven Motion

A striking, completely unanticipated cooperative process has been observed in Sn IFs deposited on Cu (111) substrate [264]. Shortly after deposition of Sn on Cu (111), 2D Sn crystals containing several hundred thousand atoms move spontaneously along the surface at 290 K. As islands move, Sn atoms within the islands randomly exchange with Cu atoms in the surface. The exchanged Cu atoms are ejected from the Sn islands in the form of ordered 2D bronze crystals.

It is worth noting that Sn atoms are bigger than Cu atoms and they are incorporated into bulk copper with difficulty, and the room temperature solubility of Sn in Cu is low. However, Sn atoms can be incorporated relatively easy into the top atomic plane of the Cu (111) surface, where the mismatch is accommodated by out-of-plane displacements. It was found that Sn atoms in single crystal Cu segregate to (111) surfaces in the form of ordered surface alloy with one Sn atom for every two Cu atoms [265, 266].

The driving force of the Sn-island motion has been traced to strong repulsion between Sn atoms incorporated into the Cu. The islands thus lower the surface free energy by moving toward unalloyed regions of the surface, that is, the process can be called surface tension driven motion.

The island trajectories were not similar to the trajectories of clusters undergoing thermal Brownian motion discussed above for much smaller metal islands. In contrast with random jumps in arbitrary directions, it was observed that Sn islands exhibit a clear tendency to continue to move in the same direction. Estimates of the steady state velocity

made by substituting thermodynamic driving force F into (67) yield the following:

$$v(R) = [\pi \cdot b(R) \cdot \varepsilon \cdot \beta_{all}]^{1/2} R \qquad (82)$$

Here ε is the free energy cost of having a single Sn atom under the island, β_{all} is the alloying rate ($[\beta_{all}] = \mathrm{m}^{-2}\mathrm{s}^{-1}$), which was assumed to be constant. As the island velocities were observed approximately independent of the island radius R, the island mobility $b(R)$ was assumed to be proportional to R^{-2}, and taking into account (80), one can obtain

$$v = (D_s \cdot s \cdot \varepsilon \cdot \beta_{all}/k_B T)^{1/2} \qquad (83)$$

Estimates of island velocity made using (83) were found to be in good agreement with experimental observations [264].

6.3. Transformation of Island Shape

The general problem of the equilibrium shape of an island on a substrate (in the case of anisotropic surface tension) can be considered conveniently using the Wulff construction [267]. In contrast to free surfaces characterized by surface tension γ, the interface between an island and the substrate should be regarded as having a tension of γ_i-γ_s, where γ_i is the interface tension between the two phases and γ_s is the surface tension of the substrate material. This definition follows from variation of the free surface energy of the island-substrate system [268].

The problem of transformation of an arbitrary island shape to the equilibrium shape was considered in the isotropic approximation [218] for SD mass transfer mechanism. It was assumed that the surface fluxes may be limited not by the actual kinetics of SD of adatoms on the island surface but also by the rate of atom detachment from parts of the surface where the curvature K is greater than the average value $\overline{K}$, or by the attachment rate to those parts of the surface where the curvature is less than average. Estimates of the characteristic time of establishing an isomeric shape have been obtained: if $D_s \ll k_s a^2 \overline{R}^2$ (k_s is the kinetic coefficient normalized to a unit surface area of the island [269]; $[k_s] = \mathrm{m}^{-2}\mathrm{s}^{-1}$; a is the lattice parameter; $\overline{R} = 2/\overline{K}$), that is, the rate shape transformation is limited by the rate of self-diffusion over the island surface, then

$$\tau \approx \frac{k_B T \overline{R}^4}{D_s \gamma \Omega^2 n_0} \qquad (84)$$

If the rate of transformation is limited by the rate of adatom acquisition or emission ($D_s \gg k_s a^2 \overline{R}^2$), then

$$\tau \approx \frac{k_B T \overline{R}^2}{k_s \gamma \cdot \Omega^2} \qquad (85)$$

Islands are frequently disk-shaped with an angle of contact less than the equilibrium value [270, 271]. In this case, relaxation of the shape towards its equilibrium configuration results in a contraction of the island and reduction of the area of contact with the substrate. This process can occur due to nucleation of new layers on the surface of the disks, which are possible until the radius of the top terrace

becomes equal to the critical radius. The nucleation can be a limiting process of the island shape transformation after the film deposition.

In contrast to relaxation of disk-shaped islands, the volume preserving relaxation of a heteroepitaxial 3D island from a nonequilibrium spherical shape to an equilibrium faceted shape occurs due to the peeling of atomic layers off the facet [272]. Experiments were carried out with 1–1.5 μm Pb crystals on Ru (0001) substrate, which after melting and subsequent solidification had a spherical shape with small (111) facets. After the sample temperature dropped from 550 to 353 K, a reshaping of the Pb crystals occurred via layer-by-layer peeling. With the temperature decrease, the total surface energy was reduced by the increase in facet size, leading to a transfer of the material to the rounded regions of the crystal surface. The temporal evolution of the top layer radius r was analyzed [273] under the assumption that the flux of atoms occurs between two concentric steps, neglecting the redistribution of mass into the curved surface regions, and the following equation

$$\frac{dr}{dt} = -\frac{D_s \alpha \Omega^2}{a^2 r \, k_B T \ln(\rho/r)} \left(\frac{1}{r} - \frac{1}{\rho} \right) \qquad (86)$$

was obtained. Here ρ is the radius of the step bounding the top facet, D_s is the SD coefficient defined in (52). At the onset of peeling, the diffusion-limited model was found to be in agreement with the experimental observations. The rate of layer peeling slowed dramatically when the radius of the top step became close to that in the equilibrium shape.

Another effect of shape transformation has been observed [274, 275] in IFs of Co deposited on Cu and Ag substrates, which are characterized by much lower surface energy than the Co particles. The Co nanoparticles with diameters of 10 nm were generated by dc magnetron spattering in argon and transferred in the gas stream to an ultra-high vacuum TEM where they deposited on the thin-film Cu (100) or Ag (100) substrates at 300 and 600 K. At room temperature, all nanoparticles remained on the surface, whereas at 600 K the majority of them burrowed into the substrate. The burrowing was driven by extremely large capillary forces appearing due to the reduction in the total free energy by exchanging the Co-vacuum interface above the surface ($\gamma_{Co} \sim 2.8$ J/m^2) [276] with a Co-substrate interface ($\gamma_{Co-Ag} \sim 0.6$ J/m^2) [31], without increasing the substrate surface area. The main mechanism of burrowing is diffusion along Co-substrate interface.

Transformation of 2D island shapes to equilibrium for various metal systems has been discussed in [277].

6.4. Diffusion Spreading and Thickening of Reactive Layers

It is known that surface diffusion of A atoms over surface B can be accompanied by a surface reaction, so that a layer of the chemical compound $A_m B_n$ is formed on the surface [278, 279]. Such process can also occur in IF of matter A on a substrate B. When the boundaries of the layers formed around adjacent islands overlap, a continuous layer of the compound will cover the substrate.

The formation of a compound layer $A_m B_n$ first starts under the island, due to the volume diffusion of component A into substrate B. At the same time, a SD zone, with a decreasing concentration of component A, starts forming on the surface (for $r > R$), resulting in the spreading of the compound layer of decreasing thickness around each island (Fig. 8).

In the general case, the kinetics of spreading can be limited either by adatom diffusion over the forming layer or by the rate of adatom exchange between the island and the surface, as previously described. The kinetics of thickening in the general case can be controlled either by the bulk diffusion through the layer $A_m B_n$ itself, or by the reactions at the interface $A_m B_n$-B. At the early stages of the process, however, when the layer thickness h is small enough, the thickening kinetics is limited by the reaction rate at the interface $A_m B_n$-B. The compound forms on the surface around the island inside the ring $R < r < R_f$, so that the value $C(R_f) = C^*$ (Fig. 8c) corresponds to some minimal supersaturation, $\sigma_{\min}$, which is necessary for nucleation and growth of the compound. At $r > R_f$, when the surface concentration $C_S < C^*$ and the supersaturation $\sigma < \sigma_{\min}$, no compound will be nucleated. Consequently, the condition $\sigma = \sigma_{\min}$ dictates the radius R_f of the lateral spreading front. These assumptions are sufficient to obtain the kinetic laws of spreading. For SD controlled spreading

$$R_f^2 \ln \frac{R_f}{R_1} - \frac{1}{2}(R_f^2 - R^2) = \frac{2D_S \delta (C_R - C^*)}{h^*} t \qquad (87)$$

where D_S is the coefficient of diffusion of A atoms along the compound surface $A_m B_n$, δ is the thickness of the surface layer where diffusion with D_S takes place, and h^* is the thickness of the compound layer at the spreading front. Equation (87) allows the computation of the product $D_S \delta$ from the lateral spreading kinetics, that is, determination of the diffusion characteristics along the compound surface. For spreading, which is controlled by atom detachment from the island periphery, the lateral-spreading rate becomes constant and the product $\beta_s \delta$ can be determined from the formula
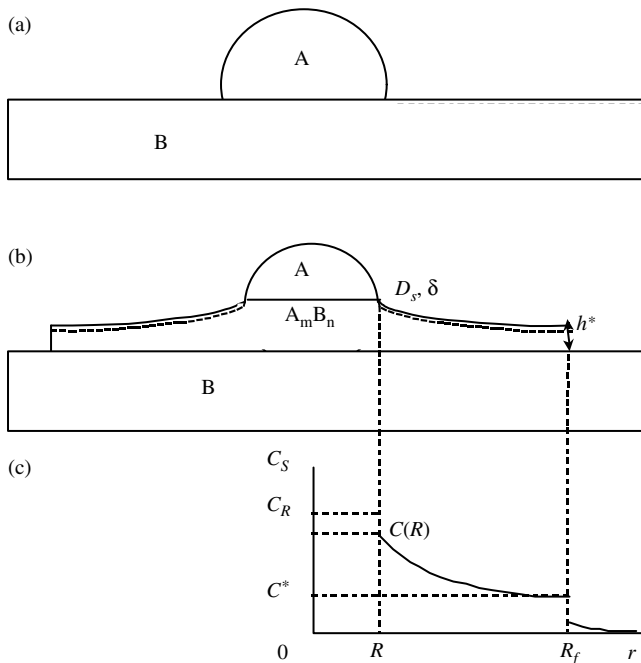
$$R_f = R + \frac{\beta_s \delta (C_R - C^*)}{h^*} t \qquad (88)$$

The kinetics of thickening of the compound layer forming between the islands on the substrate also depends on the kinetic regime of lateral spreading. The thickening rate is higher if spreading is diffusion-limited (in this case the thickness of the compound layer grows uniformly, with the same rate under and between the beads) than when it is detachment-limited.

7. SUMMARY

Two different problems of diffusion in NMs have been analyzed: GB diffusion in "bulk" NMs and SD mass transfer in nano-scale objects on singular and vicinal surfaces of single crystals.

The peculiarities of GB tracer diffusion and interdiffusion in NMs caused by the small size of their structural element and the nonequilibrium state of grain boundary structure, are analyzed in comparison with diffusion in coarse-grained polycrystals. The main features that characterize diffusion in nano-objects are the low activation enthalpies, high diffusivities, and enhanced GB solubilities of the diffusing impurity species, in comparison to the values of these parameters for the conventional GBs in coarse-grained polycrystals. These peculiarities are brought about by the nonequilibrium GB structures with enhanced free volumes in the core of GBs. The diffusion characteristics change in different temperature intervals and in the course of annealing time due to the relaxation of the nonequilibrium GB structure and grain growth, which modify the nanostructure making it closer to that of a regular polycrystal. As a result, the diffusion characteristics also change and become closer to those measured for conventional GBs in coarse-grained polycrystals.

During GB interdiffusion in binary NMs at relatively low temperatures, two partial diffusion fluxes appear along GBs in opposite directions. The GBs simultaneously act as short-circuit diffusion paths and sources (sinks) of excess vacancies, which appear due to the inequality of the partial GB diffusion coefficients. The unequal partial diffusion fluxes along GBs initiate the accompanying macroscopic effects, such as the Kirkendall and Frenkel GB effects, and the phenomenon of DIGM, which is one of the most effective mechanisms of low-temperature phase formation. The kinetics and mechanisms of the Kirkendall and Frenkel GB effects, as well as LTH caused by interdiffusion along migrating GBs, have been analyzed. Interdiffusion along GBs moving due to recrystallization at initial stages can be an even more effective mechanism of LTH than DIGM.

Low-temperature homogenization by migrating GBs is accompanied by diffusion-induced decay of layered nanostructures. Mechanisms of the decay and the stabilization of

Figure 8. Scheme of spreading compound layer. (a) Particle A is located on a substrate B; (b) the chemical compound $A_m B_n$ forms under the particle and in the surface diffusion zone; (c) surface concentration distribution.

the nanostructure by impurity inclusions acting as stoppers for migrating GBs have been discussed.

Surface diffusion mass transfer is examined both for atomically rough and atomically flat surfaces. The kinetics of flattening and coarsening of nanoscale surface structures, SD decay of needles and rods and decomposition of continuous films of nanometer thickness, are considered in continuous approximation. The driving forces and kinetic laws describing flattening of vicinal and modulated singular surfaces are critically analyzed. It is shown that surface diffusion mass transfer in nanoscale objects is mainly limited by the rate of atom attachment to steps or detachment from the steps.

Diffusion processes in nanoscale island films, such as diffusion coalescence (Ostwald ripening), kinetics and mechanisms of Brownian island mobility, surface tension driven island motion, shape transformation of islands, and reactive surface diffusion are thoroughly discussed.

GLOSSARY

Bulk nanostructural solids The polycrystals, which consist of nanometer-sized mis-oriented crystallites.

Diffusion characteristics The parameters, which figure in Arrhenius equation for diffusion coefficient: activation energy, activation volume, pre-exponential factor.

Free surface An interface between a crystal and its saturated vapor. The principal thermodynamic characteristic of free surface is a surface tension, which is the free energy per unit surface area. There are a variety of diffusion controlled processes driven by surface tension, such as flattening of corrugated surface, shape evolution of nanoscale needles and rods, decay of continuous thin films, coalescence in island film on substrate, island motion, sintering of powders, etc.

Grain boundary (GB) A two-dimensional defect, a boundary between two mis-oriented crystallites in polycrystal, having a thickness of order of $\delta \approx 5 \times 10^{-10}$ m. GB structure is characterized by lower atom density than adjacent grains and depends on grain misorientation. GB is a high diffusivity path compared to the bulk of adjacent grains.

Interface A boundary between two adjacent assembled crystallites of different chemical composition, atomic structure, and crystallographic orientation.

Interstitial heterodiffusion A migration of foreign atoms of smaller size, than constituent atoms of crystal, along crystal interstitial positions.

Nonequilibrium structure The structure which is far from equilibrium due to high density of lattice defects such as GBs, interfaces, dislocations, extra vacancies, enhanced free volumes at GBs, surface steps and corrugations.

Structural relaxation Modification of non-equilibrium atomic structure in the bulk of grains and inside GBs to lower a free energy and make nano-object closer to perfect crystal.

Substitutive heterodiffusion A migration of foreign solute atoms along lattice sites in solvent crystal with subsequent dilute substitutive alloy formation.

Tracer self-diffusion A spreading of tracer atoms from a diffusion source in a crystal, composed of atoms of the same sort.

REFERENCES

1. A. Tschöpe, R. Birringer, and H. Gleiter, *J. Appl. Phys.* 71, 5391 (1992).
2. H. Gleiter, *Nanostruct. Mater.* 6, 3 (1995).
3. H. Gleiter, *Acta Mater.* 48, 1 (2000).
4. H. Gleiter, *Nanostruct. Mater.* 1, 1 (1992).
5. Yu. R. Kolobov, R. Z. Valiev, G. P. Grabovetskaya, A. P. Zhilyaev, E. F. Dudarev, K. V. Ivanov, M. B. Ivanov, O. A. Kashin, and E. V. Naidenkin, "Grain Boundary Diffusion and Properties of Nano-Structured Materials," Nauka, 2001.
6. H. Gleiter, in "Mechanical Properties and Deformation Behavior of Materials Having Ultra-Fine Microstructures" (M. Nastasi and D. M. Parkin, Eds.) NATO Adv. Study Inst. Series E. Applied Science. Kluwer, Dordrecht, 1993, Vol. 223, p. 3.
7. U. Herr, J. Jing, U. Gonser, and H. Gleiter, *Solid St. Commun.* 76, 192 (1990).
8. C. Suryanarayana, *Inst. Metall. Rev.* 40, 41 (1995).
9. J. Weissmüller, in "Synthesis and Processing of Nanocrystalline Powder" (D. L. Bourell, Ed.), p. 3. The Minerals, Metals and Material Society, Warrendale, PA, 1996.
10. G. C. Hdjipanayis and R. W. Siegel, in "Nanophase Materials" (G. C. Hdjipanayis and R. W . Siegel, Eds.), Kluwer, Dordrecht, 1994.
11. R. W. Siegel, in "Encyclopedia of Applied Physics" (G. L. Trigg, Ed.), Vol. 11. VCH, Weinheim, 1994.
12. M. D. Baro, Yu. R. Kolobov, I. A. Ovid'ko, H.-E. Schaefer, B. B. Straumal, R. Z. Valiev, I. V. Alexandrov, M. B. Ivanov, K. Reimann, A. B. Reizis, and S. Surinach, *Rev. Adv. Mater. Sci.* 2, 1 (2001).
13. H. Gleiter, *Progr. Mater. Sci.* 33, 223 (1998).
14. C. Herring, in "Structure and Properties of Solid Surfaces" (R. Gomer and C. S. Smith, Eds.). University of Chicago Press, 1952.
15. W. W. Mullins, in "Metal Surfaces: Structure, Energetics and Kinetics" (N. A. Gjostein and W. D. Robertson Eds.). ASM, Metals Park, OH, 1963.
16. W. K. Burton and N. Cabrera, *Discuss. Faraday Soc.* 5, 33 (1949).
17. J. D. Weeks, in "Ordering in Strongly Fluctuating Condensed Matter Systems" (T. Riste, Ed.), p. 293. Plenum, New York, 1980.
18. H. Van Bueren and I. Nolden, in "Structures and Dynamics of Surfaces II" (W. Schommers and P. von Blanckenhagen, Eds.). Springer, Berlin, 1987.
19. A. Rettori and J. Villain, *J. Phys.* (France) 49, 257 (1988).
20. M. Ozdemir and A. Zangwill, *Phys. Rev. B* 42, 5013 (1990).
21. H. J. Höefler and R. S. Averback, *Scripta Metall. Mater.* 24, 2401 (1990).
22. G. W. Neiman and J. R. Weertman, in "Proc. M. E. Fine Symp." (P. K. Liaw, Ed.), p. 243. TMS, Warrendale, PA, 1991.
23. S. K. Ganapathi, D. M. Owen, and A. H. Chokshi, *Scripta Metall. Mater.* 25, 2699 (1991).
24. K. Boylan, D. Ostrander, U. Erb, G. Palumbo, and K. T. Aust, *Scripta. Metall. Mater.* 25, 2711 (1991).
25. T. R. Malow and C. C. Koch, *Acta Mater.* 45, 2177 (1997).
26. A. Kumpmann, B. Günter, and H.-D. Kunze, *Mater. Sci. Engng.* A168, 165 (1993).
27. C. Krill, "Proc. 4th Conf. Nanostruct. Mater.," Stockholm, 14–19 June 1998, p. 1.
28. Ya. E. Geguzin, L. N. Paritskaya, V. V. Bogdanov, and V. I. Novikov, *Fiz. Met. Metall.* 55, 768 (1983).
29. L. N. Paritskaya, *Powder Metall.* 6, 28 (1984).
30. W. Wanderlich, Y. Ishida, and R. Maurer, *Scripta Metall. Mater.* 24, 403 (1990).
31. L. E. Murr, "Interfacial Phenomena in Metals and Alloys." Addison–Wesley, Reading, MA, 1975.
32. V. Y. Gertsman and R. Birringer, *Scripta Metall. Mater.* 30, 577 (1994).

33. Ya. E. Geguzin, "Physik des Sinterns," VEB Deutsch. Verlag Grundstoffindustrie, Leipzig, 1973.
34. Ya. E. Geguzin and M. A. Krivoglaz, "Migration of Macroscopic Inclusions in Solids." Plenum, Consult. Bureau, London, 1973.
35. H. Hahn, J. Logas, and R. S. Averback, *Mater. Res.* 5, 609 (1990).
36. R. S. Averback, H. J. Höfler, and R. Tao, *R. Mater. Sci. Engng* A116, 169 (1993).
37. J. Weissmüller, W. Krauss, T. Haubold, R. Birringer, and H. Gleiter, *Nanostruct. Mater.* 1, 039 (1992).
38. J. W. Cahn, *Acta Metall.* 10, 789 (1962).
39. K. Lücke and H. P. Stüwe, "Recovery and Recrystallization of Metals," p. 171. Interscience, New York, 1962.
40. J. Weissmüller, *J. Nanostruct. Mater.* 3, 261 (1993).
41. J. Weissmüller, *J. Mater. Res.* 4, 9 (1994).
42. C. E. Krill, R. Klein, S. Janes, and R. Birringer, *Mater. Sci. Forum*, 179–181, 443 (1995).
43. L. G. Harrison, *Trans. Farad. Soc.* 57, 1191 (1961).
44. I. Kaur, Y. Mishin, and W. Gust, "Fundamentals of Grain and Interface Boundary Diffusion." Wiley, Chichester, NY, 1995.
45. E. W. Hart, *Acta Met.* 5, 597 (1957).
46. I. V. Belova and G. E. Murch, *Defect and Diffusion Forum* 194–199, 1223 (2001).
47. J. C. Fisher, *J. Appl. Phys.* 22, 74 (1951).
48. Yu. S. Kaganovskii and L. N. Paritskaya, *Metallofizika* 4, 103 (1982).
49. T. Suzuoka, *Trans. Jpn. Inst. Metals* 2, 25 (1961).
50. R. T. P. Whipple, *Phil. Mag.* 45, 1225 (1954).
51. Y. Mishin, *Defect and Diffusion Forum* 194–199, 1113 (2001).
52. Y. Mishin, Chr. Herzig, J. Bernardini, and W. Gust, *Inst. Mater. Rev.* 42, 155 (1997).
53. S. V. Divinski, M. Lotmann, and Chr. Herzig, *Defect and Diffusion Forum* 194–199, 1127 (2001).
54. G. S. Hartley, *Phil. Mag.* 29, 245 (1937).
55. L. Darken, *Trans. AIME* 175, 184 (1948).
56. A. D. Le Claire, *Progr. Metal Phys.* 1, 306 (1949).
57. W. Seith, "Diffusion in Metals." Springer, Berlin, 1955.
58. J. C. M. Hwang and R. W. Balluffi, *J. Appl. Phys.* 50, 1339 (1979).
59. J. C. M. Hwang, J. D. Pan, and R. W. Balluffi, *J. Appl. Phys.* 50, 1349 (1979).
60. Z. Erdelyi, Ch. Girardeaux, J. Bernardini, D. L. Beke, and A. Rolland, *Defect and Diffusion Forum* 194–199, 1161 (2001).
61. J. Horváth, R. Birringer, and H. Gleiter, *Solid State Commun.* 62, 319 (1987).
62. H. Gleiter, *Phys. Stat. Sol.* (B) 172, 41 (1992).
63. H.-E. Schaefer, R. Würschum, R. Birringer, and H. Gleiter, *Phys. Rev.* B28, 9545 (1988).
64. H. J. Höefler, R. S. Averback, H. Hahn, and H. Gleiter, *J. Appl. Phys.* 74, 3832 (1993).
65. L. Kaur, W. Gust, and L. Kozma, "Handbook of Grain and Interface Boundary Diffusion Data," p. 380. Zeigler, Stuttgart, 1989.
66. A. E. Austin, N. A. Richard, and V. E. Wood, *J. Appl. Phys.* 37, 3650 (1966).
67. S. Schumacher, R. Birringer, R. Strauss, and H. Gleiter, *Acta Metall.* 37, 2485 (1989).
68. J. M. Schoen, J. M. Poate, C. J. Doherty, and C. M. Melliar-Smith, *J. Appl. Phys.* 50, 6910 (1979).
69. L. L. Balandin, B. S. Bokshtein, V. K. Egorov, and P. V. Kurkin, *Nanostruct. Mater.* 8, 37 (1997).
70. H. J. Höefler, Ph.D. thesis, Saarbrücken, 1991.
71. R. Kirchheim, T. Mütschele, W. Kieninger, H. Gleiter, R. Birringer, and, T. D. Koblé, *Mater. Sci. Engng.* 99, 457 (1998).
72. H. Tanimoto, P. Farber, R. Würschum, R. Z. Valiev, and H.-E. Schaefer, *Nanostruct. Mat.* 12, 681 (1999).
73. H. J. Hofler, R. S. Averback, and H. Gleiter, *Phil. Mag. Lett.* 62, 99 (1993).

74. B. S. Bokstein, H. D. Brose, L. I. Trusov, and T. P. Khvostantseva, "Nanostructural Materials. Proc. 2nd Intern. Conf. on Nanostructured Materials." Germany, Stuttgart Univ., 1995.
75. K. Maier, *Phys. Stat. Sol.* (*A*) 44, 567 (1977).
76. J. Cousty, R. Peix, and B. Perraillon, *Surf. Sci.* 107, 586 (1981).
77. V. A. Gorbachev, S. M. Klotsman, Y. A. Rabovskii, V. K. Talinskii, and A. N. Timofeev, *Fiz. Met. Metall.* 44, 214 (1977).
78. S. D. Gertsriken and A. L. Revo, *Fiz. Metall.* 9, 92 (1960).
79. P. Shewmon, "Diffusion in Solids," 2nd ed. TMS, Warrendale, PA, 1989.
80. D. Chaleb and B. Perraillon, *Surf. Sci.* 162, 103 (1985).
81. M. Inman and L. Barr, *Acta. Metall.* 8, 112 (1960).
82. S. Herth, T. Michel, H. Tanimoto, M. Eggersmann, R. Dittmar, H.-E. Schaefer, W. Frank, and R. Würschum, *Defect and Diffusion Forum* 194–199, 1199 (2001).
83. S. A. Golovin, M. A. Krishtal, and A. M. Svobodov, *Fiz. Chem. Obrab. Mater.* 4, 119 (1968); cited in *Diffusion Data* 3, 133 (1969).
84. A. K. Niessen, F. R. de Boer, R. Boom, P. F. de Châtel, W. C. M. Mattens, and A. R. Miedema, *CALPHAD* 7, 51 (1983).
85. R. Würschum, S. Grub, B. Gissible, H. Natter, R. Hempelmann, and H.-E. Schaefer, *Nanostruct. Mater.* 9, 615 (1997).
86. R. Würschum, K. Reimann, S. Grab, A. Kübler, P. Scharwaechter, W. Frank, O. Kruse, H.-D. Carsanjen, and H. E. Schaefer, *Phil. Mag. B* 76, 407 (1997).
87. M. Hansen, "Constitution of Binary Alloys," 2nd ed. McGraw-Hill, New York, 1958.
88. P. Fortier, G. Palumbo, C. D. Bruce, W. A. Miller, and K. T. Aust, *Scripta Metall. and Mater.* 25, 177 (1991).
89. V. B. Rabukhin and A. S. Panikarski, *Poverhnost* 5, 150 (1986).
90. A. Petelin, S. Petelin, and O. Oreshina, *Defect and Diffusion Forum* 194–199, 1265 (2001).
91. Ya. E. Geguzin, "Diffusion Zone," Nauka, Moscow, 1979.
92. J. Manning, "Diffusion Kinetics for Atoms in Crystals." Van Nostrand, Princeton, 1969.
93. A. D. Smigelskas and E. O. Kirkendall, *Trans. AIME* 171, 130 (1947).
94. B. Ya. Pines and A. F. Sirenko, *J. Techn. Phys.* 28, 1748 (1958).
95. J. M. Cahn, J. D. Pan, and R. W. Balluffi, *Scripta Metall. Mater.* 13, 503 (1979).
96. M. Hillert and J. R. Purdy, *Acta Metall.* 26, 333 (1978).
97. Ya. E. Geguzin, Yu. S. Kaganovskii, and L. N. Paritskaya, *Fiz. Met. Metall.* 54, 137 (1982).
98. A. H. King, *Mater. Reviews* 32, 173 (1987).
99. L. N. Paritskaya, *Powder Metall.* N11, 44 (1990).
100. Ya. E. Geguzin and L. N. Paritskaya, *Fiz. Met. Metall.* 40, 85 (1975).
101. L. N. Paritskaya and Ya. E. Geguzin, *Fiz. Met. Metall.* 41, 656 (1976).
102. T. Surholt and Crh. Herzig, *Acta Mater.* 45, 3817 (1977).
103. Ya. E. Geguzin, Yu. I. Boiko, and L. N. Paritskaya, *DAN SSSR* 173, 323 (1067).
104. L. S. Palatnik, B. T. Boiko, and M. V. Lebedeva, *DAN SSSR* 213, 141 (1973).
105. T. G. Garbovitskaya, Ya. E. Geguzin, and L. N. Paritskaya, *Fiz. Met. Metall.* 42, 1214 (1976).
106. T. G. Garbovitskaya, Ya. E. Geguzin, and L. N. Paritskaya, *Fiz. Met. Metall.* 47, 1244 (1979).
107. Ya. E. Geguzin, N. A. Makarovsky, and V. V. Bogdanov, *Fiz. Met. Metall.* 45, 347 (1978).
108. R. P. Volkova, M. V. Lebedeva, L. S. Palatnik, and A. T. Pugachev, *Fiz. Met. Metall.* 53, 1038 (1982).
109. J. D. Pan and R. W. Balluffi, *Acta Metall.* 30, 861 (1982).
110. V. V. Bogdanov, V. V. Lisenko, and L. N. Paritskaya, *Fiz. Met. Metall.* N4, 117 (1990).
111. Yu. S. Kaganovskii, L. N. Paritskaya, and A. O. Grengo, *Functional Materials* 1, 30 (1994).

112. K. L. Merkle, J. F. Reddy, L. C. Wiley, and D. J. Smith, *Phys. Rev. Lett.* 59, 2887 (1989).
113. S. Trapp, C. L. Limbach, H. Gonser, C. S. Campbell, and H. Gleiter, *Phys. Rev. Lett.* 75, 3766 (1995).
114. J. Löffler, J. Weissmüller, and H. Gleiter, *Nanostruct. Mater.* 6, 567 (1994).
115. S. Ramasamy, J. Jiang, H. Gleiter, R. Birringer, and U. Gonse, *Solid. St. Commun.* 74, 851 (1990).
116. V. I. Novikov, L. I. Trusov, V. V. Lopovok, and T. P. Geileshvili, *Fiz. Tverd. Tela* 25, 3696 (1983).
117. Ya. E. Geguzin and Yu. S. Kaganovskii, "Diffusion Processes on a Crystal Surface," Energoatomizdat, Moscow, 1984.
118. L. N. Paritskaya and V. V. Bogdanov, *Sci. Sintering*, 26, 259 (1994).
119. Herring, *Phys. Rev.* 82, 87 (1951).
120. L. D. Landau and E. M. Lifshits, "Statistical Physics." Addison–Wesley, Reading, MA, 1969.
121. W. K. Burton, N. Cabrera, and F. C. Frank, *Phil. Trans. R. Soc. London, Ser. A* 243, 299 (1951).
122. A. A. Chernov, in "Modern Crystallography" (B. K. Vaynstein and A. A. Chernov, Eds.). Nova Science Publishers, New York, 1988.
123. E. E. Gruber and W. W. Mullins, *J. Phys. Chem. Solids* 67, 875 (1967).
124. C. Jayaprakash, C. Rottman, and W. F. Saam, *Phys. Rev. B* 30, 6549 (1984).
125. W. W. Mullins, *J. Appl. Phys.* 30, 77 (1959).
126. W. W. Mullins, *J. Appl. Phys.* 28, 333 (1957).
127. A. D. Brailsford and N. A. Gjostein, *J. Appl. Phys.* 46, 2390 (1975).
128. R. T. King and W. W. Mullins, *Acta. Met.* 10, 601 (1962).
129. N. A. Gjostein, in "Surfaces and Interfaces. I. Chemical and Physical Characteristics" (J. Burke, N. L. Rhead, and V. Weiss, Eds.), Syracuse, 1967, p. 271.
130. P. G. Shewmon, in "Fundamental Phenomena in the Materials Science," Plenum Press, New York, 1966, p. 111.
131. W. W. Mullins, *Phil. Mag.* 6, 1313 (1961).
132. F. A. Nichols and W. W. Mullins, *J. Appl. Phys.* 36, 1826 (1965).
133. G. Neumann and G. M. Neumann, "Surface Self-diffusion of Metals" Diffusion Information Center, Switzerland, 1972.
134. Lord Rayleigh, *Proc. London Math. Soc.* 10, 4 (1878).
135. M. Drechsler, *Japan J. Appl. Phys. Suppl.* 2, Pt. 2, 35 (1974).
136. A. E. B. Presland, G. L. Price, and D. L. Trimm, *Surf. Sci.* 29, 424 (1972).
137. E. Jiran and C. V. Thompson, *J. Electronic Mater.* 19, 1153 (1990).
138. D. J. Srolovitz and S. A. Safran, *J. Appl. Phys.* 60, 247 (1986).
139. R. Brandon and F. J. Bradshaw, Royal Aircraft Establishment Tech. Rep. No. 66095, 1966.
140. D. J. Srolovitz and S. A. Safran, *J. Appl. Phys.* 60, 255 (1986).
141. H. Wong, M. J. Miksis, P. W. Voorhees, and S. H. Davis, *Acta Mater.* 45, 2477 (1997).
142. H. Wong, P. W. Voorhees, M. J. Miksis, and S. H. Davis, *Acta Mater.* 48, 1719 (2000).
143. M. Poensgen, J. F. Wolf, G. Frohn, M. Giesen, and H. Ibach, *Surf. Sci.* 274, 430 (1992).
144. M. Giesen-Seibert, R. Jentjens, M. Poensgen, and H. Ibach, *Phys. Rev. Lett.* 71, 3521 (1993).
145. L. Kuipers, M. S. Hoogeman, J. W. M. Frenken, and H. van Bejren, *Phys. Rev. B* 52, 11387 (1995).
146. M. Giesen, G. S. Icking-Konert, D. Stapel, and H. Ibach, *Surf. Sci.* 366, 229 (1996).
147. M. S. Hoogeman, L. Kuipers, D. C. Schlosser, and J. W. M. Frenken, *Surf. Sci.* 447, 25 (2000).
148. N. C. Bartelt, J. L. Goldberg, T. L. Einstein, and E. D. Williams, *Surf. Sci.* 273, 252 (1992).
149. L. Kuipers, M. S. Hoogeman, and J. W. M. Frenken, *Phys. Rev. Lett.* 71, 3517 (1993).
150. G. L. Kellog and P. J. Feibelman, *Phys. Rev. Lett.* 64, 3143 (1990).
151. C. Chen and T. T. Tsong, *Phys. Rev. Lett.* 64, 3147 (1990).
152. R. Gomer, *Rep. Progr. Phys.* 53, 917 (1990).
153. L. J. Lauhon and W. Ho, *Phys. Rev. Lett.* 85, 4566 (2000).
154. T. Tsong. *Progr. Surf. Sci.* 67, 235 (2001).
155. A. A. Chernov. *Sov. Phys. Uspekhi* 4, 116 (1961).
156. G. A. Bassett, *Phil. Mag.* 58, 1042 (1958).
157. H. Bethge, *Nova Acta Leopoldina* 35, 125 (1970).
158. H. Bethge and K. W. Keller, *J. Cryst. Growth* 23, 105 (1970).
159. Yu. S. Kaganovskii and A. A. Onoprienko, *Sov. Phys. Solid State* 20, 1335 (1978).
160. D. R. Peale and B. H. Cooper, *J. Vac. Sci. Technol. A* 10, 2210 (1992).
161. J.-M. Wen, J. W. Evans, M. C. Bartelt, J. W. Burnett, and P. A. Thiel, *Phys Rev. Lett.* 76, 652 (1996).
162. K. Morgenstern, G. Rosenfeld, and G. Comsa, *Phys. Rev. Lett.* 76, 2113 (1996).
163. K. Morgenstern, G. Rosenfeld, E. Lægsgaard, F. Besenbacher, and G. Comsa, *Phys. Rev. Lett.* 80, 556 (1998).
164. G. L. Kellog, *Surf. Sci. Rep.* 21, 1 (1994).
165. T.-Y. Fu, Y.-R. Tzeng, and T. T. Tsong, *Phys. Rev. Lett.* 76, 2539 (1996).
166. S. C. Wang and G. Ehrlich, *Surf. Sci.* 239, 301 (1990).
167. A. Ichimiya, T. Tanaka, and K. Ishiyama, *Phys. Rev. Lett.* 76, 4721 (1996).
168. G. Ehrlich and F. G. Hudda, *J. Chem. Phys.* 44, 1039 (1966).
169. S. C. Wang and G. Ehrlich, *Phys. Rev. Lett.* 70, 41 (1993).
170. R. L. Schwoebel, *J. Appl. Phys.* 40, 614 (1969).
171. R. L. Schwoebel and E. J. Shipsey, *J. Appl. Phys.* 37, 3682 (1966).
172. V. G. Bar'yakhtar, A. E. Borovik, and Yu. S. Kaganovskii, *JETP Lett.* 47, 474 (1988).
173. H. P. Bonzel and W. W. Mullins, *Surf. Sci.* 350, 285 (1996).
174. Yu. Kaganovskii, in "Dispersed Systems and Surface Phenomena" (V. K. Miloslavsky, Ed.), p. 106. Kharkov University Press, Kharkov, 1989.
175. Yu. Kaganovskii, F. Lofaj, and V. I. Bodaleva, *Ukr. Fiz. Zh.* 35, 715 (1990).
176. W. W. Mullins, *Interface Sci.* 9, 9 (2001).
177. M. S. Hoogemann, D. C. Schlosser, J. B. Sanders, L. Kuipers, and J. W. M. Frenken, *Phys. Rev. B* 53, R13299 (1996).
178. R. Butz and H. Wagner, *Surface Sci.* 87, 85 (1979).
179. N.-J. Wu, H. Yasunaga, and A. Natori, *Surf. Sci.* 260, 75 (1992).
180. S. Surnev, P. Coenen, H. P. Bonzel, and W. W. Mullins, *Progr. Surf. Sci.* 53, 287 (1996).
181. S. Surnev, B. Voigtlander, H. P. Bonzel, and W. W. Mullins, *Surf. Sci.* 360, 242 (1996).
182. Ya. E. Geguzin, Yu. S. Kaganovskii, and N. V. Stoychev, *Fiz. Metal Metalloved.* 26, 298 (1968).
183. J. Villain and F. Lancon, *C. R. Acad. Sci. Paris* 309, 647 (1989).
184. J. Villain and F. Lancon, *Phys. Rev. Lett.* 64, 293 (1990).
185. A. Retori and J. Villain, *J. Phys. (Paris)* 49, 257 (1988).
186. M. V. R. Murty, *Phys. Rev. B* 62, 17004 (2000).
187. N. Israeli and D. Kandel, *Phys. Rev. Lett.* 80, 3300 (1998).
188. N. Israeli and D. Kandel, *Phys. Rev. B* 60, 5946 (1999).
189. M. Uwaha, *J. Phys. Soc. Jpn.* 57, 1681 (1988).
190. M. Uwaha and K. Watanabe, *J. Phys. Soc. Jpn.* 69, 497 (2000).
191. M. Giesen, G. S. Icking-Konert, and H. Ibach, *Phys. Rev. Lett.* 80, 552 (1998).
192. S. Tanaka, N. C. Bartelt, C. C. Umbach, R. M. Tromp, and J. M. Blakely, *Phys. Rev. Lett.* 78, 3342 (1997).
193. E. Bauer, *Rep. Prog. Phys.* 57, 895 (1994).
194. A. Ichimiya, K. Hayashi, E. D. Williams, T. L. Einstein, M. Uwaha, and K. Watanabe, *Phys. Rev. Lett.* 84, 3662 (2000).
195. C. Duport, A. Chame, W. W. Mullins, and J. Villain, *J. Phys. I France* 6, 1095 (1996).
196. T. Michely, M. Kalff, G. Comsa, M. Strobel, and K.-H. Heinig, *J. Phys.: Condens. Matter* 14, 4177 (2002).
197. M. Siegert and M. Plischke, *Phys. Rev. Lett.* 73, 1517 (1994).
198. M. Siegert, *Phys. Rev. Lett.* 81, 5481 (1998).

199. D. Moldovan and L. Golubovic, *Phys. Rev. E* 61, 6190 (2000).
200. J. K. Zuo and J. F. Wendelken, *Phys. Rev. Lett.* 78, 2791 (1997).
201. M. V. R. Murty, T. Curcic, A. Judy, B. H. Cooper, A. R. Woll, J. D. Brock, S. Kycia, and R. L. Headrick, *Phys. Rev. Lett.* 80, 4713 (1998).
202. L. H. Tang, P. Smilauer, and D. D. Vvedensky, *Eur. Phys. J. B* 2, 409 (1998).
203. S. Schinzer, M. Kinne, M. Biehl, and W. Kinzel, *Surf. Sci.* 439, 191 (1999).
204. J. Amar, *Phys. Rev. B* 60, R11, 317 (1999).
205. W. Ostwald, *Z. Phys. Chem. (Leipzig)* 34, 495 (1900).
206. I. M. Lifshitz and V. V. Slezov, *Sov. Phys. JETP* 8, 331 (1959).
207. I. M. Lifshitz and V. V. Slyozov, *J. Phys. Chem. Solids* 19, 35 (1961).
208. C. Wagner, *Z. Electrochem.* 65, 243 (1961).
209. B. K. Chakraverty, *J. Phys. Chem. Solids* 28, 2401 (1967).
210. Ya. E. Geguzin, Yu. S. Kaganovskii, and V. V. Slezov, *J. Phys. Chem. Solids* 30, 1173 (1969).
211. Ya. E. Geguzin and Yu. S. Kaganovskii, *Ukr. Phys. Zh.* 21, 254 (1976).
212. L. Bachmann, D. L. Sawyer, and B. M. Siegel, *J. Appl. Phys.* 36, 304 (1965).
213. J. G. Skofronick and W. B. Phillips, *J. Appl. Phys.* 38, 4791 (1967).
214. W. B. Phillips, E. A. Desloge, and J. G. Skofronick, *J. Appl. Phys.* 39, 3210 (1968).
215. H. Wegener, *Z. Phys.* 139, 464 (1954).
216. Ya. E. Geguzin, Yu. S. Kaganovskii, and V. V. Kalinin, *Sov. Phys. Solid State* 11, 203 (1969).
217. Yu. S. Kaganovskii and G. S. Ratinov, *Fiz. Met. Metalloved.* 31, 143 (1971).
218. Ya. E. Geguzin and Yu. S. Kaganovskii, *Sov. Phys. Usp.* 21, 611 (1978).
219. J.-M. Wen, S.-L. Chang, J. W. Burnett, J. W. Evans, and P. A. Thiel, *Phys. Rev. Lett.* 73, 2591 (1994).
220. J.-M. Wen, J. W. Evans, M. C. Bartelt, J. W. Burnett, and P. A. Thiel, *Phys. Rev. Lett.* 76, 652 (1996).
221. W. W. Pai, A. K. Swan, Z. Zhang, and J. F. Wendelken, *Phys. Rev. Lett.* 79, 3210 (1997).
222. J. de la Figuera, J. E. Prieto, C. Ocal, and R. Miranda, *Solid. State Commun.* 89, 815 (1994).
223. K. Morgenstern, G. Rosenfeld, B. Poelsema, and G. Gomsa, *Phys. Rev. Lett.* 74, 2058 (1995).
224. J. F. Wendelken, A. K. Swan, W. W. Pai, and J.-K. Zuo, in "Morphological Organization in Epitaxial Growth and Removal" (Z. Zhang and M. G. Lagally, Eds.), Vol. 14, p. 320, Series on Directions in Cond. Matter Phys. World Scientific, Singapore, 1998.
225. P. A. Thiel and J. W. Evans, in "Morphological Organization in Epitaxial Growth and Removal" (Z. Zhang and M. G. Lagally, Eds.), Vol. 14, p. 384, Series on Directions in Cond. Matter Phys. World Scientific, Singapore, 1998.
226. M. S. Hoogeman, M. A. J. Klik, R. van Gastel, and J. W. M. Frenken, *J. Phys.: Condens. Matter* 11, 4349 (1999).
227. J. C. Hamilton, M. S. Daw, and S. M. Foiles, *Phys. Rev. Lett.* 74, 2760 (1995).
228. S. A. Kukushkin and A. V. Osipov, *Surf. Sci.* 329, 135 (1995).
229. P. Deltour, J.-L. Barrat, and P. Jensen, *Phys. Rev. Lett.* 78, 4579 (1997).
230. S. V. Khare, N. C. Bartelt, and T. L. Einstein, *Phys. Rev. Lett.* 75, 2148 (1995).
231. N. C. Bartelt, J. L. Goldberg, T. L. Einstein, E. D. Williams, J. C. Heyraud, and J. J. Metois, *Phys. Rev. B* 48, 15453 (1993).
232. N. C. Bartelt, R. M. Tromp, and E. D. Williams, *Phys. Rev. Lett.* 73, 1656 (1994).
233. D. C. Sholl and R. T. Skodie, *Phys. Rev. Lett.* 75, 3158 (1995).
234. D. C. Sholl and R. T. Skodie, *Physica* 231A, 631 (1996).
235. A. F. Voter, *Phys. Rev. B* 34, 6819 (1986).

236. J. M. Soler, *Phys. Rev. B* 53, 10540 (1996).
237. S. V. Khare and T. L. Einstein, *Phys. Rev. B* 54, 1172 (1996).
238. G. Rosenfeld, K. Morgenstern, and G. Gomsa, in "NATO-ASI Surface Diffusion: Atomistic and Collective Processes" (M. C. Tringides, Ed.), p. 361. Plenum, New York, 1997.
239. M. Giesen-Seibert, F. Schmitz, R. Jentjens, and H. Ibach, *Surf. Sci.* 329, 47 (1995).
240. S. C. Wang, U. Kurpick, and G. Ehrlich, *Phys. Rev. Lett.* 81, 4923 (1998).
241. G. Honjo and K. Yagi, *J. Vac. Sci. Technol.* 6, 576 (1969).
242. R. Kern, A. Masson, and J. J. Metois, *Surf. Sci.* 27, 483 (1971).
243. J. J. Metois, M. Gauch, A. Masson, and R. Kern, *Surf. Sci.* 30, 43 (1972).
244. A. Masson, J. J. Metois, and R. Kern, *Surf. Sci.* 27, 463 (1971).
245. J. J. Metois, M. Gauch, A. Masson, and R. Kern, *Thin Solid Films*, 11, 205 (1972).
246. C. Chapon and C. R. Henry, *Surf. Sci.* 106, 152 (1981).
247. L. Bardotti, P. Jensen, A. Hoareau, M. Treilleux, and B. Cabaud, *Phys. Rev. Lett.* 74, 4694 (1995).
248. J. C. Zanghi, J. J. Metois, and R. Kern, *Philos. Mag.* 29, 1213 (1974).
249. J. C. Zanghi, J. J. Metois, and R. Kern, *Philos. Mag.* 31, 743 (1975).
250. J. C. Zanghi, J. J. Metois, and R. Kern, *Surf. Sci.* 52, 556 (1975).
251. R. Nötzel, J. Temmyo, T. Tamamura, T. Fukuki, and H. Hasegawa, *Europ. News* 27, 148 (1996).
252. D. Leonard, M. Krishnamurthy, C. M. Reaves, S. P. Denbaars, and P. M. Petroff, *Appl. Phys. Lett.* 63, 3203 (1993).
253. J. Oshinowo, M. Nishioka, S. Ishida, and Y. Arakawa, *Appl. Phys. Lett.* 65, 1421 (1994).
254. A. Kurtenbach, K. Eberl, and T. Shitara, *Appl. Phys. Lett.* 66, 361 (1995).
255. B. R. Bennett, R. Magno, and B. V. Shanabrook, *Appl. Phys. Lett.* 68, 505 (1996).
256. J. Tersoff, C. Teichert, and M. G. Lagally, *Phys. Rev. Lett.* 76, 1675 (1996).
257. C. Teichert, J. Tersoff, M. G. Lagally, in "Morphological Organization in Epitaxial Growth and Removal" (Z. Zhang and M. G. Lagally, Eds.), Vol. 14, p. 177, Series on Directions in Cond. Matter Phys. World Scientific, Singapore, 1998.
258. M. Pinczolits, G. Springholtz, and G. Bauer, *Appl. Phys. Lett.* 73, 250 (1998).
259. M. Pinczolits, G. Springholtz, and G. Bauer, *J. Cryst. Growth* 201/202, 1126 (1999).
260. I. N. Stranski and L. Krastanow, *Acad. Wiss. Lit. Mainz Math.-Natur Kl. 1 lb* 146, 797 (1939).
261. Y. Chen and J. Washburn, *Phys Rev. Lett.* 77, 4066 (1996).
262. A. L. Barabasi, *Appl. Phys. Lett.* 70, 2565 (1998).
263. A. Raab and G. Springholz, *Appl. Phys. Lett.* 77, 2991 (2000).
264. A. K. Schmid, N. C. Bartelt, and R. Q. Hwang, *Science*, 290, 1561 (2000).
265. J. Erlewein and S. Hofman, *Surf. Sci.* 68, 71 (1977).
266. G. Contini, V. Di Castro, N. Motta, and A. Scarlata, *Surf. Sci.* 405, L509 (1998).
267. G. Wulff, *Z. Kristallogr.* 34, 449 (1901).
268. W. L. Winterbottom, *Acta Metall.* 15, 303 (1967).
269. Ya. E. Geguzin and Yu. S. Kaganovskii, *Phys. Met. Metallogr.* 39, 94 (1975).
270. K. L. Chopra, "Thin Film Phenomena." McGraw-Hill, New York, 1969.
271. L. I. Trusov and V. A. Kholmyanskii, "Metal Island Films." Metallurgia, Moscow, 1973.
272. K. Thurmer, J. E. Reutt-Robey, E. D. Williams, M. Uwaha, A. Emundts, and H. P. Bonzel, *Phys. Rev. Lett.* 87, 186102 (2001).
273. M. Uwaha, *J. Phys. Soc. Jpn.* 57, 1681 (1998).

274. C. G. Zimmermann, M. Yeadon, K. Nordlund, J. M. Gibson, R. S. Averback, U. Herr, and K. Samwer, *Phys. Rev. Lett.* 83, 1163 (1999).
275. C. G. Zimmermann, K. Nordlund, M. Yeadon, J. M. Gibson, R. S. Averback, U. Herr, and K. Samwer, *Phys. Rev. B* 64, 085419 (2001).
276. L. Vitos, A. V. Ruban, H. L. Skriver, and J. Kollár. *Surf. Sci.* 411, 186 (1998).
277. T. Michely, G. Gomsa, in "Morphological Organization in Epitaxial Growth and Removal" (Z. Zhang and M. G. Lagally, Eds.), Vol. 14, p. 265, Ser. on Directions in Cond. Matter Phys. World Scientific, Singapore, 1998.
278. Yu. S. Kaganovskii, L. N. Paritskaya, V. V. Bogdanov, and A. O. Grengo, *Acta Mater.* 45, 3927 (1997).
279. Yu. S. Kaganovskii, L. N. Paritskaya, and W. Lojkowski, *Surf. Sci.* 454–456, 591 (2000).

Dip-Pen Nanolithography

Benjamin W. Maynor, Jie Liu

Duke University, Durham, North Carolina, USA

CONTENTS

1. INTRODUCTION/BACKROUND

The field of nanofabrication has attracted great interest recently due to the potential applications of miniaturization of devices and due to the unique properties of nanoscale materials [1]. In general, nanofabrication can be divided into two classes: bulk nanofabrication and nanoscale patterning. Bulk nanofabrication is the synthesis of molar quantities of nanostructures without regard for superstructure and ordering, such as bulk synthesis of nanoparticles [2–6], carbon nanotubes [7, 8], and nanowires [9–11]. Nanopatterning is the fabrication of nanostructures in rational architectures that could be used in device construction [12]. While bulk nanostucture synthesis will be important for many applications, nanopatterning is critical for the production of functional devices. Recently, self-assembly has been used to aid the rational superassembly of two-dimensional (2D) and 3D structures [13], but traditionally, surface patterning methods such as photolithography have been used to create functional devices. Due to the diffraction limit of light, photolithography is unable to produce structures in the nanoscale (sub-100 nm) regime. Several creative fabrication techniques, including electron-beam lithography [14], soft lithography techniques [15, 16], and scanning probe lithography (SPL) techniques [17], to name a few, have been invented to facilitate the fabrication and patterning of nanostructures.

Among these nanofabrication strategies, SPL [17] techniques provide unparalleled simplicity of use and control over nanostructure location and geometry. This lithographic method uses scanning probe imaging instruments, such as the scanning tunneling microscope [18], the near-field scanning optical microscope [19], or the atomic force microscope (AFM) [20–29], to create nanofeatures on surfaces. Scanning probe techniques rely on the fact that the scanning probe tip, which is inherently a nanosize object, is used to create the patterns on the surface. Because the patterning is localized at the tip and follows the translational motion of the tip, SPL techniques allow unparalleled flexibility in fabricating different geometries of nanostructures without photomasks or other master patterns. Typically, nanofeatures are created by mechanical deformation of the surface [22, 25], surface anodization processes such as the site-specific oxidation of silicon [20, 21, 26], or by removal or alteration of resist layers followed by subsequent processing steps [23, 24].

Recently, a new SPL technique, dip-pen nanolithography (DPN) [30, 31], was invented that allows direct-write nanopatterning of a variety of materials. In DPN, material is transferred from a coated AFM tip to a surface in an analogous process with the familiar macroscale task of writing with an ink-coated paintbrush or quill pen. In fact, the familiar nomenclature of "pen," "ink," and "paper" is readily applied to describe the AFM tip, the material to be patterned, and the surface respectively in the DPN literature.

Unlike many other SPL methods, DPN is a direct-write process that can easily fabricate many heterogeneous nanostructures on a variety of surfaces. DPN has been used to successfully pattern diverse classes of materials, ranging from inorganic compounds [32–34] to biomacromolecules [35, 36], on a wide variety of surfaces [30, 37, 38] without further chemical processing steps. DPN can also be easily incorporated with postpatterning chemical and biological techniques to study a variety of phenomena ranging from surface physical chemistry [39] to interfacial biology. [40]

DPN writing works as follows (Fig. 1): an AFM tip is coated with a molecule to be patterned, or "ink," such as an alkanethiol molecule [30]. The AFM tip is engaged with an appropriate surface and the ink molecules are transported from the tip through a layer of condensed water at the tip–surface interface [30, 41], and once they reach the surface, the ink molecules are locally chemisorbed or physisorbed

AFM Tip

Writing direction

Molecular transport

Water meniscus

Au substrate
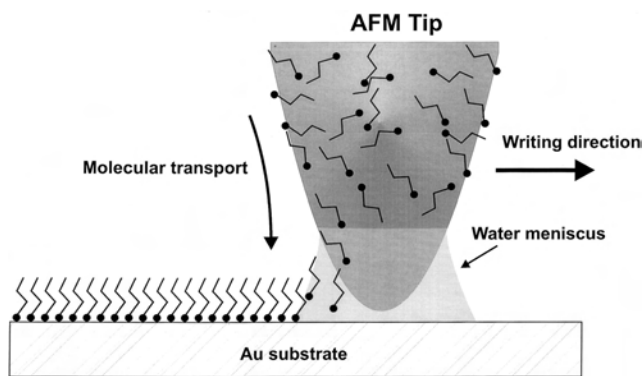
Figure 1. Schematic of the DPN process. The tip-applied ink molecules diffuse through the water meniscus and deposit on the surface to form nanostructures. Reprinted with permission from [30], R. D. Piner et al., *Science* 29, 661 (1999). © 1999, American Association for the Advancement of Science.

to form nanostructures. Material deposition tracks the position of the AFM tip and is localized around it, which gives the user great control over the morphology of the patterns. Furthermore, because the ink diffuses away from the AFM tip, feature size is directly related to writing time; one can pattern at a variety of length scales, from nanometers to micrometers, within the same experiment, by simply controlling the writing time or speed.

For a material "ink" to be successfully patterned by DPN, two criteria must be met: (1) the material must be mobile enough to release from the AFM tip and (2) there must be a driving force to initiate the formation of nanostructures and to stabilize them against surface diffusion or other dissolution processes. These requirements are not as limiting as one might expect; DPN has been used to pattern hydrophilic [42] and hydrophobic [30] materials, ionic [32, 43] and uncharged [44] materials, and high [45] and low [37] molecular weight materials, to name a few. Covalent bonding [31], physical interactions [32], electrostatic interactions [43], electrochemical reactions [46], and polymerization [47] have all been used as the driving force for nanostructure formation. The specific nature of the driving force depends on the chemical and physical properties of the ink chosen for patterning. The number of ink/surface systems that are suitable for DPN is large and novel demonstrations are appearing often in the literature.

DPN feature size can be influenced by the experimental conditions, including the writing speed (or time, in the case of dot features), the ambient temperature, and humidity. As mentioned, a characteristic feature of DPN is the radial ink diffusion from the AFM tip. Therefore, feature size is related to tip–surface contact time; if patterns are written more slowly, ink diffuses farther from the tip and the pattern feature size is larger. Several diffusion-based models have been proposed to describe this radial ink transport phenomenon [48–51]. DPN feature size is also dependent on the ambient temperature and humidity. The temperature dependence is well described by dissolution kinetics describing the detachment of individual molecules from the ink-coated AFM tip [41]. The humidity dependence of feature size arises from the fact that when imaging (or writing)

with the AFM in humid air, a spontaneous water layer, or "meniscus," forms between the AFM tip and the surface [52, 53] which can influence the transport of ink during DPN writing. Because the size of the meniscus is humidity dependent (it increases with increasing humidity) the DPN feature size can also be humidity dependent. The specific nature of this relationship depends on the chemical properties of the ink [41, 49–51]. Section 3 contains a more complete discussion of the factors that affect DPN feature size.

The evolution of DPN can be compared with that of microcontact printing [54, 55], another (microscale) material transfer lithography technique. Interestingly, proof-of-concept experiments for both techniques used the same ink/surface system, namely alkanethiol self-assembled monolayers on Au surfaces [30, 55], and many of the same material/surface systems that have been demonstrated for microcontact printing should also be suitable for DPN patterning. In fact, it has recently been shown that the same ink/surface system can be used to create metallic patterns with microcontact printing or DPN as well [34]. Since its inception, microcontact printing has been used to pattern many types of materials and has initiated development of a whole new class of soft lithographic techniques [56, 57]. DPN is beginning a similar evolution beyond its initial demonstrations toward new materials and applications. This chapter will survey the current state of DPN technology and applications and provide an indication of things to come in the next few years.

2. DEMONSTRATIONS OF DPN

As suggested, DPN has been used to pattern a variety of materials on many different surfaces. An appreciation of the breadth and flexibility of DPN patterning is obtained by examining in detail the types of systems that have been used for DPN. Here we describe some of the demonstrations of DPN patterning of different material/surface systems. Experiments where DPN was used to fabricate templates for mechanistic or other studies will be covered in later sections.

2.1. Surface-Specific Monolayers

The first demonstrations of DPN were performed using the system of alkanethiol molecules on gold surfaces. This system is well suited for DPN. The alkanethiol molecules are sufficiently mobile so that they can move relatively easily from the AFM tip to the surface and the driving force for the formation of nanostructures is the covalent bonding of the –SH moiety to the Au surface. Using DPN, continuous, well-defined, well-ordered patterns of octadecanethiol (ODT) and 16-mercaptohexadecanoic acid (MHA) were fabricated [30]. By imaging the patterns using lateral force microscopy (LFM), differences between ODT and MHA patterns were observed (Fig. 2). ODT patterns deflected the AFM tip less than the background Au surface, while MHA patterns deflected the AFM tip more than the Au surface did, showing distinct chemical differences between ODT and MHA monolayers. It was demonstrated that dot and line patterns could be fabricated and that feature size depends on the translation speed of the AFM tip. It was also suggested that
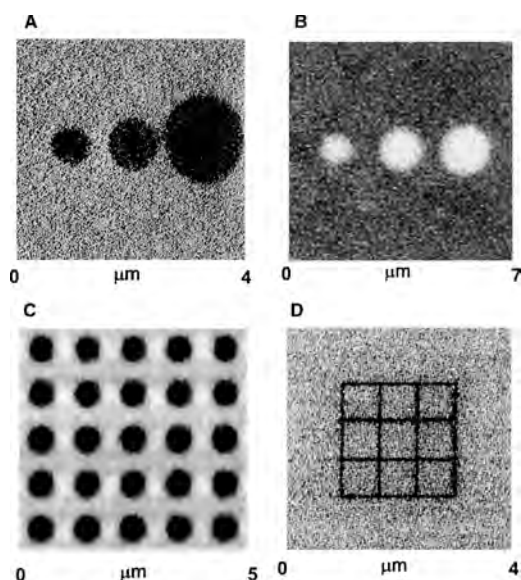
Figure 2. Lateral force microscopy images of (A) ODT dots; (B) MHA dots; (C) ODT dot array; (D) ODT grid. Reprinted with permission from [30], R. D. Piner et al., *Science* 283, 661 (1999). © 1999, American Association for the Advancement of Science.

the relative humidity of the environment plays a role in determining feature size.

Hong et al. demonstrated that multicomponent nanostructures could be formed by DPN [31]. The authors showed that ODT and MHA could be patterned serially in the same location by using DPN-generated alignment markers, termed "overwriting" (Fig. 3). Again, LFM images confirmed that ODT had lower lateral friction than MHA. The authors also demonstrated a minimum linewidth of 15 nm and a serial registration threshold of 5 nm.

By combining DPN with another AFM lithography technique, nanografting, Amro et al. showed that it was possible to selectively pattern one kind of alkanethiol within a matrix of a different alkanethiol. They described this system as a "nanopen reader and writer" (NPRW) (Fig. 4a) [58]. By scanning over a decanethiol coated Au surface at high shear forces with an AFM tip coated with a different alkanethiol, the authors were able to selectively remove the decanethiol matrix molecules while simultaneously replacing them with
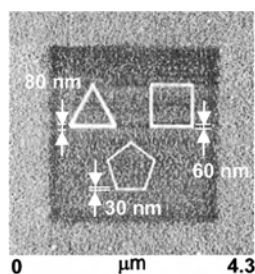
Figure 3. Multiple ink nanostructures generated by DPN. The white lines are MHA patterns, and the darker surrounding background is ODT. Reprinted with permission from [31], S. H. Hong et al., *Science* 286, 523 (1999). © 1999, American Association for the Advancement of Science.

the tip-applied alkanethiol. Replacement of the decanethiol matrix molecules was confirmed by topographic AFM and LFM (Fig. 4b).

Ivanisevic and Mirkin moved away from the alkanethiol/Au system, showing that hexamethyldisilazine (HMDS) could be patterned on silicon oxide and oxidized GaAs surfaces [37]. Like the alkanethiol/Au system, HMDS is sufficiently mobile
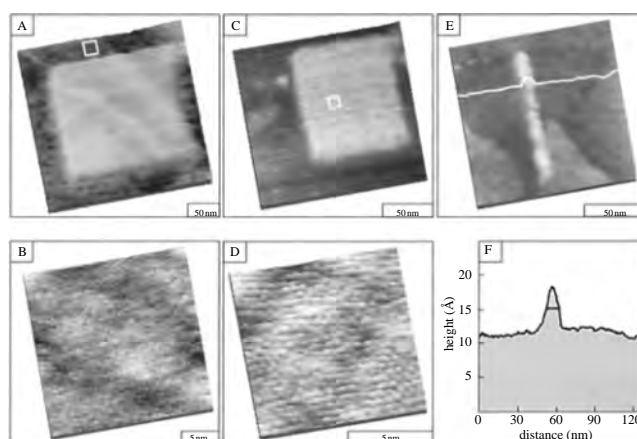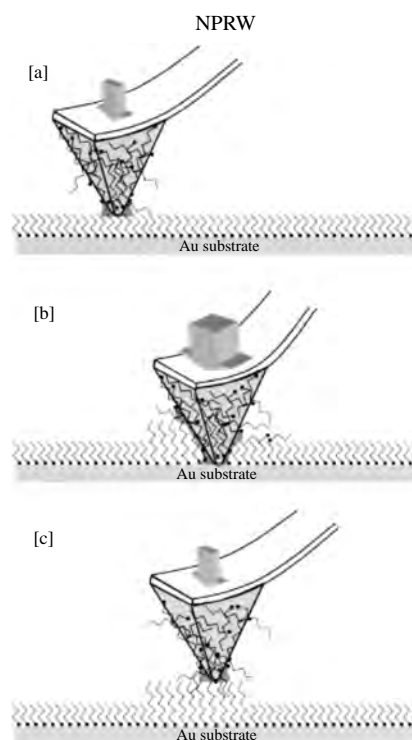
Figure 4. (a) Schematic of NPRW. (A) An alkanethiol coated AFM tip is scanned over an alkanethiol resist; (B) high shear forces remove the resist and replace it with the tip applied molecules; (C) the AFM tip is used to image the resulting patterns at lower force. (b) Nanopatterns fabricated within a decanethiol matrix using NPRW. (A) Topographic image of a square of a octadecanethiol; (B) high-resolution image of the octadecanethiol area in (A); (C) topographic image of a square of $CF_3(CH_2)_{11}(CH_2)_2SH$; (D) high-resolution image of the fluorinated thiol area in (C); (E) line of $CF_3(CH_2)_{11}(CH_2)_2SH$; (F) cross-section image of (E). Reprinted with permission from [58], N. A. Amro et al., *Langmuir* 16, 3006 (2000). © 2000, American Chemical Society.

from the AFM tip and can specifically covalently bond to oxidized silicon or GaAs, making it a suitable system for DPN patterning of these surfaces (Fig. 5). The authors also studied the ink transport kinetics of this system. Previous mechanistic studies using alkanethiol inks had shown a square root ($t^{1/2}$) relationship for dot size as a function of writing time, which was modeled as diffusive movement of the ink away from the tip (Fig. 6) [48]. (See Section 3 for further discussions on ink diffusion in DPN.) Similar $t^{1/2}$ kinetics and similar deposition morphology were observed for HMDS as for alkanethiols, though the diffusion constant was lower for HMDS patterning than for ODT.

2.2. Other Organic Molecules and Polymers

DPN patterning and simultaneous fluorescence imaging of dye molecules and luminescent polymers was reported by Noy et al. [45]. The authors patterned rhodamine 6G dye and though they could not observe the patterns using AFM, they were able to observe the photoluminescence of the dye molecules (Fig. 7). Significantly, patterned rhodamine molecules exhibited some signature characteristics of single molecule behavior, demonstrating that DPN can be used to pattern single molecules. The immobilization of the dye molecules was attributed to a stabilizing electrostatic interaction between the cationic rhodamine dye and the negatively charged glass surface. The authors also patterned fluorescently labeled human chorionic gonadotropin, a protein, and poly[2-methoxy-5-2′-(ethylhexyl)oxy-1,4-phenylenevinylene], (MEH-PPV) a well-known conducting polymer, and were able to observe their photoluminescence.

In addition to patterning rhodamine 6G dye, Su et al. also used DPN to deposit nanostructures of the fluorescent dyes coumarin 6, acid red 8 (AR8), and fluorescein [38]. The dyes were also imaged by fluorescence microscopy (Fig. 8). The authors reported the use of aminopropyltrimethoxysilane (APTES) coated Si/SiO$_x$, a cationic surface, for the patterning of the anionic AR8 and fluorescein dyes. Surprisingly, they were able to observe patterning on bare, presumably

Figure 6. Plot of the square root, or "$t^{1/2}$ dependence," of dot radius on contact time. Reprinted with permission from [48], J. Jang et al., *J. Chem. Phys.* 115, 2721 (2001). © 2001, American Institute of Physics.

anionic Si/SiO$_x$ as well, suggesting the importance of non-electrostatic interactions. The kinetics of the dye molecule inks were shown to be similar to those of covalently binding monolayers.

McKendry et al. used dendrimers, a hyperbranched polymeric structure, as a novel DPN ink [42]. They found that the deposition rate depends on both the molecular mass and the chemical composition of the dendrimer molecule (Fig. 9). It was demonstrated that for dendrimer inks, the diameter of the deposit plateaus at long tip contact times. The authors suggested that this was due to deposition of additional molecules on top of existing dendrimer molecules rather than on the periphery of the nanostructure.

Two electrically conductive polymers, self-doped sulfonated polyaniline (SPAN) and doped polypyrrole (PPy), were patterned using electrostatic attractions as the driving force for nanostructure formation (Fig. 10) [43]. In their doped state, both SPAN and PPy are anionic and cationic,

Figure 5. DPN of HMDS on (A) silicon oxide and (B) GaAs surfaces. (C) Plot of dot diameter as a function of the square root of deposition time for Au/ODT, SiO$_x$/HMDS, and GaAs/HMDS surface/ink systems. Reprinted with permission from [37], A. Ivanisevic and C. A. Mirkin, *J. Am. Chem. Soc.* 123, 7887 (2001). © 2001, American Chemical Society.
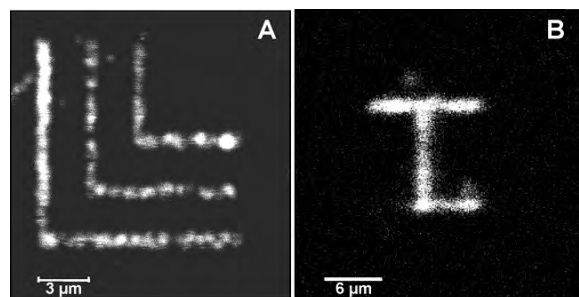
Figure 7. Scanning confocal microscopy images of (A) rhodamine 6G dye and (B) tetramethylrhodamine-labeled human chorionic gonadotropin protein. Reprinted with permission from [45], A. Noy et al., *Nano Lett.* 2, 109 (2002). © 2002, American Chemical Society.
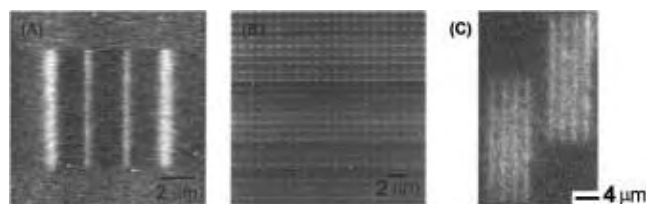
Figure 8. Topographic images of (A) rhodamine 6G lines and (B) dots; (C) fluorescence microscopy image of rhodamine 6G patterns. Reprinted with permission from [38], M. Su and V. P. Dravid, *Appl. Phys. Lett.* 80, 4432 (2002). © 2002, American Institute of Physics.

respectively. The authors exploited the charged nature of the polymers by immobilizing them on oppositely charged surfaces. No SPAN deposition was observed on negatively charged surfaces, and no PPy deposition was observed on positively charged surfaces. The deposited polymer nanofeatures showed characteristic electrochemical behavior of bulk SPAN and PPy, respectively.

Matsubara et al. used a well-known chemical addition/cyclization reaction, the Diels–Alder reaction, to react a tip-applied diene molecule with a vinyl-terminated siloxane monolayer [44]. The tip applied compound, 2-(13-hydroxy-2-oxatridecanyl)furan, added to the vinyl terminus of the monolayer, producing patterns that were topographically higher than the surrounding surface. This was the first use of carbon–carbon covalent bond formation as the driving force for DPN-induced nanostructure formation.
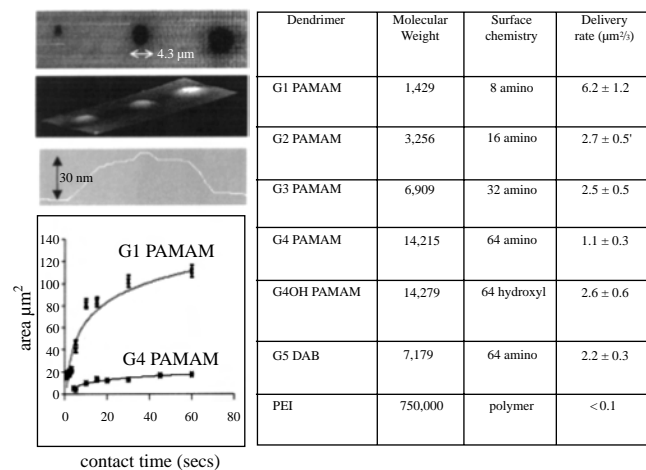
Figure 9. Upper left: topographic, surface, and cross-section images of dendrimer patterns. Lower left: plot of dot area as a function of contact time for generation 1 (G1) and generation 4 (G4) polyamidoamine dendrimers. Right: table of delivery rate for dendrimers of differing chemical compositions. Key: G1 PAMAM = generation 1 polyamidoamine dendrimer; G2 PAMAM = generation 2 polyamidoamine dendrimer; G3 PAMAM = generation 3 polyamidoamine dendrimer; G4 PAMAM = generation 4 polyamidoamine dendrimer; G4OH PAMAM = generation 4, hydroxyl terminated polyamidoamine dendrimer; G5 DAB = generation 5 polypropylene imine dendrimer; PEI = polyethylene imine polymer. Reprinted with permission from [42], R. McKendry et al., *Nano Lett.* 2, 713 (2002). © 2002, American Chemical Society.
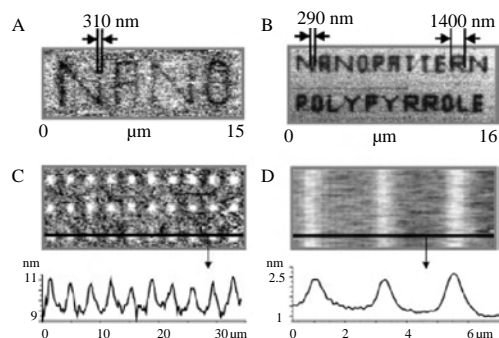
Figure 10. Lateral force microscopy images of (A) SPAN and (B) PPy patterns. Topographic images of (C) SPAN array with cross-section and (D) PPy lines with cross-section. Reprinted with permission from [43], J. H. Lim and C. A. Mirkin, *Adv. Mater.* 14, 1474 (2002). © 2002, Wiley–VCH.

2.3. Inorganic Compounds

Maynor et al. used reductive adsorption of $HAuCl_4$ on H-terminated Si surfaces as a novel driving force for DPN patterning of metallic Au nanostructures (Fig. 11) [32]. The precursor ink, $HAuCl_4$ undergoes an oxidation/reduction reaction with the Si surface; after the Au (III) ink diffuses away from the tip, it is reduced to Au (0) by the silicon surface, which is simultaneously oxidized from Si (0) to Si (IV). Immobilization of the nanostructures occurs because the Au (III) complex is mobile enough to be transported away from the AFM tip but the Au (0) is bound on the surface due to the formation of Au aggregates. Porter et al. used a similar reductive driving force to effect DPN patterning of Au nanostructures on Ge (100) surfaces [34].

A different class on inorganic nanostructures, metal oxides, was patterned using a polymer-stabilized sol–gel ink [33]. Su et al. used a ethanolic solution of block copolymers and $SiCl_4$, $AlCl_3$, or $SnCl_4$ as the ink, followed by thermal
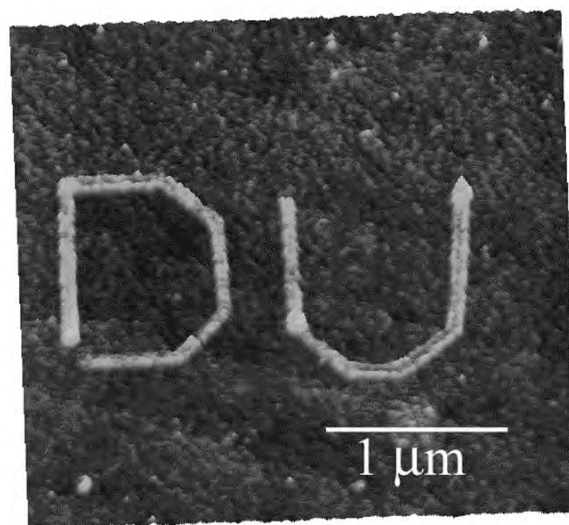
Figure 11. Topographic image of Au nanostructures forming the letters "DU." Reprinted with permission from [32], B. W. Maynor, *Langmuir* 17, 2575 (2001). © 2001, American Chemical Society.

heating to produce silica, alumina, or tin oxide nanostructures. The authors suggested that the driving force for nanostructure formation was the partial hydrolysis and polymerization of the metal chlorides in the water meniscus between the AFM tip and the surface. After thermal heating, energy dispersive X-ray analysis of the nanofeatures showed characteristic features of the metal oxides.

2.4. Biological Molecules

The first demonstration of the direct patterning of biological molecules by DPN was the patterning of collagen [35]. Collagen proteins and collagen analogues were modified with thiol-containing moieties and patterned on Au surfaces. The thiol groups were necessary to ensure surface immobilization. Significantly, the patterned collagen molecules maintained much of their native structure and even appeared to show supramolecular organization (Fig. 12). Linewidths as small as 30 nm were reported. The biological activity of the molecules was confirmed by tagging the collagen patterns with fluorescent, collagen-specific antibodies.

Demers et al. used DNA oligonucleotides as the ink for DPN patterning [36]. Using thiol- or acrylamide-modified oligonucleotides as ink, the authors were able to pattern multicomponent DNA arrays on Au and monolayer-modified SiO_2 surfaces, respectively. Selective binding to the DNA
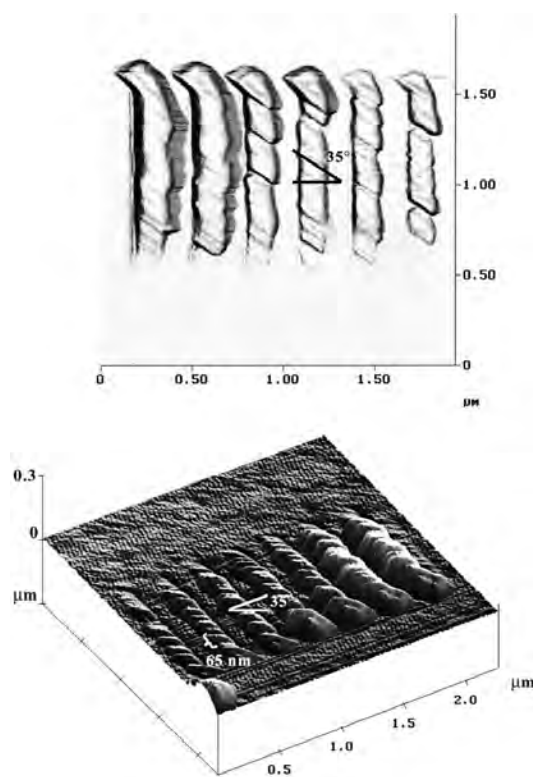
Figure 12. Topographic and surface images of collagen molecules. Note the supramolecular structure in the patterns: the individual line elements have a periodicity of 65 nm and an orientation of 35° with respect to the short axis of the line patterns. Reprinted with permission from [35], D. L. Wilson et al., *Proc. Nat. Acad. Sci.* 98, 13660 (2001). © 2001, National Academy of Sciences.

strands by Watson–Crick base pairing was demonstrated through hybridization to labeled, complementary DNA oligonucleotides. Fifty nm, biologically active DNA spots could be patterned, which is several orders of magnitude smaller than the feature size of current commercially available DNA microarrays.

2.5. Electrochemical Dip-Pen Nanolithography

Unlike the previous examples of DPN patterning, where a specific ink–surface interaction is the driving force toward nanostructure formation, electrochemical dip-pen nanolithography (E-DPN) uses an external voltage to cause the chemical change of mobile, tip-applied precursor molecules to immobile surface-bound nanostructures (Fig. 13) [46, 47]. This process is analogous to electroplating of metals or electropolymerization of conducting polymers. The lithographic process is very similar to conventional DPN writing, except that while the tip is translated across the surface, a bias voltage is applied between the tip and surface. This bias voltage causes the oxidation or reduction of mobile precursor molecules to immobile aggregates such as metal deposits or polymers. E-DPN has been used to fabricate Pt, Pd, Au, Ag, Cu, and Ge nanostructures by the externally driven reduction of precursor salts (Fig. 14) [46] and to fabricate conducting polymer nanowires by the oxidative polymerization of ethylenedioxythiophene on semiconducting and insulating surfaces (Fig. 15) [47].

The nature of the driving force for deposition determines the polarity of the external bias voltage. For example, for elemental nanostructure fabrication from higher oxidation state precursors, it is necessary to reduce the mobile metal salt precursor inks to their metallic, insoluble analogs. Therefore, a reductive (positive) bias must be applied between the AFM tip and the surface to ensure that the deposition occurs on the cathodic surface rather than on the anodic tip [46]. Likewise, for the oxidative polymerization of poly(ethylenedioxythiophene) (PEDOT), which is known to involve oxidized radical cations, it is necessary to apply an oxidative (negative) bias voltage [47]. The magnitude of the bias voltage can vary depending on the specific geometry and resistivity of the tip and the surface.

As is the case for other DPN systems, the feature size can be controlled using the writing speed because writing at slower speeds allows more time for the transport of ink,
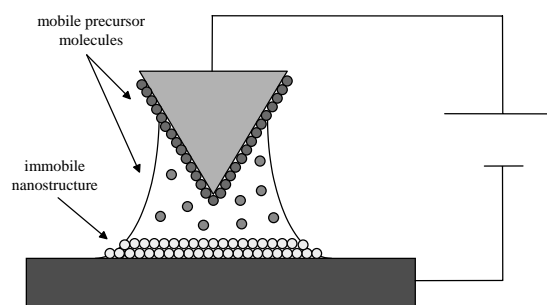
Figure 13. Schematic of E-DPN. Mobile precursor molecules (red) are transported from the tip to the surface (green), where they are reduced or oxidized to produce immobile nanostructures (yellow).
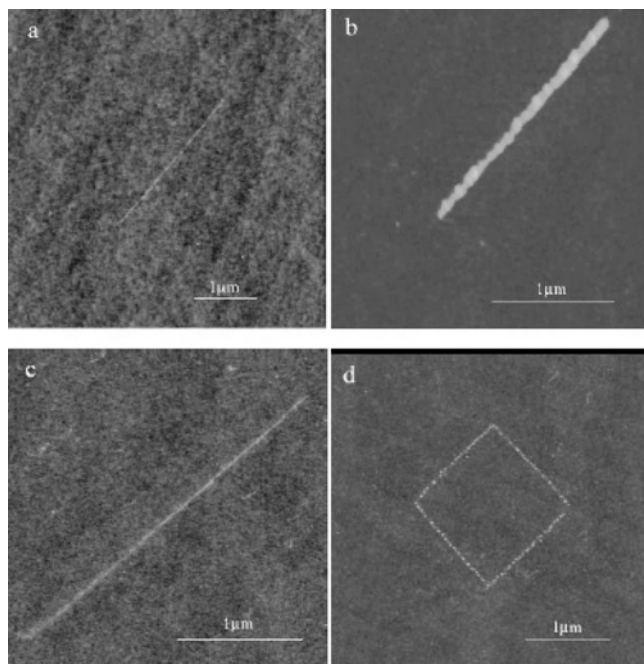
Figure 14. Elemental nanostructures produced by E-DPN. (a) Ag line, (b) Ge line, (c) Pd line, (d) Cu square. Reprinted with permission from [46], Y. Li et al., *J. Am. Chem. Soc.* 123, 2105 (2001). © 2001, American Chemical Society.

resulting in larger features (Fig. 15). For most other DPN processes, the growth of nanostructures is mostly in-plane with the surface, but for E-DPN deposition, significant growth in the vertical dimension is also observed. The feature size is also somewhat affected by the humidity and the applied voltage.
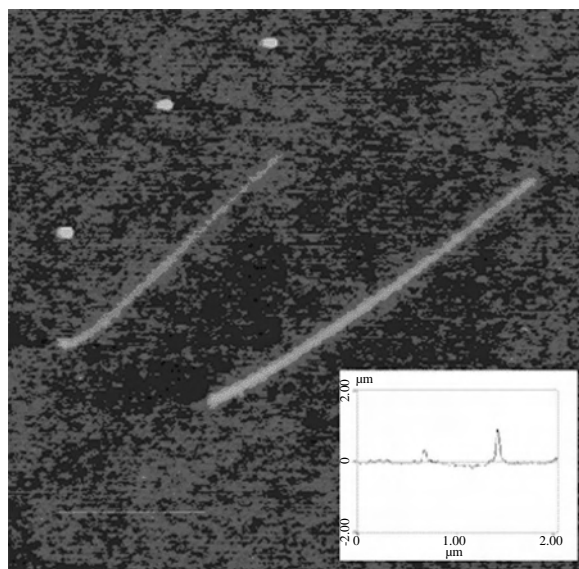
Figure 15. PEDOT lines drawn using E-DPN at different writing speeds. The leftmost line was drawn at 1 nm/sec and the rightmost line was drawn at 10 nm/sec. Inset: cross-section image of the two lines. Reprinted with permission from [47], B. W. Maynor et al., *J. Am. Chem. Soc.* 124, 522 (2002). © 2002, American Chemical Society.

3. MECHANISTIC INVESTIGATIONS OF DPN

3.1. Ink Diffusion Dynamics

Though DPN can easily pattern almost any 2D structure, the structure that lends itself most readily to theoretical interpretation is the dot. A dot is fabricated by simply placing an ink-coated AFM tip in contact with an appropriate surface for a desired length of time (the "dwell time"). While the tip is in contact with the surface the ink is transported away from the tip, resulting in nanostructure growth.

Early in the development of DPN, it was noticed that there was a linear relationship between dot area and dwell time (Fig. 6) [37, 48]. This relationship can be expressed mathematically by

$$\text{Area} = a + b * t$$

where t is the dwell time and a and b are constants. This expression directly leads to the previously cited "$t^{1/2}$ relationship" between the dot diameter and the dwell time. The $t^{1/2}$ relationship has been used to describe the deposition of many materials, including organic molecules [37, 38], DNA [36], and doped conducting polymers [43], suggesting underlying similarities in the transport of these diverse materials.

Jang et al. described the transport of ink molecules to the surface using an analytical diffusion model and a numerical "random walk" simulation of the diffusional growth of dots and lines [48]. The models assumed specific binding of the ink to the surface and a constant flux of ink molecules. Both the analytical model and the simulation demonstrated that, if the deposition of molecules was slow compared to their diffusion, the $t^{1/2}$ dependence between dot radius and dwell time was reproduced.

A different diffusion model was suggested that assumed that the tip acted as a constant concentration ink "reservoir" rather than a constant flux source for ink molecules [49]. This observation was motivated by the seemingly infinite reservoir of ink molecules on an ODT coated AFM tip. Using this model, the authors reported a better correspondence to experimental data than by using only a $t^{1/2}$ dependence.

As an alternative to these strictly diffusion-based models, Weeks et al. have developed an ink transport theory that suggests two distinct deposition regimes: (1) a kinetic regime, where deposition is dominated by the kinetics of ink desorption from and reattachment to the AFM tip ("dissolution kinetics") and (2) a molecular diffusion-controlled regime [50]. At short dwell times, feature size is dominated by ink dissolution kinetics, whereas at longer dwell times, ink dissolution reaches equilibrium and the ink transport becomes dominated by diffusion growth. This model was used to explain the observation of different linear growth coefficients for short and long dwell times. Temperature dependent experimental studies also support the idea that ink dissolution is an important factor in DPN pattern formation [41].

In addition to the analysis of dot patterns, several experimental and theoretical studies of line growth have appeared in the literature. Rozhok et al. have demonstrated that the ink deposition rate for line growth is greater than the ink

deposition rate for dot growth for MHA and ODT inks [41]. The authors attribute this observation to the important role that the ink concentration gradient between the tip and the surface plays in regulating the deposition rate. During line deposition, the ink-coated tip is continually encountering a fresh Au surface with which to bind, so therefore there is a large ink concentration gradient between the tip and surface and fast ink deposition. For dot growth, there is a lower concentration gradient between the tip and the surface because the ink must first diffuse over a passivated alkanethiol layer before it encounters bare Au. This smaller gradient leads to slower diffusion.

Several groups have also noticed a nonlinearity between linewidth and inverse writing speed. Schwartz modeled this behavior with a diffusion-based ink transport model that assumes an ink concentration gradient between a point above the apex of the AFM tip and the outer edge of the deposited line [51]. At small inverse writing speeds (high tip translation speed), the model predicts a linear dependence between width and inverse writing speed, but at higher inverse speeds (slow tip translation speed), the model behaves differently, predicting a square root dependence. Weeks et al. applied their dissolution/diffusion model to linewidth data and explained the observed nonlinearity in the width/inverse writing speed relationship as consisting of two linear regimes with different slopes [50]. More analysis is needed to determine which model most accurately describes DPN line writing.

The variety of ink transport models presented in a relatively short period of time (2001–2002) is indicative of the lack of complete understanding of the ink transport process and the lack of rigorous experimental control in DPN patterning. More reproducible experimental procedures and a better understanding of fundamental processes such as ink dissolution, diffusion, and binding is necessary before a truly complete understanding of ink dynamics can be obtained.

3.2. Temperature Dependence of DPN

All of the relevant physical processes in DPN, such as ink dissolution, diffusion, and surface binding, have temperature dependencies. Therefore, it is important to qualitatively and quantitatively understand these temperature relationships. Using the HMDS/SiO$_x$ ink/surface system, Ivanisevic and Mirkin demonstrated that the patterning rate increases significantly at elevated temperatures (Fig. 5) [37]. Schwartz found an Arrhenius temperature dependence with an activation energy of 0.74 eV for ODT [51]. Rozhok et al. have recently conducted detailed temperature-dependent experiments and found that the temperature dependence of ink transport for ODT and MHA is well described by the thermoactivated dissolution of ink from the AFM tip [41], in accordance with the transport model presented by Weeks et al. [50]. The authors also found that the temperature dependence for ODT and MHA patterning is relatively independent of dwell time and but does increase with increasing humidity. Additional temperature studies on other relevant parameters, such as meniscus formation and surface diffusion, will help clarify the DPN writing process.

3.3. Role of the Water Meniscus in DPN Patterning

Another important question is to what degree the condensed water meniscus between the AFM tip and the surface influences the rate and morphology of DPN deposition. The reason for the humidity dependence of DPN is formulated as follows: it is well known that the size of the water meniscus varies significantly with the relative humidity; since the meniscus facilitates (or inhibits) the transport of the ink to the surface, the larger the meniscus, the greater (smaller) the deposition area, resulting in larger (smaller) written nanofeatures. It has been demonstrated that the feature size/humidity relationship is strongly dependent on the chemical nature of the ink; for example, increased humidity will increase the feature size of certain inks such as MHA [41, 50, 51] and DNA [36] but can decrease the feature size of other inks, such as ODT [41, 49, 51]. The ubiquitous role of water in DPN patterning is underscored by its effect on patterning at 0% humidity [41, 49, 51]; unless water has been rigorously removed from a surface, adventitious surface-bound water can still mediate ink transport [41].

Jang et al. performed grand canonical Monte Carlo simulations to describe meniscus condensation in DPN [52]. The authors found that the dynamics of meniscus formation depend on the relative humidity, temperature, AFM tip–substrate distance, tip diameter, and the chemical natures of the tip and surface. They also investigated the thermodynamic stability of the meniscus. They demonstrated that the meniscus increases in size with relative humidity and decreases with decreasing tip diameter.

Because of the importance of chemical composition, each DPN ink will probably have a unique humidity dependence. Experiments to establish similarities and differences between the transport of different chemical inks would significantly aid the understanding of DPN. Another important area to be explored is the role of surface chemistry, which is well known to influence capillary phenomena. As with the diffusion experiments, more reproducible experimental conditions and further theoretical and experimental studies on ink–meniscus interactions may aid the understanding of the exact role of condensed water in DPN transport

3.4. AFM Tip–Ink Interactions

To date, no detailed studies have been performed to study AFM tip–ink interactions, but some information has been reported about the effect of AFM tip chemistry on DPN writing. Demers et al. reported that that chemical functionalization of the AFM tip with APTES, a cationic self-assembled monolayer, enhanced the quality and reproducibility of DNA writing [36]. The authors reported that the APTES enhanced the wettability of the tip by DNA, enabling significant patterning before the tips had to be reinked. Schwartz reported that the method of coating the tip had a dramatic impact on the DPN writing; if a tip was coated using vapor-phase MHA, it did not write, but tips coated using MHA/acetonitrile solutions wrote immediately [51]. The author hypothesized that the coadsorbed acetonitrile or other additives may play a role in the patterning process. Matsubara et al. reported that alkoxy functionalization of the furan ink was necessary to

achieve adhesion to the AFM tip for a DPN-induced Diels–Alder reaction [44], but no further discussion of the effects of chemical functionalization of the ink was reported. In simulations, Jang et al. demonstrated that the wettability of the AFM tip affects the size of the condensed water meniscus [52]. These studies suggest that AFM tip–ink interactions can play an important role in the patterning process. Further studies investigating different AFM tip chemistries and ink aggregation on the tip will increase the understanding of the ink dissolution process.

4. DPN AS A TOOL FOR TEMPLATING AND MECHANISTIC STUDIES

DPN has been shown to be capable of patterning many types of materials on a variety of surfaces. Though many unique demonstrations of DPN have appeared in the literature, in the future it will primarily be a patterning tool rather than an independent research topic. Other innovative lithographic techniques have already proven their usefulness for investigations in other areas; for instance, soft lithography has emerged as an important tool for biopatterning [57] and electron-beam lithography is routinely used for electronic investigations of nanostructures [14]. DPN is beginning to make a similar transition to become a multidisciplinary research tool. Here we describe some recent efforts where DPN is used for mechanistic studies and templating of surfaces.

4.1. Surface Self-Assembly Studies

Soon after the first demonstration of DPN, Hong et al. used DPN to study the AFM tip-directed local formation of self-assembled monolayer (SAM) films [59]. An ODT- or MHA-coated tip was raster scanned over an Au surface and simultaneous lateral force microscopy images were obtained. ODT monolayers were shown to nucleate as small islands and grow with each consecutive scan until a continuous monolayer was observed in the entire scan area. MHA monolayer films, however, did not appear to have distinct nucleation sites; uniform growth was observed over the entire scan area.

Because the AFM tip can be used as a patterning and an imaging tool, DPN can be used to study nanoscale surface deposition and assembly. An interesting example of the unique facility of DPN for these types of investigations was demonstrated by Hong et al. [60]. A "molecular corral" was fabricated using ODT and MHA patterns. A MHA dot of sufficient size was deposited in the center of the corral so that the MHA molecules could approach with the walls. If the wall was made of ODT, deposition of the MHA was confined to within the walls of the corral. If the walls were made of MHA, however, the ink could diffuse through the walls to the bare gold surface outside (Fig. 16). The ability of DPN to pattern nanometer size features with high registration makes it ideal for these types of studies where high precision and flexibility are required.

Another surface assembly study was presented by Ivanisevic et al. Combinatorial templates generated by DPN were used to study the stability of diverse alkanethiol
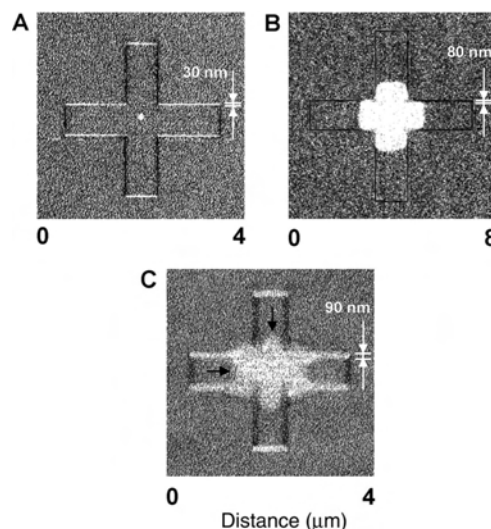
Figure 16. (A) A "molecular corral" fabricated from ODT lines (dark) and MHA lines (light). Note that the MHA in the interior of the corral will not diffuse through the ODT walls (B) but will diffuse through MHA walls. (C) Reprinted with permission from [60], S. H. Hong and C. A. Mirkin, *Science* 288, 1808 (2000). © 2000, American Association for the Advancement of Science.

molecules on Au substrates [39]. The authors explored the exchange kinetics of MHA and ferrocene-terminated monolayers with ODT molecules coated on the AFM tip. They found that the MHA patterns were significantly more stable than patterns of the ferrocene-terminated compounds because of the greater packing stability of MHA. The authors also demonstrated that SAMs formed on single-crystal gold were more stable than those formed on amorphous Au substrates.

4.2. DPN Generated Templates

One important application of lithography is pattern transfer to underlying surfaces. Photolithography, e-beam lithography, and soft lithography have been used to create relief structures using a variety of resists. Weinberger et al. used DPN patterning of alkanethiol resists and chemical etching to transfer the DPN-generated patterns to underlying Au and Si surfaces (Fig. 17) [61, 62]. Similarly generated structures have been used for the combinatorial templating of thiolated DNA [63] and for the fabrication of Au electrodes with sub-100 nm interelectrode spacing [64].

The most widely used ink for templating of surfaces is MHA. The –COOH terminal group of MHA is easily liked with other moieties using carbodiimide or other chemistries, making it ideal for templating of materials through chemical functionalization. MHA can also be used as an electrostatic template because it is negatively charged in aqueous solutions. DPN generated MHA dots have been used as a template for the electrostatic assembly of amidine-modified polystyrene particles [65] and magnetic nanoparticles [66] and for the covalent attachment of DNA [67] and biotin/streptavidin [68]. Significantly, MHA-templated biomolecules maintain their biological activity.

Ivanisevic et al. demonstrated redox-controlled nanoparticle assembly on DPN-fabricated nanofeatures [69]. The
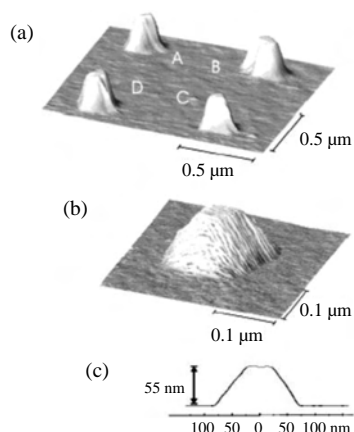
Figure 17. Topographic images of islands of Au/Ti/Si generated by pattern transfer of DPN-generated alkanethiol etch resists. (a) Four islands of (A) 65 nm, (B) 110 nm, (C) 75 nm, (D) 105 nm top diameter; (b) single island; (c) cross-section image of (b). Reprinted with permission from [61], D. A. Weinberger et al., *Adv. Mater.* 12, 1600 (2000). © 2000, Wiley–VCH.

Figure 18. Cellular spreading experiment on DPN-generated structures. (A) Schematic of cellular spreading procedure. (B) Representative image of protein arrays on DPN-templated structures for cellular adsorption. (C) Large optical micrograph of cellular adhesion. (D) Zoom in of cellular adhesion on DPN-generated template. Reprinted with permission from [40], K. B. Lee et al., *Science* 295, 1702 (2002). © 2002, American Association for the Advancement of Science.

authors wrote patterns of two redox-active ferrocene-terminated alkanethiol inks with different reduction potentials. Upon application of an appropriate voltage pulse, the ferrocene moiety became charged and was used to guide electrostatic assembly of oppositely charged nanoparticles. Orthogonal assembly of nanoparticles was demonstrated when the voltage pulses were cycled between the two redox potentials.

A DPN generated template was used to study the surface-mediated biological recognition of protein/cell systems [40]. MHA dots were patterned on a triethylene glycol terminated monolayer background. Significant protein adsorption was observed on the MHA areas, but no protein adsorption was seen on the ethylene glycol-modified background. The proteins maintained biological activity after adsorption to the MHA surface. Significantly, using DPN templating, cellular adsorption on submicrometer protein structures could be studied for the first time (Fig. 18).

Templates generated using E-DPN have been used for selective growth of other materials. Li et al. used a Pt line for the site-specific, selective chemical vapor depostion of carbon [46]. Maynor et al. showed that a poly(ethylenedioxythiophene) feature fabricated by E-DPN could be used as a template for the selective nucleation of gold nanoparticles (Fig. 19) [47].

5. PARALLEL PATTERNING WITH MULTIPLE DPN TIPS

DPN is a serial process; for many applications, this is not a drawback, but for applications where large-area (mm and larger) patterning is desired, the utility of single-tip DPN may be limited. However, it has been demonstrated that DPN with multiple AFM "pens" is possible. Multipen patterning will greatly expand the scientific and commercial utility of DPN.

Hong and Mirkin were able to use up to eight co-mounted AFM cantilevers for multitip, multi-ink DPN [60]. Significantly, only one AFM feedback-driven AFM tip was required even though writing was performed with multiple tips. The authors suggested that the reason for this observation is that capillary forces due to the condensed meniscus regulate the height of the other tips and facilitate ink transport. Therefore, if one tip is feedback controlled, the other tips move in concert with the controlling tip, enabling patterning with all
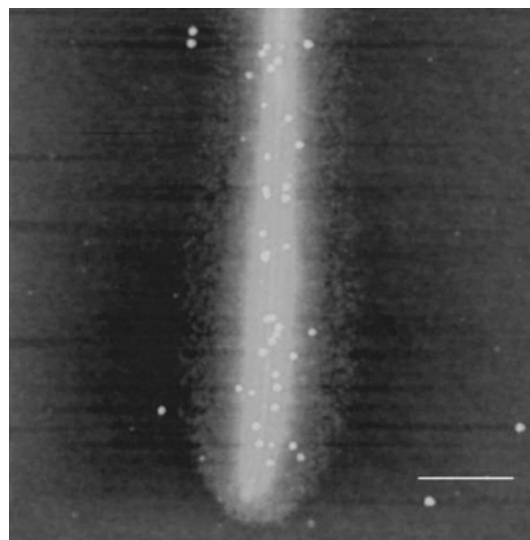
Figure 19. Topographic image of PEDOT template for preferential Au nanoparticle nucleation. The PEDOT line was generated by E-DPN and the gold nanoparticles were prepared by solution-phase reduction of HAuCl$_4$ in the presence of the template. Reprinted with permission from [47], B. W. Maynor et al., *J. Am. Chem. Soc.* 124, 522 (2002). © 2002, American Chemical Society.
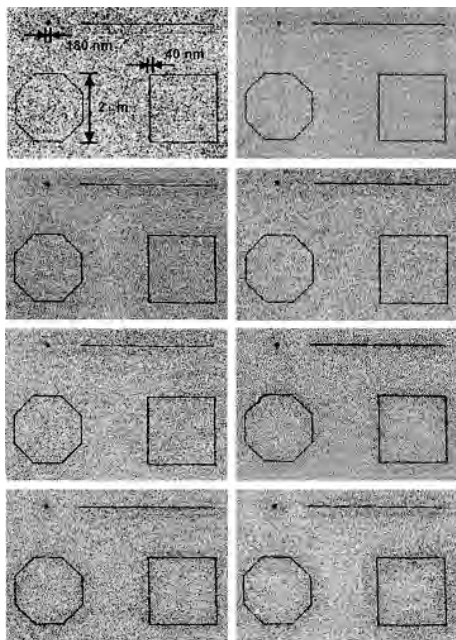
Figure 20. Lateral force microscopy images of eight identical ODT patterns generated by an eight-tip multipen DPN apparatus. Only one tip was under active AFM feedback control, while the other seven tips were passively following. Reprinted with permission from [60], S. H. Hong and C. A. Mirkin, *Science* 288, 1808 (2000). © 2000, American Association for the Advancement of Science.

tips. Multiple-ink nanostructures were fabricated using two tips and up to eight tips could be used for simultaneous patterning (Fig. 20).

Recently, progress has been made toward microfabrication of multiple AFM cantilevers for DPN-specific applications [70]. Using standard microfabrication techniques, 8 and 32 tip AFM cantilever arrays have been fabricated with cantilever spring constants and tip radii that are suitable for multipen DPN (Fig. 21). These tips have been shown to be capable of parallel DPN writing.

The flexibility of DPN would be a great advantage for patterning of many devices, such as displays, microarrays, and circuits. Though single-tip DPN may not be practical for these types of applications, multipen DPN could be a viable fabrication strategy. When practical, scalable multipen, multi-ink DPN is realized, DPN will be posed to become a flexible nano- and microfabrication tool for large scale laboratory and commercial applications [62].
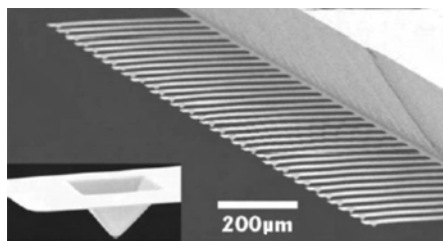
Figure 21. Thirty-two pen array fabricated for multipen DPN. Reprinted with permission from [70], M. Zhang et al., *Nanotechnology* 13, 212 (2002). © 2002, Institute of Physics.

6. SUMMARY

Dip-pen nanolithography is a flexible nanofabrication technique that has been used to pattern many types of materials on surfaces. DPN is an experimentally simple yet extraordinarily powerful technique for material patterning at a variety of length scales. Patterning of SAMs, polymers, organic molecules, inorganic substances, and biological molecules on metallic, semiconducting, and insulating surfaces has been reported. More examples are currently appearing in the literature, and as new applications for nanostructures and new DPN nanofabrication strategies are envisioned, more material/surface systems will be used for DPN patterning.

Though DPN has been demonstrated to be a very general process that works for many types of materials, the specifics of the material transport mechanism are still under debate. Further mechanistic studies need to be performed before a complete understanding of the DPN process is obtained. The mechanism of ink dissolution from the tip, ink transport, and specific ink–tip, ink–surface, and capillary interactions are important issues that need to be carefully considered. Furthermore, each ink and surface will provide unique challenges that need to be understood. These mechanistic investigations into the material transport process will further extend the flexibility and applicability of DPN patterning.

Though much of the recent work has focused on extending DPN to new systems, it is beginning to evolve into a multidisciplinary patterning and templating tool. Because DPN requires minimal equipment (only a commercial AFM), the number of research groups using DPN-patterned substrates for a variety of applications can be expected to increase rapidly. Furthermore, DPN is a direct-write technique that can simultaneously pattern at a variety of length scales simply by changing the writing speed, which makes it ideal for the generation of templates and other experimental platforms. To date, DPN generated structures have been used to characterize phenomena ranging from surface assembly to biological interactions, but these examples just scratch the surface of all the possible applications for which DPN templates could be used. Furthermore, DPN is unique in that it can be used to precisely deliver reagents to surfaces and also to characterize them by AFM imaging. This feature will enable DPN to be used to study nanoscale chemical phenomena by delivering reactants to a specific location and imaging the resulting products. Though single-tip fabrication itself is exciting, multitip DPN will facilitate large-scale patterning, thereby extending the utility of this technique beyond the laboratory and into the commercial realm.

DPN is a very exciting research area with potential applications in fields ranging from applied physics to biology. Because it is a simple technique requiring only a commercial AFM, it should be accessible to many research groups in many fields. In the 3+ years since DPN was first demonstrated, over 35 publications by several independent research groups, including 22 in 2002 alone, have reported patterning, templating, or mechanistic studies. This is indicative of the excitement currently surrounding DPN. In the coming years as it makes the transition from an interesting research topic

to a bona fide technology, DPN should become a versatile and valuable nanopatterning tool.

GLOSSARY

AFM feedback The optoelectronic and mechanical system that maintains the AFM tip at a constant height above the surface, allowing accurate tracking of the surface topography.

Arrhenius temperature dependence An exponential relationship between temperature and reaction rate.

Atomic force microscope (AFM) A specific type of SPM where contact forces between the tip and the surface are used to image the surface topography.

Capillary forces The interactions between objects caused by the liquid film between them.

Conducting polymers Conjugated macromolecules that, when oxidized or reduced, behave as electrical conductors.

Deoxyribonucleic acid (DNA) A macromolecule consisting of one or two strands of linked deoxyribonucleotides.

Dip-pen nanolithography (DPN) A scanning probe lithography technique based on the localized transfer of materials from the AFM tip to the surface.

DNA hybridization Formation of a duplex structure by two complementary single strands of DNA.

Electron-beam lithography A lithography technique where an electron beam is used to define structures on surfaces.

Fluorescence The emission of light by a substance immediately after the absorption of energy from light of usually shorter wavelength.

Lateral force microscopy (LFM) A type of AFM where the frictional properties of the surface are measured.

Lithography Rational fabrication of structures on surfaces.

Microcontact printing A lithography technique where master patterns are coated with a desired material, then pressed against another surface, resulting in transfer of the material from the master to the surface according to the master pattern.

Photolithography The technique of using optical patterns to create structures on surfaces, akin to photography.

Scanning probe microscope (SPM) An instrument that can image surface topography and/or other properties by scanning a proximal probe over the surface. Typical imaging sizes range from 10×10 nm to 100×100 micrometers.

Self-assembled monolayers (SAM) Molecules that can covalently attach to a specific surface and produce ordered, single-layer thin films, especially alkanethinol thin films on noble metal surfaces.

REFERENCES

1. Special Issue on Nanotechnology, *Chemical and Engineering News*, 16 October 2000.
2. C. B. Murray, C. R. Kagan, and M. G. Bawendi, *Ann. Rev. Mater. Sci.* 30, 545 (2000).
3. T. Trindade, P. O'Brien, and N. L. Pickett, *Chem. Mater.* 13, 3843 (2001).
4. H. Bonnemann and R. M. Richards, *Euro. J. Inorg. Chem.* 2455 (2001).
5. M. A. El-Sayed, *Acc. Chem. Res.* 34, 257 (2001).
6. G. Z. Zhang, A. Z. Niu, S. F. Peng, M. Jiang, Y. F. Tu, M. Li, and C. Wu, *Acc. Chem. Res.* 34, 249 (2001).
7. M. Su, B. Zheng, and J. Liu, *Chem. Phys. Lett.* 322, 321 (2000).
8. M. S. Dresselhaus, G. Dresselhaus, and P. Avouris, in "Topics in Applied Physics," Vol. 80. Springer, New York, 2001.
9. J. T. Hu, T. W. Odom, and C. M. Lieber, *Acc. Chem. Res.* 32, 435 (1999).
10. S. Banerjee, A. Dan, and D. Chakravorty, *J. Mater. Sci.* 37, 4261 (2002).
11. G. R. Patzke, F. Krumeich, and R. Nesper, *Angew. Chem. Inter. Ed.* 41, 2446 (2002).
12. Y. N. Xia, J. A. Rogers, K. E. Paul, and G. M. Whitesides, *Chem. Rev.* 99, 1823 (1999).
13. H. O. Jacobs, A. R. Tao, A. Schwartz, D. H. Gracias, and G. M. Whitesides, *Science* 296, 323 (2002).
14. Y. Huang, X. F. Duan, Y. Cui, L. J. Lauhon, K. H. Kim, and C. M. Lieber, *Science* 294, 1313 (2001).
15. Y. L. Loo, R. L. Willett, K. W. Baldwin, and J. A. Rogers, *J. Am. Chem. Soc.* 124, 7654 (2002).
16. S. Y. Chou, C. Keimel, and J. Gu, *Nature* 417, 835 (2002).
17. R. M. Nyffenegger and R. M. Penner, *Chem. Rev.* 97, 1195 (1997).
18. M. F. Crommie, C. P. Lutz, and D. M. Eigler, *Science* 262, 218 (1993).
19. A. Naber, H. Kock, and H. Fuchs, *Scanning* 18, 567 (1996).
20. M. Tello and R. Garcia, *Appl. Phys. Lett.* 79, 424 (2001).
21. K. Wilder, C. F. Quate, D. Adderton, R. Bernstein, and V. Elings, *Appl. Phys. Lett.* 73, 2527 (1998).
22. S. Jahromi, J. Dijkstra, E. van der Vegte, and B. Mostert, *Chem. Phys. Chem.* 3, 693 (2002).
23. S. W. Park, H. T. Soh, C. F. Quate, and S. I. Park, *Appl. Phys. Lett.* 67, 2415 (1995).
24. M. Rolandi, C. F. Quate, and H. J. Dai, *Adv. Mater.* 14, 191 (2002).
25. L. Santinacci, T. Djenizian, and P. Schmuki, *J. Electrochem. Soc.* 148, C640 (2001).
26. H. Sugimura and N. Nakagiri, *J. Vac. Sci. Technol. A* 14, 1223 (1996).
27. R. Maoz, S. R. Cohen, and J. Sagiv, *Adv. Mater.* 11, 55 (1999).
28. R. Maoz, E. Frydman, S. R. Cohen, and J. Sagiv, *Adv. Mater.* 12, 725 (2000).
29. R. Maoz, E. Frydman, S. R. Cohen, and J. Sagiv, *Adv. Mater.* 12, 424 (2000).
30. R. D. Piner, J. Zhu, F. Xu, S. H. Hong, and C. A. Mirkin, *Science* 283, 661 (1999).
31. S. H. Hong, J. Zhu, and C. A. Mirkin, *Science* 286, 523 (1999).
32. B. W. Maynor, Y. Li, and J. Liu, *Langmuir* 17, 2575 (2001).
33. M. Su, X. G. Liu, S. Y. Li, V. P. Dravid, and C. A. Mirkin, *J. Am. Chem. Soc.* 124, 1560 (2002).
34. L. Porter, C. Choi, J. Schmeltzer, A. Ribbe, L. Elliot, and J. Buriak, *Nano Lett.* 2, 1369 (2002).
35. D. L. Wilson, R. Martin, S. Hong, M. Cronin-Golomb, C. A. Mirkin, and D. L. Kaplan, *Proc. Nat. Acad. Sci.* 98, 13660 (2001).
36. L. M. Demers, D. S. Ginger, S. J. Park, Z. Lee, S. W. Chung, and C. A. Mirkin, *Science* 296, 1836 (2002).
37. A. Ivanisevic and C. A. Mirkin, *J. Am. Chem. Soc.* 123, 7887 (2001).
38. M. Su and V. P. Dravid, *Appl. Phys. Lett.* 80, 4434 (2002).
39. A. Ivanisevic, K. V. McCumber, and C. A. Mirkin, *J. Am. Chem. Soc.* 124, 11997 (2002).
40. K. B. Lee, S. J. Park, C. A. Mirkin, J. C. Smith, and M. Mrksich, *Science* 295, 1702 (2002).
41. S. Rozhok, R. Piner, and C. A. Mirkin, *J. Phys. Chem. B*, 107, 751 (2003).
42. R. McKendry, W. T. S. Huck, B. Weeks, M. Florini, C. Abell, and T. Rayment, *Nano Lett.* 2, 713 (2002).
43. J. H. Lim and C. A. Mirkin, *Adv. Mater.* 14, 1474 (2002).
44. S. Matsubara, H. Yamamoto, K. Oshima, E. Mouri, and H. Matsuoka, *Chem. Lett.* 886 (2002).

45. A. Noy, A. E. Miller, J. E. Klare, B. L. Weeks, B. W. Woods, and J. J. De Yoreo, *Nano Lett.* 2, 109 (2002).
46. Y. Li, B.W. Maynor, and J. Liu, *J. Am. Chem. Soc.* 123, 2105 (2001).
47. B. W. Maynor, S. F. Filocamo, M. W. Grinstaff, and J. Liu, *J. Am. Chem. Soc.* 124, 522 (2002).
48. J. Jang, S. Hong, G. Schatz, and M. Ratner, *J. Chem. Phys.* 115, 2721 (2001).
49. P. E. Sheehan and L. J. Whitman, *Phys. Rev. Lett.* 88, 16104 (2002).
50. B. L. Weeks, A. Noy, A. E. Miller, and J. J. De Yoreo, *Phys. Rev. Lett.* 88, 255505 (2002).
51. P. V. Schwartz, *Langmuir* 18, 4041 (2002).
52. J. Y. Jang, G. C. Schatz, and M. A. Ratner, *J. Chem. Phys.* 116, 3875 (2002).
53. R. D. Piner and C. A. Mirkin, *Langmuir* 13, 6864 (1997).
54. J. L. Wilbur, A. Kumar, E. Kim, and G. M. Whitesides, *Adv. Mater.* 6, 600 (1994).
55. A. Kumar, H. A. Biebuyck, and G. M. Whitesides, *Langmuir* 10, 1498 (1994).
56. Y. N. Xia and G. M. Whitesides, *Angew. Chem. Inter. Ed.* 37, 551 (1998).
57. G. M. Whitesides, E. Ostuni, S. Takayama, X. Y. Jiang, and D. E. Ingber, *Ann. Rev. Biomed. Eng.* 3, 335 (2001).
58. N. A. Amro, S. Xu, and G. Y. Liu, *Langmuir* 16, 3006 (2000).
59. S. Hong, J. Zhu, and C. A. Mirkin, *Langmuir* 15, 7897 (1999).
60. S. H. Hong and C. A. Mirkin, *Science* 288, 1808 (2000).
61. D. A. Weinberger, S. G. Hong, C. A. Mirkin, et al., *Adv. Mater.* 12, 1600 (2000).
62. C. A. Mirkin, S. H. Hong, and L. Demers, *Chem. Phys. Chem.* 2, 37 (2001).
63. H. Zhang, Z. Li, and C. A. Mirkin, *Adv. Mater.* 14, 1472 (2002).
64. H. Zhang, S. W. Chung, and C. A. Mirkin, *Nano Lett.*, 3, 43 (2003).
65. L. M. Demers, S. J. Park, T. A. Taton, Z. Li, and C. A. Mirkin, *Angew. Chem. Int. Ed.* 40, 3071 (2001).
66. X. G. Liu, L. Fu, S. H. Hong, V. P. Dravid, and C. A. Mirkin, *Adv. Mater.* 14, 231 (2002).
67. L. M. Demers and C. A. Mirkin, *Angew. Chem. Int. Ed.* 40, 3069 (2001).
68. J. Hyun, S. J. Ahn, W. Lee, A. Chilkoti, and S. Zauscher, *Nano Lett.* 2, 1203 (2002).
69. A. Ivanisevic, J. H. Im, K. B. Lee, S. J. Park, L. M. Demers, K. J. Watson, and C. A. Mirkin, *J. Am. Chem. Soc.* 123, 12424 (2001).
70. M. Zhang, D. Bullen, S. W. Chung, S. Hong, K. S. Ryu, Z. F. Fan, C. A. Mirkin, and C. Liu, *Nanotechnology* 13, 212 (2002).

Disulfide-Bond Associated Protein Folding

Hideki Tachibana

Kobe University, Kobe, Japan

Shin-ichi Segawa

Kwansei Gakuin University, Sanda, Japan

CONTENTS

1. INTRODUCTION

1.1. Protein Folding Problem

Proteins are linear macromolecules with a non-repeated specific covalent structure that is determined by the structures of the 20 different L-amino acids and by the order in which they are linked together into a polypeptide chain. The amino acid sequence of hen lysozyme, which is called the primary structure, is schematically shown in Figure 1. The conformation of a protein is specified by the torsion angles ϕ and ψ of each residue (Fig. 2) [1–3]. To be biologically active, a protein must adopt a specifically folded three-dimensional structure, as shown in Figure 3 for lysozyme. Almost all proteins can spontaneously refold *in vitro* after being completely unfolded, so the three-dimensional structure (tertiary structure) must be determined by the primary structure. The precision and reproducibility of this folding are so high that polypeptide chains with the same amino

acid sequence arrive at conformations sufficiently homogeneous to form macroscopic crystals. The protein folding problem refers to how a protein adopts a specific active conformation. This is a special problem because of the great many numbers of conformations possible. With an average of 8 equally probable conformations per amino acid residue [4] and 100 residues in the polypeptide chain, the total number of possible conformations of the polypeptide chain will be $8^{100} \approx 10^{90}$. How does a protein among such great number of conformations select a specific native conformation? The ultimate determinant of the native conformation is the amino acid sequence. What are the rules governing the relationship between amino acid sequence and three-dimensional structure? It had been primarily of academic interest, but has recently emerged as a pressing practical problem. The lack of understanding of how the folding of the amino acid sequences is controlled makes it difficult to interpret rapidly accumulating genetic data. This situation is highlighted by the coming of the human genome project, which will yield the sequences of thousands of genes whose protein products are of unknown function.

In this chapter, general aspects of protein folding such as the physical basis of the structure, stability of folded proteins, kinetic process or pathway of protein folding, and characteristics of the transition state for folding will be first described in Section 2.

1.2. Protein Folding Coupled with the Formation of Disulfide Bonds

Historically, the so-called "thermodynamic hypothesis," which states that the three-dimensional structure of a native protein is the one in which the Gibbs free energy of the
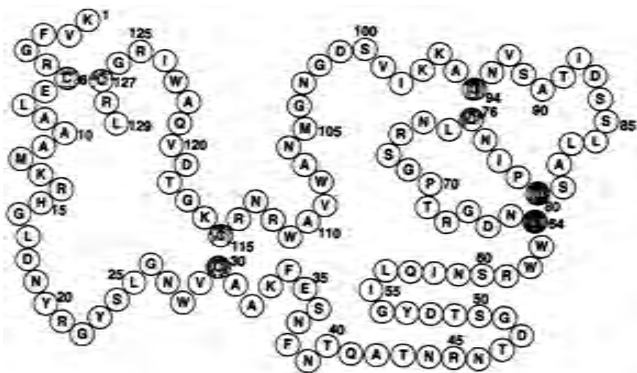
Figure 1. Schematic representation of the amino acid sequence of hen lysozyme. Each small circle denotes an amino acid residue, and is labeled with a one-letter symbol that stands for amino acid species. Hen lysozyme consists of 129 amino acid residues. Residues in proteins are linked successively through peptide bonds (see Fig. 2) to form a linear polypeptide chain. The residue number in lysozyme is also labeled in every five residues mostly. An amino group ($-NH_2$), a carboxyl group ($-COOH$), and a hydrogen atom that are bonded to a central carbon atom (termed an α-carbon; $C\alpha$) are three common constituents of α-amino acids. The fourth group that is bonded to $C\alpha$ is called "side-chain." It differs among amino acid species and depicts their physicochemical and biological properties. One-letter symbols, three-letter abbreviations, and corresponding full names of 20 amino acids are: A, Ala, alanine; C, Cys, cysteine; D, Asp, aspartic acid; E, Glu, glutamic acid; F, Phe, phenylalanine; G, Gly, glycine; H, His, histidine; I, Ile, isoleucine; K, Lys, lysine; L, Leu, leucine; M, Met, methionine; N, Asn, asparagine; P, Pro, proline; Q, Gln, glutamine; R, Arg, arginine; S, Ser, serine; T, Thr, threonine; V, Val, valine; W, Trp, tryptophan; Y, Tyr, tyrosine. In one group of amino acids, the side chains are nonpolar and aliphatic (G, A, V, L, I, P); in another group, they are polar and charged, positively (K, R, H) or negatively (D, E); in a third group, they are polar and uncharged (S, T, N, Q); in a fourth group, they are aromatic (F, Y, W); in a fifth group, they contain a sulfur atom (C, M). The diversity of physicochemical and biological properties of proteins derives from the combinatorial diversity in the sequential arrangement of the twenty amino acids of different physicochemical properties. Each residue in a protein can be specified by using the abbreviation followed by its residue position: Lys1, Val2, Phe3, or K1, V2, F3, and so on. The linkage between adjacent amino acid residues is a peptide bond (–CO–NH–), which is formed by a condensation reaction with the removal of a water molecule from the α-carboxyl group of the preceding amino acid and the α-amino group of the following amino acid. Biosynthesis of proteins on the cellular machinery, ribosome, proceeds in this direction, and the residues are correspondingly numbered. Therefore, usually, the first residue has a free α-amino group whereas the last residue has a free α-carboxyl group. In the native form of hen lysozyme, disulfide bonds are formed between the side-chains of Cys6 and Cys127, Cys30 and Cys115, Cys64 and Cys80, Cys76 and Cys94 (gray circles). In a reduced (i.e., disulfide-cleaved) form of hen lysozyme, the two Cys residues involved in the disulfide bond of the oxidized (i.e., disulfide-bonded) form of lysozyme, are not necessarily in spatial proximity.

Figure 2. Torsion angles ϕ and ψ for an amino acid residue. Each amino acid residue inside a protein has an imino group (–NH–) as well as a carbonyl group (–CO–) attached to $C\alpha$, a central, asymmetric (except for glycine) carbon atom. The torsion (or dihedral) angle ϕ of the ith residue is the rotation angle defined by the atoms C_{i-1}, N_i, $C\alpha_i$, and C_i (here, the atoms belonging to the ith residue have a suffix i): looking along the N_i–$C\alpha_i$ bond with the atom N_i in front as in Newman's projection formula, the clockwise rotation of the $C\alpha_i$–C_i bond in back with respect to the C_{i-1}–N_i bond in front is given a positive value, and counterclockwise rotation a negative value. It equals to $0°$ for *cis* form and $180°$ (or $-180°$) for *trans* form. Likewise, the torsion (or dihedral) angle ψ of the ith residue is the rotation angle defined by the atoms N_i, $C\alpha_i$, C_i, and N_{i+1}. The atoms involved in a peptide bond, N, H, C, and O, lie in a plane due to its partial double-bond character, and dihedral angle (denoted ω) defined by $C\alpha_i$, C_i, N_{i+1}, and $C\alpha_{i+1}$ is close to $180°$ (*trans* peptide) or, less frequently, to $0°$ (*cis* peptide). Thus, the four atoms in the peptide bond and two neighboring $C\alpha$ atoms are in a plane (trapezia with blue sides). As for the side chain of each residue, N, $C\alpha$, $C\beta$, and $C\gamma$ ($C\gamma$ atom is absent in the figure: the ith residue in this case is alanine) define the side chain dihedral angle χ_1; in larger side chains, the next set of four atoms shifted further by one bond to the distal end of the side chain define χ_2, and so on.

whole system is lowest, and the concept that all the information required to determine the final native conformation of a protein resides in the primary sequence of amino acids, were established through the studies on the spontaneous refolding of ribonuclease A upon removal of denaturant in the presence of thiol reagents via rearrangement of "scrambled" disulfide bonds to a native linkage [5]. Here, a unique

property of cysteine, one of the twenty amino acids that comprise proteins, was utilized.

Among the 20 amino acids, cysteine and methionine contain sulfur atoms. Cysteine was first isolated from cystolith. Cysteine is relatively rare, and its occurrence in proteins is only a few percent. Nevertheless, considerable
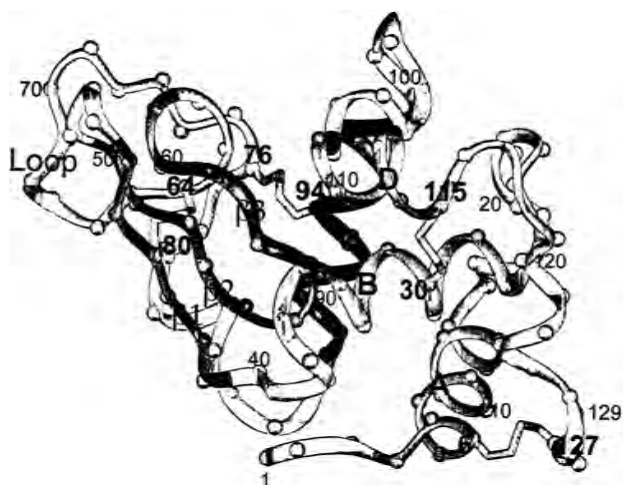
Figure 3. Ribbon diagram of the folded structure of native hen lysozyme [PDB 6LYZ]. The tertiary fold of polypeptide main chain is shown by using a ribbon, on which small balls represent the position of Cα of each amino acid residue. The residue number was labeled in every ten residues in order to follow the fold. In addition, those for the Cys residues participating in disulfide bonds were labeled in bold and large. As for the secondary structures (see Fig. 4), four α-helical segments, labeled A (residue numbers 4–15), B (24–36), C (88–99), and D (108–115), are colored magenta, while three β-strands, labeled β1 (41–46), β2 (50–55), and β3 (56–61), are blue. A loop region (62–78) appears in this figure at top left behind. Side chains are not shown except for the yellow sticks that represent (Cα)–Cβ–S–S–Cβ–(Cα) bonds in the four disulfide cross-links. The right and left halves in the structure roughly correspond to the α- and β-domains, respectively, and the C-helix behind is at the interface between them.

numbers of proteins, especially extracellular proteins, contain cysteinyl residues. Cysteine, $HSCH_2CH(NH_2)COOH$, has a sulfhydryl group, SH, in its side chain. Sulfhydryl groups are highly reactive, and combine with various reagents and metal ions [6]. The high reactivity of sulfur compound derives from the relatively low energy of the lowest unoccupied molecular orbital and high energy of the highest occupied molecular orbital [7]. The most characteristic reaction of cysteine is that two molecules can combine with each other, under oxidizing conditions, through a covalent linkage, called "disulfide bond," SS, to form a cystine molecule $HOOCCH(NH_2)CH_2SSCH_2CH(NH_2)COOH$. In proteins, formation of disulfide bonds between cysteinyl residues results in covalent cross-links within a polypeptide chain or between polypeptide chains. Such cross-links generally stabilize higher-order structure of proteins. A familiar example can be found in keratins, disulfide-rich proteins produced by epithelial cells. Skin, hair, wool, feather, nail, and horn are made up of particular families of keratin proteins, and there exists a correlation between their physical hardness and cystine content. As is well known in permanent wave treatment, disulfide bonds can be cleaved under reducing conditions and reformed with different linkages under oxidizing conditions.

However, the important role of disulfide bonds is found not only in such assemblies of proteins that are directly involved in the formation of relatively macroscopic biological structures. More fundamentally, disulfide bonds are

involved in a considerable number of cases to assist "protein folding," the acquisition of native three-dimensional structures of proteins essential for the expression of their activities. Protein folding is an elaborate nanoscale process that lies at the interface of materials science and biological science. In proteins with disulfide bonds, when all the disulfide bonds are reduced to thiol groups, they generally lose their native three-dimensional structure and biological function. When favorably coupled with the formation of three-dimensional structure of protein, the formation of disulfide bonds will stabilize the protein structure. In turn, the protein structure will stabilize disulfide bonds against cleavage.

Protein structure is made up of a number of noncovalent interactions, such as van der Waals interactions, hydrogen bonds, and electrostatic interactions. Disulfide bonding is the only covalent interaction coupled with folding of protein. In the case of ribonuclease A mentioned above, which contains eight cysteinyl residues, a total of 105 ways exist to form four disulfide bonds among them in the scrambled state. The attainment of a single native disulfide-pairing pattern out of the 105 possibilities is a good indicator of the accurate attainment of a correct three-dimensional structure. Furthermore, since disulfide bonds are stable under particular conditions that preclude reshuffling, or unreacted free sulfhydryl groups can be blocked stably, it is possible to trap and characterize intermediate species during the folding process. Moreover, by virtue of the development of site-specific mutagenesis methods in recombinant DNA technology and of related protein engineering techniques, it has been made possible, in principle, to construct recombinant analogues of any disulfide-intermediates that lack specific disulfide bond(s).

In this chapter, elementary properties of disulfide bonds in proteins and the mechanism of protein stabilization by disulfide bonds are described in Section 3. Next, the pathways of disulfide-associated folding of four representative proteins, bovine pancreatic trypsin inhibitor, ribonuclease A, hen lysoyme, and alpha-lactalbumin, are reviewed in Section 4. Then, structure and properties of the disulfide-intermediates and their analogues of these four proteins are described with implications for their folding mechanisms.

2. GENERAL ASPECTS OF PROTEIN FOLDING

2.1. Initial and Final States of Protein Folding

Different conformations of a protein differ only in the angle of rotation about the bonds of the backbone and amino acid side-chains. The folded structure of a protein can be disrupted by relatively minor alterations in pH or temperature, the addition of denaturing agents (e.g., urea), or by reduction of disulfide bond. Loss of the folded structure of proteins can be readily followed by observing changes in spectroscopic properties (absorption, circular dichroism, fluorescence, and NMR spectra). Unfolding transitions for a single-domain protein generally approximate to a two-state model in which only the fully folded native (N) and fully

unfolded denatured (U) states are populated [8]. It is represented as a chemical reaction of both first-order steps: U—N. The two-state nature of the unfolding transition results from the cooperative nature of the interactions that stabilize protein structure.

2.1.1. Unfolded State

The simplest model for a disordered polymer is known as the freely joined chain, a series of segments of constant length that are connected with a completely free joint at each junction. This is called a random coil, because consecutive segments follow a random walk pattern. A random coil approximates the ideal unfolded protein, in which the torsion angles ϕ and ψ of each residue are independent of others along the amino acid sequence. Since only certain values of ϕ and ψ are permitted because of unfavorable steric interactions between atoms of the same and neighboring residues, the conformational flexibility of a real unfolded protein is limited [1]. In spite of these restrictions, however, there are very many conformations possible even for a small protein. A collection of such chains will represent a great number of different conformations, all with about the same energy. For a protein consisting of 100 amino acids, the number of possible conformations amounts to 10^{90}, as mentioned above. If the rate constant for converting conformations is 10^{11} s^{-1}, it would require, on average, more than 10^{69} years for a polypeptide chain to sample 10^{90} conformations. It should therefore be impossible for a fully unfolded protein to fold in this way on a finite time-scale. This was the initial indication that there must be pathways for protein folding and has come to be known as the "Levinthal paradox" [9].

The unfolded state of protein means highly open and solvent exposed states. The apparent size of a chain of given length will depend markedly upon the chemical nature of both the polymer and the solvent. In a "good" solvent, a polymer chain is highly expanded because the interactions between the solvent and the units of the chain are preferred over the interactions between the chain units themselves. In a "poor" solvent, these relations are reversed and the chain contracts in an attempt to exclude contact with the solvent as far as possible [10]. From such a point of view, water is actually a poor solvent for the polypeptide chain under conditions where the native folded state is stable. Very little water is normally found within the interiors of globular proteins. Charged residues are located preferentially at the protein surface, where they can interact with water; residues in the interior are close-packed, with the solvent essentially excluded and no voids; and burying hydrophobic groups and surfaces is a major source of stabilization [11].

The ambivalent relationship between polymers and solvent for the polypeptide/water pair appears to be at the root of the unusual behavior of this system [12]. The fully unfolded state of a protein has been thought to be properly described as a random coil [8]. Indeed, in good solvents, such as strong aqueous solutions of urea or guanidium chloride (GdmCl), the radius of gyration usually indicates a highly expanded polymer chain [13, 14]. On the other hand, there is a wide variety of evidence suggesting that unfolded proteins are less unfolded under other conditions, such as extremes of pH or temperature in the absence of denaturants [10]. This is perhaps not too surprising, because a real polypeptide chain is composed of 20 different amino acids, with a variety of chemical properties. In such a case where interactions between different parts of the polypeptide chain are energetically favored over those with solvent, the polypeptide chain will tend to be more compact and less disordered than expected for a random coil. The opposite will occur in the case where there are especially favorable interactions between solvent and polypeptide. Thus, one can imagine a collection of structures in which some parts of the chain are maximally extended, while others are contracted into compact forms depending on the amino acid sequence. The undoubted fact is that a fully unfolded, random-coil polypeptide chain is not possible in practice [15]. Most importantly, unfolded proteins do not generally contain cooperative folded structures. The interactions that stabilize folded proteins would not be expected to persist in the unfolded state. Certainly, most short peptides approximate random coils in solution, and only small degrees of local nonrandom conformation are usually apparent. There is a small tendency to adopt the α-helical conformation, which depends upon the local sequence [16, 17].

2.1.2. Folded State

The native, folded conformations of proteins are complex, but known in great detail from the structures determined by X-ray crystallography [18] and more recently, by NMR [19, 20]. The interiors of folded proteins consist primarily of elements of secondary structure (α-helices and β-sheets). As shown in Figure 4a, in the α-helix with 3.6 amino acid residues per turn, every carbonyl oxygen points upward along the helix and receives a hydrogen bond from the downward-pointing amide nitrogen of the fourth residue away from it. Another common structural element is the β-pleated sheet (Fig. 4b). Here the polypeptide chain backbone is relatively extended and each residue is rotated 180° with respect to the previous residue. The strands pack side by side, forming sheets in which each amide nitrogen donates a hydrogen bond to a carbonyl oxygen in the adjacent strand. The side-chains point out from the plane of the sheet, alternating above and below, in successive residues [18]. α-Helices and β-sheets make up about half the secondary structure of globular proteins, with the remainder occurring as tight turns, small loops, and random coil. The choice between these backbone conformations must be made during the folding.

The helices and sheets are packed together through interactions between their nonpolar side-chains. Ridges formed of side-chains projecting from helix faces pack into grooves between the ridges of other helix faces. In a similar way, the packing of helices against sheet involves complementary surfaces [21–23]. Examination of these interfaces reveals clearly that the fit is very sensitive to the location and character of the side-chains. These considerations suggest that after the chain is folded into such secondary structure as helices and β-sheets, the pattern of bulky residues on the faces of these structures determines whether they can pack together successfully.

Backbone folds of globular proteins are so complicated that rotations around the bond of the backbone readily
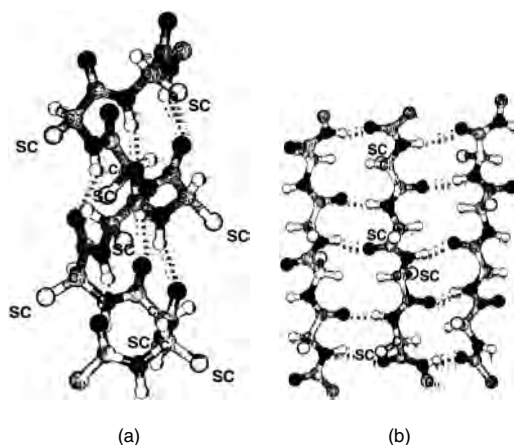
Figure 4. (a) Ball-and-stick model of a right-handed α-helix in proteins. Cα atoms and side chains (SC; only Cβ atoms are shown) are labeled. Hydrogen bonds are shown with white dotted lines. In the α-helices found in natural proteins, carbonyl groups tend to point outward and less straight at the NH groups than in the original model [2, 359]. Torsion angles ϕ and ψ for this conformation are $-62°$ and $-41°$, respectively [2]. Since all the peptide groups point in nearly the same direction, an α-helix has a macrodipole moment [360]. The side chains point away from the axis of helix. (b) Ball-and-stick model of an antiparallel β-sheet that is composed of three β-strands. Cα atoms and side-chains are indicated for the central strand, which runs downward in terms of the orientation of peptide bonds (–CO–NH–), while the left and right strands run upward, in antiparallel with the central strand. Individual β-strands are shown truncated in the figure; actually, they can derive from different regions of a single polypeptide chain or from different protein molecules. With the formation of hydrogen bonds (white dotted lines) between strands, a stable β-sheet is formed. Torsion angles ϕ and ψ for an ideal antiparallel β-sheet structure are $-139°$ and $+135°$, respectively [361]. Parallel β-sheets are also found.

cause the polypeptide chain to get tangled with itself; the rotation of torsion angles (ϕ, ψ) of a residue generally leads to the overlapping of the backbone. In order to avoid the steric overlap of the polypeptide chain, rotations around several bonds of the backbone must concertedly occur at different residues specified. Such events rarely happen. The movement of two rigid segments of structure in a protein relative to each other requires a "hinge." Although no structural units in a protein are literally rigid, some elements do tend to move as coordinated units without severe steric overlap in an attempt to rotate around the one or two bonds making up such a hinge. The sites of such flexible hinges are quite limited on the backbone, but actually found in the folded structure of proteins [24]. The region of the polypeptide chain has the potential to initiate the unfolding of compact structural units by the opening of the hinge. In such a sense, the structural elements dictated by flexible hinges might be folding units of protein. In fact, there is a good correspondence between folding units identified by the flexible hinges and structural units, "modules" found as the patterns in diagonal distance plot [25]. The modules are generally accepted to be constituent parts of globular proteins. It has been shown that module boundaries are closely correlated with the intron positions of genes that encode proteins [26].

In the folded protein, buried, labile protons undergo isotope exchange with solvent hydrogens [27], but the kinetics

of exchange are markedly slower than in unfolded polypeptides [28]. This indicates that, whereas buried protein atoms are shielded from solvent, the protein fluctuates around the time average structure and occasionally exposes buried sites to solvent [29]. Hydrogen exchange studies are carried out to characterize the nature of the fluctuations between conformational substates, or to monitor the major cooperative unfolding transition [30–32].

2.1.3. Non-Native State under Physiological Conditions

Refolding is initiated by restoring a protein from unfolding condition to refolding one. The unfolded state rearranges in the dead time (<1 ms) of a stopped-flow mixing experiment [33]. The starting state for protein folding is different from the fully unfolded state in solutions containing concentrated urea or GdmCl. This is the nonnative state under physiological conditions [10]. The properties of the starting state for folding are difficult to measure directly because it rapidly reacts to give products. But its properties can be inferred from kinetic studies and shown to be a disordered but compact state [34–37]. Such states may be related to the so-called molten-globule states [38–40]. These are compact, partly folded states of proteins that can sometimes be isolated under mildly denaturing conditions or when a cofactor or metal ion that is essential for stability has been removed. They are characterized by having few tertiary interactions, some secondary structure, and a fluctuating hydrophobic core and by being separated from the native state by a high free energy barrier. The role of this state will be considered in some detail later on.

2.2. Two-State Approximation

Both thermal and denaturant-induced unfolding are generally described adequately at equilibrium by a two-state model involving only U and N. The analysis of equilibrium unfolding requires an extrapolation of the base lines for the native (A_N) and for the unfolded protein (A_U) into the transition region to determine the fraction of native molecules, f_N, as a function of the unfolding parameter: $f_N = (A - A_U)/(A_N - A_U)$. The unfolding curve is given by plotting f_N against the concentration of a denaturant. The primary characteristic of cooperative two-state unfolding is that different probes of unfolding, such as fluorescence or absorbance measurements, circular dichroism, and viscosity give the same unfolding curve.

2.2.1. Physical Basis of Stability of Folded Proteins

Understanding the physical basis of stability of the folded state is crucial for understanding how such a conformation can be acquired. The interactions determining the tertiary structure are largely classified into two categories; they are "long-range" interactions between residues distant in the primary structure, and "short-range" interactions between groups close in the primary structure [41]. One can expect the following noncovalent interactions in proteins: van der Waals interactions, interactions between charged

groups, between polar groups (hydrogen bonds) and nonpolar groups. Each interaction energy is small, but because of the large number of interactions, the total interaction energies in the N and U states are large. Yet the N state is only marginally more stable than the U state [4]. Typical values of the difference in free energies of the N and U states for small natural proteins are -20 to -40 kJ/mol [42], so the equilibrium constant between the N and U states would have a value in the region of 10^4 to 10^7. This means that the folded state does not last forever. Folded proteins must transiently unfold completely even under the physiological condition, and then will promptly refold.

Rationalizing the stabilities of folded conformations should be careful, because the net effect is a relatively small difference between much larger individual factors. Nevertheless, it now appears that the two most important stabilizing interactions in the folded state are hydrogen bonds between polar atoms and the van der Waals interactions between nonpolar atoms [43]. The latter term is frequently called "hydrophobic interactions." The hydration around the exposed nonpolar groups is accompanied by the decrease in both entropy and enthalpy due to water ordering. These two factors result in the negative hydration free energy [44]. Therefore, the hydration itself attempts stabilizing the contacts between a nonpolar group and surrounding water, but cannot overcome the unfavorable increase in enthalpy due to breaking van der Waals interactions between nonpolar groups. This is the cause of hydrophobic interactions. These phenomena originate in a significant increase in heat capacity due to the exposure of nonpolar groups to water [4].

The contribution of hydrogen bonds to stability of the folded state might seem surprising in view of the fact that the unfolded protein undoubtedly forms an equal number of hydrogen bonds with water [45]. The largely fluctuating hydrogen bond of the protein polar group with relatively mobile water can hardly be identical to the bonds between the polar groups in the crystal-like interior of proteins. The latter can be much more stable, due to having an entropic advantage. This effect probably also accounts for the cooperativity of protein folding.

2.2.2. Cooperative Nature of Protein Stabilization

The two-state nature of unfolding transition indicates that folding is a cooperative process. It is due to the cooperativity that individually weak interactions can stabilize folded conformations; many of them work simultaneously to produce the system. The unfolding of protein has many of the characteristics of a phase transition from a crystal-like phase to a disordered phase, unlike a helix-coil transition of homopolymers based on the one-dimensional Ising model [46].

The cooperativity originates in the presence of long-range interactions in the folded structure. On the contrary, short-range interactions are noncooperative; they work independently on different sites on the polypeptide chain. When an elementary step of reaction brings some groups into proximity and orientation more favorable for interaction, not only short-range interactions at the reaction site but also long-range interactions at multiple sites are gained simultaneously. This is the cooperativity of many weak interactions. In order to make long-range interactions between

specific sites available, several folding elements must be preformed through short- and medium-range interactions. Therefore, the cooperativity of the long-range interactions is highlighted at the late stage of folding. On the other hand, little happens to the fully folded state prior to complete unfolding except for local structural fluctuations. When a global structural fluctuation happens, breaking one or more of the stabilizing interactions induces the destabilization of the other part, and consequently many sites are disrupted in a concerted manner. Within folded proteins, internal hydrogen bonds and the contacts of nonpolar surfaces are pulled apart without gaining comparable interactions with the solvent and with other surfaces, respectively. Yet the increase in conformational multiplicity in partially unfolded structures is not enough to compensate the unfavorable interactions. As a result, such partially unfolded states are largely unstable compared with the N and U states. These are the causes of the all-or-none character of unfolding transition.

The cooperativity of protein folding causes partially folded intermediates to be unstable and not populated at equilibrium, where the fully folded and fully unfolded states usually predominate. Consequently, it is necessary to study the folding process kinetically, as a function of time.

2.3. Kinetics of Protein Folding

2.3.1. Folding Scheme

A great many models have been proposed for the folding process [47]. For example, they are jigsaw puzzle model [48], nucleation/growth model [49], diffusion-collision-adhesion model [50], framework model [51], etc. The terminology is very confusing, and the differences between various models frequently appear to be small. Every folding model envisages hierarchical processes in which several preformed substructures are further assembled to build up the whole structure of protein. Points of difference are whether substructures are secondary structural elements present in the native structure or hydrophobic micro-domains, and whether substructures are assembled in a concerted manner or in a stepwise and progressive manner. It is unlikely that there is a single mechanism for protein folding. Whether folding is a concerted or stepwise process depends on the stability of individual substructures of the protein when they are decoupled from one another. The more the individual structures are stable, the more stepwise and hierarchical the folding process is.

Most models of folding imagine a sequential pathway of folding through a limited number of intermediates (the sequential model). The nucleation/rapid growth model imagines the appearance by random fluctuations of sufficiently small nucleus of structure that would not be stable but would serve as a template upon which the remainder of the polypeptide chain would fold rapidly. In this nucleation/rapid growth model, the initial nucleation event would be the rate-determining step.

In the diffusion-collision-adhesion model, individual nativelike micro-domains are recognized as being unstable in the initial unfolded protein and present with only low probabilities. The individual micro-domains will, however, stabilize each other when they interact. The rate constant

of formation of such a more stable substructure would be given by the rate at which they diffuse together.

The framework model imagines the folded structure to be formed by packing together pre-existing individual elements of secondary structure such as α-helices and β-sheets. The elements of secondary structure are imagined to have significant stability in the unfolded protein and the most difficult step to be their packing together.

There is a useful analogy between the jigsaw puzzle and the protein folding process. The pieces corresponding to amino acid residues are joined together to complete the full matrix representation. These processes mimic protein folding. If the pieces have a uniform color, then there will be no preferential starting point, each folding attempt will follow a different path, yet the final result is the same. The jigsaw puzzle model does not rule out other folding models. If the color pattern is simple and definitive, almost every folding attempt will follow the same path (i.e., the sequential model). If the color is less definitive, then a limited selection of paths will be followed with nearly the same substructures developed on each try (i.e., the framework or diffusion-collision-adhesion model).

In the hydrophobic collapse model [52], the hydrophobic effect is presumed to be the overwhelming driving force. The water is squeezed out as far as possible without any particular regard to the formation of secondary structure. Different models mentioned above can be accommodated to others. For example, the framework model might be modified so that the hydrophobic collapse is linked to the formation of secondary structural elements.

The two-state character of protein folding indicates that a single folding or unfolding transition finishes in a much shorter time than both of average life spans of N- and U-states. Whatever the distinctions of names, stable secondary and tertiary structural interactions must form concurrently to complete the folding transition.

2.3.2. Transient Folding Intermediates

In order to determine how a protein folds, we should follow the time course of the process. It would clearly be unrealistic, however, to expect to elucidate all the details of such a complex reaction. It might then be feasible to determine what is the starting state for folding, to identify the overall rate-determining step, and to characterize the most stable intermediates. To determine the mechanism and pathway of folding and unfolding, any intermediates that define and direct the pathway must be identified [53]. Such intermediates may not be stable at equilibrium, but they might be detectable as transient kinetic intermediates. The detection and characterization of kinetic folding intermediates is therefore central to studies of protein folding, but must be treated on a case-by-case basis, and can be very complex.

In the simplest general case, with a simple one-step reaction involving a homogeneous reactant and no intermediates, a single kinetic phase is expected, characterized by single rate constant. Kinetic complexities can arise from the accumulation of intermediates, when there are two or more slow steps. Kinetic intermediates will accumulate to substantial levels only if they occur before the rate-determining step of the pathway, and if their free energies are comparable

to, or lower than, that of the initial state. No other intermediates will be populated even transiently. The most difficult question to answer is whether an observed "intermediate" I is on or off the reaction pathway. That is, is there the compulsory order, U–I–N, or is I a nonproductive side product that has to unfold back to U for folding to proceed?

2.3.3. Effects of Peptidyl-Proline Isomerization on Folding Kinetics

Refolding is generally found to proceed by a series of exponential phases. Many of these exponentials are a consequence of *cis-trans* isomerization about peptidyl-prolyl bonds [54]. The equilibrium constant for the normal peptide bond in proteins favors the *trans* conformation by a factor of 10^3–10^4 or so. The peptidyl-prolyl bond is an exception that has some 5–30% of *cis* isomer in model peptides. Further, it is often found as the *cis* isomer even in native structures. The interconversion of *cis* to *trans* in solution is quite slow, having half-lives of 10–100 sec at room temperature and neutral pH. A protein that has several prolines all in the *trans* conformation in the native structure will equilibrate upon unfolding to give a mixture of *cis* and *trans* forms. On refolding, an apparent succession of slow refolding phases will be observed as the different isomers fold in parallel. That peptidyl-proline isomerization is a post-unfolding event is readily demonstrated by double-jump experiments [55].

2.3.4. Formation of Collapsed State

As mentioned earlier, refolding is initiated by restoring a protein from unfolding condition to refolding one. Immediately after that, the unfolded state U rearranges to the initial nonnative state in the refolding solution. The properties of the starting state for protein folding can be inferred from kinetic studies and shown to be a disordered but compact state [33]. For several proteins, the nature of such collapsed states has been explored in some detail. Especially, a pulsed hydrogen exchange or pulse labeling experiment succeeds to provide insight into the early stage of protein folding [56, 57]. In this approach, the protein is initially unfolded in the presence of D_2O to deuterate the exchangeable amide protons. During refolding, the proteins are exposed to a pulse of H_2O so that exposed amides become fully protonated (NH), while those that are already engaged in stable hydrogen-bonded structure remain deuterated (ND). After the proteins have completely refolded, the deuterated sites are identified by NMR techniques.

In the early stage of ribonuclease A folding, the first amide protons protected from exchange are in the region of the chain that forms a three-stranded β-sheet [58, 59] (see Fig. 9). Studies with cytochrome c suggest that helices at the N- and C-terminal ends form in the earliest phase with the time constant of 20 ms, while other regions of the chain do not become structured for the first 100 ms of refolding [60]. Pulsed hydrogen exchange and CD folding experiments on hen lysozyme [34, 35] demonstrate that the large majority of amides in the helical α-domain of lysozyme exhibit two protection phases with time constants of 7 ms and 60 ms, respectively, whereas most amides in the structurally distinct β-domain are protected more slowly on the 100-ms timescale. In the case of α-lactalbumin that is a homologue of

lysozyme, one can study the stable analogues of the kinetically formed collapsed state. Such studies suggest that the extensive secondary structure exists in the α-domain, while the β-domain remains unstructured [61–63]. All these experiments indicate that the secondary structures existing in the early collapsed state have native-like character.

Hydrogen pulse labeling procedures are elegant and powerful to provide insight into protein folding at the atomic resolution. Yet there remain some limitations in this method. For example, only amides that are protected in the final native state, which are usually involved in secondary structure, can be observed in this way. Therefore, any protection of such groups in the refolding protein will be consistent with a presumption of the refolding protein having at least some native-like secondary structure. In an attempt to elucidate the early stage of protein folding, the protection factors against the hydrogen exchange should be measured for amide protons that are not involved in intramolecular hydrogen bonds in the native state [64]. Some amides might be protected during the folding, although they are located near the surface of a protein after the completion of protein folding.

The occurrence of the molten globule (MG) in folding kinetics is generally taken to indicate that it must be a kinetic intermediate important for folding; it is assigned the kinetic role: U–MG–N [40, 65]. However, the role of MG in protein folding is not definite [66, 67]. If the average conformational properties of the unfolded protein are different in unfolding conditions such as 6 M GdmCl and in physiological conditions after the dilution of GdmCl, is such an initial change the equivalent of the formation of kinetic intermediate? Because the intermediate is more stable than U, the intermediate is, in fact, the most stable of the nonnative states under physiological conditions. It seems plausible that the MG is the compact denatured state in the refolding condition, and the starting state for folding rather than compulsory intermediates. Both native and nonnative contacts persist within the MG of α-lactalbumin [61, 68], yet folding of the polypeptide chain to the MG can have only low cooperativity. Kinetic studies with NMR spectroscopy indicate that the close packing characteristic of the native state emerges in a highly cooperative manner, following the formation of the MG state [69].

2.4. Transition State for Folding

2.4.1. A Hypothetical Transition State

The transition state cannot be observed directly in any reaction. It is a hypothetical state introduced to explain rate constants of a chemical reaction from a view of statistical mechanics. The conventional description of a transition state is a structure that is at a saddle point on a free energy surface, through which a chemical reaction irreversibly proceeds from a reactant to a product along a reaction pathway. Only a few bonds are made or broken within the transition state. These bonds are very strong, so that quantum theory has been applied [70].

However, protein folding involves the making and breaking of very many weak bonds, which can be described by classic statistical mechanics. What is the hypothetical transition state in folding and unfolding reactions of proteins?

Proteins spend most of the time either in the N or U state because of the two-state nature. A high free energy barrier stands between N and U. For the purpose of illustration, Figure 5 shows the free energy diagram of a protein as a function of internal energy of the chain, which was calculated from Monte Carlo computer simulations for an island-model protein [71, 72]. This model of protein folding is quite similar to lattice models of protein [12, 73, 74], which have been frequently used for the simulation of protein thermodynamics. The N and U states are located at both ends of the free energy diagram with the difference in internal energy of about 155 (arbitrary unit). Populations of states between N and U are negligibly small. The question is where the transition state is. Arrhenius plots of folding and unfolding rates obtained from computer simulations, in which logarithms of rate constants are plotted as a function of 1/T, give the activation energies of folding and unfolding reactions, respectively [71]: $E_f^{\neq} = -85$, $E_{uf}^{\neq} = 70$ (arbitrary unit). Interestingly, $E_{uf}^{\neq} - E_f^{\neq}$ is nearly equal to the difference in the average internal energies of the U and N states, and the transition state (TS) is very close to the state with the highest free energy. These results of computer simulations of protein folding are quite consistent with the conventional transition state theory, if the transition state is accepted as follows.

Upon climbing up the slope of free energy barrier, backward steps are very much preferable to forward ones, but the relation is reversed at the downhill. Proteins populate the states between N and TS according to statistical thermodynamics until an unfolding transition happens, and move to the U state virtually irreversibly after passing through the transition state. The transition state is probably the statistical ensemble of such critical states. It seems plausible to assume that all the states are in chemical equilibrium at least along the reaction pathway from N to TS, because the average life span of the N state is long enough for proteins to repeat conformation changes a great many times. Until a folding transition happens, the states from U to TS may be assumed to be in chemical equilibrium along the reaction pathway, although the states located off pathway are naturally exceptions. Within the transition state, elementary steps of a reaction may be assumed to be composed of breaking or forming a small number of weak bonds and one-way either
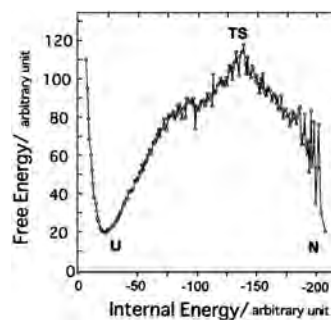
Figure 5. Free energy diagram for a folding-unfolding reaction of protein. The data were obtained from Monte Carlo computer simulations for a simplified model of protein [71]. TS represents the transition state, whose position is determined from activation energies of folding and unfolding rate constants obtained by computer simulations.

forward or backward with a rate constant k_0. Therefore, the unfolding rate (k_{uf}) is given by k_0 times the equilibrium constant $K^{\neq}_{TS-N}$ between N and TS, and similarly the folding rate (k_f) by k_0 times $K^{\neq}_{TS-U}$ between U and TS [75, 76]. If the above consideration would be proper, the activation energy obtained from the rate constants, k_{uf} and k_f, is nearly equal to the change in enthalpy associated with the process from the preceding state to the hypothetical transition state, under the assumption that the activation energy of k_0 is much smaller than the enthalpy changes mentioned above. Probably, this is the reason why the transition state determined from the activation energy is near the highest free energy barrier in the free energy diagram shown in Figure 5.

2.4.2. Characteristics of Transition States

By definition, the structure of the transition state cannot be determined by static methods. Instead, inferences about its structure are made according to the changes observed in the rate constant of a reaction when certain variables are changed. For a protein folding, these variables are either mutations or environmental parameters such as pH, temperature, and the concentration of a denaturant or a specific ligand.

Temperature dependences of folding and unfolding rate constants of hen lysozyme are shown in Figure 6a [77]. As mentioned earlier, the slopes of the tangential lines for the plots of $\ln k_{uf}$ and $\ln k_f$ as a function of $1/T$ determine the activation enthalpies of unfolding ($\Delta H^{\neq}_{TS-N}$) and folding ($\Delta H^{\neq}_{TS-U}$), respectively.

$\Delta H^{\neq}_{TS-N}$ and $\Delta H^{\neq}_{TS-U}$ are the changes in enthalpy associated with the processes from the N and U to the transition
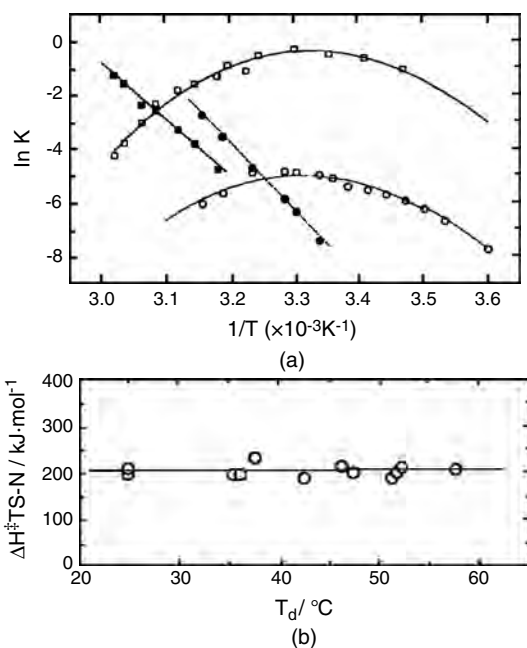
Figure 6. (a) Temperature dependences of folding and unfolding rate constants of hen lysozyme. Open and filled symbols denote folding and unfolding rate constants, respectively, at pH 2.6. Squares and circles are the data obtained in solutions containing 0.7 M and 2.4 M guanidine hydrochloride, respectively [77]. (b) Temperature dependence of activation enthalpies of unfolding ($\Delta H^{\neq}_{TS-N}$).

state, respectively. $\Delta H^{\neq}_{TS-N}$ is definitely independent of temperature, whereas $\Delta H^{\neq}_{TS-U}$ is positive at lower temperatures less than 25 °C, and negative at higher temperatures. The temperature derivatives of $\Delta H^{\neq}_{TS-N}$ and $\Delta H^{\neq}_{TS-U}$ are the heat capacity changes, $\Delta C_p{}^{\neq}{}_{TS-N}$ and $\Delta C_p{}^{\neq}{}_{TS-U}$, associated with the processes from the N and U to the transition state, respectively. From the data shown in Figure 6a, $\Delta C_p{}^{\neq}{}_{TS-N}$ and $\Delta C_p{}^{\neq}{}_{TS-U}$ are nearly equal to 0 and $-6.7 \text{ kJ} \cdot \text{mol}^{-1} \text{ K}^{-1}$, respectively. It is the process from the transition state to the U state that the increase in heat capacity, which is specific for the exposure of nonpolar groups to water, occurs. Therefore, it is clear that the second stage of unfolding is associated with the hydration of internal groups of the protein, while the first stage corresponds to the disruption of van der Waals interactions between nonpolar groups and hydrogen bonds between polar groups, which maintain a crystal-like structure in the interior of a protein. The transition state can be considered as a "dry molten globule" state [78] of the protein with diminished noncovalent interactions, but without water inside. The magnitude of $\Delta H^{\neq}_{uf}$ is substantially large and independent of temperature (about 200 kJ/mol) over a relatively wide range of temperature (Fig. 6b). These characteristics in temperature dependences of k_{uf} and k_f are also found in other proteins [79, 80].

2.4.3. Φ-Value Analysis of Transition States

A powerful approach for investigating the transition state is based on protein engineering [81]. It involves mutating specific residues and measuring the change in the rates of folding and unfolding relative to the effect on the overall stability of the protein. If a mutant folds with a rate constant $k_{f'}$, compared with k_f for wild type, then the change in activation energy on mutation is given by $\Delta\Delta G^{\neq}_{TS-U} = -RT \cdot \ln k_{f'}/k_f$. In order to examine the effect of the formation of interactions on the folding or the unfolding reaction, a function Φ_F is introduced: $\Phi_F = \Delta\Delta G_{TS-U}/\Delta\Delta G_{N-U}$. In order to illustrate the meaning of Φ_F values, energy diagrams for protein folding are shown in Figure 7. A Φ_F value of 0 means that the energy of the transition state is perturbed on mutation by the same amount as the unfolded state is perturbed. A Φ_F value of 1.0 means that the energy of the transition state is perturbed on mutation by the same amount as the native state is perturbed. It is inferred from the changes in energy that a Φ_F value of 0 means that the structure of the transition state is unfolded at the site of mutation as much as it is in the unfolded state, and a Φ_F value of 1.0 means that the structure is folded at the site of mutation as much as it is in the native state.

Barnase was extensively analyzed by measurements of more than 130 mutants [82]. Unfolded barnase collapses into an intermediate that is converted to the folded state through the rate-determining transition state. The transition state for unfolding has some regions with Φ_F values of 0, others with values close to 1.0, and a few regions with intermediate values. The main parts of barnase that are nearly completely folded in the transition state are the β-sheet, with Φ_F values of 1.0 at the center and slightly decreasing at the edges, and the α-helix1 located at the N-terminal. The hydrophobic core, which is formed by the
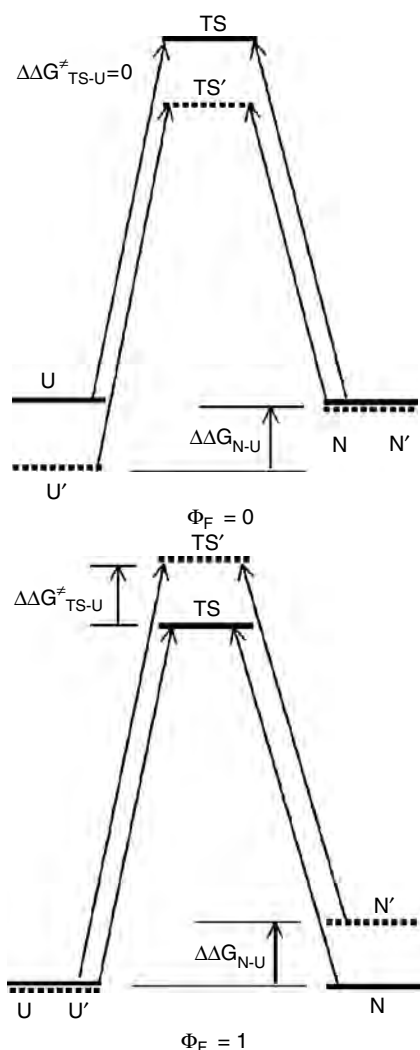
Figure 7. Free energy diagram for the illustration of Φ_F-value. The free energy levels change on mutation from N, U, TS to N′, U′, TS′, respectively. Suppose that U and TS are perturbed on mutation by the same amount, but N is not (left panel). Then it results in $\Phi_F = 0$ because $\Delta\Delta G^{\neq}_{TS-U}$ equals zero. On the contrary, if TS is perturbed on mutation by the same amount as N, but U is not (right panel), $\Phi_F = 1$. The value of Φ_F is unaffected by the change in absolute values of free energy level, because ΔG itself is the relative change in free energy. Therefore, it is not a prerequisite for $\Phi_F = 0$ that the free energy level of N is the same as that of N′. In a similar manner, the level of U′ need not be equal to that of U in the case of $\Phi_F = 1$.

docking of helix1 on the sheet, is weak, with low Φ_F values. These observations suggest that the rate-determining step in folding of barnase involves the docking of the preformed α helix1 on the preformed β sheet. The hydrophobic cores partially formed in the intermediate consolidate during the later folding events and possibly solvent is expelled. The packing of the hydrophobic residues is part of the rate-determining process.

2.4.4. Effects of Covalent Cross-Links

One experimental method of characterizing the folding transition state is examining the effects of the addition of covalent cross-links on unfolding and refolding rates. If the stabilizing effect of an added covalent cross-link is primarily entropic (i.e., if the added cross-link does not affect the enthalpy), then the effect of such an added cross-link on the folding and unfolding rates determines whether the linked segments of the protein are associated in the folding transition state of the wild-type protein. Specifically, if the added cross-link accelerates the folding but does not affect the unfolding, then the two segments are associated in the folding transition state; the added cross-link destabilizes the unfolded state, but not the native and transition states. On the contrary, if the added cross-link decelerates the unfolding but does not affect the folding, the two segments are not associated in the transition state; the added cross-link destabilizes both the unfolded and transition states, but not the native state. The study on the cross-link introduced between Lys7 and Lys41 in RNase A suggests that the N-terminal α-helix of RNase A is not associated with the major β-sheet in the folding transition state [83].

Disulfide bonds are naturally occurring covalent cross-links in proteins. The effects of deletion of specific disulfide bonds on folding kinetics have recently been systematically examined, and will be reviewed in the following sections.

3. DISULFIDE BONDS IN PROTEINS

3.1. Occurrence, Geometry, and Physicochemical Properties

The distribution, topology, conformation, and conservation of disulfide bonds in proteins of known sequence and/or three-dimensional structures have been analyzed [84–86]. The most frequent separation between the two cysteinyl residues along the amino acid sequence (primary structure) of proteins is 10 to 14 residues, and 49% of the observed disulfides are separated by less than 24 residues. For small disulfide loops, disulfide bonds with odd numbers of intervening residues have a low probability of formation compared with those with even numbers [87]. Adjacent cysteine residues, that is, in the case of zero intervening residues, can form a disulfide bond with a peptide bond that links them in a *cis* conformation [88].

Physicochemical properties of thiol and disulfide groups have been reviewed [6]. Sulfur has a larger atomic volume and is less electronegative than oxygen. Bond length and angle for CSH are 1.33 Å and 100°, respectively. Those for CSS are 1.8–2.1 Å and 105°. Studies of model compounds have shown that disulfides have a restriction in rotation around the SS bond and have preferred dihedral angles of ±90° [89]. *Ab initio* molecular orbital calculations showed that the relative energy is minimum for S-S dihedral angle of 87°, where the S–S bond length becomes minimal, 2.05 Å [90]. UV absorption maxima for undissociated thiols, dissociated thiols (thiolate anions), and disulfides occur at 190–200, 230–240, and 245–255 nm, respectively. Disulfides with asymmetric carbon atoms show much bigger optical rotations than their corresponding thiols. Cysteine has a pK value of 8.52–8.72 for the thiol group when its α-amino group is protonated. The rate of many chemical reactions in which the reactive species is thiolate anion decreases with decreasing pH. Thiols form stable complexes with metal ions

such as mercury, silver, arsenic, copper, iron, molybdenum, cobalt, and zinc. Autoxidation of thiols to disulfide is catalyzed by metal ions. The standard redox potential for cysteine is -0.22 V.

The conformation of a disulfide bond in protein is described with the side-chain torsion angles χ_1, χ_2, χ_{SS}, $\chi_{2'}$, and $\chi_{1'}$, which represent the dihedral angles around C_α–C_β, C_β–S, S–S', S'–C'_β, and C'_β–C'_α, respectively [84–86], where the prime indicates the atoms of the cysteinyl residue that is located downstream in a primary sequence of protein. Analysis of the crystal structures of disulfide-containing proteins has shown that χ_{SS} values are conserved to either $-90°$ ($\pm 20°$) or $+90°$ ($\pm 20°$), consistent with the results obtained for model compounds. Right- ($-90°$) or left-handed ($+90°$) disulfides occur almost equally. χ_1 and $\chi_{1'}$ are clustered about $-60°$ (gauche), $+60°$ (gauche), and $180°$ (trans). The distribution of χ_2 and $\chi_{2'}$ values is less well defined. In all, eight families of bridge conformation with significant occurrences have been identified [86]. The most populated family takes the "left-handed spiral" conformation ($\chi_1 = \chi_{1'} = -60°$, $\chi_2 = \chi_{SS} = \chi_{2'} = -90°$). However, significant variations in the dihedral angles exist in naturally occurring or genetically engineered proteins as described later, which lead to dihedral strain energies up to several kcal mol^{-1}.

The distance between the two C_α atom is mostly between 4.4–6.8 Å. The average C_α–$C_{\alpha'}$ distance across the left-handed disulfide bonds is 6.1 Å, while that for right-handed ones is 5.2 Å [85].

Most disulfide bonds are buried and inaccessible to solvent, although there are exceptions [84, 86]. Among the proteins that belong to a common protein family, namely the proteins with a common biological function and an ancestral gene, and with amino acid sequences that are homologous to each other, sequence positions of disulfide bonds are highly conserved [84, 91].

3.2. Formation of Disulfide Bonds in Proteins

3.2.1. Elementary Reaction Steps

When proteins are synthesized on ribosome, cysteinyl residues are in a reduced form. Disulfide bonds in proteins are formed in endoplasmic reticulum by disulfide-transfer from other molecules, the principal one of which is believed to be the oxidized form of glutathione. Glutathione, the most abundant non-protein thiol in tissue [6], is a tripeptide, γ-glutamylcystenylglycine. It is a monofunctional thiol compound. Two glutathione (GSH) molecules are linked with each other by a disulfide bond between each cysteine residue, which is called oxidized form of glutathione (GSSG). A reduced form of cysteinyl residues in a protein (P-SH) can form a mixed disulfide with GSSG, leaving GSH:

$$P\text{-SH} + GSSG \rightarrow P\text{-SSG} + GSH$$
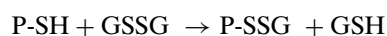
Dissociation of thiol group of protein to produce thiolate anion is necessary for this transfer reaction: namely, denoting each sulfur atom with suffix a, b, or c,

$$S_a^- + S_b S_c \rightarrow S_a S_b + S_c^-$$
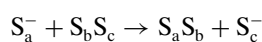
The rate of this reaction depends on the fraction of thiolate anion. Intramolecular environment of protein thiols affects their pK values. Usually, however, their values are considered to be nearly 8.7, which is the pK value of GSH [92]. If the protein contains second cysteinyl residue, intraprotein disulfide transfer from the preformed mixed disulfide to the second cysteinyl residue will result in the formation of a protein disulfide:

$$P_{SH}^{SSG} \rightarrow P_S^S + GSH$$
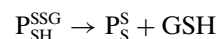
This process is governed solely by conformational properties of protein. Thus, protein disulfide formation consists of two consecutive disulfide-transfer reactions.

In the presence of excess GSH, just the reverse process will convert a disulfide bond to two cysteinyl residues:

$$P_S^S + 2GSH \rightarrow P_{SH}^{SSG} + GSH \rightarrow P_{SH}^{SH} + GSSG$$
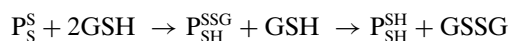
In a mixture of GSSG and GSH that are sufficiently excess to the concentration of protein thiol groups, that is, under defined redox conditions, defined fractions of oxidized (Oxi; or disulfide-formed, P_S^S), and reduced (Red; or disulfide-cleaved, P_{SH}^{SH}) proteins will equilibrate with each other:

$$[\text{Oxi}]/[\text{Red}] = K[GSSG]/[GSH]^2$$

Formation of protein disulfide bonds *in vitro* is generally conducted with 1–10 mM total glutathione concentration and [GSH]/[GSSG] ratio of less than 10. The principal redox buffer *in vivo*, that is, in endoplasmic reticulum, is glutathione, and its redox state is much more oxidized ([GSH]/[GSSG] ≈ 2) than that of the cytosol ([GSH]/[GSSG] ≈ 60) [93], which appears to enable the formation of stable disulfide bonds in that compartment. However, the direct role of glutathione to drive protein oxidation *in vivo* has been questioned [94]. Disulfide reagents such as oxidized dithiothreitol, oxidized mercaptoethanol, cystine, etc. are also used for protein oxidation *in vitro*. More details of disulfide bond formation in proteins *in vitro* have been reviewed [95, 96].

3.2.2. Effective Concentration of Protein Thiol Groups

The equilibrium constant K in the equation shown in the previous section has a dimension of concentration. It is often denoted "effective concentration" (C_{eff}) of the pair of cysteinyl thiols in the protein without the disulfide [96, 97]. It quantitatively represents the tendency of protein structure to keep the cysteinyl thiols in proximity to enable disulfide formation. It is the ratio of the equilibrium constants between otherwise identical intra- and intermolecular interactions [98]. Even if the protein concentration and therefore the cysteinyl thiol concentration are as low as $\sim\mu$M, C_{eff} is typically on the order of mM to M or more, depending on the conformational state of protein [96, 99]. In other words, protein disulfide bonds are generally more stable than those formed between structureless low molecular weight thiol compounds. High value of C_{eff} for protein thiol groups means that the two groups are near to each other by virtue of proximity in the amino acid sequence and/or proximity

in the tertiary structure. Thus, C_{eff} measurements can be a sensitive means of detecting protein tertiary structure formation as described in the next subsection. In practice, equilibrated oxidized and reduced forms of protein under defined GSSG and GSH concentrations are quenched by lowering pH, separated, and quantitated, for example, with reversed-phase HPLC under acidic conditions, and the C_{eff} value is calculated:

$$C_{eff} = ([Oxi] [GSH]^2)/([Red] [GSSG])$$

Examples of the use of C_{eff} measurements to probe the formation of highly unstable structures, or to probe the formation of a native-like fold of polypeptide main chain, will be described in later sections.

3.2.3. Linkage between Disulfide Formation and Conformational Folding

Propensity of disulfide bond formation in the unfolded state of proteins is usually lower compared with that in the folded state, provided that cysteinyl thiol groups in the folded state are not buried into the interior of the protein [100]. In an unfolded state, polypeptide chain is rather extended, and adopts a random-coil conformation, in which an averaged distance between two residues, positions i and j in a primary sequence, is proportional to $|i - j|^{1/2}$. Thus, in a three-dimensional space, the C_{eff} for such a cysteine pair is proportional to $|i - j|^{-3/2}$. In a natively folded state, pair of cysteinyl residues that are long separated in a primary sequence often come close and form a native disulfide bond, showing a significant increase in C_{eff}. Conformational folding-unfolding equilibrium thus affects propensity of disulfide formation. On the other hand, whatever conformation favored the formation of certain disulfide bond is likewise favored by the presence of the disulfide bond [96]. Disulfide-cleaved forms of protein usually show decreased stability against conformational unfolding. There exists a thermodynamic linkage relationship between the disulfide oxidation-reduction and the conformational unfolding-folding equilibria:

$$
\begin{array}{ccc}
F_{SH}^{SH} & \xrightarrow{\;K_1\;} & F_{S}^{S} \\
{\scriptstyle K_3}\big\downarrow & & \big\downarrow{\scriptstyle K_4} \qquad K_1/K_2 = K_3/K_4 \\
U_{SH}^{SH} & \xrightarrow{\;K_2\;} & U_{S}^{S}
\end{array}
$$
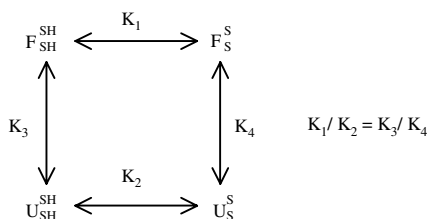
Here, horizontal arrows show disulfide reduction-oxidation equilibrium, and vertical arrows unfolding-folding equilibrium. F and U represent folded and unfolded states, respectively. This linkage relationship was also demonstrated experimentally [101]. Protein folding is usually monitored by spectroscopic means. However, in particular cases it can be indirectly monitored through the change in disulfide reduction-oxidation equilibrium and quantitatively analyzed by using the linkage relationship [101, 102]. The advantage of this approach is that the sensitivity is very high; several hundredth of change in reduced or oxidized state

in a total of microgram amount of protein can be quantitated. Recently, by combining with the principle of conventional urea-denaturation analysis of protein, this approach has been applied to know the size of highly unstable submolecular structures that are coupled with individual native disulfide formation in an early stage of oxidative folding of hen lysozyme [103].

3.2.4. Disulfide Isomers and Disulfide Rearrangements

When a protein contains more than three cysteinyl (Cys) residues, a number of disulfide isomers occur. In a simplest case of three Cys residues, there exist three ways for the formation of one disulfide bond between two Cys residues with the remaining one Cys residue keeping its thiol group free: a total of three isomers of single-disulfide (1SS) species occur. If a protein contains four Cys residues, three isomers of two-disulfide (2SS) species and six isomers of 1SS species occur. The number of ways in which $2n$ Cys residues form j disulfide bonds, $(2n)!/(2^j(2n - 2j)!j!)$, rapidly increases with increasing n values [41]: for a protein with eight Cys residues as in the case of ribonuclease A, lysozyme, or α-lactalbumin, the total number of possible disulfide isomers is 28, 210, 420, and 105, for 1SS, 2SS, 3SS, and 4SS species, respectively. Thus, for proteins with multiple disulfide bonds, to examine the disulfide linkage pattern of the refolded state or to identify the state of isomer is one of the highly sensitive means of confirming the attainment of a native tertiary structure.

A disulfide isomer can spontaneously convert to another isomer if the protein molecule contains a free Cys residue: for instance, a protein with one disulfide bond ($-S_aS_b-$) and one free cysteinyl residue ($-S_cH$; the reactive species is an ionized form) can convert to its isomer with $-S_bS_c-$ and $-S_aH$, or that with $-S_aS_c-$ and $-S_bH$, via a linear transition state [104, 105]. This process is known as "thiol-disulfide exchange" or "thiol-disulfide transfer." It occurs via a transition state in which a disulfide bond and a free thiol group come close to each other and linearly arrange. Thus, facile occurrence of thiol-disulfide exchange is a measure of protein flexibility or an indication of the absence of defined stable topology of polypeptide chain tertiary fold.

Even if a protein molecule is saturated with disulfide bonds, for example, 4SS, and does not contain any free thiol groups, in the presence of externally added thiol reagent such as GSH, the protein can be reduced partially, for example, to a 3SS state, generating free intramolecular thiol groups, thus enabling thiol-disulfide exchange to occur, resulting in another 3SS isomer. Then, in the presence of externally added disulfide reagents such as GSSG, this isomer can form a fourth disulfide bond, resulting in a 4SS isomer that is different from the original 4SS species. This process is called "disulfide rearrangement." If starting from disulfide-scrambled states formed under denaturing solution conditions, through repeated cycles of disulfide rearrangements, proteins attain, under native solution conditions, a native disulfide linkage pattern associated with a native three-dimensional structure, which is energetically most stable and resistant to further disulfide rearrangement.

3.3. Mechanism of Protein Stabilization by Disulfide Bonds

3.3.1. Thermodynamic Factors in Stabilization

Disulfide linkages confer stability to proteins primarily by reducing the stability of the unfolded state: the introduction of disulfide bonds into a polypeptide chain of a random-coil conformation decreases the conformational entropy of the chain [106, 107]. The entropy decrease is obtained by the equation [108]

$$\Delta S = -8.8 - 1.5R \ln N \ (J\,K^{-1}\,mol^{-1})$$

where N represents the number of residues contained in the loop formed by the disulfide bond. The magnitude of the first term on the right-hand side of the equation is related with the volume tolerance, that is, the volume within which the two Cys C_α atoms must reside for disulfide bonding, and depends on the estimation of the closest approach of two Cys residues; different values for this term have been used [109, 110], and the equation proposed more recently is [111]

$$\Delta S = -14.4 - 1.5R \ln N$$

The difference in equilibrium conformational stability and that in kinetics of folding/unfolding between the reduced (i.e., 0SS) and intact (1SS) forms of constant fragment of the immunoglobulin light chain [112–114], and that between the 0SS, 1SS, and 2SS (intact) forms of ribonuclease T1 [108], were explained by this mechanism.

In the above equations, the factor "1.5" derives from the relationship that the available spatial volume for a random chain of N residues without a cross-link is proportional to $N^{1.5}$. If excluded volume effect of polymer chains [115] is taken into consideration, the factor will increase to 1.8–2.4 [116, 117]. In any way, in this mechanism the stabilization is driven entropically, and is larger for increasing loop size.

Contrary to the entropic stabilization mechanism, by taking the contributions from solvent into consideration, entropic destabilization and enthalpic stabilization mechanism for the introduction of disulfide bond was proposed based on a decreased hydrophobic surface area and less favorable hydrogen bonding networks in the cross-linked denatured state of protein [118]. Also, the vibrational entropy determined by use of normal mode calculations on the folded state of bovine pancreatic trypsin inhibitor was shown to be reduced substantially on cleavage of disulfide bonds [119]. Statistical analysis has shown that the number of disulfides in proteins is negatively correlated with the content of aliphatic hydrophobic amino acid residues, which contribute to protein stabilization through hydrophobic interactions [120].

Experimental results on the destabilization upon removal of disulfide bonds and the mechanisms of destabilization have been reviewed [121]. Those concerned with the proteins that appear in Section 4 in this chapter will be described in Section 5.

3.3.2. Introduction of Novel Disulfide Bonds

Introduction of novel disulfide bonds into proteins has been carried out by using protein engineering techniques [121]. Incorporation of a disulfide bond into T4 lysozyme, a disulfide-free enzyme, increases the stability against thermal inactivation [122]. In this case, the stabilization is primarily against chemical inactivation at high temperature, such as hydrolysis of side-chain amide or peptide bonds, which is an irreversible phenomenon [123–125]. The role of disulfide bonds to reduce the ability of proteins to undergo aggregation by placing constraints on their unfolded conformations was also suggested [126]. However, a novel disulfide bond introduced into dihydrofolate reductase stabilized the protein against denaturant-induced denaturation, but not thermal denaturation [127]. Stabilization against both denaturant- and thermal-unfolding was shown on the introduction of a disulfide bond into *Escherichia coli* ribonuclease H [128].

Introduction of novel disulfide bonds into subtilisin did not impart the stabilization against irreversible inactivation compared with wild-type subtilisin [129, 130]. X-ray crystallography of the disulfide-engineered subtilisin molecules showed the existence of atypical, high-energy dihedral angles in the engineered disulfide bonds [131]. Destabilization on the introduction of a disulfide bond was also reported for cytochrome c, although the mechanism is different [132, 133].

Studies on several individual disulfide bonds introduced into T4 lysozyme indicated that a large loop size and a location that includes a flexible part of the protein molecule are important for the novel disulfide bond to stabilize the protein [134]. If a disulfide bond is introduced to a rigid part of protein, the strain energy is difficult to dissipate. When multiple disulfide bonds, each of which suffices the conditions for protein stabilization, are introduced, the resultant stabilization in terms of melting temperature was shown to be nearly additive [135]. Two different novel disulfide bonds were introduced into different parts of barnase [136]. One part becomes structured early in the folding kinetics, and the other part late (after the rate-determining step). Both increased the equilibrium stability against denaturation, although the magnitude of which was not in accord with the chain entropy theory. More importantly, although intermediate and transition states of folding are stabilized in the former construct, only the final folded form is stabilized in the latter construct. Consequently, the stability against the kinetic rate of denaturation is enhanced in the latter construct. Differential effect of the introduction of disulfide bonds at various positions, one group stabilizing local hairpins and another group connecting β-strands distant in primary sequence, on the folding kinetics of a β-sheet protein, CD2, has been reported [137]: the enhancement of the folding rate in the rate-limiting step was found to be correlated with a reduction in "contact order" [138, 139] of the molecule.

Lattice model simulations have shown that folding is accelerated when disulfides are introduced in or close to the folding nucleus, while decelerated when they are introduced outside the nucleus [120]. These are consistent with experimental results obtained for barnase [136].

4. PATHWAY OF DISULFIDE-ASSOCIATED PROTEIN FOLDING

Folding reaction of many simple proteins with multiple disulfide bonds has been reported to conform to an all-or-nothing mechanism. However, this is usually true only for the folding/unfolding reactions with all disulfide bonds intact, that is, not associated with disulfide formation. In the case of a folding reaction which starts from a reduced state of protein, and which involves the formation of disulfide bonds (called "oxidative folding"), and therefore which is closer to the folding reactions *in vivo*, the folding process is not an all-or-nothing type in most cases. A number of intermediate states with intermediate numbers of disulfide bonds ("disulfide-intermediates"), and usually with partial structure formation, are observed. Detailed studies of the pathways of oxidative folding for representative proteins are described in the following. We note that the apparent accumulation of a particular intermediate does not necessarily indicate its importance in productive folding pathways: in purely sequential reactions, "lazy" intermediates tend to accumulate more than "quick" intermediates, while in parallel reactions the flux of reaction is of course larger for more efficient pathways. The actual oxidation of proteins seems to accord with reaction schemes that involve both sequential and parallel pathways. Therefore, the role or fate of particular intermediates should be clarified by the experiments specially designed for such objectives. We also note that the extent of the attainment of protein conformational structure does not necessarily parallel with the extent of disulfide formation.

4.1. Bovine Pancreatic Trypsin Inhibitor

Bovine pancreatic trypsin inhibitor (BPTI) is a small (58 amino acids) protein, which binds to trypsin and inhibits its enzymatic action. It contains three disulfide bonds: Cys 5–Cys 55, Cys 14–Cys 38, and Cys 30–Cys 51 (Fig. 8). The detailed pathway of disulfide-associated protein folding was presented first for BPTI by Creighton [140], and a number of reviews on the pathway have been published [141–147].

4.1.1. Nonnative Intermediates and Disulfide Rearrangements

Starting from a reduced and unfolded form, initial single disulfides form nearly randomly between the six Cys residues. Among one-disulfide (1SS) intermediates, that with the Cys 30–Cys 51 disulfide bond, designated [Cys 30–Cys 51] (or simply [30–51], when this is not confused with references cited), is energetically most stable and became predominantly populated. From [Cys 30–Cys 51], three species of two-disulfide (2SS) intermediates [Cys 30–Cys 51, Cys 5–Cys 14], [Cys 30–Cys 51, Cys 5–Cys 38], and [Cys 30–Cys 51, Cys 14–Cys 38] are produced efficiently. Note that the former two 2SS intermediates contain nonnative disulfide bonds, Cys 5–Cys 14 and Cys 5–Cys 38, and are designated "nonnative intermediates." These two nonnative 2SS intermediates rearrange their disulfide bonds intramolecularly to produce a 2SS intermediate, [Cys 30–Cys 51, Cys 5–Cys 55], in which native-like stable structure is attained. The
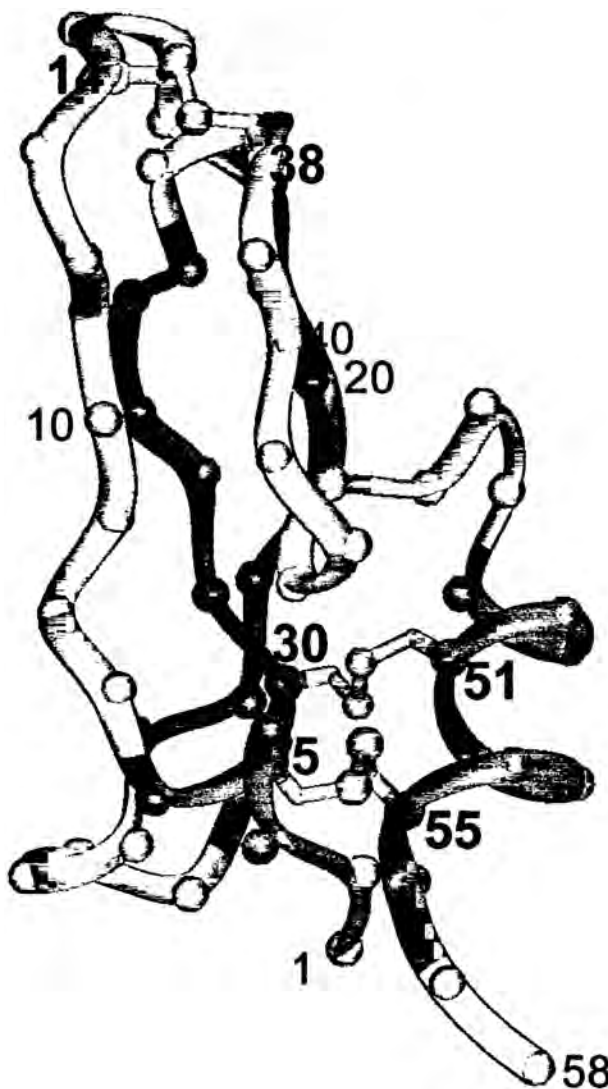
Figure 8. Ribbon diagram of the folded structure of native BPTI [PDB 1BPI]. Two major β-strands (residue numbers 18–24 and 29–35) are colored blue, and two helical segments (3–6 and 48–56) are colored magenta. Other details of graphical representation conform to those described for Figure 3.

2SS native intermediate, [Cys 30–Cys 51, Cys 14–Cys 38], which contains two native disulfide bonds, however, does not efficiently proceed to direct formation of the remaining third native disulfide bond, Cys 5–Cys 55. It must rearrange to either (or both) of the 2SS nonnative intermediates [Cys 30–Cys 51, Cys 5–Cys 14] or [Cys 30–Cys 51, Cys 5–Cys 38] to enter the productive pathway. The reaction step leading to the formation of [Cys 30–Cys 51, Cys 5–Cys 55] via disulfide rearrangements is rate determining in the whole series of reaction of the oxidative folding of BPTI [148]. From [Cys 30–Cys 51, Cys 5–Cys 55], the remaining native disulfide bond, Cys 14–Cys 38, is readily formed to produce completely oxidized native state, [Cys 30–Cys 51, Cys 5–Cys 55, Cys 14–Cys 38].

Why are such indirect means required to reach the final folded state? A hint can be found in the study employing

snake proteins that are homologous to BPTI, and with lower stability of the folded state [149]. With decreasing stability of the final native proteins, the direct pathway, in which the three native disulfide bonds are successively formed, that is, first Cys 30–Cys 51, then Cys 5–Cys 55, finally Cys 14–Cys 38, becomes significant. Since the energy of the transition state leading to the formation of [Cys 30–Cys 51, Cys 5–Cys 55] is thought to reflect the need to distort the native-like conformation [142, 150], it seems that when the final native state is more stable, the energy to distort it in the transition state may be even higher. Amino acid replacements at three different sites of BPTI (Tyr 23 → Leu, Tyr 35 → Gly, Asn 43 → Gly) have different effects on the relative stabilities of the representative classes of intermediates described in this scheme [151].

When the Cys residues 14 and/or 38 are blocked by alkylation, or replaced by serine residues with genetic engineering, the formation of 2SS intermediates at 25 °C becomes very inefficient [152, 153], in agreement with the involvement of [Cys 30–Cys 51, Cys 5–Cys 14], [Cys 30–Cys 51, Cys 5–Cys 38], and [Cys 30–Cys 51, Cys 14–Cys 38] intermediates for the disulfide rearrangement pathway of wild-type BPTI folding described earlier. However, the "direct" pathway in which [Cys 30–Cys 51, Cys 5–Cys 55] is directly produced from [Cys 30–Cys 51] exists, especially at high refolding temperatures, for variant BPTI forms in which Cys residues 14 and 38 are genetically replaced by alanine or threonine, or chemically blocked [154]. Furthermore, detailed analyses on the difference between the rates of protein disulfide formation for two different redox pairs, GSSG/GSH and oxidized DTT/reduced DTT, predicts that such direct pathway from either [Cys 30–Cys 51] or [Cys 5–Cys 55] to form [Cys 30–Cys 51, Cys 5–Cys 55] becomes significant with the use of former redox pair [155].

4.1.2. Dominance of Native Intermediates

After the pioneering work by Creighton and co-workers described earlier, oxidative-folding pathway of BPTI was reexamined by Kim group using acid quenching methods and reversed-phase high-performance liquid chromatography as a separation technique of disulfide intermediates [156]. Their results, especially those obtained at neutral pH condition (pH 7.3), showed that 1SS intermediate [Cys 5–Cys 55] also predominates in addition to [Cys 30–Cys 51]. From these 1SS intermediates, 2SS intermediates with native disulfide bonds, [Cys 30–Cys 51, Cys 14–Cys 38] and [Cys 5–Cys 55, Cys 14–Cys 38] respectively, are predominantly formed. However, these 2SS intermediates do not directly proceed to the formation of the remaining respective third native disulfide bond. Disulfide rearrangement to form the 2SS native intermediate [Cys 30–Cys 51, Cys 5–Cys 55], which has been identified by Creighton to be the immediate product of the rate-limiting step, via nonnative disulfide bond formation as required by disulfide chemistry, is necessary before reaching a fully oxidized form [Cys 30–Cys 51, Cys 5–Cys 55, Cys 14–Cys 38]. The two 2SS native intermediates, [Cys 30–Cys 51, Cys 14–Cys 38] and [Cys 5–Cys 55, Cys 14–Cys 38], are essentially natively folded as described in the next section. Stably folded state of these partially

oxidized forms can bury unoxidized thiol groups inside protein molecule and inhibit their reaction with thiol reagents, thus considerably retarding the completion of oxidative folding reaction, as was shown for the constant fragment of immunoglobulin light chain [100]. Indeed, isolated [Cys 30–Cys 51, Cys 14–Cys 38] intermediate showed accelerated rearrangement to [Cys 30–Cys 51, Cys 5–Cys 55] in the presence of increasing concentrations of denaturing agent. Thus, for the final product of oxidative folding to be obtained efficiently, there exists a case in which the unfolding of stable intermediates is required.

4.1.3. Toward a More Comprehensive View

The involvement of nonnative intermediates and dominant population of native intermediates in the pathway of oxidative folding are not contradictory to each other. The two views on the oxidative-folding pathway of BPTI, while containing several fundamental aspects in common, differ in the evaluation of the role of nonnative disulfide intermediates in the productive folding pathway [157, 158]. On the one hand, the conformational structures of the recombinant analogues of the 2SS nonnative intermediates [Cys 30–Cys 51, Cys 5–Cys 14] and [Cys 30–Cys 51, Cys 5–Cys 38] in comparison with 1SS [Cys 30–Cys 51] were shown to be consistent with their proposed role in the folding [159]. The oxidative refolding of the recombinant BPTI analogues that lack either Cys14 or Cys38 with replacement by Ser has been characterized, and it was shown that essentially all the molecules refold through the two 2SS nonnative intermediates [160]. On the other hand, rearrangement kinetics starting from the isolated 2SS nonnative species, [Cys 30–Cys 51, Cys 5–Cys 14] or [Cys 30–Cys 51, Cys 5–Cys 38], showed that these nonnative intermediates predominantly converted to [Cys 30–Cys 51, Cys 14–Cys 38] rather than to [Cys 30–Cys 51, Cys 5–Cys 55], and are not specifically involved in the productive pathway alone [161]. The reason why the 2SS native intermediate [Cys 30–Cys 51, Cys 14–Cys 38] does not efficiently proceed to direct formation of the remaining third native disulfide bond, Cys 5–Cys 55, was shown to be that the native-like structure of this intermediate decelerates not only the first step, that is, mixed disulfide formation of Cys5 or Cys55 with disulfide reagents by hundred-fold, but also the second step, that is, intramolecular thiol-disulfide transfer to form 5–55 disulfide bond by several hundredfold [162].

Theoretical and experimental studies that explicitly and extensively analyze relationships between native and nonnative intermediates of BPTI have been reported. A phenomenological theory to predict pathways of oxidative folding was developed based on a "proximity rule" in which $P(l)$, the probability of the formation of a disulfide bond with a loop size of l, is assumed to depend only on the loop size l (in such a way that $P(l)$ is negligible for $l < 7$, reaches maximum at $l \approx 10$, and $P(l) \sim l^{-2.2}$ for larger l values), and $P(l_1, l_2)$, that of simultaneous formation of two disulfide bonds with loops of l_1 and l_2, is assumed to be $P(l_1)P(l_2)$ [163]. Further, the folding was assumed to occur in three distinct stages. First, for short time regime, random formation of native and nonnative 1SS species, followed by the formation of native or nonnative second disulfide bond, occurs according to the proximity rule. Next, for medium

time regime, interconversion of nonnative and seminative 2SS species to native species occurs via cleavage of a nonnative disulfide bond (with concomitant reproduction of 1SS species) and reformation of second disulfide bond. Last, for long time regime, the rate-limiting rearrangement transition from native-like two-disulfide species to the native species ([Cys 30–Cys 51, Cys 5–Cys 55] for BPTI) occurs. The results showed that the native state is primarily obtained by the rearrangement of [Cys 30–Cys 51, Cys 14–Cys 38] to [Cys 30–Cys 51, Cys 5–Cys 55], 90% of which proceeded via nonnative transients, most notably [Cys 30–Cys 51, Cys 5–Cys 14].

Previously unidentified native 1SS intermediate, [Cys 14–Cys 38], has been shown to be formed more rapidly than any other 1SS species [164, 165], partly due to electrostatically enhanced reactivities of Cys14 and Cys38 thiols [165, 166]. The majority of [Cys 14–Cys 38], however, was not a direct precursor to either [Cys 14–Cys 38, Cys 30–Cys 51] or [Cys 14–Cys 38, Cys 5–Cys 55], but undergoes intramolecular rearrangements, via nonnative 1SS intermediates, to generate thermodynamically more stable, native 1SS intermediates, [Cys 30–Cys 51] and [Cys 5–Cys 55] [166]. Thus, whether a particular disulfide-intermediate is directly productive for subsequent folding steps or not is a question different from whether the disulfide-linkage in the intermediate is native or not.

4.2. Ribonuclease A

Bovine pancreatic ribonuclease A (RNase A; EC 3.1.27.5) is 124 amino acids long, and contains four disulfide bonds between Cys residues 26–84, 40–95, 58–110, and 65–72. Two disulfide bonds, Cys 40–Cys 95 and Cys 65–Cys 72, link together surface loops, while the other two, Cys 26–Cys 84 and Cys 58–Cys 110, link an α-helix to a β-strand in a protein core (Fig. 9) RNase A hydrolyzes a phosphodiester bond of ribonucleic acids at the 3′ side of pyrimidine nucleotide.
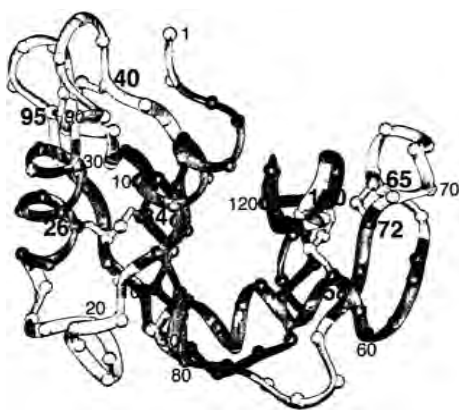
Figure 9. Ribbon diagram of the folded structure of native RNase A [PDB 1FS3]. Three α-helical segments (residue numbers 3–13, 24–33, and 50–60) are colored magenta, and seven β-strands (43–48, 79–86, and 97–104, comprising an antiparallel β-sheet on the left; 61–63, 72–74, 105–111, and 115–124, comprising another antiparallel β-sheet on the right) are colored blue.

4.2.1. Multiple versus Nonmultiple Pathways

In the oxidative folding of RNase A with GSSG and GSH redox couple, a number of intermediates appear and incorrectly formed disulfide bonds are reshuffled. Essentially all of the intermediates are disordered in conformation and have no enzymatic activity [167–169], except for a 3SS intermediate that lacks the Cys 40–Cys 95 disulfide bond [170, 171]. This is in contrast to the case of BPTI, in which only limited numbers of intermediates appear. It seems to reflect a lower stability and higher cooperativity of RNase A structure compared to BPTI.

As for the rate-limiting transition, it was shown, on the one hand, to occur at the very final stages of refolding, that is, the formation of the last correct disulfide bond [172, 173]. On the other hand, multiple rate-determining steps were proposed to exist: the intermediates of RNase A were separated into nine fractions on a carboxymethylcellulose column [174]. They collectively contain 24 intermediates, which differ from each other in the numbers of protein disulfide bonds, mixed disulfides with glutathione, and free thiol groups. The relative populations of these intermediates, which lie prior to the rate-determining steps, become constant rapidly after the start of reoxidation reaction: a stationary, or preequilibrium, state is established. The equilibrium constants among the intermediates in the preequilibrium state were determined under various concentrations of GSH and GSSG. By measuring the amounts of fully regenerated RNase A at various concentrations of GSH and GSSG, and relating the amounts to the distributions of the intermediates, multiple pathways with different rate-determining steps were identified [175–177]. These, altogether six, pathways were classified as a growth-type (the rate-limiting step involves formation of an intramolecular disulfide bond) or a rearrangement-type (the rate-limiting step involves reshuffling or disruption of a disulfide bond) [178].

Concerning the appropriateness of multiple versus nonmultiple folding pathways, criticisms and a great deal of debate were exchanged, particularly on the appropriateness of kinetic and energetic analyses, refolding conditions, quenching methods, and existence of intermediates in reductive unfolding pathways [95, 96, 179–181].

When oxidized and reduced dithiothreitol are used as redox couple, the fractionation of intermediates and subsequent kinetic analysis are greatly simplified due to practical elimination of mixed disulfide species in this redox system [155, 182]. The oxidative folding proceeds with sequential reaction steps: R → 1SS → 2SS → 3SS → 4SS, where *i*SSs represent ensembles of isomers that contain *i* disulfide bonds. These ensembles, including 4SS, are essentially unstructured with respect to protein conformation. A steady-state condition is established soon after the start of reaction. Apparent equilibrium constants, derived from steady-state populations of these SS groups and corrected for the number of chemically distinct species in each group, are nearly constant, consistent with the intermediates being globally disordered in protein conformation. Later, extensive analyses of the populations of isomers among 1SS ensemble, employing peptide mapping with mass spectrometry, showed that they are not random within each group. The 1SS native isomer [Cys 65–Cys 72] predominates (40% of the total 1SS population), and all the four 1SS isomers of native disulfide

pairings, including [Cys 65–Cys 72], have populations greater than respective theoretical populations expected for random polypeptide chains [183]. Similar analysis showed that the disulfide bond Cys 65–Cys 72 is present in about 53% of all 2SS intermediates [184].

Detailed kinetic analysis of the sequential reaction steps just described showed that the rate-determining step in the oxidative refolding of RNase A with oxidized and reduced dithiothreitol involves intramolecular disulfide rearrangement of 3SS species [185]. Rearranged 3SS species are rapidly oxidized to the final native 4SS protein. Thus, the oxidative refolding of RNase A is similar to that of BPTI in that it proceeds via disulfide rearrangement pathways, but dissimilar in that the development of conformational structure of RNase A is highly cooperative and occurs only late in the pathways.

4.2.2. Two Separate Pathways and Disulfide-Secure Species

By manipulating redox conditions after the attainment of the steady-state conditions, the 3SS species that follow the rate-determining step were trapped, isolated, and identified: one lacking the 65–72 disulfide bond (des-[65–72]), and the other lacking the 40–95 disulfide bond (des-[40–95]) [186]. The population of these two 3SS species during the time course of oxidative folding were specifically monitored by using a "reduction pulse," under which these 3SS species as well as fully regenerated native species survived unreduced [187]. About 80–86% of the regeneration occurs via des-[40–95] while the remainder occurs via des-[65–72]. The temperature dependence of the overall regeneration rates [188] reflects the stability of these 3SS intermediates with respect to the entire ensemble of 3SS species.

Examination of the reductive unfolding, which is a reverse process of oxidative folding, of RNase A over a range of pH, temperature, and concentrations of dithiothreitol has been carried out [189, 190]. As a blocking reagent, 2-aminoethyl methanethiosulfonate was used. The reductive unfolding proceeds through parallel pathways with the formation of the two 3SS intermediate species described above. The rate-limiting steps involve two distinct local unfolding events rather than a global one.

The two 3SS intermediates, des-[40–95] and des-[65–72], are productive on-pathway intermediates, while the other two 3SS intermediates with native disulfide bonds, des-[26–84] and des-[58–110], are off-pathway dead-end species, which must reshuffle their disulfide bonds to go back to the productive pathway. These different kinetic fates of intermediates can be experimentally distinguished by subjecting them to reducing reagents of appropriate concentration [191]. The former species are not sensitive to the reducing reagents, which indicates that their disulfide bonds are buried and protected. Moreover, they did not rearrange their disulfide bonds ("disulfide-secure"). By contrast, the latter species rearranged their disulfide bonds, and are reduced ("disulfide-insecure"). The reductive unfolding, oxidative folding, conformational structure in disulfide intermediates, and other aspects of the folding of RNase A have been reviewed [83, 192].

4.3. Hen Lysozyme

Lysozyme (1,4-β-N-acetylmuramidase; EC 3.2.1.17) is a bacteriolytic enzyme, which cleaves the glycosidic linkage between C-1 of N-acetylmuramic acid and the C-4 of N-acetylglucosamine in the peptidoglycan of bacterial cell wall [193]. It is found in various tissue and secretion [194] such as tears, nasal mucus, milk, and most notably in egg white. Hen lysozyme consists of 129 amino acid residues [195, 196] (Fig. 1). It contains four disulfide bonds between Cys residues 6–127, 30–115, 64–80, and 76–94 [197, 198] (Fig. 3). Among these, the 6–127 and 30–115 disulfide bonds reside in the α-domain of the molecule, the 64–80 bond in the β-domain, and the 76–94 bond at the interface between the α- and β-domains [199, 200]. Although the folding of lysozyme starting from a denatured state with its four disulfide bonds intact completes in seconds, the oxidative refolding reaction starting from a denatured and reduced state takes minutes to hours. Early history, occurrence, isolation, structure, activity, and other properties of lysozyme as well as those of α-lactalbumin, a protein closely related to lysozyme, have been reviewed [201]. Folding of lysozyme has also been reviewed [34, 202].

Optimal conditions such as pH, temperature, protein and thiol reagents concentrations for the oxidative folding of hen lysozyme have been reported [203, 204]. By optimizing the ratio of GSSG to GSH, as well as their total concentration, the oxidative refolding process *in vitro* was made considerably rapid and efficient, a half-time of 5 min or so [204]. Under such conditions, the rate-limiting process was suggested to be protein conformational changes that accompany protein thiol-disulfide interchange reactions. The analysis of disulfide-containing peptides formed during an early stage of air-oxidation of hen lysozyme apparently identified only less than one-third of the 28 possible pairs [205]. Detailed analysis in the case of oxidation with glutathione showed that two disulfide bonds involving Cys64, Cys76, Cys80, and Cys94 are formed rapidly, then the disulfide bond between Cys30 and Cys115, and presumably finally, the disulfide bond between Cys6 and Cys127 [206]. Hence, the oxidative folding of hen lysozyme was shown to proceed through a limited search of intermediates, and seems to proceed through a "direct" pathway. However, it was pointed out that there may have occurred disulfide rearrangements during quenching since the method employed was not ideal [141].

Enzymatically active fractions with native-like compact hydrodynamic volumes, which were obtained during air-oxidation reaction, were fractionated, and shown to contain 3SS derivatives that lack either 6–127, 64–80, or 76–94 disulfide bonds [207]. Using the materials obtained by reoxidation of reduced and partially as well as randomly carboxymethylated hen lysozyme, it was shown that none of the four native disulfide bonds of hen lysozyme is obligatory for *in vitro* oxidative folding to enzymatically active forms [208]. These early results on the disulfide intermediates of hen lysozyme have been reviewed [209].

4.3.1. Stages for the Appearance of Conformational Structures

It was reported that considerable amount of secondary structure was instantaneously formed in reduced lysozyme after transferring to oxidative-refolding conditions [210]. However, continuous-flow circular dichroism study [211] and improved estimation of the signal of the denatured protein in the renaturation buffer [212] have shown that there is no burst phase in the ellipticity change during the oxidative folding of reduced lysozyme, unlike the case of nonoxidative folding of disulfide-intact lysozyme which is described in the next subsection. Almost no enzymatic activity is regained until the averaged number of disulfides formed per protein molecule reaches two [206]. As described above [207, 208] and demonstrated by using recombinant analogue proteins [213], all the four 3SS intermediates with native disulfide pairing are enzymatically active. The progress curves for protein conformations, protein thiol oxidation, enzymatic activity, etc. were different between oxidative-folding reactions promoted by Cu(II) + O$_2$ and glutathione redox pair [214].

A detailed time course of the oxidative folding of hen lysozyme monitored through the population of intermediates with defined number of disulfide bonds, protein conformational structures, and enzymatic activity has been reported [212, 215]. The oxidative folding of hen lysozyme at practically high protein concentrations can be carried out by suppressing aggregation with the addition of solubilizing agents [216, 217]. Solution conditions were optimized to minimize the formation of aggregate, as well as to enable far-UV CD and fluorescence measurements during the oxidative-folding reaction [212]. Since the concentrations of GSH and GSSG were very low, the oxidation reaction was essentially irreversible, unlike the case described above for RNase A, and the formation of mixed disulfides was rate-limiting in each step of protein disulfide-bond formation. By using electrospray-mass spectrometry, the time courses of populational changes of 0SS through 4SS species during oxidative folding of hen lysozyme were obtained. Leaving aside an "off-pathway" reaction step which led to aggregates of presumably nonnatively disulfide-bonded 3SS species, the productive oxidative-folding reaction conformed to a simple four-step sequential model in which i-SS species is produced from $(i-1)$-SS species, for $i = 1$ to 4, successively. By comparing the time course of populational changes of these disulfide-intermediates with the progress of far-UV CD signal and enzymatic activity during oxidative folding, it was shown that protein secondary structure appears after the formation of 2SS species and before the appearance of 3SS species. Substantial enzymatic activity and nearly full amount of far-UV CD signal appear with the appearance of 3SS species. These conclusions are consistent with the properties of recombinant analogues of 1SS, 2SS, and 3SS intermediates of lysozyme [103, 213, 218].

Qualitatively similar pathway was reported using optical as well as NMR spectroscopies and HPLC separation techniques [219, 220]. First, a relatively large number of highly unstructured intermediates with one or two disulfide bonds, rapidly interconverting among isomers, are formed. Next, with the formation of a third disulfide bond, extensive native-like tertiary structure develops. Fully native protein with four disulfide bonds is formed via rearrangement of a highly native-like, kinetically trapped 3SS intermediate des-[76–94]. It was suggested that this particular 3SS intermediate has to unfold and reorganize in order to form the 76–94 disulfide bond and therefore to complete oxidative folding. This situation is similar to that described previously for BPTI. A significant population (about 30%), however, appears to fold more quickly via other two 3SS intermediates detected, namely des-[64–80] and des-[6–127].

Immunochemical pulsed-labeling characterization with two monoclonal antibodies that recognize native structures within the α- and β-domains, respectively, showed that the native-fold of the α-domain appears in 2SS intermediate [Cys 6–Cys 127, Cys 30–Cys 115], but not in other 2SS intermediates, while the native-fold of the β-domain appears with the formation of the third disulfide bond 64–80 [221]. Thus, although it was reported (under somewhat different redox conditions) that β-domain disulfide bonds form first during 1SS and 2SS stages [206], native folding occurs first in the α-domain, and simultaneous existence of two disulfide bonds, 6–127 and 30–115, is necessary for this to occur.

4.3.2. Pathways of Nonoxidative Folding

The kinetics of nonoxidative folding, or disulfide-intact folding, has been studied extensively for hen lysozyme [75, 222–228]. In the nonoxidative folding, the reaction is started from chemically denatured state of protein, for example, in the presence of 6 M guanidium chloride, with protein's disulfide bonds intact, and is initiated by rapidly lowering the denaturant concentration for the protein to restore its tertiary structures. Nonoxidative folding proceeds faster than oxidative folding [211]. Secondary structure forms in milliseconds and the complete tertiary structure forms in seconds. The mechanism of nonoxidative folding of lysozyme has a great deal of relevance to that of oxidative folding of lysozyme, and recent results are briefly reviewed here.

The existence of early folding intermediates with considerable amount of secondary structure but without tertiary structure in the nonoxidative folding of hen lysozyme has been shown previously [227, 228]. Competition between amide hydrogen exchange and the progress of folding showed that in the early stages of nonoxidative folding, two structural domains of lysozyme fold distinctly: exchange-protected structure accumulates faster in the α-domain than in the β-domain [229]. Pulsed hydrogen/deuterium exchange labeling and stopped-flow CD measurements have shown that within the first 2 msec rapid formation of labile α-helical structure with hydrophobic collapse occurs; then within the next 10 msec or so, protection of about 50% of the α-domain amides and 30% of the β-domain amides occurs; protection of α-domain amides completes by 100–150 msec, while that of β-domain does not complete until about 1 sec, which nearly correlates with the development of tertiary structures [230]. In addition, a transient overshoot at around 80 msec in the CD signal at 225 nm was observed, which was thought to be due to formation of some nonnative

structures. Importantly, experiments with varying labeling pulses showed that there exist parallel alternative folding pathways. Detailed stopped- and continuous-flow CD studies at different wavelengths enabled construction of the far-UV CD spectrum of the molecular species formed in the initial burst phase [231]. It strongly suggested that the complete native-like secondary structure is formed in less than 4 msec. On the other hand, the kinetics in near-UV CD showed that at 4 msec aromatic or cystinyl side-chains are not tightly packed and still in a symmetrical environment. The considerably large overshoot-type changes in the CD band centered at 228 nm in the subsequent rapid and slow phases are most likely due to transient constraints on disulfide bonds.

Stopped-flow fluorescence and absorbance studies have shown substantial quenching of tryptophan fluorescence (either Trp62 or Trp108) [232] in the intermediate that was shown to exhibit CD overshoot in the previous studies described earlier. This structure is stabilized by nonnative tertiary interactions involving Trp62 and Trp108, since two mutants in which either of these tryptophan residues was replaced by tyrosine did not show the intermediate of highly quenched fluorescence [233]. Moreover, these mutants showed accelerated rates of folding. The nonoxidative folding of human lysozyme, which is homologous to hen lysozyme, has been studied [234]. The overall rate of folding is four-fold faster than that of hen lysoyzme. The fundamental character of the folding process is preserved, but there exist significant changes in the stability and structures of the intermediates.

The use of electrospray ionization mass spectrometry to monitor and resolve intermediately hydrogen-exchanged, and therefore of intermediate masses, species during folding, has shown that, in addition to a sequential folding pathway in which α-domain is first structured followed by β-domain structure formation, there exists faster and cooperative pathway in which the two domains become structured simultaneously [235]. The active site of lysozyme is formed at the interface between the two domains. By using a fluorescent substrate analogue 4-methylumbelliferyl-N,N′-diacetyl-β-chitobiose [236], which binds to the active site, the slow phase (a time constant value around 350 msec) was shown to represent the process of integration of two domains with the formation of a functional active site, and therefore a fully native molecule [237]. In a later report, another pathway with faster formation of the active site (a time constant value of 100 msec, and amplitude of 25%) was revealed [238]. The latter pathway corresponds to the faster and cooperative pathway that has been found in hydrogen-exchange labeling studies [230, 235]. The 5 to 10-msec product in which amides groups in both α- and β-domains are protected from hydrogen-exchange is not fully natively folded. This state lacks the docking between the two domains, and is called "a near-native state."

In agreement with these observations, by using interrupted refolding experiments, which specifically monitor the amount of natively folded molecules, the major folding pathway that involves the α-domain-folded intermediate described above as well as a minor pathway in which lysozyme molecules fold faster without such an intermediate

were shown [239]. Kinetic partitioning occurs between parallel folding pathways: part of the molecules fold directly to the native state, while others are trapped in partially folded states, which decelerates their conversion to the native state [240]. The existence of the slow-folding channel implies that pre-formed secondary structure in the folding intermediate obstructs formation of the transition state of folding. At higher temperatures, the folding process becomes more cooperative and the overshoot-type unusual CD and fluorescence changes are absent, due to the destabilization of the α-domain-folded intermediate [241].

The rate of the slow phase decreased with increasing ionic strength [237], and the formation of the near-native state in the slow-folding track and subsequent docking of the α- and β-domains with the formation of a fully native molecule were decoupled [242]. Thus, the near-native state is a common intermediate found in both fast- and slow-folding tracks. Specific electrostatic interactions and anion binding appear to play important roles in the docking process.

4.4. α-Lactalbumin

Bovine α-lactalbumin (α-LA) is 123 amino acids long, and contains four disulfide bonds between Cys residues 6–120, 28–111, 61–77, and 73–91. It is homologous to lysozyme in amino acid sequence [243–245], in a disulfide linkage pattern, and in three-dimensional structure [246–248]. α-LA is a milk whey protein. As a regulatory component of a lactose synthase (UDP-D-galactose:D-glucose β-4-D-galactosyltransferase; EC 2.4.1.22) system, it alters the substrate specificity of the galactosyltransferase from N-acetylglucosamine to glucose, thus enabling lactose (β-D-galactopyranosyl-(1→4)-D-glucose) synthesis to be effected with the onset of lactation [201]. α-LA tightly binds a calcium ion [249]. The gene for α-LA seems to have diverged from that for calcium-binding lysozyme some 200 million years ago with the appearance of mammary gland (reviewed in [201, 250, 251]).

Oxidative folding of α-LA to generate the final native active protein requires calcium ion [252, 253]. Pathways of reductive unfolding and oxidative folding of bovine α-LA have been clarified in detail [147, 254]. During the oxidative folding, many 1SS, 2SS, and 3SS intermediate species appear sequentially. Most of them do not have stable native-like structures, and do not bind calcium ion. Through disulfide rearrangements among the 3SS intermediates, a particular 3SS species, des-[6–120], appears, which can bind calcium ion, and rapidly forms the fourth disulfide bond, 6–120. The binding of calcium ion is necessary for the oxidation reaction to progress beyond the 3SS stage, and the rate-determining step is the rearrangement of 3SS intermediates to produce 3SS des-[6–120].

In the reductive-unfolding pathway with the presence of calcium ion, the 6–120 and 28–111 disulfide bonds are reduced sequentially [254]. The 6–120 disulfide bond was shown to be 140 times more reactive than normal disulfide bonds in a fully accessible state, and the superreactivity arises from the geometric strain imposed on this disulfide bond by the native structure [255].

5. STRUCTURE AND PROPERTIES OF DISULFIDE INTERMEDIATES AND THEIR ANALOGUES

The elucidation of the structure and properties of the disulfide intermediates that are trapped during the folding or unfolding reaction provides valuable information about their roles in folding, and therefore about the appropriateness of the proposed folding mechanism. Apart from this objective, since most proteins with multiple disulfide bonds lose higher-order structure and enzymatic activity upon reductive cleavage of all the disulfide bonds, a natural question is how many disulfide bonds are necessary under native solution conditions for such proteins to acquire native-like structure and biological activity; and if not all the disulfide bonds are necessary, which ones are essential or dispensable? Even if it is the case that the completely folded structure can be attained in the reduced form of the protein such as that for constant fragment of the immunoglobulin light chain [112] or ribonuclease T1 [108, 256], studies of defined disulfide-intermediate species provide information about the mechanism of gain or loss in thermodynamic stability.

The development of site-directed mutagenesis and recombinant DNA technologies has made it possible to construct variant protein genes in which codons for specific Cys residues are changed to, usually, Ala or Ser residue. By expressing the variant genes in appropriate host cells such as *E. coli*, yeast, insect cells, etc., variant proteins that lack specific disulfide bonds can be prepared. With the conventional techniques of protein chemistry, it is usually difficult to prepare variant proteins that lack specific disulfide bonds. They serve as stable analogues of disulfide intermediates, and their structures and properties provide useful insights into the folding mechanism. Thus, it is now possible to explore the contribution of individual disulfide bonds to the folding and stability of proteins with multiple disulfide bonds. Another obvious merit of the use of stable analogues of disulfide variants that have fewer numbers of possible disulfide bonds than wild-type protein is that it makes the analysis of many aspects of disulfide formation much simpler since the number of possible isomers are considerably reduced as described in Section 3.2.4.

Some descriptions related to these topics have already been given in Section 4; in this section, the structure and properties of disulfide intermediates of representative proteins are reviewed comprehensively. In the titles of the following subsections, "*n*SS species" denote collectively both the disulfide intermediates and their analogues with *n* disulfide bonds.

5.1. Intermediates of Bovine Pancreatic Trypsin Inhibitor

5.1.1. BPTI 0SS Species

Fully reduced BPTI lacks its activity and stable conformations [257, 258], and appears to be largely disordered, as evidenced by the equal reactivities of individual Cys residues against alkylating reagents with the rate constant comparable to those observed with model thiol compounds [259], by the estimated amount of nonrandom conformations [260],

and by small effects of amino acid replacements on the hydrodynamic volume [261]. However, effect of urea on the C_{eff} values for individual single disulfide bonds suggested that the reduced BPTI under normal refolding conditions is not an ideal random coil [105]. Fluorescence energy transfer measurements, ANS binding, and NMR analyses including pulsed field-gradient NMR measurements have shown that the reduced BPTI or its analogue contains subpopulations with compact intramolecular distances [262, 263], has stable hydrophobic surfaces, and is more compact than a random coil [264, 265]. Although it lacks regular secondary structure [266], it contains a number of local structures that involve aromatic rings and groups nearby, turn-like conformations, and so on [267–270].

5.1.2. BPTI 1SS Species

Among the three native 1SS intermediates of BPTI, [Cys 5–Cys 55] already acquires a nearly native-like structure [271–273]. A peptide model of [Cys 5–Cys 55] seems to fold into a native-like conformation [274]. [Cys 5–Cys 55] is not a partially structured folding intermediate; rather, it is a globally structured protein with low stability. By using a recombinant analogue of 1SS [Cys 5–Cys 55] as a reference protein, almost all the residues were individually replaced by Ala residue ("alanine-scanning mutagenesis"), and the contribution of individual amino acid side-chain to the stability was examined [275]. The two hydrophobic core regions and internal hydrogen-bonding network were demonstrated to be important. Furthermore, a mutant thereof that contained 22 multiple alanine residues substituted was shown by NMR spectroscopy to fold into a native-like structure [276].

One of the other 1SS intermediates, [Cys 30–Cys 51], is partially structured and represents a typical folding intermediate [277–279]. ^{1}H and ^{15}N 2D NMR measurement on the recombinant analogue of [Cys 30–Cys 51] has clarified that part of the polypeptide chain, consisting of residues 18 to 36 and 42 to 55, is stably folded, while N-terminal 15 residues and the segment consisting of residues 37 to 41 are disordered or flexible. The folded portion includes the antiparallel β-sheet and the C-terminal α-helix, interacting as in the hydrophobic core of native BPTI. The disordered or flexible portion includes Cys residues 5, 14, and 38, which explains why during the oxidative folding the 1SS intermediate [Cys 30–Cys 51] readily forms disulfide bonds between these Cys residues. A synthetic peptide model of [Cys 30–Cys 51] contained native-like secondary and tertiary structure [280].

The third 1SS intermediate, [Cys 14–Cys 38], has the least tendency to form a native-like conformation [166]. It adopts a molten globule state in which a number of conformations interconvert with each other, with the antiparallel β-sheet in native-like conformation [264, 281, 282]. The formation of 14–38 disulfide bond is facilitated by the presence of several hydrophobic residues that form a part of the central β-sheet in the structure of native BPTI [283]. Marginal thermodynamic stability of the residual structure involving these hydrophobic residues has been estimated based on the difference in the formation rate of 14–38 disulfide bond between the variants that have mutations in these hydrophobic residue positions [284].

5.1.3. BPTI 2SS Species

All the three species of two-disulfide intermediates of BPTI with native disulfide pairings, [Cys 30–Cys 51, Cys 5–Cys 55] [277, 285–287], [Cys 5–Cys 55, Cys 14–Cys 38] [287–291], [Cys 30–Cys 51, Cys 14–Cys 38] [277, 292], attain essentially native-like structures albeit with different stabilities, subtle changes, and with the exception of the extreme N- and C-terminal regions in [Cys 30–Cys 51, Cys 14–Cys 38]. In [Cys 5–Cys 55, Cys 14–Cys 38], the thiol groups of remaining Cys residues 30 and 51 are buried in the interior of the protein molecule and unreactive with oxidizing reagents [288].

5.2. Intermediates of Ribonuclease A

As described in Section 4.2.1, essentially all of the 1SS and 2SS intermediates of RNase A are disordered in conformation and have no enzymatic activity. Native disulfide pairings, however, occur more than theoretical populations expected for random polypeptide chains.

5.2.1. RNase A 2SS Species

Analogue of 2SS intermediate of RNase A was constructed with site-directed mutagenesis, in which Cys residues 40, 65, 72, and 95 were replaced by serine or alanine [293]. All the three 2SS isomers obtained by oxidation of all reduced form of this mutant are predominantly disordered. However, a native isomer 2SS [Cys 26–Cys 84, Cys 58–Cys 110] is populated more than a statistical population, indicating the presence of specific local interactions to favor the formation of native disulfide bonds.

5.2.2. RNase A 3SS Species

The 3SS species des-[65–72] is the most highly populated intermediate in the reductive unfolding pathway of RNase A. The 2D and 3D ^{1}H NMR spectroscopic study on the stable derivative of this 3SS species obtained by partial reduction and blocking with (2-aminoethyl) methanethiosulfonate showed that while it is thermodynamically less stable than native RNase A, it has a structure that is globally similar to native RNase A [294]. Structural differences occur only in a loop region comprising residues 60–72, indicating that the rate-determining step in reductive unfolding corresponds to a local unfolding event, and not to a global unfolding process. The more precise structure of this species was studied by using the ^{13}C, ^{15}N-enriched [C65S, C72S] mutant RNase A produced in E. coli [295, 296]. Removal of the disulfide bond 65–72 resulted in the disruption of the short antiparallel β-sheet that is formed between β2 (residues 60–64) and β3 (residues 72–75) strands. Since this β-sheet comprises part of the hydrophobic core of RNase A, its disruption leads to global destabilization.

Another 3SS species, des-[40–95], which is also populated in the reductive unfolding pathway of RNase A, shows global similarity in tertiary fold, although being destabilized, with wild-type RNase A as revealed with NMR spectroscopy and crystal structure [297, 298]. Structural perturbations are localized only around the mutation sites.

The remaining two 3SS species with native disulfide linking, that is, des-[26–84] and des-[58–110], are thermally unstable and have native structures only at low temperatures [299]. These two 3SS species as well as the two 3SS species described above have enzymatic activity [295]. Thus, no single native disulfide bond is prerequisite for global folding of RNase A.

The pathway of the oxidative folding of the 3SS mutants [C65S/A, C72S/A] [300], and that of [C40A, C95A] [301] were studied. In both cases, the major rate-determining step is the oxidation step from 2SS to a 3SS species, which is a minor pathway to produce these 3SS intermediates in the oxidative folding of wild-type RNase A. The relative disulfide-bond populations of the 1SS, 2SS, and 3SS ensembles of the [C40A, C95A] under near-physiological conditions were reported [302]. A comparison of the free energy changes for the conformational (i.e., disulfide bond being kept intact) [303] and reductive [190] unfolding reactions indicates that the reduction of des-[40–95] to the 2SS species is rate-limited by global conformational unfolding, whereas that of des-[65–72] is rate-limited by local conformational unfolding. Moreover, the isomerization of Pro93 may be rate-limiting for the reduction of the 40–95 disulfide bond.

Thermodynamic stability and enzymatic activity were studied on the four recombinant analogues of the 3SS intermediates of RNase A, each lacking one of the four native disulfide bonds with amino acid replacements to alanine. Removal of either of the disulfide bonds 26–84 or 58–110, both linking an α-helix to a β-strand, primarily destabilized the global structure of protein, while the removal of either of the disulfide bonds 40–95 or 65–72, both linking surface loops, primarily decreased enzymatic activity [304]. Detailed thermodynamic analyses showed that the destabilization of the two analogue species, C40A–C95A and C58A–C110A, was driven by enthalpic factors, indicating that the loss or weakening of interactions occurs in the folded state upon the removal of a disulfide bond [305]. This was partially counterbalanced by a corresponding increase in conformational entropy of the folded state. It leads to a decreased amount of entropy change observed upon unfolding of analogue species compared to wild type, contrary to the common theoretical expectation that the destabilization due to the cleavage of disulfide cross-link is primarily through entropic stabilization of the unfolded state.

5.3. Intermediates of Lysozyme

5.3.1. Lysozyme 0SS Species

The completely reduced form of hen lysozyme or its analogues does not have enzymatic activity or rigid tertiary structure, but appears to have some residual secondary structures [204, 210, 306–312]. It should be noted that the completely reduced form as well as disulfide intermediates of lysozyme are highly prone to aggregation: detailed study on the kinetic competition between oxidative folding and aggregation of lysozyme has shown that while the commitment to oxidative refolding is a comparatively slow process, with a half-time of about 4.5 min, that to aggregation is a rapid process, which completes in less than 1 min under the protein concentration range employed [313].

5.3.2. Lysozyme 1SS Species

Four species of hen lysozyme 1SS variants with a native disulfide linkage pattern have been constructed [103]. They do not have global cooperative structures or enzymatic

activity. Under denaturing solution conditions, the dependence of C_{eff} of cysteinyl thiol groups of disulfide bonds on the loop size agreed with the expectations based on random coil conformation. The relative increase in C_{eff} accompanying the change from denaturing to native solution conditions was high for α-domain disulfides, indicating higher propensity of structure formation in the α-domain. Consistent with this, the increase in secondary structure upon the formation of each single disulfide bond was relatively large for the α-domain disulfide bonds. Analysis of urea concentration dependence of C_{eff} based on the folding-oxidation linkage relationship combined with the conventional treatment of urea-unfolding curves [314] provided information about the size and intrinsic stability of submolecular structure associated with the formation of each disulfide bond.

5.3.3. Lysozyme 2SS Species

A 2SS intermediate of hen lysozyme, presumably [Cys 30–Cys 115, Cys 64–Cys 80], was obtained by reduction of wild-type lysozyme with DTT [315]. It was enzymatically active (15%, relative to wild-type activity) and appeared to have a native-like fold. Recently, two species of the recombinant analogue of the 2SS intermediate were constructed [218]. One species, 2SS [Cys 6–Cys 127, Cys 30–Cys 115], which contains two disulfide bonds in the α-domain, had native-like amount of structures and bacteriolytic activity of 60–70% of wild-type lysozyme. By contrast, the other species, 2SS [Cys 64–Cys 80, Cys 76–Cys 94], which contained the β-domain disulfide bond as well as the interdomain one, had limited amount of secondary and little tertiary structures. Together with disulfide exchange and ^{1}H-NMR results, the α-domain of hen lysozyme was shown to be an independent folding domain at equilibrium. By using a recombinant protein that corresponds to an isolated α-domain of lysozyme, the same conclusion was drawn independently [316]. A detailed NMR structural analysis on 2SS [Cys 6–Cys 127, Cys 30–Cys 115] revealed that the structure of the α-domain is virtually the same as that of intact lysozyme, with side-chains closely packed in the hydrophobic core through the specific binding of C-helix to the N-terminal half of the α-domain (residues 1–39) [317]. On the contrary, the β-domain (residues 40–87) is largely unstructured, but the residues Ile55 and Leu56 are properly set in the hydrophobic pocket between B- and C-helices. Such interactions between the α- and the β-domains seem crucial to keep the marginal stability of the whole structure of lysozyme.

2SS [Cys 6–Cys 127, Cys 30–Cys 115] showed immunoreactivity toward the monoclonal antibody that recognizes an epitope in the α-domain [221]. The other four recombinant analogues of the 2SS intermediates that contain only one native disulfide bond in the α-domain, that is, 2SS [Cys 6–Cys 127, Cys 64–Cys 80], 2SS [Cys 6–Cys 127, Cys 76–Cys 94], 2SS [Cys 30–Cys 115, Cys 64–Cys 80], and 2SS [Cys 30–Cys 115, Cys 76–Cys 94], did not show such immunoreactivity.

5.3.4. Lysozyme 3SS Species

The 3SS intermediates which were formed during the oxidative folding of hen lysozyme and that lack either 6–127, 64–80, or 76–96 disulfide bond were isolated. They all have

enzymatic activity and native-like compact hydrodynamic volume [207].

Human lysozyme 3SS variant that lacks the 77–95 disulfide bond, which corresponds to the 76–94 disulfide bond of hen lysozyme, was produced [318] by using yeast expression system [319–321]. It was shown that the 6–128 disulfide bond in human lysozyme is a prerequisite for correct folding and secretion *in vivo* in yeast, whereas the 77–95 disulfide bond is not. Furthermore, Cys65 was shown to be indispensable, while Cys81 was dispensable, for correct folding *in vivo* [322]. The overall three-dimensional structure of des-[77–95] human lysozyme is essentially identical to that of wild type, except for the vicinity of the residue 77 [323]. A cavity was produced by the removal of the disulfide bond, which could increase the free energy of the folded state. Differential scanning calorimetry results have shown that the destabilization of this 3SS variant is caused primarily by enthalpic factors involving disappearance of van der Waals contact with sulfur atoms and increase in flexibility in the folded state [324], contrary to the theoretically expected entropic effect of cross-linking in the unfolded state. Nonoxidative folding/unfolding kinetics of this variant also showed that the 77–95 disulfide bond primarily contributes to the stabilization of the folded state, rather than the destabilization of the unfolded state [325].

On expression of several mutant human lysozymes in yeast, the attachment *in vivo* of glutathione to the thiol group of Cys95 [326] and that of 1,2-dicarboxyethyl group to the thiol group of Cys77 were observed [327].

Among hen lysozyme 3SS derivatives, that with Cys6 and Cys127 blocked by carboxymethylation [328], designated CM^{6-127} lysozyme, could be prepared in large amount [329, 330] by using the conditions originally described for the preparation of 2SS variant [315]. This 3SS species, an analogue of des-[6–127], is enzymatically nearly fully active. It has a conformation that is globally similar to native lysozyme except for local perturbation around the cleaved disulfide bond. Its thermodynamical stability is considerably lower than that of wild-type lysozyme, which is explained predominantly by the increase in chain entropy of the unfolded state of 3SS relative to the unfolded state of wild-type (4SS) lysozyme [331], simply consistent with the theoretically expected entropic effect of cross-linking in the unfolded state. A crystal structure of this 3SS lysozyme is very similar to that of unmodified lysozyme except for some displacement of the C-terminal residues [332].

All the four 3SS derivatives of hen lysozyme, in which one of the four native disulfide bonds was opened by substitution of Ser (or Ala in later studies) for Cys residues, were produced in *Escherichia coli* by expressing synthetic variant genes [213]. Since these derivatives were only obtained as insoluble form ("inclusion body") and must be denatured and reduced for solubilization, the reoxidation and formation of correct disulfide bonds are required. The reoxidation conditions previously described to be optimal for authentic lysozyme [204] were not efficient for these 3SS derivatives. Instead, the addition of glycerol, which has been known to increase the stability of the native state of proteins with the mechanism of preferential hydration [333], increased the efficiency of reoxidation [213], and enabled preparation of all the four 3SS variants in sufficient amount. The

four 3SS derivatives all showed lytic activities and secondary structures comparable to authentic lysozyme, which directly showed that none of the four native disulfide bonds is a prerequisite for correct *in vitro* folding. There exists a parallel relationship for the 3SS derivatives between the optimal refolding temperature and the thermal stability of the correctly refolded state [334]. All the four 3SS variants of hen lysozyme show native-like amount of tertiary structure, cooperative thermal as well as guanidium hydrochloride-induced unfolding, although their stabilities are considerably low compared to wild-type lysozyme [335]. They also bind a substrate analogue, tri-*N*-acetyl-D-glucosamine, like wild-type lysozyme does, except that the binding is specifically weak for the 3SS variant des-[76–94].

As a dominant 3SS intermediate during the later stages of oxidative folding of hen lysozyme, des-[76–94] has been identified and characterized [219, 220]. NMR spectroscopic study has shown that it has a highly native-like structure. The α-domain structure is essentially identical with that in wild-type lysozyme. There exist slight differences in the structure of β-domain and interfacial region between the two domains. It was suggested that Cys94 is buried in des-[76–94] in the protein interior and not accessible to oxidizing reagents, thus making this intermediate a kinetic trap in folding.

The role of individual disulfide bonds in the kinetics of lysozyme folding has been investigated. In a nonoxidative folding kinetics, the 3SS derivative CM$^{6-127}$ lysozyme does not show the phase, as monitored by absorbance and fluorescence, that is associated with the formation of nonnative tertiary interactions in the α-domain. Also, the overall folding process is faster compared with wild type [232]. Another study of the kinetics of nonoxidative folding of this 3SS derivative, monitored by hydrogen-exchange labeling, mass spectrometry, CD, and fluorescence, also demonstrated the absence of this phase, while other features of overall kinetics, such as the initial burst in secondary structure formation, slower formation of native-like tertiary interactions, and parallel pathways of folding, are similar to those of wild-type lysozyme [336]. Thus, the 6–127 disulfide bond is not required for the efficient folding of lysozyme, nor the cause of the parallel pathways. Instead, it confers stability on the partially folded intermediate, as well as on the final folded state, and directs the folding through a pathway characterized by nonnative tertiary interactions involving a tryptophan residue(s) and/or a disulfide bond(s).

The other three species of 3SS variants, that is, recombinant analogues of des-[30–115], des-[64–80], and des-[76–94], were constructed and the kinetics of the early steps of their non oxidative folding were studied [337]. All these variants showed initial burst in secondary structure formation. It was further shown that simultaneous presence of the two intra-α-domain disulfides, that is, 6–127 and 30–115, is necessary for the generation of the trapped intermediate that has nonnative tertiary interactions in the α-domain. The intra-β-domain disulfide, 64–80, stabilizes the trapped intermediate, whereas the interdomain disulfide, 76–94, destabilizes it. On the other hand, the kinetics of the late steps that concern the transition state of nonoxidative folding was studied using the four species of 3SS variants [335]. The results suggest that two segments around Ala76 and Ala94

substituted for Cys residues are associated with each other in the transition state, whereas two segments around Ala64 and Ala80 substituted for Cys residues are not. The arrangement of the loop region (around residue 76) in close proximity to the C-helix (around residue 94) seems to be part of the rate-determining process of folding. Conversely, the segment around Ala64 will be associated with that around Ala80 after passing through the rate-determining step. Thus, the role of the disulfide bond Cys 64–Cys 80 is to prevent protein from unfolding, whereas that of Cys 76–Cys 94 is to induce the structure that is necessary for the folding transition. The role of the other disulfide bridges located in the α-domain is more or less similar to that of Cys 64–Cys 80. The formation of α-helix 88–98 has been shown to be essential in the oxidative folding of hen lysozyme to the native state [338].

5.4. Intermediates of α-Lactalbumin

5.4.1. α-LA 0SS Species

The completely reduced form of bovine α-LA is close to a random coil in the absence of salt [339]. In the presence of salt, the amount of secondary structure increases to the level found in the intermediate, during nonoxidative folding, of disulfide-intact α-LA. It was therefore concluded that the disulfide bonds were not a determinant of the secondary structure formed at an early stage of folding. The completely reduced bovine α-LA is prone to aggregation in the presence of salt. The recombinant analogue of the all-reduced form of human α-LA is nearly as compact as wild-type human α-LA [340]. It contains a native-like stable helical core region. Taken together with the reported propensities of native disulfide-bond formation of human α-LA, it was concluded that the topological constraints provided by disulfide bonds are not the source of the native-like three-dimensional fold of α-LA.

5.4.2. α-LA 1SS Species

A set of 1SS variants of human α-LA were constructed and local structural preferences were investigated by means of CD spectroscopy and measurements of the effective concentration of disulfide-participating thiol groups [341]. They all lack rigid side-chain packing and adopt molten-globule state. The region surrounding the 28–111 disulfide bond had a particularly high preference (C_{eff} value of 1070 mM) to adopt a native-like structure.

5.4.3. α-LA 2SS Species

A 2SS intermediate of bovine α-LA, 2SS [Cys 61–Cys 77, Cys 73–Cys 91], was trapped during reduction of calcium-bound α-LA, isolated, and characterized [342]. Its β-domain is folded whereas its α-domain is unfolded. With removal of the bound calcium, the structure is lost to the level of molten-globule state. Concomitantly, reshuffling of disulfide bonds occurs if the remaining thiol groups are not blocked. The calcium-bound form of 2SS [Cys 61–Cys 77, Cys 73–Cys 91] shows a cooperative, reversible unfolding transition as monitored by calorimetry and CD [343], indicating that the calcium-bound β-domain of α-LA is an independent folding domain. This is in marked contrast to the results

obtained for hen lysozyme 2SS variants that the α-domain is an independent folding domain [218, 316].

A 2SS variant of human α-LA, 2SS [Cys 6–Cys 120, Cys 28–Cys 111], which contains the two α-domain disulfide bonds, adopts a molten-globule state and lacks side-chain packing [61]. Nevertheless, the study of disulfide exchange among one native and two nonnative 2SS isomer species has shown that it maintains a native-like main-chain tertiary fold in the α-domain. This was also shown for the construct of α-domain in isolation [344]. The study of the denaturant concentration dependence of disulfide exchange has suggested that the formation of secondary structure is a necessary, but not sufficient condition for the formation of the native-like main-chain tertiary fold, supporting a hierarchical model of protein folding [345]. Another 2SS variant of human α-LA, 2SS [Cys 61–Cys 77, Cys 73–Cys 91], which contains the intra-β-domain disulfide bond as well as the interdomain disulfide bond, also adopts a molten-globule state, but does not maintain a native-like main-chain tertiary fold in its β-domain in the absence of calcium. This bipartite nature in structure formation for human α-LA was also observed in the corresponding 2SS variants of hen lysozyme described in the previous subsection [218]. However, in hen lysozyme, the folded state of 2SS [Cys 6–Cys 127, Cys 30–Cys 115] is not a molten globule. Both a native-like main-chain tertiary fold and side-chain packing are established in its α-domain. This difference in the establishment of tertiary structure within the α-domain between these two homologous proteins appears to originate from the difference in the intramolecular packing density between them [218, 316]. On the contrary, when only the 28–111 (α-LA) or 30–115 (lysozyme) disulfide bond is present, the AB helix region of α-LA, and not that of lysozyme, appears to have an intrinsic ability to form structure [346]. The variant 2SS [Cys 6–Cys 120, Cys 28–Cys 111] does not bind calcium, whereas 2SS [Cys 61–Cys 77, Cys 73–Cys 91] binds calcium, leading to a cooperative formation of tertiary interactions and a native-like main-chain topology [347]. Thus, in human α-LA, the organization of the β-domain, coupled with calcium binding, comprises the locking step in its folding from the molten-globule to the native state.

By using 1SS [Cys 28–Cys 111] or 2SS [Cys 6–Cys 127, Cys 30–Cys 115] variant of human α-LA as a reference protein, further mutations relevant to protein folding problem were introduced and analyzed. Proline scanning mutagenesis showed that the native-like main-chain tertiary fold in the molten-globule state is formed by noncooperative assembly of constituent helices [348]. Replacement of all the hydrophobic residues in the α-domain by a representative amino acid, leucine, retained a native-like main-chain fold in the molten-globule state [349]. This suggests that nonspecific hydrophobic interactions may be sufficient to specify the global fold of a protein. By substituting alanine (or other hydrophobic amino acids) for a number of buried residues in the α-domain and evaluating the effect on the C_{eff} for the formation of the 28–111 disulfide bond, it was shown that a subset of hydrophobic residues that comprises a densely packed core in the wild-type structure is most important for the formation of the native-like main-chain topology [350, 351].

5.4.4. α-LA 3SS Species

The 6–120 disulfide bond of bovine and human α-LA can be selectively reduced and blocked [352–354]. The molecular basis of the hyperreactivity of this disulfide bond in bovine α-LA has been clarified in detail [255]. This analogue of the 3SS intermediate des-[6–120] of bovine or human α-LA retains native-like secondary and tertiary structures in the presence of calcium [255, 342, 343]. The equilibrium as well as kinetic intermediates with characteristics of molten globule that are similar to those found for wild-type α-LA also exist in the nonoxidative folding of this 3SS variant [355]. The molten-globule state was shown to be stabilized by the 6–120 disulfide bond, although the extent of stabilization is smaller than that for the native state. It was shown later, however, based on the analysis of the guanidine hydrochloride concentration dependence of the folding and unfolding rate constants, that the molten-globule state is not necessarily an obligatory intermediate [356]. Also it was indicated that the polypeptide loop closed by the 6–120 disulfide bond is unfolded in the transition state of the folding of α-LA. Upon the removal of bound calcium, the 3SS variant in which the free Cys residues 6 and 120 are unblocked rapidly converts to the molten-globule state with concomitant rearrangement of disulfide bonds [357]. The distribution of free thiol groups within the rearranged species was nearly uniform, which indicates the absence of a native-like main-chain tertiary topology [358].

6. SUMMARY

6.1. Protein Folding in General

Unfolding transitions for a single-domain protein generally approximate to a two-state model. It is a consequence of the cooperative nature of protein stabilization. The interactions that stabilize folded proteins are individually weak, especially in the presence of competing water. Many of them work simultaneously to stabilize folded conformations of protein. The cooperativity of these numerous interactions apparently results in partially folded conformation being much less stable than either N or U under all condition. Consequently, it is necessary to study the folding process kinetically, as a function of time. The starting state for protein folding is different from the fully unfolded state in solutions containing concentrated urea or GdmCl. It is the nonnative state under physiological conditions. The properties of the starting state for folding have been inferred from kinetic studies and shown to be a disordered but compact (molten-globule; MG) state. In some proteins, extensive secondary structure exists in the MG state prior to the formation of close-packed tertiary structure in the native state. The main barrier to folding is between MG and N so that it involves the rate-determining step of the overall folding pathway.

Is the correct secondary structure formed prior to collapse of the chain, or simultaneously with the collapse, or only when the native three-dimensional structure is formed? It seems certain that there are residual structures in nonnative states of proteins. But any such structures appear to be only marginally stable and undoubtedly rapidly fluctuating between conformational states. Are they compulsory

structures important for the folding transition? These questions are central to the elucidation of the early stage of protein folding. NMR spectroscopy may be the major technique to investigate residual structures in nonnative states of proteins. It has unique possibility to provide information with atomic resolution. For small unfolded proteins, full assignment of ^{1}H, ^{15}N, and ^{13}C resonances is often straightforward in the advanced NMR spectroscopy. Different methods have been developed to extract structural and dynamic information about nonnative states of proteins from NMR parameters. The most popular NMR method for analyzing partially folded proteins is hydrogen exchange kinetics. Next to this method, the deviations of ^{1}H or ^{13}C chemical shifts from random-coil values suggest the presence of a stable folded substructure in the nonnative state. Further, in the ^{1}H-^{15}N correlation spectrum, the finding of a set of missing H_N peaks due to severe line broadening is evidence that these residues are participating in exchange between two or more conformations at a rate of the order of 500 s^{-1}. Furthermore, ^{15}N relaxation data have been recently analyzed to explore the backbone motion of each residue. The analysis of relaxation data in a semiquantitative way suggests that hydrophobic clusters and disulfide bridges affect the dynamics of polypeptide chain in the nonnative state.

The concept of transition state appears to be applicable to protein folding. By definition, the structure of the transition state cannot be determined by direct methods. Instead, inferences about its structure are made according to the changes observed in the rate constant of a reaction when certain variables are changed. Analysis of the folding and unfolding rates of hen lysozyme suggests that the transition state is close to the native state in heat capacity and that the hydrophobic core of hen lysozyme is largely intact and unsolvated in the transition state. The large activation enthalpy of the unfolding reaction is due to the disruption of van der Waals interactions between nonpolar groups and hydrogen bonds between polar groups, which maintain a crystal-like structure in the interior of a protein. A powerful approach for investigating the structure of the transition state is based on protein engineering. It involves mutating specific residues and measuring the change in the rates of folding and unfolding relative to the effect on the overall stability of the protein. Barnase was extensively analyzed by measurements of more than 130 mutants. In hen lysozyme, effects of the deletion of a specific disulfide bridge on folding kinetics were systematically examined by replacing Cys residues with Ala or Ser residues. In these examples, structures of the transition state are inferred at the level of individual residues. It is expected that there will be increasing numbers of such systematic studies to elucidate the nature of the transition state of protein folding.

6.2. Disulfide-Associated Protein Folding

The attainment of a single native disulfide-pairing pattern out of a number of possibilities was used as an indicator of the attainment of a correct three-dimensional structure of proteins. The formation of disulfide bonds stabilizes protein structures, which in turn stabilize disulfide bonds against cleavage. Under appropriate conditions, unstable disulfide bonds can be rearranged to more stable ones. Thus, the process of the attainment of a native disulfide-pairing starting from a state of randomized pairing or from a reduced state appears to be a simple one from a thermodynamic point of view. However, as was described in previous sections, the actual pathways of oxidative folding of proteins are not so simple. For relatively stable proteins, native disulfide intermediates often do not proceed to the next step of native disulfide formation, and are "trapped." Disulfide rearrangements via the formation of nonnative disulfide bond to a "productive" native disulfide intermediate are required. Premature formation of a stable as well as globally folded state within a partially oxidized form buries unoxidized thiol groups inside the protein molecule and inhibits their reaction with thiol reagents. For relatively unstable proteins, on the other hand, intramolecular disulfide rearrangements among structureless intermediates occur frequently, and the formation of "disulfide-secure" species is an important step for entering productive pathways. The mechanism of specific stability of the disulfide-secure species among its disulfide isomers is to be elucidated.

The progress in the techniques of the quenching of free sulfhydryl groups, separation and quantification of disulfide intermediates with high-performance liquid chromatography and mass spectrometry, rapid-kinetics experiments, a double-jump kinetic study such as the subjection of oxidation intermediates to reducing agents to identify disulfide-secure species, and most notably the recombinant protein technology as well as NMR spectroscopy, enabled to provide valuable information about the disulfide-associated folding. In most cases, it appears that there exist more than single pathways for oxidative folding. In some cases, the pathways that are "hidden" for a wild-type protein become apparent for variant proteins. For hen lysozyme, it now appears that there exist close relationships between the mechanism of oxidative folding and nonoxidative folding. The mechanism of structure formation and docking of the two domains in lysozyme as well as in α-LA should further be elucidated. Systematic cleavage or introduction of a number of individual disulfide bonds has now become a practical achievement. Such series of variants are highly valuable to know the role of each disulfide bond, and therefore that of specific interactions between local and distant regions of the main chain, in static as well as kinetic aspects of protein folding. The fundamental problem whether some disulfide bonds kinetically dictate protein folding or they only statically stabilize preformed structures is to be studied furthermore. In any way, proteins are highly complex macromolecules that lie at the interface of materials science and biological science, and their folding reactions are elaborate nanoscale processes, which require correspondingly comprehensive descriptions.

Finally, biological aspects of oxidative protein folding that were not treated in this chapter are briefly mentioned: The folding and assembly of proteins within living cells occur under conditions significantly different from those used for *in vitro* experiments. They involve enzymes such as protein disulfide isomerases in the endoplasmic reticulum in eukaryotes, peptidyl-prolyl *cis-trans* isomerases, Dsb proteins in bacterial periplasm, and a number of cellular proteins collectively known as chaperones. A number of studies of the

oxidative folding of the proteins described in this chapter in the presence of these enzymes or chaperones have been reported. Protein misfolding and aggregation/fibrillogenesis are known to be linked to a number of diseases such as Creutzfeldt–Jakob disease, Alzheimer's disease, Parkinson's diseases, type II diabetes, etc. Two naturally occurring human lysozyme variants are known to be amyloidogenic. Even wild-type human or hen lysozymes form amyloid-like fibers upon various denaturing treatments. It is thought that partially folded intermediates are involved in fibrillogenesis, and the formation of amyloid-like fiber is a generic property of protein.

GLOSSARY

Conformation For proteins, a spatial arrangememt of main-chain and side-chain atoms that is interconvertible to other arrangements without breaking any covalent bonds; the diversity of conformations results from the freedom of rotation around a great number of bonds contained in a protein.

Denaturant Reagents, such as urea or guanidium chloride, that destabilize the native conformation of proteins by breaking non-covalent interactions in proteins.

Disulfide intermediate Molecular species that appears transiently during oxidative folding of protein and has less number of disulfide bonds formed than that of the final product protein; it may contain nonnative disulfide bonds.

Disulfide isomers Proteins with a common primary structure, and therefore with the same number and positions of cysteinyl residues, but with disulfide-linkage patterns different from each other.

Disulfide rearrangement Change in a disulfide-linkage pattern through thiol-disulfide transfer reactions.

Disulfide transfer A process in which a recombination among three sulfur atoms, two from a disulfide bond and one from a thiol group, that results in the formation of a new disulfide bond and a new thiol group take place; also called "thiol-disulfide transfer" or "thiol-disulfide exchange".

Effective concentration The ratio of the equilibrium constant of an intramolecular interaction between two molecular parts to that of an intermolecular interaction between the two parts under otherwise identical conditions; if arranged in appropriate proximity and orientation, intramolecular groups show an effective concentration that is much higher than the conventional concentration.

Folding For proteins, a complex reaction process in which a structureless polypeptide chain acquires, through a number of mostly noncovalent interactions, a defined and functional three-dimensional structure, that is a native conformation.

Higher-order structure Three-dimensional structure of proteins belonging to any of the three hierarchical categories, namely, secondary, tertiary, or quaternary structure.

Main chain In proteins, a chain of bonds that connect, serially, amide nitrogen, α-carbon, and carbonyl carbon atoms, that is $-N-C_\alpha-C-$, through the first and last amino acid residues of protein; also called "backbone".

Molten globule A state in which a protein has compact dimensions as well as an amount of secondary structure, both comparable to those of a folded state, but lacks tertiary structure; rapidly interconverts with a fully unfolded state, whereas is separated from a fully folded state by a high free energy barrier.

Native For proteins, retaining its intact structure and biological function, not modified artificially or denatured; in disulfide bonds, linking the same pair of cysteinyl residues as found in a native protein.

Oxidative folding The folding of protein which is coupled with the formation of disulfide bonds; as distinct from "nonoxidative folding", in which the starting protein has disulfide bonds already formed, but is unfolded with the action of denaturant; the contrary process is "reductive unfolding", in which the unfolding of protein is coupled with the cleavage of disulfide bonds.

Polylpeptide A relatively long chain of amino acids linked by peptide bonds; called "protein" if it is produced as a result of the expression of genetic information and adopts a defined three-dimensional structure.

Primary structure For proteins, the covalent structure defined by the sequence of amino acids linked by peptide bonds, disulfide-linkages among cysteinyl residues, and any other covalent modifications.

Recombinant protein A protein in which alterations in the primary structure, such as substitutions, deletions, or insertions, are artificially introduced; produced by expression of correspondingly modified genes with recombinant DNA technology; as opposed to "wild type protein"; the term "variant protein" includes not only "recombinant protein" but also naturally occurring mutant proteins.

Refolding Restoration of a folded state by the removal of unfolding agents; also called "renaturation" when the restoration of protein function is concerned.

Residue In proteins, a constitutive chemical unit derived from a single amino acid molecule with the removal of the elements of a water molecule; $-NH-CHR-CO-$, where R represents a side-chain (except for the amino- and carboxyl-terminal residues, which have an amino- and a carboxyl-group, respectively).

Secondary structure Regular, residue-by-residue conformations in protein such as α-helices, β-strands (which associate into -sheets), and turns; the former two structures contain a regular array of hydrogen bonds between main-chain amide nitrogens and carbonyl oxygens.

Side chain In proteins, a short chain of bonds, distinct from a main chain, that connect elements of the chemical group which is attached to the α-carbon of each residue and characteristic of each amino acid species.

Tertiary structure Overall three-dimensional structure of protein as viewed with special attention to the topological folding pattern of polypeptide main chain and interactions as well as packing of side chains.

Torsion angle In a chain of four atoms A, B, C, and D, and therefore of three successive bonds, AB, B—C, and C—D, not lying in a plane, the torsion angle around the second bond B—C is the angle of rotation of the third bond C—D relative to the first bond A—B looking along the second

bond; the angle between the two planes containing atoms A, B, C and B, C, D, which is usually called "dihedral angle", is identical to the torsion angle defined above; strictly speaking, a dihedral angle is the angle between the normals to these planes, and is the supplement of the torsion angle.

Unfolding A reverse process of folding; loss of a native conformation by extremes of temperature of pH, by the action of certain solutes such as urea or guanidinium, by certain organic solvents or detergents; also called "denaturation" when the loss of protein function as a result of unfolding is concerned.

ACKNOWLEDGMENTS

REFERENCES

1. G. E. Schulz and R. H. Schirmer, "Principles of Protein Structure." Springer-Verlag, New York, 1979.
2. T. E. Creighton, "Proteins: Structures and Molecular Properties," 2nd ed. W. H. Freeman, New York, 1993.
3. K. Hamaguchi, "The Protein Molecule: Conformation, Stability and Folding." Japan Scientific Societies Press/Springer-Verlag, Tokyo, Japan, 1992.
4. P. L. Privalov, *Adv. Protein Chem.* 33, 167 (1979).
5. C. B. Anfinsen, *Science* 181, 223 (1973).
6. P. C. Jocelyn, "Biochemistry of the SH Group: The Occurrence, Chemical Properties, Metabolism and Biological Function of Thiols and Disulphides." Academic Press, London, 1972.
7. C. Nagata and T. Yamaguchi, *Radiation Res.* 73, 430 (1978).
8. C. Tanford, *Adv. Protein Chem.* 23, 121 (1968).
9. C. Levinthal, *J. Chim. Phys.* 65, 44 (1968).
10. K. A. Dill and D. Shortle, *Ann. Rev. Biochem.* 60, 795 (1991).
11. F. M. Richard, *Ann. Rev. Biophys. Bioeng.* 6, 151 (1977).
12. H. S. Chan and K. A. Dill, *Ann. Rev. Biophys. Chem.* 20, 447 (1991).
13. G. Damaschun, H. Damaschun, K. Gast, C. Gernat, and D. Zirwer, *Biochim. Biophys. Acta* 1078, 289 (1991).
14. P. Calmettes, B. Roux, D. Durand, M. Desmadril, and J. C. Smith, *J. Mol. Biol.* 231, 840 (1993).
15. L. J. Smith, K. M. Fiebig, H. Schwalbe, and C. M. Dobson, *Folding & Design* 1, R95 (1996).
16. S. Marqusee, V. H. Robbins, and R. L. Baldwin, *Proc. Natl. Acad. Sci. USA* 86, 5286 (1989).
17. S. Segawa, T. Fukuno, K. Fujiwara, and Y. Noda, *Biopolymers* 31, 497 (1991).
18. C. Branden and J. Tooze, "Introduction to Protein Structure." Gerland Press, New York, 1991.
19. K. Wuthrich, "NMR of Proteins and Nucleic Acids." Wiley, New York, 1986.
20. G. M. Clore and A. M. Gronenborn, *Nature Struct. Biol.* 4, 849 (1997).
21. F. M. Richards, in "Protein Folding" (T. E. Creighton, Ed.), p. 1. W. H. Freeman, New York, 1992.
22. C. Chothia, *Ann. Rev. Biochem.* 53, 537 (1984).
23. J. S. Richardson, *Adv. Protein Chem.* 34, 167 (1981).
24. S. Segawa and F. M. Richards, *Biopolymers* 27, 23 (1988).
25. M. Go, *Proc. Natl. Acad. Sci. USA* 80, 1964 (1983).
26. M. Go, *Adv. Biophys.* 19, 91 (1985).
27. K. Linderstrom-Lang, "The Chemical Society Symposium on Peptide Chemistry," Chem. Soc. Publ. 2, 1 (1955).
28. A. Hvidt and S. O. Nielsen, *Adv. Protein Chem.* 21, 287 (1966).
29. S. W. Englander and N. R. Kallenbach, *Q. Rev. Biophys.* 16, 521 (1984).
30. C. Woodward, *Molec. Cell. Biochem.* 48, 135 (1982).
31. G. Wagner, *Q. Rev. Biophys.* 16, 1 (1983).
32. Y. Noda, Y. Fukuda, and S. Segawa, *Biopolymers* 41, 131 (1997).
33. P. S. Kim and R. L. Baldwin, *Ann. Rev. Biochem.* 59, 631 (1990).
34. C. M. Dobson, P. A. Evans, and S. E. Radford, *Trends Biochem. Sci.* 19, 31 (1994).
35. C. M. Dobson, A. Sali, and M. Karplus, *Angew. Chem. Int. Ed.* 37, 868 (1998).
36. K. Kuwajima, H. Yamaya, S. Miwa, S. Sugai, and T. Nagamura, *FEBS Lett.* 221, 115 (1987).
37. R. I. Gilmanshin and O. B. Ptitsyn, *FEBS Lett.* 223, 327 (1987).
38. M. Ohgushi and A. Wada, *FEBS Lett.* 164, 21 (1983).
39. O. B. Ptitsyn, *J. Protein Chem.* 6, 273 (1987).
40. K. Kuwajima, *Proteins: Struct. Funct. Genet.* 6, 87 (1989).
41. C. B. Anfinsen and H. A. Scheraga, *Adv. Protein Chem.* 29, 205 (1975).
42. W. Pfeil, *Molec. Cell Biochem.* 40, 3 (1981).
43. K. P. Murphy and S. J. Gill, *J. Mol. Biol.* 222, 699 (1991).
44. P. L. Privalov and S. J. Gill, *Pure Appl. Chem.* 61, 1097 (1989).
45. T. E. Creighton, *J. Phys. Chem.* 89, 2452 (1985).
46. B. H. Zimm and J. K. Bragg, *J. Chem. Phys.* 31, 526 (1959).
47. P. S. Kim and R. L. Baldwin, *Ann. Rev. Biochem.* 51, 459 (1982).
48. S. C. Harrison and R. Durbin, *Proc. Natl. Acad. Sci. USA* 82, 4028 (1985).
49. D. B. Wetlaufer, *Proc. Natl. Acad. Sci. USA* 70, 697 (1973).
50. M. Karplus and D. L. Weaver, *Biopolymers* 18, 1421 (1979).
51. R. L. Baldwin, *Trends Biochem Sci.* 14, 291 (1989).
52. K. Dill, *Biochemistry* 24, 1501 (1985).
53. F. X. Schmid, in "Protein Folding" (T. E. Creighton, Ed.), p. 197. W. H. Freeman, New York, 1992.
54. J. F. Brandts, H. R. Halvorson, and M. Brennan, *Biochemistry* 14, 4953 (1975).
55. F. X. Schmidt, *Ann. Rev. Biopys. Biomol. Struct.* 22, 123 (1993).
56. H. Roder and G. A. Elove, in "Mechanisms of Protein Folding." (R. H. Pain, Ed.), p. 26. Oxford University Press, New York, 1994.
57. S. W. Englander and L. Mayne, *Ann. Rev. Biophy. Biomol. Struct.* 21, 243 (1992).
58. J. B. Udgaonkar and R. L. Baldwin, *Nature* 335, 694 (1988).
59. J. B. Udgaonkar and R. L. Baldwin, *Proc. Natl. Acad. Sci. USA* 87, 8197 (1990).
60. H. Roder, G. A. Elove, and S. W. Englander, *Nature* 335, 700 (1988).
61. L. C. Wu, Z.-Y. Peng, and P. S. Kim, *Nature Struct. Biol.* 2, 281 (1995).
62. J. Baum, C. M. Dobson, P. A. Evans, and C. Hanley, *Biochemistry* 28, 7 (1989).
63. B. A. Schulman, C. Redfield, Z.-Y. Peng, C. M. Dobson, and P. S. Kim, *J. Mol. Biol.* 253, 651 (1995).
64. Y.-Z. Zhang, Y. Paterson, and H. Roder, *Protein Sci.* 4, 804 (1995).
65. O. B. Ptitsyn, *Adv. Protein Chem.* 47, 83 (1995).

66. T. E. Creighton, *Trends Biochem. Sci.* 22, 6 (1997).

67. A. Sali, E. Shakhnovich, and M. Karplus, *Nature* 369, 248 (1994).

68. L. A. Morozova, D. T. Haynie, C. Arico-Muendel, H. V. Van Dael, and C. M. Dobson, *Nature Struct. Biol.* 2, 871 (1995).

69. J. Balbach, V. Forge, N. J. van Nuland, S. Winder, P. J. Hore, and C. M. Dobson, *Nature Struct. Biol.* 2, 865 (1995).

70. S. Glasstone, K. J. Laidler, and H. Eyring, "The Theory of Rate Processes." McGraw-Hill, New York, 1941.

71. S. Segawa and T. Kawai, *Biopolymers* 25, 1815 (1986).

72. H. Wako and N. Saito, *J. Phys. Soc. Jpn.* 44, 1931 (1978).

73. N. Go, H. Abe, H. Mizuno, and H. Taketomi, in "Protein Folding" (R. Jaenicke, Ed.). Elsevier/North-Holland Biom. Press, Amsterdam, 1980.

74. A. Dinner, A. Sali, and M. Karplus, *Proc. Natl. Acad. Sci. USA* 93, 8356 (1996).

75. S. Segawa, Y. Husimi, and A. Wada, *Biopolymers* 12, 2521 (1973).

76. A. R. Fersht, *Curr. Opin. Struct. Biol.* 5, 79 (1995).

77. S. Segawa and M. Sugihara, *Biopolymers* 23, 2473 (1984).

78. P. L. Privalov, in "Protein Folding" (T. E. Creighton, Ed.), p. 83. W. H. Freeman, New York, 1992.

79. B. Chen, W. A. Baase, and J. A. Schellman, *Biochemistry* 28, 691 (1989).

80. M. Oliveberg and A. R. Fersht, *Biochemistry* 35, 2726 (1996).

81. A. F. Fersht, "Structure and Mechnism in Protein Science." W. H. Freeman, New York, 1999.

82. A. R. Fersht and L. Serrano, *Curr. Opin. Struct. Biol.* 3, 75 (1993).

83. W. J. Wedemeyer, E. Welker, M. Narayan, and H. A. Scheraga, *Biochemistry* 39, 4207 (2000).

84. J. M. Thornton, *J. Mol. Biol.* 151, 261 (1981).

85. J. Richardson, *Adv. Prot. Chem.* 34, 167 (1981).

86. N. Srinivasan, R. Sowdhamini, C. Ramakrishnan, and P. Balaram, *Int. J. Pept. Prot. Res.* 36, 147 (1990).

87. R. Zhang and G. H. Snyder, *J. Biol. Chem.* 264, 18472 (1989).

88. C. C. F. Blake, M. Ghosh, K. Harlos, A. Avezoux, and C. Anthony, *Nature Struct. Biol.* 1, 102 (1994).

89. R. Steudel, *Angew. Chem. Internat. Ed.* 14, 655 (1975).

90. M. Aida and C. Nagata, *Theor. Chim. Acta* 70, 73 (1986).

91. M. O. Dayhoff, "Atlas of Protein Sequence and Structure," Vol. 5, Suppl. 3. National Biomedical Research Foundation, Maryland, 1978.

92. D. M. E. Reuben and T. C. Bruice, *J. Am. Chem. Soc.* 98, 114 (1976).

93. C. Hwang, A. J. Sinskey, and H. F. Lodish, *Science* 257, 1496 (1992).

94. C. S. Sevier and C. A. Kaiser, *Nature Rev. Molec. Cell Biol.* 3, 836 (2002).

95. T. E. Creighton, *Methods Enzymol.* 107, 305 (1984).

96. T. E. Creighton, *Methods Enzymol.* 131, 83 (1986).

97. T. E. Creighton, *Biopolymers* 22, 49 (1983).

98. M. I. Page and W. P. Jencks, *Proc. Natl. Acad. Sci. USA* 68, 1678 (1971).

99. T. E. Creighton and D. P. Goldenberg, *J. Mol. Biol.* 179, 497 (1984).

100. Y. Goto and K. Hamaguchi, *J. Mol. Biol.* 146, 321 (1981).

101. T-Y. Lin and P. S. Kim, *Biochemistry* 28, 5282 (1989).

102. T-Y. Lin and P. S. Kim, *Proc. Natl. Acad. Sci. USA* 88, 10573 (1991).

103. H. Tachibana, *FEBS Lett.* 480, 175 (2000).

104. M. Aida and C. Nagata, *Chem. Phys. Lett.* 112, 129 (1984).

105. N. J. Darby and T. E. Creighton, *J. Mol. Biol.* 232, 873 (1993).

106. P. J. Flory, *J. Am. Chem. Soc.* 78, 5222 (1956).

107. D. C. Poland and H. A. Scheraga, *Biopolymers* 3, 379 (1965).

108. C. N. Pace, G. R. Grimsley, J. A. Thomson, and B. J. Barnett, *J. Biol. Chem.* 263, 11820 (1988).

109. J. A. Schellman, *Compt. Rend. Lab. Carlsberg. Ser. Chim.* 29, 228 (1955).

110. S. H. Lin, Y. Konishi, M. E. Denton, and H. Scheraga, *Biochemistry* 23, 5504 (1984).

111. P. M. Harrison and M. J. E. Sternberg, *J. Mol. Biol.* 244, 448 (1994).

112. Y. Goto and K. Hamaguchi, *J. Biochem.* 86, 1433 (1979).

113. Y. Goto and K. Hamaguchi, *J. Mol. Biol.* 156, 891 (1982).

114. Y. Goto and K. Hamaguchi, *J. Mol. Biol.* 156, 911 (1982).

115. P. J. Flory, "Principles of Polymer Chemistry." Cornell University Press, Ithaca, NY, 1953.

116. H. S. Chan and K. A. Dill, *J. Chem. Phys.* 90, 492 (1989).

117. H. S. Chan and K. A. Dill, *J. Chem. Phys.* 92, 3118 (1990).

118. A. J. Doig and D. H. Williams, *J. Mol. Biol.* 217, 389 (1991).

119. B. Tidor and M. Karplus, *Proteins Struct. Funct. Genet.* 15, 71 (1993).

120. V. I. Abkevich and E. I. Shakhnovich, *J. Mol. Biol.* 300, 975 (2000).

121. S. F. Betz, *Protein Sci.* 2, 1551 (1993).

122. L. J. Perry and R. Wetzel, *Science* 226, 555 (1984).

123. T. J. Ahern and A. M. Klibanov, *Science* 228, 1280 (1985).

124. L. J. Perry and R. Wetzel, *Biochemistry* 25, 733 (1986).

125. R. Wetzel, L. J. Perry, W. J. Baase, and W. J. Becktel, *Proc. Natl. Acad. Sci. USA* 85, 401 (1988).

126. R. Wetzel, *Trends Biochem. Sci.* 12, 478 (1987).

127. J. E. Villafranca, E. E. Howell, S. J. Oatley, N.-H. Xuong, and J. Kraut, *Biochemistry* 26, 2182 (1987).

128. S. Kanaya, C. Katsuda, S. Kimura, T. Nakai, E. Kitakuni, H. Takamura, K. Katayanagi, K. Morikawa, and M. Ikehara, *J. Biol. Chem.* 266, 6038 (1991).

129. J. A. Wells and D. B. Powers, *J. Biol. Chem.* 261, 6564 (1986).

130. C. Mitchinson and J. A. Wells, *Biochemistry* 28, 4807 (1989).

131. B. A. Katz and A. Kossiakoff, *J. Biol. Chem.* 261, 15480 (1986).

132. S. F. Betz and G. J. Pielak, *Biochemistry* 31, 12337 (1992).

133. S. F. Betz, J. L. Marmorion, A. J. Saunders, D. F. Doyle, G. B. Young, and G. J. Pielak, *Biochemistry* 35, 7422 (1996).

134. M. Matsumura, W. J. Becktel, M. Levitt, and B. W. Matthews, *Proc. Natl. Acad. Sci. USA* 86, 6562 (1989).

135. M. Matsumura, G. Signor, and B. W. Matthews, *Nature* 342, 291 (1989).

136. J. Clarke and A. R. Fersht, *Biochemistry* 32, 4322 (1993).

137. J. M. Mason, N. Gibbs, R. B. Sessions, and A. R. Clarke, *Biochemistry* 41, 12093 (2002).

138. K. W. Plaxco, K. T. Simons, and D. Baker, *J. Mol. Biol.* 277, 985 (1998).

139. A. R. Fersht, *Proc. Natl. Acad. Sci. USA* 97, 1525 (2000).

140. T. E. Creighton, *J. Mol. Biol.* 95, 167 (1975).

141. T. E. Creighton, *Prog. Biophys. Mol. Biol.* 33, 231 (1978).

142. T. E. Creighton, in "Protein Folding" (R. Jaenicke, Ed.), p. 427. Elsevier/North-Holland Biomedical Press, Amsterdam, 1980.

143. T. E. Creighton, *BioEssays* 8, 57 (1988).

144. T. E. Creighton, *Adv. Biophys.* 18, 1 (1984).

145. T. E. Creighton, *Biochem. J.* 270, 1 (1990).

146. T. E. Creighton, *Biol. Chem.* 378, 731 (1997).

147. T. E. Creighton, in "Mechanisms of Protein Folding" (R. H. Pain, Ed.), p. 250. Oxford University Press, New York, 2000.

148. T. E. Creighton, *J. Mol. Biol.* 113, 275 (1977).

149. M. Hollecker and T. E. Creighton, *J. Mol. Biol.* 168, 409 (1983).

150. D. P. Goldenberg and T. E. Creighton, *Biopolymers* 24, 167 (1985).

151. D. P. Goldenberg, R. W. Frieden, J. A. Haack, and T. B. Morrison, *Nature* 338, 127 (1989).

152. T. E. Creighton, *J. Mol. Biol.* 113, 275 (1977).

153. D. P. Goldenberg, *Biochemistry* 27, 2481 (1988).

154. C. B. Marks, H. Naderi, P. A. Kosen, I. D. Kuntz, and S. Anderson, *Science* 235, 1370 (1987).

155. D. M. Rothwarf and H. A. Scheraga, *Biochemistry* 32, 2690 (1993).

156. J. S. Weissman and P. S. Kim, *Science* 253, 1386 (1991).

157. T. E. Creighton, *Science* 256, 111 (1992).

158. J. S. Weissman and P. S. Kim, *Science* 256, 112 (1992).

159. N. J. Darby, C. P. M. van Mierlo, G. H. E. Scott, D. Neuhaus, and T. E. Creighton, *J. Mol. Biol.* 22, 905 (1992).

160. N. J. Darby, P. E. Morin, G. Talbo, and T. E. Creighton, *J. Mol. Biol.* 249, 463 (1995).
161. J. S. Weissman and P. S. Kim, *Proc. Natl. Acad. Sci. USA* 89, 9900 (1992).
162. J. S. Weissman and P. S. Kim, *Nature Struct. Biol.* 2, 1123 (1995).
163. C. J. Camacho and D. Thirumalai, *Proc. Natl. Acad. Sci. USA* 92, 1277 (1995).
164. M. Dadlez and P. S. Kim, *Nature Struct. Biol.* 2, 674 (1995).
165. M. Dadlez and P. S. Kim, *Biochemistry* 35, 16153 (1996).
166. G. Bulaj and D. P. Goldenberg, *Protein Sci.* 8, 1825 (1999).
167. R. R. Hantgan, G. G. Hames, and H. A. Scheraga, *Biochemistry* 13, 3421 (1974).
168. Y. Konishi and H. A. Scheraga, *Biochemistry* 19, 1308 (1980).
169. Y. Konishi and H. A. Scheraga, *Biochemistry* 19, 1316 (1980).
170. T. E. Creighton, *FEBS Lett.* 118, 283 (1980).
171. A. Galat, T. E. Creighton, R. C. Lord, and E. R. Blout, *Biochemistry* 20, 594 (1981).
172. T. E. Creighton, *J. Mol. Biol.* 113, 329 (1977).
173. T. E. Creighton, *J. Mol. Biol.* 129, 411 (1979).
174. Y. Konishi, T. Ooi, and H. A. Scheraga, *Biochemistry* 20, 3945 (1981).
175. Y. Konishi, T. Ooi, and H. A. Scheraga, *Biochemistry* 21, 4734 (1982).
176. Y. Konishi, T. Ooi, and H. A. Scheraga, *Biochemistry* 21, 4741 (1982).
177. H. A. Scheraga, Y. Konishi, and T. Ooi, *Adv. Biophys.* 18, 21 (1984).
178. Y. Konishi, T. Ooi, and H. A. Scheraga, *Proc. Natl. Acad. Sci. USA* 79, 5734 (1982).
179. H. A. Scheraga, Y. Konishi, D. M. Rothwarf, and P. W. Mui, *Proc. Natl. Acad. Sci. USA* 84, 5740 (1987).
180. T. E. Creighton, *Proc. Natl. Acad. Sci. USA* 85, 5082 (1988).
181. S. J. Wearne and T. E. Creighton, *Proteins Struct. Funct. Genet.* 4, 251 (1988).
182. D. M. Rothwarf and H. A. Scheraga, *Biochemistry* 32, 2671 (1993).
183. X. Xu, D. M. Rothwarf, and H. Scheraga, *Biochemistry* 35, 6406 (1996).
184. M. J. Volles, X. Xu, and H. Scheraga, *Biochemistry* 38, 7284 (1999).
185. D. M. Rothwarf and H. A. Scheraga, *Biochemistry* 32, 2680 (1993).
186. D. M. Rothwarf, Y.-J. Li, and H. Scheraga, *Biochemistry* 37, 3760 (1998).
187. D. M. Rothwarf, Y.-J. Li, and H. Scheraga, *Biochemistry* 37, 3767 (1998).
188. D. M. Rothwarf and H. A. Scheraga, *Biochemistry* 32, 2698 (1993).
189. D. M. Rothwarf and H. A. Scheraga, *J. Am. Chem. Soc.* 113, 6293 (1991).
190. Y.-J. Li, D. M. Rothwarf, and H. A. Scheraga, *Nature Struct. Biol.* 2, 489 (1995).
191. E. Welker, M. Narayan, W. J. Wedemeyer, and H. A. Scheraga, *Proc. Natl. Acad. Sci. USA* 98, 2312 (2001).
192. R. Narayan, E. Welker, W. J. Wedemeyer, and H. A. Scheraga, *Accounts Chem. Res.* 33, 805 (2000).
193. T. Imoto, L. N. Johnson, A. C. T. North, D. C. Phillips, and J. A. Rupley, in "The Enzyme" (P. D. Boyer, Ed.), Vol. 7, p. 665. Academic Press, New York, London, 1972.
194. A. Fleming, *Proc. R. Soc. London* B39, 306 (1922).
195. R. E. Canfield, *J. Biol. Chem.* 238, 2698 (1963).
196. J. Jollès, J. Jáuregui-Adell, and P. Jollès, *Biochim. Biophys. Acta* 78, 668 (1963).
197. J. R. Brown, *Biochem. J.* 92, 13 (1964).
198. R. E. Canfield and A. K. Liu, *J. Biol. Chem.* 240, 1997 (1965).
199. C. C. F. Blake, D. F. Koenig, G. A. Mair, A. C. T. North, D. C. Phillips, and V. R. Sarma, *Nature* 206, 757 (1965).
200. D. C. Phillips, *Sci. Am.* 215, 78 (1966).
201. H. A. McKenzie and F. H. White, Jr., *Adv. Protein Chem.* 41, 173 (1991).
202. B. Fischer, in "Lysozymes: Model Enzymes in Biochemistry and Biology" (P. Jollès, Ed.), p. 143. Birkhäuser, Basel, 1996.
203. C. J. Epstein and R. F. Goldberger, *J. Biol. Chem.* 238, 1380 (1963).
204. V. P. Saxena and D. B. Wetlaufer, *Biochemistry* 9, 5015 (1970).
205. S. S. Ristow and D. B. Wetlaufer, *Biochem. Biophys. Res. Commun.* 50, 544 (1973).
206. W. L. Anderson and D. B. Wetlaufer, *J. Biol. Chem.* 251, 3147 (1976).
207. A. S. Acharya and H. Taniuchi, *J. Biol. Chem.* 251, 6934 (1976).
208. A. S. Acharya and H. Taniuchi, *Proc. Natl. Acad. Sci. USA* 74, 2362 (1977).
209. A. S. Acharya and H. Taniuchi, *Mol. Cell. Biochem.* 44, 129 (1982).
210. K. Yutani, A. Yutani, A. Imanishi, and T. Isemura, *J. Biochem.* 64, 449 (1968).
211. M. E. Goldberg and Y. Guillou, *Protein Sci.* 3, 883 (1994).
212. P. Roux, M. Delepierre, M. E. Goldberg, and A.-F. Chaffotte, *J. Biol. Chem.* 272, 24843 (1997).
213. H. Sawano, Y. Koumoto, K. Ohta, Y. Sasaki, S. Segawa, and H. Tachibana, *FEBS Lett.* 303, 11 (1992).
214. J.-P. Perraudin, T. E. Torchia, and D. B. Wetlaufer, *J. Biol. Chem.* 258, 11834 (1983).
215. P. Roux, M. Ruoppolo, A.-F. Chaffotte, and M. E. Goldberg, *Protein Sci.* 8, 2751 (1999).
216. D. L. Havehan and E. De Bernardez Clark, *Biotechnol. Bioeng.* 54, 221 (1997).
217. E. De Bernardez Clark, D. L. Havehan, S. Szela, and J. Maachu-palli Reddy, *Biotechnol. Prog.* 14, 47 (1998).
218. H. Tachibana, T. Oka, and K. Akasaka, *J. Mol. Biol.* 314, 311 (2001).
219. B. van den Berg, E. W. Chung, C. V. Robinson, P. L. Mateo, and C. M. Dobson, *EMBO J.* 18, 4794 (1999).
220. B. van den Berg, E. W. Chung, C. V. Robinson, and C. M. Dobson, *J. Mol. Biol.* 290, 781 (1999).
221. N. M. Jarrett, L. Djavadi-Ohaniance, R. C. Willson, H. Tachibana, and M. E. Goldberg, *Protein Sci.* 11, 2584 (2002).
222. C. Tanford, K. C. Aune, and A. Ikai, *J. Mol. Biol.* 73, 185 (1973).
223. P. J. Hagerman, *Biopolymers* 16, 731 (1977).
224. S. Kato, M. Okamura, N. Shimamoto, and H. Utiyama, *Biochemistry* 20, 1080 (1981).
225. S. Kato, N. Shimamoto, and H. Utiyama, *Biochemistry* 21, 38 (1982).
226. K. Kuwajima and F. X. Schmid, *Adv. Biophys.* 18, 43 (1984).
227. K. Kuwajima, Y. Hiraoka, M. Ikeguchi, and S. Sugai, *Biochemistry* 24, 874 (1985).
228. M. Ikeguchi, K. Kuwajima, M. Mitani, and S. Sugai, *Biochemistry* 25, 6965 (1986).
229. A. Miranker, S. E. Radford, M. Karplus, and C. M. Dobson, *Nature* 349, 633 (1991).
230. S. E. Radford, C. M. Dobson, and P. A. Evans, *Nature* 358, 302 (1992).
231. A. F. Chaffotte, Y. Guillou, and M. E. Goldberg, *Biochemistry* 31, 9694 (1992).
232. M. E. Denton, D. M. Rothwarf, and H. A. Scheraga, *Biochemistry* 33, 11225 (1994).
233. D. M. Rothwarf and H. Scheraga, *Biochemistry* 35, 13797 (1996).
234. S. D. Hook, S. E. Radford, and C. M. Dobson, *Biochemistry* 33, 5867 (1944).
235. A. Miranker, C. V. Robinson, S. E. Radford, R. T. Aplin, and C. M. Dobson, *Science* 262, 896 (1993).
236. Y. Yang and K. Hamaguchi, *J. Biochem.* 87, 1003 (1980).
237. L. S. Itzhaki, P. A. Evans, C. M. Dobson, and S. E. Radford, *Biochemistry* 33, 5212 (1994).
238. A. Matagne, S. E. Radford, and C. M. Dobson, *J. Mol. Biol.* 267, 1068 (1997).
239. T. Kiefhaber, *Proc. Natl. Acad. Sci. USA* 92, 9029 (1995).
240. G. Wildegger and T. Kiefhaber, *J. Mol. Biol.* 270, 294 (1997).

241. A. Matagne, E. W. Chung, L. J. Ball, S. E. Radford, C. V. Robinson, and C. M. Dobson, *J. Mol. Biol.* 277, 997 (1998).

242. S. K. Kulkarni, A. E. Ashcroft, M. Carey, D. Masselos, C. V. Robinson, and S. E. Radford, *Protein Sci.* 8, 35 (1999).

243. K. Brew, F. J. Castellino, T. C. Vanaman, and R. L. Hill, *J. Biol. Chem.* 245, 4570 (1970).

244. T. C. Vanaman, K. Brew, and R. L. Hill, *J. Biol. Chem.* 245, 4583 (1970).

245. J. G. Shewale, S. K. Sinha, and K. Brew, *J. Biol. Chem.* 259, 4947 (1984).

246. K. R. Acharya, D. I. Stuart, N. P. C. Walker, M. Lewis, and D. C. Phillips, *J. Mol. Biol.* 208, 99 (1989).

247. K. R. Acharya, J. Ren, D. I. Stuart, D. C. Phillips, and R. E. Fenna, *J. Mol. Biol.* 221, 571 (1991).

248. E. D. Chrysina, K. Brew, and K. R. Acharya, *J. Biol. Chem.* 275, 37021 (2000).

249. Y. Hiraoka, T. Segawa, K. Kuwajima, S. Sugai, and N. Murai, *Biochem. Biophys. Res. Commun.* 95, 1098 (1980).

250. E. M. Prager and P. Jollès, in "Lysozymes: Model Enzymes in Biochemistry and Biology" (P. Jollès, Ed.), p. 9. Birkhäuser, Basel, 1996.

251. H. A. McKenzie, in "Lysozymes: Model Enzymes in Biochemistry and Biology" (P. Jollès, Ed.), p. 365. Birkhäuser, Basel, 1996.

252. K. R. Rao and K. Brew, *Biochem. Biophys. Res. Commun.* 163, 1390 (1989).

253. M. Wang, W. A. Scott, K. R. Rao, J. Udey, G. E. Conner, and K. Brew, *J. Biol. Chem.* 264, 21116 (1989).

254. J. J. Ewbank and T. E. Creighton, *Biochemistry* 32, 3677 (1993).

255. K. Kuwajima, M. Ikeguchi, T. Sugawara, Y. Hiraoka, and S. Sugai, *Biochemistry* 29, 8240 (1990).

256. M. Oobatake, S. Takahashi, and T. Ooi, *J. Biochem.* 86, 65 (1979).

257. T. E. Creighton, *J. Mol. Biol.* 87, 563 (1974).

258. T. E. Creighton, *J. Mol. Biol.* 87, 579 (1974).

259. T. E. Creighton, *J. Mol. Biol.* 96, 777 (1975).

260. T. E. Creighton, *Biophys. Chem.* 31, 155 (1988).

261. D. P. Goldenberg and J. X. Zhang, *Proteins Struct. Funct. Genet.* 15, 322 (1993).

262. D. Amir and E. Haas, *Biochemistry* 27, 8889 (1988).

263. V. Ittah and E. Haas, *Biochemistry* 34, 4493 (1995).

264. M. Ferrer, G. Barany, and C. Woodward, *Nature Struct. Biol.* 2, 211 (1995).

265. H. Pan, G. Barany, and C. Woodward, *Protein Sci.* 6, 1985 (1997).

266. P. A. Kosen, T. E. Creighton, and E. R. Blout, *Biochemistry* 20, 5744 (1981).

267. J. Kemmink, C. P. M. van Mierlo, R. M. Scheek, and T. E. Creighton, *J. Mol. Biol.* 230, 312 (1993).

268. J. Kemmink and T. E. Creighton, *J. Mol. Biol.* 234, 861 (1993).

269. K. J. Lumb and P. S. Kim, *J. Mol. Biol.* 236, 412 (1994).

270. H. Pan, E. Barbar, G. Barany, and C. Woodward, *Biochemistry* 34, 13974 (1995).

271. N. J. Darby, C. P. M. van Mierlo, and T. E. Creighton, *FEBS Lett.* 279, 61 (1991).

272. C. P. M. van Mierlo, N. J. Darby, D. Neuhaus, and T. E. Creighton, *J. Mol. Biol.* 222, 373 (1991).

273. J. P. Staley and P. S. Kim, *Proc. Natl. Acad. Sci. USA* 89, 1519 (1992).

274. J. P. Staley and P. S. Kim, *Nature* 344, 685 (1990).

275. M.-H. Yu, J. S. Weissman, and P. S. Kim, *J. Mol. Biol.* 249, 388 (1995).

276. Y. Kuroda and P. S. Kim, *J. Mol. Biol.* 298, 493 (2000).

277. D. J. States, T. E. Creighton, C. M. Dobson, and M. Karplus, *J. Mol. Biol.* 195, 731 (1987).

278. C. P. M. van Mierlo, N. J. Darby, and T. E. Creighton, *Proc. Natl. Acad. Sci. USA* 89, 6775 (1992).

279. C. P. M. van Mierlo, N. J. Darby, J. Keeler, D. Neuhaus, and T. E. Creighton, *J. Mol. Biol.* 299, 1125 (1993).

280. T. G. Oas and P. S. Kim, *Nature* 336, 42 (1988).

281. E. Barbar, G. Barany, and C. Woodward, *Biochemistry* 34, 11423 (1995).

282. E. Barbar, M. Hare, V. Daragan, G. Barany, and C. Woodward, *Biochemistry* 37, 7822 (1998).

283. M. Dadlez, *Biochemistry* 36, 2788 (1997).

284. K. Zdanowski and M. Dadlez, *J. Mol. Biol.* 287, 433 (1999).

285. C. I. Stassinopoulou, G. Wagner, and K. Wuthrich, *Eur. J. Biochem.* 145, 423 (1984).

286. G. Wagner, C. I. Stassinopoulou, and K. Wuthrich, *Eur. J. Biochem.* 145, 431 (1984).

287. M. R. Hurle, C. B. Marks, P. A. Kosen, S. Anderson, and I. D. Kuntz, *Biochemistry* 29, 4410 (1990).

288. D. J. States, C. M. Dobson, M. Karplus, and T. E. Creighton, *J. Mol. Biol.* 174, 411 (1984).

289. C. Eigenbrot, M. Randal, and A. Kossiakoff, *Protein Eng.* 3, 591 (1990).

290. C. Eigenbrot, M. Randal, and A. Kossiakoff, *Proteins Struct. Funct. Genet.* 14, 75 (1992).

291. Y. Liu, K. Breslauer, and S. Anderson, *Biochemistry* 36, 5323 (1997).

292. C. P. M. van Mierlo, N. J. Darby, D. Neuhaus, and T. E. Creighton, *J. Mol. Biol.* 222, 353 (1991).

293. C. C. Lester, X. Xu, J. H. Laity, S. Shimotakahara, and H. A. Scheraga, *Biochemistry* 36, 13068 (1997).

294. S. Talluri, D. M. Rothwarf, and H. A. Scheraga, *Biochemistry* 33, 10437 (1994).

295. J. H. Laity, S. Shimotakahara, and H. A. Scheraga, *Proc. Natl. Acad. Sci. USA* 90, 615 (1993).

296. S. Shimotakahara, C. B. Rios, J. H. Laity, D. E. Zimmerman, H. A. Scheraga, and G. T. Montelione, *Biochemistry* 36, 6915 (1997).

297. J. H. Laity, C. C. Lester, S. Shimotakahara, D. E. Zimmerman, G. T. Montelione, and H. A. Scheraga, *Biochemistry* 36, 12683 (1997).

298. M. A. Pearson, P. A. Karplus, R. W. Dodge, J. H. Laity, and H. A. Scheraga, *Protein Sci.* 7, 1255 (1998).

299. E. Welker, M. Narayan, M. J. Volles, and H. A. Scheraga, *FEBS Lett.* 460, 477 (1999).

300. M. Iwaoka, D. Juminaga, and H. A. Scheraga, *Biochemistry* 37, 4490 (1998).

301. X. Xu and H. A. Scheraga, *Biochemistry* 37, 7561 (1998).

302. W. J. W. J. Wedemeyer, X. Xu, E. Welker, and H. A. Scheraga, *Biochemistry* 41, 1483 (2002).

303. M. Iwaoka, W. J. Wedemeyer, and H. A. Scheraga, *Biochemistry* 38, 2805 (1999).

304. T. A. Klink, K. J. Woycechowsky, K. M. Taylor, and R. T. Raines, *Eur. J. Biochem.* 267, 566 (2000).

305. G. Graziano, F. Catanzano, and E. Notomista, *Thermochim. Acta* 364, 165 (2000).

306. Y. Ota, Y. Hibino, K. Asaba, K. Sugiura, and T. Samejima, *Biochim. Biophys. Acta* 236, 802 (1971).

307. C.-L. Lee and M. Z. Atassi, *Biochemistry* 12, 2690 (1973).

308. F. H. White, Jr., *Biochemistry* 15, 2906 (1976).

309. F. H. White, Jr., *Biochemistry* 21, 967 (1982).

310. F. H. White, Jr. and A. G. Wright, Jr., *Int. J. Pept. Protein Res.* 23, 256 (1984).

311. G. Wilson, L. Hecht, and L. D. Barron, *Biochemistry* 35, 12518 (1996).

312. H. Tachibana, *FEBS Lett.* 480, 175 (2000).

313. M. E. Goldberg, R. Rudolph, and R. Jaenicke, *Biochemistry* 30, 2790 (1991).

314. C. N. Pace, *Methods Enzymol.* 131, 266 (1986).

315. A. S. Acharya and H. Taniuchi, *Int. J. Peptide Protein Res.* 15, 503 (1980).

316. P. Bai and Z.-Y. Peng, *J. Mol. Biol.* 314, 321 (2001).

317. Y. Noda, A. Yokota, D. Horii, T. Tominaga, Y. Tanisaka, H. Tachibana, and S. Segawa, *Biochemistry* 41, 2130 (2002).

318. Y. Taniyama, Y. Yamamoto, M. Nakao, M. Kikuchi, and M. Ikehara, *Biochem. Biophys. Res. Commun.* 152, 962 (1988).
319. K. Yoshimura, A. Toibana, K. Kikuchi, M. Kobayashi, T. Hayakawa, K. Nakamura, M. Kikuchi, and M. Ikehara, *Biochem. Biophys. Res. Commun.* 145, 712 (1987).
320. Y. Yamamoto, Y. Taniyama, M, Kikuchi, and M. Ikehara, *Biochem. Biophys. Res. Commun.* 149, 431 (1987).
321. M. Kikuchi, Y. Yamamoto, Y. Taniyama, K. Ishimaru, W. Yoshikawa, Y. Kaisho, and M. Ikehara, *Proc. Natl. Acad. Sci. USA* 85, 9411 (1988).
322. Y. Taniyama, Y. Yamamoto, R. Kuroki, and M. Kikuchi, *J. Biol. Chem.* 265, 7570 (1990).
323. K. Inaka, Y. Taniyama, M. Kikuchi, K. Morikawa, and M. Matsushima, *J. Biol. Chem.* 266, 12599 (1991).
324. R. Kuroki, K. Inaka, Y. Taniyama, S. Kidokoro, M. Matsushima, M. Kikuchi, and K. Yutani, *Biochemistry* 31, 8323 (1992).
325. Y. Taniyama, K. Ogasahara, K. Yutani, and M. Kikuchi, *J. Biol. Chem.* 267, 4619 (1992).
326. Y. Taniyama, C. Seko, and M. Kikuchi, *J. Biol. Chem.* 265, 16767 (1990).
327. M. Kikuchi, Y. Taniyama, S. Kanaya, T. Takao, and Y. Shimonishi, *Eur. J. Biochem.* 187, 315 (1990).
328. A. S. Acharya and H. Taniuchi, *Biochemistry* 17, 3064 (1978).
329. S. E. Radford, D. N. Woolfson, S. R. Martin, G. Lowe, and C. M. Dobson, *Biochem. J.* 273, 211 (1991).
330. M. E. Denton and H. A. Scheraga, *J. Prot. Chem.* 10, 213 (1991).
331. A. Cooper, S. J. Eyles, S. E. Radford, and C. M. Dobson, *J. Mol. Biol.* 225, 939 (1992).
332. C. P. Hill, N. L. Johnston, and R. E. Cohen, *Proc. Natl. Acad. Sci. USA* 90, 4136 (1993).
333. K. Gekko and S. N. Timasheff, *Biochemistry* 20, 4677 (1981).
334. H. Tachibana, Y. Ohta, H. Sawano, Y. Koumoto, and S. Segawa, *Biochemistry* 33, 15008 (1994).
335. A. Yokota, K. Izutani, M. Takai, Y. Kubo, Y. Noda, Y. Koumoto, H. Tachibana, and S. Segawa, *J. Mol. Biol.* 295, 1275 (2000).
336. S. J. Eyles, S. E. Radford, C. V. Robinson, and C. M Dobson, *Biochemistry* 33, 13038 (1994).
337. V. Guez, P. Roux, A. Navon, and M. E. Goldberg, *Protein Sci.* 11, 1136 (2002).
338. T. Ueda, A. Nakashima, Y. Hashimoto, T. Miki, H. Yamada, and T. Imoto, *J. Mol. Biol.* 235, 1312 (1994).
339. M. Ikeguchi and S. Sugai, *Int. J. Peptide Protein Res.* 33, 289 (1989).
340. C. Redfield, B. A. Schulman, M. A. Milhollen, P. S. Kim, and C. M. Dobson, *Nature Struct. Biol.* 6, 948 (1999).
341. Z.-Y. Peng, L. C. Wu, and P. S. Kim, *Biochemistry* 34, 3248 (1995).
342. J. J. Ewbank and T. E. Creighton, *Biochemistry* 32, 3694 (1993).
343. T. M. Hendrix, Y. Griko, and P. Privalov, *Protein Sci.* 5, 923 (1996).
344. Z.-Y. Peng and P. S. Kim, *Biochemistry* 33, 2136 (1994).
345. S. Chakraborty and Z.-Y. Peng, *J. Mol. Biol.* 298, 1 (2000).
346. S. J. Demarest, S.-Q. Zhou, J. Robblee, R. Fairman, B. Chu, and D. P. Raleigh, *Biochemistry* 40, 2138 (2001).
347. L. C. Wu, B. A. Schulman, Z.-Y. Peng, and P. S. Kim, *Biochemistry* 35, 859 (1996).
348. B. A. Schulman and P. S. Kim, *Nature Struct. Biol.* 3, 682 (1996).
349. L. C. Wu and P. S. Kim, *Proc. Natl. Acad. Sci. USA* 94, 14314 (1997).
350. J. Song, P. Bai, L. Luo, and Z.-Y. Peng, *J. Mol. Biol.* 280, 167 (1998).
351. L. C. Wu and P. S. Kim, *J. Mol. Biol.* 280, 175 (1998).
352. K. S. Iyer and W. A. Klee, *J. Biol. Chem.* 248, 707 (1973).
353. Y. Schechter, A. Patchornik, and Y. Burstein, *Biochemistry* 12, 3407 (1973).
354. S. Gohda, A. Shimizu, M. Ikeguchi, and S. Sugai, *J. Protein Chem.* 14, 731 (1995).
355. M. Ikeguchi, S. Sugai, M. Fujino, T. Sugawara, and K. Kuwajima, *Biochemistry* 31, 12695 (1992).
356. M. Ikeguchi, M. Fujino, M. Kato, K. Kuwajima, and S. Sugai, *Protein Sci.* 7, 1564 (1998).
357. J. J. Ewbank and T. E. Creighton, *Nature* 350, 518 (1991).
358. T. E. Creighton and J. J. Ewbank, *Biochemistry* 33, 1534 (1994).
359. L. Pauling, R. B. Corey, and H. R. Branson, *Proc. Natl. Acad. Sci. USA* 37, 206 (1961).
360. A. Wada, *Adv. Biophys.* 9, 1 (1976).
361. G. N. Ramachandran and V. Sasisekharan, *Adv. Protein Chem.* 23, 283 (1968).

DNA Electronics

Massimiliano Di Ventra, Michael Zwolak

*Virginia Polytechnic Institute and State University,
Blacksburg, Virginia, USA*

CONTENTS

1. INTRODUCTION

DNA, or deoxyribonucleic acid, encodes the architecture and function of cells in all living organisms. DNA, shown in Figure 1, is made of a sequence of four bases: thymine (T), cytosine (C), adenine (A), and guanine (G) (see Fig. 2 for a schematic of each base), attached to a phosphate-sugar backbone. Any particular sequence forms a single strand of DNA. Two strands may come together through hydrogen bonding of the bases A with T (AT) and G with C (GC). This forms the double helix structure discovered by Watson and Crick [1].

Apart from its fundamental role in defining the genetic code of living organisms, DNA's electronic and self-assembly properties have been the subject of much investigation over the past decade. Both properties bear enormous importance in understanding the functionalities of DNA in living cells and indicate that DNA could be of use in nanoscience. On the one hand, the transport properties of DNA are of interest in several disciplines because of their relevance to damage and mutation in DNA [2–13]. On the other hand, the use of molecules and nanomaterials to develop new ways of detecting, manipulating, and sequencing DNA is being pursued [14–25]. The charge transport properties of DNA are central to such developments. For instance, electrochemical detection of structural changes, due to protein binding or base mismatches, is currently being examined [26–34]. It has also been suggested that new read-out schemes on DNA chips [35], which can detect for the presence of different DNA sequences, might exploit the electronic properties of DNA [36]. Finally, understanding charge transport in DNA

can shed new light on the transport properties of other systems with $\pi-\pi$ interactions, that is, molecular crystals and discotic materials [37–39].

It was suggested early on that DNA could be a conductor because of the formation of a π-band across the different bases. Many researchers subsequently looked into this possibility [40–59]. π-stacking is important in the conducting properties of several other organic molecules [60–65]. In the early 1990s, the idea that DNA might conduct started to be pursued with more vigor. When Murphy et al. [66] suggested that electron transfer through DNA was responsible for fluorescence quenching of an excited molecule, intense debate was started over the charge transport properties of DNA [36, 67–100].

Since these early investigations, many researchers have looked at the transport properties of DNA and have found that it behaves as a conductor, semiconductor, or insulator, in what seems to be contradictory conclusions. The apparent contradictions have been attributed to the large phase space in which DNA can be prepared and probed (see, e.g., [36]). Many experimental conditions and attributes of the specific DNA used, including base sequence, length, orientation, counterions, temperature, electrode contact, adsorption surface, fluctuations, and so on, could affect its conducting properties. As a consequence, although much progress has been made, DNA's transport properties are still in question.

Despite the debate on whether DNA conducts or not, its self-assembly properties are being used to create novel nanoscale structures. For instance, silver wires and palladium wires were made using a DNA template [101, 102]. Devices that exploit DNA's complex properties are currently envisioned as transistors, biosensors, molecular memories, and complex circuits [103–114].

In this chapter, we will discuss the research done in understanding charge transport in DNA, and the novel electronic structures and devices that have been made using this important biological molecule. This chapter is organized as follows: in Section 2, we discuss the complex structure of DNA and the different DNA structures used in charge transport experiments. In Section 3, we review the experiments that try to identify the transport mechanism in DNA, both directly and indirectly, and the different theoretical interpretations
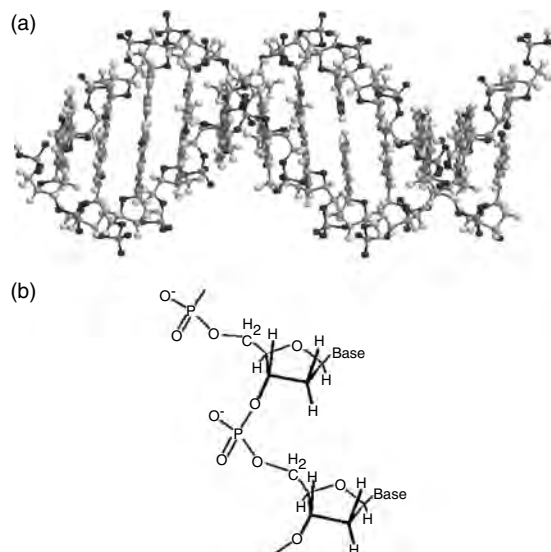
Figure 1. (a) DNA double helix. The DNA double helix is made of two strands, which are each a sequence of four bases attached to a phosphate-sugar backbone. The bases opposite each other on the two strands are bonded by hydrogen bonds. (b) Schematic of the chemical structure of the phosphate-sugar backbone of a single strand of DNA.

of charge transport that have been suggested over the years. Finally, in Section 4, we outline the possible applications of DNA in nanoscale electronics.

2. DNA STRUCTURE

DNA is a macromolecule made of four different monomers. Each monomer unit, called a nucleotide, consists of a phosphate group, a $2'$-deoxyribose (a 5-carbon sugar), and one of four bases shown in Figure 2. The monomers are attached through a phosphodiester link. The pK_a of the phosphate
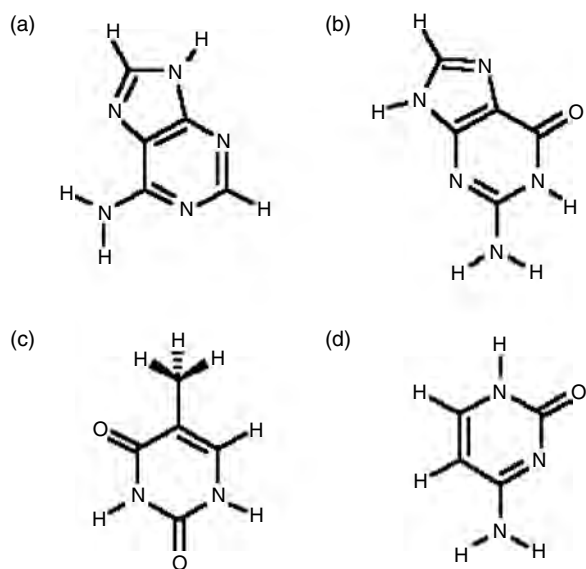
Figure 2. The four bases that compose DNA: (a) adenine, (b) guanine, (c) thymine, and (d) cytosine.

group is near one, making it a strong acid. At physiological pH, it will therefore be negatively charged in solution. This charge is partially neutralized by counterions, such as sodium (Na^+), potassium (K^+), and magnesium (Mg^{2+}). Within the monomer, the $5'$ and $3'$ carbons are the carbons attached to the phosphate group on either side.

Polynucleotides (i.e., any sequence of single nucleotides) are actually thermodynamically unstable *in vivo* (in living organisms), that is, in an aqueous environment. The hydrolyzation of the linking oxygen, that is,

$$-O- + H_2O \longrightarrow -OH + HO-$$
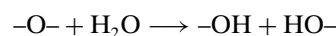
in the phosphodiester group forms the individual monomer units, which are more stable. This process, however, is extremely slow without the presence of a catalyst. Nucleases are enzymes in living organisms which act as catalysts in this reaction to break down polynucleotides in food. It is common when directly measuring current–voltage (I–V) characteristics of DNA to use these enzymes to break DNA.

Double-stranded DNA is due to hydrogen bonding between bases on two single strands. In this case, the bases come together in what is called Watson–Crick base pairing. The A base only pairs with T, and the G base only pairs with C. These pairs allow for the formation of the double helix, a secondary structure of DNA (see Fig. 1). The carbons which bond to the phosphate-sugar backbone on each side of either base pair are the same distance apart, which allows for the regular structure of the helix.

In B-DNA, the common type of DNA found in cells of living organisms, the center of the base pairs lies along the helix axis. The helix is right handed. The base pairs are slightly tilted with respect to this axis and are separated by a distance of about 3.4 Å. This is close to the 3.3 Å in stacked phthalocyanines in which charge transport is perpendicular to the plane of the molecule [60]. There are, on average, 10 base pairs with each turn of the helix, which gives an average 36-degree angle between successive base pairs. However, the base-pair sequence and interaction with other molecules (e.g., counterions, proteins) can cause deviation from these average values.

Another form of DNA, A-DNA, is quite different from B-DNA; see Figure 3. In this structure, the base pairs are more tilted with respect to the helix axis. This should
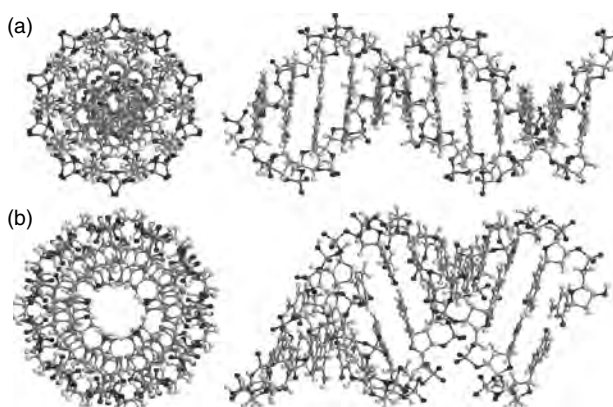
Figure 3. Top and side views of (a) B-DNA and (b) A-DNA.

significantly alter the electronic properties of DNA, especially if charge transport is through a π-channel [89]. The B-DNA is more stable than A-DNA in aqueous environments, due to water molecules that bind along the length of the chain. There are many other forms of DNA, including H-DNA, a triple helix whose formation is favored when there is a single strand of all purine bases (A and G) and a strand of all pyrimidine bases (C and T).

Single-stranded DNA has a mostly random structure. However, in some parts of the single strand there can be a secondary structure if self-complementary regions are present. In these regions, the DNA can pair up with itself and form a double helix.

A typical sequence of DNA used in charge transfer experiments is λ-DNA, which comes from a virus called Phage Lambda. The sequence consists of about 50,000 base pairs, which gives a length of about 16 μm. This is a complex sequence of DNA. Another natural sequence of DNA used in such experiments is calf-thymus DNA. Other common synthetic sequences of DNA are the homogeneous sequences, in which one strand is made of just one nucleotide and the other of its complement. These can either be poly(dG)–poly(dC) or poly(dA)–poly(dT). The DNA sequence can be cut to the length required in the experiment.

Finally, some experimental groups have used synthetic DNA hairpins to perform fluorescence and charge transfer measurements. Natural DNA hairpins are single strands of DNA which fold back onto themselves due to a self-complementary region. The synthetic DNA hairpins used are two short complementary polynucleotides linked with a fluorescent organic molecule, which stabilizes the structure.

3. CHARGE TRANSPORT IN DNA

3.1. Indirect Measurements of Charge Transport in DNA

In the early 1990s, Murphy et al. suggested that charge is transferred through DNA from an excited donor to an electron acceptor [66]. The donor and acceptor used in the experiment were metal complexes intercalated in a 15-base pair double-strand DNA. The intercalated donor complex was photoexcited in solution; in the absence of the acceptor, it would emit light. However, in the presence of the acceptor, the luminescence was found to be quenched at a high rate, suggesting that DNA carries charge from the donor to the acceptor. This was extraordinary since the estimated distance that charge was supposed to travel was about 4 nm.

In similar experiments, Brun and Harriman et al. used organic donors and acceptors [59, 115, 116]. They found that charge-transfer rates drop off fast as the length of the DNA increases; this is opposed to the findings of Murphy et al. [66]. Later on, Lincoln et al. conducted experiments with the metal complexes used by Murphy et al. [117] and modeled the data. The results suggested that the metal complexes must cooperatively bind onto the DNA, which explains the fast rate of charge transfer and its small "distance dependence" [117, 118]. After these reports, more experimental and theoretical research was done, adding to the seemingly contradictory results [96–100].

The contradictory results were attributed to various factors, including base sequence and how the charge was injected in the system (i.e., using intercalated metal complexes rather than intercalated organic molecules, etc.). More recent measurements [119, 120] were performed under more controlled conditions, and the sequence dependence of charge transfer has been systematically investigated. In many of these experiments, holes were injected into a GC pair; three GC pairs, with the G's on one strand (GGG), were the acceptors. The main findings are that DNA transfers charge over long distances of up to hundreds of angstroms [120]. However, the rate of transfer strongly depends on the base sequence. The rate of charge transfer between a hole injector (e.g., organic chromophore) and a GC pair, separated by a small number of AT pairs, drops off exponentially with the number of AT pairs. However, the rate stays relatively constant with increasing number of AT pairs when there are more than four AT pairs. This has been attributed to a change of transfer mechanism from coherent tunneling to hopping, which will be discussed in Section 3.3.

Henderson et al. covalently attached an anthraquinone derivative to a 60-base pair DNA oligomer [121]. The anthraquinone derivative was irradiated with ultraviolet light, which produces a radical cation on the GC pair attached to the quinone. The cation can then migrate down the length of DNA, where there are GG sequences in several places. The location of the charge can be detected as strand scission at these places with treatment of piperidine. This yields an exponential dependence of the charge transfer up to about 18 nm of DNA length, with a very large decay length.

Using stilbenedicarboxamide (SA) linked to a DNA hairpin, Lewis et al. examined the distance dependence of charge transfer [73]. The experiment consisted of attaching SA to the end of one sequence of T's and one sequence of A's. A GC pair was substituted for one of the AT pairs. This GC pair behaved as an acceptor. It was found that, if the GC pair was directly attached to the SA, the fluorescence of the photoexcited SA was quenched. If the GC pair moved away from the SA, the quenching rate decreased. When the GC pair had four AT pairs separating it from the SA, there would be very little quenching. This suggests a strong distance dependence of the quenching rate when there are a few AT pairs separating the donor and acceptor. However, it was found that if there are long sequences of DNA with only AT pairs, there would be thermal hopping through the AT bridge. The A base would carry the holes since it has the second smallest ionization potential [122]. Giese et al. observed that the amount of charge on a GGG triplet transferred across a bridge of n AT pairs decreases rapidly as the number of AT pairs increases from one to three [123]. However, a further increase in the number of AT pairs would only slightly reduce the amount of charge transferred [123–125]. This can be explained by the formation of the highest occupied molecular orbital band across the AT pairs, which lowers the energy barrier for hole transfer. We will discuss this mechanism in more detail in Section 3.3.

More recently, contactless measurements of the conducting properties of DNA have indicated that this molecule is not a conductor [126–130]. These experiments have been designed to minimize contact effects. The contacts could

be the source of high resistance observed in direct measurements [128]. These experiments were done by adsorbing both DNA and single-walled nanotubes on different insulating substrates. A gold electrode was then evaporated on part of the substrate. Using a scanning force microscope (SFM) tip, the DNA molecules were imaged near the electrode. The same area was reimaged with a voltage of 1.6 V applied to the tip. The nanotubes contrasted more intensely to the substrate due to electrostatic interaction. However, no additional contrast was seen in the case of λ-DNA or poly(dG)–poly(dC). DNA molecules that were not partly covered by the gold electrode, but were in contact with a nanotube, were also imaged. No additional contrast was seen in this case either. Using an oscillating SFM tip, the single-walled nanotubes and the DNA with no electrode were also scanned [128]. In this process, the frequency of the SFM tip oscillations should decrease if the specimen is conducting, due to the polarization of the sample. The decrease in frequency was actually observed for the nanotubes, but not for DNA, suggesting that the molecule behaves as an insulator [128]. However, in this case, the insulating character of DNA could be due to distortions caused by the substrate.

In another indirect measurement, Tran et al. measured the resistance of λ-DNA via the change in the quality factor of a resonant cavity when the DNA is placed in it [130]. The λ-DNA has been found to have a conductivity on the order of 1 $(\Omega\ cm)^{-1}$ or, assuming a DNA diameter of 2 nm, a resistance of about $10^{10}\ \Omega$ for the full length λ-DNA (~16 μm).

3.2. Direct Measurements of Current–Voltage Characteristics

Fink and Schonenberger performed the first direct measurement of the conducting properties of DNA [131, 132]. The resulting I–V characteristics are shown in Figure 4. It was found that λ-DNA is a good conductor, with a resistance comparable to that of conducting polymers. The experiment was done in vacuum, where a drop of solution containing DNA was placed onto a gold-covered carbon foil with 2 μm holes. Excess solution was removed with blotting paper. The holes were imaged with a low-energy electron point source (LEEPS) microscope, which is claimed to not radiatively damage DNA [131, 133]. Upon scanning, holes were occasionally found with only one DNA rope (e.g., several DNA molecules twisted together) spanning across it. The DNA ropes were then broken by using a tungsten tip. The tip was also used to apply a bias across the DNA. A 600 nm portion of a DNA rope produced a resistance of 2.5 MΩ. This provides an upper value for the resistance of DNA, since some finite contact resistance is expected to contribute. Since the experiment was done in vacuum, ionic conduction could not account for the transfer mechanism. However, this experiment does not rule out that ions trapped by the DNA might have changed its electronic structure, allowing for higher conductivity. There has also been some evidence that LEEPS imaging contaminates the DNA and can account for the conducting behavior observed in this experiment [134].

In other direct measurements, researchers have found that DNA acts as a large bandgap semiconductor. For
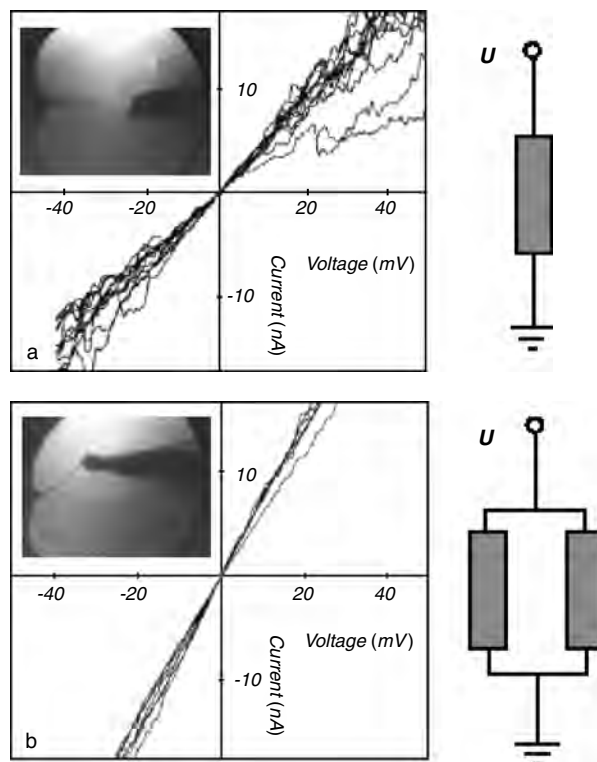
Figure 4. I–V characteristics of DNA ropes. (a) I–V curve for a single rope 600 nm long. The inset shows the LEEPS image of DNA rope attached to a tungsten tip. (b) I–V curve for two ropes in parallel. The inset shows the LEEPS image of the DNA ropes attached to the tungsten tip. Reprinted with permission from [131], H.-W. Fink and C. Schonenberger, *Nature* 398, 407 (1999). © 1999, Macmillan Magazines Ltd.

instance, Porath et al. measured the conductivity in poly(dG)–poly(dC) DNA [135]. The homogeneous sequence is ideal for overlap of π-orbitals in adjacent base pairs. These experiments were done using a DNA oligomer 30 base pairs long or, equivalently, 10.4 nm long. An electrostatically trapping technique [136, 137] was used to position single DNA molecules between two electrodes 8 nm apart (see Fig. 5). The sample was then dried with a flow of nitrogen. The I–V characteristics of this experiment are shown in Figure 5. As is clear from Figure 5, the DNA oligomer does not conduct charge for biases below about 1 V at room temperature, which shows that poly(dG)–poly(dC) DNA behaves like a semiconductor with a large bandgap. As in previous measurements, these results do not rule out the possibility that ions could be attached to the DNA, thus modifying its electronic structure. In Section 3.3, we discuss the possibility that the hybridization of the G-G π stack could induce the semiconducting behavior.

Watanabe et al. measured charge transfer in a single DNA molecule from a biological source using an atomic force microscope (AFM) with a carbon nanotube tip and a two-probe "nanotweezer" made with two multiwalled carbon nanotubes, shown in Figure 6a [138]. Vibrating the two probes of the nanotweezer ensured that the probes did not adhere to each other or the sample. Watanabe et al. reported that the probes could be positioned with roughly 2 nm accuracy. The DNA was deposited on a
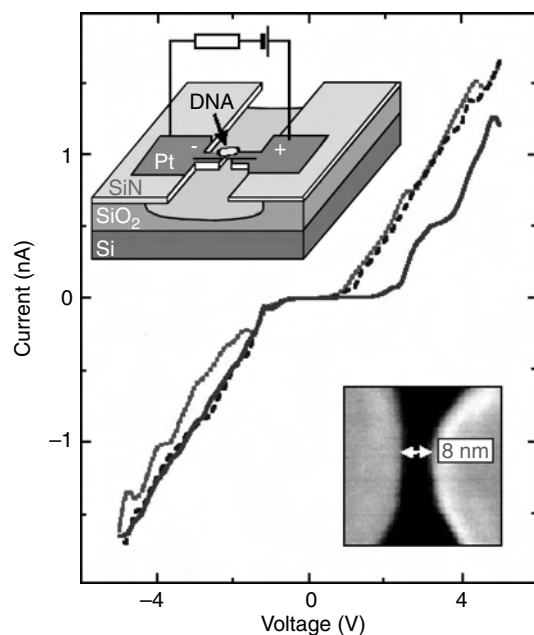
Figure 5. *I–V* characteristics for single poly(dG)–poly(dC) DNA molecules. The different curves show repeated measurements. The upper inset shows the experimental setup. The lower inset shows the electrodes separated by a 8 nm gap. Reprinted with permission from [135], D. Porath et al., *Nature* 403, 635 (2000). © 2000, Macmillan Magazines Ltd.

Figure 6. (a) AFM image (scale bar, 10 nm) of the experimental setup. p1 is the source and p2 the drain of the two-probe nanotweezer. NT is the carbon nanotube used to apply the gate voltage. (b) *I–V* characteristics of biological DNA at different gate voltages, V_G. Reprinted with permission from [138], H. Watanabe et al., *Appl. Phys. Lett.* 79, 2462 (2001). © 2001, American Institute of Physics.

SiO_2/Si(100) surface and dried under a flow of nitrogen gas. Afterwards, the sample was kept in a nitrogen atmosphere. Figure 6b shows the *I–V* characteristics at room temperature for a 25 nm separation of the source and drain. The measurements in Figure 6b indicate that double-strand DNA is semiconducting with a voltage gap of about 2 V. Applying a gate voltage with the carbon nanotube tip reduces this gap significantly. Figure 7 shows the *I–V* characteristics at room temperature if the carbon nanotube tip is placed across the DNA molecule. The tip is held at 2 V. A Coulomb blockade-like staircase is observed whose origin is still unclear.

Hwang et al. made direct measurements using gold electrodes on a SiO_2 substrate [139, 140]. A drop of a solution of 60 base pair poly(dG)–poly(dC) DNA was deposited between the electrodes and then dried with nitrogen gas. Almost linear *I–V* characteristics were found with electrodes separated by a 30 μm gap. However, when the electrode gap was reduced to 20 nm, highly nonlinear *I–V* characteristics and a large voltage gap were found.

De Pablo et al. recently performed measurements on the resistance of λ-DNA by depositing DNA on a mica surface next to a gold electrode. A gold-covered SFM tip was positioned close to one of the DNA chains to function as a second contact. Using the SFM tip at different distances from the electrode, a lower resistivity limit of 10^4 Ω cm was found for a DNA molecule. The same authors reported a lower resistivity limit of 10^6 Ω cm for a DNA molecule using a different method. These results suggest that λ-DNA is an insulator. This is in clear contradiction with previous results obtained by Fink and Schonenberger [131]. De Pablo et al. [134] suggest that the disagreement could be due to the effect of the low-energy electron beam Fink and
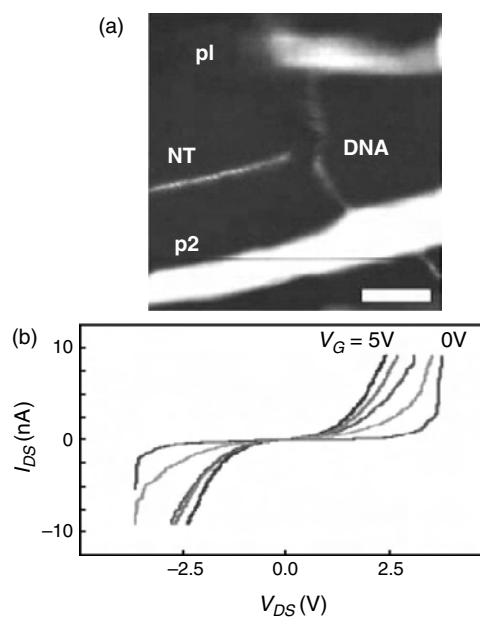
Schonenberger use to image the DNA ropes [131]. In order to prove this, de Pablo et al. irradiated their samples in a vacuum with a low-energy electron beam and found that the DNA resistivity is greatly reduced after irradiation [134]. SFM images show that the sample had indeed been contaminated by the electron beam.

Kasumov and Klinov [141] offered another possible explanation for the discrepancy. These authors suggest that the compression induced by depositing DNA on surfaces changes its electronic structure. By depositing λ-DNA on a mica substrate partially covered with platinum, Kasumov and Klinov found, by simultaneously measuring the DNA height and conductivity using an AFM, that DNA did not conduct and its height was 1 nm. However, if pentylamine vapor was diffused on the Pt/mica surface before depositing the DNA, its height was found to be about 2 nm. At the same time, the DNA was found to conduct. The authors explained this observation by the reduction of the interaction of the mica substrate with the DNA after vapor discharge. Other studies seem to support the finding that the DNA height changes on different substrates [142].

The change in conductivity due to the different compressions can be explained as follows: If the charge transport relies on a very organized DNA chain (i.e., if the transport is through the π-channel), then compression will disrupt the π-channel greatly. The compression could be of such a magnitude that the single strands in the DNA duplex are essentially independent, a case which is believed to lead to small conductivity [92].

Storm et al. measured the conductivity of single DNA molecules and bundles of DNA molecules, finding for mixed-sequence, 1.5 μm long, DNA molecules on a SiO_2 surface between two gold electrodes about 300 nm apart a
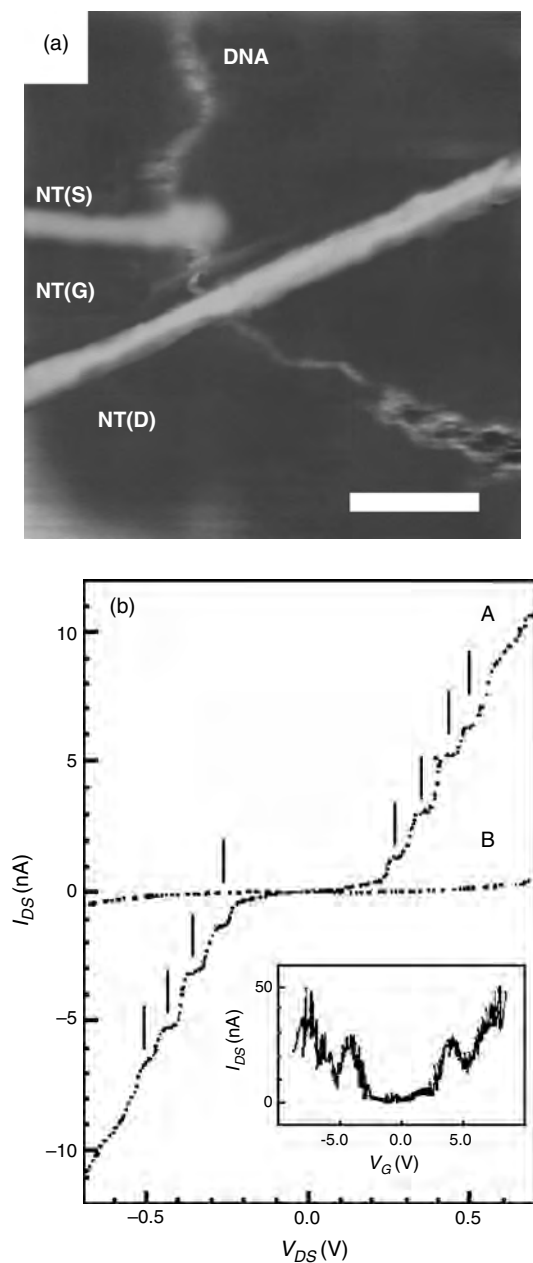
Figure 7. (a) AFM image (scale bar, 10 nm) of the experimental setup. The nanotube gate, NT(G), is placed across the DNA molecule. The source, NT(S), and drain, NT(D), are separated by 5 nm. (b) *I–V* characteristics when the carbon nanotube tip is placed across the DNA molecule. The inset shows the current versus the gate voltage at a source-drain voltage of 0.5 V. Reprinted with permission from [138], H. Watanabe et al., *Appl. Phys. Lett.* 79, 2462 (2001). © 2001, American Institute of Physics.

lower resistance limit of 10 TΩ for about 10 molecules in parallel [143]. These measurements were done at ambient conditions. The DNA was bonded to the electrodes through a thiol group. Other samples with different electrode spacing also showed large resistance. However, the DNA height was measured to be 0.5 nm, suggesting that the compression induced by the surface may play a prominent role in decreasing the conductivity in this case. A similar device

made of a mixed-sequence, 300 nm long DNA, and platinum electrodes at a distance of 40 nm on a SiO_2 substrate, also showed a resistance of 10 TΩ. Finally, poly(dG)–poly(dC) DNA with no thiol groups showed resistances greater than 1 TΩ on both SiO_2 and mica substrates.

Yoo et al. measured the conductance in poly(dG)–poly(dC) and poly(dA)–poly(dT) DNA [144]. Poly(dG)–poly(dC) DNA 1.7–2.9 μm long and poly(dA)–poly(dT) DNA 0.5–1.5 μm long were used in the experiments. DNA was electrostatically trapped [137] between electrodes 20 nm apart and dried with nitrogen. Measurements at both ambient conditions and in a vacuum were performed, with no substantial change in the results. The *I–V* characteristics for poly(dA)–poly(dT) DNA showed a large bandgap at temperatures lower than 161 K. A strong temperature dependence of the current was also observed [144]. This can be accounted for by a small polaron hopping model [145], where the current is given by

$$I \propto \sinh bV \exp\left(-E_a/k_B T\right) \qquad (1)$$

where E_a is the activation energy, T is the background temperature, $b = ea/2k_B T d$, e is the electron charge, a is the hopping distance, and d is the distance between the electrodes. Equation (1) describes the *I–V* characteristics of poly(dA)–poly(dT) DNA very well if b is taken to be independent of temperature. Poly(dG)–poly(dC) DNA displays similar temperature behavior to that of poly(dA)–poly(dT) DNA, but with a much lower resistance of 1.3 MΩ at room temperature compared to 100 MΩ for poly(dA)–poly(dT) DNA. Poly(dG)–poly(dC) DNA shows the correct temperature dependence of b. Furthermore, poly(dG)–poly(dC) DNA shows temperature dependence of the current down to 4.2 K and seems to have two molecular vibration frequencies which contribute to the polaron motion, whereas poly(dA)–poly(dT) DNA shows temperature dependence only down to 50 K and seems to support only one molecular vibration.

Yoo et al. also performed *I–V* measurements with a gate bias [144] and found that poly(dA)–poly(dT) DNA has larger conductance upon application of a positive gate voltage, while poly(dG)–poly(dC) DNA has enhanced conductance under negative gate voltage conditions. Thus, in these experiments, poly(dA)–poly(dT) DNA displays *n*-type conducting behavior, while poly(dG)–poly(dC) DNA displays *p*-type behavior.

In addition to semiconducting and insulating behavior, Kasumov et al. reported proximity-induced superconductivity (i.e., superconductivity induced by the nearby electrodes) in DNA [146]. Using sputtering techniques, Kasumov et al. deposited rhenium/carbon electrodes on a freshly cleaved mica surface [146]. The rhenium layer was 2 nm thick, and the carbon layer developed into clumps (see Fig. 8). A flow of 16 μm long λ-DNA solution parallel to the electrodes introduced about 100 to 200 DNA molecules bridging the gap between the electrodes.

The overall resistance of the structure decreased from 1 GΩ, with no DNA molecules deposited, to a few kΩ after deposition (or a few hundred ohms per DNA molecule). The structure showed no decrease in resistance when treated with the buffer solution without the DNA. Kasumov et al. used a low-powered focused laser beam to destroy
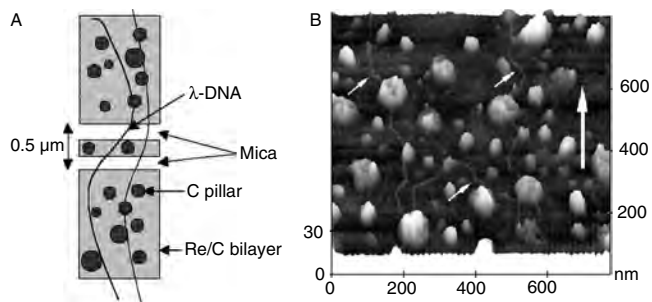
Figure 8. (a) A schematic of the rhenium/carbon electrodes. (b) AFM image of the Re/C film with deposited DNA molecules. The small arrows show the DNA molecules and the large arrow shows the direction of the solution flow. Reprinted with permission from [146], A. Yu. Kasumov et al., *Science* 291, 280 (2001). © 2001, The American Association for the Advancement of Science.

DNA molecules within the gap, except for in a narrow portion. In this way, three different samples were obtained with approximately 10 DNA chains (DNA1), 40 DNA chains (DNA2), and 2–3 DNA chains (DNA3), respectively. The resistance of all three samples increased as the temperature decreased. However, DNA1 and DNA2 decreased in resistance below the superconducting transition of the electrodes (see Fig. 9). The application of a magnetic field increased the resistance at temperatures close to the superconducting transition, which is the case for proximity-induced superconductivity [146]. The DNA3 sample showed an increased resistance even below the superconducting transition and a decreased resistance with increasing magnetic field, suggesting that this was not a case of proximity-induced superconductivity [146]. In order to prove that these unusual conducting properties are attributable to DNA bridging the electrodes, the samples were reheated to room temperature and treated with a flow of buffer solution for about 30 minutes. This did not result in a change of resistance. When DNase was added, however, the resistance increased back to that of the original electrode systems (without the DNA), showing that the transport was indeed taking place through the DNA molecule. Although not conclusive, the
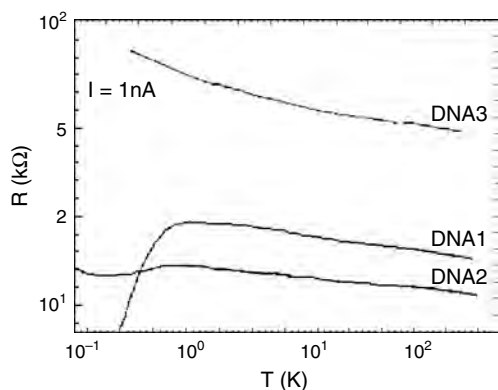
results of Kasumov et al. indicate that proximity-induced superconductivity may be realized in DNA, and that thermal hopping is an unlikely mechanism of transport in λ-DNA, since the resistance does not increase strongly with decreasing temperature.

Other researchers have measured conductivity in DNA networks. Cai et al., for instance, investigated networks of poly(dG)–poly(dC) DNA and networks of poly(dA)–poly(dT) DNA self-assembled onto a mica surface (see Fig. 10) [147]. The samples were made of a drop of a DNA solution adsorbed onto a freshly cleaved mica surface and incubated for about one minute. The excess solution was then removed and dried with a flow of nitrogen gas. The sample was also kept under vacuum conditions for 5 to 12 hours, after which the electrical characteristics were measured. The poly(dG)–poly(dC) DNA networks show a "uniform reticulated structure" opposed to poly(dA)–poly(dT) DNA which forms a cross-linked network. Details of these structures can also be controlled [148–150]. A gold electrode was evaporated to form a contact to the DNA network, as shown in Figure 10c and d. Using a conducting probe AFM, Cai et al. measured the *I–V* characteristics of these networks. Without DNA, a noise of about 1 pA was measured. Placing the AFM tip 100 nm away from the gold electrodes (see Fig. 11a), the current in poly(dG)–poly(dC) DNA displayed ohmic behavior. Poly(dG)–poly(dC) DNA also exhibited *p*-type rectifying behavior (see Fig. 11d). Poly(dA)–poly(dT) DNA, on the other hand, displayed much higher resistances. However, in this case as well, ions from the buffer solution could have changed the electronic properties of the DNA.

Figure 9. Resistance measurements as a function of temperature for λ-DNA between superconducting electrodes for the three samples discussed in the text. Reprinted with permission from [146], A. Yu. Kasumov et al., *Science* 291, 280 (2001). © 2001, The American Association for the Advancement of Science.
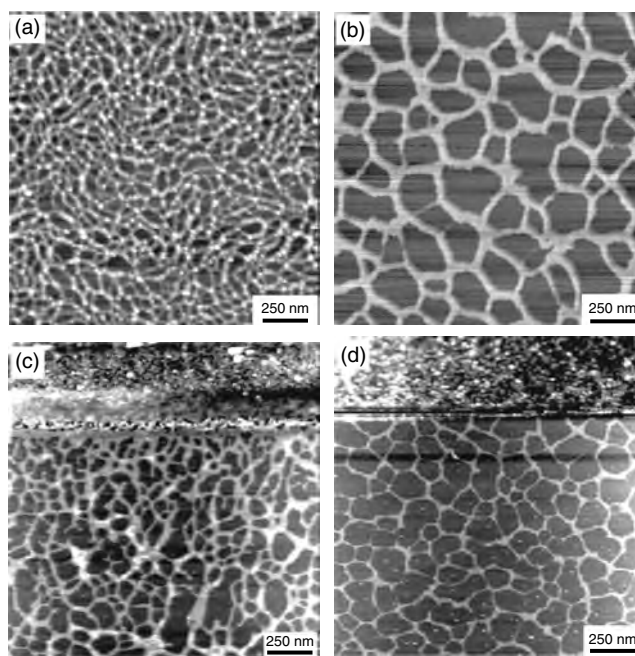
Figure 10. AFM images of self-assembled networks of (a) poly(dA)–poly(dT) DNA and (b) poly(dG)–poly(dC) DNA. (c) Poly(dA)–poly(dT) DNA with a gold electrode and (d) poly(dG)–poly(dC) DNA with a gold electrode. Reprinted with permission from [147], L. Cai et al., *Appl. Phys. Lett.* 77, 3105 (2000). © 2001, American Institute of Physics.
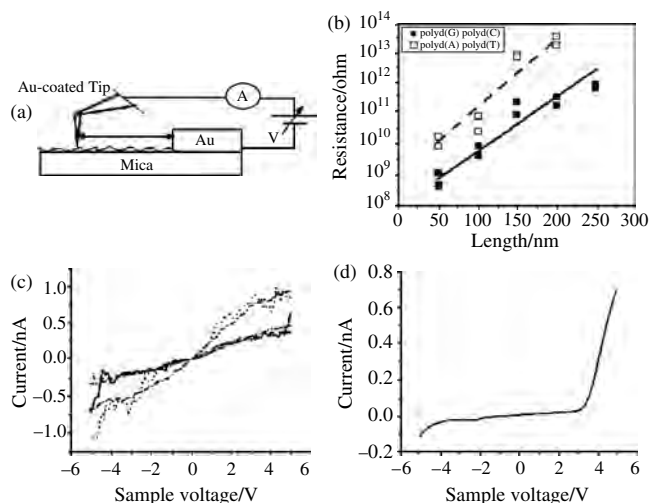
Figure 11. (a) Experimental setup. (b) Resistance versus length for poly(dG)–poly(dC) DNA and poly(dA)–poly(dT) DNA. (c) I–V characteristics for poly(dG)–poly(dC) DNA. (d) Rectifying curve for poly(dG)–poly(dC) DNA. Reprinted with permission from [147], L. Cai et al., *Appl. Phys. Lett.* 77, 3105 (2000). © 2001, American Institute of Physics.

Zhang et al. [151] recently focused on eliminating, or at least reducing, two experimental factors, contact resistance [152, 153] and ions from the solutions, which could have caused the large discrepancy between previous experimental results. Such direct measurements indicate that DNA is generally insulating. λ-DNA on a quartz substrate between 4 μm thick gold electrodes was used in these experiments. The DNA ends were modified to include a T base with a thiol group, so that the base could easily bind to the gold electrodes. The electrode distance was fixed at 4 or 8 μm. A solution of DNA molecules was applied to the electrodes and then diffused across the electrodes by a flow of solution. Mg^{2+} ions were introduced so that the DNA could stick to the quartz surface while it was rinsed with NH_4Ac to remove leftover salt from the buffer solution. The volatile NH_4Ac was then removed under vacuum. The corresponding I–V characteristics showed no conduction for an applied voltage of up to 20 V for λ-DNA between electrodes 4 μm apart. A lower resistivity limit of 10^6 Ω cm was found for biases up to 20 V.

These results suggest that the lower resistivities measured by other groups are due to ionic contamination from the buffer solution and/or from other sources. The influence of ions and humidity on both the structure and the electronic properties of DNA has also been intensively studied by other researchers [154, 155]. Lee et al. did experiments to examine the influence of both humidity and oxygen on the conductance properties of DNA [155]. Trapped oxygen has been found to dope poly(dG)–poly(dC) DNA with holes and increase its conductivity. In these experiments, 1.7–2.9 μm poly(dG)–poly(dC) DNA and 0.5–1.5 μm poly(dA)–poly(dC) DNA were placed between Au/Ti electrodes. The distance between the electrodes varied between 100 to 200 nm. A DNA solution was dropped between the electrodes and allowed to dry. I–V curves were measured under three conditions: in air with 35% humidity, in an oxygen–nitrogen (1:4 ratio) atmosphere with less than

0.1% humidity, and in a vacuum. For poly(dG)–poly(dC) DNA at 1 V, the resistance increased from about 0.8 to 7 to 100 GΩ, for the three different conditions, respectively. Finally, when poly(dG)–poly(dC) DNA was exposed to pure oxygen gas instead of air, the conductance increased by over 100 times. This shows that oxygen doping has a larger impact on the DNA resistance than water. In the case of poly(dA)–poly(dT) DNA, the conduction decreased when the sample was placed in a pure oxygen atmosphere. These results also support early findings that poly(dG)–poly(dC) DNA is a *p*-type conductor and poly(dA)–poly(dT) DNA is an *n*-type conductor [144, 147].

3.3. Charge Transport Mechanisms

The previous section reviewed the main experiments on the transport properties of DNA, showing that in several instances these experiments yielded contradictory results, even on supposedly similar system configurations. This section focuses on the interpretation of these experiments on the basis of physical models. Over the past several years, many transport mechanisms have been proposed to account for differing experimental results. This does not come as a surprise due to the wide range of conducting properties found for DNA. Specifically, three possible mechanisms for charge transport stand as the main physical processes: thermal hopping, sequential tunneling, and coherent tunneling (see Fig. 12). Polaron and soliton formation and transport have also been investigated and will be discussed at the end of this section.

In certain experiments, some of the three main mechanisms can be ruled out on the basis of the DNA configuration or experimental conditions. For instance, in the fluorescence experiments, charge could thermally hop from base to base (see Fig. 12A). However, the thermal energy required for this process is generally quite large; thus, this mechanism is unlikely in this case, as in many other cases. Charge can also sequentially tunnel from one site to the next (see Fig. 12B). After each tunneling process the coherence of the charge wavefunction is lost through dephasing processes, such as scattering with molecular vibrations. Neither of these mechanisms depends strongly on the DNA length. Finally, charge can tunnel through a whole length of DNA (see Fig. 12C). In this case, the charge wavefunction does not lose phase coherence, so the process is called coherent or unistep tunneling. This mechanism has a strong distance dependence. In the case of DNA, many researchers have
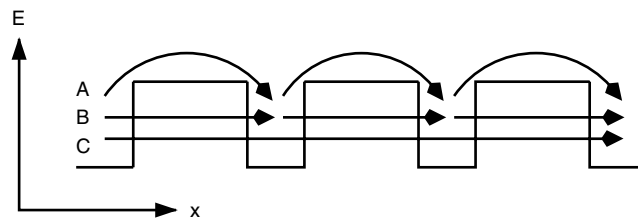
Figure 12. Schematic of three possible mechanisms for charge transfer in DNA, depicted as a series of energy barriers, (A) thermal hopping, (B) sequential tunneling, and (C) coherent or unistep tunneling. The vertical axis represents energy, E, and the horizontal axis represents the spatial position, x.

assumed that charge coherently tunnels through the whole length of DNA, with a rate of charge transfer R,

$$R \propto \exp(-\beta L) \quad (2)$$

where L is the length of the DNA and β is the inverse tunneling decay length. A large value of β means that the rate of tunneling will decrease rapidly with increasing distance. However, earlier measurements yielded seemingly contradictory values for β [96–100].

Charge transport over large distances by a single tunneling step is unlikely. Theoretical studies have shown that the rate of coherent tunneling should drop off dramatically with distance [156]. Thus, many argue that sequential tunneling is the most likely mechanism for charge transport in DNA. Within this mechanism, holes have been studied as the likely charge carrier. The G base is the most favorable site for location of holes due to the order of the ionization potentials (G < A < C < T), which is independent of nearest neighbor bases [122, 157–169]. Many models have looked into the possibility of hole transport via G bases, along with other mechanisms of charge transport [170–194].

Berlin et al. did a quantitative analysis of sequential tunneling using kinetic rate equations [171, 172]. In this work, sequential tunneling between GC pairs through a bridge of AT pairs has been studied. A G^+ radical is considered as the charge donor and the base sequence GGG as the acceptor, in close connection with the experiments by Meggers et al. [75] and Giese et al. [195]. The base sequence GGG acts as an acceptor due to the lower ionization potential compared to a single G base. The ratios of reaction yields of water between the GGG site to the first G site, and also the GGG site with all the other G sites, were calculated. Tunneling rates from short DNA chains were taken from theory and experiment [75, 188, 195] and used to calculate the ratio of reaction yields for different base sequences. A fair amount of agreement with experiments has been obtained [75, 195]. Berlin et al. found that the rate for sequential tunneling drops exponentially with distance due to the reaction with water. The β parameter was found to be 0.1 Å^{-1} for sequential tunneling, compared to a value of about 1 Å^{-1} for coherent tunneling [156].

The physical meaning of the model is as follows. A hole is generated on some G base (part of a GC pair) to obtain a G^+ radical. The hole is then assumed to hop along the length of DNA to successive G bases, or, alternatively, the G^+ radical can undergo a reaction with water. If there are some sites with a sequence of many G bases (i.e., GG...G), then the hole is assumed to be transferred to the first G base to obtain $(G^+G...G)$. This electronic configuration can relax to the lower energy state $(GG...G)^+$, trapping the hole. Alternatively, the hole can transfer to adjacent single G bases along the length of the DNA. If the time to relax from the configuration $(G^+G...G)$ to the more stable $(GG...G)^+$ is small, the hole travels along the DNA until it reaches a GG...G site, where it is trapped. On the other hand, if the relaxation time is large, the hole will continue to travel along the DNA without being trapped. The first possibility seems to explain the experimental data of [75, 195].

Berlin et al. [174] also studied the competition between coherent and hopping transport using a one-dimensional tight-binding model. In this model, the DNA sequence was chosen to be of the form $(AT)_m$–GC–$(AT)_n$–GC–$(AT)_m$. The rate for tunneling was assumed to be

$$\nu_{\text{tun}} \exp(-\beta L) \quad (3)$$

where $L = (n+1)a$ is the distance between the two GC pairs, n is the number of AT pairs, a is the distance between base pairs, β is the tunneling decay length derived from the tight-binding model, and ν_{tun} is a fitting parameter. The rate for thermal transport is assumed to be

$$\nu_{\text{therm}} \exp\left(-\frac{g_G}{k_B T}\right) \quad (4)$$

where g_G is the energy separation between the hole state on the GC pair and the bottom of the AT band, which is derived from the tight-binding model. There is a critical value of n when these two rates are equal, at which the main mechanism will switch from tunneling to thermal hopping. Using this model, it is estimated to be between three and five, depending on the value of the transfer integral between adjacent base pairs. This is in agreement with the experimental work of Giese et al. [123], where the transfer rate has been found to drop exponentially up to a bridge length of three AT pairs. This also agrees with experimental evidence that suggests some charge is localized on the AT bridge [124, 125]. In this context, the effects of fluctuations and structural distortions have also been considered [86, 173, 175, 196–202].

Long-range charge transfer has also been studied with a scattering matrix formalism and Büttiker's dephasing model [177–181]. The idea behind this approach is that in complex systems, like DNA, charge transfer is unlikely to occur in a single step. Thermal motions of the DNA structure, solvation effects, etc., can break the phase coherence of the charge carrier. The approach thus combines the coherent tunneling and sequential tunneling mechanisms, with relative amount of one to the other determined by the strength of the dephasing. This approach has been successfully employed to account for the experimental results of Porath et al. [135] on a DNA molecule with 30 GC pairs between two electrodes [179]. A good agreement between experiment and theory has been obtained by assuming partial dephasing.

Using a similar model with two different channels, one for each relative magnetic polarization of the electrodes, Zwolak and Di Ventra [203] predicted that a short poly(dG)–poly(dC) DNA molecule should behave as a spin-valve device; that is, the resistance of the molecule can be changed according to the relative magnetization of the electrodes (see Section 4). Preliminary results from Kasumov seem to confirm that spin-dependent transport can be observed in DNA [204].

Cuniberti et al. [205] used a tight-binding model which includes coupling of the base states to other states (e.g., states on the phosphate backbone) to calculate the transport properties of a 30-base pair poly(dG)–poly(dC) DNA between two electrodes. By fitting some parameters in the Hamiltonian, a fairly good agreement between the theoretical and experimental I–V characteristics has been obtained [205]. This result suggests that the large resistance

of the poly(dG)–poly(dC) DNA could be due to the hybridization of the π stack.

Finally, we need to mention that apart from the three main transport mechanisms discussed in this section, polaron [6, 87, 121, 144, 206–212] and soliton [213, 214] formation in DNA have also been investigated. The former relates to the coupling of the electronic and vibrational-mode degrees of freedom, and the latter relates to the formation of domain walls in dimerized bonds of DNA.

Schuster et al. suggested a phonon-assisted, polaronlike hopping mechanism for charge transfer [121, 208]. Since structural fluctuations of DNA are relatively fast [215–217], the local structure around a charged base is likely to rearrange. The distance in between base pairs would thus decrease; the angle between base pairs could also decrease. Other structural changes that trap the charge might occur as well. The resulting polaron could then move through the DNA via temperature-induced structural fluctuations.

Bruinsma et al. suggested, based on a tight-binding model which includes structural fluctuations, a polaronlike hopping mechanism, where the hopping is controlled by structural fluctuations [196]. Charge transfer would then increase strongly with temperature, an effect that is actually observed in some experiments [86, 130]. Barnett et al. put forth an explanation of this temperature dependence which relies on fluctuations in the location of the counterions on the DNA [218]. By performing first-principles calculations, these authors have shown that different counterion configurations can lead to localized hole states. Therefore, fluctuations of the counterions could induce movement of the holes. This would also lead to an increase of the rate of charge transfer with increasing temperature.

Yu and Song [201] explained the temperature dependence observed by Tran et al. [130]. Tran et al. found that the conductivity increases slowly with increasing temperature. However, at high temperatures, the conductivity has been found to be strongly dependent on temperature [130]. This result can be explained by invoking a "variable-range hopping" model with a temperature dependent localization length. Here, the probability of hopping is dependent on two mechanisms, both tunneling (characterized by the localization length) and a thermally activated hopping. Thus, the most probable distance for hopping is due to the competition between these two mechanisms. If this is the case, there is a critical temperature above which the most likely hopping distance becomes smaller than the distance between bases. Above this temperature, the hopping mechanism can only be thermally activated. This fact alone is enough to describe a transition from weak temperature dependence to strong temperature dependence. However, the results from this model do not fit well with experiment [130, 201]. Yu and Song thus calculated the localization length using a tight-binding Hamiltonian which includes fluctuations in the angle between adjacent base pairs. With this correction, the "variable-range hopping" model seems to give the correct temperature dependence.

Hjort and Stafstrom studied charge transfer in poly(dG)–poly(dC) DNA using a tight-binding Hamiltonian [219]. These authors found that including fluctuations of the angle between adjacent base pairs decreases the conductivity of DNA. Likewise, Grozema et al. used a tight-binding

Hamiltonian with an electronic coupling that depends on the angle and distance between adjacent base pairs to study the effect of fluctuations [175]. These authors found that the mobility of poly(dG)–poly(dC) DNA decreases by an order of magnitude when structural fluctuations are taken into account. Furthermore, Grozema et al. found that disorder in the site energies of the tight-binding chain, due to, for example, an inhomogeneous distribution of counterions on the DNA, can reduce the mobility by another order of magnitude [175].

4. DNA APPLICATIONS IN NANOSCALE ELECTRONICS

In this section, we discuss the possible application of DNA as an electronic component and its use as a self-assembling template. In the latter case, DNA has been found to aid in the assembly of novel nanoscale structures, which could not be assembled otherwise, and could potentially speed up self-assembly of existing structures.

4.1. DNA Nanoscale Wires

Braun et al. carried out an interesting application of DNA in a rudimentary nanoscale circuit [101, 220]. These authors made a silver wire using DNA as a template [101]. The fabrication method is outlined in Figure 13. Two different
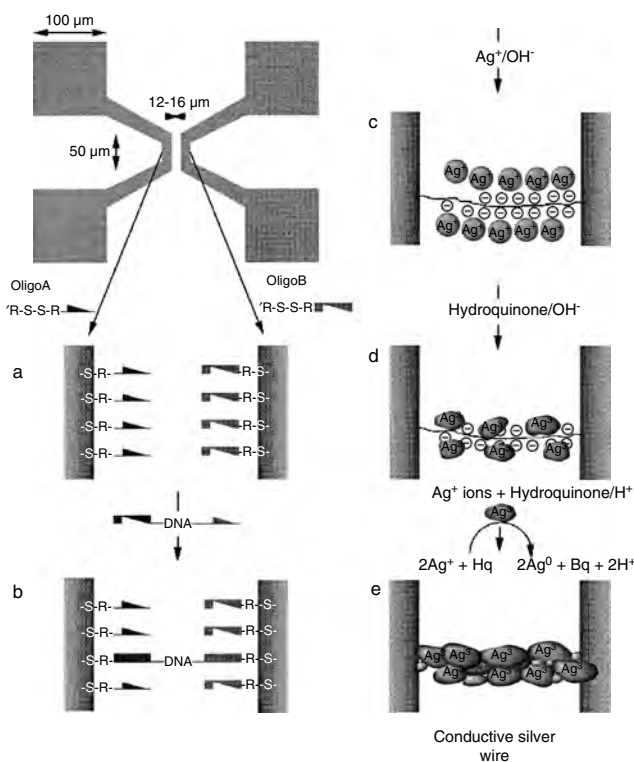
Figure 13. Assembly of a silver wire from a DNA template. (a) The electrodes with attached oligonucleotide groups. (b) A DNA molecule bridging between the two electrodes. (c) Ion exchange of sodium ions with silver ions. (d) Silver deposition onto the DNA. (e) Conductive silver wire. Reprinted with permission from [101], E. Braun et al., *Nature* 391, 775 (1998). © 1998, Macmillan Magazines Ltd.

12-base oligonucleotides are attached to one of two gold electrodes through a disulphide group at their end. The two electrodes are connected by placing them in a solution of fluorescently labeled λ-DNA. Two 12-base "sticky ends" were added to the λ-DNA. One of these ends hybridized to an electrode. The DNA was then stretched to the other electrode by flow of the solution.

Using an ion-exchange process, Na^+ ions on the DNA backbone are replaced with Ag^+. The silver ions are reduced by a basic hydroquinone solution. Extra silver metal is then deposited by addition of an acidic Ag^+/hydroquinone solution. The resulting silver wire between gold electrodes 12 μm apart is shown in Figure 14. AFM imaging has been used to verify the presence of only a single wire.

The wire, shown in Figure 14, had grains of 30–50 nm continuously placed, and overall had a width of about 100 nm and a length of 12 μm. The size and structure of the wire could be controlled during the different fabrication steps. However, wires with grain sizes of 25 nm or less were found to be discontinuous [101]. The I–V characteristics of the silver wire are shown in Figure 15. Its resistance was greater than 10^{13} Ω in the region of low bias. These curves were
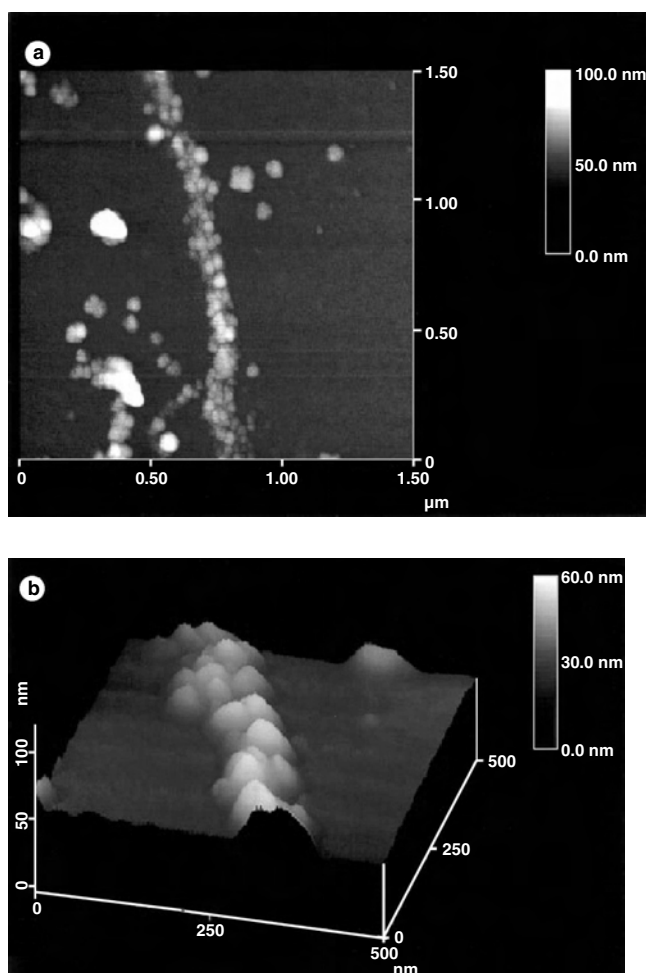
Figure 14. Silver wire fabricated from a DNA template. (a) A 1.5 μm field size image of the silver wire. (b) A 0.5 μm field size image. Reprinted with permission from [101], E. Braun et al., *Nature* 391, 775 (1998). © 1998, Macmillan Magazines Ltd.
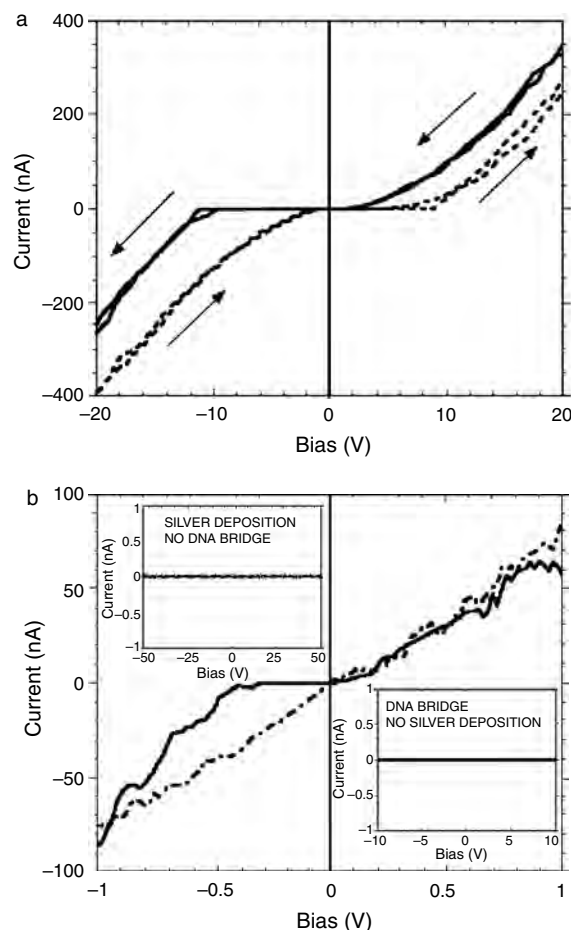
Figure 15. (a) I–V characteristics of the 12 μm long and 100 nm wide silver wire. The arrows show the direction of the voltage scan. (b) I–V characteristics of a silver wire with more silver deposited. The upper inset shows I–V curves with silver deposition and no DNA bridge. The lower inset shows the I–V curve with a DNA bridge and no silver deposition. Reprinted with permission from [101], E. Braun et al., *Nature* 391, 775 (1998). © 1998, Macmillan Magazines Ltd.

reproducible, as shown in Figure 15a, but they showed hysteresis whose origin is still unclear. Figure 15b shows a wire where more silver was deposited. A smaller current gap was found in this case, and the resistance was reduced at higher voltages from 30 to 7 MΩ, showing that the electrical conductivity can be somewhat controlled by silver deposition.

The large current gap in the first case is still unclear. It can be attributed to grain boundary effects or to Coulomb blockade. For practical applications, ohmic behavior is, however, desirable. In this respect, Richter et al. succeeded in making a palladium wire which displayed ohmic behavior [102, 221–223]. A single palladium wire is shown in Figure 16. A drop of λ-DNA solution was placed on gold electrodes. The capillary forces of the evaporating drop aligned the DNA chain between the gold surfaces. A palladium solution was then put on the sample and reduced by addition of a different solution. Finally, the sample was rinsed in order to remove clusters that formed without the DNA. Further addition of palladium solution and reducing agent caused more growth. Like the silver wire, separate metal clusters were observed which eventually became
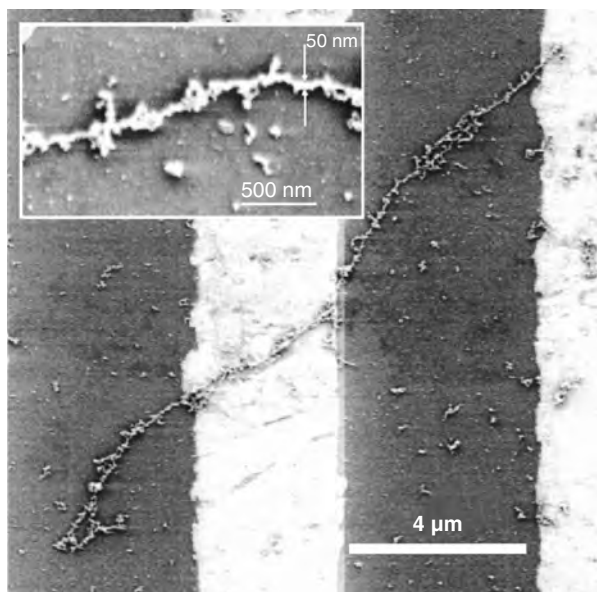
Figure 16. Palladium wire made from metallization of λ-DNA. Reprinted with permission from [102], J. Richter et al., *Appl. Phys. Lett.* 78, 536 (2001). © 2001, American Institute of Physics.

Figure 17. *I–V* characteristics of the palladium wire. Squares correspond to the wire as grown; triangles refer to the wire after it was cut. The inset shows the *I–V* characteristics at low voltages. Reprinted with permission from [102], J. Richter et al., *Appl. Phys. Lett.* 78, 536 (2001). © 2001, American Institute of Physics.

continuous with increased deposition. However, unlike the DNA-template silver wire, the grain sizes were about 3 nm, and the metal clusters aggregated into a continuous structure at about 20 nm of thickness. A linear dependence of the resistance on wire length has also been found [102, 221, 222]. Since none of the wires, including very thick ones, displayed a resistance below ∼5 kΩ, a contact resistance was likely present. This minimum resistance was significantly reduced by "pinning" further wires to the gold electrodes, using electron-beam-induced carbon lines.

Since the fabrication process generates many wires, the resistance of each wire was measured by systematically cutting each one. The resulting wires displayed ohmic behavior (see Fig. 17). The measured resistance was found to be about 700 Ω, which gives a specific conductivity of 2×10^4 S cm^{-1} (i.e., about one order of magnitude less than bulk palladium).

Richter et al. more recently measured the resistance of DNA-templated palladium wires at low temperatures [224]. Above 30 K, the resistance of these wires decreased with decreasing temperature. However, below 30 K, the resistance increased. This type of behavior is observed in two-dimensional 2D disordered metals, like palladium films of similar thickness, where localization occurs due to backscattering without loss of phase coherence of the electrons. The disorder in the palladium wires was attributed to the presence of grain boundaries. In order to decrease the amount of disorder, the DNA-templated palladium wire was annealed. After annealing, the wire no longer showed an increase of resistance at low temperatures, indicating that the resistance increase is indeed due to disorder.

Other groups have also succeeded in fabricating DNA-based nanowires [225–227]. For instance, Harnack et al. made a gold wire network on a DNA template [225]. Gold nanoparticles of 1–2 nm capped with tris(hydroxymethyl)phosphine were bound to DNA [225]. Nanowires as
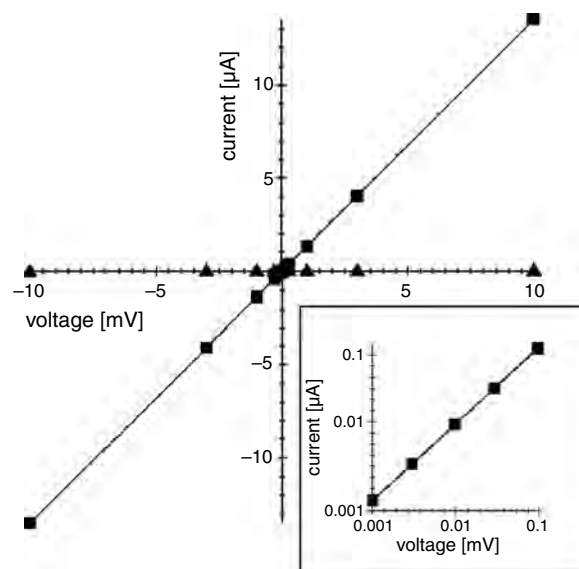
small as 30–40 nm with resistivities about 1000 times larger than bulk gold were fabricated [225]. Ford et al. were able to assemble DNA with 1 nm size platinum grains as a precursor to a larger wire [226]. In this case, the platinum was bound directly to the bases, instead of exploiting the ionic interaction with the backbone. The goal is to be able to create smaller wires with the desired *I–V* characteristics [223, 226, 228].

Kumar et al. exploited the electrostatic interactions with the DNA backbone to create linear arrays of nanoparticles, which could potentially be used to create an array of wires [229]. Lysine-capped, ∼3 nm colloidal gold particles were mixed with DNA. The DNA–gold hybrids were separated out after the solution sat for two hours. The experiment was carried out with two types of synthetic DNA and calf-thymus DNA. Figure 18A shows the transmission electron microscopy (TEM) image of a 15-base pair, synthetic DNA–gold hybrid on a carbon coated TEM grid. The linear arrays of gold nanoparticles can clearly be seen in the image. The separation of the arrays is about 9 nm. Figure 18B shows the scanning tunneling microscopy (STM) image of the 30-base pair synthetic DNA–gold hybrid on a silicon wafer. However, the electrical properties of these structures have not been measured, so no conclusion can be drawn about their conducting properties. Sastry et al. created DNA–gold hybrids using similar methods [230].

Another way of fabricating nanowires is to use M-DNA [231–233]. In M-DNA, the imino proton (a proton attached to a nitrogen which is double-bonded to a carbon) is replaced by a divalent metal atom, like Zn^{2+}, Co^{2+}, and Ni^{2+} [233]. B-DNA together with one of those ions will form M-DNA in a solution with a pH larger than 8. The metal ion not only alters the electronic structure of DNA but also its physical structure. The base pair separation is about 4 Å
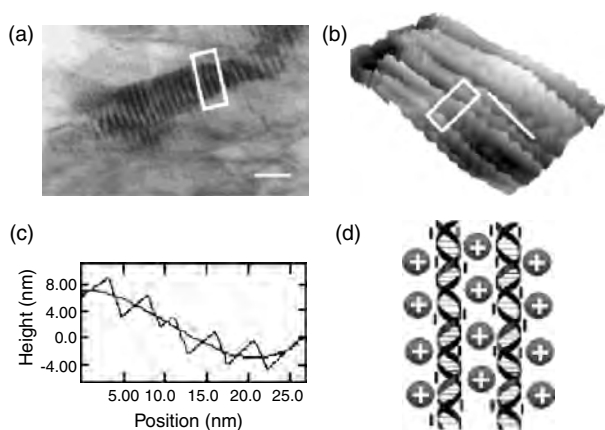
Figure 18. (A) TEM image of a 15-base pair synthetic DNA–gold hybrid on a carbon coated TEM grid. (B) STM image of the 30-base pair synthetic DNA–gold hybrid on a silicon wafer. (C) Height versus distance along the line shown in (B). (D) Schematic of the DNA–gold hybrid. Reprinted with permission from [229], A. Kumar et al., *Adv. Mater.* 13, 341 (2001). © 2001, Wiley–VCH.

in M-DNA compared to 3.4 Å in B-DNA. Figure 19 shows the base pairs in M(Zn)-DNA.

To measure the *I–V* characteristics, a DNA chain was placed across a deep gap, which kept salt bridges from forming and guaranteed that the DNA chain was the only conducting element of the device [231]. This was done by placing a drop of either B-DNA or M-DNA across the electrodes. The corresponding current–voltage characteristics in vacuum and at room temperature were measured. The B-DNA displayed semiconducting behavior, with a current gap of about 200 meV. The M-DNA, however, showed no gap but comparable behavior at higher biases. The lack of a current gap was attributed to the zinc ions bringing the edge of the DNA molecular bands closer to the Fermi level of the gold electrodes. As in the experiment of Braun et al. [101], transport through B-DNA with "sticky ends" has also been measured. In this case, large-bandgap semiconducting behavior was observed in B-DNA, reminiscent of the behavior found by Porath et al. [135]. The presence of this large current gap was attributed to the end groups limiting the current.

The same group finds that electron transfer is greatly enhanced in M-DNA compared to B-DNA from fluorescence quenching measurements [232, 234, 235]. Most recently, significant quenching at distances up to ~150 nm has been reported [232, 234, 235]. Weak distance dependence suggests that electron hopping is the main mechanism for transport in M-DNA.
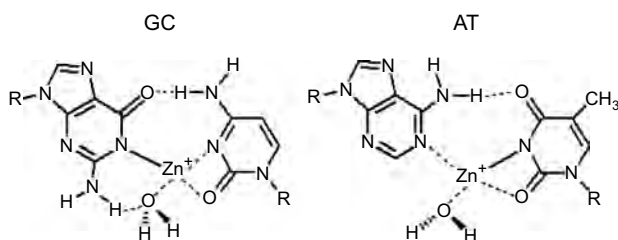
Figure 19. Base pairs in M-DNA, with Zn^{2+} as the metal ion.

Zwolak and Di Ventra recently suggested that short DNA wires can be used as spin valve devices [203]. A short poly(dG)–poly(dC) between two magnetic electrodes was studied as an example. By assuming negligible spin-flip scattering in the wire and at the contacts, magnetoresistance values of as much as 26% for Ni and 16% for Fe contacts were predicted. The magnetoresistance is defined as $(R_{anti} - R_{parallel})/R_{anti}$, where R is the resistance for each relative magnetization of the electrodes. The calculated magnetoresistance is shown in Figure 20. Kasumov recently performed experiments with DNA between permalloy electrodes [204] and actually observed spin-dependent transport in DNA.

Finally, Ben-Jacob et al. suggested, based on the idea that each phosphate group can act as a tunnel junction, that DNA could be used as a transistor or even as a quantum bit [214, 236].

4.2. DNA Self-Assembly

The different properties of DNA make it particularly versatile in several applications from computation to fueling nanomechanical devices [237–250]. In addition, DNA's recognition ability has been found to help in the self-assembly of novel nanoscale structures out of "nanoscale building blocks" (e.g., nanoparticles) [103, 251–255]. In this section, we will review the research done on assembling large-scale structures relevant to nanoscale electronics using DNA.

Ordering of nanoparticles is important to realize electronic devices and storage media. However, it is a difficult task, for instance, to order hexagonal closed-packed structures [256–260]. A DNA template, on the other hand, is flexible enough that it can be shaped in many different ways. For example, several geometrical structures of DNA have already been made, such as cubes and knots [261]. Periodic arrays are being examined as the main components in nanoscale memory devices and other electronic applications. One potential downfall of using DNA in these applications is that the resulting structures are not rigid [261]. However, this problem can be overcome by assembly onto surfaces (see, e.g., [262–265]). Before discussing different nanoparticle
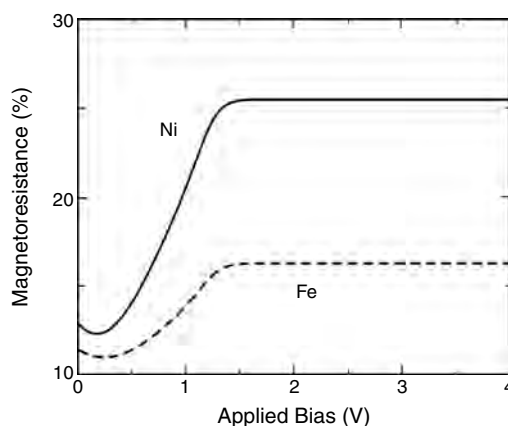
Figure 20. Theoretical magnetoresistance for 30-base pair poly(dG)–poly(dC) DNA between nickel and iron electrodes as a function of bias. Reprinted with permission from [203], M. Zwolak and M. Di Ventra, *Appl. Phys. Lett.* 81, 925 (2002). © 2001, American Institute of Physics.

structures, we review some recent work on molecular lithography (i.e., the patterning of functional devices) using DNA.

Keren et al. demonstrated molecular lithography using DNA [266]. The suggested process starts with a polymerization of RecA protein monomers with a single strand of DNA. The RecA protein mediates homologous recombination between the single strand of DNA and a double strand of DNA. Homologous recombination binds the single stranded DNA to the double-stranded DNA with an identical sequence. Thus, the sequence of the single strand of DNA will determine where it is "placed" on the double strand of DNA. As a consequence, the new double strand of DNA has a section which has the RecA protein bound to it. This section is not coated with metal in the process that will be described. A gold wire was fabricated on the DNA template as follows. The new double strand of DNA was stretched across a passivated silicon surface and then incubated in an $AgNO_3$ solution. The original double strand of DNA had aldehyde bound to it. The aldehyde allowed for small silver aggregates to form on the DNA. The DNA was then further metallized by electroless deposition of gold on top of the silver. This process produced a piece of DNA wire on an insulating surface, which had an insulating gap on the portion where the RecA was bound. It was found that the conductivity of a 50–100 nm thick gold wire, using the aforementioned process, was only about one-seventh that of bulk gold.

Small particles can also be attached to the RecA bound length. A single strand of biotin-labeled DNA binds specifically to the length of DNA that is bound to the RecA. It remains bound even after the protein is removed. This product, then, was used to specifically bind streptavidin-conjugated gold nanoparticles, which attach only to biotin-labeled DNA. After further gold deposition, a piece of metallized DNA formed between two sections of DNA.

Using a similar process, Keren et al. were also able to fabricate a gold cluster [266]. This was done by reacting the primary antibodies of RecA with the DNA that had the RecA bound length. Then secondary antibodies were used with conjugated gold particles. The latter bind to the antibodies. After further gold deposition, the result was a piece of DNA with a localized metal cluster. In addition, by using two double strands of DNA, Keren et al. were able to demonstrate the ability of RecA to create a three-arm junction at a specific location on the DNA. This work demonstrated the potential of DNA to integrate devices on the molecular scale and to create novel functional devices.

Other researchers have focused on the organization of nanoparticles [251, 252, 267, 268]. Although no specific device/structure has been created for use in molecular electronics, this research area shows tremendous potential. Alivisatos et al., for instance, have attached single-stranded DNA to gold nanoparticles. The latter self-assemble onto a complementary DNA template [252]. This approach can form complex structures. Using a similar strategy, Mbindyo et al. attached gold wires to a gold surface [267]. In these structures, single-stranded DNA was attached to specific sites of gold wires 200 nm in diameter. These strands of DNA were complementary to strands on a gold surface.

Other strategies have also been used to attach nanoparticles to surfaces [269]. As an example, Coffer et al. used DNA as a template for the formation of CdS nanoparticles [265, 270–272]. Cd^{2+} ions were added to a solution of plasmid DNA, which formed a DNA/Cd^{2+} complex via electrostatic interaction with the DNA backbone. The DNA was then bound to a solid surface. An array of CdS nanoparticles formed along the DNA upon addition of H_2S. The resulting nanoparticles were relatively monodisperse. Further study has shown that the particular sequence affects the size of the particles [271].

The use of streptavidin–biotin interactions has also been suggested to create arrays of nanoparticles and molecules [273–275]. Winfree et al. used double crossover DNA (i.e., two double-stranded DNA chains which are linked twice by a crossover junction) to create two-dimensional DNA crystals [237]. These methods were shown to be useful in the creation of regular structures.

Mirkin et al. [251] and Alivisatos et al. [252] were among the first to link nanoparticles together using DNA. Mirkin et al. attached two different oligonucleotides to different 13 nm gold particles using a thiol group [251]. Upon addition of a duplex DNA with two "sticky ends," each complementary to one of the oligonucleotides, the gold particles were networked together. Mirkin et al. found the formation of ordered 2D networks of the gold particles. If heated above the dissociation temperature of the DNA duplex, the process could be reversed. This method allows for the assembly of structures with a wide range of parameters (e.g., nanoparticle spacing, size, and composition) [276–278]. Park et al. measured the conductivity of these gold nanoparticle networks [279] and found semiconducting behavior regardless of the length of the DNA linker. This was attributed to collapse of the network upon drying. Mucic et al. even assembled binary networks of gold nanoparticles with two different sizes [276]. A similar method to those just described was extended to other types of nanoparticles as well [277].

Alivisatos et al. assembled 1.4 nm gold particles with one N-propylmaleimide attached [252]. This maleimido group could be coupled to a sulphydryl group on an oligonucleotide. Adding a single-stranded DNA as a template, these oligonucleotide substituents formed the corresponding duplex DNA. With this method, Alivisatos et al. were able to create well spaced gold particles along the DNA template.

Niemeyer et al. used streptavidin as a model particle to which only a few biotinylated DNA molecules can bind [280]. These researchers found that by changing the ionic conditions, the streptavidin–DNA network changes. Under ionic conditions, double-stranded DNA condensed into supercoils (i.e., the double helix axis is itself twisted). This caused the contour length of the DNA to decrease, thereby bringing bound streptavidin closer together, hence changing the topology of the networks. Transition in the structure of DNA is a mechanism behind nanomechanical devices based on DNA [243, 244, 249].

Dwyer et al. functionalized carbon nanotubes with DNA [281]. Open-ended, single-walled carbon nanotubes with terminal carboxylic acid groups were reacted with amino-terminated DNA strands. This reaction covalently attached the DNA to the nanotube. Exploiting DNA's self-assembly properties, these functionalized nanotubes could be assembled onto surfaces or into structured networks.

Another approach to build functional devices has relied on the modification of semiconductor surfaces with DNA. These modified surfaces can then be used to fabricate nanoscale electronic devices [282, 283]. Pike et al., for instance, used photolithography and anodic etching on a silicon surface with a carbon monolayer to attach double-stranded DNA in an organized manner [282]. However, a good electrical contact between the DNA and the surface has yet to be established.

Demers et al. used "dip-pen nanolithography" to pattern DNA on a gold surface and on a silicon oxide surface [284]. Dip-pen nanolithography consists of a silanized AFM tip, which is dipped into a "DNA ink" (i.e., a solution of 90% dimethyl-formamide/10% water containing 1 mM DNA and 0.3 M $MgCl_2$). The "AFM pen" is then used to directly "write" the DNA onto the surfaces. The DNA used consisted of hexanethiol-modified oligonucleotides. In one case, dip-pen nanolithography was used to "write" DNA onto a gold surface, where the thiol group adsorbs onto the surface [284]. The surface was then placed into a solution containing an alkane-thiol, which protects the surface from adsorption of other elements, (e.g., nanoparticles). The DNA-patterned gold surface was then used to assemble DNA modified gold nanoparticles. One benefit of this method is the ability to write patterns on the surface with different oligonucleotides, which can then be used to assemble more complicated structures. Another benefit is the ability to vary the feature size by varying the experimental conditions while writing to the surface. A change in humidity of 15% was found to change the size of the DNA spot six times [284]. Demers et al. also used this method to pattern DNA on a silicon oxide surface [284]. Here, an oxidized silicon wafer was activated by treatment with 3′-mercaptopropyltrimethoxysilane. The DNA in the "DNA ink" was an oligonucleotide modified with an acrylamide group, which reacts with the silane on the silicon surface. Finally, protection of the rest of the silicon surface was done by reaction with acrylic acid.

We conclude this section by noting that although functional nanoparticle networks for nanoscale electronics have yet to be demonstrated using DNA assembly, rapid progress in this area suggests that such goal is not so difficult to achieve. For instance, an aspect of this research that has yet to be developed, but which shows great potential for applications, is the assembly of magnetic nanoparticles using DNA. Assembling nanoparticles with coercivity large enough to maintain their magnetization at room temperature would constitute a considerable advancement in creating self-assembled nanoscale memory devices.

5. CONCLUSIONS

We have reviewed the transport properties of DNA with particular emphasis on its possible use in nanoscale electronics. DNA shows a large number of conducting properties due the large phase space in which it can be made and assembled. The physical interpretation of these properties is not completely clear yet. Notwithstanding this, DNA is already occupying an important place in nanoscale science due to its self-assembly and recognition properties. The different functional properties of this important biological molecule promise to find practical use in many electronic applications that have yet to be completely explored at the nanoscale.

GLOSSARY

Deoxyribonucleic acid (DNA) A macromolecule made of four different monomers. Each monomer unit, called a nucleotide, consists of a phosphate group, a five-carbon sugar, and one of four bases.

Fluorescence The emission of light by a substance immediately after the absorption of energy from light of usually shorter wavelength.

Molecular lithography The use of information stored in a molecular structure to direct the formation of patterned assemblies at the nanoscale.

Self-assembly Coordination of several entities to form a larger structure (e.g., the coordination of molecules and a gold surface to form a layer of molecules on that surface).

Sequential tunneling A mechanism of charge transport through a series of energy barriers. Each barrier is transversed by tunneling, and the carrier wavefunction looses all or part of its coherence before it transverses the next barrier.

Thermal hopping A mechanism of charge transport which relies on thermal excitation of charge carriers to give them the required energy to transverse an energy barrier.

Tunneling A mechanism of charge transport which relies on the quantum mechanical nature of charge carriers that allows particles to transverse an energy barrier at a lower energy than the barrier itself.

ACKNOWLEDGMENTS

REFERENCES

1. J. D. Watson and F. H. C. Crick, *Nature* (*London*) 171, 737 (1953).
2. S. Steenken, *Chem. Rev.* 89, 503 (1989).
3. E. D. A. Stemp, M. R. Arkin, and J. K. Barton, *J. Am. Chem. Soc.* 119, 2921 (1997).
4. D. B. Hall and J. K. Barton, *J. Am. Chem. Soc.* 119, 5045 (1997).
5. M. R. Arkin, E. D. A. Stemp, S. C. Pulver, and J. K. Barton, *Chem. Biol.* 4, 389 (1997).
6. D. T. Breslin, J. E. Coury, J. R. Anderson, L. McFail-Isom, Y. Kan, L. D. Williams, L. A. Bottomley, and G. B. Schuster, *J. Am. Chem. Soc.* 119, 5043 (1997).
7. W. Chen, C. Turro, L. A. Friedman, J. K. Barton, and N. J. Turro, *J. Phys. Chem. B* 101, 6995 (1997).
8. B. Demple and L. Harrison, *Annu. Rev. Biochem.* 63, 915 (1994).
9. S. Loft and H. E. Poulsen, *J. Mol. Med.* 74, 297 (1996).
10. V. Guallar, A. Douhal, M. Moreno, and J. M. Lluch, *J. Phys. Chem. A* 103, 6251 (1999).

11. S. Steenken, *Biol. Chem.* 378, 1293 (1997).

12. H. L. Chen and P. Yang, *Progr. Chem.* 14, 239 (2002).

13. A. Heller, *Faraday Discuss.* 116, 1 (2000).

14. D. R. Meldrum and M. R. Holl, *Science* 297, 1197 (2002).

15. T. A. Taton, C. A. Mirkin, and R. L. Letsinger, *Science* 289, 1757 (2000).

16. C. V. Kumar, E. H. A. Punzalan, and W. B. Tan, *Tetrahedron* 56, 7027 (2000).

17. J. J. Kasianowicz, E. Brandin, D. Branton, and D. W. Deamer, *Proc. Nat. Acad. Sci. USA* 93, 13770 (1996).

18. W. Vercoutere, S. Winters-Hilt, H. Olsen, D. Deamer, D. Haussler, and M. Akeson, *Nature Biotechnol.* 19, 258 (2001).

19. J. Li, D. Stein, C. McMullan, D. Branton, M. J. Aziz, and J. A. Golovchenko, *Nature* (*London*) 412, 166 (2001).

20. A. Meller, L. Nivon, and D. Branton, *Phys. Rev. Lett.* 86, 3435 (2001).

21. R. H. Terbrueggen, T. W. Johann, and J. K. Barton, *Inorg. Chem.* 37, 6874 (1998).

22. T. W. Johann and J. K. Barton, *Philos. Trans. Roy. Soc. London Ser. A* 354, 299 (1996).

23. D. Wemmer, *Annu. Rev. Biophys. Biomol. Struct.* 29, 439 (2000).

24. D. Wemmer, *Nat. Struct. Biol.* 5, 169 (1998).

25. A. Marziali and M. A. Akeson, *Annu. Rev. Biomed. Eng.* 3, 195 (2001).

26. A. Marshall and J. Hodgson, *Nature Biotechnol.* 16, 27 (1998).

27. S. O. Kelley, N. M. Jackson, M. G. Hill, and J. K. Barton, *Angew. Chem., Int. Ed.* 38, 941 (1999).

28. F. Lisdat, B. Ge, and F. W. Scheller, *Electrochem. Commun.* 1, 65 (1999).

29. F. Lisdat, B. Ge, B. Krause, A. Ehrlich, H. Bienert, and F. W. Scheller, *Electroanal.* 13, 1225 (2001).

30. J. J. Gooding, *Electroanal.* 14, 1149 (2002).

31. S. Kumamoto, H. Nakano, Y. Matsuo, Y. Sugie, and K. Yamana, *Electrochemistry* 70, 789 (2002).

32. E. M. Boon, J. K. Barton, P. I. Pradeepkumar, J. Isaksson, C. Petit, and J. Chattopadhyaya, *Angew. Chem., Int. Ed.* 41, 3402 (2002).

33. A. Erdem and M. Ozsoz, *Electroanal.* 14, 965 (2002).

34. R. P. Fahlman and D. Sen, *J. Am. Chem. Soc.* 124, 4610 (2002).

35. M. J. Heller, *Annu. Rev. Biomed. Eng.* 4, 129 (2002).

36. C. Dekker and M. A. Ratner, *Phys. World* 14, 29 (2001).

37. S. F. Nelson, Y.-Y. Lin, D. J. Gundlach, and T. N. Jackson, *Appl. Phys. Lett.* 72, 1854 (1998).

38. W. A. Schoonveld, J. Vrijmoeth, and T. M. Klapwijk, *Appl. Phys. Lett.* 73, 3884 (1998).

39. A. M. van de Craats, L. D. A. Siebbeles, I. Bleyl, D. Haarer, Y. A. Berlin, A. A. Zharikov, and J. M. Warman, *J. Phys. Chem. B* 102, 9625 (1998).

40. H. McConnel, *J. Chem. Phys.* 35, 508 (1961).

41. D. D. Eley and D. I. Spivey, *Trans. Faraday Soc.* 58, 411 (1962).

42. R. S. Snart, *Trans. Faraday Soc.* 59, 754 (1963).

43. H. Pohl and W. Kauzman, *Rev. Mod. Phys.* 36, 721 (1963).

44. T. A. Hoffmann and J. Ladik, *Advan. Chem. Phys.* 7, 84 (1964).

45. C. T. O'Konski, P. Moser, and M. Shirai, *Biopolymers*, Symp. No. 1, 479 (1964).

46. R. S. Snart, *Biopolymers* 6, 293 (1968).

47. B. B. Singh, *Adv. Med. Phys.* 12, 245 (1968).

48. J. Ladik, *Int. J. Quant. Chem.* 3S, 307 (1971).

49. S. Suhai, *J. Chem. Phys.* 57, 5599 (1972).

50. M. F. Lecompte, D. Muller, and M. Josefowicz, *Biopolymers* 11, 2563 (1972).

51. D. Dee and M. E. Baur, *J. Chem. Phys.* 60, 541 (1974).

52. R. Pethig, "Dielectric and Electronic Properties of Biological Materials." Wiley, New York, 1979.

53. B. C. Baguley and M. Lebret, *Biochemistry* 23, 937 (1984).

54. C. V. Kumar, J. K. Barton, and N. J. Turro, *J. Am. Chem. Soc.* 107, 5518 (1985).

55. P. Fromherz and B. Rieger, *J. Am. Chem. Soc.* 108, 5361 (1986).

56. J. K. Barton, C. V. Kumar, and N. J. Turro, *J. Am. Chem. Soc.* 108, 6391 (1986).

57. J. D. Magan, W. Blau, D. T. Croke, D. J. McConnell, and J. M. Kelley, *Chem. Phys. Lett.* 141, 489 (1987).

58. D. D. Eley, *Mol. Cryst. Liquid Cryst.* 171, 1 (1989).

59. A. M. Brun and A. Harriman, *J. Am. Chem. Soc.* 114, 3656 (1992).

60. Y. Lee, H. H. Heasley, J. A. Thompson, K. Murata, B. M. Hoffman, T. M. Haard, P. J. Hamot, W. P. Halperin, and P. Wölfle, *Europhys. Lett.* 36, 681 (1996).

61. A. M. van de Craats, J. M. Warman, M. P. de Haas, D. Adam, J. Simmerer, D. Haarer, and P. Schuhmacher, *Adv. Mater.* 8, 823 (1996).

62. A. M. van de Craats, P. G. Schouten, and J. M. Warman, *Ekisho* 2, 12 (1998).

63. A. M. van de Craats and J. M. Warman, *Adv. Mater.* 13, 130 (2001).

64. P. G. Schouten, J. M. Warman, M. P. de Haas, M. A. Fox, and H. L. Pan, *Nature* (*London*) 353, 736 (1991).

65. P. G. Schouten, J. M. Warman, M. P. de Haas, J. F. van der Pol, and J. W. Zwikker, *J. Am. Chem. Soc.* 114, 9028 (1992).

66. C. J. Murphy, M. R. Arkin, Y. Jenkins, N. D. Ghatlia, S. H. Bossmann, N. J. Turro, and J. K. Barton, *Science* 262, 1025 (1993).

67. Y. Okahata, T. Kobayashi, K. Tanaka, and M. Shimomura, *J. Am. Chem. Soc.* 120, 6165 (1998).

68. C. J. Burrows and J. G. Muller, *Chem. Rev.* 98, 1109 (1998).

69. J. Cadet, in "DNA Adducts: Identification and Significance" (K. Hemminki, A. Dipple, D. E. F. Shiker, F. F. Kadlubar, D. Segerback, and H. Bartsch, Eds.). IARC, Lyon, France, 1994.

70. M. R. Arkin, E. D. A. Stemp, R. E. Holmlin, J. K. Barton, A. Hörmann, E. J. C. Olson, and P. F. Barbara, *Science* 273, 475 (1996).

71. S. O. Kelley and J. K. Barton, *Science* 273, 475 (1996).

72. T. J. Meade and J. F. Kayyem, *Angew. Chem. Int. Ed. Engl.* 34, 352 (1995).

73. F. D. Lewis, T. Wu, Y. Zhang, R. L. Letsinger, S. R. Greenfield, and M. R. Wasielewski, *Science* 277, 673 (1997).

74. S. O. Kelley, R. E. Holmlin, E. D. A. Stemp, and J. K. Barton, *J. Am. Chem. Soc.* 119, 9861 (1997).

75. E. Meggers, M. E. Michel-Beyerle, and B. Giese, *J. Am. Chem. Soc.* 120, 12950 (1998).

76. S. O. Kelley and J. K. Barton, *Chem. Biol.* 5, 413 (1998).

77. K. Fukui and K. Tanaka, *Angew. Chem. Int. Ed. Engl.* 37, 158 (1998).

78. S. O. Kelley and J. K. Barton, *Science* 283, 375 (1999).

79. S. Priyadarshy, S. M. Risser, and D. N. Beratan, *J. Phys. Chem.* 100, 17678 (1996).

80. A. K. Felts, W. T. Pollard, and R. A. Friesner, *J. Phys. Chem.* 99, 2929 (1995).

81. A. Okada, V. Chernyak, and S. Mukamel, *J. Phys. Chem. A* 102, 1241 (1998).

82. T. L. Netzel, in "Organic and Inorganic Photochemistry" (V. Ramamurthy and K. S. Schanze, Eds.), Dekker, New York, 1998, pp. 1–54.

83. M. Ratner, *Nature* (*London*) 397, 480 (1999).

84. P. J. Dandliker, R. E. Holmlin, and J. K. Barton, *Science* 275, 1465 (1997).

85. D. B. Hall, R. E. Holmlin, and J. K. Barton, *Nature* (*London*) 382, 731 (1996).

86. C. Wan, T. Fiebig, S. O. Kelley, C. R. Treadway, J. K. Barton, and A. H. Zewail, *Proc. Natl. Acad. Sci. USA* 96, 6014 (1999).

87. S. M. Gasper and G. B. Schuster, *J. Am. Chem. Soc.* 119, 12762 (1997).

88. G. Taubes, *Science* 275, 1420 (1997).

89. J. M. Warman, M. P. de Haas, and A. Rupprecht, *Chem. Phys. Lett.* 249, 319 (1996).

90. T. Fiebig, C. Wan, S. O. Kelley, J. K. Barton, and A. H. Zewail, *Proc. Natl. Acad. Sci. USA* 96, 1187 (1999).

91. C. Wan, T. Fiebig, O. Schiemann, J. K. Barton, and A. H. Zewail, *Proc. Natl. Acad. Sci. USA* 97, 14052 (1999).

92. Y. Okahata, T. Kobayashi, H. Nakayama, and K. Tanaka, *Supramol. Sci.* 5, 317 (1998).

93. D. Dunlap, R. Garcia, E. Schabtach, C. Bustamante, *Proc. Natl. Acad. Sci. USA* 90, 7652 (1993).

94. R. Guckenberger, M. Heim, G. Cevc, H. F. Knapp, W. Wiegrabe, and A. Hillebrand, *Science* 266, 1538 (1994).

95. R. P. Fahlman, R. D. Charma, and D. Sen, *J. Am. Chem. Soc.* 124, 12477 (2002).

96. S. Priyadarshy, S. M. Risser, and D. N. Beratan, *J. Biol. Inorg. Chem.* 3, 196 (1998).

97. N. J. Turro and J. K. Barton, *J. Biol. Inorg. Chem.* 3, 201 (1998).

98. T. L. Netzel, *J. Biol. Inorg. Chem.* 3, 210 (1998).

99. F. D. Lewis and R. L. Letsinger, *J. Biol. Inorg. Chem.* 3, 215 (1998).

100. E. S. Krider and T. J. Meade, *J. Biol. Inorg. Chem.* 3, 222 (1998).

101. E. Braun, Y. Eichen, U. Sivan, and G. Ben-Yoseph, *Nature* (*London*) 391, 775 (1998).

102. J. Richter, M. Mertig, W. Pompe, I. Monch, and H. K. Schackert, *Appl. Phys. Lett.* 78, 536 (2001).

103. J. J. Storhoff and C. A. Mirkin, *Chem. Rev.* 99, 1849 (1999).

104. P. S. Weiss, *Nature* (*London*) 413, 585 (2001).

105. T. Yokoyama, S. Yokoyama, T. Kamikado, Y. Okuno, and S. Mashiko, *Nature* (*London*) 413, 619 (2001).

106. C. M. Niemeyer, *Curr. Opin. Chem. Biol.* 4, 609 (2000).

107. C. M. Niemeyer, *Angew. Chem., Int. Ed.* 40, 4128 (2001).

108. S. Mann, *Nature* (*London*) 365, 499 (1993).

109. W. Shenton, S. A. Davis, and S. Mann, *Adv. Mater.* 11, 449 (1999).

110. R. Kirsch, M. Mertig, W. Pompe, R. Wahl, G. Sadowski, K. J. Bohm, and E. Unger, *Thin Solid Films* 305, 248 (1997).

111. M. Mertig, R. Kirsch, W. Pompe, and H. Engelhardt, *Eur. Phys. J. D* 9, 45 (1999).

112. R. Wahl, M. Mertig, W. Pompe, S. Selenska-Pobell, and J. Raffi, *Adv. Mater.* 13, 736 (2001).

113. U. B. Sleytr, M. Sara, D. Pum, and B. Schuster, *Progr. Surf. Sci.* 68, 231 (2001).

114. S.-W. Lee, C. Mao, C. E. Flynn, and A. M. Belcher, *Science* 296, 892 (2002).

115. A. M. Brun and A. Harriman, *J. Am. Chem. Soc.* 116, 10383 (1994).

116. A. Harriman, *Angew. Chem. Int. Ed.* 38, 945 (1999).

117. P. Lincoln, E. Tuite, and B. Norden, *J. Am. Chem. Soc.* 119, 1454 (1997).

118. E. J. C. Olson, D. Hu, A. Hörmann, and P. F. Barbara, *J. Phys. Chem. B* 101, 299 (1997).

119. B. Giese, *Annu. Rev. Biochem.* 71, 51 (2002).

120. E. M. Boon and J. K. Barton, *Curr. Opin. Struc. Biol.* 12, 320 (2002).

121. P. T. Henderson, D. Jones, G. Hampikian, Y. Kan, and G. B. Schuster, *Proc. Nat. Acad. Sci. USA* 96, 8353 (1999).

122. A. A. Voityuk, J. Jortner, M. Bixon, and N. Rosch, *Chem. Phys. Lett.* 324, 430 (2000).

123. B. Giese, J. Amaudrut, A.-K. Kohler, M. Spormann, and S. Wessely, *Nature* (*London*) 412, 318 (2001).

124. T. T. Williams, D. T. Odom, and J. K. Barton, *J. Am. Chem. Soc.* 122, 9048 (2000).

125. V. Sartor, E. Boone, and G. B. Schuster, *J. Phys. Chem. B* 105, 11057 (2001).

126. C. Gómez-Navarro, A. Gil, M. Álvarez, P. J. de Pablo, F. Moreno-Herrero, I. Horcas, R. Fernańdez-Sánchez, J. Colchero, J. Gómez Herrero, and A. M. Baró, *Nanotechnology* 13, 314 (2002).

127. A. Gil, P. J. de Pablo, J. Colchero, J. Gómez Herrero, and A. M. Baró, *Nanotechnology* 13, 309 (2002).

128. C. Gómez-Navarro, F. Moreno-Herrero, P. J. de Pablo, J. Colchero, J. Gómez Herrero, and A. M. Baró, *Proc. Nat. Acad. Sci. USA* 99, 8484 (2002).

129. M. Bockrath, N. Markovic, A. Shepard, M. Tinkham, L. Gurevich, L. P. Kouwenhoven, M. W. Wu, and L. L. Sohn, *Nano Lett.* 2, 187 (2002).

130. P. Tran, B. Alavi, and G. Gruner, *Phys. Rev. Lett.* 85, 1564 (2000).

131. H.-W. Fink and C. Schonenberger, *Nature* (*London*) 398, 407 (1999).

132. H.-W. Fink, *Cell. Mol. Life Sci.* 58, 1 (2001).

133. H.-W. Fink, H. Schmid, E. Ermantraut, and T. Schulz, *J. Opt. Soc. Am. A* 14, 2168 (1997).

134. P. J. de Pablo, F. Moreno-Herrero, J. Colchero, J. Gómez Herrero, P. Herrero, A. M. Baró, P. Ordejón, J. M. Soler, and E. Artacho, *Phys. Rev. Lett.* 85, 4992 (2000).

135. D. Porath, A. Bezryadin, S. de Vries, and C. Dekker, *Nature* (*London*) 403, 635 (2000).

136. A. Bezryadin and C. Dekker, *J. Vac. Sci. Technol. B* 15, 793 (1997).

137. A. Bezryadin, C. Dekker, and G. Schmid, *Appl. Phys. Lett.* 71, 1273 (1997).

138. H. Watanabe, C. Manabe, T. Shigematsu, K. Shimotani, and M. Shimizu, *Appl. Phys. Lett.* 79, 2462 (2001).

139. J. S. Hwang, G. S. Lee, K. J. Kong, D. J. Ahn, S. W. Hwang, and D. Ahn, *Microelectron. Eng.* 63, 161 (2002).

140. J. S. Hwang, G. S. Lee, D. Ahn, G. S. Lee, D. J. Ahn, and S. W. Hwang, *Appl. Phys. Lett.* 81, 1134 (2002).

141. A. Yu. Kasumov and D. V. Klinov, private communication.

142. T. Muir, E. Morales, J. Root, I. Kumar, B. Garcia, C. Vellandi, D. Jenigian, T. Marsh, E. Henderson, and J. Vesenka, *J. Vac. Sci. Technol. A* 16, 1172 (1998).

143. A. J. Storm, J. van Noort, S. de Vries, and C. Dekker, *Appl. Phys. Lett.* 79, 3881 (2001).

144. K.-H. Yoo, D. H. Ha, J.-O Lee, J. W. Park, J. Kim, J. J. Kim, H.-Y. Lee, T. Kawai, and H. Y. Choi, *Phys. Rev. Lett.* 87, 198102 (2001).

145. H. Böttger and V. V. Bryksin, "Hopping Conduction in Solids." Akademie-Verlag, Berlin, 1985.

146. A. Yu. Kasumov, M. Kociak, S. Guéron, B. Reulet, V. T. Volkov, D. V. Klinov, and H. Bouchiat, *Science* 291, 280 (2001).

147. L. Cai, H. Tabata, and T. Kawai, *Appl. Phys. Lett.* 77, 3105 (2000).

148. T. Kanno, H. Tanaka, N. Miyoshi, and T. Kawai, *Jpn. J. Appl. Phys. 1* 39, 269 (2000).

149. T. Kanno, H. Tanaka, N. Miyoshi, and T. Kawai, *Appl. Phys. Lett.* 77, 3848 (2000).

150. T. Kanno, H. Tanaka, N. Miyoshi, M. Fukuda, and T. Kawai, *Jpn. J. Appl. Phys. 1* 39, 1892 (2000).

151. Y. Zhang, R. H. Austin, J. Kraeft, E. C. Cox, and N. P. Ong, *Phys. Rev. Lett.* 89, 198102 (2002).

152. K. W. Hipps, *Science* 294, 536 (2001).

153. X. D. Cui, A. Primak, X. Zarate, J. Tomfohr, O. F. Sankey, A. L. Moore, T. A. Moore, D. Gust, G. Harris, and S. M. Lindsay, *Science* 294, 571 (2001).

154. D. H. Ha, H. Nham, K.-H. Yoo, H. So, H.-Y. Lee, and T. Kawai, *Chem. Phys. Lett.* 355, 405 (2002).

155. H.-Y. Lee, H. Tanaka, Y. Otsuka, K.-H. Yoo, J.-O. Lee, and T. Kawai, *Appl. Phys. Lett.* 80, 1670 (2002).

156. D. N. Beratan, S. Priyadarshy, and S. M. Risser, *Chem. Biol.* 4, 3 (1997).

157. V. M. Orlov, A. M. Smirnov, and Y. M. Varshavsky, *Tetrahedron Lett.* 48, 4377 (1976).

158. C. A. M. Seidel, A. Schultz, and M. H. M. Sauer, *J. Phys. Chem.* 100, 5541 (1996).

159. S. Steenken and S. C. Jovanovic, *J. Am. Chem. Soc.* 119, 617 (1997).

160. N. S. Hush and A. S. Cheung, *Chem. Phys. Lett.* 34, 11 (1975).

161. H. Sugiyama and I. Saito, *J. Am. Chem. Soc.* 118, 7063 (1996).

162. I. Saito, T. Nakamura, K. Nakatani, Y. Yoshioka, K. Yamaguchi, and H. Sugiyama, *J. Am. Chem. Soc.* 120, 12686 (1998).

163. A.-O. Colson, B. Besler, M. D. Close, and M. D. Sevilla, *J. Phys. Chem.* 96, 661 (1992).

164. A.-O. Colson, B. Besler, and M. D. Sevilla, *J. Phys. Chem.* 96, 9787 (1992).

165. M. D. Sevilla, B. Besler, and A.-O. Colson, *J. Phys. Chem.* 99, 1060 (1995).

166. M. Hutter and T. Clark, *J. Am. Chem. Soc.* 118, 7574 (1996).
167. N. S. Kim and P. R. LeBreton, *J. Am. Chem. Soc.* 118, 3694 (1996).
168. H. Fernando, G. A. Papadantonakis, N. S. Kim, and P. R. LeBreton, *Proc. Natl. Acad. Sci. USA* 95, 5550 (1998).
169. F. Prat, K. N. Houk, and C. S. Foote, *J. Am. Chem. Soc.* 120, 845 (1998).
170. W. B. Davis, M. R. Wasielewski, M. A. Ratner, V. Mujica, and A. Nitzan, *J. Phys. Chem. A* 101, 6158 (1997).
171. Y. A. Berlin, A. L. Burin, and M. A. Ratner, *J. Phys. Chem. A* 104, 443 (2000).
172. Y. A. Berlin, A. L. Burin, and M. A. Ratner, *J. Am. Chem. Soc.* 123, 260 (2001).
173. Y. A. Berlin, A. L. Burin, L. D. A. Siebbeles, and M. A. Ratner, *J. Phys. Chem. A* 105, 5666 (2001).
174. Y. A. Berlin, A. L. Burin, and M. A. Ratner, *Chem. Phys.* 275, 61 (2002).
175. F. C. Grozema, L. D. A. Siebbeles, Y. A. Berlin, and M. A. Ratner, *Chem. Phys. Chem.* 3, 536 (2002).
176. Y. A. Berlin, A. L. Burin, and M. A. Ratner, *Superlattice Microstruct.* 28, 241 (2000).
177. X. Li and Y. Yan, *J. Chem Phys.* 115, 4169 (2001).
178. X. Li, H. Y. Zhang, and Y. Yan, *J. Phys. Chem. A* 105, 9563 (2001).
179. X. Li and Y. Yan, *Appl. Phys. Lett.* 79, 2190 (2001).
180. Y. Yan and H. Y. Zhang, *J. Theoretical Computational Chem.* 1, 225 (2002).
181. X. Y. Yu, H. Y. Zhang, P. Han, X. Li, and Y. Yan, *J. Chem. Phys.* 117, 2180 (2002).
182. J. Jortner, M. Bixon, T. Langenbacher, and M. E. Michel-Beyerle, *Proc. Natl. Acad. Sci. USA* 95, 12759 (1998).
183. M. Bixon, B. Giese, S. Wessely, T. Langenbacher, M. E. Michel-Beyerle, and J. Jortner, *Proc. Natl. Acad. Sci. USA* 96, 11713 (1999).
184. M. Bixon and J. Jortner, *J. Adv. Chem. Phys.* 106, 35 (1999).
185. M. Bixon and J. Jortner, *J. Phys. Chem. B* 104, 3906 (2000).
186. J. Jortner, M. Bixon, A. Voityuk, and N. Rösch, *J. Phys. Chem. A* 106, 7599 (2002).
187. A. A. Voityuk, N. Rösch, M. Bixon, and J. Jortner, *J. Phys. Chem. B* 104, 9740 (2000).
188. F. C. Grozema, Y. A. Berlin, and L. D. A. Siebbeles, *Int. J. Quantum Chem.* 75, 1009 (1999).
189. F. C. Grozema, Y. A. Berlin, and L. D. A. Siebbeles, *J. Am. Chem. Soc.* 122, 10903 (2000).
190. Y.-J. Ye, R. S. Chen, A. Martinez, P. Otto, and J. Ladik, *Solid State Commun.* 112, 139 (1999).
191. Y.-J. Ye, R. S. Chen, F. Chen, J. Sun, and J. Ladik, *Solid State Commun.* 119, 175 (2001).
192. L. Shen, Y.-J. Ye, and J. Ladik, *Solid State Commun.* 121, 35 (2002).
193. G. Brunaud, F. Castet, A. Fritsch, and L. Ducasse, *Phys. Chem. Chem. Phys.* 4, 6072 (2002).
194. D. Bicout and E. Kats, *Phys. Lett. A* 300, 479 (2002).
195. B. Giese, S. Wessely, M. Spormann, U. Lindemann, E. Meggers, and M. E. Michel-Beyerle, *Angew. Chem. Int. Ed.* 38, 996 (1999).
196. R. Bruinsma, G. Gruner, M. R. D. Orsogna, and J. Rudnick, *Phys. Rev. Lett.* 85, 4393 (2000).
197. E. W. Schlag, D.-Y. Yang, S.-Y. Sheu, H. L. Selzle, S. H. Lin, and P. M. Rentzepis, *Proc. Nat. Acad. Sci. USA* 97, 9849 (2000).
198. A. Voityuk, K. Siriwong, and N. Rösch, *Phys. Chem. Chem. Phys.* 3, 5421 (2001).
199. S. Komineas, G. Kalosakas, and A. R. Bishop, *Phys. Rev. E* 65, 061905-1 (2002).
200. W. Zhang, A. O. Govorov, and S. E. Ulloa, *Phys. Rev. B* 66, 060303(R) (2002).
201. Z. G. Yu and X. Song, *Phys. Rev. Lett.* 86, 6018 (2001).
202. R. G. Endres, D. L. Cox, R. R. P. Singh, and S. K. Pati, *Phys. Rev. Lett.* 88, 166601-1 (2002).
203. M. Zwolak and M. Di Ventra, *Appl. Phys. Lett.* 81, 925 (2002).
204. A. Yu. Kasumov, private communication.
205. G. Cuniberti, L. Craco, D. Porath, and C. Dekker, *Phys. Rev. B* 65, 241314(R) (2002).
206. D. Ly, Y. Kan, B. Armitage, and G. B. Schuster, *J. Am. Chem. Soc.* 118, 8747 (1996).
207. D. Ly, L. Sanii, and G. B. Schuster, *J. Am. Chem. Soc.* 121, 9400 (1999).
208. G. B. Schuster, *Acc. Chem. Res.* 33, 253 (2000).
209. B. Armitage, D. Ly, T. Koch, H. Frydenlund, H. Orum, H. G. Batz, and G. B. Schuster, *Proc. Natl. Acad. Sci. USA* 94, 12320 (1997).
210. E. M. Conwell and S. V. Rakhmanova, *Proc. Nat. Acad. Sci. USA* 97, 4556 (2000).
211. S. V. Rakhmanova and E. M. Conwell, *J. Phys. Chem. B* 105, 2056 (2001).
212. S. V. Rakhmanova and E. M. Conwell, *Appl. Phys. Lett.* 75, 1518 (1999).
213. V. D. Lakhno, *J. Biol. Phys.* 26, 133 (2000).
214. Z. Hermon, S. Caspi, and E. Ben-Jacob, *Europhys. Lett.* 43, 482 (1998).
215. E. B. Brauns, M. L. Madaras, R. S. Coleman, C. J. Murphy, and M. A. Berg, *J. Am. Chem. Soc.* 121, 11644 (1999).
216. Z. Liang, J. H. Freed, R. S. Keyes, and A. M. Bobst, *J. Phys. Chem. B* 104, 5372 (2000).
217. P. N. Borer, S. R. Pante, A. Kumar, N. Zanatta, A. Martin, A. Hakkinen, and G. C. Levy, *Biochemistry* 33, 2441 (1994).
218. R. N. Barnett, C. L. Cleveland, A. Joy, U. Landman, and G. B. Schuster, *Science* 294, 567 (2001).
219. M. Hjort and S. Stafstrom, *Phys. Rev. Lett.* 87, 228101 (2001).
220. Y. Eichen, E. Braun, U. Sivan, and G. Ben-Yoseph, *Acta Polym.* 49, 663 (1998).
221. W. Pompe, M. Mertig, R. Kirsch, R. Wahl, L. C. Ciacchi, J. Richter, R. Seidel, and H. Vinzelberg, *Z. Metallkd.* 90, 1085 (1999).
222. J. Richter, R. Seidel, R. Kirsch, M. Mertig, W. Pompe, J. Plaschke, and H. K. Schackert, *Adv. Mater.* 12, 507 (2000).
223. J. Richter, *Physica E*, in press
224. J. Richter, M. Mertig, W. Pompe, and H. Vinzelberg, *Appl. Phys. A* 74, 725 (2002).
225. O. Harnack, W. E. Ford, A. Yasuda, and J. M. Wessels, *Nano Lett.* 2, 919 (2002).
226. W. E. Ford, O. Harnack, A. Yasuda, and J. M. Wessels, *Adv. Mater.* 13, 1793 (2001).
227. F. Patolsky, Y. Weizmann, O. Lioubashevski, and I. Willner, *Angew. Chem. Int. Ed.* 41, 2323 (2002).
228. M. Mertig, L. C. Ciacchi, R. Seidel, W. Pompe, and A. De Vita, *Nano Lett.* 2, 841 (2002).
229. A. Kumar, M. Pattarkine, M. Bhadbhade, A. B. Mandale, K. N. Ganesh, S. S. Datar, C. V. Dharmadhikari, and M. Sastry, *Adv. Mater.* 13, 341 (2001).
230. M. Sastry, A. Kumar, S. Datar, C. V. Dharmadhikari, and K. N. Ganesh, *Appl. Phys. Lett.* 78, 2943 (2001).
231. A. Rakitin, P. Aich, C. Papadopoulos, Yu. Kobzar, A. S. Vedeneev, J. S. Lee, and J. M. Xu, *Phys. Rev. Lett.* 86, 3670 (2001).
232. P. Aich, S. L. Labiuk, L. W. Tari, L. J. T. Delbaere, W. J. Roesler, K. J. Falk, R. P. Steer, and J. S. Lee, *J. Mol. Biol.* 294, 477 (1999).
233. J. S. Lee, L. J. P. Latimer, and R. S. Reid, *Biochem. Cell Biol.* 71, 162 (1993).
234. P. Aich, H. B. Kraatz, and J. S. Lee, *J. Biomol. Struct. Dyn., Sp. Iss.* S2, 297 (2000).
235. P. Aich, R. J. S. Skinner, S. D. Wettig, R. P. Steer, and J. S. Lee, *J. Biomol. Struct. Dyn.* 20, 93 (2002).
236. E. Ben-Jacob, Z. Hermon, and S. Caspi, *Phys. Lett. A* 263, 199 (1999).
237. E. Winfree, F. Liu, L. A. Wenzler, and N. C. Seeman, *Nature (London)* 394, 539 (1998).
238. C. Mao, W. Sun, and N. C. Seeman, *J. Am. Chem. Soc.* 121, 5437 (1999).

239. F. Liu, R. Sha, and N. C. Seeman, *J. Am. Chem. Soc.* 121, 917 (1999).
240. C. Mao, W. Sun, and N. C. Seeman, *Nature* (*London*) 386, 137 (1997).
241. J. Chen and N. C. Seeman, *Nature* (*London*) 350, 631 (1991).
242. C. Mao, T. H. LaBean, J. H. Reif, and N. C. Seeman, *Nature* (*London*) 407, 493 (2000).
243. C. Mao, W. Sun, Z. Shen, and N. C. Seeman, *Nature* (*London*) 397, 144 (1999).
244. B. Yurke, A. J. Turberfield, A. P. Mills, Jr., F. C. Simmel, and J. L. Neumann, *Nature* (*London*) 406, 605 (2000).
245. I. Willner and B. Willner, *Pure Appl. Chem.* 74, 1753 (2002).
246. M. Sastry, *Pure Appl. Chem.* 74, 1609 (2002).
247. C. J. Nulf and D. R. Corey, *Nucleic Acids Res.* 30, 2782 (2002).
248. D. L. Feldheim and C. D. Keating, *Chem. Soc. Rev.* 27, 1 (1998).
249. C. M. Niemeyer and M. Alder, *Angew. Chem. Int. Ed.* 41, 3779 (2002).
250. R. Bashir, *Superlattices Microstruct.* 29, 1 (2001).
251. C. A. Mirkin, R. L. Letsinger, R. C. Mucic, and J. J. Stofhoff, *Nature* (*London*) 382, 607 (1996).
252. A. P. Alivisatos, K. P. Johnson, T. E. Wilson, C. J. Loveth, M. P. Bruchez, and P. G. Schultz, *Nature* (*London*) 382, 609 (1996).
253. D. Bethell and D. J. Schiffrin, *Nature* (*London*) 382, 581 (1996).
254. Y. Shao, Y. Jin, and S. Dong, *Electrochem. Commun.* 4, 773 (2002).
255. C. M. Niemeyer, *Science* 297, 62 (2002).
256. M. Sastry, *Curr. Sci.* 79, 1089 (2000).
257. J. H. Fendler, *Chem. Mater.* 8, 1616 (1996).
258. S. Henrichs, C. P. Collier, R. J. Saykally, and J. R. Heath, *J. Am. Chem. Soc.* 122, 4077 (2000).
259. R. L. Whetten, J. T. Khoury, M. M. Alvarez, S. Murthy, I. Vezmar, Z. L. Wang, P. W. Stephens, C. L. Cleveland, W. D. Luedtke, and U. Landman, *Adv. Mater.* 8, 428 (1996).
260. J. Fink, C. S. Kiely, D. Bethell, and D. J. Schiffrin, *Chem. Mater.* 10, 922 (1998).
261. N. C. Seeman, *Annu. Rev. Biophys. Biomol. Struct.* 27, 225 (1998).
262. G. P. Lopinski, D. D. M. Wayner, and R. A. Wolkow, *Nature* (*London*) 406, 48 (2000).
263. R. H. Austin, J. P. Brody, E. C. Cox, K. Duke, and W. Volkmuth, *Phys. Today* 50, 32 (1997).
264. C. A. Mirkin and T. A. Taton, *Nature* (*London*) 405, 626 (2000).
265. J. L. Coffer, S. R. Bigham, X. Li, R. F. Pinizzotto, Y. G. Rho, R. M. Pirtle, and I. L. Pirtle, *Appl. Phys. Lett.* 69, 3851 (1996).
266. K. Keren, M. Krueger, R. Gilad, G. Ben-Yoseph, U. Sivan, and E. Braun, *Science* 297, 72 (2002).
267. J. K. N. Mbindyo, B. D. Reiss, B. R. Martin, C. D. Keating, M. J. Natan, and T. E. Mallouk, *Adv. Mater.* 13, 249 (2001).
268. S. J. Xiao, F. R. Liu, A. E. Rosen, J. F. Hainfeld, N. C. Seeman, K. Musier-Forsyth, and R. A. Kiehl, *J. Nanopart. Res.* 4, 313 (2002).
269. D. M. Hartmann, M. Heller, S. C. Esener, D. Schwartz, and G. Tu, *J. Mater. Res.* 17, 473 (2002).
270. J. L. Coffer, S. R. Bigham, R. F. Pinizzotto, and H. Yang, *Nanotechnology* 3, 69 (1992).
271. S. R. Bigham and J. L. Coffer, *Colloids Surf. A* 95, 211 (1995).
272. J. L. Coffer, *J. Cluster Sci.* 8, 159 (1997).
273. C. M. Niemeyer, W. Burger, and J. Peplies, *Angew. Chem. Int. Ed.* 37, 2265 (1998).
274. S.-J. Park, A. A. Lazarides, C. A. Mirkin, and R. L. Letsinger, *Angew. Chem. Int. Ed.* 40, 2909 (2001).
275. M. A. Batalia, E. Protozanova, R. B. Macgregor, and D. A. Erie, *Nano Lett.* 2, 269 (2002).
276. R. C. Mucic, J. J. Storhoff, C. A. Mirking, and R. L. Letsinger, *J. Am. Chem. Soc.* 120, 12674 (1998).
277. G. P. Mitchell, C. A. Mirkin, and R. L. Letsinger, *J. Am. Chem. Soc.* 121, 8122 (1999).
278. J. J. Storhoff, A. A. Lazarides, C. A. Mirkin, R. L. Letsinger, R. C. Mucic, and G. C. Schatz, *J. Am. Chem. Soc.* 122, 4640 (2000).
279. S.-J. Park, A. A. Lazarides, C. A. Mirkin, P. W. Brazis, C. R. Kannewurf, and R. L. Letsinger, *Angew. Chem. Int. Ed.* 39, 3845 (2000).
280. C. M. Niemeyer, M. Alder, S. Lenhert, S. Gao, H. Fuchs, and L. Chi, *Chem. Bio. Chem.* 2, 260 (2001).
281. C. Dwyer, M. Guthold, M. Falvo, S. Washburn, R. Superfine, and D. Erie, *Nanotechnology* 13, 601 (2002).
282. A. R. Pike, L. H. Lie, R. A. Eagling, L. C. Ryder, S. N. Patole, B. A. Connolly, B. R. Horrocks, and A. Houlton, *Angew. Chem. Int. Ed.* 41, 615 (2002).
283. A. Pike, B. Horrocks, B. Connolly, and A. Houlton, *Aust. J. Chem.* 55, 191 (2002).
284. L. M. Demers, D. S. Ginger, S.-J. Park, Z. Li, S.-W. Chung, and C. A. Mirkin, *Science* 296, 1836 (2002).

DNA-Based Nanodevices

Friedrich C. Simmel

Ludwig-Maximilians-Universität, Munich, Germany

Bernard Yurke

Bell Laboratories, Lucent Technologies, Murray Hill, New Jersey, USA

CONTENTS

1. INTRODUCTION

Molecular machines that convert chemical energy into mechanical motion are ubiquitous within the cells of living organisms [1, 2]. The way that these machines are used to carry out the functions of life provides clues for the ways that synthetic molecular machines might be used to advantage in analogous nanotechnology applications. Biological molecular motors are responsible for most of the motions exhibited by living organisms. They drive cilia and flagella and are responsible for muscle contraction. They also actively transport substances within cells. DNA replication itself is carried out by a complex of proteins that can be viewed as a sophisticated assembly machine, which performs its function with a very low error rate and even carries out proofreading and error-correction functions [3]. Considering these examples, one expects synthetic molecular motors to find use in aiding nanoscale assembly processes and in providing micro- and nanostructures with the ability to move.

The chemical energy that drives most known biological molecular motors is supplied by adenosine triphosphate (ATP) or guanosine triphosphate (GTP) hydrolysis, although other energy sources are also known to be used. For example, the bacterial flagellar motor is essentially an electrostatic motor driven by the energy that is extracted as protons are pushed through the motor by the electric field spanning the cell wall [4]. Nanotechnology applications may allow the use of molecular motors that employ mechanisms or consume fuels not used by biological molecular motors. A number of molecular devices that undergo mechanical motion driven by chemical changes have been constructed [5] and even include a rotary motor driven by light [6].

DNA has been successfully used to construct a variety of nanostructures that exhibit motion. The motion of most of these nanostructures is driven by the energy supplied as two strands of DNA zip up to form a double helix. So far, these DNA-based devices have been used only as demonstrations of principles by which nanoscale machinery could be driven. It is likely, however, that in the near future such devices will find application as nanoscale scientific instruments and may eventually form the basis for a sophisticated nanotechnology. Here we will describe some of the considerations that go into the design of DNA-based molecular motors and review those devices that have been experimentally demonstrated to date.

2. DNA NANOTECHNOLOGY

2.1. DNA Technology

DNA has proven to be a versatile material to work with in constructing nanostructures and nanomachines [7, 8]. Not only does DNA have extraordinary molecular recognition properties, but the emergence of molecular biotechnology also provides the researcher with a variety of convenient tools for the manipulation of DNA and with custom synthesis of DNA strands with almost arbitrary sequence. DNA structures can thus be "designed" and readily translated into "hardware"; the good predictability of strand–strand interactions [9, 10] aids in the design work. With existing technology, DNA strands of arbitrary base sequences up to 100 nucleotides in length are easily synthesized. A wide variety of modifications is also available. These include the attachment of dye molecules at particular locations within a

strand of DNA or the attachment of reactive groups to DNA to facilitate the attachment of DNA to other molecules or to a substrate. Also, a wide variety of enzymes are commercially available that operate on DNA in precise ways. These include polymerase enzymes that allow the amplification of DNA strands; ligase, which allows the covalent linking of DNA strands; and restriction enzymes that cut DNA at precise locations determined by base sequence. This rich repertoire of tools has already allowed the construction of some of the most complex nanostructures and machines made to date.

2.2. DNA Self-Assembly

Within biological organisms, DNA exists primarily in a duplex form consisting of two strands of single-stranded DNA wound together in a double helix. Single-stranded DNA is a linear polymer consisting of a chain of monomers called nucleotides, which themselves consist of the sugar 2′-deoxyribose connected to one of four compounds called bases. The four resulting nucleotides are designated A, C, G, and T for the bases adenine, cytosine, guanine, and thymine, respectively. The nucleotides are chiral and are linked together through a phosphodiester bridge between the 5′ carbon of the sugar in one nucleotide and the 3′ carbon of the sugar in the next nucleotide. As a consequence, DNA is a directed molecule in which one end is chemically different from the other. Duplex DNA consists of two strands that are aligned in an antiparallel manner and are held together by base-pair bonding between A and T and between C and G. Two strands of DNA for which all the bases can be paired in this way are said to be complementary. If base mismatches are present, the binding between two strands of DNA is not as strong as that for complementary strands. If the base mismatch density between two strands of DNA is sufficiently high, a stable duplex will not form. Two such strands, brought in contact in an aqueous solution, dissociate. DNA thus exhibits a kind of molecular recognition property in that it will bind well to complementary strands but not with strands of DNA for which there are too many mismatches. This recognition property has been extensively exploited in the assembly of DNA-based nanostructures. In effect, this property allows one to construct DNA strands that behave like a set of molecular LEGO™ blocks that can only snap together in a particular manner. Such strands of DNA placed in solution will be brought in contact with each other randomly through Brownian motion, and will self-assemble into a nanostructure as pairs of complementary regions between strands zip up, that is, hybridize, into the duplex form. The characteristic length scales of DNA provide lower bounds on the size of nanostructures assembled from DNA. Duplex DNA in its native form has a diameter of 2 nm and a spacing between bases of 0.34 nm.

The vast combinatorial space of base sequences provides a large set of labels that can be used to direct the assembly of complex nanostructures [11]. A variety of structures [7, 8], including wire-frame polyhedra [12, 13] and two-dimensional sheets of DNA [14], have been constructed by exploiting this assembly strategy. This recognition property has also been exploited in DNA-based computation [15–19].

The stiffness of DNA is a property of particular relevance in the design of nanostructures. The stiffness of a polymer is often specified by its persistence length [20]. A polymer in solution is continually and randomly batted about as the solvent molecules, executing Brownian motion, bump into it. A short polymer strand will simply be displaced or rotated by these collisions. A longer section of polymer will also bend in response to these collisions. The length at which a polymer shows an appreciable amount of this bending is called the persistence length. This length is proportional to the stiffness of the polymer and thus provides a convenient way of characterizing its resistance to distortion by the continual collisions with the solvent molecules.

Single-stranded DNA has a persistence length on the order of three bases [21], that is about 1 nm. Double-stranded DNA has a persistence length of 50 nm [22]. Thus, on a 10-nm length scale, the scale that will be relevant for the DNA devices discussed here, double-stranded DNA behaves like a rigid rod as it is bombarded by collisions with solvent molecules, while single-stranded DNA behaves like a flexible string.

2.3. Force Generation

The change in stiffness that results as two floppy single-stranded DNA molecules hybridize to form a rigid double helix has been used to induce motion in DNA-based nanostructures. How hybridization can induce motion and perform mechanical work is illustrated by the thought experiment shown in Figure 1, where a weight is depicted as being lifted through the formation of base pairs. As a result of the formation of a base pair, free energy ΔG becomes available for performing work. The value of this free energy depends on the identity of the two bases involved in the pairing and also on the identity of the neighboring bases [9, 10]. A representative value for ΔG is 73 meV per base pair (or 1.8 kcal mol^{-1}) [9, 10]. In the process of forming a base pair, the weight is lifted by a distance h that is twice the spacing Δx of 0.43 nm between nucleotides in single-stranded DNA. An estimate of 15 pN for the stall force F of a DNA motor, based on DNA hybridization, is obtained by $F = \Delta G/h$. Forces of this size have been measured using atomic force microscopes [23], optical traps [24], or other means [25] to pull double-stranded DNA apart. This is also comparable to the forces developed by biological molecular motors. For example, kinesin walking on microtubules exhibits a stall force in the 5 pN range [26].
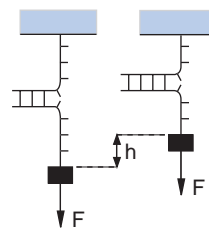
Figure 1. Here, as a thought experiment, DNA is depicted performing work by lifting a weight against the gravitational force F. The free energy of hybridization is converted into work as a base pair is formed, and the weight is lifted by twice the distance Δx between bases in single-stranded DNA, i.e., $h = 2\Delta x$.

Both the assembly of DNA-based nanostructures and the operation of DNA-based motors involves hybridization between complementary strands of DNA. This is a second-order chemical reaction process. Competing with this process is a first-order reaction in which duplex DNA dissociates into single-stranded DNA. The dissociation rate is a strong function of temperature and duplex length, whereas the association rate depends more weakly on these parameters [27]. As a consequence, the dissociation rate can be made negligible, and a reasonable association rate can be maintained by working at low temperatures and with complementary regions that are of sufficient length. For example, at 20 °C in a 1 M salt buffer, a DNA-based structure held together by duplex regions 20 bases long is for all practical purposes stable. The half time for dissociation is estimated to be 10^5 years from a simple extrapolation of data by L. E. Morrison and L. M. Stols [27]. On the other hand, under the same buffer conditions the association rate can be on the order of minutes when the DNA strands are present at 1 μM concentration. More generally, the time to half completion of the association reaction, at stoichiometry, is given by $t_{1/2} = 1/k_2[n]_0$, where k_2 is the second order rate constant and $[n]_0$ is the initial concentration of one of the strands. This time sets the scale for the time required to assemble a nanostructure through complementary base pairing. It also determines the speed with which a population of molecular motors, powered by DNA hybridization, can switch states.

2.4. Branch Migration

Most of the DNA devices discussed below utilize a phenomenon called *branch migration* to selectively displace DNA strands from a DNA nanostructure. Branch migration can occur whenever two DNA strands with the same base sequence (homologous strands) try to bind to one or two complementary strands simultaneously. One can discern between situations involving three and four strands of DNA, as depicted in Figure 2. Thermal fluctuations can break base pairs at the junction where the strands compete for binding to their complements. Subsequent formation of new base

Figure 2. Schematic representation of branch migration in the case of (a) three-stranded and (b) four-stranded DNA junctions. The branch point is indicated by a dashed line. Thermal fluctuations can cause the branch point to move to the left or to the right. The structures on the right evolve from the structures on the left by making one step to the left.

pairs can cause the branch point to move one step to the left or to the right from the original junction. The movement of the branch point along the DNA strands involved can be modeled by a random walk. The mean step time τ of this random walk is very different for three- and four-stranded junctions, and furthermore it is strongly dependent on temperature and buffer composition. Reported step times for three-stranded branch migration are on the order of 10–100 μs [28, 29], whereas four-stranded branch migration can have step times three orders of magnitude larger (i.e., milliseconds) [30, 31]. This large difference can be explained by the different structures of the branch points: In a four-stranded junction, all four strands outside of the junction are in duplex form; the three-stranded junction, however, lacks such a defined structure. As the structure of four-way junctions is strongly influenced by the presence of Mg^{2+}, high magnesium concentrations can slow down or completely inhibit branch migration.

In biological systems, strand displacement by branch migration occurs in the context of DNA recombination and DNA repair processes. In DNA recombination, a mobile four-way junction formed by strand exchange between two homologous sequences is also known as *Holliday intermediate* structure (for a review see Ref. [32]). In the following applications of this process, only three-stranded branch migration will be considered.

It is also possible to construct four-way junctions from nonhomologous DNA duplexes. In contrast to homologous crossovers, these junctions are immobile as the branch point cannot move along the strands freely. Immobile crossover junctions form the basis of supramolecular constructs, which consist of multiple crossover points (double- and triple-crossover structures) that have already been utilized for the assembly of 2-D DNA crystals [14, 33]. DNA crossover complexes have also been employed as structural elements in several of the DNA nanodevices to be discussed in the next section.

3. DNA-BASED NANODEVICES

3.1. A Device Based on the B–Z Transition

The first example of a nanomechanical device based on DNA was reported by C. Mao et al. [34]. It utilized the conformational change of dsDNA from its right-handed B-form to the left-handed Z-form—a process known as B–Z transition.

3.1.1. The B- and Z-Forms of DNA

Double-stranded DNA can assume a number of different conformations, termed, among others, the A-, B-, or Z-form of DNA. These conformations differ in handedness, twist and rise of the double helix, or in other characteristics [20]. The "canonical" DNA double helix is termed B-DNA. This form is usually adopted under physiological conditions, that is, near neutral pH and at moderate salt concentrations. B-form DNA has a right-handed double-helical structure in which the bases are stacked at a distance of approximately 0.34 nm from each other. The helix makes one turn every 10 bp (i.e., the helix pitch is 3.4 nm) and the twist between two adjacent bases is approximately 36°.
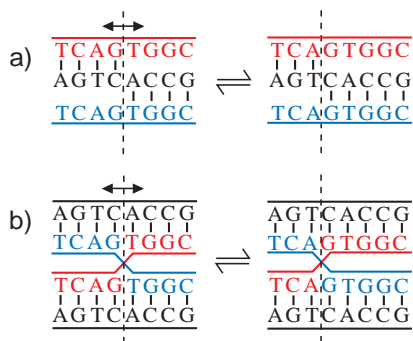
In stark contrast, Z-DNA has the structure of a left-handed double helix. It occurs with alternating purine-pyrimidine base sequences like $d(G-C)_n$. Z-DNA contains 12 bp per turn. The helix twist is $-10°$ between C and G and $-50°$ between G and C residues. This form of DNA is favored under certain buffer conditions, for example, at high salt concentrations, in particular in the presence of multi-valent cations such as cobalt hexammine ($[Co(NH_3)_6]^{3+}$) or in the presence of alcohol. In addition, the propensity for a transition from B- to Z-DNA is enhanced for methylated cytosine residues.

3.1.2. Design of the Device

The transition from B-form to Z-form DNA can be utilized to induce motion on the nanometer scale. To this end, C. Mao et al. [34] combined double-crossover (DX) structures (cf. Section 2.4.) serving as stiff lever arms with an "active" structure undergoing a B–Z transition upon a change in the buffer conditions (see Fig. 3). In the B–Z device, two DX structures are connected by a DNA strand containing a sequence $d(m^5CG)_{10}$ (with cytosine methylated at the C-5 position), which is particularly prone to a B–Z transition. A change of the concentration of $[Co(NH_3)_6]^{3+}$ from 0 mM to 0.25 mM (accompanied by a change in $[MgCl_2]$ from 10 mM to 100 mM) promotes this transition in the middle section of the device. For each d(CG) dinucleotide this corresponds to a change in twist of approximately $-128° = -10° - 50° - 2 \times 34°$, or -3.5 helix turns. From this, an overall change in the conformation of the device as depicted in Figure 3 can be expected. Most importantly, the two lever sections are rotated with respect to each other by one half-turn. The inner edges of the lever arms in Figure 3 have a distance of 7.0 nm in the B-form and 8.9 nm in the Z-form, as derived from fluorescence resonance energy transfer experiments.
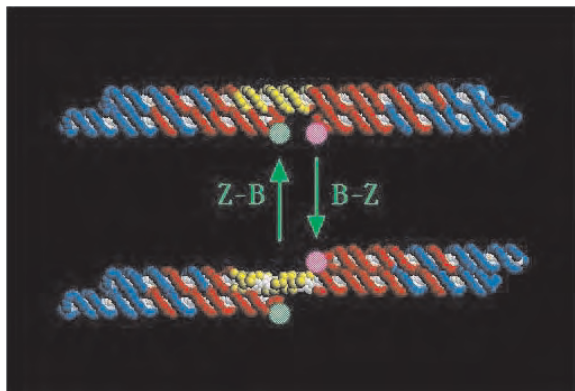
Figure 3. The B–Z device consists of two levers constructed from double-crossover junctions (blue and red strands) and an active region (yellow strand) that performs a B–Z transition when $[Co(NH_3)_6]^{3+}$ is added to or removed from the buffer. The device is depicted in the B-form in the upper part of the figure, and in the Z-form in the lower part. The green and pink dots symbolize two fluorescent dyes forming a FRET pair. The B–Z transition effectively leads to a half-turn of one handle with respect to the other. The larger distance between the dyes in the Z-form makes energy transfer between them less efficient. Reprinted with permission from [34], C. Mao et al., *Nature* **397**, 144 (1999). © 1999, Macmillan Magazines Ltd.

3.1.3. Characterization of the Device—Fluorescence Resonance Energy Transfer

The B–Z device can be switched between its two conformations essentially by raising and lowering the concentration of the cobalt hexammine complex $[Co(NH_3)_6]^{3+}$. This conformational change can be observed indirectly using a common biophysical technique called fluorescence resonance energy transfer (FRET), a widely applicable fluorescence technique for measuring distances and characterizing motion on the nanometer scale, and it is also applied to the other DNA devices discussed below. FRET can occur between two fluorescent dyes if the absorption band of one dye (the FRET acceptor) overlaps with the emission band of the other dye (the FRET donor). If the two dyes approach each other to within a distance of a few nanometers, the fluorescence of the donor is strongly quenched and the fluorescence of the acceptor is enhanced. The efficiency of the energy transfer at a distance R between the dyes is given by

$$E_T = \frac{F(D) - F(DA)}{F(D)} = \frac{1}{1 + (R/R_0)^6} \qquad (1)$$

where $F(D)$ and $F(DA)$ denote the fluorescence intensities of the donor in the absence or presence of the acceptor. R_0 is called Förster distance, or, the typical distance over which energy transfer occurs. For usual dye combinations, R_0 lies between 2 nm and 6 nm. The B–Z device in Ref. [34] was characterized using the FRET pair fluorescein (donor)/Cy3 (acceptor), which has a Förster distance of 5.6 nm. The dyes are attached to the device as indicated by the dots in Figure 3. The transition from B-form to Z-form leads to a detectable change in energy transfer efficiency from 20% to 5% due to the larger distance between the dyes in the Z-conformation. Using the FRET-technique, it could be shown that the B–Z device indeed can be cyclically switched between its two conformations and thus represents a very simple example of a molecular machine based on DNA. The same principle applied to larger and more complicated structures could probably be utilized to induce larger structural changes in supramolecular constructions.

3.2. DNA Actuators

Unlike the B–Z device, the following examples of DNA devices are driven through their mechanical states not by changes in the buffer conditions but by hybridization with "fuel strands". To enable cyclic operation of the devices, the original states have to be restored by the controlled displacement of the fuel strands with their Watson–Crick complements. This can be achieved by utilizing the DNA branch migration process discussed above.

3.2.1. DNA Tweezers

The first DNA device that uses branch migration [35] as an essential part of its operation principle has been termed "DNA tweezers" because of its resemblance to its macroscopic counterpart. The DNA tweezers are formed by three DNA strands A, B, and C. The sequences of B and C are chosen in such a way that they can hybridize to A over a

length of 18 bp each. The resulting structure consists of two 18 bp double-helical sections connected by a short four-base-long single-stranded section. From the two double-helical arms, 24-base-long single-stranded sections extend, which are the unhybridized sections of B and C. As discussed in Section 2, due to the relatively large persistence length of double-stranded DNA, the 18-bp-long double-helical sections of the tweezer structure can be regarded as stiff structural elements, whereas the single-stranded sections can act as flexible interconnects. A schematic depiction of the device and its operation cycle is shown in Figure 4. Starting from its "open" state, the device can be "closed" by the addition of a fuel strand F. The 48-base-long fuel strand consists of two 20-base-long sections complementary to the unhybridized parts of strands B and C and an 8-base-long "toehold" section. As shown in Figure 4, interaction of F with the tweezer structure pulls the two arms together. The toehold section of F remains unhybridized. At this section, the "removal" strand F̄—which is the exact Watson–Crick complement of F—can attach and wrest F off the device via branch migration and restore the open state of the tweezers. Subsequent addition of fuel and removal strand cycles the DNA device through its two conformational states—open and closed. The operation of the DNA tweezers can be checked using fluorescence resonance energy transfer (see Section 3.1.3.). This is achieved by attaching fluorescent dyes to the ends of the arms of the device that comprise a FRET pair. Depending on the distance of the two arms, the fluorescence of the FRET donor is quenched more or less strongly. In Ref. [35], the FRET pair TET and TAMRA has been used, which has a Förster distance R_0 of approximately 5 nm. A typical FRET signal recorded during the operation of the device is shown in Figure 5. In the open

Figure 5. FRET signal recorded during operation of the DNA tweezers. In the closed state, the two FRET dyes are closer to each other than in the open state. Therefore, fluorescence quenching is more efficient in the closed state, leading to a lower fluorescence signal of the FRET donor. The fluorescence maxima do not recover to the previous maximum values due to dilution effects and mismatches in the amount of F and F̄ added successively. Reprinted with permission from [35], B. Yurke et al., *Nature* 406, 605 (2000). © 2000, Macmillan Magazines Ltd.

state, the two dyes are ≈6 nm apart from each other and FRET efficiency is therefore low. Addition of F closes the structure; therefore the distance between the dyes decreases and the donor fluorescence is quenched due to FRET. In addition to FRET measurements, gel electrophoresis experiments were carried out and fully validated the schematic operation scheme depicted in Figure 4.

In principle, the accumulation of waste product FF̄ is undesirable, as this could ultimately stall the device. In each cycle, the device has to be driven out of equilibrium by the addition of unhybridized fuel and removal strands. The device then performs one cycle, and one waste duplex FF̄ is formed. In the presence of a very large amount of waste product, the back-reaction, in which FF̄ is broken down and the device is driven backwards, could inhibit the operation of the tweezers. In biological systems, the breakdown of ATP to ADP and inorganic phosphate during the operation of molecular motors is coupled to metabolic processes that restore the fuel molecule and therefore maintain the necessary disequilibrium. Another way to avoid problems with waste accumulation would be to simply remove the waste from the system (an approach taken for the device described in Section 3.3.). However, as already mentioned in Section 2.3., under ordinary experimental conditions the dissociation rate for long DNA duplexes is extremely small. For the 48 bp waste duplexes at 20 °C, this rate is essentially zero. In the current experimental setting, the accumulation of waste products therefore does not pose any problems and has no influence on the kinetics of the devices.

3.2.2. DNA Scissors

A variation of DNA tweezers are DNA scissors [36]. The structure and the operation cycle of this device are displayed in Figure 6. DNA scissors are capable of transducing the hybridization-driven closing motion in one section of the device (the "handles") to another section (the "jaws"); 13 nm away. The resulting motion resembles that of a pair

Figure 4. Design and operation cycle of the tweezers: The open tweezers are assembled from three strands A, B, and C (top structure). As indicated by the colors, a fuel strand F can hybridize to the arms of the tweezers, thereby closing the device (bottom). A short overhang section (red) serves as a toehold for the removal strand F̄, which can wrest the fuel strand F from the device via three-stranded branch migration. This restores the open state of the tweezers. In each operation cycle, one waste duplex FF̄ is produced. The red circles and triangles symbolize the two dyes of a FRET pair. In the closed state, the two dyes are very close to each other, leading to maximum energy transfer. In the open state, energy transfer is less efficient. Reprinted with permission from [35], B. Yurke et al., *Nature* 406, 605 (2000). © 2000, Macmillan Magazines Ltd.

Figure 6. Design and operation of DNA scissors: The double-helical sections of the device are connected by C3 spacers (indicated by red zigzag lines). Closing the right pair of arms of the device (the "handles") with the fuel strand F also closes the left pair of arms (the "jaws"). Addition of $\overline{F}$ restores the open state.

of scissors. This particular motion is achieved by introducing short C3 carbon linker sections (i.e., $(-CH_2-)_3$) into the device (see Fig. 6). The C3 spacers provide full rotational freedom while acting as stiff hinges rather than flexible connectors. FRET experiments [36] showed, however, that the force transduction is not perfect: The jaws are not closed as thoroughly as the handles, as also indicated in Figure 6.

3.2.3. A Three-State Device

One of the shortcomings of the DNA tweezers is the flexibility of the open state of the device. This problem is resolved for the three-state device (TSD) [37], which has two mechanically robust states and one flexible intermediate state. The TSD is also a variation of the tweezers structure. Its assembly and operation principle is depicted in Figure 7. In the relaxed state (Fig. 7a), the single-stranded extensions of the arms are joined to form a circular structure. Addition of fuel strands F_1 or F_2 transforms the relaxed structure into a stretched (Fig. 7c) or a closed state (Fig. 7b). The closing motion is very similar to the DNA tweezers operation discussed above. The stretching motion has been analyzed in detail in Refs. [38–40]. Using the appropriate removal strands, the device can be deliberately cycled through its three mechanical states. This again can be checked by fluorescence resonance energy transfer between two dyes attached to the ends of the arms of the device: In the stretched state, the dyes are approximately 14 nm apart from each other; in the relaxed state, the mean distance is 6 nm; and in the closed state, the dyes are separated by roughly 4 nm (corresponding to the diameter of two double helices). A typical fluorescence signal recorded during operation of the TSD is shown in Figure 8. In the stretched state, FRET is inefficient and the donor fluorescence is at a high level. The smaller distances between the dyes in the relaxed and the closed states lead to accordingly lower fluorescence intensities. At not too low salt concentrations, the closed and stretched states are mechanically robust [40]. It can, therefore, be expected that an operation between these two states actually could be used to transduce forces to other nanoscale structures.
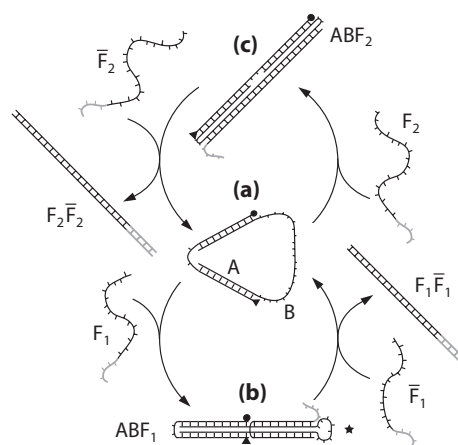
Figure 7. (a) The loop-like three-state device (TSD) is assembled from the two DNA strands A and B. (b) Addition of fuel strand F_1 closes the device, and (c) addition of fuel strand F_2 stretches the devices. From its mechanically robust closed and stretched conformations, the TSD can be returned to its relaxed state by the addition of appropriate removal strands $\overline{F}_1$ or $\overline{F}_2$. The circle and triangle again symbolize the FRET pair TET and TAMRA. Reprinted with permission from [37], F. C. Simmel and B. Yurke, *Appl. Phys. Lett.* 80, 883 (2002). © 2002, American Institute of Physics.

3.3. A Device Based on Crossover Junctions

The DNA device discussed in this section also uses strand displacement by branch migration as a means of switching between different conformations. However, the structure of the device is not based on simple double helix formation, but uses more intricate double crossover molecules composed of several linked four-way junctions (see Section 2).

3.3.1. Design and Operation Scheme of the Device

In Figure 9a, the structure of the active section of the PX device is shown [41]. It consists of four strands (two duplexes) of DNA linked together by reciprocal strand
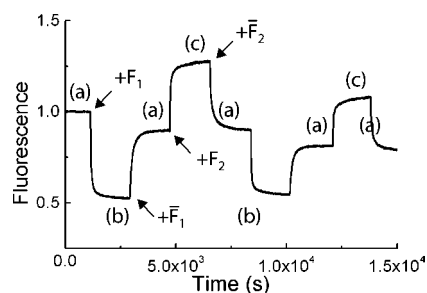
Figure 8. Operation of the TSD: The three states of the device correspond to three different fluorescence intensity levels: In the relaxed state (a), the distance of the dyes is approximately equal to the Förster distance, and the fluorescence is at an intermediate level. In the closed state (b), the two dyes are closer to each other, and FRET is more efficient, suppressing the fluorescence of the donor. In the stretched state (c), the dyes are too far apart from each other for FRET to be efficient. Reprinted with permission from [37], F. C. Simmel and B. Yurke, *Appl. Phys. Lett.* 80, 883 (2002). © 2002, American Institute of Physics.
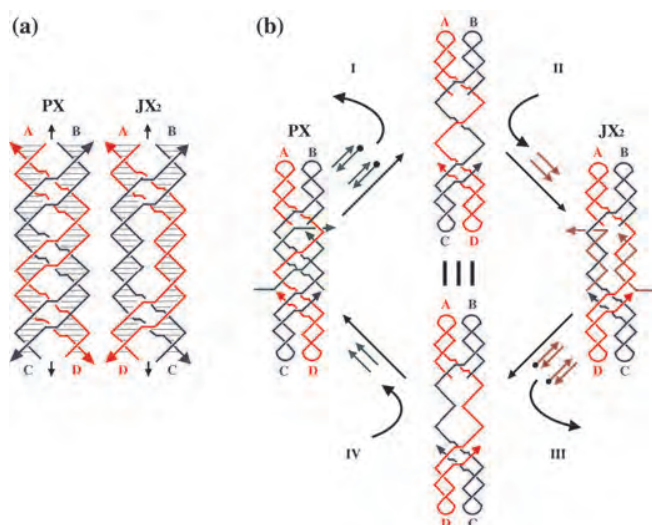
Figure 9. Active section of the PX device: (a) The operation of the device is based on the PX and JX$_2$ conformers of a multiple crossover structure formed by four DNA strands. In the PX conformer, the strands cross over at every point where the duplexes touch each other, whereas in the JX$_2$ structure the two inner junctions are missing. In the JX$_2$ conformation, the lower two duplexes (C and D) have switched positions with respect to the PX conformation. (b) The transition from PX to JX$_2$ can be utilized by forming the innermost junctions with removable strands. The structures in the middle are intermediate structures with a single-stranded inner part. Adding the appropriate fuel strands that hybridize to these sections transforms the intermediate structures into the JX$_2$ conformation (II) or the PX conformation (IV). PX and JX$_2$ can be returned to the intermediate state by branch migration using the complementary fuel strands (I and III). The removal strands are biotinylated (indicated by full circles), which facilitates removal of the waste duplexes. Reprinted with permission from [41], H. Yan et al., *Nature* 415, 62 (2002). © 2002, Macmillan Magazines Ltd.

exchange, or multiple crossover. In the PX conformation, strands cross over at every point where the two double helices touch each other. In the JX$_2$ conformer, the two inner crossovers are removed. This leads to a rotation of the lower part of the PX structure by 180°, that is, sections C and D switch position. This conformational change can be utilized to form a nanomechanical switch as shown in Figure 9b: For the PX device, the two inner crossovers are formed by two removable DNA strands. Removal is accomplished by branch migration using appropriate fuel strands, as already discussed in the previous sections. This transforms the device to a floppy intermediate state, in which the inner device section consists of single-stranded DNA. A different pair of DNA strands can now hybridize to the intermediate state (II) forcing the device to assume the JX$_2$ state. Again, these strands can be removed by the corresponding fuel strands (III), and the device can be returned to its original PX state (IV).

3.3.2. Operation and Characterization of the Device

By the addition of fuel and removal strands, the PX device can be cycled through its conformations similar to the devices described in the previous section. Due to the
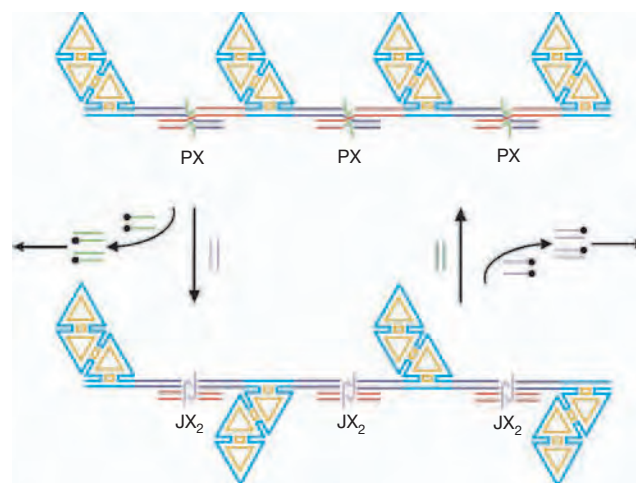
Figure 10. The PX device is composed of the active PX/JX$_2$ regions and supramolecular "pointers," also constructed from DNA. When the device is in the PX conformation, all the pointers are aligned on one side of the junctions (cis), whereas in the JX$_2$ conformation the pointers assume alternating positions with respect to the device (trans). The relative position of the pointers can be determined experimentally by atomic force microscopy. Reprinted with permission from [41], H. Yan et al., *Nature* 415, 62 (2002). © 2002, Macmillan Magazines Ltd.

enhanced stiffness of multiple crossover molecules, the PX and JX$_2$ conformations of the device represent two relatively robust mechanical states that might allow for an efficient transduction of the force generated by the device. In addition to gel electrophoresis experiments, the operation of the device was checked using atomic force microscopy (AFM). To this end, several PX devices were linked together and modified with large supramolecular "pointer" structures also constructed from DNA (see Fig. 10). These pointer structures are large enough to be imaged with the AFM (about 15 nm). Operation of the linked PX devices leads to a juxtaposition of the pointers. When the device is in its PX state, the pointers are aligned on one side of the device, whereas in the JX$_2$ conformation the pointers are in a staggered position.

As already discussed in the previous section, the buildup of a high concentration of waste products during the operation of a molecular machine eventually stalls it. In the scheme presented by H. Yan et al. [41], this problem has been solved by actively removing the waste product formed by the fuel strands: As indicated in Figure 9b, the fuel strands have been functionalized with the vitamin biotin. As biotin binds very strongly to the protein streptavidin (a very commonly used molecular linker system [42]), the waste products can be removed after each (half-) cycle using streptavidin-coated magnetic beads.

3.4. Utilization of Nonstandard Base Pairing

Apart from the canonical Watson–Crick pairs, the nucleic acid bases adenine, guanine, cytosine, thymine, or uracil can form a large variety of nonstandard hydrogen-bonded duplexes, triplexes, or even quadruplexes [20]. These nonstandard bonds allow DNA or RNA structures to fold into much more complicated secondary structures than expected
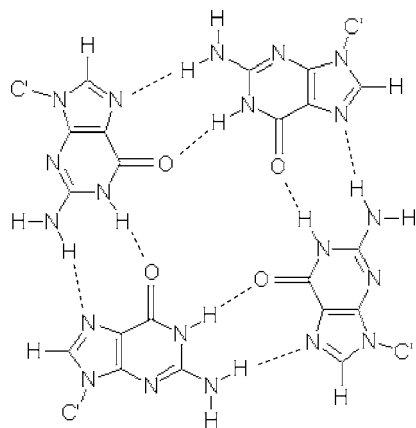
Figure 11. In a G-quartet, four guanine bases bind to each other via hydrogen bonds in a cyclic fashion. The formation of this planar structure occurs in G-rich sequences and is favored by the presence of potassium ions.

Figure 12. DUTE device based on G-quartets: The device's sequence and secondary structure are depicted on the right. In the tetraplex (TE) conformation, the device strand forms two stacked G tetrads connected by several loops. Fluorophore (F) and quencher (Q) enable fluorescent read-out of the state of the device. On the left, the operation cycle of the device is shown. Strand α forms a duplex (DU) with the device strand, disrupting the TE conformation. Strand β can attach to the toehold section (pink) of α and remove the fuel strand via branch migration. A waste product $\alpha\beta$ is formed in each cycle. Reprinted with permission from [45], J. J. Li and W. Tang, *Nano. Letters* 2, 315 (2002). © 2002, American Chemical Society.

from WC pairing alone. In biological systems, complicated RNA structures are often found in the context of ribozymes—RNA structures with a catalytic function similar to protein enzymes [43]. One of the nonstandard pairing schemes has already been utilized for the construction of another simple DNA device: the formation of guanine quartets.

3.4.1. Formation of G-Quartets

Guanine can form relatively stable hydrogen bonds with every other base, including itself. Particularly in guanine-rich sequences in the presence of monovalent cations, the formation of G-quartets can occur. In this structure, four guanine bases are aligned in a plane and connected with each other via hydrogen bonds as depicted in Figure 11. Potassium ions particularly favor the formation of G-quartets [44, 20]. G-quartet structures can be formed either by a single DNA strand via intramolecular folding, or bimolecularly or even tetramolecularly by the association of two or four DNA strands. The stability of G-quartets can equal or even exceed that of conventional WC base pairs [44]. G-quartets are actually found in the non-coding DNA sequences at the ends of eukaryotic chromosomes called telomeres. Telomeric DNA contains tandemly repeated G-rich sequences.

3.4.2. Design and Operation of the G-Quartet Device

The G-quartet device utilizes intramolecular tetraplex formation within a single strand (i.e., the device actually consists of a single strand!). Its design and operation principle is shown in Figure 12 [45]. The 17-base-long sequence of the device strand is chosen in such a way that, in the absence of any other strand, the device assumes the conformation depicted in the right part of Figure 12. The strand forms two stacked G-quartets with the guanine residues G3-G6-G12-G15 and G2-G7-G13-G16 connected by two upper loops (T4-T5 and T13-T14) and one lower loop (T8-G9-T10). The first and last residue of the 17-mer (T1 and T17) are connected to a fluorophore and a quencher molecule, respectively. Device operation is achieved by the addition

and removal of the strand α, which contains a sequence complementary to the sequence of the device strand plus a short overhang section. Hybridization of α with the device disrupts the G-tetraplex (TE) and leads to duplex (DU) formation (therefore the device has been termed DUTE device). Completely analogous to the operation principle of the DNA devices in the preceding sections, the strand α can be removed via branch migration by its WC complement β (see Fig. 12). By subsequent addition of strands α and β, the device can be cycled through its TE and DU states. Again, the state of the device can be read by fluorescence techniques: In the TE state, the dye and quencher molecules are close to each other and the fluorescence level is low. In the stretched DU conformation, the dye and the quencher are far apart from each other, yielding a high fluorescence signal.

3.5. Free-Running DNA Devices

3.5.1. Clocked and Free-Running Motors

The DNA devices presented in the previous sections can be regarded as simple molecular motors transforming the free energy of hybridization between fuel and removal strands into mechanical motion. In classifying motors, it is useful to distinguish clocked motors from free-running motors. For a clocked motor, the switching that advances the motor from one state to the next is done externally. An electrical stepper motor, for which the switching that supplies current to the various coils is done in the power supply, would be an example of such a motor. Free-running motors, in contrast, have internal switching mechanisms that advance the motor through its successive states. An example of such a motor is a DC electrical motor where brushes and a commutator

perform the switching of the current in the armature wind-ings. The motors we have described so far can be regarded as clocked motors since these motors are advanced through their cycles by the sequential addition of the fuel and the removal strands to the solution in which the motor resides. Clocked motors are particularly useful in cases were the advancement of the motor through successive states must be coordinated with events occurring external to the motor. In fact, regulatory proteins that undergo changes driven by GTP hydrolysis can be viewed as biological examples of clocked molecular motors [46].

For the DNA devices described above, the simultaneous addition of fuel strands and removal strands to the solution will not result in the efficient cycling of the motor through its various states because most of the fuel and removal strands will directly hybridize without interaction with the motor. In contrast, many biological motors are free-running since they will cycle through their complete set of states once an ATP or GTP molecule is supplied. The problem of the decay of the fuel without interaction with the motor is avoided by the fact that the fuel consists of metastable molecules that release their energy only after binding with the motor molecule. A means by which, in principle, one could construct free-running DNA-based molecular motors has been demonstrated that uses secondary structures to inhibit the the fuel strand from directly reacting with the removal strand [47, 48].

3.5.2. Hybridization Catalysis: An Operation Principle for Free-Running DNA Motors

The principle of hybridization catalysis is depicted in Figure 13. To avoid direct hybridization of fuel and removal strands F and $\overline{F}$, the fuel strand is "protected" by the strand P. F and P hybridize together to form a secondary structure consisting of two double-helical arms and a small single-stranded loop. Extensive experiments on the kinet-ics of the reaction of $\overline{F}$ with FP [47, 48] have shown that the hybridization of protected F with $\overline{F}$ is slowed down by a factor of 100 as compared to the direct reaction between F and $\overline{F}$. Then the strand C (the catalyst) is chosen in such
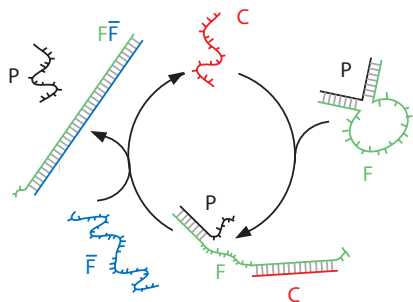
Figure 13. Hybridization catalysis: The direct hybridization of fuel and removal strands F and $\overline{F}$ is inhibited by secondary structure forma-tion with protection strand P. The catalyst C can open the complex FP and thereby catalyze the reaction FP + $\overline{F}$ → F$\overline{F}$ + P. The catalyst C is restored after each cycle. C can be thought of as a very sim-ple free-running molecular machine switching successively between a single-stranded and a double-stranded state.

a way that it can attach to the complex FP much more effi-ciently than $\overline{F}$. Hybridization of C with FP, again via branch migration, opens up the loop, making FP more accessible for $\overline{F}$. Now $\overline{F}$ can attack the complex FPC and displace both P and C from F to form the waste products F$\overline{F}$ and P. The catalyst C is recovered after one cycle. Overall, C catalyzes the reaction FP + $\overline{F}$ → F$\overline{F}$ + P. The catalyst C can actually be viewed as an extremely simple molecular machine, con-tinually switching between a relaxed, single-stranded state and a stretched double-helical state (in the complex FPC). The catalyst operation scheme is closely analogous to that of motor proteins (see previous section): The fuel is provided in a metastable form (FP together with $\overline{F}$). Upon binding to the motor (C) the stored chemical energy is released, waste products form (F$\overline{F}$ and P) and the motor returns to its original state. In fact, motor proteins are also enzymes catalyzing the hydrolysis of ATP/GTP to ADP/GDP and orthophosphate (technically, they are classified as ATPases or GTPases). From this viewpoint, the DNA motor C—as a nucleic acid with catalytic activity—could also be considered a new type of deoxyribozyme [48, 49].

4. SUMMARY

In this chapter a survey of DNA-based nanodevices that undergo motion has been presented. The forces developed by such devices should be comparable to those developed by biological molecular motors. For most of the DNA-based devices discussed here, the energy for the power stroke is supplied by DNA hybridization when a fuel strand hybridizes with the DNA of a motor domain. The device is returned to its original state through the addition of a removal strand—the complement of the fuel strand that dis-places the fuel strand from the motor domain by branch migration. These DNA nanodevices can be regarded as motors operating from the free energy of hybridization between the fuel strand and the removal strand. For many of these machines, there is a good deal of flexibility in the choice of base sequences for the motor domain. One could make structures possessing multiple motors, each operated by a different fuel and removal strand. This would allow the creation of structures capable of undergoing a complex series of motions. The sequence of the motions would be determined by the sequence with which the fuel and removal strands are supplied, that is, the sequence of motions would be programmable. Although the devices that have so far been constructed are demonstrations of principle and have been used only to move a pair of dyes relative to each other, they demonstrate a versatile means by which nanometer scale objects can be manipulated by nanometer-sized tools. The related fields of DNA self-assembly, DNA comput-ing, and DNA-based devices therefore offer all the means for a sophisticated molecular nanotechnology: the ability to assemble and manipulate matter and process information on the nanometer scale.

GLOSSARY

ATP, GTP Adenosine 5′-triphosphate and guanosine 5′-triphosphate. These molecules are the energy currency of living organisms. Energy gained by hydrolysis of ATP or

GTP is used to drive many biochemical processes, including the motion of biological molecular motors.

Bases Purine or pyrimidine molecules occuring as residues in nucleic acids. The bases adenine, cytosine, guanine, and thymine are found in DNA. Uracil replaces thymine in RNA. Hydrogen bonding between complementary bases is the origin of the molecular recognition properties of DNA.

Deoxyribonucleic acid (DNA) A macromolecule consisting of one or two strands of linked deoxyribonucleotides.

DNA hybridization Formation of a duplex structure by two complementary single strands of DNA.

Fluorescence The emission of light by a substance immediately after the absorption of energy from light of usually shorter wavelength.

Fluorescence resonance energy transfer (FRET) The non-radiative transfer of excitation energy from one fluorescent molecule to another. FRET quenches the fluorescence of the originally excited molecule and elicits the fluorescence of the absorbing molecule.

ACKNOWLEDGMENTS

REFERENCES

1. J. Howard, *Mechanics of Motor Proteins and the Cytoskeleton*. Sinauer Associates, Inc., Sunderland, 2001.
2. D. Bray, *Cell Movements*, 2nd ed. (Garland Publishing, New York, 2001).
3. B. Alberts, D. Bray, J. Lewis, M. Raff, K. Roberts, and J. D. Watson, *Molecular Biology of the Cell*, 3rd ed. Garland Publishing, New York, 1994.
4. D. Bray, in *Cell Movements*, 2nd ed., Garland Publishing, New York, 2001, pp. 259–261.
5. V. Balzani, A. Credi, F. M. Raymo, and J. F. Stoddart, *Angew. Chem., Int. Ed. Engl.* 39, 3348 (2000).
6. N. Koumura, R. W. J. Zijlstra, R. A. van Delden, N. Harada, and B. L. Feringa, *Nature* 401, 152 (1999).
7. N. C. Seeman, *Acc. Chem. Res.* 30, 357 (1997).
8. C. M. Niemeyer, *Appl. Phys. A* 68, 119 (1999).
9. J. SantaLucia, Jr., H. T. Allawi, and P. A. Seneviratne, 35, 3555 (1996).
10. D. M. Gray, *Biopolymers* 42, 795 (1997).
11. R. Deaton, M. Garzon, R. C. Murphy, J. A. Rose, D. R. Franceschetti, and S. E. Stevens, Jr., *Phys. Rev. Lett.* 80, 417 (1998).
12. J. Chen and N. C. Seeman, *Nature* 350, 631 (1991).
13. Y. Zhang and N. C. Seeman, *J. Am. Chem. Soc.* 160, 1661 (1994).
14. E. Winfree, F. Liu, L. A. Wenzler, and N. C. Seeman, *Nature* 394, 539 (1998).
15. L. M. Adleman, *Science* 266, 1021 (1994).
16. F. Guarnieri, M. Fliss, and C. Bancroft, *Science* 273, 220 (1996).
17. Q. Ouyang, P. D. Kaplan, S. Liu, and A. Libchaber, *Science* 278, 446 (1997).
18. L. M. Adleman, *Sci. Am.* 54, (1998).
19. C. Mao, W. Sun, Z. Shen, and N. C. Seeman, *Nature* 407, 493 (2000).
20. V. A. Bloomfield, D. M. Crother, and I. Tinoco, Jr., *Nucleic Acids*. University Science Books, Sausalito, CA, 2000.
21. B. Tinland, A. Pluen, J. Sturm, and G. Weill, *Macromolecules* 30, 5763 (1997).
22. S. B. Smith, Y. Cui, and C. Bustamante, *Science* 271, 795 (1996).
23. M. Rief, H. Clausen-Schaumann, and H. E. Gaub, *Nat. Struct. Biol.* 6, 346 (1999).
24. J. Liphardt, B. Onoa, S. B. Smith, I. Tinoco, Jr., and C. Bustamante, *Science* 292, 733 (2001).
25. E. Essevaz-Roulet, U. Bockelmann, and F. Heslot, *Proc. Natl. Acad. Sci. USA* 94, 11935 (1997).
26. C. M. Loppin, D. W. Pierce, L. Hsu, and R. D. Vale, *Proc. Natl. Acad. Sci. USA* 94, 8539 (1997).
27. L. E. Morrison and L. M. Stols, *Biochemistry* 32, 3095 (1993).
28. C. M. Radding, K. L. Beattie, W. K. Holloman, and R. C. Wiegand, *J. Mol. Biol.* 116, 825 (1977).
29. C. Green and C. Tibbetts, *Nucleic Acids Res.* 9, 1905 (1981).
30. A. J. Courey and J. C. Wang, *Cell* 33, 817 (1983).
31. I. G. Panyutin and P. Hsieh, *Proc. Natl. Acad. Sci. USA* 91, 2021 (1994).
32. D. M. Lilley, *Q. Rev. Biophys.* 33, 109 (2000).
33. T. H. LaBean, H. Yan, J. Kopatsch, F. Liu, E. Winfree, J. H. Reif, and N. C. Seeman, 122, 1848 (2000).
34. C. Mao, W. Sun, Z. Shen, and N. C. Seeman, *Nature* 397, 144 (1999).
35. B. Yurke, A. J. Turberfield, A. P. Mills, Jr., F. C. Simmel, and J. L. Neumann, *Nature* 406, 605 (2000).
36. J. C. Mitchell and B. Yurke, in *DNA Based Computers VII*, No. 2340 in *LNCS*, N. Jonoska and N. C. Seeman, eds. Springer-Verlag, Heidelberg, 2002.
37. F. C. Simmel and B. Yurke, *Appl. Phys. Lett.* 80, 883 (2002).
38. F. C. Simmel and B. Yurke, *Phys. Rev. E* 63, 041913 (2001).
39. F. C. Simmel and B. Yurke, in *DNA Based Computers VII*, No. 2340 in *LNCS*, N. Jonoska and N. C. Seeman, eds. Springer Verlag, Heidelberg, 2002.
40. F. C. Simmel, B. Yurke, and R. J. Sanyal, *J. Nanosc. Nanotech.* 1, 383 (2002).
41. H. Yan, X. Zhang, Z. Shen, and N. C. Seeman, *Nature* 415, 62 (2002).
42. C. M. Niemeyer, T. Sano, C. L. Smith, and C. R. Cantor, *Nucleic Acids Res.* 22, 5530 (1994).
43. T. R. Cech, *Sci. Am.* 255, 64 (1986).
44. R. Jin, B. L. Gaffney, C. Wang, R. A. Jones, and K. J. Breslauer, *Proc. Natl. Acad. Sci. USA* 89, 8832 (1992).
45. J. J. Li and W. Tang, *Nano Letters* 2, 315 (2002).
46. H. R. Bourne, D. A. Sanders, and F. McCormick, *Nature* 349, 117 (1991).
47. A. J. Turberfield, B. Yurke, and A. P. Mills, Jr., in *DNA Based Computers V*, pp. 171–182, No. 54 in *DIMACS Series*, E. Winfree and D. K. Gifford, eds. American Mathematical Society, DIMACS, ADDRESS, 2000.
48. A. J. Turberfield, B. Yurke, A. P. Mills, Jr., M. I. Blakey, J. C. Mitchell, and F. C. Simmel, to be published (2002).
49. R. R. Breaker, *Science* 290, 2095 (2000).

Doped Carbon Nanotubes

Rui-Hua Xie

Queen's University, Kingston, Ontario, Canada

Jijun Zhao

University of North Carolina at Chapel Hill, North Carolina, USA

Qin Rao

Queen's University, Kingston, Ontario, Canada

CONTENTS

1. INTRODUCTION

Diamond and graphite are two of the well-known forms of carbon. Carbon atoms with three-coordinate sp^2 hybridization form planar sheets of graphite, while carbon atoms form an extended three-dimensional network in diamond with four-coordinate sp^3 bonding. In 1985, fullerene, a new form of carbon, was discovered by Kroto et al. [1]. Fullerenes are closed-cage carbon molecules with three-coordinate carbon atoms tiling the spherical or nearly spherical surface, for example, C_{60} with a truncated icosahedral structure formed by 20 hexagonal and 12 pentagonal rings. Because of the ability to generate fullerenes in gram-scale quantities in the laboratory using a relatively simple apparatus, intense research activities [2–5] on these molecules were initiated and led to a renaissance in the study of carbon.

1.1. Carbon Nanotubes

In 1991, Iijima [6] observed nanotubules of graphite deposited on the negative electrode during the direct current arching of graphite for the preparation of fullerenes. Such carbon-based nanostructures can be obtained by rolling graphene planes. If only one graphene sheet is rolled, a single-walled carbon nanotube (SWNT) can be made [7]. Meanwhile multi-walled carbon nanotubes (MWNT) can be obtained [6] if a few stacked graphitic shells are arranged as follows: Russian doll MWNTs [5] are built from perfectly concentric cylinders, and scroll MWNTs are derived from a single graphene sheet rolled as a scroll [8]. Since the discovery of MWNTs in 1991, carbon nanotubes have been extensively studied from both theoretical and experimental sides because of their unique geometric structures and remarkable mechanical, chemical, electronic, magnetic, and transport properties. Their small diameter (scale of nanometers) and the long length (on the order of microns) lead to such large aspect ratios that the carbon nanotubes act as ideal one-dimensional systems. In the mass production of carbon nanotubes, it was found that nanotubes form nanorope bundles with close-packed two-dimensional triangular lattices [9]. These rope crystallites might offer a host lattice for intercalation and storage. All these characteristics make carbon nanotubes the focus of extensive studies in nanoscale science and technology with potential applications in various materials and devices. More details about the synthesis, physical and chemical properties, and technological applications of carbon nanotubes can be found in recent books [5, 10–19] and review articles [20–26].

1.2. Doped Carbon Nanotubes

Similar to semiconductor technology, the idea of doping carbon nanotubes is attractive because it allows control of their electronic properties by intercalation of electron donors or acceptors, substitutional doping, chemical functionalization, and others. Experimentally, doped carbon nanotubes can be

characterized by various techniques such as X-ray diffraction, ultraviolet (UV)/infrared (IR) spectroscopy, Raman spectroscopy, nuclear magnetic resonance (NMR), electron spin resonance (ESR), electron paramagnetic resonance (EPR), positron lifetime spectra, and so on. Many interesting phenomena are found in these doped carbon nanotube materials. For example, the intercalation of the MWNTs is useful in determining the type of MWNT. Electrochemical doping is used for tube-based electrodes that are applied as anodes of lithium batteries. The electronic properties of SWNTs can be engineered by doping either electron donors or electron acceptors. The resistivity of a carbon nanotube decreases upon Br_2- or K-doping. Larger third-order optical nonlinearities are found for N- or B-doped carbon nanotubes. The field emission of carbon nanotubes can be enhanced by controlled synthesis of well-aligned N-doped carbon nanotubes with higher N ratios. Doped carbon nanotubes could be good candidates for optical limiting applications. In the application of energy storage, it has been found that the hydrogen storage capacities of doped carbon nanotubes are larger than those of pristine nanotube bundle materials.

Moreover, the doped carbon nanotubes can be promising building blocks for today's molecular electronics. The field of modern microelectronics and computation are advancing at an extremely fast rate because of remarkable circuit miniaturization in semiconductor technology. However, further miniaturization of microelectronic circuits will soon reach the scale of atoms or molecules. To continue the production of faster and smaller computers, new schemes are required. Molecular electronics [27], first introduced in the mid-1970s [28] using only a few or even just one molecule to perform basic functions of digital electronics, has provided such a possibility. For example, nanotube-based n-type, p-type, n-p-n, and p-n-p transistors and n-p junctions can be constructed.

All these exciting achievements encouraged us to write this chapter on the topic of doped carbon nanotubes, while the field is still in a highly active phase of development. This chapter is organized as follows. In Section 2, we review recent spectroscopy studies of doped carbon nanotubes such as X-ray, EPR/ESR, NMR, UV/IR, Raman, and positron lifetime spectroscopy. In Section 3 we review physical properties and related applications of doped carbon nanotubes including electronic, transport, field emission, polarizability, hyperpolarizability, optical limiting, and magnetic properties and hydrogen storage. Finally, we end this chapter by giving a brief summary and outlook in Section 4. We have not included details on the synthesis of doping of MWNTs and SWNTs, which can be found in a recent review by Duclaux [29].

2. CHARACTERIZATIONS OF DOPED CARBON NANOTUBES

2.1. X-Ray Diffraction

X-rays lie in the electromagnetic spectrum between ultraviolet light and gamma radiation and have an approximate range of wavelengths of 0.1 to 100 Å [30]. They are usually produced by rapidly decelerating fast-moving electrons

and converting their energy of motion into a quantum of radiation. The wavelengths produced depend on the energy of the electrons. In 1912, the diffraction of X-rays by crystals was discovered by von Laue [31]. This discovery is one of the most fascinating chapters in the history of science. The special usage of X-ray diffraction in the study of solid substances lies in its ability to distinguish ordered phases from disordered ones. Thus, it is common knowledge that liquids or glasses produce X-ray patterns of a diffuse nature consisting of one or more halos, whereas well-crystallized substances yield patterns of numerous sharp circles or spots [30]. In this section, we review recent developments of X-ray studies of doped carbon nanotubes.

In 1996, Mordkovich et al. [32] studied K intercalation into carbon nanotubes by X-ray diffraction (XRD). The XRD pattern of pristine carbon nanotubes obtained can be indexed on the basis of hexagonal close-packed (hcp) graphite unit cells with c-axis parameters enlarged from 6.71 to 6.88 Å. After intercalation of potassium, new diffraction patterns closely matching those of the corresponding graphite intercalation compounds [33] appear. The intershell spacing expands significantly from 3.44 to 5.3 Å. Later on, based on the powder XRD patterns of K- or Cs-intercalated SWNTs, Bower et al. [34] observed reversible intercalation of SWNTs. They found that even after a long exposure time, no clear Bragg peaks were observed from either K- or Cs-intercalated samples, corresponding to the loss of crystallinity. Moreover, Duclaux et al. [35] found that the XRD pattern of K-doped MWNT is typical of a second-stage derivative with an identity period of 8.76 Å. On the other hand, Bower et al. [36] also realized reversible intercalation of SWNTs with nitric acid by XRD. However, unlike alkali metal-intercalated SWNTs, the nitric acid-intercalated SWNTs remained crystalline, and the inter-nanotube spacing within the bundle was expanded significantly after intercalation. Recently, Maurin et al. [37] studied the structural modifications induced by the intercalation of lithium into MWNTs by XRD with a Seifert diffractometer (using CuK_α radiation). The XRD pattern of the totally lithiated nanotubes shows both a remnant of the Bragg peaks of the pure nanotube and a new set of reflections. The observations of Maurin et al. [37] indicated that carbon nanotubes are partially intercalated or some of them remain unlithiated. This was confirmed by transmission electron microscopy. Maurin et al. [37] also demonstrated that the Li intercalation does not affect the MWNT's diameter.

Grigorian et al. [38] reported intercalation of charged polyiodide chains into the interstitial channels in a SWNT rope lattice. They performed XRD characterization of the tube sample by using a Rigaku diffratometer (CuK_α radiation). A lattice constant was determined to be about 1.68 nm and the average lattice spacing was about 1.472 nm. For heavy iodine intercalation, they found that the intensities of the diffraction peaks due to the rope lattice fell below the detection limit. In their deintercalated samples, the (11) peak was observed to reappear near its original position at $2\theta \approx 6°$ observed in the pristine SWNT rope, but the overall intensity distribution was different from that of the pristine samples; that is, the initial stacking of the tubes in the rope lattice did not recover entirely. The XRD result of Grigorian et al. [38] indicates that iodine acts as a chemical wedge,

entering the interstitial channels between tubes and overcoming the van der Waals attraction between the tubes to force them farther apart [38].

Xu et al. [39] reported the fabrication of Al-doped carbon nanotube composites. They used XRD to examine the structure of doped nanotubes. In their Auger electron spectroscopy study, there are additional elements (mainly oxygen) on the sample surface. However, their XRD pattern has shown that the bulk material mainly consists of Al and carbon nanotubes. Their XRD results demonstrate that the other phases are minor constituents of the Al-doped carbon nanotube composites. The observed lattice parameter of Al is very close to the reference value of 4.0491 Å.

Very recently, Rana et al. [40] performed XRD analyses on the structure and composition of Co-doped carbon nanotubes. Their XRD patterns of the doped tubes were recorded by using a Bruker AXS D8 advance powder X-ray diffractometer (using $CuK_\alpha \lambda = 1.5418$ rad). The Co-doped carbon nanotubes were found to be in the high-temperature face-centered cubic (fcc) phase rather than the hcp phase and were present at the tip of the nanotubes. The covering graphene layers could be responsible for the stabilization of the fcc phase. This is confirmed by the fact that a small amount of Co, which is still in their fcc symmetry, was found to remain even after the acid treatment. Grigorian et al. [41] used XRD to characterize the SWNT doped with transition metal impurities (for example, Cr, Mn, Co, Fe, and Ni). All of the samples exhibited an X-ray diffraction peak in the 2θ range of 5.9° to 6.1° associated with the average tube separation in a bundle. For Fe- Co- and Ni-doped cases, a mean tube diameter, about 1.3 nm, was estimated.

Very recently, Kataura et al. [42] synthesized SWNTs encapsulating fullerenes, so-called fullerene "peapods," in high yield by using diameter-selected nanotubes as pods. It is known that the (10) peak in the XRD profile of SWNT bundles is very sensitive to molecular encapsulation because the total structure factor is modified by additional electron density coming from the molecule encapsulated [43]. In the XRD measurement of C_{70} peapods, Kataura et al. [42] observed a very strong reduction of the (10) peak intensity due to fullerene encapsulation. Because the diameter of C_{70} is about half the diameter of an individual SWNT, the structure factor of the C_{70} chain has twice the period if compared with that of the SWNT. Thus, the total structure factor becomes nearly zero at the (10) peak position, whereas the other peak intensity is not largely affected [42]. In the same manner as gas adsorption inside SWNTs, the filling factors of fullerenes in peapods can be estimated from XRD results. The XRD measurements of Kataura et al. [42] indicate 72% filling for the C_{70} molecule and 85% filling for C_{60} as a total yield.

2.2. UV/IR Spectroscopy

The unique electronic structure of SWNT's (see Section 3.1) is related to a two-dimensional (2D) graphene sheet. However, the continuous electronic density of states (DOS) in graphite, due to the radial confinement of the wavefunctions, divides into a series of spikes in SWNTs, which are referred to as Van Hove singularities. It has been shown that electronic transitions between these singularities lead to prominent features in scanning tunneling spectroscopy [44, 45] and optical spectroscopy [46]. The main point of interest is the electronic structure of SWNTs around the fermi level. However, such a region of the electronic spectrum is difficult to investigate experimentally but is important in any discussion of the metallic character of SWNTs and in addressing questions related to extrinsic effects such as nanotube doping. Very recently, Itkis et al. [47] probed the DOS of SWNTs near the fermi level as a function of SWNT diameter by using far-IR transmission spectroscopy of thin films. The most striking feature in the spectra of purified SWNT films is the intense peak in the far-IR region with an absorption maximum several times higher than that of the interband absorption peaks in the near-IR region. These results can be explained by the doping effects induced in the purification procedure, in which the nitric acid used partially exfoliates and intercalates SWNT bundles [48], which results in a hole doping of the SWNTs. The hole doping serves to pin the Fermi level in the valence band, and the holes behave as free carriers and produce a strong absorption in the far-IR region. Hence, the doping effect leads to a decreased intensity and an distinct shift of the optical transition between the first pair of Van Hove singularities in the DOS to higher energies. This was confirmed upon heating of the SWNT by Itkis et al. [47]. This heating procedure removed the trapped NO_3^- counterions and refilled the valence band. Thus, the optical transition is shifted to lower energy and the intensity increases.

Jacquemin et al. [44] separately investigated the doping behavior (either acceptors Br_2 and I_2 or donors K and Cs used as dopants) of semiconducting and metallic SWNT films using optical absorption [49]. They found disappearance of the absorption bands at 0.7, 1.2 (assigned to semiconducting tubes), and 1.8 eV (assigned to metallic ones) after doping, which were attributed to electron depletion or filling in specific bands of the SWNT. This result implies that the charge transfer in semiconducting and metallic SWNTs occurs in a specific sequence: initially the transition at 0.7 eV, then around 1.2 eV, and finally at 1.8 eV, depending on the dopant density. In a subsequent study by the same group [50], it was established that the semiconducting phase of SWNT can be doped amphoterically. The new absorption peaks induced by heavy doping were explained by the low-lying valence states in the optical transition. They have also studied the effect of high pressure and found that the interband absorption peaks significantly and is reversibly broadened and shifted under high pressure up to 4.1 GPa.

The reversible behaviors of sidewall functionalized SWNTs were demonstrated in fluorinated SWNT samples [51] and in sidewall-alkylated SWNT samples [52] with heat annealing, which has been used as an effective way to recover the pristine nanotubes [53]. However, a detailed study on the recovery behaviors of sidewall functionalized SWNTs is still lacking. Very recently, Zhao et al. [54] systematically examined the thermal recovery behavior of fluorinated SWNTs by UV visible (VIS) near-IR and IR absorption spectroscopies, measured in air by using a Perkin-Elmer UV VIS near-IR spectrometer with a resolution of 2 nm and a Nicolet Magna Fourier transform-IR 550 spectrometer at a resolution of 2 cm^{-1}, respectively. They observed a decrease in the IR intensity of C–F stretch bands

centered at about 1207 cm^{-1}. This indicates that pristine SWNTs are recovered by the removal of sidewall functional groups. After annealing at 373 K in noble gas, their IR spectrum shows nanotube features of A_{2u} mode at 867 cm^{-1} and E_{1u} mode at 1579 cm^{-1}. In their UV VIS near-IR spectrum, they observed only a few features at about 640 nm (1.9 eV). At a higher annealing temperature >423 K, they observed increased intensity of the absorption feature at 640 nm of metallic nanotubes and those at 900 and 1630 nm of semiconducting nanotubes. On the other hand, their generalized 2D UV VIS near-IR spectroscopy studies revealed that thermal recovery behaviors of fluorinated semiconducting and metallic nanotubes are very similar at annealing temperatures between 423 and 623 K. These results indicate that differentiation of these nanotubes for purification is difficult under those annealing conditions.

The abundance of so-called peapods (filling of fullerenes in SWNT) [55, 56] is difficult to determine using high-resolution transmission electron microscopy because of the small sample volume. The limited point-to-point resolution is also insufficient to prove that the peas are fullerenes. Thus, Burteaux et al. [57] exploited the well-known 335 nm transition in C_{60} by performing UV VIS spectroscopy [58] on C_{60}@SWNT. Their UV VIS spectra were recorded in the range of 300–650 nm (Perkin-Elmer Lambda 9). In this region, Burteaux et al. [57] observed all the well-known C_{60} transitions. This proved that the encapsulated object in SWNTs is C_{60}. It is known that electrochemistry offers favorable conditions for both reductive and oxidative doping and the VIS near IR spectroelectrochemistry of SWNT indicates reversible and fast bleaching of the electronic transitions between Van Hove singularities at energies between about ±1.2 eV versus the Fermi level [59]. Very recently, Kavan et al. [60] showed potential dependent VIS near IR spectra of peapods C_{60}@SWNT deposited on an indium-tin oxide (ITO) electrode in 0.2 M $LiClO_4$ + acetonitrile. Their dry peapods in air showed three characteristic optical absorptions at 0.7, 1.25, and 1.8 eV due to the optical transitions between Van Hove singularities as in the empty SWNTs [59, 61, 62]. The transitions at 0.7 and 1.25 eV are assigned to singularities in semiconducting tubes and at 1.8 eV to the first pairs of singularities in metallic nanotubes. Based on the transition energies, the SWNT diameter is estimated to 1.3 nm, in agreement with the optimum diameter of SWNT to encapsulate C_{60} [55, 56]. It should be mentioned that no distinct optical transitions of C_{60} are visible [60]. Kavan et al. [60] found that contact of the peapods with the electrolyte solution shows similar optical spectra as the applied potential varies from −0.6 to 1.6 V. The electrochemical charging causes reversible bleaching of the electronic transitions [60]. The anodic polarization shifts the Fermi level accompanying the sequential depletion of the singularities, whereas the cathodic polarization results in sequential filling of the singularities. At high anodic potentials, Kavan et al. [60] found a new peak, which is red-shifted by 0.05–0.1 eV and can be assigned to a doping induced transition occurring within the partly filled valence band [59]. Upon progressive doping, Kavan et al. [60] did not detect shifts of the peaks. This is indicative of a sharp distribution of SWNT diameters in the peapod samples.

2.3. Raman Spectroscopy

Raman spectroscopy is known to be one of the most efficient tools for investigating the vibrational properties of materials in relation to their structural and electronic properties [63]. Raman scattering for carbon nanotubes is a resonant process associated with allowed optical transitions between spikes in the one-dimensional (1D) electronic density of states falling in the visible and near-infrared ranges.

2.3.1. Alkali Metal-Doped Carbon Nanotubes

Li-Doped SWNTs Claye et al. [64] performed a Raman study on Li-doped SWNTs for doping at various constant potentials. The results are shown in Figure 1. The pristine spectrum is dominated by two first-order bands at 1593.5 cm^{-1} (E_{1g} mode) and 1567 cm^{-1} (E_{2g} mode) for individual pristine tubes [65], whereas the feature at 1485 cm^{-1} is Raman scattering from the electrolyte. Upon doping between 3 and 0 V, a continuous shift and broadening of the two SWNT tangential modes were observed. Especially, an additional line at 1350 cm^{-1} appears between 3 and 1.2 V. It is a general characteristic of disorder-induced phonon scattering at the zone edge and is dominant in samples of nanocrystalline carbons. As shown in the g line of Figure 1, the shift is reversible upon de-doping despite an irreversible loss of crystallinity. Bendiab et al. [66] reported the Raman spectroscopy of thin films of Li-doped SWNTs at different controlled stoichiometries. A monotonic upshift of the tangential modes, due to a concomitant monotonic increase of the conductivity and to the persistence of the crystallinity of the tube bundles, is evidenced for Li_xC compounds ($0 \leq x \leq 0.17$). The Raman study of Maurin et al. [67] on the Li doping of MWNTs showed that lithium species only trapped at the surface of nanotubes, probably within the cavities generated by structural defects or entanglements.
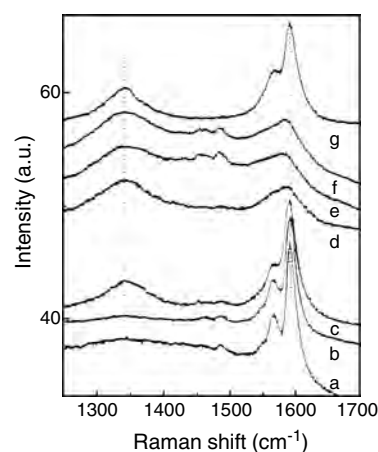
Figure 1. *In-situ* Raman scattering spectra for Li-doped SWNT at various potentials: (a) pristine sample; (b) 2 V; (c) 1.5 V; (d) 0.8 V; (e) 0.02 V; (f) electrochemically de-doped to 3 V; (g) electrochemically de-doped and washed in water and ethanol. Reprinted with permission from [64], A. Claye et al., *Chem. Phys. Lett.* 333, 16 (2001). © 2001, Elsevier Science.

K-Doped SWNTs The pioneering Raman study of K-doped SWNTs by Rao et al. [68] revealed that the tangential mode E_{2g} of the pristine SWNT exhibits a large shift from 1592 to 1550 cm^{-1} upon K-doping. Iwasa et al. [69] reported the phase identification by means of Raman scattering and X-ray photoemission spectroscopy on carefully intercalated SWNT samples. As shown in Figure 2, upon intercalation of potassium in the first 5-min reaction, the broad component disappeared, but the Raman E_{2g} peak was upshifted from 1588 to 1600 cm^{-1} (in this phase, the K/C concentration ratio at 1600 cm^{-1} was 0.04, corresponding to KC$_{27}$). Such an upshift of the Raman peak implies that K exists between the tubes (interstitial sites) rather than inside the nanotubes. Another 5-min reaction resulted in the complete disappearance of the peak at 1600 cm^{-1}, as well as a new peak observed at about 1552 cm^{-1} (in this phase, the K/C concentration ratio at 1552 cm^{-1} was 0.11, corresponding to KC$_9$) that is close to that measured by Rao et al. [68]. From Figure 2, the Raman peak corresponding to the intermediate phases KC$_x$($27 > x > 9$) was extremely broad or absent, indicating that these phases are less stable than either KC$_{27}$ or KC$_9$. Meanwhile, Claye et al. [64] examined the relation between the Raman frequencies and K dopant concentration (Fig. 3). Obviously, the reversibility of the doping-induced frequency shift was confirmed by comparing line a and line g in Figure 3.

Rb-Doped SWNTs the pioneering Raman work on Rb-doped SWNTs by Rao et al. [68] showed that the high-frequency tangential vibrational modes of the carbon atoms in the SWNTs shift substantially to lower end. Bendiab et al. [70] measured Raman spectra for Rb-doped SWNT over a broad frequency range with laser energies of 2.41 and 1.92 eV. The corresponding tangential modes are shown in Figures 4 and 5. The maximum intensity of the main structure for Rb-doped sample is located around 1547 and 1538 cm^{-1}. At 2.41 eV laser energy, the spectral profiles are close to those measured by Rao et al. [68]. Moreover, Bendiab et al. [71] performed combined *in-situ* conductivity and Raman measurements of Rb-doped SWNTs. They

Figure 3. *In-situ* Raman scattering spectra for K-doped SWNT at various K/C ratios: (a) pristine sample; (b) 0.002; (c) 0.004; (d) 0.020; (e) 0.034; (f) 0.040; (g) electrochemically de-doped, K/C = 0. Reprinted with permission from [64], A. Claye et al., *Chem. Phys. Lett.* 333, 16 (2001). © 2001, Elsevier Science.

observed striking correlations between resistance, changes of resistance under laser irradiation, and frequency of the main Raman peak.

Cs-Doped SWNTs Bendiab et al. [70] measured Raman spectra for Cs-doped SWNTs over a broad frequency range with laser energies of 2.41 and 1.92 eV and the corresponding tangential modes are shown in Figures 4 and 5. The maximum intensity of the main structure for

Figure 2. Raman spectra for the intercalation process of SWNT with potassium. Reprinted with permission from [69], Y. Iwasa et al., *Synth. Met.* 121, 1203 (2001). © 2001, Elsevier Science.
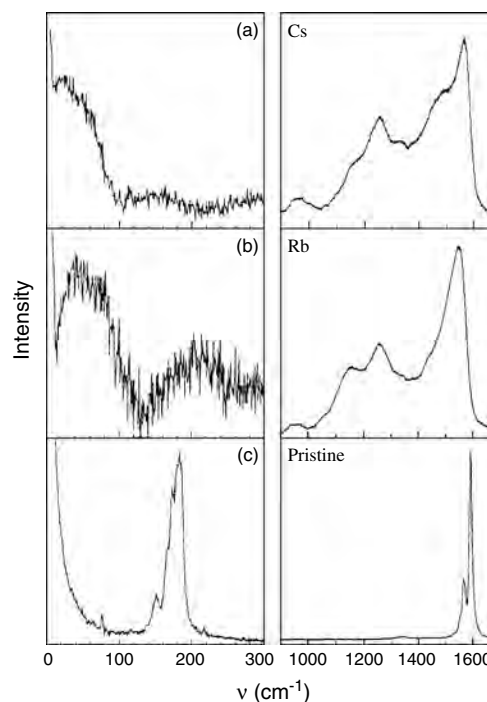
Figure 4. Low-frequency (radial breathing modes) and high-frequency (tangential modes) ranges of the Raman spectra excited at 2.41 eV for (a) Cs-doped; (b) Rb-doped, and (c) pristine SWNTs. Reprinted with permission from [70], N. Bendiab et al., *Chem. Phys. Lett.* 339, 305 (2001). © 2001, Elsevier Science.
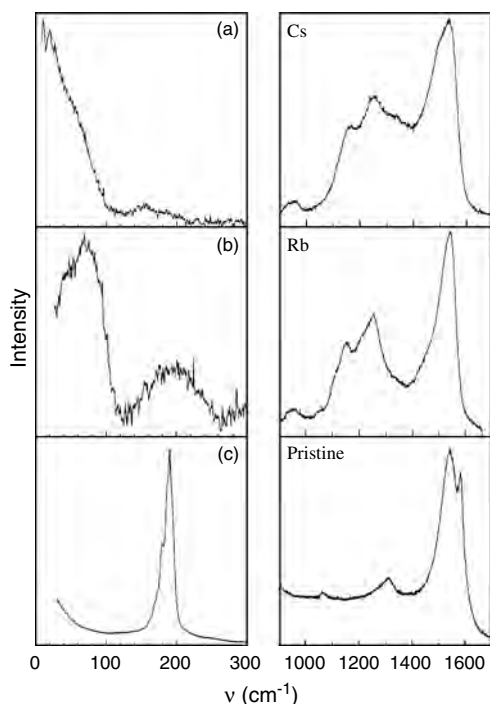
Figure 5. Low-frequency (radial breathing modes) and high-frequency (tangential modes) ranges of the Raman spectra excited at 1.92 eV for (a) Cs-doped; (b) Rb-doped, and (c) pristine SWNTs. Reprinted with permission from [70], N. Bendiab et al., *Chem. Phys. Lett.* 339, 305 (2001). © 2001, Elsevier Science.

Cs-doped sample is located around 1563 and 1534 cm^{-1} at energies of 2.41 and 1.92 eV, respectively. Obviously, the Raman spectral profiles for Li-, K-, Rb-, and Cs-doped SWNTS are similar, and the frequency shift is close. This result shows that the amount of transferred charges for saturation doping is only weakly dependent on the doping species for alkali metal. The profile is broad, asymmetric, and systematically associated with a shoulder on its low-frequency side. We have also seen a universal behavior of the doping-induced shift of the tangential modes, namely, an upshift of the tangential modes due to a concomitant monotonic increase of the conductivity and to the persistence of the crystallinity of the tube bundles. However, in contrast, the downshift of the tangential modes and the drastic changes of the Raman spectra and diffraction patterns observed for saturation-doped compounds [64, 68, 70, 71] suggest significant modifications in the structural and electronic properties of the saturated phase.

2.3.2. Br$_2$-*Doped Carbon Nanotubes*

The pioneering work of Rao et al. [68] showed that the high-frequency tangential vibrational modes of the carbon atoms in the pristine SWNTs shift substantially to higher frequencies. Because the sample contains many kinds of SWNTs with different chirality that have different electronic states [72], Kataura et al. [73] measured low-frequency resonance Raman spectra of Br$_2$-doped SWNTs using various laser lines (from 1.63 to 2.73 eV) to clarify the electronic states of the doped SWNTs. For visible excitation, two structures around 180 and 240 cm^{-1} were observed. For fully doped

samples, only one peak around 260 cm^{-1} was observed, consistent with the results of Rao et al. [68]. Actually, the structure around 240 cm^{-1} is the breathing mode of the partially doped SWNT bundles and the structure around 180 cm^{-1} can be associated with that of pristine SWNTs.

2.3.3. I$_2$-*Doped Carbon Nanotubes*

Iodine can be effectively doped into SWNTs [38, 68, 74–76]. However, it cannot be intercalated inside graphite [77] because its large van der Waals diameter (∼0.4 nm) [78] and interatomic spacing (∼0.3 nm) are incompatible with any spacing of the basal plane in graphite [79, 80]. Rao et al. [68] found that I$_2$ doping induces the smallest change in the SWNT Raman spectra. Actually, this is not surprising because I$_2$ does not intercalate into graphite. Later on, Grigorian et al. [38] analyzed the Raman scattering data for I$_2$-doped SWNT samples. Because of resonant Raman scattering from charged (I$_5$)$^-$ and (I$_3$)$^-$ linear chain complexes in the moderately doped samples, new peaks including a strong one at 175 cm^{-1} and a weaker one at 109 cm^{-1} were observed in the low-frequency region [38]. The main effect of polyiodide chain intercalation on the high-frequency Raman triplet observed in the pristine sample is an upshift of these modes by about 8 cm^{-1} because the carbon π electron transfer from the SWNTs to the iodine chains induces a contraction of the hexagonal rings along the cylindrical wall of the SWNTs. After deintercalation, the tangential and radial modes were fully recovered. Very recently, Venkateswaran et al. [81] measured the Raman spectra of I$_2$-doped SWNT bundles excited with 514.5 nm at room temperature and elevated pressure up to 7 GPa. In pristine nanotube samples, the low-frequency radial modes show a pressure-dependent shift at about 7 cm^{-1}/GPa, while that in I$_2$-doped SWNTs exhibits a very small pressure-induced frequency shift. A comparison between the pressure behavior of I$_2$-doped and pristine SWNTs suggests that polyiodide chains (i.e., I$_n^{-1}$ molecules) [38] might reside both in the interstitial channels and inside the nanotube pores in the SWNT bundles.

Very recently, Zhou et al. [82] also characterized I$_2$-doped multiwalled carbon nanotubes by means of Raman scattering. Similar to the case of SWNTs, MWNTs can be effectively doped by iodine with charge transfer. Iodine atoms form charged polyiodide chains inside tubes of different inner diameter but cannot intercalate into the graphene walls of MWNTs.

2.3.4. B-*Doped Carbon Nanotubes*

Boron, as a dopant, can substitute for the carbon atoms in nanotubes. Very recently, Maultzsch et al. [83] reported on first- and second-order Raman spectra of B-doped MWNTs. Their samples were prepared by the arc-discharge method in which the anode rod is doped with varying weight concentrations of boron. The absolute intensity of the D mode (the so-called D mode around 1300 cm^{-1} in the first-order Raman spectra of carbon nanotubes and graphite is induced by disorder in a double-resonant Raman process) in the doped MWNTs is found to be roughly constant and increase slightly from 0.5 to 1% nominal boron concentration and decreases again at 4% nominal boron concentration. The

high-energy mode (often called the G mode) as well as the D* mode (the second-order overtone mode) intensities decrease with increasing defect concentration, while the D* mode intensity decreases much faster than the G mode intensity. These results support the interpretation that the high-energy mode originates from the same defect-induced, double-resonant process as the D mode, although involving comparatively small phonon wave vectors.

2.3.5. Fullerene Peapods

The discovery of fullerene peapods like C_{60}@SWNT [55, 56] and C_{70}@SWNT [42] opened new possibilities to electrochemistry and functionalization of carbon materials. Because SWNTs and fullerenes show a specific redox response, there is a clear challenge to explore the behavior of C_{60}@SWNT and discuss the fundamental electronic and redox properties of such carbon nanostructures. Electrochemistry offers favorable conditions for both reductive and oxidative doping. Kavan et al. [60] performed measurement of *in-situ* Raman spectra of peapods excited at 2.41 or 2.54 eV as shown in Figures 6 and 7, respectively. The radial breathing mode was observed between 175 and 185 cm^{-1} for 2.41 eV excitation and between 165 and 190 cm^{-1} for 2.54 eV excitation. The intensities of radial breathing and tangential modes decrease as a result of cathodic or
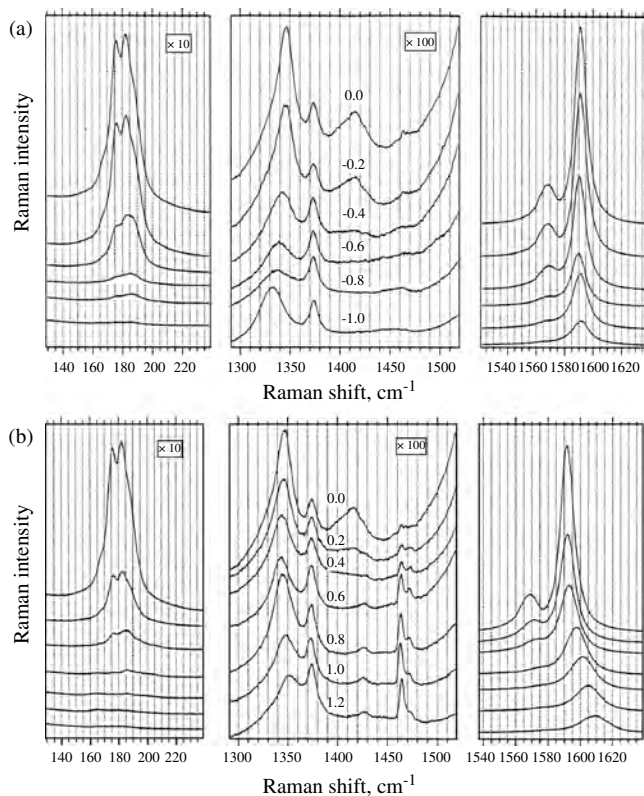
Figure 6. Potential-dependent Raman spectra of C_{60}@SWNTs on a Pt electrode excited at 2.41 eV in 0.2 M LiClO$_4$ + acetonitrile: (a) the electrode potential varies from 0 to -1.0 V; (b) potential varies from 0 to 1.2 V. The peak at 1375 cm^{-1} belongs to δC–H in acetonitrile. Reprinted with permission from [60], L. Kavan et al., *Chem. Phys. Lett.* 361, 79 (2002). © 2002, Elsevier Science.
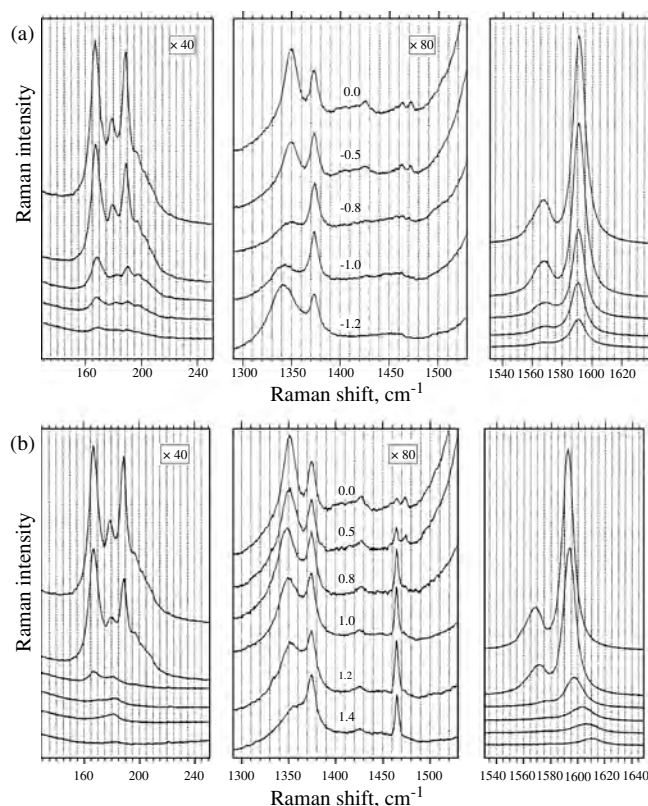
Figure 7. Potential-dependent Raman spectra of C_{60}@SWNTs on a Pt electrode excited at 2.54 eV in 0.2 M LiClO$_4$ + acetonitrile: (a) the electrode potential varies from 0 to -1.0 V; (b) potential varies from 0 to 1.4 V. The peak at 1375 cm^{-1} belongs to δC–H in acetonitrile. Reprinted with permission from [60], L. Kavan et al., *Chem. Phys. Lett.* 361, 79 (2002). © 2002, Elsevier Science.

anodic doping. An analogous effect was also shown in empty SWNTs [59, 84]. Their Raman spectroscopy results confirm a reasonable monodispersity of their sample, free from narrow tubes. The spectra excited at 2.41 eV exhibit a charging-sensitive band at 1415 cm^{-1}. As shown in Figures 6 and 7, the tangential mode band upshifts, both significantly and monotonically, with increasing anodic potential, but less sensitive to cathodic charging. The intensity of the A$_g$ mode of C_{60} exhibits considerable enhancement upon anodic doping of peapods but not at cathodic charging. This new feature is specific for peapods only, and the resistance of C_{60} toward oxidation is a key factor. Moreover, Kataura et al. [42] found that the room temperature Raman spectra of C_{60}@SWNT show 1D photopolymerization of C_{60} inside nanotubes by blue laser irradiation, which suggests molecular rotation inside them.

In the case of C_{70}@SWNT, Kataura et al. [42] found that all the Raman-active modes of C_{70} were observed even at room temperature and no photopolymerization was observed, but the relative intensity ratio of each peak is different from that in the three-dimensional (3D)-crystalline phase. This is caused by mixing of two different crystal structures in C_{70} peas. (Note: there is a mixed phase of two different structures in the C_{70} 1D crystal. So, the interaction between C_{70} molecules should differ from each other and also from the 3D crystal.) Their Raman spectra suggest

that the encapsulated molecules are deformed by interaction with the SWNT.

Grigorian et al. [41] found that Raman-scattering spectra for SWNT doped with transition metal impurities (e.g., Cr, Mn, Co, Fe, and Ni) were similar: the SWNT radial mode band exhibited an unresolved doublet with peaks at 165 and 178 cm^{-1}. Their results suggest very small differences in the mean tubule diameter from one sample to another.

2.4. NMR Spectroscopy

In common with that for other types of molecular spectroscopy, analysis of the frequency, relative intensity, and shape of high-resolution NMR spectra [85–87] yields molecular parameters that characterize the molecular intrinsic properties. These parameters include nuclear magnetic shielding σ [88] and nuclear spin–spin coupling J [89]. Both of these are determined by the electronic environments of the nuclei involved. Hence, studies of these parameters for a given molecule can provide knowledge of the electronic structure of that molecule, in particular the density of states at the Fermi level [90].

Leroux et al. [91] studied the fully Li-reacted MWNTs by carrying out solid-state ^{7}Li NMR experiments on a Bruker 360 spectrometer (^{7}Li resonance frequency of 139.9 MHz). Chemical shifts were referred to LiCl as an external standard. The presence of metallic lithium was not observed in the NMR spectra. The peak at 0 ppm was associated with the presence of the lithium salt. The peak at 12 ppm was attributed to the intercalated Li by reference with the well-known value for lithium–graphite intercalation compounds [92]. Among the heat-treated MWNTs, a downfield shift was observed with a slight increase of the reversible capacity. So the reversible capacity was assigned to particular Li sites. As the temperature increases, a change of the Li population was observed and the peak at 12 ppm was shifted to high field. Recently, Maurin et al. [67] performed high-resolution magic angle spinning ^{7}Li NMR on MWNTs using a Bruker ASX 400 spectrometer operating at a ^{7}Li resonance frequency of 116 MHz. The NMR spectrum exhibits a broad band centered around 0 ppm that is separated into two parts: a narrow band with resonance frequency of -0.8 ppm, which is assigned to the solid electrolyte interphase and to the remaining electrolyte, and a broad band with a resonance frequency shift of -0.1 ppm, which is assigned to the ionic lithium stored in reversible sites as defects at the nanotube surface. These results indicate different insertion mechanisms of lithium.

Duclaux et al. [35] investigated the modifications of electronic properties as the pristine MWNT was doped with alkali metals by using high-resolution ^{12}C NMR. It was found that the chemical shifts of the first stage KC$_8$- or CsC$_8$-MWNT ^{12}C NMR signal are practically of the same order as those in graphite-intercalated compounds (GICs) with an inversion of anisotropy attributed to the dipolar interaction of the ^{12}C nucleus with the π electrons. intercalation of K, Rb, and Cs in SWNT bundles with stoichiometry near MC$_8$ produced similar results [29]. This is a signature of charge-transfer conducting species [93], similar to GICs.

2.5. EPR/ESR Spectroscopy

A lot of experimental data on magnetic susceptibility, ESR and EPR of MWNTs have offered us undisputed evidence that those nanotubes are semimetals rather than semiconductors [94–100]. In the following, we review recent measurements on the EPR/ESR of doped carbon nanotubes.

Bandow et al. [101] studied the magnetic properties of pristine SWNTs and K-doped SWNTs by ESR. Basically, pristine SWNTs are ESR silent. But a weak ESR signal with $\Delta H \approx 2.7$ G at $g \approx 2.0026$ was observed because of the electronic states associated with the pentagonal carbon rings at the tip region of the SWNT. Considering the conduction ESR (CESR) of the pristine SWNTs and even SWNT bundles, they could not detect any signal at X-band (9.419 GHz) due to the weak magnetism of conduction electrons and the sensitivity limit of the instrument. However, after 1 h of K-doping, the observed weak ESR signal in the pristine SWNTs disappeared. After 50 h of doping, a weak Dysonian-type ESR spectrum was observed. They also observed CESR spectra at the doping times of 150 and 1000 h. The intensity of the CESRs was saturated at doping time longer than 400 h. The magnitude of χ for K-doped SWNTs was found to be about 1 order of magnitude smaller than that of the graphite [102]. Bandow et al. [101] argued that such a small χ is probably caused by the nature of the electronic structures of the pristine SWNT bundle. Because two-thirds of the SWNTs in the bundle are semiconducting, the decrease of the magnitude of χ is reasonable.

Duclaux et al. [35] performed EPR measurements on pristine and KC$_8$-MWNTs. The temperature dependence of their EPR spectra is shown in Figure 8. They found that the EPR line of the first-stage KC$_8$-MWNT is Dysonian, typical of a good conductor. In the pristine MWNTs, the g factor is temperature dependent. In the doped case, it becomes temperature independent because of the shift of the Fermi level away from the quasidegeneracy region of the π bands induced by the charge transfer. For the second stage as KC$_{24}$-MWNT, the Dysonian EPR signal was found to be narrowed compared to that of the first stage. The charge transfer is almost complete in the second-stage derivative,
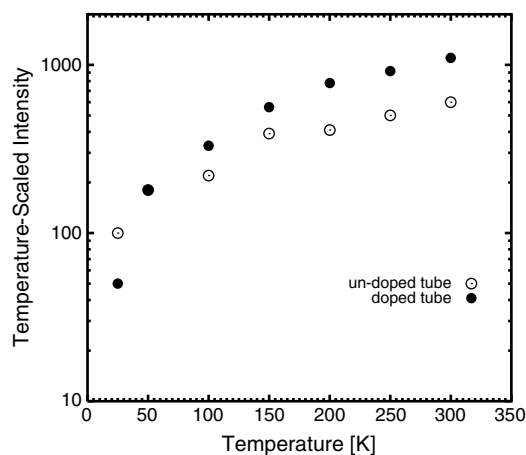
Figure 8. Temperature dependence of the intensity (I) of the EPR signal at several temperatures (T, in K). The intensity is scaled by the temperature; that is, $I = I * T$. Adapted from [35].

and the broadening due to spin-orbital interaction of the conduction electrons on alkali atoms is limited. Regarding Cs doping, the EPR signal of the first-stage CsC_8-MWNT was undetectable due to noncomplete charge transfer [103] and a large width caused by the strong spin orbital interaction on Cs.

Yokomichi et al. [104] and Hsu et al. [105] performed ESR measurements on B-doped carbon nanotubes. The ESR spectra are Dysonian. The B-doped nanotube samples exhibit free spin characteristics with a g value of 2.002 at room temperature, while the typical value for all pristine carbon nanotubes is 2.0189. The g value of the B-doped tube decreases slightly as temperature decreases [104]. Their ESR measurements revealed several distinguishing features [105]: (1) only one ESR transition is observed within the temperatures from 50 to 450 K; (2) the peak-to-peak linewidth (0.45 mT) in the first derivative does not change appreciably in the temperature range from 50 to 450 K; (3) the measured g value varies between 2.0021 and 2.0025; (4) asymmetrical spectra line shape are independent of temperature; and (5) the line absorption intensity increases linearly with temperature over the 108–200 K range and then remains constant up to 435 K. Their ESR results are strongly indicative of metallic behavior in the B-doped carbon nanotubes. They also found that the carrier density increases rapidly from 0.8×10^{16} spins/g at 108 K to 6.1×10^{16} spins/g at 253 K, then remains a constant within $\pm 0.3 \times 10^{16}$ spins/g between 253 and 435 K. Thermally activated electrons are involved in the rapid increase in carrier density from 108 to 253 K.

Kotosonov and Shilo [106] performed experimental measurements on the diamagnetic susceptibility (DMS), which is measured by using the Faraday method with an error of not over 10^{-8} emu/g, and the ESR, which is measured by using a Varian E-109 spectrometer operating at 9.3 GHz, for pristine and B-doped MWCTs in the temperature range of 100 to 900 K. The samples of MWCTs with an average diameter of 15 nm were selected from a central fibrous part of cathode deposits prepared by the arc-discharge method under optimal conditions. B-doped MWCTs were obtained by heating up to 2773 K of powder samples wetted with a weak boric acid solution. The absolute error of g factor measurement was less than 0.0001. The orbital contribution of conduction carriers, $\chi_n - \chi_a$, can be readily explained in terms of the quasi-two-dimensional graphite (QTDG) band model [107]

$$\chi_n - \chi_a = -\frac{0.00545\gamma_0^2}{T_\delta \zeta_a} \tag{1}$$

where

$$\zeta_a = 2 + e^{E_F/(\kappa_B T_\delta)} + e^{-E_F/(\kappa_B T_\delta)} \tag{2}$$

and $T_\delta = T + \delta$, $\gamma_0 \approx 3$ eV is the 2D band parameter, E_F is Fermi energy, κ_B is the Boltzman constant, T is the lattice temperature, δ is the additional parameter introduced with account of nonthermal scattering of conduction carriers by structural defects, and χ_n is the DMS component normal to the graphene sheets. The DMS value along the nanotube axis, that is, χ_p, is close to the atomic one, $\chi_a = -0.3 \times 10^{-6}$ emu/g. The observed single and narrow lines of the

ESR spectra show that the registered g factor is a result of motional averaging of the principle g factors (g_p along the nanotube axis and g_n normal to the nanotube layers, and g_p is close to the value of the free electron, $g_e = 2.0023$). The g factor shift can also be explained in terms of the QTDG band model [108]:

$$\Delta g = g_n - g_e \approx \frac{7680\gamma_0^2}{T_\delta^2 \zeta_a ln(\zeta_a)} \tag{3}$$

The above equations demonstrate that the g factor shift depends strongly on the contribution from conduction carriers, band structure, Fermi level, and temperature. The observed results show that the defects are linear in the pristine carbon nanotubes, while the defects are point types for B-doped carbon nanotubes. Because the boron atom acts as an electron acceptor, the Fermi level is more shifted into the valence band. Thus, the magnetic properties in nanotubes change. Estimation of the ESR intensity measured at 300 K shows that the B-doping results in a increase (from 0.8 to 1.2×10^{-8} emu/g) of the paramagnetic susceptibility of conduction carriers. Meanwhile, as the concentration of boron atoms changes from 0 to 29×10^{14} m^{-2}, the density of conduction carriers varies from 8 to 37×10^{14} m^{-2} and the density of localized centers changes from 0.7 to 2.0×10^{14} m^{-2}. It should be pointed out that these factors at low temperature have strong effects on the registered g factor and ESR intensity due to the strong exchange interaction between them and conduction carriers [106].

2.6. Positron Lifetime Spectroscopy

Positrons are positively charged elementary particles. If positrons are injected into a condensed material, they would be strongly repelled from the atomic nuclei of the material and prefer to be distributed in such kinds of distinguishable regions in which open-volume defects, negatively charged ions, and interstices are presented. Actually, the characteristics of positron annihilation with electrons depend on the positron and electron density distribution in a given material and the amount of overlap between the positron and electron wavefunctions. Hence, positron annihilation is able to provide us information on the electron distribution in the region where positrons annihilate through their lifetime, angular correlation of annihilation radiation and Doppler broadening. The electron–positron correlation results in an enhancement of the annihilation because of the pileup of electrons and positrons: positrons are fully thermalized at the time of annihilation, and the longitudinal-momentum component of the electron along the direction of the annihilated γ-ray emission is related to the doppler broadening of the annihilation γ-ray energy.

Traditionally, measurements of the positron lifetime and/or the Doppler broadening of the annihilation γ ray have been used for material analysis. Recently, this technique has been applied to C_{60} [109–111] and C_{70} fullerenes [112], carbon nanotubes [112, 113], and doped carbon nanotubes [113].

Murakami and Sano [113] prepared alkali metal (AM) doped carbon nanotubes (DCNTs), for example, K-DCNT, Rb-DCNT, and Cs-DCNT, from uncapped MWNTs (Bucky

BU-201) by using the method that is used for preparing alkali metal-intercalated carbon filaments grown from graphitic material in argon plasma [114]. The diameter in each DCNT is several tens of nanometers and the distance between adjacent shells is about 0.34 nm. Then they measured positron-lifetime spectra for pristine CNTs and AM-DCNTs at both 10 K and room temperature by using the positron source, ^{22}NaCl, of 0.55 MBq sealed between two Kapton films of 7500 nm thick. This source was directly dropped onto specimens packed in a glass ampoule. Their positron-lifetime spectra were observed with the aid of a conventional fast-fast coincidence system whose time resolution was 250 ps and analyzed after a positron source correction by the computer program PATFIT88 [115]. The results of lifetime spectrum analysis for AM-DCNTs are listed in Table 1. For contrast, the lifetimes for C_{60}, C_{70}, and CNTs measured by Ito and Suzuki [112] are also listed in Table 1. All positron lifetimes were represented well by a single component, which means that all of the positrons in these specimens have a rather similar history between annihilation. A positron lifetime exists for CNTs similar to that for both C_{60} and C_{70} fullerenes. The lifetimes for AM-DCNTs are shorter than the lifetime for pristine CNTs. This result reveals that the annihilation of positrons occurs in a region of higher electron density, which is expected in graphitic shells of pristine CNTs because some negative charge transfers from the alkali metal atoms (electron donors) to the graphite shells (electron acceptors) of the CNTs. The lifetime for each AM-DCNT is independent of alkali metal dopant and has the same range, for example, 360 ps at room temperature and 350 ps at 10 K. As shown in Table 1, the lifetimes observed for AM-DCNTs are found in the same range as those ascribed to lattice defects in both graphite and stage 1 potassium-intercalated graphite (PIG). Because the diffusion length is much longer than the diameter of each AM-DCNT [113], the positrons in AM-DCNTs reach trapping centers on the surface of nanotubes. The trapping centers are remotely located from the alkali metal and derived from extended lattice defects (such as edge dislocations [116] and surface steps) that are located on their negatively charged graphitic shells. It should be pointed out that in graphite, as shown in Table 1, there

are two lifetime components of 220 ± 10 ps due to positron annihilation in the bulk and 430 ± 10 ps due to positron annihilation on the surfaces or the open space of graphite [117]. In stage 1 PIG [113], the shortest life time (260 ps) is assigned to positron annihilation in the bulk, the intermediate one (530 ps) is due to positron annihilation at lattice defects, and the longest one (1400 ps) has been generally accounted for by annihilation of *ortho*-positronium [118]. However, the results for nanotubes show that the positron does not annihilate between the coaxial layers of the tubes, but rather annihilates on the surface of the tubes.

3. PROPERTIES AND APPLICATION OF DOPED CARBON NANOTUBES

3.1. Electronic Properties

Designing nanoscale materials and devices entirely from carbon nanotubes requires the control of electronic characteristics of carbon nanotubes. This involves the ability to engineer the densities and locations of specific energy levels within the electronic band structures of carbon nanotubes. It is well known that at the nanoscale, spatial variations in the local electronic structures of a nanostructure have strong effects, for example, on transport, field emission, and optical applications. Hence, it is necessary to characterize spatial variations of the electronic structure obtained from a variety of synthesis approaches to control the electronic properties of carbon nanotubes. Actually, the tailoring of electronic properties in carbon nanotubes occurs in two ways: exploiting the strong coupling between a tube's topology (intrinsic variables, e.g., tube chirality, diameter, and total curvature of the tube manifold) and its overall electronic properties [119, 120] (this way led to the idea of constructing nanoelectronic devices by joining carbon nanotubes of different topologies and electronic properties) or modifying an extrinsic variable of carbon nanotubes such as chemical modification [120]. Generally, property modification through doping is difficult when device dimensions are submicron. Carbon nanotubes [121] may offer the possibility of realizing carbon-based nanoelectronic components, which circumvent some of those difficulties met before, for example, by the introduction of donor/acceptor levels through substitutional doping of the carbon nanotubes. In the following, we shall review the electronic properties of carbon nanotubes doped with both nonmetal elements (B, N, Si, and O) and the alkali metals.

3.1.1. Doping with Nonmetal

Experiments show that B-doping [122–128] changes the electronic properties of the host carbon nanotubes. Carroll et al. [127] investigated the spatial homogeneity of electronic properties, as evidenced by the local density of states (LDOS) of pure and B-doped MWNTs, using scanning tunneling microscopy (STM) and scanning tunneling spectroscopy (STS). As shown in Figure 9, the most striking difference between the LDOS is that the pure carbon nanotubes show small bandgaps (semiconducting or semimetallic behavior) whereas for the B-doped MWNTs the bandgap is

Table 1. Observed positron lifetimes, τ_1 at 10 K and τ_2 at room temperature, for C_{60}, C_{70}, CNT, K-DCNT, Rb-DCNT, Cs-DCNT, graphite and stage 1 PIG.

Material	τ_1 (ps)	τ_2 (ps)	Ref.
C_{60}		389 ± 2	[112]
		382	[111]
		360.6	[110]
	342	356	[109]
C_{70}		384 ± 2	[112]
CNT		387 ± 1	[112]
	360 ± 2	382 ± 2	[113]
Graphite		$220 \pm 10, 430 \pm 10$	[117]
		210 (91%), 390 (9%)	[113]
Stage 1 PIG		260 (84%), 530 (14%), 1400 (2%)	[113]
K-DCNT	354 ± 2	362 ± 2	[113]
Rb-DCNT	357 ± 2	364 ± 2	[113]
Cs-DCNT	355 ± 2	362 ± 2	[113]
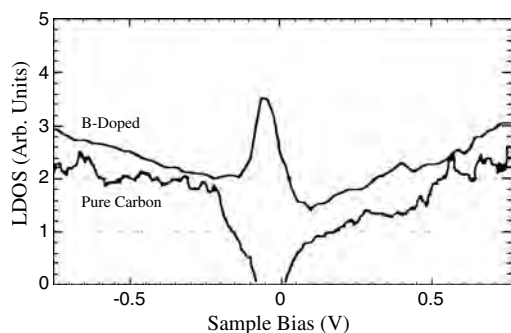
Figure 9. LDOS of pristine and B-doped MWNTs. Both spectra are from tubes of similar diameter (approximately 10 nm). Reprinted with permission from [127], D. L. Carroll et al., *Carbon* 36, 753 (1998). ©1998, Elsevier Science.

filled from the valence band side with a prominent acceptor-like peak near the Fermi level. Their observation of singular points in the doped samples is indicative of an exceptionally high structural perfection in the outmost tube cylinders probed by the STS measurement [126]. The acceptor-like states as well as the singularities are common features in all STS measurements performed on doped carbon nanotubes. *Ab initio* calculations [126] pointed out that the metallization and the strong acceptor state observed cannot be explained by isolated B substitutional atoms in the graphite network but be explained as resulting from nanodomains of BC_3 within the metallic nanotube lattice. Carroll et al. [127] observed distinct variations of the LDOS for different positions on the body of doped MWNT samples as shown in Figure 10, where the resonance is seen at about 300 meV (Figure 10, top) and 250 meV (Figure 10, bottom). For pure tubes, the characteristic difference in the LDOS between different tubes can be found, but there are no spatial variations on one tube. The spatial variations in electronic structure along the doped tube will have consequences for the application of the tubes to carrier transport as reviewed in the coming section: any hole traveling along the tube with an energy near the Fermi level will find the density of its possible states drastically changing from region to region [127]. Carroll et al. [127] indicated that the observed nonuniformity of the electronic structures is most likely related
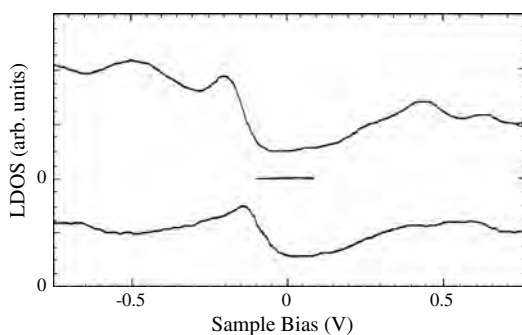
to an inhomogeneous distribution of the dopant elements in the structure. The closure of carbon nanotubes at the tube end is related to different topology compared with that of the tube sidewall. This will result in variations in electronic nature at the tube ends that is actually reflected in the LDOS. Carroll et al. [127] compared the variation of electronic structure at the tube end with that on the sidewall for both pristine and B-doped carbon nanotubes. Their results are shown in Figure 11. Because of the existence of pentagonal defects in the hexagonal lattice, responsible for inducing the curvature to close the tube [129], the width of the apparent bandgap in the pristine case is reduced by the appearance of states from the valence bandgap edge. For the B-doped case, the prominent peak close to the Fermi level is shifted to lower energies or even disappears altogether at the tube ends. It is well known that B-doping significantly increases the stiffness of carbon fibers [130] and plays an important role in the resistance to oxidation of graphitic systems [131]. These results suggest that B-doping might be a good way to produce long and well-graphitized carbon nanotubes with interesting electronic properties. Electron microscopy observations and electron diffraction patterns of Blase et al. [128] have shown that B-doping considerably increases the length of carbon tubes and results in a remarkable preferred zigzag chirality. Their first-principles static and dynamical simulations indicated that B atoms in the zigzag geometry act as a surfactant during growth, preventing tube closure, whereas this mechanism does not extend to armchair tubes, which suggests a helicity selection during growth.

Although the exact mechanisms and lattice effects of doping schemes in carbon nanotubes differ slightly from those
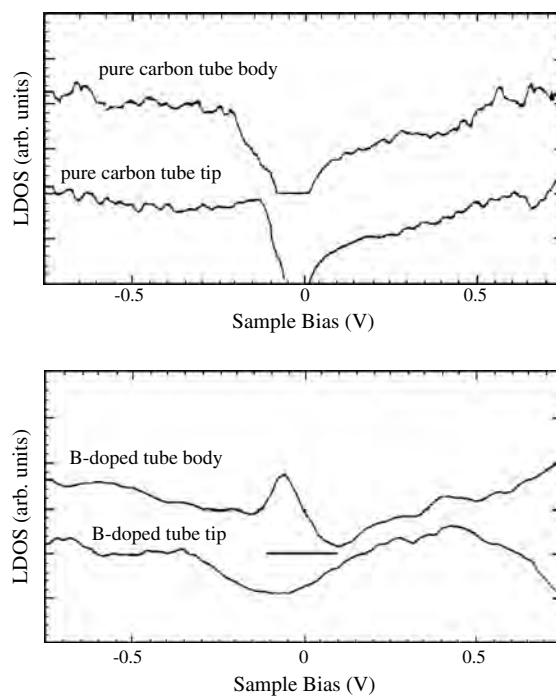
Figure 11. A comparison of the LDOS of pristine and B-doped MWNTs approaching the closure structures (tips). Both spectra are from tubes of similar diameter (approximately 10 nm). Reprinted with permission from [127], D. L. Carroll et al., *Carbon* 36, 753 (1998). © 1998, Elsevier Science.

Figure 10. A comparison of two variations in the LDOS of B-doped MWNTs. Both spectra are from tubes of similar diameter (approximately 10 nm). Reprinted with permission from [127], D. L. Carroll et al., *Carbon* 36, 753 (1998). © 1998, Elsevier Science.

of bulk materials such as Si, their similarities are striking. For a complete analogy to bulk semiconductor technology in low-dimensional materials, researchers seek to dope the materials so that n-type and p-type conduction occurs. Thus, it is necessary to introduce donor states to the system as well as acceptor states as discussed above. Recently, Czerw et al. [132, 133] synthesized N-doped carbon nanotubes using pyrolysis. It was found that N-doping of the carbon nanotube lattice resulted in the introduction of conduction band modifications, including a large electron donor state (n-type) lying approximately 0.2 eV from the Fermi level [132]. The local environment of the N within the carbon network mainly consists of N–C structures arranged in a pyridine-like configuration [132]. The tight-binding and *ab initio* calculations show that pyridine-like structures are responsible for the metallic behavior and the prominent features near the Fermi level. The studies of Czerw et al. [132, 133] suggest a way to achieve full p-n junctions, using N- and B-doped carbon nanotubes, which play a key role in the fabrication of novel carbon-based electronic devices [134, 135]. Moreover, Czerw et al. [132] noted that connections between N- and B-doped carbon nanotubes result in a barrier of about 0.5 V. Very recently, Zhi et al. [136] studied systematically the adjustable photoluminescence and field electron emission properties of large-scale highly aligned boron carbonitride nanotubes synthesized by using the bias-assisted hot filament chemical vapor deposition. Their work has verified the controllability of the electronic band structure of the boron carbonitride nanotubes by properly varying the boron or nitrogen atomic concentrations in the nanotubes; that is, the electronic band structure of such series of nanomaterials with tailored and adjustable properties are realized.

Optical absorption can detect changes in some specific electronic states of a material. Because of doping, electron depletion from or filling to specific energy bands of the pristine material in the semiconducting or metallic phase would lead to disappearance of several absorption peaks, demonstrating the amphoteric behavior of doping. Emergence of new peaks can be explained as arising from doping-induced optical transition involving high- or low-lying electronic states [61]. Kazaoui et al. [61] measured the change in optical absorption spectra of pristine SWNT thin films by p-type (I_2 and Br_2) doping. By controlling the stoichiometry, the electron transfer can be tuned so that the Fermi level coincides with specific bands of the density of states of semiconducting and metallic SWNTs accompanying the disappearance of the absorption bands at 0.68, 1.2, and 1.8 eV observed in the pristine SWNTs. Petit et al. [137] found that I_2- or Br_2-doped SWNTs are air insensitive. These redox reactions are reversible [61, 137], and the pristine materials can be recovered, for example, by exposure of the doped sample to molecules of redox potential close to that of pristine SWNTs such as benzoquinone [137] or after deintercalation by annealing under vacuum [61]. It should be noted, however, that for highly Br_2-doped SWNTs, the vanished absorption bands are only partially restored with considerable broadening after annealing at temperatures as high as 300 °C under vacuum, indicating the irreversibility of the

charge transfer, probably deriving from strong interaction between Br and SWNTs.

Zhang et al. [138] found that substitution of oxygen does not obviously change the binding energy and localized resonant states in the substitutional location, which affect the electronic and related properties of nanotubes, for example, the conductance and electron emission properties discussed in the following sections. Meanwhile, the barrier for inserting an O atom through the center of a hexagonal ring of carbon nanotubes was determined to be 13.7 eV, and under thermal conditions the O atom binds to the nanotube without a barrier, leading to one of two products: an epoxide and an adatom oxygenated nanotube[139]. It should be pointed out that tube curvature effects could lead to an increase of the epoxide binding energy with a decrease in tube diameter [139].

Predictions of the electronic properties of silicon substitutional doping in carbon nanotubes was investigated by Baierle et al. [140]. A large outward displacement of the Si atom and its nearest-neighbor carbon atom is observed. For (6, 6) and (10, 0) tubes, the formation energies of the substitutional defects are obtained at around 3.1 eV/atom. In particular, in the doped metallic nanotube, a resonant state appears at about 0.7 eV above the Fermi level, whereas the silicon for the semiconducting tube introduces an empty level at about 0.6 eV above the top of the valence band. Their results indicate that the Si substitutional impurity will be highly reactive, serving as a binding center to other atoms or molecules.

3.1.2. Alkali Metal Intercalation

So far, alkali metal intercalation into the carbon nanotube and tube bundles has been intensively studied both experimentally and theoretically, partially due to potential applications in batteries. Table 2 summarizes the Li storage capacity of different carbon-based materials. Li storage capacity up to Li_2C_6 (∼677 mAh/g) is obtained in purified SWNT bundle samples [141], significantly higher than that with LiC_6 in commercially used graphite materials (372 mAh/g). The capacity can be further improved by chemically etching [142] or ball-milling the nanotube [143], with the maximum capacity as high as $Li_{2.7}C_6$ (∼1000 mAh/g).

Zhao et al. [144] performed first-principle calculations on the intercalation energy of electronic structures of a Li-intercalated SWNT nanorope. After intercalation, almost complete charge transfer between Li and SWNTs occurs, and a small structural deformation was found [144]. Both the interior of the nanotube and the interstitial space of the nanorope are susceptible for intercalation. They have shown that the Li intercalation potential of a SWNT rope is comparable to that of graphite and independent of Li density

Table 2. Summary of Li storage capacity of different carbon-based materials.

Materials	Raw (mAh/g)	After processing (mAh/g)
Soft carbon	200–400	200–950
Hard carbon	200–300	150–680
MWNT	∼250	440
SWNT	495–677	900–1037

up to a saturation density of about Li_3C_6 [144]. The higher Li capacity in nanotube bundles can be related to the lower carbon density than that in graphite. Later on, Kar et al. [145] explored the possibilities of Li^+ ion intercalation or insertion through the sidewall or the cap region of carbon nanotubes. They found that the barrier to insert an Li^+ ion through five, six, seven, or eight-member rings depends on the ring size, and insertion is easier as the ring size increases. In particular, they noticed that a lithium ion favors two positions: either inside the tube close to the wall or outside the tube. The outside position is slightly more favorable. As two lithium ions are considered in a single-wall tube, the binding energy strongly depends on the ions' positions, and the most stable configuration is the one for which both ions are outside the tube and the binding energy is higher than for the single cationic system.

It was mentioned before that three sets of optical bands at 0.68, 1.2, and 1.7 eV are observed in the optical spectrum of the pristine SWNT sample [137]. The first two features at 0.68 and 1.2 eV originate from bandgap transitions in semiconducting tubes, while the third one at 1.7 eV comes from metallic tubes. Petit et al. [137] have shown that all these features are removed after the pristine SWNT sample is exposed to naphthalene–lithium, fluorenone–lithium, and anthraquinone–lithium, which have different redox potentials [137], by optical absorption spectroscopy. If their Li-doped samples are kept under vacuum for a few months, there is no change in the absorption spectra, indicating the perfect stability of Li-doped SWNTs, but they are unstable when exposed to air. In addition, their work demonstrated that it is possible to fill or deplete selectively the density of states of the different kinds of tube (semiconducting and metallic) that constitute the material and consequently to control their electronic properties by tuning the Fermi levels of SWNTs upon chemical doping.

Gao et al. [146] examined the position of K atoms in doped SWNT crystals for two different doping types, that is, exo-type (K atoms allowed only in between tubes) and endo-type (K atoms allowed to be inside tubes). They found that if the K atom can (cannot) penetrate the tubes, the optimum stoichiometry is KC_{10} (KC_{16}). Furthermore, it was found that the effect of K-doping on SWNT is highly sensitive to the size of nanotube [147]. For example, in the (10, 0) and (12, 0) tube, a band originating from the nearly free electron state crosses the fermi level, the state being distributed inside the tube rather than on the atomic circumference of the tube and extends to the tube direction. In the thinner (7, 0) tube, the state is located above the Fermi level. Such a spatial distribution of the nearly free electron state of nanotube suggests high conductivity via this state as reviewed in the coming section. Very recently, Jo et al. [148] investigated electronic properties of K-doped SWNT bundles. They found lattice up to 8% at $K_{0.1}C$ with negative binding energies, where distortion of tube walls is negligible up to $K_{0.25}C$ with full relaxation. Their results indicate that the Fermi level and the amount of the charge transfer increase with increasing doping concentration and saturate at large concentrations [148].

Choi et al. [149] investigated modification of the electronic structure of the vertically aligned MWNTs due to sodium doping. The change in band structure is largely associated with shifts of the Fermi level position relative to the MWNT band structure. As in Li-doping, the changes in the apparent density of states in the vicinity of the Fermi level suggested effects associated with the electron correlation energy.

3.1.3. Transition Metal Coating

A carbon nanotube with high stability and large aspect ratio can be considered to be an ideal template for fabricating 1D metal/nanotube hybrid nanostructures. Recent experiments by Zhang and Dai [150] found that titanium atoms deposited on the surface of SWNTs are capable of forming continuous wires, whereas other metals such as gold, palladium, iron, aluminum, and lead can only form incontinuous and amorphous wires outside the tube wall. Yang et al. [151] studied the binding energies and electronic structures of metal (Ti, Al, and Au) chains adsorbed on SWNTs using *ab initio* methods. They found that titanium is much more favored energetically over gold and aluminum to form a continuous chain on a variety of SWNTs. The interaction between titanium and the carbon nanotube significantly modifies the electronic structures around the Fermi energy of carbon nanotubes [151]. In particular, the delocalized 3d electrons from the titanium chain generate additional states in the bandgap regions of the semiconducting tubes, transforming them into metals [151].

3.2. Magnetic Properties

Experimentally, it is possible to fill various transition metals inside the hollow space of nanotubes [152–154]. Recently, the magnetism of SWNTs with Co and other magnetic transition metals (Fe and Cr) filled inside or covered outside were theoretically exploited by Yang et al. [155]. It was predicted that that such transition metal/nanotube hybrid structures exhibit substantial magnetic moments that are comparable to bulk value. In particular, large spin polarization at the Fermi level is found. Thus, it is possible to use the transition metal-filled/coated carbon nanotubes as 1D devices for spin-polarized transport, which is expected to provide immense applications in the emerging field of spintronics [156, 157].

Experimentally, Lafdi et al. [158] used the Kratschmer–Huffman method [159] to prepare carbon nanotubes and the discharge process to produce a higher yield of Co-DCNTs. Lafdi et al. [158] measured the magnetic properties of Co-DCNTs at 10 K by using a SQUID magnetometer (Quantum Design, Inc.). In contrast, the magnetic properties of pure CNTs, a Co powder, and a mixture of Co powder and CNT were also measured.

Very recently, Rana et al. [40] described a chemical method by which MWNTs and nanoparticles can be obtained from the decomposition products of $Co(CO)_3NO$ when the reaction is performed over MgO or a mixture of Mg and MgO. Rana et al. [40] also investigated the magnetic properties of Co-DCNTs at 300 K using a vibrating sample magnetometer with an applied field $|H| \leq 1.6$ T.

All of the measured results of Lafdi et al. [158] and Rana et al. [40] are summarized in Table 3. These studies have shown that the magnetic properties of pure CNTs are diamagnetic with negative magnetic susceptibility,

Table 3. Experimental values of saturation magnetization (M_s), ratio M_r/M_s (M_r, remanence), coercive field (H_c) and saturation field (H_s) for pure CNT, Co powder, a mixture of Co powder and CNT, Co-DCNT measured at temperature (T_m).

Sample	T_m (K)	T_r (K)	M_s (emu/g)	M_r/M_s	H_c (T)	H_s (T)	Ref.
Co powder	10		160	0.05	±0.014	1.7	[158]
CNT	10		−0.37	None	None	None	[158]
Co powder + CNT	10		3.45	0.046	±0.014	1.7	[158]
Co-DCNT	10		3.2	0.469	±0.075	0.5	[158]
	300	1273	5.8	0.2	0.0435		[40]
	300	1173	2.9	0.1	0.0197		[40]
	300	1073	1.2	0.3	0.0302		[40]

the magnetization curve of cobalt powders exhibits ferromagnetic feature with a hysteresis loop, and the magnetization curve of the mixture of cobalt powder and CNTs shows ferromagnetic behavior at low field range and then diamagnetic behavior with negative magnetic susceptibility after 1.7 T. For Co-DCNTs, the magnetization curve shows typical ferromagnetic behavior and has a higher coercive force than that of pure Co powder. From Table 3, it can be seen that the Co-DCNTs show saturation of magnetization at −0.5 T, which is much faster than that of pure CNTs at −1.7 T. The coercive field of Co-DCNTs increases by a factor of more than five compared with pure Co powder or a mixture of Co powder and CNTs. The magnetic properties of Co-DCNTs exhibit most likely superparamagnetic behavior. These intriguing magnetic properties are probably related to the low dimensionality of the cobalt entities. At room temperature, Table 3 shows that the saturation magnetization, remanence, and coercive force can be altered significantly with a change in reaction temperature. It is found that the smaller cobalt particles encapsulated at the tip positions of nanotubes show single-domain behavior with a high coercive force, whereas the nanoparticles obtained at lower temperatures are of multidomain systems. This demonstrates the importance of the chemical method used for fabricating carbon-coated cobalt particles at lower temperatures.

Altshuler–Aronov–Spivak (AAS) oscillation and weak localization are the typical phase interference effects of electron waves observed in MWNTs [5, 10]. When the sample size is smaller than both the phase coherence length and the localization length, constructive phase interference along current paths that encircle MWNTs with time-reversal symmetry would lead to weak localization [5, 10]. The presence of a resistance maximum and a negative magnetoresistance around zero magnetic field reflects the weak localization in AAS oscillation [5, 10]. Very recently, Haruyama et al. [160, 161] doped MWNTs at one end by impurity atoms from electrode materials. They found that doping of the light-mass materials, for example, carbon and aluminum, results in the weak localization in AAS oscillation, but doping of heavy-mass materials, for example, gold and platinum at a volume ratio of only about 5%, changes the weak localization to antilocalization [161]. Such effects can be understood by the drastic change of the phase interference in MWNTs [161]. (Note: This phase interference is caused by the polarized injection of spin-flipped electrons because of

spin–orbit interaction in the diffusion region [160].) For the application of this effect, a novel spintronics (electron wave phase switching) circuit [160] can be designed by using a general MWNT (exhibiting weak localization without a magnetic field) and a Au-doped MWNT (exhibiting antilocalization without a magnetic field).

3.3. Transport Properties

It is well known that SWNTs can be either semiconducting or metallic, depending on their chirality [162–165]. Thus, carbon nanotubes are considered to be conducting nanowires for investigating mecroscopic electric transport phenomena and constructing nanoscale electronics devices. Ebbesen et al. [166], in their pioneering work, studied the transport properties of individual MWNTs by contacting the nanotubes using focused-ion beam lithography. Tans et al. [167] measured electrical resistivities of individual SWNTs from cyrogenic to room temperature. Other studies on the resistivity measurements used arc-produced MWNT bundles [168] and pellets [169], oriented films of MWNTs [170], single ropes of SWNTs [72], individual MWNTs as the needle of a scanning-force microscope [171] and other materials [172–175]. In Table 4, we list the resistivities of different types of carbon nanotubes at room temperature compared with the data for other materials. In this section, we review recent developments on transport properties of doped carbon nanotubes.

Lee et al. [178] were the first to study the doping effect on the transport properties of bulk samples of SWNTs by vapor-phase reactions with bromine (a prototypical electron acceptor) and potassium (a prototypical electron donor). They found that doping decreases the resistivity at 300 K

Table 4. Resistivities (R) of different types of carbon nanotubes, doped carbon nanotubes, graphite, diamond, and aluminum at room temperature.

Materials	R (Ω cm)	Ref.
Al	3.4×10^{-6}	[39]
Diamond	10^{20}	[5]
Graphite (basal plane)	5×10^{-5}	[5]
Carbon nanotube film	2×10^{-2}	[170]
Carbon nanotube bundle	$6.5 \times 106-3$	[168]
Individual MWNTs	8×10^{-4}–1.2×10^{-2}	[171]
	5.1 to 5.8	[166]
	3×10^{-2} to 0.3	[175]
	5.3×10^{-4}–1.9×10^{-3}	[183]
Bulk MWNT sample	2×10^{-4} to 3×10^{-4}	[176]
Bulk SWNT sample	1.6×10^{-2}	[178]
Nanotube–epoxy composite	3.4×10^{-2}	[177]
Bulk Br$_2$-doped SWNT sample	10^{-3}	[178]
Bulk K-doped SWNT sample	3×10^{-4}	[178]
Individual B-doped MWNTs	7.4×10^{-5}–7.7×10^{-4}	[183]
B-doped MWNT/polystyrene	3.2×10^2	[190]
Al (1 wt %)-doped carbon nanotube	4.9×10^{-6}	[39]
Al (4 wt %)-doped carbon nanotube	6.6×10^{-6}	[39]
Al (10 wt %)-doped carbon nanotube	5.5×10^{-6}	[39]

by a factor of 30 and enlarges the region where the temperature coefficient of resistance is positive, indicative of the metallic behavior. Their results suggested that doped SWNTs represent a new family of synthetic metals. Later on, Ruzicka et al. [179] reported direct current (dc) transport and optical conductivity measurements on purified and K-doped thick films of SWNTs. The pristine sample shows a Drude component in the optical conductivity despite the nonmetallic behavior in dc resistivity measurement due to the nonmetallic tube–tube contacts. They found that the K-doping strongly in fluences the tube–tube contact regions than rather the intrinsic on-tube transport. Thus, the average dc conductivity is higher than the $\omega \to 0$ optical contribution, averaged over all directions [179]. Meanwhile, Sklovsky et al. [180] presented *in-situ* four-probe dc resistance versus pressure for pristine and K-doped SWNT buckypaper up to 90 kbar. They found that K-doped samples show quite different behavior from that of pristine samples: (1) by 10 kbar, the resistance R of doped samples drops by 40%; (2) from 10 to 45 kbar, the resistance of K-doped SWNTs decreases gradually with pressure, contrary to that of pristine nanotubes; and (3) at still higher pressure, resistance increases slightly by 2% from 45 to 90 kbar. They also found that after exposing K-doped SWNTs to air, the resistance is exactly restored to the behavior of pristine materials. This result shows that potassium vapor-transport doping is actually reversible. Further work of Lee et al. [181] pointed out that K-doping in the nanotube ropes leads to similar effects: an overall decrease in the resistance and suppression of the low-temperature divergence. For doping-induced change in V_g characteristics, their work proves that chemical doping is a charge-transfer process rather than a change in rope–rope contact properties. In addition, the work of Lee et al. [181] does support the idea that SWNT materials are inherently p-type due to tube-level inadvertent doping by exposure to air.

The simultaneous measurements of the change in optical absorption and in dc resistance for controlled stoichiometry in p-type (Br_2 and I_2) or n-type (K and Cs) doped SWNTs by Kazaoui et al. [61] demonstrated their close correspondence: disappearance of absorption bands at 0.68, 1.2, and 1.8 eV exhibited in pristine SNWTs and a concomitant decrease of dc resistance by doping, which is attributed to electron depletion from or filling to specific bands in semiconducting or metallic SWNTs, demonstrating their amphoteric doping behavior.

Rochefort and Avouris [182] studied the effects of impurity scattering on the conductance of metallic carbon nanotubes as a function of the relative separation of the impurities. They found that the conductance of a single oxygen-doped (6, 6) nanotube decreases by about 30% with respect to that of the perfect nanotube. Introducing a second oxygen atom induces strong changes in the conductance, which depends strongly on the relative position of the two oxygen atoms. They observed regular oscillations of the conductance that repeat over an O–O distance corresponding to an integral number of half-Fermi wavelength. This shows strong electron interference produced by electron scattering from the oxygen defects whose contribution to the resistance of the carbon nanotube cannot be obtained by simply summing up their individual contributions.

Wei et al. [183] investigated the resistivities of individual multi-walled pure and B-doped carbon nanotubes as the temperature varied from room temperature to 573 K. They found that a decrease in the resistivity with increasing temperature, that is, a semiconductor-like behavior, was observed for both B-doped and pure carbon nanotubes. As listed in Table 4, B-doped nanotubes have a reduced room temperature resistivity (7.4×10^{-5}–7.7×10^{-4} Ω cm) compared with that of pure nanotubes (5.3×10^{-4}–1.9×10^{-3} Ω cm). Their results indicate that the resistivity of the B-doped carbon nanotubes is comparable to those along the basal plane of graphite (Table 4). It should be mentioned that the activation energy derived from the resistivity versus temperature Arrhenius plots for B-doped MWNTs was 55–70 meV, smaller than that (190–290 meV) for the pure MWNTs. Later on, Liu et al. [184] examined the effects of doping, electron, and electron correlation on the transport properties of B-doped MWNTs. They found that the substitutional B lowers the Fermi level of the carbon nanotubes and increases the number of participating conduction channels without introducing strong carrier scattering. As the temperature varies from 300 K to about 50 K, they found that the B-doped nanotubes show metallic behavior with weak electron–phonon coupling and the resistance increases at lower temperatures, accompanying the observation of a zero-bias anomaly. Very recently, Hsu and Nakajima [185] have studied the conductivity of B-doped MWNT bundles (each bundle consisting of about 10 to 20 B-doped MWNTs). The results are shown in Figure 12. Their current–voltage relationship is characteristically linear at room temperature and the contact resistance between the bundle and the Au electrodes is about 1–2 kΩ, which is significantly lower than $G_0 = 2e^2/h = 12.9$ kΩ [186], indicating that the contact resistance does not hinder the passage of electrons through B-doped MWNT bundles. From Figure 12, the resistance/length value of the B-doped MWNT bundles is about 1.22 kΩ/μm, considerably smaller than the value (10–30 kΩ/μm) for pure MWNT bundles [166]. Figure 12 also shows the semiconductor-like behavior for the three B-doped MWNT bundles: the conductance between 77 and 300 K is about 150, 100, and 75 μS, for sample 1, sample 2, and sample 3, respectively. The derived activation energy (i.e., bandgap) is about 0.098–0.16 eV, smaller than that found for carbon nanotubes (0.1–1 eV) [187]. The electronic behavior of carbon nanotubes in the polymer matrices has attracted some attention [188, 189]. Watts et al. [190] studied the alterating current impedance of carbon nanotubes in a polystyrene matrix by introducing various materials, for example, fullerene-free carbon soot, pyrolyzed polyacetylene carbon black, graphite powder, MWNTs, and B-doped MWNTs. They found that the B-doped MWNT films exhibit a relatively low resistivity (3.2×10^2 Ω cm) and the conduction does not vary significantly upon mechanical compression and bending. Such low resistance is actually due to the intrinsic low resistance of B-doped MWNTs and to preferential networking. Besides B-doping, very recently, Kaun et al. [191] reported *ab initio* analysis of current–voltage characteristics of carbon nanotubes with nitrogen substitutional doping. They found that for zigzag semiconducting tubes, doping with a single

(a)

(b)
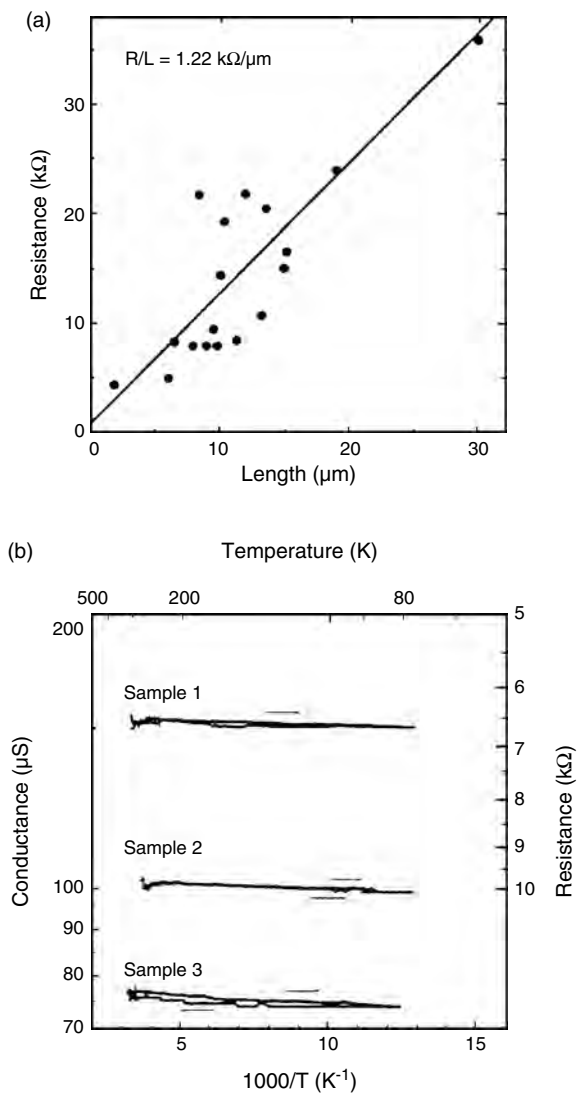
Figure 12. (a) Relationship between resistance and length for B-doped MWNT bundles; (b) relationship between conductance and temperature for B-doped MWNT bundles. Reprinted with permission from [185], W. K. Hsu and T. Nakajima, *Carbon* 40, 445 (2002). © 2002, Elsevier Science.

N atom increases current flow and for small radii tubes narrows the current gap. They pointed out that doping a N impurity per nanotube unit cell would generate a metallic transport behavior. They have also observed a negative differential resistance region for doped tubes and nonlinear current–voltage characteristics set in a high bias. For armchair metallic nanotubes, Kaun et al. [191] predicted a reduction of current with substitutional doping because of elastic backscattering caused by the N impurity.

Yuan et al. [192] investigated the electrical transport properties of single pure and Au-doped MWNTs. Their current–voltage measurement shows that single Au-doped MWNTs have a minimum resistance of 20 kΩ and a maximum of 200 kΩ, which is smaller by a factor of 5 than that of the undoped carbon nanotube. They also found that the resistance of Au-doped carbon nanotubes decreases with increasing temperature, showing a semiconducting-like

behavior. Attention has also been paid to the influence of doping such as Al, Ag, and Hg [39, 193]. For example, as shown in Figure 13, Xu et al. [39] investigated the dependence of electrical resistivity in Al-doped carbon nanotube composites on the temperature and found that Al-doped carbon nanotubes have a lower electrical conductivity than aluminum. To explain the observed conductance, it was believed that the existence of a potential barrier in the doped carbon nanotube was responsible for the electron transport. The barrier height can be determined by $E_{\text{barrier}} = E_F - E_V$, where E_F is the Fermi energy of carbon nanotube and E_V means the top energy of valence band. As an

(A)

(B)

(C)
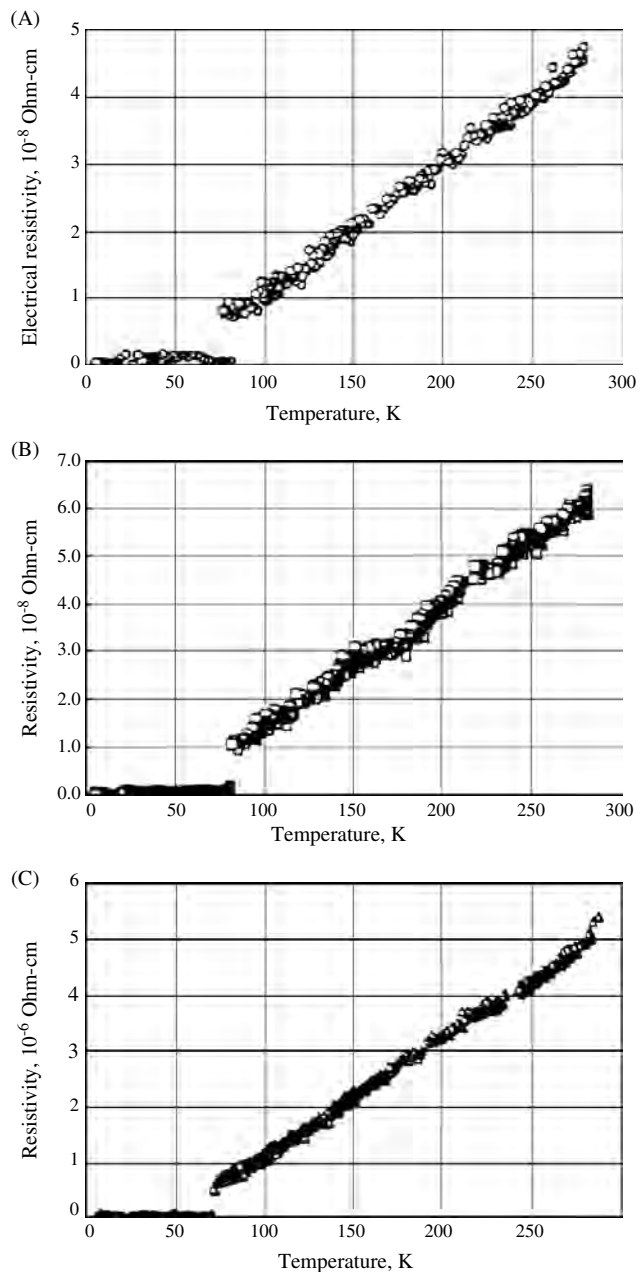
Figure 13. Dependence of electrical resistivities in Al-doped carbon nanotube composites on temperature. (A) Al 1 wt %; (B) Al 4 wt %; (C) Al 10 wt %. Reprinted with permission from [39], C. L. Xu et al., *Carbon* 37, 855 (1999). © 1999, Elsevier Science.

example, in considering the doping on the outer wall (note: the outer wall contributes mostly to electron transport), the Fermi level of the Au-doped MWNTs was modified and decreased relative to the valence and conductance band and therefore the height of the barrier was lowered. Thus, more electrons in doped carbon nanotubes can easily tunnel the potential barrier and contribute to the conductance more than in the undoped carbon nanotubes.

To date, it has proved possible to produce encapsulated LaC_2 [194], YC_2 [195, 196], LaC_2 [197], CeC_2 [197, 198], Gd_2C_3 [199, 200], TiC [199, 201], V_4C_3 [202], ZrC [202], TaC [194, 198], HfC [203], Fe_3C [199], Ni_3C [199], and carbides of Cr [199], Dy [199], and Yb [199]. Recently, Terrones et al. [169] performed four-probe and microwave conductivity measurements on carbon nanotubes with or without encapsulated materials generated by arc-discharge and electrolytic techniques. Their results indicated that most of the samples behaved as semiconductors. However, metallic transport was observed in specimens containing single conglomerated carbon nanotube bundles and B-doped carbon nanotubes. Grigorian et al. [41] have shown that the electrical transport properties of SWNTs are strongly influenced by the presence of transition metal impurities (for example, Cr, Mn, Co, Fe, and Ni) derived from the catalyst introduced to stimulate their growth. Their observed unusual transport behavior is assigned to a Kondo effect, that is, an interaction between the magnetic moment of the transition metal atom and the spin of the conduction π electrons of the nanotubes.

Carbon nanotubes are promising materials for building electronic devices, in particular, field effect transistors (FETs) [204]. SWNT FETs built from as-grown tubes are unipolar p-type; that is, there are no electron current flows even at large positive gate biases. This behavior suggests the presence of a Schottky barrier at the metal–nanotube contact. Obviously, the capability to produce n-type transistors is important technologically, as it allows the fabrication of nanotube-based complementary logic devices and circuits [205, 206]. Bockrath et al. [207] reported a controlled chemical doping of individual semiconducting nanotube ropes with potassium. Based on their scheme, they were able to control the level of doping by reversibly intercalating and deintercalating potassium and K-doping could change the carriers in the ropes from holes to electrons. They found that typical values for the carrier density are about 100–1000 electrons/μm and the effective mobility for the electrons is about 20–60 cm^2 V s, which is similar to that reported for the hole effective mobility in nanotubes [204]. Their experiments open the way for other experiments that require controlled doping such as making nanoscale p-n junctions [208, 209]. For example, Kong et al. [210] doped a 0.4 μm long semiconducting SWNT into an n-type by using potassium vapor, and their electrical measurement reveal single-electron charging at temperatures up to 60 K. Their K-doped SWNT manifests as a single quantum dot or multiple quantum dots in series depending on the range of applied gate voltage. For another example, Kong et al. [211] doped a SWNT in such a way that it consisted of two p-type sections (doping by molecular oxygen adsorbed from ambient) and a central n section (doping the SWNT central part by using potassium) and the transport measurements

of the formed p-n-p junction reveal that nanometer-scale wide tunnel barriers at the p-n junctions dominate the electrical characteristics of the system. They pointed out that at low temperature, the system manifests as a single on-tube quantum dot confined between two p-n junctions. In addition to K-doping, Martel et al. [212], Derycke et al. [205], and Liu et al. [206] showed that p- to n-type conversion of the carbon nanotube FETs can be made by simply annealing the device in an inert gas [212] or in vacuum [205, 206]. Very recently, Derycke et al. [213] compared the characteristics of carbon nanotube FETs produced by both methods and showed fundamental differences in the mechanism of the transformation. They found that the main effect of oxygen adsorption is not to dope the bulk of the carbon nanotube, but to modify the barriers at the metal–semiconductor contacts. Their studies indicated that the oxygen concentration and the level of doping of the nanotubes are complementary in controlling the carbon nanotube FET characteristics. They demonstrated the method of controlling the individual contact barriers by local heating. Meanwhile, Park and McEuen [214] used field effect doping to study both n- and p-type conduction in a semiconducting carbon nanotube. They found that in the n-type region, the ends of the tube remain p-type due to doping by the metal contacts. Thus, a p-n junction forms near the contact, creating a small, p-type quantum dot between the p-n junction and the contact.

The effects of a gas environment on the electronic and transport properties of carbon nanotube have also attracted some attention recently. The resistance of metallic nanotube bundles decreases as gas molecules (most importantly, oxygen) are removed from the sample [215]. Upon exposure to O_2 [216], NO_2, or NH_3 gas [217], the electrical conductance of the semiconducting tubes is dramatically changed. Theoretical calculations by Jhi et al. [218] showed weak hybridization between carbon and oxygen for the valence-band edge states, which leads to conducting states near the bandgap. Similar results were found for NO_2 adsorption on semiconducting SWNTs by Zhao et al. [219]. They also studied the electronic properties of SWNTs upon adsorption of various gas (NO_2, O_2, NH_3, N_2, CO_2, CH_4, H_2O, H_2, and Ar). They found that most gas molecules adsorb weakly on SWNTs and are charge donors to the nanotubes, while the electronic properties of SWNTs are sensitive to the adsorption of certain molecules, such as NO_2 and O_2, as charge acceptors. The charge-transfer and gas-induced charge fluctuations significantly affect the transport properties of SWNTs.

The insertion of C_{60} or of endohedral fullerenes into SWNTs leads to novel forms of carbon-based materials, named peapods [220–224], which have attracted great interest due to their unusual transport properties. For example, a C_{60}@(10, 10) peapod has been shown to be metallic [225] with two types of carriers, one propagating along the nanotube and the other on the C_{60} chain. Chiu et al. [226] explored the electrical transport properties of individual semiconducting nanotubes doped with metallofullerene $Dy@C_{82}$. Their samples show a transition from p-type to n-type conduction if the samples are cooled from room temperature to 265 K. Upon further cooling the samples become metal-like at 265 K. These transitions are due to

temperature-dependent charge transfer from the metallo-fullerene to the nanotube. They also found that at liquid helium temperature the tubes exhibit irregular Coulomb blockade oscillations due to being split into a series of quantum dots, presumably caused by inhomogeneous distribution of the fullerenes inside the nanotubes. Pichler et al. [227] reported doping-induced polymerization of C_{60} inside SWNTs by performing resistivity measurements as a probe. They found that the resistivity changes from semiconducting for the undoped system to metallic for the doped system. For full intercalation, they observed a chemical reaction inside the nanotubes, leading to a one-dimensional polymeric C_{60}^{-6} chain which has metallic character.

Recently, Xie et al. [228] demonstrated that $C_{60-n}B_n$ and $C_{6-m}N_m$ molecules could be engineered as acceptor/donor pairs desired for molecular electronics by properly controlling the number n and m of the substitutional dopants in C_{60}. These acceptor/donor pairs can be promising components for making nanotube-based p-type, n-type, n-p-n, and p-n-p transistors and p-n junctions. For example, placing an acceptor $C_{48}B_{12}$ [228] into a (10, 10) tube, as shown in Figure 14a, puts a $+0.23$ e charge on the SWNT, resulting in a p-type tube-based transistor; incorporating donor $C_{48}N_{12}$ [229, 230] into a (10, 10) tube, as shown in Figure 14b, leads to -0.26 e charge on the SWNT resulting in an n-type tube-based transistor. As shown in Figure 14c, doping a (17, 0) semiconducting SWNT with $C_{48}B_{12}$ and $C_{48}N_{12}$ can make a SWNT-based p-n junction.

3.4. Field Emission

Metals were initially used as electron sources in field emission displays. However, for metal emitters, there will be nanoscale protrusions growing on the emitter surfaces

Figure 14. (a) $C_{48}B_{12}$@(10,10) tube; (b) $C_{48}N_{12}$@(10,10) tube; (c) p-n junction made by filling of $C_{48}B_{12}$ and $C_{48}N_{12}$ in a (17,0) semiconducting tube.

during field emission. These protrusions result in the destruction of the emitters through a vacuum arc. That was one of the primary reasons that metal field emitters failed to reach widespread use in electron tubes. Then, it was shown that graphite fibers have much better environmental stability and can be used as field emitters in spite of their high work function ($\phi \approx 5$ eV) [231]. In comparison with graphite, the curvature and high aspect ration of carbon nanotube lead to strong field enhance effect around the local geometry of nanotube tips, making the carbon nanotubes superior field emitter. Since the first reports of electron field emission from carbon nanotubes [232, 233], carbon nanotube field emitters have been extensively studied [234–239]. These studies have shown that carbon nanotubes exhibit interesting field-emission properties such as low extraction field, high current density, and long operating time. In general, the current-voltage characteristics of carbon nanotubes are found to follow a Fowler-Nordheim type tunneling law [233–236]. It was found that electronic states localized near or at the apex of the nanotubes influence the current emission profile [240, 241]. These localized states are relatively well documented for various kinds of tube termination [242–245] and can be induced by the extraction field [246]. More details about the mechanism of field emission in carbon nanotubes can be found in the work of Mayer and Lambin [238]. In the field-emission analysis within Fowler-Nordheim model [247], the work function is a critical parameter to determine field emission properties of carbon nanotubes. Many experimental and theoretical efforts have been devoted to determine the precise value of the work functions of carbon materials [248–253]. For example, the work functions of multi-walled carbon nanotubes are about 0.1 to 0.2 eV lower than that of the graphite [249, 252–254]. The work functions of single-walled carbon nanotube bundles (about 5.0 eV) are found to be slightly higher than that graphite [250, 251]. Theoretical calculations by Zhao et al. show that the work functions of SWNTs are not sensitive to the tube size and chirality [248]. Upon alkali-metal intercalation, as shown in Table 5, the work functions of carbon nanotubes are reduced dramatically with alkali-metal concentration [248, 251]. The reduction of work function upon alkali-metal intercalation implies a significant enhancement in field emission, which was observed in recent

Table 5. Work functions (ϕ) of alkali metal-intercalated carbon nanotube bundles at various intercalation density (x in M_xC, where M = Cs, Rb, or K).

	ϕ (ev)				
	(10,10) armchair nanotube			(17,0) zigzag nanotube	
x	K_xC	Rb_xC	Cs_xC	x	Cs_xC
0.00	5.01	5.01	5.01	0.00	5.06
0.0125	4.3	4.246	4.185	0.0147	4.323
0.025	4.086	4.084	4.056	0.0294	4.034
0.0375	4.05	4.006	3.943	0.0441	3.83
0.05	3.982	3.929	3.85	0.0588	3.773
0.0625	3.898	3.834	3.78	0.0735	3.711
0.075	3.877	3.83	3.728	0.0882	3.668
0.10	3.827	3.76	3.644		

Source: Adapted from the theoretical work of Zhao et al. [248].

experiment [255]. In addition to doping, substituting the carbon atom with B or N atom through substitution reaction [256, 257] provides another way to modify the physical properties of carbon nanotubes at the atomic level. Many studies on atom substitution [258, 259] suggested that impurities can introduce impurity states near the Fermi level and influence the electronic properties of carbon nanotubes. Very recently, Zhang et al. [260] investigated the effect of introducing substitutional boron or nitrogen atoms in the nanotube tip on the field emission properties of capped SWNTs. They found that the substitution in the tip can significantly enhance the localized density of states at the Fermi level, which is important for field emission. A reduction of the work function of the tip occurs as the nitrogen atom substitutes for a carbon atom. In low-voltage field emission, both tubes with substitutional B or N could provide much larger emission current than the pure carbon nanotube. The gap between the lowest unoccupied molecular orbital and the highest occupied molecular orbital for B- or N-doped carbon nanotubes is smaller than that for a pure tube. This implies that substituting B or N in the tip enhances the localized reactivity of the tip and thus makes field emission easier. Later on, Poa et al. [261] obtained low threshold fields of 1.6 V/μm and 2.6 V/μm for field emission from MWNTs and B-doped MWNTs embedded in polystyrene, respectively. The threshold field for electron emission is markedly determined by geometry enhancement of the film surface, not by film resistivity. Poa et al. found that higher carbon nanotube concentrations result in larger effective emission areas, at the expense of a higher threshold field.

Wang et al. [262] performed field emission measurements on CN$_x$ nanotubes. They found that such tubes began to emit electrons at an electric field of 1.5 V/μm and current densities of 80 μA/cm^2 were realized at an applied field as low as 2.6 V/μm. doping carbon nanotubes with N atoms enhances their electron-conducting properties because of the presence of additional lone pairs of electrons that act as donors with respect to the delocalized π system of the hexagonal framework. Hence, their work suggests that the controllable synthesis of well-aligned CN$_x$ nanotubes with a high N concentration may open a route to improve the field emission properties of the nanotubes.

Meanwhile, Meunier et al. [263] showed that BN/C junctions are superlattices characterized by the presence of a spontaneous polarization field whose value is highly sensitive to the helicity of the underlying nanotubes. Such a polarization field can be used to lower the work function of BN/C nanotube tips, thereby increasing the field-emitting properties over carbon nanotube tips by up to 2 orders of magnitude.

Tondare et al. [264] reported field emission measurements from the nanotubes of aluminum nitride synthesized by gas-phase condensation. They found that the field emission patterns display very interesting features consisting of sharp rings. Such patterns are attributed to the open-end nanotubes of aluminum nitride. The corresponding Fowler–Nordheim plots were nonlinear in nature, reflecting the semi-insulating behavior of their field emitter. Their field enhancement factor is estimated to be 34,500, indicating that the field enhancement due to the nanometric size of the field emitter is an important cause for the observed emission in their measurement.

Kung et al. [265] demonstrated a facile gas-phase O$_2$/O$_3$ oxidation process for improvement of the field emission properties of carbon nanotube arrays via selective opening of the carbon nanotube tips in the array format with minimum damage along the tube walls. They found that the onset emission voltage of carbon nanotube arrays can be lowered to about 0.6 Vμm along with 700 to 800% enhancement in the emission current. The sharper the carbon nanotube end tip is, the lower is the onset emission voltage as well as the larger the emission current, corresponding to a good field emission behavior. The current gas-phase O$_2$/O$_3$ oxidation method is a simple, convenient, clean process that can be very easily applied to any carbon nanotube array/film to lower the carbon nanotube onset emission voltage and enhance the emission current.

Kurt et al. [266] have shown that the field emission properties of catalytically grown C/N nanotubes vary over a large range and are strongly correlated to the deposition temperature and therefore to the tube diameter, not affected by the catalyst. They found that the field emission is not governed solely by the diameter of the smallest tubes. Their results indicate that C/N nanotubes show turn-on and threshold fields comparable to these of carbon nanotubes but lead greater amplification factors, and the ability to tailor the tube diameter by temperature variations does offer an easy parameter to optimize field emission properties depending on the requirement of applications.

Although carbon nanotubes show extensive applications, their electronic characteristics may depend on tube radius and chirality, which limit their applications [267]. Overcoming of these limitations is needed to synthesize new nanotube materials or study the formation mechanism of nanotubes. Si–C–N films have been considered as the first candidate material for nanotube synthesis because of their promising characteristics [268, 269], such as higher nanohardness, UV to blue light emission, high field emission, and others. Adding additional Si sources has been shown to be important in the making of crystalline Si–C–N tubes [270, 271]. Very recently, Chang et al. [272] studied the field emission properties of carbon nanotubes and Si–C–N nanotubes. Their results are shown in Figure 15. They found that the emission current densities ($>$10 mA/cm^2 at 10 V/μm) of all nanotubes are much better than those of other field-emitting materials. Also, they noted that carbon nanotubes (samples 1 and 2) exhibit emission properties superior to those of Si–C–N nanotubes (samples 3 and 4), except for carbon nanotube 5 whose low emission current is related to a work-like part tube.

3.5. Nonlinear Optical Properties

As an external electric field is applied to a molecule, its charges will be redistributed and induced dipoles are created (or already present dipoles are oriented) [273]. The relation between the dipole moment **P** and the applied field **E** can be written as

$$\mathbf{P} = \mathbf{P}_0 + \alpha\mathbf{E} + \frac{1}{2}\beta\mathbf{E}^2 + \frac{1}{6}\gamma\mathbf{E}^3 + \cdots \tag{4}$$
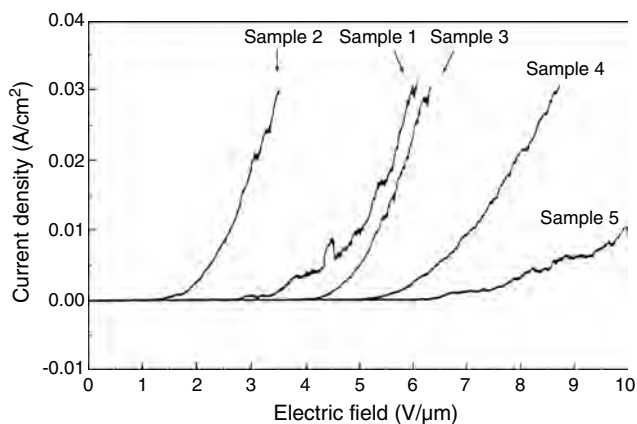
Figure 15. Current density versus electric field for carbon nanotubes (sample 1, sample 2, and sample 5) and Si–C–N tube (sample 3 and sample 4). Reprinted with permission from [272], H. L. Chang et al., *Diamond Relat. Mater.* 11, 793 (2002). © 2002, Elsevier Science.

where **E** is the electric field, $\mathbf{P}_0$ is the permanent dipole moment, α is the dipole polarizability, β is the first-order hyperpolarizability, and γ is the second-order hyperpolarizability. Explicitly, the static dipole polarizability (SDP) measures the ability of the valence electrons to find an equilibrium configuration, which screens a static external field. It has been shown that molecules with many delocalized valence electrons should display large values of SDPs [274]. The first- and second-order hyperpolarizabilities, representing the first- and second-order nonlinear polarizations, play a key role in the description of nonlinear optical phenomena because a time-varying polarization can act as the source of new components of the electromagnetic field [273].

3.5.1. Polarizability

For carbon nanotubes, the mean polarizability $\bar{\alpha}$ is defined as

$$\bar{\alpha} = \frac{\alpha_{xx} + \alpha_{yy} + \alpha_{zz}}{3} = \frac{2\alpha_1 + \alpha_2}{3} \tag{5}$$

where the nanotubes are oriented in such a way that $\alpha_{xx} = \alpha_{yy} = \alpha_1$ (perpendicular to the tube) and $\alpha_{zz} = \alpha_2$ (parallel to the tube). The anisotropy $\Delta\alpha$ is defined as

$$\Delta\alpha = \sqrt{2(\alpha_1 - \bar{\alpha})^2 + (\alpha_2 - \bar{\alpha})^2} \tag{6}$$

For the individual SWNT, the static electric polarizability tensor was calculated within the random-phase approximation based on a tight-binding model by Benedict et al. [275]. They found that the polarizability for an external field parallel to the tube axis is dependent on the details of the tube's electronic structure, while the polarizability for fields perpendicular to the axis only depends on the tube diameters. Kongsted et al. [276] calculated the static polarizability components of different BN-doped armchair nanotubes at the self-contained field (SCF) level with slater-type orbital-3G basis sets and the interaction model. At a fixed tube length (0.984 nm), varying the tube diameter from a (5, 5) tube to a (10, 10) tube results in enhanced polarizability. The polarizability component along the tube calculated at

the SCF level is lower than that of the interaction model. At a fixed tube diameter (0.807 nm for BN-doped nanotubes), increasing the tube length leads to enhanced polarizability in a nonlinear way, and both α_1 and α_2 cannot be described by an additive model. The largest relative increase in the polarizability component is along the tubes. From Table 6, it is seen that for a fixed number of atoms, the polarizability along the zigzag tube is lower than that along the armchair tube, while the polarizability perpendicular to the zigzag tube is higher than that perpendicular to the armchair tube. But the mean static polarizability is almost the same for the two conformations. The anisotropy for the zigzag configuration is lower than that for the armchair configuration. With the same geometry and number of atoms, the polarizability perpendicular and along the tube is lowered when going from a pure carbon nanotube to a BN-doped carbon nanotubes. The results of Kongsted et al. indicate that the intramolecular geometry has great influence on the polarizability of doped carbon nanotubes. Furthermore, they showed that the increase in polarizability along the tube arising from the frequency dependence was about 7%, whereas it was about 3% for the polarizability perpendicular to the tube. In general, the frequency dependence is relatively modest.

3.5.2. Second-Order Hyperpolarizability

Molecules with large second-order hyperpolarizabilities γ are required for photonic applications including all-optical switching, data processing, and eye and sensor protection [277]. However, the γ magnitudes of most third-order materials are usually smaller than those needed for photonic devices. Hence, finding third-order materials with large γ magnitudes has been a hot issue in physics and chemistry.

The conjugated π-electron organic systems are potentially important in photonics due to their large nonlinear optical (NLO) response [277, 278]. The γ values of fullerenes have been extensively studied but are relatively smaller [279–293] than those needed for photonic devices. Xie et al. [294–298] performed a numerical calculation of the NLO properties of armchair, zigzag, and chiral carbon nanotubes. Their results demonstrated that armchair, zigzag, and chiral nanotubes are potentially important in photonics owing to their large γ values. Recently, enhancement of the third-order optical nonlinearities of carbon nanotubes was experimentally observed with both 30- and 8-ns-wide neodymium:yttrium-argon-garnet (Nd:YAG) laser beams [299].

Based on a doped extended Su–Schrieffer–Heeger model, Xie et al. [293, 300, 301] calculated the static second-order

Table 6. Static polarizabilities of selected carbon nanotubes calculated from the interaction model.

Nanotube	Total no. atoms	α_1 (au)	α_2 (au)	$\bar{\alpha}$ (au)	$\Delta\alpha$ (au)
(5,5) SWNT	100	1267.7	854.4	991.2	414.7
BN-doped (5,5) SWNT	100	1049.1	710.9	823.7	338.2
BN-doped (10,0) SWNT	100	972.6	752.1	825.6	220.6
BN-doped (9,0) SWNT	90	909.6	661.6	744.3	248.0
(9,0) SWNT	90	1070.6	781.6	877.9	288.9

Source: Adapted from Kongsted et al. [276].

hyperpolarizabilities (γ^{im}) of the single substituted armchair ($C_{59+i\times10}X$) and zigzag ($C_{59+i\times18}X$) tubular fullerenes, where $X = $ B or N as the dopant. The results are shown in Figure 16. To examine the substitute doping effect, the ratio $q = \gamma^{im}/\gamma^p$ is plotted, where γ^p denotes the static γ value of the corresponding pure case, which is given by the empirical formula $\gamma^p = (1+i\times10/60)^{3.15}\gamma^{60}$ for an armchair nanotube [296] and $\gamma^p = (1+i\times18/60)^{2.98}\gamma^{60}$ for a zigzag nanotube [296], and $\gamma^{60} = 5.6\times10^{-34}$ esu is the static γ value of C_{60}. Figure 16 shows that the static γ value of $C_{59+i\times10}$B or $C_{59+i\times18}$B is several times larger than that of the corresponding pure value, and the static γ value of $C_{59+i\times10}$N or $C_{59+i\times18}$N is more than 30 times larger than that of the corresponding pure value. This shows that the substitute doping, especially for the case of $X = $ N, greatly increases the NLO polarizability of carbon nanotubes. It should be mentioned that owing to the distortion of the π electron distribution in the substituted tubules, especially around the substituted dopant B or N atoms, the difference between the z and x (or y) components of γ for those substituted tubules is much more pronounced than that for pure cases.

The dynamical NLO responses of doped armchair tubule $C_{59+9\times10}X$ and zigzag tube $C_{59+5\times18}X$ were also investigated by calculating the third-harmonic generation spectrum for $X = $ N or B, respectively, and some details of the first peaks are listed in Table 7. For an armchair tube, the first peaks are located at $3\omega = 0.129$ and 0.653 eV, respectively, and their corresponding γ magnitudes are 47.9 and 25.3 $\times$ 10^{-32} esu, which are 3 and 1.6 times larger than that ($=15.6\times10^{-32}$ esu [294]) for pure armchair tubules. Similar results are obtained for zigzag nanotubes. As in the pure case, the first peak in the γ spectrum of the substituted armchair tubule is also caused by a three-photon resonance between two energy levels (a and b) near Fermi levels with one in the conduction band and the other in the valence band; that is, $\epsilon_{ab} \approx 3\omega$. For armchair nanotubes, the strongest peaks in the γ spectra for $X = $ N or B are located at $3\omega = 0.437$ and 1.783 eV, respectively, and their corresponding γ_{max} magnitudes are about 792.45×10^{-30} and 172.18×10^{-30} esu, which are about 60 and 13 times larger than that ($=13.44\times10^{-30}$ esu [295]) of the strong peak of the pure armchair tubule. For the zigzag nanotube, the corresponding γ_{max} values for $X = $ N or B are about 50 and 20 times larger than that ($=6.66\times10^{-30}$ esu [295]) of the strongest peak of pure zigzag nanotubes. These peaks are caused by one-, two-, and three-photon resonance enhancement (OTTPRE). The other peaks with larger γ magnitudes are produced by two- or three-photon resonance. For example, the three-photon peaks with larger γ magnitudes in N-doped carbon nanotubes are located at $3\omega = 0.387, 0.423$,
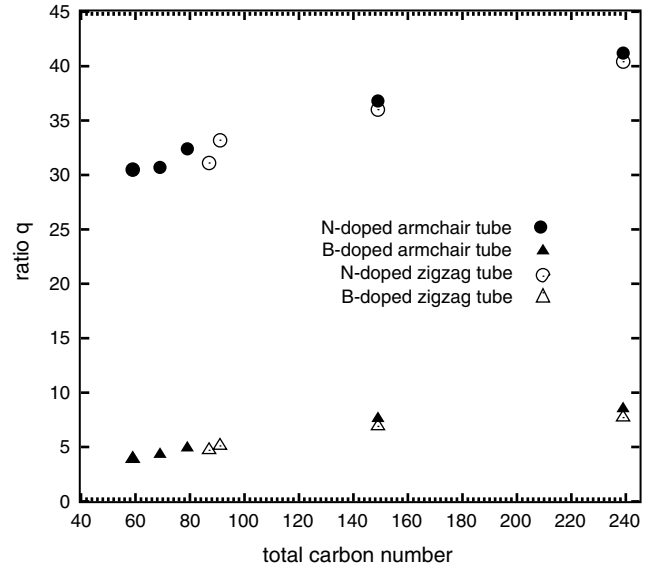
Figure 16. The ratio $q = \gamma^{im}/\gamma^p$ of several doped armchair $C_{59+i\times10}X$ ($i = 1, 2, 9, 18$) and zigzag $C_{59+i\times18}X$ ($i = 1, 2, 5, 10$) ($X = $ B or N) carbon nanotubes, where γ^{im} is the calculated static γ value of the doped nanotube and γ^p is the static γ value of the corresponding pure case and is given by the empirical formula [296] for armchair and zigzag nanotubes. Adapted from [289, 293, 296].

and 0.465 eV, and the two-photon peaks with large γ magnitudes are located at $3\omega = 0.409, 0.451$, and 0.487 eV. The major response peaks with large γ magnitudes concentrate on a narrow region, where the optical frequency is near the energy gap; that is, $3\omega \approx 3E_g$. The reason is the same as that for the pure case; that is, a lot of OTTPRE processes can be observed in the doped tubule, but only the transition processes that occur between the energy levels near Fermi levels are able to contribute large γ magnitudes. The rather larger NLO response for armchair and zigzag tubules is mainly produced by its delocalized π electronics as in conjugated polymer chains. However, their three-dimensional character, which distinguishes them from linear polymers, causes severe limitations on their NLO properties and makes their γ values smaller than those of linear polymers containing a similar number of carbon atoms. The calculations of Xie et al. [293, 300, 301] indicated that the substituted dopant ions ($X = $ B or N) attract or repel electrons and cause a distortion of π electron distribution on the tubule's surface, which mainly happens around the dopant ions (this effect can be called an inductive effect). On the other hand, the dopant ions cause greater localization of the original delocalized π electrons around them and therefore may reduce the effective space dimensions of tubules (this effect can be

Table 7. Optical frequency position (3ω), γ magnitudes, and resonant transition energies ($\epsilon_{ab} = \epsilon_a - \epsilon_b$) of the first peaks for doped armchair tube $C_{59+9\times10}X$ and zigzag tube $C_{59+5\times18}X$.

	Armchair nanotube				Zigzag nanotube		
X	E_g (ev)[a]	3ω (ev)	γ (10^{-32} esu)	ϵ_{ab} (ev)	E_g (ev)	3ω (ev)	γ (10^{-32} esu)
N	0.136	0.129	47.9	$\epsilon_{77,75} = 0.133$	0.135	0.13	32.6
B	0.647	0.653	25.3	$\epsilon_{76,74} = 0.651$	0.56	0.58	19.7

[a] Energy gap of the corresponding tubule.

called a reduction effect). Both effects make the NLO properties of the substituted tubule different from those of the corresponding pure tubule and greatly enlarge its γ magnitudes. In addition, as shown before, the localization effect of the N impurities atom is stronger than that of the B atom. So the inductive and reduction effects of the effective space dimension in the N-doped tubule are stronger than those in the B-doped tubule, which explains why the N-doped tubule has larger γ values than the B-doped tubule. Surely, it would be very interesting to see what would happen if heavier substitute doping is done. Based on the calculated results, this process will raise the γ magnitude further.

3.5.3. Optical Limiting

Laser sources are widely used in the laboratory and industry areas. However, they have a potential hazard for eyes, thermal camera, CCD and other optical sensors, for example, the possibility of damage from pulsed lasers, temporary blinding by continuous-wave lasers, and so on [302]. Hence, with nearly every wavelength being emitted by these sources, developing optical limiters and tunable filters, which can suppress undesired radiation and effectively decrease transmittance at high intensity or fluence [302], is necessary [303–310]. As an ideal optical limiter [302], it should have reasonable linear transmittance at low input fluence (at least of 70%) protecting optical sensors or eyes against laser pulses of any wavelength and pulse duration, and its output energy must remain at high fluences below the optical damage threshold of sensors or eyes. Meanwhile, optical damage threshold must be as high as possible, and the optical activating threshold must be as low as possible. Certainly, to realize this, all existing nonlinear optical materials need a tightly focused beam to initiate the effect. Thus, an optical limiter must be incorporated into an adapted optical system. Actually, there are several nonlinear effects which lead to optical limiting behavior, for example, nonlinear absorption [311], nonlinear refraction [273, 312] and nonlinear scattering [313–316]. Since the discovery of carbon nanotubes, a lot of investigations have been carried out on the optical limiting properties of carbon nanotubes. It was shown that carbon nanotubes are good candidates for optical limiting applications [317–328]. For example, Sun et al. [317] and Vivien et al. [319] have pointed out that carbon nanotubes could exhibit nonlinear scattering, similar to that of carbon black suspensions (CBS); Mishra et al. [320] discussed extensively the mechanisms responsible for the optical limiting behavior and nonlinear refraction of single-walled carbon nanotubes in ethylene glycol, water and ethanol; Riggs et al. [327] found that carbon nanotubes in solutions would exhibit much weaker optical limiting responses than those in suspensions owing to different nonlinear mechanisms. (See the review article of Vivien et al. [302] for further details.) All of these studies showed that NLO transmission in carbon nanotubes is strongly dependent on the host media, pulse width, and wavelength of the light pulse. The most reasonable mechanism for optical limiting is actually related to the creation of "micro-bubbles" in the surrounding solvent due to the local heating from the dissipation of induced currents. This is particularly enhanced in carbon nanotubes because their aspect ratios allow them to behave as effective antenna.

It should be noted that such a mechanism has been put forward to explain optical limiting in CBSs. On the other hand, the fluences in these studies are low to avoid damage to the host materials. This suggests that the exact mechanism for optical limiting in carbon nanotubes involves several "fluence regimes."

An instructive approach to understanding the mechanisms involved in the limiting behavior of suspensions is to modify the local electronic properties of the nanotubes. Over time, researchers have demonstrated that substitutional doping of MWNTs is responsible for stimulating a number of structural, electronic, and optical properties. For example, B- or N-doping plays a key role in controlling the structure of tube walls and increases the overall length and third-order optical nonlinearities of carbon nanotubes [293, 300, 301]. Very recently, Xu et al. [329, 330] performed experimental measurements on the optical limiting properties of B- and/or N-doped carbon nanotubes. Their MWNTs were prepared by two different methods. An arc-discharge dc generator was used for production of pure and B-doped MWNTs. Pyrolysis of ferrocene–melamine mixtures was used to generate N-doped MWNTs. The linear transmittance measurements of these suspensions carried out in a 1-cm thick optical cell were ~40% for both radiations: 532 and 1064 nm. CBSs with similar transmissions were measured for comparison. Their optical limiting experiments were performed with a Nd:YAG laser with pulse widths of 8 ns at wavelengths of 532 and 1064 nm. Each pulse was divided by a beam splitter into two parts: the reflected part was taken as a reference representing the incident light and the transmitted beam was focused on the sample using a 20-cm lens such that the $1/e^2$ radius of the focused beam was ~40 and 45 μm at 532 and 1064 nm, respectively. Xu et al. [329] recorded the linear transmittance spectra of pure and B- and N-doped MWNT suspensions in the visible and near-IR; range by using a Lambda 900 spectrophotometer. Their spectra are relatively flat, without any strong absorption peak in the VIS near-IR regions except for two absorption bands located at 980 and 1200 nm caused by the vibronic transitions of the O–H bond in water. Varying the incident energy and measuring the transmitted energy, Xu et al. [329, 330] obtained the optical limiting of pure and B- or N-doped MWNTs plus CBSs. MWNTs exhibit an enhanced optical limiting compared with CBSs. The limiting thresholds are about 0.8 and 1.3 J/cm^2 for MWNTs and CBSs, respectively. Carbon nanotube suspensions are not only found to be competitive optical limiters at 532 nm but also appear to be very efficient at 1064 nm. The optical limiting curves for CBSs and MWNTs at 1064 nm show that carbon nanotube suspensions also exhibit stronger optical limiting responses compared with CBSs under the same experimental measurement conditions. In comparing nonlinear transmittance versus incident fluence of pure and B- and N-doped MWNTs at 532 and 1064 nm, B- or N-doped MWNTs have better optical limiting than pure MWNTs. At 1064 nm, the thresholds are ~5.5 and 5.8 J/cm^2 for B- and N-doped carbon nanotubes, respectively, lower than that for pure MWNTs (8.1 J/cm^2). Meanwhile, at 532 nm, the doped samples have also lower thresholds compared with those for pure carbon nanotubes. A comparison of Z-scan results further confirms that doped nanotubes exhibit a greater nonlinear response

than pure MWNTs. At low input influence, pure MWNT materials show linear behavior. However, the transmittance drops down 33 and 65% when the fluence increases to 0.5 and 0.9 J/cm^2. Their results for pure and B-doped MWNTs under identical input fluence (0.5 J/cm^2) show that the transmittance drops about 60 and 33% for B-doped and pure MWNTs, respectively. The optical nonlinearity within B-doped samples is stronger than that for pure MWNTs. Moreover, Xu et al. [329, 330] found that for B-doped carbon nanotubes, there is no appreciable variation in the optical limiting behavior between the fresh and aged samples. However, for the pure MWNT sample, the optical limiting enhances with settling, compared with that for the original sample. In addition, the limiting performance of freshly agitated MWNTs can be recovered quite easily by ultrasonicating the aged samples.

However, the full mechanism for the enhanced optical limiting performance of B- or N-doped MWNTs is unclear. Jin et al. [331] found that the optical limiting behavior of MWNTs in poly(vinylidene fluoride)/dimethyformamide solution is size-dependent. The tubes with a large aspect ratio possess stronger limiting properties. Actually, the limiting is obtained by nanotube bundles not by individual tubes. Using electron microscopy, Xu et al. [329, 330] showed that for each type of their doped carbon nanotubes, the bundles exceeded 100 μm, significantly longer than the wavelength of incident light. Hence, the length of single tubes played little part in their optical limiting properties. On the other hand, Xu et al. [329, 330] found that some Fe catalyst particles are present within N-doped MWNTs, but the Fe particles show no limiting at their light range, whereas B-doped materials are made with no catalyst and show an enhancement over pure MWNTs as well. Hence, the small amount of Fe particles plays no role in the optical limiting behavior. Thus, it is possible that the enhancement of the optical limiting is caused by the presence of either B or N within MWNTs [329, 330].

3.6. Hydrogen Storage

A variety of fuels, including reformulated gasoline or diesel, methanol, ethanol, and dimethyl ether, that could help address future environmental and energy-supply challenges have been proposed. Compared with other common fuels, hydrogen has several unusual properties that significantly influence its use as a fuel [332–334]. For example, it is a low-density diatomic gas at ambient conditions which must be compressed to high pressure (typically several hundred atmospheres) or liquefied (at about 20 K) for storage in a reasonable volume, it has a low volumetric energy density that is an important challenge to compact storage on vehicles, its small size allows it to diffuse readily and it is more likely to leak than other fuels, it has the highest heating value per kilogram of any fuel which makes it usable as a rocket fuel, it has a wide range of flammability and detonability limits, and it can be used for energy applications with little or no pollution. Thus, hydrogen has been recognized as a clean and ideal energy carrier. However, one of the problems to be solved for the utilization of hydrogen energy is the difficulty of storing H$_2$ efficiently. In the beginning, metal alloys were tested for storage tanks. Although

they have sufficient storage capacity, they are expensive and heavy for commercial production focused on mobile applications. Recently, the U.S. Department of Energy Hydrogen Plan has set a standard by providing a commercially significant benchmark for the amount of reversible hydrogen absorption [335]: a system weight efficiency of 6.5 wt % hydrogen and a volumetric density of 63 kg H$_2$/m^3. Obviously, no storage technology is currently capable of meeting these goals [336]. A carbon nanotube is a light-weight material, capable of reversibly storing and releasing hydrogen in a modest range of near-ambient temperature and pressures [335]. Thus, carbon nanotubes were suggested as suitable materials for gas storage. Recently, much excitement has arisen about reports of promising results on use of carbon nanotubes for hydrogen storage [337–347]. High hydrogen absorption capacities were reported for various carbon nanotubes. The results are summarized in Table 8, where it is seen that all those H$_2$ uptake systems require high pressure, subambient temperature, or both. Further work on doped carbon nanotubes [347–349] (Table 9) has clearly shown that pure carbon nanotubes do not present sufficient storage capacity for commercial use. In the following, we review the recent developments about hydrogen storage in doped carbon nanotubes.

Chen et al. [347] introduced a H$_2$ storage system that uses K- and Li-doped carbon nanotubes as sorbents and operates at ambient pressure and moderate temperatures. The pristine carbon nanotubes were synthesized by catalytic decomposition of methane. The alkali metal doping of the carbon nanotubes was carried out by means of solid-state reaction with Li- or K-containing compounds. Then the determined the extent of hydrogen uptake by using thermogravimetry analysis (TGA) with purified H$_2$ (>99.99%) and confirmed it by using temperature-programmed desorption with H$_2$ being the only desorption product of the H$_2$-saturated carbons. They found that the H$_2$ uptake can achieve 20 wt % for Li-doped carbon nanotubes at 653 K or

Table 8. Reported gaseous H$_2$ storage capacity in pristine carbon nanotubes, graphite nanofibers (GNFs), and graphite.

Material	Temperature (K)	Pressure (MPa)	Maximum capacity (wt %)	Ref.
Graphite	298	11.35	4.52	[339]
GNFs (tubular)	298	11.35	11.26	[339]
GNFs (herringbone)	298	11.35	67.55	[339]
GNFs (platelet)	298	11.35	53.68	[339]
GNFs	298–773	0.101	0.4	[339]
SWNT (100% pure)	133	0.04	5–10	[337]
SWNT	300	0.04	4	[338]
SWNT (high purity)	Ambient	0.067	3.5–4.5	[340]
SWNT (high purity)	300	10.1	4.2	[341]
SWNT	80	7	8.25	[342]
MWNT	300–700	Ambient	0.25	[343]
SWNT–TiAl$_{0.1}$V$_{0.04}$	Ambient	0.067	7	[344]
SWNT–Ti–6Al–4V	Ambient	0.08	1.47	[345]
SWNT–Fe	Ambient	0.08	<0.005	[345]
Ball-milled SWNT	Ambient	0.08	1.0	[346]
SWNT	298–773	0.1	0.4	[347]

Source: Adapted from Ding et al. [335].

14 wt % for K-doped carbon nanotubes at room temperature. These values are comparable to those for gasoline and diesel (Table 9). The promising storage improvement with Li relative to the pristine case was attributed to adsorption by means of metal hydride interaction. The special open-edged, layered structure of the carbon nanotubes helps to improve the adsorption performance of hydrogen.

Chen et al. [347] did not report the grade of H_2 they used except to note that the purity was 99.99%. On the other hand, a change in temperature or gas composition/flow rate is accompanied by changes in buoyancy and friction forces from the gas flow, which are usually on the same order of magnitude as the signal that is being measured. Hence, special care should be taken to eliminate possible moisture contamination and caution needs to be used when TGA is used to measure adsorption or reaction kinetics. Hence, recently, Yang [348] performed rigorous calibration for all changes of hydrogen adsorption. The alkali metal-doped carbon nanotubes were prepared following the same methods of Chen et al. [347], and ultra high purity hydrogen was used to measure adsorption. Yang calibrated the weight gains and losses under the same conditions. Detailed results are summarized in Table 9 and are shown in Figures 17, through 20, where the results of H_2 adsorption with added water (2.3 vol %) are compared with those of dry H_2 adsorption. These results show that Yang [348] reproduced the features of Li-doped nanotubes observed by Chen et al. [347]. However, the total weight differential was only 2.5% rather than 20%. With moisture addition, it is seen that the total weight differential in wet H_2 was about 12%, five times larger than that in dry H_2. For K-doped carbon nanotubes, Yang [348] obtained 1.8 and 21 wt % in dry and wet H_2, respectively, whereas Chen et al. [347] reported 14 wt %. In addition, the work of Yang [348] showed that the TGA measurements strongly depended upon the concentration and rate of supply of moisture. Later on, Pinkerton et al. [349] further studied hydrogen storage in Li-doped carbon nanotubes. Similar to results reported by Chen et al. [347] and Yang [348], they found that generation of the qualified cycling feature of the TGA measurements does not need H_2 or carbon. In agreement with Yang [348], they found that the cycling species responsible for the weight changes is actually H_2O. Further, they reported that H_2 storage varied from 0.72 to 4.2 wt %, as listed in Table 9, depending on

Figure 17. TGA profile of Li-doped carbon nanotubes in 1 atm dry H_2: (a) increasing temperature from 20 to 500 °C at 5 °C/min, and (b) cooling at slower rates. The total weight of Li/C was 10 mg; ultra high purity H_2 (>99.999%) with an additional H_2O trap was used. Reprinted with permission from [348], R. T. Yang, *Carbon* 38, 623 (2000). © 2000, Elsevier Science.

the initial weight and the scan rate under 46% H_2 in Ar on Li-doped carbon nanotubes.

Why do alkali metal-doped carbon nanotubes have high H_2 uptake? To answer this question, Froudakis [350] investigated the nature of H_2 adsorption in pure and K-doped SWNTs by using a mixed quantum mechanics/molecular mechanics model. The bulk of their calculations were performed at the density function level of theory. All their computations were performed with the Gaussian 98 program

Table 9. Reported gaseous H_2 storage capacity in doped carbon nanotubes, graphite, and gasoline.

Material	Temperature (K)	Pressure (MPa)	Maximum capacity (wt %)	Ref.
Li–SWNT	473–673	0.1	20	[347]
Li–SWNT (wet H_2)	473–673	0.1	12	[348]
Li–SWNT (dry H_2)	473–673	0.1	2.5	[348]
Li–SWNT	473–663	0.1	0.72–4.2	[349]
K–SWNT	<313	0.1	14	[347]
K–SWNT (wet H_2)	<313	0.1	21	[348]
K–SWNT (dry H_2)	<313	0.1	1.8	[348]
Li–graphite	473–673	0.1	14.0	[347]
K–graphite	<313	0.1	5.0	[347]
Isooctane/gasoline	>233	0.1	17.3	[347]

Figure 18. TGA profile of Li-doped carbon nanotubes in 1 atm wet H_2: (a) increasing temperature from 20 to 500 °C at 5 °C/min, and (b) cooling at slower rates. The total weight of Li/C was 10 mg; 2.3% volume water vapor was added in H_2O. Reprinted with permission from [348], R. T. Yang, *Carbon* 38, 623 (2000). © 2000, Elsevier Science.
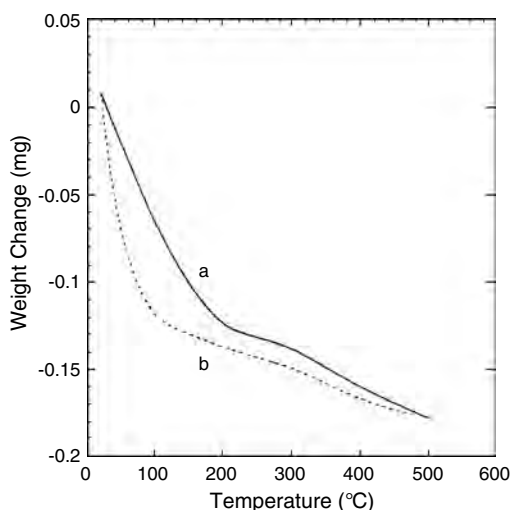
Figure 19. TGA profile of K-doped carbon nanotubes in 1 atm dry H_2: (a) increasing temperature from 20 to 500 °C at 5 °C/min, and (b) cooling at slower rates. The total weight of K/C was 10 mg; ultra high purity H_2 (>99.999%) with an additional H_2O trap was used. Reprinted with permission from [348], R. T. Yang, *Carbon* 38, 623 (2000). © 2000, Elsevier Science.

package [351] and under the ONIOM [352] two-level approach. Their results demonstrated a charge transfer from the alkali metal to the carbon nanotube that polarizes the H_2 molecule. This charge-induced dipole interaction characterizes the H_2 physisorption on alkali metal-doped carbon nanotubes and is responsible for the higher hydrogen uptake of the doped carbon nanotubes. A detailed review of *ab initio* studies on H_2 storage in pristine and alkali metal-doped nanotube bundles can be found in a recent review article [353].
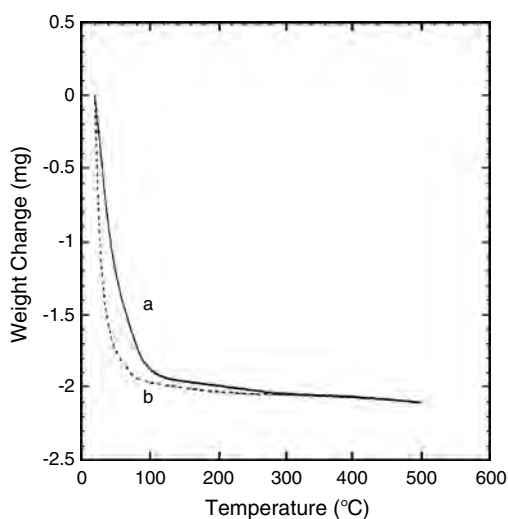
Figure 20. TGA profile of K-doped carbon nanotubes in 1 atm wet H_2: (a) increasing temperature from 20 to 500 °C at 5 °C/min, and (b) cooling at slower rates. The total weight of K/C was 10 mg; 2.3% volume water vapor was added in H_2O. Reprinted with permission from [348], R. T. Yang, *Carbon* 38, 623 (2000). © 2000, Elsevier Science.

4. SUMMARY

Doped carbon nanotubes clearly are a fascinating class of nanoscale materials and devices with a variety of novel properties and applic ations reviewed in this chapter. The unique geometric and electronic properties make the carbon nanotube ropes promising materials for batteries with high lithium capacity. The enhanced field emission properties of the doped carbon nanotubes make them viable for future development in planar displays. The large third-order optical nonlinearities of doped carbon nanotubes have potential applications as photonic devices including all-optical switching and data processing. As an ideal optical limiter, doped carbon nanotubes have reasonable linear transmittance at low input fluence, which protects optical sensors or eyes against laser pulses of any wavelength and pulse duration. A lot of experimental data on the magnetic susceptibility of doped carbon nanotubes have offered us undisputed evidence that those nanotubes are metallic or semiconducting. Our ability to manipulate such nanostructures by atomic probe microscopies reinforces this conviction, and those tubes themselves can be used as atomic force microscopy and STM tips.

The remarkable electronic and transport properties of doped carbon nanotubes make them important building block in nanoelectronics, which may speed up the development of molecular circuits and related devices. In particular, the controlled p/n doping and reversible adsorption/desorption of gas molecules that are strongly coupled with nanotube electronic states are key issues in obtaining the carbon nanotube-based devices with desirable and tunable conductance. Moreover, a nanotube can serve as a 1D template to build up metal/nanotube hybrid nanostructures, which might have novel applications in nanoelectronics and spintronics.

There are other equally interesting topics that are not included because of limited energy. For example, chemical functionalization of SWNTs [354, 355] and ionic crystalline filling of carbon nanotubes [356] are two of those promising directions to separate the carbon nanotube and to control the mechanical, electronic, and chemical properties of carbon nanotubes.

Certainly, a lot of reported information doped carbon nanotubes, for example, the optical and magnetic properties of p- and n-type doped carbon nanotubes or peapods, needs more careful and systematic study. To determine the feasibility of potential applications of doped carbon nanotubes also requires obtaining of highly reproducible preparations of doped SWNTs or MWNTs possessing the desired characteristics through a controlled manner. This also applies to the other chemical manipulations with these nanoscale materials. In addition, full understanding of the mechanism of hydrogen storage of the doped nanotubes is still needed. So far, most theoretical studies have focused on doped SWNTs. It is important and challenging to explore the electronic structure and other physical properties of doped MWNTs and find the differences between doping behaviors of SWNTs and MWNTs using accurate first-principles methods.

In the end, for many researchers who have spent a lot of time on doped nanotubes, the best and most exciting days

in this field are still ahead as they find novel properties or make discoveries, whereas for others, it will be interesting and entertaining just to sit down and look at the developments in this exciting field.

GLOSSARY

C$_{60}$ A truncated icosahedral structure formed by 20 hexagonal and 12 pentagonal rings.

Endohedral doping A doping mechanism with the dopant inside a cage molecule, for example, a fullerene or carbon nanotube.

Exohedral doping A doping mechanism with the dopant outside or between cage molecules, for example, fullerene cages or carbon nanotubes.

Multi-walled carbon nanotube (MWNT) A carbon nanotube derived from single graphene sheet rolled as a scroll or built from perfectly concentric cylinders formed by a few stacked graphitic shells.

Optical limiter A device suppressing undesired radiation and effectively decreasing transmittance at high intensity or fluence.

Peapod Filling of molecules or fullerenes into carbon nanotubes.

Positron A positively charged elementary particle.

Single-walled carbon nanotube (SWNT) A carbon nanotube formed by rolling only one graphene sheet.

Substitutional doping A doping mechanism with one or more dopants substituting for the atoms in a cage molecule, for example, a fullerene or carbon nanotube.

X-ray The electromagnetic spectrum between ultraviolet light and gamma radiation.

ACKNOWLEDGMENTS

REFERENCES

1. H. W. Kroto, J. R. Heath, S. C. O'Brien, R. F. Curl, and R. E. Smalley, *Nature* 318, 162 (1985).
2. H. W. Kroto, J. E. Fischer, and D. E. Cox, "The Fullerenes." Pergamon Press, New York, 1993.
3. P. W. Fowler and D. E. Manlopoulos, "An Atlas of Fullerenes." Clarendon Press, Oxford, 1995.
4. J. Cioslowski, "Electronic Structure Calculations on Fullerenes and Their Derivatives." Oxford University Press, Oxford, 1995.
5. M. S. Dresselhaus, G. Dresselhaus, and P. C. Eklund, "Science of Fullerenes and Carbon Nanotubes." Academic Press, New York, 1996.
6. S. Iijima, *Nature* (*London*) 354, 56 (1991).
7. S. Iijima and T. Ichiashi, *Nature* (*London*) 363, 603 (1993).
8. V. Z. Mordkovitch, M. Baxendale, S. Yoshimura, and R. P. H. Chang, *Carbon* 34, 1301 (1996).
9. A. Thess, R. Lee, P. Nikdaev, H. Dai, P. Petit, J. Robert, C. Xu, Y. H. Lee, S. G. Kim, A. G. Rinzler, D. T. Colbert, G. E. Scuseria, D. Tomanek, J. E. Fischer, and R. E. Smalley, *Science* (*Washington, DC*) 273, 483 (1996).
10. M. Endo, S. Iijima, and M. S. Dresselhaus, "Carbon Nanotubes." Pergamon Press, New York, 1996.
11. T. W. Ebbesen, "Carbon Nanotubes: Preparation and Properties." CRC Press, Boca Raton, FL, 1996.
12. R. Saito, G. Dresslehaus, and M. S. Dresselhaus, "Physical Properties of Carbon Nanotubes." Imperial College Press, London, 1998.
13. K. Tanaka, T. Yamabee, K. Fukui, T. Yamabe, and K. Fukui, "The Science and Technologies of Carbon Nanotubes." Elsevier Science, New York, 1999.
14. K. C. Venema, "Electronic Structure of Carbon Nanotubes." Delft University Press, Delft, 2000.
15. K. M. Kadish and R. S. Ruoff, Eds., "Fullerenes: Chemistry, Physics, and Technology." Wiley, New York, 2000.
16. L. P. Biro, C. A. Bernardo, and G. G. Tibbetts, "Carbon Filaments and Nanotubes: Common Origins, Differing Applications." Kluwer Academic, New York, 2001.
17. M. S. Dresselhaus, G. Dresselhaus, and Ph. Avouris, Eds., "Carbon Nanotubes: Synthesis, Structures, Properties, and Applications." Springer-Verlag, New York, 2001.
18. P. J. F. Harris, "Carbon Nanotubes and Related Structures." Cambridge University Press, New York, 2001.
19. St. Reich, J. Janina, and Ch. Thomsen, "Carbon Nanotubes." Wiley, New York, 2002.
20. J. P. Lu and J. Han, *Int. J. High Electron. Syst.* 9, 101 (1998).
21. L. Dai, *Polym. Adv. Technol.* 10, 357 (1999).
22. P. M. Ajayan, *Chem. Rev.* 99, 1787 (1999).
23. C. N. R. Rao, B. C. Satishkumar, A. Govindaraj, and M. Nath, *Chem. Phys. Chem.* 2, 78 (2001).
24. S. B. Sinnott and R. Andrews, *Crit. Rev. Solid State Mater. Sci.* 26, 145 (2001).
25. P. Avouris, *Chem. Phys.* 281, 429 (2002).
26. R. H. Baughman, A. A. Zakhidov, and W. A. de Heer, *Science* (*Washington, DC*) 297, 787 (2002).
27. C. Joachim, J. K. Gimzewski, and A. Aviram, *Nature* (*London*) 408, 541 (2000).
28. A. Aviram and M. A. Ratner, *Chem. Phys. Lett.* 29, 277 (1974).
29. L. Duclaux, *Carbon* 40, 1751 (2002).
30. G. H. Stout and L. H. Jensen, "X-Ray Structure Determination." Wiley, New York, 1989.
31. M. von Laue, *Sitz. Math. Phys. Klasse Bayer. Akad. Wiss.* 303 (1912).
32. V. Z. Mordkovich, M. Baxendale, S. Yoshimura, and R. P. H. Chang, *Carbon* 34, 1301 (1996).
33. A. Herold, in "Physics and Chemistry of Materials with Layered Structures," Vol. 6, pp. 323–421. D. Reidel, Dordrecht, the Netherlands, 1979.
34. C. Bower, S. Suzuki, K. Tanigaki, and O. Zhou, *Appl. Phys. A* 67, 47 (1998).
35. L. Duclaux, K. Metenier, J. P. Salvetat, P. Lauginie, S. Bonnamy, and F. Beguin, *Mol. Cryst. Liq. Cryst.* 340, 769 (2000).
36. C. Bower, A. Kleinhammes, Y. Wu, and O. Zhou, *Chem. Phys. Lett.* 288, 481 (1998).
37. G. Maurin, Ch. Bousquet, F. Henn, P. Bernier, R. Almairac, and B. Simon, *Chem. Phys. Lett.* 312, 14 (1999).
38. L. Grigorian, K. A. Williams, S. Fang, G. U. Sumanasekera, A. L. Loper, E. C. Dickey, S. J. Pennycook, and P. C. Eklund, *Phys. Rev. Lett.* 80, 5560 (1998).
39. C. L. Xu, B. Q. Wei, R. Z. Ma, J. Liang, X. K. Ma, and D. H. Wu, *Carbon* 37, 855 (1999).
40. R. K. Rana, X. N. Xu, Y. Yeshurun, and A. Gedanken, *J. Phys. Chem. B* 106, 4079 (2002).

41. L. Grigorian, G. U. Sumanasekera, A. L. Loper, S. L. Fang, J. L. Allen, and P. C. Eklund, *Phys. Rev. B* 60, 11309 (1999).
42. H. Kataura, Y. Maniwa, M. Abe, A. Fujiwara, T. Kodama, K. Kikuchi, H. Imahori, Y. Misaki, S. Suzuki, and Y. Achiba, *Appl. Phys. A* 74, 349 (2002).
43. Y. Maniwa, Y. Kumazawa, Y. Saito, H. Tou, H. Karaura, H. Ishii, S. Suzuki, Y. Achiba, A. Fujiwara, and H. Suematsu, *Jpn. J. Appl. Phys.* 38, L668 (1999).
44. J. W. G. Wildoer, L. C. Venema, A. G. Rinzler, R. E. Smalley, and C. Dekker, *Nature* (*London*) 391, 59 (1998).
45. T. W. Odom, J. L. Huang, P. Kim, and C. M. Lieber, *Nature* (*London*) 391, 62 (1998).
46. J. Chen, M. A. Hamon, H. Hu, Y. Chen, A. M. Rao, P. C. Eklund, and R. C. Haddon, *Science* (*Washington, DC*) 282, 95 (1998).
47. M. E. Itkis, S. Niyogi, M. E. Meng, M. A. Hamon, H. Hu, and R. C. Haddon, *Nano Lett.* 2, 155 (2002).
48. C. Bower, A. Kleinhammes, Y. Wu, and O. Zhou, *Chem. Phys. Lett.* 288, 481 (1998).
49. R. Jacquemin, S. Kazaoui, D. Yu, A. Hussanien, N. Minami, H. Kataura, and Y. Achiba, *Synth. Met.* 115, 283 (2000).
50. N. Minami, S. Kazaoui, R. Jacquemin, H. Yamawaki, K. Aoki, H. Kataura, and Y. Achiba, *Synth. Met.* 116, 405 (2001).
51. E. T. Mickelson, I. W. Chiang, J. L. Zimmerman, P. J. Boul, J. Lozano, J. Liu, R. E. Smalley, R. H. Hauge, and J. L. Margrave, *J. Phys. Chem. B* 103, 4318 (1999).
52. P. J. Boul, J. Liu, E. T. Mickelson, C. B. Huffman, L. M. Ericson, I. W. Chiang, K. A. Smith, D. T. Colbert, R. H. Hauge, J. L. Margrave, and R. E. Smalley, *Chem. Phys. Lett.* 310, 367 (1999).
53. I. W. Chiang, B. E. Brinson, R. E. Smalley, J. L. Margrave, and R. H. Hauge, *J. Phys. Chem. B* 105, 1157 (2001).
54. W. Zhao, C. Song, B. Zheng, J. Liu, and T. Viswanathan, *J. Phys. Chem. B* 106, 293 (2002).
55. B. W. Smith, M. Monthioux, and D. E. Luzzi, *Nature* (*London*) 396, 323 (1998).
56. D. E. Luzzi and B. W. Smith, *Carbon* 38, 1751 (2000).
57. B. Burteaux, A. Claye, B. W. Smith, M. Monthioux, D. E. Luzzi, and J. E. Fischer, *Chem. Phys. Lett.* 310, 21 (1999).
58. J. P. Hare, H. W. Kroto, and R. Taylor, *Chem. Phys. Lett.* 177, 394 (1991).
59. L. Kavan, P. Rapta, L. Dunsch, M. J. Bronikowski, P. Willis, and R. E. Smalley, *J. Phys. Chem. B* 105, 10764 (2001).
60. L. Kavan, L. Dunsch, and H. Kataura, *Chem. Phys. Lett.* 361, 79 (2002).
61. S. Kazaoui, N. Minami, R. Jacquemin, H. Kataura, and Y. Achiba, *Phys. Rev. B* 60, 13339 (1999).
62. S. Kazaoui, N. Minami, N. Matsuda, H. Kataura, and Y. Achiba, *Appl. Phys. Lett.* 78, 3433 (2001).
63. M. S. Dresselhaus and P. C. Eklund, *Adv. Phys.* 49, 705 (2000), and related references therein.
64. A. Claye, S. Rahman, J. E. Fischer, A. Sirenko, G. U. Sumanasekera, and P. C. Eklund, *Chem. Phys. Lett.* 333, 16 (2001).
65. A. M. Rao, E. Richter, S. Bandow, B. Chase, P. E. Eklund, K. A. Williams, S. Fang, K. R. Subbaswamy, M. Menon, A. Thess, R. E. Smalley, G. Dresselhaus, and M. S. Dresselhaus, *Science* 275, 187 (1997).
66. N. Bendiab, E. Anglaret, J. L. Bantignies, A. Zahab, J. L. Sauvajol, P. Petit, C. Mathis, and S. Lefrant, *Phys. Rev. B* 64, 245424 (2001).
67. G. Maurin, F. Henn, B. Simon, J. F. Colomer, and J. B. Nagy, *Nano Lett.* 1, 75 (2001).
68. A. M. Rao, P. C. Eklund, S. Bandow, A. Thess, and R. E. Smalley, *Nature* (*London*) 388, 257 (1997).
69. Y. Iwasa, H. Fudo, Y. Yatsu, T. Mitani, H. Kataura, and Y. Achiba, *Synth. Met.* 121, 1203 (2001).
70. N. Bendiab, A. Righi, E. Anglaret, J. L. Sauvajol, L. Duclaux, and F. Béguin, *Chem. Phys. Lett.* 339, 305 (2001).
71. N. Bendiab, L. Spina, A. Zahab, P. Poncharal, J. L. Bantignies, E. Anglaret, and J. L. Sauvajol, *Phys. Rev. B* 63, 153407 (2001).
72. A. Thess, R. Lee, P. Nikolaev, H. Dai, P. Petit, J. Robert, C. Xu, Y. H. Lee, S. G. Kim, A. G. Rinzle, D. T. Colbert, G. E. Scuseria, D. Tomanek, J. E. Fischer, and R. E. Smalley, *Science* 273, 483 (1996).
73. H. Kataura, Y. Kumazawa, N. Kojima, Y. Maniwa, I. Umezu, S. Masubuchi, S. Kazama, Y. Ohtsuka, S. Suzuki, and Y. Achiba, *Mol. Cryst. Liq. Cryst.* 340, 757 (2000).
74. A. M. Rao, S. Bandow, E. Richter, and P. C. Eklund, *Thin Solid Films* 331, 141 (1998).
75. M. S. Dresselhaus and P. C. Eklund, *Adv. Phys.* 49, 705 (2000).
76. X. Fan, E. C. Dickey, P. C. Eklund, K. A. Williams, L. Grigorian, R. Buczko, S. T. Pantelides, and S. J. Pennycook, *Phys. Rev. Lett.* 84, 4621 (2000).
77. M. S. Dresselhaus and G. Dresselhaus, *Adv. Phys.* 30, 139 (1981).
78. R. H. Baughman, S. L. Hsu, L. R. Anderson, G. P. Pez, and A. J. Signorelli, in "Molecular Metals" NATO Conference Series, Series VI: Materials Science, Vol. 1 (W. E. Hatfield, Ed.), Plenum, New York, 1979, p. 187.
79. S. Nakashima, M. Norimoto, H. Harima, Y. Hamanaka, L. S. Grigorian, and M. Tokumoto, *Chem. Phys. Lett.* 268, 359 (1997).
80. H. Werner, M. Wesemann, and R. Schlogl, *Europhys. Lett.* 20, 107 (1992).
81. U. D. Venkateswaran, E. A. Brandsen, M. E. Katakowski, A. Harutyunyan, G. Chen, A. L. Loper, and P. C. Eklund, *Phys. Rev. B* 65, 054102 (2002).
82. W. Zhou, S. Xie, L. Sun, D. Tang, Y. Li, Z. Liu, L. Ci, X. Zou, G. Wang, P. Tan, X. Dong, B. Xu, and B. Zhao, *Appl. Phys. Lett.* 80, 2553 (2002).
83. J. Maultzsch, S. Reich, C. Thomsen, S. Webster, R. Czerw, D. L. Carroll, S. M. C. Vieira, P. R. Birkett, and C. A. Rego, *Appl. Phys. Lett.* 81, 2647 (2002).
84. L. Kavan, P. Rapta, and L. Dunsch, *Chem. Phys. Lett.* 328, 363 (2000).
85. I. Ando and G. A. Webb, "Theory of NMR Parameters." Academic Press, New York, 1983.
86. R. J. Abraham, J. Fisher, and P. Loftus, "Introduction to NMR Spectroscopy." Wiley, New York, 1988.
87. B. D. N. Rao and M. D. Kemple, "NMR as a Structural Tool for Macromolecules: Current Status and Future Directions." Plenum Press, New York, 1996.
88. N. S. Ramsey, *Phys. Rev.* 78, 699 (1950).
89. N. S. Ramsey, *Phys. Rev.* 91, 303 (1953).
90. X. P. Tang, A. Kleinhammes, H. Shimoda, L. Fleming, K. Y. Bennoune, S. Sinha, C. Bower, O. Zhou, and Y. Wu, *Science* 288, 492 (2000).
91. F. Leroux, K. Méténier, S. Gautier, E. Frackowiak, S. Bonnamy, and F. Béguin, *J. Power Sources* 81, 317 (1999).
92. P. Lauginie, H. Estrade-Szwarckopf, and J. Conard, *Mater. Sci. Forum* 91, 545 (1992).
93. C. Goze-Bac, S. Latil, P. Lauginie, V. Jourdain, J. Conard, L. Duclaux, A. Rubio, and P. Bernier, *Carbon* 40, 1825 (2002).
94. J. Heremans, C. H. Olk, and D. T. Morelli, *Phys. Rev. B* 49, 15122 (1994).
95. A. P. Ramirez, R. C. Haddon, O. Zhou, R. M. Fleming, J. Zhang, S. M. Mcclure, and R. E. Smalley, *Science* 265, 84 (1994).
96. X. K. Wang, R. P. H. Chang, A. Patashinski, and J. B. Ketterson, *J. Mater. Res.* 9, 1578 (1994).
97. M. Kosaka, T. W. Ebbesen, H. Hiura, and K. Tanigak, *Chem. Phys. Lett.* 225, 161 (1994).
98. O. Chauvet, L. Forro, W. Bacsa, D. Ugarte, B. Doudin, and W. A. de Heer, *Phys. Rev. B* 52, 6963 (1995).
99. M. Kosaka, T. W. Ebbesen, H. Hiura, and K. Tanigak, *Chem. Phys. Lett.* 233, 47 (1995).
100. S. Bandow, *J. Appl. Phys.* 80, 1020 (1996).
101. S. Bandow, M. Yudasaka, R. Yamada, S. Iijima, F. Kokai, and K. Takahashi, *Mol. Cryst. Liq. Cryst.* 340, 749 (2000).

102. G. Wagoner, *Phys. Rev.* 118, 647 (1960).
103. P. Lauginie, A. Messaoudi, and J. Conard, *Synth. Met.* 56, 3002 (1993).
104. H. Yokomichi, M. Matoba, T. Fukuhara, H. Sakima, F. Sakai, and K. Maezawa, *Phys. Stat. Sol. B* 207, R1 (1998).
105. W. K. Hsu, S. Y. Chu, E. Munoz-Picone, J. L. Boldu, S. Firth, P. Franchi, B. P. Roberts, A. Schilder, H. Terrones, N. Grobert, Y. Q. Zhu, M. Terrones, M. E. McHenry, H. W. Kroto, and D. R. M. Walton, *Chem. Phys. Lett.* 323, 572 (2000).
106. A. S. Kotosonov and D. V. Shilo, *Mol. Mater.* 13, 113 (2000).
107. A. S. Kotosonov and S. V. Kuvshinnikov, *Phys. Lett. A* 229, 377 (1997).
108. A. S. Kotosonov and D. V. Shilo, *Carbon* 36, 1649 (1998).
109. Y. C. Jean, X. Lu, Y. Lou, A. Bharathi, C. S. Sundar, Y. Lyu, P. H. Hor, and C. W. Chu, *Phys. Rev. B* 45, 12126 (1992).
110. J. Kristiak, K. Kristiakova, and O. Sausa, *Phys. Rev. B* 50, 2792 (1994).
111. F. Becvar, I. Novotny, I. Prochazka, D. Rafaja, and J. Kern, *Appl. Phys. A: Mater. Sci. Process* 61, 335 (1995).
112. Y. Ito and T. Suzuki, *Phys. Rev. B* 60, 15636 (1999).
113. H. Murakami and M. Sano, *J. Phys. Soc. Jpn.* 71, 125 (2002).
114. M. Sano, N. Sato, H. Inokuchi, and S. Tamura, *Bull. Chem. Soc. Jpn.* 54, 2610 (1981).
115. P. Kirkegaard, N. J. Pedersen, and M. Eldrup, Ris M-2740, 1989.
116. O. Zhou, R. M. Fleming, D. W. Murphy, C. H. Chen, R. C. Haddon, A. P. Ramirez, and S. H. Glarum, *Science* 263, 1744 (1994).
117. Y. C. Jean, K. Vankateswaren, E. Parasai, and K. L. Cheng, *Appl. Phys. A: Solids Surf.* 35, 169 (1984).
118. H. Murakami, I. Kanazawa, M. Sano, T. Enoki, and H. Inokuchi, *Synth. Met.* 32, 135 (1989).
119. P. Lambin, A. Fonseca, J. P. Vigneron, J. B. Nagy, and A. A. Lucas, *Chem. Phys. Lett.* 245, 85 (1995).
120. L. Chico, V. H. Crespi, L. X. Benedict, S. G. Louie, and M. L. Cohen, *Phys. Rev. Lett.* 76, 971 (1996).
121. M. S. Dresselhaus, *Phys. World* 9, 18 (1996).
122. Z. Weng-Sieh, K. Cherrey, N. G. Chopra, X. Blase, Y. Miyamoto, A. Rubio, M. L. Cohen, S. G. Louie, A. Zettl, and R. Gronsky, *Phys. Rev. B* 51, 11229 (1995).
123. J. Y. Yi and J. Bernholc, *Phys. Rev. B* 47, 1708 (1993).
124. D. Goldberg, Y. Bando, K. Kurashima, and T. Sasaki, *Appl. Phys. Lett.* 72, 2108 (1998).
125. W. Q. Han, Y. Bando, K. Kurashima, and T. Sato, *Chem. Phys. Lett.* 299, 368 (1999).
126. D. L. Carroll, Ph. Redlich, X. Blase, J. C. Charlier, S. Curran, P. M. Ajayan, S. Roth, and M. Rühle, *Phys. Rev. Lett.* 81, 2332 (1998).
127. D. L. Carroll, Ph. Redlich, P. M. Ajayan, S. Curran, S. Roth, and M. Rühle, *Carbon* 36, 753 (1998).
128. X. Blase, J. C. Charlier, A. de Vita, R. Car, Ph. Redlich, M. Terrones, W. K. Hsu, H. Terrones, D. L. Carroll, and P. M. Ajayan, *Phys. Rev. Lett.* 83, 5078 (1999).
129. D. L. Carroll, P. Redlich, P. M. Ajayan, J. C. Charlier, X. Blase, A. de Vita, and R. Car, *Phys. Rev. Lett.* 78, 2811 (1997).
130. A. Agarwal, *J. Mater. Sci.* 21, 3455 (1986).
131. L. R. Radovic, M. Karra, K. Skokova, and P. A. Thrower, *Carbon* 36, 1841 (1998).
132. R. Czerw, M. Terrones, J. C. Charlier, X. Blase, B. Foley, P. Kamalakaran, N. Grobert, H. Terrones, D. Tekleab, P. M. Ajayan, W. Blau, M. Rühle, and D. L. Carroll, *Nano Lett.* 1, 457 (2001).
133. M. Terrones, P. Ajayan, F. Banhart, X. Blase, D. L. Carroll, J. C. Charlier, R. Czerw, B. Foley, N. Grobert, R. Kamalakaran, P. Kohler-Redlich, M. Rühle, T. Seeger, and H. Terrones, *Appl. Phys. A* 74, 355 (2002).
134. K. Suenaga, C. Colliex, N. Demoncy, A. Loiseau, H. Pascard, and F. Willaime, *Science* 278, 653 (1997).
135. P. Kohler-Redlich, M. Terrones, C. Manteca-Diego, W. K. Hsu, H. Terrones, M. Rühle, H. W. Kroto, and D. R. M. Walton, *Chem. Phys. Lett.* 310, 459 (1999).
136. C. Y. Zhi, J. D. Guo, X. D. Bai, and E. G. Wang, *J. Appl. Phys.* 91, 5325 (2002).
137. P. Petit, C. Mathis, C. Journet, and P. Bernier, *Chem. Phys. Lett.* 305, 370 (1999).
138. G. Zhang, W. Duan, G. Zhou, and B. Gu, *Solid State Commun.* 122, 121 (2002).
139. D. J. Mann and M. D. Halls, *J. Chem. Phys.* 116, 9014 (2002).
140. R. J. Baierle, S. B. Fagan, R. Mota, A. J. R. da Silva, and A. Fazzio, *Phys. Rev. B* 64, 085413 (2001).
141. B. Gao, A. Kleinhammes, X. P. Tang, C. Bower, L. Fleming, Y. Wu, and O. Zhou, *Chem. Phys. Lett.* 307, 153 (1999).
142. H. Shimoda, B. Gao, X. P. Tang, A. Kleinhammes, L. Fleming, Y. Wu, and O. Zhou, *Phys. Rev. Lett.* 88, 015502 (2002).
143. B. Gao, C. Bower, J. D. Lorentzen, L. Fleming, A. Kleinhammes, X. P. Tang, L. E. McNeil, Y. Wu, and O. Zhou, *Chem. Phys. Lett.* 327, 69 (2000).
144. J. Zhao, A. Buldum, J. Han, and J. P. Lu, *Phys. Rev. Lett.* 85, 1706 (2000).
145. T. Kar, J. Pattanayak, and S. Scheiner, *J. Phys. Chem. A* 105, 10397 (2001).
146. G. Gao, T. Cagin, and W. A. Goddard III, *Phys. Rev. Lett.* 80, 5556 (1998).
147. T. Miyake and S. Saito, *Phys. Rev. B* 65, 165419 (2002).
148. C. Jo, C. Kim, and Y. H. Lee, *Phys. Rev. B* 65, 035420 (2002).
149. J. Choi, I. A. Samayoa, S. C. Lim, C. Jo, Y. C. Choi, Y. H. Lee, and P. A. Dowben, *Phys. Lett. A* 299, 601 (2002).
150. Y. Zhang and H. Dai, *Appl. Phys. Lett.* 77, 3015 (2000).
151. C. K. Yang, J. Zhao, and J. P. Lu, *Phys. Rev. B* 66, 041403 (2002).
152. C. G. Piecourt, Y. L. Bouar, A. Loiseau, and H. Pascard, *Nature (London)* 372, 761 (1994).
153. S. Setaphin, D. Zhou, and J. Jiao, *J. Appl. Phys.* 80, 2097 (1996).
154. L. C. Qin, *J. Mater. Sci. Lett.* 16, 457 (1997).
155. C. K. Yang, J. Zhao, and J. P. Lu, *Phys. Rev. Lett.* 90, 257203 (2003).
156. G. A. Prinz, *Science* 282, 1660 (1998).
157. S. A. Wolf, *Science* 294, 1488 (2001).
158. K. Lafdi, A. Chin, N. Ali, and J. F. Despres, *J. Appl. Phys.* 79, 6007 (1996).
159. W. Kratschmer and D. R. Huffman, *Chem. Phys. Lett.* 170, 167 (1990).
160. J. Haruyama, I. Takesue, and T. Hasegawa, *Physica E* 12, 735 (2002).
161. J. Haruyama, I. Takesue, and T. Hasegawa, *Phys. Rev. B* 65, 033402 (2002).
162. J. W. Mintmire, B. I. Dunlap, and C. T. White, *Phys. Rev. Lett.* 68, 631 (1992).
163. N. Hamada, S. Sawada, and A. Oshiyama, *Phys. Rev. Lett.* 68, 1579 (1992).
164. R. Saito, M. Fujita, G. Dresselhaus, and M. S. Dresselhaus, *Phys. Rev. B* 46, 1804 (1992).
165. R. Saito, M. Fujita, G. Dresselhaus, and M. S. Dresselhaus, *Appl. Phys. Lett.* 60, 2204 (1992).
166. T. W. Ebbesen, H. J. Lezec, H. Hiura, J. W. Bennett, H. F. Ghaemi, and T. Thio, *Nature (London)* 382, 54 (1996).
167. S. T. Tans, M. H. Devoret, H. Dai, A. Thess, R. E. Smalley, L. J. Geerligs, and C. Dekker, *Nature (London)* 386, 474 (1997).
168. S. N. Song, X. K. Wang, R. P. H. Chang, and J. B. Ketterson, *Phys. Rev. Lett.* 72, 697 (1997).
169. M. Terrones, W. K. Hsu, A. Schilder, H. Terrones, N. Grobert, J. P. Hare, Y. Q. Zhu, M. Schwoerer, K. Prassides, H. W. Kroto, and D. R. M. Walton, *Appl. Phys. A* 66, 307 (1998).
170. W. A. de Herr, W. S. Bacsa, A. Chatelin, T. Gerfin, R. Humphrey-Baker, L. Forro, and D. Ugarte, *Science* 268, 845 (1995).

171. H. Dai, E. W. Wong, and C. M. Lieber, *Science* (*Washington, DC*) 272, 523 (1996).
172. J. P. Issi, L. Langer, J. Heremans, and C. H. Olk, *Carbon* 33, 941 (1995).
173. A. G. Rinzler, J. Liu, H. Dai, P. Nikolaev, C. B. Huffman, F. J. Rodriguez-Macias, P. J. Boul, A. H. Lu, D. Heymann, D. T. Colbert, R. S. Lee, J. E. Fischer, A. M. Rao, P. C. Eklund, and R. E. Smalley, *Appl. Phys. A* 67, 29 (1998).
174. C. L. Kane, E. J. Mele, R. S. Lee, J. E. Fischer, P. Petit, H. Dai, A. Thess, R. E. Smalley, A. R. M. Verschueren, S. J. Tans, and C. Dekker, *Europhys. Lett.* 41, 683 (1998).
175. A. Yu. Kasumov, H. Bouchiat, B. Reulet, O. Stephan, I. I. Khodos, Yu. B. Gorbatov, and C. Colliex, *Europhys. Lett.* 43, 89 (1998).
176. R. Z. Ma, C. L. Xu, B. Q. Wei, J. Liang, D. H. Wu, and D. J. Li, *Carbon*, to be published.
177. Q. H. Wang, T. D. Corrigan, J. Y. Dai, and R. P. H. Wu, *Appl. Phys. Lett.* 70, 3308 (1997).
178. R. S. Lee, H. J. Kim, J. E. Fischer, A. Thess, and R. E. Smalley, *Nature* (*London*) 388, 255 (1997).
179. B. Ruzicka, L. Degiorgi, R. Gaal, L. Thien-Nga, R. Bacsa, J. P. Salvetat, and L. Forro, *Phys. Rev. B* 61, 2468 (2000).
180. D. E. Sklovsky, V. A. Nalimova, and J. E. Fischer, *Mol. Cryst. Liq. Cryst.* 340, 763 (2000).
181. R. S. Lee, H. J. Kim, J. E. Fischer, J. Lefebvre, M. Radosavljevic, J. Hone, and A. T. Johnson, *Phys. Rev. B* 61, 4526 (2000).
182. A. Rochefort and P. Avouris, *J. Phys. Chem. A* 104, 9807 (2000).
183. B. Wei, R. Spolenak, P. Kohler-Redlich, M. Rühle, and E. Arzt, *Appl. Phys. Lett.* 74, 3149 (1999).
184. K. Liu, Ph. Avouris, R. Martel, and W. K. Hsu, *Phys. Rev. B* 63, 161404 (2001).
185. W. K. Hsu and T. Nakajima, *Carbon* 40, 445 (2002).
186. S. Frank, P. Poncharal, Z. L. Wang, and D. W. Heer, *Science* 280, 1744 (1998).
187. J. W. G. Wildöer, L. C. Venema, A. G. Rinzler, R. E. Smalley, and C. Dekker, *Nature* (*London*) 391, 59 (1998).
188. Ph. G. Colins and A. Zettl, *Appl. Phys. Lett.* 69, 1969 (1996).
189. G. Z. Chen, M. S. P. Shaffer, D. Coleby, G. Dixon, W. Zhou, D. J. Fray, and A. H. Windle, *Adv. Mater.* 12, 522 (2000).
190. P. C. P. Watts, W. K. Hsu, G. Z. Chen, D. J. Fray, H. W. Kroto, and D. R. M. Walton, *J. Mater. Chem.* 11, 2482 (2001).
191. C. C. Kaun, B. Larade, H. Mehrez, J. Taylor, and H. Guo, *Phys. Rev. B* 65, 205416 (2002).
192. H. J. Yuan, P. Xie, J. Xiang, D. P. Yu, J. Xu, S. S. Xie, and S. Q. Feng, *Solid State Commun.* 119, 573 (2001).
193. F. J. Garcia-Vidal, J. M. Pitarke, and J. B. Pendry, *Phys. Rev. B* 58, 6783 (1998).
194. M. Tomita, Y. Saito, and T. Hayashi, *Jpn. J. Appl. Phys.* 32, L280 (1993).
195. R. S. Ruoff, C. Lorents, B. C. Chan, R. Malhotra, and S. Subramoney, *Science* 259, 346 (1993).
196. Y. Saito, T. Yoshikawa, M. Okuda, M. Ohkohchi, Y. Ando, A. Kasuya, and Y. Nishima, *Chem. Phys. Lett.* 209, 72 (1993).
197. Y. Murakami, T. Shinata, K. Okuyama, T. Arai, H. Suematsu, and Y. Yoshida, *J. Phys. Chem. Solids* 54, 1861 (1994).
198. Y. Yosida, *Appl. Phys. Lett.* 62, 3447 (1993).
199. C. Guerret-Piecourt, Y. Le Bouar, A. Loisseau, and H. Pascard, *Nature* (*London*) 372, 761 (1994).
200. S. A. Majetich, J. O. Artman, M. E. WcHenry, N. T. Nuhfer, and S. W. Staley, *Phys. Rev. B* 48, 16845 (1995).
201. S. Seraphin, D. Zhou, J. Jiao, J. C. Withers, and R. Loufty, *Appl. Phys. Lett.* 63, 2073 (1993).
202. S. Bandown and Y. Saito, *Jpn. J. Appl. Phys.* 32, L1677 (1994).
203. M. Ata, K. Yamaura, and A. J. Hudson, *J. Adv. Mater.* 7, 286 (1995).
204. R. Martel, T. Schmidt, H. R. Shea, T. Hertel, and Ph. Avouris, *Appl. Phys. Lett.* 73, 2447 (1998).
205. V. Derycke, R. Martel, J. Appenzeller, and Ph. Avouris, *Nano Lett.* 1, 453 (2001).
206. X. Liu, C. Lee, C. Zhou, and J. Han, *Appl. Phys. Lett.* 79, 3329 (2001).
207. M. Bockrath, J. Hone, A. Zettl, P. L. McEuen, A. G. Rinzler, and R. E. Smalley, *Phys. Rev. B* 61, 10606 (2000).
208. K. Esfarjani, A. A. Farajian, Y. Hashi, and Y. Kawazoe, *Appl. Phys. Lett.* 74, 79 (1999).
209. C. Zhou, J. Kong, E. Yenilmez, and H. Dai, *Science* 290, 1552 (2000).
210. J. Kong, C. Zhou, E. Yenilmez, and H. Dai, *Appl. Phys. Lett.* 77, 3977 (2000).
211. J. Kong, J. Cao, H. Dai, and E. Anderson, *Appl. Phys. Lett.* 80, 73 (2002).
212. R. Martel, V. Derycke, C. Lavoie, J. Appenzeller, K. Chan, J. Tersoff, and Ph. Avouris, *Phys. Rev. Lett.* 87, 256805 (2001).
213. V. Derycke, R. Martel, J. Appenzeller, and Ph. Avouris, *Appl. Phys. Lett.* 80, 2773 (2002).
214. J. Park and P. L. McEuen, *Appl. Phys. Lett.* 79, 1363 (2001).
215. G. U. Sumanasekera, C. K. W. Adu, S. Fang, and P. C. Eklund, *Phys. Rev. Lett.* 85, 1096 (2000).
216. P. G. Collins, K. Bradley, M. Ishigami, and A. Zettl, *Science* 287, 1801 (2000).
217. J. Kong, N. R. Franklin, C. Zhou, M. G. Chapline, S. Peng, K. Cho, and H. Dai, *Science* 287, 622 (2000).
218. S. H. Jhi, S. G. Louie, and M. L. Cohen, *Phys. Rev. Lett.* 85, 1710 (2000).
219. J. Zhao, A. Buldum, J. Han, and J. P. Lu, *Nanotechnology* 13, 195 (2002).
220. B. W. Smith, M. Monthioux, and D. E. Luzzi, *Science* 396, 323 (1998).
221. B. W. Smith and D. E. Luzzi, *Chem. Phys. Lett.* 321, 169 (2000).
222. K. Suenaga, M. Tence, C. Mory, C. Colliex, H. Kato, T. Okazaki, K. Hirahara, S. Bandow, and S. Iijima, *Science* 290, 2280 (2000).
223. K. Hirahara, K. Suenaga, S. bandow, H. Kato, T. Okazaki, H. Shinohara, and S. Iijima, *Phys. Rev. Lett.* 85, 5384 (2000).
224. M. Monthioux, *Carbon* 40, 1809 (2002).
225. S. Okada, S. Saito, and A. Oshiyama, *Phys. Rev. Lett.* 86, 3835 (2001).
226. P. W. Chiu, G. Gu, G. T. Kim, G. Philipp, S. Roth, S. F. Yang, and S. Yang, *Appl. Phys. Lett.* 79, 3845 (2001).
227. T. Pichler, H. Kuzmany, H. Kataura, and Y. Achiba, *Phys. Rev. Lett.* 87, 267401 (2001).
228. R. H. Xie, G. W. Bryant, J. Zhao, V. H. Smith, Jr., A. Di Carlo, and A. Pecchia, *Phys. Rev. Lett.* 90, 206602 (2003).
229. R. H. Xie, G. W. Bryant, and V. H. Smith, Jr., *Chem. Phys. Lett.* 368, 486 (2003).
230. R. H. Xie, G. W. Bryant, L. Jensen, J. Zhao, and V. H. Smith, Jr., *J. Chem. Phys.* 118, 8621 (2003).
231. K. Okano, S. Koizumi, S. R. P. Silva, and A. J. Amaratunga, *Nature* (*London*) 381, 140 (1996).
232. A. G. Rinzler, J. H. Hafner, P. Nikolaev, L. Lou, S. G. Kim, D. Tomanek, P. Nordlander, D. T. Colbert, and R. E. Smalley, *Science* 269, 1550 (1995).
233. W. A. de Heer, A. Chatelain, and D. Ugarte, *Science* 270, 1179 (1995).
234. P. G. Collins and A. Zettle, *Phys. Rev. B* 55, 9391 (1997).
235. J. M. Bonard, J. P. Salvetat, T. Stöckli, L. Forro, and A. Chatelain, *Appl. Phys. A* 69, 245 (1999), and references therein.
236. M. J. Fransen, Th. L. van Rooy, and P. Kruit, *Appl. Surf. Sci.* 146, 312 (1999), and references therein.
237. A. Mayer, N. M. Miskovsky, and P. H. Cutler, *Phys. Rev. B* 65, 155420 (2002).
238. A. Mayer and Ph. Lambin, *Carbon* 40, 429 (2002).

239. C. Oshima, K. Mastuda, T. Kona, Y. Mogami, M. Komaki, Y. Murata, T. Yamashita, T. Kuzumaki, and Y. Horiike, *Phys. Rev. Lett.* 88, 038301 (2002).

240. Ch. Adessi and M. Devel, *Phys. Rev. B* 62, 13314 (2000).

241. K. A. Dean, O. Groening, O. M. Kuttel, and L. Schlapbach, *Appl. Phys. Lett.* 75, 2773 (1999).

242. R. Tamura and M. Tsukada, *Phys. Rev. B* 52, 6015 (1995).

243. D. L. Carroll, P. Redlich, P. M. Ajayan, J. C. Charlier, X. Blase, A. de Vita, and R. Car, *Phys. Rev. Lett.* 78, 2811 (1997).

244. A. de Vita, J. Ch. Charlier, X. Blase, and R. Car, *Appl. Phys. A* 68, 283 (1999).

245. Ph. Kim, T. W. Odom, J. L. Huang, and C. M. Lieber, *Phys. Rev. Lett.* 82, 1225 (1999).

246. S. Han and J. Ihm, *Phys. Rev. B* 61, 9986 (2000).

247. R. H. Fowler and L. Nordheim, *Proc. R. Soc. London, Ser. A* 119, 683 (1928).

248. J. Zhao, J. Han, and J. P. Lu, *Phys. Rev. B* 65, 193401 (2002).

249. H. Ago, T. Kugler, F. Cacialli, W. R. Salaneck, M. S. P. Shaffer, A. H. Windle, and R. H. Friend, *J. Phys. Chem. B* 103, 8116 (1999).

250. M. Shiraishi and M. Ata, *Carbon* 39, 1913 (2001).

251. S. Suzuki, C. Bower, Y. Matanabe, and O. Zhou, *Appl. Phys. Lett.* 76, 4007 (2002).

252. S. Suzuki, Y. Watanable, T. Kiyokura, K. G. Nath, T. Ogino, S. Heun, W. Zhu, C. Bower, and O. Zhou, *Phys. Rev. B* 63, 245418 (2001).

253. R. Gao, Z. Pan, and Z. L. Wang, *Appl. Phys. Lett.* 78, 1757 (2001).

254. P. Chen, X. Wu, X. Sun, J. Lin, W. Ji, and K. L. Tan, *Phys. Rev. Lett.* 82, 2548 (1999).

255. A. Wadhawan, R. E. Stallcup, and J. M. Perez, *Appl. Phys. Lett.* 78, 108 (2001).

256. D. Goldberg, Y. Bando, W. Han, K. Kurashima, and T. Sato, *Chem. Phys. Lett.* 308, 337 (1999).

257. W. Han, Y. Bando, K. Kurashima, and T. Sato, *Chem. Phys. Lett.* 299, 368 (1999).

258. T. Ando and T. Nakanishi, *J. Phys. Soc. Jpn.* 67, 1704 (1998).

259. A. Rochefort and P. Avouris, *J. Phys. Chem. A* 104, 9807 (2000).

260. G. Zhang, W. Duan, and B. Gu, *Appl. Phys. Lett.* 80, 2589 (2002).

261. C. H. Poa, S. R. P. Silva, P. C. P. Watts, W. K. Hsu, H. W. Kroto, and D. R. M. Walton, *Appl. Phys. Lett.* 80, 3189 (2002).

262. X. Wang, Y. Liu, D. Zhu, L. Zhang, H. Ma, N. Yao, and B. Zhang, *J. Phys. Chem. B* 106, 2186 (2002).

263. V. Meunier, C. Roland, J. Bernholc, and M. B. Nardelli, *Appl. Phys. Lett.* 81, 46 (2002).

264. V. N. Tondare, C. Balasubramanian, S. V. Shende, D. S. Joag, V. P. Godbole, S. V. Bhoraskar, and M. Bhadbhade, *Appl. Phys. Lett.* 80, 4813 (2002).

265. S. C. Kung, K. C. Hwang, and I. N. Lin, *Appl. Phys. Lett.* 80, 4819 (2002).

266. R. Kurt, J. M. Bonard, and A. Karimi, *Thin Solids Films* 398, 193 (2001).

267. M. Endo, S. Iijima, and M. S. Dresselhaus, Eds., "Carbon Nanotubes," pp. 37, 159. BPC Press, Oxford, UK, 1996.

268. H. L. Chang and C. T. Kuo, *Diamond Relat. Mater.* 10, 1910 (2001).

269. A. Badzian, T. Badzian, W. Drawl, and R. Roy, *Diamond Relat. Mater.* 7, 1519 (1998).

270. L. C. Chen, C. T. Wu, J. J. Wu, and K. H. Chen, *Int. J. Mod. Phys. B* 14, 333 (1999).

271. Z. Gong, E. G. Wang, G. C. Xu, and Y. Chen, *Thin Solid Films* 348, 114 (1999).

272. H. L. Chang, C. H. Lin, and C. T. Kuo, *Diamond Relat. Mater.* 11, 793 (2002).

273. R. W. Boyd, "Nonlinear Optics." Academic Press, New York, 1992.

274. M. Bianchetti, P. F. Buonsante, F. Ginelli, H. E. Roman, R. A. Broglia, and F. Alasia, *Phys. Rep.* 357, 459 (2002).

275. L. X. Benedict, S. G. Louie, and M. L. Cohen, *Phys. Rev. B* 52, 8541 (1995).

276. J. Kongsted, A. Osted, L. Jensen, P. O. Astrand, and K. V. Mikkelsen, *J. Phys. Chem. B* 105, 10243 (2001).

277. J. Messier, F. Kajzar, and P. N. Prasad, "Organic Molecules for Nonlinear Optics and Photonics." Kluwer Academic, Dordrecht, 1991.

278. S. R. Marder, W. E. Torruellas, M. Blanchard-Desce, V. Ricci, G. I. Stegeman, S. Gilmour, J. L. Bredas, J. Li, G. U. Bublitz, and S. G. Boxer, *Science* 276, 1233 (1997), and related references therein.

279. W. J. Blau, H. J. Byrne, D. J. Cardin, T. T. Dennis, J. P. Hare, H. W. Kroto, R. Taylor, and D. R. M. Walton, *Phys. Rev. Lett.* 67, 1423 (1991).

280. J. S. Meth, H. Vanherzeele, and Y. Wang, *Chem. Phys. Lett.* 197, 26 (1992).

281. Y. Wang and L. T. Cheng, *J. Phys. Chem.* 96, 1530 (1992).

282. S. R. Flom, R. G. S. Pong, F. J. Bartoli, and Z. H. Kafafi, *Phys. Rev. B* 46, 15598 (1992).

283. D. Neher, G. I. Stegeman, F. A. Tinker, and N. Peyghambarian, *Opt. Lett.* 17, 1491 (1992).

284. Z. Shuai and J. L. Bredas, *Phys. Rev. B* 46, 16135 (1992).

285. F. Kajzar, C. Taliani, R. Dannieli, S. Rossini, and R. Zamboni, *Phys. Rev. Lett.* 73, 1617 (1994).

286. M. Fanti, G. Orlandi, and F. Zerbetto, *J. Am. Chem. Soc.* 117, 6101 (1995).

287. M. Fanti, P. W. Fowler, G. Orlandi, and F. Zerbetto, *J. Chem. Phys.* 107, 5072 (1997).

288. H. Huang, G. Gu, S. Yang, J. Fu, P. Yu, G. K. L. Wong, and Y. Du, *Chem. Phys. Lett.* 272, 427 (1997).

289. R. H. Xie and Q. Rao, *Appl. Phys. Lett.* 72, 2358 (1998).

290. R. H. Xie and J. Jiang, *J. Appl. Phys.* 83, 3001 (1998).

291. T. Zhang, F. Wang, H. Yang, Q. Gong, X. An, H. Chen, and D. Qiang, *Chem. Phys. Lett.* 301, 343 (1999).

292. R. H. Xie, *Phys. Lett. A* 258, 51 (1999).

293. R. H. Xie, in "Handbook of Advanced Electronic and Photonic Materials and Devices" (H. S. Nalwa, Ed.), Academic Press, San Diego, 2001, Vol. 9, pp. 267–307.

294. R. H. Xie and J. Jiang, *Appl. Phys. Lett.* 71, 1029 (1997).

295. R. H. Xie and J. Jiang, *Chem. Phys. Lett.* 280, 66 (1997).

296. R. H. Xie, *J. Chem. Phys.* 108, 3626 (1998).

297. R. H. Xie and Q. Rao, *Z. Naturforsch. A* 54, 645 (1999).

298. R. H. Xie and Q. Rao, *Chem. Phys. Lett.* 313, 211 (1999).

299. X. Liu, J. Si, B. Chang, G. Xu, Q. Zhang, Z. Pan, S. Xie, P. Ye, J. Fan, and M. Wan, *Appl. Phys. Lett.* 74, 164 (1999).

300. R. H. Xie, *Z. Naturforsch. A* 54, 348 (1999).

301. R. H. Xie, *Chem. Phys. Lett.* 310, 379 (1999).

302. L. Vivien, P. Lancon, D. Riehl, F. Hache, and E. Anglaret, *Carbon* 40, 1789 (2002).

303. D. J. Harter, M. L. Shend, and Y. B. Band, *J. Appl. Phys.* 56, 865 (1984).

304. Y. B. Band, D. J. Harter, and R. Bavli, *Chem. Phys. Lett.* 126, 280 (1996).

305. L. W. Tutt and A. Kost, *Nature* (*London*) 356, 225 (1992).

306. K. Mansour, M. J. Soileau, and E. W. van Stryland, *J. Opt. Soc. Am. B* 9, 1100 (1992).

307. K. M. Nashold and W. D. Powell, *J. Opt. Soc. Am. B* 12, 1228 (1995).

308. I. C. Khoo, M. Wood, B. D. Guenther, M. Y. Shih, and P. H. Chen, *J. Opt. Soc. Am. B* 15, 1533 (1998).

309. T. Xia, A. Dogariu, K. Mansour, D. J. Hagan, A. A. Said, E. W. van Stryland, and S. Shi, *J. Opt. Soc. Am. B* 15, 1497 (1998).

310. R. C. Hollins, *Curr. Opin. Solid State Mater. Sci.* 4, 189 (1999).

311. A. A. Said, M. Sheik-Bahae, D. J. Hagan, T. H. Wei, J. Wang, J. Young, and E. W. van Stryland, *J. Opt. Soc. Am. B* 9, 405 (1992).

312. B. L. Justus, A. L. Huston, and A. J. Campillo, *Appl. Phys. Lett.* 63, 1483 (1993).

313. K. J. McEwan, P. K. Milsom, and D. B. James, *SPIE* 3472, 42 (1998).

314. K. M. Nashold and W. D. Powell, *J. Opt. Soc. Am. B* 12, 1228 (1995).

315. K. Mansour, M. J. Soileau, and E. W. van Stryland, *J. Opt. Soc. Am. B* 9, 1100 (1992).
316. V. Joudrier, P. Bourdon, F. Hache, and C. Flytzanis, *Appl. Phys. B* 70, 105 (2000).
317. X. Sun, R. Q. Yu, G. Q. Xu, T. S. A. Hor, and W. Ji, *Appl. Phys. Lett.* 73, 3632 (1998).
318. P. Chen, X. Wu, X. Sun, J. Lin, W. Ji, and K. L. Tan, *Phys. Rev. Lett.* 82, 2548 (1999).
319. L. Vivien, E. Anglaret, D. Riehl, F. Bacou, C. Journet, C. Goze, M. Andrieux, M. Brunet, F. Lafonta, P. Bernier, and F. Hache, *Chem. Phys. Lett.* 307, 317 (1999).
320. S. R. Mishra, H. S. Rawat, S. C. Methendale, K. C. Rustagi, A. K. Sood, R. Bandyopadhyay, A. Govindaraj, and C. N. R. Rao, *Chem. Phys. Lett.* 317, 510 (2000).
321. L. Vivien, E. Anglaret, D. Riehl, F. Hache, F. Bacou, M. Andrieux, F. Lafonta, C. Journet, C. Goze, M. Brunet, and P. Bernier, *Opt. Commun.* 174, 271 (2000).
322. X. Sun, Y. Xiong, P. Chen, W. Ji, L. J. Hong, S. S. Yang, D. J. Hagan, and E. W. van Stryland, *Appl. Opt.* 39, 1998 (2000).
323. L. Vivien, D. Riehl, E. Anglaret, and F. Hache, *IEEE J. Quant. Electron.* 36, 680 (2000).
324. L. Vivien, E. Anglaret, D. Riehl, and F. Hache, *Nonlinear Opt.* 27, 395 (2001).
325. L. Vivien, D. Riehl, F. Hache, and E. Anglaret, *J. Opt. Nonlinear Phys. Mater.* 9, 297 (2000).
326. L. Vivien, D. Riehl, P. Lancon, F. Hache, and E. Anglaret, *Opt. Lett.* 26, 223 (2001).
327. J. E. Riggs, D. B. Walker, D. L. Carroll, and Y. P. Sun, *J. Phys. Chem. B* 104, 7071 (2000).
328. M. Sheik-Bahae, A. A. Said, T. H. Wei, D. J. Hagan, and E. W. van Stryland, *IEEE J. Quant. Electron.* 26, 760 (1990).
329. J. F. Xu, M. Terrones, N. Grobert, R. Czerw, M. Reyes-Reyes, H. Terrones, P. M. Ajayan, and D. L. Carroll, *J. Opt. Soc. Am. B*, to be published.
330. J. F. Xu, R. Czerw, and D. L. Carroll, *Chem. Phys. Lett.*, to be published.
331. Z. Jin, L. Huang, S. H. Goh, G. Xu, and W. Ji, *Chem. Phys. Lett.* 352, 328 (2002).
332. J. Hord, *Int. J. Hydrogen Energy* 3, 157 (1976).
333. S. Kartha and P. Grimes, *Phys. Today* Nov., 54 (1994).
334. J. M. Ogden, *Phys. Today* April, 69 (2002).
335. R. G. Ding, G. Q. Lu, Z. F. Yan, and M. A. Wilson, *J. Nanosci. Nanotechnol.* 1, 7 (2001).
336. M. S. Dresselhaus, K. A. Williams, and P. C. Eklund, *Mater. Res. Soc. Bull.* Nov., 45 (1999).
337. A. C. Dillon, K. M. Jones, T. A. Bekkedahl, C. H. Kiang, D. S. Bethune, and M. J. Heben, *Nature* (*London*) 386, 377 (1997).
338. M. S. Dresselhaus, K. A. Williams, and P. C. Eklund, *MRS Bull.* 24, 45 (1999).
339. A. Chambers, C. Park, R. T. K. Baker, and N. M. Rodriguez, *J. Phys. Chem. B* 102, 4253 (1998).
340. A. C. Dillon, T. Gennett, J. L. Alleman, K. M. Jones, P. A. Parilla, and M. J. Heben, in "Proceedings of the U.S. DOE Hydrogen Program Review," 1999.
341. C. Liu, Y. Y. Fan, M. Liu, H. T. Cong, H. M. Cheng, and M. S. Dresselhaus, *Science* 286, 602 (1999).
342. Y. Ye, C. C. Ahn, C. Witham, B. Fultz, J. Liu, A. G. Rinzler, D. Colbert, K. A. Smith, and R. E. Smalley, *Appl. Phys. Lett.* 74, 2307 (1999).
343. X. B. Wu, P. Chen, J. Lin, and K. L. Tan, *Int. J. Hydrogen Energy* 25, 261 (2000).
344. A. C. Dillon, T. Gennett, J. L. Alleman, K. M. Jones, P. A. Parilla, and M. J. Heben, in "Proceedings of the U.S. DOE Hydrogen Program Review," 2000.
345. M. Hirscher, M. Becher, M. Haluska, U. Dettlaff-Weglikowska, A. Quintel, G. S. Duesberg, Y. M. Choi, P. Downes, M. Hulman, S. Roth, I. Stepanek, and P. Bernier, *Appl. Phys. A* 72, 129 (2001).
346. M. Hirscher, M. Becher, M. Haluska, A. Quintel, V. Skakalova, Y. M. Choi, U. Dettlaff-Weglikowska, S. Roth, I. Stepanek, P. Bernier, A. Leonhardt, and J. Fink, *J. Alloys Compds.* 330, 654 (2002).
347. P. Chen, X. Wu, J. Lin, and K. L. Tan, *Science* 285, 91 (1999).
348. R. T. Yang, *Carbon* 38, 623 (2000).
349. F. E. Pinkerton, B. G. Wicke, C. H. Olk, G. G. Tibbetts, G. P. Meisner, M. S. Meyer, and J. F. Herbst, *J. Phys. Chem. B* 104, 9460 (2000).
350. G. E. Froudakis, *Nano Lett.* 1, 531 (2001).
351. M. J. Frisch, G. W. Trucks, H. B. Schlegel, G. E. Scuseria, M. A. Robb, J. R. Cheeseman, V. G. Zakrzewski, J. A. Montgomery, Jr., R. E. Stratmann, J. C. Burant, S. Dapprich, J. M. Millam, A. D. Daniels, K. N. Kudin, M. C. Strain, O. Farkas, J. Tomasi, V. Barone, M. Cossi, R. Cammi, B. Mennucci, C. Pomelli, C. Adamo, S. Clifford, J. Ochterski, G. A. Petersson, P. Y. Ayala, Q. Cui, K. Morokuma, D. K. Malick, A. D. Rabuck, K. Raghavachari, J. B. Foresman, J. Cioslowski, J. V. Ortiz, A. G. Baboul, B. B. Stefanov, G. Liu, A. Liashenko, P. Piskorz, I. Komaromi, R. Gomperts, R. L. Martin, D. J. Fox, T. Keith, M. A. Al-Laham, C. Y. Peng, A. Nanayakkara, M. Challacombe, P. M. W. Gill, B. Johnson, W. Chen, M. W. Wong, J. L. Andres, C. Gonzalez, M. Head-Gordon, E. S. Replogle, and J. A. Pople, Gaussian 98, Revision A.9, Gaussian, Inc., Pittsburgh, PA, 1998.
352. S. Dapprich, I. Omaromi, K. S. Byun, K. Morokuma, and M. J. Frisch, *J. Mol. Struct.* 461, 1 (1999).
353. G. E. Froudakis, *J. Phys.: Condens. Matter* 14, 453 (2002).
354. J. L. Bahr and J. M. Tour, *J. Mater. Chem.* 12, 1952 (2002).
355. A. Hirsch, *Angew. Chem., Int. Ed. Engl.* 41, 1853 (2002).
356. J. Sloan, A. I. Kirkland, J. L. Hutchison, and M. L. H. Green, *Chem. Commun.* 1319 (2002).

Doped II–VI Semiconductor Nanoparticles

S. K. Kulkarni

University of Pune, Pune, India

CONTENTS

1. INTRODUCTION

Doped semiconductors have been widely investigated in the past. Doping is very important not only to control the transport properties of the semiconductors but also to modify their optical properties. In fact doped semiconductors constitute a major portion of a class of materials [1] known as "phosphors" or "luminescent" materials. Phosphors are the materials that can be excited with electric field, visible, ultraviolet (UV), or X-rays etc. Hence, they find applications in display screens of computer monitors, screens of cathode ray tubes (CRT), fluorescent lamps, X-ray detectors, light emitting diodes (LED), laser materials, etc. Semiconductors used in such applications are doped with metal ions, specially transition, or rare earth metal ions. Sometimes, additional metal ions are used as coactivators to enhance the emission. In recent years, there is also a lot of interest [2–4] in diluted magnetic semiconductors (DMS) that have application in "spintronics" that is, electronics in which transport properties of charge carriers are controlled not only by their charge but also by their spin. In DMS materials, small amounts of magnetic impurities or dopants (doped ions are also often referred to as "impurities") are added to a semiconductor.

Depending upon the size and charge on the ion, substitutional doping of impurity ions can produce either excess electrons or holes in a semiconductor or just lattice distortion can take place. This gives rise to localized levels in the bandgap of a semiconductor. Such states are responsible for transport properties, photo luminescence, electro luminescence, and other optical properties in these semiconductors [5].

It is now well known that below a critical size characteristics of every material, physico-chemical properties change [6–10]. This critical size is the diameter of an exciton in a semiconductor [11–15]. Charge carriers are spatially confined in small particles of nanometric dimension affecting the electronic states, and effects due to quantum confinement are observable. Semiconductor nanoparticles in the quantum confinement regime are extremely small viz. few nanometers to few tens of nanometers in most of the cases [12]. Therefore, the number of constituent atoms is also very small ($<10^4$ atoms or so). In the doped nanoparticles, the number of doped atoms therefore should be still smaller that is, just a few atoms per particle. How the electronic structure, and hence the optical and other properties become altered, of doped semiconductor nanoparticles, is an interesting area of nanoparticles research. There are attempts not only to investigate the static equilibrium properties of the doped nanoparticles but also the charge dynamics in nanoparticles.

The first report on the doped nanoparticles appeared as for back as 1983 [16]. However, it was an unintentional synthesis of nanoparticles. Wang et al. later reported in 1991 results of their work on $Zn_xMn_{1-x}S$ clusters [17]. In 1994, Bhargava et al. [18] reported a large enhancement of photoluminescence in Mn-doped ZnS nanoparticles. They further stressed that doped nanoparticles form a new class of materials in which photoluminescence efficiency increases and decay time reduces dramatically by some orders of magnitude. Following this report, many different groups reported investigations on doped semiconductor particles of various sizes as well as materials. The most important question that is being discussed is whether or not doped particles are really different than the bulk materials.

Although there are some reports on doped insulators also, in this chapter various results only on the II–VI doped semiconductor nanoparticles will be reviewed. The chapter is organized as follows. Synthesis of doped nanoparticles by

various commonly used methods will be discussed first. Specific examples of transition and rare earth metal ions doped ZnO, ZnS, ZnSe, CdS, and CdSe will be discussed. Notice that the section on ZnS doped with Mn ions is disproportionately longer in comparison to others. The reported work today is predominantly on ZnS doped with Mn than on any other nanoparticles. This in turn may be due to the importance of ZnS phosphors and ease of doping ZnS with Mn ions in general.

2. SYNTHESIS OF DOPED SEMICONDUCTOR NANOPARTICLES

Semiconductor nanoparticles can be synthesized by a variety of methods and have been are reviewed [6, 7] in the past. However, it has been found from the available literature that doped semiconductor nanoparticles have been mostly synthesized either by chemical capping, reverse micelles, sol–gel, glass, polymer, or some hybrid methods. Thin films of nanoparticles can also be obtained. Therefore, only these methods will be discussed here with a few examples. The main advantage of doping the nanoparticles is that they can be doped even at room temperature in contrast to the bulk materials for which the dopants are diffused at a relatively high temperature of a few hundred degrees Celsius [1]. The disadvantage with nanoparticles is that they need to be surface passivated in order to prevent their coalescence or aggregation. For this they need to be either capped or surface passivated with organic molecules or immobilized in some inert matrix like polymer, glass, or zeolite.

2.1. Chemical Capping

There are many reports in which doped semiconductor nanoparticles have been synthesized using "chemical capping" method. Surface atoms of nanoparticles are bonded to some organic or inorganic molecules in such a way that they would provide necessary protection of the nanoparticles without affecting essential properties of nanoparticles. The capping molecules are primarily expected to inhibit the coalescence of nanoparticles without interacting with the particles except at surface. Figure 1 shows how the particles can be attached to a variety of molecules. Usually cation and anion giving salts are dissolved in the aqueous or nonaqueous media so that resulting solutions react in the presence of the appropriate organic molecules. The solution of metal ion to be doped is also prepared by dissolving its salt in aqueous or nonaqueous medium and mixed in the cationic solution in appropriate proportion before it is reacted with the anionic solution. As properties of nanoparticles are size-dependent, it is essential to obtain them in a narrow size range.

In general, the chemical capping methods can be divided into two types, one in which reactions are carried out at elevated temperatures and the others that are carried out at room temperature.

High temperature synthesis methods [19–21] can also be subdivided into two routes viz—the one in which cold organometallic reactants are injected in hot coordinating solvent like trioctylphosphine (TOPO) at a temperature
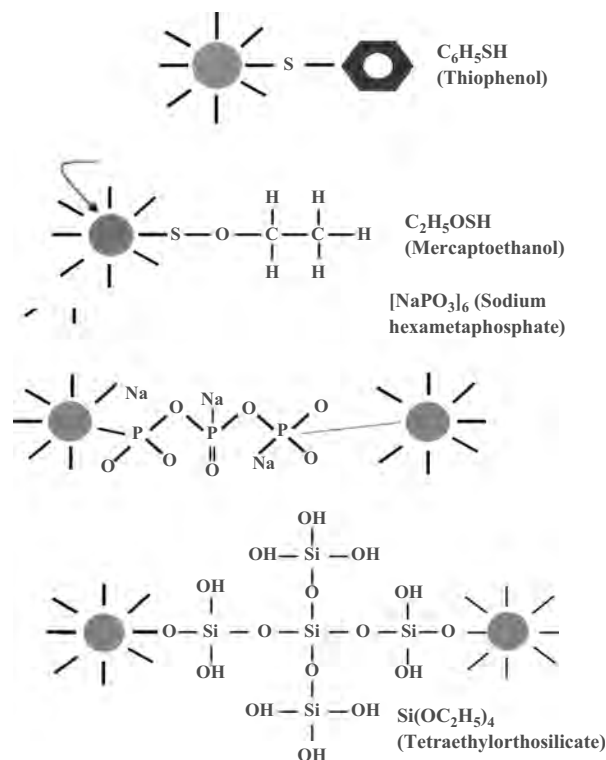
Figure 1. Chemical capping of nanoparticles.

>300 °C and the other one known as size selective precipitation in which reactions are carried out [21] at a moderate temperature of 80–150 °C. The former method, although successful in producing highly stable particles of narrow size distribution (<5%) is not very widely used for producing doped nanoparticles, probably due to high temperature synthesis. Also, expensive organometallic chemicals are often involved. Besides, there is a possibility that the dopants can outdiffuse in high temperature synthesis making their incorporation difficult. However, this high temperature organometallic synthesis route for ZnSe nanocrystallites [22] was followed by Norris et al. [23] to obtain high quality Mn-doped ZnSe nanocrystallites of various sizes. They showed that high temperature neither removed Mn ions out of nanocrystals nor were they on the surface of nanocrystallites.

The method of size selective precipitation is used in the past [21, 24] for synthesizing CdS, ZnS, etc. nanoparticles at a temperature less than about 150 °C and involves the use of a thiol (SH) group like in mercaptoethanol, thioglycerol, etc. as the surface capping agent. It is possible to collect the particles of different sizes as the reaction proceeds. Size selection is carried out from a broad distribution of particle sizes by using a proper pair of solvent-nonsolvent liquids. In the solvent solution, when a nonsolvent polar solution is added, the barrier to flocculation is reduced. This is more effective for large particles. Therefore, bigger particles tend to flocculate and others appear as supernatant solution. Bigger particles can then be separated by centrifugation and again dispersed in the solvent solution producing a clear solution. This procedure can be repeated until no further improvement occurs in the size distribution of the particles as observed from a sharp peak in the optical absorption.

The organometallic route followed by Leeb et al. [25] is similar to the chemical capping method but involves reaction at 130 °C. They reacted $ZnCl_2$ and $MnCl_2$ in a round flask containing chloroform to which tri n-butylphosphine was added which was dissolved after refluxing at 130 °C for 1 h. To the resulting dark violet solution, $(TMS)_2S$ was added at room temperature and stirred for $\sim$12 h. Final refluxing for half an hour gave colorless Mn-doped colloids. Resulting colloids were washed in heptane, redissolved in chloroform, and finally filtered through a 100-nm pore size filter. Furthermore, they synthesized Mn-doped $Zn_{1-x}Cd_xS$ nanoparticles by also adding $CdCl_2$ to as prepared Mn^{2+}:ZnS solution, by stirring for 1 h and refluxing for 15 min. This produced $Zn_2Mn_{0.01}Cd_{1.99}S$ particles.

It is also possible to obtain narrow size distribution of particles by simply reacting the essential solvents at room temperature in the presence of capping organic molecules like mercapto acids or thioglycerol molecules. This procedure of chemically capping the doped semiconductor nanoparticles has been used by many groups. However, the synthesis parameters are quite stringent, and optimization of all the parameters is time-consuming. Khosravi et al., Borse et al., and Kulkarni et al. [26–29] used this method to obtain doped ZnS particles at room temperature. The aqueous solutions of zinc, sodium, and dopant (manganese, copper, nickel, etc.) salt were prepared. Zinc salt solution, along with the dopant salt solution in the presence of mercaptoethanol, were stirred vigorously and sodium sulphide solution was added dropwise. Precipitate was washed several times, centrifuged, and dried. Resulting zinc sulphide particles were capped with mercaptoethanol molecules. Particles of different sizes were possible by controlling the concentration of reactants. Nanoparticles were quite stable in the ambient.

Lu et al. [30] reacted $Zn(CH_3COO)_2 2H_2O$, $Mn(CH_3COO)_2 \cdot 4H_2O$ and $Na_2S \cdot 9H_2O$ in ethanol at room temperature. Precipitate was obtained by centrifugation, washed in deionized water. 3-methacryloxypropyl triethoxysilane (MPTS) was added for surface passivation. To study the effect of the passivating agent, they used polyoxyethylene sorbitan monooleate (Tween® 80) for the second sample. It has a carboxylic group in its structure. The third sample was without surface modification.

Chemical capping method for CdS:Mn nanoparticles was used by Liu et al. [31]. They employed $Mn(ClO_4)_2$, $Cd(ClO_4)_2$, and Na_2S aqueous solutions in the presence of mecapto acetate. CdS:Mn particles were separated by adding 2-propanol and purified by precipitation and rinsing several times.

Inorganic chains of molecules like sodium polyphosphate were used by Bol and Meijerink [32] as well as Khosravi et al. [33], to synthesize nanocrystalline-doped ZnS and CdS particles. Differences are in the chemicals used but procedure is the same as for capping with organic molecules previously discussed.

Sun et al. [34] discussed the difficulties in the synthesis of copper doping in the ZnS nanoparticles. They suggested the use of coordination chemistry method to overcome the problem of solubility of Cu in ZnS. Thiourea and thiosulfates were used as both ligand and surfactant. These helped to stabilize Cu^+ ions in aqueous solutions. $ZnCl_2$ and thiourea (or sodium thiosulfate) solutions, plus CuCl added to thiourea (or thiosulfate), were mixed together under continuous stirring. Na_2S solution was added at a controlled rate. No difference was observed with either sodium thiosulfate or thiourea.

Chung et al. [35] synthesized Mn^{2+}-doped ZnS nanoparticles suspended in water by reacting 30 mL of 2 mM $Na_2S \cdot 9H_2O$ aqueous solution to 30 mL aqueous solution (pH-10.3) of 2 mM $Zn(NO_3)_2 \cdot 6H_2O$ and 40 μM $Mn(NO_3)_2 \cdot 6H_2O$. This resulted in a 2% Mn^{2+}-doped sample. For passivating the particles with ZnS, 2.5 mM of 40 mM $Zn(NO_3)_2 \cdot 6H_2O$ aqueous solution and 2.5 mM $Na_2S \cdot 9H_2O$ aqueous solution were added to 10 mL of Mn^{2+}-doped sample at pH 10.3. Surface passivated Mn^{2+}-doped particles of $\sim$6 nm were synthesized.

2.2. Use of Reverse Micelles

Metal, metal oxide, and semiconductor nanoparticles have been synthesized by many groups using the technique of reverse micelles. For a general review on micelles, and reverse or inverse micelles see [36] and [37]. Size, shape, and composition of the nanoparticles can be finely controlled [38] using this technique. Particles in the form of spheres, rods, discs, etc. have been obtained. As high purity particles can be obtained with this technique, good control of the doping is also imperative. In order to control the growth of the particles, surfactants (surface active reagents) or some long or short hydrocarbon chain amphiphilic molecules, monomers are used (see Fig. 2). Amphiphilic molecules have a hydrophilic (water loving) end molecule group (head) on one hand and hydrophobic (water hating, lyophilic, or oil-loving) group at the other end (tail). The head group is ionic or polar in nature and the hydrophobic group is nonpolar. Amphiphilic molecules, when dissolved in water, try to stay at the air-water interface in such a way that the head group is immersed in water and the tail group tries to stay in the air. As the concentration of amphiphilic molecules is increased beyond a certain limit, they spontaneously form the aggregates or the droplets known as "micelles" in such a way that tails come close together and the heads float outside in water. Reverse micelles on the other hand are the molecular aggregates of amphiphiles in which head groups are inside trapping some water inside and tails float in the nonpolar liquid. Reverse micelles are thus water-in-oil droplets that are stabilized by the surfactant molecules. Volumes of the water added is responsible for the size of the droplet or, ultimately the size of the nanoparticle. In the synthesis of semiconductor nanoparticles, miceller solutions of cation and anion giving salts are mixed in appropriate quantities, stirred together, usually at room temperature to give the particles as precipitate. After usual centrifugation, washing,
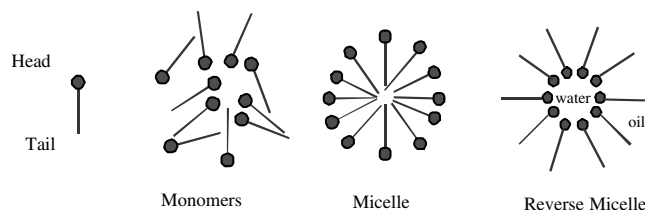
Figure 2. Nanoparticles using reverse micelles.

and drying, nanoparticle powder can be collected. In order to obtain doped nanoparticles, one needs to simply add the appropriate metal salt solution in cationic solution prior to the reaction.

Xu et al. [39] prepared ZnS:Mn, ZnS:Cu, and ZnS:Eu nanoparticles at room temperature using reverse micelles. Particles were in the size range of 3–18 nm. They used petroleum ether as the oil phase and a mixture of poly (oxyethylene)5, nonyl phenol ether (NP-5), and poly (oxyethylene)9 nonyl phenol ether (NP-9) as surfactants. Aqueous solution of $ZnCl_2$, reactants of doping and sodium sulphide were used. Further synthesis details can be found in Gan et al. [40].

A technique of reverse micelles to synthesize CdS particles doped with Mn has been used by Levy et al. Feltin et al. and Petit et al. [41–45]. They used bis (2-ethylhexyl) sulfosuccinate Na(AOT) as the surfactant and $Cd(AOT)_2$, $Mn(AOT)_2$ in predetermined ratios to obtain $Cd_{1-y}Mn_yS$ nanoparticles with a desired concentration of maganese. Size and composition could be varied independently. The effect of synthesis conditions was studied by Levy et al. [41].

Smith et al. [46] synthesized Mn-doped ZnS nanoparticles of 1.2 nm size using a similar procedure to that of Petit et al. [45].

A similar synthesis route to obtain ZnS:Mn particles as that by Levy et al. [41–43] was used by Dinsmore et al. [47]. However, they further applied a capping layer of ZnO on the surface of the nanoparticles (the particles designated as ZnS:Mn/ZnO). For this purpose, after synthesizing ZnS:Mn particles by reverse micelle route, they rinsed the particles in methanol and suspended the nanoparticles in aqueous solution of $ZnCl_2$. Drops of 0.5 M NaOH were added till pH rose to 10, forming $Zn(OH)_2$ or ZnO at the surface. After 2 min samples were washed in water, then in methanol, and lastly in dichloromethane. Powder was then dried in vacuum.

A reverse micelle method was employed by Chamarro et al. [48] to first obtain Mn-doped CdS nanoparticles. However, once the particles were separated from the solution they functionalized the particles by alkoxide. Methyl-triethoxysilane was used as the precursor to alkoxide. This procedure resulted in a mixed organic-inorganic matrix for nanoparticles.

Behboudnia and Sen [49] synthesized ZnS and $Zn_{1-x}M_xS$ (M = Mn, Fe and Ni) using a reverse micelle technique. They used $Zn(NO)_3$ and Na_2S to form reverse micelle solutions. Reverse micelles were prepared from the aqueous solutions of the salts by adding them to a matrix of sodium bis (2-ethylhexyl) sulfosuccinate (AOT), a surfactant, and an oil. Sulphate salts were used for doping Mn, Fe, and Ni.

Hofmann et al. [50] used two methods to synthesize CdS:Mn nanoparticles. One sample was obtained by reverse micelle route from AOT/water/heptane. Mixing of solutions containing metallic ion (Cd and Mn) and sulfur ions produced Mn^{2+}-doped CdS. On the surface, 4-flurothiophenolate were chemically attached. Centrifugation and washing produced fluorophenol-capped CdS:Mn nanoparticle powder. An other sample was obtained by mixing ethylene glycol solution containing metal ions and sulfur ions. Particles get aggregated forming a turbid yellow-orange solution. A ethylene glycol solution was centrifuged and nanocrystallites washed in methanol and

then put in triethylphosphate. They were then heated at 215 °C in N_2 atmosphere. By adding heptane and pyridine, the colloidal solution could be destabilized. The powders then obtained could be redispersed in other solvents like methanol, ethanol, or pyridine.

2.3. Polymer/Zeolite/Glass

One way of controlling the size of the nanoparticles is to synthesize them directly in some solid matrix or synthesize the nanoparticles as separate colloidal particles and then immobilize them by dissolving in the liquid, which is later solidified. Polymers, alumina, zeolites, and glass seem to be commonly used for this purpose. Nanoparticles embedded in glass, zeolites, or alumina have an additional advantage in that they give good mechanical support.

Bhargava et al. [18] obtained doped semiconductor nanoparticles by reacting diethylzinc and diethylmanganese with H_2S in toulene to form ZnS:Mn nanoparticles. Diethylmanganese was obtained by reacting manganese chloride with ethylmagnesium chloride in tetrahydrofuran solvent which formed diethylmanganese. Methacrylc acid was used to coat the ZnS:Mn particles prepared at R.T. in the size range 3.5–7.5 nm.

Jin et al. [51] have synthesized colloids of Mn-doped ZnS by dissolving $Zn(CH_2COO)_2$ and $Mn(CH_2COO)_2$ in alcohol, while the solutions were stirred together, H_2S gas was passed in it. Colloids were immobilized in polymethyl methacrylate.

Igarashi et al. [52, 53] have used a similar synthesis route except that they used polyacrylic acid (PAA) to get the ZnS:Mn particles of ~1.8 nm.

Murase et al. [54] also used chemical route to synthesize doped-ZnS:Mn particles but did not use any capping molecules. However, along with $Zn(NO_3)_2$ and $Mn(NO_3)_2$, they added NaOH and raised the pH from 6 to 10.3. This probably formed $Zn(OH)_2$. Na_2S solution was added to this at a constant rate while stirring the solution to obtain Mn-doped nanoparticles of ZnS. They added the above solution of ZnS to the aqueous solution of poly vinyl alcohol (PVA) so as to immobilize the nanoparticles.

Kane et al. [55] have synthesized Mn- and Tb-doped ZnS nanoparticles in microphase separated films of block copolymers via ring opening metathesis polymerization (ROMP). This was done, by following a general synthesis procedure adopted by Yue and Cohen [56]. The method involves selective sequestering of metal ions into the microdomains of a block copolymer film from a solution of metal salt or permeation of an organometallic compound. Doped particles were first produced by introducing aqueous zinc acetate and then aqueous manganese acetate or a mixture of metal salt solutions. These metal-containing domains, separated from each other, served as localized reaction sites for particle synthesis. They can be considered as "nanoreactors." When H_2S was passed through them, semiconductor sulphide clusters or particles were generated.

Yu et al. [57, 58] mixed zinc and manganese acetates in methanolic media in the presence of sodium sulfide at room temperature. Dull white fluid was obtained. Precipitate was dispersed in methacrylic acid at room temperature. The resulting powder was separated, washed in methanol

several times, and dried at 50 °C for 24 h. Particles of sizes 2.3, 2.5, and 2.7 nm were synthesized.

2.4. Ion Implantation, Sol–Gel, Hybrid, and Thin Films

Sequential ion implantation has been successfully used by Kanemitsu et al. [59] to obtain Mn-doped CdS nanoparticles. They implanted Cd^+ at 430 KeV, S^+ at 157 KeV in equal doses (4.5×10^{16} cm^{-2}) in single crystal of Al_2O_3, while it was held at 500 °C and Mn^{2+} at 250 KeV (dose 2×10^{14} cm^{-2}) by reducing the substrate temperature to 400 °C. After annealing the substrate at 1000 °C in mixture of Ar and H_2 gas atmosphere for 60 min, Mn-doped CdS nanoparticles were formed.

Morita et al. [60, 61] synthesized zirconia thin films with CdS nanoparticles doped with Mn and Eu. Particles were about 5 nm in size and were derived by a sol–gel method. CdS:Mn nanoparticles (4–7 nm) were prepared in thin films of sol–gel. The films were referred to by a general formula $xZrO_2 \cdot 100 - x$ CdS:Mn^{2+} where $x = 20$, 50, or 80. The film thickness was ~0.4 μm.

The sol–gel technique was employed by Artemyev et al. [62] to synthesize CdS:Mn nanocrystalline thin films. Cadmium perchlorate, manganese perchlorate, and sodium sulphide were dissolved in dimethylformaldide. A reaction was carried out at room temperature by mixing the solutions. Washing of the precipitate was carried out in isopropanol and the sample redissolved in 1-MPTS in isopropanol as a complexing and gelating solution. Ultrasonic treatment produced a clear viscous solution of MPTS-CdS:Mn nanoparticles. When dried on quartz substrates, it produced a thin film of MPTS gel with a CdS:Mn nanocrystals with a 1.5 nm size.

Synthesis of Mn-doped ZnS samples (3 nm) was carried out by Sohling et al. [63] and Saenger et al. [64] by dissolving $Zn(CH_3COO)_2 \cdot 2H_2O$ and $Mn(CH_3COO)_2 \cdot 4H_2O$ and hydroxypropyl alcohol in ethanol while stirring the solution at room temperature. A transparent solution of ZnS:Mn colloids was obtained by injecting H_2S in solution within 2 min during stirring. Glass substrates were dip-coated to a thickness between 0.5–50 μm by dip-coating into colloidal solution. Mn^{2+}-doping concentrations were varied from 1 to 8 mol%.

The Langmuir–Blodget technique is an accurate technique in obtaining thin films of nanoparticles. Guo et al. [65, 66] used this technique to obtain the doped nanoparticulate thin films. They first produced layers of organometallic solid by LB technique. Pure salts of Cd thioalkanoats $[CH_3(CH_2)_nCOS]_2Cd$, $n = 10$ to 24 were prepared using corresponding potassium salt, cadmium thioalkanoates were exposed to dry ammonia at R.T. The reactions were complete in 2 to 4 d, yielding CdS and alkylamide as

$$[CH_3(CH_2)_nCOS]_2Cd + 3NH_3 \rightarrow [Cd(SH)_2]$$
$$+ CH_3(CH_2)_nCONH_2 \quad (1)$$

$$Cd(SH)_2 \rightarrow CdS + H_2S \quad (2)$$
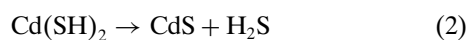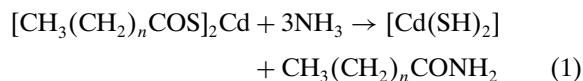
Furthermore, they proposed a novel route to organize nanoparticles of PbS, CdS, $Cd_{1-x}Mn_xS$ from solid thioalkanoates with gaseous ammonia. They provided sufficient optical, structural, and electron paramagnetic resonance (EPR) measurements to prove that Mn ions in different concentrations could be doped in CdS particles synthesized by two-step methodology. In the first step, an organometallic solid in the form of a 3D crystal or Langmuir–Blodgett was formed. The metal ions were arranged in layers or some pattern. By some gas/solid reaction, in the next step, semiconductor quantum particles were formed which retained the periodic order or pattern formed in the first step.

3. PROPERTIES OF DOPED NANOPARTICLES

In this section, results of some specific doped semiconductor nanoparticles will be reviewed. Effects of dopant concentration, structure, photoluminescence, enhancement quenching due to irradiation to UV light and effects of thermal treatment will also be discussed. As is expected, the bulk doped semiconductors like ZnS:Mn, CdS:Mn that have found applications are more thoroughly investigated and others may receive more attention in the near future due to the findings that doped nanoparticles are more efficient and can be doped at much lower temperatures than the bulk solids.

3.1. ZnO:Mn

Zinc oxide is a wide bandgap material that can crystallize in a cubic zinc blend (wurtzite) structure [5]. The direct bandgap in a bulk solid is 3.35 and 3.42 eV at 300 and 0 K, respectively. Doped ZnO Zinc oxide also has been considered as a low voltage, stable phosphor material for flat panel display application, thin films have interesting optical and magnetic properties. Although optical and structural properties of undoped ZnO nanoparticles have been reported in the past, there, is little research on doped ZnO nanoparticles. However, it is one of the likely candidates for DMS. Therefore, it would be worthwhile in the future to investigate nanoparticles of ZnO and doped ZnO as already begun by some groups.

Luminescence in manganese and europium-doped ZnO nanoparticles has been reported by Bhargava et al. [67]. Their results of bulk ZnO, ZnO:Eu, and ZnO:Mn are summarized in Table 1.

Table 1. Photoluminescence excitation and emission peaks in (a) ZnO bulk, (b) Eu^{2+}-doped ZnO nanocrystalline, and (c) Mn^{2+}-doped ZnO nanocrystalline samples.

PL	ZnO (bulk)	ZnO:Eu^{2+} (nanocrystal)	ZnO:Mn^{2+} (nanocrystal)
PL excitation Peak wavelength, nm	374	372	362
PL emission Peak wavelength, nm	513	590	520

Source: Adapted with permission from [67], R. N. Bhargava et al., *Phys. Stat. Sol. (B)* 229, 897 (2002). © 2002, Wiley-VCH.

Sapra et al. [68] have synthesized $Zn_{1-x}Mn_xO$ nanoparticles and investigated the structure and optical properties. The particle size was ~4.7 nm as determined by X-ray diffraction and bandgap measurement. As shown in Figure 3 they observed a photoluminescence peak at ~470 nm when excited with ~325 nm radiation. They also note that the addition of Mn (5%) increased the bandgap of ZnO.

3.2. Doped-ZnS Nanoparticles

3.2.1. ZnS:Mn

Optical properties of Mn-doped bulk zinc sulfide semiconductors are widely investigated due to their favorable luminescent properties [1] useful in display panels, laser, sensors, etc. It is also an important DMS due to the presence of Mn^{2+}, a localized magnetic impurity in the ZnS host. Naturally, there are many attempts to investigate whether nanoparticles of ZnS doped with Mn are better and more useful than bulk or not.

Becker and Bard [16] have studied Mn^{2+}-doped colloidal particles of ZnS which could have been nanoparticles. However, intentional synthesis of ZnS:Mn clusters or nanoparticles and their investigations started much later. Wang et al. [17] investigated optical as well as some structural properties of $Zn_{0.93}Mn_{0.07}S$ nanoparticles. By studying Mn doped ZnS nanoparticles, Bhrgava et al. [18] later claimed for the first time that there was an increase in the quantum efficiency of the nanoparticles with decreasing nanoparticle size. They also claimed that photoluminescence decay time reduced from some milliseconds in bulk ZnS:Mn to some nanoseconds in the nanoparticles. This triggered the research activity in the area of doped semiconductor nanoparticles, specially of ZnS:Mn. There are attempts to understand photoluminescence, its enhancement, or quenching, looking for applications and so on. In this section, a review on various aspects of ZnS:Mn properties will be made. In spite of the controversies about the luminescence

Figure 3. Photoluminescence of ZnO and Mn-doped ZnO nanoparticles. Reprinted with permission from [68], S. Sapra et al. *Recent Advantages in Inorganic Materials*, to appear. © Narosa Publishers.

decay lifetime in ZnS:Mn nanoparticles, that is, whether it decreases dramatically or not, there seems to be a possibility that doped nanoparticles may still be much more luminescent than bulk materials. Also because they may have some unique applications, doping of ZnS with Mn under different conditions and their investigations have been persued extensively. Some of the issues which are tackled are what is the concentration of Mn ions needed to obtain highly luminescent particles, where are Mn ions located and what is their influence on optical properties, what is the magnetic state of doped ZnS:Mn, and what is the effect of UV radiation, optical stability, etc.

Structure Zinc sulfide can occur either in cubic zinc blend (Wurtzite) or hexagonal (Sphalerite) structure. In both structures, Zn and S are tetrahedrally bonded forming layers of Zn and S. The two structures only differ in their stacking sequence of Zn-S layer pairs.

The covalent radii of Mn^{2+} and Zn^{2+} ions are 0.080 and 0.083 nm, respectively—very close to each other. Therefore, it is relatively easy to dope Mn in ZnS lattice. Under appropriate conditions, Mn^{2+} ions can replace some of the Zn^{2+} ions resulting into local field distortions around the replaced ion sites. Usually the desired doping is just a few Mn ions in about 10^3 to 10^4 Zn ions—indeed too small a concentration to alter the extended structure dramatically. However, determination of ZnS nanoparticle structure in presence or absence of Mn ion is quite important as electronic structure can get modified dramatically depending upon the structure. As discussed later, most of the research shows that the structure of Mn-doped nanoparticles is cubic zinc blend.

Structural analysis of individual particles can be done using microscopic techniques like transmission electron microscopy (TEM), scanning tunneling microscopy (STM), or atomic force microscopy (AFM). There are only a few reports [25, 30, 54, 57] in which TEM has been used for ZnS:Mn nanoparticles and all of them were used to determine particle sizes (<5 nm) and structure. The sizes of ZnS:Mn nanoparticles varied, depending upon the synthesis parameters and growth conditions, however, all found that particles were cubic zinc blend in structure.

Chen et al. [69], however, used cryo-TEM to show that Mn was indeed doped in ZnS nanoparticles. Inelastically scattered electrons were used to obtain jump ratio elemental maps and detect the presence of Mn in ZnS nanoparticles.

X-ray diffraction (XRD) is widely used as a conventional and routine technique [70] to determine the crystal structure of powder samples. However, it may not be an adequate technique to determine the nanoparticle size due to very small number of available diffracting planes in the nanoparticles. Nonetheless, XRD is an often used technique, at least to get a rough estimation of structure and average particle size determination of nanoparticles [25, 26, 53, 54, 57, 69, 71]. Scherrer's formula $d = 0.9\lambda/B\cos\theta$, where d is the average particle size, λ is the X-ray wavelength used, B is full width at half maximum (FWHM) of the diffraction peak, and θ is the corresponding Bragg angle, can be used to determine the average particle size.

Borse et al. [28] have also used X-ray diffraction analysis to determine the nanoparticle size in ZnS:Mn. However, they used a debye function analysis (DFA) method [72] to simulate the diffraction pattern and also obtain the size
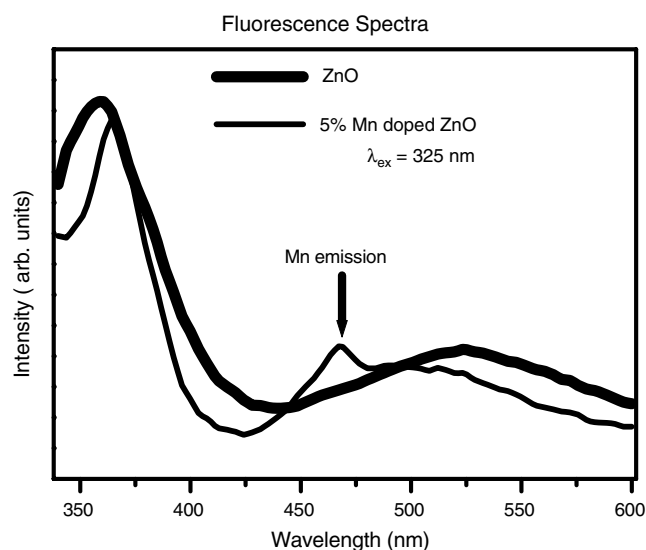
distribution. In Figure 4(a), XRD of ZnS:Mn for very low Mn concentration are showed [73]. At a concentration of ∼8.10 Mn wt%, diffraction peaks due to MnS_2 appeared (Fig. 4(b)). These results are consistent with some previously published work [28].

Dinsmore et al. [47] analyzed ZnO-capped ZnS:Mn nanoparticles using XRD. They have also annealed the particles at different temperatures. They show that the as-synthesized particles are zinc blend cubic with an average particle size ∼3.5 nm. With vacuum annealing up to 350 °C, a tetragonal distortion occurs accompanied by an increase in the particle size. Between 400 and 525 °C zinc blend and wurtzite phases coexisted with the particle size going to ∼16 nm at 525 °C.
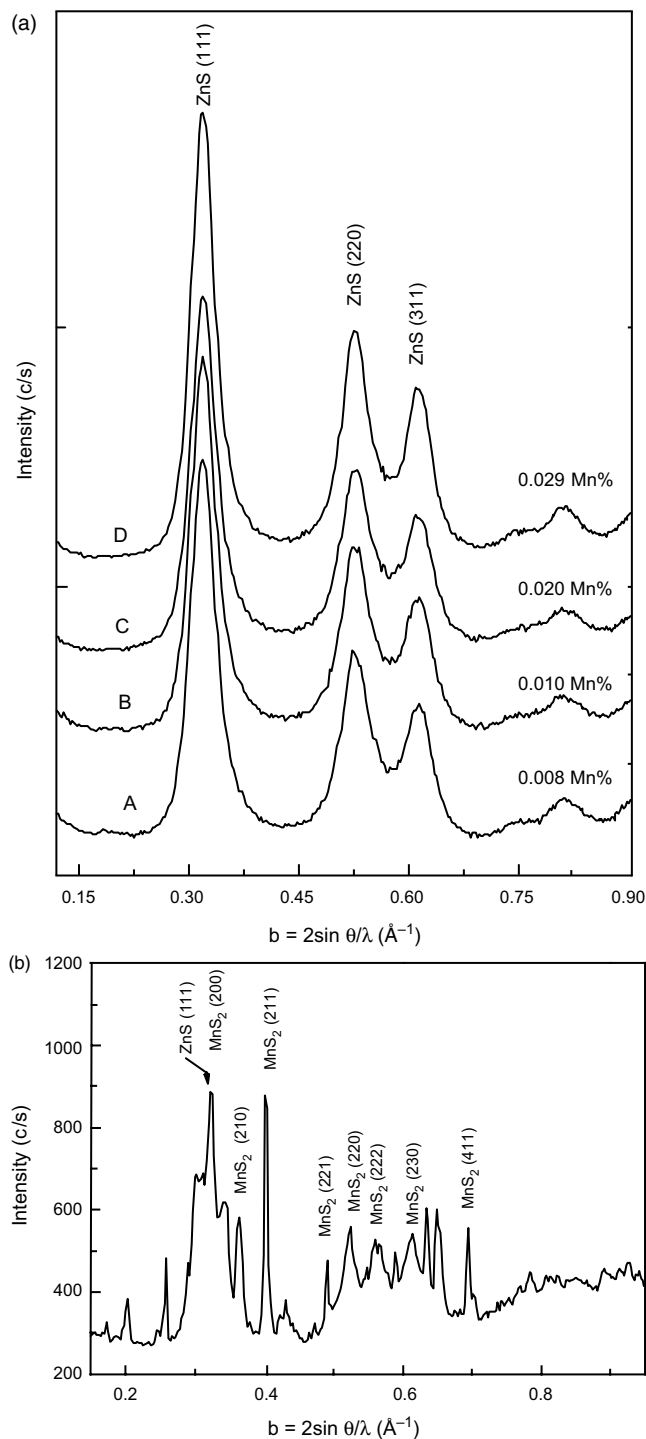
Small angle X-ray scattering (SAXS) has also been used by some groups [46, 63] to determine the particle size of ZnS:Mn nanoparticles. Extended X-ray absorption fine structure (EXAFS) is a powerful and widely used technique [74–76] to determine the coordination number, bond lengths, and local symmetry around the specific atom in a solid.

Extended X-ray absorption fine structure studies of Mn-doped clusters of 2.5-nm sized ZnS particles embedded in a glass/polymer matrix having a composition as $Zn_{0.93}Mn_{0.07}S$ were made by Wang et al. [17]. They used synchrotron radiation to obtain high flux and variable photon energy necessary to record the EXAFS with low concentration Mn ions in ZnS:Mn nanoparticles. They analyzed extended X-ray absorption fine structure at both Mn and Zn in glass containing Zn and Mn and found out that Mn ions were surrounded by six oxygen atoms. The Mn—O bond length was 2.19 Å typical for bulk MnO. When the sample was treated with H_2S to form $Zn_{0.93}Mn_{0.07}S$, cluster coordination of Mn changed from 6 to 4.6 and coordination of oxygen to sulphur with Mn-S bond distance of 2.45 Å. Zn—S bond length of 2.35 Å is shorter than that of Mn—S. Their results led to the conclusion that Mn ions substitute Zn ions and were located inside the cluster of $Zn_{0.93}Mn_{0.07}S$ and not on the particle surface.

Soo et al. [77] also carried out EXAFS and near edge extended X-ray absorption fine structure (NEXAFS) measurements on two different sizes of ZnS:Mn nanocrystals in methacrylic acid. They compared their EXAFS results with a bulk ZnS:Mn sample with the same amount of Mn doping viz. 0.5 at% and found that in nanocyrstalline samples with particle sizes 3–3.5 and 5–5.5 nm, the Mn coordination was less than four atoms and the Mn—S distance was 2.4 Å, also consistent with the bulk sample. However, in nanocrystals size-dependent bond length change occurred for Mn-S, although the Zn lattice remained unaltered. There were, however, enough indications to believe that Mn substituted Zn causes crystal field change around the Mn site (originally the Zn site). Additionally, a comparison of different Mn compounds and ZnS:Mn nanocrystals of two different sizes using NEXAFS showed size dependence. It was also inferred from this study that Mn ions were in +2 state.

Dinsmore et al. [47] have also used EXAFS to determine coordination of Mn ions in ZnS:Mn unannealed and annealed (525 °C) nanoparticles, surface passivated with ZnO. Their results are essentially in agreement with major conclusions by Soo et al. previously discussed. In Table 2, a comparison of EXAFS results on some samples reported by different groups is given.

Photoluminescence and Decay Time Zinc sulfide is a direct and wide bandgap (3.6 eV at R.T.) material. Some defect levels are usually present in the energy gap. As the dopant concentration per nanoparticle can be very small (few ions per thousands of host ions), similar to diffraction,

Figure 4. X-ray diffraction pattern of Mn-doped ZnS nanoparticles (a) from 0.008 to 0.296 and (b) 8.1 Mn wt. %.

Table 2. Comparison of EXAFS results of different groups for ZnS:Mn.

Materials	Mn-S distance	No. of near neighbors	Ref.
$Zn_{1-x}Mn_xS$ (2.5 nm)	2.45 Å	4–6	[17]
Bulk ZnS:Mn	2.42 ± 0.01 Å	4	[77]
Zn:Mn (A ∼ 5 nm)	2.39 ± 0.01 Å	3.6 ± 0.2	[77]
ZnS:Mn (B ∼ 3 nm)	2.36 ± 0.04 Å	3.2 ± 0.4	[77]
ZnS:Mn/ZnO (unannealed 3.5 nm)	2.394 ± 0.01 Å	3.73 ± 0.12	[47]
ZnS:Mn/ZnO (annealed–525 °C ∼16 nm)	2.413 ± 0.002 Å	3.78 ± 0.12	[47]
ZnS:Mn (Sanroff bulk 3–6 nm)	2.428 ± 0.004 Å		[47]

no significant changes are expected in optical absorption spectra. However, optical absorption and photoluminescence (PL) excitation peaks may differ in peak position or wavelength due to their different origins. When doped with Mn ions, defect levels due to crystal field splitting of $3d$ levels of Mn are produced in the bandgap of ZnS. As shown in Figure 5(a), in the absence of Mn ions, photoexitation of a valence electron can be followed by a transfer of electron to defect levels and subsequent broad emission around 400 nm wavelength. In Mn-doped ZnS bulk, the photoexcitation of a valence electron may be followed by its transfer to $^4T_1$ level due to Mn^{2+} as depicted in Figure 5(b). Alternatively, as depicted in Figure 5c, photoexcitation may be followed by transfer of the electron in the defect state and then transfer to $^4T_1$ level due to Mn^{2+} in the energy gap of host lattice. Subsequent transitions from $^4T_1$ to ground state level $^6A_1$ of Mn^{2+} results into PL. The $^4T_1-^6A_1$ is an otherwise spin forbidden transition, which becomes allowed due to perturbation of the host ZnS crystal. The wavelength of the emitted radiation is ∼585 nm (2.12 eV) and its half width is 0.23 eV. The PL decay time is ∼1.8 ms [78]. It is interesting to see what differences in PL and its decay time occur due to being in a nanoparticle state.

In Figure 6, typical PL spectra of mercaptoethanol capped ZnS:Mn nanoparticles [73] are illustrated. Both defects related emission at ∼425 nm and Mn^{2+} doping related emission at ∼600 nm can be seen.

Becker and Bard [16] observed orange emission in doped ZnS:Mn colloidal particles at ∼583 nm. There is no knowledge about the size of colloids. Wang et al. [17] investigated PL in $Zn_{0.93}Mn_{0.07}S$ clusters of 2.5 nm size immobilized in glass. They observed that the photo excitation peak was located at 346 nm and the emission peak was at 594 nm. However, the PL peak at ∼594 nm also showed a large shoulder at ∼700 nm, which was attributed to the presence of some defect states of unknown origin. Annealing reduced the intensity of defect emission. Shift in the excitation spectrum from 370 nm in the bulk $Zn_{1-x}Mn_xS$ with the same composition to 346 nm in nanoparticles was attributed to the quantum confinement effect [11, 12].

Bhargava et al. [18], however, were the first to claim in case of ZnS-doped Mn that the doped semiconductor nanoparticles had increased quantum efficiency of 18% in contrast to the corresponding bulk materials. It was shown that quantum efficiency increased with decreasing particle size. They also claimed that the luminescence decay time
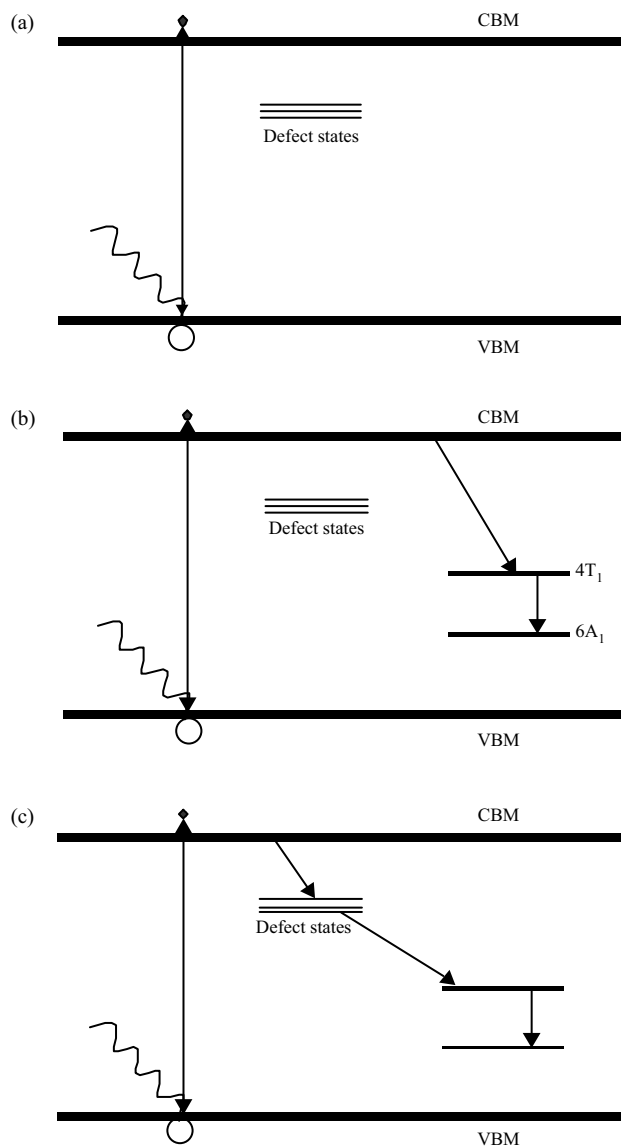
Figure 5. (a) Photoexcitation of an electron in a ZnS crystal; (b) photoexcitation followed by transfer to $^4T_1$ in ZnS:Mn; (c) photoexcitation followed by defect states and then a transfer to $^4T_1$. In both (b) and (c), electron from $^4T_1$ makes a transition to $^6A_1$. Reprinted with permission from [90], S. Sapra et al., *J. Nano. Nanotech.* 3, 392 (2003). © American Scientific Publishers, 2003.

was much faster (1.8 ns, 3.7 ns, and 20.5 nsec.) in ZnS:Mn as compared to the corresponding bulk (1.8 ms). Based on their experimental results, Sooklal et al. [79] and Yu et al. [80] also supported that luminescence decay time in ZnS:Mn were in nanoseconds. Yan et al. [81] showed theoretically that luminescence lifetime shortening is possible by five orders of magnitude in ZnS:Mn nanoparticles, supporting Bhargava et al.

The observations of Bhargava et al. [18] were very useful because they illustrated faster devices with a high saturation threshold. Bhargava et al. observed a large shift in the excitation spectrum (265 nm) due to quantum confinement effect as opposed to the bulk excitation peak at 332 nm. The emission peak for the bulk ZnS:Mn sample appeared
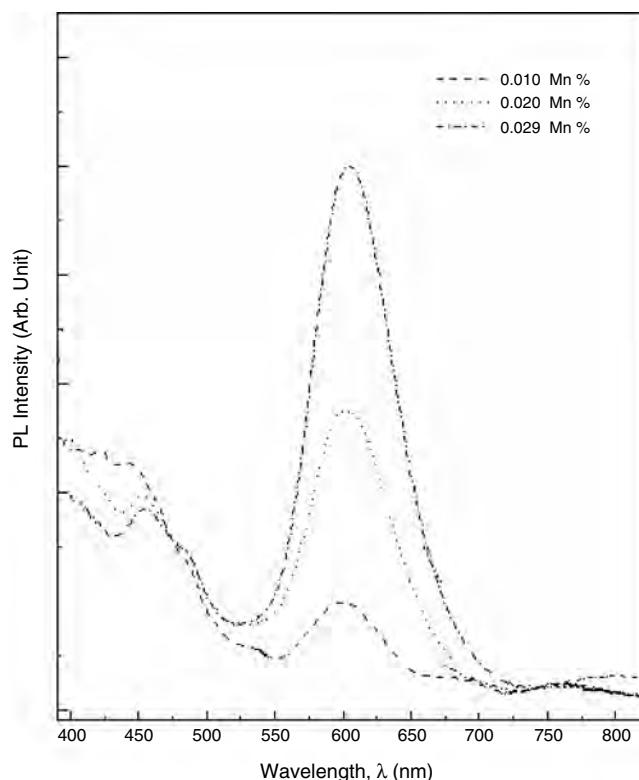
Figure 6. Photoluminescence from ZnS:Mn nanoparticles. From [122], P. H. Borse et al., unpublished.

at 584 nm and that for the nanocrystalline (3 nm) sample appeared at 590 nm. Their sample appears to be defect-free as there are no shoulders on the luminescence peak and there is no PL due to ZnS defect states at ~425 nm. However, luminescence peak is broader than that for the bulk powder sample. Larger line width was attributed to inhomogeneous broadening and presence of phonon-assisted transition. One of the observations of Bhargava et al. [18] is related to the fast decay time (about five orders of magnitude shorter and an increase in the quantum efficiency for luminescence which they related to strong coupling of sp–d electrons in nanoparticles and a strong localization of e–h pair). Therefore, in subsequent article [82, 83], they argued that doped semiconductor nanoparticles are a new class of luminescent materials. They also emphasized that undoped nanoparticles with size less than Bohr diameter are not expected to show fast decay time. This is because electron and holes in undoped particles have little or no spatial correlation. They are trapped separately at different locations and merge through a radiative or nonradiative recombination path.

The claim of Bhargava et al. [18] that PL decay time is shortened from milliseconds to nanoseconds in nanoparticles was, however, opposed by Bol and Meijerink [32, 84, 85] in a series of article. First of all, due to proposed sp–d hybridization in Mn^{2+} doped ZnS nanoparticles, one should expect a change in the position of the emission band with particle size that has not been observed. Bol and Meijerink [32] indeed showed that in ZnS:Mn nanocrystallites, there

is a short decay time but there is also a long decay time of milliseconds. They, in fact, compared ZnS:Mn particles of ~4 nm, the comparable size as used by Bhargava et al. They used a similar synthesis route or organometallic chemicals and embedded the particles in methacrylic acid as well as using an inorganic route. In inorganically synthesized samples, concentration of Mn^{2+} was varied from 2–10%. In all the samples, a broad peak around 420 nm, which can be due to recombination or free charge carriers at defect states was observed along with a peak due to Mn^{2+} emission at ~600 nm. An excitation wavelength of 308 nm was used. Lifetime measurements were carried out using excimer laser (XeCl) with a 308 nm wavelength or a fourth harmonic of a Nd-YAG laser with 266 nm wavelength. Laser pulse width was 20 ns and the time resolution of photomultiplier tube was 10 ns. The time resolution of laser set up was 50 ns. Decay time measurements were made on a digital oscilloscope. They observed for the ZnS:Mn sample for 420 nm emission, a multiexponential decay with fast initial decay ($\tau \cong 50$ ns) and a slower ($\tau \cong 200$ ns) decay components. Their set-up did not allow accurate determination of short nanoseconds, decay times. For an ~600 nm emission also, a fast multiexponential decay of $\tau \cong 40$ and 250 ns could be observed. However, decay time measurements in the millisecond time regime showed an initial fast decay of $\tau = 0.4$ millisecond and then a single decay of 1.9 millisecond. It was, therefore, proposed that earlier short nanosecond decay times reported by Bhargava et al. could be due to ZnS defect state band emission at 420 nm extending into 600 nm band due to Mn^{2+}. Due to a high repetition rate of laser pulses, only short nanosecond pulses can be observed leading to erroneous results. In order to further prove that Mn^{2+} emission in nanoparticles of ZnS has a long millisecond decay time and is not due to millisecond decay from Mn^{2+} in large ZnS particles that may be present in the sample, they recorded a time resolved emission spectra. All organic and inorganic samples showed similar results. They were excited with the YAG laser ($\lambda_{ex} - 266$ nm). Delay of 0, 3 μs, and 0.5 ms were used with 2 μs, 200 μs, and 1 ms gates, respectively. For 0 delay time, a broad emission around 420 nm with a tail extending into 600 nm was observed. This indicates that 420 nm has a very short lifetime. For a 3 μs delay and a 200 μs gate width, both 420 nm and 590 nm emission could be seen. With 0.5 ms delay, 420 nm emission disappeared completely and only a long-lived Mn^{2+} emission remained. These results clearly indicated that 420 nm emission has a short decay time and 590 nm has long decay time of milliseconds as in bulk ZnS:Mn, contradicting exactly the earlier reports of Bhargava et al. [18]. Murase et al. [54] also claim that there is no lifetime shortening due to quantum confinement effect in nanoparticles of ZnS:Mn.

Chung et al. [35] also observed one short and one long luminescence decay component. The short or fast component was attributed to surface bound Mn^{2+} and the slow decaying component to lattice-bound Mn^{2+} in ZnS host lattice. It was argued that an overall lifetime decrease with a reduction of size was due to an increase of Mn^{2+} impurities on the surface rather than quantum size effects. They also did not agree with the proposal [18, 79, 83] that strong s, p, d hybridization occurs in nanoparticles. Tanaka et al. [86] also had concluded that in ZnS:Mn nanoparticles, s–p

state does not change significantly, as compared to bulk and mixing of s, p, d states cannot be the reason for high efficiency of luminescence in nanoparticles.

Although Bol and Meijerink were able to do time-resolved experiments, their experiments were carried out with limited time resolution with 2 μs gate. Zhang and Smith [87, 88] used ZnS:Mn nanoparticles (2.5 nm) prepared by reverse micelle route and carried out PL intensity decay measurements with better resolution. They compared the absorption and luminescence (emission spectra) for ZnS undoped and Mn doped nanoparticles. For undoped particles, the absorption edge was at 278 nm and for the doped sample 269 nm and both shifted with respect to bulk ZnS due to quantum confinement. The undoped ZnS sample showed triple exponential decay with 250 picosecond, 7 picosecond, and 10 μs time constant. The ZnS:Mn sample of nanoparticles showed an additional 1.8 ms component. As 250 ps, 7 ps, and 10 μs decay time was showed by both the doped and undoped sample, it was attributed to defect state emission from ZnS and 1.8 ms decay to Mn^{2+} related emission.

Magnetic Measurements   A number of groups have used electron spin resonance (ESR) or EPR to investigate the symmetry and electronic structure of Mn ions in ZnS. Mn^{2+} has five electrons in its d shell; hence, total angular momentum is $L = 0$ and total spin is $S = 5/2$. A characteristic feature of Mn is that due to ^{55}Mn nucleus with $I = 5/2$. It produces in ESR, a six-line pattern as a result of hyperfine splitting. The spin Hamiltonian can be written as

$$H = g\beta\overline{H}\cdot\overline{S} + \frac{1}{6}a(S_x^4 + S_y^4 + S_z^4) + D\left[S_z^2 - \frac{1}{3}S(S+1)\right] + A\overline{S}\cdot\overline{I}$$
(3)

where β is the Bohr magneton, H is the applied magnetic field, and g, D, and $|A|$ are the ESR parameters. The first term in the equation is nothing but the Zeeman interaction term. The second term arises due to a cubic crystal field and the third term is due to fine structure splitting. The fourth term is due to hyperfine interaction. The Mn^{2+} ions with t_{2g}^3 e_g^2 electronic configuration, g tensor is isotropic with a value 2.0023, close to free electron spin g value. The parameter D is 0 in cubic crystal field symmetry and has finite value for lower symmetry. Considerable information can be obtained by analyzing ESR spectra.

Kennedy et al. [89] investigated 3.5 nm size nanoparticles of ZnS:Mn using ESR. Nanoparticles were synthesized using diethyl metal salts, H_2S, and methacrylic acid in their work, there was one impurity of Mn ion per particle having roughly 1000 Zn and S atoms. Although ESR spectra for bulk and nanoparticle samples of ZnS:Mn did not differ when recorded at room temperature using 9.5 GHz frequency, the spectra taken with 35 GHz frequency appeared considerably different. Spectrum of bulk powder did not show frequency dependence, but the nanoparticle sample showed a considerably resolved spectrum at a higher frequency. Furthermore, it was found that the nanocrystalline sample spectra changed with time. This may be due to more than one impurity per particle as well as aggregation of particles. They divided the ESR signal into two components, NC1 and NC2, both being six line spectra with different ESR parameters. The NC1

component had 6.9 mT splitting with $g = 2.003$ (closer to cubic) and NC2 had 9.5 mT and $g = 2.001$. The $|A|$ values for NC1 and NC2 were 64.5×10^{-4} cm^{-1} and 89×10^{-4} cm^{-1}, respectively. $|A|$ value is in general proportion to the ionicity of the Mn-ligand bond. The NC1 component of the spectrum was similar to that due to bulk ZnS:Mn and could be attributed to Mn^{2+} occupying a substitutional site in the cubic crystal. On the other hand, NC2 could be attributed to Mn^{2+} ions near the surface. NC2 peak widths were inversely proportional to the frequency used. The hyperfine splitting and g value for NC2 were different from bulk ZnS:Mn, but closer to Mn in ionic solids like $KMgF_3$. This indicated that NC2 is not related to Mn in Wurtzite lattice. The only alternative is to associate NC2 with Mn ions closer to the surface.

The effect of methacrylic acid on Mn-doped ZnS nanoparticles prepared by a chemical route and dispersed in methacrylic acid was investigated by Yu et al. [57]. Efforts were made to produce a homogenous distribution of Mn in ZnS. Particles with 2.3 nm, 2.5 nm, and 2.7 nm were obtained and characterized using XRD, TEM, XPS, UV absorption, PL, and ESR. They observed a well-resolved sextet in ESR which is an indication of the presence of isolated Mn^{2+} ions without the clustering of Mn—Mn ions. However, intensity and shape of ESR lines did not observably change with an increasing concentration of methacrylic acid. Spectra without methacrylic acid were unresolved and broad, probably due to aggregation of Mn. They also compared the ZnS:Mn sample with and without the addition of methacrylic acid before and after drying. Measurements were carried out at 170 K and 77 K for samples in the solution and dry. The results indicated that in samples with methacrylic acid, Mn^{2+} ions were well distributed and particles were well protected, leading to suppression of temperature and fluctuations. They also observed a slight blue shift in PL (579 nm) compared to bulk (585 nm). This value appears to be the shortest wavelength of luminescence in ZnS:Mn nanoparticles, the longest being 600 nm [26]. They also showed that PL intensity increased with reduction in the ZnS:Mn nanoparticle size.

Igarashi et al. [53] found agreement with the ESR results on ZnS:Mn by Kennedy et al. [89]. For 2–3 nm ZnS:Mn they observed PL at ~580 nm. Their samples were synthesized in methanol by reacting zinc and manganese acetate with sodium sulfide, and investigated as colloids as well as by modification in acrylic acid. They too could deconvolute the ESR signals into signal I and signal II. Hence, signal I (or NC1 in [89] was assigned to Mn^{2+} ions in substitutional sites as in cubic ZnS. Signal II (or NC2 in [89]) was attributed to Mn^{2+} near surface. They found that the intensity ratio of signal II to signal I increased with decreasing S/Zn. They, however, found a decrease in signal II compared to signal I when particles were modified with acrylic acid.

Murase et al. [54] investigated ZnS:Mn nanoparticles of ~4 nm size. Samples were prepared using metal nitrate salts and sodium sulfide by reacting them in aqueous medium. For particle size analysis, X-ray diffraction and TEM were used. They observed the fluorescence band at 590 nm when excited with a 266 nm wavelength of light. They found that the ESR spectra recorded at 77 K within 2 hours of sample preparation kept on changing up to 2 days and then

remained unaltered. The hyperfine structure appeared gradually and became narrow as also observed by Yu et al. [57] for samples synthesized in a different way by using methacrylic acid. This kind of variation with time, in the ESR spectra, is reported by others too. However, there was no change of particle size but possible changes in agglomeration, diffusion of ionic species, and changes in the defect concentration. The samples with PVA, however, do not show surface-related alterations in spectra with time as they are fixed by hydrogen bonding. They resolved the ESR spectra into two sets of Sextets as Mn I and Mn II responsible for two different sites for Mn ion substitution in the host ZnS nanoparticle. The intense substructure could not, however, be due to interaction of S^{2-} ligands surrounding the Mn^{2+} center as abundance of S^{2-} nuclei with nonzero nuclear spin is expected to be less than 1%. Both the sextet structures are considered to be opposing the lifetime shortening due to efficient energy transfer from sp states to d states discussed by Bhargava et al. [18]. They also observed two additional weak structures below 77 K, due to hole centers. Hole centers arise under specific synthesis conditions of samples. Similar to Bol and Meijerink [32], they also found that the luminescence bands at ~400 nm and 600 nm were due to nano and millisecond decay times, respectively, and concluded that a short life time component at ~600 nm may be originating from the tail of blue emission at ~400 nm due to a ZnS nanocrystal with a large defect density. However, blue emission at ~400 nm appeared to be absent in the ZnS:Mn nanocrystals reported by Bhargava et al. [18]. Therefore, Murase et al. [54] concluded that the lifetime shortening may differ in differently prepared ZnS:Mn nanoparticles.

Temperature-dependent ESR experiments on ZnS:Mn ~3.6 nm size particles by Igarashi et al. [52] throw more light on the fluorescence efficiency increase in nanocrystals. For this they studied a sample of ZnS:Mn of sub micron particles (SMP) and other nanocrystallites (NC) in acrylic acid. They found that the luminescence intensity in the NC sample was much larger than that in the SMP, which can only be due to higher efficiency in nanoparticles. The ESR spectra in both samples showed sextets. Lattice distortion was larger in the NC as compared to the SMP. Two kinds of Mn^{2+} sites were identified corresponding to two signals I and II. Signal I was due to Mn^{2+} inside the particle and II was due to that on the surface. Signal II, which was assigned to Mn^{2+} on the surface, was observed only for NC and not in SMP. Signal II was prominent at a higher frequency. Temperature dependence of a average line width of a sextet signal, ΔHpp was plotted as a function of temperature. For SMP, signal I decreased with temperature. For NC, no temperature dependence in ΔHpp was noticed for both signals I and II. ΔHpp depends on spin-lattice interaction. Its lower value and decrease at a low temperature in SMP sample means that spin-lattice interaction is weaker in SMP as compared to that in NC. Thus, in agreement with Bhargava et al. [18] overlapping of Mn^{2+} and S^{2-} orbitals was considered in existence in nanocrystals which would increase spin-lattice interaction. Lower symmetry of a crystal field in NCs increases hybridization between sp^3 and d orbitals. The same arguments were considered valid for the absence of temperature dependence of ΔHpp for signal II in NC. This indicates strong coupling

of poly acrylic acid (PAA) and cations of Zn and Mn. This probably explains effective energy transfer between Mn^{2+} and ZnS as well as Mn^{2+} and PAA. Igarashi et al. however, remarked that more experiments were necessary to understand increased efficiency.

Dinsmore et al. [47] also analyzed ZnS:Mn/ZnO unannealed, and samples annealed up to 525 °C using ESR with 9 GHz and 35 GHz frequencies. The unannealed samples have ~3.5 nm diameter. The sample annealed at 300 °C, 350 °C, 400 °C, and 525 °C has average particle size as 6.0, 8.4, 17.1, and 16.0 nm, respectively. The frequency dependency of spectra and larger hyperfine splitting with peaks near the edges of 35 GHz data were obvious as before [89]. They found from their ESR spectra that Mn^{2+} is replacing some of the Zn^{2+} ions inside the particles of ZnS. However, by annealing the samples at 350 °C, the contributions of the Mn^{2+} ion signal from near surface location appeared to have vanished.

Chen et al. [69] have also carried out ESR measurement of ZnS:Mn nanoparticles synthesized in ultrastable zeolite-Y (USY). Their other samples were synthesized in methacrylic acid (MAA) and a mixture of methacrylic acid and citric acid. Electronic spin resonance spectra of Mn^{2+}/USY, ZnS:Mn/USY, and ZnS:Mn/MAA of 3.5 nm, 4.5 nm and 10 nm are quite different from each other but all show presence of Mn^{2+}. Chen et al. also confirm that there are two different sites for Mn^{2+} ions evident from two ESR signals. Bulk like, the ESR signal decreased in intensity with a decrease in particle size, and the intensity of near surface site signal increased. However, uncapped 10-nm size particles proved to be an exception as near surface site ESR intensity was stronger than bulk-like signal. This could be due to the presence of more surface defects in uncapped particles. All this leads to the conclusion that distribution of Mn^{2+} was not only related to particle size but also to surface modification. Furthermore, they emphasize that ZnS:Mn nanoparticles in USY showed only hyperfine structure forbidden for cubic symmetry and associated to Mn^{2+} surface sites.

Electron spin resonance investigations were carried out by Borse et al. [28] for different samples with various Mn concentrations. The particles were similarly synthesized as in [26], but had an average size of 2.8 nm. As shown in Figure 7(a), the ESR spectra showed dramatic changes with Mn concentration. Electronic spin resonance spectra were fitted with four components—S_I, S_{II}, S_{III}, and S_{IV}—which enabled the understanding of the observed spectral changes in ESR spectra with Mn ion concentration. Two examples are showed in Figure 7(b) and 7(c) for low and high concentrations of Mn in ZnS nanoparticles of the same size. These contributions on Mn ions are identified as Mn (S_I) in tetrahedral cationic substitution with T_d symmetry, isolated Mn ions at the surface or interstitial locations S_{II} with octahedral symmetry (O_h), Mn—Mn dipolar interactions S_{III} and exchange coupled Mn clusters (S_{IV}) in various proportions. Line widths for all these S_I–S_{IV} differ. Identification of the S_I–S_{IV} components enabled the discovery that the component S_I is responsible for the PL increase, whereas S_{II}–S_{IV} are responsible for luminescence quenching. Relative contribution of these S_I–S_{IV} components varied with Mn concentration. At low Mn concentration (S_I), some particles are
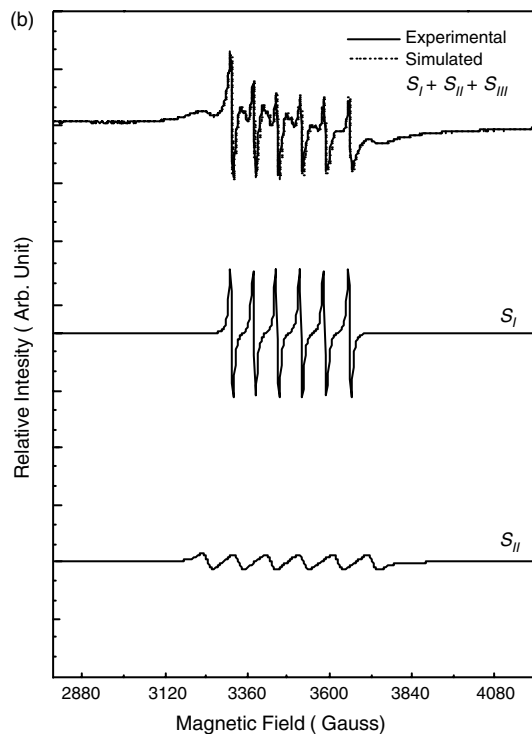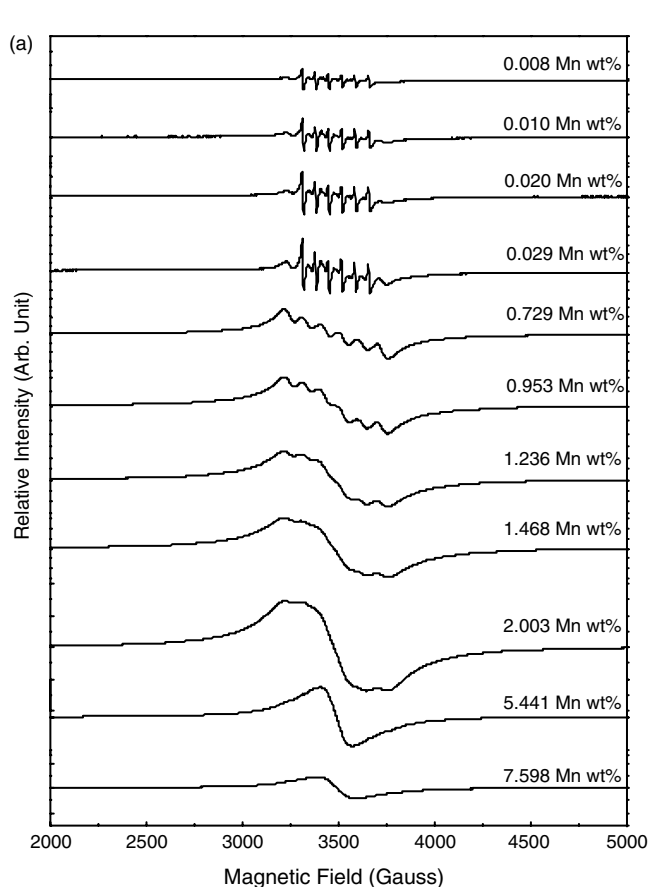
Figure 7. (a) ESR spectra of ZnS:Mn with various Mn nanoparticles with various Mn concentrations; (b) fitted components of ESR spectra for 0.02 Mn Wt %; and (c) 5.441 Mn Wt %. From [122], P. H. Borse et al., unpublished.
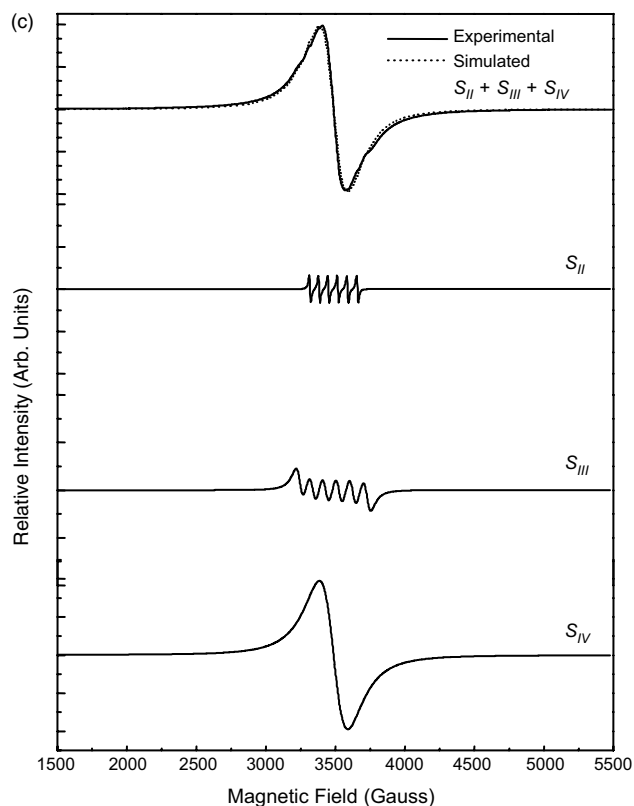
Figure 7. Continued.

doped and some are not. With increasing Mn concentration, more and more particles are doped resulting in an increase in photoluminescense intensity. At a higher concentration of Mn, contributions due to S_{II}, S_{III}, and S_{IV} increase. This was accompanied by photoluminscence quenching.

There are only a few reports on the measurement of magnetic susceptibility of ZnS:Mn nanoparticles. Wang et al. [13] presented some preliminary magnetic susceptibility data from 2.3 to 314 K on $Zn_xMn_{1-x}S$ clusters and concluded that clusters were paramagnetic with effective magnetic moment of 5.43, in close agreement with effective value of 5.9 on Mn^{2+} ion.

Sapra et al. [90] have recently carried out magnetic susceptibility measurements on 2.4 nm ZnS:Mn nanoparticles. The particles were doped with 2, 5.5, 9, and 13% Mn, keeping the size constant. Suceptibility against the temperature behavior has been shown in Figure 8. The χ^{-1} against $1/T$ plots exhibited perfect Curie behavior indicating that the interaction between Mn^{2+} ions was minimal. They could also show that the Mn concentration determined by susceptibility data and EDAX agreed well.

Effect of Mn Concentration The concentration of dopants may have an effect on the PL or cathedoluminescence intensity, ESR spectra, etc. and has been investigated by many groups. The effect of Mn concentration on ESR has already been discussed in the previous section.

Khosravi et al. [28] investigated the Mn-doped ZnS nanoparticles capped with mercaptoethanol. The crystalline particles with an average size 2.1 nm were investigated for their

Susceptibility
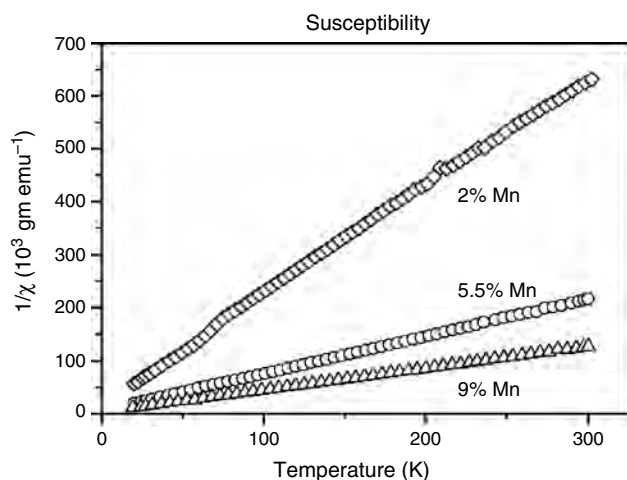
Figure 8. Curie behavior of Mn-doped ZnS nanoparticles doped with different concentrations of Mn. Reprinted with permission from [68], S. Sapra et al., *Recent Advances in Inorganic Materials*, to appear. Narosa Publishers.

PL properties. It was found that excitation with 312 nm produced a PL peak at ∼600 nm, an intensity which varied with Mn% in the sample (see Fig. 9). The nanoparticles with approximately 0.12 at wt% showed maximum intensity, and luminescence quenching occurred at a higher concentration. Correspondingly, the ESR spectra also changed dramatically. The luminescence quenching effect was also observed at a high concentration of Mn ions in nanoparticles as is usually observed in bulk ZnS:Mn [91].

Similar trends in PL were observed by Sooklal et al. [79] for 5 nm particles of ZnS:Mn with 1–5 % Mn^{2+} ion doping. Both 435 nm emission due to defect states in the host ZnS and 585 nm emission due to Mn^{2+} in ZnS nanoparticles were detected. They have also observed band-edge UV emission (transition from conduction to valence band edge) when Mn^{2+} ions were residing on the nanoparticle's surface. However, both the peaks showed Mn concentration dependence
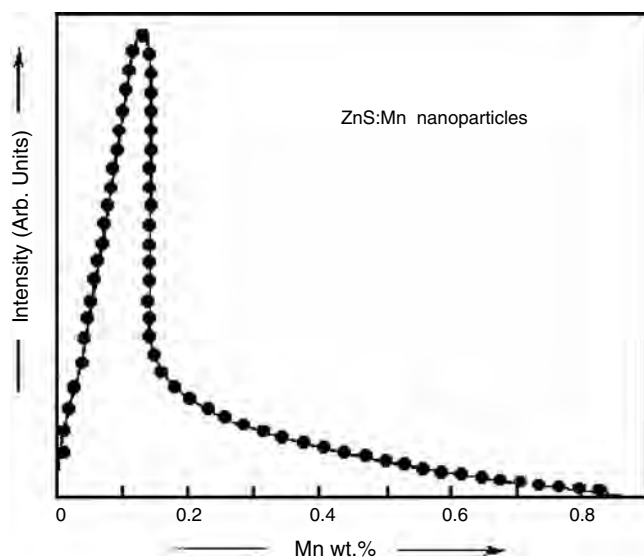
Figure 9. Variation of PL intensity with Mn wt % in ZnS nanoparticles.

on PL intensity. The highest intensity 435 nm radiation occurred at 1% Mn doping, and for 585 nm occurred when 2% Mn doping, was made. Both PL emission lifetimes were insensitive to the doping.

Chen et al. [69] investigated the effect of Mn^{2+} concentration in ZnS nanoparticles on the 580 nm PL peak position as well as intensity. They did not observe any peak position shift with an increase in an initial Mn concentration of 3%, 5%, and 7% in 3.5 nm size Zns:Mn particles. Intensity of the peak, however, increased from 3 to 7% Mn increase.

Bol and Meijerink [84] made a different observation that the quantum efficiency of luminescence for Mn^{2+} related emission at ∼590 nm of their sample with 300 nm excitation wavelength did not show the concentration quenching effect. In their samples, the quantum efficiency increased with a Mn/Zn increase, in nanoparticles (4nm) passivated with Na(PO$_3$)$_n$, but stabilized around 3 to 3.5% efficiency.

Effect of Radiation There are many attempts to observe the effect of UV irradiation on nanoparticles of ZnS:Mn with the purpose of finding out if observed PL gets affected by UV irradiation.

Bol and Meijerink [84] have investigated the increase in quantum efficiency for ZnS:Mn nanoparticles when irradiated with UV radiation. For example, in Figure 10, the emission and excitation spectra of nanoparticles passivated with methacrylic acid (MA) without and after UV radiation for different durations, are illustrated. In general, it was found that PL intensity increased initially and then remained constant. They defined % increase as

$$\%\text{Increase} = (\text{quantum efficiency after UV}$$
$$\text{irradiation} - \text{quantum efficiency before UV}$$
$$\text{irradiation/quantum efficiency before}$$
$$\text{irradiation}) \times 100 \qquad (4)$$

In Table 3, the % increase for different polymer coatings are given. Increase in polyvinylbutyral (PVB), MA, PVA, and (PP) could be attributed to UV-induced-increased cross-linking in these polymers which further passivates the nanoparticles. For PP, no further polymerization takes place but photooxidation takes place. This can result in reduced particle size and increased quantum efficiency as predicted by Bhargava et al. [18].

It was observed by Jin et al. [51] that there was UV irradiation induced enhancement of PL peak at ∼600 nm in ZnS:Mn colloides (3.6 nm), which was wavelength-dependent. They observed that the ratio of intensity of sample exposed to a particular wavelength of a Xenon lamp of an unirradiated sample changed with wavelength. The shape of excitation and peak position also changed due to irradiation. However, the shape of the PL peak did not change except that there was a small blue shift for the irradiated sample (590.42 to 585.6 nm). There was no size change of nanoparticles due to UV irradiation. Enhancement in the PL intensity was attributed to surface modification due to UV radiation.

Ultraviolet radiation using a mercury lamp was done by Sohling et al. [63] for ZnS:Mn nanoparticles (3 ± 0.5 nm) stabilized using hydroxypropyl cellulose (HPC). Initially, there was an increase in the PL intensity for the 590 nm
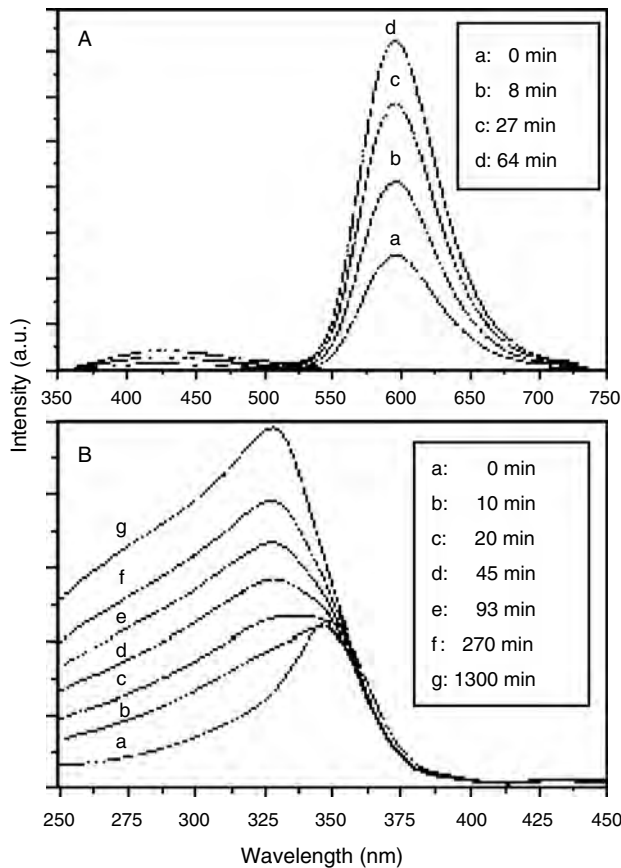
Figure 10. (a) Emission spectra ($\lambda_{ex} - 300$ nm) of nanocrystalline ZnS:Mn passivated with MA after different times of UV irradiation (b) excitation spectra recorded at an emission wavelength of 590 nm of nanocrystalline ZnS:Mn without polymer as function of UV irradiation times. Reprinted with permission from [84], A. A. Bol and A. Meijerink, *Phys. Stat. Sol. B* 224, 291 (2001). © 2001, Wiley-VCH.

wavelength due to Mn^{2+} in ZnS but reduced with longer exposure. This was true for 50 μW or 200 μW power of UV radiation. The optical absorption spectra also showed a reduction in absorption intensity with increasing UV irradiation. However, a PL intensity maximum at ~590 nm was reached faster for higher irradiation intensity. The initial rise in PL intensity could be due to better surface passivation. This also occurs faster when UV intensity is higher. By exposure to UV, the particles get photo oxidized leading to

Table 3. Photoluminescence quantum efficiency comparison for ZnS:Mn nanoparticles uncoated and polymer-coated samples before and after UV-radiation.

	PVB	MA	PVA	PP	Without polymer
Quantum efficiency before UV irradiation	3.5	1.0	2.7	4.5	0.3
% increase in quantum efficiency	250	240	230	60	10

Source: Adapted with permission from [84], A. A. Bol and A. Meijerink, *Phys. Stat. Sol. (B)* 224, 291 (2001). © 2001, Wiley-VCH.

a decrease in absorbance of exciting radiation leading to a reduction in emission intensity.

Effect of Temperature The effect of temperature on PL of ZnS:Mn nanoparticles was investigated by some groups [13, 57, 64, 71, 86]. There is a general agreement that blue luminescence at ~425 nm arising due to host ZnS lattice defects decreases with an increasing temperature. However, Mn^{2+} related yellow/orange emission depends upon the sample preparation.

Wang et al. [17] investigated the temperature dependence (Fig. 11) of PL intensity and found that below 50 K PL intensity was constant but dropped down rapidly with an increasing temperature. The temperature dependence was discussed in terms of the multiphonon-induced radiationless transition theory [92].

Temperature-dependent PL spectra were recorded for sol–gel prepared ZnS:Mn nanoparticles by Saenger et al. [64]. The intensity of absorption (a) and emission (b) peak reduced with an increasing temperature accompanied by a red shift in the absorption spectra and a blue shift in the PL spectra. They disagree with Bhargava et al. [18] that fast and efficient relaxation is a result of coupling of Mn^{2+} derived states with ZnS derived states. They state that in nanoparticles, there is an increased probability that electron and hole pair see Mn center, which is responsible for not decaying via surface states. Saenger et al. [64] observed in ZnS:Mn nanoparticles stabilized in hydroxypropyl cellulose that by increasing the temperature from 20 K to 298 K, the emission peak at ~600 nm blue shifted slightly with a substantial reduction in the PL intensity.

Yu et al. [93] observed for ZnS:Mn nanoparticles (3.6 nm) embedded in PVB that the PL at ~590 nm due to Mn^{2+} ions in ZnS increased with increasing temperature as shown in Figure 12 from 7.8 K to 270 K and then decreased by 297 K. This behavior is certainly different from a powder sample
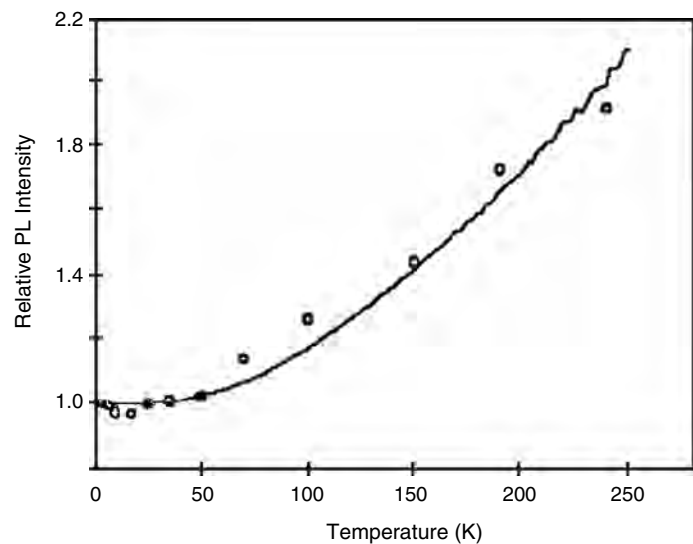
Figure 11. The relative luminescence intensity at 594 nm, (temperature = 3.7 K/I(t)), plotted as a function of temperature for 2.5 nm $Zn_{0.93}Mn_{0.07}S$ nanoparticles in glass. The solid curve is a theoretical fit. Reprinted with permission from [17], Y. Wang et al., *Sol. St. Comm.* 77, 32 (1991). © 1991, Elsevier Science.
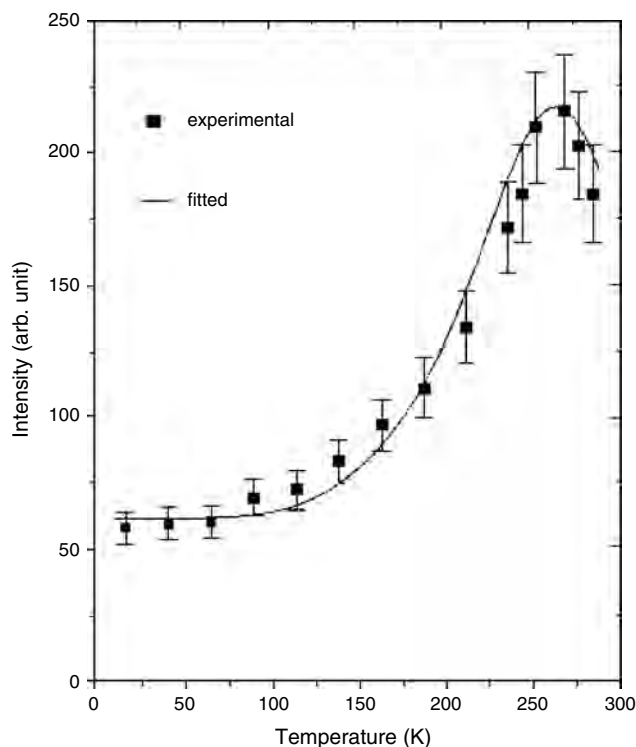
Figure 12. Luminescence intensity at 590 nm versus temperature for ZnS:Mn nanoparticles. Reprinted with permission from [93], J. Yu et al., *J. Lumin.* 76–77, 252 (1998). © 1998, Elsevier Science.

Figure 13. Temperature dependence of the intensity of the orange luminescence of (a) nanocrystals and (b) bulk powder excited by 260 nm (open circles) and 488 nm (crosses). The solid line is the fitting curve, taking into account the nonradiative loss channel with an activation energy of 57 meV. Reprinted with the permission from [94], M. Tanaka and Y. Masumoto, *Chem. Phys. Lett.* 324, 249 (2000). © 2000, Elsevier Science.

(e.g., [64]) where PL intensity decreases with increases in temperature. Different mechanisms were explored but the one in which phonon-assisted energy transfer occurs was considered to be more appropriate.

A similar observation has been reported by Suyver et al. [71]. The PL intensity related to a ZnS host decreased and that related to Mn^{2+} increased with an increasing temperature from ~20 to 300 K. However, they interpreted the temperature dependence of the Mn^{2+} and ZnS host lattice related emission by modes in which sulphur vacancies are involved in the defect luminescence.

Tanaka and Masumoto [94] observed (Fig. 13) a very weak temperature dependence in the 9 K to 300 K temperature range for the PL at ~600 nm due to Mn^{2+} in ZnS. They used an excitation wavelength of 260 nm, which was sufficient enough to cause an interband transition of the host lattice. In the same temperature range, bulk powder of ZnS:Mn shows a strong temperature dependence and the luminescence decreases substantially with increases in temperature. However, excitation of Mn^{2+} by 488 nm wavelength through d–d transition viz. $^6A_1$ (^6S) to $^4T_1(^4G)$ had negligible temperature dependence in the same range, both in nanocrystalline and in a bulk sample. The difference in the same luminescence with different excitation wavelength has been discussed in terms of thermally induced dissociation of the exciton, the exciton-phonon interaction, and the rate of energy transfer from exciton to Mn ion. Excitons in nanoparticles are spatially confined and not dissociated easily as in bulk materials. Exciton-phonon interaction in nanoparticles is weaker than in bulk materials. They also

confer that energy transfer from exciton to Mn^{2+} is faster in nanoparticles.

Hot Luminescence Yu et al. [95] reported for the first time an observation of the two split bands around the usual Mn^{2+}-related luminescence band at ~590 nm position in ZnS:Mn nanocrystals. The samples were the nanoparticles ~3.6 nm in size embedded in PVB. Samples were excited with laser pulses of 40 ns width having a wavelength of 248 nm and the energy deposited per pulse was 180 mJ. Emission spectra were observed for different delay time as shown in Figure 14, with a gate width of 2 μ seconds at room temperature. The two bands observed for short decay time were discussed to have the origin due to transition from the classical turning points of high vibration levels of excited electronic ground state of Mn^{2+} in ZnS. With very high excitation density as used in their experiments "hot spot" can be formed, which in turn produce long (μs) relaxation times. Relaxation time was found to increase with a increase in excitation density in agreement with the "hot spot" model. Such a split pair of bands was not observed at room temperature in ZnS:Mn powder with micrometer-size grains. The confinement of phonons in nanoparticles is particularly favored for the creation of "hot spot" in these nanoparticulate samples. However, Donega et al. [96] did
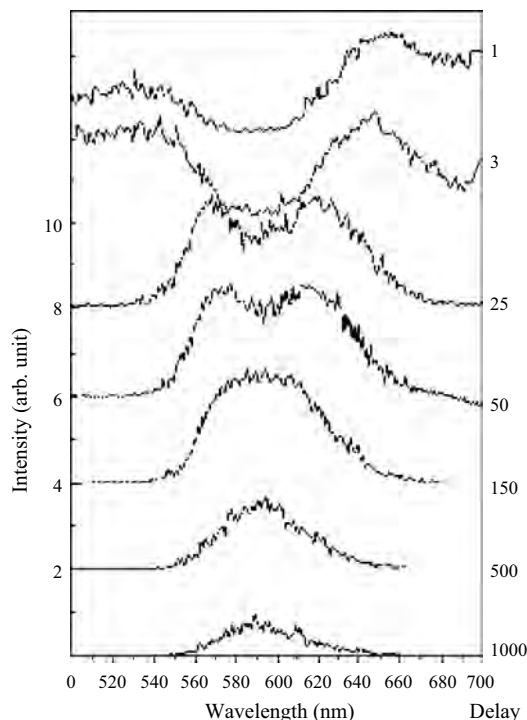
Figure 14. Time resolved emission spectra of ZnS:Mn nanoparticles at different delay time. Excitation: 248 nm excimer laser beam, pulse width 40 ns, 2 Hz, excitation density 5.6 mJ/cm^2. Gate width 2μs. Room temperature studies. Reprinted with the permission from [95], J. Yu et al., *J. Lumin.* 79, 191 (1998). © 1998, Elsevier Science.

not find any evidence for Mn^{2+} hot luminescence in 4.5 nm ZnS:Mn of two different Mn concentrations.

Cathodoluminescence Powders containing about a few micrometer-size particles are commercially used as phosphors. Doped ZnS phosphors are widely used as screens of cathode ray tubes and other display panels [1]. However, for better resolution a smoother coating with finer particles would be preferred [83]. It is also necessary in field emission display (FED) that the coating should efficiently operate with a pulsed electron beam without saturation for as high as ~100 μA/cm^2 current density. Dinsmore et al. [47] have investigated cathodoluminescence of Mn-doped ZnS nanoparticles under various conditions and compared them with commercially available phosphor samples (Sanroff Corporation, Princeton, NJ, USA) having ~3 to 6 μm size. Commercial samples exhibited completely wurtzite structure. But nanocyrstalline unannealed ZnS:Mn/ZnO particles synthesized by Dinsmore et al. were zinc blend at room temperature. Their unannealed sample showed a maximum in CL intensity at ~600 nm. But the commercial sample and the nanophosphor sample annealed at ~525 °C had peak at ~580 nm. Nanoparticle samples used in their experiments were surface passivated with ZnO and labeled as ZnS:Mn/ZnO. They found that CL efficiency increased substantially when particles were coated with ZnO. They tried MgO also to passivate the nanoparticles of ZnS:Mn, but found that CL efficiency of nanoparticles was better with a ZnO passivated surface.

The luminescence and CL efficiency of Sanroff, nano ZnS:Mn,cu/ZnO, and nano ZnS:Mn/ZnO were plotted as a function of electron beam accelerating voltage [97]. Low cathedoluminescence efficiency below about 2 kV of a commercial sample was attributed to nano-luminescent "dead layer" as the particle surfaces. At low voltages, electrons penetrate nonluminescent outer surface layers due to a low penetration depth of low energy electrons. However, as the energy of the electrons increases, they are able to penetrate more in micrometer-sized particles, making the particles give more luminescence from bulk layers. With nanoparticles, the situation has to be different, as with their much smaller size high energy electrons will be able to penetrate more particles. An increase in CL efficiency, even in nanoparticles, was therefore attributed to a extremely thin deep layer. Furthermore, it was found that the nanoparticles saturated less compared to large (bulk) particles, available commercially. At large currents (>20 μA) the CL efficiency of nanoparticles approached that of commercial phosphors. This aspect of nanoparticles in CL efficiency may turn out to be very useful.

Igarashi et al. [98] have also observed the reduction in CL degradation of ZnS:Ag, Cl microparticles due to ZnO-coated nanoparticles. The addition of CuSO$_4$ to the precursor solution of ZnS:Mn nanoparticles also resulted in CL efficiency of ~40% as that of commercial phosphors.

Core-Shell Particles of ZnS:Mn As discussed in the Section 2, surfaces of nanoparticles need to be passivated so that the particles do not grow into larger particles, changing their size-dependent properties. Surface passivation, however, may not be perfect [99, 100]. As shown using photoelectron spectroscopy [101–103] particles may even be oxidized to some extent or degrade with time. A variety of defects including surface defects can be present in nanoparticles and are discussed for ZnS:Mn [104] reducing their utility. It is therefore useful to protect the nanoparticles by growing the shells around them. Such particles termed as "core-shell" particles are expected to be of future interest in nanoparticles research.

ZnS:Mn nanoparticles were surface protected by growing an additional ZnS shell by Cao et al. [105]. They synthesized a ZnS:Mn core of 2.15 nm coated with a 0.75-nm thick ZnS. They found that the PL of core shell particles was seven times more than that of uncoated particles. Their calculations indicated that Mn^{2+} ions were preferably occupying the surface sites. They further suggested that the ZnS shell and UV treatment blocked the nonradiative transition path leading to luminescence enhancement.

Photoluminescence enhancement was also observed by Ethiraj et al. [106] for ZnS:Mn core shell particles. They, however, used silica shell to encapsulate the ZnS:Mn nanoparticles. They observed that with increasing reaction time of ZnS:Mn, thioglycerol capped nanoparticles (~1.7 nm size) got entrapped first into a silica matrix and then in spherical silica particles as showed in Figure 15. Particles as large as ~900 nm were formed in which ZnS:Mn particles were trapped as confirmed by a variety of techniques like Raman spectroscopy, PL, energy dispersive analysis of X-rays (EDAX), and photoelectron spectroscopy. Silica shells were found to be semi-transparent to UV and visible light.
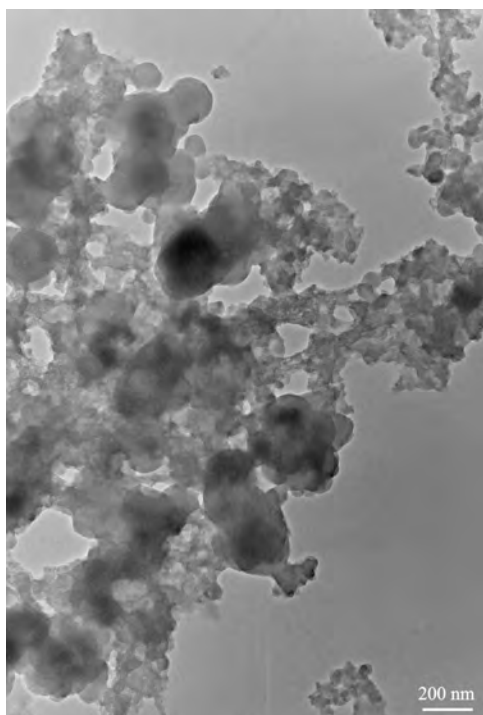
(a)
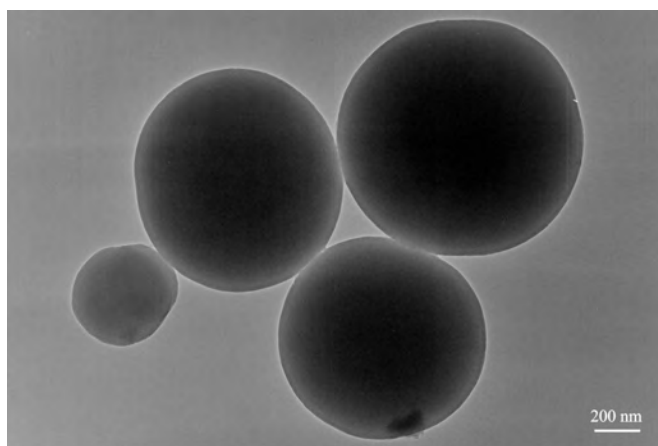
(b)

Figure 15. TEM of ZnS:Mn@SiO$_2$, 10 min reaction, entrapment of ZnS:Mn nanoparticles in silica matrix; (b) TEM of ZnS:Mn@SiO$_2$, 180 min reaction, large particles formation.

3.2.2. ZnS:Cu

Bulk ZnS:Cu phosphor has been widely investigated since 1866 when Sidot [107] observed phosphorescence from ZnS. Although the origin of green luminescence from ZnS was not understood in Sidot's time, by 1920 it was considered to be due to inclusion of a small amount of copper in ZnS lattice. ZnS:Cu along with different coactivators like Al, In, Ag, Cl, and I has been considered to be an important photo- and electroluminescent material for light emitting diodes and display screen coatings, for example, in a CRT tube. Earlier work on ZnS:Cu bulk phosphor has been well discussed in some review articles [108–110]. Copper-doped ZnS has emission bands in UV, blue, green, red, and IR regions.

Copper is substituted as Cu^{2+} ($3d^9$) in a tetrahedral site. In bulk ZnS, there can occur delocalized shallow or deep localized levels below the conduction band minimum. The Cu^{2+} level also splits due to a crystal field into $^2T_2$ and ^2E levels as shown in Figure 16.

Photoexcited electrons from a valence band can make various radiative transitions to Cu^{2+}-derived states producing green, red, or IR radiation. Blue and UV luminescence may be due to a transition from defect levels of a ZnS host to its valence band or some defects produced by interstitial incorporation of copper ions in a ZnS host matrix. In spite of their importance as phosphors copper-doped nanoparticles of ZnS have been reported only by a few groups [33, 34, 111, 112]. This may be due to difficulties in synthesizing Cu-doped nanoparticles due to low stability of Cu in ZnS [34]. However, by proper control of reacting chemicals, it is indeed possible to synthesize copper-doped nanoparticles.

Khosravi et al. [33] succeeded in doping $\sim$2.1 $\pm$ 0.02 nm ZnS nanoparticles with Cu ions. Absorption spectra and X-ray diffraction for undoped and doped samples are similar suggesting that a low concentration of dopants does not change the particle size of host ZnS. However, as shown in Figure 17 excitation and emission spectra for copper-doped ZnS nanoparticles sample is quite different. The emission at $\sim$420 nm (λ_{ex} – 326 nm) is usually present for undoped nanoparticles due to a presence of defect states, but ZnS:Cu nanoparticles showed the luminescence at $\sim$480 nm (λ_{ex} – 312 nm). The luminescence due to Cu ions in a ZnS nanoparticles host was close to that of a ZnS:Cu bulk discussed by Peka and Schulz [78]. However, instead of a transition of photo-excited electron from a conduction band to a copper-induced t_2 level in a bandgap of ZnS, transition from defect states present due to anion vacancies to t_2 level was considered. If this were not the case, size-dependent large change in the PL peak position should have been detected. For ZnS:Cu two decay times, viz. 2.9 ns and 54.2 ns, were observed at a 500 nm wavelength of emission excited with a 310 nm wavelength. However, in view of the recent understanding in the case of ZnS:Mn, it would be necessary to do further experiments about luminescence decay time in ZnS:Cu also.

Sun et al. [34, 113] and Wang et al. [114] found two different PL emission peaks from copper-doped nanoparticles.
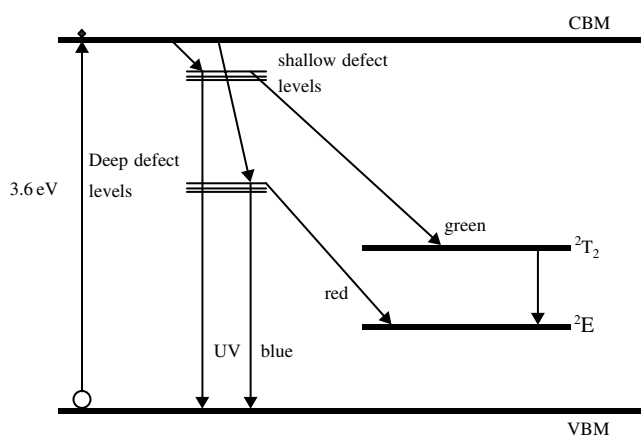
Figure 16. Energy level diagram for Cu-doped ZnS.
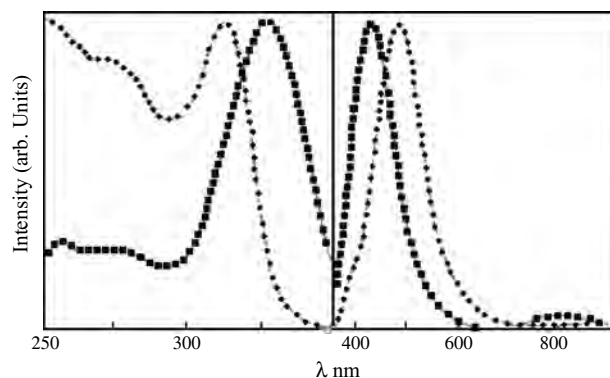
Figure 17. Excitation and emission spectra of undoped (squares) and copper-doped (circles) ZnS nanoparticles.

They studied particles of 3.4 and 3.8 nm stabilized, using thiourea and thiosulphate, respectively. With low concentration (0.2%) copper doping for both the passivants luminescence at ~450 nm (blue) and ~510–520 nm (green), emissions were detected. The blue emission got quenched with an increasing concentration of the Cu^+ dopant. For the same amount of dopant concentration, an emission intensity of thiosulfate stabilized particles was found to be larger than that for thiourea stabilized particles. A blue emission was attributed to Cu ions going into intrestitial sites of ZnS nanoparticles and green emission due to a substitution of Cu^{2+} into Zn^{2+} sites.

The ZnS:Cu particles of different sizes, viz. 1.8 nm and 3.0 nm synthesized by Zhang et al. [111] produced a PL at 466 nm. Their nanoparticles were stabilized with methacrylic acid and showed an increase in intensity with a decreasing particle size as in the case of Mn-doped ZnS [18, 57].

Huang et al. [112] and Que et al. [115] have been successful in observing even electroluminescence from ZnS doped with copper. The ZnS:Cu nanoparticles (3 nm) by Huang et al. [112] were embedded in a polymer network of sulphonated polystyrene.

They observed a PL peak at ~415 nm and slightly red-shifted electroluminescence peak at ~430 nm. However, these peaks are very close to ZnS defect emission bands. Nonetheless, they have used ZnS:Cu nanoparticles to fabricate a light-emitting diode (LED) described in Section 3.6. Slightly larger nanoparticles (9 nm) of ZnS:Cu have been synthesized by Que et al. [115] and broad PL and EL bands observed at ~520 nm. They too could employ these nanoparticles in fabricating a LED to be discussed later.

Temperature-dependent PL and luminescence decay time measurements in ZnS:Cu nanoparticles of various sizes has been carried out by Bol [116]. Unlike other measurements on ZnS:Cu nanoparticles, they found that there is a possibility of red (~600 nm) band also along with the green band (~470 nm) previously observed. They studied particles in the range of 3.1 nm to 7.4 nm. It was noticed that PL intensity was reduced with an increase in temperature from 4 K to room temperature. However, the luminescence reduced more for green band at a much lower temperature compared to red band. The origin of different PL bands was

discussed and decay time measurements also made. It was found that the lifetime for red emission at 4K was longer (40 μs) and that for green emission was shorter (20 μs) at the same temperature. It further decreased at room temperature (0.5 μs).

Co-doping of Mn and Cu in ZnS was carried out by Yang et al. [117]. In the presence of Mn, the PL observed in the wavelength range ~520–540 nm increased considerably.

3.2.3. ZnS:Fe and Ni

Borse et al. [27] have doped mercaptoethanol capped ZnS nanoparticles (2 ± 0.2 nm) with various concentrations of Fe and Ni. They observed a progressive decrease in defect luminescence intensity due to ZnS host lattice at ~425 nm as the concentration of Fe or Ni ions increased. However, no luminescence was detected due to ZnS:Fe or ZnS:Ni in the visible range. An extremely small amount of Mn^{2+}, undetected in atomic absorption measurements was detected by ESR in undoped ZnS. Fe-doped ZnS samples indicated clustering of Fe ions. However, more PL experiments over a wide range and valency determination in these systems is necessary.

Behboudnia and Sen [49] have also doped ZnS nanoparticles (less than 10 nm) with various concentrations of Fe and Ni using reverse micelle technique. They pointed out that compared to doping of Mn, substitution of Fe (or Ni) was difficult in ZnS lattice. This is because ZnS and MnS are isostructural with tetrahedral geometry, but sulfide of Fe and Ni crystallize in NiAs structure. In NiAs structure, each S atom is coordinated by six metal atoms and each metal atom has six S atoms and two metal atoms. This may affect the incorporation of dopant in ZnS lattice. They observed that the bandgap of nanoparticles was dependent on Fe or Ni concentration in the doped particles synthesized by them.

Green luminescence at 520 nm was detected by doping Ni in ZnS by Yang et al. [118]. They noticed the dependence of luminescence efficiency on the concentration of Ni^{2+} in doped ZnS nanoparticles.

3.2.4. ZnS:Pb

Lead ions have been doped in bulk ZnS as early as 1928 [119]. Emission of blue, green, yellow and orange bands is possible [120] from ZnS:Pb.

However, there is little work thus far on ZnS:Pb. Some work on ZnS:Pb nanoparticles has been reported by Bol and Meijerink [121] and Borse et al. [122]. Bol and Meijerink showed that there are white and red emission bands possible, depending upon the wavelength of excitation in the case of ZnS:Pb^{2+} nanoparticles. In their temperature-dependent PL investigations they observed that red emission quenches at lower temperature than that for white emission. A mechanism based on photoionization was suggested to explain the results. Temperature dependence of luminescence decay time was such that a longer decay time (ms) occurred at a lower temperature (4 K) compared to higher temperatures (room temperature) by several microseconds.

As shown in Figure 18, Borse et al. observed a concentration-dependent quenching of ZnS:Pb particles for the white band they observed [122].
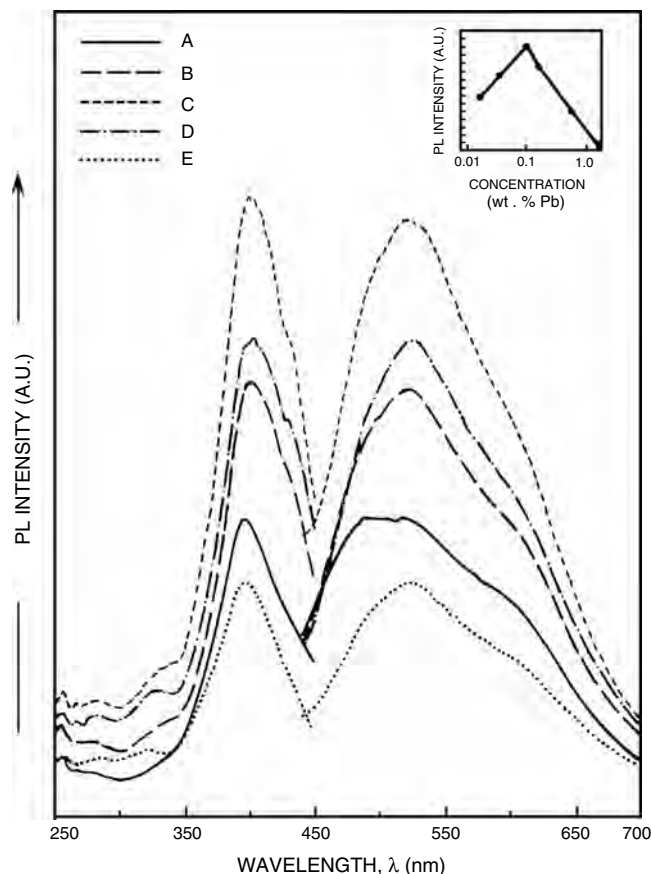
Figure 18. Concentration-dependent quenching of PL in ZnS:Pb nanoparticles. Concentration of Pb increases from sample A to E as shown in the inset [122]. Below 450 nm are excitation and above that are emission spectra.

3.2.5. ZnS:Eu,Tb

Luminescence due to rare earth ions in bulk solids has been reviewed [1]. In rare earth ions (usually trivalent), $4f$ electrons participate in the luminescence. These are hardly influenced by their ligands due to the presence of $5s$ and $5p$ outer electrons surrounding them. Therefore, crystal field effects, observable in $3d$ transition metal ions, are not feasible in the case of rare earth ions. Excited charge carriers from the host lattice are transferred very slowly to $4f$ states. The lifetime of luminescence decay is generally a few milliseconds and luminescence efficiency is very low. However, rare earth ion-doped solids can phosphor in the visible range and have attracted research efforts of various groups.

Doping of rare earth ions in ZnS nanoparticles has been discussed by Bhargava [83]. As shown in Figure 19, the ZnS host is able to produce red, green, and blue luminescence due to Tm^{3+}, Tb^{2+}, and Eu^{3+} doping, and would therefore be very useful for display screens, provided that they are efficient and do not saturate. He pointed out that in ZnS nanoparticles, with particle size less than about 5 nm (the size below which quantum confinement effects prevail for ZnS), rare earth ion doping can be useful in producing efficient phosphor materials with a gamut of colors. Slow trapping sites or nonradiative recombination sites can be removed in nanoparticles by appropriate surface passivation. Moreover,
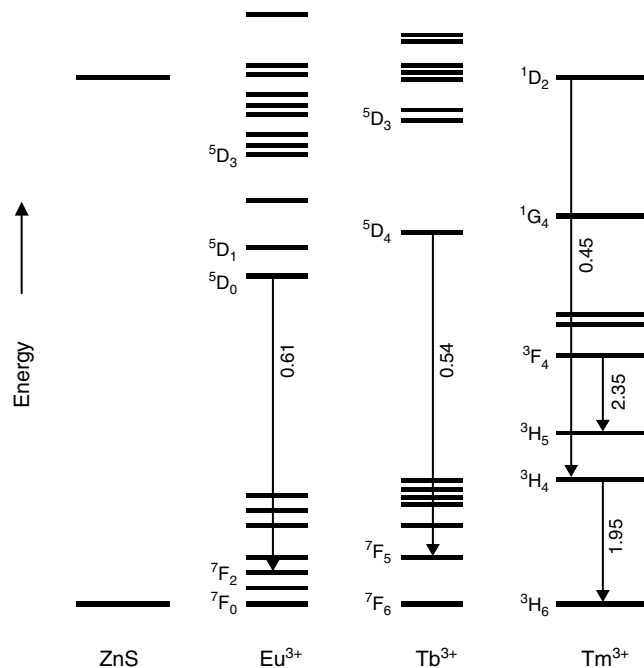
Figure 19. Energy level diagram of rare earth activators in relation to ZnS.

the electronic structure in nanoparticles is believed to be very different from that of bulk materials. Usually d–d or d–f transitions in the rare earth ions are spin or parity forbidden, either completely or partially. Partially forbidden transitions with decay time of a few milliseconds are responsible for low efficiency and saturation in rare earth doped solids. However, the forbidden transitions are relaxed in nanoparticles due to the hybridization of host ZnS s–p states with d–f states of rare earth ions. Very fast (a few nanoseconds) transitions with increased efficiency for luminescence were detected in ZnS doped with rare earth ions [83].

Europium can be doped either as Eu^{2+} or Eu^{3+} in solids. Doping of Eu^{2+} in different solids like $BaMgAl_{10}O_{17}$ or SrS_4O_7 has been widely investigated in bulk solids as luminescence has been found to be host dependent extending from UV to a red region in the electromagnetic spectrum. Therefore, these materials have applications in plasma display panels, UV light for medical application, etc.

Eu^{2+}-doped ZnS nanoparticles of ~3nm size were investigated by Chen et al. [123]. They observed a luminescence band at ~530 nm, which could be transformed into that due to Eu^{3+} by heating in air. The excitation wavelength was by a 260-nm wavelength, but the emission band position or shape was unaffected by the change of excitation wavelengths to 340 or 390 nm. However, intensity of a 530-nm peak was maximum for a 260-nm excitation. The energy gap for 3 nm-size ZnS nanoparticles was estimated to be ~4.5 eV. Thus, excitation of valence electrons was possible in ZnS nanoparticles of a 3-nm size only with a 260-nm wavelength. The emission arising from a 340 or 390 nm wavelength excitation was due to intraion transition. Direct transition in Eu^{2+} nanoparticles was possible because with an increasing energy gap due to quantum effects in nanoparticles of ZnS smaller

than 3–5 nm the first excited state of Eu^{2+} lies below the conduction band. Thus, both direct and indirect transitions from a $4f^6 5d^1$ to $4f^7$ level of Eu^{2+} are possible in particles smaller than the 3–5 nm size. However, indirect transition in which a ZnS host is excited appears to be a more efficient process. Size dependence of luminescence was observed by Chen et al. [124]. It is quite clear that emission band blue shifts with a reduction in the ZnS particle size is a truly quantum confinement effect. However, this could not be attributed to the concentration effects, that is, Eu^{2+}—Eu^{2+} interaction nor hybridization of *sp* states of ZnS and *d–f* states of Eu. If the mixing would have occurred, then the luminescence peak would have red shifted with decreasing particle size rather than blue shifted, as was observed. The size-dependent blue shift of luminescence was explained in terms of the decrease in electron phonon coupling and reduced crystal field strength.

Structurally and optically stable nanoparticles of ZnS: Eu^{2+} with a mean size of about 3–5 nm were prepared by the chemical precipitation method by adding α-methacrylic acid as the stablizier by Qu et al. [125]. The authors compared four samples with no doping, 1%, 2%, and 5% in a molar ratio of Eu^{3+}. They carried out XRD, TEM, and PL investigations. Transmission electron microscopy images indicated that particles were spherical with a $\sim$4–5 nm diameter, whereas the mean diameter estimated from XRD was $\sim$3 nm. It was found that the peak of higher energy, shifted to higher energy with an increase of the doping level without much change in the intensity. However, the intensity of the low energy peak changed substantially. It was suggested that the blue shift of a higher energy peak was a consequence of lattice distortion due to Eu^{3+} going into Zn^{2+} sites and subsequent change in the bandgap emission of ZnS. A sharp peak due to hybridization of electronic states was also observed.

ZnS nanoparticles ($\sim$4 nm) were also doped with Eu^{3+} ions and embedded in a polymer matrix [126]. It was argued that the introduction of Eu^{3+} greatly enhanced the ZnS-related PL at $\sim$420 nm by exciting with a 315-nm wavelength. By exciting with 395-nm peaks at 586 nm and 617 nm, due to $^5D_0-^7F_1$ and $^5D_0-^7F_2$ transitions, respectively, for free Eu^{3+} were observed.

Bhargava et al. [82] investigated the optical properties of Tb^{3+}-doped ZnS nanoparticles synthesized by the precipitation in polymer film of polyethylene oxide. The ZnS particle size was $\sim$6 nm. The luminescence excitation peak was symmetric around 304 nm, whereas emission was in the visible range with four distinct narrow peaks at $\sim$480, 543, 580, and 610 nm—peak at 543 nm being the strongest in intensity. Similar results were obtained by Kane et al. [55], who synthesized doped ZnS nanoparticles with Tb in microphase separated films of diblock copolymers containing carboxylic acid units on one of the blocks. Emission peaks were the result of $^5D_4-^7F_n$ transitions. The effect of UV irradiation was to increase the luminescence intensity. Lifetime measurements showed that it was shortened to 7 ns in nanoparticles as compared to 3 ms in bulk materials. The quantum efficiency of Tb-doped ZnS nanocrystals was found to be much larger than green phosphor LaOBr doped with Tb.

3.3. ZnSe:Mn

Suyver et al. [127] synthesized and investigated $ZnSe:Mn^{2+}$ nanoparticles $\sim$3–4 nm in size. They observed two peaks in PL emission. The peak located at $\sim$430 nm was weak in Mn^{2+}-doped ZnSe and ascribed to subband luminescence due to a ZnSe lattice. The peak at 560 nm was due to a $^4T_1 \rightarrow ^6A_1$ transition in the Mn^{2+} excited by the host lattice. However, there was no peak in the 600- to 640-nm range as observed in the bulk $ZnSe:Mn^{2+}$, indicating that the concentration of self-activated pairs was low in ZnSe nanoparticles. With an increase in Mn^{2+} concentration in ZnSe nanoparticles, the Mn^{2+} related emission red shifted. This could be due to the formation of Mn^{2+} ion pairs. Lifetime measurements supported this observation. In all the samples of ZnSe with different concentrations of doping, a radiative lifetime close to 200 μs was observed. The temperature-dependent lifetime was investigated which showed that the lifetime decreased with an increase in temperature. The photoluminescence peak at 430 nm in $ZnSe:Mn^{2+}$ nanoparticles was found to be red shifted, whereas, due to Mn^{2+} emission at $\sim$560 nm, they were blue shifted.

Norris et al. [23] and Shim et al. [128] also synthesized the $ZnSe:Mn^{2+}$ nanoparticles ($\sim$2.7 to 6.3 nm). However, in order to determine the location of Mn^{2+} in nanoparticles, that is, whether on the surface or inside the nanoparticles, in addition to absorption and PL measurements, they also carried out magnetic circular dichroism (MCD) and ESR studies of $ZnSe:Mn^{2+}$ samples. They found the luminescence at $\sim$585 nm rather than $\sim$500 nm due to Mn^{2+} in ZnSe as in [127]. Electron spin resonance spectra showed six line spectra characteristics of Mn embedded inside the nanoparticle. A hyperfine splitting of $60.4 * 10^{-4}$ cm^{-1} was consistent with Mn-doped bulk ZnSe [129]. The signal from lower symmetry was much smaller. They have extensively discussed the problems related to Mn doping in high temperature synthesis of nanoparticles to obtain highly crystalline, defect-free nanoparticles of uniform size distribution and showed that indeed, it is possible to dope Mn^{2+} inside the interior of ZnSe nanoparticles. Further evidence for Mn^{2+} being inside the nanoparticle, and not on the surface, could be obtained from Zeeman splitting. A very large Zeeman splitting can be obtained in case of a overlap of electron-hole wavefunction and Mn *d* levels. If Mn^{2+} is on the surface, the splitting is lower. Thus, Zeeman splitting can be used to decide the location of Mn^2. Magnetic circular dichroism measurements on 5.3 nm ZnSe:Mn at 1.5 K were carried out. An effective g factor of 475 was obtained. The internal magnetic field of $>$400 T is expected. Induced splitting is larger than thermal energy at room temperature.

3.4. Doped CdS Nanoparticles

3.4.1. CdS:Mn

CdS is structurally very similar to ZnS and belongs to the same II–VI group of semiconductors. Bulk CdS has a large and direct bandgap of 2.42 and 2.56 eV at 300 and 0 K, respectively [5]. For nanoparticles of CdS, the energy gap widens [12].

Mn-doped CdS nanoparticles have been investigated, although to a lesser extent than ZnS. Structure, PL, ESR,

and the effect of concentration of Mn dopant on CdS nano-particles has been investigated by a few groups.

Structure CdS bulk solid similar to bulk ZnS solid can occur either in the zinc blend or in the hexagonal structures. The same is true for pure CdS nanoparticles [130, 131].

There are some reports on chemically synthesized CdS:Mn nanoparticles, which indicated that they were of a zinc blende structure [65, 132, 133]. Levy et al. [132] have also reported from TEM measurements that CdS:Mn nano-particles synthesized by them had a zinc blende structure. Morita et al. [60, 61] also reported the cubic structure for CdS:Mn nanoparticles embedded in ZrO_2 films.

Ordered layers of $Cd_{1-x}Mn_xS$ nanoparticles [65] were obtained by a Langmuir–Blodgett (LB) technique. The par-ticles of ∼3 to 4 nm in diameter were obtained. These par-ticles had also a cubic structure as determined by XRD.

Kanemitsu et al. [59] have observed the formation of a CdS:Mn hexagonal structure in their ∼17 nm nanoparticles obtained by ion implantation.

It is an important issue in the doped nanoparticles to know the site of the dopant. The dopants can enter a sub-stitutional or interstitial site in the bulk of the nanoparticle or reside in the surface region. It is interesting to know if the substitution is random or nonrandom. Extended X-ray Absorption Fine Structure being an atom-specific technique, capable of yielding bond length information, number of first, second, etc. coordinating shell atoms, was used by Levy et al. [134] to determine the structural properties of $Cd_{1-y}Mn_yS$ nanoparticles. They could show that $Cd_{1-y}Mn_yS$ formed a solid solution.

PL and Decay Time In general, there can be a large number of defect states or surface states present in nano-particles. Photoluminescence spectra exhibit a contribution from defect states as well as from dopants. A schematic dia-gram (Fig. 7) used to discuss PL in ZnS:Mn is also valid for CdS doped with Mn^{2+}. Thus, in some cases of CdS doped with Mn, defect or surface state related emission has been reported to occur and in some cases PL related only to Mn has been considered.

Photoluminescence and other optical properties of CdS:Mn have been investigated by many [31, 41, 48, 62]. Levy et al. [41] observed for 4-nm size $Cd_{0.95}Mn_{0.05}S$ parti-cles the PL peak at 580 nm. With an increase in tempera-ture from 77 K to 250 K, the PL intensity quenching occurs. Chamarro et al. [48] observed for $Cd_{0.99}Mn_{0.01}S$ particles a PL peak at 2.13 eV, that is, ∼582 nm. Liu et al. [31] also observed PL when excited with 420-nm wavelength due to Mn^{2+} at 585 nm. They agree that initially, the host CdS is excited and the energy is transferred to a $^4T_1$ level of Mn^{2+}. Transition takes place between $^4T_1$ and $^6A_1$ to give yellow emission. Levy et al. [43] noted that energy transfer from the conduction band to isolated Mn^{2+} states ($^4T_1$–$^6A_1$, 585 nm), as well as to defect states (trap state emission, 700 nm) with the excitation of a host with higher energy, is possible in order to reach higher states of Mn^{2+} and then transfer energy to $^4T_1$, with a subsequent radiative transition characteristic of $^4T_1$–$^6A_1$ at 585 nm.

Counio et al. [135] also investigated $Cd_{1-x}Mn_xS$ ($x < 5\%$) nanoparticles for luminescence and its lifetime. They were able to isolate contributions from particles containing zero,

one, or more Mn^{2+} ions. The distribution of dopants was found to be random.

Ordered $Cd_{1-x}Mn_xS$ nanoparticles [65], deposited by LB technique, showed PL at ∼570 nm when suspended in tou-lene. However, the PL spectra of the nanoparticles, mea-sured directly in reacted C22 thioalkanoate, exhibited an additional peak at ∼700 nm. While the peak at 570 nm was due to the $^4T_1$–$^6A_1$ transition within the Mn^{2+} levels, the one at 700 nm was attributed to the PL of CdS nanoparticles. Photoluminescence measurements were carried out at 4.2 K.

Photoluminescence of CdS:Mn nanoparticles synthesized by sequential deposition [59] exhibited green and yellow PL bands at ∼500 nm, respectively, when excited with a 457.9-nm wavelength of an Ar laser. A green wavelength at ∼500 nm was obtained as in-phase and the one at ∼570 nm as out of phase wavelength by phase shifter and lock-in amplifier. The decay dynamics of these two luminescence bands suggested that the PL band around 500 nm was due to free excitons and shallow impurity levels in CdS. The band at ∼570 nm was due to d–d interactions of Mn^{2+} ions in agreement with an earlier discussion. The authors note, however, that Mn^{2+}-related PL at 570 nm had a long life-time of ∼1.1 ms.

Time-resolved PL spectra of undoped CdS nanoparticles and Mn-doped CdS nanoparticles were compared by Chamarro et al. [48]. The particle size in both the cases was ∼3 nm. Luminescence was excited at 2.95 eV (λ-420 nm) and the spectra recorded after 500 ns for undoped CdS par-ticles (curve a) and after 500 ns (curve b), as well as 40 μs (curve c) in case of CdS:Mn particles. The undoped CdS spectrum recorded after 500 ns had features similar to the continuous spectrum, but only reduced in intensity and red shifted. The PL band was due to the recombination on deep defects and surface traps. The spectrum of CdS:Mn after 500 ns at 1.9 eV (λ-652 nm) was essentially similar to that of undoped CdS nanoparticles. However, after 40 μs, this band disappeared, and only a relatively narrow band at ∼2.2 eV (λ-564 nm) due to Mn^{2+} survived. It was, therefore, inferred that emission due to Mn^{2+} in nanoparticles did not differ from the bulk.

Time-resolved PL, excitation, and decay profiles were studied by Morita et al. [60] over a temperature regime 10 K to 300 K, in case of CdS:Mn embedded in zirconia thin films. The broad emission band was found to be composed of four components viz, due to the band-edge emission of host CdS nanoparticles, ligand-to-metal-charge transfer (LMCT) center (ZrO_2), and deep centers due to surface and intra-Mn^{2+} ion transitions. The luminescence lifetime reduced at 10 K and was a fraction of a nanosecond at room tem-perature. Luminescence also depended upon the annealing temperature, and fast decay (0.5 ns to 1.8 ns) was observed as compared to bulk.

Artemyev et al. [62] investigated CdS:Mn nanoparticles of 3.6-nm size synthesized by a chemical precipitation route and then obtained the thin films using a sol–gel technique. The particle size was determined using an excitation peak position in the optical absorption spectrum and inserting the corresponding energy gap value in the tight-band calcu-lation. They observed a broad emission band at ∼640 nm (the excitation wavelength was 415 nm). This emission band appears to be considerably red shifted as compared to that

reported by some others [43, 48, 60]. Artemyev et al. also investigated at various wavelengths viz near 540, 560, 580, 600, 620, and 640 nm in a PL emission spectra, the time-resolved behavior. The fast decay component was attributed to a recombination at surface traps and a slow component to the transition between states due to Mn^{2+} ions in the bandgap of CdS. They observed that the slow component has a 2.3-millisecond time constant for all the wavelengths. This value is close to that reported by Chamarro et al. [48]. It was concluded that there is no order of magnitude reduction in the luminescence decay time in nanoparticles as compared to bulk.

Magnetic Measurements Electron spin resonance or EPR spectra were recorded by Levy et al. [131] for various compositions of $Cd_{1-y}Mn_yS$ (3.2-nm nanoparticles) for $y < 0.03$ to $y = 1$. The hyperfine structure could be seen in the spectrum. However, with increasing Mn concentration of Mn, a broadening of the EPR spectrum takes place along with the disappearance of the hyperfine structure. For pure MnS, the EPR linewidth is as large as 624 Gauss, and for $Cd_{0.97}Mn_{0.03}S$ as 300 Gauss. The line width of the EPR signal varied with y^2, indicating that Mn ions were randomly distributed inside the nanoparticles. A correlation was observed between the Mn—Mn ion distance and the EPR signal line width by these authors. Levy et al. [136] also observed isolated Mn ions in tetrahedral sites in CdS nanoparticles at rather large concentrations. This was due to the presence of an aging layer. They also noted that magnetic interactions increased in nanoparticles compared to those in the bulk phase. They observed the variations of luminescence and a hyperfine structure of isolated Mn ions with a number of atoms in the aged layer.

Levy et al. [41] have also investigated energy-gap variation of CdS:Mn nanoparticles with concentration of Mn Figure 20. Energy bandgap also depends upon temperature and magnetic susceptibility through

$$E_g(y, T) = E_g(CdS) - AT^2/(T + B) + \Delta Ey - b\chi(y)T \tag{5}$$
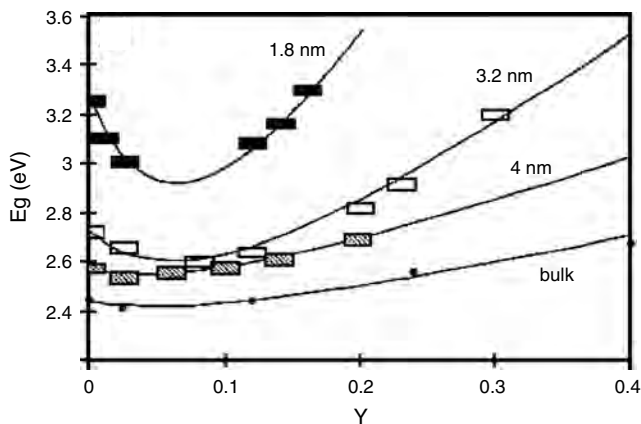
Figure 20. Variation of bandgap energy with composition for various particle sizes in the bulk phase and thin films of CdS:Mn. The line is obtained from the best fit between experimental data and Eq. (2) in [41]. Reprinted with permission from [41], L. Levy, N. Feltin, D. Ingert, and P. Pileni, *J. Phys. Chem. B* 101, 9153 (1997). © 1997, American Chemical Society.

where $\chi(y)$ is the magnetic susceptibility, T is temperature, and y is the concentration of magnetic ion. A, B are constants, dependent on material. The parameter b accounts for exchange interaction.

Feltin et al. [44] have also measured the susceptibility of Mn-doped CdS nanoparticles using super conducting quantum interference device (SQUID). They showed that similar to bulk phase above 60 K, susceptibility followed the Curie–Weiss law in case of $Cd_{1-y}Mn_yS$

$$X(y, T) = C_o y/T + \Theta_o y \tag{6}$$

In Table 4, C_o, Θ and b values along with ΔHpp for two different sizes of particles along with that for the bulk, are given. The factor b, which is an indication of increased Mn^{2+}—Mn^{2+} interaction and Θ_o, the Curie temperature has increased with decreased particle size. It was also shown that magnetic susceptibility increased with Mn^{2+} ion concentration, but unlike in $Zn_{1-y}Mn_yS$ [17], decreased with decreasing particle size. The comparison of magnetization in 4-nm $Cd_{1-y}Mn_yS$ nanoparticles and a corresponding bulk phase see Table 3 in the original reference led to the conclusion that S_{eff}, that is, effective spin values in nanoparticles, were smaller than in the corresponding bulk. For Mn^{2+}, maximum spin value can be 5/2. Antiferromagnetic coupling tends to reduce S_{eff} due to the formation of spin pairs. This suggests that in $Cd_{1-y}Mn_yS$ nanoparticles, Mn^{2+}—Mn^{2+} interactions become stronger as compared to the bulk materials of the same composition. Also, for a given particle size, the interaction increases with increasing dopant concentration. Interaction also becomes strong, the lower the temperature. Electron paramagnetic resonance spectra of $Cd_{1-y}Mn_yS$ consisted of two parts viz, a hyperfine structure consisting of six lines characteristic of tetrahedrally bonded isolated Mn^{2+} ions with a hyperfine splitting of 69 G. With an increasing Mn^{2+} concentration, the intensity of peaks decreased and structure disappeared at $y = 0.2$. The observed broad peak was due to Mn^{2+}—Mn^{2+} interactions and peak-to-peak line width ΔHpp increased with decreasing particle size. They further recorded magnetization curves at various compositions ($0.006 < y < 0.2$) for different sizes of nanoparticles (1.8 to 4 nm). No saturation in the magnetization was observed either at 3 K or 10 K. They also found that S_{eff}, that is, the mean spin of Mn^{2+} ions, was always smaller than 5/2 and decreased in nanocrystals compared to bulk. This implies that antiferromagnetically correlated spins are larger in nanoparticles, and for

Table 4. C_o[K] and θ_0 values derived from χ^{-1} extrapolation; variation of the parameter b derived from simulation of bandgap evolution by Eq. (3) in the original [44]. Experimental line widths ΔHpp are of $Cd_{0.9}Mn_{0.1}S$ nanoparticles.

	C_o [K]	θ_0 [emu.g.K^{-1}]	b [eV.g.Oe.emu^{-1}K^{-1}]	ΔHpp [Gauss]
1.8 nm	0.015	700	1250	400
4 nm	0.03	409	150	182
Bulk	0.03	280	120	

Source: Adapted with permission from [44], N. Feltin et al., *Adv. Mater.* 11, 398 (1999). © 1999, Wiley-VCH.

fixed Mn concentration, decreased with decreasing particle sizes. The S_{eff} also decreases with decreasing temperature due to near neighbor interactions.

Hoffman et al. [50] have investigated two samples of CdS nanoparticles (average size 2.5 nm) doped with Mn (~1%). Their sample A was having 4-fluorothiophenol and sample B had triethylphosphate as capping molecules. The distribution of Mn ions in both the samples differed as was evident from the differences in the EPR spectra for sample A and sample B. However, both had six line hyperfine peaks characteristics of isolated manganese ions in tetrahedral sites. Intense peaks, due to forbidden transitions as well as an underlying structureless resonance line, were also observed for both sample A and sample B. They carried out electron double resonance (ENDOR) measurements on different parts of the EPR spectra. Their analysis showed that the sharp six line pattern could be attributed to manganese ions located mostly in the center of the nanoparticles, and those residing in the surface region contributed to the broad ESR lines.

Effect of Mn Concentration Levy et al. [41–43, 132, 134, 136] have published a series of article on CdS nanoparticles doped with Mn. Using Mn-doped CdS nanoparticles obtained by inverse micelle route of nanoparticles synthesis, they investigated the effect of doping on the properties of nanoparticles. They varied the particle size in one set and the concentration in the other, keeping particle size constant. The average composition was determined using energy dispersive spectroscopy (EDS). Structure and size of the particles was determined using TEM. In the host lattice, Cd and S were tetrahedrally bonded producing zinc blende structure, and Mn^{2+} ions were in cationic substitutional sites. The chemical formula could, in general, be written as $Cd_{1-y}Mn_yS$. Nanoparticles were observed to be quite stable in solutions for several weeks and as powders for several months as far as size, polydispersity, or composition was concerned.

Energy gap determined [41], using optical absorption spectra and an effective mass absorption equation [12], showed an increase with a decreasing particle size, a picture consistent with a quantum confinement effect in nanoparticles. As shown in Figure 20, a minimum occurred around 5% Mn doping, even in the case of bulk CdS, but it became progressively pronounced with decreasing particle size. It was clear from the same figure that bandgap does not vary monotonically with particle size. In the same figure, variation of Mn^{2+} concentration (y) was also varied for 1.8 nm, 3.2 nm, and 4.0 nm size along with bulk CdS. In bulk, the variation in bandgap due to change in concentration was interpreted as due to statistical fluctuations in crystal potential in an alloy as a consequence of chemical disorder. However, it is clear from what was shown later by the same group [44], that there is no correlation between experimental observation for 3.2 nm sized particles and simulated curves for different compositions of Mn and energy gap. Therefore, it was concluded that a minimum in the bandgap cannot be due to chemical disorder. However, it is likely that there is a strong interaction between d electrons of Mn^{2+} and sp electrons of CdS. In fact, this type of interaction is expected to be increasingly stronger with reduction

in particle size. However, they remark that the Mn^{2+}—Mn^{2+} interactions that take place with decreasing particle size are not easy to explain and theoretical models in this respect are needed in the future.

3.4.2. CdS:Zn

Kulkarni et al. [29] investigated nanoparticles of CdS, $Cd_{0.75}Zn_{0.25}S$, $Cd_{0.50}Zn_{0.50}S$, $Cd_{0.25}Zn_{0.75}S$, and ZnS. As shown in Figure 21 they find a systematic blue shift of the PL band from ~700 nm to 400 nm as composition varied from CdS to ZnS. A similar trend was also noted for optical absorption. Detailed investigations were also made of the nanoparticle surfaces by high-resolution, photoelectron spectroscopy using variable photon energy from a synchrotron source.

Temperature dependence of Mn-doped $Cd_xZn_{1-x}S$ ($x = 0, 0.8,$ and 0.7) nanoparticles has also been investigated by Bol et al. [137]. Excitation and emission spectra measured at 4 K showed a systematic variation as one goes from CdS:Mn to $Cd_{0.7}Zn_{0.3}S$:Mn. Emission around 700 nm was related to defects in CdS nanoparticles and around 600 nm to Mn^{2+} intralevels. Interestingly, temperature dependence of a PL band at ~600 nm for CdS:Mn^{2+}, $Cd_{0.8}Zn_{0.2}S$:Mn^{2+}, and $Cd_{0.7}Zn_{0.3}S$:Mn^{2+} followed a similar trend. Thus, increase in the bandgap due to substitution of Cd ions by Zn ions in CdS host lattice did not have any influence on the Mn^{2+}-related emission. This could be well explained by assuming that after excitation of CdS or $Cd_{1-x}Zn_xS$ host lattice the charge carriers are transferred to defect states where they are transferred to the $^4T_1$ level of Mn^{2+}. The radiative transfer from $^4T_1$ to $^6A_1$ of Mn^{2+} is therefore rarely influenced by the host lattice. Decay time measurements supported this mechanism.

3.4.3. CdS:Co

$Cd_{0.991}Co_{0.009}S$ nanoparticles between 3.5–29.5 nm were investigated using nuclear magnetic resonance (NMR) by Ladizhansky and Vega [138]. They observed substantial differences with particle size in ^{113}Cd MAS NMR spectra as shown in Figure 22.
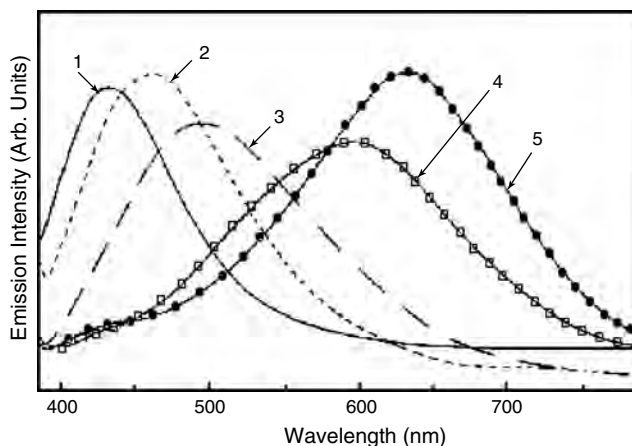
Figure 21. Photoluminescence spectra of (1) ZnS, (2) $Cd_{0.25}Zn_{0.75}S$, (3) $Cd_{0.50}Zn_{0.50}S$, (4) $Cd_{0.75}Zn_{0.25}S$, and CdS nanoparticles. Excitation wavelength of 300 nm was used.
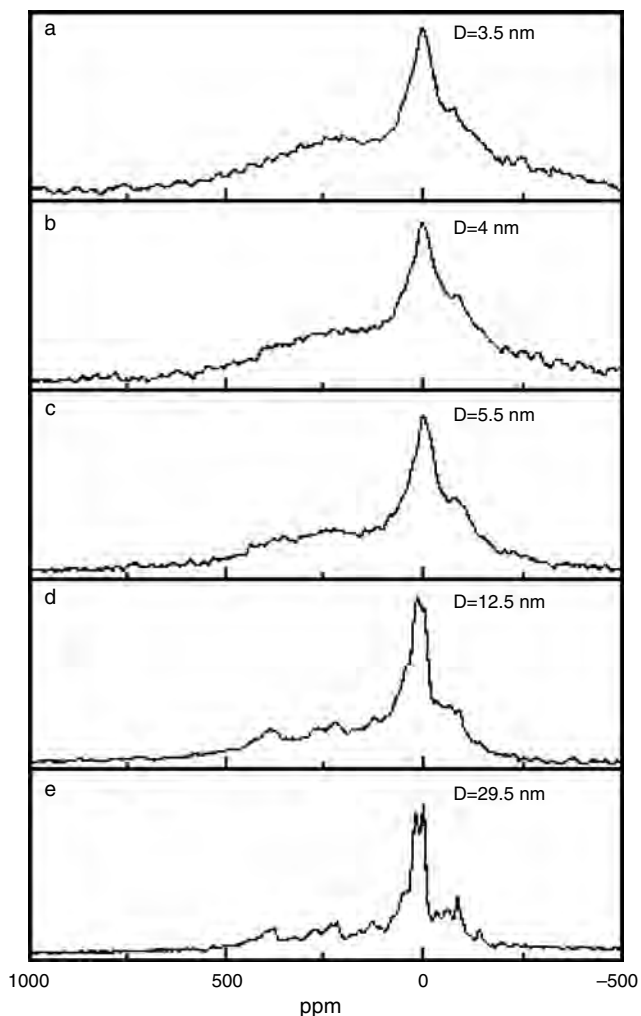
Figure 22. ^{113}Cd MAS NMR spectra of $Cd_{0.991}Mn_{0.009}S$ nanoparticles with average diameter D, as indicated in the figure. The spinning speed was 2.46 kHz. The repetition time was 300 ms in these experiments and much shorter than the T_1 of the main peak. Reprinted with permission from [138], V. Ladizhansky and S. Vega, *J. Phys. Chem. B* 104, 5237 (2000). © 2000, American Chemical Society.

3.5. Doped CdSe Nanoparticles

3.5.1. CdSe:Mn

Doping of CdSe nanoparticles by Mn ions has been reported by Yanata et al. [139]. They observed an interesting effect viz. a monotonous increase in the energy shift of the fluorescence with increasing magnetic field strength. This effect could be explained by considering the interactions of exciton with Mn^{2+}.

Mikulec et al. [140] also doped CdSe nanoparticles synthesized using a high-temperature chemical route. They performed optical as well as magnetic measurements. It was shown that dopant atoms resided in surface layers and dramatically affected the NMR spectra as shown in Figure 23. They also detected a new state in optical absorption at a very low temperature (<3 K), establishing the presence of an optically dark exciton predicted by Efros et al. [141] in a CdSe quantum dot.
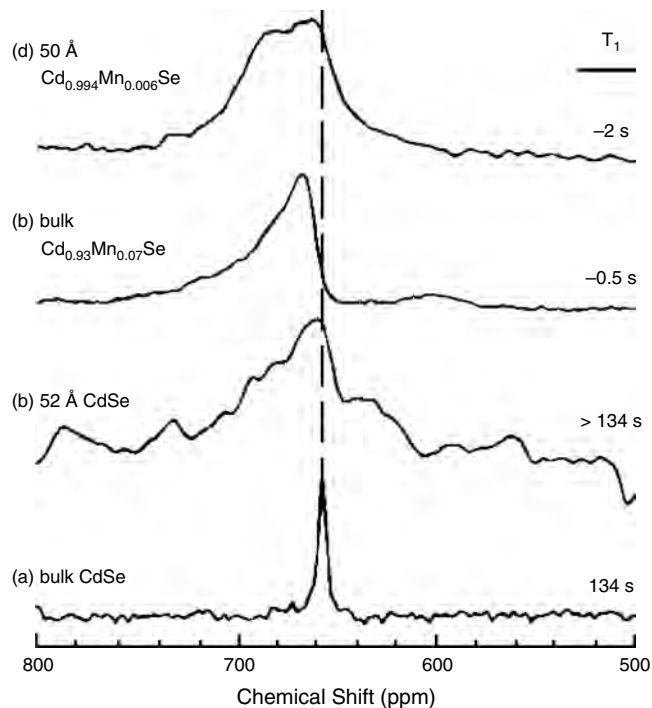
Figure 23. Solid state NMR spectra of (a) bulk CdSe, (b) 5.2 nm CdSe, (c) bulk $Cd_{0.93}Mn_{0.07}Se$, and (d) $Cd_{0.93}Mn_{0.07}Se$ nanoparticles. Smaller chemical shift values correspond to higher field strengths. Reprinted with permission from [140], F. V. Mikulec et al., *J. Am. Chem. Soc.* 122, 2532 (2000). © 2000, American Chemical Society.

3.5.2. CdSe:Co

In their investigations on doped CdSe with Co ions, Hanif et al. [142] performed SQUID, Raman, PL, and X-ray diffraction measurements. They varied the concentration of cobalt ions (x) from 0 to 0.30 in $Cd_{1-x}Co_xSe$. They noted that with an increasing concentration of Co^{2+}, which displaced Cd^{2+} ions, a lattice of CdSe contracted linearly.

4. DEVICES BASED ON DOPED NANOPARTICLES

There have been some attempts to fabricate light-emitting device using ZnS:Cu nanoparticles. Que et al. [115] fabricated ZnS:Cu nanoparticles/polymer composite, single-layer electroluminescent devices. They synthesized ZnS:Cu nanoparticles in an inverse microemulsion by a hydrothermal route. They used polymethyl methacrylate (PMMA) polymer for embedding the ZnS:Cu nanoparticles. Both PL and electroluminescence (EL) emission bands were observed in the 490–530-nm range at R.T. with a large half-width of ~60 nm. The peak shapes however, were different for PL and EL. They also found a low onset voltage for the ZnS:Cu/polymer composite device fabricated by them with nearly symmetric I–V characteristic indicating that direction of an applied bias was not important for the electrical properties of the device made by them.

Huang et al. [112] synthesized ZnS:Cu particles with an average size about 3 nm. The size was estimated from tight

binding calculations. The EL device was fabricated on the indium tin oxide (ITO)-coated glass substrate. Indium tin oxide served as an anode on which ZnS:Cu nanoparticles embedded in polymer were spin-coated to a thickness of about 50 nm. A 300-nm thick aluminium cathode was vacuum deposited on this layer. Electroluminescence was observed at 4 V bias with the EL peak at 430 nm (blue), the intensity reaching to 15 cd/m^2, corresponding to a current density of ∼100 mA/cm^2, at 8 V. The EL peak was shifted from PL peak, which appeared at 415 nm (blue). This could be due to a diffusion of Al in a polymer layer, which can then act as a donor defect. Luminescence can then be due to a radiative recombination of electrons and holes from both Al and Cu or the local heating of an emitting layer resulting in a poor thermal conductivity.

An organic/inorganic multilayer structure in which ZnS:Mn nanoparticles of ∼3 to 4 nm were used, has been reported by Yang et al. [143]. They showed that blue light emitting poly (N-vinylcarbazole), (PVK) and yellow light emitting ZnS:Mn both contributed to the electroluminescent emission spectrum. However, their contributions depended on the applied voltage with increasing PVK emission with increasing applied voltage. It was shown that variation of Mn concentration from 0.40 to 2.14 mol % did not have any effect on the PL peak position or shape.

5. CONCLUSIONS

Doped semiconductor nanoparticles form an interesting class of nanomaterials. Although a large amount of published work is now available on Mn-doped ZnS nanoparticles on various optical and magnetic aspects, research on other systems like CdS:Mn, rare earth doped nanoparticles, etc. is still in frequent. There still appears to be no definite understanding of quantum efficiency for photo- and electro-luminescence in doped nanoparticles. More research in the future on size effect and concentration effect while keeping nanoparticle size constant is necessary. Diluted magnetic semiconductor nanoparticles would be an interesting area of future research due to some observations of giant magnetic fields and increased magnetic interactions [44, 144] in the doped nanoparticles.

GLOSSARY

Agglomeration   Clustering of particles.

Alkoxide   Compounds containing RO group, R = a group with general formula $C_nH_{2n_2}$ with one H-atom removed, e.g. CH_3ONa.

Amphiphilic   Substance which has affinity for both water and oil.

Annealing   A heating process in which a substance is heated at a particular temperature for some time.

Bond-length   The distance at which atoms or molecules are held.

Cathedoluminescence   Light emitted by a substance when hit by electrons. (Also see luminescence.)

Cationic solution   A liquid that will provide positively charged ions to form a compound.

Centrifugation   Sedimentation of particles by high speed rotation of a container with liquid having dispersed particles.

Chemical capping   A chemical synthesis process in which some solid particles are surface passivated so that they do not coalesce into each other.

Colloids   Heterogeneous mixtures of two or more phases in which one is a dispersion medium e.g. solid particles (one phase) and other is liquid (dispersed phase).

Co-ordinate number   A group of atoms, ions or molecules, surrounding a given atom, ion or molecule.

Crystal field   Splitting of inner orbitals, specially of 'd' orbitals of an atom or ion occurs if it is surrounded by some ions or molecules. Field set up by surrounding ions or molecules responsible for this splitting is known as crystal field.

Dark exciton   A non-radiative exciton (electron-hole pair forming an exciton can normally combine giving out radiation).

Decay time   The time taken from initial intensity to an intensity of l/e after initial excitation.

Deconvolution   Splitting into components.

Deep defects   Defect states lying well below (closer to valence band) conduction band.

Direct band gap   A direct band gap is said to exist when transitions of all valence electrons to conduction band (or conduction band to valence band) is possible without change of wave vector **k**.

Direct transition   A transition occurring without change of wave vector **k** of initial and final state.

Dopant   An intentionally added impurity atom/ion.

Doping   Addition of some atoms or ions carried out to control charge or set up some localized energy levels in the energy gap of a material is known as doping.

Electroluminescence   Luminescence occuring due to application of an electric field to the substance. Also see luminescence.

Exciton   A bound electron-hole pair.

Flocculation   Phenomenon of small particles aggregating into bigger ones.

Fluorescence   Radiation given out by a material after absorbing some energy.

Hybridization of electronic states   A process by which one can consider different electronic states of nearly same energy combine to form new electronic states.

Hydrophilic   Loving water.

Hydrophobic   Hating water.

Indirect bandgap   When transition of valence electrons to conduction band (or other way) cannot take place, unless wavevector is changed (may be by absorption or emission of a phonon), indirect bandgap is said to be present.

Indirect transition   Transition occurring between initial and final state with change of wave vector **k**.

Interstitial site   Vacant place between group of atoms/ions/ molecules in a solid.

Ion implantation   Deposition of some ions by accelerating them with high energy (keV to MeV) in a solid.

Langmuir–Blodgett technique A technique developed by Langmuir and Blodgett to deposit on a solid substrates regular arrays of molecules dissolved in some liquid.

Ligand A group of molecules surrounding metal ions.

Local symmetry Geometrical symmetry around an atom, ion or molecule in a molecule or solid.

Luminescence A phenomenon in which electromagnetic radiation is given out by an excited substance.

Lyophillic Affinity for solvent.

Magnetic-susceptibility Ability to get magnetized.

Microdomain Regions of few micrometer (10^{-6} m) sizes.

Monomer Simple, basic group of small number of atoms.

Nanocrystallites Crystalline material with size of few nanometers (10^{-9} m).

Nanoreactors Nanometer size region in which reaction takes place.

Nonradiative recombination Electron and hole can combine without giving out visible electromagnetic radiation.

Organometallic Compound or molecules in which a metal ion is bonded to organic molecules.

Phosphors Materials giving fluorescence or phosphorescence. Fluorescence has said to occur when decay time is very short ($\sim 10^{-8}$ to 10^{-9} seconds) while phosphorescence can take place from few milliseconds to seconds.

Photoexcitation Excitation occurring due to incident photon.

Photoluminescence Luminescence obtained as result of excitation by incident photons, also see luminescence.

Photon Quantum of electromagnetic radiation travelling at the same speed as light.

Polar solution A solution or liquid in which molecules have permanent dipole moments on them, e.g. water.

Polydispersity A material (or powder) having grains or particles of different sizes.

Polymer A large molecule formed due to repetition of some group of atoms or monomers. Both synthetic and natural polymers exist.

Polymerization A process by which monomers or some basic group of atoms stick together to form a long repeat unit.

Precursor A chemical useful to form another chemical by a chemical reaction.

Quantum confinement When an electron and hole pair are spatially trapped so that their wave functions start overlapping, a quantum confinement is said to occur. Size dependent properties start appearing when quantum confinement occurs.

Quantum efficiency for luminescence Ratio of photons emitted to that of absorbed.

Quantum dot A particle showing quantum confinement or size effects.

Radiative transfer Transfer of energy by emitting radiation.

Recombination In an excitation process by incident photon, electron or application of electric field, an electron-hole pair is formed which combines again with certain probability.

Reverse micelles At high concentration of amphiphilic monomers they aggregate forming micelles, in which polar hydrophilic heads are outside. Reverse micelles trap water inside with their polar heads inside and tails floating in liquid.

Saturation threshold A value above which saturation of a process occurs that is further input has no effect.

Shallow impurity level Impurity levels formed close to conduction band minimum in an energy gap.

Sol–gel A jelly like dispersion with colloidal particles.

Sphalerite A zinc-blend or ZnS type of crystalline structure.

Substitutional site An impurity atom/ion can occupy under certain conditions the position of atom/ion in a crystalline solid.

Surface traps Atoms or ions in surface region are deficient of coordinating atoms or bonds. They can readily trap or catch a charge or atom/molecule and are known as surface traps.

Surfactants Surface active agents and can wet and lower surface tension. Some surfactants help to protect the surfaces and avoid coalescence between particles.

Synchrotron radiation An accelerated charged particle produces electromagnetic radiation.

Tetragonal A structure in which two unit cell sides are equal but third side is different. All the angles between crystal sides are 90°.

Turbid Muddy, not clear or disordered.

Ultrasonic treatment A treatment using ultrasonic waves. Ultra sonic waves are sound waves with frequencies above 20,000 Hz.

Viscous With less fluidity.

Wurtzite A hexagonal crystalline structure.

Zeeman splitting Splitting of energy levels of an atom under the application of magnetic field.

Zeolite Kind of hydrated aluminosilicates. They occur naturally and also synthesized to exploit their porous structure.

ACKNOWLEDGMENTS

REFERENCES

1. S. Shionoya and William M. Yen, Eds. "Phosphor Handbook," CRC Press, Boca Raton, FL, 1998.
2. S. A. Wolf, D. D. Awschalom, R. A. Buhrman, J. M. Daughton, S. von Molnar, M. L. Roukes, A. Y. Chtchelkanova, and D. M. Treger, *Science* 294, 1488 (2001).
3. H. Munekata, H. Ono, S. von Molnar, A. Segmuller, L. L. Chang, and L. Esaki, *Phys. Rev. Lett.* 63, 1849 (1989).
4. J. K. Furdyna and J. Kossut, "Semiconductors and Semimetals," Vol. 25, Academic Press, New York, 1988.

5. S. M. Sze, "Physics of Semiconductor Devices." John Wiley & Sons, New York, 1981.
6. H. Gleiter, *Prog. Mat. Sci.* 33, 223 (1989).
7. R. Vyeda, *Prog. Mat. Sci.* 35, 1 (1991).
8. A. Henglein, *Topics in Curr. Chem.* 143, 113 (1988).
9. H. Weller, *Angew. Chem.* 32, 42 (1993).
10. A. P. Alivisatos, *J. Phys. Chem.* 100, 132266 (1996).
11. Al. L. Efros and Al. Efros, *Sov. Phys. Semicond.* 16, 772 (1982).
12. L. E. Brus, *J. Chem. Phys.* 80, 4403 (1984).
13. Y. Wang and N. Herron, *J. Phys. Chem.* 95, 525 (1991).
14. S. V. Gaponenko, "Optical Properties of Semiconductor Nanocrystals,." Cambridge University Press, Cambridge UK, 1998.
15. U. Woggon, "Optical Properties of Semiconductor Quantum Dots." Springer-Verlag, Berlin. 1997.
16. W. G. Becker and A. J. Bard, *J. Chem. Phys.* 87, 4888 (1983).
17. Y. Wang, N. Herron, K. Moller, and T. Bein, *Sol. St. Comm.* 77, 32 (1991).
18. R. N. Bhargava, D. Gallagher, X. Hong, and A. Numikko, *Phys. Rev. Lett.* 72, 416 (1994).
19. C. B. Murray, D. J. Norris, and M. G. Bawendi, *J. Am. Chem. Soc.* 115, 8706 (1993).
20. X. Peng, J. Wickham, and A. P. Alvisatos, *J. Am. Chem. Soc.* 120, 5343 (1998).
21. T. Vossmayer, L. Katsikas, M. Giersig, I. G. Popovic, K. Diesner, A. Chemseddine, A. Eychmuller, and H. Weller, *J. Phys. Chem.* 98, 7655 (1994).
22. M. A. Hines and P. Guyot-Sionnest, *J. Phys. Chem. B* 102, 3655 (1998).
23. D. J. Norris, N. Yao, F. T. Charnock, and T. A. Kennedy, *Nano Lett.* 1, 3 (2001).
24. C. B. Murray, C. R. Kagan, and M. G. Bawendi, *Ann. Rev. Mat. Sci.* 30, 545 (2000).
25. J. Leeb, V. Gebhardt, G. Muller, D. Haarer, D. Su, M. Giersig, G. McMahon, and L. Spanhel, *J. Phys. Chem. B* 103, 7839 (1999).
26. A. A. Khosravi, M. Kundu, B. A. Kuruvilla, G. S. Shekhawat, R. P. Gupta, A. K. Sharma, P. D. Vyas, and S. K. Kulkarni, *Appl. Phys. Lett.* 67, 2506 (1995).
27. P. H. Borse, N. Deshmukh, R. F. Shinde, S. K. Date, and S. K. Kulkarni, *J. Mat. Sci.* 34, 6087 (1999).
28. P. H. Borse, D. Srinivas, R. F. Shinde, S. K. Date, W. Vogel, and S. K. Kulkarni, *Phys. Rev. B* 60, 8659 (1999).
29. S. K. Kulkarni, U. Winkler, N. Deshmukh, P. H. Borse, R. Fink, and E. Umbach, *Appl. Surf. Sci.* 169–170, 438 (2001).
30. S. W. Lu, B. I. Lee, Z. L. Wang, W. Tong, B. K. Wagner, W. Park, and C. J. Summers, *J. Lumin.* 92, 73 (2001).
31. S. M. Liu, F. Q. Liu, H. Q. Guo, Z. H. Zhang, and Z. G. Wang, *Sol. State Comm.* 115, 615 (2000).
32. A. Bol and A. Meijerink, *Phys. Rev. B* 58, R15997 (1998).
33. A. A. Khosravi, M. Kundu, L. Jatwa, S. K. Deshpande, U. A. Bhagwat, M. Sastry, and S. K. Kulkarni, *Appl. Phys. Lett.* 67, 2702 (1995).
34. L. Sun, C. Liu, C. Liao, and C. Yan, *J. Mat. Chem.* 9, 1655 (1999).
35. J. H. Chung, C. S. Ah, and D. J. Jang, *J. Phys. Chem. B* 105, 4128 (2001).
36. K. Shinoda, *Adv. Coll. Int. Sci.* 4, 281 (1975).
37. J. Fendler, *J. Chem. Rev.* 87, 877 (1987).
38. M. P. Pileni, *Langmuir* 13, 3266 (1997).
39. S. J. Xu, S. J. Chua, B. Liu, L. M. Gan, C. H. Chew, and G. Q. Xu, *Appl. Phys. Lett.* 73, 1478 (1998).
40. L. M. Gan, B. Liu, C. H. Chew, S. J. Xu, S. J. Chua, G. L. Loy, and G. Q. Xu, *Langmuir* 13, 6427 (1997).
41. L. Levy, N. Feltin, D. Ingert, and P. Pileni, *J. Phys. Chem. B* 101, 9153 (1997).
42. L. Levy, D. Ingert, N. Feltin, and M. P. Pileni, *J. Cryst. Growth* 184–185, 377 (1998).
43. L. Levy, D. Ingert, N. Feltin, and M. P. Pileni, *Adv. Mat.* 10, 53 (1998).
44. N. Feltin, L. Levy, D. Ingert, and M. P. Pileni, *Adv. Mat.* 11, 398 (1999).
45. C. Petit, P. Lixon, and M. P. Pileni, *J. Phys. Chem.* 94, 1598 (1990).
46. B. A. Smith, J. Z. Zhang, A. Joly, and J. Liu, *Phys. Rev. B* 62, 2021 (2000).
47. A. D. Dinsmore, D. S. Hsu, S. B. Qadri, J. O. Cross, T. A. Kennedy, H. F. Gray, and B. R. Ratna, *J. Appl. Phys.* 88, 4985 (2000).
48. M. A. Chamarro, V. Voliotis, R. Grousson, P. Lavallard, T. Gacoin, G. Counio, J. P. Boilot, and R. Cases, *J. Cryst. Growth* 159, 853 (1996).
49. M. Behoudnia and P. Sen, *Phys. Rev. B* 63, 35316 (2001).
50. D. M. Hofmann, A. Hofstaetter, U. Leib, B. K. Meyer, and G. Counio, *J. Cryst. Growth* 184–185, 383 (1998).
51. C. Jin, J. Yu, L. Sun, K. Dou, S. Hou, J. Zhao, Y. Chen, and S. Huang, *J. Lumin.* 66–67, 315 (1996).
52. T. Igarashi, M. Ihara, T. Kusunoki, K. Ohno, T. Isobe, and M. Senna, *J. Nanopart. Res.* 3, 51 (2001).
53. T. Igarashi, T. Isobe, and M. Senna, *Phys. Rev. B* 56, 6444 (1997).
54. N. Murase, R. Jagannathan, Y. Kanematsu, M. Watanabe, A. Kurita, K. Hirata, T. Yazawa, and T. Kushida, *J. Phys. Chem. B* 103, 754 (1999).
55. R. S. Kane, R. E. Kohen, and R. Silbey, *Chem. Mater.* 11, 90 (1999).
56. J. Yue and R. E. Cohen, *Supermol. Sci.* 1, 117 (1994).
57. I. Yu, T. Isobe, and M. Senna, *J. Phys. Chem. Sol.* 57, 373 (1996).
58. I. Yu and M. Senna, *Appl. Phys. Lett.* 66, 424 (1994).
59. Y. Kanemitsu, H. Matsubara, and C. W. White, *Appl. Phys. Lett.* 81, 535 (2002).
60. M. Morita, M. Baba, H. Fujii, D. Rau, M. Yoshita, H. Akiyama, and M. Herren, *J. Lumin.* 94–95, 191 (2001).
61. M. Morita, D. Rau, H. Fujii, Y. Minami, S. Murakami, M. Baba, M. Yoshita, and H. Akiyama, *J. Lumin.* 87–89, 478 (2000).
62. M. V. Artemyev, L. I. Gurinovich, A. K. Stupak, and S. V. Gaponenko, *Phys. Stat. Sol. (B)* 224, 191 (2001).
63. U. Sohling, G. Jung, D. U. Saenger, S. Lu, B. Kutsch, and M. Mennig, *J. Sol. Gel. Sci. Tech.* 13, 685 (1998).
64. D. U. Saenger, G. Jung, and M. Mennig, *J. Sol–Gel Sci. Tech.* 13, 635 (1998).
65. S. Guo, L. Konopny, R. P. Biro, H. Cohen, M. Sirota, E. Lifshitz, and M. Lahav, *Adv. Mat.* 12, 302 (2000).
66. S. Guo, L. Konopny, R. P. Biro, H. Cohen, H. Porteanu, E. Lifshitz, and M. Lahav, *J. Am. Chem. Soc.* 121, 9589 (1999).
67. R. N. Bhargava, V. Chhabra, T. Som, A. Ekimov, and N. Taskar, *Phys. Stat. Sol. (B)* 229, 897 (2002).
68. S. Sapra, R. Viswanatha, J. Nanda, and D. D. Sarma (unpublished).
69. W. Chen, R. Sammynaiken, Y. Huang, J. O. Malm, R. Wallenberg, J. O. Bovin, V. Zwiller, and N. A. Kotov, *J. Appl. Phys.* 89, 1120 (2001).
70. B. D. Culity, "Elements of X-Ray Diffraction, 2nd Ed.," Addison–Wesley,
71. J. F. Suyver, S. F. Wuister, J. J. Kelly, and A. Meijerink, *Nano Lett.* 1, 429 (2001).
72. V. Gnutzmann and W. Vogel, *J. Phys. Chem.* 94, 4991 (1990).
73. P. H. Borse, Ph. D. thesis, Univesity of Pune, India 1999.
74. D. E. Sayers, E. A. Stern, and F. W. Lytle, *Phys. Rev. Lett.* 27, 1204 (1971).
75. B. Lengeler and P. Eisenberger, *Phys. Rev. B* 21, 4507 (1980).
76. J. Rockenberger, L. Troger, A. Kornowski, T. Vossmeyer, A. Eychmuller, J. Feldhaus, and H. Weller, *J. Phys. Chem. B* 101, 2691 (1997).
77. Y. L. Soo, Z. H. Ming, S. W. Huang, Y. H. Kao, R. N. Bhargava, and D. Gallagher, *Phys. Rev. B* 50, 7602 (1994).

78. P. Peka and H. J. Schulz, *Physica B* 193, 57 (1994).
79. K. Sooklal, B. S. Cullum, S. M. Angel, and C. J. Murphy, *J. Phys. Chem.* 100, 4551 (1996).
80. J. Yu, H. Liu, Y. Wang, F. E. Fernandez, W. Jia, L. Sun, C. Jin, D. Li, J. Liu, and S. Huang, *Opt. Lett.* 22, 913 (1997).
81. K. Yan, C. Duan, Y. Ma, S. Xia, and J. C. Krupa, *Phys. Rev. B* 58, 13585 (1998).
82. R. N. Bhargava, D. Gallagher, and T. Welker, *J. Lumin.* 60–61, 275 (1994).
83. R. N. Bhargava, *J. Lumin.* 70, 85 (1996).
84. A. A. Bol and A. Meijerink, *Phys. Stat. Sol.* (*B*) 224, 291 (2001).
85. A. A. Bol and A. Meijerink, *J. Lumin.* 87–89, 315 (2000).
86. M. Tanaka, J. Qi, and Y. Masumoto, *J. Lumin.* 87–89, 472 (2000).
87. J. Z. Zhang, *J. Phys. Chem. B* 104, 7239 (2000).
88. B. A. Smith, J. Z. Zhang, A. Joly, and J. Liu, *Phys. Rev. B* 62, 2021 (2001).
89. T. A. Kennedy, E. R. Glaser, P. B. Klein, and R. N. Bhargava, *Phys. Rev. B* 52, R14356 (1995).
90. S. Sapra, J. Nanda, A. Anand, S. V. Bhat, and D. D. Sarma, *J. Nanosci. Nanotech.* 3, 392 (2003).
91. H. E. Gumlich, *J. Lumin.* 23, 76 (1981).
92. F. K. Fong, "Theory of Molecular Relaxation, Applications in Chemistry and Biology." Wiley, New York, 1975.
93. J. Yu, H. Liu, Y. Wang, F. E. Fernandez, and W. Jia, *J. Lumin.* 76–77, 252 (1998).
94. M. Tanaka and Y. Masumoto, *Chem. Phys. Lett.* 324, 249 (2000).
95. J. Yu, H. Liu, Y. Wang, and W. Jia, *J. Lumin.* 79, 191 (1998).
96. C. de Mello Donega, A. A. Bol, and A. Meijerink, *J. Lumin.* 96, 87 (2002).
97. A. D. Dinsmore, D. S. Hsu, H. F. Gray, S. B. Quadri, Y. Tian, and B. R. Ratna, *Appl. Phys. Lett.* 75, 802 (1999).
98. Igarashi et al. *MRS Bull.* 36, 1317 (2001).
99. P. Mulvaney, L. M. Liz-Marzan, M. Giersig, and T. Ung, *J. Mater. Chem.* 10, 1259 (2000).
100. D. V. Talapin, A. L. Rogash, M. Haase, and H. Weller, *J. Phys. Chem. B* 105, 12278 (2001).
101. U. Winkler, D. Eich, Z. H. Chen, R. Fink, S. K. Kulkarni, and E. Umbach, *Chem. Phys. Lett.* 306, 95 (1999).
102. U. Winkler, D. Eich, Z. H. Chen, R. Fink, S. K. Kulkarni, and E. Umbach, *Phys. Stat. Sol.*
103. J. E. B. Katari, V. L. Colvin, and A. P. Alivisatos, *J. Phys. Chem.* 98, 4109 (1994).
104. D. Denzler, M. Olschewski, and K. Sattler, *J. Appl. Phys.* 84, 2841 (1998).
105. L. Cao, J. Zhang, S. Ren, and S. Huang, *Appl. Phys. Lett.* 80, 4300 (2002).
106. A. S. Ethiraj, N. Hebalkar, S. K. Kulkarni, R. Pasricha, J. Urban, C. Dem, M. Schmitt, W. Kiefer, L. Weinhardt, S. Joshi, R. Fink, C. Heske, C. Kumpf, and E. Umbach, *J. Chem. Phys.* 118 (2003) in press.
107. E. Becquerel, *C. R. Acad. Sci.* 62, 999 (1866).
108. G. F. J. Garlick and M. J. Dumbleton, *Proc. Phys. Soc. B* 67, 442 (1954).
109. F. E. Williams, *J. Opt. Soc. Am.* 39, 648 (1949).
110. R. Heitz, A. Hoffmann, P. Thurian, and I. Broser, *J. Phys. Condens. Mat.* 4, 157 (1992).
111. H. Zhang, Z. Wang, L. Zhang, Y. Li, and, J. Yuan, *J. Mater. Sci.* 21, 1031 (2002).
112. J. Huang, Y. Yang, S. Xue, B. Yang, S. Liu, and J. Shen, *Appl. Phys. Lett.* 70, 2335 (1997).
113. L. Sun, C. Liu, C. Liao, and C. Yan, *Sol. Stat. Comm.* 111, 483 (1999).
114. M. Wang, L. Sun, X. Fu, C. Liao, and C. Yan, *Sol. Stat. Comm.* 115, 493 (2000).
115. W. Que, Y. Zhou, Y. L. Lam, Y. C. Chan, C. H. Kam, B. Liu, L. M. Gan, C. H. Chew, G. Q. Xu, S. J. Chua, S. J. Xu, and F. V. C. Mendis, *Appl. Phys. Lett.* 73, 2727 (1998).
116. A. A. Bol, http://www.lumi.phys.uu.nl/Ageeth/thesis.html (Chap. 7).
117. P. Yang, M. Lu, D. Xu, D. Yuan, and G. Zhou, *Appl. Phys. A* 73, 455 (2001).
118. P. Yang, M. Lu, D. Xu, D. Yuan, G. Zhou, and M. Pan *Appl. Phys. A* 74, 257 (2002).
119. P. Lenard, F. Schmidt, and R. Tomascher, "Handbook der Experimentelle Physik, Vol. 3, Chap. 1, Akademische Verlagsgesellschaft, Leipzig, 1928, p. 39.
120. Y. Uehara, *J. Chem. Phys.* 51, 4385 (1969).
121. A. A. Bol and A. Meijerink, *Phys. Stat. Sol.* (*B*) 224, 173 (2001).
122. P. H. Borse, W. Vogel, and S. K. Kulkarni (unpublished).
123. W. Chen, J. O. Malm, V. Zwiller, Y. Huang, S. Liu, R. Wallenberg, J. O. Bovin, and L. Samuelson, *Phys. Rev. B* 61, 11021 (2000).
124. W. Chen, J. O. Malm, V. Zwiller, R. Wallenberg, and J. O. Bovin, *J. Appl. Phys.* 89, 2671 (2001).
125. S. C. Qu, W. H. Zhou, F. Q. Liu et al. *APL* 80, 3605 (2000).
126. D. D. Papakonstantinou, J. Huang, and P. Lianos, *J. Mat. Sci. Lett.* 17, 1571 (1998).
127. J. F. Suyver, S. F. Wuister, J. J. Kelly, and A. Meijerink, *Phys. Chem. Chem. Phys.* 2, 5445 (2000).
128. M. Shim, C. Wang, D. J. Norris, and P. G. Sionnest, *MRS Bulleten*, Dec. 2001, p. 1005.
129. G. W. Ludwig and H. H. Woodburg, "in Solid State Physics," (F. Seitz and D. Turnbull, Eds.). Vol. 13, p. 298. Academic Press, New York, 1962.
130. W. Vogel, J. Urban, M. Kundu, and S. K. Kulkarni. *Langmuir* 13, 827 (1997).
131. J. Nanda, K. S. Narayan, B. A. Kuruvilla, G. L. Murthy, and D. D. Sarma, *Appl. Phys. Lett.* 72, 1335 (1998).
132. L. Levy, J. F. Hochepied, and M. P. Pileni, *J. Phys. Chem.* 100, 18322 (1996).
133. S. M. Liu, F. Q. Liu, H. Q. Guo, Z. H. Zhang, and Z. G. Wang, *Sol. Stat. Comm.* 115, 615 (2000).
134. L. Levy, D. Ingert, N. Feltin, V. Briois, and M. P. Pileni, *Langmuir* 18, 1490 (2002).
135. G. Counio, T. Gacoin, and J. P. Boilot, *J. Phys. Chem. B* 102, 5257 (1998).
136. L. Levy, N. Feltin, D. Ingert, and M. P. Pileni, *Langmuir* 15, 3386 (1991).
137. A. A. Bol, http://www.lumi.phys.uu.nl/Ageeth/thesis.html (Chap. 5).
138. V. Ladizhansky and S. Vega, *J. Phys. Chem. B* 104, 5237 (2000).
139. K. Yanata, K. Suzuki, and Y. Oka, *J. Appl. Phys.* 73, 4595 (1993).
140. F. V. Mikulec, M. Kuno, M. Bennati, D. A. Hall, R. G. Griffin, and M. G. Bawendi, *J. Am. Chem. Soc.* 122, 2532 (2000).
141. A. L. Efros, M. Rosen, M. Kuno, M. Nirmal, D. J. Norris, and M. Bawendi, *Phys. Rev. B* 54, 4843 (1996).
142. K. M. Hanif, R. W. Meulenberg, and G. F. Strouse, *J. Am. Chem. Soc.* 124, 11495 (2002).
143. H. Yang, P. H. Holloway, and B. B. Ratna, *J. Appl. Phys.* 93, 586 (2003).
144. D. M. Hoffman, B. K. Meyer, A. I. Ekimov, I. A. Merkulov, Al. L. Efros, M. Rosen, G. Couino, T. Gacoin, and J. P. Boilot, *Sol. Stat. Comm.* 114, 547 (2000).

Double- and Triple-Decker Phthalocyanines/Porphyrins

Tatyana N. Lomova, Marija E. Klyueva

Russian Academy of Sciences, Ivanovo, Russian Federation

CONTENTS

1. INTRODUCTION

Phthalocyanine (H_2Pc) and porphyrins (H_2P) are macrocyclic aromatic compounds forming complexes of different structures with metals. Cations with a large radius and coordination number give complexes of nanostructures $M(HPc)(Pc)$ (**1**), $M(Pc)_2^{\bullet}$, and $M_2(Pc)_3$ (**2**) more readily than those of planar structure $M(Pc)$ or $(X)_{n-2}M(Pc)$ (**3**) (X, axial ligand of acido type in the inner coordination sphere; *n*, formal charge of the metal cation). This relates first of all to lanthanides and actinides, which are the subject of this review. Metallophthalocyanines have very stable coordination bonds, in contrast to the great majority of complexes of other known ligands. Synthesis of metallophthalocyanines with sandwich structure was described for the first time in 1965 [1] and then in 1971 and 1974 [2, 3]. The double-decker structure of diphthalocyanine complexes of lanthanides was confirmed with X-ray crystallography data for $NdPc_2$ [4]. According to these data, the Nd atom in the molecule is situated between two parallel phthalocyanine ligands, which are turned to 45° about each other. Each of the eight Nd-N bond distances is equal to 2.39–2.49 Å. One of the phthalocyanine ligands has a saucer-like conformation and the other is planar. At present there is also information about the structures of $Ga(Pc)_2$ [5], $Er^{III}(Pc)_2$ [6], $Ce^{IV}(Pc)_2$ [7], and others. Data

on sandwich complexes whose structure has been studied by X-ray crystallography are listed in Table 1. As for triple-decker phthalocyanine complexes, there are structural data only on $In_2(Pc)_3$ [35] and Lu complex with tetra-15-crown-5-phthalocyanine (Fig. 1) [36]. The central ligand in the latter is turned to 43.7° about external ligands. The average distance between macrocycle planes is 2.923 Å. Lu ions are localized between the ligands. The average distance between Lu atoms and coordinating N atoms of the external ligands is 2.305 Å. Analogous distances to the central ligand N atoms are much larger (2.560 Å). Several sandwich complexes with porphyrins and those with different phthalocyanine and porphyrin macrocycles in one and the same molecule (heteroleptic compounds) were described as well [53] (Table 1). The results of the cited works prove the molecular structure of both double-decker and triple-decker phthalocyanine and porphyrin complexes of rare-earth metals. On the whole, data for triple-decker complexes are not numerous, whereas double-decker complexes have been studied intensively [54–56]. Basic spectral and applied properties of the complexes have been investigated [57, 58]. From the point of the possibility of practical use of the compounds, their stability to chemical, thermal, and photochemical influence is very important. The present work is a review of publications of recent decades on double- and triple-decker phthalocyanines and porphyrins, where special attention is given to the synthesis, structure, and spectral characteristics of the compounds, as well as to ways of increasing complex stability.

2. ACIDO PHTHALOCYANINE METAL COMPLEXES $(X)_{n-2}M(Pc)$

Phthalocyanine complexes with $(X)_{n-2}M(Pc)$ composition for cations able to from double and triple deckers with the Pc^{2-} dianion as well are under consideration in this section. These are cations of group IV of the periodic table and those of the rare earth elements.

Table 1. Structural data for double- and triple-decker phthalocyanines/porphyrins.

Compound	T (K)	Ref.
$Ga(Pc)_2$	295	[5]
$In^{III}(Pc)_2$	298	[8]
$Sn^{IV}(Pc)_2$ γ-form	295	[9]
$Sn^{IV}(Pc)_2$ monoclinic β-form	300	[10]
$Bi^{III}(Pc)_2 \cdot CH_2Cl_2$	208	[11]
$[Ti^{IV}(Pc^{+\bullet})_2] [I_3]_{0.66}$	113	[12]
$Zr^{IV}(Pc)_2$	295	[13]
$Y(Pc)_2 \cdot CH_2Cl_2$	173	[14]
$La^{III}(Pc)_2 \cdot CH_2Cl_2$	243	[15]
$[Ph_3PNPPh_3][La^{III}(Pc)_2]$	293	[16]
$Ce^{IV}(Pc)_2$	295	[7]
$[Ce^{IV}(Pc)_2][BF_4]_{0.33}$	295	[17]
$Pr(Pc)_2$ $\beta1$ phase	295	[18]
$Pr(Pc)_2$ α-phase	295	[19]
$[Pr^{III}(Pc)_2][Br_3]_{0.75}$	295	[20]
$Nd(Pc)_2$	295	[21]
$Nd(Pc)_2$ α-form	296	[22]
$Nd(Pc)_2$ α-phase	295	[23]
$Nd(Pc)_2$ β-phase	295	[24]
$[Bu_4N][Nd^{III}(Pc)_2]$	296	[25]
$[Sm^{III}(Pc)_2][Br]_{1.45}$	295	[26]
$[Sm^{III}(Pc)_2][ClO_4]_{0.63}$	295	[26]
$[Bu_4N][Gd^{III}(Pc)_2]$	296	[25]
$[Ph_3PNPPh_3][Gd^{III}(Pc)_2] \cdot 0.3H_2O$	293	[16]
$[Bu_4N][Ho^{III}(Pc)_2] \cdot H_2O$	296	[25]
$Er^{III}(Pc)_2$	293	[6]
$[Ph_3PNPPh_3][Tm^{III}(Pc)_2] \cdot 1/2H_2O$	293	[16]
$Lu^{III}(Pc)_2 \cdot CH_2Cl_2$	293	[27]
$Lu^{III}(HPc)(Pc)_2$	173	[28]
$[Bu_4N][Lu^{III}(Pc)_2] \cdot H_2O$	296	[25]
$[Bu_4N][Lu^{III}(Pc)_2] \cdot 2C_3H_7NO$	173	[28]
$Lu^{IV}(Pc)_2$ γ-phase	295	[29]
$Th^{IV}(Pc)_2$	295	[30]
$Th^{IV}(Pc)_2$	295	[31]
$Th^{IV}(Pc)_2$	295	[24]
$Th^{IV}(Pc)_2$	295	[32]
$Th^{IV}(Pc)_2 \cdot C_7H_8$	248	[32]
$Th^{IV}(Pc)_2 \cdot C_7H_8$	248	[33]
$[Th^{IV}(Pc)_2][SbCl_6] \cdot 2C_7H_8 \cdot CH_2Cl_2$	295	[32]
$[Th^{IV}(Pc)_2][SbCl_6] \cdot 2C_7H_8 \cdot CH_2Cl_2$	295	[33]
$U^{IV}(Pc)_2$	295	[34]
$U^{IV}(Pc)_2$	295	[30]
$In_2^{III}(Pc)_3$	300	[35]
$Lu_2(tetra-15-crown-5-Pc)_3$	295	[36]
$Zr^{IV}(OEP)_2 \cdot 2C_2H_6OS$	173	[37]
$Zr^{IV}(TPP)_2 \cdot CH_2Cl_2$	300	[38]
$Zr^{IV}(TPP)_2 \cdot CH_2Cl_2$	300	[39]
$Zr^{IV}(TPP)_2 \cdot 4H_2O$	295	[40]
$[Zr^{IV}(TPP^{+\bullet})_2][SbCl_6]_2 \cdot 3CH_2Cl_2$	295	[41]
$[Zr^{IV}(TPP^{+\bullet/2})_2][SbCl_6]_2 \cdot 3CH_2Cl_2$	173	[41]
$Zr^{IV}(5,10,15,20\text{-tetraaza-OEP})_2$	213	[42]
$Ce^{IV}(OEP)_2$	173	[43]
$Eu^{III}(OEP)_2$	173	[44]
$Th(TPP)_2 \cdot C_7H_8$	298	[33]
$[Th(TPP)_2][SbCl_6] \cdot 2C_7H_8 \cdot CH_2Cl_2$	298	[33]
$Zr^{IV}(OEP)(5,10,15,20\text{-tetraaza-OEP})$	213	[42]
$La^{III}(Pc)(TPP) \cdot 2CH_2Cl_2$	173	[45]
$[La^{III}(Pc)(TpyP)][OH] \cdot CHCl_3 \cdot CH_3OH$	295	[46]
$Ce^{IV}(OEP)(TPP) \cdot 1.5C_5H_5N$	173	[47]

continued

Table 1. Continued

Compound	T (K)	Ref.
$Ce^{IV}(TPOMeP)(Pc) \cdot 2CHCl_3 \cdot nC_5H_{12}$	173	[48]
$[Ce^{IV}(TPP)^{+\bullet}(Pc)][SbCl_6]$	173	[48]
$Sm^{III}(OEP)(H)(TPP) \cdot C_7H_8$	295	[49]
$[Gd^{III}(Pc)(TPP)][SbCl_6] \cdot 2CH_2Cl_2 \cdot H_2O$	173	[45]
$Ce_2^{III}(OEP)_3 \cdot C_6H_3Cl_3$	295	[43]
$(TPP)Ce^{III}(2,3,9,10,16,17,23,$ $24\text{-octamethyl-Pc})Ce^{III}(TPP) \cdot 6CH_2Cl_2$	173	[50]
$(Pc)Ce^{III}(TPOMeP)Ce^{III}(Pc) \cdot 2C_7H_8$	173	[50]
$(Pc)Nd^{III}(Pc)Nd^{III}(TPOMeP) \cdot 2C_2H_4Cl_3$	295	[51]
$(TPP)Ce^{III}(Pc)Gd^{III}(OEP) \cdot C_6H_5Cl$	295	[52]
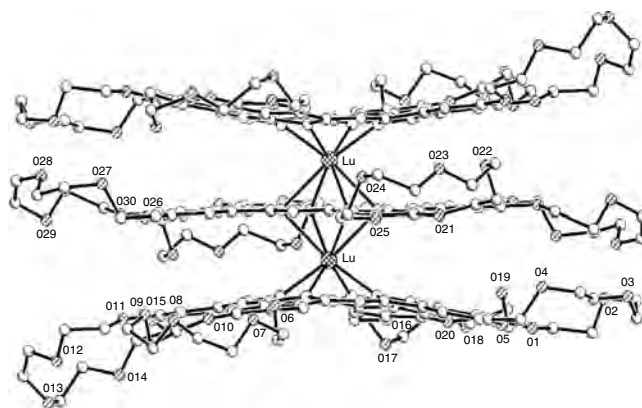
Figure 1. X-ray structure of triple-decker Lu complex with tetra-15-crown-5-phthalocyanine. Reprinted with permission from S. I. Troyanov et al., *Dok. Akad. Nauk.* 367, 644 (1999).
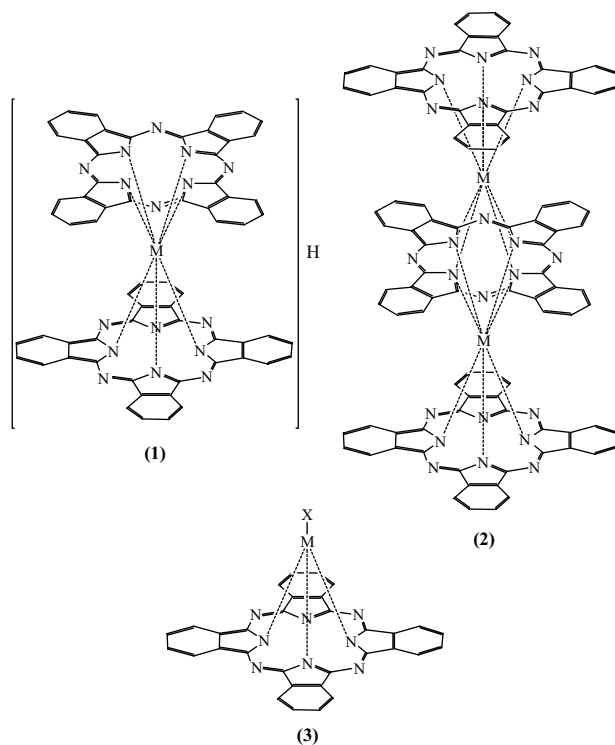
2.1. Synthesis

Template synthesis from phthalic acid and its derivatives [59] (phthalodinitrile, phthalimid, phthalic anhydride) in the presence of a complexing atom (Scheme 1) is a universal method of metallophthalocyanine synthesis including metallophthalocyanine acido-complexes. Independently of the nature of the reagent, the synthesis is always going through the stage of phthalic acid dinitrile formation. Metals and their salts and oxides could be used as complexations.

The final stage includes grouping around the metal ion of bipolar iminoisoindoline ions, which closes the cycle. The reaction proceeds in a melt of dry reagents by caking or in a high-boiling solvent: nitrobenzene, 1-chloronaphthalene, o-dichlorobenzene, or ethylene glycol [60].

When a metal was used as a matrix the extra-complexes of tin $(X)_2Sn(Pc)$ were obtained [59]; from chlorides of metals M(III) and M(IV) the extra-complexes (Cl)In(Pc), $(Cl)_2Zr(Pc)$, and $(Cl)_2Hf(Pc)$ were synthesized [61].

The described template synthesis of metallophthalocyanine acido-complexes $(X)_{n-2}M(Pc)$ demands a long, high temperature influence on the reaction mixture. During electrochemical template assembly of metallophthalocyanines M(Pc) [62], the reaction proceeds in organic solvents (dimethylformamide (DMF), absolute ethanol) at room temperature. Using UO_2^{2+} as a complexating agent in methanol led to H_2Pc formation [62].

Metallophthalocyanines can be obtained by the reaction of Li substitution in $Li_2(Pc)$ by another metal in ethanol solution in the absence of moisture to prevent the hydrolysis of initial metal salts. When using $SnCl_2$ or $ThCl_4$, which undergo hydrolysis, H_2Pc is the final product [60].

Complexes of the rare earth elements (Y, Sc, lanthanides from La to Lu besides promethium) with phthalocyanines can have a composition of 1:1, 2:1, 1:2, or 2:3. Monophthalocyanine complexes (1:1 and 2:1) are obtained [63] by substitution reaction from $Li_2(Pc)$. Reaction with lanthanide
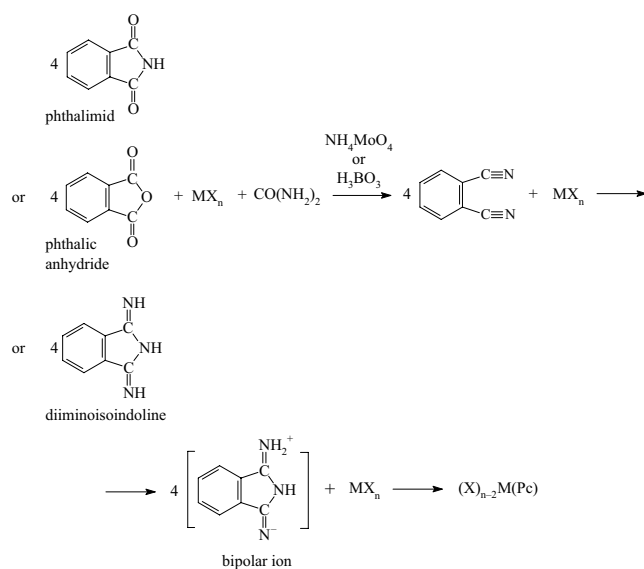
β-diketonate occurs in boiling dry organic solvent, such as methanol, tetrahydrofuran, or acetone. Depending on the reagent ratio, the lanthanide, and the nature of the solvent, complexes with a 1:1 or 2:1 composition can be obtained (Scheme 2).

Authors of the present review synthesized complexes of lanthanides (X)Ln(Pc) from $Li_2(Pc)$ and the corresponding lanthanide salts in boiling dimethyl sulfoxide (DMSO) according to the method of [63]. This method is characterized by high yield of the complexes (about 90%) and is simple in realization [64]. $Li_2(Pc)$ and chloride or acetate of lanthanide in a 1:2.5 mole ratio were refluxed in DMSO for 15–20 min, depending on Ln. The reaction mixture was cooled and diluted with a double volume of water. The sediment obtained was filtered, washed with water, and dried in air. $Li_2(Pc)$ was synthesized from H_2Pc and butyl lithium, and H_2Pc from o-phthalodinitrile [63].

In contrast to lanthanide phthalocyanine complexes of different compositions, it is much more difficult to obtain phthalocyanine complexes of cations of metals of groups III and IV of the periodic table with high yield. Chloride extra-complexes of In, Zr, and Hf were synthesized from 1,3-diiminoisoindoline [61]. The simplest method of $(Cl)_2M(Pc)$ (M = Sn, Zr, Hf, Ti, or Pb) synthesis is interaction of a metal chloride with o-phthalodinitrile, leading to diphthalocyanines of metals in 64% yield [65]. It is established in the cited work that monophthalocyanine complexes are formed as intermediate compounds of the reaction. To obtain $(Cl)_2M(Pc)$ as a desired product, the reaction of o-phthalodinitrile with a metal salt must be carried out at a 1:5 mole ratio of the reagents at 473 K for 30 min.

2.2. Spectroscopic Characterization

In contrast to phthalocyanine d-metal complexes, those of lanthanides $((X)_{n-2}Ln(Pc))$ are soluble in organic solvents (Table 2). UV-vis spectra of lanthanide complexes are

Scheme 1.

Note: When diiminoisoindoline using the urea presence is not necessary.
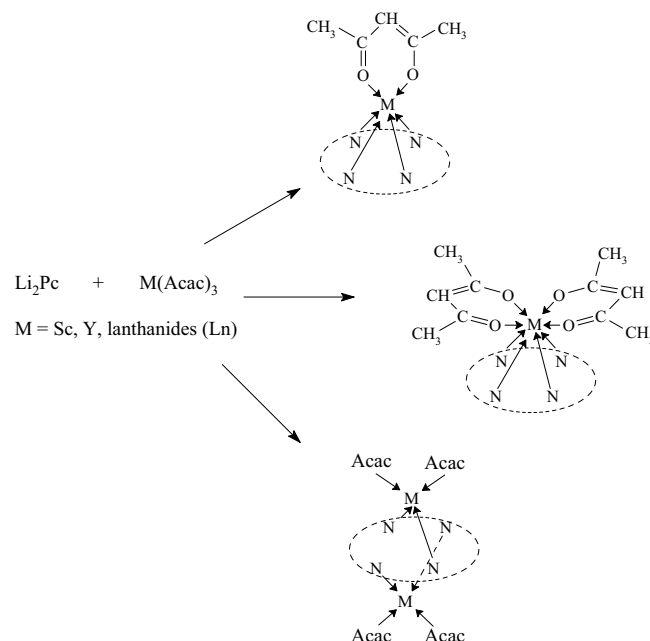
Scheme 2.

Table 2. Long wave absorption band position in UV-vis spectra of (X)Ln(Pc), λ_{max}.

Solvent	(OAc)TbPc	(OAc)DyPc	(OAc)HoPc	(OAc)ErPc	(OAc)TmPc	(Cl)YbPc	(OAc)LuPc
DMSO	676.9	674.9	678.6	674.6	673.4	677.5	673.8
DMF	669.7	671.1	672.6	—	671.6	670.8	665.3
Benzene	671.5	671.9	672.6	672.6	677.5	674.3	674.3
Acetone	667.9	667.8	670.2	666.8	666.7	666.7	663.1
Pyridine	675.2	675.4	674.4	674.4	675.7	674.4	674.4
Benzonitrile	719.1	720.5	719.0	719.0	718.4	716.9	714.9
	691.2	690.6	691.2	691.2	691.2	691.2	691.2
Acetonitrile	669.0	669.0	663.0	669.0	663.1	669.0	669.0
CHCl₃	675.2	671.6	671.3	676.8	675.7	676.7	675.3
(C₂H₅)₂O	668.1	669.6	668.2	667.1	670.2	667.8	667.8

Values are in nanometers.

similar as a whole to M(Pc) spectra (Table 3, Fig. 2). A typical UV-vis spectrum of metal phthalocyanine in organic solvent has a long-wave maximum I in the region 670–700 nm ($\pi \rightarrow \pi^*$ transition [66]) and its oscillation component of lower intensity at about 610 nm. An intensive Soret band is disposed at 330–390 nm. For the raw lanthanides the UV-vis spectra show low dependence on Ln and acido-ligand nature (Table 2). Thus complexes with 1:1 composition differ from double and triple deckers, which will be considered next. The data in Table 2 show a notable solvatochromic effect in the UV-vis spectra of $(X)_{n-2}$Ln(Pc).

It is established experimentally that $(X)_{n-2}$Ln(Pc) gives molecular solutions in ethanol and other coordinating solutions when the complex concentration is 10^{-4} to 10^{-5} mole/liter. The independence of long-wave absorption band position of metal and acido ligand nature points to the existence of coordinationally saturated particles $[(\text{Solv})_{n-2}\text{Ln}(\text{Pc})]^+$ in the solution, where n is the maximum coordination number of Ln in the given conditions. This makes ethanol a fit medium for investigating the dissociation of complexes in the presence of acid.

2.3. Structure

The composition and structure of metallophthalocyanines complexed with elements of the main third group of the periodic table can be expressed by the general formula (X)M(Pc) (X = monovalent anion) or (Y)[M(Pc)]₂ (Y = divalent anion). Until now only a few crystal structures with trivalent metals have been described [27, 35, 74, 75]. Unfortunately, many of the polymorphs of phthalocyanines are difficult to grow in large enough crystals for single-crystal analysis. However, the structure of such a crystal could be obtained from powder X-ray diffraction data by Rietveld analysis [76–78].

According to data of [74, 78], the metal atom in (X)M(Pc) (M = Al, Ga) is moved from the plane of four N-iso (N-iso, isoindole N atom) toward an acido-ligand; the distance depends on X and M. Positional parameters of (OH)Ga(Pc) and (Cl)Ga(Pc) with respect to the triclinic axes made by Rietveld analysis are discussed in [78], and the nonplanar structure of the molecules in the crystals is obtained.

In the complexes of M(IV) with trans-positioned acido-ligands, the metal atom is situated in the center of the

Table 3. UV-vis spectra of metallophthalocyanines with 1:1 composition.

$(X)_{n-2}$M(Pc)	Solvent	λ_{max} (nm) (log ε)				Ref.
		I	II	III	Soret	
Zn(Pc)	Pyridine	672	646	607	348	[67]
		(5.45)	(4.56)	(4.59)	(4.81)	
(Cl)In(Pc)[a]	Nitrobenzene	700	629	605	365	[68]
		(4.93)	(4.25)	(3.57)	(3.50)	
(Cl)₂Sn(Pc)	1-Chloronaphthalene	701			363	[69]
(OH)₂Ti(Pc)	Benzonitrile	701	631		387	[69]
(Cl)₂Zr(Pc)	DMF	678				[70]
(Cl)₂Hf(Pc)	DMF	678				[71]
(Cl)Nd(Pc)	o-Dichlorobenzene	673	—	610	344	[72]
		(4.98)		(4.40)	(4.65)	
(Cl)Lu(Pc)	o-Dichlorobenzene	672	—	606	344	[72]
		(4.97)		(4.25)	(4.54)	
(OAc)Lu(Pc)	CH₂Cl₂	673	645	608	342	[27]
		(5.14)	(shoulder)	(4.32)	(4.67)	
(Acac)₂Th(Pc)	Benzonitrile	684	—	617	353	[73]
		(5.32)		(4.60)	(4.80)	
(Acac)₂U(Pc)	Benzonitrile	689	—	620	351	[73]
		(5.22)		(4.53)	(4.76)	

[a] There are also absorption bands at 668 (4.15) and 585 (3.40) nm.
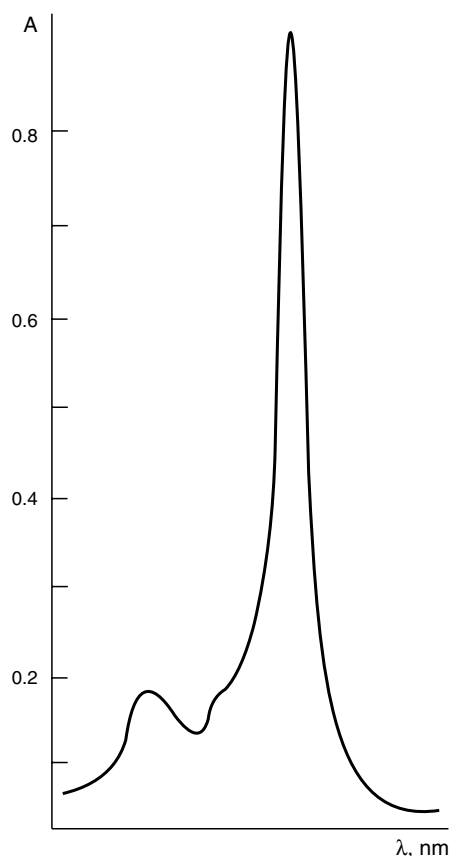
Figure 2. UV-vis spectra of $(OAc)_{n-2}Ln(Pc)$ in ethanol. λ^I_{max} for complexes of metals (nm): Tb, 670.6; Dy, 671.1; Ho, 670.6; Er, 671.0; Tm, 670.2; Yb, 670.6 ((Cl)Yb(Pc)); Lu, 669.7.

macrocycle plane. For example, in the tin phthalocyanine complex, the Sn atom is in the center of a square with a side of 2.78 Å, which is made by the isoindole nitrogens of the phthalocyanine ring [79]. The coordination center in $[(I)(Py)Ir^{III}(Pc)] \cdot Py$ has an analogous structure. Ir^{III} is in the center of a slightly distorted phthalocyanine ligand and coordinates pyridine (Py) and iodide in a trans-arrangement. The average Ir–N-iso distance is 1.995 Å; the Ir–N_{Py} and Ir–I distances are 2.102 and 2.657 Å, respectively [75]. In lutetium(III) monophthalocyanine derivative, $[(H_2O)_2(OAc)Lu^{III}(Pc)] \cdot H_2O \cdot CH_3OH$, the coordination geometry is again a slightly distorted square antiprism [27]. The donor atoms consist of the four isoindole nitrogens of the phthalocyanine ring, two oxygen atoms of one acetate anion, and two oxygens of two water molecules. The acetate anion and two water molecules are at one and the same side of the macrocycle. The four Lu–N-iso bond distances range from 2.333 to 2.359 Å with a mean value of 2.345 Å. The four isoindole nitrogen atoms of the phthalocyanine ring are coplanar. The Lu atom lies 1.26 Å away from the four N-iso mean plane.

2.4. Properties

A varying acido-ligand nature could change the stability of the coordination compounds of this type. Our investigations were carried out in two ways: for complexes of one and the same metal (Gd) with a set of acido-ligands X^- (Cl^-, Br^-, AcO^-) and for acidophthalocyanine complexes of different metal cations of one type (lanthanides) with one and the same X^-. In the last case correlations between parameters of the complexes and chemical-physical parameters of the complexation atoms could be obtained, allowing the establishment of the type of donor-acceptor bonds and contributions to complex stability.

$[(C_2H_5OH)_{n-2}Ln(Pc)]^+$ dissociation in mixtures of ethanol with 15–60% AcOH leads to formation of H_2Pc soluble in the reaction mixture; sediment formation is not observed during the reaction process:

$$[(C_2H_5OH)_{n-2}LnPc]^+ + 2C_2H_5OH_2^+$$
$$\rightarrow H_2Pc + [Ln(C_2H_5OH)_n]^{3+} \qquad (1)$$
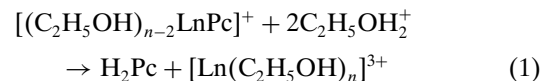
The rate constant of $(X)_{n-2}Ln(Pc)$ dissociation at standard temperature 298 K k^{298} is the main fundamental characteristic of the complex stability in the absence of data on equilibrium constants of the reaction [59, 80]. When obtaining the real k^{298} values is impossible, the observed value k^{298}_{obs} for one and the same composition of the acid solvent simultaneously acting as a reagent could be used.

k^{298}_{obs} values for $(X)_{n-2}Ln(Pc)$-derived extrapolation k_{obs} temperature dependence change nonlinearly with changing AcOH content in a wide range of the mixed solvent compositions (Fig. 3). For labile complexes of phthalocyanine with lanthanum subgroup lanthanides, the $k^{298}_{obs} - f(C^0_{AcOH})$ dependence is linear from 0 to 2.5 mol/liter AcOH concentration in ethanol. In this case a value of the tangent of the inclination angle of a straight line in $k^{298}_{obs} - f(C^0_{AcOH})$ coordinates can be used as a universal (with regard to mixed
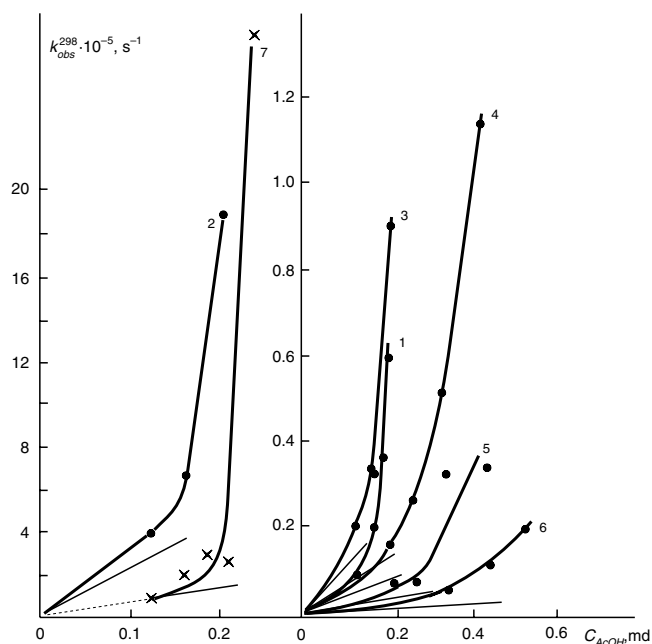
Figure 3. Dependence of dissociation rate constants of (X)M(Pc) on initial AcOH concentration. M: 1, Tb; 2, Dy; 3, Ho; 4, Er; 5, Tm; 6, Yb; 7, Y. Reprinted with permission from [80], T. N. Lomova and L. G. Andrianova, *Zh. Neorg. Khim.* 39, 2011 (1994).

solvent composition) criterion of the complex stability. This value is proportional to k: $K_a \times k$, where K_a is the acid ionization constant of AcOH in ethanol. The tangent of the inclination angle of the tangent line to the curve on Figure 3 (tg α), drawn through the origin, has the same meaning as the $K_a \times k$ parameter in the case of phthalocyanine complexes with elements from La to Gd. Thus, making use of tg α values proportional to the k value for Tb-Lu phthalocyanine complexes, we obtain the dependence of the physical-chemical parameter of the complex from the lanthanide ordinal number (Z) through the entire row (Fig. 4). According to Figure 4 data, the phthalocyanine lanthanide stability changes with Z growth through a concave curve with "gadolinium fracture" directed down. It must be pointed out that k_{obs}^{298} dependence from Z for one and the same solvent composition is analogous (Fig. 4). In spite of the complex composition of the investigated compounds, the dependence under consideration has a "canonical" type in a whole [81] and is analogous to the dependencies obtained when stability constants for Ln^{3+} complexes with chelate and simple molecular ligands are studied. It is known [81, 82] that "gadolinium fracture" is connected with peculiarities of Ln^{3+} f-shells and is determined by contributions of spin and orbital angular moments of quantity of motion of the base states of lanthanide cations. Detailed analysis of the dependency in Figure 4 (curve 1) shows that in addition to the presence of partially filled f-orbitals in (X)Ln(Pc), the non-monotonous character of complex stability change in the lanthanide row is connected with the action of supplementary factors in the cases of complexes of Ce^{3+} and Tb^{3+}. The sharp increase in kinetic stability at the beginning of every subgroup—from La to Ce and from Gd to Tb—indicates participation of $4f^1$ and $4f^8$ electrons in dative π-connection Ln→N in the complex. This could be connected with striving of the pointed atoms in the complexes for stable f^0 and f^7 configurations correspondingly and with the presence of vacant π-orbitals of low energy in the macrocycle.
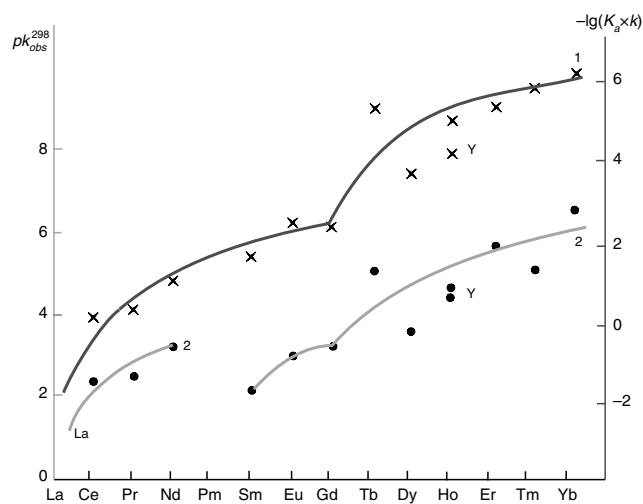
The considered data show that phthalocyanine complexes of rare-earth elements are not pure ionic complexes. Covalent contribution to donor-acceptor interaction is carried out with the participation of $4f$-orbitals as well as external s-orbitals. The last is proved by comparison of the stability of complexes of M^{3+} cations with a closed s^2p^6 outer shell without f orbitals (Al^{3+}, Sc^{3+}, Y^{3+}) and complexes of La^{3+}, Gd^{3+}, Lu^{3+} cations with f^0, f^7, and f^{14} electron configuration. The stability series, made with the help of data on the acidity of media where the complexes dissociate at a measurable rate [80, 83], is Al > Sc > Y > La < Gd < Lu. The complexes in the series are settled as Z increases. Deviation from monotony for Gd and Lu complexes is obviously connected with the so-called f-effect [84], which is a decrease in energy of the outer s-orbitals and their participation in the formation of covalent bonds with the ligand orbitals.

Dependence of the dissociation reaction rate of gadolinium phthalocyanine complexes with a set of different acido ligands X^- upon the X^- nature is evidence of the acido ligand presence in the first coordination shell of gadolinium(III). The dissociation rate increases in a series, (OAc)Gd(Pc) < (Br)Gd(Pc) < (Cl)Gd(Pc), corresponding to a parameter of electronegativity of donor atoms of X^-. Thus the complex stability could be changed in a necessary direction by acido ligand change.

The second process of complex stability increase is connected with high phthalocyanine macrocycle polarizability, which allows change in the complex stability through introduction of the substituents to benzene rings [85]. However, a maximum effect of the change in metallophthalocyanine stability could be achieved by coordination center steric screening, that is, going from $(X)_{n-2}M(Pc)$ to more complex compounds.

3. PHTHALOCYANINE DOUBLE DECKERS

3.1. Synthesis

Diphthalocyanines of lanthanides could be obtained in two forms: a mono-proton form, Ln(HPc)(Pc), where the tree-charged Ln^{3+} cation replaces three protons of NH bonds and the fourth proton remains unsubstituted or in oxidized radical form, Ln(Pc)$_2^{\bullet}$, where one π-electron is moved off and the H atom is absent [86, 87].

A mixture of (X)Ln(Pc), Ln(HPc)(Pc) (or Ln(Pc)$_2^{\bullet}$), and $Ln_2(Pc)_3$ (**1–3**) complex compounds with different contents of individual complexes, depending on the nature of the metal, is obtained when lanthanide phthalocyanines are synthesized according to traditional methods [86, 88, 89], that is, when o-phthalodinitrile is heated with a rare-earth metal salt in a 8:1 mole ratio at 563 K. In [90], with a sample of Lu complexes, it is shown that the optimum conditions for synthesis of metallophthalocyanines with double-decker structure from substituted o-phthalodinitrile (dicyanobenzo-15-crown-5) are the following: caking of $Lu(OAc)_3 \cdot 4H_2O$ with substituted dinitrile in a 1:8 ratio at 538 K for 40 min. The yield of the Lu double-decker complex is 35%. The radical structure of the compound (Lu(tetra-15-crown-5-Pc)$_2^{\bullet}$) is established on the basis of its UV-vis, infrared (IR), and electron paramagnetic resonance (EPR)

Figure 4. Dependence of lg($K_a \times k$) (1) and pk_{obs}^{298} in ethanol–25% AcOH (2) from lanthanides number (for La-Nd complexes k_{obs}^{298} values in ethanol–1% AcOH is presented). Reprinted with permission from [80], T. N. Lomova and L. G. Andrianova, *Zh. Neorg. Khim.* 39, 2011 (1994).

spectroscopy investigations. If the pointed conditions are disturbed, H_2(crownPc) and monophthalocyanine complex (OAc)Lu(crownPc) appear in the products of the synthesis as well.

Another form of double-decker lutetium complex (protonated form Lu(HPc)(Pc), described for the first time in [90]) is obtained in [28] by a multistage synthetic procedure. A solution of [Lu(Pc)$_2$][Na⊂18c.6] was prepared with 20 mg (7.5×10^{-2} mmol) of 18-crown-6 and 100 mg (20 mmol) of sodium hydride (dispersion in oil) for 80 mg (6.7×10^{-2} mmol) of green Lu(Pc)$_2$, and chlorobenzene was used as a solvent. After filtration, 10 ml of methanol was added to 50 ml of the solution. Concentration under vacuum and subsequent addition of pentane led to blue crystals of Lu(HPc)(Pc) [28]. The green form of Lu diphthalocyanine, Lu(Pc)$_2$, which has a sandwich structure with one phthalocyanine ring oxidized in a radical cation, was prepared from Lu(OAc)$_3$(H$_2$O)$_x$ by procedures published in [27].

One of the authors of the present review investigated [91] the influence of o-phthalodinitrile:Ln salt ratio on the yield of double- and triple-decker metallophthalocyanines in a single-stage reaction (template synthesis) for the whole lanthanide series (except Pm) and Sc and Y. The goal of the work was to obtain phthalocyanine complexes of double and triple structure with optimal yields in one and the same reaction. The maximum Ln$_2$(Pc)$_3$ yield is achieved in the reaction of o-phthalodinitrile with a rare-earth metal chloride in a 6:1 mole ratio at 563 K for 1 h. Diphthalocyanines of lanthanides (Ln(HPc)(Pc)) are almost always present as the products of the synthesis. Ln$_2$(Pc)$_3$ yield decreases from the beginning to the end of the lanthanides raw, whereas Ln(HPc)(Pc) yield changes in a reverse succession. For example, for Yb complexes the yield of double decker is 19.1% and that of triple decker is 10.3%. For Nd complex the triple decker is the only product of the synthesis. After the reaction mixture was cooled, double and triple deckers could be divided by dissolving in dimethyl flouride (DMF) and preparative chromatography procedure on Al$_2$O$_3$. Two well-divided zones of green and blue colors were observed.

A simple method of synthesis of double-decker phthalocyanine complexes with microwave irradiation has been suggested [92]. In this work rare-earth phthalocyanines were produced from tetrahydrated Tb, Dy, and Lu acetates and different phthalic acid derivatives. The attempts were focused on the production of individual mono- and bisphthalocyanines by varying the phthalogen:salt ratio (4:1, 8:1, 12:1) and the time of synthesis. With increasing time of synthesis the proportion between mono- and diphthalocyanine yields is shifted toward the diphthalocyanine. The activity of phthalogenes increases slightly in the order phthalic acid < phthalic anhydride < phthalimide, but the main final product was monophthalocyanine, even if the reagents were taken in the ratio optimal for diphthalocyanine synthesis. However, the reaction with phthalodinitrile as a precursor gives diphthalocyanine as the main final product, which was formed even at a phthalodinitrile:salt ratio of 4:1. Thus, depending upon the nature of the phthalogen, its proportion to the metal salt, and the duration of microwave irradiation, it is possible to control the yield of the final

products. The yield of the tert-butyl-substituted phthalocyanines of rare-earth elements under microwave irradiation was much smaller than that of unsubstituted phthalocyanine analogues. The yield of unsubstituted diphthalocyanines synthesized from rare-earth acetates was 7–10 times higher than that of tert-butyl phthalocyanines and accounted for more than 70%.

LnPc$_2^\bullet$ [93] can be synthesized [54, 86] by the interaction of 10 g of o-phthalodinitrile with 1 g of lanthanide acetate at 560–570 K for 1 h. The blue-green product is kept in a vacuum at 620 K for 1 h and then dissolved in DMF (150 ml) with the addition of hydrazine hydrate. The solution is filtered and undergoes electrolysis with constant current in a cell with a graphite cathode and Pt anode. The crystals obtained are filtered, washed with acetone, and dried at 370 K in air.

As for other tree-charged metal cations, the synthesis of a double-decker complex of In^{III} has been described [8]. Indium diphthalocyanine was prepared from InMg alloy and o-phthalonitrile in 1:2 weight proportion, mixed together, and pressed into pellets. The pellets were inserted into an evacuated glass ampule and sealed. The ampule was heated at 483 K for 1 day, which yielded good quality blue-violet rectangular crystals with an edge up to 1 mm and a blue polycrystalline material. The polycrystalline material was identified as MgPc.

Double-decker phthalocyanine complexes of four-charged metal cations (Zr(IV), Hf(IV) [65], Th(IV), U(IV) [54]) have been synthesized. It was found [94] that the heating of a reaction mixture consisting of phthalodinitrile and hafnium and zirconium salts at 523–553 K for several hours was necessary for the formation of sandwich-like complexes of these metals. In [92] this reaction was accomplished over a few minutes under exposure to 650–700-W microwave irradiation, and the amount of by-products was lower, which made the final purification simpler. A single purification procedure with the use of column chromatography gives individual compounds with a high degree of purity, as is evident from thin-layer chromatography, elemental analysis, and UV and visible spectra.

U(IV) phthalocyanine double-decker was obtained in [54] by a method that was slightly modified from one described earlier in [95]. Three grams of Na$_2$(Pc) and 0.9 g of UCl$_4$ were allowed to react in boiling 1-chloronaphthalene (30 ml) for 12 h. The solution was filtered while hot, and, after cooling, the solid was precipitated from solution with heptane. The yield of U(Pc)$_2$ was 0.25 g (7.4%). The Th(IV) diphthalocyanine complex was obtained by the same method [54]. In a typical experiment, 3 g of Na$_2$(Pc) and 1.72 g of ThCl$_4$ gave 0.18 g of Th(Pc)$_2$ (6.2% yield).

It is evident that template synthesis is the main method of synthesis of double-decker phthalocyanine complexes. The reaction of complexation of H$_2$Pc, prepared before, with metal salts is of minor significance.

3.2. Spectroscopic Characterization

Electron absorption spectra of stable Ln diphthalocyanines in concentrated sulfuric acid (Table 4) have one wide band in the region of 400 nm. λ_{max} in 17.7 M H$_2$SO$_4$ changes from 443 nm for the Pr complex to 395 nm for Tm, Yb,

Table 4. Position (λ_{max}) and intensity ($\log \varepsilon$) of adsorption bands in Ln(Pc)$_2^{\bullet}$ UV-vis spectra in 17.7 M H$_2$SO$_4$.

Diphthalocyanine	λ_{max} nm ($\log \varepsilon$)						
	I	II	III	IV	V	VI	VII
Pr(Pc)$_2^{\bullet}$	837 (5.16)	775 (5.02)	745[a]	690[a]	443 (4.51)	305 (4.90)	250
Nd(Pc)$_2^{\bullet}$	837 (5.11)	775 (4.96)	745[a]	690[a]	442 (4.47)	305 (4.85)	250
Sm(Pc)$_2^{\bullet}$	—	783 (3.26)	—	—	410 (4.32)	—	250
Eu(Pc)$_2^{\bullet}$	—	—	—	—	410 (4.00)	—	250
Gd(Pc)$_2^{\bullet}$	—	—	—	—	407 (4.00)	315[a]	250
Tb(Pc)$_2^{\bullet}$	—	—	—	—	397 (4.43)	285 (4.78)	250
Dy(Pc)$_2^{\bullet}$	—	—	—	—	397 (4.52)	287 (4.79)	250
Ho(Pc)$_2^{\bullet}$	—	—	—	—	397 (4.50)	287 (4.77)	250
Er(Pc)$_2^{\bullet}$	—	—	—	—	397 (4.26)	287 (4.50)	250
Tm(Pc)$_2^{\bullet}$	—	—	—	—	395 (4.60)	285 (4.85)	253 (5.03)
Yb(Pc)$_2^{\bullet}$	—	—	—	—	395 (4.63)	285 (4.88)	253 (5.04)
Lu(Pc)$_2^{\bullet}$	—	—	—	—	395 (4.60)	285 (4.83)	253 (4.99)

Note: Intensity ($\log \varepsilon$) is in parentheses.
[a] Shoulder.

and Lu complexes. Such absorption bands are absent from the spectra of monophthalocyanine complexes and are considered a reliable indicator of phthalocyanine complexes of double-decker structure.

When the Ln(Pc)$_2^{\bullet}$ (Ln = Pr, Nd, Sm) concentration in sulfuric acid solution is increased from 2×10^{-5} to 1×10^{-4} mol/liter, the UV-vis spectrum changes (Fig. 5, compare curves 11 and 1). The absorption band of the diphthalocyanine Ln(Pc)$_2^{\bullet}$ (420 nm) is shifted bathochromically and decreases in intensity with increasing complex concentration. High-energy absorption bands (838, 775 nm) become more intensive. This spectrum is characteristic for dimer diphthalocyanine complexes [83, 87]. With heating

in concentrated sulfuric acid solutions these complexes undergo dissociation.

UV-vis spectra of lanthanide diphthalocyanines of La and Y subgroups display large differences (Table 4). Spectra of freshly prepared sulfuric acid solutions of diphthalocyanines of lanthanides of the first group contain intensive absorption bands at 700–900 nm (Fig. 6). Over several hours at room temperature (or several minutes at 320 K) the spectra of Sm, Eu, Gd complexes change and become analogous in character to spectra of complexes of lanthanides from Tb to Lu (Ln(Pc)$_2^{\bullet}$) (Table 4). The number of bands in the spectra of Pr and Nd complexes does not change in time, but the intensity of the absorption bands decreases because
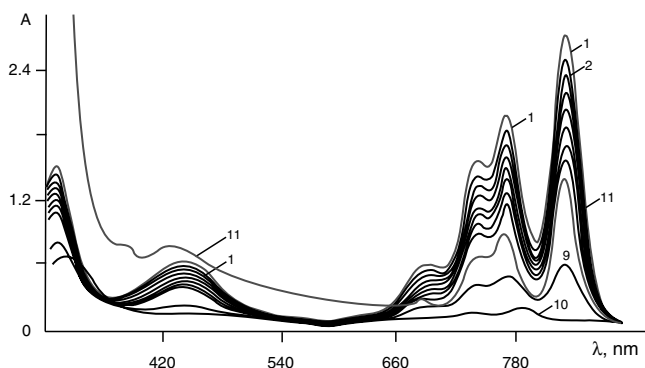
Figure 5. Electron absorption spectra of Nd(Pc)$_2^{\bullet}$ in 17.7 M H$_2$SO$_4$ for [NdPc$_2^{\bullet}$] $\cong 1 \times 10^{-4}$ (1–10) and 2×10^{-5} (11) mol/liter at 298 K; time: 1 and 11, 0; 10, 24 h; 2–9, intermediate moments.
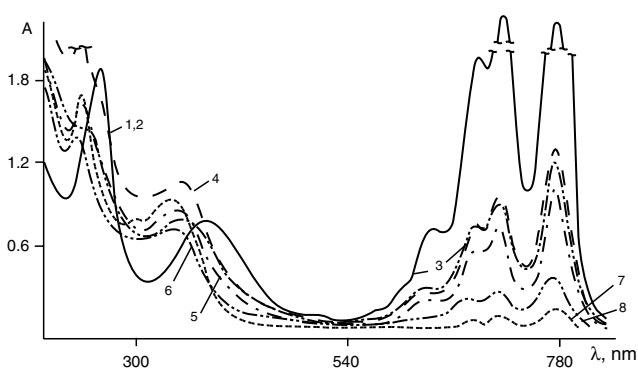
Figure 6. Electron absorption spectra of freshly prepared solutions of diphthalocyanines in 17.2 M H$_2$SO$_4$. 1, Pr; 2, Nd; 3, Sm; 4, Eu; 5, Gd; 6, Tb; 7, Ho, 8, Yb. [Ln(Pc)$_2^{\bullet}$] = 2×10^{-5} mol/liter.

of the complex dissociation. The transformation of diphthalocyanine spectra over time is obviously connected with the formation of dimers of diphthalocyanines in freshly prepared solutions. According to the opinion of the author of [55], $Ln(Pc)_2^\bullet$ complexes exist as dimers in a solid state. The dimers transfer to monomeric diphthalocyanines, $Ln(Pc)_2^\bullet$, when they are dissolved in concentrated H_2SO_4, which has a high dielectric constant. This is the cause of the spectra change over time or during heating. Spectral data (Table 4, Fig. 6) show that the complexes of lanthanides of the second half of the row are less inclined toward dimer formation, which could be connected with their larger susceptibility to unpaired electron delocalization as compared with the complexes of the La subgroup.

Data on the state of diphthalocyanine complexes in H_2SO_4 and the data of [55] suggest a total scheme of mutual transformations of different forms of double-decker lanthanides (Scheme 3).

Diphthalocyanine complexes of M(IV) exist in only one form, $M^{IV}(Pc)_2$. Because of the several forms of complexes of M^{III}, their electron absorption spectra in organic solvents are divided into two types: with a single Q(0,0) band in the region of 615–690 nm and with a Q(0,0) band split into two components, with $\Delta\lambda \sim 60$ nm. In the second case the intensity of long-wave band I is much lower compared with that of II. Spectra of the first type belong to complexes with nonequivalent macrocycles—nonsymmetrical hydrogen-containing oxidized forms $M^{III}(HPc)(Pc)$ and $M^{III}(Pc)_2^\bullet$ (Fig. 7). Symmetrical $M^{IV}(Pc)_2$ has a split Q(0,0) band. Resonance dipole-dipole interaction between the aromatic systems of the two macrocycles is considered the cause of the splitting [55]. Spectra of $U(Pc)_2$ and $Th(Pc)_2$ are good examples (Table 5). An additional weak absorption band at 450–480 nm is one more characteristic feature of nonsymmetrical complex spectra (Fig. 7, Table 5).

3.3. Structure

The central atoms in metallodiphthalocyanines of the general formula $M(Pc)_2$ have a coordination number of eight [8]. The metallodiphthalocyanines exist in different crystalline modifications. For instance, α-tetragonal and β-monoclinic forms of $Nd(Pc)_2$ and β-monoclinic and γ-orthorhombic forms of $Sn(Pc)_2$ are known [9, 10, 24]. $Nd(Pc)_2$ also crystallizes in orthorhombic γ-form, for which the lattice parameters obtained from the powder diffraction diagram correspond to the known orthorhombic form of $Sn(Pc)_2$ [9].

The crystal of the indium(III)diphthalocyanine complex consists of discrete $In(Pc)_2$ molecules [8]. The indium atom
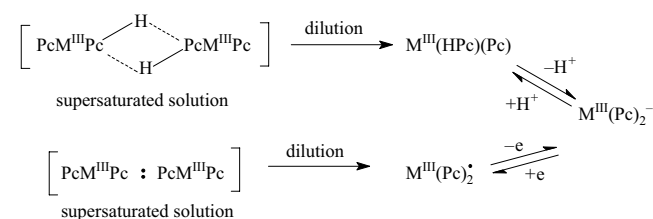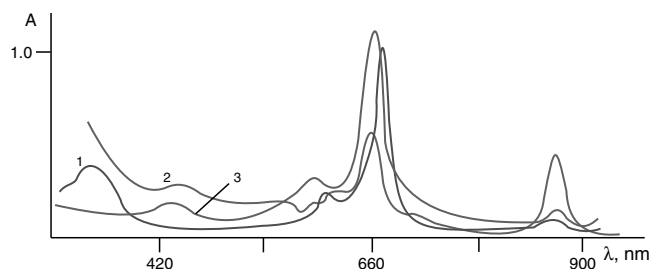
Figure 7. UV-vis spectra of (X)Tm(Pc) (1), Tm(HPc)(Pc) (2), and $Tm_2(Pc)_3$ (3) in benzene. Reprinted with permission from [91], T. N. Sokolova et al., *Koord. Khim.* 20, 637 (1994).

is located between two saucer-shaped isoindole phthalocyaninato units and is coordinated by eight nitrogen isoindole atoms, which form an irregular square antiprism. The ring systems are rotated by 41.2° with respect to one another [8]. The two opposite squares of isoindole nitrogen atoms are 2.741 Å apart.

In monoclinic crystals of $Sn(Pc)_2$ (β-form) the two phthalocyanine rings form a sandwich-type complex with a tin atom in the center of the molecule [10]. The distance between phthalocyanine planes in this sandwich-type macromolecule is equal to 2.57 Å. The two phthalocyanine moieties are rotated about 38° with respect to one another. The tin atom, in coordination with eight isoindole nitrogen atoms, forms a square antiprism. The Sn-N bond distances range from 2.312 to 2.330 Å [10].

According to crystallographic data [28], Lu(HPc)(Pc) molecules also have a sandwich-type (double-decker) structure. The coordination polyhedron of the metal is a slightly distorted square antiprism. The mean value of the Lu–N-iso bond lengths is 2.366 Å with one ring and 2.376 Å with the other ring. Each phthalocyanine ring is rotated by 41° with respect to the other. The acidic hydrogen of Lu(HPc)(Pc) could not be located. It is most probably linked to a methine nitrogen and disordered over both rings.

X-powder diffraction of $Pa(Pc)_2$ [95] shows the compound to be isostructural with $Th(Pc)_2$ and $U(Pc)_2$.

Summary table of crystallographic data (Table 1) on double-decker phthalocyanine complexes is presented in the Introduction. From the results it can be seen that the structure of double-decker phthalocyanine complexes for all of the investigated compounds is of one type. The metal atom is coordinated by eight isoindole nitrogen atoms (N-iso) and is situated between two phthalocyanine macrocycles (Fig. 8). Macrocycles undergo distortion and become nonplanar but saucer-shaped with benzene rings bent outward. The degree of distortion as well as M-N-iso distances and rotation of the macrocycles with respect to one another are determined by the nature and radius of the metal cation.

We should point out one more type of phthalocyanine double-decker [12, 96, 97] in which the two C-C σ bonds are present, "stapling" together the two phthalocyaninato moieties at the opposite sites of the metal ion. For such structures a shorter distance between the two opposite N-isoindole planes is observed (2.32 Å for $Ti(Pc)_2C_{10}H_7Cl$) as compared with the previously described complexes [8].

Scheme 3.

Table 5. UV-vis spectra of solutions and solid films of phthalocyanine double deckers.

Chemical formula of the compound	Solvent or solid film	λ_{max} (nm)(log ε)	Ref.[c]
La(Pc)$_2^-$	Dichlorobenzene	340 (5.05), 646 (5.01), 686 (4.42)	
La(Pc)$_2^-$	Methanol	639	
La(Pc^t)$_2^a$	Dichlorobenzene	318 (4.90), 462 (4.12), 646 (4.63), 686 (4.80)	
Pr(Pc)$_2^-$	Methanol	334 (5.03), 644 (5.05), 682 (4.47)	
Pr(Pc^t)$_2$	Dichlorobenzene	324 (4.94), 480 (4.15), 610 (4.34), 644 (4.69), 682 (4.82)	
Nd(Pc)$_2^-$	DMF + 1 vol.% hydrazine hydrate	640, 660 shoulder	
Nd(Pc)$_2^-$	Methanol	635	
Nd(Pc)$_2^•$	Benzene	464, 610, 680, 905	
Nd(Pc)$_2^•$	Solid film	470, 618, 690, 908	
Sm(Pc^t)$_2^-$	Dichlorobenzene	340 (5.01), 644 (5.03), 680 sh. (4,61)	
Sm(Pc)$_2^-$	Methanol	630	
Sm(Pc^t)$_2$	Dichlorobenzene	330 (5.04), 340 (5.02), 502 (4.16), 644 (4.60), 679 (4.86)	
Eu(Pc)$_2^-$	DMF + 1 vol.% hydrazine hydrate	633, 680 sh.	
Eu(Pc)$_2^•$	Benzene	460, 606, 676, 908	
Eu(Pc)$_2^•$	Solid film	468, 614, 688, 915	
Eu(HPc)(Pc)	Chloronaphthalene	350 (4.87), 463 (4.38), 610 (4.54), 677 (5.10)	
Gd(Pc^s)$_2^{-b}$	H$_2$O (pH 10–11)	640 (5.04)	
Gd(Pc)$_2$	Methanol	628	
Gd(Pc^t)$_2^-$	Dichlorobenzene	328 sh. (5.12), 330 (5.25), 634 (5.24), 674 sh. (5.06)	
Tb(Pc)$_2^-$	Methanol	626	
Dy(Pc)$_2^-$	Methanol	625	
Ho(HPc)(Pc)	H$_2$SO$_4$	224 (4.94), 250 (5.00), 288 (4.80), 396 (4.56)	
Ho(Pc)$_2^-$	Methanol	624	
Er(Pc)$_2^-$	DMF	624	
Er(Pc)$_2^-$	Methanol	623	
Tm(Pc)$_2^-$	Methanol	620	
Yb(Pc)$_2^-$	Methanol	620	
Lu(HPc)(Pc)	Chloronaphthalene	350 (4.76), 460 (3.94), 607 (4.38), 668 (5.09)	
Lu(Pc)$_2^-$	DMF + 1 vol.% hydrazine hydrate	620, 720	
Lu(Pc^s)$_2^-$	H$_2$O (pH 10–11)	635 (5.02)	
Lu(Pc)$_2^•$	Benzene	458, 592, 660, 912	
Lu(Pc)$_2^•$	Solid film	470, 610, 682, 930	
Lu(Pc^t)$_2$	Dichlorobenzene	328 (5.02), 342 (4.99), 462 (4.49), 599 (4.20), 634 (4.57), 662 (5.21)	
Y(Pc^s)$_2^-$	H$_2$O (pH 10–11)	638 (4,96)	
Y(Pc)$_2^-$	DMF	623	
Sc(Pc)$_2^-$	DMF	334 (5.24), 560 sh., 615 (5.20), 730 (4.82)	
Th(Pc)$_2$	DMF + 1 vol.% hydrazine hydrate	592 sh., 646, 688	
Th(Pc)$_2$	Benzene	592 sh., 646, 688 sh.	
Th(Pc)$_2$	Solid film	560 sh., 675	
Pa(Pc)$_2$	Chloronaphthalene	350 (4.49), 590 sh., 650 (5.23), 700 sh	
U(Pc)$_2$	Quinoline	649	
U(Pc)$_2$	Chloronaphthalene	355 (4.91), 590 sh., 650 (5.18), 715 sh.	
U(Pc)$_2$	Solid film	244 (5.07), 270 sh., 428 (4.68),662, 732 sh.	
Np(Pc)$_2$	Chloronaphthalene	343, 646, 698	
Pu(Pc)$_2$	DMF + 1 vol.% hydrazine hydrate	641, 682 sh.	
Pu(Pc)$_2$	Benzene	642, 690 sh.	
Pu(Pc)$_2$	Solid film	664	
Pu(Pc)$_2$	Chloronaphthalene	344, 642, 690	
Am(Pc)$_2^-$	DMF + 1 vol.% hydrazine hydrate	642, 662 sh.	
Am(Pc)$_2^•$	Benzene	476, 610, 676, 908	
Hf(Pc)$_2$	Chloronaphthalene	350 (4.97), 580 sh., 631 (5.13), 757 (4.65)	
Lu(HPc)(Pc)	Chlorobenzene	324 (4.85), 614 (4.82), 694 (3.95)	[28]
Lu(crownPc)$_2^•$	CHCl$_3$	367 (5.17), 476 (4.66), 602 (4.50), 655 (5.20)	[89]
Th(Pc)$_2$	CH$_2$Cl$_2$	330 (5.09), 585 sh., 640 (5.26), 689 sh.	[54]
Th(Pc)$_2$	Chloronaphthalene	343.5, 645.5, 682	[96]
Pa(Pc)$_2$	Chloronaphthalene	344, 643.5, 680	[96]
U(Pc)$_2$	CH$_2$Cl$_2$	332 (4.83), 593 sh., 638 (4.95), 700 (4.32)	[54]
U(Pc)$_2$	Chloronaphthalene	342.5, 642.5, 708	[96]
Zr(Pc)$_2$	o-dichlorobenzene	274 (4.90), 335 (5.03), 571 (4.20), 628 (5.21),746 (4.76)	[65]
Hf(Pc)$_2$	o-dichlorobenzene	334 (4.84), 626 (5.01), 744 (4.51)	[65]

[a] Pc^t, *tert*-butylphthalocyanine dianion.
[b] Pc^s, sulforized phthalocyanine dianion.
[c] Lines without references are taken from [55].
Source: Reprinted with permission from [55], P. N. Moskalev, *Koord. Khim.* 16, 147 (1990).
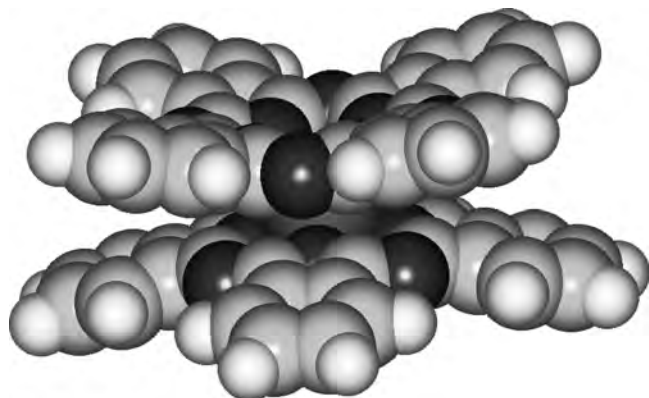
Figure 8. Molecular structure of Th(Pc)$_2$ according to geometrical optimization data, using molecular mechanics method MM+.

3.4. Properties

Properties of double deckers are studied intensively. Lanthanide and actinide porphyrin and phthalocyanine sandwich complexes have provided an ideal series of molecules for studying the electronic structure and dynamism of interacting macrocycles [54]. The electrochemistry of 26 different neutral and singly oxidized actinide double-decker complexes is reported [54]. The investigated compounds are presented as $[M(P)_2]^n$, $[M(P)(P')]^n$, $[M(Pc)_2]^n$, and $[M(P)(Pc)]^n$, where $n = 0$ or $+1$ and M = U or Th. Cationic singly oxidized double-decker derivatives were chemically generated and isolated as a $SbCl_6^-$ salt. The initial neutral species can undergo up to six reversible one-electron transfers in nonaqueous media, and U(IV) or Th(IV) compounds with porphyrin and phthalocyanine macrocycles could be electrogenerated in up to seven different oxidation states. M(Pc)$_2$ derivatives undergo initial one-electron oxidations and reductions that are localized not at a single phthalocyanine ring but rather at orbitals involving both macrocycles. No π-π interactions were observed for the singly oxidized diphthalocyanine species, and electron spin resonance spectra of $[Th(Pc)_2]^+$ suggest simple monomeric cation radicals, both as $SbCl_6^-$ salts in the solid state and in frozen solutions of CH_2Cl_2 or pyridine at 110 K [54].

Tetra-crown substituted diphthalocyanines of metals, M(tetra-15-crown-5-Pc)$_2$, have liquid-crystal properties [98]. They form mesophases where crown-ether rings lying one over another create channels through which transport of ions is possible [99]. Thus, a possibility of accumulation and transformation of information is created.

Diphthalocyanine complexes of rare-earth metals of double-decker structure possess many useful properties, such as electrochromism (Lu complexes [60, 100, 101]), semiconductor properties, and others, which are being intensively investigated [102]. In this connection questions about the chemical stability of the compounds are of special importance.

The results of the first quantitative investigations of stability in solutions of lanthanide phthalocyanines with a 1:2 composition of lanthanide ion-phthalocyanine were published in [93]. In this paper the properties of sulfuric acid solutions and dissociation reactivity of oxidized diphthalocyanines of Sc, Y, Pr, Nd, and lanthanides from Sm to Lu

were systematically considered. The properties of oxidized Ln diphthalocyanines change essentially along a series from La to Lu. That is why La and Y subgroups will be described separately.

When sulfuric acid solutions of the complexes are kept at temperatures higher than 338 K (Sm, Eu, Gd) or 300 K (Pr, Nd), a decrease in Ln(Pc)$_2^{\bullet}$ concentration is observed, and there are no other colored forms in the solutions according to UV-vis spectra. Reprecipitation of the reaction mixture during the reaction process ($\tau_{1/2}$) to ice gives the same result. The dissociation process is accompanied by rapid destruction of the macrocycle. The total scheme of the transformations of the complexes is

$$LnPc_2^{\bullet} + (n-2)H_3O^+ \Leftrightarrow LnPc_2^{\bullet} \cdots (n-2)H_3O^+ \quad (2)$$

$$LnPc_2^{\bullet} \cdots (n-2)H_3O^+ + 2H_3O^+$$
$$\rightarrow [(H_2O)_2LnPc]^+ + H_2Pc^{\bullet} \cdots (n-2)H_3O^+ \quad (3)$$

$$[(H_2O)_2LnPc]^+ + 2H_3O^+ \rightarrow [(H_2O)_4Ln]^{3+} + H_2Pc_{Solv} \quad (4)$$

$$H_2Pc_{Solv} \rightarrow \text{destruction products} \quad (5)$$
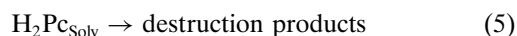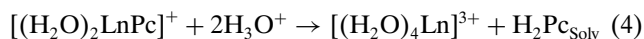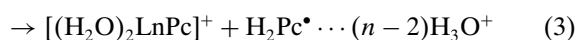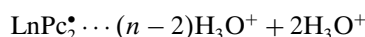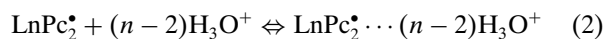
An order of diphthalocyanine Ln(Pc)$_2^{\bullet}$ dissociation on $[H_3O^+]$ (n) changes when the temperature changes and depends upon the nature of the metal cation. For one and the same complex n is smaller at the higher temperature. At 298 K the reaction order decreases in a series Eu > Gd > Sm > Pr, Nd, in a reverse succession compared with lgk^{298} (Fig. 9) and the E values change. Like monophthalocyanine complex dissociation in ethanol-AcOH mixtures, the rate of diphthalocianine complex dissociation in sulfuric acid decreases in the lanthanide row. Gd complex is an exception.
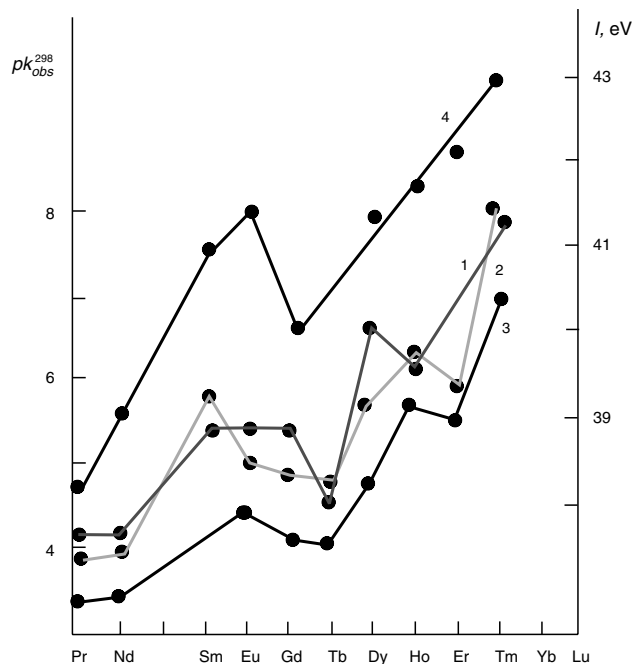
Figure 9. Dependence of pk_{obs}^{298} on LnPc$_2^{\bullet}$ dissociation (1–3) and summary of the third potential of ionization of rare-earth metals (4) from lanthanide number. H_2SO_4 concentration: 1, 17.7 M; 2, 16.9 M; 3, 15.9 M.

This is connected basically with peculiarities of the structure of electron f-shells of the metal cation and essential covalence of the complexes. $Ln(Pc)_2^{\bullet}$ transformation to monophthalocyanine complex (reactions (2) and (3)) is a result of solvo-protolytical dissociation of Ln-N bonds under the action of H_3O^+ cations, but not owing to splitting one of two macrocycles of $Ln(Pc)_2^{\bullet}$.

Tb, Dy, Ho, Er, and Tm diphthalocyanines are stable in 16–18 M H_2SO_4 at 298 K and in 100% H_2SO_4, even at 400 K. In more diluted H_2SO_4 (12 M) $Ln(Pc)_2^{\bullet}$ dissolves with destruction. When a solution of diphthalocyanine in 16–18 M H_2SO_4 is heated, a progressive decrease in intensity of the visible absorption band is observed. Dissociation rate constants grow with increasing temperature and with decreasing H_2SO_4 concentration. lg k_{obs}^T values are proportional to lg$[H_3O^+]^n$ values. The reaction order on $[H_3O^+]$ (n) is higher in most cases and varies when the nature of the metal is varied. n is higher for higher pk values of diphthalocyanine dissociation.

As already shown, in the dissociation conditions the complexes exist in the form of monomeric sandwich molecules (radicals). Proton absence (i.e., Ln(HPc)(Pc) particle absence) is shown by ^{1}H NMR spectra investigations (signals are not observed in D_2SO_4 solutions, tetramethylsilane internal standard, in region $+11 \div -5$ m.d.).

Nonconstant order on $[H_3O^+]$ of reaction (3) does not allow use of the pk^{298} value for comparative estimation of the complex stability. Because of this the pk_{obs}^{298} values for the same H_2SO_4 concentration for different complexes are shown in Figure 9. The character of pk_{obs}^{298}-Z dependence is the same as the ionization potential changing in the lanthanide row (Fig. 9). In all of the investigated media a deep minimum for Gd and Tb complexes is observed, and the Eu complex is kinetically more stable than neighboring $Gd(Pc)_2^{\bullet}$. Thus it could be concluded that, first, lanthanide diphthalocyanines must be regarded as covalent complexes and, second, that f-orbitals of metal take part in covalent Ln-N interaction. The complex of Gd (f^7) is essentially less stable than $Eu(Pc)_2^{\bullet}$, in which one electron must be added to the metal f-orbital to create a stable f^7 state. The last apparently promotes an electron density transfer from macrocycle π-orbitals to metal (dative π-bond N→Ln). We should point out that the "tetrade effect" found for the dissociation of sulfur derivatives of lanthanide diphthalocyanines in acid aqueous media [55] is not corroborated by the data presented here.

4. TRIPLE-DECKER METALLOPHTHALOCYANINES

4.1. Synthesis

In the infrequent communications on phthalocyanine complexes of triple-decker structure [36, 51, 55, 91], two main methods of their synthesis are reported: from o-phthalodinitrile and chlorides of the rare-earth elements (classic template phthalocyanine synthesis) and from the corresponding diphthalocyanine, metal salt, and phthalodinitrile or monophthalocyanine complex and $Li_2(Pc)$. In [35] an original method of $In_2(Pc)_3$ synthesis is described. The triple-decker complex was prepared from $InSn_4$ filings

($InSn_4$ alloy was obtained by melting indium and tin, in stoichiometric proportion, both 99.999% pure, under vacuum in a glass ampule) and o-phthalodinitrile, in 1:2 weight proportion, mixed together and pressed into pellets. The pellets were inserted into an evacuated glass ampule, which was sealed. The ampule was heated at 480 K for 2 days, which yielded two kinds of good-quality crystals. One kind was identified as Sn(Pc), the second as $In_2(Pc)_3$.

The template synthesis is described in the previous section. Triple-decker phthalocyanine complexes of Sm, Gd, Tm, and Lu were obtained according to this method [91]. As already shown (Section 3.1), the $Lu_2(Pc)_3$ complex is formed in a mixture with the corresponding diphthalocyanine Ln(HPc)(Pc), which could be devided easily on an Al_2O_3 column with DMF (green zone). The main product, $Ln_2(Pc)_3$, forms the second zone, which is blue in color. Compounds of the blue zone are triple-decker metallophthalocyanines (**2**). In earlier publications it was suggested that analogous products of the template synthesis are either metallophthalocyanines with formal metal charge $4 + Ln^{IV}(Pc)_2$ [103, 104]; or products of one-electron reduction of diphthalocyanines, $Ln^{III}(Pc)_2^-$ [100]; or products of their dimerization [105, 106]; or a binuclear complex with the composition $Ln(Pc)_2^- Ln(Pc)^+$ [86, 88, 107, 108]. In [36, 91] it is proved that the structure of this complex is of the triple-decker type, corresponding to the formula $(Pc)Ln^{III}(Pc)Ln^{III}(Pc)$ or $Ln_2(Pc)_3$. Each of the two metal atoms is covalently bound with two macrocycles. Two equivalent external macrocycles are not adequate to the third, central macrocycle. This structure is confirmed by all of the obtained experimental data. For instance, there is no signal of the proton of the NH-group in the ^{1}H NMR spectrum of Tm_2Pc_3. The ^{13}C NMR spectrum shows more than four signals of carbon, that is, there are macrocycles of two types in the sample (one central and two equal external macrocycles) (Fig. 10).

Triple-decker $Ln_2(Pc)_3$ dissociates in the mixed ethanol-H_2SO_4 (20:1) solvent at 298 K, giving double-decker Ln(HPc)(Pc) and H_2Pc. The last is insoluble in the experimental conditions and falls to sediment that is blue-green in color over several hours. The low stability of $Ln_2(Pc)_3$ complexes in comparison with $Ln(Pc)_2^{\bullet}$ is obviously connected with mutual pushing off the macrocycles in the coordination sphere of the triple-decker complexes.

$Ln_2(Pc)_3$ complexes are insoluble in water and do not undergo dissociation in it. They are weakly dissolved in the coordinating solvents. Thus the initial complex is not an ionic compound, as the authors of [86, 88, 107, 108] suppose. Analogous conditions of dissociation (ethanol-H_2SO_4 mixtures) of $Ln_2(Pc)_3$ complexes (to $Ln(Pc)_2$ and H_2Pc) and their mono-phthalocyanine (X)Ln(Pc) analogs (to Ln^{3+}, X^-, and H_2Pc) are more evidence of the covalent nature of donor-acceptor bonds in $Ln_2(Pc)_3$.

4.2. Spectroscopic Characterization

UV-vis spectra of complexes Ln(HPc)(Pc) and $Ln_2(Pc)_3$ differ from those of (X)Ln(Pc) (Fig. 7). Ln(HPc)(Pc) and $Ln_2(Pc)_3$ have two intensive absorption bands at 660 and 870 nm in the visible region of the spectra, but the ratios of the intensities of the bands are different.
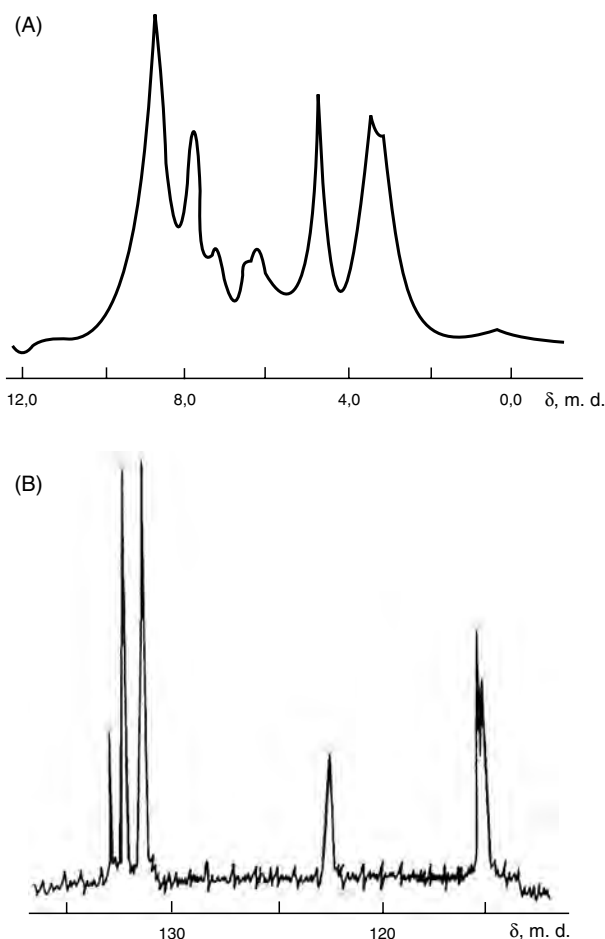
Figure 10. ^{1}H NMR (A) and ^{13}C NMR (B) spectra of $Tm_2(Pc)_3$ in $CDCl_3$.

IR spectra of the triple-decker compounds correspond to metallophthalocyanine spectra [109]. There are differences in the IR spectra of Ln(HPc)(Pc) and $Ln_2(Pc)_3$ in the region of ν(CH) benzene ring vibrations (2800–3080 cm^{-1}). An example is shown in Table 6. The IR spectrum of triple-decker $Tm_2(Pc)_3$ contains a larger number of bands than the Tm(HPc)(Pc) spectrum. This could be connected with the presence of one more phthalocyanine ligand. Macrocycles of

different types (central planar and external deformed) show different IR vibrations.

4.3. Structure

The structure of triple-decker phthalocyanine complexes is proved by crystallographic investigations. Complexes of Lu with tetra-15-crown-5-phthalocyanine [36] and $In_2(Pc)_3$ [35] were studied. The first structure is presented in Figure 1. The $In_2(Pc)_3$ macromolecule consists of two indium atoms and three phthalocyanine ligands. The indium atoms are located between phthalocyanine planes. The peripheral saucer-shaped phthalocyanine unit is coordinated through four nitrogen isoindole atoms, and the central phthalocyanine moieties by two nitrogen isoindole atoms. All of the atoms in the peripheral unit lie below the isoindole nitrogen atom plane. The intramolecular distance between two phthalocyanine ligand planes is 2.954 Å. The two peripheral phthalocyanine planes are parallel and 5.818 Å apart; the third ring is rotated by 37.5° with respect to them. The isoindole nitrogens belonging to the same ring form a square with a side 2.78 Å in length. The In atoms are located closer to the peripheral phthalocyanine plane than to the central phthalocyanine plane, the distances being 1.005 and 1.838 Å, respectively. The corresponding average indium-nitrogen distances are 2.223 and 2.350 Å. It appears that the indium atoms are more strongly connected to the peripheral phthalocyanine rings than to the central phthalocyanine ring.

4.4. Properties

$Ln_2(Pc)_3$ complexes that have an octacoordinated cation with valence 3 Ln^{III} are very stable coordination compounds. They do not change in weak acid solutions as well as Ln(HPc)(Pc) and $Ln(Pc)_2^\bullet$ complexes. But when they are dissolved in concentrated H_2SO_4, $Ln_2(Pc)_3$ complexes lose one of their macrocycle ligands and are transformed into Ln(HPc)(Pc) [91]. Rates of $Ln_2(Pc)_3$ dissociation in H_2SO_4 are equal to the rates of the corresponding Ln(HPc)(Pc) complex dissociation. The observed kinetic parameters for the dissociation of Ln(HPc)(Pc) complexes formed when $Ln_2(Pc)_3$ is dissolved are close to the values [93] obtained for Ln(HPc)(Pc) synthesized by the traditional method [86, 88]. Lowering the stability of $Ln_2(Pc)_3$ as compared with $Ln(Pc)_2$ is connected

Table 6. Frequencies of main absorption bands (ν, cm^{-1}) in IR spectra of Tm(HPc)(Pc) and $Tm_2(Pc)_3$ (KBr tablets).

$TmPc_2H$	Tm_2Pc_3	Attribution [109, 110]	$TmPc_2H$	Tm_2Pc_3	Attribution [109, 110]
275	275	ν(Tm-N)	1304	1320	
360	360		1364	1364, 1384	Pyrrole ring-N_{meso}
472	472	ν(Tm-N)	1448	1448	ν(C≈C) pyrrole rings
528	528		1496	1490	
544	544		1524	1524	ν(C≈C) benzene rings
640	644		1570		The same
720	736	γ(C-H)	1590	1590	The same
768	772		1608	1608	The same
	1024		1732	1732	
1056	1056		2816	2784, 2800	ν(C-H)
1056	1056		2920	2968	
1116	1116		2984	3010	The same
1148	1148		3080	3040, 3080	The same

to our opinion about strains of the central macrocycle, which is in coordination spheres of two Ln^{3+} cations.

5. DOUBLE- AND TRIPLE-DECKER PORPHYRINS

5.1. Synthesis

Four-charged ions of zirconium, hafnium, cerium, and actinides, as well as three-charged ions of lanthanides, form double-decker porphyrin complexes. The lanthanide bis-porphyrins are easier to isolate and more stable with the larger lanthanide cations than with those with the smaller lanthanide cations [47, 111–113].

Neutral lanthanide bisporphyrins as well as bisphthalocya-nines can contain a hydrogen atom ($LaH(P)_2$ [114]) or be in an oxidized state ($Ln(P)_2$ [44, 115]). Most probably when the complexes are synthesized by the so-called acetylacetonate method, the lanthanide bisporphyrins are oxidized by air oxygen to form neutral radical form $Ln(P)_2$. The $Ln(OEP)_2$ complexes ($Ln = Ce^{IV}$, Eu^{III}, Nd^{III}, La^{III}, octaethylporphyrin dianioin (OEP)) were prepared [115] by refluxing H_2OEP and the appropriate Ln^{III}(acetylacetonate)$_3 \cdot x H_2O$ in 1,2,4-trichlorobenzene under an inert atmosphere. Prolongation of the refluxing Eu^{III}(acetylacetonate)$_3 \cdot H_2O$-containing reaction mixture to 20 h led to the formation of double-decker and triple-decker complexes, $Eu(OEP)_2$ and $Eu_2(OEP)_3$, at the same time, with 79% and 16% yields, respectively [44]. $Dy(TPP)_2$ and $Dy_2(TPP)_3$ complexes (TPP, tetraphenylporphyrin dianion) were synthesized from dys-prosium tetraphenylporphyrinate prepared *in-situ* [111]. The double-decker compound was obtained by direct oxidation of the $HDy(TPP)_2$ intermediate. The existence of the radical anion, $(TPP)^{\bullet-}$, in the double-decker product was confirmed by EPR spectrometry. In contrast to other lanthanides, cerium is in the oxidizing state +4 in a double-decker complex, whereas in a triple-decker complex $Ce_2(P)_3$ is in the same oxidizing state as the other lanthanides. $Ce^{IV}(OEP)_2$ and $(Ce^{III})_2(OEP)_3$ were synthesized in a manner similar to that of complexes of other lanthanides by reaction of H_2OEP with cerium acetylacetonate in boiling 1,2,4-trichlorobenzene for 19 h [43]. The authors assumed that in this case a Ce^{III} monoporphyrin $Ce(OEP)(acac)$ is formed, which then is partially converted to the Ce^{III} double-decker $CeH(OEP)_2$ by reaction with H_2OEP (Scheme 4, reaction 2). Such a hydrogen lanthanide(III) bisporphyri-nate has been isolated in the cases of $PrH(TPP)_2$ [111] and $LaH(P)_2$ [114] but never in the case of cerium. Therefore it seems likely that the hydrogen cerium(III) bis-porphyrinates are easily autoxidized under the reaction conditions to yield cerium(IV) bisporphyrinates (Scheme 4, reaction 3). $CeH(OEP)_2$ may undergo condensation reaction 4 (Scheme 4) with the monoporphyrin $Ce(OEP)(acac)$ to yield the triple-decker $Ce_2(OEP)_3$ [43].

Use of lithiated porphyrins, $Li_2(P)$, instead of metal-free porphyrins, H_2P, in the synthesis of water-soluble cerium bis-porphyrins increased the yield of $Ce(P)_2$ (Eqs. (6)–(8)) [116]:

$$2H_2P + 4n\text{-BuLi} \rightarrow 2Li_2(P) + 4n\text{-BuH} \quad (6)$$

$$2Li_2(P) + Ce(acac)_3 \rightarrow CeLi(P)_2 \quad (7)$$

$$4CeLi(P)_2 + O_2 + 2H_2O \rightarrow 4Ce(P)_2 + 4LiOH \quad (8)$$
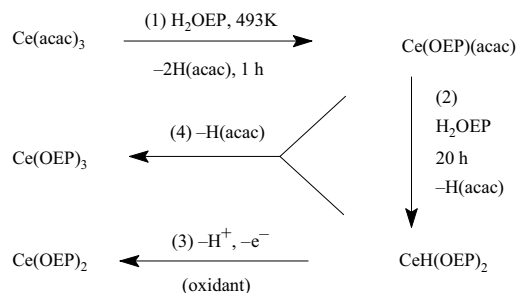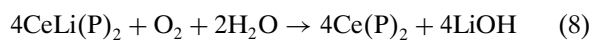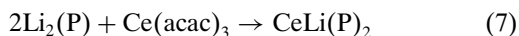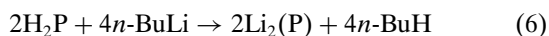
Scheme 4.

Neutral and singly oxidized U and Th double-decker complexes are reported [33, 54, 117]. They were obtained by reaction of the diethylamide complexes with H_2TPP or H_2OEP.

One of the authors of the present review found that the reaction between H_2TPP and $UO_2(OAc)_2$ in a 1:10 molar ratio in a refluxing benzonitrile medium for 19 h yields two complexes, $U(TPP)_2$ and $U_2(TPP)_3$. The complexes were divided by thin-layer chromatography with a benzene-chloroform (1:4) mixture. Individual complexes can also be obtained when the reaction mixture is dissolved in ethanol after benzonitrile evaporation. The complex $U(TPP)_2$ is sol-uble in ethanol, whereas the $U_2(TPP)_3$ complex stays in a solid phase.

By an analogous synthetic procedure, double- and triple-decker thorium tetraphenylporphyrins were obtained for the first time in 1991 [118].

There are only a few works on double-decker porphyrin complexes with d-metal cations (Zr, Hf) [37, 38, 41, 119]. Zr and Hf complexes were synthesized by reaction of the diethylamide complexes with H_2TPP or H_2OEP.

5.2. Spectroscopic Characterization

The optical absorption spectrum of $Eu^{III}(OEP)_2$ [44] has bands at 543 and 676 nm that are typical for π-radicals. The complex also has a strong band at 1280 nm (near-infrared region) with a molar extinction coefficient of 7800. This band is absent in the $Eu_2(OEP)_3$ spectrum and must be a property of the electron-deficient sandwich system [44]. According to [115] data in the absorption spectra of $Eu^{III}(OEP)_2$, $Nd^{III}(OEP)_2$, and $La^{III}(OEP)_2$, a broad Soret band near 400 nm and low-intensity Q bands in the region of 500–700 nm are observed. These features are atypical for neutral porphyrins but are typical of porphyrin π-cation radicals. The similarity of the general features of UV-vis spectra of $Ln^{III}(OEP)_2$ and $Ce^{IV}(OEP)_2^+$ is indicative of the hole in the π system of the neutral lantanide bisporphyrins $Ln^{III}(OEP)_2$. The presence of a hole in the porphyrin π system of the Ln^{III} double deckers is further confirmed by the appearance of the near-IR absorption band at 1200–1400 nm [115].

The double-decker and triple-decker M(IV) complexes have different UV-vis and IR spectra. For uranium complexes, according to the data of the authors of the review, λ_{max} are 595.3, <u>556.9</u>, 516.0, <u>422.5</u>, 410.0 nm in ethanol and <u>657.9</u>, 599.5, <u>462.1</u>, <u>422.3</u> nm in benzene (intensive bands are noted); $\nu_{U\text{-}N}$, is 430 and 436 cm^{-1} for $U(TPP)_2$ and

$U_2(TPP)_3$, respectively. IR spectra of double- and triple-decker complexes are more complicated in regions 700 (γ_{C-H} of benzene rings), 800 (γ_{C-H} of pyrrole rings), 990–1010 (δ_{C-H}, ν_{C-C}, ν_{C-N} of pyrrole rings), and 1540–1550 cm^{-1} (pyrrole ring stretching) than in the case of lanthanide complexes (X)LnTPP.

In the region of 200–500 cm^{-1} IR spectra of double-decker porphyrins of M^{IV} can also be distinguished from spectra of complexes with 1:1 composition (X)LnP (Table 7). Frequencies of vibrations νTh-N (436 cm^{-1}) are higher than those of Ln-N (excepting Ce-N), which is connected to the growth of the strength constant of the Th-N bond in bisporphyrins. There is no band at 212–216 cm^{-1} (νM-Cl, M-O) in the spectrum of Th^{IV}(TPP)$_2$ because of the absence of acidoligands X (Cl or C$_6$H$_5$COO) in the complex.

Th^{IV}(TPP)$_2$ is soluble in ethanol, whereas the triple-decker complex Th$_2^{III}$(TPP)$_3$ is insoluble in ethanol. UV-vis spectra of both complexes (Fig. 11) have specific features compared with the spectra of (X)Th(TPP). There is an additional intensive band at 426 nm in the Th(TPP)$_2$ spectrum and a wide band at 699 nm with low intensity in the Th$_2$(TPP)$_3$ spectrum. Soret bands in both spectra are split in two with λ_{max} equal to 411 and 398 nm. Visible absorption bands in the Th(TPP)$_2$ spectrum are bathochromically shifted compared with those of Th$_2$(TPP)$_3$. Analogous regularities are observed for the Ce(OEP)$_2$ and Ce$_2$(OEP)$_3$ complexes [43]. The authors of [43] explain the appearance of wide absorption bands in the region higher than 650 nm in the spectra of metalloporphyrins with two and more macrocycles by resonance interaction of the porphyrin ligands.

Data on optical absorption spectra of double- and triple-decker porphyrins are shown in Table 8.

5.3. Structure

The magnetic moment of Eu$_2$(OEP)$_3$ at room temperature is 3.17 μ_B/Eu^{III} [44]. There is no problem with the valence of the lanthanide central ions. The ^{1}H NMR spectrum clearly shows the resonances of two external rings and the internal porphyrin ring in the expected 2:1 intensity ratio. The Eu(OEP)$_2$ formula is corroborated [44] by the mass spectrum and the crystallographic data. In the crystalline state Eu(OEP)$_2$ is isomorphous with Ce(OEP)$_2$ and consists of discrete sandwich molecules linked solely by van der Waals contacts; there are no unusually short intermolecular contacts. The Eu^{III} ion is octacoordinate; the eight
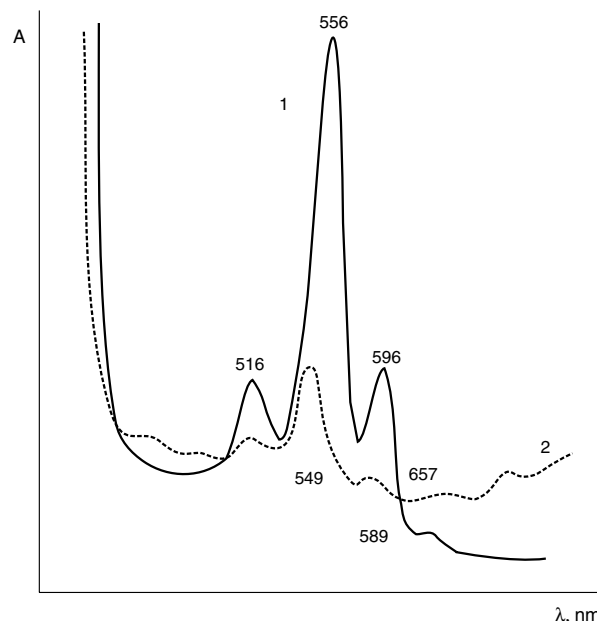
Figure 11. UV-vis spectra of Th(TPP)$_2$ in ethanol (1) and Th$_2$(TPP)$_3$ in benzene (2).

porphyrin nitrogen atoms form a nearly square antiprism. The angle of rotation of the porphyrin rings from the eclipsed position is 41.3°. The average Eu-N bond length is 2.510 Å [44].

The Ce^{IV} ion in Ce(OEP)$_2$ is surrounded by the eight nitrogen atoms of the two porphyrin rings, and its coordination polyhedron is nearly a square antiprism: the porphyrin rings are rotated by an angle of 41.8° with respect to their eclipsed position [43]. Thus, this polyhedron is very similar to those found in the bisphthalocyaninates such as Sn(Pc)$_2$, U(Pc)$_2$, Nd(Pc)$_2$, and Lu(Pc)$_2$. The four pyrrole nitrogen atoms of each of the macrocycles are coplanar within experimental error. The cerium ion lies 1.376 Å from the 4N mean planes. The separation of the two 4N mean planes is nearly 2.752 Å. The eight Ce-N bond lengths do not significantly differ from each other and have a mean value of 2.475 Å. Both macrocycles are convex and severely distorted from planarity. Triple-decker Ce$_2$(OEP)$_3$ crystallizes with 1,2,4-trichlorobenzene molecules [43]. Discrete Ce$_2$(OEP)$_3$ and 1,2,4-trichlorobenzene molecules are

Table 7. Absorption band frequencies (ν, cm^{-1}) in IR spectra of metalloporphyrins (X)Ln TPP and Th(TPP)$_2$ in KBr.

| H$_2$TPP | Complexing atom, acido-ligand | | | | | | | | | | Attribution |
	Ce, Br	Sm, Cl	Gd, Cl	Tb, OAc	Dy, Cl	Ho, Br	Er, Cl	Yb, Cl	Lu, Cl	Th	
—	216	—	212	212	212	Not studied	214	—	212	—	νLn-Cl νLn-O
216	220	216	222	223	220		220	216	222	216	KBr
236	232	232	232	232	234	232	232	232	232	236	KBr
—	—	244	—	—	—	—	—	244	—	—	
—	252	252	252	240	252	252	256	252	252	252	νLn-N δC-C-N
384	415	365	—	395	350	386	392	372	375	384	δC-C-N νC-N
416	430	385	392	400	394	396	400	396	396	395	δC-C-N
—	456	424	421	423	424	427	429	427	427	436	νLn-N νTh-N

Table 8. UV-vis spectra of double- and triple-decker porphyrins.

Compound	Solvent	λ_{max} (nm) (log ε)	Ref.
La$_2$(OEP)$_3$	CH$_2$Cl$_2$	386 (5.29), 530 (4.27), 567 (4.03), 629 (3.83), 728 (3.59)	[115]
Ce$_2$(OEP)$_3$	CH$_2$Cl$_2$	387 (5.28), 529 (4.24), 568 (4.14), 631 (3.85), 743 (3.59)	[115]
Eu$_2$(OEP)$_3$	CH$_2$Cl$_2$	382 (5.25), 530 (4.03), 572 (3.92), 658 (3.67), 800 (3.05)	[115]
Eu$_2$(OEP)$_3$	Diethylene-glycol-diethyl ether	381 (5.27), 532 (3.75), 574 (3.74), 664 (3.32), 800 (3.03)	[44]
Eu(OEP)$_2$	Cyclohexane	340 (4.59sh), 376 (5.04), 543 (3.67), 676 (3.36)	[44]
Ce$_2$(OEP)$_3$	Diethylene-glycol-diethyl ether	387, 530, 571, 639, 755	[43]
Ce(OEP)$_2$	Cyclohexane	378, 467(sh), 530, 573	[43]
Ce(TPP)$_2$	CH$_2$Cl$_2$	338 (4.64), 396 (5.32), 486 (4.12), 540 (4.00), 630 (3.46)	[116]
Ce(TPyP)$_2$[a]	CH$_2$Cl$_2$	334.4 (4.64), 392.8 (5.22), 486.2 (4.04), 538.9 (3.90), 636 (3.47), 720 (3.17)	[116]
Ce(TMeCPP)$_2$[b]	CH$_2$Cl$_2$	336.8 (4.48), 398 (5.18), 487 (3.98), 542.8 (3.86), 645.6 (3.45), 718 (3.17)	[116]
[Th(TPP)$_2$][SbCl$_6$]	CH$_2$Cl$_2$	396 (the Soret band)	[33]
[U(TPP)$_2$][SbCl$_6$]	CH$_2$Cl$_2$	392	[33]
U(TPP)$_2$	CH$_2$Cl$_2$	404, 485, 550, 620	[117]
[Zr(TPP)$_2$][SbCl$_6$]$_2$	CH$_2$Cl$_2$	372 (4.98), 433 (sh), 505 (33.96), 780 (3.82)	[41]
Zr(OEP)$_2$	Toluene	358, 382, 489, 594, 742	[119]
Hf(OEP)$_2$	Toluene	357, 379, 491, 595, 750	[119]
Y(OEP)$_2$	Cyclohexane	374 (5.10), 538 (3.88), 674 (3.38)	[120]
La(OEP)$_2$	Cyclohexane	394 (5.15), 494 (3.75), 540 (3.85), 576 (3.70)	[120]
Ce(OEP)$_2$	Cyclohexane	378 (5.08), 467 (3.92), 530 (3.77), 573 (4.24), 661 (3.16)	[120]
Pr(OEP)$_2$	Cyclohexane	391 (5.18), 490 (3.72), 540 (3.80), 576 (3.64), 670 (3.21)	[120]
Nd(OEP)$_2$	Cyclohexane	390 (4.81), 488 (3.53), 542 (3.97), 577 (3.48), 668 (3.08)	[120]
Sm(OEP)$_2$	Cyclohexane	390 (5.11), 489 (3.79), 544 (3.86), 578 (3.78), 674 (3.21)	[120]
Gd(OEP)$_2$	Cyclohexane	380 (4.88), 542 (3.71), 674 (3.26)	[120]
Tb(OEP)$_2$	Cyclohexane	378 (5.00), 492 (3.80), 544 (3.81), 580 (3.70), 680 (3.30)	[120]
Dy(OEP)$_2$	Cyclohexane	386 (5.09), 494 (3.82), 546 (3.84), 582 (3.77), 679 (3.27)	[120]
Ho(OEP)$_2$	Cyclohexane	376 (5.10), 494 (3.89), 546 (3.91), 582 (3.83), 684 (3.24)	[120]
Er(OEP)$_2$	Cyclohexane	374 (5.05), 494 (3.78), 544 (3.79), 582 (3.67), 679 (3.24)	[120]
Tm(OEP)$_2$	Cyclohexane	388 (5.08), 494 (3.77), 546 (3.76), 584 (3.78), 672 (3.31)	[120]
Yb(OEP)$_2$	Cyclohexane	370 (4.98), 498 (3.75), 530 (3.76), 672 (3.21)	[120]
Lu(OEP)$_2$	Cyclohexane	370 (5.02), 490 (3.76), 534 (3.77), 674 (3.36)	[120]

[a] 5,10,15,20-Tetrakis(4-pyridyl)porphyrin.
[b] 5,10,15,20-Tetrakis(4-(methoxycarbonyl)phenyl)porphyrin.

linked by van der Waals interactions and do not show any unusual intermolecular contacts. For each Ce$_2$(OEP)$_3$ entity there are two 1,2,4-trichlorobenzene solvent molecules in the crystal. Each Ce$_2$(OEP)$_3$ molecule lies on a crystallographically imposed inversion center located between the two Ce^{III} ions. The Ce-N distances fall into two classes: those of the pyrrole nitrogen atoms of the external rings, mean value 2.501 Å, slightly lengthened compared with those found in double-decker Ce(OEP)$_2$, and those of the pyrrole atoms of the internal ring, with a mean value of 2.758 Å. The mean value of all Ce-N distances is 2.63 Å and is considerably larger than the corresponding value in Ce(OEP)$_2$, reflecting the fact that the former molecule contains two Ce^{III} ions, whereas the latter one encompasses the smaller Ce^{IV} ion. The external porphyrinates are bent away from the cerium ions in a saucer-like shape, whereas the internal porphyrinate is planar [43].

The coordination geometry of Th(TPP)$_2$ is a distorted square-antiprism where the thorium center is displaced 1.47 Å from each of the porphyrin N$_4$ planes; the porphyrin N$_4$ planes are therefore separated by 2.94 Å [32]. In analogous octaethylporphyrin complex, Th(OEP)$_2$, the two porphyrin planes are separated by 2.89 Å in a nearly perfect square-antiprismatic coordination geometry around the thorium center. The porphyrin macrocycles, held in such close proximity, interact electronically as shown by a blue shift in

the porphyrin Soret band and by unusually low oxidation potentials relative to related monoporphyrin species [32].

Total information about work on X-ray crystallography data for double- and triple-decker complexes is given in Table 1.

The molecular structure of Zr(TPP)$_2$ has been determined crystallographically in [38]. The Zr-N distances of 2.40 Å and the porphyrin-porphyrin interplanar spacing of 2.56 Å are the shortest such distances in all known M(P)$_2$ complexes. X-ray structures of [Zr(TPP)$_2$][SbCl$_6$] and [Zr(TPP)$_2$][SbCl$_6$]$_2$ [41] reveal that the interporphyrin distances shorten progressively as one proceeds from the neutral to the dication species. The structural features are consistent with the spectroscopic data and confirm that the π-π interaction between the two porphyrin rings is enhanced by oxidation.

5.4. Properties

Spectral and chemical properties of double- and triple-decker porphyrin complexes are essentially different.

Complexes U(TPP)$_2$ and U$_2$(TPP)$_3$ dissociate at a spectrophotometrically measured rate in ethanol or benzene media only in the presence of HOAc in concentrations above 5.5 mol/liter at 330–350 and 300–320 K, respectively (reactions (9), (10), (11)). Values of constants of the dissociation rate of formally the first order (k_{obs}^{298K}) at 50% HOAc

concentration in the mentioned solvents are 10^{-4} and 0.5×10^{-3} s^{-1} for U(TPP)$_2$ and U$_2$(TPP)$_3$, respectively:

$$U(TPP)_2 + 8H^+_{Solv} \rightarrow U^{4+}_{Solv} + 2H_4TPP^{2+} \qquad (9)$$

$$U_2(TPP)_3 + 5H^+_{Solv} \rightarrow UH(TPP)_2$$
$$+ H_4TPP^{2+} + U^{3+}_{Solv} \quad (10)$$

$$UH(TPP)_2 \rightarrow U(TPP)_2 \qquad (11)$$
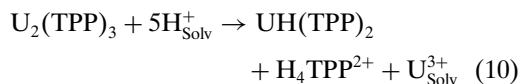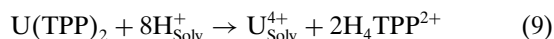
Thorium(IV) complexes with a Th(TPP)$_2$ composition and thorium(III) complexes with Th$_2$(TPP)$_3$ differ not only in solubility and UV-vis spectra but in their reactivity with acids as well [118]. Th(TPP)$_2$ dissociates in ethanol-AcOH as well as in benzene-AcOH solutions with an acid content of 50–90 vol%. Th$_2$(TPP)$_3$ dissociates at a measurable rate in the same mixtures with lesser acid content (25–60 vol%). Dissociation occurs analogously to uranium complex dissociation (Eqs. (10) and (11)). $k^{298\,K}_{obs}$ is 0.31×10^{-3}, 0.50×10^{-3}, and 0.80×10^{-3} s^{-1} for HOAc concentrations of 40%, 50%, and 60%, respectively.

Porphyrin and phthalocyanine complexes of lanthanides and actinides with double- and triple-decker structures have many useful practical properties and could be used as components of new materials [102].

6. HETEROLEPTIC SANDWICH-TYPE COMPLEXES

6.1. Synthesis

The preparation and properties of several heteroleptic sandwich-type complexes, (TPP)Ce^{IV}(Pc) [48], (TPP)Ce^{IV}·(OEP) [47], (T(p-CH$_3$P)P)Ce^{IV}(OEP) [121], (P)U^{IV}(Pc), (P)Th^{IV}(Pc) (P = OEP, TPP, or T(p-CH$_3$P)P) [54], (TPP)M^{III}(Pc) (M = La, Pr, Nd, Eu, Gd, Er, Lu, or Y) [45], have been reported. It is shown that in [(TPP)Ce^{IV}(Pc)]$^+$ the electronic hole preferentially resides on the phthalocyanine ring [122]; in [(TPP)Ce^{IV}(OEP)]$^+$ and (TPP)Eu^{III}(OEP) it resides on the octaethylporphyrin rings [47, 112]. These results are consistent with the oxidation potentials known for monomeric metallophthalocyanine and metallooctaethyl-porphyrin derivatives relative to the oxidation potentials of the metallotetraphenylporphyrin complexes.

Two approaches to the synthesis of heteroleptic double- and triple-decker complexes of lanthanides and actinides and Zr and Hf double-deckers were realized. In the first of them monophthalocyanine complexes were caked together with phthalic acid dinitrile. Use of various substituted phthalonitriles in the reaction leads to formation of the corresponding heteroleptic (asymmetrical) diphthalocyanines of the rare-earth elements. Pure individual compounds were obtained after a preparative chromatographic procedure on an Al$_2$O$_3$ column. By this method complexes with different phthalocyanine ligands of similar structure and complexes with phthalo- and naphthalocyanine ligands were synthesized [63, 72]. An analogous approach was used [45] for the synthesis of complexes with the (TPP)M(Pc) structure for all of the lanthanide series. The authors have adopted two different strategies: with the larger metal cations (La-Gd) they reacted the metal-free tetraphenylporphyrin H$_2$TPP with the

monophthalocyanine derivative (Pc)M(acac). The dilithium phthalocyanine Li$_2$(Pc) with the monoporphyrin complex (TPP)Ln(acac) was reacted (Scheme 5) with the smaller metal cations (M = Er, Lu, Y).

Most probably, the protonated forms (TPP)MH(Pc) are a common intermediate [45]. However, such an intermediate could only be isolated with M = La. With the other metal cations, the neutral form (TPP)M(Pc) contains a tetrapyrrole monoanion as a ligand, which results, most probably, from oxidation of the protonated forms by O$_2$ (Scheme 5). The yields of formation of the neutral form of the heteroleptic sandwiches increase when the metal cation radii decrease. The preparation becomes almost quantitative, with the metal cation displaying the smallest radius (Lu). By analogous approach, triple-decker structures (TPP)Gd(Pc)Gd(TPP), (TPP)Gd(Pc)Gd(Pc), and their oxidized forms, as well as (TPP)Ce^{III}(Pc)Ce^{III}(TPP) and (Pc)Ce^{III}(TPP)Ce^{III}(Pc), were synthesized [122].

The second approach is based on the fact that dinitrile of sterically strained phthalic acid in the presence of unsubstituted phthalonitrile forms tetra- and octaphenyl-substituted monophtyalocyanine complexes; in the last case substituted benzene fragments are in remote positions of the macrocycle. With caking of a mixture of tetraphenylphthalonitrile, o-phthalonitrile, and zirconium tetrachloride (in 8:4:1 ratio) over a gradual temperature increase from 493 to 563 K and maintaining the mixture for 3 h, the four main fractions were obtained and isolated: (Ph$_8$Pc)Zr(PcPh$_8$), (Ph$_8$Pc)Zr(PcPh$_4$), (Ph$_4$Pc)Zr(PcPh$_4$) and (Ph$_8$Pc)Zr(Pc) and (Ph$_4$Pc)Zr(Pc) mixture [65, 94].

6.2. Spectroscopic Characterization

Breach of symmetry in diphthalocyanines of the rare-earth elements with two different phthalocyanine ligands leads to changes in their electron absorption spectra. When two ligands of similar structure are in the molecule, one basic
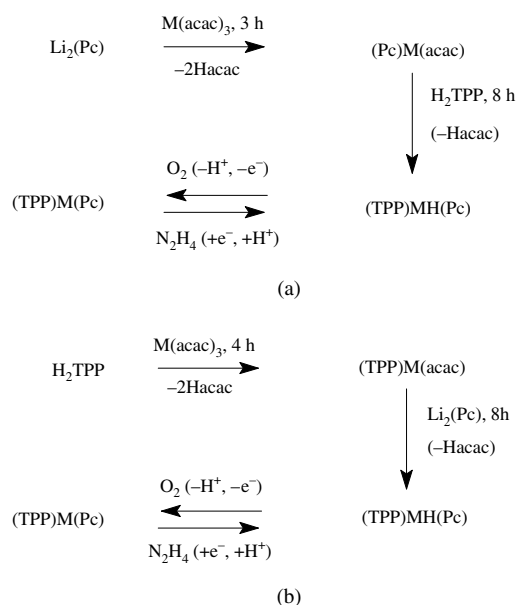
Scheme 5.

absorption band with a maximum at intermediate position as compared with symmetrical diphthalocyanines is observed [63, 72]. For instance, λ_{max} for Lu(Pc)$_2$, (Pc)Lu(Pc^t), and Lu(Pc^t) is 658, 660, and 662 nm, correspondingly. If two ligands for which the absorption maximums are far from each other are combined in one molecule, there is no blending of two maximums into one, but a displacement as compared with absorption band position of the corresponding monophthalocyanine and symmetrical diphthalocyanine complexes is observed.

In the case of heteroleptic porphyrin-phthalocyanine complexes, the band lying between 324 and 328 nm in the spectra of (TPP)M(Pc) derivatives is attributed to the phthalocyanine Soret band, and the band appearing between 396 and 412 nm is attributed to the porphyrin Soret band [45]. The phthalocyanine Q bands lying between 500 and 700 nm in the spectra of the diphthalocyanine tervalent-metal derivatives (Pc)M(Pc) are absent in the absorption spectra of the heteroleptic (TPP)M(Pc) derivatives. In contrast, two bands lying, respectively, between 468 and 484 nm and 965 and 1067 nm appear in these spectra (Table 9). The bands in spectra of (TPP)M(Pc) sandwich derivatives can be attributed to an electron hole localized on the phthalocyanine ring. Futhermore, a broad band appears in the near-IR in the spectra of the heteroleptic sandwich derivatives between 1211 and 1535 nm. It can be ascribed to an intramolecular charge transfer transition in which the TPP^{2-} dianionic ligand acts as an electron donor and the monoanionic Pc$^{\bullet-}$ radical as the electron acceptor [45].

(TPP)Ce^{III}(Pc)Ce^{III}(TPP) and (Pc)Ce^{III}(TPP)Ce^{III}(Pc) can be visualized as two (TPP)Ce^{III}(Pc) units sharing the same inner tetraphenylporphyrin moiety [122]. As a consequence of the strong interaction of the porphyrin ring with the two phthalocyanine ligands, the porphyrin Soret band at 407 nm is drastically weaker in intensity and the Q

bands are strongly red-shifted. The maximum of the Soret bands of the two outer phthalocyanine rings remains practically uncharged, and their Q bands are less shifted to the red than for the corresponding inner phthalocyanine macrocycle in (TPP)Ce^{III}(Pc)Ce^{III}(TPP). Similar behavior was observed for Ce$_2^{III}$(OEP)$_3$, but the red band was not specifically attributed to the inner ring [122].

6.3. Structure

References to work on X-ray investigation of heteroleptic double and triple deckers are given in Table 1. (TPP)La(Pc)·2CH$_2$Cl$_2$ [45] metal cation is octacoordinated: it is bonded to four pyrrole nitrogens of the porphyrin ring and to four isoindole nitrogens of the phthalocyanine ring. Tetrapyrrole rings adopt a staggered orientation with a relative rotation angle of 45.7°. The coordination environment of the metal cation is a slightly distorted square antiprism. The average metal-nitrogen distances are La-N$_p$ = 2.520 and La-N-iso = 2.590 Å. The metal cation lies 1.425 Å above the four pyrrole nitrogen mean planes and 1.656 Å below the four isoindole nitrogen mean planes. The porphyrin ring is slightly distorted. The phthalocyanine macrocycle is domed and displays a saucer shape. Despite the probable localization of the π-radical on the phthalocyanine ring in (TPP)La(Pc)·2CH$_2$Cl$_2$ the structure of this ring is not significantly different from those found in several divalent metallophthalocyanines in which these rings are dianionic ligands [45, 124].

In the triple-decker heteroleptic compound (P)Nd(Pc)Nd(Pc) where P = T(4-OCH$_3$)PP, the Nd atoms are sandwiched between two phthalocyanine macrocycles and one porphyrin macrocycle [51]. Thus, both metal atoms are eightfold coordinated to eight nitrogens, either to four porphyrinato and four phthalocyaninato nitrogen atoms (Nd1)

Table 9. UV-vis and near-IR band maxima of heteroleptic double- and triple-decker porphyrins/phthalocyanines in CH$_2$Cl$_2$.

Compound	λ_{max} (nm) (log ε)	Ref.
(TPP)La(Pc)	324 (4.65), 412 (5.37), 484 (4.15), 965 (3.24), 1535 (3.38)	[45]
(TPP)Pr(Pc)	325 (4.72), 410 (5.28), 480 (3.98), 968 (3.27), 1469 (3.36)	[45]
(TPP)Nd(Pc)	326 (4.66), 410 (5.39), 476 (4.07), 995 (3.31), 1434 (3.43)	[45]
(TPP)Eu(Pc)	326 (4.69), 408 (5.26), 476 (4.13), 1002 (3.25), 1350 (3.41)	[45]
(TPP)Gd(Pc)	327 (4.71), 406 (5.31), 472 (3.87), 1005 (3.21), 1321 (3.39)	[45]
(TPP)Y(Pc)	328 (4.65), 402 (5.18), 472 (4.21), 1053 (3.23), 1285 (3.37)	[45]
(TPP)Er(Pc)	328 (4.71), 400 (5.20), 470 (3.88), 1057 (3.19), 1255 (3.35)	[45]
(TPP)Lu(Pc)	328 (4.68), 396 (5.13), 468 (3.97), 1067 (3.22), 1211 (3.38)	[45]
(TPP)Ce^{III}(Pc)	333[a], 385, <u>422</u>, 482.5, 585, 625, 600, <u>755</u>	[122]
(TPP)Ce^{III}(Pc)Ce^{III}(TPP)	295, <u>359</u>, <u>417</u>, 486, 547, 602.5, 800, 890	[122]
(Pc)Ce^{III}(TPP)Ce^{IV}(Pc)	290, <u>342</u>, 407, 450, 500, 585, 617, <u>645</u>, 770	[122]
(Pc)Ce^{III}(TPP)Ce^{III}(Pc)	287, <u>337</u>, 407, 457, 500, <u>615</u>, 645, 752.5, 832	[122]
(P)Nd(Pc)Nd(Pc)[b]	338 (5.03), 418 (5.00), 515 sh, 550 sh, 620 (4.60), 704 (4.35)	[51]
(P)Eu(Pc)Eu(Pc)[b]	340 (4.98), 418 (4.80), 518 sh, 545 sh, 617 (4.53), 724 (4.26)	[51]
(P)Gd(Pc)Gd(Pc)[b]	340 (5.17), 417 (5.03), 520 sh, 538 sh, 618 (4.84), 730 (4.54)	[51]
(TPP)Zr(Pc)[c, d]	340 (6.65), 400 (6.91), 457 (3.54), 468 (3.47), 579 (1.76), 600 (2.78)	[123]
(OEP)Zr(Pc)[d]	342 (10.84), 383 (9.86), 450 (2.79), 549 (2.67), 644 (4.44)	[123]
(TPP)Hf(Pc)[d]	336 (6.19), 398 (6.85), 457 (3.60), 466 (3.51), 578 (1.72), 600 (2.26)	[123]
(OEP)Hf(Pc)[d]	339 (10.48), 381 (8.82), 447 (2.95), 553 (2.63), 646 (3.87)	[123]

[a] Intensive bands are underlined.
[b] P = T(4-OCH$_3$)PP.
[c] 340-Pc, 400-Soret, 457, 468-Q'', 579, 600-Q'.
[d] In parentheses $\varepsilon \times 10^{-4}$.

or to eight phthalocyaninato nitrogens (Nd2). The coordination polyhedron of Nd1 is a distorted cube. This geometry minimizes the nonbonding interactions between the four *p*-methoxyphenyl groups of the tetraanisylporphyrin and the inner phthalocyanine ring [51]. The porphyrin ring is slightly domed. The outer phthalocyanine ring is also convex. The inner phthalocyanine ring is almost planar. One phthalocyanine ring is rotated with respect to the other by 42.8°.

6.4. Properties

In the work on heteroleptic double- and triple-decker porphyrin-phthalocyanine complexes, optical and redox properties were investigated. Along with spectral characteristics of neutral complexes, analogous characteristics of singly oxidized and singly reduced states are presented [45, 47, 48, 54, 63, 65, 72, 94, 112, 121, 122]. The stability of the compounds in acid media was not investigated.

7. CONCLUSION

The quantity of work on the investigation of double- and triple-decker porphyrin and phthalocyanine complexes has grown in recent years [125–129] and will increase further because of the elaboration of convenient methods of their synthesis and their properties, such as the high stability of neutral and oxidized forms, solubility in organic media, their ability to self-organize in solid layers, and a great number of applied properties [102, 130, 131]. Heteroleptic complexes are the most interesting because of the possibility of direct combination of phthalocyanine and porphyrin properties in one compound, in contrast to dimers and trimers of other structures [132–134]. Development in this direction is just beginning.

GLOSSARY

Acido-ligand The acid anion, having affinity to metal cation.

Acido phthalocyanine/porphyrin metal complex Mixed ligand complex containing one macrocyclic and 1–3 acido-ligands.

Double decker complex Coordination compound of metal cation with planar aromatic macrocyclic ligands with composition 1:2 in which 1 metal atom is located between two macrocycles.

Heteroleptic sandwich type complexes Coordination compound of a metal cation containing both phthalocyanine and porphyrin macrocycles.

Kinetic stability of the complex Parameter that is determined by the constant of the dissociation rate of the complex to metal cation and ligand at 298 K and 1 atm.

Macrocyclic compound Chemical compound with closed contour built from 9 or more atoms, 3 or more of which have electron donor function.

Phthalocyanine Aromatic macrocyclic compound consisting from four isoindole fragments and four aza-groups.

Phthalocyanine/porphyrin extra-complex
Phthalocyanine/porphyrin metal complex containing acido- or molecular ligands parallel with macrocyclic ligand.

Porphyrin Aromatic macrocyclic compound consisting from four pyrrole fragments and four methine bridges.

Reaction of complex formation with porphyrins Process of interaction of metal cation with porphyrin.

Template synthesis of complexes Process in which a metal cation acts as a template, matrix for forming the only possible or prevailing in the reaction conditions products from the corresponding initial substances.

Triple decker complex Coordination compound of metal cations with planar aromatic macrocyclic ligands with composition 2:3 in which each metal atom is located between two macrocycles.

REFERENCES

1. I. S. Kirin, P. N. Moskalev, and Yu. A. Makashev, *Russ. J. Inorg. Chem.* 10, 1065 (1965).
2. S. Misumi and K. Kasuga, *J. Chem. Soc. Jpn., Pure Chem.* 92, 335 (1971).
3. A. G. MacKay, J. F. Boas, and G. J. Troup, *Aust. J. Chem.* 27, 955 (1974).
4. K. Kasuga, M. Tsutsui, R. S. Petterson, K. Tatsumi, N. van Ophenbosch, G. Pepe, and E. F. Meyer, Jr., *J. Am. Chem. Soc.* 102, 4835 (1980).
5. M. Moussavi, A. De Cian, J. Ficher, and R. Weiss, *Inorg. Chem.* 27, 1287 (1988).
6. G. Ostendorp, J.-P. Werner, and H. Homborg, *Acta Crystallogr., Sect. C* 51, 1125 (1995).
7. M. S. Haghighi, C. L. Teske, and H. Z. Homborg, *Z. Anorg. Allg. Chem.* 608, 73 (1992).
8. J. Janczak, R. Kubiak, and A. Jezierski, *Inorg. Chem.* 34, 3505 (1995).
9. W. E. Bennett, D. E. Broberg, and N. C. Baenziger, *Inorg. Chem.* 12, 930 (1973).
10. J. Janczak and R. Kubiak, *Alloys Compd* 204, 5 (1994).
11. G. Ostendorp and H. Homborg, *Z. Anorg. Allg. Chem.* 622, 873 (1996).
12. A. Capobianchi, C. Ercolany, A. M. Paoletti, G. Pennesi, G. Rossi, A. Chiesi-Villa, and C. Rizzoli, *Inorg. Chem.* 32, 4605 (1993).
13. J. Silver, P. Lukes, S. D. Howe, and B. Howlin, *J. Mater. Chem.* 1, 29 (1991).
14. J. L. Paillaud, M. Drillon, A. De Cian, J. Fischer, R. Weiss, R. Poinsot, and A. Herr, *Physica B* 175, 337 (1991).
15. G. Ostendorp and H. Homborg, *Z. Naturforsch. B* 50, 1200 (1995).
16. M. S. Haghighi, A. Franken, and H. Homborg, *Z. Naturforsch. B* 49, 812 (1994).
17. G. Ostendorp, H. W. Rotter, and H. Homborg, *Z. Naturforsch. B* 51, 567 (1996).
18. A. Darovsky, L. Wu, P. Lee, and H. S. Sheu, *Acta Crystallogr., Sect. C* 47, 1836 (1991).
19. A. Darovsky, V. Keserashvili, R. Harlow, and I. Mutikainen, *Acta Crystallogr., Sect. B* 50, 582 (1994).
20. M. S. Haghighi, M. Rath, H. W. Rotter, and H. Homborg, *Z. Anorg. Allg. Chem.* 619, 1887 (1993).
21. J. Jullien, M. Mossoyan Deneux, M. Pierrot, J. P. Sorbier, A. Fournel, and D. Benlian, *C. R. Acad. Sci., Ser. 2* 303, 669 (1986); *Chem. Abstr.* 105, 201246v (1986).
22. A. N. Darovsky, O. V. Frank-Kamenetskaya, and V. S. Fundamenskii, *Kristallografiya* 31, 901 (1986); *Chem. Abstr.* 105, 236208m (1986).
23. A. Darovsky, V. Keserashvili, R. Harlow, and I. Mutikainen, *Acta Crystallogr., Sect. B* 50, 582 (1994).
24. A. N. Darovsky, A. K. Tsutsenko, O. V. Frank-Kamenetskaya, V. S. Fundamenskii, and P. N. Moskalev, *Kristallografiya* 29, 455 (1984); *Chem. Abstr.* 101, 46753e (1984).

25. N. Koike, H. Uekusa, Y. Ohashi, C. Harnoode, F. Kitamura, T. Ohsaka, and K. Tokuda, *Inorg. Chem.* 35, 5798 (1996).

26. G. Ostendorp, H. W. Rotter, and H. Homborg, *Z. Anorg. Allg. Chem.* 622, 235 (1996).

27. A. De Chian, M. Moussavi, J. Fisher, and R. Weiss, *Inorg. Chem.* 24, 3162 (1985).

28. M. Moussavi, A. De Chian, J. Fisher, and R. Weiss, *Inorg. Chem.* 27, 1287 (1988).

29. A. N. Darovsky, O. V. Frank-Kamenetskaya, V. S. Fundamenskii, and A. M. Golubev, *Kristallografiya* 31, 279 (1986); *Chem. Abstr.* 104, 197557g (1986).

30. I. S. Kirin, A. B. Kolyadin, and A. A. Lychev, *J. Struct. Chem. Russ.* 15, 415 (1974).

31. T. Kobayashi, *Bull. Inst. Chem. Res. Kyoto Univ.* 56, 204 (1978); *Chem. Abstr.* 89, 224285x (1978).

32. G. S. Girolami, P. A. Gorlin, S. N. Milam, K. S. Suslick, and S. R. Wilson, *J. Coord. Chem.* 32, 173 (1994).

33. G. S. Girolami, S. N. Milam, and K. S. Suslick, *J. Am. Chem. Soc.* 110, 2011 (1988).

34. A. Gieren and W. Hoppe, *J. Chem. Soc., Chem. Commun.* 413 (1971).

35. J. Janczak and R. Kubiak, *J. Chem. Soc., Dalton Trans.* 3809 (1993).

36. S. I. Troyanov, L. A. Lapkina, V. E. Larchenko, and A. Yu. Tsivadze, *Dok. Chem.* 367, 192 (1999).

37. J. W. Buchler, A. De Cian, S. Elschner, J. Fischer, P. Hammerschmitt, and R. Weiss, *Chem. Ber.* 125, 107 (1992).

38. K. Kim, W. S. Lee, H. J. Kim, S. H. Cho, G. S. Girolami, P. A. Gorlin, and K. S. Suslick, *Inorg. Chem.* 30, 2652 (1990).

39. K. Kim, W. S. Lee, H. J. Kim, S.-H. Cho, G. S. Girolami, P. A. Gorlin, and K. S. Suslick, *Inorg. Chem.* 31, 716 (1991).

40. J. W. Buchler, A. De Chian, J. Fisher, P. Hammerschmitt, and R. Weiss, *Chem. Ber.* 124, 1051 (1991).

41. H. J. Kim, D. Whang, J. Kim, and K. Kim, *Inorg. Chem.* 31, 3882 (1992).

42. J. P. Collman, J. L. Kendall, J. L. Chen, T. A. Eberspacher, and C. R. Moylan, *Inorg. Chem.* 36, 5603 (1997).

43. J. W. Buchler, A. De Cian, J. Fischer, M. Kihn-Botulinski, H. Paulus, and R. Weiss, *J. Am. Chem. Soc.* 108, 3652 (1986).

44. J. W. Buchler, A. De Cian, J. Fisher, M. Kihn-Botilinski, and R. Weiss, *Inorg. Chem.* 27, 339 (1988).

45. D. Chabach, M. Tahiri, A. De Cian, J. Fischer, R. Weiss, and M. El Malouli-Bibout, *J. Am. Chem. Soc.* 117, 8548 (1995).

46. M. Tahiri, D. Chabach, M. El Malouli-Bibout, A. De Cian, J. Fischer, and R. Weiss, *Ann. Chim.* 20, 81 (1995); *Chem. Abstr.* 123, 216783p (1995).

47. J. W. Buchler, A. De Cian, J. Fisher, P. Hammerschmitt, J. Loffler, B. Scharbert, and R. Weiss, *Chem. Ber.* 122, 2219 (1989).

48. M. Lachkar, A. De Cian, J. Fisher, and R. Weiss, *New J. Chem.* 12, 729 (1988).

49. G. A. Spyroulias, A. G. Coutsolelos, C. P. Raptopoulou, and A. Terzis, *Inorg. Chem.* 34, 2476 (1995).

50. D. Chabach, M. Lachkar, A. De Cian, J. Fisher, and R. Weiss, *New J. Chem.* 16, 431 (1992).

51. M. Moussavi, A. De Chian, J. Fisher, and R. Weiss, *Inorg. Chem.* 25, 2107 (1986).

52. D. Chabach, A. De Cian, J. Fischer, R. Weiss, and M. El Malouli-Bibout, *Angew. Chem. Int., Ed. Engl.* 35, 898 (1996).

53. M. O. Senge, in "The Porphyrin Handbook" (K. M. Kadish, K. M. Smith, and R. Guilard, Eds.), Vol. 10. Academic Press, San Diego, 2000.

54. K. M. Kadish, G. Moninot, Y. Hu, D. Dubois, A. Ibnlfassi, J. M. Barbe, and R. Guilard, *J. Am. Chem. Soc.* 115, 8153 (1993).

55. P. N. Moskalev, *Koord. Khim.* 16, 147 (1990).

56. M. A. Ovseevich, L. G. Tomilova, E. G. Kogan, and N. S. Zefirov, *Mendeleev Commun.* 5, 186 (1998).

57. M. J. Stellman and T. Nyokong, in "Phthalocyanines: Properties and Applications" (C. C. Leznoff and A. B. P. Lever, Eds.), Vol. 1, p. 133. VCH, New York, 1989.

58. C. C. Leznoff and A. B. P. Lever, Eds., "Phthalocyanines: Properties and Applications," Vol. 4. VCH, New York, 1996.

59. B. D. Berezin, "Coordination Compounds of Porphyrins and Phthalocyanine." Wiley, New York/Toronto, 1981.

60. K. Kasuga and M. Tsutsui, *Coord. Chem. Rev.* 32, 67 (1980).

61. G. P. Shaposhnikov, V. P. Kulimich, and V. E. Maizlish, in "Uspehi khimii porfirinov" (O. A. Golubchikov, Ed.), Vol. 2, p. 190. S-Pb., State University, 1999.

62. C. H. Yang, S. F. Lin, H. L. Chen, and C. T. Chang, *Inorg. Chem.* 19, 3541 (1980).

63. N. B. Subbotin, L. G. Tomilova, N. A. Kostromina, and E. A. Luk'yanetz, *Zh. Obshch. Khim.* 56, 397 (1986).

64. T. N. Lomova and L. G. Andrianova, *Russ. J. Phys. Chem.* 74, 1432 (2000).

65. L. G. Tomilova, E. V. Cherugkh, N. A. Ovchinnikova, and E. A. Luk'yanets, "The Synthesis and Properties of III and IV Groups Diphthalocyanines. Chemistry of Functional Dyes," p. 234. Mita Press, Tokyo, 1989.

66. V. A. Kuz'mitzkiy, K. N. Solov'ev, and M. P. Zvirko, in "Spektroskopiya i kvantovaya khimiya porfirinov" (N. S. Enikolopyan, Ed.), p. 7. Nauka, Moscow, 1987.

67. A. B. P. Lever, *Adv. Inorg. Chem. Radiochem.* 7, 27 (1965).

68. D. Colaitis, *Bull. Chim. Soc. Fr.* 1, 23 (1962).

69. P. Sayer, M. Gouterman, and C. R. Connell, *Acc. Chem. Res.* 15, 73 (1982).

70. Yu. M. Osipov, G. P. Shaposhnikov, V. P. Kulinich, A. B. Korzhenevsky, and R. P. Smirnov, *Izv. Vuzov. Khim. Khim. Tehnol.* 30, 29 (1987) (in Russian).

71. Yu. M. Osipov, M. K. Islyaikin, G. P. Shaposhnikov, V. P. Kulinich, and R. P. Smirnov, *Izv. Vuzov. Khim. Khim. Tehnol.* 31, 31 (1988) (in Russian).

72. N. B. Subbotin, L. G. Tomilova, N. A. Kostromina, and E. A. Luk'yanetz, *Zh. Obsch. Khim.* 56, 297 (1986) (in Russian).

73. R. Guilard, A. Dormond, and M. Belkalem, *Inorg. Chem.* 26, 1410 (1987).

74. K. J. Wynne, *Inorg. Chem.* 23, 4658 (1984).

75. H. Huckstadt and H. Homborg, *Z. Naturforsch. B-A* 52, 728 (1997).

76. H. M. Rietveld, *J. Appl. Crystallogr.* 2, 65 (1969).

77. B. G. Malmros and J. O. Thomas, *J. Appl. Crystallogr.* 10, 7 (1977).

78. K. Yamasaki, O. Okada, K. Inami, K. Oka, M. Kotani, and H. Yamada, *J. Phys. Chem. B* 101, 13 (1997).

79. R. Kubiak and J. Janczak, *J. Alloys Compd.* 189, 107 (1992).

80. T. N. Lomova and L. G. Andrianova, *Zh. Neorg. Khim.* 39, 2011 (1994) (in Russian).

81. G. V. Ionova, G. V. Vohnin, and V. I. Spitzin, "Zakonomernosti izmananiya svoistv lantanidov i actinidov." Nauka, Moscow, 1990.

82. S. B. Meshkova, N. S. Poluektov, Z. M. Topilova, and M. M. Danilovic, *Koord. Khim.* 12, 481 (1986).

83. T. N. Lomova and T. N. Sokolova, in "Uspehi khimii porfirinov" (O. A. Golubchikov, Ed.), Vol. 2, p. 167. S.-Pb., 1999.

84. K. B. Yatzimirsky, N. A. Kostromina, and P. F. Tzheka, "Khimiya kompleksnich soedineniy redkozemel'nich elementov." Naukova Dumka, Kiev, 1966.

85. T. Sokolova, T. Lomova, V. Mayzlish, G. Shaposhnikov, M. Korina, T. Mezintzeva, L. Stolyarova, and M. Klyueva, in "6th European Symposium on Organic Reactivity. Book of Abstracts," p. 112. Louvain-la-Neuve University, Brussels, 1997.

86. I. S. Kirin, P. N. Moskalev, and I. V. Ivannikova, *Russ. J. Inorg. Chem.* 12, 369 (1967).

87. P. N. Moskalev, G. N. Shapkin, and A. N. Darovskih, *Zh. Neorg. Khim.* 24, 340 (1979).

88. M. M'Sadac, J. Roncalay, and F. Carrier, *J. Chim. Phys. Phys.-Chim. Biol.* 83, 211 (1986).

89. E. O. Tolkacheva, A. Yu. Tsivadze, Sh. G. Bitiev, Yu. G. Gorbunova, V. I. Zhilov, and V. V. Minin, *Zh. Neorg. Khim.* 40, 984 (1995).

90. P. N. Moskalev and I. S. Kirin, *Russ. J. Phys. Chem.* 46, 1019 (1972).

91. T. N. Sokolova, T. N. Lomova, V. V. Morozov, and B. D. Berezin, *Koord. Khim.* 20, 637 (1994).

92. E. G. Kogan, A. V. Ivanov, L. G. Tomilova, and N. S. Zefirov, *Mendeleev Commun.* 54 (2002).

93. T. N. Lomova, T. N. Sokolova, E. G. Mozhzhukhina, P. N. Moskalev, and B. D. Berezin, *Zh. Fisitcheskoi Khim.* 66, 1240 (1992).

94. N. A. Ovchinnikova, L. G. Tomilova, N. V. Seregina, V. V. Minin, G. M. Larin, and E. A. Luk'yanets, *Russ. J. Gen. Chem.* 62, 1340 (1992).

95. F. Lux, O. F. Beck, H. Kraub, D. Brown, and T. C. Tso, *Z. Naturforsch. B* 35, 564 (1980).

96. L. A. Lapkina, E. Niskanen, X. Renkkomyaki, V. E. Larchenko, E. O. Tolkacheva, K. I. Popov, and A. Yu. Tzivadze, *Russ. J. Coord. Chem.* 24, 598 (1998).

97. C. Ercolani, A. M. Paoletti, G. Pennesi, G. Rossi, A. Chiese-Villa, and C. Rizzoli, *J. Chem. Soc., Dalton Trans.* 1971 (1990).

98. C. Sirlin, I. Basio, and J. Simon, *Chem. Phys. Lett.* 139, 362 (1987).

99. J. Simon and C. Sirlin, *Pure Appl. Chem.* 61, 1625 (1989).

100. G. A. Corker, B. B. Grant, and N. J. Clecak, *J. Electrochem. Soc.* 126, 1339 (1979).

101. G. C. S. Collin and D. J. Schiffrin, *Electroanal. Chem. Interfacial Electrochem.* 139, 335 (1982).

102. C. C. Leznoff and A. B. P. Lever, "Phthalocyanines: Properties and Application" (C. C. Leznoff and A. B. P. Lever, Eds.), Vols. 1, 2, and 3. VCH, New York, 1989, 1990, 1992.

103. L. G. Tomilova, E. V. Chernich, N. T. Ioffe, and E. A. Luk'yanetz, *Zh. Obshch. Khim.* 53, 2594 (1983).

104. V. I. Burkov, I. B. Talanina, and V. M. Mokshin, *Opt. Spektrosk.* 61, 786 (1986).

105. V. I. Gavrilov, V. A. Vazhina, A. P Konstantinov, and I. V. Shelepin, *Elektrokhimiya* 22, 1112 (1986).

106. V. I. Gavrilov, A. P Konstantinov, E. A. Luk'yanetz, and I. V. Shelepin, *Elektrokhimiya* 22, 1667 (1986).

107. P. N. Moskalev, V. A. Mishin, E. M. Rubtzov, and I. S. Kirin, *Zh. Neorg. Khim.* 21, 2259 (1976).

108. M. M'Sadac, J. Roncaly, and F. Garrier, *J. Electroanal. Chem.* 189, 99 (1985).

109. A. N. Sidorov and I. P. Kotl'ar, *Opt. Spektrosk.* 11, 175 (1961).

110. W. Wang, X. Yang, and J. Zhang, *J. Appl. Chem.* 36, 58 (1986).

111. J. W. Buchler, H. G. Kapellmann, M. Knoff, K. L. Lay, and S. Pfeifer, *Z. Naturforsch. B* 38, 1339 (1983).

112. J. W. Buchler and J. Loffler, *Z. Naturforsch. B* 45, 531 (1990).

113. J. W. Buchler, P. Hammerschmitt, I. Kaufeld, and J. Loffer, *J. Chem. Ber.* 124, 2151 (1991).

114. J. W. Buchler, M. Kihnbotulinski, J. Loffer, and B. Scharbert, *New J. Chem.* 16, 545 (1992).

115. J. K. Duchowski and D. F. Bocian, *J. Am. Chem. Soc.* 112, 3312 (1990).

116. J. W. Buchler and M. Nawra, *Inorg. Chem.* 33, 2830 (1994).

117. G. S. Girolami, S. N. Milam, and K. S. Suslick, *Inorg. Chem.* 26, 343 (1987).

118. L. N. Lomova, L. G. Andrianova, and B. D. Berezin, *Zh. Neorg. Khim.* 36, 641 (1991).

119. P. C. Martin, J. Arnold, and D. F. Bocian, *J. Phys. Chem.* 97, 1332 (1993).

120. J. W. Buchler and B. Scharbert, *J. Am. Chem. Soc.* 110, 4272 (1988).

121. O. Bilsel, J. Rodrigues, and D. Holten, *J. Phys. Chem.* 94, 3508 (1990).

122. T. H. Tran-Thi, T. Mattioli, D. Chabach, A. De Chian, and R. Weiss, *J. Phys. Chem.* 98, 8279 (1994).

123. R. Guilard, J.-M. Barbe, A. Iblnfassi, A. Zrineh, V. A. Adamian, and K. M. Kadish, *Inorg. Chem.* 34, 1472 (1995).

124. B. F. Hoskins, S. A. Mason, and J. B. C. White, *J. Chem. Soc., Chem. Commun.* 554 (1969).

125. M. P. Donzello, C. Ercolani, and P. J. Lukes, *Inorg. Chim. Acta* 256, 171 (1997).

126. J. Jiang, U. Cornelissen, D. P. Arnold, X. Sun, and H. Homborg, *Polyhedron* 20, 557 (2001).

127. N. Pana, L. Rinyoulb, D. P. Arnold, and J. Jiang, *Polyhedron* 21, 1905 (2002).

128. N. Ishikawa, *J. Porphyrins Phthalocyanines* 5, 87 (2001).

129. V. M. Negrimovskii, M. Bouvet, E. A. Luk'yanets, and J. Simon, *J. Porphyrins Phthalocyanines* 5, 423 (2001).

130. F. Fernandez-Alonso, P. Marovino, A. M. Paoletti, M. Righini, and G. Rossi, *Chem. Phys. Lett.* 356, 607 (2002).

131. A. K. Ray, J. Exley, Z. Ghassemlooy, D. Crowther, M. T. Ahmet, and J. Silver, *Vacuum* 61, 19 (2001).

132. N. Kobayashi, *Coord. Chem. Rev.* 227, 129 (2002).

133. Yu. V. Korovin, N. V. Rusakova, Z. I. Zhilina. Yu. V. Ishkov, S. V. Vodzinsky, and V. P. Dotsenko, *Mendeleev Commun.* 12, 151 (2002).

134. N. Ishikawa, T. Iino, and Yo. Kaizu, *J. Am. Chem. Soc.* 124, 11220 (2002).

Doubly Connected Mesoscopic Superconductors

B. J. Baelus, F. M. Peeters

Universiteit Antwerpen, Antwerpen, Belgium

CONTENTS

1. INTRODUCTION

Thanks to recent progress in microfabrication and measurement techniques, it has become possible to study the properties of single superconducting samples with sizes comparable to the penetration depth λ and the coherence length ξ. The penetration length is a measure of the distance over which the magnetic field penetrates the superconductor, whereas the coherence length is a measure of the size of the Cooper pair (and of a vortex). Bulk superconductors are divided into two classes, that is, type I and type II superconductors. In type I superconductors only the Meissner state nucleates, where the magnetic field is expelled from the superconductor. In type II superconductors the mixed state also exists, the magnetic field can penetrate through the superconductor, creating vortices. The energetically most favorable vortex configuration in bulk superconductors is the triangular

Abrikosov vortex lattice. The properties of mesoscopic samples are considerably influenced by confinement effects. This was most dramatically shown by recent experiments of Geim et al. (see, e.g., [1]) on Al superconducting disks. Whereas bulk Al is a type I material, depending on the size, mesoscopic superconductors were found to be type I, type II, or a mixture of both. This clearly showed that the vortex state is strongly influenced by the size and the geometry of the sample and that the bulk value for $k = \lambda/\xi$ becomes less relevant.

Singly connected mesoscopic superconductors, that is, superconducting samples with one closed superconductor/insulator boundary, have been studied extensively during the past few years. Most of the studies concentrated on superconducting disks. Experimentally, the magnetization of superconducting disks was measured as a function of the externally applied magnetic field [1–3]. Several transitions between different superconducting states were found, and the magnetization depends sensitively on size and temperature. Most theoretical studies covered disks [4–12] of zero thickness. In this case one can neglect the magnetic field induced by the supercurrents, and one assumes that the total magnetic field equals the external applied magnetic field, which is uniform. A limited number of studies considered disks [13–18] with *finite* thickness. Then, the finite thickness of the disks influences the magnetic field profile, and it is necessary to take into account the demagnetization effects. Often only the (circular symmetric) giant vortex states or the superconducting/normal transition was investigated. Even in type I superconductors, multivortex states in disks [5–9, 16, 17] were predicted. It was found that if the disk is large enough, the giant vortex nucleates into a multivortex state in which the vortices are situated on a ring.

Mesoscopic superconductors with noncircular geometries have attracted less attention. Moshchalkov et al. [19] measured the superconducting/normal transition in superconducting lines, squares, and square rings using resistance measurements. Bruyndoncx et al. [20] calculated the $H - T$ phase diagram for a square with zero thickness in the framework of the linearized Ginzburg–Landau theory, which

is only valid near the superconducting/normal boundary. They compared their results with the $H - T$ phase boundary obtained from resistance measurements. Schweigert and Peeters [15, 18] calculated the nucleation field as a function of the sample area for disks, squares, and triangles with zero thickness. Jadallah et al. [21] computed the superconducting/normal transition for mesoscopic disks and squares of zero thickness. Chibotaru et al. investigated the vortex entry and the nucleation of antivortices in infinite thin superconducting squares [22] and triangles [23] using the linearized Ginzburg–Landau theory. Within this linear theory they studied the superconducting/normal transition and they found near this transition the nucleation of multivortices, antivortices, and combinations of these two instead of the expected surface superconductivity. They found that the appearance of those antivortices is a consequence of the fact that the vortex state tries to preserve the symmetry of the sample boundary. Bonča and Kabanov [24] studied the $\kappa \to \infty$ limit and extended those results to thin superconducting squares, focusing on the nonlinear Ginzburg–Landau theory. Within this nonlinear theory they showed that the vortex/antivortex configuration becomes rapidly unstable when moving away from the superconducting/normal transition. We confirmed this conclusion for arbitrary values of κ and studied also the vortex states deep inside the superconducting phase. Interesting vortex configurations were found with the coexistence of giant and multivortex states [25]. Misko et al. [26, 27] studied stable vortex and antivortex configurations in mesoscopic superconducting triangles. They found that a stable vortex–antivortex "molecule" can appear in effectively type I superconductors due to the interplay between two factors: a repulsive vortex–antivortex interaction in type I superconductors and the vortex confinement in the triangle.

During the past few years, doubly connected mesoscopic superconductors, that is, mesoscopic superconductors with a hole in its inside, gained considerable interest. What is the effect of the hole on the critical parameters and on the vortex configuration? The goal of this chapter is to give an overview of the theoretical and experimental work on these doubly connected mesoscopic superconductors.

2. GINZBURG–LANDAU THEORY

Ginzburg and Landau developed a phenomenological theory [28] to describe the superconducting state, which is based on the theory of second-order phase transitions as developed by Landau. They assumed that the wavefunction of the superconducting electrons $\Psi(\vec{r})$ is the order parameter, and they chose the normalization of this wavefunction such that $|\Psi(\vec{r})|^2$ gives the density of Cooper pairs:

$$|\Psi(\vec{r})|^2 = n_s/2 \qquad (1)$$

where n_s is the density of the superconducting electrons.

The theory is based on an expansion of the free energy in powers of the order parameter, which is small close to the superconducting/normal transition at the critical temperature T_c. In this way, it is immediately clear that the Ginzburg–Landau (GL) theory is, in principle, valid only near T_c.

2.1. Free Energy

Near T_c the Gibbs free energy density can be expanded as [29]

$$G_{sH} = G_n + \alpha|\Psi|^2 + \frac{\beta}{2}|\Psi|^4 + \frac{1}{2m^*}\left|\left(-i\hbar\vec{\nabla} - \frac{2e}{c}\vec{A}\right)\Psi\right|^2$$
$$+ \frac{H^2}{8\pi} - \frac{\vec{H} - \vec{H}_0}{4\pi} \cdot \vec{H}_0 \qquad (2)$$

where H is the microscopic field at a given point of the superconductor, H_0 is the externally applied field, and G_n is the free energy density of a superconductor in the normal state when no field is applied. When a field is applied, the free energy density of a superconductor in the normal state is given by $G_{nH} = G_n + H_0^2/8\pi$, where $H_0^2/8\pi$ is the magnetic energy density.

- The first part of Eq. (2) is the expansion of the free energy density for a homogeneous superconductor in the absence of an external magnetic field in powers of $|\Psi|^2$ near the zero-field critical temperature $T_{c0} \equiv T_c(H_0 = 0)$,

$$G_n + \alpha|\Psi|^2 + \frac{\beta}{2}|\Psi|^4 \qquad (3)$$

where α and β are some phenomenological expansion coefficients that are characteristics of the material. The coefficient α is negative and depends on the temperature as $\alpha \propto (T - T_{c0})$, while β is a positive constant. From Eq. (3) the Cooper pair density corresponding to the free energy minimum at temperatures below T_{c0} can be calculated as

$$|\Psi_0|^2 = -\alpha/\beta \qquad (4)$$

- The next term is the kinetic energy of the Cooper pairs:

$$\frac{1}{2m^*}\left|\left(-i\hbar\vec{\nabla} - \frac{2e}{c}\vec{A}\right)\Psi\right|^2 \qquad (5)$$

where the mass of a Cooper pair m^* is two times the mass of an electron m and the charge of the Cooper pair is twice the charge of the electron e. In quantum mechanics, the kinetic energy density of a particle of mass m^* is

$$\frac{1}{2m^*}|-i\hbar\vec{\nabla}\Psi|^2 \qquad (6)$$

For a particle of charge $2e$ moving in the field with vector potential $\vec{A}$, the operator $-i\hbar\vec{\nabla}$ in the expression for the kinetic energy density has to be modified:

$$-i\hbar\vec{\nabla} \to -i\hbar\vec{\nabla} - \frac{2e}{c}\vec{A} \qquad (7)$$

- The next to last term simply represents the magnetic energy density, that is,

$$\frac{H^2}{8\pi} \qquad (8)$$

- The last term describes the reduction of the magnetic field due to the penetration of the field, that is,

$$-\frac{\vec{H} - \vec{H}_0}{4\pi} \cdot \vec{H}_0 \qquad (9)$$

Without this term, expression (1) would be the free energy F. For a superconductor in the presence of an external field, it is the Gibbs free energy G,

$$G = F - \frac{\vec{H} - \vec{H}_0}{4\pi} \cdot \vec{H}_0 \qquad (10)$$

which has to be minimized to obtain the ground state of the superconductor [30].

The overall Gibbs free energy of a superconductor is

$$\mathcal{G}_{sH} = \mathcal{G}_{nH} + \int \left\{ \alpha|\Psi|^2 + \frac{1}{2}\beta|\Psi|^4 + \frac{1}{2m^*}\left|\left(-i\hbar\vec{\nabla} - \frac{2e}{c}\vec{A}\right)\Psi\right|^2 \right.$$
$$\left. + \frac{H^2}{8\pi} + \frac{H_0^2}{8\pi} - \frac{\vec{H} \cdot \vec{H}_0}{4\pi} \right\} dV \qquad (11)$$

where the integration is carried out over the entire space V. Note that $\mathcal{G}_{sH}$ is a functional of $\Psi(\vec{r})$ and $\vec{A}(\vec{r})$. Minimizing $\mathcal{G}_{sH}$ with respect to these two functions leads to the Ginzburg–Landau equations, which will be derived below.

2.2. First Ginzburg–Landau Equation

To obtain the minimum of the total Gibbs free energy, we vary expression (11) with respect to Ψ^* [29]:

$$\int \left\{ \alpha\Psi\delta\Psi^* + \beta\Psi|\Psi|^2\delta\Psi^* + \frac{1}{2m^*}\vec{\varphi} \right.$$
$$\left. \cdot \left(i\hbar\vec{\nabla} - \frac{2e}{c}\vec{A}\right)\delta\Psi^* \right\} dV' = 0 \qquad (12)$$

where

$$\vec{\varphi} = \left(-i\hbar\vec{\nabla} - \frac{2e}{c}\vec{A}\right)\Psi \qquad (13)$$

After minimization we obtain the first equation of the Ginzburg–Landau theory and its boundary condition:

$$\alpha\Psi + \beta|\Psi|^2\Psi + \frac{1}{2m^*}\left(-i\hbar\vec{\nabla} - \frac{2e}{c}\vec{A}\right)^2\Psi = 0 \qquad (14)$$

$$\vec{n} \cdot \left(-i\hbar\vec{\nabla} - \frac{2e}{c}\vec{A}\right)\Psi\Big|_{\text{boundary}} = 0 \qquad (15)$$

where $\vec{n}$ is the unit vector normal to the surface of the super-conductor.

2.3. Second Ginzburg–Landau Equation

To obtain the minimum of the Gibbs free energy, we vary Eq. (11) with respect to $\vec{A}$ [29]:

$$\frac{1}{2m^*}\int\left[\left(-\frac{2e}{c}\delta\vec{A}\Psi^*\right)\cdot\left(-i\hbar\vec{\nabla}\Psi - \frac{2e}{c}\vec{A}\Psi\right)\right.$$
$$\left. + \left(i\hbar\vec{\nabla}\Psi^* - \frac{2e}{c}\vec{A}\Psi^*\right)\cdot\left(-\frac{2e}{c}\delta\vec{A}\Psi\right)\right]dV$$
$$+ \frac{1}{4\pi}\int(rot\,\vec{A} - \vec{H}_0)\cdot rot\,\delta\vec{A}dV = 0 \qquad (16)$$

with $\vec{H} = rot\,\vec{A}$ and V is the volume of the entire space.

Because the current density $\vec{j}_S$ in the superconductor is given by the Maxwell equation

$$\vec{j}_S = \frac{c}{4\pi} rot\,rot\,\vec{A} \qquad (17)$$

the minimization finally leads to the second Ginzburg–Landau equation:

$$\vec{j}_S = -\frac{i\hbar e}{m^*}(\Psi^*\vec{\nabla}\Psi - \Psi\vec{\nabla}\Psi^*) - \frac{4e^2}{m^*c}|\Psi|^2\vec{A} \qquad (18)$$

2.4. Characteristic Length Scales

The Ginzburg–Landau theory introduces two important characteristic length scales: the coherence length $\xi(T)$ and the penetration depth $\lambda(T)$. The coherence length $\xi(T)$ indicates the typical length scale over which the size of the order parameter can vary (Fig. 1). The typical length scale over which the magnetic field $\vec{H}$ can vary is the penetration depth $\lambda(T)$ (Fig. 1).

2.5. Boundary Condition

The boundary condition for the order parameter in a super-conductor in contact with an insulator or with a vacuum is given by Eq. (15), where $\vec{n}$ is the unit vector normal to the surface of the superconductor. This condition expresses the fact that no supercurrent can pass perpendicular to the sample boundary (Neumann boundary condition).
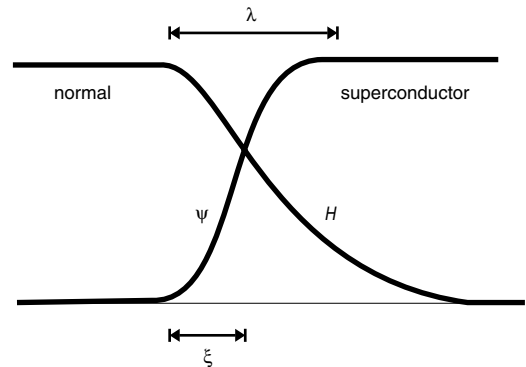
Figure 1. The radial dependence of the order parameter Ψ and the magnetic field H at the superconducting/normal surface boundary.

For a superconductor–normal metal interface the boundary condition must be modified. The more general expression, which assures that no supercurrent passes perpendicular to the sample boundary, can be written as [31]

$$\vec{n} \cdot \left(-i\hbar \vec{\nabla} - \frac{2e}{c} \vec{A} \right) \Psi \Big|_{\text{boundary}} = \frac{i}{b} \Psi \Big|_{\text{boundary}} \tag{19}$$

with b being the extrapolation length over which the order parameter becomes zero in the normal metal (Fig. 2). Notice that for a superconductor–normal metal interface b is positive.

The value of the extrapolation length is determined by the medium adjacent to the superconductor:

1. For vacuum or an insulator: $b \to \infty$.
2. For normal metals: $b > 0$, and for ferromagnets: $b \to 0$.
3. For a superconducting layer with a higher T_c: $b < 0$.

The latter case is of theoretical interest because then the order parameter near the surface will increase, which will lead to higher critical fields and larger critical temperatures.

3. TYPE I AND TYPE II SUPERCONDUCTORS

3.1. Bulk Superconductors

Bulk superconductors can be separated into two types through their Ginzburg–Landau parameter $\kappa = \lambda(T)/\xi(T)$:

$$\kappa < 1/\sqrt{2} \to \text{ type I superconductors}$$

$$\kappa > 1/\sqrt{2} \to \text{ type II superconductors}$$

All superconducting elements except niobium are type I superconductors. Niobium and all superconducting alloys and chemical compounds are type II. The high T_c superconductors also belong to the second group. The dependence of the superconducting characteristics on the value of κ is shown in Figure 3.

For $\kappa < 0.42$ the superconductor is a type I superconductor. For fields below the thermodynamical critical field H_c the superconductor is in the Meissner state and all flux
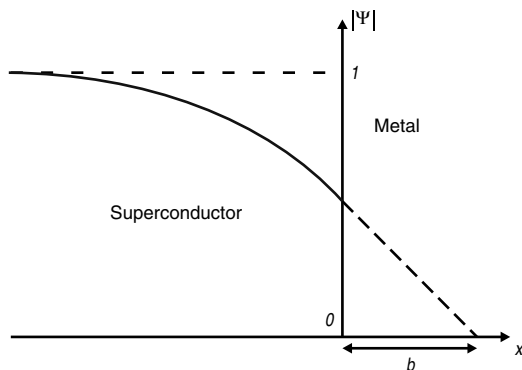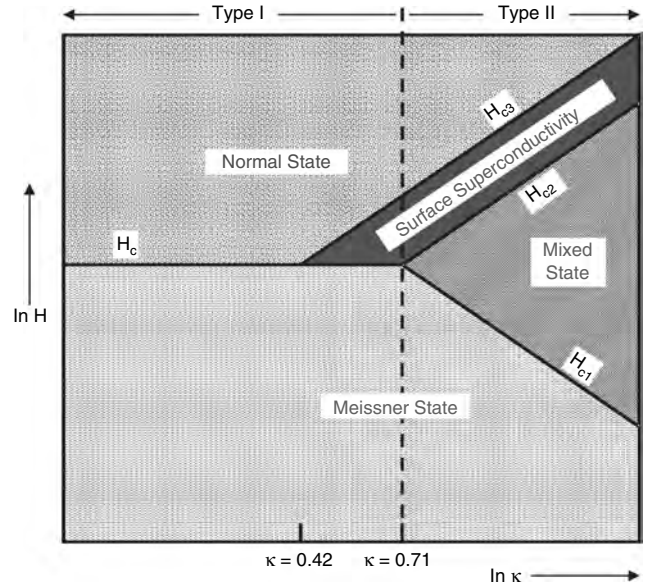
Figure 3. The dependence of the characteristics of semi-infinite superconductors on the value of the Ginzburg–Landau parameter κ. H_{c3} is the surface superconducting field when the field is parallel to the surface. Modified from [32].

is expelled from the sample. At the critical field the magnetic field penetrates the sample, the superconductivity is destroyed, and the sample becomes normal. For $0.42 < \kappa < 1/\sqrt{2} \simeq 0.71$ the superconductor is still a type I superconductor, but now the Meissner state does not change immediately into the normal state with increasing field. At the field H_c flux can penetrate the inner part of the sample, while a layer remains superconducting near the surface of the sample. At the surface critical field H_{c3} the surface becomes normal too and the sample is in the normal state.

In type II superconductors ($\kappa > 1/\sqrt{2}$), on the other hand, a fourth possible state exists. In equilibrium, the Meissner state is only observed at applied fields H_0 below the first critical field H_{c1}. In the region between the first critical field H_{c1} and the second critical field H_{c2} the magnetic flux is able to penetrate the sample in quantized units of the flux quantum $\phi_0 = hc/2e$, called vortices. Abrikosov [33] found that these vortices form a triangular lattice inside the superconductor, the so-called Abrikosov vortex lattice. The state is called the Abrikosov vortex state or mixed state. In the region $H_{c2} < H_0 < H_{c3}$ superconductivity only exists at a thin layer near the sample edges, while the inner side of the sample is in the normal state. For bulk type II superconductors the third critical field H_{c3} is approximately equal to $1.69H_{c2}$. For larger fields superconductivity is destroyed, and the entire sample is in the normal state.

The critical fields H_c, H_{c1}, H_{c2}, and H_{c3} depend on the temperature. The $H - T$ phase diagrams for type I and type II bulk superconductors are shown in Figure 4.

The magnetization behavior as a function of the external magnetic field is also different for both types. This can be seen from Figure 5. The magnetization of a superconductor is defined as

$$\vec{M} = \frac{1}{4\pi}(\vec{B} - \vec{H}_0) \tag{20}$$

Figure 2. Schematic presentation of the spatial dependence of the superconducting order parameter $|\Psi|$ at the interface between a superconducting and a normal metal. The extrapolation length b is indicated.
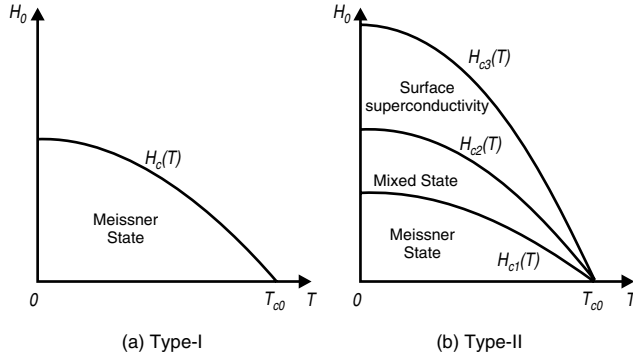
Figure 4. $H - T$ phase diagrams for type I (a) and a type II (b) bulk superconductors.

where $\vec{B} = \langle \vec{H} \rangle$ is the magnetic induction and $\vec{H}_0$ is the applied magnetic field.

At $H_0 < H_c$ a type I bulk superconductor is in the Meissner state, and all flux is expelled from the sample: $\langle \vec{H} \rangle = 0$ and $-4\pi \vec{M} = \vec{H}_0$. At larger fields, the applied field penetrates into the superconductor, which becomes normal: $\langle \vec{H} \rangle = \vec{H}_0$ and $\vec{M} = 0$. Type II superconductors are in the Meissner state at $H_0 < H_{c1}$ and $-4\pi \vec{M} = \vec{H}_0$. In the mixed state ($H_{c1} < H_0 < H_{c2}$) the absolute value of the magnetization $|\vec{M}|$ decreases with increasing field until it vanishes at the second critical field.

Also the surface energy is different for type I and type II superconductors (see, for example, [30]). The expulsion of the external field increases the energy of a superconductor by $H^2/8\pi$ per unit volume. It is energetically more favorable that the volume will be divided up into alternate normal and superconducting regions. The creation of such normal regions requires a negative interface surface energy σ_{ns} whose magnitude is such that its contribution exceeds the gain in magnetic energy. The two types of superconductors have a different behavior with respect to the surface energy:

$$\text{Type I} : \sigma_{ns} > 0,$$
$$\text{Type II} : \sigma_{ns} < 0.$$

3.2. Mesoscopic Superconductors

In thin superconducting films the distinction between type I and type II superconductivity depends not only on the Ginzburg–Landau parameter κ but also on the sample
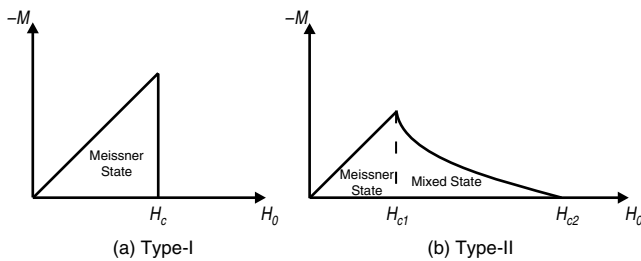
Figure 5. The magnetization as a function of the applied magnetic field for type I and type II bulk superconductors.

thickness. Because the effective London penetration depth $\Lambda = \lambda^2/d$ increases considerably in films with thickness $d \ll \lambda$, the vortex state can appear in thin films made from a material with $\kappa < 1/\sqrt{2}$. In this case one introduces the effective Ginzburg–Landau parameter $\kappa^* = \Lambda/\xi$, which defines the type of superconductivity: type I when $\kappa^* < 1/\sqrt{2}$ and type II when $\kappa^* > 1/\sqrt{2}$. In mesoscopic samples the distinction between type I and type II superconductors is determined not only by κ and the thickness d, but also by the lateral dimensions of the sample (see, e.g., [16, 34]).

In confined mesoscopic samples there is a competition between the triangular Abrikosov distribution of vortices, being the lowest energy configuration in bulk material and thin films, and the sample boundary, which tries to impose its geometry on the vortex distribution. For example, a circular disk will favor vortices situated on a ring near the boundary and only far away from the boundary does its influence diminish and the triangular lattice may reappear.

Multivortex versus Giant Vortex State

Depending on the geometry, the size, the applied field, and the temperature, different kinds of vortex states can nucleate in mesoscopic samples: giant vortex states and multivortex states or a mixture of both of them, for example, in triangular and square superconductors (see, e.g., [25]).

The **multivortex** state in mesoscopic confined samples is the analogon of the Abrikosov vortex state in bulk superconductors. The flux penetrates the sample at several positions where vortices are created. These vortices can be very close to each other and overlap, but they are defined by their separate zeros of the Cooper pair density. On the other hand, when the sample is sufficiently small, the vortices will overlap so strongly that it is more favorable to form one **giant vortex**, corresponding with only one minimum in the Cooper pair density. The shape of the giant vortex also depends on the sample geometry. Figure 6a and b shows the Cooper pair density for a multivortex state and a giant vortex state in a superconducting disk with radius $R/\xi = 6.0$. High Cooper pair density is given by dark regions and low by light regions. This means that in Figure 6a the white spots are the vortices.

Vorticity

For a given mesoscopic sample, different superconducting states (giant vortex states and multivortex states) can nucleate for a particular magnetic field. These states have a different free energy and a different vortex configuration, and they can be characterized by their **vorticity** L. For multivortex states the vorticity is nothing other than the number of vortices. To determine the vorticity of the giant vortex state one has to look at the phase of the order parameter. Along a closed path around the vortex, the phase of the order parameter always changes with L times 2π. Figure 6c shows the contour plot of the phase of the order parameter for the multivortex state of Figure 6a. Light regions indicate phases near zero and dark regions phases near 2π. By encircling the disk near the boundary of the disk, the phase changes 5 times with 2π. This means that the total vorticity of the disk is $L = 5$. By going around one single vortex the phase changes with 2π and $L = 1$. In Figure 6d the phase of the
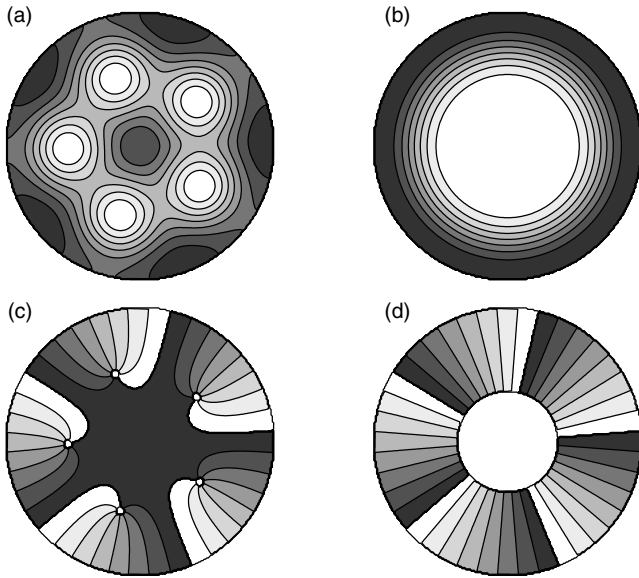
Figure 6. The Cooper pair density for the multivortex state (a) and the giant vortex state (b) and the phase of the order parameter for the multivortex state (c) and the giant vortex state (d) with vorticity $L = 5$ in a superconducting disk with radius $R/\xi = 6.0$. High (low) Cooper pair density is given by red (blue) regions. Phases near 2π (0) are given by dark (light).

order parameter is shown for the giant vortex configuration of Figure 6b. By going around the giant vortex, the phase of the order parameter changes 5 times with 2π, which means that the giant vortex state has vorticity $L = 5$.

4. LITTLE–PARKS EFFECT

In 1962 Little and Parks [35, 36] measured the shift of the critical temperature $T_c(H)$ of a thin-walled Sn microcylinder in an axial magnetic field H. The $T_c(H)$ phase boundary showed a periodic component, with the magnetic period corresponding to the penetration of a superconducting flux quantum $\Phi_0 = hc/2e$. The Little–Parks oscillations in $T_c(H)$ are a straightforward consequence of the fluxoid quantization constraint, which was predicted by London [37]. Inserting the order parameter $\Psi = |\Psi|\exp(i\varphi)$ into the current operator we obtain

$$\vec{j} = \frac{e\hbar}{m}|\Psi|^2\left(\vec{\nabla}\varphi - \frac{2e}{\hbar c}\vec{A}\right) \qquad (21)$$

which after integration over a closed contour C inside the superconductor leads to

$$\oint_C \frac{mc}{2e^2|\Psi|^2}\vec{j} \cdot d\vec{l} + \oint_C \vec{A} \cdot d\vec{l} = L\Phi_0 \qquad (22)$$

where $\oint_C \vec{A} \cdot d\vec{l} = \int rot\vec{A} \cdot d\vec{S} = \int \vec{H} \cdot d\vec{S} = \Phi$ using the Stokes theorem. In other words, when the external flux Φ is not an integer times the flux quantum Φ_0, induced supercurrents are necessary to fulfill Eq. (22). The integer number L is the vorticity.

5. GIANT VORTEX STATES IN RINGS

In small superconducting rings, the sample boundary imposes its symmetry on the vortex configuration. Therefore, the vortex configuration is axially symmetric and only giant vortex states nucleate. In a first step, Bruyndoncx et al. [38] studied the superconducting/normal transition of superconducting rings with zero thickness. To this aim, they were allowed to simplify the problem by linearizing the first Ginzburg–Landau equation and neglecting the second one. Later, we solved the complete set of nonlinear Ginzburg–Landau equations assuming axial symmetry [39].

5.1. Linear Theory

Bruyndoncx et al. [38] studied the phase boundary $T_c(H)$ of superconducting disks with a hole in the center. Concentrating on the phase boundary they used the linear Ginzburg–Landau theory and neglected the second GL equation which describes the demagnetization effects. The linearized first Ginzburg–Landau equation was solved to find $T_c(H)$:

$$\frac{1}{2m^*}\left(-i\hbar\vec{\nabla} - \frac{2e}{c}\vec{A}\right)^2 \Psi = |-\alpha|\Psi \qquad (23)$$

The eigenenergies can be written as

$$|-\alpha| = \frac{\hbar^2}{2m^*\xi^2(T)} = \frac{\hbar^2}{2m^*\xi^2(0)}\left(1 - \frac{T}{T_{c0}}\right) \qquad (24)$$

where T_{c0} is the critical temperature in the zero magnetic field. The boundary condition for the order parameter is given by Eq. (15), which expresses the fact that the supercurrent does not have a component perpendicular to the sample boundary.

For loop geometries the cylindrical coordinate system (r, φ) and the gauge $\vec{A} = Hr/2\vec{e}_\varphi$ are used, where $\vec{e}_\varphi$ is the tangential unit vector. They found that the exact solution of the first Ginzburg–Landau equation has the following form:

$$\Psi(\Phi, \varphi) = e^{-iL\varphi}\left(\frac{\Phi}{\Phi_0}\right)^{L/2} \exp\left(-\frac{\Phi}{2\Phi_0}\right)$$
$$\times K\left(-n, L+1, \frac{\Phi}{\Phi_0}\right) \qquad (25)$$

where $K(a, c, y) = c_1 M(a, c, y) + c_2 U(a, c, y)$ with $M(a, c, y)$ and $U(a, c, y)$ as the two confluent hypergeometric functions and $\Phi = H\pi r^2$ is the applied magnetic flux through a circle of radius r. The integer n determines the energy eigenvalue. The sample topology determines the values of c_1, c_2, and n through the boundary condition.

The eigenenergies of the first Ginzburg–Landau Eq. (23) are

$$|-\alpha| = \frac{2e\hbar H}{2m^*}(2n+1) = \hbar\omega\left(n + \frac{1}{2}\right) \qquad (26)$$

where $\omega = 2eH/m^*$ is the cyclotron frequency. The parameter n depends on the vorticity L. With Eq. (24) this can be rewritten as

$$\frac{r_0^2}{\xi^2(T_c)} = \frac{r_0^2}{\xi^2(0)}\left(1 - \frac{T_c(H)}{T_{c0}}\right) = 4\left(n + \frac{1}{2}\right)\frac{\Phi}{\Phi_0}$$

$$= \epsilon(H_{c3}^*)\frac{\Phi}{\Phi_0} \qquad (27)$$

where $\Phi = H\pi r_o^2$.

The bulk Landau levels can be found when $n = 0, 1, 2, \ldots$ is substituted in Eqs. (26) and (27), meaning that the lowest level $n = 0$ corresponds to the upper critical field $H_{c2}(T) = \Phi_0/[2\pi\xi^2(T)]$. Note that the lowest Landau level ($n = 0$) for a bulk superconductor is degenerate in the phase winding number L, and therefore the eigenfunction can be expanded as $\Psi = \sum c_L\Psi_L$. Interference patterns between the different functions Ψ_L give rise to aperiodic vortex states [40].

The boundary condition can be written in cylindrical coordinates as

$$\left.\frac{\partial|\Psi(r)|}{\partial r}\right|_{r=r_0, r_i} = 0 \qquad (28)$$

with r_i and r_o, respectively, as the inner and outer radius of the ring. Using $dM(a, c, y)/dy = a/cM(a+1, c+1, y)$ and $dU(a, c, y)/dy = -aU(a+1, c+1, y)$ for the derivates of the first and second types of Kummer functions and inserting Eq. (25) into Eq. (28) gives

$$c_1\left[\left(L - \frac{\Phi}{\Phi_0}\right)M\left(-n, L+1, \frac{\Phi}{\Phi_0}\right)\right.$$
$$\left. - \frac{2n}{L+1}\frac{\Phi}{\Phi_0}M\left(-n+1, L+2, \frac{\Phi}{\Phi_0}\right)\right]$$
$$+ c_2\left[\left(L - \frac{\Phi}{\Phi_0}\right)U\left(-n, L+1, \frac{\Phi}{\Phi_0}\right)\right.$$
$$\left.\left. + 2n\frac{\Phi}{\Phi_0}U\left(-n+1, L+2, \frac{\Phi}{\Phi_0}\right)\right]\right|_{r=r_o, r_i} = 0 \quad (29)$$

which has to be solved numerically for each integer value of L, resulting in a set of values $n(L, \Phi)$ with $\Phi = H\pi r_0^2$. Notice that one can choose $c_1 = 1$.

Figure 7 shows the Landau level scheme (dashed curves) calculated from Eqs. (27) and (29) for loops with two different inner radii: $x = 0.5$ (a), and $x = 0.9$ (b). The applied magnetic flux $\Phi = \mu_0 H\pi r_o^2$ is defined with respect to the outer sample area. The $T_c(H)$ boundary is composed of Ψ solutions with a different phase winding number L and is drawn as a solid cusp-like curve in Figure 7. At $\Phi \approx 0$, the state with $L = 0$ is formed at $T_c(H)$ and one by one consecutive flux quanta L enter the loop as the magnetic field increases. Each state L approximately has a parabolic dependence, close to $T_c(H)$. Like for the disk [1, 4, 41], where $\Phi \approx \Phi_0(L + L^{1/2})$, one has $L\Phi_0 \leq \Phi$ here as well, indicating the overall diamagnetic response of the sample. As x increases, the oscillations in $T_c(\Phi)$ change from cusp-like to very pronounced local extrema for $x = 0.9$. In the limit of vanishing wire width ($x \to 1$), L is the integer closest to Φ_m/Φ_0, and therefore the response of the loop is alternating between diamagnetic and paramagnetic, as the flux
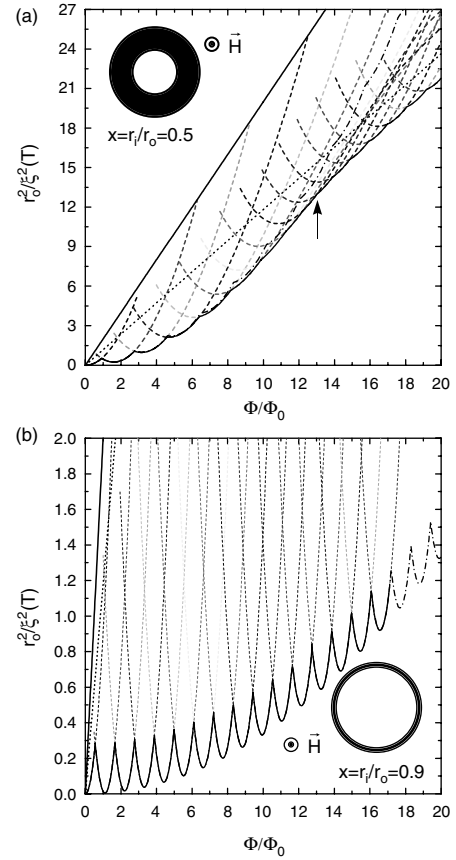
Figure 7. Calculated energy level scheme (dashed curves) for a superconducting loop with different ratio of inner to outer radius $x = r_i/r_o$: (a) $x = 0.5$ and (b) $x = 0.9$. The lowest level for each magnetic flux Φ/Φ_0 corresponds to the highest possible temperature $T_c(H)$ for which superconductivity can exist. A state with phase winding number $L = 0$ is formed at $T_c(\Phi \approx 0)$, and at each cusp in $T_c(H)$ the system makes a transition $L \to L + 1$, indicating the entrance of an extra vortex. The solid and dotted lines correspond to $H_{c2}(T)$ and $H_{c3}(T)$, respectively. Reprinted with permission from [38], V. Bruyndoncx et al., *Phys. Rev. B* 60, 10468 (1999). © 1999, American Physical Society.

varies. The solid and dotted straight curves in Figure 7 are the bulk upper critical field $H_{c2}(T)$ and the surface critical field $H_{c3}(T)$ for a semi-infinite slab, respectively.

The energy levels below the H_{c2} line (solid straight curve in Fig. 7) could be found by fixing a certain L and solving Eq. (29) for a small Φ until a set (n, c_2) is found with $n < 0$. These values were always put in as starting values for a slightly higher Φ. A trivial solution of Eq. (29) is obtained for $n = 0, 1, 2, \ldots$. Both confluent hypergeometric functions reduce to $M(-N, L+1, \Phi/\Phi_0) = 1$ and $U(-N, L+1, \Phi/\Phi_0) = 1$, and thus $c_2 = -c_1$. Inserting this into Eq. (25) gives $\Psi(\Phi, \varphi) = 0$ everywhere. With this method, one is able to find solutions with $n < 0$ numerically. Note that the lowest Landau level always has a lower energy $|-\alpha(\Phi)|$ than that for a semi-infinite superconducting slab. The dash–dotted curve in Figure 7 gives the result obtained with the London limit [42]. For $x = 0.5$ (Fig. 7a) the London limit is valid up to $\Phi \approx 8\Phi_0$ and for $x = 0.9$ (Fig. 7b) the assumption of a spatially constant $|\Psi|$ gives a $T_c(\Phi)$, which cannot be distinguished from the exact solution of Eq. (23).

For $x = 0.5$ (Fig. 7a) $T_c(H)$ has a rather *parabolic* background for flux $\Phi \lesssim 14\Phi_0$ and becomes quasi-linear at higher flux. In Figure 7b the background is parabolic in the entire flux regime. Simultaneously, as x increases, the cusps in $T_c(H)$ become more and more pronounced, until the usual Little–Parks effect is recovered for $x = 0.9$, where sharp local minima and clear maxima in $T_c(H)$ are seen.

The $|\Psi|$ profiles for a loop with $x = 0.5$ are shown in Figure 8 for different values of vorticity. ϕ is chosen to be equal to $9\Phi_0$, and the normalization $|\Psi(r_o)| = 1$. For $L = 2$ (Fig. 8a), $|\Psi|$ has a maximum at $r = r_i$. For higher L the order parameter distribution flattens until it reaches $L = 4$. Then, for the ground state energy ($L = 5$) (Fig. 8b), the maximum in $|\Psi|$ moves outward, but we should notice that superconductivity nucleates in a quasi-uniform way. Indeed, the exact $T_c(\Phi)$ and the London limit result are still very close to each other at $\Phi = 9\Phi_0$ (see Fig. 7a). Although multiple flux quanta L are threading the middle opening of the loop, we cannot, in the strict sense, speak about a giant vortex state here. First of all, there is no real "normal core" within the sample area, and secondly we are not dealing with a surface superconducting state in this case. The surface-to-volume ratio is so large that the whole sample area becomes superconducting at once. On the contrary, for the disk, strong spatial gradients of $|\Psi|$ are responsible for the spontaneous breaking of superconductivity in the giant vortex core, while only a surface sheath is superconducting.

It is worth noting that for all of the states shown in Figure 8 with $x = 0.5$ the different L states correspond to $w < 2.1\xi(T)$ (see also Fig. 7a). At this point we want to remind the reader that in a thin film of thickness d in a parallel field H, a dimensional crossover is found at $d = 1.84\xi(T)$. For low fields (high ξ) $T_c(H)$ is parabolic [two-dimensional (2D)], and for higher fields vortices start penetrating the film and consequently $T_c(H)$ becomes linear [three-dimensional (3D)] [43]. In Figure 7a the arrow indicates the point on the phase diagram $T_c(\Phi)$ where $w = 1.84\xi(T)$. For the loop with $x = 0.9$ this point lies outside the flux regime of the calculation. A dimensional transition from 2D to 3D shows up approximately at this point, although the vortices are not penetrating the sample area in the 3D regime. Instead, the middle loop opening contains an integer number of flux quanta $L\Phi_0$. In the present case, the 2D–3D crossover roughly occurs at the value Φ where the London limit result fails to describe the exact $T_c(\Phi)$.

Next, the periodicity $\Delta\Phi$ of $T_c(\Phi)$ is discussed for the different L states in the loops. These results are shown in Figure 9. For the disk the first transition occurs at $\Phi = 1.92\Phi_0$, so $\Delta\Phi(L = 0) = 3.85\Phi_0$. The period $\Delta\Phi$ goes down for increasing L, until it reaches the asymptotic limit [2]:

$$\Delta\Phi = \Phi_0(1 + (2\,\eta\Phi/\Phi_0)^{-1/2}) \tag{30}$$

The filled squares are the periods for the filled disk. The periodicity of $T_c(\Phi)$ in the case of loops behaves differently: for $x = 0.1$ (filled up-triangles in Fig. 9) $\Delta\Phi(L = 1) = 1.82\Phi_0$ is larger than for the disk, and then $\Delta\Phi(L = 2)$ jumps below the corresponding value for the disk; and for higher $L \geq 3$, the period $\Delta\Phi$ matches the disk behavior. Consequently, the giant vortex state builds up for $L \geq 3$; that is, $\Phi \gtrsim 5\Phi_0$. A similar analysis can be carried out for a loop with $x = 0.5$ (filled down-triangles in Fig. 9). For low L, $\Delta\Phi \approx 1.8\Phi_0$, and then $\Delta\Phi(L)$ decreases substantially below the value for the disk, before increasing again until the same period $\Delta\Phi(L)$ is reached for $L \geq 12$. The loop is in the giant vortex state when $\Phi \gtrsim 17\Phi_0$. For loops made of even thinner wires ($x = 0.7$ and $x = 0.9$) (open symbols in Fig. 9), $T_c(\Phi)$ stays periodic up to $L = 13$. The constant period $\Delta\Phi$ corresponds to $\Delta\Phi_m = ((1 + x)/2)^2\Delta\Phi = 1\Phi_0$, as it should be in the London limit for $x \to 1$.

5.2. Nonlinear Theory

But what happens away from the superconducting/normal transition, that is, deeper inside the superconducting state? To study this we solved the complete set of Ginzburg–Landau equations, assuming axial symmetry, which implies that the Ginzburg–Landau equations are solved for a fixed value of the angular momentum or vorticity L. Therefore, the order parameter has the form

$$\Psi(\rho, \phi) = f(\rho)e^{iL\phi} \tag{31}$$

a) $L = 2$ b) $L = 5$ c) $L = 6$

Figure 8. Order parameter distribution $|\Psi|$ for $x = 0.5$, at a fixed $\Phi = 9\Phi_0$. (a) $L = 2$, (b) $L = 5$, and (c) $L = 6$. The state with $L = 5$ is only slightly modulated ($|\Psi| \approx$ constant: $\beta_A = 1.01$) and corresponds to the ground state level $|-\alpha_{LLL}(9\Phi_0)|$. Reprinted with permission from [38], V. Bruyndoncx et al., *Phys. Rev. B* 60, 10468 (1999). © 1999, American Physical Society.
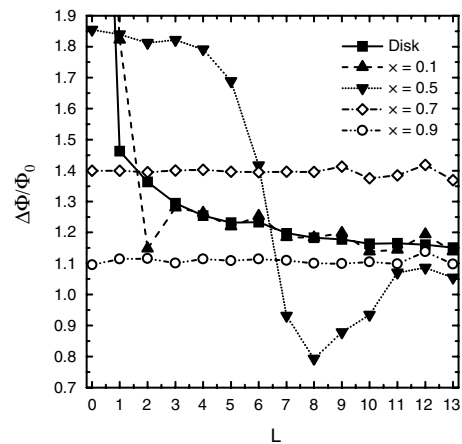
Figure 9. The period $\Delta\Phi$ of the phase boundary $T_c(\Phi)$ in units of the flux quantum Φ_0 as a function of the phase winding number L. The data for several of the loops are shown as a symbol and are compared to the period in a filled disk (filled squares). The interconnecting lines are only a guide to the eye. Reprinted with permission from [38], V. Bruyndoncx et al., *Phys. Rev. B* 60, 10468 (1999). © 1999, American Physical Society.

and, consequently, both the vector potential and the superconducting current are directed along $\vec{e}_\phi$. For a fixed angular momentum L, the Ginzburg–Landau equations can be reduced to

$$-\frac{1}{\rho}\frac{\partial}{\partial\rho}\rho\frac{\partial f}{\partial\rho} + \left\langle\left(\left(\frac{L}{\rho} - A\right)^2\right)\right\rangle f = f(1 - f^2) \qquad (32)$$

and

$$-\kappa^2\left(\frac{\partial}{\partial\rho}\frac{1}{\rho}\frac{\partial\rho A}{\partial\rho} + \frac{\partial^2 A}{\partial z^2}\right) = \left(\frac{L}{\rho} - A\right)f^2\theta\left(\frac{\rho}{R}\right)\theta\left(\frac{2|z|}{d}\right) \qquad (33)$$

where $\theta(x) = 1$ for $x < 1$ and $\theta(x) = 0$ for $x > 1$, $\vec{A} = A\vec{e}_\phi$, and $\langle\,\rangle$ means averaging over the disk thickness $\langle g(r)\rangle = \frac{1}{d}\int_{-d/2}^{+d/2} g(z,r)dz$.

The boundary condition for the order parameter (15) can be written as

$$\left.\frac{\partial f}{\partial\rho}\right|_{\rho=R_o} = 0, \qquad \left.\frac{\partial f}{\partial\rho}\right|_{\rho=R_i} = 0 \qquad (34)$$

where R_i and R_o are the inner and outer radius of the ring.

To solve the system of Eqs. (32) and (33) numerically, a finite difference representation is applied on the space grid ρ_i, z_i. Because the size of the simulation region exceeds by far the size of the disk, this space grid will be nonuniform outside the disk region to diminish computation time. Outside the disk region, the grid space increases exponentially with the distance. Because of this, it becomes possible to use the same number of grid points inside and outside the disk.

Integrating over the line $\rho_{i-1/2} < \rho < \rho_{i+1/2}$, where $\rho_{i+1/2} = (\rho_{i+1} + \rho_i)/2$, the first Ginzburg–Landau equation (32) becomes

$$-\frac{2}{\rho_{i+1/2}^2 - \rho_{i-1/2}^2}\left(\rho_{i+1/2}\frac{f_{i+1} - f_i}{\rho_{i+1} - \rho_i} - \rho_{i-1/2}\frac{f_i - f_{i-1}}{\rho_i - \rho_{i-1}}\right)$$
$$+ \left\langle\left(\frac{L}{\rho} - A\right)^2\right\rangle_i f_i = f_i - f_i^3 \qquad (35)$$

where $f_i = f(\rho_i)$. The steady-state solution of the Ginzburg–Landau equations was obtained using an iteration procedure. Therefore, an upper index k is introduced to denote the iteration step. To speed up the convergency an iteration parameter η_f is added and the nonlinear term is expanded in $(f_i^k)^3 = (f_i^{k-1})^3 + 3(f_i^{k-1})^2(f_i^k - f_i^{k-1})$, which leads to the first Ginzburg–Landau equation in finite difference form:

$$\eta_f f_i^k - \frac{2}{\rho_{i+1/2}^2 - \rho_{i-1/2}^2}\left(\rho_{i+1/2}\frac{f_{i+1}^k - f_i^k}{\rho_{i+1} - \rho_i} - \rho_{i-1/2}\frac{f_i^k - f_{i-1}^k}{\rho_i - \rho_{i-1}}\right)$$
$$+ \left\langle\left(\frac{L}{\rho} - A\right)^2\right\rangle_i f_i^k - f_i^k + 3(f_i^{k-1})^2 f_i^k$$
$$= \eta_f f_i^{k-1} + 2(f_i^{k-1})^3 \qquad (36)$$

To obtain the finite difference representation of the second Ginzburg–Landau Eq. (32), we integrated this equation over the square $z_{j-1/2} < z < z_{j+1/2}$, $\rho_{i-1/2} < \rho < \rho_{i+1/2}$. By introducing the upper index k denoting the iteration step and the iteration parameter η_a to speed up the convergence,

the finite difference representation of the second Ginzburg–Landau equation becomes

$$\eta_a A_{j,i}^k - \frac{2\kappa^2}{\rho_{i+1/2} - \rho_{i-1/2}}\left(\frac{\rho_{i+1}A_{j,i+1}^k - \rho_i A_{j,i}^k}{\rho_{i+1}^2 - \rho_i^2} - \frac{\rho_i A_{j,i}^k - \rho_{i-1}A_{j,i-1}^k}{\rho_i^2 - \rho_{i-1}^2}\right)$$
$$- \frac{2\kappa^2}{z_{j+1/2} - z_{j-1/2}}\left(\frac{A_{j+1,i}^k - A_{j,i}^k}{z_{j+1} - z_j} - \frac{A_{j,i}^k - A_{j-1,i}^k}{z_j - z_{j-1}}\right)$$
$$- \left(\frac{L}{\rho_i} - A_{j,i}^k\right)(f_i^k)^2 = \eta_a A_{i,j}^{k-1} \qquad (37)$$

The iteration parameters η_f and η_a correspond to an artificial time relaxation of the system to a steady state with time steps $1/\eta_f$ and $1/\eta_a$. For typical values of the iteration parameters $\eta_f = 2$, $\eta_a = 5$ convergency is reached after a few hundred iteration steps.

The ground state free energy F of a superconducting disk with radius $R_o = 2.0\xi$ and thickness $d = 0.005\xi$ and GL parameter $\kappa = 0.28$ is shown in Figure 10 for a hole in the center with radius $R_i/\xi = 0.0, 0.5, 1.0$, and 1.5. The situation with $R_i = 0$ corresponds to a superconducting disk without a hole, which was already studied in [13]. With increasing hole radius R_i, we find that the superconducting/normal transition (this is the magnetic field where the free energy equals zero) shifts appreciably to higher magnetic fields, and more transitions between different L states are possible before superconductivity disappears. Furthermore, the thin dotted curve gives the free energy for a thicker ring with thickness $d = 0.1\xi$ and $R_i = 1.0\xi$. In comparison with the previous results for $d = 0.005\xi$, the free energy becomes more negative, but the transitions between the different L states occur almost at the same magnetic fields. Thus increasing the thickness of the ring increases superconductivity, which is a consequence of the smaller penetration of the magnetic field into the superconductor.

Experimentally, using magnetization measurements one can investigate the effect of the geometry and the size of the sample on the superconducting state. To investigate the magnetization of a single superconducting disk Geim et al.
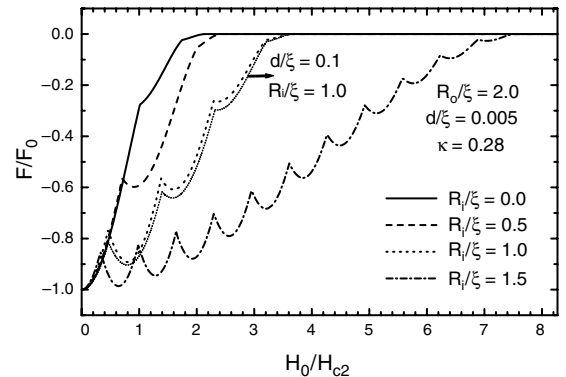
Figure 10. The ground state free energy as a function of the applied magnetic field H_0 of a superconducting disk with radius $R_o = 2.0\xi$, thickness $d = 0.005\xi$, and $\kappa = 0.28$ for a hole in the center with radius $R_i/\xi = 0.0, 0.5, 1.0$, and 1.5, respectively. The thin dotted curve gives the free energy of a thicker ring with thickness $d = 0.1\xi$ and $R_i = 1.0\xi$. The free energy is in units of $F_0 = H_c^2 V/8\pi$. Reprinted with permission from [39], B. J. Baelus et al., *Phys. Rev. B* 61, 9734 (2000). © 2000, American Physical Society.

[1] used submicron Hall probes. The Hall cross acts like a magnetometer, where in the ballistic regime the Hall voltage is determined by the average magnetic field through the Hall cross region [44]. Hence, by measuring the Hall resistance, one obtains the average magnetic field and, consequently, the magnetic field expelled from the Hall cross [Eq. (20)], which is a measure for the magnetization of the superconductor [14]. As for a superconducting disk [14], the field distribution for thin superconducting rings is extremely nonuniform inside as well as outside the sample and therefore the detector size will have an effect on the measured magnetization. To understand this effect of the detector, we calculate the magnetization for a superconducting ring with outer radius $R_o = 2.0\xi$, thickness $d = 0.005\xi$, and two values of the inner radius $R_i = 0.5\xi$ and $R_i = 1.5\xi$ by averaging the magnetic field [see Eq. (20)] over several detector sizes S. The results are shown in Figure 11a and b as a function of the applied magnetic field for $R_i = 0.5\xi$ and $R_i = 1.5\xi$, respectively. The solid curve [curve (i)] shows the calculated magnetization if we average the magnetic field over the superconducting volume, and curve (ii) is the magnetization after averaging the field over a circular area with radius R_o, that is, superconductor and hole. Notice that in the Meissner regime, that is, $H_0/H_{c2} < 0.7$ where $L = 0$, the magnetization of superconductor + hole is larger

than that of the superconductor alone, which is due to flux expulsion from the hole. For $L \geq 1$ the reverse is true because now flux is trapped in the hole. Experimentally, one usually averages the magnetic field over a square Hall cross region. Therefore, we calculated the magnetization by averaging the magnetic field over a square region [curve (iii)] with width equal to $2R_o$, that is, the diameter of the ring. Curve (iv) shows the magnetization if the sides of the square detector are equal to $(2 + 1/2)R_o$. Increasing the size of the detector decreases the observed magnetization because the magnetic field is averaged over a larger region, which brings $\langle H \rangle$ closer to the applied field H_0.

Having the free energies of the different giant vortex configurations for several values of the hole radius varying from $R_i = 0.0\xi$ to $R_i = 1.8\xi$, we construct an equilibrium vortex phase diagram. Figure 12 shows this phase diagram for a superconducting disk with radius $R_o = 2.0\xi$, thickness $d = 0.005\xi$, and $\kappa = 0.28$. The solid curves indicate where the ground state of the free energy changes from one L state to another, and the thick solid curve gives the superconducting/normal transition. The latter exhibits a small oscillatory behavior, which is a consequence of the Little–Parks effect. Notice that the superconducting/normal transition is moving to higher fields with increasing hole radius R_i and more flux can be trapped. In the limit $R_i \rightarrow R_o$, the critical magnetic field is infinite, and there are an infinite number of L states possible, which is a consequence of the enhancement of surface superconductivity for very small samples [15, 18, 45–47]. Because of the finite grid, we were not able to obtain accurate results for $R_i \approx R_o$. The dashed lines connect our results for hole radius $R_i = 1.8\xi$ with the results for $R_i \rightarrow R_o$ [48], where the transitions between the different L states occur when the enclosed flux is $\phi = (L + 1/2)\phi_0$, where $\phi_0 = ch/2e$ is the elementary flux quantum. Notice that for rings of nonzero width, that is, $R_i \neq R_o$, the $L \rightarrow L + 1$ transition occurs at higher magnetic field than predicted from the condition $\phi = (L + 1/2)\phi_0$. The discrepancy

Figure 11. The magnetization as a function of the applied magnetic field H_0 for a superconducting disk with radius $R_o = 2.0\xi$ and thickness $d = 0.005\xi$ and $\kappa = 0.28$ for a hole in the center with radius $R_i/\xi = 0.5$ (a) and $R_i/\xi = 1.5$ (b). Curve (i) is the calculated magnetization if we average the magnetic field over the superconducting volume, curve (ii) after averaging the field over the area with radius R_o, that is, superconductor and hole, and curves (iii) and (iv) after averaging the magnetic field over a square region with widths equal to $2R_o$ and $(2 + 1/2)R_o$, respectively. Reprinted with permission from [39], B. J. Baelus et al., *Phys. Rev. B* 61, 9734 (2000). © 2000, American Physical Society.

Figure 12. Phase diagram: the relation between the hole radius R_i and the magnetic fields H_0 at which giant vortex transitions $L \rightarrow L + 1$ takes place for a superconducting disk with radius $R_o = 2.0\xi$ and thickness $d = 0.005\xi$ and for $\kappa = 0.28$. The solid curves indicate where the ground state changes from one L-state to another one and the thick solid curve gives the superconducting/normal transition. Reprinted with permission from [39], B. J. Baelus et al., *Phys. Rev. B* 61, 9734 (2000). © 2000, American Physical Society.

increases with increasing width of the ring and with increasing L. Starting from $R_i = 0$ we find that with increasing R_i the Meissner state disappears at smaller H_0. The hole in the center of the disk allows for a larger penetration of the magnetic field which favors the $L = 1$ state. This is the reason why the $L = 0 \to L = 1$ transition moves to a lower external field while the $L = 1 \to L = 2$ transition initially occurs for larger H_0 with increasing R_i. When the hole size becomes of the order of the width of one vortex the $L = 1 \to L = 2$ transition starts to move to lower fields and the $L = 2$ state becomes more favorable.

The effect of the thickness of the ring on the phase diagram is investigated in Figure 13. The thin solid curves indicate where the ground state of the free energy changes from one L state to another, while the thick curve gives the superconducting/normal transition. Notice that the transition from the $L = 0$ to the $L = 1$ state and the superconducting/normal transition depends weakly on the thickness of the ring. For increasing thickness d, the $L = 2$ state becomes less favorable and disappears for $d \gtrsim 0.7\xi$. In this case, there is a transition from the $L = 1$ state directly to the normal state. Increasing d stabilizes the different L states up to larger magnetic fields. This is due to the increased expulsion of the applied field from the superconducting ring [15].

In the next step, we investigate three very important and mutually dependent quantities: the local magnetic field H, the Cooper pair density $|\Psi|^2$, and the current density j. We will discuss these quantities as a function of the radial position ρ. For this study we distinguish two situations; that is, $R_i \ll R_o$ and $R_i \lesssim R_o$. In the first case the sample behaves more like a superconducting disk and in the second case like a superconducting loop.

First, we consider a superconducting disk with radius $R_o = 2.0\xi$ and thickness $d = 0.1\xi$ with a hole with radius $R_i = 0.5\xi$ in the center. The free energy and the magnetization (after averaging over the superconductor + hole) for such a ring are shown in Figure 14. The dashed curves
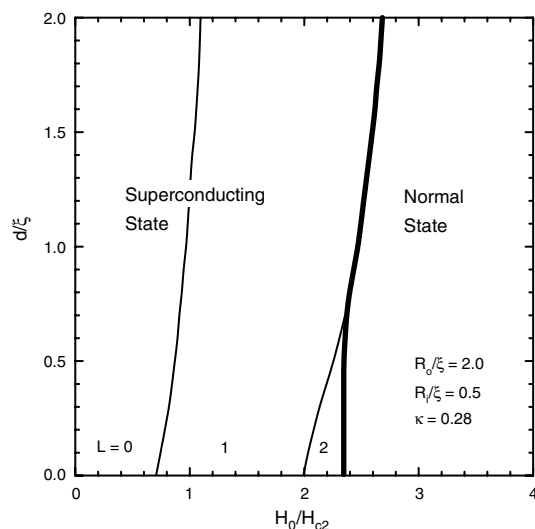
Figure 13. The same as Figure 12 but for varying thickness d of the ring for fixed $R_o = 2.0\xi$, $R_i = 0.5\xi$, and $\kappa = 0.28$. Reprinted with permission from [39], B. J. Baelus et al., *Phys. Rev. B* 61, 9734 (2000). © 2000, American Physical Society.
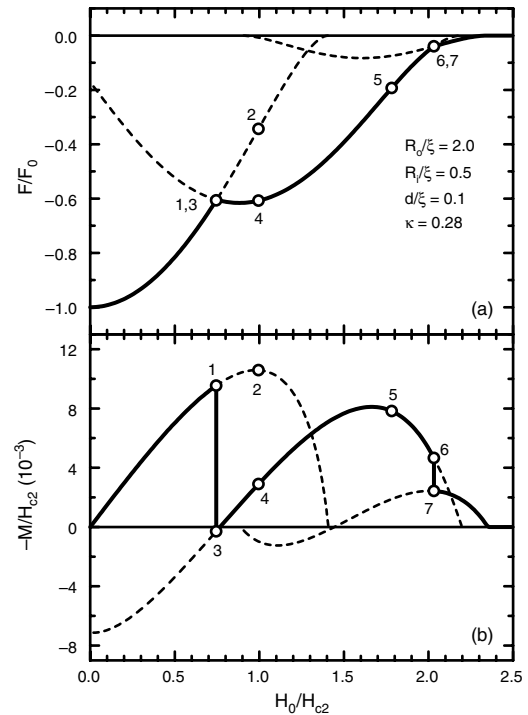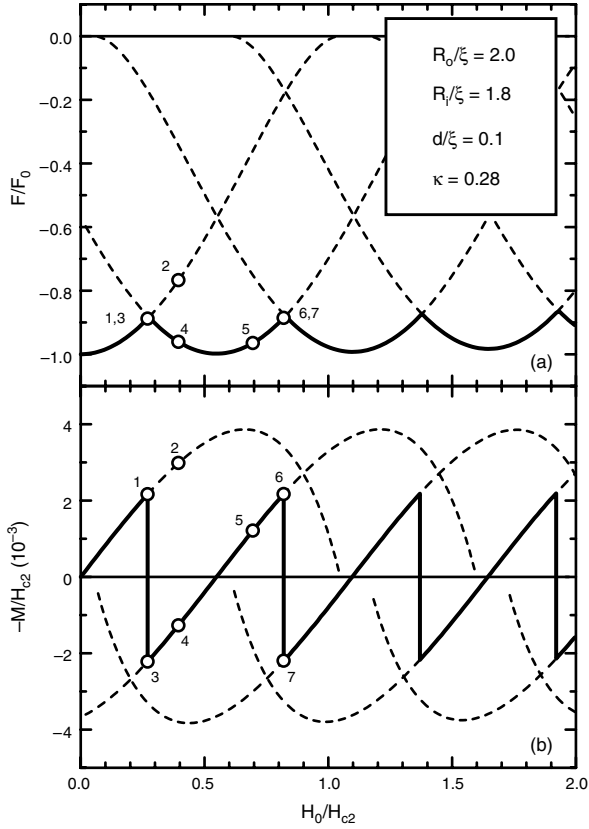

Figure 14. The free energy (a) and the magnetization after averaging over the superconductor + hole (b) as a function of the applied magnetic field for a superconducting disk with outer radius $R_o = 2.0\xi$ and thickness $d = 0.1\xi$ with a hole with radius $R_i = 0.5\xi$ in the center ($\kappa = 0.28$) for the different L states (dashed curves) and for the ground state (solid curves). The open circles are at (1) $L = 0$, $H_0/H_{c2} = 0.745$; (2) $L = 0$, $H_0/H_{c2} = 0.995$; (3) $L = 1$, $H_0/H_{c2} = 0.745$; (4) $L = 1$, $H_0/H_{c2} = 0.995$; (5) $L = 1$, $H_0/H_{c2} = 1.7825$; (6) $L = 1$, $H_0/H_{c2} = 2.0325$; and (7) $L = 2$, $H_0/H_{c2} = 2.0325$. Reprinted with permission from [39], B. J. Baelus et al., *Phys. Rev. B* 61, 9734 (2000). © 2000, American Physical Society.

give the free energy and the magnetization for the different L states, and the solid curve is the result for the ground state. Figure 15a and b shows the local magnetic field H, Figure 15c and d the Cooper pair density $|\Psi|^2$, and Figure 15e and f the current density j as a function of the radial position ρ for such a ring at the L states and magnetic fields as indicated by the open circles in Figure 14a and b.

For low magnetic field, the system is in the $L = 0$ state, that is, the Meissner state, and the flux trapped in the hole is considerably suppressed. Hence, the local magnetic field inside the hole is lower than the external applied magnetic field as is shown in Figure 15a by curves 1 and 2. Please notice that the plotted magnetic field is scaled by the applied field H_0. In the $L = 0$ state the superconductor expels the magnetic field by inducing a supercurrent that tries to compensate the applied magnetic field in the superconductor and inside the hole. This is called the diamagnetic Meissner effect. As long as L equals zero, the induced current has only to compensate the magnetic field at the outside of the ring and, therefore, the current flows in the whole superconducting material in the same direction and the size of the current increase with increasing field. This is clearly shown in Figure 15e by curves 1 and 2, where the current density j becomes more negative for increasing H_0/H_{c2}. Notice also that the current density is more negative at the outside than
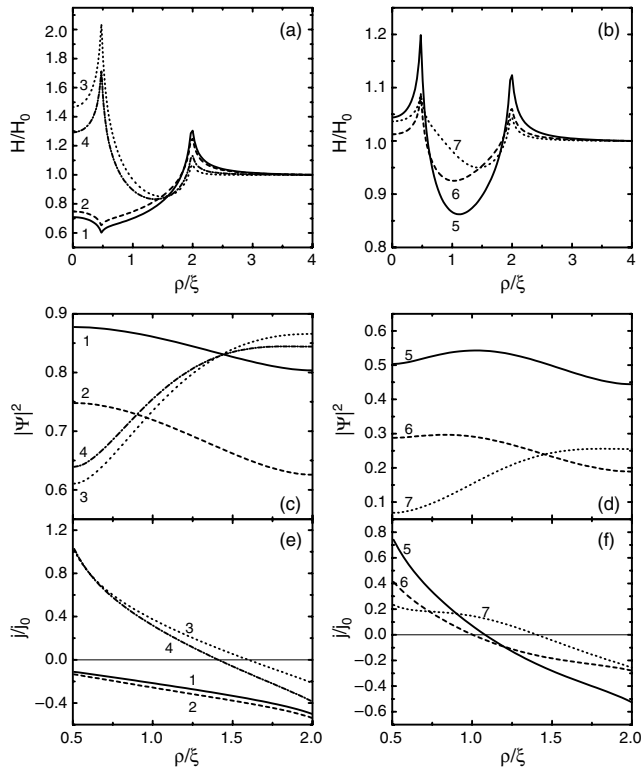
Figure 15. The local magnetic field H (a and b), the Cooper pair density $|\Psi|^2$ (c and d) and the current density j (e and f) for the situations indicated by the open circles in Figure 14 as a function of the radial position ρ for a superconducting disk with radius $R_o = 2.0\xi$ and thickness $d = 0.1\xi$ with a hole with radius $R_i = 0.5\xi$ in the center ($\kappa = 0.28$). Reprinted with permission from [39], B. J. Baelus et al., *Phys. Rev. B* 61, 9734 (2000). © 2000, American Physical Society.

at the inside of the superconducting ring, which leads to a stronger depression of the Cooper pair density at the outer edge compared to the inner edge of the ring (see curves 1 and 2 in Fig. 15c).

At $H_0/H_{c2} = 0.745$, the ground state changes from the $L = 0$ to the $L = 1$ state (see Fig. 14a). Suddenly more flux becomes trapped in the hole (compare curve 1 with curve 3 in Fig. 15a), the local magnetic field inside the hole increases and becomes larger than the external magnetic field H_0. In the $L = 1$ state, there is a sharp peak in the magnetic field at the inner boundary because of demagnetization effects. Consequently, more current is needed to compensate the magnetic field near the inner boundary than that near the outer boundary (see curve 3 in Fig. 15e). The sign of the current near the inner boundary becomes positive (the current direction reverses), but the sign of current near the outer boundary does not change. This can be explained as follows. Near the inner boundary ($\rho \gtrsim 1.0\xi$) the magnetic field is compressed into the hole (paramagnetic effect), whereas near the outer boundary ($\rho \lesssim 2.0\xi$) the magnetic field is expelled to the insulating environment (diamagnetic effect). The sign reversal of j occurs at $\rho = \rho^*$, and later we will show that the flux through the circular area with radius ρ^* is exactly quantized. At the $L = 0$ to the $L = 1$ transition the maximum in the Cooper pair density (compare curves 1 and 3 in Fig. 15c) shifts from $\rho = R_i$ to $\rho = R_o$. Further

increasing the external field increases the Cooper pair density near the inner boundary initially (compare curves 3 and 4 in Fig. 15c), because the flux in the hole has to be compressed less. The point ρ^*, where $j = 0$, shifts toward the inner boundary of the ring. By further increasing the external magnetic field, the Cooper pair density starts to decrease (see curves 5 and 6 in Fig. 15d) and attains its maximum near the inner boundary. The current near the inner boundary becomes less positive (see curves 5 and 6 in Fig. 15f), that is, less shielding of the external magnetic field inside the hole (see curves 5 and 6 in Fig. 15b), and near the outer boundary j becomes less negative, which shields the magnetic field from the superconductor + hole. Thus at the outer edge the local magnetic field has a local maximum, which decreases with applied magnetic field H_0.

At $H_0/H_{c2} \approx 2.0325$, the ground state changes from the $L = 1$ state to the $L = 2$ state and extra flux is trapped in the hole. The changes in the magnetic field distribution, the Cooper pair density and the current density are analogous to the changes at the first transition. For example, the magnetic field inside the hole increases compared to the external magnetic field (curve 7 in Fig. 15b), the radius ρ^* increases substantially (curve 7 in Fig. 15f), and the maximum in the Cooper pair density shifts to the outer boundary (curve 7 in Fig. 15d).

For $R_i \ll R_o$ and $L > 0$, the superconducting state consists of a combination of the paramagnetic and the diamagnetic Meissner state, like for a disk. For $R_i \lesssim R_o$ we expect that the sample behaves like a loop and, hence, the superconducting state is in a pure paramagnetic Meissner state or a pure diamagnetic Meissner state.

We consider a superconducting disk with radius $R_o = 2.0\xi$ and thickness $d = 0.1\xi$ with a hole with radius $R_i = 1.8\xi$ in the center. The free energy and the magnetization (after averaging over the superconductor + hole) for such a ring are shown in Figure 16. The dashed curves give the free energy and the magnetization for the different L states, and the solid curve is the result for the ground state. Figure 17a and b shows the local magnetic field H and Figure 17c and d the current density j as a function of the radial position ρ for such a ring at the L states and magnetic fields as indicated by the open circles in Figure 16a and b. The Cooper pair density has almost no structure and is practically constant over the ring and will, therefore, not be shown. For $L = 0$, the situation is the same as that for $R_i \ll R_o$. The magnetic field is expelled from the superconductor and the hole to the outside of the system, that is, a diamagnetic Meissner effect. The current flows in the whole superconducting material in the same direction (curves 1 and 2 in Fig. 17a) and the size increases with increasing external field H_0 (curves 1 and 2 in Fig. 17c). At $H_0/H_{c2} = 0.27$, the ground state changes from the $L = 0$ state to the $L = 1$ state and suddenly more flux is trapped in the hole. The local magnetic field inside the hole becomes larger than the external field H_0, and there is a sharp peak near the inner boundary (curves 3 and 4 in Fig. 17a). In contrast to the situation for $R_i \ll R_o$, there is no peak near the outer boundary, which means that the magnetic field is only expelled to the hole, that is, a paramagnetic Meissner effect. The induced current flows in the reverse direction in the whole superconductor (curves 3 and 4 in Fig. 17c). For increasing external magnetic field, the

Figure 16. The free energy (a) and the magnetization after averaging over the superconductor + hole (b) as a function of the applied magnetic field for a superconducting disk with outer radius $R_o = 2.0\xi$ and thickness $d = 0.1\xi$ with a hole with radius $R_i = 1.8\xi$ in the center ($\kappa = 0.28$) for the different L states (dashed curves) and for the ground state (solid curves). The open circles are at (1) $L = 0$, $H_0/H_{c2} = 0.27$; (2) $L = 0$, $H_0/H_{c2} = 0.395$; (3) $L = 1$, $H_0/H_{c2} = 0.27$; (4) $L = 1$, $H_0/H_{c2} = 0.395$; (5) $L = 1$, $H_0/H_{c2} = 0.695$; (6) $L = 1$, $H_0/H_{c2} = 0.82$; and (7) $L = 2$, $H_0/H_{c2} = 0.82$. Reprinted with permission from [39], B. J. Baelus et al., *Phys. Rev. B* 61, 9734 (2000). © 2000, American Physical Society.

magnetic field inside the hole, the height of the demagnetization peak, and hence the size of the current decrease (see curves 3 and 4 in Fig. 17a and c). With a further increase in the field, the superconducting state transforms into a diamagnetic Meissner state. The magnetic field is now expelled to the outside of the sample (curves 5 and 6 in Fig. 17b) and the direction of the current is the same everywhere in the ring (curves 5 and 6 in Fig. 17d). At $H_0/H_{c2} = 0.82$, the ground state changes from the $L = 1$ state to the $L = 2$ state. The changes in the magnetic field distribution (see curve 7 in Fig. 17b) and the current density (see curve 7 in Fig. 17c) are analogous to the changes at the first transition. The diamagnetic state transforms into a paramagnetic state.

6. FLUX QUANTIZATION

Zharkov and Arutunyan [49, 50] found that in a thin-walled hollow cylinder the flux is not quantized through the hole, but through a circular area with (effective) radius equal to the geometric mean square of the inner and outer radius of
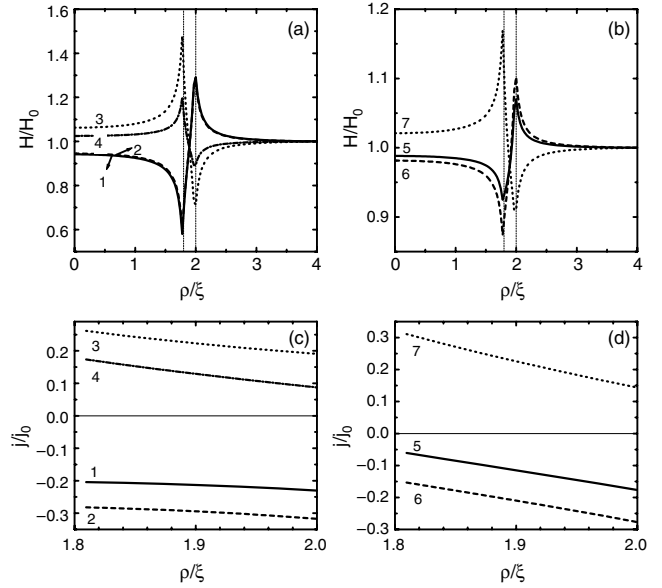
Figure 17. The local magnetic field H (a and b) and the current density j (c and d) for the situations indicated by the open circles in Figure 16 as a function of the radial position ρ for a superconducting disk with radius $R_o = 2.0\xi$ and thickness $d = 0.1\xi$ with a hole with radius $R_i = 1.8\xi$ in the center ($\kappa = 0.28$). Reprinted with permission from [39], B. J. Baelus et al., *Phys. Rev. B* 61, 9734 (2000). © 2000, American Physical Society.

the hollow cylinder; that is, $\rho^* = \sqrt{R_i R_o}$. These results were obtained within the London limit.

We investigated the flux quantization in the fat ring. Figure 18 shows the flux through the hole (a) and through the superconductor + hole (b) as a function of the applied magnetic field H_0 for a superconducting disk with radius $R_o = 2.0\xi$ and thickness $d = 0.1\xi$ with a hole in the center with radius $R_i = 1.0\xi$. The dashed curves show the flux for the different L states, the solid curve for the ground state, and the thin solid line is the flux through the hole if the sample is in the normal state. It is apparent that the flux through the hole (or through the superconducting ring + hole) is *not quantized* (see Fig. 18a). At $H_0/H_{c2} = 0.4575$ suddenly more flux enters the hole and the ground state changes from the $L = 0$ state to the $L = 1$ state. At this transition also the flux increase through the hole is not equal to one flux quantum ϕ_0. It is generally believed that the flux through a superconducting ring is quantized. But as was shown in [42], this is even no longer true for hollow cylinders when the penetration length is larger than the thickness of the cylinder wall. The present result is a generalization of this observation to mesoscopic ring structures. Note that for the case in Figure 18 the penetration length is $\lambda/\xi = 0.28$ and the effective penetration length $\Lambda/\xi = 0.78$ is comparable to the width of the ring $(R_o - R_i)/\xi = 1.0$.

For $L > 0$, the superconducting current equals zero at a certain "effective" radial position $\rho = \rho^*$. It is the flux through the circular area with radius ρ^* that is quantized and not necessarily the flux through the hole of our disk. Inserting the order parameter $\Psi = |\Psi| \exp(i\varphi)$ into the current operator, we obtain

$$\vec{j} = \frac{e\hbar}{m}|\Psi|^2\left(\vec{\nabla}\varphi - \frac{2e}{\hbar c}\vec{A}\right) \qquad (38)$$
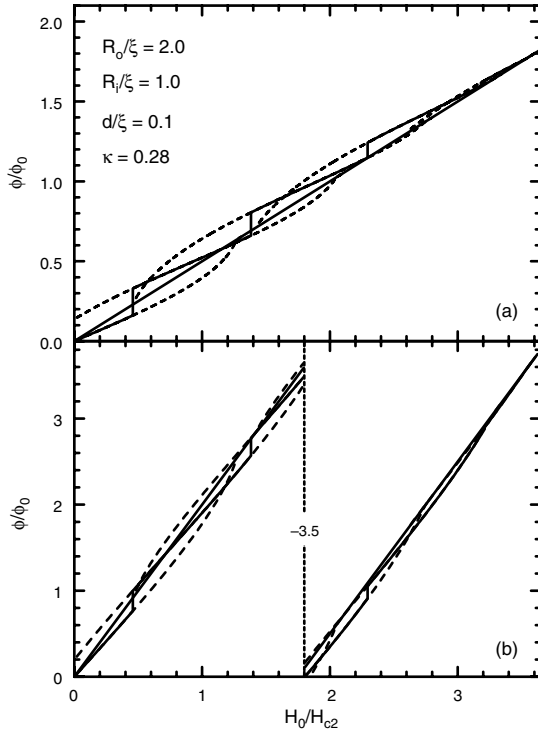
Figure 18. The flux through (a) the hole and (b) the superconductor + the hole as a function of the applied magnetic field H_0 for a superconducting disk with radius $R_o = 2.0\xi$ and thickness $d = 0.1\xi$ with a hole in the center with radius $R_i = 1.0\xi$. The dashed curves show the flux for the different L states and the solid curve for the ground state. The thin solid line is the flux in the absence of superconductivity. Reprinted with permission from [39], B. J. Baelus et al., *Phys. Rev. B* 61, 9734 (2000). © 2000, American Physical Society.

which after integration over a closed contour C inside the superconductor leads to

$$\oint_C \left(\frac{mc}{2e^2|\Psi|^2} \vec{j} + \vec{A} \right) \cdot d\vec{l} = L\phi_0 \qquad (39)$$

When the contour C is chosen along a path such that the superconducting current is zero we obtain, using Stokes' theorem,

$$L\phi_0 = \oint_C \vec{A} \cdot d\vec{l} = \int rot\,\vec{A} \cdot d\vec{S} = \int \vec{H} \cdot d\vec{S} = \phi \qquad (40)$$

which tells us that the flux through the area encircled by C is quantized. In our wide superconducting ring the current is nonzero at the inner boundary of the ring and, consequently, the flux through the hole does not have to be quantized.

To demonstrate that this is indeed true, we show in Figure 19a the current density as a function of the radial position ρ and in Figure 19b the flux through a circular area with radius ρ for a superconducting disk with radius $R_o = 2.0\xi$ and thickness $d = 0.1\xi$ with a hole in the center with radius $R_i = 1.0\xi$ in the presence of an external magnetic field $H_0/H_{c2} = 1.6075$ for the case of three different giant vortex states; that is, $L = 1, 2$, and 3. In the $L = 1$ state, the current density equals zero at a distance $\rho^*/\xi \approx 1.16$ from the center and the flux through an area with this radius is
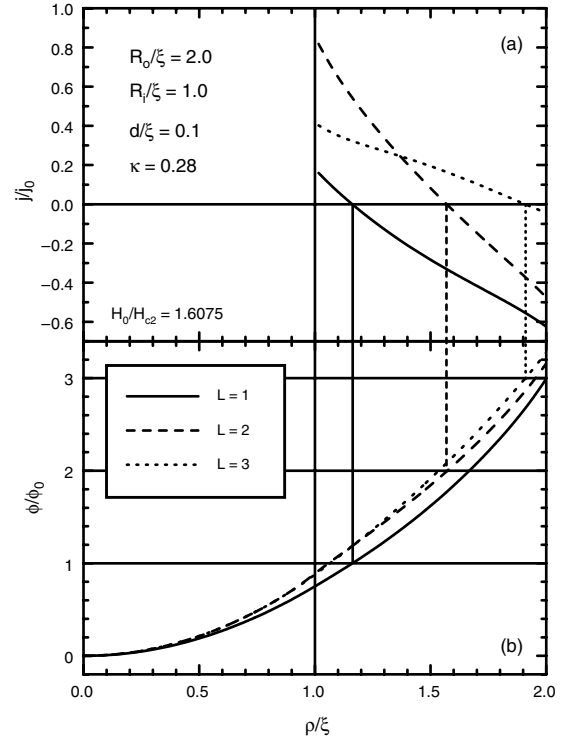
Figure 19. The current density (a) and the flux (b) as a function of the radial position ρ for a superconducting ring with $R_o = 2.0\xi$, $R_i = 1.0\xi$, $d = 0.1\xi$, and $\kappa = 0.28$ for $L = 1$ (solid curves), $L = 2$ (dashed curves), and $L = 3$ (dotted curves) at an applied magnetic field $H_0/H_{c2} = 1.6075$. Reprinted with permission from [39], B. J. Baelus et al., *Phys. Rev. B* 61, 9734 (2000). © 2000, American Physical Society.

exactly equal to one flux quantum ϕ_0. For $L = 2$ and $L = 3$, the current density j equals zero at $\rho^*/\xi \approx 1.56$ and 1.91, respectively, and the flux through the area with this radius ρ^* is exactly equal to $2\phi_0$ and $3\phi_0$, respectively. We find that ρ^* depends on the external applied magnetic field and on the value of L, contrary to the results of Arutunyan and Zharkov [49, 50], which for the case in Figure 20a would give $\rho^* = 1.41\xi$. The dependence of ρ^* as a function of the applied magnetic field is shown in Figure 20a. The dashed curves give the ρ^* of the different L states. For increasing magnetic field and fixed L, the value of ρ^* decreases; that is, the "critical" radius moves toward the inner boundary. The solid curve gives ρ^* for the ground state. At the $L \to L + 1$ transitions, ρ^* jumps over a considerable distance toward the outside of the superconducting ring, and the size of the jumps decreases with increasing L. The dotted lines in the figure give the two boundaries of the superconducting ring: the outer boundary $R_o = 2.0\xi$ and the inner boundary $R_i = 1.0\xi$. Note that in Figure 20 there is no ρ^* given for the $L = 0$ state, because only the external magnetic field has to be compensated so that the current has the same sign everywhere inside the ring. In Figure 20b we repeated this calculation for a hole with radius $R_i = 1.5\xi$, where superconductivity remains to higher magnetic fields and many more $L \to L + 1$ transitions are possible. The result of [49, 50] gives in this case $\rho^* = 1.73\xi$. Note that the results for the $L = 1$ and the $L = 2$ states are not connected. The reason is that just before the $L = 1 \to L = 2$ transition the critical
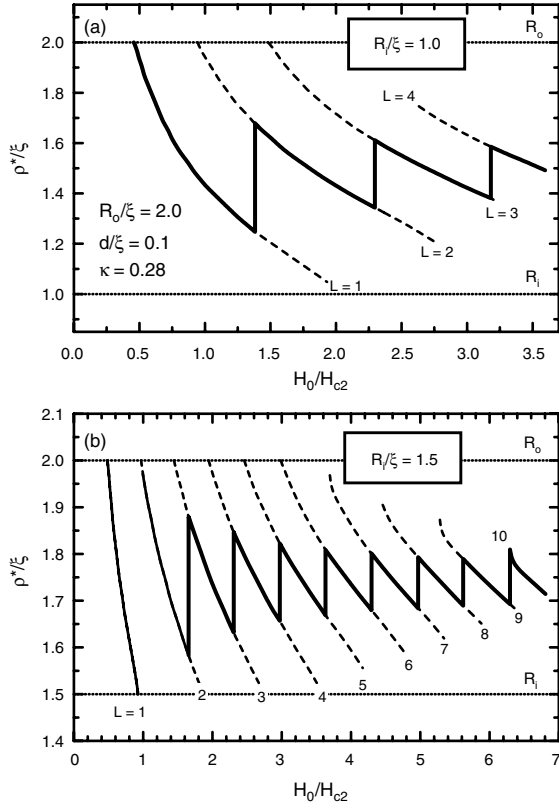
Figure 20. The dependence of the effective radius ρ^* as function of the applied magnetic field for a superconducting disk with radius $R_o = 2.0\xi$ and thickness $d = 0.1\xi$ with a hole in the center with radius $R_i = 1.0\xi$ (a), and $R_i = 1.5\xi$ (b). The dashed curves show ρ^* for the different L states and the solid curve is for the ground state. Reprinted with permission from [39], B. J. Baelus et al., *Phys. Rev. B* 61, 9734 (2000). © 2000, American Physical Society.

current for the $L = 1$ state is strictly positive in the whole ring and hence ρ^* is not defined. Notice that the results in Figure 20a and b oscillate around the average value $\rho^* = \sqrt{R_i R_o}$.

For even narrower rings the current in the ring is mostly diamagnetic or paramagnetic and the region in the magnetic field over which both directions of current occur in the ring becomes very narrow. This is illustrated in Figure 21 for a ring with outer radius $R_o = 2.0\xi$ and inner radius $R_i = 1.8\xi$. We plot in Figure 21a the flux through the hole, which becomes very close to the external flux, that is, the flux without any superconductor. In Figure 21b the value of the current at the inner and the outer side of the ring is shown, which illustrates nicely the fact that over large ranges of the magnetic field the current in the ring can flow in one direction. The free energy becomes minimal (Fig. 21c) at a magnetic field where the current in the rings can flow in both directions.

7. MULTIVORTEX STATES

Until now, we considered only small rings. In such rings, the confinement effect dominates, and we found that only the giant vortex states are stable. Now we will consider larger wide superconducting rings in which multivortex states can
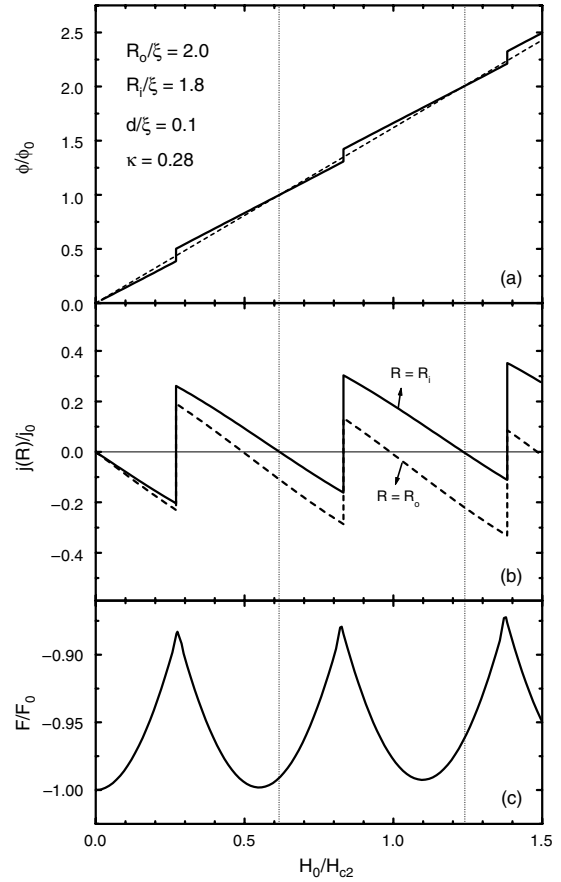
Figure 21. (a) The flux through the hole of the ring as a function of the applied magnetic field. The thin dashed line is the applied flux. (b) The current at the inner side (solid curve) and at the outer side (dashed curve) of the ring and (c) the free energy of the ground state as function of the applied magnetic field. Reprinted with permission from [39], B. J. Baelus et al., *Phys. Rev. B* 61, 9734 (2000). © 2000, American Physical Society.

nucleate for certain magnetic fields. This means that we are no longer allowed to assume axial symmetry for the order parameter.

For thin disks ($d \ll \xi, \lambda$) it is allowable to average the GL equations over the disk thickness. Using dimensionless variables and the London gauge $div\vec{A} = 0$ for the vector potential $\vec{A}$, we write the system of GL equations in the following form

$$(-i\vec{\nabla}_{2D} - \vec{A})^2 \Psi = \Psi(1 - |\Psi|^2) \qquad (41)$$

$$-\Delta_{3D}\vec{A} = \frac{d}{\kappa^2}\delta(z)\vec{j}_{2D} \qquad (42)$$

where

$$\vec{j}_{2D} = \frac{1}{2i}(\Psi^*\vec{\nabla}_{2D}\Psi - \Psi\vec{\nabla}_{2D}^*\Psi) - |\Psi|^2\vec{A} \qquad (43)$$

is the density of superconducting current. The superconducting wavefunction satisfies the following boundary conditions

$$(-i\vec{\nabla}_{2D} - \vec{A})\Psi|_{\vec{r}=\vec{R}_i} = 0 \qquad (44)$$

$$(-i\vec{\nabla}_{2D} - \vec{A})\Psi|_{\vec{r}=\vec{R}_o} = 0 \qquad (45)$$

and $\vec{A} = \frac{1}{2}H_0\rho\vec{e}_\phi$ far away from the superconductor. Here the distance is measured in units of the coherence length ξ, the vector potential in $c\hbar/2e\xi$, and the magnetic field in $H_{c2} = c\hbar/2e\xi^2 = \kappa\sqrt{2}H_c$. The ring is placed in the plane (x, y), the external magnetic field is directed along the z axis, and the indices $2D$ and $3D$ refer to two- and three-dimensional operators, respectively.

To solve the system of Eqs. (41) and (42), we generalized the approach of [15] for disks to our fat ring configuration. We apply a finite difference representation of the order parameter and the vector potential on a uniform Cartesian space grid (x, y), with a typical grid spacing of 0.15ξ and use the link variable approach [51] and an iteration procedure based on the Gauss–Seidel technique to find Ψ. The vector potential is obtained with the fast Fourier transform technique, where we set $\vec{A}_{|x|=R_S,|y|=R_S} = H_0(x, -y)/2$ at the boundary of a larger space grid (typically, $R_S = 4R_o$).

To find the different vortex configurations, which include the metastable states, we search for the steady-state solutions of Eqs. (41) and (42) starting from different randomly generated initial conditions. Then we increase/decrease slowly the magnetic field and recalculate each time the exact vortex structure. We do this for each vortex configuration in a magnetic field range where the number of vortices stays the same. By comparing the dimensionless Gibbs free energies of the different vortex configurations

$$F = V^{-1}\int_V[2(\vec{A} - \vec{A}_0)\cdot\vec{j}_{2d} - |\Psi|^4]d\vec{r} \qquad (46)$$

where integration is performed over the sample volume V, and $\vec{A}_0$ is the vector potential of the uniform magnetic field, we find the ground state. The dimensionless magnetization, which is a direct measure of the expelled magnetic field from the sample, is defined as

$$M = \frac{\langle H\rangle - H_0}{4\pi} \qquad (47)$$

where H_0 is the applied magnetic field. $\langle H\rangle$ is the magnetic field averaged over a sample/detector surface area S.

As an example we take a fat ring with outer radius $R_o = 4.0\xi$, thickness $d = 0.005\xi$, $\kappa = 0.28$, and different values of the inner radius. Figure 22a shows the free energy for such a ring with inner radius $R_i = 0.4\xi$ as a function of the applied magnetic field H_0. The different giant vortex states are given by the thin solid curves and the multivortex state by the thick solid curves. The open circles indicate the transitions from the multivortex state to the giant vortex state. In such a ring, multivortex states exist with winding number $L = 3$ up to 7. For $L = 3, 4$, and 5 multivortices occur both as metastable states and in the ground state, while for $L = 6$ and 7 they are only found in the metastable state. Notice there is no discontinuity in the free energy at the transitions from the multivortex state to the giant vortex state for fixed winding number L. Figure 22b shows the magnetization M for this ring as a function of H_0 after the field H is averaged over the superconducting ring (without the hole). The dashed curves give the results for the different L states, the thin solid curves are the results for the ground state, the thick solid curves are the results for the multivortex states,
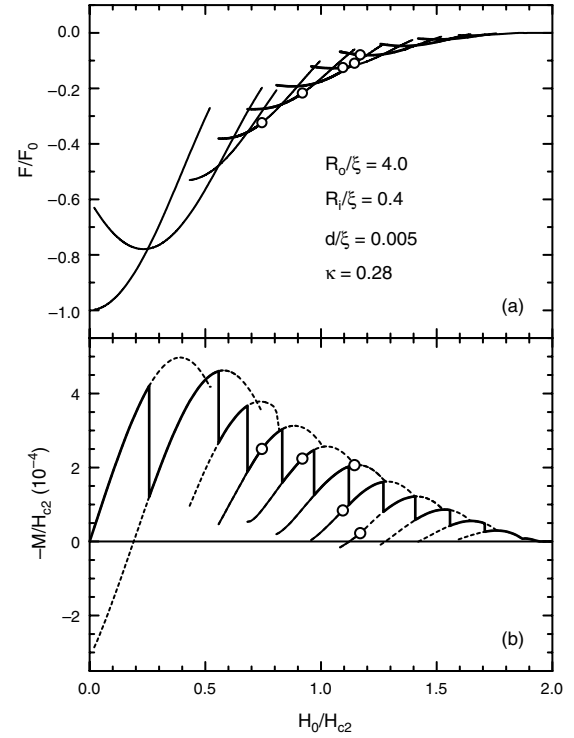
Figure 22. (a) The free energy as a function of the applied magnetic field for a superconducting ring with $R_o = 2.0\xi$, $R_i = 0.4\xi$, $d = 0.005\xi$, and $\kappa = 0.28$. The different giant vortex states are shown by the thin solid curves and the multi-vortex states by the thick solid curves. (b) The magnetization for the same sample after averaging over the superconducting ring only. The different L states are given by the dashed curves, the ground state by the thin solid curves, and the multivortex states by the thick solid curves. The transitions from the multivortex state to giant vortex state are indicated by the open circles. Reprinted with permission from [39], B. J. Baelus et al., *Phys. Rev. B* 61, 9734 (2000). © 2000, American Physical Society.

and the open circles indicate the transition from the multivortex state to the giant vortex states. Notice that the latter transitions are smooth; there are no discontinuities in the magnetization.

Now, we investigate the flux ϕ through the hole for the $L = 4$ multivortex and giant vortex state for the case of the above ring. Figure 23 shows the flux ϕ through a circular area of radius ρ for different values of the applied magnetic field H_0. Curves 1, 2, 3, and 4 are the results for $H_0/H_{c2} = 0.72$, 0.795, 0.87 (i.e., multivortex states), and 0.945 (i.e., giant vortex state), respectively. There is no qualitative difference between the four curves, that is, no qualitative difference between the multivortex states and the giant vortex state. In the inset, we show the flux through the hole with radius $R_i = 0.4\xi$ and through the superconductor + hole as a function of the applied magnetic field for a fixed value of the winding number; that is, $L = 4$. The solid circles indicate the magnetic fields considered in the main figure and the open circle indicate the position of the transition from multivortex state to giant vortex state. The slope of the curves increases slightly at the applied magnetic field, where there is a transition form the multivortex state to the giant vortex state. This agrees with the result for a disk [16] that
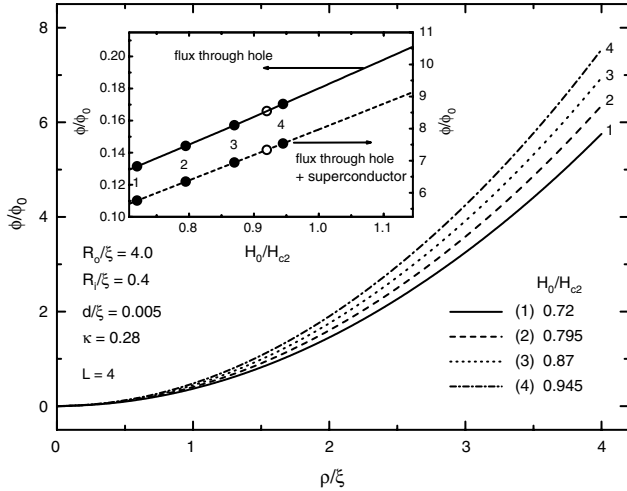
Figure 23. The flux ϕ through a circular area of radius ρ for different values of the applied magnetic field, H_0. Curves 1, 2, 3, and 4 give the results for $H_0/H_{c2} = 0.72$ (1), 0.795 (2), 0.87 (3) (i.e., multi-vortex states), and 0.945 (4) (i.e., giant vortex state), respectively. The inset shows the flux through the hole with radius $R_i = 0.4\xi$ and through the superconductor + hole as a function of the applied magnetic field for a fixed value of the winding number, that is, $L = 4$. The solid circles indicate the magnetic fields considered in the main figure, and the open circles indicate the transition from the multivortex state to the giant vortex state. Reprinted with permission from [39], B. J. Baelus et al., *Phys. Rev. B* 61, 9734 (2000). © 2000, American Physical Society.

Figure 24. The Cooper pair density corresponding to the four situations of Figure 23: $H_0/H_{c2} = 0.72$ (a); $H_0/H_{c2} = 0.795$ (b); $H_0/H_{c2} = 0.87$ (c); and $H_0/H_{c2} = 0.945$ (d). Dark regions indicate high density and light regions low density. The thick circles indicate the inner and the outer edge of the ring. Reprinted with permission from [39], B. J. Baelus et al., *Phys. Rev. B* 61, 9734 (2000). © 2000, American Physical Society.

the giant $\leftrightarrow$ multivortex transition is a second-order phase transition.

The Cooper pair density $|\psi|^2$ for the previous four configurations is shown in Figure 24. The darker the region, the larger the density and thus vortices are located at the white regions. At the magnetic field $H_0/H_{c2} = 0.72$ (Fig. 24a) we clearly see three vortices. With increasing magnetic field, these vortices start to overlap and move to the center (Fig. 24b and c) and finally they combine to one giant vortex in the center (Fig. 24d). Please note that a theory based on the London limit will not be able to give such an intricate behavior, because in such a theory vortices are point-like objects.

The free energies of the different vortex configurations were calculated for different values of the hole radius which we varied from $R_i = 0$ to $R_i = 3.6\xi$. From these results we constructed an equilibrium vortex phase diagram. First, we assumed axial symmetry, where only giant vortex states occur and the order parameter is given by $\Psi(\vec{\rho}) = F(\rho)e^{iL\theta}$. In the phase diagram (Fig. 25) the solid curves separate the regions with different numbers of vortices (different L states). In the limit $R_i \rightarrow 0$ we find the previous results of [16] for a superconducting disk. The radius of the giant vortex R_L in the center of the disk increases with increasing L, because it has to accommodate more flux; that is, $R_L/\xi \sim \sqrt{L/(H_0/H_{c2})}$. Hence, if we make a little hole in the center of the disk, this will not influence the $L \rightarrow L+1$ transitions as long as $R_i \ll R_L$ as is apparent from Figure 25. For a sufficiently large hole radius R_i, the hole starts to influence the giant vortex configuration and the magnetic field needed to induce the $L \rightarrow L+1$ transition increases. For example, the transition field from the $L = 7$ state to the

$L = 8$ state reaches its maximum for a hole radius $R_i \approx 2.0\xi$ which occurs for $H_0/H_{c2} \approx 1.5$. The above rough estimate gives $R_L/\xi \sim 2.16$, which is very close to $R_L/\xi \sim 2.0$. Further increasing R_i, the hole becomes so large that more and more flux is trapped inside the hole, and consequently a
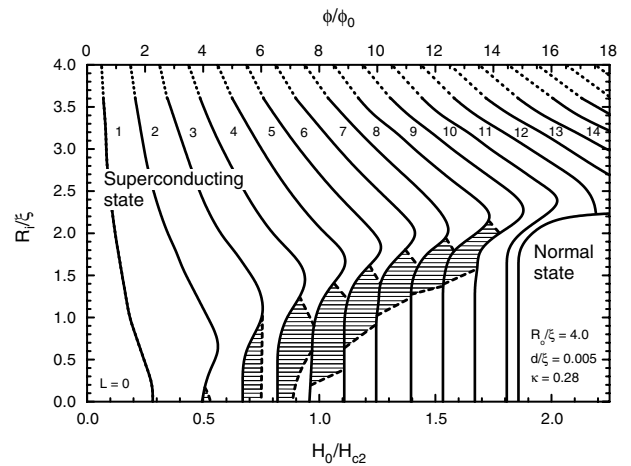
Figure 25. Equilibrium vortex phase diagram for a superconducting disk with radius $R_o = 4.0\xi$ and thickness $d = 0.005\xi$ with a hole with radius R_i in the center. The solid curves show the transitions between the different L states, the thick solid curve shows the superconducting/normal transition, and the dotted lines connect the results for $R_i = 3.6\xi$ with the results in the limit $R_i \rightarrow R_o$. The shaded regions indicate the multivortex states, and the dashed curves separate the multivortex states from the giant vortex states. Reprinted with permission from [39], B. J. Baelus et al., *Phys. Rev. B* 61, 9734 (2000). © 2000, American Physical Society.

smaller field is needed to induce the $L \rightarrow L + 1$ transition. Because of our finite grid size, we were limited to $R_i \leq 3.6\xi$. The results we find for $R_i = 3.6\xi$ are extrapolated to $\phi = (L + 1/2)\phi_0$ for $R_i = R_o$. The thick curve in Figure 25 gives the superconducting/normal transition. For low values of R_i, this critical magnetic field is independent of R_i, because the hole is smaller than the giant vortex state in the center and hence the hole does not influence the superconducting properties near the superconducting/normal transition. For $R_i \gtrsim 2.0\xi$, this field starts to increase drastically. Therefore, more and more L states appear. In the limit $R_i \rightarrow R_o$, the critical magnetic field is infinite and there are an infinite number of L states, which is a consequence of the enhancement of surface conductivity for very small superconducting samples [18].

Next, we consider the general situation where the order parameter is allowed to be a mixture of different giant vortex states and thus we no longer assume axial symmetry of the superconducting wavefunction. We found that the transitions between the different L states are not influenced by this generalization, but that for certain magnetic fields the ground state is given by the multivortex state instead of the giant vortex state. In Figure 25 the shaded regions correspond to the multivortex states and the dashed curves are the boundaries between the multivortex and the giant vortex states. For $L = 1$, the single vortex state and the giant vortex state are identical. In the limit $R_i \rightarrow 0$, the previous results of [16] for a superconducting disk are recovered. For increasing hole radius R_i, the $L = 2$ multivortex state disappears as a ground state for $R_i > 0.15\xi$. If R_i is further increased, the ground state for $L = 5$ up to $L = 9$ changes from giant vortex state to multivortex state and again to giant vortex state. For example, for $R_i = 2.0\xi$ the multivortex state exists only in the $L = 9$ state. Notice that for small R_i the region of multivortex states increases and consequently the hole in the center of the disk stabilizes the multivortex states, at least for $L > 2$. For large R_i, that is, narrow rings, the giant vortex state is the energetic favorable one because confinement effects start to dominate, which impose the circular symmetry on ψ. For fixed hole radius $R_i \leq 2.0\xi$ and increasing magnetic field we find always at least one transition from giant vortex state to multivortex state and back to giant vortex state (re-entrant behavior). Note that the ground state for $L \geq 10$ is in the giant vortex state irrespective of the value of the magnetic field. Near the superconducting/normal transition the superconducting ring is in the giant vortex state because now superconductivity exists only near the edge of the sample and consequently the superconducting state will have the same symmetry as the outer edge of the ring and thus it will be circular symmetric.

Finally, for $L \geq 3$ the multivortex state does not necessarily consist of L vortices in the superconducting material. Often it consists of a combination of a big vortex trapped in the hole and some multivortices in the superconducting material. This is clearly shown in Figure 26 where a contour plot of the local magnetic field is given for a superconducting disk with radius $R_o = 4.0\xi$ and thickness $d = 0.005\xi$ with a hole in the center with radius $R_i = 0.6\xi$ (Fig. 26a) and $R_i = 1.0\xi$ (Fig. 26b). As usual we took $\kappa = 0.28$. The dashed thick circle is the outer radius, while the small solid black

circle is the inner radius of the ring. Low magnetic fields are given by light regions and darker regions indicate higher magnetic fields. In this way, multivortices in the superconducting area are dark spots. In Figure 26a the local magnetic field is shown for an applied magnetic field $H_0/H_{c2} = 0.895$. Although the winding number is $L = 4$, there are only three vortices in the superconducting material and one vortex appears in the hole in the center of the disk. The phase difference is always given by $\Delta\varphi = L \times 2\pi$, with L as the winding number. In Figure 26b a contour plot of the local magnetic field is shown for a ring with $R_i = 1.0\xi$, which leads to $L = 6$ at $H_0/H_{c2} = 1.145$. Only four vortices are in the superconducting material and one giant vortex is in the center (partially in the hole) with $L = 2$. Note that the flux ϕ through the hole equals $\phi \approx 0.19\phi_0$ for the case of
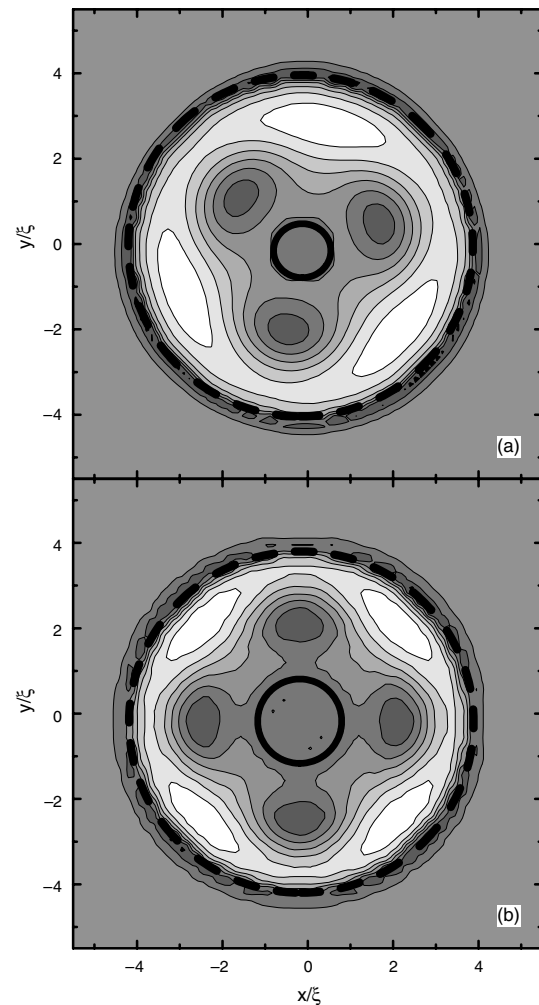
Figure 26. Contour plot of the local magnetic field for a superconducting disk with radius $R_o = 4.0\xi$ and thickness $d = 0.005\xi$ ($\kappa = 0.28$) with a hole in the center with (a) radius $R_i = 0.6\xi$ at $H_0/H_{c2} = 0.895$ for $L = 4$ and (b) radius $R_i = 1.0\xi$ at $H_0/H_{c2} = 1.145$ for $L = 6$. The dashed thick circle is the outer radius; the small solid thick circle in the inner radius. Low magnetic fields are given by light regions and dark regions indicate higher magnetic fields. Reprinted with permission from [39], B. J. Baelus et al., *Phys. Rev. B* 61, 9734 (2000). © 2000, American Physical Society.

Figure 26a and $\phi \approx 0.36\phi_0$ for the case of Figure 26b and is thus not equal to a multiple of the flux quantum ϕ_0.

8. ASYMMETRIC RINGS

So far, we gave an overview of the influence of the size of the hole on the vortex configuration and the critical parameters for superconducting rings of different sizes. For small rings, only the axially symmetrical situation occurs, that is, the giant vortex states. For large rings the multivortex state can be stabilized for certain values of the magnetic field. In the next step, the axial symmetry is purposely broken by moving the hole away from the center of the superconducting disk over a distance a.

As an example, we consider a superconducting disk with radius $R_o = 2.0\xi$ and thickness $d = 0.005\xi$ with a hole with radius $R_i = 0.5\xi$ moved over a distance $a = 0.6\xi$ in the x direction. Figure 27 shows the free energy and magnetization (defined through the field expelled from the
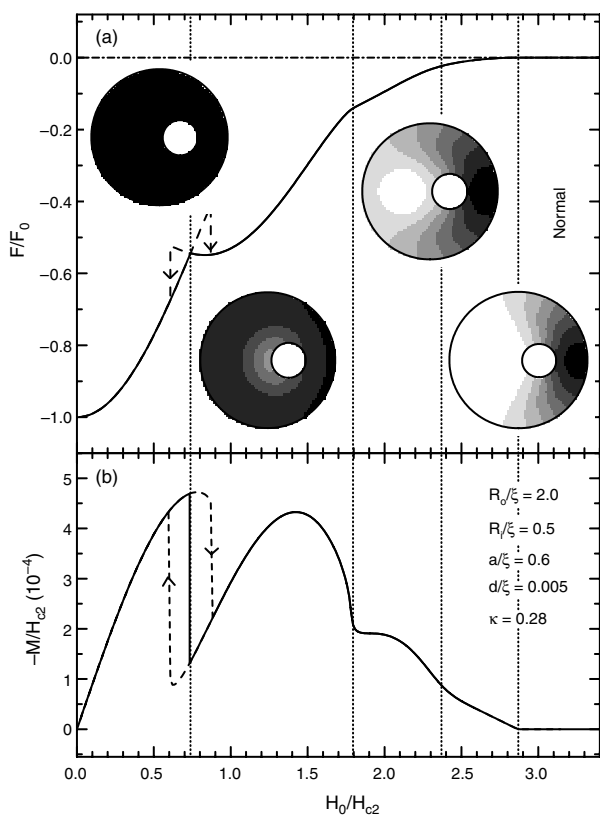
Figure 27. The free energy (a) and magnetization after averaging over the superconducting ring only (b) as function of the applied magnetic field for a superconducting disk with radius $R_o = 2.0\xi$ and thickness $d = 0.005\xi$ with a hole with radius $R_i = 0.5\xi$ moved over a distance $a = 0.6\xi$ in the x direction. The solid curve indicates the ground state; the dashed curve indicates the results for increasing and decreasing field. The vertically dotted lines separate the regions with different vorticity L. The insets show the Cooper pair density at magnetic field $H_0/H_{c2} = 0.145$, 1.02, 2.145, and 2.52, where the ground state is given by a state with $L = 0$, 1, 2, and 3, respectively. High Cooper pair density is given by dark regions, while light regions indicate low Cooper pair density. Reprinted with permission from [39], B. J. Baelus et al., *Phys. Rev. B* 61, 9734 (2000). © 2000, American Physical Society.

superconducting ring without the hole) as a function of the magnetic field. The solid curve indicates the ground state, while the dashed curves indicate the metastable states for increasing and decreasing fields. The vertically dotted lines separate the regions with different winding number L. Notice that hysteresis is only found for the first transition from the $L = 0$ to the $L = 1$ state and not for the higher transitions, which are continuous. At the transition from the $L = 1$ state to the $L = 2$ state and further to the $L = 3$ state, the free energy and the magnetization vary smoothly (see Fig. 27a and b). In the insets of Fig. 27a, we show the Cooper pair density for such a sample at the magnetic fields: $H_0/H_{c2} = 0.145$, 1.02, 2.145, and 2.52, where the ground state is given by a state with $L = 0$, 1, 2, and 3, respectively. High Cooper pair density is indicated by dark regions, whereas light regions indicate low Cooper pair density. For $H_0/H_{c2} = 0.145$, we find a high Cooper pair density in the entire superconducting ring. There is almost no flux trapped in the circular area with radius smaller than R_o. After the first transition at $H_0/H_{c2} \approx 0.75$, suddenly more flux is trapped in the hole, which substantially lowers the Cooper pair density in the superconductor. Notice that the trapped flux tries to restore the circular symmetry in the Cooper pair density and that the density of the superconducting condensate is largest in the narrowest region of the superconductor. The next inset shows the Cooper pair density of the $L = 2$ state where an additional vortex appears. Some flux is passing through the hole (i.e., winding number equals 1 around the hole), while one flux line is passing through the superconducting ring and a local vortex (the normal region with zero Cooper pair density) is created. In the $L = 3$ state superconductivity is destroyed in part of the sample which contains flux with winding number $L = 2$ and the rest of the flux passes through the hole. Hence, by breaking the circular symmetry of the system, multivortex states are stabilized. Remember that for the corresponding symmetric system, that is, $a = 0$, only giant vortex states were found.

Having the magnetic fields for the different $L \to L + 1$ transitions for superconducting rings with different positions of the hole, that is, different values of a, we constructed the phase diagram shown in Figure 28. The thin curves (solid curves when the magnetization is discontinuous and dashed curves when the magnetization is continuous) indicate the magnetic field at which the transition from the L state to the $L + 1$ state occurs, while the thick solid curve gives the superconducting/normal transition.

To show that the stabilization of the multivortex state due to an off-center hole is not peculiar for $R_o = 2.0\xi$, we repeated the previous calculation for a larger superconducting disk with radius $R_o = 5.0\xi$ and thickness $d = 0.005\xi$ containing a hole with radius $R_i = 2.0\xi$. In Figure 29a the Cooper pair density is shown for such a system with the hole in the center, while in Figure 29b the hole is moved away from the center over a distance $a = 1.0\xi$ in the negative y direction. The externally applied magnetic field is the same in both cases, $H_0/H_{c2} = 0.77$, which gives a winding number $L = 4$ and $L = 5$ for the ground state of the symmetric and the nonsymmetric geometry, respectively. The assignment of the winding number can be easily checked from Figure 29c and d which shows contour plots of the
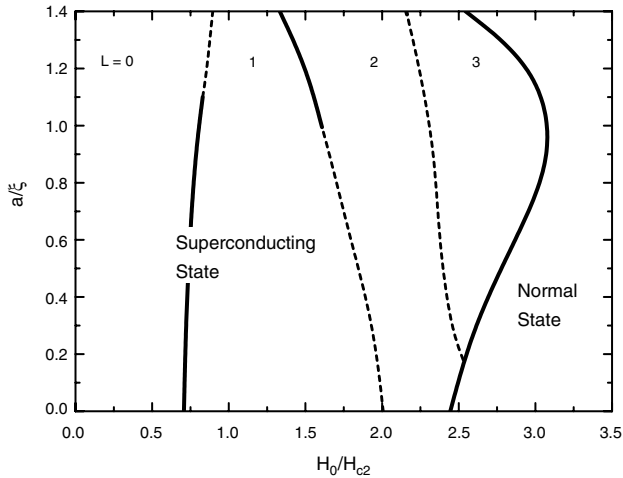
Figure 28. The relation between the displacement a and the transition magnetic fields for a superconducting ring with $R_0/\xi = 2.0$, $d/\xi = 0.005$, $R_i/\xi = 0.5$, and $\kappa = 0.28$. The thin solid curves give the $L \rightarrow L+1$ transition when it corresponds to a first-order phase transition while a dashed curve is used when it is continuous. The thick solid curve is the superconducting/normal transition. Reprinted with permission from [39], B. J. Baelus et al., *Phys. Rev. B* 61, 9734 (2000). © 2000, American Physical Society.
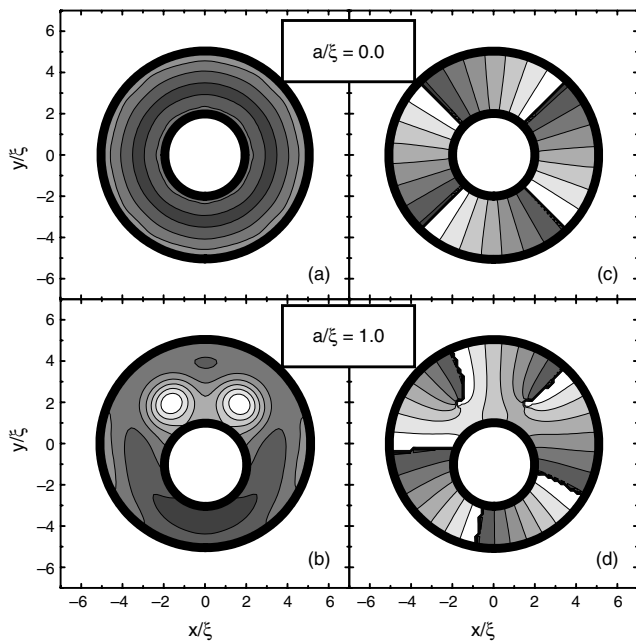
Figure 29. The Cooper pair density for a superconducting disk with radius $R_o = 5.0\xi$ and thickness $d = 0.005\xi$ with a hole with radius $R_i = 2.0\xi$ (a) in the center and (b) moved away form the center over a distance $a = 1.0\xi$ in the negative y direction. The applied magnetic field is the same in both cases: $H_0/H_{c2} = 0.77$. High Cooper pair density is given by dark regions and low Cooper pair density by light regions. The corresponding contour plot of the phase of the superconducting wavefunction is given in (c) and (d). Reprinted with permission from [39], B. J. Baelus et al., *Phys. Rev. B* 61, 9734 (2000). © 2000, American Physical Society.

corresponding phase of the superconducting wavefunction. If the hole is at the center of the disk, the ground state is a giant vortex state. If the center of the hole is moved to the position $(x/\xi, y/\xi) = (0, -1)$, two vortices appear in the superconducting material while the hole contains three vortices. Notice that in this case, although the magnetic field is kept the same and the amount of superconducting material is not altered, changing the symmetry of the system alters the winding number.

9. SADDLE POINT STATES

Up to now we only discussed stable vortex configurations, which correspond to minima in the free energy landscape. These minima are separated from each other by saddle points (Fig. 30). Therefore, the states corresponding to the saddle points (i.e., the saddle point states) describe the transition from one vortex state to another. In other words, by studying the saddle point states, we can investigate the flux entree and expulsion in mesoscopic rings; that is, how does the vortex enter or leave the superconductor?

We considered superconducting rings with inner radius R_i, outer radius R_o, and thickness d [52]. These mesoscopic superconducting systems are immersed in an insulating medium in the presence of a perpendicular uniform magnetic field H_0. To solve this problem, we follow the numerical approach of Schweigert and Peeters [8]. For very thin rings, that is, $Wd \ll \lambda^2$, with $W = R_o - R_i$ as the width of the ring, the demagnetization effects can be neglected and the Ginzburg–Landau functional can be written as

$$G = G_n + \int d\vec{r} \left(\alpha |\Psi|^2 + \frac{\beta}{2}|\Psi|^4 + \Psi^* \widehat{L} \Psi \right) \quad (48)$$
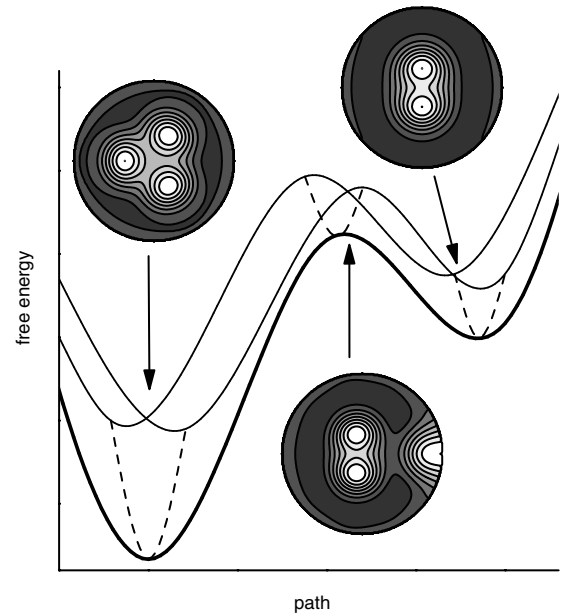
Figure 30. Schematical view of the free energy in functional space depicting two minima with $L = 2$ and $L = 3$ and the saddle point connecting them. The Cooper pair densities of these three states are shown in the insets. High (low) Cooper pair density is given by dark (light). Reprinted with permission from [8], V. A. Schweigert and F. M. Peeters, *Phys. Rev. Lett.* 83, 2409 (1999). © 1999, American Physical Society.

where G and G_n are the free energies of the superconducting and the normal states, Ψ is the complex order parameter, and α and β are the GL coefficients which depend on the sample temperature. $\hat{L}$ is the kinetic energy operator for Cooper pairs of charge $e^* = 2e$ and mass $m^* = 2m$; that is,

$$\hat{L} = (-i\hbar\vec{\nabla} - e^*\vec{A}/c)/2m^* \qquad (49)$$

where $\vec{A} = \vec{e}_\phi H_0\rho/2$ is the vector potential of the uniform magnetic field H_0 written in cylindrical coordinates ρ and ϕ.

By expanding the order parameter $\Psi = \sum_i C_i\varphi_i$ in the orthonormal eigenfunctions of the kinetic energy operator $\hat{L}\varphi_i = \epsilon_i\varphi_i$ [5, 6, 15, 16], the difference between the superconducting and the normal state Gibbs free energy can be written in terms of complex variables as

$$F = G - G_n = (\alpha + \epsilon_i)C_iC_i^* + \frac{\beta}{2}A_{kl}^{ij}C_i^*C_j^*C_kC_l \qquad (50)$$

where the matrix elements $A_{kl}^{ij} = \int d\vec{r}\varphi_i^*\varphi_j^*\varphi_k\varphi_l$ are calculated numerically. The boundary condition for these φ_i, corresponding to zero current density in the insulator media, is given by Eq. (15). These eigenenergies ϵ_i and the eigenfunctions φ_i depend on the sample geometry. For thin axial symmetric samples the eigenfunctions have the form $\varphi_{j=(n,l)}(\rho, \phi) = \exp(il\phi)f_n(\rho)$, where l is the angular momentum and the index n counts different states with the same l and equals the number of nodes in the radial direction. Thus, the order parameter Ψ can be written as

$$\psi = \sum_n \sum_l C_{n,l}\varphi_{n,l} \qquad (51)$$

We do not restrict ourselves to the lowest Landau level approximation (i.e., $n = 1$) and expand the order parameter over all eigenfunctions with energy $\epsilon_i < \epsilon_*$, where the cutting parameter ϵ_* is chosen such that increasing it does not influence the results. The typical number of complex components used is in the range $N = 30$–50. Thus the superconducting state is mapped into a 2D cluster of N particles with coordinates $(x_i, y_i) \leftrightarrow (\text{Re}(C_i), \text{Im}(C_i))$, whose energy is determined by the Hamiltonian (50). The energy landscape in this $2N + 1$ dimensional space is studied where the local minima and the saddle points between them will be determined together with the corresponding vortex states.

To find the superconducting states and the saddle point states we use the technique described in [8]. A particular state is given by its set of coefficients $\{C_i\}$. We calculate the free energy in the vicinity of this point $\delta G = G(C^n) - G(C)$ where $\{C^n\}$ is the set of coefficients of a state very close to the initial one. This free energy is expanded to second order in the deviations $\delta = C^n - C$,

$$\delta G = F_m\delta_m^* + B_{mn}\delta_n\delta_m^* + D_{mn}\delta_n^*\delta_m^* + c.c. \qquad (52)$$

where

$$F_m = (\alpha + \epsilon_i)C_m + \beta A_{kl}^{mj}C_jC_k^*C_l \qquad (53)$$

$$B_{mn} = (\alpha + \epsilon_m)I_{mn} + 2\beta A_{kl}^{mn}C_kC_l^* \qquad (54)$$

$$D_{mn} = \beta A_{kl}^{mn}C_kC_l \qquad (55)$$

and I_{mn} is the unit matrix. Using normal coordinates $\delta_m = x_kQ_m^k$ we can rewrite the quadratic form as $\delta G = 2(\gamma_k x_k + \eta_k x_k^2)$. To find the eigenvalues η_k and the eigenvectors γ_k we solve numerically the equation

$$\begin{vmatrix} B + \text{Re}(D) & \text{Im}(D) \\ \text{Im}(D) & B - \text{Re}(D) \end{vmatrix} \cdot \begin{vmatrix} \text{Re}(Q^k) \\ \text{Im}(Q^k) \end{vmatrix} = \eta_k \begin{vmatrix} \text{Re}(Q^k) \\ \text{Im}(Q^k) \end{vmatrix} \qquad (56)$$

Starting from a randomly chosen initial set of coefficients, we calculate a nearby minimum of the free energy by moving in the direction of the negative free energy gradient $-\gamma_k$. The set of coefficients of this minimum then determines the ground state or a metastable state. Starting from the initial set of coefficients we can also calculate a nearby saddle point state by moving to a minimum of the free energy in all directions, except the one that has the lowest eigenvalue. In this direction we move to a local maximum. Repeating this procedure for many randomly chosen initial sets of coefficients $\{C_i\}$ for fixed magnetic field, we find the different possible superconducting states and saddle point states. To calculate the magnetic field dependence we start from a superconducting state at a certain field and we change the applied field by small increments. By moving into the direction of the nearest minimum or saddle point, the corresponding state will be found for the new magnetic field, provided that the field step is small enough.

Just like for the discussion of the stable states, we also make a distinction between small and large rings for the discussion of the saddle point states. As mentioned above, in small rings only giant vortex states are stable, while in larger rings it is possible that multivortex states are stabilized.

9.1. Small Rings: Giant Vortex State

As an example, we consider a superconducting ring with radius $R_o = 2.0\xi$ and hole radius $R_i = 1.0\xi$. In Figure 31 the free energy is shown as a function of the applied magnetic field for the different L states (solid curves) together with the saddle point states (dashed curves). We find giant vortex states with $L = 0, 1, 2, 3$, and 4. Comparing this result with the result for a disk with radius $R = 2.0\xi$, we find that more L states are possible and the superconducting/normal transition moves to larger magnetic fields [39]. The inset shows the energy barrier U for the transitions between the different L states as a function of the difference between the applied magnetic field H_0 and the $L \to L + 1$ transition field $H_{L\to L+1}$. For increasing L, the height of the energy barrier and the difference between the penetration and the expulsion field decreases. The energy barrier near its maximum can be approximated by $U/F_0 = U_{max}/F_0 + \alpha(H - H_{max})/H_{c2}$, and we determined the slope $\alpha_{L\to L+1}$; $\alpha_{0\to 1} = -0.8$ for $H \lesssim H_{max}$ and 0.9 for $H \gtrsim H_{max}$, $\alpha_{1\to 2} = -0.6$ for $H \lesssim H_{max}$ and 0.75 for $H \gtrsim H_{max}$, $\alpha_{2\to 3} = -0.3$ for $H \lesssim H_{max}$ and 0.42 for $H \gtrsim H_{max}$, and $\alpha_{3\to 4} = -0.013$ for $H \lesssim H_{max}$ and 0.038 for $H \gtrsim H_{max}$. The slope decreases again for increasing L and the absolute value of the slope for $H \lesssim H_{max}$ is smaller than that for $H \gtrsim H_{max}$ for every L.

Next, we investigate the $2 \leftrightarrow 3$ saddle point. At $H_0/H_{c2} = 2.01$ (expulsion field) and 2.535 (penetration field) the saddle point state equals the giant vortex states with $L = 3$ and $L = 2$, respectively. The transition between these two
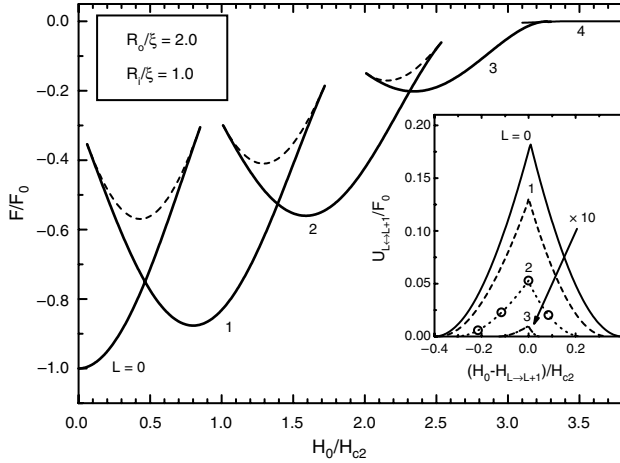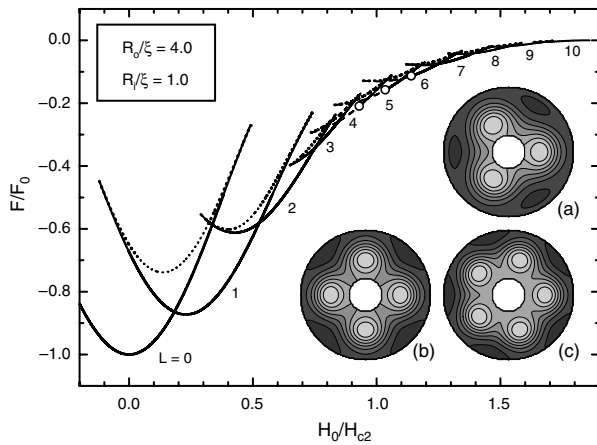
Figure 31. The free energy for a superconducting ring with radius $R_o = 2.0\xi$ and hole radius $R_i = 1.0\xi$ as a function of the applied magnetic field for the different giant vortex states (solid curves) and for the saddle point states (dashed curves). The inset shows the energy barrier U for the transitions between different L states as a function of the difference between the applied magnetic field H_0 and the $L \to L + 1$ transition field $H_{L \to L+1}$. Reprinted with permission from [52], B. J. Baelus et al., *Phys. Rev. B* 63, 144517 (2001). © 2001, American Physical Society.

giant vortex states is illustrated in Figure 32a–d which shows the spatial distribution of the superconducting electron density $|\Psi|^2$ corresponding with the open circles in the inset of Figure 31 at $H_0/H_{c2} = 2.1$, 2.2, 2.315 (i.e., the barrier maximum), and 2.4, respectively. High (low) density is given by dark (light) regions. With increasing field one vortex moves from inside the ring, through the superconducting material, to outside the ring. From Figure 32c one may infer that the Cooper pair density is zero along a radial line and that the vortex is, in fact, a sort of line. That this is not the case can be seen from the left inset of Figure 33, which shows the Cooper pair density $|\psi|^2$ along this radial line for $H_0/H_{c2} = 2.315$. The Cooper pair density in the superconducting material is zero only at the center of the vortex, which is situated at $x_{min}/\xi \approx 1.5$, and $|\Psi|^2$ is very small otherwise; that is, $|\Psi|^2 < 0.01$. In Figure 33 the position of the vortex (i.e., of x_{min}) is shown as a function of the applied field. Over a narrow field region the vortex moves from the inner boundary toward the outer boundary. From $H_0/H_{c2} = 2.01$–2.25 the center of the vortex is still situated in the hole, but the vortex already influences the superconducting state (see, e.g., Fig. 32a and b). From $H_0/H_{c2} = 2.36$–2.535 the center of the vortex lies outside the ring, but it still has an influence on the saddle point (see, e.g., Fig. 32d). In the region $H_0/H_{c2} = 2.25$–2.36 the center of the vortex is situated inside the conductor. This is also illustrated by the contour plot (right inset of Fig. 33) for the phase of the order parameter at $H_0/H_{c2} = 2.315$, corresponding with the open circle in Figure 33. When encircling the superconductor near the inner boundary of the ring, we find that the phase difference $\Delta\varphi$ is equal to $2 \times 2\pi$ which implies vorticity $L = 2$. When encircling the superconductor near the outer boundary, we find vorticity $L = 3$. If we choose a path around the vortex (located at x_{min}), the phase changes with 2π and thus $L = 1$. At the transition field ($H_0/H_{c2} = 2.315$) the center of the vortex of the saddle point is clearly not
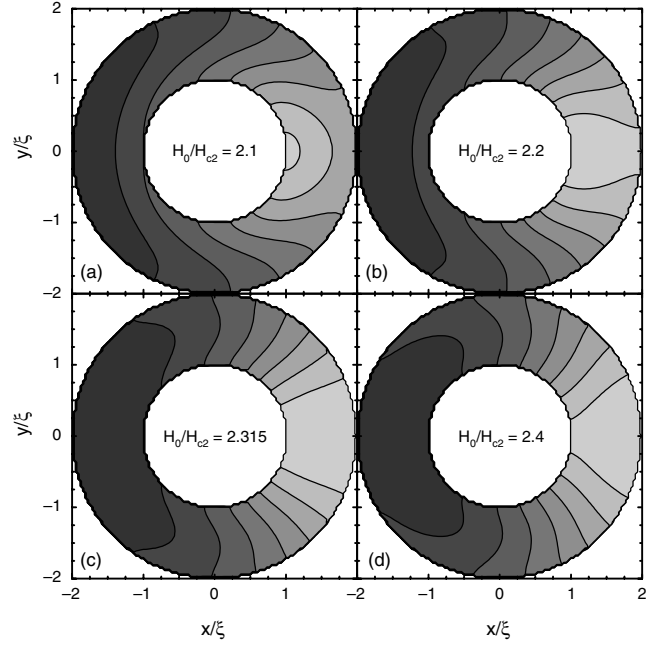
Figure 32. The spatial distribution of the superconducting electron density $|\Psi|^2$ of the transition between the giant vortex states with $L = 2$ and $L = 3$ for a superconducting ring with $R_o = 2.0\xi$ and $R_i = 1.0\xi$ at $H_0/H_{c2} = 2.1$ (a), 2.2 (b), 2.315 (c), and 2.4 (d). High density is given by dark regions and low density by light regions. Reprinted with permission from [52], B. J. Baelus et al., *Phys. Rev. B* 63, 144517 (2001). © 2001, American Physical Society.

situated at the outer boundary as was the case for superconducting disks (see e.g., [8, 52]).

9.2. Large Rings: Multivortex States

First, we consider superconducting rings with radius $R_o = 4.0\xi$ and hole radius $R_i = 1.0\xi$. In Figure 34 the free energy is shown as a function of the applied magnetic field. The different L states are given by solid curves for giant vortex
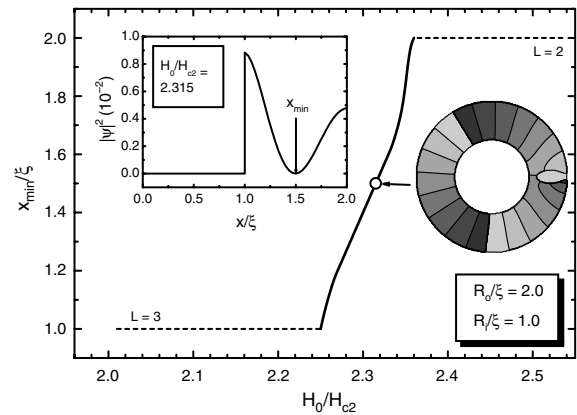
Figure 33. The radial position of the vortex line in the saddle point for the $2 \leftrightarrow 3$ transition through the superconductor with radius $R_o = 2.0\xi$ and $R_i = 1.0\xi$. The left inset shows the Cooper pair density along the x-direction at $H_0/H_{c2} = 2.315$, and the right inset is a contour plot of the phase of the order parameter at $H_0/H_{c2} = 2.315$. Reprinted with permission from [52], B. J. Baelus et al., *Phys. Rev. B* 63, 144517 (2001). © 2001, American Physical Society.

states and dashed curves for multivortex states, and the saddle point states are given by the dotted curves. The open circles correspond to the transition between the multivortex state and the giant vortex state for fixed L. These transitions occur at $H_{MG}/H_{c2} = 0.93$, 1.035, and 1.14 for $L = 4$, 5, and 6, respectively. Notice that for such a small hole in the disk the maximum number of L (i.e., $L = 10$) is the same as for the disk case without a hole. The spatial distribution of the superconducting electron density $|\Psi|^2$ is depicted in the insets (a–c) of Figure 34 for the multivortex state with $L = 4$ at $H_0/H_{c2} = 0.8$, $L = 5$ at $H_0/H_{c2} = 0.9$, and $L = 6$ at $H_0/H_{c2} = 1.0$, respectively. High (low) Cooper pair density is given by dark (light) regions. Notice that there are always $L - 1$ vortices in the superconducting material and one vortex appears in the hole, that is, in the center of the ring.

The energy barriers for the transitions between the different L states are shown in Figure 35 as a function of the applied magnetic field. By comparing this with the energy barriers for a disk with no hole [52], we see that the barrier heights and the transition fields are very different. Therefore we show in the insets of Figure 35 the maximum height of the energy barrier U_{max} and the $L \leftrightarrow L + 1$ transition field H_{tr} as a function of L for superconducting disks with no hole (squares) and with a hole of radius $R_i = 1.0\xi$ (circles), 2.0ξ (triangles), and 3.0ξ (stars). In all cases the height of the energy barrier decreases and the transition fields increase with increasing L. By comparing the situation with no hole and that with a small hole with $R_i = 1.0\xi$, we see that the barriers for $L \leq 1$ are higher for the disk with a hole with $R_i = 1.0\xi$ than for $R_i = 0.0\xi$, whereas they are smaller when $L > 1$. Notice also that the value of the $L \to L + 1$ transition field is sensitive to the presence of the hole with radius

Figure 35. The energy barrier U for the transitions between the different L states in a superconducting ring with $R_o = 4.0\xi$ and $R_i = 1.0\xi$ as a function of the applied magnetic field. The insets show the maximum height of the energy barrier U_{max} and the transition field H_{tr} as a function of L for rings with $R_o = 4.0\xi$ and $R_i = 0.0$, 1.0, 2.0, and 3.0ξ. Reprinted with permission from [52], B. J. Baelus et al., *Phys. Rev. B* 63, 144517 (2001). © 2001, American Physical Society.

$R_i = 1.0\xi$ for small L and insensitive for larger L. The reason is that for small $L > 0$ such a central hole always has one vortex localized inside, which favors certain vortex configurations above others, whereas for larger L in both cases only giant vortices appear with sizes larger than the hole size and the presence of the hole no longer matters. For larger holes the energy barrier decreases more slowly, because the free energy of the different L states shows a more parabolical type of behavior as a function of the magnetic field. The transition field has a much smaller dependence on the radius of the hole. Notice that the transition field for $R_i = 3.0\xi$ is linear as a function of L for small holes and $L \leq 9$. This is in good agreement with the results in the narrow ring limit, where the transition between states with different vorticity L occurs when the enclosed flux ϕ equals $(L + 1/2)\phi_o$ [48].

Next, we investigate the saddle point states in these superconducting rings. We make a distinction between different kinds of saddle point states: (1) between two giant vortex states, (2) between a multivortex and a giant vortex state, (3) between two multivortex states with the same vorticity in the hole and different vorticity in the superconducting material, and (4) between two multivortex states with the same vorticity in the superconducting material but different vorticity in the hole. The first saddle point transition was already described for the case of small superconducting rings (see Figs. 32 and 33). Next, we study the saddle point state between a multivortex state with $L = 5$ and a giant vortex state with $L = 4$ for the previously considered ring with radius $R_o = 4.0\xi$ and hole radius $R_i = 1.0\xi$. Figure 36a–f shows the Cooper pair density for these saddle point states at $H_0/H_{c2} = 0.83$, 0.88, 0.93, 0.965 (i.e., the barrier maximum), 1.03, and 1.06, respectively. High (low) Cooper pair density is given by dark (light) regions. For increasing field one vortex moves to the outer boundary, while the others move to the center of the ring where they create a giant vortex state. Note that the giant vortex state is larger than

Figure 34. The free energy for a superconducting ring with $R_o = 4.0\xi$ and $R_i = 1.0\xi$ as a function of the applied magnetic field for the different L states (solid curves for giant vortex states and dashed curves for multivortex states) and the saddle point states (dotted curves). The open circles correspond to the transition between the multivortex state and the giant vortex state for fixed L. The inset shows the spatial distribution of the superconducting electron density $|\Psi|^2$ for the multivortex state with $L = 4$ at $H_0/H_{c2} = 0.8$ (a), $L = 5$ at $H_0/H_{c2} = 0.9$ (b), and $L = 6$ at $H_0/H_{c2} = 1.0$ (c). High Cooper pair density is given by dark regions; low Cooper pair density by light regions. Reprinted with permission from [52], B. J. Baelus et al., *Phys. Rev. B* 63, 144517 (2001). © 2001, American Physical Society.

Figure 36. The Cooper pair density for the saddle point state transition between a multivortex state with $L = 5$ and a giant vortex state with $L = 4$ at $H_0/H_{c2} = 0.83$ (a), 0.88 (b), 0.93 (c), 0.965 (d), 1.03 (e), and 1.06 (f). High Cooper pair density is given by dark regions and low Cooper pair density by light regions. Reprinted with permission from [52], B. J. Baelus et al., *Phys. Rev. B* 63, 144517 (2001). © 2001, American Physical Society.

the hole and therefore it is partially situated in the superconductor itself.

To study saddle point transitions between different multivortex states we have to increase the radius of the ring to favor the multivortex states. Therefore, we consider a ring with radius $R_o = 6.0\xi$ and hole radius $R_i = 2.0\xi$. Figure 37 shows the free energy of multivortex states with $L = 8$ and $L = 9$. In both cases three vortices are trapped in the hole. The lower insets show the spatial distribution of the superconducting electron density $|\Psi|^2$ at the transition field $H_0/H_{c2} = 0.695$ for $L = 8$ and $L = 9$. It is clear that there are only five and six vortices in the superconducting material, respectively. The free energy of these multivortex states is shown by solid curves, whereas the saddle point energy between these states is given by the dashed curve. Notice further that there is no transition from the multivortex states to the giant vortex states with $L = 8$ and 9 as long as these states are stable. The spatial distribution of the superconducting electron density $|\Psi|^2$ for this saddle point state is depicted in the upper insets at the magnetic fields $H_0/H_{c2} = 0.63$, 0.695 (the barrier maximum), and 0.76, respectively.
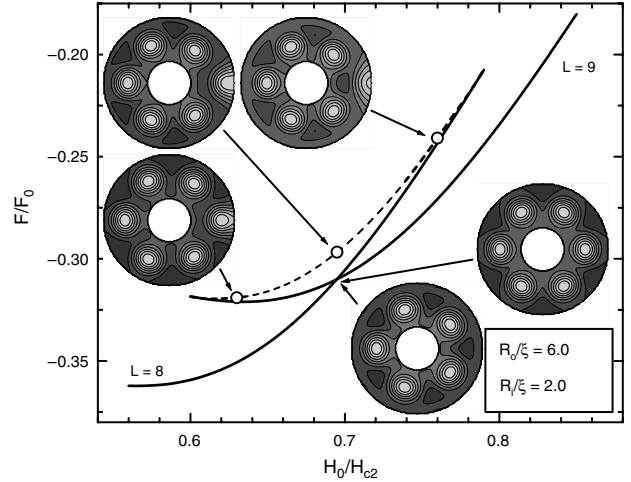
Figure 37. The free energy of the multivortex states with $L = 8$ and $L = 9$ (solid curves) and the saddle point state (dashed curves) between these multivortex states for a superconducting ring with $R_o = 6.0\xi$ and $R_i = 2.0\xi$ as a function of the applied magnetic field. The lower insets show the spatial distribution of the superconducting electron density $|\Psi|^2$ at the transition field $H_0/H_{c2} = 0.695$ for $L = 8$ and $L = 9$. The upper insets show the spatial distribution of the superconducting electron density $|\Psi|^2$ for the saddle point states indicated by the open circles, that is, at $H_0/H_{c2} = 0.63$ (a), 0.695 (b), and 0.76 (c). High Cooper pair density is given by dark regions and low Cooper pair density by light regions. Reprinted with permission from [52], B. J. Baelus et al., *Phys. Rev. B* 63, 144517 (2001). © 2001, American Physical Society.

For increasing field one vortex moves from the superconducting material to the outer boundary and hence the vorticity changes from $L = 9$ to $L = 8$. Notice that the vorticity of the interior boundary of the ring does not change.

The fourth type of saddle point state to discuss is the $L \to L + 1$ transition between two multivortex states with the same vorticity in the superconducting material but with a different vorticity in the hole. For $R_o/\xi = 4$ and $R_o/\xi = 6$ we did not find such transitions regardless of the hole radius. This means that at least for these radii there is no transition between such states that describes the motion of one vortex from the hole through the superconducting material toward the outer insulator.

Finally, we investigated the influence of the hole radius on the barrier for a fixed outer ring radius. Figure 38a shows the maximum barrier height, that is, the barrier height at the thermodynamic equilibrium $L \to L + 1$ transition, as a function of the hole radius R_i for a ring with radius $R_o = 4.0\xi$ for the transition between the Meissner state and the $L = 1$ state (solid curve) and for the transition between the $L = 1$ state and the $L = 2$ state (dashed curve). For increasing hole radius, the barrier height of the first transition rapidly increases in the range $R_i = 0.1\xi$ to $R_i = 1.5\xi$ and decreases slowly afterward. For a superconducting disk with radius $R_o = 4.0\xi$ with a hole in the center with radius $R_i = 1.5\xi$ the maximum barrier height for the $0 \to 1$ transition is twice as large as that for a superconducting disk without a hole. The barrier height of the second transition first decreases, then rapidly increases in the range $R_i = 0.6\xi$ to $R_i = 2.5\xi$ and then slowly decreases again. In this case the maximum barrier height for a superconducting disk with
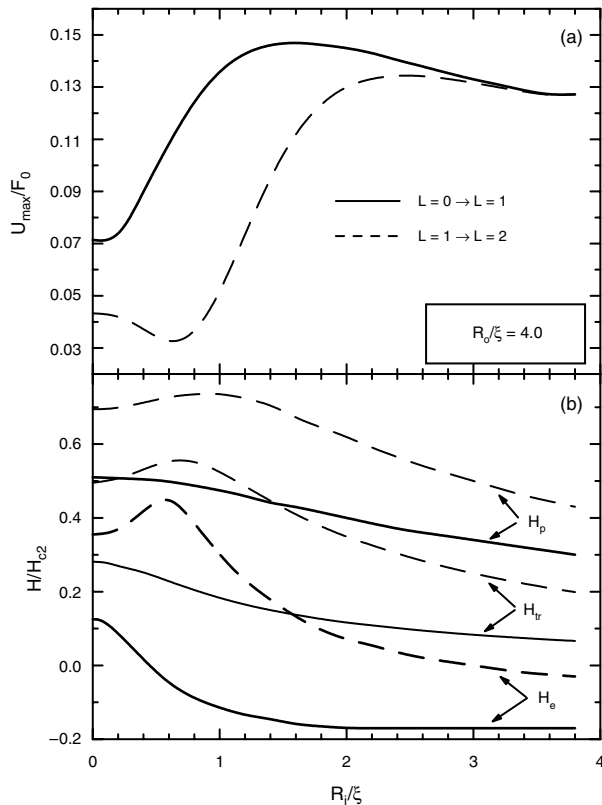
Figure 38. (a) The maximum barrier height as a function of the hole radius R_i for a ring with radius $R_o = 4.0\xi$ for the transition between the Meissner state and the $L = 1$ state (solid curve) and the transition between the $L = 1$ state and the $L = 2$ state (dashed curve) and (b) the transition magnetic field H_{tr}, the expulsion magnetic field H_e, and the penetration magnetic field H_p as a function of the hole radius R_i for the transition between the Meissner state and the $L = 1$ state (solid curve) and the transition between the $L = 1$ state and the $L = 2$ state (dashed curve). Reprinted with permission from [52], B. J. Baelus et al., *Phys. Rev. B* 63, 144517 (2001). © 2001, American Physical Society.

a hole with radius $R_i = 2.5\xi$ is three times as large as that for a superconducting disk without a hole. Hence, changing the hole radius strongly influences the maximum height of the barrier. In Figure 38b we plot the characteristic magnetic fields of the barrier as a function of the hole radius (i.e. the transition magnetic field H_{tr}), the expulsion magnetic field H_e, and the penetration magnetic field H_p for the $0 \to 1$ transition by solid curves and for the $1 \to 2$ transition by the dashed curve. For the $0 \to 1$ transition the characteristic magnetic fields decrease with increasing hole radius. For the $1 \to 2$ transition the characteristic magnetic fields first increase to a maximum and then decrease. This behavior was already encountered in Figure 25. Notice that the position of the minimum in U_{max} coincides with the position of the maximum in H_{tr}.

10. EXPERIMENTAL RESULTS

Two different types of experiments have been performed on single mesoscopic rings: resistivity measurements and magnetization measurements.

To measure the resistivity, leads are attached to the sample and a transport current is applied through the leads. By measuring the resistivity of the non-fully superconducting state one can obtain information about the superconducting/normal transition. Most of the time this information is plotted in a $H - T$ phase diagram, which shows transitions between vortex states with different vorticity L. With this technique it is possible to investigate the dependence of the critical magnetic field and temperature, but it does not provide any information about the real vortex structure. Another restriction is that the leads can influence the result.

Hall magnetometry is revealing itself as a powerful tool for obtaining information on a single mesoscopic superconductor away from the superconducting/normal phase boundary, that is, deep inside the superconducting state. Thin superconducting samples are placed on top of a Hall probe created in a two-dimensional electron gas. In the ballistic regime the Hall resistance is directly proportional to the average of the magnetic field through the junction [44]. The averaged value of the magnetic field $\langle \vec{H} \rangle$ in the junction area is determined by the expulsion of the field by the superconductor, which is placed on top of the junction. Because the magnetization is given by the difference between the averaged field and the applied field, one can obtain the magnetization of single superconductors and compare them with the theoretical values (see, e.g., [13, 14]). By using this technique, it has been possible to show that a single mesoscopic superconductor in a magnetic field does not exhibit the standard magnetization dependencies of bulk superconductors.

10.1. Resistivity Measurements

Moshchalkov et al. [19] performed resistivity measurements on a square Al dot and on a square Al ring with connected leads (see the insets of Fig. 39). The sample geometry was
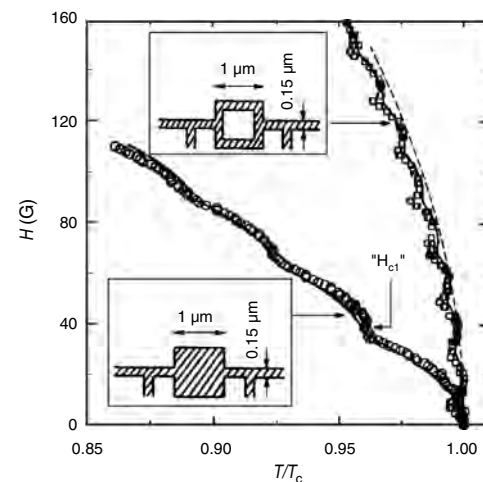
Figure 39. The measured superconducting phase boundary in the $H - T/T_c$ plane for a 1 μm$\times$1 μm Al square ring (square symbols) and by a 1 μm$\times$1 μm filled Al square (circular symbols). The solid lines correspond to calculations based on the linear Ginzburg–Landau theory. The dashed line shows the phase boundary for a straight wire. Reprinted with permission from [19], V. V. Moshchalkov et al., *Nature* 373, 319 (1995). © 1995, Macmillan Magazines Ltd.

defined by combining electron beam lithography and lift-off techniques. The resistance of the 25-nm-thick Al samples was measured using a four-probe technique with an alternating current resistance bridge. The normal state resistivity $\rho \approx 4.5 \times 10^{-6}$ Ω cm of the Al structures as well as the resistance ratio $R(300 \text{ K})/R(4.2 \text{ K}) \approx 2.1$ indicate a pronounced metallic character. Detailed atomic force microscopy and scanning electron microscopy studies of the Al films confirm the presence of a smooth and continuous film surface.

The normal superconductivity phase boundary was constructed in the $H - T$ phase diagram by measuring the temperature shift of the midpoint of the normal-to-superconducting resistive transition at different magnetic fields. The latter was always applied perpendicular to the plane of the sample. The square symbols in Figure 39 give the superconducting phase boundary in the $H - T/T_c$ plane for the 1 μm $\times$ 1 μm Al square ring and the circular symbols for the 1 μm $\times$ 1 μm filled Al square. The solid lines in Figure 39 correspond to calculations based on the linear Ginzburg–Landau theory. The dashed line shows the phase boundary for a straight wire. The phase boundary for the square ring shows classic Little–Parks oscillations, which are related to fluxoid quantization in the ring.

The phase boundary for the ring can be obtained by averaging the one-dimensional result [31] over the different radii imposed by the finite linewidth of the ring [48]. Such a calculation results in

$$\frac{T_c(H) - T_c(H = 0)}{T_c(H = 0)} = \left(\frac{\pi \xi(0) w H}{\sqrt{3} \Phi_0} \right)^2$$
$$= \frac{\xi^2(0)}{R_i R_o} \left(L - \frac{\pi H R_i R_o}{\Phi_0} \right)^2, \quad (57)$$

where R_i and R_o are the inner and outer boundaries of the ring, respectively. The first term gives a monotomic shift of $T_c(H)$. The second term describes the oscillatory $T_c(H)$ variation caused by the change of orbital quantum number L with increasing magnetic flux. Using the actual sample dimensions the theoretical phase boundary was calculated (see the solid lines in Fig. 39), which agrees well with the experimental data.

10.2. Magnetization Measurements

Pedersen et al. [3] performed magnetization measurements of a micron-sized superconducting aluminium loop placed on top of a μ-Hall magnetometer. The μ-Hall magnetometer was etched out of a GaAs/Ga$_{0.7}$Al$_{0.3}$As heterostructure. A symmetrical 4 μm $\times$ 4 μm Hall geometry was defined by standard electron beam lithography on top of the heterostructure. In a later processing step a lift-off mask was defined on top of the μ-Hall probe by electron beam lithography. After deposition of a $d = 90$-nm-thick layer of aluminium and lift-off the sample looked as shown in Figure 40. The mean radius of the aluminium loop is $R = 2.16$ μm and the average wire width w is 316 ± 40 nm. The superconducting coherence length was estimated to be approximately $\xi_o = 180$ nm, corresponding to a bulk critical field of $H_{c2} = \Phi_0/2\pi\xi_o^2 \approx 100$ G. By using the expression

$$n\Phi_0 = n\frac{h}{2e} = \Delta(\mu_0 H)\pi R^2 \quad (58)$$
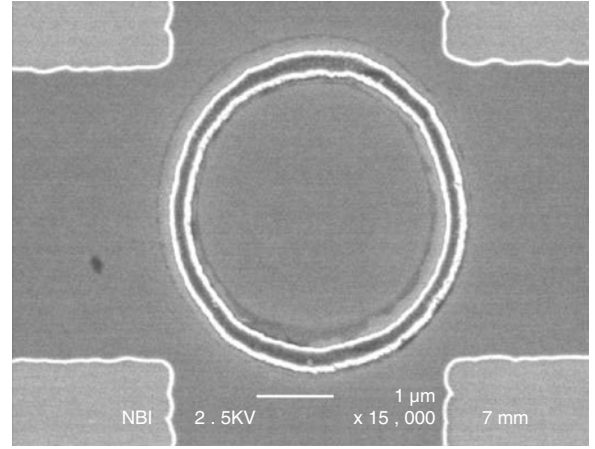
Figure 40. Scanning electron microscope image of a μ-Hall probe, the cross-section of the etched μ-Hall probe is 4×4 μm^2. The mean radius of the superconducting aluminium loop deposited on top of the μ-Hall magnetometer is 2.16 μm, and the difference between the outer and inner radius is 314 nm. Reprinted with permission from [3], S. Pedersen et al., *Phys. Rev. B* 64, 104522 (2001). © 2001, American Physical Society.
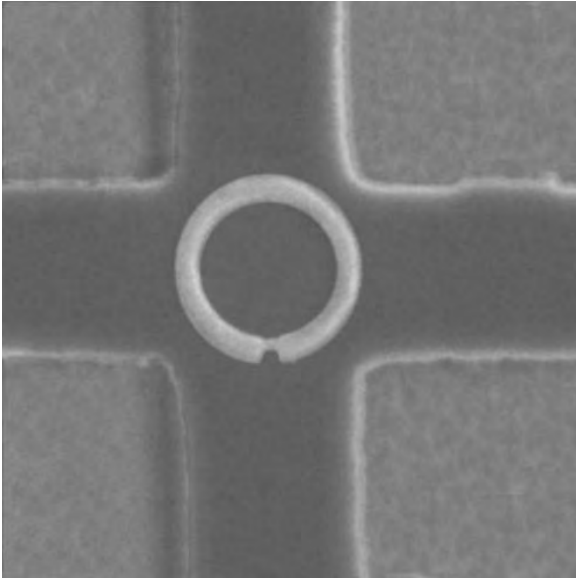
where $A = \pi R^2$ is the area of the loop given by its mean radius R, it is found that a single flux jump ($n = 1$) corresponds to a magnetic field periodicity given by $\Delta(\mu_0 H) = 1.412$ G for the ring shown in Figure 40.

In Figure 41 the measured local magnetization $\mu_0 M$ detected by the μ-Hall is shown as a function of magnetic field intensity $\mu_0 H$. The measurement was performed at $T = 0.36$ K on the device of Figure 40. The curve shows a series of distinct jumps corresponding to abrupt changes in the magnetization of the superconducting loop. The difference in the magnetic field intensity between two successive flux jumps is approximately given by $\Delta(\mu_0 H) = 1.4$ G or $\Delta(\mu_0 H) = 2.8$ G which corresponds to either single or double flux jumps ($n = 1$ or $n = 2$). Large flux jumps ($n > 1$) or flux avalanches
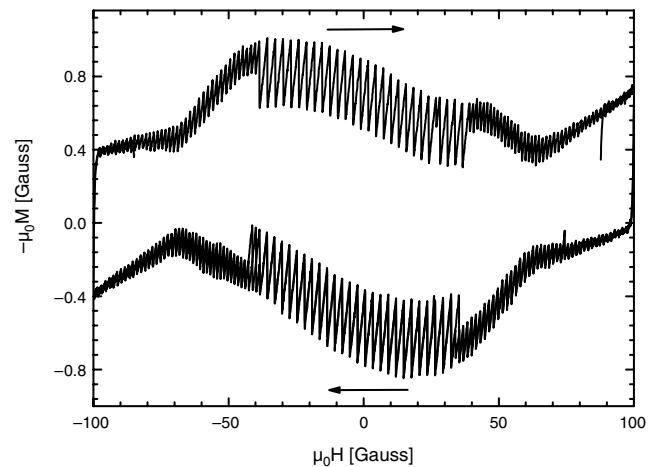
Figure 41. Measured magnetization $\mu_0 M$ detected by the μ-Hall probe as a function of magnetic field intensity $\mu_0 H$ of the device presented in Figure 40. The curve displays distinct jumps corresponding to the abrupt changes in magnetization of the superconducting loop when the system changes state. The measurements were performed at $T = 0.36$ K. Reprinted with permission from [3], S. Pedersen et al., *Phys. Rev. B* 64, 104522 (2001). © 2001, American Physical Society.

occur when the system is trapped in a metastable state. It was generally observed that these flux avalanches become more pronounced with decreasing temperature, at low magnetic field intensities, and for wide loops. Furthermore the flux avalanches were sensitive to the cooling procedure. The energy barrier causing the metastability of the eigenstates of the loop is due to either the Bean–Livingston surface barrier or the volume barrier, or even an interplay of both [53–55].

In Figure 42 the magnetic field intensity difference between successive jumps $\Delta(\mu_0 H)$ is given as a function of the magnetic field intensity. One can see that the magnetic field intensity difference between the observed jumps is, to a high degree of accuracy, given by integer values of 1.412 G, that is, the flux quantum. For magnetic fields lower than 40 G double flux jumps dominate, whereas at higher magnetic fields only single flux jumps are observed. The figure shows both an up-sweep and a down-sweep as indicated by the arrows. Pedersen et al. [3] also studied thicker loops where the flux avalanches are much more pronounced.

In Figure 42 it is seen that a small systematic variation of the value of the flux jumps occurs when the magnetic field intensity is changed. This fine structure appears as a memory effect in the sense that with increasing (decreasing) magnetic field intensity the size of the flux jumps decreases (increases). Thus these deviations depend not only on the size of the magnetic field intensity, but also on which direction the magnetic field intensity was swept during measurements. The data presented in Figure 42 have been replotted in Figure 43 in the following way. Eq. (58) is used to calculate the effective radius R of the superconducting loop and this radius was plotted as a function of the magnetic field. The dotted horizontal lines in Figure 43 represent the mean inner R_i and outer radius R_o determined from the scanning electron microscope picture. It is seen that as the magnetic

field intensity is changed from negative to positive values, the effective radius, as defined from the flux quantization condition of the loop, changes from inner to outer radius and vice versa. This is in agreement with the results of [39].

For a superconducting loop at low magnetic field intensities, it is expected that the appropriate effective radius is given by the geometrical mean value of the outer and inner radius $R = \sqrt{R_i R_o}$ [39, 50, 56] (see also Section 6). This is indeed in good agreement with the observed behavior around zero magnetic field (Fig. 43). In the regime of high magnetic field the concept of surface superconductivity becomes important and the giant vortex state will nucleate on the edges of the loop [38, 39, 56]. In this regime two degenerate current carrying situations are possible [48]; hence the giant vortex state can either circulate the loop clockwise or anti-clockwise.

Later, Vodolazov et al. [57] studied multiple flux jumps and irreversible behavior of thin Al superconducting rings using ballistic Hall magnetometry. The technique employs small Hall probes microfabricated from a high-mobility 2D electron gas. The rings, having radii $R \simeq 1$ μm and width w ranging from 0.1 to 0.3 μm, were placed directly on top of the microfabricated Hall crosses, which had approximately the same width b of about 2 μm (see micrograph in Fig. 44 for a ring with an artificial defect, i.e., an indentation). These experimental structures were prepared by multistage electron beam lithography with in accuracy of alignment between the stages of better than 100 nm. The rings studied in this work were thermally evaporated and exhibited
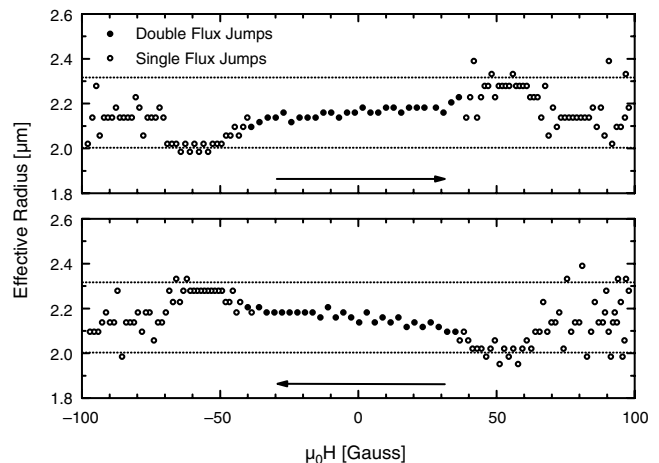
Figure 43. Effective radius R calculated by using Eq. (58). The data points are the same as those presented in Figure 42. Because the measurements were performed by stepping the magnetic field intensity with a finite step, the effective radius is only measured with a precision of approximately 40 nm. The filled (open) dots correspond to single flux jumps $n = 1$ (double flux jumps $n = 2$). The horizontal lines correspond to the outer and inner radius determined from the SEM pictures. The arrows indicate sweep direction. It is seen that as the magnetic field intensity is changed the effective radius changes between inner and outer radius of the loop, a change that depends on sweep direction and magnetic field intensity. The large spread of the data at high magnetic fields corresponds to regions where the amplitude of the oscillations measured by the Hall probe are small. Reprinted with permission from [3], S. Pedersen et al., *Phys. Rev. B* 64, 104522 (2001). © 2001, American Physical Society.

Figure 42. The magnetic field intensity difference $\Delta(\mu_0 H)$ between two successive jumps in magnetization given in units of 1.412 G corresponding to a single flux quantum $\Phi_0 = h/2e$. The plotted jumps are given as a function of magnetic field intensity. The measurement was performed at $T = 0.36$ K. The positive (negative) flux values correspond to the case in which $\mu_0 H$ was decreased (increased) during the measurements. Arrows indicate sweep direction. Reprinted with permission from [3], S. Pedersen et al., *Phys. Rev. B* 64, 104522 (2001). © 2001, American Physical Society.

Figure 44. A micrograph of the superconducting ring placed on top of a Hall bar. An artificial defect (narrowing of the ring cross-section) is intentionally made by electron beam lithography. Reprinted with permission from [57], D. Y. Vodolazov et al., *Phys. Rev. B* 67, 054506 (2003). © 2003, American Physical Society.

a superconducting transition at about 1.25 K. The superconducting coherence length was $\xi(T = 0) \simeq 0.18 \ \mu$m. The latter was calculated from the electron mean free path $l \simeq 25$ nm of macroscopic Al films evaporated simultaneously with the Al rings.

Rings with and without an artificial defect were studied. In Figure 45a and b the full magnetization loop of such a ring with parameters $R = 1.0 \pm 0.1 \ \mu$m and $w = 0.25 \pm 0.05 \ \mu$m is shown for, respectively, a ring without and with an artificial defect at $T \simeq 0.4$ K. The experimental value for the coherence length obtained from the mean free path is given by $\xi(0) \simeq 0.18 \ \mu$m. In Figure 46 the low free part of the virgin magnetization curve is presented for a ring without (solid curve) and with (dotted curve) an artificial defect. From the figures one can notice the nonunity of the vorticity jumps for the ring without artificial defects; that is, $\Delta L = 3$ in the low magnetic field region, $\Delta L = 2$ in the intermediate H region, and $\Delta H = 1$ near $H_{\max}$. In the ring with approximately the same mean radii and width but containing an intentionally introduced artificial defect, jumps with $\Delta L = 1$ are mostly observed.

To understand the multiflux jumps one has to go beyond theories based on thermodynamical equilibrium states. Not only metastable states have to be considered but also the transitions between them. This necessitates the study of time-dependent phenomena [57, 58] which will be presented in the next section.

11. DYNAMIC TRANSITIONS BETWEEN METASTABLE STATES

For systems that exhibit a series of metastable states and that may be brought far from equilibrium, the dynamics will be very important. For such systems the fundamental problem is to determine the final state to which the system will
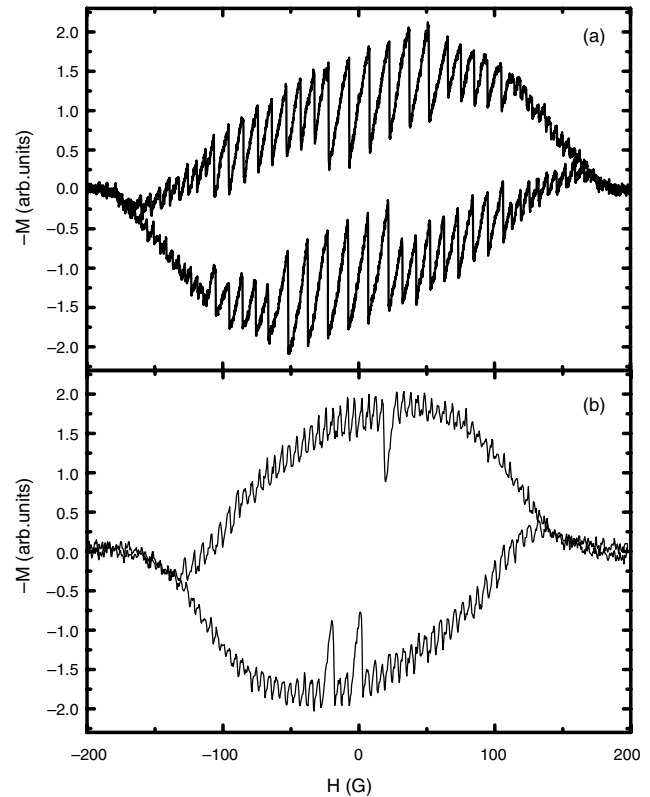
Figure 45. Magnetic field dependence of the magnetization of the ring without (a) and with (b) an artificial defect at $T \simeq 0.4$ K. Parameters of the rings (width and radii) are the same within experimental accuracy. Reprinted with permission from [57], D. Y. Vodolazov et al., *Phys. Rev. B* 67, 054506 (2003). © 2003, American Physical Society.

transit (see, e.g., [59]). Vodolazov et al. [58] presented a detailed study of the dynamics in a mesoscopic superconducting ring [58]. This system is a typical example of the above mentioned systems in which a set of metastable states exist. They showed that the final state depends crucially on
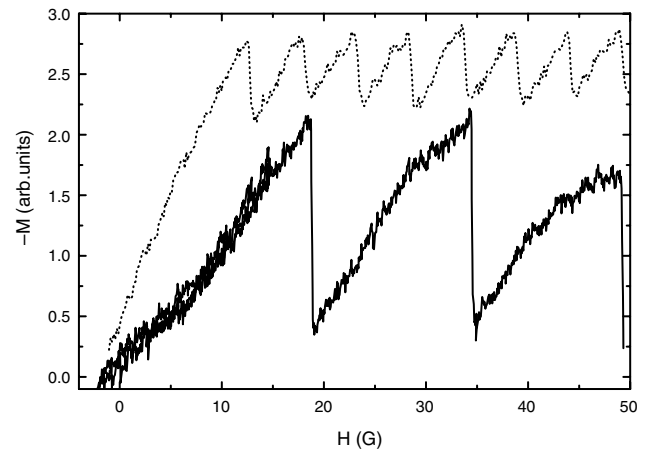
Figure 46. Magnetic field dependence of the virgin magnetization of a ring without (solid curve) and with (dotted curve) an artificial defect. The dotted curve is shifted for clarity by 0.6. Reprinted with permission from [57], D. Y. Vodolazov et al., *Phys. Rev. B* 67, 054506 (2003). © 2003, American Physical Society.

the ratio between the relaxation time of the absolute value of the order parameter and the relaxation time of the phase of the order parameter.

To solve this problem a numerical study of the time-dependent Ginzburg–Landau equations was presented in [58]. In their approach the self-field of the ring (which is valid if the width and thickness of the ring are less than λ, the London penetration length) could be neglected and hence the distribution of the magnetic field and the vector potential are known functions. The time-dependent GL equations in this case are

$$u\left(\frac{\partial\psi}{\partial t} + i\varphi\psi\right) = (\nabla - i\mathbf{A})^2\psi + \psi(1 - |\psi|^2) + \chi \quad (59)$$

$$\Delta\varphi = \mathrm{div}(\mathrm{Im}(\psi^*(\nabla - i\mathbf{A})\psi)) \quad (60)$$

where $\psi = |\psi|e^{i\phi}$ is the order parameter, the vector potential A is scaled in units $\Phi_0/(2\pi\xi)$ (where Φ_0 is the quantum of magnetic flux), and the coordinates are in units of the coherence length $\xi(T)$. In these units the magnetic field is scaled by H_{c2} and the current density, j, by $j_0 = c\Phi_0/8\pi^2\lambda^2\xi$. Time is scaled in units of the Ginzburg–Landau relaxation time $\tau_{GL} = 4\pi\sigma_n\lambda^2/c^2$, the electrostatic potential, φ, is in units of $c\Phi_0/8\pi^2\xi\lambda\sigma_n$ (σ_n is the normal state conductivity), and u is a relaxation constant. In their numerical calculations they used the new variable $U = \exp(-i\int\mathbf{A}\,d\mathbf{r})$ which guarantees gauge invariance of the vector potential on the grid. They also introduced small white noise χ in their system, the size of which is much smaller than the barrier height between the metastable states.

The parameter u is considered as an adjustable parameter, which is a measure of the different relaxation times (for example, the relaxation time of the absolute value of the order parameter) in the superconductor. This approach is motivated by the following observations. From an analysis of the general microscopic equations, which are based on the BCS model, the relaxation constant u was determined in two limiting cases: $u = 12$ for dirty gapless superconductors [60] and $u = 5.79$ for superconductors with weak depairing [61, 62]. However, this microscopic theory is built on several assumptions, for example, that the electron–electron pairing interaction is of the BCS form, which influences the exact value of u. On the other hand, the stationary and time-dependent Ginzburg–Landau equations, Eqs. (59) and (60), are in some sense more general and their general form does not depend on the specific microscopic model, but the values of the parameters, of course, are determined by the microscopic theories. (For a discussion of this question see also [63, 64] and for a review of different types of time-dependent Ginzburg–Landau equations we refer to [48, 65–67].)

11.1. One-Dimensional Rings

If the width of the ring is much smaller than ξ and $\lambda_\perp = \lambda^2/d$ (d is the film thickness), it is possible to consider the ring, of radius R, as a one-dimensional object and the strictly one-dimensional Eqs. (59) and (60), which model the dynamics of a ring with small width, have to be solved. The vector potential is equal to $A = HR/2$, where H is the applied magnetic field.

As shown in [68, 69] the transition of the superconducting ring from a state with vorticity $L = \oint \nabla\phi\,ds/2\pi$ (which in general can be a metastable state) to a state with a different vorticity occurs when the absolute value of the gauge-invariant momentum $\mathbf{p} = \nabla\phi - \mathbf{A}$ reaches the critical value

$$p_c = \frac{1}{\sqrt{3}}\sqrt{1 + \frac{1}{2R^2}} \quad (61)$$

For simplicity, consider that the magnetic field is increased from zero (with initial vorticity of the ring $L = 0$) to the critical H_c where p becomes equal to p_c (for $L = 0$ one has $H_c = 2p_c/R$). In this case $\mathbf{p} = -\mathbf{A}$ and Eq. (61) can be written as

$$\Phi_c/\Phi_0 = \frac{R}{\sqrt{3}}\sqrt{1 + \frac{1}{2R^2}} \quad (62)$$

For this value of the flux the thermodynamical equilibrium state becomes $L_{eq} = \mathrm{Int}(\Phi_c/\Phi_0)$. For example, if $R = 10\xi$ one finds $L_{eq} = 6$ (Fig. 47). The fundamental question one wants to answer is *What will be the actual value of the vorticity of the final state*? Will it be the thermodynamic equilibrium state or a metastable one? This answer is obtained from a numerical solution of the time-dependent Ginzburg–Landau equations.

In the numerical calculation Vodolazov et al. considered two different rings with radius $R = 10\xi$ and $R = 15\xi$. These values were chosen such that the final state exhibits several metastable states and, in principle, transitions can occur with jumps in L that are larger than unity. For $R = 10\xi$, ΔL may attain values between 1 and 6 and for $R = 15\xi$ it may range from 1 to 9. Smaller rings have a smaller range of possible ΔL values. They found that rings larger than $R = 15\xi$ did not lead to new effects. In their numerical simulations they increased H gradually from zero to a value $H_c + \Delta H$ (they took $\Delta H = 0.036H_c$ for $R = 10\xi$ and $\Delta H = 0.012H_c$ for $R = 15\xi$) during a time interval Δt, after which the magnetic field was kept constant. The magnetic field ΔH and time Δt range were chosen sufficiently large to speed up the initial time for the nucleation of the phase slip process but still
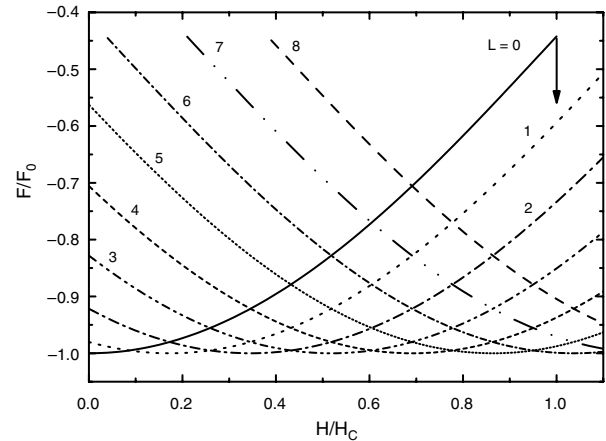
Figure 47. Dependence of the free energy of the one-dimensional ring (with $R = 10\xi$) on the applied magnetic field for different vorticity L. Reprinted with permission from [58], D. Y. Vodolazov and F. M. Peeters, *Phys. Rev. B* 66, 054537 (2002). © 2002, American Physical Society.
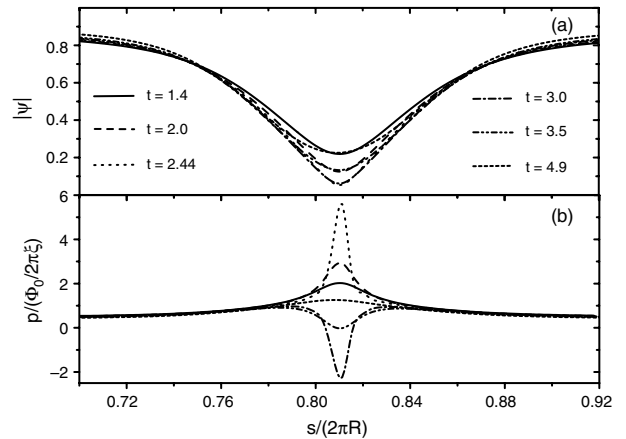
sufficiently small to model real experimental situations in which H is increased during a time much larger than $u \cdot \tau_{GL}$ (e.g., for Al $\tau_{GL}(T=0) \simeq 10^{-11}$ s). A change of ΔH and Δt, within realistic boundaries, did not have an influence on their final results.

Their detailed numerical analysis showed that the vorticity L of the final state of the ring depends on the value of u and is not necessarily equal to L_{eq}. The larger u is, the larger the vorticity after the transition. The final state is reached in the following manner. When the magnetic field increases, the order parameter decreases (inset of Fig. 48a). First, in a single point of the ring a local suppression of the order parameter occurs, which deepens gradually with time during the initial part of the development of the instability. This time scale is taken as the time in which the value of the order parameter decreases from 1 to 0.4 in its minimal point. When the order parameter reaches the value ~ 0.4 in its minimal point the process speeds up considerably and the order parameter starts to oscillate in time at this particular point of the ring (Fig. 48a). Also at the same time oscillatory behavior of the superconducting $j_s = \mathrm{Re}(\psi^*(-i\nabla - \mathbf{A})\psi)$

Figure 48. Dependence of the order parameter (a), the superconducting j_s (b), and the normal j_n (c) current density in the point where the minimal (thick curves) and the maximal (thin curves) values of the order parameter are reached as a function of time for $u = 3$, $R = 10$ (dotted curves), and $R = 15$ (solid curves). For both rings we took $\Delta t = 100$, the time interval over which the magnetic field is increased to its value H_c [inset of (a)]. Reprinted with permission from [58], D. Y. Vodolazov and F. M. Peeters, *Phys. Rev. B* 66, 054537 (2002). © 2002, American Physical Society.

(Fig. 48b) and the normal $j_n = -\nabla\varphi$ (Fig. 48c) current density is found at the point where the minimal value of the order parameter is found. At other places in the ring such oscillatory behavior is strongly damped (see, e.g., the thin curves in Figure 48). After some time the system evolves to a new stable state, which in the situation of Figure 48 is $L = 3$ for $R = 10$ and $L = 5$ for $R = 15\xi$.

In [58] the dependence of the dynamics of $|\psi|$ on u in the minimal point was also investigated. With increasing value of u it was found that (1) the number of phase slips (or equivalently the number of oscillations of the order parameter at its minimal point) increases and hence ΔL also increases, and (2) the amplitude of those oscillations decreases with increasing u.

The above results lead to the conclusion that in a superconducting ring there are two characteristic time scales. First, there is the relaxation time of the absolute value of the order parameter $\tau_{|\psi|}$. The second time scale is determined by the time between the phase slips (PSs), that is, the period of oscillation of the value of the order parameter in its minimal point. Below it is shown that the latter time is directly proportional to the time of change of the phase of the order parameter τ_ϕ and is connected to the relaxation time of the charge imbalance in the system.

In Figure 49 the distribution of the absolute value of the order parameter ψ and the gauge-invariant momentum p are shown near the point where the first PS occurs for a ring with radius $R = 10\xi$ and $u = 3$ at different times: just before and after the first PS which occurs at $t \simeq 2.7\tau_{GL}$. Before the moment of the phase slip the order parameter decreases while after the PS it increases. To understand this different behavior, Eq. (59) is rewritten separately for the absolute value $|\psi|$ and the phase ϕ of the order parameter

$$u\frac{\partial|\psi|}{\partial t} = \frac{\partial^2|\psi|}{\partial s^2} + |\psi|(1 - |\psi|^2 - p^2), \qquad (63)$$

$$\frac{\partial\phi}{\partial t} = -\varphi - \frac{1}{u|\psi|^2}\frac{\partial j_n}{\partial s}. \qquad (64)$$

Figure 49. Distribution of the absolute value of the order parameter (a) and gauge-invariant momentum (b) near the phase slip center at different moments of time for a ring of $R = 10\xi$ and with $u = 3$. The phase slip occurs at $t \simeq 2.7\tau_{GL}$. Reprinted with permission from [58], D. Y. Vodolazov and F. M. Peeters, *Phys. Rev. B* 66, 054537 (2002). © 2002, American Physical Society.

Here s is the arc coordinate along the ring, and we used the condition $\operatorname{div}(j_s + j_n) = 0$. It is obvious from Eq. (63) that if the right-hand side (RHS) of Eq. (63) is negative $|\psi|$ decreases in time and if the RHS is positive $|\psi|$ will increase in time. Because the second derivative of $|\psi|$ is always positive [at least near the phase slip center (Fig. 49a)] the different time dependence of $|\psi|$ is governed by the term $-p^2|\psi|$. From Figure 49b it is clear that after the phase slip the value of p is less than before this moment, with practically the same distribution of $|\psi|$. This fact is responsible for an increase of the order parameter just after the moment of the phase slip. But at some moment of time the momentum p can become sufficiently large, making the RHS of Eq. (63) negative and as a consequence $|\psi|$ starts to decrease.

Based on their numerical calculations they stated that for every value of the order parameter in the minimal point, there exists a critical value of the momentum $p_c^{\min}$ such that if the value of the momentum in this point is less than $p_c^{\min}$, the order parameter will increase in time. In the opposite case the order parameter decreases, which leads ultimately to the phase slip process. Therefore, after a phase slip p increases fast enough such that at some moment the condition $p^{\min} > p_c^{\min}$ is fulfilled, the order parameter will start to decrease, which leads then to a new phase slip process.

Vodolazov et al. [58] concluded that the change of p (or phase of the order parameter) with time and of $|\psi|$ with time has a different dependence on u. They found that with increasing u the time relaxation of $|\psi|$ becomes larger with respect to the relaxation time for p (e.g., the amplitude of the oscillations in $|\psi|$ decreases). Moreover, the relaxation time for p depends not only on u but also on the history of the system: the larger the number of phase slips which have occurred in the system the longer the time becomes between the next two subsequent phase slips. To understand such behavior one has to turn to Eq. (64).

Numerical analysis shows that the second term in the RHS of Eq. (64) is only important for some distance close to the PS center. This distance scale is nothing either than the length over which the electric field penetrates the superconductor. This can be checked directly by solving Eqs. (59) and (60) for this situation. But this length is the decay length λ_Q of the charge imbalance in the superconductor (see, e.g., [48, 67]). Numerically it is found that λ_Q varies with u (in the range $u = 1 - 100$) as $\lambda_Q \sim u^{-0.27}$, which means that the relaxation time of the charge imbalance is $\tau_Q \sim \lambda_Q^2 \sim u^{-0.54}$.

If we take the derivative $\partial/\partial s$ on both sides of Eq. (64) and integrate it over a distance of λ_Q near the PS center (far from it we have $j_n \sim 0$) we obtain the Josephson relation (in dimensionless units)

$$\frac{d\Delta\phi}{dt} = V \sim j_n(0)\lambda_Q \tag{65}$$

where $\Delta\phi = \phi(+\lambda_Q) - \phi(-\lambda_Q)$ is the phase difference over the PS center which leads to the voltage $V = -(\varphi(+\lambda_Q) - \varphi(-\lambda_Q))$ and where $j_n(0)$ is the normal current (or electric field in our units) in the point of the phase slip. From Eq. (65) it follows immediately that the relaxation time for the phase of the order parameter near the PS center is

$$\tau_\phi \sim \frac{1}{\lambda_Q \langle |j_n(0)| \rangle} \tag{66}$$

where $\langle \cdot \rangle$ means averaging over time between two consecutive phase slips. This result allows one to qualitatively explain the numerical results. Indeed, from Figure 48c it is apparent that $\langle |j_n(0)| \rangle$ decreases after each PS and as a result it leads to an increase of τ_ϕ. With increasing u, λ_Q decreases and τ_ϕ increases. Fitting the data (Fig. 50) leads to the dependencies $\tau_\phi \sim u^{0.21}$ and $\tau_\phi \sim u^{0.23}$ for rings with radius $R = 10\xi$ and $R = 15\xi$, respectively (here τ_ϕ was defined as the time between the first and the second PS). This is close to the expected dependencies that follow from Eq. (66) and from the above dependence of $\lambda_Q(u)$. In addition, Eq. (66) allows us to explain the decrease of τ_ϕ with increasing radius of the ring (see inset in Fig. 50). Namely, during the time between two PSs the gauge-invariant momentum decreases as $\Delta p \sim 1/R$ (because $\nabla\phi$ increases as $\sim 2\pi/2\pi R$) in the system. Far from the PS center the total current becomes practically equal to $j_s \sim p$. Because $\operatorname{div}(j_s + j_n) = 0$ in the ring, one finds directly that during this time the normal current density in the point of the PS also decreases as $\sim 1/R$. Taking into account Eq. (66) one can conclude that τ_ϕ should vary as $\sim 1/R$ (at least for a large radius and for the first PS). The behavior shown in the inset of Figure 50 is very close to such a dependence (it is interesting to note that in contrast to τ_ϕ the time $\tau_{|\psi|}$ is practically independent of R).

On the basis of their results Vodolazov et al. [58] made the following statement: when the period of oscillation (time of change of the phase of the order parameter) becomes of the order, or larger, than the relaxation time of the absolute value of the order parameter the next PS becomes impossible in the system.
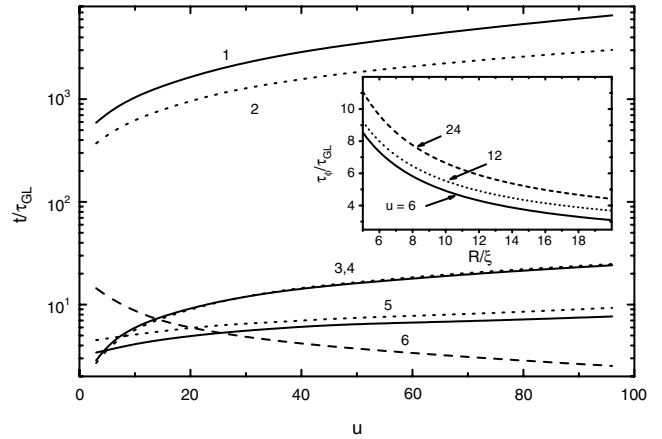
Figure 50. Dependence of the initial nucleation time t_0 (curves 1 and 2), the relaxation time of the order parameter $\tau_{|\psi|}$ (which for definiteness we defined as the time of variation of the order parameter from 0.4 until the first PS (curves 3 and 4), and the relaxation time of the phase of the order parameter τ_ϕ [we defined it here as the time between the first and second PS (curves 5 and 6)] are shown as function of the parameter u. Dotted (solid) curves are for a ring with radius $R = 10 (15)$. The dashed curve corresponds to the relaxation time of the charge imbalance (as obtained from the expression $\tau_Q = 5.79\lambda_Q^2$). In the inset, the dependence of τ_ϕ on the ring radius is shown for different values of the parameter u. Reprinted with permission from [58], D. Y. Vodolazov and F. M. Peeters, *Phys. Rev. B* 66, 054537 (2002). © 2002, American Physical Society.

Above it was found that the time scale governing the change in the phase does not coincide with the relaxation time of the absolute value of the order parameter. This difference is essentially connected with the presence of an electrostatic potential in the system. To demonstrate this the following numerical experiment was performed. Vodolazov et al. neglected φ in Eq. (59) and found that the number of PSs is now independent of u and R, and ΔL equals unity. Moreover, it turned out that the time scale t_0 is an order of magnitude larger. This clearly shows that the electrostatic potential is responsible for the appearance of a second characteristic time which results in the above mentioned effects.

In an earlier paper [68] the question of the selection of the metastable state was already discussed for the case of a superconducting ring. However, Tarlie and Elder neglected the effect of the electrostatic potential and found that transitions with $\Delta L > 1$ can occur only when the magnetic field (called the induced electromoving force (emf) in [68]) increases very quickly. In their case these transitions were connected to the appearance of several nodes in ψ along the perimeter of the ring and in each node a single PS occurred. Vodolazov et al. [58] reproduced those results and found such transitions also for larger values of ΔH. However, simple estimates show that to realize such a situation in practice it is necessary to have an extremely large ramp of the magnetic field. For example, for Al mesoscopic samples with $\xi(0) = 100$ nm and $R = 10\xi$ the corresponding ramp should be about 10^3–10^4 T/s. With such a ramp the induced normal currents in the ring are so large that heating effects will suppress superconductivity.

The transitions between the metastable states in the ring are not only determined by u and R, but also the presence of defects plays a crucial role. Their existence leads to a decrease of ΔL. This is mainly connected to the fact that with decreasing p_c (as a result of the presence of a defect) the value of $\langle |j_n(0)| \rangle$ decreases even at the moment of the first PS (because $\langle |j_n(0)| \rangle$ cannot be larger than $\langle |j_s(0)| \rangle \simeq p_c$) and hence τ_ϕ increases. This can also be explained in terms of decreasing degeneracy of the system. For example, if one decreases p_c with a factor of two (e.g., by the presence of defects) it leads to a twice smaller value for Φ_c and L_{eq}. But the numerical analysis of Vodolazov et al. showed that the effect of defects is not only restricted to a decrease of p_c and L_{eq}. To show this they simulated a defect by including another material with a smaller or zero T_c. This is done by inserting in the RHS of Eq. (59) an additional term $\rho(r)\psi$ where $\rho(r)$ is zero except inside the defect where $\rho(r) = \alpha < 0$. The magnetic field was increased up to H_c of the ideal ring case. It was found that the number of PSs was smaller compared with these for a ring without defects. The calculations were done for defects such that p_c was decreased by less than a factor of 2 in comparison to the ideal ring case. In contrast, a similar calculation for a ring with nonuniform thickness/width showed that, even for "weak" nonuniformity (which decreases p_c by less than 20%), ΔL was larger than for the ideal ring case and the final vorticity approaches L_{eq}. This remarkable difference between the situation for a defect and the case of a nonuniformity may be traced back to the difference in the distribution of the order parameter: even in the absence of an

external magnetic field the defect leads to a nonuniform distribution of the order parameter, which is not so for the nonuniform ring case.

11.2. Two-Dimensional Rings

The results of the previous section were based on a one-dimensional model that contains the essential physics of the decay and recovery of the superconducting state in a ring from a metastable state to its final state. However, even when the effect of the self-field can be neglected, the finite width of the ring may still lead to important additional effects (e.g., a finite critical magnetic field). To include the finite width of the ring into our calculation Vodolazov et al. [58] considered the following model. They took a ring of mean radius $R = 12\xi$, width 3.5ξ, and thickness less than ξ and λ. These parameters are close to those of the ring studied experimentally in [3] (see Section X) and they are such that the self-field of the ring can still be neglected. The magnetization curves obtained for such a ring are shown in Figure 51 as a function of the magnetic field and for two values of u. Those results were obtained from a numerical solution of the two-dimensional Ginzburg–Landau equations [Eqs. (59) and (60)]. The magnetic field was changed with steps ΔH over a time interval that is larger than the initial part of the phase slip process t_0.

From Figure 51 it can be noted that the value of the vorticity jumps, ΔL, depends sensitively on the parameter u. The PSs occur in one particular place along the perimeter of the ring. However, in contrast to the previous one-dimensional case, ΔL depends also on the applied magnetic field. The reason is that for a finite width ring the number of metastable states decreases with increasing magnetic field [70]. It means that the system cannot be moved far from equilibrium with a large superconducting current density (because the order parameter is strongly suppressed by the external field) at high magnetic field. Hence, the value
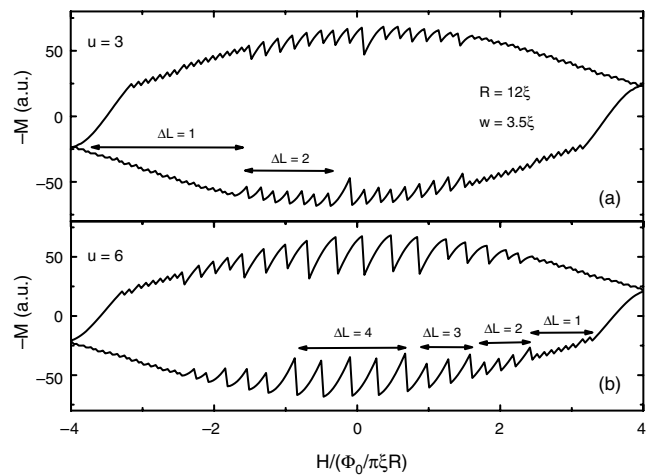
Figure 51. Dependence of the magnetization of a finite width ring on the external magnetic field for two values of the parameter u. The results are shown for a sweep up and sweep down of the magnetic field. Reprinted with permission from [58], D. Y. Vodolazov and F. M. Peeters, *Phys. Rev. B* 66, 054537 (2002). © 2002, American Physical Society.

of $\langle |j_n(0)|\rangle$ will be much smaller in comparison to the one at low magnetic fields, and τ_ϕ is larger or comparable with $\tau_{|\psi|}$ even for high values of u and even for the first PS. Thus, the effect of a large magnetic field for a finite width ring is similar in some respects to the effect of defects for a one-dimensional ring.

The numerical results are in *qualitative* agreement with the experimental results of Pedersen et al. [3] (see Fig. 41). Unfortunately, no *quantitative* comparison is possible because of a number of unknowns, for example, the value of p_c [it is necessary to have the dependence of $M(H)$ as obtained starting from zero magnetic field]; the value of ξ is not accurately known, and hence the ratio R/ξ can only be estimated. The values of both these parameters have a strong influence on the value of the vorticity jumps ΔL.

For the two-dimensional ring the modified critical momentum can be written as [57]:

$$ p_c = \frac{1}{\sqrt{3}} \sqrt{1 - \left(\frac{H}{H_{\max}}\right)^2 + \frac{1}{2R^2}} \tag{67} $$

Note that now p_c decreases with increasing magnetic field. This automatically leads to a decreasing value of the jump in the vorticity ΔL at high magnetic field, because in [58] it was shown that

$$ \Delta L_{\max} = \text{Nint}(p_c R) \tag{68} $$

where $\text{Nint}(x)$ is the nearest integer of x.

To check the validity of Eq. (67) a numerical simulation of the two-dimensional Ginzburg–Landau equations [Eqs. (59) and (60)], was performed for a ring with $R = 5.5\xi$ and $w = 1.5\xi$ (for these parameters the theoretical findings fit the experimental results of Geim et al. [57]). In Figure 52 the magnetization, the order parameter and the gauge-invariant momentum p are shown as function of the applied magnetic field. The magnetic field was cycled up and down from $H < -H_{\max}$ to $H > H_{\max}$. The condition (67) leads to an hysteresis of $M(H)$ and to a changing value of the jump in the vorticity in accordance with the change in p_c. The main difference between the theoretical prediction (67) and the results of the numerical calculations of Vodolazov et al. appears at fields close to $H_{\max}$. Apparently it is connected to the fact that for the considered ring the distribution of the order parameter along the width of the ring is appreciably nonuniform at $H \simeq H_{\max}$ and as a consequence the one-dimensional model breaks down.

Finally, Vodolazov et al. also considered the same ring with a defect. The effect of the defect was modelled by introducing in the RHS of Eq. (59) the term $-\rho(s)\psi$ (s is the arc coordinate) where $\rho(s) = -1$ inside the defect region with size ξ and $\rho(s) = 0$ outside. This leads to the results shown in Figure 53 for $M(H)$, $|\psi|(H)$, and $p(H)$. Due to the presence of the defect, p_c already differs from Eq. (67) at low magnetic field [$p_c(H = 0) \simeq 0.33$ at given "strength" of the defect] and as a result only jumps with $\Delta L = 1$ are possible in such a ring. In this case the p_c and $|\psi|$ also depend on the applied magnetic field with practically the same functional dependence on H as Eq. (67).

The numerical results of Vodolazov et al. can be compared to the experimental results of Geim et al. [57].
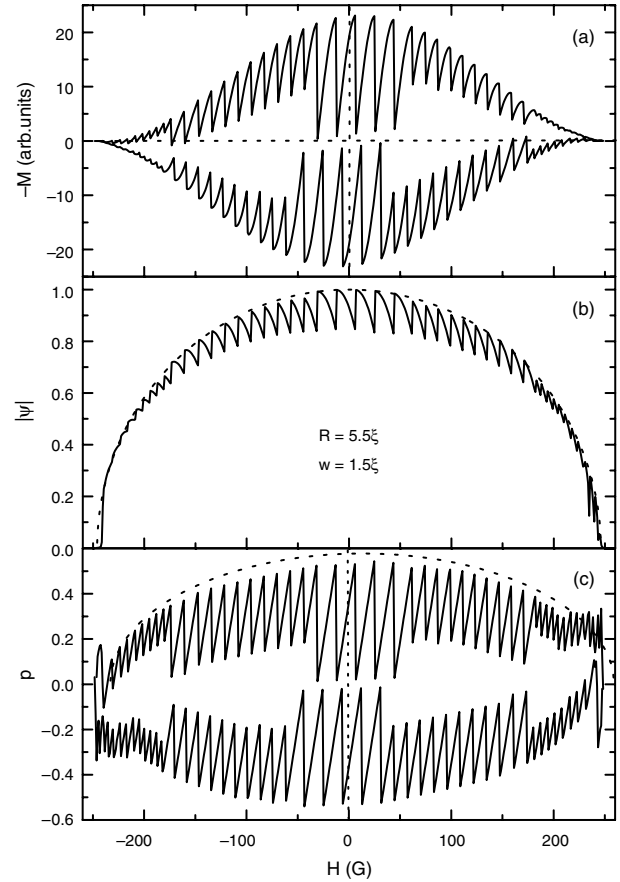
Figure 52. Magnetic field dependence of the magnetization (a), the order parameter (b), and the gauge invariant momentum (c) in the middle of the ring. Dotted curve in (b) is the expression $\sqrt{1 - (H/H_{\max})^2}$. The dotted curve in (c) is the expression $\sqrt{1 - ((H - H_0)/H_{\max})^2}/\sqrt{3}$, where $H_0 \simeq 13G$ is the displacement of the maximum of $M(H)$ from the $H = 0$ line. Reprinted with permission from [57], D. Y. Vodolazov et al., *Phys. Rev. B* 67, 054506 (2003). © 2003, American Physical Society.

Figures 52a and 45a are qualitatively very similar. For example, the theory describes: (1) the hysteresis; (2) the nonunity of the vorticity jumps, that is, $\Delta L = 3$ in the low magnetic field region, $\Delta L = 2$ in the intermediate H region, and $\Delta L = 1$ near $H_{\max}$ [theoretically (experimentally) one found 6(5), 13(21), and 22(18) jumps with respectively, $\Delta L = 3$, 2, and 1]; and (3) the nonsymmetric magnetization near $\pm H_{\max}$ for a magnetic field sweep up and down.

In the ring with approximately the same mean radii and width but containing an intentionally introduced artificial defect, jumps with $\Delta L = 1$ are mostly observed (see Fig. 45b). The reason is that an artificial defect considerably decreases the critical value p_c (and hence the field H_{en}; see dotted curve in Fig. 46). From Figures 52(c) and 53(c) it is clear that the maximum value $p_c^{id} \simeq 0.54$ for a ring without a defect and $p_c^d \simeq 0.35$ for a ring with a defect. The ratio $p_c^d/p_c^{id} \simeq 0.65$ is close to the ratio of the field of the first vortex entry $H_{en}^d/H_{en}^{id} \simeq 0.67$ obtained from experiment (see Fig. 46). From Figure 52c it is easy to see that for a ring without a defect at $p \simeq 0.35$ there are only jumps with $\Delta L = 1$. But if we slightly increase p then jumps with $\Delta L = 2$ can appear in the system. So one can conclude that $p = 0.35$ is
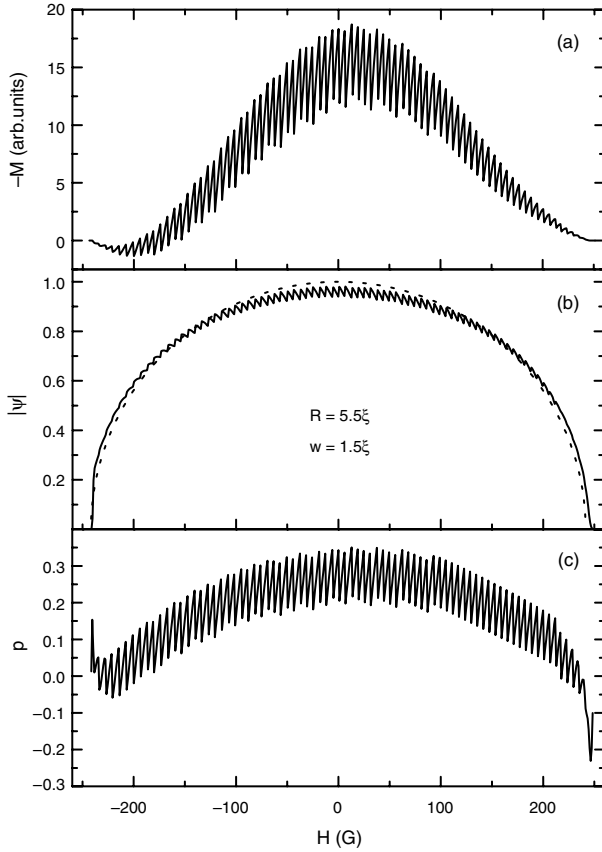
Figure 53. Magnetic field dependence of the magnetization (a), the order parameter (b), and the gauge invariant momentum (c) (in the middle of the ring) of a ring containing one defect. The dotted line in (b) is the expression $\sqrt{1 - (H/H_{max})^2}$. Reprinted with permission from [57], D. Y. Vodolazov et al., *Phys. Rev. B* 67, 054506 (2003). © 2003, American Physical Society.

close to the border value that separates regimes with jumps in vorticity of $\Delta L = 1$ and $\Delta L = 2$. Thermal fluctuations may influence the value of ΔL and in particular for a p_c value close to this border value. This is probably the reason why in the experiment (Fig. 45b) occasional jumps with $\Delta L = 2$ are observed, which are absent in the simulation (Fig. 53a).

12. PHASE SLIP STATES

The nonuniform superconducting state in a ring in which the order parameter vanishes at one point is called the phase slip state. This state is characterized by a jump of the phase by π at the point where the order parameter becomes zero. In uniform rings such a state is a saddle-point state and consequently unstable. However, for nonuniform rings with, for example, variations of geometrical or physical parameters or with attached wires, this state can be stabilized and may be realized experimentally.

In recent years [70–72] the existence of a single-connected state in a ring was proposed theoretically. Such a state implies that the relation between the phase ϕ of the order parameter $\psi = f e^{i\phi}$, the current density j, and the magnetic

flux Φ through the ring (which follows from the single valuedness of ψ; see, [73]),

$$\oint \frac{j}{f^2} \, ds = 2\pi n - \Phi \tag{69}$$

is no longer valid (the flux is expressed in $\Phi_0/2\pi$ and the current density in $j_0 = c\Phi_0/4\pi^2\lambda^2\xi$; λ is the London penetration length, ξ is the coherence length, and Φ_0 is the quantum of magnetic flux). The reason is that the order parameter in such a single-connected state is zero at one point. Moreover, it was claimed that under certain conditions, that is, radius of the ring less than ξ and the flux through the ring of about $(n + 1/2)\Phi_0$, this state may become metastable in some range of magnetic fields [73].

Together with Vodolazov we revisited this problem [75] and we showed that a state where the order parameter vanishes in one point is still double-connected and that Eq. (69) remains valid for such a state. We propose to call such a state a one-dimensional vortex state (ODV state), because like for an ordinary 2D Abrikosov vortex, there is a jump in the phase of the order parameter of π at the point where $\psi = 0$. In contrast to a 2D Abrikosov vortex the ODV is an unstable structure in an uniform ring. However, if some inhomogeneities are present in the ring (defects, nonuniform thickness or nonuniform width of the ring, on attached superconducting wires) the ODV structure can be stabilized and may consequently be realized experimentally.

Consider a ring with thickness $d \lesssim \lambda$ and width $w \lesssim \xi$. In addition, let the radius of the ring R be much larger than w. Under these conditions we can neglect the screening effects and the problem is reduced to a one-dimensional one. The distribution of the current density j and the order parameter ψ of the system at a temperature not far from the critical temperature T_c is described by the one-dimensional Ginzburg–Landau equation (plus the condition div**j** = 0)

$$\frac{d^2 f}{ds^2} + f(1 - f^2 - p^2) = 0 \tag{70}$$

$$\frac{dj}{ds} = \frac{d}{ds} f^2 p = 0 \tag{71}$$

where the gauge-invariant momentum $p = \nabla\phi - A$ is scaled in units of $\Phi_0/(2\pi\xi)$, the length of the ring is $L = 2\pi R$, and the circular coordinate s is in units of the coherence length ξ. In these units, the magnetic field is scaled in units of the second critical field, H_{c2}, and the magnetic flux in $\Phi_0/2\pi$.

The coupled Eqs. (70) and (71) have to be solved with the boundary condition $\psi(-L/2) = \psi(L/2)$. We use the method proposed in [76] (see also [55]). These equations have the first integral

$$\frac{1}{2}\left(\frac{df}{ds}\right)^2 + \frac{f^2}{2} - \frac{f^4}{4} + \frac{j^2}{2f^2} = E \tag{72}$$

From a formal point of view, Eq. (72) is nothing other than the condition of conservation of energy for some "particle" with "coordinate" f and "momentum" j. The role of "time" is played [76] by the circular coordinate s. In

Figure 54 we show the dependence of the "potential energy" of this system

$$U(f) = \frac{f^2}{2} - \frac{f^4}{4} + \frac{j^2}{2f^2} \qquad (73)$$

for different values of j. Possible solutions of Eqs. (70) and (71) are in the region where confined "trajectories" of our virtual particle exist. This is possible for currents $0 < j \leq j_c$ ($j_c = \sqrt{4/27}j_0$ is the depairing current density).

Using Eq. (72) we can immediately write the solution of Eqs. (70) and (71) for the ring

$$\sqrt{2}s = \int_{t_0}^{t} \frac{dt}{\sqrt{(t - t_0)(t_1 - t_0)(t_2 - t_0)}}$$

$$= \frac{2}{\sqrt{t_2 - t_0}} F\left(\sin^{-1}\sqrt{\frac{t - t_0}{t_1 - t_0}}, \sqrt{\frac{t_1 - t_0}{t_2 - t_0}}\right) \qquad (74)$$

where $t(s) = f^2(s)$, $F(\theta, m)$ is the elliptic integral of the first kind and $t_0 \leq t_1 \leq t_2$ are the solutions of the cubic equation

$$t^3 - 2t^2 + 4Et - 2j^2 = 0 \qquad (75)$$

Using the boundary condition for f we may conclude that for a given current there exist a maximum number of three solutions. There are two uniform solutions [in the points of the minimum $E = E_{min}$ and the maximum $E = E_{max}$ of the "potential energy" (73)] and one nonuniform solution with energy $E_{min} < E < E_{max}$, which is defined by the equation

$$L = \sqrt{\frac{8}{t_2 - t_0}} K\left(\sqrt{\frac{t_1 - t_0}{t_2 - t_0}}\right) \qquad (76)$$

where $K(m)$ is the complete elliptic integral of the first kind. Numerical analysis of Eq. (76) for $0 < j < j_c$ shows that there is a minimal value for the ring length L_{min} for which there exists a solution for this equation. When $j \to j_c$, $L_{min} \to \infty$ and in the opposite limit $j \to 0$ one can show that $L_{min} \to \pi$. The latter corresponds to a ring radius
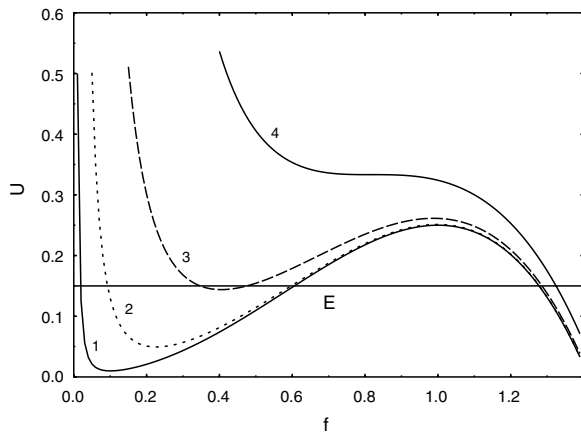
Figure 54. Dependence of the "potential energy" $U(f)$ for different values of the current j: (1) $j = 0.01$, (2) $j = 0.05$, (3) $j = 0.15$, and (4) $j = j_c = \sqrt{4/27}$. Reprinted with permission from [75], D. Y. Vodolazov et al., *Phys. Rev. B* 66, 054543 (2002). © 2002, American Physical Society.

$R = 1/2$ (or $\xi/2$ in dimensional units). For a radius $R > 1/2$ metastable states may exist and superconductivity is present for any value of the magnetic flux (at least in our one-dimensional model) [73, 77].

In principle, Eqs. (74)–(76) define the nonuniform solution of Eqs. (70) and (71) for a ring. Unfortunately, even using the explicit Kordano expressions for the roots of Eq. (75) the results are rather complicated for arbitrary values of the current j. However a tractable analytical solution is possible if we consider the case for low currents $j \ll 1$ for which the roots of Eq. (75) are simplified to

$$t_0 \simeq j^2/2E, \qquad (77)$$

$$t_1 \simeq 1 - \sqrt{1 - 4E} \qquad (78)$$

$$t_2 \simeq 1 + \sqrt{1 - 4E} \qquad (79)$$

After inserting these results into Eq. (76) we obtain the "energy." For $L \gg \pi$ the "energy" $E \simeq 1/4$ is practically independent of L [e.g., for $L = 8$ the difference $1/4 - E(L = 8)$ is less than 0.002]. Also in the limit $L - \pi \ll 1$ we found that the "energy" E is independent of j

$$E(L) \simeq \frac{1}{2}\left(\frac{L - \pi}{\pi/8}\right)^2 \qquad (80)$$

In the limit $j \ll 1$ we can also find the dependence of $t(s)$ near the minimum point of $t(s)$

$$t(s) = 2j^2 + s^2/2, \qquad L \gg \pi, \quad s \ll 1 \qquad (81)$$

$$t(s) = j^2/2E + 2Es^2, \qquad L - \pi \ll 1, \quad s \ll 1 \qquad (82)$$

Using Eqs. (81) and (82) it is easy to show that in the limit $j \to 0$ the gauge-invariant momentum is given by

$$p(s) = j/t(s) = \frac{j}{|j|}(\pi + 2\pi m)\delta(s) \qquad (83)$$

where $\delta(s)$ is the Dirac delta function and m is an integer. As a result the integral

$$\lim_{j \to 0} \oint \frac{j}{f^2} ds = \lim_{j \to 0} \oint p(s) ds$$

$$= \phi(+\epsilon) - \phi(-\epsilon) = \Delta\phi = \pm(\pi + 2\pi m) \qquad (84)$$

for arbitrary ring size. Combining Eq. (84) with Eq. (69) it is easy to show that if $\Phi = (k + 1/2)\phi_0$ (k is an integer) a solution of Eq. (70) can be found which vanishes at one point.

In previous studies of this state [71–73], Eq. (83) was not taken into account (only the absolute value of the order parameter was found). Furthermore, in [73] it was claimed that for small rings there is a magnetic field region in which such a state exists and is metastable. But we find that in this region this state even does not exist (except in one point) because Eq. (69) is not fulfilled!

The distribution of the order parameter as obtained in [75] may also be applied to a ring in which some part of the ring consists of a normal metal. Then at the boundary between the normal metal and the superconductor the condition $\psi \simeq 0$ is fulfilled (if the normal part is longer than ξ)

and the distribution of the density $|\psi(s)|^2$ coincides with the one obtained in [73] (but the phase $\phi(s)$ will be different for our previous ring geometry). Besides we cannot call such a state single-connected as in [71–73] because the relation (69) is valid even for this case. Therefore, it is better to call this state a ODV state because like the 2D Abrikosov vortex there is a point where $|\psi| = 0$ and the phase of the order parameter exhibits a jump equal to $k\pi$ (as the Abrikosov vortex with orbital momentum $2\pi k$). A numerical calculation shows that, as in the case for an ordinary Abrikosov vortex in superconductors where such a state is stable, the phase jump is always equal to π; that is, $k = 1$.

The numerical analysis of the time-dependent Ginzburg–Landau equations showed that this state is unstable for a uniform ring. However for rings with nonuniform width (thickness) or attached wires a nonuniform distribution of the order parameter becomes possible [71, 72, 78, 79] and for small rings with $L \sim \pi$ this state is realized in practice (besides for the case of a ring, a ODV state can also exist in the Wheatstone bridge [80, 81]). In Figure 55 the distribution of the absolute value and the phase of the order parameter is shown for different values of the magnetic field for a nonuniform ring. We used the model of [71] in which

the width of the ring was varied as

$$w(s) = 1 + w_0 \sin\left(\frac{2\pi s}{L}\right) \tag{85}$$

The parameters used are $w_0 = 0.1$ and $L = 3.25$. It is seen that with increasing magnetic flux the magnitude of the order parameter f decreases in the thinner part of the ring (at $s/L = 3/4$) and becomes zero when $\Phi/\Phi_0 = 1/2$. In [72] it was found that the ODV state is only possible at $\Phi = (n + 1/2)\Phi_0$. The reason is now clear—only at this value of the magnetic flux were the phase difference near the point where the order parameter is zero be compensated for by the term $2\pi n - \Phi$ and the current density will be equal to zero. It is interesting to note that the current density is also zero for $\Phi = n\Phi_0$ even in the case of a nonuniform ring, but for values of the flux where the ODV state does not exist. At these values of the magnetic flux the order parameter is uniform along the ring and the term $2\pi n$ is completely compensated for by the term Φ in Eq. (69).

Above we showed that the ODV state can be realized by varying the geometrical parameters of the ring. But there are two alternative experimental approaches to realize the ODV state in the ring. First, it is possible to include an other phase in the ring. This leads to the appearance of a weak link in the sample and if the radius of the ring is less than some critical value (about ξ) it also leads to the existence of the ODV state in the ring at $\Phi = (n + 1/2)\Phi_0$. We modeled this situation by introducing an additional term $\rho(s)f$ in Eq. (70), and, as an example, we took $\rho(s) = -\alpha\delta(s)$ and $\alpha = 1$ (it should be noted that qualitatively the results do not depend on the specific value of α). We will not present the numerical results of the modified Ginzburg–Landau equations, but we found that they are qualitatively similar to the behavior of f and ϕ shown in Figure 56. When approaching the flux $\Phi = (n + 1/2)\Phi_0$ the order parameter reaches zero in the defect point and a jump in the phase equal to π occurs. Secondly, such a ODV state should also appear in small rings with attached wire(s). As was shown in [78, 79] an attached wire leads to a nonuniform distribution of the order parameter in the ring. In Figure 56 the dependence of the current j in such a ring on the flux through the ring is shown (see also [79]). As for nonuniform rings, where the parameters chosen such that the ODV state may exist, there is no hysteresis in such a system [72]. In addition, for rings with an attached wire the dependence $dj/d\Phi$ on Φ has two maxima in the range $(0, 1)$ for small L in contrast to the case for nonuniform rings (see [72]).

Small inhomogeneities in rings give us the unique possibility to study states close to the ODV state because there is no sharp transition from the state with finite order parameter to a state with vanishing order parameter at one point (see Fig. 55). The latter is, in some sense, a "frozen" slip phase state. A small variation of the flux through the ring near $\Phi = \Phi_0/2$ leads to a change of $\Delta\phi$ by 2π (from $-\pi$ to $+\pi$ with a concomitant change of the current from -0 to $+0$; see Fig. 55b). As a result an additional phase circulation $\oint \nabla\phi ds = 2\pi$ appears in the system, not because the magnetic flux Φ is changed, but because the term $\oint j/f^2 ds$ changes from $-\pi$ to $+\pi$ [see Eq. (69)]. When such a jump occurs $\nabla\phi$ does not change in the ring, except near the point
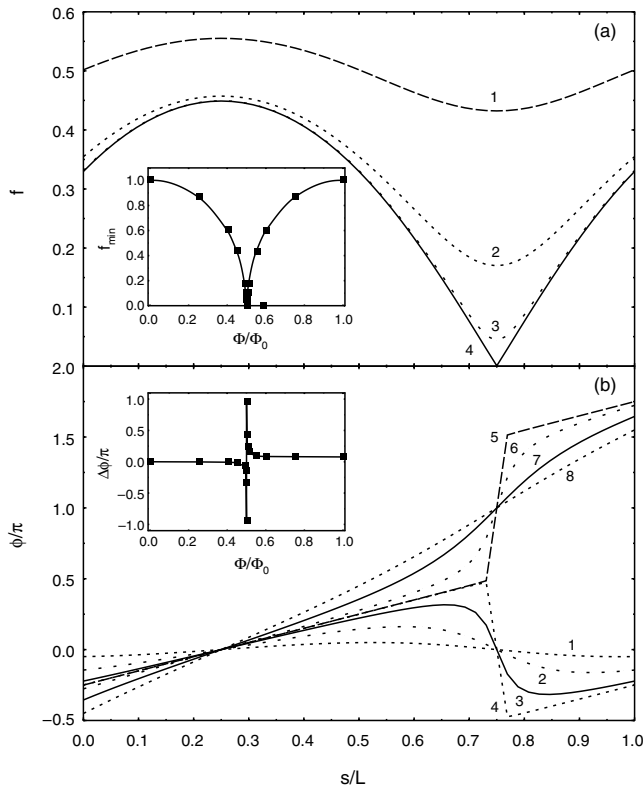
Figure 55. Distribution of the absolute value (a) and phase (b) of the order parameter at different values of the magnetic flux: (1) $\Phi = 0.45\Phi_0$, (2) $\Phi = 0.49\Phi_0$, (3) $\Phi = 0.498\Phi_0$, (4) $\Phi = (0.5 - 0)\Phi_0$, (5) $\Phi = (0.5 + 0)\Phi_0$, (6) $\Phi = 0.502\Phi_0$, (7) $\Phi = 0.51\Phi_0$, and (8) $\Phi = 0.55\Phi_0$. Note that the order parameter for $\Phi = \Phi_0/2 + \alpha$ is the same as that for $\Phi = \Phi_0/2 - \alpha$ when $\alpha < \Phi_0/2$. In the insets (a) f_{min} and (b) the phase difference $\Delta\phi$ near the point $s/L = 3/4$ are shown as a function of Φ. Reprinted with permission from [75], D. Y. Vodolazov et al., *Phys. Rev. B* 66, 054543 (2002). © 2002, American Physical Society.
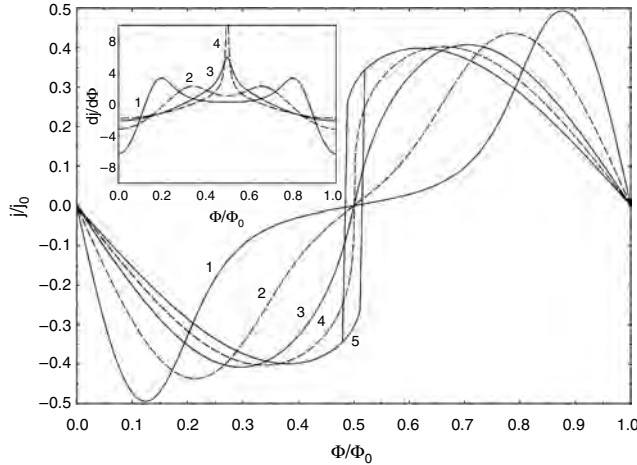
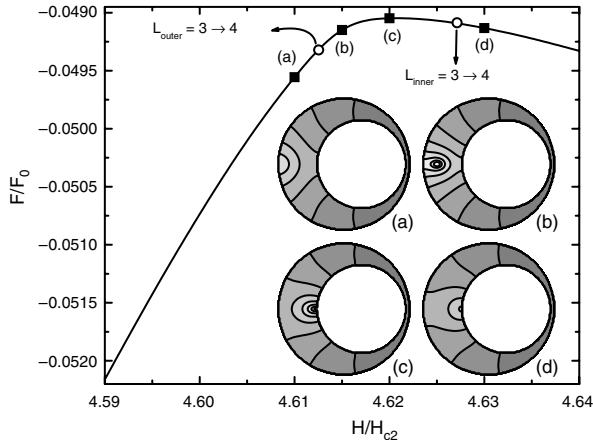**Figure 56.** The current in the ring as a function of the flux. The different curves are for different circumference of the ring: (1) $L = 1$, (2) $L = 2$, (3) $L = 3$, (4) $L = 3.5$, and (5) $L = 4$. For $L = 4$ the ODV state does not exist in the ring and hysteresis appears. In the inset the dependence of $dj/d\Phi$ on the flux Φ is shown for rings with lengths $L = 1, 2, 3$, and 3.5 (curves 1, 2, 3, and 4, respectively). Note that there are two maxima in the range $(0, 1)$. With increasing length the two maxima merge into one and when one approaches the critical length $dj/d\Phi$ diverge at $\Phi = \Phi_0/2$. Reprinted with permission from [75], D. Y. Vodolazov et al., *Phys. Rev. B* 66, 054543 (2002). © 2002, American Physical Society.

where $f = 0$, and as a result the current density in the system changes continuously. In the usual case transitions of the vorticity from a state with phase circulation $2\pi n$ to a state with phase circulation $2\pi(n + 1)$ leads to a jump in the current *everywhere* in the ring because $\oint \nabla \phi\, ds$ changes by 2π and the order parameter and the current density are finite *everywhere* in the system.

To supplement the above study we also made a numerical study of a nonuniform ring of finite width and thickness by implementing our previous finite difference solution of the coupled nonlinear Ginzburg–Landau equations [52]. As an example we took the following parameters: outer radius of the ring $R_o = 2\xi$, radius of the hole $R_i = 1.5\xi$, displacement of the hole from the center $a = 0.4\xi$, ring thickness $d = 0.001\xi$, and Ginzburg–Landau parameter $\kappa = 2$. In Figure 57 the dependence of the Gibbs free energy F and the magnetization $M = -\partial F/\partial H$ of this system on the magnetic field are shown. As in the case of our one-dimensional ring these dependencies are reversible, and there are magnetic fields at which the magnetization is equal to zero (at these points the free energy has a local maximum). We found that the distribution of the order parameter and the phase in the ring (see inset of Fig. 58) is similar to analogous distributions for the above one-dimensional ring (Fig. 55) at low magnetic fields. However, a difference with the one-dimensional system is that the phase circulation increase of 2π [between points (2) and (3) in Fig. 58] does not occur at the magnetic field value where the free energy has a local maximum (and zero magnetization). With decreasing width of the ring this point shifts toward the local maximum in the free energy.

It is interesting to note that for the system corresponding to Figure 57 the vortex enters through the thinnest part
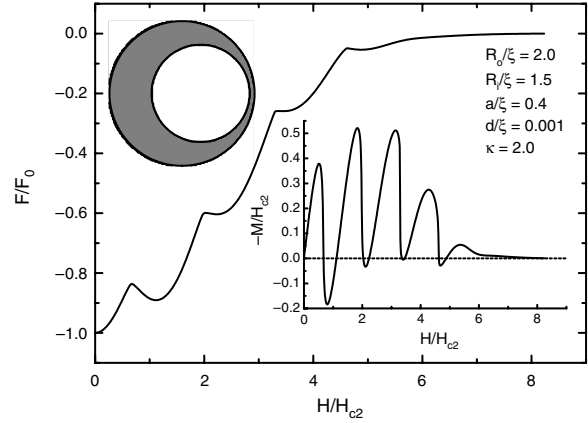
Figure 57. The Gibbs free energy and the magnetization (right lower inset) of the asymmetric ring (upper inset) as function of the applied magnetic field. Reprinted with permission from [75], D. Y. Vodolazov et al., *Phys. Rev. B* 66, 054543 (2002). © 2002, American Physical Society.

of the ring for the first three maxima in the free energy while for the highest magnetic field maxima (i.e., $H/H_{c2} \simeq 4.6$) the vortex enters through the thickest part of the ring (see Fig. 59). Because the width of the thicker part of the ring ($=0.9\xi$) is considerable larger than that of the thinner part ($=0.1\xi$) and is of order ξ, the ODV for $H/H_{c2} \simeq 4.6$ becomes the usual two-dimensional vortex. As a result the order parameter is equal to zero only in one point along the radial coordinate and the circulation of the phase of the order parameter now is also a function of this coordinate (see Fig. 59). When the vortex enters/exits the ring at low magnetic fields there is also a slow dependence of the order parameter on the radial coordinate along the thinnest part of the ring. Therefore, we can conclude that in a ring with finite width the one-dimensional vortex is transformed into the usual two-dimensional vortex.
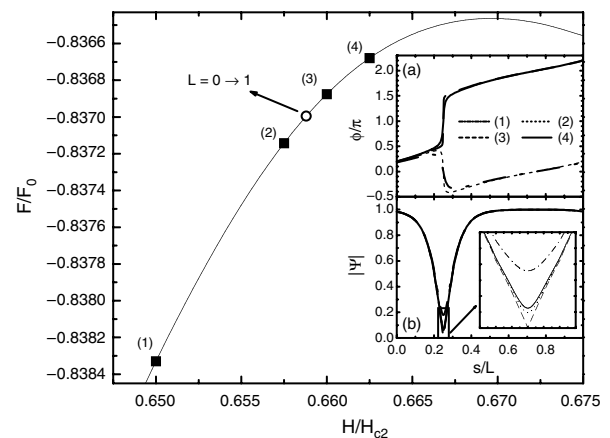
Figure 58. The Gibbs free energy $F(H)$ near the first maximum. In the inset the phase and the order parameter distribution at different values of the applied magnetic field [indicated by the squares on the $F(H)$ curve] are shown. The phase was calculated along the outer perimeter of the ring. The open circle on $F(H)$ indicates the position at which the vorticity increases from 0 to 1. Reprinted with permission from [75], D. Y. Vodolazov et al., *Phys. Rev. B* 66, 054543 (2002). © 2002, American Physical Society.

The process of the appearance of a stable vortex in a ring with finite width is similar to the creation of a phase slip in wires of finite width in the presence of a transport current. In the latter case the distribution of the gauge-invariant momentum is not exactly uniform over the wire width. The maximum value of p is obtained at the edges and as a result the order parameter vanishes first in these points. When a phase slip is created the distribution of the order parameter is not uniform over the width. With decreasing wire width this nonuniformity decreases, but it will be uniform, strictly speaking, only in the limit $w \to 0$. With increasing wire width the phase slip transforms to the ordinary process of vortex/antivortex pair nucleating at the edges, penetrating deep into the superconductor and annihilating. In nonuniform rings the distribution of p over the width is nonuniform and in contrast to wires with transport current, it is nonsymmetric with respect to the ring width. Suppression of the order parameter first occurs only on the outer side (when increasing the magnetic field) or on the inner side (when the magnetic field is decreasing). As in the case of an one-dimensional ring we may call this state a stable ("frozen") phase slip state if the width of the ring, where the vortex penetrates, is less than ξ.

The ODV state of a nonuniform ring is very similar to the saddle-point state as found in [52] for a uniform ring of finite width and in [8] for the case of a disk. Note that for an uniform ring with zero width the nonuniform solution [Eq. (75)] corresponds to a saddle point of $F(\psi)$. In Figure 60 the gradual decrease of the hysteresis with increasing displacement a of the hole from the center of the ring is shown. It is seen that with increasing a the region where metastable states exist decreases and ultimately vanishes for some critical displacement a_c. The saddle point states (only shown for $a = 0$, by the thin full curve) approach the stable phase slip state when $a = a_c$.

In [39] nonuniform superconducting rings of finite width were also investigated, but with a larger ring radius (see also
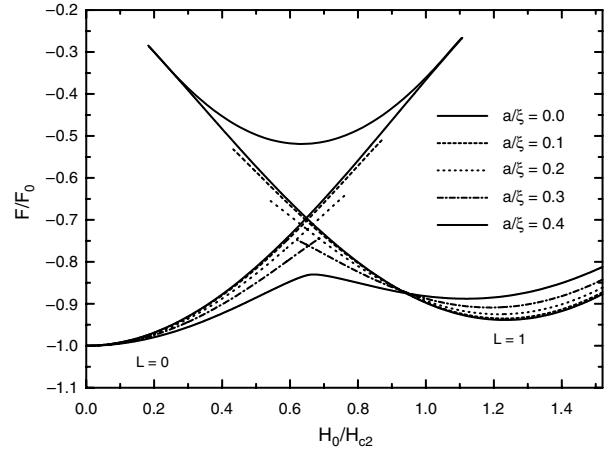
Section 8). It was found that for low magnetic fields $F(H)$ is irreversible but for high magnetic fields the dependence $F(H)$ was reversible. In high fields the transition from a state with vorticity one to another state occurred through the same scenario as discussed above. A similar state was also considered in [82, 83] in the framework of the linearized Ginzburg–Landau equations for a nonuniform ring of finite width. In such a system the vortex may be stable in some magnetic field region. In [83] analytical results for the magnetic field ranges where the vortex enter through the thinner part of the ring and through the thicker part were obtained. Our calculations generalize this result to lower temperatures (i.e., where the nonlinear Ginzburg–Landau equations have to be used) and with inclusion of the nonzero demagnetization factor of the ring. We found dependence of the Gibbs free energy (and magnetization) of this sample on the applied magnetic field. Our results also allowed us to compare the results of the one-dimensional model with the full two-dimensional one.

The ODV (or stable phase slip) state may be observed by magnetic experiments. Magnetic susceptibility is proportional [55] to $dj/d\Phi$ and the ODV state exhibits some characteristic peculiarities as was shown in the inset of Figure 56. Magnetization M is proportional to the current j and hence $M(H)$ is reversible, for samples where the ODV state exists (see Fig. 56 and inset of Fig. 58). Furthermore $M = 0$ at $\Phi \simeq (n+1/2)\Phi_0$. Alternatively, because at $\Phi = (n+1/2)\Phi_0$ there is a point in the ring where the order parameter is equal to zero, this state may be found by transport measurements. For example, in [84] the dependence of the resistance of a hollow cylinder with radius of order ξ was studied at temperature $T < T_c$ far from T_c. At $\Phi = \Phi_0/2$ the resistance (R) exhibited a maximum but the value of R was a factor of 3 less than the normal state resistance R_n. If the cylinder has a nonuniform thickness the ODV state can be realized as a stable state when $\Phi = \Phi_0/2$, and it will lead to a resistive (but superconducting) state even for very small currents and naturally the resistance of such a state will be less than R_n as was found by Liu et al. [84].

GLOSSARY

Giant vortex state State in which all the vortices are combined in the center into one big vortex corresponding with one minimum in the Cooper pair density.

Mesoscopic superconductors Superconductors with sizes comparable to the coherence length and the penetration depth.

Multivortex state State in which all the vortices are separated from each other.

Phase slip center The point in a quasi-one dimensional (with cross-section less than ξ) superconductor where a jump by 2π in the phase occurs when the order parameter becomes equal zero. The appearance of a phase slip center in superconducting wires with transport current leads to a finite resistivity of the sample.

ACKNOWLEDGMENTS

REFERENCES

1. A. K. Geim, I. V. Grigorieva, S. V. Dubonos, J. G. S. Lok, J. C. Maan, A. E. Filippov, and F. M. Peeters, *Nature* (*London*) 390, 256 (1997).
2. O. Buisson, P. Gandit, R. Rammal, Y. Y. Wang, and B. Pannetier, *Phys. Lett. A* 150, 36 (1990).
3. S. Pedersen, G. R. Kofod, J. C. Hollingbery, C. B. Sørensen, and P. E. Lindelof, *Phys. Rev. B* 64, 104522 (2001).
4. R. Benoist and W. Zwerger, *Z. Phys. B* 103, 377 (1997).
5. J. J. Palacios, *Physica B* 256–258, 610 (1998).
6. J. J. Palacios, *Phys. Rev. B* 58, R5948 (1998).
7. J. J. Palacios, *Phys. Rev. Lett.* 84, 1796 (2000).
8. V. A. Schweigert and F. M. Peeters, *Phys. Rev. Lett.* 83, 2409 (1999).
9. S. V. Yampolskii and F. M. Peeters, *Phys. Rev. B* 62, 9663 (2000).
10. E. Akkermans, D. M. Gangardt, and K. Mallick, *Phys. Rev. B* 62, 12427 (2000).
11. E. Akkermans and K. Mallick, *Physica C* 332, 250 (2000).
12. E. Akkermans and K. Mallick, *J. Phys. A* 32, 7133 (1999).
13. P. Singha Deo, V. A. Schweigert, F. M. Peeters, and A. K. Geim, *Phys. Rev. Lett.* 79, 4653 (1997).
14. P. Singha Deo, F. M. Peeters, and V. A. Schweigert, *Supperlattice Microstruct.* 25, 1195 (1999).
15. V. A. Schweigert and F. M. Peeters, *Phys. Rev. B* 57, 13817 (1998).
16. V. A. Schweigert, F. M. Peeters, and P. Singha Deo, *Phys. Rev. Lett.* 81, 2783 (1998).
17. V. A. Schweigert and F. M. Peeters, *Physica C* 332, 426 (2000).
18. V. A. Schweigert and F. M. Peeters, *Phys. Rev. B* 60, 3084 (1999).
19. V. V. Moshchalkov, L. Gielen, C. Strunk, R. Jonckheere, X. Qiu, C. Van Haesendonck, and Y. Bruynseraede, *Nature* (*London*) 373, 319 (1995).
20. V. Bruyndoncx, J. G. Rodrigo, T. Puig, L. Van Look, V. V. Moshchalkov, and R. Jonckheere, *Phys. Rev. B* 60, 4285 (1999).
21. H. T. Jadallah, J. Rubinstein, and P. Sternberg, *Phys. Rev. Lett.* 82, 2935 (1999).
22. L. F. Chibotaru, A. Ceulemans, V. Bruyndoncx and V. V. Moshchalkov, *Nature* (*London*) 408, 833 (2000).
23. L. F. Chibotaru, A. Ceulemans, V. Bruyndoncx, and V. V. Moshchalkov, *Phys. Rev. Lett.* 86, 1323 (2001).
24. J. Bonča and V. V. Kabanov, *Phys. Rev. B* 65, 012509 (2002).
25. B. J. Baelus and F. M. Peeters, *Phys. Rev. B* 65, 104515 (2002).
26. V. R. Misko, V. M. Fomin, J. T. Devreese, and V. V. Moshchalkov, *Physica C* 369, 361 (2002).
27. V. R. Misko, V. M. Fomin, J. T. Devreese, and V. V. Moshchalkov, *Phys. Rev. Lett.* 90, 147003 (2003).
28. V. L. Ginzburg and L. D. Landau, Zh. Eksp Teor. Fiz. 20, 1064 (1950).
29. V. V. Schmidt, P. Müller, and A. V. Ustinov, "The Physics of Superconductors: Introduction to Fundamentals and Applications." Springer-Verlag, Berlin/Heidelberg, 1997.
30. D. Saint-James, G. Sarma, and E. J. Thomas, "Type II Superconductivity." Pergamon Press, Oxford, 1969.
31. P. G. de Gennes, "Superconducting of Metals and Alloys." Benjamin, New York, 1966.
32. A. C. Rose-Innes and E. H. Rhoderick, "Introduction to Superconductivity." Pergamon Press, Oxford, 1969.
33. A. A. Abrikosov, *Sov. Phys. JETP* 5, 1175 (1957).
34. G. F. Zharkov, V. G. Zharkov, and A. Yu. Zvetkov, *Phys. Rev. B* 61, 12293 (2000).
35. W. A. Little and R. D. Parks, *Phys. Rev. Lett.* 9, 9 (1962).
36. R. D. Parks and W. A. Little, *Phys. Rev.* 133, A97 (1964).
37. F. London, "Superfluids." Wiley, New York, 1950.
38. V. Bruyndoncx, L. Van Look, M. Verschuere, and V. V. Moshchalkov, *Phys. Rev. B* 60, 10468 (1999).
39. B. J. Baelus, F. M. Peeters, and V. A. Schweigert, *Phys. Rev. B* 61, 9734 (2000).
40. V. V. Moshchalkov, M. Dhalle, and Y. Bruynseraede, *Physica C* 207, 307 (1993).
41. A. K. Geim, S. V. Dubonos, J. G. S. Lok, M. Henini, and J. C. Maan, *Nature* (*London*) 396, 144 (1998).
42. R. P. Groff and R. D. Parks, *Phys. Rev.* 176, 567 (1968).
43. H. J. Fink, *Phys. Rev.* 177, 732 (1969).
44. F. M. Peeters and X. Q. Li, *Appl. Phys. Lett.* 72, 572 (1998).
45. V. M. Fomin, J. T. Devreese, and V. V. Moshchalkov, *Europhys. Lett.* 42, 553 (1998).
46. V. M. Fomin, J. T. Devreese, and V. V. Moshchalkov, *Europhys. Lett.* 46, 118 (1999).
47. A. P. van Gelden, *Phys. Rev. Lett.* 20, 1435 (1968).
48. M. Tinkham, "Introduction to Superconductivity." McGraw Hill, New York, 1975.
49. G. F. Zharkov, in "Superconductivity, Superdiamagnetism, Superfluidity" (V. L. Ginzburg, ed.), p 126. MIR, Moscow, 1987.
50. R. M. Arutunyan and G. F. Zharkov, *J. Low Temp. Phys.* 52, 409 (1983).
51. R. Kato, Y. Enomoto, and S. Maekawa, *Phys. Rev. B* 47, 8016 (1993).
52. B. J. Baelus, F. M. Schweigert, and V. A. Schweigert, *Phys. Rev. B* 63, 144517 (2001).
53. P. Singha Deo, V. A. Schweigert, and F. M. Peeters, *Phys. Rev. B* 59, 6039 (1999).
54. C. P. Bean and J. D. Livingston, *Phys. Rev. Lett.* 12, 14 (1964).
55. X. Zhang and J. C. Price, *Phys. Rev. B* 55, 3128 (1997).
56. F. M. Peeters, V. A. Schweigert, B. J. Baelus, and P. S. Deo, *Physica C* 332, 255 (2000).
57. D. Y. Vodolazov, F. M. Peeters, S. V. Dubonos, and A. K. Geim, *Phys. Rev. B*, 67, 054506.
58. D. Y. Vodolazov and F. M. Peeters, *Phys. Rev. B* 66, 054537 (2002).
59. M. C. Cross and P. C. Hohenberg, *Rev. Mod. Phys.* 65, 851 (1993).

60. L. P. Gor'kov and G. M. Eliashberg, *Zh. Eks. Teor. Fiz.* 54, 612 (1968) [*Sov. Phys. JETP* 27, 328 (1968)].

61. A. Schmid, *Phys. Kondens. Mater.* 5, 302 (1996).

62. L. Kramer and R. J. Watts-Tobin, *Phys. Rev. Lett.* 40, 1041 (1978).

63. T. J. Rieger, D. J. Scalapino, and J. E. Mercereau, *Phys. Rev. B* 6, 1734 (1972).

64. A. T. Dorsey, *Phys. Rev. B* 46, 8376 (1992).

65. B. I. Ivlev and N. B. Kopnin, *Usp. Fiz. Nauk* 142, 435 (1984) [Sov. Phys. Usp. 27, 206 (1984)].

66. A. L. de Lozanne and M. R. Beasley, "Nonequilibrium Superconductivity" (D. N. Langenberg and A. I. Larkin, Eds.), p. 111. North-Holland, Amsterdam, 1986.

67. A. M. Kadin and A. M. Goldman, "Nonequilibrium Superconductivity" (D. N. Langenberg and A. I. Larkin, Eds.), p. 253. North-Holland, Amsterdam, 1986.

68. M. B. Tarlie and K. R. Elder, *Phys. Rev. Lett.* 81, 18 (1998).

69. D. Y. Vodolazov and F. M. Peeters, *Physica C* 400/3-4, 165 (2003).

70. J. Berger, *Phys. Rev. B* 67, 014531 (2003).

71. J. Berger and J. Rubinstein, *Phys. Rev. Lett.* 75, 320 (1995).

72. J. Berger and J. Rubinstein, *Phys. Rev. Lett.* 56, 5124 (1997).

73. E. M. Horane, J. J. Castro, G. C. Buscaglia, and A. Lopez, *Phys. Rev. B* 53, 9296 (1995).

74. M. Tinkham, *Phys. Rev.* 129, 2413 (1963).

75. D. Y. Vodolazov, B. J. Baelus, and F. M. Peeters, *Phys. Rev. B* 66, 054543 (2002).

76. J. S. Langer and V. Ambegaokar, *Phys. Rev.* 164, 498 (1967).

77. A. Bezryadin, A. Buzdin, and B. Pannetier, *Phys. Rev. B* 51, 3718 (1995).

78. H. J. Fink and V. Grunfeld, *Phys. Rev. B* 33, 6088 (1986).

79. H. J. Fink and V. Grunfeld, *Phys. Rev. B* 31, 600 (1985).

80. H. J. Fink, *Phys. Rev. B* 45, 4799 (1992); 48, 3579 (1993).

81. C. Ammann, P. Erdös, and S. B. Haley, *Phys. Rev. B* 51, 11739 (1995).

82. J. Berger and J. Rubinstein, *Phys. Rev. B* 59, 8896 (1999).

83. J. Berger, "Connectivity and Superconductivity" (J. Berger and J. Rubinstein, Eds.), p. 138. Springer-Verlag, New York, 2000.

84. Y. Liu, Yu. Zadorozhny, M. M. Rosario, B. Y. Rock, P. T. Carrigan, and H. Wang, *Science* (*Washington, DC*) 294, 2332 (2001).

Drug Nanocrystals of Poorly Soluble Drugs

Rainer H. Müller

Pharmasol GmbH, Berlin, Germany

Aslihan Akkar

Free University of Berlin, Berlin, Germany

CONTENTS

1. INTRODUCTION

Poor solubility of a drug is in most cases associated with poor bioavailability, at least bioavailability problems. About 10% of the present drugs are poorly soluble, about 40% of the drugs in the pipeline possess a poor solubility, and even 60% of drugs coming directly from synthesis have a solubility below 0.1 mg/mL [1]. The problem is even more pronounced than in the past because more and more new drugs are poorly soluble in aqueous media and simultaneously in organic media. This excludes previous formulation approaches such as dissolution of the drugs in solvent mixtures (e.g., ethanol/water) or dissolving them in oils or the lipophilic phase of microemulsions. In the case of too low oral bioavailability of poorly soluble drugs, in most cases, parenteral administration is not an alternative. Injection volumes are either too high because of the very low solubility, or the drugs cannot be dissolved at all. The injection of crystalline microparticulate drug dispersions would even worsen the situation compared to oral administration because the body fluid volume at the injection site is very limited. From this, new smart technological formulations for improved delivery are required to overcome this problem of most newly developed drugs, and to make them available to the patient. Improved formulations are even necessary at a much earlier state in the drug discovery process. A pharmacological screening for activity and side effects is not possible without having reached a sufficient availability in the blood.

According to the biopharmaceutical classification, drugs with poor solubility fall either in class II or class IV. Class II drugs show poor solubility, but good permeability, which means that their bioavailability problems can be overcome when improving the solubility. Class IV drugs are characterized by simultaneously poor solubility and low permeability. In this case, improving the solubility will not or will little improve the bioavailability. Therefore, the attempts to find improved formulations are mainly targeting class II drugs. The "specific" formulation approaches are characterized in that they are working only with a very limited number of specific molecules which "fit." For example, molecules need to fit in size to be complexed by cyclodextrins or for efficient solubilization by mixed micelles. The molecules need to have the right structure to sufficienty interact with the surfactants forming the micelles. This limited applicability is clearly proven by the very low number of products on the market being based on such formulation principles. Much more attractive are the "generalized" formulation approaches; a very simple and effective one is micronization. Any drug can be micronized independent of its structure. In the past, this worked for quite a number of drugs; however, it is not effective anymore for the new drugs exhibiting even lower saturation solubilities. Consequently, the next step after "micronization" was "nanonization," which means that, instead, producing ultrafine drug microparticles (mean diameter approximately 2–10 μm), one produces

superfine drug nanocrystals (approximately 100 nm to just below 1000 nm). To be more precise, a drug showing poor solubility means that it has a low saturation solubility which is typically correlated with a low dissolution velocity dc/dt. The terms "solubility" and "saturation solubility" are used synonymously. In case a drug—despite having a low saturation solubility—dissolves very fast and has a good permeability, this should not cause any bioavailability problems. However, this is normally not the case with poorly soluble drugs because, according to the law of Noyes–Whitney, the dissolution velocity dc/dt is directly correlated to the saturation solubility c_s. The principle of micronization is to increase the surface area A to which dc/dt is also directly correlated. Nanonization is taking the increase in surface area A one dimension further than micronization. There are also some additional features of drug nanocrystals improving the dissolution velocity (increase in dissolution pressure, reduction of diffusional distance h), discussed below, which further improve the enhancement of bioavailability.

There is a limited number of technologies around to produce drug nanocrystals; basically, one can differentiate between "bottom-up" techniques and "top-down" techniques. All of them are patent protected, which means that it is a "closed market" and dominated by only a few companies. The different technologies are briefly discussed and compared, and advantages and disadvantages highlighted. The main focus is on drug nanoparticles produced by milling or by high-pressure homogenization using preferentially piston-gap homogenizers. Special emphasis is given to the large-scale production, including regulatory aspects—important criteria for entering the market with a product.

2. GENERAL FEATURES OF DRUG NANOCRYSTALS

The law of Noyes–Whitney describes the dissolution velocity [2]:

$$\frac{dm}{dt} = \frac{DA}{h}(c_S - c_x) \quad (1)$$

D is the diffusion coefficient, A is the surface area, c_s is the saturation solubility, c_x is the bulk concentration, and h is the so-called "diffusional distance" over which the concentration gradient occurs (note: division of the equation by the volume v leads to dc/dt). It is obvious that an increase in A increases the dissolution velocity. To illustrate this, the surface area was calculated for a 100 mg dose of drug assuming that the drug powder is a finely milled powder of 50 μm particles, micronized powder of 5 μm particles, and nanonized powder of 200 nm particles (assumed drug density 2.0 g/cm^3):

- 50 μm particles: 6.03×10^{-3} m^2
- 5 μm particles: 0.0599 m^2
- 200 nm particles: 1.50 m^2.

The Kelvin equation [3] describes the vapor pressure above very fine liquid droplets in a gas phase, for example, during the spray drying process. It describes the vapor pressure as a function of the droplet radius, which means as a function of the droplet curvature:

$$\ln \frac{P_r}{P_\infty} = \frac{2\gamma M_r}{rRT\rho} \quad (2)$$

where P_r is the dissolution pressure of a particle with the radius r, P_∞ is the dissolution pressure of an infinitely large particle, γ is the surface tension, R is the gas constant, T is the absolute temperature, r is the radius of the particle, M_r is the molecular weight, and ρ is the density of the particle.

The basic information is that the vapor pressure above a flat surface and a slightly curved surface are identical; going to a strongly curved surface (i.e., typically particles below 1–2 μm) leads to an increase in vapor pressure (Fig. 1).

The situation at the liquid–gas interface can directly be transferred to the situation at the solid–liquid interface, which means that the vapor pressure of the liquid corresponds to the dissolution pressure of the solid (drug). It is known that different liquids have different vapor pressures; for example, comparing ether, water, and oil (Fig. 2), the same compound-specific differences are, of course, valid for solid materials. Consequently, different drugs have different dissolution pressures at identical particle size.

Based on the Kelvin equation, the relative increase in vapor pressure as a function of decreasing particle size was calculated [4]; as model compounds, three liquids were chosen having distinct differences in vapor pressure. Oleic acid has a relatively low vapor pressure (boiling point: 350 °C) [5], water has a relatively high vapor pressure (boiling point: 100 °C) [6], and ether, as a highly volatile liquid, possesses the highest vapor pressure (boiling point: 35 °C) [7]. The vapor pressure was normalized, which means that only the relative increase was calculated when reducing the size leading to characteristic functions (Fig. 2).

Water and ether represent compounds of good and very good solubility; the relative increase takes place below the known threshold size of approximately 1.0 μm, but is not very pronounced. Oleic acid represents the poorly soluble drug (low vapor pressure = low dissolution pressure). The first slight increase is already observed below approximately 2.0 μm, being very distinct below the well-known 1.0 μm and highest below 200 nm (Fig. 2, upper curve). It is noteworthy that the increase in relative pressure going from 200 nm

Dissolution pressure ($\Delta p \sim 1/r$) $\longrightarrow$ Cs$_N$ > Cs$_M$

Substance layer (flat surface)   Large particle (slight curvature)   Nanosuspension (strong curvature)
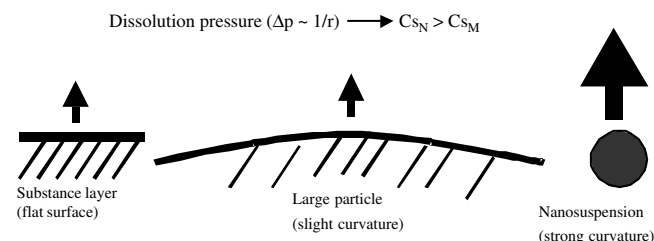
Figure 1. Vapor pressure above differently curved surfaces of liquids occurring at the liquid–gas interface, corresponding to the dissolution pressure at the interface solid–liquid, as a function of the curvature (drug, Cs_M/Cs_N—saturation solubility of microparticles and nanoparticles, respectively). Modified with permission from [10], R. H. Müller et al., "Emulsions and Nanosuspensions for the Formulation of Poorly Soluble Drugs," 1998. © 1998, Medpharm Scientific Publishers.
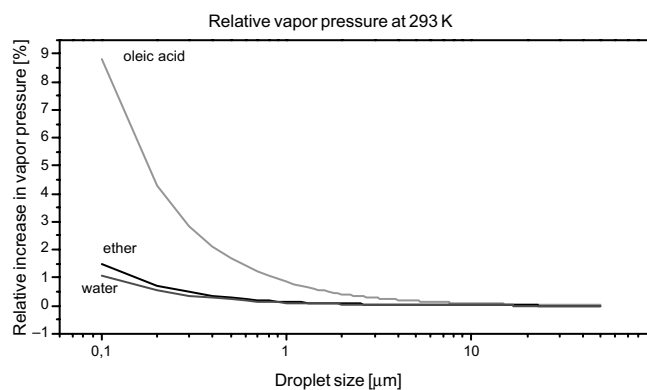
Figure 2. Compound-specific differences in the vapor pressure (dissolution pressure) of different liquids (different drugs) as a function of droplet (particle) size.

down to 100 nm is similarly large as going from 1.0 μm to 200 nm. That means, to obtain extremely fast dissolving particles in the blood, a size of 100 nm (or even below) would be ideal.

According to the textbooks, the saturation solubility is a compound-specific constant depending only on the temperature. This is valid for the powders of daily life. However, as outlined above, it changes below a particle size of approximately 1–2 μm. Saturation solubility is an equilibrium of molecules dissolving and molecules recrystallizing; the increase in dissolution pressure shifts the equilibrium, thus resulting in a higher saturation solubility. Therefore, drug nanoparticles are characterized by an increase in saturation solubility c_s. According to Noyes–Whitney, the increase in c_s—in addition to A—further increases the dissolution velocity. The final saturation solubility achieved is, of course, compound-specific based on the differences in compound-specific dissolution pressures (cf. Fig. 2).

The dissolution velocity is reversly proportional to the diffusional distance h_H, which means that reducing h_H leads to a further increase in dissolution velocity. According to the Prandtl equation, the diffusional distance h_H decreases for very small particles [8]:

$$h_H = k(L^{1/2}/V^{1/2}) \qquad (3)$$

In this equation, h_H is the hydrodynamic boundary layer thickness, k is a constant, L is the length of the surface in the direction of the flow, and V is the relative velocity of the flowing liquid against a flat surface.

However, due to some parameters which cannot be specified as actual figures, the decrease in h_H can hardly be calculated. Therefore, publications dealing with h_H focus rather on direct measurement of the increase in dissolution velocity to have an idea of the quantity of this effect [8].

To clarify the definitions, we must differentiate between dissolution rate (velocity) and the so-called "intrinsic dissolution rate." The dissolution rate just quantifies the observed dissolution velocity of the powder; therefore, for example, rock candy sugar has a slower dissolution rate than the same amount of sugar in a crystalline form. However, when expressing it as an intrinsic dissolution rate, the intrinsic dissolution rates are identical because the intrinsic dissolution

rate refers to the respective surface unit. Based on the surface unit, the intrinsic dissolution rates for both sugars are identical. Based on the outline above regarding the increases in dissolution pressure, the increase in saturation solubility and the reduction in diffusional distance h, the intrinsic dissolution rate increase when one moves in the range below approximately 1 μm. Therefore, the nanonization not only increases the measured dissolution rate due to enlargement of the surface A, but additionally the intrinsic dissolution rate as well [9, 10].

It should be noted that the described effects are valid for any identically sized drug nanocrystal independent of its method of production. It does not matter if the drug nanocrystal has been produced, for example, by precipitation, pearl milling, or high-pressure homogenization. For a crystal of a given size (and identical physical state, crystallinity), the same physical effects occur. Therefore, no production method can claim that its nanocrystal has a special feature because it is produced in a certain way.

However, differences in identically sized drug nanocrystals can occur when they show differences in their crystalline character, which means the polymorphic form or the fraction of an amorphous drug. It is well documented in the literature that amorphous drugs have a higher saturation solubility than crystalline forms. Therefore, in theory, it is beneficial to have an amorphous drug nanocrystal. However, there are two major challenges for these systems:

1. to provide a reproducible and functioning technology to produce 100% amorphous particles, and
2. to guarantee its unchanged amorphous character during the shelf life of the product.

There is the general feeling that things are much easier when one immediately begins with a 100% crystalline nanoparticle. The question of shelf-life stability is therefore the major concern with regard to these technologies for amorphous particles—despite the very attractive feature of a further increase in dissolution rate. From the viewpoint of physics, the increase in saturation solubility of amorphous products can be explained by the Ostwald–Freundlich equation. The Ostwald–Freundlich equation is derived from the Kelvin equation, and describes the saturation solubility as a function of the particle size [11]:

$$(1 - \alpha n)\frac{RT}{M} \ln \frac{S_2}{S_1} = \frac{4\delta}{\xi}\left(\frac{1}{d_2} - \frac{1}{d_1}\right) \qquad (4)$$

The parameters are as follows:

α = dissociation grade
n = number of ions
R = gas constant
M = molecular weight
S_1 = saturation concentration of population 1
S_2 = saturation concentration of population 2
δ = interfacial energy
ζ = density
d_1 = diameter of population 1
d_2 = diameter of population 2.

In a simplified way, amorphous products can be considered as powders with a very small (indefinite) particle size, thus

exhibiting a higher saturation solubility compared to crystalline particles. As an aside, to complete the theoretical considerations, the Ostwald–Freundlich equation also contains the interfacial tension γ (solid/liquid interface). Thus, it explains and describes the different saturation solubilities obtained with polymorphic forms. The polymorphic forms have different energy contents; consequently, they are different in the interfacial tension at the solid/liquid interface, thus resulting in different saturation solubilities.

It should also be considered that energy input to create drug nanocrystals can theoretically lead to a change in polymorphic forms. In tabletting technology, it is described that high compression pressures can induce a transform of a lower energetic form to a higher energetic form (e.g., partial transition from I to II) [12]. Therefore, when producing drug nanocrystals, intensive characterization of the crystalline character after production and—in the case of totally or partially amorphous nanoparticles or nanocrystals of higher polymorphs—the monitoring of the crystalline status during the shelf life of the product are important. Again, the most convenient approach is to create drug nanocrystals that are completely crystalline, and preferentially having the polymorph I. It should be noted that about 50% of the drugs exhibit polymorphism; therefore, this characterization is of great importance.

3. "BOTTOM-UP" TECHNOLOGIES FOR DRUG NANOCRYSTAL PRODUCTION (HYDROSOLS, NanoMorph™)

Bottom-up technology means that one starts from the molecular level, and goes via molecular association to the formation of a solid particle. That means that we are discussing classical precipitation techniques by reducing the solvent quality, for example, by pouring the solvent into a nonsolvent or changing the temperature or a combination of both. Precipitation is a classical technique in pharmaceutical chemistry and technology. The Latin terminology is *via humida paratum* (v.h.p.) [13], which means being prepared via a liquid process (solutions are made to obtain a fine powder (precipitate) dispersed in a "wet" environment). Well-known old examples of the pharmacopea are the mercury ointments (e.g., Unguentum Hydrargyri cinereum, German Pharmacopea no.6, 1926). Because it is a long-known process in pharmacy, a clear outline is necessary to document the innovative height of patent applications based on this process.

The soundness of a patent regarding such a technology (of course, the soundness of patents in general), and especially in case they are challenged, is a very important factor for companies when deciding to place a formulation development on such a technology.

The so-called "hydrosols" were developed by Sucker and co-workers [14–17] at the Sandoz Company (nowadays Novartis). The drug is dissolved in a solvent, and the solvent is added to a nonsolvent to initiate the fast precipitation of a finely dispersed product. To achieve this, it is necessary to pass the so-called Ostwald–Mier area very quickly, which means reducing the solvent quality very quickly [18]. This is achieved by adding the solvent to a nonsolvent; doing it the

other way around would lead to larger crystals. The formed crystals need to be stabilized by surfactants or polymers to avoid growth of the nanocrystals to microcrystals. In general, it is recommended to lyophilize the product to preserve the nanometer character of the particles [16]. The technology is to some extent complex (e.g., the preservation of particle size), and excludes all molecules which are poorly soluble in aqueous and organic media. To our knowledge, no products based on this technology are marketed by Novartis. An additional problem is, for example, solvent residues; removal makes the process more costly.

The particles generated by precipitation, as, for example, by Sucker, are in most cases crystalline in nature; in contrast to this, the company Knoll (nowadays owned by Abbott) creates amorphous particles by a precipitation technique [19]. The product is NanoMorph™. As outlined above, an additional positive feature is a further increase in the dissolution velocity due to the amorphous character of the product. The precipitation in the amorphous form is achieved by an aqueous polymer solution (company brochure; www.soliqs.com). However, for a commercial product, it is necessary to preserve the amorphous character during the shelf life to avoid changes in bioavailability caused by a reduction in the dissolution velocity due to the transfer of the amorphous drug to a crystalline drug.

A precipitation technology was also described by Müller and co-workers (Kiel University, Germany), dissolving the drug in a water-miscible solvent, for example, isopropanol or acetone [20, 21]. The particles are stabilized in the nanometer range by selecting stabilizers possessing optimal affinity to the particle surface, and stabilizing the precipitated particles in the nanometer range. Examples of stabilizers are agar, calcium caseinate, dextran 200, gelatin A, hydroxyethylcellulose, hydroxyethylstarch, hydroxypropylcellulose, polyvinylpyrrolidone, and polyvinylalcohol [22]. The optimum stabilizer might differ from one drug to the next because each drug nanocrystal shows differences in surface properties, such as the presence of functional groups on the surface, surface hydrophobicity, and surface wetability. To transform the particles into a dry product, spray drying is described [23, 24].

The advantage of the precipitation techniques is that relatively simple equipment can be used. For example, the solvent can be poured into the nonsolvent with a constant velocity in the presence of a high-speed stirrer. Very elegant approaches are the use of static mixers or micromixers [25, 26] which simulate the precipitation conditions in a small volume (i.e., simulating lab scale conditions), but being simultaneously a continuous process. In the case of micromixers, scaling up can be performed in a simple way just by so-called "numbering up," which means arranging many micromixers in parallel [27, 28]. The equipment is relatively simple, and in the case of large conventional static mixers, of relatively low cost (this is not necessarily valid for the micromixers). However, there are some major general disadvantages of the precipitation techniques.

1. The drug needs to be soluble in at least one solvent (thus excluding all new drugs that are simultaneously poorly soluble in aqueous and in organic media).
2. The solvent needs to be miscible with at least one nonsolvent.

3. Solvent residues need to be removed, thus increasing production costs.
4. It is a little bit tricky to preserve the particle character (i.e., size, especially the amorphous fraction).

In general, it is recommended that a second consecutive process be performed for particle preservation, that is, spray drying or lyophilization.

4. "TOP-DOWN" TECHNOLOGIES

There are basically two "top-down" techniques, which means starting from a large powder and performing a size diminution:

1. pearl ball milling [13] and
2. high pressure homogenization.

The milling technique was developed and patented by the Nanosystems Company, which was acquired by the élan Company a few years ago. There are two techniques based on high-pressure homogenization in water: the microfluidizer technology developed by the RTP Company [29], and the DissoCubes® technology developed by Mülller et al. [30], nowadays both owned by the company SkyePharma PLC (www.skyepharma.com). Recently, SkyePharma PLC acquired RTP Pharma, which means that the high-pressure homogenization in water is on hand. The third technique is homogenization in media, other than 100% water, which means the Nanopure technology, which is currently owned by Pharmasol GmbH (www.pharmasol-berlin.com).

4.1. Pearl Milling (Nanocrystals™)

Liversidge and co-workers developed the milling process to yield the so-called (Nanocrystals™) [31]. The mills used by the élan Company are basically containers with small pearls, beads, or balls which can have different sizes, a typical size being 1–2 mm (Fig. 3). The drug powder is dispersed in a surfactant solution, and the obtained suspension is poured into the mill. In the milling process, the pearls are moved, either by using a stirrer or by moving the mill container itself. The drug particles are disintegrated between the moving pearls. This process is accompanied by the erosion of milling material from the pearls, a phenomenon well known for these mills and documented in the literature [32].
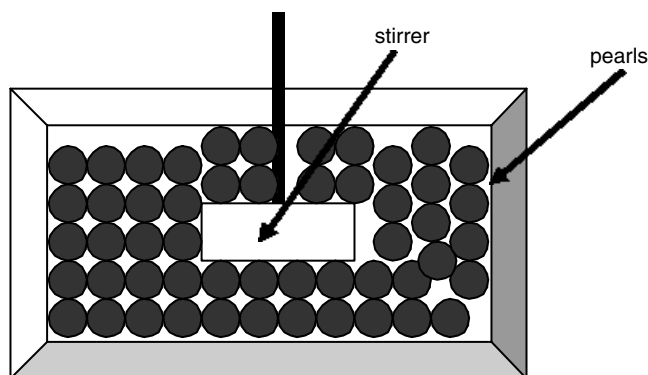
Figure 3. Principle of pearl mill type; pearls are moved by the stirrer.

Typical milling materials are glass or zirconium oxide. Buchmann et al. reported on the generation of glass particles with a size of a few micrometers during the milling process. The accepted contamination in a product originating from the production equipment used is normally limited in the very low parts-per-million range (e.g., 10 ppm). Depending on the desired small size, the hardness and the crystallinity of the material, and milling forces present, the milling procedure can last from hours or days up to one week. Of course, the contamination increases with the milling time and hardness of the drug material. Some years ago, the NanoSystems Company replaced zirconium oxide by hard polystyrene beads as the milling material. The milling technique clearly has some advantages:

1. simple technology
2. low-cost process regarding the milling itself
3. large-scale production possible to some extent (batch process).

Large-scale production is stated only to "some extent." This should be explained by a model calculation. A pearl mill of 1000 L volume containing milling pearls in hexagonal packaging has 76% pearls (760 L) and 24% void volume available for the drug suspension (240 L). The solid concentration in the suspension is limited; it should not be too pasty because such a highly viscous system is no longer processable. Assuming a suspension with 20% solid would mean that 20% of the 240 L suspension is drug (48 L). This is equivalent to 96 kg of drug (assumed drug density: 2.0 g/mL). Depending on the density of the milling material used (glass: approximately 2–3 g/mL, zirconium oxide: 5.9 g/mL, and hard polystyrene: 1.05 g/mL), the weight of the milling material and suspension will be in the range of 1–2 tons plus the weight of the mill itself. The batch cannot be increased by just multiplying the dimensions of pearl mills [33].

As disadvantages, we can see:

1. potential erosion from the milling material leading to product contamination
2. duration of the process not being very production friendly
3. potential growth of germs in the water phase when milling for a long time
4. time and costs associated with the separation procedure of the milling material from the drug nanoparticle suspension, especially when producing parenteral sterile products.

The contamination issue is controversially discussed between the believers in the technology and colleagues who are more skeptical. The company SkyePharma PLC presented data wherein they found 70 ppm contamination in a drug suspension when milling with zirconium oxide pearls [34]. Recently, the élan Company made an oral presentation about intravenous drug nanocrystal suspensions, giving a figure of 70 ppm solid contamination (polystyrene) in the produced drug nanosuspension [35]. The solid contamination was determined by dissolving all of the other parts of the particle suspension, and subsequent filtering of the solution through a 0.2 μm filter to collect nondissolved contamination (i.e., eroded polystyrene). It should be kept in mind that the

concentration of the contamination increases when removing the water phase of a nanocrystal suspension to obtain a dry product. Of course, the contamination is "diluted" when incorporating the drug nanocrystals into the matrix of a tablet or of pellets. Regarding the figure given by élan, it was not specified how hard the drug was and how long the milling time was, two factors affecting the extent of contamination. Irrespective of the discussion of the contamination issue, élan was successful in getting the first oral product approved, Rapamune®. According to the Rapamune® information package, the tablet is the "dry" alternative to an orally administered solution of Rapamune®. Compared to the solution, the oral bioavailability of the nanocrystal tablet is even slightly higher (approximately 27% higher relative to the oral solution). The bioavailabilities of the nanocrystal tablet and solution are in a similar range; production of the nanocrystal tablet is therefore mainly seen for reasons of convenience, which means easier administration, and less as a final approach to reach sufficiently high bioavailability of a poorly soluble drug. Independent of this, from our point of view, Rapamune® can be seen as a very important milestone because it demonstrates that the drug nanoparticles/nanocrystals are a suitable technology for the pharmaceutical market. It is an important proof of principle for the drug nanocrystal itself—independent of which technology was used to produce it.

4.2. Homogenization in Water (DissoCubes®)

Homogenization in water is performed either using the Microfluidizer® as a high-pressure homogenizer (RTP) [36] or, alternatively, piston-gap homogenizers (SkyePharma PLC) [30]. The Microfluidizer® (Fig. 4) realizes the jet stream principle, which means that two streams of liquid/suspension hit each other on the front, leading to particle disintegration [26]; different types of interaction chambers are available ("Y" type and "Z" type) (Fig. 5, upper and lower part, respectively). The smallest particle size obtained depends on the power density achieved in the disintegration volume. The power density is defined as power/volume unit (watt/m^3). A measure for the power is the homogenization pressure. Homogenization pressure in Microfluidizer® machines are, for example, 40,000 psi/2760 bar, and for the lab scale mode 120B Microfluidizer®, 15,000 psi/1035 bar. Maximum pressures achievable with piston-gap homogenizers are, for example, 1600 bar with the LAB 40 and Gaulin 5.5, and 2000 bar with the Rannie 118 from APV (APV, Unna, Germany). The Stansted Company can produce homogenizers up to 3500 bar and above [37]. From this, in principle, with given material, the microfluidizer 120B cannot produce such a small particle size as the other lab scale homogenizers with their higher power densities. The examples in the Mikrofluidizer patent [36] described the use of 50 or even up to 100 homogenization cycles to produce drug nanoparticles. This leads to high production times, and is not friendly for the production process. From our investigations, we observed disintegration to real drug nanoparticles only with "soft" drugs. For hard crystalline drugs, the mean diameter stayed in the very low micrometer range. According to the theoretical considerations above
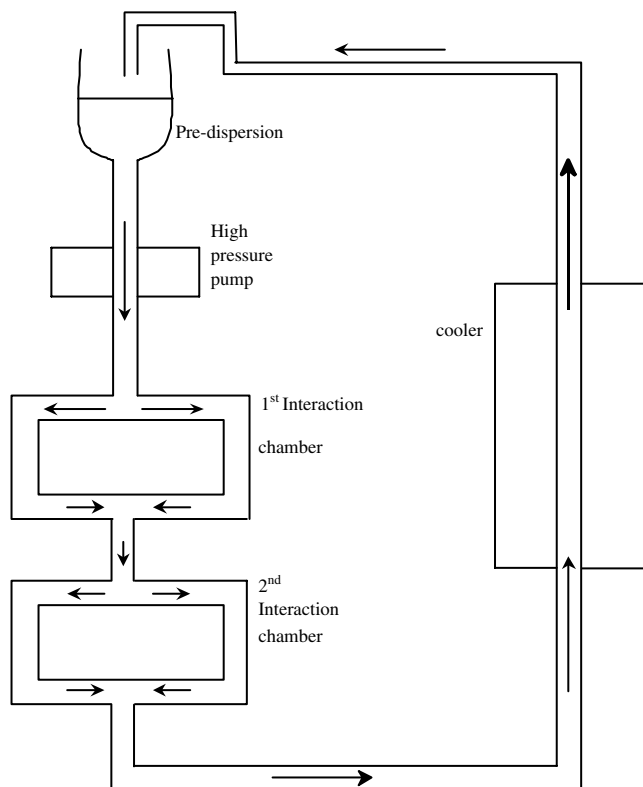
Figure 4. Basic principle of Microfluidizer® with the first interaction chamber plus second interaction chamber.

(cf. Section 2), this does not utilize all of the benefits of the real drug nanoparticles. In addition, it might be easier to obtain similar particle sizes with other techniques. In the case of highly efficient jet milling, laser diffractometery particle diameters of 2–3 μm (diameter 50%) can be obtained. Regarding potential product contamination, no published data were available to us when writing this chapter. Clear disadvantages can be summarized [38]:

1. a relatively high number of required homogenization cycles (up to 100), leaving the production technology user unfriendly
2. a potentially larger content of microparticle diameters above 1 μm, not fully providing real drug nanoparticles.

Piston-gap homogenizers are based on a different homogenization principle. Liquid/suspension is streaming through a narrow gap with a very high streaming velocity. A typical arrangement for this technology is to place the dispersion (emulsion or suspension) in a cylinder with a piston; a pressure is applied to the piston, pressing the suspension through a gap at the end of the cylinder (Fig. 6). In the Micron LAB 40, the cylinder has a diameter of 3.0 cm, and the narrow gap just has a width of only 25 μm; this narrowing by a factor of 120,000 leads to extremely high flow velocities up to 200–300 m/s [39]. For some homogenizer types, velocities up to 1000 m/s are given. According to the patent of DissoCubes®, the reason for disintegration of the particles is the cavitation occurring in this gap. According to the Hagen–Poiseulle equation, the flow rate in the system
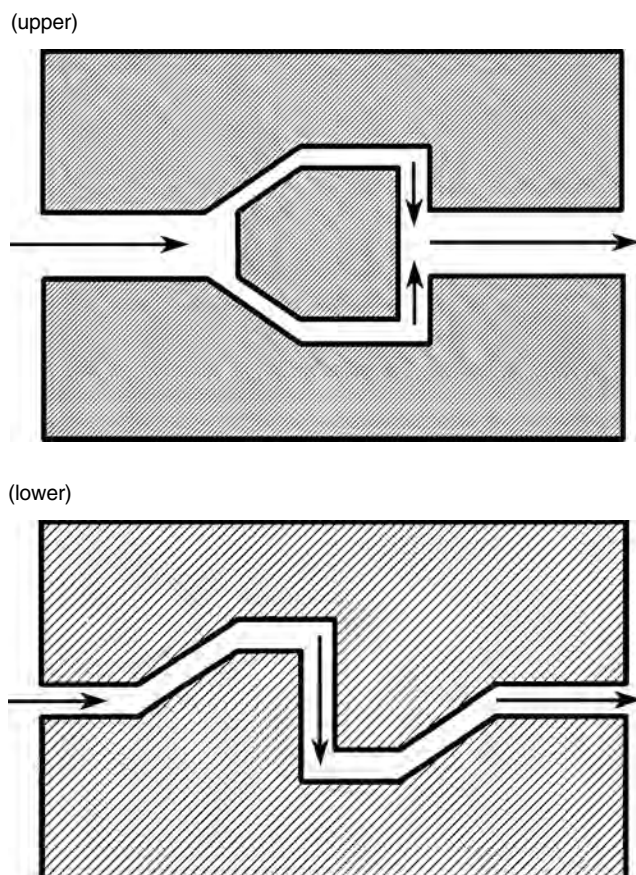
(upper)

(lower)

Figure 5. The "Y" interaction chamber (upper) and the "Z" interaction chamber (lower) of the Microfluidizer®. Adapted with permission from [26], R. H. Müller and B. H. L. Böhm, "Dispersion Techniques for Laboratory and Industrial Scale Processing," 2001. © 2001, Wissenschaftliche Verlagsgesellschaft mbH.

of different diameters is equal at each diameter. According to the Bernoulli equation, the sum of static and dynamic pressure is constant at each diameter of the system [40]:

$$P_s + \frac{1}{2} \rho V^2 = K \qquad (5)$$

where P_S is the static pressure, $1/2\rho V^2$ is the dynamic pressure (P_{dyn}), and K is a constant.
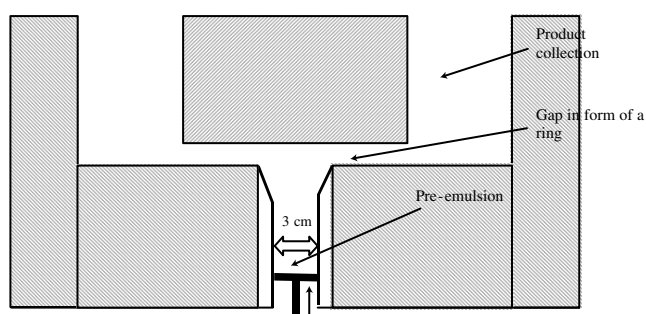
Figure 6. Principle arrangement in piston-gap homogenizer of LAB type (note: some parts are out of proportion (piston, gap) for reasons of clarity).

In the gap, the dynamic pressure drastically increases (i.e., also streaming velocity), and simultaneously, the static pressure decreases and falls below the vapor pressure of the water at room temperature (Fig. 7). This leads to the boiling of the water at room temperature, the formation of gas bubbles which implode when the liquid leaves the gap being under the normal pressure conditions again (=cavitation). The formation of gas bubbles and their implosion cause shock waves, leading to the destruction of the droplets in the case of an emulsion and the diminution of particles in the case of a suspension. Nowadays, bubble formation and not the implosion is considered as the major reason for diminution. There are advantages of the piston-gap homogenization technique:

1. the effective particle diminution
2. production lines can be qualified and validated
3. production lines already exist in industry, for example, production of parenterals, and so on
4. no contamination, for example, iron content is below 1 ppm [41]
5. off-shelf equipment
6. simple process
7. low-cost process/low-cost equipment.

To summarize: homogenization with piston-gap homogenizers has good potential to be used as a production technique because it fulfills the key industrial features such as large-scale production and various regulatory aspects [42–44].

The definition includes the term "homogenization" reduction of particle or droplet size and simultaneous narrowing of the size distribution, that is, making the particle population not only smaller, but simultaneously more homogeneous in size [45, 46]. Figure 8 shows an EM graph of a drug compound produced by high-pressure homogenization; the crystals are relatively homogeneous in size and of rather cuboid shape. The homogeneity in size is an essential prerequisite for the physical long-term stability, which means avoiding Ostwald ripening and crystal growth. Ostwald ripening is caused by different saturation solubilities in the vicinity of differently sized particles (cf. aspects of dissolution pressure and saturation solubility of differently sized particles outlined above). Figure 9 shows the situation in the case where very differently sized particles are present. Each particle is surrounded by a layer of saturated solution. Due to the smaller size, the saturation solubility in the vicinity of the small particle (Cs_N) is higher then the saturation solubility in the vicinity of the microparticle (Cs_M),
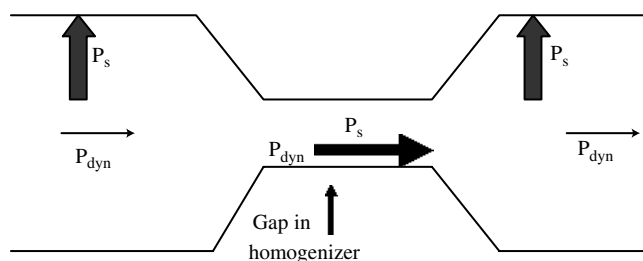
Figure 7. Change of static pressure (P_s) and dynamic pressure (P_{dyn}) as a function of tube diameter according to Bernoulli.
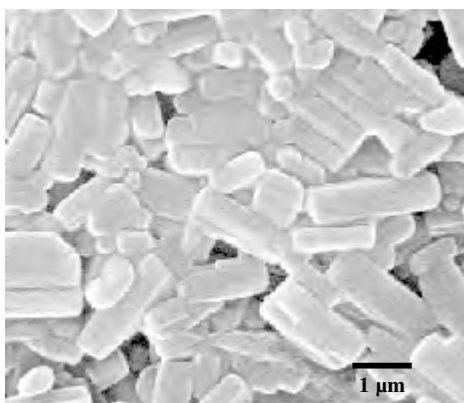
Figure 8. EM graph of the model drug RMBB 98. Modified with permission from [61], B. H. L. Böhm, Ph. D. Dissertation, 1999. © 1999, Free University of Berlin.

which means that there is a concentration gradient between the higher concentrated solution around the small particle to the vicinity of the larger particle. Based on the gradient, drug diffuses from the surrounding of the small particle to the surrounding of the large particle. In this case, in the surrounding of the small particle, the solution is no longer saturated, which means that more drug dissolves, and the size of the small particles reduces. Due to drug diffusion in the vicinity of the large particle, a supersaturated solution results, which leads to precipitation of the drug to the particle surface and crystal growth of the large particle. To avoid this, it is necessary to have a uniform particle size, which is achieved by the homogenization process. In the last ten years of our drug nanocrystal research, we never observed crystal growth in a nanosuspension produced by homogenization. In case larger particles occurred during storage, they were only aggregates of small drug nanocrystals due to a suboptimal choice of surfactant or surfactant mixture. The absence of Ostwald ripening is an amazing effect when considering the high disperitivity and energy of the system.

Ostwald ripening is promoted in case a drug has a higher solubility, and also shows pronounced solubility increases/decreases as a function of temperature. Nanocrystals are made from poorly soluble drugs; therefore, the saturation solubility is a priori low, and in general, they show
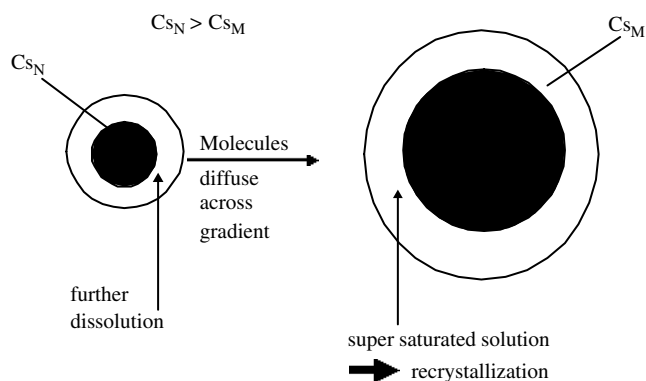
little increase in solubility with an increase in temperature, which means that temperature fluctuations during storage will not lead to relevant increases or decreases with fluctuating temperature. There is a general experience; when differently sized particles are partially dissolved by an increase in temperature, recrystallization occurring during a subsequent temperature decrease will preferentially take place on the large crystals, which means that, during temperature cycling processes, small particles dissolve and the larger ones grow.

4.3. Homogenization in Water–Liquid Mixtures and Nonaqueous Media (Nanopure®)

The DissoCubes® patent describes homogenization in pure water as a dispersion medium; the rationale behind that is—as explained in detail in the patent [30]—the cavitation is seen as being responsible for the diminution of the particles. To obtain cavitation in the dispersion medium, one needs to have a high vapor pressure of the dispersion fluid at room temperature. This is fulfilled with water, but not with other liquids such as oils or liquid polyethylene glycol (PEG) 600. In addition, homogenization at higher temperatures (e.g., 80 °C) should be much more efficient than at room temperature because the vapor pressure of water is much higher at 80 °C, thus leading to more extensive cavitation. The basics of the Nanopure® technology [47] is that homogenization was performed against these teachings, leading to a comparable or even improved product. Under the Nanopure® technology, not only drugs, but also polymers can be processed, leading to a product [48–56] with a mean diameter in the nanometer range (nanoparticles) or a size of a few micrometers (both particle ranges are covered).

At the beginning of the Nanopure® development, drug suspensions in nonaqueous media were prepared, for example, drug nanocrystals of cyclosporine (Table 1) and of RMKP 22, the latter drug also being described in the DissoCubes® patent [30]. Also for RMKP 22, a finely dispersed product was achieved (Table 2).

Based on the state of the art that homogenization with 100% water leads to a finely dispersed product, after homogenization with 0% water (e.g., liquid PEG), the range with a water content between 0 and 100% water was investigated. The drug RMKP22 was dispersed in dispersion media with increasing water content, which means starting with glycerol (0% water) and going up in water concentration stepwise. An increase in the water content should promote cavitation, and thus lead to more efficient diminution. The result was that no product-relevant differences were found (Table 3 [47]).

As pointed out above, the Nanopure® technology covers drugs and polymers to be transferred to nanoparticles or

$Cs_N > Cs_M$

Molecules diffuse across gradient

super saturated solution

➡ recrystallization

Figure 9. Principle of Ostwald ripening and crystals growth (for explanation, see text).

Table 1. PCS characterization data of 1 and 5% cyclosporine drug nanocrystal dispersion (dispersion medium: 1% Tween 80 in propylenglycol).

Cyclosporine concentration (%)	PCS diameter (nm)	Polydispersity index
1	203	0.132
5	182	0.131

Table 2. LD diameters D 50% and D 95% of RMKP 22 homogenized in aqueous surfactant solution at 1500 bar (ten cycles).

RMKP22 concentration (%)	D 50% (μm)	D 95% (μm)
1	0.94	2.74
3	1.24	3.78

microparticles with a size of a few micrometers. The teaching in the patent literature [57] was that disintegration of polymeric material is more efficient:

1. when higher temperatures above the glass transition temperature of the polymers are employed, for example, 80 °C, and
2. that the use of plasticizers promotes the diminution of polymers.

The rationale behind these two points was that soft polymers can be easier disrupted. Polymers are getting softer above their glass transition temperature or when admixing a plasticizer. In the Nanopure® technology, just the opposite was done, which means reducing the temperature below room temperature. Examples were prepared at different temperatures, showing that there was no product-relevant difference in the obtained particle sizes of polymer particles (Fig. 10).

Based on these results, high-pressure homogenization at and below the freezing point of water was performed, for example, charcoal homogenized at −20 °C.

From the data, one can conclude that the temperature has no obvious effect. It rather appears that, by using the low temperature, polymeric material is less elastic and more brittle; nonelastic material appears easier to be broken than a flexible, more elastic one such as a softened polymer.

What are the advantages of suspensions produced by the Nanopure® technology? Nonaqueous dispersion media can be used to produce oral formulations, for example, drug nanocrystals dispersed in liquid PEG 600 or miglyol/MCT oil can be directly filled into soft gelatin capsules or sealed hard gelatine capsules. Nanosuspensions in mixtures of water with water-miscible liquids (e.g., ethanol, isopropanol) can be used in the granulation process for tablet production; the solvent mixture evaporates much better than water. Drugs that are susceptible to hydrolysis in water can be prepared as nonaqueous suspensions, for example, glycerol or propyleneglycol. Prior to intravenous injection, the glycerol drug nanosuspensions can be diluted with water for injection to yield an isotonic suspension. Alternatively, isotonic water–glycerol mixtures can be directly homogenized. In the first patent [30], cavitation was considered as the dominating factor for particle diminution; therefore, homogenization was

Table 3. Drug RMKP22 homogenized in water-free medium (glycerol) and media of increasing water content (glycerol–water).

% water	D 50% (μm)	D 95% (μm)
0% (=100% glycerol)	1.28	3.85
30%	1.33	3.58
50%	1.19	3.09
100% (=pure water)	0.94	2.77
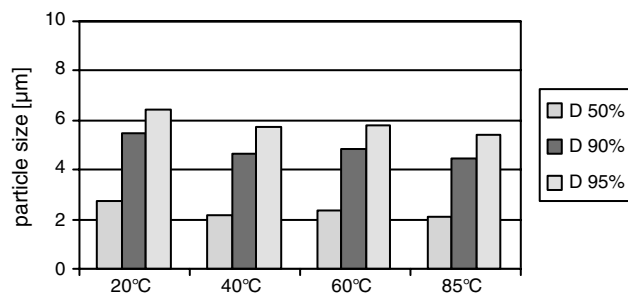
Figure 10. Particle size characterization data of the polymer ethylcellulose (laser diffractometry data, diameters 50, 90, and 95%) produced by high-pressure homogenization at different temperatures. Adapted with permission from [47], R. H. Müller et al., PCT Application PCT/EP00/06535, 2000. © 2000,

only performed in pure water, and glycerol was added afterwards to avoid an impairment of particle diminution efficiency. Another option of the Nanopure® technology is the production of aqueous polymer particle dispersions with a diameter of a few micrometers. This could be an alternative to polymer dispersion (e.g., Surelease, ethylcellulose) for the coating of tablets which are now produced by using solvents. Aqueous shellack dispersions produced have already been described [58].

5. COMBINATION OF "BOTTOM-UP" AND "TOP-DOWN" TECHNOLOGY (Nanoedge®)

In 2001, the Baxter Company presented their Nanoedge® technology at the annual meeting of the American Association of Pharmaceutical Scientists (AAPS) in Denver, Co. Nanoedge® is an aqueous suspension of drug nanoparticles suitable for intravenous injection. The particles are prepared basically by a high-pressure homogenization process, which means either by microfluidization (RTP technology), homogenization in water using piston-gap homogenizers [30], or alternatively, by a new production process developed by Baxter [59]. This process is called the "microprecipitation method," and is a combination of precipitation followed by a process with energy input (e.g., homogenization). According to [59], the process includes three steps:

1. dissolving the organic compound in a water-miscible first solvent to form a solution
2. mixing this solution with the second solvent to obtain a "presuspension"
3. adding energy to this "presuspension" to form particles having an average effective particle size of 400 nm–2.0 μm.

The method can be applied to all drugs that are poorly water soluble, that is, possess a solubility which is greater in the water-miscible first solvent compared to the second solvent which comprises an aqueous phase. Examples for the first solvent are, for example, methanol, ethanol, glycerol, and acetone. Adding the solvent to the nonsolvent is a classical precipitation process. A second energy-addition step follows, which leads to a particle suspension being crystalline in

nature and having an improved physical stability compared to a precipitated product.

According to the patent, the process can be separated into three general categories; in addition there are two basic preparation methods, A and B.

The steps of the process are identical for each of the categories, the categories themselves are distinguished based on the physical properties of the drug after precipitation (prior to the energy-addition step) and after the energy-addition step.

Category I: The drug particles in the presuspension are in an amorphous form, semicrystalline form, or a supercooled melt.

Category II: The drug in the presuspension is in a crystalline form.

Category III: The organic compound is in a crystalline form that has many imperfections, which means, it is friable.

In each of the three categories, after the energy-addition step, the drug nanocrystals are in a crystalline form, which means a physically stable low-energy form with few imperfections. The energy-addition step is more effective, and leads to smaller particles than the drug crystals in the presuspension which are, for example, in an amorphous form (category I) or a crystalline form with a high friability (category III). The physical properties of the drug particles are characterized by DSC or X-ray. Which category of particles is formed depends on many factors, for example, the chemical nature and melting point of the drug, precipitation rate, surfactants present, and precipitation temperature. By adding energy, the physical stability of the suspension is improved, that is, by altering the lattice structure of the crystal to a low-energy form. In addition, the added energy seems to have an effect on the coating (surfactant layer) of the particle, leading to a rearrangement and improved stabilizing effect. The latter is concluded when comparing the physical stability of precipitated suspensions with suspensions being exposed to an additional energy-addition step, both dispersions having a similar effective particle size between 200 nm and 2.0 μm.

In method A, the drug is dissolved in the first solvent. A second aqueous solution is prepared containing one or more surfactants; if necessary, the pH is adjusted to yield optimum precipitation conditions. Then the first solution is added to the second solution, the addition rate is chosen depending on the batch size and precipitation kinetics for the organic compound, and the solutions are under constant agitation. If desired, the resulting particles can undergo an annealing step to convert category I particles (amorphous, semicrystalline, and supercooled) into a more stable solid state. In the next step, energy is added, for example, by subjecting the presuspension to sonication, homogenization (piston-gap), microfluidization, or other suitable methods providing cavitation, shear, or impact forces. Homogenizers used are, for example, the Avestin apparatus EmulsiFlex-C 160 to promote a desired phase change into a more perfect crystal; the sample might be subjected to higher temperatures from about 30 to 100 °C during the energy-addition step (annealing step). That means that annealing is basically performed by adding energy (homogenization, etc.), and additionally by variation of temperature.

In method B—different from method A—the surfactant or surfactant mixture is added to the first solution. In the second step, the first solution is added to the second solution. This leads to a formation of more uniform, finer particles compared to having the surfactant in the second solution [60]. Drug examples processed are itraconazole and carbamazepine.

A disadvantage of the microprecipitation method by Baxter is that additional process steps are required compared to direct homogenization of jet-milled drug powder (e.g., Nanopure® technology). The drug needs to be dissolved, precipitated, and then the solvent needs to be removed again, including analysis for solvent residues.

The advantages of the Baxter method are that the problem of the precipitation technique—continuing crystal growth after precipitation—has been overcome because the particles are only an intermediate product to undergo subsequent diminution/annealing. In addition, by optimal choice of precipitation conditions, more friable particles (semicrystalline, amorphous) can be produced which allow more effective diminution in the subsequent high-pressure homogenization step. This is of special importance when the available jet-milled drug is highly crystalline and simultaneously possesses a very hard crystal structure (high Mohs degree). In such cases, the direct homogenization of the jet-milled powder can require a higher number of homogenization cycles, that is, longer production times. In the case of very hard crystals, the maximum homogenization pressure applicable during production (e.g., 2000 bar) might potentially lead to a maximum dispersivity being rather close to 1 μm, and not in the preferred nanometer range.

At present, Baxter has various homogenization technologies, which means, depending on the properties of the drug and the desired target, the optimal process method can be chosen to minimize production time and costs.

6. PERSPECTIVES OF THE DRUG NANOCRYSTAL TECHNOLOGY

As outlined above, there is a definite need to find a smart formulation to overcome the bioavailability problems of poorly soluble drugs. There will be a huge market for such a formulation when looking at the percentages of the drugs being poorly soluble. Preferentially, the formulation solution should also cover drugs which are poorly soluble in aqueous media and simultaneously in nonaqueous, for example, organic, media. Nanonization, that is, production of drug nanocrystals by bottom-down technologies, definitely appears as the most promising approach. The striking reasons for this is that it is a general technology which can be applied to any drug independent of its solubility properties; in addition, the production process is simple in the case of bottom-down techniques.

The area of pearl/ball milling is extensively covered by élan/Nanosystems. The technology has a potential to be used for oral products. Contamination issues might be less of a problem when the milling times are short in the case of less hard crystalline drugs or when contamination is removed by a purification process. The feasibility has been proven by the tablet Rapamune® being on the market. The technology

appears more critical for parenteral products, for example, IV, because higher regulatory requirements need to be met.

An alternative production technique, homogenization in water, has been covered by the previously competing companies RTP (Microfluidizer®) and SkyePharma PLC (piston-gap homogenizer). This situation was clarified in the first half of 2002 by SkyePharma PLC finally taking over RTP. By the takeover, competition was reduced, leaving only two in this market of drug nanocrystals. The Baxter Company is also using homogenization in water for its product Nanoedge®.

Nanopure® technology is the new third way to produce drug nanocrystals in this densely covered market. Nanopure® allows producing any product as produced by SkyePharma PLC just by simply admixing water with a non-aqueous medium, for example, a mixture of 10% ethanol and 90% water. The ethanol is not critical at all for oral products because, generally, the suspensions are spray dried. In the case of using glycerol–water mixtures $(97.5 + 2.5)$, directly isotonic suspension for intravenous injection is obtained. In addition, it has some interesting features when homogenizing in water-free media. Drug nanocrystal suspensions in miglyol/MCT oil or PEG 600 can directly be filled into soft gelatine capsules. The drug nanocrystal suspension can also be produced in melted PEG 6000; after solidification of the PEG 6000, the drug nanocrystals are fixed, and the powder can be coarsely milled and filled into hard gelatine capsules. The coverage of low temperature in water-free media is of interest for temperature-sensitive drugs or molecules being susceptible to hydrolysis or/and high temperature. To summarize, Nanopure® provides the possibility to make at least an identical product or even an improved product. Drug nanocrystal suspensions which are not long term stable as aqueous suspensions can be formulated as glycerol or oily suspensions. The Nanopure® technologies indeed provide an alternative choice for companies with formulation problems, in addition to the other technologies on the market.

There is a definite need for a novel formulation of poorly soluble drugs. In the laboratories, the drug nanocrystals—independent of which top-down technology is employed for their production—proved to be such a formulation; many convincing data are available. The final criterion for a technology is its feasibility, proven by the appearance of products on the market. Polymeric nanoparticles have been investigated for almost 30 years; despite this huge input, to our knowledge, no product is on the market (only polymeric microparticles). In contrast to this, the first nanoparticle/nanocrystal product Rapamune® has recently been launched. Due to the huge number of drug candidates in the pipeline, a high number of products should follow.

GLOSSARY

Drug nanocrystal Particle with a diameter between approximately 5–10 nm up to 1000 nm, composed of a pure drug without any matrix material. Drug nanoparticles can be completely crystalline in nature, partially crystalline, or amorphous, and are produced either by bottom-up technologies or top-bottom technologies.

Drug nanosuspension Nanosuspension composed of drug nanocrystals (cf. nanosuspension).

Nanosuspension In the strict sense, a suspension of drug nanocrystals in a dispersion medium. Typically, the suspension is stabilized by surfactants or polymeric stabilizers (stearic stabilization). The dispersion medium can be water, mixtures of water with other water-miscible liquids, or nonaqueous media such as oils, liquid polyethyleneglycol (PEG).

REFERENCES

1. E. Merisko-Liversidge, "Particles 2002," Orlando, FL, Abstract 45, 2002, p. 49.
2. A. T. Florence and D. Attwood, "Physichochemical Principles of Pharmacy." Chapman and Hall, New York, 1981.
3. D. J. W. Grant and H. G. Brittain, in "Physical Characterization of Pharmaceutical Solids" (H. G. Britain, Ed.). New York: Marcel Dekker, 1995.
4. R. H. Müller, K. Krause, and S. Anger (publication in preparation).
5. http://physchem.ox.ac.uk/MSDS/OL/oleic_acid.html.
6. "The Merck Index," 12th ed. Merck & Co., Inc., Whitehouse Station, NJ, 1996.
7. "Remington," 15th ed. Mack Publishing, Easton, PA, 1975.
8. M. Mosharraf and C. Nyström, *Int. J. Pharm.* 122, 35 (1995).
9. C. Nyström and M. Bisrat, *Int. J. Pharm.* 47, 223 (1988).
10. R. H. Müller, S. Benita, and B. H. L. Böhm, Eds., "Emulsions and Nanosuspensions for the Formulation of Poorly Soluble Drugs." Medpharm Scientific Publishers, Stuttgart, 1998.
11. R. Voigt, "Lehrbuch der Pharmazeutischen Technologie." Verlag Chemie, Berlin, 1984.
12. H. Kala, U. Haak, U. Wenzel, G. Zessin, and P. Pollandt, *Pharmazie* 42, 524 (1987).
13. "Hagers Handbuch der Pharmazeutischen Praxis." Springer-Verlag, Berlin, 1925.
14. M. List and H. Sucker, Patent GB 2200048, 1988.
15. P. Gassmann, M. List, A. Schweitzer, and H. Sucker, *Eur. J. Pharm. Biopharm.* 40, 64 (1994).
16. R. H. Müller and G. E. Hildebrand, Eds., "Pharmazeutische Technologie: Moderne Arzneiformen 2. Aufl. Wissenschaftliche." Verlagsgesellschaft mbH, Stuttgart, 1998.
17. P. Gaßmann and H. Sucker, GB Patent 2200048; GB Patent 2269536, 1994.
18. P. H. List, "Arzneiformenlehre, p. 205." Wissenschaftliche, Verlagsgesellschaft GmbH, Stuttgart, 1982.
19. M. R. Violante and H. W. Fischer, U.S. Patent 4, 997, 454, 1991.
20. S. Schenderlein, M. Husmann, M. Lück, H. Lindler, and B. W. Müller, "Proceedings of the 13th Symposium on Microencapsulation." Angers, France, Sept. 7 2001, p-074.
21. B. W. Müller, EP 0 605 933, 1998.
22. N. Rasenack and B. W. Müller, *Pharm. Res.* 19, 1894 (2002).
23. R. Buscall and R. H. Otewill, pp. 141–217. Elsevier Applied Science Publishers, London, 1986
24. R. H. Müller, K. Peters, and D. Craig, "International Symposium on Control. Rel. Bioact. Material," 1996, Vol. 23, pp. 925–926.
25. G. E. Hildebrand, J. Tack, and S. Harnisch, Patent WO 072955A1, 2000.
26. R. H. Müller and B. H. L. Böhm, "Dispersion Techniques for Laboratory and Industrial Scale Processing." Wissenschaftliche Verlagsgesellschaft mbH, Stuttgart, 2001.
27. K. Schalper, S. Harnisch, R. H. Müller and G. E. Hildebrand, "4th World Meeting on Pharmaceutics, Biopharmaceutics and Pharmaceutical Technology (APV, APGI)," Florence, 2002.
28. K. Schalper, Herstellen hochdisperser Systemen mit Kontunierlichen Mikromischern, Ph.D. Dissertation, Dept. of Pharm.

Technology, Biotechnology & Quality Management, Free University of Berlin, 2003.

29. K. J. Illig, R. L. Mueller, K. D. Ostrander, and R. Jon, *Pharm. Technol.* (Oct. 1996).

30. R. H. Müller, R. Becker, B. Kruss, and K. Peters, U.S. Patent 5, 858, 410, 1999.

31. G. G. Liversidge, K. C. Cundy, J. F. Bishop, and D. A. Czekai, U.S. Patent 5,145,684, 1992.

32. S. Buchmann, W. Fischli, F. P. Thiel, R. Alex, and Mainz, "Proceedings of the Annual Congress of the International Association for Pharmaceutical Technology (APV)," 1994, p. 124.

33. R. H. Müller and K. Peters, "International Symposium on Control. Rel. Bioact. Materials," 1997, Vol. 24, pp. 863–864.

34. G. Vergnault, "Workshop 'Nanobiotech Medicine,' Nanobiotech 2001," Münster, 2001.

35. M. R. Hilborn, "Particles 2002," Orlando, FL, 2002, Abstract 48, p. 50.

36. P. Indu and S. Ulagaraj, U.S. Patent 5,922,355.

37. M. Freeman, *New Drugs* 2, 13 (2001).

38. B. H. L. Böhm, M. J. Grau, G. E. Hildebrand, A. F. Thünemann, and R. H. Müller, "International Symposium on Control. Rel. Bioact. Materials," 1998, Vol. 25, pp. 956–957.

39. Company brochure, Niro-Soavi Deutschland, 2000.

40. H. Stricker, "(Hrsg.), Physikalische Pharmazie," Wissenschaftliche Verlagsgesellschaft GmbH, Stuttgart, Auflage, 1987.

41. K. P. Krause, O. Kayser, K. Mäder, R. Gust, and R. H. Müller, *Int. J. Pharm.* 196, 169 (2000).

42. K. Krause and R. H. Müller, *Int. J. Pharm.* 214, 21 (2001).

43. R. H. Müller, K. Peters, R. Becker, and B. Kruss, "1st World Meeting on Pharmaceutics, Biopharmaceutics and Pharmaceutical Biotechnology (APGI/APV)," Budapest, 1995, pp. 491–492.

44. K. Peters and R. H. Müller, "Proceedings of the European Symposium on Formulation of Poorly Available Drugs for Oral Administration, APGI/APV," Paris, 1996, pp. 330–333.

45. B. Böhm and R. H. Müller, *Pharm. Sci. Technol. Today* 2, 336 (1999).

46. R. H. Müller, B. H. L. Böhm, and M. J. Grau, *Pharm. Ind.* 61, 74 (1999).

47. R. H. Müller, K. Mäder, and K. Krause, PCT Application PCT/EP00/06535, 2000.

48. R. H. Müller and K. Peters, *Int. J. Pharm.* 160, 229 (1998).

49. C. Jacobs, O. Kayser, and R. H. Müller, *Int. J. Pharm.* 196, 161 (2000).

50. B. H. L. Böhm, D. Behnke, and R. H. Müller, "2nd World Meeting on Pharmaceutics, Biopharmaceutics and Pharmaceutical Biotechnology (APGI/APV)," Paris, 1998, pp. 621–622.

51. M. J. Grau, O. Kayser, and R. H. Müller, *Int. J. Pharm.* 196, 155 (2000).

52. R. H. Müller, C. Jacobs, and O. Kayser, *Adv. Drug Del. Rev. (ADDR)* 47, 3 (2001).

53. C. Jacobs and R. H. Müller, *Pharm. Res.* 19, 189 (2002).

54. R. H. Müller and C. Jacobs, *Int. J. Pharm.* 237, 151 (2002).

55. A. Akkar and R. H. Müller, "Access of Therapeutics to the Brain, 8th UKICRS Symposium," Belfast, 2003, Abstract Book, Poster 12.

56. K. Krause and R. H. Müller, *Int. J. Pharm.* 223, 89 (2001).

57. B. W. Müller, U.S. Patent application 08/531, 283, 20.09, 1995.

58. K. P. Krause and R. H. Müller, "28th International Symposium on CRS," San Diego, 2001, p. 722.

59. J. E. Kipp et al., U.S. Patent application 20020168402 A1, Nov. 14, 2002.

60. F. Sylvan, J. E. Lofroth, and B. Levon, U.S. Patent 5,780,062.

61. B. H. L. Böhm, "Herstellung und Characterisierung von Nanosuspensionen als neue Arzneiform für Arzneistoffe mit geringer Bioverfügbarkeit," Ph.D. Dissertation, Dept. of Pharm. Technology, Biotechnology & Quality Management, Free University of Berlin, 1999.

Dye/Inorganic Nanocomposites

A. Lerf

Walther-Meissner-Institut für Tieftemperaturforschung, Garching, Germany

P. Čapková

Charles University, Prague, Czech Republic

CONTENTS

1. INTRODUCTION

Pigments based on inorganic framework structures and intercalated species have been known for a long time and used by mankind for centuries: the semiprecious stone lapis lazuli and Mayan blue. The first one is a natural occurring mineral, which can be used for the preparation of a valuable and very expensive pigment. Its application in ancient Egypt is questioned [1], but the original stone has been used in many art objects for more than 5000 years (an example is shown in Fig. 1) [2]. The origin of the blue color was solved only recently [2]. The main component is a framework silicate based on the sodalite-type cage. The colored species is very probably the S_3^- radical anion [3]. The second material mentioned has been used as a pigment for murals and other art objects (an example is shown in Fig. 2 [4, 5]). It is of purely artificial origin and its application goes back in pre-Columbian times [4–6]. The blue color seems to be caused by the intercalation of indigo in the channel-type clay

mineral palygorskite and/or sepiolite [4–6]. The brilliance of the pigment could be influenced by metal nanoparticles deposited on the pigment during preparation [6].

The most recent interest in dye/inorganic composites has been devoted to the optic properties of the dyes and their changes during adsorption/intercalation on inorganic materials. Apart from the possible applications in photocatalysis, photoelectrochemistry, nonlinear optics, and optoelectronics the photophysical properties of the dyes can be easily monitored by ultraviolet-visible (UV-vis) spectroscopy and allow some insight in the guest–guest interactions under the conditions of constrained microenvironments in the interlayer space of layered hosts or in the mesopores of three-dimensional open frameworks as in zeolites or in other meso- and microporous materials [7–19]. A prerequisite for application of UV-vis spectroscopy is that the solids are transparent for UV or visible light. Nearly all materials discussed in the following are electric insulators with a rather big bandgap, thus fulfilling this condition.

An enormous amount of material has been collected in the last 20 years in this field of research and the interest in dye/inorganic composites is still increasing. In order to cope with this huge amount of literature we will cite as much as possible previous review articles [7–19]. Original papers are only cited if they appeared after the excellent review of Ogawa and Kuroda [14] or if we need it for a peculiar argumentation.

2. DYE/INORGANIC COMPOSITES

Adsorption and/or intercalation of organic molecules or molecular cations is nearly as old as the field of intercalation; thus it dates back to the 1930s [20, 21]. At this time intercalation of organic compounds was restricted to clay minerals. The adsorption of various organic substances by natural and chemically altered or heat-treated clays can produce color changes in the clay. Well pronounced is the

Figure 1. Photograph of an art piece containing lapiz lazuli (bracelet with a scarabaeus, piece from the buriel chamber of Tutenchamun). Photography provided by Dr. D. Wildung [2].

coloration of clays, which have been loaded with aromatic amines. The coloration is caused by oxidation with oxygen and/or by structural iron ions after intercalation via cation exchange [22–26]. In [22] an exhaustive list of color forming amines is given. However, only the color reaction of benzidine has been studied in greater detail [24–26]. The formation of crystal violet was observed as early as 1941, if clays have been treated with dimethylaniline vapor [23]. Colored complexes have also been obtained by the adsorption of certain aromatic molecules on montmorillonites saturated with transition metals in the interlayer space [27, 28]. A further method to get coloration is by an acid–base reaction in which the natural or the acid-treated clay behaves as an acid and the adsorbed molecules, known as an acid–base indicator, accept protons and change their color [24, 29]. Without any chemical reaction clays became colored when loaded with organic dye molecule cations or colored metal chelate complexes via ion exchange. Staining of clays with dyes has been used for the determination of the cation exchange capacity, monitoring the surface acidity, colloidal properties,

Figure 2. Mural painting from Cacaxtla: The blue color is made from the so-called Mayan blue; it is a intercalation complex of indigo in the framework clay mineral palygorskite [4–6]. Reprinted with permission from [4], C. Reyes-Valerio, http://www.azulmaya.com.

and redox active sites. These types of application have been reviewed several times and shall not be discussed in detail here [20, 21, 30–33].

For aniline and some aromatic heterocycles the color reaction due to oxidation is only an intermediate state toward the final formation of conducting polymers. The transformation of aniline to polyaniline can be achieved by the external acting oxidant sodium peroxodisulfate (e.g., in case of a zeolite [33]) or by treating Cu^{2+} or Fe^{3+} loaded clays and zeolites with aniline, pyrrol, or thiophene vapors [34–41].

The second wave of interest on the intercalation of colored/or color forming species was devoted to those dye systems, which are photosensitive and/or redox active. It started soon after 1975 when Balzani et al. [42] proposed several cyclic reactions involving transition metal complexes, which would result in the net photodecomposition of water either to H_2, O_2, or both (please note the temporal coincidence with the first oil market crisis!). The key compound in constructing redox cycles for photodecomposition of water became the $[Ru(bpy)_3]^{2+}$ complex because of several attractive features [43–45]. The principal design of such a water-splitting redox cycle is as follows [46–49]:

$$D + h\nu \longrightarrow D^* \qquad (D = \text{dye sensitive to visible light}$$
$$= \text{donor)} \qquad (1)$$

$$D^* + A \longrightarrow D_{ox} + A_{red} \qquad (2)$$

$$D_{ox} + OH^- \longrightarrow D + \frac{1}{4}O_2 + \frac{1}{2}H_2O \qquad (3)$$

$$A_{red} + H^+ \longrightarrow A + \frac{1}{2}H_2 \qquad (4)$$
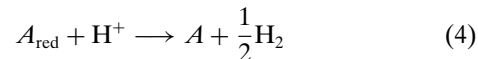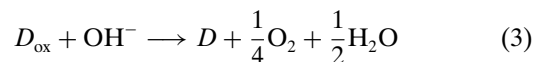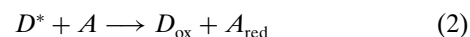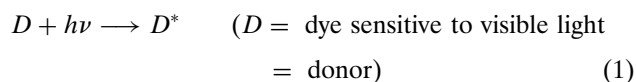
Oxidation and reduction catalysts are necessary for steps (3) and (4) in order to reduce the overpotentials of these reactions. In Lehn's experiments Pt and RuO_2 played this role [46, 47]. It became clear very soon that systems based on this reaction sequence have little chance to be effective unless one designs their architecture at a supramolecular level in such a way to promote the electron transfer from D^* to A, to separate D_{ox} and A_{red} to avoid recombination, to separate catalytic sites for H_2 and O_2 [49, 50]. A crucial step in these redox cycles is the electron flow from the excited sensitizer to the first electron acceptor. First, metal complexes have been used for this purpose [46–50]. Also semiconductors have been proposed as a way of achieving charge separation and have led to molecularly sensitized cyclic water cleavage systems [51]. Nijs et al. introduced clay minerals to solve the "architectural" problem. As electronically insulating but negatively charged solids they can support the catalysts and control the position of the ionic species in the medium [49]. About 1981 the methyl viologen system was introduced in the redox cycles as the first electron acceptor of the excited electrons of the sensitizers, maybe due to its fortunate redox potential and its high stability against further chemical modifications [52]. Later on the search for suitable, more complex architectures of redox cycles for the photodecomposition of water has been extended to further intercalating layered and framework structures (see Sections 3 and 6.3).

The previous reaction cycle is the shortest functional cyclic redox system (Fig. 3b, middle and bottom), which can
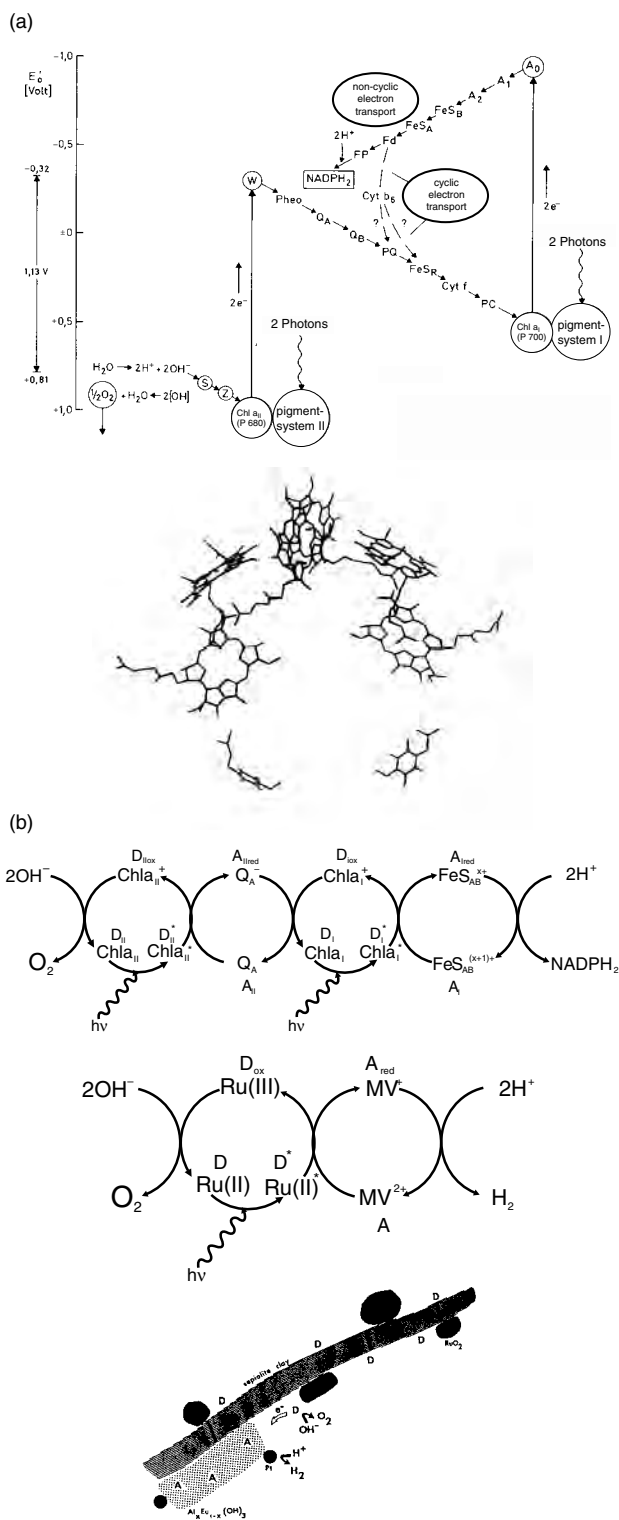
(a)

(b)

Figure 3. Light driven redox reaction cycles in plant photosynthesis and artificial water splitting system. (a) Electron transfer chains in plant photosynthesis [53] (top) and the arrangement of pigments in the reaction center of the photosynthesis unit of Rhodopseudomonas sphaeroides [54] (bottom). (b) Simplified representation of the redox system shown in (a), top, using the terminology of Eqs. (1)–(4) (top), cyclic representation of the equations applied to an artificial photochemical system (middle), and a sketch showing the component assembly in the mixed colloid system which is able to split water under illumination [49].

be used to mimic the light driven reaction sequence of plant photosynthesis. Neglecting that the electron transfer steps in plant photosynthesis (Fig. 3a) are much more complex than those given in Eqs. (1)–(4) one will realize immediately that there are two coupled simple redox cycles [cf. Fig. 3a (top) and Fig. 3b (top)]. The first one is connected with the photosystem (PS) I and the second with PS II. The electron of the excited sensitizer of PS I ($Chla_I$-P700) is transferred through some intermediate steps to the first stable electron acceptor A—an Fe–S protein—and finally used for the production of reducing equivalents $NADPH_2$ (instead of H_2). This process corresponds with Eq. (4). The oxidized state of the donor ($Chla_I$-P700$^+$ = D_{ox}) is brought back to the initial state D = $Chla_I$-P700 by the electron transfer from the first stable electron acceptor of the PS II and not directly from water; this reduced acceptor is a reduced quinone. It is reduced due to the electron transfer from the excited state of the $Chla_{II}$-P680 = D_{II}^+ belonging to PS II. The oxidized state of P680$^+$ gets its electron back from water under oxygen deliberation. Figure 3a (bottom) shows the photosynthetic reaction center of Rhodopseudomonas sphaeroides, which is very similar to the reaction center of the LHCII of plants [53, 54]. It is the place for charge separation and its proper function depends crucially on the right architecture and spacing of the various antenna and electron acceptor molecules. Compared with this the solid-state model for reaction sequence Eqs. (1)–(4) is rather "primitive" (Fig. 3b, middle and bottom). However, it is really astonishing that it works so well, even if it did not come to a technical application.

Despite the disappointing result of the efforts to mimic photosynthesis it remains a valuable "by-product" of these trials that the photophysical investigation of various light sensitive and redox active systems brought insight in the organization of complex molecules on the external and internal surfaces of intercalating hosts. In addition some of the dyes investigated found applications as electron mediators in photocatalytic processes and clay-modified electrodes [55, 56].

A new boost to the field of dye-inorganic composites comes from the demand of functional supramolecular arrangements in the strongly growing nanosciences. This boost is also accompanied with a shift of interest, from photocatalysis to lasing, second harmonic generation (nonlinear optics), spectral hole burning, quantum confinement, and quantum superstructures. Before we get into the details of these new developments we would like to remind the reader about early trials to produce supramolecular functional units by a sort of self-assembly.

Kuhn used in the 1960s the long-known Langmuir–Blodgett technique [57–59] to produce organized arrangements of molecules, which show properties depending on this arrangement [60–63]. In his seminal article written in 1965 he formulated the principles of supramolecular chemistry [60]. Since his original text is so well written and clear we cannot resist repeating here his original version [60]:

Die im folgenden zu beschreibenden Versuche gehen von der Zielsetzung aus, einfachste organisierte Systeme von Molekülen zu bauen, das heißt Anordnungen einzelner Moleküle, welche Eigenschaften haben, die durch die Besonderheit der Anordnung bedingt sind. Während die Moleküle schon in einfachsten biologischen Strukturen in hoch organisierter Weise assoziiert sind,

fehlt es dem Chemiker an Methoden, um Moleküle in vorausgeplanter Weise aneinanderzufügen. Er kann sehr komplizierte Moleküle synthetisieren, aber er kann nicht wie die Natur Aggregate von verschiedenen Molekülen in geplanter Ordnung bauen.

Man kann das ferne Ziel der Herstellung größerer organisierter Assoziate von Molekülen in zwei Aspekten sehen. Einerseits wird man bestrebt sein, einfache biologische Strukturen nachzuahmen; andererseits wird man sich bemühen, ganz unabhängig vom Vorbild der Natur irgendwelche der Phantasie entspringende Anordnungen von Molekülen herzustellen, die nützliche, von der genauen Anordnung der Moleküle im Aggregat abhängige Eigenschaften haben und die somit Werkzeuge mit molekular dimensionierten Bauelementen darstellen.

Kuhn and co-workers studied the photochemical properties of synthetic dye molecules (mainly cyanins) embedded in membrane-like multilayer assemblies. These dye molecules carry long-chain alkyl residues, which fit them in the membrane forming amphiphiles. The authors studied mainly the influence of the distance between the sensitizer molecules and the acceptors on the fluorescence and phosphorescence of the prime photon acceptors. A typical arrangement is shown in Figure 4. It shows also a schematic view of the Langmuir trough, the equipment used for preparation of these assemblies. From the historical point of view it is of interest to give also the sketch of Pockels showing her assembly for measuring dense packing of monolayers. Figure 4d is a microscope view of a ferritin assembly made by the same technique and showing a highly ordered hexagonal arrangement of the iron oxide cores. It corresponds very well with recent arrangements of quantum dots [64]. These studies have been continued by many other scientists in different fields of applications, like nonlinear optics, piezoelectric devices, photoelectron transfer processes, photovoltaic effects, electrochromic, thermochromic, and photochromic devices, field effect devices, and various types of sensors [65, 66]. As far as we know real applications of these systems have not been achieved up to date, maybe due to problems with long-term stability of these molecular assemblies, especially in aqueous media.

This may be one of the reasons the assembly of metal-organic or organic dye species within inorganic crystalline host materials by intercalation processes has been investigated. These inorganic hosts (mainly two-dimensional anisotropic or zeolite-type materials) may lead to an increased stability of the organic species, keep them separated from other components in the surrounding medium, and may support preorientation of the guest molecules which could be of advantage for various applications. However, the uptake of bulky organic species in natural or synthetic preformed hosts is rather limited and their orientation is often dominated by the interaction of the π-electron systems with the inorganic intracrystalline surfaces, thus preventing guest–guest interactions. On the other hand the question arises whether the arrangement of the dye molecules in the interlayer space is really of importance for electrochemical and photofunctional applications. Cyclovoltaic studies of clay modified electrodes gave some evidence that the capture of the redox mediators in the interlayer galleries prevents the diffusion in the electrolyte medium, but the amount of electroactive species is very low; thus only those species very near the outer surface of the crystals are really involved in the electrochemical processes
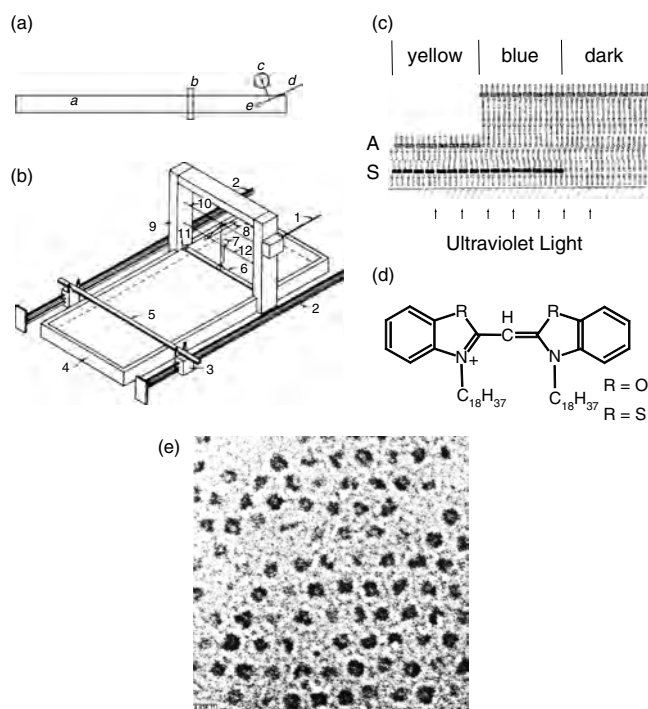
Figure 4. Langmuir–Blodgett technique: (a) Drawing by A. Pockels showing her film balance. Reprinted with permission from [?], A. Pockels. (b) Sketch of a modern Langmuir–Blodgett trough [65]. (c) Cut through a Langmuir–Blodgett assembly made of cyanins shown in (d); the assembly is irradiated by UV light which is absorbed by the sensitizer S. Zone 1, energy transfer from S to the acceptor A at a distance of 50 Å, yellow fluorescence; zone 2, distance S to A of 150 Å, no energy transfer, blue fluorescence of sensitizer S; zone 3, sensitier S omitted, no fluorescence because the light is not absorbed. If irradiated with blue visible light, which is absorbed by A all three compartments show yellow fluorescence of A. Reprinted with permission from [62], H. Kuhn and D. Möbius, *Angew. Chem.* **83**, 672 (1971); *Int. Ed. Eng.* **10**, 620 (1971). © 1971, VCH, Weinheim. (d) Structural formula of the cyanins used to build the Langmuir–Blodgett assembly shown in (c). In the sensitizer S oxygen is the second heteroatom in the five-membered ring (R = O). In the acceptor A the heteroatom R corresponds to sulfur. (e) Ferritin assembly adsorbed on a stearicacidmethylester/trimethyldodeclammoniumsulfate film. Dense packing of the proteins as detected by the ferritin cores in an electron microscope view [62].

[56, 67, 68]. Photophysical investigations have been carried out mainly on dye molecules adsorbed to clay or Zr–phosphate colloids prior to precipitation [14, 15]. Thus the loading with the dyes is below the cation exchange capacity. In these studies metachromic shifts of the absorption bands have been observed which can be interpreted in terms of dye aggregate formation [14, 15, 19, 32]. Since the space limitations in the interlayer galleries prevents mainly aggregate formation several authors conclude that these aggregates are formed on the external surfaces of the colloids or in the mesopores within the tactoid aggregates of partially restacked layers of the host colloidal layers [14, 15]. Apart from these problems of dye distribution in intra-crystalline and external surfaces there is only information about the layer distances which gives some idea about whether we have dye molecules in the interlayer space or not.

In case of co-adsorption/co-intercalation of more than one dye species, which is of interest for the formation of photofunctional units, the situation is even worse (see Section 6.2). From the aforementioned problems one can conclude that the distribution of both species in the intracrystalline and external surfaces may be more or less random unless there is a preferred aggregation of AB pairs with respect to AA or BB interactions, or vice versa. Even if there is such a preferred aggregation it is not quite certain that such AB pairs will be unchanged if they are inserted in the interlayer space, though the chance to plan the arrangement of sensitizers and photon or electron acceptors is much lower than in the case of the Langmuir–Blodgett multilayers.

In the inorganic/organic composites there is not only the problem of planned distribution of different functional units but also the problem of orientation of the dye loaded solid particles. Due to the uniform size of the membrane forming amphiphiles the dense packing of the molecules is possible under the conditions of the Langmuir–Blodgett technique, even in a macroscopic area. In case of the inorganic particles one has a particle size distribution, which does not have be very regular. In case of anisotropic solids with a fortunate aspect ratio the orientation of the particles parallel to the layers should be without problems, at least in the proper electrolyte medium. However, the orientation within the layers is nearly impossible if there is a particle distribution. It will be hard also to have a dense packing of the particles without any macroscopic voids.

In order to overcome all these problems completely new preparation procedures have been developed: layer-by-layer deposition [19, 69–72] and the *in-situ* synthesis of the organic/inorganic composites [19, 73–75]. The prerequisite for both techniques is a new class of dye molecule derivative which shows great potential to form stable well-ordered assemblies on an inorganic solid template and in aqueous solutions, respectively. In almost all cases they consist of the aromatic dye unit with an elongated shape (azo-benzenes, styryl compounds), with strong charge transfer interactions (porphyrins or phtalocyanines without and with complexing metals) or they are modified in such a manner that they are substituted with long tails of alkyl chains and positively or negatively charged head groups. The chromophor is in the center of the molecule. Some systems used recently are shown in the scheme. Up to now the first technique has been applied to clay minerals, Zr-phosphate, and some layered oxide systems forming new forms of clay modified electrodes [71, 72] or photofunctional units with charge separation after illumination [69].

The second is rather new. Structure directing assemblies containing chromophores have been used as templates in hydrothermal processes, in which the inorganic material is deposited on the surfactant system. This follows the lines of synthesis of the large pore zeolite analogs of MCM type. In this procedure new dye/inorganic composites have been obtained with the following inorganic matrices: M41S [73, 74] and anionic clays [75]. In these samples completely new arrangements of the chromophores have been realized and the packing density seems to be higher than in the normal intercalation compounds.

Both methods may help to design the dye organization but do not solve the problem of particle orientation and the formation of micropores. One trial to tackle the problem of particle orientation is the successful directed growth of zeolites with one-dimensional channels [13, 16, 76]. The as-grown crystals are arranged in such a manner that the channels are aligned perpendicular to the solid support.

The previous discussion was devoted mainly to the layered dye–inorganic host composites. Since about 1985 there has been growing interest on dye species inserted in framework structures like silica gels, zeolites, and zeolite-like frameworks [8, 13, 16–19]. Due to the diameter of channels or supercages the dye–dye interactions are much more restricted than in the case of layer composites and also the dimension of the inserted dye molecules is restricted by the size of the pores. In many cases only linear arrangements of the long axis of the dye molecules in parallel channels are possible. The rigid walls of the channels prevent large-scale rotations and the diffusion of the molecules. These peculiar and strongly restricted preorientations may be of advantage for applications in quantum superstructures and other optic and electronic devices. This preorientation is visualized in the response to light of preferred polarization as shown in
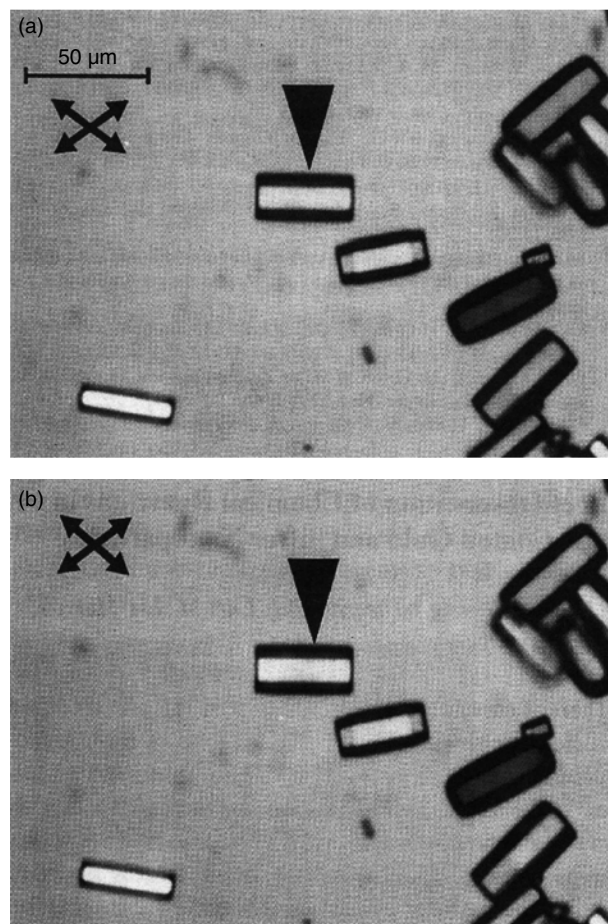

Figure 5. Azobenzene loaded $AlPO_4$-5 crystals between polarizers crossed at an angle of 70°, which gives optimal visual contrast (the directions of polarization are indicated by the crossed arrows). One crystal marked with a pointer was irradiated: before (top) and after (bottom) irradiation. Reprinted with permission from [77], K. Hoffmann et al., *Adv. Mat.* 9, 567 (1997). © 1997, VCH, Weinheim.

Figure 5. The special microenvironment in these materials may prevent also the diffusion out of the channel and will lead to a higher chemical stability of the dye molecules. The inclusion of rather big dyes during synthesis of the frameworks will improve the stability and could be of advantage for the application of the dye–zeolite composites as new pigments. The new mesoporous systems with rather big channel diameters are now accessible for a larger number of dyes even those with more bulky shape [18].

3. HOST LATTICES AND GUEST SPECIES

3.1. Layered Host Lattices

Layered structures represent a very suitable matrix for insertion of various guest species, because they are able to accommodate very large guest molecules in the interlayer space by the free adjustment of the interlayer space [78–83]. The number of host systems investigated with respect to the uptake of dye molecular species is much more restricted than the number of host systems known to undergo intercalation processes. Those host lattices for which dye intercalation has been described are collected in Table 1 (whereas a comprehensive list of layered host lattices for intercalation is given in [83]). With the exception of 2H-TaS$_2$ all compounds listed in Table 1 are electronic insulators or wide gap semiconductors.

The most important layered host materials are the so-called 2:1 clay minerals, natural and synthetic ones. They consist of two flat corner-shared Si–O tetrahedral networks whose apices points toward each other and take part in the formation of the central metal-oxide/hydroxide layer, which is of the brucite-type structure (see Fig. 6). In the ideal case all the octahedral holes are occupied by Mg (talc) or Al ions (pyrophyllite) only (trioctahedral or dioctahedral, respectively). Normally some of these ions are replaced by other metal ions of the same or different positive charges. Also the Si ions in the tetrahedral layers can be substituted by Al^{3+} or Fe^{3+} ions. The substitution by other valent ions leads to an overall negative charge of the clay layers, which has to be compensated by hydrated cations in the interlayer space (not shown in Fig. 6). These interlayer cations (normally alkali metal ions) can be exchanged easily by other inorganic and a huge number of organic cations, including cationic dyes. In addition these interlayer cations undergo very peculiar interactions with neutral solvating species. The well-developed intercalation chemistry of clay minerals is the subject of many review articles, for example [20, 21, 83, 85–87]. The majority of the clays which have been used for dye intercalation belong to the class of smectites characterized by a low negative charge. The most frequently used minerals are the montmorillonites (dioctahedral); others are the trioctahedral minerals hectorite, fluorohectorite (mostly synthetic), saponites, and the synthetic laponite (similar to hectorite) [14, 32]. Applications of higher charged 2:1 clay minerals in dye intercalation are rare and restricted to some vermiculites [32] and the synthetic fluoro-taeniolite [88, 89]. Most of the investigations concerning dye intercalation are carried out in colloidal solutions of the clays because the uptake of the dyes can be controlled much more easily than the ion exchange of complex molecules in crystalline materials [14, 15, 20, 21, 32] and easily monitored by UV-vis spectroscopy. This is the reason montmorillonite dominates in

Table 1. Layered solids used as hosts for dye intercalation reactions.

Solid type	Formula of examples (mineral name)	Ref.
(i) Uncharged layers		
Metal dichalcogenides	2H-TaS$_2$	[130–132]
Metal phosphorous chalcogenides	MPS$_3$ = Mn, Cd	[223–225]
Oxides	V$_2$O$_5$	[122–127]
Metal oxyhalides	FeOCl	[128, 129]
Metal phosphates/phosphonates	α-Zr(HPO$_4$)$_2$	
	α-Zr(RPO$_3$)$_2$; R= organic residue	
(ii) Charged layers		
(a) Positively charged hydroxides [Hydrotalcite type compounds ("anionic clays")]	[M$^{II}_{1-x}$M$^{III}_x$(OH)$_2$][A$_{x/n}$]mH$_2$O M^{II} = Mg, Fe, Co, Ni, Mn, Zn; M^{III} = Al, Fe, Cr, Mn, V; A^n = inorganic or organic anions	[14, 105–108]
(b) Negatively charged clays	Na$_x$(Al$_{2-x}$Mg$_x$)(Si$_4$O$_{10}$)(OH)$_2$ (montmorillonite)	[14]
	Ca$_{x/2}$(Mg$_3$)(Al$_x$Si$_{4-x}$O$_{10}$)(OH)$_2$ (saponite)	[14]
	M(I)$_{0.67}$(Mg$_{2.65}$Li$_{0.34}$)(Si$_4$O$_{10}$)(OH,F)$_2$ (hectorite)	[14]
	Li$_{0.8}$(Mg$_{2.2}$Li$_{0.8}$)(Si$_4$O$_{10}$)(F)$_2$ [fluorohectorite (synth.)]	
	(Mg)$_x$(Mg$_{3-u}$Al$_y$Fe$^{2+}_v$Fe$^{3+}_w$) (Si$_{4-z}$Al$_z$O$_{10}$)(OH)$_2$; $u = y + v + w$; $x = z - y - w$ (vermiculite)	[32]
	Li(Mg$_2$Li)(Si$_4$O$_{10}$)F$_2$ (taeniolite)	[88, 89]
Layered silicic acids	Na$_2$Si$_4$O$_{29}$ · nH$_2$O (magadiite)	[93]
Oxides	Na$_2$Ti$_3$O$_7$, K$_2$Ti$_4$O$_9$	[111–120]
	K$_4$Nb$_6$O$_{17}$ · 3H$_2$O	
	K[Ca$_2$Na$_{n-3}$Nb$_n$O$_{3n+1}$], 3 < n < 7	

Note: Their structures and intercalation chemistry are described in [78–83]. Literature directly related to dye intercalation is given in the table.
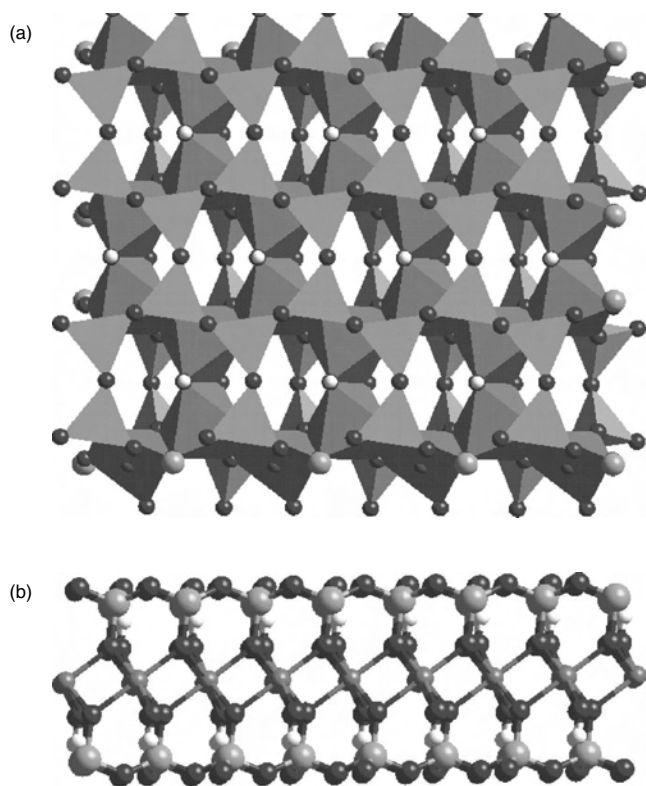
Figure 6. Structure of an isolated monolayer in 2:1 clays shown: perpendicular (a) and parallel (b) to the layers. The drawing is made with a *Cerius*[2] modeling unit. The crystallographic parameters adapted from [84].

Figure 7. Perspective view of structure of α-zirconium phosphate, α-Zr(HPO$_4$)$_2$ · H$_2$O (parallel to the layers) prepared with DIAMOND—Visuelles Informationssystem für Kristallstrukturen (Professor Dr. G. Bergerhoff, Bonn, Germany). The red dots in the interlayer space are water molecules. Crystallographic data adapted from [95].

dye–clay composite research: It can be transferred easily in the colloidal state and its colloidal solutions are well understood and very stable [90–92]. Dyes to intercalate in clay minerals have to be cationic. Very recently the first intercalation of a dye in the layered polymerized silicic acid mineral magadiite has been described [93]. (Please note this silic acid is structurally related to the tetrahedral layers of the clay mineral host lattice [94].)

The next important layered host compounds are the layered Zr–phosphates/phosphonates. The α-modification of Zr(HPO$_4$)$_2$ · xH$_2$O, whose structure is shown in Figure 7, is the most important member of this family of compounds with respect to intercalation chemistry. The intercalation chemistry of this host lattice is described several times [96–99]. In Table 1 it is counted as a neutral compound. Its intercalation chemistry is dominated by the presence of weak Bronstedt acid groups. Compounds with functional groups able to accept protons are the preferred guests and for this reason the intercalation of complex species such as the cyclodextrins or porphyrins has been achieved using their amino derivatives. Ion exchange is possible in a medium controlling the pH and is supported by the hydration water or by other species propping open the interlayer space. For example, the half-exchanged phase with the composition ZrNaH(PO$_4$)$_2$ · 5H$_2$O is formed at a pH > 2, whereas the fully exchanged phase appeared at a pH > 6. In contrast less hydrated large monovalent ions like Cs or highly hydrated divalent ions are not able to replace protons at slightly

acidic or basic media [99]. They can form also colloidal solutions [88], which can be used for the oriented deposition of organic inorganic composites. Unique for all intercalating systems is the following property of the Zr–phosphate system: If phosphoric acid is replaced by organic phosphonates (the chromophore is part of the organic moiety) and these are brought to reaction with Zr ions [71, 72] a solid is formed which has the same arrangement of the Zr–PO$_4$ units as in the purely inorganic α-Zr(HPO$_4$)$_2$ · xH$_2$O. Thus, the Zr^{4+}/phosphate/phosphonate system is an ideal candidate for layer-by-layer deposition of inorganic/organic multilayer assemblies. Their structure is not only determined by the bonding restrictions of the Zr–phosphate arrangement but also by the structure directing influence of the organic counterpart. However, it should be noted that the product of this assembly is no longer an intercalation compound but a three-dimensional covalent network with alternating inorganic/organic layers [69, 71, 72].

A very interesting and versatile class of host lattices is the so-called "anionic clays" [100, 101]. Their chemical composition is given by the general formula $[(M^{2+})_{1-x}(M^{3+})_x(OH)_2]^{x+}(A^{m-})_{x/m}$ · nH$_2$O where M^{2+} = Mg, Ni, Fe and M^{3+} = Al, Cr, Fe. The preferred anion in these compounds is CO$_3^{2-}$, which can be replaced easily by other ions, even very complex ones via ion exchange reactions [100, 101]. A strongly related group of intercalation

compounds can be achieved, if gibbsite is treated with an excess of Li salts [102–104]. The resulting composition of this reaction is [LiAl$_2$(OH)$_6$]X · nH$_2$O with X = Cl, Br, NO$_3^-$. The structure of both series of compounds consists of a brucite-type hydroxide layer structure and the anions are inserted between these hydroxide layers. In case of the gibbsite the Li ions are inserted in the empty octahedral lattice sites of the Al(OH)$_3$/gibbsite layers. Figure 8 shows this structure for the example [LiAl$_2$(OH)$_6$]NO$_3$. Apart from porphyrin derivatives dye anions have been intercalated in the layered hydroxides only recently [105–108]. Because these compounds can be prepared at relatively moderate temperature it is possible to obtain dye–MOH composites by direct synthesis in the presence of the organic moiety as structure directing medium [75]. In order to be inserted in these compounds the chromophore systems should be modified with functional groups giving them an excess negative charge.

There is a large number of layered ternary or quaternary oxides of titanium and mixed systems containing titanium and niobium [14, 109, 110]. The layers consist of Ti/Nb-oxygen octahedra sharing edges and corners. The most compact slabs are observed for oxides A$_x$Ti$_{2-x}$M$_x$O$_4$; they consist of a double plane of edge-sharing octahedra similar to the array observed along the (110) plane of the sodium chloride structure. The layers of the other compounds are deduced from that structure by shearing the layers in the direction perpendicular to its plane every second, third, or

fourth octahedron [109]. Thus the layers are no longer flat but corrugated as shown in Figure 9 for Na$_2$Ti$_3$O$_7$. Very peculiar is the structure of K$_4$Nb$_6$O$_{17}$ · 3H$_2$O: the corrugated Nb-oxygen layers are stacked in such a manner that two types of alternating interlayers with different reactivities are formed (Fig. 9) [112–114]. The interlayer galleries of these oxides are accessible for guest species only, if the potassium ions have been replaced with hydrated protons [109]. For the intercalation of more complex species it is
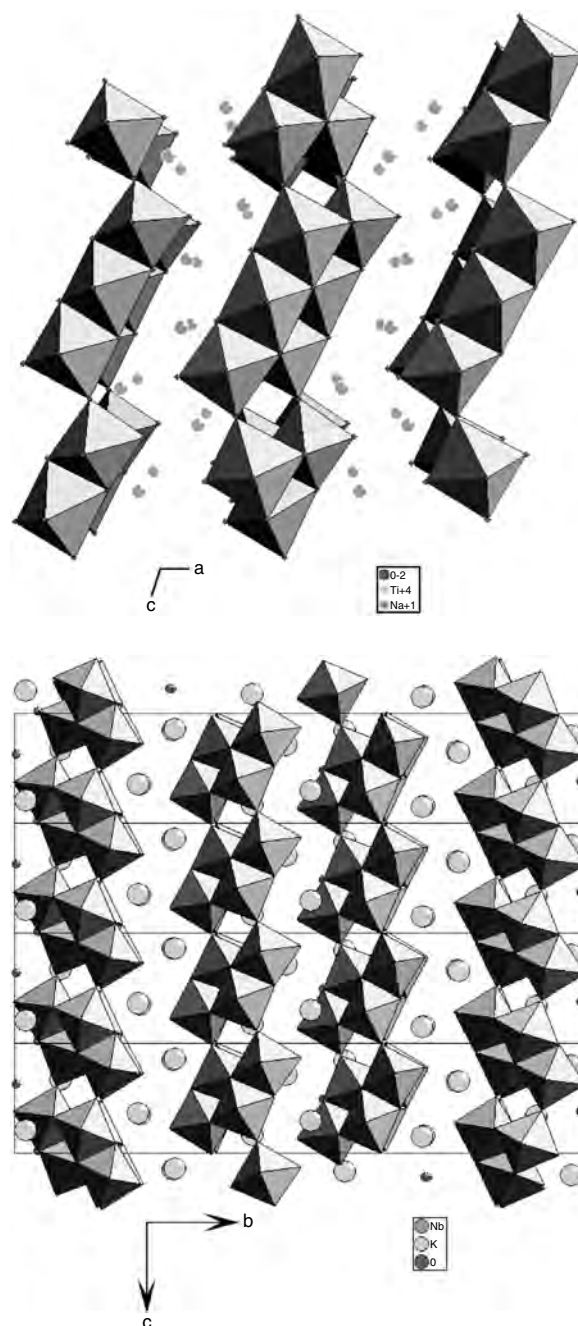
Figure 9. Perspective view of the structure of: Na$_2$Ti$_3$O$_7$ (top) and K$_4$Nb$_6$O$_{17}$ · 3H$_2$O (bottom) prepared with DIAMOND. Please note the two kinds of interlayer space which behave differently in intercalation processes. Crystallographic data adapted from [111, 112].

Figure 8. Perspective view of the structure of [LiAl$_2$(OH)$_6$]NO$_3$, prepared with DIAMOND. The metalhydroxide layers are built by a hexagonal dense packing of OH and metal atoms occupying all octahedral holes. It is isomorphous with the structure of CdJ$_2$ or the TiS$_2$ layers. The nitron atoms (blue balls) are surrounded by six oxygen atoms (red balls) in the interlayer galleries. This is due to the rotation symmetry of the triangular NO$_3^-$. Crystallographic data adapted from [104].

of advantage to use organo-ammonium-exchanged materials as intermediates (propping-open method [83]). The number of dye species intercalated, of course cationic species only, is rather small [14]. The reason they found attention in context of photochemistry was their ability to split water [14, 115–118]. The deposition of Pt and/or NiO may support this process [115, 118]. Some of these oxides can form colloidal solutions, which allow the layer-by-layer assembly [72, 119, 120].

The just mentioned binary oxide (V_2O_5) is applied in intercalation reactions as a xerogel which exhibits a layered structural organization by stacking of the V_2O_5 sheets separated by water layers. The insertion of ions and organic molecules is governed by a variety of interaction mechanisms: hydrogen bonding, protonation, and charge transfer. Its intercalation chemistry has been reviewed by Livage [121]. Apart from the formation of conducting polymers [122, 123] and the intercalation of benzidine [124] and the electron donor tetrathiafulvalene [125] the intercalation of dye species is rather new [126, 127].

The other uncharged host lattices mentioned in Table 1 play a minor role in the intercalation of dye species. The metal phosphorous chalcogenides [78] are known to intercalate just the hemicyanine/stilbazolium and the $[Ru(bpy)_3]^{2+}$ complex [14]. The intercalation of cationic species in this host lattice is accompanied by a loss of structural metal atoms. To the best of our knowledge FeOCl is known to intercalate TTF derivatives and no other dye species [128, 129]. The uptake of this donor leads to a reduction of the host iron atoms. It cannot be excluded that further dye species can be intercalated in these host lattices.

$2H-TaS_2$ is the only metal-like conductor in the compounds listed in Table 1. Up to now only the intercalation of crystal violet [130], methyl viologen [131], and methylene blue [132] has been demonstrated. Because the sample is an electronic conductor the intercalation can be carried out electrochemically. It is interesting to note that in case of methylene blue the packing density and the arrangement of the dye molecules can be influenced depending on the reaction conditions [132] (see also Section 4). The resulting products are superconductors with rather high T_c values in comparison to other organic intercalates [131, 133].

3.2. Framework Structures

The framework structures used for the formation of dye/inorganic nanocomposites are collected in Table 2. Most of these frameworks are based on the main the group elements Si, Al, P. These elements are surrounded by four oxygen ions in tetrahedral coordination and these tetrahedra share corners with neighboring tetrahedra. Due to the kind of linking of the tetrahedra a huge number of amorphous and crystalline phases can be imagined and many of them are realized [134]. The variety based on Si only and Si/Al is enormous. Whereas in case of the silica gels the occluded wholes vary in size and the linkage of the tetrahedra is more or less random, the crystalline phases show very regular distribution of cages, supercages, and channels depending on the preparation conditions and the size of the template used during synthesis. In case of the pure silica systems the species formed are the so-called chrathrasils

[135]. In order to insert dye species they have to be applied as templates during synthesis. These systems are inclusion compounds where the structure of the host is directed from the included guest and the guest cannot leave after synthesis. Only some metal complexes with interesting photofunctions have been inserted in such sort of frameworks [16, 136].

Replacing part of the silicon atoms by aluminum lead to the huge family of natural and synthetic zeolites [134, 137]. Due to this replacement the framework carries negative charges, which has to be compensated by cations in the cages. The Si–Al–O networks in the zeolites are built in such a way that two- or three-dimensionally intersecting channels allow exchange with chemical species in the surrounding of the solids. At the intersection of channel systems large supercages appear which allow the *in-situ* synthesis ("ship in a bottle" strategy) of rather complex molecules from smaller building units. The size of the species, which can be inserted from the outside, is, however, restricted by the smallest dimension of the channels. The channel width of most natural zeolites is normally too small for the uptake of the rather big dye species. Therefore, the zeolites used for dye insertion are the synthetic variants with pore size in the order of 7 Å. Table 2 gives a collection of them with the relevant channel and cage dimensions. A frequently used framework is ZSM 5 whose structure is shown in Figure 10. Isostructural to this framework is silicalite, the end-member of the ZSM family without any Al in the structure [139].

In 1982 a new class of microporous framework was discovered replacing Si by Al and P [140]. The compounds are isoelectronic to SiO_2 and the overall structure is dominated from tetrahedral networks [134, 141]. However, new theoretically possible structures are realized and some of them have rather big channel diameters of about 11 Å (Table 1). In all the systems of this family ($AlPO_4$-5, $AlPO_4$-11, VPI-5) used in the preparation of dye–inorganic nanocomposites the channels are arranged parallel to each other as shown in Figure 11. It is possible to replace a small fraction of aluminum by Si, Fe, or other transition metals. In case of Si the framework again gets a negative charge, which is compensated by cations in the channels [146–148]. The structure seems to be unchanged. Up to now mainly those systems have been used for dye insertion, which has the same structure as $AlPO_4$-5 [149, 150].

A new family of molecular sieves (M41S) with an open pore diameter of 15 to 100 Å has been described in 1992 [151, 152]. They are based on silica and are grown in the presence of amphiphilic ammonium ions as templates, which are applied in such a concentration that they form hexagonal cylinders. The resulting silica solids are arranged in a honeycomb packing of channels with an open pore diameter of 15 to 100 nm. The inorganic matrix is stable after removal of the template at least to temperatures up to 500 °C. The empty channel can be filled easily with other organic species. In these large pore systems there is nearly no restriction of the shape of the guests. In addition rather complex dye species can be dissolved in the surfactants and, thus, inserted during synthesis [19, 153–156, 178, 179].

Using the method applied to the synthesis of phthalocyanine encapsulated in MCM 41 Zhou et al. could get similar mesoporous dye-loaded systems with VO_x, FeO_x, MoO_3,

Table 2. Framework structures [10, 134].

Compound	Effective window size (Å)	Pore shape and size (Å)	Dimensionality
Sodalite	2.3	cage (6.6)	three
Zeolite A	4.2	cage (11.4)	three
Zeolites X, Y	7.4	cage (11.8)	three
ZSM-5	5.3×5.6; 5.1×5.5	channel	two, intersecting
Mordenite	7.0×6.7; 2.6×5.7	channel	two, intersecting
Zeolite L	7.1	lobe (7.5)	single
Silicalite-1	5.5	channel	three
AlPO$_4$-5	7.3	channel	single
AlPO$_4$-11	3.9×6.3	channel	single
VPI-5 [215]	12–13	channel	single
SAPO-5 (AlPO$_4$-5)	8	channel	single
SAPO-34 (chabazite)	4.3	channel	three
FAPO-5 (AlPO$_4$-5)	7.3	channel	single
Nonasil [135, 136]	—	cage (4.1)	zero
Octadecasil [136]	—	cage (4.05)	zero
Dodecasil 1H [136]	—	cage (4.7)	zero
MCM 41			
MCM 50			
Sepilolite	3.7×10.6		
Palygorskite	3.7×6.4		

and WO$_3$ frameworks [154–156]. However, the metal coordination and the formation mechanisms of these frameworks are not clearly established [157].

Other framework structures with parallel running channels are palygorskite and sepiolite (see Fig. 12). They are considered phyllosilicates because they contain a continuous two-dimensional tetrahedral network of composition Si$_2$O$_5$, but they differ from the layered 2:1 aluminosilicates in lacking continuous octahedral sheets [158]. The structures of these minerals can be considered as consisting of 2:1 phyllosilicate ribbons, one ribbon being linked to the next by inversion of the SiO$_4$ tetrahedra along a set of Si–O–Si bonds. The channels thus created are running parallel to the fiber axis. The intercalation chemistry of these minerals is still in its infancy, but it got some attention by the discovery that the ancient pigment Maya blue can be considered an intercalation compound of indigo into palygorskite [4–6]; the proposed structure is shown in Figure 12 (bottom). Only recently has the intercalation compound of indigo in sepiolite been studied in greater detail [159].

Figure 10. Structure of zeolites. Right: supercage assembly of faujasite structure (top) and possible position of sodium ions [216]; the synthetic zeolites X and Y have the same structure as the natural counterpart faujasite. Left: view of the ZSM-5 structure along the crystallographic *b*-axis showing the more regular channel windows. This view is prepared with DIAMOND. Crystallographic data adapted from [138].

Figure 11. Structures of various AlPO$_4$ compounds used in the preparation of dye–inorganic nanocomposites: The view shows the arrangement and shape of the parallel channels in these compounds. The viewgraphs are prepared with DIAMOND. Crystallographic data adapted from [142–145].
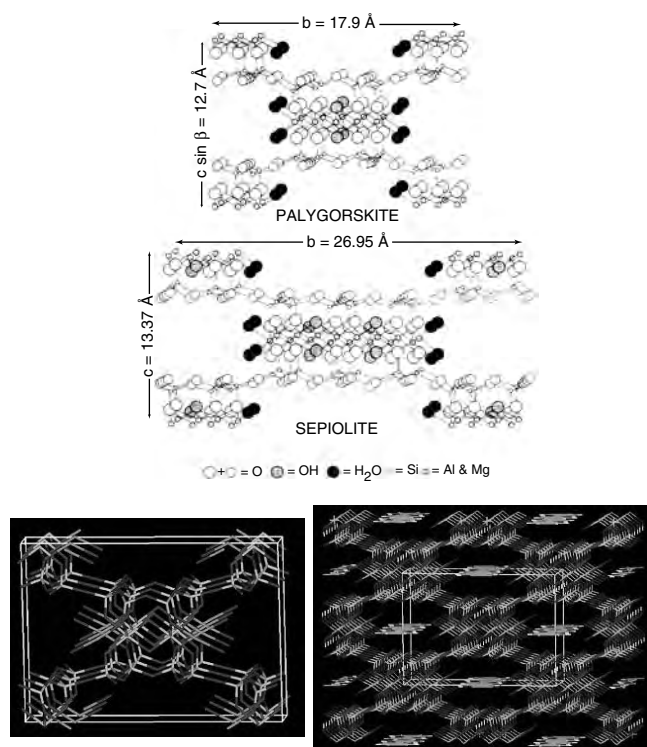
Figure 12. Structure of sepiolite and/or palygorskite. Top: Ball and stick drawing of the crystallographic structure of the minerals sepiolote and palygorskite. Bottom: Modeling structures of palygorskite (left) and the proposed Mayan Blue structure (right). Reprinted with permission from [4], C. Reyes-Valerio, http://www.azulmaya.com.

3.3. Guest Species

Species of nearly any class of organic dyes have been inserted in inorganic solids: acridine, xanthen, phenazine, phenoxazine, and phenothiazine type compounds, porphyrins and phthalocyanins, and only recently azo-compounds and cyanine derivatives. In addition there are some metal compounds which belong in the context of this chapter. Three major phenomena induced by light absorption are discussed with respect to possible applications: (a) electron transfer, (b) photochromism [160], and (c) second harmonic generation [161, 162]. These effects are related to the molecular structure of the dyes and can be assigned roughly to different classes of dyes: Compounds inducing electron transfer should be redox active irrespective of the influence of light, the redox reactions involved should be fully reversible, and light absorption may change the redox potential. Compounds fulfilling these conditions are, for example, the metal chelate complexes, porphyrins and phthalocyanines, and the phenothiazines. Photochromism means a reversible transition between two states with different light absorption spectra, where the transition should be induced by light at least in one direction. Known organic photochromic systems are based on *cis–trans* isomerizations (e.g., in stilbenes, azobenzenes, indigo, or retinal—the visual pigment of our eyes), pericyclic reactions (spiropyranes), on redox reactions (e.g., thionine, viologens). Second harmonic generation (SHG) affords molecules, which show strong dipole moments. Such systems are benzene or stilbene molecules carrying simultaneously electron-pushing and electron-withdrawing substituents. In order to get a SHG effect the molecules must be incorporated in non-centro-symmetric environments.

Since the inorganic matrices used for immobilization or orientation of the organic dyes can be neutral (zeolite related materials like $AlPO_4$ modifications, silicalite) or charged, these dyes are inserted preferentially, which correspond with the charge status of the solid. The overwhelming number of hosts is negatively charged; thus dye cations will be inserted preferentially. There are many dye species which are cationic in nature and thus fulfill this condition. If this is not the case it is always possible to incorporate in the periphery of the chromophore substituents with the right charging of the resulting molecules without influencing too much the absorption behavior. Examples are as follows. (a) Whereas pyridyl or anilinium subsituents make porphyrines more soluble, the uptake in negatively charged zeolites or clay minerals SO_3^- groups allow easier insertion in the positively charged double hydroxide hosts. (b) Methyl orange and methyl yellow are azo-compounds; the first one is neutral or protonated and can be inserted in framework structures and negatively charged hosts and the second one carries an additional SO_3^- group suitable for the uptake in the double hydroxides.

3.3.1. Metal Complexes

Although organic dyes are the focus of this chapter, it is worth mentioning a few metal–organic systems (see Table 3). The cobaltocinium cation is the first metal–organic complex which acts as a template in the synthesis of microporous solids. Since the framework used is of the chlathrasil type the fluoride counterion of the metal complex has to be included in the solid in order to keep the overall charge neutrality [136, 163]. This inclusion complex shows an electric field induced SHG effect [164].

Transition metal bipyridine and phenanthroline complexes found widespread interest in clay chemistry because of their optical activity and the potential application in adsorption and asymmetric synthesis [165]. Soon after the proposed value of metal complexes in photoelectrolysis of water [42] tris(2,2′-bipyridine)ruthenium(II) $\{[Ru(bpy)_3^{2+}]\}$ became the most important photosensitizer in all artificial

Table 3. Colored metal chelate complexes in dye/inorganic nanocomposites [14, 18, 19, 165].

2,2′-Bipyridine complexes	1,10-Phenanthroline complexes	Various ligands
$[Cr(bpy)_3]^{3+ a}$	$[Fe(phen)_3]^{2+}$	Co(saloph) [166]
$[Fe(bpy)_3]^{2+}$	$[Ni(phen)_3]^{2+}$	Co(salen)
$[Ru(bpy)_3]^{2+}$	$[Ru(phen)_3]^{2+}$	
$[Cu(bpy)_3]^{2+}$	$[Cu(phen)_2]^{2+}$	
$[Cu(bpy)_2]^+$		$Co^{III}(Cp)_2F$ [136, 163, 164]
	$[Ru(BPS)_3]^{4-}$ [167]	

Note: Underlined references refer to intercalation in framework structures. References behind a species are additional references to those given in the headlines.
[a] bpy = 2,2′-pipridyl, phen = 1,10-phenanthroline, BPS = 4,7-diphenyl-1,10-phenanthrolinedisulfonate, saloph = N,N-bis(salicylidene)-1,2-phenylendiamine, salen = N,N'-bis(salicylidene)-ethylenediamine, cp = cyclopentadienyl.

water splitting assemblies [14, 18, 43–52, 69] because of its unique combination of chemical stability, long excited state lifetime, and redox properties. Its photofunctional properties are well characterized and it may be the metal complex, which has been intercalated in as many inorganic hosts as possible. The intercalation of this Ru complex in smectites has been described by Traynor et al. as early as 1978 [168].

3.3.2. Porphyrins and Phthalocyanines

The naturally occurring porphyrin chlorophyll is the most important light harvesting antenna in the biosphere [53]. Whereas porphyrin complexes play an essential role in artificial organic supramolecular systems mimicking photosynthesis [51, 194], they could not compete with the Ru complex in the inorganic models [51]. Nevertheless intercalation compounds in clays have been known for many years due to their potential importance in biogeochemistry [169, 170]. Quite interesting with respect to prebiotic chemistry is the formation of phorphins from aldehydes and pyrrols in the interlayer space [171]. In most cases synthetically modified porphyrins has been used carrying charged substituents on the $=CH$ groups (Table 4 and Scheme 1). The positive charge can be increased further by proton uptake of some of the pyrrol units [170–174]. Thus, each of the porphyrin molecules can compensate the charge of at least four cations and thus it should be enough space for these rather big molecules. Depending on the cation in the interlayer galleries the porphyrins: a) are inserted in the interlayer space; b) remove metal atoms out of the interlayer space and form complexes with them in solution (in case of copper ions); c) form complexes with metals in the interlayer space; or d) are co-intercalated to remaining metals [170–174]. Bathochromic shifts of UV-vis-absorption bands are mainly interpreted as the appearance of different protonated states in the interlayer space as function of water acidity in the presence of certain metal atoms. In most of these cases the porphyrin molecules are laying parallel to the host layers. Only in the case of the exchange of preformed porphyrin–metal complexes (Fe^{3+}, Co^{2+} complexes of TAP and TMPyP) into montmorillonite

Table 4. porphyrins and phthalocyanins in dye/inorganic nanocomposites [14, 19, 170–174].

Metal-free systems
Hematoporphyrin IX [*187*]
TPP = *meso*-tetraphenylporphyrin [191]
TpyP = *meso*-tetrapyridylporphyrin [191]
TMPyP = *meso* tetrakis-(1-methyl-4-pyridyl) porphyrin [183, 190, 191]
THPyP = *meso* tetrakis-(1-hexyl-4-pyridyl) porphyrin [19, 180]
TAP = TMAP = *meso* tetrakis-(*N*,*N*,*N*-trimethyl-4-anilinium)porphyrin [190]ᵃ
TAHPP = *meso*-tetrakis(4-(6-trimethylammino)hexyloxy)phenylporphyrin [73]
TTMAPP = *meso*-tetrakis(5-trimethylaminopentyl)porphyrin [179]
POR = 5,15-di(*p*-thiolphenyl)-10,20-di(*p*-tolyl)porphyrin [192]
TSPP = *meso* tetrakis(4-sulfophenyl)porphyrin [184, 189]
pTCPP = *meso* tetrakis(4-carboxyphenyl)porphyrin [189]
oTCPP = *meso* tetrakis(2-carboxyphenyl)porphyrin [189]
Pc = phthalocyanine [154, 156]
TSPc = 2,9,16,23-tetrasulfophthalocyanine [19, 180]
TMPyoPc = 2,9,16,23-tetrakis[3-(*N*-methylpyridyloxy)] phthalocyanine [19, 180, 186]
TMPyPaz = tetra[*N*-methylpyrido(2,3-b:2′,3′-g:2″,3″-1:2‴,3‴*q*)]porphyrazine [19, 180]
TEPyPaz = tetra[*N*-ethylpyrido(2,3-b:2′,3′-g:2″,3″-1:2‴,3‴*q*)]porphyrazine [19, 180]
15-crown-5-PC = 4,5,4′,5′,4″,5″,4‴,5‴-[tetrakis(1,4,7,10,13-pentaoxatridecamethylene)]

Metal-containing systems
Sn^{4+}–TTP, Fe^{3+}–TPP, VO–TTP, Mn^{3+}–TTP, Mg–TTP, Zn–TTP, Cu–TTP
Sn^{4+}–TpyP; Fe^{3+}–TpyP
Fe^{3+}–TMPyP [190], Co^{2+}–TMPyP [180], Zn^{2+}–TMPyP [19, 179, 180]; Cu–TMPyP [182, 190]
Zn^{2+}–THPyP [19, 180]
Fe^{3+}–TMAP [174, 185]; Zn–TMAP [19, 176–178]; Cu–TMAP [179]
Cu–TAHPP [73]
Chl = chlorophyll [154, 188]
ZOR = 5,15-di(*p*-thiolphenyl)-10,20-di(*p*-tolyl)porphyrin–Zn [192]
Cu–Pc [154–156]
Zn–TMPyoPc [19, 180, 186]
Cu-tetra-4-dimetylaminophthalocyanine [175]
Zn–TEPyPaz [19, 180]
Zn–TTMAPP [179]
Co–TSPc [181]
Cu–TSPc [193]

Note: Underlined references refer to intercalation in framework structures; italic references refer to encapsulation in gels. References behind a species are additional references to those given in the headlines.
ᵃ Different acronyms have been used in the literature.
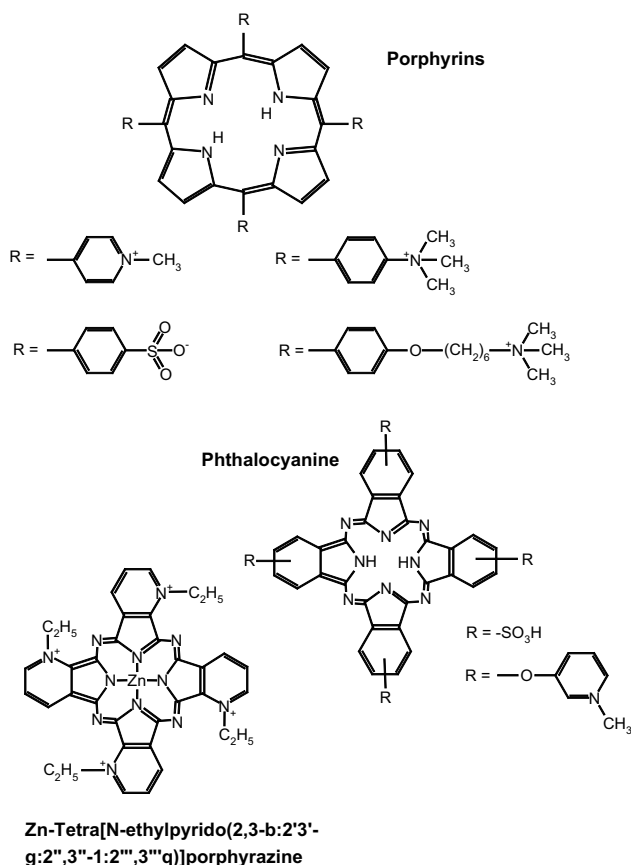
Scheme 1.

and fluorohectorite are the complexes oriented in upright positions allowing porphyrin–porphyrin interactions [174]. In very recent publications the bathochromic shift of absorption bands is explained by a flattening of the TMPyP molecules due to rotation of the pyridyl side-groups to a coplanar arrangement with respect to the porphyrin ring system and an enhanced bonding to the clay layers [176, 177]. This change in configuration shall lead to the formation of a densely packed monolayer on the external and internal surfaces of the clay particles ("size-matching effect"). The fluorescence lifetime of the porphyrins in this arrangement seems to be sufficiently long to be used as sensitizers [177]. Photochemical energy transfer between porphyrins adsorbed on the same clay sheet and those adsorbed on adjacent sheets has been observed recently [178]. The question arises as to whether these new observations are related to the use of synthetic clays. Whereas porphyrins and phthalocyanines are too big to be inserted in classic zeolites they have been incorporated into micro- and mesostructured materials after synthesis or during synthesis of the mesostructures [19, 153–156, 179, 180]. With a new porphyrin derivative, which acts as a structure directing amphiphile, a new layered M41S mesostructure has been prepared consisting of an alternative stacking of the porphyrin and the silica layers [73]. Apart from applications as sensitizers, porphyrins and phtalocyanines incorporated in solids could find applications in SHG and information storage [180]. Up to now the hole burning effect has been shown in a Zn–phthalocyanine/AlPO$_4$-5 system [187].

3.3.3. Viologens

Viologens form an outstanding group of chromophores (some of them are shown in Scheme 2; those systems interesting in the context of this chapter are collected in Table 5) because their electrochemical behavior is in the center of interest, not their photophysical properties. Easily accessible are only the dicationic RV^{2+} salts. RV^{2+} undergoes reversible reduction to the deeply colored monoradical RV$^{+\bullet}$ and in a second one-electron step to the neutral biradical RV$^{\bullet\bullet}$ [195]. Therefore, viologens received much attention as redox indicators in biochemistry, as electron transfer mediators in electrochemistry [55, 56, 195], and as a first electron acceptor in photoinduced redox processes like artificial photosynthesis [18, 51, 69]. This latter application is based on the observation that colloidal Pd led to the disappearance of the MV$^{+\bullet}$ radical (obtained by reduction of MV^{2+} with CrCl$_2$) with concomitant formation of H$_2$ [197]. This metal catalyzed water splitting with MV as the electron transfer system was applied to light induced processes around 1980 [51]. As a consequence of this success MV^{2+} got the most studied electron acceptor in photofunctional redox arrangements with Ru(bipyr)$_3^{2+}$ as the photosensitizer in the presence of various electron donors [51], even in the presence of clays [15, 198], as well as in corresponding zeolite systems [16–18].

The intercalation of methyl viologen was first studied when it was observed that soil clays inhibit the herbicide effect of methyl viologen (=paraquat) action in agricultural applications [199]. Subsequent studies (reviewed in [87]) led to a detailed model of the MV^{2+} arrangement in the interlayer space of vermiculites [200]. To the best of our knowledge this could be the first successful structure determination for a dye/inorganic nanocomposite.

Because the reduction is accompanied by color formation viologens could be of interest as redox mediated photochromic materials. Only a few publications are devoted to
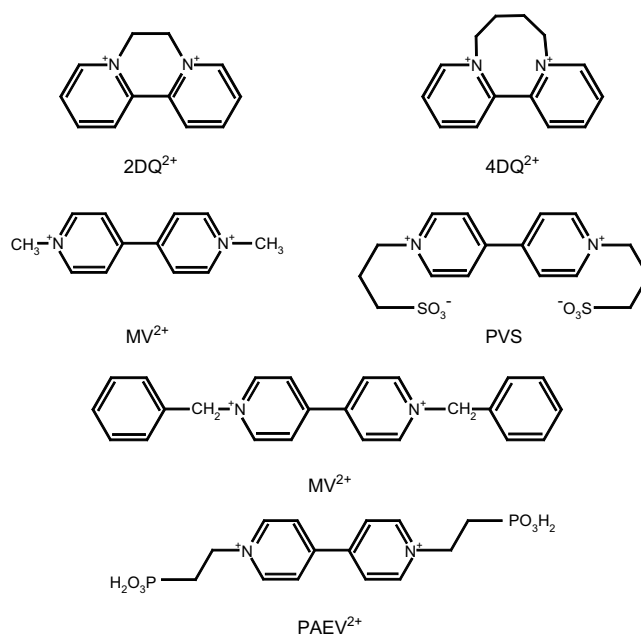
Scheme 2.

Table 5. Viologen derivatives in dye/inorganic nanocomposites [14, 18].

Methylviologen = paraquat = 1,1′dimethyl-4,4′-bipyridilium
Diquat = N,N'-ethylene-2,2′bipyridylium = 2DQ^{2+}
N,N'-tetramethylene-2,2′bipyridylium = 4DQ^{2+}
Benzylviologen = 1,1′dibenzyl-4,4′-bipyridilium = BV^{2+}
Propyl-viologen sulfate = PVS
Ethylviologen diphosphonic acid = PAEV^{2+} [192]

Note: Underlined references refer to intercalation in framework structures. References behind a species are additional references to those given in the headlines.

this topic (see [14] and Table 10, shown later). However, the viologen chromophor can be modified easily by the exchange of the organic residue on the pyridine nitrogen atoms. Depending on the shape and the functional groups at the end of these substituents they can form densely packed arrangements and thus be used as structure directing agents in molecular self-assembly. The potential with this respect has been demonstrated several times [69, 72].

The great potential of viologens as an electron mediator in electrochemical and photoelectrochemical processes led to trials to intercalate viologens in a great number of host lattices (see Table 10).

3.3.4. Anthracene Related Heterocycles

There is a series of heterocycles which are related formally to anthracene and where the CH groups in positions 9 and 10 are replaced by heteroatoms N, O, and S. X = N are the

acridines, X = O are the xanthenes; X = Y = N lead to the so-called phenazines, X = N, Y = O the phenoxazines, and X = N, Y = S the phenothiazines. There are a great number of compounds distinguished by substitution of various functional groups in other ring positions. All of them are strongly colored dyes, which are easily soluble in water. The compounds inserted in inorganic host lattices are summarized in Table 6; the molecular structure of some of them is shown in Scheme 3.

Methylene blue (MB) is one of the most studied compounds and it has been used in clay chemistry for a rather long time [14, 32, 225–235] to investigate surface charge density and ion exchange capacity. In nearly all studies the methylene blue lay parallel to the host lattices preventing any aggregate formation in the interlayer space. Only in 2H-TaS$_2$ [132] and in clays containing residual metal ions [226] have higher layer distances been observed indicating higher packing densities and an arrangement with molecules tilted toward the layers. Photophysical studies are restricted to the investigation of methylene blue aggregation and methylene blue clay interaction (including colloidal dispersions) [14, 225–235]. (Reference [234] gives an excellent overview on the investigation of methylene blue clay interactions up to 2001.) As many other dyes of the anthracene related heterocycles, especially the phenothiazines, MB is redox active

[238–240]. Despite its electrochemical properties and its possible role as photosensitizer and/or electron acceptor it has been used in photofunctional redox chains only rarely [227, 241]. This may be related to the fact that the reduced form of methylene blue is a water insoluble neutral species which forms a conductive film on the surface of electrodes and whose behavior in electrochemical cycles is not well understood up to now [240]. Its intercalation (and also of other phenoxazin, phenothiazin, and related compounds; see Table 6) in zeolites has been studied recently [19, 149, 150, 213, 224].

Other species of this type, which have been investigated more thoroughly, are various rhodamines. Its arrangement in the interlayer space of clays and other layered material cannot be as simple as in the case of methylene blue because of the bulky phenyl substituent (see [88, 89, 206–208] and Section 4.4.2). Rhodamines are interesting pigments and are used as dyes for lasing and show the photochromic effect. These promising aspects may trigger the study of rhodamine/solid interactions.

3.3.5. Triphenylmethane Dyes

Triphenylmethane dyes form a very important class of commercial dyes. They were among the first of the synthetic dyes to be developed and find applications in many fields [242]. Only a small amount of this type of dye has been brought in contact with inorganic solids relevant in this chapter (see Table 7); the most important is crystal violet (CV) (Scheme 4). Most of the studies concerned with CV/clay interactions are carried out at concentrations strongly below the cation exchange capacity (staining effects) [32, 210]. Thus, the aggregation phenomena observed with photophysical methods (metachromasy) are indicative more for adsorption than for intercalation. A series of publications is devoted to the competition of CV adsorption with respect to other dyes [202, 244, 245]. True intercalation as indicated by changes in layer distances has been observed for 2H-TaS$_2$ [130] and α-Zr–phosphate [243].

3.3.6. Azo-Compounds and Stilbenes

Due to its molecular shape these species have a strong polarity, which makes them ideal components for SHG [14, 161, 162]. The presence of *trans*-double-bonds allows photoinduced isomerizations; the concomitant change in light absorption makes them interesting photochromic materials [14, 160]. The elongated shape of these molecules in combination with suitable functional groups at head and tail makes them ideal building blocks for the formation of mesostructures [74] and more complex supramolecular assemblies [69–72, 259, 260]. The compounds inserted in hosts or in inorganic/dye assemblies are collected in Tables 7 (charged species) and 8 (neutral species); the structural formulas of some of them are shown in Scheme 5. A very peculiar system is the donor–acceptor-substituted stilbene DAMS$^+$. This type of stilbene forms the largest class of organic compounds with large second-order-harmonic polarizabilities [161, 162]. The intercalation of this cation via ion exchange into CdPS$_3$ and MnPS$_3$ induces a spontaneous poling giving rise to an efficiency of 750 times that of urea in second-harmonic generation. The manganese derivative displays a permanent

Table 6. Anthracen shaped heterocylcic dyes in dye/inorganic nanocomposites [14, 15, 19, 32].

Acridine-type dyes	Xanthene-type dyes	Xanthene-type dyes
Proflavine	pyronine Py$^+$ [215]	fluorescein [106]
Acridine orange [203, 210, 232, 236, 237]	pyronineY [216]	fluorescein 548 [205]
	rhodamine B [204, 250]	erythrosin B [205]
Acridine yellow	rhodamine 3B [204, 201]	eosin Y [205, 219]
	rhodamine 590 [208]	
	rhodamine 640 [88, 89]	
	rhodamine 6G [88, 89, 206, 207, 217, 218, 220, 221]	
	rhodamine BE50 [204]	
	rhodamine 110 [222]	
Phenazine-type dyes		
Safranine T [209]	oxazine 4 [88, 213]	thionine [211–213]
Janus green	oxonine Ox$^+$ [215]	monomethyl thionine
	Nile blue A	dimethyl thionine
	cresyl violet	trimetylthionine
	neutral species	methylene blue [126, 149, 150, 202, 213, 224, 225–235]
	Nile red [223]	new methylene blue
	resorufin [214]	tetraethyl thionine
		toluidine blue

Note: Underlined references refer to intercalation in framework structures; italic references refer to encapsulation in gels. References behind a species are additional references to those given in the headlines.

magnetization below 40 K. Thus these materials exhibit a large optical nonlinearity and magnetic ordering [249–251]. Other stilbene derivatives (called also hemicyanine dyes) have been intercalated or included recently in Na–fluorine mica [252] and in mesoporous materials [19].

The closely related azo-benzene based dyes with amine-functional groups have been intercalated in layered hosts like V$_2$O$_5$ [127] or directly produced in the mesoporous

Scheme 3.

Y-zeolitebs [254]. The unsubstituted azo-benzene has been inserted in AlPO$_4$-5 and ZSM-5 [255]. The need for better organization of organic chromophores in layered inorganic/organic composites leads to the intercalation of single chain ammonium amphiphiles having an azo-benzene chromophor in the hydrophobic chain [93, 256–258].

3.3.7. Other Types of Dyes

There are numerous other dyes which have been inserted in solid hosts. Because they belong to various classes of organic compounds and they are not studied in depth they are mentioned only for the sake of completeness and are collected in Tables 7 and 8. The structural formulas of the more interesting species are given in Scheme 6. In the following we will give only a few comments on special examples or groups of compounds.

Whereas cyanine dyes play an essential role as photoactive components in Langmuir–Blodgett assemblies [60–63, 65, 66], intercalation of cyanine dyes in layered compounds have been rare up to now [264, 265].

The extent of intercalation of aromatic ammonium compounds (e.g. naphthyl, pyrenyl ammonium) is rather low because of their hydrophobicity [14, 15, 263]. If, however, the solid is preloaded with a surfactant system the extent of adsorption increases dramatically [14, 15, 263]. Using the photophysical properties of the aromatic amines it is possible to probe their aggregation behavior and the surface properties of the inorganic support. It is not necessary to use the aromatic amines; one can also use the corresponding aromatic hydrocarbons instead if the surface is made hydrophobic by preadsorption of surfactant species. One of the most interesting probe molecules is pyrene due to the high quantum yield of fluorescence, excimer-forming capacity, and great sensitivity of its photophysical behavior to its
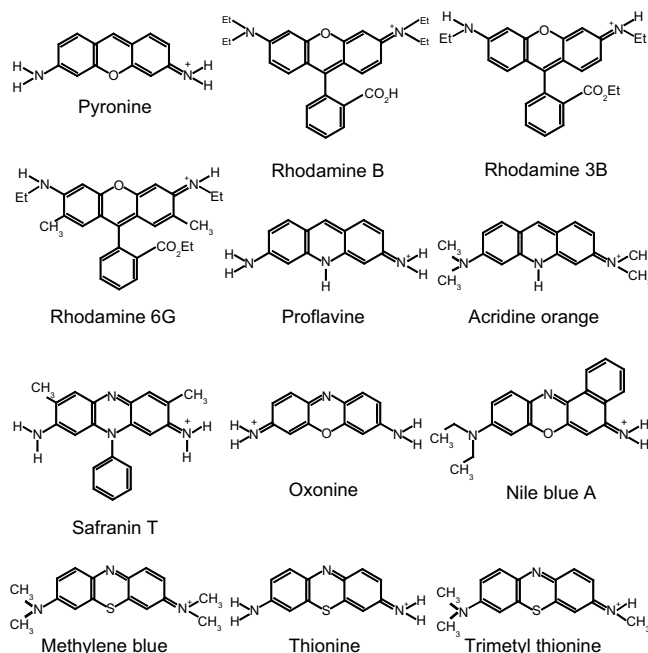
Table 7. Positively and negatively charged dye species in dye/inorganic nanocomposites.

| Triphenylmethane derivatives [32, 14, 15]		
$^+CPh_3$ [130]	fuchsine	pararoseaniline
Michler's hydrol blue [247]	crystal violet [210, 243, 247, 248]	ethyl violet
	methylgreen [245, 247]	malachite green [210, 246, 248]
		brilliant green [210]

Stilbenes or hemicyanins
DAMS [249–251] = 4DASPI [97] = *trans*-4-[4-(dimethyl-amino)styryl]-1-methylpyridinium
2DASPI [252] = 2-[4-(dimethyl-amino)styryl]-1-methylpyridinium
LD698 [252] = 1-ethyl-2-(4-(*p*-dimethylamino)phenyl-1,3-butadienyl)pyridinium
LD722 [252] = 1-ethyl-4-(4-(*p*-dimethylamino)phenyl-1,3-butadienyl)pyridinium
Stilbene 32 [19]
Stilbene 33 [19]
Stilbene 34 [19]

Azo-compounds
Methyl yellow [127]
Methyl-orange [105]
4-[*N*-ethyl-*N*-(2-hydroxyethyl)]amino-4′-nitroazobenzene [*253*]
$C_{12}AzoC_5N^+$ = *p*-(ω-trimethylammoniopentyloxy)-*p*′-(dodecyloxy)azobenzene [93, 256–258]
$C_8AzoC_{10}N^+$ = *p*-(ω-trimethylammoniodecyloxy)-*p*′-(octyloxy)azobenzene [257, 258]
$C_nAzoC_mN^+$ [74]
Chrysoidine = dimethylaminoazobenzene [254]
Basic blue 159 [19]
Basic red 18:1 [19]
4-(2-Pyridylazo)resorcinol [261]
4-{4-[*N*,*N*-bis(2-hydroxyethyl)amino]phenylazo}benzylphosphonic acid [259, 260]
(4-{(4-(4-(4-(2-hydroxyethyl)sulfonyl)phenylazo}phenyl)piperazinyl)phenyl)phosphonic acid [260]
(3-{(4-((4-(2-cyano-(2-hydroxyethyl)carbonyl)ethenyl)phenylazo}phenyl)*N*-methylamino)-
propyl)phosphonic acid [260]
New coccine = Na_3-7-hydroxy-8-[(4-sulph-1-naphthalenyl)azo]-1,3-naphthalenedisulphonate [262]

Arylammonium systems [15]
$C_{10}H_7CH_2NH_3^+$ [263]
$C_{14}H_9CH_2NH_3^+$ [263]
$C_{16}H_9NMe_3^+$ [263]
$C_{16}H_9(CH_2)_nNMe_3^+$, with n = 3, 4, 8
$C_{16}H_9(CH_2)_4NH_3^+$ [263]
PBITS [75] = *N*,*N*′-di(phenyl-3,5-disulphonicacid)-perylene-3,4:9,10-tetracarboxydiimide

Various compounds
Cyanin [264, 265]
2,4,6-Triphenylpyrylium [19, 266]
Thioflavine T [202, 245]
Coumarin [267]
Basic yellow 40 (coumarin 40) [19]
Indigo carmine [262]
Anthraquinone sulfonate [272]
8-Hydroxy-5,7-dinitro-2-naphtalene-sulfonicacid [273]
8-Hydroxy-quninoline [274]

Note: Underlined references refer to intercalation in framework structures; italic references refer to encapsulation in gels. References behind a species are additional references to those given in the headlines.

surroundings (see [14] and a series of original publications [290–295]). Many of the phenomena observed will happen at outer crystalline surfaces and not in the interlayer galleries. This seems to be different in case of the solid-state uptake of pyrene in intercalation compounds of long-chain alkylammonium ions [296]. In this context it should be mentioned that dye assembly [212] and formation of charge transfer complexes (between hydrophilic various pyridinium containing ions and hydrocarbons) occur also in supercages of some framework structures [10, 297]. For these aggregation phenomena the influence of residual water has to be taken into account [212].

A very interesting class of molecules is the neutral disubstituted benzenes with the functional groups in para-position (Table 8). These species are highly polar and show in the solid state or in suitable matrices the effect of second harmonic generation. Intercalated in hydrophobic (neutral) framework structures with parallel running channels they are highly oriented [8, 268–271]. If in addition the structures are not centrosymmetric the SHG effect can be strongly amplified.
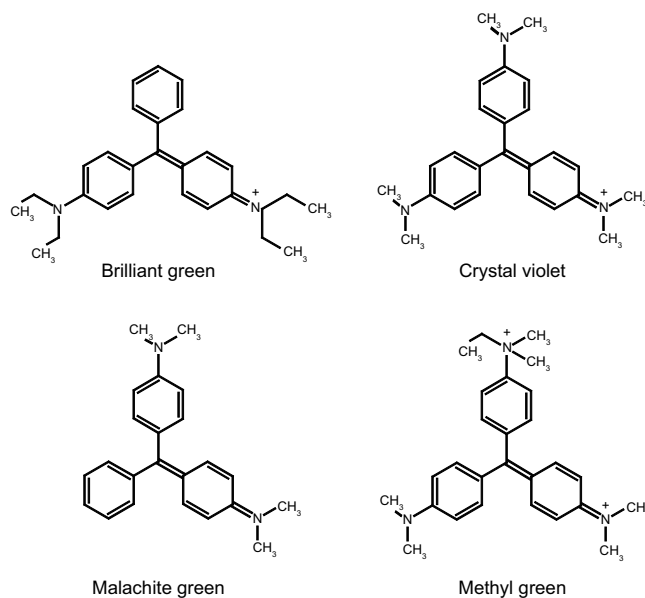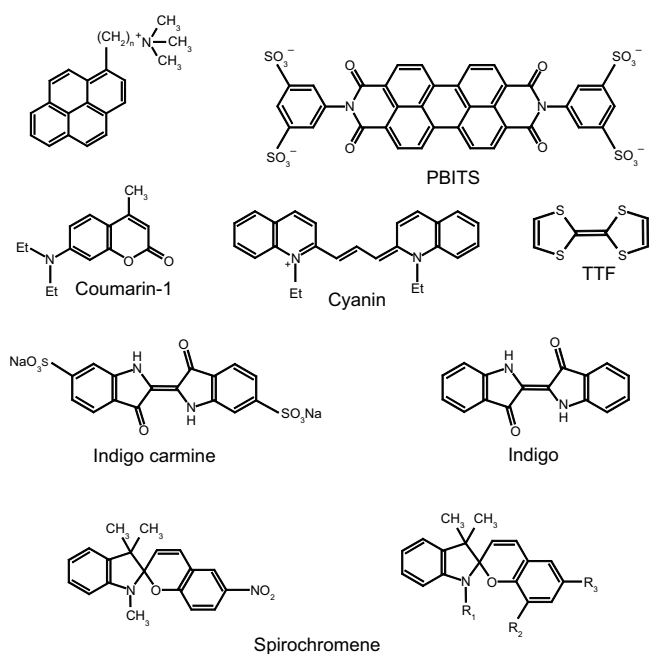
Scheme 4.
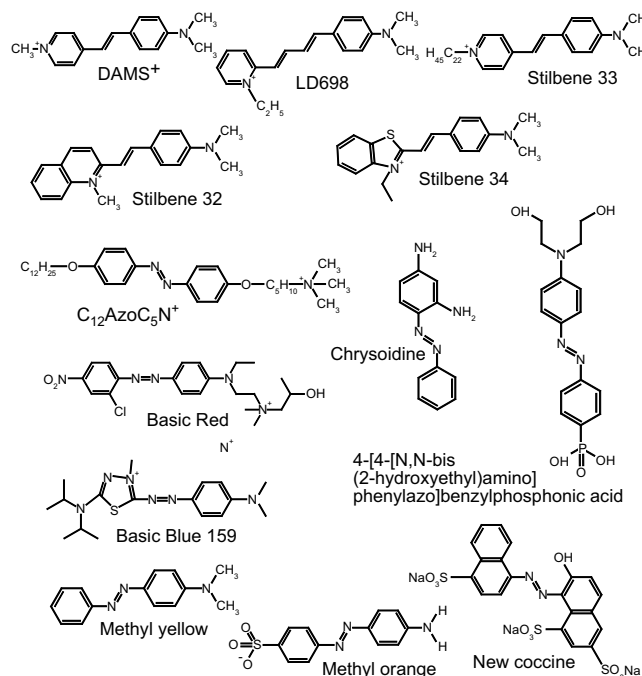
Scheme 5.

Table 8. Neutral systems inserted in inorganic matrices.

Small bipolar donor acceptor substituted organic chromophores [8, 19, 268]	
p-Nitroaniline [269]	*p*-dimethylaminobenzonitrile [270, 271]
N-methyl-*p*-nitroaniline	2-amino-4-nitropyridine
p-Nitrodimethylaniline	2-amino-4-nitropyrimidine
2-Methyl-4-nitroaniline	*p*-nitropyridine-*N*-oxide

Phenol dyes	Aromatic imids
Phenol red [275]	*N*-methylphtalimide [246]
Cresol red [275]	perylene red [220]
Bromophenol [275]	perylene orange [220]

Azocompounds	
trans-Azobenzene [255]	diethylazodicarboxylate [280]
	diisopropylazodicarboxylate [280]
	dibenzylazodicarboxylate [280]

Heterocyclic compounds	
Indigo [4–6, 159]	2H-spiro[6]nitrochromene-2,2′-[1,3,3]trimethylindoline [276, 277, 278–280]
Thioindigo [283]	1,3-dihydro-1,3,3-trimethylspiro[2*H*]-indole-2,3′-[3*H*]naphth[2,1-b][1,4]oxazine (SO) [277]
	other spiropyranes [277, 278, 280]
	1,4-diketo-2,5-dimethyl-3,6-diphenylpyrrolo[3,4-c]pyrrole; R = H, CH₃ [281]

Strong electron donors; cation forming species [125, 128, 129, 284–289]	
TTF = tetrathiafulvalene	
Tetramethyl-TTF	
TTT = tetrathiatetracene	
TTN = tetrathianaphthalene	
ET = bis(ethylenedithia)tetrathiafulvalene	
DBTTF	

Note: Underlined references refer to intercalation in framework structures; italic references refer to encapsulation in gels. References behind a species are additional references to those given in the headlines.

Scheme 6.

The spiropyranes are the most widely studied photochromic dyes [298]. Photochromic materials have potential for optical switching and information storage. The immobilization in a clay/didodeceyldimethylammonium matrix was tried as early as 1991 [278]. Recently these interesting species have been encapsulated in inorganic and organic matrices [276, 277].

Very interesting is the intercalation of electron donors including TTF, the most famous donor for preparing organic conductors. However, the intercalation of these species is restricted to silicates [284], FeOCl [128, 129], V_2O_5 [125], and some MPS_3 compounds [285, 286], hosts which show a redox potential positive enough to accept electrons from these donors or do not lead to a reduction of the cation intercalated. The proposed intercalation of DBTTF into layered dichalcogenides [287] is hard to evaluate with respect to this condition. In case of Zr–P surfactant long-chain alcohols have been used to expand the host structure allowing the intercalation of partially charged TTF [289]. Just the cations can be considered as dyes. There are no further investigations of the photophysical properties of these intercalation compounds.

4. PREPARATION OF DYE–INORGANIC HOST COMPOSITES

The methods of preparation of dye intercalation compounds are the same as used in the intercalation processes of inorganic ions and small organic molecules [19–21, 78–83]:

- **Adsorption of organic neutral compounds:** This can be achieved by treating the solid with the species to be inserted in the gas, the liquid, and the solid state, or out of a solution. It should be carried out at moderate temperature because the species adsorbed is in equilibrium

with the surrounding. If the species intercalated is very volatile some precautions against outgassing have to be undertaken. Solid compounds with low vapor pressure can be inserted out of solutions or by solid-state reactions as shown for the intercalation of pyrene in clays preloaded with surfactants [296]. The species of interest in this chapter can be taken up only in host lattices with a hydrophobic surface, which means it is restricted to special frameworks of the $AlPO_4$ family [8, 19, 268–271]. In the latter case the uptake of volatile dyes is restricted to those for which the smallest diameter is smaller than and or of the same size as the effective window size of the channels.

- **Ion exchange [19–21, 79, 83]:** This is the most convenient procedure for intercalation of the cationic and anionic dyes and is carried out by soaking the solid with an aqueous solution of the dyes. The reaction is carried out normally at room temperature. Since many of the dye ions are bulky the uptake in the interlayer space is slow unless there is a strong interaction of the electron system with the surface of the host lattices. Due to this hindered uptake in the interlayer space the adsorption on external surfaces competes with it (especially if the particles are in the μm range or the interaction with the organic species is very strong). This method can be applied for the intercalation of nearly all dye ions in many of the charged layered host compounds and also for zeolites or zeolite related materials as long as the frameworks have an excess negative charge. However, in the latter case the uptake is again restricted to those dyes for which the smallest diameter is smaller than or of the same size as the effective window size of the channels.

- **Adsorption on dispersed solids:** This is a very reasonable method for all layered host systems which form colloidal dispersions [83, 90–92]. In the ideal case all layers are separated from each other and form monolayer dispersions. In this case the surfaces of all particles can be considered as external, at least below the critical flocculation concentration (often identical with the cation exchange capacity = cec). This state is ideally suited to investigate the dye/solid and the dye/dye aggregation phenomena by visible light [7, 9, 14, 15, 290–296]. In real systems not all layers will be separated from each other, but there will be distribution of stacks with different numbers of individual layers (Fig. 13). Thus the uptake in the interlayer space competes with the adsorption on external surfaces. Since the dye molecules interact very strongly with the surfaces of the inorganic hosts, at concentration higher than the cec dye species will be found on the external surface of the solid particles, in the interlayer space, and in voids of tactoids formed during flocculation. This method is ideally suited for the preparation of inorganic/organic composites with very bulky dye molecules, if the orientation of the species is not of importance.

- **"Ship in the bottle" synthesis [18, 19]:** The construction of molecules in the zeolite itself is a further strategy to overcome the problem of the finite size of the accessible window. With this approach it is possible
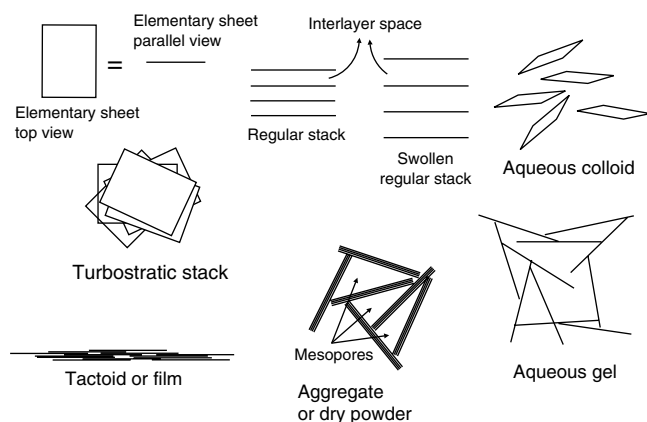
Figure 13. Sketch of the various forms of clay dispersions and their flocculation products.
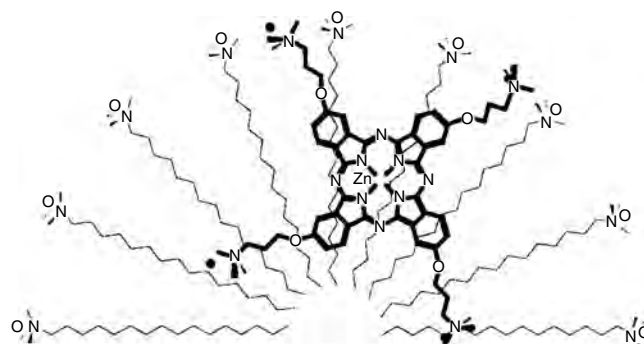

Figure 14. Sketch of the arrangement of a modified Zn–phthalocyanine in the hexadecyltrimethylammonium micelles used in the synthesis of mesoporous Si-MCM-41 and Ti-MCM-41 frameworks. Adapted from [153].

to get bulky species in the interior of the solid. It is applied for example to the synthesis of porphyrins in clay minerals [170], of polypyridine complexes of transition metals [18, 19], the synthesis of a spiran molecule within synthetic faujasites [276], the azo coupling in zeolite Y [254], the synthesis of Nile red in zeolites [223], and the formation of the triphenylpyrylium cation (an interesting electron-transfer sensitizer) in zeolite Y [266]. The species produced are so bulky that they cannot escape out of the solid; thus these compounds should be considered inclusion compounds and not intercalation compounds [83].

- **Dye species as templates:** A breakthrough for the insertion of dye species in framework structures is the *in situ* inclusion of these organic complexes during synthesis of the frameworks [19]. Thus, methylene blue [19, 224] or the cobaltocinium complex [136, 163] has been used as template. In case of the methylene blue one methyl group is missing after synthesis. To avoid the decomposition of sensitive dyes in the highly aggressive hydrothermal media a change of gel composition and the assistance of microwaves (reducing the reaction time and temperature) is helpful [19]. Another approach is the modification of the dyes with such substituents that they can be included in the template micelles. This method has been applied for the synthesis porphyrin-loaded mesoporous solids [153]. Figure 14 shows a sketch of the phthalocyanin arrangement in the hexadecyltrimethylammonium chloride micelles. The phthalocyanins have also be used as templates in the synthesis of new mesoporous solids based on some transition metal oxides [154–156]. In recent publications chromophores have been substituted with long tails of alkyl chains with polar head groups. These new classes of dyes are amphiphilic and act as structure forming templates in molecular sieve synthesis [73–75]. It should be mentioned that this technique was applied for the first time in 1991 to form an intercalation compound of porphyrin in a synthetic clay [184].
- In case of the electronically conducting 2H-TaS$_2$ the intercalation can be carried out electrochemically [83, 131]. A complete reaction can be achieved under

galvanostatic conditions overnight at room temperature. Normally the reaction is carried out with 2H-TaS$_2$ crystals of a few millimeters in diameter. This gives intercalated samples with a residual resistance ratio in the order of 10 to 40. Depending on the intercalation current a different packing density of the dye molecules can be realized, at least for the case of methylene blue intercalation.

In almost all these cases one gets powder materials without preferred orientation. For many applications highly ordered macroscopic assemblies are desired. The following methods have been developed in order to get macroscopic assemblies:

- **Oriented aggregate technique:** Colloidal dispersions can be used to deposit thin films of solids on suitable substrates (glass, ITO coated glass, metal electrodes, etc.) by evaporating to dryness a 2% suspension. Such oriented supported or self-supporting films have been applied in clay chemistry for many years [83, 87, 88, 172, 173, 201, 209, 267, 299, 300]. Such films can be loaded easily with desired species. However, there is again the problem of competition of external adsorption and deposition in mesoporous voids and in the interlayer space as in case of the colloid preparation mode (for structure see Fig. 13). A very recent application of such dye-loaded films is the preparation of clay-modified electrodes [55, 56, 196].
- **layer-by-layer deposition [72, 301]:** The idea of preparing electrostatically bound thin films was introduced by Iler in 1966 [302]. He showed that surfaces modified with positively charged boehmite colloids or cationic amphiphiles could bind negatively charged colloidal silica or latex particles (for a schematic view of such a deposit see Fig. 15). This method was applied later for sequential adsorption of alternatively charged polyelectrolytes [301, 303, 304]. It can be adapted to the sequential layering of inorganic polyanions (obtained by exfoliation of layered intercalation compounds: clays, ternary oxides, Zr-phosphates [92]) with a variety of polymeric cations [72, 304–310]. The first inorganic polyanionic layer has to be deposited on a self-assembled organic bifunctional layer anchored by covalent bonding to a solid substrate as shown in
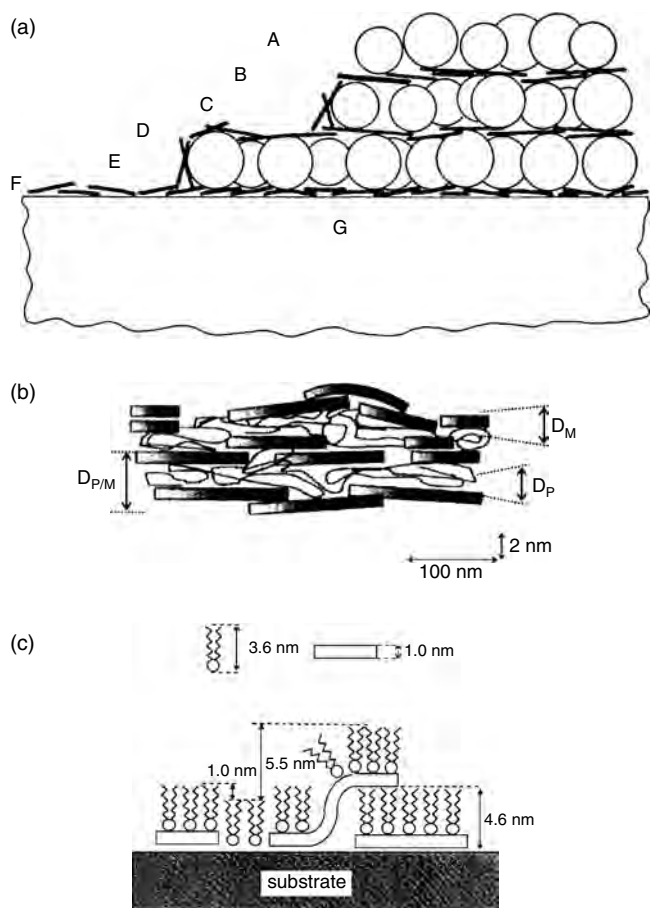
Figure 15. Layer by layer deposits. Schematic views of various types of deposits: (a) The classic schematic cross-section of a multilayer film; A, C, and E represent layers of 100 μm silica; B, D, and F represent layers of colloidal boehmite fibers; G the glass substrate. Adapted from [302]. (b) An oversimplified representation of a polymer/montmorillonite layer: $D_{P/M}$ is the mean repeating distance of a P/M layer, D_M is the mean thickness of a montmorillonite layer, and D_P is the mean thickness of a polymer layer. Adapted from [309]. (c) Schematic drawing of a hybrid film consisting of a synthetic lithium hectorite and a Ru/bipyridine complex, carrying long aliphatic side-groups at the bipyridine ligand. Adapted from [319].

Scheme 7. On this assembly the first layer of a polymeric cation can be adsorbed followed by the second inorganic sheet. In repeating adsorption/washing procedures subsequent layers of alternative charge can be deposited. However, the real multilayer deposits will not be as regular as expected. (a) Again the real colloids will not be so monodisperse that only monolayers are present in the solutions. (b) It will be impossible to tune the deposition in such a manner that only a regular monolayer of the disperse system will be formed. A tactoidlike arrangement is more probable. (c) An interdigiting of the polymer and the colloid particles can also not be excluded. Just these sorts of defects have been observed recently [309, 310], and the term "fuzzy assembly" has been introduced for this sort of multilayer architectures. For the purpose of this chapter it is important to note that it was possible to form a clay/polymer/dye film by this method recently [311].
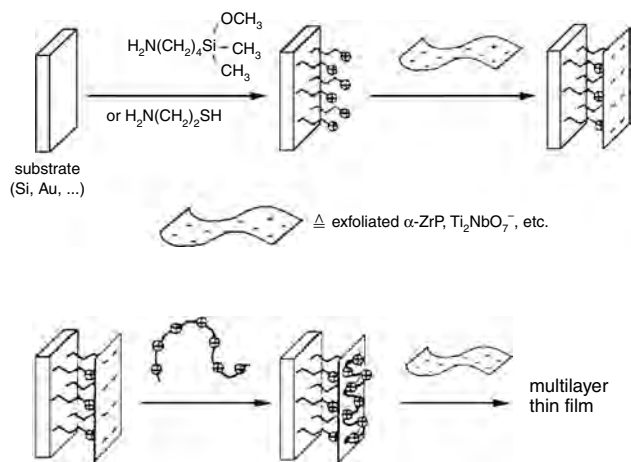
Scheme 7.

In case of the very peculiar Zr–phosphate phosphonate system it could be shown that the technique discussed before can be used for the self-assembly of low molecular species also [71, 72]. This is based on the following experimental facts: during precipitation of the Zr–phosphate the phosphoric acid can be replaced with phosphonic to a considerable amount without severe changes of the inorganic backbone formed; the affinity of the zirconium metal ions to the phosphate groups is exceptionally high and, thus, the solubility of the building blocks extremely low. From structural analogy of Zr–phosphonates with aliphatic chains and Langmuir–Blodgett films it was concluded that it should be possible to prepare multilayer assemblies on a solid substrate if it is possible to form stable assemblies of phosphonic acids on a solid substrate. Cao and co-workers demonstrated this in 1988, for the first time [71]. Since then many multilayer assemblies of this Zr–phosphonate system have been obtained including many with chromophores in the organic backbone of the phosphonic acid. Typical chromophores are azobenzene derivatives and viologens (typical examples are shown in Fig. 16). A very interesting multilayer assembly has been prepared with a viologen spacer [69, 314]: it contains halide ions compensating the positive charges of the pyridinium nitrogen atoms. If this sample is irradiated in vacuum or under argon the viologen is reduced immediately as indicated by the blue color of the viologen radical.

- **Langmuir–Blodgett technique:** This method is based on the self-assembly tendencies of membrane building amphiphilic molecules. In 1993 Lvov et al. combined this method with the polycation/polyanion based layer-by-layer deposition. Polyelectrolytes form stable complexes by electrostatic interactions with some amphiphiles, which spread to a homogeneous film at the water–air interface. These complexes can be transferred by the Langmuir–Blodgett (LB) technique to solid substrates [315]. In a very similar manner clay particles intercalated and embedded with bulky amphiphilic cations. The clay can be spread (out of a solution in volatile organic solvent like chloroform)
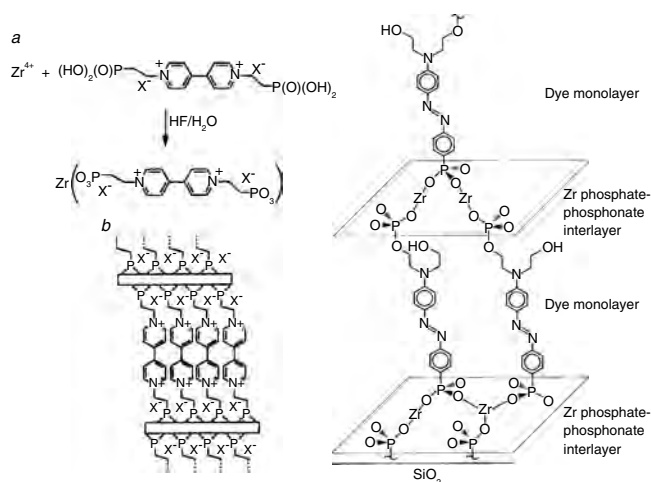
Figure 16. Schemtaic structural view of Zr–phosphonate multilayers. Left: Layer-by-layer deposit made from substituted viologens and Zr ions; by illumination a stable charge separation can be produced. Right: Layer-by layer deposit of an Zr–diphosphonate containing azobenzene groups; this system exhibits SHG. Adapted from [312].

on the water surface in an LB trough. This spread clay film can be transferred on hydrophobic glass or carbon [316, 317]. Even alkyl ammonium cations with short alkyl chains (C_4–C_{12}) form hybrid monolayers with clay particles at the air–water interface [318]. In the meantime it was also possible to spread a clay/Ru(phen)$_2$(dC$_{18}$)bpy complex at the air–water interface to form a multilayer film of this complex by the LB technique [319].

- **Orientation and oriented growth of framework crystals**: For applications of dye/inorganic complexes in framework structures it is not enough to have the photosensible organic dyes aligned in parallel channels of frameworks, but it is also necessary to have aligned the whole crystals. Various methods for aligning crystals of zeolites have been discovered since about 1990 [320]. The materials obtained were of interest for catalysis, sensor applications, and separation technologies. We would like to mention only two examples, which are of interest in the context of this chapter: the crystal growth of AlPO$_4$ on an organophosphate film [76, 321] and the alignment of ZSM-5 and AlPO$_4$-5 in an applied electric field [322]. After aligning the crystals are fixed by water glass. Such oriented crystals loaded with *p*-nitro aniline show a SHG intensity of 100%, which is a factor of 5 higher than in a random powder assembly [322].

5. STRUCTURE AND STRUCTURE SIMULATION

The knowledge of structure and understanding of the structure–property relationship is crucial for the design of new intercalation compounds with desired properties. These properties can be tuned by the proper choice of the host–guest combination, the guest concentration, and co-intercalation of further guest species. However, the structure analysis of layered intercalates brings specific problems. As the intercalation is in fact an insertion of a known molecule

into a known layered crystal structure, we have to determine the positions, orientations, and arrangement of the guest molecules in the interlayer space, the way of layer stacking, and possible changes in conformation of guest molecules. Intercalated structures exhibit very often various degrees of disorder in arrangement of guest molecules and in layer stacking. Consequently the characterization of the disorder usually belongs to the structure analysis of intercalates.

The crystal packing of intercalated structures is a result of the host–guest complementarity [323–325], which reflects the character of the host–guest interaction and the geometry of the host structures and guest species in the pristine state. Factors governing the crystal packing in intercalates can be summarized as follows.

- the nature of the active sites on the host structure and guest species (i.e., the charge distribution on the host structures and guest species, the type of functional groups, etc.)
- the ratio between the host–guest and guest–guest interaction energy
- the topology of host structure (i.e., the distances and ordering of functional groups, the presence of steric barriers for the diffusion of guest molecules, etc.)
- the size and shape of the guest molecules, especially the ratio between the size of guests and distances of the active sites in the host structure
- the rigidity (or flexibility) of host structure and guest species (i.e., the tendency to distortions in the host structure and to conformational changes of guest molecules due to intercalation)

These factors act sometimes in concert and sometimes in conflict. As a result of this interplay we can get a perfectly ordered intercalated structure in case of perfect host–guest complementarity. The requirement of structure ordering is of great importance in a design of new intercalates for special applications, in which one has to control the porosity in intercalated layered structures (selective sorbents, molecular sieves), or to control photofunctions of guest molecules, etc. On the other hand, the departure from the perfect host–guest complementarity leads to various degrees of disorder in an intercalated structure.

5.1. Method and Strategy of Structure Analysis

Intercalated layered structures exhibit very often various degrees of disorder in positions and orientation of guest molecules and consequently in layer stacking. This disorder obstructs the structure analysis based only on the diffraction method. Intercalation of organic guests into an inorganic host structure introduces an additional specific problem into the diffraction analysis of intercalates. Scattering amplitudes of carbon, oxygen, and hydrogen are small in comparison with the atoms building the inorganic host structures and consequently the contribution of guest molecules to the total intensity diffracted from the crystal is too small. This fact complicates the precious localization of guests in the intercalated compounds.

For disordered guest molecules, which in addition contribute very little to the diffracted intensities, the diffraction analysis fails. In such a case the molecular modeling

(molecular mechanics and molecular dynamics) represents a very powerful tool in structure analysis, provided that the modeling is combined with an experiment. Experiment plays an important role in creation of the modeling strategy and in corroboration of modeling results. In present work we combine the modeling in *Cerius*[2] [326] with X-ray powder diffraction and infrared (IR) spectroscopy. Using the combination of structure simulation and experiment can provide us with a detailed structure model including the characterization of the disorder. In addition to diffraction analysis we get the total crystal energy, the total sublimation energy, and the host–guest and guest–guest interaction energy.

5.2. Modeling of Intercalates

Molecular modeling (molecular mechanics) is a method of optimization of the structure and bonding geometry using minimization of the total potential energy of the crystal or molecular system. The energy of the system in molecular mechanics is described by an empirical force field [327, 328]. This simplified description of the crystal energy enables us to model large supramolecular systems, which cannot be treated using *ab initio* calculations. The energy terms describing the valence interactions (i.e., the bond stretching, angle bending, dihedral torsion, and inversion) may differ in various force fields [326] and it is evident that the choice and test of the force field belong to the most important part of the modeling strategy.

Two methods are used to test a force field. First of all the comparison of force field calculations with experiment is the most reliable test of the force field. For this purpose one can use the known structure from the database, which is similar to the investigated structure. In case of intercalation compounds it is difficult to find related structures in databases and then we have to use the limited number of structure parameters obtained from the X-ray powder diffraction pattern affected by a disorder. The second method of force field testing is comparison with the results of *ab initio* calculations for a small fragment of structure [329]. The force field library in *Cerius*[2] [326] contains the universal force field [330] and several special force fields designed for modeling of organic supramolecular systems [331, 332], polymers [333], and sorption of organic molecules into silicates and zeolites [334]. In the *Cerius*[2] modeling environment the atomic charges are calculated using the Qeq (charge equilibration) method [335] and the Ewald summation method [336, 337] is used to calculate the Coulomb energy. The Lennard-Jones potential is used for calculation of van der Waals interactions.

Classical molecular dynamics calculates the dynamic trajectory of the system solving the classical equations of motion for a system of interacting atoms [326–328]. The temperature and the distribution of atomic velocities in the system are related through the Maxwell–Boltzmann equation. Introducing the temperature and pressure controlled molecular dynamics enables one to study temperature dependent processes and to explore the local conformational space. However, for crossing large energy barriers, molecular dynamics at high temperatures can be used.

All the computational methods searching for the global energy minimum have to generate the large number of initial models using three different methods [327, 338]:

- deterministic method for generation of starting models, performing the systematic grid search that covers all areas of the potential energy surface [338–340]
- molecular dynamics generating the starting geometry [326–328]
- stochastic methods (Monte Carlo [328], genetic algorithm [341])

The first method, performing the systematic grid search, can be used easily to generate starting models in case of small or rigid large guests and rigid host layers. On the other hand molecular dynamics is very well suited for generation of starting models in case of large flexible organic guest molecules. For modeling of layered intercalates it is useful to combine the systematic grid search with the molecular dynamics to generate the staring models. The strategy of modeling consists of: the building of initial models, the setup energy expression, the choice and test of the force field, the definition of rigid fragments, and the setup of fixed and variable structure parameters, etc. Reliable results of modeling can be obtained providing that all the steps in the modeling strategy are based on available experimental data.

5.3. X-Ray Diffraction and Vibration Spectroscopy

Because of the disorder in intercalated structures, it is usually impossible to prepare a single crystal of reasonable size suitable for X-ray diffraction measurements. The powder diffraction pattern, which is influenced by disorder and a small scattering contribution of guest molecules, is in addition affected by the sample effects like preferred orientation of crystallites [342] and absorption in surface roughness [343]. In spite of these difficulties, the diffraction pattern can always provide us with some information useful for the strategy of modeling. At least we can get the basal spacing (interlayer distance), indicate the disorder, and recognize the type of disorder. In more favorable cases we can even get the lattice parameters of the intercalated structure. These experimental data are useful for the building of the initial models. Comparing the diffraction pattern for the intercalated and host structures one can deduce the changes of structure after intercalation and consequently to set up the most suitable modeling strategy (variable and fixed structure parameters, rigid fragments, rigidity of layers, etc.). The diffraction line profiles indicate a possible lattice strain due to the disorder in arrangement of guests and the disorder in layer stacking.

Comparing the vibration (IR/Raman) spectra of the intercalate, the pristine guest compound, and the host compound we can see possible changes in the bonding geometry and the conformation of guest molecules and host layers, which may occur during the intercalation. If the spectral bands corresponding to the host layers exhibit the same positions and profiles in the spectrum of host structure and intercalate, one can conclude that there are no changes in bonding geometry of host layers during intercalation. This is a very

important conclusion for the modeling strategy, as in such a case the host layers can be treated as rigid units during energy minimization. The same conclusion can be derived for the guest molecules. In case of rigid host layers and rigid guests we obtain the IR spectrum for this intercalate as a superposition of the host structure and guest compound spectra. The rigidity of host layers is the crucial assumption in modeling of layered intercalates, as in case of inorganic covalently bonded host layers the force field calculations cannot be used to reveal possible changes in their bonding geometry.

5.4. Examples of Structure Analysis

The perfect three-dimensional (3D) order in intercalated structure requires the perfect ordering of guest molecules in the interlayer space and consequently the perfect order in the layer stacking. The ordering of guests requires the regular network of active sites on the host layer which means the presence of functional groups or regularity in charge distribution on the host layer. This effect will be illustrated on three examples: tantalum sulphide intercalated with methylene blue, monmtorllonite intercalated with rhodamine B, and vermiculite intercalated with anilinium.

5.4.1. Tantalum Sulphide Intercalated with Methylene Blue

Tantalum sulphide $2H\text{-}TaS_2$ has been found as a suitable host lattice for intercalation of organic or organometallic molecules (for reviews see [78–83]). The discovery of superconductivity in the intercalation compound of $2H\text{-}TaS_2$ initiated a very broad investigation of these compounds [344, 345]. Recently, it was shown that electrointercalation of MB [131, 346] into $2H\text{-}TaS_2$ leads to three different phases indicated by different basal spacings and superconducting transition temperatures T_c. (The intercalation compounds will be denoted in the forthcoming text as $MB\text{-}TaS_2$.) The first phase, $I\text{-}MB\text{-}TaS_2$, exhibits an interlayer distance 9.07 Å, obtained from X-ray powder diffraction (XRPD) measurements. Since this phase shows the two-layer stacking as the host structure $2H\text{-}TaS_2$, the parameter periodicity d_{001} in the direction perpendicular to the layers is $2 \times 9.07 \text{ C} = 18.14$ Å. The T_c for this phase is 5.21 K (slow cooling) and/or 4.47 K (fast cooling). (For more details see [131, 346].) For the second phase, $II\text{-}MB\text{-}TaS_2$, the interlayer distance obtained from XRPD measurements is 11.9 Å and the T_c for this phase is 4.92 K. For the third phase, $III\text{-}MB\text{-}TaS_2$, the interlayer distance obtained from XRPD measurements is 16.80 Å. The T_c for this phase is 4.24 K. From experience with $2H\text{-}TaS_2$ intercalation compounds we conclude that phase II and phase III should also have a two-layer periodicity in the direction perpendicular to the layers.

The initial models of $MB\text{-}TaS_2$ were built using the known structure data for the host compound $2H\text{-}TaS_2$ (hexagonal, space group $P6_3/mmc$ with Ta in trigonal-prismatic coordination by S) [347]. The unit cell (cell parameters: $a = 3.314$ Å and $c = 12.097$ Å, and $Z = 2$, i.e., two formula units TaS_2 per unit cell) contains two TaS_2 layers mutually shifted. The supercell $3a \times 5b \times 1c$ was built for the intercalation

of MB cations (for MB cations see Fig. 17a). The concentration of the MB cations in the initial models was set up according to the chemical analysis, performed in previous work [346], which means:

- For the phase $I\text{-}MB\text{-}TaS_2$ there are two MB cations per one two-layer $3a \times 5b \times 1c$ supercell.
- For the phase $II\text{-}MB\text{-}TaS_2$ there are four MB cations per one two-layer $3a \times 5b \times 1c$ supercell.
- For the phase $III\text{-}MB\text{-}TaS_2$ there are six MB cations per one two-layer $3a \times 5b \times 1c$ supercell.

A systematic grid search combined with molecular dynamics was used to generate the series of initial models for energy minimization in $Cerius^2$. The energy minimization of all initial models was carried out in the space group $P1$ under the following conditions: the host layers were treated
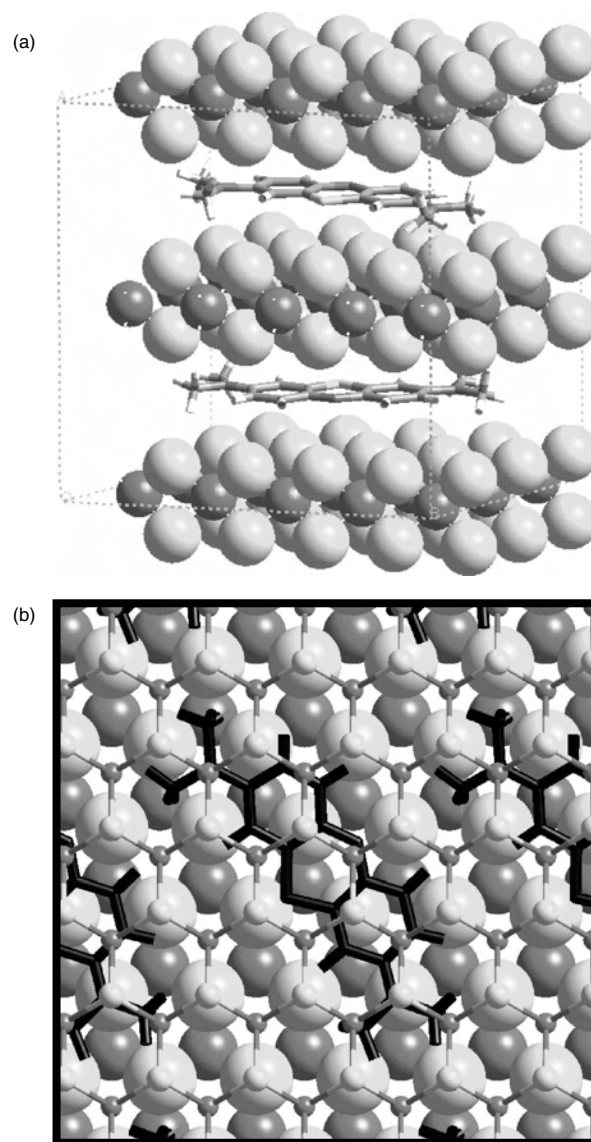

Figure 17. (a) Structure of tantalum sulfide intercalated with methylene blue phase $I\text{-}MB\text{-}TaS_2$, side view of one $3a \times 5b \times 1C$ supercell. (b) Top view of structure of the phase $I\text{-}MB\text{-}TaS_2$, illustrating the position of the MB cation on the TaS_2 host layer and the layer stacking.

as rigid bodies, but they were allowed to shift with respect to each other. The cell parameters a, b and angle γ were kept fixed. Variable parameters were the supercell parameters c, α, β, and the bonding geometry, position, and orientation of the MB cations were also variable. (For more details see [132].)

The structure of the phase I-MB-TaS$_2$ obtained as a result of molecular modeling is shown in Figure 17a,b. This model represents the global minimum of the crystal energy. No multiple minima have been detected; that means the structure exhibits the perfect 3D ordering. As one can see from the figure, the planar MB cation resides just in the central plane in the interlayer space, perfectly parallel with the host layers. The calculated interlayer distance $d = 8.99$ Å is in good agreement with the experimental value 9.07 Å. The calculated supercell parameters are $A = 10.02$ Å, $B = 16.70$ Å, $C = 17.98$ Å, $\alpha = 90.0°$, $\beta = 90.0°$, and $\gamma = 60°$.

Figure 17b shows in detail the position of the MB cation with respect to the lower and upper host layers. This position is a result of the predominant electrostatic host–guest interaction in this intercalate, where the negatively charged atoms in the MB cation tend to avoid the negatively charged sulfur atoms in the host layer. Figure 17b illustrates in addition the layer stacking in the phase I-MB-TaS$_2$.

Figure 18 shows the structure of the phase II-MB-TaS$_2$, the side view of the two-layer $3a \times 5b \times 1c$ supercell with four MB cations obtained as a result of molecular
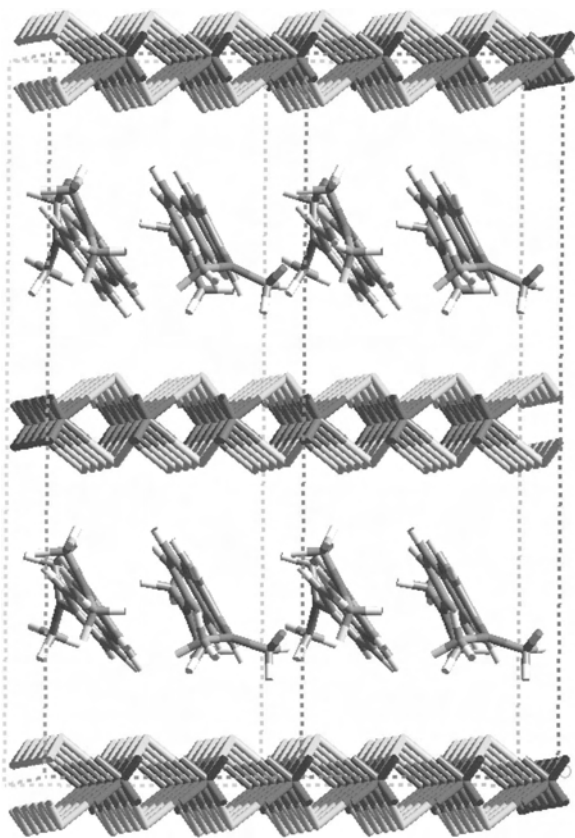
simulation. The calculated supercell parameters are $A = 10.05$ Å, $B = 16.75$ Å, $C = 25.36$ Å, $\alpha = 90.0°$, $\beta = 90.0°$, and $\gamma = 60°$; this means the interlayer distance is 12.68 Å. The MB cations are tilted with respect to the host layer creating pairs of discrete cations $[C_{16}H_{18}N_3S]^+$ in antiparallel arrangement. This pairlike arrangement of MB cations with the same relative positions and orientations occurs also in the crystal structure of MB-thiocyanate [348]. According to the results of modeling the structure of II-MB-TaS$_2$ is ordered. Energy minimization for the series of initial models led always to the same perfectly ordered layer stacking and to the same orientation and position of MB cations with respect to the TaS$_2$ layers. As one can see in Figure 18, the longer edge of the planar MB cation resides in the groove between the rows of sulfur atoms. This arrangement of guests results in a layer stacking different from phase I-MB-TaS$_2$, as one can see comparing Figures 17 and 18. (For details see [132].) Comparing the values of the sublimation energy per supercell, one can see that phase II-MB-TaS$_2$ is significantly less stable than phase I-MB-TaS$_2$. This result of modeling is in agreement with the experimental results [346].

The arrangement of the MB cations in phase III-MB-TaS$_2$ is illustrated in Figure 19. Energy minimization for the series of initial models led always to same layer stacking and to the same orientation and position of MB cations with respect to the TaS$_2$ layers. That means that the structure of this phase is ordered. The calculated supercell parameters are $A = 10.05$ Å, $B = 16.75$ Å, $C = 33.33$ Å, $\alpha = 90.52°$, $\beta = 93.48°$, and $\gamma = 60°$. The calculated interlayer distance of 16.63 Å is in good agreement with the experimental value of 16.8 Å. Phase III-MB-TaS$_2$ keeps the same character of layer stacking, as phase II-MB-TaS$_2$. The supercell in this case is not rectangular ($\alpha = 90.52°$, $\beta = 93.48°$) and consequently two successive layers are mutually slightly shifted from the ideal arrangement in Figure 17. The total sublimation energy for phase II-MB-TaS$_2$ is nearly the same as in case of phase III-MB-TaS$_2$.
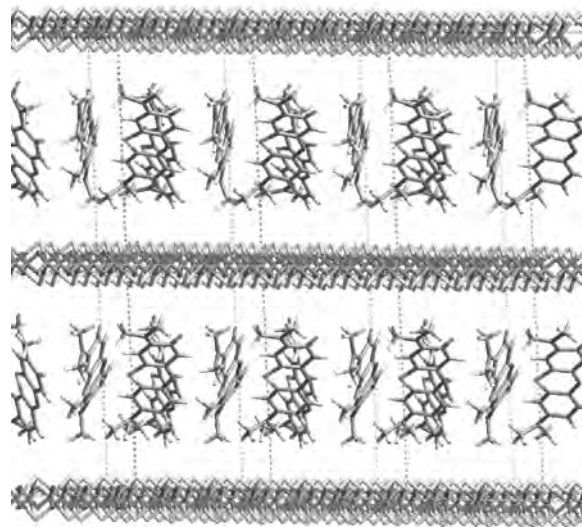

Figure 18. Structure of tantalum sulfide intercalated with methylene blue phase II-MB-TaS$_2$.

Figure 19. Structure of tantalum sulfide intercalated with methylene blue phase III-MB-TaS$_2$.

5.4.2. Montmorillonite Intercalated with Rhodamine B

The intercalation of xanthene dyes in the smectite-type clays is followed by the changes observed in the absorption spectrum (the so-called metachromic effect), whereby the main absorption band is shifted to higher energies [206, 207, 216]. This effect is explained by:

(i) the interaction between the alumino-silicate layers and the dye (i.e., the interaction between the electron lone-pairs of clay surface oxygen and the dye π-system) and

(ii) the interaction between the dye molecules in the interlayer space of the clay structure (i.e., dimerization and the π–π interaction between two monomers in the dimer).

Rhodamine dyes are considered good probe molecules to study the clay–dye complexes because they can be easily intercalated into the clay structure via a cation-exchange mechanism and their photophysics depends on the environmental factors.

The molecular mechanics and dynamics simulations have been performed in *Cerius*[2] to investigate the structure of montmorillonite intercalated with rhodamine B cation. Montmorillonite belongs to the 2:1 dioctahedral layer silicates with prevailing octahedral substitutions in the silicate layer. The octahedral and tetrahedral substitutions in the silicate layers lead to charge fluctuations in the surface oxygen sheet and the resulting charge distribution is important factor ruling the arrangement of guests in the intercalated structure. It is evident from the silicate layer structure that the charge fluctuations in the surface oxygen sheet due to the octahedral substitutions are lower than fluctuations due to the tetrahedral substitutions. Molecular modeling in *Cerius*[2] shows that in case of montmorillonite layers with prevailing octahedral substitutions the charge on the surface oxygen sheet is almost evenly distributed with only small fluctuations within the range -0.03 el. Consequently there are no strong pronounced active sites for the anchoring of guests on the silicate layer. This leads to irregular anchoring of guests on the silicate layer and to disorder in layer stacking in structures of intercalated montmorillonites [349].

The starting model for building the montmorillonite layer is based on the structure data published by Tsipursky and Drits [84]. The unit cell parameters according to Méring and Oberlin [350] have been used to define the planar unit cell dimensions: $a = 5.208$ Å, $b = 9.020$ Å. The composition of the montmorillonite layer according to the chemical analysis was $(Al_{1.53}Mg_{0.23}Fe^{3+}_{0.25})(Si_{3.89}Al_{0.10}Ti_{0.01})O_{10}(OH)_2$. To create a supercell of reasonable size for calculations the structure formula was slightly modified. Consequently the supercell $3a \times 2b \times 1c$ with the layer composition $(Al_{18}Mg_3Fe^{3+}_3)(Si_{47}Al_1)O_{120}(OH)_{24}$ was built with the total negative layer charge (-4). The c values in the initial model were set up according to the basal spacings obtained from X-ray powder diffraction [351, 352].

Modeling results led to two types of interlayer structure with the basal spacing 18.1 (phase 18 Å) and ~23 Å (phase 23 Å) [351, 352]. The existence of these two phases was corroborated by experiment (X-ray powder diffraction). Both phases differ significantly in the interlayer structure; anyway they exhibit certain common features. First of all no regular ordered positions of the rhodamine B anchoring to the silicate layers have been found, neither for phase 18 Å nor for 23 Å. The intramolecular rotation about the xanthene–amine bonds has been observed in both phases. The carboxyphenyl rings may rotate about the xanthene–phenyl bonds in both phases and in all arrangements of rhodamine B cations. The carboxyl groups can rotate about the phenyl–carboxyl (C–C) bonds. The slight distortion of the planar xanthene part of the rhodamine B cation has been observed in both phases 18 Å and 23 Å and confirmed by IR spectroscopy.

Phase 18 Å ($d_{001} = 18.1$ Å) The rhodamine B cations form a bilayer arrangement. In both guest layers the long axis of the xanthene ring along the N–N line is nearly parallel with the silicate layers. The phase 18 Å exhibits two types of interlayer structures with the same basal spacing and nearly the same total sublimation energy: dimeric sandwich type and monomeric bilayer arrangement [351, 352].

Dimeric Sandwich-Type H-Dimers These were reported also in [208, 353] (see Fig. 20a, b). In H-dimers the rhodamine B cations interact with each other via the carboxyl groups. A detailed view of the H-dimer is seen in Figure 20b. One can see the carboxyl groups pointed to the oxygen atom in the xanthene ring of the neighboring rhodamine B cation. It is also evident from Figure 20b that the double xanthene = amine bonds of both cations in the dimer are oriented in the same direction (head-to-head arrangement). The total sublimation energy per one supercell of montmorillonite $3a \times 2b \times 1c$ is 876 kcal/mol.
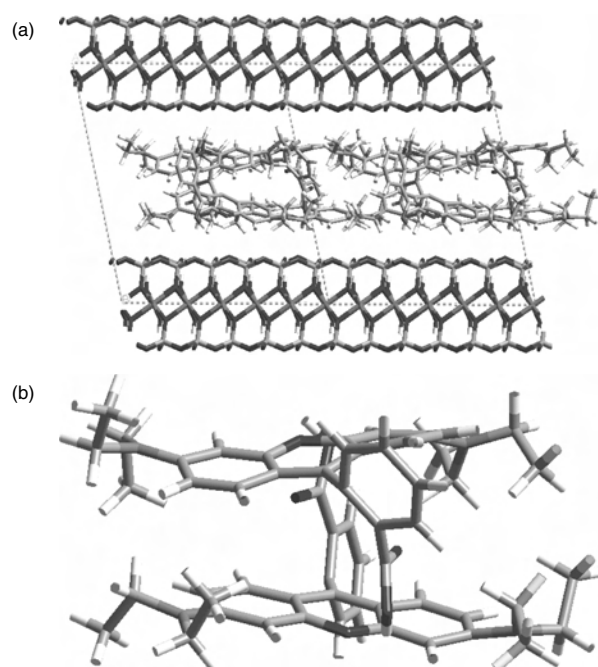

Figure 20. (a) Montmorillonite intercalated with [rhodamine B]$^+$, phase 18 Å with bilayer dimeric arrangements of rhodamine B, H-dimers. (b) The detailed view of H-dimer intercalated in montmorillonite in the phase 18 Å.

Monomeric Bilayer Arrangement This is shown in Figure 21a, b. Figure 21a shows the side view of the $3a \times 2b \times 1c$ supercell with monomeric bilayer arrangement of rhodamine B cations. The top view of the guest structure is given in Figure 21b. In this structure only weak interactions between the guests were detected. The basal spacing for this model is the same as for the H-dimeric structure 18.1 Å. The total sublimation energy per supercell $3a \times 2b \times 1c$ is slightly lower, ~842 kcal/mol.

The inclusion of the water molecules into the interlayer space of the phase 18 Å leads to a significant increase of the total sublimation energy. Thus it is very probable that the sorption of water is stabilizing the structure. This conclusion of modeling agrees with experimental observations. The modeling of monomeric arrangement in the interlayer space of montmorillonite led to: (i) the bilayer guest structure (phase 18 Å) previously described and (ii) the monolayer

arrangement of tilted monomers with basal spacing within 21–25 Å, which we denoted as "phase 23 Å" [351, 352].

Phase 23 Å This was observed by X-ray diffraction in samples prepared using intercalation solutions with very low concentrations of rhodamine B with prevailing monomeric arrangement. The modeling result of this structure is shown in Figure 22a. In this phase the rhodamine B cations are tilted with respect to the silicate layers. The tilting angles are in the range 40°–60°. This wide range of positions and orientations of rhodamine B cations in the interlayer results in disorder and strain in the interlayer space. There is a mixture of monomers and dimers in the interlamellar space. Two types of dimers observed are shown in Figure 22b: a head-to-tail sandwich type of dimer and a head-to-tail J-dimer. (For more details see [351, 352].) Insertion of water molecules into the interlayer structure of the phase 23 Å leads to the fluctuations of the basal spacing, within the range 21–25 Å.

5.4.3. Vermiculite Intercalated with Anilinium

Vermiculite is a widely used host structure for the intercalation of various organic species. In contrast to intercalated smectites intercalated vermiculites exhibit ordered
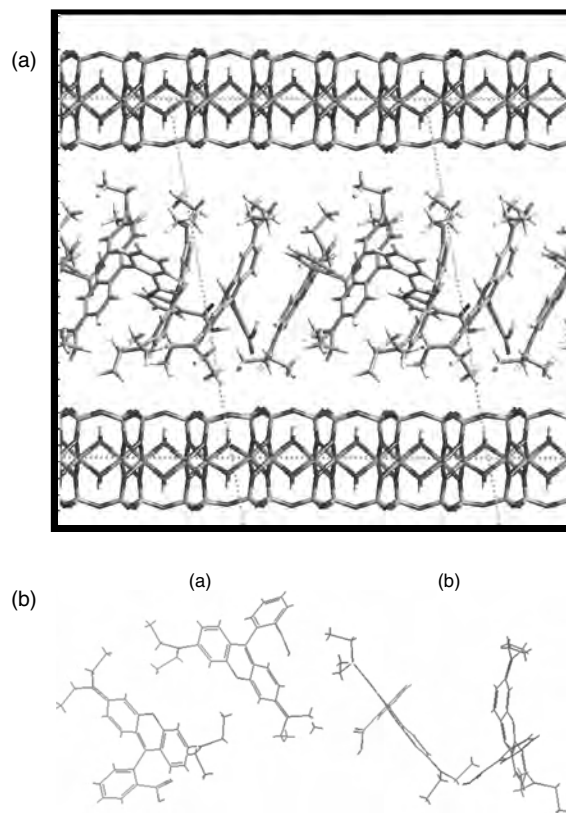

Figure 21. (a) The structure of montmorillonite intercalated with [rhodamine B]$^+$, phase 18 Å with monomeric bilayer arrangement of guests. (b) The top view of the interlayer guest structure of [rhodamine B]$^+$ in the phase 18 Å with monomeric bilayer arrangement of guests.

Figure 22. (a) Structure of montmorillonite intercalated with [rhodamine B]$^+$, phase 23 Å with monolayer arrangement of guests, which can occur in monomeric and dimeric arrangement (J-dimers, head-to-tail dimers, H-dimers, monomers). (b) Detailed view of the head-to-tail dimer (a) and J-dimer (b) in monolayer arrangement of the phase 23 Å.

structures, which could be solved using single crystal diffraction [354–356]. Vermiculite is a 2:1 trioctahedral layer silicate. The layer charge in the vermiculite comes from the tetrahedral substitution (replacement of Si by Al). Compared with the trioctahedral saponite the layer charge in vermiculites is higher due to the higher concentration of tetrahedral replacements. The higher concentration of replacements and their tendency to separation leads to a higher degree of ordering in the silicate layer [357] and consequently to a more regular charge distribution in the surface oxygen sheet. This is a favorable condition for the ordering of guest cations in the intercalated structure. Due to the higher layer charge and consequently higher guest concentration the guest–guest interaction becomes more important for the guest arrangement in vermiculites than in smectites. The ordering of the guests in vermiculite is a result of interplay between the host–guest and the guest–guest interaction.

The ordered structure of vermiculite intercalated with anilinium cations was investigated using modeling with an empirical force field in *Cerius*[2] [358]. The results of modeling have been compared with the single crystal X-ray diffraction data published by Slade and Stone [356]. The initial model of anilinium–vermiculite was built using the structure data presented by Slade and Stone [356]: space group $C2/m$ with the cell parameters $a = 5.33$ Å, $b = 9.268$ Å, $c = 14.89$ Å, and $\beta = 97°$. The host structure was Na-saturated Llano vermiculite from Llano County, Texas. The structural formula of the silicate layer was $(Mg_{5.62}Al_{0.16}Fe^{III}_{0.13}Ti_{0.04}Mn_{0.01})(Si_{5.79}Al_{2.21})O_{20}(OH)_4$. In order to create a unit cell of reasonable size for modeling, we had to simplify the structure formula of one unit cell, taking into account not only the layer charge but also the reported C and N contents in the intercalate. Two aniline cations have been placed into the single unit cell with the layer formula $(Mg_6)(Si_6Al_2)O_{20}(OH)_4$, carrying the charge -2 and corresponding to the fully exchanged vermiculite.

The result of modeling is presented in Figure 23a, b. The anilinium cations are positioned over the ditrigonal cavities in the silicate layers to which the C–N bonds are perpendicular. The anilinium cations alternate in anchoring their terminal NH_3^+ groups to the lower and upper silicate layers. The three amine–hydrogen atoms of aniline are involved in hydrogen bonds to the surface oxygen in adjacent silicate layers. The arrangement of anilinium cations in the interlayer space and the mutual positions of two successive silicate layers are illustrated in Figure 23b. This arrangement of anilinium cations in the calculated model corresponds very well to the electron density map obtained from the single crystal diffraction data, by Slade and Stone [356]. A comparison of the calculated cell parameters with the experimental structure data of Slade and Stone [356] is given in Table 9.

The ditrigonal cavities in adjacent silicate layers are positioned opposite each other and this order in layer stacking is controlled by the well-defined positions of the anilinium cations. This regular layer stacking has also been confirmed by X-ray single crystal diffraction measurements in the Slade–Stone model [356]. The average N–O distance (averaged over six oxygens surrounding the adjacent ditrigonal cavity) in our calculated model $d_{N–O}$ is 3.01 Å; in the experimental Slade–Stone model $d_{N–O} = 3.03$ Å.
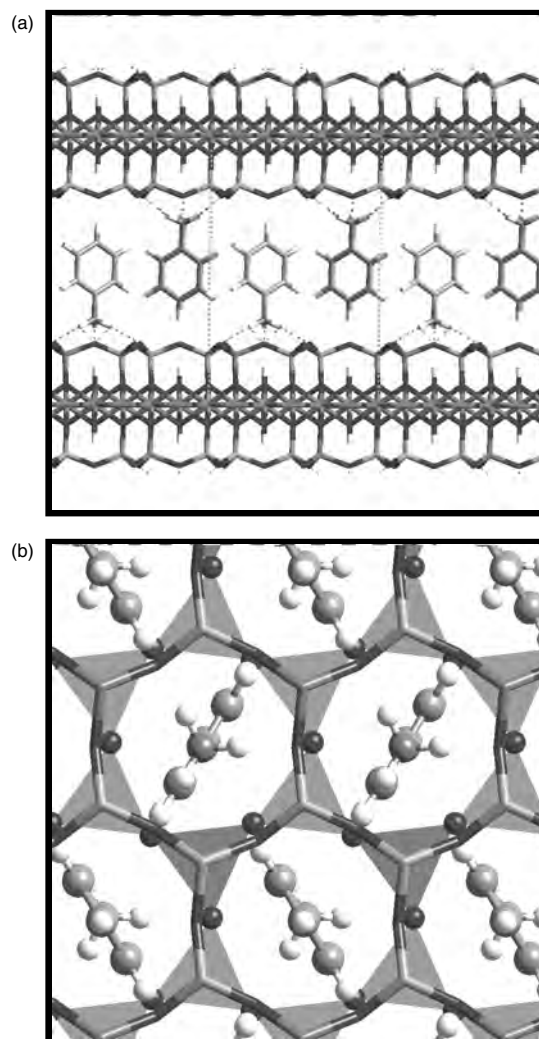

Figure 23. (a) Vermiculite intercalated with anilinium. Hydrogen bonds between the anilinium hydrogen and surface oxygen on the silicate layer are marked by a broken line. (b) The regular arrangement of anilinium in the interlayer space of vermiculite. The top view illustrates the regular stacking of the host layers. Two adjacent tetrahedral sheets are visualized as polyhedra (lower silicate layer) and cylinders (upper silicate layer).

In a subsequent paper Slade et al. [359] discussed the following problems with the structure determination. (a) The packing density of the anilinium is not as high as expected from the structural model presented earlier and the ion exchange capacity of the Llano vermiculite. (b) Therefore, there are additional water and inorganic cations in the structure (anilinium content too low with respect to the cation exchange capacity). However, it is difficult to

Table 9. Comparison of cell parameters for anilinium–vermiculite.

	c (Å)	α (°)	β (°)	d (Å)
Experimental	14.89	90.00	97.00	14.78
Modeling	14.84	90.53	97.17	14.72

Note: Experimental values have been taken from X-ray single crystal diffraction data of Slade and Stone [157]. The calculated values have been obtained by modeling using *Cerius*[2] [159].

determine the absolute positions of these inorganic cations, the water molecules, and the organic cations. Based on three-dimensional data the author introduces the simultaneous presence of anilinium rich and anilinium pure regions to overcome these problems. The first one shows the arrangement of aniline as discussed in the previous paper [356] and in this chapter. This packing motive is also found for benzidine ions in Young River (Western Australia) vermiculite [360]. In the anilinium poor domains triangular groups of water molecules about the inorganic cations and the anilinium ions form together a close-packed array.

The anilinium loaded Llano vermiculite is dark and lilac-blue colored indicating that anilinium has been oxidized by the low amount of structural iron [360]. Since the anilinium ions in the interlayer space are highly organized, the question arises as to where the oxidation takes place and what the oxidation products are. One explanation could be that the color arises from anilinium radicals and the arrangement of the anilinium ions prevents the oligomerization. Another possibility is that the oxidation is only a side reaction of the formation of the intercalation complex and it takes place on the external crystal surfaces and the products remained there because they are too big to diffuse in the interlayer space.

5.4.4. [Ru(bipy)₃]²⁺/Saponite

As pointed out the $[Ru(bpy)_3]^{2+}$ complex is the most studied photosensitizer in biomimetic artificial photoelectrochemistry and a widely used electron transfer mediator in organic electrochemistry. Apart from that Yamagishi has shown that some chiral transition metal (mainly Fe^{2+}, Ni^{2+}, Ru^{2+}) complexes with chelate ligands like phenanthroline, bipyrdine, or 1-(2-pyridylazo)-2-naphthol intercalated in low charged smectites exhibit remarkable chiral recognition phenomena despite the fact that the silicates are achiral [165]. Thus, a racemic mixture of the $[Fe(phen)_3]^{2+}$ complex is taken up in montmorillonite in an amount twice as high as the cation exchange capacity of the clay and twice as high as the pure enantiomers. The layer expansion of the product is in the order of 20 Å indicating the uptake of metal-complex double layers, whereas only a monolayer of the pure enantiomer complexes is adsorbed. In case of the $[Ru(bpy)_3]^{2+}$ the opposite effect is observed: bilayer adsorption of the pure enantiomer complex and monolayer adsorption for the racemic mixture [361]. The preferential uptake of racemic pairs is confirmed further by the observation that the addition of clay to a partially resolved mixture of both enantiomers changes the optical purity of the solution after filtration [165]. In addition the following other effects has been discovered: induction of optical activity in a less stable chiral chelate complex by preadsorption of an enantiomeric chelate complex, chromatographic separation of enantiomeric pairs with clays loaded with an enantiomeric chelate complex, and asymmetric synthesis. However, the reason for this preferred formation of racemic pairs is still a matter of debate [362], since it was not possible to determine the structure of a clay loaded with racemic or enantiomeric chelate complexes. It is clear that the complexes are arranged in the interlayer space with their pseudo C_3 symmetry axis perpendicular to the clay layers. The protons of the aromatic rings are keying in three neighboring

ditrigonal cavities on the Si–O tetrahedral network [165, 362]. Modeling of the possible arrangements of $[Ru(bpy)_3]^{2+}$ in a (saponite) gave different packing motifs for the pure enantiomer and the racemic complex. Whereas the enantiomer shows the generally assumed hexagonal pattern, the arrangement of the racemic mixture is of tetragonal symmetry. The distance between complexes of the same chirality is slightly shorter along the b-axis and the neighboring molecules penetrate each other. This interpenetration of the optical antipodes is feasible only due to the clay mediated alignment of the complexes (parallel C_3 axis) [362] and is indicative for a stronger guest–guest interaction. This result confirms the peculiar interactions within a racemic pair, but it is in disagreement with the assumed packing for the Fe–phenanthroline complexes and with the assumption that racemic pair formation has to be accompanied by the formation of a double layer arrangement [165]. This structure simulation is performed for a loading level high enough to yield a close packed monolayer. For designing microporous materials it is necessary to know how reducing the layer charge will affect the interlamellar arrangement of the Ru complexes. In a subsequent investigation the same authors clarified this point and highlighted the complexity of the interplay of the host–guest and guest–guest interactions [349]. In this study the overall charge of the host is reduced by more than a factor of two with respect to the previous study (0.22 per formula unit vs 0.5). For the $[Ru(bpy)_3]^{2+}$ intercalated into a homogeneously charged saponite (negative charges due to substitution in the tetrahedral layers) the energy minimum for both enantiomeric and racemic interlayers is observed with the hexagonal arrangement of the complexes (E1 and R1 in Fig. 24). The picture changes when switching to the very similar pillar $[Ru(phen)_3]^{2+}$. For enantiomeric interlayers E1 is still energetically favored over any other cluster investigated. However, with the racemic complexes π-stacks can be realized between aromatic ligands of neighboring cations. Due to the parallel alignment of the C_3-axes, as required by the host–guest interaction, the cation distances and orientations induced by the clay surface corrugation the guest–guest interactions are stronger for larger π-systems (phen as compared to bpy) and even large clusters like one-dimensional chains became lower in energy than the hexagonal pattern (R4 in Fig. 24). Moving the permanent silicate charge from the tetrahedral to the octahedral layer and hence further away from the interlayer cations increases the weight of the guest–guest interaction, which makes clustering more feasible. The difference of E1 and E4 declines when going from saponite to hectorite. For the racemic mixture pairs of $[Ru(bpy)_3]^{2+}$ (R2) have energies so close to that of the hexagonal pattern that ordering cannot be ruled out. In case of the enantiomeric interlayers the influence of a nonrandom charge distribution in the host structure has been investigated. Two charge models have been compared. In one of them the substitution follows the pillars in model E4; in the second one it reflects the maximum Löwensteinian clustering of isomorphous substitution. Starting simulations with a prevalent mismatch between the isomorphous substitution pattern in the host and the pillar arrangement in the interlayer are far from any local energy minimum. On the other hand, configurations where pillar arrangement and substitution pattern
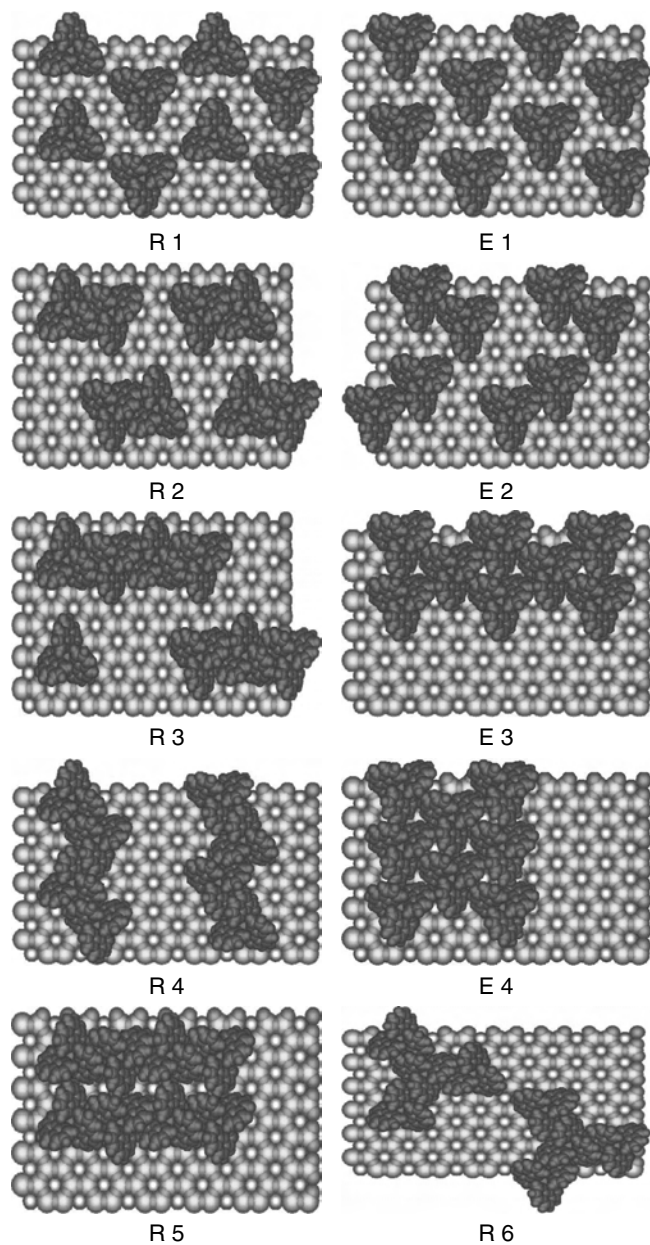
Figure 24. Possible arrangements of $[Ru(bpy)_3]^{2+}/[Ru(phen)_3]^{2+}$ confined between homogeneously charged saponite. The configurations correspond to local energy minima for the enantiomeric [E] and racemic (R) complexes [349].

correspond have local minima close to the starting structures. Despite the increased clustering between both models the pillar arrangement does not change significantly because short-range guest–guest and/or host–guest interactions do not allow denser packing. These results put the focus on the following points. (a) The electrostatic energy is the leading term in host–guest interactions. (b) Constructing supercells with a homogeneous substitution pattern creates highly organized structure in the interlayer. (c) Unless there is good reason to assume such an ordering, this approach can introduce severe artifacts; it will be essential to know the charge distribution and to synthesize monophasic, homoge-

neously charged host materials in order to be able to construct highly organized intercalation compounds.

Therefore when working with natural smectites, the characterization of exchange properties solely by bulk cation exchange capacities will make a conclusive interpretation and reproduction difficult. This point can be illustrated by the conflicting results of luminescence behavior of racemic and enantiomeric $[Ru(bpy)_3]^{2+}$ and $[Ru(phen)_3]^{2+}$ intercalated in smectites [363–366].

5.5. Examples of Structure Analysis in Framework Structures

As for the layered host–dye complexes the knowledge of dye arrangement in framework structures is rather limited. The structure determination has been carried out by X-ray powder diffraction, Rietveld refinement, and structure simulation with commercial programs ($Cerius^2$ and ChemX); only in case of p-nitroaniline (PNA)/H-ZSM-5 was a single crystal structure analysis possible. The position of the guest molecules depends on the preparation method, the size and shape of the molecules inserted, and the pore structure in the frameworks. If the available space is too big, the inserted dyes are in close contact to the channel walls (methyl viologen in zeolite L). When inserting the species during synthesis of the framework, they are squeezed in the open windows between neighboring supercages (methylene blue and thioindigo in zeolites X/Y). Even the deformation of the framework cannot be excluded (p-nitroaniline in H-ZSM-5). In none of these examples is there a remarkable guest–guest interaction, which plays an essential role in layered intercalation compounds.

5.5.1. H-ZSM-5 Loaded with p-Nitroaniline

If a crystal of H-ZSM-5 is loaded with PNA coexisting domains of different symmetries are formed depending on the reaction time [367]. At very long loading times crystals containing only one type of domain can be prepared. The PNA molecules are located in the intersections of the straight and the sinusoidal channels [367]. Figure 25c shows the orientation of PNA along the straight channels. The long axis of the molecules is arranged parallel toward the channel axis (crystallographic b-axis), but tilted by about 9° with respect to it. The angle between the normal on the aromatic ring plane and the a-axis is around 45°. Due to the adsorption of the PNA the straight channel pores are strongly elliptically deformed while the sinusoidal channels are nearly not affected by the adsorption [compare structures of the pristine ZSM-5 (Fig. 10) and the loaded system (Fig. 25a)]. This structure refinement is based on the centrosymmetric space group $Pnma$ and not the acentric $Pn2_1a$ assumed in an earlier paper [369]. This increase in symmetry does not affect the position and orientation of the molecules seriously. Neighboring molecules are only loosely connected as can be seen in the N $\cdots$ O distances of about 4 Å, which is too long for hydrogen bonds [367]. The nitro group is shifted away from the straight channel-10 ring and preferentially related to the neighboring molecules by a twofold screw axis along b (non-centro-symmetric structure), to avoid the short O $\cdots$ O contact. If this chain is interrupted by empty

(a) metyl viologen in zeolite L   (b) thioindigo in a faujasite type zeolite

(c) *p*-nitroaniline in H-ZSM-5   (d) methylene blue in faujasite
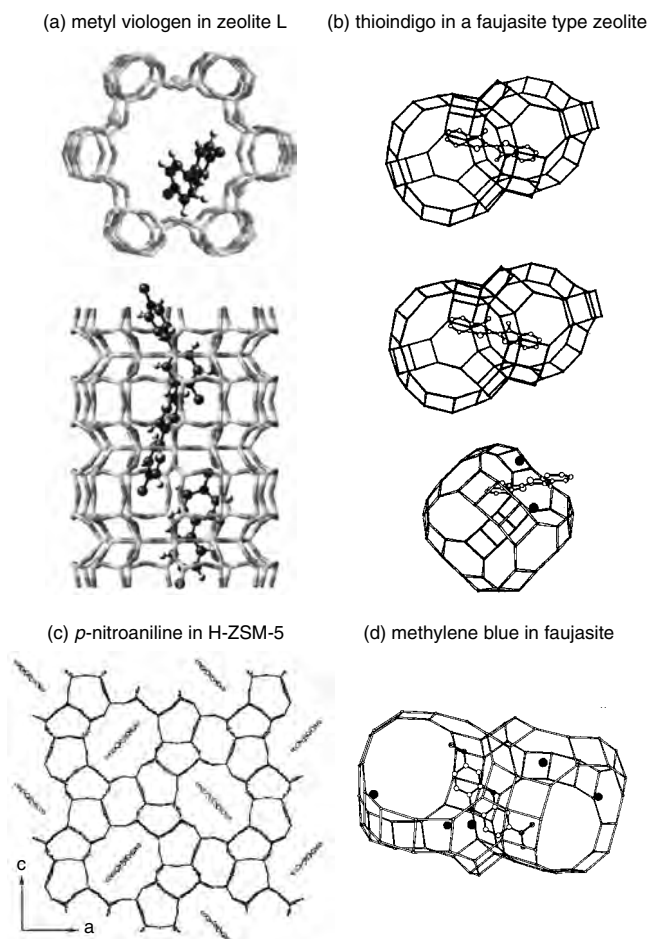
Figure 25. (a) Arrangement of methylene blue in NaY [216]. (b) Arrangement of thioindigo in faujasite [258]. (c) Arrangement of methyl viologen in zeolite L [370]. (d) Arrangement of *p*-nitroaniline in H-ZSM-5 [346]. The PNA molecules are located in the intersections of the straight and the sinuoidal channels. The orientation of the molecules is shown along the straight channels running parallel to the crystallographic *b*-axis.

cross-sections the chain polarity can change and destroy the long-range order of the PNA molecules leading to the loss of acentricity and the higher symmetric space group *Pmna*. This missing long-range order is in conflict with the previous structure determination [369]. The reason for this difference is not quite clear and therefore also the influence on the SHG effect observed previously [368, 369] (see Section 6.4).

5.5.2. NaX, NaY-Encaged Thioindigo and Methylene Blue

Thioindigo [283] as well as methylene blue [224] has been inserted in the X/Y zeolites during hydrothermal synthesis and in both cases the molecules are located in the 12-membered rings which form the windows connecting neighboring supercages (see Fig. 25b and d). If methylene blue is inserted by ion exchange it became located in the supercage of the zeolite structure very near the place of the sodium ion in S_{IV} sites (cf. Fig. 10, top) [224]. In case of the methylene blue one methyl group is missing;

thus it is transferred to trimethylthionine. The incorporation of MB/trimethylthionine is accompanied with a complete loss of Na at S_I sites (cf. Fig. 10, top). Whereas MB/trimethylthionine is located in the center of the effective window between neighboring supercages, the position of thioindigo depends on the condition of solvent removal. By a mild removal of solvents (in air at room temperature) the molecule is located in the center of the window. The occupation factors, exhibiting values <1 for the cation position (S_I' and S_{II}), and the water molecules reflect a displacement of sodium ions and water molecules [283]. After drying in a dryer at 350 K thioindigo is shifted toward the window walls, the more the longer the drying procedure (Fig. 25d). This attachment to the walls is related to an increasing strength of coordination by sodium ions. Prolonged heating leads to migration of sodium from S_{II}' to S_{III} and a chelation of Na by thioindigo. The increased bonding of the dye to sodium prevents the *trans* to *cis* photoisomerization [283].

5.5.3. Methyl Viologen in Zeolite L

Methyl viologen inserted in the rather large channels of zeolite L is located near the channel wall (see Fig. 25d) [370]. The shortest distances between the molecule and the framework oxygens are around 3 Å, indicating possible C–H$\cdots$O hydrogen bridges. The two pyridinium moieties are twisted toward each other by 36.6°. (A twist of the rings in the same order (37.8°) is observed in the iridium(I) maleonitriledithiolate complex with MV^{2+} [371]; this angle amounts to 19.6° in the salt MV^{2+}/2-dicyanomethylene-1,1,3,3-tetracyanopropandiide [372]. In most of the salts within organic and organic cations the rings are coplanar probably due to packing effects; *ab initio* calculations gave an dihedral angle of about 60° for an isolated MV^{2+} cation [373]. Even in intercalation compounds of MV^{2+} in the Llano vermiculite the rings can be twisted [200], whereas the molecules are almost flat in case of MV^{2+} intercalation compounds of montmorillonite [200] and $2H\text{-}TaS_2$ [131].)

The angle between the main molecular axis and the *c*-axis of the zeolite amounts to 27° with the MV^{2+} lying along the channel wall. Neighboring MV^{2+} cations are rotated by 120° around the six-fold axis to get normal contact distances of 3.3–3.4 Å (see Fig. 25a) [370].

This rather rigid arrangement of methyl viologen in a channel structure with a large effective window seems to be in conflict with the suggestion that the MV^{2+} rotation around the single C–C bond connecting both pyridinium rings experiences different degrees of freedom when incorporated in zeolites with different void dimensions [374].

6. PHOTOPHYSICAL BEHAVIOR AND POTENTIAL APPLICATIONS

The previous investigation of the photophysical properties of dye/inorganic composites is overwhelming and is increasing continuously [7–21, 32]. However, as far as we can see it cannot compete with the investigation on the pure organic dyes and their Langmuir–Blodgett–Kuhn assemblies or polymer composites. Browsing through the literature we also got the impression that these all-organic composites are much

nearer to potential applications than the dye/inorganic nanocomposites. However, the potential of the inorganic composites is not really exhausted and the situation may change, if we consider the most recent developments [217, 221, 277, 409–412].

In this section we will discuss a few principal photophysical phenomena which could be of importance for future applications. Since applications are not really around the corner we will focus on the relationship of the photophysical properties with the structural arrangement of the dyes in the inorganic matrices. If possible the information for layered and for framework structures shall be compared. For selected topics the achievements in dye/inorganic nanocomposites shall be discussed with respect to the all-organic supramolecular assemblies. Before going into the details Table 10 shall give the reader a compilation of photophysical phenomena observed on the most studied dyes inserted in various inorganic matrices.

6.1. Photoluminescence and Supramolecular Organization

Absorption of light and the fate of the excited state not only depend on the energy difference of the electronic structure of the ground and excited state, but also on the environment, in which the light-absorbing molecule is encaged. The interaction between identical molecules and/or the matrix in which the light absorbing system is occluded can lead to a shift of the absorption frequency; blue- and redshifts have been observed in many of the chromophores mentioned in this chapter.

Blueshift is attributed to the face-to-face association (dimer or H-aggregate formation) of flat aromatic or heteroaromatic dye ions [235, 413–415]. This association can occur in solution with increasing concentration of the dyes or by adsorption at interfaces. The redshift is caused by the formation of so-called J- or Scheibe aggregates with head-to-tail interactions between the dye cations [210, 235, 414–419]. (The two types of aggregate are sketched in Fig. 26a.) It is also observed if steric constraints prevent the twisting of bulky substituents as, for example, in methylviologen [394, 395] or the pyridyl rings in substituted porphyrins [176–178, 420]. Even protonation of some dyes can lead to redshift [171–173, 228–230, 234, 421].

The energy of the electronically excited state can be lost or distributed in a variety of ways as shown in Scheme 8. The most common fate of an excited state is the nonradiative decay, in which the excess energy is transferred into vibration, rotation, and translation of the excited and the surrounding molecules. These processes convert the excitation energy to heat (i.e., thermal motion). An excited molecule may also take part in chemical reactions. This sort of degradation shall not be discussed further in this chapter. Photochemical processes of species inserted in inorganic frameworks have been discussed thoroughly by Ramamurthy and others [12, 17, 412].

The radiative decay occurs via fluorescence or phosphorescence. The excitation and the reverse process of fluorescence may not occur at the same energy (frequency). Both transitions (excitation and emission) are vertical with respect to the reaction coordinate: the excitation and emission normally do not occur in the same vibronic states of the system and the molecule will interact differently with the surrounding in the ground and the excited state. Thus, fluorescence occurs normally at a lower frequency than the incident radiation because the emissive transition occurs after some vibrational energy has been discarded into the surrounding. If an excited system has undergone a singlet–triplet crossover, the radiative transition to the ground state is strongly delayed because it is spin-forbidden. However, spin–orbit coupling that was responsible for the intersystem crossing can break the selection rule. This delayed transition out of a triplet state is called phosphorescence.

However, the fluorescence can be destroyed ("quenched") completely because of the interaction of the excited molecule with its surrounding. A classification of quenching processes into two general pathways—energy and electron transfer—has been established [422]. Quenching by energy transfer can take place by two different mechanisms: (i) in the electron exchange mechanism two single electron transfers—one in each direction—result in formation of the sensitizers ground state and quenchers excited state; (ii) energy transfer by the dipole–dipole mechanism operates by Coulombic resonance interactions, in which the oscillating electrons of an excited state sensitizer are coupled with those of the quencher by an induced dipole interaction (see Kuhn and Möbius [62]). Quenching by electron transfer is a one-electron reaction, in which an electron jumps from an occupied orbital of one reactant to the unoccupied orbital of the other. The sensitizer's excited state can be an electron donor or acceptor. In either case, electron transfer between uncharged species leads to a radical ion pair or a charge transfer complex.

All three phenomena have been studied in dye/inorganic photochemistry. We will discuss them for a few selected examples. The blueshift is observed in clay/phenothiazine (i.e., methylene blue [32, 224, 226–234] and thionine [32, 423]; in the latter case also in a zeolite complex [212]), clay/phenazine (acridine orange [32, 195, 202, 380]) systems, in some clay/triphenylmethane dye complexes [32, 210], and in azobenzene/magadiite [258].

In case of MB absorption the appearance of the blueshift has been attributed to the deposition of dimers (the organization of the dimers can be seen in Fig. 18), oligomers, and higher aggregates on the clay surface [224, 226–234]. To the contrary Yariv and co-workers assigned the blueshift to a strong π-interaction of the flat lying MB cations with the oxygen plane of the clay layers (this interpretation was applied first to the acridine orange intercalation compounds and then extended to other intercalation compounds of this type of dye) [32, 203, 236, 237]. In the most recent papers the adsorption of dyes on reduced charge montmorillonites at very low loading (only up to 5% of the cec) has been described [231, 234, 235]. The blueshift is observed immediately after adsorption out of solutions containing only monomeric species. Different types of aggregates occur and vary in their amounts as a function of time. The amounts of higher aggregates decrease with decreasing surface charge density of the clay particles. An additional redshifted absorption peak has been observed on low loading with MB and has been assigned to protonated MBH^{2+} [228–230, 234] or

Table 10. Compilation of the (photo)physical properties of selected dye/host systems.

Dye	Host	Property	Ref.
$[Ru(bpy)_3]^{2+}/$ $[Ru(phen)_3]^{2+}$	hectorite	luminescence quenching	[300]
	bentonite	electron transfer quenching	[375]
	low-iron montmorillonite	electron transfer quenching	[375]
	hectorite	electron transfer quenching	[375]
	hectorite	photoxidation of water	[376]
	hectorite (and other clays)	excited state properties depending on entantiomer/racemic	[365]
	laponite	luminescence quenching at internal and external surfaces	[380]
	laponite (bpy/phen)	luminescence quenching	[377]
	ZRP	luminescence quenching	[378, 379]
	LDH (modified phen)	fluorescence self-quenching	[167]
	zeolite Y	luminescence quenching	[381]
	zeolite Y	photoinduced electron transfer	[18, 382, 383]
	zeolite Y	photoinduced charge separation along a redox chain	[18, 384]
	zeolite Y, L, mordenite	photoinduced electron transfer via donor–acceptor diads/triads	[18, 385, 386]
	silica gel matrices	luminescence quenching	[387]
Porphyrins and phthalocyanins (Pc)	synth. saponite	energy transfer	[176–178]
	saponite	hole burning	[388]
	Zr–phosphonate	photoinduced charge transfer	[313]
	TaS_2 (Pc)	superconductivity	[175]
	$H_2Ti_4O_9$	fluorescence self-quenching	[116, 183]
	zeolite L	photoinduced hydrogen evolution	[389]
	$AlPO_4$-5	photostability	[180]
	$AlPO_4$-5 (Pc)	hole burning	[186]
	FSM mesoporous silica	photostability	[188]
	silica gel	fluorescence, energy transfer	[187]
	silica/titania gel	fluorescence, energy transfer	[187]
Methylene blue	hectorite	sensitizer for photoxidation	[227]
	laponite	sensitizer for photoxidation	[227]
	V_2O_5	reduction, dimerization	[126]
	ZRP	dye-modified electrode	[390]
	2H-TaS_2	superconductivity	[131, 133]
	faujasite Y	hole burning	[213]
	faujasite X	hole burning	[213]
Methyl viologen	montmorillonite	photochromism	[391]
		photoreduction of water	[190]
	bentonite	fluorescence decay	[396, 397]
	hectorite	fluorescence decay	[396, 397]
	2H-TaS_2	superconductivity	[131–133]
	MPS_3 (M = Mn,Fe,Zn,Cd)	chemochromism	[398–400]
	V_2O_5	dye-electroreduction	[394]
	ZrP	photoinduced electron transfer	[313, 314]
	ZrP	photocurrent generation	[192]
	$K_4Nb_6O_{17}$, HNb_3O_8	photoinduced electron transfer	[116, 392]
	$H_2Ti_4O_9$	photoinduced electron transfer	[116, 393]
	$HTiNbO_5$	photoinduced electron transfer	[116]
	zeolite L	photoreduction of water	[389]
	zeolite Y	dye-modified electrodes	[395, 401]
		fluorescence, photolysis	[374, 402]
		electron/charge transfer	[10, 297]
	ZSM-5	fluorescence, photolysis	[374, 402]
	mordenite	fluorescence, photolysis	[374, 402]
Rhodamines	saponite	fluorescence	[201, 216]
	laponite	energy transfer	[244]
	$AlPO_4$-5	fluorescence quenching	[204]
	mesoporous silica fiber	lasing	[217]
	silica gel	fluorescence lifetime	[222]
	silica/block copolymer	lasing	[221]

Table 10. Continued.

Dye	Host	Property	Ref.
Crystal violet	montmorillonite	electric linear dichroism	[247]
	montmorillonite K10	electric linear dichroism	[248]
Azobenzenes/hemicyanins, cf. Table 7	magadiite	photomechanical effect	[258]
	$MnPS_3$, $CdPS_3$	SHG, magnetism	[249–251]
	ZrP	SHG, controversial results	[259, 260]
	M41S	solvent induced lattice expansion	[74]
	$AlPO_4$-5	photoswitchable birefringence	[255, 403]
Spiropyranes	montmorillonites	photochromism	[278–280]
	faujasites (HY, DAY)	photochromism	[276]
	SiMCM-41	photochromism	[276]
	SBA-15	photochromism	[277]
	silica gel	photochromism	[404]
	aluminosilicate gel	photochromism	[405]
	organic/silica gel	photochromism	[406–408]
	polymer/silica	photochromism	[277]

to J-aggregates [210, 234]. The dye loading in these experiments is so low that all of the dye cations could be attached to the surface with their aromatic rings parallel to the clay sheets. In addition the space demand of the aggregates is much lower than that of flat lying molecules (adsorbed flat 135 $Å^2$, adsorbed edgewise 75 $Å^2$; when tilted 85–100 $Å^2$ depending on the tilt angle). Thus one would expect domains of different aggregates, flat lying dye cations, and dye-free surface and not the idealized H- and J-aggregates [231, 234, 235]. This conclusion is in agreement with a very recent molecular simulation work of MB arrangements in the interlayer space of beidelites and on external surfaces of micas [423]. These authors show conclusively that water influences strongly the type of aggregation formed and thus increases the complexitiy of the whole system.

Thus—despite enormous effort—a conclusive interpretation of all experimental facts is still lacking and the exact mechanisms of how MB adsorbs to clay minerals are still unknown and are expected to be rather complex. At the moment the following scenario could be reasonable: It is known that the aggregate formation of MB and similar dye cations is strongly influenced by the ionic strength of the solution, though it would not be surprising if dye aggregation would be triggered by the peculiar electrolyte situation in the Gouy–Chapman layer around the clay particles as soon as dye monomers (out of a very thin solution) enter in the near surrounding of the clay particles. The electrostatic attraction of the MB cations to the negatively charged clay particles leads to an enrichment near the particles, which favors also aggregate formation. (It is worth noting that the final state of the MB adsorbate on kaolinite is not influenced by the presence of aggregates in solution [424] and that on laponites—a synthetic clay mineral with low layer charge caused by substitution in the octahedral layers only—no aggregation has been observed. This indicates clearly the importance of the layer charge density for the aggregation tendency.) If attached to the surface MB cations in the aggregates will not be very mobile due to their size or their arrangement in domains. It should be noted that most of the experiments to intercalate these dye species have been started from highly dispersed clay suspensions. Thus the uptake is not necessarily a diffusion process in the bulk but more of an adsorption and flocculation process on external surfaces. If there is a stacking mediated by flat lying dye molecules a partial rearrangement of the MB and water may occur leading to a measurable layer distance. However, the precipitates or films of the dye/clay composite should be considered as highly disordered tactoid, containing voids filled with externally adsorbed dye–water clusters of various sizes (Scheme 9 is a trial to visualize the complex structure). Xiang et al. described peculiar macroscopic structures of such precipitates with $[Ru(bpy)]^{2+}$ and MV^{2+} [425].

Methylene blue in zeolite Y occurs only in the monomer form and its position depends on the preparation procedure (see Section 5.5.2). The loss of one methyl group leads to an additional absorption peak, which is also blueshifted [426]. Thus, the question arises whether all blueshifted spectral features in the MB/clay complexes are due to aggregation or are caused at least in part by demethylated MB. It is known that MB loses methyl groups under acidic or basic conditions [427] (the acidic character of the clay surfaces may be documented by the MBH^{2+} formation). In case of thionine insertion we have very similar features as in case of MB: aggregation by adsorption on clays [428] and monomer uptake in zeolite Y [211]. However, there is an additional effect not observed in case of MB. Equilibrating the thionine/zeolite Y complex in water vapor leads to a dramatic blueshift of the thionine absorption peak [212]. Thus, the uptake of water is assumed to trigger a rearrangement of the thionine cations to dimers located in the supercages of this zeolite [212]. This may happen to minimize the interface of the hydrophobic aromatic rings toward the water surrounding. It seems to be a general rule that the anthracene shaped heterocyclic dyes show a tendency to aggregation in clay systems [32] (at least on the outer surfaces) and are inserted as monomers in framework structures [211–216].

Inspite of the peculiar features of the rhodamine configuration (the phenyl ring is rotated toward the xanthene ring by nearly 90°) the tendency to form aggregates is not excluded completely. Whereas Arbeloa et al. assume the existence of J-aggregates (dimers and trimers) of rhodamine 3B on external surfaces [208], Japanese scientists discuss the formation of H-aggregates of rhodamine 6G (see model in Fig. 20b) in the interlayer space of the synthetic
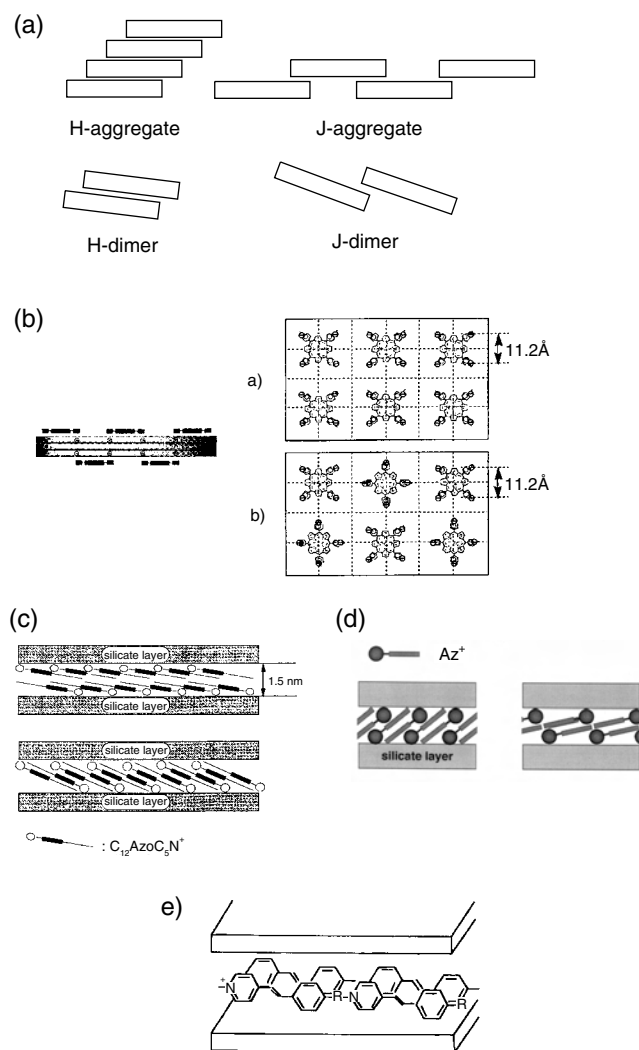
(a)

H-aggregate   J-aggregate

H-dimer   J-dimer

(b)

a)   11.2Å

b)   11.2Å

(c)   (d)

silicate layer   Az+

1.5 nm

silicate layer

silicate layer

silicate layer

○—■ : $C_{12}AzoC_5N^+$ silicate layer

e)

Figure 26. Schematic structural arrangements of aggregates in various dye-intercalation compounds: (a) Simplified visualisation of H-aggregate and J-aggregate assemblies. (b) Schematic view of a porphyrin–synthetic saponite complex visualizing the proposed size mathing effect. Left: View parallel to the layers. Right: Top view indicating to different assemblies of the porphyrin units. Adapted from [177]. (c) Different models of arrangements for the $C_{12}AzoC_5N^+$ azobenzene in montmorillonite [257]. (d) Proposed models for azobenzene/magadiite complex [258]. Left: Interdigited arrangement. Right: Bilayer arrangement. The first one is more probable because of the observed photomechanical layer expansion. (e) Tentative model of the DAMS$^+$ arrangement in the interlayer galleries of MPS$_3$. Adapted from [429].

fluor-taeniolite [89]. The molecular simulation discussed in Section 5.4.2 indicates that H- and J-aggregates of rhodamine B can exist only or simultaneously with monomers in the interlayer space in intercalation compounds with various layer expansions. Aggregates have also been found for fluorescine intercalation in a layered double hydroxide [106]. H- and J-aggregates of a rhodamine derivative have been observed also in silica gels depending on the concentration of the dye [222]. The transition from J dimers to H dimers was found for a specific concentration. In the concentration
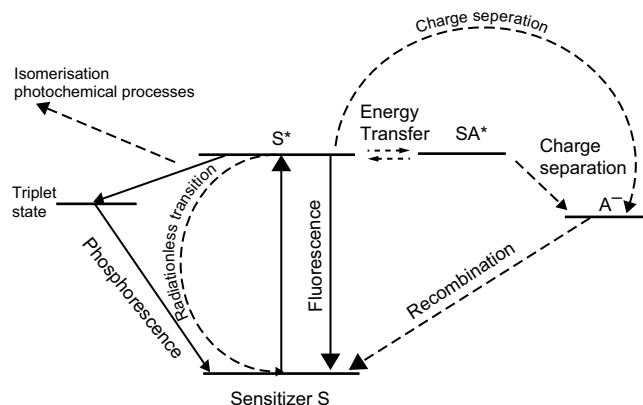
Scheme 8.

range of the J dimer there is a large tunability both in the emission spectrum as well as in the lifetime values of the excited state. This tunability makes these systems good candidates for preparation of Rh 110 solid tunable laser dyes [222]. In the rhodamine inclusion compounds of AlPO$_4$-5 an aggregate formation is prohibited due to the channel size, but there is a strong blueshift which has been attributed to a very strong host–guest interaction [204].

In the crystal violet intercalation compound of zirconiumphosphate aggregate formation (causing blueshift) has been observed with increasing dye concentration. The process of uptake starts with a sequence of various protonated states of this dye cation (well pronounced redshifts), the appearence of the unprotonated monocation, the dimer, and ends up with the formation of stacked $(CV^+)_n$ species [243]. For optimal π–π interaction the dye cations should be arranged perpendicular to the host layers, which has been found in computer assisted model building. Blueshift accompanied with the formation of H-stacks has also been observed in intercalation compounds of crystal violet in smectites [32].

In a recent study of the porphyrin interaction with a synthetic saponite no aggregation of the porphyrins has been observed [176–178]. The observed redshift is explained by the flattening of the bulky side groups as proposed earlier [191, 420]. The very peculiar monolayer adsorption seems to
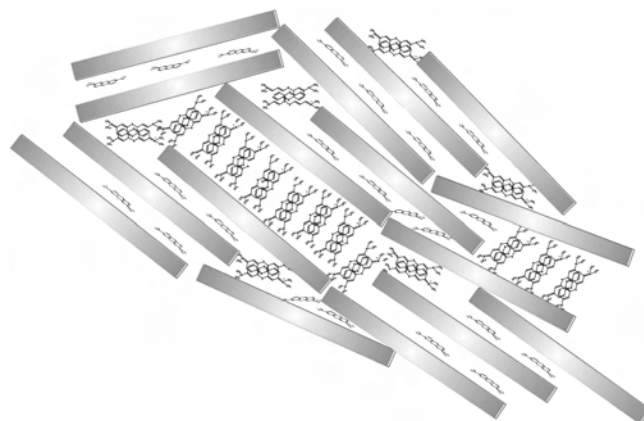
Scheme 9.

be caused by an ideal matching of the charge distribution on the clay layers and on the porphyrin molecules (see Fig. 26b) [176]. Porphyrins are too big to be incorporated in zeolites or other framework structures except the mesoporous systems of the MCM41 type. Even in these large pore systems (pore diameter 35 Å) there are no indications for aggregation [153, 179]. The trial to incorporate porphyrins and phthalocyanins into $AlPO_4$-5 shows that these rather big molecules are not incorporated in the channels of the $AlPO_4$-5 structure (channel width 7.4 Å) but included in mesopores. The molecules are occluded in monomeric form also and show a remarkable photostability [180].

Aggregation phenomena have been observed also in azobenzene and hemicyanine type intercalation compounds in layered host lattices. Recently Ogawa and Ishikawa reported the successful intercalation of alkoxysubstuted azobenzenes into montmorillonites ($C_{12}AzoC_5N$ and $C_8AzoC_{10}N$; see Table 7 and Scheme 5) [256, 257]. The intercalation of these amphiphilic azodyes alters the surface properties of montmorillonite to strongly organophilic. Consequently these intercalation compounds swell in organic solvents like toluene or chloroform. The absorption bands assigned to the azo-moiety of the intercalation compounds are shifted toward higher wavelength with respect to the corresponding absorption bands of the unintercalated azo-compounds in aqueous solution indicating J-aggregate formation in the interlayer space. The difference in redshift has been assigned by the authors to different tilt angles of the azo-groups with respect to the clay layers leading to a varying extent of azobenzene interaction of neighboring molecules (see Fig. 26c [257]). Very similar results have been observed for magadiite intercalation compounds [93]. Due to the higher layer charge of the silicic acid the layer distance becomes larger as well as the tilt angle of the azobenzene chromophore and thus leads to a lower redshift of the absorption band. In a very recent publication, Ogawa was successful in intercalating another azobenzene derivative in magadiite [258], carrying only one shorter substitutional alkoxy group on one of the benzene rings. The absorption band of this intercalation compound shows a slight blueshift relative to that of the unintercalated species in ethanolic solution, indicating the formation of H-aggregates. It is assumed that these cations form an interdigited monolayer with face-to-face interaction of neighboring azobenzene chromophores, thus the H-aggregates (see Fig. 26d) [258].

J-aggregate formation has been observed also in those stilbazolium (hemicyanine-type, most interesting species DAMS$^+$) intercalation compounds in $MnPS_3$, which show a SHG effect. In these compounds the molecular plane is arranged perpendicular to the host layers, so that the $\pi-\pi$ interaction between neighboring DAMS cations is possible [429]. It is questionable whether the assumed stacking (Fig. 26e) is compatible with the J-aggregate formation deduced from the redshift of the absorption spectrum. The situation is quite different in case of the DAMS$^+$ intercalation in the fluorine taeniolite [252]. The intercalation leads to a strong broadening of the absorption spectrum as for the solid iodide salt of DAMS. The broadening is extended to lower as well as to higher wavelengths. From a peak at the lower wavelength region (with respect to the

spectrum in solution) one could deduce a tendency to form H-aggregates, opposite to the situation in the $MnPS_3$ intercalation compound.

Up to now the discussion was devoted exclusively to self-organization of the adsorbed/inserted dye on the internal and external surfaces and their interaction with these surfaces. Now we look at the competitive or cooperative effects between different adsorbates. Information about these effects comes from photophysical and from adsorption studies. The coadsorption systems investigated can be divided in the following categories: (i) charge complexes of pyridinium acceptors and aromatic donors [10]; (ii) the alkylammonium/pyrene coadsorbates (see Section 3.3.7 [14, 15, 290–295]); (iii) the competive co-adsorption of two or more dye species.

Only the third category shall be treated in detail stressing mainly the aspects related to energy and electron transfer. Competitive adsorption has been studied for the following dye couples: MB/TFT [202, 421], MB/proflavine [421], and MB/acridine yellow [232, 421]. These couples have been chosen to avoid spectral interference. In the simultaneous uptake of MB/TFT both dyes are adsorbed to a similar extent up to the cec; above the cec TFT is adsorbed preferently accompanied with a slight loss of the MB content. In a sample previously loaded with MB the additionally adsorbed TTF cannot replace MB to an extent expected from the binding coefficient of the pure MB/clay system. The overall uptake of both dyes in the experiment exceeds that of the cec by a factor 1.5 [202] to 2 [421]; that means most of the material must be deposited on external surfaces of the clay. The presence of TTF seems to change the MB species present in the pure system (from dimers to monomers and a higher content of MBH^{2+}). In the MB/acridine absorption the nonadditivity of the absorption spectra of the individual dyes is attributed to the formation of mixed aggregates on the clay particles [232]. Significant spectral variations with time were observed: for suspensions containing the SWy-1 montmorillonite they were mainly due to the reorganization of the dye molecules on the clay particles; for systems containing laponite the spectral changes were ascribed to association processes of the clay particles. A further study of coadsorption of dyes was devoted primarily to how coadsorbed species influence the energy transfer between a donor (here rhodamine 6G) and various acceptors. In the case of co-adsorption of rhodamine 6G and crystal violet the energy transfer (i.e., fluorescence quenching) is most efficient when the donor is surrounded by acceptor species only [244].

To optimize the electron transfer or other desired photofunctions it is essential to know how the fate of the dye excited state is influenced by the immediate surrounding of the dye and how to control it. The central point of these investigations is the determination of the luminescence properties, mainly lifetime and decay mechanisms. The various parameters of importance shall be discussed for the well investigated sensitizer $[Ru(bpy)_3]^{2+}$. First of all oxygen is one of the most important luminescence quenchers and has to be excluded in all experiments to determine luminescence properties, irrespective of the dye under investigation. Another crucial quencher is iron. It plays an essential role when natural clays are applied as matrices for dye/inorganic

composites [300, 375]. It is interesting to note that the structural iron (although 4 Å apart) is more effective than Fe^{3+} in the interlayer galleries. To circumvent this problem one has to use those natural clays with a very low iron content or purely synthetic clays without any trace of iron. In the $[Ru(bpy)_3]^{2+}$/layered host composites (see Table 10 and [167, 375–380]) as well as in many other dye/inorganic systems [14] the emission kinetics can be fitted with a double exponential decay. This behavior is assumed to be caused by different sites on the solid surface. However, in the case of the $[Ru(bpy)_3]^{2+}$/clay system the results can be fitted with a single exponential decay if the measurements have been carried out under low-level illumination using the time-correlated single-photon counting (see Table 11) [375]. The slightly longer lifetime compared to that in water is in accord with the ~30% increase in emission quantum yield. The missing concentration dependence of the self-quenching rate (quenching by other $[Ru(bpy)_3]^{2+}$ complexes in close distance) has been attributed to a nonrandom distribution of the complex ions in the interlayer space. This situation would result if at low loadings a given interlayer would be completely saturated with $[Ru(bpy)_3]^{2+}$ whereas neighboring interlayers are not occupied at all. The large effective concentration in the intercalated domains would explain the high self-quenching efficiencies. A $[Ru(bpy)_3]^{2+}$ complex diluted by $[Zn(bpy)_3]^{2+}$, which is photochemically silent under proper illumination conditions, leads to a decrease of the self-quenching rate [375]. A similar reduction of the self-quenching rate has been observed if the $[Ru(bpy)_3]^{2+}$ complex has been diluted with a polymer [431]. The influence of the strong electron acceptor viologen has also been tested [375] using two different types of viologens with

Table 11. A selection of lifetime data for excited states of dye/inorganic complexes under various conditions.

Host	Guest	τ_1 (μs)	τ_2 (μs)	Ref.
	$[Ru(bpy)_3]^{2+}$, water	~0.65		[430]
	$[Ru(bpy)_3]^{2+}$, dichloride, crystalline	0.43		
Hectorite	$[Ru(bpy)_3]^{2+}$,	0.062	0.350	[375]
		0.8		[375]
	$+[Zn(bpy)_3]^{2+}$, 2×10^5 M,	0.076	0.714	[375]
	6×10^5 M	0.098	0.788	[375]
TMS	33 mmol $[Ru(bpy)_3]^{2+}$ per 100 g TSM-PVP	0.24	0.992	[431]
TMS	1 mmol $[Ru(bpy)_3]^{2+}$ per 100g TSM-PVP	0.265	1.54	[431]
Laponite	0.30 meq/g	1.12		[430]
Montmorillonite	0.05 meq/g	1.52		[430]
Nontronite		0.319		[386]
	0.05 meq/g	1.20		[430]
	0.05 meq/g	1.20		[430]
	0.10 meq/g	1.98		[430]
$[Mg_{2.98}Al_{1.04}(OH)_8]^-$	$[Ru(BPS)_3]^{4-}/[Zn(BPS)_3]^{4-}$ 1:0	0.544	2.96	[360]
	1:1	4.31		
	1:9	5.6		
Zeolite Y	6.9 $[Ru(bpy)_3]^{2+}$/u.c.	0.266		[381]
	3.2 $[Ru(bpy)_3]^{2+}$/u.c.	0.58		
	H_2TMAP^{4+}, in water	0.0093		[177]
	Zn_2TMAP^{4+}	0.0018		[177]
Synthetic saponite	H_2TMAP^{4+}, externally	0.0041		[177]
	H_2TMAP^{4+}, intercalated	0.0032		[177]
	Zn_2TMAP^{4+}, externally	0.0007		[177]
	Zn_2TMAP^{4+}, intercalated	0.0004	0.0001	[177]
	H_2TMPyP^{4+} in water	0.0041		[182]
		0.0051		[176]
	H_2TMPyP^{4+} in methanol	0.0072		[182]
	H_2TMPyP^{4+} in glycerol	0.0108	0.0012	[182]
	H_2TMPyP^{4+} 4I	0.0057		[182]
	Zn_2TMPyP	0.0013		[176]
$H_xTi_4O_9$	H_2TMPyP^{4+}	0.006	0.0012	[182]
Synthetic saponite	H_2TMPyP^{4+}, external	0.0038	0.0007	[176]
	H_2TMPyP^{4+}, intercalated	0.0032	0.0002	[176]
	Zn_2TMPyP^{4+}, external	0.0006	0.0002	[176]
	Zn_2TMPyP^{4+}, intercalated	0.0005		[176]

Note: TSM = fluorotetrasilicic mica; PVP poly(vinylpyrrolidone).

the same redox potential: the zwitterionic system propylviologen sulfonate and MV^{2+}. Whereas there is a complete lack of quenching in the presence of MV^{2+}, clear evidence of electron transfer mediated quenching by PVS has been observed. This difference in behavior has been explained by a complete segregation of the positively charged MV^{2+} ions from $[Ru(bpy)_3]^{2+}$ upon intercalation/adsorption. Table 11 summarizes some lifetime data for $[Ru(bpy)_3]^{2+}$ under various conditions. In contrast to the clay intercalation compound there is a strong inverse relationship between emission intensity and concentration for the zeolite encaged $[Ru(bpy)_3]^{2+}$ complex [381]. In the sample with the highest complex concentration ($[Ru(bpy)_3]^{2+}$-Y(6.9)) the formal concentration corresponds to 0.77 M in free solution and the extremities of the complexes are almost in contact with one another through the 12-membered rings separating the large cavities. In a sample containing half as much of $[Ru(bpy)_3]^{2+}$ the lifetime of the excited state is the same as in an aqueous solution (see Table 11), and it is expected to exceed 600 ns in a more dilute sample but would not be greatly different from the lifetime of the complex in aqueous solution. The presence of water influences the lifetime also. Although water is not a ligand in the $[Ru(bpy)_3]^{2+}$ complex, the OH vibrations must couple with the excited complex such that radiationless transitions occur [381]. Self-quenching by neighboring dye cations has been observed also in the porphyrin/clay system (see Table 11) [177, 178]. In general one can sum up that the variation of lifetimes in dye/layered systems is about ± 1 order of magnitude higher/lower than in the aqueous solution of the free dye.

The unavoidable close contact of dyes in layered systems, the tendency to from domains corresponding with a concentration of the dye, and the often-observed aggregate formation are unfavorable conditions to elongate the luminescence lifetimes. Thus, to increase the quantum efficiency of fluorescence it is necessary to isolate the dye species from contact with other dye molecules, reduce the host–guest interaction, and restrict nonradiative processes due to molecule tumbling and internal rotational motions. Now there is overwhelming evidence that framework structures like zeolites, zeolite related compounds, silica gels, and ormosils are much more suitable matrices for this purpose than the layered host materials. This has been demonstrated just recently with the invention of new laser materials based on rhodamine 6G/ormosil type gels [217, 221] or rhodamine 110/silica gel [222]. Calzaferri et al. have shown that dye molecules in the channels of hexagonal zeolite L crystals provide fascinating possibilities for building an artificial antenna device which consists of highly concentrated monomeric dye molecules of up to 0.4 M with a high luminescence quantum yield in a specific arrangement (see Section 6.2) [215, 410, 411, 432, 433].

6.2. Light Harvesting Antennas, Charge Separation, and Artificial Photosynthesis

To establish artificial photosynthetic systems the total problem can be divided into partial goals. For each of these partial problems simple chemical model systems have been created and their photophysical and photochemical properties investigated. In that way insight in the mechanism

of the underlying processes and the requirements for the optimal design have been obtained. Based on these results and on the growing knowledge about the structure and the photophysical properties of the natural photosynthetic nanomachines (see, e.g., for the photosystem II of plants [434]) the models have been improved continuously over the last 30 years. The development of these artificial architectures is a paradigmatic example of the growing field of supramolecular chemistry. Table 12 shall give an overview about the partial goals, the chemical models, and the main inventors of this field. Apart from the efforts made with dye/inorganic nanocomposites essential inventions are included which were closely related to our systems of interest.

In the first trials to mimic photosynthesis, the antenna system has been replaced with a photosensitive compound, which can undergo reversible redox reactions and which is stable enough toward light induced chemical side reactions. In combination with electron acceptors the essential steps in the reaction center of the natural photosynthetic systems can be simulated. However, the choice of a suitable electron acceptor is a difficult goal since the electron exchange is determined by many factors whose interplay is not easy to figure out [422]: the ionization potential of the donor, the electron affinity of the acceptor, the tendency to form free radicals, contact ion pairs, or charge transfer complexes, the interaction with the environment (i.e., the solvents for the educts, the photosensitized states, and the products), and possible orbital overlap or the topology of the nuclei. A useful guideline is the difference in the electrochemical potentials in the excited and ground states and their change with solvents and other experimental conditions. Other crucial points for the photoinduced electron transfer are the following: (i) the electron transfer has to be faster than any luminescence or self-quenching processes of the sensitizer; (ii) the backtransfer of the electron from the reduced acceptor to the sensitizer has to be retarded below the level of diffusion controlled backreaction.

Since the first trials to mimic photosynthetic solar energy transduction $[Ru(bpy)_3]^{2+}$ and other closely related Ru complexes became the most used photosensitizers [18, 51, 69, 436, 442–444]. The electron acceptors, which won out against other candidates [442], are MV^{2+} or other viologen systems [18, 51, 52, 69, 436]. The electron transfer rate constant in aqueous solution is near the diffusion-controlled limit, nearly independent of the charge of the viologen (MV^{2+} vs the zwitterionic species PVS) [52]. The situation changes drastically if adsorption processes come into play: the quenching rate for the electron transfer to PVS is not changed seriously by addition of the SiO_2 colloid [52] or of the hectorite [375]; but for MV^{2+} it is enhanced by nearly two orders of magnitude to 5×10^{10} in case of the SiO_2 colloid [52] and lowered by the same order if hectrorite has been added [375]. The latter effect has been explained by a strong segregation of $[Ru(bpy)_3]^{2+}$ and MV^{2+} on the hectorite surface (see Section 6.1). The backtransfer in homogeneous solutions is in the same order as the forward reaction. In case of the SiO_2 gel it is retarded by two orders of magnitude (compared to the homogeneous system) because the negatively charged PVS^- radical is pushed away from the negatively charged SiO_2 surfaces [52].

Table 12. Supramolecular assemblies designed for mimicking photosynthesis.

Partial goals	Chemical models	Inventors, year, Ref.
Antenna (light harvesting)	$(P_{ZP})_3$-P_{ZC}-P-C_{60}	Gust et al., 1997 [435]
	dye energy transfer cascades-zeolite L	Calzaferri et al. [410, 411]
	ZrP($HTiNbO_5$)coumarin-fluorescein-porphyrin- ZrP($HTiNbO_5$)-MV^{2+}	Kaschak et al. [450]
Reaction center (charge separation)	$[Ru(bpy)_3]^{2+}$/$Fe(H_2O)_6^{3+}$ and other electron transfer quenchers	Whitten et al., 1975ff. [43, 436]
		Sutin et al., 1976 [44]
	$[Ru(bpy)_3]^{2+}$-MV^{2+}	Bock et al., 1974 [437]
	TEOA-$[Ru(bpy)_3]^{2+}$-PVS^0-SiO_2-colloid	Willner et al. [52]
	TEOA-$ZnTMPyP^{4+}$-PVS^0-SiO_2-colloid	Willner et al. [52]
	$[Ru(bpy)_3]^{2+}$-MV^{2+}(PVS^0)-hectorite	Ghosh and Bard, 1983 [375]
	$[Ru(bpy)_3]^{2+}$-MV^{2+}-Zeolite Y	Dutta and Turbeville, 1992 [383]
	$[Ru(bpy)_3]^{2+}$-MV^{2+}-dyads-Zeolite L	Krueger et al., 1988 [385, 386]
	$[Ru(bpy)_3]^{2+}$-DQ^{2+}-Zeolite Y-PVS	Borija and Dutta, 1993 [384]
	$[Ru(bpy)_2(bpz)]^{2+}$-$[Ru(mmb)_3]^{2+}$-DQ_{55}^{2+}-Zeolite Y-PVS	Sykora and Kincaid, 1997 [447, 448]
	viologen^{2+}-Cl^-(Br^-)-Zr-P	Vermeulen and Thompson [314]
Hydrogen evolving systems	TEOA-$[Ru(bpy)_3]^{2+}$-$[Rh(bpy)_3]^{3+}$-Pt	Lehn et al., 1977 [46]
	EDTA-$[Ru(bpy)_3]^{2+}$-MV^{2+}-Pt	Keller et al., 1980 [438]
	EDTA-$[Ru(bpy)_3]^{2+}$-MV^{2+}-sepiolite-RuS_2	Van Damme et al., 1986 [50]
	TEOA-$[Ru(bpy)_3]^{2+}$-MV^{2+} montmorillonite	Villemure et al., 1986 [198]
	EDTA-$ZnTMPyP^{4+}$-MV^{2+}-zeolite L-Pt	Persaud et al., 1987 [389]
	viologen^{2+}-Cl^-(Br^-)-ZrP-Pt	Snover and Thompson, 1994 [439]
	RuL_3^{2+}-$K_{4-x}H_xNb_6O_{17}$-Pt	Kim et al., 1991 [441, 456]
	H^+/$K_4Nb_6O_{17}$	Abe et al., 1997 [120]
	$H_2Ti_2O_5$ and $Cs_2Ti_2O_5$	Kudo and Kondo, 1997 [117]
	$H_2Ti_2O_5$-Pt	Kudo and Kondo, 1997 [117]
Oxygen evolving systems	RuO_2/$[Ru(bpy)_3]^{2+}$-$[Co(NH_3)_5Cl]^{2+}$	Lehn et al., 1979 [47]
	hectorite-$[Ru(bpy)_3]^{2+}$-$[Co(NH_3)_5Cl]^{2+}$-$[Ru(bpy)_3]^{3+}$-zeolite Y	Nijs et al., 1982 [376]
		Dutta, 1997 [18]
Artificial photosynthesis	$[Ru(bpy)_3]^{2+}$ monolayers	Whitten et al., 1976 [440]
	sepiolote-RuO_2-$[Ru(bpy)_3]^{2+}$/Eu^{3+}-$Al(OH)_{3gel}$-Pt	Nijs et al., 1983 [49]
	$K_4Nb_6O_{17}$-Ni/NiO	Kudo et al., 1988 [115]
	$A_{2-x}La_2Ti_{3-x}Nb_xO_{10}$-Ni/NiO	Takata et al. [118]
Proton gradients	C-P-Q triad-liposome vesicle	Gust et al., 1997 [435]

The photoelectron transfer within a zeolite exhibits a behavior quite distinct from that of other microheterogeneous supports [383]. The size of the $[Ru(bpy)_3]^{2+}$ complex ensures that it is trapped within the supercages of zeolite Y. Its density is adjusted to a value so that 1 out of 14 supercages is occupied by the complex. The other cages are filled with methyl viologen. It can migrate through the zeolite network. The formation of the $MV^{+\bullet}$ radical occurs on the 15 ns time scale. Two pathways are observed for the fate of the transferred electron: rapid backtransfer is observed on the microsecond time scale; a slower process leads to charge separation and stabilization of the redox pairs for extended periods. The latter process has been explained by diffusion of methyl viologen through the cages. Due to particular orientations of these molecules (in principle two MV species could occupy one supercage) electron hopping along adjacent molecules could occur leading to charge separation. The kinetics of this process is influenced by diffusion of cocations, necessary to balance the charge of the migrating photoelectron.

A strong increase of the electron transfer rate has been achieved by covalent linking of the $[Ru(bpy)_3]^{2+}$ complex and the viologen moiety (diads) [445]. In case of the diads the forward reaction depends on the length of the spacer and the conformation of the molecule [18, 446]. The time scale of this process varied from picoseconds to hundreds of nanoseconds. Back electron transfer in the diads is a factor of 10 faster than the forward reaction. However, if these diads had been inserted in the channels of zeolite frameworks (see Fig. 27) the backreaction would have been lowered by as much as 10^4 for five CH_2 units as compared to that in solution [386]. Up to now no experiments concerning the intercalation of these diads in clay systems have been carried out.

The back electron transfer can be prevented if a sacrificial donor like triethanolamine (TEOA) or EDTA is added to the solution, which reduces the $[Ru(bpy)_3]^{3+}$ formed during the electron transfer from the excited state to the acceptor. A further possibility is to transfer the electron from the first acceptor to another one or to consume it
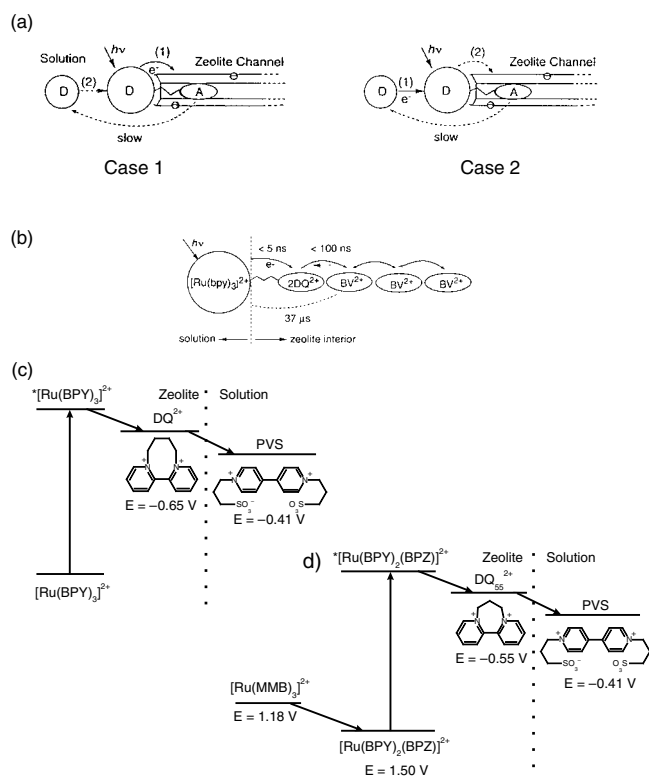
Figure 27. Schematic drawings of various charge separation assemblies: (a) Possible diad assemblies in zeolite L. The diads consist of a viologen (A) covalently attached to a Ru–bipyridine complex (D). D in the smaller circles means sacrificial donors. The cases a and 2 are described in the text. Adapted from [18]. (b) A triad zeolite L assembly. Adapted from [18]. (c) Redox cascade with sensitizer and first electron acceptor in zeolite Y, redrawn according to [18]. (d) Modified redox cascade with a sacrificial electron donor and sensitizer arranged in neighboring supercages of zeolite Y, redrawn following [447, 448].

for irreversible chemical reduction reactions (i.e., hydrogen formation by water splitting; see later). The electron transfer to other acceptors is realized in the natural photosynthesis system (see Fig. 3). It has been simulated in some framework structures based on the $[Ru(bpy)_3]^{2+}–(CH_2)_n–MV^{2+}$ diad/zeolite L systems [18, 385, 386]. The authors used as a donor promethazine (PMZ^+, a thionine derivative). This cation is able to reduce Ru^{3+} but not Ru^{2+*}, resulting in a final charge separated state $PMZ^{2+\bullet}–[Ru(bpy)_3]^{2+}–(CH_2)_n–MV^{+\bullet}$ (see Fig. 27a, case 1) [18, 386]. This charge-separated state collapses back to the ground state indicating that the $PMZ^{2+\bullet}$ on the surface has access to the $MV^{+\bullet}$. Thus, the $MV^{+\bullet}$ in the supercages is somehow exposed to the zeolite–solution interface. Case 2 in Figure 27a was observed with $[W(CN)_8]^{4-}$ in solution, which quenched $[Ru(bpy)_3]^{2+\bullet}$ forming $[Ru(bpy)_3]^+$. This reaction is followed by a fast second electron transfer to MV^{2+}, resulting in $[W(CN)_8]^{3-}–[Ru(bpy)_3]^{2+}–(CH_2)_n–MV^{+\bullet}$. The quantum yield of charge separation for this system was 10%, significantly higher than in all other systems discussed so far.

Mallouk and co-workers also reported on the molecular system $[Ru(bpy)_3]^{2+}–(CH_2)_n–2DQ^{2+}–BV^{2+}$ formed at the zeolite–solution interface by ion exchange of the system $[Ru(bpy)_3]^{2+}–(CH_2)_n–2DQ^{2+}$ diad into a benzylviologen

loaded zeolite L (see Fig. 27b) [18, 385]. Photoexcitation leads to efficient quenching of the $[Ru(bpy)_3]^{2+\bullet}$ by the covalently bound DQ^{2+}. The lifetime of this charge separated state amounts to 0.44 μs, whereas it lives less than 5 ns in solution. There is a subsequent charge transfer from the more strongly reducing agent $DQ^{+\bullet}$ to BV^{2+}. The $Ru^{3+}–BV^{+\bullet}$ thus formed decays considerably slowly ($\sim$37 μs), leading to a long lived charge separated state. In another ternary system intrazeolitic electron transfer occurs between encapsulated $[Ru(bpy)_3]^{2+}$ and $4DQ^{2+}$ with a higher reduction potential than MV^{2+}, followed by a second electron transfer to the zwitterionic neutral viologen PVS present in the surrounding solution (see Fig. 27c) [18, 384]. While the quantum yield is very low (5×10^{-4}), this system is quite important because it represents the first photochemical electron cascade assembly that leads to permanent charge separation in the absence of a sacrificial electron donor. The charge separation efficiency can be greatly improved, if a potential donor is properly positioned in the cage adjacent to the sensitizer (see Fig. 27d) [447, 448]. The role of this donor is kept by $[Ru(mmb)_3]^{2+}$. The trivalent oxidation state of this donor is favored over $[Ru(bpy)_2(bpz)]^{3+}$. Upon selective excitation of the $[Ru(bpy)_2(bpz)]^{2+}$ sensitizer an initial photoproduct $[Ru(bpy)_2(bpz)]^{3+} \cdot DQ_{55}^{+\bullet}$ is formed. Reductive quenching of the oxidized sensitizer by $[Ru(mmb)_3]^{2+}$ leads to a the charge separated pair $[Ru(mmb)_3]^{3+} \cdot DQ_{55}^{+\bullet}$, which is separated by a reduced sensitizer molecule. Since the undesirable back electron transfer is strongly suppressed in this arrangement, the $DQ_{55}^{+\bullet}$ can be oxidized by PVS in solution. The extent of reduction of PVS upon prolonged irradiation is enhanced dramatically with respect to that of Duttas arrangement. In order to produce the $[Ru(mmb)_3]^{2+}/[Ru(bpy)_2(bpz)]^{2+}$ couple in adjacent supercages an effective synthetic scheme has been applied which exploits the susceptibilty of coordinated 2,2′-bipyrazine (bpz) to attachment of secondary metal complexes. A zeolite loaded with $[Ru(bpy)_2(bpz)]^{2+}$ is treated with a solution of $[(H_2O)Ru(NH_3)_5](PF_6)_2$, whereupon a $Ru(NH_3)_5$ fragment is attached to one of the peripheral nitrogens of the coordinated bpz; this material, when treated with excess 5′-mono-methyl-2,2′-bipyridine (mmb), yields a zeolite sample which contains the two complexes entrapped in neighboring supercages.

Vermeulen and Thompson could realize a permanent charge separation in the layer-by-layer deposited ZrP–dialkylviologen–halide system shown schematically in Figure 16 [69, 314], clearly visualized by the blue color of the viologen radical. Photoreduction of viologen in these thin-film samples is very efficient [449]. The primary photoprocess involves a viologen centered excitation, followed by oxidation of the halide anion. Subsequent structural rearrangements lead to the ultimate charge-separated state whose chemical nature is still uncertain. Ungashe et al. were successful in forming multilayer assemblies with alternating sheets of phosphonophenylporphyrin and phosphonoalkylviologens [313]. The fluorescence of the porphyrin layer is diminished by ca. 60% in the presence of the viologen layers. No significant quenching is observed when a layer of 1,12-dodecanediylphosponicacid was deposited between the donor and the acceptor sheets. Data on the
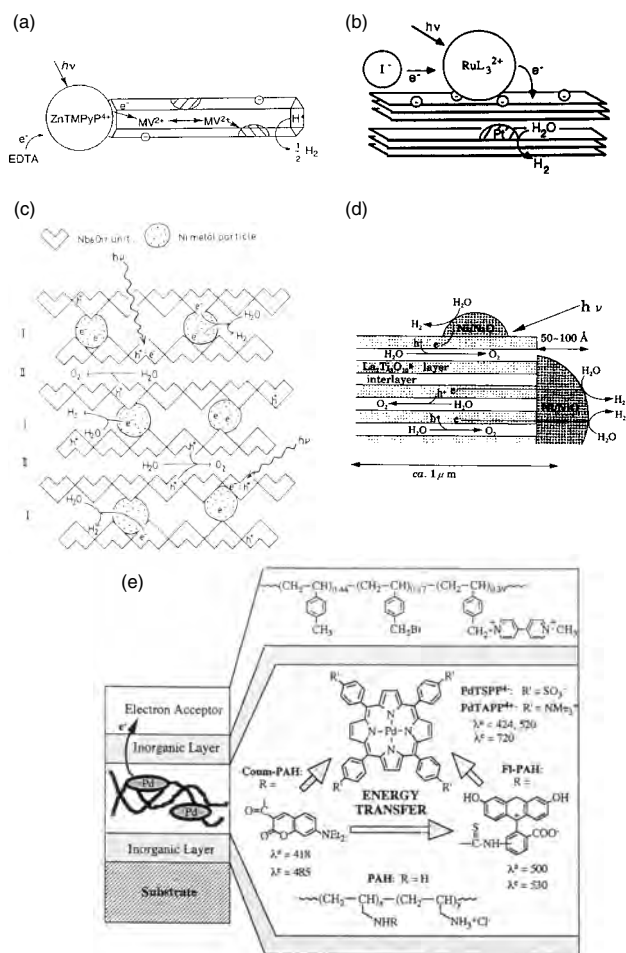
Figure 28. Tentative sketches of supramolecular assemblies for water splitting and charge separation: (a) Hydrogen evolving system based on Pt loaded zeolite L with MV²⁺ as an electron acceptor intercalated in the zeolite. Sensitizer is a Zn–porphyrin arranged as a stopcock at the end of the zeolite channels. Adapted from ref. [18]; originally published by Persaud et al. [389]. (b) Hydrogen evolving system based on the layered oxide $K_{4-x}H_xNb_6O_{17}$, loaded with as catalyst in the interlayer space. Sensitizer is a Ru complex RuL_3^{2+}. Adapted from [441]. (c) Water splitting unit based on $K_4Nb_6O_{17}$. Ni particles are formed in the interlayer space of type I. The oxide serves as the light harvesting system. Oxygen is deliberated in the interlayers of type II. Adapted from [115]. (d) Water splitting unit based on a layered perovskite. Ni particles are formed at the external surfaces of the oxide. The oxide serves as the light harvesting system. Oxygen is deliberated in the interlayer space. Hydrogen evolved at the Ni particles at the interface solid/solution. Adapted from [118]. (e) Deposited layer system unifying a light harvesting antenna based on a polymer–porphyrin assembly and an electron acceptor separated by inorganic layers. Charge separation lasts for a millisecond. Apapted from [450].

lifetime of the photoinduced charge separation have not been given. A modified multilayer assembly of viologen zirconium bisphosphonate on copper dithiolate multilayer containing porphyrin units shows an improved photoinduced charge separation with higher quantum efficiency and a better fill factor of the photoelectrode. Upon illumination with visible light a permanent and stable photocurrent can be produced [192].

Applying the same preparation method (see also Scheme 7) a photoredox "onion" can be grown by sequentially adsorbing polymer bound viologen, α-ZrP, and polymer bound $[Ru(bpy)_3]^{2+}$ layers onto amine-derivatized silica particles [450]. In this simple assembly there is no quenching of the $[Ru(bpy)_3]^{2+}$ excited state by viologen. The modest driving force of this reaction (ca. 0.28 V) is not sufficient for electron transfer on the time scale of the excited state (600 ns) over a relatively long donor–acceptor distance imposed by the α-ZrP sheets. However, addition of the anionic electron donor *p*-methoxyanilinedi(ethylsilfonate) to the suspension causes efficient excited state quenching. The reduced $[Ru(bpy)_3]^+$ generated in this process is a substantially stronger reducing agent than the excited $^*[Ru(bpy)_3]^{2+}$, and consequently rapid reduction of the viologen polymer occurs across the α-ZrP layers. The charge separated state is relatively long-lived (~40 μs), because the backreaction must occur across a $[Ru(bpy)_3]^{2+}$ polymer and α-ZrP layers.

The same authors have designed a multilayer film that consists of a three-chromophore light harvesting layer, separated by an inorganic spacer from an electron acceptor layer (see Fig. 28e) [450]. The three chromophores (fluorescein, coumarin, porphyrin) were chosen to maximize spectral overlap. The coumarin and fluorescein molecules are covalently bound to PAH. In the case of PdTAPP⁴⁺ all three cations are adsorbed simultaneously and in the case of PdTSPP⁴⁻ a cation–anion–cation sequence is used. The assembly containing the anionic porphyrin, which is a stronger triplet state reducing agent, shows an electron transfer reaction, as indicated by the disappearance of the porphyrin phosphorescence. Interestingly, when an HTiNbO₅ spacer layer is substituted for α-ZrP (47%), the same assembly has a higher overall quantum yield for the four-component energy/electron transfer cascade (61%). While the α-ZrP-containing sample shows a first-order decay with a lifetime of 150 μs, the decay with the HTiNbO₅ spacer is biexponential, and there is a substantial component with a much longer (900 μs) lifetime. A plausible explanation of this difference is that the semiconducting HTiNbO₅ spacers play an active role in the reaction, by mediating electron transfer between the porphyrin and the viologen.

Some of these charge separation systems based on ZrP hosts [192, 313, 450] are the first dye/inorganic composites in which porphyrins have been used as sensitizers, whereas the development of organic supramolecular systems mimicking photosynthesis have started with porphyrins as the light harvesting systems [194, 435]. In these systems the electron acceptor is normally a quinone like in the natural photosynthetic reaction centers.

To set up a continuous photosynthetic energy transduction means that the oxidized sensitizer and the reduced acceptor are lead back to their initial forms. This can be achieved by applying sacrificial donors (TEOA or EDTA [18, 46, 47, 198, 442]) and irreversible reduction of a chemical species, respectively. To mimic the natural process water should be used for both processes: water oxidation (oxygen liberation) for reduction of the sensitizer and water reduction (hydrogen evolution) to convert the acceptor. Water splitting is an energy consuming process accompanied with strong overpotentials on both electrodes, if carried out electrochemically [51, 442], though it is not surprising that both processes need

some electrode pretreatment or the application of very specific catalysts in order to reduce these overpotentials. The same is true for the artificial systems discussed here. In natural photosynthesis hydrogen evolution is replaced by the formation of NADPH, which is carried out by an enzyme [53, 434]. The water splitting under liberation of oxygen has been carried out also by a special enzyme, which contains a manganese complex as the effective unit [53, 444]. In case of the artificial systems various catalysts has been used. One should note that only a few inorganic solids are known to act as catalysts for these reactions. Pt, RuO_2, RuS, or Ni/NiO$_x$ supports the hydrogen evolution [51, 442]. Suitable catalysts for oxygen liberation are much more restricted, mainly to RuO_2 and Ru metal [51]. These are the same systems which are known to reduce the overpotentials in electrochemical splitting of water.

More effort has been devoted to hydrogen evolving systems, because hydrogen would be an interesting fuel to replace the decreasing resources of oil and gas. Thus we will discuss first the few trials to get oxygen evolution and then the experiments concerning photoreduction. The first attempts to photoxidize water were performed with a hectorite supported RuO_2 catalyst loaded with $[Ru(bpy)_3]^{2+}$ as a sensitizer and $[Co(NH_3)_5Cl]^{2+}$ as a sacrificial acceptor. However, this system failed to produce oxygen [50]. According to the authors the reason could be that both species are intercalated in the interlayer space whereas the catalyst is located on the external surface due to its size and mobility. Thus the oxidized sensitizer has no access to the catalyst. Pretreating the hectorite–RuO_2 samples in hydrogen at 600 °C before adsorbing the sensitizer leads to a collapse of most of the interlayer spaces and to a strong reduction of the accessible surface. The $[Ru(bpy)_3]^{2+}$ ions are forced to remain on the external surface where they can react with water over the catalyst particles. Due to the pretreatment the RuO_2 has been reduced to Ru metal; thus the active catalyst is this metal or metal particles coated with a few monolayers of oxide. These accessibility problems do not arise with sepiolite, which gives considerable oxygen evolution when loaded with RuO_2 and the sensitizer and acceptor used in the hectorite system. The species cannot be taken up in the channels of this peculiar 2:1 clay mineral. Oxygen evolution was also observed in a clay system using $[Ru(bpy)_2(H_2O)_2]^{2+}$ as a catalyst [376]. In case of $[Ru(bpy)_3]^{2+}$ encapsulated in zeolite Y oxygen evolution has been observed when the zeolite is exposed to an aqueous solution of pH 12 [18]. In this case the $[Ru(bpy)_3]^{3+}$ is reduced to the two valent state by a direct reaction with water via many reaction steps with covalent bonding of water to one of the bpy rings [18]. Quayle and Lundsford found CO_2 formation instead of oxygen evolution [451]. Only recently have attempts been made to use manganese complexes covalently bound to the Ru–polypyridine sensitizers as the sacrificial donors and catalyst for water splitting [444]. However, the manganese complexes were not active in water splitting.

As one can see in Table 12 there are much more trials to realize reduction of water. No significant hydrogen evolution was observed with $[Ru(bpy)_3]^{2+}$ and MV^{2+} coadsorbed on a Pt/smectite or RuO_2 smectite due to the aforementioned segregation phenomena [50]. To avoid these segregation phenomena sepiolite was used, but the activity for

hydrogen evolution remained low. One reason is the application of EDTA as a sacrificial donor, since this donor is repelled from the negatively charged silicate surfaces. Second, the light induced electron transfer results in the formation of a less charged reduced acceptor, which is less strongly bound to the highly charged Ru complexes. Thus, the more diffuse adsorption layer is prevented from reacting with the catalyst on the silicate surface. The stratification of the adsorption layer (surface/$[Ru(bpy)_3]^{2+/3+}$/MV^+/EDTA) could enhance also a backtransfer of electrons to the Ru complex. All these problems could be circumvented by a new design of the clay–sensitizer–acceptor arrangement [198]. Villemure et al. replaced EDTA with the neutral donor triethanolamine [198]. In addition they loaded the clay (montmorillonite) first with MV^{2+} and afterward with the Ru complex. It could be shown that the complex can displace only a rather limited amount of MV^{2+}; this is in agreement with X-ray data indicating a monolayer of methyl viologen. $[Ru(bpy)_3]^{2+}$ is thus located only on the external surfaces of the clay particles. Maximum hydrogen evolution is reached if one dication out of three on the external surface is $[Ru(bpy)_3]^{2+}$. It should be noted that there is no additional catalyst present in this experiment. The authors assume that the coexistence of electron acceptor sites at the crystal edges and electron-donating sites, such as reduced transition metals, may affect the electronic transfer to the protons [198].

Hydrogen evolution has been demonstrated also in case of the framework structure zeolite L as the support. To realize a suitable reaction chain Persaud et al. generated in the first step small Pt particles inside the zeolite channels (see Fig. 28a) [389]. The electron transport chain was composed of EDTA, ZnTMPy as the sensitizer, and MV^{2+} as the electron acceptor. Since the porphyrin is too large to penetrate into the 7 Å channels, it is ion exchanged onto the zeolite interface. Upon photolysis the intrazeolitic viologen molecules quench the excited singlet state of the porphyrin. The electron donor EDTA, which has free excess to the positively charged porphyrin, is oxidized by the porphyrin, thus stabilizing the MV^+ radical. Significant hydrogen evolution results only for high loading levels of MV^{2+}.

Nijs et al. designed the only system based on dye/inorganic composite showing water splitting [49, 50]. Based on a disappointing experience in the development of a hydrogen evolving system they combined their oxygen evolving system with a new positively charged aluminum hydroxide colloid containing a metal ion with a suitable redox potential as the electron acceptor and Pt deposited on the external surface (see schematic view of the structure in Fig. 3b). Both colloids undergo a spontaneous association in the pH range 3–6. This system shows hydrogen and oxygen evolution simultaneously, but the turnover numbers are quite low. The authors are quite pessimistic with respect to the future of these systems due to the irreversible character of the A^{3+}/A^{2+} redox couples.

The mechanism of water splitting in the layered oxides differs completely from all other examples discussed to now. Upon illumination of methyl viologen intercalation compounds a coloration of the samples occurs indicating a photoinduced electron transfer [116, 392, 393]. Since there is no dye sensitizer in the system, the oxide layers themselves

have to have taken over the role of the sensitizer. This is related with their electronic structure. In contrast to all other inorganic matrices we dealt with (which are insulators) the layered transition metal oxides are semiconductors with a bandgap in the order of 3.5 eV (corresponding to the wavelengths of blue light to the UV) [452]. The water splitting capability of these oxides is much higher than that of other oxides [51, 115, 455]. Catalysts supporting the hydrogen liberation, Pt [117, 453] or Ni/NiO [115, 118, 120, 454], enhance the efficiency of the reaction. In the two most efficient systems the proposed mechanism of the reaction is as follows (see Fig. 28): Upon illumination electron–hole pairs have been created in the oxide layers. The electrons flow to the metal catalysts and initiate the hydrogen liberation [118, 454]. The holes have been annihilated from electrons originating from the water splitting in the interlayer galleries. In case of the layered perovskites the Ni particles are deposited only on the external surface of the oxides (see Fig. 28d) [118], whereas in $K_4Nb_6O_{17}$ there is some evidence that the Ni particles are located in type I interlayer galleries (see Fig. 28c) [454]. In this compound only the potassium ions in this galleries can be hydrated and exchanged by other ions. In forming this hydrogen splitting assembly hydrated Ni ions have been exchanged in the interlayer space and afterward are transferred to the Ni metal by a heat treatment in hydrogen and oxygen subsequently [115, 454]. According to the authors the oxygen liberation should proceed in the type II interlayer galleries [454]. However, the uptake of water in these galleries can be achieved only if some of the potassium ions have been replaced with protons during the various preparation steps. This mechanism deserves additional experimental checking. The efficiency for water splitting could be improved further if the two-dimensional niobate layers obtained from exfoliation of $H^+/K_4Nb_6O_{17}$ were precipitated on MgO fine particles [120]. There is one exception from the general scheme discussed for the layered oxides. Layered niobates (KNb_3O_8 and $K_4Nb_6O_{17}$) and titanoniobates ($KTiNbO_5$ and $CsTi_2NbO_7$) were internally platinized, acid-exchanged, and sensitized with ruthenium polypyridyl complexes (see Fig. 28b) [441, 456]. These assemblies were active for HI photolysis with visible light (quantum efficiencies up to 0.3%) forming H_2 and I_3^-. The iodide ion reduces the oxidised sensitizer. The hydrogen evolution rate decreased sharply as the average layer spacing increased, indicating that the competition between charge recombination and electron tunneling between layers determines the efficiency of the photolysis reaction.

A photonic antenna is an organized multicomponent arrangement in which several chromophores absorb the incident light and channel the excitation energy to a common acceptor component. Attempts to build an artificial antenna system are based on organic supramolecular chemistry [194, 435]. Trials to design antennas with dye/inorganic composites have been described just recently [65, 410, 411, 433, 450]. The antenna system assembled by the layer-by-layer method has been discussed in the context of charge separation systems. The most recent dye/inorganic antenna system is based on zeolite L as a host and specially organized dye molecules [410, 411, 433]. This system is of bidirectional type and able to collect and transport excitation energy. The two cationic dyes, Py^+ as a donor and Ox^+

(see Table 6 and Scheme 3) as an acceptor, were found to be very versatile to demonstrate photonic antenna functionalities [411]. They can be incorporated into zeolite L by means of ion exchange, where they are present as monomers because of the restricted space. In this form they have a high fluorescence quantum yield and favorable spectral properties. An assembly has been constructed where a Py^* loaded zeolite L is modified by Ox^+ located at the channel ends. Ox^+ becomes excited by radiationless energy transfer from the excited Py^+ moieties at the center of the crystals. The fluorescence decay of the donor becomes much faster in the presence of the acceptor, because of the depopulation due to the irreversible energy transfer to the acceptors. The fluorescence intensity stemming from the acceptors initially increases because excited states must first be populated via energy transfer from the donors. It therefore reaches a maximum before it decays. A sophisticated bidirectional antenna with three dyes has also been realized [433].

The synthesis principle is based on the diffusion of molecules into the individual channels. This means that under appropriate conditions, the molecules can leave the zeolite in the same manner. It is desirable to block their way out, so as to stabilize the structure. This can be done, by adding "closure" molecules after insertion of the other antenna components. A variety of closure molecules can be used depending on the requirements. One approach is to add "stopcock" molecules as illustrated in Figure 29. A stopcock molecule consists of three components: a head, a spacer, and a label. The head moiety has a lateral extension that is larger than the channel width and prevents the head from penetrating into the channels. The main function of the stopcocks is to connect the antenna with its surrounding. Direct linkage to a semiconductor surface, embedding into semiconducting polymers, or linkage to sites of biological interest are possibilities. If either the insertion
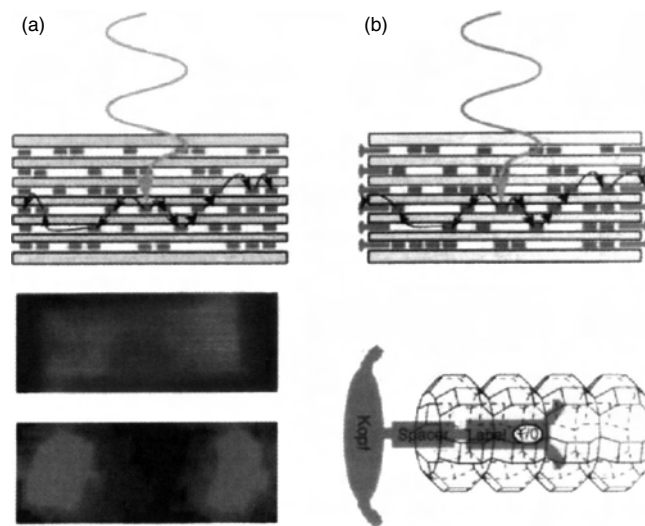

Figure 29. Dye/zeolite L light harvesting antenna system. (A) Blue is the luminescence of the donor in the channels of the zeolite. The donor transfers energy to the red emitting acceptor molecules located at the end of the channels. (B) Antenna system with stopcock molecules at the end of the channels. Shown in an enlarged form. The stopcock consists of a spacer and a label. Adapted from [457].

of the dyes into the zeolite crystals is controlled such that molecules can penetrate the channels only from one side or crystals containing different dyes are organized appropriately, monodirectional antenna systems can also be created [411]. Applications of these antenna systems as educational tools, nanoscaled lasers, dye sensitized solar cells, and light-emitting diodes have been realized or proposed [411].

6.3. Photochromism

As stated earlier photochromism means a reversible transition between two states with different light absorption spectra, where the transition should be induced by light at least in one direction. For applications in information storage and optical switching a high-contrast color change should occur under illumination. This condition is fulfilled for the viologens and the spiropyranes, the systems whose photochromic behavior in inorganic matrices has been studied preferentially. In addition the response time should be very high, in case of switching in both directions. There should be a high quantum yield and a high fatigue resistance (can be cycled many times without significant loss of performance). Both forms should show a high thermal stability. For data storage the reverse reaction should be strongly suppressed and the readout process should be nondestructive. If the coloration reaction is accompanied by a strong change in molecule configuration as in the case of photoinduced *trans–cis* isomerization of double bands (azobenzenes, stilbenes, or carotene) or by the ring-opening reactions toward linear merocyanins (e.g., spiropyranes) the response time and other properties depend strongly on the environment of the photosensitive moieties, which means the free space, the packing density, alignment, and polarity of the medium. In case of the viologens the coloration is caused by a reduction of the RV^{2+} dication to the colored monoradical cation $RV^{+\bullet}$. The reduction can be induced by illumination in the presence of an electron donor or directly by electric current [160]. Thus, this system is also electrochromic. In order to keep the colored state stable the exclusion of oxidizing agents like oxygen is essential. The advantage of inorganic/viologen composites is that the inorganic matrix prevents or retards the access of oxygen to the dye radical cation.

With respect to the overwhelming literature on all organic photochromic systems [458] the corresponding inorganic dye nanocomposites are rather restricted. We will discuss first the photochromic systems based on viologen/inorganic composites, then those of the spiropyrane intercalation/insertion compounds, and at the end the photochromic behavior of the azobenzene intercalation compounds which have been prepared just recently.

Miyata et al. reported the photochromism of some viologens (1,1'-dialkyl-4,4-bipyridninum ions) cointercalated with polyvinylpyrrolidone (PVP) into montmorillonite [391]. By irradiation with the light of an Hg lamp the viologen radicals are formed as indicated by their characteristic blue color. The cointercalated PVP is considered to act as an electron donor for the reduction of the viologen. After finishing the irradiation the color fades away continuously. But this process is much slower than that in the PVP matrix. It takes 4 to 6 hours to obtain completely faded samples even in

thin films. In thicker samples the color remained for several days. The coloration/decoloration process is reversible, but the extent of coloration is reduced cycle by cycle. There seems to be no photochromic effect in the PVP-free intercalation compound.

Photochromic behavior is also observed in the intercalation compounds of MV^{2+} in a series of layered transition metal oxides (see Table 10) [116, 392, 393]. In this case the semiconducting host layers act as an electron donor. In all examples the blue color fades away after finishing illumination. The lifetime of the colored state depends on the arrangement of the intercalated viologens in the interlayer space. It is in the order of minutes in those intercalation compounds, in which all interlayer spaces are completely filled with MV^{2+} species. The colored state is more stable in $MV^{2+}/K_2Nb_6O_{17}$ where the viologens can be intercalated only in each second interlayer space (cf. Section 3.1 and Fig. 9). The stability was enhanced even further when the viologens were further diluted by photoinactive species like potassium or propylammonium ions. Thus, the authors supposed that the lifetime of the colored species depends on an effective suppression of the electron hopping between adjacent $MV^{2+}/MV^{+\bullet}$.

Photochromism of various spiropyranes has been observed in the interlayer space of montmorillonites, one Mg/Al layered double hydroxide, and framework structures [14, 276–280]. The color change of the spiropyrane (SP) is based on the ring-opening isomerization of the spiro system and the concommitant formation of a zwitterionic merocyanin (MC) according to the following scheme ("normal photochromism").
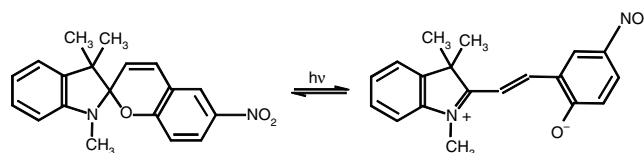
Under acidic conditions the zwitterionic form of the merocyanine is transferred to a cationic form in which the phenolate group becomes protonated. This cationic merocyanine undergoes a reversible isomerization to the *cis*-form, which is colorless ("reverse photochromism") [276].

The extent of spiropyrane intercalation into clays depends on the kinds of substituents. Unsubstituted spiropyrane (see Scheme 6: $R_1 = CH_3$; $R_2 = R_3 = H$) and the pyridine derivative (see Scheme 6: $R_1 = CH_3$; $R_2 = CH_2$-py; $R_3 = NO_2$) were intercalated easily, whereas the nitroform is inefficiently taken up. Protonation of the neutral forms increases the content of the dye further, dramatically in case of the nitro-form ($R_1 = CH_3$; $R_2 = H$; $R_3 = NO_2$; see structural formula in Scheme 6). In any case the species intercalated preferentially is the MC form [280]. In contrast a preferential adsorption of the spiro-form is observed when cetyltrimethylammonium was coadsorbed with Py^+–SP, H–SP, and NO_2–SP [280]. This is an agreement with the general experience that thermal equilibria between SP and MC are dependent on the polarity of the surrounding and MC becomes the major product with increasing polarity.

Seki and Ichimura have investigated the kinetics of the thermal backreaction from the irradiation generated MC to the SP form in solid films built up from dialkylammonium bilayers and clay layers and polystyrenesulfonate (PSS) as counterions [279]. The nitro-spiropyrane was incorporated in the film, which has been prepared by casting the chloroform suspension of the polyion complexes onto a quarz or glass plate. The $2C_{18}2C_1N^+$–montmorillonite films show a more ordered structure than the $2C_{18}2C_1N^+$–PSS films. In the latter case the ordering can be increased by annealing the films at 60–70 °C, in 100% relative humidity for a few hours. The rate of the decoloration reaction increased abruptly near the crystal to liquid crystal phase transition. The rate change at this phase transition is larger in case of the montmorillonite films, probably due to a more homogeneous reaction environment. If substituted spiropyranes carrying alkyl chains in position R_1 and R_2 are immobilized in didoceyldimethylammonium montmorillonite, the merocyanine forms produced by illumination with UV light form J- and H-aggregates which show a high thermal stability against the backreaction to the spiro-form [278]. The origin of aggregate formation as well as the nature of these aggregates is not clear at present [278].

The investigation of the photochromism of spiropyrane in crystalline framework structures has been developing recently [276, 277]. In faujasites (HY and DAY) and low-loaded Si-MCM-41 only the open MC forms have been detected as in layered compounds (without cointercalated surfactants) [276]. Due to their zwitterionic character the MC forms are stabilized via strong interactions to the polar host structures. The various colored isomers can range from the open *cis*- to *trans*-forms and can comprise additionally various protonated isomers depending on the acidity of the framework OH groups. In MCM-41, the framework with the lowest acidity among the investigated hosts, the dye can be deprotonated resulting in a significant fraction of ring closure to the SP form. In the mesoporous molecular sieve of the SBA-15 type spiropyrane exists exclusively in the SP form [277]. This may be due to the hydrophobic parts in this framework silicate.

In the more acidic framework reverse photochromism occurs upon irradiation (excitation wavelengths above 400 nm) leading to decoloration. The thermal relaxation of the *cis* to the *trans* MC proceeds very slowly. The attainment of the final state would have required several weeks but can be speeded up by photoexcitation using a wavelength of 347 nm. The patterns of the final states of the dye-loaded MCM-41 composites exhibit significant differences to the faujasite system. The irradiation leads to the formation of the SP form (closed ring) whereas the thermal relaxation to the initial state is much faster as in all the faujasites investigated. In the SBA-15 complex irradiation produces the *trans* MC form which switches back to the initial SP form very rapidly [277].

More detailed knowledge has been elaborated for spiropyrane/amorphous silica (aluminosilica and zirconia) composites [404–409]. In case of the pure silica gels, prepared by hydrolysis/condensation reaction of a methanol/dye/tetramethyl orthosilicate solution, there are continuous environmental changes along the gel/xerogel transition. These are reflected in the gradual changes of the photochromic behavior of the trapped molecules [404, 409]. In particular, the photochromism changes at a certain point to reversed photochromism. These changes are interpreted as reflecting a gradual shift in the equilibrium between the adsorbed and dissolved molecules within the cage, enriching the system with the former as the reaction proceeds. This shift is caused by the change in the composition of the cage-trapped solvent from methanol/water, by solvent evaporation, and by gradual shrinking in the cage size. If the spiropyranes are incorporated in organically modified silica matrices (or if less volatile solvents are used for incorporation) the closed SP form as well as the open merocyanine form has been observed [405, 406]. The dye is accommodated preferentially in a nonaggregated state as can be deduced from the ready luminescence [405, 406].

In block-copolymer/silica mesostructures the spiropyranes are located within the organic part of the composite and show direct photochromism without competition of reverse photochromism [277]. The composites become colored upon UV illumination and bleach back thermally to their colorless closed SP forms. The response times of the spirooxazine (SO) loaded system are very fast [277]. As these silica/block-copolymer materials can be processed in any desired shape (fibers, films, monoliths) they are promising candidates for application as optical shutters and light modulators.

Schaudel et al. embedded spiropyrane and spirooxazine in hybrid matrices formed from hydrolysis and cocondensation between diethoxydimethylsilane and zirconium propoxide and between methyldiethoxysilane (DH) and triethoxysilane (TH), respectively [407]. The nature and the kinetics of the photochromic response depend on the hydrophobic/hydrophilic balance of the hybrid material. This balance controls the competition between direct and reverse photochromism. The photochromic behavior of the strongly hydrophobic spirooxazine-doped DH/TH coatings is direct, highly efficient, reversible, and extremely fast.

Ogawa and Kuroda have demonstrated for the first time the appearance of photochromism in a cointercalation phase of *p*-aminoazobenzene (*p*-AZ) and dodecylammonium in montmorillonite [14]. The uptake of the azobenzene by a solid-state reaction with the dodecylammonium loaded montmorillonite leads to an increase of the layer distance from 18 to ca. 30 Å. By irradiation with UV light the absorption band at 395 nm ascribed to the *trans*-*p*-AZ decreases continuously but recovers in the dark after illumination. The thermal *cis*- to *trans*-reaction is very slow. Also the intercalation compounds of alkoxysubstituted azobenzenes (see Section 6.1) show *trans*–*cis* isomerization upon irradiation with UV light. The stationary state after illumination contains about 60% *cis*-isomer. This degree of isomerization is quite remarkable if one considers the layer distances (lower than in the cointercalated system discussed previously) and the azobenzene chromophore aggregation. Both effects will lead to a lack of free volume for the isomerization process. Very similar results have been observed for magadiite intercalation compounds of these azobenzenes [93]. The $C_{12}AzoC_5N^+$/magadiite system is effectively photoisomerized when irradiated with UV and visible light. After 10 min irradiation the intensity of the *trans*-isomer decreased and the absorption bands due to the *cis*-isomer appeared at 318

and 444 nm. The absorption band of the *trans*-isomer recovered to the same intensity as that of the original spectrum under visible light illumination [93]. In the recently found intercalation compound of another azobenzene derivative (carrying only one shorter substitutional alkoxy group on one of the benzene rings; see Section 6.1) the irradiation leads again to a *trans* to *cis* isomerization. It is worth noting that in contrast to the other examples this isomerization leads to a reversible shrinking of the layer separation [258]. Thus we have light induced mechanical shrinking and expanding of a crystalline system.

Photochromic behavior of the unsubstituted azobenzenes has been observed also in the framework structures ZSM-5 and AlPO$_4$-5 [255, 403]. The half-life-time of the *cis*-form in the AlPO$_4$-5 composite is found to be about 100 h, whereas azobenzene in ZSM-5 shows a considerably lower *cis*-state lifetime of 6 h. According to the authors the role of the acidic sites in *cis–trans* relaxation is very likely to be crucial for the understanding of the host lattice effects. The photoisomerization is highly reversible if carried out in both directions by irradiation with light of the wavelengths 360 and 436 nm, respectively. A scale of reversibility of photoswitchable compounds is the number of repetitions after which the switching effect decreases to one-half of the value of the first cycle. For the azobenzene/AlPO$_4$-5 composite this value is about 300 (for comparison this value is around 80 for the spiropyrane/DAY composite [276]; unfortunately no such numbers are available for the spiropyrane or azobenzene intercalation compounds of clay minerals). This very good reversibility demonstrates that the *trans–cis* conversion takes place without significant side reactions.

Photoisomerization and the thermal backreaction have been studied also for azobenzenes immobilized in silica gels [409, 459, 460]. In sol–gel films hydrogen bonds are formed between the azo groups and silanol groups in matrices prepared with a relatively high water concentration [459]. The rigidity of the matrix depends on the water content of the solution from which it was prepared. In the case of [H$_2$O]/[TEOS] = 1, the photoisomerization takes place readily in a gel film possibly because of inefficient network formation. In a sol–gel glass prepared from a solution with [H$_2$O]/[TEOS] $\geq$ 2 the azobenzene probes are of three different types: (i) at sites within smaller pores in which the *trans*-to-*cis* isomerization is quenched; (ii) at sites in which the *cis* isomer is formed in a strained conformation enhancing the thermal reversion; (iii) at sites in which the thermal reversion is reduced by the hydrogen bonding between the guest molecules and silanol groups. The *cis* to *trans* thermal isomerization in a sol–gel bulk obeyed first-order kinetics at a rate similar to that of the solution chemistry, whereas the isomerization in a glass film deviated from the first-order kinetics [460]. The steric constraint due to the matrix decreased in the following order: sol–gel films > PMMA > sol–gel bulk [460].

6.4. Second Harmonic Generation

Second harmonic generation is a nonlinear optical process that converts an input optical wave into an out wave of twice the input frequency. To gain insight into the origin of nonlinear optical effects it is helpful to look at the nature of

polarization induced in a molecule by a local electric field [461]. The polarization P can be expended in powers of the electric field E,

$$P = \alpha E + \beta E^2 + \gamma E^3 + \cdots \tag{5}$$

The first term α in the expansion is the linear polarization and is the origin of the refractive index if the field E is associated with an electromagnetic wave in the optical frequency range. The coefficients are actually complex numbers. The real part of α corresponds to the index of refraction, and the imaginary part corresponds to absorption of a photon by the molecule. When an electromagnetic field interacts with a medium consisting of many molecules, the field polarizes the molecules. These, in turn, act as oscillating dipoles broadcasting electromagnetic radiation, which can then be detected at some point in space outside of the medium. In a nonlinear medium the induced polarization is a nonlinear function of the applied field and is related to the nonlinear term β (its real part is the molecular hyperpolarizability), which makes the most significant contribution to the induced frequency components. It is nonzero only in non-centro-symmetric media. (γ is the first nonzero nonlinear term in centrosymmetric media.) If the response P is asymmetric, an appropriate summation of the even harmonics describes the function P (SHG). Nonlinear optical properties are measured on macroscopic samples that consist of many individual molecules. Although it is possible to infer the values of the molecular hyperpolarizabilities from measurements on macroscopic samples, great care must be taken to determine the values of the internal electric fields and the propagation characterisitcs of the generated fields. In the design of materials with large second-order nonlinear optical coefficients and other useful properties the molecular hyperpolarizabilities must be optimized and then oriented in a medium so that the propagating field can be transmitted from the medium.

Recent studies have revealed large molecular hyperpolarizabilities of certain organic materials (see Section 3.3) leading to anomalously large optical nonlinearities relative to those of conventional inorganic substances (like LiNbO$_3$) [161, 162, 461]. Major research efforts are directed toward (a) identifying new molecules possessing large nonlinear polarizability and (b) controlling the molecular orientation on a microscopic level. The following part of this section will be devoted to the contribution of intercalation in inorganic framework to the latter point.

Cooper and Dutta have reported the first evidence for SHG in a layered intercalation compound [462]. They have inserted 4-nitrohippuric acid (NO$_2$C$_6$H$_4$CONHCH$_2$ · COOH = NHA) into the layered lithium aluminate [LiAl$_2$(OH)$_6$]$^+$ (see Fig. 8). From the observed basal spacing of the product ($d = 18$ Å) the guest species are thought to be stacked perpendicular to the host lattice sheets. From optical spectroscopic data it has been concluded that the NHA molecules are held in the interlayer space as carboxylic acids. The material exhibits frequency-doubling characteristics generating a 532 nm radiation from incident 1064 nm. This is particularly interesting, since crystals of pure NHA do not exhibit any nonlinear optical properties due to the centrosymmetric packing of the crystals. Thus,

the dipoles of the NHA molecules must be aligned very strongly and the arrangement must be very particular and non-centro-symmetric, while the host lattice itself is also centrosymmetric.

Lacroix et al. have reported SHG in intercalation compounds of DAMS$^+$ (see Section 3.3.6, Table 7 and Scheme 6) in MPS$_3$, where M is either Mn^{2+} or Cd^{2+} [249, 250]. In their first report on this system the authors prepared this compound by using the potassium intercalation compound K$_{2x}$(H$_2$O)$_y$Cd$_{1-x}$PS$_3$ as an intermediate. This product gave only a small SHG response on the same order as that of urea, whereas the DAMS$^+$ chromophore can be 10^3 times more efficient than urea. This disappointing poor SHG signal was thought to originate from grain surface effects and low crystallinity of the intercalation compound. The authors could optimize the synthesis by direct reaction between MPS$_3$ powder and an ethanolic solution of DAMS$^+$ at 130 °C in the presence of pyridinium chloride. Pyridinium chloride played a role in generating *in-situ* an intermediate pyridinium intercalation compound that underwent rapid exchange with DAMS$^+$. The products obtained had the composition (DAMS)$_{0.28}$Cd$_{0.86}$PS$_3$ and (DAMS)$_{0.28}$Mn$_{0.86}$PS$_3$, respectively, and exhibited a significantly increased SHG activity (750 and 300 times, respectively, that of urea) [249]. In a more thorough investigation of the optical properties of MPS$_3$ intercalation compounds with various stilbene derivatives it could be shown that only those compounds show a significant SHG effect, which form J-aggregates (see Section 6.1 and Fig. 26; the adjacent DAMS$^+$ molecules are oriented with their long axis parallel to the host layer planes and the benzene rings perpendicular to the MPS$_3$ sheets) [251, 429]. This is the case nearly exclusively for the two aforementioned compounds. Since the original host lattice is centrosymmetric there must be a very dense packing of the DAMS$^+$ cations within a non-centro-symmetric superstructure. However, X-ray studies did not give evidence for such a superstructure or other structural changes from one intercalate to the other, other than small differences in the host interlayer space [429]. Thus, there seems to be no long-range order, but for an effective SHG to occur aggregates or ordered domains of a sufficient size of coherence (around 1 μm) should be present. For the detailed characterization of the optical properties as well as their practical applications as photonic devices, the compounds should be available as single crystals or oriented thin films.

Such an assembly has been realized with an organic Zr–diphosphonate prepared by means of the layer-by-layer method (see Fig. 16) [312]. Instead of the hemicyanine chromophore in the aforementioned compound an azobenzene moiety is used (cf. Table 7 [259, 260], Scheme 5). The chromophores with asymmetric head and tail groups (to produce a high dipole moment) are oriented perpendicular to the inorganic layers. The nonlinearities of this system are on the same order of magnitude as those of LiNbO$_3$, one of the widely used inorganic nonlinear materials. The SHG shows that the multilayers have polar order that does not decrease with increasing numbers of monolayers in the film. The inorganic interlayers impart excellent orientational stability to the dye molecules, with the onset of orientational randomization above 150 °C. Relatively large values for some of the hyperpolarizability tensors indicate that it is inappropriate

to view this dye as an isolated linear molecule with a single hyperpolarizability along its long axis. The polar order of the films is greater using a rigid chromophore than with a more flexible one [260]. However, SHG activity can be lost through H-aggregation, if the component molecules are both highly ordered and very polar [260]. (The other donors used in [260] are mentioned in Table 7.) The SHG in the film using the phosphonate shown in Scheme 5 is not well understood. The film does not exhibit linear dichroism and X-ray diffraction studies indicate the absence of a well-structured surface [259, 461]. In addition, ellipsometry studies of the interlayer system on silicon indicate that each deposited layer is approximately 16 Å thick, which is 4 Å thinner than calculated based on typical bond lengths [312]. The difference in layer thickness was attributed to nonideal packing and an average molecular tilt angle of ∼35°. Some of these inconsistencies may be due to loss of Zr^{4+} from the surface and some "self-healing" during subsequent exposure to layer formation solutions [463]. (Note also the tendency for hydrolysis of the Zr–phosphate layers [450]!) That the film formation is not as ideal as generally assumed is further confirmed by angle-resolved photoacoustic spectroscopy [259]. The curvature of the photoacoustic amplitude as function of the electric field angle increases with increasing number of deposited layers, indicating a change in molecular orientation as a function of coverage. The authors assume that incomplete interlayers are formed during each exposure and that subsequent exposures result in improved coverage for the bottom layer as well as formation of an incomplete upper layer.

SHG has been observed also for PNA and related aromatic polar molecules (Table 8) inserted in aluminophosphate molecular sieves (AlPO$_4$-5, AlPO$_4$11, VPI-5). Models supported by Fourier transform infrared evidence shows that the aggregates could be chains of molecules with a large net dipole that form within the molecular sieve channels. The polar host then aligns the aggregates to produce a large bulk dipole moment and the observed SHG signal [8, 268] if the SHG effect of PNA/AlPO$_4$ becomes significantly larger when measured on a single crystal sample or in crystals aligned in the electric field [322]. Measurements of the pyroelectric effect show that the PNA dipoles are oppositely directed into halves of a single crystal, forming two macroscopic regions of opposite polarization. It is concluded that the preferred direction of the dipole chains in the channel is a result of the adsorption process of the molecules in the channels [269]. However, because of the macroscopic extent of each of the two regions (comparable with half of the crystal length) being much larger than the wavelength of the incident laser light, the second harmonic order light from both regions does not interfere [322]. The PNA molecules adsorbed in ZSM-5 also exhibit the SHG effect. This is not a trivial finding, since in contrast to the AlPO$_4$-5 case where reorientations are excluded for steric reasons, the bimodal and bidirectional MFI framework could *a priori* allow reorientation of the PNA molecules in the channel intersections [368]. The angular dependence of the SHG signal together with the position of the ZSM-5 crystal in the laser beam show that the SHG signal detected originates exclusively from PNA molecules that are aligned parallel with their long molecular axes to the straight channels [368].

X-ray single crystal structure analysis is in good agreement with these findings (see also Section 5.5.1) [367, 369]. The PNA molecules are located in the intersections of the two interconnected channel systems. However, there is disagreement about the symmetry of the composite. In the previous paper the crystal structure has been solved in a non-centro-symmetric space group, with symmetry lower than that of the empty host lattice [369]. This result could not be confirmed later [367]. The loss of acentricity is explained by empty intersections, which destroy the long-range coherence of the polar chains [367]. Maybe it is enough for SHG that there are ordered non-centro-symmetric domains with a size larger than the wavelength of the incident light, as seems to be the case in other SHG materials discussed in this section.

PNA has been intercalated also in tetramethylammonium-saponite. The free space between the TMA ions is just as large as the PNA molecules [464]. These additional guests are oriented with their long axes parallel to the silicate layers. During thermal intercalation the dipoles are oriented randomly in the ab plane and do not show an apparent SHG effect. However, when the intercalation has been carried out in an applied electric field, the sample exhibits an SHG effect with an intensity 10^5 higher than that for a compound without electric field. This indicates that the applied electric field caused the alignment of PNA dipoles with non-centro-symmetry in the interlayer space. In this experiment the SHG effect is used as analytical tool to monitor the orientation of the highly polar molecules.

For dimethylaminobenzonitrile (DMABN) in the straight pores of $AlPO_4$-5 two components of the SHG effect have been observed [270]. One component of the frequency-doubled radiation is polarized to the long axis of the crystal (z-axis, $\Phi_2 = 0°$) and exhibits the maximum of intensity when the excitation beam has the same polarization. The second component is polarized perpendicularly to the z-axis ($\Phi_2 = 90°$) and shows the maximum efficiency for mixed excitation ($\Phi_2 = 45°$). The reason for the different tensor elements is the two close-lying lowest excited states in DMABN having transition dipole matrix elements perpendicular to each other. Whereas PNA loaded molecular sieves are able to mix waves of the same polarization only, for the DMABN-based materials a mixing of waves with different polarizations is observed. This is a promising property for phase matching as a prerequisite for technical applications.

The investigations described were mainly motivated by the search for new materials for nonlinear optics. However, all the results give insight in the orientation of molecules in solid matrices. Two papers, which remain to be discussed, are devoted exclusively to showing application of the SHG as an analytical tool in surface chemistry. Yan and Eisenthal reported a SHG signal in aqueous suspension of clay particles loaded with 4-(2-pyridylazo)resorcinol (PR) [261]. Since montmorillonite has a centrosymmetric structure, SHG cannot be generated from the bulk of the sample. Because of the coherence properties of SHG, the SHG efficiency greatly depends on the size of the particles. Since the diameter of the clay particles is on the length scale of the light wavelength, while the thickness of the particles is much smaller than the wavelength, only the edges separated by roughly the diameter of the particles contribute to the SHG effect [261]. The origin of the SHG effect in the clay suspension must be the polarization of water molecules by surface charges located at the edges of the clay particles. On addition of PR to the clay aqueous dispersion a strong SHG signal originating from PR molecules adsorbed onto the edge surfaces was observed.

The nonlinear optical properties of a glass/clay/PDDA/NAMO films were found to depend on the adsorbed amount of NAMO (a negatively charged phenylazobenzenesulfonic acid derivative) and its non-centro-symmetric organization [311]. These factors are in turn governed by the substrate type, the clay type, and the PDDA (poly-diallyldimethylammonium) concentration. Optimized SHG for the glass/laponite/PDDA/NAMO films was found, when the clay articles are deposited on a (3-aminopropyl)trimethoxysilane modified glass surface and PDDA chains are adsorbed from a 0.1 M solution. At high PDDA loading the length of unbound polymer strands provides enough structural flexibility for the dipole moments of the dye. The overall non-centro-symmetric organization decreases together with the SHG intensity.

7. CONCLUSIONS AND FUTURE PERSPECTIVES

- Despite the huge number of dye/inorganic composites studied only a few of them found greater attention and are promising for applications: the $[Ru(bpy)_3]^{2+}$ complex as a photosensitizer (in organic supramolecular assemblies and in nature porphyrins do that job), methyl viologen (in natural systems quinines) as the most widely used electron acceptor, rhodamines in lasing, azobenzenes, spiropyranes, and viologens (perhaps) for photochromism, and azobenzenes and stilbenes for SHG. This is normal in many other areas of applied chemistry (for example, 1 out 10,000 compounds is pharmaceutically active and applicable; 5 out of 5000 compounds are applied superconductors).

- Many of the dyes discussed in this chapter show the tendency for aggregate formation. For many applications this is an unfortunate property because it reduces the quantum efficiency of luminescence, reduces the lifetime of the excited state, and influences energy and electron transfer. Encapsulation in organic or inorganic matrices is the method to circumvent these unfortunate side reactions.

- Framework structures with channel diameters of the dye size provide the constrained space for preventing aggregate formation, restricted motion, and an alignment of the dye molecules. If alignment is the essential property as is the case in application in nonlinear optics dye/zeolite composites are a good choice. If the contact between neighboring dye molecules has to be reduced as in the formation of light antennas zeolite encapsulated dyes have some advantages. If free space is of advantage as in photoisomerization processes (photochromism) encapsulation into gels is an interesting alternative.

- Despite the perspectives for application photophysical investigations are valuable tools for studying guest–guest and guest–host interactions, even in systems with missing long-range order in the dye arrangement.

- The knowledge of the arrangement of dye species is rather limited despite the huge number of investigations of dye/inorganic composites. Lack of long-range order, disorder, and mobility lead to enormous difficulties in structure determination by diffraction methods. The situation seems better in the case of the highly crystalline molecular sieves and in vermiculites. Note that most structural data of intercalated organic compounds are obtained for vermiculite intercalation compounds. The situation may improve further when applying synthetic clays for structural work [465, 466]. Since the middle of the 1990s highly sophisticated new tools for structure simulation have gained more and more importance in structure determination and will support strongly structure determination.

- Despite the demonstration that artificial multilayer assemblies can be obtained, knowledge about reproducibility of assembly preparation, comparability of the physical properties in various preparation runs, and stability of highly sophisticated assemblies is rather low. The structural view of the artificial composites seems to be very idealized. Most of the systems discussed will be metastable states far from equilibrium. Many questions arise concerning the kinetic stability, the degree of disorder, the types of defects, and their annealing behavior at room temperature.

- Great progress has been made in orientation of zeolite crystals.

- Whereas layered compounds, especially clays, were the first host lattices for the preparation of dye/inorganic composites, and a wealth of knowledge about intercalate arrangement is now available, the products are far removed from applications of dye/zeolite and dye/gel composites. This is due to the very strong guest–guest and guest–host interactions and the missing organization of the intercalation compounds. It is worth mentioning that most of the dye/layered host composites are prepared via flocculation of colloid dispersion; thus badly organized tactoids are formed. In addition, the packing density of the dyes in the interlayer space and the tendencies for aggregation detracted from increases in quantum efficiency and optimization of other relevant optical properties.

- To keep the layered materials in the business it is crucial to control the coadsorption/cointercalation of photosensitive electron donors, electron acceptors, and other functional molecules. Application of the concepts of organic supramolecular chemistry [435, 467–471] may help one to find better assemblies. However, one should have in mind that for mimicking, say biological photolysis/photosynthesis, it may be necessary to arrange different sorts of antenna molecules and electron transfer shuttles in a highly organized but flexible arrangement, probably all of the species in very different concentrations (cf. the most recent success in constructing light antennas on the basis of dye/zeolite composites [410, 411, 432, 433]). Structure directing chromophores as used in the hydrothermal *in-situ* syntheses of dye inorganic composites may be of advantage for this goal. Suitably modified molecules could be arranged in the constrained space of solids and the

functional units constructed in this frame (ship in a bottle synthesis). Another interesting aspect is the formation of amphiphilic organic–inorganic heterostructures as prepared for the first time by Jido et al. [472–474]. Breu et al. obtained highly ordered intercalation compounds and heterostructures with synthetic fluorohectorites [465, 466]. Cointercalation of surfactants may also allow a better organization of intercalated species, if demixing can be avoided [14, 475]. The organization of the platelets [248] and even of the intercalated species [464] could be improved also by the application of an electrical field.

GLOSSARY

Classical molecular dynamics Introduces the kinetic energy into the system, where the temperature and velocities are related via Maxwell–Boltzmann equation. Potential energy is described using empirical force field.

Empirical force field The set of empirical force constants, parametrizing the bonding (bond stretching, bending, torsion, deformation etc.) and nonbonding interactions (van der Waals, H- bonds, etc.), which are described using simple analytical expressions.

Host-guest complementarity The set of geometrical and chemical factors characterizing the ability of both molecules to create an ordered inclusion intercalated structure.

Intercalation The reversible uptake of atoms, ions, molecular cations or molecules at low temperature while the structure of the host lattices is conserved. The term "intercalation" does not tell anything about the nature of the chemical reaction underlying this process. It stresses mainly the topological relationships between the host and the final product of the reaction.

Laugmuir–Blodgett technique Produces organised arrangements of amphiphilic molecules on a solid substrate.

Layer-by-layer-deposition A preparative method applied for sequential adsorption of alternatively charged polyelectrolytes. It can be adapted to the sequential layering of inorganic polyanions (obtained by exfoliation of layered intercalation compounds: clays, ternary oxides, Zr-phosphates) with a variety of polymeric cations.

Molecular mechanics In molecular mechanics the potential energy of the system is described using empirical force field.

Molecular simulations The optimization of structure and bonding geometry based on energy minimization.

Photochromism A reversible transition between two states with different light absorption spectra, where the transition should be induced by light at least in one direction.

Photodecomposition of water The light induced splitting of water for the production of hydrogen and/or oxygen. It is the energy supplying process for the assimilation of CO_2 in photosynthesis.

Second harmonic generation A nonlinear optical process that converts an input optical wave into an out wave of twice the input frequency.

Sensitizer A light sensitive dye, which can transfer in the excited the electron to an electron acceptor.

REFERENCES

1. W. Noll, *Fortschr. Miner.* 57, 203 (1979).

2. D. Wildung, Ägyptische Staatssammlung München.

3. F. Seel, G. Schäfer, H.-J. Güttler, and G. Simon, *Chem. Zeit.* 8, 65 (1974).

4. Very interesting with respect to Mayan blue is the following homepage: http://www.azulmaya.com. Part of the information given in this homepage concerning the X-ray crystal structure refinement has now been published; C. Chiari, R. Giustetto, and G. Ricciardi, *Eur. J. Miner.* 15, 21 (2003).

5. C. Reyes-Valerio, "De Bonampak al Templo Mayor, El Azul Maya en Mesoamérica." Siglo XXI editores, Mexico, 1993.

6. M. José-Yacamán, L. Rendón, J. Arenas, and M. C. Serra-Puche, *Science* 273, 223 (1996).

7. J. K. Thomas, *Acc. Chem. Res.* 21, 275 (1988).

8. G. D. Stucky, *Progr. Inorg. Chem.* 40, 99 (1992).

9. J. K. Thomas, *Chem. Rev.* 93, 301 (1993).

10. K. B. Yoon, *Chem. Rev.* 93, 321 (1993).

11. S. Suib, *Chem. Rev.* 93, 803 (1993).

12. V. Ramamurthy, R. G. Weiss, and G. S. Hammond, *Adv. Photochem.* 18, 67 (1993).

13. J. Caro, F. Marlow, and M. Wübbenhorst, *Adv. Mater.* 6, 413 (1994).

14. M. Ogawa and K. Kuroda, *Chem. Rev.* 95, 399 (1995).

15. R. A. Schoonheydt, in "Comprehensive Supramolecular Chemistry" (G. Alberti and T. Bein, Eds.), Vol. 7. Pergamon, Oxford, 1996.

16. P. Behrens and G. D. Stucky, "Comprehensive Supramolecular Chemistry" (G. Alberti and T. Bein, Eds.), Vol. 7. Pergamon, Oxford, 1996.

17. V. Ramamurthy and M. A. Garcia-Garibay, "Comprehensive Supramolecular Chemistry" (G. Alberti and T. Bein, Eds.), Vol. 7. Pergamon, Oxford, 1996.

18. P. K. Dutta and M. Ledney, *Progr. Inorg. Chem.* 44, 209 (1997).

19. G. Schulz-Ekloff, D. Wöhrle, B. van Duffel, and R. A. Schoonheydt, *Microporous Mesoporous Mater.* 51, 91 (2002).

20. R. E. Grim, "Clay Mineralogy," 2nd ed. McGraw–Hill, New York, 1968.

21. B. K. G. Theng, "The Chemistry of Clay-Organic Reactions." Hilger, London, 1974.

22. E. A. Hauser and M. B. Leggett, *J. Amer. Chem. Soc.* 62, 1811 (1940).

23. D. Krüger and F. Oberlies, *Ber.* 74, 1711 (1941).

24. H. Weil-Maherbe and J. Weiss, *J. Chem. Soc.* 2164 (1948).

25. D. H. Solomon, B. C. Loft, and J. D. Swift, *Clay Miner.* 7, 389 (1968).

26. D. T. B. Tennakoon, J. M. Thomas, and M. J. Tricker, *J. Chem. Soc. Dalton Trans.* 2211 (1974).

27. M. M. Mortland and T. J. Pinnavaia, *Nature* 229, 75 (1971).

28. Y. Soma, M. Soma, and I. Harada, *J. Phys. Chem.* 89, 738 (1985).

29. T. Tanabe, "Solid Acids and Bases." Kodansha/Academic Press, Tokyo/New York, 1970.

30. R. C. Mielenz and M. E. King, *Proc. Am. Soc. Test. Mater.* 55, 1213 (1951).

31. D. H. Solomon and D. G. Hawthorne, "Chemistry of Pigments and Fillers." Wiley, New York, 1983.

32. S. Yariv, in "Organo-Clay Complexes and Interactions" (S. Yarif and H. Cross, Eds.). Dekker, New York, 2002.

33. P. Enzel and T. Bein, *J. Phys. Chem.* 93, 6270 (1989).

34. A. Moreale, P. Coos, and C. Badot, *Clay Miner.* 20, 29 (1985).

35. V. Mehrotra and E. P. Giannelis, *Solid State Commun.* 77, 155 (1991).

36. M. Ilic, E. Koglin, A. Pohlmeier, H. D. Narres, and M. J. Schwuger, *Langmuir* 16, 8946 (2000).

37. T. H. Chao and H. A. Erf, *J. Catal.* 100, 492 (1986).

38. T. Bein and P. Enzel, *Angew. Chem. Int. Ed. Engl.* 28, 1692 (1989).

39. Y. Soma, M. Soma, Y. Furukawa, and I. Harada, *Clays Clay Miner.* 35, 53 (1987).

40. P. Enzel and T. Bein, *J. Chem. Soc. Chem. Commun.* 1326 (1989).

41. J. V. Caspar, V. Ramamurthy, and D. R. Corbin, *J. Am. Chem. Soc.* 113, 600 (1991).

42. V. Balzani, L. Moggi, M. F. Manfrin, F. Bolletta, and M. Gleria, *Science* 189, 852 (1975).

43. C. R. Bock, T. J. Meyer, and D. G. Whitten, *J. Am. Chem. Soc.* 97, 2909 (1975).

44. C. Creutz and N. Sutin, *Inorg. Chem.* 15, 496 (1976).

45. C. T. Lin and N. Sutin, *J. Phys. Chem.* 80, 97 (1976).

46. J. M. Lehn and H. P. Sauvage, *Nouv. J. Chim.* 1, 449 (1977).

47. J. M. Lehn, H. P. Sauvage, and R. Ziessel, *Nouv. J. Chim.* 3, 423 (1979).

48. M. Calvin, *Acc. Chem. Res.* 11, 369 (1978).

49. H. Nijs, J. J. Fripiat, and H. van Damme, *J. Phys. Chem.* 87, 1279 (1983).

50. H. Van Damme, F. Bergaya, and D. Challal, in "Homogeneos and Heterogeneous photocatalysis" (E. Pelizetti and N. Serpone, Eds.), Reidel, Dordrecht, 1986, p. 479.

51. J. Kiwi, K. Kalyanasundaram, and M. Graetzel, *Structure Bonding* 49, 37 (1982).

52. I. Willner, J. M. Jand, C. Laane, J. W. Otwos, and M. Calvin, *J. Phys. Chem.* 85, 3277 (1981).

53. P. Sitte, H. Ziegler, F. Ehrendorfer, and A. Bresinsk, "Lehrbuch der Botanik für Hochschulen." Gustav Fischer Verlag, Stuttgart, 1991.

54. C. H. Chang, D. Tiede, J. Tang, U. Smith, J. Norris, and M. Schiffer, *FEBS Lett.* 205, 82 (1986).

55. P. K. Ghosh and A. J. Bard, *J. Am. Chem. Soc.* 105, 5691 (1983).

56. A. Fiche, *Clays Clay Miner.* 38, 391 (1990).

57. A. Pockels, cited in W. Ostwald, *Kolloid-Z.* 58, 1 (1932); Lord Rayleigh, *Philos. Mag.* 48, 337 (1899).

58. I. Langmuir, *J. Am. Chem. Soc.* 39, 1848 (1917).

59. K. B. Blodgett, *J. Am. Chem. Soc.* 57, 1007 (1935).

60. H. Kuhn, *Pure Appl. Chem.* 11, 345 (1965).

61. H. Kuhn, *Naturwissenschaften* 54, 429 (1967).

62. H. Kuhn and D. Möbius, *Angew. Chem.* 83, 672 (1971); *Int. Ed. Eng.* 10, 620 (1971).

63. H. Kuhn, D. Möbius, and H. Bücher, in "Techniques of Chemistry" (A. Weissberger, Ed.), Vol. I, Part IIIb (Physical Methods of Chemistry). Wiley-Interscience, New York, 1972.

64. U. Simon and G. Schön, in "Handbook of Nanostructured Materials and Nanotechnology" (H. S. Nalwa, Ed.), Vol. 3, p. 131. Academic Press, San Diego, 2000.

65. J. H. Fendler, "Membrane Mimetic Chemistry." Wiley, New York, 1982.

66. A. Ulman, "An Introduction to Ultrathin Organic Films. From Langmuir–Blodgett to Self-Assembly." Academic Press, Boston, 1991.

67. D. Petridis, P. Falaras, and T. J. Pinnavaia, *Inorg. Chem.* 31, 3530 (1992).

68. Y. Xiang and G. Villemure, *J. Phys. Chem.* 100, 7143 (1996).

69. L. A. Vermeulen, *Progr. Inorg. Chem.* 44, 143 (1997).

70. D. Rong, Y. I. Kim, and T. E. Mallouk, *Inorg. Chem.* 29, 1531 (1990).

71. G. Cao, H. G. Hong, and T. E. Mallouk, *Acc. Chem. Res.* 25, 420 (1992).

72. T. E. Mallouk, H.-K. Kim, P. J. Ollivier, and S. W. Keller, in "Comprehensive Supramolecular Chemistry" (G. Alberti and T. Bein, Eds.), Vol. 7, Ch. 6, p. 189. Pergamon, Oxford, 1996.

73. P. Behrens and A. M. Glaue, *Monatsh. Chem.*, in press.

74. P. Behrens, A. M. Glaue, and O. Oellrich, submitted for publication.

75. J. Bauer, P. Behrens, M. Speckbacher, and H. Langhals, submitted to publication.

76. S. Feng and T. Bein, *Nature* 368, 834 (1994).

77. K. Hoffmann, F. Marlow, and J. Caro, *Adv. Mater.* 9, 567 (1997).
78. "Intercalation Chemistry" (M. S. Whittingham and A. J. Jacobson, Eds.). Academic Press, New York, 1982.
79. R. Schöllhorn, in "Inclusion Compounds" (J. L. Atwood, J. E. D. Davies, and D. D. MacNicol, Eds.), p. 249. Academic Press, New York, 1984.
80. A. J. Jacobson, in "Solid-State Chemistry Compounds" (A. K. Cheetham and P. Day, Eds.), Ch. 6, p. 182. Clarendon, Oxford, 1992.
81. D. O'Hare, in "Inorganic Materials" (D. W. Bruce and D. O'Hare, Eds.), Ch. 4, p. 165. Wiley, Chichester, 1992.
82. "Progress in Intercalation Research" (W. Müller-Warmuth and R. Schöllhorn, Eds.). Kluwer, Dordrecht, 1994.
83. A. Lerf, in "Handbook of Nanostructured Materials and Nano-technology" (H. S. Nalwa, Ed.), Vol. 5, p. 1. Academic Press, San Diego, 2000.
84. S. J. Tsipursky and V. A. Drits, *Clay Miner.* 19, 177 (1984).
85. J. M. Thomas, in "Intercalation Chemistry" (M. S. Whittingham and A. J. Jacobson, Eds.), p. 55. Academic Press, New York, 1982.
86. K. Jasmund and G. Lagaly, "Tonminerale und Tone." Steinkopff Verlag, Darmstadt, 1993.
87. "Organo-Clay Complexes and Interactions" (S. Yarif and H. Cross, Eds.). Dekker, New York, 2002.
88. T. Fujita, N. Iyi, T. Kosugi, A. Ando, T. Degushi, and T. Sato, *Clays Clay Miner.* 45, 77 (1997).
89. R. Sasai, T. Fujita, N. Iyi, H. Itoh, and K. Takagi, *Langmuir* 18, 6578 (2002).
90. S H. van Olphen, "Clay Colloid Chemistry. For Clay Technologists, Geologists, and Soil Scientists." Wiley, New York, 1977.
91. G. Lagaly, in "Developments in Ionic Polymers" (A. D. Wilson and J. Prosser, Eds.), Vol. 2, Ch. 2, p. 77. Elsevier, London, 1986.
92. A. J. Jacobson, in "Comprehensive Supramolecular Chemistry" (G. Alberti and T. Bein, Eds.), Vol. 7, Ch. 10, p. 315. Pergamon, Oxford, 1996.
93. M. Ogawa, M. Yamamoto, and K. Kuroda, *Clay Miner.* 36, 263 (2001).
94. G. Lagaly, *Adv. Coll. Interf. Sci.* 11, 105 (1979).
95. J. M. Troup and A. Clearfield, *Inorg. Chem.* 16, 3311 (1977).
96. G. Alberti, in "Comprehensive Supramolecular Chemistry" (G. Alberti and T. Bein, Eds.), Vol. 7, Ch. 5, p. 151. Pergamon, Oxford, 1996.
97. G. Alberti, M. Casciola, U. Costantino, and R. Vivani, *Adv. Mater.* 8, 291 (1996).
98. A. Clearfield, in "Progress in Intercalation Research" (W. Müller-Warmuth and R. Schöllhorn, Eds.). Kluwer, Dordrecht, 1994.
99. A. Clearfield and U. Costantino, in "Comprehensive Supramolecular Chemistry" (G. Alberti and T. Bein, Eds.), Vol. 7, Ch. 4, p. 107. Pergamon, Oxford, 1996.
100. F. Cavani, F. Trifirò, and A. Vaccari, *Catal. Today* 11, 173 (1991).
101. F. Trifirò and A. Vaccari, in "Comprehensive Supramolecular Chemistry" (G. Alberti and T. Bein, Eds.), Vol. 7, Ch. 8, p. 251. Pergamon, Oxford, 1996.
102. T. Sato, *J. Appl. Chem.* 14, 303 (1964).
103. J. P. Thiel, C. K. Chiang, and K. R. Poepelmeier, *Chem. Mater.* 5, 297 (1993).
104. A. V. Besserguenev, A. M. Fogg, R. J. Francis, S. J. Price, D. O'Hare, V. P. Isupov, and B. P. Tolochko, *Chem. Mater.* 9, 241 (1997).
105. G. G. Aloisi, N. Coletti, U. Costantino, F. Elisei, L. Latterini, and M. Nocchetti, *Langmuir* 15, 4454 (1999).
106. G. G. Aloisi, N. Coletti, U. Costantino, F. Elisei, L. Latterini, and M. Nocchetti, *Langmuir* 16, 10351 (2000).
107. G. G. Aloisi, U. Costantino, F. Elisei, L. Latterini, and M. Nocchetti, *Phys. Chem. Chem. Phys.* 4, 2792 (2002).
108. G. G. Aloisi, U. Costantino, F. Elisei, L. Latterini, C. Natali, and M. Nocchetti, *J. Mater. Chem.* 12, 3316 (2002).
109. B. Raveau, *Rev. Chim. Miner.* 21, 391 (1984).
110. B. Raveau, *Rev. Inorg. Chem.* 9, 37 (1987).
111. S. Andersson and A. D. Wadsley, *Acta Cryst.* 14, 1245 (1961).
112. M. Gasperin and M. T. Bihan, *J. Solid State Chem.* 33, 83 (1980).
113. M. Gasperin and M. T. Bihan, *J. Solid State Chem.* 43, 346 (1982).
114. N. Kinomura, N. Kumada, and F. Muto, *J. Chem. Soc. Dalton Trans.* 2349 (1985).
115. A. Kudo, A. Tanaka, K. Domen, K.-I. Maruya, K.-I. Aika, and T. Ohishi, *J. Catal.* 111, 67 (1988).
116. T. Nakato and K. Kuroda, *Eur. J. Sol. State Inorg. Chem.* 32, 809 (1995).
117. A. Kudo and T. Kondo, *J. Mater. Chem.* 7, 777 (1997).
118. T. Takata, Y. Furumi, K. Shinohara, A. Tanaka, M. Hara, J. N. Kondo, and K. Domen, *Chem. Mater.* 9, 1063 (1997).
119. M. M. C. Treacy, S B. Rice, A. J. Jacobson, and J. T. Lewandowski, *Chem. Mater.* 2, 279 (1990).
120. R. Abe, K. Shinohara, A. Tanaka, M. Hara, J. N. Kondo, and K. Domen, *Chem. Mater.* 9, 2179 (1997).
121. J. Livage, *Chem. Mater.* 3, 578 (1991).
122. M. G. Kanatzidis and C. G. Wu, *J. Am. Chem. Soc.* 111, 4139 (1989).
123. M. G. Kanatzidis, C. G. Wu, H. O. Marcy, D. C. DeGroot, and C. R. Kannewurf, *Chem. Mater.* 2, 222 (1990).
124. H. Masbah, D. Tinet, M. Crespin, R. Erre, R. Setton, and H. van Damme, *J. Chem. Soc. Chem. Commun.* 935 (1985).
125. H. Van Damme, M. Letellier, D. Tinet, B. Kihal, and R. Erre, *Mater. Res. Bull.* 19, 1635 (1984).
126. B. Ackermans, R. A. Schoonheydt, and E. Ruiz-Hitzky, *J. Chem. Soc. Faraday Trans.* 92, 4479 (1996).
127. T. Kuwahara, H. Tagaya, and J. Kadokawa, *Inorg. Chem. Comm.* 4, 63 (2001).
128. S. M. Kauzlarich, B. K. Teo, and B. A. Averill, *Inorg. Chem.* 25, 1209 (1986).
129. J. F. Bringley, J. M. Fabre, and B. A. Averill, *J. Amer. Chem. Soc.* 112, 4577 (1990).
130. C. Riekel, H. G. Reznik, and R. Schöllhorn, *J. Solid State Chem.* 34, 253 (1980).
131. A. Hauptmann, A. Lerf, and W. Biberacher, *Z. Naturf. B* 51, 1571 (1996).
132. P. Čapková, M. Pospíšil, and A. Lerf, *Solid State Sci.* 4, 671 (2002).
133. A. Schlicht, M. Schwenker, W. Biberacher, and A. Lerf, *J. Phys. Chem. B* 105, 4867 (2001).
134. S. V. Smith, *Chem. Rev.* 88, 149 (1988).
135. H. Gies and B. Marler, "Comprehensive Supramolecular Chemistry" (D. D Mac Nicol, F. Toda, and R. Bishop, Eds.), Vol. 6. Pergamon, Oxford, 1996.
136. G. Van de Goor, C. Freyhardt, and P. Behrens, *Z. Anorg. Allg. Chem.* 621, 311 (1995).
137. W. M. Meier and W. A. Olson, "Atlas of Zeolite Structure Types," 2nd revised ed. Butterworths, Cambridge, UK, 1987.
138. D. H. Olson, G. T. Kokotallo, S. L. Lawton, and W. M. Meier, *J. Phys. Chem.* 85, 2238 (1981).
139. E. M. Flanigen, J. M. Bennett, R. W. Grose, J. P. Cohen, R. L. Patton, R. M. Kirchner, and J. V. Smith, *Nature* 271, 512 (1978).
140. S. T. Wilson, B. M. Lok, C. A. Messina, T. R. Cannon, and E. M. Flanigen, *J. Am. Chem. Soc.* 104, 1146 (1982).
141. J. M. Bennett, W. J. Dytrych, J. J. Pluth, J. W. Richardson, and J. V. Smith, *Zeolites* 6, 349 (1986).
142. J. W. Richardson, J. J. Pluth, and J. V. Smith, *Acta Cryst. C* 43, 1469 (1987).
143. J. W. Richardson, J. J. Pluth, and J. V. Smith, *Acta Cryst. B* 44, 367 (1988).
144. M. E. Davis, C. Saldarriaga, C. Montes, J. Garces, and C. Crowder, *Nature* 331, 698 (1988).
145. L. B. McCusker, C. Baerlocher, E. Jahn, and M. Bülow, *Zeolites* 11, 308 (1991).
146. B. M. Lok, C. A. Messina, R. L. Patton, R. T. Gajek, T. R. Cannon, and E. M. Flanigen, *J. Am. Chem. Soc.* 106, 6092 (1984).

147. N. Rajić, V. Kaučič, and D. Stojaković, *Zeolites* 10, 169 (1990).

148. C. M. Cardile, N. J. Trapp, and N. B. Milestone, *Zeolites* 10, 90 (1990).

149. S. Wohlrab, R. Hoppe, G. Schulz-Ekloff, and D. Wöhrle, *Zeolites* 12, 862 (1992).

150. R. Hoppe, G. Schulz-Ekloff, D. Wöhrle, E. S. Shpiro, and O. P. Tkachenko, *Zeolites* 13, 222 (1993).

151. C. T. Cresge, M. E. Leonowicz, W. J. Roth, J. C. Vartuli, and J. S. Beck, *Nature* 359, 710 (1992).

152. G. Øye, J. Sjöblom, and M. Stöcker, *Adv. Coll. Interf. Sci.* 89–90, 439 (2001).

153. M. Wark, A. Ortlam, M. Ganschow, G. Schulz-Ekloff, and D. Wöhrle, *Ber. Bunsenges. Phys. Chem.* 102, 1548 (1998).

154. H. S. Zhou and I. Honma, *Adv. Mater.* 11, 683 (1999).

155. H. S. Zhou, H. Sasabe, and I. Honma, *J. Mater. Chem.* 8, 515 (1998).

156. I. Honma and H. S. Zhou, *Chem. Mater.* 10, 103 (1998).

157. X. He and D. Antonelli, *Angew. Chem.* 114, 222 (2002); *Int. Ed. Engl.* 41, 214 (2002).

158. B. F. Jones and E. Galan, in "Hydrous Phyllosilicates" (S. W. Bailey, Ed.), Reviews in Mineralogy, Vol. 19. Miner. Soc. Am., Washington, DC, 1988.

159. C. Detellier et al., submitted for publication

160. H. Dürr, *Angew. Chem.* 101, 427 (1989); *Int. Ed. Engl.* 28, 413 (1989).

161. T. J. Marks and M. A. Ratner, *Angew. Chem.* 107, 167 (1995); *Int. Ed. Engl.* 34, 155 (1995).

162. N. J. Long, *Angew. Chem.* 107, 37 (1995); *Int. Ed. Engl.* 34, 21 (1995).

163. G. Van de Goor, B. Lindlar, J. Felsche, and P. Behrens, *J. Chem. Soc. Chem. Commun.* 2559 (1995).

164. F. Marlow, G. van de Goor, and P. Behrens, *Adv. Mater.* 11, 238 (1999).

165. A. Yamagishi, *J. Coord. Chem.* 16, 131 (1987).

166. M.-H. Ryoo and H. Chon, *Microporous Mater.* 10, 35 (1997).

167. E. P. Giannelis, D. G. Nocera, and T. J. Pinnavaia, *Inorg. Chem.* 26, 203 (1987).

168. M. F. Traynor, M. M. Mortland, and T. J. Pinnavaia, *Clays Clay Miner.* 26, 318 (1978).

169. A. Weiss and G. Roloff, *Z. Naturf. B* 19, 533 (1964).

170. F. Bergaya and H. Van Damme, *Geochim. Cosmochim. Acta* 46, 349 (1982).

171. S. S. Cady and T. J. Pinnavaia, *Inorg. Chem.* 17, 1501 (1978).

172. H. Van Damme, M. Crespin, F. Obrecht, M. I. Cruz, and J. J. Fripiat, *J. Coll. Interface Sci.* 66, 43 (1978).

173. S. Abdo, M. I. Cruz, and J. J. Fripiat, *Clays Clay Miner.* 28, 125 (1980).

174. K. A. Carrado and R. E. Winans, *Chem. Mater.* 2, 328 (1990).

175. V. B. Preobrazhensky, Z. J. Zhernova, A. P. Babichev, I. K. Kobrin, E. A. Lukyanez, and O. L. Kalija, *Solid State Comm.* 27, 127 (1978).

176. S. Takagi, T. Shimada, T. Yui, and H. Inoue, *Chem. Lett.* 128 (2001).

177. S. Takagi, T. Shimada, M. Eguchi, T. Yui, H. Yoshida, D. A. Tryk, and H. Inoue, *Langmuir* 18, 2265 (2002).

178. S. Takagi, D. A. Tryk, and H. Inoue, *J. Phys. Chem. B* 106, 5455 (2002).

179. B. T. Holland, C. Walkup, and A. Stein, *J. Phys. Chem. B* 102, 4301 (1998).

180. D. Wöhrle, A. K. Sobbi, O. Franke, and G. Schulz-Ekloff, *Zeolites* 15, 540 (1995).

181. L. Ukrainczyk, M. Chibwe, T. J. Pinnavaia, and S. A. Boyd, *J. Phys. Chem.* 98, 2668 (1994).

182. E. P. Giannelis, *Chem. Mater.* 2, 627 (1990).

183. T. Nakato, Y. Iwata, K. Kuroda, M. Kaneko, and C. Kato, *J. Chem. Soc. Dalton Trans.* 1405 (1993).

184. I. Y. Park, K. Kuroda, and C. Kato, *Chem. Lett.* 2057 (1989).

185. K. A. Carrado, P. Thiyagarajan, R. E. Winans, and R. E. Botto, *Inorg. Chem.* 30, 794 (1991).

186. M. Ehrl, F. W. Deeg, C. Bräuchle, A. Sobbi, G. Schulz-Ekloff, and D. Wöhrle, *J. Phys. Chem.* 98, 47 (1994).

187. J. M. Krüger and H. D. Brauer, *Ber. Bunsenges. Phys. Chem.* 102, 1554 (1998).

188. T. Itoh, K. Yano, Y. Inada, and Y. Fukushima, *J. Mater. Chem.* 12, 3304 (2002).

189. S. Bonnet, C. Forano, A. de Roy, J. P. Besse, P. Maillard, and M. Momentau, *Chem. Mater.* 8, 1962 (1996).

190. K. A. Carrado and S. R. Wassermann, *Chem. Mater.* 8, 219 (1996).

191. Z. Chernia and D. Gill, *Langmuir* 15, 1625 (1999).

192. F. B. Abdelrazzaq, R. C Kwong, and M. E. Thompson, *J. Am. Chem. Soc.* 124, 4796 (2002).

193. K. A. Carrado, J. E. Forman, R. E. Botto, and R. E. Winans, *Chem. Mater.* 5, 472 (1993).

194. M. R. Wasielewski, *Chem. Rev.* 92, 435 (1992).

195. C. L. Bird and A. T. Kuhn, *Chem. Soc. Rev.* 10, 49 (1981).

196. H. J. Schäfer, *Top. Current Chem.* 142, 101 (1987).

197. L. Michaelis and E. S. Hill, *J. Gen. Physiol.* 16, 859 (1933).

198. G. Villemure, H. Kodoma, and C. Detellier, *Can. J. Chem.* 63, 1139 (1985).

199. J. B. Weber and D. C. Scott, *Science* 152, 1400 (1966).

200. M. Raupach, W. W. Emerson, and P. G. Slade, *J. Coll. Interface Sci.* 69, 398 (1979).

201. T. Endo, T. Sato, and M. Shimada, *J. Phys. Chem. Solids* 47, 799 (1986).

202. L. Margulies, H. Rozen, and S. Nir, *Clays Clay Miner.* 36, 270 (1988).

203. R. Cohen and S. Yariv, *J. Chem. Soc. Faraday Trans. I* 80, 1705 (1984).

204. M. Bockstette, D. Wöhrle, I. Braun, and G. Schulz-Ekloff, *Microporous Mesoporous Mater.* 23, 83 (1998).

205. S. K. Lam and D. Lo, *Chem. Phys. Lett.* 281, 35 (1997).

206. M. J. T. Estévez, F. L. Arbeloa, T. L. Arbeloa, and I. L. Arbeloa, *J. Colloid Interface Sci.* 171, 439 (1995).

207. M. J. T. Estévez, F. L. Arbeloa, T. L. Arbeloa, and I. L. Arbeloa, *J. Colloid Interface Sci.* 162, 412 (1994).

208. F. L. Arbeloa, R. Chaudhuri, T. L. Arbeloa, and I. L. Arbeloa, *J. Colloid Interface Sci.* 246, 281 (2002).

209. H. Van Damme, M. Crespin, M. I. Cruz, and J. J. Fripiat, *Clays Clay Miner.* 25, 19 (1977).

210. J. Bujdák and N. Iyi, *Clays Clay Miner.* 50, 446 (2002).

211. G. Calzaferri and N. Gfeller, *J. Phys. Chem.* 96, 3428 (1992).

212. V. Ramamurthy, D. D. Sanderson, and D. F. Eaton, *J. Am. Chem. Soc.* 115, 10438 (1993).

213. M. Ehrl, H. W. Kindervater, F. W. Deeg, and C. Bräuchle, *J. Phys. Chem.* 98, 11756 (1994).

214. D. Brühwiler, N. Gfeller, and G. Calzaferri, *J. Phys. Chem. B* 102, 2923 (1998).

215. N. Gfeller, S. Megelski, and G. Calzaferri, *J. Phys. Chem. B* 102, 2433 (1998).

216. T. Endo, N. Nakada, T. Sato, and M. Shimada, *J. Phys. Chem. Solids* 49, 1423 (1988).

217. F. Marlow, M. D. McGehee, D. Zhao, B. F. Chmelka, and G. D. Stucky, *Adv. Mater.* 11, 632 (1999).

218. U. Narang, R. Wang, P. N. Prasad, and F. V. Bright, *J. Phys. Chem.* 98, 17 (1994).

219. D. Levy and D. Avnir, *J. Photochem. Photobiol. A: Chem.* 57, 41 (1991).

220. A. Dubois, M. Canva, A. Brun, F. Chaput, and J.-P. Boilot *Synth. Met.* 81, 305 (1996).

221. G. Wirnsberger and G. D. Stucky, *Chem. Mater.* 12, 2525 (2000).

222. F. Del Monte and D. Levy, *J. Phys. Chem. B* 103, 8080 (1999).

223. J. L. Meinershagen and T. Bein, *J. Am. Chem. Soc.* 121, 448 (1999).

224. R. Hoppe, G. Schulz-Ekloff, D. Wöhrle, C. Kirschock, H. Fuess, L. Uyterhoeven, and R. A. Schoonheydt, *Adv. Mater.* 7, 61 (1995).

225. K. Bergman and C. T. O'Konski, *J. Phys. Chem.* 67, 2169 (1963).
226. P. T. Hang and G. W. Brindley, *Clays Clay Miner.* 18, 203 (1970).
227. J. Cenens and R. A. Schoonheydt, *Clay Miner.* 23, 205 (1988).
228. J. Cenens and R. A. Schoonheydt, *Clays Clay Miner.* 36, 214 (1988).
229. R. A. Schoonheydt and L. Heughebaert, *Clay Miner.* 27, 91 (1992).
230. F. Gessner, C. Schmitt, and M. G. Neumann, *Langmuir* 10, 3749 (1994).
231. J. Bujdák and P. Komadel, *J. Chem. Phys. B* 101, 9065 (1997).
232. A. P. P. Cione, M. G. Neumann, and F. Gessner, *J. Coll. Interf. Sci.* 198, 106 (1998).
233. K. Y. Jacobs and R. A. Schoonheydt, *J. Coll. Interf. Sci.* 220, 103 (1999).
234. J. Bujdák, M. Janek, J. Madejovà, and P. Komadel, *Clays Clay Miner.* 49, 244 (2001).
235. J. Bujdák, N. Iyi, and T. Fujita, *Clay Miner.* 37, 121 (2002).
236. D. Garfinkel-Shweky and S. Yariv, *J. Coll. Interf. Sci.* 188, 168 (1997).
237. D. Garfinkel-Shweky and S. Yariv, *Clay Miner.* 34, 459 (1999).
238. L. Michaelis and S. Granick, *J. Am. Chem. Soc.* 63, 1636 (1941).
239. K. Schwabe and H. Berg, *Z. Phys. Chem.* 204, 78 (1955).
240. S. H. de Araujo-Nicolai, P. R. P. Rodrigues, S. M. L. Agostinho, and L. C. Rubin, *J. Electroanal. Chem.* 527, 103 (2002).
241. S. Ameta, S. Khamesra, A. K. Cittora, and K. M. Gangotri, *Int. J. Energ. Res.* 13, 643 (1989).
242. D. F. Duxbury, *Chem. Rev.* 93, 381 (1993).
243. R. Hoppe, G. Alberti, U. Costantino, C. Diongi, G. Schulz-Ekloff, and R. Vivani, *Langmuir* 13, 7252 (1997).
244. D. Avnir, Z. Grauer, S. Yariv, D. Huppert, and D. Rojanski, *Nouv. J. Chim.* 10, 153 (1986).
245. L. Margulies, H. Rozen, and E. Cohen, *Clays Clay Miner.* 36, 159 (1988).
246. D. N. Simon, R. Czolk, and H. J. Ache, *Thin Solid Films* 260, 107 (1995).
247. Z. Chernia, D. Gill, and S. Yariv, *Langmuir* 10, 3988 (1994).
248. K. Yamaoka and R. Sasai, *J. Coll. Interf. Sci.* 225, 82 (2000).
249. P. G. Lacroix, R. Clement, K. Nakatani, J. Zyss, and I. Ledoux, *Science* 263, 658 (1994).
250. I. Lagadic, P. G. Lacroix, and R. Clement, *Chem. Mater.* 9, 2004 (1997).
251. D. Gonbeau, T. Coradin, and R. Clement, *J. Phys. Chem. B* 103, 3545 (1999).
252. J. Kim, M. Lee, J. H. Yang, and J. H. Choy, *J. Phys. Chem. A* 104, 1388 (2000).
253. K. Izawa, N. Okamoto, and O. Sugihara, *Jpn. J. Appl. Phys.* 32, 807 (1993).
254. C. Schomburg, D. Wöhrle, and G. Schulz-Ekloff, *Zeolites* 17, 232 (1996).
255. K. Hoffmann, U. Resch-Genger, and F. Marlow, *Microporous Mesoporous Mater.* 41, 99 (2000).
256. M. Ogawa, *Chem. Mater.* 8, 1347 (1996).
257. M. Ogawa and A. Ishikawa, *J. Mater. Chem.* 8, 463 (1998).
258. M. Ogawa, *J. Mater. Chem.* 12, 3304 (2002).
259. S. K. Doughty, G. J. Simpson, and K. L. Rowlen, *J. Am. Chem. Soc.* 120, 7997 (1998).
260. H. E. Katz, W. L. Wilson, and G. Scheller, *J. Am. Chem. Soc.* 116, 6636 (1994).
261. E. C. Y. Yan and K. B. Eisenthal, *J. Phys. Chem. B* 103, 6056 (1999).
262. I. Y. Park, K. Kuroda, and C. Kato, *J. Chem. Soc. Dalton Trans.* 3071 (1990).
263. C. V. Kumar, A. Chaudhari, and G. L. Rosenthal, *J. Am. Chem. Soc.* 116, 403 (1994).
264. D. W. Murphy and G. W. Hull, *J. Chem. Phys.* 62, 967 (1975).
265. N. Miyamoto, K. Kuroda, and M. Ogawa, *J. Am. Chem. Soc.* 123, 6949 (2001).
266. A. Corma, V. Fornés, H. García, M. A. Miranda, J. Primo, and M.-J. Sabater, *J. Am. Chem. Soc.* 116, 2276 (1994).
267. T. Endo, N. Nakada, T. Sato, and M. Shimada, *J. Phys. Chem. Solids* 50, 133 (1989).
268. S. D. Cox, T. E. Gier, and G. D. Stucky, *Chem. Mater.* 2, 609 (1990).
269. F. Marlow, M. Wübbenhorst, and J. Caro, *J. Phys. Chem.* 98, 12315 (1994).
270. F. Marlow, J. Caro, L. Werner, J. Kornatowski, and S. Dähne, *J. Phys. Chem.* 9, 11286 (1993).
271. K. Hoffmann, F. Marlow, J. Caro, and S. Dähne, *Zeolites* 16, 138 (1996).
272. W. K. Kuk and Y.-D. Huh, *J. Mater. Chem.* 7, 1933 (1997).
273. S. Miyata, *Clays Clay Miner.* 31, 305 (1983).
274. N. Khaorapapong, K. Kuroda, and M. Ogawa, *Clays Clay Miner.* 50, 428 (2002).
275. B. D. Gupta and D. K. Sharma, *Optics Commun.* 140, 32 (1997).
276. C. Schomburg, M. Wark, Y. Rohlfing, G. Schulz-Ekloff, and D. Wöhrle, *J. Mater. Chem.* 11, 2014 (2001).
277. G. Wirnsberger, B. J. Scott, B. F. Chmelka, and G. D. Stucky, *Adv. Mater.* 12, 1450 (2000).
278. H. Tomioka and T. Itoh, *J. Chem. Soc. Chem. Commun.* 532 (1991).
279. T. Seki and K. Ichimura, *Macromolecules* 23, 31 (1990).
280. K. Takagi, T. Kurematsu, and Y. Sawaki, *J. Chem. Soc. Perkin Trans. 2* 1517 (1991).
281. N. Röhrlich, E. Löffler, B. Zibrowius, L. Chassot, and W. F. Hölderich, *J. Chem. Soc. Fararday Trans.* 94, 609 (1998).
282. L.-T. Yuen, J. S. Geilfuss, and S. I. Zones, *Microporous Mater.* 12, 229 (1997).
283. R. Hoppe, G. Schulz-Ekloff, D. Wöhrle, C. Kirschhock, and H. Fuess, *Langmuir* 10, 1517 (1994).
284. H. Van Damme, F. Obrecht, and M. Letellier, *Nouv. J. Chim.* 8, 681 (1984).
285. P. Lacroix, J. P. Audière, and R. Clement, *J. Chem. Soc. Chem. Comm.* 536 (1989).
286. L. Lomas, P. Lacroix, J. P. Audière, and R. Clement, *J. Mater. Chem.* 1, 475 (1991).
287. T. E. Sutto, B. A. Averill, and J. M. Fabre, *Synth. Met.* 55–57, 2019 (1993).
288. S. M. Kauzlarich, J. L. Stanton, J. Faber, and B. A. Averill, *J. Am. Chem. Soc.* 108, 7946 (1986).
289. R. Backov, B. Bonnet, D. J. Jones, and J. Rozière, *Chem. Mater.* 9, 1812 (1997).
290. R. A. DellaGuardi and J. K. Thomas, *J. Phys. Chem.* 88, 964 (1984).
291. P. Labbé and G. Reverdy, *Langmuir* 4, 419 (1988).
292. X. Liu and J. K. Thomas, *Langmuir* 7, 2808 (1991).
293. R. J. Kavanagh, K. K. Iu, and J. K. Thomas, *Langmuir* 8, 3008 (1992).
294. X. Liu, K. K. Iu, and J. K. Thomas, *Langmuir* 8, 539 (1992).
295. B. Brahimi, P. Labbé, and G. Reverdy, *Langmuir* 8, 1908 (1992).
296. M. Ogawa, T. Aono, K. Kuroda, and C. Kato, *Langmuir* 9, 1529 (1993).
297. K. B. Yoon, T. J. Huh, D. R. Corbin, and J. K. Kochi, *J. Phys. Chem.* 97, 6492 (1993).
298. G. Berkovic, V. Krongauz, and V. Weiss, *Chem. Rev.* 100, 1741 (2000).
299. W. F. Bradley, R. E. Grim, and G. L. Clark, *Z. Kristallogr.* 97, 216 (1937).
300. D. Krenske, S. Abdo, H. Van Damme, M. Cruz, and J. J. Fripiat, *J. Phys. Chem.* 84, 2447 (1980).
301. G. Decher, in "Comprehensive Supramolecular Chemistry" (J. P. Sauvage and M. W. Hosseini, Eds.), Vol. 9, Ch. 14, p. 507. Pergamon, Oxford, 1996.
302. R. K. Iler, *J. Coll. Interf. Sci.* 21, 569 (1966).
303. J. Schmitt, T. Grünewald, G. Decher, P. S. Persham, K. Kjaer, and M. Lösche, *Macromolecules* 26, 7058 (1993).
304. Y. Lvov, K. Ariga, I. Ichinose, and T. Kunitake, *J. Amer. Chem. Soc.* 117, 6117 (1995).

305. S. W. Keller, H.-N. Kim, and T. E. J. Mallouk, *Amer. Chem. Soc.* 116, 8817 (1994).
306. G. S. Ferguson and E. R. Kleinfeld, *Adv. Mater.* 7, 414 (1995).
307. J. H. Fendler and F. C. Meldrum, *Adv. Mater.* 7, 607 (1995).
308. J. H. Fendler, *Chem. Mater.* 8, 1616 (1996).
309. N. A. Kotov, T. Haraszti, L. Turi, G. Zawala, R. E. Geer, I. Dékány, and J. Fendler, *J. Am. Chem. Soc.* 119, 6821 (1997).
310. B. van Duffel, R. Schoonheydt, C. P. M. Grim, and F. C. DeSchryver, *Langmuir* 15, 7520 (1999).
311. B. van Duffel, T. Verbiest, S. Van Elshocht, A. Persoons, F. C. DeSchryver, and R. Schoonheydt, *Langmuir* 17, 1243 (2001).
312. H. E. Katz, G. Scheller, T. M. Putvinski, M. L. Schilling, W. L. Wilson, and C. E. D. Chidsey, *Science* 254, 1485 (1991).
313. S. B. Ungashe, W. L. Wilson, H. E. Katz, G. Scheller, and T. M. Putvinski, *J. Am. Chem. Soc.* 114, 8717 (1992).
314. L. A. Vermeulen and M. E. Thompson, *Nature* 358, 656 (1992).
315. Y. Lvov, F. Essler, and G. Decher, *J. Phys. Chem.* 97, 13773 (1993).
316. K. Inukai, Y. Hotta, M. Taniguchi, S. Tomura, and A. Yamagishi, *J. Chem. Soc. Chem. Commun.* 959 (1994).
317. N. Kotov, A. Meldrum, F. C. Fendler, J. H. Tombácz, and I. Dekany, *Langmuir* 10, 3797 (1994).
318. Y. Umemura, A. Yamagishi, R. Schoonheydt, A. Persoons, and F. DeSchryver, *Langmuir* 17, 449 (2001).
319. K. Tamura, H. Setsuda, M. Taniguchi, and A. Yamagishi, *Langmuir* 15, 6915 (1999).
320. A. Tavolaro and E. Driolo, *Adv. Mater.* 11, 975 (1999).
321. S. Feng and T. Bein, *Science* 265, 1839 (1994).
322. J. Caro, G. Finger, J. Kornatowski, J. Richter-Mendau, L. Werner, and B. Zibrowius, *Adv. Mater.* 4, 273 (1992).
323. J. M. Lehn, *Angew. Chem. Int. Ed. Engl.* 29, 1304 (1990).
324. A. Nangia and G. R. Desiraju, *Acta Cryst. A* 54, 934 (1998).
325. A. Gavezzotti, *J. Am. Chem. Soc.* 113, 4622 (1991).
326. *Cerius²* documentation Molecular Simulations Inc. (CD-ROM), San Diego, June 2000.
327. P. Comba and T. W. Hambley, "Molecular Modeling of Inorganic Compounds." VCH, Weinheim, 1995.
328. D. Frenkel and B. Smit, "Understanding Molecular Simulation." Academic Press, San Diego, 1996.
329. P. Čapková, J. V. Burda, Z. Weiss, and H. Schenk, *J. Mol. Model* 5, 8 (1999).
330. A. K. Rappé, C. J. Casewit, K. S. Colwell, W. A. Goddard III, and W. M. Skiff, *J. Am. Chem. Soc.* 114, 10024 (1992).
331. P. Dauber-Osguthorpe, V. A. Roberts, D. J. Osguthorpe, J. Wolff, M. Genest, and A. T. Hagler, *Proteins: Structure, Function Genetics* 4, 31 (1988).
332. M. Clark, R. D. Cramer III, and N. Van Opdenbosh, *J. Comp. Chem.* 10, 982 (1989).
333. H. Sun, *J. Comp. Chem.* 15, 752 (1994).
334. S. L. Mayo, B. D. Olafson, and W. A. Goddard III, *J. Phys. Chem.* 94, 8897 (1990).
335. A. K. Rappé and W. A. Goddard III, *J. Phys. Chem.* 95, 3358 (1991).
336. P. P. Ewald, *Ann. Phys.* (*Leipzig*) 64, 253 (1921).
337. N. Karasawa and W. A. Goddard III, *J. Phys. Chem.* 93, 7320 (1989).
338. P. Koudelka and P. Čapková, *J. Mol. Model* 8, 184 (2002).
339. P. Erk, in "Crystal Engineering: From Molecules and Crystals to Materials" (D. Braga and G. Orpen, Eds.), p. 143. Kluwer Academic, Dordrecht, 1999.
340. P. Verwer and F. J. J. Leusen, *Rev. Comput. Chem.* 12, 327 (1998).
341. K. D. M. Harris, B. M. Kariuki, and R. L. Johnston, in "Advances in Structure Analysis" (R. Kužel and J. Hašek, Eds.), p. 190. Czech and Slovak Crystallographic Association, Prague, 2001.
342. W. A. Dollase, *J. Appl. Cryst.* 19, 267 (1986).
343. P. Suortti, *J. Appl. Cryst.* 5, 325 (1972).
344. F. R. Gamble, F. J. DiSalvo, R. A. Klemm, and T. H. Geballe, *Science* 168, 568 (1970).
345. R. H. Friend and A. D. Yoffe, *Adv. Phys.* 36, 1 (1987).
346. A. Schlicht, Thesis, TU München, 1999.
347. A. Meetsma, G. A. Wiegers, R. J. Haange, and J. L. De Boer, *Acta Cryst. C* 46, 1598 (1990).
348. A. Kahn-Harari, R. E. Ballard, and E. K. Norris, *Acta Cryst. B* 29, 1124 (1973).
349. J. Breu, N. Raj, and C. R. A. Catlow, *J. Chem. Soc. Dalton Trans.* 6, 835 (1999).
350. J. Méring and A. Oberlin, *Clays Clay Miner.* 27, 3 (1967).
351. M. Pospíšil, Complex Structure Analysis of Intercalates Using Molecular Simulations, Thesis, Charles University, Prague, 2002.
352. M. Pospíšil, P. Čapková, H. Weissmannová, Z. Klika, M. Trchová, M. Chmielová, and Z. Weiss, *J. Mol. Model*, in press.
353. R. Chaudhuri, F. L. Arbeloa, and I. L. Arbeloa, *Langmuir* 16, 1285 (2000).
354. A. Vahedi-Faridi and S. Guggenheim, *Clay Clay Miner.* 45, 859 (1997).
355. A. Vahedi-Faridi and S. Guggenheim, *Clay Clay Miner.* 47, 338 (1999).
356. P. G. Slade and P. A. Stone, *Clay Clay Miner.* 32, 223 (1984).
357. J. Méring, in "Soil Components" (J. E. Gieseking, Ed.), Vol. 2, p. 110. Springer-Verlag, Berlin, 1975.
358. P. Čapková, J. V. Burda, Z. Weiss, and H. Schenk, *J. Mol. Model.* 5, 8 (1999).
359. P. G. Slade, C. Dean, P. K. Schultz, and P. G. Self, *Clays Clay Miner.* 35, 177 (1987).
360. P. G. Slade and M. Raupach, *Clays Clay Miner.* 30, 297 (1982).
361. G. Villemure, *Clays Clay Miner.* 38, 623 (1990).
362. J. Breu and C. R. A. Catlow, *Inorg. Chem.* 34, 4504 (1995).
363. V. Joshi, D. Koktar, and P. K. Gosh, *Proc. Indian Acad. Sci: Chem. Sci.* 102, 203 (1990).
364. R. A. Schoonheydt, P. Depauw, D. Vliers, and F. C. DeSchryver, *J. Phys. Chem.* 88, 5113 (1984).
365. P. V. Kamat, K. R. Gopidas, T. Mukherjee, V. Joshi, D. Koktar, V. S. Pathak, and P. K. Gosh, *J. Phys. Chem.* 95, 10009 (1991).
366. N. Shimizu, S. Hashimoto, T. Takemura, M. Kawasaki, and A. Yamagishi, Clays controlling the environment, in "Proc. 10th International Clay Conference" (G. J. Churchman, R. W. Fitzpatrick, and R. A. Eggleton, Eds.). CSIRO, Melbourne, 1995.
367. H. Van Koningsveld and J. H. Koegler, *Microporous Mater.* 9, 71 (1997).
368. L. Werner, J. Caro, G. Finger, and J. Kornatowski, *Zeolites* 12, 658 (1992).
369. G. Reck, F. Marlow, J. Kornatowski, W. Hill, and J. Caro, *J. Phys. Chem.* 100, 1698 (1996).
370. B. Hennesy, S. Megelski, C. Marcolli, V. Shklover, C. Bärlocher, and G. Calzaferri, *J. Phys. Chem. B* 103, 3340 (1999).
371. E. H. Megehee, C. E. Johnson, and R. Eisenberg, *Inorg. Chem.* 28, 2423 (1989).
372. K. Nakamura, Y. Kai, N. Yasuoka, and N. Kasai, *Bull. Chem. Soc. Jpn.* 54, 3300 (1981).
373. H. Wolkers, R. Stegemann, G. Frenking, K. Dehnicke, D. Fenzke, and G. Baum, *Z. Naturf.* 48b, 1341 (1993).
374. M. Alvaro, G. A. Facey, H. García, S. García, and J. C. Scaiano, *J. Phys. Chem.* 100, 18173 (1996).
375. P. K. Ghosh and A. J. Bard, *J. Phys. Chem.* 88, 5519 (1984).
376. H. Nijs, M. I. Cruz, J. J. Fripiat, and H. van Damme, *Nuov. J. Chim.* 6, 551 (1982).
377. N. J. Turro, C. V. Kumar, Z. Grauer, and J. K. Barton, *Langmuir* 3, 1056 (1987).
378. D. P. Vliers, D. Collin, R. A. Schoonheydt, and F. C. DeSchryver, *Langmuir* 2, 165 (1986).
379. D. P. Vliers, R. A. Schoonheydt, and F. C. DeSchryver, *J. Chem. Soc. Faraday Trans.* 81, 2009 (1985).
380. T. Nakamura and J. K. Thomas, *Langmuir* 1, 568 (1985).
381. W. De Wilde, G. Peeters, and J. H. Lundsford, *J. Phys. Chem.* 84, 2306 (1980).

382. P. K. Dutta and J. A. Incavo, *J. Phys. Chem.* 91, 4443 (1987).

383. P. K. Dutta and W. Turbeville, *J. Phys. Chem.* 96, 9410 (1992).

384. M. Borja and P. K. Dutta, *Nature* 362, 43 (1993).

385. J. S. Krueger, J. E. Mayer, and T. E. Mallouk, *J. Am. Chem. Soc.* 110, 8332 (1988).

386. E. H. Yonemoto, Y. I. Kim, R. H. Schmehl, J. O. Wallin, B. A. Shoulders, B. K. Richardson. J. F. Haw, and T. E. Mallouk, *J. Am. Chem. Soc.* 116, 10557 (1994).

387. K. F. Mongey, J. G. Vos, B. D. MacCraith, and C. M. McDonagh, *Coord. Chem. Rev.* 185–186, 417 (1999).

388. K. Sakoda and K. Kominami, *Chem. Phys. Lett.* 216, 270 (1993).

389. L. Persaud, A. J. Bard, A. Campion, M. A. Fox, T. E. Mallouk, S. E. Webber, and J. M. White, *J. Am. Chem. Soc.* 109, 7309 (1987).

390. Y. Yang, P. Wang, and G. Zhou, *Anal. Bioanal. Chem.* 372, 712 (2002).

391. H. Miyata, Y. Sugahara, K. Kuroda, and C. Kato, *J. Chem. Soc. Faraday Trans. 1* 83, 1851 (1987).

392. T. Nakato, K. Kuroda, and C. Kato, *Chem. Mater.* 4, 128 (1992).

393. H. Miyata, Y. Sugahara, K. Kuroda, and C. Kato, *J. Chem. Soc. Faraday Trans. 1* 84, 2677 (1988).

394. A. Bose, P. He, C. Liu, B. D. Ellman, R. J. Twieg, and S. D. Huang, *J. Am. Chem. Soc.* 124, 4 (2002).

395. Z. Li, C. M. Wang, L. Persaud, and T. E. Mallouk, *J. Phys. Chem.* 2592 (1988).

396. G. Villemure, C. Detellier, and A. G. Szabo, *J. Am. Chem. Soc.* 108, 4658 (1986).

397. G. Villemure, C. Detellier, and A. G. Szabo, *Langmuir* 7, 1215 (1991).

398. O. Poizot, C. Sourisseau, and Y. Mathey, *J. Chem. Soc. Faraday Trans. I* 80, 3257 (1984).

399. O. Poizot, C. Sourisseau, and C. Giannotti, *Chem. Phys. Lett.* 122, 129 (1984).

400. O. Poizot, C. Sourisseau, and J. Corset, *J. Mol. Struct.* 143, 203 (1986).

401. G. Calzaferri, M. Lanz, and J. W. Li, *J. Chem. Soc. Chem. Commun.* 1313 (1995).

402. M. Alvaro, H. García, S. García, F. Márquez, and J. C. Scaiano, *J. Phys. Chem. B* 101, 3043 (1997).

403. F. Marlow and K. Hoffmann, *Ber. Bunsenges. Phys. Chem.* 101, 1731 (1997).

404. D. Levy and D. Avnir, *J. Phys. Chem.* 92, 4734 (1988).

405. D. Preston, J. C. Pouxviel, T. Novinson, W. C. Kasca, B. Dunn, and J. I. Zink, *J. Phys. Chem.* 94, 4167 (1990).

406. J. Biteau, F. Chaput, and J.-P. Boilot, *J. Phys. Chem.* 100, 9024 (1996).

407. B. Schaudel, C. Guermeur, C. Sanchez, K. Nakatani, and J. A. Delaire, *J. Mater. Chem.* 7, 61 (1997).

408. H. Tagaya, T. Nagaoka, T. Kuwahara, M. Karasu, J.-I. Kadokawa, and K. Chiba, *Microporous Mesoporous Mater.* 21, 395 (1998).

409. D. Levy, *Chem. Mater.* 9, 2666 (1997).

410. G. Calzaferri, D. Brühwiler, S. Megelski, M. Pfenninger, M. Pauchard, B. Hennesy, H. Maas, A. Devaux, and U. Graf, *Solid State Sci.* 2, 421 (2000).

411. G. Calzaferri, M. Pauchard, H. Maas, S. Huber, A. Khatyr, and T. Schaafsma, *J. Mater. Chem.* 12, 1 (2002).

412. H. García and H. D. Roth, *Chem. Rev.* 102, 3947 (2002).

413. G. Scheibe, *Angew. Chem.* 49, 563 (1936).

414. L. Antonov, G. Gergov, V. Petrov. M. Kubista, and J. Nygren, *Talanta* 49, 99 (1999).

415. H. Kuhn, *Coll. Surf. A* 171, 3 (2000).

416. G. Scheibe, *Angew. Chem.* 50, 51 (1937).

417. E. E. Jelley, *Nature* 138, 1009 (1936).

418. E. E. Jelley, *Nature* 139, 631 (1937).

419. D. Möbius, *Adv. Mater.* 7, 437 (1995).

420. V. G. Kuykendall and J. K. Thomas, *Langmuir* 6, 1350 (1990).

421. C. Breen and B. Rock, *Clay Miner.* 29, 179 (1994).

422. G. J. Kavarnos and N. J. Turro, *Chem. Rev.* 86, 401 (1986).

423. C.-H. Yu, S. Q. Newton, M. A. Norman, D. M. Miller, L. Schäfer, and B. J. Teppen, *Clays Clay Miner.* 48, 665 (2000).

424. M. J. Avena, L. E. Valenti, V. Pfaffen, and C. P. De Pauli, *Clays Clay Miner.* 49, 168 (2001).

425. Y. Xiang, G. Villemure, and C. Detellier, *Clays Clay Miner.* 40, 362 (1992).

426. R. Hoppe, G. Schulz-Ekloff, D. Wöhrle, M. Ehrl, and C. Bräuchle, in "Zeolite Chemistry and Catalysis" (P. A. Jacobs, N. I. Jaeger, L. Kubelková, and B. Wichterlová, Eds.), p. 199. Elsevier, Amsterdam, 1991.

427. W. J. MacNeal and J. A. Killian, *J. Am. Chem. Soc.* 48, 740 (1926).

428. C. B. Sunwar and H. Bose, *J. Coll. Interf. Sci.* 136, 54 (1990).

429. T. Coradin, R. Clement, P. G. Lacroix, and K. Nakatani, *Chem. Mater.* 8, 2153 (1996).

430. A. Habti, D. Keravis, P. Levitz, and H. van Damme, *J. Chem. Soc. Faraday Trans. 2* 80, 67 (1984).

431. M. Ogawa, M. Inagaki, N. Kodama, K. Kuroda, and C. Kato, *J. Phys. Chem.* 97, 3819 (1993).

432. N. Gfeller, S. Megelski, and G. Calzaferri, *J. Phys. Chem. B* 103, 1250 (1999).

433. M. Pauchard, A. Devaux, and G. Calzaferri, *Chem. Eur. J.* 6, 3456 (2000).

434. G. Renger, in "Concepts in Photobiology: Photosynthesis and Photo-morphogenesis" (G. S. Singhal, G. Renger, S. K. Sopory, K.-D. Irgang, and Govindjee, Eds.). Narosa, New Dehli, 1999.

435. D. Gust, T. A. Moore, and A. L. Moore, *Acc. Chem. Res.* 34, 40 (2001).

436. D. G. Whitten, *Acc. Chem. Res.* 13, 83 (1980).

437. C. R. Bock, T. J. Meyer, and D. G. Whitten, *J. Am. Chem. Soc.* 96, 4710 (1974).

438. P. Keller, A. Moradpour, E. Armouyal, and H. B. Kagan, *Nouv. J. Chim.* 4, 377 (1980).

439. J. L. Snover and M. E. Thompson, *J. Am. Chem. Soc.* 116, 765 (1994).

440. G. Sprintschnik, H. W. Sprintschnik, P. P. Kirsch, and D. G. Whitten, *J. Am. Chem. Soc.* 98, 2337 (1976).

441. Y. I. Kim, S. Salim, M. J. Huq, and T. E. Mallouk, *J. Am. Chem. Soc.* 113, 9561 (1991).

442. M. Kirch, J.-M. Lehn, and J.-P. Sauvage, *Helv. Chim. Acta* 62, 1345 (1979).

443. V. Balzani, A. Juris, M. Venturi, S. Campagna, and S. Serroni, *Chem. Rev.* 96, 759 (1996).

444. L. Sun, L. Hammarström, B. Åkermark, and S. Styring, *Chem. Soc. Rev.* 30, 36 (2001).

445. R. Lomoth, T. Häupl, O. Johansson, and L. Hammarström, *Chem. Eur. J.* 8, 102 (2001).

446. E. H. Yonemoto, G. B. Saupe, R. H. Schmehl, S. M. Hubig, R. R. Riley, B. L. Iverson, and T. E. Mallouk, *J. Am. Chem. Soc.* 116, 4786 (1994).

447. J. R. Kincaid, *Chem. Eur. J.* 6, 4055 (2000).

448. M. Sykora and J. R. Kincaid, *Nature* 387, 162 (1997).

449. L. A. Vermeulen, J. L. Snover, L. S. Sapochak, and M. E. Thompson, *J. Am. Chem. Soc.* 115, 11767 (1993).

450. D. M. Kaschak, S. A. Johnson, C. C. Waraksa, J. Pogue, and T. E. Mallouk, *Coord. Chem. Rev.* 185–186, 403 (1999).

451. W. H. Quayle and J. H. Lunsford, *Inorg. Chem.* 21, 97 (1982).

452. T. Sekine, J. Yoshimura, A. Tanaka, K. Domen, K.-I. Maruya, and T. Onishi, *Bull. Chem. Soc. Jpn.* 63, 2107 (1990).

453. K. Sayama, A. Tanaka, K. Domen, K. Maruya, and T. Onishi, *J. Phys. Chem.* 95, 1345 (1991).

454. A. Kudo, K. Sayama, A. Tanaka, K. Asakura, K. Domen, K. Maruya, and T. Onishi, *J. Catal.* 120, 337 (1989).

455. J.-M. Lehn, J.-P. Sauvage, and R. Ziessel, *Nouv. J. Chim.* 4, 623 (1980).

456. Y. Kim. S. J. Atherton, E. S. Brigham, and T. E. Mallouk, *J. Phys. Chem.* 97, 11802 (1993).

457. H. Maas and G. Calcaferri, *Angew. Chem.* 114, 2389 (2002).

458. Special issue of *Chemical Reviews* devoted exclusively to "Photochromism: Memories and Switches" (M. Irie, guest editor), *Chem. Rev.* 100(5) (2000).

459. M. Ueda, H.-B. Kim, T. Ikeda, and K. Ishimura, *Chem. Mater.* 4, 1229 (1992).

460. M. Ueda, H.-B. Kim, and K. Ishimura, *Chem. Mater.* 6, 1771 (1994).

461. D. J. Williams, *Angew. Chem. Int. Ed. Engl.* 23, 690 (1984).

462. S. Cooper and P. K. Dutta, *J. Phys. Chem.* 94, 114 (1990).

463. T. M. Putvinski, M. L. Schilling, H. E. Katz, C. E. D. Chidsey, A. M. Mujsce, and A. B. Emerson, *Langmuir* 6, 1567 (1990).

464. M. Ogawa, M. Takahashi, and K. Kuroda, *Chem. Mater.* 6, 715 (1992).

465. J. Breu, A. Stoll, K. G. Lange, and T. Probst, *Phys. Chem. Chem. Phys.* 3, 1232 (2001).

466. J. Breu, W. Seidl, A. Stoll, K. G. Lange, and T. U. Probst, *Chem. Mater.* 13, 4213 (2001).

467. J.-M. Lehn, "Supramolecular Chemistry." VCH, Weinheim, 1995.

468. J. C. Scaiano and H. García, *Acc. Chem. Res.* 32, 783 (1999).

469. R. T. Hayes, M. R. Wasielewski, and D. Gosztola, *J. Amer. Chem. Soc.* 122, 5563 (2000).

470. A. S. Lukas, S. E. Miller, and M. R. Wasielewski, *J. Phys. Chem. B* 104, 931 (2000).

471. H. Imahori, H. Norieda, H. Yamada, Y. Nishimura, I. Yamazaki, Y. Sakata, and S. Fukuzumi, *J. Amer. Chem. Soc.* 123, 100 (2001).

472. W. L. Jido, T. Lee, and T. Pinnavaia, *Adv. Mater.* 8, 79 (1996).

473. W. L. Jido and T. Pinnavaia, *J. Solid State Chem.* 139, 281 (1998).

474. W. L. Jido and T. Pinnavaia, *Chem. Mater.* 11, 3227 (1999).

475. M. E. Hagerman, S. J. Salomone, R. W. Herbst, and A. L. Payeur, *Chem. Mater.* 15, 443 (2003).

Dynamic Processes
in Magnetic Nanostructures

B. Hillebrands, S. O. Demokritov

Technische Universität Kaiserslautern, Kaiserslautern, Germany

CONTENTS

1. INTRODUCTION

The subject of this review is the dynamic properties of small magnetic elements made by patterning magnetic films and multilayers. Such elements generally receive very high attention, as they constitute, for example, magnetic sensors in magnetic read heads in hard discs or in magnetic random access memory. Because of the demand for higher speed of such sensors, the physical properties of fast magnetization processes came into the focus of interest in the last years. As one fundamental property, and this is the main subject of this review, the eigenexcitation spectrum of such elements in the linear excitation regime is of central interest. The availability of this basic knowledge is mandatory to understand dynamic processes, in particular those involved in fast switching of the magnetization direction, in general.

Magnetic elements show a large variety of dynamic excitations. The most fundamental one is the uniform precession, where the magnetization precesses about a common direction given by the direction of the internal field. Such a precession is sensed by the method of ferromagnetic resonance, a technique known since the 1970s.

A uniform precession can be regarded as a spin wave with zero wavevector. Modes with nonzero wavevector may exist as well. However, boundary conditions at the edges of the elements exist, which will cause a characteristic quantization into a discrete set of excitation modes, similar to the fundamental mode and the overtone modes of a guitar string.

It is the subject of this chapter to discuss the fundamental properties of the magnetic excitation spectrum in patterned magnetic elements. There exists a characteristic peculiarity in magnetic systems: since the elements are magnetized, they generate a magnetic stray field outside the elements. The interaction of the stray field with the internal distribution of magnetization results in an intrinsic inhomogeneity of the internal field distribution. Therefore magnetization dynamics demands an explicit consideration of spatially varying internal fields, which, on one hand, makes the problem more complex, on the other hand, results in new phenomena, like the localization of modes in certain regions within the element.

Magnetic phenomena in small objects are driven by two interactions: the exchange interaction, which inside the element leads to ferromagnetic order, and dipolar interaction. Stray fields usually play a very important role, and, although the stray field energy is orders of magnitude lower than exchange energy, we observe a large variety of effects, like coupling and particular modes. Exchange interaction, taking place on small distances below several nanometers only, appears in the spectra through the existence of short-wavelengths modes.

The outline of the chapter is as follows. After a short description of the preparation of patterned magnetic structures, we will describe in detail the spin wave spectrum in a restricted geometry. One central tool is the Brillouin light scattering technique, which will be discussed in Section 4. With increasing degree of complexity, we next discuss the excitation spectrum in various restricted geometries, beginning with the quantization of spin waves due to the lateral edges in magnetic stripes (Section 5) and in

dots (Sections 6–8). As an important side step, we discuss the static magnetic coupling in arrays of rectangular dots (Section 6) and the dynamic interdot coupling in arrays of circular dots (Section 7). An important physical phenomenon is the appearance of localization effects of spin waves in small elements due to the inhomogeneity of the internal field. This effect, which is reminiscent of localization effect in a potential in quantum mechanics, will be discussed in detail in Section 8. Section 9 concludes this review.

2. PREPARATION OF PATTERNED MAGNETIC STRUCTURES

The technology for fabrication of high-quality patterned magnetic structures with lateral extensions on the micrometer, submicrometer, and nanometer length scale has been perfected to a remarkable degree in the past decade [1–3].

Lateral magnetic structures are conveniently fabricated from magnetic films using lithographic patterning procedures. In the following, for simplicity, we will call structures with one restricted lateral dimension "stripes," and those with two restricted dimensions circular "dots" or rectangular "elements" following the usual conventions, although, as will be one of the subjects of this review, no real reduction of dimensionality is given since both in "stripes" and "dots" the magnetization is not constant over each magnetic object along a direction of restricted dimension.

It is usually extremely difficult to study a single magnetic element, since it challenges the sensitivity of the measurement setup [4]. To avoid this problem the elements under investigation are usually assembled in arrays. Changing the distance between elements in an array, one can additionally investigate the interaction between the elements.

Metallic Fe [5], FeNi [6–8], or Co [9, 10] films are mainly used for patterning. For fundamental studies FeNi films are preferable due to their smallness of the coercive field, the weak intrinsic magnetocrystalline anisotropy, and magnetostriction. The saturation fields of FeNi films are small, and the vanishing intrinsic anisotropy does not inhibit the observation of sometimes minute anisotropy effects caused by, for example, the shape of the elements or interactions between elements. However, patterned structures made on the basis of Co films allow one to investigate the interesting case of perpendicularly magnetized dots or stripes [9].

The patterning process is most often performed by means of electron beam lithography (EBL) [11–13], X-ray lithography (XRL) [14], and laser interference lithography (LIL) [15], followed by ion beam etching for pattern transfer. High-quality samples can be fabricated using all three processes, but each of them has its characteristic advantages and disadvantages.

The EBL technique is very versatile, and can provide a very high resolution down to 10 nm, but due to its serial character it is time consuming, in particular for large patterned areas. Figure 1 shows scanning electron micrographs of a dense array of permalloy magnetic rectangular elements demonstrating the quality which can be achieved by EBL.

In the XRL technique a resist is exposed to synchrotron radiation through a metallic mask. The technique possesses the potential to pattern large areas for standard magnetic
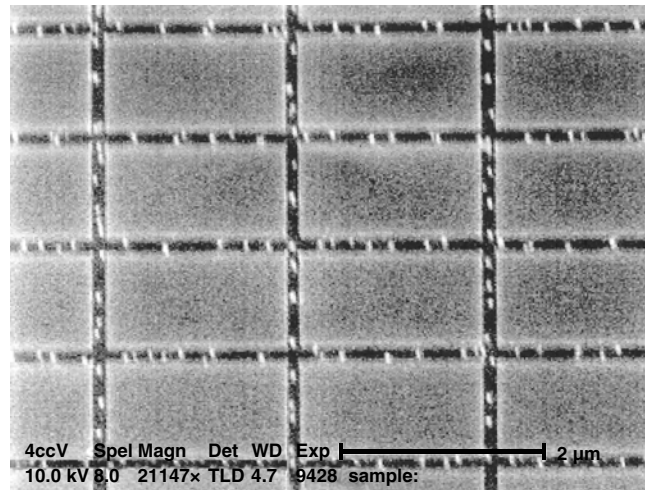
Figure 1. Scanning electron micrograph of an array of rectangular 1×1.75 μm^2 permalloy elements with a spacing of 0.1 μm. The structure is obtained by EBL. Reprinted with permission from [64], S. O. Demokritov and B. Hillebrands, *J. Magn. Magn. Mater.* 200, 706 (1999). © 1999, Elsevier Science.

measurements, and one can achieve a high fabrication yield for systematic studies versus, for example, film thickness or material composition. A resolution as low as 50 nm can be achieved using XRL [16] which allows the exploration of mesoscopic magnetic phenomena. The key step in XRL is the mask fabrication, which is performed using EBL. This is a rather complicated and time-consuming procedure. However, once prepared, a mask can be used for XRL patterning of hundreds of samples. Thus, XRL is a fast and convenient method, but the need of a synchrotron radiation source and a mask fabrication step restricts its applicability. Figures 2 and 3 show scanning electron micrographs of an array of stripes and circular dots, respectively, prepared by XBL.

LIL is a fast and easy process well suited for generating periodic arrays of stripes or ellipsoidally shaped dots on large areas with high coherency. Here the magnetic film coated with a photoresist is exposed to the interference pattern produced by two laser beams. Double exposure with a rotation of the sample of 90° or 120° generates patterns with fourfold or hexagonal symmetry.

Very recently ion beam [3, 17] and electron beam [18] irradiation were used for patterning of the magnetic properties of Co/Pt multilayers. The advantage of both techniques is that the patterning process does not affect the meso- and macroscopical roughness of the surface and the optical properties of the film. The ion beam irradiation technique takes advantage of a low-density displacement of atoms by light ion irradiation. The microscopical mechanism which causes the changes of the magnetic properties of a film by electron beam bombardment is still not clear [18, 19]. Ion/electron-beam-induced magnetic patterning allows one to create adjoining regions with very different magnetic properties, such as perpendicular versus in-plane magnetization.
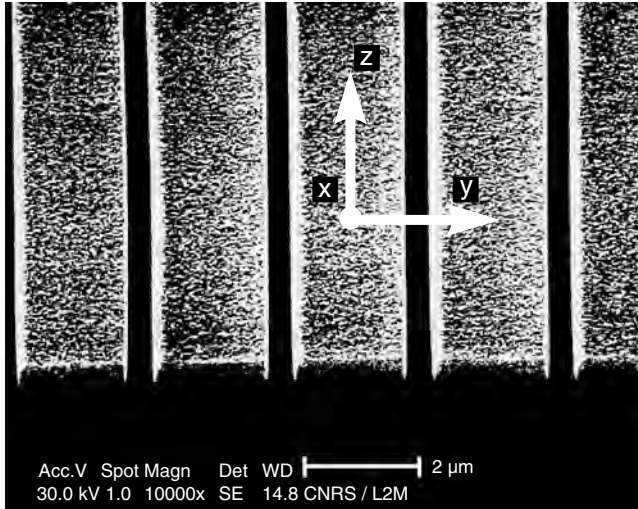
Figure 2. Scanning electron micrographs of permalloy stripes with a width of 1.8 μm and a separation of 0.7 μm. The structure is obtained by XBL. The orientation of the Cartesian coordinate system used for calculations is shown as well. Reprinted with permission from [64], S. O. Demokritov and B. Hillebrands, *J. Magn. Magn. Mater.* 200, 706 (1999). © 1999, Elsevier Science.

3. SPIN WAVE SPECTRUM IN RESTRICTED GEOMETRIES

The problem of the calculation of a spin wave spectrum for an axially magnetized infinite ferromagnetic stripe with a rectangular cross section has never been solved analytically (see, e.g., comments in [20]). However, in the particular case of a thin stripe with $d \ll w$, where d is the thickness of the stripe and w is its width, the spectrum of long-wavelength magnetic excitations can be calculated approximately using the theory of dipole-exchange spin waves in a magnetic film [21].
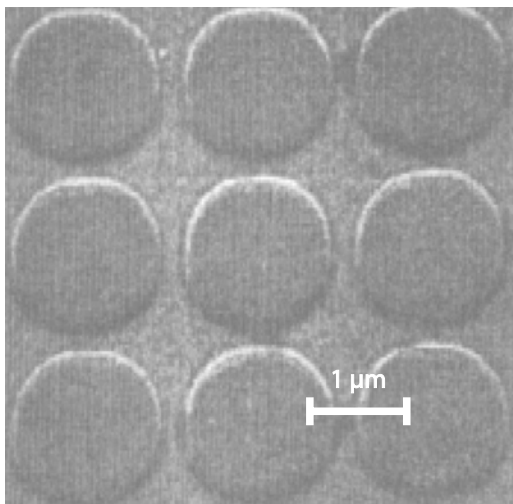
Figure 3. Scanning electron micrographs of the permalloy dots with a diameter of 1 μm and a separation of 0.1 μm. The structure is obtained by XBL. Reprinted with permission from [64], S. O. Demokritov and B. Hillebrands, *J. Magn. Magn. Mater.* 200, 706 (1999). © 1999, Elsevier Science.

The dipole-exchange spin wave spectrum in an unlimited ferromagnetic medium is given by the Herring–Kittel formula [22]

$$\nu = \frac{\gamma}{2\pi} \left[\left(H + \frac{2A}{M_S} Q^2 \right) \left(H + \frac{2A}{M_S} Q^2 + 4\pi M_S \sin^2 \theta_Q \right) \right]^{1/2} \tag{1}$$

where γ is the gyromagnetic ratio, A is the exchange stiffness constant, H and M_S are the applied magnetic field and the saturation magnetization both aligned along the z-axis, Q is the three-dimensional wavevector, and θ_Q is the angle between the directions of the wavevector and the magnetization.

In a magnetic film with a finite thickness d, the spin wave spectrum is modified due to the fact that the translational invariance of an infinite medium is broken in the vicinity of the film surfaces. An approximate expression for spin wave frequencies of a film can be written in the form, analogous to Eq. (1) (see Eq. (45) in [21]):

$$\nu = \frac{\gamma}{2\pi} \left[\left(H + \frac{2A}{M_S} Q^2 \right) \left(H + \frac{2A}{M_S} Q^2 + 4\pi M_S \cdot F_{pp}(q_\| d) \right) \right]^{1/2} \tag{2}$$

where

$$Q^2 = q_y^2 + q_z^2 + \left(\frac{p\pi}{d} \right)^2 = q_\|^2 + \left(\frac{p\pi}{d} \right)^2 \tag{3}$$

Here the normal to the film surface points along the x-direction. $q_\|$ is the continuously varying in-plane wavevector, $F_{pp}(q_\|, d)$ is the matrix element of the magnetic dipole interaction, and $p = 0, 1, 2, \ldots$ is a quantization number for the so-called perpendicular standing spin waves. Equation (3) is obtained under boundary conditions of "unpinned" spins on the film surfaces for the dynamic part m of the magnetization:

$$\left| \frac{\partial m}{\partial x} \right|_{x = \pm d/2} = 0 \tag{4}$$

For a general description of the spin wave modes one can use a more complicated boundary condition instead of the above one [23]:

$$\pm \frac{\partial m}{\partial x} + Dm|_{x = \pm d/2} = 0 \tag{5}$$

where the so-called pinning parameter D is determined by the effective surface anisotropy, k_S, and the exchange stiffness constant A: $D = k_S/A$. In the following the approximation $D = 0$ is justified by the small values of anisotropies in permalloy.

If the spin wave is propagating in the film plane, but perpendicular to the bias magnetic field ($q_z = 0$, $q_\| = q_y$), the expression for the matrix element of the dipole-dipole interaction $F_{pp}(q_\| d)$ has the form [21]

$$F_{pp} = 1 + \frac{4\pi M_S}{H + \frac{2A}{M_S} Q^2} (P_{pp}(1 - P_{pp})) \tag{6}$$

where the function $P_{pp}(q_\parallel, d)$ for the lowest thickness mode ($p = 0$) is given by [21]

$$P_{00} = \frac{1 - \exp(-q_\parallel d)}{q_\parallel d} \tag{7}$$

The explicit expressions for $P_{pp_\perp}$ when $p > 0_\perp$ are also given in [21] (see Eq. (A12) in [21]).

In a long-wavelength approximation ($q_\parallel d < 1$) neglecting exchange ($A = 0$), the dispersion equation for the lowest thickness mode ($p = 0$) obtained from Eqs. (6), (7) gives results that are very similar to the results obtained by Damoun and Eshbach [24]:

$$\nu_{DE} = \frac{\gamma}{2\pi} \cdot [H \cdot (H + 4\pi M_S) + (2\pi M_S)^2 \cdot (1 - e^{-2q_\parallel d})]^{1/2} \tag{8}$$

Thus, if the film is magnetized in-plane and $q_\parallel \perp M_S$, the spin wave modes described by Eqs. (3), (4), (6), (7) can be divided into the dipole dominated surface mode ($p = 0$, so-called Damon–Eshbach (DE) mode) and exchange dominated, thickness- or perpendicular standing spin wave (PSSW) modes ($p > 0$). The frequency of the former is determined by either Eq. (2) (with $p = 0$) or Eq. (8), while the frequencies of the PSSW modes ($p > 0$) can be approximately calculated from the expression

$$\begin{aligned}
\nu_p = \frac{\gamma}{2\pi} \Bigg[& \left(H + \frac{2A}{M_S}q_\parallel^2 + \frac{2A}{M_S}\left(\frac{p\pi}{d}\right)^2 \right) \\
& \cdot \left(H + \left[\frac{2A}{M_S} + H\left(\frac{4\pi M_S/H}{p\pi/d}\right)^2 \right] q_\parallel^2 \right. \\
& \left. + \frac{2A}{M_S}\left(\frac{p\pi}{d}\right)^2 + 4\pi M_S \right) \Bigg]^{1/2}
\end{aligned} \tag{9}$$

which is obtained from Eq. (2) in the limit $q_\parallel d \ll 1$ using the expressions for the dipole-dipole matrix elements $F_{pp}(q_\parallel d)$ calculated in [21]. It is clear from Eq. (9) that the $\nu_p(q_\parallel)$ dependence is rather weak for $q_\parallel \ll p\pi/d$. In the general case of $q_\parallel d > 1$, a numerical approach is usually used for the determination of the spin wave frequencies [25].

Equations (3), (6)–(9) provide a proper description of the spin wave frequencies apart from the intervals of mode crossing ($\nu_0 \approx \nu_p$), where an essential mode hybridization takes place. In these regions numerical calculations are also necessary to obtain the correct spin wave spectrum of the film [21, 25].

Let us consider a magnetic stripe magnetized in-plane along the $\hat{z}$-direction and having a finite width w along the $\hat{y}$-direction as shown in Figure 2. A boundary condition similar to Eq. (4) at the lateral edges of the stripe should be imposed:

$$\left| \frac{\partial \boldsymbol{m}}{\partial y} \right|_{y = \pm w/2} = 0 \tag{10}$$

An additional quantization of the y-component of $\boldsymbol{q}_\parallel$ is then obtained:

$$q_{y,n} = \frac{n\pi}{w} \tag{11}$$

where $n = 0, 1, 2, \dots$. Using Eqs. (2), (8), and (9) and the quantization expression (11), one can calculate the frequencies of these so-called width (or laterally quantized) modes. The profile of the dynamic part of the magnetization $\boldsymbol{m}$ in the nth mode can be written as

$$\boldsymbol{m}_n(y) = \boldsymbol{a}_n \cdot \cos\left(q_{y,n}\left(y + \frac{w}{2} \right) \right), \quad -\frac{w}{2} < y < \frac{w}{2} \tag{12}$$

Equation (12) describes a standing mode consisting of two counterpropagating waves with quantized wavenumbers, $q_{y,n}$. Note here, that due to the truncation of the cos-function at the stripe boundaries the modes are no longer infinite plane waves and the quantized value $q_{y,n}$ is not a true wavevector.

Taking into account the nonuniform dynamic part of the dipole dynamic field near the edges of the stripes $y = \pm w/2$, one obtains a boundary condition similar to Eq. (5) with the constant k_S determined by the aspect ratio of the stripe cross section [26]. The mode profiles in this case, however, cannot be written in a simple way as above.

The spin wave modes described above all possess a zero wavevector component along the stripe axis. If this is not the case, the spin wave quantization becomes much more complicated. Calculations of the quantized dipole-dominated surface modes in the case of an axially magnetized elliptical cylinder, somehow simulating a stripe, have been performed by de Wames and Wolfram [27, 28]. They showed that all modes can be characterized by a positive integer number and the wavevector component along the axis of the cylinder, q_z. The calculated surface mode frequencies are closely related to the Damon–Eshbach (DE) modes of an infinite film. For $q_z \neq 0$ no simple quantization scheme can be used, because a quantization parameter cannot be defined independent of q_z.

The above result gives an indication that spin wave quantization in magnetic elements with both lateral directions quantized is much more complicated than that of stripes. The development of an analytical theory describing spin wave quantization in circular dots is just beginning [29]. An essential complexity connected with the calculation of the spin wave spectrum of a dot is the nonuniform demagnetizing field within the dot. Contrary to a magnetic stripe magnetized along its axis, most parts of the side wall are noncollinear with the magnetization. Near these locations the demagnetizing field increases dramatically causing a nonuniform static magnetization near the edge even at moderate applied fields. In one-dimensional case the effect of the nonuniform internal field can be analyzed analytically. As it will be described below, a strongly inhomogeneous internal field causes a creation of spin wave wells. Up to now there is no full theory describing spin waves under such circumstances in two dimensions.

4. THE BRILLOUIN LIGHT SCATTERING TECHNIQUE

Two basic techniques, ferromagnetic resonance (FMR) and Brillouin light scattering (BLS), are mainly used for spin wave studies. In the field of patterned structures BLS has a number of advantages over FMR. These are (i) the potential to investigate spin waves with different absolute values

and orientations of their wavevectors; (ii) detection of thermally excited spin waves, that is, no need to excite spin waves with suitably high wavevectors; (iii) high spatial resolution defined by the size of the laser beam focus, which is 10–30 μm in diameter. The latter circumstance allows one to investigate small patterned areas, which simplifies the patterning procedure.

Brillouin light scattering is a spectroscopic method for investigating excitations with frequencies in the gigahertz regime. As illustrated in Figure 4, photons of energy $\hbar\omega_I$ and momentum $\hbar q_I$ interact with the elementary quanta of spin waves $(\hbar\omega, \hbar q)$, which are the magnons. The scattered photon gains an increase in energy and momentum:

$$\hbar\omega_S = \hbar(\omega_I + \omega)$$
$$\hbar q_S = \hbar(q_I + q) \tag{13}$$

if a magnon is annihilated. From Eq. (13) it is evident that the wavevector $q_S - q_I$, transferred in the scattering process, is equal to the wavevector q of the spin wave. A magnon can also be created by energy and momentum transfer from the photon, which in the scattered state has the energy $\hbar(\omega_I - \omega)$ and momentum $\hbar(q_I - q)$. For room temperature $(T_R \gg \hbar\omega/k_B \approx 1 \text{ K})$ both processes have about the same probability. In a classical treatment the scattering process can be understood as follows. Due to magneto-optical effects a phase grating is created in the material by a spin wave, which propagates with the phase velocity of the spin wave. Light is Bragg-reflected from the phase grating with its frequency Doppler-shifted by the spin wave frequency.

The differential light scattering cross section $d^2\sigma / d\Omega\, d\omega_S$, that is, the number of photons scattered into the solid angle $d\Omega$ in the frequency interval between ω_S and $\omega_S + d\omega_S$ per unit incident flux density, can be written as follows [30]:

$$\frac{d^2\sigma}{d\Omega\, d\omega_S} \propto \langle \delta\epsilon^*(q_I - q_S)\delta\epsilon(q_I - q_S)\rangle_{\omega_I - \omega_S} \tag{14}$$
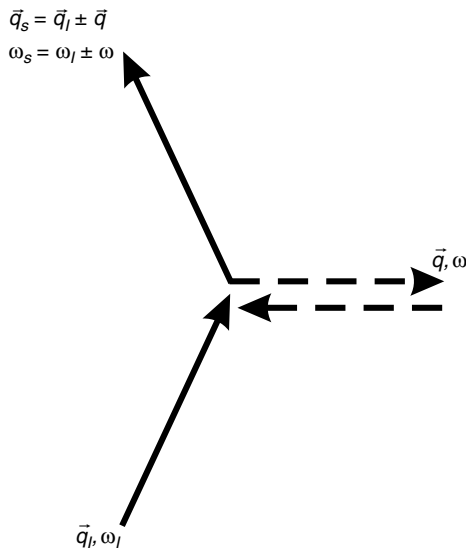
Figure 4. Scattering process of photons from spin wave excitations.

with $\delta\epsilon$ the dynamic (fluctuating) part of the dielectric permittivity, which is caused by the spin waves due to magneto-optical effects and which gives rise to the scattering. $\delta\epsilon$ is proportional to the dynamic part of the magnetization m of the spin wave. The correlation function is given by

$$
\begin{aligned}
\langle \delta\epsilon^*(q)\delta\epsilon(q)\rangle_\omega &= \int d(t_2 - t_1)d^3(r_2 - r_1) \\
&\quad \times \exp[-i\omega t - iq(r_2 - r_1)] \\
&\quad \times \langle \delta\epsilon^*(r_1, t_1)\delta\epsilon(r_2, t_2)\rangle \\
&\propto \int d(t_2 - t_1)d^3(r_2 - r_1) \\
&\quad \times \exp[-i\omega t - iq(r_2 - r_1)] \\
&\quad \times \langle m^*(r_1, t_1)m(r_2, t_2)\rangle
\end{aligned}
\tag{15}
$$

with $\langle \cdots \rangle$ the statistical average. If light is scattered from a spin wave propagating in an infinite medium, the spatial integration volume is the entire space. In this case the correlation function in Eq. (15) is nonzero only if the relations $\omega = \omega_S - \omega_I$ and $q = q_S - q_I$ are fulfilled, yielding the conservation laws of energy and momentum, described by Eq. (13). However, since for a spin wave mode propagating in a film the integration volume is bounded by the two film surfaces, the conservation conditions are fulfilled only for the two in-plane components of the wavevector, $q_\parallel$. In the backscattering geometry, when $q_S = -q_I$, $q_\parallel$ is determined by the angle of incidence of the light, θ: $q_\parallel = 2q_I \sin\theta$. The third component perpendicular to the film, q_n, is not well defined by the conservation law because the system does not possess the symmetry of translational invariance perpendicular to the film. The uncertainty in q_n is, apparently, inversely proportional to t, the thickness of the film or of the mode localization region, or the penetration depth of the light. It is negligible, if $(q_S - q_I)_n t \gg 2\pi$.

If now the *in-plane* translational invariance of the magnetic film is broken by patterning, the in-plane wavevector, $q_\parallel$, is no longer fully conserved in a light scattering process. In the case of a spin wave mode localized in a stripe, for example, the only conserved component is the component of $q_\parallel$ along the stripe axis. It is clear from Eq. (15) that the dependence of the differential light scattering cross section on the component of $q_\parallel$ perpendicular to the stripes is determined by the Fourier components of $m(y)$. We will discuss this in more detail later.

A typical experimental setup for BLS studies is schematically shown in Figure 5. Light of a frequency stabilized laser is focused onto the sample by an objective lens. The light scattered from the sample (elastic and inelastic contributions) is collected and sent through a spatial filter for suppressing background noise before entering the interferometer. The central part of the interferometer consists of two Fabry–Perot etalons FP1 and FP2. The tandem arrangement avoids ambiguities in the assignment of inelastic peaks to the corresponding transmission order [31, 32]. In order to obtain the high contrast necessary to detect the weak inelastic signals, the light is sent through both etalons several times using a system of retroreflectors and mirrors. The frequency selected light transmitted by the interferometer is detected by a photomultiplier or an avalanche photodiode
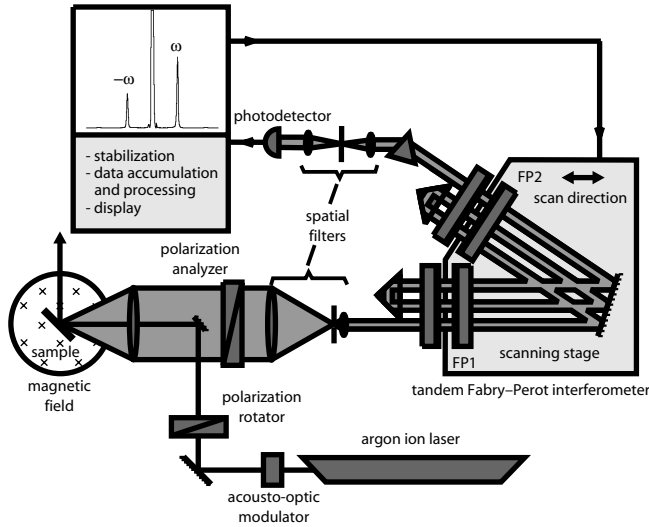
Figure 5. Schematic view of a Brillouin light scattering setup.

after passing through a second spatial filter for additional background suppression. A prism or an interference filter between the second spatial filter and the detector serves for suppression of inelastic light from common transmission orders outside the frequency region of interest. Data collection is performed by a personal computer or by a multichannel analyzer.

5. SPIN WAVE QUANTIZATION IN STRIPES

The spin wave excitation spectrum of arrays of ferromagnetic stripes was recently investigated by several groups [8, 10, 33–36].

An early investigation of BLS from spin waves in an array of magnetic stripes made of permalloy was performed by Gurney et al. [34]. The stripe thickness and width were 30 nm and 0.55 μm, respectively. The authors have observed a splitting of the spin wave spectrum into several discrete modes, but they were not able to identify the nature of the modes.

Ercole et al. [8] investigated arrays of stripes, fabricated from 60-nm-thick, Au captured FeNi films grown on GaAs (001) substrates. Stripe arrays were produced with stripe widths between 0.4 and 10 μm; the individual stripes were separated by twice their width. The spin wave frequencies were found to be sensitive to the size of the stripes, as well as to the in-plane angle of the wavevector of the spin waves demonstrating a clear twofold symmetry, obviously introduced by the symmetry of the stripe shape. Both effects have a magnetic dipolar origin and are due to demagnetizing fields caused by the stripe edges. The magnetic easy axis corresponds to the case when the stripes are parallel to the applied field. No evidence of any mode splitting was reported. The authors have simulated their experimental results by solving the Landau–Lifshitz torque equation with the dynamic magnetization profiles assumed to be homogeneous in each stripe. As a result, an expression for the spin wave frequency was obtained, which is similar to Eq. (17), describing the $q = 0$ resonance in finite samples.

Cherif et al. [10] studied spin waves in arrays of 40-nm-thick Co stripes with widths and periodicities on the micrometer scale. Contrary to FeNi, Co films possess an essential magnetic anisotropy with an effective field $H_a = 2.6$ kOe. Under a magnetic field parallel to the stripes, the frequency of the DE mode is higher than in the unpatterned film. For a magnetic field perpendicular to the stripe a significant variation of the frequency is observed, which is related to the size-dependent demagnetizing field. An additional, low-frequency mode which is not seen in the infinite film, was observed. The authors connect this mode with the uniform precession mode, which gives rise to a measurable BLS intensity in patterned, highly anisotropic structures.

Mathieu et al. [35] and Jorzick et al. [37] investigated spin wave excitations by BLS in arrays of FeNi stripes. In addition to demagnetization effects, a quantization of the spin wave mode in several dispersionless modes was observed and quantitatively described. This quantization is caused by a confinement effect of the spin waves in each stripe. It was not seen in the geometry when the wavevector of the detected mode was parallel to the stripes. Since these experiments provide the first account for a quantitative understanding of ($q \neq 0$) spin wave quantization effects in lateral structures, let us consider them in more detail.

The samples were made of 20-nm- and 40-nm-thick $Ni_{81} \cdot Fe_{19}$ films deposited in UHV onto a Si(111) substrate by means of e-beam evaporation. Patterning was performed using XRL with a following lift-off process with Al coating and ion milling [14]. The procedure is a high-quality patterning process, which provides a superb quality of the stripe boundaries. Several types of periodic arrays of stripes with stripe widths $w = 1, 1.7$, and 1.8 μm and with different stripe separations 0.2–2.3 μm were prepared. The length L of the stripes was 100–500 μm. The patterned area was 500×500 μm^2. One of the arrays studied in [35] and [37] is shown in Figure 2. An investigation of the magnetization reversal behavior of the structures, performed by Kerr magnetometry, showed that the magnetic easy axis of the array was along the stripe axis.

In a BLS experiment with backscattering geometry the in-plane wavevector $\boldsymbol{q}_{\parallel} = (\boldsymbol{q}_S - \boldsymbol{q}_I)_{\parallel}$, transferred in the light scattering process, was oriented perpendicular to the stripes, and its value was varied by changing the angle of light incidence, θ, measured from the surface normal: $q_{\parallel} = (4\pi/\lambda_{Laser}) \cdot \sin \theta$. The wavevector was oriented perpendicular to the stripe axes or along one of the edges of the elements. The absolute value of $q_{\parallel}$ was varied in the range of $(0–2.5) \cdot 10^5$ cm^{-1}. An external magnetic field $\mathbf{H}_e$ was applied in the plane of the samples. The collection angle of the scattered light was chosen small enough to ensure a reasonable resolution in $q_{\parallel}$ of $\pm 0.8 \cdot 10^4$ cm^{-1}. It is important to mention here once more that, strictly speaking, due to spin wave confinement in a stripe the transferred wavevector $\boldsymbol{q}_{\parallel}$ cannot be considered as the wavevector of the spin waves mode taking part in the scattering process and, thus, tested in the experiment. Because of the confinement the spin wave mode does not possess a well-defined wavevector.

Figure 6 shows a typical BLS spectrum for the sample with a stripe width of 1.8 μm and a separation between the stripes of 0.7 μm. A transferred wavevector $q_{\parallel} = 0.3 \cdot 10^5$ cm^{-1} was oriented perpendicular to the stripes, while an external field
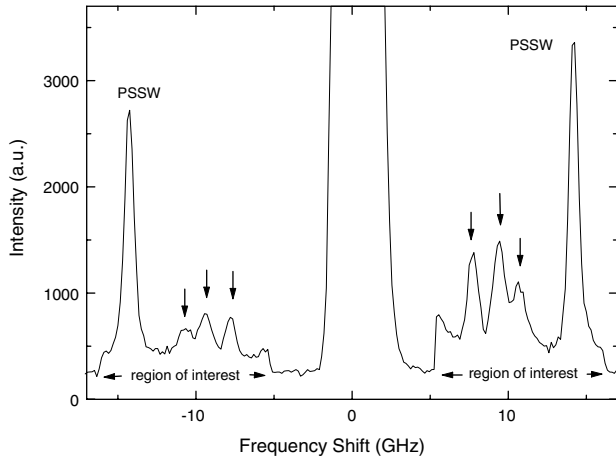
Figure 6. Experimental Brillouin light scattering spectrum obtained from the stripe array with a stripe thickness of 40 nm, a stripe width of 1.8 μm, and a separation between the stripes of 0.7 μm. The applied field is 500 Oe orientated along the stripe axis. The transferred wavevector of $q_{\parallel} = 0.3 \cdot 10^5$ cm^{-1} is oriented perpendicular to the stripes. The discrete spin wave modes are indicated by arrows. In the so-called region of interest (5–17 GHz) the scanning speed was reduced by a factor of 3, increasing the number of recorded photons by the same factor. Reprinted with permission from [64], S. O. Demokritov and B. Hillebrands, *J. Magn. Magn. Mater.* 200, 706 (1999). © 1999, Elsevier Science.

of 500 Oe was applied along the stripe axis. As it is seen in Figure 6, the spectrum contains four distinct modes near 7.8, 9.3, 10.4, and 14.0 GHz. Note here that in the region of interest (5–17 GHz), the scanning speed of the interferometer was reduced by a factor of 3 to increase the accumulation time in this region and, thus, to improve the signal-to-noise ratio. By varying the applied field the spin wave frequency for each mode was measured as a function of the field. The observed dependence of all frequencies on the field confirms that all detected modes are magnetic excitations.

To identify the nature of the observed modes, the dispersion of the modes was obtained by varying the angle of light incidence, θ, and, thus the magnitude of the transferred wavevector, $q_{\parallel}$. The results are displayed in Figure 7 for two samples with the same stripe thickness of 40 nm and width of 1.8 μm, but with different stripe separations of 0.7 μm (open symbols) and 2.2 μm (solid symbols). The dispersion measured on the arrays with the same lateral layout but with a stripe width of 20 nm is presented in Figure 8. It is clear from Figure 7 that one of the detected modes presented by circles (near 14 GHz) is the PSSW mode, corresponding to $p = 1$ in Eq. (9) (it is not seen in Fig. 8 due to its much higher frequency caused by the smaller stripe thickness). In the region of low wavevectors the spin wave modes show a disintegration of the continuous dispersion of the DE mode of an infinite film into several discrete, resonance-like modes with a frequency spacing between the lowest lying modes of approximately 0.9 GHz for $d = 20$ nm and 1.5 GHz for $d = 40$ nm. As it is clear from Figures 7 and 8, there is no significant difference between the data for the stripes with a separation of 0.7 μm and 2.2 μm. This fact indicates that the mode splitting is purely caused by the quantization of the spin waves in a single stripe due to its finite width.
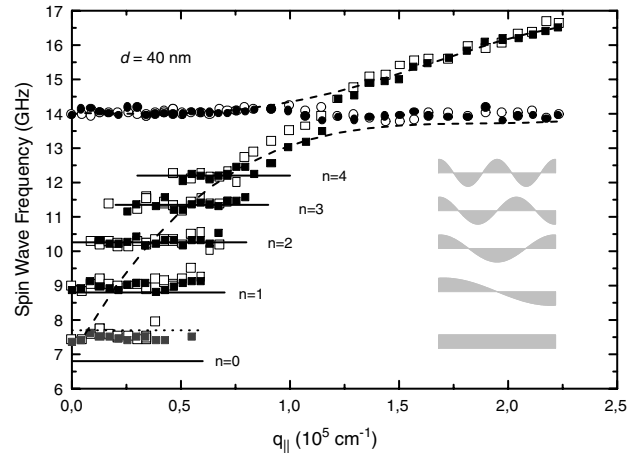
Figure 7. Obtained spin wave dispersion curves for an array of stripes with a stripe thickness of 40 nm, a stripe width of 1.8 μm, and a separation between the stripes of 0.7 μm (open symbols) and 2.2 μm (solid symbols). The external field applied along the stripes axis is 500 Oe. The solid horizontal lines indicate the results of a calculation using Eq. (8) with the quantized values of $q_{\parallel}$. The dotted horizontal line indicates the result of calculations for the mode $n = 0$ using Eq. (17). The dashed lines showing the hybridized dispersion of the Damon–Eshbach mode and the first perpendicular standing spin wave mode were calculated numerically for a continuous film with a thickness of 40 nm. On the right-hand side the mode profiles are illustrated. Reprinted with permission from [64], S. O. Demokritov and B. Hillebrands, *J. Magn. Magn. Mater.* 200, 706 (1999). © 1999, Elsevier Science.
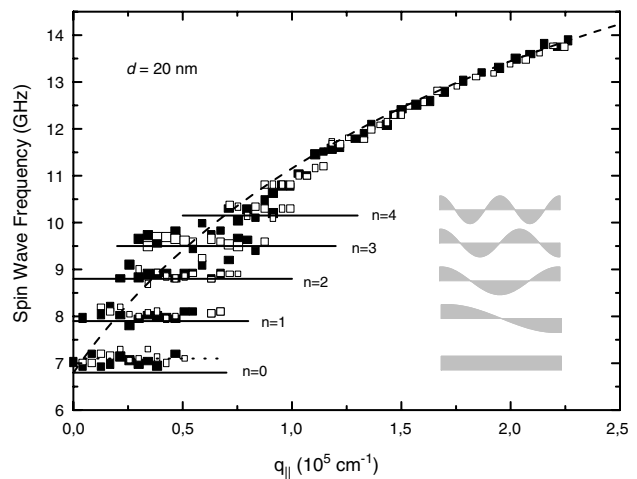
Figure 8. Obtained spin wave dispersion curves for an array of stripes with a stripe thickness of 20 nm, a stripe width of 1.8 μm, and a separation between the stripes of 0.7 μm (open symbols) and 2.2 μm (solid symbols). The external field applied along the stripes axis is 500 Oe. The solid horizontal lines indicate the results of a calculation using Eq. (8) with the quantized values of $q_{\parallel}$. The dotted horizontal line indicates the result of calculations for the mode $n = 0$ using Eq. (17). The dashed lines, showing the hybridized dispersion of the Damon–Eshbach mode and the first perpendicular standing spin wave mode, were calculated numerically for a continuous film with a thickness of 20 nm. On the right-hand side the mode profiles are illustrated. Reprinted with permission from [64], S. O. Demokritov and B. Hillebrands, *J. Magn. Magn. Mater.* 200, 706 (1999). © 1999, Elsevier Science.

As it is seen in Figure 7, the first PSSW mode ($p = 1$) was observed in the arrays with a stripe thickness of 40 nm for the entire investigated range of $q_\parallel$. It was used as a reference for relative measurements of the BLS scattering cross section, as it is described below.

Having a closer look at the dispersion curves and the BLS cross-section profiles of the magnetic stripes, one can summarize the main features as follows: (i) For low wavevector values (0–$0.8 \cdot 10^5$ cm^{-1}) the discrete modes do not show any noticeable dispersion, behaving like standing wave resonances. (ii) Every discrete mode is observed over a continuous range of the transferred wavevector $q_\parallel$. (iii) The lowest two modes appear very close to zero wavevector; the higher modes appear at higher values. (iv) The frequency splitting between two neighboring modes is decreasing for increasing mode number. (v) There is a transition regime ($q_\parallel = (0.8$–$1.0) \cdot 10^5$ cm^{-1}) where the well-resolved dispersionless modes converge towards the dispersion of the continuous film (see dashed lines in Figs. 7 and 8). (vi) There is no noticeable difference for the samples with the same stripe width w but different stripe separations (0.7 μm and 2.2 μm).

In order to understand the above experimental findings we need (i) to explain why every discrete mode is observed over a characteristic continuous range of transferred wavevectors, and (ii) to calculate the frequencies of the observed eigenmodes.

Since the discrete, dispersionless spin wave modes observed for small wavevectors converge towards the dispersion of the DE mode of the continuous film, it is natural to assume that these modes result from a width-dependent quantization of the in-plane wavevector of the DE mode, as discussed. As it was shown, the profile of the dynamic part of the magnetization, $\boldsymbol{m}$, in the nth mode is well approximated by a cosine-like shape (see Eq. (12)). On the other hand, the component of the transferred in-plane wavevector along the stripe axis, $q_{\parallel,z}$, is fully conserved in the light scattering process. Since in the described experiments $\boldsymbol{q}_\parallel$ was oriented perpendicular to the stripes, only the spin wave modes with $q_z = 0$, that is, $\boldsymbol{m}(z) = $ const, can take part in the scattering process. This and the fact that $d \ll w$ justifies writing Eq. (12) in a one-dimensional form, where $\boldsymbol{m}$ is considered to be a function of y only. In this case Eq. (15), which determines the light scattering intensity $I(q)$, can be essentially simplified:

$$I(q) \propto \frac{d^2\sigma}{d\Omega \, d\omega_S} \propto \langle \delta\epsilon^*(q)\delta\epsilon(q) \rangle \propto |m_q|^2$$

$$= \left| \int_{-w/2}^{w/2} m(y) \cdot \exp(-iqy) \, dy \right|^2 \qquad (16)$$

Note here that since the integration is performed only within the stripe, the Fourier transform m_q is nonzero over a continuous interval of q and, thus, the discrete modes are observed over a finite interval of the transferred wavevector $q_\parallel$. Substituting Eq. (12) in Eq. (16) and using Eq. (11), one can calculate the light scattering intensity $I_n(q)$ for each standing lateral mode. The results of this calculation and comparison with the experimental results for the stripes with their width $w = 1.8$ and 1 μm, normalized for the best fit of the $n = 0$ mode, are shown in Figure 9.
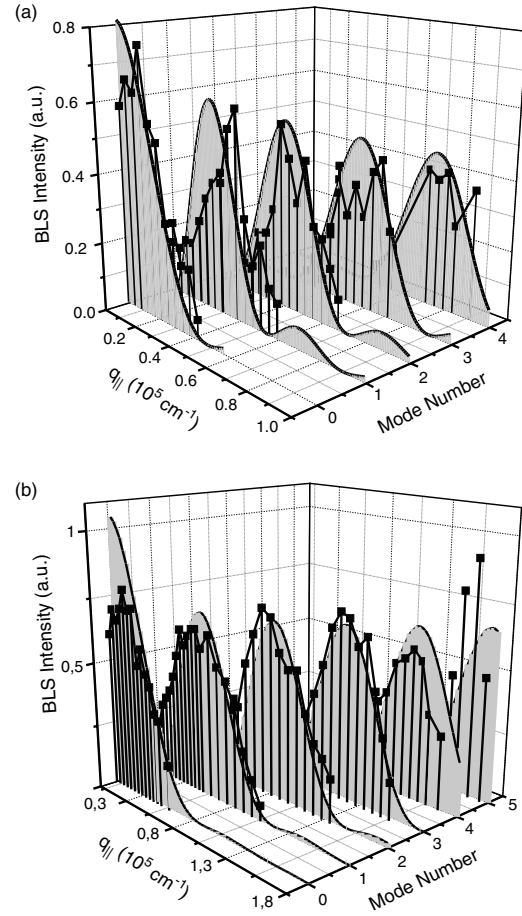
Figure 9. Measured relative BLS intensities (black squares) of the in-plane quantized spin wave modes as a function of the wavevector $q_\parallel$ and the mode number n in comparison to the calculated results based on Eq. (16) (gray colored curves). (a) Stripe width is 1.8 μm, (b) stripe width is 1 μm.

The measured light scattering intensity for these modes are also presented in Figure 9. Due to possible variations in the transmission of the interferometer during the course of the measurements, it is, in general, very difficult to measure absolute values of the BLS scattering cross section. To overcome this problem, the PSSW mode, registered for the entire investigated range of $q_\parallel$, was used as a reference for relative measurements of the BLS scattering cross section. The BLS intensity corresponding to each in-plane mode was normalized to the intensity of the PSSW mode. The relative intensities obtained in this way were very reproducible and were used for measuring the lateral distribution of the dynamic magnetization through the stripe using the approach discussed above. They are shown in Figure 9 by black squares. The very good agreement between the experimental data and the results of the calculation justifies the chosen boundary condition and confirms that the observed spin wave modes are in fact the quantized DE modes.

The frequency of the observed modes can be derived by substituting the obtained quantized values of the wavevector, $q_{y,n}$, into the dispersion equation of the DE mode, Eq. (8). The results of these calculations are shown for two arrays of stripes in Figures 7 and 8 by the solid horizontal

lines. For the calculation the geometrical parameters (stripe thickness $d = 20$ or 40 nm, stripe width $w = 1.8$ μm) and the independently measured material parameters $4\pi M_S = 10.2$ kG and $\gamma/2\pi = 2.95$ GHz/kOe were used. Without any fit parameters the calculation reproduces all mode frequencies with $n > 0$ very well, and for the $n = 0$ mode a reasonable agreement is achieved. Since the group velocity $V_g = 2\pi \partial\nu/\partial q$ of the DE spin wave (cf. Eq. (8)) decreases with increasing wavevector, the frequency splitting of neighboring, width-dependent discrete spin wave modes, which are equally spaced in q-space ($q_{y,n} = n\pi/w$), becomes smaller with increasing wavevector $q_{y,n}$, until the mode separation is smaller than the frequency resolution in the BLS experiment and/or the natural line width, and the splitting is no longer observable in Figures 7 and 8.

Although the spatial distribution and the frequencies of the observed modes are well reproduced, the above approach ignores the correction of dynamic dipole fields due to the finite width of the stripes. Since the magnetic dipole interaction is a long-range one, the strength of the field at a given position is determined not only by the amplitude of the dynamic magnetization in the vicinity of this position, but also by the spatial distribution of the dynamic magnetization far from this position. Therefore, due to finite size effects caused by the side walls, the dipole fields accompanying a quantized mode in the stripe differ from those of the DE mode of the infinite film with the same wavevector. This correction, which is small in any case for the stripes with a high aspect ratio, is negligible for all modes with sufficiently high quantum numbers (i.e., for modes with either p or n larger than zero). It is, however, observable for the lowest, uniform mode ($p = 0$, $n = 0$). The finite size effect can be easily taken into account for long stripes with ellipsoidal cross section since the dynamic dipole field is homogeneous in this case. The corresponding frequency is given by the Kittel formula [38]:

$$\nu = \frac{\gamma}{2\pi} \cdot [(H + (N_x - N_z) \cdot 4\pi M_S)$$
$$\cdot (H + (N_y - N_z) \cdot 4\pi M_S)]^{1/2} \qquad (17)$$

where N_x, N_y, and N_z are the demagnetizing factors along the $\hat{x}$-, $\hat{y}$-, and $\hat{z}$-direction in the stripe cross section (note here that the demagnetizing factor along the stripe, N_z, is negligible). In the particular case of a stripe with a rectangular cross section Eq. (17) is not exactly applicable, since the dynamic demagnetizing field is not homogeneous. However, since the thickness of the stripe is much smaller than its width ($d \ll w$), one can consider this field to be approximately homogeneous over the main part of the stripe in agreement with the analytical solution for demagnetizing fields of a rectangular prism found by Joseph and Schlömann [39]. The corresponding demagnetizing factors are: $N_y = 2d/\pi w$, $N_x = 1 - N_y$, $N_z = 0$. The calculated value of N_y is in good agreement with that obtained from static measurements. The frequency of the lowest mode calculated on the basis of Eq. (17) using the above demagnetizing factors is shown by a dotted horizontal line in Figures 7 and 8. The agreement with the experiment is convincing. It is much more complicated to take into account the finite size effects for the nonuniform modes. However, from the

qualitative considerations it is obvious that the correction of the demagnetizing fields (or demagnetizing factors) due to the finite size of the stripe rapidly decreases with increasing mode number. Therefore, good reproduction of the mode frequencies for $n > 0$ just on the basis of Eq. (17) is not surprising.

6. STATIC MAGNETIC COUPLING IN ARRAYS OF RECTANGULAR DOTS

Before we discuss in more detail the dynamics in films patterned in two dimensions, we first need to visit the static properties. This is the subject of this section. We present a study of the static magnetic properties of dense arrays, consisting of micron-size rectangular magnetic elements with small interelement spacings. Special attention is paid to the influence of the magnetic dipole coupling on the magnetization curves and magnetic domain configurations.

The rectangular elements with a thickness of 35 nm and lateral dimensions of 1×1 μm^2, 1×1.2 μm^2, and 1×1.75 μm^2 respectively were prepared for these studies. The spacing d between the elements was always chosen the same in both lateral directions. In addition several arrays with the same element size (1×1.75 μm^2) and different interelement spacings ($\delta = 0.1$ μm, 0.2 μm, 0.5 μm, and 1 μm) were prepared. The elements were arranged in arrays with overall dimensions of 800×800 μm^2. The high quality of the patterning process is evident from Figure 1, where a scanning electron micrograph of the elements with lateral dimensions of 1×1.75 μm^2 and a spacing of 0.1 μm is shown. Measurements of the magnetization curves were performed using longitudinal magneto-optic Kerr effect (MOKE) magnetometry with the magnetic field applied in the plane of the sample. The measured signal in this case is proportional to the in-plane magnetization component parallel to the applied field. The domain structures of the elements were monitored at room temperature by magnetic force microscopy (MFM). For imaging, two MFM microscopes, Solver MFM from NT-MDT and NanoScope IIIa from Digital Instruments, were used. The MFM tips were magnetized along the tip axis, that is, normal to the sample surface, making the MFM sensitive to the vertical component of the stray fields.

The unpatterned films are characterized by square shape magnetization loops with coercivities less than 2 Oe, which reflect the high quality of the films. Measured at different in-plane orientations of the applied magnetic field, the magnetization curves demonstrate quasi-isotropic properties of the films, an in-plane anisotropy field being below 1 Oe. The magnetization curves of the patterned arrays show higher coercivities and much higher saturation fields between 30 and 250 Oe. Typical examples of the magnetization curves measured by MOKE for the magnetic field applied along the long and short sides of the rectangles are presented in Figure 10.

The pronounced difference between the two curves reflects the anisotropic nature of static magnetic properties of the array. An arrow in Figure 10 indicates the experimentally determined saturation field $\mathbf{H_S}$ as an averaged value over two saturation fields H_{S1} and H_{S2} measured for different parts of the hysteresis loop. Such an averaging compensates the effect of the hysteresis.
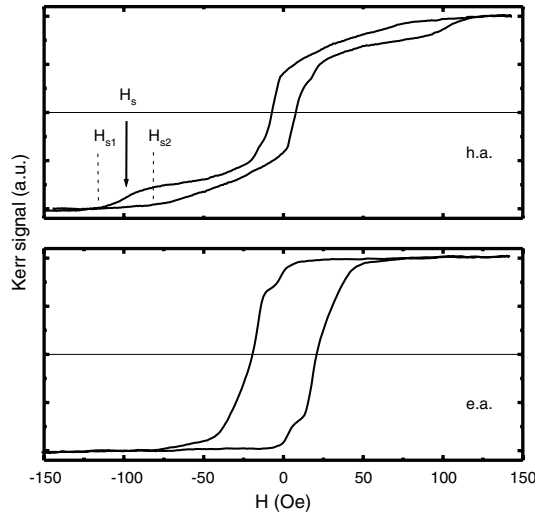
Figure 10. Typical magnetization curves of the array of $1 \times 1.75 \ \mu m^2$ elements with a spacing of $0.1 \ \mu m$ measured along their easy (e.a.) and hard (h.a.) axes using MOKE. The arrow indicates the value of the measured saturation field for the hard-axis curve determined as an averaged value of H_{S1} and H_{S2} measured for different parts of the hysteresis loop (shown is only H_S for the hard-axis curve).

Figure 11 shows the obtained saturation field versus the in-plane angle of the applied field for the arrays with different lateral dimensions of the elements, but with a fixed separation between the elements of $0.1 \ \mu m$. For the arrays of rectangles a twofold anisotropy with the easy axis lying along the long axis of the elements is clearly seen. The experimentally determined magnitude of the saturation field depends on the lateral dimensions of the elements, on the in-plane orientation of the applied field with respect to the rectangle sides, and on the distance between the elements in the array. To saturate the sample the applied field needs to be higher than the demagnetizing field which is determined by the
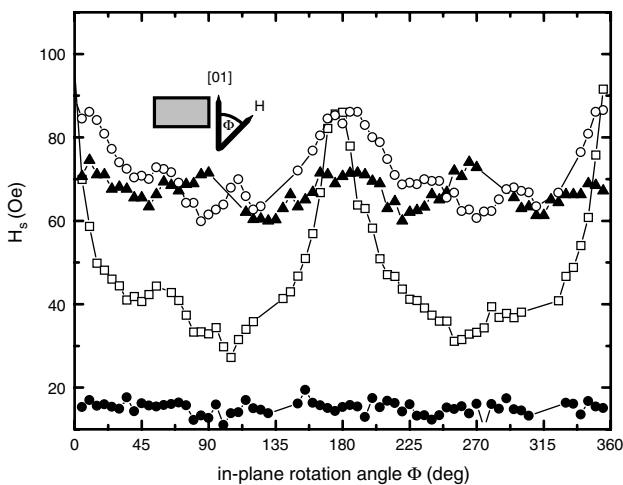
shape of the elements and the interelement distance. The effect is attributed to the element shape, as corroborated by a larger anisotropy observed for the elements with a higher lateral aspect ratio. For the array of squares a weak fourfold anisotropy caused by the inhomogeneity of the demagnetizing field is observed (configurational anisotropy), while the continuous film is almost isotropic in the plane, as is seen from the solid circles in Figure 11.

Although the observed magnetic anisotropy is strongly correlated with the shape of a single element, it depends on the interelement distance as well. The circles and the squares in Figure 12 show the saturation fields along the easy and hard axis (the long and short sides of the rectangles) measured as a function of the interelement spacing for the array of elements with the lateral size of $1 \times 1.75 \ \mu m^2$. For "zero spacing," that is, a continuous film, the data are shown for reference. A sizeable increase in the saturation field with increasing spacing and nearly a constant saturation field at higher spacing values demonstrate the fact that the interaction between the elements influences drastically the magnetization process of the array. For large spacings, that is, well above $1 \ \mu m$, the elements can be considered as noninteracting. In this case the saturation field of the arrays is determined by the demagnetizing field of an individual element. With decreasing separation between the elements, the demagnetizing fields of the neighboring rectangles partly compensate each other and the saturation field of the array is decreasing. The obvious limit of zero spacing is a nonstructured film with a very low saturation field, which is determined by the intrinsic coercivity of the film.

The influence of the magnetostatic interaction between the elements can be understood from the analysis of the magnetic dipole field of the interacting elements. For a uniformly magnetized array of rectangular elements this can be done rigorously using the approach developed in [40]. For calculating the dipolar fields we assume Cartesian coordinates with the x- and y-axes lying along the rectangle sides

Figure 11. The saturation field H_S as a function of the in-plane angle measured with respect to the short axis of the element: ●—unstructured film; —array of square $1 \times 1 \ \mu m^2$ elements with spacing $\delta = 0.1 \ \mu m$; □—array of $1 \times 1.75 \ \mu m^2$ elements with spacing $\delta = 0.1 \ \mu m$; and —array of $1 \times 1.2 \ \mu m^2$ elements with spacing $\delta = 0.1 \ \mu m$.
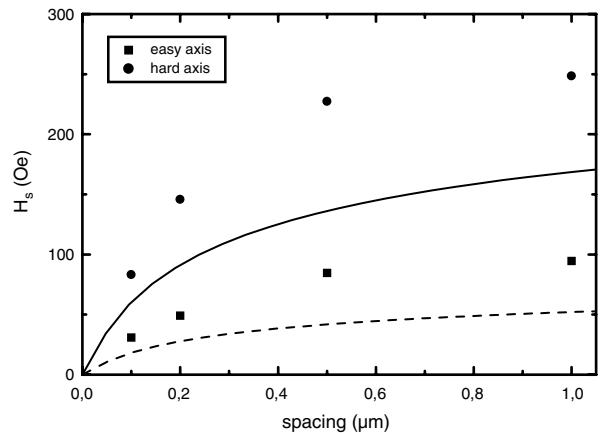
Figure 12. Measured (symbols) and calculated (lines) values of the saturation field H_S for the array of $1 \times 1.75 \ \mu m^2$ rectangular elements as a function of the interelement spacing δ. ● and the solid line—the field is along the short edge of the element (hard axis), ■ and the dashed line—the field is along the long edge of the element (easy axis). Reprinted with permission from [64], S. O. Demokritov and B. Hillebrands, *J. Magn. Magn. Mater.* 200, 706 (1999). © 1999, Elsevier Science.

of the size l_x and l_y, respectively, and the z-axis lying along the surface normal, as is shown in Figure 1. The origin of the system is placed in the center of an element, that is, the element occupies the volume of $-l_x/2 < x < l_x/2$, $-l_y/2 < y < l_y/2$, and $-h/2 < z < h/2$. The magnetization is assumed to be homogeneous across the element and oriented along the y-direction. The scalar potential which is produced by an infinitely thin layer of the array, lying within the xy-plane at height z, can be found using the following expression:

$$d\Phi(x, y, z') = dz' \int_{-\infty}^{\infty} dk_x \int_{-\infty}^{\infty} dk_y \frac{iMk_y}{\sqrt{k_x^2 + k_y^2}}$$
$$\times e^{-\sqrt{k_x^2+k_y^2}|z-z'|} \tilde{\xi}(k_x, k_y) e^{-ik_x x} e^{-ik_y y} \quad (18)$$

where the Fourier component of the two-dimensional array structure $\xi(x, y)$ is

$$\xi(k_x, k_y) = \frac{1}{2\pi} \int_{-\infty}^{\infty} e^{ik_x^x} dx \int_{-\infty}^{\infty} e^{ik_y^y} dy \xi(x, y),$$
$$= \frac{1}{2\pi} \left(\sum_{n=-\infty}^{\infty} \int_{nL_x-l_x/2}^{nL_x+l_x/2} e^{ik_x^x dx} \right)$$
$$\cdot \left(\sum_{m=-\infty}^{\infty} \int_{mL_y-l_y/2}^{mL_y+l_y/2} e^{ik_y^y dy} \right) \quad (19)$$

with the translation vectors of the array in the x- and y-direction $L_x = l_x + \delta$ and $L_y = l_y + \delta$. Substituting $\xi(x, y)$ in [1] and integrating over k_x and k_y, one obtains

$$d\Phi(x, y, z - z') = \frac{8\pi M \, dz'}{L_x L_y} \sum_{n,m=-\infty}^{\infty} \frac{ie^{-iq_x x} e^{-iq_y y}}{qq_x}$$
$$\times \sin\left(\frac{q_x l_x}{2}\right) \sin\left(\frac{q_y l_y}{2}\right) e^{-q|z-z'|} \quad (20)$$

where $q_x = \frac{2\pi}{L_x} n$, $q_y = \frac{2\pi}{L_y} m$ and $\sqrt{q_x^2 + q_y^2}$ are the vectors of the reciprocal lattice of the array. In order to calculate the potential of the entire structure, the expression (20) should be integrated over z' from $-h/2$ to $h/2$. For $-h/2 < z < h/2$, the result of the integration is written as follows:

$$\Phi(x, y, z) = \frac{8\pi M l_x l_y}{L_x L_y} \sum_{n,m=-\infty}^{\infty} \frac{ie^{-iq_x x} e^{-iq_y y}}{q^2 q_x} \sin\left(\frac{q_x l_x}{2}\right) \left(\frac{q_y l_y}{2}\right)$$
$$\times [2 - e^{-q(z+h/2)} - e^{q(z-h/2)}] \quad (21)$$

The magnetic field can be found by differentiating this expression in accordance with $\mathbf{H} = -\nabla\phi$. The y-component of the field $H_y(x, y, z)$, which is antiparallel to the magnetization and is therefore decisive for the remagnetization process, can be written as follows:

$$H_y(x, y, z) = -\frac{\partial\Phi}{\partial y} = \frac{8\pi M}{L_x L_y} \left\{ \sum_{m=l}^{\infty} \frac{l_x}{q_y} \sin(q_y y) \cos\left(\frac{q_y l_y}{2}\right) \right.$$
$$\times [2 - e^{q_y(z+h/2)} - e^{q_y(z-h/2)}] - \sum_{n,m=l}^{\infty} \frac{4q_y}{q^2 q_x}$$

$$\times \sin(q_x x) \sin(q_y y) \cos\left(\frac{q_x l_x}{2}\right) \cos\left(\frac{q_y l_y}{2}\right)$$
$$\left. \times [2 - e^{q_y(z+h/2)} - e^{q_y(z-h/2)}] \right\} \quad (22)$$

The calculated profile of the demagnetizing field over a single element in the array of the $1 \times 1.75 \ \mu m^2$ elements with $\delta = 0.1 \ \mu m$ is shown in Figure 13 for the magnetization lying along the short side of the element. Since the elements have a rectangular, nonellipsoidal shape, the demagnetizing field is not homogeneous. It is significantly enhanced in the zones near the edges of the element perpendicular to the magnetization. Thus, the saturation of the entire element occurs at higher fields compared to the demagnetizing field in the center of the element H_{d0}. The process of the element magnetization can be divided into three steps: (i) the applied field is below H_{d0}—a domain walls movement and/or a rotation of the magnetization in the domains take place; (ii) the applied field exceeds H_{d0}—the main part of the element is magnetized into the new field direction; (iii) the applied field approaches and then exceeds the much higher value of the demagnetizing field near the edges—the entire element is saturated. Thus, from the experimental point of view, a fast increase of the element magnetization during step (ii), followed by a very slow saturation at high fields, can be considered as a partial saturation of the main part of the element.

The calculated demagnetizing field H_{d0} in the center of the element, that is, for $x = y = 0$, averaged over z, is plotted in Figure 12 as a function of the distance between the elements δ. This field mainly determines the experimentally measured saturation field, which is also shown in Figures 12 and 13. As it is seen in Figure 12, both fields gradually increase with increasing δ. This increase reflects the fact that magnetic poles of opposite sign, which belong to neighboring rectangles, become more and more separated, reducing
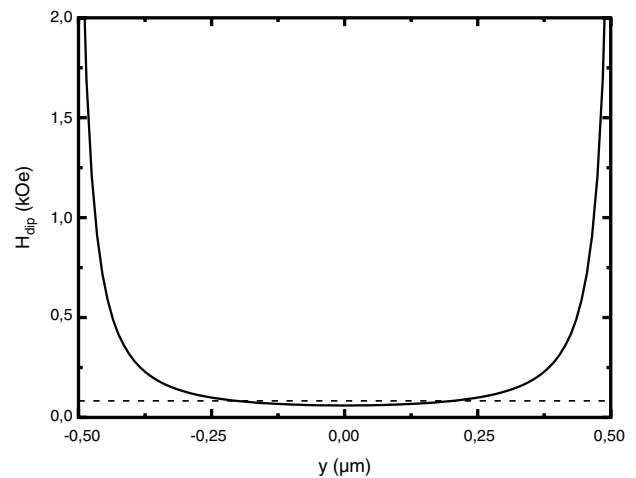
Figure 13. The profile of the magnetic dipolar field across the element at $x = 0$ for the array of $1 \times 1.75 \ \mu m^2$ elements with spacing $\delta = 0.1 \ \mu m$ for the magnetization lying along the short side of the element. The dipolar field is averaged over the thickness of the element h. Note that the field is oriented opposite to the magnetization direction. The dashed horizontal line indicates the experimentally measured value of the saturation field.

the diminishing effect on the resulting dipolar field. In the limit of large separations the calculated dipolar field of the array saturates and it becomes characteristic for an individual rectangular prism [41]. The calculated dipolar field H_{d0} reproduces qualitatively the behavior of the measured saturation field: both fields grow with increasing δ and become almost constant for $\delta > 0.7$ μm. The lack of the quantitative agreement is a consequence of the inhomogeneity of the demagnetizing field over the element dimensions, as it is discussed above. To take this into account one needs to solve the problem self-consistently implying a nonuniform distribution of the magnetization.

For a deeper insight into the magnetic ground state of a single rectangular element, MFM images of the samples were measured at zero field. It was found that the remanent domain structure depends drastically on the demagnetization history. If a moderate magnetic field of 100–150 Oe is applied along the long edge of the element, the so-called S- and C-domain states are observed. If the field is applied along the short edge of the element, the Landau state is observed on the majority of the elements. In addition the MFM imaging process slowly changes the domain pattern. After several imaging cycles many elements show a diamond-like domain pattern. This pattern completely avoids 180° walls and consists of 90° walls only. The observed domain patterns are presented in the upper panel of Figure 14. It is worth noting here that the MFM tips covered by carbon caps do not affect the domain patterns. For a relatively large separation between the elements the observed domain patterns can be simulated by considering the micromagnetic behavior of a single element. The numerical approach, based on a direct solution of the Landau–Lifshitz–Gilbert torque equation, was applied for this purpose (OOMMF program package [42]). It is evident from Figure 14 that the modeling demonstrates excellent agreement between the calculated and measured domain configurations (compare the top and bottom
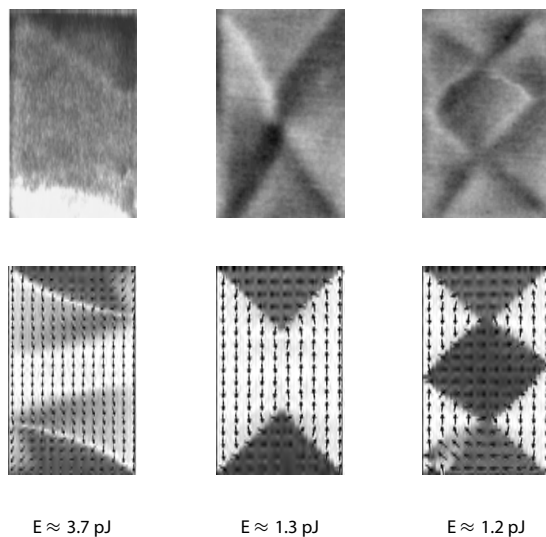
panels in Fig. 14). As was found by the modeling, the three domain configurations have different energies, the lowest energy given by the diamond-like configuration. This implies that the S-domain structure and the Landau structure are metastable and can be brought to the diamond-like state by a corresponding perturbation. In our case the stray field of the MFM tip is such a perturbation.

A significant interelement interaction in the arrays with small spacings becomes obvious from the MFM images. Figure 15 shows two MFM images (6.5×9 μm^2) for the array of 1×1.75 μm^2 elements with $\delta = 0.1$ μm at two different external fields. In order to magnetize the array, a high field of 120 Oe was applied along the long side of the elements before imaging. As is evident from Figure 15, the magnetization close to the short edges of the elements tends to rotate towards the direction parallel to these edges, forming the S-domain structure. At high fields (not shown) these edge domains are rather narrow, but in remanence they cover extended triangular areas, as can be seen in Figure 15. The resulting magnetic charges are positioned close to the short edges of the elements and are imaged in the dark and light shades. Their respective positions for each individual element indicate the dominant direction of the magnetization within the elements. Figure 15a shows the domain configuration, which was recorded after decreasing the external field and reaching a weak reverse field
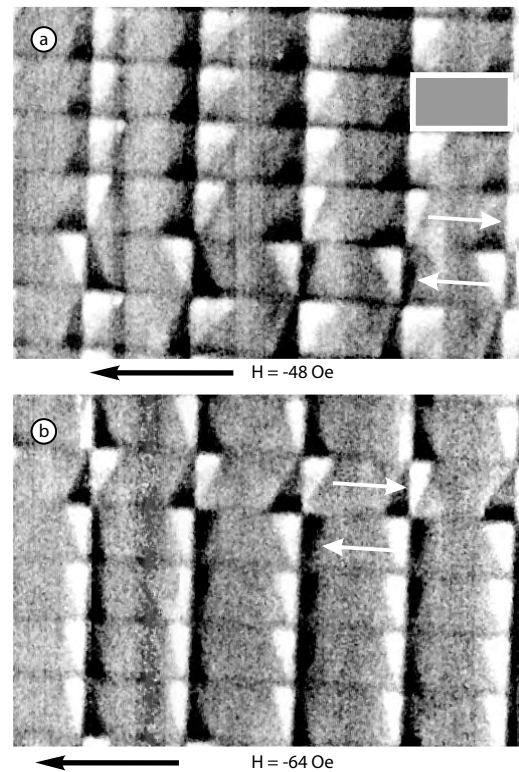

Figure 15. MFM images (6.5×9 μm^2) of the array of the 1×1.75 μm^2 rectangular elements recorded during a magnetization reversal process. The sample was magnetized at 120 Oe. (a) MFM image taken at -48 Oe. The gray rectangle indicates a single element; the white arrows indicate the main orientation of the magnetization within the element. (b) MFM image taken at -64 Oe.

E ≈ 3.7 pJ   E ≈ 1.3 pJ   E ≈ 1.2 pJ

Figure 14. Comparison between the experimental (upper panel) and simulated domain patterns (lower panel) of 1×1.75 μm^2 rectangular elements. The total energies of the pattern obtained in the simulations are also shown.

of 48 Oe. The fact that the magnetization reversal process has been already initiated manifests itself in the second row of elements from the bottom. Here the entire row has been switched to the opposite magnetization direction. An increase in the reverse field up to 64 Oe results in switching all the rows excluding the second row from the top, which remains in the initial configuration.

Figure 15 demonstrates a significant intrarow interaction, which keeps the elements within one row in a common magnetization direction. In this case the inter-row interaction strength is much weaker. Nevertheless, it can be observed after ac demagnetization of the sample. Figure 16a and b displays two zero-field MFM images, recorded after demagnetizing the sample in an ac field along the long and short axes of the elements, respectively. As is seen from Figure 16a, each individual element still carries a net magnetization and shows the triangular edge domains, similar to those in Figure 15. A significant intrarow interaction is evident from the fact that all the elements in a row are found in the same magnetization direction, that is, each row still carries macroscopic nonzero magnetization. By comparing the black-white contrast for the rows one finds, however, that the magnetization alternates in most cases from pointing to the right to pointing to the left for the neighboring rows. As a result, although the elements and even the rows still carry the net magnetization, the overall magnetization of the sample is compensated to zero by the alternating magnetization directions of the rows. The presence of an inter-row interaction is also evidenced by a high number of cases where the edge domains of four neighboring islands

Figure 16. Remanence MFM images (6.5×9 μm^2) of the array of the 1×1.75 μm^2 rectangular elements after demagnetizing in ac fields. (a) Demagnetizing field is along the long edge of the element. (b) Demagnetizing field is along the short edge of the element.

show a strong correlation between the rows. They tend to form a structure with an alternating black-white contrast, which allows an effective flux closure on a local scale.

One might expect that a configuration with a demagnetized state for each single element is energetically more favorable. As is obvious from Figure 16b, such a situation can indeed be generated after ac-demagnetizing the sample along the short axis. Now one finds the elements in the Landau state with some of the elements displaying a single cross-tie to be present within the central 180° wall, as it was also seen for isolated permalloy elements [43]. Since the net magnetization of the Landau state is smaller than that of the S-state, the interelement coupling is not apparent in Figure 16b.

7. DYNAMIC INTERDOT COUPLING IN ARRAYS OF CIRCULAR DOTS

Up to now there exist very few studies of spin waves in magnetic dot arrays [5–7, 44]. This is definitely connected to the fact that, on one hand, it is much more difficult to prepare dots with a well-defined shape. On the other hand, the magnetic signal from dots is lower than that from stripes simply due to the lower coverage of the surface by the magnetic material.

Grimsditch et al. [5] investigated submicron Fe magnetic dot arrays by BLS with dots of ellipsoidal shape. They showed that the shape anisotropy of individual dots is a dominant source of anisotropy, measured both by static magnetometry and BLS. The measured spin wave frequencies are in good agreement with values calculated on the basis of isolated ellipsoids using Eq. (17). No interdot coupling was observed.

Hillebrands et al. [6, 44] investigated spin wave properties of square lattices of micron-sized circular dots of permalloy with varying dot separations. Different samples comprising circular dots arranged in a 1×1 mm^2 square lattice with a diameter/separation of 1/0.1, 1/1, 2/0.2, and 2/2 μm, respectively, patterned into 500- and 1000-Å-thick films were prepared. Special care was taken to avoid a touching of neighboring dots even for the smallest separation. This was confirmed by depth profile measurements. The measured spin wave frequencies of the different dot arrays as a function of the applied field are shown in Figure 17. For each dot array the spin wave frequencies decrease with decreasing field, and they disappear below certain critical applied fields. The strong reduction of the spin wave frequencies with decreasing aspect ratio L/d is also seen in Figure 17. This is caused by size-dependent demagnetizing fields, that is, the demagnetizing factor $N_\parallel$ of each magnetic dot decreases with the aspect ratio. The solid lines in Figure 17 are calculated on the basis of Eq. (8), where the applied magnetic field is substituted by the internal field in the dot. The latter is calculated using demagnetizing factors of spheroids with axial ratios taken from the aspect ratios of the magnetic dots. Although spheroids are a crude approximation to the real three-dimensional shape of the dots, the calculation is in reasonably good agreement with the experimental data for $H > N_\parallel \cdot 4\pi M_s$.

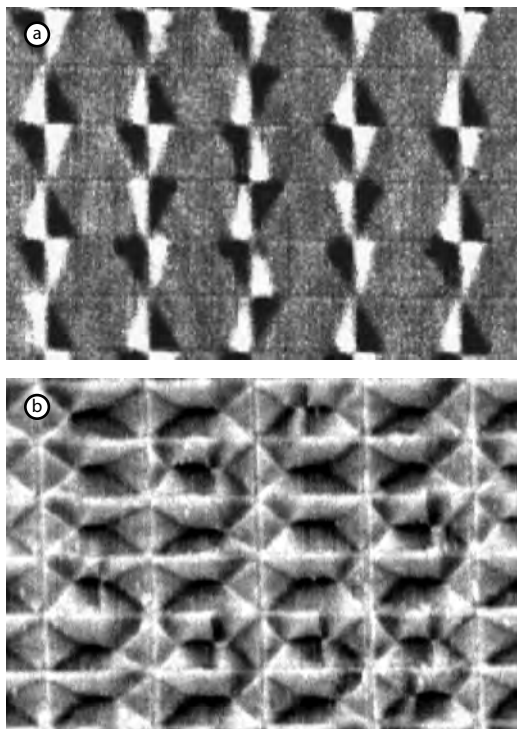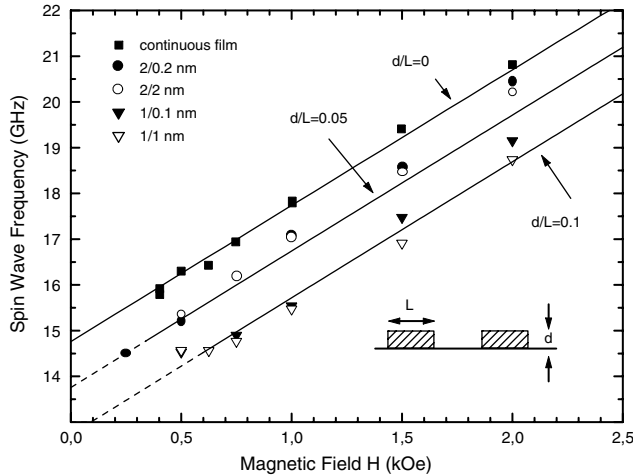To investigate the problem of an in-plane interdot coupling, the spin wave frequencies were measured as a function

Figure 17. Measured spin wave frequencies of the dot arrays with a dot thickness of $d = 100$ nm as a function of the magnetic field. The solid lines represent the calculated frequencies on the basis of Eq. (8) with substitution of the applied field by the internal field in the dot. Reprinted with permission from [64], S. O. Demokritov and B. Hillebrands, *J. Magn. Magn. Mater.* 200, 706 (1999). © 1999, Elsevier Science.

of the angle of the in-plane applied field, Φ_H, with respect to a reference [10]-direction of the lattice arrangement. For the smallest dot separations of 0.1 μm a fourfold anisotropic behavior was found, which was seen neither for larger dot separations nor for the unpatterned reference film. This is displayed in Figure 18 for the 1/0.1 μm and, for comparison, for the 1/1 μm lattices of the sample of 100 nm thickness at an applied field of 1 kOe. Note here that the easy axes (maximum frequencies) of the observed anisotropy are along the [11]-directions of the lattice. To determine quantitatively the
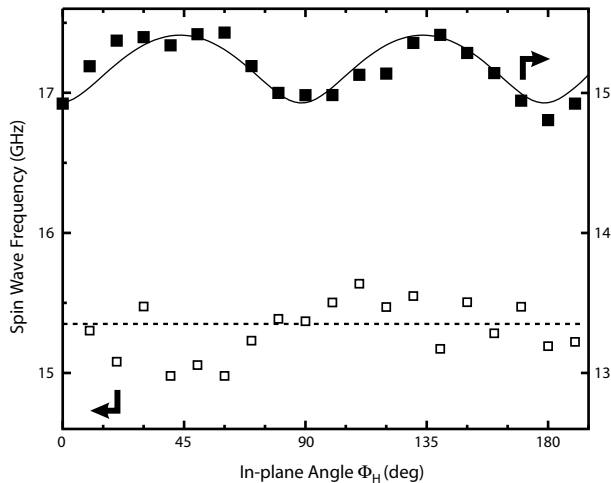
Figure 18. Dependence of the spin wave frequencies on the in-plane direction of the applied field for the 1/0.1 mm (full squares) and, for comparison, for the 1/1 mm (open squares) dot arrays of 100 nm thickness. The solid line is a fit for the data. Note that maximum values of the spin wave frequencies indicate an easy axis. Reprinted with permission from [64], S. O. Demokritov and B. Hillebrands, *J. Magn. Magn. Mater.* 200, 706 (1999). © 1999, Elsevier Science.

anisotropy constant, the free energy expression is

$$F = K^{(4)} \sin^2 \Phi \cdot \cos^2 \Phi \qquad (23)$$

with Φ the angle between the direction of magnetization with respect to the [10]-direction, and $K^{(4)}$ the constant of a fourfold in-plane anisotropy. A model fit using Eq. (23) and a numerical procedure to calculate the spin wave frequencies [45] is displayed in Figure 18 as a solid line for the 1/0.1 μm lattice. For both 1/0.1 μm samples with thicknesses of 50 nm and 100 nm, the anisotropy contribution $K^{(4)}$ was determined for several values of the applied magnetic field.

The obtained values of $K^{(4)}$ decrease with increasing field, and they saturate within the investigated field range at $K^{(4)} = -0.6 \cdot 10^5$ erg/cm^3, which corresponds to an effective anisotropy field $H_{ani} = 150$ Oe, at the same reduced field value of about $H/H_d = 5$ with H_d the demagnetizing field. As a function of the reduced field, H/H_d, the data of both dot thicknesses fall onto one common curve within the error margins indicating that the coupling strength scales with the demagnetizing field.

The observed fourfold anisotropy can be understood as being caused by a magnetic dipolar interaction between residual unsaturated parts of the dots. This effect is known as "configurational anisotropy" [46]. Because of the large distance of 0.1 μm between the dots, a direct exchange mechanism via conduction electrons or via electron tunneling can be excluded. A dipolar interaction of completely magnetized dots also cannot account for the observed anisotropy, because the corresponding dipolar energy can be expressed as a bilinear form of the components of the magnetization vector. Such an expression can only yield an uniaxial, but not a fourfold anisotropy contribution, since in a bilinear form the direction cosines appear quadratic in highest order and add to a constant if a fourfold symmetry is given. But, if the dots are not completely saturated, the magnetic dipolar interaction energy cannot be expressed in the above bilinear form, and the fourfold anisotropy is no longer forbidden. The large observed decrease of the coupling anisotropy constant with increasing field, forcing the alignment of the magnetization with the field, corroborates this assumption. Similar effect of higher-order magnetic anisotropies caused by the shape of the dot has been recently observed in static measurements [46].

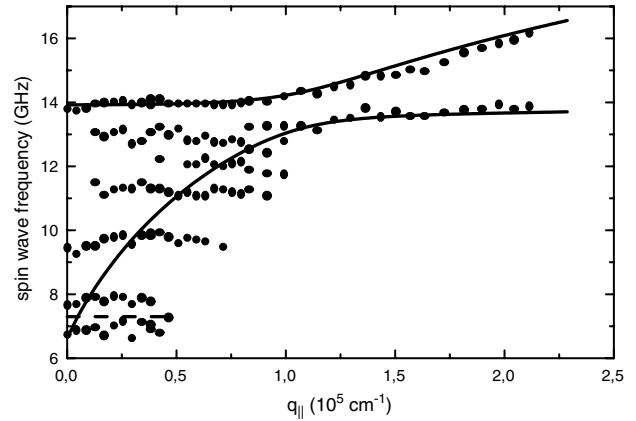Cherif et al. [7] studied magnetic properties in periodic arrays of square permalloy dots. The spin wave frequencies were found to be sensitive to the size of the dots and, for the smallest structures, to the in-plane direction of the applied field. While the size dependence can be reasonably explained to originate from the demagnetizing field effect, the in-plane anisotropy should be discussed in more detail. The authors observed a fourfold anisotropy in the spin wave frequencies as a function of the in-plane angle of the external field. The spin wave frequencies show maxima for the magnetic field applied along the edges of the squares, indicating easy axes of anisotropy along the edges. Contrary to the results of Hillebrands et al. [6, 44], the authors did not demonstrate that the observed anisotropy is caused by inter-dot interaction; instead they argue that it may be a single-dot effect. In fact, dots of square shape possess a lower symmetry compared to circular shaped dots. Therefore, shape

effects (corner effects for the magnetization, confinement of the spin wave mode, etc.) can cause this anisotropy. The spin wave mode splitting caused by confinement of the spin waves and corresponding quantization of the wavevector was not observed as well.

Jorzick et al. [47] investigated square lattices of circular permalloy micron dots, similar to those used in [6, 44]. The only difference was the smaller thickness of the dots of $d = 40$ nm. Figure 19 shows the anti-Stokes side of a typical BLS spectrum for $q_\parallel = 0.42 \cdot 10^5$ cm^{-1} of an array with a dot diameter of 2 μm and a dot spacing of 0.2 μm at $H = 600$ Oe. Similar to the results obtained from the studies of magnetic stripes, several peaks, corresponding to in-plane quantized spin wave modes, as well as an exchange dominated, perpendicular standing spin wave mode are seen in Figure 19. By changing the angle of light incidence the value of $q_\parallel$ is varied and the dispersion of the observed mode is obtained as demonstrated in Figure 20 for the array of dots with 2 μm dot diameter and 0.2 μm dot separation. As it is seen in the figure, at least seven discrete dispersionless modes are detected in the wavevector interval, $q_\parallel = (0–0.8) \cdot 10^5$ cm^{-1}. For large values of $q_\parallel$ ($>1 \cdot 10^5$ cm^{-1}) only two well-defined spin wave modes are observed. Using a numerical procedure [45], the frequencies of the DE mode and the first perpendicular standing spin wave mode for a continuous film of same thickness ($d = 40$ nm) were calculated. The results of the calculation are plotted in Figure 20 as full lines. A good agreement between the experimentally measured and the calculated dispersion curves for $q_\parallel > 1 \cdot 10^5$ cm^{-1} demonstrates the fact that for large transferred wavevectors ($2\pi/q_\parallel \ll D$) the measured dispersion converges to the dispersion of a continuous film of the same thickness.

In the transition region between well-resolved multiple modes and the dispersion of the continuous film ($q_\parallel \cong (0.8–1) \cdot 10^5$ cm^{-1}) the mode separation is close to the BLS

Figure 20. Obtained spin wave dispersion curve for a square array of dots with a dot thickness of 40 nm, a dot diameter of 2 μm, and a dot separation of 0.2 μm. An external field of 600 Oe was applied in-plane along the axis of the array lattice. The solid lines show the results of a spin wave calculation for a continuous film of the same thickness as the dots. The dashed line marks the calculated frequency of the uniform mode of a single dot. Reprinted with permission from [64], S. O. Demokritov and B. Hillebrands, *J. Magn. Magn. Mater.* 200, 706 (1999). © 1999, Elsevier Science.

instrumental line width, and therefore separate modes cannot be resolved. Broad peaks are observed in the BLS spectra. A decrease of the frequency splitting between the modes observed at high values of wavevectors has been found for magnetic stripes [35]. It is due to the fact that the group velocity $V_g = \delta\omega/\delta q$ of the DE mode decreases with increasing wavevector. In the case of stripes, where the spin wave modes are characterized by quantized equidistant wavenumbers $q_{\parallel, n}$ (see previous section), this fact necessarily leads to a monotonical decreasing frequency splitting between the neighboring modes. Two-dimensional quantization conditions in a circular dot are not so simple, as are those for the stripes. Therefore, the splitting between the quantized modes in the dots does not follow the simple rule, but still we observe a small splitting at high wavevectors in dots as well.

The frequency of the uniform mode of a single disc ($\omega = 7.35$ GHz) calculated by means Eq. (17), using the values of the demagnetizing factors obtained from separate static magneto-optic Kerr magnetometry, is shown as a horizontal dashed line in Figure 20. The calculations clearly demonstrate that the two lowest quantized modes have frequencies near the frequency of the uniform mode.

The five lowest spin wave modes of arrays of dots with the same dot thickness $d = 40$ nm as presented in Figure 20, but with a smaller dot diameter ($D = 1$ μm), are shown in Figure 21 for two different dot spacings. From a comparison of the data presented in Figures 20 and 21 it is seen that the wavevector interval, where each mode is observed, scales approximately as the inverse dot diameter, D^{-1}. For example, the two lowest modes of the dots with the diameter of 2 μm are observed in the wavevector interval $q_\parallel \cong (0–0.5) \cdot 10^5$ cm^{-1}, whereas the same modes of the dots with the diameter of 1 μm are observed at $q_\parallel \cong (0–1) \cdot 10^5$ cm^{-1}. This result is in agreement with the theoretical analysis performed in [35], which has shown that the

Figure 19. Obtained BLS spectrum for a square array of dots with a dot diameter of 2 μm and a dot separation of 0.2 μm for the transferred wavevector $q_\parallel = 0.21 \cdot 10^5$ cm^{-1} with an external field of 600 Oe applied in-plane demonstrating the existence of several discrete spin wave modes. The peaks corresponding to laterally quantized modes are indicated by arrows. In the so-called region of interest the scanning speed was reduced by a factor of 8, increasing the number of of recorded photons by this factor. Reprinted with permission from [64], S. O. Demokritov and B. Hillebrands, *J. Magn. Magn. Mater.* 200, 706 (1999). © 1999, Elsevier Science.
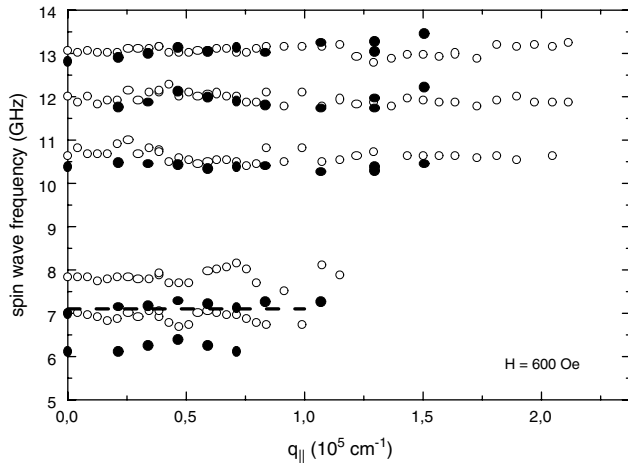
Figure 21. Dispersion of the five lowest spin wave modes measured on two square arrays of dots with the same dot thickness of 40 nm and the same dot diameter of 1 μm. Open symbols indicate data for a dot separation of 0.1 μm, full symbols of 1 μm. Note the difference between the frequencies of the lowest modes for the two samples. The dashed horizontal line indicates the calculated frequency of the uniform mode of a single dot. Reprinted with permission from [64], S. O. Demokritov and B. Hillebrands, *J. Magn. Magn. Mater.* 200, 706 (1999). © 1999, Elsevier Science.

light scattering intensity from a given spin wave mode confined to an island is determined by the Fourier transform of the mode profile over the island. Changing the thickness of the dots for a constant dot diameter (the data are not shown), one observes that the frequency splitting between neighboring modes decreases with decreasing dot thickness, in accordance with the fact that the group velocity of the Damon–Eshbach mode at a given $q_\parallel$ decreases with decreasing film thickness.

The above presented experimental findings lead us to the conclusion that the observed dispersionless, resonance-like modes are the Damon–Eshbach spin waves, quantized due to lateral confinement in a single dot. Earlier studies of the magnetostatic modes of *in-plane* magnetized macroscopic discs using a ferromagnetic resonance technique [48] do not present any comparison of the experimental findings with the theory. Surprisingly, despite numerous publications on inhomogeneous magnetostatic modes in finite-size magnetic samples (see, e.g., [49] and references therein), there is no appropriate theoretical description of such modes up to now. This can be probably explained by the low symmetry of the problem. In fact, in his pioneering work, Walker [50] considered an axially magnetized spheroid. Due to axial symmetry, the analytic solution of the Walker equation is possible in this case and it can be expressed in terms of Legendre functions. The magnetization direction of an in-plane magnetized dot breaks the axial symmetry of the Walker equation, and, correspondingly, that of possible mode profiles [51]. The solution (analytical or numerical) of the Walker equation corresponding to an in-plane magnetized disc is still needed.

Since the considered spin waves are the magnetostatic modes, and since the magnetic dipole interaction is long-range, the question of possible interdot mode coupling is of importance. Also, from the practical point of view, interdot

coupling restricts the density of dot arrays in, for example, magnetic memory applications. Figure 21 shows the frequencies of the spin wave modes, obtained on arrays having the same dot thicknesses and dot diameters, but with different interdot distances, δ. A clear frequency upshift of the two lowest modes of the sample with $\delta = 0.1$ μm documents the existing interdot coupling.

8. SPIN WAVE WELLS

In this section we discuss dynamic excitations in small magnetic items (long stripes and rectangular elements) with a large inhomogeneity of the internal field. It is known that in a nonellipsoidal element the internal field decreases near the edges of the element [39]. In some cases zones with zero internal fields can be created [52]. The problem of inhomogeneous internal field has been avoided in the previously discussed geometry used for the studies of the spin wave quantization in stripes, since the external field was applied along the long axis of the stripes.

In the following discussion we assume a Cartesian coordinate system in which the x-axis is perpendicular to the plane of the elements, and the y-axis is along the long axes of the stripes. The wave vector $\boldsymbol{q}$ is chosen along the z-axis, that is, perpendicular to the stripes. Figure 22 shows two typical BLS spectra obtained from an array of stripes of width
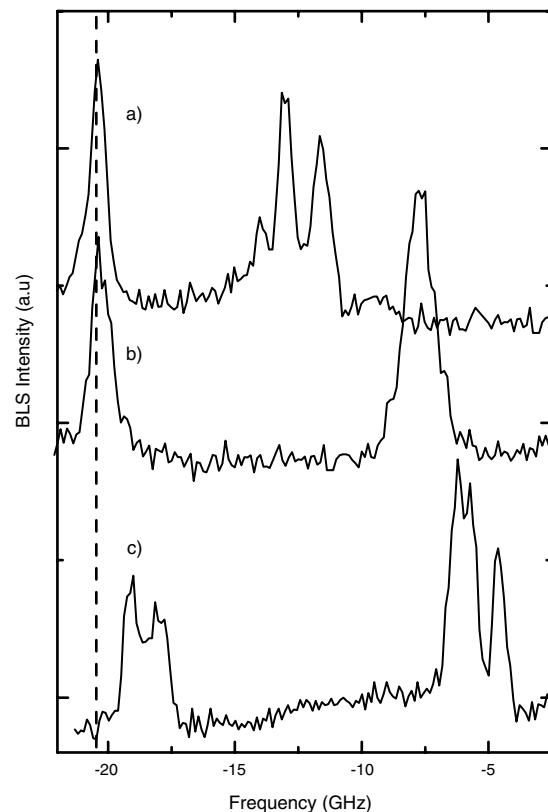

Figure 22. BLS spectra obtained on the stripe array for $q = 1 \cdot 10^5$ cm^{-1} at $H_e = 500$ Oe. Panels (a) and (c) correspond to different experimental geometries as described in the text. Panel (b) represents the spectrum of a unpatterned film.

$w = 1\ \mu$m, a length of 90 μm, and a distance between the stripes of 0.5 μm for the external in-plane magnetic field $H_e = 500$ Oe for different orientations of the field. Spectrum (a) is obtained for $\mathbf{H}_e$ oriented along the y-axis, thus presenting the DE geometry, discussed above. Spectrum (b) represents the unpatterned film. Spectrum (c) is recorded with both q and $\mathbf{H}_e$ aligned along the z-axis. As it is seen in Figure 22, spectra contain several distinct peaks corresponding to spin wave modes. The high-frequency peaks indicated as PSSW can be easily identified as exchange dominated perpendicular standing spin wave modes also observed in unpatterned films. Their frequencies are determined by the exchange interaction and the internal field. To investigate the nature of the other observed excitations, the dispersion was measured by varying q. It is displayed in Figures 23 and 24 for both orientations of $\mathbf{H}_e$.

Figure 23 representing the DE geometry clearly demonstrates the lateral quantization of the DE spin waves, resembling a typical "staircase" dispersion, discussed in Section 5. The interval of the observation of each mode in the q-space $\Delta q \approx (0.8-1.0) \cdot 10^5$ cm^{-1} is in agreement with the width of the stripe $w = 1\ \mu$m, giving $2\pi/w = 0.63 \cdot 10^5$ cm^{-1}. The frequency of the PSSW mode coincides with that of the PSSW mode for the unpatterned film and corresponds to an internal field of $H = H_e = 500$ Oe, thus corroborating negligible demagnetizing effects in the stripes magnetized along their long axes.

The dispersion presented in Figure 24 for $\mathbf{H}_e$ parallel to the z-axis (i.e., $\mathbf{H}_e \| \boldsymbol{q}$, so-called backward volume magnetostatic spin wave (BWVMS) geometry) differs completely from that shown in Figure 23. First, the PSSW mode is split into two modes, with frequencies corresponding to internal fields of $H = 300$ Oe and $H = 0$ Oe, respectively. This corroborates the well-known fact that the internal field is determined by essential demagnetizing effects and can be zero near the stripe edges [52]. Second, a broad peak is seen in the spectra in the frequency range 5.5–7.5 GHz over the entire accessible interval of q. The shape of the peak varies
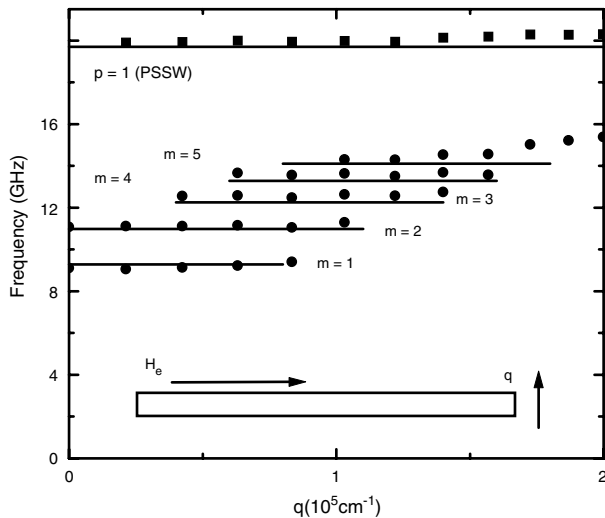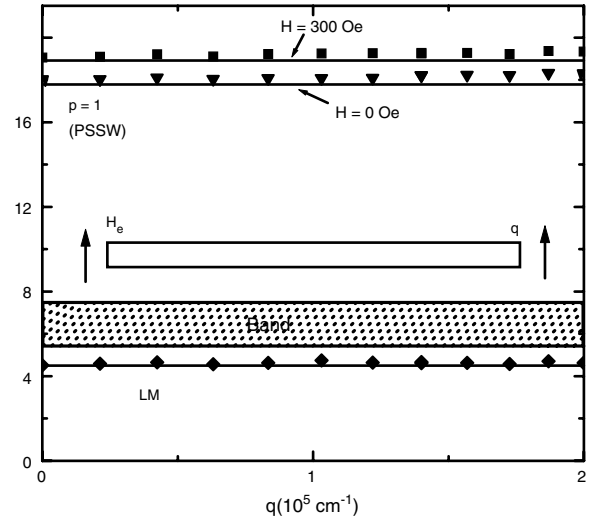

Figure 24. Spin wave dispersion of the stripe array measured at $H_e = 500$ Oe for the BWVMS geometry. The solid lines represent the results of calculation.

with q, thus indicating different contributions of unresolved laterally quantized modes to the scattering cross section at different q. Third, a separate, low-frequency, dispersionless mode with a frequency near 4.6 GHz (indicated as "LM" in Fig. 24) is observed over the entire accessible wavevector range ($q_{lim} = 2.5 \cdot 10^5$ cm^{-1}) with almost constant intensity. This is a direct confirmation of a strong lateral localization of the mode within a region with the width $\Delta r < 2\pi/q_{lim} = 0.25\ \mu$m. From the low frequency of the mode one can conclude that it is localized near the edges of the elements, since these are the field-free regions [39, 52].

Further evidence is provided by the observation of a corresponding mode in rectangular elements (not shown). For example, the frequency of the lowest mode for the rectangular elements with the lateral sizes $1 \times 1.75\ \mu$m^2, the distance between the elements $\delta = 0.2\ \mu$m, and the thickness $d = 33$ nm is 5.3 GHz.

A quantitative analytical description of the spin wave modes observed in the stripes is made as follows. According to Eq. (2), the frequency ν of the spin wave is then given by

$$\nu(Q) = \frac{\gamma}{2\pi}\left[\left(H + \frac{2A}{M_S}Q^2\right) \right.$$
$$\left. \times \left(H + \frac{2A}{M_S}Q^2 + 4\pi M_S \cdot F_{pp}(q \cdot d)\right)\right]^{1/2} \quad (24)$$

where H is the internal static magnetic field, M_S is the magnetization, A is the exchange constant, and $F_{pp}(qd)$ is the matrix element of dipole-dipole interaction [21]. Here we have written the spin wave wavevector as $\boldsymbol{Q} = q_p\mathbf{e}_x + \mathbf{q}$ consisting of the perpendicular part $q_p = p\pi/d$ quantized due to the finite film thickness, and the in-plane part $\mathbf{q} = q_y\mathbf{e}_y + q_z\mathbf{z}$.

If, for reference, $\mathbf{H}_e \| \mathbf{e}_y$ and $\mathbf{q} \| \mathbf{e}_z$ (DE geometry), the analysis of spin wave quantization is straightforward [37]. One assumes a quantization condition for q: $q = m\pi/w$, where $m = 1, 2, 3 \ldots$. The frequencies of these quantized modes calculated using Eq. (2) for $p = 0$, $m = 1, 2, 3, 4, 5$

Figure 23. Spin wave dispersion of the stripe array measured at $H_e = 500$ Oe for the DE geometry. The solid lines represent the results of calculation.

(laterally quantized modes) and for $p = 1$ and $m = 0$ (PSSW) are in good quantitative agreement with the results of the experiments as shown in Figure 23. The material parameters used are: $4\pi M_S = 10.2$ kOe, $A = 10^{-6}$ erg/cm^2, $\gamma/2\pi = 2.95$ GHz/kOe.

If $\mathbf{H}_e \| \mathbf{e}_z$, the effect of demagnetization due to the finite stripe width is very large, and the internal magnetic field is strongly inhomogeneous and differs from H_e. It can be evaluated as [39, 52]:

$$H(x, y, z) = H_e - N_{zz}(x, y, z) \cdot 4\pi M_S \qquad (25)$$

where $N_{zz}(x, y, z)$ is the demagnetizing factor. As will be discussed, this inhomogeneous field creates a potential well for spin waves resulting in localization. The averaged value of $H(z)$ obtained by integrating Eq. (25) along the axes x and y over the stripe cross section is shown in Figure 26. For $H > 0$ the magnetization is parallel to $\mathbf{H}_e$. Near the edges, however, regions with $H = 0$ and with continuously rotating magnetization are formed [52]. Since the rotation of the static magnetization dramatically changes the dispersion of spin waves [53], regions with zero internal field reflect spin waves propagating from the middle of the stripe towards these regions. On the other hand, a spin wave propagating in an inhomogeneous field might encounter the second turning point even if the magnetization is uniform. In fact, for large enough values of the internal field there are no allowed real values of q, consistent with the spin wave dispersion [54]. Thus, a potential well for propagating spin waves is created. Similar to the potential well in quantum mechanics, the conditions determining the frequencies ν_n of possible spin wave states in the well created by the inhomogeneous internal field are determined by the equation

$$2 \int q[H(z), \nu] \, dz = 2r\pi \qquad (26)$$

where $r = 1, 2, 3, \ldots$ and $q[H(z), \nu]$ is found from the spin wave dispersion. It states that the total phase shift of a wave propagating from one turning point to another and then returning back is a multiple of 2π. As will be discussed, additional phase jumps can appear at the turning points. These jumps are firstly neglected in our analysis for the sake of clarity.

We will illustrate these ideas in the following. The dispersion curves for spin waves with $\mathbf{q} \| \mathbf{H}$ and $p = 0$ calculated using Eq. (2) for different constant values of the field are presented in Figure 25. A dashed horizontal line shows the frequency of the lowest spin wave mode $\nu_1 = 4.5$ GHz obtained from Eq. (26) for $r = 1$ in good agreement with the experiment. It can be seen from Figure 25 that, for $H > 237$ Oe, there are no spin waves with the frequency $\nu_1 = 4.5$ GHz. Therefore, the lowest mode can only exist in the spatial regions in the magnetic stripe where 0 Oe $< H <$ 237 Oe. The corresponding turning points are indicated in Figure 26 by the vertical dash lines. Thus, the lowest mode is localized in the narrow region Δz near the lateral edges of the stripe where $0.26 < |z/w| < 0.39$. The mode is composed of exchange dominated plane waves with $q_{\min} < q < q_{\max}$, as indicated in Figure 25.

The higher-order spin wave modes with $r > 1$ having their frequencies above 5.3 GHz are not strongly localized and
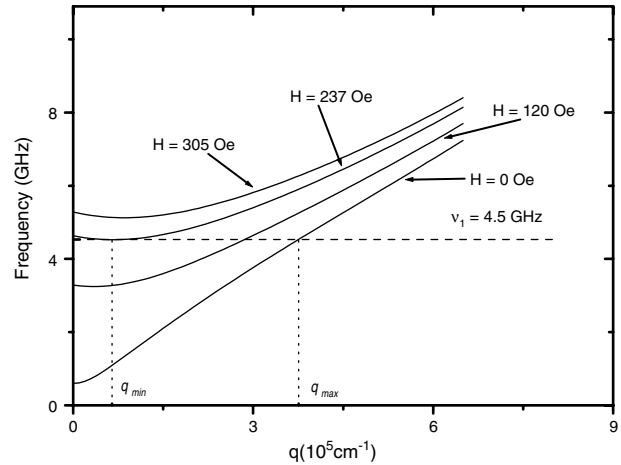

Figure 25. Dispersion of plane spin waves in the BWVMS geometry at constant internal fields as indicated.

exist anywhere in the stripe where the internal field is positive ($0 < |z/w| < 0.39$). In the experiment they show a band, since the frequency difference between the ν_r and ν_{r+1} modes is below the frequency resolution of the BLS technique.

The above presented one-dimensional analytical approach is applicable to long magnetic stripes. To describe the spin wave modes of two-dimensional rectangular magnetic elements, micromagnetic simulations of nonuniform magnetic excitations in such elements have been performed [55]. The method used is based on the Langevin dynamics, and the time evolution of the magnetization distribution in the magnetic element, which is discretized into $N_x \times N_z = 100 \times 180$ cells with magnetic moments $\boldsymbol{\mu}_i$, is simulated using the stochastic Landau–Lifshitz–Gilbert (LLG) equation [55]. The effective field $\mathbf{H}_i^{\text{eff}}$ acting on the ith moment consists of a deterministic part $\mathbf{H}_i^{\text{det}}$ (which includes external magnetic field and the fields created by the exchange and dipolar interactions between different cell moments) and a fluctuating part $\mathbf{H}_i^{\text{fl}}(t)$. The correlation properties of this fluctuating field, which is intended to simulate the influence of thermal fluctuations, may be quite complicated in
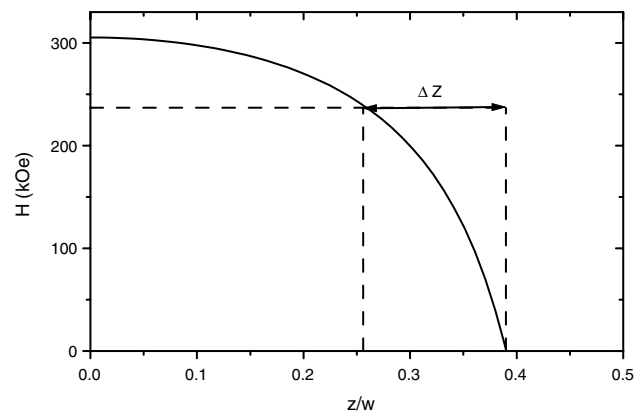

Figure 26. The profile of the internal field in a stripe. Δz shows the region of the lowest mode localization.

the micromagnetic system with interaction, in contrast to the standard single-particle situation [56]. These properties are not studied so far. It is, however, common practice to use a simple approximation describing the fluctuating field in the form of δ-correlated random noise [55, 57, 58]. We believe that the results of simulations with such a delta-correlated noise should provide at least qualitatively a correct picture of the spatial distribution of different magnetic eigenmodes in the system. In frame of this approximation the noise power has been calculated for a system of interacting magnetic cells as in [57]. The stochastic LLG equation has then been solved using the modified Bulirsch–Stoer method (details of the method are given elsewhere).

The results of the simulation are presented in Figure 28. Figure 27 presents a scanning force microscope image of the rectangular elements studied and the distribution of the static magnetization obtained by solving the LLG equation without any fluctuations and used as a starting point for the dynamic simulation. Next the field $\mathbf{H}_i^{fl}(t)$ has been turned on. After the thermodynamic equilibrium state of the system has been reached, the obtained values of all cell moments were recorded. Afterwards, using Fourier analysis, the oscillation spectrum of the total magnetic moment of the element was obtained. In the frequency interval 3–20 GHz, this Fourier spectrum demonstrates several maxima. The Fourier components of *each* cell magnetization $\boldsymbol{\mu}_{i,\omega}$ corresponding to these maxima were calculated and squared, to compare them with the measured spin wave intensities. As an example, the obtained spatial distributions for the frequencies $\nu = 5.3$ GHz and $\nu = 12.2$ GHz are presented in Figure 28. It is clear from Figure 28 that the low-frequency mode is strongly localized in the narrow regions near the edges of the elements that are perpendicular to the applied field. In contrast, and for comparison, the mode with $\nu = 12.2$ GHz shown in Figure 28 is not localized.

Thus, we have shown that a strong inhomogeneity of the internal field causes the creation of "spin wave wells" (SWW) in magnetic stripes and rectangular elements and the localization of spin wave modes in these wells. It is clear from the above consideration that the number of the states localized in the well depends on the depth of the well, which is controlled by the value of the applied external field. This is demonstrated in Figure 29.

Shown is a BLS spectrum for a transferred wavevector $q = 0.47 \cdot 10^5$ cm^{-1} for a higher external field of $H_e = 800$ Oe instead of $H_e = 500$ Oe as it is the case for Figure 22. As it is seen, in addition to the PSSW modes, the spectrum contains two spin wave eigenstates of the SWW (instead of one in Fig. 22).
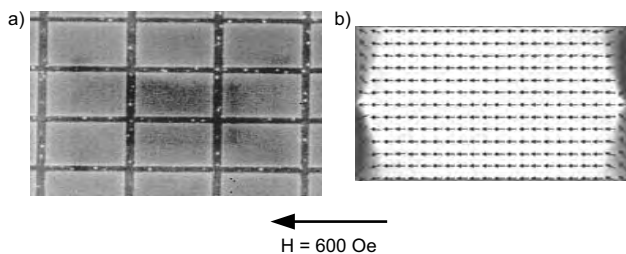

a) b)

H = 600 Oe

Figure 27. (a) AFM image of rectangular elements; (b) calculated distribution of static magnetization in an element.
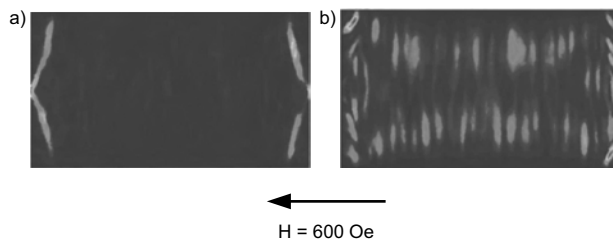

a) b)

H = 600 Oe

Figure 28. (a) Mode profile of a low-frequency spin wave mode with $\nu = 5.3$ GHz (note the mode localization near the edges) in the rectangular elements; (b) mode profile of a spin wave mode with $\nu = 12.2$ GHz.

Figure 30 shows the dependence of the frequencies of the observed modes on H_e. While the magnitude of H_e is small and not sufficient to saturate the stripe, only a single PSSW mode corresponding to $H_i = 0$ is present in the spectrum. At some critical field $H_e = H^*$ the PSSW peak begins to split. The first peak corresponding to $H_i = 0$ retains its frequency, but loses its intensity with increasing H_e. The frequency of the second peak (which appears at $H_e = H^*$) increases with the applied field, indicating the increase of H_i in the central part of the stripe. The observed value of the critical field $H^* = 220$ Oe is in agreement with the calculated demagnetizing field in the stripe center, $H_d(y = 0)$, based on the approach presented in [59]. Static magnetometry also shows a sharp increase of the stripe magnetic moment for $H_e > H^*$, indicating partial magnetic saturation of the stripe.

For $H_e > H^*$, a broad band of nonresolved spin wave excitations is seen [60] in the low-frequency part of experimental spectra. At higher H_e, at first one and then more narrow peaks are observed in addition to the band. To understand the appearance of several multiple states in a SWW, one should take into account that the depth of the well strongly depends on H_e. In fact, the bottom of the well corresponds to $H_i = 0$ independently of H_e. The field, which determines the position of the top of the well, however, can be roughly estimated as $H_e - H_d(y = 0) \approx H_e - H^*$. For a
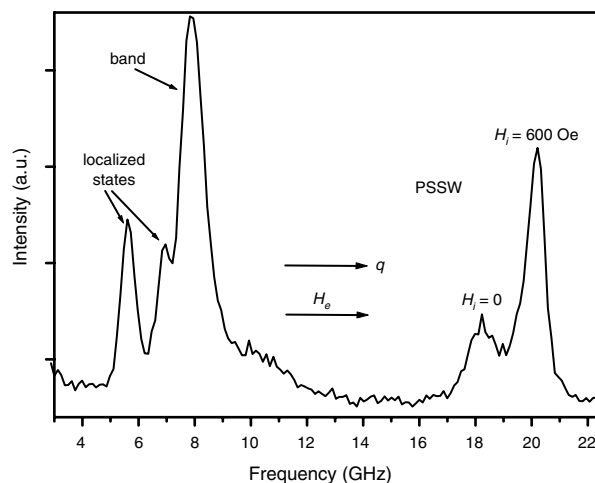

Figure 29. BLS spectrum for a transferred wavevector $q = 0.47 \cdot 10^5$ cm^{-1} and an external field of $H_e = 800$ Oe. PSSW indicates the perpendicular standing spin wave. The inset shows the used experimental geometry.
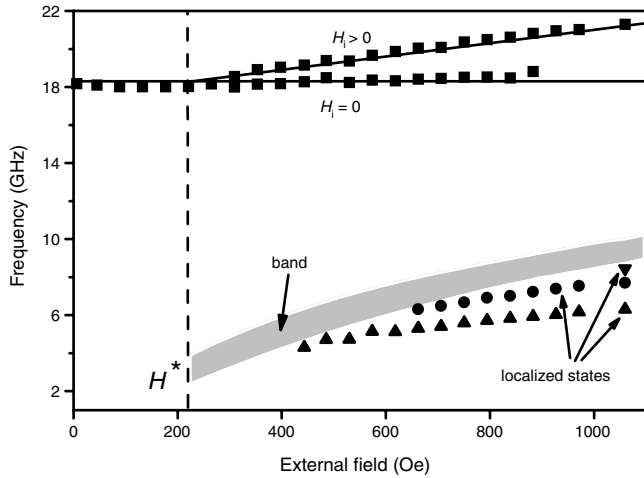
Figure 30. Frequencies of the modes observed in the stripes at $q = 0.47 \cdot 10^5$ cm^{-1} as a function of H_e. The vertical dashed line marks the critical field H^*. Note the constant frequency of one PSSW mode and the increase in frequency for the other mode for $H_e > H^*$. The gray region illustrates the band of nonresolved laterally quantized excitations.

small difference $H_e - H^*$ the well is too shallow, and there is no room in the well for a localized spin wave state. With increasing H_e the well becomes deeper, and as a result of that, at first one, and then more localized spin wave states appear in the well.

To obtain a complete quantization condition for localized spin wave states in a SWW, we need to modify Eq. (26) by adding phase jumps at the turning points of the SWW:

$$\Delta\phi_l + \Delta\phi_r + 2 \times \int_{y_l}^{y_r} q(H_i(y), \nu)\, dy = 2n\pi \qquad (27)$$

where $n = 1, 2, 3 \ldots$ and $\Delta\phi_l, \Delta\phi_r \in [0, \pi]$ are the phase jumps at the left and right turning points, respectively. Henceforth we will call the third term in Eq. (27) the quantization integral. Note that since the dispersion of a spin wave differs from that of an electron, the results for the phase jumps obtained for an electron in a quantum well may not be used for SWW. However, the difference between the quantization integrals calculated for two successive modes should be equal to 2π, if $\Delta\phi_l$ and $\Delta\phi_r$ are the same for all the localized modes.

To determine the turning points and the quantization integrals for the different spin wave states in the SWW, the profile of H_i in the saturated region (see solid curve in Fig. 31) has been calculated using the approach proposed in [59]. The equation $\nu = \nu(q(y), H_i(y))$ [61] has been numerically solved for the experimentally measured values of ν. As is discussed, the point at which the solution $q(y)$ does not exist for real $q(y)$ is the turning point. The second turning point was assumed to be at the boundary between the saturated and zero-field regions. Based on the obtained dependencies $q(y)$, the quantization integrals for the modes have been calculated.

The main results of the calculation can be summarized as follows. (a) The calculated quantization integrals for the localized states in the SWW decrease with increasing external field, probably due to the field dependence of $\Delta\phi_l, \Delta\phi_r$.
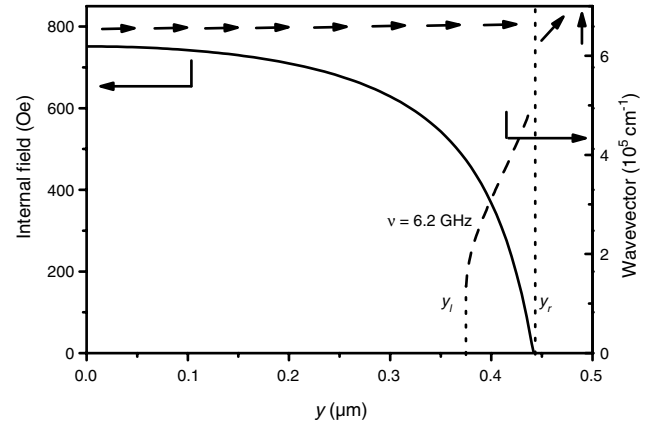

Figure 31. Internal field (solid line) and wavevector of the observed states (dashed lines) calculated as functions of y for an applied field of 970 Oe. y_l and y_r are the turning points of the localized modes with the frequencies as indicated. The arrows at the top of the figure illustrate the orientation of the static magnetization.

(b) The localization length $\xi = y_r - y_l$ is about 50 nm for the lowest localized state and 200–300 nm for the states having higher frequency. The localization lengths decrease with increasing H_e. (c) Although the quantization integrals for two lowest localized modes depend on H_e, their difference is almost constant and equal to $(4.2 \pm 0.4)\pi$. This is a direct confirmation of the applicability of the quasi-classical quantization conditions Eqs. (26) and (27) to the spin wave modes localized in a SWW.

The fact that the difference between the quantization integrals corresponding to the two lowest localized spin wave states in the SWW is close to 4π (and not to 2π) suggests that only the two odd-numbered modes ($n = 1$ and $n = 3$) are detected having a similar (symmetrical) distribution of the spin wave intensity about the center of the well. The reason why only the symmetric modes in the BLS experiment are seen is related to the strong spatial localization of these modes: $q\xi \ll 1$, where $q = (1 - 2) \cdot 10^5$ cm^{-1} is a typical wavevector transferred in the BLS process. This inequality means that the light fields are practically homogeneous on the spatial scale of the spin wave mode localization length and, similar to the case of standing spin wave resonance experiments [62], only the odd (symmetric) spin wave states contribute to the observed BLS intensity [63].

9. CONCLUSIONS

In this review we have discussed the field of magnetization dynamics in confined objects. This field is currently tremendously expanding and we could only scratch here some fundamental properties. As a basic system, we have extensively discussed the quantized excitation spectrum in magnetic stripes with the field parallel and perpendicular to the stripe axis, showing the fundamental properties of spin wave quantization and localization. The extensions to square and circular objects naturally were less detailed, as currently research is massively going on and a deep understanding still needs to be achieved. Progress is expected from the combined action of a better analytical understanding of the basic

wave functions, better numerical analysis, and in particular by advanced experiments. This is an exciting field with likely many new discoveries and potential applications to come.

GLOSSARY

Brillouin light scattering A spectroscopic technique to measure the spin wave dispersion using a Fabry-Pérot interferometer. The spin wave dispersion is obtained by scattering laser light inelastically from the spin waves under energy and partially under wavevector conserva-tion. The frequency shift equals the spin-wave frequency, and the change in wavevector equals certain wavevector components of the spin wave. For films the wavevector compo-nents parallel to the film is conserved, but not the component perpendicular to it.

Dipolar interaction Coupling between two magnetic moments (or even magnetic objects such as films) via the dipolar stray fields. The interaction energy varies with the cubed in-verse distance between the moments.

Exchange interaction Coupling between two spins of two electrons (or even magnetic enti-ties such as films) due to superposition of the wave functions of the spins and the application of the Pauli's principle. The origin is Coulomb interaction, which is different for spatially symmetric and antisymmetric wavefunctions. Since the total wavefunction of a Fermi particle like an electron must be antisymmetric, the difference in Coulomb energy translates directly into a difference in energy (so-called exchange energy) between the parallel and antiparallel orientation of the two spins. The exchange interaction is short-range and often approximated by a nearest-neighbour interaction.

Internal field Field existing inside a magnetic object. The internal field is the external field minus the demagnetising field caused by the field generated by the magnetization distribution in the object and the poles of the magnetization at the surface of the object.

Landau-Lifshitz torque equation Equation describing the precessional motion of a spin or a magnetic moment in a magnetic field. It is based on the balance between the torques acting on the magnetic moment and the torque provided by the change in time of the magnetic mo-ment, i.e., the time derivative of the angular momentum related to the magnetic moment.

Localization effects in magnetic films The internal field is inhomogeneous in almost all magnetic objects, the only exemptions are ellipsoids such as spheres, cylinders or infinitely extended films. The inhomogeneity is generated by the magnetic poles at the surface, where magnetic field lines enter or exit the object. The spin wave dispersion depends on the internal field. Situations occur, where spin wave prop-agation is forbidden in certain regions of the object due to the locally different internal field. Here the spin wave is con-fined to the other regions.

Magnetic coupling Interaction between different spins, moments or entire magnetic objects such as magnetic films. Two mechanisms contribute to magnetic coupling, the dipole-dipole interaction caused by magnetic stray fields, and the exchange interaction.

Magnetic domain Area in a magnetic object of uniform magnetization direction. Magnetic domains are separated by magnetic domain walls, where the magnetization changes direction.

Magnetic force microscopy A scanning probe microscopy tool to measure the magnetic stray fields with high spa-tial resolution. The stay fields are measured by the dipolar interac-tion with a scanning magnetic tip.

Magnetic multiplayer A stack of magnetic layers, often separated by nonmagnetic spacer layers. Magnetic inter-action between the magnetic layers, such as dipolar or exchange inter-action may result in novel ground states, such as so-called artificial antiferromagnets, where an antiferro-magnetic exchange interaction between neighboured ferro-magnetic layers results in an alternating sequence of the direction of magnetization from layer to layer.

Magnetization curve Magnetization of a magnetic object as a function of the applied mag-netic field. In general the component of the magnetization in the direction of the applied field is used. Ordered magnetic systems show hysteretic behaviour. Important parameters derived from a magnetization curve are the saturation magnetization obtained for large applied field strengths, the remnant mag-netization obtained at zero applied field, and the coercive field, which is the field, where the magnetization crosses the zero line.

Magneto-optic Kerr effect An optical technique to mea-sure magnetic properties. Polarized light is reflected from a magnetic surface. The change in the polarization state (polarization and ellipticity) reflects the amount and direc-tion of the magnetization.

Patterned magnetic element Usually a magnetic object obtained from a magnetic film by lithography.

Spin wave Dynamic collective excitation of a magnetic sys-tem, reminiscent to phonons as the lattice excitations. Clas-sically the spin wave dispersion is well described by the

ACKNOWLEDGMENTS

REFERENCES

1. D. D. Awschalom and D. P. DiVeincenzo, *Phys. Today* 48, 43 (1995).
2. M. Hehn, K. Ounadjela, J. P. Bucher, F. Rousseaux, D. Decanini, B. Bartenlian, and C. Chappert, *Science* 272, 1782 (1996).
3. C. Chappert, H. Bernas, J. Ferre, V. Kottler, J.-P. Jamet, Y. Chenm, E. Cambril, T. Devolder, F. Rousseaux, V. Mathet, and H. Launois, *Science* 280, 1919 (1998).
4. W. Wernsdorfer, K. Hasselbach, D. Mailly, B. Barbara, A. Benoit, L. Thomas, and G. Suran, *J. Magn. Magn. Mater.* 145, 33 (1995).
5. M. Grimsditch, Y. Jaccard, and I. K. Schuller, *Phys. Rev. B* 58, 11539 (1998).

6. B. Hillebrands, C. Mathieu, M. Bauer, S. O. Demokritov, B. Bartenlian, C. Chappert, D. Decanini, F. Rousseaux, and F. Carcenac, *J. Appl. Phys.* 81, 4993 (1997).

7. S. M. Cherif, C. Dugautier, J. F. Hennequin, and P. Moch, *J. Magn. Magn. Mater.* 175, 227 (1997).

8. A. Ercole, A. O. Adeyeye, J. A. C. Bland, and D. G. Hasko, *Phys. Rev. B* 58, 345 (1998).

9. T. Aign, P. Meyer, S. Lemerle, J. P. Jamet, J. Ferré, V. Mathet, C. Chappert, J. Gierak, C. Vieu, F. Rousseaux, H. Laumois, and H. Bernas, *Phys. Rev. Lett.* 81, 5656 (1998).

10. S. M. Cherif, Y. Roussigne, P. Moch, J. F. Hennequin, and M. Labrune, *J. Appl. Phys.* 85, 5477 (1999).

11. P. R. Kraus and S. Y. Chou, *J. Vac. Sci. Technol. B* 13, 2850 (1995).

12. M. H. New, R. F. W. Pease, and R. L. White, *J. Vac. Sci. Technol. B* 13, 1089 (1995).

13. R. O. Barr, S. Y. Yamomoto, and S. Schultz, *J. Appl. Phys.* 81, 4730 (1997).

14. F. Rousseaux, D. Decanini, F. Carcenac, E. Cambril, M. F. Ravet, C. Chappert, N. Bardou, B. Bartenlian, and P. Veillet, *J. Vac. Sci. Technol. B* 13, 2787 (1995).

15. A. Fernandez, P. J. Bedrossian, S. L. Baker, S. P. Vermon, and D. R. Kania, *IEEE Trans. Magn.* 32, 4472 (1996).

16. Y. Chen, R. K. Kupka, F. Rousseaux, F. Carcenac, D. Decanini, M. F. Ravet, and H. Launois, *J. Vac. Sci. Technol. B* 12, 3959 (1994).

17. T. Devolder, C. Chappert, Y. Chen, E. Cambril, H. Bernas, J.-P. Jamet, and J. Ferre, *Appl. Phys. Lett.* 74, 3383 (1999).

18. R. Allenspach, A. Bischof, U. Dürig, and P. Grütter, *Appl. Phys. Lett.* 73, 3598 (1998).

19. S. Demokritov, J. A. Wolf, and P. Grünberg, *Appl. Phys. Lett.* 63, 2147 (1993).

20. A. G. Gurevich and G. A. Melkov, CRC Press, New York, 1996.

21. B. A. Kalinikos and A. N. Slavin, *J. Phys. C: Solid State Phys.* 19, 7013 (1986).

22. C. Herring and C. Kittel, *Phys. Rev.* 81, 869 (1951).

23. G. T. Rado and J. R. Weertman, *J. Phys. Chem. Solids* 11, 315 (1959).

24. R. W. Damon and J. R. Eshbach, *J. Phys. Chem. Solids* 19, 308 (1961).

25. B. Hillebrands, *Phys. Rev. B* 37, 9885 (1988).

26. B. Hillebrands, A. N. Slavin, K. Yu. Guslienko, and S. O. Demokritov, *Phys. Rev. B* 66, 132402 (2002).

27. R. D. de Wames and T. Wolfram, *Appl. Phys. Lett.* 16, 305 (1970).

28. R. D. de Wames and T. Wolfram, *J. Phys.* 32, C1 (1971).

29. K. Yu. Guslienko, J. Jorzick, C. Krämer, S. O. Demokritov, B. Hillebrands, E. Søndergard, M. Bailleul, C. Fermon, and A. N. Slavin, to be published.

30. L. D. Landau and E. M. Lifshitz, Pergamon Press, Oxford, 1960.

31. J. R. Sandercock, M. Cardona, and G. Güntherodt, Eds., Springer Verlag, Berlin, Heidelberg, New York, 1982.

32. B. Hillebrands, *Rev. Sci. Instr.* 70, 1589 (1999).

33. A. O. Adeyeye, J. A. C. Bland, C. Daboo, J. Lee, U. Ebels, and H. Ahmed, *J. Appl. Phys.* 79, 6120 (1996).

34. B. A. Gurney, P. Baumgart, V. Speriosu, R. Fontana, A. Patlac, T. Logan, and P. Humbert, "Digest of the International Conference on Magnetic Films and Surfaces in Glasgow" 1991, p. 474.

35. C. Mathieu, J. Jorzick, A. Frank, S. O. Demokritov, B. Hillebrands, B. Bartenlian, C. Chappert, D. Decanini, F. Rousseaux, and E. Cambril, *Phys. Rev. Lett.* 81, 3968 (1998).

36. B. Hillebrands, S. O. Demokritov, C. Mathieu, S. Riedling, O. Büttner, A. Frank, B. Roos, J. Jorzick, A. N. Slavin, B. Bartenlian, C. Chappert, F. Rousseaux, D. Decanini, E. Cambrill, A. Müller, and U. Hartmann, *J. Magn. Soc. Jap.* 23, 670 (1999).

37. J. Jorzick, S. O. Demokritov, C. Mathieu, B. Hillebrands, B. Bartenlian, C. Chappert, F. Rousseaux, and A. N. Slavin, *Phys. Rev. B* 60, 15194 (1999).

38. C. Kittel, *Phys. Rev.* 73, 155 (1948).

39. R. I. Joseph and E. Schlömann, *J. Appl. Phys.* 36, 1579 (1965).

40. E. Y. Tsymbal, *J. Magn. Magn. Mater.* 130, L6 (1994).

41. R. I. Joseph and E. Schloemann, *J. Appl. Phys.* 36, 1679 (1965).

42. http://math.nist.gov/oommf/.

43. S. McVitie and J. N. Chapman, *IEEE Trans. Magn.* 24, 1778 (1988).

44. C. Mathieu, C. Hartmann, M. Bauer, O. Büttner, S. Riedling, B. Roos, S. O. Demokritov, B. Hillebrands, B. Bartenlian, C. Chappert, D. Decanini, F. Rousseaux, A. Müller, B. Hoffman, and U. Hartmann, *Appl. Phys. Lett.* 70, 2912 (1997).

45. B. Hillebrands, *Phys. Rev. B* 41, 530 (1990).

46. R. P. Cowburn, *J. Phys. D: Appl. Phys.* 33, R1 (2000).

47. J. Jorzick, S. O. Demokritov, B. Hillebrands, B. Bartenlian, C. Chappert, D. Decanini, F. Rousseaux, and E. Cambril, *Appl. Phys. Lett.* 75, 3859 (1999).

48. J. F. Dillon, *J. Appl. Phys.* 31, 1605 (1960).

49. R. D. McMichael and P. E. Wigen, in "Nonlinear Phenomena and Chaos in Magnetic Materials" (P. E. Wigen, Ed.). World Scientific, Singapore, 1994.

50. L. R. Walker, *Phys. Rev.* 105, 390 (1957).

51. J. F. Dillon, H. Kamimura, and J. P. Remeika, *J. Appl. Phys.* 34, 1240 (1963).

52. P. Bryant and H. Suhl, *Appl. Phys. Lett.* 54, 2224 (1989).

53. R. W. Damon and J. R. Eshbach, *J. Phys. Chem. Solids* 19, 308 (1961).

54. E. Schlomann and R. I. Joseph, *J. Appl. Phys.* 35, 167 (1964).

55. J. L. Garcia-Palacios and F. J. Lazaro, *Phys. Rev. B* 58, 14937 (1998).

56. W. F. Brown, Jr., *Phys. Rev.* 130, 1677 (1963).

57. H.-B. Braun, P. Entel, and D. Wolf, Eds., "Structure and Dynamics of Heterogeneous Systems." World Scientific, Singapore, 2000.

58. G. Brown, M. A. Novotny, and P. A. Rikvold, *Phys. Rev. B* 64, 134422 (2001).

59. R. I. Joseph and E. Schloemann, *J. Appl. Phys.* 36, 5 (1965).

60. J. Jorzick, S. O. Demokritov, B. Hillebrands, D. Berkov, N. L. Gorn, K. Guslienko, and A. N. Slavin, *Phys. Rev. Lett.* 88, 047204 (2002).

61. B. A. Kalinikos and A. N. Slavinm, *J. Phys. C* 19, 7013 (1986).

62. C. Kittel, *Phys. Rev.* 110, 1295 (1958).

63. J. Jorzick, S. O. Demokritov, C. Mathieu, B. Hillebrands, B. Bartenlian, C. Chappert, F. Rousseaux, and A. N. Slavin, *Phys. Rev. B* 60, 15194 (1999).

64. S. O. Demokritov and B. Hillebrands, *J. Magn. Magn. Mater.* 200, 706 (1999).

Dynamics of Metal Nanoclusters

Paul-Gerhard Reinhard

Universität Erlangen, Erlangen, Germany

Eric Suraud

Université Paul Sabatier, Toulouse, France

CONTENTS

1. INTRODUCTION

Clusters are an important class of nanoparticles. They bridge the gap between molecules and the solid state. Like solids, they consist out of multiple replicas of the same building block. Like molecules, they cover a finite number of atoms. Furthermore, they are arbitrarily scalable and exist for any number of building blocks. This makes them extremely interesting objects for basic scientific investigations. And one can also view clusters as being nanoparticles, sharing with all nanoscience promising perspectives for technical applications. Taking all aspects together hints that cluster science is a truly interdisciplinary field in between physics, chemistry, and technology which makes it even more interesting. In fact, clusters have been around for a long time. Think, for example, of the age old techniques of coloring glass with embedded noble-metal clusters [1]. However, the focus on clusters came rather late (only about the last three decades) to systematic physical and chemical research, partially because that option was not noticed earlier and partially because cluster research requires advanced experimental techniques for proper identification and analysis. The late arrival was compensated by a rapid growth of the field. In the meantime, there exists a vast manifold of investigations for any sort of material and for a huge variety of aspects thereof (structure, thermal properties, dynamics, . . .). This chapter takes only a thin slice of this huge area. It is confined in two respects: it considers only the special subspecies of metal clusters and concentrates on their basic dynamical properties.

Research on metal clusters has been brought forward in the pioneering work of [2, 3]. The first phase of studies mainly dealt with revealing the shell structure and studying optical absorption. It is interesting to note that both features could well be sorted by theories which had been developed much earlier. The shell structure, and particularly the appearance of supershells, was conjectured in [4] and the pronounced surface plasmon resonances were considered much earlier in [5]. These findings are summarized in several review articles and books (see, e.g., [1, 6–10]). In recent years, the rapid development of laser technology made powerful femtosecond (fs) lasers readily available. This has inspired many novel investigations in the nonlinear regime of electron dynamics, time resolved explorations of ionic motion, and refined studies of basic properties. This phase of studies is still going on. An early review of cluster dynamics with bias on theoretical description was given in [11].

This chapter aims to report on those emerging and promising lines of development in research on dynamics of metal clusters. For reasons of space, it concentrates on a discussion of basic features and results while skipping technical details (experimentally as well as theoretically). The chapter is outlined as follows: In the starting Section 2, we discuss typical energy, time scales, and forces in simple metal clusters. In Section 3, we briefly discuss the various theoretical methods to describe cluster dynamics. In Section 4, we recall the basic features of optical response which are to be considered as the doorway to more elaborate processes in the nonlinear domain. In Section 5, we come to the nonlinear domain dealing with the more violent processes which reach high ionization states or even lead to complete destruction. Finally, in Section 6, we present future directions of research in cluster structure and dynamics.

2. BASIC SCALES

2.1. Sorting Energies and Distances

As compared to atoms, metal clusters are loosely bound structures composed of ions and quasi-free valence electrons. Alkaline clusters, and in particular sodium, constitute archetypes of such objects. Many experiments and correlatively many theoretical developments have thus been devoted to these systems. Electrons behave quantally and move at a rapid time scale below 1 fs, while ions, which are much heavier than electrons, can be considered as classical objects: they move at a relatively slow pace in the range of hundreds of fs or even ps.

Ion–ion interactions may safely be reduced to a mere point charge interaction, because ions are relatively far away from each other. Electron–ion interactions, in turn, require some care, as only a (usually small) shell of valence electrons do effectively take part in the global binding of the system. The majority of electrons (core electrons) remain bound to their parent nucleus and can be accounted for in the interaction between ions and valence electrons via pseudo-potentials, which allow a proper modelization of the screening of the nuclear charge by core electrons. The electron–electron contributions can be split into three components (direct, exchange, and correlations). The "direct" contribution is the standard Hartree term. To a large extent, the three (infinite range) ion–ion, ion–electron, and direct electron–electron contributions cancel each other, in a neutral cluster. As in a bulk metal, most of the binding comes from the "attractive" exchange and correlation contributions, themselves, to a large extent, of local nature. The exchange contribution just stems from the indistinguishability of electrons. Finally, the correlation term reflects the fact that the two-body density matrix which should enter the calculation of the electron–electron potential energy does not reduce to a mere (even antisymmetrized) product of one-body densities.

To a large extent, in particular in alkaline clusters, valence electrons constitute a quasi-free Fermi gas, which allows one to fix scales. The Fermi energy ϵ_F (~ 3 eV in sodium) can be related to a key quantity of the bulk material, the Wigner–Seitz radius r_s ($\simeq 4a_0$ in sodium) ($\epsilon_F \propto \rho_F^{2/3} \propto r_s^2$). The Wigner–Seitz radius r_s represents the radius of the average sphere occupied by one atom in the bulk (see the systematics of radii in finite clusters $R \sim r_s n^{1/3}$). The Fermi energy also provides the Fermi velocity v_F ($\sim 25 a_0$ fs^{-1} for sodium), which yields a microscopic time scale $\tau_\mu \sim 2 r_s/v_F$ (~ 0.3 fs in sodium), fixing a typical microscopic scale in the system. These basic quantities are summarized in Table 1 in the case of alkaline clusters.

2.2. Time Scales

Various dynamical processes compete in metal clusters. First come the all dominating Mie surface plasmon oscillations, in which the electron cloud collectively oscillates with respect to the ionic background, in response to an external electromagnetic excitation. These oscillations quickly couple to single electron excitations which leads to Landau damping (damping of the collective mode due to its coupling to the mean field) and direct electron emission. The thus generated

Table 1. Gross properties of alkaline systems: Wigner Seitz radius r_s, Fermi energy ϵ_F, and microscopic time scale r_s/ϵ_F.

	Li	Na	K	Rb	Cs
r_s [a_0]	3.3	4.0	4.9	5.2	5.6
ε_F [eV]	4.7	3.2	2.1	1.9	1.6
$\dfrac{r_s}{v_F}$ [fs]	0.13	0.20	0.30	0.35	0.40

turbulence in the electron cloud gives rise to electron–electron collisions which adds further damping and associated internal heating. The thermal energy of the electron cloud is transferred to ionic thermalization or released much later in terms of electron evaporation. The excited electron cloud also shakes the ions which react, of course, somewhat slower due to their comparatively huge mass. A typical time scale is here set by the cycle of ionic vibrations, keeping in mind that first effects of ionic motion can already be seen in the first quarter cycle. Subsequent ionic processes like fragmentation or monomer evaporation usually take much longer (several ionic cycles) but become faster with increasing violence of the excitation (as, e.g., in a Coulomb explosion). Times scales for these various processes are sketched in Figure 1 for alkaline clusters. For reasons of transparency, we have skipped the (basically horizontal) lines for Landau damping as well as direct electron emission and indicated the range by the associated key words. Note that all electronic time scales from the different materials are gathering close together when expressed in the natural units of the electron cloud. The ionic time scales, on the other hand,
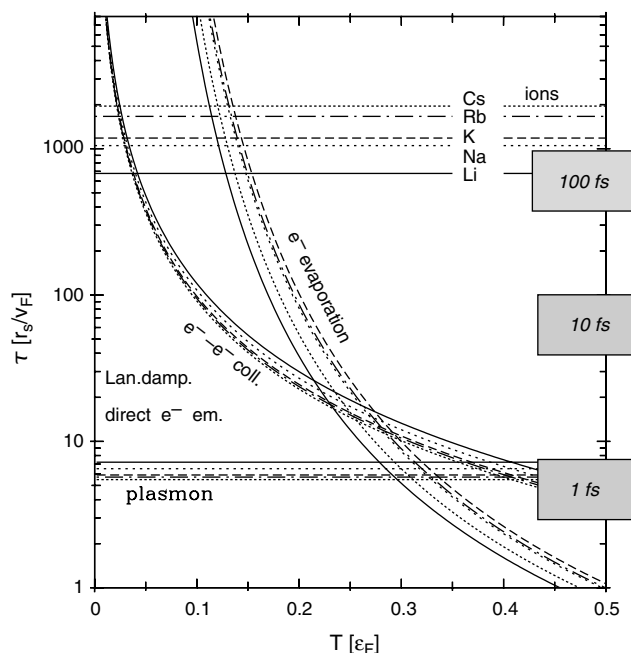

Figure 1. Time scales for alkaline clusters drawn versus internal excitation in terms of temperature T. Times and energies are expressed in natural units of each material according to the table on top. Orders of magnitude of the times in fs are given for completeness on the right part of the figure. Not drawn are the relaxation times for Landau damping and for direct electron emission. They reside at 20–40 r_s/v_F and are almost independent of T.

are dominated by the independent parameter of ionic mass and thus show a larger spread among the materials. Still, ionic time scales group themselves in a time range well separated from basic electronic scales, as expected in view of the large mass difference between ions and electrons. The different dynamical processes depend differently on the degree of internal excitation. This means that the balance between different reaction channels changes dramatically with the violence of the process. For example, electron–electron collisions are of minor importance in the linear regime of small excitations but compete with single electron times for temperatures around 2000 K.

The internal time scales of a cluster are to be complemented by the time scale of the excitation processes. Nanosecond lasers are beyond any time shown in Figure 1. That is a regime where the frequency hence plays the dominant role. Collisions with highly charged and fast ions are below any time scale shown (typically in the fs or sub-fs range). That covers the opposite regime where frequencies are unimportant and only forces count. Femtosecond lasers have just the time scales which interfere with the various time scales of metal clusters. It is obvious that this gives rise to a huge variety of accessible dynamical processes which can thus be triggered by laser experiments.

2.3. Forces and Dynamical Regimes

Besides times and frequencies, one has also to keep track of forces in the regime of intense laser excitations. Figure 2 sketches these relations for the example of Na clusters as a function of laser intensity I. The force (F) exerted by an external laser field (E) is drawn as guiding line ($I \propto E$, $F \propto E$). A critical regime is reached around $I = 10^{14}$ W/cm^2 where the laser field equals the binding forces for valence electrons and can thus at once ionize
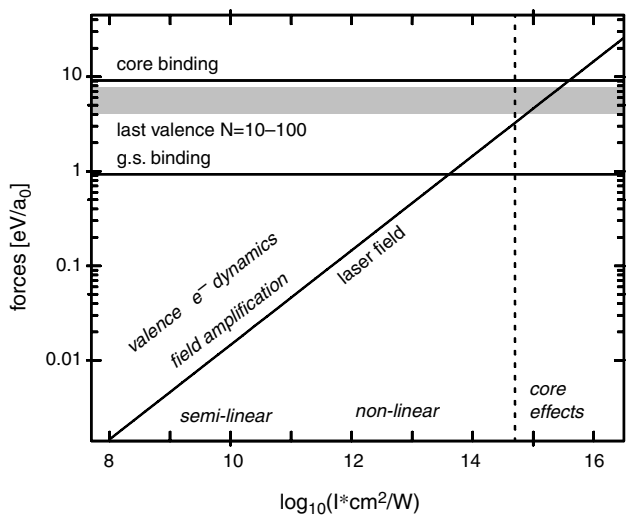

Figure 2. Typical forces in Na clusters compared with the external force of a laser and drawn versus laser intensity I. The binding forces of the valence electrons are shown at several levels, for the ground state binding of a neutral cluster and for nearly fully ionized clusters (indicated by "last valence") of several sizes N. This is to be compared with the binding of the core electrons in the $2s$–$2p$ shell.

the cluster. Below that we have a regime where the actual dynamics sensitively depends on the interplay between electron response and laser. This gives rise to mechanisms like field amplification, second-harmonic generation, or multiphoton emission. A more detailed discussion of that can be found in [12]. More violent ionization grows when approaching the critical regime. The first process here is rapid ionization of the valence electrons. For intensities one order of magnitude higher, one reaches a regime where the laser accedes directly the core electrons. This is the nanoplasma regime where details of the material become unimportant. That regime is discussed in more detail in the chapter by M. Belkacem et al. in this Encyclopedia. Note also that the valence-ionization and core-ionization regimes are well separated for small Na clusters while these regime overlap for large ones. Similarly, core ionization comes much earlier for noble metals where the d shell stays rather close to the valence s shell.

3. THEORETICAL DESCRIPTION

There is a huge manifold of methods to describe the structure of metal clusters. All techniques from molecular physics can and are applied, such as *ab initio* calculations at the level of configuration interaction (CI) [13], density-functional theory (DFT) [7, 11], or tight-binding approaches [14, 15]. The viewpoint that clusters are small pieces of bulk metal has motivated the jellium approach for the ionic background which is mainly used in connection with DFT. The nuclear shell model also inspired simple oscillator models for the shell structure of metal clusters [6]. The phenomenon of supershells, first identified in metal clusters [16], can be interpreted in terms of semiclassical periodic-orbit theory [4, 17].

The choice of methods is strongly reduced if one aims to describe dynamics. Optical response in the linear regime is still accessible to CI calculations [18] and all DFT methods can be applied as well [7]. A simple dielectric description which was initiated in [5] is, for example, extremely useful to describe the gross features of optical response [1]. Tight-binding approaches are well suited to describe ionic dynamics of clusters in a regime where electron emission still remains low. The regime of highly excited clusters with nonlinear electron response, sizeable ionization, and correspondingly hefty ionic motion is the most demanding of all. Up to now, it has only been attacked by DFT methods [11]. One actually reaches soon a regime where semiclassical dynamical approaches become valid; for these see the chapter by M. Belkacem et al. in this Encyclopedia.

A few words on the DFT methods are in order here. The valence electrons of the cluster are described by single-electron wavefunctions φ_α ($\alpha = 1, \ldots, N_{\text{el}}$) while the ions are treated as classical point particles $\mathbf{R}_I, \mathbf{P}_I$. The starting point is an energy-density functional $E_{\text{kin, el}}(\varphi_\alpha) + E_{\text{kin, ion}}(\mathbf{P}_I) + E_{\text{pot}}(\rho_{\text{el}}, \mathbf{R}_I)$ where $\rho_{\text{el}}(\mathbf{r}) = \sum_\alpha |\varphi_\alpha(\mathbf{r})|^2$ is the local electron density. The mean-field equations for the electrons are obtained by variation with respect to φ_α^* and the complementing ionic equations-of-motion are drawn from variation of the total energy with respect to electronic wavefunctions. This is called the time-dependent local-density

approximation (TDLDA) for the electronic dynamics coupled to molecular dynamics for the ions. It provides coupled electronic and ionic propagation which is capable of dealing with the demanding situations triggered by intense laser fields: high excitations, large amplitude motion, and dynamics far off the Born–Oppenheimer surface. The TDLDA can also be applied to compute optical response in the linear regime. To that end, one can keep ions fixed. The electronic dynamics is initialized by an instantaneous boost of the electron cloud, a protocol of the subsequent time-dependent dipole signal is taken, and the distribution of dipole strength is obtained from Fourier transform of the dipole signal into the frequency domain [19, 20]. The alternative is an explicit linearization of the dynamical equations in terms of a response function formalism, sometimes called linearized TDLDA or random-phase approximation (RPA). We prefer the notation RPA to distinguish the method from the fully fledged TDLDA. RPA is the option which is advantageous in restricted symmetries. It has been used in the pioneering work of [21, 22] and in most other early studies of optical response [7, 23].

4. NONDESTRUCTIVE DYNAMICS

Optical absorption was one of the first features studied in the physics of metal clusters. The case is meanwhile well understood for free clusters. Nonetheless, optical response is always the first thing to be looked at. It constitutes, so to say, the doorway to the further dynamics of clusters. And it remains a basic analyzing tool even in the more elaborate scenarios, such as pump and probe experiments. We thus briefly discuss the crucial pattern of optical response before proceeding to more advanced applications in the further sections.

4.1. Optical Response in Alkaline Clusters

The simplest picture of the surface plasmon resonance in metal clusters is the Mie model [5]. It shows the collective oscillations of the electron cloud against a homogeneous positive background in a metallic sphere. This yields the estimate $\omega_{Mie} = \omega_{plas}/\sqrt{3}$ where ω_{plas} is the (volume) plasmon frequency of the material. Refined versions of the Mie model take into account the detailed surface profile of the ionic background as well as of the electron cloud and yield a very good first guess for the resonance position [7]. In turn, the pure (original) Mie model corresponds to "macroscopic" cases in which the number of active electrons is very large, thus washing out detailed finite size effects.

The microscopic structure of the plasmon resonance is, of course, more involved than in the simple Mie model. Figure 3 tries to illustrate its composition for a medium to large Na cluster (with a diameter of about 2 nm). The static mean-field ground state provides a sequence of single electron levels. Dipole excitations within the static mean-field potential generate one-particle–one-hole (1ph) states (i.e., transitions from an occupied to an empty electron level). The lowest small panel of the figure shows the energies of 1ph states accessible by such dipole transitions. This defines the configuration space for the computation of excited states in linearized TDLDA (=RPA). Panel (c)
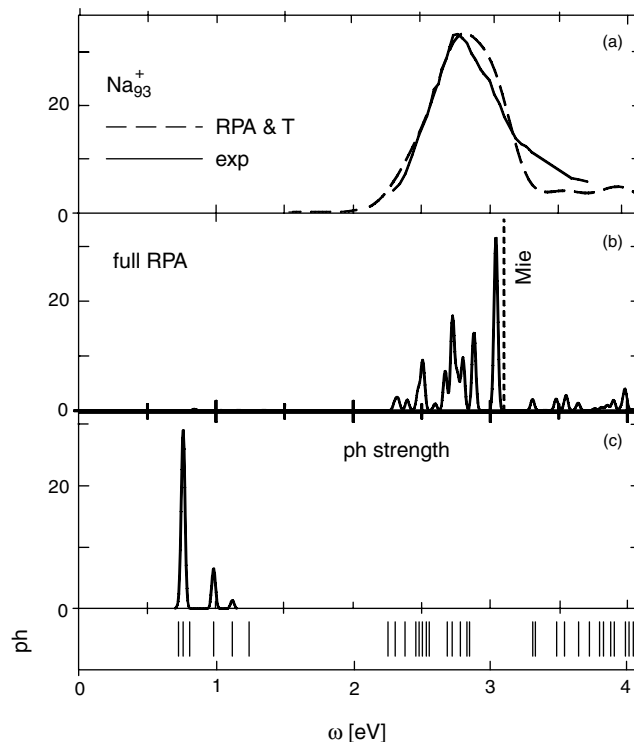

Figure 3. Composition of Mie plasmon resonance. Test case is Na_{93}^{+} with a soft jellium background ($r_s = 3.93a_0$, $\sigma_{jel} = 0.9a_0$). The dipole strength distributions are shown at various stages of calculation. Lowest panel: the 1ph states as such. (c) Dipole strength from pure 1ph states. (b) Strength distribution from TDLDA at small amplitude (=RPA); the position of the Mie frequency is indicated by a vertical dotted line. (a) Experimental strength (full) modified from [108] and TDLDA results folded with a Gaussian of width 0.15 eV to simulate thermal line broadening.

shows the actual dipole strength distribution from pure 1ph states. (The obtained discrete levels have been smoothed by a small width to provide a smooth and plottable shape.) This pure 1ph distribution gathers at rather low excitation energies (here around 1 eV) corresponding to transitions over one shell. It is far from the experimentally observed spectrum. Unlike the case of atoms, the pure 1ph states are not at all an approximation to the excitation spectrum of a metal cluster. They merely serve as expansion basis for the true excited states which can be thought of as coherent superpositions over all the 1ph states.

The key ingredient is the Coulomb force which recouples the 1ph states. Its strong repulsion moves the peak of dipole strength to dramatically higher energies. The essence of that is correctly described in the Mie model as indicated in panel (b). But the new position of the dipole resonance resides in a region where plentiful 1ph states are around (compare with the lowest panel). Linearized TDLDA (=RPA) correctly incorporates all microscopic details of the single particle structures (i.e., all features of a coherent superposition of 1ph states). The result is shown in panel (b). The resonance peak is obviously distributed over a set of nearby 1ph states. This is called Landau fragmentation in analogy to Landau damping in the continuous electron gas [24].

The surface plasmon resonance in large Na clusters thus gathers already some width due to Landau fragmentation. This is obviously not enough to explain the full experimentally observed width; see panel (a). The point is that this measurement was performed at a rather high temperature of about 400 K. This causes large fluctuations of the cluster shape. The resonance changes with shape (see later discussion) and a broader peak is obtained from incoherent superposition of all these different spectra. We simulate the thermal broadening by folding the RPA result with a Gaussian having a full width at half maximum of 0.14 eV [25]. The result agrees very nicely with the experimental spectrum. The figure thus demonstrates the various contributions from which the optical absorption strength is composed. TDLDA embraces the dominant (collective) effect of the Coulomb repulsion and all details of 1ph structure. Thermal effects have to be added in terms of incoherent superposition of TDLDA results at various shapes.

4.2. Case of Noble Metals

We thus have seen that clusters of simple metals (alkalines, earth-alkalines) have spectra with one pronounced surface plasmon peak. There are more involved cases. Consider for example noble metals (Cu, Ag, Au). They have also one valence electron in a s shell. But the next core state below that is a d shell which is energetically not so well separated as in alkalines. The d shell is loosely bound and easily polarizable. The ensemble of d shells of all atoms in a cluster together build also a collective dipole mode where all core dipoles oscillate coherently. We thus have two strong dipole modes. One is from the d states and the other one is the Mie resonance of the valence electron. These two modes interact with each other and recouple to two new hybrid modes. The optical absorption spectrum of a cluster from noble metals thus shows two regions of strong response. Figure 4 exemplifies that for Ag_8. There is obviously a plasmon peak at 3.6 eV quite close to the prediction of the Mie model. But the peak is not as isolated as it used to be for simple metals. There resides appreciable strength above the Mie resonance and more is to follow for larger energies, not shown on the
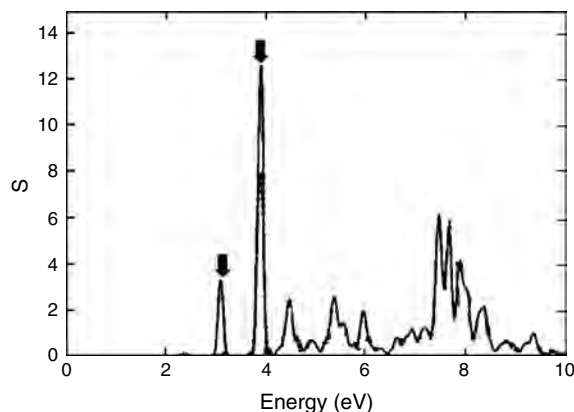
plot. The hybridization of two basic dipoles modes has been worked in detail in [26]. The situation is very similar in all Ag clusters. The actual numbers for Ag_8, in particular, are the following. The 4s valence electrons alone place a surface plasmon resonance at 5.18 eV and the collective oscillations of the d states at 10.7 eV. The dipole–dipole interaction couples these two modes and this places eventually the Mie plasmon at 3.6 eV which, however, carries only about 16% of the total dipole strength. The upper mode is shifted up and resides in a region of high density of states thus becoming very broad. This more involved composition of dipole resonances requires reconsideration of effects discussed, such as deformation splitting or Landau damping. Very little of that task has been worked up until now. There is an interesting approach which may help to simplify those considerations. One can replace the treatment of the the d-shell core electrons by the dielectric function of this core [27]. This works well in the linear regime. The capability of that approach has not yet been fully exhausted.

4.3. Shapes

The example of Na_{93}^+ dealt with a spherical cluster to keep things simple in a first step. Most clusters are deformed. An unavoidable small deformation is, in fact, always present due to detailed ionic structure. But the systematics of deformations of metal clusters shows huge fluctuations of deformation. This concerns particularly the quadrupole momentum which plays the leading role in quantifying deformation. Spontaneous ground state deformation of metal clusters is a shell effect very similar to the Jahn–Teller effect in molecules [28]. Certain electron numbers are associated with an ambiguous ground state at symmetric shape. The system undergoes deformation to render the ground state unique again. These electronic shell effects can reliably be well estimated in a simple oscillator model [29] and they are no longer confirmed by microscopic calculation.

The question arises as to how one could identify the cluster deformation. It is to be noted that the quadrupole deformation has consequences for the Mie resonance. It is split into three different modes corresponding to the three principal axes of the cluster. The mode oscillating along the shortest axis has the highest frequency while a longer axis produces a lower frequency. This produces a collective splitting of the Mie resonance which is very visible in small metal clusters where Landau fragmentation is still negligible. Most clusters are deformed but still axially symmetric. One has then two axes with the same extension and correspondingly two modes with the same frequency. Prolate (cigar shape) clusters have the degenerated (=strong) mode at the high frequency end while oblate (pancake shape) clusters have it at low frequencies. The splitting is used to assess experimentally the shape of a metal cluster. As an example, Figure 5 shows the systematics of the Mie plasmon peaks for small Na clusters. The experimental spectra generally show clearly two pronounced peak regions. The two peak positions can be well fitted by two Gaussians. The resulting peak frequencies are shown in the upper panel. The full line shows the stronger peaks where two modes coincide. This allows one to sort prolate and oblate clusters. A spherical cluster is distinguished by coincidence of all three modes.
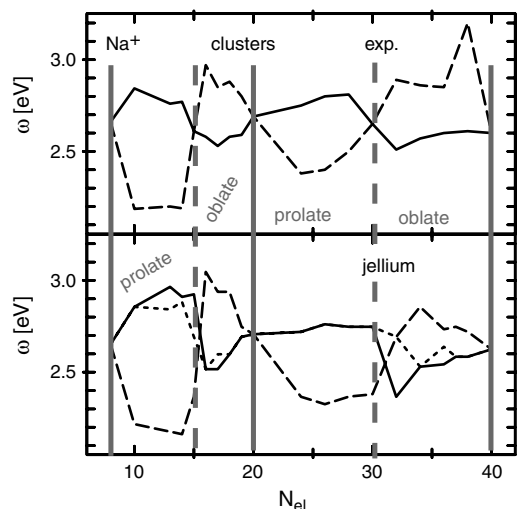

Figure 4. Photoabsorption spectrum of Ag_8 for ground state (full line) and isomer (dashed line) computed with TDLDA, taken from [26]. Arrows show the positions of excitations observed in argon-matrix clusters. Modified from [109]. See also Figure 9.

Figure 5. Illustration of deformation splitting of the Mie resonance for singly charged Na clusters. Theoretical calculations are done with (TD)LDA using soft jellium for the ionic background. Upper panel: The frequencies of the two dominant peaks (major peak = full, minor peak = dashed) in the experimental spectra, modified from [110, 111]. Lower panel: Results from TDLDA calculations on deformed jellium background modified from [112]; shown are the frequencies of the Mie resonance peaks for the three modes along x, y, and z axes.

The experimental results show the systematics of prolate and oblate shapes in agreement with microscopic models of cluster shell structure [6, 7]. The lower panel of Figure 5 shows theoretical results produced from RPA on a deformed jellium model where the ground state deformation had been optimized by energy minimization. The detailed information from these calculations allows one to distinguish all three basic resonance modes. Thus results for the modes in the x, y, and z direction are drawn separately. Two of them are degenerated for axially symmetric clusters (which are the majority). Three separate peaks indicate a triaxial shape which is a rather rare event and occurs, understandably, just at the transition between prolate and oblate clusters. One observes a very good agreement between theory and experiment which confirms the theoretical deformation systematics and the underlying theoretical interpretation in terms of deformation splitting of the Mie resonance. However, the occurrence of triaxial shapes is not yet clearly discriminated by experimental data. It is extremely hard to disentangle the triple splitting in the rather broad absorption spectra. Note that this immediate access to deformations applies only to small clusters. Landau fragmentation of the spectra takes over for larger Na clusters around $N = 40$ [23] which inhibits this simple interpretation [30].

5. NONLINEAR DYNAMICS

The widespread applicability of powerful fs lasers has open the door to the study of nonlinear effects in clusters. For still moderate laser intensities, one remains in the so-called semilinear regime where one counts in orders of one-, two-, three-, ... photon processes. Typical examples here are second harmonic generation (SHG) and multiphoton emission. We will discuss both with one test case each. Enhancing

the laser intensity quickly leads to the regime of destructive processes. There are many experiments where destruction is used as a tool for selection or analysis. We will discuss that with two examples. Finally, lasers are more flexible than just allowing variation of frequency and intensity. The whole time profile can be shaped in a flexible manner. From the world of scenarios which are possible then, we will discuss a most typical example (i.e., pump-and-probe experiments). This all together hopefully serves to get a rough idea of the rich variety of explorable scenarios in the nonlinear domain.

5.1. Second Harmonic Generation

SHG is meanwhile a well understood phenomenon in nonlinear optics and it is regularly used for frequency doubling in laser setups. These standard applications employ bulk material containing macroscopic amounts of nonlinearly reacting molecules. The theoretical description of SHG on clusters by means of dielectric theory is straightforward [31]. The experimental situation is much less favorable because there are very few and small scattering centers producing only faint SHG output signals. The situation improves for clusters on surfaces because it becomes possible to pack them more closely yielding a higher density of scatterers. Moreover, surfaces are crucial to break reflection symmetry and this symmetry breaking is required to obtain a second harmonic. There exist several SHG studies for metal clusters on surfaces. Most often, it is used as an analyzing tool to suppress background which would be abundant when dealing with the original laser input frequency. That way it has helped, for example, the analysis of growth dynamics [32, 33] and is widely used in combination with pump-and-probe experiments; see Section 6.6. Figure 6 stems from a rather early attempt on that subject and discusses features of SHG as such [34]. In particular, it nicely demonstrates the effect of symmetry breaking. The laser light is reflected under varying angles. The SHG signal vanishes if the laser beam comes in orthogonal to the surface. The signal grows with the deflection angle turned on. The interpretation is obvious. The clusters have more or less symmetric shapes
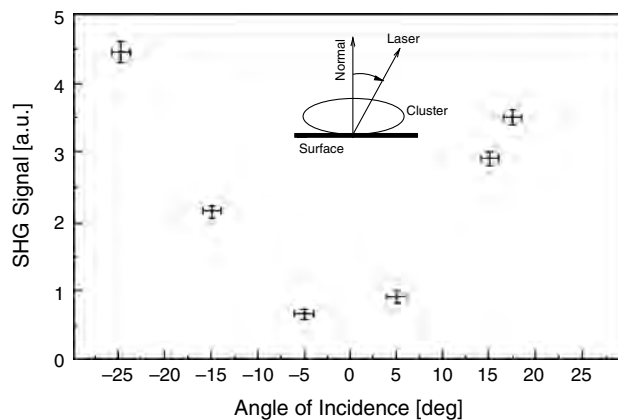

Figure 6. Dependence of the SHG output signal on the angle between laser beam and normal to the surface (the angle of incidence is measured with respect to the normal to the surface). Test cases are large Na clusters ($R > 100$ nm) on the LiF surface. The wavelength of the incident laser pulse was 1064 nm. Modified from [34].

when viewed from a position orthogonal to the surface. They are strongly deformed when seen as a cut through the surface because the interface potential acts only on one side of the cluster. In spite of that achievement, metal clusters will probably not become the preferred source for large scale frequency doubling. But SHG has found widespread application as an analyzing tool. All that has to stay in the non-destructive regime and this requires a subtle balance to have sufficiently large laser intensity but to stay below the regime of strong ionization [35].

5.2. Photoelectron Spectroscopy

Photoelectron spectroscopy as a useful tool for structure analysis was already mentioned in the previous section. New aspects come into play when considering multiphoton processes. This is a broad, opening field of research in atomic physics known there as above threshold ionization (ATI) (for reviews see, e.g., [36, 37]). Studies of multiphoton ionization have also been performed for Na clusters [38] and for Ag nanoclusters attached to a surface [39]. We consider here a case in C_{60}. The analysis becomes particularly telling when resolving the kinetic energy spectra of the emitted electrons. An example is shown in Figure 7. A laser pulse with fixed intensity but varying pulse length was applied (left panels). The shortest pulse leaves the cluster basically intact and one sees the succession of multiphoton peaks nicely resolved. Longer pulses pump more energy into the C_{60} which leads to a substantial broadening of the peak. It is an effect of the total absorbed energy. That was counterchecked in the right panels where the intensity was reduced to leave the fluence approximately constant. The ATI structure is thus somewhat recovered in panel (d). But the overall slope shrinks and even more so in panel (e). That is due to the fact that the probability for multiphoton processes scales with I^{ν} (where ν is the number of involved photons) independently of pulse length. The figure thus demonstrates nicely how the change of two laser parameters can change the resulting spectra in two different ways. It was argued in [40] that the more energetic cases show a transition to thermal emission. A different mechanism is worked out in a theoretical study of ATI from Na clusters [41]. The continuous quasi-thermal patterns are explained as an effect of ongoing ionization which yields a sliding threshold and thus to a superposition of ATI spectra with a different onset. The case is still a matter of debate (as almost every example in this section). More experimental information can help in that matter. There are, for example, simultaneous measurements of kinetic energy spectra and angular distributions of emitted electrons in W clusters [42]. These show isotropic emission for the thermal (=exponentially decreasing) part of the kinetic energy spectrum while the nonthermal part is directed along the axis of laser polarization. A theoretical survey of this double analysis has yet to be worked out.

ATI offers further interesting possibilities. For example, there is a discussion about the competition between direct and sequential emission in atomic physics [43]. This is a challenging topic for clusters as well and it would add new aspects due to the dominance of the plasmon in metal clusters [44].
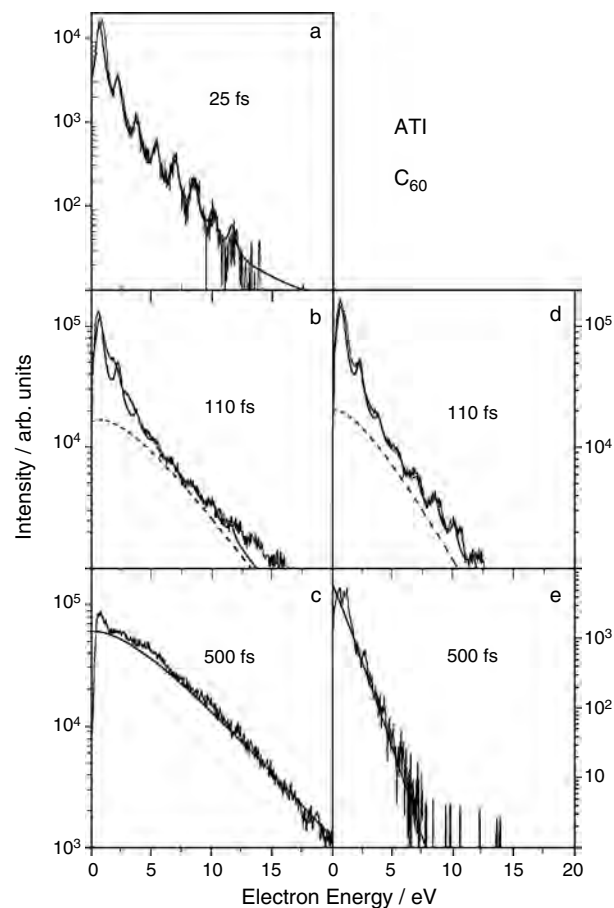

Figure 7. Photoelectron spectra from C_{60} irradiated by a laser with wavelength of 790 nm and various pulse lengths as indicated. The laser intensity was $I = 8 \times 10^{13}$ W/cm^2 for all left panels and reduced to $I = 3 \times 10^{13}$ W/cm^2 for (d) and $I = 8 \times 10^{12}$ W/cm^2 for (e). Curves are fitted to data with a sum of Lorentzian peaks over the thermal background. Modified from [40].

5.3. Coupling Electronic and Ionic Dynamics

The interplay between laser frequency and cluster resonances has also been directly exploited in a dynamical scenario. Consider a laser which is strong enough to remove initially a few electrons from a cluster. The thus released Coulomb pressure will drive the cluster to a slow expansion at ionic time scales (hundreths of fs). The cluster thus changes its resonance conditions as a function of time. Dramatic ionization may arise at a later stage if the laser is still irradiating and if the cluster moves into resonance with the laser. On the contrary, nothing will happen if the laser is switched off before that point. Such an experiment had been reported in [45] and the results are summarized in Figure 8. The pulse width of the laser was varied systematically while the fluence ($\propto$intensity times pulse width = total energy exposed to the cluster) was kept constant. Nonetheless, the final ionization state shows a remarkable evolution as a function of pulse length with a peak around a pulse width of 600 fs. One has to assume that the ionic expansion, proceeding always at its typical long time scale, drives the cluster into resonant conditions around a time of 600 fs. Shorter pulses are less efficient because they do not reach
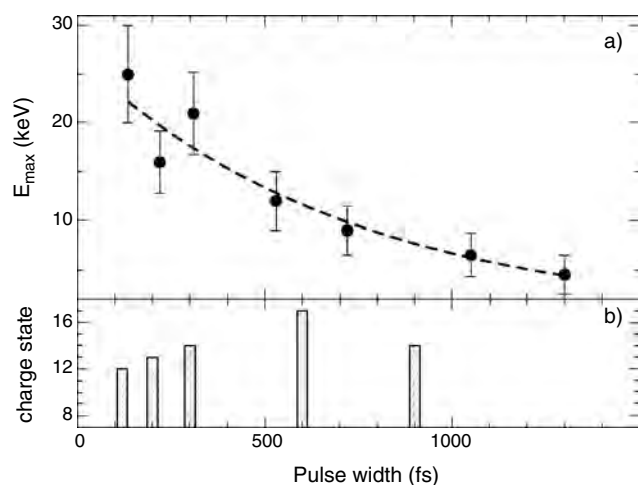
Figure 8. Coulomb explosion of small Pt clusters induced by a laser with frequency of 1.54 eV and energy of 15 mJ. Experiments have been done with systematically varied pulse length. Results are drawn versus pulse length. Lower panel: Net charge state reached. Upper panel: Maximum kinetic energy of emitted ions. Modified from [45].

the optimum time for resonance, even though the initial ionization is larger due to larger intensity. Longer pulses become inefficient again because the initial ionization is weaker and the Coulomb pressure does not suffice any more to deliver the required expansion. The question remains as to what process these resonant conditions are related to. The dominance of the Mie plasmon suggests that the Mie frequency moves into resonance with the laser because expansion of the radius R is known to yield a redshift $\omega_{Mie} \propto R^{-3/2}$ [46]. This mechanism was studied in detail for Na clusters in [12]. The experimentally studied case of Pt, however, is more involved because weakly bound core electrons (which exist in all noble metals) take part in the dynamics and may be released in quantities. An alternative resonance mechanism has been proposed in [47] which relies on field assisted tunneling appearing precisely if a certain (large) ionic distance is reached. The rather high laser intensity used in the experiments speaks in favor of that model. The case is yet open for discussion.

6. PROMISING FUTURE DIRECTIONS

6.1. Clusters in Matrices

In the previous section, we dealt with the most basic features of cluster dynamics. The doorway here was the case of optical response which has been intensely studied in the early phase of cluster physics and seems to be well understood by now. However, there are still several open ends and less well understood aspects even in this seemingly simple area. One of those is the influence of interfaces on the optical properties of a cluster. The leading effect for clusters on surface is that the interface interaction changes the shape dramatically as compared to a free cluster. This has consequences on the spectrum, as any shape change has (see previous discussion). This has been demonstrated in detail for Na clusters on the rather inert NaCl substrate [48]. A further crucial effect is the polarization interaction with

the other atoms [49]. This has been studied recently in a systematic manner for Ag clusters embedded in different rare gas layers. The small cluster Ag_8 still has a well defined resonance peak (see also Fig. 4). Results for the peak position as function of coverage and for different surrounding rare gases are shown in Figure 9. The results nicely demonstrate the impact of the surroundings. This is a rather fresh result. Theoretical explanations can be found systematically with fully fledged microscopic calculations. But these grow quickly unmanageable, even when reducing the environment to a minimum of necessary neighbor atoms [50]. Simple and yet reliable approaches using appropriate pseudo-potentials and effective electron–atom interactions are underway (see, e.g., [51] for an environment of He drops) but have yet to be worked out for the many conceivable combinations of materials. The modeling should be open for effects beyond linear response to cover also the more intense excitations discussed later.

SHG has been discussed as a prominent nonlinear optical effect for clusters on surfaces in Section 5.1. Nonlinear response is also observed for metal clusters embedded in glass matrices [52]. A higher densities of clusters can be reached here. Tools for shaping and handling embedded clusters are under development (see, e.g., Section 6.5). This may allow design of optical switches as a promising future application of metal nanocluster dynamics [52].

6.2. Clusters on Surfaces

Clusters embedded in matrices and clusters at surfaces have much in common where handling of cluster–environment interaction is concerned. But they do also display significant differences concerning their structural and dynamical pattern. For example, the cluster shape, the cluster–cluster interaction, and the mobility on a surface are different from those in a matrix. This has many interesting consequences. One is the appearance of treelike structures in growth of Ag clusters on surfaces [53]. Figure 10 shows these exciting structures. Closer analysis of size distributions shows
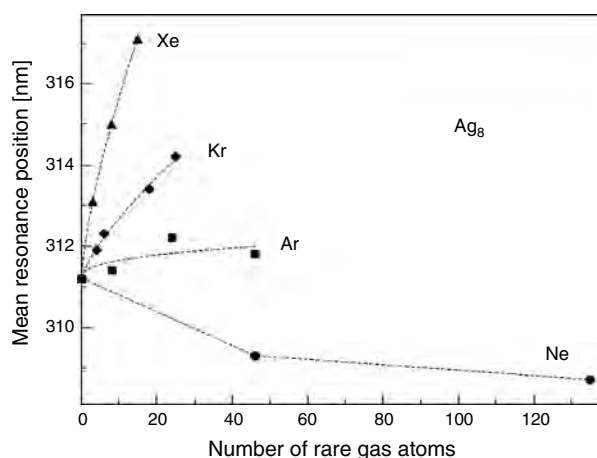

Figure 9. Mie resonance frequency for Ag_8 surrounded by layers of different rare gases and embedded finally in a liquid He drop. The frequency is drawn versus number of attached rare gas atoms. Modified from [113].
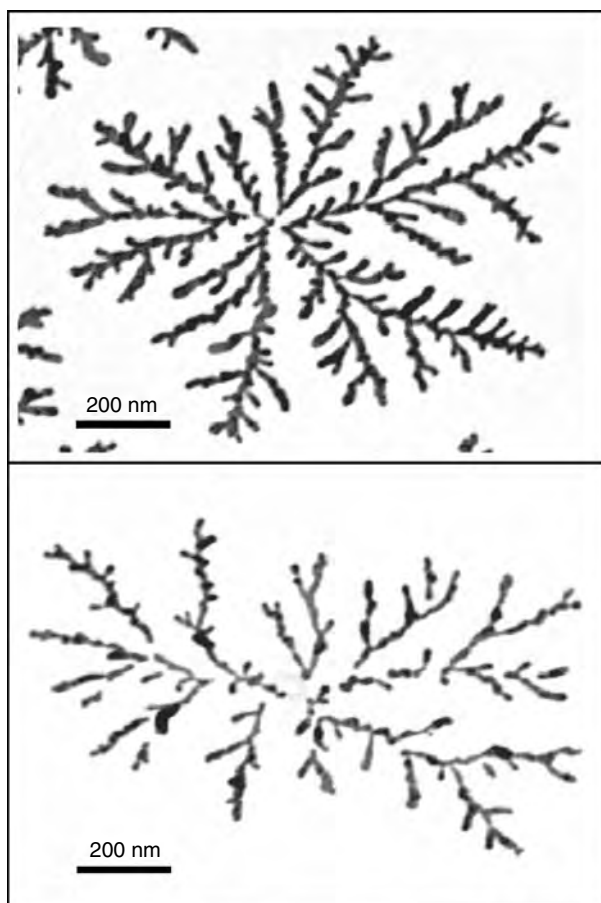
Figure 10. Distributions of connected Ag clusters on a graphite surface grown with two different coverages: upper panel = 6 monolayers in the average, lower panel = 2 monolayers. Modified from [53].

that these are, in fact, of fractal structure with an effective dimension of about 1.7. The pattern reappears consistently under many varied growth conditions (and for many different combinations of materials [54]). And they can be understood within a simple model of the fragmentation instability of elongated clusters on a surface. The findings have consequences for technology of growth of nanowires and self-organizing structures, yet to be worked out.

This example concerns predominantly the topic of structure of deposited clusters (although the fragmentation dynamics is a crucial input for the results). It demonstrates that even questions of cluster structure can reveal surprisingly new features. The quest to understand catalysis is one further motivating example [55]. This holds even more so when considering the magnetic properties of embedded clusters [56] or of deposited metal clusters (see, e.g., [57, 58] and for a review [59]), not to forget that the technology of producing as well as handling clusters on surfaces is a rich field of its own (for reviews see [59–63]) going far beyond the limits of this chapter.

The emphasis in this chapter is on dynamics. And indeed, still many more possibilities open up in that field for clusters on surfaces. The dynamics of cluster deposit as such has attracted great attention. Most considerations concentrate on ionic motion; particularly theoretical simulations prefer

to deal with effective atom–atom potentials to keep the very complex processes manageable [63–65]. However, electronic dynamics is not always negligible. For example, electron emission and electron transfer during cluster deposit have been observed experimentally [66, 67]. It is yet a challenge for theoretical simulations to describe that properly.

An even wider field of dynamical effects opens up when considering excitation by external sources (applied constant voltage or oscillating laser field). Examples will be presented in subsequent sections (see, e.g., Sections 6.4–6.6).

6.3. Thermodynamics

A basic feature of a many-body system is the specific heat although the experimental assessment of it for a finite and not too large cluster requires very elaborate methods. In an impressive series of diligent experiments, the systematics of caloric curves for positively charge Na clusters has been established down to sizes in the range of $N = 50$. An example is shown in Figure 11. One clearly recognizes the step of the internal energy at the melting point. The results have raised a lot of interesting issues. First of all, there is the general challenge of thermodynamics in finite systems [68]. The particularly exciting feature is the appearance of negative specific heat around the melting point which has been much discussed in several publications (see, e.g., [69, 70]). In spite of the hefty discussion, there are still several features not yet fully understood from the theoretical side (e.g., pronounced peaks in the systematics of the melting temperature which cannot be simply associated with electronic or atomic shell closures).

6.4. Conductivities

A key quantity in constructing nanodevices is the conductivity. The situation is somehow similar to caloric properties. Conductivity is a concept from bulk matter and the transfer to small systems raises many intriguing new questions. For example, detailed structure, orientation, and shaping of the interface all play a role. There is nothing like conductivity as such. The result depends on the whole setup in all
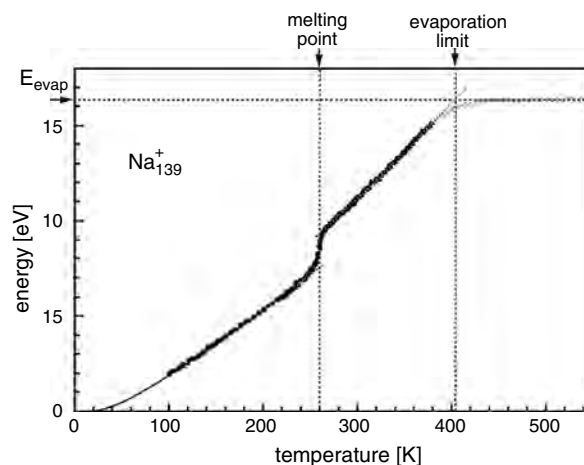

Figure 11. Internal energy of a Na_{139}^+ cluster as function of temperature. Modified from [114].

its details. Much experience has been acquired already in materials similar to metals, namely in polymers and carbon nanotubes [71]. Studies on metal clusters are on the way. Figure 12 shows results for the conductivity of deposited Au nanoclusters [72, 73]. The current–voltage diagrams differ from on-cluster sites to off-clusters sites which demonstrates clearly the impact of cluster conductivity. These studies are still in a developing stage. It is obvious that particularly tailored cluster arrangements will allow a huge variety of response functions which can be exploited for building switches at nanoscale. Such developments need to be accompanied by theoretical methods to cut a path through the swamp of possibilities. Standard methods for electrical circuits become unsafe at nanoscale because surface and quantum effects play a major role. This holds for any geometry; for an example from layered nanostructures see [74]. And it is even more critical for dots and clusters which display different sites. Fully quantum mechanical and microscopic calculations are required here. Examples are the DFT calculations for the condictivity of small, deposited Na clusters in various configurations where linear response techniques were used to obtain the conductivity [75]. One sees a strong dependence of the computed conductivities on cluster size, orientation, and isomeric state, due to pronounced electronic shell effects. This hints that proper tuning of circuitry with nanoclusters will require combined theoretical and experimental effort.

6.5. Laser Burning

With slightly increased laser intensity comes a regime where substantial ionization takes place while the clusters response is still in the (nonlinear) plasmon regime, sensitive to the laser frequency. Thus all the resonance features discussed in Section 4 apply. That means that the resonance position depends on cluster size and on deformation. Now consider an ensemble of clusters attached to a surface. That will cover a certain distribution of sizes and shapes. A powerful laser with well defined frequency will couple only to a fraction of the clusters, namely those whose resonance position happens to come close to the laser frequency. The laser will ionize
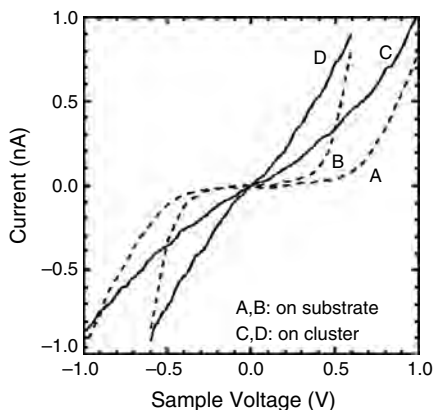
and heat up those clusters to which it is in resonance and these will thus dissappear. One is literally burning a hole into the spectral distribution (i.e., into size and deformation space). The effect is shown in Figure 13. A dip is digged into the given spectral distribution of an ensemble of Ag nanoparticles on a sapphire surface. The depth of the dip increases with increasing energy deposit from the laser. This effect can be exploited to produce cluster ensembles with sharp size distribution and/or well defined orientation. To that end one has to apply successive laser pulses with different frequencies which burn away all the unwanted species.

The method is, of course, more widely applicable. Bleaching of the optical response of mixed clusters, Au capped by CdS, has been reported in [76]. Dedicated destruction and destructive spectral selection has also been applied to change the size and shape of silver clusters embedded in a glass matrix [77]. A new effect appears here. The destruction of a given embedded Ag cluster cannot send the fragments to asymptotically nowhere. They start to move away from the hot cluster but tend to get stuck after a short travel through the glass. Thus they typically remain as a halo of small Ag fragments in the vicinity of a few tens of nm of the original cluster. This can modify the resonance properties by polarization interaction, typically yielding a slight redshift and a broadening.

6.6. Pump and Probe Dynamics

Varying the pulse width is the simplest way to modify the time profile of a laser. Much more information can be gained in pump and probe scenarios where two short pulses follow each other within a well defined and tunable time interval. The method is widely used in molecular physics and
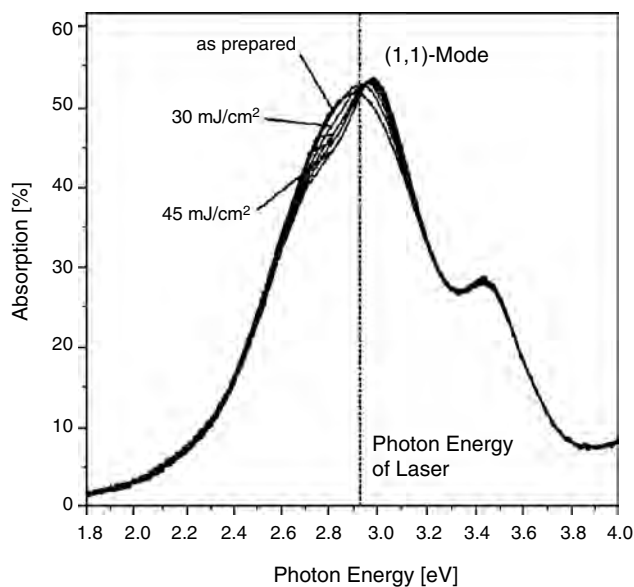
Figure 12. Current–voltage diagrams for Au nanoclusters on a GaAs surface. The measurement was done with a scanning tunneling microscope at different sites (see figure) and for different voltages. Modified from [72].

Figure 13. Optical absorption spectra of large Ag clusters on sapphire substrate under various conditions. First "as prepared" by deposition at room temperature, and further on after application of a strong laser pulse with fluence as labeled. The frequency of the "burning laser" is indicated by a vertical line. Modified from [115].

chemistry. It allows time resolved tracking of molecular reactions and even dedicated switching of them. For an extensive discussion see, for example, [78]. Very detailed information can be extracted for small molecules or compounds with few and well understood reaction channels (for a review see, e.g., [79]). The case of clusters is more demanding in that respect because they possess usually a large amount of accessible degrees of freedom which we still do not know so well. Nonetheless, one has seen several recent promising studies on pump and probe scenarios in metal clusters (see, e.g., [80, 81] for experiments and [82, 83] for theoretical explorations). Figure 14 reports a particularly intriguing case with Hg clusters where a mix of laser ionization experiments and accompanying pump and probe studies were used to eludicate the laser induced nonlinear dynamics. The figure shows the pump and probe signal for several size and charge selected Hg clusters. One is surprised to see almost the same pattern in each case with only a slight variation of the frequency. This suggests that the same subunit is responsible for the process in the different clusters. Collecting information from variation of laser parameters (frequency, intensity) allowed one to confine that to a covalently bound Hg_2 dimer which acts as chromophore and which is placed into a Rydberg state by multiphoton processes. This exerts a pressure on the surrounding Hg atoms of the cluster which then, as a whole, performs a breathing mode. The long time pump and probe signal (not shown here) hints at dissociation and reassembling of the Hg_2 chromophore. Somewhat similar scenarios have been observed with a NO molecule in hydrogen matrix [84].
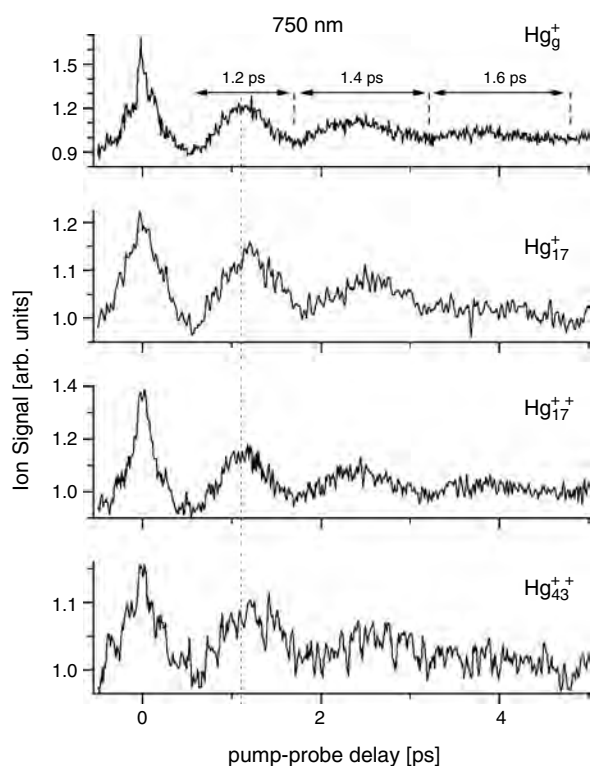
This example dealt with a pump and probe experiment on free clusters. Much more published experiments exist for supported or embedded nanoclusters. The analysis is often combined with SHG (see Section 5.1) to suppress background signals. That way, many relaxation times for supported metal nanoclusters have been measured (e.g., plasmon lifetimes and phonon relaxation for Na_n clusters on an insulating surface [85–87], or plasmon lifetimes for Ag nanoclusters on a surface [39], or ionic relaxation times for Ag clusters in a glass matrix [77, 88]). In fact, pump and probe experiments on or in substrate have the advantages that the orientation is well defined and that temperature can be better controlled. The capabilities of this scenario are yet open for many further studies.

6.7. Other Directions

The previous sections presented mainly future aspects for dynamics in the nonlinear regime. And yet there are as many interesting new features and analyzing tools coming up in less violent excitations. We collect here briefly several examples. Remember that the two regimes are closely linked in that a good knowledge of linear response properties is required for understanding the nonlinear regime while some nonlinear processes, such as SHG, offer useful tools for analyzing structure and weak responses.

Metals in contact with He droplets have given access to new surveys on metal clusters. A seemingly simple system like Mg clusters has been systematically measured only recently with the help of accumulation and production out of He droplets. This revealed a surprising electronic shell structure [89] which cannot be easily explained by standard theoretical models [90] and which thus has triggered an ongoing debate. Another experiment used the spin-selectivity of Na attached to He surfaces to produce Na clusters with totally aligned spin [91], a species which is worth further investigation.

A big step forward in handling of free metal clusters and precision of analysis is attained by experiments in a trap. We mention here two examples, the model free determination of the systematics of dissociation energies [92] and the direct observation of radiative cooling in vanadium clusters which was made possible by the long lifetime of the cluster beam in a trap [93]. That sort of precision experiment will continue to serve as an invaluable complement of the more direct methods on clusters in vapor, on surfaces, or in substrate.

Much progress has been made concerning photoelectron spectroscopy in the linear regime of one-photon processes. This requires laser frequencies well above the ionization threshold and allows then a more or less direct mapping of the single electron levels in the cluster. The method has been used for a long time but was formerly restricted to cluster anions [6]. Modern ultraviolet sources give access to cations, which has already revealed a lot of interesting information on the density of states in free Na_n^+ clusters [94]. A much larger part of the electron spectrum (core states) is accesible by X-rays. These are available now in a versatile manner from synchrotron radiation where frequency and pulse shape can be tuned in a very broad range. Photoelectron spectroscopy with X-rays has already been used successfully to identify the effect of the cluster binding and

Figure 14. Fragmentation yield after pump and probe for different Hg clusters as indicated. Modified from [116].

substrate on the core states of supported Au clusters [95, 96]. One has even disentangled in that way exciton satellites in the spectrum which emerge from coupling of a cluster to excitons in the surrounding substrate [97]. The increasing brilliance and availability of synchrotron radiation will make that a widely used tool for basic cluster research and analysis of nanocluster materials.

Among the advanced analyzing tools is also Raman scattering from supported embedded clusters. The comparatively low density of scatterers in case of cluster ensembles has hindered such experiments for a long while. Meanwhile it seems to be possible to produce sufficient strength of signal and resolution. Examples are successful measurements of monopole plasmon modes in embedded clusters [98]. Note that this mode and all other modes besides the dipole excitations are inaccessible in standard optical absorption experiments due to the dominance of the dipole there. Raman spectroscopy opens the door to unfold the large variety of excitation modes of clusters, monopole or quadrupole plasmon, or the various magnetic excitation modes such as spin modes [99, 100], scissors modes [101], or twist modes [102]. This will provide invaluable new information on cluster dynamics which, in turn, can be exploited for design of nanostructures.

Last not least, there emerge exciting prospects from combination of metal nanoclusters with biological materials. It was shown that metal clusters have a much more enduring luminescence in an organic environment [103], a feature which could possibly be exploited for tagging biochemical reactions in living bodies. Surface effects by interaction with surrounding organic molecules modify the plasmon resonance of metal clusters significantly. That can be exploited to build electro-optical sensors for fast biochemical analysis [104]. In turn, tunable regular structures of proteins can be used as templates to build well defined arrays of metal nanoclusters [105, 106]. Such arrays are very promising switching devices in nanotechnology, having tunable optical response from dielectric cluster–cluster interaction [107] and similarly rich facets of pattern in conductivity [73].

7. CONCLUSIONS

Metal clusters had been the preferred objects of investigations in the early stages of cluster physics due to their pronounced electronic shell structure and the impressive Mie plasmon resonance in the dynamical response. They allowed one for the first time to assess experimentally the phenomenon of supershells. Equally interesting are the optical properties with well understood dependence on size, shape, and material. In spite of the enormous successes of these early studies (which, after all, are only one to two decades old), there remains a rich open field for research with metal clusters, particularly in connection with (nonlinear) cluster dynamics where most of the tools stay just at the start of their career. This holds, for example, for pump and probe studies on clusters, shaping of nanoparticles with dedicated laser beams as practical tools, using the second harmonics from cluster response (in combination with pump and probe) to assess more precisely electronic lifetimes in large clusters, and photoelectron spectroscopy (complemented by

measuring also angular distributions). And even in the seemingly well settled grounds of structure analysis and optical response in the linear regime, there are a lot of intriguing problems. Think, for example, of the thermodynamics of small clusters or the huge field of clusters in contact with other materials (on a surface or embedded into a matrix). After all, we hope to have shown the interesting physics which can be done with metal clusters and the rich future prospects of such research.

GLOSSARY

ATI Above Threshold Ionization (typically in intense laser fields).

Chromophore Light sensitive molecule.

Core electrons Electrons not participating in binding.

Density-functional theory (DFT) Many body theory based on Hohenberg and Kohn theorem stating that the ground state energy of an electronic system can be expressed from the electronic density only in terms of a universal energy-density functional.

Field amplification Non linear amplification of laser field in a (nearly) resonant system.

FWHM Full width at half maximum.

Jellium Approximation to the ionic background through a homogeneous positive background.

Landau damping Damping of the collective mode (e.g. dipole resonance) due to its coupling to the single-particle degrees of freedom.

Local-density approximation (LDA) Approximation of the exchange and correlation functional by taking the infinite-gas energy at the local density of the inhomogeneous system.

Nano-plasma Model for the dynamics of clusters at and after interaction with very intense laser fields, assuming that a large fraction of the core electrons has been locally ionized and sums up to a common electron cloud.

Oblate Pancake shape, i.e. axially symmetric ellipsoid with two longer axes and one shorter axis.

One-particle-one-hole ($1ph$) Single electron excitation from one occupied to another one unoccupied level.

Optical response Photo-absorption strength, imaginary part of the dynamical polarizability (particularly pronounced in metals, see "plasmon").

Photo-electron spectroscopy Measurement of the distribution of kinetic energies from electrons emitted by a cluster through photo-excitation.

Plasmon (Mie surface plasmon) Dominant dipole mode in metals, collective oscillation of the metallic electron cloud with respect to ions.

Prolate Cigar shape, axially symmetric ellipsoid with two shorter axes and one longer axis.

Pseudo-potentials Effective potential for the valence electrons summarizing the efect of core electrons which are elsewise eliminated from the actual calculation.

Pump-and-probe Analysis of dynamics by means of two successive laser pulses; pump pulse excites the system, probe pulses with well defined time offset explore the response.

ACKNOWLEDGMENTS

REFERENCES

1. U. Kreibig and M. Vollmer, "Optical Properties of Metal Clusters." Springer Series in Materials Science, Vol. 25. Springer-Verlag, Berlin, 1993.

2. W. D. Knight, K. Clemenger, W. A. de Heer, W. A. Saunders, M. Y. Chou, and M. L. Cohen, *Phys. Rev. Lett.* 52, 2141 (1984).

3. W. D. Knight, K. Clemenger, W. A. de Heer, and W. A. Saunders, *Phys. Rev. B* 31, 2539 (1985).

4. R. Balian and C. Bloch, *Ann. Phys.* (*NY*) 85, 514 (1974).

5. G. Mie, *Ann. Phys.* (*Leipzig*) 25, 377 (1908).

6. W. A. de Heer, *Rev. Mod. Phys.* 65, 611 (1993).

7. M. Brack, *Rev. Mod. Phys.* 65, 677 (1993).

8. "Clusters of Atoms and Molecules 1—Theory, Experiment, and Clusters of Atoms" (H. Haberland, Ed.), Springer Series in Chemical Physics, Vol. 52. Springer-Verlag, Berlin, 1994.

9. "Clusters of Atoms and Molecules 2—Solvation and Chemistry of Free Clusters, and Embedded, Supported and Compressed Clusters" (H. Haberland, Ed.), Springer Series in Chemical Physics, Vol. 56. Springer-Verlag, Berlin, 1994.

10. "Metal Clusters" (W. Ekardt, Ed.). Wiley, Chicester, UK, 1999.

11. F. Calvayrac, P.-G. Reinhard, E. Suraud, and C. A. Ullrich, *Phys. Rep.* 337, 493 (2000).

12. P.-G. Reinhard, F. Calvayrac, C. Kohl, S. Kümmel, E. Suraud, C. A. Ullrich, and M. Brack, *Euro. Phys. J. D* 9, 111 (1999).

13. V. B. Koutecký, P. Fantucci, and J. Koutecký, *Chem. Rev.* 91, 1035 (1991).

14. M. E. Garcia, G. M. Pastor, and K. H. Benneman, *Phys. Rev. Lett.* 67, 1142 (1991).

15. F. Spiegelmann and R. Poteau, *Comments At. Mol. Phys.* 31, 395 (1995).

16. J. P. S. Bjornholm, J. Borggreen, K. Hansen, T. P. Martin, and H. D. Rasmussen, *Nature* 353, 733 (1991).

17. M. Brack, *Sci. Am.* 277, 50 (1997).

18. V. Bonacic-Koutecky, J. Pittner, C. Fuchs, P. Fantucci, M. F. Guest, and J. Koutecky, *J. Chem. Phys.* 104, 1427 (1996).

19. K. Yabana and G. F. Bertsch, *Phys. Rev. B* 54, 4484 (1996).

20. F. Calvayrac, P.-G. Reinhard, and E. Suraud, *Ann. Phys.* (*NY*) 255, 125 (1997).

21. W. Ekardt, *Phys. Rev. Lett.* 52, 1925 (1984).

22. W. Ekardt and Z. Penzar, *Phys. Rev. B* 43, 1331 (1991).

23. P.-G. Reinhard, O. Genzken, and M. Brack, *Ann. Phys.* (*Leipzig*) 5, 576 (1996).

24. E. M. Lifschitz and L. P. Pitajewski, "Physikalische Kinetik," Vol. X of Lehrbuch der Theoretischen Physik. Mir, Moscow, 1988; see section on Landau damping.

25. J. Babst and P.-G. Reinhard, *Z. Phys. D* 42, 209 (1997).

26. K. Yabana and G. F. Bertsch, *Phys. Rev. A* 58, 2604 (1998).

27. L. Serra and A. Rubio, *Phys. Rev. Lett.* 78, 1428 (1997).

28. R. Englman, "The Jahn–Teller Effect in Molecules and Crystals." Wiley, London, 1972.

29. K. Clemenger, *Phys. Rev. B* 32, 1359 (1985).

30. V. O. Nesterenko, W. Kleinig, and P.-G. Reinhard, *Euro. Phys. J. D* 19, 57 (2002).

31. T. Müller, P. H. Vaccaro, F. Balzer, and H. G. Rubahn, *Opt. Comm.* 153, 103 (1997).

32. F. Balzer, S. D. Jett, and H.-G. Rubahn, *Thin Solid Films* 372, 78 (2000).

33. F. Balzer and H.-G. Rubahn, *Nanotechnology* 12, 105 (2001).

34. T. Goetz, M. Buck, C. Dressler, F. Eisert, and F. Traeger, *Appl. Phys. A* 60, 607 (1995).

35. C. Kohl, P. G. Reinhard, and E. Suraud, *Euro. Phys. J. D* 11, 115 (2000).

36. M. Protopaps, C. H. Keitel, and P. I. Knight, *Rep. Progr. Phys.* 60, 389 (1997).

37. C. J. Joachain, M. Dörr, and N. Kylstra, *Adv. Atom. Mol. Opt. Phys.* 42, 225 (2000).

38. R. Schlipper, R. Kusche, B. von Issendorff, and H. Haberland, *Phys. Rev. Lett.* 80, 1194 (1998).

39. M. Merschdorf, W. Pfeiffer, A. Thon, S. Voll, and G. Gerber, *Appl. Phys. A* 71, 547 (2000).

40. E. Campbell, K. Hansen, K. Hoffmann, G. Korn, M. Tchaplyguine, M. Wittmann, and I. V. Hertel, *Phys. Rev. Lett.* 84, 2128 (2000).

41. A. Pohl, P.-G. Reinhard, and E. Suraud, *Phys. Rev. Lett.* 84, 5090 (2000).

42. B. Baguenard, J. C. Pinar, C. Bordas, and M. Broyer, *Phys. Rev. A* 63, 023204 (2001).

43. T. Weber, M. Weckenbrock, A. Staudte, L. Spielberger, O. Jagutzki, V. Mergel, A. Afaneh, G. Urbasch, M. Vollmer, H. Giessen, and R. Dörner, *J. Phys. B* 33, L127 (2000).

44. A. Pohl, P.-G. Reinhard, and E. Suraud, *J. Phys. B* 34, 4969 (2001).

45. S. Teuber, T. Döppner, T. Fennel, J. Tiggesbäumker, and K. H. Meiwes-Broer, *Euro. Phys. J. D* 16, 59 (2001).

46. P.-G. Reinhard, O. Genzken, and M. Brack, *Ann. Phys.* (*Leipzig*) 5, 1 (1996).

47. U. Saalmann and M. Rost, *Phys. Rev. Lett.* 89, 133401 (2002).

48. C. Kohl, F. Calvayrac, P.-G. Reinhard, and E. Suraud, *Surf. Sci.* 405, 74 (1998).

49. A. Rubio and L. Serra, *Phys. Rev. B* 48, 18222 (1993).

50. T. Jacob, S. Fritzsche, W.-D. Sepp, B. Fricke, and J. Anton, *Phys. Lett. A* 300, 71 (2002).

51. F. Ancilotto and F. Tagio, *Z. Phys. B* 98, 309 (1995).

52. E. Cattaruzza, G. Battaglin, F. Gonella, R. Polloni, G. Mattei, C. Maurizio, P. Mazzoldi, C. Sada, M. Montagna, C. Tosello, and M. Ferrari, *Philos. Mag. B* 82, 735 (2002).

53. C. Bréchignac, P. Cahuzac, F. Carlier, C. Colliex, J. Leroux, A. Masson, B. Yoon, and U. Landman, *Phys. Rev. Lett.* 88, 196103 (2002).

54. L. Badotti, P. Jensen, A. Horeau, M. Treilleux, and B. Cabaud, *Phys. Rev. Lett.* 74, 4694 (1995).

55. A. Sanchez, S. Abbet, U. Heiz, W.-D. Schneider, H. Häkkinen, R. N. Barnett, and U. Landman, *J. Phys. Chem.* 103, 9573 (1999).

56. P. Alvarado, J. Dorantes-Davila, and G. M. Pastor, *Phys. Rev. B* 58, 12216 (1998).

57. J. Bansmann, V. Senz, R.-P. Methling, R. Röhlsberger, and K. H. Meiwes-Broer, *Mater. Sci. Eng. C* 19, 305 (2000).

58. R.-P. Methling, V. Senz, E.-D. Klinkenberg, T. Diederich, J. Tiggesbäumker, G. Holzhöter, J. Bansmann, and K. H. Meiwes-Broer, *Euro. Phys. J. D* 16, 173 (2001).

59. C. Binns, *Surf. Sci. Rep.* 44, 1 (2001).

60. G. E. Engelmann, J. C. Ziegler, and D. M. Kolb, *Surf. Sci. Lett.* 401, L420 (1998).

61. T. A. Winninghama, H. P. Gillisb, D. A. Choutovc, K. P. Martinc, J. T. Moorea, and K. Douglasa, *Surf. Sci.* 406, 221 (1998).

62. D. B. Janes, M. Batistuta, S. Datta, M. R. Melloch, R. P. Andres, J. Liu, N.-P. Chen, T. Lee, R. Reifenberger, E. H. Chen, and J. M. Woodall, *Superlat. Microstruct.* 27, 555 (2000).

63. C. Xirouchaki and R. E. Palmer, *Vacuum* 66, 167 (2002).

64. H. Haberland, Z. Insepov, and M. Moseler, *Z. Phys. D* 26, 229 (1993).

65. Q. Hou, M. Hou, L. Bardotti, B. Prevel, P. Melinon, and A. Perez, *Phys. Rev. B* 62, 2825 (2000).

66. O. Speer, M. E. Garcia, B. W., and K. H. Meiwes-Broer, *Surf. Sci.* 443, 195 (1999).

67. M. Fallavier, R. Kirsch, J. C. Poizat, J. Remillieux, and J. P. Thomas, *Nucl. Instrum. Methods B* 164–165, 920 (2000).

68. D. H. E. Gross, "Microcanonical Thermodynamics." World Scientific, Singapore, 2001.

69. G. Bertsch, *Science* 277, 1619 (1997).

70. S. Berry, *Nature* 393, 212 (1998).

71. A. B. Kaiser, *Rep. Progr. Phys.* 64, 1 (2001).

72. T. Lee, J. Liu, D. B. Janes, V. R. Kolagunta, J. Dicke, R. P. Andres, J. Lauterbach, M. R. Melloch, D. McIntruff, J. M. Woodall, and R. Reifenberger, *Appl. Phys. Lett.* 76, 212 (2000).

73. T. Lee, J. Liu, N.-P. Chen, R. P. Andres, D. B. Janes, and R. Reifenberger, *J. Nanopart. Res.* 2, 345 (2000).

74. L. Shifren and D. K. Ferry, *Physica B* 314, 72 (2002).

75. R. Gutierrez, F. Grossmann, O. Knospe, and R. Schmidt, *Phys. Rev. A* 64, 013202 (2001).

76. P. V. Kamat and B. Shangkavi, *J. Phys. Chem. B* 101, 7675 (1997).

77. G. Seifert, M. Kaempfe, K.-J. Berg, and H. Graener, *Appl. Phys. B* 71, 795 (2000).

78. A. H. Zewail, "Femtochemistry," Vols. I and II. World Scientific, Singapore, 1994.

79. B. M. Garraway and K.-A. Suominen, *Rep. Progr. Phys.* 58, 365 (1995).

80. T. Leisner, S. Vajda, S. Wolf, and L. Wöste, *J. Chem. Phys.* 111, 1017 (1999).

81. R. Heinicke and J. Grotemeyer, *Appl. Phys. B* 71, 419 (2000).

82. M. Hartmann, J. Pittner, V. Bonacic-Koutecky, A. Heidenreich, and J. Jortner, *J. Chem. Phys.* 108, 3096 (1998).

83. K. Andrae, P.-G. Reinhard, and E. Suraud, *J. Phys. B* 35, 1 (2002).

84. C. Jeannin, M. T. Portella-Oberli, F. Vigliotti, and M. Cherugi, *Chem. Phys. Lett.* 279, 65 (1997).

85. J.-H. Klein-Wiele, P. Simon, and H.-G. Rubahn, *Phys. Rev. Lett.* 80, 45 (1997).

86. J.-H. Klein-Wiele, P. Simon, and H.-G. Rubahn, *Phys. Rev. Lett.* 80, 45 (1998).

87. J.-H. Klein-Wiele, P. Simon, and H.-G. Rubahn, *Opt. Comm.* 161, 42 (1999).

88. C. Voisin, D. Christofilos, N. D. Fatti, F. Vallée, B. Prövel, E. Cottancin, J. Lermé, M. Pellarin, and M. Broyer, *Phys. Rev. Lett.* 85, 2200 (2000).

89. T. Diederich, T. Döppner, J. Tiggesbäumker, and K.-H. Meiwes-Broer, *Phys. Rev. Lett.* 86, 4807 (2001).

90. L. Serra, P.-G. Reinhard, and E. Suraud, *Euro. Phys. J. D* (2002).

91. C. P. Schulz, P. Class, and F. Stienkemeier, preprint, 2002.

92. M. Vogel, K. Hansen, A. Herlert, and L. Schweikhard, *Phys. Rev. Lett.* 87, 013401 (2001).

93. C. Walther, G. Dietrich, W. Dostal, K. Hansen, S. Kruckeberg, K. Lutzenkirchen, and L. Schweikhard, *Phys. Rev. Lett.* 83, 3816 (1999).

94. G. Wrigge, M. A. H., and B. v Issendorff, *Phys. Rev. A* 65, 063201 (2002).

95. D. Dalacu, E. Klemberg-Sapieha, and L. Martinu, *Surf. Sci.* 472, 33 (2001).

96. T. Ohgi and D. Fujita, *Phys. Rev. B* 66, 115410 (2002).

97. U. Hergenhahn, A. Kolmakov, M. Riedler, A. R. B. de Castro, O. Lofken, and T. Moller, *Chem. Phys. Lett.* 351, 235 (2002).

98. H. Portales, L. Saviot, E. Duva, M. Fujii, S. Hayashil, N. D. Fatti, and F. Vallée, *J. Chem. Phys.* 115, 3444 (2001).

99. L. Serra, R. A. Broglia, M. Barranco, and J. Navarro, *Phys. Rev. A* 47 (1993).

100. C. Kohl, S. M. El-Gammal, F. Calvayrac, E. Suraud, and P.-G. Reinhard, *Euro. Phys. J. D* 5, 271 (1999).

101. V. O. Nesterenko, W. Kleinig, F. F. de Souza Cruz, and N. L. Iudice, *Phys. Rev. Lett.* 83, 57 (1999).

102. J. R. Marinelli, V. Nesterenko, F. F. de Souza-Cruz, W. Kleinig, and P.-G. Reinhard, *Phys. Rev. Lett.* 85, 3141 (2000).

103. M. B. Jr, M. Moronne, P. Gin, S. Weiss, and A. P. Alivisato, *Science* 281, 2013 (1998).

104. C. Mayer, R. Palkovits, G. Bauer, and T. Schalkhammer, *J. Nanopart. Res.* 3, 361 (2001).

105. M. Mertig, R. Kirsch, W. Pompe, and H. Engelhardt, *Euro. Phys. J. D* 9, 45 (1998).

106. A. Mertig, R. Wahl, M. Lehmann, P. Simon, and W. Pompe, *Euro. Phys. J. D* 16, 317 (2001).

107. V. Russier and M. P. Pileni, *Surf. Sci.* 425, 313 (1999).

108. T. Reiners, C. Ellert, M. Schmidt, and H. Haberland, *Phys. Rev. Lett.* 74, 1558 (1997).

109. S. Fedrigo, W. Harbich, and J. Buttet, *Phys. Rev. B* 47, 10706 (1993).

110. J. Borggreen, P. Chowdhury, N. Kebaili, L. Lundsberg-Nielsen, K. Luetzenkirchen, M. B. Nielsen, J. Pedersen, and H. D. Rasmussen, *Phys. Rev. B* 48 (1993).

111. H. Haberland and M. Schmidt, *Euro. Phys. J. D* 6, 109 (1999).

112. P.-G. Reinhard and E. Suraud, in "Resonance Dynamics in Metal Clusters and Nuclei" (W. Ekardt, Ed.). Wiley, New York, 1999.

113. T. Diederich, J. Tiggesbümker, and K. H. Meiwes-Broer, *J. Chem. Phys.* 116, 3263 (2002).

114. M. Schmidt, T. Hippler, J. Donges, W. Kronmüller, B. v Issendorff, H. Haberland, and P. Labastie, *Phys. Rev. Lett.* 87, 203402 (2001).

115. T. Vartanyan, J. Bosbach, F. Stietz, and F. Träger, *Appl. Phys. B* 73, 391 (2002).

116. B. Bescos, B. Lang, J. Weiner, V. Weiss, E. Wiedemann, and G. Gerber, *Euro. Phys. J. D* 9, 399 (1999).

Elastic Models for Carbon Nanotubes

C. Q. Ru

University of Alberta, Edmonton, Canada

CONTENTS

1. INTRODUCTION

Nanotechnology is rapidly developing into engineering disciplines and is predicted to spark a series of industrial revolutions in the next decades [1–3]. A most significant breakthrough that could accelerate this process is the discovery of carbon nanotubes (CNTs) in 1991 [4]. CNTs are only few nanometers in diameter and possess many superior electronic and mechanical properties over any other known material [5–10]. To mention a few, CNTs are about 6 times lighter and 10 times stronger than steel, can conduct electricity better than copper and transmit heat better than diamonds, and can sustain large elastic strain more than 5%. CNTs hold substantial promise as the leading candidate material for nanoelectronics [11–15], nanodevices [16–20], and superstrong nanocomposites [21–26].

Most potential applications of CNTs are heavily based on a thorough understanding of their mechanical behavior. For example, experiments and molecular dynamics simulations showed that electronic properties of CNTs can be changed by mechanical deformations up to several orders of magnitude [27–32]. This can explain why the study of mechanical behavior of CNTs has been one topic of major concern [33–50]. Among various methods, solid mechanics (such as elastic beam or shell) models have been widely and successfully used to study CNTs. Many studies indicated "the laws of continuum mechanics are amazingly robust and allow one to treat even intrinsically discrete objects only a few atoms in diameter" [6]. Particularly, elastic models provide simple formulas in many important cases which clearly identify major factors affecting mechanical behavior of carbon nanotubes. Indeed, because controlled experiment at

nanoscale is usually difficult, and molecular dynamics simulation remains expensive and formidable especially for large sized atomic systems, solid mechanics models offer a cost-effective alternative method for the study of CNTs. On the other hand, owing to new phenomena at nanoscale, traditional solid mechanics models cannot be applied to CNTs in many cases of practical and academic interest. This has raised a major challenge to solid mechanics.

This chapter gives an overview of elastic models for CNTs. Comparison between elastic models and available experiments or molecular dynamics simulations is highlighted. This overview will be limited to reversible and relatively small elastic deformations of CNTs and thus will not cover other topics such as plastic yielding [6, 51, 52] and fracture [6, 21, 40, 53, 54] of CNTs. Examples given below will clearly demonstrate the effectiveness of elastic models to CNTs. On the other hand, many complex physical phenomena due to intertube displacements in CNTs and the associated van der Waals forces require new and more ingenious elastic models.

2. ELASTIC BEAM MODELS

CNTs are only few nanometers in diameter, while as long as a few mm. Therefore, the aspect ratio of CNTs is usually very large, up to 1000 or beyond, although shorter CNTs of aspect ratio as small as 10 or 20 are also used in some cases, such as CNT-based nanotweezers [18] and atomic force microscope (AFM) tips [16, 55, 56]. In all these cases, because there are large number of atoms along the longitudinal direction, the elastic rod or elastic beam model is adequate for overall mechanical deformation of CNTs. It is known that transverse dynamics of an elastic beam under axial force F and transverse distributed pressure $p(x)$ (per unit axial length) is governed by [57, 58]

$$p(x) + F\frac{\partial^2 w}{\partial x^2} = EI\frac{\partial^4 w}{\partial x^4} + \rho A\frac{\partial^2 w}{\partial t^2} \qquad (1)$$

where x is the axial coordinate, t is time, $w(x,t)$ is the deflection of the beam, I and A are the moment of inertia and the area of the cross-section of the beam, and E and ρ

are Young's modulus and the mass density (per unit volume). Thus, (ρA) is the mass density per unit axial length, (EI) represents the bending stiffness of the beam, and (EA) represents the axial stiffness which is defined by the axial force divided by the axial strain [the latter does not appear explicitly in Eq. (1)]. In addition, bending moment M and transverse shear force V are given by

$$M = EI\frac{\partial^2 w}{\partial x^2} \qquad V = EI\frac{\partial^3 w}{\partial x^3} \qquad (2)$$

These equations provide a complete description of elastic beam model with appropriate boundary conditions (such as pinged, clamped, and free ends).

In order to apply elastic beam model (1) to CNTs, it is sufficient to know the mass density per unit axial length (ρA), the bending stiffness (EI), and the axial stiffness (EA). Once the three parameters are known, the deflection of CNTs can be determined by (1) even without knowing the details of the cross-sectional geometry (such as I and A). Recognition of this simple fact is important for understanding applicability of the elastic beam model to one-dimensional nanoscale structures, such as CNTs or DNA molecules [59, 60] which are only few atoms in diameter and thus questionable as far as applicability of continuum models across their cross-sections. For instance, there have been different opinions on the thickness of single-wall nanotubes (SWNTs). Although most researchers have adopted the equilibrium interlayer spacing between adjacent nanotubes (about 0.34 nm) as the representative thickness of SWNTs combined with a Young modulus of about 1 TPa, some authors have suggested a much smaller thickness (say, 0.07 nm; see Yakobson et al. [6, 34]) combined with a Young's modulus of about 5 TPa. It is obvious that axial stiffness (EA) remains unchanged if the Young's modulus is 5 times larger and, at the same time, the thickness is 5 times smaller. Furthermore, it is readily seen that these different definitions of thickness do not significantly affect the value of bending stiffness (EI) provided the cross-section of SWNTs is treated as a thin annulus. Thus, the governing equation (1) and the overall deflection of SWNTs remain essentially unchanged when these different thicknesses of SWNTs are adopted.

2.1. Single-Beam Models

Elastic beam models have been effectively applied to CNTs by many researchers. As will be shown below, elastic models offer simple general formulas in many important cases which clearly summarize major factors affecting basic mechanical properties of CNTs. Usually, such simple formulas cannot be achieved by other methods.

2.1.1. Static Deflection

For a cantilever beam of length L under a concentrated force P at a point $x = a$ measured from the fixed end, the deflection at any point between $x = a$ and the free end $x = L$ is (see [61], p. 892)

$$y = \frac{Pa^2}{6EI}(3x - a) \qquad a \le x \le L \qquad (3)$$

The $1/a^3$ dependency of P/y when $x = a$ predicted by this formula has been confirmed by the experimental data for CNTs [35]. As another example, maximum deflection of a simple beam under a concentrated force P applied at its midway is (see [61], pp. 707 and 895)

$$y = \frac{PL^3}{48EI} \qquad (4)$$

where the number 48 becomes 192 for a clamped beam. This relation has been used [62] to estimate the Young's modulus of CNTs based on experimental data of the maximum deflection. The estimated value $(E = 0.81$ TPa) is in good agreement with the values obtained by other methods. It is emphasized that the thickness of SWNTs in these studies has been taken as 0.34 nm and the thickness of multiwall nanotubes (MWNTs) has been calculated by the difference of the outermost radius R_{out} and the innermost radius R_{in}, and thus $I = \pi(R_{\text{out}}^4 - R_{\text{in}}^4)/4$.

2.1.2. Column Buckling

Dai et al. [16] used MWNTs as AFM tips and treated them as a hinged elastic column, and thus the maximum axial force MWNTs could sustain is estimated by the Euler force given by [61]

$$P = \frac{\pi^2 EI}{L^2} \qquad (5)$$

Assuming $E = 1$ TPa, for example, these authors found that the Euler force for a 250-nm-long, 5-nm-diameter MWNT (treated as a column of solid circular cross-section) is about 5 nN. The Euler force is also estimated by Yao and Lordi [63] for some other examples of CNTs. In particular, the Young's modulus of CNTs has been estimated by comparing the values of Euler force obtained by molecular dynamics simulations with those given by (5); see Garg et al. [64]. Their results confirmed that the Young's modulus estimated by such a comparison is around 1 TPa, in satisfactory agreement with the values obtained by other methods. Yakobson et al. [6] studied SWNTs as clamped column and calculated the Euler force from the above formula (5) multiplied by a factor of 4 to its right-hand side [61]. On the other hand, CNTs as AFM tip to very smooth surface could be modeled as a cantilever elastic column. In that case, a factor of $\frac{1}{4}$ will have to be multiplied to the right-hand side of (5) [61], and thus the Euler force for a cantilever column is just 25% of that given by (5) for a hinged column. Indeed, the sensitivity of the Euler force of CNTs to the end conditions should be examined in more detail.

2.1.3. Buckling-Driven Debonding of CNT Ropes

As a major form of CNTs, CNT ropes composed of aligned CNTs with narrow distribution of diameters and geometries have been widely used in the study of CNTs. An interesting theoretical issue which has not been addressed in the literature is buckling-driven debonding of individual CNTs from a CNT rope. For instance, consider a CNT rope consisting of a large number of CNTs under axial compression. Because the Euler strain for column buckling is roughly proportional

to the squared radius of the cross-section, the Euler strain for the rope should be much larger than the Euler strain for a single CNT, and thus column buckling of the rope as a whole will not occur when the applied axial strain exceeds the Euler strain for a single CNT but is well below the Euler strain for the rope. It is the intertube van der Waals adhesive energy that keeps individual CNTs together and prevents Euler buckling of individual CNTs from the rope. In this case, the difference between the elastic energy stored in a straight (unbuckled) single CNT and the elastic energy of its bucked state offers a driving force for debonding and buckling of a single CNT from the rope. For example, the linear bucked deflection of a clamped single CNT under an axial strain ε (exceeding its Euler strain ε_{cr}) can be estimated by [65, 66]

$$w(x) = \frac{w_0}{2}\left[1 + \cos\frac{2\pi x}{L}\right] \qquad w_0^2 = (\varepsilon - \varepsilon_{cr})\left(\frac{2L}{\pi}\right)^2 \qquad (6)$$

where the origin $x = 0$ is at the midway of the CNT of length L. It can be verified that the elastic energy stored in a straight (unbuckled) single CNT and the elastic energy of its bucked state are

$$U_1 = \frac{1}{2}EAL\varepsilon^2 \qquad U_2 = \frac{EAL}{2}\left[2\varepsilon\varepsilon_{cr} - \varepsilon_{cr}^2\right] \qquad (7)$$

respectively, where A is the across-sectional area of the bucked CNT. Thus, an individual CNT could split from the rope only when the difference between the two energies exceeds the van der Waals adhesive energy between the CNT and the rope, namely

$$\Delta U = U_1 - U_2 = \frac{EAL}{2}[\varepsilon - \varepsilon_{cr}]^2 \geq \gamma L \qquad (8)$$

where γ is the adhesive energy per unit length of the bucked CNT. For instance, the adhesive energy is about 0.01–0.03 eV/C-atom, and the average area of a C-atom is about 2.6×10^{-20} m^2 [67–70]. Thus, if the contact width between an outermost SWNT and the SWNT rope is estimated roughly by the radius R of the SWNT, then condition (8) is satisfied when $(\varepsilon - \varepsilon_{cr})$ is significantly larger than 0.01. This implies that debonding of individual SWNTs could occur prior to Euler buckling of the rope as a whole when the aspect ratio of the ropes is small enough (say, around 10) that the Euler axial strain of the rope is significantly larger than 0.01.

Furthermore, if debonding growth of a preexisting debond of length L is considered, the growth condition is that the energy release rate is greater than the adhesive energy per unit length, namely

$$G = \frac{EA}{2}\varepsilon^2 - \frac{\partial U_2}{\partial L} = \frac{EA}{2}[\varepsilon - \varepsilon_{cr}](\varepsilon + 3\varepsilon_{cr}) \geq \gamma \qquad (9)$$

It is obvious that satisfaction of (8) ensures satisfaction of (9), which implies that debonding would be unstable once it is initiated. To our best knowledge, these interesting issues for CNTs have not been studied in the literature.

2.1.4. Winkler Model

CNTs have been suggested as reinforcement fibers for superstrong composites [21–26]. Therefore, the role of surrounding elastic medium in mechanical behavior of embedded CNTs is a significant topic. A simplified model for the surrounding elastic medium is provided by the Winkler-like model [71, 72] which assumes that interaction pressure acting on the embedded CNT per unit length is given by

$$p = -ky(x) \qquad (10)$$

where $y(x)$ is the deflection of the embedded CNT, and k is a spring constant of the surrounding elastic medium which may depend not only on the Young's modulus of the surrounding elastic medium and the outermost diameter of the CNT, but also on the wave-length of the deformed CNT. The minus sign on the right-hand side indicates that the interaction pressure is opposite to the deflection. This simplest model has been used to study column buckling of embedded CNTs by Lourie et al. [21] and Ru [44], and vibration of embedded MWNTs by Yoon et al. [73].

2.1.5. Resonant Frequencies

The n-order resonant (circular) frequency of a MWNT of length L, given by the single-beam model [33, 37, 49, 57, 58], has the form

$$\omega_n = \frac{\beta_n^2}{L^2}\sqrt{\frac{EI}{\rho A}} = \frac{\beta_n^2}{2L^2}\sqrt{\frac{E(R_{\text{out}}^2 + R_{\text{in}}^2)}{\rho}} \qquad (11)$$

where ρ is the mass density (per unit volume) of CNTs, I and A are the moment of inertia and the area of the cross-sectional of MWNT, and R_{out} and R_{in} are the outermost and the innermost radii. In addition, β_n is a constant depending on the number n and end conditions. For instance, for fixed end conditions (that is, all nested individual tubes of the MWNT are clamped at both ends), $\beta_1 = 4.73$, $\beta_2 = 7.85$, $\beta_3 = 10.996$. For cantilever end conditions, $\beta_1 = 1.875$, $\beta_2 = 4.694$, $\beta_3 = 7.855$; see [57, 58]. If the CNT is embedded in an elastic medium characterized by the Winkler model (10), the n-order resonant (circular) frequency is [57, 73]

$$\omega_n = \sqrt{\frac{\frac{\beta_n^4}{L^4}EI + k}{\rho A}} \qquad (12)$$

Prior experiments [33, 37, 49] have convincingly shown that resonant frequencies of CNTs can be calculated by the formula (11). For example, for a CNT tested in [37], the experimental ratio ω_2/ω_1 is 5.68, in good agreement with the theoretical ratio 6.2 predicted by (11). In addition, the second-order vibrational mode was observed in [37], and the experimental value of a characteristic length is $0.76L$, in good agreement with the theoretical value $0.8L$.

2.1.6. Sound Wave Speeds

It is well known that longitudinal and transverse sound wave speeds (phase velocity) in an elastic beam are [74]

$$v_L = \sqrt{\frac{E}{\rho}} \qquad v_T = \left(\frac{EI\omega^2}{\rho A}\right)^{1/4} \qquad (13)$$

In particular, the transverse speed v_T depends on both the frequency ω and the cross-sectional shape, while the longitudinal speed v_L depends on none of them. Popov et al. [39] have used these formulas to calculate sound speeds along CNTs. The value of Young's modulus of CNTs obtained by (13) based on a comparison with another method is about 1 TPa, in good agreement with the known values. This indicates that the classic elastic beam formulas (13) can be applied to sound wave propagation in CNTs [39, 75, 76].

2.2. Multiple-Beam Models

Carbon MWNTs are different from traditional elastic beams due to their hollow multilayer structure and the associated interlayer van der Waals forces. On one hand, it is known that friction between adjacent tubes in MWNTs is so low that the adjacent tubes could easily slide to each other [19, 77, 78]. On the other hand, although the van der Waals repulsive forces resist any reduction of interlayer spacing between adjacent tubes in MWNTs, it is not clear whether the magnitude of the repulsive forces in CNTs is so strong that the change in interlayer spacing in MWNTs can always be neglected even in some extreme cases. In spite of this, all previous beam models, such as those mentioned above, have ignored interlayer radial displacements in MWNTs and treated a MWNT as a single elastic beam. The single-beam model [38, 46] assumes that all originally concentric tubes of a MWNT remain coaxial during deformation and thus can be described by a single deflection curve. In reality, however, individual tubes of a MWNT could deform individually with nonzero interlayer radial displacements, while their individual deformations are coupled through the interlayer van der Waals interaction.

2.2.1. Column Buckling of MWNTs

In order to identify the condition under which interlayer radial displacements between adjacent tubes in MWNTs cause new physical phenomena and thus are not negligible, a multiple-elastic beam model has been developed in [44] to study column buckling of carbon MWNTs embedded within an elastic medium. In contrast to the existing single-beam model, the multiple-elastic beam model assumes that each of the nested, originally concentric SWNTs is an individual elastic beam, and the deflections of all elastic beams are coupled through the van der Waals interaction between adjacent nanotubes. Thus, Eq. (1) is applied to each nested tube of the MWNT. Assuming that the interaction between the outermost tube and the surrounding elastic medium is described by a Winkler model (10), it is found [44] that the noncoincidence of the deflected axes is negligible provided the half wavelength of the buckling mode is much larger than the outermost diameter. Under this condition, the existing single-beam model gives a satisfactory estimate of the critical axial strain. However, the single-beam model is invalid when the half wavelength is comparable to the outermost radius. This study reveals that the single-beam model for MWNTs becomes invalid when the characteristic wavelength of MWNTs is comparable to their outermost diameter.

2.2.2. Noncoaxial Vibration of MWNTs

In many proposed applications, shorter CNTs of smaller aspect ratio are often used [16, 18, 55, 56]. In this case, because the characteristic wavelengths of higher-order modes are just few times the outermost diameter, it is anticipated that the interlayer radial displacements of MWNTs would come to play a significant role and give rise to new resonant frequencies and associated noncoaxial intertube vibration. Although the noncoaxial intertube vibration would not significantly affect overall deflection of the outermost tube, it could cause noncoaxial deformation and distort otherwise concentric geometry of MWNTs. In particular, noncoaxial distortion could significantly affect some important physical (especially electronic and optical) properties of MWNTs [20, 79–88]. Hence, it is relevant to study when vibration of MWNTs becomes substantially noncoaxial.

To clearly demonstrate essential concepts of noncoaxial vibration of MWNTs, let us consider a double-wall nanotube (DWNT) [89–91] of length L; see Figure 1. The interaction pressure between the inner and outer tubes can be estimated by the known van der Waals interaction between a carbon atom and a flat graphite sheet [67], and the van der Waals normal pressure between the inner and outer tubes at any point is assumed to depend on the interlayer spacing at that point. Thus, the coefficient of interaction pressure can be estimated using recent date given in [89], with the result

$$c = \frac{3.2 \times 10^2 \text{ ergs/cm}^2}{0.16d^2} \qquad d = 0.142 \text{ nm} \qquad (14)$$

which is slightly bigger than that used in [48]. Here, the curvature effect has been ignored because it is usually small for MWNTs of larger innermost radius [92–94]. Thus, the interaction coefficient per unit length of MWNTs between any two adjacent SWNTs is proportional the diameter of the inner tube and is given by

$$c = \frac{3.2 \times 10^2(2R_{\text{in}}) \text{ ergs/cm}^2}{0.16d^2} \qquad d = 0.142 \text{ nm} \qquad (15)$$

where R_{in} is the radius of the inner tube. Applying Eq. (1) to each of the two concentric tubes, the multiple-beam model gives the equations for vibration of a DWNT as [95]

$$c[w_2 - w_1] = EI_1\frac{\partial^4 w_1}{\partial x^4} + \rho A_1\frac{\partial^2 w_1}{\partial t^2}$$
$$-c[w_2 - w_1] = EI_2\frac{\partial^4 w_2}{\partial x^4} + \rho A_2\frac{\partial^2 w_2}{\partial t^2} \qquad (16)$$

where $w_1(x, t)$ and $w_2(x, t)$ are the deflections of the inner tube and the outer tube, I_k and A_k $(k = 1, 2)$ are their
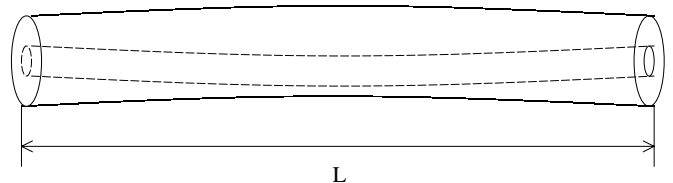

Figure 1. Noncoaxial vibration of a double-wall carbon nanotube.

moment of inertia and the area of the cross-section, respectively, and the two tubes have the same Young's modulus E and the mass density ρ per unit volume. It is seen from (16) that vibration of the inner tube is coupled with vibration of the outer tube through the van der Waals interaction. Equation (16) is mathematically similar to the governing equations for vibration of an elastically connected double-beam system [96], or coupled harmonic oscillators [97, 98]. Here, let us consider the case in which the inner and outer nanotubes have the same end conditions. Thus, the inner and outer tubes share the same vibrational mode $Y(x)$ determined by

$$\frac{d^4 Y(x)}{dx^4} = \lambda^4 Y(x) \tag{17}$$

with the given end conditions. The value λ and the associated mode $Y(x)$ are determined as the eigenvalue and associated eigenfunction of (17) with the given end conditions. For instance, for fixed end conditions, the first three eigenvalues of (17) are $\lambda_1 L = 4.73$, $\lambda_2 L = 7.85$, and $\lambda_3 L = 10.996$. For cantilever end conditions, $\lambda_1 L = 1.875$, $\lambda_2 L = 4.694$, and $\lambda_3 L = 7.855$ [57, 58]. Thus, for the n-order vibrational mode $Y_n(x)$ [$n = 1, 2, \ldots$, defined by the eigenfunction associated with the nth eigenvalue of (17)], the frequency equation can be obtained by substituting $w_1 = a_1 e^{i\omega t} Y_n(x)$, $w_2 = a_2 e^{i\omega t} Y_n(x)$ to (16), where a_1 and a_2 represent the amplitudes of the inner and the outer tubes, respectively, and ω is the (circular) frequency. It turns out that, in contrast to the only n-order resonance frequency (11) given by the single-beam model [33, 37, 49], the multiple-beam model [95] predicts two n-order resonant (circular) frequencies as

$$\omega_{n1}^2 = \frac{1}{2}\left(\alpha_n - \sqrt{\alpha_n^2 - 4\beta_n}\right) \qquad \omega_{n2}^2 = \frac{1}{2}\left(\alpha_n + \sqrt{\alpha_n^2 - 4\beta_n}\right) \tag{18}$$

where

$$\begin{aligned} \alpha_n &= \frac{EI_1 \lambda_n^4 + c}{\rho A_1} + \frac{EI_2 \lambda_n^4 + c}{\rho A_2} > \sqrt{4\beta_n} \\ \beta_n &= \frac{EI_1 EI_2 \lambda_n^8}{\rho^2 A_1 A_2} + c\lambda_n^4 \frac{EI_1 + EI_2}{\rho^2 A_1 A_2} \end{aligned} \tag{19}$$

Here, ω_{n1} is the lower n-order resonant frequency, and ω_{n2} is the higher n-order resonant frequency.

It is found in [95] that (1) the lower n-order resonant frequency ω_{n1} is always close to the frequency (11) given by the single-beam model, and the associated amplitude ratio a_1/a_2 is very close to unity and thus the associated vibrational mode is almost coaxial; (2) the higher n-order resonant frequency ω_{n2} is insensitive to the mode number n, the length of the MWNTs, and the end conditions and is substantially noncoaxial characterized by negative amplitude ratio a_1/a_2 which indicates that the deflection of the inner tube is opposite to the deflection of the outer tube. When the aspect ratio of the MWNTs is very large (say, >100), the noncoaxial resonant frequency ω_{n2} is much higher than the lower one ω_{n1} and the frequency (11) given by the single-beam model. In this case, the influence of the noncoaxial mode associated with the resonant frequency ω_{n2} can usually be ignored and thus the single-beam model is accurate enough

for (almost coaxial) vibration of MWNTs of larger aspect ratio, such as those studied in [33, 37, 49]. However, for shorter CNTs of relatively small aspect ratio (say, between 10 and 25 [55, 56]), the noncoaxial resonant frequency ω_{n2} is comparable to the first few high-order frequencies given by (11) (say, for $n = 3, 4$, or 5), and thus vibration of MWNTs is essentially noncoaxial and cannot be described by the single-beam model. For example, for a DWNT of inner diameter 0.7 nm [89–91, 95] and aspect ratio 10, the noncoaxial (circular) frequency ω_{n2} (for $n = 1, 2, 3, 4$, or 5) is around 10 THz, comparable to the third-order classic frequency given by (11), 7.2 THz, and the fourth-order classic frequency, 10.6 THz. This implies that noncoaxial internal resonance will be excited at the higher natural frequencies and MWNTs cannot keep their concentric structure at ultrahigh frequencies. In this case, the noncoaxial vibration would lead to nonconcentric distortion of MWNTs and thus crucially alter some important physical properties of MWNTs.

Similar results have been drawn for MWNTs of more than two layers [95] and MWNTs embedded within an elastic medium [73]. Further research subjects in this direction may include the effect of individual end conditions (for instance, all inner tubes of a MWNT are hinged or free at the ends, while the outermost tube is clamped) and forced noncoaxial vibration of MWNTs.

2.2.3. Sound Wave Propagation in MWNTs

In view of rapid advances in nanoelectromechanical systems [99, 100] and rapidly growing interest in terahertz physics of nanoscale materials and devices [101–106], a relevant open problem is terahertz sound wave propagation in CNTs. The multiple-beam model has been used to study terahertz sound wave propagation in MWNTs [107]. For instance, for a sinusoid propagating in an infinite DWNT, the transverse sound wave speed can be studied by substituting $w_1 = a_1 e^{i(kx-\omega t)}$, $w_2 = a_2 e^{i(kx-\omega t)}$ to (16), where a_1 and a_2 are the amplitude coefficients of the inner and outer tubes, respectively, and k and ω are the wave number and the frequency. For given (circular) frequency ω, in contrast to the only sound speed of a DWNT given by the single-beam model (13) [39], the multiple-beam model [107] predicts that a DWNT could have two sound speeds given by

$$v_1 = \frac{\sqrt[4]{2}\,\omega}{\sqrt[4]{\alpha + \sqrt{\alpha^2 - 4\beta}}} \qquad v_2 = \frac{\sqrt[4]{2}\,\omega}{\sqrt[4]{\alpha - \sqrt{\alpha^2 - 4\beta}}} \tag{20}$$

where ($\alpha^2 \geq 4\beta$)

$$\begin{aligned} \alpha &= \left(\frac{\rho A_1}{EI_1} + \frac{\rho A_2}{EI_2}\right)\omega^2 - \left(\frac{1}{EI_1} + \frac{1}{EI_2}\right)c \\ \beta &= \frac{\rho^2 A_1 A_2}{EI_1 EI_2}\omega^4 - c\omega^2 \frac{\rho(A_1 + A_2)}{EI_1 EI_2} \end{aligned} \tag{21}$$

and the coefficient c is given by (15). It can be verified that v_1 given by (20) is always positive, while v_2 is real only for sufficiently high frequency. Thus, there is a critical frequency above which both v_1 and v_2 given by (20) are positive. This critical frequency, somewhat similar to the

so-called "cutoff frequency" in some elastic beam structures [58], is given by

$$\omega_{cr} = \sqrt{\frac{(A_1 + A_2)c}{\rho A_1 A_2}} \qquad (22)$$

Notice here that the critical frequency (22) is very close to the noncoaxial resonant frequency of DWNTs predicted by [95]. In particular, similar to the latter, the critical frequency (22) is insensitive to the radii of DWNTs.

For frequency below the critical frequency (22), only one speed exists, which is v_1 given by (20), and the associated amplitude ratio a_1/a_2 is very close to unity and thus the associated vibrational mode is almost coaxial. In this case, the sound speed and the associated vibrational mode are very close to that given by the single-beam model. When the frequency is higher than the critical frequency (22), however, there are two different sound speeds v_1 and v_2 given by (20), and a new noncoaxial vibrational mode emerges which propagates at a speed v_2 much higher than the speed (13) given by the single-beam model. Therefore, the single-beam model, which has been effectively applied to sound wave propagation in SWNTs [39], fails for MWNTs at ultra-high frequencies where noncoaxial vibration comes to play a dominant role. For example, for a DWNT of inner diameter 0.7 nm, the critical (circular) frequency given by (22) is 8 THz, and the corresponding transverse sound speed is close to 10^4 m/s. Similar results are drawn for MWNTs of more than two layers [107]. It is found that there are $(N-1)$ critical frequencies for an N-wall CNT. Sound wave propagation is essentially coaxial only when the frequency is much below all critical frequencies, and it becomes substantially noncoaxial when the frequency is higher than at least one of the $(N-1)$ critical frequencies. In the latter case, the sound speeds predicted by the multiple-beam model [107] are significantly higher or lower than that given by the existing single-beam model (13), depending not only on the frequency but also on the vibrational modes. In particular, when the frequency is higher than all $(N-1)$ critical frequencies, N different sound speeds will exist simultaneously with their respective noncoaxial vibtrational modes. Since noncoaxial vibration would crucially alter some important physical properties of MWNTs, it is anticipated that new complex physical phenomena would occur in terahertz sound wave propagation in MWNTs.

In summary, the preceding results for vibrations and sound waves in MWNTs show that internal degrees of freedom of MWNTs become essential when the characteristic wavelength of vibrational modes is just a few times larger than the outermost diameter of MWNTs. Indeed, for a DWNT of inner diameter 0.7 nm, the wavelengths of the higher-order modes (say $n = 3, 4,$ or 5) are just few times the outermost diameter when the aspect ratio of the DWNT is about or below 20, and the wavelength of transverse sound waves at the critical (circular) frequency (22) is just a few (about 6–7) times the outermost diameter of the DWNT. In this case, the single-beam model fails, and a more accurate elastic model that considers interlayer radial displacements of MWNTs is required. Another issue that is probably significant in this case is the effect of rotary inertia and shear deformation. For this reason, relevance of the Timoshenko beam model [57] to CNTs is an interesting topic for future work [108].

3. ELASTIC SHELL MODELS

When aspect ratios of CNTs are small, or local deformation is concerned, CNTs should be treated as elastic shell rather than elastic beam. To apply elastic shell models to CNTs, a basic quantity which has to be understood appropriately is the representative thickness of carbon SWNTs. Almost all previous researchers defined the equilibrium interlayer spacing between adjacent nanotubes (about 0.34 nm) as the representative thickness of a carbon SWNT. Based on this concept, MWNTs have been treated as cylindrical shells whose thicknesses are determined by the difference between the outermost radius and the innermost radius. In particular, it has been tacitly assumed by some researchers that the bending stiffness of MWNTs would be proportional to the cube of the representative thickness. Unfortunately, as stated by Yakobson et al. [34], the actual bending stiffness of carbon SWNTs is much lower than that given by the classic bending stiffness formula for elastic shells if the representative thickness defined above is used. In fact, the effective bending stiffness of a carbon SWNT is about 0.85 eV, while its in-plane stiffness is 360 J/m^2 [109]. If the classic relationship between the bending stiffness and the shell thickness is retained, the thickness of carbon SWNTs would be 0.066 nm, which is about five times smaller than the suggested thickness 0.34 nm. If such a definition of small thickness is adopted in the elastic shell model for each layer of MWNTs, a huge interior gap exists between any two adjacent layers.

This discrepancy is apparently due to the single atom-layer structure of SWNTs. In fact, the classic bending stiffness formula for elastic shells is based on the assumption that an elastic shell can be divided infinitesimally into many thin layers without interlayer slips, and flexural strains at any point are proportional to the distance between that point and the middle face. For a SWNT, however, the single atom layer cannot be divided into any thin layers, and flexural stresses are actually concentrated in a narrow region around the middle face of the atom layer, rather than distributed linearly over the entire representative thickness. This clearly explains why the actual bending stiffness of carbon SWNTs is much (about 25 times) smaller than that predicted by the classic bending stiffness formula when the representative thickness 0.34 nm is used. Therefore, it is proposed [42, 45] that the effective bending stiffness of SWNTs should be regarded as an independent material parameter, not necessarily related to the representative thickness through the classic bending stiffness formula. Thus, a carbon SWNT could be treated as an isotropic elastic shell with an effective bending stiffness different from that predicted by the classic shell theory. Since the elastic shell theory does not essentially rely on the relation between the shell thickness and the bending stiffness, almost all equations of elastic shell theory remain valid, with or even without a slight modification. For instance, in the absence of any tangential external force, elastic buckling of a SWNT modeled as an isotropic cylindrical shell of radius R can be described by the Donnell equation [110–112]

$$D\nabla^8 w = \nabla^4 p(x, \theta) + F_x \frac{\partial^2}{\partial x^2}\nabla^4 w + 2\frac{F_{x\theta}}{R}\frac{\partial^2}{\partial x \partial \theta}\nabla^4 w$$
$$+ \frac{F_\theta}{R^2}\frac{\partial^2}{\partial \theta^2}\nabla^4 w - \frac{Eh}{R^2}\frac{\partial^4 w}{\partial x^4} - \rho h\frac{\partial^2}{\partial t^2}\nabla^4 w \qquad (23)$$

where x and θ are axial coordinate and circumferential angular coordinate, respectively, t is time, w is the radial (inward) deflection due to buckling, $p(x, \theta)$ is the net normal (inward) pressure caused by buckling, F_x and F_θ are the known uniform axial and circumferential membrane forces, $F_{x\theta}$ is the known uniform shear membrane force, D and h are the effective bending stiffness and thickness of the shell, and E and ρ are Young's modulus and mass density per unit volume. Here, the effective bending stiffness D can be a material parameter independent of the thickness h and thus not necessarily proportional to h cube.

3.1. Single-Shell Models

Single-shell models have been applied to CNTs. Almost all published related studies have focused on buckling behavior of CNTs under various mechanical loadings.

3.1.1. Axially Compressed Buckling of SWNTs

Axially compressed buckling of SWNTs was studied in [34, 42] using the elastic shell model. In this case, F_x is the only nonzero uniform membrane force prior to buckling. As shown in [42], under fairly general conditions, the critical axial strain for buckling of a simply supported cylindrical shell is

$$\frac{-F_x}{Eh} = \frac{2}{R}\sqrt{\frac{D}{Eh}} \qquad (24)$$

while the axial and circumferential half-wave numbers, m and n, of the buckling mode are determined by the single condition

$$\frac{1}{m^2}(m^2 + \beta^2)^2 = \frac{L^2}{R\pi^2}\sqrt{\frac{Eh}{D}} \qquad \beta \equiv \frac{nL}{2\pi R} \qquad (25)$$

These results remain valid even when the effective bending stiffness D is independent of the thickness h and thus not necessarily proportional to h cube. If the classic relation between the bending stiffness and the thickness (see (1) of [42]) is adopted, the critical axial strain is [34, 42]

$$\frac{-F_x}{Eh} = \frac{h}{R\sqrt{3(1-\nu^2)}} \qquad (26)$$

where ν is the Poisson ratio introduced through the classic bending stiffness formula of elastic shells. If the axisymmetric buckling mode ($n = 0$) is further assumed, the axial wavelength of the buckling mode is [36, 42]

$$\frac{2L}{m} = 2\pi\sqrt{Rh}\left[\frac{1}{12(1-\nu^2)}\right]^{1/4} \qquad (27)$$

The critical axial strain (24) has been compared to several available results obtained by molecular dynamics simulations [34, 113–115]. For example, the critical strain for SWNTs of diameter 1 nm obtained by molecular dynamics simulations is 0.05 [34] or 0.08 [114], in good agreement with the value 0.075 predicted by the above formula (24) (where $D = 0.85$ eV, $Eh = 360$ J/m^2; see [34, 109]). For SWNTs of diameter 2.2 or 3.3 nm, the critical strains obtained by

molecular dynamics simulations [113] are about 0.037 and 0.025, respectively, in good agreement with the values 0.034 and 0.023 predicted by the above formula (24).

On the other hand, in contrast to the formula (27) based on the axisymmetric mode, molecular dynamics simulations of SWNTs clearly indicated that the actual buckling mode is not axisymmetric [113, 115]. Hence, it is suggested [42] that the axial wavelength of SWNTs should be estimated by the nonaxisymmetric mode for which the axial wavelength is equal to the circumferential wavelength. In doing so, the axial wavelength is given by

$$\frac{2L}{m} = 4\pi\sqrt{R}\left[\frac{D}{Eh}\right]^{1/4} \qquad (28)$$

For example, the wavelength predicted by the formula (28) for a SWNT of radius 0.67 nm is about 1.2 nm, which is in good agreement with the value 1.3 nm obtained in [115] by molecular dynamics simulations. Hence, it seems that the single-layer isotropic elastic shell model can satisfactorily predict the critical axial strain and the associated wavelength of SWNTs under axial compression, although more careful studies are still needed to clarify some unclear issues, such as the role of anisotropic atomic structure and end conditions of SWNTs.

3.1.2. Buckling under Bending

Elastic buckling of CNTs under bending has been observed in a number of experiments or molecular dynamics simulations [6, 21, 23, 116–120]. One most remarkable result is due to Falvo et al. [36]. Classic buckling theory of elastic tube or shell under bending [112] shows that buckling occurs when the compressive stress on the compressed side of the shell reaches the critical value for axially compressed buckling of cylindrical shells given by (26). Hence, the critical bending moment and the associated wavelength would be predicted by the formulas (26) and (27). Falvo et al. compared the observed wavelength of MWNTs under bending with the theoretical value predicted by (27) and found that the wavelength observed for an eight-layered MWNT is about 68 nm, which is almost four times the theoretical value 18 nm given by formula (27). This discrepancy has been cited by some authors to question the applicability of elastic shell model to CNTs.

For carbon MWNTs, as argued in [42], the friction between adjacent layers is essential for their effective bending stiffness. In some special circumstances, the friction could be so high that interlayer slips between adjacent layers is actually prohibited, and thus the bending stiffness of carbon MWNTs can be well described by the classic bending stiffness formula of elastic shells [42]; see Figure 2.
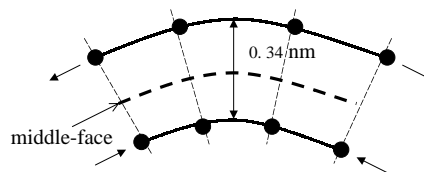

Figure 2. Bending deformation of a double-wall carbon nanotube in the absence of interlayer slips.

It is further argued that such a phenomenon could have occurred for MWNTs under bending. In fact, bending of a tube or shell of originally circular cross-section causes substantial ovalization of the cross-section, which could lead to a change as large as 20% in the diameters prior to the onset of buckling [112]. As a result, the interlayer spacing between adjacent layers would be reduced by 20% at the top and bottom of the cross-section, which could lead to very high friction and thus largely restrict interlayer slips between adjacent layers; see Figure 3. If such an assumption holds, the single-layer elastic shell model can be applied to large-strain bending buckling of carbon MWNTs. Thus, the above paradox raised by Falvo et al. can be explained by two corrections: (1) The wavelength formula used by Falvo et al. [36] is exactly the formula (27) which is valid only for axisymmetric mode ($n = 0$). As mentioned before, molecular dynamics simulations of CNTs have indicated that the actual buckling mode of CNTs is nonaxisymmetric. In particular, the above discussion has shown that the predicted axial wavelength based on the modified formula (28) is in good agreement with the results obtained by molecular dynamics simulations. Thus, the axial wavelength should be estimated by (28) rather than (27). This gives a factor of 2 to the axial wavelength. (2) On the other hand, as stressed by Calladine (see p. 609 in [112]), the curvature radius appearing in the formulae for bending buckling should be understood as the deformed local radius, rather than the original one. According to bending buckling theory, the deformed local radius is twice the initial one when buckling occurs. Thus, because the axial wavelength is proportional to the square root of the radius, this correction contributes another factor of 1.4 to the axial wavelength. In summary, the theoretical axial wavelength should be about 3 times that predicted by the formula (27), which gives a value of 54 nm for the example discussed in Falvo et al. [36]. This modified theoretical value is in good agreement with the observed value of 68 nm. Therefore, it seems that buckling of MWNTs under bending can be described by single-layer shell model.

An interesting open problem is bending of thick MWNTs embedded within an elastic medium. The Bower et al. experiments [23] indicated that, in contrast to the observed wavelength for a relatively thin freestanding MWNT (whose innermost radius-to-thickness ratio is about 4) which is few times larger than that predicted by (27), the wavelength observed for embedded thick MWNTs (whose innermost radius-to-thickness ratio is around 1) is few times smaller than that predicted by (27). In our opinion, a possible explanation is that the assumed interlayer locking, which
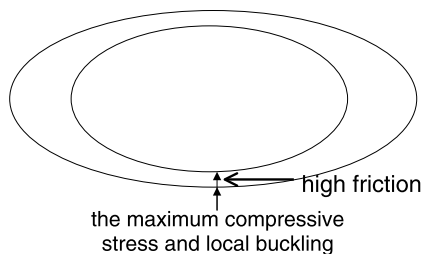
dominates the entire thickness of relatively thin MWNTs, could not occur throughout the entire thickness of thick MWNTs from the outermost layer to the innermost layer. As a result, the interlayer locking would occur only in few outermost layers of thick MWNTs, and thus the actual thickness which determines the observed wavelength in the outermost layer should be the thickness of the few interlocked outermost layers, which should be much smaller than the entire thickness of MWNTs. This could explain why the observed wavelength for embedded thick MWNTs is much smaller than that predicted by (27). Apparently, detailed study is needed before a conclusion may be made. In addition, the effect of interlayer van der Waals energy or an internal/external pressure on the critical bending moment and the wave length of MWNTs under bending deserves further study.

3.1.3. SWNT Ropes under High Pressure

Since the discovery of efficient methods that produce SWNT ropes composed of aligned SWNTs with narrow distribution of diameters, SWNT ropes have become a major form of CNTs. An interesting phenomenon of SWNT ropes is the pressure-induced abrupt changes observed for vibrational modes and electric conductivity when the applied external pressure reached a critical value ranging from 1.5 to 1.9 GPa [121–123]. Hence, an understanding of the intrinsic mechanism behind these pressure-induced abnormalities of SWNT ropes is needed.

Local flattening of tube walls due to van der Waals attraction is a well-known phenomenon [68, 69, 124]. Owing to this phenomenon, it was observed that SWNTs of larger diameter (larger than 2.5 nm) exhibit a honeycomblike geometrical structure, while SWNTs of smaller diameter remain circular [68]. It is assumed in [43] that when SWNT ropes are exposed to high pressure, such a shape change from circular to honeycomb could occur even for SWNT ropes of smaller diameters (say, 1.3 nm), and thus the latter would exhibit a honeycomblike geometrical shape under high pressure; see Figure 4. This assumed pressure-enhanced flattening (not because of the van der Waals attraction) has been confirmed qualitatively by other independent molecular dynamics simulations [125–127]. Based on this assumption, the geometry of SWNT ropes of even smaller radius under high pressure can be approximated by elastic honeycombs. Thus, the analysis of elastic buckling of conventional elastic honeycombs
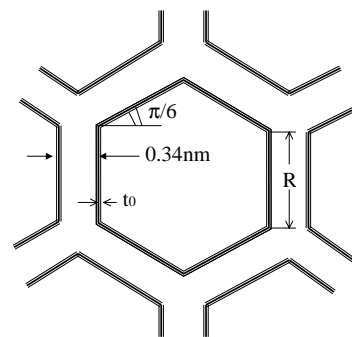

Figure 3. Ovalization of the cross-section of multiwall nanotubes under bending and the induced high interlayer friction.

Figure 4. The idealized cross-section of a single-wall carbon nanotube in the nanotube ropes under high pressure.

(see, e.g., [128]) is modified and applied to the honeycomb-like structure of SWNT ropes under high pressure. In doing so, the critical pressure for elastic buckling of SWNT ropes is found to be given by

$$P_{cr} = 0.32 \frac{E_0 t_0^3}{R^3 \left(1 + \frac{0.34 \text{ nm}}{\sqrt{3}R}\right)}$$

$$t_0 = 0.066 \text{ nm} \qquad E_0 = 5.5 \text{ TPa} \qquad (29)$$

where R is the radius of SWNTs. This result reduces to Eq. (4) of [43] when the radius R is considerably larger than 0.34 nm and thus the factor 0.34 nm/($\sqrt{3}R$) can be neglected. It turns out that the above formula (29) is in good agreement with known experimental data. For example, for SWNT ropes of diameters 1.3 nm, the critical pressure predicted by (29) is about 1.8 GPa, in excellent agreement with the known data ranging from 1.5 to 1.9 GPa [121–123]. On the other hand, Kazaoui et al. [129] studied SWNT ropes under high pressure, of diameter 1.2 and 0.8 nm, respectively. They found that optical properties of SWNT ropes undergo abrupt change when the applied external pressure reaches 1.5 and 3 GPa, respectively. The critical pressure of SWNT ropes predicted by (29) is 1.7 GPa for $R = 0.6$ nm, and 4.6 GPa for $R = 0.4$ nm, both of which are in reasonable agreement with the Kazaoui et al. experimental values. Here, we would mention that some experimental results have been reported for a seemingly new type of structural instability of SWNT ropes when the applied pressure reaches another much higher critical value ranging from 10 to 20 GPa [130–132]. A possible mechanism responsible for this phenomenon is the so-called "second buckling" of the elastic honeycomb under hydrostatic pressure [128], characterized by catastrophic structural change.

3.1.4. Complete Flattening of CNTs

The van der Waals attractive forces of opposite edges offer a potential driving force for collapse of CNTs under large radial deformation [133–136]. Chopral et al. [133] examined complete flattening of CNTs of larger radius based on an analysis of elastic energy and the attractive van der Waals energy. The elastic energies per unit length of CNTs, before and after complete flattening, are estimated by

$$E_{\text{tube}} = \pi k/R \qquad E_{\text{flat}} = ka/r^2 \qquad (30)$$

respectively, where R is the original (average) radius of CNT before flattening, r is the radius of the highly curved part at the two edges of flattened CNT (see Fig. 4 of [133]), a is the arc length of the highly curved part (thus a/r is always larger than π), and the curvature modulus of CNTs $k = 1.4$ eV [133]. Since R is usually much larger than r, the elastic energy after flattening is larger than the elastic energy before flattening. This forms a energy barrier for flattening. On the other hand, the reduction of the van der Waals attractive energy per unit length of CNTs due to flattening is estimated by

$$E_{\text{vdW}} = \gamma_{\text{vdW}}(\pi R - a) \qquad \gamma_{\text{vdW}} \approx 0.02 \text{ eV/C} \qquad (31)$$

which provides the driving force for flattening. Thus, flattening could occur when the reduction of the van der Waals

energy exceeds the increase of elastic energy due to flattening. Since the van der Waals energy scales with R, while r and a are not sensitive to the radius R, flattening will occur more likely for CNTs of larger radius. The critical radius of CNTs for flattening based on this simple elastic model depends on the number of layers n. For instance, Chopra et al. estimated the critical radius $R = 8d$ when $n = 1$, while $R = 19d$ when $n = 8$, where d is the equilibrium interlayer separation (about 0.34 nm). Theoretical predictions based on this elastic model are in reasonable agreement with the observed data [133]. In spite of this, it should be noticed that the above elastic model compares the energies between the original CNT and the completely flattened state only, without a detailed analysis of any intermediate states which could offer a higher energy barrier for flattening.

Finally, dynamics of CNTs modeled as single-layer elastic shells has received very little attention [45, 137, 138], especially for MWNTs in which the interlayer radial displacements and the associated van der Waals interaction could play a significant role.

3.2. Multiple-Shell Models

To apply elastic shell models to MWNTs, it is crucial to notice that MWNTs are different than conventional single-layer elastic shells due to their multilayer structure and the interlayer van der Waals forces. In some special cases, interlocking between all adjacent layers could occur and thus MWNTs can be described by single-layer shell model, as shown above for buckling of MWNTs [36] under bending. In addition, some studies have shown that inter-layer friction in MWNTs largely depends on interlayer commensurability and could lead to significant interlocking for commensurate adjacent layers [139–142]. In general, however, it is well known that interlayer friction in MWNTs is so low that adjacent layers can slide to each other almost freely [19, 77, 78]. In site of this, almost all previous elastic shell models for MWNTs have overlooked the interlayer slips and treated a MWNT as a single-layer elastic shell whose thickness is equal to the difference between the outermost radius and the innermost radius. In doing so, particularly, it has been tacitly assumed that the bending stiffness of a MWNT is proportional to the cube of its thickness defined above. For example, a consequence of such a model is that the critical axial strain of a DWNT should be twice the critical axial strain of a SWNT of the same radius.

It is clear that such an oversimplified model completely neglects the crucial role of interlayer slips and could lead to qualitatively incorrect results. In an effort to study this issue, a multiple-shell model has been developed [41, 47, 48] to study the role of interlayer slips in axially compressed buckling of MWNTs, in which each of the concentric SWNTs is modeled as an individual elastic shell and the normal deflections of all concentric SWNTs are coupled through the normal van der Waals interaction.

3.2.1. Axially Compressed Buckling of MWNTs

To demonstrate essential features of the multiple-shell model, let us consider a simply supported DWNTs of length L, as shown in Figure 5. Let p_{12} be the (inward) pressure
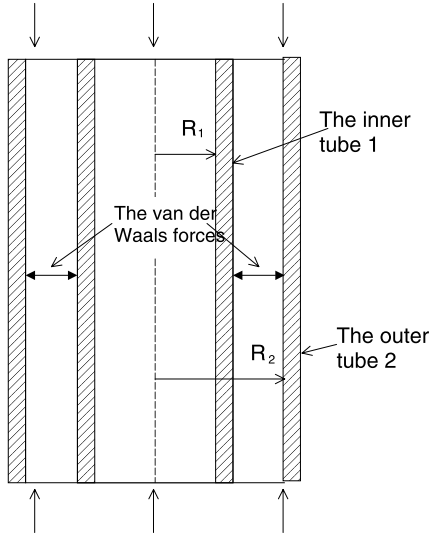
Figure 5. A double-shell model for axially compressed buckling of double-wall carbon nanotube.

on the inner tube due to the outer tube during buckling, let p_{21} be the (inward) pressure on the outer tube due to the inner tube during buckling, and thus they are related by

$$R_1 p_{12} = -R_2 p_{21} \tag{32}$$

where R_1 and R_2 are the radii of the inner tube and the outer tube, respectively. Here, the pressure p_{12} due to buckling is determined by the difference of the deflections of the inner tube and the outer tube due to buckling as

$$p_{12} = c[w_2 - w_1] \tag{33}$$

where w_1 and w_2 are the deflections of the inner tube and the outer tube due to buckling, and the interaction coefficient c is given by (14). Applying (23) to each of the inner and outer tubes, axially compressed buckling of the DWNT under a uniform axial stress is governed by

$$D_1 \nabla_1^8 w_1 = \nabla_1^4 p_{12} + F_x \frac{\partial^2}{\partial x^2} \nabla_1^4 w_1 - \frac{E t_1}{R_1^2} \frac{\partial^4 w_1}{\partial x^4}$$

$$D_2 \nabla_2^8 w_2 = \nabla_2^4 p_{21} + F_x \frac{\partial^2}{\partial x^2} \nabla_2^4 w_2 - \frac{E t_2}{R_2^2} \frac{\partial^4 w_2}{\partial x^4} \tag{34}$$

where initial interlayer pressure prior to buckling (which was considered in [41, 47]) is ignored and thus the applied axial force F_x is the only nonzero membrane force, D_k and t_k are the bending stiffness and thickness of the two tubes, E is Young's modulus of CNTs, and

$$\nabla_k^2 = \frac{\partial^2}{\partial x^2} + \frac{1}{R_k^2} \frac{\partial^2}{\partial \theta^2} \qquad k = 1, 2 \tag{35}$$

Based on this model, an explicit expression can be derived for the axial buckling strain (see Eq. (16) of [47]). When the difference between the two radii is negligible compared to the radii, it is found [41, 47] that the critical axial strain of a DWNT is the same as the critical axial strain of a SWNT of the same radius, although the total critical axial force of

the former almost doubles the latter due to the increase in the cross-sectional area. This conclusion is in sharp contrast to the single-shell model of MWNTs which predicts that the critical axial strain of a cylindrical shell is proportional to its thickness and thus the critical axial strain of a DWNT should double the critical axial strain of a SWNT of the same radius. This result clearly demonstrated that interlayer slips, which are ignored by the single-shell model, have a crucial effect on buckling behavior of MWNTs.

Axially compressed buckling of a DWNT embedded within an elastic medium is studied in [47] with a Winkler-like model for the elastic medium. It is found that the critical axial strain of a DWNT surrounded by an elastic medium of the spring constant d is equal to the critical axial strain of a SWNT of the same radius surrounded by an elastic medium of the spring constant $d/2$. This means that embedded MWNTs would be even more susceptible to infinitesimal axially compressed buckling than embedded SWNTs. Furthermore, for a MWNT of larger radius-to-thickness ratio (say, bigger than 5), it is shown [48] that an N-wall CNT can be treated approximately as an elastic shell whose bending stiffness is N times the effective bending stiffness of SWNTs. In particular, the critical axial strain of an N-wall CNT is almost the same as the critical axial strain of a SWNT of the same radius, which is about $5N$ times lower than the critical axial strain predicted by the single-shell model. These theoretical predictions have to be verified by experiments or molecular dynamics simulations. Unfortunately, to our best knowledge, no detailed experimental results or molecular dynamics simulations on the critical axial strain of MWNTs have been available in the literature. This is apparently due to the fact that experiments at the nanoscale are extremely difficult, and molecular dynamics simulation of MWNTs remains a formidable task.

3.2.2. Externally Pressured MWNTs

Recently, MWNTs under high pressure have been studied [143–147]. In particular, Tang et al. [144] studied electronic properties of a specific group of MWNTs of about 20 layers (with the innermost radius 1.5 nm, and the outermost radius 8 nm) under high pressure. They observed that an abrupt change of conductivity of MWNTs occurs when the applied external pressure reaches a critical value about 1.5 GPa. In their experiment, helium was used as pressure medium and some helium molecules existed inside the MWNTs. Thus, as suggested by Thomsen and Reich [147], the role of helium molecules inside MWNTs could be modeled approximately by an internal pressure within the interior of MWNTs. In an effort to explain the pressure-induced abrupt change observed by Tang et al. [144], an elastic buckling analysis has been given by Wang et al. [148] based on the multiple-shell model [48]. According to the radius-to-thickness ratio, the multiwall carbon nanotubes studied in [148] are classified into three types: thin, thick, and (almost) solid. The results of Wang et al. [148] indicate that

1. A thin N-wall nanotube (defined by a radius-to-thickness ratio larger than 4) is approximately equivalent to a single-layer elastic shell whose effective bending stiffness and thickness are N times the effective bending stiffness and thickness of SWNTs.

2. Based on this result and those obtained in [48], an approximate method is suggested to substitute a MWNT of many layers by a multilayer elastic shell of fewer layers. The effectiveness and accuracy of this approximate method are demonstrated with examples.

3. The critical pressure predicted for the specific MWNTs tested in [144] is about 1 GPa, which is insensitive to the magnitude of the internal pressure beyond a certain value. This predicted critical pressure is in reasonably good agreement with the experimental result 1.5 GPa [144]. The small discrepancy between the predicted value and the experimental value could be attributed to the low interlayer friction, which is ignored in the multiple-shell model but could have a accumulative effect on the critical pressure for MWNTs of 20 layers. This reasonable agreement between theory and experiment offers evidence for the relevance of the multiple-elastic shell model for MWNTs.

3.2.3. MWNTs under Combined Loadings

Elastic buckling of CNTs under combined mechanical loadings has not been examined in the literature. Very recently, axially compressed buckling of SWNTs filled with other molecules has been studied by Ni et al. [149]. These authors found that the critical axial strain increases by 10–20% for different filling molecules at low density, and up to 45% for filling molecules at high density. As mentioned above, the role of filling molecules can be modeled approximately by an internal pressure. Although the value of this equivalent internal pressure depends on filling molecules and the density and thus cannot be determined exactly, its magnitude can be assumed to be of the order of magnitude of the critical radial external pressure [147] (the latter is about 5% of the critical axial stress for SWNTs [42, 43]). Therefore, one could assume that filled SWNTs can be approximately modeled as SWNTs with an internal radial pressure comparable to 5% of their critical axial stress.

Motivated by the above ideas, a systematic study of axially compressed buckling of MWNTs subjected to an internal or external radial pressure is given by Wang et al. [150]. The main results of [150] can be summarized as follows.

1. *Pure axial stress*. There always is more than one combination of the axial and circumferential wave numbers of the buckling mode which corresponds to the same critical axial stress. On the other hand, the critical axial stress of a thin MWNT is approximately equal to the critical axial stress of a SWNT of the average radius of the MWNT, while the critical axial stress of a thick or solid MWNT is bounded, from above and below, respectively, by the critical axial stress of a SWNT of the innermost radius of the MWNT, and the critical axial stress of a SWNT of the outermost radius of the MWNT.

2. *Combined axial stress and internal pressure*. The internal pressure has a significant effect on the critical axial stress for nonaxisymmetric buckling modes, while it has no effect on the axisymmetirc buckling mode. In addition, for nonaxisymmetric modes, the effect of internal pressure on the critical axial stress is strong for thin MWNTs, moderate for thick MWNTs, and negligible for solid MWNTs. In particular, for SWNTs of diameter 1.3 nm, the predicted critical axial stress increases by 10%, 20%, and 45% when the internal pressure-to-axial stress ratio is 0.04, 0.07, and 0.14, respectively. Therefore, the relative increase of the critical axial stress due to filling molecules observed by Ni et al. [149], which is about 10–20% at low density or up to 45% at high density, could be explained by an equivalent internal pressure about 5% or 14% of the critical axial stress. Therefore, the present theoretical result appears to be in qualitative agreement with the Ni et al. results obtained by molecular dynamics simulations [149].

3. *Combined axial stress and external pressure*. The buckling mode can be determined uniquely in this case. In addition, the critical condition for buckling, expressed as a relation between the axial stress and the external pressure, is strongly nonlinear for all examples studied in [150]. The disagreement between this strongly nonlinear relation and the well-known nearly linear relation for elastic thin shells [111, 112, 151] is due to the fact that the radius-to-thickness ratio for the examples of MWNTs studied in [150] is too small as compared to that of conventional elastic thin shells. Indeed, as shown in [150], the nonlinear relation for SWNTs reduces to a nearly linear one when the radius-to-thickness ratio of SWNTs is sufficiently large.

Here, we would mention that CNTs are known to be susceptible to twisting deformation [27, 152, 153]. In spite of this, to our best knowledge, buckling of CNTs under torsion has not been studied in the literature. For example, the effect of the interlayer van der Waals forces on the critical torque of MWNTs is an interesting subject for future work.

Finally, as mentioned at the beginning, this overview does not cover nonelastic deformations of CNTs, such as nucleation of defects and related plastic deformations [6, 51, 52] and crack growth and fracture [6, 21, 40, 53, 54]. In addition, contact mechanics of CNTs interacting with other materials [154–160] is another related topic which has not been covered here. For potential industrial applications of CNTs, see [1–3, 8–12, 161–163]. In particular, two recent articles have particularly addressed technical challenges of CNTs to mechanical engineers [164, 165].

4. CONCLUDING REMARKS

CNTs hold substantial promise for nanotechnology, and the potential applications stretch in almost all directions. It is no longer a question of whether CNTs will become useful in the future, but merely a question of how and when. Recently, industry has begun to take notice of the unique properties of CNTs. However, the study of CNTs is still in its infancy, applications for carbon nanotubes progress slowly, and many technical hurdles need to be overcome before large scale applications reach the market.

As we mentioned at the beginning of this chapter, almost all potential applications of CNTs require thorough understanding of mechanical behavior of CNTs. The examples shown here clearly indicate that elastic models provide a

powerful and cost-effective approach for CNTs and could play an indispensable role in the study of CNTs. In particular, elastic models offer relatively simple general formulas which clearly identify major factors affecting mechanical behavior of CNTs. Such simple formulas cannot usually be expected with other methods. The merits of elastic models allow researchers to develop new and more accurate elastic models for more complex physical phenomena of CNTs, which have the potential to predict new physical phenomena, identify related key issues, and stimulate and guide further experimental studies and molecular dynamics simulations. On the other hand, CNTs are distinguished from traditional elastic beams or shells especially due to their multilayered hollow structures and the associated intertube van der Waals interaction. This is largely responsible for many technical difficulties in the study of mechanical behavior of individual MWNTs, CNT ropes, CNT composites, and CNTs interacting with other materials. Indeed, existing elastic models cannot directly be applied to CNTs in many cases of theoretical and practical significance. This would raise significant challenges and exciting opportunities for the solid mechanics community.

GLOSSARY

Carbon nanotubes   A carbon nanotube is a hexagonal network of carbon atoms that has been rolled into a seamless cylindrical shell. Carbon nanotubes are only few nanometers in diameter and can be single-layer or multi-layer. Owing to their unique atomic structure, carbon nanotubes have superior electrical, mechanical and other physical properties, and are predicted to play a pivotal role in Nanotechnology.

Elastic beam   A slender, elastically deformable solid structure whose length is at least one order of magnitude larger than the dimensions of its cross-section. A carbon nanotube can be modeled as an elastic beam of uniform cross-section.

Elastic shell   A thin, elastically deformable solid structure whose thickness is much (say, at least ten or five times) smaller than its other dimensions. A singlewall carbon nanotube can be modeled as an elastic cylindrical shell of constant thickness, and a multiwall carbon nanotube can be modeled as some concentric elastic cylindrical shells.

Multiwall carbon nanotubes (MWNTs)   MWNTs are composed of a number of concentric singlewall nanotubes which nest almost perfectly one inside the other. The concentric tubes are held together by van der Waals forces between any two nearest nanotubes. The interlayer spacing between adjacent tubes is about 0.34 nm and can vary slightly depending on the diameter and number of nested tubes in MWNTs.

van der Waals forces   The van der Waals forces represent the weak (secondary) interaction between adjacent molecule or atoms, and arise from their electric dipoles. The van der Waals forces are long-range (even for distances larger than tens of nanometers), and may be attractive or repulsive depending on the distance between interacting atoms or molecules. In particular, the van der Waals forces between nearest nanotubes become attractive when the distance is larger than the equilibrium distance, or repulsive when the distance is smaller than the equilibrium distance.

The van der Waals forces between nearest nanotubes play a crucial role in physical properties of multiwall carbon nanotubes and singlewall carbon nanotube ropes.

ACKNOWLEDGMENT

REFERENCES

1. R. S. Williams, *Physics World* (December), 49 (1999).
2. C. Macilwain, *Nature* 405, 730 (2000).
3. R. Compano and A. Hullmann, *Nanotechnology* 13, 243 (2002).
4. S. Iijima, *Nature* 354, 56 (1991).
5. T. W. Ebbesen, *Annu. Rev. Mater. Sci.* 24, 235 (1994).
6. B. I. Yakobson and R. E. Smalley, *Am. Sci.* 85, 324 (1997).
7. M. Dresselhaus, G. Dresselhaus, and R. Saito, *Phys. World* (January), 33 (1998).
8. P. Ball, *Nature* 414, 142 (2001).
9. H. Dai, *Surface Sci.* 500, 218 (2002).
10. R. H. Baughman, A. A. Zakhidov, and W. A. de Heer, *Science* 297, 787 (2002).
11. C. Dekker, *Physics Today* 52, 22 (1999).
12. P. G. Collins and P. Avouris, *Sci. Am.* (December), 69 (2000).
13. T. Rueckers, K. Kyounghan, E. Joselevich, G. T. Tseng, C. L. Cheung, and C. M. Lieber, *Science* 289, 94 (2000).
14. V. Derycke, R. Martel, J. Appenzeller, and P. Avouris, *Nanoletters* 1, 453 (2001).
15. A. Bachtold, P. Hadley, T. Nakanishi, and C. Dekker, *Science* 294, 1317 (2001).
16. H. Dai, J. H. Hafner, A. G. Rinzler, D. T. Colbert, and R. E. Smalley, *Nature* 384, 147 (1996).
17. P. G. Collins, A. Zettl, H. Bando, A. Thess, and R. E. Smalley, *Science* 278, 100 (1997).
18. P. Kim and C. M. Lieber, *Science* 286, 2148 (1999).
19. J. Cumings and A. Zettel, *Science* 289, 602 (2000).
20. M. Ahlskog, P. Hakonen, M. Paalanen, L. Roschier, and R. Tarkiainen, *J. Low Temperature Phys.* 124, 335 (2001).
21. O. Lourie, D. M. Cox, and H. D. Wagner, *Phys. Rev. Lett.* 81, 1638 (1998).
22. P. Calvert, *Nature* 399, 210 (1999).
23. C. Bower, R. Rosen, L. Jin, J. Han, and J. Zhou, *Appl. Phys. Lett.* 74, 3317 (1999).
24. D. Qian, E. C. Dickey, R. Andrews, and T. Rantell, *Appl. Phys. Lett.* 76, 2868 (2000).
25. E. T. Thostenson, Z. Ren, and T. W. Chou, *Composite Sci. Technol.* 61, 1899 (2001).
26. K. T. Lau and D. Hui, *Composites B* 33, 263 (2002).
27. C. L. Kahn and E. J. Mele, *Phys. Rev. Lett.* 78, 1932 (1997).
28. M. B. Nardelli and J. Bernhole, *Phys. Rev. B* 60, R16338 (1999).
29. L. Yang and J. Han, *Phys. Rev. Lett.* 85, 154 (2000).
30. T. W. Tombler, C. Zhou, L. Alexseyev, J. Kong, H. Dai, L. Liu, C. S. Jayanshi, M. Tang, and S. Y. Wu, *Nature* 405, 769 (2000).
31. L. Liu, C. S. Jayanthi, and S. Y. Wu, *Phys. Rev. B* 64, 033412-1 (2001).
32. A. Maiti, A. Svizhenko, and M. P. Anantram, *Phys. Rev. Lett.* 88, 126805-1 (2002).
33. M. J. Treacy, T. W. Ebbesen, and J. M. Gibson, *Nature* 381, 678 (1996).
34. B. I. Yakobson, C. J. Brabec, and J. Bernholc, *Phys. Rev. Lett.* 76, 2511 (1996).
35. E. W. Wong, P. E. Sheehan, and C. M. Lieber, *Science* 277, 1971 (1997).

36. M. R. Falvo, G. J. Clary, R. M. Taylor II, V. Chi, F. P. Brooks, Jr., S. Washburn, and R. Superfine, *Nature* 389, 582 (1997).
37. P. Poncharal, Z. L. Wang, D. Ugarte, and W. A. de Heer, *Science* 283, 1513 (1999).
38. S. Govindjee and J. L. Sackman, *Solid State Comm*. 110, 227 (1999).
39. V. N. Popov, V. E. Van Doren, and M. Balkanski, *Phys. Rev. B* 61, 3078 (2000).
40. M. F. Yu, O. Lourie, M. J. Dyer, K. Moloni, T. F. Kelly, and R. S. Ruoff, *Science* 287, 637 (2000).
41. C. Q. Ru, *J. Appl. Phys.* 87, 7227 (2000).
42. C. Q. Ru, *Phys. Rev. B* 62, 9973 (2000).
43. C. Q. Ru, *Phys. Rev. B* 62, 10405 (2000).
44. C. Q. Ru, *Phys. Rev. B* 62, 16962 (2000).
45. D. Kahn and K. W. Kim, *J. Appl. Phys.* 89, 5107 (2001).
46. V. M. Harik, *Solid State Comm*. 120, 331 (2001).
47. C. Q. Ru, *J. Mech. Phys. Solids* 49, 1265 (2001).
48. C. Q. Ru, *J. Appl. Phys.* 89, 3426 (2001).
49. Z. L. Wang, R. P. Gao, Z. W. Pan, and Z. R. Dai, *Adv. Eng. Mater.* 3, 657 (2001).
50. D. Qian, G. J. Wagner, W. K. Liu, M. F. Yu, and R. S. Ruoff, Mechanics of carbon nanotubes, *Applied Mechanics Review*, in press.
51. P. Zhang, P. E. Lammert, and V. H. Crespi, *Phys. Rev. Lett.* 81, 5346 (1998).
52. M. B. Nardelli, B. I. Yakobson, and J. Bernholc, *Phys. Rev. Lett.* 81, 4656 (1998).
53. T. Belytschko, S. P. Xiao, G. C. Schatz, and R. S. Ruoff, *Phys. Rev. B* 65, 235403-1 (2002).
54. P. Zhang, Y. Huang, H. Gao, and K. C. Huang, *J. Appl. Mech.* 69, 454 (2002).
55. E. S. Snow, P. M. Campbell, and J. P. Novak, *Appl. Phys. Lett.* 80, 2002 (2002).
56. M. Ishikawa, M. Yoshimura, and K. Ueda, *Appl. Surface Sci.* 188, 456 (2002).
57. S. Timoshenko, "Vibration Problems in Engineering." Wiley, New York, 1974.
58. J. F. Doyle, "Wave Propagation in Structures." Springer-Verlag, Berlin, 1989.
59. C. Bustamante, S. B. Smith, J. Liphardt, and D. Smith, *Curr. Opin. Struct. Biol.* 10, 279 (2000).
60. G. Bao, *J. Mech. Phys. Solids* 50, 2237 (2002).
61. J. M. Gere, "Mechanics of Materials," 5th ed. Brooke/Cole, 2001.
62. J. P. Salvetat, A. J. Kulik, J. M. Bonard, G. A. D. Briggs, T. Stockli, K. Meitenier, S. Bonnamy, F. Beguin, N. A. Burnham, and L. Forro, *Adv. Mater.* 11, 161 (1999).
63. N. Yao and V. Lordi, *Phys. Rev. B* 58, 12649 (1998).
64. A. Garg, J. Han, and S. Sinnott, *Phys. Rev. Lett.* 81, 2260 (1998).
65. H. Chai, C. D. Babcock, and W. G. Knauss, *Int. J. Solids Struct.* 17, 1069 (1981).
66. L. M. Kachanov, "Delamination Buckling of Composite Materials." Kluwer Academic, Dordrecht, 1988.
67. L. A. Girifalco and R. A. Lad, *J. Chem. Phys.* 25, 693 (1956).
68. J. Tersoff and R. S. Ruoff, *Phys. Rev. Lett.* 73, 676 (1994).
69. J. C. Charlier, X. Gonze, and J. P. Michenaud, *Europhys. Lett.* 29, 43 (1995).
70. L. X. Benedict, N. G. Chopra, M. L. Cohen, A. Zettl, S. G. Louie, and V. H. Crespi, *Chem. Phys. Lett.* 286, 490 (1998).
71. Y. Lanir and Y. C. B. Fung, *J. Composite Mater.* 6, 387 (1972).
72. A. D. Kerr, *Ingenieur-Archiv* 54, 455 (1984).
73. J. Yoon, C. Q. Ru, and A. Mioduchowski, *Composites Sci. Technol*., in press.
74. L. D. Landau and E. M. Lifshitz, "Theory of Elasticity." Pergamon, Oxford, 1995.
75. J. Yu, R. K. Kalia, and P. Vashishta, *J. Chem. Phys.* 103, 6697 (1995).
76. M. S. Dresselhaus and P. C. Eklund, *Adv. Phys.* 49, 705 (2000).
77. J. C. Charlier and J. P. Michenaud, *Phys. Rev. Lett.* 70, 1858 (1993).
78. A. N. Kolmogorov and V. H. Crespi, *Phys. Rev. Lett.* 85, 4727 (2000).
79. C. Schonenberger and L. Forro, *Phys. World* 13, 37 (2000).
80. S. Paulson, M. R. Falvo, N. Snider, A. Helser, T. Hudson, A. Seeger, R. M. Taylor, R. Superfine, and S. Washburn, *Appl. Phys. Lett.* 75, 2936 (1999).
81. R. Gao, Z. Pan, and Z. L. Wang, *Appl. Phys. Lett.* 78, 1757 (2001).
82. Y. P. Zhao, B. Q. Wei, P. M. Ajayan, G. Ramamath, T. M. Lu, G. C. Wang, A. Rubio, and S. Roche, *Phys. Rev. B* 64, 201402 (2001).
83. K. Suenaga, C. Colliex, and S. Iijjima, *Appl. Phys. Lett.* 78, 70 (2001).
84. A. Hassanien, A. Mrzel, M. Tokumoto, and D. Tomanek, *Appl. Phys. Lett.* 79, 4210 (2001).
85. Y. Miyamoto, S. Saito, and D. Tomanek, *Phys. Rev. B* 65, 041402 (2001).
86. P. G. Collins, M. Hersam, M. Aronld, R. Martel, and P. Avouris, *Phys. Rev. Lett.* 86, 3128 (2001).
87. W. Lu, J. Dong, and Z. Li, *Phys. Rev. B* 63, 033401 (2000).
88. Z. Jin, X. Sun, G. Xu, S. H. Goh, and W. Ji, *Chem. Phys. Lett.* 318, 505 (2000).
89. R. Saito, R. Matsuo, T. Kimura, G. Dresselhaus, and M. S. Dresselhaus, *Chem. Phys. Lett.* 348, 187 (2001).
90. B. W. Smith and D. E. Luzzi, *Chem. Phys. Lett.* 321, 169 (2000).
91. S. Bandow, M. Takizawa, K. Hirahara, M. Yudasaka, and S. Iijima, *Chem. Phys. Lett.* 337, 48 (2001).
92. C. H. Kiang, M. Endo, P. M. Ajayan, G. Dresselhaus, and M. S. Dresselhaus, *Phys. Rev. Lett.* 81, 1869 (1998).
93. G. Zhou, W. Duan, and B. Gu, *Chem. Phys. Lett.* 333, 344 (2001).
94. O. Gulseren, T. Yildirim, and S. Ciraci, *Phys. Rev. B* 65, 153405 (2002).
95. J. Yoon, C. Q. Ru, and A. Mioduchowski, *Phys. Rev. B* 66, 233402-1 (2002).
96. J. M. Seelig and W. H. Hoppmann, *J. Appl. Mech.* 31, 621 (1964).
97. E. Majorana and Y. Ogawa, *Phys. Lett. A* 233, 162 (1997).
98. B. L. Burrows and M. Cohen, *Molecular Phys.* 98, 1083 (2000).
99. H. G. Craighead, *Science* 290, 1532 (2000).
100. M. Roukes, *Physics World* (February), 25 (2001).
101. C. Sirtori, *Nature* 417, 132 (2002).
102. T. Jeon and K. Kim, *Appl. Phys. Lett.* 80, 3403 (2002).
103. G. A. Antonelli and H. J. Maris, *J. Appl. Phys.* 91, 3261 (2002).
104. W. Knap, V. Kachorovskii, Y. Deng, S. Rumyantsev, J. P. Lu, R. Gaska, and M. S. Shur, *J. Appl. Phys.* 91, 9346 (2002).
105. E. B. Brauns, M. IL. Madaras, R. S. Coleman, C. J. Murphy, and M. Berg, *Phys. Rev. Lett.* 88, 158101 (2002).
106. M. Y. Su, S. G. Carter, M. S. Sherwin, A. Huntington, and L. A. Coldren, *Appl. Phys. Lett.* 81, 1564 (2002).
107. J. Yoon, C. Q. Ru, and A. Mioduchowski, *J. Appl. Phys.*, in press.
108. J. Yoon, C. Q. Ru, and A. Mioduchowski, in preparation.
109. D. Robertson, D. Brenner, and J. Mintmire, *Phys. Rev. B* 45, 12592 (1992).
110. L. H. Donnell, "Beams, Plates and Shells." McGraw–Hill, New York, 1976.
111. S. Timoshenko and S. Woinowsky-Krieger, "Theory of Plates and Shells." McGraw–Hill, New York, 1959.
112. C. R. Calladine, "Theory of Shell Structures." Cambridge Univ. Press, Cambridge, UK, 1983.
113. C. F. Cornwell and L. T. Wille, *Solid State Comm*. 101, 555 (1997).
114. D. Srivastava, M. Menon, and K. Cho, *Phys. Rev. Lett.* 83, 2973 (1999).
115. T. Ozaki, Y. Iwasa, and T. Mitani, *Phys. Rev. Lett.* 84, 1712 (2000).
116. J. F. Despres, E. Daguerre, and K. Lafdi, *Carbon* 33, 87 (1995).
117. R. S. Ruoff and D. L. Lorents, *Carbon* 33, 925 (1995).
118. S. Iijima, C. Brabec, A. Maiti, and J. Bernholc, *J. Chem. Phys.* 104, 2089 (1995).

119. T. Kuzumaki, T. Hayashi, H. Ichinose, K. Miyazawa, K. Ito, and Y. Ishida, *Philos. Mag. A* 77, 1459 (1998).

120. T. Kizuka, *Phys. Rev. B* 59, 4646 (1998).

121. U. D. Venkateswaran, A. M. Rao, E. Richter, M. Menon, A. Rinzler, R. E. Smalley, and P. C. Eklund, *Phys. Rev. B* 59, 10928 (1999).

122. M. J. Peters, L. E. Mcneil, J. P. Lu, and D. Kahn, *Phys. Rev. B* 61, 5939 (2000).

123. R. Gaal, J. P. Salvetat, and L. Forro, *Phys. Rev. B* 61, 7320 (2000).

124. R. S. Ruoff, J. Tersoff, D. G. Lorenta, S. Subramoney, and B. Chan, *Nature* 364, 514 (1993).

125. J. Tang, L. Qin, T. Sasaki, M. Yudasaka, A. Matsushita, and S. Iijima, *Phys. Rev. Lett.* 85, 1887 (2000).

126. S. Rols, I. N. Goncharenko, R. Almairac, J. L. Sauvajol, and I. Mirebeau, *Phys. Rev. B* 64, 153401 (2001).

127. M. Popov, M. Kyotani, R. J. Nemanich, and Y. Koga, *Phys. Rev. B* 65, 033408 (2002).

128. L. J. Gibson and M. F. Ashby, "Cellular Solids: Structures and Properties." Cambridge Univ. Press, Cambridge, UK, 1997.

129. S. Kazaoui, Nanotechnology Research Institute, Japan, private communication.

130. P. V. Teredesai, A. K. Sood, D. V. S. Muthu, R. Sen, A. Govindaraj, and C. N. R. Rao, *Chem. Phys. Lett.* 319, 296 (2000).

131. T. Yildirim, O. Gulseren, C. Kilic, and S. Ciraci, *Phys. Rev. B* 62, 12648 (2001).

132. S. M. Sharma, S. Kurmakar, S. K. Sikka, P. V. Teredesai, A. K. Sood, A. Govindaraj, and C. N. R. Rao, *Phys. Rev. B* 63, 205417-1 (2001).

133. N. G. Chopra, L. X. Benedict, V. H. Grespi, M. L. Cohen, S. G. Louie, and A. Zettl, *Nature* 377, 135 (1995).

134. V. Lordi and N Yao, *J. Chem. Phys.* 109, 2509 (1998).

135. I. Stepanek, G. Maurin, P. Bernier, J. Grvillet, A. Loiseau, R. Edward, and O. Jaschinski, *Chem. Phys. Lett.* 331, 125 (2000).

136. P. E. Lammert, P. Zhang, and V. H. Crespi, *Phys. Rev. Lett.* 84, 2453 (2000).

137. S. Erdin and V. Pokrovsky, *Int. J. Modern Phys. B* 15, 3099 (2001).

138. G. D. Mahan, *Phys. Rev. B* 65, 235402-1 (2002).

139. M. R. Falvo, R. M. Taylor, A. Helser, F. P. Brooks, S. Washburn, and R. Superfine, *Nature* 397, 236 (1999).

140. M. F. Yu, B. I. Yakobson, and R. S. Ruoff, *J. Chem. Phys.* 104, 8764 (2000).

141. M. R. Falvo, J. Steele, R. M. Taylor, and R. Superfine, *Phys. Rev. B* 62, R10665 (2000).

142. K. Miura, T. Takagi, S. Kamiya, T. Sahashi, and M. Yamauchi, *Nanoletters* 1, 161 (2001).

143. C. Thomsen, S. Reich, H. Jantoljak, I. Loa, K. Syassen, M. Burghard, G. S. Dueberg, and S. Rothet, *Appl. Phys. A* 69, 309 (1999).

144. D. S. Tang, Z. X. Bao, L. J. Wang, L. C. Chen, L. F. Sun, Z. Q. Liu, W. Y. Zhou, and S. S. Xie, *J. Phys. Chem. Solids* 61, 1175 (2000).

145. D. S. Tang, L. C. Chen, L. J. Wang, L. F. Sun, Z. Q. Liu, G. Wang, W. Y. Zhou, and S. S. Xie, *J. Mater. Res.* 15, 560 (2000).

146. U. D. Venkateswaran, E. A. Brandsen, U. Schlecht, A. M. Rao, E. Richter, I. Loa, K. Syassen, and P. C. Eklund, *Phys. Status Solidi B* 223, 225 (2001).

147. C. Thomsen and S. Reich, *Phys. Status Solidi B* 225, R18 (2001).

148. C. Y. Wang, C. Q. Ru, and A. Miodachowski, *J. Nanoscience and Nanotechnology*, in press.

149. B. Ni, S. B. Sinnott, P. T. Mikulski, and J. A. Harrison, *Phys. Rev. Lett.* 88, 205505-1 (2002).

150. C. Y. Wang, C. Q. Ru, and A. Mioduchowski, submitted for publication.

151. S. Timoshenko and J. M. Gere, "Theory of Elastic Stability." McGraw–Hill, New York, 1964.

152. W. Clauss, D. J. Bergeron, and A. T. Johnson, *Phys. Rev. B* 60, R4266 (1998).

153. M. F. Yu, T. Kowalewski, and R. S. Ruoff, *Phys. Rev. Lett.* 86, 87 (2001).

154. T. Hertel, R. E. Walkup, and P. Avouris, *Phys. Rev. B* 58, 13870 (1998).

155. A. Buldum and J. P. Lu, *Phys. Rev. Lett.* 83, 5050 (1999).

156. P. Avouris, T. Hertel, R. Martel, T. Schmidt, H. R. Shea, and R. E. Walkup, *Appl. Surface Sci.* 141, 201 (1999).

157. A. Maiti, *Chem. Phys. Lett.* 331, 21 (2000).

158. S. Decossas, G. Cappello, G. Poinnat, L. Patrone, A. M. Bonnot, F. Comin, and J. Chevriler, *Europhys. Lett.* 53, 742 (2001).

159. C. Q. Ru, *J. Appl. Mech.* 69, 97 (2002).

160. R. Czerw, B. Foley, D. Tekleab, A. Rubio, P. M. Ajayan, and D. L. Carroll, *Phys. Rev. B* 66, 033408-1 (2002).

161. S. Mirsky, *Sci. Am.* (June), 40 (2000).

162. W. A. Heer and R. Martel, *Physical World* (June), 49 (2000).

163. P. Smaglik, *Nature* 408, 621 (2000).

164. P. Sharke, *Mech. Eng. ASME* (February), 42 (2001).

165. A. Majumdar, *Mech. Eng. ASME* (March), 46 (2001).

ENN
Encyclopedia of Nanoscience and Nanotechnology
www.aspbs.com/enn

Electrically Detected Magnetic Resonance

Carlos F. O. Graeff

Universidade de São Paulo, Ribeirão Preto, Brazil

CONTENTS

1. INTRODUCTION

Magnetic resonance techniques have attracted considerable attention in many research fields, and are commonly used, for example, in medical imaging. Advantages compared to other techniques are among others, high sensitivity and selectivity. In general, the technique can be used to investigate local static and dynamic interactions, or in other words, the microscopic surroundings of the spin. In this article, we shall be discussing only Magnetic resonance techniques based on the detection of electron spins, also known as paramagnetic resonance. Zavoisky [1] was the first to observe electron spin resonance (ESR) or electron paramagnetic resonance (EPR) in 1945. It soon developed into a powerful tool in many areas of research and of special interest to nanotechnology in the area of solid-state electronics [2]. Unfortunately, though ESR has a high sensitivity as already mentioned, it is not sufficient when one wants to investigate, for example, submicrometer-sized transistors found in today's computer microprocessors. In a Pentium 4 processor using 0.13 μm technology, the dimension of a typical transistor's active channel is around 10^{-9} cm^2. On the other hand, the density of paramagnetic states in the interface SiO$_2$/Si used in complementary metal oxide semiconductor (CMOS) technology is about 10^{10} to 10^{12} cm^{-2}. Thus, in this typical transistor, there are between 10 and 1000 paramagnetic spins. The detection limit of modern high sensitivity ESR spectrometers is about 10^9 spins per Gauss linewidth. In the case of Si and SiO$_2$, ESR linewidths are of the order of 10 G, which means that in the best situation, 10^{10} paramagnetic spins can be measured using conventional ESR. Compared to the expected number of active spins in

the transistor just mentioned (10–1000 spins), the lack of sensitivity is clear. Electrically detected magnetic resonance (EDMR) is many orders of magnitude more sensitive than conventional ESR. Thus, the higher sensitivity combined with other characteristics that will be discussed ahead, makes EDMR one of the few magnetic resonance techniques available nanoscience/nanotechnology. We shall be using EDMR in a broader sense, as all techniques that involve a combination of conventional ESR with electrical characterization techniques such as (photo)conductivity, capacitance, or electronic noise spectroscopy. However we shall be using this definition only when the transport/recombination of charge carriers in the sample of interest is spin dependent. Spin dependent transport/recombination will be the subject of the next section. According to this definition, EDMR is found in the literature with the following denominations: resistivity change due to electron spin resonance, spin dependent conductivity (SDC), spin-dependent photoconductivity (SDPC), spin-dependent trapping, spin-dependent Hall effect, spin-dependent transport, spin dependent polarizabilities, electrical detection of paramagnetic resonance (EDPR), conductivity-detected resonance, photovoltaic detection of magnetic resonance (PDMR), electrical detection of electron nuclear double resonance, capacitively detected magnetic resonance (CDMR), noise-detected magnetic resonance (NDMR), time domain measurement of spin-dependent recombination (TSR), among others.

The first observations of EDMR were made by Honig and Maxwell in crystalline silicon [3, 4], and simultaneously by Schmidt and Solomon [5]. Maxwell and Honig observed an increase in conductivity at low temperatures attributed to the spin-dependent scattering of conduction electrons with paramagnetic phosphorous atoms, while Schmidt and Solomon have observed a change in photoconductivity at low temperatures, due to spin-dependent recombination. After those early works, EDMR has been applied to a variety of systems. Table 1 contains references to all materials and structures/devices investigated by EDMR, known to the author, not directly connected to nanoscience/nanotechnology. The relevant EDMR studies to nanoscience/nanotechnology will be discussed in greater detail in Section 3. For those more interested in the

Table 1. Materials, devices and structures investigated by EDMR, excluding those more relevant to nanoscience/nanotechnology.

Material	Structure/Device	Ref.
c-Si	Thin-film on sapphire	[6, 7]
	Bulk, surface	[3, 4, 8–39]
	MOSFET	[26, 40–48]
	p-n diode	[26, 35, 49–69]
	Photovoltaic devices	[7, 70–72]
Poly-(or micro-) crystalline Si	Thin film	[73–78]
c-Ge	Bulk n-type	[79]
c-SiC	LED	[80]
c-GaAs	Bulk	[80–82]
c-GaP	Bulk, LED	[80, 83]
c-(Al,In)GaN	Film, LED	[80, 84–87]
c-ZnSe	Schottky diode	[88]
c-InSb	Bulk n-type	[89]
Diamond	Thin film	[90, 91]
a-Si	Thin film	[76, 92–105]
	Ion implantation	[106]
	Diode, solar cell	[7, 99, 107–111]
	TFT	[112–114]
a-Si:H/a-Ge:H	Multilayers	[115]
a-Ge:H	Thin film	[116]
a-SiGe:H	Thin film	[116]
SiO_2	Thin film	[117]
Polyparaphenylenevinylene (PPV) and derivatives	LED	[118–123]
	Thin film, photodiode	[124]
2,5-Dialkoxy derivatives of poly(p-phenylene-acetylene) (PPA)	LED	[125]
Poly(p-phenyleneethynylene) (PPE)	LED	[126]
Polyaniline	Thin films	[127–130]
Polyacetylene	Thin film	[127]

theoretical attempts to describe EDMR, the most relevant references are [8, 11, 12, 16, 31, 34, 39, 60, 61, 64, 93, 103, 135, 137, 142].

2. BASIC PHYSICS OF EDMR

To understand EDMR, let us first remember some basic aspects of electron spin resonance, taking the simple case of a single electron (S = 1/2). From quantum mechanics, the spin of an isolated single electron subject to an external magnetic field H_0 will have two possible energy levels to occupy, corresponding to $m_s = \pm 1/2$. The Zeeman splitting gives the energy difference between these states: $g\mu_B H_0$, where μ_B is the Bohr magneton and g is 2.00225 for a free electron. Generally, g is a tensor similar to the effective mass, reflects the various magnetic interactions/coupling that this

particular electronic spin is subject to. Transitions between these levels can be induced by applying an alternating magnetic field H_1, perpendicular to H_0, when the frequency of oscillation of H_1 is equal to the resonance frequency $\nu_0 = g\mu_B H_0/h$. In thermal equilibrium, the lowest energy level ($m_s = -1/2$) has a higher occupation when compared to the $m_s = +1/2$ level. The transitions induced by H_1 changes this condition and tends to equalize the number of spins in both levels. For a strong enough H_1, the two levels will be equally occupied. This condition is called saturation. For intermediate values of H_1, the occupation of $m_s = -1/2$ level; will always be smaller than in thermal equilibrium. In conventional ESR, it is possible to measure changes in magnetization of the sample induced by the spin transitions just described. The measurements are made monitoring the sample's microwave (H_1 photons) absorption.

On the other hand, in an EDMR experiment, the occupation of spin levels is in general probed through changes in the electronic conductivity of the sample under study. To understand how the conductivity will depend on electron spin resonance, let us take, for example, the hopping transport through localized states in the presence of H_0. A spin in a singly occupied state (paramagnetic) will hop to another singly occupied state only if spin selection rules are not violated (see Figure 1). This means that a transition will be allowed as long as no spin flip (no transition from $m_s = -1/2$ to $m_s = +1/2$ or vice versa) is necessary. This condition is commonly described as a pair of interacting spins forming singlet and triplet states. It is important to notice that in most cases, distant pairs are formed; so strictly speaking, these are pairs of parallel and antiparallel states, and not singlet and triplet states. However, we shall use the terms singlet and triplet states in the following to describe the phenomena of spin-dependent transport. The spin in a singlet (S = 0) is allowed to hop, since the final state is also S = 0 state (Figure 1a), while the spin in the triplet configuration (S = 1) is forbidden to hop (Figure 1b). Thus out of resonance, triplets have a much longer lifetime than singlets, and then in steady state the number of charges (spins) "trapped" in triplets can be quite significant. When one of the spins from a triplet is brought into resonance condition it will flip and thus transform into a singlet, and consequently transport takes place. In other words, "trapped" charges (spin) are released when the spin system is in magnetic resonance;
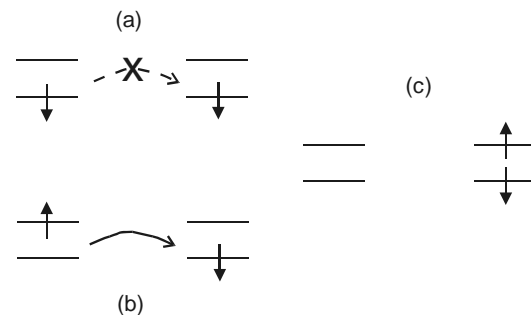

Figure 1. Schematic diagram of possible spin states before (a) and (b), and after (c) a spin-dependent electronic transitions of two independent S=1/2 states. (a) Represents a forbidden transition, while (b) allowed.

therefore, in this specific case conductivity increases when conducting spins are in resonance.

Several transport/recombination processes have been identified as spin-dependent, which can be summarized as:

1. Spin-dependent scattering: Not commonly observed, in this case free electrons suffering collisions with either localized states (such as donors) or other free electrons will have different collision cross-sections depending on the spin states of both. Similarly to what is presented in Figure 1, it is expected from Pauli exclusion principle that if both spins are parallel (triplet state), the collision cross-section should be higher than in the antiparallel case. In a simple and imprecise view, parallel magnetic dipoles tend to repel, while antiparallel ones attract each other.
2. Spin-dependent hopping: This was the mechanism described previously to explain the basic principles of EDMR.
3. Spin-dependent recombination: Probably the most commonly described spin dependent effect. An excited electron in the conduction band or in a donor level, after recombination with a deep defect or acceptor level, will doubly occupy the final level. Thus from Pauli exclusion principle, the final state is a singlet. Triplet states will be spin forbidden to recombine.

Notice that in the last spin-dependent process, recombination of excited electrons in semiconductors is in many cases followed by light emission. The luminescence is thus in a similar way spin-dependent. The technique, which explores the spin-dependent luminescence, is optically detected magnetic resonance (ODMR). In this work, we shall not deal with ODMR.

Electron spin resonance and EDMR have important differences; an EDMR experiment always involves a spin transition that leads to charge transport. The first consequence is an increase in sensitivity. Signals in most ESR spectrometers comes from microwave rectification in a diode. In such a system, thermal noise limits detection. The spin selection rule governing EDMR is not as sensitive to thermal noise due to the weak magnetic coupling of the spins with the lattice. Remember that the Zeeman splitting is normally just a few μeV, although typical relaxation time of those levels is in the ms range. In other words, spins can normally be treated as isolated states with weak interactions. In EDMR, it is as if we were using this characteristic doubly, to investigate the magnetic and transport properties of our sample, and as a very sensitive microwave detection scheme. The increased sensitivity has been experimentally confirmed using a commercial p-channel MOSFET [48]. In this investigation the spin dependent changes in capacitance were observed. Knowing the CV characteristics of the device, they have obtained that the spin dependent changes in capacitance came from 400 ± 50 charges (or spins). This is 8 orders of magnitude more sensitive than ESR, as mentioned in the introduction, for a similar situation, the detection limit of ESR is 10^{10} spins." In principle there is no limit to the sensitivity, EDMR being ultimately able to detect a single spin as already demonstrated in the case of ODMR

[133]—as already mentioned, a very relevant characteristic for nanotechnology.

Electrically detected magnetic resonance detects only spins that are participating in charge transport/recombination. Spins that contribute to the magnetization of the sample or sample holder, but not to the electronic conduction, are seen by ESR but not by EDMR. This property has important implications, since in a number of systems, it is not trivial to know the role of an ESR active state in the transport/recombination characteristics of the sample under study. Another consequence is that restriction in sample substrates are not an issue in an EDMR measurement. Electronic spin resonance tubes or sample holders must be signal-free which restricts the materials that can be used, as for example quartz. However, nanodevices are normally embedded in a matrix that is not always ESR inactive, EDMR presenting thus again advantages over ESR. The selectivity has been useful in many situations; recent examples are found in π-conjugated polymers [126, 130].

Electrically detected magnetic resonance spectra contain information of at least two spins. Remember that any of the two spins in the "trapped" triplet state that flips will convert the pair to a singlet, changing the conductivity of the sample. In principle, EDMR allows the microscopic identification of both spin states of the triplet. Note, however, that there are situations where only one spin resonance signal is observed by EDMR. One example of it is spin-dependent transport paths involving indistinguishable spins states, such as the interchain hopping of polarons in (semi)conducting polymers [126]. Another typical situation is when the spin states in the triplet has largely different line widths coming, as, for example, from differences in g-strain. In this case, the broader component may be hard to detect.

Electrically detected magnetic resonance has also disadvantages; an important one has its origin in the fact that the signal observed comes from an increase in transition rates (hopping or recombination) or a decrease in scattering cross-section when the system is in resonance. This considerably reduces the possibilities normally available by ESR when analyzing the magnetic properties of the sample. Continuous wave ESR can measure either the absorption or the dispersion component of the magnetization. The dispersion component does not involve spin flip transitions, being thus inaccessible to EDMR. The different nature of ESR versus EDMR signal is especially noticeable in pulsed or time-domain ESR. The interest in pulsed ESR comes from the possibility to manipulate the magnetization by different pulse sequences, while measuring the transversal component of the magnetization with very short ($\approx$ns) time resolutions. Spin echo, two-dimensional spectra and many other more complex measuring schemes are thus available using pulsed ESR. Electronically detected magnetic resonance measures changes in spin flip rates. Thus the transversal component of the magnetization is in principle inaccessible to EDMR, making fruitless the use of complex pulse sequences. Still, EDMR measurements in the time domain are possible and useful [75].

As a last comment, notice that EDMR signals are presented as a normalized change in some quantity, as, for example, the conductivity in (σ_r) and out (σ_{out}) of resonance: $\sigma_r - \sigma_{out}/\sigma_{out}$ or $\Delta\sigma/\sigma_{out}$. The changes are normally small, in the range of 10^{-8} to 10^{-2}, and to simplify EDMR, signals are presented as $\Delta\sigma/\sigma$. So, contrary to ESR where the intensity of the signal is the relevant quantity, in EDMR the amplitude of the signal is treated as the relevant quantity. Surprisingly, this question is scarcely discussed in the literature [116], though any spectroscopist knows the advantages of using signal intensity instead of amplitude, especially when comparing spectra with distinct line widths.

Several attempts to develop general theories of EDMR can be found in the literature. The most relevant are cited in the end of Section 1 and are connected to spin-dependent changes in the conductivity. The focus of these attempts was to model the amplitude of the spin dependent conductivity changes. Electronic spin resonance can be complicated enough to describe—EDMR involves magnetic resonance *and* electronic transport/recombination. Electrically detected magnetic resonance experiments involve necessarily nonequilibrium conditions since in EDMR a spin is about to "jump" from one orbital to another which generally belongs to different nuclei, molecules, or polymers. In this case, transport relaxation times, as well as spin relaxation times (T_1, T_2), are important in determining the intensity/amplitude of the signal. The processes involved, transport or recombination, and their respective dynamics will have a significant role on EDMR, making quantitative analysis a challenging task. Electronic spin resonance measures the magnetization, which is proportional to the number of spins present in the sample. Electrically detected magnetic resonance measures changes in spin flip rates in and out of resonance, which is not directly connected to the absolute number of spins participating in the process. Remember that this characteristic is the one that boosts the sensitivity of EDMR when compared to ESR! Nevertheless, the best theoretical attempts to describe EDMR fall into basically two categories derived from the work of Lepine [9] and Kaplan et al. [12].

In Lepine's model, an excess of triplet states is formed exclusively by $\mathbf{H}_0 \cdot H_0$ splits the Zeeman levels, and in thermal equilibrium there will be an excess of $m_s = -1/2$ for both spins as represented in Figure 1(a). Using conventional statistics

$$\frac{N_+}{N_-} = \exp\left(-\frac{E_+ - E_-}{kT}\right) = \exp\left(-\frac{h\nu_0}{kT}\right) \approx 1 - \frac{h\nu_0}{kT} = 1 - P$$

where N_+, N_- are the occupation numbers of the spin states, and $P \equiv h\nu_0/kT$. Now, assuming identical spins, the probability that these spins are antiparallel is given by

$$p_s = \frac{N_+ N_-}{N^2} + \frac{N_- N_+}{N^2} = 2\frac{N_+ N_-}{N^2}$$

Similarly, the probability for formation of parallel spins is

$$p_t = \frac{N_+ N_+}{N^2} + \frac{N_- N_-}{N^2} = \frac{N_+^2 + N_-^2}{N^2}$$

Thus, due to the presence of an external magnetic field, the surplus of triplet states will be given by

$$p_t - p_s = \left(\frac{N_+ - N_-}{N_+ + N_-}\right)^2 = \left(\frac{-P}{2 - P}\right)^2 \approx \left(\frac{P}{2}\right)^2 = \left(\frac{h\nu_0}{2kT}\right)^2$$

In this model, $\Delta\sigma/\sigma$ is expected to be no greater than the population change induced by the resonance condition. Thus, the maximum change with respect to the equilibrium will happen when the system is in resonance and under saturation condition, when both $m_s = -1/2$ and $m_s = +1/2$ are equally populated, or in other words, $p_t - p_s = 0$. Since according to our earlier discussion, magnetic resonance "releases" charged carriers in triplet states, it is now straightforward to write the expression for the relative change of $\Delta\sigma/\sigma$;

$$\frac{\Delta\sigma}{\sigma} = (p_t - p_s)_{out} - (p_t - p_s)_r \leqslant \left(\frac{h\nu_0}{kT}\right)^2$$

In X-band at 300K, $\Delta\sigma/\sigma$ is at maximum 6×10^{-7}. This result is in clear contradiction to data found, for example, in Si where $\Delta\sigma/\sigma$ can be as high as 10^{-2} in the same conditions! Notice, however, that Lepine's model does give satisfactory results in some special situations [116, 134]. To explain the relatively high values of $\Delta\sigma/\sigma$ found in common semiconductors, Kaplan et al. have centered their explanation on spin pair recombination dependent on the relative orientation of the two spins [12]. The other important aspect introduced in this model is the possibility of spin dissociation prior to recombination. The model of Kaplan et al., has been further developed by many authors, for example, Barabanov et al. [31] introduced quantum kinetic equations describing the recombination of charge carriers in the presence of both static and high-frequency magnetic fields. For the sake of brevity, we shall not develop either Kaplan's or Barabanov's model; however, in both cases $\Delta\sigma/\sigma$ are found as large as 10^{-1}, in good agreement with experimental findings.

3. EDMR IN NANOTECHNOLOGY

As can be seen in Table 1, EDMR has been exclusively applied to semiconductors, though wide bandgap semiconductors can also be classified as insulators. From our present understanding, there should be no restriction on the use of EDMR, so long as there are paramagnetic states and the possibility of injecting/extracting electronic carriers in the material or device. The technique has been successfully applied both to nanostructures as well as to nanostructured materials. In selecting the relevant EDMR work to nanoscience/nanotechnology, the author has made an arbitrary choice of what should be included in this section. The technique has been used since 1966, and many structures such as thin films are in some cases 100 nm thick or less; in metal oxide, semiconductor, field effect transitors (MOSFET), the relevant physics is happening just a few nanometers away from the Si/SiO$_2$ interface; polymers in many cases can be described as one-dimensional nanostructures. Thus, in the case of nanomaterials, we shall restrict our examples to fullerenes and nanocrystals. Concerning nanostructured

materials, the examples will concentrate on structures where quantum confinement is important and to submicron (or nano) electronics.

3.1. Nanomaterials

3.1.1. Fullerenes

Fullerenes have been studied by EDMR since 1996 by several groups [135–138]. Experiments have been performed in thin films of C_{60} and C_{70} [136], in heterostructured photodiodes made of fullerenes and oligothiophene [135] or H_2-phtalocyanine [137], as well as in polymer fullerene blends [138]. A representative heterostructure used in EDMR investigations is presented in Figure 2. Typically two resonance lines are observed in these heterostructures as shown in Figure 3. Though the origin of the signals is not completely understood, it appears that they are coming from the polymer part of structure. The observation of EDMR signatures from fullerenes were possible in the simplest structure, the one comprised of only C_{60} or C_{70}. In this case, a line with $g \approx 2.003$ was observed and attributed to the exchange of coupled positive polarons. Eickelkamp et al./[136] have proposed a theoretical model and used spectra simulation to qualitatively, as well as quantitatively, describe the exchange interaction between the two polarons, their dipolar coupling as well as the anisotropy of the g-tensor. From their results, they estimated that the two exchanged coupled polarons that give rise to the EDMR signal are about 2 nm apart.

3.1.2. Si Nanocrystals

Another class of nanomaterials that has been recently explored by EDMR is polymorphous silicon [139]. Hydrogenated polymorphous silicon (pm-Si:H) is a class of thin-film material intermediate between hydrogenated amorphous silicon (a-Si:H) and microcrystalline silicon (μc-Si:H). It consists of an amorphous matrix in which ordered silicon clusters and/or crystallites are embedded [140]. The size/diameter of such inclusions is about 3 nm as deduced from high-resolution transmission electron microscope images. In this system, two EDMR signals were observed as can be seen in Figure 4. The first signal was found just at low temperatures, $T < 100$ K. This signal has $g = 2.01$ and was assigned to hopping of holes through the disordered a-Si:H matrix. The second signal with $g = 2.005$ was assigned to the recombination of conduction electrons
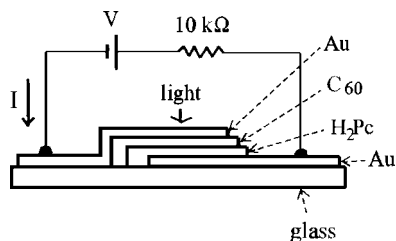
Figure 3. X-band EDMR spectrum of H_2-phthalocyanine/C_{60} heterojunction at 169 K. Bias voltage V = −10 V. The broken line is a simulated one by an overlap of two Lorentzian lines which are shown by the dotted lines. Reprinted with permission from [137], I. Hiromitsu et al., *Phys. Rev. B* 59, 2151 (1999). © 1999, American Physical Society.

with neutral dangling bonds in the crystallites. One of the interesting results from the EDMR investigation was that when both signals were observed, no exchange narrowing was found. This result shows that amorphous and nanocrystalline regions are distinct, and play different roles in what concerns transport and recombination of charges.

3.2. Nanostructured Materials and Devices

3.2.1. Two-Dimensional Electron Gas in Si

Silicon-based quantum-confined electron systems have been explored using EDMR in different structures. We shall use the Si-based systems as examples; however, work has also been done on GaAs/AlGaAs-based heterostructures [143, 144]. In the first report of Ghosh and Silsbee [141], the scattering of spin conduction electrons off neutral impurities in a two-dimensional electron gas was studied. The two-dimensional gas was formed in a Si metal-oxide-semiconductor field effect transistor, with a n-channel accumulation layer that operated at 4K. The EDMR spectrum consisted of a broad central feature with g = 2 and a pair of narrow hyperfines separated by 42G. The central feature is found to be influenced by three sources: (1) conduction electron spins, (2) exchange narrowed clusters of weakly coupled donor impurities, and (3) impurity spins that are strongly

Figure 2. Scheme of the H_2-phthalocyanine/C_{60} heterojunction. Reprinted with permission from [137], I. Hiromitsu et al., *Phys. Rev. B* 59, 2151 (1999). © 1999, American Physical Society.
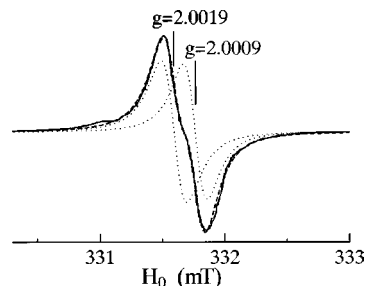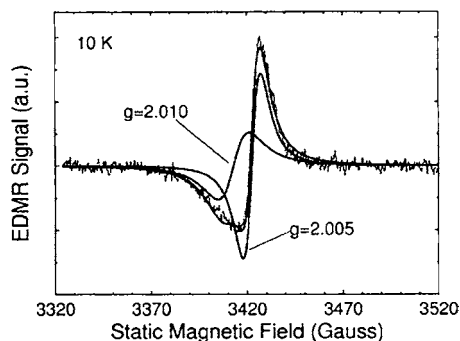

Figure 4. EDMR results for pm-Si:H at 10 K. The spectrum was fitted with two Lorentzian lines with g = 2.010 and g = 2.005. Reprinted with permission from [139], W. Bronner et al., *J. Non-Cryst. Solids* 299–302, 551 (2002). © 2002, Elsevier Science.

coupled to conduction spins. The split pair was assigned to the impurity electron spin system alone. The expected anisotropy in g-factor of conduction electrons in Si were not observed, as will be described later. However they were able to estimate the difference in singlet and triplet scattering cross-sections as a function of Fermi energy of the two-dimensional electron gas. This difference is greater than 4×10^{-13} cm^2 at a density of 5.7×10^{12} cm^{-2}.

In the second case, Si/Si$_{0.75}$Ge$_{0.25}$ heterostructures were investigated [134]. The EDMR signal in this case was assigned to the scattering between conduction electrons. The samples were grown by solid source e-beam evaporation, molecular beam epitaxy (MBE) on weakly p-type Si(100) substrates. The layer sequence of the structure is shown in Figure 5. The two-dimensional electron gas is formed in these structures from the anisotropy in the strain-induced splitting of the conduction band valleys [134]. The lattice mismatch between Si and Ge is approximately 4%. Thus, when a thin Si layer is sandwiched between SiGe layers, it suffers a tensile strain. This tensile strain lifts the degeneracy of the six silicon conduction-band valleys of bulk silicon. As a consequence, and as shown in Figure 5, the two Si conduction band valleys with their major axis parallel to the [100] growth direction have a conduction-band energy minimum $\Delta(2)$ lower than the conduction band minimum of the SiGe layer $\Delta(6)$, while the other four valleys of the strained Si layer (with major axes parallel to [010] or [001]) have a higher energy, $\Delta(4)$. Notice that the confinement in this case is restricted to the conduction band.

Due to this special configuration, where only the conduction-band minima in the [100] direction are occupied by the two-dimensional gas, the g anisotropy was undoubtedly observed as seen in Figure 6. Notice that in Figure 6, the EDMR spectra of a Si/Si$_{0.75}$Ge$_{0.25}$-heterostructure are shown as a function of the relative orientation of the external magnetic field H_0, with respect to the sample growth direction [100]. An angle of 0° thus corresponds to H_0
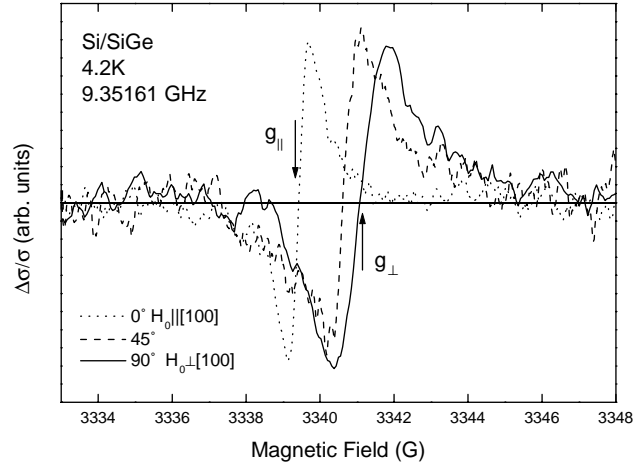
Figure 6. Typical EDMR signals for a sample without gate under different orientations of the sample growth direction with respect to the magnetic field H_0. Reprinted with permission from [134], C. F. O. Graeff et al., *Phys. Rev. B* 59, 13242 (1999). © 1999, American Physical Society.

parallel to the growth direction and an angle of 90° to H_0 perpendicular.

The linewidths in this system are exceptionally narrow, as small as 70 mG, which substantially increased the precision in the determination of the g-tensor. Without providing details, the magnetic resonance linewidths of either EDMR or ESR signal is in many cases, inversely proportional to the relaxation time, in particular, more precisely to the transversal relaxation time. Due to weak spin-orbit coupling, the conduction electrons have a *g*-factor very close to 2 and very slow spin relaxation.

The anisotropy reflects the axial symmetry of the conduction-band valleys of Si. For an axially symmetric *g*-tensor, with main components $g_\parallel$ and $g_\perp$, the orientation-dependent g-factor is given by

$$g^2 = g_\parallel^2 \cos^2\theta + g_\perp^2 \sin^2\theta \qquad (1)$$

where θ is the angle between the applied field H_0 and the major valley axis (parallel to [100]). From a least square fit to the g-value anisotropy observed for the Si/SiGe heterostructure (Fig. 7), $g_\parallel$ is found to be 2.0007 ± 0.0001 and $g_\perp = 1.9999 \pm 0.0001$, which leads to a dispersion of $\Delta g = g_\parallel - g_\perp = (8 \pm 2) \times 10^{-4}$. This value for Δg is in good agreement with experimental results for doped Si under uniaxial stress by Wilson and Feher, who in 1961 [142] determined $\Delta g = (11 \pm 1) \times 10^{-4}$ for the case of complete repopulation into the $\Delta(2)$ valleys. It should be noted, however, that these authors have deduced their value of Δg via extrapolation from g-factor shifts observed under small applied strains ($\leq 0.1\%$). In the EDMR results, as already mentioned, the valleys are only partly occupied and the anisotropy can be observed directly without the need of extrapolation.

In this particular system, as well as the one studied by Gosh et al., a simple modification of Lepine's model [8] for spin-dependance gave good agreement with experimental findings.
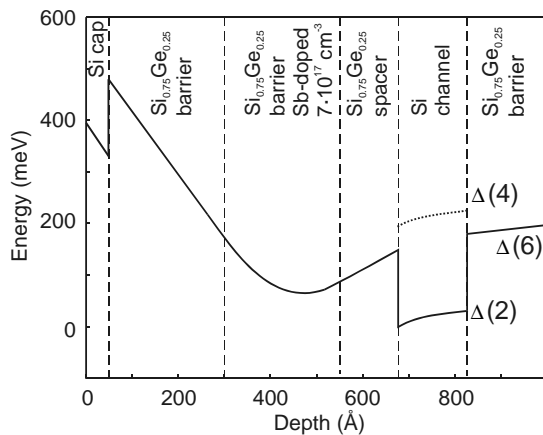

Figure 5. Schematic diagram of the conduction band of the Si/SiGe heterostructures studied in this work. $\Delta(n)$ indicates the degeneracy of the conduction band minima in the unstrained and strained layers. Reprinted with permission from [134], C. F. O. Graeff et al., *Phys. Rev. B* 59, 13242 (1999). © 1999, American Physical Society.
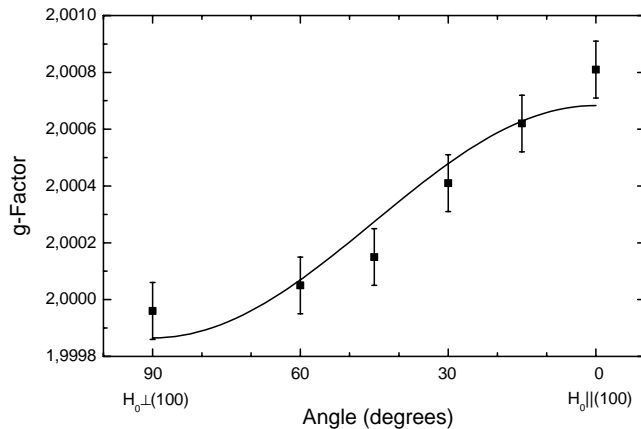
Figure 7. *g*-factor as a function of the relative orientation between the magnetic field H_0 and the sample growth direction. The fit of the *g*-factor anisotropy was done using Eq. (1). The clear anisotropy indicates that only electrons in the conduction-band valleys with the long axis parallel to the sample growth direction [100] contribute to the spin-dependent transport path.

3.2.2. Si-Based Submicron Devices

For dynamic random access memories (DRAMs), leakage currents in reverse-biased p-n junctions have to be suppressed in order to keep the capacitor charges (or memory working) as long as possible. A typical schematic view of the memory device structure is shown in Figure 8 [145]. As sources of leakage current in reverse-bias, defects in the n-p junctions are considered to be important. Thus, this type of memory device is very susceptible to residual defects in 0.3 μm ultralarge-scale integrated circuits (ULSIs). However, as already mentioned in the introduction, only EDMR is sensitive enough to detect defects in these devices, and in fact has been successfully used to study such devices [145, 146] A typical EDMR spectrum in reverse bias is shown in Figure 9(a). The spectrum consists of two parts: one main broad resonance at g = 2.0055 and weak multilines at both sides. The main line was assigned to Si dangling bonds found, for example, in amorphous silicon. The multilines seen in Fig. 9(a) were assigned to a combination of the P2 and A14 centers, from the strong dependence they have on magnetic field orientation as shown in Figure 10. The
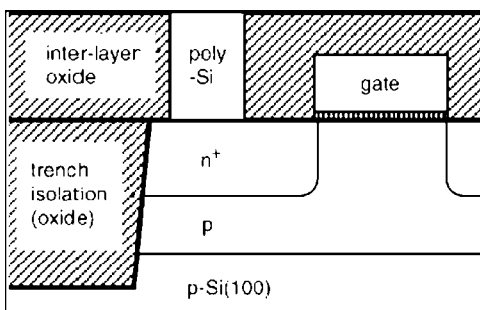
Figure 8. Sample structure of the DRAM cell. The p- and n-type regions were produced by the implantation of B and P in a p-type (100) Si wafer. Reprinted with permission from [145], T. Umeda et al., *Physica B* 308–310, 1169 (2001). © 2001, Elsevier Science.
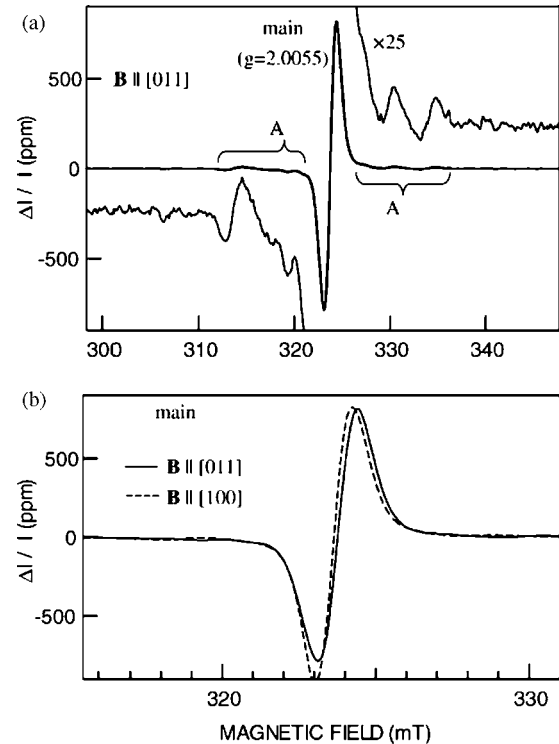

Figure 9. (a) EDMR spectra for the junction leakage current of the DRAM cells, and (b) the main signal. Reprinted with permission from [145], T. Umeda et al., *Physica B* 308–310, 1169 (2001). © 2001, Elsevier Science.

P2 and A14 centers are a defect system known as a divancancy coupled to one oxygen in the case of A14 and to two oxygen atoms in the case of P2 [147]. From the knowledge of how these devices are made, the authors could identify the fabrication step, which could be improved to avoid such defects—the phosphorous implantation.
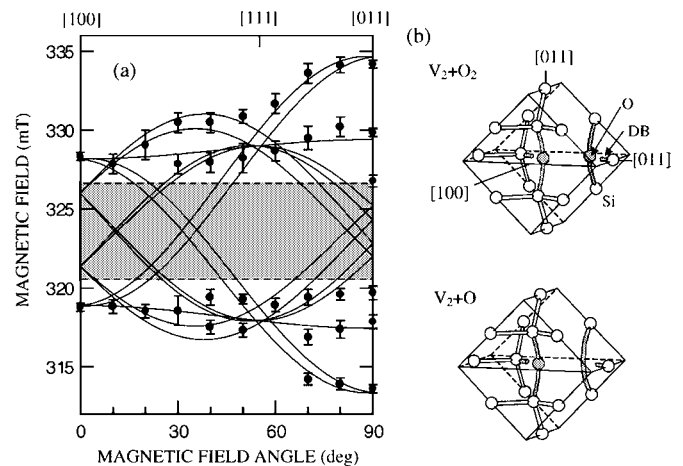

Figure 10. (a) Angular dependence of the signal *A* shown in Figure 9(a). In the gray area, this signal is not clearly resolved due to overlapped main signal. (b) The microscopic origins of the signal just mentioned. Reprinted with permission from [145], T. Umeda et al., *Physica B* 308–310, 1169 (2001). © 2001, Elsevier Science.

GLOSSARY

Complementary metal oxide semiconductor (CMOS) A semiconductor technology used in making integrated circuits, based on the insulating capacity of silicon dioxide. When compared to other semiconductor technologies, CMOS is favored for portable computers and other battery-powered devices because of its low power consumption.

Dynamic random access memories (DRAM) Computer memory available to the user for creating, loading, or running programs and for the temporary storage and manipulation of data, in which time of access to each item is independent of the storage sequence.

Electrically detected magnetic resonance (EDMR) A spectroscopic technique that investigates the phenomena of ESR through spin-dependent changes in the electrical characteristics of conductivity, capacitance, and electronic noise.

Electron spin resonance (ESR) A spectroscopic technique that investigates transitions between electron spin states under a magnetic field, and using microwave photons as the probe.

Light emitting diode (LED) Electronic device used as a source of light by direct conversion of electronic current into photons.

Metal oxide semiconductor field effect transistor (MOSFET) Transistor used in the CMOS technology.

Molecular beam epitaxy (MBE) An ultra-high vacuum deposition technique, where a beam of atoms or molecules created through a highly controlled evaporation, is deposited in a substrate. This deposition technique allows the deposition of nanostructures.

Polaron A conducting electron in an ionic crystal (or polymer) together with the induced polarization of the surrounding lattice (or polymeric chain).

Ultra-large scale integrated circuits (ULSI) A high-density circuit of transistors, resistors, and capacitors constructed on a single semiconductor wafer or chip, in which the components are interconnected to perform a given function.

Thin film transistor (TFT) A transistor in the form of a thin film used for example as the active matrix that controls the pixels in notebook computers displays.

ACKNOWLEDGMENTS

REFERENCES

1. E. Zavoisky, *J. Phys. USSR* 9, 211 (1945).
2. G. D. Watkins, *Semiconduct. Semimet.* 51, 1 (1998).
3. A. Honig, *Phys. Rev. Lett.* 17, 188 (1966).
4. R. Maxwell and A. Honig, *Phys. Rev. Lett.* 17, 188 (1966).
5. J. Schmidt and I. Solomon, *Compt. Rend. Acad. Sci. Paris* 263, 169 (1966).
6. C. O'Raifeartaigh, L. Bradley, R. C. Barklie, A. M. Hodge, E. D. Richmond, *Semicond. Sci. Tech.* 10, 1595 (1995).
7. R. Müller, P. Kanschat, S. von Aichberger, K. Lips, and W. Fuhs, *J. Non-Cryst. Solids* 266–269, 1124 (2000).
8. D. J. Lepine and J. J. Prejan, "Proceedings of the 10th ICPS" (S. P. Keller, J. C. Hensel, and F. Stern, Eds.). Conf.-700801 U.S. A.E.C. Division of Technical Information, Springfield, VA, 1970, 805.
9. Y. Toyoda and Y. Hayashi, *J. Phys. Soc. Japan* 33, 718 (1972).
10. N. Kishimoto and K. Morigaki, *J. Phys. Soc. Japan* 42, 137 (1976).
11. R. M. White and J. F. Goyet, *Phys. Rev. B* 16, 3596 (1977).
12. D. Kaplan, I. Solomon, N. F. Mott, *J. Phys. (Paris)* 39, L51 (1978).
13. V. S. Lvov, O. V. Tretyak, and I. A. Kolomiets, *Sov. Phys.-Semicond.* 11, 661 (1977).
14. I. A. Kolomiets, L. S. Mima, V. I. Strikha, and O. V. Tretyak, *Sov. Phys.-Semicond.* 13, 253 (1979).
15. L. S. Mima, V. I. Strikha, and O. V. Tretyak, *Sov. Phys.-Semicond.* 14, 1328 (1980).
16. V. S. Lvov, L. S. Mima, and O. V. Tretyak, *Sov. Phys. JETP* 56, 897 (1982).
17. J. Ruzytto, I. Shiota, N. Miyamoto, and J. Nishizawa, *J. Electrochem. Soc.* 123, 26 (1976).
18. G. Mendz and D. Haneman, *J. Phys. C* 11, L197 (1978).
19. D. Neubert, K. Hoffmann, H. Teichmann, and R. Schlief, *Solid State Electron.* 21, 1445 (1978).
20. V. S. Lvov and O. V. Tretyak, *Sov. Phys. JETP* 60, 136 (1984).
21. R. Haberkorn and W. Dietz, *Solid State Commun.* 35, 505 (1980).
22. D. Haneman, *Prog. Surf. Sci.* 15, 85 (1984).
23. P. M. Lenahan and W. K. Schubert, *Solid State Commun.* 47, 423 (1983).
24. P. M. Lenahan and W. K. Schubert, *Phys. Rev. B* 30, 1544 (1984).
25. C. H. Seager, E. L. Venturini, and W. K. Schubert, *J. Appl. Phys.* 71, 5059 (1992).
26. D. Vuillaume, D. Deresmes, and D. Stievernard, *Appl. Phys. Lett.* 64, 1690 (1994).
27. S. Greulich-Weber, *Mat. Sci. Forum* 143–147, 1337 (1994).
28. B. Stich, S. Greulich-Weber, and J. M. Spaeth, *J. Appl. Phys.* 77, 1546 (1995).
29. L. S. Vlasenko, Y. V. Martynov, T. Gregorkiewiczz, and C. A. J. Ammerlaan, *Phys. Rev. B* 52, 1144 (1995).
30. B. Stich, S. Greulich-Weber, and J. M. Spaeth, *Appl. Phys. Lett.* 68, 1102 (1996).
31. A. V. Barabanov, O. V. Tretiak, and V. A. Lvov, *Phys. Rev. B* 54, 2571 (1996).
32. M. M. Afanasjev, R. Laiho, L. S. Vlasenko, and M. P. Vlasenko, *Solid State Commun.* 102, 595 (1997).
33. T. Mchedlidze and K. Matsumoto, *J. Appl. Phys.* 83, 4042 (1998).
34. A. V. Barabanov, V. A. Lvov, and O. V. Tretyak, *Phys. Stat. Sol. B* 207, 419 (1998).
35. T. Sato, H. Yokoyama, H. Ohya, and H. Kamada, *J. Magn. Reson.* 139, 422 (1999).
36. T. Mchedlidze, K. Matsumoto, T. C. Lin, and M. Suezawa, *Physica B* 274, 404 (1999).
37. T. Sato, H. Yokoyama, H. Ohya, and H. Kamada, *Rev. Sci. Instrum.* 71, 486 (2000).
38. B. Langhanki, S. Greulich-Weber, J. M. Spaeth, V. P. Markevich, L. I. Murin, T. McHedlidze, and M. Suezawa, *Physica B* 302–303, 212 (2001).
39. K. Fukui, T. Sato, H. Yokoyama, H. Ohya, and H. Kamada, *J. Magn. Reson.* 149, 13 (2001).
40. M. C. Chen and D. V. Lang, *Phys. Rev. Lett.* 51, 427 (1983).
41. B. Henderson, *Appl. Phys. Lett.* 44, 228 (1984).
42. R. L. Vranch, B. Henderson, and M. Pepper, *Appl. Phys. Lett.* 52, 1161 (1988).
43. R. L. Vranch, B. Henderson, and M. Pepper, *Appl. Phys. Lett.* 53, 1299 (1988).
44. M. A. Jupina and P. M. Lenahan, *IEEE Trans. Nucl. Sci.* 36, 1800 (1989).
45. B. Henderson, M. Pepper, and R. L. Vranch, *Semicond. Sci. Technol.* 4, 1045 (1989).

46. P. M. Lenahan and M. A. Jupina, *Coloids and Surfaces* 45, 191 (1990).

47. J. T. Krick, P. M. Lenahan, and G. J. Dunn, *Appl. Phys. Lett.* 59, 3437 (1991).

48. M. S. Brandt, R. T. Neuberger, and M. Stutzmann, *Appl. Phys. Lett.* 76, 1467 (2000).

49. I. Solomon, *Solid State Commun.* 20, 505 (1976).

50. W. Szkielko, *Phys. Status Solidi B* 90, K81 (1978).

51. F. I. Borisov, V. I. Strikha, and O. V. Tretyak, *Sov. Phys. Semicond.* 15, 1149 (1981).

52. Z. Kachwalla and D.J. Miller, *J. Appl. Phys.* 62, 2848 (1987).

53. D. Kaplan and M. Pepper, *Solid State Commun.* 34, 803 (1980).

54. F. Rong, E. H. Poindexter, M. Harmatz, W. R. Buchwald, and G. J. Gerardi, *Solid State Commun.* 76, 1083 (1990).

55. F. C. Rong, W. R. Buchwald, E. H. Poindexter, W. L. Warren, and D. J. Keeble, *Solid State Electron.* 34, 835 (1991).

56. P. Christmann, C. Wetzel, B. K. Meyer, A. Asenov, and A. Endrös, *Appl. Phys. Lett.* 60, 1857 (1992).

57. F. C. Rong, G. J. Gerardi, W. R. Buchwald, E. H. Poindexter, M. T. Umlor, D. J. Keeble, and W. L. Warren, *Appl. Phys. Lett.* 60, 610 (1992).

58. E. H. Poindexter, F. C. Rong, W. R. Buchwald, G. J. Gerardi, D. J. Keeble, and W. L. Warren, *Colloid Surface A* 72, 119 (1993).

59. B. Stich, S. Gruelich-Weber, J. M. Spaeth, and H. Overhof, *Semicond. Sci. Technol.* 8, 1385 (1993).

60. Z. Xiong and D. J. Miller, *Appl. Phys. Lett.* 63, 352 (1993).

61. M. Lannoo, D. Vuillaume, D. Deresmes, and D. Stievenard, *Microelectron. Eng.* 22, 143 (1993).

62. W. Gehlhoff, N. T. Bagraev, and L. E. Klyachkin, *Mater. Sci. Forum* 196, 467 (1995).

63. P. Christmann, W. Stadler, and B. K. Meyer, *Appl. Phys. Lett.* 66, 1521 (1995).

64. Z. Xiong and D. J. Miller, *J. Appl. Phys.* 77, 5201 (1995).

65. Z. Xiong and D. J. Miller, *J. Appl. Phys.* 78, 4895 (1995).

66. Y. Kamigaki, T. Miyazaki, N. Yoshihiro, K. Watanabe, and K. Yokogawa, *J. Appl. Phys.* 84, 2193 (1998).

67. T. Wimbauer, Y. Mochizuki, K. Ito, M. Horikawa, and T. Kitano, *Appl. Surf. Science* 159–160, 72 (2000).

68. T. Wimbauer, K. Ito, Y. Mochizuki, K. Ito, M. Horikawa, T. Kitano, M. S. Brandt, and M. Stutzmann, *App. Phys. Lett.* 76, 2280 (2000).

69. E. T. Hornmark, S. A. Lyon, E. H. Poindexter, and C. F. Young, *Solid State Commun.* 116, 279 (2000).

70. M. X. Yan, K. P. Homewood, and B. C. Cavenet, *J. Phys. C: Solid State Phys.* 19, L189 (1986).

71. B. C. Cavenett and M. X. Yan, *Semicond. Sci. Technol.* 1, 180 (1986).

72. C. H. Seager, E. L. Venturini, and W. K. Schubert, *Appl. Phys. Lett.* 60, 1732 (1992).

73. W. K. Schubert and P. M. Lenahan, *Appl. Phys. Lett.* 43, 497 (1983).

74. K. Lips, P. Kanschat, D. Will, C. Lerner, and W. Fuhs, *J. Non-Cryst. Solids* 227–230, 1021 (1995).

75. C. Boehme, P. Kanschat, and K. Lips, *Nucl. Instr. and Meth. in Phys. Res. B* 186, 30 (2002).

76. P. Kanschat, K. Lips, and W. Fuhs, *J. Non-Cryst. Solids* 266–269, 524 (2000).

77. M. Stutzmann, M. S. Brandt, and M. W. Bayerl, *J. Non-Cryst. Solids* 266–269, 1 (2000).

78. W. Bronner, M. Mehring, and R. Brüggemann, *Phys. Rev. B* 65, 165212 (2002).

79. K. Morigaki and M. Onda, *J. Phys. Soc. Japan* 33, 1031 (1972).

80. N. M. Reinacher, M. S. Brandt, and M. Stutzmann, *Mat. Sci. For.* 196–201, 1915 (1995).

81. K. Krambrock, M. V. Pinheiro, and S. M. Medeiros, *Mater. Sci. Forum* 258–262, 957 (1997).

82. M. S. Brandt, M. W. Bayerl, N. M. Reinacher, T. Wimbauer, and M. Stutzmann, *Mater. Sci. Forum* 258–2, 963 (1997).

83. N. M. Reinacher, M. S. Brandt, and M. Stutzmann, *J. Appl. Phys.* 80, 4541 (1996).

84. W. E. Carlos, E. R. Glaser, T. A. Kennedy, and S. Nakamura, *J. Electron. Mater.* 25, 851 (1996).

85. W. E. Carlos and S. Nakamura, *Appl. Phys. Lett.* 70, 2019 (1997).

86. M. W. Bayerl, M. S. Brandt, and M. Stutzmann, *Phys. Status Solidi A* 159, R5 (1997).

87. M. W. Bayerl, M. S. Brandt, H. Angerer, O. Ambacher, and M. Stutzmann, *Phys. Status Solidi B* 210, 389 (1998).

88. B. C. Cavenett and R. Brunwin, *Solid State Commun.* 31, 659 (1979).

89. I. Solomon, "Proceedings of the 11th ICPS." Elsevier, Amsterdam, 1972, 27.

90. C. F. O. Graeff, E. Rohrer, C. E. Nebel, M. Stutzmann, H. Güntler, and R. Zachai, *Mater. Res. Soc. Symp. Proc.* 423, 495 (1996).

91. T. Graf, M. S. Brandt, C. E. Nebel, M. Stutzmann, and S. Koizumi, *Physica B* 308, 593 (2001).

92. I. Solomon, D. K. Biegelsen, and J. C. Knights, *Solid State Commun.* 22, 505 (1977).

93. B. Movaghar, B. Ries, and L. Schweitzer, *Phil. Mag. B* 41, 141 (1980). B. Movaghar, B. Ries, and L. Schweitzer, *Phil. Mag. B* 41, 159 (1980).

94. N. Kishimoto, K. Morigaki, and K. Murakami, *J. Phys. Soc. Japan* 50, 1970 (1981).

95. R. Street, *Phil. Mag. B* 46, 273 (1982).

96. H. Dersch, L. Schweitzer, and J. Stuke, *Phys. Rev. B* 28, 4678 (1983).

97. H. Dersch and L. Schweitzer, *Phil. Mag. B* 50, 397 (1984).

98. M. S. Brandt and M. Stutzmann, *Phys. Rev. B* 43, 5184 (1991).

99. K. Lips and W. Fuhs, *J. Non-Cryst. Solids* 137 & 138, 255 (1991).

100. K. Lips, S. Schütte, and W. Fuhs, *Phil. Mag. B* 65, 945 (1992).

101. M. Stutzmann and M. S. Brandt, *J. Non-Cryst. Solids* 141, 97 (1992).

102. M. S. Brandt and M. Stutzmann, *J. Non-Cryst. Solids* 164–166, 547 (1993).

103. K. Lips, C. Lerner, and W. Fuhs, *J. Non-Cryst. Solids* 200, 267 (1996).

104. M. S. Brandt, M. W. Bayerl, M. Stutzmann, and C. F. O. Graeff, *J. Non-Cryst. Solids* 227–230, 343 (1998).

105. S. T. B. Goennenwein, M. W. Bayerl, M. S. Brandt, and M. Stutzmann, *Phys. Rev. Lett.* 84, 5188 (2000).

106. A. A. Karanovich, A. V. Dvurechenskii, I. E. Tyschenko, and G. A. Kachurin, *Nucl. Instrum. Meth. B* 55, 630 (1991).

107. K. P. Homewood, B. C. Cavenet, W. E. Spear, and P. G. Le Comber, *J. Phys. C* 16, L427 (1983).

108. M. S. Brandt, M. Stutzmann, and J. Kocka, *J. Non-Cryst. Solids* 164–166, 693 (1993).

109. K. Lips and W. Fuhs, *J. Appl. Phys.* 74, 3993 (1993).

110. C. Lerner, K. Lips, and W. Fuhs, *J. Non-Cryst. Solids* 227–230, 1177 (1998).

111. M. S. Brandt, R. T. Neuberger, M. W. Bayerl, and M. Stutzmann, *Jpn. J. Appl. Phys.* 38, L1172 (1999).

112. C. F. O. Graeff, M. S. Brandt, M. Stutzmann, and M. J. Powell, *Phys. Rev. B* 52, 4680 (1995).

113. G. Kawachi, C. F. O. Graeff, M. S. Brandt, and M. Stutzmann, *Phys. Rev. B* 54, 7957 (1996).

114. G. Kawachi, C. F. O. Graeff, M. S. Brandt, and M. Stutzmann, *Jpn. J. Appl. Phys.* 36, 121 (1997).

115. C. F. O. Graeff, M. Stutzmann, and S. Miyazaki, *J. Appl. Phys.* 79, 9166 (1996).

116. C. F. O. Graeff, M. Stutzmann, and M. S. Brandt, *Phys. Rev. B* 49, 11028 (1994).

117. J. H. Stathis, *Appl. Phys. Lett.* 68, 1669 (1996).

118. L. S. Swanson, J. Shinar, A. R. Brown, D. D. C. Bradley, R. H. Friend, P. L. Burn, A. Kraft, and A. B. Holmes, *Phys. Rev. B* 46, 15072 (1992).

119. L. S. Swanson, J. Shinar, A. R. Brown, D. D. C. Bradley, R. H. Friend, P. L. Burn, A. Kraft, and A. B. Holmes, *Synthetic Met.* 55–57, 241 (1993).
120. V. Dyakonov, N. Gauss, G. Rosler, S. Karg, and W. Riess, *Chem. Phys.* 189, 687 (1994).
121. N. C. Greenham, J. Shinar, J. Partee, P. A. Lane, O. Amir, F. Lu, and R. H. Friend, *Phys. Rev. B* 53, 13528 (1996).
122. G. B. Silva, L. F. Santos, R. M. Faria, and C. F. O. Graeff, *Physica B* 308–310, 1078 (2001).
123. G. B. Silva, L. F. Santos, R. Biachi, R. M. Faria, and C. F. O. Graeff, *Mol. Cryst. Liq. Cryst.* 374, 135 (2002).
124. V. Dyakonov, G. Rösler, M. Schwoerer, S. Blumstengel, and K. Lüders, *J. Appl. Phys.* 79, 1559 (1996).
125. L. S. Swanson and J. Shinar, *Synthetic Met.* 55–57, 1 (1993).
126. J. Shinar, in "Handbook of Organic Conductive Molecules and Polymers: Vol. 3. Conductive Polymers: Spectroscopy and Physical Properties" (H. S. Nalwa, Ed.). John Wiley & Sons Ltd., New York, 1997, p. 320.
127. C. F. O. Graeff, M. S. Brandt, R. M. Faria, and G. Leising, *Phys. Stat. Sol. B* 162, 713 (1997).
128. C. F. O. Graeff, C. A. Brunello, and R. M. Faria, *Synthetic Met.* 101, 805 (1999).
129. C. F. O. Graeff and C. A. Brunello, *J. Non-Cryst. Solids* 273, 289 (2000).
130. C. F. O. Graeff and C. A. Brunello, *Synthetic Met.* 119, 327 (2001).
131. C. S. Sunandana, *Bull. Mater. Sci.* 21, 1 (1998).
132. W. M. M. Chen, *Thin Solid Films* 364, 45 (2000).
133. J. Köhler, J. A. J. M. Disselhorst, M. C. J. M. Donckers, E. J. J. Groenen, J. Schmidt, and W. E. Moerner, *Nature* 363, 242 (1993).
134. C. F. O. Graeff, M. S. Brandt, M. Stutzmann, M. Holzmann, G. Abstreiter, and F. Schäffler, *Phys. Rev. B* 59, 13242 (1999).
135. A. Maier, A. Grupp, and M. Mehring, *Solid State Commun.* 99, 623 (1996).
136. T. Eickelkamp, M. Mehring, and S. Roth, *Mol. Phys.* 95, 967 (1998).
137. I. Hiromitsu, Y. Kaimori, M. Kitano, and T. Ito, *Phys. Rev. B* 59, 2151 (1999).
138. M. C. Scharber, N. A. Schultz, C. J. Brabec, and N. S. Sariciftci
139. W. Bronner, J. P. Kleider, R. Brüggemann, P. Roca i Cabarrocas, D. Mencaraglia, and M. Mehring, *J. Non-Cryst. Solids* 299–302, 551 (2002).
140. P. Roca i Cabarrocas, S. Hamma, S. N. Sharma, J. Costa, and E. Bertran, *J. Non-Cryst. Solids* 227–230, 871 (1998).
141. R. N. Ghosh and R. H. Silsbee, *Phys. Rev. B* 46, 12508 (1992).
142. D. K. Wilson and G. Feher, *Phys. Rev.* 124, 1068 (1961).
143. T. Wimbauer, M. S. Brandt, M. W. Bayerl, N. M. Reinacher, M. Stutzmann, D. M. Hofmann, Y. Mochizuki, and M. Mizuta, *Phys. Rev. B* 58, 4892 (1998).
144. T. Wimbauer and Y. Mochizuki, *Nec. Res. Develop.* 40, 405 (1999).
145. T. Umeda, Y. Mochizuki, K. Okonogi, and K. Hamada, *Physica B* 308–310, 1169 (2001).
146. K. Ikeda, *Microelectron. Reliab.* 41, 1525 (2001).
147. Y. H. Lee and J. W. Corbett, *Phys. Rev. B* 13, 2653 (1976).

Electrochemical Fabrication of Metal Nanowires

Huixin He

Rutgers University, Newark, New Jersey, USA

Nongjian J. Tao

Arizona State University, Tempe, Arizona, USA

CONTENTS

1. INTRODUCTION

The development of ever more powerful electronics depends on continued progress in miniaturizing their components. However, the laws of quantum mechanics, the limitations of fabrication techniques, and the increasing cost of the fabrication facilities may soon prevent us from the further scaling down of conventional silicon technology. The quest for alternative technologies has stimulated a surge of interest in nanometer-scale materials and devices in recent years. Metal nanowires are one of the most attractive materials because of their unique properties that may lead to a variety of applications. Examples include interconnects for nanoelectronics, magnetic devices, chemical and biological sensors, and biological labels. Metal nanowires are also attractive because they can be readily fabricated with various techniques. An important fabrication technique that will be discussed in this article is the electrochemical method.

The diameters of metal nanowires range from a single atom to a few hundreds of nm, and the lengths vary over even a greater range: from a few atoms to many microns. Because of the large variation in the aspect ratio (length-to-diameter ratio), different names have been used in literature to describe the wires in order to reflect the different shapes. For example, wires with large aspect ratios (e.g., >20) are called nanowires, while those with small aspect ratios are called nanorods. When short "wires" are bridged between two larger electrodes, they are often referred to as nano-contacts. These definitions are intuitive, but somewhat arbitrary. For this reason and also because of the fact that all the wires have diameters on the nanometer scale, they are sometimes all loosely referred to as nanowires.

In terms of electron transport properties, metal wires have been described as classical wires and quantum wires. The electron transport in a classical wire obeys the classical relation

$$G = \sigma \frac{A}{L} \qquad (1)$$

where G is the wire conductance, and L and A are the length and the cross-sectional area of the wire, respectively. σ in Eq. (1) is the conductivity, which depends on the material of the wire. The classical behavior arises because the wires are much longer than the electron mean-free path, and much thicker than the electron Fermi wavelength. The former condition means that conduction electrons experience many collisions with phonons, defects, and impurities when they traverse along a wire. The second condition smears out the effects due to the quantum-size confinement in the transverse direction of the wire. For a typical metal, such as Cu, at room temperature, the mean-free path is a few tens of nm and the electron wavelength is only a fraction of nm, comparable to the size of an atom. Many metal nanowires behave like a classical conductor despite their nanometer-scale diameters.

When the wire is shorter than the electron mean-free path, the electron transport is ballistic, that is, without collisions along the wire. If, in addition, the diameter of the wire is comparable to the electron wavelength, quantum-size confinement becomes important in the transverse direction, which results in well-defined quantum modes. The

conductance of the system measured between two bulk electrodes is described by the Landauer formula [1]

$$G = \frac{2e^2}{h} \sum_{i,j=1}^{N} T_{ij}, \qquad (2)$$

where e is the electron charge, h is Planck's constant, and T_{ij} is the transmission probability of an electron from ith mode at one side of the wire to the jth mode at the other side. The summation is overall the quantum modes, and N is the total number of modes with nonzero T_{ij} values, which is determined by the number of standing waves at the narrowest portion of the wire. In the ideal case, T_{ij} is 1 for $i = j$ and 0 for all other cases, so Eq. (2) is simplified as $G = NG_0$, where $G_0 = 2e^2/h \sim 77.5$ μS is the conductance quantum. So the conductance is quantized and the wire is referred to as a quantum wire.

In this chapter, we provide an overview of electrochemical fabrication and discuss some applications of both classical and quantum wires. While we focus mainly on electrochemical or related fabrication techniques, we would like to point out that many other methods have also been rapidly developed in recent years. Examples include wet chemistry [2–14], electron beam lithography [15–20], focused ion beam techniques [21], and atomic-beam holography [17, 22, 23]. We divide the rest of the chapter into the following sections. In Section 2, we describe the fabrications and applications of classical nanowires. Because rather different approaches are used to fabricate metallic quantum wires, we discuss the fabrication of quantum wires separately in Section 3. In Section 4, a brief summary is provided.

2. CLASSICAL NANOWIRES

We divide this section into two parts. The first part is focused on the electrochemical fabrication of the nanowires. In this part, we discuss the fabrication of various templates first, and then the fabrication of metal nanowires with the templates. The second part discusses various applications of the nanowires.

2.1. Electrochemical Fabrication of Classical Nanowires

A widely used approach to fabricate metal nanowires is based on various templates, which include negative, positive, and surface step templates. We discuss each of the approaches below.

2.1.1. Negative Template Methods

Negative template methods use prefabricated cylindrical nanopores in a solid material as templates. By depositing metals into the nanopores, nanowires with a diameter predetermined by the diameter of the nanopores are fabricated. There are several ways to fill the nanopores with metals or other materials to form nanowires, but the electrochemical method is a general and versatile method. If one dissolves away the host solid material, free-standing nanowires are obtained. This method may be regarded as a "brute-force"

method because the diameter of the nanowires is determined by the geometrical constraint of the pores rather than by elegant chemical principles [24]. However, it is one of the most successful methods to fabricate various nanowires that are difficult to form by conventional lithographic process.

Fabrication of suitable templates is clearly a critical first step. To date, a number of methods have been developed to fabricate various negative templates. Examples include alumina membranes, polycarbonate membranes, mica sheets, and diblock polymer materials. These materials contain a large number of straight cylindrical nanopores with a narrow distribution in the diameters of the nanopores.

The Templates

Track-Etched Membranes When a heavy-charged particle from a nuclear radiation resource passes through certain materials, such as a mica film, it leaves a track of radiation damage in the mica film via a so-called Coulomb explosion phenomenon (Fig. 1A). The minimum width of the track is only 2.5 nm. The track can be selectively etched in a suitable reagent, such as hydrofluoric acid, a technique that was originally introduced for the detection of charged radiation particles [25, 26]. The reagent "develops" and "fixes" the tracks, which results in fine cylindrical pores in the mica along the tracks, while leaving the rest of the material essentially unchanged (Figs. 1B and 1C). The pores are randomly distributed in the mica film but with a rather uniform diameter along their entire length. The diameter of the pores can be controlled by controlling the etching time. In 1969, Possin used the mica film with nanopores to fabricate metal nanowires with a diameter as small as 40 nm [27]. The fabrication technique was refined later by Williams and Giordano who obtained Ag wires with diameters as thin as 8 nm [28]. The works by Martin et al. marked the beginning of a surge in the development and application of the methods in recent years [29–51]. They have demonstrated that various nanostructures, including metal and conducting polymer nanowires and nanotubes, can be fabricated using the negative templates, which may lead to many novel applications [29–51].

The ion-track method has been applied to create nanopores in plastic membranes, such as polycarbonate and polyester [52, 53]. Instead of using acid, alkaline solvent is used to "develop" the ion tracks in polycarbonate membranes [54]. Membranes with pore diameters as small as 10 nm have been fabricated and become commercially available. An important advantage of these plastic templates over the mica films is that their surface wetting properties can be
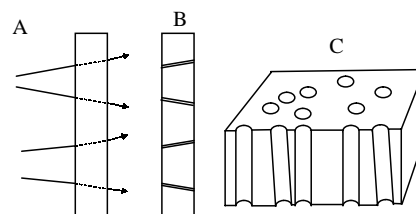

Figure 1. Track-etch process for nanoporous membranes. (A) Tracks of the high-energy fission fragments. (B) Nanopores formed after developing the damaged tracks. (C) Top view of the nanopore membrane.

tailored, which is important for many applications. Another advantage is that they can be more easily dissolved without affecting the nanowires formed in the pores. Despite the great success, these track-etched membranes have some drawbacks when they are used to fabricate nanowires. First, the pore density is rather low (10^9 pores/cm^2), which limits the yield of the nanowires. The pores are randomly positioned and not always parallel to each other (Fig. 1C). While these problems may be tolerable in many applications, they can complicate the interpretations of measured properties [55]. To circumvent the problems, Sun et al. have fabricated nanoporous templates using mica single crystals [56, 57]. The pores in the crystals are diamond-shaped with well-defined crystal axes that are related to the crystal structure of the mica. The improved collimation of the pores, the uniform pore cross-section, and the low density of overlapping pores resulted in significant enhancement in the magnetic anisotropy, in comparison to nanowires of the same dimension formed in polycarbonate membranes.

Anodic Porous Alumina Anodic porous alumina is another commonly used negative template. The nanopores in the template are formed by anodizing aluminum films in an acidic electrolyte. The individual nanopores in the alumina can be ordered into a close-packed honeycomb structure (Fig. 2). The diameter of each pore and the separation between two adjacent pores can be controlled by changing the anodization conditions. The fabrication method of anodic porous alumina can be traced back to the work done in the 1950's, which involves a one-step anodization process. This original one-step anodization method is still used to fabricate most commercial alumina membranes [58, 59]. The anodic porous alumina has a much higher pore density ($\sim 10^{11}$ pores/cm^2), which allows one to fabricate a large number of nanowires at one time. Another interesting feature of the porous alumina template is that the chemistry of the pore walls can be altered via reaction with silane compounds [60].

The distribution of nanopores in anodic porous alumina is usually not as perfect as the one shown in Figure 2. To achieve highly ordered pores, high-purity aluminum films (99.999%) are used. In addition, they are first preannealed to remove mechanical stress and enhance the grain size. Subsequently, the films are electropolished in a 4:4:2 (by
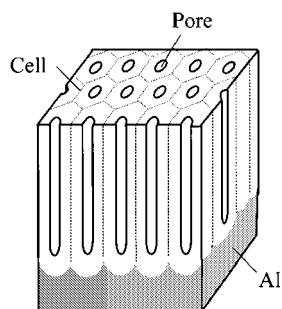
weight) mixture of H_3PO_4, H_2SO_4, and H_2O to create homogeneous surfaces. Without the preannealing and electropolishing steps, it is hard to form well-ordered pores [61]. The order of the pores depends also on other anodization conditions, such as anodization voltage and electrolyte. It has been reported that anodization over a long period at an appropriate constant voltage can produce an almost ideal honeycomb structure over an area of several μm [61, 62]. The optimal voltage depends on the electrolyte used for the anodization [61–64]. For example, the optimal voltage for long-range ordering is 25 V in sulfuric acid, 40 V in oxalic acid, and 195 V in phosphoric acid electrolyte, respectively [61, 65, 66].

The diameter and depth of each pore, as well as the spacing between adjacent pores can be also controlled by the anodizing conditions. Both the pore diameter and the pore spacing are proportional to the anodizing voltage with proportional constants of 1.29 nm V^{-1} and 2.5 nm V^{-1}, respectively. The dependence of the diameter and the spacing on the voltage is not sensitive to the electrolyte, which is quite different from the optimal voltage for ordered distribution of the pores as discussed above [67–69]. This property has been exploited to make size-selective microfiltration membranes and to control the diameter of nanowires formed in the pores. By properly controlling the anodization voltage and choosing the electrolyte, one can make highly ordered nanopores in alumina with desired pore diameter and spacing.

The order of the pores achieved by anodizing an aluminum film over a long period is often limited to a domain of several μm. The individual ordered domains are separated by regions of defects. Recently, a novel approach has been reported to produce a nearly ideal hexagonal nanopore array that can extend over several millimeters [70, 71]. The approach uses a pretexturing process of Al in which an array of shallow concave features is initially formed on Al by indentation. These concave features serve as nucleation sites for the formation of pores during the initial stage of anodization. The pore spacing can be controlled by the pretextured pattern and the applied voltage. Another widely used method to create highly ordered nanopore arrays is a two-step anodization method [65, 72–75]. The first step involves a long-period anodization of high purity aluminum to form a porous alumina layer. Subsequent dissolution of the porous alumina layer leads to a patterned aluminum substrate with an ordered array of concaves formed during the first anodization process. The ordered concaves serve as the initial sites to form a highly ordered nanopore array in a second anodization step.

Acidic anodization of Al normally results in a porous alumina structure which is separated from the aluminum substrate with a so-called barrier layer of Al_2O_3. The barrier layer and aluminum substrate can be removed to form a free-standing porous alumina membrane. The aluminum can be removed with saturated $HgCl_2$ and the barrier layer of Al_2O_3 with a saturated solution of KOH in ethylene glycol. An alternative strategy to separate the porous alumina from the substrate is to take advantage of the dependence of pore diameter on anodization voltage. By repeatedly decreasing the anodization voltage several times at 5% increments, the barrier layer becomes a tree-root-like network with fine

Figure 2. Schematic drawing of an anodic porous alumina template. Reprinted with permission from [71], H. Asoh et al., *J. Electrochem. Soc.* 148, B152 (2001). © 2001, The Electrochemical Society, Inc.

pores. Since the root-like network has a higher exposed surface area than the primary large pores, dissolution occurs there first when immersing the sample in a concentrated acid. The dissolution of the network then results in the separation of the porous oxide film from the aluminum substrate [24].

Other Nanoporous Materials   Thurn-Albrecht et al. showed a simple and robust chemical route to fabricate ultra high-density arrays of nanopores with high aspect ratios using diblock copolymer [76, 77]. The method is based on self-assembly of incompatible block copolymers into well-ordered structures of molecular dimension [78–80]. Block copolymers are long-chain molecules built up from different types of monomers, say A and B, that are grouped in blocks. These blocks are often incompatible and are separated into A-rich and B-rich domains. Depending on the length, connectivity, and interactions between different blocks, the domains can form periodically arranged spheres, cylinders, lamellae, and other structures. The typical repeating distance of the structures is in the range between 10–100 nm, which is attractive for applications in the area of nanotechnology [81, 82]. For the purpose of fabricating metal nanowires, the cylindrical domains are of the obvious interest. Thurn-Albrecht et al. fabricated nanopores using diblock copolymers composed of polymethylmethacrylate (PMMA) and polystyrene (PS). The molecular weight and volume fraction of styrene are chosen such that the copolymer self-assemble into arrays of 14-nm-diameter PMMA cylinders hexagonally packed in the PS matrix with a lattice constant of 24 nm in bulk. The PMMA cylinders are oriented parallel to each other by applying an electric field, while the copolymer film is heated above the glass transition temperature. Deep ultraviolet exposure degrades the PMMA domains and simultaneously cross-links the PS matrix. By rinsing the film with acetic acid, the PMMA domains are selectively removed, which results in a PS film with ordered nanopores. Similar nanopores in other diblock copolymers have also been reported [81, 83]. One of the attractive features of the diblock copolymer template method is that it is compatible with current lithographic techniques and amendable to multilayered device fabrication.

Hong et al. reported that calix[4]hydroquinones (CHQs) form chessboard-like arrays of rectangular pores when they are soaked in $AgNO_3$ aqueous solution [84]. The rich π-electron density of hydroquinones (HQ) moieties in the CHQ nanopores can capture metal ions, such as Ag^+, with high affinity via cation-π interactions. Once Ag^+ ions are captured inside the pores, the redox process between Ag^+ and CHQ takes place spontaneously. Because the reduced neutral Ag atoms do not exhibit strong interactions with the HQ moieties, single-crystalline Ag nanowire arrays with a diameter of 0.4 nm and a length of μm-scale are formed. The atomically thin wires are very stable under ambient air and aqueous environments, because they are confined in the pores and protected by the organic material. Considering the oxidation potential of the HQ moieties in the CHQ and the reduction potentials of metal ions, it should be possible to prepare nanowires of other elements, such as Au, Pd, and Pt, using this method.

Tonucci et al. described a method to fabricate arrays of nanopores in glass [85]. The pores are arranged in a two-dimensional hexagonal close-packed configuration with pore diameter as small as 33 nm and pore density as high as 3×10^{10} pores/cm^2. Because of the high-temperature stability of the nanopore arrays in glass, they are well suited as hosts or templates for nanowire arrays for high temperature studies. Other porous template materials, such as mesoporous silica [86, 87] and niobium oxide [88] have been also reported.

Fabrication of Metal Nanowires   Using the membrane templates previously described, nanowires of various metals, semiconductors [41] and conducting polymers [51, 89], have been fabricated. These nanostructures can be deposited into the pores by either electrochemical deposition or other methods, such as chemical vapor deposition (CVD) [90], chemical polymerization [43, 47], electroless deposition [91], or by sol–gel chemistry [41]. Electrodeposition is one of the most widely used methods to fill conducting materials into the nanopores to form continuous nanowires with large aspect ratios. One of the great advantages of the electrodeposition method is the ability to create highly conductive nanowires. This is because electrodeposition relies on electron transfer, which is the fastest along the highest conductive path. Structural analysis showed that the electrodeposited nanowires tend to be dense, continuous, and highly crystalline in contrast to other deposition methods, such as CVD. Yi and Schwarzacher demonstrated that the crystallinity of superconducting Pb nanowires can be controlled by applying a potential pulse with appropriate parameters [92]. The electrodeposition method is not limited to nanowires of pure elements. It can fabricate nanowires of metal alloys with good control over stoichiometry. For example, by adjusting the current density and solution composition, Huang et al. controlled the compositions of CoPt and FePt nanowires to 50:50 in order to obtain the high anisotropic face-centered tetragonal phases [93]. Similar strategies have been used in other magnetic nanowires [94, 95] and in thermoelectronic nanowires [50, 96]. Another important advantage of the electrodeposition method is the ability to control the aspect ratio of the metal nanowires by monitoring the total amount of passed charge. This is important for many applications. For example, the optical properties of nanowires are critically dependant on the aspect ratio [37, 38, 97]. Nanowires with multiple segments of different metals in a controlled sequence can also be fabricated by controlling the potential in a solution containing different metal ions [98].

Electrodeposition often requires one to deposit a metal film on one side of the freestanding membrane to serve as a working electrode on which electrodeposition takes place. In the case of large pore sizes, the metal film has to be rather thick to completely seal the pores on one side. The opposite side of the membrane is exposed to an electrodeposition solution, which fills up the pores and allows metal ions to reach the metal film. However, one can avoid using the metal film on the backside by using anodic alumina templates with the natural supporting Al substrate. The use of the supported templates also prevents one from breaking the fragile membrane during handling. However, it requires one

to use AC electrodeposition [99–102]. This is because of the rather thick barrier layer between the nanopore membrane and the Al substrate.

Detailed studies of the electrochemical fabrication process nanowires have been carried out by a number of groups [103, 104]. The time dependence of the current curves recorded during the electrodeposition process reveal three typical stages. Stage I corresponds to the electrodeposition of metal into the pores until they are filled up to the top surface of the membrane. In this stage, the steady-state current at a fixed potential is directly proportional to the metal film area that is in contact with the solution, as found in the electrodeposition on bulk electrodes. However, the electrodeposition is confined within the narrow pores, which has a profound effect on the diffusion process of the metal ions from the bulk solution into the pores before reaching the metal film. The concentration profiles of Co ions in the nanopores of polycarbonate membranes during electrodeposition of Co have been studied by Valizadeh et al. [105]. After the pores are filled up with deposited metal, metal grows out of the pores and forms hemispherical caps on the membrane surface. This region is called stage II. Since the effective electrode area increases rapidly during this stage, the electrochemical current increases rapidly. When the hemispherical caps coalescence into a continuous film, stage III starts, which is characterized by a constant value again. By stopping the electrodeposition process before stage I ends, an array of nanowires filled in the pores is formed.

The current-time curves are not always as well behaved as the one described above [103]. For example, the current may vary during the first stage, so that stages I, II, and III may merge together and become difficult to separate. One plausible explanation of this observation is that the pores in the membranes are not aligned parallel but have a considerable angular distribution ($\pm 34°$). The angular distribution means a large length distribution of the pores, such that the pores with different lengths fill up with nanowires at different times. Another possible reason is inhomogeneous growth rates in different pores, due to different degrees of wetting of different pores. The wetting problem tends to be more severe for membranes with smaller pores because of the increased difficulty to wet all the pores before electrodeposition. One way to reduce the wetting problem is to treat polycarbonate membranes with polyvinylpyrrolidone (PVP) [103]. Adding ethanol or methanol into the electrolyte is also found to reduce the wetting problem [77]. Another method is to perform the electrodeposition in an ultrasound bath to facilitate the mass transport of ions through the pores of the membrane [106].

When freely standing nanowires are desired, one has to remove the template hosts after forming the nanowires in the templates. This task is usually accomplished by dissolving away the template materials in a suitable solvent. Methylene chloride can readily dissolve away track-etched polycarbonate film and 0.1M NaOH removes anodic alumina effectively. If one wants to also separate the nanowires from the metal films on which the nanowires are grown, a common method is to first deposit a sacrificial metal. For example, in order to fabricate freely standing Au nanowires, one can deposit a thin layer of Ag onto the metal film coated on one side of

the template membrane before filling the pores with Au. The Ag layer can be etched away later in concentrated nitric acid, which separates the Au nanowires from the metal film.

While DC electrodeposition can produce high-quality nanowires, it is challenging to obtain an ordered nanowire array. Normally only 10–20% of the pores in the membrane are filled up completely using the simple DC method [107]. Using AC electrodeposition with appropriate parameters [99–102], a high filling ratio can be obtained which results in a uniform nanowire array. For example, Yin et al. reported that a high filling ratio can be obtained using a sawtooth wave, triangle wave, or sine wave, but not with a square wave [108]. Furthermore, they found that the filling ratio increases with the AC frequency. A possible reason is that nuclei formed at higher frequencies are more crystalline, which makes the metal deposition easier in the pores and promotes homogeneous growth of nanowires. Nielsch and Sauer et al. developed a pulsed electrodeposition method [109, 110]. After each potential pulse, a relatively long delay follows before application of the next pulse. The rationale is that the long delay after each pulse allows ions to diffuse into the region where ions are depleted during the deposition (pulse). They demonstrated that the pulsed electrodeposition is well suited for a uniform deposition in the pores of porous alumina with a nearly 100% filling rate.

It is interesting to point out that the membrane templates have also been used to fabricate other nanostructures such as nanoparticles [24] and hollow nanotubules [44]. When conducting polymers are synthesized (either chemically or electrochemically) in the pores of the track-etched polycarbonate membranes, the polymer preferentially nucleates and grows on the pore walls. By controlling the polymerization time, tubules with different wall thickness can be obtained. By filling up the polymer tubules with a metal, metal nanowires with polymer sheaths have been fabricated [111]. Metal nanotubules can be fabricated by modifying the pore walls with molecular anchors that allow the deposited metal to form a thin skin on the pore walls [29, 31]. These metal tubules are useful for chemical separations [39, 40].

2.1.2. Positive Template Method

The positive template method uses wire-like nanostructures, such as DNA and carbon nanotubes as templates, and nanowires are formed on the outer surface of the templates. Unlike negative templates, the diameters of the nanowires are not restricted by the template sizes and can be controlled by adjusting the amount of materials deposited on the templates. By removing the templates after deposition, wire-like and tube-like structures can be formed. We discuss some of the positive templates below.

Carbon Nanotube Template Fullam et al. demonstrated a method to fabricate Au nanowires using carbon nanotubes as positive templates. The first step is to self-assemble Au nanocrystals along carbon nanotubes [112]. After thermal treatment, the nanocrystal assemblies are transformed into continuous polycrystalline Au nanowires over many μm. Carbon nanotubes have also been used as templates to fabricate Mo-Ge superconducting nanowires [113] and other metal nanowires [114, 115]. Choi et al. [116] reported

a highly selective electroless deposition of metal nanoparticles on single wall carbon nanotubes (SWNTs). Because $HAuCl_4$ (Au^{3+}) or Na_2PtCl_4 (Pt^{2+}) have much higher reduction potentials than SWNTs, they are reduced spontaneously and form Au or Pt nanoparticles on the sidewalls of SWNTs (Fig. 3). This is different from the traditional electroless deposition because no reducing agents or catalysts are required. Charge transfer during the reaction is probed electrically as it causes significant changes in the electrical conductance of the nanotubes by hole doping. The nanoparticles decorated on the nanotube can coalesce and cover the entire surface of the nanotube. By removing the nanotube via heating, a Au tube-like structure with a outer diameter <10 nm can be fabricated.

DNA Template   DNA is another excellent choice as a template to fabricate nanowires because its diameter is ~2 nm and its length and sequence can be precisely controlled [117–127]. Coffer and coworkers synthesized micrometer-scale CdS rings using a plasmid DNA as a template [128]. Richter et al. [129] reported a two-step electroless deposition process to fabricate Pd nanowires using DNA as templates. The first step is to treat DNA in a Pd acetate solution. The second step is to add reducing agent, dimethylamine borane, which reduces Pd ions into Pd along the DNA chains. If the reduction time is short, it leads to individual isolated Pd clusters with a diameter of 3–5 nm. Increasing the reduction time, Pd clusters aggregate and form a quasi-continuous Pd nanowire. This metallization method has been applied to both DNA in solution and DNA immobilized on a solid surface. Braun et al. [130] fabricated a Ag nanowire of ~100 nm in diameter and ~15 μm in length using a linear DNA template.

The procedure used by Braun et al. is illustrated in Figure 4. The first step is to fix a DNA strand between two electrical contacts. The DNA is then exposed to a
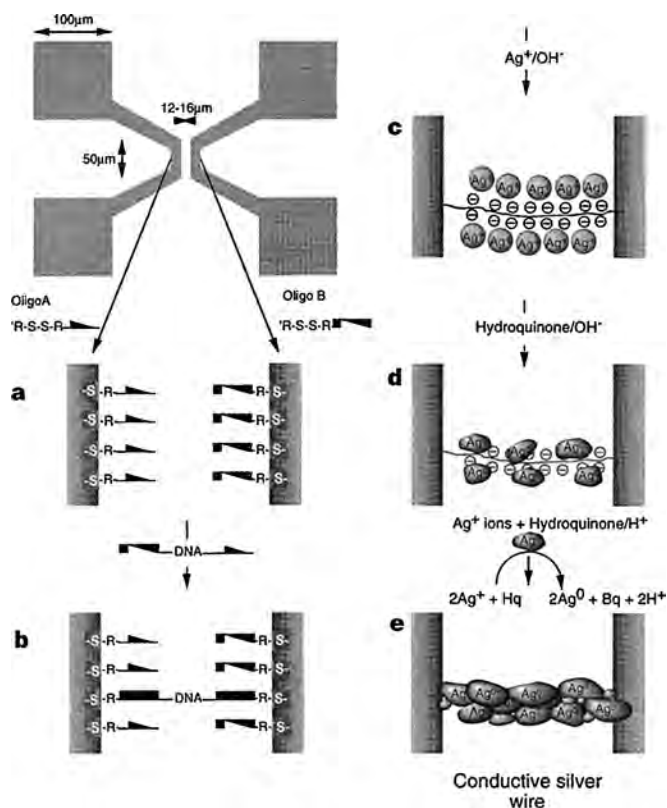

Figure 4. Construction of an Ag wire connecting two gold electrodes using DNA as template. The top left image shows the electrode pattern used in the experiments. The two 50-μm-long parallel electrodes are connected to four (100×100 μm) bonding pads. (a) Oligonucleotides with two different sequences attached to the electrodes. (b) λ-DNA bridge connecting the two electrodes. (c) Ag-ion-loaded DNA bridge. (d) Metallic Ag aggregates bound to the DNA skeleton. (e) Fully developed Ag wire. Reprinted with permission from [130], E. Braun et al., *Nature* 391, 775 (1998). © 1998, Macmillan Magazines Ltd.

Figure 3. AFM images of metal nanoparticles formed on a SWNT template. (a) Au nanoparticles spontaneously and selectively formed on an individual SWNT after immersion in a Au^{3+} solution for 3 min. (b) Pt nanoparticles formed on a SWNT after 3 min exposure to a Pt^{2+} solution. (c) Diagram showing the Fermi energy (E_F) of a SWNT, and the reduction potentials of Au^{3+} and Pt^{2+} versus SHE, respectively. The reduction potentials of most other metal ions lie above E_F, except for Ag^+. Reprinted with permission from [116], H. C. Choi et al. *J. Am. Chem. Soc.* 124, 9058 (2002). © 2002, American Chemical Society.

solution containing Ag^+ ions. The Ag^+ ions bind to DNA and are then reduced by a basic hydroquinone solution to form Ag nanoparticles decorating along the DNA chain. In the last step, the nanoparticles are further "developed" into a nanowire using a standard photographic enhancement technique. The nanowire is highly resistive because they are composed of individual Ag clusters of ~50 nm in diameter. Recently, they developed a DNA sequence-specific molecular lithography to fabricate metal nanowires with a predesigned insulating gap [131]. The approach utilizes homologous recombination processes and the molecular recognition capability of DNA. Homologous recombination is a protein-mediated reaction by which two DNA molecules possessing some sequence homology cross over at equivalent sites. In the lithography process, RecA proteins are polymerized on a single strand DNA (ssDNA) probe to form a nucleoprotein filament. Then the nucleoprotein filament binds to an aldehyde-derivatized double strand DNA (dsDNA) substrate at a homologous sequence. Incubation of the formed complex in $AgNO_3$ solution results in the formation of Ag aggregates along the substrate DNA molecules at regions unprotected by RecA. The Ag aggregates serve as catalysts for specific Au deposition, converting

the unprotected regions to conductive Au wires. Thus, a Au nanowire with an insulating gap is formed. The position and size of the insulating gap can be tailored by choosing the template DNA with the special sequence and length.

Ford et al. [132] demonstrated a method to synthesize colloidal Pt-DNA composite via chemical reduction of platinated DNA with borohydride ions. "Platination" here is referred to as the process of direct ("covalent") bonding of the Pt^{2+} to electron pair "donor" atoms (e.g., N and O) in DNA, a reaction that has been widely studied because of their relevance to the mechanism of anti-cancer drugs based on coordination complexes of Pt^{2+}. The reduction results in Pt particles that do not form aggregates. This is probably because the electrostatic repulsion between the highly charged DNA molecules prevents the particles from contacting each other. This unique feature is quite important in the fabrication of metal nanowires or other nanostructures using platinated-DNA as templates. The Pt particles decorated along the DNA can be used as nucleation sites for electroless deposition of Au.

Another DNA template approach is to attach Au nanoparticles to a DNA chain via electrostatic interaction between the positively charged particles and the negatively charged phosphate groups of the DNA [133, 134]. A surprise found by Harnach et al. is that negatively charged tris(hydroxymethyl)-phosphine-capped Au nanoparticles also bind densely to DNA [135]. The immobilized Au colloidal particles can serve as catalysts and nucleation sites for the subsequent electroless deposition of Au, resulting in nanowires as thin as 30–40 nm and longer than 2 μm. Electron transport of these nanowires follows the classical Ohm's law with resistivity of $\sim 10^{-5}$ Ωm.

Polymer Templates In addition to DNA, many other polymer chains can also be excellent choices as positive templates for nanowire fabrications. Minko et al. developed a method using single synthetic flexible polyelectrolyte molecules, poly2-vinylpyridine (P2VP) as templates to fabricate nanowires [136]. Since these polymers are thinner than DNA, it is possible to fabricate thinner nanowires. Under appropriate conditions, the polymer chains are stretched into worm-like coils due to the electrostatic repulsion between randomly distributed positive charges along the chain. This stretched conformation is frozen when the polymer is attached to a solid substrate. Exposing the polymer to palladium acetate acidic aqueous solution, Pd^{2+} is then coordinated to the polymer template via an ion exchange reaction. In the following step, Pd^{2+} is reduced by dimethylamine borane. The procedure results in metal nanoparticles of 2–5 nm in diameter, which decorate along the template into a wire-like structure.

Djalali et al. [137] utilized the core-shell cylindrical polymer brushes as templates to synthesize metal cluster arrays and wires (Fig. 5). The starting material of the templates is methacryloyl end-functionalized block copolymers, consisting of styrene and vinyl-2-pyridine, which are polymerized to poly(block comacromonomer)s. The formed poly(block comacromonomer)s exhibit an amphipolar core-shell cylindrical brush structure with a core of vinylpyridine and a shell of polystyrene. The vinylpyridine cores of the cylindrical brushes are loaded with $HAuCl_4$ in toluene or methylene
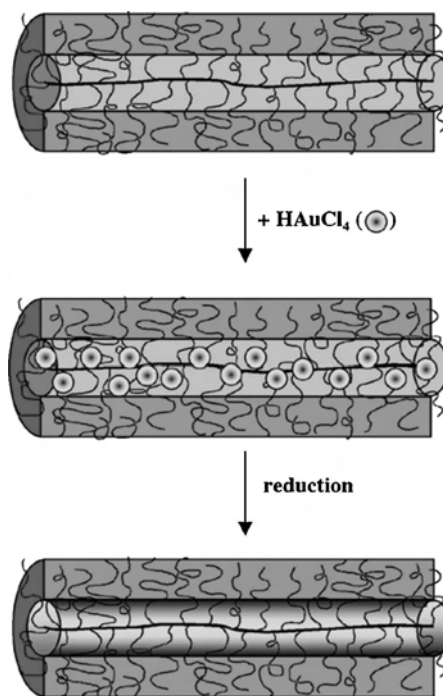

Figure 5. Fabrication of nanowires with a polymer template. (a) Coreshell cylindrical brushes with a PVP core and PS shell. (b) Loading the core with $HAuCl_4$. (c) Subsequent reduction $HAuCl_4$ yields a onedimensional Au wire within the macromolecular brush. Reprinted with permission from [137], D. Djalali et al., *Macromolecules* 35, 4282 (2002). © 2002, American Chemical Society.

chloride followed by reduction of the Au salt by the electron beam, UV light, or chemical-reducing agents. Depending on the amount of $AuCl_4^-$ ions loaded in the cores and the reduction conditions, either a linear array of Au clusters or a continuous Au nanowire is formed within the core of the cylindrical brushes. The resulting Au metal nanowires are much longer than the individual core-shell macromolecules, which are caused by a yet unexplained specific end-to-end aggregation of the cylindrical polymers upon loading with $HAuCl_4$. Since the metal formation occurs within the cores of the polymers, the polystyrene shells may serve as the electrically insulating layers.

Other Positive Templates There are a number of other positive templates that have been used for nanowire fabrications. An interesting example is quantum wells in a semiconductor multilayer structure prepared by molecular beam epitaxy (MBE). Figure 6 shows such a template used by Fasol and Runge [138]. The quantum well is a 4-nm thin InAs layer embedded in a semiconductor multilayer structure, since the Fermi level of the InAs layer is pinned within the conduction band and the surface depletion layer customary in GaAs-based materials is avoided. The thin edge of the conducting quantum well is exposed to an electrolyte and acts as a template electrode for selective electrodeposition, leading to the fabrication of extremely thin metal wires. Service [139] fabricated a quantum well superlattice that consists of a stack of atomically thin layers of different semiconductors with MBE. Using the superlattice as templates, they are able to grow an array of
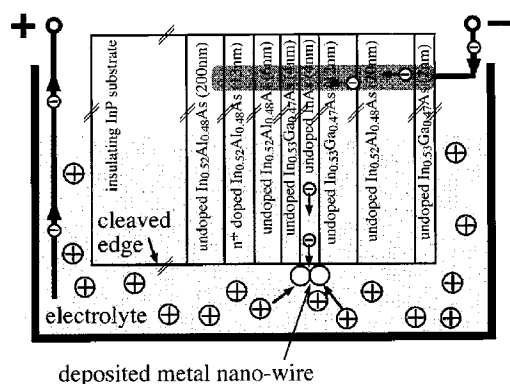
Figure 6. Fabrication of nanowires with a quantum well template. The template is the cleaved edge of a 4-nm InAs quantum well embedded into a layered semiconductor structure. The conductive InAs quantum well is connected to the negative current contact during electrodeposition, leading to the selective growth of an extremely thin magnetic metal wire. Reprinted with permission from [138], G. Fasol and K. Runge, *Appl. Phys. Lett.* 70, 2467 (1997). © 1997, American Institute of Physics.

parallel conducting nanowires whose diameters and spacing are controlled by the superlattice. The nanowires are then transferred to a substrate. By repeating the process, a second set of nanowires is fabricated and deposited on top of the first set in the perpendicular direction to form an array of crossing nanowires. When organic molecules are sandwiched between the crossing wires, an array of molecular junctions is formed, which may be used in molecular electronics.

Song et al. [140] demonstrated an elegant redox chemistry method to synthesize long freestanding metal nanowires. The method starts with a $LiMo_3Se_3$ wire template with a diameter between 2–100 nm, which is formed by dissolving a quasi-one-dimensional $LiMo_3Se_3$ crystal in a polar solvent, such as methanol and dimethyl sulfoxide (DMSO). The $LiMo_3Se_3$ nanowire is then exposed to aqueous solution containing metal ions (e.g., $AuCl_4^-$, Ag^+, $PdCl^{2-}$, $PtCl_4^{2-}$) (Fig. 7). Because of the reducing capability of the $LiMo_3Se_3$ nanowire template, metal ions are reduced by the template, which results in a continuous and uniform metal nanowire. During the process, the $LiMo_3Se_3$ template is oxidized into Mo_3Se_3 and then dissolves in water. Metal nanowires fabricated with this approach displayed liner current vs. voltage
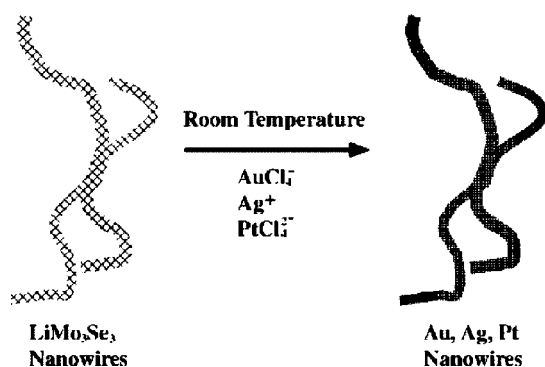
characteristics with low resistivity. Using Cu_2S nanowires as positive templates, Wen et al. fabricated Au nanowires and nanotubes [141]. They electrochemically deposited Au onto the template surfaces to form Cu_2S/Au core/sheath nanowires. For relatively thick Au sheaths, the Cu_2S cores can be etched away in 6M HCl to yield Au nanotubes.

2.1.3. Surface Step-Edge Templates

Atomic-scale step edges on a crystal surface can be used as templates to grow nanowires [142]. The method takes the advantage of the fact that deposition of many materials on a surface often starts preferentially at defect sites, such as surface step-edges. For this reason, the method is sometimes called "step edge decoration." Using the step edges of highly oriented pyrolytic graphite (HOPG) as templates, Noll et al. fabricated conducting polypyrrole nanowires by electrodeposition [143]. Several other groups prepared metal nanowires on vicinal single crystal surfaces, such as Si, using the physical vapor deposition (PVD) method [144–146]. Blanc, Nichols, Morin, El Meguid, and Dekoster et al. [147–151], Gambardella et al., and Dallmeyer et al. fabricated metal nanowires of 1–2 atomic layer high with a controlled "width" and wire spacing [152, 153]. These nanowires cannot be easily removed from the surfaces on which they are deposited, which can be a serious limit for some applications.

Penner's group [154] demonstrated that metal nanowires could be obtained by selectively electrodepositing conductive metal oxide at the step edges of HOPG, followed by reduction of the metal oxide to form metal nanowires. The nanowires can be removed from the HOPG surface. Their strategy, called electrochemical step-edge decoration (ESED), is illustrated in Figure 8. It involves electrodeposition of metal oxide nanowires at graphite step-edges as a "precursor," and the subsequent reduction of the "precursor" in hydrogen leads to metal nanowires. They have fabricated Mo nanowires in this way. The "precursors," MoO_x nanowires, are brittle and poorly conductive, but they are highly uniform in diameter (20–500 nm). The "precursor" nanowires are then reduced in H_2 at 500 °C to produce metallic Mo nanowires that are highly conductive. The Mo nanowires are also mechanically resilient, which can withstand the mechanical stress associated with the process of transferring the nanowires to an insulating substrate.
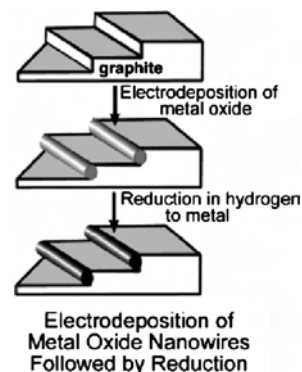

Figure 7. Fabrication of metal nanowires with $LiMo_3Se_3$ nanowire as template. Reprinted with permission from [140], J. H. Song et al., *J. Am. Chem. Soc.* 123, 10397 (2001). © 2001, American Chemical Society.

Figure 8. Fabrication of metal nanowires using step-edge decoration method. Reprinted with permission from [156], E. C. Walter et al., *J. Phys. Chem. B* 44, 11407 (2002). © 2002, American Chemical Society.

The method is expected to work also for other metals with stable conductive metal oxides, such as Cu_2O and Fe_2O_3. However, this strategy cannot be directly applied to metals that do not form stable and conductive oxide. In the case of noble metals, although they can be directly electrodeposited to the step edges, it usually produces discontinuous nanowires, consisting of individual clusters [155]. In order to obtain continuous noble metal nanowires, Penner's group developed a three-voltage pulse method [156, 157]. The first pulse has amplitude that is optimized to oxidize the graphite step edges just prior to deposition. The oxidation is believed to produce some oxygen-containing functionalities preferentially at steps, which increases the affinity of the step edges to metal adatoms, and thus reducing the nucleation overpotential and increasing the nucleation density along the step edges. The second voltage pulse supplies a large overpotential for a short period of time, which increases the nucleation density and initiates the nanowire growth. After this nucleation pulse, a third pulse is applied at the smallest possible overpotential that allows the nucleation sites to grow into nanowires. This method has, so far, been successfully used for four metals, Cu, Ni, Au, and Pd. The metal nanowires are composed of rough grains, which is in contrast to the smooth MoO_2 nanowires prepared by potentiostatic electrodeposition. The individual metal grains have diameters approximately equal to the diameters of the nanowires, as revealed in the SEM images.

Metal nanowires prepared by ESEM can be removed from the graphite surface by embedding them in an epoxy film. During this removal process, metal nanowires retain the parallel ordering of the graphite step edges. After this transfer process is complete, arrays of metal nanowires can be electrically characterized and prepared for device applications.

2.2. Applications of the Nanowires

Metal nanowires are promising materials for many novel applications, ranging from chemical and biological sensors to optical and electronic devices. This is not only because of their unique geometry, but also because they possess many unique physical properties, including electrical, magnetic, optical, as well as mechanical properties. While most efforts to date have focused on developing better methods to fabricate the nanowires and on characterizing the various properties, applications are becoming an important area of research and development. Some of the applications are discussed below.

2.2.1. Magnetic Materials and Devices

The electrodeposition methods described above have been used to fabricate magnetic nanowires of a single metal [104], multiple metals in segments [158–160], as well as alloys [161]. Since the pioneering works nearly a decade ago [104, 158, 160], much progress has been made in understanding the magnetic properties of the nanowires [105, 162]. A recent review provides a detailed description of the properties [163]. For magnetic nanowires (Fe, Co, and Ni) with relative large aspect ratios (e.g., >50), they exhibit an easy axis along the wires. An important parameter that describes magnetic properties of materials is the remanence ratio, which measures

the remanence magnetization after switching off the external magnetic field. The remanence ratios of the Fe, Co, and Ni nanowires can be larger than 0.9 along the wires and much smaller in the perpendicular direction of the wires. This finding clearly shows that the shape anisotropy plays an important role in the magnetism of the nanowires. Another important parameter that describes the magnetic properties is coercivity, which is the coercive field required to demagnetize the magnet after full magnetization. The magnetic nanowires exhibit greatly enhanced magnetic coercivity [164, 165]. In addition, the coercivity depends on the wire diameter and the aspect ratio, which shows that it is possible to control the magnetic properties of the nanowires by controlling the fabrication parameters. The diameter dependence of the coercivity reflects a change of the magnetization reversal mechanism from localized quasi-coherent nucleation for small diameters to a localized curling like nucleation as the diameter exceeds a critical value [100].

Another technically important novel property observed in the magnetic nanowires is giant magnetoresistance (GMR) [158, 160, 161, 166, 167]. For example, Evans et al. have studied Co-Ni-Cu/Cu multilayered nanowires and found a magnetoresistance ratio of 55% at room temperature and 115% at 77K for current perpendicular to the plane (along the direction of the wires) [167]. Giant magnetoresistance has also been observed in semimetallic Bi nanowires fabricated by electrodeposition [168–170]. Hong et al. have studied GMR of Bi with diameters between 200 nm and 2 μm in magnetic fields up to 55T and found that the magnetoresistance ratio is between 600–800% for magnetic field perpendicular to the wires and ~200% for the field parallel to the wires [169]. The novel properties and small dimensions have potential applications in the miniaturization of magnetic sensors and the high-density magnetic storage devices.

The alignment of magnetic nanowires in an applied magnetic field can be used to assemble the individual nanowires [171, 172]. Tanase et al. studied the response of Ni nanowires in response to magnetic field [171]. The nanowires are fabricated by electrodeposition using alumina templates and functionalized with luminescent porphyrins so that they can be visualized with a video microscope. In viscous solvents, magnetic fields can be used to orient the nanowires. In mobile solvents, the nanowires form chains in a head-to-tail configuration when a small magnetic field is applied. In addition, they demonstrated that three-segment Pt-Ni-Pt nanowires can be trapped between lithographically patterned magnetic microelectrodes [172]. The technique has a potential application in the fabrication and measurement of nanoscale magnetic devices.

2.2.2. Optical Applications

Dickson and Lyon studied surface plasmon (collective excitation of conduction electrons) propagation along 20 nm-diameter Au, Ag, and bimetallic Au-Ag nanowires with a sharp Au/Ag heterojunction over a distance of tens of μm [173]. The plasmons are excited by focusing a laser with a high numerical aperture microscope objective, which propagate along a nanowire and reemerge as light at the other end of the nanowire via plasmon scattering. The propagation depends strongly on the wavelength of the incident laser

light and the composition of the nanowire. At the wavelength of 820 nm, the plasmon can propagate in both Au and Ag nanowires, although the efficiency in Ag is much higher than that in Au. In the case of bimetallic nanowire, light emission is clearly observed from the Ag end of the nanowire when the Au end is illuminated at 820 nm. In sharp contrast, if the same bimetallic rod is excited at 820 nm via the Ag end, no light is emitted from the distal Au end. The observation suggests that the plasmon mode excited at 820 nm is able to couple from the Au portion into the Ag portion with high efficiency, but not from the Ag portion into Au. The unidirectional propagation has been explained using a simple two-level potential model. Since surface plasmons propagate much more efficiently in Ag than in Au, the Au $\rightarrow$ Ag boundary is largely transmissive, thus enabling efficient plasmon propagation in this direction. In the opposite direction, however, propagation from Ag to Au "sees" a much steeper potential wall, allowing less optical energy to couple through to the distal end. Their experiments suggest that one can initiate and control the flow of optically encoded information with nanometer-scale accuracy over distances of many microns, which may find applications in future high-density optical computing.

2.2.3. Biological Assays

We have mentioned that by sequentially depositing different metals into the nanopores, multisegment or striped metal nanowires can be fabricated [106]. The length of each segment can be controlled by the charge passed in each plating step and the sequence of the multiple segments is determined by the sequence of the plating steps. Due to the different chemical reactivities of the "stripe" metals, these stripes can be modified with appropriate molecules. For example, Au binds strongly to thiols and Pt has high affinity to isocyanides. Interactions between complementary molecules on specific strips of the nanowires allow different nanowires to bind to each other and form patterns on planar surfaces. Using this strategy, nanowires could assemble deterministically into cross- or T-shaped pairs, or into more complex shapes [174]. It is also possible to use specific interactions between selectively functionalized segments of these nanowires to direct the assembly of nanowire dimers and oligomers, to prepare two-dimensional assembly of nanowire-substrate epitaxy, and to prepare three-dimensional colloidal crystals from nanowire-shaped objects [117, 175]. As an example, single-stranded DNA can be exclusively modified at the tip or any desired location of a nanowire, with the rest of the wire covered by an organic passivation monolayer. This opens the possibility for site-specific DNA assembly [106].

Nicewarner-Pena et al. showed that the controlled sequence of multisegment nanowires can be used as "barcodes" in biological assays [176]. The typical dimension of the nanowire is $\sim$200 nm thick and $\sim$10 μm long. Because the wavelength dependence of reflectance is different for different metals, the individual segments are easily observed as "stripes" under an optical microscope with unpolarized

white-light illumination. Different metal stripes within a single nanowire selectively adsorb different molecules, such as DNA oligomers, which can be used to detect different biological molecules simultaneously. These multisegment nanowires have been used like metallic barcodes in DNA and protein bioassays.

The optical scattering efficiency of the multisegment nanowires can be significantly enhanced by reducing the dimensions of the segment, such that the excitation of the surface plasmon occurs. Mock et al. [177] have studied the optical scattering of multisegment nanowires of Ag, Au, and Ni that have diameters of $\sim$30 nm and length up to $\sim$7 μm. The optical scattering is dominated by the polarization-dependant plasmon resonance of Ag and Au segments. This is different from the case of the thicker nanowires used by Nicewarner-Pena et al., where the reflectance properties of bulk metals determine the contrast of the optical images [176]. Because of the large enhancement by the surface plasmon resonance, very narrow ($\sim$30 nm diameter) nanowires can be readily observed under white light illumination and the optical spectra of the individual segments are easily distinguishable [177]. The multisegment nanowires can host a large number of segment sequences over a rather small spatial range, which promises unique applications.

2.2.4. Nanoelectronic and Nanoelectrochemical Applications

In addition to multisegment metal nanowires, one can also fabricate a metal/organic film/metal junction [178] and metal/nanoparticle/metal junctions [179] in a single nanowire, which have been used to study electron transport properties of the small amount of molecules and nanoparticles. It has been demonstrated that a Au nanowire containing 4-{[2-nitro-4 (phenylethynyl) phenyl ethynyl}benzenethiol molecule junction exhibits negative differential resistance at room temperature [180], while a 16-mercaptohexadecanoic acid nanojunction exhibits a coherent nonresonant tunneling [178, 181, 182]. If some of the metal segments or "stripes" are being replaced with semiconductor, colloidal, and polymer layers, one can introduce rectifying junctions, electronic switching, and photoconductive elements in the composite nanowires. If selectively modifying the nanowire further, using the distinct surface chemistry of different stripes, the nanowires can be positioned on a patterned surface to fulfill nano-logic and memory circuits by self-assembling [179, 183–185].

An array of metal nanowires can be used as a nano-electrode array for many electrochemical applications [30, 35, 46, 49, 186]. For this purpose, a large array of nanowires with long-range hexagonal order fabricated with the anodic alumina templates is particularly attractive.

2.2.5. Chemical Sensors

Penner, Handley, and Dagani et al. exploited hydrogen sensor applications using arrays of Pd nanowires [187–190]. Unlike the traditional Pd-based hydrogen sensor that detects a drop in the conductivity of Pd upon exposure to hydrogen, the Pd-nanowire sensor measures an increase in the conductivity (Fig. 9a). The reason is because the Pd wire consists of
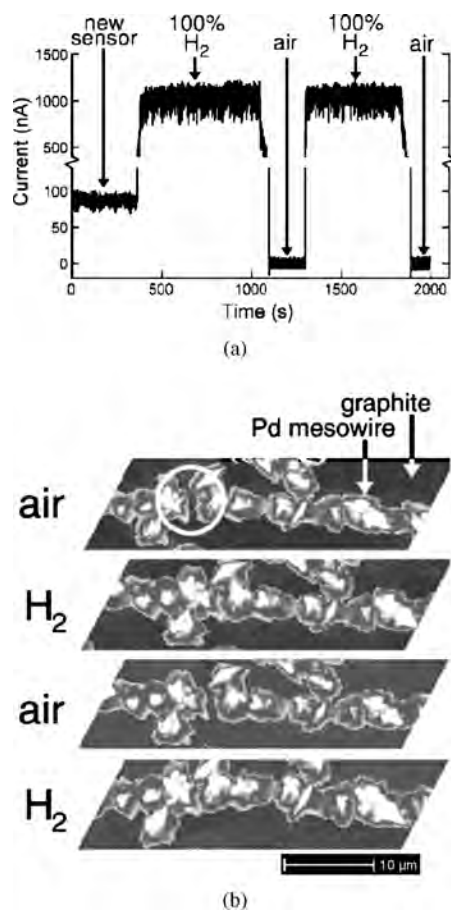
Figure 9. Chemical sensor application of Pd nanowires. (a) Plot of sensor current versus time for the first exposure of a Pd nanowire sensor to hydrogen and one subsequent H_2/air cycle. (b) AFM image of a Pd nanowire on a graphite surface. These images were acquired either in air or in a stream of H_2 gas, as indicated. A hydrogen-actuated break junction is highlighted (circle). Reprinted with permission from [188], E. C. Walter et al., *Anal. Chem.* 74, 1546 (2002). © 2002, American Chemical Society.

a string of Pd particles separated with nanometer-scale gaps. These gaps close to form a conductive path in the presence of hydrogen molecules as Pd particles expand in volume (Fig. 9B). The volume expansion is well known, which is due to the disassociation of hydrogen molecules into hydrogen atoms that penetrate into the Pd lattice and expand the lattice. Although macroscopic Pd-based hydrogen sensors are readily available, they have the following two major drawbacks. First, their response time is between 0.5 s to several minutes, which is too slow to monitor gas flow in real time. Second, they are prone to the poisoning of a number of gas molecules, such as methane, oxygen, and carbon monoxide, which adsorb onto the sensor surfaces and block the adsorption sites for hydrogen molecules. The Pd nanowires offer remedies to the above problems. They have a large surface-to-volume ratio, so the response time can be as fast as 20 ms. The large surface-to-volume ratio also make the nanowire sensor less prone to the poisoning by common contaminations.

3. QUANTUM WIRES

The electron transport in the nanowires previously described obeys the classical behaviors as found for macroscopic metal wires. This is because the dimensions of the nanowires are still significantly greater than the characteristic lengths, the electron mean-free path, and the electron wavelength. When the length is shorter than the electron mean-free path, the electron transport is ballistic along the wire. In addition if the diameter of the wire is comparable to the electron wavelength, the effect of quantum-size confinement becomes important in the transverse direction, which results in quantum modes. Connecting such a wire to the outside world (electron reservoirs), the conductance of the system is quantized in the ideal case.

The phenomenon of quantization of conductance was first clearly demonstrated in semiconductor devices containing a two-dimensional electron gas confined into a narrow constriction by the gate voltage, where $\lambda_F \sim 40$ nm is much larger than the atomic scale [191, 192]. A similar conductance quantization has been observed in three-dimensional metallic wires [193–197]. Since the wavelength of conduction electrons in a typical metal is only 0.1–0.3 nm, comparable to the size of an atom, a metal wire with conductance quantized at the lowest steps must be atomically thin. This conclusion has been directly confirmed by high-resolution transmission electron microscopy [198]. Because the metal wires that exhibit conductance quantization are usually very short, they are often called atomic-scale contacts or simply nanocontacts. They are also referred to as metal quantum wires or atomic-scale metal wires.

3.1. Fabrication Metal Quantum Wires

There are two approaches that one can use to fabricate metal quantum wires: one is the mechanical method and the other one is based on electrochemical etching and deposition. We provide a brief description of them below.

3.1.1. Mechanical Methods

Mechanical methods create a metal quantum wire by mechanically separating two electrodes in contact. During the separation process, a metal neck is formed between the electrodes due to strong metallic cohesive energy, which is stretched into an atomically thin wire before breaking. One such method is based on a scanning tunneling microscope (STM) (Fig. 10a) [193–195, 199–202], in which the STM tip is driven into the substrate and the conductance is recorded while the tip is gradually pulled out of the contact with the substrate. The first experiment of this type was reported by Gimzewski et al. to study the transition in the electron transport between tunneling and ballistic regimes [193]. Figure 10b shows several conductance traces during stretching of a Au wire with a STM setup. The conductance decreases in a stepwise fashion. The steps tend to occur near the integer multiples of G_0, indicating the origin of conductance quantization. However, they can deviate significantly from the simple integer multiples. For this reason, a conductance histogram is often constructed from thousands of individual conductance traces to show the occurrence of the steps at difference conductance values (Fig. 10c). For metals
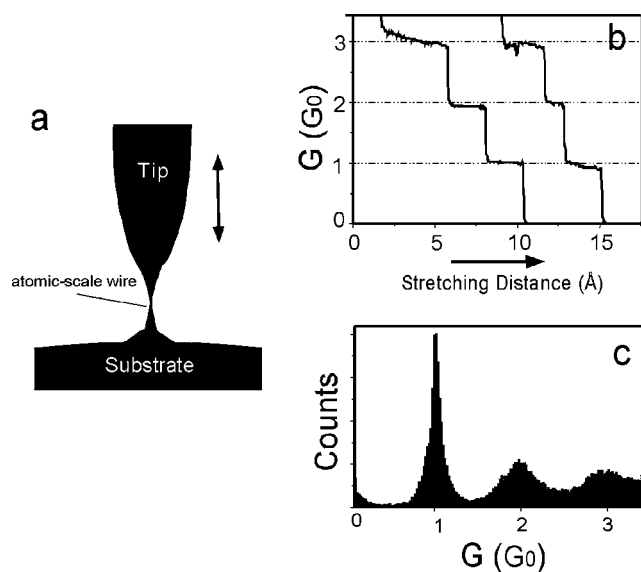
Figure 10. (a) Mechanical fabrication of a metal quantum wire with a STM setup. A STM tip is first pressed into a metal substrate and then pulled out of contact during which an atomically thin wire is formed before breaking. (b) Typical conductance versus stretching distance traces that show the quantized variation in the wire conductance. (c) Conductance histogram of Au wires in 0.1M NaClO$_4$. The well-defined peaks near integer multiples of $G_0 = 2e^2/h$ have been attributed to conductance quantization. Each histogram was constructed from over 1000 individual conductance traces like the ones shown in (b).

such as Au, Na, and K, well-defined peaks near the integer multiples are found. For Na and K, the peaks near $2G_0$ and $4G_0$ are missing, which is expected because of the mode degeneracy for a cylindrical symmetry of a wire in free electron gas model. The observation, therefore, demonstrates beautifully that these metal wires can be described as free electron gas models in cylindrical wires. Not all metals show pronounced histogram peaks near the integer conductance values. Most other metals show only a broad first peak that is not an integer value. For example, Nb has a first peak near $2.5G$ G_0.

The transition in conductance from one step to another during mechanical stretching of a wire is usually abrupt, due to sudden rearrangements of the atoms in the wire upon stretching. That is, upon stretching, the stress is accumulated in the metallic bonds between atoms. When the accumulated elastic energy is large enough, the atomic configuration becomes unstable and collapsed into a new atomic configuration that has a thinner diameter. This atomic arrangement during mechanical stretching has been directly observed by simultaneously measuring the force with the atomic force microscope (AFM) and conductance with STM [203].

Another tool to fabricate atomic-scale metal wires is to use a mechanically controllable break-junction (MCB) [204, 205]. The MCB technique creates a clean fracture surface by mechanically breaking a metal and can provide better stability than the STM method. Other methods include the use of a tip and plate [206], two macroscopic electrodes in contact [196], and mechanical relay [197]. The mechanical methods can repeatedly fabricate (and break) a large number of wires within a relatively short time, which is

particularly convenient for statistical analysis, such as conductance histograms. However, the methods form one wire at a time and use piezoelectric or other mechanical transducers, which are not desirable for device applications. It has been recently demonstrated that metal wires with quantized conductance can be fabricated with electrochemical etching and deposition [207–212], which can fabricate arrays of atomic-scale wires supported on solid substrates, thus overcoming some of the drawbacks that the mechanical methods have. The electrochemical methods are discussed below.

3.1.2. Electrochemical Methods

Snow et al. [213] reported on an AFM-based anodic oxidation method to fabricate Al point contacts. In the method, AFM is first used to anodize a 1-μm-wide Al thin film into a 40-nm-wide by 500-nm-long nanowire. The anodization is similar to conventional electrochemical anodization, except that the AFM tip is used as the cathode and water from the ambient humidity is used as electrolyte. The point contacts are formed by further anodizing a section of the nanowire. In order to achieve the control necessary to fabricate atomic-sized features, *in situ* electrical measurements are used as feedback to control the anodization. As the conductance of the point contact is reduced below $\sim 5 \times 10^{-4}$ S, the conductance starts to decrease in discrete steps of $2e^2/h$. In some of the samples, the conductance can be stabilized at the lowest few quantum steps for a long time, which corresponds to the formation of an atomic-sized wire.

Li and Tao demonstrated an electrochemical method to fabricate metal quantum wires using an electrochemical STM setup [207]. In the method, a STM tip is first held at a fixed distance (10–150 nm) from a Au substrate electrode in a plating solution (Cu). Cu is then selectively electroplated onto the sharp STM tip. The selective plating onto the tip is achieved by keeping the substrate potential slightly more positive than the bulk deposition potential. When the growing Cu reaches the substrate, a contact is formed between the tip and the substrate, which is reflected by a sharp increase in the current that flows between the tip and substrate. By slowly dissolving away the deposited Cu contact, a Cu quantum wire is formed between the tip and the substrate electrodes. The conductance of the wire changes in a stepwise fashion with a preference to occur near integer multiples of $G_0 = 2e^2/h$. The electrochemical method does not need mechanical stretching to form the wires, but the STM setup used to achieve a small initial separation between two metal electrodes makes the method prone to thermal drift and mechanical noise.

The undesired instability problem is removed in an improved electrochemical method, in which the STM setup is replaced by a metal wire supported on solid substrate (Fig. 11) [208]. The metal wire with an initial diameter of a few tens of μm is glued onto a glass slide. The glue covers the entire wire except for a small portion that is exposed to electrolyte for electrochemical deposition and etching. The exposed portion is less than a few μm so that ionic conduction through the electrolyte is negligible compared to the electronic conduction through the wire. By electrochemical etching, the diameter of the wire is reduced to the atomic scale, at which the conductance becomes
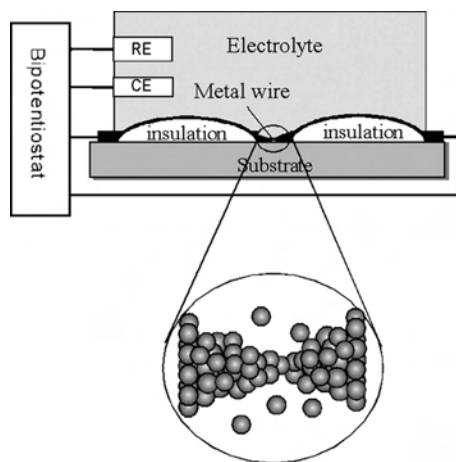
Figure 11. Electrochemical fabrication of a metal quantum wire. A metal wire is attached to the bottom surface of a plexiglas solution cell. The wire is coated with wax except for a small section that is exposed to electrolyte for etching. The electrochemical potential of the wire is controlled by a bipotentiostat with a reference electrode (RE) and a counter electrode (CE).

quantized. The process can be reversed to increase the diameter by electrochemical deposition. The electrochemical etching and deposition are controlled with a bipotentiostat that can simultaneously control the etching rate and measure the conductance of the wire. In order to form a wire with a desired conductance, a feedback loop has been demonstrated to control the electrochemical etching by comparing the measured conductance with a preset value. When the conductance is greater than the preset value, etching is activated to reduce the diameter of the wire. When the conductance is smaller than the preset value, deposition is turned on to increase the diameter. These atomic-scale wires can last from minutes to days. Further improvement of the stability may be achieved by "coating" the wire with appropriate molecules. The method has been used to fabricate atomic-scale Au, Ag, Cu, and Ni wires with conductance quantized at different steps.

Morpurgo et al. observed conductance quantization during the formation metal contact between two Au electrodes by electrodeposition [209]. The initial Au electrodes are fabricated with electron beam lithography and separated with a gap of a few tens nm. Nakabayashi et al. fabricated quantum wires by electrochemically growing a Zn fractal into contact with a Cu ring electrode [212]. The Zn fractal is synthesized at an immiscible interface between water and 4-methyl-2-pentanone so that it is quasi two-dimensional. Li et al. showed that Cu, Ag, Ni, Pd, and Pb quantum wires can be formed between two Au electrodes by electrochemical deposition and etching [210, 214]. A nice feature of the approach is that the Au electrodes can be reused by dissolving away the quantum wires. Their experiment indicates that while Cu, Ag, Ni, and Pd can form stable wires with conductance quantized near 1 G_0, conductance quantization of Pb wires is rather unstable.

Elhoussine et al. have reported on conductance quantization in magnetic nanowires (Ni) electrodeposited in the nanopores of track-etched polymer membranes [211]. The

magnetic nanocontacts are formed at the extremity of a single Ni nanowire either inside or outside of the nanopores. As expected for ferromagnetic metals without spin degeneracy, their experiment shows that the conductance of the contacts is quantized in units of $0.5G_0$ ($G_0 = 2e^2/h$). This system might be useful for studying ballistic spin transport through electrodeposited nanocontacts and tunneling through controllable magnetic nanogaps.

The method described above can fabricate atomic-scale wires for many measurements, but a simpler method has been demonstrated by Boussaad and Tao [215]. The method does not require a bipotentiostat and feedback control, and it can *simultaneously* fabricate a large array of wires. The principle is illustrated in Fig. 12(a). It starts with a pair of electrodes separated with a relative large gap in an electrolyte. When applying a bias voltage between the two electrodes, metal atoms are etched off from the anode and deposited onto the cathode. The etching takes place all over the anode surface, but the deposition is localized to the sharpest point on the cathode, due to a high electric field and a metal ion concentration near the sharpest point. Consequently, the gap narrows and disappears eventually when a point contact is formed between the two electrodes.

In order to control the formation of the contact between the electrodes, the etching and deposition processes must be terminated immediately after a desired contact is formed. While a feedback mechanism may be used for this purpose, they introduced a much simpler self-termination mechanism by connecting one electrode in a series with an external
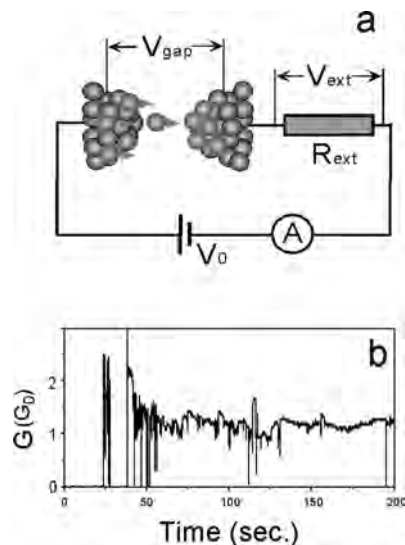

Figure 12. Fabrication of metal nanowires with a self-terminated electrochemical method. (a) Metal atoms etched off the left electrode are deposited onto the right electrode by applying a voltage between the electrodes with an external resistor (R_{ext}) in series. As the gap between the two electrodes shrinks, the gap resistance decreases, which results in a drop in etching/deposition voltage and eventually terminates the etching/deposition processes. (b) Choosing a $R_{ext} < 12.7$ kΩ, a wire with quantized conductance can be fabricated. The conductance change during the formation of a contact ($R_{ext} = 3$ kΩ and $V_0 = 1.2$ V). The large conductance fluctuations corresponding to constant breakdown and reformation of the contact are due to electromigration.

resistor (R_{ext}). So the effective voltage (or overpotential) for etching and deposition is given by

$$V_{gap} = \frac{R_{gap}}{R_{gap} + R_{ext}} V_0 \qquad (3)$$

where R_{gap} is the resistance between the two electrodes, and V_0 is the total applied bias voltage. Initially, the gap is large, so no tunneling current flows across it and R_{gap} is solely determined by ionic conduction (leakage current) between the electrodes. By coating the electrodes with an insulation layer, such as Si_3N_4, the unwanted leakage current can be reduced below 1 pA, which gives rise to a large initial R_{gap} ($\gg R_{ext}$). According to Eq. (3), $V_{gap} \sim V_0$ initially, so the etching and deposition take place at maximum speed and the gap quickly narrows. When the gap is reduced to a few nm or less, R_{gap} begins to decrease because of electron tunneling across the gap. Eventually, a contact with quantized conductance is formed between the two electrodes. By choosing an appropriate R_{ext}, one can form either a small gap or a contact (quantum wire) with quantized conductance. If R_{ext} is greater than $h/2e^2$, the resistance for a single atom contact between two electrodes terminates with a small tunneling gap between the electrodes. On the other hand, if R_{ext} is smaller than $h/2e^2$, it terminates with an atomic-scale contact between the electrodes.

Figure 12(b) shows the conductance (normalized against G_0) between two Cu electrodes during electrochemical etching and deposition in water with R_{ext} preset at 3 kΩ (<12.7 kΩ). The initial conductance due to ionic conduction is negligibly small compared to G_0. A few minutes after applying a 1.2 V voltage, the conductance suddenly jumps to $\sim 2G_0$ and the deposition terminates itself as a contact is formed between the electrodes. However, the initial contact breaks within seconds and the conductance drops back to zero. Once the contact is broken, the voltage across the electrodes goes back to the maximum value, according to Eq. (3), and the etching and deposition starts over again. Indeed, several seconds later, a new contact with conductance near 1 G_0 is reformed, so the method has a self-repairing mechanism. The measured I–V characteristic curves of the contacts show that the current is linearly proportional to the bias voltage for the contacts. This simple Ohmic behavior was also found by Hansen et al. in the atomic-scale wires formed by STM [216].

3.2. Applications

Since the discovery of conductance quantization, most studies have been directed towards a better understanding of the phenomenon. However, a number of applications based on the phenomenon have been proposed and explored, and more are expected to follow in the future.

Smith demonstrated both analog and digital switches using atomic-scale point contacts formed between a Ni wire and a Au substrate [201]. The switches were activated by repeatedly moving the Ni wire into contact with the Au using a piezoelectric actuator over a distance of 0.2 nm. The Ni and Au electrodes together with the piezoelectric actuator form a three-terminal device. The device exhibits good discrimination between high and low states and possesses the important property of power gain.

Motivated by the possibility for chemical sensing applications, molecular and ionic adsorption onto atomic-scale metal wires have been studied [217, 218]. Xu et al. have determined the potential-induced conductance modulation in electrolytes containing, F^-, Cl^-, Br^-, and I^- [219]. These anions are known to adsorb onto Au electrodes with different strengths [220]. At very negative potentials, the conductance modulations are the same for all the electrolytes, since no substantial anion adsorption takes place. Increasing the potential, however, the induced conductance modulation increases as anions adsorb onto the wire. The dependence of the conductance change on the potential correlates well with the adsorption strengths of the anions, in the sequence of $F^- < Cl^- < Br^- < I^-$, which is consistent with measurements performed on classical metal films [221–226]. The significant increase in the conductance modulation upon anion adsorption is attributed to the scattering of the conduction electrons in the wire by the adsorbed anions [227–230]. Because the wire is typically a few atoms long, enough to accommodate only a few ions, the sensitive dependence of the conductance on the adsorption suggests a method to detect a single or a few ions.

It has also been observed that the conductance of the atomic-scale wires drops abruptly to a fractional value upon molecular adsorption (Fig. 13) [217, 231]. The largest conductance drop occurs for the wires with conductance at the lowest quantum step, and the drop diminishes quickly at higher steps as the quantum ballistic regime is replaced by the classical diffusive regime. Similar to anions, the conductance change correlates with the binding strength of the molecules to the metal wires. The adsorbate scattering mechanism mentioned above naturally explains the decreases in the conductance [230], but it fails to explain a number of other facts. For example, the mechanical stability of the wires is strongly dependant on molecular adsorption. It has been found that the binding of a molecule onto an atomic-scale wire enhances the mechanical stability of the wire [232]. So by choosing the right molecules, one might be able to fabricate atomic-scale wires with long-term stability. The large conductance change upon molecular adsorption suggests the possibility of studying single molecules.

Like the classical nanowires, magnetoresistance of ferromagnetic wires has been measured [233, 234]. Because
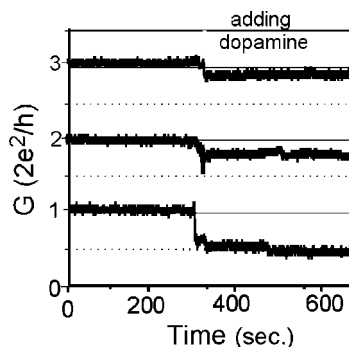

Figure 13. Conductance change of Cu wires with conductance quantized at $1G_0$, $2G_0$, and $3G_0$ upon adsorption of dopamine from the electrolyte.

the electron transport in these wires is ballistic, the magnetoresistance effect is referred to as ballistic magnetoresistance (BMR). A BMR effect as large as 400–700% has been observed in Ni point contacts fabricated by electrodeposition [235]. The effect has been explained in terms of spin-scattering of ballistic electrons at atomically sharp domain walls and enhanced polarization due to a magnetic "dead" layer at the point contact. Chopra and Hua reported a remarkably BMR effect that is greater than 3000% in Ni point contact at room temperature and in a weak magnetic field (a few hundred oersteds) [233]. These findings are anticipated to lead applications in magnetic storage devices and spintronics.

4. SUMMARY

Because of its simplicity and flexibility, electrochemical methods have been widely used to fabricate various nanowires. The diameters of the nanowires can be made as thin as a single atom, and the length can vary from a few atoms to many μm. For nanowires with large aspect ratios, a template is usually used in the fabrication. To date, several types of templates have been successfully developed, which include positive templates, negative templates, surface step-edge templates, and soft templates (wet chemistry). Most of the metal nanowires (with the exception of Bi at low temperatures), fabricated with the template methods, exhibit the classical Ohm's law behavior and are regarded as classical wires. However, they do possess unique physical properties, such as the small dimensions, high surface-to-volume ratios, and novel optical and magnetic properties. In order to observe quantum transport properties, metal nanowires have to be shorter than a few tens of nm and thinner than a few nm. Such metal nanowires can be fabricated using electrochemical deposition and etching without the use of templates. In this case, instead of directly controlling the dimensions of the nanowires, one controls the signature of quantum transport and conductance quantization during the fabrication process. Electrochemical methods have also some drawbacks depending on the specific applications. One is that the materials must be conductive. A number of complementary fabrication techniques have been developed to fabricate insulating and semiconducting nanowires.

To date, most of the research effort has been directed towards the fabrication of the nanowires and characterization of their properties. However, the unique properties of the nanowires have been explored by researchers around the world for various applications, from chemical and biological nanosensors to magnetic, optical, and electronic nanodevices. As the fabrication techniques become mature and more and more interesting properties are revealed, more exciting applications are anticipated in the coming years.

GLOSSARY

Classical metal nanowire Nanowire whose conductance obeys the classical relation, i.e., proportional to the cross sectional area and inversely proportional to the length of the wire.

Conductance quantization A quantum phenomenon that occurs when the diameter of a wire is comparable to the wavelength of the conduction electrons and the length is shorter than the electron mean free path.

Negative template A template with, usually, hollow channels that determines the dimension of the fabricated nanowires.

Positive template A template with a wire-like structure that guides the growth of a nanowire. The dimension of the nanowire is controlled by the experimental condition rather than by the template.

Quantum metal nanowire A metal nanowire whose conductance exhibits conductance quantization.

Surface step-edge template Well-defined surface step edges on a solid surface to guide the growth of a nanowires.

ACKNOWLEDGMENTS

REFERENCES

1. R. Landauer, *IBM J. Res. Dev.* 1, 223–231 (1957).
2. Y. Y. Yu, S. S. Chang, C. L. Lee, and C. R. C. Wang, *J. Phys. Chem. B* 101, 6661 (1997).
3. S. S. Chang, C. W. Shih, C. D. Chen, W. C. Lai, and C. R. C. Wang, *Langmuir* 15, 701 (1999).
4. C. Y. Wang, M. H. Chen, G. M. Zhu, and Z. G. Lin, *J. Colloid. Interf. Sci.* 243, 362 (2001).
5. L. M. Huang, H. T. Wang, Z. B. Wang, A. Mitra, K. N. Bozhilov, and Y. S. Yan, *Adv. Mater.* 14, 61 (2002).
6. D. B. Zhang, L. M. Qi, J. M. Ma, and H. M. Cheng, *Chem. Mater.* 13, 2753 (2001).
7. J. J. Zhu, Q. F. Qiua, H. Wang, J. R. Zhang, J. M. Zhu, and Z. Q. Chen, *Inorg. Chem. Commun.* 5, 242 (2002).
8. N. R. Jana, L. Gearheart, and C. J. Murphy, *J. Phys. Chem. B* 105, 4065 (2001).
9. N. R. Jana, L. Gearheart, and C. J. Murphy, *Chem. Commun.* 617 (2001).
10. N. R. Jana, L. Gearheart, and C. J. Murphy, *Langmuir* 17, 6782 (2001).
11. N. R. Jana, L. Gearheart, and C. J. Murphy, *Adv. Mater.* 13, 1389 (2001).
12. N. R. Jana, L. Gearheart, and C. J. Murphy, *Chem. Mater.* 13, 2313 (2001).
13. N. R. Jana, L. Gearheart, S. O. Obare, and C. J. Murphy, *Langmuir* 18, 922 (2002).
14. C. J. Murphy and N. R. Jana, *Adv. Mater.* 14, 80 (2002).
15. J. Fujita, Y. Ohnishi, Y. Ochiai, and S. Matsui, *Appl. Phys. Lett.* 68, 1297 (1996).
16. J. Fujita, Y. Ohnishi, Y. Ochiai, E. Nomura, and S. Matsui, *J. Vac. Sci. Tech. B* 14, 4272 (1996).
17. J. Sone, J. Fujita, Y. Ochiai, S. Manako, S. Matsui, E. Nomura, T. Baba, H. Kawaura, T. Sakamoto, C. D. Chen, Y. Nakamura, and J. S. Tsai, *Nanotechnology* 10, 135 (1999).
18. D. L. Klein, R. Roth, A. K. L. Lim, A. P. Alivisatos, and P. L. McEuen, *Nature* 389, 699 (1997).
19. D. L. Klein, P. L. McEuen, J. E. B. Katari, R. Roth, and A. P. Alivisatos, *Appl. Phys. Lett.* 68, 2574 (1996).
20. M. C. Hersam, A. C. F. Hoole, S. J. O'Shea, and M. E. Welland, *Appl. Phys. Lett.* 72, 915 (1998).

21. J. Gierak, A. Septier, and C. Vieu, *Nucl. Instrum. Meth. A.* 427, 91 (1999).
22. M. Morinaga, M. Yasuda, T. Kishimoto, F. Shimizu, J. Fujita, and S. Matsui, *Phys. Rev. Lett.* 77, 802 (1996).
23. J. Fujita, M. Morinaga, T. Kishimoto, M. Yasuda, S. Matsui, and F. Shimizu, *Nature* 380, 691 (1996).
24. C. A. J. Foss, "Metal Nanoparticles Synthesis Characterization and Applications." Marcel Dekker, 2002.
25. P. B. Price and R. M. Walker, *J. Appl. Phys.* 33, 3407 (1962).
26. R. L. Fleischer, P. B. Price, and R. M. Walker, *J. Appl. Phys.* 34, 510 (1963).
27. P. E. Possion, *Rev. Sci. Instrum.* 41, 772 (1970).
28. W. D. Williams and N. Giordano, *Rev. Sci. Instrum.* 55, 410 (1984).
29. C. J. Brumlik and C. R. Martin, *J. Am. Chem. Soc.* 113, 3174 (1991).
30. C. J. Brumlik, C. R. Martin, and K. Tokuda, *Anal. Chem.* 64, 1201 (1992).
31. C. J. Brumlik, V. P. Menon, and C. R. Martin, *J. Mater. Res.* 9, 1174 (1994).
32. Z. Cai and C. R. Martin, *J. Am. Chem. Soc.* 111, 4138 (1989).
33. Z. Cai, J. Lei, W. Liang, V. Menon, and C. R. Martin, *J. Chem. Mater.* 3, 960 (1991).
34. V. M. Cepak, J. C. Hulteen, G. Che, K. B. Jirage, B. B. Lakshmi, E. R. Fisher, and C. R. Martin, *Chem. Mater.* 9, 1065 (1997).
35. I. F. Cheng, L. D. Whiteley, and C. R. Martin, *Anal. Chem.* 61, 762 (1989).
36. S. De Vita and C. R. Martin, *Chem. Mater.* 10, 1738 (1998).
37. C. A. Foss, Jr., G. L. Hornyak, J. A. Stocket, and C. R. Martin, *J. Phys. Chem.* 96, 7497 (1992).
38. C. A. Foss, Jr., G. L. Hornyak, J. A. Stocket, and C. R. Martin, *J. Phys. Chem.* 98, 2963 (1994).
39. J. C. Hulteen, K. B. Jirage, and C. R. Martin, *J. Am. Chem.Soc.* 120, 6603 (1998).
40. K. B. Jirage, J. C. Hulteen, and C. R. Martin, *Anal. Chem.* 71, 4913 (1999).
41. B. B. Lakshmi, P. K. Dorhout, and C. R. Martin, *Chem. Mater.* 9, 857 (1997).
42. C. R. Martin, L. S. Van Dyke, Z. Cai, and W. Liang, *J. Am. Chem. Soc.* 112, 8976 (1990).
43. C. R. Martin, R. Parthasarathy, and V. Menon, *Synth. Met.* 55–57, 1165 (1993).
44. C. R. Martin, *Science* 266, 1961 (1994).
45. C. R. Martin, *Chem. Mater.* 8, 1739 (1996).
46. V. P. Menon and C. R. Martin, *Anal. Chem.* 67, 1920 (1995).
47. R. Parthasarathy and C. R. Martin, *Nature* 369, 298 (1994).
48. R. M. Penner and C. R. Martin, *J. Electrochem. Soc.* 133, 2206 (1986).
49. R. M. Penner and C. R. Martin, *Anal. Chem.* 59, 2625 (1987).
50. S. A. Sapp, B. B. Lakshmi, and C. R. Martin, *Adv. Mater.* 11, 402 (1999).
51. L. S. Van Dyke and C. R. Martin, *Langmuir* 6, 1123 (1990).
52. R. P. Fleischer, P. B. Price, R. M. Walker, and E. L. Hubbard, *Phys. Rev.* 156, 353 (1967).
53. T. M. Whitney, Thesis, Johns Hopkins University, 1992.
54. W. Kautek, S. Reetz, and S. Pentzien, *Electrochim. Acta* 40, 1461 (1995).
55. R. Ferre, K. Ounadjela, J. M. George, L. Pirauz, and S. Dubois, *Phys. Rev. B* 56, 14066 (1997).
56. L. Sun, C. L. Chien, and P. C. Searson, *J. Mater. Sci.* 35, 1097 (2000).
57. L. Sun, P. C. Searson, and C. L. Chien, *Appl. Phys. Lett.* 74, 2803 (1999).
58. F. Keller, M. S. Hunter, and D. L. Robinson, *J. Electrochem. Soc.* 100, 411 (1953).
59. J. P. O'Sullivan and G. C. Wood, *Proc. R. Soc. London, Ser. A* 317, 511 (1970).
60. C. R. Martin, *Acc. Chem. Res.* 28, 61 (1995).
61. O. Jessensky, F. Muller, and U. Gosele, *Appl. Phys. Lett.* 72, 1173 (1998).
62. H. Masuda and K. Fukuda, *Science* 268, 1466 (1995).
63. H. Masuda, K. Yaka, and A. Osaka, *Jpn. J. Appl. Phys. Part 2* 37, L1340 (1998).
64. H. Masuda and F. Hasegwa, *J. Electrochem. Soc.* 144, L127 (1997).
65. S. Shingubara, O. Okino, Y. Sayama, H. Sakaue, and T. Takahagi, *Jpn. J. Appl. Phys.* 36, 7791 (1997).
66. F. Li, L. Zhang, and R. M. Metzger, *Chem. Mater.* 10, 2470 (1998).
67. A. R. Despic, *J. Electroanal. Chem. Interfacial Electrochem.* 191, 417 (1985).
68. R. C. Furneaux, W. R. Rigby, and A. P. Davidson, *Nature* 337, 147 (1989).
69. D. Crouse, Y.-H. Lo, A. E. Miller, and M. Crouse, *Appl. Phys. Lett.* 76, 49 (2000).
70. H. Masuda, H. Yamada, M. Satoh, H. Asoh, M. Nakao, and T. Tamamura, *Appl. Phys. Lett.* 71, 2770 (1997).
71. H. Asoh, N. Kazuyuki, M. Nakao, T. Tamanura, and H. Masuda, *J. Electrochem. Soc.* 148, B152 (2001).
72. H. Masuda and M. Satoh, *Jpn. J. Appl. Phys.* 35, L126 (1996).
73. A.-P. Li, F. Muller, A. Birner, K. Nielsch, and U. Gosele, *Adv. Mater.* 11, 483 (1999).
74. A.-P. Li, F. Muller, and U. Gosele, *Electrochem. Solid-State Lett.* 3, 131 (2000).
75. A.-P. Li, F. Muller, A. Birner, K. Nielsch, and U. Gosele, *J. Vac. Sci. Technol. A* 17, 1428 (1999).
76. T. Thurn-Albrecht, R. Steiner, J. DeRouchey, C. M. Stafford, E. Huang, M. Bal, M. Tuominen, C. J. Hawker, and T. P. Russell, *Adv. Mater.* 12, 787 (2000).
77. T. Thurn-Albrecht, J. Schotter, G. A. Kastle, N. Emley, T. Shibauchi, L. Krusin-Elbaum, K. Guarini, C. T. Black, M. T. Tuominen, and T. P. Russell, *Science* 290, 2126 (2000).
78. G. Krausch, *Mater. Sci. Eng. Rep.* 14, 1 (1995).
79. M. J. Fasolka and A. M. Mayes, *Annu. Rev. Mater. Res.* 31, 323 (2001).
80. G. Krausch and R. Magerle, *Adv. Mater.* 14, 1579 (2002).
81. M. Park, C. Harrison, P. M. Chaikin, R. A. Register, and D. H. Adamson, *Science* 276, 1401 (1997).
82. P. Mansky, P. Chaikin, and E. L. Thomas, *J. Mater. Sci.* 30, 1987 (1995).
83. P. Mansky, C. K. Harrison, P. M. Chaikin, R. A. Register, and N. Yao, *Appl. Phys. Lett.* 68, 2586 (1996).
84. B. H. Hong, S. C. Bae, C.-W. Lee, S. Jeong, and K. S. Kim, *Science* 294, 348 (2001).
85. R. J. Tonucci, B. L. Justus, A. J. Campillo, and C. E. Ford, *Science* 258, 783 (1992).
86. M. H. Huang, A. Choudrey, and P. Yang, *Chem. Commun.* 1063 (2000).
87. C. M. Yang, H. S. Sheu, and K. J. Chao, *Adv. Funct. Mater.* 12, 143 (2002).
88. B. Ye, M. Trudeau, and D. Antonelli, *Adv. Mater.* 13, 29 (2001).
89. C.-G. Wu and T. Bein, *Science* 264, 1757 (1994).
90. G. Che, B. B. Lakshmi, C. R. Martin, E. R. Fisher, and R. S. Ruoff, *Chem. Mater.* 10, 260 (1998).
91. M. Wirtz, M. Parker, Y. Kobayashi, and C. R. Martin, *Chem. Eur. J.* 8, 353 (2002).
92. G. Yi and W. Schwarzacher, *Appl. Phys. Lett.* 74, 1746 (1999).
93. Y. H. Huang, H. Okumura, and G. C. Hadjipanayis, *J. Appl. Phys.* 91, 6869 (2002).
94. C. Z. Wang, G. W. Meng, Q. Q. Fang, X. S. Peng, Y. W. Wang, Q. Fang, and L. D. Zhang, *J. Phys. D* 35, 738 (2002).
95. D. H. Qin, C. W. Wang, Q. Y. Sun, and H. L. Li, *Appl. Phys. A-Mater.* 74, 761 (2002).
96. M. S. Sander, A. L. Prieto, R. Gronsky, T. Sands, and A. M. Stacy, *Adv. Mater.* 14, 665 (2002).
97. C. K. Preston and M. J. Moskovits, *J. Phys. Chem.* 97, 8495 (1993).

98. K. Liu, K. Nagodawithana, P. C. Searson, and C. L. Chien, *Phys. Rev. B* 51, 7381 (1995).

99. K. H. Lee, H. Y. Lee, W. Y. Jeung, and W. Y. Lee, *J. Appl. Phys.* 91, 8513 (2002).

100. H. Zeng, R. Skomki, L. Menon, Y. Liu, S. Bandyopadhyay, and D. J. Sellmyer, *Phys. Rev. B* 65, 134426 (2002).

101. P. Forrer, F. Schlottig, H. Siegenthaler, and M. Textor, *J. Appl. Electrochem.* 30, 533 (2000).

102. V. Caboni, Vol. 339 Italian Patent, 339232, p. 232.

103. C. Schönenberger, B. M. I. van der Zande, L. G. J. Fokkink, M. Henny, C. Schmid, M. Kruger, A. Bachtold, R. Huber, H. Birk, and U. Staufer, *J. Phys. Chem. B* 101, 5497 (1997).

104. T. M. Whitney, J. S. Jiang, P. C. Searson, and C. L. Chien, *Science* 261, 1316 (1993).

105. S. Valizadeh, J. M. George, P. Leisner, and L. Hultman, *Electrochim. Acta* 47, 865 (2001).

106. B. R. Martin, D. J. Dermody, B. D. Reiss, M. M. Fang, L. A. Lyon, M. J. Natan, and T. E. Mallouk, *Adv. Mater.* 11, 1021 (1999).

107. A. L. Prieto, M. S. Sander, M. S. Martin-Gonzalez, R. Gronsky, T. Sands, and A. M. Stacy, *J. Am. Chem. Soc.* 123, 7160 (2001).

108. A. J. Yin, J. Li, W. Jian, A. J. Bennett, and J. M. Xu, *Appl. Phys. Lett.* 79, 1039 (2001).

109. K. Nielsch, F. Müller, A.-P. Li, and U. Gösele, *Adv. Mater.* 12, 582 (2000).

110. G. Sauer, G. Breshm, S. Schneider, K. Nielsch, R. B. Wehrspohn, J. Choi, H. Hofmeister, and U. Cosele, *J. Appl. Phys.* 91 (2002).

111. H. Q. Cao, Z. Xu, H. Sang, D. Sheng, and C. Y. Tie, *Adv. Mater.* 13, 121 (2001).

112. S. Fullam, D. Cottell, H. Rensmo, and D. Fitzmaurice, *Adv. Mater.* 12, 1430 (2000).

113. A. Bezryadin, C. N. Lau, and M. Tinkham, *Nature* 404, 971 (2000).

114. Y. Zhang and H. J. Dai, *Appl. Phys. Lett.* 77, 3015 (2000).

115. W. S. Yun, J. Kim, K. H. Park, J. S. Ha, Y. J. Ko, K. Park, S. K. Kim, Y. J. Doh, H. J. Lee, J. P. Salvetat, and L. Forro, *J. Vac. Sci. & Technol. A* 18, 1329 (2000).

116. H. C. Choi, M. Shim, S. Bangsaruntip, and H. J. Dai, *J. Am. Chem. Soc.* 124, 9058 (2002).

117. J. K. N. Mbindyo, B. D. Reiss, B. R. Martin, C. D. Keating, M. J. Natan, and T. E. Mallouk, *Adv. Mater.* 13, 249 (2001).

118. J. J. Storhoff and C. A. Mirkin, *Chem. Rev.* 99, 1849 (1999).

119. J. J. Storhoff, R. Elghanian, R. C. Mucic, and C. A. Mirkin, *J. Am. Chem. Soc.* 120, 1959 (1998).

120. R. Elghanian, J. J. Storhoff, R. C. Mucic, R. L. Letsinger, and C. A. Mirkin, *Science* 277, 1078 (1997).

121. C. A. Mirkin, R. L. Letsinger, R. C. Mucic, and J. J. Storhoff, *Nature* 382, 607 (1996).

122. R. C. Mucic, J. J. Storhoff, C. A. Mirkin, and R. L. Letsinger, *J. Am. Chem. Soc.* 120, 12674 (1998).

123. G. P. Mitchell, C. A. Mirkin, and R. L. Letsinger, *J. Am. Chem. Soc.* 121, 8122 (1999).

124. L. He, M. D. Musick, S. R. Nicewarner, F. G. Salinas, S. J. Benkovic, M. J. Natan, and C. D. Keating, *J. Am. Chem. Soc.* 122, 9071 (2000).

125. P. G. Schultz, *Nature* 382, 609 (1996).

126. C. J. Loweth, W. B. Caldwell, X. Peng, A. P. Alivisatos, and P. G. Schultz, *Angew. Chem. Int. Ed.* 33, 1808 (1999).

127. S. J. Park, T. A. Taton, and C. A. Mirkin, *Science* 295, 1503 (2002).

128. J. L. Coffer, S. R. Bigham, X. Li, R. F. Pinizzotto, Y. G. Rho, R. M. Pirtle, and I. L. Pirtle, *Appl. Phys. Lett.* 69, 3851 (1996).

129. J. Richter, R. Seidel, R. Kirsch, M. Mertig, W. Pompe, J. Plaschke, and H. K. Schackert, *Adv. Mater.* 12, 507 (2000).

130. E. Braun, Y. Eichen, U. SIvan, and G. Ben-Yoseph, *Nature* 391, 775 (1998).

131. K. Keren, M. Krueger, R. Gilad, G. Ben-Yoseph, U. Sivan, and E. Braun, *Science* 297, 72–75 (2002).

132. W. E. Ford, O. Harnack, A. Yasuda, and J. M. Wessels, *Adv. Mater.* 13, 1793 (2001).

133. A. Kumar, M. Pattarkine, M. Bhadbhade, A. B. Mandale, K. N. Ganesh, S. S. Datar, C. V. Dharmadhikari, and M. Sastry, *Adv. Mater.* 13, 341 (2001).

134. M. Sastry, A. Kumar, S. Datar, C. V. Dharmadhikari, and K. N. Ganesh, *Appl. Phys. Lett.* 78, 2943 (2001).

135. O. Harnach, W. E. Ford, A. Yasuda, and J. M. Wessels, *Nano Lett.* 2, 919 (2002).

136. S. Minko, A. Kiriy, G. Gorodyska, and M. Stamm, *J. Am. Chem. Soc.*, 124, 10192 (2002).

137. D. Djalali, S. Y. Li, and M. Schmidt, *Macromolecules* 35, 4282 (2002).

138. G. Fasol and K. Runge, *Appl. Phys. Lett.* 70, 2467 (1997).

139. R. F. Service, *Science* 295, 2398 (2002).

140. J. H. Song, Y. Y. Wu, B. Messer, H. Kind, and P. D. Yang, *J. Am. Chem. Soc.* 123, 10397 (2001).

141. X. G. Wen and S. H. Yang, *Nano Lett.* 2, 451 (2002).

142. A. Brodde, G. Wilhelmi, D. Badt, H. Wengelnik, and H. Neddermeyer, *J. Vac. Sci. Tech. B* 9, 920 (1991).

143. J. D. Noll, M. A. Nichloson, P. G. Vanpatten, C. W. Chung, and M. L. Myrick, *J. Electrochem. Soc.* 145, 3320 (1998).

144. F. J. Himpsel, T. Jung, A. Kirakosian, J. L. Lin, D. Y. Petrovykh, H. Rauscher, and J. Viernow, *MRS Bulletin* 24, 20 (1999).

145. F. J. Himpsel, *Appl. Phys. A* 61, 467 (1995).

146. D. Y. Petrovykh, F. J. Himpsel, and T. Jung, *Surf. Sci.* 407, 189 (1998).

147. M. Blanc, K. Kuhnke, V. Marsico, and K. Kern, *Surf. Sci.* 414, L964 (1998).

148. R. J. Nichols, D. M. Kolb, and R. J. Behm, *J. Electroanal. Chem.* 313, 109 (1991).

149. S. Morin, A. Lachenwitzer, O. M. Magnussen, and R. J. Behm, *Phys. Rev. Lett.* 83, 5066 (1999).

150. E. A. Abd El Meguid, P. Berenz, and H. Baltruschat, *J. Electroanal. Chem.* 467, 50 (1999).

151. J. Dekoster, *Appl. Phys. Lett.* 75, 938 (1999).

152. P. Gambardella, M. Blanc, H. Brune, K. Kuhnke, and K. Kern, *Phys. Rev. B* 61, 2254 (2000).

153. A. Dallmeyer, C. Carbone, W. Eberhardt, C. Pampuch, O. Rader, W. Gudat, P. Gambardella, and K. Kern, *Phys. Rev. B* 61, R5133 (2000).

154. M. P. Zach, K. H. Ng, and R. M. Penner, *Science* 290, 2120 (2000).

155. H. Liu and R. M. Penner, *J. Phys. Chem. B* 104, 9131 (2000).

156. E. C. Walter, B. J. Murray, J. Favier, G. Kaltenpoth, M. Grunze, and R. M. Penner, *J. Phys. Chem. B* 44, 11407 (2002).

157. E. C. Walter, M. P. Zach, J. Favier, B. J. Murray, K. Inazu, J. C. Hemminger, and R. M. Penner, *Chem. Phys. Chem.* 4, 131 (2003).

158. L. Piraux, J. M. George, J. F. Despres, C. Leroy, E. Ferain, R. Legras, K. Ounadjela, and A. Fert, *Appl. Phys. Lett.* 65, 2484–2486 (1994).

159. S. Dubois, C. Marchal, J. M. Beuken, L. Piraux, J. L. Duvail, A. Fert, J. M. George, and J. L. Maurice, *Appl. Phys. Lett.* 70, 396 (1997).

160. A. Blondel, J. P. Meier, B. Doudin, and J.-P. Ansermet, *Appl. Phys. Lett.* 65, 3019 (1994).

161. S. Dubois, J. M. Beuken, L. Piraux, J. L. Duvail, A. Fert, J. M. George, and J. L. Maurice, *J. Magn. Magn. Mater.* 165, 30 (1997).

162. S. Pignard, G. Goglio, A. Radulescu, and L. Piraux, *J. Appl. Phys.* 87, 824 (2000).

163. D. J. Sellmyer, M. Zheng, and R. Skimski, *J. Phys. Condens. Matter* 13, R433 (2001).

164. C. L. Chien, *J. Appl. Phys.* 69, 5267 (1991).

165. T. Thurn-Albrecht, J. Schotter, C. A. Kastle, N. Emley, T. Shibauchi, L. Krusin-Elbaum, K. Guarini, C. T. Black, M. T. Tuominen, and T. P. Russell, *Science* 290, 2126 (2000).

166. K. Liu, K. Nagodawithana, P. C. Searson, and C. L. Chien, *Phys. Rev. B* 51, 7381 (1995).

167. P. R. Evans, G. Yi, and W. Schwarzacher, *Appl. Phys. Lett.* 76, 481 (2000).

168. K. Liu, C. L. Chien, P. C. Searson, and Y. Z. Kui, *Appl. Phys. Lett.* 73, 1436 (1998).
169. K. Hong, F. Y. Yang, K. Liu, D. H. Reich, P. C. Searson, C. L. Chien, F. F. Balakirev, and G. S. Boebinger, *J. Appl. Phys.* 85, 6184 (1999).
170. Y. M. Lin, S. B. Cronin, J. Y. Ying, M. S. Dresselhaus, and J. P. Heremans, *Appl. Phys. Lett.* 76, 3944 (2000).
171. M. Tanase, L. A. Bauer, A. Hultgren, D. M. Silevitch, L. Sun, D. H. Reich, P. C. Searson, and G. J. Meyer, *Nano Lett.* 1, 155 (2001).
172. M. Tanase, D. M. Silevitch, A. Hultgren, L. A. Bauer, P. C. Searson, G. J. Meyer, and D. H. Reich, *J. Appl. Phys.* 91, 8549 (2002).
173. R. M. Dickson and L. A. Lyon, *J. Phys. Chem. B* 104, 6095 (2000).
174. B. D. Reiss, J. N. K. Mbindyo, B. R. Martin, S. R. Nicewarner, T. E. Mallouk, M. J. Natan, and C. D. Keating, *MRS Symp. Proc.* 635, C6.2.1 (2001).
175. J. S. Yu, J. Y. Kim, S. Lee, J. K. N. Mbindyo, B. R. Martin, and T. E. Mallouk, *Chem. Commun.* 2445 (2000).
176. S. R. Nicewarner-Pena, R. G. Freeman, B. D. Reiss, L. He, D. J. Pena, I. D. Walton, R. Cromer, C. D. Keating, and M. J. Natan, *Science* 294, 137 (2001).
177. J. J. Mock, S. J. Oldenburg, D. R. Smith, D. A. Schultz, and S. Schultz, *Nano Lett.* 2, 465 (2002).
178. J. K. N. Mbindyo, T. E. Mallouk, J. B. Mattzela, I. Kratochvilova, B. Razavi, T. N. Jackson, and T. S. Mayer, *J. Am. Chem. Soc.* 124, 4020 (2002).
179. N. I. Kovtyukhova, B. R. Martin, J. K. N. Mbindyo, T. E. Mallouk, M. Cabassi, and T. S. Mayer, *Mater. Sci. & Eng. C* 19, 255 (2002).
180. I. Kratochvilova, M. Kocirik, A. Zambova, J. Mbindyo, T. E. Mallouk, and T. S. Mayer, *J. Mater. Chem.* 12, 2927 (2002).
181. I. Kratochvilova, A. Zambova, J. Mbindyo, B. Razavi, and J. Holakovsky, *Modern Phys. Lett. B* 16, 161 (2002).
182. V. Mujica and M. A. Ratner, *Chem. Phys.* 264, 365 (2001).
183. N. I. Kovtyukhova and T. E. Mallouk, *Chem. Euro. J.* 8, 4355 (2002).
184. N. I. Kovtyukhova, B. R. Martin, J. K. N. Mbindyo, P. A. Smith, B. Razavi, T. S. Mayer, and T. E. Mallouk, *J. Phys. Chem. B* 105, 8762 (2001).
185. D. J. Pena, J. K. N. Mbindyo, A. J. Carado, T. E. Mallouk, C. D. Keating, B. Razavi, and T. S. Mayer, *J. Phys. Chem. B* 106, 7458 (2002).
186. K. Uosaki, K. Okazaki, H. Kita, and H. Takahashi, *Anal. Chem.* 62, 652 (1990).
187. F. Favier, E. C. Walter, M. P. Zach, T. Benter, and R. M. Penner, *Science* 293, 2227 (2001).
188. E. C. Walter, F. Favier, and R. M. Penner, *Anal. Chem.* 74, 1546 (2002).
189. J. Handley, *Anal. Chem.* 74, 196 A (2002).
190. R. Dagani, *Chem. Eng. News* 79, 14 (2001).
191. D. A. Wharam, T. J. Thornton, R. Newbury, M. Pepper, H. Ahmed, J. E. F. Frost, D. G. Hasko, D. C. Peacock, D. A. Ritchie, and G. A. C. Jones, *J. Phys. C* 21, 209 (1988).
192. B. J. van Wees, H. van Houten, C. W. J. Beenakker, J. G. Williams, L. P. Kouwenhowen, D. van der Marel, and C. T. Foxon, *Phys. Rev. Lett.* 60, 848 (1988).
193. J. K. Gimzewski and R. Moller, *Phys. Rev. B* 36, 1284 (1987).
194. J. I. Pascual, J. Mendez, J. Gomez-Herrero, A. M. Baro, N. Garcia, and V. T. Binh, *Phys. Rev. Lett.* 71, 1852 (1993).
195. L. Olesen, E. Lægsgaard, I. Stensgaad, F. Besenbacher, J. Schiotz, P. Stoltze, K. W. Jacobsen, and J. K. Norskov, *Phys. Rev. Lett.* 72, 2251 (1994).
196. J. L. Costa-Kramer, N. Garcia, P. Garcia-Mochales, and P. A. Serena, *Surf. Sci.* 342, L1144 (1995).
197. H. Yasuda and A. Sakai, *Phys. Rev. B* 56, 1069 (1997).
198. H. Ohnishi, Y. Kondo, and K. Takayanagi, *Nature* 395, 780 (1998).
199. N. Agrait, J. G. Rodrigo, and S. Vieira, *Phys. Rev. B* 52, 12345 (1993).
200. J. I. Pascual, J. Mendez, J. Gomez-Herrero, A. M. Baro, N. Garcia, U. Landman, W. D. Luedtke, E. N. Bogachek, and H.-P. Cheng, *Science* 267, 1793 (1995).
201. D. P. E. Smith, *Science* 269, 371 (1995).
202. Z. Cai, Y. He, H. Yu, and W. S. Yang, *Phys. Rev. B* 53, 1042 (1996).
203. G. Rubio, N. Agrait, and S. Vieira, *Phys. Rev. Lett.* 76, 2302 (1996).
204. C. J. Muller, J. M. van Ruitenbeek, and L. J. de Jongh, *Phys. Rev. Lett.* 69, 140 (1992).
205. J. M. Krans, C. J. Muller, I. K. Yanson, T. C. M. Govaert, R. Hesper, and J. M. van Ruitenbeek, *Phys. Rev. B* 48, 14721 (1993).
206. U. Landman, W. D. Luedtke, B. E. Salisbury, and R. L. Whetten, *Phys. Rev. Lett.* 77, 1362 (1996).
207. C. Z. Li and N. J. Tao, *Appl. Phys. Lett.* 72, 894 (1998).
208. C. Z. Li, A. Bogozi, W. Huang, and N. J. Tao, *Nanotechnology* 10, 221 (1999).
209. A. F. Morpurgo, C. M. Marcus, and D. B. Robinson, *Appl. Phys. Lett.* 14, 2082 (1999).
210. J. Z. Li, T. Kanzaki, K. Murakoshi, and Y. Nakato, *Appl. Phys. Lett.* 81, 123 (2002).
211. F. Elhoussine, S. Matefi-Tempfli, A. Encinas, and L. Piraux, *Appl. Phys. Lett.* 81, 1681 (2002).
212. S. Nakabayashi, H. Sakaguchi, R. Baba, and E. Fukushima, *Nano Lett.* 2, 507 (2001).
213. E. S. Snow, D. Park, and P. M. Campbell, *Appl. Phys. Lett.* 69, 269 (1996).
214. J. Z. Li, Y. Yamada, K. Murakoshi, and Y. Nakato, *Chem. Commun.* 21, 2170 (2001).
215. S. Boussaad and N. J. Tao, *Appl. Phys. Lett.* 80, 2398 (2002).
216. K. Hansen, S. K. Nielsen, M. Brandbyge, E. Lægsgaard, I. Stensgaard, and F. Besenbacher, *Appl. Phys. Lett.* 77, 708 (2001).
217. C. Z. Li, H. Sha, and N. J. Tao, *Phys. Rev. B* 58, 6775 (1998).
218. C. Z. Li, H. X. He, A. Bogozi, J. S. Bunch, and N. J. Tao, *Appl. Phys. Lett.* 76, 1333 (2000).
219. B. Q. Xu, H. X. He, and N. J. Tao, *J. Am. Chem. Soc.* 124, 13568 (2002).
220. J. Lipkowski, Z. C. Shi, A. C. Chen, B. Pettinger, and C. Bilger, *Electrochim. Acta* 43, 2875 (1998).
221. G. A. Fried, Y. Zhang, and P. W. Bohn, *Thin Solid Films* 401, 171 (2001).
222. R. I. Tucceri and D. Posadas, *J. Electroanal. Chem.* 191, 387 (1985).
223. R. I. Tucceri and D. Posadas, *J. Electroanal. Chem.* 270, 415 (1989).
224. R. I. Tucceri and D. Posadas, *J. Electroanal. Chem.* 283, 159 (1990).
225. C. Hanewinkel, A. Otto, and T. Wandlowski, *Surf. Sci.* 429, 255 (1999).
226. H. Winks, D. Schumacher, and A. Otto, *Surf. Sci.* 400, 44 (1998).
227. K. Fuchs, *Proc. Cambridge Philos. Soc.* 34, 100 (1938).
228. E. H. Sondheimer, *Adv. Phys.* 1, 1 (1952).
229. R. G. Tobin, *Surf. Sci.* 502, 374 (2002).
230. B. N. J. Persson, *J. Chem. Phys.* 98, 1659 (1993).
231. A. Bogozi, O. Lam, H. X. He, C. Z. Li, N. J. Tao, L. A. Nagahara, I. Amlani, and R. Tsui, *J. Am. Chem. Soc.* 123, 4585 (2001).
232. H. X. He, C. Shu, C. Z. Li, and N. J. Tao, *J. Electroanal. Chem.* 522, 26 (2002).
233. H. D. Chopra and S. Z. Hua, *Phys. Rev. B.* 66, Art. No. 020403 (2002).
234. N. Garcia, G. G. Qiang, and I. G. Saveliev, *Appl. Phys. Lett.* 80, 1785 (2002).
235. N. Garcia, M. Munoz, G. Qian, H. Rohrer, I. Saveliev, and Y. Zhao, *Appl. Phy. Lett.* 79, 4550 (2001).

ENN
Encyclopedia of Nanoscience and Nanotechnology
www.aspbs.com/enn

Electrochemical Insertion of Lithium in Carbon Nanotubes

G. Maurin

Royal Institution of Great Britain, London, United Kingdom

F. Henn

Université Montpellier II, Montpellier, France

CONTENTS

1. INTRODUCTION

One of the most crucial problems for our environment is the emission of gas. This problem is more accentuated in big cities where cars are responsible for a large part of the CO_2 emission. Therefore, it has been more necessary, for the two last decades, to search for alternative energy sources, especially for vehicles. Besides, the market for new electronic devices (cell phones, computers, etc.) which demands more energy and more power, along with light, small, and reliable energy sources, increased tremendously. So it becomes clear that the development of new electrochemical energy sources is one of the most important technical challenges for the coming years [1].

Consequently, huge research efforts have been focused on rechargeable batteries, supercapacitors, and fuel cells [2, 3]. In all these power sources, carbon materials are used to a large extent. The most powerful rechargeable battery system, commercially named lithium-ion, uses carbon electrodes in which lithium cations (Li$^+$) can be inserted and reversibly de-inserted [4]. Likewise, the supercapacitor electrodes can be made of carbons whose performances rely on their surface properties. In fuel cells, electrodes are also made of carbon materials, but in that case they act both as the catalyst support and the current collector. Carbons might also be used for their potential ability to adsorb hydrogen and therefore to be involved in a "safe" H_2 reservoir.

Carbon materials exist under many various forms which have, of course, different physical and chemical properties [5]. This is the reason they are used in so many applications. Diamond and graphite are of the well known crystalline structures. However, carbons can be partially or totally disordered depending on the reactant products, synthesis methods, and heating treatment. In this way, it is possible to create thousands of different carbons by adjusting their degree of disorder and/or their porosity. This is what has been known as "carbon science," until Kroto et al. [6] in 1985 discovered a new type of carbon: fullerenes or C_{60}. This discovery was a new kick-off for the physics and chemistry of carbon, and a few years later, in 1991, Iijima [7] found another new form of carbon: carbon nanotubes (CNTs). Since Iijima's discovery a large amount of work has been devoted to the production and the applications of CNTs [8–12].

Apart from diamond, all the other forms of carbon can potentially be used as materials for hosting significant quantities of lithium cations and, consequently, as materials for Li-ion batteries. Investigations searching for the potential ability of these new nanoforms of carbon to intercalate or insert Li$^+$ were then undertaken. More particular work has been carried out to study the electrochemical insertion of lithium and to evaluate the performance of the carbon

nanotubes as materials for advanced rechargeable Li-ion battery applications. It must also be mentioned that insertion of ions, atoms, or molecules in these carbon nanostructures is a subject [13] which opens up a multitude of connected subjects whose scientific interest is impressively broad.

Prior to entering into the world of CNTs, it must be kept in mind that this material, especially if one wants to purchase a high quality and pure sample, is, to date, very expensive. Nowadays, the as-synthesized CNTs samples can be purchased for "only" $60 g^{-1} while highly pure nanotubes cost about 10 times more [8]. Although this price may sound reasonable for high-technology applications, it remains too expensive for making CNTs a good candidate in many industrial domains, that is, for Li-ion batteries, where the carbon materials currently used cost about 1000 times less. Then even if the electrochemical properties of CNTs would appear to be outstanding, many developments for producing them at an industrial scale and at a competitive price would be still far ahead of us.

In this chapter, the focus is on the state-of-the-art of the electrochemical Li$^+$ insertion in CNTs. In order to make this subject more accessible for nonexpert readers, a summary of the different forms of carbon nanotubes and the various methods developed for their production will be given. The fundamental principles for the electrochemical intercalation of lithium in graphite which is, so far, used as a model for carbon materials will also be recalled. The experimental procedures and methods used for characterizing the electrochemical process will be briefly described. Likewise, a short description of the different techniques used for following the evolution of the properties of the carbon nanotubes during the whole insertion process will be provided. The theoretical work which has been carried out will also be briefly reported, underlining how the predictions gained from the simulations can be helpful for experimentalists that attempt to understand the mechanisms involved in the insertion of lithium. Finally, we will summarize the various results obtained and published in the literature before drawing some perspectives about the expected performances of these materials which are currently subject to extensive research, the evolution of which is fast, and which have been and are still often claimed to be potentially attractive for energy storage.

2. STRUCTURE AND PRODUCTION OF CARBON NANOTUBES

2.1. Structure

Carbon nanotubes were discovered by Iijima [7] in 1991 as a by-product of the synthesis of fullerene [14] and were then first produced in significant quantities by Ebbesen and Ajayan [15]. Two basic types of carbon nanotubes has been discovered so far: the single and multiwalled. Both structures can be described starting from a graphene sheet. A graphene sheet is made of unsaturated hexagonal carbon (C$_6$) cycles, like benzene, connected to each other so that they form a two-dimensional pattern (Fig. 1a). Graphite is made of a parallel stacking of graphene sheets (Fig. 1b).
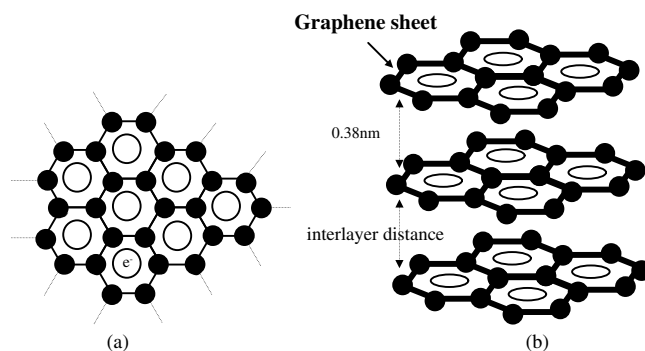

Figure 1. Schematic representation of a graphene layer where full circles represent carbon atoms, lines represent the C–C bonds, and the empty circles at the center of the hexagons represent the π electrons clouds (a) and of the graphite structure (b).

Single walled carbon nanotubes (SWCNTs) [16, 18] can be seen as "a narrow strip of nanoscale graphene... rolled up in a seamless cylinder" [18]. The graphene strip can be rolled up in different ways (Fig. 2) and then SWCNTs with different symmetries (e.g., chirality) and specific electronic or mechanical properties [19] can be produced. The diameter of the tube varies from about 1 to 10 nm and their length can exceed several micrometers depending on the synthesis methods. The inner part (i.e., the central core) of the tube is supposed to be empty and this is the main reason it appears to be promising a "object" for storing chemical species. Single walled carbon nanotubes can be found isolated although, most of the time, they gather in a "compact" and ordered way to make bundles or ropes (Fig. 3), the cohesion of which
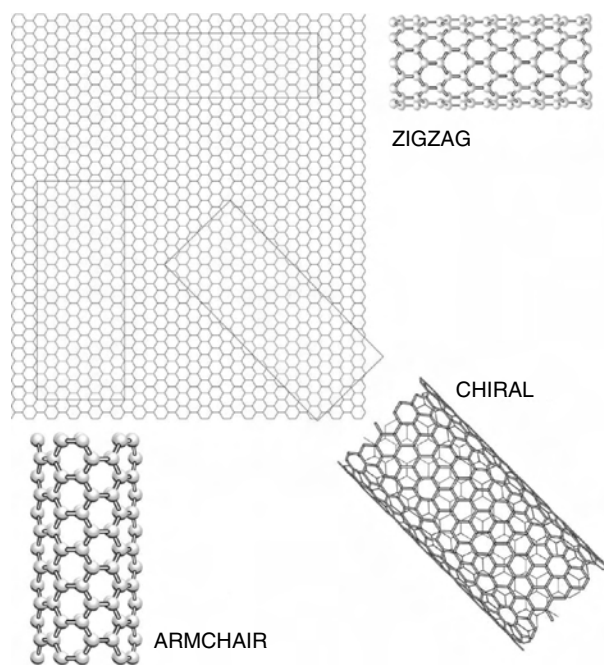

Figure 2. Schematic representation of a graphene sheet and of the various ways to roll up a seamless tube with respect to the hexagonal lattice. Electronic properties depend on the chirality. Reprinted with permission from [18], J. E. Fischer, *Chem. Innov.* 30, 21 (2000). © 2000, American Chemical Society.
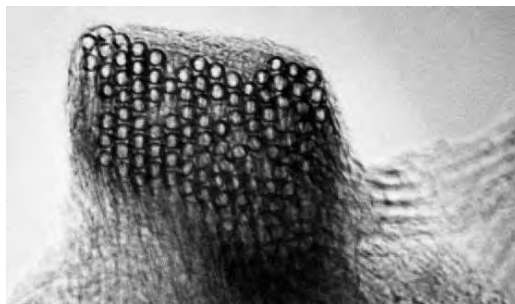
Figure 3. A high resolution TEM picture of SWCNTs packed into a triangular lattice bundle. Diameter of each SWCNT is about 1.5 nm. Reprinted with permission from http://www.ruf.rice.edu/~smalleyg/images/ropes_1c.jpg.

is due to weak interactions (i.e., dipole–dipole van der Walls interaction). Up to about several hundreds of SWCNTs can then form bundles which have a two-dimensional triangular symmetry and diameters can be as large as several tens of nanometers [20, 21].

Multiwalled carbon nanotubes (MWCNTs) are made of several tubes fitted into each other in a nesting or "Russian doll" fashion [22] (Fig. 4). The number of walls can be very large (several tens) and the distance between them is about 0.34 nm. Nowadays, a better control of the synthesis method can be achieved and nanotubes with a given number of walls can be made. As for SWCNTs, the diameter of the central tube can vary. Consequently, both the number of walls and the diameter of the inner tube cause the diameter of a MWCNT to be large (i.e., 5–100 nm). MWCNT ends are not necessarily closed and their sidewall can exhibit many defects (Fig. 5) [23]. Likewise, each individual tube constituting a MWCNT can have different symmetry (see Fig. 2) [24].

Diameters, lengths, and symmetries much depend in all cases on the synthesis procedure as well as on the post-treatment of the nanotubes. In all the studies reported on the electrochemical storage of Li^+ in either single or multi-walled nanotubes, it is likely that the samples were characterized by a rather broad distribution of these parameters. Consequently, it is somewhat difficult to relate these parameters to the insertion capabilities of the tubes. Nevertheless,
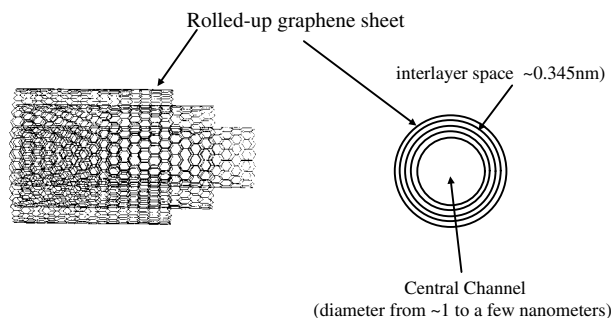
Figure 4. Schematic representation of a MWCNT made of single tubes inserted into each other (Russian doll model) (a). The distance between each wall is about 0.345 nm. The diameter of the central tube can reach several nanometers (b).
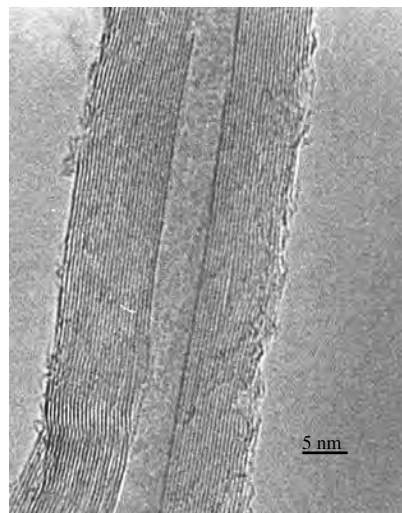

Figure 5. TEM picture of a MWCNT obtained by catalytic decomposition of acetylene on zeolites. Reprinted with permission from [48], G. Maurin et al., *Carbon* 39, 1273 (2001). © 2001, Elsevier Science.

it has already been reported that the diameter of the tubes could influence the insertion of potassium [25]. However, as we will see in this chapter, the nature of the chemical species bonded either at their external surface or at their extremities plays a key role. In other words, Li^+ insertion mechanisms and storage properties appear to be more strongly influenced by the defects than by diameter, length, and symmetry of the single and multiwalled carbon nanotubes.

2.2. Production

For the last decades, much effort has been devoted to the synthesis, purification, and postsynthesis treatment methods. Of course, the main target of all these investigations is the development of experimental procedures able to produce nanotubes in quantities large enough to perform all kinds of experiments, and if industrial applications became the norm, the production scale should be extended to kilos or tons. Furthermore it is crucial to provide materials as pure as possible. Almost all carbon nanotubes synthesis methods produce a non-negligible amount of other carbonaceous species, more or less porous and amorphous [5], extremely complicated to separate from the carbon nanotubes. Also, many procedures require the use of metal catalysts (Fe, Ni, Co, Y) and of substrats (porous alumina, porous silica, or zeolites) which must be removed once the synthesis is completed. Therefore, purification is a necessary step before investigating the properties of the nanotubes. Finally, once we can obtain pure single or multiwalled carbon nanotubes, it appears quite tempting to perform physical or chemical transformations by heating under different types of gas (oxidizing or reducing atmosphere) or by treating the sample with various chemical agents. The latter procedure, often called functionalization, seems to be a promising approach for adjusting the properties of the tubes to the desired applications [26]. It is noteworthy that the functionalization of the CNTs is often achieved, certainly not on purpose and in a very noncontrolled manner, when purifying the pristine samples.

2.2.1. Synthesis Methods

We can classify the various synthesis procedures into two families: on the one hand, the methods based on the sublimation of carbon materials (mainly graphite) under inert atmosphere and on the other hand the methods based on chemical vapor deposition (CVD) principles. In the former, carbon materials are sublimed due to an electric arc [21, 28], a laser [20, 28, 29], or a solar furnace [30]. In the second case, it consists of a gas reaction assisted by a catalyst which can be accomplished in various manners: catalytic decomposition of gaseous hydrocarbon compounds [31–35], electrolysis [36], pyrolysis [37], and more recently aerosol [38] methods.

So far, only the electric arc, laser ablation, and decomposition of hydrocarbon methods have been able to produce reasonably large quantities of carbon nanotubes and have been used for the electrochemical application we are interested in.

It is possible to synthesize single and multiwalled nanotubes separately. The main factor is the composition of the carbonaceous phase and the addition of metal catalysts. For instance, if the carbonaceous material used in the electric arc and laser ablation methods is made of graphite powder only, then MWCNTs are synthesized. However, if this material also contains metallic particles of Ni, Co, and Y then single walled carbon nanotubes are obtained. For CVD based methods, it is always necessary to use catalyst for both single and multiwalled production. In that case, the main factor is the size of the catalyst particle.

2.2.2. Purification

Carbon materials obtained via these different routes always contain impurities that represent in certain cases up to 50% of the synthesized matter. They are various types of solid carbon phases and the remaining catalyst particles [39]. When silica [23], alumina [33], or zeolite [40] supports are used in the CVD process, they also must be eliminated. This is carried out by dissolving the support with solutions of fluoridric, nitric, or sulfuric acid. The undesirable carbonaceous phases can be eliminated by heating under oxygen atmosphere or by acid oxidation since poorly organized carbons are less stable and are expected to be removed more easily than carbon nanotubes. Oxidation in strong acid can often be used for eliminating the catalyst particle. Also, as-synthesized material can be purified by maintaining the carbon nanotubes in suspension using ultrasound and filtering the undesirable carbonaceous phases through a micropore membrane [41]. Most of the time, all these reported methods are used in subsequent steps.

It must be kept in mind that the purification route is long and increases drastically the cost of the synthesis. Furthermore, each oxidizing heating or chemical treatment changes the structure and the surface of the nanotubes. Likewise a non-negligible amount of matter, including carbon nanotubes, is lost at each step of the procedure. So purification must be thought of as a crucial step in the production of carbon nanotubes.

2.2.3. Surface Defects and Functionalization

In the ideal case, the outer surface of carbon nanotubes would be made of carbon atoms only linked to each other. Thus, we could expect carbon nanotubes to be as chemically inert as graphite [42]. However, their sidewalls as well as their extremities contain a certain amount of chemical or physical defects which are created during the synthesis or the purification routes and which greatly influence their properties [43] and more particularly their capability to insert lithium cations. Therefore, one of the most challenging aspects in the research and development of carbon nanotubes during the coming years will probably be the acquisition of a better knowledge and control of the defects.

Some physical defects can be directly observed by transmission electronic microscopy (TEM) on MWCNTs produced for instance by catalytic decomposition (Fig. 5). In that case, they mainly consist of noncontinuous carbon layers and open tips [23]. At the atomic scale, physical defects can be identified as broken bonds or nonhexagonal carbon cycles such as squares (C_4), pentagons (C_5), heptagons (C_7), and octagons (C_8) that can be located at the extremities or at the sidewall of the tubes (Fig. 6). These local defective structures imply stress that modifies the mechanical and electrical properties. They can also act as doorways (i.e., C_7, C_8, ...) for inserting small ions [44] or molecules.

Physical defects can be cured by heating at high temperature under inert gas. Frackowiak et al. [23] showed clearly how a post-treatment at 2800 °C can realign the walls and close the extremities of their MWCNTs. By contrast, increasing the physical defect density, shortening the tube, or opening the tips can enhance some properties such as field emission [45] or insertion. This can be achieved by using strong chemical oxidation [46] or a mechanical process such as abrasive treatment [47, 48] and ball milling [49].

Chemical defects are essentially associated with the presence of oxygen or hydrogen atoms that are bonded to the carbon atoms. The C–H bonds can be introduced during the synthesis (especially when CNTs are produced by CVD) while oxygen impurities can also come from the reaction with air when carbon nanotubes are extracted from the reactor and when they are purified. For instance, the presence of –C=O, –C–OH, or even –COOH groups was detected [50]. Also, it has been shown that SWCNTs and MWCNTs
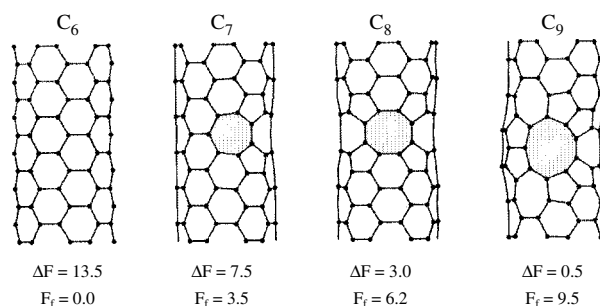

C_6	C_7	C_8	C_9
$\Delta F = 13.5$	$\Delta F = 7.5$	$\Delta F = 3.0$	$\Delta F = 0.5$
$F_f = 0.0$	$F_f = 3.5$	$F_f = 6.2$	$F_f = 9.5$

Figure 6. Representation of some possible topological defects at the nanotube walls. ΔF (in eV) and F_f (in eV) are the diffusion barrier and the formation energy corresponding to each defect respectively. Reprinted with permission from [135], V. Meunier et al., *Phys. Rev. Lett.* 88, 075506 (2002). © 2002, American Physical Society.

could be fluorinated [51, 52] at high temperature and defluorinated by diverse chemical treatment. From all these chemical groups attached to the carbon nanotubes, controlled chemical [53] or electrochemical [54] functionalization can be imagined, thus leading to an extraordinarily wide domain of investigations. It has even been demonstrated that it is possible to shape CNTs by using the chemical properties of their functionalizing groups [55].

3. ELECTROCHEMICAL INSERTION IN CARBONS

3.1. Principles

In this section, we propose a brief encounter with the basic electrochemical principles needed for understanding the following sections.

Formally, the redox reaction of the lithium species can be written as followed:

$$\text{Li}^+ + x\text{C} + 1e^- \quad \Longleftrightarrow \quad \text{LiC}_x \quad (1)$$
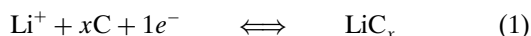
When the reaction proceeds from the left to the right, Li^+ is reduced and it is oxidized in the opposite direction. The potential associated to this reaction can be measured in an electrochemical cell by comparing the potential of the carbon electrode where reaction (1) and only reaction (1) takes place (working electrode) to another electrode where the potential is constant and therefore used as a reference. Most of the time, the reference electrode is a lithium metallic foil where the following redox reaction takes place:

$$\text{Li}_{\text{metal}} \quad \Longleftrightarrow \quad \text{Li}^+ + 1e^- \quad (2)$$
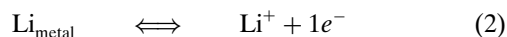
Therefore, combining reactions (1) and (2), one can write the global reaction:

$$\text{Li}_{\text{metal}} + x\text{C} \quad \Longleftrightarrow \quad \text{LiC}_x \quad (3)$$

A schematic representation of an electrochemical cell combining reactions (1) and (2) is given in Figure 7. If a current i flows in such a way that reaction (3) is pushed toward the right (insertion) then the cell is discharged. If the current flows in the opposite direction, deinsertion proceeds and the cell is charged.
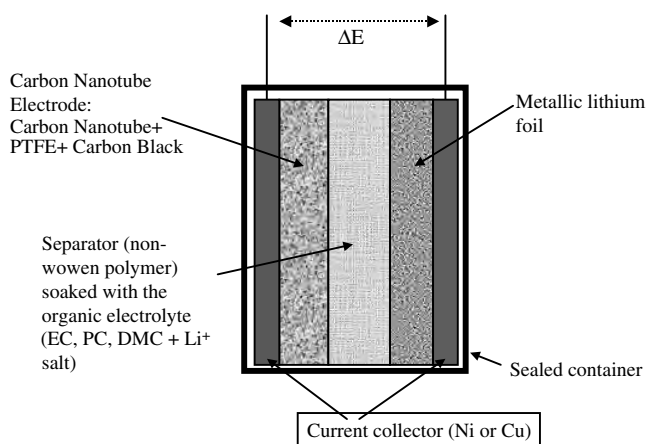
Two specific parameters can be investigated: the difference of potential ΔE measured between each electrode and the quantity of electronic charges (i.e., the faradic capacity Q) exchanged during the reaction. For the sake of comparison between experiments, Q must be divided by the mass of electrochemical active carbon contained in the electrode and then given as a specific value often expressed in mAh g^{-1}. At a constant pressure and temperature, it can be demonstrated that ΔE accounts for the thermodynamical characteristic of the intercalated phase LiC_x. Therefore, the variation of ΔE, measured upon intercalation or deintercalation, provides information about the electrochemical phases which are formed. The faradic capacity Q related to the redox reactions is obtained at any time t by integrating the product $i\,dt$. As charge and discharge are frequently performed at constant current, then $Q = it$. If reaction (3) is the only one occurring in the electrochemical cell then the value of Q allows us to calculate the amount of Li^+ that has been intercalated (or deintercalated) in the carbon network. For instance, providing that 1 g of metallic lithium oxidized in Li^+ exchanges 0.14 mole of electrons then the total capacity Q corresponding to this oxidation is about 13,500 Coulomb or 3800 mAh. The reversible capacity is the capacity which can be recovered from the previous step. (N.B. Be aware of the fact that this is not the thermodynamical reversibility. The later is measured by comparing the potential of the cell upon charging and discharging at a given value of Q.)

Theoretically, the electrochemical cell described in Figure 7 is easy to set up. Practically, it appears more difficult because of the extreme chemical reactivity of the lithium species with water. The electrochemical cell must then be assembled and studied under water-free atmosphere (i.e., in a glove box). Likewise, the electrolyte which insures the Li^+ migration from one electrode to the other must be totally anhydrous. Furthermore, it must be chemically and electrochemically inert. If it is oxidized and/or reduced at the electrodes, then an additional electric current will flow and consequently will lead to a measured capacity Q which is different from that induced by reaction (3). In most of the experiments reported in this chapter as well as in the commercial Li-ion batteries, the electrolyte is a mixture of organic solvents: dimethyl carbonate and ethylene and propylene carbonate in which lithium salts such as LiPF_6 or LiClO_4 are dissolved at a concentration of about 1 mole per liter.

As for the electrolyte, all the other nonactive elements of the cell must be chemically and electrochemically inactive. If not, additional currents can occur and make the measurement of ΔE and Q unreliable. This stands more particularly for the materials which are combined with carbons, the metal used as current collector, and the microporous separator into which the electrolyte is absorbed. Usually, the carbon electrode is made of a mixture which contains about 90% in mass of the electroactive carbon (i.e., CNTs), 5% of black carbon for increasing the conductivity, and 5% of a binder. The later is a polytetrafluoroethylene or a polyvinylidene fluoride, the separator is a nonwoven mat of polypropylene, and the current collector is a grid of nickel.

Figure 7. Schematic representation of an electrochemical cell used for characterizing the redox reactions between Li^+ and the electrode which contains the active carbon (i.e., graphite, CNTs, etc.).

3.2. Electrochemical Methods

As previously mentioned, the intercalation or insertion properties can be investigated from the curve which represents the evolution of ΔE with Q [56] at a given current density j (the current i divided by the mass of active carbon). A schematic representation of the procedures used when a constant current (i.e., galvanostatic conditions) is applied to the electrochemical cell is given in Figure 8a. The main advantage of this so-called galvanostatic method is that it can quickly be carried out (i.e., one or more insertion/deinsertion cycle can be performed per day depending on the current density). Moreover, this technique allows direct access to the reversible and irreversible capacity, the evolution of these capacities upon cycling, and finally the thermodynamical irreversibility measured by the difference of potential at a given value of Q between the charge and the discharge. Further, as is the case for instance in graphite (Fig. 9), the occurrence of different intercalation steps can be pointed out. If the plateaus are not as pronounced as for graphite, then the curve $\Delta E = f(Q)$ can be derived. Complementary methods such as cyclic voltammetry can also be used. It consists of measuring the evolution of the current i when the applied potential ΔE is ramping. Usually, the potential varies linearly at a given scan rate between two selected limits (i.e., 0–3 V versus Li/Li$^+$) such as it is possible to investigate the various redox reactions [33, 57–60]. One advantage of this method is also to assess the modifications induced by the scan rate. Capacitance effects can then be emphasized and qualitatively characterized [23]. However, galvanostatic and cyclic voltammetry techniques do not provide all the information about the mechanisms responsible for the electrochemical behavior. For instance, it is not possible to readily access the kinetic of insertion (i.e., the diffusion processes). Impedance spectroscopy [61, 62] and relaxation techniques as galvanostatic or potentiostatic intermittent titration techniques (GITT [63] or PITT [64, 65]) can be employed for that purpose.

The analysis of the impedance spectra is based on the schematic representation of the studied system by means of resistance and capacitance equivalent circuits. The theoretical values of the real and imaginary parts of the impedance
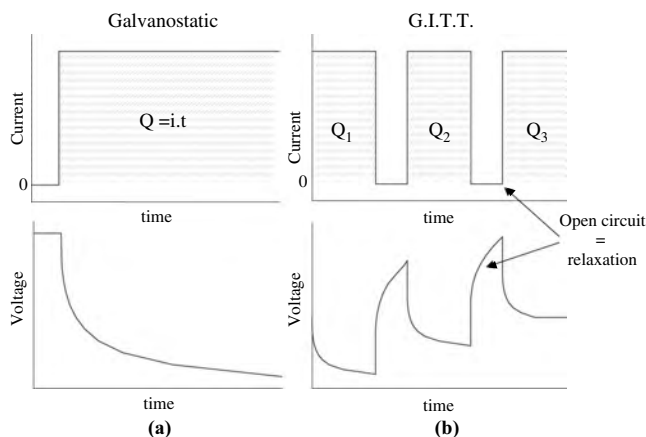

Figure 8. Schematic representation of the galvanostatic and GITT procedure used for measuring the capacity Q and the evolution of the voltage upon the application of a current.
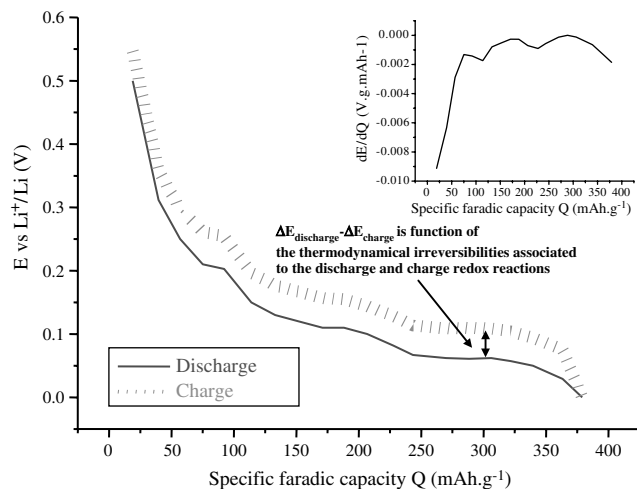

Figure 9. A typical discharge curve $E = f(Q)$ obtained for graphite. Insert is the derivative of the potential as a function of the specific faradic capacity Q. The potential plateaus (or the broad peaks in the dE/dQ curve) correspond to the various intercalation states.

circuit can be expressed and fitted to the experimental one. The fitting of the so-called Nyquist curves which report the evolution of the real part Z' as a function of the imaginary part Z'' of the impedance allows us to calculate the resistance and capacitance of the different components of the circuit. Then, different characteristic values of the system can be determined (e.g., the double layer capacitance which is proportional to the reactive surface of the sample). It can also yield the value of the diffusion coefficient [57, 66–68].

GITT consists of applying periodically a constant current followed by an open circuit period (Fig. 8b). The system is charged or discharged while the current remains constant and when it is switched off, the system relaxes until it reaches a pseudo-equilibrium state which is characterized by a voltage plateau. PITT involves the application, step by step, of a potential. At each step, we measure the current i as a function of time. As for GITT, the measured signal tends toward a steady state.

These techniques yield two main facts. First, it is possible to calculate by integration the charge or discharge capacity after each current or potential pulse and therefore to associate this capacity Q to the pseudo-equilibrium potential measured at the end of the relaxation period. As for the galvanostatic experiment already described, a $\Delta E = f(Q)$ curve can then be plotted and derived if necessary. However, as this representation corresponds to the pseudo-equilibrium states, a much better resolution is obtained. The drawback of this method is that it can demand several weeks just to complete a charge/discharge cycle. Second, the relaxation period can be used for analyzing the potential decay. A model proposed by Honders and co-workers [69] provides an expression relating the potential decay function measured from GITT to the diffusion coefficient D_{li^+}. Therefore, it makes possible the evaluation of the diffusion coefficient after each current pulse, that is to say, at every given value of Q upon charge or discharge [70]. Similar methods are proposed from PITT data [71].

It is worth noting that all these methods employed for calculating the diffusion coefficient require the introduction of

constant parameters, such as the length of the diffusion path, whose the exact value is not known. For instance, this length is frequently assigned to the electrode thickness. Our thinking is that it is not always necessarily true. Consequently, it is not surprising that the D_{li^+} values reported in the literature vary over several decades since they would strongly depend on the experimental method and the intrinsic parameters used for the fits of the data. Meanwhile, information can be gained from the qualitative evolution of D_{li^+} with Q.

4. PHYSICAL METHODS FOR ANALYZING CARBON NANOTUBES

The electrochemical techniques previously described provide information about the electrochemical characteristics of the insertion process and about the electrochemical performances of the CNTs. However, we cannot extract information about the structure of the nanotubes during the whole insertion process. Likewise, they are not sufficient to understand how the lithium ions interact with the carbon structure of the tubes. For instance, the knowledge of the electron transfer between Li and CNTs is crucial for a better understanding of the electronic conductivity of the intercalated tubes. To answer to these questions, physicists have adapted some techniques. The purpose of this section is to enumerate the methods commonly employed. No details about the principles of these techniques will be given. They are well known and can be extensively found in the literature.

Basically, the main problem faced by the experimentalist who aims to analyze its samples is that the lithiated samples are sensitive to moisture. Therefore, precautions must be taken to prevent the contamination of the sample with water contained in the air. This can be quite straightforwardly undertaken with some techniques, but not with others.

4.1. Electron Microscopy and Elemental Analysis

About 99% of the articles concerning CNTs contain pictures obtained by electron microscopy. It can be scanning electron microscopy (SEM) which provides a direct image of the studied material (Fig. 10). The best resolution (resolving power) usually obtained with this technique is between 4 to 10 nm. It is useful for obtaining an overview of the material at the μm scale. It allows us to (i) appreciate how the tubes or the bundles are arranged (they can be aligned or entangled), (ii) evaluate the shape, length, and diameter of the tubes or of the bundles, and (iii) examine the shape and the quantity of carboneous or catalyst particles.

The other important technique is TEM. It enables us to visualize the structures and the morphologies of the tubes at a smaller scale. In the high resolution mode, the carbon layers can be observed (Fig. 5). It is thus possible to measure the interlayer distance and the internal and external diameters and to observe both the extremities and the structural defects. The main drawback of TEM and SEM is the same for all types of microscopy: they analyze only a given part of the sample which may not necessarily be the most representative of the whole material.
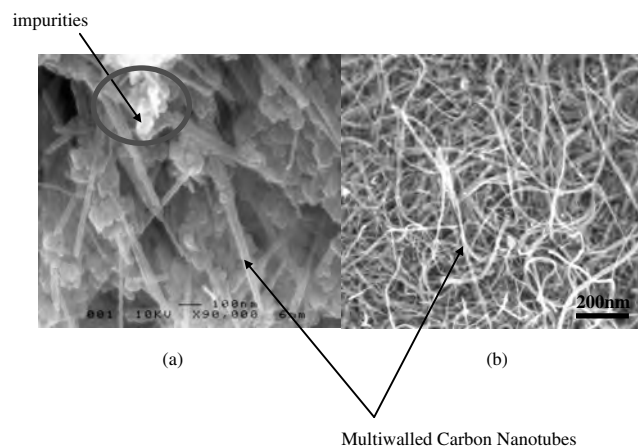

Figure 10. Typical SEM pictures of MWCNTs obtained by catalytic decomposition of acetylene on a zeolite support; detail which shows the tubes and the remaining particles (catalyst and diverse disordered carbons) (a) and overview from which tube length can be measured (b).

Chemical analysis can be achieved by burning the sample and by analyzing the emitted gas. These basic chemical methods are reliable in most cases but are destructive. Moreover, they just give the composition of the materials and it is not possible to gain further details about the molecular entities which could pollute the sample. This is the reason why chemical analysis is very often performed using the nondestructive physical techniques found in many electron microscopes nowadays. Electron or X-ray based analysis methods like energy dispersive X-ray spectrometry, X-ray photoelectron spectroscopy (XPS), and electron energy loss spectroscopy which can probe chemical elements or entities at the micrometer scale are the most common methods. As an example, XPS is a powerful tool for analyzing the oxygen groups attached at the surface of the tubes [23, 73]. It must also be mentioned that infrared spectroscopy is also often employed for determining the nature of the functionalized groups [50].

4.2. X-Ray Diffraction

X-ray diffraction (XRD) is a widely used technique since it enables us to characterize the structure of the carbon nanotubes. In contrast to electron microscopy, XRD does not correspond to a local analysis. Therefore, it provides the response of the whole sample. As an illustration, the asymmetric peak (0,0,2) located around 13 $°\theta$ (θ is the diffraction angle) characterizes the tubular morphology of the MWCNT sample [22, 24] (Fig. 11). The exact position of the peak allows us to determine the interlayer distance. The half-width of this peak is inversely proportional to the coherent scattering length. This length characterizes the dimension of the diffracting structure. In the case of MWCNTs, it can be associated with the thickness of their walls and consequently their diameter. If it is much lower than those directly measured by TEM, it means that the stacking of the graphene rolls is highly disordered leading to a turbostratic character of the tubes. The latter point can be confirmed by the asymmetry of the (1,0) peak at around 22θ. Any new LiC_x phase, if ordered, exhibits new peaks on the XRD pattern.
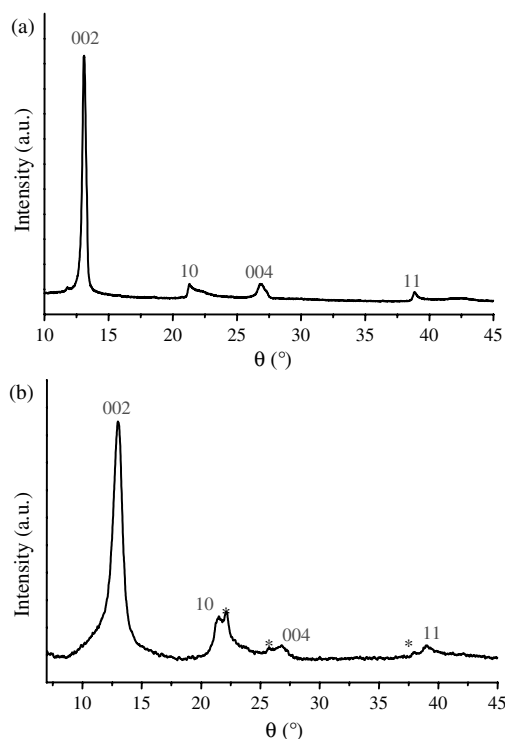
Figure 11. X-ray diffraction patterns obtained on as-synthesized MWC-NTs produced by the electric arc technique (a) and by catalytic decomposition of acetylene (b). ∗ denotes the peaks attributed to the remaining cobalt particles.

The XRD pattern of SWCNTs provides information about the structural organization of the two-dimensional lattice of the nanotube bundles by means of (h,k) lines [73–75]. We can then deduce, for instance, from the position of the (0,0,2) peak and its broadness, the parameter and the crystallinity of the lattice of the SWCNTs respectively. Furthermore, a shift of the (h,k) lines for inserted nanotubes can yield the expansion of the two-dimensional lattice associated with the Li$^+$ insertion mechanism [57, 76].

4.3. Raman, NMR, and ESR Spectroscopy

Raman spectroscopy has often been used to characterize carbonaceous materials. Many studies have been carried out on MWCNTs [77–81] and SWCNTs [82–86]. Recent investigations [87, 88] concerning both MWCNTs and SWCNTs show that it can be a fruitful technique since the charge transfer between Li and the carbon nanotube can be identified by the shift of the high frequency tangential vibrational mode, usually named the G band, situated around 1580 cm^{-1}. Another band located around 1330 cm^{-1}, called D, is due to different kinds of structural carbon defects. Therefore, the ratio of the G and D band intensities can be employed to quantify the degree of disorder of the nanotube (Fig. 12). Moreover, in the case of SWCNTs, low frequency Raman modes are found which can be related to the diameter distribution of the bundles. This frequency domain is also explored during the insertion process and can be useful for a better understanding of the alkali–alkali or alkali–carbon interactions [87, 89].
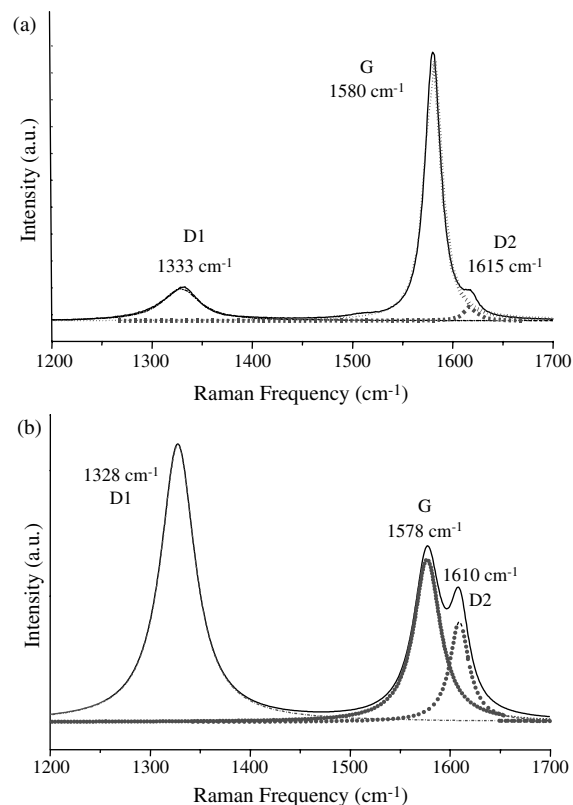

Figure 12. Micro-Raman (confocal technique) obtained on as-synthesized MWCNTs produced by the electric arc technique (a) and by catalytic decomposition of acetylene (b).

Likewise, solid state ^{7}Li nuclear magnetic resonance (NMR) can be helpful for understanding the nature of the Li–CNT bond. Its has been widely used in graphite [90–95] and in other types of carbonaceous materials. Depending on the location of the inserted lithium atom and consequently on the specific charge transfer between Li and the carbon network, the resonance will be shifted to a given value. For instance, the broad band centered at 43.5 ppm versus LiCl reference is characteristic of Li$^+$ intercalated between graphene sheets (Fig. 13). Furthermore, solid state ^{13}C NMR can provide information about the electronic state of the sample by considering the anisotropic shift of a sp^2 carbon during the insertion process [96, 97].

Finally, electron spin resonance is also used to characterize the "electronic" behavior of the MWCNTs and SWCNTs upon the insertion of alkali ions. It has been reported that the occurrence of a dysonian shape signal and a temperature independent Pauli paramagnetism for K-doped MWCNTs and SWCNTs can be interpreted as a metallic state [97, 98].

5. INSERTION AND INTERCALATION OF Li$^+$ IN CARBON MATERIALS

First of all, two terms must be properly defined. Intercalation should be used only when the lithium cations penetrate into the interlayer space of the structure (i.e., the empty space between two adjacent graphene sheets) or into the
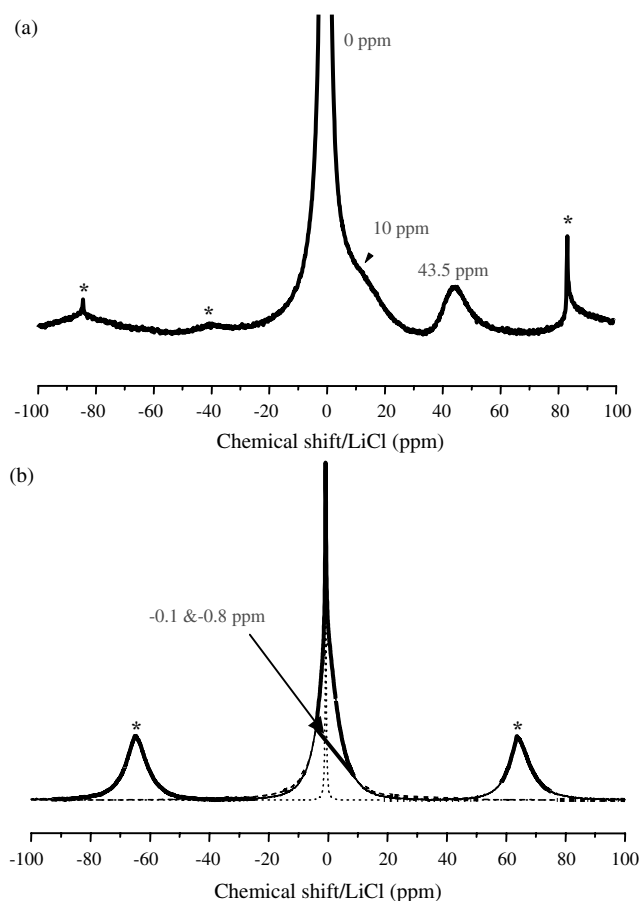
Figure 13. ^{7}Li MAS NMR spectra obtained on fully lithiated as-synthesized MWCNTs produced by the electric arc technique (a) and by catalytic decomposition of acetylene (b). * denotes the spinning side bands. The 10 ppm band can be ascribed to Li$^+$ adsorbed at the surface of disordered carbons. The 43.5 ppm band, the so-called Knight shift, is characteristic of Li$^+$ intercalated between graphene sheets (a). In spectrum (b), the narrow band at -0.8 ppm is ascribed to Li$^+$ inserted in the SEI while the broad band centered at -0.1 ppm is likely due to Li$^+$ adsorbed at the nanotube surface. As for Figures 17 and 18, these plots clearly show the different mechanism of insertion/intercalation between both types of MWCNTs.

central core of the nanotubes. If Li$^+$ is bonded to the carbon atoms at the outer surface or to any other interstitial sites, then insertion is the relevant term. Readers must be aware that this distinction is not often clearly made and that misunderstanding is possible.

Many investigations on alkali insertion or intercalation in various types of carbonaceous solids were undertaken [99–101]. The aim of these studies is to search for a material which can store, in a reversible manner, the largest quantity of alkali into the carbonaceous network. Beyond this first requirement, the material must also sustain as many as possible insertion/deinsertion cycles. To sum up, a carbon material which would exhibit a high irreversible capacity coupled with a low number of insertion/deinsertion cycles sustainability would not be a good candidate for rechargeable batteries.

Among the various alkali atoms, lithium insertion was the most studied because of its highest electrochemical standard

potential which means the highest energy stored per inserted atom.

Insertion can proceed via chemical or electrochemical routes. We will mainly focus on the latter. In principle, insertion capacity and reversibility depend strongly on the chemical composition and on the ordered/disordered state of the carbon material. For instance, it was shown that an increase of the hydrogen/carbon atomic ratio leads to an increase of the insertion capacity [102]. Likewise, according to Dahn et al. [5], it seems that "... the best microporous carbons for lithium-ion batteries are those ... with the minimum value of R and R_g." Here, R is associated with the number of stacked graphene sheets and R_g is a parameter characteristic of the pore size. So it is clear that both the composition and the micro- and macrostructure of carbons are relevant parameters for their insertion properties.

It would be too tedious to make an extensive presentation of all the different possible mechanisms for Li$^+$ insertion in these materials. Therefore, for the sake of simplicity, we shall begin with the description of Li$^+$ intercalation in graphite which is the well-known ordered carbon form and for which a detailed image of the intercalation is given. Starting from this point, a further attempt to draw the main differences that we may expect for the intercalation or insertion in CNTs will be presented.

5.1. Li$^+$ Intercalation in Graphite

The studies of Li$^+$ intercalation in graphite, either by chemical [103] or electrochemical routes [104], show that lithium reacts with the hosting carbon network by successive steps. This can be clearly seen from the evolution of the potential ΔE as a function of the capacity Q where plateaus appear (Fig. 9). Each of them accounts for the occurrence of a new solid phase. This phenomenon means that different crystalline states exist upon the intercalation process. In other words, the interlayer spaces are not filled randomly. The different intercalation states are named according to the number of graphene sheets which separate two layers of intercalated lithium (Fig. 14a). Daumas and Herold [105] refined the model initially due to Rüdorff and Schulze [106] and proposed a model in which the second state takes into account the possible deformation of the graphene layer (Fig. 14b). The stoichiometry of state 1 is LiC$_6$. The expansion of the interlayer distance is less than 10% [61] making the successive intercalation and deintercalation reactions reversible under certain experimental circumstances.

The specific faradic capacity Q measured when very low current densities are applied approaches the theoretical capacity of LiC$_6$ (i.e., 372 mAh g^{-1}) [104]. The main drawback of graphite is that its structure can be exfoliated if small molecules penetrate the interlayer space. This was observed with certain solvents in which Li$^+$ was dissolved. In those cases, the irreversible capacity reached 1000 mAh g^{-1} and the graphite structure collapsed after a few intercalation/deintercalation cycles [107]. It has been claimed that the theoretical capacity of 372 mAh g^{-1} can be improved by oxidation or mechanical treatments [108–111]. Exfoliation can also occur when the discharge voltage is pushed below 0 V (vs Li/Li$^+$) [112].
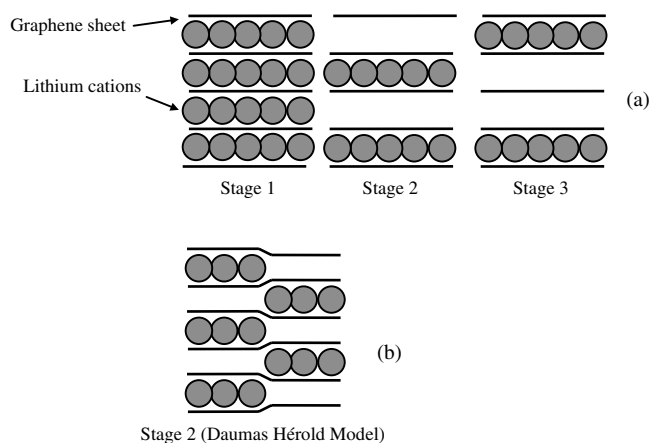
Figure 14. Schematic representation of the subsequent intercalated states of graphite. Lines correspond to the graphene sheets and full circles to the intercalated Li^+.

The intercalation of Li^+ involves an electronic charge transfer from the carbon atoms to the lithium ions such that Li^+ is reduced to lower oxidation states. As was recalled in Section 4, this can be followed by different spectroscopies [91–93, 113–115]. Likewise, the various stages of the intercalation have been investigated by X-ray diffraction [61, 116, 117]. It is then possible to assign each potential plateau to the coexisting phases (ΔE is given versus the Li/Li^+ reference electrode):

  i. $\Delta E = 0.21$ V: State 1 (LiC_6) diluted in State 4 whose composition is not clearly defined
 ii. $\Delta E = 0.14$ V: State 2 (LiC_{18}) diluted in State 3 (LiC_{24})
iii. $\Delta E = 0.12$ V: State 2 (LiC_{18}) diluted in State 2 (LiC_{12})
 iv. $\Delta E = 0.08$ V: State 2 (LiC_{12}) diluted in State 1 (LiC_6)

5.2. Li^+ Intercalation in Disordered Carbons

These materials come from the pyrolitic reaction (reaction with oxygen in a flame) of various organic compounds. Their properties depend both on the heteroatoms remaining attached to C (H, O, N, and S) and on the number of graphitelike clusters which are formed into the amorphous structure. Some of these disordered carbons can be transformed into graphite by heating at around 3000 °C under inert atmosphere (soft carbons), while some others cannot be converted to graphite even at high temperature (hard carbons). Their ability to insert lithium can exceed that of graphite [92, 118, 119]. This more effective behavior can be schematically explained by the superposition of different mechanisms; it can be either by the Li^+ intercalation into the graphitelike cluster [120, 121], the Li^+ insertion at the boundaries of these clusters [122–124], the formation of Li metallic cluster into the porosity of these disordered structure [125, 126], the occupation of porosity created by the removal of heteroatoms during the heating process [127, 128], and finally interactions with either hydrogen [129] or heteroatoms [130]. Unfortunately, this higher insertion/intercalation capacity often comes with important irreversibility that can be unsuitable for their use in Li-ion batteries.

6. INSERTION AND INTERCALATION OF Li^+ IN CARBON NANOTUBES

CNTs are thought to be attractive hosts for lithium because of their particular structure. First of all, it may be assumed that a large amount of Li^+ ions can be stored in the central core, the interlayer space (case of MWCNTs), or the empty space between the SWCNTs when they are assembled in bundles. As was reported for disordered carbons, we can also envisage a non-negligible amount of Li^+ bonded to the external walls of these structures. Likewise, it is most likely that the structural and chemical defects of the CNTs play a key role in their ability to intercalate and insert lithium. To date, all these assumptions have been checked. The purpose of this chapter is therefore to provide an up-to-date review of the theoretical and experimental work which has been collected since 1998/1999 when the first electrochemical measurements were reported [23, 33, 49, 131–134].

6.1. Theoretical Predictions

Ab initio [44, 135] and semiempirical Hartree–Fock [136] calculations have recently been carried out and have concluded that the electrochemical intercalation of Li^+ through the walls of the nanotube is unfeasible. For instance, the potential barrier that a Li cation must cross to pass through a C_6 cycle would be in the order of 10 eV ($\sim$1000 kJ mol^{-1}). This value decreases significantly to about 50–300 kJ mol^{-1} if the cation goes through a C_8 cycle [45, 136], but the presence of such C_8 entities is unlikely (Fig. 6). Needless to say, these energy values emphasize that Li^+ cannot penetrate the tube under standard conditions if the tube extremities are closed and if there are no structural defects at the sidewall. Defective CNTs would then have to be synthesized in order to obtain a higher insertion capacity.

These calculations show that CNTs act as Li^+ attractors. When lithium is adsorbed near the CNT walls, it is reduced to about $Li^{+0.7}$. It is suggested that the CNT system is slightly more stabilized when Li^+ is adsorbed at the outer surface of the tube. This is still more significant when two lithium cations are adsorbed: the most stable configuration is obtained when both cations are outside the tube (Fig. 15). This means that adsorption at the outer surface is more favorable than intercalation inside the central channel and that the Lithium insertion capacity would strongly depend on the specific surface of the sample. The average distance between the adsorbed cation and the sidewall has been evaluated to be equal to about 0.2–0.3 nm.

It is also demonstrated that the diffusion of Li^+ intercalated inside the central core is almost free [135, 137]. Very weak potential barriers (about 0.04 eV) are encountered by Li^+ when it moves inside the tube such that its residence time could be rather short (a few microseconds for a 1 μm long CNT).

Finally, it is pointed out that the presence of preadsorbed Li^+ on the outer surface of CNTs allows hydrogen molecules to be adsorbed via the occurrence of stable $Li–H_2$ entities [136, 138]. These results would confirm that Li^+-inserted CNTs are much better candidates for hydrogen adsorption [139, 140] than pristine CNTs [141].
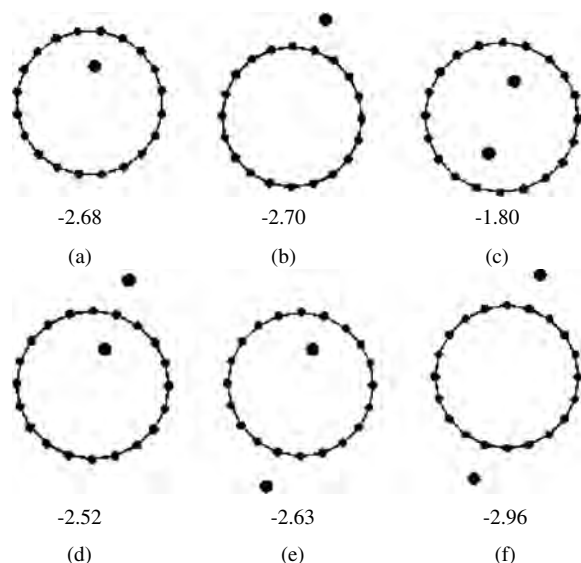
Figure 15. Optimized structures and binding energies (eV) of different isomers of one (a & b) and two Li$^+$ (c–f) ions at the sidewall of a nanotube. Reprinted with permission from [44], T. Kar et al., *J. Phys. Chem. A* 105, 10397 (2001). © 2001, American Chemical Society.

6.2. Chemical Li Intercalation

Prior to reviewing the electrochemical insertion, let us recall the main information gained from the chemical intercalation that can be performed via a gaseous (a high pressure of alkali vapor) or a liquid phase (a molten salt or metal) [13]. The latter also corresponds to redox reactions between the carbon nanotubes and solutions containing tetrahydrofuran solvent and various organic radical anions as naphthalene, benzophenone, and benzoquinone characterized by different redox potentials, with lithium ion as a counterion [142, 143]. The composition of the lithiated phases was thus obtained by determining the number of electrons transferred from the solution to the carbon material. This can be estimated from the variation of the concentration of the radical ions induced by the redox reactions.

Most of these studies preceded the first results reported on the electrochemical intercalation. Consequently, the interpretation of the results obtained by the electrochemical route are greatly influenced by the conclusions drawn from the previous chemical intercalation investigations. So it seems to us important to write a brief report about it.

6.2.1. Multiwalled Carbon Nanotubes

In 1994, Zhou et al. [22] studied, for the first time, the chemical intercalation of potassium and rubidium in MWCNTs produced by the electrical arc technique. This intercalation process seems to proceed via the structural defect located at the outer surface of the tubes. Later, Suzuki and Tomita [25] reported the observation by TEM of a well defined intercalated state corresponding to the stoichiometry KC$_{24}$ similar to state 2 of the Daumas/Herold classification for graphite. They pointed out that MWCNTs having a diameter larger than 10 nm were more reactive toward the potassium

vapor. Mordkovich et al. [144–146] observed an heterogeneous K-intercalated structure looking like a necklace of pearls. It was then assumed that a given MWCNT could be intercalated in some specific regions and not in other ones. The first work with high pressure of lithium vapor was carried out by Nalimova et al. [147] and showed the occurrence of an unstable LiC$_2$ phase with MWCNTs produced by catalytic decomposition. This phase has the same periodicity as LiC$_6$ with highly dense layers of lithium. Finally, it was reported by Chen et al. [140] that a LiC$_{15}$ phase could be obtained by mixing MWCNTs and lithium carbonate and that this phase could store up to 20% in mass of H$_2$. This result was not confirmed by Yang [139] who obtained "only" 2% of adsorption, using the same conditions. (Readers who are interested in the H$_2$ uptake in CNTs must be aware of the fact that the experimental data reported in the literature are highly controversial and that no general agreement exits on the CNTs' ability to store a large quantity of molecular hydrogen.)

6.2.2. Single Walled Carbon Nanotubes

More studies have been undertaken on the chemical intercalation of alkali in SWCNTs [142, 143, 148] since the presence of alkali increases the electronic conductivity of the tubes [83, 149]. MC$_7$, MC$_8$, MC$_{24}$ (M = K or Cs) [29, 149–151], and LiC$_{10}$ [152] phases have been obtained. An expansion of the bundles network is observed, meaning that K and Cs would be preferentially adsorbed into the interstices of the bundles between the SWCNTs. This result is in good agreement with the calculations reported in the previous section. However, the complete occupation of these interstitial sites would lead to MC$_{16}$ stoichiometry [153]. In this case, MC$_8$ and MC$_7$ phases could not be explained from this simple assumption. We must then assume that each interstitial site is occupied by more than one lithium atom or that lithium atoms also penetrate the central core. As explained in Section 6.1, the latter event is rather unlikely, unless the SWCNTs have opened tips or the pressure and temperature conditions allow the alkali to cross the potential barrier.

6.3. Electrochemical Li$^+$ Intercalation

Many investigations have been reported on this subject [23, 33, 46, 48, 49, 57, 60, 65, 68, 70, 71, 76, 87, 88, 131–134, 153–166]. First of all, it must be underlined that there are non-negligible discrepancies between the various articles, not that the authors are responsible for it. It is most likely because the physical and chemical characteristics of CNTs vary from sample to sample, though they can be produced and treated by the same methods. Other factors play important roles: (i) the way the CNT electrodes are prepared, (ii) the size (surface and thickness) and the porosity of these electrodes, (iii) the nature of the electrolyte, and finally (iv) all the selected parameters for the electrochemical tests (current density, voltage range, and scanning rate in cyclic voltammetry, relaxation time in GITT or PITT,...). The combination of all these variable factors is so broad that it is not so surprising to notice discrepancies. Nevertheless, some general trends can be drawn.

6.3.1. Multiwalled Carbon Nanotubes

Typical $E = f(Q)$ curves [133, 165], of the first discharge and of the subsequent charge and discharge, are reported in Figure 16. (N.B. Basically $E = f(Q)$ is obtained by the application of a current density in the order of 5 to 10 mA g^{-1} of nanotubes.) These data were collected on MWCNTs produced by the electric arc (Fig. 15a) and by catalytic decomposition (Fig. 16b) synthesis methods. From these plots, it is possible to determine the irreversible and reversible capacity. It can be noticed that they vary greatly from one sample to another. Electric arc MWCNTs exhibit much lower reversible ($Q_{rev} = 145$ mAh g^{-1}) and irreversible ($Q_{irrev} = 190$ mAh g^{-1}) capacities compared to catalytic decomposition MWCNTs ($Q_{rev} = 190$ mAh g^{-1} and $Q_{irrev} = 1150$ mAh g^{-1}). It is noteworthy that very similar $E = f(Q)$ curves were reported elsewhere [23, 60, 154], except that in some cases reversible capacities as high as about 400 mAh g^{-1} were obtained [134, 155].

In almost every case, we can observe that the higher the irreversible capacity, the higher the initial reversible capacity. However, it seems that a high initial capacity is followed by a more important decrease of the reversible capacity upon cycling. Basically, it is observed that the irreversible capacity is directly related to the specific area of the sample whereas the reversible capacity is clearly dependent on the ordering degree of the MWCNTs. When the nanotubes are treated at high temperature, the suppression of the physical defects located at the sidewalls, as well as at the inner

tube surface, is associated with a significant loss of reversible capacity [23].

A deeper analysis of the $E = f(Q)$ or $dQ/dE = f(Q)$ curves emphasizes that the only plateau noticed appears at potentials higher than 0.5 V during the first discharge and vanishes afterward. We demonstrated from various analysis methods that at potentials higher than 0.2–0.1 V, though the first discharge capacity is already large, there is no trace of intercalated Li inside the tube [133]. A pseudo-plateau (not really flat) was observed in electric arc MWCNTs, at about 0.1 V. It was assigned to the intercalation of Li$^+$ into the CNT structure which turns out, in that case, to look like a necklace of pearls (Fig. 17) as was already observed by chemical insertion [144]. The only way to account for this particular shape is to assume that Li$^+$ penetrates the tube via the physical defects present at the surface. The ~0.1 V pseudo-plateau seems not to be exhibited by catalytic decomposition MWCNTs (Fig. 16b). The different mechanisms of insertion/intercalation in MWCNTs produced by electric arc and catalytic decomposition can be seen on the XRD patterns of the samples at the end of the discharge (Fig. 18). Electric arc nanotubes exhibit new diffraction peaks which can be assigned to the occurrence of a new phase similar to the stage 2 of graphite [61, 116, 117]. On the contrary, no new peak appears in the lithiated MWCNTs obtained by catalytic decomposition. The same trends are observed from the Raman (Fig. 18) and from NMR (Fig. 19) spectra.

Mukhopadhyay et al. [160] report, in a recent article, cyclic voltammetry obtained at a very low scanning rate (4 μV s^{-1}) on electric arc MWCNTs where distinct peaks occur in the 0–0.3 V potential range. These peaks are interpreted as arising from various intercalation stages. This is the only work where such a graphitelike behavior is seen. Nevertheless, the reversible capacity (Q equals about
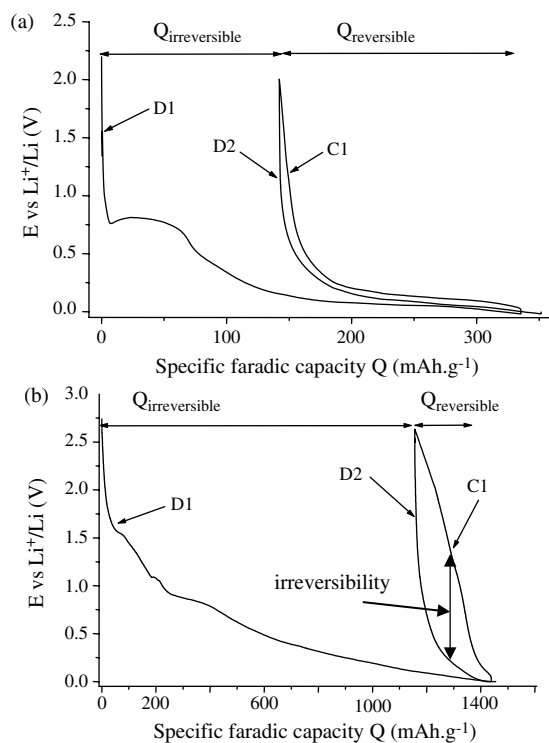

(a)

(b)

Figure 16. First discharge (D1), charge (C1), and second discharge (D2) obtained on as-synthesized MWCNTs produced by the electric arc technique (a) and by catalytic decomposition of acetylene (b). One can note the huge irreversible faradic capacity measured in the second case along with a larger hysteresis. In both cases, the current density applied to the cell was equal to 10 mA g^{-1}.
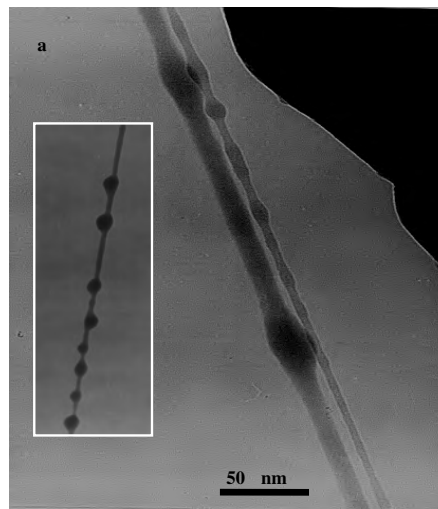

Figure 17. TEM picture of an intercalated MWCNT produced by the arc electric method. The "necklace" morphology indicates that Li$^+$ intercalates the tube through its sidewall defects and not the central channel. This intercalation mechanism leads to weak reversible capacities but to weak overvoltages (see Fig. 16a) as in graphite. Reprinted with permission from [133], G. Maurin et al., *Chem. Phys. Lett.* 312, 14 (1999). © 1999, Elsevier Science.
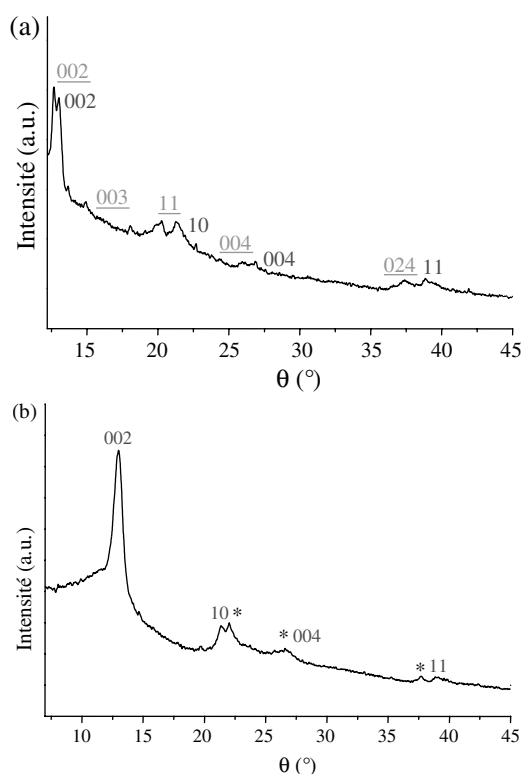
Figure 18. X-ray patterns obtained on fully lithiated as-synthesized MWCNTs produced by the electric arc technique (a) and by catalytic decomposition of acetylene (b). ∗ denotes the peaks attributed to the remaining cobalt particles. Comparison with XRD patterns plotted in Figure 10 shows the occurrence of new peaks in case (underlined) (a) but not in case (b).
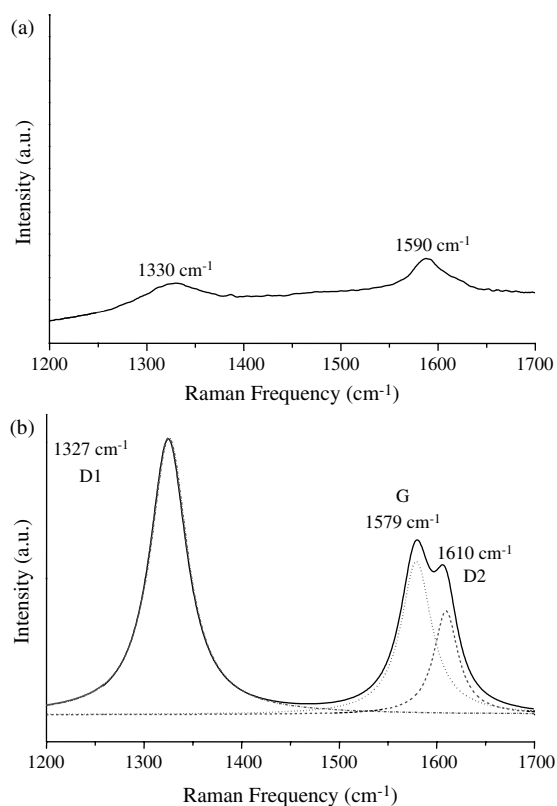
Figure 19. Micro-Raman (confocal technique) obtained on fully lithiated as-synthesized MWCNTs produced by the electric arc technique (a) and by catalytic decomposition of acetylene (b). Comparison with Figure 12 denotes a significant variation of the Raman signal of the electric arc nanotubes while the response of the catalytic decomposition nanotubes remains unchanged.

160 mAh g^{-1}) measured on these MWCNTs is again much lower than in graphite.

The intercalation of Li^+ in MWCNTs would not always be, as we could have expected, similar to the intercalation in graphite. Apart from the work of Mukhopadhyay et al. no intercalation state has ever been observed. This result is different from the observation reported on the chemical insertion where some well defined intercalated phases become visible.

The correlation between the specific area and the capacity is likely to be due to the irreversible and reversible redox reactions of lithium with the surface of the tube. The origin of the irreversible capacity is usually assumed to be related to the formation of a passivating layer, the so-called solid electrolyte interphase (SEI). It can be made of various lithium alkyl carbonates formed by the redox reaction of Li^+ with the solvent molecules [167, 168] or from the reduction of some oxygenated groups attached to the surface of the CNTs. In the later case, lithium oxide can even be formed [130, 169]. The formation of these compounds is highly irreversible and usually occurs at potentials ranging from 3 to 0.5 V. The better resolution of the $E = f(Q)$ curves (or its derivative) obtained by GITT enables us to point out the subsequent redox steps associated with the formation of SEI [70].

The other noticeable feature of the Li^+ insertion in MWCNTs, compared to graphite, is the large hysteresis

measured between the discharge and charge potential (see Fig. 16). It is quite clear that the amplitude of this effect is much larger when the irreversible capacity is high. Therefore, it must also be connected to some reactions at the surface of the CNTs, that is to say, to SEI. As SEI contains species which are electronically insulating, it strongly limits the electron transfer between Li^+ and the carbon structure. This obstruction implies an increase of the redox potential, so-called overvoltage, which makes the system unsuitable for industrial applications. Frackowiak et al. [23] have also performed cyclic voltammetry on their low temperature treated (900 °C) MWCNTs and have detected a strong capacitance character in the 1.5–3 V potential range. This capacitance, equal to about 35 F g^{-1}, acts as a thermokinetic barrier which hinders the electronic transfer and thus enhances the overvoltage. Although this effect is undesirable for battery applications, it can be of great relevance for supercapacitors [166].

The increase of capacity induced by the surface chemical activity and the physical defects of the tubes incited some authors [48, 157] to open their MWCNTs by mechanical treatment. Unfortunately, though these treatments increased the irreversible capacity, the reversible capacity remains at about the same level as the closed MWCNTs.

The evolution of the Li^+ diffusion coefficient upon deinsertion (Fig. 20a), calculated from GITT experiments in
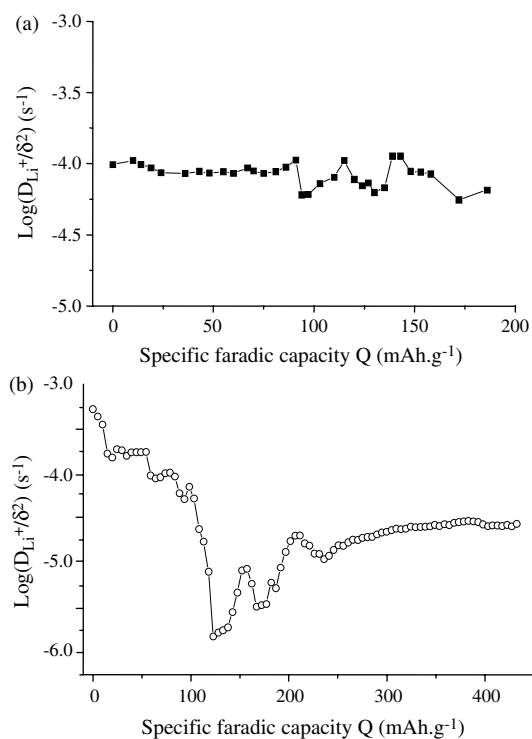
Figure 20. Diffusion coefficient as a function of the specific faradic capacity measured from the GITT method on as-synthesized MWCNTs produced by the electric arc technique (a) and by catalytic decomposition of acetylene (b). The diffusion coefficient is given with respect to δ, the length of the diffusion path. GITT was performed, upon charge, by applying periodically a current density of 5 mA g^{-1} for 1 hour followed by 2 hours of relaxation.

MWCNTs produced by electric arc, shows no strong dependence [70]. This behavior is different for graphite which exhibits a significant decrease of D_{li+} along with the occurrence of the intercalation stages [170–173]. This decrease is assumed to arise from the electrostatic repulsion between the intercalated Li$^+$.

The same experiment undertaken on MWCNTs produced by chemical vapor deposition shows a rather distinct behavior with D_{li+} minima (Fig. 20b). These minima, already observed in some disorder carbons [174], can be ascribed to the different redox kinetics associated with distinct adsorption sites (i.e., functional groups or interstices) present at the surface of the tube. This result corroborates that the Li$^+$ insertion is, in that case, mainly related to the redox reactions taking place at the surface of the tube.

To sum, Li$^+$ insertion in MWCNTs is much more interrelated to the diverse surface reactions than to a "true" intercalation between the graphene layers or inside the central channel of the MWCNT. Although there is some evidence for Li$^+$ intercalation and for the occurrence of different intercalated phases, the reversible capacity, in that case, is very low compared to the insertion at the surfaces and much lower than the capacity (i.e., 372 mAh g^{-1}) corresponding to the intercalated LiC$_6$ graphite-based compound. The contrast of behavior between the electric arc and CVD MWCNTs could be due to the fact that intercalation is possible only if the sidewalls have physical defects but no chem-

ical groups attached at the surface. The oxygenated groups, present in much higher quantity on the CVD MWCNTs, lead to the formation of SEI which hinders the Li$^+$ diffusion toward the sidewall of the tubes.

Finally, it must be emphasized that the experimental observations summarized in this section are supported by the theoretical predictions.

6.3.2. Single Walled Carbon Nanotubes

The $E = f(Q)$ curves reported on SWCNTs look like those exhibited by MWCNTs (see Fig. 16) [49, 57, 156]. The first discharge is characterized by rapid decrease of the potential, then a plateau at around 1 V, and finally a slow decrease toward 0 V. However, in most of the reported results, the 1 V plateau is much longer than for MWCNTs. It can cover several hundreds of mAh g^{-1}. As for MWCNTs, this plateau which does not occur on the subsequent charges and discharges can be assigned to the formation of SEI. This essentially contributes to the irreversible capacity which turns out in some cases to be as large as 1000 mAh g^{-1}. This huge capacity is directly associated with the high specific surface of SWCNTs which is on the order of 300 m^2 g^{-1} (compared to the 10–20 m^2 g^{-1} generally reported for MWCNTs). The electrochemical reaction involving functional groups at the SWCNT surface is demonstrated by Barisci et al. [58] from cyclic voltammetry in aqueous and organic solvent and from the measurement of SWCNT electrical resistance upon Li$^+$ insertion in two different organic solvent [76]. Nevertheless, it is clear from all the published results that the reversible capacity is larger in SWCNTs than in MWCNTs. Values of about 500 mAh g^{-1} are often obtained in purified but nontreated SWCNTs. Because of the important surface electrochemical activity of SWCNTs, large hysteresis is always observed between the charge and discharge potential. Again, it seems that a correlation exists between the irreversible capacity and the amplitude of the hysteresis which makes the SWCNTs investigated to date unusable for battery applications. Meanwhile, attempts to increase the reversible capacity were carried out by opening or cutting the samples. Although this solution yielded unsatisfactory results for MWCNTs, it appeared to be very efficient in the case of SWCNTs. First, Gao et al. [49] measured much higher reversible capacities upon processing their SWCNTs by ball milling. So reversible capacities as high as 1000 mAh g^{-1} were obtained. Besides, the irreversible capacity was lowered as a consequence of the specific surface decrease induced by the ball milling process. This result would mean that the opening of the tube allows Li$^+$ to reversibly intercalate the central core of SWCNTs. This assumption is in agreement with the theoretical calculations [153]. In a more recent article, Shimoda et al. [46] reported reversible capacities of about 700 mAh g^{-1} (corresponding to the LiC$_3$ stoichiometry) when SWCNTs are etched by strong acidic treatment which opens the tube and reduces their length. It is remarkable that, for the first time, two potential plateaus clearly appear on the $E = f(Q)$ plots at the second and further discharges when SWCNT lengths are shortened to 0.5 μm. These plateaus would then be the signature of staging intercalation mechanisms and would then confirm that the central core of the tube can be occupied

by Li$^+$ when SWCNTs are open and short enough. However, as these plateaus were not reported after ball milling which is also assumed to open the tubes, confirmation of Li$^+$ intercalation in the central core and of defined staging stoichiometry is still needed.

When SWCNTs have close caps, *in-situ* XRD studies [76] showed that the insertion of Li$^+$ irreversibly destroyed the bundle triangular structure. This indicates that Li$^+$ is inserted in the interstices of the bundles, strongly modifies the symmetry of the cohesion forces which ensure the stability of the bundles, and as a consequence breaks their organized structure. It is noteworthy that the triangular structure which is not recovered upon deinsertion can be recovered after a thermal treatment.

No kinetic investigation has been reported from GITT or PITT measurements. However, electrochemical impedance spectroscopy has been used [67]. A diffusion coefficient equal to about 10^{-12} cm^2 s^{-1} was thus determined on nontreated SWCNTs and assigned to the kinetic of insertion into the interstices or at the surface of the SWCNT bundle. This result supports the assumption that Li$^+$ is only inserted at the external and internal surface of the bundles but not into the central channel of the pristine SWCNTs.

6.3.3. Discussion

To summarize, it can be said that nontreated SWCNTs behave very similarly to MWCNTs since Li$^+$ electrochemical insertion mainly proceeds at the external surface of the tube. The increase of reversible and irreversible capacities would arise from the higher specific area of the SWCNTs, but it is likely that the intercalation mechanisms which involve, in both cases, the reaction of Li$^+$ with the CNT external surface, and more particularly with the chemical groups attached to it, are the same. Intercalation in MWCNTs, via the defects of the external wall, has also been reported, but it appears as a secondary phenomena which does not enhance significantly the capacity. However, intercalation of Li$^+$ into the central channel of SWCNTs when they are broken by mechanical treatments or etched by a strong acid solution seems possible and related to double faradic capacity, but direct evidence has not been definitively provided yet.

In almost every case, overvoltage appears to be very large. This characteristic which seems to increase with the reversible capacity impedes the use of CNTs in Li$^+$ batteries. So far, though it was shown that the reversible capacity was maintained upon a few charge/discharge cycles, no data have been reported about the "real" cycling life of CNTs. Industrial purposes require up to 1000 cycles. Longer tests then have to be carried out in order to prove the ability of CNTs to sustain such a long electrochemical life.

Finally, it can be emphasized that chemical and electrochemical routes for Li$^+$ intercalation yield different results. None of the well defined stoichiometry reported for the chemical insertion has been reported for the electrochemical one. This could result from (i) the chemical reaction which implies the nanotube surface and the organic solvent used for the electrochemical route and/or (ii) the fact that Li, in the vapor or a liquid state, used in some chemical insertion does not have the same chemical potential as Li$^+$ dissolved in the organic electrolyte.

7. CONCLUSION

Although we now have experimental evidence, supported by theoretical calculations, that Li$^+$ can undoubtedly be electrochemically inserted into CNTs, it remains very difficult to provide a simple and single image of the mechanisms involved. By contrast with the case of graphite, it is not yet clearly established whether CNTs can be intercalated step by step with the occurrence of a well defined state. In this way, only a few indications are given by the various authors and it stays a subject of controversy.

This lack of clear understanding lies in the strong difficulty to compare the various samples with each other. The ways they have been produced, purified, and eventually treated create so many different configurations at the molecular scale that disparities occur. We are then facing, to some extent, the same difficulties that have already been encountered about the lithium insertion in the disordered carbons for which various interpretation can be given [175].

However, some general trends can be drawn. First of all, the specific faradic capacities Q, both reversible and irreversible, appear to be closely related to the specific area of the studied sample. This indicates that the nature of the physical and chemical defects existing at the surface of the tubes plays a key role both in the quantity of lithium which can be reversibly inserted and in the insertion mechanism itself. The formation of the solid electrolyte interphase, by reaction of the nanotube surface with the organic electrolyte, would control most of the insertion process. If the nanotube surface is covered with large quantities of oxygenated groups then the SEI is likely to be thick and uniform and thus to act as a barrier which hinders lithium intercalation. For instance, Li$^+$ intercalation between the walls of MWCNTs has been observed but it was on nontreated tubes produced by the electric arc method, that is to say, on MWCNTs having the least possible amount of oxygenated groups at their surface. Unfortunately, the amount of intercalated lithium was much lower than in graphite because the tubes do not have many "gates" through which Li$^+$ can penetrate the structure. The idea was then to create doorways (i.e., physical defects) by opening and cutting the tubes, but the procedures used, if they effectively create defects, also increase the chance to cover the tubes with oxygenated group which will then block the intercalation. In principle, it is possible to get rid of the oxygenated group by treating the tubes at high temperature under a controlled reducing atmosphere. However, such a treatment, if efficient enough, would help the tube to cure its physical defects and as a consequence to close the access to its inner parts. The solution of this dilemma is rather intricate and, as far as we know, has not be found yet. Therefore, one could take advantage of the fact that a non-negligible part of the lithium insertion at the surface is reversible. CNTs could then be used, not because of their apparently open hosting structure as was thought at the beginning, but thanks to their surface properties. New forms of "carbon-nanotube-like" structures with more favorable mesoporosity and surface reactivity are under investigation [176]. Larger capacities have even been recently reported on oxidized CNTs [177]. The major drawback is, however, that the reversible faradic capacity due to the insertion at

the surface goes along with high thermodynamic irreversibility (i.e., the overvoltage), which makes their application in Li-ion batteries irrelevant.

The solution could then be to produce CNTs coated or assembled with chemically inert (viz. the electrolyte) compounds which would be capable of inserting lithium in a truly reversible manner. In such a case, CNTs could not be seen as the electroactive matter but as a highly conducting substrate able to drain electrons from the active matter to the external circuit. Recent examples have been reported where SWCNTs are mixed with vanadium oxide [178] and Sn_2Sb [163]. Further, the possibilities provided by the electrofunctionalization [54] or metal electrodeposition techniques should open new investigation routes.

Anyway, as was outlined in the Introduction, we are still far from the industrial production of CNTs, doped or non-doped, that will be able to supply materials whose the ratio performance/price could compete with the actual carbons used in lithium-ion batteries.

This is a rather pessimistic view, but it only concerns the main application we could have expected for CNTs. However, the electrochemical insertion of lithium, or other species, into the various forms of CNTs, especially where they are treated, remains an exciting subject for fundamental research which will surely open new perspectives for various applications.

GLOSSARY

Ab initio OR "from the beginning." Resolution of Schrödinger's equation (fundamental equation of quantum mechanics) when only the atomic number of the considered atoms, the mass, and the charge of the electron are input into the calculation.

Alkali The family name of the elements (from lithium to cesium) of the first column of the periodic table.

Alumina Solid compound whose chemical formula is Al_2O_3. It exists under various crystalline forms.

Amorphous It qualifies the absence of order or symmetry of a solid network. Basically, it is the opposite of crystalline.

Carbon nanotube (CNT) A nanoscopic tubular structure made of carbon (see Fig. 2).

Catalyst A chemical compound that makes possible a chemical reaction which would not take place or would be too slow without its presence.

Chemical vapor deposition (CVD) A widely used synthesis technique for producing thin films or nanostructures. Basically, it consists of mixing gases in a reactor under well controlled pressure and temperature conditions such as they react or crack to form a solid or a mixture of solid phases. Schematically, the reaction proceeds i) in the gas phase and the materials thus formed are deposited onto the wall of the reactor or ii) it takes place at the surface of a substrate placed into the reactor and maintained at a suitable temperature.

Cluster Small particle made of a few atoms.

Current density Defined by the ratio of the current over the cross-sectional surface of the electrode. In principle, electrochemical capacity should only be compared for a given value of current density. Also bear in mind that the surface of the electrode is a parameter which is not as simple as it sounds, especially for porous electrodes.

D_{li^+} Diffusion coefficient of Li^+ ($m^2 s^{-1}$). The diffusion coefficient, defined from Ficks' laws, accounts for the ability of a given species (i.e., Li^+) to migrate into a given matter. It is the coefficient of proportionality between the current density induced by the displacement of Li^+ and the force (electric field, gradient of concentration, . . .) which gives rise to this displacement.

DMC, EC, PC Dimethyl carbonate, ethylene carbonate, and propylene carbonate are water-free organic solvents with high dielectric constants (>40). They can then dissolve a reasonably high content of lithium salts and therefore be used as electrolytes for lithium batteries. Furthermore, they are relatively inert viz. the materials used in the battery and they are neither reduced nor oxidized upon charge or discharge of the battery (under normal operation conditions).

Double layer capacitance Capacitance formed by one layer of ions adsorbed at the surface of the current collector and whose the charge is opposite to the collector.

Electrochemical It concerns chemical reactions which are controlled by electron exchange at a current collector (usually a metal).

Electrochemical potential (V) (E) It characterizes the ability of a species under given conditions (temperature, concentration, oxidation state) to give (i.e., to be oxidized) or to accept (i.e., to be reduced) electrons. In other words, it schematically corresponds to the electrical measurement of the energy needed for the oxidation or reduction of a given species.

Electrolysis When a chemical compound is decomposed by oxidation or reduction (i.e., water electrolysis gives oxygen and hydrogen gases).

Electrolyte It can be a solution, a molten salt, or a solid containing mobile ions. Its ionic conductivity must be as high as possible whereas it must be an electronic insulator.

Electron energy loss spectroscopy (EELS) It is an electron beam microanalysis based on the energy loss (inelastic diffusion) of the electrons which are transmitted through the sample. The energy loss spectrum exhibits peaks which identify the elements present in the sample. This analysis method is coupled with TEM.

Electron spin resonance (ESR) A method whose principle is to measure the response of unpaired electrons placed in a magnetic field.

Energy dispersive X-ray spectrometry (EDX) It is an electron beam microanalysis based on the excitation of characteristic X-rays which identify the element present (atomic number >3) and whose the intensity is proportional to the relative amount of the investigated element. This analysis method is often coupled with SEM.

Galvanostatic intermittent titration technique (GITT) It is a electrochemical method which consists of applying to an electrode a constant current during a short period of time and then of measuring the evolution of the electrode potential when the current is switched off. This operation can be repeated as many times as necessary. In other words,

it is a step by step constant current charge or discharge procedure.

Graphite This is the most stable form of crystallized carbon. It is a good electronic conductor, it is highly inert viz. many chemical compounds. Its layered crystalline structure allows the intercalation of small ions and chemical compounds (see Fig. 1b).

Hartree–Fock Method for the resolution of Schrödinger's equation. It can also be called self-consistent field method. It is a semi-empirical method where experimental values as ionization energies are input into the calculation.

Insertion When molecules, atoms, or ions penetrate the structure of a given solid. Structure as to be understood in a very broad meaning; it can be the structure at the atomic scale (insertion in empty sites in the bulk or at the surface of the solid network) as well as at the nanometric scale (nano- or mesoporosity, large defects at the surface, . . .).

Intercalation As for insertion but in a more restricted way. Intercalation is limited to the insertion of molecules, atoms, or ions into the empty interlayer space of a layered structure. In CNTs, it corresponds to the insertion in between the walls of MWCNTs or in the central channel of MWCNTs or SWCNTs.

Laser ablation Sublimation of a solid compound when it is irradiated with a laser beam.

Lithium It is the first alkali metal. Its atomic mass is 7 and its ground electronic state configuration is $1s^2\ 2s^1$. Its ability to lose one electron (to be oxidized to Li^+) is very high, so that its redox potential ($E_0 = 3.04$ V) makes it the most appealing element for energy storage.

Multiwalled carbon nanotubes (MWCNT) Made of several single walled carbon nanotubes fitted into each other such as in a nesting or "Russian dolls" pattern (see Fig. 4).

Nuclear magnetic resonance (NMR) A widely used method whose principle is to measure the response of a given atomic nucleus when it is placed in a magnetic field. This response strongly depends on the atomic electronic state and its atomic environment, hence yielding fruitful information about its surrounding structure.

Oxidation Chemical reaction which corresponds to a loss of electron.

Polytetrafluoroethylene (PTFE) Also known as Teflon®. It is a very resistive polymer. It is chemically and electrochemically inert. Further, it exists in liquid suspension which can be readily mixed, in very small quantity, to a powder in order to form a paste. Once the paste is dried, it forms a binding network which ensures cohesion between the grains of the powder, giving rise to a material with a reasonably good elasticity. It is very often used as a binder in electrodes.

Potentiostatic intermittent titration technique (PITT) As for GITT, except that in that case, the electrode is submitted to a constant potential during a given period of time and the information is contained in the time evolution of the current.

Pyrolysis When a compound is thermally decomposed in the absence of oxygen.

Q Faradic capacity (C or Ah; 1 Ah = 3600 C). It corresponds to the quantity of electrons released or received by the electrode. It is calculated by integrating the product $i\ dt$.

Raman spectroscopy The Raman effect is an inelastic scattering of light. It occurs when energy is transferred between the light and the vibrational modes of the solid network or of the molecule.

Reduction Chemical reaction which corresponds to a gain of electron.

Scanning electron microscopy (SEM) Images of a sample from the secondary or elastically backscattered electrons when it is submitted to an electron beam. The resolution is about 2–3 nm.

Silica Solid compound whose chemical formula is SiO_2. It exists under various crystalline or amorphous forms.

Single walled carbon nanotubes (SWCNT) A narrow strip of nanoscale graphene rolled up into a seamless cylinder (see Fig. 2).

Solid electrolyte interphase (SEI) The phase formed at the interface between the electrode material and the electrolyte. This phase is not inert and can play a key role on the electrochemical behavior of the electrode.

Sublimation Corresponds to the solid to gas transformation of a pure compound. Sublimation depends on the temperature and the pressure.

Supercapacitor Power source made of high surface electrodes separated by an electrolyte. When an electric field is applied, the system is polarized by the accumulation of ions at the surface of the electrodes. This usually corresponds to a weak amount of energy. However, this system is capable of releasing, when short-circuited, the accumulated charges during a very short time and hence of giving rise to high power delivery.

Transmission electron microscopy (TEM) Images of a sample when an electron beam is focalized and sent through it. The sample dimension must not exceed 1 μm thickness. The resolution is about 0.2 nm.

X-ray diffraction (XRD) Probably the most widely used technique for studying atoms arrangement in solids. It is based on the diffraction principle of waves. In that case, the wavelength is in the order of the atomic scale so that the diffraction reflects the atomic building of the investigated matter. Structure of crystals is determined by X-ray diffraction.

X-ray photoelectron spectroscopy (XPS) X-ray beam microanalysis based on the excitation of characteristic photoelectrons which identify the element present and its environment.

Zeolite Porous solid compounds built from silica and alumina units. It exists under various crystalline forms which can be found in soils and which can be synthesized.

ACKNOWLEDGMENTS

REFERENCES

1. *Physics World* 15–7, 25 (2002).
2. "Modern Batteries: An Introduction to Electrochemical Power Sources" (C. A. Vincent and B. Scrosati, Eds.). Arnold, London, 1997.
3. Z. S. Wronski, *Int. Mater. Rev.* 46, 1 (2001).
4. Y. Nishi, *J. Power Sources* 100, 101 (2001).
5. J. R. Dahn, W. Xing, and Y. Gao, *Carbon* 35–6, 825 (1997).
6. H. W. Kroto, J. R. Heath, S. C. O'Brien, R. F. Curl, and R. E. Smalley, *Nature* 318, 162 (1985).
7. S. Iijima, *Nature* 354, 56 (1991).
8. R. Baughman, A. A. Zakhidov, and W. A. de Heer, *Science* 297, 787 (2002).
9. General information about carbon nanotubes and suppliers can be also found at http://www.personal.rdg.ac.uk/~scsharip/tubebooks.htm.
10. See the special issue on carbon nanotubes, *Carbon* 40 (2002).
11. C. N. R. Rao, B. C. Satishkumar, A. Govindaraj, and M. Nath, *Chem. Phys. Chem.* 2, 78 (2001).
12. P. M. Ajayan, *Chem. Rev.* 99, 1787 (1999).
13. L. Duclaux, *Carbon* 40, 1751 (2002).
14. M. S. Dresselhaus, G. Dresselhaus, and P. E. Eklund, "Science of Fullerene and Carbon Nanotubes." Academic Press, San Diego, 1996.
15. T. W. Ebbesen and P. M. Ajayan, *Nature* 358, 220 (1992).
16. S. Iijima and T. Ichihashi, *Nature* 363, 603 (1993).
17. D. S. Bethune, C. H. Kiang, M. S. de Vries, G. Gorman, R. Savoy, J. Vasquez, and R. Beyers, *Nature* 363, 605 (1993).
18. J. E. Fischer, *Chem. Innov.* 30, 21 (2000).
19. A. Hassanien, M. Tokumoto, Y. Kumazawa, Y. Maniwa, S. Suzuki, and Y. Achiba, *Appl. Phys. Lett.* 73, 3839 (1998).
20. A. Thess, R. Lee, P. Nikolaev, H. Dai, P. Petit, J. Robert, C. Xu, Y. H. Lee, S. G. Kim, A. G. Rinzler, D. T. Colbert, G. E. Scuseria, D. Tomanek, J. E. Fischer, and R. Smalley, *Science* 273, 483 (1996).
21. C. Journet, W. K. Maser, P. Bernier, A. Loiseau, M. Lamy de la Chapelle, S. Lefrant, P. Deniard, R. Lee, and J. E. Fischer, *Nature* 388, 756 (1997).
22. O. Zhou, R. M. Fleming, D. W. Murphy, C. H. Chen, R. C. Haddon, A. P. Ramirez, and S. H. Glarum, *Science* 263, 1744 (1994).
23. E. Frackowiak, S. Gautier, H. Gaucher, S. Bonnamy, and F. Béguin, *Carbon* 37, 61 (1999).
24. Y. Saito, T. Yoshikawa, S. Bandow, M. Tomita, and T. Hayashi, *Phys. Rev. B* 48, 1907 (1993).
25. S. Suzuki and M. Tomita, *J. Appl. Phys.* 79, 3739 (1996).
26. A. Hirsh, *Angew. Chem. Int. Ed.* 41, 1853 (2002).
27. W. Krätschmer, L. D. Lamb, K. Fostiropoulos, and D. R. Huffman, *Nature* 347, 354 (1990).
28. T. Guo, P. Nikolaev, A. Thess, D. T. Colbert, and R. E. Smalley, *Chem. Phys. Lett.* 243, 49 (1995).
29. C. Bower, S. Suzuki, K. Tanigaki, and O. Zhou, *Appl. Phys. A* 67, 47 (1998).
30. D. Laplaze, P. Bernier, W. K. Maser, G. Flamant, T. Guillard, and A. Loiseau, *Carbon* 36, 685 (1998).
31. M. J. Yacaman, M. M. Yoshida, L. Rendon, and J. G. Santiesteban, *Appl. Phys. Lett.* 62, 202 (1993).
32. A. Hamwi, H. Alvergnat, S. Bonnamy, and F. Beguin, *Carbon* 35, 723 (1997).
33. G. Che, B. B. Lakshmi, E. R. Fisher, and C. R. Martin, *Nature* 393, 346 (1998).
34. P. Nikolaev, M. Bronikowski, R. K. Bradley, F. Rohmund, D. T. Colbert, K. A. Smith, and R. E. Smalley, *Chem. Phys. Lett.* 313, 91 (1999).
35. L. C. Qin, *J. Mater. Sci. Lett.* 16, 457 (1997).
36. W. K. Hsu, J. P. Hare, M. Terrones, H. W. Kroto, D. R. M. Walton, and P. J. F. Harris, *Nature* 377, 687 (1995).
37. Y. L. Li, Y. D. Yu, and Y. Liang, *J. Mater. Res.* 12, 1678 (1997).
38. M. Glerup, H. Kanzow, R. Almerac, and P. Bernier, *AIP Conf. Proc.* 633, 161 (2002).
39. I. W. Chiang, B. E. Brinson, R. E. Smalley, J. L. Margrave, and R. H. Hauge, *J. Phys. Chem. B* 105, 1157 (2001).
40. J. F. Colomer, P. Piedigrosso, I. Willems, C. Journet, P. Bernier, G. Van Tendeloo, A. Fonseca, and J. B. Nagy, *J. Chem. Soc. Faraday Trans.* 94, 3753 (1998).
41. K. B. Shemilov, R. O. Esenaliev, A. G. Rinzler, C. B. Huffmann, and R. E. Smalley, *Chem. Phys. Lett.* 282, 429 (1998).
42. J. Aihara, *J. Phys. Chem.* 98, 9773 (1994).
43. S. M. Lee, Y. H. Lee, Y. G. Hwang, J. R. Hahn, and H. Kang, *Phys. Rev. Lett.* 82, 217 (1999).
44. T. Kar, J. Pattanayak, and S. Scheiner, *J. Phys. Chem. A* 105, 10397 (2001).
45. G. Z. Yue, Q. Qiu, B. Goa, Y. Cheng, J. Zhang, H. Shimoda, S. Chang, J. P. Lu, and O. Zhou, *Appl. Phys. Lett.* 81, 355 (2002).
46. H. Shimoda, B. Gao, X. P. Tang, A. Kleinhammes, L. Fleimg, Y. Wu, and O. Zhou, *Phys. Rev. Lett.* 88, 015502 (2002).
47. P. M. Ajayan, T. Ichihashi, and S. Iijima, *Nature* 162, 522 (1993).
48. G. Maurin, I. Stepanek, P. Bernier, J. F. Colomer, J. B. Nagy, and F. Henn, *Carbon* 39, 1273 (2001).
49. B. Gao, A. Kleinhammes, X. P. Tang, C. Bower, L. Fleming, Y. Wu, and O. Zhou, *Chem. Phys. Lett.* 307, 153 (1999).
50. D. B. Mawhinney, V. Naumenko, A. Kuznetsova, J. T. Yates, Jr., J. Liu, and R. E. Smalley, *Chem. Phys. Lett.* 324, 213 (2000).
51. E. T. Mickelson, C. B. Huffman, A. G. Rinzler, R. E. Smalley, R. H. Hauge, and J. L. Margave, *Chem. Phys. Lett.* 296, 188 (1998).
52. H. Touhara, J. Inahara, T. Mizuno, Y. Yokoyama, S. Okanoa, K. Yanagiuch, I. Mukopadhyay, S. Kawasaki, F. Okino, H. Shirai, W. H. Xu, and A. Tomita, *J. Fluor. Chem.* 114, 181 (2002).
53. C. Velasco Santos, A. L. Martinez Hernandez, M. Lozada Cassou, A. Alvarez Castillo, and V. M. Castaño, *Nanotechnology* 13, 495 (2002).
54. J. L. Bahr, J. Yang, D. Kosynkin, M. J. Bronikowski, R. E. Smalley, and J. T. Tour, *J. Am. Chem. Soc.* 123, 6536 (2001).
55. M. Sano, A. Kamino, J. Okamura, and S. Shinkai, *J. Inclusion Phenom. Macrocyclic Chem.* 41, 49 (2001).
56. As Q is directly related to the amount of Li inserted into the carbon, the coordinate Q can be replaced by the stoichiometric factor $x(LiC_x)$.
57. A. S. Claye, J. E. Fischer, C. B. Huffmann, A. G. Rinzler, and R. E. Smalley, *J. Electrochem. Soc.* 147, 2845 (2000).
58. J. N. Barisci, G. G. Wallace, and R. H. Baughman, *J. Electrochem. Soc.* 147, 4580 (2000).
59. I. Mukhopadhyay, N. Hoshino, S. Kawasaki, W. K. Hsu, and H. Touhara, *J. Electrochem. Soc.* 149, A39 (2002).
60. Z. Yang and H. Wu, *Mater. Chem.* 71, 7 (2001).
61. J. R. Dahn, *Phys. Rev. B* 44, 9170 (1991).
62. M. D. Levi, E. A. Levi, and D. Aurbach, *J. Electroanal. Chem.* 421, 89 (1997)
63. W. Weppner and R. A. Huggins, *J. Electrochem. Soc.* 124, 1569 (1977).
64. P. Papanek, M. Radosavljevic, and J. E. Fischer, *Chem. Mater.* 8, 1519 (1996).
65. H. C. Shin, M. Liu, B. Sadanadan, and A. M. Rao, *J. Power Sources* 112, 216 (2002).
66. C. Ho, I. D. Raistrick, and R. A. Huggins, *J. Electrochem. Soc.* 127, 343 (1980).
67. A. Claye, J. E. Fischer, and A. Metrot, *Chem. Phys. Lett.* 330, 61 (2000).
68. Z. Yang and H. Wu, *Chem. Phys. Lett.* 343, 235 (2001).
69. A. Honders, J. M. der Kinderen, A. H. Van Heeren, J. H. W. de Wit, and G. H. J. Broers, *Solid State Ion.* 15, 265 (1985).
70. G. Maurin, Ch. Bousquet, F. Henn, and B. Simon, *Ionics* 5, 156 (1999).

71. D. D. Aurbach, J. S. Gnanaraj, M. D. Levi, E. A. Levi, J. E. Fischer, and A. Claye, *J. Power Sources* 97–98, 92 (2001).

72. M. Holzinger, A. Hirsch, F. Hennrich, M. M. Kappes, A. Dziakova, L. Ley, and R. Graupner, *AIP Conf. Proc.* 633, 96 (2002).

73. M. Bockrath, J. Hone, A. Zettl, P. L. Mc Ewen, A. G. Rinzler, and R. Smalley, *Phys. Rev. B* 61, R 10606 (2000).

74. R. S. Lee, H. J. Kim, J. E. Fischer, J. Lefevre, M. Radosavljevic, and J. Hone, *Phys. Rev. B* 61, 4526 (2000).

75. M. Baxendale, V. Z. Mordkovitch, and S. Yoshumura, *Phys. Rev. B* 56, 2161 (1997).

76. A. Claye and J. E. Fischer, *Mol. Cryst. Liq. Cryst.* 340, 743 (2000).

77. W. Li, H. Zhang, C. Wang, Y. Zhang, L. Xu, K. Zhu, and S. Xie, *Appl. Phys. Lett.* 70, 2684 (1997).

78. J. Kastner, T. Pichler, H. Kuzmany, S. Curran, W. Blau, D. N. Weldon, M. Delamesiere, S. Draper, and H. Zandbergen, *Chem. Phys. Lett.* 221, 53 (1994).

79. H. Hiura, T. W. Ebbesen, K. Tanigaki, and H. Takahashi, *Chem. Phys. Lett.* 202, 509 (1993).

80. P. V. Huong, R. Cavagnat, P. M. Ajayan, and O. Stephan, *Phys. Rev. B* 51, 10048 (1995).

81. W. S. Bacsa, D. Ugarte, A. Chatelain, and W. A. de Heer, *Phys. Rev. B* 50, 15473 (1994).

82. P. C. Eklund, J. M. Holden, and R. A. Jishi, *Carbon* 33, 959 (1995).

83. A. M. Rao, P. C. Eklund, S. Bandow, A. Thess, and R. E. Smalley, *Nature* 388, 257 (1997).

84. S. Bandow, S. Asaka, Y. Saito, A. M. Rao, L. Grigorian, E. Richter, and P. C. Eklund, *Phys. Rev. Lett.* 80, 3779 (1998).

85. A. M. Rao, S. Bandow, E. Richter, and P. G. Eklund, *Thin Solid Films* 331, 141 (1998).

86. G. S. Duesberg, W. J. Blau, H. J. Byrne, J. Muster, M. Burghard, and S. Roth, *Chem. Phys. Lett.* 310, 8 (1999).

87. A. Claye, S. Rahman, J. E. Fischer, A Sirenko, G. U. Sumanasekera, and P. C. Eklund, *Chem. Phys. Lett.* 333, 16 (2001).

88. G. Maurin, Ch. Bousquet, F. Henn, P. Bernier, R. Almairac, and B. Simon, *Solid State Ion.* 136–137, 1295 (2000).

89. N. Bendiab, A. Righi, E. Anglaret, J. L. Bantignies, A. Zahab, J. L. Sauvajol, P. Petit, C. Mathis, and S. Lefrant, *Phys. Rev. B* 64, 245424 (2001).

90. J. Conard and H. Estrade, *Mater. Sci. Eng.* 31, 173 (1977).

91. J. Conard, V. A. Nalimova, and D. Guérard, *Mol. Cryst. Liq. Cryst.* 245, 25 (1994).

92. S. Yamazaki, T. Hashimoto, T. Iriyama, Y. Mori, H. Shiroki, and N. Tamura, *J. Mol. Struct.* 441, 165 (1998).

93. C. Menachem, Y. Wang, J. Flowers, E. Peled, and S. G. Greenbaum, *J. Power Sources* 76, 25 (1994).

94. N. Imanishi, K. Kumai, H. Kokugan, Y. Takeda, and O. Yamamoto, *Solid State Ion.* 107, 135 (1998).

95. K. Zaghib, K. Tatsumi, Y. Sawada, S. Higuchi, H. Abe, and T. Ohsaki, *J. Electrochem. Soc.* 146, 2784 (1999).

96. L. Duclaux, K. Metenier, J. P. Salvetat, P. Lauginie, S. Bonnamy, and F. Beguin, *AIP Conf. Proc.* 544, 408 (2000).

97. L. Duclaux, A. M. Faugere, J. Conard, S. Flandrois, and P. Lauginie, *Mol. Cryst. Liq. Cryst.* 340, 167 (2000).

98. S. Bandow, M. Yudasaka, R. Yamada, S. Iijima, F. Kokai, and K. Takahashi, *Mol. Cryst. Liq. Cryst.* 340, 749 (2000).

99. Y. Liu, J. S. Xue, T. Zhen, and J. R. Dahn, *Carbon* 34, 193 (1996).

100. E. Buiel and J. R. Dahn, *J. Electrochem. Soc.* 145, 1977 (1998).

101. Y. C. Chang, H. J. Sohn, Y. Korai, and Y. Mochida, *Carbon* 36, 1653 (1998).

102. T. Zheng, Q. Zhong, and J. R. Dahn, *J. Electrochem. Soc.* 142, L211 (1995).

103. D. Guerard and A. Herold, *Carbon* 13, 337 (1975).

104. R. Yazami and P. H. Touzain, *J. Power Sources* 9, 365 (1983).

105. N. Daumas and A. Herold, *C.R. Acad. Sci. Paris C* 268, 373 (1969).

106. W. Rüdorff and E. Schulze, *Z. Angew. Chem.* 66, 35 (1954).

107. R. Fong, U. Von Sacken, and J. R. Dahn, *J. Electrochem. Soc.* 137, 2009 (1990).

108. E. Peled, C. Menachem, D. Bar-Tow, and A. Melman, *J. Electrochem. Soc.* 143, L4 (1996).

109. Y. Ein-Eli and V. R. Koch, *J. Electrochem. Soc.* 144, 2968 (1997).

110. F. Disma, L. Aymard, L. Dupont, and J. M. Tarascon, *J. Electrochem. Soc.* 143, 12 (1996).

111. F. Salver-Disma, C. Lenain, B. Beaudoin, L. Aymard, and J. M. Tarascon, *Solid State Ion.* 98, 145 (1997).

112. Q. Xu, C. Schwandt, G. Z. Chen, and D. J. Fray, *J. Electroanal. Chem.* 530, 16 (2002).

113. P. C. Eklund, G. Dresselhaus, M. S. Dresselhaus, and J. E. Fischer, *Phys. Rev. B* 21, 4705 (1980).

114. G. L. Doll, P. C. Eklund, and J. E. Fischer, *Phys. Rev. B* 36, 4940 (1987).

115. M. Inaba, H. Yoshida, Z. Ogumi, T. Abe, Y. Mizutani, and M. Asano, *J. Electrochem. Soc.* 142, 20 (1995).

116. D. Billaud, F. X. Henry, and P. Willmann, *Mater. Res. Bull.* 28, 477 (1993).

117. T. Ohzuku, Y. Iwakoshi, and K. Sawai, *J. Electrochem. Soc.* 140, 2490 (1993).

118. K. Guérin, M. Ménétrier, A. Février-Bouvier, S. Flandrois, B. Simon, and P. Biensan, *Solid State Ion.* 127, 187 (2000).

119. S. Yata, M. Kinoshita, M. Komori, N. Ando, T. Kashiwamura, T. Harada, K. Tanaka, and T. Yamabe, *Synth. Met.* 62, 153 (1994).

120. K. Tatsumi, N. Iwashita, H. Sakaebe, H. Shioyama, S. Higuchi, A. Mabuchi, and H. Fujimoto, *J. Electrochem. Soc.* 142, 716 (1995).

121. K. Tatsumi, T. Akai, K. Zaghib, N. Iwashita, S. Higuchi, and Y. Sawada, *J. Electrochem. Soc.* 143, 1923 (1996).

122. T. Zheng, Y. Liu, E. W. Fuller, S. Tseng, U. Von Sacken, and J. R. Dahn, *J. Electrochem. Soc.* 142, 2581 (1995).

123. J. R. Dahn, T. Zheng, L. Yinghu, and J. S. Xue, *Science* 270, 590 (1995).

124. H. Q. Xiang, S. B. Fang, and Y. Y. Jiang, *J. Electrochem. Soc.* 144, L187 (1997).

125. I. Mochida, C. H. Ku, S. H. Yoon, and Y. Korai, *J. Power Sources* 75, 214 (1998).

126. K. Sato, M. Noguchi, A. Demachi, N. Oki, and M. Endo, *Science* 264, 556 (1994).

127. I. Mochida, C. H. Ku, and Y. Korai, *Carbon* 39, 399 (2001).

128. T. Zheng, W. R. McKinnon, and J. R. Dahn, *J. Electrochem. Soc.* 143, 2137 (1996).

129. N. Takami, A. Satoh, T. Ohsaki, and M. Kanda, *Electrochim. Acta* 42, 2537 (1997).

130. Y. Matsumura, S. Wang, and J. Mondori, *J. Electrochem. Soc.* 142, 2914 (1995).

131. A. G. Rinzler, J. Liu, P. Nikolaev, C. B. Huffman, E. J. Rodriguez-Macias, P. J. Boul, A. H. Lu, D. Heymann, D. T. Colbert, R. S. Lee, J. E. Fischer, A. M. Rao, P. C. Eklund, and R. E. Smalley, *Appl. Phys. A* 67, 29 (1998).

132. G. T. Wu, C. S. Wang, X. B. Zhang, H. S. Yang, Z. F. Qi, and W. Z. Li, *J. Power Sources* 75, 175 (1998).

133. G. Maurin, Ch. Bousquet, F. Henn, P. Bernier, R. Almairac, and B. Simon, *Chem. Phys. Lett.* 312, 14 (1999).

134. G. T. Wu, C. S. Wang, X. B. Zhang, H. S. Yang, Z. F. Qi, P. M. He, and W. Z. Li, *J. Electrochem. Soc.* 146, 1996 (1999).

135. V. Meunier, J. Kephart, C. Roland, and J. Bernholc, *Phys. Rev. Lett.* 88, 075506 (2002).

136. P. Dubot and P. Cenedese, *Phys. Rev. B* 63, 241402 (2001).

137. J. Young, H. J. Liu, and C. T. Chan, *Phys. Rev. B* 64, 085420 (2001).

138. E. C. Lee, Y.-S. Kim, Y. G. Liu, and K. J. Chang, *Phys. Rev. B* 66, 073415 (2002).

139. R. T. Yang, *Carbon* 38, 623 (2000).

140. P. Chen, X. Wu, J. Lin, and K. L. Tan, *Science* 285, 91 (1999).

141. M. Hirscher, M. Becher, M. Haluska, A. Quintel, V. Skakalova, Y. M. Choi, U. Dettlaff-Weglikowska, S. Roth, I. Stepanek, P. Bernier, A. Leonhardt, and J. Fink, *J. Alloys Compounds* 330, 654 (2002).

142. P. Petit, E. Jougelet, J. E. Fischer, A. G. Rinzler, and R. E. Smalley, *Phys. Rev. B* 56, 9275 (1997).

143. E. Jougelet, C. Mathis, and P. Petit, *Chem. Phys. Lett.* 318, 561 (2000).

144. V. Z. Mordkovich, M. Baxendale, M. Yudasaka, S. Yoshimura, J. Y. Dai, and R. P. H. Chang, *Mol. Cryst. Liq. Cryst.* 310, 159 (1998).

145. V. Z. Mordkovitch, M. Baxendale, R. P. Chang, and H. Yoshimura, *Synth. Met.* 86, 2049 (1997).

146. V. Z. Mordkovitch, M. Baxendale, S. Yoshimura, and R. P. Chang, *Carbon* 34, 1301 (1996).

147. V. A. Nalimova, D. E. Sklovsky, G. N. Bondarenko, H. Alvergnat-Gaucher, S. Bonnamy, and F. Béguin, *Synth. Met.* 88, 89 (1997).

148. P. Petit, C. Mathis, C. Journet, and P. Bernier, *Chem. Phys. Lett.* 305, 370 (1999).

149. R. S. Lee, H. J. Kim, J. E. Fischer, A. Thess, and R. E. Smalley, *Nature* 388, 255 (1997).

150. S. suzuki, C. Bower, and O. Zhou, *Chem. Phys. Lett.* 285, 230 (1998).

151. T. Pichler, M. Sing, M. Knupfer, M. S. Golden, and J. Fink, *Solid State Comm.* 109, 721 (1999).

152. R. Yazami, H. Gabrisch, and B. Fultz, *J. Chem. Phys.* 115, 10585 (2001).

153. G. Gao, T. Cagin, and W. A. Goddart, *Phys. Rev. Lett.* 80, 5560 (1998).

154. T. Ishihara, A. Kawahara, H. Nishigushi, M. Yoshio, and Y. Takita, *J. Power Sources* 97–98, 129 (2001).

155. F. Leroux, K. Menetier, S. Gautier, E. Frackwiak, S. Bonnamy, and F. Beguin, *J. Power Sources* 81–82, 317 (1999).

156. B. Gao, C. Bower, J. D. Lorentzen, L. Fleming, A. Kleinhammes, X. P. Tang, L. E. McNeil, Y. Wu, and O. Zhou, *Chem. Phys. Lett.* 327, 69 (2000).

157. Z. Yang and H. Wu, *Solid State Ion.* 143, 173 (2001).

158. O. Zhou, B. Gao, C. Bower, L. Fleming, and H. Shimoda, *Mol. Cryst. Liq. Cryst.* 340, 541 (2000).

159. J. E. Fischer, A. S. Claye, and R. Lee, *Mol. Cryst. Liq. Cryst.* 340, 737 (2000).

160. I. Mulhopadhyay, N. Hoshino, S. Kawasaki, F. Okino, W. K. Hsu, and H. Touhara, *J. Electrochem. Soc.* 149, A39 (2002).

161. Q. Wang, L. Q. Chen, and X. J. Huang, *Electrochem. Solid State Lett.* 5, A188 (2002).

162. Z. H. Yang, H. Q. Wu, and B. Simard, *Electrochem. Comm.* 4, 574 (2002).

163. W. X. Chen, J. Y. Lee, and Z. Liu, *Electrochem. Comm.* 4, 260 (2002).

164. H. Q. Peng, Z. N. Gu, J. P. Yang, J. L. Zimmerman, and P. A. Willis, *Nanoletters* 1, 625 (2001).

165. G. Maurin, F. Henn, B. Simon, J. F. Colomer, and J. B. Nagy, *Nanoletters* 1, 75 (2001).

166. E. Frackowiack and F. Beguin, *Carbon* 40, 1775 (2002).

167. Q. Liu, T. Zhang, C. Bindra, J. E. Fischer, and J. Y. Josefowicz, *J. Power Sources* 68, 287 (1997).

168. D. Aurbach, Y. Ein-Eli, B. Markovsky, and A. Zaban, *J. Electrochem. Soc.* 142, 2873 (1995).

169. W. Xing and J. R. Dahn, *J. Electrochem. Soc.* 144, 1195 (1996).

170. Y. C. Chang and H. J. Sohn, *J. Electrochem. Soc.* 147, 50 (2000).

171. T. Piao, S. M. Park, C. H. Doh, and S. I. Moon, *J. Electrochem. Soc.* 146, 2794 (1999).

172. S. Pyun and Y. G. Ryu, *J. Power Sources* 70, 34 (1998).

173. M. D. Levi and D. Aurbach, *J. Phys. Chem.* 101, 4641 (1997).

174. H. Higuchi, K. Uenae, and A. Kawakami, *J. Power Sources* 68, 212 (1997).

175. A. Claye and J. E. Fischer, *Electrochem. Acta* 45, 107 (1999).

176. K. Moriguchi, Y. Itoh, S. Munetoh, K. Kamei, M. Abe, A. Omaru, and M. Nagamine, *Physica B* 323, 127 (2002).

177. T. Prem Kumar, A. Manuel Stephan, P. Thayananth, V. Subramanian, S. Gopukumar, N. G. Rengenathan, M. Raghavan, and N. Muniyandi, *J. Power Sources* 97, 118 (2001).

178. J. S. Sakamoto and B. Dunn, *J. Electrochem. Soc.* 149, A26 (2002).

ENN
Encyclopedia of Nanoscience and Nanotechnology
www.aspbs.com/enn

Electrochemical Nanoelectrodes

Irina Kleps

National Institute for Research and Development in Microtechnologies, Bucharest, Romania

CONTENTS

1. INTRODUCTION

Because of the progress in nanoscience and nanotechnology, a new field—electrochemical nanotechnology—has recently developed [1–4]. This chapter is a review focused on the properties, fabrication technologies, and main applications of nanoelectrodes (NEs) and nanoelectrode arrays (NEAs) as working electrodes in an electrochemical cell; it does not deal with NEs as electrical conductors in nanoelectronics or molecular electronics.

The terms and dimensions of the electrodes are not strictly delimited in the specialized literature. Generally, one NE element has one dimension lower than 500 nm. Electrodes with one dimension between 0.5 and 1 μm are known as submicroelectrodes; electrodes with dimensions of micrometers or tens of micrometers are ultramicroelectrodes (UMAs) or microelectrodes; other higher electrodes are known as macroelectrodes.

Various scientific fields, such as nanofabrication technology, electrochemistry, surface and material sciences, electronics, and biology, are involved in NE fabrication and applications, including working electrodes or elements of electrochemical or biochemical sensors (amperometric, potentiometric, or conductimetric probes). The working NEs can be individual (called NEs or nanoprobes), or they can be connected in an array, and in this case they are known as NEAs or nanoelectrode ensembles (NEEs).

There are various fields of application of electrochemical micro- and nanoelectrodes, such as the study of chemical reaction mechanisms; materials science; analytical chemistry (environment pollution control); medicine, biology, and biochemistry; scanning electrochemical microscopy (SECM) [5–12]; etc.

2. BASIC ELECTROCHEMISTRY

Two types of processes occur at the electrode-solution interface. One involves electron transfer between the electrode and the electrolyte; such processes are called faradaic. The other involves processes such as adsorption and desorption, where no charges cross the interface, called nonfaradaic. Faradaic currents are proportional to the concentration of the reactants and are of interest in sensor applications. During nonfaradaic processes, although no charges cross the interface, external transient currents can flow when the potential, electrode area, or solution composition changes; these currents flow to charge or discharge the interfacial region between the electrode and the electrolyte. Both faradaic and nonfaradaic processes occur when electrode reactions take place. The transient currents due to nonfaradaic processes can be minimized with the use of micro- and nanoelectrodes.

The faradaic currents or electrode reaction rates are governed by the rates of the following processes: (a) mass transfer rate from the bulk solution to the electrode surface; (b) electron transfer rate at the electrode surface; (c) chemical reaction rates preceding or following the electron transfer; (d) other surface reactions such as adsorption, desorption, or electrodeposition.

When a steady-state current is obtained, the rates of all of these processes must be constant. The magnitude of the current is limited by the slowest process in the sequence, which is called the rate-determining step. The simplest reactions are rate limited by the mass transfer of a reactant to the electrode; this means that the kinetics of all electron transfers and associated chemical reactions are very rapid by comparison with those of the mass transfer process. This allows for a relationship between the current magnitude and

the quantity of reactant present. The mass transfer in solution is a function of three phenomena: diffusion, migration, and convection. Diffusion is the motion of species under the influence of a chemical potential gradient, for example, a concentration gradient; molecules or ions move from a region of high concentration to a region of low concentration, to equalize concentration gradients in the solution. Migration is the motion of charged species under the influence of an electrical field; charged particles move to equalize potential gradients in the solution. Convection is an agitation or hydrodynamic transport; material is moved by an external force such as flow. Generally, the flow is induced by natural convection (convection due to the density gradient) or by forced convection; this flow can be laminar or turbulent.

Each of these three components can be described mathematically. The effects of all three modes of mass transport can be summed with the generalized Nernst–Planck equation. The flux J_i of species i given by the Nernst–Plank equation is

$$J_i = -D_i \operatorname{grad} c_i - \frac{z_i F}{RT} D_i c_i \operatorname{grad} \phi + c_i \bar{\nu}$$

where D_i is the diffusion coefficient, c_i is the concentration, z_i is the charge, grad c_i is the concentration gradient of the species i, grad ϕ is the potential gradient in the solution, F is the Faraday constant, and R, T, and ν are the gas constant, the temperature, and the hydrodynamic flow, respectively. Diffusion is the preferred method of transport for analytical measurements, as it ensures that the current magnitude is proportional to the analyte concentration.

If the kinetics of electron transfer are rapid, the concentrations of the oxidized and reduced species at the electrode surface can be assumed to be at equilibrium. Thermodynamically reversible reactions correspond to an equilibrium potential between the oxidized and reduced species, which is described by the Nernst equation.

During a standard electroanalytical measurement, the conditions are favorable for maximizing the diffusion current, as opposed to the other two mass transport phenomena, migration and convection.

To maintain a diffusion-controlled reaction it is important that the diffusion rate is dominant over other mass transfer processes. The following conditions must be fulfilled to have a reaction under diffusion control: (i) an inert supporting electrolyte of high concentration to be added in solution to ensure a constant ionic strength during the measurement; (ii) detection to be made in a stagnant solution or under controlled convection.

Under these circumstances, the equation of the mass transport is simplified and can be expressed by Fick's laws:

(i) Fick's first law expresses the relation between current density (J_i) and concentration (c_i):

$$J_i = -D_i \operatorname{grad} c_i$$

(ii) Fick's second law represents the evolution of concentration as a function of time (t):

$$\frac{\partial c}{\partial t} + \operatorname{div}(-D_i \operatorname{grad} c) = 0$$

Mass transport control implies fast kinetics; hence the surface reaction is reversible and the potential is given by the Nernst equation applied to the surface concentrations.

3. NANOELECTRODE ELECTROCHEMISTRY

3.1. Nanoelectrode Properties

Normal electrodes used in electrochemistry are on the order of millimeters. There are benefits to downscaling electrode sizes toward micrometers and nanometers. There are a lot of papers that deal with microelectrode properties [13–26]. These properties are also valuable for NEs, but because of their low dimensions a lot of specific problems, deviations from the theory and different behaviors, can occur; these will be discussed separately.

By measuring the limiting current versus the applied voltage potential, it is possible to determine both the concentration and species type in a solution. One of the complicating factors in this measurement is the existence of nonfaradaic currents due to the charging/discharging of the double-layer capacitance. This charging current is a source of noise and becomes a significant part of the overall current when very low concentrations of analyte are being measured. Since the double-layer capacitance is directly proportional to the electrode surface area, a reduction in electrode radius, r, will result in a capacitance decrease proportional to r^2. The decrease in electrode size also reduces the faradaic component of the measured current, the limiting current. But because the limiting current is directly proportional to the radius, its value decreases at a slower rate and the ratio of the limiting current to the charging current grows with decreasing electrode size [14, 27].

So, although the total current goes down, the net result is an increase in the signal-to-noise (S/N) ratio. On the other hand, this magnitude can be increased with the use of arrays as discussed below.

Another benefit of miniaturization involves the *potential drop* in the solution. A reduction of the electrode surface area also tends to decrease the quantity *IRs* by reducing the current, I [28]. The steady-state limiting current can be difficult to measure if the electrode is of nanometric size. The very low steady-state limiting current of one NE can be multiplied with NEAs, making it possible to take sensitive measurements in nonaqueous and low-conductivity solutions [29, 30].

When multiple electrodes are connected in parallel, the original current will be broken into n equal parallel currents and the total voltage drop in solution will be lowered. This configuration is known as an array. Summing these currents in parallel, via interconnection of a large group of NEs, results in a measurable current output while maintaining a high S/N ratio and a diminished potential drop. To maintain the NE behavior, the individual NEs in the array must be spaced far enough from each other so that their diffusion layers do not overlap within the time scale of interest.

Fan and Bard [31] and Ingram [32] have shown a coulombic staircase response by using electrodes of nanometer dimensions.

The NE, in a conducting liquid, represents a point with *spherical* (*radial*) diffusion of the active species; this leads to a decrease in the surface-to-volume ratio and to an increase in the current density at the electrode surface [13–26, 33].

NEs offer higher sensitivity than macroelectrodes of conventional size, because an electroactive molecule can approach the NE from every direction (Fig. 1). Therefore, the flux of electroactive molecules toward the electrode is much greater for a micro/nanoelectrode than for a macro-electrode, for which the diffusion is planar [34–38].

Mathematical solutions for each kind of electrode response (macro and nano) predict the superior electrode sensitivity of NEs [39, 40].

In Figure 2 a cyclic voltammogram (CV) of the NE with spherical diffusion is presented. Generally, NE voltammo-grams have a well-defined sigmoid shape, and the forward and reverse scans retrace each other exactly. As expected, the current associated with the charging/discharging of the double layer is invisible. The shape of the wave indicates that the current reaches a steady state in which the current is independent of time.

The study of NE behavior involves not only electrode size and shape, but also the kinetic parameters of the electroan-alytical technique employed that govern the thickness of the diffusion layer developed (e.g., the potential scan rate for cyclic voltammetry). The sigmoid shape of the CV is main-tained even at a potential scanning rate of 1 V s^{-1}, indicating that the NE tip is well sealed by the polymer insulation, as in the case of a carbon microelectrode with an effective radius of 1 nm [41].

Theoretical aspects related to coupled radial-linear diffu-sion recessed electrodes were developed by Bond et al. [42].

3.1.1. NEAs

In the analysis of the diffusional regimes for NEAs, three sit-uations are observed, depending on the kinetic parameters of the electroanalytical technique employed [43]: (i) linear regime (very high scanning rate, very short time) (at a suf-ficiently short time, any planar electrode behaves as an infinitely large planar electrode) (Fig. 3a); (ii) radial regime (high scanning rate, short time) (at short analysis times for an array of N NEs, the current response is dominated by nonlinear diffusion to the individual NEs) (Fig. 3b); (iii) overlapping regime (very low scanning rate, very long time) (the value of the overlap factor depends on the elec-trode geometry and the time of electrolysis) (Fig. 3c); at a longer time, overlap of diffusion layers occurs and diffusion becomes linear on the entire surface of the array [44]. Thus, at low scan rates, the NEA behaves like a macroelectrode,
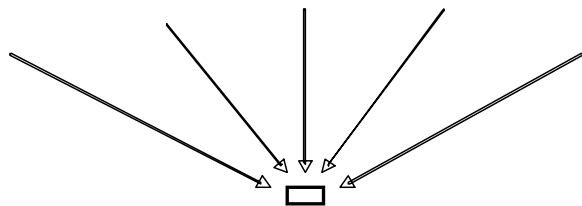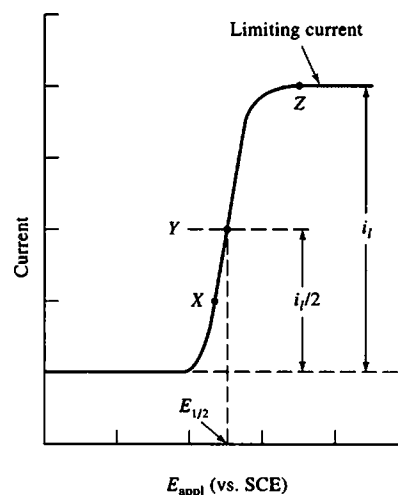

Figure 2. The voltammogram for the nanoelectrode.

while at high scan rates the NEs act independently. This is an important feature for real-time in vivo sensing and other electroanalytical applications [8].

The nature of the faradaic currents observed at a NEA depends on the distance between the electrode elements and the time scale (in cyclic voltammetry, scan rate) of the exper-iment [45–48]. Three principal cases can be distinguished
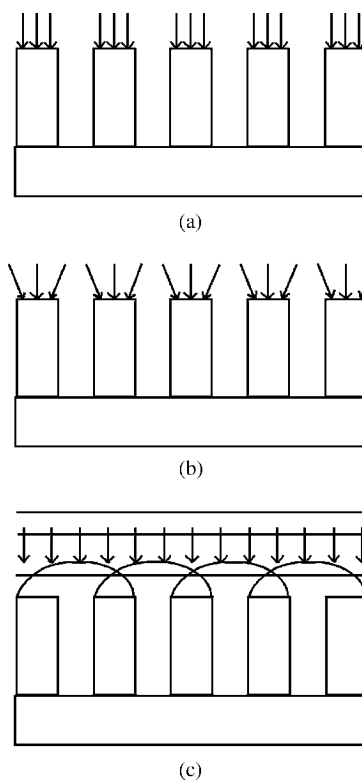

Figure 3. Diffusional regimes for nanoelectrode arrays. (a) Linear regime. (b) Radial regime. (c) Overlapping regime.

Figure 1. Radial diffusion of the electroactive molecules toward the nanoelectrode.

when the diffusional flux toward a NEA is considered [14, 45–51]:

(i) If the distance between two consecutive electrodes (D) is wide compared with the diffusion layer thickness (ρ), the electrodes do not affect one another and the overall current measured is the sum of the currents passing through the individual electrodes.

(ii) If $D < \rho$, the diffusion layers of the individual electrodes partially overlap. The overall current is smaller than the sum of the currents passing through the electrodes when they operate independently.

(iii) If $D \ll \rho$, the diffusion layers of the individual electrodes totally overlap. The behavior of such electrodes is similar to that of macroelectrodes; under these conditions, the signal is proportional to the surface area of the whole array, while noise is proportional only to the area of the electrodes. Thus, the S/N ratio is greatly improved.

It can be summarized that the electrochemically active area of the NEA depends on the electrode size and array geometry and on the measurement conditions. As the distance between two electrodes increases, the current density decreases. Only at low current densities is the current response optimum, as in theory.

Experimental works suggested that the separation distances should be 10 times the diameter of the electrode [52, 53].

NEAs operating in total-overlap regime show enhanced electroanalytical detection limits, as opposed to a conventional macroelectrode [54]. This is due to the fact that the faradaic current is proportional to the total geometric area of the NEA, while the background currents (double-layer charging currents) are proportional to the sum of the areas of the electrode elements in the NEA [45, 55]. As a result, the ratio of the faradaic-to-background currents can be as much as three orders of magnitude higher for the NEA than for the macroelectrode [45]. This enhancement in signal-to-background ratio results in conventional peak-shaped voltammograms and enhanced electroanalytical detection limits [45, 55, 56].

Several articles in the literature discuss the theoretical analytical response of NEs and the parameters that affect it [57–60]. Morf and de Rooij [58] presented theoretical calculations for the current output of arrays of different packing densities, using steady-state and chronoamperometric responses. In another paper, Morf [61] presented a theoretical approach to the steady-state behavior of multiple electrode arrays consisting of spherical, hemispherical, and disk-shaped or hemicylindrical electrodes. Rigorous analytical and numerical solutions for the transient current at the hemirecessed and protruded electrodes have recently been reported [62]. One special and very important feature of the NE is that it allows for detection in a very confined space, which has the same volume as a biological cell [63].

NEs have some useful properties because of the increased importance of mass transport to the edges of the electrode. Their main NE properties, as in the case of microelectrodes [13, 14], can be summarized as follows:

- A steady state of the current for a faradaic process is attained very rapidly.

- The small sizes of the electrodes permit measurements in very small solution volumes.
- Voltammetry can be conducted at steady state where the current (and hence the ohmic drop) is lower than with a transient method; this means that NEs can be used to perform electrochemistry in high resistive media.
- The faradaic-to-charging current ratio, I_F/I_C, is improved, as the charging current decreases in proportion to the decrease of the electrode area, while the steady-state faradaic current is proportional to the same electrode area; this allows the use of higher scan rates in potential sweep experiments such as cyclic voltammetry.
- The limiting current density increases as the electrode size decreases.
- The mass transport rate to a NE is higher than that which can be achieved with larger electrodes.
- The detection limits are lower because of the higher signal-to-background ratio.
- Chemical or electrochemical processes that are too fast for larger electrodes can be studied with a NE; the quick response of NEs allows for monitoring of the low-frequency fluctuation of signals and rapid recording of steady-state polarization curves.
- The very low level of Faraday current results in the beneficial effect of a very small ohmic potential drop.
- The current output is practically insensitive to conventional flow in solution.

Numerous advantages are attained by making the electrodes smaller: faster equilibration with the solution, smaller capacitance, higher packing density, and the ability to be integrated into on-chip microanalytical systems.

3.2. Nanoelectrode Particularities

Some experimental works on voltammetric characterization of NEs emphasized deviations from the microelectrode theory. The deviations from the theory could be due to the similar dimensions of the NE and the redox molecule undergoing oxidation or reduction in addition to the effect of molecular transport that takes place within the interfacial double-layer region where the fluid properties are considerably different from those of the bulk electrolyte. Moreover, the approximation of electroneutrality used in developing models of the voltammetric response of electrodes is believed not to be valid for electrodes of very low dimensions because of charge separation in the depletion layer caused by electric fields generated by the flux of ions through the electrolyte and the comparable dimensions of the depletion layer and the double layer [64, 65]. Some cases of NE deviation behavior are presented in detail.

3.2.1. Steady-State Voltammograms in the Absence of Supporting Electrolyte

The steady-state voltammetric response at NEs in the absence of a supporting electrolyte was theoretically predicted by incorporating the contribution of migration into the steady-state current [66]; this theoretical assumption was found to be applicable to the voltammetric behavior

of most redox couples [67]. However, large deviations from the expected theory have been reported in some cases [54, 68–74], as in the case of the reduction of ferricyanide on a precious metal or carbon nanoelectrode. Penner et al. [69] evaluated the rate constant of ferrocene at an electrode 1.6 nm in radius to be 220 cm s^{-1}, which is much larger than the value theoretically predicted. The ferricyanide reduction in the absence of the supporting electrolyte is almost completely suppressed at electrodes with an electroactive radius of about 100 nm, which is far greater than the characteristic thickness of the diffuse layer at these concentrations.

In the case of ferricyanide reduction, it is not clear whether the larger value of the rate constant is due to an intrinsic increase in the rate at the molecular level or an overestimation caused by the complicated processes of diffusion and migration [70]. Moreover, steady-state voltammograms, in the absence of supporting electrolyte, become rather ill defined as the electroactive radius of the electrodes decreases. Different interpretations of this behavior were made. The Debye length, k^{-1}, in diluted solution is on the order of 1 nm, and the diffuse double layer is $5k^{-1}$, so the inhibition effect should occur at an electrode size of about 10 nm. However, some authors [29, 67, 71] suggested that the effect of the diffuse double layer on the NE reaction in the dilute solution is the major reason for the inhibition of the ferricyanide reduction in the absence of the electrolyte. Furthermore, the electroneutrality assumption used in developing the voltammetric theory is not valid in the case of such small electrodes [72]. A similar behavior was observed in the case of hexaamineruthenium (III) reduction [69, 73]. If the reaction takes place in the presence of a supporting electrolyte, the voltammetric curves showed close to ideal electrochemical behavior, with the forward and reverse branches overlapping, while in the absence of the supporting electrolyte a non-adsorbing redox couple with a high rate of electron transfer was observed; however, in hexaamineruthenium (III) such deviation occurs only for electrodes with effective radii of 20 nm or less [73].

3.2.2. Deviation from the Microelectrode Theory in the Case of Single NE Tips

Deviation from the microelectrode limiting current is a general trend in NEs and is the result of the NE dimension being similar to the size of the redox probe. Deviation from the theory in the case of nanoband electrodes in comparison with microband ones has been extensively studied by various authors [74–78].

White [75, 76], Fritsch [77], and Wightman [78] and their co-workers have shown that nanoband electrodes with widths less than approximately 25 nm exhibited limiting currents less than that predicted in the case of microband electrodes. In 1985, Wightman and co-workers suggested [78] that the equation of the current response of the electrode with one geometric dimension in the micrometric range is inappropriate for an electrode of small size (5 nm). White and co-workers [75] proposed a theory that explains these deviations. The proposed theory is based on the idea that transport of the redox species to an electrode of near-equivalent dimensions is strongly influenced by changes in the fluid properties of the electrolyte near the electrified

interface. In addition, the diffusional transport equations were derived for isotropic fluid structure [75]. The diffusion property can be explained by stating that the diffusion layer of a nanoscopic band electrode is similar to that of the region near a surface where changes occur in the viscosity and density of the electrolyte medium. With this assumption, the change in concentration of a redox species from the bulk value to a surface value of zero is incorrect. Redox species approaching electrodes of comparable size encounter a buildup due to the highly structured solvent/electrolyte environment and the physical impossibility of having their concentration change from bulk values to zero at the electrode surface over distances of a few molecular diameters. Under these circumstances, it is clear that the current response equation must be reassessed.

The observations of Caston and McCarley [74] are in accordance with previous data recorded for Pt nanoscopic band electrodes [75, 76]. The similarity of Caston's results obtained for Au bands [75] to those of White and co-workers for Pt bands [75, 76] and those of Nagale and Fritsch for Au micromachined bands [77] is important because the deviation is not specific to the type of material used for the nanoband electrode. Thus, the observed deviation from the microelectrode limiting current is a general trend and is the result of the dimension of the band being similar to the size of the redox probe.

3.2.3. Deviations in the Case of NEAs

Pt-TiO$_2$ composite materials can be considered ensembles of NEs or Pt-NEAs, and the voltammetric curves recorded at various electrode compositions display features typical for a quasi-reversible electron transfer process [79]. In particular, peak-to-peak separation, which is related to the reversibility of the process, has been found to be, in all cases, greater than the theoretical value (59 mV) for a fully reversible process. Daniele [79] attributes the apparent kinetic limitation of the electrode process to the size of each active site of the various composites. This behavior can be explained, assuming that the electron transfer process occurs only at very small particles of platinum embedded within a TiO$_2$ layer; the fractional surface of the dielectric is probably inactive.

Similar voltammetric behaviors were reported for ensembles of NEs [45, 80] and for self-assembled organized monolayers of surfactants on conventional electrodes, where only a fraction of the total area was active [81]. Under these conditions, because of the very small electrode size, a kinetic limitation was apparent [80–82], and the heterogeneous rate constant k_{ap} decreased to an extent that depended either on the dimensions of the nanoelectrodes from the ensembles, or on the fractional area blocked by the insulating material.

In the context of the above results, if the electron transfer process occurs only in the case of small Pt particles, the electron transfer process is inhibited to various extents, depending on the TiO$_2$ content, particles of which partially block the electrode surface.

A strange behavior of interdigital ultramicroelectrode arrays (ID-UMEAs) was reported by Min and Baeumner [83]. The S/N was significantly different (S/N of gold ID-UMEAs and platinum ID-UMEAs were 1000 and 11.6, respectively, for 50 μM potassium ferro/ferrihexacyanide in 0.2 M potassium phosphate buffer); since the background

signal of gold ID-UMEAs was negligible, that of platinum ID-UMEAs was in the range of 20 nA. This is an unusual result, since platinum is the better electrochemical material. It was observed that the electrode height also influenced the overall current and S/N. The overall signal height increased with the height of the electrodes; however, the S/N was optimal at a 50-nm height [83].

3.2.4. Electrochemistry in Small Volumes

Recent developments have shown that in ultrasmall volumes (<100 pl), electrodes are reaching the limit of their standard behavior [84, 85]. This distortion from classical microelectrode theory is also observed when the electrode is placed close to an insulating wall (1 to 150 μm), as in the SECM technique [86, 87].

Special attention has been paid to understanding the effect of microchannel geometry on electrochemical detection with both experimental and numerical simulations, which have recently been used to understand the electrochemical response of recessed [88] and protruding microelectrodes [89]. A comprehensive study of the numerical simulation can be found in Ferrigno's Ph.D. thesis [90].

4. NANOELECTRODE FABRICATION

Techniques of ultramicroelectrode fabrication were gradually developed [91–99]. Recent nanotechnology developments allow the construction of NEs with well-known geometries. Various technologies have been developed for NE fabrication:

- Lithographic techniques for electrode definition
- Template-synthesized nanomaterials
- Carbon-based nanoelectrodes: single-walled carbon nanotubes (SWCNTs), fullerenes, functionalized carbon nanotubes, synthetic nanowires, etc.
- Embedded nanoparticles
- Pyramidal NEs made on silicon-etched structures
- Self-assembled monolayers (SAMs) on metallic surfaces
- Single wire/band nanoelectrodes

4.1. Lithographic Techniques for Nanoelectrode Definition

Photolithographic techniques are versatile and permit the preparation of electrodes with a broad range of shapes and sizes, in both single and electrode arrays. Most of the electrodes realized through lithographic techniques reported in the literature have micrometer dimensions [100–102].

Platinum and gold ID-UMEAs for electrochemical biosensor transducers were recently reported [83]. Optimized ID-UMEAs were made of gold and had 400 fingers with a finger width of 2.7 μm, a finger height of 50 nm, and a gap size of 0.3 μm.

Recent lithographic techniques led to new practical and ultimate limits in the nanometric range [103–104] (Table 1), and they are expected to penetrate more into the nanoelectrode fabrication technology.

The use of scanning tunneling microscopy (STM) has demonstrated that ultrasmall structures of a single or a few

Table 1. Lithographic technique limits.

Lithography type	Practical limit (nm)	Ultimate limit (nm)
Ultraviolet light contact/proximity	2500	125
Ultraviolet light projection	150	150
Extreme ultraviolet projection (soft X-ray projection)	150	30
X-ray proximity	70	10
Ion beam	30–50	10
Electron beam (low-energy beam arrays)	40–50	7–20
Electron beam (scapel)	90	35
Imprinting	20–40	8–10
Inking	30–50	10
Scanning probe methods (STM/AFM)	15	0.5

atomic layers can be built on a semiconductor surface such as silicon [105].

4.2. Template-Synthesized Nanoelectrodes

Many groups from all over the world are working in the template-NE field. This involves two processing steps: (i) template preparation as a dielectric support for NEAs and (ii) filling the template pores with the electrode material.

Depending on the material and the chemistry of the pore wall, this nanocylinder can be solid (a fibril or nanowire) or hollow (a tubule). Nanofibers and nanotubules composed of metals, polymers, semiconductors, carbons, and Li$^+$ intercalation materials have been prepared. A schematic representation of a NEA obtained through this method can be seen in Figure 4.

Dr. Martin's group, from the University of Arizona Department of Chemistry, developed a template method for realizing nanopores in a host membrane as a dielectric support for monodisperse nanoscopic particles of a desired electrode material [106, 107].

4.2.1. The Polymeric Template

Various polymeric membranes, such as polycarbonate, polymethylmethacrylate, polyethylene, etc., can be used as templates for NE preparation [8, 33, 45–47, 54–57, 108–116].

Polycarbonate Membrane as a Template Commercially available polycarbonate filters that have cylindrical pores with monodisperse diameters were used as template membranes. The diameter of the pores in the template
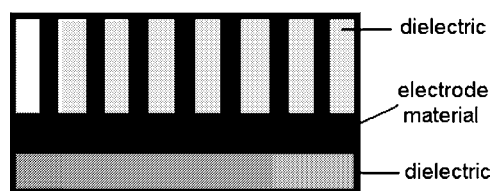

Figure 4. Schematic representation of the nanoelectrode array.

determines the diameter of the Au-disk nanoelectrode elements that make up the NEA. The density of the pores in the template determines the number of Au-disk nanoelectrode elements per square centimeter of NEA surface and, correspondingly, the average distance between the nanoelectrode elements [45, 46, 54, 56].

The nature of the faradaic currents observed at NEE was discussed in section 1 [45–47, 57]. Most template membranes used to prepare the NEAs have high pore densities (in excess of 10^8 pores cm^{-2}), and the corresponding NEAs operate in the total-overlap response regime. In this regime, the diffusion layers at the individual electrode elements overlap to produce a diffusion layer that is linear on the entire area of the NEA. As a result, conventional peak-shaped voltammograms and enhanced electroanalytical detection limits, relative to a conventional macroelectrode, are obtained [45–47, 57].

An electroless plating method was used to prepare ensembles of gold nanodisk electrodes with a disk diameter as small as 10 nm within the pores of a polycarbonate membrane; the plating process must be sufficiently long that solid nanowires can be produced; if the plating is done for shorter times, ensembles of gold nanotubules that span the complete thickness of the template membrane can be obtained [117–120]. The inside diameters of the Au nanotubules can be controlled at will, down to molecular dimensions (<1 nm), by control of the Au deposition time. Because the nanotubules have inside diameters of molecular dimensions, these membranes can be used to separate small molecules on the basis of their molecular size. When an analyte with molecules of dimensions comparable to the inside diameter of the nanotubules is added to one of the half-cells, these molecules enter the nanotubules and partially occlude the pathway for ion conduction across the membrane. As a result, the transmembrane current drops. The magnitude of the drop in the transmembrane current is proportional to the concentration of the analyte. Detection limits as low as 10^{-11} M were obtained [55, 108].

Copolymers as a Template Nanoporous array templates can be prepared with the use of thin films of asymmetric diblock copolymers of polystyrene and polymethylmethacrylate (P(S-b-MMA)). The template can be made of any chosen thickness in the range of 20 nm to 10 μm, since the polymer is initially applied by spin-coating. Two methods were developed to orient the PMMA cylinders perpendicular to the substrate, with the use of either controlled interfacial interactions [110] or an external electric field [111]. Subsequent UV or electron-beam irradiation followed by an acetic acid rinse facilitates the removal of the PMMA while simultaneously cross-linking the polystyrene. This results in a film with a periodic hexagonal array of nanopores. These geometric parameters can be controlled and tuned by the copolymer molecular weight and block fraction.

4.2.2. Alumina and Zeolites as Templates

Other template membranes studied as a support for NEs were alumina (Al$_2$O$_3$) [121–125] (Fig. 5) and zeolites [126]. Recently, Wang et al. [123] found a novel route for preparing
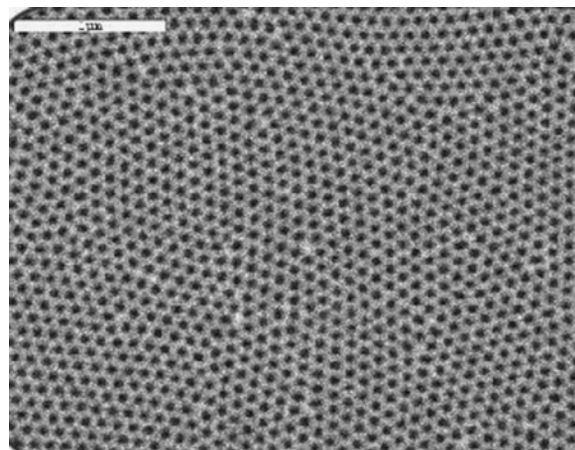

Figure 5. Scanning electron micrograph of the surface of a microporous alumina template membrane prepared in the laboratory of Dr. Charles R. Martin. Reprinted with permission from Dr. Charles R. Martin, Department of Analytical, Bioanalytical, and Materials Chemistry, University of Florida.

nano-Hg$_2$Cl$_2$ in the pores of alumina membrane. This nano-Hg$_2$Cl$_2$ structure has a potential application as a NE. Conductive polymer (polyaniline) nanowires realized in zeolites as templates were reported by Rolison and Bessel [126]. Zeolites can be modified with either redox solutes or nanocrystalline particles [127].

4.3. Carbon-Based Nanoelectrodes

Carbon is a versatile electrode material that can undergo various chemical and electrochemical modifications because of its flexible surface, ranging from purely inert to highly active. Carbon-based nanoelectrodes include SWCNTs/fullerenes, nanoparticles chemically linked to carbon nanotubes, carbon fibers with nanometric size tip, synthetic nanowires, etc.

Water proved to be a suitable environment for studying redox processes at the carbon/electrolyte interface because of the dominant voltammetric wave of the water at half-potentials close to -0.8 V relative to the Ag/AgCl reference electrode. This is the well-known redox reaction of protons in weak acids leading to reproducible voltammetric scans.

4.3.1. Carbon Single Nanoprobes

The development of microelectrodes for use in SECM has demonstrated the utility and importance of such probes at increasingly small length scales. Bard et al. [128] have reviewed a wide range of important issues where the small size of an electrochemical probe is critical in determining the physics and chemistry of electrode surfaces. Very recently, single-walled nanotubes, of precisely known atomic structure with a specific chemical derivatization of the tip optimized to the last atom for the intended probing purpose, were developed [129–130]. With the use of these molecular tips as a direct replacement for the W and Pt STM wires, new probing techniques were developed, including nanoelectrodes for electrochemical studies of living cells.

The nanoscale thinness and great length of carbon nanotubes suggest applications in electrode technology for direct probing of biological systems in vivo. For this purpose means of applying an uniform insulating polymer to the side of the nanotube were developed, so that the only contact of the conducting electrode with the electrolytic medium takes place at the tip. Nanometric-size electrochemical probes can be realized through this procedure. Additionally, the feasibility of turning such probe into ion-selective electrodes was explored, by leaving the tip of the nanotube open and then sealing off this tip with an appropriate ion-selective membrane such as Nafion [131]. Such nanoelectrodes have the potential of making a great impact in a wide variety of areas.

New probes are based on fullerene nanotubes individually mounted on macroscopic electrodes with the goal of developing these mounted nanotubes as transducers [132].

Carbon fibers were extensively used as single NEs [41, 133–140]. Generally, such NEs were fabricated with the use of ion-beam, conically etched carbon fibers with tip diameters ranging from 100 to 500 nm. Zhang et al. [136, 137, 139, 140] reported a cone-shaped, nanometric-sized, single-electrode preparation from carbon fibers, as follows: carbon fibers (7 mm in diameter and 15 mm in length, Goodfellow, Oxford, UK) that had been cleaned and dried were positioned in the center of the target of the ion beam thinner and etched with an argon beam. A single etched carbon fiber was mounted on the end of a copper wire (0.2 mm in diameter and 8 cm in length) and fixed by means of high-purity silver epoxy resin.

Carbon fiber NEs 10–100 μm long, with tip diameters of about 100 nm, can be uninsulated [133] or insulated by a polymeric film. NE insulation was ensured by the electrochemical deposition of polyaniline [134] or polyacrylnitrile [135] films on the carbon fiber nanometer-size electrode. The polyaniline film was deposited from HCl solution containing the aniline monomer, by cycling the potential between -0.2 and $+1.0$ V [134].

Recently, Chen and Kucernak [41] developed a new technology for the fabrication of carbon electrodes with a 1-nm radius by using electrochemically etched carbon fibers, partially insulated by a polymeric film that was electrophoretically deposited.

Carbon microband electrodes with one dimension less than 50 nm were also reported [141].

4.3.2. Carbon Nanoelectrode Arrays

Plasma-assisted catalytic chemical vapor deposition (CVD), in combination with well-defined nanoporous template methods, was used to grow micropatterned multiwalled carbon nanotube arrays with controlled densities and purities for nanoelectrode ensemble applications (Fig. 6).

The aligned carbon nanotubes from the nickel nanoparticles were grown by plasma-enhanced hot filament chemical vapor deposition [142] or by CVD [143]. Pulse current electrochemical deposition has been used to prepare nickel nanoparticles that are used as the catalysts for the growth of aligned carbon nanotubes. The nucleation site density of the nickel nanoparticles was controlled by the amplitude and duration of the pulse current. The site density of the
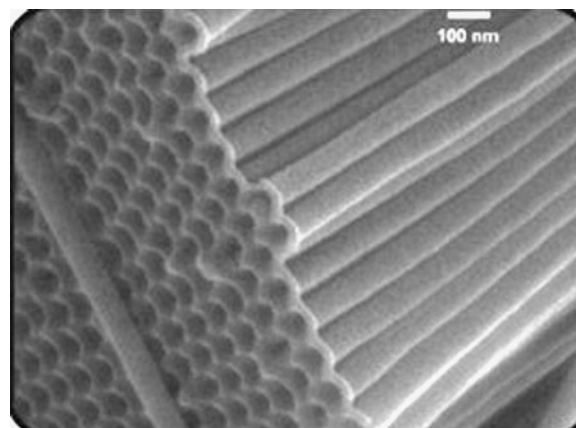

Figure 6. Scanning electron micrograph of an array of CVD template synthesized carbon nanotubes prepared in the laboratory of Dr. Charles R. Martin. Reprinted with permission from Dr. Charles R. Martin, Department of Analytical, Bioanalytical, and Materials Chemistry, University of Florida.

aligned carbon nanotubes varied from 10^5 to 10^8 cm^{-2} [142]. The achievement of controlling the site density is significant for applications of carbon nanotube NEAs. Electrochemical properties of carbon nanotube ensembles were described by various authors (Nguyen et al. [144], Ren et al. [145–148], etc).

Carbon nanofiber electrode arrays for integration into on-chip electrochemical biosensor systems were also developed [149].

4.3.3. Nanostructured Carbon Electrodes

New electrode nanostructured materials, such as boron-doped diamond (BDD), were recently developed [79, 150–157] for various electrochemical applications [152–156]; BDD is structurally and chemically robust [157], allowing it to be useful over a wide potential window (about 3.5 V) in aqueous media. BBD film electrodes were used for lead and copper determination [158]. By the doping of diamond-like carbon (DLC) films with metals, a two-dimensional array of metal clusters within the DLC matrix was obtained. Such composite nanostructures are also of interest for use as NEs in electrochemistry [69].

Chromium-doped carbon films were studied by Fan et al. [159]. DLC films of 0.1–5.0-μm thickness were grown on alumina substrates with a plasma chemical deposition technique [159]. The doping of chromium (Cr) was performed by co-evaporation of chromium into the reactor volume while the carbon film was grown [160–161]. At low doping ($\sim$6 at.% Cr), Cr was uniformly distributed within the C matrix; at high doping ($\sim$12 at.% Cr), chromium carbide clusters were formed. The structure and chemistry of Cr-doped DLCs were investigated with Z-contrast electron imaging and electron energy loss spectroscopy (EELS). It was found that Cr tends to be metallic-like when it is uniformly distributed in a C matrix and carbide-like in the Cr-rich clusters. The carbon is more diamond-like at low doping and more graphite/carbide-like at high doping according to the sp^2/sp^3 electron percentage measurements;

the residual Cr between the clusters remains metallic-like, but C loses its sp³-type bonding [161].

4.4. Nanoparticles Dispersed in a Dielectric Layer

NE arrays can be prepared in a very simple way by dispersing sufficiently small particles of a conductive material in an insulator [9, 162–167]. From an electrochemical point of view, small metallic aggregates, such as Pt, Pd, Au, Co, Cu/Au, or RuO_2 particles, separated by a dielectric layer, form an ultramicro- or even nanoelectrode array. Such electrodes with dimensions smaller than the Nernst diffusion layer have some important advantages, which were pointed out earlier.

Recent research related to Pt nanoparticles embedded in TiO_2 has been done by Battiston and Gerbasi [79, 163]. Pt-TiO_2 films were grown at a temperature of 400 °C with the simultaneous use of platinum bisacetylacetonate (Pt(acac)$_2$) and titanium tetraisopropoxide (Ti(OiPr)$_4$) as precursors in the presence of oxygen. With varying platinum precursor sublimation temperature (130–155 °C) or TiO_2 precursor evaporation temperature (50–60 °C), thin films were obtained over a Pt:Ti atomic ratio range of 1:10 to 1:80. The voltammetric behavior of these nanostructured electrodes has been investigated with the Ru(NH$_3$)$_6^{3+/2+}$ redox couple. These electrodes behave as ensembles of Pt NEs, and electrochemical measurements have shown that the active sites of the investigated composites are smaller than 10 nm [163].

Gold nanoparticles as NEAs were extensively studied by Foss's group [109, 164–166].

Another interesting approach is related to carbon ceramic nanocomposite electrodes. As an example, carbon ceramic electrodes bulk-modified with nanoparticles of ferrocenebutyrate-intercalated Mg-Al layered double hydroxide were reported [167]. Nanoparticles of ferrocenebutyrate anion (FcLDH) in deionized water were first adsorbed to the surface of graphite powder to prepare graphite powder-supported FcLDH, which was then dispersed into methyltrimethoxysilane-derived gels to yield a conductive composite. The composite was used as an electrode material to fabricate highly stable ceramic nanocomposite electrodes containing the electroactive ferrocenyl group.

Nanoscale Pt or RuO_2 particles as ensembles of ultramicroelectrodes for controlled potential electrolyses were enclosed in the structure of zeolites [168]. Pt and RuO_2 NE-modified zeolites were reported by various groups [168–171].

The surface of the Au (111) electrode was modified with Cu nanoclusters with a STM [172].

4.5. Pyramidal Nanoelectrodes Made by Silicon Etching

Pyramidal NEs were realized on the pyramidal shape structures SiO_2/Si or Si_3N_4/Si fabricated by standard Si device processes on Si wafer substrates [173–179]. A schematic representation of the pyramidal NEA can be seen in Figure 7.

It is important to point out some advantages of these electrodes: (i) this kind of NEs can be fabricated through
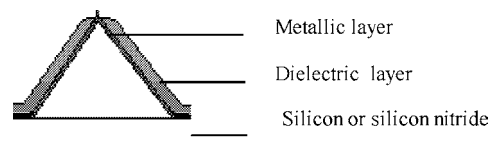

Figure 7. Pyramidal nanoelectrode schematic structure.

the common photolithographic technique of ultraviolet light proximity and does not involve other special lithographic techniques; (ii) these electrodes are never recessed; (iii) the array consists of a series of NEs separated by an insulating material with sufficient spacing to avoid overlap of the diffusion layers.

The technological sequences are presented in Figure 8. The electrode material, gold (Au), plasma vapor-deposited film (200 nm), or platinum (Pt), was deposited on the pyramidal dielectric structures through physical vapor deposition (PVD) or metal oxide chemical vapor deposition (MOCVD). These structures were covered by a dielectric layer, and finally the structure tip was uncovered. If the radius of the electrode top is higher than 20 nm, a short UV exposition process without a mask was performed, to release the top of the electrode. For structures that have the radius of the electrode top lower than 20 nm, the dielectric layer was etched through the photoresist cracks that occurred because of stress.

In such electrode arrays, all electrodes are at the same potential and the active electrode aria is constituted by the sum of the little pyramidal areas from the structure top. Various NE array geometries were realized by this method, with top radii of 5–250 nm. The scanning electron microscopic (SEM) image of a NEA after the etching of the SiO_2 isolation layer on the structure top can be seen in Figure 9.

4.6. Organic Monolayers on Metallic Surfaces

In the field of interfacial electrochemistry, the formation of organic monolayers, such as Langmuir-Blodgett films, polymeric films, and self-assembled monolayers, on metallic surfaces has attracted much attention.
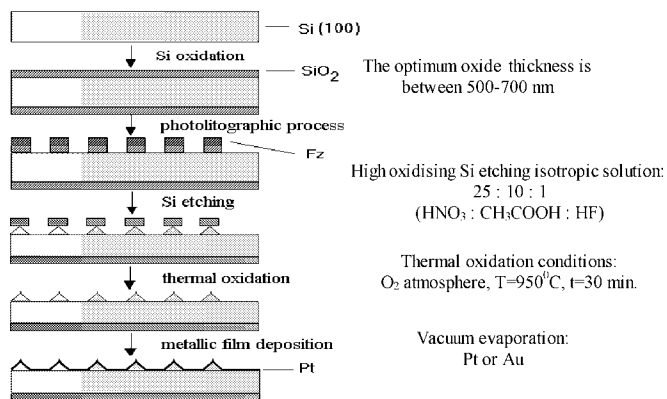

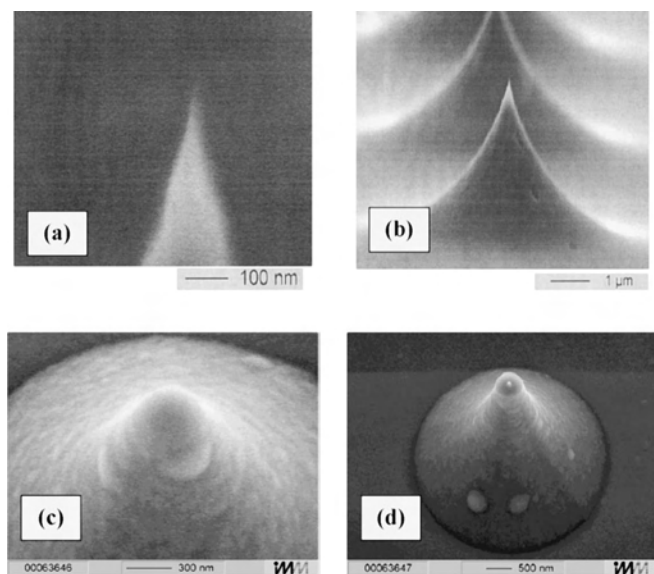**Figure 8.** Technological sequences of the pyramidal nanoelectrode array fabrication.

Figure 9. SEM image of one nanoelectrode from the NEA in different fabrication sequences. (a) Si pyramidal structure. (b) Pt/Si structure. (c) SiO$_2$/Pt/Si. (d) Final structure.

A promising approach to the preparation of micro- and nanoelectrode arrays involves the passivation of the electrode surface with a nonconductive Langmuir-Blodgett film and the formation of conductive channels in the film by uniformly dispersing in it molecules of a suitable substance. Single-molecule electron and ion gate sites can thus be obtained, forming a random array [180, 181].

Clay-modified carbon ultramicroelectrodes were realized by Thurzo et al. [182]. Carbon fiber ultramicroelectrodes ($d = 7$ μm) were coated by 10 monolayers of Laponite clay with the Langmuir-Blodgett method. The electrochemical behavior of both untreated and clay-coated working electrodes was tested by means of double-step voltcoulometry and steady-state and derivative voltammetry in deionized water (pH $\approx$ 5.8). The clay-coated electrodes, if compared
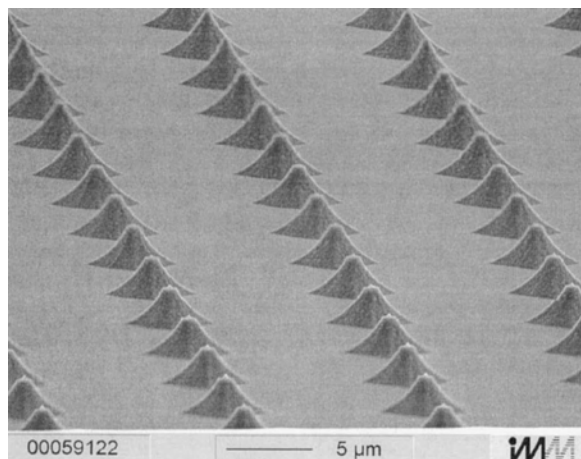
Figure 10. SEM image of the nanoelectrode array after the etching of the SiO$_2$ isolation layer on the structure top.

with the virgin ones, exhibited not only significantly lower steady-state limiting (faradaic) currents, but also strong changes in the kinetic coefficient of the transient charge.

Ugo et al. [56] demonstrated that a NEA coated with a thin film of Kodak ion-exchange polymer shows enhanced electroanalytical detection limits relative to an uncoated NEA.

Self-Assembled Monolayers on Metallic Surfaces

Molecules such as n-alkanethiols spontaneously assemble into ordered SAMs on gold surfaces [183, 184]. The formation of SAMs is partly driven by the strong Au-S covalent bond and partly by hydrophobic effects of the long alkyl chains.

SAMs of poly(3-alkylthiophene) on gold electrodes were examined by cyclic voltammetry in solutions containing electroactive species [2, 4, 185]. Two well-separated electron transfer processes, electron tunneling through the monolayer and electron exchange at pinholes (defects) of the monolayer, were observed. The voltammetric responses of the pinhole electron transfer process take place around the standard potential of the electroactive species and resemble those of a NE ensemble of independent individual NEs [185].

The electrochemical behavior of organothiol monolayers on gold surfaces was studied by Sabatani and Rubinstein [81]. They demonstrated an improved S/N ratio on a SAM-coated electrode for the voltammetry of Ru(bpy)$_3^{2+/3+}$ (bpy $= 2,2'$-bipyridine) in the presence of gold oxidation and oxide reduction.

For practical applications it is necessary to control the density and size of the pinholes in the SAMs [186]. Mixed SAMs composed of a long-chain alkane thiol and a short thiol form phase-separated domains of the short thiol. The mixed SAMs show a preferential response to neutral redox species over charged ones, suggesting the presence of adsorption or permselectivity through the hydrophobic SAMs [187–189].

These SAM electrodes exhibit greater response for hydrophobic redox couples than for hydrophilic ones.

Kind and co-wokers [190] have investigated Pd and Co nanometer-sized islands. They experimented with Pd growing by electroless deposition (ELD) in nanometer-sized islands on self-assembled aminothiolate layers on Au(111) electrodes. The Pd island density has been varied over a large range by changing the amine concentration. On these Pd islands nanometer-sized Co islands were deposited through ELD. The size of such islands, from 1–3 nm up to 60 nm in diameter, can be controlled by the oxygen concentration in the Co plating bath.

Another interesting approach for NEA fabrication is related to SAMs prepared on a gold electrode surface, using thiolated β-cyclodextrin (β-CD) and n-alkanethiol, mixed in appropriate proportions [191–197]. The thiolated β-CD molecules make an almost ideal SAM when the unoccupied space between β-CD molecules is sealed with n-hexadecanethiol molecules that are also strongly adsorbed to the gold surface. Recently, Lee and Park [192, 197] have demonstrated that β-CD cavities can be separated from

each other by controlling the molar ratios of thiolated β-CD and n-hexadecanethiol. Each β-CD cavity can be isolated in thick forests of n-hexadecanethiol and, therefore, can act as a nanoelectrode array. In such SAMs, n-hexadecanethiol molecules act as an electron- and mass-transfer blocking layer, while the β-CD molecules act as electron-transfer sites, introducing openings in the alkanethiol SAMs. When thiolated α- and β-CD molecules formed SAMs on gold electrodes, they showed molecular size selectivity for electroactive compounds. Choi's results [196–198] suggest that chemical selectivity can be successfully designed by employing appropriate molecules for the formation of SAMs on gold electrodes.

A new method of preparing nanopores in a SAM of alkanethiol has been developed by Oyamatsu et al. [199] on the basis of their previous findings that underpotential deposition of Ag on alkanethiol SAM-coated Au makes numerous islands of Ag atomic monolayers; also, the underpotential deposition of Ag or Cu on SAM-coated Au stabilizes the adsorbed alkanethiol molecules against their reductive desorption in an alkaline solution. The analysis of the resulting electrode surface with a STM revealed that the size and number of the nanopores can be controlled by changing the Ag deposition time. This method was also made available for nanopore preparation in other alkanethiol SAMs by replacing decanethiol with the desired alkanethiol [199].

Moreover, SAM techniques can be used to fabricate silicon-based devices with appropriate ligands, enzymes, and other chemically functional arrays, directly on-chip [200–203].

4.7. Single Tip Nanoelectrodes/Nanoprobes

The simplest and most popular single-wire electrode is the nanodisc electrode, which can be made by sealing a fine wire in glass/plastic and polishing the end. Another popular geometry is the nanoband. This can be fabricated in a similar way—by sealing a thin layer of foil between two blocks and polishing the edge. Alternatively, nanobands can be fabricated by lithography. Such electrodes require an elevated insulation procedure, and many groups deal with this. Single carbon-based nanoprobes are presented in Section 4.3.1.

4.7.1. Single-Wire Nanoelectrodes

Single metallic NEs are essentially metal STM tips coated with an insulating polymer layer so that only a nanometer-size fraction of the sharp end of the tip is exposed to the solution. Instead of measuring the tunneling current, this tip is used as an electrode [204]. This kind of electrode was developed for SECM and is discussed in Section 5.4. Different tip geometries (hemispherical, conical, spherical, ring) have been considered, particularly for those electrodes in the nanometer range [29, 69, 70, 98, 205–211].

Individual Pt electrodes with electrochemically active radii as small as several tens of nanometers, and even down to a few nanometers, have been reported [29, 69, 70, 98].

Several insulation methods were used, such as translating with controlled speed the etched tip in a molten glass [69], or using a laser micropipette puller [70]. Compared with these approaches, the method employing the electrophoretic deposition of a polymer paint (EDP) [29, 98, 210] is more practical since a complicated experimental setup is not required.

The deposition of electrophoretic paint, a method called the "inverted deposition" technique, developed by Chen [41], allows for a complete insulation of the whole body of the NE except the tip, leaving an electrochemically active area with an effective diameter as small as a few nanometers.

Thus, nanometer-sized electrodes were fabricated by electrochemically etching a Pt wire with a 20-μm diameter and then coating the Pt tip with anodic-electrophoretic paint (ZQ84-3225) including polyacrylic acid, according to the procedure developed by Slevin et al. [98]. Chen and Aoki [68] further developed the electrophoretic insulation. According to their procedure, the exposed portion of the Pt wire tip was immersed in dilute aqueous paint solution (50:1) and positioned at the center of a Pt coil; a DC potential of +2.1 V was applied between the Pt wire and the Pt coil to initiate the oxidation of water; the coating took place from the support of the Pt wire toward the tip; finally, the paint was treated and stabilized. In this process [68], the paint can only cover the junction between the insulating glass and the Pt wire, leaving the tip exposed to air, because the paint shrinks during the heating. For a better covering, iterative coating processes are required.

A new single NE (for potential measurements), based on an electrochemically etched Pt/Ir needle, has been produced by Schwank et al. [212]. In accordance with their procedure, the needle was electrically insulated with a thin (15 to 20 nm) insulation film made of diamond-like carbon (DLC), deposited on the electrode by a plasma deposition process. In order for the needle to be used as an electrode, the tip had to be made conductive again with the use of a local oxygen plasma. The localization of the plasma was achieved in a specially designed STM, working in a high-pressure oxygen atmosphere.

4.7.2. Nanoband Electrodes

Only a few papers on Au bands (<50 nm) have been reported [75, 77]. This relatively low number of voltammetric studies with Au electrodes is most likely due to the fact that evaporated Au tends to form discontinuous films (islands) below a 15-nm gold thickness [213]. However, with the use of appropriate modifiers on glass surfaces, it was shown that small-grained, electrically conductive Au films as thin as 3 nm can be obtained [214]. These films can be used to construct nanoband electrodes by merely insulating the top side of the Au film with an appropriate dielectric. Enzyme-modified nanoscopic band electrodes for electrochemical sensors show great promise for use in small volumes [215].

Most of the reported NEs [45, 69, 70, 77, 98, 216], except those reported in [136], are housed in large insulating and supporting electrode bodies. As a result, the overall physical tip dimensions are in the millimeter range and therefore cannot be used for measurements in small volumes or at the single-cell level.

5. NANOELECTRODE APPLICATIONS

5.1. Nanoelectrodes and the Electrochemical Reaction Mechanism

The invention of ultramicroelectrodes and NEs had a significant impact on the field of electrode kinetics. Moreover, NEAs offer advantages for both analytical and kinetic studies because the electrode capacitance is greatly reduced and mass transfer is greatly enhanced relative to micro- and macroelectrode faradaic processes. Heinze [217, 218] extensively investigated the electrode processes. The rate of mass transport to and from the electrode surface increases with decreasing electrode size; the high transport rates mean that with very small electrodes this process can take place faster than in the case of heterogeneous charge transfer; in these conditions the reaction becomes kinetically controlled, as opposed to being diffusion controlled [217]. Unlike the diffusion-controlled case, the corresponding stationary current-voltage curves shift with minor changes in their shapes, depending on the rate of electron transfer; the transfer rate, k_S, can be determined from the potential shift of the curves [22, 23, 25, 219]. By applying a suitable set of NEs of different sizes to obtain steady-state voltammograms, one can determine the kinetic parameters of the heterogeneous charge transfer (the transfer coefficient α and the transfer rate k_S), as well as the thermodynamic standard redox potential [218].

For fast reactions, most of the analyte will react at the working electrode surface. This type of reaction is reversible, and no advantage will be gained by increasing the applied potential. For slow reactions, not all of the analyte that reaches the working electrode surface has time to react. To drive the electrolytic reaction at a faster rate, a much higher potential must be used. Slow reactions are essentially irreversible. This results in a greater noise and a poorer limit of detection.

In the past, the time constant of the cell was in the range of 100 μs or more, and electrode kinetics were restricted to investigations of processes that were much slower than that studied in other areas of chemical kinetics. With the use of NEs, the time constant could be reduced to nanoseconds and the rates of electrode reactions could be investigated up to the diffusion jump limit [219]. Thus NEs can be used to study fast chemical reactions. Consequently, micro- and nanoelectrodes are powerful tools for understanding the behavior mechanism of an electrochemical reaction and the kinetics of fast reactions [3, 23–26, 32, 34, 69, 70, 75, 220–224]. More recently, NEs have been introduced in the study of ultrafast electrode processes. The time constant of the NE may be even as small as 1 ns. This opens the possibility for the study of solvent relaxation phenomena at the electrode surface [75, 204, 220].

The use of NEAs for the determination of standard heterogeneous rate constants was reported for the first time by Brunetti et al. [54].

5.2. Nanoelectrodes in Biomedicine

The most important NE development is related to the biomedical field, and it is presented in this section. However, because of the huge quantity of information, the examples that are described are not exhaustive, the purpose of this section being only to demonstrate the diversity of applications.

5.2.1. The Importance of Nanoelectrodes for Biological Investigations

Recently, the bionanoscience field has developed rapidly and found many novel applications. The high number of recent workshops, conferences, symposia, congresses (the Conference on Molecular Nanotechnology; BioMEMS & Biomedical Nanotechnology World; the Symposium on Bio-Nano Electronics; Nanotechnology and Biosience for the 21st Century; the International Meeting on Nanobiology; the International Conference on Molecular Electronics and Bioelectronics; the International Congress on Bio-Nanointerface; Summer School: Cell Adhesion and Migration, the Interface with Tissue Engineering; EuroConference: Computational Biophysics, Integrating Theoretical Physics and Biology; the European Conference on Biomaterials; the Annual Protein Informatics; BIOMED—the International Symposium on Biomedical Science & Technology; the International Biomaterials Days; the Asian Symposium on Biomedical Optics and Photomedicine), reviews, and books [26, 225, 226] attest to the fact that many of these novel developments will be extended rapidly in the near future, especially in the fields of biochemical sensing and analyses, molecular recognition, and signal transduction [227].

The connection between biological self-assembly and non-biological molecules is very important for nanotechnology applications. Biological molecules and systems have a number of properties that make them highly suitable for nanotechnology applications [225]. Enzymes and proteins (hirudin, mellitin, actinoxanthin, cytochrome b and c, flavodoxin, azurin, high potential iron protein, plastocyanin, hemoglobin, leucine-binding protein, galactoze-binding protein, myoglobin, uteroglobin, calcium-binding protein, b-lactamase, pepsin, immunoglobulin, etc.) have sizes in the 5–10-nm range. Very small NE structures, with dimensions less than the Stokes radius of a small protein (which is approximately 2–3 nm), can be obtained through STM [104, 105].

On the other hand, new measurement tools make use of current developments and the recent progress in the fields of micro- and nano-manufacturing and nanodevices, molecular design, and polymer technology.

An excellent review of Lawrence et al. [228] including 206 references, in the field of voltammetric analysis of small biologically relevant compounds, reveals the problems that will require more attention in the future: (i) insufficient selectivity; (ii) overlapping signals; (iii) an unresolved voltammetric peak in a multicomponent mixture, if one component is in excess; (iv) poor electrode sensitivity as a consequence of slow electrode kinetics or electrode surface contamination.

There is also a need to move detection away from the ensemble, to the single-molecule scale. This includes driving instrumentation toward single-molecule spectroscopy, chemical analysis of nanoliter volumes [229], nanoscale electrode and chemical probes, chemical sensing and detection technology [230], and chemical analysis of single cells [225].

The high flexibility in the design and shape of nanoprobes, as well as the large number of various probe materials and functionalization layers, offers a high potential for a wide variety of applications, such as (i) biomedical detection, in diagnostics and analysis of various fluids, including on-line analysis of blood electrolytes like K^+, Na^+, and Ca^{2+} and blood metabolites like glucose and L-lactate, and measurements of the intracellular free ion concentrations of important inorganic ions; (ii) cell investigation: membrane cell properties study, including the level of single ion channels, and study of cell architecture and connections between cells by injection of markers; (iii) investigation of the mechanism of transducing DNA hybridization into electronic signals by electrochemical methods; and (iv) the integration of nanoelectrodes into genoelectronics-based genechips.

New methods of fabricating nanomaterials such as carbon nanotubes and mesoporous catalyst templates were developed in recent years, and these materials were integrated into useful nanodevices by combining nanofabrication and chemical functionalization, particularly NE assemblies interfaced with biomolecules.

5.2.2. Electrochemical Measurements in the Field of Biology

Voltammetric Analysis in Small Volumes NEs allow for detection in very confined spaces with the same volume as a biological cell [228, 229]. For example, the integration of NEs in picoliter vials has been investigated for single-cell analysis [69, 216, 231–237] or for measurements in living tissue, as they cause minimal physical damage [216].

Recent advances in the development of nanoscale analytical techniques have allowed minute amounts of compounds of biological interest to be monitored in microenvironments. Voltammetric NE techniques, such as amperometry and fast-scan cyclic voltammetry, are ideally suited for monitoring transiently occurring chemical events in cellular and subcellular processes because of their rapid response times and small structural dimensions [238]. The principles and applications of these techniques in single-cell analysis have been presented by Chen and Ewing [239]. The redox-active species were measured as a function of cellular dynamics.

For these electrochemical measurements in microvolumes, two main strategies have been proposed, either precisely positioning external nanoelectrodes in the small volume or integrating the electrodes in the nanoliter device. The first approach has the advantage of being easier to implement in microvolumes but requires very precise and reproducible placement of the NEs [84, 232]. The second strategy provides a better stability in the measurements and does not require a difficult placement procedure before the analysis [231].

Recent research has exploited steady-state voltammetry for very small electrodes and ion transfer to micropipettes, to facilitate the study of binding small molecules to DNA [240–242].

Pantano and Walt [243] developed optical sensors with nanovials for immuno- and DNA sensors attached at the ends of fiber optics.

Redox cycling of an individually addressable electrode array can provide an enhanced current intensity [244–246].

The analyte is oxidized at one electrode (referred to as the generator) and is subsequently reduced at the neighboring electrode (the collector). The small distance between electrodes within the array (typically nanometer to micrometer) allows for the diffusion of the analyte between the electrodes, thus inducing a redox cycle that amplifies the current.

NEs for sensitive measurements of very small amounts of important molecules such as neurotransmitters, carbohydrates, pollutants, and proteins can be incorporated into "labs on chips"—microdevices capable of reactions, separation, and detection.

As was previously specified, most of the reported NEs are housed in large insulating and supporting electrode bodies and therefore cannot be used for measurements at the single-cell level.

Analyses in vitro and in vivo *In vivo* measurements in the central nervous system constitute a new and exciting direction of modern electrochemistry [247, 248]. The small sizes of micro- and nanoelectrodes allow novel applications *in vitro* and *in vivo*, where neurotransmitters can be accurately analyzed [249–252]. Such electrodes can be used to stimulate or monitor the response of individual nerve cells, allowing experimental research into the central nervous system in both medicine [250] and zoology [251]. Voltammetric techniques may then be used to monitor the concentration of neurotransmitters in the extracellular fluid space following stimulated synaptic release.

In vivo voltammetry provides unique information concerning the kinetics of drug administration or emphasizes changes in the brain chemistry related to physiological processes such as drinking or feeding. Carbon fiber microelectrodes that support enzyme-containing redox polymer gels permit the amperometric detection of glutamate, choline, and glucose. These devices are of interest for *in vivo* neurochemical monitoring because their small dimensions permit highly localized measurements within small brain nuclei.

Ultramicroelectrodes also find applications in the study of secretion of molecules such as histamines or neurotransmitters from a single biological cell *in vitro*.

A new Pt/Ir nanoprobe for intracellular potential measurements was developed [158]. The functioning of this new type of electrode was tested by measuring the transmembrane potential of mouse liver cells *in vitro*.

5.2.3. Electrode Material for Biological Applications

A number of excellent reviews have been compiled on the electroanalytical versatility of the electrode materials used in the field of biology; the reader is directed to these for more comprehensive information [253, 254].

In biology, the appropriate choice of the electrode material is critical. For example, carbohydrates [255–257] and amino acids (with the exception of tyrosine, tryptophan, and cysteine) [258–262] cannot be electrochemically investigated with conventional electrode materials, but they display marked reactivity at copper surfaces.

Metallic Nanoelectrodes for Biomedical Applications Metal alloys (Cu/Ni [263], Pt/Ir [264], Ni/Cr [265], Ni/Ti [266]) give poorer performances, and their use is limited to

specific areas. Min and Baeumner [83] have developed a biosensor for the detection of pathogenic organisms at the single-cell level, based on Au and Pt ID-UMEAs with the following sizes: gap sizes of 0.3, 0.9, 1, 2, 5 μm; widths of 2.7, 3.7, 5.7 μm; and heights of 10, 25, 50, 100, 150 nm. Applications of ID-UMEAs for the quantitative analysis of dopamine, one of the most important neurotransmitters, have been reported [267]; in this system, a detection limit of 100 pM was reported [268]. Subfemtomole detection of dopamine with an IDA carbon microelectrode was reported [102].

Carbon-Based Nanoelectrodes for Biomedical Applications Carbon electrodes have a wider potential window and larger overpotential for water than noble metal electrodes; in most cases their electrochemical reaction is faster and they are expected to improve sensitivity for redox-active biological molecules.

Carbon Nanotubes (CNTs) offer the potential of making probes with very precise mechanisms. The use of CNTs as NEs in the field of biomedicine includes both potential measurements and ion concentration determinations. The main research in this field is focused on (i) measuring the potential across a cell membrane, focusing on the quality of the electrical seal between the nanotube and the membrane; (ii) measuring the potential across organelle membranes, particularly the nucleus and mitochondria; (iii) measuring the local neurosecretion upon stimulation of a neuron; (iv) locally measuring specific ion concentrations in the cytoplasm (e.g., Ca^{2+}) by appropriately derivatizing the nanotube tip.

CNTs can be used as connections between the electrode and the active center of the enzyme. The purification of SWCNTs with oxidizing acids such as nitric acid creates surface acid sites that are mainly carboxylic and possibly phenolic on both the internal and external surfaces of the oxidized nanotubes [144, 269–271]. The CNT high surface area, possessing abundant acidic sites, offers special opportunities for the adsorption and entrapment of chemical/biological molecules [272–277]. The immobilization of DNA, proteins, and enzymes on CNT and the helical crystallization and interaction of proteins with CNT contributed to the development of new biosensors [272–278]. In such devices the CNT acts as a host by trapping and supporting the biological molecules, and the surface acidic sites can serve to enhance the binding of the biomolecules.

Chen et al. [279] reported CNTs aligned on a cysteamine-modified gold electrode. The enzyme or enzyme active center can be attached to the other end of the tube. The initial immobilized enzyme was microperoxidase, which has an active site close to the surface, thus facilitating a direct electron transfer to the enzyme. A direct electron transfer where the redox active centre is located deep within the proteins was also reported [279].

Malinski's invention [280] is related to the microelectrode sensors and NE sensors, using, for example, the edges of carbon films and suitable metal films, as well as carbon fibers. Because of their mechanical properties as well as the possibility of controlled miniaturization, carbon fibers are the preferred support materials for microsensors in

single-cell applications [281–282]. Zhang et al. [133] developed a glucose nanosensor based on Prussian-blue-modified carbon-fiber cone nanoelectrodes. Much research is related to carbon fiber surface modifications for biological purposes [283–289].

Electrode Surface Derivatization for Biological Purposes The molecular building blocks of life—proteins, nucleic acids, lipids, carbohydrates, and their nonbiological counterparts—are examples of materials that possess unique properties determined by their size, folding, and nanoscale patterns. The most common groups that are exploited as quantifiable redox labels are phenolics, aromatic amines, thiols, heterocyclics, quinoids, and the nitro and nitroso groups. Redox modifying compounds can be immobilized on a nanoelectrode surface to improve the selectivity and sensitivity of the electrode arrays to biological agents.

To study electron transfer processes in individual proteins, Pemberton et al. [290–292] proposed the following procedure for NE fabrication: (i) the attachment of 3-mercaptopropyl trimethoxysilane (3MPT) on a Ag or Au/Si support; (ii) the deposition of a tetramethyl orthosilicate (TMOS)-based sol–gel on the Ag/Au surface; (iii) the atomic force microscope (AFM) NE definition; (iv) the protein attachment. After the protein attachment to the NE, the electrochemistry of a small number of cytochrome *c* molecules is probed by SECM, which also provides spatial resolution of these surfaces [290–292].

Submicron-sized domains of a carbon surface can be derivatized with antibodies by biotin/avidin technology [253, 293]. These sites are spatially segregated from and directly adjacent to electron transfer sites on the same electrode surface. The distance between these electron transfer sites and enzyme-loaded domains is kept to a minimum (e.g., less than a micrometer) to maintain the high sensitivity required for the measurement of enzyme-linked cofactors in an enzyme-linked immunoassay.

5.2.4. Nanoelectrode Biosensors

Nanostructures with biomaterials such as enzymes, DNA, receptors, and antibodies are coupled to nanobiosensors. Several reviews have been written on this subject [294–297].

Molecular biosensors, based on antibodies, enzymes, ion channels, or nucleic acids, are briefly reviewed in [298]. The first application of nanofibers in the field of biosensors was reported by Alarie and Vo-Dinh [299]. They developed and characterized antibody-based nanobiosensors for the detection of benzo[a]pyrenetetrol (BPT), a DNA adduct of the carcinogen benzo[a]pyrene. A simple three-step procedure was used to create these biosensors. The first step involved pulling and coating a nanofiber with a thin coating of Ag ($\sim$200 nm) to optimize the delivery of light to the end of the fiber. After this, the fiber was silanized to create attachment sites for the antibodies; the antibodies were attached to the fiber by covalent binding. It was found that the absolute detection limit of these nanobiosensors for BPT was $\sim$300 zeptomoles (10^{-21} moles).

Although enzymes had previously been exploited in the field of biosensors for their ability to be regenerated, Vo-Dinh and Cullum [294] realized for the first time an enzyme nanosensor. This sensor represents a significant tool

for the field of neurophysiology. Glutamate is one of the major neurotransmitters in the central nervous system, and, through monitoring of the glutamate levels produced by individual cells, a better understanding might be achieved of the mechanisms by which sensations are transmitted throughout the human body. When glutamate is bound to glutamate dehydrogenase, NAD is reduced to NADH and the fluorescence of the NADH can be readily measured [294]. Because the receptor of this biosensor is an enzyme, it should be possible to continuously monitor glutamate release from individual cells.

Electrochemical sensors based on enzyme-modified nanoscopic band electrodes show great promise for use in small volumes [214]. To achieve direct communication between enzymes and electrodes the electrode must be brought inside the enzyme to the redox active center [279].

Several other optical nanobiosensors have been developed over the past few years for the analysis of various biologically relevant species [300–306]. These have included nanobiosensors for the detection of nitric oxide through fluorescence detection of cytochrome c_9 or fluorescently labeled cytochrome c_9 [300], as well as enzyme-based nanobiosensors for indirect detection of glutamate [301].

Nanobiosensors for intracellular measurements have been developed. Measurements involving the smallest cells to be probed with a fiber-optic nanosensor have been reported in a study by Vo-Dinh et al. [302], in which nanobiosensors for BPT were prepared as described earlier and used to measure intracellular concentrations of BPT in the cytoplasm of two different cell lines, human mammary carcinoma cells and rat-liver epithelial cells.

A pH NE sensor for body fluids (serum, urine) and low-ionic-strength water samples (rain, deionized water, and tap-water) was developed by Zhang et al. [134]. The proposed pH NE displayed a high ion selectivity for K^+, Na^+, Ca^{2+}, and Li^+. The proposed pH NE demonstrates attractive properties and seems particularly promising for use under physiological conditions.

Zhang et al. [137] developed a new NO nanosensor, with a tip dimension as small as 100 nm. This sensor technology is based on the etching of a carbon fiber electrode, which is further modified with multiple membranes. A composite polymer of nafion and NO selective membranes demonstrates superior sensitivity, selectivity, and stability for NO detection. The new nanosensor displays a high sensitivity to NO with a detection limit of 2 nM. It is free from most interfering species found in biological samples. The use of this nanosensor is very promising in applications for the *in-situ*, *in vivo*, and real-time detection of NO at the single-cell and microcapillary levels.

NE arrays can serve as individual electronic protein "receptors" (or detectors); they can be used to detect, characterize, and quantify many different proteins on a single chip. NEAs were used by Brunetti et al. [54] to investigate the electrochemistry of three electron-transfer mediators: two phenothiazines (Azure A and B) and methylviologen in biosensors based on reductase enzymes. They investigated the effects of background currents associated with proton reduction on the detection limits. The lower detection limits obtained with the NEA allow the use of lower

mediator concentrations, and the unwanted adsorption process observed at macroelectrodes can be eliminated in the case of NEAs. The use of lower concentrations of reactants (both mediator and enzyme) in a NEA-based sensor offers some important advantages: (i) it can be beneficial because the employed mediators are often toxic, (ii) it can be beneficial because enzymes are often expensive and difficult to purify, and (iii) problems associated with protein aggregation are minimized.

5.2.5. SECM Development in the Field of Biology

SECM was used for biological applications such as the transport of species through membranes, tissues, and pores [307]. Specific applications were developed related to the quantitative imaging of transport through dentine [308] and to the imaging of the localized transport and permeability in cartilage [309]. The charge transfer through bilayer lipid membranes was also investigated by SECM [310].

The combination of AFM and SECM makes it possible to obtain more information on transport phenomena through membranes (e.g., biological tissues). Hence, a combined probe with improved lateral resolution permits biomedical investigations, including drug delivery through membranes (e.g., cell membranes), cellular communication processes (e.g., exocytosis), and neurophysiologically relevant signaling events. Fields of application include cancer research, neurophysiology, pharmaceutical applications, and mental disease research (Parkinsonism, Alzheimer's disease).

The ultimate detection limit of the single molecule has already been achieved [311, 312]. Recent research is related to detection with the use of biomolecules or biomodified electrodes and probe redox couples in solution. Opportunities for establishing calibration and measurement standards lie in the determination of concentrations, diffusion coefficients, and electron transfer rates for electroactive biomolecules in solution and a morphological current map of biosamples attached to modified electrodes.

SECM was applied to image the localized mass transport of oxygen and electroactive ions in cartilage and ionic fluxes through skin. SECM was used to map the concentration profile of hydrogen peroxide [313, 314], cell activity [315], and enzymatic activity [316]. Other studies on the fluxes of calcium and other ions from the cells known as osteoclasts, which are responsible for the resorption and remodeling of bone, are reported [317–319]. The SECM NE is positioned over an osteoclast attached to a bone slice, to monitor the resorptive activity of the cell in response to various biochemical stimuli.

Various chemical processes occurring in living cells (e.g., electron transfer reactions, molecular diffusion of oxygen, proton pumping across the membrane) have been imaged with a submicrometer spatial resolution. The imaging is difficult because the SECM probe is small (i.e., the tip radius is much smaller than the cell dimensions). At the same time, such small probes are required to obtain high (submicrometer scale) spatial resolutions [128]. The mapping of intracellular redox activity, combined with potentiometric measurements employing a scanning pH probe, can provide

information about cell metabolism, respiration, photosynthesis, and other important biochemical processes [315, 320–331]. The topography and redox reactivity of human breast cells have been imaged by SECM [321]. SECM was used to probe the redox activity of purple bacteria (*Rhodobacter sphaeroides*). The two groups of redox mediators (i.e., hydrophilic and hydrophobic redox species) were used to shuttle the electrons between the SECM tip electrode in solution and the redox centers inside the cell [328, 329].

5.2.6. New Hybrid Techniques

The applicability of a recent technique, sonoelectrochemistry, which aids the analysis of organic compounds (ascorbate [330], dopamine [331], and 5-aminosalicylic acid [332]), has been demonstrated. Liquid chromatography and capillary electrophoretic systems with electrochemical detection in biological media are described in [333–335].

5.3. Electroanalytical Detection

Voltammetry is useful for both qualitative analysis (identification of analytes) and quantitative analysis (concentration measurements). Moreover, the oxidation state of the analyte (e.g., how much Fe(II) and how much Fe(III) are present) can be determined through voltammetry analyses. A very interesting review related to microelectrode contributions to analytical studies employing voltammetric detection has been written [336].

NE voltammetric techniques have come to be used more and more in metallic trace analysis. At trace levels, most elements are essential to life. However, some of them, especially heavy metals, are toxic even at very low concentrations; they do not degrade with time and thus tend to accumulate in living organisms. Maximum heavy metal contents should be in the range of 1 to 50 ppb (parts per billion or μg/liter) [337].

Quantitative measurements are usually obtained with spectroscopic analytical techniques such as atomic absorption or fluorimetry, but these methods require expensive equipment and are not easily adaptable as portable probes for *in-situ* determinations. In contrast, electrochemical methods require nonsophisticated instrumentation and are well adapted to quantitative measurements [338].

Voltammetry, including polarography, presents many advantages for trace metal determination in water or in liquid food:

- The simultaneous determination of more than one metal (e.g., the determination of lead and cadmium in food through anodic stripping voltammetry (AVS) is very common). Cu, Cd, Zn, and Pb can be determined during the same polarographic scan. The time saved by determining two or more metals simultaneously is evident.
- The trace metal technique (<100 ppb) is performed with the same instrumentation that is used to determine many other ions, such as ascorbic acid or nitrate. Subfemtomole detection of dopamine with an IDA carbon microelectrode has been reported [102]. Stripping voltammetry is a very common analysis technique that can also be considered in the case of NE tools; in

this case, the size of a single Hg hemispherical droplet formed on a flat surface, calculated from the deposition charge and from the limiting CV current, is about 4.5×10^{-6} m [339–340], which could limit its usage.

In Table 2 some of the detection limits in voltammetric analysis using electrodes of various materials and sizes and various voltammetric techniques are presented. Because of the different measuring conditions, it is not possible to compare these data. In any case, the sensitivity can be improved by a suitable choice of the electrode and electrochemical measurement conditions. It is remarkable that some types of NEs are developed as commercial products with very high performances related to the detection limits [341–343].

5.4. Nanoelectrodes in Scanning Electrochemical Microscopy

SECM provides *in-situ* electrochemical, chemical, and biochemical information on surfaces and interfaces. The unique advantage of integrating NEs into conventional AFM tips is based on the fact that complementary electrochemical or activity information is obtained in combination with any of the state-of-the-art measurement techniques in AFM, such as chemical force imaging, force imaging, or phase imaging. The scanning electrochemical microscope is a scanned probe microscope (SPM) related to the familiar STM and AFM. All SPMs operate by scanning the surface to be imaged with the tip of a small probe. In SECM, imaging is performed in an electrolyte solution with an electrochemically active UME or NE; the nanoprobe signal is a faradaic current obtained from the electrolysis of solution species. This NE can then be used to scan a surface, and the current, measured as a function of position, can be used to acquire an electrochemical topographic map of the substrate. Obviously, the response of the SECM is governed by the mass transport characteristics between the UME and the sample and the electrochemical reactions occurring at the sample surface. Although not as spatially resolved as in the case of an AFM or STM, because of the relatively long range of the tip (electrochemical substrate interactions accounting for a poorer resolution), the SECM can probe both the topography and reactivity of the surface with a resolution governed by the tip dimensions.

In 1998, Fan and Bard [344] have shown that the detection of a ferrocenyl molecule in solution is possible with a tip of nanometer proportions.

Fabricating techniques for submicroelectrodes have been gradually developed [69, 70, 73, 235, 345–349], which has led to the extensive development of SECM techniques using nanoprobes [2, 29, 130, 136, 350–359]. Some SECM experiments use an ion-selective electrode as a tip [360].

Two features distinguish SECM from related methods such as electrochemical STM or AFM: the chemical sensitivity of the SECM tip and the use of solution phase ions or molecules as the imaging signal. The surface properties of the substrate influence the electrochemical response of the electrode, providing information on the nature of the substrate. Because of the difficulty in positioning electrodes at a nanometer range, SECM offers limited lateral resolution compared with STM and AFM [361–362].

Table 2. Detection limits in voltammetric analysis using various electrodes.

Reference	Electrode type	Technique	Detection limits
ΩMETROHM ion analysis Ltd. CH-9101 Herisau (Switzerland) [341]	Unspecified	DP, SWV, CV	Sb^{III}/Sb^{v} 500 ppt; As^{III}/As^{v} 100 ppt; Bi 500 ppt; Cd 50 ppt; Cr 25 ppt; Co 50 ppt; Cu 50 ppt; Fe 200 ppt; Pb 50 ppt; Hg 100 ppt; Mo 50 ppt; Ni 50 ppt; Pt 0.1 ppt; Rh 0.1 ppt; Tl 50 ppt; W 200 ppt; U 25 ppt; Zn 50 ppt
Trace detect [342]	Nanoband electrode	ASV, CSV, CV	Part per million is instantaneous Part per billion in 20 s or less Part per trillion takes 1–3 min Pb, Cu, Zn, Cd, Tl, Bi, Sn, Sb, As, Ag, Ga, Se, Co, Ni, Cr, S, Cl, Br, I
Min et al. [83]	Interdigital UMEA		0.1 μM ferro/ferrihexacyanide
Takahashi et al. [268]	Interdigital UMEA IDA carbon electrode	CV	100 pM for dopamine 0.5 fmol for 5 μl of dopamine (100 pM)
Prado et al. [158]	Boron-doped diamond film macroelectrodes	CV ASV SWV	2.5×10^{-5} M solution of Pb^{2+} in 0.1 M HNO_3, scan rate 50 mV s^{-1} 2.5×10^{-5} M solution of Cu^{2+} in 0.1 M HNO_3, scan rate 50 mV s^{-1}
Brunetti et al. [54]	Macroelectrode	CV	2.4 μM Azure A 2.5 μM Azure B 10 μM Methylviologen
	NEA	CV scan rate: 20 mV s^{-1} 10^{-2} M phosphate buffer at pH 7.4.	2.4 μM Azure A 2.5 μM Azure B 10 μM Methylviologen
Zhang et al. [137]	Nanoelectrode tip diameter of 100 nm	Amperometric measurements	10 nM to 1 μM NO in stirring 0.1 PBS buffer solution (pH 7.4).
Gamma analysen technik GMBH, Bremerhaven, Germany [343]	Hanging mercury drop electrode (HMDE)	All typical voltammetric/polarographic analysis methods	Cd 0.05 ppb; Cr 0.01 ppb; Cu 0.05 ppb; Hg 0.03 ppb; Ni 0.01 ppb; Pb 0.05 ppb; Zn 0.05 ppb; Co 0.01 ppb; As 0.1 ppb; Se 1 ppb; Mn 0.5 ppb; Tl 0.03 ppb; Fe 30 ppb; NO_2^- 10 ppb; NO_3^- 50 ppb; NH_4^+ 60 ppm; Cl^- 1 ppb; PO_4^{3-} 20 ppm; SO_4^{2-} 20 ppb; S^{2-} 10 ppb;
Kleps et al. [176]	NEA (900 electrodes) tip diameter of 100 nm; 0.1 M HCl	SWV	Pb^{2+}, Cd^{2+}-10^{-9} M

The trend of using nanoelectrodes for enhanced spatial resolution and the use of micro/nanosensors as SECM tips demand innovative approaches to the manufacture and positioning of the SECM probe.

Recent attempts to combine SECM with AFM have been reported in the literature [363].

Lugstein et al. [361, 364] introduced the concept of integrated multifunctional scanning probes. They realized the first reproducible integration of submicro- and nanoelectrodes in commercial AFM tips through microfabrication techniques. Using such a system, laterally resolved electrochemical information on homogeneous or heterogeneous electron transfer processes at the sample surface can be obtained simultaneously during AFM imaging. Micro- or nanoelectrodes are integrated into standard AFM cantilevers through nanofabrication techniques. Consequently, electrochemical processes can be imaged or induced at the nanoscale during simultaneous AFM measurements [364].

Recently, Lugstein et al. [361] proposed the extension of this concept to multifunctional scanning probes/sensors, combining, for example, SECM with AFM and scanning near-field optical microscopy (SNOM) into a single trifunctional tip or integrating multiple electrode/sensor systems.

The construction of SECM/AFM tips is based entirely on micro- or nanofabrication processes [361–364]. The main processing steps include the deposition of the electrode material (60–100 nm) on a cantilever surface by sputtering. In the case of a conducting tip, a prior deposition of an insulation layer is required. Commonly used electrode materials include gold, platinum, and modified carbon. Subsequent insulation is achieved by chemical vapor deposition of silicon nitride, mixed silicon nitride/oxide, or parylene. Exposing the micro/nanoelectrode at the required working distance to the sample surface is achieved by means of a three-step focused ion beam (FIB) cutting/milling process.

SECM can be applied to the measurement of fluxes of ions [365] and redox-active molecules [366] through porous media [98]. Slevin et al. [98] have obtained SECM Pt nanoprobes with effective radii varying from 1 μm to 10 nm, with a technology presented in Section 4.7.1. When the tip is an ion-selective electrode, it can be used to map the concentration of an ion and to monitor particular reactions

occurring at the substrate, for example, the activity of immobilized enzymes and cells such as the osteoclast [321, 367–368].

SECM employs a very low-dimension electrode above the sensing surface. The diffusion and generation of redox-active molecules are perturbed by the conductivity of the surface. Since SECM uses a scanning electrode, the time resolution is limited by the mechanical scanning speed. Other methods employing a multimicroelectrode array have also been reported [369–371]. These kinds of image measurement provide a huge number of discrete measurements instantly.

5.4.1. Nanocluster Deposition

The electrochemical nucleation and growth of metal clusters and low-dimensional metal structures can be achieved locally at predefined positions on a substrate surface by using the tip of a STM as an electrochemical nanoelectrode. The deposition of nanometer-sized clusters and the local etching of a metal surface have been achieved by applying ultrashort voltage pulses between the SECM probe tip and the surface [221, 372–374]. Schindler [375–377] demonstrated that nanostructures such as Co on Au(111) and Pb on *n*-Si(111):H can be grown with a controlled aspect ratio and with lateral diameters even below 10 nm. The width and height of the clusters were determined by the diameter of the tip apex, the distance between the tip and the substrate, the substrate potential, and the amount of Co transferred to the substrate through the tip [131].

6. CONCLUSIONS

The spotlight in this review is on electrodes or probes as well as electrode arrays of nanometric dimensions. However, there are some reasons to occasionally mention higher size electrodes, such as UMEs, microelectrodes, and submicroelectrodes: (i) behavior and applications of NEs are very close to those of microelectrodes; (ii) the chronological development of the electrode fabrication technology was from the micro to the nano domain; (iii) one aim is to compare or emphasize advantages or drawbacks.

The general properties of microelectrodes are extensively reviewed in the literature and can be considered as well for NEs. Moreover, the microelectrode theory and modeling of microelectrode processes are well consolidated.

The flux of electroactive molecules toward the electrode is much greater for a NE than for a macroelectrode, because of the radial diffusion. This confers important properties on the NE: (i) the steady state for a faradaic process is attained very rapidly; (ii) the applied potential can be scanned very rapidly because the charging current is suppressed; (iii) with the use of NE arrays, the amperometric signal (i.e., the current intensity) is enhanced; (iv) there are lower detection limits due to the higher signal-to-background ratio; (v) the small sizes of the electrodes permit measurements in very limited solution volumes.

Unlike microelectrodes, the use of NEs confers more sensitivity to the electrochemical measurements and the possibility of integration into nanosensors. Sometimes NE/NEA behavior is greatly different from microelectrode theory, depending on many factors: the electrode size, geometry,

and material; the distance between two consecutive electrodes in an array; the kinetic parameters of the electroanalytical technique employed, etc. Some NE particularities and deviations from the theory described in the literature are presented.

The recent improvement in nanotechnology tools and procedures permits the preparation of very small electrodes, in the range of 100–10 nm, or even 1 nm. Actually, nanoelectrodes of different sizes and geometries can be fabricated with lithographic techniques, template-synthesized nanomaterials, silicon-etched pyramidal structures, embedded nanoparticles, carbon nanotubes, etc. In the case of NEA, an optimum current response occurs at low current densities, and for high distances between the electrodes. Only NEAs realized by lithographic techniques, or those fabricated on silicon-etched pyramidal structures, behave in accordance with the theory. The fabrication of the pyramidal NEAs is very simple, being based on standard Si device processes on Si wafer substrates. Pyramidal NEAs can be fabricated with a common photolithographic technique, ultraviolet light proximity, and does not involve other special lithographic techniques.

There are some drawbacks of electrochemical NE tools, as follows: (i) the difficulty of achieving an efficient NE insulation, in order to release only the tip of the electrode in contact with the solution; (ii) the discordance between the NE size and the dimensions of the mounting case; (iii) deviation from the ideal behavior, due to many causes; (iv) not enough reproducibility of the measurements; (v) the difficulty of systems using arrays of NEs in achieving widespread application, due to the complexity of their construction.

Nevertheless, NEs represent an exciting domain and a real challenge because of their unique performance, high sensitivity, and low dimensions that allow *in vivo* measurements.

NEs have applications in various fields: electroanalytical determinations, bioanalyses, medicine, scanning electrochemical microscopy, and investigation of the chemical reaction mechanism. More recently, NEs have been introduced to study ultrafast electrode processes. The time constant of the NE may even be as small as 1 ns. Great attention was given to NE biomedical applications, a field with a huge potential for expansion in the future. Voltammetric NE techniques, such as amperometry and fast-scan cyclic voltammetry, are ideally suited for monitoring transiently occurring chemical events in cellular and subcellular processes. Furthermore, applications of NEs in diagnostics, biomedical detection, and analysis of various fluids are becoming common. NEAs with high NE densities, such as template-synthesized nanoelectrodes, nanoparticles embedded in dielectric layers, or SAM electrodes, can be easily functionalized for biomedical applications.

NEAs that behave in accordance with the theory, such as those realized by photolithographic processes, or on pyramidal structures or single NEs, are very appropriate for electroanalytical determinations; NE voltammetric techniques are coming to be used more and more in metallic trace analysis; NEs are even commercial tools for selective identification of toxic chemical compounds at ultratrace levels in liquid media.

Single NEs or nanoprobes are widely used in SECM tools. The recent NE applicability in new hybrid techniques, such as AFM/SECM, AFM/SNOM/SECM, sonoelectrochemistry, liquid chromatography, and capillary electrophoresis with electrochemical detection, will increase the interest in the advance of NE technology.

The varied and immense quantity of information related to NE use, especially in biomedical or SECM fields, made a very strict classification of applications difficult; the purpose of this review is only to emphasize the great potential and the large aria of applicability.

Some commercial NE tools have been developed; however, it may be unrealistic to expect in the near future a widespreading use of all NE-based electrochemical tools or devices.

Nevertheless, based on the continuous improvements in this field, it is reasonable to be confident about NE performance and implementation; it is obvious that the methods discussed and continuing advances can eliminate some misconceptions concerning the inapplicability of NEs. The great interest in NEs and nanoprobes is proved by the huge number of review papers and book chapters, as well as conference, symposium, and workshop sessions being organized in this emerging field.

GLOSSARY

Bionanosensors Combine the selectivity of biology with the processing power of modern micro/nanoelectronics and optoelectronics to offer powerful new analytical tools with major applications in medicine, environmental diagnostics, and processing industries.

Biosensor An analytical tool combining a biochemical recognition component with a physical transducer. The biological sensing element can be an enzyme, antibody, DNA sequence, or even a microorganism. The transducer converts the biochemical event into a measurable signal, thus providing the means for detecting it.

Electrochemical nanoelectrode (NE) The working electrode in an electrochemical cell, having one dimension in the nanometric range, usually lower than 500 nm. Operational definition: A nanoelectrode is any electrode whose characteristic dimension is, under the given experimental conditions, comparable to or smaller than the diffusion layer thickness. Under these conditions, a current steady state or a pseudo-steady state is attained.

Electrochemical nanoprobe Similar to the nanoelectrode; this term is used specially in microscopy; it is also widely used in biomedicine and in bioelectrochemistry.

Electrode surface derivatization Redox modifying compounds that can be attached to the nanoelectrode surface to improve the selectivity and sensitivity of the electrode array to various agents.

Nanoelectrode array (NEA) The working electrode constituted of a group of many electrodes at the same potential, separated from each other by dielectric material; the area of the active electrode is the sum of the areas of all electrodes from the array.

Pyramidal nanoelectrode Nanoelectrode realized by insulating pyramidal shape nanostructures such as metal/dielectric/Si.

Scanning electrochemical microscopy (SECM) Microscopic technique that can provide information on both the topography and reactivity of a surface or an interface (liquid/solid, liquid/liquid, and liquid/gas), with a resolution governed by the dimensions of the electrochemical tip. The SECM tip is a submicronic-size electrochemical probe, and the tip signal is a faradaic current generated by the electrolysis of the solution species.

Self-assembled monolayers (SAMs) Ordered, chemically and thermally stable two-dimensional aggregates that are formed spontaneously by the adsorption of surface active molecules to a solid; the spontaneous molecular adsorption brings molecules close enough together and allows for the short-range van der Waals forces to become important.

Single-wire nanoelectrode Nanoelectrode realized by adequate insulation of the carbon fiber or metallic wire with a nanometric size tip.

Template-synthesized nanoelectrode Nanoelectrode realized by filling the pores of a dielectric material template with the electrode material.

Voltammetry An electrochemical measuring technique used for electrochemical analysis or for the determination of the kinetics and mechanism of electrode reactions. The potential of the working electrode is typically controlled with a potentiostat, and the current flowing through the electrode is measured. Cyclic voltammetry (CV) is a linear-sweep voltammetry with the scan continued in the reverse direction at the end of the first sweep. Voltammogram: Graphical representation of the results of a voltammetric measurement.

Working electrode One of the electrodes in a two-electrode/three-electrode cell where the electrochemical reaction takes place. It can serve as either an anode or a cathode, depending on the applied polarity. The working electrode can be the "measuring," "indicator," or "sensing" electrode, for example, in a potentiometric electroanalytical setup where the potential of the measuring electrode (relative to the reference electrode) is a measure of the concentration of a species in the solution.

ACKNOWLEDGMENTS

REFERENCES

1. X. W. Cai, J. S. Gao, Z. X. Xie, Z. Q. Tian, and B. W. Mao, *Langmuir* 14, 2508 (1998).
2. G. Staikov and W. Lorenz, in "Electrochemical Nanotechnology: *In-Situ* Local Probe Techniques at Electrochemical Interfaces" (W. J. Lorenz and W. Plieth, Eds.). Wiley/VCH, New York, 1998.
3. S. E. Creager and P. T. Radford, *J. Electroanal. Chem.* 500, 21 (2001).
4. W. S. Baker and R. M. Crooks, *J. Phys. Chem. B* 102, 10041 (1998).
5. A. J. Bard and C. G. Zoski, *Anal. Chem.* 72, 346A (2000).
6. S. J. Green, J. J. Stokes, M. J. Hostetler, J. Pietron, and R. W. Murray, *J. Phys. Chem. B* 101, 2663 (1997).
7. S. Chen, R. S. Ingram, M. J. Hostetler, J. J. Pietron, R. W. Murray, T. G. Schaaff, J. T. Khoury, M. M. Alvarez, and R. L. Whetten, *Science* 280, 2098 (1998).
8. E. Jeoung, T. H. Galow, J. Schotter, M. Bal, A. Ursache, M. T. Tuominen, C. M. Stafford, T. P. Russell, and V. M. Rotello, *Langmuir* 17, 6396 (2001).
9. C. M. Demaille, M. T. Brust, and A. J. Bard, *Anal. Chem.* 69, 2323 (1997).
10. C. Amatore, *Spectra* 151, 43 (2000).
11. C. Amatore, R. S. Kelly, E. W. Kristensen, W. G. Kuhr, and R. M. Wightman, *J. Electroanal. Chem.* 213, 31 (1986).
12. C. Amatore, *C. R. Acad. Sci. Ser. B.* 323, 757 (1996).
13. K. Štulík, C. Amatore, K. Holub, V. Mareček, and W. Kutner, *Pure Appl. Chem.* 72, 1483 (2000).
14. N. R. Sharma, Fabrication and Testing of an Integrated Microelectrode Chemical Sensor Array on Silicon, M.S. Electrical Engineering Thesis, University of Washington, 1995.
15. A. G. Ewing, M. A. Dayton, and R. M. Wightman, *Anal. Chem.* 53, 1842 (1981).
16. R. J. Forster, *Chem. Soc. Rev.* 23, 289 (1994).
17. M. Tian and X. L. Jing, *Electroanalysis* 19, 718 (1997).
18. K. B. Oldham and J. C. Myland, "Fundamentals of Electrochemical Science." Academic Press, San Diego, 1994.
19. K. B. Oldham, in "Microelectrodes: Theory and Applications" (M. I. Montenegro, M. A. Queiros, and J. L. Daschbach, Eds.). Kluwer Academic Publishers, Dordrecht, 1991.
20. K. B. Oldham, in "Microelectrodes: Theory and Applications" (M. I. Montenegro, M. A. Queiros, and J. L. Daschbach, Eds.). Kluwer Academic Publishers, Dordrecht, 1991.
21. R. D. Lafleur, J. C. Myland, and K. B. Oldham, in "Microelectrodes" (J. Wang, Ed.), VCH, New York, 1990, pp. 49–54.
22. K. B. Oldham, in "Ultramicroelectrodes" (M. Fleischmann, S. Pons, D. R. Rolison, and P. P. Schmidt, Eds.). Datatech Systems Publishers, Morganton, NC, 1987.
23. K. B. Oldham and C. G. Zoski, in "Comprehensive Chemical Kinetics." (C. H. Bamford and R. G. Compton, Eds.). Elsevier, Amsterdam, 1986.
24. C. Amatore, in "Microelectrodes: Theory and Applications" (M. I. Montenegro, M. A. Queiros, and J. L. Daschbach, Eds.), NATO ASI Series, Ser. E, Vol. 197, pp. 269–282. Kluwer Academic Press, Dordrecht, 1991.
25. K. B. Oldham, C. G. Zoski, A. M. Bond, and D. A. Sweigart, *J. Electroanal. Chem.* 248, 467 (1988).
26. C. Amatore, in "Molecular Electrochemistry of Inorganic, Bioinorganic and Organometallic Compounds" (A. J. L. Pombeiro and J. McCleverty, Eds.), NATO ASI Series, Ser. C, Vol. 385, pp. 625–644. Kluwer Academic Press, Dordrecht, 1993.
27. P. Hopper and W. G. Kuhr, *Anal. Chem.* 66, 1996 (1994).
28. C. A. Amatore, in "Physical Electrochemistry" (I. Rubinstein, Ed.), M. Dekker, New York, 1995, p. 131.
29. M. Ciszkowska and Z. Stojek, *J. Electroanal. Chem.* 466, 129 (1999).
30. C. Amatore, M. R. Deakin, and R. M. Wightman, *J. Electroanal. Chem.* 225, 49 (1987).
31. F. F. Fan and A. J. Bard, *Science* 277, 1791 (1997).
32. R. S. Ingram, *J. Am. Chem. Soc.* 119, 9279 (1997).
33. J. C. Hulteen, V. P. Menon, and C. R. Martin, *J. Chem. Soc., Faraday Trans. 1* 92, 4029 (1996).
34. C. Amatore, in "Ultramicroelectrodes" (M. Fleischmann, S. Pons, D. Rolinson, and P. P. Schmidt, Eds.), Chap. 5, pp. 169–183. Datatech Science, Morganton, NC, 1987.
35. J. Galceran, S. L. Taylor, and P. N. Bartlett, *J. Electroanal. Chem.* 506, 65–81 (2001).
36. C. Amatore, S. Szunerits, L. Thouin, and J. S. Warkocz, *Electrochem. Commun.* 2, 353 (2000).
37. C. Amatore, B. Fosset, K. M. Maness, and R. M. Wightman, *Anal. Chem.* 65, 2311 (1993).
38. R. C. Engstrom, M. Weber, D. J. Wunder, R. Burgess, and S. Winguist, *Anal. Chem.* 58, 844 (1986).
39. K. Aoki, *Electroanalysis* 5, 627 (1998).
40. M. V. Mirkin and A. J. Bard, *J. Electroanal. Chem.* 323, 1 (1992).
41. S. Chen and A. Kucernak, *Electrochem. Commun.* 4, 80 (2002).
42. A. M. Bond, D. Luscombe, K. B. Oldham, and C. G. Zoski, *J. Electroanal. Chem.* 249, 1 (1988).
43. B. R. Scharitker, in "Microelectrodes, Theory and Applications" (M. I. Montenegro, M. A. Queiros, and J. L. Daschbach, Eds.), Vol. 197. Kluwer, Dordrecht, the Netherlands, 1990.
44. S. Bellomi, in "Caratterizzazione elettroanalitica e voltammetria di scambio ionico su ensemble di nanoelettrodi." Ph.D. thesis, Dept. of Physical Chemistry, University of Venice, Italy, 10 (1995).
45. V. P. Menon and C. R. Martin, *Anal. Chem.* 67, 1920 (1995).
46. J. C. Hulteen, V. P. Menon, and C. R. Martin, *J. Chem. Soc., Faraday Trans.* 92, 1029 (1996).
47. R. M. Penner and C. R. Martin, *Anal. Chem.* 59, 2625 (1987).
48. S. Pons and M. Fleischmann, *Anal. Chem.* 59, 1391A (1987).
49. M. Mosbach, T. Laurell, J. Nilsson, E. Csoregi, and W. Schuhmann, *Anal. Chem.* 73, 2468 (2001).
50. H. Ju, H. Chen, and G. Hong, *J. Electroanal. Chem.* 341, 35 (1992).
51. P. Tomčík, S. Jursa, D. Bustin, and V. Tvarožek, *Chem. Listy* 92, 626 (1998).
52. C. Belmont, M. L. Tercier, J. Buffle, G. Fiaccabrino, and M. Koudelka-Hep., *Anal. Chim. Acta* 329, 203 (1996).
53. A. West, *J. Electrochem. Soc.* 140, 134 (1993).
54. B. Brunetti, P. Ugo, L. M. Moretto, and C. R. Martin, *J. Electroanal. Chem.* 491, 166 (2000).
55. C. R Martin and D. T. Mitchell, *Anal. Chem.* 70, 322A (1998).
56. P. Ugo, L. M. Moretto, S. Bellomi, V. P. Menon, and C. R. Martin, *Anal. Chem.* 68, 4160 (1996).
57. I. F. Cheng, L. D. Whiteley, and C. R. Martin, *Anal. Chem.* 61, 762 (1989).
58. W. E. Morf and N. E. de Rooij, *Sens. Actuators, B* 44, 538 (1997).
59. N. E. de Rooij and W. E. Morf, *Sens. Actuators, A* 51, 89 (1995).
60. S. G. Weber, *Anal. Chem.* 61, 295 (1989).
61. W. E. Morf, *Anal. Chim. Acta* 330, 139 (1996).
62. L. Rajendran and S. P. Ananthi, *Electrochem. Commun.* 4, 72 (2002).
63. P. R. Unwin and A. J. Bard, *Anal. Chem.* 64, 113 (1992).
64. J. Li, R. Stevens, L. Delzeit, H. T. Ng, A. Cassell, J. Han, and M. Meyyappan, *Appl. Phys. Lett.* 81, 910 (2002).
65. J. Li, A. Cassell, L. Delzeit, J. Han, and M. Meyyappan, *J. Phys. Chem. B* 106, 9299 (2002).
66. C. Amatore, B. Fosset, J. Barteli, M. R. Deakin, and R. M. Wightman, *J. Electroanal. Chem.* 226, 255 (1988).
67. C. Lee and F. C. Anson, *J. Electroanal. Chem.* 323, 381 (1992).
68. J. Chen and K. Aoki, *Electrochem. Commun.* 4, 24 (2002).
69. R. M. Penner, M. J. Heben, T. L. Longhin, and N. S. Lewis, *Science* 250, 1118 (1990).
70. Y. Shao, M. V. Mirkin, G. Fish, S. Kokotov, D. Palanker, and A. Lewis, *Anal. Chem.* 69, 1627 (1997).
71. C. Beriet and D. Pletcher, *J. Electroanal. Chem.* 72, 3486 (2000).

72. K. B. Oldham and A. M. Bond, *J. Electroanal. Chem.* 508, 28 (2001).
73. J. L. Conyers and H. S. White, *Anal. Chem.* 72, 4441 (2000).
74. S. L. Caston and R. L. McCarley, *J. Electroanal. Chem.* 529, 124 (2002).
75. R. B. Morris, D. J. Franta, and H. S. White, *J. Phys. Chem.* 91, 3559 (1987).
76. J. D. Seibold, E. R. Scott, and H. S. White, *J. Electroanal. Chem.* 264, 281 (1989).
77. M. P. Nagale and I. Fritsch, *Anal. Chem.* 70, 2902 (2000).
78. K. R. Wehmeyer, M. R. Deakin, and R. M. Wightman, *Anal. Chem.* 57, 1913 (1985).
79. S. Daniele, C. Bragato, G. A. Battiston, and R. Gerbasi, *Electrochim. Acta* 46, 2961 (2001).
80. C. R. Martin, M. J. Tierney, I. F. Cheng, L. S. Van Dyke, Z. Cai, J. R. McBride, and C. J. Brumlik, in "Nanostructure Physics and Fabrication," pp. 461–465. Academic Press, New York, 1989.
81. E. Sabatani and I. Rubinstein, *J. Phys. Chem.* 91, 6663 (1987).
82. C. Amatore, J. M. Saveant, and D. Tessier, *J. Electroanal. Chem.* 147, 39 (1983).
83. J. Min and A. J. Baeumner, "Characteristics of Interdigitated Ultramicroelectrode Arrays as Electrochemical Biosensor Transducers," NNUN Abstracts, Biology & Chemistry, p. 7. 2002.
84. R. A. Clark and A. G. Ewing, *Anal. Chem.* 70, 1119 (1998).
85. R. Kshyap and M. Gratzl, *Anal. Chem.* 70, 1468 (1998).
86. R. C. Engstrom, T. Meany, R. Tople, and R. M. Wightman, *Anal. Chem.* 59, 2005 (1987).
87. A. J. Bard, F.-F. F. Fan, J. Kwak, and O. Lev, *Anal. Chem.* 61, 132 (1989).
88. P. N. Bartlett and S. L. Taylor, *J. Electroanal. Chem.* 453, 49 (1998).
89. R. Ferrigno, P.-F. Brevet, and H. H. Girault, *J. Electroanal. Chem.* 430, 235 (1997).
90. R. Ferrigno, Ph.D. Dissertation, EPFL, Lausanne, 1997.
91. R. Sonnenfeld and P. Hansma, *Science* 232, 221 (1986).
92. H. Liu, F.-R. Fan, C. W. Lin, and A. J. Bard, *J. Am. Chem. Soc.* 108, 3838 (1986).
93. D. J. Trevor, C. E. Chiclsey, and D. N. Loiacono, *Phys. Rev. Lett.* 62, 929 (1989).
94. A. A. Gewirth, D. H. Graston, and A. J. Bard, *J. Electroanal. Chem.* 261, 477 (1989).
95. M. P. Greer, K. J. Hanson, D. A. Scherson, X. Xing, M. Richter, P. N. Ross, R. Carr, and I. Lindau, *J. Chem. Phys.* 93, 2181 (1989).
96. C. M. Vitus, S.-C. Chang, B. C. Schardt, and M. J. Weaver, *J. Phys. Chem.* 95, 7559 (1991).
97. C. E. Bach, R. J. Nichols, W. Beckmann, and H. Meyer, *J. Electrochem. Soc.* 140, 1281 (1993).
98. C. J. Slevin, N. J. Gray, J. V. Macpherson, M. A. Webb, and P. R. Unwin, *Electrochem. Commun.* 1, 282 (1999).
99. J. W. Schultze and A. Bressel, *Electrochim. Acta* 47, 3 (2001).
100. R. Feeney, J. Herdan, M. A. Nolan, S. H. Tan, V. V. Tarasov, and S. P. Kounaves, *Electroanalysis* 10, 89 (1998).
101. R. Feeney and S. P. Kounaves, *Electroanalysis* 12, 677 (2000).
102. Y. Iwasaki and M. Morita, *Curr. Separations* 14, 1 (1995).
103. "European Community Report on Nanotechnology." 2001.
104. J. K. Schoer, F. P. Zamborini, and R. M. Crooks, *J. Phys. Chem.* 100, 11086 (1996).
105. J. P. Peeters, U.S. Patent 6,325,904, December 4, 2001.
106. C. R. Martin, *Chem. Mater.* 8, 1739 (1996).
107. J. C. Hulteen and C. R. Martin, *J. Mater. Chem.* 7, 1075 (1997).
108. V. M. Cepak, J. C. Hulteen, C. Guangli, K. B. Jirage, B. B. Lakshmi, E. R. Fisher, and C. R. Martin, *Chem. Mater.* 9, 1065 (1997).
109. N. Al-Rawashdeh, M. L. Sandrock, C. J. Seugling, and C. A. Foss, Jr., *J. Phys. Chem. B* 102, 361 (1998).
110. P. Mansky, Y. Liu, E. Huang, T. P. Russell, and C. Hawker, *Science* 275, 1458 (1997).
111. T. Thurn-Albrecht, J. DeRouchey, C. M. Stafford, E. Huang, M. Bal, M. Tuominen, T. Russell, and C. J. Hawker, *Adv. Mater.* 12, 787 (2000).
112. T. Thurn-Albrecht, J. Schotter, G. A. Kästle, N. Emley, T. Shibauchi, L. Krusin-Elbaum, K. Guarini, C. T. Black, M. Tuominen, and T. P. Russell, *Science* 290, 2126 (2000).
113. M. Tuominen, T. Russell, and J. Penelle, "NSF Partnership in Nanotechnology Conference Proceedings," Arlington, VA, January 29–30, 2001, p. 13.
114. C. R. Martin and D. T. Mitchell, "Electroanalytical Chemistry," Vol. 21, pp. 1–74. Dekker, New York, 1999.
115. G. M. Kim, A. Kovalgin, and J. Holleman, *J. Nanosci. Nanotechnol.* 2, 55 (2002).
116. S. Valizadeh, J. M. George, and P. Leisner, *Electrochim. Acta* 47, 865 (2001).
117. M. Wirtz, S. F. Yu, and C. R. Martin, *Analyst* 127, 871 (2002).
118. C. R Martin, M. Nishizawa, and K. Jirage, *J. Phys. Chem. B* 105, 1925 (2001).
119. C. R Martin, M. Nishizawa, and K. Jirage, *Adv. Mater.*, 13, 1351 (2001).
120. S. B. Lee and C. R. Martin, *Chem. Mater.* 13, 3236 (2001).
121. H. Masuda, M. Yotsuya, and M. Ishida, *Jpn. J. Appl. Phys. Pt.* 2 37 (9AB), L1090 (1998).
122. P. Forrer, F. Schlottig, and H. Siegenthaler, *J. Appl. Electrochem.* 30, 533 (2000).
123. Y. H. Wang, J. M Mo, and W. L. Cai, *Chem. Lett.* 434 (2001).
124. M. Mikhaylova, M. Toprak, D. K. Kim, Y. Zhang, and M. Muhammed, *Mater. Res. Soc. Symp. Proc.* 704 (2002).
125. K. Nielsch, R. B. Wehrspohn, S. F. Fischer, H. Kronmüller, J. Barthell, J. Kirschner, T. Schweinböck, D. Weiss, and U. Gösele, *Mater. Res. Soc. Symp. Proc.* 705, Y9.3.1 (2002).
126. D. R. Rolison and C. A. Bessel, *Acc. Chem. Res.* 33, 737 (2000).
127. C. Z. Li, H. X. He, and N. J. Tao, *Appl. Phys. Lett.* 77, 3995 (2000).
128. A. J. Bard, F.-R. Fan, and M. V. Mirkin, in "Electroanalytical Chemistry" (A. J. Bard, Ed.), Dekker, New York, 1994, pp. 244–370.
129. J. Chlistunoff, D. E. Cliffel, and A. J. Bard, *Thin Solid Films* 257, 166 (1995).
130. J. K. Campbell, L. Sun, and R. M. Crooks, *J. Am. Chem. Soc.* 121, 3779 (1999).
131. B. Fabre, S. Burlet, R. Cespuglio, and G. Bidan, *J. Electroanal. Chem.* 426, 75, (1997).
132. D. T. Colbert, J. Zhang, S. M. McClure, P. Nikolaev, Z. Chen, J. H. Hafner, D. W. Owens, P. G. Kotula, C. B. Carter, J. H. Weaver, A. G. Rinzler, and R. E. Smalley, *Science* 266, 1218 (1994).
133. X. Zhang, J. Wang, B. Ogorevc, and U. E. Spichiger, *Electroanalysis* 11, 945 (1999).
134. X. Zhang, B. Ogorevc, and J. Wang, *Anal. Chim. Acta* 452, 1 (2002).
135. D. Shi, N. Liu, H. Yang, J. Gao, Y. Jiang, S. Pang, X. Wu, and Z. Ji, *MRS Bull.* 12, 2543 (1997).
136. X. J. Zhang, W. M. Zhang, X. Y. Zhou, and B. Ogorevc, *Anal. Chem.* 68, 3338 (1996).
137. X. Zhang, Y. Kislyak, J. Lin, A. Dickson, L. Cardosa, M. Broderick, and H. Fein, *Electrochem. Commun.* 4, 11 (2002).
138. A. Schulte and R. H. Chow, *Anal. Chem.* 70, 985 (1998).
139. X. J. Zhang and B. Ogorevc, *Anal. Chem.* 70, 1646 (1998).
140. X. J. Zhang, B. Ogorevc, M. Rupnik, M. Kreft, and R. Zorec, *Anal. Chim. Acta* 378, 135 (1999).
141. J. Wang, A. Brennsteiner, A. P. Sylwester, and C. L. Renschler, *Electroanalysis* 3, 505 (1991).
142. J. H. Chen, Z. P. Huang, D. Z. Wang, J. G. Wen, and Z. F. Ren, *Electrochem. Soc. Proc.* 2001-11, 362 (2001).
143. G. Che, B. B. Lakshmi, C. R. Martin, E. R. Fisher, and R. S. Ruoff, *Chem. Mater.* 10, 260 (1998).

144. C. V. Nguyen, L. Delzeit, A. M. Cassell, J. Li, J. Han, and M. Meyyappan, *NanoLetters* 2, 1079 (2002).
145. Z. F. Ren, Z. P. Huang, J. W. Xu, J. H. Wang, P. Bush, M. P. Siegal, and P. N. Provencio, *Science* 282, 1105 (1998).
146. Z. P. Huang, J. W. Xu, Z. F. Ren, J. H. Wang, M. P. Siegal, and P. N. Provencio, *Appl. Phys. Lett.* 73, 3845 (1998).
147. Z. F. Ren, Z. P. Huang, J. W. Xu, D. Z. Wang, J. G. Wen, J. H. Wang, L. Calvet, J. Chen, J. F. Klemic, and M. A. Reed, *Appl. Phys. Lett.* 75, 1086 (1999).
148. Y. Tu, Z. P. Huang, D. Z. Wang, J. G. Wen, and Z. F. Ren, *Appl. Phys. Lett.* 80, 4019 (2002).
149. L. Hernández, P. Hernández, F. Paton, and Y. Ballesteros, *Electroanalysis* 9, 235 (1997).
150. A. J. Saterlay, C. Agra-Gutierrez, M. P. Taylor, F. Marken, and R. G. Compton, *Electroanalysis* 11, 1083 (1999).
151. G. M. Swain, A. B. Anderson, and J. C. Angus, *MRS Bull.* 23, 56 (1998).
152. F. Bonamrame, A. Tadjeddine, R. Tene, J. E. Butler, R. Kalish, and C. LeviClement, *J. Phys. Chem. B* 102, 134 (1998).
153. T. Yano, D. A. Tryk, K. Hashimoto, and A. Fujishima, *J. Electrochem. Soc.* 145, 1870 (1998).
154. J. S. Xu, Q. Y. Chen, and G. M. Swain, *Anal. Chem.* 70, 3146 (1998).
155. C. H. Goeting, F. Jones, J. S. Foord, J. C. Eklung, F. Marken, R. G. Compton, P. R. Chalher, and C. Johnston, *J. Electroanal. Chem.* 442, 207 (1998).
156. O. Chaiapakul, E. Popa, H. Tai, B. V. Sarada, D. A. Tryk, and A. Fujishima, *Electrochem. Commun.* 2, 422 (2000).
157. J. Xu, M. C. Garnger, Q. Chen, J. W. Strojek, T. E. Lister, and G. M. Swain, *Anal. Chem.* 69, 591A (1997).
158. C. Prado, S. J. Wilkins, F. Marken, and R. G. Compton, *Electroanalysis* 14, 262 (2002).
159. X. Fan, E. C. Dickey, S. J. Pennycook, and M. K. Sunkara, *Appl. Phys. Lett.*, 75, 2740 (1999).
160. V. F. Dorfman and B. N. Pypkin, *Surf. Coat. Technol.* 48, 193 (1991).
161. M. Sunkara, E. Yeap, S. V. Babu, V. G. Ralchenko, B. N. Pypkin, and B. L. Shubekin, in "Diamond Materials V" (J. L. Davidson, W. D. Brown, A. Gicquel, B. V. Spitsyn, and J. C. Angus, Eds.), pp. 297–308. Electrochemical Society, Pennington, NJ, 1997.
162. P. Koduri, M. Sunkara, E. C. Dickey, C. Frasier, and S. V. Babu, in "Proceedings of Twelfth International Symposium on Surface Modification Technologies" (T. S. Sudarshan, K. A. Khor, and M. Jeandin, Eds.), pp. 357–364. Institute of Materials and American Society of Metals, London, 1998.
163. S. Daniele, C. Bragato, M. Antonietta Baldo, G. Battiston, and R. Gerbasi, "Electrochemical Behaviour of Pt-TiO2 Nanocomposites Prepared by MOCVD in Acidic Aqueous Solution," Materials Science Forum, Contemporary Studies in Advanced Materials and Processes, (D. P. Uskoković, G. A. Battiston, S. K. Milonjić, and D. I. Raković, Eds.), p. 147. Trans Tec Publications Ltd., Switzerland, 2002.
164. A. H. Ali and C.A. Foss, Jr., *J. Electrochem. Soc.* 146, 628 (1999).
165. M. El-Kouedi, M. L. Sandrock, C. J. Seugling, and C. A. Foss, Jr., *Chem. Mater.* 10, 3287 (1998).
166. A. H. Lu, G. H. Lu, A. M. Kessinger, and C. A. Foss, Jr., *J. Phys. Chem. B* 101, 9139 (1997).
167. P. Wang and G. Zhu, *Electrochem. Commun.* 4, 36 (2002).
168. C. A. Bessel and D. R. Rolison, *J. Electroanal. Chem.* 439, 97 (1997).
169. D. R. Rolison, E. A. Hayes, and W. E. Rudzinski, *J. Phys. Chem.* 93, 5524 (1989).
170. T. Kyotani, T. Nagai, S. Inoue, and A. Tomita, *Chem. Mater.* 9, 609 (1997).
171. A. J. Bard and T. Mallouk, in "Molecular Design of Electrode Surfaces," Techniques of Chemistry, Vol. 22 (R. W. Murray, Ed.), pp. 271–312. Wiley-Interscience, New York, 1992.

172. D. M. Kolb, R. Ullmann, and T. Will, *Sci. Mag.* 275, 1097 (1997).
173. A. I. Kleps, A. S. Angelescu, M. Miu, M. Avram, and M. Simion, in "Proceedings of the International Conference on Semiconductors CAS," Sinaia, Romania, 2001, pp. 39–43.
174. M. Avram, A. S. Angelescu, A. I. Kleps, M. Miu, and A. Popescu, in "Proceedings of the International Conference on Semiconductors CAS," Sinaia, Romania, 2001, pp. 43–46.
175. A. I. Kleps, A. S. Angelescu, M. Miu, M. Avram, and M. Simion, in "Micro and Nano Engineering Proceedings, MNE 2001," Grenoble, France, 2001.
176. I. Kleps, A. Angelescu, M. Miu, M. Simion, A. Bragaru, and M. Avram, in "NATO–ASI: Synthesis, Functional Properties and Applications of Nanostructures." 2002.
177. I. Kleps, A. Angelescu, and M. Miu, *Mater. Sci. Eng. C* 19, 219 (2002).
178. I. Kleps, A. Angelescu, M. Avram, M. Miu, and M. Simion, *Microelectron. Eng.* 61–62, 675 (2002).
179. I. Kleps, A. Angelescu, R. Vasilco, and D. Dascalu, *Biomed. Microdevices* 3, 29 (2001).
180. R. Bilewicz and M. Majda, *J. Am. Chem. Soc.* 113, 5464 (1991).
181. R. Bilewicz, T. Sawaguchi, R. V. Chamberlain, and M. Majda, *Langmuir* 11, 2256 (1995).
182. I. Thurzo, K. Gmucová, J. Orlický, and J. Pavlásek, *Rev. Sci. Instrum.* 70, 3723 (1999).
183. D. Yang, M. Zi, B. Chen, and Z. Gao, *J. Electroanal. Chem.* 470, 114 (1999).
184. A. Ulman, *Chem. Rev*. 96, 1533 (1996).
185. Z. Gao, K. S. Siow, and H. Chan, *Synth. Met.* 75, 5 (1995).
186. H. O. Finklea, in "Encyclopedia of Analytical Chemistry" (R. A. Meyers, Ed.), Vol. 11, pp. 10090–10115. Wiley, New York, 2000.
187. W. A. Hayes, H. Kim, X. Yue, S. S. Perry, and C. Shannon, *Langmuir* 13, 2511 (1997).
188. O. Chailapakul and R. M. Crooks, *Langmuir* 9, 884 (1993).
189. O. Chailapakul and R. M. Crooks, *Langmuir* 11, 1329 (1995).
190. H. Kind, A. M. Bittner, O. Cavalleri, K. Kern, and T. Greber, *J. Phys. Chem. B* 102, 7582 (1998).
191. W. L. Cheng, S. J. Dong, and E. K. Wang, *Anal. Chem.* 74, 3599 (2002).
192. J.-Y. Lee and S.-M. Park, *J. Phys. Chem. B* 102, 9940 (1998).
193. J.-Y. Lee and S.-M. Park, *J. Electrochem. Soc.* 147, 4189 (2000).
194. S.-J. Choi, D.-H. Woo, N. Myung, H. Kang, and S.-M. Park, *J. Electrochem. Soc.* 148, C569 (2001).
195. D.-H. Woo, S.-J. Choi, D.-H. Han, H. Kang, and S.-M. Park, *Chem. Phys.* 3, 3382 (2001).
196. S.-J. Choi and S.-M. Park, *Adv. Mater.* 12, 1547 (2000).
197. S.-M. Park, J.-Y. Lee, and S.-J. Choi, *Synth. Met.* 121, 1297 (2001).
198. S.-J. Choi and S.-M. Park, *Bull. Korean Chem. Soc.* 23, 699 (2002).
199. D. Oyamatsu, H. Kanemoto, and S. Kuwabata, *J. Electroanal. Chem.* 497, 97 (2001).
200. G. C. Cleland, B. R. Horrocks, and A. Houlton, *J. Chem. Soc., Faraday Trans.* 91, 4001 (1995).
201. R. A. Eagling, J. E. Bateman, N. J. Goodwin, W. Henderson, B. R. Horrocks, and A. Houlton, *J. Chem. Soc., Dalton Trans.* 1273 (1998).
202. J. E. Bateman, R. D. Eagling, D. R. Worrall, B. R. Horrocks, and A. Houlton, *Angew. Chem. Int. Ed.* 37, 2683 (1998).
203. J. E. Bateman, R. D. Eagling, B. R. Horrocks, and A. Houlton, *J. Phys. Chem. B*, 104, 5557 (2000).
204. J. Lipkowski, *Can. Chem. News* 12–14 (2000).
205. Y. Selzer and D. Mandler, *Anal. Chem.* 72, 2383 (2000).
206. P. Sun, Z. Zhang, J. Guo, and Y. Shao, *Anal. Chem.* 73, 5346 (2001).
207. R. E. Gyurcsanyi, E. Pergel, R. Nagy, I. Kapui, B. T. T. Lan, K. Toth, I. Bitter, and E. Lindner, *Anal. Chem.* 73, 2104 (2001).
208. G. Shi, L. F. Garfias-Mesias, and W. H. Smyrl, *J. Electrochem. Soc.* 145, 2011 (1998).

209. P. James, N. Casillas, and W. H. Smyrl, *J. Electrochem. Soc.* 143, 3853 (1996).
210. G. Schurmann, P. F. Indermuhle, and U. Staufer, *Surf. Interface Anal.* 27, 299 (1999).
211. C. E. Bach, R. J. Nichols, H. Meyer, and J. O. Besenhard, *Surf. Coat. Technol.* 67, 139 (1994).
212. M. Schwank, U. Muller, R. Hauert, R. Rossi, M. Volkert, and E. Wintermantel, *Sens. Actuators, B* 56, 6 (1999).
213. J. W. Geus, in "Chemisorption and Reactions on Metallic Films" (J. R. Anderson, Ed.), Academic Press, London, 1971, Chap. 3, pp. 129–224.
214. D. J. Dunawayad and R. L. McCarley, *Langmuir* 10, 3598 (1994).
215. J. Wang, N. Naser, and C. L. Renschler, *Anal. Lett.* 26, 1333 (1993).
216. D. K. Y. Wong and L. Y. F. Xu, *Anal. Chem.* 67, 4086 (1995).
217. J. Heinze, *Angew. Chem. Int. Ed. Engl.* 32, 1268 (1993).
218. J. Heinze, in "Microelectrodes: Theory and Applications" (M. I. Montenegro, M. A. Queiros, and J. L. Daschbach, Eds.), NATO ASI Ser. E, p. 197. Kluwer Academic Publishers, Dordrecht, 1991.
219. K. B. Oldham, J. C. Myland, C. G. Zoski, and A. M. Bond, *J. Electroanal. Chem.* 270, 79 (1989).
220. A. S. Baranski and A. Moyna, *Langmuir* 12, 3295 (1996).
221. R. Schuster, V. Kirchner, X. H. Xia, A. M. Bittner, and G. Ertl, *Phys. Rev. Lett.* 80, 5599, (1998).
222. C. Amatore, in "Chemical Reactivity in Liquids: Fundamental Aspects" (M. Moreau and P. Turq, Eds.), Plenum, New York, 1988, pp. 73–88.
223. C. Amatore, A. Jutand, and F. Pflüger, *J. Electroanal. Chem.* 218, 361 (1987).
224. M. J. Schöning, G. Buß, F. Faßbender, O. Glück, G. Schmitt, J. W. Schultze, and H. Lüth, in "Technical Digest of 7th International Meeting on Chemical Sensors (IMCS) Conference," Beijing, July 27–30, 1998, pp. 100–102.
225. L. Jelinski, Biologically Related Aspects of Nanoparticles, Nanostructured Materials, and Nanodevices, in Nanostructure Science and Technology, A Worldwide Study Prepared under the guidance of the Interagency Working Group on Nanoscience Engineering and Technology (IWGN), National Science and Technology Council (NSTC), (R. W. Siegel, E. Hu, and M. C. Roco, Eds.), Chap. 7, pp. 113–130. WTEC, Loyola College, Baltimore, 2001.
226. H. C. Hoch, L. W. Jelinski, and H. G. Craighead, Eds., "Nanofabrication and Biosystems," Cambridge University Press, New York, 1996, p. 423.
227. K. M. Roth, J. S. Lindsey, D. F. Bocian, and W. G. Kuhr, *Langmuir* 18, 4030 (2002).
228. N. S. Lawrence, E. L. Beckett, J. Davis, and R. G. Compton, *Anal. Biochem.* 303, 1 (2002).
229. P. B. Hietpas, S. D. Gilman, R. A. Lee, M. R. Wood, N. Winograd, and A. G. Ewing, in "Nanofabrication and Biosystems: Integrating Materials Science, Engineering and Biology" (H. H. Hoch, L. W. Jelinski, and H. Craighead, Eds.), Cambridge University Press, New York, 1996, Chap. 7, 139–158.
230. H. M. McConnell, in "Nanofabrication and Biosystems, Integrating Materials Science, Engineering, and Biology" (Harvey C. Hoch, Lynn W. Jelinski, and Harold G. Craighead, Eds.), Cambridge University Press, New York, 1996, Chap. 6, pp. 115–139.
231. C. D. T. Bratten, P. H. Cobbold, and J. M. Cooper, *Anal. Chem.*, 69, 253 (1997).
232. R. A. Clark, P. B. Hietpas, and A. G. Ewing, *Anal. Chem.* 69, 259 (1997).
233. W.-R. Schlue, W. Kilb, and D. Günzel, *Electrochim. Acta* 42, 3197 (1997).
234. J. S. Rossier, M. A. Roberts, R. Ferrigno, and H. H. Girault, *Anal. Chem.* 71, 4294 (1999).
235. B. D. Pendley and H. D. Abruna, *Anal. Chem.* 62, 782 (1990).
236. A. Schulte and R. H. Chow, *Anal. Chem.* 68, 3054 (1996).
237. J. C. Ball, J. K. Lumpp, S. Daunert, and L. G. Bachas, *Electroanalysis* 12, 685 (2000).
238. D. M. J. Cannon, N. Winograd, and A. G. Ewing, *Annu. Rev. Biophys. Biomol. Struct.* 29, 239 (2000).
239. G. Chen, and A. G. Ewing, *Crit. Rev. Neurobiol.* 11, 59 (1997).
240. C. Price, M. Aslanoglu, C. J. Isaac, M. R. J. Elsegood, W. Clegg, B. R. Horrocks, and A. Houlton, *J. Chem. Soc., Dalton Trans.* 21, 4115 (1996).
241. B. R. Horrocks and M. V. Mirkin, *Anal. Chem.* 70, 4653 (1998).
242. M. Aslanoglu, C. J. Isaac, A. Houlton, and B. R. Horrocks, *Analyst* 125, 1791 (2000).
243. P. Pantano and D. R. Walt, *Chem. Mater.* 8, 2832 (1996).
244. D. Diamond, *Electroanalysis* 5, 795 (1993).
245. O. Niwa, *Electroanalysis* 7, 606 (1995).
246. E. Linder, V. V. Cosofret, R. P. Buck, T. A. Johnson, R. B. Ash, M. R. Neuman, W. J. Kao, and J. M. Anderson, *Electroanalysis* 7, 864 (1995).
247. J. Cui, N. V. Kulagina, and A. C. Michael, *J. Neurosci. Methods* 104, 183 (2001).
248. S. E. Zerby and A. G. Ewing, *J. Neurochem.* 66, 651 (1996).
249. J. B. Zimmerman and R. M. Wightman, *Anal. Chem.* 63, 24 (1991).
250. M. Buda and F. G. Gonon, in "Voltammetry in the Neurosciences" (J. B. Justice, Jr., Ed.), pp. 239–272. Humana, Clifton, NJ, 1987.
251. R. Menzel, in "Handbook of Physiology" (H. Autrum, Ed.), Vol. VII-6A. Springer-Verlag, Berlin, 1979.
252. P. S. Cahill, Q. D. Walker, J. M. Finnegan, G. E. Mickelson, E. R. Travis, and R. M. Wightman, *Anal. Chem.* 68, 180 (1996).
253. L. Gorton, *Electroanalysis* 7, 23 (1995).
254. A. Walcarius, *Electroanalysis* 10, 1217 (1998).
255. G. Weber and J. Messerschmidt, *Fresenius J. Anal. Chem.* 367, 356 (2000).
256. I. M. Fitsev, Y. N. Bakanina, I. F. Abdullin, and G. K. Budnikov, *Ind. Lab.* 64, 426 (1998).
257. R. P. Baldwin and J. Ye, *J. Chromatogr., A* 687, 141 (1994).
258. J. M. Zen, A. S. Kumar, and M. R. Chang, *Electrochim. Acta* 45, 1691 (2000).
259. K. Stulik, V. Pacakova, K. Le, and B. Hennissen, *Talanta* 35, 455 (1988).
260. P. F. Luo, F. Z. Zhang, and R. P. Baldwin, *Anal. Chem.* 62, 752 (1991).
261. Y. Q. Xie and C. O. Huber, *Anal. Chem.* 63, 1714 (1991).
262. S. Prabhu and R. P. Baldwin, *Anal. Chem.* 61, 2258 (1989).
263. M. J. Moorcroft, L. Nei, J. Davis, and R. G. Compton, *Anal. Lett.* 33, 3127 (2000).
264. N. Villeneuve, F. Bedioui, K. Voituriez, S. Avaro, and J. P. Vilaine, *J. Pharmacol. Toxicol. Methods* 40, 95 (1998).
265. I. L. De Mattos, D. Melo, and E. A. G. Zagatto, *Anal. Sci.* 15, 537 (1999).
266. K. Sato, J. Y. Jin, T. Takeuchi, T. Miwa, Y. Takekoshi, S. Kanno, and S. Kawase, *Talanta* 53, 1037 (2001).
267. O. Niwa, M. Morita, and H. Tabei, *Electroanalysis* 3, 163 (1991).
268. M. Takahashi, M. Morita, O. Niwa, and H. Tabei, *J. Electroanal. Chem.* 335, 253 (1992).
269. A. Thess, R. Lee, P. Nikolaev, H. Dai, P. Petit, J. Robert, C. Xu, Y. H. Lee, S. G. Kim, A. G. Rinzler, D. T. Colbert, G. E. Scuseria, D. Tomanek, J. E. Fischer, and R. E. Smalley, *Science* 273, 483 (1996).
270. J. Liu, A. G. Rinzler, H. Dai, J. H. Hafner, R. K. Bradley, P. J. Boul, A. Lu, T. Iverson, K. Shelimov, C. B. Huffman, F. Rodriguez-Macias, Y.-S. Shon, T. R. Lee, D. T. Colbert, and R. E. Smalley, *Science* 280, 1253 (1998).
271. R. H. Baughman, C. Cui, A. A. Zakhidov, Z. Iqbal, J. N. Barisci, G. M. Spinks, G. G. Wallace, A. Mazzoldi, D. De Rossi, A. G. Rinzler, O. Jaschinski, S. Roth, and M. Kertesz, *Science* 284, 1340 (1999).

272. J. J. Davis, M. L. H. Green, H. A. O. Hill, Y. C. Leung, P. J. Sadler, J. Sloan, A. V. Xavier, and S. C. Tsang, *Inorg. Chim. Acta* 272, 9 (1998).

273. Z. Guo, P. J. Sadler, and S. C. Tsang, *Adv. Mater.* 10, 701 (1998).

274. L. Dong, A. B. Fischer, M. Lu, M. T. Martin, D. Moy, and D. Simpson, *J. Mol. Recognit.* 9, 383 (1996).

275. O. P. Matyshevska, A. Y. Karlash, Y. V. Shtogun, A. Benilov, Y. Kirgizov, K. O. Gorchinskyy, E. V. Buzaneva, Y. I. Prylutskyy, and P. Scharff, *Mater. Sci. Eng., C* 15, 249 (2001).

276. R. J. Chen, Y. Zhang, D. Wang, and H. Dai, *J. Am. Chem. Soc.* 123, 3838 (2001).

277. F. Balavoine, P. Schultz, C. Richard, V. Mallouh, T. W. Ebbesen, and C. Mioskowski, *Angew. Chem., Int. Ed.* 38, 1912 (1999).

278. A. Guiseppi-Elie, C. Lei, and R. H. Baughman, *Nanotechnology* 13, 559 (2002).

279. J. Chen, H. Liu, W. A. Weimer, M. D. Hall, D. H. Waldeck, and G. C. Walker, *J. Am. Chem. Soc. Commun.* 124, 9034 (2002).

280. T. Malinski, D. A. Wink, J. Younathan, R. W. Murray, M. Sullivan, and T. J. Meyer, U.S. Patent 5,603,820, February 18, 1997.

281. W. Lawrence, I. Dobrucki, A. Burewicz, and T. Malinski, *Anal. Sci.* 17, 583 (2001).

282. F. Bailey, T. Malinski, and F. Keichle, *Anal. Chem.* 63, 395 (1991).

283. W. G. Kuhr, V. Barrett, M. R. Gagnon, P. Hopper, and P. Pantano, *Anal. Chem.* 65, 612 (1993).

284. P. Pantano and W. G. Kuhr, *Anal. Chem.* 63, 1413 (1991).

285. P. Pantano and W. G. Kuhr, in "Monitoring Molecules in Neuroscience" (H. Rollema, B. Westerink, and W. J. Drijfhout, Eds.), pp. 117–120. University Center for Pharmacy, Groningen, the Netherlands, 1991.

286. S. E. Rosenwald, W. B. Nowall, N. Dontha, and W. G. Kuhr, *Anal. Chem.* 72, 4914 (2000).

287. A. Akitane, *Anal. Chem.* 57, 1518 (1985).

288. A. Brajter-Toth, K. Abou El-Nour, E. T. Cavalheiro, and R. Bravo, *Anal. Chem.* 72, 1576 (2000).

289. K. Abou El-Nour and A. Brajter-Toth, *Electroanalysis* 12, 805 (2000).

290. M. H. Schoenfisch and J. E. Pemberton, *Langmuir* 15, 509 (1999).

291. J. E. Pemberton, L. L. Wood, and G. Ghoman, *J. Chem. Ed.* 76, 253 (1999).

292. C. E. Taylor, J. E. Pemberton, G. G. Goodman, and M. H. Schoenfisch, *Appl. Spectrosc.* 53, 1212 (1999).

293. N. Dontha, W. B Nowall, and W. G. Kuhr, *J. Pharm. Biomed. Anal.* 19, 83 (1999).

294. T. Vo-Dinh and B. M. Cullum, *J. Anal. Chem.* 366, 540 (2000).

295. J. Davis, D. H. Vaughan, and M. F. Cardosi, *Enzyme Microb. Technol.* 17, 1030 (1995).

296. T. McCormack, "Biomaterials for Biosensors in Principles of Chemical and Biological Sensors" (D. Diamond, Ed.), p. 158. Wiley–Interscience, New York, 1998.

297. B. M. Cullum and T. Vo-Dinh, *Trends Biotechnol.* 18, 388 (2000).

298. J. J. Pancrazio, J. P. Whelan, D. A. Borkholder, W. Ma, and D. A. Stenger, *Ann. Biomed. Eng.* 27, 697 (1999).

299. J. P. Alarie and T. Vo-Dinh, *Polycyclic Aromat. Compd.* 8, 45 (1996).

300. S. L. R. Barker and R. Kopelman, *Anal. Chem.* 70, 971 (1998).

301. J. Cordek, X. Wang, and W. Tan, *Anal. Chem.* 71, 1529 (1999).

302. T. Vo-Dinh, J. P. Alarie, B. Cullum, and G. D. Griffin, *Nat. Biotechnol.* 18, 76 (2000).

303. H. A. Clark, M. Hoyer, M. A. Philbert, and R. Kopelman, *Anal. Chem.* 71, 4831 (1999).

304. H. A. Clark, R. Kopelman, R. Tjalkens, and M. A. Philbert, *Anal. Chem.* 71, 4837 (1999).

305. H. A. Clark, S. L. R. Barker, M. Brasuel, M. T. Miller, E. Monson, S. Parus, Z. Y. Shi, A. Song, B. Thorsrud, R. Kopelman, A. Ade, W. Meixner, B. Athey, M. Hoyer, D. Hill, R. Lightle, and M. A. Philbert, *Sens. Actuators, B* 51, 12 (1998).

306. H. Xu, J. W. Aylott, R. Kopelman, T. J. Miller, and M. A. Philbert, *Anal. Chem.* 73, 4124 (2001).

307. R. Brown, J. Gallop, and M. Milton, Review of Techniques for Single Molecule Detection in Biological Applications, in NPL Report COAM 2, National Physical Laboratory, Queens Road, Teddington, Middlesex, TW1 0LW, 2001.

308. J. V. Macpherson, M. A. Beeston, P. R. Unwin, N. P. Hughes, and D. Littlewood, *Langmuir* 11, 3959 (1995).

309. M. Gonsalves, A. L. Barker, J. V. Macpherson, P. R. Unwin, D. O'Hare, and C. P. Winlove, *J. Biophys.* 78, 1578 (2000).

310. M. Tsionsky, J. F. Zhou, S. Amemiya, F. R. F. Fan, A. J. Bard, and R. A. W. Dryfe, *Anal. Chem.* 71, 4300 (1999).

311. F.-R. F. Fan and A. J. Bard, *Science* 267, 871 (1995).

312. A. J. Bard and F.-R. F. Fan, *Acc. Chem. Res.* 29, 572 (1996).

313. B. R. Horrocks, D. Schmidtke, A. Heller, and A. J. Bard, *Anal. Chem.* 65, 3605 (1993).

314. O. D. Uitto and H. S. White, *Anal. Chem.* 73, 533 (2001).

315. T. Yasukawa, Y. Kondo, I. Uchida, and T. Matsue, *Chem. Lett.* 767 (1998).

316. D. T. Pierce, P. R. Unwin, and A. J. Bard, *Anal. Chem.* 64, 1795 (1992).

317. C. E. M. Berger, B. R. Horrocks, and H. K. Datta, *J. Endocrinol.* 158, 311 (1998).

318. C. E. M. Berger, B. R. Horrocks, and H. K. Datta, *Electrochim. Acta* 44, 2677 (1999).

319. C. E. M. Berger, B. R. Horrocks, and H. K. Datta, *Mol. Cell. Endocrinol.* 149, 53 (1999).

320. B. Liu, W. Cheng, S. A. Rotenberg, and M. V. Mirkin, *J. Electroanal. Chem.* 500, 590 (2001).

321. B. Liu, S. A. Rotenberg, and M. V. Mirkin, *Proc. Natl. Acad. Sci. USA* 97, 9855 (2000).

322. B. R. Horrocks and G. Wittstock, in "Scanning Electrochemical Microscopy" (A. J. Bard and M. V. Mirkin, Eds.). Dekker, New York, 2002.

323. L. Stryer, *Biochemistry* W. H. Freeman, New York, 1995.

324. J. D. Rabinowitz, J. F. Vacchino, C. Beeson, and H. M. McConnell, *J. Am. Chem. Soc.* 120, 2464 (1998).

325. C. M. Lee, J. Y. Kwak, and A. J. Bard, *Proc. Natl. Acad. Sci. USA* 87, 1740 (1990).

326. M. Tsionsky, Z. G. Cardon, A. J. Bard, and R. B. Jackson, *Plant Physiol.* 113, 895 (1997).

327. T. Yasukawa, T. Kaya, and T. Matsue, *Anal. Chem.* 71, 4637 (1999).

328. C. Cai, B. Liu, M. V. Mirkin, H. A. Frank, and J. F. Rusling, *Anal. Chem.* 74, 114 (2002).

329. T. Yasukawa, Y. Kondo, I. Uchida, and T. Matsue, *Chem. Lett.* 767 (1998).

330. R. P. Akkermans, M. Wu, and R. G. Compton, *Electroanalysis* 10, 814 (1998).

331. E. L. Beckett, N. S. Lawrence, Y. C. Tsai, J. Davis, and R. G. Compton, *J. Pharm. Biomed. Anal.* 26, 995 (2001).

332. E. L. Beckett, N. S. Lawrence, R. G. Evans, J. Davis, and R. G. Compton, *Talanta* 54, 871 (2001).

333. S. M. Sabry and H. Mahgoub, *J. Pharm. Biomed. Anal.* 21, 993 (1999).

334. P. Mattila, M. Lehtonen, and J. Kumpulainen, *J. Agric. Food Chem.* 48, 1229 (2000).

335. K. Inoue, K. Kato, Y. Yoshimura, T. Makino, and H. Nakazawa, *J. Chromatogr., B* 749, 17 (2000).

336. A. M. Bond, *Analyst* 119, R1 (1994).

337. *Official Journal of the European Community* 22, L327 (2000).

338. J. Herdan, R. Feeney, S. P. Kounaves, A. F. Flannery, C. W. Storment, G. T. Kovacs, and R. B. Darling, *Environ. Sci. Technol.* 32, 131 (1998).

339. H. P. van Leeuwen and R. M. Town, *J. Electroanal. Chem.* 523, 16 (2002).

340. M. Corbetta, M. A. Baldo, S. Daniele, and G. A. Mazzocchin, *Ann. Chim.* 86, 77 (1996).
341. http://www.metrohm.com/.
342. http://www.tracedetect.com/products/measure.htm.
343. http://www.upchurch.com/products/DistDetail.asp?vRecID=648.
344. R. F. Fan and A. J. Bard, "Considerations in Scanning Electrochemical Microscopy at Nanometer-Size Electrodes," Abstracts of Papers of the American Chemical Society, 215, 130-COLL (1998).
345. A. J. Bard and L. R. Faulkner, in "Electrochemical Methods: Fundamentals and Applications," 2nd ed., pp. 669–677. Wiley, New York, 2001.
346. C. Lee, C. J. Miller, and A. J. Bard, *Anal. Chem.* 63, 78 (1991).
347. K. T. Kawagoe, J. A. Jankowski, and R. M. Wightman, *Anal. Chem.* 63, 1589 (1991).
348. T. G. Strein and A. G. Ewing, *Anal. Chem.* 64, 1368 (1992).
349. M. V. Mirkin, F.-R. F. Fan, and A. J. Bard, *Science* 257, 364 (1992).
350. C. Kranz, B. Mizaikoff, A. Lugstein, and E. Bertagnolli, in "Electrochemical Methods for the Environmental Analysis at Trace Element Biogeochemistry" (M. Taillefert and T. F. Rozan, Eds.), American Chemical Society Symposium, 2002. pp. 320–336.
351. C. Hess, K. Borgwarth, C. Ricken, D. G. Ebling, and J. Heinze, *Electrochim. Acta* 42, 3065 (1997).
352. G. Wittstock, R. Hesse, and W. Schuhmann, *Electroanalysis* 9, 746 (1997).
353. E. L. H. Heintz, C. Kranz, B. Mizaikoff, H.-S. Noh, P. Hesketh, A. Lugstein, and E. Bertagnolli, in "Proceedings Nanotechnology '01 IEEE Conference," 2001.
354. M. V. Mirkin, F. R. F. Fan, and A. J. Bard, *J. Electroanal. Chem.* 328, 47 (1992).
355. W. Li, J. A. Virtanen, and R. M. Penner, *J. Phys. Chem.* 96, 6529 (1992).
356. H. J. Dai, J. H. Hafner, A. G. Rinzler, D. T. Colbert, and R. E. Smalley, *Nature* 384, 147 (1996).
357. Y. H. Shao and M. V. Mirkin, *J. Am. Chem. Soc.* 119, 8103 (1997).
358. C. Wei, A. J. Bard, and S. W. Feldberg, *Anal. Chem.* 69, 4627 (1997).
359. S. D. Campbell and A. C. Hillier, *Langmuir* 15, 891 (1999).
360. C. Wei, A. J. Bard, I. Kapui, G. Nagy, and K. Tóth, *Anal. Chem.* 68, 2651 (1996).
361. A. Lugstein, E. Bertagnolli, C. Kranz, and B. Mizaikoff, *Surf. Interface Anal.* 33, 146 (2002).
362. J. P. Smith, *Anal. Chem.* 73, 39 A (2001).
363. J. V. Macpherson and P. R. Unwin, *Anal. Chem.* 73, 550 (2001).
364. C. Kranz, G. Friedbacher, B. Mizaikoff, A. Lugstein, J. Smoliner, and E. Bertagnolli, *Anal. Chem.* 73, 2491 (2001).
365. Y. H. Shao and M. V. Mirkin, *J. Phys. Chem. B* 102, 9915 (1998).
366. B. D. Bath, H. S. White, and E. R. Scott, *Anal. Chem.* 72, 433 (2000).
367. B. R. Horrocks and M. V. Mirkin, *J. Chem. Soc., Faraday Trans.* 94, 1115 (1998).
368. M. V. Mirkin and B. R. Horrocks, *Anal. Chim. Acta* 406, 119 (2000).
369. H. Meyer, H. Drewer, B. Gruendig, K. Cammann, R. Kakerow, Y. Manoli, W. Mokwa, and M. Rospert, *Anal. Chem.* 67, 1164 (1995).
370. M. G. Sullivan, H. Utomo, P. J. Fagan, and M. D. Ward, *Anal. Chem.* 71, 4369 (1999).
371. K. Hayashi, T. Horiuchi, R. Kurita, K. Torimitsu, and O. Niwa, *Biosens. Bioelectron.* 15, 523 (2000).
372. W. Plieth, in "Electrochemical Nanotechnology" (W. J. Lorenz, Ed.), pp. 257–292. Wiley-VCH, Weinheim/New York, 1998.
373. J. R. LaGraff and A. A. Gewirth, in "Nanoscale Probes of the Solid/Liquid Interface" (A. A. Gewirth and H. Siegenthaler, Eds.), p. 83. Kluwer Academic Publishers, Dordrecht, 1995.
374. K. Uosaki, in "Solid–Liquid Electrochemical Interfaces" (G. Jerkoiewicz, Ed.), p. 189. American Chemical Society, Washington, DC, 1997.
375. W. Schindler, P. Hugelmann, and A. Hugelmann, *J. Electroanal. Chem.* 522, 49 (2002).
376. W. Schindler, D. Hofmann, and J. Kirschner, *J. Electrochem. Soc.* 148, C124 (2001).
377. W. Schindler, D. Hofmann, and J. Kirschner, *J. Appl. Phys.* 87, 7007 (2000).

Electrochemical Self-Assembly of Oxide/Dye Composites

Tsukasa Yoshida

Gifu University, Gifu, Japan

Derck Schlettwein

Universität Oldenburg, Oldenburg, Germany

CONTENTS

1. INTRODUCTION

1.1. Interest in Nanocrystalline Electrodes

Studies on dye-sensitization in the field of photoelectrochemistry began in the late 1960s by using a single crystal zinc oxide (ZnO) electrode in an aqueous electrolyte solution containing the photosensitizer dyes [1, 2]. Although spectral sensitization of semiconductors had been known much earlier from photographic technologies, dye-sensitized photocells evoked high interest among researchers because they provide means to utilize wide bandgap semiconductors for solar energy conversion which showed to be quite resistive against otherwise considerable photocorrosion. However, early systems provided quite poor efficiency, because most of the photons incident on the cell were absorbed by dye molecules in the solution, which do not serve as sensitizers but tend to decompose. As it had been revealed that only the dyes directly adsorbed on the semiconductor surface act as sensitizers [3], Tsubomura et al. significantly improved the cell performance by using a sintered pellet of ZnO with a large surface area and adsorbing dyes before it was put into an aqueous I^-/I_3^- redox electrolyte [4]. However, no substantial improvements were made later

and the studies on dye sensitization virtually ceased in the 1980s, despite the fact that the importance of the electrode porosity had been known [5] and the idea of using a carboxylated polypyridine Ru complex for firm chemical attachment of the sensitizer on the oxide surface had been reported [6]. The revival of dye sensitization had to wait until the 1990's, when O'Regan and Grätzel developed a new electrode material with an extremely high surface area, that is, a porous thick film made by spreading colloidal paste of TiO_2 nanocrystals on transparent conductive substrates such as F-doped SnO_2 (FTO) coated glass and sintering it between 400 and 500 °C [7, 8]. They also developed specially designed polypyridine Ru complexes as sensitizers and used water-free electrolyte solutions. From these improvements, a light to electric power conversion efficiency of 10% has been achieved and the dye-sensitized photocells, which now can be called dye-sensitized solar cells (DSSCs), have finally demonstrated their high promises as solar power devices.

There have been a lot of active studies on DSSCs in the last decade. Thanks to the development of pulse laser spectroscopy and time-/frequency-resolved photoelectrochemical techniques, significant progress has been made in understanding how DSSCs operate [9–26]. Unique features of charge separation/recombination and charge transport in nanoporous networks have been elucidated. On the other hand, there have also been a lot of studies seeking alternative materials for DSSCs including other semiconductors [28–36], dyes [30, 33, 37–47], and electrolytes (hole conducting materials) [34, 48–54]. Various kinds of metal oxides such as ZnO [27, 28, 32, 33], Fe_2O_3 [29], In_2O_3 [32, 33], SnO_2 [30, 32, 33], CeO_2 [31], Nb_2O_5 [32, 33], and their combinations either as mixtures [34] or as core–shell structured composites [35, 36] have proven their capability as electrode material for DSSCs when they are used as

porous films. Although their performance often appeared to be inferior to TiO$_2$, comparisons under exactly the same conditions especially for the crystal size and the film porosity have barely been possible, so that "the best material" is still in question. Various dyes, some of them already studied decades ago, were investigated again as sensitizers of nanocrystalline porous semiconductor electrodes and were found to perform much better than in early studies [33, 39, 42]. Molecular engineering was used to substitute the anchoring groups for firm attachment of the sensitizers on the semiconductor surface and to modify the energetic structure of the chromophore to broaden their spectral sensitivity. Improved cell efficiencies were obtained, indicating a further potential to improve the performance of DSSCs by appropriate design of the dye molecules [37, 38, 40]. Among promising dyes, also several naturally occurring molecules have exhibited rather high activities as sensitizers and were discussed to be cheap and nontoxic alternatives [46–48]. On the electrolyte side, aside from optimization of the electrolyte composition for maximum output of the cells [8], (quasi)solidification of the cells has been studied in an attempt to improve the long-term stability of the cells, using molten salt electrolytes [49], polymer gel electrolytes [34, 50, 51], solid hole-conducting polymers [52, 53], or inorganic p-conductors [54, 55]. Simply speaking about the efficiency of the cell, however, none of these new systems has exhibited superior performance when compared with the "Grätzel cell" [8].

It should be mentioned that almost all of the recent studies related to DSSCs employed the same preparation method for porous oxide semiconductor films (i.e., colloid coating on FTO glass followed by sintering). The history in the field, however, may teach us that substantial improvements occurred only when new methods were adopted for the preparation of semiconductor electrodes [1, 4, 7].

Improvement of the cell performance, however, is not the only driving force to study new synthetic methods. In order to provide alternatives of manufacturing DSSCs, recently several new methods of film preparation were reported such as low temperature (=100 °C) sintering of spin-coated aqueous TiO$_2$ sol [56], electrophoretic deposition of semiconductor nanoparticles [57], electrodeposition [58, 59], sputtering [60], and compression of powdered samples at high pressure [61]. Although these methods did not yield better cell characteristics than the conventional technique, such new techniques, especially those allowing low temperature fabrication of porous semiconductor films, are important in order to realize flexible DSSCs using conductive plastic substrates [56, 61]. Since the conventional technique needs a heat treatment at 400 to 500 °C, the choice of transparent substrates is essentially limited to glass. Since the cost of glass sheets typically occupies a significant part of the total cost [62], elimination of the heat treatment for substitution of glass by plastic films is an important step to reduce the cost of a device. Beyond this, however, it will reduce the weight and will also allow newly accessible geometries of solar cells. Another important feature of these new methods in the case of electrodeposition and sputtering consists in the aspect that the film growth occurs in an ordered structure, because these processes "build up" a film from very small units such as ions

or clusters [59, 60]. The colloid-based methods inherently results in a formation of randomly structured films since preformed particles are used, unless the shape and size of the particles are well controlled, so that their physical contact leads to an ordered packing [63]. Control of film structure especially with respect to the pore size distribution is highly relevant for the performance and stability of DSSCs. Limitation of the photocurrent by the transport of redox electrolyte through narrow pores can decrease the efficiency in spite of a high surface area and desorption and decomposition of the oxidized dye molecules can lead to degradation of the cells [64].

1.2. Level of Control in Electrochemical Depositions

Electrochemically induced depositions of solids are well-established technical procedures and play key roles in a number of technologies [65]. Most prominent here are processes of metal plating. Electroplating has been established as a traditional way of coating any conductive substrate in particular by Cu. In the past these techniques have been well established and optimized and a number of additives were found that led to an increased smoothness and more shiny finish of the coatings which were desired in most cases. A scientific understanding of the role of these additives [66] evolved considerably later and to date today it remains of highly relevant research interest [67]. Beyond flat coatings on a given sample geometry, electroplating of metals in channels or pores has become a very important step in modern microprocessor technology because a number of interconnects, vertical or lateral, can be prepared by electroplating [68–72]. Here it has become of major importance to be able to deposit through narrow pores, deposit metal in the trough of a pore first, and then subsequently fill it to the opening and beyond it (super conformal deposition). Since interconnect pores get more and more narrow with decreasing chip dimensions (i.e., increased microprocessor performance), dimensions have become so small that the diffusion profile and the heterogeneous deposition kinetics have to be controlled in great detail, both on a microscopic [73–81] and reactor [82] level. An understanding of the traditional additives and of newly developed additives was obtained on a molecular level which was essential to tune the morphology of the deposited metal to the extent necessary in this demanding field. This can serve as an example of the level of control that can be obtained in electrochemical depositions.

Of course other metals can also be electrodeposited cathodically and a similar level of control is often needed. Super conformal or at least conformal depositions have also been worked out for Ag [83] and Ni [84]. Sequential and alternating depositions even from a single, mixed electrolyte can be obtained by careful tuning of the reaction rates and diffusion profiles by means of the applied potential [85]. Pulsed depositions, for example, are established methods to control diffusion profiles in a well defined way, as shown, for example, to deposit nanoparticles [86], metal alloys [87–89], or metal multilayers [85, 87–90] from a given mixed bath.

1.3. Electrochemical Crystallization of Oxide Films

To form oxide films by eletrochemical means one would at first sight think of anodic reactions at a given metal electrode. This concept is well established [91] and often studied in corrosion reactions and in the case of passive oxides (e.g., Al_2O_3 or TiO_2). On the other hand, compound semiconductor thin films can be directly deposited from solutions and, aside from their economical advantage and versatility in application to various materials in complex shapes [92–98], solution phase techniques often allow highly ordered crystal growth, when they are properly controlled [93]. Epitaxial growth of several metal sulfides [93, 94, 99], selenides [100, 101], and oxides [102, 103] has been observed, which is a clear manifestation of the high quality of the materials grown from solutions. Heteroepitaxial deposition using substrates with geometrical matching to the deposit is the usual way to achieve precise control of the film structure [104]. However, such an approach typically limits the choice of the substrates to expensive single crystals. Moreover, such a heteroepitaxial effect typically is valid only for extremely thin films. As the films grow thicker, the anisotropy of the stability of the deposits caused by surface adsorption of coexisting ions, molecules, and even simply by solvation becomes so enormous that the control of the film growth by such chemical events at the solid/solution interface comes into play [98]. Precipitation from solutions can be performed under equilibrium conditions, if the chemical stability of the solvated ions and that of the solid are comparable. Under such conditions, film growth can occur under active control of the film structure. As examples of such an approach to control of the film structure, we have demonstrated electrochemically induced chemical deposition [93, 97] of nanoparticulate cadmium sulfide (CdS) thin films by introduction of mercaptoethanol to the bath [95], which strongly coordinates to the surface reaction sites of CdS, and by using acetonitrile as solvent [96], which permits only limited solubility of CdS, as in both cases the growth of bulk CdS is suppressed.

Because of the interesting features and practical advantages to growing semiconductor films electrochemically from solutions, the films prepared by such methods are attractive candidates as photoelectrode materials for DSSCs. Anodic [105] and cathodic [106] electrodeposition of TiO_2 from aqueous solutions has been reported and we have recently proven that electrodeposited TiO_2 thin film electrodes have decent properties for application to DSSCs [58]. To obtain reasonably porous, crystalline films, however, the as-deposited amorphous films had to be heated above 300 °C and this heat treatment does not permit the use of plastic substrates, making the electrodeposition technique not very attractive in the case of TiO_2. Zinc oxide (ZnO), on the other hand, can be directly crystallized by cathodic electrodeposition from solutions owing to a higher solubility than TiO_2 [107–112], and it is one of the most promising materials for DSSCs, probably next to TiO_2 [28, 33]. The electrochemical growth of ZnO thin films proceeds in an atomic layer-by-layer fashion, as evident from the fact that a long-range epitaxial growth was possible [102]. Such a character of the film growth provides a good chance to control the structure of ZnO thin films, including the crystal size, crystal orientation, and pore size. Recently, as in the case of metal depositions, nonstationary conditions have also been applied to modify the morphology of ZnO either toward porous or smooth electrodes [113, 114]. ZnO nanoparticles were deposited by an electrophoretic method to yield nanowire arrays [115]. Boron could be incorporated into the ZnO crystalline thin films by means of a mixed electrolyte [116]. Reaction conditions were worked out to further contact the ZnO layer by subsequent metal deposition on top of it [117]. These conditions provide a good starting point to utilize electrochemically deposited ZnO layers as dye-sensitized electrodes.

1.4. Control by Structure-Directing Agents in Chemical Crystallizations

The level of control that can be reached in the structure and morphology of mineral crystallization is most impressively shown in fields as different as biomineralization and the synthesis of molecular sieves. In both of these examples the growing mineral network is constructed by means of templates (i.e., molecules that are critical during synthesis but that are not included into the covalent oxide network and are dispensable at the end of the synthesis). Acid–base and metal–ligand interactions are dominating the bonds between template molecules and mineral precursors that then lead to the structure–directing character of the template molecules on the resulting mineral. Peptides and (glyco)proteins as well as phospholipids play the most important roles in the mineralization in biological systems [118, 119] whereas in the synthesis of mesoporous materials or molecular sieves the most important structure-directing agents consist of aliphatic amines, tetraalkylammonium salts, or oligoethers [120, 121]. It is far beyond the scope of this chapter to review the literature in these fields but some aspects should be highlighted that carry a significance for electrochemical self-assembly.

Those molecules controlling many reactions in biomineralization, for example, carry acidic functionalities. The kinetics of site-specific nucleation and crystal growth as well as the interface energy as reflected in the surface tension are influenced by these molecules [122, 123]. This control works to an extent that even chiral morphologies can be obtained for nonchiral crystals, just by such an influence of a chiral molecule (e.g., aspartic acid) [118, 124]. Such a level of control over the morphology of crystals and films is challenging the traditional chemistry of materials. Concepts based upon chemical reactions with or under control of biomolecules already have entered the field of materials science [125, 126], even using the enormous complexity of information provided by molecules like DNA. Interfacial interactions with biomolecules also have to be considered in purely inorganic crystallization reactions when interaction of a medically implanted material with biominerals is discussed (e.g., in the growth of TiO_2 on implanted Ti and subsequent biomineralization of hydroxyapatite and fluorapatite on TiO_2) [127].

The use of covalent or coordination bonds of oxides and of organic molecules can, aside from the template effect mentioned, lead to the formation of hybrid materials. Very

well-defined mixed crystals could be obtained for an inter-action of an aromatic ligand like 2,6-bis(hydroxymethyl)-*p*-cresol with Ti (IV) alkoxides [128]. Further, if such hybrid organic/inorganic precursors are used in condensation reactions similar to the sol–gel route, highly ordered hybrid materials can be obtained with the organic portions still in a covalent backbone network [129]. Also dye molecules could be incorporated into mesoporous materials already during their synthesis, if the dye molecules were soluble in the reaction mixtures, carried functional groups that were compatible with the template molecules, and could chemically withstand the rather harsh environment of molecular sieve synthesis [121]. In turn the incorporated dye molecules can also influence the structure of the host molecular sieves. If the size of the dye molecules, for example, exceeded the pore size of the molecular sieve, mesopores were formed as defects of the molecular sieve or even new oxide phases were formed as a consequence of chemical interactions with the dye molecules [121].

2. ELECTROCHEMICAL CRYSTALLIZATION OF OXIDE/DYE HYBRID FILMS

The electrodeposited ZnO electrodes appeared to be potentially useful candidates for dye-sensitized electrodes, because of their high crystallinity which is usually beneficial to an efficient charge transport. In an attempt to adsorb dye molecules to electrodeposited ZnO films, however, dye adsorption could not be observed at an appreciable amount, most likely due to a rather small surface area of the electrodeposited crystalline ZnO films. Only when the dye molecules were already added into the $Zn(NO_3)_2$ bath of the electrode synthesis, did we succeed in obtaining crystalline ZnO thin films intensively colored by the added dyes [17, 18, 130–140]. Various water soluble dyes have been tested and resulted in formation of thin films with various colors, proving the versatility of this method. The formulae of the dye molecules are shown in Figure 1 which includes tetrasulfonated metallophthalocyanines (TSPcMt) [17, 18, 130–132], the family of xanthene dyes such as eosinY (EY) [133–136], the triphenylmethane dye tetrabromophenol blue (TB) [137, 138], *cis*-dithiocyanato bis(4,4′-dicarboxylic acid-2,2′-bipyridine)ruthenium(II) (N3) [139, 140] which is known as the best sensitizer in the Grätzel cell [8], and riboflavin 5-phosphate (R5P) which is one of the few commercial phosphonated dyes. These dye molecules have carboxylic, sulfonic, or phosphonic acid groups which are not only needed to provide solubility in water but also are expected to act as anchors of the dyes to the ZnO surface. Because dye adsorption takes place on the growing surface of ZnO during the electrodeposition, the added dye molecules modify the structure of ZnO in various ways as it is revealed in the following sections. The act of dye molecules in this respect finds similarity to the role of organic additives in electrochemical metal plating or the templates and structure-directing agents in the solution processing of molecular sieves. In case of ZnO/dye hybrid electrodeposition, however, the dye molecules do not need to be removed as their function can be directly utilized in the resulting materials.
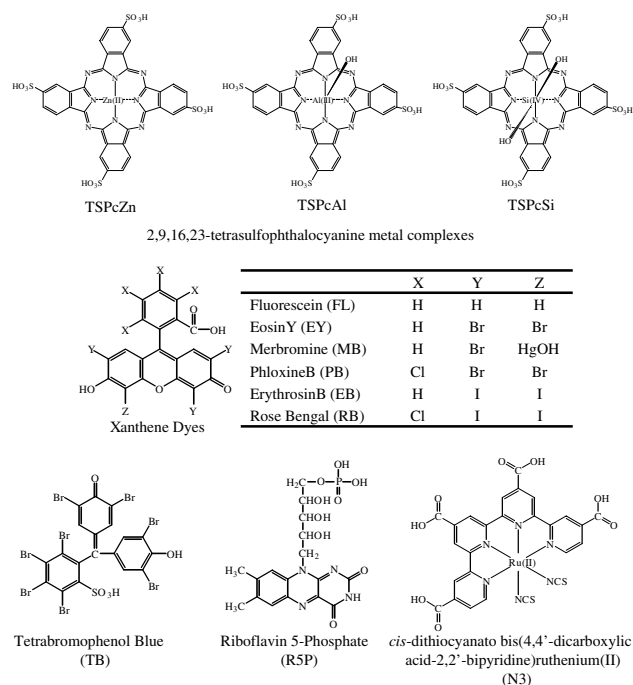
Figure 1. Formulae of the dyes used.

2.1. Impact of Dye Addition on Crystallization of ZnO

2.1.1. Electrochemical Aspects

Cathodic electrodeposition of crystalline ZnO from an aqueous $Zn(NO_3)_2$ bath proceeds at temperatures above 60 °C and at electrode potentials more negative than −0.7 V relative to the saturated calomel electrode (SCE) [107, 131]. Although the reaction turned out to consist of a multi-component complex equilibrium it can be thought of as a sequence of steps for the purpose of simplicity. As a first step, nitrate is reduced to nitrite and partly to ammonia to generate hydroxyl ions [131]:
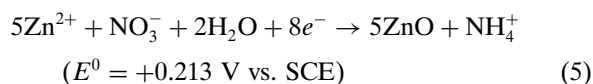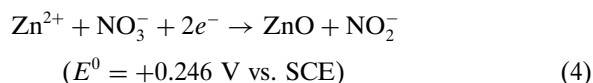
$$NO_3^- + H_2O + 2e^- \rightarrow NO_2^- + 2OH^-$$
$$(E^0 = -0.240 \text{ V vs. SCE}) \qquad (1)$$
$$NO_3^- + 6H_2O + 8e^- \rightarrow NH_3 + 9OH^-$$
$$(E^0 = -0.373 \text{ V vs. SCE}) \qquad (2)$$
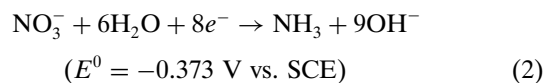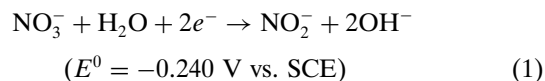
The E^0 values are calculated from the Gibbs free energy of formation (ΔG_f) of each chemical species appearing in the equations. The hydroxyl ions are expected to react with Zn^{2+} to precipitate as zinc hydroxide, which subsequently is dehydrated to give ZnO [109];

$$Zn^{2+} + 2OH^- \rightarrow Zn(OH)_2 \rightarrow ZnO + H_2O \qquad (3)$$
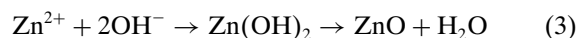
However, there is no evidence of $Zn(OH)_2$ formation as an intermediate. Since the elemental reaction steps are difficult

to know, we prefer to describe in overall expressions as follows:

$$Zn^{2+} + NO_3^- + 2e^- \rightarrow ZnO + NO_2^-$$
$$(E^0 = +0.246 \text{ V vs. SCE}) \tag{4}$$
$$5Zn^{2+} + NO_3^- + 2H_2O + 8e^- \rightarrow 5ZnO + NH_4^+$$
$$(E^0 = +0.213 \text{ V vs. SCE}) \tag{5}$$

It is noticed from the calculated E^0 values that these reactions are thermodynamically feasible owing to the high stability of ZnO.

The addition of dye molecules to the solution often hinders the crystal growth of ZnO. In some of the systems studied, the film deposition was completely inhibited when the deposition was carried out under moderate overpotentials and when dyes were added at high concentrations [131, 135, 140]. The effect of dye addition to the current during the electrodeposition in case of EY is shown in Figure 2 [135]. Chronoamperograms measured during the electrolyses at -0.7, -0.8, and -0.9 V (vs SCE) in the absence and presence of 55 μmol dm^{-3} EY (Fig. 2A) show that the current decreases by the addition of EY at all potentials. When the electrode potential is fixed at -0.9 V (vs SCE) and the concentrations of EY is varied (Fig. 2B), a systematic decrease of current is seen upon increasing the concentration of EY. Colorless and translucent thin films of ZnO can be deposited at all potentials in the absence of EY. In the presence of EY,

the electrolysis at -0.7 or -0.8 V (vs SCE) led to the deposition of red colored thin film, although the film at -0.7 V (vs SCE) was only partly covering the substrate. The electrolysis at -0.9 V (vs SCE) in the presence of EY at concentrations below 100 μmol dm^{-3}, on the other hand, resulted in a deposition of colorless thin films, which, however, gradually turned into red when kept in air after the deposition. This color change is caused by the electrochemical reduction of EY molecules during the film deposition and its importance to the hybrid formation will be discussed later in detail.

In the absence of EY and at -0.9 V (vs SCE) [Fig. 2A(a)], the current sharply rises at the beginning of the electrolysis and falls to a steady value of ca. 1 mA cm^{-2}, creating a current peak at $t = 1.5$ min. This behavior is typically expected when the film growth takes place by initial nuclei formation and subsequent growth of these seed crystals [141]. At the high concentration (0.1 mol dm^{-3}) of Zn(NO$_3$)$_2$ used in the present study, the observed small current can not be ascribed to the limitation by the transport of Zn^{2+} or NO$_3^-$ [109] but is limited by the kinetics of charge transfer and crystallization. This is interesting to note since it points at the complex reaction conditions mentioned that the reduction of nitrate cannot be seen as independent of the "subsequent" reactions with Zn^{2+}. Formation of ZnO is a crucial step in the overall electrochemical reaction and it is this step which limits the current: at the beginning of the deposition, the seed crystals grow three-dimensionally to increase the active surface area, thus leading to the observed increase of current. As the crystals grow, they merge together so that the lateral crystal growth ceases and the film growth becomes one-dimensional (i.e., in the direction perpendicular to the substrate). Consequently, the current falls to a constant value. When more positive potentials were applied, the current peak was broadened and moved toward later times, along with a decrease of the steady-state current. A smaller number of nuclei can be formed at a smaller overpotential, so that the transition from the three-dimensional to the one-dimensional growth occurs at a later time [141]. The smaller steady-state current is also expected by the slowdown of the charge transfer kinetics under a smaller overpotential.

If eosinY is added to the bath, the current peaks are broadened and shifted to larger t, compared with the corresponding reaction without dye, and a decrease of the steady-state current is noticed. The partial coverage of the substrate in the case of -0.7 V (vs SCE) is explained by a significant decrease of the current by inefficient seed formation and slow rate of the subsequent growth due to local inhibition by the dye molecules. When the potential was fixed at -0.9 V (vs SCE) and the dye concentration was changed, systematic broadening of the nucleation peak, its shift to larger t, and a decrease of the steady-state current were observed upon increasing the dye concentration (Fig. 2B). When the dye concentration was higher than 100 μmol dm^{-3}, no film was deposited. These results indicate that the addition of EY hinders the nucleation as well as the crystal growth of ZnO and it clearly confirms that no independent reduction of nitrate occurs.

Figure 2. Chronoamperograms measured during cathodic electrolyses at indium tin oxide (ITO) coated glass electrodes in aqueous solutions of 0.1 mol dm^{-3} Zn(NO$_3$)$_2$ with or without addition of 55 μmol dm^{-3} EY and at different electrode potentials of -0.7, -0.8, and -0.9 V (vs SCE) as indicated in (A), those measured at -0.9 V (vs SCE) in solutions containing different concentrations of EY as indicated in (B). All measurements were carried out under air and at 70 °C. Reprinted with permission from [135], T. Yoshida et al., *Electrochemistry* 70, 470 (2002). © 2002, Electrochemical Society of Japan.

2.1.2. Change of Surface Morphology

The addition of dye to the deposition bath significantly affects the crystal growth of ZnO and alters the film morphology in various ways. Figure 3 shows scanning electron
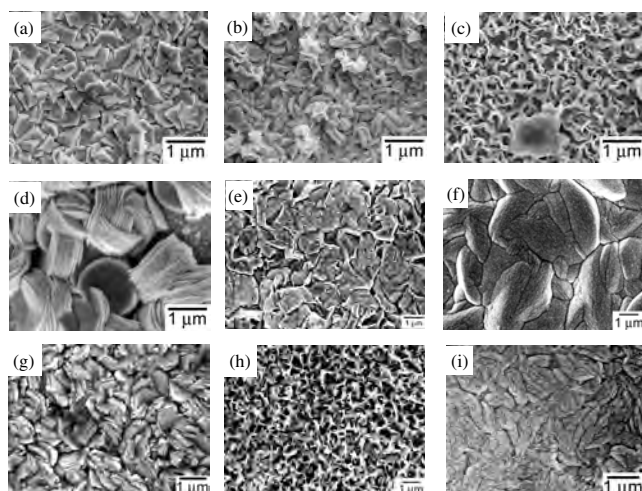
Figure 3. Variation of surface morphology of the electrodeposited ZnO/dye hybrid thin films; pure ZnO thin film electrodeposited at −0.9 V for 60 min from a 0.1 M Zn(NO₃)₂ aqueous solution (70 °C) (a), ZnO/TSPcZn hybrid thin film (b), ZnO/TSPcAl hybrid thin film (c), ZnO/TSPcSi hybrid thin film (d), ZnO/EY hybrid thin film (e), ZnO/PB hybrid thin film (f), ZnO/TB hybrid thin film (g), ZnO/N3 hybrid thin film (h), and ZnO/R5P hybrid thin film (i).

microscopy (SEM) images of films prepared under different conditions. Figure 3a depicts the pure ZnO thin film electrodeposited from a dye-free $Zn(NO_3)_2$ bath which consists of hexagonally shaped particles. The film morphology is completely changed when the same electrolysis is carried out after minor addition of TSPcZn (b) [130, 131], TSPcAl (c) [131], TSPcSi (d) [131, 132], EY (e) [133–135], PB (f) [134], TB (g) [137], N3 (h) [138], and R5P (i) [140]. All of the dye loaded films consist of crystalline ZnO as seen in X-ray diffraction (XRD) measurements, although they are colored by the dyes unlike the pure ZnO. As shown in the previous section, the electrodeposition of ZnO is not completely hindered when proper concentration of dye is chosen. In fact, the films prepared in the presence of dyes are often thicker than the pure ZnO under the given deposition conditions, because the films often become porous in structure. The hybrid films with dyes such as TSPcAl (c) and N3 (h) are obviously porous. However, one should pay attention to the fine internal structure seen in the deposits. For example, the ZnO/PB hybrid thin film (f) appears rather flat and dense in Figure 3. But careful observation reveals a nanosized internal structure within the grains which are several micrometers large [134]. The film with EY (e) has a disordered structure as a whole, but domains which appear as assemblies of nanosized particles can be recognized [133, 135]. The structure of ZnO/TSPcSi hybrid thin film (d) is particularly interesting as the deposits look like stacked thin platelets which stand with their edge on the substrate [131, 132]. These unique morphologies reflect the history of the film growth, more precisely, the anisotropy of the crystal growth of ZnO caused by the addition of dyes. The observed film morphologies in the micrometer regime do relate to the crystal shape, size, and orientation of ZnO, which in some cases were still observed on a nanometer scale.

2.1.3. Crystallographic Orientation

As predicted in the previous section, the orientation of ZnO crystallites in the ZnO/dye hybrid thin films differs from that of pure ZnO. The change of the crystallographic orientation by the dye addition can be studied by analyzing the relative peak intensities in the XRD pattern of the films and an example is given for the series of hybrid thin films with TSPcZn, TSPcAl, and TSPcSi in comparison with the pure ZnO in Figure 4. All films show sharp diffraction peaks assigned to ZnO, aside from the peaks arising from the ITO substrate. It is noticed that the relative intensities of major diffractions arising from (100), (002), and (101) planes for the ZnO/TSPcMt films are different from those for the pure ZnO. While the peak intensity from the (002) planes decreases, the (100) peak becomes larger for the films deposited with TSPcMts. This indicates the tendency that the ZnO crystallites in the hybrid thin films are oriented with their c-axis parallel with the substrate so that the diffraction from the (100) planes increases since they lie parallel to the substrate. When the degree of such preferential orientation is estimated quantitatively by calculating orientation indices taking the standard powder sample as the reference, the highest influence has been found for TSPcZn, which is followed by TSPcSi [131]. The observed preference of the crystallographic orientation implies that the edge of the disklike deposits found in the SEM picture of Figure 3d corresponds to the (100) face of ZnO, while the plane of the disk to the (002). This was confirmed by observing the microstructure of the deposits by transmission electron microscopy (TEM) (Fig. 5). The samples were prepared by mechanically scratching the ZnO/TSPcSi thin film off the ITO substrate. Several large particles which do not permit penetration of electron beams were found as seen in the lower part of Figure 5, and they correspond to the disk stacks. Fortunately, several thin and flat platelets were also found as shown in the upper part of Figure 5. It supposedly
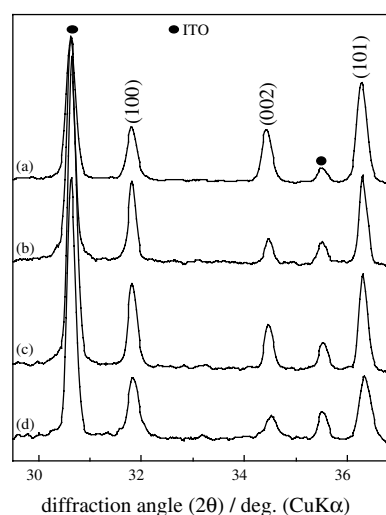

Figure 4. X-ray diffraction patterns of the pure ZnO (a), ZnO/TSPcZn (b), ZnO/TSPcAl (c), and ZnO/TSPcSi (d) hybrid thin films electrodeposited at −0.9 V. Reprinted with permission from [131], T. Yoshida et al., *Chem. Mater.* 11, 2657 (1999). © 1999, American Chemical Society.
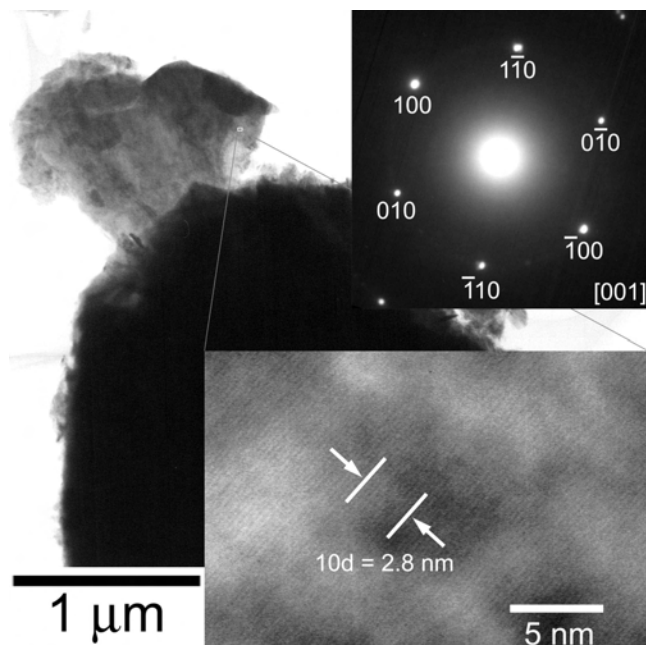
Figure 5. TEM photograph of the "discs" consisting the ZnO/TSPcSi thin film seen in Figure 3d in a view vertical to the disc plane together with the high magnification image (lower inset) showing the lattice fringe with ca. 2.8 Å interspace corresponding to the (100) planes of ZnO and the complementary SAED pattern (upper inset) showing six-fold diffraction spots indexed by taking the [001] zone axis. Reprinted with permission from [131], T. Yoshida et al., *Chem. Mater.* 11, 2657 (1999). © 1999, American Chemical Society.

is the building unit (the disk) of the disk stack. In the high magnification image of the disk can be found a uniform lattice image with ca. 2.8 Å spacing over the entire deposit, as shown in the lower inset of Figure 5. This corresponds to the lattice fringe created by lateral projection of the (100) planes of ZnO. The complementary selected area electron diffraction pattern is shown as the upper inset of Figure 5 and it clearly exhibits diffraction spots in a six-fold symmetry. They are indexed by taking the [001] zone axis as shown in the figure. The spot pattern assignable with unique zone axis indicates the single crystalline nature of the disklike deposit. The relationship between the zone axis and the structure of the deposit confirms that the disk plane corresponds to the (002) face of ZnO as expected from the SEM photograph and the XRD. This structure was also confirmed from the TEM image for a lateral projection of the disk stacks [131].

It is interesting to note that the crystallinity of ZnO in the electrodeposited ZnO/dye hybrid thin films is generally as high as that of the electrodeposited pure ZnO, although the adsorption of dye molecules is expected to hinder the crystal growth of ZnO. In many cases, the XRD peaks of the hybrid thin films do not exhibit any broadening even for the ZnO/EY hybrid thin film which appears to consist of nanosized particles (Fig. 3e). These nanosized building blocks in fact are interconnected to form spongelike porous crystals, as confirmed from the TEM image of this film, which showed continuous lattice fringes appearing over the assembly of nanosized structures [135]. The stacking of the disklike ZnO for the ZnO/TSPcSi system mentioned also

indicates a certain driving force to assemble these platelets. The addition of a dye significantly modifies how the crystals grow but does not block the crystal growth completely, so that these building units grow to be connected and maintain a complete structure of ZnO in their assembly.

2.1.4. Growth Model of ZnO/TSPcMt Hybrid Films

Considering the impact of dye addition to the crystal growth of ZnO, a model for the growth of hybrid thin films can be derived as depicted in Figure 6 for the case of the ZnO/TsPcMt system. The attachment of a TSPcMt molecule onto the surface of ZnO is expected to occur through its sulfonic acid groups, since a formation of sulfonic ester linkage was also indicated in the Fourier transform infrared analysis of a sol–gel processed TiO_2/TSPcCo composite [142]. The adsorption of dye through a sulfonic acid group was also suggested in the ZnO/TB hybrid thin film prepared by one-step electrodeposition, for which the pH-dependent color change along with the change of molecular structure into the lactone form was prohibited [137]. Such adsorption of dye molecules in the case of TSPcMts seems to take place preferentially onto the (002) faces of ZnO, so that the crystal growth along the c-axis is hindered. Consequently, the crystal growth occurs predominantly along the a- and b-axes. Following the initial period of seed formation, the growth direction is defined by reactant transport and hence proceeds vertical to the surface. Therefore those ZnO crystallites with their a- and b-axes perpendicular to the substrate will grow faster and represent the preferential crystal orientation of the final film.

The stability of dye adsorption to each crystallographic face of ZnO is expected to differ from dye to dye and these
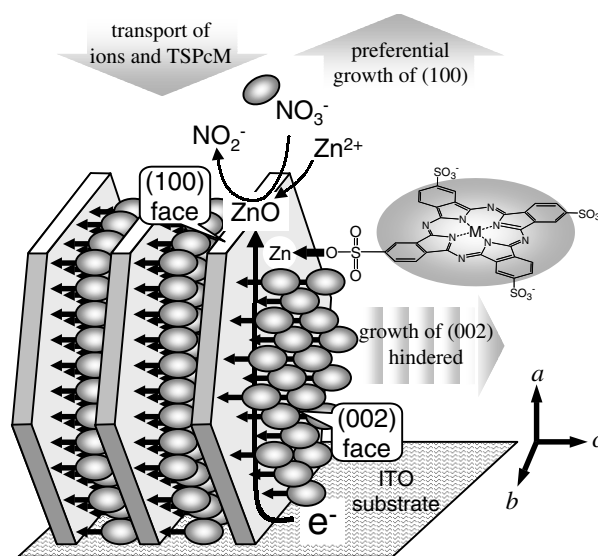

Figure 6. Illustration of the electrochemical self-assembly of the ZnO/TSPcMt thin films, showing the preferential adsorption of TSPcMt molecules onto the (002) planes of ZnO and consequent preferential growth of (100) planes to create the stacking "discs" aligned vertical to the substrate. Reprinted with permission from [131], T. Yoshida et al., *Chem. Mater.* 11, 2657 (1999). © 1999, American Chemical Society.

differences lead to the characteristics in the anisotropy of the crystal growth. The variation of the film morphology shown in Figure 3 can therefore be explained as arising from the different interactions of the dye molecules with the surface of ZnO.

2.2. Ordered Dye Assemblies in ZnO/Dye Hybrid Films

The added dye molecules not only interact with the surface of ZnO but also among themselves to form molecular assemblies in ordered structures. The intermolecular electronic interaction can be nicely studied by measuring ultraviolet-visible (UV-vis) absorption spectra, because the interaction of the chromophores in condensed dye assemblies leads to specific changes of the electronic structures [143–145]. This was discussed in detail for the electrodeposited ZnO/TSPcZn hybrid thin film [131].

In Figure 7 are shown the absorption spectra of the ZnO/TSPcZn thin films electrodeposited at −0.7 and −0.9 V (vs SCE), compared with those of the pure ZnO thin film, an aqueous solution of TSPcZn, an aqueous solution of TSPcZn with added CTAC (=cetyltrimethylammoniumchloride), a dry mixture of solid TSPcZn and ZnO powders, and ZnO powder to which TSPcZn is adsorbed by refluxing it in an aqueous solution of TSPcZn.

The electrodeposited pure ZnO thin film only exhibits a sharp increase of the absorption below ca. 380 nm attributable to the bandgap absorption of ZnO, aside from the gradual increase of apparent absorption with decreasing wavelength due to light scattering (a). Both of the ZnO/TSPcZn thin films deposited at −0.7 and −0.9 V were
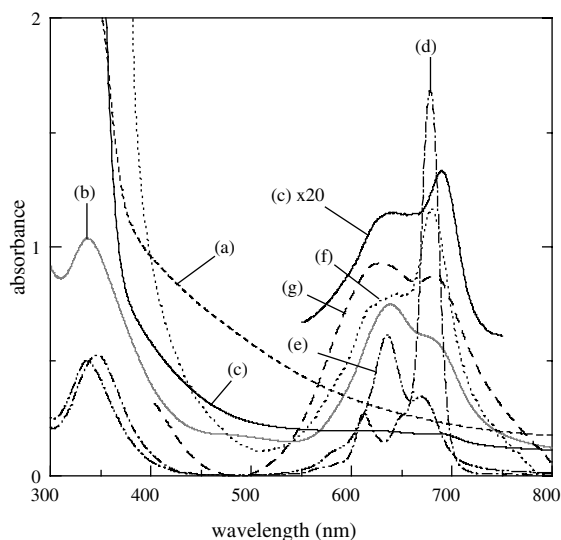
Figure 7. UV-vis absorption spectra of the ZnO thin film electrodeposited at −0.9 V (a), the ZnO/TSPcZn hybrid thin films electrodeposited at −0.7 V (b) and −0.9 V (c), the aqueous solutions of TSPcZn in its monomeric form measured in the presence of cetyltrimethylammonium chloride (CTAC) (d), and dimeric form without CTAC (e), the physical mixture of dry powders of ZnO and TSPcZn (f), and the ZnO powder to which TSPcZn is chemically adsorbed from its aqueous solution (g). Reprinted with permission from [131], T. Yoshida et al., *Chem. Mater.* 11, 2657 (1999). © 1999, American Chemical Society.

blue and more transparent than the pure ZnO. However, a clear difference can be noticed in the character of the absorption peaks in the visible range, namely those arising from the loaded TSPcZn molecules. The film deposited at −0.7 V obviously contains a higher amount of dye and exhibits absorption maxima at 337 and 639 nm, and a shoulder at around 680 nm (b), whereas the film deposited at −0.9 V was pale blue and has a Q-band absorption peak at 690 nm and a shoulder at around 630 nm, as clearly seen in the enlarged spectrum (c). The relative intensity of the blue side and the red side peaks of the Q-band clearly oppose these two films.

The intermolecular attraction due to the strong π-electronic affinity between TSPcZn molecules leads to the formation of dimers in a face-to-face arrangement of the Pc ring system even when dissolved in water [145]. Formation of such assemblies of Pc molecules can be characterized by a blueshift of the Q-band absorption peak from that of the monomer, due to the π-electronic interaction in a parallel arrangement of the chromophores [143, 144]. This π-stacking of TSPcZn molecules can only be suppressed in the presence of a cationic detergent (CTAC) [145]. An absorption spectrum of monomeric TSPcZn is therefore obtained only for an aqueous solution mixed with CTAC, which exhibits a sharp Q-band absorption peaking at 678 nm and a Soret-band absorption at 347 nm (d). The absorption spectrum of dimeric TSPcZn is obtained for an aqueous solution of TSPcZn without CTAC, for which both of the two absorption peaks are blueshifted to 635 and 336 nm, respectively (e).

Clear resemblance between the absorption spectra of the ZnO/TSPcZn film deposited at −0.7 V and the dimeric TSPcZn in water indicates formation of π-stacking aggregates for the TSPcZn molecules in the ZnO/TSPcZn film. The aggregates in the film obviously differ from solid TSPcZn which was precipitated in water by adding ethanol (f). The solid TSPcZn exhibits an absorption peak at 679 nm, close to that of monomeric TSPcZn in water, although the absorption peak is significantly broadened. Such spectral characteristics speak for an amorphous structure of solid TSPcZn, for which random intermolecular interaction is expected to cause a simple broadening of the absorption spectrum. The electrodeposition obviously does not result in the formation of such a random solid of TSPcZn but generates ordered aggregates.

Formation of ordered assemblies of TSPcZn on the ZnO surface was further proven by preparing a TSPcZn-modified ZnO powder by refluxing commercial ZnO powder in an aqueous solution of TSPcZn. Its absorption spectrum has a very similar character to the ZnO/TSPcZn film deposited at −0.7 V, exhibiting absorption maxima at 633 and 681 nm (g). TSPcZn is again adsorbed as π-stacking aggregates on the ZnO surface. Formation of such ordered dye aggregates on inorganic surfaces was also reported by Nüesch et al. for merocyanine dyes adsorbed on TiO₂, Al₂O₃, and ZrO₂, as a consequence of chemical interactions between the dye molecules and the ordered surface of inorganic materials as well as that among the neighboring dye molecules [146].

Chemical adsorption of TSPcZn to ZnO and the electrodeposition of ZnO/TSPcZn hybrid thin films with a small overpotential allowed formation of ordered dye aggregates.

On the contrary, the electrodeposition with a high overpotential, namely, at -0.9 V, results in a dye loading in its monomer form as noticed from the Q-band absorption character similar to that of the monomer (c and d). It should be noted that TSPcZn is dissolved as dimers in the deposition bath, since it does not contain CTAC. Dimers of TSPcZn in this case are split into monomers during the film growth probably because of the increased pH at the vicinity of the electrode due to the reduction of nitrate, which should result in a higher solubility of TSPcZn [145]. It is interesting to note that washing the ZnO/TSPcZn hybrid thin film deposited at -0.7 V and TSPcZn modified ZnO powder prepared by reflux treatment with CTAC solution lead to partial desorption of TSPcZn molecules and converted their absorption spectra to those very similar to that of the hybrid thin film deposited at -0.9 V [131]. Such a change clearly indicates formation of dye multilayers due to the dye/dye interaction in the as-deposited films. At the bottom of such dye multilayers, however, TSPcZn molecules are present that are chemically attached to ZnO and that cannot be washed away by the CTAC treatment.

Besides TSPcZn, many of the dyes we studied such as EY [133, 135] and TB [137] also showed a tendency to form ordered aggregates in the electrodeposited ZnO/dye layer. The added dye molecules not only act as structure-directing agents for the crystal growth of ZnO but also self-assemble in ordered structures. The process can therefore be considered as an electrochemically induced self-assembly of three dimensional ZnO/dye hybrid structures determined by the constituent ions and molecules.

2.3. Role of Electrochemical Reductions of Dye Molecules

It has been elucidated in the previous sections that the addition of surface adsorbing dye molecules in the bath results in electrochemical self-assembly of ZnO/dye hybrid thin films. The added dye molecules in fact are not simply passively adsorbed but also can actively participate in the electrochemical charge transfer processes since some of the dyes can be reduced at the potentials typically used for the deposition of ZnO.

Among such dyes, the family of xanthene dyes shows especially unique electrochemical behavior in the presence of Zn^{2+}. Figure 8 shows a set of cyclic voltammograms measured in aqueous solutions containing EY of a constant concentration and $Zn(NO_3)_2$ with various strengths [135]. In the absence of Zn^{2+}, a couple of reversible redox peaks centered at -1.07 V (vs SCE) are seen, which correspond to the reversible reduction and reoxidation of EY. Increase of the Zn^{2+} concentration causes a systematic positive shift of the cathodic peak of EY reduction, aside from the increase of the cathodic current in the more negative potential range, which is related to the formation of ZnO. At the same time, the reoxidation peak of EY disappears. The cathodic peak potentials are plotted vs the logarithm of the Zn^{2+} concentration in the inset of Figure 8. It is clearly seen that the peak potential remains almost constant up to a certain concentration of Zn^{2+} and the further addition of Zn^{2+} causes a linear positive shift. The slope of the shifting part has been
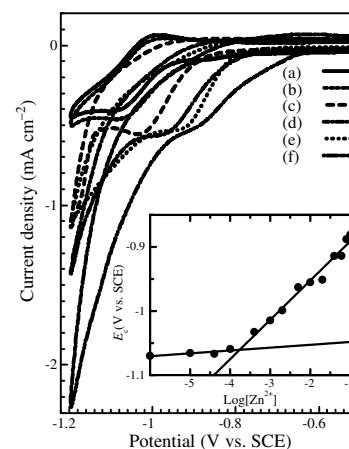

Figure 8. Cyclic voltammograms measured at an ITO coated glass electrode in aqueous solutions prepared by mixing 0.1 mol dm^{-3} Zn(NO$_3$)$_2$ and 0.2 mol dm^{-3} KNO$_3$ at various ratios to maintain an ionic strength of 0.2 mol dm^{-3} while varying the strength of Zn^{2+} as 0 (a), 0.4 (b), 1 (c), 10 (d), 60 (e), and 100 (f) mmol dm^{-3}. All of these solutions contain EY at a constant concentration of 0.5 mmol dm^{-3}. The solutions were saturated by Ar and maintained at 70 °C. Potential sweep rate was fixed to 500 mV s^{-1}. The inset shows the relationship between the cathodic potential of EY reduction and logarithmic strength of Zn^{2+}. The slope of the shifting part is 64 mV/decade and thus indicates coupling of a Zn^{2+} ion with electrochemical reduction of an EY molecule. The borderline Zn^{2+} strength is referred to the stability of the resultant complex between reduced eosinY and Zn^{2+} (pK_{Zn} = 3.76) (see text). Reprinted with permission from [135], T. Yoshida et al., *Electrochemistry* 70, 470 (2002). © 2002, Electrochemical Society of Japan.

determined as ca. 64 mV/decade, which indicates a Nernstian behavior of a Zn^{2+}-coupled reduction of EY under high concentrations of Zn^{2+} that can be written as

$$EY + e^- + Zn^{2+} \rightarrow (EY^-)(Zn^{2+}) \qquad (6)$$

The reduced form of EY is stabilized against reoxidation by complex formation with Zn^{2+}. Such complex formation can well explain why these molecules can be loaded into the film at a high amount [135]. Since electrodeposition of ZnO/EY hybrid thin films is typically carried out at -0.9 V (vs SCE) in a 0.1 M Zn(NO$_3$)$_2$ containing EY, electroreduction of EY molecules does take place during the film growth. The freshly deposited thin film is in fact colorless and it only gradually turns into red on its exposure to air, because the reduced EY molecules are reoxidized by atmospheric oxygen [135].

The borderline between the regions where the reduction potential of EY is dependent and independent on the Zn^{2+} strength is referred to the stability of the $(EY^-)(Zn^{2+})$ complex, which dissociates into free EY^- and Zn^{2+} at an equilibrium constant, K_{Zn}, as written by the equations
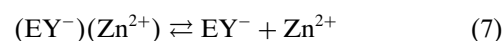
$$(EY^-)(Zn^{2+}) \rightleftarrows EY^- + Zn^{2+} \qquad (7)$$

$$K_{Zn} = \frac{[EY^-][Zn^{2+}]}{[(EY^-)(Zn^{2+})]} \qquad (8)$$

The stability constant of pK_{Zn} = 3.76 is therefore determined from the borderline between the $[Zn^{2+}]$ dependent and independent parts in Figure 8. In a series of similar

experiments, a pK_{Zn} value of 2.8 has been determined for the complex formation of phloxineB (PB) which is also a member of xanthene dyes [134]. The higher value of pK_{Zn} for the $(EY^-)(Zn^{2+})$ complex indicates its higher stability than the $(PB^-)(Zn^{2+})$ complex. The electrochemical reduction of EY generates the nucleophilic EY^- species which form stable and colorless complexes with Zn^{2+}. The EY molecule stays reduced when attached to ZnO during the film growth but can be slowly reoxidized to the red form by atmospheric oxygen when the film is exposed to air after the deposition is finished.

2.4. Extraction of Dye Molecules

The process of electrochemical self-assembly can yield highly crystallized porous ZnO and achieve dye loading at a high amount. Now, a question arises about the location of dye molecules in the hybrid structure, because dye molecules have to be attached to the surface of ZnO and not entrapped inside of ZnO grains in order for them to perform as photosensitizers for the solar cell applications. Although the exact hybrid structure on the molecular level has not been determined yet, the accessibility of the dye molecules can be easily checked by dipping the films in mild alkaline solutions, to cleave the ester bond between the dye and ZnO and to detect the dye in the solution.

When a ZnO/EY hybrid thin film electrodeposited at -0.9 V (vs SCE) from a 0.1 M $Zn(NO_3)_2 + 55\ \mu M$ EY mixed aqueous solution was dipped in a 0.1 M KOH solution, the EY molecules were almost completely extracted from the film. The film was completely bleached by this treatment as one can see in the change of the UV-vis absorption spectra shown in Figure 9. The absorption peak in the visible range arising from the loaded EY molecules almost completely disappears after the alkaline treatment. In this process, the

film thickness (about 1.2 μm for this sample) did not change, since dissolution of ZnO does not take place at this pH. The undamaged ZnO structure can also be seen in the SEM picture of the film after the alkaline treatment (Fig. 10). The surface morphology of the film is almost unchanged before and after the treatment. These results clearly indicate that the loaded EY molecules exist only on the surface of ZnO accessible from the KOH solution. This is encouraging in view of its application to solar cells, because the redox electrolytes used there should also reach the dye molecules. It is supposed that the stable complex formation between the reduced EY molecule and Zn^{2+} ion mentioned previously locally terminates the crystal growth of ZnO, so that the adsorbed EY molecules are not trapped inside of ZnO. However, this is of course not always the case for all kinds of dye molecules. For example, only a part of the loaded dyes could be extracted by the alkaline treatment of ZnO/TSPcMt hybrid thin films.

2.5. Chemical Composition of ZnO/Dye Hybrid Films

Finally, the chemical and volumetric compositions of ZnO/dye hybrid thin films are discussed for the example of ZnO/EY hybrid thin films.

Cathodic electrolysis at -0.9 V (vs SCE) for 60 min in a 0.1 M $Zn(NO_3)_2 + 55\ \mu M$ EY aqueous mixed solution consumed about 2.7 C cm^{-2} of cathodic charge. The thickness and the dye loading for the resultant film were 1.7 μm and 4.8×10^{-8} mol cm^{-2}, respectively. The dye concentration in the solid film assuming homogeneous distribution of dye molecules is calculated as 0.28 mol dm^{-3}, which is far greater than that of the Ru complex adsorbed on the porous TiO_2 films prepared by colloid based processes as those typically used in DSSCs (0.13 mol dm^{-3}) [7]. The dye loading at a very high amount is a unique feature of the electrodeposited ZnO/EY thin film. In fact, simple chemical adsorption of EY to a 9 μm thick colloid based porous ZnO film

Figure 9. UV-vis absorption spectra of a ZnO/EY hybrid thin film electrodeposited at -0.9 V (vs SCE), for 60 min, under air and at 70 °C from an aqueous mixed solution of 0.1 mol dm^{-3} $Zn(NO_3)_2$ and 55 μmol dm^{-3} EY measured at its fully reoxidized state (a), and the same sample measured after dye extraction by dipping the film in a 0.1 mol dm^{-3} aqueous KOH solution (b). Reprinted with permission from [135], T. Yoshida et al., *Electrochemistry* 70, 470 (2002). © 2002, Electrochemical Society of Japan.
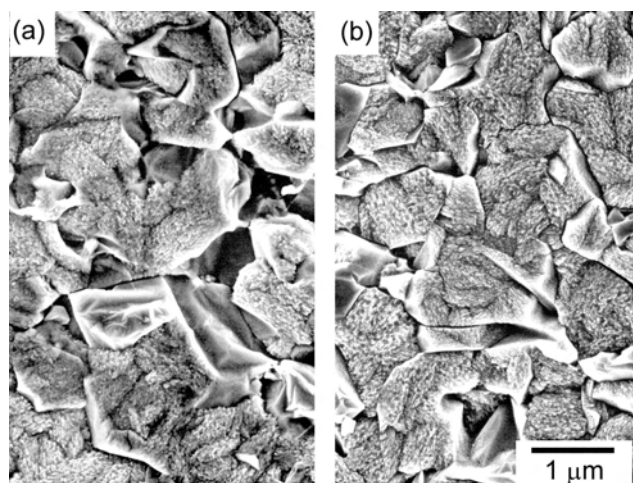

Figure 10. Change of surface morphologies of a ZnO/EY hybrid thin film before (a) and after (b) dye extraction. The same samples as those in Figure 9 were observed. Reprinted with permission from [135], T. Yoshida et al., *Electrochemistry* 70, 470 (2002). Electrochemical Society of Japan.

allowed dye loading only at 0.029 mol dm^{-3}, suggesting a rather poor stability for the chemical adsorption of EY in its neutral oxidation state onto ZnO. The high loading of dyes in the electrochemical self-assembly process could be explained by the stable complex formation between reduced EY molecules and Zn^{2+}. The amount of deposited ZnO determined by inductively coupled plasma atomic emission spectroscopy was ca. 8.0×10^{-6} mol cm^{-2}. Since the amount of charge consumed for dye reduction should be negligibly small, a faradaic efficiency of 57% for ZnO formation according to Eq. (4) is derived from the comparison of the consumed charge and the amount of ZnO for the electrodeposition of the ZnO/EY hybrid thin films, which is somewhat smaller than that for the pure ZnO growth from solutions of Zn(NO$_3$)$_2$ (around 70%).

Judged from the amounts of electrodeposited ZnO and EY in the hybrid material, its composition can be determined as EY:ZnO = 1:170 in molar ratio. However, their volume ratio is quite different from this. The volume of electrodeposited ZnO calculated by using the formula weight (=81.46) and the density (=5.606 g cm^{-3}) of bulk ZnO reveals that about 66% of the total volume of the film is occupied by ZnO. If we approximate the density of adsorbed EY by a value of 1 g cm^{-3}, a typical bulk value for halogenated aromatic compounds, the volume of the loaded EY is calculated as 1.66×10^{-5} cm^3 per cm^2 of the projected film area, which is as much as 10% of the total film volume. It is therefore concluded that the remaining 24% corresponds to the overall pore volume in the film.

In summary of the structural characterization, we can conclude that the process of electrochemical self-assembly can yield ZnO/dye hybrid thin films which are highly crystallized, are highly porous, and contain high amounts of dyes adsorbed on the inner surface of ZnO. All of these characteristics are favorable for their applications as photoelectrodes in dye-sensitized solar cells.

3. PHOTOELECTROCHEMICAL CHARACTERIZATION

The general goal in the ongoing and future photoelectrochemical work can be summarized in the task of preparing highly porous electrodes of high structural order covered by a monolayer of strongly absorbing dyes [147]. Ultrafast electron transfer from the dye to the electrode and a suppression of backtransfer to the dye (recombination) or the electrolyte as compared to hole transfer from the dye to the electrolyte are further prerequisites for efficiently working and chemically stable electrodes [10, 12–14, 19, 64, 148–150].

Kinetic information about charge transfer, trapping in interface states, and recombination can be best obtained by time-resolved measurements, or by the frequency-resolved methods of IMPS (intensity-modulated photocurrent spectroscopy) or IMVS (intensity-modulated photovoltage spectroscopy). These methods have turned out to be valuable tools in studies of charge transfer at semiconductor surfaces [15, 16, 151] in the case of molecular semiconductors [152–154] and especially in the case of dye-sensitized oxide semiconductors [14, 22, 23, 155–157].

The sensitization properties of electrochemically self-assembled ZnO/dye composite films were studied in detail

by photocurrent spectra, time-resolved photocurrent measurements, IMPS, and IMVS [17, 18, 133–135, 137–140, 158]. One important parameter is the incident-photon-to-current-conversion efficiency (IPCE). It is calculated from photocurrent spectra as the ratio of the transferred electron density (calculated from Faraday's constant and the photocurrent at the working electrode) to the photon density incident on the cell. An entity similar to a quantum efficiency is obtained. However, incident rather than absorbed photons are considered. The IPCE characterizes the overall efficiency of an electrode in its light absorption, electron injection to the semiconductor, charge transport therein, and hole transfer to the electrolyte.

3.1. Nanoparticulate ZnO–TSPc Hybrid Electrodes

The TSPc/ZnO hybrid films were intensely colored by adsorbed dye molecules. Intermolecular interactions in assemblies of organic molecules can be monitored conveniently in optical spectra. Whereas monomeric solutions of phthalocyanines are characterized by narrow absorption bands in the Soret- (about 350 nm) and especially in the Q-band region (about 680 nm), samples of dimers already showed a considerable shift to around 630 nm of the Q-band maximum [145]. A strongly broadened and split Q-band is typical for solid crystalline samples [143]. The absorption at 640 nm seen in Figure 11a showed the dominance of aggregated dye only in the case of TSPcZn when grown at −0.7 V vs SCE [17, 18, 130, 158]. Under these conditions the growth rate of ZnO is still rather low, allowing the formation of dye aggregates. Under identical conditions, but at −0.9 V vs SCE, the rate of film formation was enhanced obviously
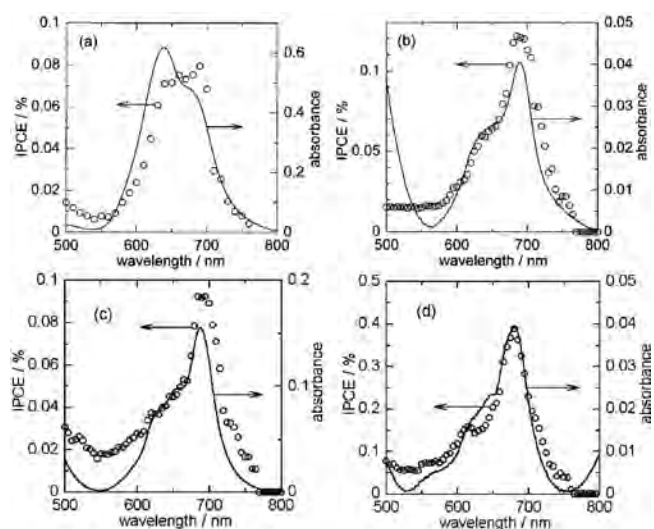

Figure 11. Optical absorption spectra (lines) and photocurrent action spectra in the oxidation of iodide at −0.2 V vs Ag/AgNO$_3$ (circles) measured at films of ZnO–TSPcZn grown at −0.7 V vs SCE (a) and at −0.9 V vs SCE (b), ZnO–TSPcAl(OH) (c), and ZnO–TSPcSi(OH)$_2$ (d), both grown at −0.9 V vs SCE. Reprinted with permission from [158], D. Schlettwein et al., *Proc. SPIE* 4465 (2002). © 2002, The International Society for Optical Engineering.

leading to lower steady-state concentrations of the dyes and hence monomer adsorption.

Light absorption of the adsorbed phthalocyanine molecules led to sensitized photocurrents in contact to an organic I_2/I_3^- electrolyte. Many experiments were performed in a conventional three-electrode arrangement with the deposited hybrid thin films as working electrode, a Pt counterelectrode, and a $Ag/AgNO_3$ reference electrode as the electrolyte, 0.5 M KI in acetonitrile/ethylenecarbonate (1:4 by volume) was used.

Results of photocurrent spectra are directly compared to the optical absorption spectra in Figure 11. Among TSPc of different central groups, significantly higher conversion efficiencies were found for monomeric as compared to aggregated TSPc adsorbed on the ZnO surface [17, 18, 158]. This was also the case for electrodes having mostly aggregated TSPcZn, although these aggregates dominated the absorption spectra. A considerably higher quantum efficiency of monomeric dye when compared with aggregated dye was thereby shown.

When the values of the IPCE are considered it has to be noted that the values reached by ZnO–TSPc hybrid thin films were generally low. Among the materials, however, clear differences could be detected showing the strong influence of the central group. $TSPcSi(OH)_2$ proved to be the most efficient sensitizer since a peak IPCE of 0.4% was reached at an absorbance of only 0.04. This indicated a quantum efficiency about a factor of 3 higher when compared to monomers of TSPcZn (0.12% at similar absorbance) and about a factor of 17 higher when compared to TSPcAl(OH) reaching the lowest values of the TSPc monomers in spite of the highest absorbance. These differences are only in part explained by a more suitable position of the frontier orbitals of $TSPcSi(OH)_2$ and it has to be assumed that a stronger interaction with the ZnO surface through interactions with the additional OH- groups of TSPcSi or an enhanced accessibility of the sensitizers caused by differences in the morphology of the films played a decisive role [18, 158].

Time-resolved photocurrent measurements in the ms regime were performed to analyze the kinetics of light-induced charge transfer at the ZnO–TSPc thin film electrodes and to discuss the role of charge-carrier recombination (Fig. 12). A fast increase of the photocurrent shortly after the beginning of illumination was seen for the electrodes. The maxima of the photocurrents appear about 10 ms after the beginning of illumination. This reflects the opening time of the shutter (i.e., the time needed to achieve full illumination of the electrode). Although the size-quantization effect should only significantly decrease the conduction in nanocrystalline semiconductors below a particle size of about 10 nm [159], a slow electron transport can often be observed in nanocrystalline oxide electrodes, which leads to a slow increase of the photocurrent during a light pulse and photocurrent rise times of several tens or hundreds of milliseconds have been reported in these cases [16]. The photocurrent rise time of $\leq$10 ms, however, shows that electron transport in ZnO is not hindered significantly in the electrodes investigated here. When the photocurrents observed at electrodes of TSPcZn monomers on ZnO were compared with those of aggregates on ZnO,
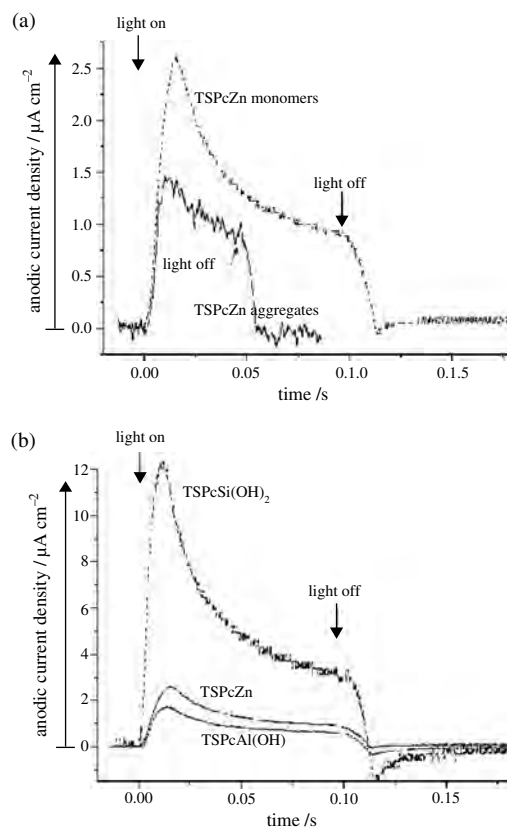

Figure 12. Photocurrent transients observed at -200 mV vs $Ag/AgNO_3$ in contact to 0.5 M KI in acetonitrile/ethylenecarbonate (1:4 by volume). Comparison between aggregated and monomeric forms of TSPcZn (a), and of the influence of the central group in monomeric TSPc (b). Reprinted with permission from [158], D. Schlettwein et. al., *Proc. SPIE* 4465 (2002). © 2002, The International Society for Optical Engineering.

a significantly different shape was observed. The monomer electrodes led to a more pronounced overshoot of the photocurrent above the stationary value when the light was switched on and significant cathodic currents when the beam was shut, whereas the electrodes in which also aggregates were present showed a more rectangular response consisting of anodic currents only. This behavior is consistent with the assumption of a more facile transfer of electrons from I_3^- to the aggregates compared with the monomers [17]. The slower re-reduction of the oxidized dye following electron transfer from the excited dye to the conduction band of ZnO led to a significantly higher concentration of oxidized dye in the stationary state with the consequence of the observed cathodic currents during the re-reduction by electrons from the ZnO valence band when the light beam was shut. The low efficiency of TSPcZn aggregates is not caused by slow electrode kinetics but either by a low concentration of excited dye molecules due to fast radiationless decay within TSPcZn aggregates or by a slower electron injection rate into the conduction band of ZnO. Although electron transfer from I_3^- to the aggregates occurred significantly faster, the electrodes were significantly less efficient.

The different TSPc monomers showed transients which were qualitatively similar in shape indicating rather similar relative rates of electron injection and re-reduction. As compared to ZnO–TSPcSi(OH)$_2$, however, smaller ratios of charging/steady-state and discharging/steady-state currents were observed at ZnO–TSPcZn and ZnO–TsPcAl(OH) electrodes (Fig. 12) [17, 18, 158]. This would speak for a faster charge transfer from TSPcZn or TSPcAl(OH) to the electrolyte. On the other hand, lower steady-state values are observed when compared with TSPcSi. Since the crystallinity of ZnO and the preference of its orientation were found to be comparable for ZnO–TSPcZn, ZnO–TSPcAl(OH), and ZnO–TSPcSi(OH)$_2$ films [131], differences in the conductivity of the ZnO are unlikely to be the reason. It is therefore suggested that a faster and more efficient electron injection from TSPcSi as compared to TSPcZn and TSPcAl(OH) into ZnO led to the higher efficiency of the ZnO–TSPcSi(OH)$_2$ electrodes. The more efficient charge transfer to the electrolyte from TSPcZn and TSPcAl(OH) compared with TSPcSi(OH)$_2$ can be explained by differences in the morphology of the films [131]. ZnO–TSPcZn films showed a porous morphology similar to that of ZnO–TSPcAl(OH) (Fig. 3), so that it can be assumed that most TSPcZn and TSPcAl(OH) adsorbed on ZnO is accessible from the electrolyte. On the other hand, ZnO–TSPcSi(OH)$_2$ showed a much lower surface area (Fig. 3). Furthermore, it has to be assumed that most of the TSPcSi(OH)$_2$ molecules are located between the disklike ZnO stacks seen in Figure 3, with no or small contact to the electrolyte. These molecules were able to inject electrons into the conduction band of ZnO, leading to a charging current, but the holes remaining in these molecules cannot undergo charge transfer to the electrolyte and will recombine eventually.

3.2. ZnO–Eosin Porous Single Crystals

Films which were prepared in the presence of Eosin Y in the deposition bath also were intensely colored by the characteristic red color of Eosin Y (Fig. 13). Aqueous solution spectra of the dye showed a single absorption band at 518 nm with only a small shoulder at 490 nm [133]. The characteristics of this spectrum were almost preserved but redshifted and broadened when Eosin Y was adsorbed at ZnO powder samples from solutions [133]. For Eosin adsorbed during the film preparation (Fig. 13), however, a spectrum was observed with the shoulder at shorter wavelength now being of almost identical intensity when compared with the main absorption band [133, 135, 158]. For dimers of Eosin Y the absorption at shorter wavelength was predicted to be the main absorption band [160] and we conclude that during electrochemical deposition of the ZnO–Eosin Y hybrid films Eosin is adsorbed in a relative arrangement of chromophores similar to that in dimers. The photocurrent spectrum (Fig. 13) almost matched the absorption spectrum indicating that only one form of Eosin aggregates exists in the films rather than a mixture of monomers and dimers since it is rather unlikely to observe identical quantum yields for monomers and dimers.

The IPCE observed for ZnO–Eosin Y films was significantly higher than that in the case of ZnO–TSPc films by about a factor of 100. When compared with TSPcSi(OH)$_2$, the most efficient TSPc, it is seen that this increase is mainly
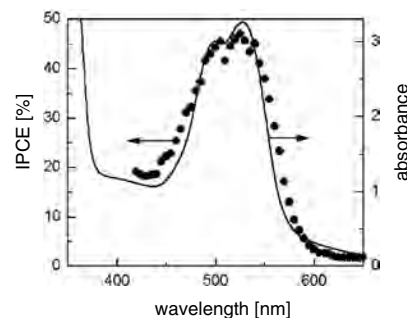

Figure 13. As in Figure 11, but for ZnO/EY grown at −0.9 V vs SCE. Reprinted with permission from [158], D. Schlettwein et al., *Proc. SPIE* 4465 (2002). © 2002, The International Society for Optical Engineering.

caused by an increased absorption at almost constant quantum efficiency. It is remarkable that a high quantum efficiency of photocurrent generation cold be preserved at such significantly increased dye load, and in fact for aggregated Eosin Y.

Facile electron transfer from Eosin Y to ZnO and from I$_3^-$ to the oxidized Eosin Y could also be concluded from time-resolved photocurrent measurements (Fig. 14) [133, 135, 158]. An almost rectangular photocurrent response was obtained with almost no overshoot above the stationary value indicating only a small amount of surface charging. When the illuminating beam was shut, a small cathodic current was observed speaking for a somewhat hindered electron transfer from I$_3^-$ to the oxidized Eosin Y. Based on the considerably higher currents, however, the reaction can be estimated to occur significantly faster when compared with the transfer to TSPc. It may be coincidence, but it should be kept in mind that Eosin exists as aggregates in the films and that also for aggregates of TSPcZn the transfer of electrons from I$_3^-$ to the oxidized dye was found to be considerably faster when compared with monomers of TSPcZn. A general trend may be observed here which would be reasonable since an aggregate has a distribution of energy levels
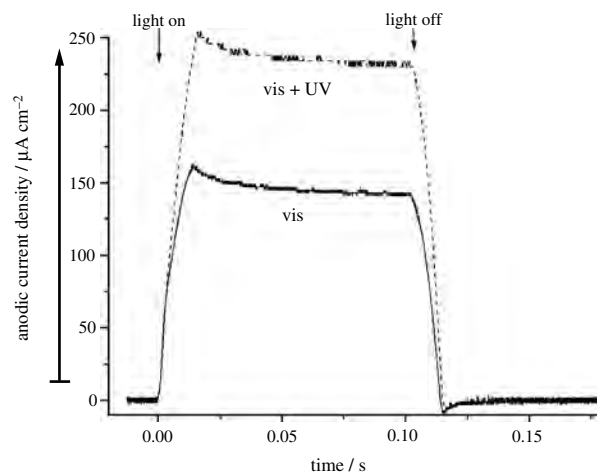

Figure 14. As in Figure 12, but for ZnO/EY grown at −0.9 V vs SCE. Comparison between illumination by the full lamp spectrum or by the visible part only. Reprinted with permission from [158], D. Schlettwein et al., *Proc. SPIE* 4465 (2002). © 2002, The International Society for Optical Engineering.

to offer as opposed to quite well-defined individual levels of monomers.

Also compared in Figure 14 are results obtained during illumination with the visible part of the lamp spectrum only as opposed to the full lamp spectrum which also contained a contribution in the UV. As opposed to light in the visible part in the spectrum, UV light is efficiently absorbed in ZnO. ZnO is known to be an efficient photoelectrode and for TSPc, for example, the photocurrent that could be reached under illumination in the visible range always was much lower than that obtained under illumination by the full lamp spectrum, caused by the small IPCE (albeit in part high quantum efficiency) of ZnO–TSPc electrodes in the visible range. From Figure 14 it becomes clear, however, that the IPCE reached with ZnO–Eosin is high enough to let the sensitized photocurrents dominate over the photocurrents obtained by direct excitation of ZnO [135, 158].

Since the Eosin-modified electrodes looked quite promising in their photoelectrochemical characteristics, also IMPS and IMVS have been used to analyze in detail the underlying photoelectrochemical kinetics [135]. These experimental techniques have proven to be very useful in the analysis of photoelectrochemical reactions at pure inorganic semiconductors and, in particular, at dye-sensitized electrodes [15, 16, 22, 23]. In these methods, a modulated light beam is superimposed to a continuous source of illumination and the change (amplitude A and phase φ) of either the photocurrent (IMPS) or the photovoltage (IMVS) that is caused by this modulated part of the illumination is registered, typically by a lock-in amplifier or a frequency response analyzer. By means of these methods, electrode kinetics are studied for electrodes that are permanently illuminated allowing one to study the electrochemical kinetics at an almost constant electrical situation of the electrodes, different from the situation of transient measurements during illumination pulses. Another big advantage is the fact that the modulation frequency of the light can be easily varied in a frequency range spanning 0.1 Hz to 100 kHz, allowing one to study reaction rates in a wide range of time scales. Results of IMPS or IMVS are typically presented as plots in the complex plane with the amplitude A of the signal corresponding to the distance of a given data point (at a given modulation frequency) from the origin and the phase φ corresponding to the angle of a line from the origin with the real axis [16]. For dye-sensitized electrodes, IMPS is in particular suitable to quantitatively study recombination steps in photoelectrochemical reactions beyond the level of transient methods whereas IMVS can be used to analyze the lifetime τ_n of free electrons in the semiconductor electrode [15, 16, 22, 23]. The results of IMPS and IMVS at electrodes of ZnO/Eosin Y in contact to an organic electrolyte with iodide as the redox- active component are represented in the complex plain plots of Figures 15 and 16 [135].

In Figure 15 a series of frequency-dependent experiments is shown for different electrode potentials. Generally higher photocurrents were observed at more positive potentials leading to circles of higher radii. The maximum in the first quadrant shows the recombination current also indicated in the photocurrent transients. For a given light intensity, the maximum was found at a constant modulation frequency (in the example of Fig. 15 at 133 Hz). It was thereby shown
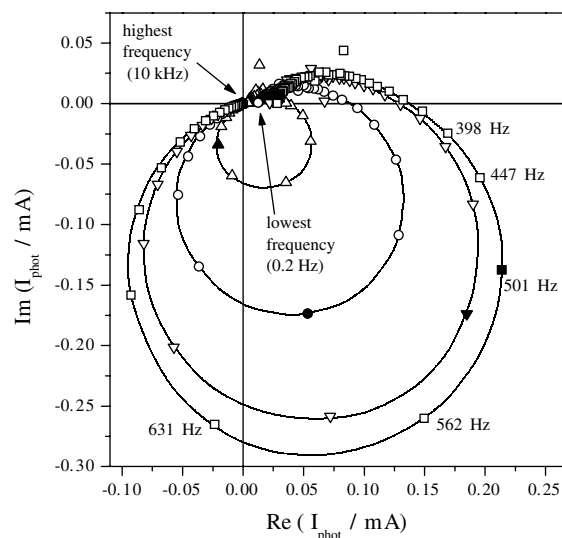

Figure 15. IMPS plots of a ZnO/EY hybrid thin film electrodeposited at −0.9 V (vs SCE) with a deposition time of 60 minutes and a dye concentration of 55 μmol dm^{-3} in the bath. IMPS was performed in contact to 0.5 mol L^{-1} KI in a mixture of acetonitrile/ethylenecarbonate (1:4 by volume) illuminated with 530 nm light of 0.3 mW cm^{-2} that was modulated by 10% in order to detect the corresponding modulation of the photocurrent. The currents were plotted as vectors from the origin of the plot. The length of the vector corresponds to the amplitude of the photocurrent, the angle with the real axis to the phase shift relative to the light intensity. The electrode potentials were −100 (square), −300 (inverted triangle), −500 (circle), and −700 mV (triangle) (vs Ag/Ag$^+$). The results at 501 Hz are plotted as solid symbols as an orientation mark. Reprinted with permission from [135], T. Yoshida et al., *Electrochemistry* 70, 470 (2002). © 2002, Electrochemical Society of Japan.

that no electric field exists in the porous electrodes that would change with the applied potential and thereby lead to changes in the concentration of free electrons at the surface. A decreased light intensity, however, directly leads to a decreased surface concentration of free electrons, as shown
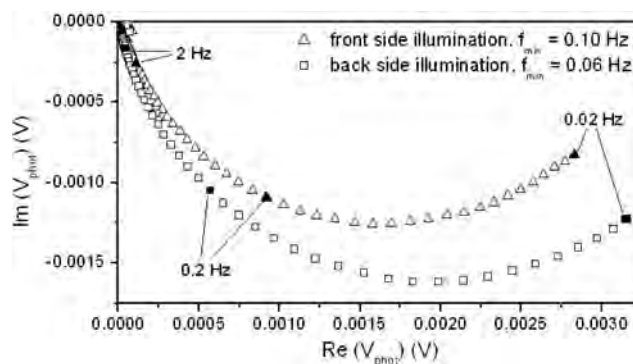

Figure 16. Complex plane plots (see explanation in the legend of Fig. 15) of the open-circuit photovoltage measured in an IMVS experimental series at a ZnO/EY hybrid thin film electrode in contact to 0.5 mol L^{-1} KI and 1.5 mmol L^{-1} I$_2$ in acetonitrile/ethylenecarbonate (1:4 by volume) measured with 0.1 mW cm^{-2} of 530 nm light. The measurements were made under front side or back side illumination as indicated. Reprinted with permission from [135], T. Yoshida et al., *Electrochemistry* 70, 470 (2002). © 2002, Electrochemical Society of Japan.

by maxima at lower modulation frequencies, speaking for a decreased rate of recombination [135]. The frequency of the minimum in the fourth quadrant of the IMPS plot was discussed as characteristic for the *RC* time of the cell since in this case no systematic dependence on the light intensity could be detected and a clear potential dependence was observed. An *RC* time of about 0.3–0.4 ms was derived, a value typical for nanoporous electrodes [20]. The finding further speaks for a transit time faster than the *RC* time, showing fast diffusion of electrons in the porous single- crystalline ZnO [135]. The frequency of the minimum imaginary part of the photovoltage at open circuit in an IMVS plot can be used to determine the average lifetime of free electrons, determined only by the backreaction of free electrons with the acceptor in solution, I_3^- [22, 23]. Values of the electron lifetime of about two seconds were determined from the data in Figure 16 for ZnO/Eosin Y [135]. A slightly lower frequency and hence a slightly longer electron lifetime were found for illumination from the back side of the electrode, probably caused by a slightly less efficient illumination. When compared with previous data, it was concluded that the lifetime of the free electrons in the porous single crystal of ZnO is considerably larger than that in nanoparticulate ZnO [20] and comparable to TiO_2 typically used in the most efficient dye-sensitized solar cells [26]. Also from this analysis, the thin films of porous single crystals of ZnO as obtained by electrodeposition of ZnO under structural control by Eosin Y can be considered promising electrode materials.

4. CONCLUSIONS

The electrodeposited colored ZnO thin films can perform as sensitized photoanodes [17, 18, 133–135, 137–140, 158]. Since dyes with various absorption ranges can be loaded, the hybrid thin film photoelectrodes can be furnished in many color variations. Deposition of stacked layers with dyes in three primary colors, yellow, magenta, and cyan, can create any desired color without mixing the dyes. Such an aspect of the hybrid electrodeposition process gives a unique feature in the design flexibility of the solar cells unlike the conventional inorganic solar cells. Because the process does not need any heat treatment at high temperatures, the material is directly applicable to non-heat-resistant substrates such as conductive plastic films for the realization of flexible DSSCs.

GLOSSARY

Dye-sensitized solar cells (DSSC) A concept to utilize chemically stable wide-bandgap semiconductors as charge-transporting part and highly colored organic dye-molecules as light-harvesting centers of photovoltaic cells.

Eosin yellow (EY) One suitable dye and structure-directing agent in the presently reviewed work.

Fuorine-doped tin oxide and indium-tin oxide (FTO and ITO) Transparent conductors suitable as back contacts for DSSC.

Incident photon to current conversion efficiency (IPCE) A measure of an electrodes efficiency determined by the ratio of harvested electrons divided by incoming photons. It combines the efficiency of light absorption and quantum efficiency of the overall cell.

Intensity-modulated photocurrent spectroscopy (IMPS) A method that monitors the amplitude and phase shift of the observed photocurrent during modulation of the incoming light at different frequency and electrode potential and allowing to determine details of the electrode kinetics.

Intensity-modulated photovoltage spectroscopy (IMVS) A method like IMPS but monitoring the photovoltage under conditions of no net current (at open circuit).

Saturated calomel electrode (SCE) A reference electrode commonly used in electrochemical experiments to provide a common reference potential for a series of experiments.

Transmission electron microscopy (TEM) A method to determine the detailed morphology of thin solid particles and, by observation of the diffraction pattern, their crystallographic structure.

TSPcAl, TSPcSi, TSPcZn TetraSulfonated PhthaloCyanines with different central metals, one group of sensitizers for the red part of the visible spectrum.

X-ray diffraction (XRD) An experimental method to determine the crystal structure and crystal orientation of films.

ACKNOWLEDGMENTS

REFERENCES

1. H. Gerischer and H. Tributsch, *Ber. Bunsenges. Physik. Chem.* 72, 437 (1968).
2. H. Tributsch and M. Calvin, *Photochem. Photobiol.* 14, 95 (1971).
3. H. Gerischer, *Photochem. Photobiol.* 16, 243 (1972).
4. H. Tsubomura, M. Matsumura, Y. Nomura, and T. Amamiya, *Nature* 261, 402 (1976).
5. M. Matsumura, S. Matsudaira, H. Tsubomura, M. Takata, and H. Yanagida, *Ind. Eng. Chem. Prod. Res. Dev.* 19, 415 (1980).
6. S. Anderson, E. C. Constable, M. P. Dare-Edwards, J. B. Goodenough, A. Hamnett, K. R. Seddon, and R. D. Wright, *Nature* 280, 571 (1979).
7. B. O'Regan and M. Grätzel, *Nature* 353, 737 (1991).
8. M. K. Nazeeruddin, A. Kay, I. Rodicio, R. Humphry-Baker, E. Müller, P. Liska, N. Vlachopoulos, and M. Grätzel, *J. Am. Chem. Soc.* 115, 6382 (1993).

9. J. M. Rehm, G. L. McLendon, Y. Nagasawa, K. Yoshihara, J. Moser, and M. Grätzel, *J. Phys. Chem.* 100, 9577 (1996).

10. T. Hannappel, B. Burfeindt, W. Storck, and F. Willig, *J. Phys. Chem. B* 101, 6799 (1997).

11. R. J. Ellingson, J. B. Asbury, S. Ferrere, H. N. Gosh, J. R. Sprague, T. Lian, and J. Nozik, *Z. Phys. Chem.* 212, 77 (1999).

12. S. Y. Huang, G. Schlichthörl, A. J. Nozik, M. Grätzel, and A. J. Frank, *J. Phys. Chem. B* 101, 2576 (1997).

13. S. A. Haque, Y. Tachibana, D. R. Klug, and J. R. Durrant, *J. Phys. Chem. B* 102, 1745 (1998).

14. A. Solbrand, H. Lindström, H. Rensmo, A. Hagfeldt, S.-E. Lindquist, and S. Södergren, *J. Phys. Chem. B* 101, 2514 (1997).

15. L. M. Peter, *Chem. Rev.* 90, 753 (1990).

16. L. M. Peter and D. Vanmaekelbergh, in "Advances in Electrochemical Science and Engineering" (R. C. Alkire and D. Kolb, Eds.), Vol. 6, Wiley–VCH, Weinheim, 1999.

17. D. Schlettwein, T. Oekermann, T. Yoshida, M. Tochimoto, and H. Minoura, *J. Electroanal. Chem.* 481, 42 (2000).

18. T. Oekermann, T. Yoshida, D. Schlettwein, T. Sugiura, and H. Minoura, *Phys. Chem. Chem. Phys.* 3, 3387 (2001).

19. L. Dloczik, O. Ileperuma, I. Lauermann, L. M. Peter, E. A. Ponomarev, and G. Redmond, *J. Phys.Chem. B* 101, 10281 (1997).

20. P. E. de Jongh, E. A. Meulenkamp, D. Vanmaekelbergh, and J. J. Kelly, *J. Phys. Chem. B* 104, 7686 (2000).

21. E. A. Meulenkamp, *J. Phys. Chem. B* 103, 7831 (1999).

22. G. Schlichthörl, S. Y. Huang, J. Sprague, and A. J. Frank, *J. Phys. Chem. B* 101, 8141 (1997).

23. G. Franco, J. Gehring, L. M. Peter, E. A. Ponomarev, and I. Uhlendorf, *J. Phys. Chem. B* 103, 692 (1999).

24. Y. Liu, A. Hagfeldt, X. R. Xiao, and S. E. Lindquist, *Sol. Energy Mater. Sol. Cells* 55, 267 (1998).

25. G. Schlichthörl, N. G. Park, and A. J. Frank, *J. Phys. Chem. B* 103, 782 (1999).

26. A. C. Fisher, L. M. Peter, E. A. Ponomarev, A. B. Walker, and K. G. U. Wijayantha, *J. Phys. Chem. B* 104, 949 (2000).

27. G. Redmond, D. Fitzmaurice, and M. Grätzel, *Chem. Mater.* 6, 686 (1994).

28. K. Keis, J. Lindgren, S.-E. Lindquist, and A. Hagfeldt, *Langmuir* 16, 4688 (2000).

29. U. Björkstén, J. Moser, and M. Grätzel, *Chem. Mater.* 6, 858 (1994).

30. S. Ferrere, A. Zaban, and B. A. Gregg, *J. Phys. Chem. B* 101, 4490 (1997).

31. A. Turković and Z. Crnjak Orel, *Sol. Energy Mater. Sol. Cells* 45, 275 (1997).

32. K. Sayama, H. Sugihara, and H. Arakawa, *Chem. Mater.* 10, 3825 (1998).

33. K. Hara, T. Horiguchi, T. Kinoshita, K. Sayama, H. Sugihara, and H. Arakawa, *Sol. Energy Mater. Sol. Cells* 64, 115 (2000).

34. K. Tennakone, G. K. R. Senadeera, V. P. S. Perera, I. R. M. Kottegoda, and L. A. A. De Silva, *Chem. Mater.* 11, 2474 (1999).

35. A. Zaban, S. G. Chen, S. Chappel, and B. A. Gregg, *Chem. Commun.* 2231 (2000).

36. K. Tennakone, J. Bandara, P. K. M. Bandaranayake, G. R. A. Kumara, and A. Konno, *Jpn. J. Appl. Phys. 2*, 40, L732 (2001).

37. P. Péchy, F. P. Rotzinger, M. K. Nazeeruddin, O. Kohle, S. M. Zakeeruddin, R. Humphry-Baker, and M. Grätzel, *J. Chem. Soc., Chem. Commun.* 65 (1995).

38. M. Yanagida, L. P. Singh, K. Sayama, K. Hara, A. Katoh, A. Islam, H. Sugihara, H. Arakawa, M. K. Nazeeruddin, and M. Grätzel, *J. Chem. Soc., Dalton. Trans.* 2817 (2000).

39. O. Enea, J. Moser, and M. Grätzel, *J. Electroanal. Chem.* 259, 59 (1989).

40. K. Hara, K. Sayama, Y. Ohga, A. Shinpo, S. Suga, and H. Arakawa, *Chem. Commun.* 569 (2001).

41. Y. Shen, L. Wang, Z. Lu, Y. Wei, Q. Zhou, H. Mao, and H. Xu, *Thin Solid Films* 257 144 (1995).

42. M.K. Nazeeruddin, R. Humphry-Baker, M. Grätzel, D. Wöhrle, G. Schnurpfeil, G. Schneider, A. Hirth, and N. Trombach, *J. Porph. Phtalocyanines* 3, 230 (1999).

43. G. K. Boschloo and A. Goossens, *J. Phys. Chem.* 100, 19489 (1996).

44. A. Ehret, L. Stuhl, and M. T. Spitler, *Electrochim. Acta* 45, 4553 (2000).

45. D. Zhang, W. Wang, Y. Liu, X. Xiao, W. Zhao, B. Zhang, and Y. Cao, *J. Photochem. Photobiol. A* 135, 235 (2000).

46. K. Tennakone, G. R. R. A. Kumara, I. R. M. Kottegoda, V. P. S. Perera and P. S. R. S. Weerasundara, *J. Photochem. Photobiol. A* 117, 137 (1998).

47. Q. Dai and J. Rabani, *Chem. Commun.* 2142 (2001).

48. D. Zhang, T. Yoshida and H. Minoura, *Trans. Mater. Res. Soc. Jpn.*, 27, 811 (2002).

49. H. Matsumoto, T. Matsuda, T. Tsuda, R. Hagiwara, Y. Ito, and Y. Miyazaki, *Chem. Lett.* 26 (2001).

50. F. Cao, G. Oskam, and P. C. Searson, *J. Phys. Chem.* 99, 17071 (1995).

51. W. Kubo, K. Murakoshi, T. Kitamura, Y. Wada, K. Hanabusa, H. Shirai, and S. Yanagida, *Chem. Lett.* 1241 (1998).

52. K. Murakoshi, R. Kogure, Y. Wada, and S. Yanagida, *Chem. Lett.* 471 (1997).

53. U. Bach, D. Lupo, P. Comte, J. E. Moser, F. Weissörtel, J. Salbeck, H. Spreitzer, and M. Grätzel, *Nature* 395, 583 (1998).

54. K. Tennakone, G. R. R. A. Kumara, I. R. M. Kottegoda, and K. G. U. Wijayantha, *Semicond. Sci. Technol.* 12, 128 (1997).

55. B. O'Regan and D. T. Schwartz, *J. Appl. Phys.* 80, 4749 (1996).

56. F. Pichot, S. Ferrere, R. J. Pitts, and B. A. Gregg, *Langmuir* 16, 5626 (1999).

57. Stanley, B. Verity, and D. Matthews, *Sol. Energy Mater. Sol. Cells* 52, 141 (1998).

58. S. Karuppuchamy, D. P. Amalnerkar, K. Yamaguchi, T. Yoshida, T. Sugiura, and H. Minoura, *Chem. Lett.* 78 (2001).

59. B. O'Regan, D. T. Schwartz, S. M. Zakeeruddin, and M. Grätzel, *Adv. Mater.* 12, 1263 (2000).

60. M. M. Gomez, J. Lu, E. Olsson, A. Hagfeldt, and C. G. Granqvist, *Sol. Energy Mater. Sol. Cells* 64, 385 (2000).

61. H. Lindström, A. Holmberg, E. Magnusson, S.-E. Lindquist, L. Malmqvist, and A. Hagfeldt, *Nano Lett.* 1, 97 (2001).

62. G. Smestad, C. Bignozzi, and R. Argazzi, *Sol. Energy Mater. Sol. Cells* 32, 259 (1994).

63. S. D. Burnside, V. Shklover, C. Barbé, P. Comte, F. Arendse, K. Brooks, and M. Grätzel, *Chem. Mater.* 10, 2419 (1998).

64. R. Grünwald and H. Tributsch, *J. Phys. Chem. B* 101, 2564 (1997).

65. D. Landolt, *J. Electrochem. Soc.* 149, S9 (2002).

66. A. Bittner, M. Wanner, and K. Weil, *Ber. Bunsenges. Phys. Chem.* 96, 647 (1992).

67. A. H. Whitehead, J. M. Elliott, J. R. Owen, and G.S. Attard, *Chem. Commun.* 331 (1999).

68. P. F. J. de Leon, E. V. Albano, R. C. Salvarezza, and H. G. Solari, *Phys. Rev. E* 66, 42601 (2002).

69. Ch. Henninot, C. Vallieres, S. Rode, and M. Matlosz, *Electrochem. Soc. Proc.* 99–34, 333 (1999).

70. D. Josell, D. Wheeler, W. H. Huber, and T. P. Moffat, *Phys. Rev. Lett.* 87, 16102 (2001).

71. M. Hayase, M. Taketani, K. Aizawa, T. Hatsuzawa, and K. Hayabusa, *Electrochem. Solid State Lett.* 5, C98 (2002).

72. T. P. Moffat, D. Wheeler, C. Witt, and D. Josell, *Electrochem. Solid-State Lett.* 5, C110 (2002).

73. A. Milchev, "Electrocrystallization—Fundamentals of Nucleation and Growth." Kluwer, Boston, 2002.

74. B. R. Scharifker, J. Mostany, M. Palomar-Pardave, and I. Gonzales, *J. Electrochem. Soc.* 146, 1005 (1999).

75. K. M. Takahashi and M. E. Gross, *J. Electrochem. Soc.* 146, 4499 (1999).

76. Y. Cao, P. C. Searson, and A. C. West, *J. Electrochem. Soc.* 148, C376 (2001).

77. M. Georgiadou, D. Veyret, R. L. Sani, and R. C. Alkire, *J. Electrochem. Soc.* 148, C54 (2001).

78. D. Josell, W. Wheeler, W. H. Huber, J. E. Bonevich, and T. P. Moffat, *J. Electrochem. Soc.* 148, C767 (2001).

79. Y. Cao and A. C. West, *J. Electrochem. Soc.* 149, C223 (2002).

80. T. J. Pricer, M. J. Kushner, and R. C. Alkire, *J. Electrochem. Soc.* 149, C396 (2002).

81. V. R. Subramanian and R. E. White, *J. Electrochem. Soc.* 149, C498 (2002).

82. D. de Kubber, L. Bortels, J. Deconinck, and T. E. G. Daenen, *Electrochim. Acta* 47, 91 (1999).

83. T. P. Moffat, B. Baker, D. Wheeler, J. E. Bonevich, M. Edelstein, D. R. Kelly, L. Gan, G. R. Stafford, P. J. Chen, W. F. Egelhoff, and D. Josell, *J. Electrochem. Soc.* 149, C423 (2002).

84. D. Josell, B. Baker, C. Witt, D. Wheeler, and T. P. Moffat, *J. Electrochem. Soc.* 149, C637 (2002).

85. C. Schröter and T. Solomun, *Ber. Bunsenges. Phys. Chem.* 100, 1257 (1996).

86. H. Natter, T. Krajewski, and R. Hempelmann, *Ber. Bunsenges. Phys. Chem.* 100, 55 (1996).

87. E. Toth-Kadar, L. Peter, T. Becsei, J. Toth, L. Pogany, T. Tarnoczi, P. Kamasa, G. Lang, A. Cziraki, and W. Schwarzacher, *J. Electrochem. Soc.* 147, 3311 (2000).

88. L. Peter, A. Cziraki, L. Pogany, Z. Kupay, I. Bakonyi, M. Uhlemann, M. Herrich, B. Arnold, T. Bauer, and K. Wetzig, *J. Electrochem. Soc.* 148, C168 (2001).

89. Q. Huang, D. P. Young, J. Y. Chan, J. Jiang, and E. J. Podlaha, *J. Electrochem. Soc.* 149 (2002).

90. E. Chassaing, A. Morrone, and J. E. Schmidt, *J. Electrochem. Soc.* 146, 1794 (1999).

91. G. H. A. Therese and P. V. Kamat, *Chem. Mater.* 12, 1195 (2000).

92. H. Minoura, T. Kajita, K. Yamaguchi, Y. Takahashi, and D. P. Amalnerker, *Chem. Lett.* 339 (1994).

93. K. Yamaguchi, T. Yoshida, T.Sugiura, and H. Minoura, *J. Phys. Chem. B* 102, 9677 (1998).

94. T. Yoshida, K. Yamaguchi, T. Kazitani, T. Sugiura, and H. Minoura, *J. Electroanal. Chem*. 473, 209 (1999).

95. K. Yamaguchi, T. Yoshida, N. Yasufuku, T. Sugiura, and H. Minoura, *Electrochemistry* 67, 1168 (1999).

96. T. Yoshida, K. Kondo, G. Ohta, K. Yamaguchi, T. Sugiura, and H. Minoura, *Trans. Mater. Res. Soc. Jpn.* 24, 405 (1999).

97. K. Yamaguchi, P. Mukherjee, T. Yoshida, and H. Minoura, *Chem. Lett.* 864 (2001).

98. T. Yoshida, S. Ide, T. Sugiura, and H. Minoura, *Trans. Mater. Res. Soc. Jpn.* 25, 1111 (2000).

99. M. Froment, M. Claude, R. Cortes, B. Mokili, and D. Lincot, *J. Electrochem. Soc.* 142, 2642 (1995).

100. H. Cachet, R. Cortes, M. Froment, and G. Maurin, *J. Solid State. Electrochem.* 1, 100 (1997).

101. S. Menezes, *Electrochem. Solid State Lett.* 5, C79 (2002).

102. Th. Pauporté and D. Lincot, *Appl. Phys. Lett.* 75, 24 (1999).

103. E. W. Bohannan, M. G. Shumsky, and J. A. Switzer, *Chem. Mater.* 11, 2289 (1999).

104. A. Gichuhi, B. E. Boone, U. Demir, and C. Shannon, *J. Phys. Chem. B* 102, 6499 (1998).

105. L. Kavan, B. O'Regan, A. Kay, and M. Grätzel, *J. Electroanal. Chem.* 346, 291 (1993).

106. C. Natarajan and G. Nogami, *J. Electrochem. Soc.* 143, 1547 (1996).

107. M. Izaki and T. Omi, *Appl. Phys. Lett.* 68, 2439 (1996).

108. S. Peulon and D. Lincot, *Adv. Mater.* 8, 166 (1996).

109. S. Peulon and D. Lincot, *J. Electrochem. Soc.* 145, 864 (1998).

110. Th. Pauporté and D. Lincot, *J. Electrochem. Soc.* 148, C310 (2001).

111. D. Gal, G. Hodes, D. Lincot, and H.-W. Schock, *Thin Solid Films* 361–362, 79 (2000).

112. B. O'Regan, V. Sklover, and M. Grätzel, *J. Electrochem. Soc.* 148, C498 (2001).

113. M. Izaki, *J. Electrochem. Soc.* 146, 4517 (1999).

114. K. Nomura, N. Shibata, and M. Maeda, *J. Electrochem. Soc.* 149, F76 (2002).

115. Y.-C. Wang, I.-C. Liu, and M.-H. Hon, *Electrochem. Solid State Lett.* 5, C53 (2002).

116. M. Izaki and J. Katayama, *J. Electrochem. Soc.* 147, 210 (2000).

117. M. Izaki, A. Murasumi, M. Chigane, M. Ishikawa, M. Yamashita, J. Katayama, H. Takahashi, and H. Nakamura, *Electrochem. Solid State Lett.* 3, 501 (2000).

118. C. A. Orme, A. Noy, A. Wierzbicki, M. T. McBride, M. Grantham, H. H. Teng, P. M. Dove, and J. J. DeYoreo, *Nature* 411, 775 (2001).

119. S. R. Letellier, M. J. Lochhead, A. A. Campbell, and V. Vogel, *Biochim. Biophys. Acta* 1380, 31 (1998).

120. J. Ying, C. P. Mehnert, and M. S. Wong, *Angew. Chem. Int. Ed.* 38, 56 (1999).

121. G. Schulz-Ekloff, D. Wöhrle, B. van Duffel, and R. A. Schoonheydt, *Micropor. Mesopor. Mat.* 51, 91 (2002).

122. G. H. Noncollas and W. Wu, *J. Cryst. Growth* 211, 137 (2000).

123. H. H. Teng, P. M. Dove, and J. J. DeYoreo, *Geochim. Cosmochim. Acta* 63, 2507 (1999).

124. L. Addadi and S. Weiner, *Nature* 411, 753 (2001).

125. C. M. Niemeyer, *Angew. Chem.* 113, 4254 (2001).

126. E. Dujardin and S. Mann, *Adv. Mater.* 14, 775 (2002).

127. W. Wu and G. H. Nancollas, *Colloids Interfaces B* 10, 87 (1997).

128. A. Rammal, F. Brisach, and M. Henry, *J. Am. Chem. Soc.* 123, 5612 (2001).

129. S. Guan, S. Inaki, T. Ohsuna, and O. Terasaki, *J. Am. Chem. Soc.* 122, 5660 (2000).

130. T. Yoshida, K. Miyamoto, N. Hibi, T. Sugiura, H. Minoura, T. Oekermann, G. Schneider, and D. Wöhrle, *Chem. Lett.* 7, 599 (1998).

131. T. Yoshida, M. Tochimoto, D. Schlettwein, D. Wöhrle, T. Sugiura, and H. Minoura, *Chem. Mater.* 11, 2657 (1999).

132. T. Yoshida and H. Minoura, *Adv. Mater.* 12, 1219 (2000).

133. T. Yoshida, K. Terada, D. Schlettwein, T. Oekermann, T. Sugiura, and H. Minoura, *Adv. Mater.* 12, 1214 (2000).

134. K. Okabe, T. Yoshida, T. Sugiura, and H. Minoura, *Trans. Mater. Res. Soc. Jpn.* 26, 523 (2001).

135. T. Yoshida, T. Oekermann, K. Okabe, D. Schlettwein, K. Funabiki, and H. Minoura, *Electrochemistry* 70, 470 (2002).

136. Th. Pauporte, T. Yoshida, A. Goux, and D. Lincot, *J. Electroanal. Chem.* 534, 55 (2002).

137. T. Yoshida, J. Yoshimura, M. Matsui, T. Sugiura, and H. Minoura, *Trans. Mater. Res. Soc. Jpn.* 24, 497 (1999).

138. S. Karuppuchamy, K. Nonomura, T. Yoshida, T. Sugiura, and H. Minoura, *Solid State Ionics*, 151, 19 (2002).

139. K. Nonomura, T. Yoshida, D. Schlettwein and H. Minoura, *Electrochim. Acta.* 48, 3071 (2003).

140. S. Karuppuchamy, T. Yoshida, T. Sugiura, and H. Minoura, *Thin Solid Films* 397, 63 (2001).

141. B. Cavana and D. Lincot, *J. Appl. Electrochem.* 30, 711 (2000).

142. U. Schubert, A. Lorenz, N. Kundo, T. Stuchinskaya, L. Gogina, A. Salanov, V. Zaikonovskii, V. Maizlish, and G. P. Shaposhnikov, *Chem. Ber./Recl.* 130, 1585 (1997).

143. M. J. Stillman and T. Nyokong, in "Phthalocyanines" (C. C. Leznoff and A. B. P. Lever, Eds.), Vol. 1, pp. 133–289. New York, 1989.

144. C. A. Hunter and K. M. Sanders, *J. Am. Chem. Soc.* 112, 5525 (1990).

145. G. Schneider, D. Wöhrle, W. Spiller, J. Stark, and G. Schulz-Ekloff, *Photochem. Photobiol.* 60, 333 (1998).

146. F. Nüesch, J. E. Moser, V. Shklover, and M. Grätzel, *J. Am. Chem. Soc.* 118, 5420 (1996).

147. A. J. Nozik and R. Memming, *J. Phys. Chem.* 100, 13061 (1996).

148. M. Hilgendorff and V. Sundström, *J. Phys. Chem. B* 102, 10505 (1998).

149. R. J. Ellingson, J. B. Asbury, S. Ferrere, H. N. Ghosh, J. R. Sprague, T. Lian, and A. J. Nozik, *J. Phys. Chem. B* 102, 6455 (1998).

150. H. N. Ghosh, J. B. Asbury, and T. Lian, *J. Phys. Chem. B* 102, 6482 (1998).

151. P. E. de Jongh and D. Vanmaekelbergh, *J. Phys. Chem. B* 101, 2716 (1997).

152. T. Oekermann, D. Schlettwein, and N. I. Jaeger, *J. Electroanal. Chem.* 462, 222 (1999).

153. T. Oekermann, D. Schlettwein, N. I. Jaeger, and D. Wöhrle, *J. Porphyrins Phthalocyanines* 3, 444 (1999).

154. T. Oekermann, D. Schlettwein, and N. I. Jaeger, *J. Phys. Chem. B* 105, 9524 (2001).

155. H. Gerischer and F. Willig, *Top. Curr. Chem.* 61, 31 (1976).

156. T. Yamase, H. Gerischer, M. Lübke, and B. Pettinger, *Ber. Bunsenges. Phys. Chem.* 83, 658 (1979).

157. M. T. Spitler, *J. Phys. Chem.* 90, 2156 (1986).

158. D. Schlettwein, T. Oekermann, T. Yoshida, T. Sugiura, H. Minoura, and D. Wöhrle, *Proc. SPIE* 4465 (2002).

159. A. P. Alivisatos, *J. Phys. Chem. B* 100, 13226 (1996).

160. K. K. Rohatgi and A. K. Mukhopadhyay, *Photochem. Photobiol.* 14, 551 (1971).

Electrochemical Synthesis
of Semiconductor Nanowires

Dongsheng Xu, Guolin Guo

Peking University, Beijing, People's Republic of China

CONTENTS

1. INTRODUCTION

One-dimensional (1D) nanostructure materials have been the focus of extensive research in recent years due to their potential applications in fabricating nanoscale electronic, optoelectronic, and sensing devices [1, 2]. Besides the general drive toward miniaturization, a lot of unique and fascinating properties have been proposed and demonstrated for this class of materials. For example, electrical transport measurements have shown that single-walled carbon nanotubes can behave as low-temperature single-electron transistors [3, 4] and room-temperature field-effect transistors [5, 6], and can exhibit power-law behavior characteristic of a strongly interacting Tomanaga–Luttinger liquid [7, 8]. Optical studies of semiconductor nanowires show higher luminescence efficiency [9, 10] and order-of-magnitude polarization anisotropy in photoluminescence measurements [11, 12]. Room-temperature ultraviolet lasing in ZnO nanowire arrays show that 1D semiconductors can lower the lasing threshold [13–16]. 1D materials can also be used as building blocks to construct a new generation of nanoscale electronic circuits and photonics [17–19].

The synthesis of 1D materials is critical to work directed toward understanding their fundamental properties and developing nanotechnologies. Various growth techniques have been studied for the formation of nanorods and nanowires. A well-accepted mechanism of nanowire growth via gas phase reaction is the so-called vapor–liquid–solid (VLS) process proposed by Wagner and Eillis in 1960s, during studies of large single-crystalline whisker growth [20]. According to this mechanism, the anisotropic growth is promoted by the presence of a liquid alloy–solid interface, in which a gaseous target source diffuses into a drop of the molten alloy to nucleate and grow from the droplet. Nanowires of element semiconductors (Si, Ge, Se) [21–23], binary and ternary III–V, II–VI, and I–IV group materials [24–26], and metal oxide semiconductors [15, 27, 28] have been prepared in bulk quantities as high purity single crystals. A critical feature of this method is that the catalyst used to define 1D growth and thus the metal is always observed at the nanowire end. Laser ablation or thermal evaporation of oxide powders has also been demonstrated as a means of forming nanowires that contain an amorphous oxide shell and Si(Ge) cores and ribbonlike nanostructures of various oxides [29–31].

Another common fabrication method for 1D nanostructure materials is the template-based synthesis technique, pioneered by Martin [32–35], Rouketevitch et al. [36], and Whitney et al. [37]. In this method, a porous membrane with cylindrical pore geometry is used as a template for growing the desired materials. It has been demonstrated that this technique is a general and versatile method for preparing nanostructural materials including both nanotubules and nanofibrils composed of conductive polymers, metals, carbon, oxide, semiconductors, and other materials [32–37]. Due to cylindrical pore geometry and monodisperse diameters, corresponding cylindrical and oriented nanostructural materials with a narrow diameter distribution are obtained. In general, typical concerns that need to be addressed when developing new template synthesis methods include the following [34]: (1) will the precursor solutions used to prepare

the material wet the pore (i.e., hydrophobic/hydrophilic consideration); (2) will the deposition reaction proceed too fast resulting in pore blockage at the membrane surface before tubule/fibril growth can occur within the pores; (3) will the host membrane be stable (i.e., thermally and chemically) with respect to the reaction condition? Until now, various chemical strategies have been developed for template synthesis of ID materials. For example, Lakshmi et al. [38] first conducted sol–gel synthesis within the pores of the anodic aluminum oxide (AAO) template to create both fibrils and tubules of oxides, using a simple immersion method. Li et al. [39] have developed a chemical bath deposition method to produce ordered CdS nanowires in porous AAO membranes, in which the membranes were immersed into a cadmium acetate aqueous solution under reduced pressure in a flask first and then the flask was exposed to the atmosphere to pour the solution into the pores due to the pressure differentiation. Template-assisted chemical vapor deposition synthesis through a VLS growth mechanism can also be used for the formation of nanotubes and nanowires [23, 40]. Commonly, this process begins with the formation of metal nanoparticles within the template pores and then a vapor or reactant gases are passed into the pores of the membranes containing metal nanoparticles to deposit the desired materials.

Another method used for template-assisted growth of nanowires is direct electrochemical deposition [32]. This technique is accomplished by coating one face of the membrane with a metal film and using this metal film as an electrode for electroplating. In the past few years, electrochemical synthesis in template has become one of the most efficient methods in controlling the growth of nanowires and is used to produce a variety of metal [37, 41–45], conducting polymer [32, 46], oxide, and compound semiconductor nanowire arrays [47–86]. It offers a simple and viable alternative to the cost-intensive methods such as laser ablation or thermal evaporation synthesis. In particular, it affords precise process control due to its electrical nature, in which the lengths or aspect ratios of the materials can be controlled by the amount of material deposited.

In this chapter, we summarize the works on electrochemical synthesis of semiconductor nanowires (SNWs) to date. In Section 2, we will describe the types of templates used for electrochemical synthesis of SNWs. Next, a general outline of seven representative chemical strategies that have been used in electrochemical synthesis of SNWs will be presented in Section 3. Finally, we will discuss characterization and fundamental properties of these SNWs in Sections 4 and 5.

2. TEMPLATES USED

2.1. Porous AAO Membranes

Anodic aluminum oxide film can be produced upon aluminum metal when aluminum is made the anode in an electrolyte, which has been studied in detail over the last five decades [87]. The type of anodic oxide film depends upon several factors, the most important of which is the nature of the electrolyte [88]. For strongly acidic solution, the formed oxide film is slightly soluble and corresponds to produce porous-type films, in contrast to the formation of barrier-type

films in which the formed oxide film is completely insoluble. The typical electrolytes commercially used for the formation of porous AAO membranes are sulfuric, phosphoric, chromic, and oxalic acids at almost any concentration. The essential points of the structure of porous AAO membranes are that pores of virtually tubular shape with semispherical bottoms and a more or less hexagonal outside alumina cell are a logical consequence of expending circles, evenly distributed over the surface in a (111) type of arrangement (starting from active sites), and merging after their perimeters hit each other. Since the pores nucleate at the surface at almost random positions, the pore arrangements fabricated are disordered.

Recently, a two-step or self-organization anodization process has been developed to fabricate densely regular hexagonal pore arrays [89–94], as shown in Figure 1A. Pore densities as high as 10^{11} pores cm^{-2} can be achieved and the pores in these membranes have little or no tilt with respect to the surface normal resulting in an isolating, nonconnecting pore structure. In general, the structure of the porous AAO membranes depends on the anodizing condition including the electrolyte composition, voltage, and temperature. Importantly, the pore diameter was reported as being independent of the anodizing voltage and the time of
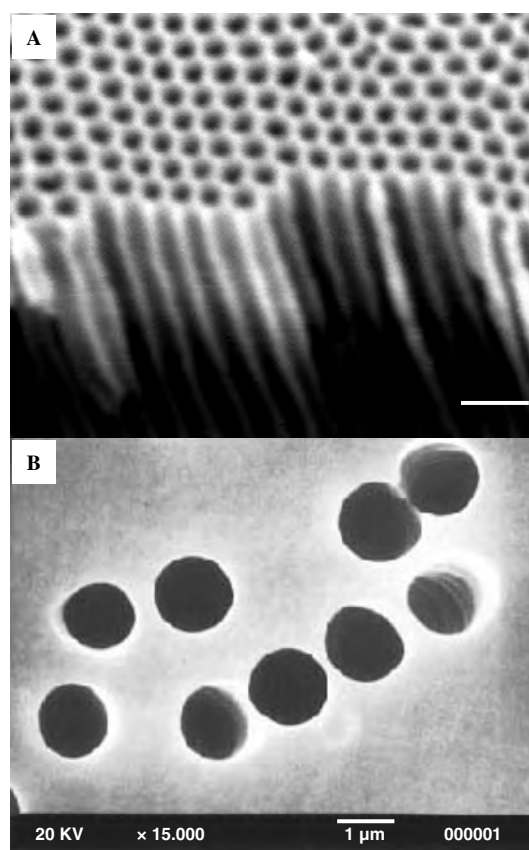

Figure 1. Scanning electron micrographs of two kinds of templates used for electrochemical syntheses of SNWs: (A) cross-sectional view of a 50-nm pore AAO membrane [94], and (B) polycarbonate membrane with 1 μm diameter pores. The scar bar in (a) is 100 nm. Reprinted with permission from [34], J. C. Hulteen and C. R. Martin, *J. Mater. Chem.* 7, 1075 (1997). © 1997, Royal Society of Chemistry.

the film formation, and to be dependent only on the electrolyte used. Commonly, pore diameters of 5–30, 30–90, and more than 100 nm were formed in 1–20% sulfuric acids, 2–4% oxalic acids, and 2–10% phosphoric acids, respectively.

Owing to the regular hexagonal pore structures, higher pore density, highly thermal and chemical stability (i.e., neutral aqueous and organic baths), and easy removal by strong acids or bases, the AAO membranes have been used as an important template material. However, the compact barrier layer between the porous AAO and Al substrate is insulating and obstructs the passage of direct current. For electrochemical template synthesis, this barrier layer is mostly removed to form through-hole membranes. A detailed report on the preparation of through-hole membranes can be found in [50–52, 89–94]. First, high purity aluminum foils were degreased in acetone, cleaned in mixed solution of $HF/HNO_3/HCl/H_2O$, annealed under nitrogen ambient at 400 °C, and then electropolished in a mixture of $HClO_4$ and C_2H_5OH. Second, the aluminum foils were anodized in aqueous acidic solutions such as sulfuric, oxalic, and phosphoric acids. Third, after the anodization, the remaining aluminum was removed by a 20% HCl–$0.1 \, mol \, l^{-1}$ $CuCl_2$ mixed solution or a saturated $HgCl_2$ solution. Finally, the pore bottoms were opened by chemical etching in 5 wt% aqueous phosphoric or 20 wt% H_2SO_4 acids.

2.2. Track-Etched Polymer Membranes

Microporous and nanoporous polymer membranes are commercially available filters, which are prepared by the track-etch method. This method entails bombarding a nonporous sheet of the desired material with nuclear fission fragments to create damage tracks in this material and then chemically etching these tracks into pores [95]. A broad range of pore diameters (down to 10 nm) is available, and pore densities approaching 10^9 pores cm^{-2} can be obtained. The pores in these membranes are randomly distributed across the membrane surfaces with uniform diameters (Fig. 1B). However, due to the random nature of the pore-production process, the pores have tilt with respect to the surface normal, and a number of pores may actually intersect within the membrane [32].

3. ELECTROCHEMICAL SYNTHESIS STRATEGIES OF SNWs

Electrochemical deposition (ED) of a material within the pores is a simple and versatile method for synthesizing one-dimensional nanostructural material. Table 1 gives the summary of the deposition parameters used in electrochemical synthesis of a variety of SNWs as well as the crystalline structures. In general, this technique is accomplished by coating one face of the membrane with a metal film and using this metal film as an electrode for electroplating. The following is a general outline of seven representative chemical strategies that have been used in electrochemical template synthesis of SNWs by now.

3.1. Direct-Current Electrochemical Deposition

3.1.1. General

In general, the synthesis of SNW arrays within the pores of the AAO template by direct-current electrochemical deposition (DCED) involves three steps (Fig. 2) [51]: first, a metal film was deposited by vacuum evaporation or ion sputtering onto the back of the template membrane; second, semiconductor materials were cathodically deposited on the metal surface at the pore bottom from a solution containing the metal ion (e.g., Cd^{2+}) and another anion (e.g., sulfur and selenium); and finally, the AAO template was dissolved in strong acid or base (i.e., H_3PO_4 and NaOH). The deposition was commonly performed potentiostatically or galvanostatically in a three-electrode configuration. By this strategy, a variety of highly ordered and crystallized metal [37, 41–45], conductor polymers [32], and metal chalcogenide SNW arrays have been prepared [47–62].

Sander et al. [63b] suggested improving the DCED approach to reproducibly fabricate high density and high aspect ratio Bi_2Te_3 nanowire arrays over large areas (Fig. 3). In this approach, first, an Ag film is sputter-deposited onto one surface of an Al foil that is mechanically polished and the thermal oxide layer is chemically removed. Then, the Al foil is anodized to produce a nanoporous AAO membrane for nanowire array fabrication. Before DCED, the AAO template is allowed to soak in a 1 M HNO_3 solution in order to dissolve the barrier layer at the base of the pores. They proposed that several processing steps that lead to template damage or contamination have been eliminated. However, this approach may be unsuited for AAO membranes with thick barrier layers.

There are some important considerations, however, in the choice of electrochemical reaction routes and the operational parameters of DCED synthesis. Electrodeposition occurs closer to equilibrium than those high-temperature vacuum deposition methods. It affords precise process control due to its electrical nature (i.e., the lengths or aspect ratios of the nanowires can be controlled by the amount of material deposited). Also, it enables good control over stoichiometry. However, contamination of the target material with impurity phases is often a problem with electrodeposition as is the morphological quality of the product. In particular, both the greater number of active species in the solution and the by-reaction render the composition modulation a little trickier. On the other hand, the important point to emphasize is that the electrochemical reaction routes have a key role in the growth of nanowires.

Significant improvements have also been claimed in the morphological quality of the resultant nanowires using nonaqueous media [48–58]. For example, highly aligned and crystallized CdS and CdSe nanowires have been prepared by DCED in porous AAO template from dimethylsulfoxide (DMSO) solution containing $CdCl_2$ and S (Se) [48–52]. There have been proponents of the use of nonaqueous solvents. The proclivity of the chalcogen to exist predominantly in low oxidation states in these baths and the attendant lack of complications in the electrodeposition chemistry have been the principal motivating factors in evaluation of nonaqueous media. For example, CdSe nanowires by DCED

Table 1. An overview of the deposition routes and the structures of a variety of SNWs by electrochemical synthesis.

Nanowires/ nanorods	Deposition route			Structure (comments)		
	Method	Bath	Template	Crystallinity	Size (nm)	Ref.
CdS	DCED	DMSO	AAO	(002), W	15–100	[49–51]
		aqueous	AAO		15–100	[50]
	ACED	DMSO	AAO	W, C	9–35	[36, 66–69]
	EID	aqueous	AAO	W	5–100	
	HECS		AAO	W	50	[84]
Ag_2S	DCED	DMSO	AAO	M	40	[56]
	HECS		AAO	M	35–90	[83]
Bi_2S_3	DCED	DMSO	AAO	O	40	[57]
CdSe	DCED	DMSO	AAO	(002), W	20–100	[50, 52]
	ACED	aqueous	AAO	W	9–35	[66]
	DCED	aqueous	AAO	W	60	[59]
				C	200–250	[60]
PbSe	DCED	aqueous	AAO	C	40–60	[58]
$Ag_{2+x}Se$	DCED	aqueous	AAO	O, (002)	20–50	[61]
	DCED	DMSO	AAO	O	20–50	[55]
	DCED	aqueous	AAO	O	200–350	[62]
CdTe	DCED	ethylene glycol	AAO	(002), W	15–50	[50, 53]
$Ag_{2+x}Te$	DCED	DMSO	AAO	M	20–50	[54]
	HECS		AAO	M	60–70	[82]
Bi_2Te_3	DCED	aqueous	PC	R, (002)	280 ± 30	[47]
			AAO	R, (110)	25–75	[63]
$CdSe_xS_{1-x}$	ACED	DMSO	AAO	W	9–35	[66]
$Cd_xZn_{1-x}S$	ACED	DMSO	AAO	W	9–35	[66]
$Ag_2Se_{1-x}Te_x$	DCED	DMSO		M	20–100	[55]
GaAs	ACED	aqueous	AAO			[66]
ZnO	HECS		AAO		60	[78]
	DCED	aqueous	AAO		40–90	[64]
	EPD	sol	AAO		200	[74]
SnO_2	HECS		AAO		60	[79]
In_2O_3	HECS		AAO		60	[80]
MgO	HECS		AAO		20–50	[81]
NiO	HECS		AAO		20–50	[81]
TiO_2	EPD	sol	AAO, PC	anatase	125–200	[71–73]
	EISGD	aqueous	AAO	anatase	10–50	[75]
					15–60	[77]
	HECS		AAO	anatase	20–50	[81]
SiO_2	EPD	sol	PC	nanowires	125–200	[71–73]
		sol	PC	mesoporous, hierarchic	125–200	[73]
	EISGD	aqueous	AAO	nanowires, nanotubes	10–50	[76]
Cu_2O	DCED	aqueous	PC		200	[65]
	ESA		LCP	cuprite	25–100	[85]
$BaTiO_3$	EPD	sol	PC		125–200	[72]
$SrNb_2O_6$	EPD	sol	PC		125–200	[72]
$Pb(Zr, Ti)O_3$	EPD	sol	PC	perovskite PZT	125–200	[71–73]

Note: DCED—direct current electrodeposition, ACED—alternating current electrodeposition, EID—electrochemically induced deposition, EISGD—electrochemically induced sol–gel deposition, EPD—electrophoretic deposition, HECS—hybrid electrochemical/chemical synthesis, ESA—electrochemical self-assembly, PC—polycarbonate, LCP—liquid crystalline phase, W—wurtzite, C—cubic, M—monoclinic, O—orthorhombic, R—rhombohedral.
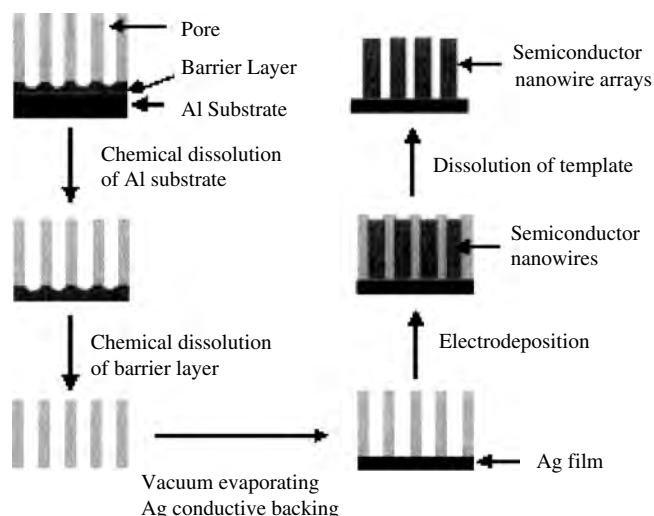
Figure 2. Dc electrochemical synthesis scheme for SNWs. Reprinted with permission from [50], D. S. Xu et al., *Pure Appl. Chem.* 72, 127 (2000). © 2000, International Union of Pure and Applied Chemistry.

in porous AAO template from DMSO solution containing $CdCl_2$ and Se are highly (002) oriented, and the atomic composition of Cd and Se is very close to a 1:1 stoichiometry [52]. However, in $CdCl_2$ and SeO_2 ammonia alkaline solutions, the deposited CdSe nanowires are randomly oriented and the ratio of Se to Cd depends on the pH of the deposition bath [59, 60]. Another important factor is that interference from solvent electrochemistry is circumvented in aprotic media; this proves to be crucial in the electrodeposition synthesis of relatively difficult systems such as ZnX (S, Se, Te).

3.1.2. Metal Sulfide Nanowires

CdS Nanowires Nanowires of CdS were cathodically deposited at a constant direct current density of $2.5 \, \text{mA cm}^{-2}$ from a nonaqueous DMSO solution containing 0.055 M $CdCl_2$ and 0.19 M element S [49–51]. The deposition temperature was keep at 110 °C by immersing the cell in an oil bath. These nanowires have uniform diameters of about 20 and 100 nm, which is in good agreement with the pore diameters of the templates used, and lengths are up to tens of micrometers. The X-ray energy dispersion analysis (EDAX) shows that the atomic composition of S and Cd is very close to a 1:1 stoichiometry. Electron diffraction pattern and high resolution transmission electron microscopy (HRTEM) images demonstrated that these CdS nanowires have a uniform crystalline structure of hexagonal CdS [51].

Nanowires of CdS were also cathodically deposited in aqueous solution consisting of 0.5 M $CdSO_4$, 0.1 M EDTA, and 0.5 M $S_2O_3^{2-}$ in a pH range of 5–6 at a constant current density of 1 mA/cm^2 for 60 min [50]. The length of the nanowire array is up to 30 μm and the diameters of the nanowires are about 90 nm. However, for the as-deposited samples, these nanowires are of poor crystallinity.

Ag₂S Nanowires Electrodeposition of Ag_2S nanowires has been reported from DMSO solutions containing $AgNO_3$ and element S [56]. In this case, the depositions were carried
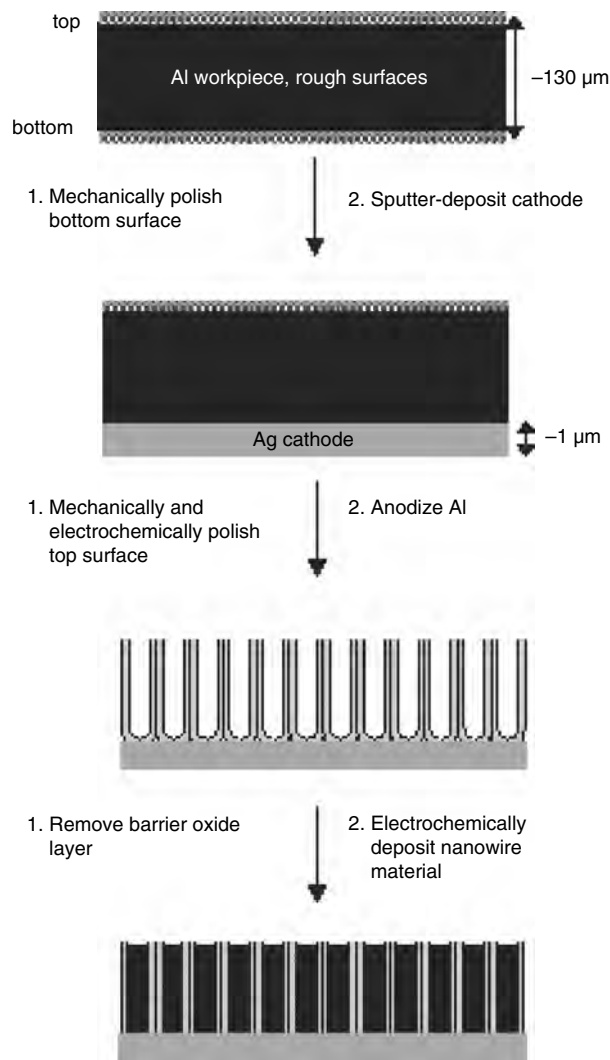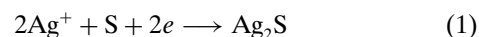

Figure 3. Schematic of the improving process employed to produced nanowire arrays by DCED. Reprinted with permission from [63b], M. S. Sander et al., *Adv. Mater.* 14, 665 (2002). © 2002, Wiley–VCH.

out at 120 °C and a potentiostatic voltage of −0.8 V relative to Ag/Ag⁺ reference electrode. The electrode reaction is

$$2Ag^+ + S + 2e \longrightarrow Ag_2S \tag{1}$$

This reaction pathway could be expressed in the following manner:

$$2Ag^+ + 2e \longrightarrow 2Ag \tag{2}$$

$$S + 2Ag \longrightarrow Ag_2S \tag{3}$$
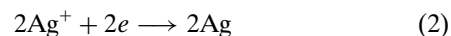
The lengths of the nanowires are about 5 μm after growing for 60 min. The annealed nanowires are monoclinic Ag_2S (β-Ag_2S) structure with constant of $a = 0.423$ nm, $b = 0.693$ nm, $c = 0.786$ nm, and $\beta = 99.61°$.

Bi₂S₃ Nanowires Electrodeposition of Bi_2S_3 nanowires was carried out in a solution containing of 0.055 M $BiCl_3$ and 0.19 M element S dissolved in DMSO at 120 °C and −0.1 V relative to the Ag/AgCl reference electrode for

60 min [57]. The porous AAO membranes with channel diameters of about 40 nm were taken as templates. X-ray diffraction (XRD) and selected area electron diffraction (SAED) investigations demonstrate that the Bi_2S_3 nanowires have a uniform orthorhombic structure. Electromicroscopy results show that the nanowires are quite ordered with diameters of about 40 nm and lengths up to 5 μm. Optical absorption studies reveal that the annealed Bi_2S_3 nanowires have an optical band edge (direct) of about 1.56 eV.

3.1.3. Metal Selenide Nanowires

CdSe Nanowires Electrodepositions of CdSe nanowires have been carried from both the aqueous and nonaqueous solution baths. Xu et al. have prepared CdSe nanowires by cathodical deposition from a DMSO solution containing $CdCl_2$ as Cd source and elemental Se as selenium source [50, 52]. The electrode reaction for CdSe deposition is

$$Cd^{2+} + Se + 2e \longrightarrow CdSe \qquad (4)$$
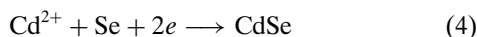
The deposition was carried out at a constant direct current density of 0.85 $mA\,cm^{-2}$ for 30–60 min. The solution was held at 160 °C. The length, diameter, and direction of growth of these CdSe nanowires are quite uniform. Characterizations by XRD, electron diffraction, and HRTEM indicated that the c-axis of hexagonal crystals is preferentially aligned along the direction normal to the substrate rather than oriented randomly [52].

Peng et al. [59] fabricated CdSe nanowires from an ammonia alkaline solution containing 0.1 M $CdCl_2$, 0.002 M SeO_2, and 0.1 M Na_2SO_4. Shen et al. [60] prepared polycrystalline CdSe nanowires from an acidic bath consisting of 0.25 M $CdSO_4$, 0.01 M H_2SeO_3, and 0.25 M Na_2SO_4. The pH value of the bath is 2.5. The deposition potential applied was −0.70 V (SCE). The deposited CdSe nanowires are cubic polycrystalline and randomly oriented, and the ratio of Se to Cd varied with the pH of the bath [59].

PbSe Nanowires Ordered PbSe crystalline nanowire arrays have been fabricated in the nanochannels of AAO membrane by DCED [58]. XRD and SAED investigations demonstrate that the PbSe nanowires have a uniform cubic structure. The nanowires are quite ordered with diameters of about 50 nm and lengths up to 5 μm. EDAX data indicate that Pb:Se is very close to 1:1. The optical absorption spectrum of these PbSe nanowires shows that there exist two peaks at 280 and 434 nm, respectively, attributed to excitonic absorption peaks.

Ag_2Se Nanowires Silver chalcogenides (Ag_2Se and Ag_2Te) belong to the $A_2^IB^{VI}$ group of compound semiconductors with narrow bandgaps. Their high temperature phases are superionic conductor materials [96], and large positive magnetoresistance has been discovered in self-doped $Ag_{2+\delta}Se$ and $Ag_{2+\delta}Te$ [97]. Chen et al. [61] have synthesized near stoichiometric Ag_2Se nanowires by cathodic electrolysis from aqueous baths containing 0.5 M KSCN, 5.0 mM $AgNO_3$, 0.05 M KNO_3, and 2.5 mM SeO_2. The electrode reactions that take place are

$$2Ag(SCN)_n^{1-n} + Se + 2e \longrightarrow Ag_2Se + 2nSCN^- \qquad (5)$$

or

$$2Ag(SCN)_n^{1-n} + HSeO_3^- + 5H^+ + 6e$$
$$\longrightarrow Ag_2Se + 3H_2O + 2nSCN^- \qquad (6)$$
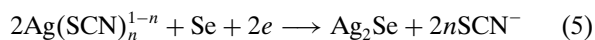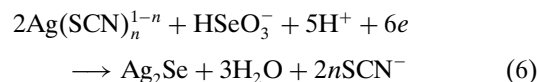
Meanwhile, the deposition would be accompanied by the formation of silver. The deposited silver can participate in the electrode reaction and transform to Ag_2Se according to

$$2Ag + HSeO_3^- + 5H^+ + 4e \longrightarrow Ag_2Se + 3H_2O \qquad (7)$$
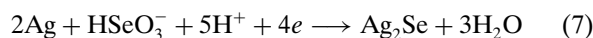
The pH values of the solutions were adjusted to 2.60 with HNO_3 aqueous solution. At this pH SeO_2 is in the form of selenous acid (H_2SeO_3 and $HSeO_3^-$) in aqueous solutions. SCN^- was used to complex Ag^+ in order to lower the redox potential of Ag^+/Ag and to prevent the precipitation of insoluble Ag_2SeO_3. Silver selenide was deposited into the pores of the template at a constant potential of −0.70 V vs SCE. The nanowires are continuous and of about 10 μm length, in which the growth rate is about 2.5 μm h^{-1} at a potential of −0.70 V vs SCE. These nanowires align with uniform lengths, diameters, and growth directions. The as-deposited nanowires are polycrystalline orthorhombic β-Ag_2Se. After being annealed and slowly cooled, highly [002] oriented orthorhombic Ag_2Se nanowires were formed, which was demonstrated by XRD, SAED, and HRTEM. Importantly, the ratio of excess Ag can be controlled by adjusting the bath compositions and the deposition potentials. The slight excess of Ag in the deposited film can be transformed into Ag_2Se by annealing in Se vapor.

Glanville et al. [62] reported a two-step electrodeposition method for synthesis of Ag_2Se nanowires. In this approach, a 9 μm layer of Ag was first directly electrodeposited into the pores of the template membrane and then the deposited Ag nanowires were electrochemically converted to Ag_2Se nanowires at a constant current density of 0.8 mA/cm^2 in an aqueous bath of 0.3 M SeO_2 and 0.03 M H_2SO_4 according to Eq. (7). Finally, the Ag_2Se nanowire/alumina membrane was chemically etched in a 50% HNO_3 solution removing all excess silver, leaving just the Ag_2Se nanowires standing in the membrane.

Stoichiometric Ag_2Se [55] nanowires have also been electrodeposited from a nonaqueous DMSO solution. The electrolyte solution consists of 0.1 M $NaNO_3$, 5.0 mM $AgNO_3$, and 4.0 mM $SeCl_4$. In this case of depositing Ag_2Se, the $SeCl_4$ was used as a selenium source. The reactions can be expressed as

$$2Ag^+ + SeCl_4 + 6e \longrightarrow Ag_2Se + 4Cl^- \qquad (8)$$
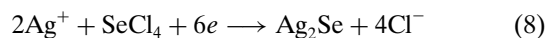
The deposition was carried out at a potential of −0.95 to −1.05 V vs SCE. The as-deposited nanowires are polycrystalline orthorhombic β-Ag_2Se with an [002] orientation, which is quite different from the nanowires deposited in aqueous baths.

3.1.4. Metal Telluride Nanowires

CdTe Nanowires CdTe nanowires have been prepared by electrochemical deposition into the pores of anodic aluminum oxide templates from an ethylene glycol bath containing $CdCl_2$, $TeCl_4$, and KI [53]. The electrodeposition was carried out by potentiostatic electrolysis in the potential range between -0.59 to -0.85 V vs SCE at 160–175 °C. The AAO templates with about 10, 20, and 50 nm pore diameters have been used. The electrolyte solution consisted of 1.00 M $CdCl_2$, 0.01 M $TeCl_4$, and 0.3 M KI in glycol. Highly ordered CdTe nanowire arrays have been obtained, in which the length, diameter, and direction of growth of the nanowires are quite uniform. XRD, TEM, and HRTEM investigations demonstrate that these nanowires have a crystalline structure of hexagonal CdTe single crystal with a uniform [002] growth direction.

Ag₂Te Nanowires Silver telluride nanowires were synthesized by cathodic electrolysis into porous AAO membranes from nonaqueous DMSO solutions containing 0.1 M $NaNO_3$, 5.0 mM $AgNO_3$, and 6.0 mM $TeCl_4$ [54a]. DMSO would be both an electrochemical solvent, which easily dissolves $TeCl_4$ to form $(2DMSO \cdot TeCl_3)^+ \cdot Cl^-$, and a weak complexing agent of Ag^+. The electrode reaction for deposition of Ag_2Te is

$$2Ag^+ + TeCl_4 + 6e \longrightarrow Ag_2Te + 4Cl^- \qquad (9)$$
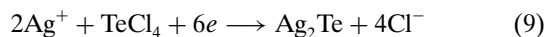
The deposition temperature was 80 ± 1 °C. The deposition time is 40–50 min. XRD and SAED patterns of the as-prepared nanowires were indexed to be a monoclinic structure of Ag_2Te. Near stoichiometric Ag_2Te nanowires were obtained at a potential range between -0.55 and -0.65 V vs Ag/AgCl. Furthermore, the composition of the nanowires can be controlled continuously from Ag-rich to Te-rich mainly by changing the concentration of $TeCl_4$ in the solutions. Interestingly, single-crystalline Ag_7Te_4 nanowire arrays were obtained by electrodeposition from DMSO solutions containing 0.1 M $NaNO_3$, 5.0 mM $AgNO_3$, and 7.5 mM $TeCl_4$ at -0.65 V (vs Ag/AgCl) [54b].

Bi₂Te₃ Nanowires Bismuth telluride is currently the most efficient thermoelectric material at room temperature. Highly crystalline nanowires of Bi_2Te_3 have been deposited directly by electrochemical reduction of Bi^{3+} and $HTeO_2^+$ in acidic aqueous solutions [47, 62, 63]. The electrode reaction for deposition of Bi_2Te_3 is

$$2Bi^{3+} + 3HTeO_2^+ + 9H^+ + 18e \longrightarrow Bi_2Te_3 + 6H_2O \quad (10)$$
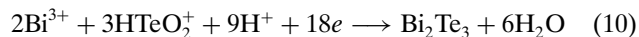
The deposition solution was prepared by dissolving elemental Te and Bi in 1 M HNO_3. The depositions were carried out by both potentiostatic control with potentials more negative than -0.45 V vs Hg/Hg_2SO_4 and a galvanostatic process with a current density of 3.5 mA/cm². The as-deposited nanowires by galvanostatic electrodeposition are a random polycrystalline orthorhombohedral Bi_2Te_3 structure. But the nanowires by potentiostatic deposition have a preferred [110] orientation of orthorhombohedral Bi_2Te_3 [62].

3.1.5. Metal Oxide Nanowires

ZnO Nanowires Semiconductor metal oxide films can be prepared through a one-step electrodeposition approach from an aqueous solution only of metal nitrate and dissolved oxygen as the oxygen precursor. For example, when a cathodic potential of typically -0.9 V (vs SCE) is applied to a conductive substrate in an aqueous solution of 0.1 M zinc nitrate maintained at 70 °C, nucleation of ZnO takes place almost instantaneously and further electrolysis promotes further crystal growth, resulting in a film composed of hexagonal faceted crystals. The electrode reaction is expressed as

$$Zn^{2+} + \frac{1}{2}O_2 + 2e \longrightarrow ZnO \qquad (11)$$
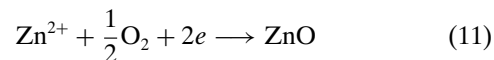
This method has been employed to prepare dye-modified ZnO films [98] and obtain epitaxial growth of metal oxide films [99–101].

Zheng et al. have demonstrated that semiconductor zinc oxide nanowires can also be prepared by this one-step electrodeposition [64]. The electrodeposition was performed at 1 V (vs Ag/AgCl), with a zinc sheet serving as the counterelectrode. Electron diffraction patterns show that these nanowires are not single crystals. In principle, other metal oxide nanowires including thallium, zirconium, copper, bismuth, and iron oxides can also been fabricated by this one-step electrodeposition.

Cu/Cu₂O Composite Nanowires Arrays of Cu/Cu_2O nanowires were grown by electrodeposition in the nanopores of track-etched polymer membranes [65]. If an appropriate solution is used, the electrode potential spontaneously oscillates during the application of a constant cathodic current. Both the period of the oscillations and the composition of the nanowires can be controlled by varying the applied current density. A nanocomposite of copper and cuprous oxide is deposited at an applied current over which oscillations occur. In contrast, pure Cu or Cu_2O nanowires are obtained at a deposition current out of the range of oscillation. Electrical transport measurements were also performed on these nanowires.

3.1.6. GaAs Nanowires

Electrodeposition of GaAs nanowires into the pores of the AAO template from an aqueous chloride bath containing $GaCl_3$ and As_2O_3 has been studied by Routkevitch et al. [66]. They have investigated the effect of the Ga(III)/As(III) ratio and pH on the deposition of GaAs. For pH < 2.5, no GaAs is deposited. Arsenic is found to be the main deposited component under those conditions on Pt, indium tin oxide, or AAO substrates, and H_2 evolution was the primary side reaction. This is in agreement with the fact that Ga electrodeposition is possible only at pH > 2.5 at the onset of hydrolysis. With solutions of 0.05 M of Ga(III) at pH $= 2.5$ and Ga(III)/As(III) ratio $= 2.1$, a reddish–yellow sample was generated which produced resonance Raman spectra with well defined peaks at about 280 cm^{-1} characteristic of GaAs. However, XRD did not reveal crystalline GaAs. Samples lost their colors over a period of several hours.

3.1.7. Ternary Semiconductor Nanowires

CdS_xSe_{1-x} Nanowires An attractive feature of the electrochemical synthesis approach is the ease with which alloy nanowires may be generated. Routkevitch et al. have fabricated ternary compound CdS_xSe_{1-x} nanowires in a DMSO solution containing 0.055 M $CdCl_2$ and 0.19 M of the elemental chalcogens (S and Se) using an ac ACED technique [66]. In order to vary the Se/S ratio in the nanowire, solutions with Se/S ratios ranging from 20:1 to 1:20 were used. The composition of the electrolytes (Se/S ratios) determines the nanowire composition, with the XRD pattern changing from that of hexagonal CdS to that of hexagonal CdSe. Normalized absorption spectra of AAO/CdS_xSe_{1-x} as a function of Se/S ratio in electrolyte illustrate that the control over ternary semiconductor CdS_xSe_{1-x} composition allowed us to produce nanowires with widely varying values of the optical bandgap [66].

$Cd_xZn_{1-x}S$ Nanowires Deposition of the $Cd_xZn_{1-x}S$ nanowires was carried out in a DNSO solution containing 0.055 M ($CdCl_2 + ZnCl_2$), and 0.19 M elemental S using ACED [66]. The co-deposition of ZnS with CdS was found to occur only at high deposition voltage (50 V). Likewise the various phases of $Cd_xZn_{1-x}S$ could only be produced with high deposition temperatures. Similar to the deposition of CdS_xSe_{1-x} nanowires [66], the composition of the electrolytes (Zn/Cd ratios) determines the nanowire composition.

$Ag_{2+\delta}Se_{1-x}Te_x$ Nanowires Ternary compound $Ag_{2+\delta} \cdot Se_{1-x}Te_x$ nanowires have been direct current electrodeposited at the co-deposition potentials of Ag_2Se and Ag_2Te using DMSO as a solvent and $CdCl_2$, $SeCl_4$, and $TeCl_4$ as Cd, Se, and Te sources respectively [55]. By varying the concentrations of $SeCl_4$ and $TeCl_4$ in DMSO solutions, ternary $Ag_{2+\delta}Se_{1-x}Te_x$ compounds with tunable compositions were prepared.

3.2. Alternating Current Electrochemical Deposition

The compact barrier layer between the porous AAO and Al substrate is insulating, which obstructs the passage of direct current. Thus, it is difficult for materials to be directly deposited on the AAO/Al substrate by DCED. Routkevitch et al. demonstrated that the rectifying properties of the oxide barrier layer that separates the bottom of the pores from the underlying aluminum substrate make it possible to use ac deposition [36]. On the other hand, for samples with very narrow pore diameters the DCED strategy only works when the anodic films are free from cracks and defects; otherwise, the electrochemistry becomes dominated by processes in the much more accessible cracks. Fabricating templates of such structural perfection is commonly difficult. By retaining the barrier layer and using ac electrolysis, this problem is avoided even with very small pore diameter since the rectification only occurs inside the pores while at defects the electrochemical processes occurring during the cathodic half-cycle are reversed, more or less, during the anodic half-cycle. When the anodization was complete, the anodizing voltage was decreased stepwise in 5 V intervals over a period of 5 min in order to reduce the thickness of the barrier layer. In the case of ac electrolysis of CdS nanowires, deposition was carried out in a DMSO solution containing 0.0055 M $CdCl_2$ and 0.19 M S at 100–160 °C and 30–50 V ac (60–500 Hz) applied between the Al/AAO working electrode and a graphite counterelectrode. The deposited CdS nanowires are found to be hexagonal CdS with the c-axis preferentially oriented along the length of the pore. On average the thicker wires (with diameters larger than 12 nm) consist of a large number of crystallites in the axial direction and rather few in the radial direction [36, 66–69]. Other semiconductor nanowires, such as CdSe, $Cd_xZn_{1-x}S$, CdS_xSe_{1-x}, and GaAs, have also been fabricated by this strategy [66].

ACED is a simple method to fabricate aligned nanowires in AAO template while retaining the compact barrier layer [36]. A major disadvantage of this synthesis route is that there are large numbers of stacking faults and twinned segments in the deposited nanowire and the structure of the nanowire appears to be mainly the hexagonal form, interleaved with domains of cubic structure [68]. In general, for the case of electrodeposition in the pore of the AAO templates, the direction of the diffusion is limited on one dimension. The diffusion rate may be much slower than the surface electrochemical reaction and the diffusion process would limit the nanowire growth. For the ac process, the rate and the direction of the diffusion would vary with the alternation of the electric field and thus make a high density of defects and small polycrystalline CdS structure in the nanowires [36, 68]. On the other hand, it is easy to reach a steady diffusing process under the DCED condition. Thus, the defects in the nanowires by DCED are largely decreased and produce perfect and highly crystalline nanowires.

3.3. Electrochemically Induced Deposition

Although direct electrochemical deposition can afford precise process control and enables good control over stoichiometry, both the greater number of active species in the solution and the by-reaction render the composition modulation a little trickier. Meanwhile, the deposition of the nanowires controlled by the electrochemical reaction usually results in a polycrystalline structure. It can be expected that these problems can be avoided while the deposition is controlled by chemical reaction rather than by the electrode kinetics.

Xu et al. have reported an electrochemically induced deposition method to prepare CdS single-crystal nanowires from acidic chemical bath containing 0.05 M $CdCl_2$ and 0.10 M thioacetamide (TAA) [70]. This process involves electroreduction of protons on conductive substrates and chemical bath deposition of materials on the electrode/solution interface in the pores of the template. The component processes may be represented by the following equations:

$$2H_2O + 2e = 2OH^- + H_2 \tag{12}$$

$$CH_3CSNH_2 + 2OH^- = CH_3COONH_4 + S^{2-} \tag{13}$$

$$S^{2-} + Cd^{2+} = CdS \tag{14}$$
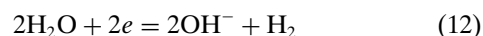
The deposition of CdS was performed potentiostatically at a potential value of -0.65 V (vs SCE) in a three-electrode

configuration in a glass cell at 70 °C. It is interesting that the growth rate of the CdS nanowires deposited in the pores increases with decreasing pore size of the template. After deposition in 20 nm AAO template for 8 h, the length of the nanowire is up to 10 μm, while the nanowires with 2–3 μm lengths are found in 90 nm template (Fig. 4A and B). HRTEM images reveal that these nanowires have a uniform hexagonal CdS single-crystal structure (Fig. 4C). The single-crystal nanowires with diameters smaller than 5 nm have also been prepared (Fig. 4D).

This method differs from direct ED in that the deposition does not involve reduction of Cd^{2+} or TAA but requires the reduction of the protons at a low current density. The
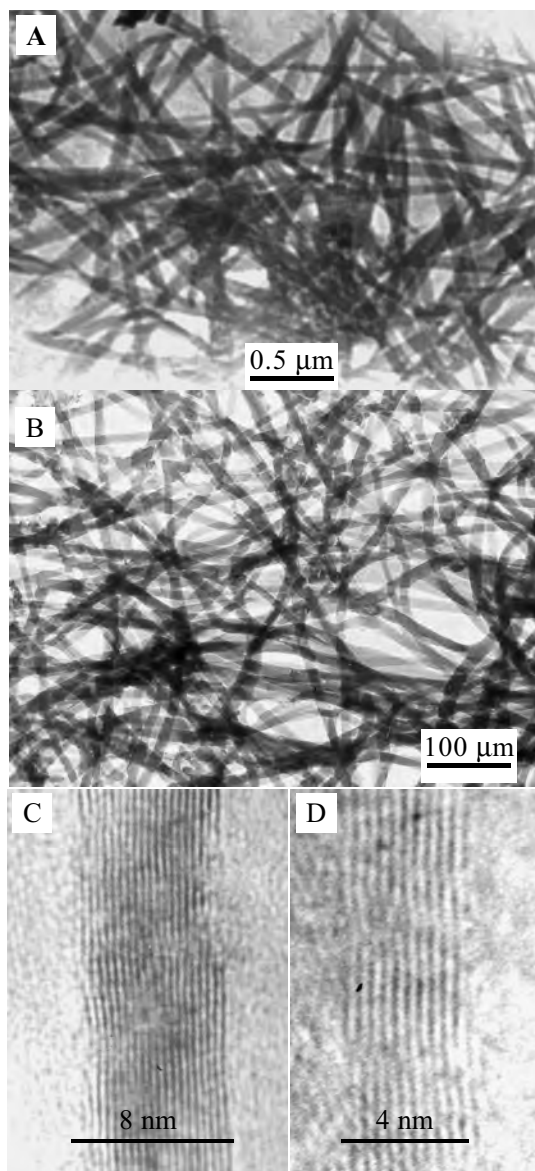
Figure 4. TEM images of CdS nanowires prepared by electrochemically induced deposition in the AAO templates with diameters of about 90 nm (A) and 20 nm (B), and the HRTEM images of individual nanowires with different diameters of (C) 8 nm and (D) 4 nm. Reprinted with permission from [70], D. S. Xu et al., *Adv. Mater.* 12, 520 (2000). © 2000, Wiley–VCH.

electroreduction of protons imposes a pH gradient at the vicinity of the substrate to reduce the activation barrier for the hydrolysis of TAA. In this case, the CdS nanowire growth is not controlled by the electrode kinetics and is not disturbed by the reactions in the solution phase. Therefore, this method allows one to deposit single crystal CdS nanowires. Of course, the same approach may also be valid in the deposition of other metal sulfide single crystal nanowires.

3.4. Sol–Gel Electrophoretic Deposition

Sol–gel chemistry has evolved into a general and powerful approach for preparing inorganic materials [102, 103]. This method typically entails hydrolysis of a solution of a precursor molecule to obtain first a suspension of colloidal particles (the sol) and then a gel composed of aggregated sol particles. The gel is then thermally treated to yield the desired material. This approach for the synthesis of inorganic materials has advantages in the preparation of both high-purity materials at a lower temperature and homogenous multicomponent systems by mixing precursor solutions. Lakshmi et al. [38] first conducted sol–gel synthesis within the pores of the AAO template to create both fibrils and tubules of the desired material, using a simple immersion method. First, the AAO membrane is immersed into a sol for a given period of time, and the sol deposits on the pore walls. After thermal treatment, either a nanotubule or nanofibril is formed within the pores. Whether tubules or fibrils are obtained is determined by the immersion time, the temperature of the sol, and the electric properties of the pore walls. Longer immersion times yield solid fibrils while brief immersion times produced tubules. For the templates with smaller pore sizes, solid fibrils are always obtained in the pores [38]. By this method, nanostructures (nanowires and nanotubules) of a variety of oxides, complex oxide materials [104–108], and other semiconductors have been synthesized [109].

However, there are some potential limitations to this technique. For example, since the only driving force of this technique is capillary action, for the sol with higher concentration, the filling of the pores would be difficult (at the same time destabilization of the sol remain a big problem), but low concentration leads to nanomaterials with serious shrinkage and cracking. Sol–gel electrophoretic growth of nanowires by Limmer et al. throws some light on overcoming the limitations of the direct sol filling method [71, 72]. First, a proper sol contains solid nanoclusters of the desired stoichiometric chemical composition. If the sol is electrostatically stabilized, then the charged nanoclusters will have an oriented diffusion, parallel to the field direction, when an electric field is applied to the sol. While using this sol–gel electrophoresis in the template-assisted growth of nanorods, an electric field was applied to draw the charged sol nanoclusters into the template pores. The nanoclusters will migrate and deposit at the bottom of the pore under an applied electric field. Simultaneously, the counterions move in the opposite direction. As time increases, the densely packed sol particles fill more of the pore, until the pore is completely filled.

Limmer et al. have applied this sol–gel electrophoretic method to grow both single metal oxides (TiO$_2$, ZnO, SiO$_2$) and complex oxides [BaTiO$_3$, Sr$_2$Nb$_2$O$_7$, and

Pb(Zr$_{0.52}$Ti$_{0.48}$)O$_3$] [71–73]. For positively charged sol particles, an anode of Pt mesh is immersed in the sol, and the cathode used is aluminum. For negatively charged sol particles, the electrodes are reversed. The PC membrane is attached to the electrode with a piece of double-sided conductive tape, to provide a conductive path from the membrane to the cathode. For the electrophoretic growth, a potential of 5 V is applied between the electrodes and held for up to 3 h. The desired crystal structure of the oxide nanorods was achieved by a heat treatment (500–700 °C for 15–30 min) for crystallization and densification. Interestingly, they have prepared nanorods of hierarchically structured mesoporous silica by this electrophoretic deposition [73].

Wang et al. have studied the effect of the colloid characteristics on the formation of ZnO nanowire arrays by electrophoretic deposition in porous AAO templates [74]. It was found that both the morphology and the deposition rate of ZnO nanowire arrays were influenced by the pH of the suspension and the applied voltage. The particle surface charge and size changed with the pH of the suspension, which in turn affected the deposition characteristics. The deposition rate of nanowire arrays was high at the initial stage, then approached a saturation value, and also increased with increasing zeta potential of the particles and the applied voltage. On the other hand, they observed that the morphologies of the products depended on the applied voltages; the lower deposition voltage could produce nanofibrils and at the higher voltage, the product changes from fibril to tubule form.

It has been demonstrated that sol–gel electrophoresis deposition is widely applicable and can be used for the template growth of a number of different oxide nanorods, especially of complex oxide nanorods. However, this sol–gel electrophoresis growth of nanowires is still limited by the pore size of the templates used. Synthesis of nanorods with diameters less than 50 nm is unsuccessful, due to the difficulty of diffusion of nanoclusters in the small nanosized pores [71–74]. Serious shrinkage and cracking are also observed in these nanorods by electrophoresis deposition [71–73]. In addition, HRTEM images and electron diffraction patterns reveal that theses nanorods are polycrystalline, with small grains that are ∼5 nm in size [73].

3.5. Electrochemically Induced Sol–Gel Synthesis

Miao et al. reported an electrochemically induced sol–gel method to prepare TiO$_2$ single-crystalline nanowire arrays (Fig. 5) [75]. At first, the hydroxyl ion is generated due to the cathodic reduction, and then the generation of OH$^-$ ions increases the local pH at the electrode surface resulting in titanium oxyhydroxide gel formation in the pores of the template. Finally, subsequent heat treatment and the removal of the AAO template results in the formation of TiO$_2$ single-crystalline nanowire arrays. During this electrochemically induced sol–gel process, both the formation of sol particles and the gelation process take place in the AAO pores.

This method offers many advantages for the formation of nanowires and nanotubes. First, the sol–gel preparation of nanowires within the templates that have very small pores
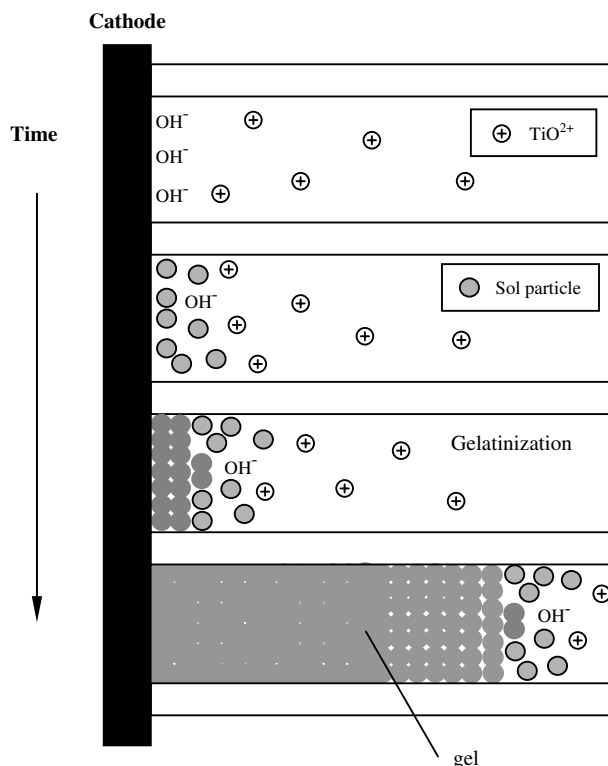

Figure 5. This schematic demonstrates the progress of the electrochemically induced sol–gel process. It can be seen that both the formation of sol particles and the gelatin process take place in the AAO pores; lastly, the pores are filled with homogeneous titanium oxyhydroxide gel. Reprinted with permission from [75], Z. Miao et al., *Nano Lett.* 2, 717 (2002). © 2002, American Chemical Society.

(less than 20 nm or even small) would be readily achievable by using this technique (Fig. 6A and B). Second, the length of the nanowires can be well controlled by varying the deposition time and potential of the working electrode. Third, less shrinkage and cracking will occur during the heat treatment of nanowires. The transport of ions through the voids of packed sol particles and the tiny pores in the titanium oxyhydroxide gel network courses the expansion of gel in the AAO pores and aging of the gel that has already formed. The AAO template with pores of nanoscaled size can restrict the diffusion of OH$^-$ in solution, so it is easy to construct high local pH and long diffusion depth in the AAO pores, resulting a higher packing density gel.

Further, one-dimensional silica nanostructures, such as nanotubes, "bamboolike" structure, and nanowires, have also been synthesized by such an electrochemically induced sol–gel deposition [76]. It was demonstrated that the growth of these nanostructures is strongly dominated by the electrochemical process. The lower cathode voltage is favored to produce nanotubes while the nanowires were formed at a higher cathode voltage. Zhang et al. [77] reported the fabrication of single-crystalline TiO$_2$ nanowires by anodic oxidative hydrolysis of TiCl$_3$ in the pores of the AAO templates. They found that the diameter of TiO$_2$ nanowires is much smaller than the pore diameter of the template used [77]. Hence, electrochemically induced sol–gel deposition is a general method for the growth of 1D nanostructures of a variety
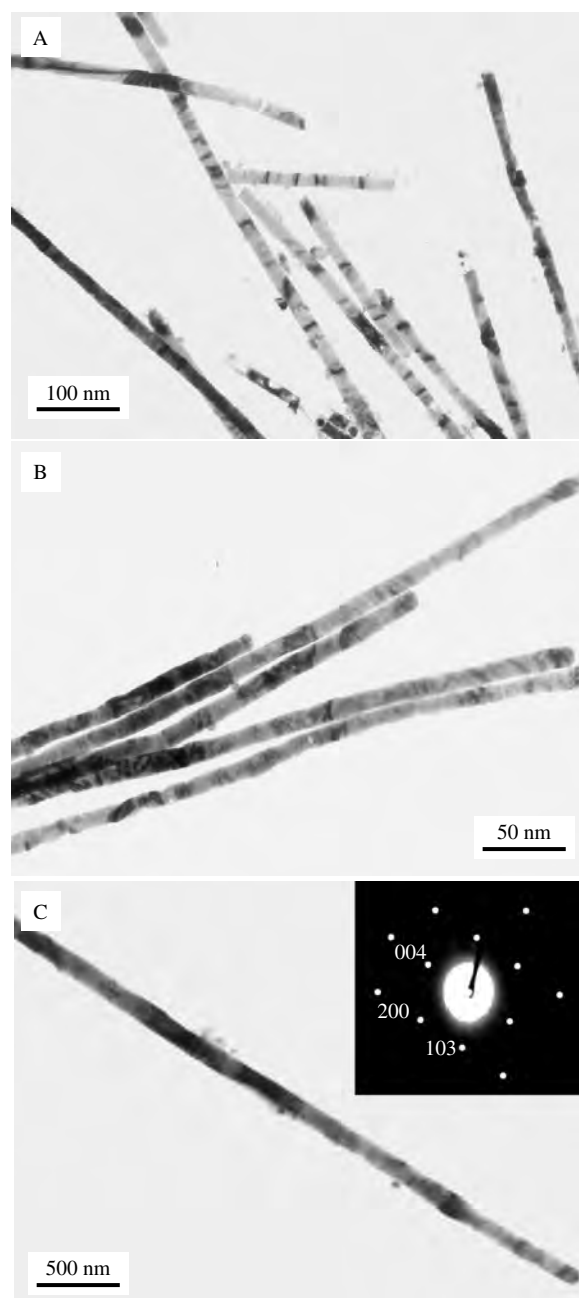
Figure 6. TEM images of TiO_2 nanowires grown in AAO membranes with pore diameters of (A) 22, (B) 12, and (C) 50 nm by electrochemical sol–gel deposition. The inset plot in (C) gives the corresponding selected area diffraction pattern of the single nanowire. Reprinted with permission from [75], Z. Miao et al., *Nano Lett.* 2, 717 (2002). © 2002, American Chemical Society.

of inorganic oxide (single or complex) materials in small-pore templates.

3.6. Hybrid Electrochemical/Chemical Synthesis

Although direct electrochemical deposition has successfully been applied in preparation of metal chalcogen nanowires, control of the composition is still a problem in these nanowires. In addition, it is difficult to fabricate metal oxide nanowires by this approach. The hybrid electrochemical/chemical synthesis of SNWs involves two steps: first, metal nanowires are prepared by DCED in the pores of the template; second, the metal nanowires are reacted with other reactants to yield metal compound nanowires. By now, there are four reaction routes for hybrid electrochemical/chemical synthesis.

3.6.1. Metal Oxide Nanowires by Thermal Oxidation of Metal Nanowires

This approach involves thermal oxidation of metal nanowires embedded in the pores of the AAO template, resulting in the formation of metal oxide nanowires. Various metal oxide SNWs, including ZnO [78], SnO_2 [79], In_2O_3 [80], TiO_2, MgO, and NiO [81], have been fabricated by this electrochemical deposition and thermally oxidizing methods. The key point is that the composition of the metal oxide nanowires is decided by the annealing temperature and the oxidation time. Zheng et al. [79] reported that there are three phases (Sn, SnO, and SnO_2) coexisting in the thermally oxidized nanowires at 823 K; however, only the SnO_2 cassiterite phase is detected under annealing at 923 K.

3.6.2. Ag_2Te Nanowires by Reaction of Te Nanowires with Aqueous $AgNO_3$ Solutions

The hybrid electrochemical/chemical synthesis of Ag_2Te nanowires begins with the electrodeposition of Te nanowires in the pores of the AAO template. After removing the AAO template, the metal Te nanowires were then converted into monoclinic Ag_2Te nanowires by reacting with aqueous $AgNO_3$ solutions. Gates et al. [110] reported a template-directed reaction, in which single crystalline nanowires of trigonal Se were quantitatively converted into Ag_2Se nanowires by reacting with aqueous $AgNO_3$ solutions. In the case of conversion of Te nanowires, after treatment with 5 mM $AgNO_3$ solution at 60 °C for 24 hours, the Te nanowires have been converted into Ag_2Te nanowires, and the average diameters of the converted nanowires have an increase of 20–30% [82]. The reaction involved in this converting process can be presented as the following:

$$3Te + 4Ag^+ + 3H_2O \longrightarrow 2Ag_2Te + TeO_3^{2-} + 6H^+ \quad (15)$$
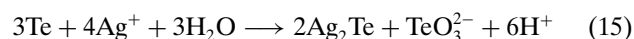
3.6.3. Ag_2S Nanowires by Reaction of Ag Nanowires with Aqueous Na_2S Solutions

It has been demonstrated that the cationic metal nanowires can also be used as a template for template-directed reaction [83]. For example, Ag nanowires can be converted into monoclinic Ag_2S nanowires by reaction with Na_2S aqueous solutions in air at room temperature [83]. The morphology of the template nanowires of Ag was almost retained in the product Ag_2S nanowires, and the average diameters of the nanowires have an increase of 70–80%. This large expansion of the volume, in some cases, would result in breaking of the nanowires.

3.6.4. Metal Sulfide Nanowires by Sulfurization of Metal Nanowires

Similar to the metal oxide nanowires by oxidation of metal nanowires, semiconductor CdS nanowires have also been fabricated by sulfurization of metal nanowires [84]. The deposition of Cd nanowires was carried out by dc potentiostatic elctrodeposition embedded in the AAO membranes. Then, Cd nanowires were sulfurized by S vapor at 300 °C for 30 hours. Due to the large volume of anionic S, the time needed for sulfurization of metal nanowires would be longer than that for the oxidation process. Another example is the conversion of metal Ag to Ag_2Se in Se vapor. The fact that excess Ag in the electrodeposited Ag_2Se nanowires was reduced and even disappeared by annealing in Se vapor implies that annealing in Se vapor may be used for the transformation of Ag_2Se nanowires from Ag nanowires [61].

3.7. Electrochemical Self-Assembly Synthesis

Conventional host–guest molecular systems and self-assembly have been hot topics in chemistry and biology in the last couple of years [111–114]. Self-assembly usually refers to assemblies formed by spontaneous recognition of strongly interacting sites and molecular shapes, often reinforced by cooperative effects and thermodynamic transitions. Electrochemical self-assembly synthesis of nanowires involves both molecular recognition and a spontaneous electrochemical synthesis on the surface of the electrode. It should be noted that unlike template-assisted electrochemical synthesis of nanowires wherein the electrochemical synthesis of the desired materials is confined in the nanochannel of the template, adsorption of organic molecules to growing surface has a significant impact on nanowire growth. However, few works have reported the preparation of nanowires or nanorods by this electrochemical self-assembly strategy. Yoshida et al. [98] reported that cathodic electrodeposition in an aqueous mixed solution of zinc nitrate and water-soluble organic dye molecules, resulting in a self-assembled growth of ZnO thin films. It has been found that anisotropy in the dye stability of the adsorption results in a preferential growth of ZnO into specific crystallographic direction to create morphologies. Zhu et al. [115] have prepared Ag nanorods by an electrodeposition technique from an aqueous solution of $AgNO_3$ in the presence of polyethylene glycol, in which the polyethylene glycol may be taken as a soft template to confine the growth of the nanowires. These works throw some light on the electrochemical self-assembled synthesis of semiconductor nanowires.

On the other hand, semiconductor nanowires can be electrochemically synthesized from surfactant mesophases with 1D aqueous channels as space-confined microreactors. Surfactant mesophases, including liquid crystals, vesicles, micelles, microemulsions, and so on, have proved to be useful and versatile "soft" templates, in contrast to porous "hard" templates such as AAO membranes, track-etched polycarbonate and mica, zeolite/mesoporous silica, diblock copolymer matrix, etc. Huang et al. [85] reported that Cu_2O nanowires with diameters of 25–100 nm were electrodeposited from anionic surfactant sodium bis(2-ethylhexyl) sulfosuccinate hexagonal liquid crystalline phase. The nanowires can be grown to up to tens of micrometers in length by simply changing the electrodeposition time. It was found that the connectivity of the aqueous channels and alignment of the liquid crystal could be improved with the application of electric field during electrodeposition, leading to the production of nanowires with high aspect ratio. Meanwhile, they have synthesized counductive polyaniline nanowires in emeraldine form by potentiodynamic electropolymerization and single-crystalline silver nanowires from the same reverse hexagonal liquid crystalline phase [86, 121].

4. CHARACTERIZATION OF SNWs BY ELECTROCHEMICAL SYNTHESIS

4.1. Morphology

In the template-assisted electrochemical synthesis approaches, the nanowire materials are assembled with a morphology complementary to that of the template. Owing to their cylindrical pore geometry, monodisperse diameters, higher pore density, and regular hexagonal 1D channel arrangements, electrochemical synthesis in AAO templates would result in corresponding cylindrical and oriented nanowire arrays. Figure 7 presents scanning electron microscope (SEM) images of CdTe nanowire arrays prepared by DCED from an ethylene glycol bath containing $CdCl_2$, $TeCl_4$, and KI [53]. This images show that these nanowires are size monodisperse and are perpendicularly arranged on the substrate, forming a highly ordered array in morphology. It is also can be seen that these nanowires have a smooth surface and the diameters are uniform in the whole wire length. In some cases, after removal of the template membrane, the top of the arrays may be shrunk and aggregated [36, 84].

The diameters of the nanowires by electrochemical synthesis are usually in good agreement with the pore sizes of the template used [47–70]. However, the diameters of the oxide nanowires prepared by electrochemical sol–gel synthesis strategies are smaller than the pore diameter of the template used, due to the shrinking of the nanowires during a heat treatment process [71–74]. In addition, for hybrid electrochemical/chemical synthesis of nanowires, the diameters of the converted nanowires are larger than the pore diameter of the template [82, 83].

4.2. Crystal Structure

Using the template-assisted electrochemical synthesis strategies, a variety of highly ordered SNW arrays have been fabricated. However, the crystal structure of the semiconductor nanowires (e.g., single crystal, polycrystalline, or amorphous) plays a key role in nanodevices and other applications. Electron diffraction, X-ray diffraction, and HRTEM have been employed to determine the crystal structure.

One important feather is that the SNWs prepared by DCED from a nonaqueous bath mostly crystallized as a uniform orientation (i.e., [001]) as well having as highly ordered arrangement in morphology. Figure 8A shows a TEM image of a bundle of 20 nm diameter CdSe nanowires prepared
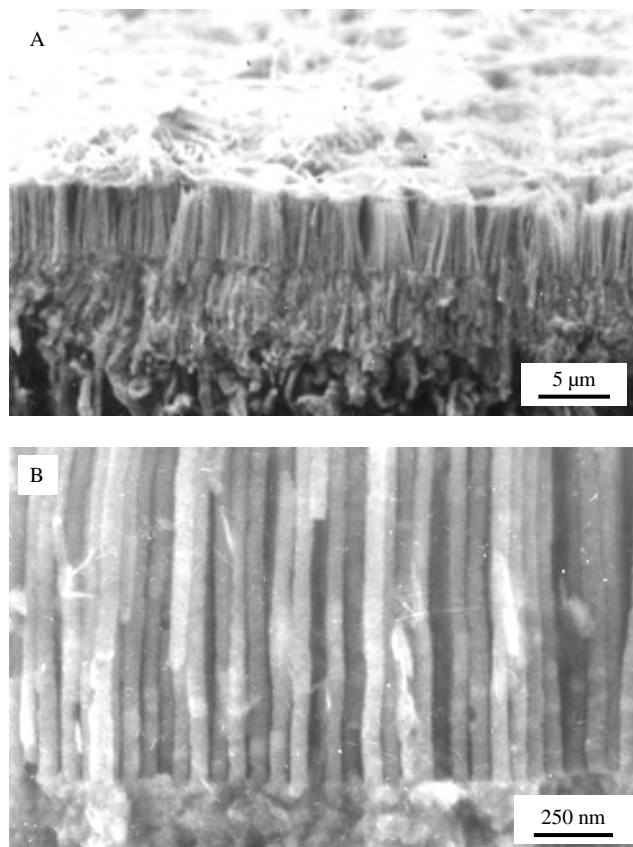
Figure 7. (A) Low magnification and (B) higher magnification SEM images of the CdTe nanowires electrodeposited in the AAO template with a diameter of ∼50 nm. Reprinted with permission from [53], D. S. Xu et al., *J. Mater. Res.* 17, 1711 (2002). © 2002, Materials Research Society.

by dc electrodeposition from a nonaqueous electrolyte bath [52]. These CdSe nanowires have a uniform width and are nearly parallel to each other. The electron diffraction pattern taken from these nanowires is shown in the inset on the upper right of the micrograph, which respectively corresponded to (002), (101), and (103) diffraction planes of the hexagonal CdSe single crystal. The diffraction pattern with somewhat dispersed and elongated spots implies that the nanowires grow with dominant direction and uniform crystal structure.

The X-ray diffractogram of the CdSe nanowire arrays is shown in Figure 8B. These XRD data indicate that the nanowires have diffraction patterns corresponding to the hexagonal phase of CdSe. The interplanar diffraction spacing (d_{hkl}) of CdSe nanowires with diameters of 20 nm differs slightly from those reported for polycrystalline CdSe. The relative intensity of the 002 diffraction peak, which corresponds to interplane distances $d = 3.49–3.51(\text{A}°)$, is greater than that of the polycrystalline CdSe powder. This fact indicates that the c-axis of hexagonal crystals is preferentially aligned along the direction normal to the substrate rather than oriented randomly. Furthermore, the dimensions of the crystallites of the CdSe nanowires were estimated from the widths of the major diffraction peaks observed in Figure 8B
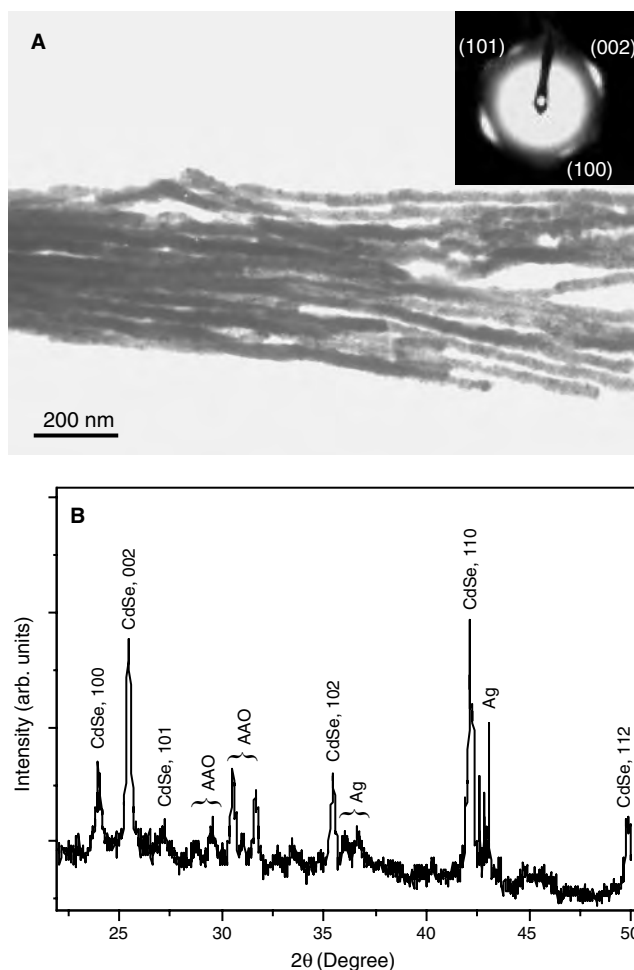
Figure 8. (A) TEM image and (B) X-ray diffractogram of the CdSe nanowires grown in an AAO membrane with 20 nm pore diameters by dc electrodeposition. The inset plot in (A) is the corresponding selected area diffraction pattern of the nanowires, which can be indexed as the hexagonal CdSe crystal structure. Reprinted with permission from [52], D. S. Xu et al., *J. Phys. Chem. B* 104, 5061 (2000). © 2000, American Chemical Society.

through the Scherrer formula

$$D_{hkl} = k\lambda/(\Delta_{hkl} \cdot \cos\theta) \qquad (16)$$

Where D_{hkl} is the linear dimension of the coherent diffracting domain along a direction normal to the diffraction plane (*hkl*), λ is X-ray wavelength in angstroms (1.5405 Å in this case), k is a crystal constant (0.9), θ is the angle of reflection of the peak, and Δ is the corrected full width at half maximum (FWHM) of the peak in radians, which was calculated as the square root of the difference between the squares of the sample's and the reference's FWHM. The dimensions of the CdSe crystallites calculated from the widths of the XRD reflections in Figure 11B are listed in Table 2. These results show that the crystallite domains of the CdSe nanowires are c-axis oriented and the crystallite dimension in the radial direction is very close to the pore sizes of the template used. An aspect ratio of 5:1 calculated from the crystallite dimensions along [002] and

Table 2. Mean crystallite sizes D_{hkl} (nm) along the [100], [002], [101], [102], and [110] zone axes in electrodeposited CdSe nanowires.

Diffraction plane	Peak position	Peak areas	D_{hkl}
(hkl)	(d, Å)	(I, %)	(nm)
(100)	3.705	38	22
(002)	3.496	80	120
(101)	3.285	12	15
(102)	2.532	35	58
(110)	2.142	100	30

Source: Reprinted with permission from [52], D. S. Xu et al., *J. Phys. Chem. B* 104, 5061 (2000). © 2000, American Chemical Society.

[100] axes is obtained. Similar crystalline orientations have also been observed on other semiconductor nanowires prepared by dc electrodeposition from nonaqueous baths [53, 54]. However, in aqueous baths, the deposited nanowires are randomly oriented [59, 61].

The crystallinity of the nanowires by electrodeposition can be largely improved by thermal annealing at high temperature. For example, the unit cell of the as-deposited CdS nanowire was found to be compressed with respect to that of polycrystalline. The interplanar spacing, d_{002}, of as-deposited samples shows a nonmonotonic dependence on diameter. Annealing at 500 °C for 1 h successfully relieved this distortion, leaving a slight residual increase in d_{002} with nanowire diameter, and caused the grain sizes of the CdS deposit to increase, except for nanowires with small diameters [36]. The degree of the crystalline orientation also increased by annealing. Figure 9 presents the XRD patterns of the Ag_2Se nanowires embedded in the AAO template by DCED. For the as-deposited nanowires, the diffraction peaks can be indexed to (120), (112), (121), and (013) of orthorhombic β-Ag_2Se, respectively. The lattice constants deduced from the diffraction data were $a = 4.46$, $b = 6.96$, $c = 7.76$ Å, which are consistent with that of the polycrystalline bulk Ag_2Se standard. After annealing and a slow cool, (002) and (004) diffraction peaks of β-Ag_2Se appeared with strong intensities. Meanwhile, the intensities of other primary diffraction peaks [e.g., (112) and (121)] are almost suppressed in comparison with the XRD pattern before annealing. For electrochemical sol–gel synthesis, the annealing process is very important to obtain condensed and highly crystalline nanowires. However, in some cases, annealing caused serious shrinkage and cracking in the nanorods due to the low density of the gel deposits [71–73].

The deposition of the nanowires controlled by electrochemical reaction usually results in a polycrystalline structure. It has been demonstrated that these problems can be avoided if the deposition is controlled by chemical reaction rather than by the electrode kinetics. For example, single-crystalline CdS nanowires have been prepared by electrochemically induced deposition (Fig. 4C–D) [70]. Another example is single-crystal anatase TiO_2 nanowires by an electrochemically induced sol–gel strategy [75]. The TEM images of the TiO_2 nanowires prepared by electrochemically induced sol–gel process shown in Figure 6A and B indicate that these wires have uniform diffraction contrast, relatively straight morphologies, and smooth surfaces. The sharp diffraction spots of the SAED pattern of
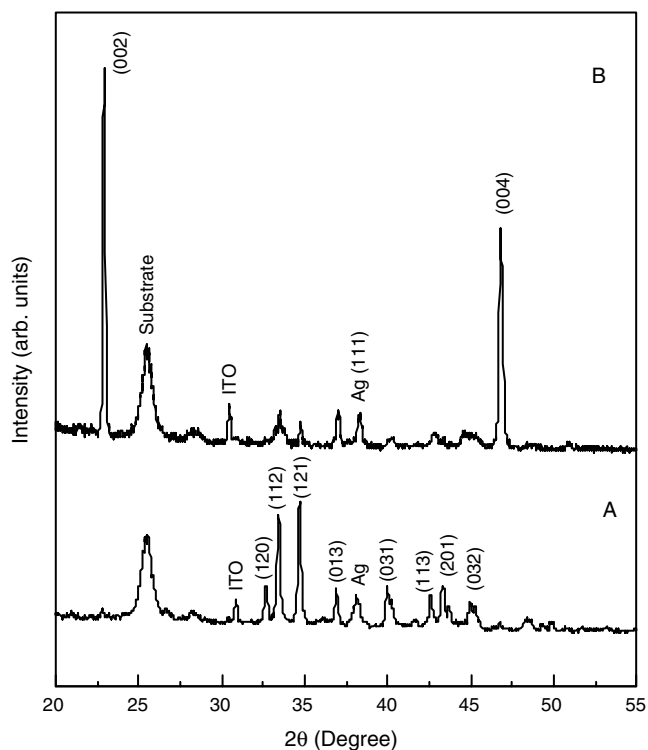

Figure 9. X-ray diffractogram of the Ag_2Se nanowires embedded in the AAO template with pore diameters of about 50 nm prepared by dc electrodeposition: (A) as-deposited, (B) annealed in Ar atmosphere. Reprinted with permission from [61], R. Z. Chen et al., *J. Electrochem. Soc.* 150, G183 (2003). © 2003, American Electrochemical Society.

a 40 nm TiO_2 nanowire in Figure 6C were indexed as 004, 200, and 103 of tetragonal anatase TiO_2. The same electron diffraction patterns were obtained from different areas throughout the entire length of the nanowire. In contrast to the single-crystalline TiO_2 nanowires by electrochemically induced sol–gel deposition, the TiO_2 nanowires by sol–gel electrophoretic deposition are polycrystalline with grains that are ~5 nm in sizes, characterized by HRTEM and electron diffraction patterns [73].

4.3. Bandgap Energy

The bandgap energy is one of the most important parameters characterizing a semiconductor nanowire. Its value determines many of the gross electronic and optical properties that the semiconductor possesses. The most straightforward to determine the bandgap energy is the measurement of the low-energy optical absorption band edge. Aside from varying the nature of the semiconductor nanowire itself, it is also possible to control the bandgap energy of a given semiconductor by restricting the dimensions to values below that of the excitonic Bohr diameter [116]. Peng et al. have measured the optical absorption of the DCED fabricated Bi_2S_3 nanowire arrays embedded in the AAO membranes [57]. They considered that the excitation band is not likely to be present and the absorption is due to a band-to-band transition. The extrapolation of the plot of $(\alpha h\nu)^2$ versus $h\nu$ to the energy axis gives a value of about 1.56 eV as the

bandgap of Bi_2S_3 nanowires, in which the bandgap of bulk Bi_2S_3 is about 1.3 eV. Routkevitch et al. [66] reported that normalized absorption spectra of AAO/CdS_xSe_{1-x} show a function of Se/S ratio in electrolyte. This illustrates that the control over ternary semiconductor (e.g., CdS_xSe_{1-x}) composition could produce nanowire arrays with widely varying values of the optical bandgap. Meanwhile, the XRD pattern would change from that of CdS to that of CdSe, with varying the Se/S ratio in electrolyte from 0 to 1.

Polarized resonance Raman spectroscopy (RRS) has been used to investigate qualitatively the effect of the nanowire diameter on the bandgap energy of the nanowires by electrochemical synthesis [66, 67, 69, 70, 75]. Routkevitch et al. [66, 67] have measured the RRS spectra of the ac deposited CdS nanowires and described them for quantitatively determining the exciton wavelength dependence of these spectra. The measure RRS spectra are dominated by overtones of the longitudinal optical (LO) phonon. They found that the intensities of the overtones in the Raman spectra of semiconductor clusters depend strongly on the particle diameter and are related to the value of the bandgap, and annealing dramatically increases the intensity of the RRS spectra. Also the LO phonon frequencies were found to be decreased with the nanowire diameter (Fig. 10), which is expected to be due to phonon confinement. However, polarization seemed to have little effect on the RR spectra. The exciton energies determined with RRS polarized across the long axis of the wires ranged from 2.376 eV for the large pore diameters to 2.417 eV for the smallest pore diameter and was well behaved as a function of the nanowire diameter.

5. PROPERTIES AND DEVICE APPLICATIONS

5.1. Photoluminescence

A lot of unique and fascinating properties have been proposed and demonstrated for SNW materials, such as oriented transport of carriers, order-of-magnitude polarization anisotropy of photoluminescence (PL), and laser emission [2]. For SNW arrays prepared by electrochemical synthesis in AAO membranes, the characteristics of these nanowires, such as high alignment and high crystallinity, suggest that they could have very important applications in chemical and biosensors, photocatalysis, and solar conversion devices as well as optoelectronic applications.

Luminescent emissions from SNWs by electrochemical synthesis have been observed. For instance, a blue and a blue–green PL band were observed in ZnO [78] and In_2O_3 [80] nanowires, respectively. The PL intensity and peak position depend on the annealing temperature, which is mainly attributed to the singly ionized oxygen vacancy in the nanowires. Due to the high density and highly regular arrangement, these nanowire arrays could also be used as luminescent emitters for the planar displayer. The size of the emitter would be greatly decreased and the amount of the emitters in the unit would be largely increased, which is expected to increase the resolution and improve the stability of the displayer.

On the other hand, these aligned SNW arrays could be used for the nanowire lasers. Recently, room-temperature
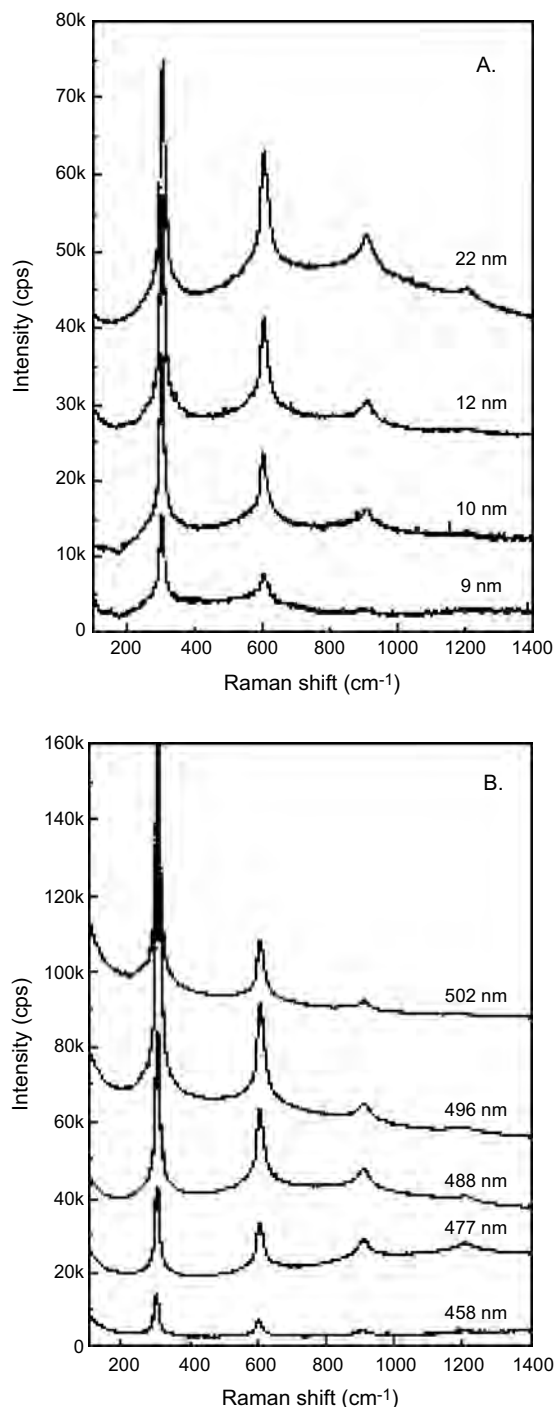

Figure 10. (A) Resonance Raman spectra of AAO/CdS nanowire arrays with different diameters excited with an *s*-polarized 488 nm laser. (B) Resonance Raman spectra of 22 nm diameter nanowire excited with an *s*-polarized laser at different frequencies. The luminescence due to the AAO has been subtracted. Reprinted with permission from [67], D. Routkevitch et al., *Chem. Phys.* 210, 343 (1996). © 1996, Elsevier Science.

ultraviolet lasing in (0001) oriented zinc oxide nanowire arrays grown on sapphire substrates, which are expected to serve as miniaturized light sources for microanalysis, information storage, and optical computing, has been demonstrated by Huang et al. [15] and Johnson et al. [16]. In this

case, these single-crystalline, well-faceted nanowires were considered as natural resonance cavities, in which one end is the epitaxial interface between the sapphire and ZnO, whereas the other end is the sharp (0001) plane of the ZnO nanocrystals. The giant oscillator strength effect, which can occur in high-quality nanowire crystals with dimensions larger than the exciton Bohr radius but smaller than the optical wavelength, enables the excitonic stimulated emission in these nanowire arrays. Also, due to their highly crystalline and well-oriented properties, SNW arrays by template-assisted electrochemical synthesis, such as ZnO, CdS, CdSe, CdTe, etc., are good candidates for excitonic laser action.

5.2. Photovoltaics and Photocatalysis

These nanowire arrays could also be used as a new class of semiconductor electrodes for photovoltaics [28]. One of the important applications of these nanowire electrodes could be the "Grätzel solar cell." A conventional cell is based on nanoporous and nanocrystalline TiO_2 on which a monolayer of a photosensitizer is absorbed. Replacing nanoparticles with nanowires could remove one of the electron transport bottlenecks occurring in the conventional Grätzel cell (i.e., the tunneling process between neighboring oxide nanocrystals). With nanowire electrodes, electrons can be transport directly to the conducting substrate without going through the multiple steps of the tunneling process, which is expected to be able to greatly decrease the probability of recombination across the large heterogeneous interface and improve the overall efficiency of the solar cell. In addition, it has been demonstrated that semiconductor CdSe nanorods can be used to fabricate readily processed and efficient hybrid solar cells together with polymers [117]. As the aspect ratio of the nanorods increases from 1 to 10, the charge transport must improve substantially to yield an external quantum efficiency enhancement by a factor of approximately 3.

Furthermore, these nanowire arrays could be used as a photocatalyst for the light-induced redox process. The photocatalytic reaction involves absorption of an ultraviolet photon by a semiconductor (i.e., TiO_2 and SiO_2) to produce an electron–hole pair and then trapping of the electron or hole by scavengers or surface defects. The valence band holes are powerful oxidants while the conduction band electrons are good reductants. For example, the generated holes have been used to oxidize organic molecules for environmental remediation applications. Also, owing to the increased surface area of the SNW arrays, the decomposition rate of the organic molecules correspondingly increases. Lakshmi et al. [38a] have investigated the decomposition of salicylic acid over time on an array of immobilized TiO_2 fibers with exposure to sunlight. They observed a marked increase in decomposition rate of salicylic acid for the template-synthesized TiO_2 fibers.

5.3. Nanodevices

The motivations for interesting in 1D nanostructures with functional electronic characteristic are the changes in properties that arise from quantum confinement and the potential applications of nanowires in very dense logic, memory,

optoelectronic, and sensing devices. Although a number of successful efforts have been reported, the established lithographic techniques seem to have approached their technological and economic limits, especially when high-density nanoarrays are needed. These challenges have forced many to look for new approaches to nanomanufacturing, especially ones which grow nanostructure directly rather than those depending on material removal. Using a focused ion beam or a scanning probe microscope looks promising for making devices in small batches but becomes unrealistic when a large area or a large throughput is needed.

An alternative approach is the direct nanofabrication by selective deposition in the openings of a self-organized template. For example, the AAO templates allow one to manipulate the nanowires arrays and to incorporate them into a variety of potential designs of nanodevices. Routkevitch et al. [66] illustrated some of the fabrication steps possible based on an ACED method. First, metal or semiconductor electrodeposition produces the array of the nanowires in the pores of the AAO templates. Second, the composition of the nanowires can be modulated at this stage along its length, resulting in the formation of *p–n* junction or heterojunctions. The next step is the partial etching of the AAO template to expose the nanowire tips for further processing, which includes (1) a nanowire array with contacts to one (tip emitters) or both ends, (2) a nanowire array sandwiched between two insulating tunneling junctions, and (3) an array of the metal/semiconductor nanoheterojuctions. Using this strategy, they fabricated a two-terminal device consisting of a 10 nm CdS nanowire array sandwiched between metal contact layers. Periodic conductance oscillations were observed in this sandwiched structure with CdS nanowires.

Peña et al. [118] have fabricated metal–CdSe–metal nanowires by electrochemical replication of the AAO and polycarbonate track-etch membranes, as shown in Figure 11. The semiconductor is sandwiched between Au or Ni segments (Fig. 12). The end-on junction between the semiconductor and the metal makes it possible to align these nanowires between metal contact pads and to make contact exclusively to the metal segments. They found that electronic conductivity of individual CdSe nanowires increases by a factor of 15 when they are illuminated by visible light (Fig. 13). This photoconductivity can be switched on and off reversibly by modulating the light. Yoon and Suh [119] reported that aligned CdS/Co heterostructured nanowires were prepared by ac electrodeposition in the anodic aluminum oxide templates. By varying the preparation conditions, a variety of CdS/Co nanowire arrays were fabricated, whose dimensional properties could be adjusted.

Kovtyukhova et al. [120] described a combined membrane replication/layer-by-layer synthetic approach to preparing nanoscale rod-shaped rectifiers, as shown in Figure 14. Wet layer-by-layer self-assembly of nanoparticle (TiO_2 or ZnO)/polymer multilayer films was performed inside the membrane pores in two ways: (1) growing the film between metal electrodeposition steps to give in-wire junctions; (2) first coating the membrane walls with multilayer films, and then growing nanowires inside the resulting tubules to give concentric structures. TiO_2/PSS, ZnO/PSS (PSS = polystyrenesulfonate) and ZnO/PAN (PAN = polyaniline) assembly was driven by electrostatic
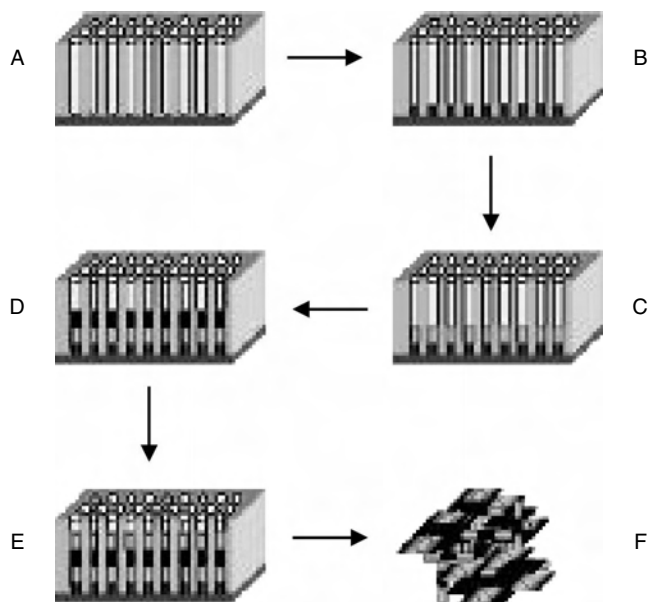
Figure 11. Schematic of template growth and release of Au–CdSe–Au nanowires. An AAO or polycarbonate template is coated on one side with Ag (A). The template is filled with approximately 1 μm of Ag (B). An Au segment is then deposited (C), followed by the CdSe layer (D) and another Au layer (E). Finally, the Ag backing and the membrane are dissolved, leaving freestanding nanowires (F). Reprinted with permission from [118], D. J. Peña et al., *J. Phys. Chem. B* 106, 7458 (2002). © 2002, American Chemical Society.

Figure 13. I–V curves of a Au–CdSe–Au nanowire taken in the light and the dark and with the light switched on and off at 5-s intervals during the voltage sweep. Reprinted with permission from [118], D. J. Pena et al., *J. Phys. Chem. B* 106, 7458 (2002). © 2002, American Chemical Society.

Figure 12. SEM images of 350-nm diameter Au–CdSe–Au nanowires (A) and a 70-nm diameter Ni–CdSe–Ni nanowire (B). Reprinted with permission from [118], D. J. Peña et al., *J. Phys. Chem. B* 106, 7458 (2002). © 2002, American Chemical Society.
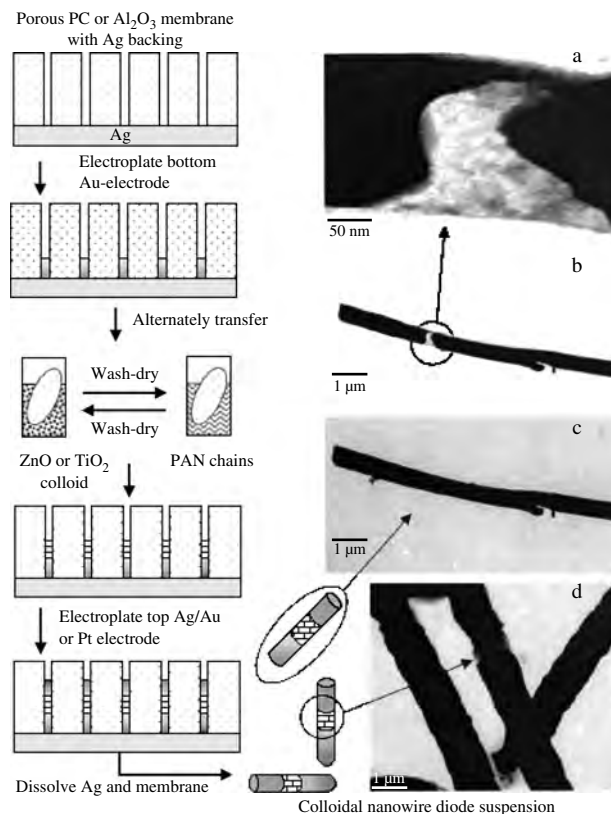
Figure 14. Left: Scheme for the preparation of in wire semiconductor thin-film devices. Right: (a)–(c) High and low resolution TEM images of the 4C Au/(TiO$_2$/PAN)$_{10}$/2C Ag/4C Au device prepared using the alumina membrane treated with ethyltriethoxyl silnae. (a, b) Nanoparticle junction (end of the bottom Au electrode on the right). These TEM images were taken after focusing the electron beam for several seconds. (c) The image taken immediately after focusing the electron beam. (d) TEM image of an Au/Ag/(ZnO/PAN)$_9$TiO$_2$/Au nanowire prepared in a PC membrane. The nanoparticle junction is seen between the two metals. Reprinted with permission from [120a], N. I. Kovtyukhova et al., *Mater. Sci. Eng. C* 19, 255 (2002). © 2002, Elsevier Science.

and covalent–coordination interactions, respectively. The current–voltage (I–V) characteristics of nanowires containing semiconductor nanoparticles show current rectifying behavior. Current rectification appears to arise at the oxide semiconductor–metal interface. Switching behavior and hysteresis, which was found in all devices, was particularly evident in junctions containing anionic PSS and cationic TiO_2 particles and was less evident in ZnO-containing devices.

6. CONCLUSION

In the past few years, electrochemical synthesis in template has been taken as one of the most efficient methods in controlling the growth of 1D semiconductor nanostructural arrays and a broad range of SNWs have been fabricated. Electrochemical synthesis offers a simple and viable alternative to the cost-intensive methods such as laser ablation or thermal evaporation synthesis and can afford precise process control due to its electrical nature. These SNWs are size monodisperse and have a highly ordered arrangement in morphology. The characteristics of these nanowires, such as high alignment and high crystallinity, suggest that they could have very important applications in nanosensors, nanowire lasers, photocatalysis, solar conversion devices, and planar displayers.

GLOSSARY

Electrochemical self-assembly   A self-assembly method which involves both molecular recognition and a spontaneous electrochemical synthesis on the surface of the electrode.

Electrophoretic deposition   A deposition process designed to preparation of coating and laminated materials by which charged particles in a suspension is moved and then deposited on the oppositely charged electrode under the influence of an electric field.

Giant magnetoresistance effect (GMR)   A kind of physical phenomenon that is there is a dramatic increasing of electric resistance of a material under an applied magnetic field.

Gratzel solar cell   A device designed to conversion of solar energy to electric power based on nanoporous and nanocrystalline TiO_2 on which a monolayer of a photosensitizer is absorbed.

Photocatalysis   A catalytic process induced by light irradiation, involving absorption of a photon by semiconductor to produce an electron-hole pair and then trapping of the electron or hole by scavengers or surface defects.

Single-electron transistor   A transistor that single-electron charging and resonant tunneling through quantized energy levels regulate transport through small structures such as quantum dots, nanoparticles, nanowires, nanotubes, and single molecules.

Sol–gel procedure   A wet chemical technique to nanostuctured materials via hydrolysis of a solution of a precursor molecular to obtain first a suspension of colloidal particles (the sol) and then gel composed of aggregated sol particles.

Tomanaga-Luttinger liquid   A liquid to be distinctly different from Fermi-liquid. Tunneling into a Luttinger liquid at energies near the Fermi level is predicted to be strongly suppressed.

Vapor-liquid-solid process   A anisotropic growth promoted by the presence of a liquid alloy-solid interface, in which a gaseous target source diffuses into a drop of the molten alloy to nucleate and grow from the droplet.

ACKNOWLEDGMENTS

REFERENCES

1. "Handbook of Nanostructured Materials, and Nanotechnology" (H. S. Nalwa, Ed.), Vols. 1–5, Academic Press, San Diego, 2000.
2. "Nanowires and Nanobelts: Materials, Properties and Devices" (Z. L. Wang, Ed.). Kluwer, Dordrecht, 2003.
3. S. J. Tans, M. H. Devoret, H. J. Dai, A. Thess, R. E. Smalley, L. J. Geerligs, and C. Dekker, *Nature* 386, 474 (1997).
4. M. Bockrath, D. H. Cobden, P. L. McEuen, N. G. Chopra, A. Zettl, A. Thess, and R. E. Smalley, *Science* 275, 1922 (1997).
5. S. J. Tans, R. M. Verschueren, and C. Dekker, *Nature* 393, 49 (1998).
6. R. Martel, T. Schmidt, H. R. Shea, T. Hertel, and Ph. Avouris, *Appl. Phys. Lett.* 73, 2447 (1998).
7. M. Bockrath, D. H. Cobden, J. Lu, A. G. Rinzler, R. E. Smalley, T. Balents, and P. L. McEuen, *Nature* 397, 598 (1999).
8. Z. Yao, H. W. C. Postma, L. Balents, and C. Dekker, *Nature* 402, 273 (1999).
9. L. T. Canham, *Appl. Phys. Lett.* 57, 1046 (1990).
10. J. D. Holmes, K. P. Johnston, R. C. Doty, and B. A. Korgel, *Science* 287, 1471 (2000).
11. J. Wang, M. S. Gudiksen, X. Duan, Y. Cui, and C. M. Lieber, *Science* 293, 1455 (2001).
12. H. Kind, H. Q. Yan, B. Messer, M. Law, and P. D. Yang, *Adv. Mater.* 14, 158 (2002).
13. Y. Arakawa and H. Sakaki, *Appl. Phys. Lett.* 40, 16631 (1996).
14. Y. Miyamoto, Y. Miyake, M. Asada, and Y. Suematsu, *IEEE J. Quantum Electron.* 25, 851 (1989).
15. M. H. Huang, S. Mao, H. Feick, H. Q. Yan, Y. Y. Wu, H. Kind, E. Weber, R. Russo, and P. D. Yang, *Science* 292, 1897 (2001).
16. J. C. Johnson, H. Q. Yan, R. D. Schaller, L. H. Haber, R. J. Saykally, and P. D. Yang, *J. Phys. Chem. B* 105, 11387 (2001).
17. Y. Cui and C. M. Lieber, *Science* 291, 851 (2001); Y. Huang, X. F. Duan, Q. Q. Wei, and C. M. Lieber, *Science* 291, 630 (2001); Y. Huang, X. F. Duan, Y. Cui, L. J. Lauhon, K. H. Kim, and C. M. Lieber, *Science* 294, 1313 (2001); X. F. Duan, Y. Huang, Y. Cui, J. F. Wang, and C. M. Lieber, *Nature* 409, 66 (2001); T. Rueckes, K. Kim, E. Joselevich, G. Y. Tseng, C. L. Cheung, and C. M. Lieber, *Science* 289, 94 (2000).
18. M. S. Fuhrer, J. Nygard, L. Shih, M. Forero, Y. Yoon, M. S. C. Mazzoni, H. J. Choi, J. Ihm, S. Louie, A. Zettle, and P. L. McEuen, *Science* 288, 494 (2000).
19. S. Noda, K. Tomoda, N. Yamamoto, and A. Chutinan, *Science* 289, 604 (2000).
20. R. S. Wagner and W. C. Eillis, *Appl. Phys. Lett.* 4, 889 (1964).
21. A. M. Morales and C. M. Lieber, *Science* 279, 208 (1998).
22. Y. Y. Wu and P. D. Yang, *J. Am. Chem. Soc.* 123, 3165 (2001).
23. X. Y. Zhang, L. D. Zhang, G. W. Meng, G. H. Li, N. Y. Jin-Phillipp, and F. Phillipp, *Adv. Mater.* 13, 1238 (2001).
24. X. F. Duan and C. M. Lieber, *Adv. Mater.* 12, 298 (2000); X. F. Duan and C. M. Lieber, *J. Am. Chem. Soc.* 122, 188 (2000).

25. Z. W. Pan, Z. R. Dai, C. Ma, and Z. L. Wang, *J. Am. Chem. Soc.* 124, 1817 (2002).
26. Y. W. Wang, G. W. Meng, L. D. Zhang, C. H. Liang, and J. Zhang, *Chem. Mater.* 14, 1773 (2002); C. H. Ye, G. W. Meng, Y. H. Wang, Z. Jiang, and L. D. Zhang, *J. Phys. Chem. B* 106, 10338 (2002); C. H. Ye, G. W. Meng, L. D. Zhang, and Y. H. Wang, *Chem. Phys. Lett.* 363, 34 (2002).
27. Y. W. Wang, G. W. Meng, L. D. Zhang, C. H. Liang, and J. Zhang, *Chem. Mater.* 14, 1773 (2002); C. H. Liang, G. W. Meng, G. Z. Wang, Y. W. Wang, L. D. Zhang, and S. Y. Zhang, *Appl. Phys. Lett.* 78, 3202 (2001); X. S. Peng, G. W. Meng, X. F. Wang, Y. W. Wang, J. Zhang, X. Liu, and L. D Zhang, *Chem. Mater.* 14, 4490 (2002); C. H. Liang, G. W. Meng, Y. Lei, F. Phillipp, and L. D. Zhang, *Adv. Mater.* 13, 1330 (2001).
28. Y. Y. Wu, H. Q. Yan, and P. D. Yang, *Top. Catal.* 19, 197 (2002).
29. D. P. Yu, C. S. Lee, I. Bello, X. S. Sun, Y. H. Tang, G. W. Zhou, Z. G. Bai, Z. Zhang, and S. Q. Feng, *Solid State Commun.* 105, 403 (1998); S. T. Lee, N. Wang, Y. F. Zhang, and Y. H. Tang, *Mater. Res. Soc. Bull.* 24, 36 (1999); Z. G. Bai, D. P. Yu, H. Z. Zhang, Y. Ding, Y. P. Wang, X. Z. Gai, Q. L. Hang, G. C. Xiong, and S. Q. Feng, *Chem. Phys. Lett.* 303, 311 (1999); D. P. Yu, Q. L. Hang, Y. Ding, H. Z. Zhang, Z. G. Bai, J. J. Wang, Y. H. Zou, W. Qian, G. C. Xiong, and S. Q. Feng, *Appl. Phys. Lett.* 73, 3076 (1998).
30. Z. W. Pan, Z. R. Dai, and Z. L. Wang, *Science* 291, 1947 (2001).
31. Z. L. Wang, Z. R. Dai, R. P. Gao, Z. G. Bai, and J. L. Gole, *Appl. Phys. Lett.* 77, 3349 (2000); Z. L. Wang, R. P. Gao, J. L. Gole, and J. D. Stout, *Adv. Mater.* 12, 15 (2000).
32. C. R. Martin, *Science* 266, 1961 (1994).
33. C. R. Martin, *Acc. Chem. Res.* 28, 61 (1995).
34. J. C. Hulteen and C. R. Martin, *J. Mater. Chem.* 7, 1075 (1997).
35. C. R. Martin, *Chem. Mater.* 8, 1739 (1996).
36. D. Routkevitch, T. Bigioni, M. Moskovits, and J. M. Xu, *J. Phys. Chem.* 100, 14037 (1996).
37. T. M. Whitney, J. S. Jiang, P. C. Searson, and C. L. Chien, *Science* 261, 1316 (1993).
38. (a) B. B. Lakshmi, P. K. Dorhout, and C. R. Martin, *Chem. Mater.* 9, 857 (1997). (b) B. B. Lakshmi, C. J. Patrissi, and C. R. Martin, *Chem. Mater.* 9, 2544 (1997).
39. Y. Li, D. S. Xu, Q. M. Zhang, F. Z. Huang, D. P. Chen, Y. J. Xu, G. L. Guo, and Z. N. Gu, *Chem. Mater.* 11, 3433 (1999).
40. J. Zhang, L. D. Zhang, X. F. Wang, C. H. Liang, X. S. Peng, and Y. W. Wang, *J. Chem. Phys.* 115, 5714 (2001); G. S. Cheng, S. H. Chen, X. G. Zhu, Y. Q. Mao, and L. D. Zhang, *Mater. Sci. Eng. A* 286, 165 (2000); G. S. Cheng, L. D. Zhang, S. H. Chen, Y. Li, L. Li, X. G. Zhu, Y. Zhu, G. T. Fei, and Y. Q. Mao, *J. Mater. Res.* 15, 347 (2000); G. S. Cheng, L. D. Zhang, Y. Zhu, G. T. Fei, L. Li, C. M. Mo, and Y. Q. Mao, *Appl. Phys. Lett.* 75, 2455 (1999).
41. M. J. Tierney and C. R. Martin, *J. Phys. Chem.* 93, 2878 (1989); C. J. Brumlik and C. R. Martin, *J. Am. Chem. Soc.* 113, 3174 (1991); C. J. Brumlik, C. R. Martin, and K. Tokuda, *Anal. Chem.* 64, 1201 (1992); C. A. Foss, Jr., G. L. Hornyak, J. A. Stockert, and C. R. Martin, *J. Phys. Chem.* 96, 7497 (1992); C. A. Foss, Jr., G. L. Hornyak, J. A. Stockert, and C. R. Martin, *Adv. Mater.* 5, 135 (1993); C. A. Foss, Jr., G. L. Hornyak, J. A. Stockert, and C. R. Martin, *J. Phys. Chem.* 98, 2963 (1994).
42. A. J. Yin, J. Li, W. Jian, A. J. Bennett, and J. M. Xu, *Appl. Phys. Lett.* 79, 1039 (2001).
43. P. C. Searson, R. C. Cammarata, and C. L. Chien, *J. Electron. Mater.* 24, 955 (1995).
44. G. Sauer, G. Brehm, S. Schneider, K. Nielsch, R. B. Wehrspohn, J. Choi, H. Hofmeister, and U. Gosele, *J. Appl. Phys.* 91, 3243 (2002).
45. Y. W. Wang, L. D. Zhang, G. W. Meng, X. S. Peng, Y. X. Jin, and J. Zhang, *J. Phys. Chem. B* 106, 2502 (2002).
46. L. Liang, J. Liu, C. F. Windisch, G. J. Exarhos, and Y. H. Lin, *Angew. Chem. Int. Ed.* 41, 3665 (2002).
47. S. A. Sapp, B. B. Lakshmi, and C. R. Martin, *Adv. Mater.* 11, 402 (1999).
48. J. D. Klein, R. D. Herrick, D. Palmer, M. J. Sailor, C. J. Brumlick, and C. R. Martin, *Chem. Mater.* 5, 902 (1993).
49. Y. J. Xu, D. S. Xu, D. P. Chen, G. L. Guo, and C. J. Li, *Acta Phys.-Chem. Sinica* 15, 577 (1999).
50. D. S. Xu, D. P. Chen, Y. J. Xu, X. S. Si, G. L. Guo, L. L. Gui, and Y. Q. Tang, *Pure Appl. Chem.* 72, 127 (2000).
51. D. S. Xu, Y. J. Xu, D. P. Chen, G. L. Guo, L. L. Gui, and Y. Q. Tang, *Chem. Phys. Lett.* 325, 340 (2000).
52. D. S. Xu, X. S. Si, G. L. Guo, L. L. Gui, and Y. Q. Tang, *J. Phys. Chem. B* 104, 5061 (2000).
53. D. S. Xu, Y. G. Guo, D. P. Yu, G. L. Guo, and Y. Q. Tang, *J. Mater. Res.* 17, 1711 (2002).
54. (a) R. Z. Chen, D. S. Xu, G. L. Guo, and Y. Q. Tang, *J. Mater. Chem.* 12, 2435 (2002). (b) R. Z. Chen, D. S. Xu, G. L. Guo, and Y. Q. Tang, *Chem. Phys. Lett.* 377, 205 (2003).
55. R. Z. Chen, D. S. Xu, G. L. Guo, and L. L. Gui, *Electrochem. Commun.* 5, 579 (2003).
56. X. S. Peng, G. W. Meng, J. Zhang, X. F. Wang, L. X. Zhao, Y. W. Wang, and L. D. Zhang, *Mater. Res. Bull.* 37, 1369 (2001).
57. X. S. Peng, G. W. Meng, J. Zhang, L. X. Zhao, X. F. Wang, Y. W. Wang, and L. D. Zhang, *J. Phys. D* 34, 3224 (2001).
58. X. S. Peng, G. W. Meng, J. Zhang, X. F. Wang, X. Liu, and L. D. Zhang, *J. Mater. Res.* 17, 1283 (2001).
59. X. S. Peng, J. Zhang, X. F. Wang, Y. W. Wang, L. X. Zhao, G. W. Meng, and L. D. Zhang, *Chem. Phys. Lett.* 343, 470 (2001).
60. C. M. Shen, X. G. Zhang, and H. L. Li, *Mater. Sci. Eng. A* 303, 19 (2001).
61. R. Z. Chen, D. S. Xu, G. L. Guo, and L. L. Gui, *J. Electrochem. Soc.* 150, G183 (2003).
62. Y. J. Glanville, D. G. Narehood, P. E. Sokol, A. Amma, and T. Mallouk, *J. Mater. Chem.* 12, 2433 (2002).
63. (a) A. L. Prieto, M. S. Sander, M. S. Martin-Gonzalez, R. Gronsky, T. Sands, and A. M. Stacy, *J. Am. Chem. Soc.* 123, 7160 (2001). (b) M. S. Sander, A. L. Prieto, R. Gronsky, T. Sands, and A. M. Stacy, *Adv. Mater.* 14, 665 (2002). (c) M. S. Sander, A. L. Prieto, R. Gronsky, T. Sands, and A. M. Stacy, *Chem. Mater.* 15, 335 (2003).
64. M. J. Zheng, L. D. Zhang, G. H. Li, and W. Z. Shen, *Chem. Phys. Lett.* 363, 123 (2002).
65. S. Kenane and L. Piraux, *J. Mater. Res.* 17, 401 (2002).
66. D. Routkevitch, A. A. Tager, J. Haruyama, D. Almawlawi, M. Moskovits, and J. M. Xu, *IEEE Trans. Electron Devices* 43, 1646 (1996).
67. D. Routkevitch, T. L. Haslett, L. Ryan, T. Bigioni, C. Douketis, and M. Moskovits, *Chem. Phys.* 210, 343 (1996).
68. J. L. Hutchison, D. Routkevitch, M. Moskovits, and R. R. Nayak, *Inst. Phys. Conf. Ser.* 157, 389 (1997).
69. J. S. Suh and J. S. Lee, *Chem. Phys. Lett.* 281, 384 (1997).
70. D. S. Xu, Y. J. Xu, D. P. Chen, G. L. Guo, L. L. Gui, and Y. Q. Tang, *Adv. Mater.* 12, 520 (2000).
71. S. J. Limmer, S. Seraji, M. J. Forbess, Y. Wu, T. P. Chou, C. Nguyen, and G. Z. Cao, *Adv. Mater.* 13, 1269 (2001).
72. S. J. Limmer, S. Seraji, Y. Wu, M. J. Forbess, T. P. Chou, C. Nguyen, and G. Z. Cao, *Adv. Funct. Mater.* 12, 59 (2002).
73. S. J. Limmer, T. L. Hubler, and G. Z. Cao, *J. Sol–Gel Sci. Tech.* 26, 577 (2003).
74. Y. C. Wang, I. C. Leu, and M. H. Hon, *J. Mater. Chem.* 12, 2439 (2002); Y. C. Wang, I. C. Leu, and M. H. Hon, *J. Crystal Growth* 237, 564 (2002); Y. C. Wang, I. C. Leu, and M. H. Hon, *Electrochem. Solid-State Lett.* 5, C53 (2002).
75. Z. Miao, D. S. Xu, J. H. Ouyang, G. L. Guo, X. S. Zhao, and Y. Q. Tang, *Nano Lett.* 2, 717 (2002).
76. D. S. Xu, Y. X. Yu, Z. Miao, G. L. Guo, and Y. Q. Tang, *Electrochem. Commun.* 5, 673 (2003).

77. X. Y. Zhang, B. D. Yao, L. X. Zhao, C. H. Liang, L. D. Zhang, and Y. Q. Mao, *J. Eelectrochem. Soc.* 148, G398 (2001); X. Y. Zhang, L. D. Zhang, W. Chen, G. W. Meng, M. J. Zheng, and L. X. Zhao, *Chem. Mater.* 13, 2511 (2001).

78. Y. Li, G. W. Meng, L. D. Zhang, and F. Phillipp, *Appl. Phys. Lett.* 76, 2011 (2000); Y. Li, G. S. Cheng, and L. D. Zhang, *J. Mater. Res.* 15, 2305 (2000).

79. M. J. Zheng, G. H. Li, X. Y. Zhang, S. Y. Huang, Y. Lei, and L. D. Zhang, *Chem. Mater.* 13, 3859 (2001).

80. M. J. Zheng, L. D. Zhang, X. Y. Zhang, J. Zhang, and G. H. Li, *Chem. Phys. Lett.* 334, 298 (2001).

81. D. S. Xu, Y. X. Yu, G. L. Guo, and Y. Q. Tang, unpublished data.

82. R. Z. Chen, D. S. Xu, G. L. Guo, and Y. Q. Tang, in preparation.

83. R. Z. Chen, D. S. Xu, G. L. Guo, and Y. Q. Tang, unpublished data.

84. J. C. Fan, T. Gao, G. W. Meng, Y. W. Wang, X. N. Liu, and L. D. Zhang, *Mater. Lett.* 57, 656 (2002).

85. L. M. Huang, H. T. Wang, Z. B. Wang, A. P. Mitra, D. Zhao, and Y. H. Yan, *Chem. Mater.* 14, 876 (2002).

86. L. M. Huang, Z. B. Wang, H. T. Wang, X. L. Chen, A. P. Mitra, and Y. H. Yan, *J. Mater. Chem.* 12, 388 (2002).

87. F. Keller, M. S. Hunter, and D. L. Robinson, *J. Electrochem. Soc.* 100, 411 (1953).

88. Diggle, T. C. Downie, and C. W. Goulding, *Chem. Rev.* 69, 365 (1969).

89. H. Masuda and K. Fukuda, *Science* 268, 1466 (1995).

90. H. Masuda, F. Hasegawa, and S. Ono, *J. Electrochem. Soc.* 144, L127 (1997).

91. O. Jessensky, F. Muller, and U. Gosele, *Appl. Phys. Lett.* 72, 1173 (1998).

92. A. P. Li, F. Muller, A. Birner, K. Nielsch, and U. Gosele, *J. Appl. Phys.* 84, 6023 (1998).

93. J. S. Suh and J. S. Lee, *Appl. Phys. Lett.* 75, 2047 (1999).

94. C. Mu, D. S. Xu, and K. Wu, unpublished data.

95. R. L. Fleisher, P. B. Price, and R. M. Walker, "Nuclear Tracks in Solids." Univ. of California Press, Berkeley, CA, 1975.

96. V. Damodara Das and D. Karunakaran, *J. Appl. Phys.* 68, 2105 (1990).

97. R. Xu, A. Husmann, T. F. Rosenbaum, and M. L. Saboungi, *Nature* 390, 57 (1997).

98. T. Yoshida, M. Tochimoto, D. Schlettwein, D. Wohrle, T. Sugiura, and H. Minoura, *Chem. Mater.* 11, 2657 (1999); T. Yoshida, K. Terada, D. Schlettwein, T. Oekermann, T. Sugiura, and H. Minoura, *Adv. Mater.* 12, 1214 (2000).

99. M. Izaki and T. Omi, *Appl. Phys. Lett.* 68, 2439 (1996).

100. Th. Pauporte and D. Lincot, *Appl. Phys. Lett.* 75, 3817 (1999).

101. J. A. Switzer, M. G. Shumsky, and E. W. Bohannan, *Science* 284, 293 (1999).

102. C. J. Brinker and G. W. Scherer, "Sol–Gel Science." Academic Press, New York, 1990.

103. L. L. Hench and J. K. West, *Chem. Rev.* 90, 33 (1990).

104. Y. K. Zhou and H. L. Li, *J. Mater. Chem.* 12, 681 (2002).

105. B. A. Hernandez, K. S. Chang, E. R. Fisher, and P. K. Dorhout, *Chem. Mater.* 14, 480 (2002).

106. Y. K. Zhou, C. M. Shen, and L. H. Li, *Solid State Ion.* 146, 81 (2002).

107. M. Zhang, Y. Bando, and K. Wada, *J. Mater. Res.* 16, 1408 (2001).

108. C. Hippe, M. Wark, E. Lork, and G. Schulz-Ekloff, *Microporous Mesoporous Mater.* 31, 235 (1999).

109. H. Q. Cao, Z. Xu, X. W. Wei, X. Ma, and Z. L. Xue, *Chem. Commun.* 541 (2001).

110. B. Gates, Y. Y. Wu, Y. D. Yin, P. D. Yang, and Y. N. Xia, *J. Am. Chem. Soc.* 123, 11500 (2001).

111. J. M. Lehn, *Angew. Chem. Int. Ed.* 29, 1304 (1990).

112. L. F. Lindoy and I. M. Atkinson, "Self-Assembly in Supramolecular Systems." Royal Society of Chemistry, Cambridge, UK, 2000.

113. J. de Mendoza, *Chem. Eur. J.* 4, 1373 (1998).

114. G. M. Whitesides, J. P. Mathias, and C. T. Seto, *Science* 254, 1312 (1991).

115. J. J. Zhu, X. H. Liao, X. N. Zhao, and H. Y. Chen, *Mater. Lett.* 49, 91 (2001).

116. L. E. Brus, *J. Chem. Phys.* 80, 4403 (1994).

117. W. U. Huynh, J. J. Dittmer, and A. P. Alivisatos, *Science* 295, 2425 (2002).

118. D. J. Peña, J. K. Mbindyo, A. J. Carado, T. E. Mallouk, C. D. Keating, B. Razavi, and T. S. Mayer, *J. Phys. Chem. B* 106, 7458 (2002).

119. C. H. Yoon and J. S. Suh, *Bull. Kor. Chem. Soc.* 23, 1519 (2002).

120. (a) N. I. Kovtyukhova, B. R. Martin, J. K. N. Mbindyo, T. E. Mallouk, M. Cabassi, and T. S. Mayer, *Mater. Sci. Eng. C* 19, 255 (2002). (b) N. I. Kovtyukhova and T. E. Mallouk, *Chem. Eur. J.* 8, 4355 (2002).

121. L. M. Huang, H. T. Wang, Z. B. Wang, A. Mitra, K. N. Bozhilov, and Y. S. Yan, *Adv. Mater.* 14, 61 (2002).

Electrochemistry of Silicate-Based Nanomaterials

Alain Walcarius

Université Henri Poincaré Nancy I, Villers-les-Nancy, France

CONTENTS

1. INTRODUCTION

1.1. Chemically Modified Electrodes

Chemically modified electrodes (CMEs) are integrated chemical systems that combine in a single device an intelligently designed chemical component in close connection to an electrode surface, enabling one to couple the intrinsic properties of the modifier to a particular redox process. At the beginning, CMEs were mainly developed by the Murray group [1–4]. They have been extensively studied for the past 25 years, as reported in plenty of well-documented reviews [5–106].

CMEs are basically classified into three main categories. (1) Monolayer modified electrodes [5–10] can be prepared as Langmuir–Blodgett films, self-assembled monolayers, adsorbed molecules, or covalently attached moieties on solid electrode surfaces such as alkanethiols on gold. (2) Homogeneous multimolecularly layered electrodes [10–20] are produced by coating the surface of solid electrodes with polymer layers such as redox polymers [15, 18, 19], ion exchange polymers [13, 14], or conducting polymers [12, 17]. (3) Composite electrodes based on multicomponent heterogeneous matrixes that are constituted by either (bio)organic [21–27] or inorganic [27–29] modifiers; electrodes modified with clays [34–39], zeolites [38–48], silica, or silica-based materials [49–61] form subclasses of this category.

Among the wide range of applications involving CMEs, those related to electroanalysis and electrochemical biosensors have been especially developed [14, 16, 17, 21, 23, 27, 29, 37, 44, 47, 52–55, 58–95]. They involve, for example, selective recognition or discrimination, amperometric detection after preconcentration, selective determination by electrocatalysis, indirect amperometric detection, potentiometric sensors, ... Other kinds of applications are in the fields of electrocatalysis [48, 96–100], photoelectrochemistry and optoelectronics [101–104], power sources [105], and large-scale electrolysis [106].

This chapter focuses on the silicate-based materials such as clays, zeolites, silica, and organically modified silicas, as they are used in modified electrode studies or directed toward electrochemical applications. Numerous overviews are provided for readers that are interested in other kinds of CMEs [5–33, 62–106].

1.2. Interest of Silicate-Based Materials in Electrochemical Science

1.2.1. Clays

Clays [107–110] are colloidal, layered hydrated aluminosilicates, which are composed of stacked sheets of "SiO_4" tetrahedra and "AlO_6" octahedra. Most of them occur naturally and belong to the class of phyllosilicates (e.g., montmorillonites, kaolinites, nontronites, and hectorites). One can distinguish 1:1 and 2:1 layered minerals on the basis of stacking: 1:1 clays are made of one silicate layer on one aluminate layer while 2:1 clays are formed by one octahedral sheet sandwiched between two tetrahedral sheets. Because of isomorphous substitutions for Si and/or Al within the layers, these minerals display a net charge (usually negative) that is counterbalanced via electrostatic interaction by exchangeable ions (usually cations). The total amount of exchangeable cations represents an important parameter characterizing the clay properties and is expressed as the cation exchange capacity (i.e., typically in the range 70–100 meq per 100 g for most clays used as electrode

modifiers). Clays containing many substitution sites are subjected to significant swelling depending on the hydration state. Such expanding layer minerals are known as smectite clays, for which the interlayer spacing between the tetrahedral and octahedral sheets undergoes a progressive increase upon exposition to high humidity due to ingress of water molecules within the interlayer region. Clays usually appear in the form of micrometric-sized particles arising from spatial arrangement of plates made of several layers stacked parallel to one another. Clays can be pillared by introducing robust bulky cations between the layer, leading to materials with molecular sieving properties due to the existence of pores and channels of fixed dimension. In addition, the clay-related solids exhibiting anion exchange properties (hydrotalcite type) extend the scope of application of layered materials [111, 112]. These are called layered double hydroxides (LDH) and are made of positively charged brucite-like layers containing compensating anions in the interlayer region.

The attractiveness of clay modified electrodes is apparent in two main fields [36]. First, the electrochemical behavior of electroactive species located within the clay structure would help in illuminating the transport issues of various substances in these layered materials. This might lead to a better understanding of pollutant migration in the environment, allow optimization of soil remediation processes, or induce advanced applications in selective recognition or solid/liquid separations. Second, the intrinsic properties of clays can be advantageously exploited in combination with redox processes when associating in a single device such minerals with an electrode material. For example, the binding ability of clays to a wide range of inorganic ions or organic species can be used to accumulate them prior to electrochemical quantification of these elements at trace levels. These porous solids are also good candidates to support biomolecules or electrocatalysts that are often employed to modify electrode surfaces. Most commonly used clays at electrochemical interfaces involve montmorillonites, nontronites, hectorites, and vermiculites (smectites), as well as kaolinites and LDHs.

1.2.2. Zeolites

Zeolites [113–115] are crystalline, hydrated aluminosilicates, most of which belong to the class of tectosilicates. Zeolite minerals occur naturally, but most of those actually used for practical applications are synthetic. They are characterized by a regular three-dimensional structure made of cages and channels of molecular size (typically between 3 and 8 Å), which arise from an extending network of "SiO_4" and "AlO_4" tetrahedra linked to each other by sharing all of the oxygen. This induces size selectivity properties to zeolites, as the entrance to the microporous structure is only afforded to species small enough to fit inside the pores and channels. Tetrahedral sites centered with Al^{3+} ions are negatively charged, these negative charges in the framework being neutralized by the presence of cations in the channels and interconnected voids. These cations are mobile and most often hydrated. The general chemical composition of zeolites can be expressed by the formula (i.e., crystallographic unit cell)

$$M_a D_b T_c [Al_{(a+2b+3c)} Si_{[x-(a+2b+3c)]} O_{2x}] \cdot m H_2 O \qquad (1)$$
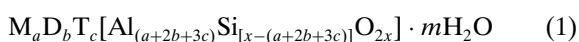
where M, D, and T represent monovalent, divalent and trivalent cations, respectively.

Charge-compensating cations include the alkaline (Na^+, K^+, Rb^+, Cs^+) and alkaline earth (Mg^{2+}, Ca^{2+}) cations, NH_4^+, H^+, tertaalkylammonium, and other nitrogen-containing organic cations, and the rare-earth and noble metal ions. These can be exchanged, to various degrees, by other cations, leading to another important property of zeolites: the ion exchange capacity [115]. The latter is directly related to the Si/Al ratio, defining the amount of negative charge in the framework. The minimal Si/Al ratio is unity, which occurs in zeolite A, and corresponds to the maximum substitution of Si^{4+} for Al^{3+}; increasing this ratio leads to a decrease in the ion exchange capacity. Zeolites can be dehydrated (and rehydrated) without significant change in their three-dimensional structure, unlikely to the swelling of layered clays.

Zeolites are attractive electrode modifiers because they constitute a quite unique family of materials displaying both ion exchange capacity and size selectivity in a single component, unlikely to other polymer-based ion exchangers. This would allow one, for example, to discriminate between positively charged electroactive species on the basis of their size, to encapsulate organometallic complexes in zeolite cages by physical entrapment (e.g., by ship-in-a-bottle synthesis [116]) and use them as supported electrocatalysts, or to promote charge transfer in microporous media by self-organized electron transfer chains. This last point is supported by the huge amount of work devoted to redox, photoredox, and electron transfer processes in zeolites and related microporous media [117, 118]. In addition, the extra-large pore zeolites [119] and the discovery of ordered mesoporous silicas [120] have extended the scope of applications of zeolites toward molecular sieving and selective recognition at higher dimensions. Zeotypes derived from isomorphous substitution of Si^{4+} and/or Al^{3+} centers (e.g., titanosilicates, metallosilicates and -aluminates, aluminophosphates, silicoaluminophosphates, . . . [121, 122]) might also be of special interest, especially if the substituting element can undergo a charge transfer. The most commonly used zeolites in connection to electrochemistry are those characterized by a rather high ion exchange capacity, such as zeolites A, X, Y, L, and mordenite, among others.
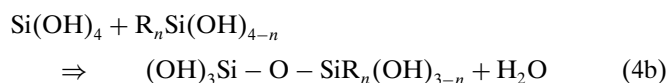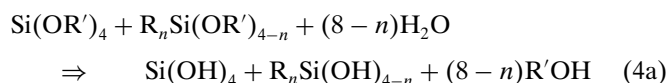
1.2.3. Porous Silicas and Organically Modified Silicas

Notwithstanding the very simple chemical formula of silicon dioxide, silica does exist under a very broad variety of forms [123], as either crystalline (often natural) or amorphous (mainly synthetic) materials. Most porous silicas belong to this latter class, displaying an open three-dimensional structure made of "SiO_4" tetrahedra linked to each other, defining void spaces interconnected to each other, resulting in high specific surface areas (i.e., 200–1500 m^2 g^{-1}). Both external and internal surfaces contain active functions (siloxane moieties and weakly acid silanol groups) that govern most properties of the material. Synthesis, characterization, and surface reactivity of porous silicas have been largely reviewed in the literature [123–136]. Modification of the silica surface can be achieved in various

ways, including immobilization of reagents by surface complexation or adsorption, coverage with metal oxide layers, impregnation with organic molecules or macromolecules, or covalent bonding of organic groups via grafting with organofunctional alkoxysilanes or chlorosilanes. Of special interest is the sol–gel process [126, 137–140] which provides a versatile way to prepare a wide range of ceramic-based materials through the hydrolysis and subsequent condensation of metal alkoxides [see Eqs. (2) and (3) for examples of the early stage of silica formation]. Reactions are usually

$$Si(OR)_4 + 4H_2O \quad \Rightarrow \quad Si(OH)_4 + 4ROH \qquad (2)$$

$$Si(OH)_4 + Si(OH)_4 \quad \Rightarrow \quad (OH)_3Si - O$$
$$- Si(OH)_3 + H_2O \qquad (3a)$$

$$Si(OH)_4 + Si(OR)_4 \quad \Rightarrow \quad (OH)_3Si - O$$
$$- Si(OR)_3 + ROH \qquad (3b)$$
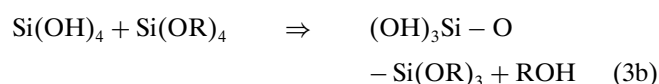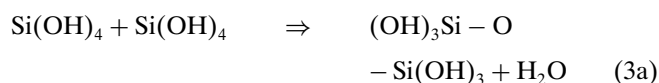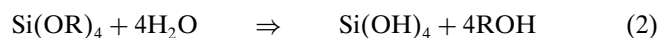
performed in hydroalcoholic medium in the presence of an acid or a base catalyst. The sol-to-gel transition is due to the formation of a three-dimensional network. Aerogels or xerogels can be obtained after solvent removal. Most importantly, sol–gel processing is fully compatible with the production of organic–inorganic hybrid materials of both class I (weak interactions between organic and inorganic components) and class II (strong bond between the two components). Hybrids of class I can be obtained by doping the starting sol with an appropriate reagent (e.g., organic molecule or polymer) that is physically entrapped in the inorganic lattice resulting from the condensation of silicon alkoxides. An elegant way to prepare hybrid of class II results from the use of functional alkoxysilanes [$R_nSi(OR')_{4-n}$, $n = 1-3$, R = organic group, R$'$ = alkyl] as one or more of the precursors for the sol–gel reaction. The polymerization mechanism still involves the "hydrolysis–condensation" sequence, leading to the following global reaction for an initial 1:1 mixture of alkoxysilane and organoalkoxysilane [Eqs. (4a) and (4b)]. By tailoring the nature and the structure of the organic group R, chemical,

$$Si(OR')_4 + R_nSi(OR')_{4-n} + (8-n)H_2O$$
$$\Rightarrow \quad Si(OH)_4 + R_nSi(OH)_{4-n} + (8-n)R'OH \quad (4a)$$

$$Si(OH)_4 + R_nSi(OH)_{4-n}$$
$$\Rightarrow \quad (OH)_3Si - O - SiR_n(OH)_{3-n} + H_2O \qquad (4b)$$

mechanical, optical, or electrical properties of the resulting composite materials can be greatly modified. The sol–gel process is also compatible with the formation of ceramic-based thin films on solid substrates, by dipping or spin-coating the starting sol and allowing it to gelify on the support [141–144]. In addition, it is now well established that biomolecules (e.g., enzymes) can be immobilized by encapsulation in sol–gel-derived materials without preventing their biological activity, leading to various applications in the field of biosensors [145–149]. One should finally mention the ordered mesoporous silicas, which were discovered some 10 years ago [120, 150], obtained by the sol–gel synthesis of

silica in the presence of self-assembled surfactants as a template. These materials display an exceptionally uniform and open structure with pores of monodisperse size (15–100 Å) and can be readily prepared in an organically modified form either by postsynthesis grafting or by the co-condensation route [151–155]. In spite of the rather complex chemistry depending on many experimental parameters, sol–gel-processed materials, and especially the organic–inorganic hybrids, have led to a great diversity of applications in various fields and have attracted the interest of a variety of scientists, as described in many excellent reviews [49, 54–57, 154–182].

These materials exhibit chemical and physicochemical features that might be readily exploited when used to modify electrode surfaces. The mechanically stable porous structure with high specific surface area would promote high diffusion rates and easy access of target analytes to a large number of accessible binding sites, which constitute the rate-determining steps in electrochemical sensing devices based on modified electrodes. The regular structure of ordered mesoporous silica-based materials is expected to further enhance these processes. Silica can be used as a support for immobilized or covalently grafted organic ligands that enable solid–liquid extraction of various species (e.g., heavy metals) present at trace levels in aqueous media [183–199]. Composites based on interpenetrating inorganic–organic polymers can be manufactured to exhibit either ionic or electronic conductivity or to facilitate electron transfer reactions in confined medium [200–207]. The sol–gel process permits encapsulation of bioactive molecules, alone or together with charge-transfer mediators or catalysts, which opens the door to applications in the field of electrochemical biosensors. Moreover, the versatility of sol–gel chemistry offers advantages in the design of electrode devices and microscopic electrochemical reactors.

This chapter aims at giving a brief overview (yet containing most literature citations) of the implication and applications of clays, zeolites, silicas, and organically modified silicates, in electrochemistry. The reader interested in more in-depth coverage of selected topics is directed to the numerous well-documented reviews that have appeared recently, dealing with clay modified electrodes [34–39], zeolite modified electrodes [38–48], and silica-based and sol–gel-derived materials as used as electrode modifiers [49–61].

Fundamentals of clay modified electrodes have been thoroughly reviewed by Fitch and Macha [34, 36], while the analytical applications were considered in more detail in other reports [35, 37–39]. The electrochemistry of anionic clays was treated by Therias and Mousty [208]. Bard and Mallouk [38] and Baker and Senaratne [39] provide mixed reviews dealing with all the aspects of both clay and zeolite modified electrodes. General reviews on zeolite modified electrodes have been written by Rolison [41, 42] and Roué et al. [46], while the analytical applications have been described by Walcarius [44, 47]. Extended views of electron transfer reactions in zeolites have been provided by Dutta and co-workers [45, 118]. Sol–gel electrochemistry was thoroughly reviewed by Lev et al. [49] and Alber and Cox [50]. Applications of silica-based materials in chemical analysis [51], electroanalysis and sensors [53, 59, 209], and electrochemical biosensors

[54] were extensively reviewed. Special attention to organically modified silicates in analytical chemistry was given by Collinson [52, 55, 61]. Ceramic–carbon composite electrodes were also described [58], as well as other ceramic-based solid electrolytes [60]. Fundamentals of redox processes in porous media [56, 210] and in electrically conductive oxide aerogels [211] can be found elsewhere.

2. PREPARATION OF ELECTRODES

Most aforementioned silicate-based materials are electronic insulators so that their use in connection to electrochemistry would require close contact to an electrode feeder material. Depending on the nature of the modifier (layered clays, crystalline zeolites, silica particles, sol–gel-processed materials, . . .), different strategies have been applied to build suitable integrated electrochemical devices. They were directed either to allow the exploitation of the intrinsic properties of these solids in various fields of electrochemistry or to enable the electrochemical characterization of materials.

2.1. Clay Modified Electrodes

A straightforward route to clay modified electrodes is the physical attachment of a clay film to a solid electrode surface (e.g., glassy carbon, Pt, Au, SnO$_2$), which is promoted by the fact that most clays exhibit self-adhesive properties toward polar surfaces, most probably via ion bridges [36]. A typical procedure involves the preparation of a 0.5–1% clay suspension (submicrometer- up to micrometer-sized particles in distilled water or organic solvent) of which a few microliters portion is dropped or spin-coated on the electrode surface and allowed to dry. The thickness of the resulting layer ranges from submicrometer to a few micrometers. Both conventional cation exchanging clays and anionic clays (LDHs) can be attached to electrode surfaces according to this approach [36, 208], as well as pillared clays [212–214]. The drying step applied during the preparation of clay films on electrode surfaces is a crucial parameter that strongly affects their structure. For example, fast drying tends to produce a "house of cards" structure, while face-to-face orientation of the clay sheets is favored in case of slow evaporation of the solvent. Spin-coating would also promote face-to-face interactions [215, 216]. Upon immersing a clay modified electrode into an aqueous solution, the dry film may re-swell. Re-swelling depends on the nature, composition (especially type of cations), and pH of the permeating solution. The extent and rate of swelling are not only functions of the solution composition but also of the cation exchange capacity of the clay [217, 218]. The wetting process may induce structural changes in the clay film, which is expected to affect significantly diffusion processes in this porous medium and, hence, the ionic conductivity [216] and the electrochemical behavior of intraclay electroactive species [219]. Clay–polymer composite films have also been prepared on electrode surfaces, involving mainly conducting polymers, which can be notably obtained by electropolymerization in the presence of clay [220–223].

Following the pioneering work by Ghosh and Bard [224], most investigations on clay modified electrodes have been performed with film-based devices [225–330]. Some other procedures for bringing clay structures at electrochemical interfaces have been described [331–383]. The direct covalent attachment of clay sheets to a solid electrode surface was achieved via silane bonding involving the surface hydroxyl groups on the clay [331]. More recently, this kind of reactivity was exploited to prepare organically modified clay films on electrodes using reactants such as organosilasesquioxane or organotrialkoxysilane as coupling agents [332, 333]. Other strategies based on the Langmuir–Blodgett technique, self-assembly, or even electrophoretic deposition were also applied to form very thin clay films on various electrode substrates [334–339]. Another approach is the dispersion of clay particles into carbon paste electrodes, leading to clay modified carbon paste electrodes [340–368], which represent more complicated heterogeneous systems than those based on thin films. To get good quality for this kind of modified electrode, clay particles must be wetted prior to the paste preparation to avoid leaching of them out of the composite electrode as a consequence of volume expansion during swelling; appropriate wetting is obtained after several days in vapor-saturated atmosphere at room temperature [351]. Later on, the Zen group extended this approach to the production of disposable clay–carbon-based thick film sensors obtained by screen-printing technology [369–372]. Other electronically conducting clay–carbon-based composites have been prepared as solid electrolytes in electrical power sources [373–375]. Finally, one should mention the clay and clay–polymer membranes that were designed as potentiometric sensing devices [376–380].

2.2. Zeolite Modified Electrodes

Contrary to the layered clays, the crystalline zeolite particles (solid crystals of μm dimension) are not compatible with the formation of a homogeneous, mechanically stable overlayer on solid electrode surfaces. The unique successful attempt in this direction was achieved by Calzaferri and co-workers [384, 385] who deposited a dense monograin layer of zeolite particles of monodisperse size and regular shape onto a planar electrode, but this packed zeolite layer suffered from lack of mechanical stability and required the overcoating of a thin polymer film to ensure more durable immobilization of the zeolite particles on the electrode surface.

The two main strategies applied to prepare zeolite modified electrodes can be summarized as follow: (1) formation of a zeolite–polymer composite film on solid electrode and (2) dispersion of zeolite particles into a conductive composite matrix. Several electrode configurations have been described on the basis of these two generic approaches (Fig. 1).

- *Zeolite-polymer films* (*Fig. 1A*) [384–424] can be easily deposited on solid electrodes by evaporation of an organic suspension of zeolite particles and dissolved organic polymer such as polystyrene. The polymer ensures adhesion of zeolite particles to the electrode surface and between them. Configurations based on zeolite particles sandwiched between the electrode surface and a polymer film have also been described, in the form of dense monograin layers [384, 385] or dense zeolite multilayers [406, 408]. Alternatives to
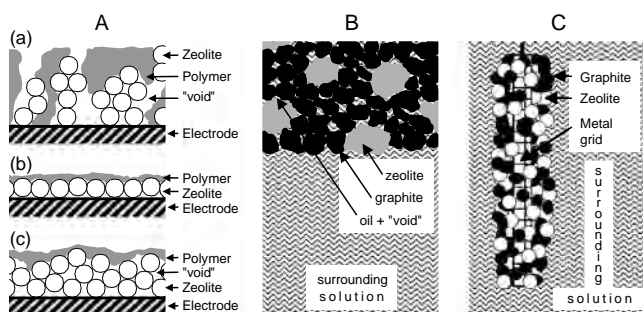
Figure 1. Schematic representation of the most common zeolite modified electrodes. (A) Film-based ZMEs: (a) zeolite-polymer film obtained by evaporation of zeolite particles suspended in a polymer solution; (b) zeolite monograin layer covered with a thin polymer film; (c) zeolite multilayer covered with a thin polymer film. (B) Zeolite modified carbon paste electrode. (C) ZME made of a "zeolite + carbon" mixture pressed on a metallic grid.

this approach are electrophoretic deposition of zeolite particles [425, 426], electrodeposition of organics in the presence of zeolite particles [427–429], or electropolymerization from zeolite–monomer suspensions [430, 431]. Carbon particles can be introduced into the film to increase its electrical conductivity [397, 432–436]. Thin films of zeolite grown on conductive substrates are also reported [437–439].

• *Zeolite modified carbon paste electrodes* (*Fig. 1B*) [390, 407, 417, 440–469] are obtained by mixing zeolite and carbon particles together with a mineral oil acting as a binder. As is common for other chemically modified carbon paste electrodes [78], their surface can be renewed by simple mechanical smoothing. An alternative to this graphite–zeolite paste is the more robust, zeolite-containing carbon–polystyrene–divinylbenzene composite electrode [470–472]. Applying the thick-film technology (screen-printing) by using a carbon ink doped with zeolite particles has led to the production of disposable zeolite modified electrodes [464, 473, 474].

• *Devices based on pressed zeolites* [475–510] are made as follows: binder-free zeolite modified electrodes are prepared by pressing zeolite–carbon mixtures on a stainless steel grid (Fig. 1C) [386, 475–494], enabling the use of resulting electrodes in organic media. Pressed pellets of pure zeolite were also used, either inserted between two solid electrodes [495–499] or as solid electrolyte [500–508], or even as a membrane [509, 510].

• *Nonconducting polymer–zeolite membranes* [511–520] are made of zeolite dispersion into inert organic resin for potentiometric measurements.

• *Covalent bonding of zeolite particles via silane coupling* [521] occurs similarly to clay linkage on indium-tin oxide electrodes [331].

• *Electrode modified zeolites* [48, 522–531] are made of metal micro- and nanostructures supported within and on zeolite particles that are then dispersed by a gas

flow into an aqueous solutions, in a rather high electric field maintained between two feeder electrodes, which behave as an ensemble of ultramicroelectrodes.

2.3. Silica Modified Electrodes

Applying silica based materials in electrochemistry is rather recent and the field of silica modified electrodes was mainly developed by the so-called organic–inorganic hybrids. The latter based on silicon oxides are organically modified silicas, which are usually classified with respect to the bond strength between the organic and inorganic components, such as class I (weak bond) and class II (strong linkage) hybrids [156]. Most silica modified electrode devices exploit the versatility of the sol–gel process, either to prepare intended materials (with given composition, structure, and properties) that are then incorporated in a suitable electrode material, or to build directly the modified electrode (as bulk conductive composites, or as silica-based coatings on conventional electrodes) [49–59]. Of particular interest is the possibility to immobilize a broad range of reagents at the electrode surface, including, for example, organic functions, ligands, catalysts, biomolecules, metal particles, macromolecules, and polymers.

Silica modified electrodes can be classified as follows.

• *Thin films deposited on solid electrode surfaces* [532–606]: the sol–gel process was largely exploited for coating the surface of a solid electrode with a silicate-based film. It is quite easily performed by dropping an aliquot of the starting sol solution on the electrode surface and allowing it to gelify and to dry. Sol deposition can be also achieved by spin-coating or dip-coating. Addition of an appropriate additive in the starting sol [i.e., poly(vinyl)alcohol-grafted-poly(vinyl)pyridine, poly(ethylene)-glycol, cetyltrimethylammonium, *N*-methyl-2-pyrrolidone] was often realized to limit shrinkage effects occurring during solvent evaporation and to produce crack-free films [560, 579, 595, 606]. Several kinds of film have been reported. Pure silicate films, most often doped with small electroactive species, have been deposited on glassy carbon and platinum electrodes [532–545]. Interpenetrating organic–inorganic polymer films were used to bring ion exchange properties at the electrode surface and/or to stabilize the silicate layer [546–562]. Both class I and II organically modified silicate films containing smaller organic groups were also prepared to get ion exchange and/or permselective behaviors [309, 563–567], ligand properties [568, 569], or even electroactive moieties attached to the material [570–576]. All these films involve either the encapsulation of the active organic component within the silica matrix, or the covalent linkage of reactive groups to the inorganic backbone via the use of an appropriate organo-alkoxysilane in the sol–gel process. Physical entrapment of enzymes or other biomolecules in the sol–gel film can be performed without preventing their biological activity, by doping the starting sol with the bioactive compound. Several works have been reported on such films coated on electrode surfaces, containing the biological material either alone [577–590] or associated

with a charge transfer mediator [577, 591–594] into the film. Finally, silicates and enzymes have been combined in multilayered film configurations on solid electrodes, such as "electrode/enzyme/silicate" [595–597], "electrodey/silicate/enzyme/silicate" [598–601], or "electrode/mediator/enzyme/silicate" [602–605].

- *Silica modified carbon paste electrodes* [606–658]: a simple route to prepare silica modified electrode is the dispersion of as-synthesized silica-based materials into carbon paste (mixture of graphite particles and organic binder). One advantage of this approach is the possibility to use materials with particular structure and properties, which cannot be produced as easily as sol–gel-processed thin films on electrode surfaces (i.e., ordered mesoporous solids [606–613]). This strategy was applied to prepare electrode containing unmodified silicas [614–623], silica gels grafted with organic ligands [608, 612, 613, 624–635], silica gels coated with inorganic layer(s) supporting adsorbed catalysts [636–648], silica-based materials with immobilized enzymes [649–654], and some other complex systems [655–658].

- *Ceramic–carbon composite electrodes* [58, 659–719]: the ceramic–carbon composite electrode (CCE) is an electrochemical device that directly arises from the sol–gel technology. It has been introduced and largely developed by Lev and co-workers and consists basically of a continuous bulk silica framework comprising physically entrapped carbon particles, originating from gelation of a starting sol containing graphite particles in suspension in a water–alcohol medium in the presence of a tetraalkoxysilane precursor [659–670]. The ceramic part imparts physical robustness while conductivity is ensured by percolation between the carbon particles, and the desired chemical reactivity can be adjusted by adding an appropriate modifier in the staring sol [58]. Examples are available with either inorganic solid catalysts (e.g., phospho- and silicomolybdates, metal or metal oxides, zirconium phosphate, . . .) used as dopants [666–669, 671–682] or small organic species or organometallic complexes [608, 683–694]. Film CCEs have also been reported [695–698]. The wetted section of such electrodes can be controlled by adjusting the hydrophobic–hydrophilic balance, which can be achieved by selecting a suitable ratio between tetraalkoxysilane and organosilane in the starting sol [673]. Preparation of CCEs is compatible with encapsulation of biomolecules, alone or associated with a charge transfer mediator, leading to various robust enzyme-containing CCEs [699–711]. Metal–ceramic composite electrodes [712–719] have been produced by applying a strategy similar to that followed to prepare CCEs, but replacing the carbon by metal particles. Finally, one may associate with this family the thick-film screen-printed silicate-containing electrodes that have been introduced as disposable electrochemical devices [720–726].

- *Silicate-containing membranes* [727–737]: they are made of ceramic–polymer composites encapsulating various kinds of ionophores that have been introduced in the material during sol–gel processing of the ceramic part [729–731]. They have been essentially applied to potentiometric sensing, most often as deposited on ion-sensitive field effect transistor devices [732–737].

- *Solid electrolytes* [738–770]: organically modified electrolytes or organically modified ceramics have been produced as solid electrolytes in power sources. They are often made of interpenetrating poly(ethylene or propylene)glycol and sol–gel silica doped with an inorganic acid or a lithium salt [738–758]. Ionic conductor monoliths based on class I organic–inorganic hybrids have also been reported [759–768], as well as related solid electrolytes with embedded electroactive moieties such as ferrocene [769, 770].

- *Miscellaneous*: other strategies were sparingly elaborated to confine silica-based materials at electrode/solution interfaces, such as electro-assisted deposition, polymerization or precipitation of siloxane films, organically modified silica monolith including microelectrode assembly, epoxy–carbon–ceramic composite, among others [771–788].

3. FUNDAMENTALS

3.1. Interplay between Charge Transfer and Mass Transport in Clays

Most basic investigations of clay modified electrodes have been performed using clay films deposited on the surface of a solid conductive substrate (Fig. 2A). When suitably prepared to promote face-to-face interactions between the clay sheets [215, 216], such a device is characterized by a unique pore architecture at the electrode surface, which arises from the spatial arrangement of clay aggregates that define various kinds of "void" spaces (Fig. 2B). Those being perpendicular to the electrode surface have been described as "elevators," those interparticle spaces that are parallel to the electrode surface are "corridors," and the layer spaces located within the particle between each clay sheet are called "rooms" and constitute the clay interlayer region [36]. When immersing the electrode into an electrolyte solution, this microstructure considered as dynamic because of the swelling property of most clays, which might result in significant modification of distances between the clay sheets and particles, as a function of the solution composition. Establishing an appropriate model for such film is therefore not an easy task. It was proposed, however, that one may distinguish five different species when soaking a clay modified
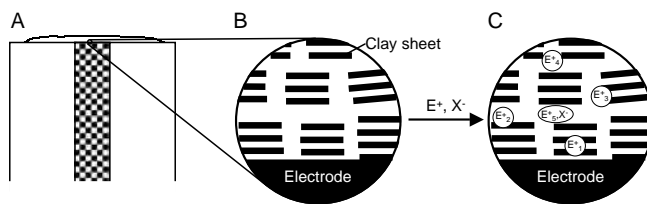

Figure 2. Schematic representation of (A) a solid electrode surface covered with a clay film, (B) an enlargement of the electrode/clay interface showing possible arrangement of clay sheets, and (C) the same interface after soaking in a solution containing an electroactive species, E^+, which is expected to occupy at least five distinct sites in the clay film.

electrode into a solution containing an electroactive species, E^+ (Fig. 2C): intercalated species that strongly interact at ion exchanging sites (E_1^+), surface- or edge-adsorbed species that are in weaker interactions with the aluminosilicate (E_2^+ and E_3^+), species located in channels or pores (E_4^+) in "elevators" or "corridors"), and ion-paired species (E_5^+, X^-) [38]. Due to their various degrees of stabilization, these species are expected to exhibit different electrochemical activities accounting for their various nano- and microscopic environments in the film. This has been extensively studied by cyclic voltammetry, chronoamperometry, and linear scan voltammetry on rotating disk electrodes. For example, information about the interaction between redox species and clay layers can be obtained from cyclic voltammetric experiments, by monitoring the differences in peak potentials of electroactive species incorporated into the clay film in comparison to those in solution [228, 233, 237, 242, 245, 251, 254, 268, 282]. Note that such a shift in peak potentials can also result from changes in the extent of loading in the clay film, the nature and concentration of the electrolyte solution, and temperature [237, 248, 268, 293]. For example, variation in the supporting electrolyte concentration in the solution might induce variation of the same parameter in the clay film, which can lead to peak potential shifts [233, 237, 293] in a similar way as that observed for electrodes modified with ion exchange polymers (e.g., redox reactions in Nafion [789]).

Several redox probes have been studied with clay modified electrodes, including metal cations or complexes [Ag^+, Cu^{2+}, Fe^{2+}, $Ru(NH_3)_6^{3+}$, ...], organometallic complexes [$Fe(bpy)_3^{2+}$, $Ru(bpy)_3^{2+}$, $Os(bpy)_3^{2+}$, $Cr(bpy)_3^{3+}$, with bpy = bipyridine], organic ions or molecules (methylviologen, MV^{2+}, tetrathiafulvalenium, TTF^+, hydroquinone, H_2Q, ...), and anions or anionic complexes [$Fe(CN)_6^{3-/4-}$, $Ru(CN)_6^{4-}$, $Mo(CN)_8^{4-}$, $IrCl_6^{4-}$, $HgCl_4^{2-}$, Br^-, ...)]. Due to favorable interaction, electroactive cations were essentially studied at electrodes modified with cation exchanging clays [36, 293] while anions were mostly involved with LDH modified electrodes [208]. Most often, only 10–30% of those incorporated into the clay film upon soaking the modified electrode in a solution of the species are electroactive [215, 228, 230, 233, 234, 237, 251, 278]. In particular, the electroactive fraction is very dependent on the film preparation conditions, the method of species incorporation, and the nature and composition of the surrounding solution. It can be measured by cyclic voltammetry at a slow scan rate, under thin layer conditions, where total charge passed in electrolyzing the film component can be easily determined by integration of peak current [790]. Cations strongly bound to the ion exchange sites in the interlayer region are electrochemically "silent" (e.g., clay pretreated with species before electrode preparation [234]). As a consequence, the electrochemical response of clay modified electrodes is essentially due to the access of redox species from the soaking solution through the clay film to the electrode surface. An elegant way of characterizing film filling is to record multisweep cyclic voltammograms (Fig. 3); increasing the number of potential scan results in increasing the soaking time and, therefore, the propagation of the diffusion front from the bulk solution/clay interface to the electrode surface, which leads to a progressive increase of voltammetric peaks up to a stationary state corresponding to equilibrium. The speed
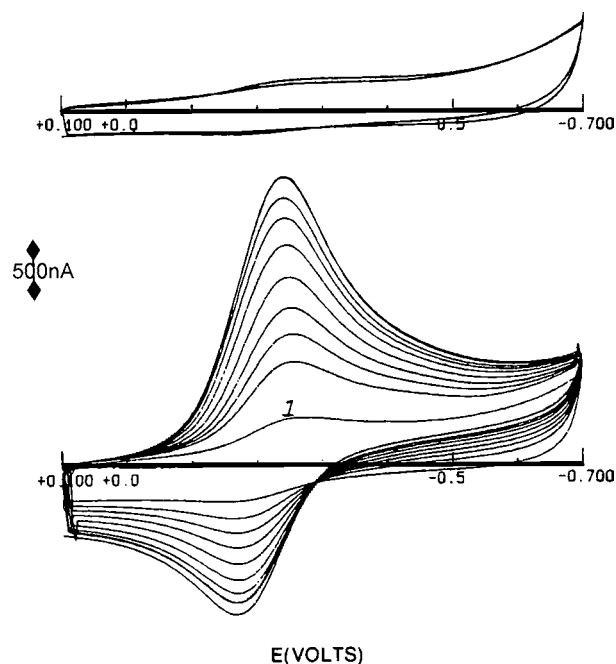

Figure 3. Multisweep cyclic voltammograms recorded in 10^{-5} M $Ru(NH_3)_6^{3+}$ (+0.01 M Na_2SO_4). Top: bare platinum electrode. Bottom: the same electrode covered with a montmorillonite film, using 5 minute intervals between each potential scan over a 50 minute time period. Reprinted with permission from [293], T. Wielgos and A. Fitch, *Electroanalysis* 2, 449 (1990). © 1990, Wiley–VCH.

at which this equilibrium is reached is related to the diffusion rate of redox species within the clay film, which is affected by the size of species, the number and accessibility of binding sites, the tortuosity of the porous film, and charge effects [218]. Peak height in cyclic voltammetry obeys to the Randles–Sevcik equation [790]: for a target electroactive species at a given electrode surface area, it is directly proportional to the concentration of this species, C, and the square root of its diffusion coefficient, $D^{1/2}$. The fact that peak currents can be much higher at clay modified electrodes than at unmodified electrodes (Fig. 3) implies that $C_{clay} \times (D_{clay})^{1/2}$ is much higher than $C_{sol} \times (D_{sol})^{1/2}$. As diffusion coefficient of species in the clay film, D_{clay}, is expected to be smaller than in solution because of restricted motion in this porous medium, the aforementioned observation implies that concentration in the film, C_{clay}, is much higher than that in the external solution, C_{sol}.

Electron transfer mechanisms at clay modified electrodes involve either physical diffusion of redox species in the porous film [251, 268], charge motion by electron hopping between adjacent redox sites [242, 251], or both [36]. Anyway, each type of mechanism requires charge compensation, which is most often realized by diffusion of a counterion originating from the electrolyte [see, e.g., Eq. (5) for oxidation of a cationic species, E^{n+}, in the presence of an electrolyte, C^+X^-]:

$$E^{n+}(nA^-)_{clay} + (C^+, X^-)_{sol} - e^-$$
$$\Rightarrow E^{(n+1)+}(nA^-)_{clay} + (X^-)_{clay} + (C^+)_{sol} \quad (5)$$
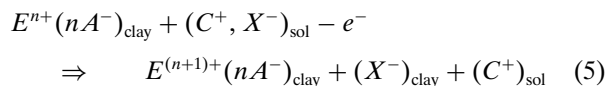
Diffusion coefficients in the clay film, D_{clay}, are thus considered as apparent because they can be affected by diffusion of these counterions, associated with either translational motion of the species to the electrode surface or to electron hopping from site to site among the electroactive species located in the whole film. It is therefore not surprising that the electrochemical activity of bound redox probes is strongly affected by the supporting electrolyte [208]. D_{clay} values have been reported to range between 10^{-12} and 10^{-11} cm^2 s^{-1} [38]. Higher values have been reported for neutral electroactive species that are also able to penetrate the clay layer [215, 225]. Ion paired species present in excess of the ion exchange capacity of clays were also found to be electroactive, either via travelling through the interparticle pores to the electrode surface, or acting as charge shuttle to immobilized cations at strong binding sites situated far from the substrate electrode [234, 250, 251, 263, 281, 282]. Their presence was experimentally evidenced by quartz crystal microbalance experiments [278].

Efforts have been made to increase both mass and charge transfer at clay modified electrodes. Mass transport into clay films can be improved by using pillared clays at the electrode surface [212, 214, 230, 331], in which inorganic or organic rigid pillars are formed between the clay sheets, allowing control of the thickness of the interlayer region. This resulted in limited swelling, molecular sieving effects, higher mass transfer rates, or preferential soaking of target species. Surfactant-containing clay modified electrodes belong to this category [34, 379]. On the other hand, charge transfer could benefit from the intrinsic electrochemical activity of redox centers that are naturally or synthetically built inside the clay lattice, as structural iron(II) that occurs in natural clays, or cobalt(II) or copper(II) containing clays, which resulted in higher currents due to assisted charge delivering to the redox active sites in the clay film coated electrode [252, 260, 272, 273, 320]. Intrinsically electroactive LDHs were especially attractive from this point of view [321, 322, 339, 381]. Electroactive polymers formed within the clay coatings can also help in the charge transfer process [220–222, 282].

3.2. Electrochemistry with Zeolites

Just as clays, zeolite particles immobilized at an electrode surface exhibit preconcentration properties toward electroactive cations that are present in the soaking solution. This results in voltammetric peak currents at zeolite modified electrodes (ZMEs) higher than those sampled at the corresponding bare electrodes. Data are available in the literature for several analytes [Ag$^+$, Cu^{2+}, Pb^{2+}, Cd^{2+}, Ru(NH$_3$)$_6^{3+}$, methyl- and heptylviologen, dopamine], three zeolite types (A, X, Y), and three electrode configurations (zeolite modified carbon paste, zeolite–carbon–copolymer composite, zeolite film on glassy carbon) [387, 390, 407, 426, 446, 471]. Enhancement with respect to bare electrodes is directly related to the ion exchange capacity of the zeolite and to the speed at which the redox species are diffusing to these sites. These processes are affected by several parameters [390, 407]: peak currents were in general higher when using zeolites displaying high cation exchange capacity, large pores, and small particle size, for cationic analytes of small hydrated size and great positive charge,

and for long soaking times especially at film ZMEs. Preconcentration efficiency was low in the presence of a high concentration of other cations in the medium (e.g., electrolyte cations) because of competition for the exchanging sites. Of course, size-excluded electroactive cations (those of size larger than the zeolite pore aperture) and charge-excluded species (anions) did not result in any enhancement of the voltammetric peaks.

In contrast to clay modified electrodes, ZMEs prepared with zeolite particles previously loaded with a redox species gave rise to significant electrochemical responses. In fact, most investigations on ZMEs have been carried out in that way, for which a distinction should be made between the small redox species incorporated within the zeolite framework by ion exchange (highly mobile species) and those bigger species which were physically entrapped as "ship-in-a-bottle" complexes in the zeolite cages (species with restricted motion).

Let us first consider the electrochemical activity of small electroactive ions exchanged in zeolites that were subsequently immobilized at an electrode surface. When immersing such a ZME into a fresh electrolyte solution (free of redox-active species), well-defined signals are usually observed in cyclic voltammetry (CV), but they progressively decrease either upon continuous cycling potentials (Fig. 4), or by increasing the soaking time of the electrode in the solution before recording the CV curve. This is explained by the continuous depletion of redox species as long as the electrode is soaked in the electrolyte solution because of ion exchange for the electrolyte cations in the zeolite particles located at the electrode surface [384, 387, 390, 399, 401, 402, 406, 432, 445, 449]. The leaching process is rather fast, increasing when raising the electrolyte concentration
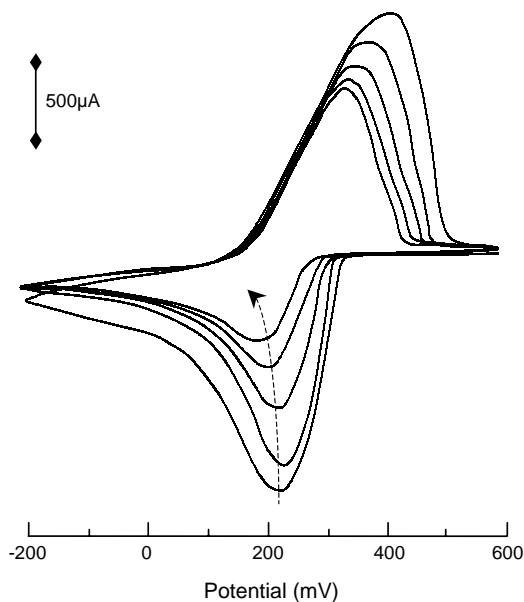

Figure 4. Cyclic voltammetry of fully exchanged silver zeolite Y, recorded in 0.1 M LiClO$_4$. Scan speed 5 mV/s. The decrease in current for each scan (arrow) is due to ion exchange with the supporting electrolyte ion. Reprinted with permission from [432], M. D. Baker and J. Zhang, *J. Phys. Chem.* 94, 8703 (1990). © 1990, American Chemical Society.

and/or when using electrolyte cations of smaller hydrated size, which led to voltammetric currents of smaller intensities [398, 402, 409, 445, 461, 475]. Using an electrolyte solution with size-excluded cations prevents the leaching process by ion exchange because they are too big to enter the zeolite pores, and this resulted in very low electrochemical activity [398]. This highlights the critical influence of ion exchange on the electrochemistry of ZMEs. Also, performing the voltammetric experiments at various scan rates has indicated that reactions were diffusion-controlled [446], in agreement with the ion exchange processes in zeolites [113]. For example, the importance of ion exchange on the electrochemistry of ZMEs was deeply considered for the methylviologen–zeolite Y system [387, 405, 422, 445, 449, 464]. Some complications, however, have been reported in several cases, especially when redox species are (or can be) located in distinct ion exchange sites in the zeolite: an eloquent example is the case of silver(I) at zeolites A, X, and Y. In these cases, depending on the cation location, the zeolite type, the nature of supporting electrolyte, and the type of ZME, distinct voltammetric peaks have been observed, the origin of which has been extensively discussed in the literature [398, 400, 401, 404, 409, 411, 416, 432, 475] and will not treated here in detail. Similar effects have been reported for copper(II) [402] and cobalt(II) [398, 477]. Finally, solvent can affect the CV response of ZMEs, often by acting on the rate of ion exchange processes [396, 406, 413].

The electrochemical behavior of encapsulated redox species (i.e., physically entrapped within the zeolite cages) is fundamentally different from that of small ion-exchanged cations. In spite of their strongly restricted mobility, these encapsulated complexes gave rise to non-negligible electrochemical response [43, 46]. Most studied species are positively charged organometallic complexes, such as metal tris-bipyridine (metal = Fe, Ru, Os, Co), metal phthalocyanine (metal = Fe, Co, Cu, Rh), and metal–schiff base complexes [412, 419, 435, 476–483, 485–487, 493, 527, 531]. They can be either located in the bulk zeolite, simply bound to the external surface of zeolite particles, or even occluded within the first layer of complete or broken cages situated at the particle boundary. Those species located at the outermost surfaces are expected to contribute to a large extent to the electron transfer reactions, as those located deeply in the bulky isolating structure can only be reached via electron hopping between the adjacent redox species, which implies a high density of these sites [791]. This explains why broken zeolite particles loaded with encapsulated complexes (by grinding or by acid treatment) gave rise to higher voltammetric currents compared to undamaged zeolites [412, 792]. Most complexes encapsulated in the bulk zeolite are electrochemically "silent." Note that species located at the outermost surface of zeolite grains can promote charge transfer to the complexes encapsulated deeper in the porous medium, the surface-adsorbed species acting then as electrocatalysts [388, 389, 521]. In the case of strong interactions between the organometallic complex and the zeolite lattice, a shift in peak potentials (or peak splitting) can be observed during cyclic voltammetry experiments, with respect to the behavior of the same redox species at bare electrodes, and such a change is dependent on the preparation mode of the entrapped complex and type of ZME (Fig. 5) [406, 477, 527].
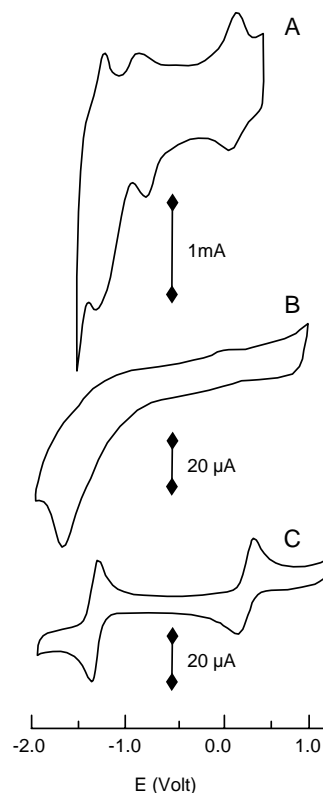

Figure 5. Cyclic voltammograms of Co(salen) in acetonitrile. (A) Recorded in 0.1 M tetrabutylammonium tetrafluoroborate, at a scan rate of 10 mV/s, with using a pressed powder composite electrode prepared with graphite and zeolite Co(salen)–NaY. (B) Recorded in 0.1 M LiClO$_4$, at a scan rate of 50 mV/s, using a film zeolite modified electrode made of graphite + zeolite Co(salen)–NaY coated on glassy carbon and covered with an acrylic-based polymer. (C) Recorded in homogeneous Co(salen) solution +0.1 M LiClO$_4$, at a scan rate of 50 mV/s, with using an unmodified glassy carbon electrode. (A) Reprinted with permission from [477], F. Bedioui et al., *J. Chem. Soc. Faraday Trans.* 87, 383l (1991). © 1991, The Royal Society of Chemistry. (B) and (C) Reprinted with permission from [406], C. Senaratne et al., *J. Phys. Chem.* 100, 5849 (1996). © 1996, American Chemical Society.

Some zeolites, or zeotypes, contain electroactive centers in their framework lattice (intrinsic composition). When immobilized at an electrode surface, such materials exhibit voltammetric responses that have been attributed to redox processes involving the framework species; examples are available for titanosilicalites [444, 448, 467], iron–silicalites [424, 469], and vanadium–silicalites [433, 489, 492]. Anodically induced degradation of mordenite was also reported [793]. Finally, electrochemistry involving the molecular sieve alone (without solvent) was possible at elevated temperatures (i.e., 200–500 °C) where extra-framework metal cations become electroactive [495–498].

3.3. Electron Transfer Mechanisms at Zeolite Modified Electrodes

As zeolites are electronic insulators, the question of the origin of charge transfer reactions at zeolite modified electrodes is very important. This question has led to intriguing observations and controversial discussions in the literature

[42, 46, 406, 490, 491, 493, 529, 794–796]. Actually, one can consider that at least three mechanisms are operating to explain the electrochemical response of redox species incorporated in ZMEs [797], which take into account the overflowing literature dealing with this fundamental question [387, 400–405, 409, 411, 412, 417, 419, 422, 446, 454, 483, 484, 486, 487, 493, 527]. These are represented by the following equations.
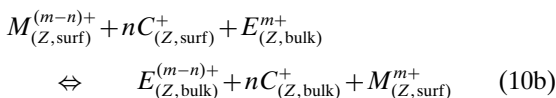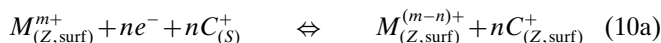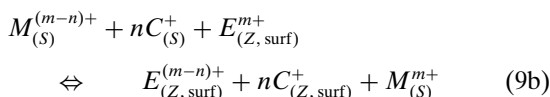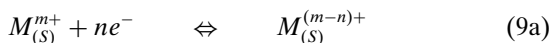
Mechanism I:

$$E^{m+}_{(Z)} + ne^- + nC^+_{(S)} \quad \Leftrightarrow \quad E^{(m-n)+}_{(Z)} + nC^+_{(Z)} \quad (6)$$

Mechanism II:

$$E^{m+}_{(Z)} + mC^+_{(S)} \quad \Leftrightarrow \quad E^{m+}_{(S)} + mC^+_{(Z)} \quad (7a)$$

$$E^{m+}_{(S)} + ne^- \quad \Leftrightarrow \quad E^{(m-n)+}_{(S)} \quad (7b)$$

Mechanism III (*three subgroups*):

$$E^{m+}_{(Z,\mathrm{surf})} + ne^- + nC^+_{(S)} \quad \Leftrightarrow \quad E^{(m-n)+}_{(Z,\mathrm{surf})} + nC^+_{(Z,\mathrm{surf})} \quad (8a)$$

$$E^{(m-n)+}_{(Z,\mathrm{surf})} + nC^+_{(Z,\mathrm{surf})} + E^{m+}_{(Z,\mathrm{bulk})}$$
$$\Leftrightarrow \quad E^{(m-n)+}_{(Z,\mathrm{bulk})} + nC^+_{(Z,\mathrm{bulk})} + E^{m+}_{(Z,\mathrm{surf})} \quad (8b)$$

$$M^{m+}_{(S)} + ne^- \quad \Leftrightarrow \quad M^{(m-n)+}_{(S)} \quad (9a)$$

$$M^{(m-n)+}_{(S)} + nC^+_{(S)} + E^{m+}_{(Z,\mathrm{surf})}$$
$$\Leftrightarrow \quad E^{(m-n)+}_{(Z,\mathrm{surf})} + nC^+_{(Z,\mathrm{surf})} + M^{m+}_{(S)} \quad (9b)$$

$$M^{m+}_{(Z,\mathrm{surf})} + ne^- + nC^+_{(S)} \quad \Leftrightarrow \quad M^{(m-n)+}_{(Z,\mathrm{surf})} + nC^+_{(Z,\mathrm{surf})} \quad (10a)$$

$$M^{(m-n)+}_{(Z,\mathrm{surf})} + nC^+_{(Z,\mathrm{surf})} + E^{m+}_{(Z,\mathrm{bulk})}$$
$$\Leftrightarrow \quad E^{(m-n)+}_{(Z,\mathrm{bulk})} + nC^+_{(Z,\mathrm{bulk})} + M^{m+}_{(Z,\mathrm{surf})} \quad (10b)$$
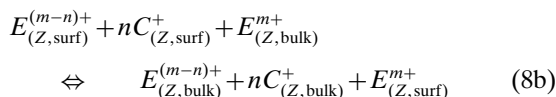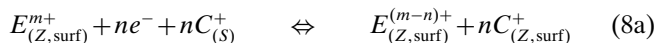
where E is the electroactive species with charge $m+$, C^+ represents the electrolyte cation (chosen as monovalent for convenience), M is a mediator (chosen with charge $m+$ for convenience), the subscripts z and s refer to the zeolite phase and the solution, respectively, and the subscripts surf and bulk to the zeolite surface (either external surface or outermost subsurface layer of cages) and bulk ion exchange sites.

Mechanism I is purely intrazeolitic, where the electroactive species undergoes intracrystalline electron transfer while charge balance is maintained by solution-phase electrolyte cations entering the zeolite framework [Eq. (6)]. Note that this mechanism does not distinguish between species located deeply in the bulk zeolite and those situated in the boundary region of the zeolite grains. Mechanism II is purely extrazeolitic and involves the ion exchange of the electroactive probes for the electrolyte cations [Eq. (7a)] prior to their electrochemical transformation in the solution phase [Eq. (7b)]. The group of mechanisms III distinguishes between the electroactive probes located in the bulk zeolite and those situated at the external boundary of the particle. The first case is the direct electron transfer to electroactive species situated at the outer surface of the zeolite particles (i.e., those easily accessible to the electrons),

charge compensation being ensured by the electrolyte cation [Eq. (8a)]. This step can be (but is not necessarily) followed by electron hopping to the probes located in the bulk of the solid, with concomitant migration of the electrolyte cation inside the zeolite structure [Eq. (8b)]. In the presence of a charge transfer mediator either dissolved in solution or adsorbed on the zeolite surface, electrochemical transformation [Eqs. (9a) and (9a)] can lead to indirect charge transfer to either surface-confined or bulk-located electroactive probes [Eqs. (10a) and (10a)].

Evidence to support one of these mechanisms, depending of the electrode systems, has been described in the literature. Without entering into the details, one can consider that the extrazeolitic mechanism [Eqs. (7a) and (7b)] is the main pathway responsible for explaining charge transfer at ZMEs incorporating ion exchangeable electroactive species [387, 398, 400, 402, 403, 409, 411, 446]. The case of encapsulated complexes is less unequivocal but must involve in great majority the electroactive species located at the outermost boundary of zeolite particles [Eqs. (8)–(10)], which are called either intrazeolitic (interacting with the zeolite framework) or extrazeolitic (located outside of the bulk zeolite), depending on the authors [42, 46, 490, 796].

3.4. Electrochemistry in Silica Gels and Xerogels

Electrochemistry oriented investigations of oxides and oxide films are widespread [798–800]. Attention is given here only to those related to silica gels and xerogels. In particular, the eletrochemical techniques can be exploited to get information on the sol–gel process (e.g., probing the sol-to-gel-to-xerogel transition [801, 802]), and to characterize the structure and properties of both wet oxide gels and xerogels [532, 540, 575, 769, 783–786, 803–805].

Electrochemistry into wet oxide gels doped with free electroactive probes (e.g., ferrocene, ferrocene–methanol) was used as a tool for the investigation of sol–gel polymerization, by exploiting the fact that the voltammetric response of the redox probe is related to its mobility in the material [783, 786, 802, 803]. Three successive phases can be distinguished (Fig. 6): (1) constant diffusion of the probe during the gelling period, (2) decrease of the probe mobility during the first stage of gel aging because of densification of the network, which then grows up again as a consequence of the decrease of the microviscosity of the interstitial liquid phase, and (3) a situation where the probe mobility is constant over a prolonged period of time corresponding to the last part of the drying process [802]. During this last phase, the probe diffusion was found to be strongly dependent on its charge: electroactive anions gave rise to constant currents, while diffusion of redox cations (and to lesser extent neutral molecules) underwent a slow decrease because of stronger interactions with the negatively charged silica surface [783, 786]. Stability of sol–gel derived silicate films on electrodes can be monitored this way and was found to be dependent on drying time and relative humidity [540]. Interaction of the electroactive probe with the gel matrix was also evidenced by voltammetry in the case of uranium(V) in silica gels [533].
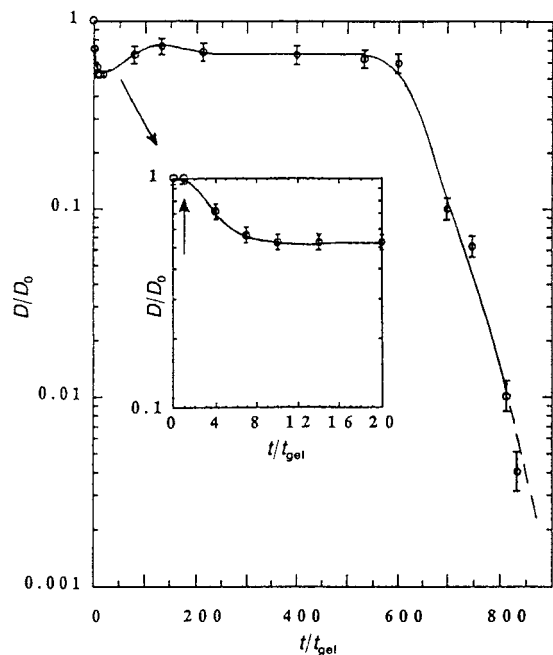
Figure 6. Dependence of reduced diffusion coefficient of ferrocene in the gel on reduced gelation time for silica gel. Reprinted with permission from [802], P. Audebert et al., *J. Mater. Chem.* 1, 699 (1991). © 1991, The Royal Society of Chemistry.

Xerogels are dried gels from which the gelation solvent has been extracted. Like gels, xerogels can be turned electroactive by insertion of or functionnalization by redox active systems. Again, the electrochemical behavior of such electroactive species in this confined media is indicative of its intrinsic properties. In this case, however, physical diffusion of the probe is not the main factor affecting the redox processes, but it can be combined to, or even totally outclassed by, electron exchange between adjacent redox sites (electron pseudo-diffusion), which becomes the rate-determining step, similar to what occurs at electrodes coated with redox polymers [806–808]. The related theories have been recently adapted to the case of silicate films on electrodes, based on a fractal distribution of redox sites in the thin layer [809]. From the practical point of view, the apparent diffusion coefficients of redox probes encapsulated within silica monoliths can be determined by a calibration-free method based on coupling cyclic voltammetry and chronoamperometry at ultramicroelectrode assemblies [783–785]. When dealing with redox active groups covalently attached to the silica backbone (i.e., ferrocene moieties), nonisotropic distribution of them in the xerogel have been observed [575, 804], in comparison to the isotropic distribution of weakly bonded redox species in gels [573].

3.5. Electrochemical Behavior of Organic–Inorganic Hybrid Polymers

Preparation and chemistry of conducting polymer nanocomposites, including the hybrids based on silicates, have attracted considerable attention in many fields [207] including electrochemistry [49]. Combining organic polymers and

silicate gels at the molecular level, in a single polymerization procedure, is not trivial because it would require the coexistence of nucleophilic functions (inorganic gel) and cation-radical precursors (conducting polymer), which are expected to interact with each other. Nevertheless, this combination is highly desirable in view of improving the properties of conducting polymers by combination to those of inorganic materials (mechanical stability, adhesion, enhanced transport issues, ...). Efforts have then been made to produce interpenetrating organic–inorganic hybrids in which sol–gel plays a leading role [810]; some of them involve electrochemistry as described hereafter. For example, mechanical stability of conducting polymers can be improved by encapsulation of rigid particles of silica or other inorganic solids, while composites based on sol–gel silica and conducting polymers resulted in faster mass and charge transfer reactions (due to three-dimensional structuration of the polymer) and exhibited better adhesion to, for example, indium tin oxide electrode (because of the presence of silanized functions) [202, 811, 812].

One can basically distinguish four approaches to synthesize inorganic-conducting polymer hybrids in one step. The most straightforward way is to dissolve the organic polymer into an organic solvent, mixing it with the starting sol, and allowing the mixture to gelify and then to dry to get the final composite film (e.g., silica-aniline based hybrids [812, 813]). An alternative is the electrochemical polymerization of the conducting polymer (polypyrrole, polythiophene, or polyaniline) in the presence of silica particles [207]. An elegant approach is the use of a reagent acting as both a precursor for the sol–gel process and a monomer to lead to conducting polymer, such as the N-[3-(trimethoxysilyl)propyl]pyrrole or 2,5-bis(trimethoxysilyl)-mono-, bi-, and terthiophene:

(with n = 1, 2, 3)
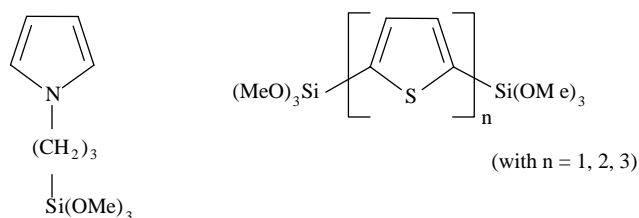
These precursors are then allowed to polymerize, to form an inorganic lattice via the sol–gel process and a conducting polymer via either chemical or electrochemical oxidation of the organic component [200, 201]. They gave good electrochemical activity but suffered from rather low stability. Electrogenerated polypyrrole–silica hybrid films have been obtained by copolymerization of a sol–gel precursor (e.g., tetra-ethoxysilane) and the pyrrole monomer, which was achieved by electropolymerization of pyrrole together with the inorganic polycondensation [774, 814]. Finally, composite films can also be prepared by electroassisted polymerization of the organic conducting polymer inside a silicate-based xerogel film preformed onto an electrode surface, as was reported for polyaniline and polypyrrole [203, 815, 816].

In addition to what occurs in conducting polymer–silica composites, long-range charge transfer in hybrid
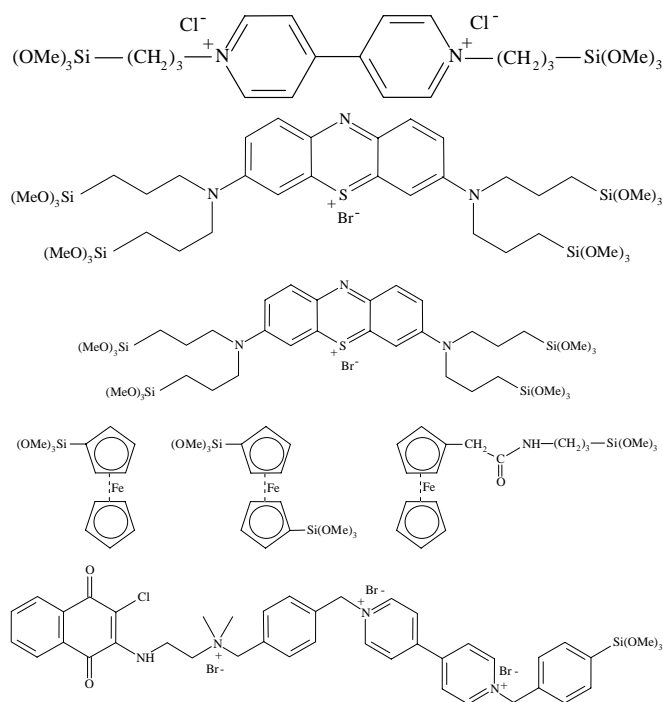
films can also be achieved in redox polymers that are produced by hydrolysis and subsequent condensation of organo-alkoxysilanes containing a redox active group [572, 573, 575, 702, 772, 775, 817]. The precursors include derivatives with various functions, such as methylviologen, phenothiazin, ferrocene, or naphtoquinone, as exemplified hereafter. These can be polymerized alone or co-condensed with a tetraalkoxysilane, acting as a cross-linking agent. The co-condensation approach leads to films displaying lower rates of charge transport compared to those prepared from the pure organosilane because of "dilution" of the active sites in the redox polymer [772, 817]. Other redox polymers based on organically modified ceramics have been prepared by binding redox active functions to a preformed organo-polysiloxane, that is, by hydrosililation of a molecule containing a vinyl function attached to a redox-active group with one alkylhydrosiloxane homopolymer or copolymer [570, 571, 655–657], or by allowing chlorocarbonyl–ferrocene derivatives to react with (aminopropyl)methylsiloxane–dimethylsiloxane [98, 773]. The electrochemical activity of all these systems involves the competitive participation of physical diffusion and electron exchange between adjacent redox sites, but this latter process is often the main one (rate-determining).

4. APPLICATIONS

4.1. Electrocatalysis

4.1.1. General Principle

Some electrochemical transformations require the application of overpotentials to occur because of strong limitations in the rate of electron transfer. An elegant way to overcome this problem is the use of charge transfer co-factors (mediators). The principle of mediated electrocatalysis is described by Eqs. (11)–(13) in the case of the reduction of a substrate S_{Ox} into a product P_{Red}. Basically, if electrochemical reduction of S_{Ox} [Eq. (11)] occurs at high overpotentials ($E_S^{o'} \ll E_S^o$), the use of a mediator couple (M_{Ox}/M_{Red}) allows one to lower the overpotential barrier by electrogenerating M_{Red} at $E_M^{o'} = E_M^o$ [Eq. (13)], which then reacts chemically with S_{Ox} [Eq. (12)]. The overall process therefore results in the electrochemical transformation of S_{Ox} at a much lower overpotential than the initial substrate in the absence of mediator ($E_M^{o'} \gg E_S^{o'}$):

$$S_{Ox} + ne^- \rightarrow P_{Red} \qquad (E_S^{o'} \ll E_S^o) \tag{11}$$

$$S_{Ox} + M_{Red} \rightarrow P_{Red} + M_{Ox} \quad \text{(occurring if } E_S^o > E_M^o) \tag{12}$$

$$M_{Ox} + ne^- \rightarrow M_{Red} \qquad (E_M^{o'} \cong E_M^o) \tag{13}$$
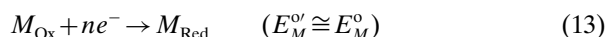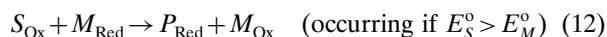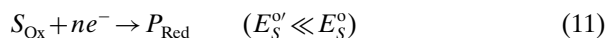
The mediator can of course be added directly in solution but, for practical reasons, it is more convenient to immobilize it at an electrode surface, to get a reagent-free device. Electrodes modified with clays, zeolites, and silica-based materials have been used for this purpose.

4.1.2. Immobilized Catalysts on Electrodes

Clays, zeolites, and silica-based materials are good support for the immobilization and/or spatial organization of catalytic centers, which are in turn applied to improve some electrochemical experiments. Examples are available, dealing with either catalysis in organic chemistry or in the analytical field, via enhancement in both selectivity and/or sensitivity of amperometric detection. This latter scope was especially of concern in the development of second generation biosensors (see Section 4.5.3).

Metal complexes encapsulated in zeolites or clays [383, 488] can contribute to electroassisted oxidation or reduction of organic substrates. For example, cobalt–salen complexes entrapped in zeolite Y were found to facilitate the reduction of benzyl bromide and benzyl chloride, with a higher efficiency than that observed for the same catalyst in solution [477, 531]. Iron phthalocyanine encapsulated in the same zeolite was a good electrocatalyst for either hydrazine oxidation or molecular oxygen reduction [435]. Oxygen reduction was also improved by a similar catalyst adsorbed on polypyrrole–silica composite [633], by Mn–salen [479] or methylviologen [442] supported within zeolite Y particles, or by $Ru(bpy)_3^{2+}$ and cobalt complexes immobilized on Nafion–clay composites [280]. Reductive dehalogenation of dibromobiphenyl was achieved with $Co(bpy)_3^+$ or Co-phthalocyanine in micellized clays [235, 818].

Other applications rely on the ability of the immobilized catalysts to improve the selectivity of electroanalytical determinations by lowering the overpotential of the target analyte while turning most interferences electrochemically "silent," or to enhance the sensor sensitivity by increasing the current response by continuous electrogeneration–consumption of the active intermediate. A huge part of the work in these directions was performed with carbon paste electrodes comprising silica gel particles covered by metal oxides (TiO_2, ZrO_2, Nb_2O_5, Al_2O_3, ...) or titanium phosphate, on which a wide range of catalysts can be durably

immobilized (e.g., metal phthalocyanines and porphyrins or organic dye mediators such as Meldola's blue, methylene blue, methylene green, Nile blue, toluidine Blue, ...) [636–648, 819–823]. These systems were used for improving the direct electrochemical detection of various analytes, such as hydrazine, cysteine, NADH, oxalic acid, ascorbic acid, among others. Ceramic–carbon composite electrodes were also largely used for these purposes because of their ability to trap many kinds of electrocatalysts by exploiting the versatility of the sol–gel process: immobilization can be achieved either by physical entrapment (doping the starting sol with a selected mediator, either organic or organometallic [683–692], or inorganic [666–670, 674–682]), or by covalent binding to the ceramic lattice (allowing an appropriate organosilane to co-condense with the starting alkoxysilane) [702, 703], or even by dispersing catalytic metal particles into the composite ceramic-based structure [671–673, 712–719]. These composite electrodes are usually robust and therefore mechanically stable; the hydrophobicity of their surface can be controlled by a suitable choice of methyl-trialkoxysilane in the starting sol, and they often offer long-term stability due to low or negligible leaching of the catalyst out of the electrode into the external solution [58]. On the contrary, clays and zeolites, in spite of their ability to retain catalysts in their structure by ion exchange or adsorption, have been much less applied to this end because of nondurable immobilization (catalyst leaching in solution) [47]. The only available examples are the determinations of ascorbic acid and dopamine, at electrodes modified with zeolite Y respectively exchanged with iron(III) [434, 456] or triphenylpyrylium [418], as well as the electrocatalytic reduction of oxygen at a montmorillonite film doped with $Ru(bpy)_3^{2+}$ ions [280]. Most interesting are the hydrotalcite-like materials that possess in their framework some electroactive centers that can directly act as electron shuttles to improve the charge transport processes [320, 321, 328–330]. The mostly studied compounds were Ni/Al–X hydrotalcites, where Ni(II) species were the catalytic centers, but LDHs containing Co(II) or Mn(II) centers in their structure have been also exploited as electron transfer mediators [321]. This is illustrated in Figure 7 where Mn$^{(II)}$-containing LDH clearly enhances the redox transformation of $Mo(CN)_8^{4-}$ as compared to an LDH free of any electrocatalytic center. Examples of electrocatalytic detection at Ni/Al–X hydrotalcite films coated on glassy carbon electrodes have been reported for the amperometric sensing of alcohols [327, 381, 382]. Similar improvements have been reported for cation-exchanging clays possessing iron(II), cobalt(II), or copper(II) centers in their framework [252, 257, 260, 272, 273, 275, 824]. Finally, it should be emphasized that oxidation of phenol derivatives can be catalyzed by the presence of unmodified zeolite particles [466], bentonite clay [457], or silica gel [825].

4.1.3. Electrode Modified Zeolites

In addition to zeolite modified electrodes, the concept of "electrode modified zeolites" was introduced. They are based on metal or metal oxide nanocrystallites supported in/on zeolite particles, acting as ultramicroelectrodes [524] when they are brought in a strong electric field (i.e., as dispersed in solution between two feeder electrodes; see
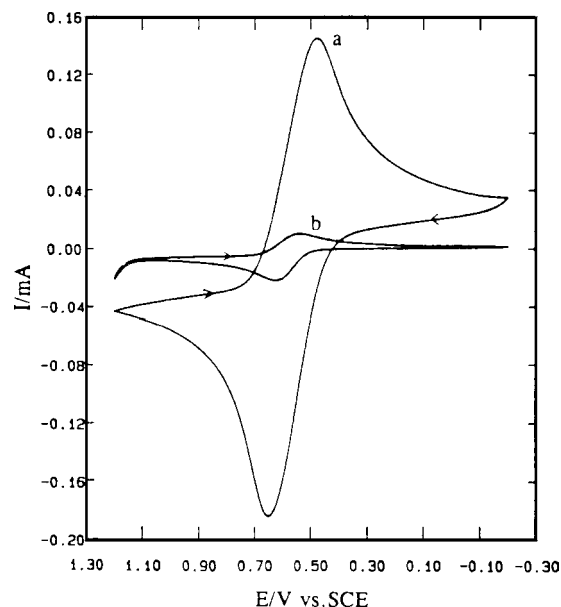
Figure 7. Cyclic voltammograms recorded in 10^{-4} M $Mo(CN)_8^{4-}$ (+0.1 M KCl), using electrodes modified with a LDH film: (a) Mg–Mn–CO$_3$ and (b) Zn–Al–Cl. Reprinted with permission from [321], J. Qiu and G. Villemure, *J. Electroanal. Chem.* 428, 165 (1997). © 1997, The Royal Society of Chemistry.

Fig. 8). They have been applied to large-scale electrolysis catalyzed by the supported nanoelectrodes and to the catalytic transformation of organic compounds via electrochemical activation by microheterogeneous dispersion of doped zeolites [48].

Zeolite-supported platinum nanoparticles are efficient catalysts for the electrolysis of water, giving higher current densities than other platinum immobilized systems [523–525]. Moreover, the particular behavior of ultramicroelectrodes can be exploited here to perform the electrolysis in the absence of added electrolyte. This kind of electrolysis at electrochemically activated microheterogeneous interfaces can also be applied to solute transformations, as exemplified
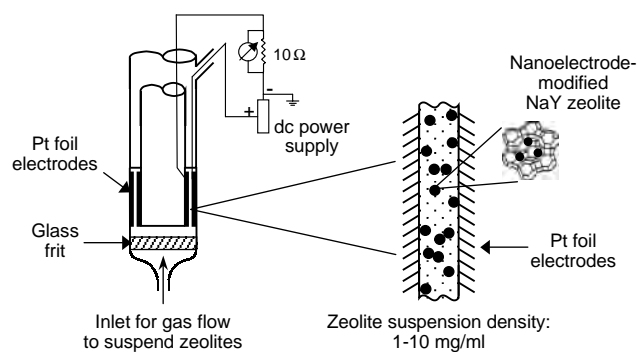
Figure 8. Schematic representation of electrode modified zeolites. Dispersion electrolysis cell showing the electrode particles contained between feeder electrodes with an exploded view of intra/extracrystalline Pt supported on zeolite Y. Reprinted with permission from [48], D. R. Rolison and C. A. Bessel, *Acc. Chem. Res.* 33, 737 (2000). © 2000, American Chemical Society.

for the $Fe(CN)_6^{3-/4-}$ couple using zeolite-supported platinum and ruthenium dioxide [530].

Electrochemically induced organic reactions can be catalyzed by the microheterogeneous dispersions. For example, pure zeolite suspensions were found to enhance the potentiostatic oxidative decomposition of toxic chlorinated aromatics and chlorofluorocarbons [826]. Selective oxidation of propene into propylene oxide was achieved at low ionic strength by using dispersions of Pd(II)–Cu(II)–zeolite Y as heterogeneous catalysts [527]. Reaction of benzylchloride with carbon dioxide was also catalyzed by electrochemistry at microheterogeneous dispersions of zeolite Y particles containing encapsulated cobalt–salen complexes [531].

4.2. Preconcentration Analysis

A common way to increase sensitivity of electrochemical detection at chemically modified electrodes [64–66, 78, 80], and to get down the detection limits, is to preconcentrate the analyte at the electrode surface prior to performing the voltammetric quantification. The usual procedure is depicted in Figure 9 and involves several steps that must be optimized to achieve the best performance for this method of preconcentration electroanalysis. Preconcentration is performed via chemical accumulation at an open circuit, usually under stirring to improve mass transport; it should be as fast as possible and highly selective with respect to the target analyte. After a certain period of time, the electrode is removed from the accumulation medium, rinsed with pure water, and immersed into the analysis cell containing an appropriate electrolyte that will allow the voltammetric quantification of the previously accumulated analyte species. This step could require the desorption of the analyte, especially when the electrode modifier is not electrically conducting (i.e., the case of clays, zeolites, silica, and most organically modified silicates). In the goal to perform successive experiments, a fourth step could be necessary to recover the initial state of the electrode: the regeneration of the electrode surface, which is ideally carried out chemically (by treatment in an appropriate medium), but it could require a mechanical renewing step in case of strong memory effects (e.g., irreversible binding of some active species to the electrode modifier).
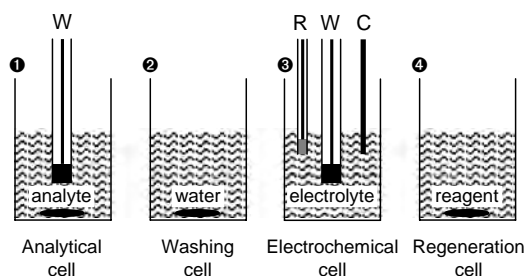

Figure 9. Schematic illustration of the four successive steps usually involved in a typical voltammetric analysis performed at a chemically modified electrode after preconcentration. W, R, and C refer to the working electrode, the reference electrode, and the counterelectrode, respectively.

4.2.1. Accumulation by Ion Exchange

As most zeolites and clays are ion exchangers, it is not surprising that the correspondingly modified electrodes have been largely applied to voltammetric detection of ionic species after their accumulation by ion exchange at the electrode surface [37, 44, 47]. Regeneration between measurements at such devices can be carried out by the reverse exchange, that is, by immersing the electrode in a washing solution containing the initial co-cation of the aluminosilicate, at least if the soaking solution does not lead to memory effects by diffusing deeply in the electrode microstructure, as observed in the case of zeolite modified carbon paste electrodes [445].

Several examples of preconcentration analysis at zeolite modified electrodes have been reported for trace analysis of electroactive cations, such as Ag^+ [441], Cu^{2+} [407, 452, 455], Hg^{2+} [440], Zn^{2+} [410], dopamine [451], or paraquat [463, 464]. Most of these applications are based on zeolite modified carbon paste electrodes because of their faster response in comparison to film-based electrodes [457]. Regeneration was often performed by mechanical smoothing of the electrode surface in order to limit the effect of solution impregnation during both the accumulation and measurement steps. The resort to disposable zeolite modified screen-printed electrodes was also reported [464]. Several zeolite types have been used and those displaying the largest pores were found to be the most efficient as they allowed fast diffusion of the analytes, which is the rate-determining step during both the accumulation and voltammetric detection stages.

Clay modified electrodes were largely used for detecting a wide range of charged species after accumulation by ion exchange within the clay [37]. Again, most of these applications have been performed with clay modified carbon paste electrodes, the choice of clay films on solid electrodes being mostly devoted to the analysis of mass transport reactions in the clay-based materials, even if ion exchange voltammetry at clay film-based electrodes have been investigated [293]. An exception is the determination of positively charged dopamine after accumulation in clay films [297–301], the latter acting as a protective layer preventing interference by ascorbic acid (repulsed from the electrode surface by unfavorable electrostatic interactions). Renewal of the clay modified carbon paste electrode surface can be achieved either by mechanical smoothing [351], chemical regeneration by reverse ion exchange [344], or even more complex chemical procedures [350]. Preconcentration efficiencies at clay modified electrodes were often better than those obtained with the corresponding zeolite modified electrodes [37]. Metal ion species such as Cu^{2+} [350–352], Ag^+ [356], Hg^{2+} [356], Cd^{2+} [361], or Fe^{3+} [344] have been successfully determined with using carbon paste electrodes modified with montmorillonite, vermiculite, or bentonite. In spite of the cation exchange properties of montmorillonite, this clay has been used to preconcentrate anionic chloro-complexes of mercury or gold prior to their voltammetric detection [360, 364, 367], leading to both cation and anion exchange on clay modified electrodes [365]. It is noteworthy that anion exchanging clays (LDHs) are more suited to the voltammetric sensing of anions after preconcentration at correspondingly modified electrodes [323, 380].

Accumulation by ion exchange can be performed in sol–gel films coated on solid electrode when the silicate-based material contains a net charge. This is the case of organic–inorganic hybrids for which the organic component is charged. Both class I and class II hybrids have been used for this purpose. The first family relies on interpenetrated ion exchange polymers and ceramic binder involving both cation exchangers (e.g., polyethylene- or polystyrene–sulfonate and Nafion [549, 551, 554]) and cation exchange polymers (e.g., poly(dimethyldiallylammonium) or poly(vinylbenzyl-trimethylammonium) [204, 553]). They were applied as thin composite films for the detection of anions $[Fe(CN)_6^{3-/4-}]$ or cations (such as methylviologen, $Ru(NH_3)_3^{3+}$, $Ru(bpy)_3^{2+}$, $[Re^I(DMPE)_3]^+$ with DMPE = 1,2-bis-(dimethyl-phosphino)ethane). Interestingly, dispersing the organic polymer in sol–gel derived silica matrix improves diffusion processes of the analyte, in comparison to the lower mass transfer rates usually observed in pure organic resins (polymeric ion exchangers), as illustrated in Figure 10 for $[Re^I(DMPE)_3]^+$ in Nafion. Sol–gel films containing charged organic groups covalently attached to the silica framework (e.g., ammonium or carboxylate moieties) [332, 563, 565, 568] have also been used for the charge selective determination of ionic species $[Fe(CN)_6^{3-/4-}$, $Ru(NH_3)_6^{3+}]$, with the advantage of a permanent binding of the reactant immobilized at the electrode surface. Note that accumulation by ion exchange at electrodes modified with pure silica gels, which were deprotonated beforehand, can also be performed, as reported for the detection of $Cu(NH_3)_4^{2+}$ or $Hg(NH_3)_4^{2+}$ species [607, 618, 619].
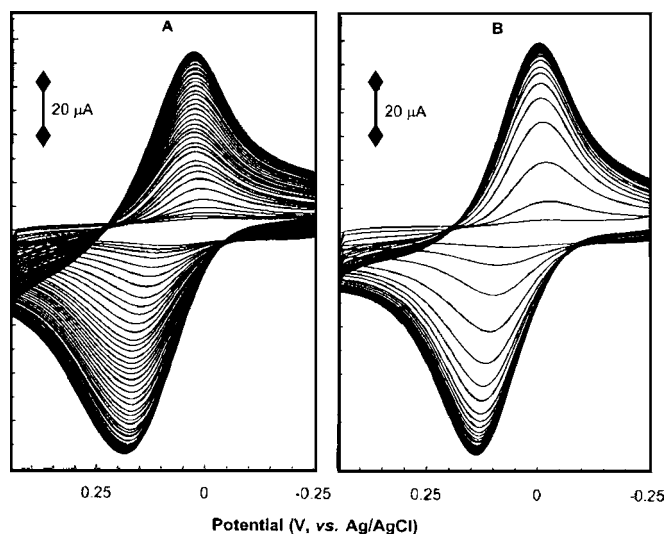

Figure 10. Cyclic voltammograms of $[Re^I(DMPE)_3]^+/[Re^I(DMPE)_3]^{2+}$ [with DMPE = 1,2-bis-(dimethyl-phosphino)ethane; 10^{-4} M in 0.14 M NaCl] at (A) Nafion and (B) Nafion–silica composite-modified spectroscopic graphite electrodes. Voltammetric parameters: 2-s prescan quiet time; 14-s cyclic voltammetric scan at 100 mV/s with an initial potential of −0.25 V and a switching potential of 0.45 V; and 224-s postscan open-circuit quiescence. A total of 50 potential cycles for each of the coatings; as shown, faster equilibration was observed with the composite film. Reprinted with permission from [550], Z. Hu et al., *Anal. Chem.* 70, 5230 (1998). © 1998, American Chemical Society.

4.2.2. Complex Formation

Accumulation of metal ions by complexation with immobilized organic ligands constitutes another attractive way to preconcentrate these analytes at an electrode surface, with the intention to get high selectivity by means of the appropriate choice of the ligand. However, this approach requires the durable immobilization of the ligand at the electrode surface (ensuring no leaching during the experiments) while maintaining its accessibility to the target analyte. The silica-based organic–inorganic hybrids are very promising for this purpose.

A simple course is to exploit the ability of the sol–gel process to physically trap a selected ligand into a ceramic matrix during its preparation, resulting in class I hybrids that can be associated to an electrode material either as a thin film or as carbon–ceramic composites. Examples are available for preconcentration analysis of Fe(III), Ni(II), Pb(II), or Os(IV), at electrodes containing, respectively, dimethylphenanthroline [606], dimethylglyoxime [684], diphenylthiocarbazone [725], or phenyl-fluorone [688] as the immobilized reagents. Even more interesting are the immobilized ligands that can be covalently attached to the silica framework (either by post-synthesis grafting or during the hybrid preparation by co-condensation with an organosilane), because they are leak-free reagents. Such class II hybrids therefore enable one to circumvent the activity loss of sensors based on simply encapsulated ligands. Applications in electroanalysis include the detection of Cu(II) and Hg(II) species after accumulation by complexation with amine- or sulfur-containing functions covalently attached to a silica matrix [566, 569, 608, 634]. An important parameter affecting the preconcentration efficiency is the accessibility (and rate of access) of the target element to the binding sites, which should be as fast as possible to get high detection sensitivity [610, 612, 613]. The ordered mesoporous organic–inorganic hybrid materials are extremely promising in this respect because they allow a homogeneous distribution of accessible organic functions in a regular porous structure made of channels of monodisperse size [613]. Therefore, preparing such ordered functional hybrid materials has led to increasing mass transfer kinetics; when bringing them to an electrode surface, much higher sensitivities were obtained in comparison to those based on amorphous and less open materials (Fig. 11).

4.2.3. Accumulation by Adsorption

Voltammetric determinations of organic analytes have been performed after accumulation by adsorption, essentially by using clay and silica modified electrodes. Separating the preconcentration medium from the detection one enables one to analyze target species in rather complex matrices without requiring any separation beforehand. However, strong adsorption to the modified electrode surface may induce some difficulties in the regeneration process and generate undesirable memory effects.

Several drugs or biological metabolites (e.g., flunitrazepam [827], clozapine [828], uric acid [297]), pesticides (dinocap [342], linuron [345], endosulfan [347], tetramethrin [343], amitrole [370]), and other organics (phenol, catechol and related alcohols [341], nitrobenzene and other nitro derivatives [457, 829], aniline [340]) have been determined after accumulation by adsorption at clay modified
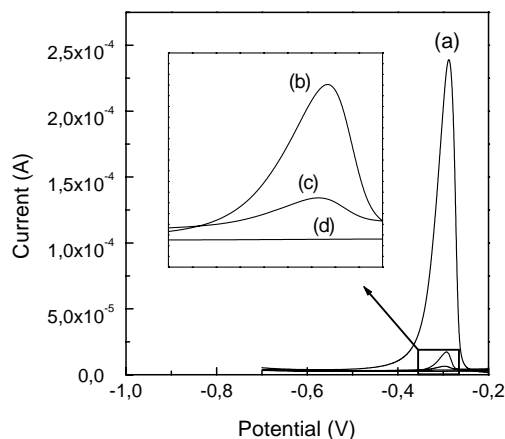
Figure 11. Typical voltammetric curves obtained for the analysis of 1×10^{-6} M Hg^{II} (at pH 1) using carbon paste electrodes modified with various silica samples bearing mercaptopropyl groups: (a) ordered solid with large pores, (b) amorphous solid with large pores, (c) poorly ordered solid with small pores, and (d) amorphous solid with small pores. Preconcentration time: 2 min. Detection: anodic stripping differential pulse voltammetry after 1 min electrolysis in 0.1 M HCl +5% thiourea. Reprinted with permission from [612], S. Sayen et al., *Electroanalysis*, 14, 1521 (2002). Wiley–VCH.

electrodes, most often by the sensitive differential pulse voltammetry technique. Clays such as sepiolite, bentonite, or nontronite were mainly used as additives to carbon paste electrodes for these applications. Various electrochemical treatments were applied to renew the electrode surface between each measurements with the goal of allowing successive analyses [341, 342, 345, 827, 829].

Silica modified carbon paste electrodes have been applied to the sensitive detection of various organics (e.g., pharmaceuticals, herbicides, ... [614, 615, 830–832]) and heavy metal species [620, 623], by exploiting the adsorption properties of silica gels toward these analytes prior to their voltammetric quantification. This approach was extended to the use of silica gel grafted with C$_{18}$ groups, a stationary phase commonly utilized for chromatographic separations, which was dispersed into carbon paste electrodes and then applied to the preconcentration analysis of some organic molecules (Tifluadom [624], methyl parathion [625], bendiocarb [626], ephedrine [629]).

4.3. Selective Recognition/Discrimination at Electrode Surfaces

4.3.1. Permselective Films

It was mentioned in Section 4.2.1, bringing a material containing ionized groups (i.e., clay, zeolite) to an electrode/solution interface enables one to accumulate either positively or negatively charged redox species (respectively in polyanionic and polycationic solids), while repelling those having the same charge as in the film. An illustrative example is the detection of the positively charged dopamine in the presence of the negatively charged ascorbic acid in both clay or zeolite modified electrodes [297, 451]. In addition to this kind of selective recognition/discrimination based on

the intrinsic electric charge of the modifier, other permselective films have been prepared to improve the selectivity of the electrochemical detection of charged species. Most of them are exploiting the versatility of the sol–gel technology to prepare hybrid materials with ionized groups durably immobilized in a porous silica matrix. Organically modified silicate film containing either –NH$_3^+$ or –COO$^-$ groups covalently linked to the silica framework have been deposited on glassy carbon electrodes. Whereas the silicate–NH$_3^+$ electrode resulted in large voltammetric currents for an anionic analyte such as Fe(CN)$_6^{3-}$, nearly complete suppression of the electrochemical response was observed with using the silicate–COO$^-$ electrode. Complementary behavior was exhibited for the positively charged Ru(NH$_3$)$_6^{3+}$ or methylviologen [563]. The extent of permselectivity is affected by the structure of the material [568]. Another approach to modulate the permeability of organic–inorganic layered coatings on electrode surfaces consists of the intercalation of polycationic silasesquioxane oligomers into a laponite clay film, which induces mesoporosity in the resulting clay modified electrode [309].

4.3.2. Molecular Sieving, Molecular Imprinting, and Chiral Recognition

Recognition at the molecular level is achieved with zeolite modified electrodes because of the size and shape selectivity exhibited by these solids, allowing one to distinguish between small electroactive species that can fit inside the molecular sieve and excluded redox species that are electrochemically "silent" [41, 42, 390, 398, 407, 438]. The latter need a more open structure, like that of ordered mesoporous solids, to be really electroactive [833]. To a lesser extent, such molecular sieving behavior has also been seen at pillared clay modified electrodes [212, 214].

An elegant approach to induce molecular recognition at the electrode surface is the design of molecularly imprinted coatings, which are based on the preparation of a polymer film structured around a target analyte that is used as a template. Removing this template generates inside the material some well-defined free spaces that are liable to "recognize" selectively the analyte later on (i.e., during a preconcentration experiment). Most of these systems that have been experienced at electrode surfaces are based on organic polymers and suffer from rather long response time [834]. Improvement can be achieved by designing sol–gel films displaying a molecular imprint. An example is available, based on a dopamine-templated film that was obtained by hydrolysis and co-condensation of phenyltrimethoxysilane and tetramethoxysilane in the presence of this analyte, which enables selective recognition of dopamine over ascorbic acid [835]. When coated on glassy carbon, the resulting electrode has led to the selective preconcentration and voltammetric detection of dopamine in the presence of structurally related molecules [565], with a satisfactory response time, and nearly complete selectivity over ascorbic acid (Fig. 12).

With the goal to create a chiral atmosphere at an electrode surface, special attention was given to the ability of some clays to impart the spatial organization of adsorbed species. In particular, it was found that the intercalation of Ru(bpy)$_3^{2+}$ species in smectite clays is rather unusual and

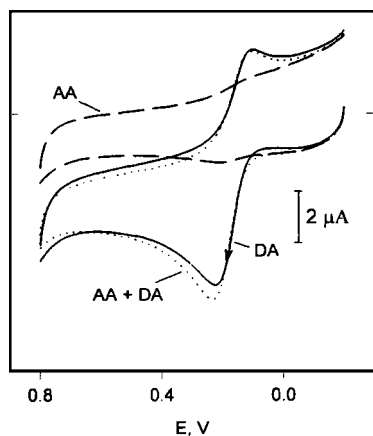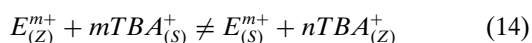**Figure 12.** Cyclic voltammograms of 10^{-4} M ascorbic acid (AA), 10^{-4} M dopamine (DA), 10^{-4} M AA and 10^{-4} M DA, at a dopamine-templated silica film coated on glassy carbon electrodes (0.1 M phosphate buffer at pH 7.4; scan rate: 100 mV/s). Reprinted with permission from [565], R. Makote and M. M. Collinson, *Chem. Mater.* 10, 2440 (1998). © 1998, American Chemical Society.

that these species have tendency to aggregate as a racemic pair rather than as a pure enantiomer [836, 837]. This has led to distinction of chiral mixtures at clay modified electrodes [217, 227, 237].

4.3.3. Indirect Amperometric Detection at Zeolite Modified Electrodes

A unique peculiarity of zeolites is that they combine in a single material both ion exchange properties and size selectivity. This has allowed the emergence of an elegant application of zeolite modified electrodes: the (indirect) amperometric detection of nonelectroactive cations [397, 398, 401, 413, 449, 458, 461, 462, 465].

The general principle [Eqs. (14) and (15)] involves the use of a zeolite modified electrode doped with an electroactive cation, E^{m+}, exchanged in the zeolite particles:

$$E^{m+}_{(Z)} + mTBA^+_{(S)} \neq E^{m+}_{(S)} + nTBA^+_{(Z)} \qquad (14)$$

$$E^{m+}_{(Z)} + mC^+_{(S)} \quad \Leftrightarrow \quad E^{m+}_{(S)} + mC^+_{(Z)} \qquad (15a)$$

$$E^{m+}_{(S)} + ne^- \quad \Leftrightarrow \quad E^{(m-n)+}_{(S)} \qquad (15b)$$

where the subscripts Z and S refer to the zeolite phase and the solution, respectively. When immersing such an electrode in an electrolyte solution containing a cation too large to enter the zeolite framework (e.g., tetrabutylammonium, TBA^+), no electrochemical activity of E^{m+} was observed because charge balance cannot be maintained [Eq. (14), Fig. 13A]. However, when injecting a certain amount of non-size-excluded cations (for example C^+) at the electrode surface, an equivalent amount of E^{m+} species is liberated by ion exchange [Eq. 15(a)] and can be detected amperometrically [Eq. (15b), Fig. 13B]. The current signal is due to the reduction of the mediator, but its intensity is directly proportional to the concentration of the C^+ sample. As such, this corresponds to the indirect amperometric detection of the usually nonelectroactive C^+ species.
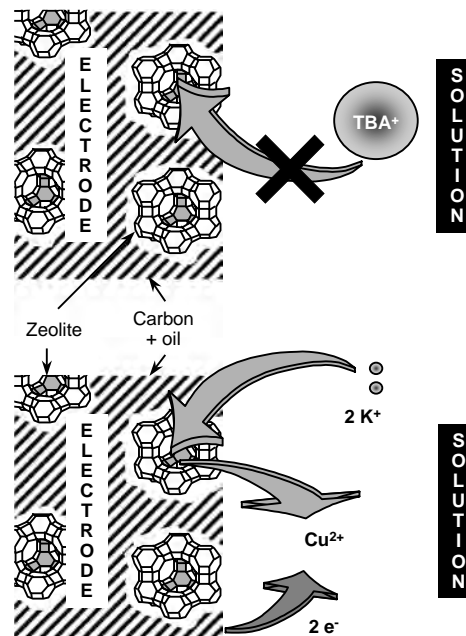

Figure 13. Schematic view of the detection principle for the indirect amperometry at a copper-doped zeolite modified carbon paste electrode (case of K^+). Reprinted with permission from [461], A. Walcarius, *Anal. Chim. Acta* 388, 79 (1999). © 1999, Elsevier Science.

Feasibility of the process was demonstrated in both aqueous [449, 461, 462] and nonaqueous [397, 398, 401, 413] media, respectively with methylviologen- or Cu^{II}-exchanged zeolite Y and Ag^I-exchanged faujasites. The intensity of the current response was inversely proportional to the size of the (hydrated) cationic analyte (i.e., selectivity series as $Cs^+ > K^+ > Na^+ > Li^+$) [413], and this selectivity was unaffected by the zeolite type [461] but dependent on the location of the redox probe in the zeolite [401]. The amperometric signals are fully controlled by diffusion and are, therefore, more intense with zeolites displaying the larger pore apertures [461]. When applied in organic medium, this detection mode was extremely sensitive to trace water [396], which made it suitable for determination of water content in organic solvents in the 1–10 ppm concentration range with a detection limit at 20 ppb [838, 839].

Indirect amperometric sensing at ZMEs was also applied to the detection of mixtures of cation after separation by ion chromatography (IC) [458, 465]. Suppressor-free detection was first realized using the methylviologen-exchanged zeolite Y modified carbon paste electrode in the presence of a mobile phase made of tetrabutyl-ammonium bromide, but this rather unusual electrolyte (chosen because of its size-excluded cation, TBA^+) gave rise to poor results [458]. Better performance was achieved when performing the IC separation with a conventional mobile phase and the amperometric detection after chemical suppression, in electrolyte-free solutions [465]. As shown in Figure 14, the indirect amperometric detection was equally efficient as that applied using the classical conductivity detector. This has opened the door to the use of other ion exchangers (without molecular
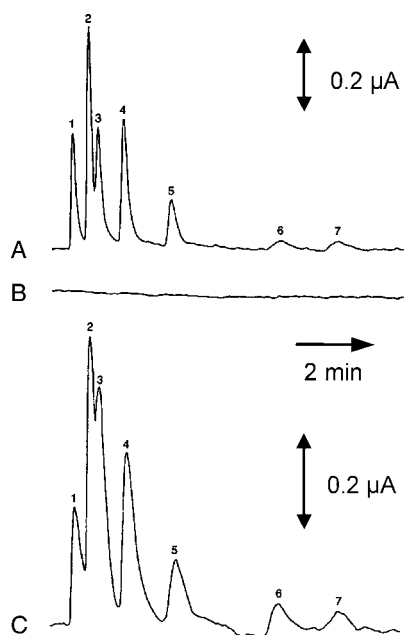
Figure 14. Chromatograms obtained using (A) a classical conductivity detector, (B) a NaY zeolite modified carbon paste electrode, and (C) a copper-exchanged zeolite Y modified carbon paste electrode, for a standard mixture of cations: 0.7 mM Li^+ (1), 0.2 mM Na^+ (3), 0.3 mM NH_4^+ (3), 0.13 mM K^+ (4), 0.04 mM Cs^+ (5), 0.2 mM Mg^{2+} (6), and 0.13 mM Ca^{2+} (7); mobile phase, 3×10^{-3} M $HNO_3 + 10^{-4}$ M EDTA; flow rate, 1 ml/min; applied potential [for (B) and (C)], −0.4 V. Reprinted with permission from [465], A. Walcarius et al., *Electroanalysis* 11, 393 (1999). ©1999, Wiley–VCH.

sieving properties) for performing such indirect amperometry, which has led to detection of both anions and cations at the output of an IC apparatus [840].

Indirect amperometry involving ZMEs was also performed via zeolite rectification of electrochemical ion transfer by exploiting the molecular sieving effects [438, 439].

4.4. Chemical Sensors Based on Direct Electrochemical Detection

In the wide range of electrochemical devices applied to the determination of a target analyte, those referred to as electrochemical sensors are based on the one-step detection of the analyte, without any other associated event (e.g., preconcentration).

4.4.1. Gas Sensors

Gas phase analysis using solid-state amperometric sensors is a current area of interest [28]. In this respect, xerogel films containing liquid microphases, coated on solid electrodes, have been applied to the electrochemical sensing of CO [663] and gaseous H_2O_2 [664], with less dependence to humidity changes than the corresponding Nafion-based sensors. Upon doping with iron(II) or a mixed valence–ruthenium oxide, this solid electrolyte coating acted as a mediator for the oxidation and simultaneous amperometric detection of gaseous monomethyl hydrazine [665].

Composite ceramic–carbon electrodes can also function as gas electrodes when doped by appropriate catalysts, such as cobalt phthalocyanines or porphyrins [683] or inert metal particles [671, 672], for oxygen sensing. Their main advantage is that the porous inorganic network provides a rigid open structure permitting gas permeability while the organic part induces hydrophobicity at the electrode surface and thus minimizes flooding of the liquid phase (Fig. 15). It is otherwise possible to control the wetted section of such composite electrodes [473]. Another related gas electrode for oxygen reduction and hydrogen peroxide generation is based on CCE containing covalently attached naphtoquinone derivatives acting as electrocatalysts [841].

Electrochemical gas sensors based on clay modified electrodes are nonexistent, while those based on zeolite modified electrodes are not widespread. Catalytic detection of ethanol and ammonia vapors was performed with the aid of gold deposits on zeolitic membranes [509], and semiconductors made of C60 encapsulated in zeolite cages have been applied to oxygen sensing [842].

4.4.2. Detection in Flowing Streams

On-line electrochemical monitoring is highly desirable with respect to multiple analyses (automation) and continuous detection in flowing streams (e.g., after chromatographic separation). One important requirement when considering flow injection analysis at chemically modified electrodes is related to the sensor stability, both chemical (i.e., durable immobilization of reagents) and mechanical (i.e., no degradation). Some achievements have been reported in this field with clay-, zeolite-, and silica-based materials used as electrode modifiers.

Most works have been performed with sol–gel-derived materials and related organic–inorganic hybrids because
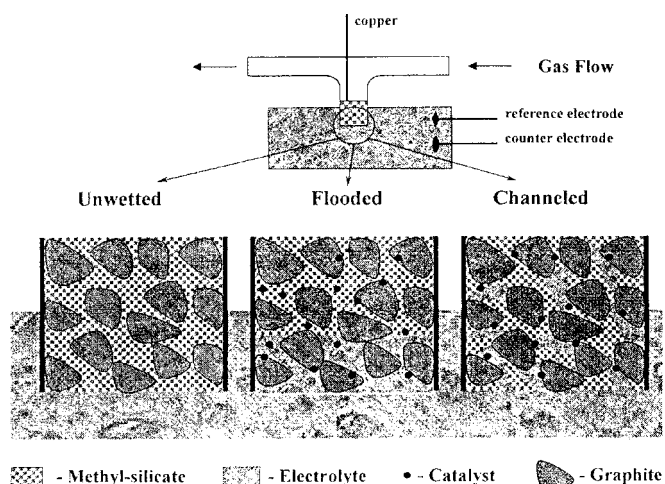

Figure 15. Gas permeable hydrophobic, sol–gel derived composite ceramic carbon electrodes. The external surface or a limited section near the bottom part of the electrode is wetted by the electrolyte. The wetted section can contain fingerlike wetted channels or can be uniformy flooded by the electrolyte. Reprinted with permission from [58], L. Rabinovich and O. Lev, *Electroanalysis* 13, 265 (2001). © 2001, Wiley–VCH.

they can be manufactured as robust composites, either coated on solid electrodes or as bulky composite ceramic–carbon electrodes. The simplest electrochemical detection in flow injection analysis (FIA) implies a direct detection without any pretreatment. It is not surprising therefore that FIA was mainly involved in determinations based on electrocatalysis. Examples are available for amperometric detection at film-based [533, 545, 663–665] and ceramic–carbon composite electrodes [685, 692, 843] doped with an appropriate catalyst. Other examples include sol–gel-based biosensors containing immobilized enzymes with or without mediator [582, 585, 821, 844], and ionophore-bearing ceramic membranes for potentiometric sensing [729, 731]. Electrodes based on ceramic–carbon composites are the most interesting with respect to FIA because they combine in a single material high mechanical stability, good conductivity, possible control of the hydrophobic–hydrophilic balance, stability in organic medium, and the possibility to immobilize durably various reactants. These are some reasons that have led to their use in wall-jet configurations, as new electrochemical detectors for both liquid chromatography [662, 688, 689] and capillary electrophoresis (e.g., detection of dopaminergic compounds [666, 668] and carbohydrates [667, 669]).

Some FIA experiments involving detection of clay modified electrodes have been also reported, involving either electrocatalysis [845], disposable sensors with adsorption properties [370, 372], and biosensors [846, 847]. Indirect amperometric detection of zeolite modified electrodes has mostly been performed under flowing conditions [449, 461, 462] or at the output of a chromatographic system [458, 465]. Combining on-line preconcentration and voltammetric detection at ZME after a selected delay time has allowed the selective detection of dopamine in the presence of ascorbic acid [451].

4.4.3. Disposable Sensors

Screen-printing microfabrication technology (Fig. 16) is widely used for the mass production of highly reproducible, yet inexpensive, disposable chemically modified electrodes. This approach has been applied in the field of silica modified electrodes by preparing sol–gel-derived carbon inks, for which low temperature curing is compatible with encapsulation of biomolecules [713, 720–725]. An attractive feature is the possibility to control the microstructure of these strips by monitoring the sol–gel process, which cannot be realized using conventional carbon inks [721]. A single-use pH sensor based on a screen-printed sol–gel ceramic carbon composite
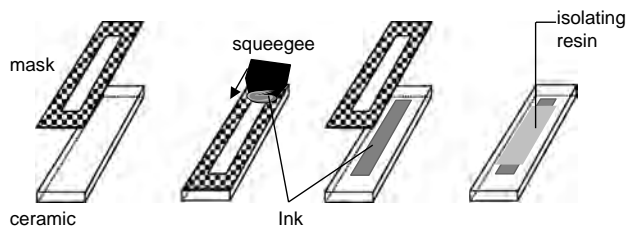

Figure 16. Schematic representation of the screen printing technology applied to the mass production of disposable electrodes.

comprising zeolite particles was also reported [474]. Zeolite-containing screen-printed electrodes gave rise to superior behavior (i.e., less memory effects) than the corresponding zeolite modified carbon paste electrodes [464]. Clay modified screen-printed electrodes have been used for detecting codeine in urine [372] and as humidity sensors [848], while conventional screen-printed electrodes covered with a clay film served as detecting pesticides [369, 370].

4.4.4. Potentiometry Detection-Ion sensors

Since the pioneering works demonstrating the usefulness of either zeolite [511] or clay [849] membranes for the potentiometric determination of alkali-metal cations, and the following report on size-selective detection of sodium ions in the presence of tetraethylammonium at zeolite A membrane [512], several other potentiometric devices based on zeolites or clays have been designed. Solid cation-exchange membrane electrodes, prepared by incorporating stilbite or bentonite clay and ammonium-phosphomolybdate in a cellulose nitrate inert matrix, were applied to the determination of the activities of Na^+, K^+, and NH_4^+ [377]. Composite membranes made of mordenite dispersion into a low viscosity epoxy resin gave rise to a near-Nernstian response to cesium ions with marked preference over other alkali metal ions [513, 514]. Optimizing the membrane preparation procedure, and especially the zeolite–polymer adhesion, resulted in Nernstian responses [427, 515, 516]. Potentiometric detection of surfactants was also performed with the aid of heterogeneous membranes containing either zeolite particles [517, 520] or laponite clay [379]. Anion-exchanging clays were exploited as ionophores in the development of anion potentiometric sensors [380]. Pure zeolite pressed to form a solid membrane has been applied to potentiometric sensing in organic medium [510]. The selectivity of clinoptilolite toward ammonium species was otherwise exploited to carry out the highly selective sensing of ammonium in water by means of a polymeric membrane comprising the zeolite deposited on an ion-sensitive field-effect transistor device [518], its high sensitivity (10 nM detection limit) enabling its use as the sensing component of a urea biosensor [519]. Finally, one should mention that adsorptive potentiometric stripping analysis was also performed on a nontronite-Nafion modified electrode and applied to the detection of dopamine [300].

Many potentiometric-sensing devices have been reported dealing with the use of silica-based materials, and especially organic–inorganic hybrid composites, which exploit the possibility to immobilize selective ionophores [535, 536, 566, 567, 727–737]. They may involve silica gels grafted with ionized groups and deposited on graphite-epoxy membranes [727, 728], organically modified silica films coated on conventional electrode surfaces for pH measurement [535, 567] or K^+ determination [536, 566], or as both class I and class II hybrid layers on ion-sensitive field-effect transistor devices, in which the ionophore can be simply entrapped in the sol–gel film [729, 730, 734, 737] or directly attached by covalent binding to the silica substrate by using an appropriate organotrialkoxysilane [733, 734] (some examples of ionophore-containing precursors follow). This category belongs to the leak-free sensors.
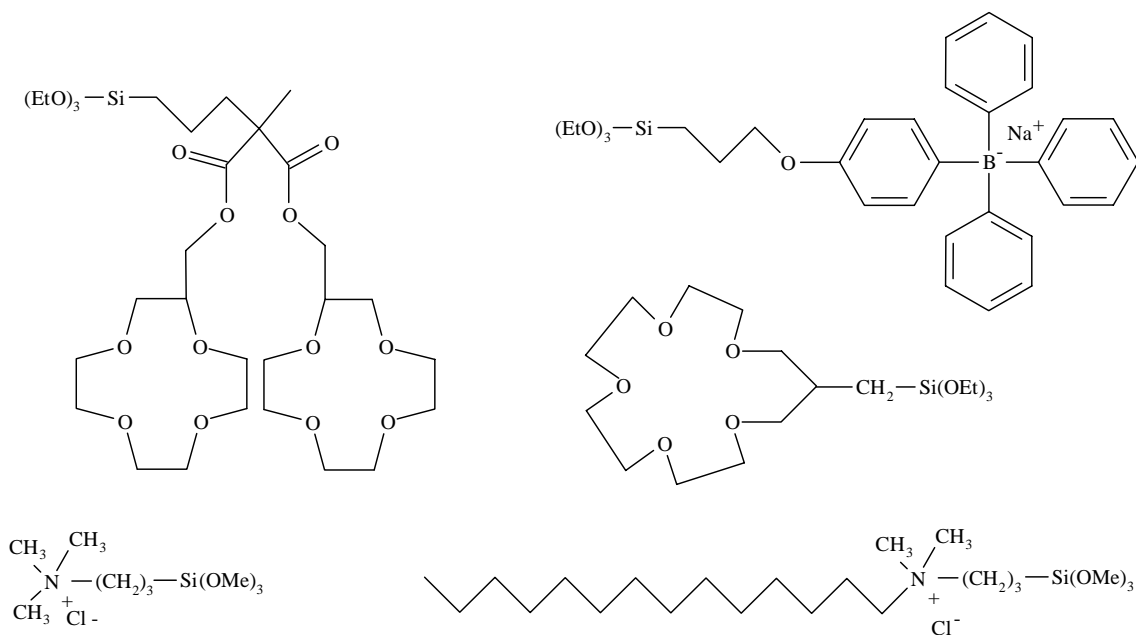
4.5. Electrochemical Biosensors

4.5.1. Basic Requirements

A biosensor is a sensing device made of three components, a biological detection system, a transducer that converts the biological recognition into a physicochemical parameter, and an output system [850]. Most biosensors have been electrochemical biosensors, based on the measurement of current, potential, or charge mobility. An electrochemical biosensor in an analytical device containing an immobilized sensitive biomaterial (mainly an enzyme, but also antibody, antigen, organelles, DNA, whole cells, or tissues) in close contact with an electrochemical transducer that is able to convert a biological event into a quantitatively measurable electric signal. Although an overwhelming number of investigations have appeared during the last decades, and some successful achievements have soared, very few "ideal" electrochemical biosensors were reported, displaying perfect selectivity, adequate detection limit, reversible response in sufficient time, acceptable robustness, and long-term stability for the target application.

Therefore, many efforts have been directed to design new devices for producing electrochemical biosensors with improved response and enhanced performance. One will focus later on describing briefly the contribution of nanostructured silicate-based materials in this field (e.g., clays, zeolites, sol–gel-processed silica, silica-based organic–inorganic hybrids). At least three key factors should be optimized to tend to the "ideal" biosensor. First, the biomolecule should be durably immobilized in close connection to an electrode surface (to ensure proper electrochemical transduction), in a configuration that does not prevent its biological activity. Second, attention should be given to ensure fast electron transfer between the electrode surface and the redox species generated during the biological event or the redox-active center of the biomolecule

itself; this might require the use of charge transfer mediators (Section 4.5.3). Third, the electrochemical biosensor should benefit from a stable response over prolonged periods, which would imply long-term stability of the biomolecule activity as well as durable immobilization of all the biosensor components.

4.5.2. First-Generation Biosensors

The first-generation electrochemical biosensors are those involving the direct electrochemical detection of the redox species produced or consumed during the biological recognition event.

Since the discovery of sol–gel bioencapsulation, which was recently reviewed [149, 177], the versatility of the sol–gel process to prepare a wide range of materials in various configurations (films, CCEs, monoliths, . . .) entrapping biomolecules was largely exploited in the realm of electrochemical biosensors. Various enzymes have been encapsulated into ceramic matrices, including glucose oxidase, peroxidase, tyrosinase, and urease, which were then coated on solid electrodes and applied to the detection of glucose [577–579, 851], hydrogen peroxide [582, 585], phenols [586, 592], and urea [583, 584], respectively. The film preparation procedure implies gelification of a starting sol that has been previously deposited on the solid electrode substrate by dropping, dip-coating, or spin-coating. Addition of an organic polymer into the starting sol was often require to produce crack-free films; poly(ethylene oxide) and poly(vinyl alcohol)-g-poly(4-vinylpyridine) were widely used to this end [579, 582–586]. Disposable ceramic-based bioelectrodes have been also produced [723]. Addition of gold nanoparticles during the film formation resulted in higher sensitivity and selectivity of the resulting film electrodes because of their catalytic action [713–716]. Other devices include the formation of an enzyme layer sandwiched between

the electrode surface and a ceramic overcoating to prevent enzyme leaching in the external solution [560, 595, 596]. Such bioceramic films coated on electrode surfaces are promising candidates for implantable biosensors as they have been found to be biocompatible [852, 853]. One should also mention that as-synthesized silica particles have also been used to stabilize enzymes at an electrode surface [776, 854–857], some of them being reported to enhance the amperometric signals [858, 859].

Clay films were also reported to participate to enzyme immobilization on an electrode surface. The hydrophilic character of laponite was exploited for this purpose and led to the extensive development of both aqueous and organic phase biosensors directed to the detection of glucose [306, 309], phenol or catechol [312], cholesterol [304], and hydrogen peroxide [860]. Some of them also involved clay–polypyrrole composite films that display improved enzyme entrapment [307, 310]. Trienzymatic arrangement in a clay film was recently applied to biosensing of inorganic phosphate [315]. Both anionic and cationic clays have been used together to immobilize urease on an electrode surface, and the resulting urea biosensor constitutes the first implication of LDH in the field of electrochemical biosensors [316], which is expected to grow in the future because of the intrinsic electrocatalytic properties of these materials. Electron transfer processes of redox proteins (C-type cytochromes) have also been studied at clay modified electrodes [311, 313, 314]. Finally, one should mention the use of zeolite particles that have been added to enzyme-containing carbon paste electrodes in order to increase their sensitivity by exposing the enzyme contained in the interior of the composite electrode, by solution impregnation, as a consequence of the hydrophilic character of the zeolite [450, 460]. The effect was less pronounced when increasing hydrophobicity of the material by dealumination [453]. After an appropriate hydrothermal treatment, zeolite Y can host small enzymes such as glucose oxidase and lead to glucose sensing when deposited as a film onto a platinum electrode [408].

4.5.3. Second-Generation Biosensors

The second-generation electrochemical biosensors are those involving the use of charge transfer mediators or electroactivated catalysts that act as electron shuttles between the electrode surface and the redox species produced or consumed during the biological recognition event. These mediators are often necessary to lower the overpotentials usually observed during the electrochemical detection of redox species, which can induce a significant lack of selectivity because of the presence of other redox-active derivatives in the medium that may affect the amperometric signal of the biosensor (interference). Of course, these charge transfer cofactors must be durably immobilized at the electrode surface, but they must keep sufficient mobility to play their role as electron shuttle between the electrode surface and the enzymatically controlled redox species. Various strategies have been proposed to confine biomolecule–mediator couples at electrode surfaces for biosensing applications.

Because of their ion exchange properties, zeolites and clays are liable to support positively charged mediators by electrostatic binding. Both zeolite [576, 578, 642, 653] and

clay [305, 308, 377] particles doped with various mediators have been coimmobilized with enzymes on electrode surfaces or within bulky composite electrodes and subsequently applied to biosensing. Even if efficient electrocatalysis was always observed, such kinds of integrated systems suffer from the lack of long-term stability due to possible leaching of the mediator into the external solution, as a consequence of reverse ion exchange with the electrolyte cations.

Silica-based materials and organic–inorganic hybrids are more promising for such purposes. Organic mediators are easily introduced in a starting sol which, upon gelification and drying, leads to the physical entrapment of them into a ceramic-based composite material: examples are available for both thin films on solid electrode surfaces [577, 591, 592] as well as bulk ceramic–carbon composite electrodes [700, 701, 706–708]. Operational second-generation biosensors were also obtained from carbon paste electrodes in which the enzyme was introduced together with chemically modified silica gel particles containing adsorbed mediators [649–654]. The mediators simply adsorbed on or entrapped within silica matrices are subjected to rather weak interactions so that they could undergo some leaching upon long exposure to solution [659–661]. Two strategies have been suggested to overcome this problem: (1) the preparation of multilayered electrode systems (electrode/mediator/enzyme/ceramic) [602–605] or (2) the covalent bonding of the mediator to the ceramic matrix, as exemplified with ceramic–ferrocene-based thin film [658] or carbon composite [702, 703] (Fig. 17). Alternatives to these approaches involve the attachment of the mediator directly to the enzyme [699–701] or to the graphite particles that constitute the ceramic–carbon composite electrode [861].
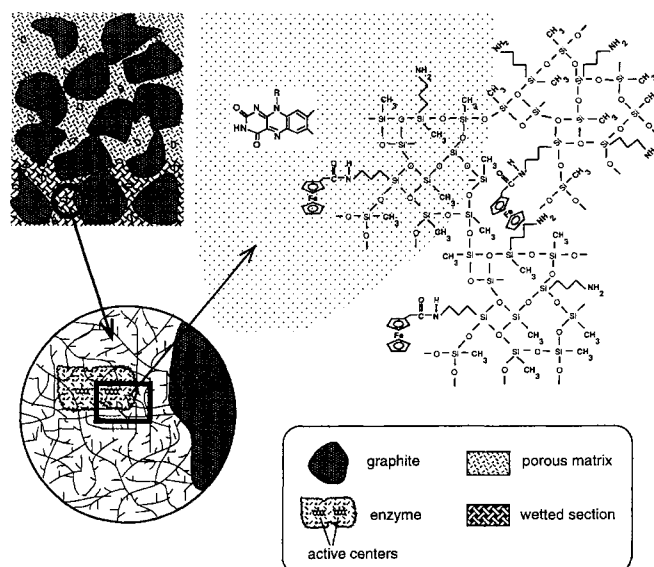

Figure 17. A scheme for glucose oxidase doped and amine-, methyl-, and redox-modified silicate–graphite composite electrodes. Reprinted with permission from [702], J. Gun and O. Lev, *Anal. Chim. Acta* 336, 95 (1996). © 1996, Elsevier Science.

4.6. Spectroelectrochemistry and Photoelectrochemistry

4.6.1. Spectroelectrochemical Sensing and Multimode Selectivity

A very nice application of hybrid films made of interpenetrated silica and ion exchange polymers coated on a transparent electrode has been proposed by the group of Heineman. It consists in a novel type of sensor based on spectroelectrochemical techniques possessing three modes of selectivity [546, 547]. The concept can be described as follow. A spectroelectrochemical device is constructed by incorporating attenuated totally reflected (ATR) light spectroscopy at an optically transparent electrode, which is coated with a selective film based on an ion exchange silica-based hybrid material. The two first levels of selectivity are achieved by conventional spectroelectrochemistry (applied potential and optical absorbance), while the third one is provided by the selective film. The latter allows access only to ionic species of a specific charge whereas it repels the opposite ones and also acts as a preconcentration layer for the analyte, which contributes to enhance the sensitivity of the detection and its detection limit. For the same goal of improving sensitivity of the optical detection mode, the light is forced to pass through the entire length of the thin layer electrode via internal reflection. The analyte partitioned into the film can undergo electrochemical modulation and the resulting oxidation or reduction product is optically monitored as the device signal. Selectivity of the detection is monitored at three levels, by a judicious choice of the coating material, the electrolysis potential, and the wavelength for optical sensing.

The concept was first demonstrated for the model analyte $Fe(CN)_6^{4-}$, which was detected by monitoring the transmittance change of the ATR beam resulting from its electrochemical oxidation after partitioning into a selective film (Fig. 18). The la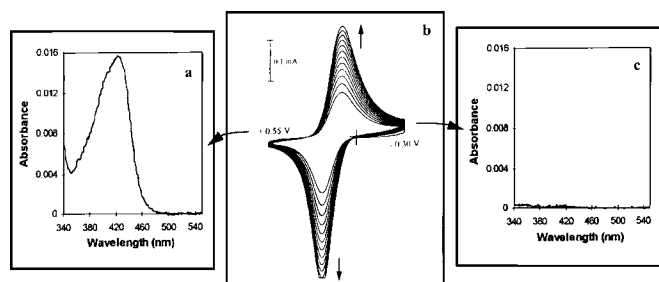tter was made of an anion exchange composite formulated by entrapping poly(dimethyldiallylammonium chloride, PDMDDAC) in a cross-linked silica network [547]. The application of suitable potential steps or waveforms results in the generation of optically detectable $Fe(CN)_6^{3-}$ species, the intensity of the ATR signal being related to the concentration of the starting $Fe(CN)_6^{4-}$ analyte. Selectivity for $Fe(CN)_6^{4-}$ species, in the presence of a competing electroactive anion [e.g., $Ru(CN)_6^{4-}$] that also displays significant permeation into the film, was obtained by restricting the electrolysis potential window to the sole $Fe(CN)_6^{4-}$ oxidation. Alternatively, an appropriate selection of the wavelength to record the ATR signal can lead to selectivity for $Ru(CN)_6^{4-}$ species [546]. Selective partitioning of cations was achieved by using a silicate/polymer composite characterized by cation exchange properties (e.g., ion exchange polymer = Nafion), while excluding anions, leading to, for example, the selective detection of $Ru(bpy)_3^{2+}$ over $Fe(CN)_6^{4-}$ [553]. Good sensitivity in the μM to mM concentration range was achieved. Averaging the optical response upon continuously cycling the potential resulted in significant improvement of the signal-to-noise ratio, contributing therefore to lowering further the detection limit [552]. Various excitation potential waveforms have been evaluated and optimized by a simulation program [555]. Two types of prototype waveguide spectroelectrochemical sensors were also developed to replace the multiple internal reflection optic consisting of the simple modified ITO (Indian Tim Oxide) electrode/glass substrate bilayer [557, 561]. The method can be applied to the detection of nonabsorbing analytes such as ascorbic acid or ascorbate if an appropriate mediator [e.g., $Ru(bpy)_3^{2+}$] is incorporated in the device [556]. The $Re(dmpe)_3^+$ compound [where dmpe = 1,2-bis(dimethylphosphino)ethane] was also detected by this method [551]. Extension of the approach to a poly(vinyl alcohol) (PVA)–polyelectrolyte blend, where ceramic binder was replaced by PVA, was also described [558]. Further works are still in progress to extend the scope of applications and to develop field portable spectroelectrochemical sensors [862].

Figure 18. (b) Series of cyclic voltammograms recorded with a PDMDDAC-silica (see text for explanation) coated indium–tin oxide electrode sensor during the uptake of $Fe(CN)_6^{4-}$. Voltammograms were recorded by cycling the sensor in 5×10^{-5} M $Fe(CN)_6^{4-}$ (scan rate: 20 mV/s). (a) Absorbance spectrum of the sensor at the positive potential limit of +0.55 V. (c) Absorbance spectrum of the sensor at the negative potential limit of −0.30 V. The absorbance measurements were performed in a single-pass transmission geometry (normal incidence) after the sensor was immersed in 10^{-3} M $Fe(CN)_6^{4-}$. Reprinted with permission from [547], Y. Shi et al., *Anal. Chem.* 69, 3679 (1997). © 1997, American Chemical Society.

4.6.2. Electrogenerated Chemiluminescence and Electrochromism

Electrochemiluminescence is defined as the generation of light induced by the reaction of an electrogenerated species with a sensitizer. The complex ruthenium–tris(bipyridine), which emits light at 610 nm, belongs to this category. When $Ru(bpy)_3^{2+}$ is incorporated into Nafion–silica composite films [559], chitosan–silica gel membranes [777], or (polyhydroxyethyl)methacrylate/sol–gel/silica composite films [780], respectively coated onto solid electrode surfaces, electrochemiluminescence can be produced. Very stable electrogenerated chemiluminescence was observed from a solid-state device based on $Ru(bpy)_3^{2+}$ encapsulated within a silica monolith comprising an immobilized ultramicroelectrode assembly and containing entrapped tripropylamine as the reductant, because such a device ensures relative immunity of the reactants to water and oxygen [782, 784]. Luminescence quenching in these systems was suggested to provide information about the interactions experienced by

the reactants in the nanostructured silicate host [785]. Clay modified electrodes prepared with iron-containing clay particles (montmorillonite K10) were able to promote electrogenerated chemiluminescence in a solution containing luminol and hydrogen peroxide [287], with enhanced stability as compared to the nonimmobilized system (Fig. 19). A linear relation between the signal and the H_2O_2 was observed under certain conditions and exploited for the detection of glucose after further modification with glucose oxidase, with high sensitivity due to the electrocatalytic action of iron centers in the clay [863]. Finally, it should be mentioned that no electrogenerated chemiluminescence has been reported to date at zeolite modified electrodes, even if zeolites have been used as an immobilization matrix for chemiluminescent precursors [117].

A persistent and reversible change of color that is electrochemically induced is ascribed to electrochromism. Among the wide range of all solid-state smart windows and switchable displays, those based on sol–gel technology have received considerable attention [49, 800, 864]. A limited number of them have been devoted to organic–inorganic hybrids, based either on the dispersion of organic dyes within a ceramic matrix (to extend the spectral color change) or on ceramic–organic polymer composites in which the organic polymer can be the electrochemically sensitive component (e.g., conducting polymer) or the structure-tuning agent [865–869].
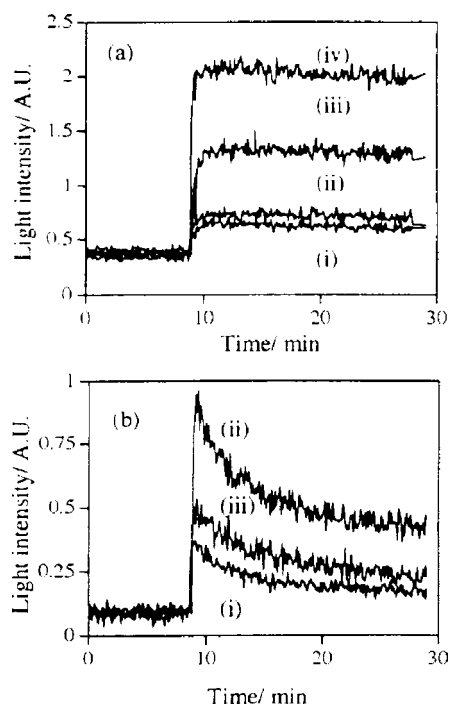

Figure 19. Transient emission spectra recorded with (a) immobilized luminol and glucose oxidase in a clay modified electrode, for the analysis of glucose at (i) 1 μM; (ii) 10 μM; (iii) 100 μM; (iv) 1 mM. (b) Spectra for 2 mM of free luminol and 1 mM of glucose with various amounts of glucose oxidase in solution: (i) 20 mg; (ii) 40 mg; (iii) 100 mg, pH 10. Reprinted with permission from [287], C. S. Ouyang and C. M. Wang, *J. Electroanal. Chem.* 474, 82 (1999). © 1999, Elsevier Science.

4.6.3. Photocatalysis

Photoelectrochemistry of molecules in zeolite and clays has been reviewed [383, 870]. Zeolites and clays are excellent templates for the fabrication of multicomponent electron transfer systems. Charge trapping behavior was observed at both zeolite and clay modified electrodes where spatial ordering of three redox species was organized [331, 388, 389, 521, 870, 871]. Photodriven catalysis of water splitting was often realized with using clay particles acting as hosts for positively charged sensitizers or mediators [36]. Photocatalytic reduction of molecular oxygen was performed using $Ru(bpy)_3^{2+}$ supported on clays and a cobalt complex as the charge transfer mediator [280, 872, 873]. Zeolites were also used for photocatalytic purposes. The zeolite AgA modified electrode immersed in chloride solution results in the formation of AgCl clusters at the electrode surface, which enables the photocatalytic oxidation of water to molecular oxygen due to the electroassisted regeneration of the metallic silver produced during the process [874]. A combined photochemical and electrochemical study of silver(0)–zeolite Y exchanged with methylviologen was reported, which was applied to photoreduction of intrazeolitic methylviologen by silver clusters stabilized in/on zeolite Y [875]. Electron transfer photocatalysis was demonstrated with $Ru(bpy)_3^{2+}/TiO_2$-codoped zeolites, for which it was found that the TiO_2 nanoparticles located in close vicinity to the zeolite particles play the role of electron relay to reach the electroactive species entrapped in the aluminosilicate [468].

4.7. Solid Electrolytes in Power Sources

Solid electrolyte electrochemistry is becoming a wide area of research, involving the production and characterization of all solid-state electrochemical devices that have found applications in various fields and, among them, the power sources (i.e., batteries, capacitors, fuel cells) [876–879]. Conductivity in these media is due to ionic motion mechanisms involving diffusion of charged species in an amorphous liquidlike environment [880]. Efforts have been concentrated on increasing the conductivity of solid electrolytes (or to generate new systems displaying enhanced conductivities). In this respect, both nanostructured materials [881] and sol–gel approaches for solid electrolytes [49, 882] offer promising in meeting several application requirements.

Solid electrolytes based on zeolite–polymer [502, 505, 506, 883] and clay–polymer [884, 885] composites benefit from the ion exchange properties of the minerals that contribute to increase the conductivity of ions (e.g., Li^+ in lithium batteries). Pure zeolites were also used for this purpose, as a host for Li^+ ions in lithium batteries [504, 505, 507, 508], for Zn^{II} in zinc-manganese oxide batteries [886], for Pb^{II} in lead-acid batteries [503], for Cu^{2+} and Zn^{2+} in a modified form of the Daniell battery [500], or for Na^+ to prepare sodium anodes [887]. Moreover, zeolites are attractive in manufacturing batteries because of their desiccant properties, enabling removal of trace water in the device after assembly of the cell [504]. Dehydrated zeolite crystals were used as host structures for liquid and/or volatile electrochemically active species in designing solid-state batteries that can be readily applied at room temperature, for example, zeolite/iodine or zeolite/sulfur (or selenium) cathodes

[502, 887, 888]. Zeolite modification of organic cathodes was recently proposed as a clean technology for improved cycle life of the zinc-chloranil organic secondary battery [889]. Zeolite-supported noble metal nanostructures have found applications as catalysts in fuel cell electrodes [890–892]. Zeolites NaX, NaA, and AgA have been used as catalysts in oxygen–methanol fuel cells [893–895]. Improved efficiency of methanol fuel cells operating at elevated temperature can be achieved by inserting a zeolite membrane between the anode and cathode compartments to prevent the escape of methanol in the atmosphere [896].
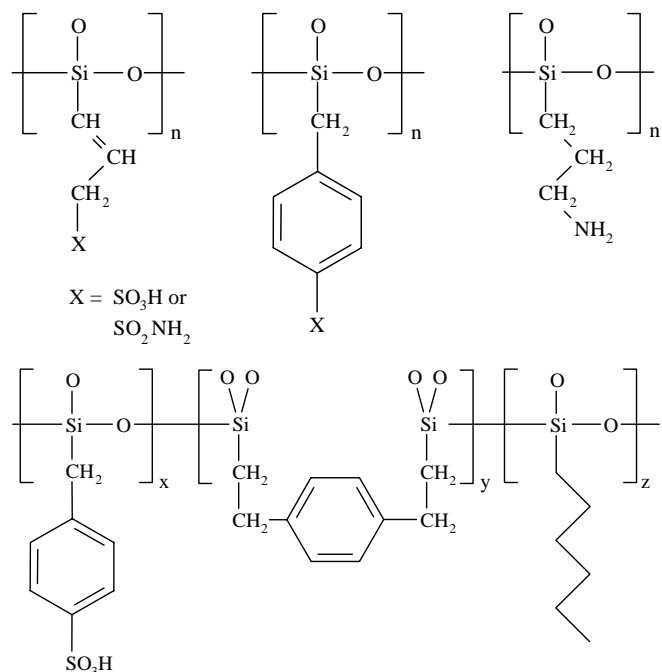
Even if much of the interest in preparing solid electrolytes by the sol–gel method for application in power sources relies on electroactive metal oxides (V, Ce, Ru, or Ti oxides) involving protonic, sodium-, and lithium-based ionic conductors [49, 50], some achievements have been reported in the field of silica-based materials. In particular, organically modified ceramics have been found to be very attractive for the production of protonic or lithium ion conductors, because the classically used polymer electrolytes [mostly poly(ethylene oxide) or Nafion doped with an acid or a lithium salt] may suffer from some drawbacks (e.g., decrease in conductivity due to some crystalline regions in the material). Several strategies have been reported to prepare solid electrolytes with high conductivity on the basis of silica-containing organic–inorganic hybrids. Numerous class I hybrids have been obtained simply by adding silica particles into a plasticizer doped with protons [740, 743, 746, 747, 753] or with a lithium salt [742, 750, 765]. They always display improved charge transfer properties as compared to the pure organic polymer doped with the same ions. An alternative consists of forming a silica network into the plasticizer by sol–gel processing [744, 748, 752]. Even more interesting are hybrids of class II that are characterized by a covalent bond between the organic and

ceramic components because the sol–gel process allows the production of solid electrolyte with tailor-made composition and structure [738, 745, 751, 897–899]. Examples are given for proton conductors, including poly(allyl sulfonic acid)siloxane, poly(allyl sulfonamide)siloxane, poly(benzyl sulfonic acid)siloxane, poly(benzyl sulfonamide) siloxane, poly(aminopropyl)siloxane, and poly(benzyl sulfonic acid–diethylbenzene-hexyl)siloxane. On the other hand, lithium-conducting electrolytes for all solid-state electrochemical devices have been produced in the form of nanocomposites based on poly(ethylene glycol) or poly(propylene glycol) covalently attached to a silica network comprising a lithium salt [759–763, 766]. High ionic conductivity was observed in these hybrids at room temperature, which was found to be maximal for a [O]/[Li] ratio of about 15 [761]. Note that related hybrids based on interpenetrated copolymers of poly(ethylene, propylene glycol)–polysiloxane that are not covalently bonded to each other, doped with an appropriate lithium salt, gave rise to higher conductivities, most probably because of higher polymer chain mobility contributing to the overall ionic motion [766]. Proton conductivity can be induced in these hybrids by replacing the lithium salt with either peroxopolytungstic acid [764] or monododecyl phosphate [749], or with $NaClO_4$ to get a sodium ion conductor [768].

4.8. Electrochemical Characterization of Reactions in Nanostructured Materials

4.8.1. Ion Exchange in Zeolites and Clays

Electrochemistry at clay modified electrodes can provide information on the ion exchange properties of clay minerals. A temptative model was proposed on the basis of the vermiculite modified carbon paste electrode for the preconcentration of silver(I) and copper(II) ions [900]. By considering a simplified ion exchange process involving the negatively charged centers in the clay, it was shown how the equilibrium constant associated with the ion exchange reaction can be estimated from the electrochemically determined concentrations of metal ions in the clay at the equilibrium. Variation of current dependence with time is also useful to characterize metal ion binding on clay materials [353]. In addition, the isopotential points observed by multisweep cyclic voltammetry at clay modified electrodes have been used to gain information on ion exchange reaction mechanisms in clays [244].

As the electrochemical behavior of small redox species at zeolite modified electrodes implies their ion exchange for the electrolyte cation before the charge transfer is taking place, the voltammetric response of the electrode is directly affected by this reaction. This was exploited to draw the normalized ion exchange isotherm corresponding to the methylviologen–sodium exchange in zeolite Y, by measuring the equivalent fraction of methylviologen in the zeolite after equilibration in a solution containing a selected equivalent fraction of solution-phase methylviologen (selected MV^{2+}/Na^+ ratio) [463]. As only the zeolite particles located at the electrode surface (few μg) contact the external solution (typically 50 ml) during the experiment, the macroscopic composition of the solution remains

unchanged during the equilibration process (the MV^{2+}/Na^+ ratio in solution is known at any time). The isotherm is thus constructed very rapidly by plotting the equivalent fraction of methylviologen in the zeolite, which is obtained by electrochemistry, as a function of the same parameter in solution, which remains constant during the process because of the very low solid-to-solution ratio. In addition, accurate determination of intrazeolite diffusion coefficients can be performed by chronoamperometry at a zeolite-modified electrode containing partially exchanged electroactive species [411]. This has been demonstrated for silver(I) in zeolite X and Y, for which the electrochemical activity of silver ions located in the small sodalite cages requires their diffusion to the large surpercages and then to the electrode surface, the former being the rate-determining step. Values of $(2-4) \times 10^{-8}$ cm^2 s^{-1} have been calculated from simulation of the chronoamperometric curves.

4.8.2. Adsorption on Silica

According to the same protocol applied to characterize ion exchange in zeolites, the choice of carbon paste electrodes modified with silica gel enables one to construct adsorption isotherms for heavy metals (i.e., Hg^{II}) on that solid and related materials [620]. The principle is based on the electrochemical monitoring of the amount of adsorbed Hg^{II} species as a function of pH. It takes again advantage of the very low solid-to-solution ratio, which allows one to avoid the use of buffers to adjust pH (which may induce deleterious effects on the sorption processes). By working in the presence of chloride at a concentration close to that of mercury, it was found that only the Hg^{II} species bearing at least one hydroxyl group were able to adsorb on the silica surface by condensation with the surface silanol groups, in the form of a surface complex. This is illustrated in Figure 20, by superimposing typical results of the electrochemical monitoring to a diagram depicting the various chemical species in solution. Similar conclusions have been established for the binding of Hg^{II} species in ordered mesoporous silica, displaying a very high selectivity for this element between pH 4 and 7 [609]. This approach is expected to be applicable to other systems and especially to the study of complexation processes on organically modified silicates.

4.8.3. Mass Transport in Clays and Soils

Clay modified electrodes have sometimes been proposed to serve as a model for the study of mass transport phenomena that occur in soils. Of course, these media are much more complicated than pure clay, involving also other minerals, a large quantity of organic matter, and a huge amount of microorganisms. In addition to the fact that electrochemistry performed at clay modified electrodes enables the characterization of adsorption and ion exchange rates in clays (see Section 3.1), some other investigations have appeared, dealing with systems closer to real geochemical situations.

One example is the study of copper(II) accumulation at a vermiculite-modified electrode in the presence of organic ligands in solution [352]. The copper(II) uptake was found to be affected by these ligands only if they were able to form a stable complex with the metal ion, otherwise no effect was observed. Moreover, it has been possible to evaluate by
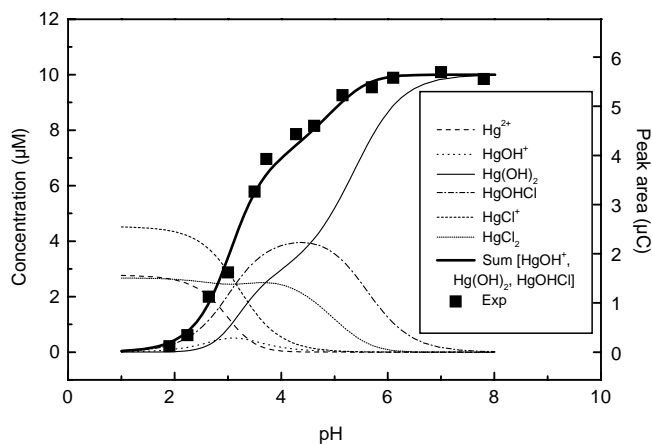

Figure 20. Adsorption isotherm obtained by electrochemistry for mercury on silica gel. Data were obtained as a function of pH at a silica-modified carbon paste electrode after 5 min accumulation from a 1.0×10^{-5} M mercury solution in the presence of 1.0×10^{-5} M of chloride; detection was performed by anodic stripping square wave voltammetry (in 0.2 M HNO$_3$) after 1 min electrolysis at -0.2 V. Comparison to the distribution diagram of mercury species, calculated using the PSEQUAD software, indicates clearly those species liable to interact with the silica surface. Reprinted with permission from [620], A. Walcarius et al., *Environ. Sci. Technol.* 33, 4278 (1999). © 1999, American Chemical Society.

this approach the interactions between heavy metal ions and some soil samples by using electrodes modified with soils in their native form [363]. The soil-modified carbon paste electrode was even suggested as a promising device for on-site characterization of soils, but great care should be taken with the various parameters that would affect the electrochemical response in such a complex system, making the interpretation of the results intricate. Another example aims at understanding the interaction of solutes in clay–humic acid systems, by comparing the behavior of copper(II) at carbon paste electrodes containing either mixtures of clay and humate or the clay alone [354]. For these systems, depending on the clay type, the electrochemical response to copper(II) was useful to distinguish between clays that interact strongly with humate and those for which no structural changes were induced by the organic matter. Similarly, it was found that humic substances reduce access to the inner regions of the clays by clogging access pores and by competitive binding cations [266].

5. CONCLUDING REMARKS

Nanostructured materials, such as layered clays, crystalline zeolites, amorphous or ordered silicas, and silica-based organic–inorganic hybrids, are attractive solids for the chemical modification of electrode surfaces. This arises from their interesting intrinsic properties that can be advantageously coupled to redox processes in designing new applications (or improving old ones) in various fields, including analytical chemistry and (bio)sensors, electrocatalysis, materials science, spectroelectrochemistry, and solid electrolytes, among others. However, even if several successful applications have been reported, the fundamentals associated with

the electrochemistry of this kind of material are not fully understood to date, most probably because of the difficulty in getting an appropriate model for such heterogeneous electrode systems. Nevertheless, the enormous potential to create new nanostructured materials with tailor-made composition, structure, and properties will undoubtedly contribute to increasing their applications in electrochemical science in the near future.

GLOSSARY

Chemically modified electrode (CME) An electrochemical device integrating an electrode surface and a chemical reagent or material, enabling to combine its intrinsic properties with the electron transfer reaction.

Electroactive species Chemical species that can undergo a charge transfer reaction.

Electroanalysis The involvement of Electrochemistry in Analytical Chemistry.

Electrocatalysis Concept relying on the methods used to increase the rate of electron transfer between electroactive species and an electrode surface.

Flow injection analysis (FIA) Quantitative monitoring of a target analyte by injection in a flowing stream.

Organic–inorganic hybrid materials Nanocomposites materials made of inorganic and organic components that are mixed at the nanometric scale.

Voltammetry Ensemble of electrohemical techniques based on the measurement of current that is generated during the application of a particular potential waveform.

REFERENCES

1. R. W. Murray, *Acc. Chem. Res.* 13, 135 (1980).
2. R. W. Murray, in "Electroanalytical Chemistry" (A. J. Bard, Ed.), Vol. 13, p. 191. Dekker, New York, 1984.
3. R. W. Murray, A. G. Ewing, and R. A. Durst, *Anal. Chem.* 59, 379A (1987).
4. R. W. Murray, Molecular design of electrodes surfaces, in "Techniques of Chemistry," Vol. 22. Wiley, New York, 1992.
5. A. E. Kaifer, *Israel J. Chem.* 36, 389 (1996).
6. A. E. Kaifer, *Progr. Colloid Polym. Sci.* 103, 193 (1997).
7. K. Uosaki, in "New Challenges in Organic Electrochemistry" T. Osa, Ed.), pp. 99–111. Gordon & Breach, Amsterdam, 1998.
8. X. Zhang and J. C. Shen, *Adv. Mater.* 11, 1139 (1999).
9. A. J. Downard, *Electroanalysis* 12, 1085 (2000).
10. J. Leddy, *Electrochem. Soc. Interface* 9, 41 (2000).
11. A. Merz, *Top. Curr. Chem.* 152, 49 (1990).
12. A. Deronzier and J.-C. Moutet, *Curr. Top. Electrochem.* 3, 159 (1994).
13. R. Harth, D. Ozer, J. Hayon, R. Ydgar, and A. Bettelheim, *Curr. Top. Electrochem.* 3, 531 (1994).
14. G. Bontempelli, N. Comisso, R. Toniolo, and G. Schiavon, *Electroanalysis* 9, 433 (1997).
15. A. R. Mount, *Res. Chem. Kinet.* 4, 1 (1997).
16. K. Brainina, G. Henze, N. Stojko, N. Malakhova, and C. Faller, *Fresenius J. Anal. Chem.* 364, 285 (1999).
17. S. Cosnier, C. Gondran, and A. Senillou, *Synth. Met.* 102, 1366 (1999).
18. A. R. Hillman, H. L. Bandey, P. M. Saville, R. W. Wilson, S. Bruckenstein, and J. G. Vos, in "Polymer Surfaces and Interfaces III" (R. W. Richards and S. K. Peace, Eds.), Wiley, Chichester, UK, 1999, pp. 165–190.
19. A. W. Bott, *Curr. Sep.* 19, 71 (2001).
20. D. Leech, in "Electroactive Polymer Electrochemistry, Part II: Methods and Applications" (M. E. G. Lyons, Ed.), p. 269. Plenum Press, New York, 1996.
21. J.-M. Kauffmann, Ed., Special issue of *Bioelectrochem. Bioenerg.* 42 (1997).
22. L. Echegoyen and L. E. Echegoyen, *Acc. Chem. Res.* 31, 593 (1998).
23. T. D. Chung and H. Kim, *J. Inclusion Phenom. Mol. Recogn. Chem.* 32, 179 (1998).
24. P. Buehlmann, H. Aoki, K. P. Xiao, S. Anemiya, K. Tohda, and Y. Umezawa, *Electroanalysis* 10, 1149 (1998).
25. F. Bedioui, S. G. Granados, and C. Bied-Charreton, *Recent Res. Devel. Electrochem.* 2, 91 (1999).
26. A. Ferancova and J. Labuda, *Fresenius J. Anal. Chem.* 370, 1 (2001).
27. I. Svancara, K. Vytras, J. Barek, and J. Zima, *Crit. Rev. Anal. Chem.* 31, 311 (2001).
28. K. S. Alber, J. A. Cox, and P. J. Kulesza, *Electroanalysis* 9, 97 (1997).
29. P. J. Kulesza and J. A. Cox, *Electroanalysis* 10, 73 (1998).
30. K. Itaya, I. Uchida, and V. D. Neff, *Acc. Chem. Res.* 19, 162 (1986).
31. D. H. Karweik, C. W. Miller, M. D. Porter, and T. Kuwana, *ACS Symp. Ser.* 199, 89 (1982).
32. J. G. Redepenning, *Trends Anal. Chem.* 6, 18 (1987).
33. H. D. Abruna, *Coord. Chem. Rev.* 86, 135 (1988).
34. A. Fitch, *Clays Clay Minerals* 38, 391 (1990).
35. D. Petridis, *NATO ASI Ser. C* 400, 433 (1993).
36. S. M. Macha and A. Fitch, *Mikrochim. Acta* 128, 1, (1998).
37. Z. Navratilova and P. Kula, *Electroanalysis*, in press
38. A. J. Bard and T. E. Mallouk, in "Molecular Design of Electrode Surfaces" (R. W. Murray, Ed.). Wiley, New York, 1992.
39. M. D. Baker and C. Senaratne, in "The Electrochemistry of Novel Materials" (J. Lipkowski and P. N. Ross, Eds.). VCH, New York, 1994.
40. G. A. Ozin, A. Kuperman, and A. Stein, *Angew. Chem., Int. Ed. Engl.* 28, 359 (1989).
41. D. R. Rolison, *Chem. Rev.* 90, 867 (1990).
42. D. R. Rolison, *Stud. Surf. Sci. Catal.* 85, 543 (1994).
43. F. Bedioui, *Coord. Chem. Rev.* 144, 39 (1995).
44. A. Walcarius, *Electroanalysis* 8, 971 (1996).
45. P. K. Dutta and M. Ledney, *Progr. Inorg. Chem.* 44, 209 (1997).
46. L. Roué, E. Briot, and F. Bedioui, *Canad. J. Chem.* 76, 1886 (1998).
47. A. Walcarius, *Anal. Chim. Acta* 384, 1 (1999).
48. D. R. Rolison and C. A. Bessel, *Acc. Chem. Res.* 33, 737 (2000).
49. O. Lev, Z. Wu, S. Bharathi, V. Glezer, A. Modestov, J. Gun, L. Rabinovich, and S. Sampath, *Chem. Mater.* 9, 2354 (1997).
50. K. S. Alber and J. A. Cox, *Mikrochim. Acta* 127, 131 (1997).
51. J. Lin and C. W. Brown, *Trends Anal. Chem.* 16, 200 (1997).
52. M. M. Collinson, *Mikrochim. Acta* 129, 149 (1998).
53. A. Walcarius, *Electroanalysis* 10, 1217 (1998).
54. J. Wang, *Anal. Chim. Acta* 399, 21 (1999).
55. M. M. Collinson, *Crit. Rev. Anal. Chem.* 29, 289 (1999).
56. M. M. Collinson, in "Handbook of Advanced Electronic and Photonic Materials and Devices" (H. S. Nalwa, Ed.), Vol. 5, pp. 163–194. Academic Press, San Diego, 2001.
57. A. Walcarius, *Chem. Mater.* 13, 3351 (2001).
58. L. Rabinovich and O. Lev, *Electroanalysis* 13, 265 (2001).
59. A. Walcarius, *Electroanalysis* 13, 701 (2001).
60. V. Linkov, L. Petrik, G. Vaivars, A. Maluleke, and G. Gericke, *Macromol. Symp.* 178, 153 (2002).
61. M. M. Collinson, *Trends Anal. Chem.* 21, 30 (2002).

62. M. D. Imisides, G. G. Wallace, and E. A. Wilke, *Trends Anal. Chem.* 7, 143 (1988).

63. G. G. Wallace, in "Chemical Sensors" (T. E. Edmonds, Ed.). Blackie, London, 1988.

64. J. Wang, in "Electroanalytical Chemistry" (A. J. Bard, Ed.), Vol. 16. Dekker, New York, 1989.

65. S. Dong and Y. Wang, *Electroanalysis* 1, 99 (1989).

66. K. Kalcher, *Electroanalysis* 2, 419 (1990).

67. P. W. Stoecker and A. M. Yacynych, *Selective Electrode Rev.* 12, 137 (1990).

68. E. Wang, H. Ji, and W. Hou, *Electroanalysis* 3, 1 (1991).

69. J. Wang, *Electroanalysis* 3, 255 (1991).

70. L. Gorton, G. Bremle, E. Csöregi, G. Jönsson-Pettersson, and B. Persson, *Anal. Chim. Acta* 249, 43 (1991).

71. L. Gorton, E. Csöregi, E. Dominguez, J. Emnéus, G. Jönsson-Pettersson, G. Marko-Varga, and B. Persson, *Anal. Chim. Acta* 250, 203 (1991).

72. R. P. Baldwin and K. N. Thomsen, *Talanta* 38, 1 (1991).

73. J. A. Cox, R. K. Jaworski, and P. J. Kulesza, *Electroanalysis* 3, 869 (1991).

74. S. A. Wring and J. P. Hart, *Analyst* 117, 1215 (1992).

75. J. Labuda, *Selective Electrode Rev.* 14, 33 (1992).

76. D. W. M. Arrigan, *Analyst* 119, 1953 (1994).

77. J. Gilby, *Sensor Rev.* 14, 30 (1994).

78. K. Kalcher, J.-M. Kauffmann, J. Wang, I. Svancara, K. Vytras, C. Neuhold, and Z. Yang, *Electroanalysis* 7, 5 (1995).

79. L. Gorton, *Electroanalysis* 7, 23 (1995).

80. P. Ugo and L. M. Moretto, *Electroanalysis* 7, 1105 (1995).

81. M. A. T. Gilmartin and J. P. Hart, *Analyst* 120, 1029 (1995).

82. C. A. Galan-Vidal, J. Munoz, C. Dominguez, and S. Alegret, *Trends Anal. Chem.* 14, 225 (1995).

83. J. A. Cox, M. E. Tess, and T. E. Cummings, *Rev. Anal. Chem.* 15, 173 (1996).

84. S. Alegret, *Analyst* 121, 1751 (1996).

85. P. Fabry and E. Siebert, Electrochemical sensors, in "The CRC Handbook of Solid State Electrochemistry" (P. J. Gellings and H. J. M. Bouwmeester, Eds.). CRC, Boca Raton, 1997.

86. P. Bühlmann, H. Aoki, K. P. Xiao, S. Amemiya, K. Tohda, and Y. Umezawa, *Electroanalysis* 10, 1149 (1998).

87. J. Janata, M. Josowicz, P. Vanysek, and D. M. DeVaney, *Anal. Chem.* 70, 179R (1998).

88. J. F. Cassidy, A. P. Doherty, and J. G. Vos, *Chem. Anal.* 150, 73 (1998).

89. F. L. Dickert and O. Hayden, *Trends Anal. Chem.* 18, 192 (1999).

90. G. G. Wallace, M. Smyth, and H. Zhao, *Trends Anal. Chem.* 18, 245 (1999).

91. S. Dong and Q. Deng, *Adv. Biosensors* 4, 1 (1999).

92. J. Labuda, M. Vanickova, M. Buckova, and E. Korgova, *Chem. Pap.* 54, 95 (2000).

93. J.-M. Zen and A. S. Kumar, *Acc. Chem. Res.* 34, 772 (2001).

94. H. Maeda, Y. Yamauchi, and H. Ohmori, *Curr. Topics Anal. Chem.* 2, 121 (2001).

95. N. Totir, C. Luca, S. Lupu, C. Lete, A. C. Ion, and I. Ion, *Rev. Roumaine Chim.* 46, 555 (2002).

96. J. Zak and T. Kuwana, *J. Electroanal. Chem.* 150, 645 (1983).

97. T. D. Jarvi and E. M. Stuve, in "Electrocatalysis" (J. Lipkowski and P. N. Ross, Eds.), pp. 75–133. Wiley–VCH, New York, 1998.

98. C. M. Casado, I. Cuadrado, M. Moran, B. Alonso, B. Garcia, B. Gonzalez, and J. Losada, *Coord. Chem. Rev.* 185–186, 53 (1999).

99. A. Malinauskas, *Synth. Met.* 107, 75 (1999).

100. L. Gorton and E. Dominguez, *Rev. Mol. Biotechnol.* 82, 371 (2002).

101. R. Ramaraj, *Proc. Indian Acad. Sci. Chem. Sci.* 108, 181 (1996).

102. M. A. Fox, M. O. Wolf, and R. S. Reese, *NATO ASI Ser. C* 485, 143 (1996).

103. I. Willner and B. Willner, *J. Mater. Chem.* 8, 2543 (1998).

104. Y. Sakata, H. Imahori, and K.-I. Sugiura, *J. Inclusion Phenom. Macrocyclic Chem.* 41, 31 (2001).

105. H. Buqa, R. I. R. Blyth, P. Golob, B. Evers, I. Schneider, M. V. S. Alvarez, F. Hofer, F. P. Netzer, M. G. Ramsey, M. Winter, and J. O. Besenhard, *Ionics* 6, 172 (2000).

106. H. Lund, in "Organic Electrochemistry" (H. Lund and O. Hammerich, Eds.), 4th ed. Dekker, New York, 2001.

107. H. Van Olphen, "An Introduction to Clay Colloid Chemistry," 2nd ed. Wiley, New York, 1977.

108. H. Van Olphen and J. J. Fripiat, "Data Handbook for Clay Materials and Other Non-Metallic Minerals." Pergamon Press, Oxford, 1979.

109. R. W. Grimshaw, "The Chemistry and Physics of Clays and Other Ceramic Material," 4th ed. Benn, London, 1980.

110. M. L. Occelli and H. E. Robson, "Expanded Clays and Other Microporous Solids." Van Nostrand Reinhold, New York, 1992.

111. D. Tichit and A. Vaccari, *Appl. Clay Sci.* 13 (1998).

112. F. Basile, M. Campanati, E. M. Serwicka, and A. Vaccari, *Appl. Clay Sci.* 18 (2001).

113. D. W. Breck, "Zeolite Molecular Sieves. Structure, Chemistry and Uses." Wiley, New York, 1974.

114. R. M. Barrer, "Zeolites and Clay Minerals as Sorbents and Molecular Sieves." Academic Press, London, 1978.

115. A. Dyer, "An Introduction to Zeolite Molecular Sieves." Wiley, Chichester, UK, 1988.

116. K. J. Balkus, Jr. and A. G. Gabrielov, *J. Inclusion Phenom. Mol. Recognition Chem.* 21, 159 (1995).

117. K. B. Yoon, *Chem. Rev.* 93, 321 (1993).

118. A. S. Vaidyalingam, M. A. Coutant, and P. K. Dutta, in "Electron Transfer in Chemistry" (V. Balzani, Ed.), Vol. 4, pp. 412–486. Wiley–VCH, Weinheim, 2001.

119. M. E. Davis, *Ind. Eng. Chem. Res.* 30, 1675 (1991).

120. C. T. Kresge, M. E. Leonowicz, W. J. Roth, J. C. Vartuli, and J. S. Beck, *Nature* 359, 710 (1992).

121. R. Szostak, "Molecular Sieves, Principles of Synthesis and Identification." Van Nostrand Reinhold, New York, 1989.

122. S. T. Wilson, B. M. Lok, C. A. Messina, T. R. Cannan, and E. M. Flanigen, *J. Am. Chem. Soc.* 104, 1146 (1982).

123. R. K. Iler, "The Chemistry of Silica." Wiley, New York, 1979.

124. K. K. Unger, "Porous Silica." Elsevier, Amsterdam, 1979.

125. A. P. Legrand, H. Hommel, A. Tuel, A. Vidal, H. Balard, E. Papirer, P. Levitz, M. Czernichowski, R. Erre, H. Van Damme, J. P. Gallas, J. F. Hemidy, J. C. Lavalley, O. Barrès, A. Burneau, and Y. Grillet, *Adv. Colloid Interface Sci.* 33, 91 (1990).

126. L. L. Hench and J. K. West, *Chem. Rev.* 90, 33 (1990).

127. M. F. Hochella, Jr. and A. F. White, Eds., Mineral–water interface geochemistry, in *Rev. Mineral.* 23, (1990).

128. L. T. Zhuravlev, *Coll. Surf. A* 74, 71 (1993).

129. P. H. Ribbe, Ed., Silica: Physical behavior, geochemistry, and materials applications, in *Rev. Mineral.* 29, (1994).

130. W. J. Miles and R. D. Hamilton, *Anal. Chim. Acta* 286, 3 (1994).

131. E. F. Vansant, P. Van der Voort, and K. C. Vrancken, "Characterisation and Chemical Modification of the Silica Surface." Elsevier, Amsterdam, 1995.

132. D. Levy and L. Esquivias, *Adv. Mater.* 7, 120 (1995).

133. P. Van der Voort and E. F. Vansant, *J. Liquid Chromatogr.* 19, 2723 (1996).

134. S. Sjöberg, *J. Non-Cryst. Solids* 196, 51 (1996).

135. A. P. Robertson and J. O. Leckie, *J. Colloid Interface Sci.* 188, 444 (1997).

136. A. P. Legrand, Ed., "The Surface Properties of Silicas." Wiley, Chichester, 1998.

137. "Sol–Gel Technology" (L. Klein, Ed.). Noyes, Park Ridge, NJ, 1988.

138. J. Livage, M. Henry, and C. Sanchez, *Progr. Solid State Chem.* 18, 259 (1988).

139. C. J. Brinker and G. W. Scherer, "Sol–Gel Science." Academic Press, San Diego, 1990.

140. "Sol–Gel Silica: Properties, Processing and Technology Transfer" (L. L. Hench, Ed.). Noyes, Westwood, NY, 1998.

141. C. McDonagh, F. Sheridan, T. Butler, and B. D. MacCraith, *J. Non-Cryst. Solids* 194, 72 (1996).

142. J. Oh, H. Imai, and H. Hirashima, *J. Non-Cryst. Solids* 241, 91 (1998).

143. K. Tsukuma, T. Akiyama, N. Yamada, and H. Imai, *J. Non-Cryst. Solids* 231, 161 (1998).

144. P. Mezza, J. Phalippou, and R. Sempere, *J. Non-Cryst. Solids* 243, 75 (1999).

145. S. Braun, S. Rappoport, R. Zusman, D. Avnir, and M. Ottolenghi, *Mater. Lett.* 10, 1 (1990).

146. D. Avnir, *Acc. Chem. Res.* 28, 328 (1995).

147. D. Avnir and S. Braun, Eds., Special issue of *J. Sol–Gel Sci. Technol.* 4 (1996).

148. I. Gill and A. Ballesteros, *J. Am. Chem. Soc.* 120, 8587 (1998).

149. I. Gill, *Chem. Mater.* 13, 3404 (2001).

150. J. S. Beck, J. C. Vartuli, W. J. Roth, M. E. Leonowicz, C. T. Kresge, K. D. Schmitt, C. T.-W. Chu, D. H. Olson, E. W. Sheppard, S. B. McCullen, J. B. Higgins, and J. L. Schlenker, *J. Am. Chem. Soc.* 114, 10834 (1992).

151. S. L. Burkett, S. D. Sims, and S. Mann, *Chem. Commun.* 1367 (1996).

152. D. J. Macquarrie, *Chem. Commun.* 1961 (1996).

153. M. H. Lim and A. Stein, *Chem. Mater.* 11, 3285 (1999).

154. K. Moller and T. Bein, *Chem. Mater.* 10, 2950 (1998).

155. A. Stein, B. J. Melde, and R. C. Schroden, *Adv. Mater.* 12, 1403 (2000).

156. C. Sanchez and F. Ribot, *New J. Chem.* 18, 1007 (1994).

157. D. A. Loy and K. J. Shea, *Chem. Rev.* 95, 1431 (1995).

158. U. Schubert, N. Hüsing, and A. Lorentz, *Chem. Mater.* 7, 2010 (1995).

159. J. E. Mark, C. Y.-C. Lee, and P. A. Bianconi, *ACS Symp. Ser.* 585 (1995).

160. T. Saegusa, *Macromol. Symp.* 98, 719 (1995).

161. J. D. Mackenzie, *ACS Symp. Ser.* 585, 226 (1995).

162. R. J. P. Corriu and D. Leclercq, *Angew. Chem. Int. Ed.* 35, 1420 (1996).

163. J. Wen and G. L. Wilkes, *Chem. Mater.* 8, 1667 (1996).

164. P. Judeinstein and C. Sanchez, *J. Mater. Chem.* 6, 511 (1996).

165. A. Vioux and D. Leclercq, *Heterog. Chem. Rev.* 3, 65 (1996).

166. M. P. Andrews, *Proc. SPIE* 2997, 48 (1997).

167. J. Livage, *Curr. Opinion Solid State Mater. Sci.* 2, 132 (1997).

168. R. J. P. Corriu and D. Leclercq, *Comments Inorg. Chem.* 19, 245 (1997).

169. S. Mann, S. L. Burkett, S. A. Davis, C. E. Fowler, N. H. Mendelson, S. D. Sims, D. Walsh, and N. T. Whilton, *Chem. Mater.* 9, 2300 (1997).

170. A. N. Seddon, *Crit. Rev. Opt. Sci. Technol.* 68, 143 (1997).

171. N. Hüsing and U. Schubert, *Angew. Chem. Int. Ed.* 37, 22 (1998).

172. G. Cerveau and R. J. P. Corriu, *Coord. Chem. Rev.* 178–180, 1051 (1998).

173. E. Bescher and J. D. Mackenzie, *Mater. Sci. Eng. C* 6, 145 (1998).

174. J. J. E. Moreau and M. Wong Chi Man, *Coord. Chem. Rev.* 178–180, 1073 (1998).

175. J. Livage, *Bull. Mater. Sci.* 22, 201 (1999).

176. E. H. Lan, B. C. Dave, J. M. Fukuto, B. Dunn, J. I. Zink, and J. S. Valentine, *J. Mater. Chem.* 9, 45 (1999).

177. I. Gill and A. Ballesteros, *Trends Biotechnol.* 18, 282 (2000).

178. A. D. Pomogailo, *Russian Chem. Rev.* 69, 53 (2000).

179. C. Sanchez, B. Lebeau, F. Ribot, and M. In, *J. Sol–Gel Sci. Technol.* 19, 31 (2000).

180. E. Ruiz-Hitzki, B. Casal, P. Aranda, and J. C. Galvan, *Rev. Inorg. Chem.* 21, 125 (2001).

181. P. Gomez-Romero, *Adv. Mater.* 13, 163 (2001).

182. C. Sanchez, G. J. de A. A. Soler-Illia, F. Ribot, T. Talot, C. R. Mayer, and V. Cabuil, *Chem. Mater.* 13, 3061 (2001).

183. D. E. Leyden and G. H. Luttrell, *Anal. Chem.* 47, 1612 (1975).

184. D. E. Leyden, G. H. Luttrell, G. E. Sloan, and N. J. DeAngelis, *Anal. Chim. Acta* 84, 97 (1976).

185. C. Kantipuly, S. Katragadda, A. Chow, and H. D. Gesser, *Talanta* 37, 491 (1990).

186. J. C. Moreira, L. C. Pavan, and Y. Gushikem, *Mikrochim. Acta* 3, 107 (1990).

187. M. E. Mahmoud, *Anal. Lett.* 29, 1791 (1996).

188. M. E. Mahmoud, *Talanta* 45, 309 (1997).

189. N. L. Dias Filho and Y. Gushikem, *Sep. Sci. Technol.* 32, 2535 (1997).

190. N. L. Dias Filho, Y. Gushikem, D. W. Franco, M. S. Schultz, and L. C. G. Vasconcellos, *Colloids Surf. A* 141, 181 (1998).

191. N. L. Dias Filho, *Colloids Surf. A* 144, 219 (1998).

192. P. de Magalhaes Padilha, L. A. de Melo Gomes, C. C. Federici Padilha, J. C. Moreira, and N. L. Dias Filho, *Anal. Lett.* 32, 1807 (1999).

193. O. A. Zaporozhets, O. M. Gawer, and V. V. Sukhan, *Colloids Surf. A* 147, 273 (1999).

194. O. A. Zaporozhets, N. Petruniock, and V. V. Sukhan, *Talanta* 49, 899 (1999).

195. O. A. Zaporozhets, N. Petruniock, and V. V. Sukhan, *Talanta* 50, 865 (1999).

196. R. Singh, A. R. Khwaja, B. Gupta, and S. N. Tandon, *Talanta* 48, 527 (1999).

197. M. E. Mahmoud, *Anal. Chim. Acta* 398, 297 (1999).

198. M. E. Mahmoud and G. A. Gohar, *Talanta* 51, 77 (2000).

199. M. E. Mahmoud, M. M. Osman, and M. E. Amer, *Anal. Chim. Acta* 415, 33 (2000).

200. R. J. P. Corriu, J. J. E. Moreau, P. Thepot, M. W. Chi Man, C. Chorro, J.-P. Lere-Porte, and J.-L. Sauvajol, *Chem. Mater.* 6, 640 (1994).

201. C. Sanchez, B. Alonso, F. Chapusot, F. Ribot, and P. Audebert, *J. Sol–Gel Sci. Technol.* 2, 161 (1994).

202. G.-W. Jang, C.-C. Chen, R. W. Gumbs, Y. Wei, and J.-M. Yeh, *J. Electrochem. Soc.* 143, 2591 (1996).

203. M. M. Verghese, K. Ramanathan, S. M. Ashraf, M. N. Kamalasanan, and B. D. Malhotra, *Chem. Mater.* 8, 822 (1996).

204. Y. Shi and C. R. Seliskar, *Chem. Mater.* 9, 821 (1997).

205. R. A. Zoppi and S. P. Nunes, *J. Electroanal. Chem.* 445, 39 (1998).

206. M. J. Adeogun and J. N. Hay, *Chem. Mater.* 12, 767 (2000).

207. R. Gangopadhyay and A. De, *Chem. Mater.* 12, 608 (2000).

208. S. Therias and C. Mousty, *Appl. Clay Sci.* 10, 147 (1995).

209. P. C. Pandey, *ACS Symp. Ser.* 762, 139 (2000).

210. B. C. Dave, B. Dunn, and J. I. Zink, in "Access in Nanoporous Materials" (T. J. Pinnavaia and M. F. Thorpe, Eds.), pp. 141–159. Plenum, New York, 1995.

211. D. R. Rolison and B. Dunn, *J. Mater. Chem.* 11, 963 (2001).

212. K. Itaya and A. J. Bard, *J. Phys. Chem.* 89, 5565 (1985).

213. B. Keita, A. Belhouari, and L. Nadjo, *J. Electroanal. Chem.* 355, 235 (1993).

214. D. Petridis, P. D. S. Kaviratna, and T. J. Pinnavaia, *J. Electroanal. Chem.* 410, 93 (1996).

215. D. Ege, P. K. Ghosh, J. R. White, J.-F. Equey, and A. J. Bard, *J. Am. Chem. Soc.* 107, 5644 (1985).

216. S. A. Lee and A Fitch, *J. Phys. Chem.* 94, 4998 (1990).

217. A. Fitch and R. J. Krzysik, *J. Electroanal. Chem.* 379, 129 (1994).

218. A. Fitch, J. Du, H. Gan, and J. W. Stucki, *Clays Clay Miner.* 43, 607 (1995).

219. A. Fitch and S. A. Lee, *J. Electroanal. Chem.* 344, 45 (1993).

220. F. R. Fan and A. J. Bard, *J. Electrochem. Soc.* 133, 301 (1986).

221. C. M. Castro-Acuna, F. R. Fan, and A. J. Bard, *J. Electroanal. Chem.* 234, 347 (1987).

222. H. Inoue and H. Yoneyama, *J. Electroanal. Chem.* 233, 291 (1987).

223. W. E. Rudzinski, C. Figueroa, C. Hoppe, T. Y. Kuromoto, and D. Root, *J. Electroanal. Chem.* 243, 367 (1988).

224. P. K. Gosh and A. J. Bard, *J. Am. Chem. Soc.* 105, 5691 (1983).

225. P. K. Ghosh, A. W.-H. Mau, and A. J. Bard, *J. Electroanal. Chem.* 169, 315 (1984).
226. P. V. Kamat, *J. Electroanal. Chem.* 163, 389 (1984).
227. A. Yamagishi and A. Aramata, *J. Chem. Soc. Chem. Commun.* 452 (1984).
228. H.-Y. Liu and F. C. Anson, *J. Electroanal. Chem.* 184, 411 (1985).
229. J. R. White and A. J. Bard, *J. Electroanal. Chem.* 197, 233 (1986).
230. W. Rudzinski and A. J. Bard, *J. Electroanal. Chem.* 199, 323 (1986).
231. N. Oyama and F. C. Anson, *J. Electroanal. Chem.* 199, 467 (1986).
232. K. Itaya, H.-C. Chang, and I. Uchida, *Inorg. Chem.* 26, 624 (1987).
233. M. T. Carter and A. J. Bard, *J. Electroanal. Chem.* 229, 191 (1987).
234. R. D. King, D. G. Nocera, and T. J. Pinnavaia, *J. Electroanal. Chem.* 236, 43 (1987).
235. J. F. Rusling, C.-N. Shi, and S. L. Suib, *J. Electroanal. Chem.* 245, 331 (1988).
236. A. Fitch and C. L. Fausto, *J. Electroanal. Chem.* 257, 299 (1988).
237. A. Fitch, A. Lavy-Feder, S. A. Lee, and M. T. Kirsh, *J. Phys. Chem.* 92, 6665 (1988).
238. H. Inoue, S. Haga, C. Iwakura, and H. Yoneyama, *J. Electroanal. Chem.* 249, 133 (1988).
239. C. Shi, J. F. Rusling, Z. Wang, W. S Willis, A. M. Winiecki, and S. L. Suib, *Langmuir* 5, 650 (1989).
240. B. Brahimi, P. Labbe, and G. Reverdy, *J. Electroanal. Chem.* 267, 343 (1989).
241. G. Villemure and A. J. Bard, *J. Electroanal. Chem.* 282, 107 (1990).
242. A. Fitch, *J. Electroanal. Chem.* 284, 237 (1990).
243. G. Villemure and A. J. Bard, *J. Electroanal. Chem.* 283, 403 (1990).
244. G. J. Edens, A. Fitch, and A. Lavy-Feder, *J. Electroanal. Chem.* 307, 139 (1991).
245. T. Okajima, T. Ohsaka, and N. Oyama, *J. Electroanal. Chem.* 315, 175 (1991).
246. A. Fitch and J. Du, *J. Electroanal. Chem.* 319, 409 (1991).
247. P. Subramanian and A. Fitch, *Environ. Sci. Technol.* 26, 1775 (1992).
248. T. Okajima, T. Ohsaka, O. Hatozaki, and N. Oyama, *Electrochim. Acta* 37, 1865 (1992).
249. B. Brahimi, P. Labbe, and G. Reverdy, *Langmuir* 8, 1908 (1992).
250. D. Petridis, P. Falaras, and T. J. Pinnavaia, *Inorg. Chem.* 31, 3530 (1992).
251. P. de S Kaviratna and T. J. Pinnavaia, *J. Electroanal. Chem.* 332, 135 (1992).
252. Y. Xiang and G. Villemure, *Canad. J. Chem.* 70, 1833 (1992).
253. P. Falaras and D. Petridis, *J. Electroanal. Chem.* 337, 229 (1992).
254. A. Fitch and P. Subramanian, *J. Electroanal. Chem.* 362, 177 (1993).
255. B. Shen, T. Peng, and H. Wang, *Electrochim. Acta* 39, 527 (1994).
256. J. A. Stein and A. Fitch, *Electroanalysis* 6, 23 (1994).
257. Y. Xiang and G. Villemure, *J. Electroanal. Chem.* 370, 53 (1994).
258. G. K. Vengatajalabathy and R. Ramaraj, *J. Chem. Soc., Dalton Trans.* 2445 (1994).
259. P. Joo and N. Nagy, in "Proc. 6th Conf. Colloid Chem." (F. Csempesz, Z. Horvolgyi, and I. Paszli, Eds.), pp. 108–111. Hung. Chem. Soc., Budapest, 1993.
260. Y. Xiang and G. Villemure, *J. Electroanal. Chem.* 381, 21 (1995).
261. K. Yao, K. Shimazu, and A. Yamagishi, *Chem. Lett.* 161 (1995).
262. J. A. Stein and A. Fitch, *Anal. Chem.* 67, 1322 (1995).
263. P. D. Kaviratna and T. J. Pinnavaia, *J. Electroanal. Chem.* 385, 163 (1995).
264. Y. Hotta, A. Yamagishi, A. Aramata, and M. Enyo, in "Clays Controlling the Environment, Proc. 10th Int. Clay Conf." (G. J. Churchman, R. W. Fitzpatrick, and R. A. Eggleton, Eds.), pp. 166–168. Commonwealth Scientific and Industrial Research Organization, East Melbourne, Australia, 1995.
265. A. Fitch, in "Access in Nanoporous Materials, Proc. Symp. Access Nanoporous Mater." (T. J. Pinnavaia and M. F. Thorpe, Eds.), pp. 93–110. Plenum, New York, 1995.
266. A. Fitch and J. Du, *Environ. Sci. Technol.* 30, 12 (1996).

267. J.-M. Zen, S.-H. Jeng, and H.-J. Chen, *J. Electroanal. Chem.* 408, 157 (1996).
268. A. Fitch, J. Song, and J. A. Stein, *Clays Clay Miner.* 44, 370 (1996).
269. J. A. Stein and A. Fitch, *Clays Clay Miner.* 44, 381 (1996).
270. A. Fitch, Y. Wang, S. Park, and M. Marjanski, in *New Directions Electroanal. Chem.* 96–9, 248 (1996).
271. P. Joo and A. Fitch, *Environ. Sci. Technol.* 30, 2681 (1996).
272. Y. Xiang and G. Villemure, *J. Phys. Chem.* 100, 7143 (1996).
273. Y. Xiang and G. Villemure, *Clays Clay Miner.* 44, 515 (1996).
274. P. Joo, A. Fitch, and S.-H. Park, *Environ. Sci. Technol.* 31, 2186 (1997).
275. S.-C. Shyu and C. M. Wang, *J. Electroanal. Chem.* 440, 27 (1997).
276. J. Premkumar and R. Ramaraj, *J. Solid State Electrochem.* 1, 172 (1997).
277. K. Yao, K. Shimazu, M. Nakata, and A. Yamagishi, *J. Electroanal. Chem.* 443, 253 (1998).
278. K. Yao, K. Shimazu, M. Nakata, and A. Yamagishi, *J. Electroanal. Chem.* 442, 235 (1998).
279. V. Borek and M. J. Morra, *Environ. Sci. Technol.* 32, 2149 (1998).
280. K. V. Gobi and R. Ramaraj, *J. Electroanal. Chem.* 449, 81 (1998).
281. P. Falaras and F. Lezou, *J. Electroanal. Chem.* 455, 169 (1998).
282. P. Joo, *Colloids Surf. A* 141, 337 (1998).
283. P. Joo and K. Antal, *Colloids Surf. A* 141, 365 (1998).
284. M. Pecorari and P. Bianco, *Electroanalysis* 10, 181 (1998).
285. S. Macha, G. Zayia, J. Du, J. Stein, and A. Fitch, *Appl. Clay Sci.* 15, 153 (1999).
286. X. Chen, N. Hu, Y. Zeng, J. F. Rusling, and J. Yang, *Langmuir* 15, 7022 (1999).
287. C. S. Ouyang and C. M. Wang, *J. Electroanal. Chem.* 474, 82 (1999).
288. J.-M. Sequaris, *Langmuir* 16, 1368 (2000).
289. A. Ramasubbu, A. Vanangamudi, S. Muthusubramanian, M. S. Ramachandranand, and S. Sivasubramanian, *Electrochem. Commun.* 2, 56 (2000).
290. P. Falaras, F. Lezou, P. Pomonis, and A. Ladavos, *J. Electroanal. Chem.* 486, 156 (2000).
291. V. Ganesan and R. Ramaraj, *J. Electroanal. Chem.* 490, 54 (2000).
292. C. Swearingen, S. Macha, and A. Fitch, *J. Electrochem. Soc.* 149, E103 (2002).
293. T. Wielgos and A. Fitch, *Electroanalysis* 2, 449 (1990).
294. A. Fitch, *J. Electroanal. Chem.* 332, 289 (1992).
295. P. Labbe, B. Brahimi, G. Reverdy, C. Mousty, R. Blankespoor, A. Gautier, and C. Degrand, *J. Electroanal. Chem.* 379, 103 (1994).
296. J.-M. Zen, S.-H. Jeng, and H.-J. Chen, *Anal. Chem.* 68, 498 (1996).
297. J.-M. Zen and P.-J. Chen, *Anal. Chem.* 69, 5087 (1997).
298. J.-M. Zen and P.-J. Chen, *Electroanalysis* 10, 12 (1998).
299. J.-M. Zen, S.-H. Jeng, C.-W. Lo, P.-J. Chen, G. Ilangovan, and H.-J. Chen, *Proc. Natl. Sci. Council Rep. China A* 22, 447 (1998).
300. J.-M. Zen, W.-M. Wang, and G. Ilangovan, *Anal. Chim. Acta* 372, 315 (1998).
301. M. Lacroix, P. Bianco, and E. Lojou, *Electroanalysis* 11, 1068 (1999).
302. J.-M. Zen, H.-Y. Lin, and H.-H. Yang, *Electroanalysis* 13, 505 (2001).
303. D. Orata and P. W. Ondachi, *Catal. Lett.* 72, 125 (2001).
304. J.-L. Besombes, S. Cosnier, P. Labbe, and G. Reverdy, *Anal. Chim. Acta* 317, 275 (1995).
305. J.-M. Zen and C.-W. Lo, *Anal. Chem.* 68, 2635 (1996).
306. S. Poyard, N. Jaffrezic-Renault, C. Martelet, S. Cosnier, P. Labbe, and J.-L. Besombes, *Sensors Actuators B* B33, 44 (1996).
307. J.-L. Besombes, S. Cosnier, and P. Labbe, *Talanta* 44, 2209 (1997).
308. J.-M. Zen, C.-W. Lo, and P.-J. Chen, *Anal. Chem.* 69, 1669 (1997).
309. L. Coche-Guerente, V. Desprez, and P. Labbe, *J. Electroanal. Chem.* 458, 73 (1998).
310. A. Senillou, N. Jaffrezic, C. Martelet, and S. Cosnier, *Anal. Chim. Acta* 401, 117 (1999).

311. C. Lei, F. Lisdat, U. Wollenberger, and F. W. Scheller, *Electroanalysis* 11, 274 (1999).

312. L. Coche-Guerente, V. Desprez, P. Labbe, and S. Therias, *J. Electroanal. Chem.* 470, 61 (1999).

313. Y. Sallez, P. Bianco, and E. Lojou, *J. Electroanal. Chem.* 493, 37 (2000).

314. C. Lei, U. Wollenberger, C. Jung, and F. W. Scheller, *Biochem. Biophys. Res. Commun.* 268, 740 (2000).

315. C. Mousty, S. Cosnier, D. Shan, and S. Mu, *Anal. Chim. Acta* 443, 1 (2001).

316. J. V. de Melo, S. Cosnier, C. Mousty, C. Martelet, and N. Jaffrezic-Renault, *Anal. Chem.* 74, 4037 (2002).

317. Y. Chevalier, L. Coche-Guerente, and P. Labbe, *Mater. Sci. Eng. C* C21, 81 (2002).

318. B. Keita, A. Belhouari, and L. Nadjo, *J. Electroanal. Chem.* 314, 345 (1991).

319. C. Mousty, S. Therias, C. Forano, and J.-P. Besse, *J. Electroanal. Chem.* 374, 63 (1994).

320. J. Qiu and G. Villemure, *J. Electroanal. Chem.* 395, 159 (1995).

321. J. Qiu and G. Villemure, *J. Electroanal. Chem.* 428, 165 (1997).

322. S. Therias, B. Lacroix, B. Schollhorn, C. Mousty, and P. Palvadeau, *J. Electroanal. Chem.* 454, 91 (1998).

323. B. Ballarin, M. Gazzano, R. Seeber, D. Tonelli, and A. Vaccari, *J. Electroanal. Chem.* 445, 27 (1998).

324. K. Yao, M. Taniguchi, M. Nakata, M. Takahashi, and A. Yamagishi, *Langmuir* 14, 2890 (1998).

325. K. Yao, M. Taniguchi, M. Nakata, K. Shimazu, M. Takahashi, and A. Yamagishi, *J. Electroanal. Chem.* 457, 119 (1998).

326. K. Yao, M. Taniguchi, M. Nakata, and A. Yamagishi, *J. Electroanal. Chem.* 458, 249 (1998).

327. B. Ballarin, R. Seeber, D. Tonelli, and C. Zanardi, *Electroanalysis* 12, 434 (2000).

328. J.-X. He, K. Kobayashi, Y.-M. Chen, G. Villemure, and A. Yamagishi, *Electrochem. Commun.* 3, 473 (2001).

329. R. Roto and G. Villemure, *J. Electroanal. Chem.* 527, 123 (2002).

330. E. Scavetta, M. Berrettoni, M. Giorgetti, and D. Tonelli, *Electrochim. Acta* 47, 2451 (2002).

331. D. Rong, Y. I. Kim, and T. E. Mallouk, *Inorg. Chem.* 29, 1329 (1990).

332. L. Coche-Guerente, S. Cosnier, V. Desprez, P. Labbe, and D. Petridis, *J. Electroanal. Chem.* 401, 253 (1996).

333. Y. Hotta, M. Taniguchi, K. Inukai, and A. Yamagishi, *Langmuir* 12, 5195 (1996).

334. Y. Hotta, M. Taniguchi, K. Inukai, and A Yamagishi, *Clay Miner.* 32, 79 (1997).

335. Y. Hotta, K. Inukai, M. Taniguchi, and A. Yamagishi, *J. Electroanal. Chem.* 429, 107 (1997).

336. Y. Hotta, K. Inukai, M. Taniguchi, M. Nakata, and A Yamagishi, *Langmuir* 13, 6697 (1997).

337. C. Song and G. Villemure, *J. Electroanal. Chem.* 462, 143 (1999).

338. K. Okamoto, K. Tamura, M. Takahashi, and A.Yamagishi, *Colloids Surf. A* 169, 241 (2000).

339. J.-X. He, K. Kobayashi, M. Takahashi, G. Villemure, and A. Yamagishi, *Thin Solid Films* 397, 255 (2001).

340. L. Hernandez, P. Hernandez, and Z. Sosa Ferrera, *Fresenius J. Anal. Chem.* 329, 756 (1988).

341. L. Hernandez, P. Hernandez, and Z. Sosa Ferrera, *Fresenius J. Anal. Chem.* 331, 525 (1988).

342. L. Hernandez, P. Hernandez, E. Lorenzo, and Z. Sosa Ferrera, *Analyst* 113, 621 (1988).

343. P. Hernandez, J. Vicente, and L. Hernandez, *Fresenius J. Anal. Chem.* 334, 550 (1989).

344. J. Wang and T. Martinez, *Electroanalysis* 1, 167 (1989).

345. P. Hernandez, J. Vicente, M. Gonzalez, and L. Hernandez, *Talanta* 37, 789 (1990).

346. L. Hernandez, P. Hernandez, and E. Lorenzo, *Electroanalysis* 2, 643 (1990).

347. L. Hernandez, P. Hernandez, and E. Lorenzo, in "Proc. ElectroFinnAnalysis Int. Conf. Electroanal. Chem." (A. Ivaska, A. Lewenstam, and R. Sara, Eds.), Vol. 205–11. Plenum, New York, 1990.

348. P. W. Faguy, W. Ma, J. A. Lowe, W. P. Pan, and T. Brown, *J. Mater. Chem.* 4, 771 (1994).

349. M. Chicharro, A. Zapardiel, E. Bermejo, J. A. Perez-Lopez, and L. Hernandez, *Analysis* 23, 131 (1995).

350. B. Ogorevc, X. Cai, and I. Grabec, *Anal. Chim. Acta* 305, 176 (1995).

351. P. Kula and Z. Navratilova, *Fresenius J. Anal. Chem.* 354, 692 (1996).

352. I. G. Svegl, B. Ogorevc, and V. Hudnik, *Fresenius J. Anal. Chem.* 354, 770 (1996).

353. P. Kula and Z. Navratilova, *Acta Univ. Carolin. Geol.* 38, 295 (1996).

354. P. Kula, Z. Navratilova, M. Chmielova, P. Martinec, Z. Weiss, and Z. Klika, *Geol. Carpathica Clays* 5, 49 (1996).

355. S. Therias, C. Mousty, C. Forano, and J.-P. Besse, *Langmuir* 12, 4914 (1996).

356. I. G. Svegl, M. Kolar, B. Ogorevc, and B. Pihlar, *Fresenius J. Anal. Chem.* 361, 358 (1998).

357. G. Raber, K. Kalcher, and M. Stadlober, *Sci. Pap. Univ. Pardubice Ser. A* 3, 163 (1998).

358. Z. Navratilova and P. Kula, *Sci. Pap. Univ. Pardubice Ser. A* 3, 195 (1998).

359. A. Domenech, A. Ribera, A. Cervilla, and E. L. Lopis, *J. Electroanal. Chem.* 458, 31 (1998).

360. P. Kula, Z. Navratilova, P. Kulova, and M. Kotoucek, *Anal. Chim. Acta* 385, 91 (1999).

361. V. Marchal, F. Barbier, F. Plassard, R. Faure, and O. Vittori, *Fresenius J. Anal. Chem.* 363, 710 (1999).

362. J.-M. Zen, A. S. Kumar, and H.-W. Chen, *Electroanalysis* 12, 542 (2000).

363. I. G. Svegl and B. Ogorevc, *Fresenius J. Anal. Chem.* 367, 701 (2000).

364. Z. Navratilova and P. Kula, *Fresenius J. Anal. Chem.* 367, 369 (2000).

365. Z. Navratilova and P. Kula, *J. Solid State Electrochem.* 4, 342 (2000).

366. A. Walcarius, G. Lefevre, J.-P. Rapin, G. Renaudin, and M. François, *Electroanalysis* 13, 313 (2001).

367. P. Kula and Z. Navratilova, *Electroanalysis* 13, 795 (2001).

368. D. Ozkan, K. Kerman, B. Meric, P. Kara, H. Demirkan, M. Polverejan, T. J. Pinnavaia, and M. Ozsoz, *Chem. Mater.* 14, 1755 (2002).

369. Y. Shih and J.-M. Zen, *Anal. Chim. Acta* 412, 63 (2000).

370. J.-M. Zen, H.-P. Chen, and A. Senthil Kumar, *Anal. Chim. Acta* 449, 95 (2001).

371. J.-M. Zen, Y.-Y. Lai, H.-H. Yang, and A. Senthil Kumar, *Sensors Actuators B* 84, 237 (2002).

372. Y. Shih, J.-M. Zen, and H.-H. Yang, *J. Pharm. Biomed. Anal.* 29, 827 (2002).

373. T. Kanbara, T. Yamamoto, H. Ikawa, T. Tagawa, and H. Imai, *J. Mater. Sci. Lett.* 6, 1195 (1987).

374. T. Kanbara, K. Nishimura, T. Yamamoto, and K. Tokuda, *J. Power Sources* 32, 165 (1990).

375. L. Duclaux, E. Frackowiak, T. Gibinski, R. Benoit, and F. Beguin, *Mol. Cryst. Liq. Cryst. Sci. Technol. A* 340, 449 (2000).

376. B. K. Pain and S. K. Mukherjee, *J. Indian Soc. Soil Sci.* 17, 209 (1969).

377. S. D. Pandey and P. Tripathi, *Electrochim. Acta* 27, 1715 (1982).

378. C. J. Coetzee, in "Inorg. Ion Exch. Chem. Anal." (M. Qureshi and K. G. Varshney, Eds.), pp. 143–175. CRC, Boca Raton, FL, 1991.

379. C. Baillarger, A. Mayaffre, M. Turmine, P. Letellier, and H. Suquet, *Electrochim. Acta* 39, 813 (1994).

380. B. Ballarin, M. Morigi, E. Scavetta, R. Seeber, and D. Tonelli, *J. Electroanal. Chem.* 492, 7 (2000).
381. B. Ballarin, R. Seeber, D. Tonelli, and A. Vaccari, *J. Electroanal. Chem.* 463, 123 (1999).
382. E. Scavetta, M. Berrettoni, R. Seeber, and D. Tonelli, *Electrochim. Acta* 46, 2681 (2001).
383. R. Ramaraj, *Res. Chem. Intermediates* 27, 407 (2001).
384. G. Calzaferri, K. Hädener, and J. Li, *J. Chem. Soc. Chem. Commun.* 653 (1991).
385. P. Lainé, R. Seifert, R. Giovanoli, and G. Calzaferri, *New J. Chem.* 21, 453 (1997).
386. B. de Vismes, F. Bedioui, J. Devynck, and C. Bied-Charreton, *J. Electroanal. Chem.* 187, 197 (1985).
387. H. A. Gemborys and B. R. Shaw, *J. Electroanal. Chem.* 208, 95 (1986).
388. Z. Li and T. E. Mallouk, *J. Phys. Chem.* 91, 643 (1987).
389. Z. Li, C. M. Wang, L. Persaud, and T. E. Mallouk, *J. Phys. Chem.* 92, 2592 (1988).
390. B. R. Shaw, K. E. Creasy, C. J. Lanczycki. J. A. Sargeant, and M. Tirhado, *J. Electrochem. Soc.* 135, 869 (1988).
391. C. Iwakura, S. Miyazaki, and U. Yoneyama, *J. Electroanal. Chem.* 246, 63 (1988).
392. J. Cassidy, E. O'Donoghue, and W. Breen, *Analyst* 114, 1509 (1989).
393. J. Cassidy, W. Breen, E. O'Donoghue, and M. E. G. Lyons, *Electrochim. Acta* 36, 383 (1991).
394. K. L. N. Phani and S. Pitchumani, *Electrochim. Acta* 37, 2411 (1992).
395. S. Bharathi, K. L. N. Phani, J. Joseph, S. Pitchumani, D. Jeyakumar, G. P. Rao, and S. K. Rangarajan, *J. Electroanal. Chem.* 334, 145 (1992).
396. C. Senaratne and M. D. Baker, *J. Electroanal. Chem.* 332, 357 (1992).
397. M. D. Baker and C. Senaratne, *Anal. Chem.* 64, 697 (1992).
398. M. D. Baker, C. Senaratne, and J. Zhang, *J. Chem. Soc. Faraday Trans.* 88, 3187 (1992).
399. J. Li and G. Calzaferri, *J. Chem. Soc. Chem. Commun.* 1430 (1993).
400. M. D. Baker, C. Senaratne, and J. Zhang, *J. Phys. Chem.* 98, 1668 (1994).
401. C. Senaratne and M. D. Baker, *J. Phys. Chem.* 98, 13687 (1994).
402. J. Li and G. Calzaferri, *J. Electroanal. Chem.* 377, 163 (1994).
403. M. D. Baker, J. Zhang, and M. McBrien, *J. Phys. Chem.* 99, 6635 (1995).
404. J. Li, K. Pfanner, and G. Calzaferri, *J. Phys. Chem.* 99, 2119 (1995).
405. G. Calzaferri, M. Lanz, and J. Li, *J. Chem. Soc. Chem. Commun.* 1313 (1995).
406. C. Senaratne, J. Zhang, M. D. Baker, C. A. Bessel, and D. R. Rolison, *J. Phys. Chem.* 100, 5849 (1996).
407. A. Walcarius, T. Barbaise, and J. Bessière, *Anal. Chim. Acta* 340, 61 (1997).
408. B. Liu, R. Hu, and J. Deng, *Anal. Chem.* 69, 2343 (1997).
409. D. H. Brouwer and M. D. Baker, *J. Phys. Chem. B* 101, 10390 (1997).
410. L. Mogensen and L. Kryger, *Electroanalysis* 10, 1285 (1998).
411. M. D. Baker, M. McBrien, and I. Burgess, *J. Phys. Chem. B* 102, 2905 (1998).
412. V. Ganesan and R. Ramaraj, *Langmuir* 14, 2497 (1998).
413. C. Senaratne, J. Zhang, J. Fox, I. Burgess, and M. D. Baker, *Microporous Mesoporous Mater.* 33, 281 (1999).
414. C. F. Chen and C. M. Wang, *J. Electroanal. Chem.* 466, 82 (1999).
415. B. Liu, F. Yan, J. Kong, and J. Deng, *Anal. Chim. Acta* 386, 31 (1999).
416. M. D. Baker and C. Senaratne, *Phys. Chem. Chem. Phys.* 1, 1673 (1999).
417. A. Doménech, I. Casades, and H. Garcia, *J. Org. Chem.* 64, 3731 (1999).
418. A. Doménech, M. T. Doménech-Carbo, H. Garcia, and M. S. Galletero, *Chem. Commun.* 2173 (1999).
419. A. Doménech, P. Formentin, H. Garcia, and M. J. Sabater, *Eur. J. Inorg. Chem.* 1339 (2000).
420. A. Doménech, A. Corma, H. Garcia, and S. Valencia, *Topics Catal.* 11/12, 401 (2000).
421. Y.-J. Li and C.-Y. Liu, *J. Electroanal. Chem.* 517, 117 (2001).
422. T-W. Hui and M. D. Baker, *J. Phys. Chem. B* 105, 3204 (2001).
423. T-W. Hui and M. D. Baker, *J. Phys. Chem. B* 106, 827 (2002).
424. A. Domenech, J. Perez-Ramirez, A. Ribera, G. Mul, F. Kapteijn, and I. W. C. E. Arends, *J. Electroanal. Chem.* 519, 72 (2002).
425. C. B. Ahlers and J. B. Talbot, *J. Electrochem. Soc.* 146, 3259 (1999).
426. C. B. Ahlers and J. B. Talbot, *Electrochim. Acta* 45, 3379 (2000).
427. D. R. Rolison, R. J. Nowak, T. Welsh, and C. G. Murray, *Talanta* 38, 27 (1991).
428. C. G. Murray, R. J. Nowak, and D. R. Rolison, *J. Electroanal. Chem.* 164, 205 (1984).
429. V. Ganesan and R. Ramaraj, *J. Appl. Electrochem.* 30, 757 (2000).
430. K. L. N. Phani, S. Pitchumani, and S. K. Ravichandran, *Langmuir* 9, 2455 (1993).
431. Y.-X. Jiang, W.-B. Song, Y. Liu, N. Lü, M.-Z. Zou, H.-D. Xu, and A.-L. Zhang, *Chem. J. Chinese Univ.* 20, 717 (1999).
432. M. D. Baker and J. Zhang, *J. Phys. Chem.* 94, 8703 (1990).
433. N. Venkatathri, M. P. Vinod, K. Vijayamohanan, and S. Sivasanker, *J. Chem. Soc. Faraday Trans.* 92, 473 (1996).
434. Y. Jiang, M. Zou, K. Yuan, and H. Xu, *Electroanalysis* 11, 254 (1999).
435. M. P. Vinod, T. K. Das, A. J. Chandwadkar, K. Vijayamohanan, and J. G. Chandwadkar, *Mater. Chem. Phys.* 58, 37 (1999).
436. K. Lee, C. Lee, J. W. Park, Y. S. Park, and K. B. Yoon, *Bull. Korean Chem. Soc.* 20, 1365 (1999).
437. K. E. Creasy, Y. P. Deng, J. Park, E. V. R. Borgstedt, S. P. Davis, S. L. Suib, and B. R. Shaw, *Mater. Res. Soc. Symp. Proc.* 233, 157 (1991).
438. R. A. W. Dryfe and S. M. Holmes, *J. Electroanal. Chem.* 483, 144 (2000).
439. G. C. Lillie, R. A. W. Dryfe, and S. M. Holmes, *Analyst* 126, 1857 (2001).
440. P. Hernandez, E. Alda, and L. Hernandez, *Fresenius J. Anal. Chem.* 327, 676 (1987).
441. J. Wang and T. Martinez, *Anal. Chim. Acta* 207, 95 (1988).
442. K. E. Creasy and B. R. Shaw, *Electrochim. Acta* 33, 551 (1988).
443. N. El Murr, M. Kerkeni, A. Sellami, and Y. Bentaarit, *J. Electroanal. Chem.* 246, 461 (1988).
444. S. de Castro-Martins, S. Khouzami, A. Tuel, Y. Bentaarit, N. El Murr, and A. Sellami, *J. Electroanal. Chem.* 350, 15 (1993).
445. A. Walcarius, L. Lamberts, and E. G. Derouane, *Electrochim. Acta* 38, 2257 (1993).
446. A. Walcarius, L. Lamberts, and E. G. Derouane, *Electrochim. Acta* 38, 2267 (1993).
447. M. Xu, W. Horsthemke, and M. Schell, *Electrochim. Acta* 38, 919 (1993).
448. S. de Castro-Martins, A. Tuel, and Y. Bentaarit, *Zeolites* 14, 130 (1994).
449. A. Walcarius, L. Lamberts, and E. G. Derouane, *Electroanalysis* 7, 120 (1995).
450. J. Wang and A. Walcarius, *J. Electroanal. Chem.* 404, 237 (1996).
451. J. Wang and A. Walcarius, *J. Electroanal. Chem.* 407, 183 (1996).
452. C. Bing and L. Kryger, *Talanta* 43, 153 (1996).
453. G. Marko-Varga, E. Burestedt, C. J. Svensson, J. Emnéus, L. Gorton, T. Ruzgas, M. Lutz, and K. K. Unger, *Electroanalysis* 8, 1121 (1996).
454. A. Walcarius and L. Lamberts, *J. Electroanal. Chem.* 422, 77 (1997).
455. B. Chen, N.-K. Goh, and L.-S. Chia, *Electrochim. Acta* 42, 595 (1997).

456. M. Z. Zou, H. D. Xu, J. Lu, and Q. H. Ru, *Chinese Chem. Lett.* 8, 247 (1997).

457. I. N. Rodriguez, J. A. Munoz-Leyva, and J. L. Hidalgo-Hidalgo de Cisneros, *Anal. Chim. Acta* 344, 167 (1997); *Analyst* 122, 601 (1997).

458. A. Walcarius and L. Lamberts, *Anal. Lett.* 31, 585 (1998).

459. S. V. Guerra, C. R. Xavier, S. Nakagaki, and L. T. Kubota, *Electroanalysis* 10, 462 (1998).

460. B.-H. Liu, R.-Q. Hu, H.-Y. Liu, and J.-Q. Deng, *Acta Chim. Sinica* 56, 682 (1998).

461. A. Walcarius, *Anal. Chim. Acta* 388, 79 (1999).

462. A. Walcarius, V. Vromman, and J. Bessière, *Sensors Actuators B* 56, 136 (1999).

463. A. Walcarius, P. Mariaulle, and L. Lamberts, *J. Electroanal. Chem.* 463, 100 (1999).

464. A. Walcarius, S. Rozanska, J. Bessière, and J. Wang, *Analyst* 124, 1185 (1999).

465. A. Walcarius, P. Mariaulle, C. Louis, and L. Lamberts, *Electroanalysis* 11, 393 (1999).

466. M. Cordero-Rando, M. Barea-Zamora, J. M. Barbera-Salvador, I. N. Rodriguez, J. A. Munoz-Leyva, and J. L. Hidalgo-Hidalgo de Cisneros, *Mikrochim. Acta* 132, 7 (1999).

467. S. Bodoardo, F. Geobaldo, N. Penazzi, M. Arrabito, F. Rivetti, G. Spano, C. Lamberti, and A. Zecchina, *Electrochem. Commun.* 2, 349 (2000).

468. S. H. Bossmann, C. Turro, C. Schnabel, M. R. Pokhrel, L. M. Payawan, Jr., B. Baumeister, and M. Wörner; *J. Phys. Chem. B* 105, 5374 (2001).

469. L. Prandi, S. Bodoardo, N. Penazzi, and B. Fubini, *J. Mater. Chem.* 11, 1495 (2001).

470. B. R. Shaw and K. E. Creasy, *Anal. Chem.* 60, 1241 (1988).

471. B. R. Shaw and K. E. Creasy, *J. Electroanal. Chem.* 243, 209 (1988).

472. B. R. Shaw and K. E. Creasy, US Patent 4, 957, 593, 1990.

473. H. Kotte, B. Gründig, K.-D. Vorlop, B. Strehlitz, and U. Stottmeister, *Anal. Chem.* 67, 65 (1995).

474. J.-P. Li, T.-Z. Peng, and C. Fang, *Anal. Chim. Acta* 455, 53 (2002).

475. J.-P. Pereira-Ramos, R. Messina, and J. Perichon, *J. Electroanal. Chem.* 146, 157 (1983).

476. F. Bedioui, E. de Boysson, J. Devynck, and K. J. Balkus, Jr., *J. Electroanal. Chem.* 315, 313 (1991).

477. F. Bedioui, E. de Boysson, J. Devynck, and K. J. Balkus, Jr., *J. Chem. Soc. Faraday Trans.* 87, 3831 (1991).

478. K. Mesfar, B. Carré, F. Bedioui, and J. Devynck, *J. Mater. Chem.* 3, 873 (1993).

479. L. Gaillon, N. Sajot, F. Bedioui, J. Devynck, and K. J. Balkus, Jr., *J. Electroanal. Chem.* 345, 157 (1993).

480. F. Bedioui, L. Roué, L. Gaillon, J. Devynck, S. L. Bell, and K. J. Balkus, Jr., *Prepr.-Am. Chem. Soc. Div. Pet. Chem.* 38, 529 (1993).

481. F. Bedioui, L. Roué, E. Briot, J. Devynck, S. L. Bell, and K. J. Balkus, Jr., *J. Electroanal. Chem.* 373, 19 (1994).

482. A. G. Gabrielov, K. J. Balkus, Jr., S. L. Bell, F. Bedioui, and J. Devynck, *Microporous Mater.* 2, 119 (1994).

483. F. Bedioui, L. Roué, J. Devynck, and K. J. Balkus, Jr., *J. Electrochem. Soc.* 141, 3049 (1994).

484. L. Gaillon, F. Bedioui, and J. Devynck, *J. Mater. Chem.* 4, 1215 (1994).

485. F. Bedioui, L. Roué, J. Devynck, and K. J. Balkus, Jr., *Stud. Surf. Sci. Catal.* 84, 917 (1994).

486. K. J. Balkus, Jr., A. G. Gabrielov, S. Bell, F. Bedioui, L. Roué, and J. Devynck, *Inorg. Chem.* 33, 67 (1994).

487. F. Bedioui, L. Roué, E. Briot, J. Devynck, K. J. Balkus, Jr., and J. F. Diaz, *New J. Chem.* 20, 1235 (1996).

488. K. J. Balkus, Jr., A. K. Khanmamedova, K. M. Dixon, and F. Bedioui, *Appl. Catal. A* 143, 159 (1996).

489. F. Bedioui, E. Briot, J. Devynck, and K. J. Balkus, Jr., *Mater. Res. Soc. Symp. Proc.* 431, 45 (1996).

490. F. Bedioui, J. Devynck, and K. J. Balkus, Jr., *J. Phys. Chem.* 100, 8607 (1996).

491. E. Briot and F. Bedioui, *Curr. Topics Electrochem.* 4, 87 (1997).

492. F. Bedioui, E. Briot, J. Devynck, and K. J. Balkus, Jr., *Inorg. Chim. Acta* 254, 151 (1997).

493. E. Briot, F. Bedioui, and K. J. Balkus, Jr., *J. Electroanal. Chem.* 454, 83 (1998).

494. M. A. N. D. A. Lemos, P. Sousa, F. Lemos, A. J. L. Pombeiro, and F. R. Ribeiro, *Stud. Surf. Sci. Catal.* 122, 443 (1999).

495. M. V. Susic and N. Petranovic, *Electrochim. Acta* 23, 1271 (1978).

496. M. V. Susic, *Electrochim. Acta* 24, 535 (1979).

497. N. Petranovic and M. V. Susic, *Zeolites* 3, 271 (1983).

498. K. E. Creasy and B. R. Shaw, *J. Electrochem. Soc.* 137, 2353 (1990).

499. N. Petranovic and D. Minic, *Ceram. Int.* 22, 317 (1996).

500. D. C. Freeman, U.S. Patent 3, 186, 875, 1965; British Patent 999, 948, 1965.

501. C. C. Liang, German Patent 2, 228, 843, 1973.

502. M. M. Thackeray and J. Coetzer, *Solid State Ionics* 6, 135 (1982).

503. Furukawa Battery Co., Ltd., Japanese Patent 58, 012, 263, 1983.

504. Sanyo Electric Co., Ltd., Japanese Patent 58, 103, 776, 1983.

505. S. Slane and M. Salomon, *J. Power Sources* 55, 7 (1995).

506. N. Munichandraiah, L. G. Scanlon, R. A. Marsh, B. Kumar, and A. K. Sircar, *J. Appl. Electrochem.* 25, 857 (1995).

507. F. Gao, P. H. Mitchell, J. Barker, and J. Swoyer, U.S. Patent 5, 728, 489, 1998.

508. D. H. Jang, S. H. Kim, H. J. Kim, and S. M. Hong, World Patent 2000, 038, 263, 2000.

509. O. Enéa, *Electrochim. Acta* 34, 1647 (1989).

510. R. A. W. Dryfe, P. Hayes, and S. M. Holmes, *Analyst* 126, 733 (2001).

511. C. E. Marshall, *J. Phys. Chem.* 43, 1155 (1939).

512. R. M. Barrer and S. D. James, *J. Phys. Chem.* 64, 417 (1960).

513. G. Johansson, L. Risinger, and L. Fälth, *Anal. Chim. Acta* 119, 25 (1980).

514. G. Johansson, L. Fälth, and L. Risinger, *Hung. Sci. Instrum* 49, 47 (1980).

515. M. Demertzis and N. P. Evmiridis, *J. Chem. Soc. Faraday Trans. I* 82, 3647 (1986).

516. N. P. Evmiridis, M. A. Demertzis, and A. G. Vlessidis, *Fresenius J. Anal. Chem.* 340, 145 (1991).

517. S. Matysik, F.-M. Matysik, J. Mattusch, and W.-D. Einicke, *Electroanalysis* 10, 98 (1998).

518. M. L. Hamlaoui, R. Kherrat, M. Marakchi, N. Jaffrezic-Renault, and A. Walcarius, *Mater. Sci. Eng. C* 21, 25 (2002).

519. M. L. Hamlaoui, K. Reybier, M. Marakchi, N. Jaffrezic-Renault, C. Martelet, R. Kherrat, and A. Walcarius, *Anal. Chim. Acta* 466, 39 (2002).

520. S. Matysik, F.-M. Matysik, and W.-D. Einicke, *Sensors Actuators B* 85, 104 (2002).

521. Z. Li, C. Lai, and T. E. Mallouk, *Inorg. Chem.* 28, 178 (1989).

522. J. Sarradin, J.-M. Louvet, R. Messina, and J. Perichon, *Zeolites* 4, 157 (1984).

523. M. Fleischmann, J. Ghoroghchian, D. R. Rolison, and S. Pons, *J. Phys. Chem.* 90, 6392 (1986).

524. D. R. Rolison, R. J. Nowak, S. Pons, J. Ghoroghchian, and M. Fleischmann, in "Molecular Electronic Devices" (F. L. Carter, R. E. Siatkowski, and H. Wohltjen, Eds.), pp. 401–410. Elsevier/North-Holland, Amsterdam, 1988.

525. D. R. Rolison, E. A. Hayes, and W. E. Rudzinski, *J. Phys. Chem.* 93, 5524 (1989).

526. J. S. Krueger and T. E. Mallouk, *Surf. Sci. Ser.* 38, 461 (1991).

527. D. R. Rolison and J. Z. Stemple, *J. Chem. Soc. Chem. Commun.* 25 (1993).

528. D. N. Blauch and D. R. Rolison, *J. Electroanal. Chem.* 370, 305 (1994).

529. C. A. Bessel and D. R. Rolison, *J. Phys. Chem. B* 101, 1148 (1997).

530. C. A. Bessel and D. R. Rolison, *J. Electroanal. Chem.* 439, 97 (1997).
531. C. A. Bessel and D. R. Rolison, *J. Am. Chem. Soc.* 119, 12673 (1997).
532. M. M. Collinson, C. G. Rausch, and A. Voigt, *Langmuir* 13, 7245 (1997).
533. M. E. Tess and J. A. Cox, *J. Electroanal. Chem.* 457, 163 (1998).
534. J. A. Cox and K. S. Alber, *J. Electrochem. Soc.* 143, L126 (1996).
535. R. Makote and M. M. Collinson, *Anal. Chim. Acta* 394, 195 (1999).
536. P. C. Pandey, S. Upadhyay, H. C. Pathak, and C. M. D. Pandey, *Electroanalysis* 11, 950 (1999).
537. W. Song, X. Chen, Y. Jiang, Y. Liu, C. Sun, and X. Wang, *Anal. Chim. Acta* 394, 73 (1999).
538. W. Song, N. Lu, Y. Jiang, Y. Liu, X. Wang, J. Liu, H. Xu, and C. Sun, *Microchem. J.* 62, 344 (1999).
539. W. Song, Y. Liu, N. Lu, H. Xu, and C. Sun, *Electrochim. Acta* 45, 1639 (2000).
540. M. M. Collinson, H. Wang, R. Makote, and A. Khramov, *J. Electroanal. Chem.* 519, 65 (2002).
541. S. L. P. Dias, Y. Gushikem, E. S. Ribeiro, and E. V. Benvenutti, *J. Electroanal. Chem.* 523, 64 (2002).
542. P. N. Deepa and S. S. Narayanan, *Bull. Electrochem.* 17, 259 (2001).
543. B. Wang, L. Cheng, and S. Dong, *J. Electroanal. Chem.* 516, 17 (2001).
544. H. Yi and A. Ichimura, *Anal. Sci.* 17, a353 (2001).
545. J. L. Cohen, J. Wydera, and J. A. Cox, *Electroanalysis* 14, 231 (2002).
546. Y. N. Shi, C. J. Seliskar, and W. R. Heineman, *Anal. Chem.* 69, 4819 (1997).
547. Y. Shi, A. F. Slaterbeck, C. J. Seliskar, and W. R. Heineman, *Anal. Chem.* 69, 3679 (1997).
548. S. Zamponi, A. M. Kijak, A. J. Sommer, R. Marassi, P. J. Kulesza, and J. A. Cox, *J. Solid State Electrochem.* 6, 528 (2002).
549. B. Barroso-Fernandez, M. T. Lee-Alvarez, C. J. Seliskar, and W. R. Heineman, *Anal. Chim. Acta* 370, 221 (1998).
550. Z. Hu, C. J. Seliskar, and W. R. Heineman, *Anal. Chem.* 70, 5230 (1998).
551. Z. Hu, A. F. Slaterbeck, C. J. Seliskar, T. H. Ridgway, and W. R. Heineman, *Langmuir* 15, 767 (1999).
552. A. F. Slaterbeck, T. H. Ridgway, C. J. Seliskar, and W. R. Heineman, *Anal. Chem.* 71, 1196 (1999).
553. L. Gao, C. J. Seliskar, and W. R. Heineman, *Anal. Chem.* 71, 4061 (1999).
554. Z. Hu and W. R. Heineman, *Anal. Chem.* 72, 2395 (2000).
555. A. F. Slaterbeck, M. G. Stegemiller, C. J. Seliskar, T. H. Ridgway, and W. R. Heineman, *Anal. Chem.* 72, 5567 (2000).
556. J. M. DiVirgilio-Thomas, W. R. Heineman, and C. J. Seliskar, *Anal. Chem.* 72, 3461 (2000).
557. S. E. Ross, C. J. Seliskar, and W. R. Heineman, *Anal. Chem.* 72, 5549 (2000).
558. M. Maizels, C. J. Seliskar, and W. R. Heineman, *Electroanalysis* 12, 1356 (2000).
559. A. Khramov and M. M. Collinson, *Anal. Chem.* 72, 2943 (2000).
560. S. H. Jang, M. G. Han, and S. S. Im, *Synth. Met.* 110, 17 (2000).
561. M. Maizels, M. Stegemiller, S. Ross, A. F. Slaterbeck, Y. Shi, T. H. Ridgway, W. R. Heineman, C. J. Seliskar, and S. A. Bryan, *ACS Symp. Ser.* 778, 364 (2001).
562. H. Wang, G. Xu, and S. Dong, *Electroanalysis* 14, 853 (2002).
563. C. C. Hsueh and M. M. Collinson, *J. Electroanal. Chem.* 420, 243 (1997).
564. M. D. Petit-Dominguez, H. Shen, W. R. Heineman, and C. J. Seliskar, *Anal. Chem.* 69, 703 (1997).
565. R. Makote and M. M. Collinson, *Chem. Mater.* 10, 2440 (1998).
566. Y. Guo, A. R. Guadalupe, O. Resto, L. F. Fonseca, and S. Z. Weisz, *Chem. Mater.* 11, 135 (1999).
567. R. V. S. Alfaya, A. A. S. Alfaya, Y. Gushikem, S. Rath, and F. G. R. Reyes, *Anal. Lett.* 33, 2859 (2000).
568. H. Wei and M. M. Collinson, *Anal. Chim. Acta* 397, 113 (1999).
569. Y. Guo and A. R. Guadalupe, *J. Pharm. Biomed. Anal.* 19, 175 (1999).
570. T. Inagaki, H. S. Lee, T. A. Skotheim, and Y. Okamoto, *J. Chem. Soc.*, Chem. Commun. 1181 (1989).
571. S. Ikeda and N. Oyama, *Anal. Chem.* 65, 1910 (1993).
572. G. Cerveau, R. J. P. Corriu, and N. Costa, *J. Non-Cryst. Solids* 163, 226 (1993).
573. P. Audebert, P. Calas, G. Cerveau, R. J. P. Corriu, and N. Costa, *J. Electroanal. Chem.* 372, 275 (1994).
574. A. Merz and H. Bachmann, *J. Am. Chem. Soc.* 117, 901 (1995).
575. P. Audebert, G. Cerveau, R. J. P. Corriu, and N. Costa, *J. Electroanal. Chem.* 413, 89 (1996).
576. J. Wang and M. M. Collinson, *J. Electroanal. Chem.* 455, 127 (1998).
577. U. Künzelmann and H. Böttcher, *Sensors Actuators B* 38–39, 222 (1997).
578. S. Yang, Y. Lu, P. Atanossov, E. Wilkins, and X. Long, *Talanta* 47, 735 (1998).
579. B. Wang, B. Li, Q. Deng, and S. Dong, *Anal. Chem.* 70, 3170 (1998).
580. P. C. Pandey, S. Upadhyay, and H. C. Pathak, *Sensors Actuators B* 60, 83 (1999).
581. P. C. Pandey, S. Upadhyay, H. C. Pathak, I. Tiwari, and V. S. Tripathi, *Electroanalysis* 11, 1251 (1999).
582. B. Wang, B. Li, Z. Wang, G. Xu, Q. Wang, and S. Dong, *Anal. Chem.* 71, 1935 (1999).
583. W.-Y. Lee, K. S. Lee, T.-H. Kim, M.-C. Shin, and J.-K. Park, *Electroanalysis* 12, 78 (2000).
584. W.-Y. Lee, S.-R. Kim, T.-H. Kim, K. S. Lee, M.-C. Shin, and J.-K. Park, *Anal. Chim. Acta* 404, 195 (2000).
585. B. Wang, J. Zhang, G. Cheng, and S. Dong, *Anal. Chim. Acta* 407, 111 (2000).
586. B. Wang and S. Dong, *J. Electroanal. Chem.* 487, 45 (2000).
587. B. Wang, J. Zhang, and S. Dong, *Biosens. Bioelectron.* 15, 397 (2000).
588. E. I. Iwuoha, S. Kane, C. Ovin Ania, M. R. Smyth, P. R. Ortiz de Montellano, and U. Fuhr, *Electroanalysis* 12, 980 (2000).
589. Y. Miao and S. N. Tan, *Anal. Chim. Acta* 437, 87 (2001).
590. S.-M. Lee and W.-Y. Lee, *Bull. Korean Chem. Soc.* 23, 1169 (2002).
591. B. Wang, B. Li, Z. Wang, G. Cheng, and S. Dong, *Anal. Chim. Acta* 388, 71 (1999).
592. B. Wang and S. Dong, *Talanta* 51, 565 (2000).
593. J. Niu and J. Y. Lee, *Sensors Actuators B* 82, 250 (2002).
594. X. Chen, B. Wang, and S. Dong, *Electroanalysis* 13, 1149 (2001).
595. J. Li, S. N. Tan, and H. Ge, *Anal. Chim. Acta* 335, 137 (1996).
596. J. Li, S. N. Tan, and J. T. Oh, *J. Electroanal. Chem.* 448, 69 (1998).
597. J. Li, S. Chia, N. K. Goh, and S. N. Tan, *Anal. Chim. Acta* 362, 203 (1998).
598. U. Narang, P. N. Prasad, F. V. Bright, K. Ramanathan, N. D. Kumar, B. D. Malhotra, M. N. Kamalasanan, and S. Chandra, *Anal. Chem.* 66, 3139 (1994).
599. J. Li, S. Chia, N. K. Goh, S. N. Tan, and H. Ge, *Sensors Actuators B* 40, 135 (1997).
600. S. L. Chut, J. Li, and S. N. Tan, *Analyst* 122, 1431 (1997).
601. P. C. Pandey, S. Upadhyay, and H. C. Pathak, *Electroanalysis* 11, 59 (1999).
602. T.-M. Park, E. I. Iwuoha, M. R. Smyth, and B. D. MacCraith, *Anal. Commun.* 33, 271 (1996).
603. T.-M. Park, E. I. Iwuoha, M. R. Smyth, R. Freaney, and A. J. McShane, *Talanta* 44, 973 (1997).
604. T.-M. Park, E. I. Iwuoha, and M. R. Smyth, *Electroanalysis* 9, 1120 (1997).
605. T.-M. Park, *Anal. Lett.* 32, 287 (1999).
606. Z. Ji and A. R. Guadalupe, *Electroanalysis* 11, 167 (1999).
607. A. Walcarius, C. Despas, P. Trens, M.-J. Hudson, and J. Bessière, *J. Electroanal. Chem.* 453, 249 (1998).

608. A. Walcarius, N. Luthi, J.-L. Blin, B.-L. Su, and L. Lamberts, *Electrochim. Acta* 44, 4601 (1999).

609. A. Walcarius and J. Bessière, *Chem. Mater.* 11, 3009 (1999).

610. M. Etienne, S. Sayen, B. Lebeau, and A. Walcarius, *Stud. Surf. Sci. Catal.* 141, 615 (2002).

611. L. Li, W. Li, C. Sun, and L. Li, *Electroanalysis* 14, 368 (2002).

612. S. Sayen, M. Etienne, J. Bessière, and A. Walcarius, *Electroanalysis*, 14, 1521 (2002).

613. A. Walcarius, M. Etienne, S. Sayen, and B. Lebeau, *Electroanalysis*, in press.

614. A. Arranz, S. F. de Betono, J. M. Moreda, A Cid, and J. F. Arranz, *Mikrochim. Acta* 127, 273 (1997).

615. A. Arranz, M. F. Villalba, S. F. de Betono, J. M. Moreda, and J. F. Arranz, *Fresenius J. Anal. Chem.* 357, 768 (1997).

616. H. Liu, Z. Zhang, Y. Fan, M. Dai, X. Zhang, J. Wei, Z. Qiu, H. Li, X. Wu, J. Deng, and D. Qi, *Fresenius J. Anal. Chem.* 357, 297 (1997).

617. W. Luo, H. Liu, H. Deng, K. Sun, C. Zhao, D. Qi, and J. Deng, *Anal. Lett.* 30, 205 (1997).

618. A. Walcarius, and J. Bessière, *Electroanalysis* 9, 707 (1997).

619. A. Walcarius, C. Despas, and J. Bessière, *Anal. Chim. Acta* 385, 79 (1999).

620. A. Walcarius, J. Devoy, and J. Bessière, *Environ. Sci. Technol.* 33, 4278 (1999).

621. A. M. Bond, W. Miao, T. D. Smith, and J. Jamis, *Anal. Chim. Acta* 396, 203 (1999).

622. A. A. S. Alfaya and Y. Gushikem, *J. Colloid Interface Sci.* 209, 428 (1999).

623. A. Walcarius, J. Devoy, and J. Bessière, *J. Solid State Electrochem.* 4, 330 (2000).

624. E. Gonzalez, P. Hernandez, and L. Hernandez, *Anal. Chim. Acta* 228, 265 (1990).

625. L. Hernandez, P. Hernandez, and J. Vicente, *Fresenius J. Anal. Chem.* 345, 712 (1993).

626. P. Hernandez, O. Nieto, F. Galan, and L. Hernandez, *Quim. Anal.* 12, 18 (1993).

627. L. M. Aleixo, M. B. Souza, O. E. S. Godinho, G. de Oliveira Neto, Y. Gushikem, and J. C. Moreira, *Anal. Chim. Acta* 271, 143 (1993).

628. L. L. Lorencetti and Y. Gushikem, *J. Braz. Chem. Soc.* 4, 88 (1993).

629. M. Chicharro, A. Zapardiel, E. Bermejo, J.A. Perez, and L. Hernandez, *Anal. Lett.* 27, 1809 (1994).

630. C. A. Borgo, R. T. Ferrari, L. M. S. Colpini, C. M. M. Costa, M. L. Baesso, and A. C. Bento, *Anal. Chim. Acta* 385, 103 (1999).

631. E. S. Ribeiro and Y. Gushikem, *Electroanalysis* 11, 1280 (1999).

632. S. T. Fujiwara and Y. Gushikem, *J. Braz. Chem. Soc.* 10, 389 (1999).

633. E. S. Ribeiro and Y.Gushikem, *Electrochim. Acta* 44, 3589 (1999).

634. M. Etienne, J. Bessière, and A. Walcarius, *Sensors Actuators B* 76, 531 (2001).

635. S. Sayen, C. Gérardin, L. Rodehuser, and A. Walcarius, *Electroanalysis*, in press

636. L. T. Kubota, Y. Gushikem, J. Perez, and A. A. Tanaka, *Langmuir* 11, 1009 (1995).

637. C. R. M. Peixoto, L. T. Kubota, and Y. Gushikem, *Anal. Proc.* 32, 503 (1995).

638. Y. Gushikem, C. R. M. Peixoto, U. P. Rodrigues Filho, L. T. Kubota, and E. Stadler, *J. Coll. Interface Sci.* 184, 236 (1996).

639. L. T. Kubota, F. Gouvea, A. N. Andrade, B. G. Milagres, and G. de Oliveira Neto, *Electrochim. Acta* 41, 1465 (1996).

640. R. F. Rocha, S. S. Rosatto, R. E. Bruns, and L. T. Kubota, *J. Electroanal. Chem.* 433, 73 (1997).

641. E. F. Perez, G. de Oliveira Neto, A. A. Tanaka, and L. T. Kubota, *Electroanalysis* 10, 111 (1998).

642. E. F. Perez, L. T. Kubota, A. A. Tanaka, and G. de Oliveira Neto, *Electrochim. Acta* 43, 1665 (1998).

643. C. A. Pessôa and Y. Gushikem, *J. Electroanal. Chem.* 477, 158 (1999).

644. A. M. Castellani and Y. Gushikem, *J. Coll. Interface Sci.* 230, 195 (2000).

645. C. U. Ferreira, Y. Gushikem, and L. T. Kubota, *J. Solid State Electrochem.* 4, 298 (2000).

646. A. M. Castellani, J. E. Goncalves, and Y. Gushikem, *Electroanalysis* 13, 1165 (2001).

647. G. Zaitseva, Y. Gushikem, E. R. Ribeiro, and S. S. Rosatto, *Electrochim. Acta* 47, 1469 (2002).

648. A. S. Santos, L. Gorton, and L. T. Kubota, *Electrochim. Acta* 47, 3351 (2002).

649. B. G. Milagres, L. T. Kubota, and G. de Oliveira Neto, *Electroanalysis* 8, 489 (1996).

650. C. A. B. Garcia, G. de Oliveira Neto, L. T. Kubota, and L. A. Grandin, *J. Electroanal. Chem.* 418, 147 (1996).

651. L. T. Kubota, B. G. Milagres, F. Gouvea, and G. de Oliveira Neto, *Anal. Lett.* 29, 893 (1996).

652. L. T. Kubota, M. U. Kleinke, C. Mello, M. I. Bueno, and G. de Oliveira Neto, *Chem. Phys. Lett.* 264, 662 (1997).

653. J. Kulys, *Biosens. Bioelectron.* 14, 473 (1999).

654. S. S. Rosatto, L. T. Kubota, and G. de Oliveira Neto, *Anal. Chim. Acta* 390, 65 (1999).

655. P. D. Hale, T. Inagaki, H. I. Karan, Y. Okamoto, and T. A. Skotheim, *J. Am. Chem. Soc.* 111, 3482 (1989).

656. L. Gorton, H. I. Karan, P. D. Hale, T. Inagaki, Y. Okamoto, and T. A. Skotheim, *Anal. Chim. Acta* 228, 23 (1990).

657. P. D. Hale, L. I. Boguslavsky, T. Inagaki, H. I. Karan, H. S. Lee, T. A. Skotheim, and Y. Okamoto, *Anal. Chem.* 63, 677 (1991).

658. P. Audebert and C. Sanchez, *J. Sol–Gel Sci. Technol.* 2, 809 (1994).

659. G. Gun, M. Tsionsky, and O. Lev, *Anal. Chim. Acta* 294, 261 (1994).

660. M. Tsionsky, G. Gun, V. Glezer, and O. Lev, *Anal. Chem.* 66, 1747 (1994).

661. G. Gun, M. Tsionsky, and O. Lev, *Mater. Res. Soc. Symp. Proc.* 346, 1011 (1994).

662. P. V. A. Pamidi, C. Parrado, S. A. Kane, J. Wang, M. R. Smyth, and J. Pingarron, *Talanta* 44, 1929 (1997).

663. M. E. Tess and J. A. Cox, *Anal. Chem.* 70, 187 (1998).

664. S. D. Holmstrom and J. A. Cox, *Electroanalysis* 10, 597 (1998).

665. S. D. Holmstrom, Z. D. Sandlin, W. H. Steinecker, and J. A. Cox, *Electroanalysis* 12, 262 (2000).

666. L. Hua, L. S. Chia, N. K. Goh, and S. N. Tan, *Electroanalysis* 12, 287 (2000).

667. L. Hua and S. N. Tan, *Anal. Chim. Acta* 403, 179 (2000).

668. L. Hua and S. N. Tan, *Anal. Chem.* 72, 4821 (2000).

669. L. Hua and S. N. Tan, *Fresenius J. Anal. Chem.* 367, 697 (2000).

670. M. Cordero-Rando, J. L. Hidalgo-Hidalgo de Cisneros, E. Blanco, and I. Naranjo-Rodriguez, *Anal. Chem.* 74, 2423 (2002).

671. J. Gun, M. Tsionsky, L. Rabinovich, Y. Golan, I. Rubinstein, and O. Lev, *J. Electroanal. Chem.* 395, 57 (1995).

672. L. Rabinovich, J. Gun, M. Tionsky, and O. Lev, *J. Sol–Gel Sci. Technol.* 8, 1077 (1997).

673. L. Rabinovich, O. Lev, and G. A. Tsirlina, *J. Electroanal. Chem.* 466, 45 (1999).

674. P. Wang, X. Wang, Y. Yuan, and G. Zhu, *J. Non-Cryst. Solids* 277, 22 (2000).

675. P. Wang, X. Wang, L. Bi, and G. Zhu, *Analyst* 125, 1291 (2000).

676. P. Wang, X. Wang, X. Jing, and G. Zhu, *Anal. Chim. Acta* 424, 51 (2000).

677. P. Wang, X. Wang, and G. Zhu, *Electrochim. Acta* 46, 637 (2000).

678. P. Wang, X. Wang, and G. Zhu, *Electroanalysis* 12, 1493 (2000).

679. P. Wang, X. Jing, W. Zhang, and G. Zhu, *J. Solid State Electrochem.* 5, 369 (2001).

680. S. N. Tan and L. Hua, *Anal. Chim. Acta* 450, 263 (2001).

681. P. Wang, Y. Yuan, and G. Zhu, *J. Electroanal. Chem.* 519, 130 (2002).

682. Y. Yuan, P. Wang, and G. Zhu, *Anal. Bioanal. Chem.* 372, 712 (2002).

683. M. Tsionsky and O. Lev, *Anal. Chem.* 67, 2409 (1995); *J. Electrochem. Soc.* 142, 2154 (1995).
684. J. Wang, P. V. A. Pamidi, V. B. Nascimento, and L. Angnes, *Electroanalysis* 9, 689 (1997).
685. J. Wang, P. V. A. Pamidi, C. Parrado, D. S. Park, and J. Pingarron, *Electroanalysis* 9, 908 (1997).
686. M. E. Tess and J. A. Cox, *Electroanalysis* 10, 1237 (1998).
687. S. Sampath and O. Lev, *J. Electroanal. Chem.* 446, 57 (1998).
688. J. A. Cox, S. D. Holmstrom, and M. E. Tess, *Talanta* 52, 1081 (2000).
689. J. Seneviratne, S. D. Holmstrom, and J. A. Cox, *Talanta* 52, 1025 (2000).
690. S. D. Holmstrom and J. A. Cox, *Anal. Chem.* 72, 3191 (2000).
691. Z. Yang, P. Wang, W. Zhang, and G. Zhu, Fresenius J. *Anal. Chem.* 371, 337 (2001).
692. S. B. Khoo and R. Ye, *Electroanalysis* 14, 420 (2002).
693. M. Opallo and M. Saczek-Maj, *Electrochem. Commun.* 3, 306 (2001).
694. M. Saczek-Maj and M. Opallo, *Electroanalysis* 14, 1060 (2002).
695. L. Coche-Guérente, S. Cosnier, and P. Labbe, *Chem. Mater.* 9, 1348 (1997).
696. G. Oskam and P. C. Searson, *J. Phys. Chem. B* 102, 2464 (1998).
697. L. Rabinovich, J. Gun, O. Lev, D. Aurbach, B. Markovsky, and M. D. Levi, *Adv. Mater.* 10, 577 (1998).
698. D. Aurbach, M. D. Levi, O. Lev, J. Gun, and L. Rabinovich, *J. Appl. Electrochem.* 28, 1051 (1998).
699. I. Pankratov and O. Lev, *J. Electroanal. Chem.* 393, 35 (1995).
700. S. Sampath, I. Pankratov, J. Gun, and O. Lev, *J. Sol–Gel Sci. Technol.* 7, 123 (1996).
701. S. Sampath and O. Lev, *Electroanalysis* 8, 1112 (1996).
702. J. Gun and O. Lev, *Anal. Chim. Acta* 336, 95 (1996).
703. J. Gun and O. Lev, *Anal. Lett.* 29, 1933 (1996).
704. S. Sampath and O. Lev, *Anal. Chem.* 68, 2015 (1996).
705. S. Sampath and O. Lev, *J. Electroanal. Chem.* 426, 131 (1997).
706. J. Li, L. S. Chia, N. K. Goh, and S. N. Tan, *J. Electroanal. Chem.* 460, 234 (1999).
707. J. J. Niu and J. Y. Lee, *Anal. Commun.* 36, 81 (1999).
708. J. J. Niu and J. Y. Lee, *Sensors Actuators B* 62, 190 (2000).
709. F. Tian, B. Xu, L. Zhu, and G. Zhu, *Anal. Chim. Acta* 443, 9 (2001).
710. F. Tian and G. Zhu, *Anal. Chim. Acta* 451, 251 (2002).
711. L. Zhu, Y. Li, F. Tian, B. Xu, and G. Zhu, *Sensors Actuators B* 84, 265 (2002).
712. S. Bharathi and O. Lev, *Chem. Commun.* 2303 (1997).
713. J. Wang and P. V. A. Pamidi, *Anal. Chem.* 69, 4490 (1997).
714. S. Bharathi and O. Lev, *Anal. Commun.* 35, 29 (1998).
715. S. Bharathi, N. Fishelson, and O. Lev, *Langmuir* 15, 1929 (1999).
716. S. Bharathi and M. Nogami, *Analyst* 126, 1919 (2001).
717. D. Ravishankaran, N. Uehara, and T. Kato, *Anal. Sci.* 18, 935 (2002).
718. F. Tian and G. Zhu, *Sensors Actuators B* 86, 266 (2002).
719. D. Ravishankaran, N. Uehara, and T. Kato, *Anal. Bioanal. Chem.* 374, 412 (2002).
720. J. Wang, P. V. A. Pamidi, and D. S. Park, *Anal. Chem.* 68, 2705 (1996).
721. J. Wang, D. S. Park, and P. V. A. Pamidi, *J. Electroanal. Chem.* 434, 185 (1997).
722. J. Wang, P. V. A. Pamidi, and D. S. Park, *Electroanalysis* 9, 52 (1997).
723. J. Wang, P. V. A. Pamidi, and M. Jiang, *Anal. Chim. Acta* 360, 171 (1998).
724. J. Wang, P. V. A. Pamidi, and K. R. Rogers, *Anal. Chem.* 70, 1171 (1998).
725. Y. Guo and A. R. Guadalupe, *Sensors Actuators B* 46, 213 (1998).
726. S. Andreescu, L. Barthelmebs, and J.-L. Marty, *Anal. Chim. Acta* 464, 171 (2002).
727. J. R. Fernandes, L. T. Kubota, Y. Gushikem, and G. de Oliveira Neto, *Anal. Lett.* 26, 2555 (1993).
728. L. L. Lorencetti, Y. Gushikem, L. T. Kubota, G. de Oliveira Neto, and J. R. Fernandes, *Mikrochim. Acta* 117, 239 (1995).
729. W. Kim, S. Chung, S. B. Park, S. C. Lee, C. Kim, and S. D. Sung, *Anal. Chem.* 69, 95 (1997).
730. W. Kim, D. D. Sung, G. S. Cha, and S. B. Park, *Analyst* 123, 379 (1998).
731. M. F. S. Teixeira, L. A. Ramos, E. Almeida Neves, and O. Fatibello-Filho, *Fresenius J. Anal. Chem.* 367, 86 (2000).
732. K. Kimura, T. Sunagawa, and M. Yokoyama, *Chem. Commun.* 745 (1996).
733. K. Kimura, T. Sunagawa, S. Yajima, S. Miyake, and M. Yokoyama, *Anal. Chem.* 70, 4309 (1998).
734. K. Kimura, H. Takase, S. Yajima, and M. Yokoyama, *Analyst* 124, 517 (1999).
735. W. Wroblewski, M. Chudy, A. Dybko, and Z. Brzozka, *Anal. Chim. Acta* 401, 105 (1999).
736. J. Liu, X. Wu, Z. Zhang, S. Wakida, and K. Higashi, *Sensors Actuators B* 66, 216 (2000).
737. M. Ben Ali, R. Kalfat, H. Sfihi, J. M. Chovelon, H. Ben Ouada, and N. Jaffrezic-Renault, *Sensors Actuators B* 62, 233 (2000).
738. M. Popall and X.-M. Du, *Electrochim. Acta* 40, 2305 (1995).
739. M.-H. Lee, H. J. Kim, S. B. Rhee, and M. J. Moon, *Solid State Ionics* 85, 91 (1996).
740. M. Watanabe, H. Uchida, Y. Seki, M. Emori, and P. Stonehart, *J. Electrochem. Soc.* 143, 3847 (1996).
741. M.-H. Lee, S. T. Ko, K. S. Lee, and S. B. Rhee, *Mol. Cryst. Liq. Cryst.* 294, 229 (1997).
742. D.-W. Kim, *J. Power Sources* 76, 175 (1998).
743. A. Matsuda, H. Honjo, M. Tatsumisago, and T. Minami, *Solid State Ionics* 113–115, 97 (1998).
744. S. Skaarup, K. West, B. Zachau-Christiansen, M. Popall, J. Kappel, J. Kron, G. Eichinger, and G. Semrau, *Electrochim. Acta* 43, 1589 (1998).
745. L. Depre, J. Kappel, and M. Popall, *Electrochim. Acta* 43, 1301 (1998).
746. A. Matsuda, H. Honjo, K. Hirata, M. Tatsumisago, and T. Minami, *J. Power Sources* 77, 12 (1999).
747. P. L. Antonucci, A. S. Arico, P. Creti, E. Ramunni, and V. Antonucci, *Solid State Ionics* 125, 431 (1999).
748. C. Wang, Y. Wei, G. R. Ferment, W. Li, and T. Li, *Mater. Lett.* 39, 206 (1999).
749. I. Honma, S. Hirakawa, K. Yamada, and J. M. Bae, *Solid State Ionics* 118, 29 (1999).
750. K.-H. Lee, Y.-G. Lee, J.-K. Park, and D.-Y. Seung, *Solid State Ionics* 133, 257 (2000).
751. L. Depre, M. Ingram, C. Poinsignon, and M. Popall, *Electrochim. Acta* 45, 1377 (2000).
752. B. Baradie, J. P. Dodelet, and D. Guay, *J. Electroanal. Chem.* 489, 101 (2000).
753. B. Bonnet, D. J. Jones, J. Rozière, L. Tchicaya, G. Alberti, M. Casciola, L. Massinelli, B. Bauer, A. Peraio, and E. Ramunni, *J. New Mater. Electrochem. Syst.* 3, 87 (2000).
754. M. Popall, R. Buestrich, G. Semrau, G. Eichinger, M. Andrei, W. O. Parker, S. Skaarup, and K. West, *Electrochim. Acta* 46, 1499 (2001).
755. N. Miyake, J. S. Wainright, and Savinell, *J. Electrochem. Soc.* 148, A898 (2001).
756. I. Honma, S. Nomura, and H. Nakajima, *J. Membrane Sci.* 185, 83 (2001).
757. I. Honma, O. Nishikawa, T. Sugimoto, S. Nomura, and H. Nakajima, *Fuel Cells* 2, 52 (2002).
758. H. Nakajima, S. Nomura, T. Sugimoto, S. Nishikawa, and I. Honma, *J. Electrochem. Soc.* 149, A953 (2002).

759. K. Dahmouche, M. Atik, N. C. Mello, T. J. Bonagamba, H. Panepucci, M. A. Aegerter, and P. Judeinstein, *Mater. Res. Soc. Symp. Proc.* 435, 363 (1996).

760. K. Dahmouche, M. Atik, N. C. Mello, T. J. Bonagamba, H. Panepucci, M. A. Aegerter, and P. Judeinstein, *J. Sol–Gel Sci. Technol.* 8, 711 (1997).

761. K. Dahmouche, M. Atik, N. C. Mello, T. J. Bonagamba, H. Panepucci, P. Judeinstein, and M. A. Aegerter, *Solar Energy Mater. Solar Cells* 54, 1 (1998).

762. K. Dahmouche, P. H. de Souza, T. J. Bonagamba, H. Panepucci, P. Judeinstein, H. Pulcinelli, and C. V. Santilli, *J. Sol–Gel Sci. Technol.* 13, 909 (1998).

763. R. F. Bianchi, P. H. Souza, T. J. Bonagamba, H. Panepucci, and R. M. Faria, *Synth. Met.* 102, 1186 (1999).

764. N. Groselj, M. Gaberscek, U. Opara Krasovec, B. Orel, G. Drazic, and P. Judeinstein, *Solid State Ionics* 125, 125 (1999).

765. H. J. Walls, J. Zhou, J. A. Yerian, P. S. Fedkiw, S. A. Khan, M. K. Stowe, and G. L. Baker, *J. Power Sources* 89, 156 (2000).

766. N. C. Mello, T. J. Bonagamba, H. Panepucci, K. Dahmouche, P. Judeinstein, and M. A. Aegerter, *Macromolecules* 33, 1280 (2000).

767. U. L. Stangar, B. Orel, N. Groselj, P. Judeinstein, F. Decker, and P. Lianos, *Monats. Chem.* 132, 103 (2001).

768. J. A. Chaker, K. Dahmouche, C. V. Santilli, S. H. Pulcinelli, V. Briois, A.-M. Flank, and P. Judeinstein, *J. Non-Cryst. Solids* 304, 109 (2002).

769. M. Opallo and J. Kukulka, *Electrochem. Commun.* 2, 394 (2000).

770. M. Opallo and J. Kukulka-Walkiewicz, *Electrochim. Acta* 46, 4235 (2001).

771. D. C. Bookbinder and M. S. Wrighton, *J. Electrochem. Soc.* 130, 1080 (1983).

772. L. J. Kepley and A. J. Bard, *J. Electrochem. Soc.* 142, 4129 (1995).

773. C. M. Casado, M. Moran, J. Losada, and I. Cuadrado, *Inorg. Chem.* 34, 1668 (1995).

774. M. Onoda, T. Moritake, T. Matsuda, and H. Nakayama, *Synth. Met.* 71, 2255 (1995).

775. G. T. R. Palmore, D. K. Smyth, and M. S. Wrighton, *J. Phys. Chem. B* 101, 2437 (1997).

776. D. Martorell, F. Céspedes, E. Martinez-Fàbregas, and S. Alegret, *Anal. Chim. Acta* 337, 305 (1997).

777. C.-Z. Zhao, N. Egashira, Y. Kurauchi, and K. Ohga, *Anal. Sci.* 194, 439 (1998).

778. L. Gao and C. J. Seliskar, *Chem. Mater.* 10, 2481 (1998).

779. R. Shacham, D. Avnir, and D. Mandler, *Adv. Mater.* 11, 384 (1999).

780. P. E. Michel, P. D. van der Wal, G. C. Fiaccabrino, N. F. de Rooij, and M. Koudelka-Hep, *Electroanalysis* 11, 1361 (1999).

781. J. P. Cloarec, J. R. Martin, C. Polychronakos, I. Lawrence, M. F. Lawrence, and E. Souteyrand, *Sensors Actuators B* 58, 394 (1999).

782. M. M. Collinson and S. A. Martin, *Chem. Commun.* 899 (1999).

783. M. M. Collinson, P. J. Zambrano, H. Wang, and J. S. Taussig, *Langmuir* 15, 662 (1999).

784. M. M. Collinson, J. S. Taussig, and S. A. Martin, *Chem. Mater.* 11, 2594 (1999).

785. M. M. Collinson, B. Novak, S. A. Martin, and J. S. Taussig, *Anal. Chem.* 72, 2914 (2000).

786. A. R. Howells, P. J. Zambrano, and M. M. Collinson, *Anal. Chem.* 72, 5265 (2000).

787. I. Markovich and D. Mandler, *J. Electroanal. Chem.* 484, 194 (2000).

788. N. W. Barnett, R. Bos, H. Brand, P. Jones, K. F. Lim, S. D. Purcell, and R. A. Russel, *Analyst* 127, 455 (2002).

789. R. Naegeli, J. Redepenning, and F. C. Anson, *J. Phys. Chem.* 90, 6227 (1986).

790. A. J. Bard and L. R. Faulkner, "Electrochemical Methods: Fundamentals and Applications." Wiley, New York, 1980.

791. M. Vitale, N. B. Castagnola, N. J. Ortins, J. A. Brooke, A. Vaidyalingam, and P. K. Dutta, *J. Phys. Chem. B* 103, 2408 (1999).

792. C. A. Bessel and D. R. Rolison, *Stud. Surf. Sci. Catal.* 98, 114 (1995).

793. G. Shi, G. Xue, W. Hou, J. Dong, and G. Wang, *J. Electroanal. Chem.* 344, 363 (1993).

794. M. D. Baker, C. Senaratne, and M. McBrien, *J. Phys. Chem.* 99, 12367 (1995).

795. J. Li, K. Pfanner, and G. Calzaferri, *J. Phys. Chem.* 99, 12368 (1995).

796. D. R. Rolison, C. A. Bessel, M. D. Baker, C. Senaratne, and J. Zhang, *J. Phys. Chem.* 100, 8610 (1996).

797. A. Walcarius, in "Handbook of Zeolite Catalysts and Microporous Materials" (S. M. Aurbach, K. A. Carrado, and P. K. Dutta, Eds.), Dekker, New York, 2003, Chap. 14, pp. 721–783.

798. D. Camino, D. Deroo, and D. Salardenne, *Sol. Energy Mater. Sol. Cells* 39, 349 (1995).

799. S. M. Jones and S. E. Friberg, *J. Mater. Sci. Lett.* 15, 1172 (1996).

800. M. A. Aegerter, C. R. Avellaneda, A. G. Pawicka, and M. Atik, *J. Sol–Gel Sci. Technol.* 8, 689 (1997).

801. B. N. Olivier, L. A. Coury, J. O. Egekeze, C. S. Sosnoff, Y. Zhang, R. W. Murray, C. Keller, and M. X. Umana, in "Biosensor Technology: Fundamentals and Applications" (R. P. Buck, W. E. Hatfield, M. X. Umana, and E.F. Bowden, Eds.), pp. 117–135. Dekker, New York, 1990.

802. P. Audebert, P. Griesmar, and C. Sanchez, *J. Mater. Chem.* 1, 699 (1991).

803. P. Audebert, P. Griesmar, P. Hapiot, and C. Sanchez, *J. Mater. Chem.* 2, 1293 (1992).

804. H. Cattey, C. Sanchez, and P. Audebert, *New J. Chem.* 20, 1023 (1996).

805. P. Audebert, H. Cattey, C. Sanchez, and P. Hapiot, *J. Phys. Chem. B* 102, 1193 (1998).

806. C. P. Andrieux and J.-M. Savéant, *J. Electroanal. Chem.* 111, 337 (1980).

807. E. Laviron, *J. Electroanal. Chem.* 112, 143 (1980).

808. D. Blauch and J.-M. Savéant, *J. Am. Chem. Soc.* 114, 3323 (1992).

809. C. P. Andrieux and P. Audebert, *J. Phys. Chem. B* 105, 444 (2001).

810. J. E. Mark, *Heterogen. Chem. Rev.* 3, 307 (1996).

811. M. A. Habib and S. Maheswari, *J. Electrochem. Soc.* 138, 1692 (1991).

812. Y. Wei, J.-M. Yeh, D. Jin, X. Jia, and J. Wang, *Chem. Mater.* 7, 969 (1995).

813. B. R. Mattes, E. T. Knobbe, P. D. Fuqua, F. Nishida, E.-W. Chang, B. Dunn, and R. B. Kaner, *Synth. Met.* 41, 3183 (1991).

814. S. Komaba, F. Fujihana, T. Osaka, S. Aiki, and S. Nakamura, *J. Electrochem. Soc.* 145, 1126 (1998).

815. S. Roux, P. Audebert, J. Pagetti, and M. Roche, *New J. Chem.* 24, 885 (2000).

816. S. Roux, P. Audebert, J. Pagetti, and M. Roche, *New J. Chem.* 26, 298 (2002).

817. N. Leventis and M. Chen, *Chem. Mater.* 9, 2621 (1997).

818. J. F. Rusling, *Acc. Chem. Res.* 24, 75 (1991).

819. C. A. Pessoa, Y. Gushikem, and S. Nakagaki, *Electroanalysis* 14, 1072 (2002).

820. S. T. Fujiwara, C. A. Pessoa, and Y. Gushikem, *Anal. Lett.* 35, 1117 (2002).

821. A. R. de Lucca, A. S. Santos, A. C. Pereira, and L. T. Kubota, *J. Colloid Interface Sci.* 254, 113 (2002).

822. A. S. Santos, A. C. Pereira, and L. T. Kubota, *J. Braz. Chem. Soc.* 13, 495 (2002).

823. A. S. Santos, L. Gorton, and L. T. Kubota, *Electroanalysis* 14, 805 (2002).

824. Y.-W. Teng, I.-J. Chang, and C. M. Wang, *J. Phys. Chem. B* 101, 10386 (1997).

825. V. Stara and M. Kopanica, *Electroanalysis* 1, 251 (1989).

826. E. A. Hayes, J. Z. Stemple, and D. R. Rolison, in "Water Purification by Photoelectrochemical, Photochemicaln and Electrochemical Processes" (T. L. Rose and O. J. Murphy, Eds.), pp. 121–130. Electrochemical Society, Pennington, NJ, 1994.

827. L. Hernandez, P. Hernandez, M. H. Blanco, E. Lorenzo, and E. Alda, *Analyst* 113, 1719 (1988).

828. L. Hernandez, E. Gonzalez, and P. Hernandez, *Analyst* 113, 1715 (1988).

829. E. Lorenzo, E. Alda, P. Hernandez, M. H. Blanco, and L. Hernandez, *Fresenius J. Anal. Chem.* 330, 139 (1988).

830. R. J. Barrio, Z. G. de Balugera, J. F. Arranz, and M. A. Goicolea, *Electroanalysis* 3, 429 (1991).

831. M. A. Ruiz Barrio and J. M. Pingarron, *Fresenius J. Anal. Chem.* 344, 34 (1992).

832. R. J. Barrio, Z. G. de Balugera, and M. A. Goicolea, *Anal. Chim. Acta* 273, 93 (1993).

833. G. Villemure and T. J. Pinnavaia, *Chem. Mater.* 11, 789 (1999).

834. D. Kriz, O. Ramström, and K. Mosbach, *Anal. Chem.* 69, 345A (1997).

835. R. Makote and M. M. Collinson, *Chem. Commun.* 425 (1998).

836. D. Kotkar, V. Joshi, and P. K. Ghosh, *Proc. Indian Natl. Sci. Acad. A* 52, 736 (1986).

837. A. Yamagishi, *Chem. Aust.* 54, 278 (1987).

838. M. D. Baker, *Canad. Chem. News* 44, 16 (1992).

839. M. D. Baker and C. Senaratne, British Patent GB 2, 252, 831, 1992.

840. P. Mariaulle, F. Sinapi, L. Lamberts, and A. Walcarius, *Electrochim. Acta* 46, 3543 (2001).

841. L. Rabinovich, V. Glezer, Z. Wu, and O. Lev, *J. Electroanal. Chem.* 504, 146 (2001).

842. K. Tanaka, C.-K. Choo, S. Sumi, Y. Kamitani, T. Fujii, K. Satoh, K.-I. Fukuda, R. Nakata, M. Yoshimune, Y. Yoshinaga, and T. Okuhara, *J. Phys. Chem. B* 106, 4155 (2002).

843. M. Kopanica and V. Stara, *Talanta* 37, 1067 (1990).

844. J. Li and S. N. Tan, *Anal. Lett.* 33, 1467 (2000).

845. S.-C. Shyu and C. M. Wang, *J. Electrochem. Soc.* 144, 3419 (1997).

846. S.-C. Shyu and C. M. Wang, *J. Electrochem. Soc.* 145, 154 (1998).

847. N. Oyama, T. Ohsaka, and S. Ikeda, *J. Macromol. Sci. Chem. A* 27, 1203 (1990).

848. J. E. Moneyron, A. de Roy, C. Forano, and J. P. Besse, *Appl. Clay Sci.* 10, 163 (1995).

849. C. E. Marshall and A. D. Ayer, *J. Am. Chem. Soc.* 70, 1297 (1948).

850. A. F. Collings and F. Caruso, *Rep. Progr. Phys.* 60, 1397 (1997).

851. K. Ogura, K. Nakaoka, M. Nakayama, M. Kobayashi, and A. Fujii, *Anal. Chim. Acta* 384, 219 (1999).

852. M. Gerritsen, A. Kros, V. Sprakel, J. A. Lutterman, R. J. M. Nolte, and J. A. Jansen, *Biomaterials* 21, 71 (2000).

853. A. Kros, M. Gerritsen, V. Sprakel, N. A. J. M. Sommerdijk, J. A. Jansen, and R. J. M. Nolte, *Sensors Actuators B* 81, 68 (2001).

854. P. Johnson and T. L. Whateley, *J. Colloid Interface Sci.* 37, 557 (1971).

855. Q. Yang, P. Atanasov, E. Wilkins, and R. C. Hughes, *Anal. Lett.* 28, 2439 (1995).

856. R. Krishnan, P. Atanasov, and E. Wilkins, *Biosensors Bioelectron.* 11, 811 (1996).

857. M. M. M. B. Duarte, G. de Oliveira Neto, L. T. Kubota, J. L. L. Filho, M. P. Pimentel, F. Lima, and V. Lins, *Anal. Chim. Acta* 350, 353 (1997).

858. J. Wang and J. Liu, *Anal. Chim. Acta* 284, 385 (1993).

859. J. Wang and N. Naser, *Electroanalysis* 6, 571 (1994).

860. S. Cosnier, F. Lambert, and M. Stoytcheva, *Electroanalysis* 12, 356 (2000).

861. S. Sampath and O. Lev, *Adv. Mater.* 9, 410 (1996).

862. W. R. Heineman, C. J. Seliskar, and J. N. Richardson, *Austral. J. Chem.*, in press.

863. C. S. Ouyang and C. M. Wang, *J. Electrochem. Soc.* 145, 2654 (1998).

864. J. Livage and D. Ganguli, *Sol. Energy Mater. Sol. Cells* 68, 365 (2001).

865. N. Hagfeld, N. Vlachopouls, S. Gilbert, and M. Grätzel, *Proc. SPIE* 2255, 297 (1994).

866. B. Orel, N. Groselj, U. O. Krasovec, R. Jese, and A. Georg, *J. Sol–Gel Sci. Technol.* 24, 5 (2002).

867. I. D. Brotherston, D. S. K. Mudigonda, J. M. Osborn, J. Belk, J. Chen, D. C. Loveday, J. L. Boehme, J. P. Ferraris, and D. L. Meeker, *Electrochim. Acta* 44, 2993 (1999).

868. J.-H. Choy, Y.-I. Kim, B.-W. Kim, N.-G. Park, G. Campet, and J.-C. Grenier, *Chem. Mater.* 12, 2950 (2000).

869. H. P. Oliveira, C. F. O. Graeff, C. A. Brunello, and E. M. Guerra, *J. Non-Cryst. Solids* 273, 193 (2000).

870. J. S. Krueger and T. E. Mallouk, *Surfactant Sci. Ser.* 38, 461 (1991).

871. D. Rong, H. G. Hong, Y. Kim, J. S. Krueger, J. E. Mayer, and T. E. Mallouk, *Coord. Chem. Rev.* 97, 237 (1990).

872. K. V. Gobi and R. Ramaraj, *J. Chem. Soc., Chem. Commun.* 1436 (1992).

873. K. V. Gobi and R. Ramaraj, *J. Electroanal. Chem.* 368, 77 (1994).

874. G. Calzaferri, N. Gfeller, and K. Pfanner, *J. Photochem. Photobiol. A* 87, 81 (1995).

875. W. S. Szulbinski, *Inorg. Chim. Acta* 269, 253 (1998).

876. R. Collongues, A. Kahn, and D. Michel, *Annu. Rev. Mater. Sci.* 9, 123 (1979).

877. T. Dickinson, *IEE Energy Ser.* 1, 464 (1980).

878. J. R. Owen, *Power Sources* 8, 77 (1981).

879. J. Schoonman and E. M. Kelder, *J. Power Sources* 68, 65 (1997).

880. M. A. Ratner, *Acc. Chem. Res.* 15, 355 (1982).

881. S. L. Swartz, M. M. Seabaugh, and W. J. Dawson, *Proc. Electrochem. Soc.* 99–13, 199 (1999).

882. B. Dunn, G. C. Farrington, and B. Katz, *Solid State Ionics* 70–71, 3 (1994).

883. J. Rocha and M. W. Anderson, *Eur. J. Inorg. Chem.* 5, 801 (2000).

884. T. Kanbara, M. Inami, and T. Yamamoto, *J. Power Sources* 36, 87 (1991).

885. H.-W. Chen, C.-Y. Chiu, and F.-C. Chang, *J. Polym. Sci. B* 40, 1342 (2002).

886. W. Yang, H. Yang, and J. Zhang, *Dianchi* 21, 3–5 (1991).

887. J. Coetzer, German Patent 2, 810, 320, 1978; 2, 928, 863, 1980; 2, 935, 686, 1980; 2, 942, 764, 1980; French Patent 2, 492, 173, 1982.

888. J. Coetzer, *Electrochim. Acta* 23, 787 (1978).

889. D. Kalaiselvi and R. Renuka, *J. Chem. Technol. Biotechnol.* 75, 285 (2000).

890. A. M. Moos, U.S. Patent 3, 097, 115, 1963; German Patent 1, 302, 003, 1969.

891. A. S. Berchielli and R. F. Chireau, German Patent 2, 938, 523, 1980.

892. M. Shelef, U.S. Patent 6, 117, 581, 2000.

893. M. Cruceanu, E. Popovici, and A. Vasile, *Rom. Rev. Chim.* 32, 973, 1981.

894. M. Cruceanu, E. Popovici, and A. Vasile, Romanian Patent 78, 511 1982.

895. A. Vasile, E. Popovici, and M. Cruceanu, *Rom. Rev. Chim.* 47, 847 (1996).

896. G. J. Bratton, T. Naylor, and A. C. C. Tseung, World Patent 9, 852, 243, 1998.

897. Y. Charbouillot, D. Ravaine, M. B. Armand, and C. Poinsignon, *J. Non-Cryst. Solids* 103, 325 (1989).

898. I. Gautier-Luneau, A. Denoyelle, J. Y. Sanchez, and C. Poinsignon, *Electrochim. Acta* 37, 1615 (1992).

899. J. Y. Sanchez, A. Denoyelle, and C. Poinsignon, *Polym. Adv. Technol.* 4, 99 (1993).

900. K. Kalcher, I. Grabec, G. Raber, X. Cai, G. Tavcar, and B. Ogorevc, *J. Electroanal. Chem.* 386, 149 (1995).

Electrodeposited Nanogranular Magnetic Cobalt Alloys

Valery Fedosyuk

Academy of Sciences, Minsk, Belarus

CONTENTS

1. INTRODUCTION

In recent years, one of the most interesting and intensely investigated classes of materials has been that of nanoscaled magnetic materials. Magnetic nanosized materials that are based on transition metals may be divided into six main groups [1]: films with columnar type of crystal structure, multilayers, granular or so-called inhomogeneous alloyed films, quasi-granular films, nanocrystalline films, and nanowires.

Among the magnetic nanostructure [2] granular films, which represent nanoinclusions of ferromagnetic material (Co, Fe, Ni) in dia- (f.e. Cu) or paramagnetic (f.e. Re) matrix, are extremely promising. Originally, the interest in inhomogeneous films, formed from alloys of transition metals of the iron group with Cu, arose from the possibility of applying these materials as substitutes for various, currently used, conventional, magnetoresistive sensors which are based on permalloy transducers. In comparison with the latter, these inhomogeneous, granular alloy films are far more promising due to the fact that they possess, under certain conditions, an isotropic giant magnetoresistance (GMR) in addition to significantly lower noise; this latter property is due to the absence of domain walls in these materials, which is contrary to the situation for ferromagnetic alloys [3]. However, quite recently, granular coatings have also come to be regarded as a material for super-high-density magnetic recording [4]. In this context, a comprehensive investigation of these granular films becomes highly appropriate.

A variety of techniques has been applied for the preparation of these materials including molecular beam epitaxy, sputtering, vapor deposition, and, later, laser ablation [5–186]. While these state-of-the-art techniques are very effective in producing good quality films and multilayers, they are extremely sophisticated and therefore costly in comparison with the relatively simple technique of electrodeposition (ED) [187–277]. Although ED has been known for many years, it is only fairly recently that it has been applied with any great success to the production of magnetic nanomaterials [1–3].

2. GRANULAR FILMS PRODUCED FROM IMMISCIBLE ELEMENTS

The CuCo system is one which has, in the past, attracted considerable attention. This is partly due to the fact that at room temperature there is almost zero solubility of Co in Cu and the system is therefore well suited as a candidate for the production of metastable alloys. As early as 1958 Knappwost and Illenger [278] reported magnetic measurements on Co particles precipitated from Cu in bulk samples and Kneller [279] reported results on thin films of CuCo evaporated at room temperature. More recently, Berkowitz et al. [280] and Xiao et al. [281] have observed GMR in heterogeneous CuCo alloys and thin films, respectively, both produced by dc sputtering. We also [282–300] have investigated a range of Cu- and Co-based nanogranulars produced by ED.

In previous works on CoFeP [301] and CoW [302], which are only partially soluble, and also some other systems where ED films had been produced under constant deposition conditions, it was found that all films were homogeneous. It thus seemed likely that in the CuCo system, produced under similar conditions, we should again obtain the same degree of homogeneity. However, as we show, in the case of the CuCo system, we produced samples with a range of inhomogeneities.

The films were electrodeposited onto both Cu- and Al-foil substrates and also on to ceramic substrates which had previously been coated with a nonmagnetic layer of NiP. The electrolytic composition was $CuSO_4 \cdot 5 H_2O$—30 g/l, $CoCl_2 \cdot 6H_2O$—3.3 g/l, H_3BO_3—6.6 g/l, $MgSO_4 \cdot 7H_2O$—23.3 g/l, $CoSO_4 \cdot 7H_2O$—10 to 30 g/l. The composition range of the samples investigated was obtained by varying the $CoSO_4$ concentration in the electrolyte; all other chemical concentrations were held constant. The electrolyte had a pH value of 6.0 and deposition was performed at 20 °C with a current density of 5 mA/cm^2.

The film composition was determined by both X-ray and chemical analysis. For the X-ray analysis we used CoK_α radiation with a graphite monochromator and a Dron-3M instrument. Transmission electron microscope (TEM) measurements were made using an EMV-1004M machine and a 300 keV Jeol 3010 machine with an accelerating voltage up to 300 keV.

Magnetic measurements, which were mainly made on films deposited onto Cu substrates, were performed in the temperature range 2–300 K and in fields of up to 5 T using a Quantum Design SQUID magnetometer MPMS5. Fields were applied in the plane of the film and could be set to an accuracy of $\pm 10^{-6}$ T; temperatures could be controlled to within $\pm 10^{-2}$ K. Measurements of magnetic moment as a function of field for various temperatures were made, together with the technique of zero-field-cooled (ZFC) and field-cooled (FC) low-field susceptibility measurements [301–304]. In this latter type of measurement, the sample was cooled in zero field from room temperature to 2 K and then a measuring field of 5 mT was applied; measurements were then made in this constant field while the temperature was increased. The sample was then cooled down to 2 K in the same field (5 mT) while, again, measurements were made of the moment.

In order to estimate the diamagnetic contribution of the Cu substrate, an uncoated substrate of known mass was measured. Subsequent measurements on ED films were then corrected for the substrate contribution by weighing the whole sample and then subtracting off an appropriately scaled value for the uncoated substrate. It was assumed that the film itself made a negligible contribution to the total mass. Measurements were made on the film immediately after preparation (no anneal) and then after annealing for 30 minutes at 200, 400, and 600 °C. For these anneals, the samples were sealed-off in quartz ampoules in a vacuum of better than 10^{-3} Pa.

Since we wished to make a precise check on the samples to see whether they satisfied the criteria of SPM, careful measurements were also made on identical Cu sheets on which no films had been deposited and also on the actual substrates used for deposition after mechanically removing the CuCo film. These results were used to correct for the effects of the substrate, which made a small contribution to the SQUID signal, especially at high fields and low temperatures. In order to investigate whether the films exhibited any anisotropy due to the directional nature of their growth, measurements were also made at 300 K while rotating the sample from an orientation with the field in-plane to that with it perpendicular to the plane of the sample.

Four different samples were investigated; their compositions were determined by X-ray and chemical analysis and the results are given in Table 1. In all samples investigated, the X-ray diffraction patterns showed distinct lines corresponding to the face-centered cubic (fcc) Cu structure. Only in one sample, 718, was it possible to detect a very weak satellite line corresponding to pure Co; this was the sample with the highest Co concentration. This is understandable since here we expect the Co inclusions to be the largest of any of the samples. The presence of only a faint Co line suggests that the sizes of the Co regions are very small, of the order 100 nm or less.

Magnetization loops were measured for all samples in the temperature range from 5 to 300 K; all loops had similar characteristics. Some typical results, for sample 715, are given in Figure 1. The hysteretic behavior at low temperatures, combined with the reversible part of the magnetization curve, which extends over a wide field-range (Fig. 1a), suggests that we have a mixture of ferromagnetic and superparamagnetic particles, whereas at higher temperatures (Fig. 1b) above the blocking temperature, we observe only superparamagnetism. It is also important to note, in this context, that no sample could be magnetically saturated, even at a temperature of 5 K and the maximum applied field of 5 T.

The temperature dependence of the remanence (Fig. 2) is different from that observed by Thompson et al. [305] in CoAg alloys in that, in the present work, we observe curves of continuously varying slope which also differ from sample to sample. This suggests that we have a range of blocking temperatures, depending upon the Co concentration. We have attempted to estimate the maximum blocking temperature for each sample by extrapolating the remanence curves to zero; the maximum blocking temperature increases with increasing Co concentration. The fact that all the remanence curves, except that for sample 718, show strong curvatures suggests a range of blocking temperatures for each sample and a corresponding range of particle sizes present in the films, which we are able to control by varying the deposition conditions. This also indicates, in our opinion, that we have been successful in producing, immediately after deposition, inhomogeneous alloy systems. The linear variation of the remanence for sample 718 suggests an approximately uniform size of particles in that film.

Earlier work on the system CoNi (Ni 40 to 70 at%) has shown that Co retains its hexagonal close packed (hcp) structure, whereas small additions of Fe cause the fcc phase

Table 1. Summary of the results obtained for a series of CuCo films produced by electrodeposition.

Sample	T_B, Kc (K)	Diameter (nm)	at% Co
725	55 + 5	7.6	6
722	80 ± 10	8.7	8
715	210 + 20	12.0	11
718	260 ± 25	12.8	20

Note: The values quoted for the Co concentrations are the averages of chemical and X-ray analyses.

Source: Reprinted with permission from [282], H. J. Blythe and V. M. Fedosyuk, *J. Phys. Status Solidi A* 146, 1113 (1994). ©1994, Wiley-VCH.
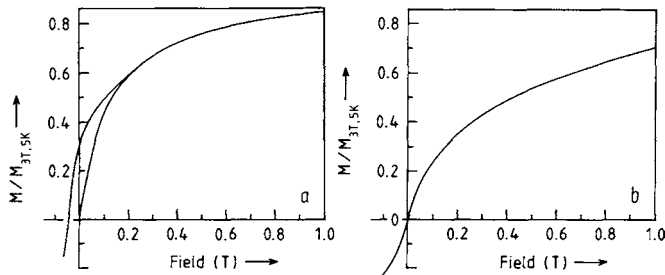
Figure 1. Typical reduced magnetization curves for sample 715: (a) 5 K, (b) 300 K. Reprinted with permission from [282], H. J. Blythe and V. M. Fedosyuk, *J. Phys. Status Solidi A* 146, 1113 (1994). © 1994, Wiley–VCH.
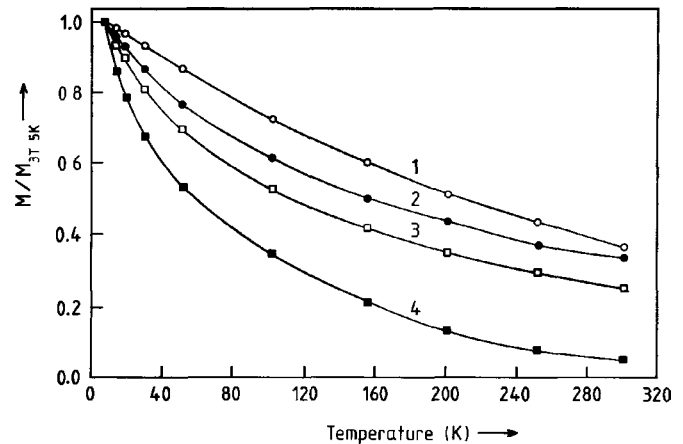

Figure 3. Temperature dependence of the magnetization of the various samples investigated as measured in a field of 3 T and normalized to their values at 5 K. (1) 718, (2) 715, (3) 722, (4) 725. Reprinted with permission from [282], H. J. Blythe and V. M. Fedosyuk, *J. Phys. Status Solidi A* 146, 1113 (1994). © 1994, Wiley–VCH.

to be stable [287]. We believe that an amount of the order of 3 to 5 at% of Cu is sufficient to stabilize the fcc phase and it thus seems very likely that, in our present measurements, the Co is in the fcc phase.

In order to estimate the maximum particle size in each sample, we have used the well-known expression [307] $K_A v = 25 k_B T_B$, where K_A is the anisotropy energy density, v is the critical particle volume, and T_B is the blocking temperature. A value of K_A appropriate for fcc Co has been assumed [308]. The results are summarized in Table 1.

The temperature dependence of the magnetization is given in Figure 3. It is interesting to note that for the sample with the highest Co concentration, 718, it is quasi-linear. Such a linear dependence of magnetization on temperature can be an indication of two-dimensional magnetism [309]. This suggests that the ferromagnetic inclusions of Co in the Cu matrix could be in the form of long needlelike inclusions.

2.1. Electrodeposited $Cu_{0.94}Co_{0.06}$ Film by SQUID Magnetometry

In order to be able to optimize the parameters which control GMR, it is essential to have a basic understanding of the physical properties of these systems. Also, for any potential

Figure 2. Temperature dependence of the remanence for the various samples investigated; values have been normalized with respect to the magnetization at 3 T and 5 K. (1) 718, (2) 715, (3) 722, (4) 725. Reprinted with permission from [282], H. J. Blythe and V. M. Fedosyuk, *J. Phys. Status Solidi A* 146, 1113 (1994). © 1994, Wiley–VCH.

application, it is a great advantage if the system is not only relatively easy to fabricate but also consists of readily available elements. The CuCo system is one which exhibits GMR and, in the past, this system has been widely investigated. More recently, there have been a number of measurements reported on thin films of granular or multilayer CuCo samples. These, however, have almost all been prepared by such techniques as sputtering [310, 311], melt spinning [312, 313], and laser ablation [314] or various types of deposition involving high-vacuum conditions. All the above-mentioned preparation methods are relatively complicated or expensive. In contrast to this, up to the present time, almost no one has used ED for the preparation of thin films of inhomogeneous alloys, despite the great advantages of simplicity and cost.

In an earlier section we have demonstrated the possibility of producing heterogeneous $Cu_{1-x}Co_x$ alloyed films by the technique of ED using conditions of constant current (i.e., the nonpulsed regime). These films were heterogeneous immediately after deposition and no postdeposition annealing was necessary. This fact is in marked contrast not only to films produced by other techniques but also to films produced using ED by other workers [315], where it has been necessary to subject samples to a heat treatment before they were in an inhomogeneous state. It should also be mentioned, perhaps, that recently Alper et al. [316] have observed GMR in short-period Cu/Co–Ni–Cu superlattices grown by ED. Our films [9, 10] consist mainly of Co-rich particles in the Cu matrix for $x \leq 0.06$–0.50 and Cu particles in a Co matrix for $x \geq 0.50$ [316].

In the present part of this chapter magnetic measurements on the alloy $Cu_{0.94}Co_{0.06}$ will be reported. In view of the results of other workers on similar systems with comparable Co concentrations [305, 313, 317], it seemed likely that we could expect to produce a film which exhibits pure superparamagnetism (SPM). However, we find this not to be the case and have to consider interaction effects. These interactions will clearly increase with increasing Co concentration.

Figure 4 shows the high- and low-field hysteresis loops measured at 5 K. It is important to note that, even at a temperature of 5 K and an applied field of 5 T, the sample could not be magnetically saturated. Figure 5 shows the temperature dependence of the remanence as determined from the hysteresis loops. An extrapolation of this curve to zero remanence gives a value of 55 ± 5 K for T_B, the maximum blocking temperature of the sample. This result is in excellent agreement with the previous value quoted for an identically prepared film [282] and is a good indication of the reproducibility of our samples.

Figure 6 gives the magnetization measurements for a sample measured at 150, 200, 250, and 300 K, temperatures which are well above the maximum blocking temperature of the film. These data have been corrected, as mentioned earlier, for the diamagnetic contribution of the Cu substrate. At these temperatures, no hysteretic effects were observed and, again, saturation is not achieved. This nonsaturation, even at 5 K, we interpret as being evidence for the existence of a wide range of particle sizes in the sample. At low temperatures and high fields, the relatively large particles will saturate, but if very small Co clusters and isolated Co

Figure 5. Temperature dependence of the remanence for a $Cu_{0.94}Co_{0.06}$ film as derived from the corresponding hysteresis loops where a field of 5 T was applied at each temperature. The remanence is normalized to its value at 2 K. Reprinted with permission from [283], H. J. Blythe and V. M. Fedosyuk, *J. Phys. Condens. Matter* 7, 3461 (1995). © 1995, IOP Publishing.

atoms are present in the Cu matrix, they will give rise to the observed nonsaturation, even in a field of 5 T.

As is well known, there are two experimental conditions which have to be satisfied for true SPM: first, there must be no hysteresis loop above the maximum blocking temperature and, second, the magnetization curves must superimpose when plotted as a function of reduced field (i.e., as a function of H/T). In order to test this second criterion, in Figure 7 we plot such curves. It can be seen that the curves do not superimpose, even after correction for the

Figure 4. Hysteresis loop for a $Cu_{0.94}Co_{0.06}$ film measured at 5 K. (a) High field, (b) low field. The magnetization has been normalized to its value at 5 T. Reprinted with permission from [283], H. J. Blythe and V. M. Fedosyuk, *J. Phys. Condens. Matter* 7, 3461 (1995). © 1995, IOP Publishing.
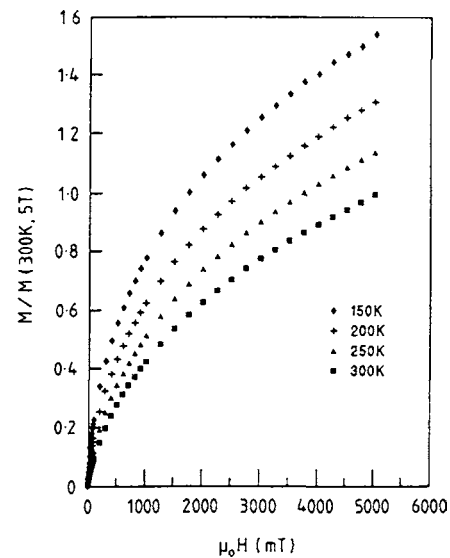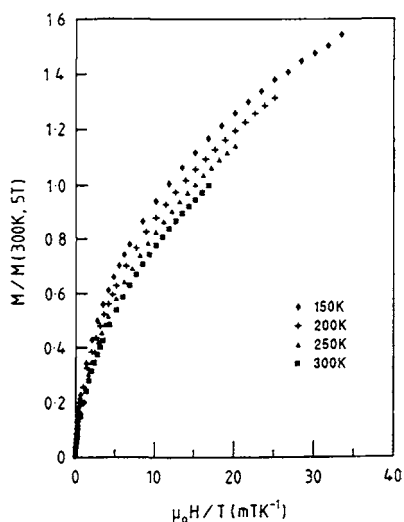

Figure 6. Magnetization of a $Cu_{0.94}Co_{0.06}$ film as a function of the magnetic field. The results have been corrected for the contribution of the diamagnetic Cu substrate and are normalized to the value of the magnetization at a temperature of 300 K and a field of 5 T. Reprinted with permission from [283], H. J. Blythe and V. M. Fedosyuk, *J. Phys. Condens. Matter* 7, 3461 (1995). © 1995, IOP Publishing.

Figure 7. Magnetization of a $Cu_{0.09}Co_{0.06}$ film plotted as a function of reduced field; the magnetization has been normalized to its value at a temperature of 300 K and a field of 5 T. The data are from Figure 6. Reprinted with permission from [283], H. J. Blythe and V. M. Fedosyuk, *J. Phys. Condens. Matter* 7, 3461 (1995). © 1995, IOP Publishing.

diamagnetic contribution of the Cu substrate. We thus conclude that here we are not dealing with a sample which exhibits pure SPM. This means that we have to consider magnetic interactions between particles.

An analysis of the remanence curve of Figure 5 gives us a further method of obtaining information about our sample. By taking the derivative of this curve, we are able to gain information about the energy barrier distribution within the sample [301] which, in turn, is related to the particle size distribution. Figure 8 shows the derivative of the remanence of curve of Figure 5. This indicates a wide distribution of energy barriers. These energy barriers to magnetic reversal of moments in real systems are influenced by effects such as interactions between SPM particles, the presence of interacting spin–glass structures, and variations in K_A due, for
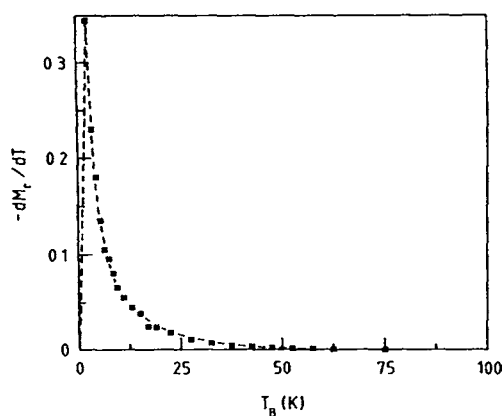
example, to localized strain at defects and boundaries. However, the experimental points show no evidence of a peak within the temperature range of our measurements and presumably the maximum occurs below the lower limit of the measurements. This suggests that the peak in the curve representing particle size distribution corresponds to a blocking temperature below 2 K.

As a further means of investigating the range and distribution of blocking temperatures, we have measured the moment (effectively the initial susceptibility) in a small, constant applied field, in this case 5 mT, after zero-field cooling the sample from well above the maximum blocking temperature. Measurements were then made at increasing temperatures from 5 to 300 K. We then field cooled the sample, still at 5 mT, measuring from 300 to 5 K. Such measurements have been found to be extremely sensitive to particle interactions [303, 304, 328, 329] and are also a good method of investigating the energy barrier distribution. The results of these measurements are shown in Figure 9. The position of the bifurcation between the two curves (250 K) is an indication of the maximum blocking temperature, whereas the position of the peak in the ZFC curve gives us a value of 35 K for the mean blocking temperature.

According to Bean and Livingstone [307], we may use the now well-known expression $K_A V = 25 k_B T_B$ to make an estimate of particle size. This expression assumes that the particles, of volume v, exhibit uniaxial anisotropy and it is based on a measuring time of 100 s, which is of the same order of magnitude as the SQUID measuring time. If we now assume that the Co-rich particles are present in the matrix as an fcc phase [282] and take a value for K_A of 5.55×10^{17} eV cm^{-3} [320] (the exact value of K_A is somewhat arbitrary, since it is strongly temperature dependent and also presumably shape and strain anisotropies play an important role), we are able to estimate the particle diameter corresponding to the maximum blocking temperature of 55 K, derived directly from the remanence curve (Fig. 8) to be 7 nm, whereas the
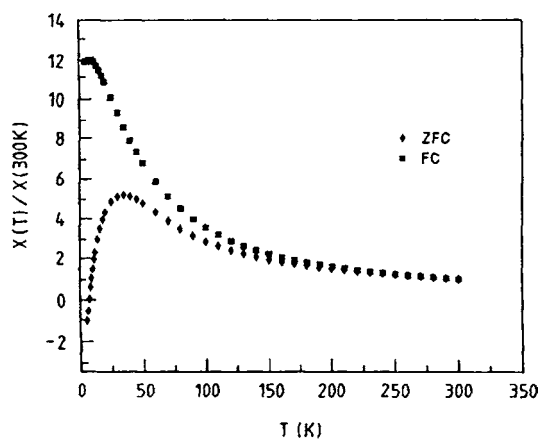

Figure 8. Derivative of the temperature dependence of the remanence for a $Cu_{0.094}Co_{0.06}$ film. The data are from Figure 5. The curve given is a guide for the eye only. Reprinted with permission from [283], H. J. Blythe and V. M. Fedosyuk, *J. Phys. Condens. Matter* 7, 3461 (1995). © 1995, IOP Publishing.

Figure 9. Magnetization of a $Cu_{0.94}Co_{0.06}$ film as measured in a field of 5 mT. The lower curve is for the film initially cooled to 5 K in zero magnetic field (ZFC), while the upper curve is for the sample cooled in the measuring field 5 mT (FC). The results are normalized to the value of the magnetization at 300 K. Reprinted with permission from [283], H. J. Blythe and V. M. Fedosyuk, *J. Phys. Condens. Matter* 7, 3461 (1995). © 1995, IOP Publishing.

mean particle diameter, which is related [302] to the peak in the ZFC curve (35 K), we find to be 6 nm. Finally, the maximum particle diameter, according to the position of the bifurcation in the ZFC/FC curves, is found to be 12 nm. This discrepancy is not unexpected, since we are applying different measuring techniques and also both the shape of the ZFC curve and the temperature at which the bifurcation occurs are dependent upon measuring field. A similar variation has also been observed by other workers [301]. The present results are in good qualitative agreement with the measurements of Dieny et al. [313] on melt-spun CuCo samples.

The apparent wide range of particle sizes, according to the ZFC/FC measurements, may be due to the fact that, in the present system, we have to take particle interactions into account. Such interactions may effectively increase the particle size via a coupling mechanism between particles (i.e., two particles, while metallurgically separate, may experience a ferromagnetic coupling, thus behaving magnetically as a single particle). There is also the possibility, as a consequence of the method of film preparation, that we have nonspherical particles which are elongated in the direction of the film growth. This seems unlikely, however, as an investigation of the variation of magnetization of the film as a function of the angle between film plane and applied field showed the magnetization to be independent of orientation when demagnetizing effects had been allowed for.

The origin of the peak of the ZFC curve lies in the increase in the fraction of particles that become unblocked with increasing temperature, while simultaneously their value of susceptibility decreases due to thermal fluctuations. This ZFC curve is reproducible but irreversible, in contrast to the FC curve which is both reproducible and reversible. This is because, whereas the shape of the ZFC curve is determined by blocking effects (and is also, strictly speaking, dependent on both field and time) plus the effects of particle interactions, when we cool the sample in a field and measure in a steady field, as the temperature is reduced the particles are blocked so as to be aligned in the field. Thus, even though a particle is below its blocking temperature, it will still make its full contribution to the magnetic moment of the sample. Hence, we are able to use the FC curve to investigate the influence of particle interactions in the absence of blocking effects.

The temperature dependence of the reciprocal of the initial susceptibility as measured in a field of 5 mT and after FC is shown in Figure 10. At high temperatures there is an almost linear dependence on temperature and, by extrapolation of the high-temperature region to zero, we obtain a positive interaction temperature, T_{int}, of 20 ± 2 K. Following the remarks of O'Grady et al. [301] we treat this determination with some caution. However, it does indicate that of the two distinct contributions of particle blocking and interactions, the latter is the dominant process. We have obtained an estimate of 1.72×10^{-3} eV for the interaction energy simply by equating it to $k_B T_{int}$. This value is comparable to the value of 4.3×10^{-2} eV for the anisotropy energy assuming the value of K_A quoted earlier.

Childress and Chien [311] have also investigated the $Cu_{1-x}Co_x$ system, producing samples using magnetron sputtering. For values of x in the range 0.10 to 0.20, the ZFC/FC

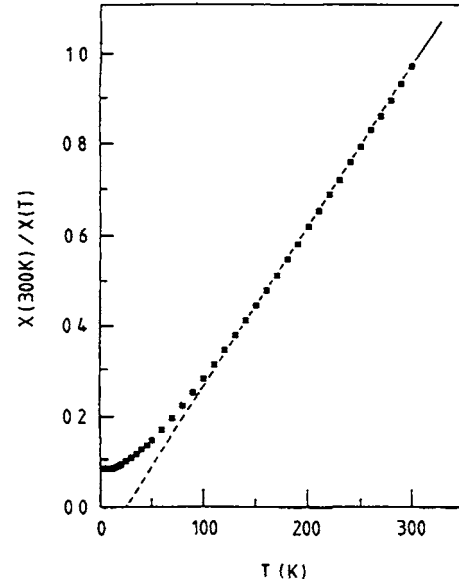**Figure 10.** Temperature dependence of the reciprocal of the reciprocal susceptibility, normalized to its value at 300 K, for a $Cu_{0.94}Co_{0.06}$ alloy; the data are from Figure 9. Reprinted with permission from [283], H. J. Blythe and V. M. Fedosyuk, *J. Phys. Condens. Matter* 7, 3461 (1995). © 1995, IOP Publishing.

curves are very similar to our present results, apart from the fact that our ZFC/FC curves do not coalesce, due to the presence of blocked SPM particles. The nearly flat FC curve below 15 K observed by Childress and Chien is very similar to the FC curve found in the present work and this generally constitutes the signature of a spin–glass transition. Any regions of the matrix exhibiting spin–glass behavior will, of course, contribute to the remanence below this temperature and affect energy barrier distribution measurements.

For more concentrated alloys, it is expected that the interaction temperature, T_{int}, and the corresponding interaction energies will be considerably enhanced. Such investigations on $Cu_{1-x}Co_x$ with values of x in the range 0.08 to 0.85 will be reported in the next sections.

2.2. Annealing Effect

There are several important factors which influence the GMR behavior of heterogeneous films. These include the size, separation, and distribution of the magnetic particles in the nonmagnetic matrix, together with the composition profile in the vicinity of the interface of the particles. All of these parameters are sensitive not only to the method of preparation but also to the influence of anneal, since in metastable, immiscible systems this generally initiates the precipitation and subsequent growth of the small particles and also affects their composition. Indeed, in most of these systems, the maximum value of GMR is only attained after anneal. Clearly then, it is essential to have a basic understanding of the magnetic behavior of these materials on anneal.

In the previous section we have reported on the magnetic behavior of the thin CuCo films produced by ED and have shown that, even at such a low Co concentration as

$Cu_{94}Co_6$, the film does not exhibit pure SPM but that interaction effects have to be considered. In the present chapter, we have investigated the influence of anneal on the magnetic properties of the film, since the physical properties of these films, and fine-particle systems generally, depend strongly upon their method of preparation and the resulting microstructure.

A transmission electron diffraction pattern from an unannealed sample is shown in Figure 11a, together with a key to the main reflections present. Reflections from at least two fcc phases may be identified with lattice parameters of $0.362 + 0.002$ and $0.424 + 0.002$ nm. The former corresponds—within experimental error—to that of Cu (0.3615 nm). The second phase is more problematic in that the estimated lattice constant falls midway between that of Cu_2O (0.4220 nm) and CoO (0.4260 nm) which differ by only 1%. It seems certain that the second set of reflections arises from one of these oxides but, in view of the experimental error involved, it is not possible to decide between them. However, the disproportionate content of Cu in the samples naturally favors an oxide of this metal. Cu_2O is a stable oxide whose growth could possibly be promoted in the aqueous environment in which the films were prepared. Since the oxide was not detected with X-ray diffraction, a technique which samples the bulk, it seems more likely that the oxidation is a surface phenomenon, perhaps encouraged by the ion-milling thinning procedure.

Some other comments are worthy to note with regard to Figure 12a. The oxide rings are of more uniform intensity than the Cu rings—which are distinctly spotty—suggesting that the grain size of the former is much smaller. It will be noticed from the indexing that some rings of each phase either overlap or have very similar d spacings. Consequently,

Figure 12. Bright-field micrographs of "as-received" sample of $Cu_{0.94}Co_{0.06}$. The central portion of (a) is shown at higher resolution in (b). Reprinted with permission from [284], H. J. Blythe et al., *J. Mater. Sci.* 31, 6431 (1996). © 1996, Kluwer Academic Publishers.

the separation of each phase with dark-field microscopy is rendered more difficult. Finally, even after the identification of Cu and Cu_2O, some low-angle reflections could not be accounted for. The intensity of these rings varied from point to point on the sample.

The failure to observe reflections attributable to either fcc or hcp Co is not surprising in the light of previous work. In his seminal paper Kneller [279] concluded that evaporated films comprise a metastable disordered fcc phase; no distinct Co reflections were observed. More recently, Rabedeau et al. [321] could detect the presence of segregated spherical Co clusters in unannealed co-evaporated $Co_{0.16}Cu_{0.84}$ films (but not sputtered films) only by small-angle X-ray scattering at grazing incidence; electron microscopy and conventional diffraction techniques proved ineffective. Similarly, Yu et al. [322] observed no Co reflections from melt-spun $Co_{15}Cu_{85}$ or Co_5Cu_{95} alloys and Wan et al. [323] failed to detect diffraction lines from Fe in FeAg sputtered films. Moreover, since the Co content of our films is so low, it is likely that even if phase segregation were to occur, it would not be detectable with electron diffraction.

Figure 12a is an electron micrograph of an unannealed specimen and reveals some interesting features. Several large areas are seen which have either dominant light or dark contrast separated by well-defined boundaries. These gross variations of contrast are not due to thickness gradations but rather to diffraction contrast. Dark-field microscopy indicates that they are associated with Cu rings and we suggest that they are a reflection of the underlying grain structure of the Cu substrate which, in some areas, is replicated directly into the electrodeposited film. Evidence for this phenomenon has recently been reported by Daniel et al. [324]. Such areas possessing some degree of common crystallographic texture would account for the spots on the Cu reflections (Fig. 11a). Further confirmation of these ideas comes from high-resolution micrographs which show the direction of lattice planes to be roughly conserved within a particular area of dark or light contrast.

Within the large Cu grains are found smaller features varying in extent up to 50 nm. While it might be tempting to associate these features with clusters of Co or Co-rich material, the factors discussed above preclude this possibility. Their size, irregular shape, and strong contrast suggest

Figure 11. Electron diffraction patterns of (a) "as-received" and (b) annealed films of $Cu_{94}Co_6$. The unprimed reflections are common to both films, namely oxide reflections—1: (1 1 1); 2: (200); 5: (220); 7: (311); 8: (222) and copper reflections—3: (111); 4: (200); 6: (220); 9: (3 1 1). The primed reflections are unique to one or other of the film. The annealing temperature was 600 °C. Reprinted with permission from [284], H. J. Blythe et al., *J. Mater. Sci.* 31, 6431 (1996). © 1996, Kluwer Academic Publishers.
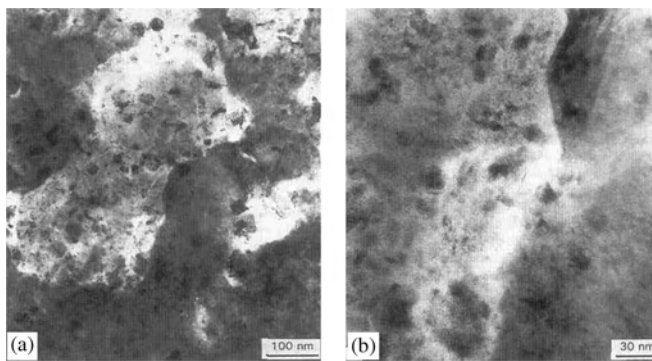
that they are small crystals rendered visible through conventional diffraction contrast and, indeed, dark-field microscopy shows that they are grains of oxide (Cu_2O). Such a range of grain size is consistent with the continuous nature of the diffraction rings. In Figure 12b, at much higher magnification, it can be seen that the edges of the oxide grains are not well defined but somewhat diffuse.

The electron diffraction pattern of an annealed sample is shown in Figure 11b—below that of the unannealed sample in order to facilitate comparison. Again, reflections from the two phases noted previously are present, although it should be remarked that the oxide rings now contain some spots. On the other hand, the prominent, unidentified, low-angle reflections in Figure 11a have vanished, although two other rings with "d" spacings of 0.283 and 0.162 nm are present. These correspond, within 1.5%, to the (220) and (422) reflections of Co_3O_4, which also has an fcc structure. In view of the comparatively large discrepancy, we do not place undue confidence on this identification, particularly as other rings which might be expected from this phase are absent. As with the as-received samples, the intensity of these extra rings depends on the particular area viewed. Again, no reflections from Co (either fcc or hcp) could be detected.

It proved difficult to prepare uniformly thin samples from annealed foils; when examined in the microscope, the specimens portrayed a distinctly lumpy or pebbly aspect. This is illustrated in Figure 13a and b which is a pair of micrographs taken from a heavily etched area of material close to the perforation in the foil. An attempt was made to isolate an oxide reflection to give the dark-field image shown in Figure 13b. Some prominent oxide particles are revealed in strong contrast: these are larger (>100 nm) and better defined than in the unannealed state, an observation that accords with the spots on the oxide rings. Other, smaller contrast features (down to 1 nm) are also evident, particularly in the dark-field micrograph. These are frequently associated with a larger oxide grain and the presumption must be that they are of this phase rather than, say, a Co cluster. The most obvious reason for the nonuniform thickness
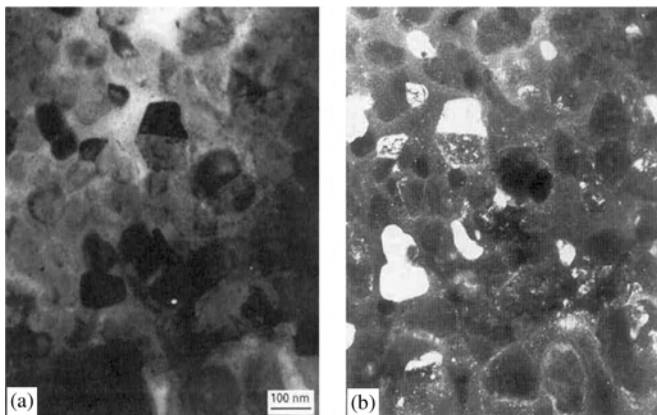
is preferential etching of the Cu (*vis-à-vis* oxide) during the ion-milling process.

In thicker regions of the specimen, areas of the Cu matrix dominate, as is shown in Figure 14a. The large circular patches to the left and right sides of the micrograph are the result of thickness variations. Of more interest are the smaller, weaker contrast features, roughly circular in form and of fairly uniform size (ca. 4 nm), which are clearly visible over the entire micrograph. At higher magnification (Fig. 14b) the small patches remain discernable but the lattice planes of the alloy are also resolved. As expected, these retain the same direction throughout the matrix grain and also pass through the darker contrast regions. These regions may be a postmilling artifact but it is also possible that they are the products of a clustering process; they have the shape and size observed by Rabedeau et al. [321]. Moreover, they are coherent with the main lattice and so will not give rise to separate reflections, which is in agreement with experiment. However, a problem does arise with this interpretation in so far as Co has a smaller atomic scattering factor for electrons than Cu. Hence, a local excess of Co atoms should result in a diminution of electron scattering, whereas the opposite situation appears to prevail here.

It must be admitted that the inconclusive outcome of the electron microscope investigations with regard to the presence of clusters is disappointing, particularly so as the interpretation of the magnetic results (below) is predicated on their existence. This ambivalence of testimony does, however, accord with previous literature. As stated above, Rabedeau et al. [321] were unable to obtain direct, electron microscope confirmation of Co-rich clusters in as-prepared and annealed films of a $Cu_{0.16}Co_{0.84}$ alloy—although they yielded to an alternative technique. On the other hand, Berkowitz et al. [325] do claim to observe microscopically such clusters in annealed, sputtered $Co_{0.19}Cu_{0.81}$ films. In their report [325] on sputtered $Cu_{0.22}Co_{0.78}$ granular films, they clearly show bright-field micrographs of Co granules about 10 nm in diameter embedded in an Ag matrix. In this case, the dissimilar scattering factors for Co and Ag lend themselves more easily to microscope observation than Co and Cu. It is of interest to note that in these CoAg films, the Co granules which have the lower scattering factors are in dark contrast. On this basis, the small, dark features in Figure 14b could be clusters of Co-rich material. The weak contrast may be due to low crystalline order as suggested by Wan et al. [323] in their study of FeAg alloys.

Figure 15a shows the variation of remanence as a function of temperature for a $Cu_{94}Co_6$ sample. These results were

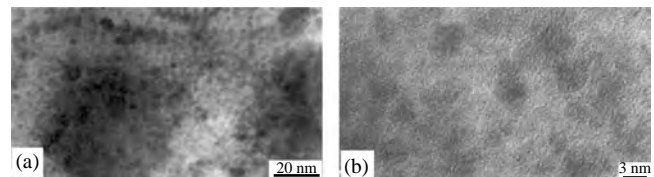**Figure 13.** Bright-field (a) and dark-field (b) micrographs of a sample of $Cu_{0.94}Co_{0.06}$, annealed at 600 °C. The particles diffracting in (b) are oxide. Reprinted with permission from [284], H. J. Blythe et al., *J. Mater. Sci.* 31, 6431 (1996). © 1996, Kluwer Academic Publishers.

Figure 14. Bright-field micrographs of a sample of $Cu_{0.94}Co_{0.06}$ annealed at 600 °C, showing weak contrast features (a). In (b) the Cu lattice fringes traverse the weak contrast features. Reprinted with permission from [284], H. J. Blythe et al., *J. Mater. Sci.* 31, 6431 (1996). © 1996, Kluwer Academic Publishers.
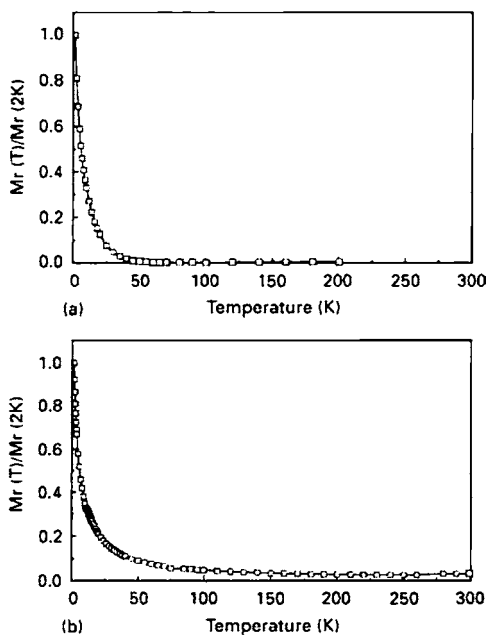
Figure 15. Temperature dependence of the remanence for an unannealed $Cu_{94}Co_6$, film (a). The values of remanence are derived from the corresponding HLRs where a field of 5 T was applied at each temperature (b). The values of TRM are derived by applying a field of 5 T at 2 K, removing the field, and then slowly warming up the sample. In both experiments, the remanence is normalized to its value at 2 K. Reprinted with permission from [284], H. J. Blythe et al., *J. Mater. Sci.* 31, 6431 (1996). © 1996, Kluwer Academic Publishers.

determined from the appropriate hysteresis loops, when a field of up to 5 T was applied at each temperature. We shall refer to these measurements of remanence as hysteresis loop remanences (HLRs). The maximum blocking temperature, T_B, of the sample is determined as being that temperature at which the extrapolated remanence intercepts the temperature axis; for the unannealed sample, this yields a value of T_B equal to 55 ± 5 K.

It is interesting to compare this temperature dependence of the remanence, and the associated maximum blocking temperature, with that determined from a different, but commonly employed, technique. Figure 15b shows the temperature dependence of the so-called thermoremanence (TRM) of the same sample. These data were obtained by cooling the sample from room temperature to 2 K in zero field, applying a field of 5 T at this temperature, removing the field, and measuring the remanence. The sample was then slowly warmed up to room temperature, measuring the residual magnetization (TRM) without any reapplication of the field.

In contrast to the previous determination of the temperature dependence of the remanence (HLR), it is not easy to draw conclusions about the maximum blocking temperature, since the sample shows a small but finite value of remanence even at 300 K. Such different behavior is also seen in more concentrated CuCo alloys [296–298]. However, it is not suggested that this behavior is a characteristic of the CuCo alloy system but rather that it is general feature of the two different types of measurement. However, to the best of the authors' knowledge, attention has not previously

been drawn to this effect by making both types of measurement on the same sample. We attribute the difference in behavior of the two types of measurement to the influence of interaction effects since, clearly, in the absence of interactions, we should expect a coincidence between them. It is possible that, in the TRM measurement, when the external field is initially removed at the lowest temperature, the small magnetic particles are able to orient their magnetizations in such a manner as to form flux-closure loops which, nevertheless, give rise to a finite remanence; the associated energy has both a local and a global minimum. If the temperature is now increased without the application, and subsequent removal, of a field, these energetically, initially favorable configurations are undisturbed and remain in a metastable or local, as opposed to a global, energy minimum, which is only attained after a field cycle in a full hysteresis loop.

Figure 16 shows the variation of HLR as a function of anneal. In this sequence of measurements, the remanence was measured from a starting temperature of 5 K. On anneal at 200 °C, there is an increase both in the HLR at any temperature and also in the corresponding maximum blocking temperature to 100 ± 10 K (i.e., above this temperature, the sample exhibits SPM). There is also a corresponding increase in the value of the TRM at any given temperature.

Further anneals at 400 and 600 °C result in strong increases in the remanence, with the HLR exhibiting a finite value at 300 K; the coercivity also exhibits a similar strong increase on anneal. This behavior is in general agreement with the work of Dieny et al. [327] who, in an investigation of melt-spun CuCo ribbons, found a particle size of 25 nm after a 10 mm anneal at 950 K. They also observed a drastic increase in the magnetization on annealing between 650 and 750 K, which they were able to associate with structural changes in their ribbons due to the coalescing and formation of larger Co precipitates.

Figure 17 shows the high- and low-field hysteresis loops, measured at 5 K, of a $Cu_{0.94}Co_{0.06}$ film both before any anneal and also after a final anneal at 600 °C. For the unannealed sample, a very narrow loop is observed, together with nonsaturation of the magnetization, even in a field of 5 T. On anneal at intermediate temperatures, there is a gradual
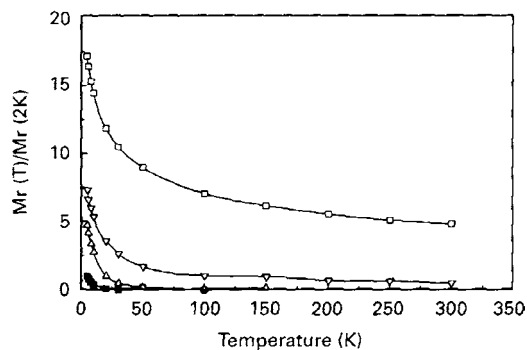

Figure 16. Temperature dependence of the remanence (HLR) for a $Cu_{0.94}Co_{0.06}$ sample as a function of anneal. Values are normalized to that of the unannealed sample at 5 K; 1—no anneal, 2—200 °C, 3—400 °C, 4—600 °C. Reprinted with permission from [284], H. J. Blythe et al., *J. Mater. Sci.* 31, 6431 (1996). © 1996, Kluwer Academic Publishers.
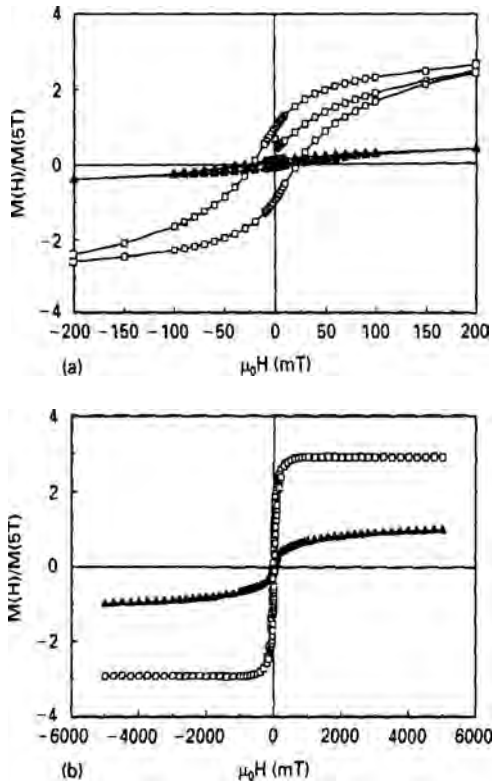
Figure 17. Hysteresis loop for an unannealed $Cu_{0.94}Co_{0.06}$ film measured at 5 K: (a) low field, (b) high-field. The magnetization has been normalized to its value at 5 T for the unannealed sample. 1—No anneal; 2—600 °C. Reprinted with permission from [284], H. J. Blythe et al., *J. Mater. Sci.* 31, 6431 (1996). © 1996, Kluwer Academic Publishers.

change in the shape of the loop. The hysteresis loop after anneal at 600 °C is much squarer and has a larger area, and the magnetization saturates in a field of about 1 T. There is also a marked increase in the value of the magnetization at any given field.

Figure 18 gives the variation of magnetization of a sample as a function of applied field, at a temperature of 5 K
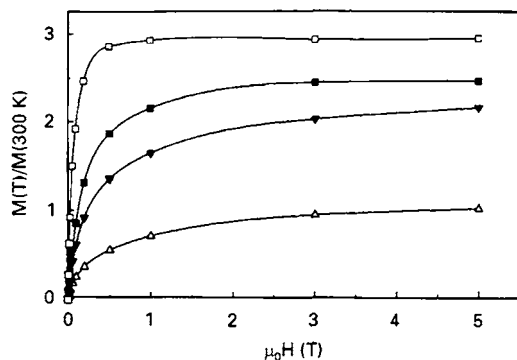
Figure 18. Magnetization of a $Cu_{0.94}Co_{0.06}$ film as a function of the magnetic field and measured at a temperature of 5 K. The results have been corrected for the contribution of the diamagnetic Cu substrate and are normalized to the value of the magnetization for the unannealed sample at a temperature of 300 K and a field of 5 T. 1—No anneal; 2—200 °C, 3—400 °C; 4—600 °C. Reprinted with permission from [284], H. J. Blythe et al., *J. Mater. Sci.* 31, 6431 (1996). © 1996, Kluwer Academic Publishers.

and its variation on anneal. The behavior gradually changes from nonsatuation, in the case of the unannealed sample, to a state where saturation is achieved in the 400 and 600 °C annealed samples in gradually lower values of applied field. Previous measurements on the unannealed sample [283] showed that even at temperatures in the range 150 to 300 K, temperatures well above T_B (55 ± 5 K), the films did not exhibit pure SPM, since plots of magnetization as a function of reduced field (H/T) did not superimpose; such scaling is a crucial test of SPM. This behavior correlates well with the observation of a finite remanences (TRM) even at 300 K in unannealed samples (Fig. 15b) and which we have earlier attributed to interaction effects.

Our interpretation of the results is based on the fact that in the unannealed sample, there must be a distribution of Co-rich particles in the Cu-rich matrix, notwithstanding the lack of direct evidence from TEM or diffraction. These particles have blocking temperatures which range from well below the minimum temperature of 2 K attained in the present work, and corresponding to both isolated Co atoms and very small Co-rich particles, up to particles with blocking temperatures of $55 + 5$ K. If we assume a value of 5.55×10^{17} eV/cm^3 for the value of K_A for fcc Co [308] for these particles (the exact value for K_A is somewhat arbitrary, since presumably both shape and strain anisotropy play an important role) and use the Livingstone and Bean expression [307] $K_A v = 25 k_B T_B$, where v is the particle volume, we are able to estimate a maximum particle diameter of 7 nm. The presence of the very small Co particles in the Cu-rich matrix is the reason for the observation that, in the unannealed sample, saturation is not achieved (Fig. 17) even in a field of 5 T. On anneal, there is a diffusion of the isolated Co atoms to the Co-rich particles to produce a "ripening" effect (i.e., a growth of the Co-rich particles). Thus, this increase in the particle size results in a corresponding increase in blocking temperature and a larger value of remanence. The absence of the isolated Co atoms, and also the smaller, Co-rich particles in the annealed sample, is also an explanation for the change in shape of the hysteresis loop, since it is the smaller SPM particles which produce the nonsaturation, whereas the larger particles give rise to the magnetic saturation.

After anneal at 400 °C the films become ferromagnetic, exhibiting a finite remanence as determined by HLR, even at room temperature (Fig. 16). More precisely, it seems that after anneal at 400 °C, part of the film becomes ferromagnetic, even at 300 K. This means that, after anneal, large Co-rich particles are formed in which a multidomain state exists. Consequently, the size of the Co particles must not be less than 50–70 nm [329].

In order to investigate the influence of anneal on particle size, we have performed ZFC/FC measurements on the samples. Figure 19a shows the results for the unannealed sample. Here, the maximum in the ZFC curve, which is related to the mean particle size, occurs at 35 K and the bifurcation between the ZFC and FC curves at 250 K. The position of the bifurcation is generally taken to be an indication of the maximum blocking temperature of the sample [303]; this corresponds to particles of diameter 12 nm.

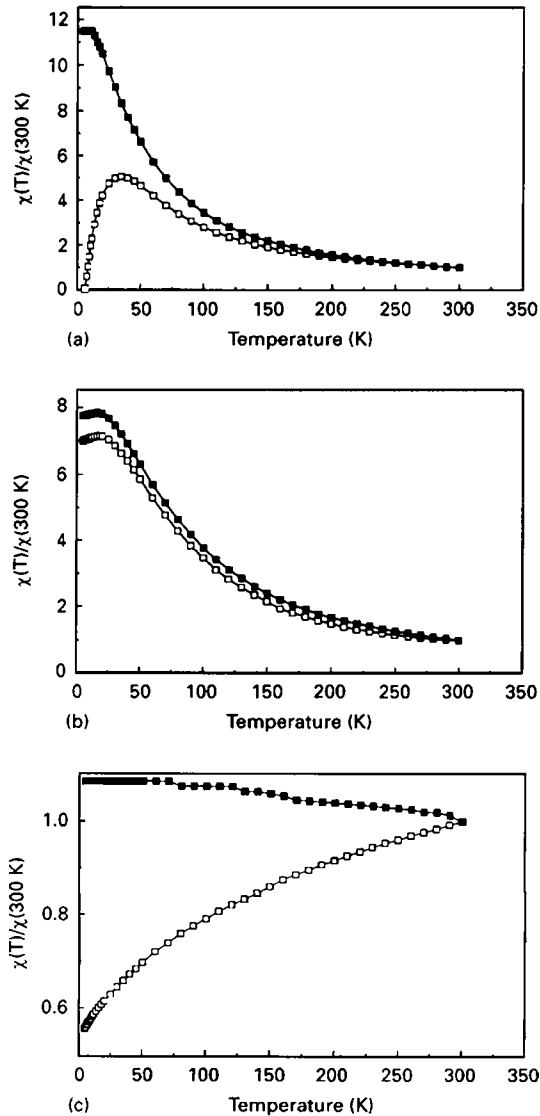Although ZFC/FC measurements have been made on samples after anneal at each temperature, since the results

Figure 19. Magnetization of a $Cu_{0.94}Co_{0.06}$ film as measured m a field of 5 mT. The lower curve (1) is for the film initially cooled to 5 K in zero magnetic field (ZFC), while the upper curve (2) is for the sample cooled in the measuring field 5 mT (FC). The results are normalized to the values of the magnetizations at 300 K. (a) Unannealed sample, (b) annealed 30 min at 400 °C, (c) annealed 30 min at 600 °C. Reprinted with permission from [284], H. J. Blythe et al., *J. Mater. Sci.* 31, 6431 (1996). © 1996, Kluwer Academic Publishers.

for the 200 °C anneal are intermediate between the unannealed and the 400 °C sample, they will not be given here. The ZFC/FC curves for the 400 °C annealed sample (Fig. 19b) exhibit a strongly enhanced value of magnetization with the peak in the ZFC curve occurring at 20 K, whereas the bifurcation is at 300 K. This anomalous shift of the ZFC peak to lower temperatures on anneal is unexpected, since we would expect a growth in particle size, as is indicated by the increase of the remanence (Fig. 16) to shift the peak to higher temperatures. Such behavior, however, has also been observed by Berkowitz et al. [330] and Slade et al. [331] in CoAg granular alloys prepared by dc sputtering, when it was suggested that this effect could reflect a depletion of Co in the matrix, shifting the freezing

temperature of the disordered matrix to lower values [330]. A similar effect has also been observed in a melt-spun $Cu_{85}Co_{15}$ alloy [312, 313], although not in $Cu_{95}Co_5$ [314].

After a final anneal at 600 °C (Fig. 19c) no maximum is observed in the ZFC curve, which suggests that it lies outside the temperature range of the measurements and, on cooling from 300 K, there is an immediate divergence between the ZFC and FC curves. This indicates that both the peak in the ZFC curve and the bifurcation temperature are well above 300 K, corresponding to a particle size of greater than 15 nm. We subsequently extended the measurements on the 600 °C annealed sample up to 600 K, but were still unable to detect a peak in the ZFC curve.

In measurements made well above the blocking temperature of the samples, in the SPM region, we expect to see a Curie–Weiss-like behavior of the susceptibility, χ, of the film; that is, $\chi \propto (T - T_{int})^{-1}$ where T_{int} is an interaction temperature which may be positive or negative, depending upon the nature of the interparticle interaction [303, 332]. In order to investigate this, in Figure 20 we have plotted the reciprocals of the FC curves as a function of temperature for the unannealed and 400 °C annealed samples.

Plotting the FC curve, rather than the ZFC curve, has the advantage that, since the FC curve is both reversible and reproducible, whereas the ZFC is reproducible but irreversible, we are able to eliminate blocking effects and therefore only have to consider interaction effects. By extrapolation of the high temperature, linear region of this curve to
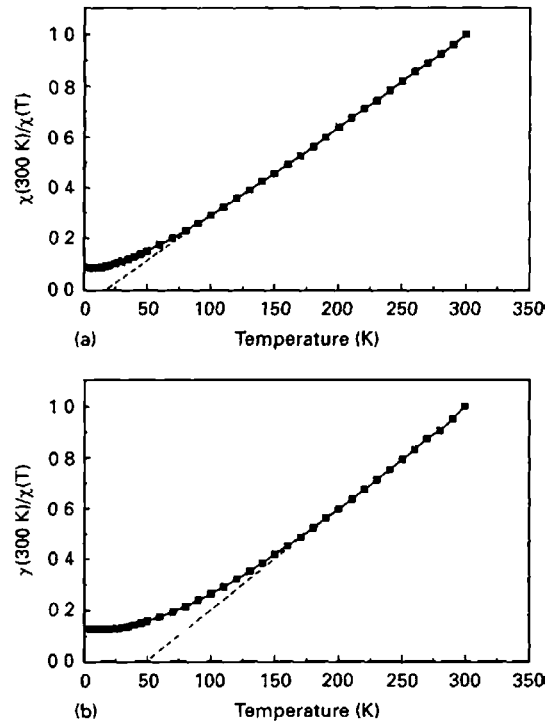

Figure 20. Temperature dependence of the reciprocal of the FC susceptibility of a $Cu_{0.94}Co_{0.06}$ sample normalized to its value at 300 K. (a) No anneal; the data are that of Figure 19a. (b) Annealed to 400 °C; the data are that of Figure 19b. Reprinted with permission from [284], H. J. Blythe et al., *J. Mater. Sci.* 31, 6431 (1996). © 1996, Kluwer Academic Publishers.

zero moment, we obtain an interaction temperature, T_{int}, of 20 ± 2 K for the unannealed sample, whereas for the 400 °C annealed sample, we obtain a value of 50 ± 5 K. If we define an interaction energy by the product $k_B T_{int}$ then there is an increase in this quantity from 1.7×10^{-3} eV in the unannealed sample to 9.0×10^{-3} eV after anneal at 400 °C.

2.3. Nanogranular CoCu Films on Co Surfaces

CoCu films with $x = 0$–0.8 were deposited from the following bath (in g/dm^3): CoSO$_4 \cdot$ 7H$_2$O—30; CoCl$_2 \cdot$ 6H$_2$O—3.3; H$_3$BO$_3$—6.6; MgSO$_4 \cdot$ 7H$_2$O—23.3; Na$_3$C$_6$H$_5$O$_7 \cdot$ 5H$_2$O—150; C$_6$H$_4$SO$_2$NHCO—5; CuSO$_4 \cdot$ 5H$_2$O—0 to 50 at pH = 6.95 to 5.0, $T = 20$ °C; deposition current density $D_K = 7$ to 25 mA/cm^2. X-ray fluorescence analysis shows that at the concentration of CuSO$_4$ in solution is 1, 3, 5, 10, 20, 30, and 50 g/dm^3; Co content in CoCu films amounts to 85, 73, 65, 52, 36, 25, and 20 at%, respectively. For CuSO$_4$ concentration 1 g/dm^3 (Co$_{0.85}$Cu$_{0.15}$), there are only reflections of hcp Co: (100) at $2\theta = 48.9°$, (002) at $2\theta = 52.1°$, and (101) at $2\theta = 55.3°$.

As in the case of films with columnar-type structure [1, 2], at small deposition current densities ($D_K \leq 10$ mA/cm^2) (002) hcp Co texture is dominant (i.e., the most compact planes of hcp Co are parallel to the film surface). At D_K 15 mA/cm^2, a redistribution of peak intensities takes place in favor of (100) texture (i.e., most compact planes of hcp Co are mainly perpendicular to the film plane). At the CuSO$_4$ concentration 3 g/cm^3 (Co$_{0.73}$Cu$_{0.27}$), a biphase mixture of hcp and fcc Co is observed. The hcp cobalt structure is dominant at higher D_K and vice versa. For 5 g/cm^3 CuSO$_4$ (Co$_{0.65}$Cu$_{0.36}$) the situation is similar to that at 3 g/cm^3 concentration.

Reflections from the pure Cu lattice are still not distinguished (i.e., we have a similar situation as for CuCo films) [1, 282, 283], when we were unable to see the reflections of Co for a similar range of its content in Cu matrix: at such compositions, Cu particles in Co matrix are still too small to be detected by X-rays. For CuSO$_4$ concentration 10 g/cm^3 (Co$_{0.52}$Cu$_{0.48}$), broad strong peaks are observed at $2\theta = 51°$, $2\theta = 60$–$59.8°$ and $2\theta = 89.5°$. We suppose that those reflections are related to both Co and Cu: (111) fcc Co ($2\theta = 51.6°$); (200) fcc Co ($2\theta = 60°$); (220) fcc Co ($2\theta = 91.3°$); (111) fcc Cu ($2\theta = 50.9°$); (200) fcc Cu ($2\theta = 59.4°$); (220) fcc Cu ($2\theta = 89.1°$). Due to small separation of reflexes and small particle sizes of Co and Cu, their corresponding reflexes are broadened and united. This suggestion is approved already after first anneal of films at 200 °C during 30 min. The above-mentioned broadened reflections become clearly subdivided into separate ones. At CuSO$_4$ concentrations 20, 30, and 50 g/cm^3 (Co$_{0.36}$Cu$_{0.64}$, Co$_{0.25}$Cu$_{0.75}$, and Co$_{0.2}$Cu$_{0.8}$ respectively), only Cu reflexes are observed. That is, changing the bath composition and, respectively, that of the film, we have observed subsequent phase transitions: first from pure hcp Co phase to hcp + fcc Co, then to fcc Co + fcc Cu, and finally to fcc Cu only.

The most interesting aspects from the viewpoint of magnetic properties are such compositions in the middle range. We have determined the normalized remanent magnetization $M_r = M(T \text{ K})/M(5 \text{ K})$ as a function of temperature. We have found some nontrivial behavior of curves
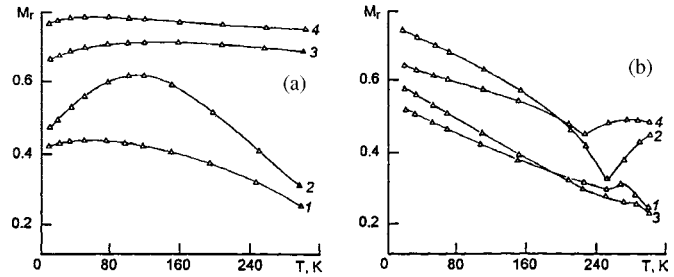

Figure 21. Temperature dependence of normalized remanent magnetization for Co–Cu films with composition Co$_{0.65}$Cu$_{0.35}$ (a) and Co$_{0.36}$Cu$_{0.64}$ (b) before annealing (1), after annealing under 200 (2), 400 °C (3), 600 ° (4). Reprinted with permission from [287], V. M. Fedosyuk et al., *J. Funct. Mater.* 4, 512 (1997). © 1997, National Academy of Science of Ukraine.

(Fig. 21a, b). Earlier we reported a similar increase of remanent magnetization in a certain low-temperature region from 10 to 50 K for Cu$_{0.85}$Co$_{0.15}$ alloy: where remanent magnetization should decrease, it increased. As for films more enriched with Co, such increase of M_r can be seen more clearly. At the composition mentioned in Figure 21, the maximum magnetization also behaves peculiarly: for an annealed sample it is $M_{max} = M(5 \text{ K}, 5 \text{ T}) = 2.94 \times 10^{-2}$ mT, after 200 °C anneal it decreases to 2.85×10^{-2} mT, then after 400 °C anneal it decreases further down to 2.64×10^{-2} mT, but finally, after 600 °C anneal, it is almost returned to previous one at 2.93×10^{-2} mT.

As seen in Figure 21, films more enriched with Co, such a trend is more pronounced, especially after annealing. Such an increase of M_r and M_{max} is more or less typical for all compositions investigated, being manifested in different temperature ranges and to a different extent. As an example, the Co$_{0.36}$Cu$_{0.64}$ composition can be mentioned (Fig. 21b). A possible explanation is that the relatively high pH values used made possible the formation of Co oxides and this possibility is increased with increasing Co ion concentration in solution and in films [1–3, 333].

2.4. Giant Magnetoresistance

For magnetoresistive measurements, films were deposited onto Al substrates, which were subsequently dissolved in a 10% solution of NaOH, and also onto ceramic substrates coated with a thin layer of nonmagnetic NiP. A comparison has shown that the results of measurement on these two types of substrates are very similar on account of the thin coating ($\sim$500 Å) and relatively high resistivity of the NiP, as compared with that of the transition metals. Resistance measurements were made using a standard, four-point method in the temperature range 5–300 K and fields up to 1.3 T. Three configurations with different orientations of current J, field H, and film plane were used: $\Delta R_{\parallel}$ if J and H are parallel and in the plane of the film, $\Delta R_{\perp}$ if J is perpendicular to H and in the plane of the film, and $\Delta R_{\parallel, \perp}$ if J is in plane and H is perpendicular to the film. ΔR was calculated as $\Delta R = 100 \times [R(0) - R(H)]/R(H)$, where $R(0)$ and $R(H)$ are the resistances in zero and finite fields. Sample annealing was performed in a vacuum of better than 5×10^{-6} mbar.

Figure 22 shows the magnetoresistance ratio of a Cu$_{0.80}$Co$_{0.20}$ before annealing no saturation is achieved in

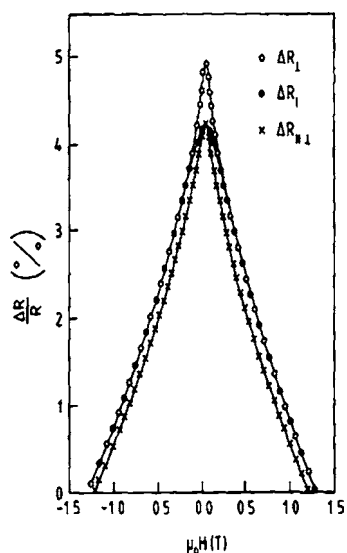**Figure 22.** Magnetoresistance of an as-deposited $Cu_{0.80}Co_{0.20}$ film measured at 5 K as a function of magnetic field for the various orientations indicated. Reprinted with permission from [293], V. M. Fedosyuk et al., *J. Magn. Magn. Mater.* 156, 345 (1996). © 1996, Elsevier Science.

Figure 23. The temperature dependence of the magnetoresistance as a function of annealing for 30 mm at the temperatures indicated for a $Cu_{0.80}Co_{0.20}$ film measured with $J \perp H$ and both in the film plane. Reprinted with permission from [293], V. M. Fedosyuk et al., *J. Magn. Magn. Mater.* 156, 345 (1996). © 1996, Elsevier Science.

the maximum available field. The fact that the magnetoresistance is both negative and isotropic (i.e., $\Delta R_\parallel \approx \Delta R_\perp \approx \Delta R_{\parallel, \perp}$) in contrast to the usual anisotropic magnetoresistance for bulk, ferromagnetic transition metals are evidence for true GMR.

The size of the magnetic particles depends upon both the electrolytic composition and the detail of the deposition parameters, but typical values [2, 3] are 7 nm for $x = 0.06$, 12 nm for $x = 0.12$, and 15 nm for $x = 0.35$ [282, 283] (i.e., they are of the same order of magnitude as the electron mean-free path in transition metals). This is clearly the reason that the spin-dependent component of the electrical conductivity tensor is predominant and this is the basis of the GMR mechanism [334, 335]. Similar variations of GMR in electrodeposited CuCo alloys have also been observed by Ueda and Ito [336].

On annealing of the samples, there is an increase in the GMR (Fig. 23), although even after annealing at 600 °C, there is no saturation observed in the available field (1.3 T). This is in contrast to the magnetization which, after a corresponding anneal, both increases and saturates in fields of less than 1 T; there is also an increase of the coercivity. This can be understood in terms of a growth of magnetic particle size on annealing.

It is well established that the magnitude of the GMR is determined by magnetic cluster sizes, their distribution, and also the sharpness of the composition profile in the vicinity of the particle–matrix boundary; these factors are strongly dependent upon annealing.

2.5. Chemically Deposited CuCo Granular Films

Despite its simplicity, the electrodeposition technique has the disadvantage that deposition can only be performed onto conducting substrates. In view of the potential technological applications of these GMR materials, it would be very useful
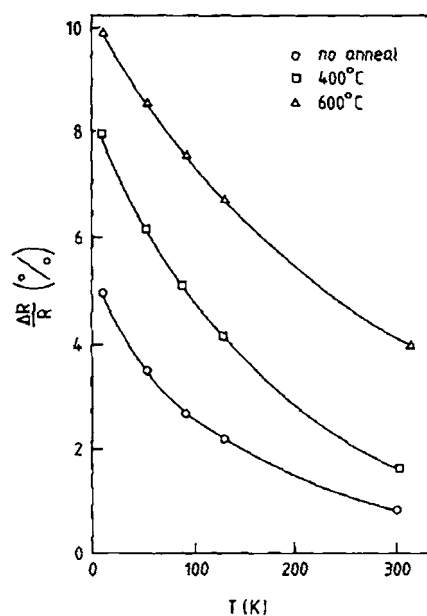
to have the flexibility of being able to deposit onto nonconducting substrates and also onto complicated geometrical shapes (the so-called method of conformal coating). One such technique, which is ideally suited to such requirements, is that of chemical deposition. The aim, therefore, was to investigate the possibility of producing granular CuCo alloyed films by the method of chemical deposition.

Thin films of CuCo were chemically deposited from a solution having the following composition: $CuSO_4 \cdot 5 H_2O$—15 g/l, $KNaC_4 \cdot 7H_6O_6 \cdot 4H_2O$—60 g/l, $CoSO_4 \cdot 7H_2O$—2 to 45 g/l, NaOH—15 g/l, Na_2CO_3—3 g/l, HCHO—15 ml/l. The solution had a pH of 12 and deposition was performed at room temperature. The films were deposited onto both Cu and ceramic substrates. Depending upon the concentration of $CoSO_4$ in the solution, $Cu_{1-x}Co_x$ films could be deposited with x in the range 0.03 to 0.50. The thickness of the film deposited depends upon deposition time but, in the present work, was typically of the order 1 μm.

We shall confine our attention to the results for the single composition, $Cu_{0.75}Co_{0.25}$. Figure 24 shows the magnetization curves for a typical sample. It can be seen that the magnetization does not saturate, even in the maximum field of 5 T and at a temperature of 5 K. Low-field magnetization measurements show that there is a weak coercive force until a temperature of 20 K. This behavior can be explained on the basis of superparamagnetism if we assume that we have a distribution of particle sizes, such that the larger particles are blocked until 20 K, thereby giving rise to the hysteresis loop, whereas the smaller particles are still unblocked and superparamagnetic even at 5 K, thus causing the nonsaturation of the magnetization. If we take the expression due to Bean and Livingstone [307], this enables us to estimate a particle size of 4.9 nm for the maximum particle
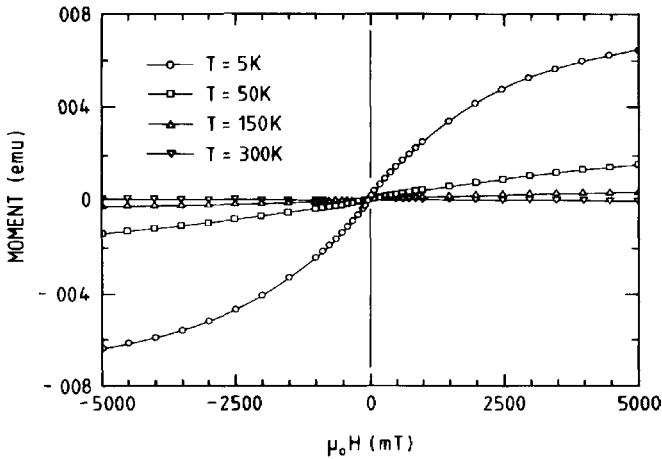
Figure 24. Magnetization curves measured at various temperatures for a $Cu_{0.75}Co_{0.25}$ thin film; granular alloy produced by chemical deposition and before any anneal. Reprinted with permission from [285], H. J. Blythe et al., *Mater. Sci. Lett.* 26, 69 (1996). © 1996, Kluwer Academic Publishers.

Figure 25. Hysteresis loops measured at various temperatures for a $Cu_{0.75}Co_{0.25}$ thin film, granular alloy produced by chemical deposition and after anneal at 400 °C. Reprinted with permission from [285], H. J. Blythe et al., *Mater. Sci. Lett.* 26, 69 (1996). © 1996, Kluwer Academic Publishers.

diameter, corresponding to the maximum blocking temperature of 20 K.

Similar behavior was recently observed by us in an alloy of comparable composition, $Cu_{0.80}Co_{0.20}$, produced by electrodeposition [282, 283], when nonsaturation of the magnetization was also observed, again even at 5 K and in a field of 5 T. However, the maximum blocking temperature found in that case was 260 K; this corresponded to a particle diameter of 12.8 nm.

It seems, therefore, that the particle size distribution and thus the magnetic properties of a given composition depend upon the method of film preparation. It might be expected that chemical deposition would produce a finer range of particles than electrodeposition, since the directionality associated with electrodeposition, which may tend to produce oriented or elongated particles, is absent in the case of chemical deposition.

Plots of magnetization as a function of reduced field (i.e., H/T) for the present chemically deposited sample were found not to be coincident. Such a plot is generally taken to be a test of superparamagnetism. However, similar nonscaling behavior was also observed in earlier measurements on electrodeposited samples, but for much more dilute Co concentrations, $Cu_{0.94}Co_{0.06}$, when it was found that interaction effects played an important role. It seems very probable, therefore, that interaction effects also have to be considered in the present chemically deposited samples.

Annealing the sample for 30 min at 200 °C in a vacuum of better than 10^{-6} mbar has negligible effects on the magnetic behavior. However, Figure 25 shows the low-field behavior after an anneal at 400 °C. The sample saturates at 5 K in a field of 5 T and shows a finite value of coercivity, even at 300 K. This behavior corresponds to a growth in particle size on annealing, with particles having blocking temperatures above room temperature. The saturation of the magnetization at 5 K, after anneal, indicates that the very small particles present originally in the unannealed samples have been eliminated from the Cu-rich matrix. Figure 26 shows
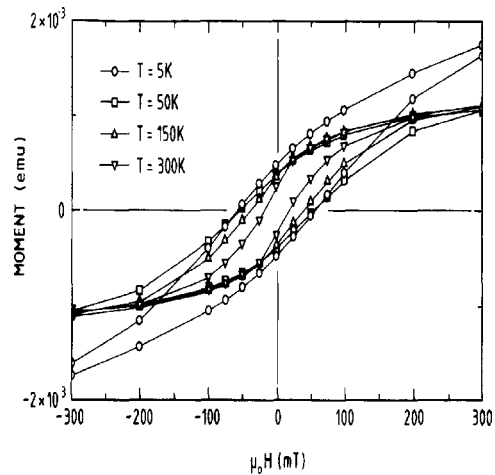
the influence of anneal on the GMR, which attains a maximum value of slightly less than 4% after anneal at 300 °C and clearly depends on particle size.

3. GRANULAR FILMS PRODUCED FROM SOLUBLE ELEMENTS

It is obvious that magnetoresistive properties of inhomogeneous alloys are determined mainly by the particle size distribution of the magnetic clusters in the nonmagnetic matrix, interparticle distance, and the sharpness of the interface of chemical composition between grains and matrix. From the scientific point of view it would be very interesting to produce and investigate the permanent transition for the same composition from granular (i.e., inhomogeneous alloyed state) to the homogeneous one. In that event it would be possible, at least in principle, to obtain direct
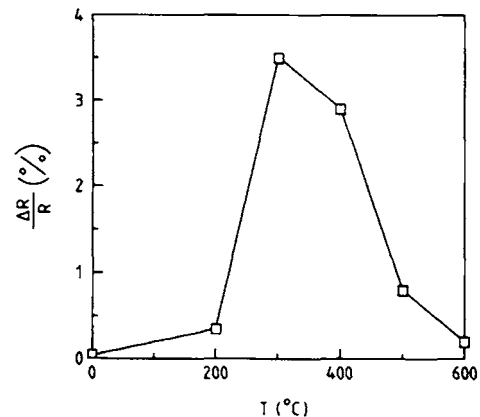

Figure 26. Variation of the GMR on anneal for a $Cu_{0.75}Co_{0.25}$ chemically deposited sample. Reprinted with permission from [285], H. J. Blythe et al., *Mater. Sci. Lett.* 26, 69 (1996). © 1996, Kluwer Academic Publishers.

information about the influence of the above-mentioned factors on the mechanism of GMR. Measurements similar to the ones already performed on CuCo and CuFe films are under the investigation. However, some technological difficulties can arise during the preparation of homogeneous alloyed films from complete mutually insoluble of Cu in Co and Fe matrixes at normal conditions. On the other hand, for the CoRe system, it could possibly be difficult to get inhomogeneous (i.e., granular) alloys on account of their complete solubility over the whole range of concentrations. Nevertheless, taking into account our previous experience with partially soluble Co–W and similar systems [337] we believe that through the choice of optimal conditions of electrodeposition and also different kinds of post-treatment (in the first place by annealing), achieving and investigating the permanent transitions from the granular (inhomogeneous) state to the homogeneous one and vice versa in CoRe system would be easier realized than in the, of course, more interesting (at least from the point of view that we have done already there relatively a lot) system of CuCo alloys [282–290], where such a task is a long-term goal perspective. We suppose that also without any post-treatment, only by choice of electrodeposition conditions, it could be possible to get different types of alloys—homogeneous or granular if we follow the next choice of ED—to produce granular alloy from immiscible elements. We need to work near the equilibrium conditions of ED [1, 338]; from immiscible ones to get a homogeneous alloy, we must work very far from the equilibrium (e.g., for the CoCu system this means high D_k and high pH). From soluble elements to produce granular films, we must be not near equilibrium; we must be absolutely in equilibrium. Why? Only in this case at the initial stage of formation of the initial "embryo" of the crystal will they grow separately despite their complete miscibility. In all other cases the films will be the mixed alloy or homogeneous only.

3.1. ReCo Films: Structure and Magnetic Properties

Films of $Re_{100-x}Co_x$ composition with $x = 100 - 4$ at% were deposited on the Cu-foil substrates of 1 μm thickness for magnetic measurements and on Al-foil and ceramic with a chemically deposited amorphous nonmagnetic NiP sublayer for X-ray and magnetoresistance measurements. The following solution was used, in g/l: $CoSO_4 \cdot 7H_2O$—30, $CoCl_2 \cdot 6H_2O$—3.3, H_3BO_3—6.6, $MgSO_4 \cdot 7H_2O$—23.3, $Na_3C_6H_5O_7 \cdot 5.5H_2O$—150, $C_6H_4SO_2NHCO$—5, $NaReO_4$—0–20. Deposition was carried out at pH = 6.95, bath temperature $T = 50$ °C, and cathodic current density $D_k = 7.5$ mA/cm^2. The film's composition was established by concentration of $NaReO_4$ in the solution and for $NaReO_4 = 0$, 0.1, 0.3, 0.5, 1, 5 and 10 g/l was correspondingly 0, 7, 30, 34, 50, 95, and 96 at% of Re in CoRe films.

For relatively low concentrations of Re in the films (less than 30 at%; the concentration of $NaReO_4$ in this case is 0.3 g/l) the crystal structure of deposited films is characterized by a hexagonal close lattice of compact hcp-Co type. The (100) and (101) reflections of hcp-Co are clearly distinguished. With increasing concentration of $NaReO_4$ the hcp-Co reflections are broadened and simultaneously shifted to

smaller angles. For the composition $Co_{0.66}Re_{0.34}$ (concentration of $NaReO_4$ in the bath is 0.5 g/l) this shift is already about 1.5 degrees. So the interplanar separation of the hcp lattice is essentially increased due to the appearance of a solid solution produced by introducing Re into the Co lattice. We note that both Co and Re are of the equilibrium structure of hcp lattice type and Co and Re have complete mutual solubility over the whole range of compositions. For the films with concentrations greater than 50 at% Re a "halolike" reflection is observed in X-ray diffraction patterns with two broad maxima. These correspond to the basic structural reflexes of hcp-Co and hcp-Re (Fig. 27). In such a way, the X-ray measurements, combined with the results of our previous TEM of investigations, allow us to draw the conclusion that the CoRe films with Re concentration greater than 50 at% are characterized by an amorphous state. According to the TEM data the average grain size is about 5 nm. Let us now discuss in more detail the actual mechanism of Re incorporation into the deposited film. Taking into account our preliminary investigations of crystal growth of electrodeposited films with the base of metals of ion group (Co, Ni, or Fe) with W [291] we assume that on introducing Re atoms in the films, the volume can be described by the "radical-film" model [340, 341]. The Re ions from the $NaReO_4$ salt form complicated complexes with hydroxide groups. Due to the relatively high pH of the bath, the possibility of such an occurrence is very great and Re cannot be electrodeposited separately but only together with other metals.

According to the above description of the mechanism of Re alloy electrode position, it is possible to expect that for a CoRe film similar types of crystal structure and similar transitions between them as those for the Co–W alloys occur [337]. Let us discuss this possibility in more detail.

We consider the process of structure formation of the Re–Co alloy films in terms of the elementary mechanism of crystal growth [341]. It is recognized [341, 342] that the probability that the atom (A) is added onto the crystal, in this case, depends upon the binding energy (E) of atoms at this position; that is, $A \sim \exp(E/kT)$. The binding energy is determined by the density of atoms at these faces and
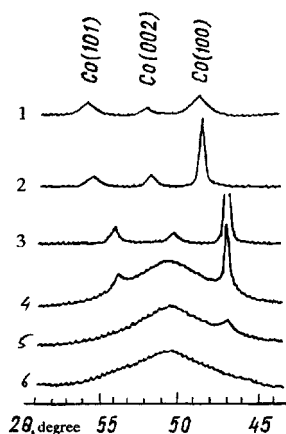

Figure 27. X-ray diagrams of ReCo films with different concentrations of $NaReO_4$ with electrolyte g/l: (1) 0; (2) 0, 1; (3) 1; (4) 2; (5) 10; (6) 20. Reprinted with permission from [286], V. M. Fedosyuk et al., *Phys. Low-Dim. Struct.* 9/10, 159 (1999). © 1999, VSV Rapid International.

is the largest for the least close packed faces [343]. Consequently, the likelihood of adding of atoms to the least close packed faces is the highest, and therefore they grow more rapidly than other faces of the crystal. In agreement with the mechanism considered, once the conditions of crystallization lead to the reduction of the dislocation density at the crystal faces presented to the solution, the growth rate of these faces in the direction of growth rises. When the lattice compresses (the packing density at the faces increases) the growth rate of this crystal decreases. In conditions of cobalt reduction (pH = 6.95, D_k = 7.5 mA/cm^2) hydrogen is released at the cathode to form Co(OH)$_2$ hydroxides in the vicinity of the cathode [339]. Large hydroxide molecules are predominantly driven to the boundaries by the growing crystallites, thus inhibiting the coherent twinning and merging of neighboring crystallites (i.e., promoting the formation of the columnar structure of the deposited film) [1–3, 339].

Hydrogen is adsorbed at the surface of the growing crystallites and is partially included into the lattice to form a supersaturated implantation solution [71]. On incorporating hydrogen into the crystallite, the lattice deforms and the lattice periodicity increases (i.e., the density of the cobalt atom distribution at the crystallite faces decreases). The latter enhances the probability of metallic atoms adding to the crystallites (i.e., the growth rate of the deposited film increases). Hence, hydrogen as well as hydroxides assists in the formation of the crystallite columnar structure of cobalt films. The surface active substances (SASs) adsorb preferentially onto the extended deposited sections at more deformed and rapidly growing sites of the crystallites (protuberances). The SASs (mainly sulphur) are partly included into the crystallite volume. Since the atomic radius of sulphur (0.104 nm) is smaller than that of cobalt (0.125 nm), the inclusion of sulphur into the metal matrix is responsible for the decrease in the cobalt lattice parameter due to its compression.

The mechanism considered assumes that the compression causes a reduction in the rate of growth of the faster growing crystallite regions. Nevertheless, the growth of the deposit persists in other regions of the crystallite. The impurity particles of SASs and hydroxides not incorporated into the microprotuberances are preferentially forced into the areas with stunted growth, thus resulting in areas being broken up into small crystals. In such a manner, the structure of small crystals of cobalt films is obtained by introducing 5 g/l of saccharin into the electrolytic solution. The cobalt crystal lattice deformation, due to the inclusion of hydrogen, results in the incorporation of rhenium atoms into the crystallite. Since the atomic radius of rhenium (r = 0.137 nm) is larger than that of cobalt, the incorporation of the rhenium atoms into the cobalt lattice increases the lattice parameter of the alloy. This, according to the mechanism considered, favors an increase in the growth rate of the deposited film, as well as that of the crystal size (Fig. 28). As the rhenium concentration in the deposited film becomes higher than that of the cobalt concentration, the cobalt atoms (whose atomic radius is less than that of rhenium) incorporating into the lattice cause its compression. In this event, the availability of cobalt in the solution acts as SASs (i.e., serves to smooth the surface of the deposited film). That is why the deposited surface
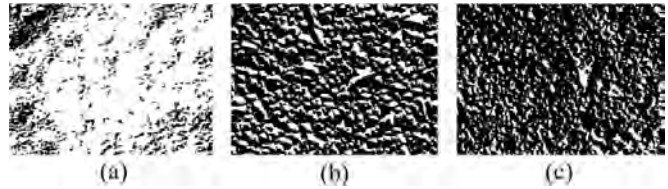

Figure 28. Morphology of ReCo films as a function of Re concentration, at%: (a) 0; (b) 7; (c) 50. Magnification 30,000 ×. Reprinted with permission from [286], V. M. Fedosyuk et al., *Phys. Low-Dim. Struct.* 9/10, 159 (1999). © 1999, VSV Rapid International.

becomes smooth at a rhenium concentration of about 50 at% (Fig. 28b).

The transformation of electrolytic cobalt into an amorphous state stems from the doping of the deposit with metals and metalloids. In this case, the doping concentration is to be less than 15 at% and its atomic radius differs from that of cobalt by no less than ~15%. The atomic radius of rhenium is larger than that of cobalt by 9.6%. Therefore, the doping of cobalt with rhenium should not, under normal conditions, give rise to formation of an amorphous structure.

Under the electrodeposition conditions adopted in this work, however, sulphur enters the cobalt lattice along with rhenium (the difference in the atomic radii of sulphur and cobalt is about 18%); this reduces the lattice parameter. Hydrogen and large hydroxide molecules are partially incorporated into cobalt to produce the crystal lattice expansion. Owing to the opposing actions of the indicated dopants the transformation in the Co–Re alloy films from the ultrafine to the amorphous state only occurs when the rhenium concentration in the deposit reaches more than ~50 at% (Figs. 28, 29).

As is obvious from the previous discussion, the buildup of the rhenium concentration in the deposited film increases the size of the crystallite, with the degree of the lattice deformation gradually increasing. The crystallite regions with a more deformed lattice are enriched with Re, S, and Co(OH)$_2$, whereas in other regions with a lower degree of lattice deformation, the formation of the crystal phase with the hcp lattice dominates. The areas enriched with impurities and dopants transform more rapidly than the less distorted crystallite areas into the amorphous state as the rhenium concentration rises. Therefore, each crystallite
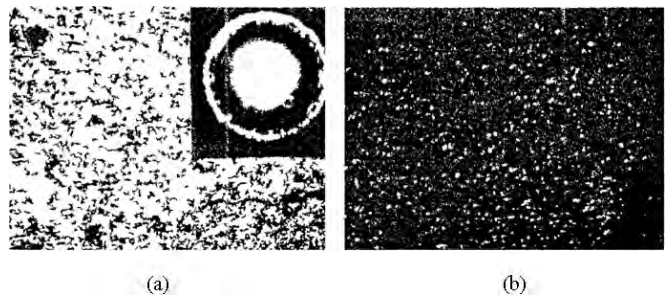

Figure 29. Bright field (a) and dark field (b) of the structure of Co$_{0.3}$Re$_{0.7}$ films. Magnification 40,000 ×. Reprinted with permission from [286], V. M. Fedosyuk et al., *Phys. Low-Dim. Struct.* 9/10, 159 (1999). © 1999, VSV Rapid International.

transforms to an aggregate made up of alternating crystalline and amorphous ranges of ~5 nm in size when the NaReO$_4$ concentration in the solution becomes equal to 2–10 g/l. As the rhenium concentration increases further in the deposited film, the areas with the crystalline phase transform into the amorphous state and the crystal aggregate changes tone which is peculiar for an amorphous structure.

Thus, the transition "polycrystalline–amorphous" structure of the Co–Re alloy films is realized according to the scheme columnar–ultrafine–aggregate–amorphous. We can obtain additional information concerning the structural state of films with Re concentrations greater than 50 at% from an analysis of their magnetic properties. If we were to find that the behavior of Co$_{100-x}$Re$_x$ with x greater than 50 at% was more typical of superparamagnetism than for ferromagnetism, it would be more probable that the main (largest) part (volume) of ReCo film is the granular (inhomogeneous) alloy, that is, the system in which nanosized single-domain particles of magnetic Co inclusions are dissolved in a non-magnetic (paramagnetic) Re matrix.

Magnetization (M), remanence (M_r), and coercivities (H_c) of Co$_x$Re$_{1-x}$ films of different compositions are found to decrease with increasing temperature. As can be seen from Figure 30, the higher the Re content of the film, the more sensitive magnetization and as a consequence M_r and H_c of the films are to temperature. The compositions Co$_{0.04}$Re$_{0.96}$ and Co$_{0.05}$Re$_{0.95}$ show behaviors of the M_r and H_c which are very similar to that of CoCu films with similar concentration of Co in Cu matrix [282, 283]. They look rather like superparamagnetics with blocking temperatures (T_b) in the region of 30 K; this corresponds, using the famous relation between T_b and the volume of a magnetic clusters [307], to Co clusters in Re matrix of the size of the order ~6.2 nm. Magnetization loops of Co$_{0.04}$Re$_{0.96}$ alloyed films confirm this point of view. Above the blocking temperature, they are reversible and unsaturated and below the blocking temperature exhibit an irreversible hysteresis (Fig. 31).

The negative slope of magnetization curves for temperatures above ~50 K (Fig. 32) could possibly be explained by the increasing influence of the response from the diamagnetic Cu substrate as compared with the decreasing magnetic signal from the Co$_{0.06}$Re$_{0.94}$ film which is above their blocking temperatures. However, such large negative slopes
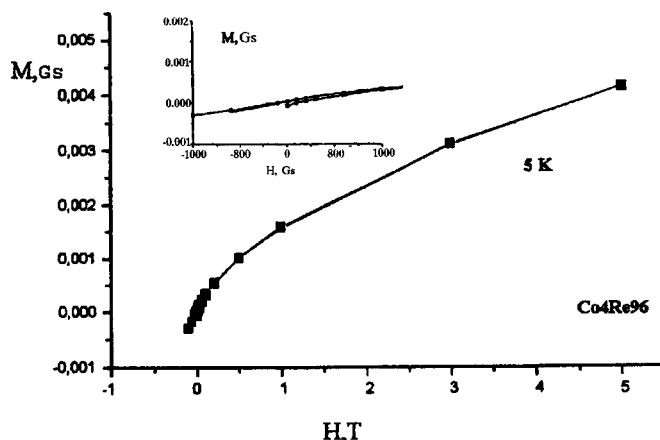
Figure 31. Magnetization loop of Co$_{0.04}$Re$_{0.96}$ at 5 K. Reprinted with permission from [286], V. M. Fedosyuk et al., *Phys. Low-Dim. Struct.* 9/10, 159 (1999). © 1999, VSV Rapid International.

(Fig. 32) are somewhat unexpected for us. For similar cobalt compositions in the CuCo system [282–284], this effect was much reduced. Furthermore, this cannot be explained by the influence of the Re matrix. It should be remembered that Cu is relatively weakly diamagnetically with a susceptibility $\chi_{Cu} = -5.41 \times 10^{-9}$ m^3 [kMol] at 300 K, whereas Re is relatively strongly paramagnetically with $\chi_{Re} = 65 \times 10^{-9}$ m^3 [kMol] [346]. Furthermore, we have performed a series of measurements to check the quality of our Cu-substrate material from the point of view of its magnetic properties. It was found to be comparable in quality with that of 99.9999% spectrographically pure copper. Our first reaction, therefore, that the noncoincident Co$_{0.06}$Re$_{0.94}$ alloyed film when plotted as a function of reduced magnetic field (B/T) above the blocking temperatures (a criterion of superparamagnetism [345]) was due to the influence of the substrate, was therefore not fulfilled. Their noncoincidence was due to the interaction of Co clusters in Cu matrix [282, 283]. In *Co*Re films, we observe a similar situation. We observe noncoincidence of M versus (B/T) not only, as is expected, for Co-rich compositions Co$_{0.7}$Re$_{0.3}$ (Fig. 32c) and Co$_{0.5}$Re$_{0.5}$ (Fig. 32b) but even for the Co$_{0.04}$Re$_{0.96}$ alloyed film (Fig. 32a). This yields information about the existence of strong interactions in CoRe films. However, we shall return to this aspect of the measurements later. More detailed information can be obtained using the ZFC-FC technique. ZFC-FC curves for the compositions Co$_{0.04}$Re$_{0.96}$, and Co$_{0.15}$Re$_{0.85}$ are similar (Fig. 33a). From a first inspection of these curves they appear to contradict our previous assumption that the Co$_{0.04}$Re$_{0.96}$ system is a granular one. We do not observe the traditional maximum near the blocking temperature that we should expect if we had ZFC curves, if we had a more or less uniform (homogeneous) distribution of magnetic Co clusters by size and inter-particle separation in the Re matrix. But the magnetization remanence and coercivity in the first instance characterize the maximum blocking temperatures which, in turn, characterize the maximum volume (size) of the magnetic clusters. The ZFC-FC technique gives us the mean values. As can be concluded from Figure 33a, the mean (average) blocking temperature of the Co$_{0.15}$Re$_{0.85}$ alloyed film is less than 5 K. There is
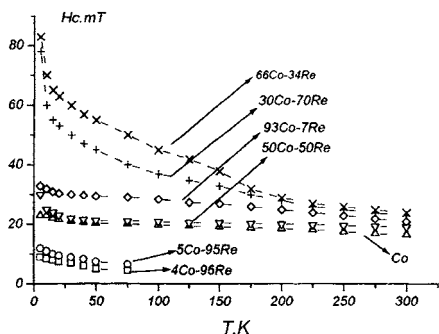

Figure 30. Coercive field of ReCo films as a function of temperature. Reprinted with permission from [286], V. M. Fedosyuk et al., *Phys. Low-Dim. Struct.* 9/10, 159 (1999). © 1999, VSV Rapid International.
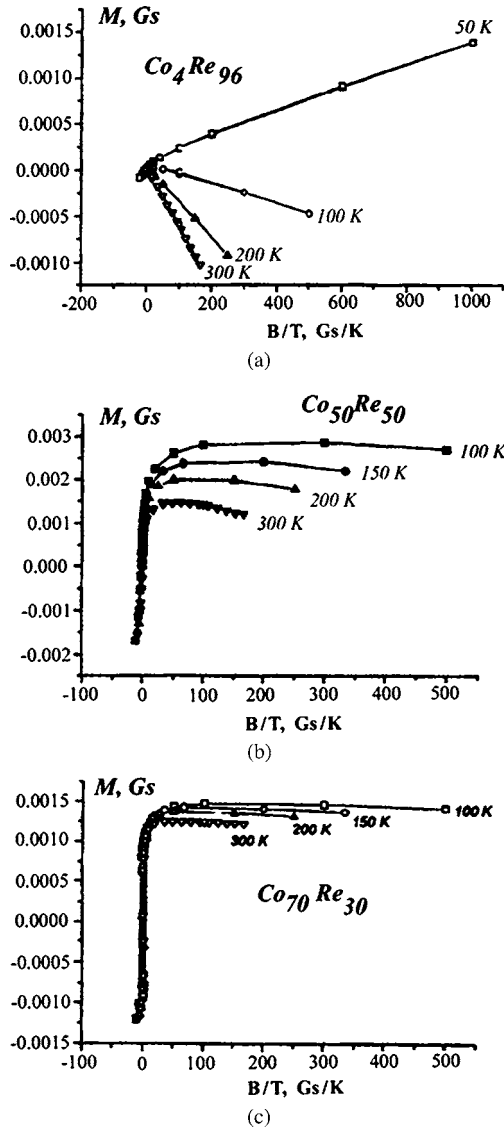
Figure 32. Magnetization versus reduced field (B/T): (a) $Co_{0.04}Re_{0.96}$, (b) $Co_{0.5}Re_{0.5}$, (c) $Co_{0.7}Re_{0.3}$. Reprinted with permission from [286], V. M. Fedosyuk et al., *Phys. Low-Dim. Struct.* 9/10, 159 (1999). © 1999, VSV Rapid International.

Figure 33. ZFC-FC curves of (a) $Co_{0.15}Re_{0.85}$ and (b) $Co_{0.3}Re_{0.7}$ films and the reciprocal susceptibility (c). Reprinted with permission from [286], V. M. Fedosyuk et al., *Phys. Low-Dim. Struct.* 9/10, 159 (1999). © 1999, VSV Rapid International.

also another important anomaly of the ZFC-FC curves for $Co_{0.15}Re_{0.85}$ film (Fig. 33a). This is that they are practically coincident at the temperatures higher than, as we suppose, the average blocking temperature ($T_b < 5$ K).

This behavior is redolent of "spin–glass" systems, that is, a system in which magnetic atoms (Co) are homogeneously distributed in nonmagnetic (Re) matrix. However, in this case, the characteristic temperature should be called the freezing temperature rather than blocking temperature [346]. For pure spin–glass behavior, the FC curves should be parallel to the temperature axis at temperatures below the freezing temperature (in our case below 5 K) [346]. We conclude that the situation in the case of $Co_{0.15}Re_{0.85}$ composition is rather complex. Plotting the reciprocal of the susceptibility as a function of temperature [307] [together with above-mentioned criterion of superparamagnetism for the coincidence of $M = M(B/T)$ (Fig. 32)] leads us to
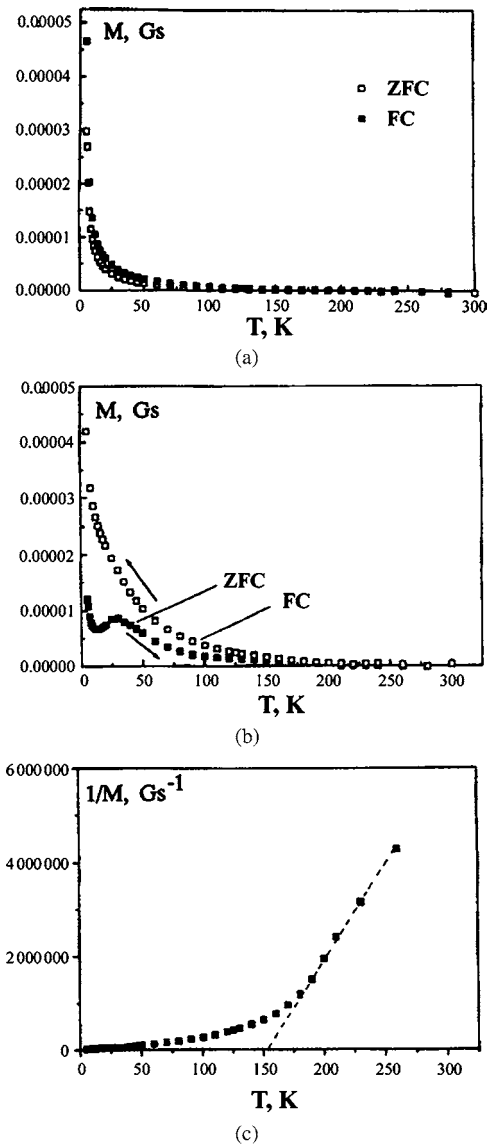
the obvious conclusion that there exist interactions between magnetic clusters (Fig. 33c). As compared with the CoCu system, these larger interaction values are possibly due to the higher concentration of dissolved Co in Re due to their complete mutual miscibility. Therefore, taking into account all the information available, we believe that both for the $Co_{0.04}Re_{0.96}$ and $Co_{0.15}Re_{0.85}$ systems, we have a mix of homogeneous and inhomogeneous alloyed states. As a consequence, we observe anomalies both for granular (Figs. 30–32) and for spin–glass (Fig. 33a) states by their volume. Such situations are also more or less typical for alloys with higher Co concentrations (e.g., $Co_{0.3}Re_{0.7}$, $Co_{0.5}Re_{0.5}$, and $Co_{0.7}Re_{0.3}$ films). The ZFC-FC curves for the alloy composition $Co_{0.7}Re_{0.3}$ and the corresponding ZFC-FC curves are shown in Figure 33b. Magnetization curves exhibit hysteresis at temperatures lower than the blocking temperature.

Furthermore, they are also unsaturated at higher temperatures. The traditional maximum of the ZFC-FC curves can be clearly distinguished in Figure 33b. The average blocking temperature for granular $Co_{0.7}Re_{0.3}$ film is about 30 K; this corresponds to an average size of Co clusters in the Re matrix of $\sim$6.2 nm. These clusters interact with each other (Fig. 33c). The interaction energy is of the order of $\sim$12.9 $\times$ 10^{-3} eV (for $T_{int} \sim$ 155 K). However, at low temperatures the ZFC-FC curves exhibit a relatively sharp increase of magnetization for both the ZFC and FC components. (Fig. 33b). This behavior is typical of a "spin–glass" material containing only small amounts of Co, for example, in $Co_{0.15}Re_{0.85}$ films (Fig. 33a) [346]. Therefore, on the whole, for the largest part of volume of $Co_{0.3}Re_{0.7}$ alloyed film a granular state is characteristic (main state), but it is obvious that there is also some part of the $Co_{0.3}Re_{0.7}$ films where Co and Re atoms are homogeneously intermixed and they thus introduce into the magnetic behavior of $Co_{0.3}Re_{0.7}$ films the "spin–glass"-like part homogeneously alloyed state. With increase of Co concentration in the CoRe films they begin to behave more like a ferromagnet with reduced Curie temperature. However, the $Co_{0.7}Re_{0.3}$ alloy still has some anomalies which are typical of spin–glass and granular states. From the ZFC curves, we can also distinguish a sharp increase of magnetization at low temperatures. The reciprocal susceptibility provides us with information about the interactions between grains. The interaction energy is $\sim 7.7 \times 10^{-3}$ eV for $T_{int} \sim$ 90 K. This is typical for granular CuCo films [282–290, 347]. It seems, therefore, that on the whole, we can draw the preliminary conclusion that in freshly prepared CoRe films over a wide range of compositions we observe both homogeneous and inhomogeneous states. It is also clear that we can regulate their relative proportions in the film by a choice of the appropriate parameters for electrodeposition and by the subsequent treatment of the film, in the first instance, by annealing.

GLOSSARY

Blocking temperature The temperature at which superparamagnetism becomes ferromagnetism at decreasing temperature. At this point the magnetic moments of ferromagnetic clusters (nanoinclusions) in nonmagnetic matrix (di- or paramagnetic) become parallel since their interection energy becomes higher than the temperature fluctuation energy.

Giant magnetoresistance (GMR) Changing of electrical resistance under applied magnetic field which is much higher compared with usual ferromagnetic materials. And it is always negative and isotropical. GMR is typical for multilayered films and granular alloys (see above).

Granular alloy Randomly distributed nanoinclusions (tens of nanometer and less by size) of ferromagnetic metal (Co, Ni, Fe, and their alloys) in di- (Cu, Ag, etc.) or paramagnetic (Re, Al etc.) matrix.

Multilayered film Film with periodically changing magnetic (ferromagnetic) and nonmagnetic (di- or paramagnetic) layers with very small thicknesses (tens of nanometers and less).

Superparamagnetic Material with magnetic succeptibility (changing of magnetic moment under applied magnetic field) much higher (thousand times) compared to usual paramagnetics at temperatures higher than the blocking temperature. At lower temperatures superparamagnetism becomes ferromagnetism. Usually such behavior is typical for granular alloys (see above).

ACKNOWLEDGMENTS

REFERENCES

1. V. M. Fedosyuk and T. A. Tochitskii, "Electrodeposited Nanostructures," BSU, Minsk, 2002.

2. V. M. Fedosyuk, *NATO ASI Ser.* 78, 85 (2000).

3. V. M. Fedosyuk, "Multilayered Magnetic structures." BSU, Minsk, 2000.

4. H. Mizuseki, K. Kikuchi, and K. Tanaka, *Jpn. J. Appl. Phys.* 37, 2155 (1996).

5. C. L. Chien, J. Q. Xiao, and J. S. Jiang, *J. Appl. Phys.* 73, 5309 (1993).

6. S. Zang, *J. Appl. Phys.* 61, 1855 (1992).

7. S. Zang and P. M. Levy, *J. Appl. Phys.* 73, 5315 (1993).

8. A. B. Pakhomov, D. S. McLachlan, I. I. Oblakova, and A. M. Virnik, *J. Phys.: Condens. Matter* 5, 5313 (1993).

9. H. Sato, K. Honda, Y. Aoki, N. Kataoka, I. J. Kim, and K. Fukamichi, *J. Magn. Magn. Mater.* 152, 109 (1996).

10. V. Franko, X. Batlle, A. Labarta, M. L. Watson, and O. O'Grady, *J. Appl. Phys.* 81, 4593 (1997).

11. Y. Luo, M. Moske, A. Kaeufler, T. Lopenz, and K. Samwer, *J. Appl. Phys.* 81, 4589 (1997).

12. A. Maraner, F. Toninato, S. Vitae, and P. Tiberto, *J. Appl. Phys.* 81, 3975 (1997).

13. A. B. Pakhomov, X. Yan, and Y. Xu, *J. Appl. Phys.* 79, 6140 (1996).

14. L. Sheng, R. Y. Gu, D. Y. Xing, Z. D. Wang, and J.-X. Zhu, *J. Appl. Phys.* 79, 6255 (1996).

15. M. Urbaniak, J. Gościańska, and H. Ratajczar, *Phys. Status. Solidi A* 160, 121 (1997).

16. A. Gavrin, M. H. Kelley, J. Q. Xiao, and C. L. Chien, *J. Appl. Phys.* 79, 5306 (1996).

17. J. Q. Xiao and C. L. Chien, *J. Appl. Phys.* 79, 5306 (1996).

18. J.-Q. Wang and G. Xiao, *J. Appl. Phys.* 79, 5587 (1996).

19. S. Ohnuma, H. Fujimori, S. Mitani, and T. Masumoto, *J. Appl. Phys.* 79, 5130 (1996).

20. M. Urbaniak, I. Goscianska, and H. Ratajczak, *Phys. Status Solidi A* 161, 121 (1997).

21. T. Sugiyama and O. Nittono, *J. Magn. Magn. Mater.* 156, 143 (1996).

22. R. Ohigashi, E. Kita, M. B. Salamon, and A. Tasaki, *Jpn. J. Appl. Phys.* 36, 684 (1997).

23. M. Nawate, M. Itogawa, and S. Honda, *J. Magn. Magn. Mater.* 156, 383 (1996).

24. By P. Allia, P. Tiberto, and F. Vinai, *Philos. Mag. B* 76, 447 (1997).

25. C. Peng, S. Zhang, G. Li, and D. Dai, *J. Appl. Phys.* 72, 998 (1994).

26. M. Rubinstein, B. N. Das, N. C. Koon, D. B. Chrisey, and J. Horwitz, *Phys. Rev. B* 50, 184 (1994).

27. E. A. M. van Alphen and W. J. M. de Jonge, *Phys. Rev. B* 51, 8182 (1995).

28. I. Navarro, M. El Ghannami, C. Gómez-Polo, M. Vázquez, and A. Hernando, *J. Magn. Magn. Mater.* 140–144, 361 (1995).

29. C. Peng and D. Dai, *J. Appl. Phys.* 76, 2986 (1994).

30. M. Rubinstein, J. Tejada, and X. X. Zhang, *J. Appl. Phys.* 75, 6557 (1994).

31. G. Xiao and J.-Q. Wang, *J. Appl. Phys.* 75, 6604 (1994).

32. J. H. Du, Q. Li, L. C. Wang, H. Sang, S. Y. Zhang, Y. W. Du, and D. Feng, *J. Phys.: Condens. Matter* 7, 9425 (1995).

33. H. Sang, S. Y. Zhang, H. Chen, G. Ni, J. M. Hong, X. N. Zhao, Z. S. Jiang, and Y. W. Du, *J. Appl. Phys.* 67, 2017 (1995).

34. B. J. Hickey, M. A. Howson, S. O. Musa, G. J. Tomka, B. D. Rainfard, and N. Wiser, *J. Magn. Magn. Mater.* 147, 253 (1995).

35. A. Gavrin, M. H. Kelley, J. Q. Xiao, and C. L. Chien, *J. Appl. Phys.* 66, 1683 (1995).

36. D. J. Kubinski, H. Holloway, and J. Hangas, *J. Appl. Phys.* 77, 3331 (1995).

37. D. J. Kubinski and H. Holloway, *J. Appl. Phys.* 77, 2508 (1995).

38. T. Bitoh, K. Ohba, M. Takamatsu, T. Shirane, and S. Chikazawa, *J. Phys. Soc. Japan* 64, 1305 (1995).

39. H. Sato, Y. Kobayashi, Y. Aoki, and H. Yamamoto, *J. Phys.: Condens. Matter* 7, 7053 (1995).

40. P. Allia, M. Knobel, P. Tiberto, and F. Vinai, *Phys. Rev. B* 52, 15398 (1995).

41. R. H. Yu, X. X. Zhang, J. Tejada, and J. Zhu, *Phys. Rev. B.* 52, R6987 (1995).

42. D. M. Kolb, R. Ullmann, and T. Will, *Science* 275, 1097 (1997).

43. B. Barbara, *J. Magn. Magn. Mater.* 156, 123 (1996).

44. S. Maekawa and J. Inoue, *J. Magn. Magn. Mater.* 156, 315 (1996).

45. A. D. C. Viegas, J. Geshev, L. F. Schelp, and J. E. Schmidt, *J. Appl. Phys.* 82, 2466 (1997).

46. T. Hihara, K. Sumiyama, K. Vakoh, and K. Suzuki, *Sci. Rep. RITU A* 42, 303 (1996).

47. M. Lijima, Y. Shimizu, N. Kojima, A. Tanaka, and K. Kobayashi, *J. Appl. Phys.* 79, 5602 (1996).

48. Y. Kobayashi, K. Honda, Y. Aoki, H. Sato, T. Ono, T. Sninjo, S. A. Makhlouf, K. Sumiyama, and K. Suzuki, *J. Magn. Magn. Mater.* 176, 164 (1997).

49. H. Zaman, S. Ikeda, and Y. Ueda, *IEEE Trans. Magn.* 33, 3517 (1997).

50. E. M. Kakuno, N. Mattoso, W. H. Schreiner, D. H. Mosca, and M. P. Cantão, *J. Electrochem. Soc.* 144, 3624 (1997).

51. A. D. C. Viegas, J. Gashev, L. S. Dorneles, J. E. Schmidt, and M. Knobel, *J. Appl. Phys.* 82, 3047 (1997).

52. B. J. Hickey, M. A. Howson, S. O. Musa, G. J. Tomka, B. D. Rainford, and N. Wiser, *J. Magn. Magn. Mater.* 147, 253 (1995).

53. H. Mizuseko, K. Kikuchi, K. Tanaka, M. Ishihara, and Y. Kawazoe, *Jap. J. Appl. Phys.* 37, 2155 (1998).

54. D. Altbir, P. Vargas, J. d'Albuquerque de Castro, and U. Raff, *Phys. Rev. B* 57, 13604 (1998).

55. A. N. Pohorilyi, A. F. Kravetz, E. V. Shipil, A. Ya. Vovk, C. S. Kim, and H. R. Khan, *J. Magn. Magn. Mater.* 186, 87 (1998).

56. A. Gerber, A. Milner, I. Ya. Korenblit, M. Karpovsky, A. Gladkikh, and A. Sulpice, *Phys. Rev. B* 57, 13667 (1998).

57. Y. D. Zhang, J. I. Budnick, W. A. Hines, C. L. Chien, and J. Q. Xiao, *Appl. Phys. Lett.* 72, 2053 (1998).

58. M. El-Hilo, K. O'Grady, and R. W. Chantrell, *J. Magn. Magn. Mater.* 114, 295 (1992).

59. M. El-Hilo, K. O'Grady, and R. W. Chantrell, *J. Magn. Magn. Mater.* 114, 307 (1992).

60. T. J. Jackson, S. B. Palmer. H. J. Blythe, and A. S. Halim, *J. Magn. Magn. Mater.* 159, 269 (1996).

61. B. J. Hickey, M. A. Howson, S. O. Musa, and N. Wiser, *Phys. Rev. B* 51, 667 (1995).

62. T. Lucinski and F. Stobiecki, *Phys. Status Solidi A* 163, 195 (1997).

63. S. Honda, M. Nawate, M. Tanaka, and T. Okada, *J. Appl. Phys.* 82, 764 (1997).

64. T. Hihara, K. Sumiyama, M. Sakurai, H. Onodera, K. Wakon, and K. Suzuki, *J. Phys. Soc. Jpn.* 66, 1450 (1997).

65. N. Wiser, *J. Magn. Magn. Mater.* 159, 119 (1996).

66. F. Badia, X. Batlle, A. Labarta, M. L. Watson, A. B. Johnson, and J. N. Chapman, *J. Appl. Phys.* 82, 677 (1997).

67. J. Xu, B. J. Hickey, M. A. Howson, D. Greig, R. Cochrane, S. Mahon, C. Achilleos, and N. Wiser, *Phys. Rev. B* 56, 14602 (1997).

68. E. F. Ferrari, F. C. S. da Silva, and M. Knobel, *Phys. Rev. B* 56, 6086 (1997).

69. S. Honda, T. Okada, and M. Nawate, *Phys. Rev. B* 56, 1466 (1997).

70. H. Zaman, S. Ikeda, and Y. Ueda, *IEEE Trans. Magn.* 33, 3517 (1997).

71. P. Allia, P. Tiberto, F. Vinai, L. Pareti, and G. Turilli, *J. Magn. Magn. Mater.* 196–197, 56 (1999).

72. N. Peleg, S. Shtrikman, G. Gorodetsky, and I. Felner, *J. Magn. Magn. Mater.* 191, 349 (1999).

73. R. H. Yu, X. X. Zhang, J. Tejada, M. Knobel, P. Tiberto, and P. Allia, *J. Phys.: Condens. Matter* 7, 4081 (1995).

74. T. Bitoh, K. Ohba, M. Takamatsu, T. Shirane, and S. Chikazawa, *J. Phys. Soc. Jpn.* 64, 1311 (1995).

75. C. L. Chien, J. Q. Xiao, and J. S. Jiang, *J. Appl. Phys.* 73, 5309 (1993).

76. A. E. Berkowitz, J. R. Mitchell, M. J. Carey, A. P. Yong, D. Rao, A. Starr, S. Zhang, F. E. Spada, F. T. Parker, A. Hutten, and G. Thomas, *J. Appl. Phys.* 73, 5320 (1993).

77. J. R. Childress and C. L. Chien, *Phys. Rev. B* 43, 8089 (1991).

78. J. Wecker, R. von Helmolt, L. Schultz, and K. Samwer, *Appl. Phys. Lett.* 62, 1985 (1993).

79. R. H. Yu, X. X. Zhang, J. Tejada, M. Knobel, P. Tiberto, and P. Allia, *J. Appl. Phys.* 78, 392 (1995).

80. G. A. Gehring, J. F. Gregg, S. M. Thompson, and M. L. Watson, *J. Magn. Magn. Mater.* 140–144 (1995).

81. T. A. Rabedeau, M. F. Toney, R. F. Marks, S. S. P. Parkin, R. F. Farrow, and G. R. Harp, *Phys. Rev. B* 48, 16810 (1993).

82. B. J. Hickey, M. A. Howson, S. O. Musa, and N. Wiser, *Phys. Rev. B* 51, 667 (1995).

83. F. Conde, C. Gomez-Polo, and A. Hernando, *J. Magn. Magn. Mater.* 138, 123 (1994).

84. V. Madurga, R. J. Ortega, V. N. Korenivski, H. Medelius, and K. V. Rao, *J. Magn. Magn. Mater.* 140–144, 465 (1995).

85. M. B. Stearns and Y. Cheng, *J. Appl. Phys.* 75, 6894 (1994).

86. S. B. Slade, F. T. Parker, and A. E. Berkowitz, *J. Appl. Phys.* 75, 6613 (1994).

87. J. R. Mitchel and A. E. Berkowitz, *J. Appl. Phys.* 75, 6912 (1994).

88. K. Pettit, E. Kita, K. Araga, A Tassaki, and M. B. Salamon, *J. Appl. Phys.* 75, 6918 (1994).

89. J. H. Hsu and Y. H. Huang, *J. Appl. Phys.* 75, 6616 (1994).

90. K. Ounadjela, A. Herr, R. Poinsot, J. M. D. Coey, A. Fagan, C. R. Staddon, D. Daniel, J. F. Gregg, S. M. Thompson, K. O'Grady, and S. Grieves, *J. Appl. Phys.* 75, 6921 (1994).

91. N. Thangaraj, C. Echer, Kannan M. Krishnan, R. F. C. Farrow, R. F. Marks, and S. S. S. Parkin, *J. Appl. Phys.* 75, 6900 (1994).

92. G. Xiao and J.-Q. Wang, *J. Appl. Phys.* 75, 6604 (1994).

93. R. Krishnan, H. Lassri, M. Seddat, M. Tessier, S. Guruswamy, and S. Sahay, *J. Appl. Phys.* 75, 6607 (1994).

94. C. Peng, S. Zhang, Guozhong, and D. Dai, *J. Appl. Phys.* 76, 998 (1994).

95. Y. Huai, M. Chaker, H. Pepin, S. Boily, X. Bian, and R. W. Cochrane, *J. Magn. Magn. Mater.* 136, 204 (1994).

96. L. Piraux, M. Cassart, E. Grivei, M. Kinany-Alaoui, Bayot, J. S. Jiang, J. Q. Xiao, and C. L. Chien, *J. Magn. Magn. Mater.* 136, 221 (1994).

97. M. Lederman and S. Shultz, *Phys. Rev. Lett.* 73, 1986 (1994).

98. S. Thamm and J. Hesse, *J. Magn. Magn. Mater.* 154, 254 (1996).

99. K. O'Grady and M. L. Watson, *J. Magn. Soc. Jpn.* 18, 379 (1994).

100. K. O'Grady, M. EL-Hilo, and R. W. Chantrell, *IEEE Trans. Magn.* 29, 2608 (1993).

101. M. EL-Hilo and K. O'Grady, *IEEE Trans. Magn.* 26, 1807 (1990).

102. M. El-Hilo, K. O'Grady, and R. W. Chantrell, *J. Magn. Magn. Mater.* 117, 21 (1992).
103. M. El-Hilo, K. O'Grady, and R. W. Chantrell, *J. Magn. Magn. Mater.* 114, 295 (1992).
104. R. W. Chantrell, M. El-Hilo, and K. O'Grady, *IEEE Trans. Magn.* 27, 3470 (1991).
105. S. Gangopadhyay, G. C. Hadjipanayis, C. M. Sorensen, and K. J. Klabunde, *IEEE Trans. Magn.* 29, 6, 2602 (1993).
106. H. Errahmani, A. Berrada, G. Schmerber, and A. Dinia, *Mater. Lett.* 51, 48 (2001).
107. G. Yan, J. Ariake, T. Kiya, N. Honda, and K. Ouchi, *J. Magn. Magn. Mater.* 235, 110 (2001).
108. K. Kamei, M. Yonemura, and K. Hanafusa, *J. Mater. Sci.* 12, 569 (2001).
109. G. R. Pattanaik, D. K. Pandya, and S. C. Kashyap, *J. Magn. Magn. Mater.* 234, 294 (2001).
110. Y. J. Chen, J. Ding, L. Si, W. Y. Cheung, S. P. Wong, I. H. Wilson, and T. Suzuki, *J. Appl. Phys. A* 73, 103 (2001).
111. R. Lopez Anton, M. L. Fdez-Gubieda, M. Insausti, A. Garca-Arribas, and J. Herreros, *J. Non-Cryst. Solids* 287, 26 (2001).
112. J. Vergara and Madurga, *J. Non-Cryst. Solids* 287, 385 (2001).
113. W. H. Flores, S. R. Teixeira, J. B. M. da Cunha, M. C. M. Alves, H. Tolentino, and A. Traverse, *J. Magn. Magn. Mater.* 233, 100 (2001).
114. U. K. Roszler, J. Noetzel, A. Tselev, K. Nenkov, A. Handstein, D. Eckert, and K.-H. Muller, *Sensors Actuators A* 91, 169 (2001).
115. M. Angelakeris, P. Poulopoulos, O. Valassiades, N. K. Flevaris, D. Niarchos, and A. Nassiopoulou, *Sensors Actuators A* 91, 180 (2001).
116. N. Gang, X. Qingyu, Y. Xiaobo, S. Hai, T. Shaolong, and D. Youwei, *Scripta Mater.* 44, 1437 (2001).
117. C. Binns, K. W. Edmonds, S. H. Baker, M. J. Maher, S. C. Thornton, and M. D. Upward, *Scripta Mater.* 44, 1303 (2001).
118. S. Ohnuma and T. Masumoto, *Scripta Mater.* 44, 1309 (2001).
119. M. Holdenried, B. Hackenbroich, and H. Micklitz, *J. Magn. Magn. Mater.* 231, 13 (2001).
120. W.-W. Yang, H. Sun, X.-y. Zhu, and W.-J. Song, *Physica B* 299, 77 (2001).
121. H. Errahmani, A. Berrada, S. Colis, G. Schmerber, A. Dinia, and D. Muller, *Nucl. Instrum. Methods B* 178, 69 (2001).
122. Y. Ju, C. Xu, and Z.-Y. Li, *J. Magn. Magn. Mater.* 223, 267 (2001).
123. K. Tonooka and O. Nishimura, *Appl. Surface Sci.* 169–170, 500 (2001).
124. Y. Ju and Z. Li, *Phys. Lett. A* 277, 169 (2000).
125. V. Franco-Puntes, X. Batlle, and A. Labarta, *J. Magn. Magn. Mater.* 221, 45 (2000).
126. P. Chen and Y. W. Du, *J. Magn. Magn. Mater.* 219, 265 (2000).
127. E. H. C. P. Sinnecker, I. S. Oliveira, P. Tiberto, and A. P. Guimaraes, *J. Magn. Magn. Mater.* 218, 132 (2000).
128. S. P. Wong, M. F. Chiah, W. Y. Cheung, N. Ke, J. B. Xu, and X. X. Zhang, *Nucl. Instrum. Methods B* 169, 166 (2000).
129. R. Yang and W. W.-J. Song, *Physica B* 279, 181 (2000).
130. K. Takanashi, S. Mitani, H. Fujimori, J.-G. Ha, and K. Yakushiji, *J. Magn. Magn. Mater.* 212, 75 (2000).
131. X. Batlle, A. Labarta, and Franco, *J. Magn. Magn. Mater.* 210, 295 (2000).
132. S.-Y. Wang, Z.-C. Shen, W.-M. Zheng, R.-J. Zhang, Y.-X. Zheng, S.-M. Zhou, and L.-Y. Chen, *Physica B* 279, 109 (2000).
133. Z.-Y. Li and C. Xu, *Phys. Lett. A* 260, 381 (1999).
134. J. Lu, H. Chen, M. Wang, Y. W. Du, Q. Y. Xu, H. Sang, X. B. Yin, and G. Ni, *J. Magn. Magn. Mater.* 204, 73 (1999).
135. M. Holdenried, S. Rubin, and H. Micklitz, *J. Magn. Magn. Mater.* 203, 97 (1999).
136. A. Labarta, K. M. Krishnan, B. J. Hattink, X. Batlle, and C. Echer, *J. Magn. Magn. Mater.* 203, 120 (1999).
137. E. Agostinelli, A. M. Testa, and D. Fiorani, *J. Magn. Magn. Mater.* 203, 196 (1999).
138. R. Kumaritova, S. Ohnuma, M. Kuzmichov, A. Bogoroditsky, and E. Gan'shina, *J. Magn. Magn. Mater.* 203, 241 (1999).
139. K. Takanashi, J.-G. Ha, M. Ohnuma, H. Fujimori, S. Mitani, and K. Hono, *J. Magn. Magn. Mater.* 198–199, 21 (1999).
140. Z. Zhang, S. Ge, and C. Li, *J. Magn. Magn. Mater.* 198–199, 30 (1999).
141. K. Hono, S. Mitani, S. Maekawa, K. Yakushiji, N. Kobayashi, K. Takanashi, J.-G. Ha, S. Ohnuma, S. Takahashi, T. Masumoto, M. Ohnuma, and H. Fujimori, *J. Magn. Magn. Mater.* 198–199, 179 (1999).
142. F. Itoh, H. Sakurai, Y. Moriya, O. Morizono, Y. Shimodaira, M. Fujimoto, and H. Oike, *J. Magn. Magn. Mater.* 198–199, 207 (1999).
143. L.-Y. Chen, B.-Y. Li, Y.-M. Yang, D.-L. Qian, S.-Y. Wang, Y.-X. Zheng, and W.-M. Zheng, *J. Magn. Magn. Mater.* 198–199, 210 (1999).
144. W. Zhang and R. Yang, *Phys. Lett. A* 255, 343 (1999).
145. J. B. Sousa, M. M. Pereira de Azevedo, J. G. Marques, Y. G. Pogorelov, J. C. Soares, C. M. De Jesus, J.-C. Ousset, M. F. Da Silva, E. Snoeck, M. S. Rogalski, and L. M. Redondo, *J. Magn. Magn. Mater.* 196–197, 13 (1999).
146. N. A. Lesnik, G. V. Bondarkova, G. N. Kakazei, A. F. Kravetz, Y. G. Pogorelov, M. M. Pereira de Azevedo, J. B. Sousa, and V. I. Silantiev, *J. Magn. Magn. Mater.* 196–197, 29 (1999).
147. J. B. Sousa, V. S. Amaral, G. N. Kakazei, Y. G. Pogorelov, A. F. Kravetz, and M. M. Pereira de Azevedo, *J. Magn. Magn. Mater.* 196–197, 40 (1999).
148. E. F. Ferrari, J. M. Broto, N. Negre, M. Goiran, G. J. Bracho Rodriguez, H. Rakoto, M. N. Baibich, M. G. M. Miranda, M. Knobel, F. C. S. da Silva, and A. B. Antunes, *J. Magn. Magn. Mater.* 196–197, 45 (1999).
149. F. Vinai, G. Turilli, P. Allia, L. Pareti, and P. Tiberto, *J. Magn. Magn. Mater.* 196–197, 56 (1999).
150. J. Vergara and Madurga, *J. Magn. Magn. Mater.* 196–197, 91 (1999).
151. V. Franco, X. Batlle, and A. Labarta, *J. Magn. Magn. Mater.* 196–197, 465 (1999).
152. J. Colino, J. M. Riveiro, and J. P. Andres, *J. Magn. Magn. Mater.* 196–197, 493 (1999).
153. H. Yamane, M. Nishino, S. Honda, and M. Nawate, *J. Magn. Magn. Mater.* 193, 492 (1999).
154. G. Gorodetsky, I. Felner, N. Peleg, and S. Shtrikman, *J. Magn. Magn. Mater.* 191, 349 (1999).
155. G. Gorodetsky and N. Peleg, *J. Magn. Magn. Mater.* 191, 354 (1999).
156. M. F. Chiah, N. Ke, J. B. Xu, W. Y. Cheung, and S. P. Wong, *Nucl. Instrum. Methods B* 148, 813 (1999).
157. H. Sang, W. J. Liu, Q. Li, Y. W. Du, D. Feng, S. Y. Zhang, and J. H. Du, *J. Magn. Magn. Mater.* 191, 17 (1999).
158. T. Sugiyama and O. Nittono, *Thin Solid Films* 334, 206 (1998).
159. S. Mitani, N. Kobayashi, H. Fujimori, S. Murakami, S. Ohnuma, and T. Masumoto, *J. Magn. Magn. Mater.* 188, 30 (1998).
160. A. Lopez, J. L. Garca-Palacios, F. J. Lazaro, R. von Helmolt, H. Cerva, and J. Wecker, *J. Magn. Magn. Mater.* 187, 221 (1998).
161. Y. Rong and W. J. Song, *Phys. Lett. A* 244, 139 (1998).
162. G. Thomas, T. S. Oh, and W. K. Choo, *Acta Mater.* 46, 3813 (1998).
163. H. R. Khan, A. F. Kravetz, A. N. Pohorilyi, A. Y. Vovk, C. S. Kim, and E. V. Shipil, *J. Magn. Magn. Mater.* 186, 87 (1998).
164. S. Luby, E. Majkova, M. Spasova, M. Jergel, R. Senderak, E. D'Anna, A. Luches, M. Martino, and M. Brunel, *Thin Solid Films* 311, 15 (1997).
165. S.-H. Ge, Z.-Z. Zhang, Y.-Y. Lu, and C.-X. Li, *Thin Solid Films* 311, 33 (1997).
166. Y. Kobayashi, K. Honda, Y. Aoki, H. Sato, T. Ono, T. Shinjo, S. A. Makhlouf, K. Sumiyama, and K. Suzuki, *J. Magn. Magn. Mater.* 176, 164 (1997).
167. W. Yang, Z. S. Jiang, Y. W. Du, and W. N. Wang, *Solid State Comm.* 104, 479 (1997).

168. B. Zhao and X. Yan, *Physica A* 241, 367 (1997).
169. A. Gerber, A. Milner, B. Groisman, M. Karpovsky, and A. Sulpice, *Thin Solid Films* 304, 319 (1997).
170. S.-H. Ge, Y.-Y. Lu, Z.-Z. Zhang, C.-X. Li, T. Xu, and J.-Z. Zhao, *J. Magn. Magn. Mater.* 168, 35 (1997).
171. Z.-Q. Li, Y. Hashi, and Y. Kawazoe, *J. Magn. Magn. Mater.* 167, 123 (1997).
172. R. H. Yu, X. X. Zhang, J. Tejada, M. Knobel, P. Tiberto, P. Allia, and F. Vinai, *J. Magn. Magn. Mater.* 164, 99 (1996).
173. E. A. Gan'shina, A. B. Granovsky, V. S. Guschin, N. S. Perov, and A. A. Radkovskaya, *J. Magn. Magn. Mater.* 160, 335 (1996).
174. T. J. Jackson, S. B. Palmer, H. J. Blythe, and A. S. Halim, *J. Magn. Magn. Mater.* 159, 269 (1996).
175. T. Lorenz, M. Moske, H. Geisler, R. V. Helmolt, M. Weiss, and K. Samwer, *Thin Solid Films* 275, 220 (1996).
176. T. Sugiyama and O. Nittono, *J. Magn. Magn. Mater.* 156, 143 (1996).
177. M. Nawate, M. Itogawa, and S. Honda, *J. Magn. Magn. Mater.* 156, 383 (1996).
178. K. Sumiyama, K. Suzuki, S. A. Makhlouf, K. Wakoh, T. Kamiyama, S. Yamamuro, T. J. Konno, M. Sakurai, T. Hihara, and Y. F. Xu, *J. Non-Cryst. Solids* 192–193, 539 (1995).
179. A. Azizi, S. M. Thompson, K. Ounadjela, J. Gregg, P. Vennegues, A. Dinia, J. Arabski, and C. Fermon, *J. Magn. Magn. Mater.* 148, 313 (1996).
180. M. Sakurai, S. A. Makhlouf, T. Hihara, K. Sumiyama, K. Wakoh, and K. Suzuki, *Physica B* 208–209, 614 (1995).
181. C. Yu, Y. Wang, W. Lai, and Z. Wang, *J. Magn. Magn. Mater.* 145, 239 (1995).
182. K. Sumiyama, S. A. Makhlouf, S. Yamamuro, Y.-F. Xu, T. J. Konno, K. Wakoh, T. Hihara, and K. Suzuki, *J. Magn. Magn. Mater.* 140–144, 563 (1995).
183. Y. Asano, J. Inoue, S. Maekawa, and A. Oguri, *J. Magn. Magn. Mater.* 140–144, 505 (1995).
184. H. Sang, Z. S. Jiang, G. Guo, J. T. Ji, Y. W. Du, and S. Y. Zhang, *J. Magn. Magn. Mater.* 140–144, 589 (1995).
185. P. Auric, B. Dieny, A. Chamberod, S. R. Teixeira, and O. Redon, *J. Magn. Magn. Mater.* 146, 153 (1995).
186. K. Sumiyama, Y. Xu, K. Wakoh, and K. Suzuki, *J. Magn. Magn. Mater.* 146, 220 (1995).
187. C. A. Ross, *Annu. Rec. Mater. Sci.* 24, 159 (1994).
188. Y. Ueda and Ito, *Jpn. J. Appl. Phys.* 33, L1403 (1994).
189. S. K. L. Lenczowski, C. Schönenberger, M. A. M. Gijs, and W. L. M. de Jonge, *J. Magn. Magn. Mater.* 148, 455 (1995).
190. E. A. M. van Alphen, A. H. J. Colaris, S. K. J. Lenczowski, C. Schönenberger, and W. J. M. de Jonge, *J. Magn. Magn. Mater.* 156, 29 (1996).
191. R. D. McMichael, U. Atzmony, C. Beauchamp, L. H. Benett, L. J. Swartzendruber, D. S. Lashmore, and L. T. Romankiw, *J. Magn. Magn. Mater.* 113, 149 (1992).
192. Y. Jyoko, S. Kashiwabara, and Y. Hayashi, *J. Electrochem. Soc.* 144, L5 (1997).
193. S. K. L. Lenczowski, C. Schönenberder, M. A. M. Gijs, and W. J. M. de Jonge, *J. Magn. Magn. Mater.* 148, 455 (1995).
194. Y. Ueda, N. Hataya, and H. Zaman, *J. Magn. Magn. Mater.* 156, 350 (1996).
195. Y. Yeda, S. Ikeda, S. Hama, and A. Yamada, *J. Magn. Magn. Mater.* 156, 353 (1996).
196. G. Nabiyouni and W. Schwarzacher, *J. Magn. Magn. Mater.* 156, 355 (1996).
197. Y. Jyoko, S. Kashiwabara, and Y. Hayashi, *J. Magn. Magn. Mater.* 156, 35 (1996).
198. V. Georgescu, V. Mazur, and O. Cheloglu, *J. Magn. Magn. Mater.* 156, 25 (1996).
199. I. Bakonyi, E. Toth-Kadar, T. Becsei, J. Toth, T. Tarnoczi, A. Cziraki, I. Geröcs, G. Nabiyouni, and W. Schwarzacher, *J. Magn. Magn. Mater.* 156, 347 (1996).
200. P. Nallet, E. Chassaing, M. G. Walls, and M. J. Hÿtch, *J. Appl. Phys.* 79, 6884 (1996).
201. C.-C. Yang and H. Y. Chen, *J. Electrochem. Soc.* 142, 3034 (1995).
202. C.-C. Yang and H. Y. Chen, *J. Electrochem. Soc.* 142, 3040 (1995).
203. E. Chassaing, P. Nallet, and M. Trichet, *J. Electrochem. Soc.* 143, L98 (1996).
204. L. Wang, P. Fricoteaux, K. Yu-Zhang, M. Troyon, P. Bonhomme, J. Douglade, and A. Metrot, *Thin Solid Films* 261, 160 (1995).
205. Y. Ueda and M. Ito, *Jpn. J. Appl. Phys.* 33, L1403 (1994).
206. B. Löchel and A. Maciossek, *J. Electrochem. Soc.* 143, 3343 (1996).
207. Y. Huttel, E. Chassaing, M. Rosso, and B. Sapoval, *Mater. Res. Soc. Symp. Proc.* 367, 177 (1995).
208. M. Ebn Touhami, M. Cherkaoui, A. Srhiri, A. ben Bachir, and E. Chassaing, *J. Appl. Electrochem.* 26, 487 (1996).
209. E. Chassaing, M. P. Roumegas, and M. F. Trichet, *J. Appl. Electrochem.* 25, 667 (1995).
210. J. N. Chazalviel, M. Rosso, E. Chassaing, and Fleury, *J. Electroanal. Chem.* 407, 61 (1996).
211. E. Beltowska-Lehman, P. Ortega, and E. Chassaing, *Surface Coating Technol.* 78, 233 (1996).
212. J. N. Hilfiker, D. W. Glenn, S. Heckens, and J. A. Woolam, *J. Appl. Phys.* 79, 6193 (1996).
213. Y. Ueda, N. Hataya, and H. Zaman, *J. Magn. Magn. Mater.* 156, 350 (1996).
214. P. Nallet, E. Chassaing, M. G. Walls, and M. J. Hÿtch, *J. Appl. Phys.* 79, 6884 (1996).
215. T. P. Moffat, *J. Electrochem. Soc.* 142, 11, 3767 (1995).
216. Y. Jyoko, S. Kashiwabara, and Y. Hayashi, *J. Electrochem. Soc.* 14, L5 (1997).
217. Ö. F. Bakkaloğlu, I. H. Karahan, H. Efeoğlu, M. Yıldırım, U. Çevik, and Y. K. Yoğurtcu, *J. Magn. Magn. Mater.* 190, 198 (1998).
218. H. Zaman, A. Yamada, H. Fakuda, and Y. Ueda, *J. Electrochem. Soc.* 145, 565 (2001).
219. A. P. O'Keeffe, O. I. Kasyutich, and W. Schwarzacher, *Appl. Phys. Lett.* 73, 1 (1998).
220. E. Chassaing, *J. Electrochem. Soc.* 144, L328 (1999).
221. A. Cziraki, I. Gerocs, B. Fogarassy, B. Arnold, M. Reibold, K. Wetzig, E. Toth-Kadar, and I. Bakonyi, *Z. Metallkd.* 88, 781 (1997).
222. A. Cziraki, V. Pierron-Bohnes, C. Ulhaq-Bouillet, E. Toth-Kadar, and I. Bakonyi, *Thin Solid Films* 318, 239 (1998).
223. S. Valizadeh, G. Holmbom, and P. Leisner, *Surface Technol.* 105, 213 (1998).
224. J. Yahalom, *Surface Technol.* 105, VII (1998).
225. D. R. Gabe and W. A. Green, *Surface Technol.* 105, 195 (1998).
226. S. Roy, *Surface Technol.* 105, 202 (1998).
227. A. R. Despic, V. D. Jovic, and N. Tosic, *Surface Technol.* 105, 206 (1998).
228. P. L. Cavalotti, N. Lecis, H. Fauser, A. Zielonka, J. P. Celis, G. Wouters, J. Machado da Silva, J. M. Brochado Oliveira, and M. A. Sa, *Surface Technol.* 105, 232 (1998).
229. V. D. Papachristor, C. N. Panagopoulos, P. Leisner, M. B. Olsen, and U. Wahlstrom, *Surface Technol.* 105, 224 (1998).
230. Ge Yi and W. Schwarzacher, *Appl. Phys. Lett.* 74, 1746 (1999).
231. G. E. Engelmann, J. C. Ziegler, and D. M. Kolb, *Surface Sci.* 401, L420 (1998).
232. K. J. Bryden and J. Y. Ying, *J. Electrochem. Soc.* 145, 3339 (1998).
233. R. Lopez, J. Herreros, A. Garcia-Arribas, J. M. Barandiaran, and M. L. Fdez-Gubeieda, *J. Magn. Magn. Mater.* 196–197, 53 (1999).
234. O. Devos, O. Aaboubi, J.-P. Chopart, E. Merienne, A. Olivier, and J. Amblard, *J. Electrochem. Soc.* 145, 4135 (1998).
235. K. Sieradzki, S. B. Brancovic, and N. Dimitrov, *Science* 284, 138 (1999).
236. L. Peter, A. Cziraki, L. Pogany, Z. Kupay, I. Bakonyi, M. Uhlemann, M. Herrich, B. Arnold, T. Bauer, and K. Wetzig, *J. Electrochem. Soc.* 148, C168 (2001).

237. Y. Jyoko, S. Kashiwabara, and Y. Hayashi, *J. Magn. Magn. Mater.* 126, 52 (1993).
238. W. Schwarzacher, *J. Interface* 8, 20 (1999).
239. M. Alper, K. Attenborough, Baryshev, R. Hart, D. S. Lashmore, and W. Schwarzacher, *J. Appl. Phys.* 75, 6543 (1994).
240. M. Alper, K. Attenborough, R. Hart, S. J. Lane, D. S. Lashmore, C. Younes, and W. Schwarzacher, *Appl. Phys. Lett.* 63, 2144 (1993).
241. M. Onoda, K. Shimizu, T. Tsuchiya, and Tohru Watanabe, *J. Magn. Magn. Mater.* 126, 595 (1993).
242. A. R. Despić, D. Jović, and S. Spaić, *J. Electrochem. Soc.* 136, 1651 (1989).
243. D. T. Schwarts, P. Stroeve, and B. G. Higgins, *AIChE J.* 35, 1315 (1989).
244. S. Menezes and D. P. Anderson, *J. Electrochem. Soc.* 137, 440 (1990).
245. S. Z. Hua, D. S. Lashmore, L. Salamanca-Riba, W. Schwarzacher, R. D. McMichael, L. H. Bennett, and R. Hart, *J. Appl. Phys.* 76, 6519 (1994).
246. R. D. McMichael, U. Atzmony, C. Beauchamb, L. H. Bennett, L. J. Swartzendruber, D. S. Lashmore, and L. T. Romankiw, *J. Magn. Magn. Mater.* 113, 149 (1992).
247. J. A. Switzer, M. J. Shane, and R. J. Phillips, *Science* 247, 444 (1990).
248. L. H. Bennett, L. J. Swartzendruber, H. Ettedgui, and U. Atzmony, *J. Appl. Phys.* 67, 4904 (1990).
249. W. Abdul-Razzaq, *J. Appl. Phys.* 67, 4907 (1990).
250. K. D. Bird and M. Schlesiger, *J. Electrochem. Soc.* 137, L65 (1990).
251. R. Hart and R. Schrebber, *Thin Solid Films* 388, 201 (2001).
252. T. Miyake, M. Kume, K. Yamaguchi, D. P. Amalnerkar, and H. Minoura, *Thin Solid Films* 397, 83 (2001).
253. K. Kudo, K. Kobayakawa, and Y. Sato, *Electrochim. Acta* 47, 353 (2001).
254. E. Jartych, D. Chocyk, M. Budzynski, and M. Jalochowski, *Appl. Surface Sci.* 180, 246 (2001).
255. J. M. D. Coey and G. Hinds, *J. Alloys Compounds* 326, 238 (2001).
256. H. Lassri, H. Ouahmane, H. El Fanity, M. Bouanani, F. Cherkaoui, and A. Berrada, *Thin Solid Films* 389, 245 (2001).
257. I. Kazeminezhad and W. Schwarzacher, *J. Magn. Magn. Mater.* 226, 1650 (2001).
258. C. N. Panagopoulos, V. D. Papachristos, U. Wahlstrom, P. Leisner, and L. W. Christoffersen, *Scripta Mater.* 43, 677 (2000).
259. L. Cagnon, A. Gundel, T. Devolder, A. Morrone, C. Chappert, J. E. Schmidt, and P. Allongue, *Appl. Surface Sci.* 164, 22 (2000).
260. L. Perez, O. de Abril, M. C. Sanchez, C. Aroca, E. Lopez, and P. Sanchez, *J. Magn. Magn. Mater.* 215–216, 337 (2000).
261. L. F. Kiss, Pierron-Bohnes, A. Dinia, E. Toth-Kadar, I. Bakonyi, and J. Toth, *J. Magn. Magn. Mater.* 198–199, 243 (1999).
262. S. Ikeda, T. Houga, N. Kikuchi, and Y. Ueda, *J. Magn. Magn. Mater.* 198–199, 740 (1999).
263. L. Salamanca-Riba, R. D. McMichael, M. Shima, and T. P. Moffat, *J. Magn. Magn. Mater.* 198–199, 52 (1999).
264. W. Schwarzacher and G. Nabiyouni, *J. Magn. Magn. Mater.* 198–199, 116 (1999).
265. Q. Xue, W. Zhang, and X. Zhang, *Wear* 214, 74 (1998).
266. Y. Hayashi, S. Kashiwabara, and Y. Jyoko, *Physica B* 239, 35 (1997).
267. S. Kashiwabara, Y. Jyoko, and Y. Hayashi, *Physica B* 239, 47 (1997).
268. C. Bonhote and D. Landolt, *Electrochim. Acta* 42, 2407 (1997).
269. J. B. Oliveira, M. A. Sa, J. M. Machado da Silva, J. P. Celis, and G. Wouters, *J. Alloys Compounds* 239, 41 (1996).
270. N. Lebbad, B. Nguyen, E. Chainet, and J. Voiron, *Thin Solid Films* 275, 216 (1996).
271. V. Georgescu and Mazur, *J. Magn. Magn. Mater.* 156, 27 (1996).
272. Y. Ueda, S. Ikeda, S. Hama, and A. Yamada, *J. Magn. Magn. Mater.* 156, 353 (1996).
273. G. Wouters, M. Bratoeva, J.-P. Celis, and J. R. Roos, *Electrochim. Acta* 40, 1439 (1995).
274. L. Wang, P. Fricoteaux, K. Yu-Zhang, M. Troyon, P. Bonhomme, J. Douglade, and A. Metrot, *Thin Solid Films* 261, 160 (1995).
275. M. C. Sanchez, C. Favieres, C. Aroca, E. Lopez, and P. Sanchez, *J. Magn. Magn. Mater.* 140–144, 591 (1995).
276. L. Seligman, M. L. Sartorelli, A. A. Pasa, W. Schwarzacher, and O. I. Kasyutich, *J. Magn. Magn. Mater.* 226, 752 (2001).
277. G. Borghs, J. De Boeck, J.-P. Celis, K. Attenborough, and H. Boeve, *Sensors Actuators A* 81, 9 (2000).
278. A. Knappwost and A. Illenger, *Naturwissenschaften* 45, 238 (1958).
279. E. Kneller, *J. Appl. Phys.* 33, 1355 (1962).
280. A. E. Berkowitz, J. R. Mitchel, M. J. Carey, A. P. Young, S. Zhang, F. E. Spada, F. T. Parker, A. Hutten, and G. Thomas, *Phys. Rev. Lett.* 68, 3745 (1992).
281. J. Q. Xiao, J. S. Jiang, and C. L. Chien, *Phys. Rev. Lett.* 68, 3749 (1992).
282. H. J. Blythe and V. M. Fedosyuk, *J. Phys. Status. Solidi A* 146, k13 (1994).
283. H. J. Blythe and V. M. Fedosyuk, *J. Phys. Condens. Matter* 7, 3461 (1995).
284. H. J. Blythe, V. M. Fedosyuk, and G. A. Jones, *J. Mater. Sci.* 31, 6431 (1996).
285. H. J. Blythe, M. Fedosyuk, and O. I. Kasyutich, *Mater. Sci. Lett.* 26, 69 (1996).
286. V. M. Fedosyuk, H. J. Blythe, and O. I. Kasyutich, *Phys. Low-Dim. Struct.* 9/10, 159 (1999).
287. V. M. Fedosyuk, O. I. Kasyutich, and H. J. Blythe, *J. Funct. Mater.* 4, 512 (1997).
288. H. J. Blyte and V. M. Fedosyuk, *J. Magn. Magn. Mater.* 155, 352 (1996).
289. H. J. Blythe, V. M. Fedosyuk, W. Schwarzacher, and O. I. Kasyutich, *J. Magn. Magn. Mater.* 208, 251 (2000).
290. T. P. Moffat, *Mater. Res. Soc. Symp. Proc.* 457, 413 (1997).
291. T. ATochitskii, H. J. Blythe, G. A. Jones, and V. M. Fedosyuk, *J. Magn. Magn. Mater.* 224, 221 (2001).
292. W. Schwarzacher, V. M. Fedosyuk, and O. I. Kasyutich, *J. Magn. Magn. Mater.* 188–189, 185 (1999).
293. V. M. Fedosyuk, O. I. Kasyutich, H. J. Blythe, and D. Ravinder, *J. Magn. Magn. Mater.* 156, 345 (1996).
294. V. M. Fedosyuk, O. I. Kasyutich, and W. Schwarzacher, *Phys. Low-Dim. Struct.* 9/10, 1 (1999).
295. V. M. Fedosyuk, G. A. Jones, and H. J. Blythe, *J. Magn. Magn. Mater.* 184, 28 (1998).
296. V. M. Fedosyuk, T. A, Tochitskii, and O. I. Kasyutich, *J. Phys. Status. Solidi A* 16, 631 (1997).
297. V. M. Fedosyuk, H. J. Blythe, and O. I. Kasyutich, *J. Funct. Mater.* 4, 512 (1997).
298. V. M. Fedosyuk, H. JBlythe, and O. I. Kasyutich, *J. Funct. Mater.* 4, 505 (1997).
299. V. M. Fedosyuk, H. J. Blythe, and O. I. Kasyutich, *J. Funct. Mater.* 4, 69 (1997).
300. H. J. Blythe, G. A. Jones, and V. M. Fedosyuk, *J. Mater. Sci.* 31, 6431 (1996).
301. K. O'Grady, M. El-Hilo, and R. W. Chantrell, *IEEE Trans. Magn.* 29, 2608 (1993).
302. M. El-Hilo, K. O'Grady, and R. W. Chantrell, *J. Magn. Magn. Mater.* 117, 21 (1992).
303. M. El-Hilo, K. O'Grady, and R. W. Chantrell, *J. Magn. Magn. Mater.* 114, 295 (1992).
304. R. W. Chantrell, M. El-Hilo, and K. O'Grady, *IEEE Trans. Magn.* 124, 3570 (1991).
305. S. M. Thompson, J. F. Gregg, C. R. Staddon, D. Daniel, S. J. Dawson, K. Oundajela, J. Hammann, C. Fermon, G. Saux, J. M. D. Coey, and A. Fagan, *Philos. Mag. B* 68, 923 (1993).

306. V. M. Fedosyuk, *Electrochemistry* 11, 17 (1993).
307. C. P. Bean and J. D. Livingstone, *J. Appl. Phys.* 30, 120 (1959).
308. L. F. Ilyushenko, "Electrodeposited Magnetic Films." Nauka (Science), Minsk, 1979.
309. C. Rau, *Appl. Phys. A* 49, 579 (1990).
310. S. S. P. Parkin, R. Bhadra, and K. P. Roche, *Phys. Rev. Lett.* 66, 2152 (1991).
311. J. R. Childress and C. L. Chien, *Phys. Rev. B* 43, 8089 (1991).
312. J. Wecker, R. von Helmholt, and L. Schultz, *Appl. Phys. Lett.* 62, 1985 (1995).
313. B. Dieny, A. Chamberod, C. Cowache, J. B. Genin, S. R. Teixeira, R. Ferre, and B. J. Barbara, *J. Magn. Magn. Mater.* 135, 191 (1994).
314. Y. Huai, M. Chaker, H. Pépin, S. Boily, X. Bian, and R. W. Cochrane, *J. Magn. Magn. Mater.* 136, 20 (1994).
315. Y. Ueda and M. Ito, *Japan. J. Appl. Phys.* 33, L1403 (1994).
316. M. Alper, K. Attenborough, R. Hart, S. J. Lane, D. S. Lashmore, C. Younes, and W. Schwarzacher, *Appl. Phys. Lett.* 63, 2144 (1993).
317. F. Conde, C. Gómez-Polo, and A. Hernando, *J. Magn. Magn. Mater.* 138, 123 (1994).
318. M. Mohie-Eldm, R. Frankel, and L. J. Gunther, *J. Magn. Magn. Mater.* 135, 65 (1994).
319. S. Linderoth, L. Balcells, A. Labarta, J. Tejada, P. V. Hendrikson, and S. A. Sethi, *J. Magn. Magn. Mater.* 124, 269 (1993).
320. R. S. Tebble and D. J. Craig, "Magnetic Materials." Wiley-Interscience, London, 1969.
321. T. A. Rabedau, M. F. Toney, R. F. Marks, S. S. P. Parkin, R. F. C. Farrow, and G. R. Harp, *Phys. Rev. B* 48, 16810 (1993).
322. R. H. Yu, X. X. Zhang, J. Tejada, M. Knobel, P. Tiberto, and P. Allia, *J. Phys. Condens. Matter.* 7, 4081 (1995).
323. H. Wan, A. Tsoukatos, G. C. Hadjipanay1s, Z. G. Li, and J. Liu, *Phys. Rev. B* 49, 1524 (1994).
324. M. P. Daniel, D. S. Lashmore, and L. H. Bennett, in "Magnetic Multilayers" (L. H. Bennett and R. E. Watson, Eds.), p. 373. World Scientific, London, 1994.
325. A. E. Berkowitz, J. R. Mitchell, M. J. Carey, A. P. Young, S. Zhang, F. E. Spada, F. T. Parker, A. Hutten, and G. Thomas, *Phys. Rev. Lett.* 68, 3754 (1992).
326. H. Sang, S. Y. Zhang, H. Chen, G. Ni, J. M. Hong, X. N. Xhao, Z. S. Jiang, and Y. W. Du, *Appl. Phys. Lett.* 67, 2017 (1995).
327. B. Dieny, A. Chamberod, C. Cowache, J. B. Genin, S. R. Teixeira, R. Ferre, and B. Barbara, *J. Magn. Magn. Mater.* 135, 191 (1994).
328. R. S. Tebble and D. J. Craig, "Magnetic Materials." Wiley-Interscience, London, 1969.
329. E. Kneller, "Ferromagnetismus." Springer-Verlag, Berlin, 1962.
330. A. E. Berkowitz, J. R. Mitchell, M. J. Carey, A. P. Young, D. Rao, A. Starr, S. Zhang, F. E. Spada, F. T. Parker, A. Hutten, and G. Thomas, *J. Appl. Phys.* 73, 5320 (1993).
331. S. B. Slade, F. T. Parker, and A. E. Berkowitz, *J. Appl. Phys.* 75, 6613 (1994).
332. M. El-Hilo, K. O'Grady, and R. W. Chantrell, *J. Magn. Magn. Mater.* 114, 307 (1992).
333. V. M. Fedosyuk and O. I. Kasyutich, *J. Electrochem. Soc.* 137, 395 (1989).
334. B. J. Hickey, M. A. Howson, S. O. Musa, and N. Wiser, *Phys. Rev. B* 51, 667 (1995).
335. G. A. Gehring, J. F. Gregg, S. M. Thompson, and M. L. Watson, *J. Magn. Magn. Mater.* 140–144, 501 (1995).
336. Y. Ueda and M. Ito, *Jpn J. Appl. Phys.* 33, L1403 (1994).
337. V. M. Fedosyuk and J. M. Riveiro, *J. Non. Cryst. Solids* 204, 99 (1996).
338. L. F. Ilyushenko, M. U. Sheleg, and A. V. Boltushkin, "Electrolitically Deposited Magnetic Films," p. 277. Nauka i technika, Minsk, 1977.
339. V. M. Fedosyuk, M. U. Sheleg, and O. I. Kasyutich, *Phys. Status Solidi A* 115, 279 (1989).
340. A. T. Vas'ko, "Elektrochemistry of W-group Metals," p. 160. Tekhnika, Kiev, 1987.
341. V. L. Kotov, *Chem. Chem. Technol.* 28, 85 (1986) [in Russian].
342. T. A. Tochitskii, V. M. Fedosyuk, A. V. Boltushkin, and A. E. Dmitrieva, *Elektrochemistry* 30, 201 (1996).
343. N. A. Pangarov, "Crystal Growth." Moscow, 1974.
344. V. V. Povetkin and N. M. Kovetskii, "Struktura i svoistva elektroliticheskikh splavov," p. 233. Moscow, 1992.
345. O. A. Shmetko and G. V. Usov, "Structure and Magnetic Properies of Metals and Alloys," p. 509. Naukova Dumka, Kiev, 1987.
346. B. J. Hickey, M. A. Hawson, and S. Musa, *J. Magn. Magn. Mater.* 147, 253 (1995).
347. V. M. Fedosyuk, H. J. Blythe, and G. A. Jones, *Phys. Low-Dim. Struct.* 4/5, 159 (1996).